ISSN 1304-7191
E-ISSN 1304-7205

sigma

Journal of Engineering and Natural Sciences

Mühendislik ve Fen Bilimleri Dergisi

Volume 44
Number 1
Year 2026

YTÜ PRESS

www.sigma.yildiz.edu.tr

E-ISSN 1304-7205

Sigma
Journal of Engineering and Natural Sciences
Mühendislik ve Fen Bilimleri Dergisi

Volume 44 Number 1 Year 2026 - February

EDITOR-IN-CHIEF

Ahmet Selim DALKILIÇ
Department of Mechanical Engineering, Yıldız Technical University, İstanbul, Turkey

ASSOCIATE EDITORS

İhsan KAYA
Department of Industrial Engineering, Yıldız Technical University, İstanbul, Turkey

Nergis ARSU
Department of Chemistry, Yıldız Technical University, İstanbul, Turkey

SECTION EDITORS

Ali ERDOĞMUŞ
Department of Chemistry, Yıldız Technical University, İstanbul, Turkey

Alper YILMAZ
Department of Bioengineering, Yıldız Technical University, İstanbul, Turkey

Azmi Seyhun KIPÇAK
Department of Chemical Engineering, Yıldız Technical University, İstanbul, Turkey

Banu MANSUROĞLU
Department of Moleculer Biology and Genetics, Yıldız Technical University, İstanbul, Turkey

Emel AKYOL
Department of Chemical Engineering, Yıldız Technical University, İstanbul, Turkey

Eyüp DEBİK
Department of Enviromental Engineering, Yıldız Technical University, İstanbul, Turkey

Fatih AKYOL
Department of Metallurgical and Materials Engineering, Yıldız Technical University, İstanbul, Turkey

Gülhayat GÖLBAŞI ŞİMŞEK
Department of Statistics, Yıldız Technical University, İstanbul, Turkey

Hakan YILMAZER
Department of Metallurgy and Malterials Engineering, Yıldız Technical University, İstanbul, Turkey

Hasan KÖTEN
Department of Mechanical Engineering, İstanbul Medeniyet University, İstanbul, Turkey

Hayriye SUNDU PAMUK
Department of Physics, Kocaeli University, Kocaeli, Turkey

Mesut AKGÜN
Department of Chemical Engineering, Yıldız Technical University, İstanbul, Turkey

Metin TÜLÜ
Department of Chemistry, Yıldız Technical University, İstanbul, Turkey

Muhammet Kasım ŞENER
Department of Chemistry, Yıldız Technical University, İstanbul, Turkey

Müslüm ARICI
Department of Mechanical Engineering, Kocaeli University, Kocaeli, Turkey

Nader JAVANI
Department of Mechanical Engineering, Yıldız Technical University, İstanbul, Turkey

Osman Nuri UÇAN
Department of Electrical and Electronics Engineering, Altınbaş University, İstanbul, Turkey

Ömer Said TOKER
Department of Food Engineering, Yıldız Technical University, İstanbul, Turkey

E-ISSN 1304-7205

Sigma Journal of Engineering and Natural Sciences
Mühendislik ve Fen Bilimleri Dergisi

Volume 44 Number 1 Year 2026 - February

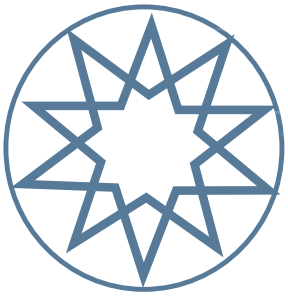
Necmiye Özlem ÜNVERDİ
Department of Electronics and Communication Engineering, Yıldız Technical University, İstanbul, Turkey
Selçuk ÇEBİ
Department of Industrial Engineering, Yıldız Technical University, İstanbul, Turkey
Sevil YÜCEL
Department of Bioengineering, Yıldız Technical University, İstanbul, Turkey
Vildan ÇETKİN
Department of Mathematics, Kocaeli University, Kocaeli, Turkey
Yasemin BUDAMA KILINÇ
Department of Bioengineering, Yıldız Technical University, İstanbul, Turkey

REGIONAL EDITORS

Abdelraheem Mahmoud ALY
South Valley University, Egypt
Abdullahi YUSUF
Federal University Dutse, Nigeria;
Biruni University Istanbul, Turkey
Adem KILICMAN
Department of Mathematics, University Putra, Malaysia
Amin SHAHSAVAR
Kermanshah University of Technology, Iran
Chandramohan V.P.
National Institute of Technology Warangal, India
Gobinath RAVINDAN
SR University, India
Hijaz AHMAD
University of Engineering and Technology Peshawar, Khyber Pakhtunkhwa, Pakistan
Md. Sabir HOSSAIN
Chittagong University of Engineering and Technology, Bangladesh
Mohammad Reza SAFAEI
Department of Civil and Enviromental Engineering, Florida International University, USA
Mostafa Safdari SHADLOO
Insa of Rouen, France
Muthu Poosan MOOPANAR
Department of Mathematics, National Institute of Technology, Warangal, India
Oscar CASTILLO
Tijuana Institute of Technology, Mathematics Division, Mexico
Pravin KATARE
Marathwada Mitra Mandal's College of Engineering, India
Ravindar KUMAR
Lovely Professional University, India
Sania QURESHI
Department of Basic Sciences and Related Studies, Mehran University of Engineering and Technology, Pakistan
Siamak HOSEINZADEH
Department of Planning, Design, and Technology of Architecture, University of Roma, Italy
Shengda ZENG
School of Mathematics and Statistics, Yulin Normal University, Yulin, China;
Faculty of Mathematics and Computer Science, Jagiellonian University in Krakow, Krakow, Poland
Taha M. RABABAH
Department of Nutrition and Food Technology, Jordan University of Science and Technology, Jordan

E-ISSN 1304-7205





Volume 44 Number 1 Year 2026 - February

ADVISORY EDITORS

Bestami ÖZKAYA
Department of Civil Engineering, Yıldız Technical University, İstanbul, Turkey

Cengiz KAHRAMAN
Department of Industrial Engineering, İstanbul Technical University, İstanbul, Turkey

Erol TUTUMLUER
Department of Civil Engineering, University of Illinois Urbana-CHampaign, USA

Hari Mohan SRIVASTAVA
Department of Mathematics and Statistics, University of Victoria, Canada

Mohsen SHEIKHOLESLAMI
Babol Noshirvani University of Technology, Iran

Melike Elif BİLDİRİCİ
Department of Economics, Yıldız Technical University, İstanbul, Turkey

Somchai WONGWISES
Department of Mechanical Engineering, King Mongkut's University of Technology, Thonburi, Thailand

Umut Rıfat TUZKAYA
Department of Industrial Engineering, Yıldız Technical University, İstanbul, Turkey

Zekai ŞEN
İstanbul Medipol University, İstanbul, Turkey

Zeynep IŞIK
Department Civil Engineering, Yıldız Technical University, İstanbul, Turkey

SECRETARY

Senol BİLGİN
Yıldız Technical University, İstanbul, Turkey

Abstracting and Indexing:
- Directory of Open Access Journals (DOAJ)
- EBSCO Host Online Research Databases
- Emerging Sources Citation Index (ESCI)
- Scopus
- MIAR
- Scilit
- OUCI
- Research4Life
- Ideal Online

Journal Description: The journal is supported by Yıldız Technical University officially, and is a blind peer-reviewed free open-access journal, published bimontly (February-April-June-August-October-December).

Owner: Yıldız Technical University

Editor-in-Chief: Ahmet Selim Dalkiliç

Language of Publication: English

Frequency: Bimontly (6 issues per year)

Publication Type: Online e-version

Publisher: Kare Publishing

E-ISSN 1304-7205

Sigma Journal of Engineering and Natural Sciences
Mühendislik ve Fen Bilimleri Dergisi

Volume 44 Number 1 Year 2026 - February

CONTENTS

Research Articles

1 **Enhancing sound quality through audio beam formation: A MVDR algorithm approach with linear microphone arrays**
Swapnil S. JADHAV, Pranali B. KASHID, Lalit N. PATIL, Sayali S. JADHAV, Pooja KOLI, Vikash AGRAWAL, Subhash GADHAVE, Santosh D. SANCHETI, Yashraj M. PATIL, Atul A. PATIL

11 **Intelligent fruit sorter for quality evaluation of guava fruit using image analysis**
Tejas G. PATIL, Sanjay P. SHEKHAWAT, Lalit K. TOKE, Lalit N. PATIL, Atul A. PATIL

23 **Classifications of artificial ıntelligence trading systems by using WASPAS approach based on picture fuzzy soft aggregation operators**
Tahir MAHMOOD, Jabbar AHMMAD

42 ***Commiphora myrrha*-functionalızed bacterial cellulose as a potential wound healing biomaterial**
Seda GENÇ ŞİMŞEK, Cenk DENKTAŞ, Nelisa TÜRKOĞLU

55 **Clustering business news for strategic insight: An unsupervised learning approach**
Gaurav V. DAHAKE, M. S. ALI

74 **Audio fingerprinting for song identification using discrete wavelet transform**
Swati Mukesh DIXIT, Daulappa Guranna BHALKE

83 **The effect of eccentricity and asymmetry in the plan on the performance level in existing steel buildings with a medium bending frame**
Kaveh NEZAMISAVOJBALAGHI

93 **Multiclass anemia classification based on multivariate adaptive regression spline method: Developing a decision support system for doctors**
Nagihan YAĞMUR, Idiris DAĞ

E-ISSN 1304-7205

sigma
Journal of Engineering and Natural Sciences
Mühendislik ve Fen Bilimleri Dergisi

Volume 44 Number 1 Year 2026 - February

105 **Properties of N, acetylamide-rich biopolymers from five different aquatic invertebrates**
Oluwashina Philips GBENEBOR, Abimbola Patricia POPOOLA

115 **Study of improved quantum particle swarm optimization for modeling of wasted surgical mask**
Subhojit CHATTARAJ, Sk Tanbir ISLAM, Pijush DUTTA, Mahuya DAS

127 **Metaheuristic and cryptographic approaches with upgraded discrete and lifting wavelet transform for effective data security in steganography**
S. SARATHA, V. MURUGAN, P. Arockia Jansi RANI

140 **Metaheuristic algorithms for multi objective vehicle routing problem**
İlknur TÜKENMEZ, Onur KAYA

153 **Electricity energy consumption forecasting using LSTM and NAR**
Parastou BEHGOUY, Abbas UĞURENVER

162 **Screening of *Trichoderma* spp. for biofertilizer and biocontrol potential in vitro**
Kemal KARACA, Rengin ELTEM

174 **Structural, thermal, morphological, and rheological properties of yeast extracts obtained from *Saccharomyces cerevisiae, Saccharomyces boulardii,* and *Kluyveromyces marxianus***
Furkan DEMİRGÜL, Ömer ŞİMŞEK, Enes DERTLİ, Osman SAĞDIÇ

184 **Technological developments and sustainable construction in Iraqi architecture**
Osamah A AL-TAMEEMI

200 **Evaluation of the effects of sustainable development goals on improvement of air quality in cities**
Şahin KORKMAZ, Damla MUSTAFAOĞLU, Zeynep CEYLAN

210 **An innovative group decision-making approach utilizing picture fuzzy hypersoft expert set**
Muhammad IHSAN, Muhammad SAEED, Muhammad Yasir HAYAT MALIK

E-ISSN 1304-7205

Sigma
Journal of Engineering and Natural Sciences
Mühendislik ve Fen Bilimleri Dergisi

Volume 44 Number 1 Year 2026 - February

222 **Investigation of civil engineering students' general disaster preparedness beliefs**
Esra Zehra BİÇER ÖZDEMİR, Özlenur CESUR AKIN, Egemen ÜNAL, Salih MOLLAHALİLOĞLU

234 **Impact of halloysite clay on the thermal degradation behaviour, kinetics analysis, and pyrolysis product distribution during catalytic pyrolysis of bakelite**
Chinmaya KAR, Achyut KUMAR PANDA, Pabitra MOHAN MAHAPATRA

252 **Simultaneous electricity generation and removal of Sars-Cov-2 from wastewater in microbial fuel cells**
Sıla ARSLAN, Tunç ÇATAL

262 **An exact analysis of chemical reaction and porosity effects for mixed convective magnetohydrodynamics Casson fluid**
Nur Fatihah MOD OMAR, Zulkhibri ISMAIL, Rahimah JUSOH, Muhammad Azrin AHMAD, Ahmad Qushairi MOHAMAD

273 **Image segmentation for semi-supervised fuzzy clustering with KL-divergence using Kernel method**
Muthulakshmi K, Jayalakshmi M

292 **Optimization of precision machine part manufacturing by integration of Grey-Taguchi method with principal component analysis**
Kübra EROL, Selda KAPAN ULUSOY, Ercan ŞENYİĞİT

309 **Improved error limits for numerical integration via some perturbed trapezoidal inequalities**
Duygu DÖNMEZ DEMİR, Gülsüm ŞANAL

318 **Hall current's effect on MHD boundary layer compressible flow of fluid past a stretching sheet with viscous dissipation**
Bandita DAS, Sunmoni MUDOI, Dipak SARMA

329 **Classification of cluster analysis techniques by using hesitant bipolar complex fuzzy multi-attribute decision-making approach based on dombi prioritized aggregation operators**
Hafiz Muhammad WAQAS, Tahir MAHMOOD, Ubaid ur REHMAN

E-ISSN 1304-7205

sigma
Journal of Engineering and Natural Sciences
Mühendislik ve Fen Bilimleri Dergisi

Volume 44 Number 1 Year 2026 - February

351 **Harnessing AI for real-time detection and mitigation of technostress in digital epoch**
Rachana PARIKH, Vishal DAHIYA

360 **Semantic algorithm for land segmentation and building recognition to protect the Egyptian cultıvated land based on u-NET and CNN**
Mahmoud ROKAYA, Majed ALWATEER 360

375 **Computational fracture analysis of 3Y-TZP dental ceramics with low Al_2O_3 using peridynamics**
Alireza MORADKHANI, Mohammad HOSEINPOUR GOLLO

388 **Enhancing bidirectional gated recurrent unit with activation mechanism for anomaly classification for network security**
N. Senthil MADASAMY, A. Noble Mary JULIET, P. Boopathi RAJAN

404 **Predicting survival rates of patients with cardiovascular diseases using ensemble techniques**
Bharati KARARE, Anushree Anand PANDE, Pratibha WAGHALE, Amruta Tapas PAUL, Chanchla TRIPATHI, Lalit DAMAHE

423 **Development of plant extract-loaded electrospun nanofiber for the prevention of biofilm-associated infections**
Sevim Feyza ERDOĞMUŞ, Cengiz SARIKURKCU

439 **Electric bus preference with analytical hierarchy process and grey relational analysis combination in public transportation considering modern trend criteria: Kayseri, Türkiye case study**
Aslan İNAN, Huzeyfe KARA

453 **Vibration-based fault detection in induced draft fans using unsupervised machine learning approaches**
Ramesh BHANDARE, Pankaj BELDAR, Shyam MOGAL

465 **Formation and analysis of thermal images for infrared radiations from top of the atmosphere**
Usama Ayub YOUSUFZAI, Muhammad Jawed IQBAL, Faisal AFRIDI

E-ISSN 1304-7205

sigma
Journal of Engineering and Natural Sciences
Mühendislik ve Fen Bilimleri Dergisi

Volume 44 Number 1 Year 2026 - February

478 **Unmasking sarcasm to understand depression: A machine learning exploration using news headlines**
Vanita Ganesh KSHIRSAGAR, Sunil Kumar YADAV, Nikhil KARANDE

490 **Influence diagnostic in beta ridge regression model: Simulation and application**
Javaria Ahmad KHAN, Atif AKBAR, B M Golam KIBRIA

501 **Comparative assessment of novel hooped and conventional Pelton wheel turbine runner using downcomer nozzles of different materials and exit diameter through experimental investigations**
H. N. LAKDAWALA, V. K. PATEL, G. C. CHAUDHARI, S. A. CHANNIWALA, T. R. PATEL

528 **Metaheuristic-based machine learning models for accurate battery remaining useful life prediction in renewable energy storage system**
Shravani GANDHI, Ashlesha CHOPANE, Anushka PARKHI, Sakshi DESHMUKH, Smita KULKARNI

545 **SWARA & EDAS integration using spherical fuzzy sets in agricultural field**
Betül KARA, Muhammed Zakir DENİZ, Umut AYDIN, Melis Almula KARADAYI

559 **Mechanical vibration-assisted enhancement of weldment mechanical properties**
Japhia Sudarsan NALLA, Basanta Kumar PALAI, P. Govinda RAO

575 **Molecular dockings of secondary metabolites to evaluate anthelmintic potential**
Dilara KARAMAN, Oya GİRİŞGİN, Ahmet Onur GİRİŞGİN

592 **Analysis of efficient solar operated air cooling system for cold storage warehouses**
Prakash P. THOMBARE, Ravindra D. PATIL

Review Articles

605 **Artificial intelligence, machine learning, and deep learning applications in the engineering fields – A comprehensive review**
Haneen DARWISH, Walaa DARWISH, Hiba DARWISH, Abdallah DARWISH, Issa W. ALHMOUD, Osamah ALSHRAIDEH, Ahmad ALZUBAIDI

637 **A comprehensive review on traditional and cutting-edge approaches for wind speed/ power forecasting**
Muskaan AHUJA, Sanju SAINI

E-ISSN 1304-7205

Journal of Engineering and Natural Sciences
Mühendislik ve Fen Bilimleri Dergisi

Volume 44 Number 1 Year 2026 - February

663 **A review of photovoltaic plants and battery energy storage systems in terms of power systems stability**
Bora ÇAVDAR, Eda KARACA, Hatice OKUMUŞ, Fatih Mehmet NUROĞLU

680 **An overview of optimum calcination parameters for improved pozzolanic activity in biomass ash**
Manoj Ashok SADAFALE, Mangesh Vasant MADURWAR

698 **The role of hybrid nanofluids in optimizing parabolic trough concentrator performance: A comprehensive review**
Sanjeev Kumar GUPTA, Soni KUMARI

720 **Advancements in thermal management of polymer composites and sandwich structures: Insights and innovations**
Sandip K. KADU, Palash SONI

Sigma Journal of Engineering and Natural Sciences
Web page info: https://sigma.yildiz.edu.tr
DOI: 10.14744/sigma.2025.00000

Research Article

Enhancing sound quality through audio beam formation: A MVDR algorithm approach with linear microphone arrays

Swapnil S. JADHAV[1,*], Pranali B. KASHID[2], Lalit N. PATIL[3], Sayali S. JADHAV[4], Pooja KOLI[2], Vikash AGRAWAL[7], Subhash GADHAVE[8], Santosh D. SANCHETI[6], Yashraj M. PATIL[7], Atul A. PATIL[4]

[1]Department of Mechanical Engineering, Adarsh Institute of Technology and Research Centre, Vita, 06304, India
[2]Padmabhooshan Vasantraodada Patil Institute of Technology, Budhgaon, Sangli, 413008, India
[3]School of Mechanical and Manufacturing Science, Faculty of Science and Technology, JSPM University, Pune, 411033, India
[4]Department of Mechanical Engineering, Annasaheb Dange College of Engineering and Technology, Ashta, Sangli, 06283, India
[5]Department of Mechanical Engineering, Dr. D. Y. Patil Institute of Technology, Pune, 411018, India
[6]Department of Mechanical Engineering, SNJB's, Late Sau. Kantabai Bhavarlalji Jain College of Engineering, Chandwad, 423101, India
[7]Department of Automation and Robotics, Dr. D. Y. Patil Institute of Technology, Pune, 413008, India
[8]Department of Mechanical Engineering, Padmabhooshan Vasantraodada Patil Institute of Technology, Bavdhan, Pune, 416304, India

ARTICLE INFO

Article history
Received: 10 August 2024
Revised: 09 September 2024
Accepted: 14 October 2024

Keywords:
Audio Beam Formation; Acoustic; Microphone Array; Sound Source Localization; MATLAB

ABSTRACT

Achieving high-quality sound in noisy environments is a significant challenge in audio applications, particularly in areas such as communications, broadcasting, and healthcare. This study explores the use of the Minimum Variance Distortionless Response (MVDR) algorithm in conjunction with a linear microphone array to improve audio beamforming. The objective is to enhance the signal-to-noise ratio (SNR) of desired signals while minimizing interference and reverberation. The MVDR algorithm is applied in the research using MATLAB to create directional beams that help isolate the target signal, and background noise is reduced. Comparative analysis against the traditional delay-and-sum beamformer shows that the MVDR scheme is much better in SNR, particularly in the multiple sources of interference environment. The major findings are that as the number of microphones increases to 20, the mean squared error (MSE) reduces by up to 33.8 dB and that the microphones work best when the spacing between them is carefully adjusted. These results indicate that MVDR-based beamforming would be able to offer excellent solutions to improving sound clarity in numerous realistic scenarios, including teleconferencing, sonar, and medical imaging.

Cite this article as: Jadhav SS, Kashid PB, Patil LN, Jadhav SS, Koli P, Agrawal V, Gadhave S, Sancheti SD, Patil YM, Patil AA. Enhancing sound quality through audio beam formation: A MVDR algorithm approach with linear microphone arrays. Sigma J Eng Nat Sci 2026;44(1):1–10.

***Corresponding author.**
*E-mail address: swapniljadhav.9001@gmail.com

This paper was recommended for publication in revised form by Editor-in-Chief Ahmet Selim Dalkilic

Published by Yıldız Technical University Press, İstanbul, Turkey
© Author. This is an open access article under the CC BY-NC license (http://creativecommons.org/licenses/by-nc/4.0/).

INTRODUCTION

The The act of combining multiple signals captured from the sensors in a sensor array is the main concept in beam forming technique. It is a signal processing technique used in sensor arrays for directional signal transmission or reception. This technique basically approaches the problem from a spatial point of view [1]. It combines the elements in a phased array in such a way that signals at particular angles experience constructive interference while others experience destructive interference. Beam forming can be used at both the transmitting and receiving ends in order to achieve spatial selectivity. This has improved the directivity of elements as compared to the unidirectional reception/ transmission [2].

Beam formation has been studied in many areas such as radar, sonar, seismology and wireless communications, to name but a few. It can be used for a variety of purposes, such as detecting the presence of a signal, estimating the direction of arrival, and enhancing a desired signal from its measurements corrupted by noise, competing sources and reverberation [3]. Typical use of beam forming arise in RADAR, SONAR, communications, imaging, geophysical exploration, biomedical and also in acoustic source localization [4].

In acoustics this concept can be adopted to form a noise free beam of the incoming corrupted signal by using array of microphones. Beam forming combines the output audio signals of the microphone array in such a way that it will make the microphone array to act as a highly directional microphone [5]. Actually, beam forming has been adopted by the audio research society, mostly to separate or extract speech for noisy environment [6]. A microphone array is used to form a spatial filter which can extract a signal from a specific direction and reduce the contamination of signals from other directions. In other words, beam forming provides a "listening beam" which points to a particular sound source while often filtering out other sounds [7, 8].

Spatially propagating signals encounter the presence of interfering signals and noise signals. If the desired signal and the interfering signals occupy the same temporal frequency band, then temporal filtering cannot be used to separate the signal from the interferers. However the desired and the interfering signals generally originate from different spatial locations. This spatial separation can be exploited to separate the signals from the interference using a beam former [9, 10]. A beam former consists of an array of sensors in a particular configuration. The output of each sensor is properly filtered and the filtered outputs of all the sensors are added up. Typically a beam former linearly combines the spatially sampled waveform from each sensor in the same way a FIR filter linearly combines temporally sampled data [11, 12].

When low frequency signals are used, then an array of sensors can synthesize a much larger spatial aperture than a single physical antenna or sensor [13, 14]. A second very significant advantage of using an array of sensors is the spatial filtering versatility offered by discrete sampling. In many applications it is necessary to change the spatial filtering function in real time to maintain effective suppression of interfering signals [15]. Changing the spatial filtering function of a continuous aperture antenna is impractical. Use of an array of sensors makes this possible to implement [16, 17].

In this paper, basic fundamentals of beam formation, certain beam formation techniques, microphone array geometries and effect of various factors on beam former's performance are discussed in subsequent chapters. The aim is to study traditional delay and sum beam former and MVDR (Minimum Variance Distortion less Response) beam former [18, 19]. It consists of performance checking of beam former output by varying various parameters. In this Paper, sound source localization algorithm is not implemented which is required to steer the beam to that direction. Instead of that, certain direction for sound source and interference signal is assumed and then beam formation is implemented in MATLAB [20, 21].

Beamforming is a method that is widely applied in communications and radar systems in order to generate a focused beam of the required signal and minimize interference of background noise [22]. This is also reflected in the science of acoustics, in which good sound in ambient noise and reverberation is very essential. Signal integrity is also paramount in most of the voice applications, such as communications, broadcasting, and healthcare. However, traditional single-channel audio systems often have difficulty improving signal-to-noise ratio (SNR) and improving signal quality [23, 24]. Therefore, techniques such as sound beam generation are needed to solve these problems. Beamforming based on the use of microphone arrays with geometry designs has been shown to have great potential in amplification of the desired signal and reduction of unwanted noise and echo [25, 26]. This article investigates electronic beam forming using the minimum displacement distortion-free response (MVDR) algorithm and linear microphone array configuration (implemented in MATLAB) [27, 28]. This research aims to improve signal clarity and signal-to-noise ratio by focusing on the sound field and optimizing the response, thus demonstrating the effectiveness of beam forming technology in various fields such as sonar, radar, wireless communications, astronomy, etc. and biomedicine [29, 30].

The whole research is organized as follows: the introductory information about the beam formation is presented in Section I. Whole system is presented in section II. In section III deals with the concept of wave front. In section IV and V discuss the delay calculation and MVDR respectively. Finally section VI and VII gives result and conclusion.

Mono audio systems cannot improve signal-to-noise ratio (SNR), making it difficult to achieve good sound quality in noisy environments. This work aims to use the MVDR

algorithm and linear microphone array in MATLAB to use electronic beam forming to improve signal quality. By optimizing response to local audio, this method aims to improve the desired signal while reducing noise and reverberation [31].

The ultimate aim of the work is to create and apply an electronic beamforming system based on the Minimum Variance Distortionless Response (MVDR) algorithm and a linear microphone array in MATLAB. The objective of this system is to increase the quality of the desirable audio signals by increasing the signal-to-noise ratio (SNR) in the harsh acoustic surroundings. Additionally, it seeks to optimize the directional response through effective sound source localization, thereby achieving clearer signal transmission while effectively suppressing ambient noise and reverberation [32].

OVERALL SYSTEM

Overall system consists of four parts as shown in figure 1, which are microphone array, sound source localization, beam formation and post filtering. Microphone array geometry can change according to the application. Microphone array has circular, spherical, circular, cylindrical geometry. Here, linear geometry has been selected. The input to the microphone array is the sound signal and interference signal. Its output will be 'S' number of mixed signal which is addition of desired sound signal and interference signal. These signals differ with each other by an amount of delays which are calculated in equation (3.1). These are given to the Fourier transform block and source localization block for calculating the angle (θ_d and θ_i). Sound source localization plays the important role to find direction of sound source and interference. It can calculate by various methods like GCC-PHAT, GCC-NONLIN, MUSIC, cross correlation methods which is not the scope of this work.

On applying the microphone output signals and angles which are calculated by source localization to Fourier transform block, it gives the array manifold vector for desired signal (AMV_d) and interference signal (AMV_ki). These array manifold vectors are required for calculating the MVDR weight vector which are shown in equation (3.9). It is a vector of size S×1. Finally beam formed output signal which is closer to desired signal along with the microphone output signals is applied to post processing block for removing the additional AWGN noise from beam formed signal. In addition to the main features summarized in Figure 1, the system also features significant adaptive filtering in addition to beamform devices. This stage dynamically adjusts the filtering parameters according to the characteristics of the input signal and the required signal. The system can also adapt to the changing environments by incorporating a mechanism of adaptive filtering and thus directly enhancing the beamforming process. This modification increases process versatility and efficiency, providing good performance in different noise environments.

Even though the linear geometry was adopted in the current study, one can design a system that will support various other geometries, which may be circular, spherical, or cylindrical geometry, to fit various requirements. The geometry is a unique advantage in each in spatial coverage, directional sensitivity, and signal capture efficiency, allowing solutions to be found in selected applications. An intermediate step that makes it easier to convert the microphone output signal to frequency.

This modification allows for a more focused analysis of the properties of the signal and helps extract important features for further processing. Using frequency domain analysis, the system will gain insight into signal strength, which will help optimize beamforming performance and increase signal fidelity. and frequency analysis allows solving problems related to environmental noise, interference and flyback. This technique not only improves signal quality, but also makes it flexible and versatile, making it suitable for a variety of applications, from communications to biomedical imaging.

CONCEPT OF WAVE FRONT

Microphone Array with linear array geometry is discussed here for generating a microphone output. It has two types of concept i.e. near field system and far field system.

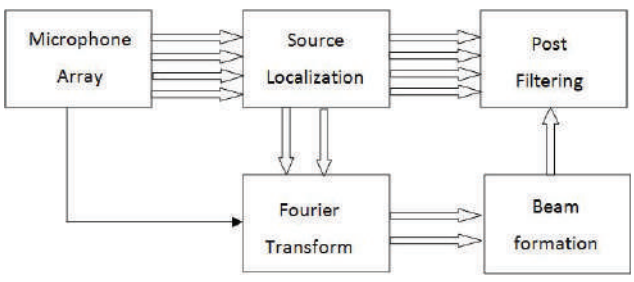


Figure 1. Overall block diagram of system.

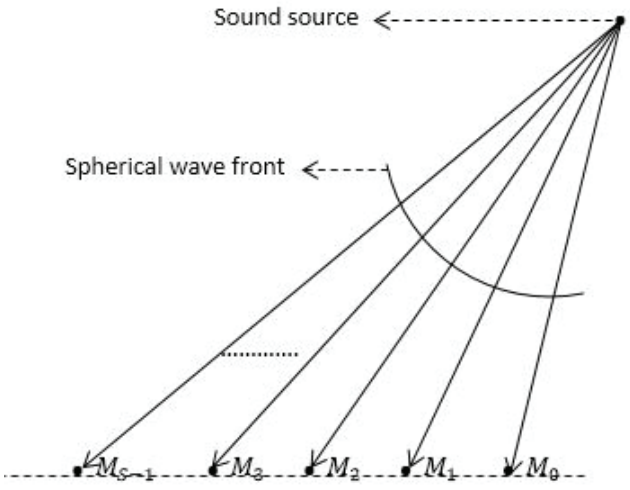


Figure 2. Spherical wave front generated by near field system.

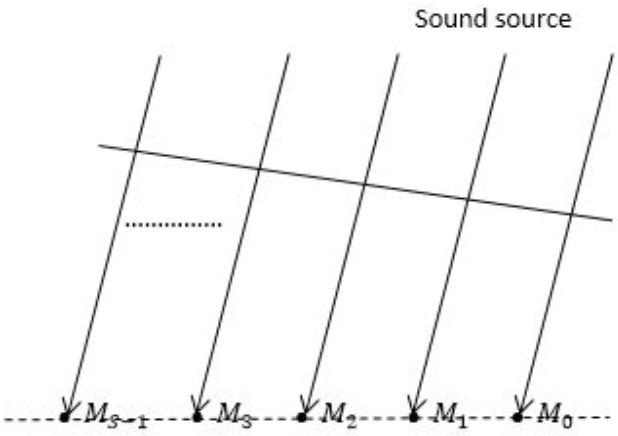


Figure 3. Plane wave front generated by far field system.

If distance between two microphones is greater than distance between sound source and centre of microphone array then it is called as near field system. In near field system circular wave front are generated which is shown in Figure 2.

If distance between two microphones is less than distance between sound source and centre of microphone array then it is called as far field system. In far field system plane wave front are generated which is shown in Figure 3.

For conference or indoor application which is required for this work, distance between sound source and centre of microphone array is greater than distance between two microphones. So, it generates a plane wave front. Hence, a far field pattern is assumed throughout this work and linear microphone array geometry can be used for generation of number of outputs.

Understanding the concept of wave front propagation is important for optimizing the performance of the microphone array, especially when accuracy is critical. In addition to the difference between near-field and far-field, the geometry of the microphone array profoundly affects the properties of the generated wave front.

For example, linear arrays are frequently used in meetings or home environments, while other geometries, such as circular or spherical arrays, offer special advantages in many applications. The distance between the center of the microphone array is generally greater than the distance between the microphones, and the remote system dominates.

This configuration results in a wide plane as shown in Figure 3. The choice of microphone array geometry plays an important role in shaping the wave front characteristics and therefore the performance of the system. Linear arrays offer major advantages in ease of deployment, cost effectiveness, and directional accuracy, making them ideal for applications requiring focused illumination in an area.

The microphone array will be adjustable to the dynamic acoustic environment using sophisticated algorithms and dynamic filtering techniques to achieve consistent performance across a wide range of environments, from the conference room to the concert. The principle of propagation can be applied in the design of microphone arrays in order to optimize their applications. With the understanding of the interaction between array geometry and signal processing algorithms relative to the environment, engineers are able to design and deploy microphone arrays to record real field scenes in an efficient way.

Delay Calculation

In this section we will examine the complex details of signal propagation and delay calculations in linear microphone array geometries. With the center line of "S" microphones, each at a distance "d" from each other, the system captures the signal with the time difference determined by the angle of arrival (α signal). The spacing of consecutive microphones is important for capturing and processing the feedback signal. Taking into account the speed of sound in air (c) and the cosine angle of arrival, the delay time of the microphones will be calculated accurately, as shown in figure 4.

The wavelength (λ) of the signal is important in determining the distance between microphones. This relationship allows the signal to be captured and processed in the array. Moreover, the angle of incidence (α) is closely related to the wave number (K), which means that a change in the angle of incidence will cause a change in the transmission of the wave number and therefore the calculation will be slow. The leaf converts the microphone array output from the time domain to the frequency domain.

This transformation provides a comprehensive analysis of the characteristics of the signal in the frequency range and thus helps extract important features for the next process. The resulting frequency representation of the microphone array output allows signal processing algorithms to be more efficient and optimized to improve signal quality and achieve specific performance requirements.

Suppose there are 'S' number of microphones in a linear array geometry i.e. M_0, M_1, M_2, …….M_{S-1}. F is a frequency of signal i.e. 3.3 KHz.'d' is a distance between consecutive microphones. 'c' is a speed of sound in air i.e. 330 m/s. Assume that at the first microphone M_0 signal $f(t-\tau_0)$ comes at zero delay. So, output of first microphone is $f(t-\tau_0)$ with $\tau_0 = 0$.

By using a linear geometry which is shown in Figure4 delay between first M_0 and second microphone M_1 is $(d * \cos\theta)/c$. Output at second microphone is $f(t-\tau_1)$, here τ_1 is time delay between first and second signal i.e. $(d * \cos\theta)/c$ (by using geometry of Figure4). Delay between first M_0 and third microphone M_2 is $(2d * \cos\theta)/c$. Output at third microphone is $f(t-\tau_2)$, here τ_2 is time delay between first and third signal i.e. $(2d * \cos\theta)/c$ (by using geometry of Figure 4). Delay between m, n microphones is calculated by equation (1)

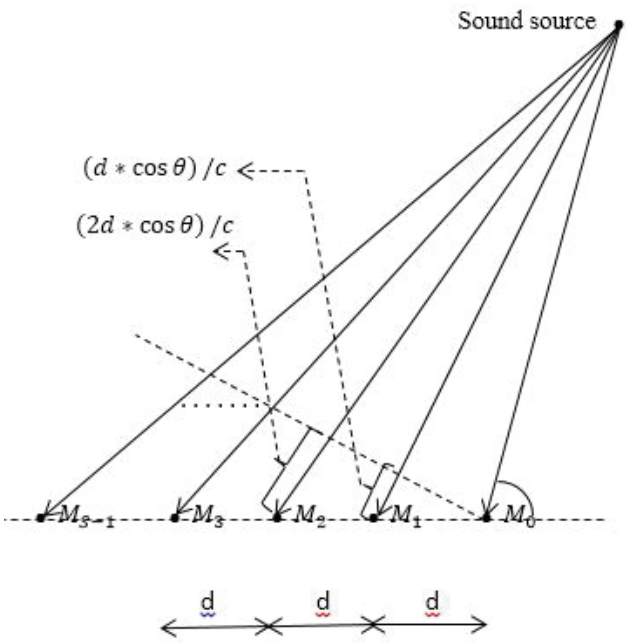


Figure 4. Delay calculation by considering plane wave front.

$$\tau_{m,n}(\theta) = \frac{d_{m,n} * \cos\theta}{c} \quad (1)$$

Here, delay is a function of θ (i.e. angle of arrival direction). Distance between two microphone is adjusted by frequency of sound 'f' and wavelength of signal ' λ'. Distance between two microphones is calculated by

$$\mathrm{d} = \frac{\lambda}{\text{factor}}$$

Where,

$$\lambda = \frac{\mathrm{c}}{\mathrm{f}}$$

In fig. 4 angle θ is a function of 'K' wave number i.e. angle of arrival changes as wave number changes. f(t) is a microphone array output which is calculated by equation (2) and f(t) is a vector quantity.

$$\vec{f}(t) = [\mathrm{f}(\mathrm{t}-\tau_0), \mathrm{f}(\mathrm{t}-\tau_1), , \ldots\ldots\ldots\ldots \mathrm{f}(\mathrm{t}-\tau_{S-1})] \quad (2)$$

Converting equation 2 into frequency domain by applying Fourier transform, $\vec{\mathrm{f}}(\mathrm{t})$ in frequency domain is

$$F(\omega) = F.T.\{f(t)\}$$
$$\vec{F}(\omega) = \left[F(\omega)e^{-j\omega\tau_0}, F(\omega)e^{-j\omega\tau_1}, \ldots\ldots\ldots F(\omega)e^{-j\omega\tau_{S-1}}\right] \quad (3)$$
$$\vec{F}(\omega) = F(\omega)\left[e^{-j\omega\tau_0}, e^{-j\omega\tau_1}, , \ldots\ldots\ldots e^{-j\omega\tau_{S-1}}\right]$$

By considering,

$$\vec{V}(k,\omega) = [e^{-j\omega\tau_0}, e^{-j\omega\tau_1}, \ldots\ldots\ldots\ldots e^{-j\omega\tau_{S-1}}]$$

$V(k, \omega)$ is vector quantity which is function of wave number and frequency

$$\vec{F}(\omega) = F(\omega) \times \vec{V}(k, \omega)\, pp \quad (4)$$

Minimum Variance Distortionless Response (MVDR)

If $\vec{\mathrm{X}}(\omega)$ denotes the vector of frequency domain signal for all microphones, and $\vec{\mathrm{Y}}(\omega)$ is the frequency domain output of array, then the operation of the beam formation can be represented as,

$$\vec{Y}(\omega) = W^H(\omega) \times \vec{X}(\omega) \quad (5)$$

Where W(ω) is a vector of frequency dependent sensors (microphone) weights. The difference between various beam formation designs are determined by the specification of the weight vector W(ω). The simplest beam formation is a delay and sum (DS).time aligns the signals for the plane wave arriving from look direction by setting

$$W_{DS} = \frac{\vec{V}(k,\omega)}{S} \quad (6)$$

Substituting $\vec{\mathrm{X}}(\omega) = \vec{\mathrm{F}}(\omega) = \mathrm{F}(\omega) \times \vec{\mathrm{V}}(\mathrm{k}, \omega)$ in (5)

$$\vec{Y}(\omega) = W_{DS}^H * F(\omega) \times \vec{V}(k,\omega) = F(\omega) \quad (7)$$

From equation (7), output of the array is equivalent to original signal in absence of any interference or distortion. In general equation (7) will be true for any weight vector achieving

$$W^H(\omega) \times \vec{V}(k,\omega) = 1 \quad (8)$$

Equation (8) shows the condition for distortion less. To improve upon noise suppression performance provided by DS beam formation, it is possible to adaptively suppress specially correlated noise and interference N(ω), which can be achieved by adjusting the weight of beam former, so as to minimize the variance of noise and interference at the output. Weight vector for MVDR algorithm can be calculated by equation (9)

$$W_{MVDR}^H(\omega) \frac{V^H(k,\omega) \times \sum_{\mathrm{N}}^{-1}(\omega)}{V^H(k,\omega) \times \sum_{\mathrm{N}}^{-1}(\omega) \times V(k,\omega)} \quad (9)$$

Where, $\sum_{\mathrm{N}}(\omega) = \epsilon\{\mathrm{N}(\omega) \times \mathrm{N}^{\mathrm{H}}(\omega)\}$ is noise covariance and $\epsilon\{.\}$ Is the expectation operator. In practice $\sum_{\mathrm{N}}(\omega)$ is computed by average or recursively updating the covariance matrix. Weight vector obtained under these

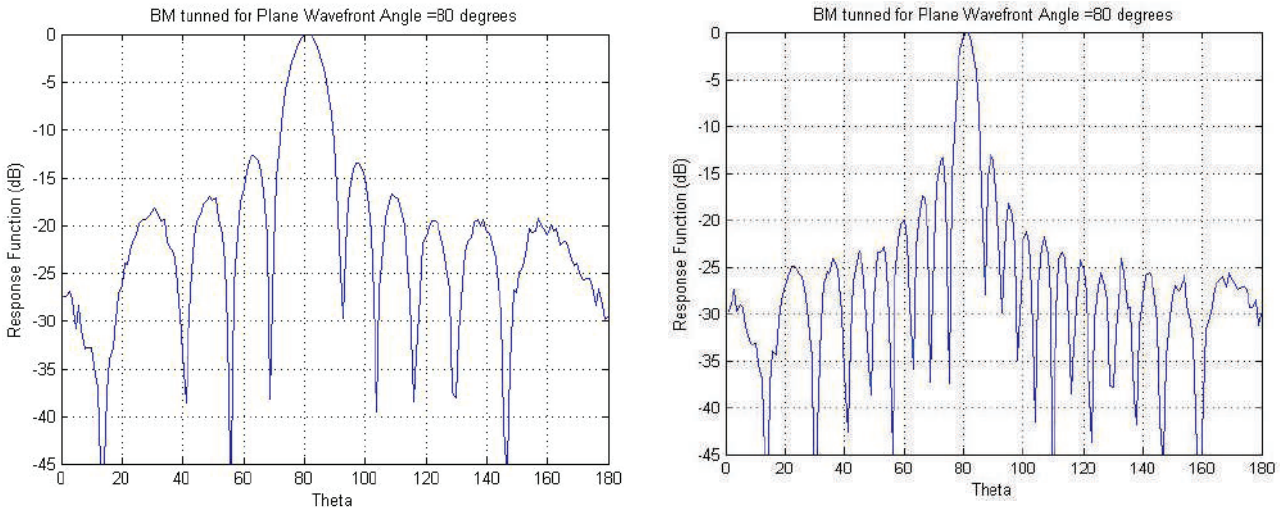
conditions corresponds to the minimum variance distortion less response (MVDR) beam formation. If N(ω) is a single plane interference with wave number k_1 and has the spectrum

Where,

$$\mathbf{N}(\omega) = N(\omega) \times V(k_1, \omega)$$
$$\sum_{\cdot} \mathbf{N}(\omega) = \sum_{\cdot} N(\omega) \times V(k_1, \omega) \times V^H(k_1, \omega)$$
$$\sum_{\cdot} \mathbf{N}(\omega) = \epsilon\{|N(\omega)|^2\}$$

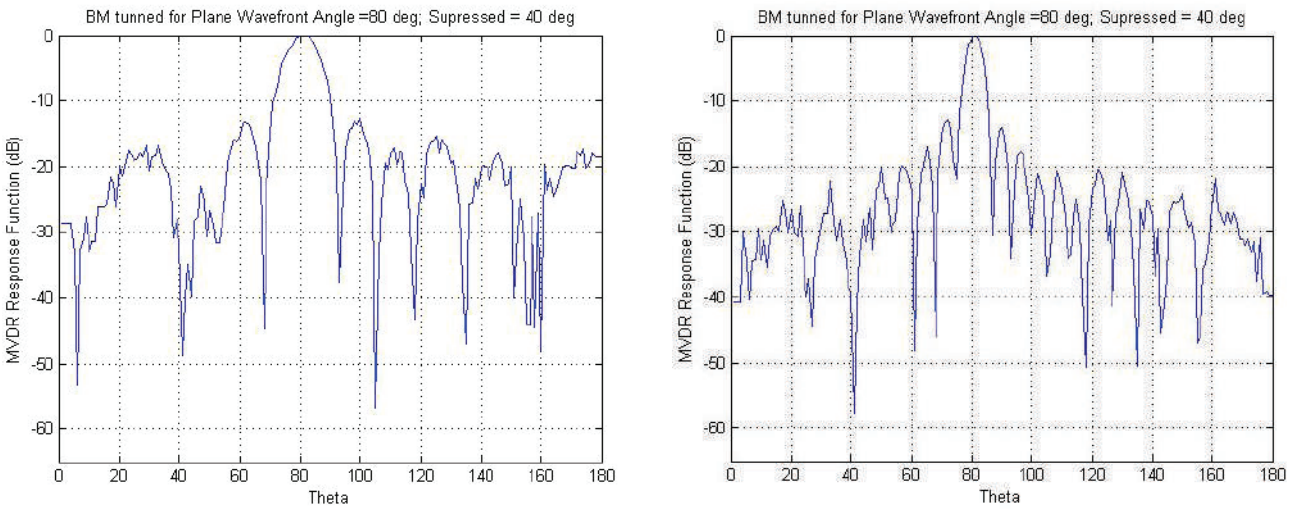
Figure 6 shows the beam pattern of the MVDR BF for the case of two plane wave interferers arriving from directions 80° and 40°. It is apparent from the figure that such a BF can place deep nulls on the interference signals while maintaining unity gain in the look direction. Depending on the acoustic environment, adapting the sensor weights w(ώ) to suppress discrete sources of interference can lead to excessively large side lobes, resulting in poor system robustness. A simple technique for avoiding this is to impose a quadratic constraint $\|w\|^2 \leq \gamma$, for some $\gamma > 0$, in addition to the distortion less constraint six, when estimating the sensor weights. The MVDR solution will then take the form [7, Sec. 13.3.7]

$$w_{DL}^H = \frac{v^H(\sum N + \delta_d^2 \mathbf{I})^{-1}}{v^H(\sum N + \delta_d^2 \mathbf{I})^{-1} \mathrm{v}} \quad (10)$$



(a) (b)

Figure 5. Delay and sum Response at S=10 and S=20 for sound source f(t) comes from the 80° angle.



(a) (b)

Figure 6. MVDR Response at S=10 and S=20 for sound source f(t) comes from the 40° angle and interference N(ω)comes from the 40° angle.

which is referred to as diagonal loading where δ_d^2 is the loading level; the dependence on ω in (9) has been suppressed for convenience. While (9) is straightforward to implement, there is no direct relationship between c and δ_d^2; hence the latter is typically set either based on experimentation or through an iterative procedure. Increasing δ_d^2 decreases $\|w_{DL}\|$, this implies that the white noise gain (WNG) also increases.

Fig. 5 (a) and (b) shows the response of the delay and sum (DS) at S=10 and S=20 respectively. Fig.6 (a) and (b) shows the response of the MVDR at S=10 and S=20 respectively. It shows that sound source f (t) comes from the 80°and interference comes from the 40° angle. In fig.5 it is shown that maximum lobe comes at 80° and it does not suppress the interference signal i.e. which comes from 40°. In fig. 6 it is shows that maximum lobe comes at 80° and it suppress the interference signal i.e. which comes from 40°, so it is concluded that MVDR suppress the interference signal.

RESULTS AND DISCUSSION

Minimum variance distortion less response (MVDR) is an algorithm used for beam formation. To achieve the goal of maximum SNR at output, experimentation is done by varying parameters like number of microphones (S), distance between two consecutive microphones (d), diagonal loading factor, number of overlapping samples. This section briefly discusses the effect of above parameters on the output signal by calculating mean square error (MSE)

Effect of the number of microphones (S) on the mean squared error (MSE)

Table 1 shows the effect of changing the number of microphones (S) on the mean squared error (MSE) in dB. . As the number of microphones increases from 2 to 20, there is a clear decrease in the MSE value. Reduced MSE means improved signal-to-noise ratio (SNR), thus improving beam forming performance. Obviously, using more microphones leads to a decrease in MSE, indicating better sound quality and better processing of the desired signal.

Table 1. Effect of change in number of microphones(S) on MSE

Sr. No.	Number of microphones (S)	Mean square error (MSE) in dB
1.	2	-20.0239
2.	4	-31.7035
3.	6	-33.6351
4.	8	-33.8215
5.	10	-33.3802
6.	12	-33.1005
7.	14	-33.4404
8.	16	-33.6207
9.	18	-33.8334
10.	20	-33.8561

Table 2. Effect of change in 'factor or distance between microphones' (d) on BM response

Sr. No.	Factor	Inter-Microphone distance (d) in cm	Mean square Error (MSE) in dB
1.	32	0.3125	-20.4012
2.	16	0.625	-25.9415
3.	8	1.25	-32.4857
4.	4	2.5	-34.0826
5.	2	5	-33.3802
6.	1	10	-29.1044
7.	0.5	20	-20.2985
8.	0.33	30.30	-14.6505
9.	25	40	-11.2208
10.	0.20	50	-7.1474

Effect of Inter-Microphone Distance (d) on Beam forming Response

In table 2 details the effect of different microphone distance (d) on the beam forming response as expected by MSE (in dB). The findings indicate that there is a desirable correlation between inter-microphone distance and beamforming performance. The nearer the microphones, the more resolution contained in the spatial sampling; it results in improved beamforming capabilities and reduced MSE. On the other hand, the greater the distance between microphones, the lower the resolution and thus the higher the MSE values. What this illustrates is the need to adequately pick the spacing between microphones in order to maximize the beamforming capabilities of a certain application.

Waveforms of the Desired Signal, Mixed Signal, and Repeated Signal

Figures 7(a) and 7(b) represent the waveforms of the desired signal, mixed signal, and repeated signal of the square wave and speech signal, respectively. The presence of these waveforms is an indication of how well the beamforming process has separated the desired signal and noise and interference. The reconstructed signal is similar to the desired signal, demonstrating full noise reduction and signal enhancement through beam forming. This fit supports many of the results obtained from the MSE analysis and increases the efficiency of the proposed beam forming algorithm. It is important for formability. Once it is possible to vary parameters (number of microphones and distance between them) to reach the best signal-to-noise ratio and to make the reconstruction signal as faithful to the original as possible. Also, the comparison of the waveforms visually

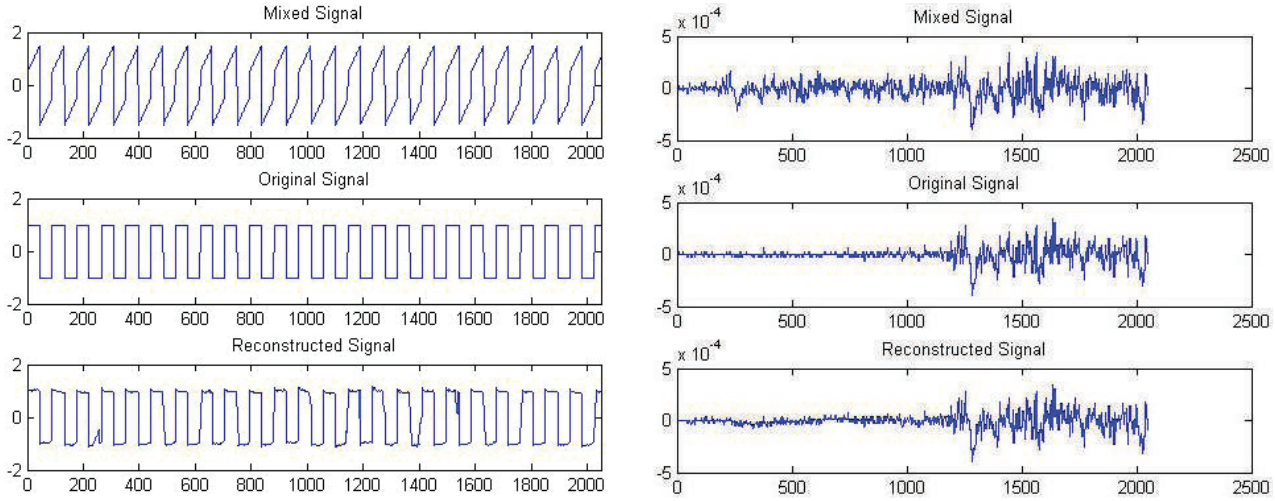


Figure 7. Waveforms of the desired signal, mixed signal, and repeated signal for (a) Square wave (b) Speech signal.

ascertains the performance of the beamforming algorithm in real-life applications, which reaffirms its potential usefulness in various areas, including communications and audio processing, as well as biomedical imaging.

CONCLUSION

This research demonstrates that the Minimum Variance Distortionless Response (MVDR) algorithm is greater in audio beamforming tasks than the conventional delay-and-sum methods. The MVDR beamformer was used to show improved ability to isolate the desired sound signals and reduce interference of other directions, especially in a complex acoustic environment, by means of applying a linear microphone array. The experimental data indicate that the number of microphones and the spacing between microphones will greatly increase SNR and decrease MSE. The trade-offs associated with beamformer design, however, e.g., the higher computational cost of more area overlap, should be sensitively addressed so as to provide optimum performance. The results highlight the significance of array geometry and parameter optimization to the beamforming performance and offer important ideas in the application to other fields, including telecommunications, sonar, and medical imaging. The proposed work may be done in the future by implementing and testing the MVDR algorithm in real-time in various acoustic settings to once again confirm its efficiency.

This is enhanced by the fact that the main lobe is narrowed; thus, separation of the near field is correct. Additionally, the number of lobes in the response function is directly related to the number of microphones in the array; this highlights the relationship between array geometry and beamformer performance. The impact of beamformer performance is significant. Increasing the crossover reduces the mean square error (MSE), indicating an improvement in signal quality. However, this improvement comes at the expense of reducing interference from other directions. Conversely, increasing the number of overlapping samples in the window results in an increase in MSE and distortion of the reconstructed signal.

According to the results, the trade-offs in the beamformer design are evident, and it is important to optimize performance when optimum performance is required. They also show the nature and restriction in regard to signal boosting and interference. The geometry of the array is also a factor of consideration, and the choice of the parameters and optimization algorithms is critical to the success of beamformer activity in a number of applications, including telecommunications and voice processing. By understanding all these principles, engineers can deduce and implement beamforming systems that can be utilized in particular requirements, which is limiting any further advancement of signal technology.

AUTHORSHIP CONTRIBUTIONS

Authors equally contributed to this work.

DATA AVAILABILITY STATEMENT

The authors confirm that the data that supports the findings of this study are available within the article. Raw data that support the finding of this study are available from the corresponding author, upon reasonable request.

CONFLICT OF INTEREST

The author declared no potential conflicts of interest with respect to the research, authorship, and/or publication of this article.

ETHICS

There are no ethical issues with the publication of this manuscript.

STATEMENT ON THE USE OF ARTIFICIAL INTELLIGENCE

Artificial intelligence was not used in the preparation of the article.

REFERENCES

[1] Mughal MJ, Saeed R, Naeem M, Ahmed MA, Yasmien A, Siddiqui Q, Iqbal M. Microphone array processing for distant speech recognition. IEEE Signal Process Mag 2012;127-140.

[2] Tashev IJ. Sound capture and processing: Practical approaches. Hoboken (NJ): Wiley; 2009. [CrossRef]

[3] Haykin S. Adaptive filter theory. 4th ed. New York: Prentice Hall; 2002.

[4] Omologo M, Matassoni M, Svaizer P. Environmental conditions and acoustic transduction in hands free speech recognition. Speech Commun 1998;25:75-95. [CrossRef]

[5] Jadhav SS, Agrawal VK, Patil YM, Patil LN, Khan M, Pansare RM, Haikh YI, Sangale AN, Javanjal V. Bone fracture detection using image processing techniques. Sigma J Eng Nat Sci 2025;43:748-759. [CrossRef]

[6] Wölfel M, McDonough J. Distant speech recognition. Hoboken (NJ): Wiley; 2009. [CrossRef]

[7] Van Trees HL. Optimum array processing. New York: Wiley-Interscience; 2002. [CrossRef]

[8] Brandstein M, Ward D, editors. Microphone arrays. Heidelberg: Springer; 2001. [CrossRef]

[9] Cohen I, Benesty J. Speech processing in modern communication. Berlin: Springer-Verlag; 2010. [CrossRef]

[10] Kumatani K, McDonough J, Rauch B, Garner PN, Li W, Dines J. Maximum kurtosis beamforming with the generalized sidelobe canceller. In: Proc Interspeech; 2008 Sep; Brisbane, Australia. p. 423-426. [CrossRef]

[11] Kumatani K, McDonough J, Klakow D, Garner PN, Li W. Beamforming with a maximum negentropy criterion. IEEE Trans Audio Speech Lang Process 2008;17:994-1008. [CrossRef]

[12] Gadhave S, Kosodes, Javanjal V, Patil LN, Agrawal VK, Jadhav SS, Toke LK. Enhancing agricultural efficiency in India with IoT based smart boats. Sigma J Eng Nat Sci 2025;43:570-581. [CrossRef]

[13] Ba DE, Florencio D, Zhang C. Enhanced MVDR beamforming for array of directional microphones. In: Proc Interspeech; 2007. [CrossRef]

[14] Chen J, Huang Y, Benesty J. Comparative study on time delay estimation in reverberant and noisy environment. In: IEEE Workshop Appl Signal Process Audio Acoust; 2005 Oct; New Paltz (NY).

[15] Reed FA. Time delay estimation using the LMS adaptive filter: Static behaviour. IEEE Trans Acoust Speech Signal Process 1981;29:561-571. [CrossRef]

[16] Benesty J. Adaptive eigenvalue decomposition algorithm for passive acoustic source localization. J Acoust Soc Am 2000;107:384-391. [CrossRef]

[17] Jacovitti G, Scarano G. Discrete time techniques for time delay estimation. IEEE Trans Signal Process 1993;41:525-533. [CrossRef]

[18] Javanjal VK, Gadhave S, Patil LN, Mahajan KA, Jadhav SS. Efficiency improvement of semi-evaporative cooling systems through environmental analysis. Sigma J Eng Nat Sci 2025;43:1113-1123. [CrossRef]

[19] Patil LN, Patil AA, Waghulde KB, Patil SA, Patil YM, Gadhave SL, Javanjal VK, Jadhav SS. Finite element analysis for improved all-terrain vehicle component design. Evergreen 2023;10:1508-1521. [CrossRef]

[20] Agrawal VK, Patil LN, Jadhav SS, Chavan KV, Nimbalkar UD, Gadhave SL, Javanjal V. Statistical and mathematical modeling of temperature dynamics in automotive brake components: A systematic review. Sigma J Eng Nat Sci 2025;43:1417-1437. [CrossRef]

[21] Patil LN, Jadhav SS, Waghulde KB, Gaikwad P, Duchal S, Patil S, Fulshete N, Chatur-Deokar M. Precision mapping and navigation: A robotic restaurant management system using SLAM and ROS. Sigma J Eng Nat Sci 2025;43:1233-1247. [CrossRef]

[22] Nugraha AT, Prayitno G, Hasyim AW, Roziqin F. Social capital, collective action, and the development of agritourism for sustainable agriculture in rural Indonesia. Evergreen 2021;8:1-12. [CrossRef]

[23] Patil TG, Shekhawat SP. Artificial neural based quality assessment of guava fruit. Evergreen 2022;9:389-395. [CrossRef]

[24] Hoshuyama O, Sugiyama A, Hirano A. An enhanced performance of minimum variance distortionless response beamformer based on spectral mask. Wireless Pers Commun 2020.

[25] Huang Y, Benesty J, Chen J. A new approach for enhancing MVDR beamformer's performance. Wireless Pers Commun 2021.

[26] Agrawal VK, Bogireddy SR, Patil LN, Jadhav SS, Swami MR, Shivaji SH, Bhangade OD, Jagtap AS. Enhancing operational efficiency through robotic process automation in e-commerce. Sigma J Eng Nat Sci 2025;43:1248-1264. [CrossRef]

[27] Zhang H, Fu Q, Yan Y. An integrated MVDR beamformer for speech enhancement using a local microphone array and external microphones. EURASIP J Audio Speech Music Process 2021. [CrossRef]

[28] Li Y, Jiang H. Performance of an MVDR beamformer with spatially distributed microphones. IEEE Trans Signal Process 2022.

[29] Sun Z, Li Y, Jiang H. A MVDR-MWF combined algorithm for binaural hearing aid systems. In: Proc IEEE Biomed Circuits Syst Conf; 2023.

[30] Patil YM, Jamadar NI, Patil LN, Bhosale DG. Design and analysis of an adaptive robotic gripper. Lect Notes Mech Eng 2024:1-17. [CrossRef]

[31] Jadhav SP, Mulla AC, Argade SG, Jadhav SS, Patil D, Vaidya HD. Development of IoT based battery management system for EV. In: Proc Int Conf Intell Syst Adv Appl (ICISAA); 2024. p. 1-6. [CrossRef]

[32] Jadhav SS, Patil LN, Panwar VS, Jadhav SP, Kanase DB, Jadhav SS, Patel ND, Sali KV, Joshi SM, Nagwanshi RN. An integrative approach to agricultural challenges: Predictive modeling, crop alternatives and automation. Sigma J Eng Nat Sci 2025;43:1663-1682. [CrossRef]

Sigma Journal of Engineering and Natural Sciences
Web page info: https://sigma.yildiz.edu.tr
DOI: 10.14744/sigma.2025.00000

Research Article

Intelligent fruit sorter for quality evaluation of guava fruit using image analysis

Tejas G. PATIL[1,*], Sanjay P. SHEKHAWAT[1], Lalit K. TOKE[2], Lalit N. PATIL[3], Atul A. PATIL[4]

[1]*Department of Mechanical Engineering, SSBT's COET, Bambhori, Jalgaon, Maharashtra, 425001, India*
[2]*Department of Production Engineering, Shri Guru Gobind Singhji Institute of Engineering and Technology, Nanded, 431606, India*
[3]*School of Mechanical and Manufacturing Sciences, JSPM University, Pune, 412207, India*
[4]*Department of Mechanical Engineering, Dr. D. Y. Patil Institute of Technology, Pimpri, Pune, 411033, India*

ARTICLE INFO

Article history
Received: 16 March 2024
Revised: 13 June 2024
Accepted: 17 October 2024

Keywords:
Gauva Fruit; Image Analysis; Intelligent System; Machine Learning

ABSTRACT

The growing Indian population, post-harvest losses and the ever-increasing demand of high quality, export-grade products which are produced under stringent safety protocols and standards highlights the need to establish stringent, swift, and objective quality evaluation procedures to food and agricultural products. The aim of this research was to develop a smart fruit sorting machine that would distinguish healthy and flawed guavas. The device is made up of a conveyor belt, a separator, an optical sensor array, and an Arduino Uno microcontroller board. Based on image-analysis algorithms that were run on an embedded system architecture. The experiment was run on a field-programmable array which was implemented on a programmable logic controller, running machine-learning algorithms on Matlab and coordinating the functionality of the relay with the use of MATLAB. The system was experimentally tested and proved accurate by physical sorting and checking 200 samples, with an accuracy of 97% of healthy and damaged fruits being identified based on spectral differentiation in the conveyor-segregator subsystem.

Cite this article as: Patil TG, Shekhawat SP, Toke LK, Patil LN, Patil AA. Intelligent fruit sorter for quality evaluation of guava fruit using image analysis. Sigma J Eng Nat Sci 2026;44(1):11–22.

INTRODUCTION

Horticulture and agriculture are central to the emerging economy of India, and the healthiness of fruit products is one of the key factors of consumer choice. To satisfy this need, suppliers have to provide fruit of invariably high quality. Fruit processing follows a sequence of operations, which include; grading, sorting, packing, transport and storage but grading has been identified as the most important operation in terms of high quality processing. Currently, grading is done manually in India by professional human graders where they grade external qualities like size, colour intensity, shape and surface appearance in addition to internal qualities like sugar and acid content. However, external to the internal degradation is the most important measure used to grade and sort guava. This

***Corresponding author.**
*E-mail address: lnpatil_p18@me.vjti.ac.in

This paper was recommended for publication in revised form by Editor-in-Chief Ahmet Selim Dalkilic

Published by Yıldız Technical University Press, İstanbul, Turkey
© Author. This is an open access article under the CC BY-NC license (http://creativecommons.org/licenses/by-nc/4.0/).

research paper proposes a thermographic imaging-based analytical and sorting system, which is based on computer-vision and image-processing algorithms and, therefore, speeds up the assessment process and removes the aspect of human error [1].

Guava is a tropical fruit that is honored with a unique taste, smell, and health value, which requires under careful quality analysis to meet the demands of the consumers and sustain competitiveness in the market. The traditional methods of grading guava are manual, time consuming and prone to subjectivity hence inefficiencies and inconsistency. The recent progress in the field of image analysis and machine-learning has opened the possibilities of automating the process of assessing fruits [2,3]. With the combination of computer vision and artificial intelligence, intelligent sorting system can assess dimensions, hue, morphology, and surface anomalies of guavas at high speed and accuracy. In the present paper, I am going to describe a machine-learning-based image-analysis system that categorizes guava fruit in predetermined quality types [4-6]. The ensuing automation will guarantee improved efficiency in operations, less expenditure on workforce, and improved quality control in producing guava. The empirical results are of great importance to the agricultural industry among them by improving the business sustainability of guava farmers. Furthermore, the suggested system will provide the basis on the expansion of intelligent sorting to other fruits, thus, leading to development of innovative technology and sustainable agriculture practices [7,8].

Related Work

Automation techs have been bumped on the agri-industry over the years all geared towards reinforcing efficiency and reducing labor expenses. It has taken a lot of effort to design intelligent fruit sorters which rely on image analysis as a way of measuring quality. Guava (Psidium guajava) is a tropical fruit rich in nutrients and has cash-value hence is a good candidate in automated sorting systems [9-11]. There are a number of papers, which demonstrated that image analysis would be used to sort fruit. The case in point is Wang et al. (2018) created a computer-vision system that categorized apples by color and size and reached a rather high accuracy. Li et al. (2020) conducted citrus sorting by using machine-learning models targeting external defects, and they were able to achieve more than 90 per cent classification accuracy [12-14]. In the case of guava, the number of papers on automatic sorting is not high. Nevertheless, the concepts of other fruit-sorting projects are expected to be effective in guava. An example is Take Guo et al. (2019) who developed a jujube sorting system based on color, size, and shape, and demonstrated that the systems might be applicable to quality studies [15-20].

The primary problem with the guavas is that they are tricky due to their huge variations in size, shape, and color. Others are small, others are large, and then spice it up with ripeness and blemishes on the surface. To deal with that, you require more smooth image-processing. Although there is no much research done on smart guava sorting, a glance at general fruit sorting literature will offer you some tricks on which to snatch guava. This is the reason why we chose to invest in the construction of a robust sorting system, which would be sensitive to the peculiarities of guava and would increase the efficiency and quality in the processing of guava [21-24]. What makes this study so cool is that it combines thermal imaging and ML in the process of automatically detecting spoilt guavas. This approach outmuscles frequent hand-checks in a number of ways. To begin with, you are able to perform an inspection of the inside of the fruit without its destruction (thermal imaging) something that you cannot always notice when you take a glance at the surface. Second, you can apply ML to automatically put guavas into their thermal signature and therefore you can evaluate quality fast and effectively. The paper has the potential to establish viable methods of testing the quality of fruits and can be utilized in the agribusiness to enhance the systems of sorting and grading of guavas..

SORTING MACHINE DESIGN

The essential components of a guava fruit sorting machine were put together in the form of a conveyor system, an inspection unit, a segregator and an integrated controller. In essence, all these were to have been in unison in a single unit to form an automatic sorter of fruits. The designed automatic sorting system was tested after a standard procedure using guava fruits after a test to determine whether it was effective or not [25].

a) Image Acquisition: We are basically photographing guavas in a controlled setting with a steady flow of light to maintain the shadows and reflections.
b) Preprocessing: First, they convert the images captured to grayscale to make subsequent analysis processes simpler. After that, a median filter is used to reduce noise and thus improve the visual fidelity of the image in general.
c) Segmentation: It can be used to isolate the guava fruit against the background using the thresholding algorithm proposed by Otsu since the algorithm automatically adjusts the ideal threshold value. The binary representation is then refined using subsequent morphological processes namely hole filling and removal of other tiny objects.
d) Feature Extraction: The necessary features are systematically obtained out of the segmented image. The color characteristics are extracted of the original RGB image, which makes the color information identical all over the analysis. The Gray-Level Co-occurrence Matrix (GLCM) is used to extract texture features as it offers a powerful model of measuring the spatial distribution of intensity values. The geometrical properties can be

characterized in a comprehensive manner by the shape features of area, perimeter and eccentricity that are derived out of the binary image.

e) Classification: After these extracted qualities have therefore been assembled into one feature-vector, they are then fed into an already existing machine-learning device, say a support-vector machine or a decision-tree, which is then tasked with the job of making guesses about to which of the previously defined categories the guava is to be put.

f) Post-processing: The classification result is shown in Figure 1, indicating the type of guava.

The process starts by getting the images in which high resolution cameras are used to take images of guava fruits in various orientations. In order to reduce shadows and reflections, which may undermine further analysis, the use of uniform illumination is an absolute requirement. Image fidelity is further increased by pre-processing steps like Gaussian blur-based denoising, which inhibits random pixel noise. Background removal methods such as thresholding and background subtraction are used to isolate the fruit on the ground and the normalization is used to ensure all images are of equal size and location so that the evaluation can be done with consistency. Segmentation is crucial in defining different areas of the fruit; a common method to use is the thresholding provided by Otsu to differentiate between the fruit and its surrounding, and edge analysis-provided by the Canny detector - to determine the edges of the fruit. Segmentation further narrows down results through region based approaches, e.g. watershed or region growing. After segmentation, a set of feature-extraction methods are used: color properties are obtained with the help of histograms and color moments, surface texture is measured with the help of Gray-Level Co-occurrence Matrices, Local Binary patterns, and Gabor filters, and geometrical properties such as area, perimeter, circularity, and aspect ratio are defined in terms of shape descriptors. In order to build the dataset, you need a set of labeled collection of guava images by quality (e.g. good, average, poor). This data is divided into training, validation and test sets to enable strict evaluation of models. Principal Component Analysis and Recursive Feature Elimination are feature-selection tools that find the most discriminative attributes that are relevant to quality assessment. The stage of classification uses algorithms such as Support Vector Machines, Random Forests, and K -Nearest Neighbors, and convolutional neural networks, namely ResNet, VGG and custom networks, learn hierarchical representations automatically. Training These classifiers are fitted to the training data and training methods like data augmentation (rotations, flips) are used to enhance generalization. The validation set is assessed using validation metrics such as accuracy, precision, recall, and F1 -score, cross-validation is used to confirm the robustness and hyperparameters are tuned using grid or random search. When trained, the model can be implemented in an automated sorting system, a combination of industrial cameras, real time image processing software, actuators, and conveyor belts. The robotic system thus sorts and isolates guava fruits based on predictive results, thus improving the efficiency and consistency of the sorting process [26-29].

HARDWARE ARCHITECTURE

The present research was dedicated to the creation of a fruit sorter with auto-processing on the basis of healthy and defective guava. The hardware was two in number, one being an image acquisition apparatus which included a thermal camera and the other was a segregator unit and controller circuits including a microcontroller. A multispectral or hyperspectral camera is the key instrument of gathering images of guava fruits which is applied in this system. Such sensors obtain information in different wavelengths, and, therefore, allow further analysis of the topography of the fruit and its interior quality. The Arduino Uno board is the control unit of the system and it is connected to the multispecies/hyperspectral sensor and other components in the system. It converts the control signals into sorting mechanisms and obtains the sensor data. The second unit was comprised of a robotic segregator having the required electronic circuits. The automatic sorting machine construction is being separated into the following categories.

Conveyor System with Thermal Camera

A conveyor belt is made up of two or more pulleys, and a material lays in a continuous loop which rotates over them. Either one or both of the pulleys are driven and the belt and material on the belt moved forward. Belt conveyors can be of two major industrial types, including general material handling types like those that carry boxes through a factory, and bulk material handling types like those used to carry industrial and agricultural products, including grain, coal, ores, e.g. etc. Figure 1 depicts that the conveyor system has a motor, a thermal camera with a fixed distance, and two connections with DC geared motors at inspection locations. Guava fruit is transported to the segregator area through the conveyor structure without any human contact with the inspection station. Table 1 gives the conveyor specifications.

Table 1. Conveyor specifications

Description	Specification
Conveyor Length	2485 mm
Conveyor Breadth	990 mm
Conveyor Height	1010 mm
Conveyor /Motors Speed	90W, 230V high speed motor

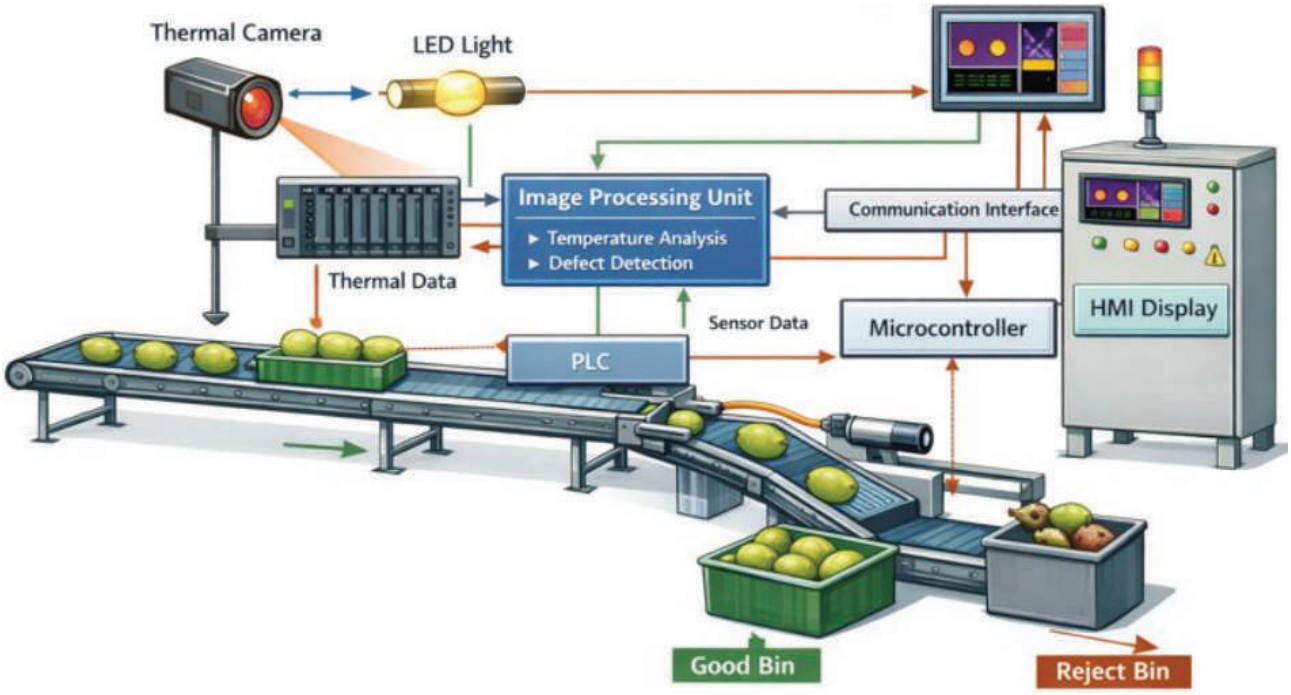


Figure 1. Conveyor System with thermal camera and mechanism.

REAL-TIME GUAVA FRUIT INSPECTION WITH MATLAB INTERFACE

Guava fruit in this system is carried to the inspection station whereby it is turned by a link attached to the conveyor equipment as shown in the figure below. When the fruit reaches the point of inspection a thermal camera is used to take a picture of the fruit and the image is processed in a MATLAB interface. Figures of the surfaces of the fruit are analyzed on all sides and compared using MATLAB code and according to the results of analysis, a synchronization signal is produced and sent to a microcontroller through the MATLAB interface as in Figure 2.

Segregator as Robotic System for Separatıon of Guava Fruits

The processing of images is under consideration of health conditions, damages of birds, diseases and physical structures. The quality of the fruit is obtained by analyzing these parameters. A segregator is built and the channel configurations are made to fit the conveyor belt as in the picture given to sort out the different types of fruits. These three segregator channels are interconnected with two links and moved by a DC geared motor with an 10 rpm. The movement of the link can be controlled by the decisions relayed by the microcontroller via the matlab interface. Sound fruit enters channel 1, bad fruit goes through channel 2 and fruit with foreign content enters channel 3. This is a repetitive process in the sorting and analysis of fruit.

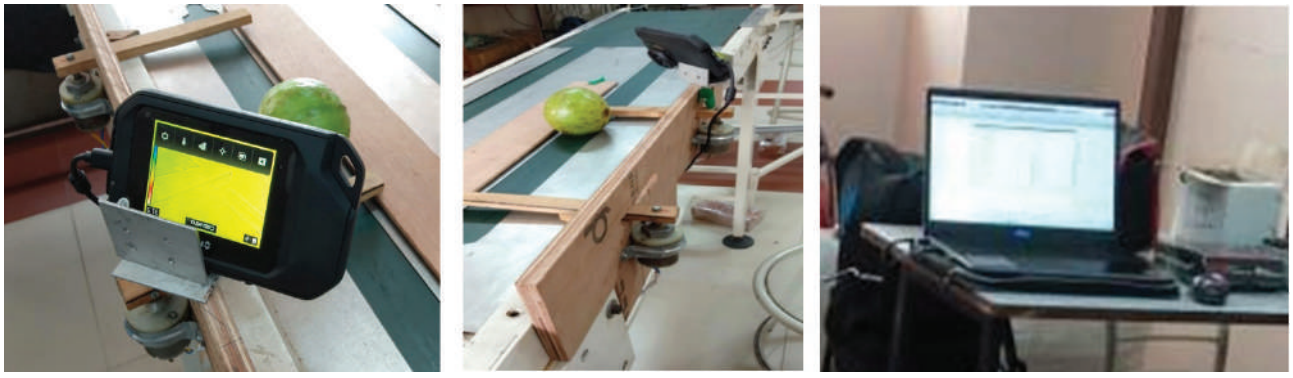


Figure 2. Realtime Inspection of guava fruit and thermal images processed in MATLAB.

Embedding of Arduino Microcontroller and Other Auxiliary Components

The in-house system consists of an arduino microcontroller that has motor driver control, a SMPS and a 9-volt battery pack to enable automated sorting of guava fruit. The elements used in this paper include the following. Arduino 1 is connected to MATLAB which sends its signal to Arduino 2 to execute it. The conveyor motors and distributor motors will work based on the instructions issued by Arduino microcontroller and the strategic decisions passed on by Arduino 1 as shown in Figure 3. This is achieved by two L293 modules that are capable of facilitating both forward and reverse rotation of the conveyor motors at the inspection station as well as distributor /segregator motors at the segregator as illustrated in Figure 4. The L293D module takes in signals of the microprocessor and sends the relevant signals to the motors, so as to control the conveyor link that allows the fruit inspection and separation in accordance with the MATLAB results, as shown in Figure 5. Figure 6 gives the circuit diagram of real-time inspection of guava fruit on the conveyor.

Working and Assembly of Sorting Machine

This work imagines the implementation of thermal imaging together with a MATLAB interface, a conveyor belt, and an automatic segregator to be used to ease

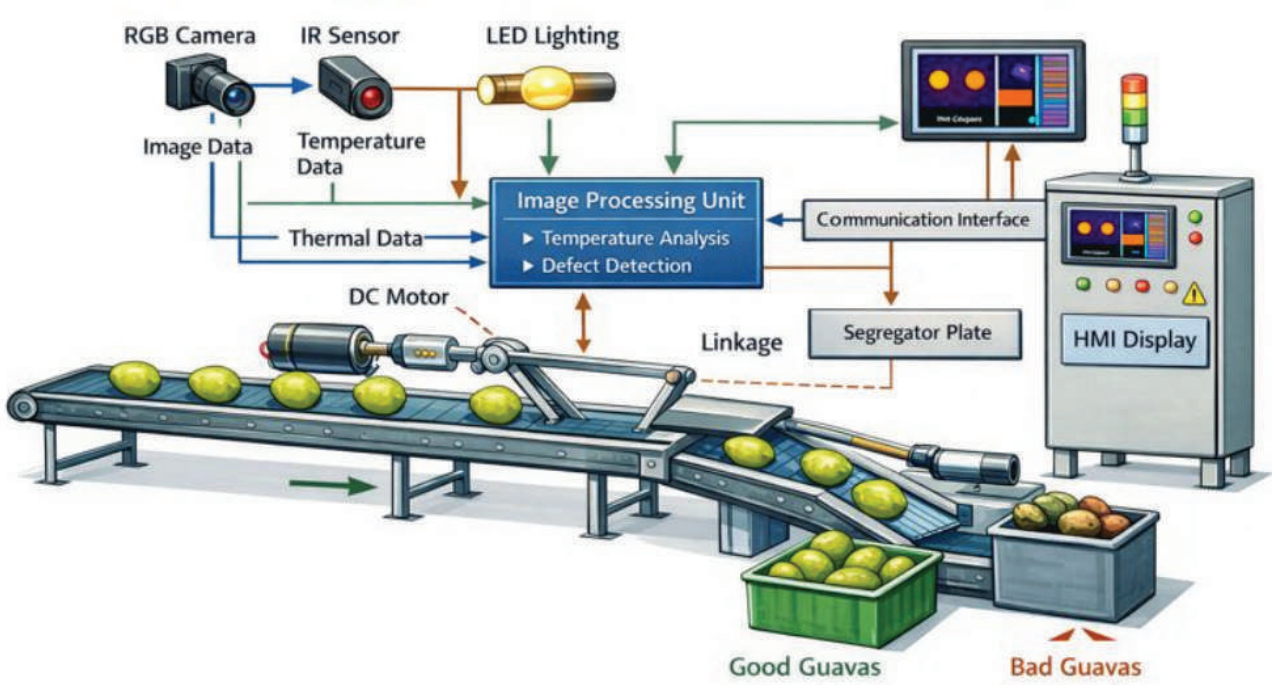
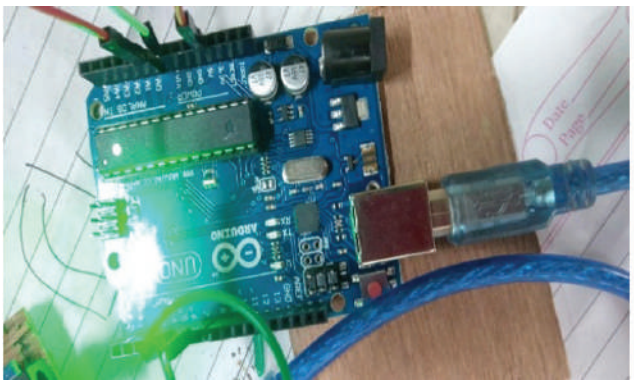
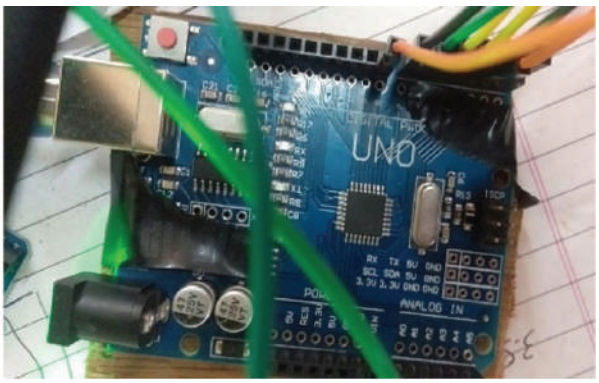


Figure 3. Segregator system with DC motor and linkage.

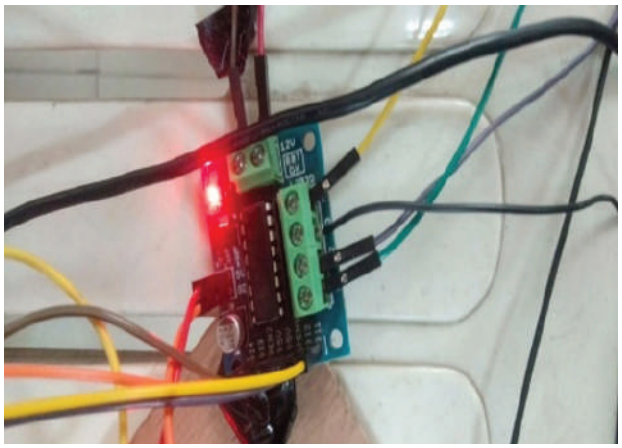


Arduino 1 – MATLAB operation

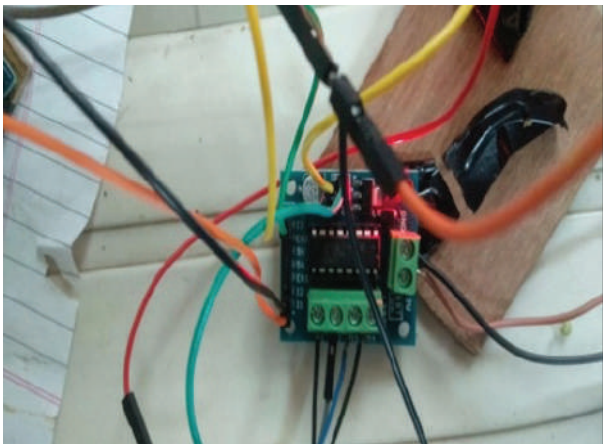


Arduino 2 – DC Motor Operation

Figure 4. Segregator system with DC motor and linkage.



L293D Module – 1 – for Conveyor DC motor



L293D Module – 2 – for Segregator DC motor

Figure 5. Module for DC motor.

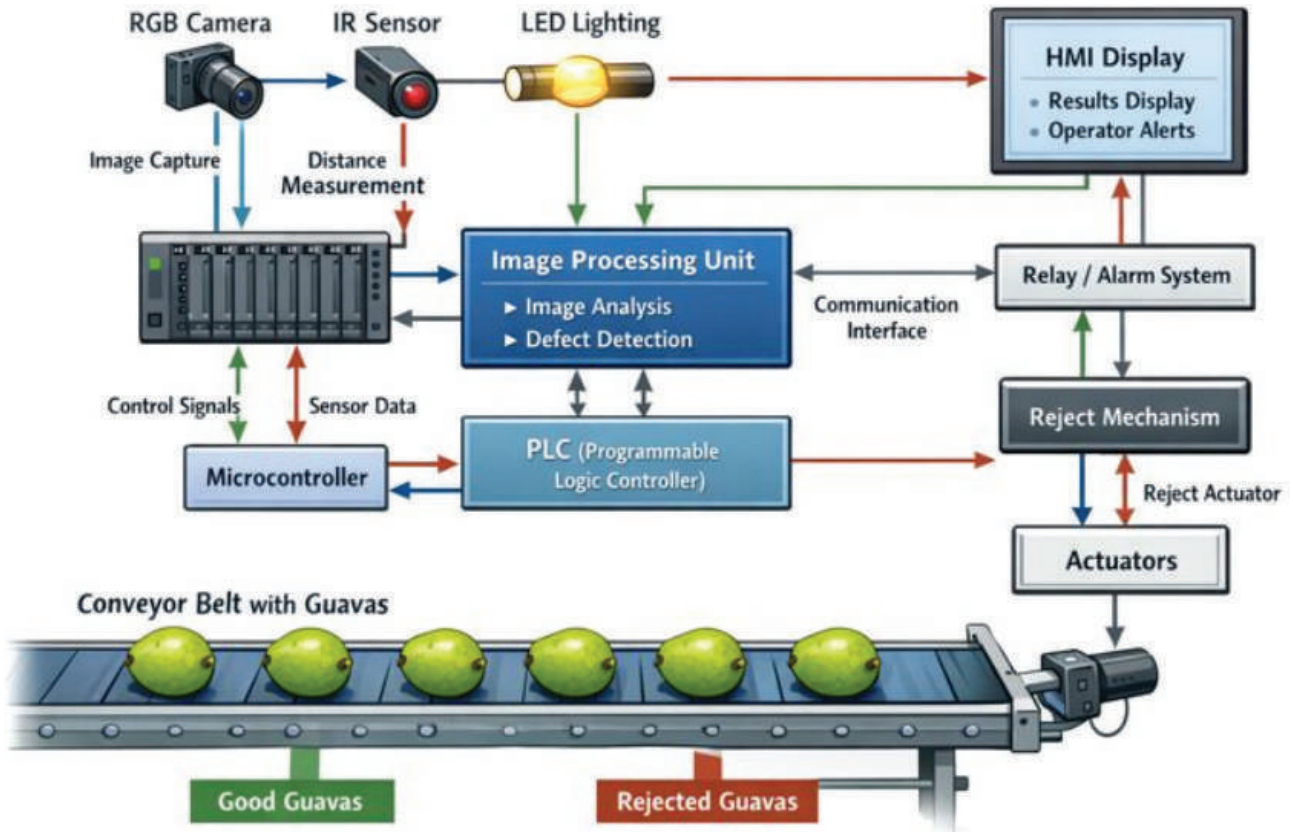


Figure 6. Circuit diagram for real-time inspection of guava fruit on conveyor.

extraction of bad guava fruit in real-time in a conveyor. An Arduino microcontroller is important in aligning all the working parts as shown in Figure 7. On activation, the conveyor motor starts rotating, which controls the movement of the guava-feeding belt. A variety of fruit type is taken at one end of the belt. The fruit is then transported to the inspection center using a 2-link system which is operated by a DC motor. The program that comes with it is designed in such a way that it does not allow the next link to develop until the entire guava that is already there is inspected and no other fruit has reached. The initial connection in turn arrests the guava, which is then transferred sequentially to

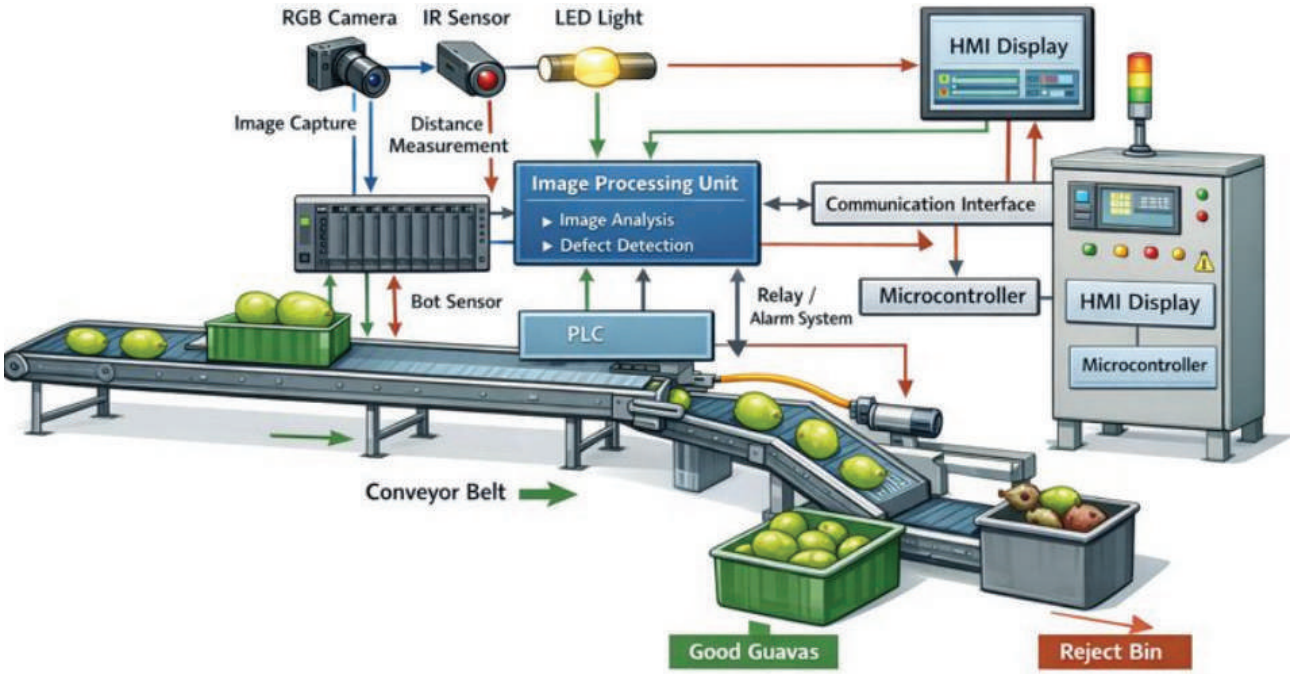


Figure 7. Schematic diagram for Guava sorting machine.

the second connection which serves as the inspection station. In the second connection, the fruit is put on a platform that is meant to process the images to measure its external quality. Thermal camera module gets the picture of the fruit and does the quality check. The embedded system then delivers a signal to the sorting mechanism which is dictated upon by embedded programming. The sorting/segregating mechanism receives the fruit through the conveyor. This is a mechanism that has a linkage that turns with the signal of the embedded module. When the fruit enters the terminal segregating unit, it drops onto the segregator because of the force of gravity. The connection initiates after getting the signal and lays the fruit in the right channel based on its quality as shown in Figure 7.

The system involves three different channels of distribution specifically designed in the segregation of guava fruits into healthy and defective ones. Two DC motors are used to activate each channel as directed by a decision signal produced by an embedded control unit. In this arrangement, processing time is significantly reduced and throughput is increased through the constant running of the analysis and sorting system. The assembled design of these components is shown in Figure 8. The core of this structure is a MATLAB interface with an Arduino microcontroller. This integrative scheme involves using the high data processing and graphic abilities of MATLAB and the direct communication capabilities of Arduino so that more complex systems can be designed with Arduino collecting sensor information, processing it and sending control instructions to actuators and MATLAB simultaneously decoding sensor information streams and sending control instructions to the Arduino. In order to communicate with an Arduino board, it is necessary to use MATLAB Arduino support package that can support a wired (USB) and wireless connection. This package provides sensor acquisition routines, pin-level output routines and bilateral data exchange between the MATLAB and the Arduino firmware. Photographs taken by the multispectral or hyperspectral cameras are handled in this context, and spectral imaging operations are performed using MATLAB and spectral signatures are extracted and machine-learning algorithms run to label the guava fruits based on quality. The sorting scheme is a real-time PLC controlled element which is fed with classification results by Matlab. After the classification process, the quality class of each fruit was passed to the PLC. The communication protocol is often based upon common industrial protocols like Modbus, OPC (OLE for Process Control), or direct I/O connecting, based on system architecture and need. Classification data are supplied to the PLC which, using preset ladder logic or structured text, triggers relays that provide motive to the appropriate sorting devices, such as conveyor belts, robotic arms or pneumatic systems. When a fruit is considered to be high-quality, PLC activates the relay of the high-quality bin, and vice versa. Such a close coordination guarantees that sorting is both fast and accurate, which can be attributed to the fact that MATLAB is able to perform computational processing of image analytics and PLC does mechanical processing. The smart system of sorting fruits is specifically designed with a user-friendly graphical user interface that makes interaction amongst operators possible. The focus on simplicity and ease of navigation is the number one priority; the interface will contain

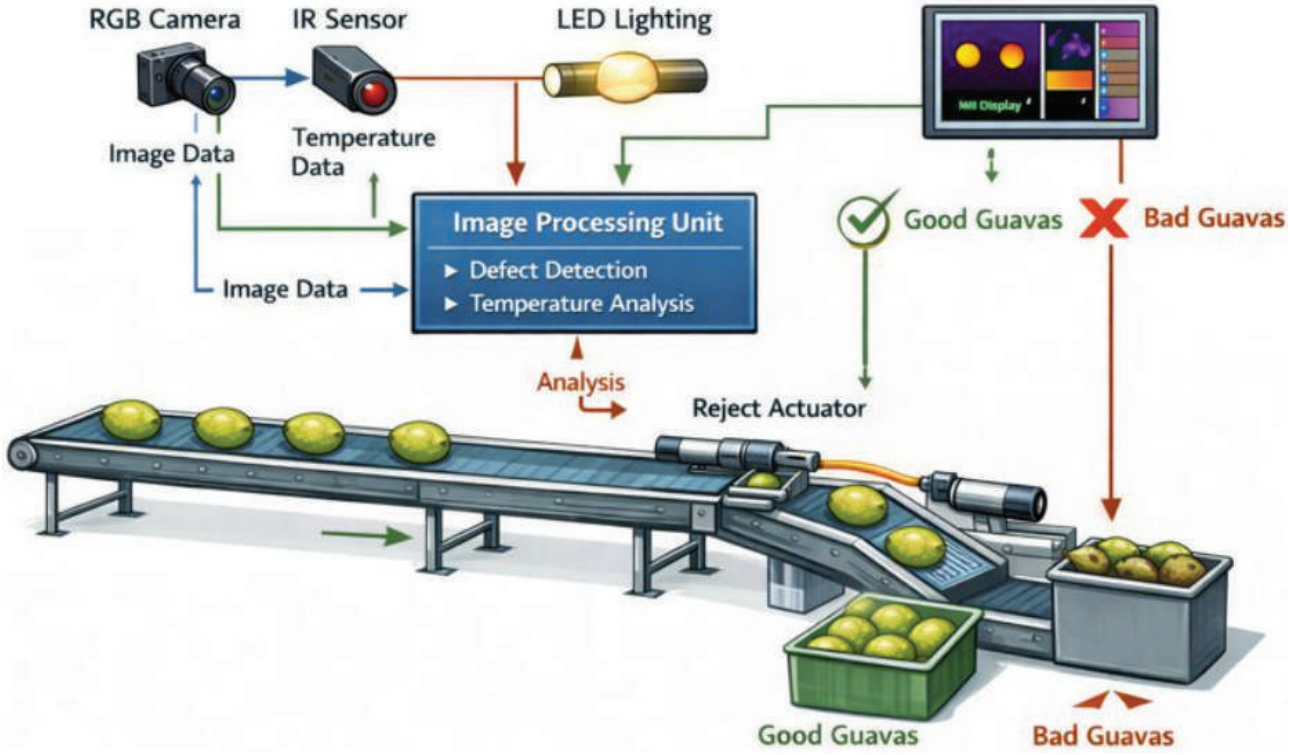


Figure 8. Inspection and segregation process.

a dashboard, control panel, alert/notification modules, real-time monitoring, data logging, and reporting features. The dashboard provides an overview of the status of the system, shows the number of fruits processed, quality metrics distribution, and live sorting, using visual representation like graphs and charts to facilitate understanding. The operators can begin, pause, or stop the sorting process as well as change system parameters through the control panel - such as illumination settings, camera calibration and sorting thresholds. The workflow of inspection and segregation is illustrated in Figure 8.

OUTLINE OF A MACHINE LEARNING ALGORITHM

The machine learning algorithm can effectively distinguish between Healthy Guava, Bird Eaten Guava, Physically Damaged, and Diseased guava types following the approach given:

1. Data Collection: Collect and label a diverse dataset of guava images.
2. Feature Engineering: Extract meaningful features such as color, texture, and shape.
3. Model Selection: Choose an appropriate model like SVM, Random Forest, or CNN.
4. Training: Train the model on the labeled dataset.
5. Evaluation: Assess model performance using accuracy, precision, recall, F1-score, and confusion matrix.
6. Optimization: Fine-tune the model to enhance its performance.

PLC Theory Used in Guava Separation

The sensors within the framework of this concept obtain the information related to guavas; the data obtained is then processed in a Programmable Logic Controller (PLC) to screen the fruit according to the established criteria. The PLC controls the sorting equipment, hence bringing to reality the segregation of guavas into separate categories. This way, consistency and accuracy of categorizing and sorting is reflected in the strength and reliability of PLCs in factories.

1. Sensors, Data Acquisition.

Varied sensors are installed to get information about the guava, these include, but are not limited to, chromatic sensors, morphological sensors and possibly crude imaging systems depending on whether they are compatible with the PLC. An example illustrating this is the color sensor is able to distinguish the color of a healthy guava and other colours that might indicate damage or pathology.

2. Signal Processing

The obtained raw data is processed to extract important information. This involves non-digital to digital representation, noise removal and normalizing the data set. With a color sensor, the PLC would be required to convert RGB values into understandable color measure that is amenable to classifications.

3. Feature Extraction

PLCs are coded to quantify certain qualities obtained out of the sensor data. An example would be the measurement of reflectance properties over the surface of the fruit, which would give information about the conformation of the fruit.

4. Decision-Making Logic

The logic, which is part of the PLC, categorizes the guavae based on the attributes that are extracted. The classification criteria are based on the thresholds or decision rules that are obtained as a result of sensor outputs. Strong sensitivity of the color sensor, say, might indicate the guava is sick, but abnormalities of the shape sensor might indicate physical damage.

5. Control Actions

Thereafter, the PLC controls actuators that separate the guava into different bins, healthy specimen in one bin, affected by the avian in the other, and so on, according to the categories applied.

6. User Interface

The PLC is also incorporated with a Human-Machine interface to provide real-time feedback and give the operators the leeway to either override or fine-tune the decision-making parameters. Precision, recall and confusion matrices are evaluation measures that are inevitable indicators of system performance and thus justifies the important inclusion.

Evaluation Metrics

1. Precision and Recall:

Precision: It estimates the exactitude of the positives being predicted. This is the ratio of correctly identified positive instances to the total number of instances classified as positive.

Recall: A measure that calculates the completeness of the positive predictions. It measures what proportion of positive instances are correctly identified from all actual positive instances in the dataset.

2. Confusion Matrix:

A confusion matrix is a table that gives the detailed breakdown of the system's predictions against the actual outcomes. It contains:

True Positive: Correctly classified high-quality guava fruits.

True Negative TN: Correctly classified low-quality guava fruits, if any.

FP (False Positive): those incorrectly classified as high-quality even though they are not. False Negative (FN): Misclassified as low quality while actually they are not.

RESULTS AND DISCUSSION

The 200 samples were carefully selected to represent various aspects of guava fruits that affect quality assessment. This selection process considered factors such as:

1. Size Variation: The dataset includes guava fruits of different sizes, ranging from small to large, to account for size-related quality attributes such as maturity and sweetness distribution.

2. Color Variation: Guava fruits exhibit a spectrum of colors as they ripen, from green to yellow and sometimes red or pink hues. The dataset encompasses this color diversity to train the system in identifying color-related quality indicators.

3. Defect Types: Common defects such as bruising, spots, cracks, and irregular shapes were included in the dataset. This ensures that the system is trained to detect and classify these defects accurately, which is critical for sorting out inferior quality fruits.

Representativeness

Samples were obtained in different sources as well as different production batches to cover a variety of geographical areas and cultivation environments to make sure that the dataset is representative. The approach eliminates bias and guarantees the trained model to generalise well within a range of guava varieties and agronomic practices. Strict quality-assurance checks were applied to each specimen to ensure the product is of the required size, colour, and defects. The system uses computer-vision algorithms to measure and categorize guava fruits as either healthy or defective (the latter that is, dinged, avian-eaten, or diseased fruit), based on the set criteria. There is sorting that is done based on certain parameters. The accuracy of system performance was checked through sorting and inspection of 200 specimens, which led to a 97 per cent correct determination of healthy and defective fruit. It involves the use of a conveyor belt and a segregating mechanism. Figure 9 illustrates a graphical form of the accuracy of the sorting trial. Comparative outcomes of the fruit categories are pointed out in Table 2.

The experimental outcomes show that, on average, throughout the stated quantity of trials, the guava sorting system was able to assign all the fruits to a relevant compartment, which, in its turn, would accumulate them in the

Table 2. Comparative results of fruits

Sr No.	Type of Fruit quality tested	Total no. of fruit tested	Manual inspection results	Testing of developed system
1	Healthy Guava	50	50	50
2	Bird Eaten Guava	50	50	49
3	Physical Damaged	50	50	48
4	Disease guava	50	50	49
5	Random guava Sample	200	200	194

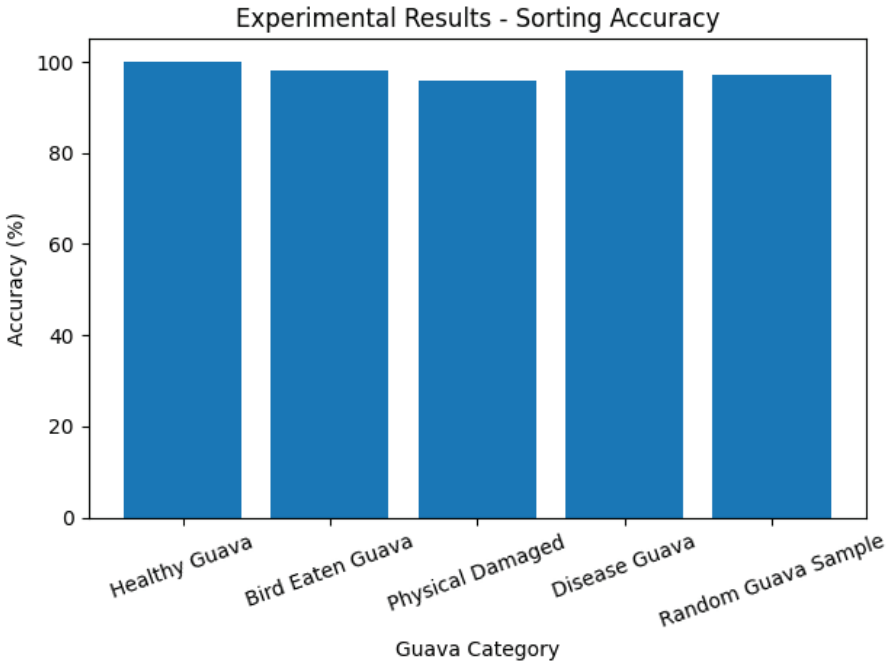


Figure 9. Graphical representation of accuracy percentage of sorting trial.

relevant baskets at the end of every sorting channel. The average time that it took to process each fruit was about 24 seconds and the inspection was in a continuous, consecutive manner where the items were positioned on the conveyor belt.

The suggested device works by identifying external texture features, thus separating and eliminating flawed guavas out of the conveyor belt. This could be used to improve quality control of products in the food-processing industry. To determine the performance of the system, there were four quality classes, namely healthy, damaged, bird-eaten, and diseased. Newly picked guavas of different grades were fed to the automated sorber and each batch was measured as per grading efficiency, production capability and percentage of defected fruits including those that were infested by birds and/or diseased.

Grading accuracy was measured by the rating of fifty specimen of each category of guava (healthy, damaged, bird-eaten, and diseased). The resulting efficiencies were 100, 98, 96 and 98 percent respectively of the healthy, bird-eaten, physically damaged and diseased groups. The grading efficiency when 200 guavas were randomly processed was at 97 on average. As a result, the constructed sorter has an adequate performance and its implementation may be expanded to various realm of spherical and oblate fruits at the farm level. The efficiency variation that was minor and was observed among three trials was attributed to manual loading of fruits.

A comparative evaluation of the intelligent sorter with the traditional manual or other automated processing devices shows that the new technology is superior in speed, accuracy, and flexibility to changes in size, colour and defect profiles. The use of multispectral/hyperspectral imaging and further analysis of images with the help of MATLAB in conjunction with PLC-controlled actuators will be a technological advancement to the conventional methods. The combination of real-time data processing, adaptative control approach, and machine-learning algorithms to assess quality will be estimated to result in increased accuracy. The expected benefits of operations are that they will be dependent less on manual labour, the sorting output will be consistent, the wastage will be reduced because of proper identification of defects, and the whole operation will save money in labor and quality maintenance.

The smart sorter, which is based on the advanced image analysis, is a modern solution to the fruit sorting, which is done based on their size, colour, and flaws. The high-resolution cameras and advanced machine-learning models make it possible to achieve proper segregation and, hence, reduce labour costs and improve throughput. The efficiency, accuracy, and productivity of agricultural sorting processes are increased since the users can comfortably monitor and manipulate the operations using a convenient interface. A heterogeneous and comprehensive set of data will be used to ensure that the system is not sensitive to real-life changes in guava morphology and condition to ensure that the system is robust and has the same performance across various batches and manufacturing conditions.

Wavelength differential detection theory is based on the concept of using differences in the spectral characteristics

of reflected or transmitted light to use between different classes of guava as healthy, bird-eaten, physically damaged, and diseased. The system categorizes the fruit using certain wavelength ranges by examining surface reflectance spectra that change depending on pigment composition, texture, and the moist content in the fruit. Multispectral or hyperspectral cameras are used to capture images in the visible (400-700nm), near infrared (700-1000nm), and short wavelength infrared (1000-2500nm) regimes. The spectral signature of every pixel is complete, and discriminative features, like the ripeness or the presence of a defect, may be extracted. Baseline signatures are set by calibration using reference samples, and spectral fidelity is increased by preprocessing, namely normalisation and noise reduction.

Thermal imaging is a technology that uses infrared thermography to identify temperature variations that are caused by internal and surface conditions to indicate defects like bird pecks, mechanical, or disease. Accuracy, precision, recall, and F1 -score are the performance metrics. The temperature contours in healthy guavas are symmetric, and thermal irregularities are observed in peck sites of fruits eaten by birds. Guavas that are damaged physically depict severe temperature variances near the areas of damages and unhealthy fruit displays wider temperature variances due to the variation in water content and metabolic activities. Thermographic data combined with machine-learning classifiers allows reliable defect-detection, which allows quality packing and distribution of products and avoids the need to inspect the product manually and enhances consumer satisfaction. In addition, it has the capability of early disease detection, and this means that intervention is done in time, preventing a loss in yield.

Main constraints of the existing system reside in the fact that the system relies on the constant illumination; changes to illumination may affect image segmentation and feature extraction, thus necessitating the additional expenses to obtain the necessary lighting infrastructure. Also, the system does not support irregularly shaped or partially covered fruits and thus will experience segmentation failures and misclassifications with large volume processing. The need to rely on high-resolution imaging devices and advanced electronics also raise the cost and maintenance requirements, making it difficult to implement in small or resource-based environments. The degradation of the hardware may affect the performance, and regular maintenance is required.

In an attempt to overcome these issues, further studies ought to be carried out to create illumination-invariant algorithms, use of adaptive thresholding, enhanced noise-reduction methods and dynamic and machine-learned illumination modulation. Multispectral imaging can be incorporated to enhance the resistance of the classification to changing light. Better segmentation techniques, including convolutional neural networks with more advanced topology, are to be considered in order to address complex shapes and occlusions. Finer shape and volume estimates can be given by three-dimensional imaging helping to sort finer. With the system, the accessibility can be made more accessible by cutting down on the high cost of hardware and customizing software to operate with low-cost cameras that are abundant in the market. Scalability will be enabled by lightweight, real-time enabled algorithms designed to fit to lower power devices, edge computing, and integration with IoT. Lastly, the user interface will be iteratively enhanced with the help of operator feedback to create increased intuitiveness and user satisfaction to make the implementation more widespread.

CONCLUSION

Feasibility studies indicated that the proposed design for a guava sorting machine was suitable for detailed development. Thermal cameras and other equipment proved effective in identifying and segregating healthy and defective guava fruits. Implementation of a belt conveyor helps prevent physical damage to fruits and improves the grading efficiency of the machine.

1. The developed sorting system is highly efficient in grading guava fruits and thus may serve beneficial for industries that require automatic sorting.
2. The effectiveness of grading by the proposed automatic sorting system was investigated using a testing machine with 50 guava fruits for each variety: healthy, damaged, bird-eaten, and diseased. The grading efficiency of the automated sorter with each quality sample of guava fruit variety was 100%, 98%, 96%, and 98%, respectively.
3. Sorting the guava into healthy and defective compartments with a grading efficiency of 97% was done for 200 guava samples.
4. The most appropriate conveyor speed was estimated to be 10.5 cm/s, considering the thermal camera's ability to accurately capture and analyze the image in MATLAB of one guava at a time. The time taken to carry one guava for sorting was 23 seconds.

AUTHORSHIP CONTRIBUTIONS

Authors equally contributed to this work.

DATA AVAILABILITY STATEMENT

The authors confirm that the data that supports the findings of this study are available within the article. Raw data that support the finding of this study are available from the corresponding author, upon reasonable request.

CONFLICT OF INTEREST

The author declared no potential conflicts of interest with respect to the research, authorship, and/or publication of this article. ETHICS There are no ethical issues with the publication of this manuscript.

STATEMENT ON THE USE OF ARTIFICIAL INTELLIGENCE

Artificial intelligence was not used in the preparation of the article.

REFERENCES

[1] Dhanabal T, Debabrata S. Computerized spoiled tomato detection. Int J Res Eng Technol 2013;2:38–41. [CrossRef]

[2] Satone M, Diwakar S, Joshi V. Automatic bruise detection in fruits using thermal images. Int J Adv Res Comput Sci Softw Eng 2017;7:727–732. [CrossRef]

[3] Jawale D, Deshmukh M. Real time automatic bruise detection in apple fruits using thermal camera. In: Proc Int Conf Commun Signal Process; 2017; Chennai, India. p. 1080–1085. [CrossRef]

[4] Ayan O, Demirez DZ, Kiziloz HK, Inci G, Isleyen S, Ergin. The detection of spoiled fruits on a conveyor belt using image processing techniques and OPC server software. Int J Comput Exp Sci Eng 2018;4:11–15. [CrossRef]

[5] Najeeb T, Safar M. Dates maturity status and classification using image processing. In: Proc Int Conf Comput Sci Eng; 2018; Kuwait. p. 1–6. [CrossRef]

[6] Vaidya A, Bagade A. Automatic fruit detection, counting and sorting using computer vision and machine learning algorithms. Int J Comput Eng Appl 2018;12:1–9.

[7] Yogesh, Dubey AK, Arora RR. A comparative approach of segmentation methods using thermal images of apple. In: Proc Int Conf Reliab Infocom Technol Optim; 2018; Noida, India. p. 412–418. [CrossRef]

[8] Naik S, Patel B. Machine vision based fruit classification and grading: A review. Int J Comput Appl 2017;170:22–34. [CrossRef]

[9] Feng J, Zeng L, He L. Apple fruit recognition algorithm based on multi-spectral dynamic image analysis. Sensors 2019;19:1–13. [CrossRef]

[10] Jiao LZ, Wu WB, Zheng WG, Dong DM. The infrared thermal image-based monitoring process of peach decay under uncontrolled temperature conditions. J Anim Plant Sci 2015;25:202–207.

[11] Varith J, Hyde GM, Baritelle AL, Fellman JK, Sattabongkot T. Non-contact bruise detection in apples by thermal imaging. Innov Food Sci Emerg Technol 2013;4:211–218. [CrossRef]

[12] Gonçalves BJ, Giarola TMO, Pereira DF, Vilas Boas EVB, Resende JV. Using infrared thermography to evaluate the injuries of cold-stored guava. J Food Sci Technol 2016;53:1063–1070. [CrossRef]

[13] Nugraha AT, Prayitno G, Hasyim AW, Roziqin F. Social capital, collective action, and the development of agritourism for sustainable agriculture in rural Indonesia. Evergreen 2021;8:1–12. [CrossRef]

[14] Zulkefly NS, Hishamuddin H, Rashid FAA, Razali N, Saibani N, Ab Rahman MN. The effect of transportation disruptions on cold chain sustainability. Evergreen 2021;8:262–270. [CrossRef]

[15] Patil LN, Khairnar HP. Investigation of human safety based on pedestrian perceptions associated to silent nature of electric vehicle. Evergreen 2021;8:280–289. [CrossRef]

[16] Hamid SR, Cheong CB, Alina S. Sustainable development practices in services sector: A case of the Palace Hotel from Malaysia. Evergreen 2021;8:693–705. [CrossRef]

[17] Umar HA, Sulaiman SA, Majid MABA, Said MA, Gungor A, Ahmad RK. An outlook on tar abatement, carbon capture and its utilization for a clean gasification process. Evergreen 2021;8:717–731. [CrossRef]

[18] Dief TN, Yoshida S. System identification for quad-rotor parameters using neural network. Evergreen 2016;3:6–11. [CrossRef]

[19] Nugraha GD, Sudiarto B, Ramli K. Machine learning-based energy management system for prosumer. Evergreen 2020;7:309–313. [CrossRef]

[20] Weake N, Pant M, Sheoran A, Haleem A, Kumar H. Optimising parameters of fused filament fabrication process to achieve optimum tensile strength using artificial neural network. Evergreen 2020;7:373–381. [CrossRef]

[21] Bashir HA, Abu-Goukh ABA. Compositional changes during guava fruit ripening. Food Chem 2003;80:557–563. [CrossRef]

[22] Lim YY, Lim TT, Tee JJ. Antioxidant properties of guava fruit: Comparison with some local fruits. Sunway Acad J 2006;3:9–20.

[23] Daza A, García-Galavís PA, Grande MJ, Santamaría C. Fruit quality parameters of 'Pioneer' Japanese plums produced on eight different rootstocks. Sci Hortic 2018;118:206–211. [CrossRef]

[24] Manna M, Paul A. Studies on genetic variability and characters association of fruit quality parameters in tomato. HortFlora Res Spectr 2012;1:110–116.

[25] Jadhav RS, Patil SS. A fruit quality management system based on image processing. IOSR J Electron Commun Eng 2013;8:1–5. [CrossRef]

[26] Razzak MI, Naz S, Zaib A. Deep learning for medical image processing: Overview, challenges and the future. In: Classification in bioapps: Automation of decision making. 2018. p. 323–350.

[27] Jiao L, Zhao J. A survey on the new generation of deep learning in image processing. IEEE Access 2019;7:172231–172263. [CrossRef]

[28] Demir Y, Bingöl Ö. Detection of pneumonia from pediatric chest X-ray images by transfer learning. Sigma J Eng Nat Sci 2023;41:1264–1271. [CrossRef]

[29] Baysal K, Taşkin D. Blocking harmful images with a deep learning based next generation firewall. Sigma J Eng Nat Sci 2024;42:1133–1147. [CrossRef]

Sigma Journal of Engineering and Natural Sciences
Web page info: https://sigma.yildiz.edu.tr
DOI: 10.14744/sigma.2025.00000

Research Article

Classifications of artificial ıntelligence trading systems by using WASPAS approach based on picture fuzzy soft aggregation operators

Tahir MAHMOOD[1,*], Jabbar AHMMAD[2]

[1]Department of Mathematics and Statistics, International Islamic University Islamabad, 44000, Pakistan
[2]Department of Mathematics, Faculty of Engineering and Computing, National University of Modern Languages (NUML), Islamabad, 44000, Pakistan

ARTICLE INFO

Article history
Received: 27 March 2024
Revised: 18 July 2024
Accepted: 07 December 2024

Keywords:
Average and Geometric Aggregation Operators; Picture Fuzzy Soft Set Structure; WASPAS Technique

ABSTRACT

Artificial intelligence stock trading uses machine learning, sentiment analysis, and advanced algorithmic forecasts to examine millions of details and carry out transactions at the lowest price. To reduce risks and increase returns, artificial intelligence traders also accurately and effectively assess future markets. A beneficial and original method for assessing or presenting the valuable decision from the accumulation of valuable information is the weighted aggregated sum product assessment approach. The notion of picture fuzzy soft set is dominant to intuitionistic fuzzy soft because it uses extra information in the form of abstinence grade that makes this structure more valuable and superior as compared to intuitionistic fuzzy soft set. It means that when data contains abstinence grade then the idea of intuitionistic fuzzy soft set fails to handle such kind of information. Moreover, in this case, the decision-making approach becomes limited. In many decision-making situations, we have to utilize a more advanced structure to avoid any kind of data loss. Hence in the case of an intuitionistic fuzzy soft set the chance of data loss increases. To avoid this kind of situation in decision-making scenarios, in this framework, we have delivered the notion of weighted averaging, ordered weighted averaging, weighted geometric, and ordered weighted geometric aggregation operators under the environment of a picture fuzzy soft set. Moreover, we have delivered properties like Idempotency, Boundedness, Shift-invariance and Homogeneity of these developed notions. We have delivered the WASPAS method for picture fuzzy soft information and employed this technique for the classification of artificial intelligence trading systems. Additionally, we provide a few scenarios using the multi-attribute decision-making technique to confirm and demonstrate the utilization of the aforementioned information and try to find the best artificial intelligence trading system. Additionally, to increase the value of the evaluated information, we compare the derived operators with a variety of currently used or existing methods.

Cite this article as: Mahmood T, Ahmmad J. Classifications of artificial ıntelligence trading systems by using WASPAS approach based on picture fuzzy soft aggregation operators. Sigma J Eng Nat Sci 2026;44(1):23–41.

***Corresponding author.**
*E-mail address: tahirbakhat@iiu.edu.pk

This paper was recommended for publication in form by Editor-in-Chief Ahmet Selim Dalkilic

Published by Yıldız Technical University Press, İstanbul, Turkey
© Author. This is an open access article under the CC BY-NC license (http://creativecommons.org/licenses/by-nc/4.0/).

INTRODUCTION

AI Trading System

Trade can be defined as the exchange of goods, services, or both in its most basic form. The essential basis of trade was the direct interchange of items and services. As long as people have needed to exchange goods, they have engaged in trading with one another. For example, around 2260 B.C., grain futures were used in ancient Mesopotamia. Rapid technological developments over the following few decades bring about the newest significant trade innovations. To analyze historical stock and market data, generate investment ideas, and automatically execute trades, artificial intelligence, and machine learning are utilized. Investors may now spend more time supervising trades and offering advice to their clients by automating research and data-driven decision-making using AI trading. AI trading makes conclusions using past financial data, so there is less chance for human error. An AI trading system may gather data from social media and news sources to predict market fluctuations. Hundreds of traders, experts, and consultants may be engaged by traditional investing firms, but the use of AI trading technology can duplicate some of the tedious tasks that need to be done by people. AI algorithms can continuously monitor the stock market around the clock. Different researchers utilize AI according to their research as Ferreira et al. [1] provided an organized survey of the literature on the use of AI in stock market investments. Moreover, Luo et al. [2] discovered the ideal policy algorithm called the "Deep Deterministic Policy Gradient" (DDPG) algorithm. Yin et al. [3] proposed the trading modes of AI in international trade. Also, Azzutti [4] studied the AI trading and limits of EU law enforcement in deterring market manipulation.

In classical set theory (CST), which only addresses the two options that an object either belongs to a set or does not, there is no third possibility. In this kind of idea, an object's membership grade (MG), which can only take one of two values 0 or 1 may be assigned. However, there are certain limitations to this idea because many phenomena, such as height and age cannot be explained by CST. Zadeh [5] developed the idea of a fuzzy set (FS) to deal with these complications. In FS, there is a requirement that MG belongs to a unit interval [0, 1]. There are some concerns about how we handle non-membership grade (NMG) in the context of FS theory because FS has only been designed to deal with MGs, not NMGs. Atanassov [6] suggested the concept of an intuitionistic FS (IFS) to address this. The foundation of IFS is MG "Ŧ" and NMG "Ê" with the restriction that the total of MG and NMG does not exceed 1. Based on the introduced idea of IFS, researchers benefit from the use of AOs, which are structural tools for describing the whole amount of information into a single value. Numerous researchers put out their theories and created some AOs based on IFS, including the IF weighted geometric [7] and IF weighted average AOs. [8] IF geometric Heronian mean AOs [9], and IF Hamacher AOs [10]. The utilization of IFS in trade is remarkable as Zhou and Xu [11] utilized the IFS for score hesitation trade-offs and portfolio selection. An intuitive quantitative trading system based on an intuitionistic-GRU fuzzy neural network was proposed by Wang and Luo [12].

Notice that the idea of IFS has many drawbacks and complications because it only discusses MG and NMG without mentioning abstinence grades (AG). As a result, we are unable to utilize the structure of IFS for some unique problems that contain three types of information, such as during elections when each voter has four different options for casting a ballot: for someone, against someone, abstinent, or refuse. Such issues are incompatible with IFS, so Cuong [13] developed the notion of picture FS (PFS), a modified form of IFS and it contains the MG "Ŧ", NMG "Ê" and abstinence grade (AG) "Ψ" with the condition that $0 \leq Ŧ + Ψ + Ê \leq 1$. Based on PFS, Dutta and Ganju [14] proposed some aspects of PFSs. Additionally, some PF-weighted geometric AOs were developed by Wang et al. [15], and some PF average AOs were studied in [16, 17].

Literature Review of Soft Set Structures

The idea of a soft set ($S_{ft}S$) was first introduced by Molodtsov [18] as a fundamental tool for dealing with ambiguous data. Many new developments have been delivered that show the importance of $S_{ft}S$ with some other FS structures as fuzzy soft set ($FS_{ft}S$)[19], fuzzy N-soft set [20] and IF soft set ($IFSS_{ft}$) [21]. Additionally, Arora [22] developed a few IFS_{ft} AOs based on Einstein norms and their applications in DM. Albailty et al. [23] delivered the impact of machine learning and AI in business by using the environment of IFS_{ft} WASPAS approach. Different researchers utilize the notion of $IFS_{ft}S$ in different fields and they have produced the new structures in this regard. Garg and Arora [24] produced generalized Maclaurin symmetric means AOs based on Archimedean t-norm under the notion of $IFS_{ft}Ss$. Moreover, Garg and Arora [25] delivered the novel scaled prioritized IFS_{ft}interaction average AOs and invented their application to MCDM problems. Hayat et al [26] invented AOs based on group-based generalized $IFS_{ft}S$. Shahzadi and Akram [27] invented the notion of IFS_{ft} graphs and proposed their applications. Many other generalized structures like the Pythagorean fuzzy soft set ($PyFS_{ft}S$) and q-ring orthopair fuzzy soft set ($q - ROFS_{ft}S$) have been developed that use more advanced conditions than that of the $IFS_{ft}S$. It means that the notion of $PyS_{ft}S$ [28] and $q - ROFS_{ft}S$ [29] provides more space for decision-makers and as a result, more advanced data can be handled. Moreover, there is no chance of data loss in the case of $PyFS_{ft}S$ and $q - ROFS_{ft}S$.

Motivation for Using $PFS_{ft}S$

Notice that all the above structures of $IFS_{ft}S$, $PyFS_{ft}S$ and $q - ROFS_{ft}S$ can only use the MG and NMG in their ideas. This property ranks these notions to limited structures because there are many decision-making situations where we have to discuss AG along with MG and NMG. Although

the notion of $IFS_{ft}S$, $PyFS_{ft}S$ and $q-ROFS_{ft}S$ can discuss the parametrization tool but these are limited notions due to a lack of considering the AG in their structure. For example, we can see that when the phenomenon of voting occurs, one can vote in favor of some candidates, vote against some candidates, refuse to vote, or abstain from voting. To cover this kind of real-life situation, the notion of $IFS_{ft}S$, $PyFS_{ft}S$ and $q-ROFS_{ft}S$ cannot discuss it properly. Keeping in view this drawback, there was a need for the literature to invent such kind of information or idea that can discuss the MG, NMG and AG in one structure. So Yang et al. [30] discovered the idea of picture fuzzy soft set ($PFS_{ft}S$). After the invention of $PFS_{ft}S$, many new developments have been made in this regard like some Bonferroni means AOs have been delivered by Yang et al. [31]. Also, Mahmood et al. [32] delivered the idea of PFS_{ft} power average and geometric AOs and provided their applications in thermal energy sectors. Ahmmad et al. [33] delivered the idea of PFS_{ft} prioritized AOs and established their application in medical diagnosis.

Literature Review of the WASPAS Approach

Zavadskas et al. [34-35] developed the WASPAS approach which is a beneficial and original method for analyzing or outlining the beneficial decision from the gathering of beneficial information. The WASPAS approach has a wide range of applications. Albailty et al. [36] discuss the impact of machine learning and AI in business based on IFS_{ft} WASPAS approach. Lukic [37] introduced the WASPAS method and utilized these notions for the evaluation of the performance of the trading companies. Gorcun et al. [38] utilized the WASPAS Bonferroni approach in a type 2 neutrosophic fuzzy environment for the selection of appropriate Ro-Ro vessels in the secondhand market. Pamucar et al. [39] initiated the notion of a multicriteria LNN WASPAS model for evaluating the work of advisors in the transport of hazardous goods. Yontar and Derse [40] utilized the WASPAS technique for the prioritization of carbon strategies in the cargo industry. Lukic [41] initiated the analysis of the trade performance of the European Union and Serbia based on the FF-WASPAS and WASPAS methods.

Methodology of the Introduced Work

The WSM and the WPM are two distinct concepts that were essential in the development of the WASPAS approach. We observed that despite these being highly difficult challenges for researchers, none could deduce the theory of the WASPAS approach or the AOs for $PFS_{ft}S$. Based on the aforementioned data, we extract the following data in this framework, including the notion of $PFS_{ft}WA$, $PFS_{ft}OWA$, $PFS_{ft}WG$ and $PFS_{ft}OWG$ AOs and delivered the properties of this developed approach. We have also derived the theory of the WASPAS technique for PFS_{ft} data. Moreover, we have used this method for the classification of AI trading systems. We have provided a few examples using the MADM technique to demonstrate the superiority of the aforementioned information. To improve the usefulness of the evaluated information, we also try to compare the derived operators with various current or previous methodologies.

Issues Related to AI Trading Systems and Utilization of introduced Work

AI trading system is facing some notable issues given in Table 1.

Table 1. Issues related to the AI trading system

Data Quality and Availability	Extensive datasets are essential to AI trading algorithms. Predictions and trading decisions that are not correct can result from low-quality data or restricted access to real-time data. Furthermore, the system may be misled by noise or out-of-date information in the data.
Market Volatility	The volatility of markets can be attributed to their abrupt shifts in prices and trends. If AI models are not correctly managed, they may not be able to swiftly adjust to such volatility, which could result in severe losses.
Ethical and regularity concerns	The volatility of markets can be attributed to their abrupt shifts in prices and trends. If AI models are not correctly managed, they may not be able to swiftly adjust to such volatility, which could result in severe losses.
Execution Risk	Even in cases where an AI model predicts the market correctly, trade execution challenges like latency, slippage, or liquidity constraints may arise. These could lessen the AI's strategy's effectiveness.
Resource Intensity	AI trading systems demand a large amount of processing power and resources to operate in real-time and train the models. This can be expensive and could make it harder for smaller businesses to compete with bigger establishments.
Model Drift	Because the financial markets are always changing, strategies that have worked in the past might not work now. To adapt to shifting market conditions, AI models must be continuously retrained and updated. However, there is always a chance that the model will deviate from peak performance.
Adversarial Attacks	Adversarial attacks, in which minute, well-planned modifications to the input data result in inaccurate outputs, can affect AI systems. This may apply to trading, where it would involve purposeful manipulation of market data to trick the AI into making poor trades.

1) To resolve these issues raised in Table 1, we have proposed a mathematical framework that can handle such kinds of issues and study these problems.
2) To discuss the WASPAS approach for the advanced idea of $PFS_{fi}S$ that can handle more advanced information.
3) WASPAS technique can combine weighted product and weighted sum model that keep this notion more accurate and valuable for MCDM approaches. The basic characteristics of the WASPA approach are given in Figure 1.

Objective and Contribution of Proposed work

The notion of picture fuzzy soft set is the fundamental notion that can generalize the idea of intuitionistic fuzzy soft set because it can consider the AG along with MG and NMG. The advantage of the more advanced idea is that it can cover more generalized information as compared to previous theories. The selection of the best AI trading system is the MCDM approach that is utilized in fuzzy set theory. FS theory can cover such kinds of problems through different methodologies based on aggregation theory. Aggregation operators are the fundamental idea that can convert the overall information in a single to help with DM problems and to reach an appropriate decision. The main objective of utilizing the notion of PFSS is that this notion is valuable in those situations where AG plays a vital role. The objective of utilizing picture fuzzy soft sets in an AI trading system is to enhance decision-making processes by incorporating more nuanced levels of uncertainty and preference in financial data analysis. Picture fuzzy soft sets, which extend fuzzy soft sets by allowing degrees of positive, neutral, and negative membership, are particularly useful in

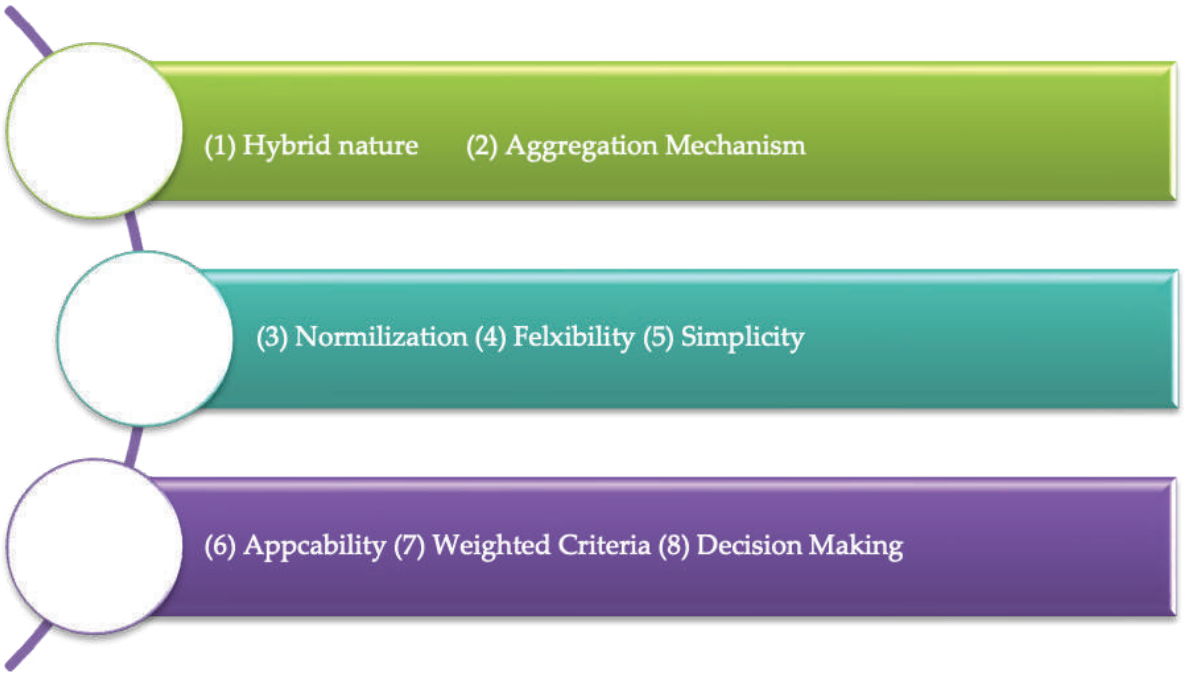


Figure 1. Advantages of using the WASPAS approach.

Table 2. Key Objective of the proposed theory

To Enhance Decision making	By representing complex market conditions more accurately, picture fuzzy soft sets allow the AI system to make more informed trading decisions.
To improve risk management	With better representation of market conditions, the AI trading system can more effectively assess and manage risks, leading to more robust trading strategies.
To customize trading strategies	The ability to model trader preferences and market sentiments more precisely enables the development of customized trading strategies.
To integrate multiple indicators	Picture fuzzy soft sets allow the integration of multiple indicators, each with different levels of influence, to form a comprehensive view of the market.
To Handle Uncertainty	Picture fuzzy soft sets offer a more flexible way to model this uncertainty by capturing not just the likelihood of events but also the degrees of hesitation, which traditional fuzzy sets might overlook.



Figure 2. Graphical representation of objectives of this study.

situations where traditional binary or fuzzy logic is insufficient. Some key objectives are given in Table 2.

The graphical representation of these objectives is given in Figure 2.

Now based on these objectives the main contribution of the proposed study is (1) To develop basic operational laws that can help to define aggregation theory (2) To define basic aggregation operators like $PFS_{ft}WA$ and $PFS_{ft}WG$ AOs (3) To develop a mathematical frame called WASPAS technique to show the importance of the developed theory (4) To utilize the notion of $PFS_{ft}S$ in the environment of the AI trading system (5) To provide the comparative analysis of the developed theory to discuss the importance of the initiated work.

The graphical representation of the main contribution of the initiated idea is given in Figure 3.

Arrangement of the Study

The order of the derived work is as follows: We have revised the idea of the division of two PFNs, $PFS_{ft}S$ and the WASPAS approach for classical set theory in Section 2. Also basic operational rules for $PFS_{ft}S$ and score function and accuracy function are revised in Section 2. The structure of the $PFS_{ft}WA$, $PFS_{ft}OWA$, $PFS_{ft}WG$ and $PFS_{ft}OWG$ AOs are further discussed in Section 3, along with a focus on determining their important properties. In Section 4, we gave an example to demonstrate how the newly introduced operators function. We developed the idea of the WASPAS technique for PFS_{ft} information and examined its useful aspects in Section 5 along with illustrative examples. In section 6, we have provided a comparative study of the delivered approach. Section 7 discusses the concluding remarks.

Preliminaries

Here, we revise the concept of PFN-based division operators. Additionally, we have debated on the notion of $PFS_{ft}S$ and WASPAS method for classical information.

Definition 1 [14]: Let Let $PFN_1 = \{(\mathfrak{T}_1(\upsilon), \Psi_1(\upsilon), \hat{\mathfrak{E}}_1(\upsilon)) : \upsilon \in \mathcal{Y}\}$ and $PFN_2 = \{(\mathfrak{T}_2(\upsilon), \Psi_2(\upsilon), \hat{\mathfrak{E}}_2(\upsilon)) : \upsilon \in \mathcal{Y}\}$ denote two PFNs, then division for two PFNs is defined by

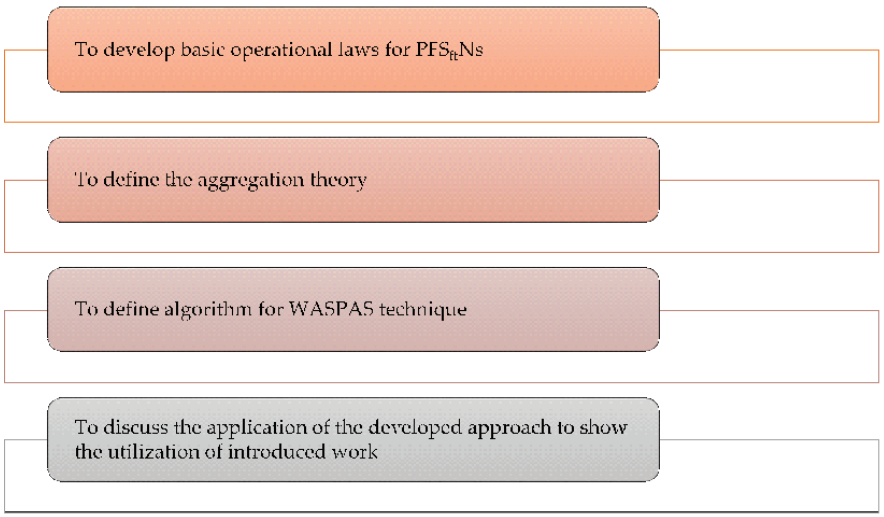


Figure 3. Graphical representation of the main contribution of the developed approach.

$$\frac{PFN_1}{PFN_2} = \left\{min\left(\mathrm{T}_1(\upsilon), \mathrm{T}_2(\upsilon)\right), \max\left(\Psi_1(\upsilon), \Psi_2(\upsilon)\right), \max\left(\hat{\mathrm{E}}_1(\upsilon), \hat{\mathrm{E}}_2(\upsilon)\right),\right\}$$

Definition 2: [**30**] Assume that $\mathcal{Y}$ denotes the universal set and S is the set of parameters. Let $P(\mathcal{Y})$ represent power set of *PFSs*. Let $A \subseteq S$. A pair (F,A) is called $PFS_{ft}S$ over $\mathcal{Y}$, where $F: A \to \hat{\mathrm{H}}(\mathcal{Y})$.

The WASPAS methodology, which was created by Zavadskas et al. [34, 35], is a useful and innovative way to assess or reveal useful decisions from the gathering of useful information. We also presented the WASPAS theory for classical set theory. The foundational elements of the WAPAS technique are WSM and WPM. The primary steps of the WASPAS technique are as follows:

Step 1: Compute the decision matrix based on cost and benefit types of information.

Step 2: The normalizing procedure is given by

Case I: For benefit type criteria

$$\bar{\mathrm{G}}'_{\mathrm{i}\mathrm{j}} = \frac{\bar{\mathrm{G}}_{\mathrm{i}\mathrm{j}}}{\max\limits_{\mathrm{i}} \bar{\mathrm{G}}_{\mathrm{i}\mathrm{j}}}$$

Where

$$\max_{\mathrm{i}} \bar{\mathrm{G}}_{\mathrm{i}\mathrm{j}} = \left\{\max_{\mathrm{i}} \mathrm{T}_{\mathrm{i}\mathrm{j}}, \min_{\mathrm{i}} \Psi_{\mathrm{i}\mathrm{j}}, \min_{\mathrm{i}} \hat{\mathrm{E}}_{\mathrm{i}\mathrm{j}}\right\}$$

And

$$\frac{\bar{\mathrm{G}}_{\mathrm{i}\mathrm{j}}}{\max\limits_{\mathrm{i}} \bar{\mathrm{G}}_{\mathrm{i}\mathrm{j}}} = \left\{\min\left(\mathrm{T}_{\mathrm{i}\mathrm{j}}, \max_{\mathrm{i}} \mathrm{T}_{\mathrm{i}\mathrm{j}}\right), \max\left(\Psi_{\mathrm{i}\mathrm{j}}, \min_{\mathrm{i}} \Psi_{\mathrm{i}\mathrm{j}}\right), \max\left(\hat{\mathrm{E}}_{\mathrm{i}\mathrm{j}}, \min_{\mathrm{i}} \hat{\mathrm{E}}_{\mathrm{i}\mathrm{j}}\right)\right\}$$

Case 2: For cost-type criteria

$$\bar{\mathrm{G}}'_{\mathrm{i}\mathrm{j}} = \frac{\min\limits_{\mathrm{i}} \bar{\mathrm{G}}_{\mathrm{i}\mathrm{j}}}{\bar{\mathrm{G}}_{\mathrm{i}\mathrm{j}}}$$

Where

$$\min_{\mathrm{i}} \bar{\mathrm{G}}_{\mathrm{i}\mathrm{j}} = \left\{\min_{\mathrm{i}} \mathrm{T}_{\mathrm{i}\mathrm{j}}, \max_{\mathrm{i}} \Psi_{\mathrm{i}\mathrm{j}}, \max_{\mathrm{i}} \hat{\mathrm{E}}_{\mathrm{i}\mathrm{j}}\right\}$$

And

$$\frac{\min\limits_{\mathrm{i}} \bar{\mathrm{G}}_{\mathrm{i}\mathrm{j}}}{\bar{\mathrm{G}}_{\mathrm{i}\mathrm{j}}} = \left\{\min\left(\min_{\mathrm{i}} \mathrm{T}_{\mathrm{i}\mathrm{j}}, \mathrm{T}_{\mathrm{i}\mathrm{j}}\right), \max\left(\max_{\mathrm{i}} \Psi_{\mathrm{i}\mathrm{j}}, \Psi_{\mathrm{i}\mathrm{j}}\right), \max\left(\max_{\mathrm{i}} \hat{\mathrm{E}}_{\mathrm{i}\mathrm{j}}, \hat{\mathrm{E}}_{\mathrm{i}\mathrm{j}}\right)\right\}$$

Step 3: Calculate the WSM value by the formula as

$$\mathfrak{G}_{\mathrm{i}}^{WS} = \sum_{\mathrm{j}=1}^{m} W_{\mathrm{j}} \bar{\mathrm{G}}'_{\mathrm{i}\mathrm{j}}$$

Step 4: Calculate the WPM value such as

$$\mathfrak{G}_{\mathrm{i}}^{WP} = \sum_{\mathrm{j}=1}^{m} \left(\bar{\mathrm{G}}'_{\mathrm{i}\mathrm{j}}\right)^{W_{\mathrm{j}}}$$

Step 5: Determine the score data

$$\mathfrak{G}_{\mathrm{i}} = \mathfrak{P} * \mathfrak{G}_{\mathrm{i}}^{WS} + (1 - \mathfrak{P})\mathfrak{G}_{\mathrm{i}}^{WP}$$

If $\mathfrak{P} = 1$, then $\mathfrak{G}_{\mathrm{i}}$ will be $\mathfrak{G}_{\mathrm{i}}^{WS}$ and if $\mathfrak{P} = 0$, then $\mathfrak{G}_{\mathrm{i}}$ will be $\mathfrak{G}_{\mathrm{i}}^{WP}$.

Step 6: Rank the alternatives and obtain the best choice.

Definition 3 [31]: Let $\hat{\mathrm{H}}_{S_{11}} = \left\{\left(\mathrm{T}_{11}(\upsilon), \Psi_{11}(\upsilon), \hat{\mathrm{E}}_{11}(\upsilon)\right) : \upsilon \in \mathcal{Y}\right\}$, $\hat{\mathrm{H}}_{S_{12}} = \left\{\left(\mathrm{T}_{12}(\upsilon), \Psi_{12}(\upsilon), \hat{\mathrm{E}}_{12}(\upsilon)\right) : \upsilon \in \mathcal{Y}\right\}$ be two $PFS_{ft}Ns$ and $\mathfrak{G} > 0$ be any real number, then we have

1) $\hat{\mathrm{H}}_{S_{11}} \oplus \hat{\mathrm{H}}_{S_{12}} = \left\{\left(\mathrm{T}_{11}(\upsilon) + \mathrm{T}_{12}(\upsilon) - \mathrm{T}_{11}(\upsilon)\mathrm{T}_{12}(\upsilon)\right), \left(\Psi_{11}(\upsilon)\Psi_{12}(\upsilon)\right), \left(\hat{\mathrm{E}}_{11}(\upsilon)\hat{\mathrm{E}}_{12}(\upsilon)\right)\right\}$
2) $\hat{\mathrm{H}}_{S_{11}} \otimes \hat{\mathrm{H}}_{S_{12}} = \left\{\begin{matrix}\left(\mathrm{T}_{11}(\upsilon)\mathrm{T}_{12}(\upsilon)\right), \left(\Psi_{11}(\upsilon) + \Psi_{12}(\upsilon) - \Psi_{11}(\upsilon)\Psi_{12}(\upsilon)\right), \\ \left(\hat{\mathrm{E}}_{11}(\upsilon) + \hat{\mathrm{E}}_{12}(\upsilon) - \hat{\mathrm{E}}_{11}(\upsilon)\hat{\mathrm{E}}_{12}(\upsilon)\right)\end{matrix}\right\}$
3) $\mathfrak{G}\hat{\mathrm{H}}_{S_{11}} = \left\{\left(1 - \left(1 - \mathrm{T}_{11}(\upsilon)\right)^{\mathfrak{G}}\right), \left(\Psi_{11}(\upsilon)\right)^{\mathfrak{G}}, \left(\hat{\mathrm{E}}_{11}(\upsilon)\right)^{\mathfrak{G}}\right\}$
4) $\hat{\mathrm{H}}_{S_{11}}{}^{\mathfrak{G}} = \left\{\left(\mathrm{T}_{11}(\upsilon)\right)^{\mathfrak{G}}, \left(1 - \left(1 - \Psi_{11}(\upsilon)\right)^{\mathfrak{G}}\right), \left(1 - \left(1 - \hat{\mathrm{E}}_{11}(\upsilon)\right)^{\mathfrak{G}}\right)\right\}$

Definition 4 [31]: Assume that $\hat{\mathrm{H}}_S = \{(\mathrm{T}(\upsilon), \Psi(\upsilon), \hat{\mathrm{E}}(\upsilon)) : \upsilon \in \mathcal{Y}\}$ is a $PFS_{ft}N$, then SF and AF are given by

$$Scr.\left(\hat{\mathrm{H}}_S\right) = \mathrm{T}(\upsilon) - \Psi(\upsilon) - \hat{\mathrm{E}}(\upsilon)$$

$$Acur.\left(\hat{\mathrm{H}}_S\right) = \mathrm{T}(\upsilon) + \Psi(\upsilon) + \hat{\mathrm{E}}(\upsilon)$$

Definition 5 [31]: Assume that $\hat{\mathrm{H}}_{S11} = \{(\mathrm{T}_{11}(\upsilon), \Psi_{11}(\upsilon), \hat{\mathrm{E}}_{11}(\upsilon)) : \upsilon \in \mathcal{Y}\}$ and $\hat{\mathrm{H}}_{S12} = \{(\mathrm{T}_{12}(\upsilon), \Psi_{12}(\upsilon), \hat{\mathrm{E}}_{12}(\upsilon)) : \upsilon \in \mathcal{Y}\}$ are two $PFS_{ft}Ns$ then

1) If $Scr.\left(\hat{\mathrm{H}}_{S_{11}}\right) < Scr.\left(\hat{\mathrm{H}}_{S_{12}}\right)$ then $\hat{\mathrm{H}}_{S_{11}} < \hat{\mathrm{H}}_{S_{12}}$.
2) If $Scr.\left(\hat{\mathrm{H}}_{S_{11}}\right) > Scr.\left(\hat{\mathrm{H}}_{S_{12}}\right)$ then $\hat{\mathrm{H}}_{S_{11}} > \hat{\mathrm{H}}_{S_{12}}$.
3) If $Scr.\left(\hat{\mathrm{H}}_{S_{11}}\right) = Scr.\left(\hat{\mathrm{H}}_{S_{12}}\right)$ then
    1) If $Acur.\left(\hat{\mathrm{H}}_{S_{11}}\right) < Acur.\left(\hat{\mathrm{H}}_{S_{12}}\right)$ then $\hat{\mathrm{H}}_{S_{11}} < \hat{\mathrm{H}}_{S_{12}}$.
    2) If $Acur.\left(\hat{\mathrm{H}}_{S_{11}}\right) = Acur.\left(\hat{\mathrm{H}}_{S_{12}}\right)$ then $\hat{\mathrm{H}}_{S_{11}} = \hat{\mathrm{H}}_{S_{12}}$.

Average and Geometric AOs Based on PFS_{ft} Data

This section has delivered the notion of $PFS_{ft}WA$, $PFS_{ft}OWA$, $PFS_{ft}WG$ and $PFS_{ft}OWG$ AOs. We have also established the properties of these developed notions.

Definition 6: Assume that $\hat{\mathrm{H}}_{S\mathrm{j}} = (\mathrm{T}_{\mathrm{j}}, \Psi_{\mathrm{j}}, \hat{\mathrm{E}}_{\mathrm{j}})$ be the family of $PFS_{ft}Ns$; $\mathrm{j} = 1, 2, \ldots, \mathrm{m}$, $\mathrm{j} = 1, 2, \ldots, \mathrm{n}$. Also let w_{j}, v_{j} represent the weight vectors (WVs) for parameters s_{j} and experts e_{j} respectively with the constraint that $\mathrm{w}_{\mathrm{j}} > 0$, $\mathrm{v}_{\mathrm{j}} > 0$ and $\sum_{\mathrm{j}=1}^{\mathrm{n}} \mathrm{w}_{\mathrm{j}} = 1, \sum_{\mathrm{j}=1}^{\mathrm{m}} \mathrm{v}_{\mathrm{j}} = 1$. $PFS_{ft}WA: \ddot{\mathrm{O}}^{\mathrm{m}} \to \ddot{\mathrm{O}}$ AO is given as

$$PFS_{ft}WA\left(\hat{\mathrm{H}}_{S_{11}}, \hat{\mathrm{H}}_{S_{12}}, \ldots, \hat{\mathrm{H}}_{S_{\mathrm{m}\mathrm{n}}}\right) = \oplus_{\mathrm{j}=1}^{\mathrm{n}} \mathrm{w}_{\mathrm{j}} \left(\oplus_{\mathrm{j}=1}^{\mathrm{m}} \mathrm{v}_{\mathrm{j}} \hat{\mathrm{H}}_{S_{\mathrm{j}}}\right)$$

Theorem 1: Let $\hat{\mathrm{H}}_{S\mathrm{j}} = (\mathrm{T}_{\mathrm{j}}, \Psi_{\mathrm{j}}, \hat{\mathrm{E}}_{\mathrm{j}})$ be the family of $PFS_{ft}Ns$; $\mathrm{j} = 1, 2, \ldots, \mathrm{m}$, $\mathrm{j} = 1, 2, \ldots, \mathrm{n}$. Then aggregated result by using definition (6) is again $PFS_{ft}N$ given by

$$PFS_{ft}WA\left(\hat{\mathrm{H}}_{S_{11}}, \hat{\mathrm{H}}_{S_{12}}, \ldots, \hat{\mathrm{H}}_{S_{\mathrm{m}\mathrm{n}}}\right) =$$

$$\left(1 - \prod_{\mathrm{j}=1}^{\mathrm{n}} \left(\prod_{\mathrm{i}=1}^{\mathrm{m}} \left(1 - \mathrm{T}_{\mathrm{i}\mathrm{j}}\right)^{\mathrm{v}_{\mathrm{j}}}\right)^{\mathrm{w}_{\mathrm{j}}}, \prod_{\mathrm{j}=1}^{\mathrm{n}} \left(\prod_{\mathrm{i}=1}^{\mathrm{m}} \left(\Psi_{\mathrm{i}\mathrm{j}}\right)^{\mathrm{v}_{\mathrm{j}}}\right)^{\mathrm{w}_{\mathrm{j}}}, \prod_{\mathrm{j}=1}^{\mathrm{n}} \left(\prod_{\mathrm{i}=1}^{\mathrm{m}} \left(\hat{\mathrm{E}}_{\mathrm{i}\mathrm{j}}\right)^{\mathrm{v}_{\mathrm{j}}}\right)^{\mathrm{w}_{\mathrm{j}}}\right) \quad (1)$$

Proof: Use $\mathrm{m} = 1$ and $\mathrm{v}_1 = 1$.

$$PFS_{ft}WA\left(\hat{H}_{S_{11}}, \hat{H}_{S_{12}}, \ldots, \hat{H}_{S_{m\mathfrak{n}}}\right) = \oplus_{j=1}^{\mathfrak{n}} \mathfrak{q}_j \hat{H}_{S_{1j}}$$

$$= \left(1 - \prod_{j=1}^{\mathfrak{n}} (1 - \mathfrak{T}_{1j})^{\mathfrak{q}_j}, \prod_{j=1}^{\mathfrak{n}} (\Psi_{1j})^{\mathfrak{q}_j}, \prod_{j=1}^{\mathfrak{n}} (\hat{\mathfrak{E}}_{1j})^{\mathfrak{q}_j}\right)$$

$$= \left(1 - \prod_{j=1}^{\mathfrak{n}} \left(\prod_{i=1}^{1} (1 - \mathfrak{T}_{ij})^{\mathfrak{v}_i}\right)^{\mathfrak{q}_j}, \prod_{j=1}^{\mathfrak{n}} \left(\prod_{i=1}^{1} (\Psi_{ij})^{\mathfrak{v}_i}\right)^{\mathfrak{q}_j}, \prod_{j=1}^{\mathfrak{n}} \left(\prod_{i=1}^{1} (\hat{\mathfrak{E}}_{ij})^{\mathfrak{v}_i}\right)^{\mathfrak{q}_j}\right)$$

For $\mathfrak{n} = 1$, we get $\mathfrak{q}_1 = 1$.

$$PFS_{ft}WA\left(\hat{H}_{S_{11}}, \hat{H}_{S_{21}}, \ldots, \hat{H}_{S_{m1}}\right) = \oplus_{i=1}^{m} \mathfrak{v}_i \hat{H}_{S_{i1}}$$

$$= \left(1 - \prod_{i=1}^{m} (1 - \mathfrak{T}_{i1})^{\mathfrak{v}_i}, \prod_{i=1}^{m} (\Psi_{i1})^{\mathfrak{v}_i}, \prod_{i=1}^{m} (\hat{\mathfrak{E}}_{i1})^{\mathfrak{v}_i}\right)$$

$$= \left(1 - \prod_{j=1}^{1} \left(\prod_{i=1}^{m} (1 - \mathfrak{T}_{ij})^{\mathfrak{v}_i}\right)^{\mathfrak{q}_j}, \prod_{j=1}^{1} \left(\prod_{i=1}^{m} (\Psi_{ij})^{\mathfrak{v}_i}\right)^{\mathfrak{q}_j}, \prod_{j=1}^{1} \left(\prod_{i=1}^{m} (\hat{\mathfrak{E}}_{ij})^{\mathfrak{v}_i}\right)^{\mathfrak{q}_j}\right)$$

So the result is valid for $m = 1$ and $\mathfrak{n} = 1$

Assume that the result is valid when $\mathfrak{n} = \mathfrak{c}_1 + 1$, $m = \mathfrak{c}_2$ and $\mathfrak{n} = \mathfrak{c}_1$, $m = \mathfrak{c}_2 + 1$.

$$\oplus_{j=1}^{\mathfrak{c}_1+1} \mathfrak{q}_j \left(\oplus_{i=1}^{\mathfrak{c}_2} \mathfrak{v}_i \hat{H}_{S_{ij}}\right)$$

$$= \begin{pmatrix} 1 - \prod_{j=1}^{\mathfrak{c}_1+1} \left(\prod_{i=1}^{\mathfrak{c}_2} (1 - \mathfrak{T}_{ij})^{\mathfrak{v}_i}\right)^{\mathfrak{q}_j}, \prod_{j=1}^{\mathfrak{c}_1+1} \left(\prod_{i=1}^{\mathfrak{c}_2} (\Psi_{ij})^{\mathfrak{v}_i}\right)^{\mathfrak{q}_j}, \\ \prod_{j=1}^{\mathfrak{c}_1+1} \left(\prod_{i=1}^{\mathfrak{c}_2} (\hat{\mathfrak{E}}_{ij})^{\mathfrak{v}_i}\right)^{\mathfrak{q}_j} \end{pmatrix}$$

And

$$\oplus_{j=1}^{\mathfrak{c}_1} \mathfrak{q}_j \left(\oplus_{i=1}^{\mathfrak{c}_2+1} \mathfrak{v}_i \hat{H}_{S_{ij}}\right)$$

$$= \begin{pmatrix} 1 - \prod_{j=1}^{\mathfrak{c}_1} \left(\prod_{i=1}^{\mathfrak{c}_2+1} (1 - \mathfrak{T}_{ij})^{\mathfrak{v}_i}\right)^{\mathfrak{q}_j}, \prod_{j=1}^{\mathfrak{c}_1} \left(\prod_{i=1}^{\mathfrak{c}_2+1} (\Psi_{ij})^{\mathfrak{v}_i}\right)^{\mathfrak{q}_j}, \\ \prod_{j=1}^{\mathfrak{c}_1} \left(\prod_{i=1}^{\mathfrak{c}_2+1} (\hat{\mathfrak{E}}_{ij})^{\mathfrak{v}_i}\right)^{\mathfrak{q}_j} \end{pmatrix}.$$

Now for $\mathfrak{n} = \mathfrak{c}_1 + 1$, $m = \mathfrak{c}_2 + 1$, we have

$$\oplus_{j=1}^{\mathfrak{c}_1+1} \mathfrak{q}_j \left(\oplus_{i=1}^{\mathfrak{c}_2+1} \mathfrak{v}_i \hat{H}_{S_{ij}}\right) = \oplus_{j=1}^{\mathfrak{c}_1+1} \mathfrak{q}_j \left(\oplus_{i=1}^{\mathfrak{c}_2} \mathfrak{v}_i \hat{H}_{S_{ij}} \oplus \mathfrak{v}_{\mathfrak{c}_2+1} \hat{H}_{S_{(\mathfrak{c}_2+1)j}}\right)$$

$$= \oplus_{j=1}^{\mathfrak{c}_1+1} \oplus_{i=1}^{\mathfrak{c}_2} \mathfrak{q}_j \mathfrak{v}_i \hat{H}_{S_{ij}} \oplus_{j=1}^{\mathfrak{c}_1+1} \mathfrak{q}_j \mathfrak{v}_{(\mathfrak{c}_2+1)} \hat{H}_{S_{(\mathfrak{c}_2+1)j}}$$

$$= \begin{pmatrix} 1 - \prod_{j=1}^{\mathfrak{c}_1+1} \left(\prod_{i=1}^{\mathfrak{c}_2} (1 - \mathfrak{T}_{ij})^{\mathfrak{v}_i}\right)^{\mathfrak{q}_j} \oplus 1 - \prod_{j=1}^{\mathfrak{c}_1+1} \left((1 - \mathfrak{T}_{(\mathfrak{c}_2+1)j})^{\mathfrak{v}_{(\mathfrak{c}_2+1)}}\right)^{\mathfrak{q}_j}, \\ \prod_{j=1}^{\mathfrak{c}_1+1} \left(\prod_{i=1}^{\mathfrak{c}_2} (\Psi_{ij})^{\mathfrak{v}_i}\right)^{\mathfrak{q}_j} \oplus \prod_{j=1}^{\mathfrak{c}_1+1} \left((\Psi_{(\mathfrak{c}_2+1)j})^{\mathfrak{v}_{(\mathfrak{c}_2+1)}}\right)^{\mathfrak{q}_j}, \\ \prod_{j=1}^{\mathfrak{c}_1+1} \left(\prod_{i=1}^{\mathfrak{c}_2} (\hat{\mathfrak{E}}_{ij})^{\mathfrak{v}_i}\right)^{\mathfrak{q}_j} \oplus \prod_{j=1}^{\mathfrak{c}_1+1} \left((\hat{\mathfrak{E}}_{(\mathfrak{c}_2+1)j})^{\mathfrak{v}_{(\mathfrak{c}_2+1)}}\right)^{\mathfrak{q}_j} \end{pmatrix}.$$

$$= \begin{pmatrix} 1 - \prod_{j=1}^{\mathfrak{c}_1+1} \left(\prod_{i=1}^{\mathfrak{c}_2+1} (1 - \mathfrak{T}_{ij})^{\mathfrak{v}_i}\right)^{\mathfrak{q}_j}, \prod_{j=1}^{\mathfrak{c}_1+1} \left(\prod_{i=1}^{\mathfrak{c}_2+1} (\Psi_{ij})^{\mathfrak{v}_i}\right)^{\mathfrak{q}_j}, \\ \prod_{j=1}^{\mathfrak{c}_1+1} \left(\prod_{i=1}^{\mathfrak{c}_2+1} (\hat{\mathfrak{E}}_{ij})^{\mathfrak{v}_i}\right)^{\mathfrak{q}_j} \end{pmatrix}.$$

So, the result is true when $\mathfrak{n} = \mathfrak{c}_1 + 1$ and $m = \mathfrak{c}_2 + 1$, and so valid for all $\mathfrak{n}, m \geq 1$.

Remark 1: If only one parameter s_1 is used i.e., $\mathfrak{n} = 1$, then *PFS$_{ft}$WA* AO reduces to PFWA AO given in [16, 17].

$$PFWA\left(\hat{H}_{S_{11}}, \hat{H}_{S_{12}}, \ldots, \hat{H}_{S_{m\mathfrak{n}}}\right)$$

$$= \left(1 - \prod_{i=1}^{m} (1 - \mathfrak{T}_{i1})^{\mathfrak{v}_i}, \prod_{i=1}^{m} (\Psi_{i1})^{\mathfrak{v}_i}, \prod_{i=1}^{m} (\hat{\mathfrak{E}}_{i1})^{\mathfrak{v}_i}\right)$$

Example 1: To describe the attractiveness of a house, let $\hat{H} = \{f_1, f_2, f_3, f_4\}$ denote the set of experts and $S = \{s_1, s_2, s_3\}$ denote the set of parameters. Let the data of the decision analyst be in the shape of *PFS$_{ft}$Ns* $(P,S) = (\mathfrak{T}_{ij}, \Psi_{ij}, \hat{\mathfrak{E}}_{ij})$ against each parameter is

$$(P, S) = \begin{bmatrix} (0.30, 0.20, 0.10) & (0.40, 0.10, 0.40) & (0.30, 0.30, 0.20) \\ (0.20, 0.30, 0.40) & (0.20, 0.50, 0.10) & (0.20, 0.20, 0.40) \\ (0.20, 0.20, 0.20) & (0.10, 0.50, 0.20) & (0.30, 0.20, 0.30) \\ (0.10, 0.40, 0.30) & (0.10, 0.30, 0.40) & (0.50, 0.10, 0.10) \end{bmatrix}$$

Let $\mathfrak{q} = (0.340, 0.410, 0.250)$ and $\mathfrak{v} = (0.300, 0.290, 0.220, 0.190)$ denote WVs of parameters and experts respectively. Utilizing equation (1), we get

$$PFS_{ft}WA\left(\hat{H}_{S_{11}}, \hat{H}_{S_{12}}, \ldots, \hat{H}_{S_{43}}\right)$$

$$= \begin{pmatrix} 1 - \prod_{j=1}^{3} \left(\prod_{i=1}^{4} (1 - \mathfrak{T}_{ij})^{\mathfrak{v}_i}\right)^{\mathfrak{q}_j}, \prod_{j=1}^{3} \left(\prod_{i=1}^{4} (\Psi_{ij})^{\mathfrak{v}_i}\right)^{\mathfrak{q}_j}, \\ \prod_{j=1}^{3} \left(\prod_{i=1}^{4} (\hat{\mathfrak{E}}_{ij})^{\mathfrak{v}_i}\right)^{\mathfrak{q}_j} \end{pmatrix}$$

$$= \begin{pmatrix} 1 - \begin{pmatrix} \{(1-0.3)^{0.30}(1-0.2)^{0.29}(1-0.2)^{0.22}(1-0.1)^{0.19}\}^{0.34} \\ \{(1-0.4)^{0.30}(1-0.2)^{0.29}(1-0.1)^{0.22}(1-0.1)^{0.19}\}^{0.41} \\ \{(1-0.3)^{0.30}(1-0.2)^{0.29}(1-0.3)^{0.22}(1-0.5)^{0.19}\}^{0.25} \end{pmatrix}, \\ \begin{pmatrix} ((0.2)^{0.30}(0.3)^{0.29}(0.2)^{0.22}(0.4)^{0.19})^{0.34}((0.1)^{0.30}(0.5)^{0.29}(0.5)^{0.22}(0.3)^{0.19})^{0.41} \\ ((0.3)^{0.30}(0.2)^{0.29}(0.2)^{0.22}(0.1)^{0.19})^{0.25} \end{pmatrix}, \\ \begin{pmatrix} ((0.1)^{0.30}(0.4)^{0.29}(0.2)^{0.22}(0.3)^{0.19})^{0.34}((0.4)^{0.30}(0.1)^{0.29}(0.2)^{0.22}(0.4)^{0.19})^{0.41} \\ ((0.2)^{0.30}(0.4)^{0.29}(0.3)^{0.22}(0.1)^{0.19})^{0.25} \end{pmatrix} \end{pmatrix}$$

$$= (0.2475, 0.2383, 0.2255).$$

In our further discussion in the application section, we will execute the formula of *PFS$_{ft}$WA* AO in a similar fashion.

Now we define the characteristics of the above-developed notions

Theorem 2: Assume that $\hat{H}_{S_{ij}} = (\mathfrak{T}_{ij}, \Psi_{ij}, \hat{\mathfrak{E}}_{ij})$ be the family of *PFS$_{ft}$Ns*; $i = 1, 2, \ldots, m$, $j = 1, 2, \ldots, \mathfrak{n}$. Then *PFS$_{ft}$WA* AO has the following properties

1) (Idempotency): Let $\hat{H}_{S_{ij}} = (\mathfrak{T}_{ij}, \Psi_{ij}, \hat{\mathfrak{E}}_{ij})$ be the family of *PFS$_{ft}$Ns*; $i = 1, 2, \ldots, m$, $j = 1, 2, \ldots, \mathfrak{n}$. Also $\hat{H}_S = (\mathfrak{T}, \Psi, \hat{\mathfrak{E}})$

Then

$$PFS_{ft}WA\left(\hat{H}_{S_{11}}, \hat{H}_{S_{12}}, \ldots, \hat{H}_{S_{43}}\right) = \hat{H}_S$$

Proof: As all $\hat{H}_{S_{ij}} = \hat{H}_S = (\mathfrak{T}, \Psi, \hat{\mathfrak{E}})$ then we get

$$PFS_{ft}WA\left(\hat{H}_{S_{11}}, \hat{H}_{S_{12}}, \ldots, \hat{H}_{S_{m\mathfrak{n}}}\right)$$

$$= \begin{pmatrix} 1 - \prod_{j=1}^{\mathfrak{n}} \left(\prod_{i=1}^{m} (1 - \mathfrak{T})^{\mathfrak{v}_i}\right)^{\mathfrak{q}_j}, \prod_{j=1}^{\mathfrak{n}} \left(\prod_{i=1}^{m} (\Psi)^{\mathfrak{v}_i}\right)^{\mathfrak{q}_j}, \\ \prod_{j=1}^{\mathfrak{n}} \left(\prod_{i=1}^{m} (\hat{\mathfrak{E}})^{\mathfrak{v}_i}\right)^{\mathfrak{q}_j} \end{pmatrix}$$

$$= \begin{pmatrix} 1 - \left((1 - \mathfrak{T})^{\sum_{i=1}^{m} \mathfrak{v}_i}\right)^{\sum_{j=1}^{\mathfrak{n}} \mathfrak{q}_j}, \left((\Psi)^{\sum_{i=1}^{m} \mathfrak{v}_i}\right)^{\sum_{j=1}^{\mathfrak{n}} \mathfrak{q}_j}, \\ \left((\hat{\mathfrak{E}})^{\sum_{i=1}^{m} \mathfrak{v}_i}\right)^{\sum_{j=1}^{\mathfrak{n}} \mathfrak{q}_j} \end{pmatrix}$$

$$= \left(1 - (1 - \mathfrak{T}), \Psi, \hat{\mathfrak{E}}\right) = \hat{H}_S.$$

Hence proof is complete.

2) (Boundedness): Let

$$\hat{H}^{-}{}_{S_{ij}} = \left(\min_j \min_i(\mathrm{T}_{ij}), \max_j \max_i(\Psi_{ij}), \max_j \max_i(\hat{E}_{ij})\right)$$

and

$$\hat{H}^{+}{}_{S_{ij}} = \left(\max_j \max_i(\mathrm{T}_{ij}), \min_j \min_i(\Psi_{ij}), \min_j \min_i(\hat{E}_{ij})\right),$$

then

$$\hat{H}^{-}{}_{S_{ij}} \le PFS_{ft}WA\left(\hat{H}_{S_{11}}, \hat{H}_{S_{12}}, \dots, \hat{H}_{S_{mn}}\right) \le \hat{H}^{+}{}_{S_{ij}}$$

Proof: As $\hat{H}_{S_{ij}} = (\mathrm{T}_{ij}, \Psi_{ij}, \hat{E}_{ij})$ denote $PFS_{ft}N$, then

$$\min_j \min_i(\mathrm{T}_{ij}) \le (\mathrm{T}_{ij}) \le \max_j \max_i(\mathrm{T}_{ij})$$

$$\Rightarrow 1 - \max_j \max_i(\mathrm{T}_{ij}) \le 1 - (\mathrm{T}_{ij}) \le 1 - \min_j \min_i(\mathrm{T}_{ij})$$

$$\Leftrightarrow \left(1 - \max_j \max_i(\mathrm{T}_{ij})\right)^{\mathrm{v}_i} \le \left(1 - (\mathrm{T}_{ij})\right)^{\mathrm{v}_i} \le \left(1 - \min_j \min_i(\mathrm{T}_{ij})\right)^{\mathrm{v}_i}$$

$$\Leftrightarrow 1 - \max_j \max_i(\mathrm{T}_{ij}) \le \prod_{i=1}^{m}\left(1 - (\mathrm{T}_{ij})\right)^{\mathrm{v}_i} \le 1 - \min_j \min_i(\mathrm{T}_{ij})$$

$$\Leftrightarrow \left(1 - \max_j \max_i(\mathrm{T}_{ij})\right)^{\sum_{j=1}^{m}\mathrm{v}_j} \le \prod_{j=1}^{n}\left(\prod_{i=1}^{m}(1 - \mathrm{T}_{ij})^{\mathrm{v}_i}\right)^{\mathrm{v}_j} \le \left(1 - \min_j \min_i(\mathrm{T}_{ij})\right)^{\sum_{j=1}^{m}\mathrm{v}_j}$$

That is

$$1 - \max_j \max_i(\mathrm{T}_{ij}) \le \prod_{j=1}^{n}\left(\prod_{i=1}^{m}(1 - \mathrm{T}_{ij})^{\mathrm{v}_i}\right)^{\mathrm{v}_j} \le 1 - \min_j \min_i(\mathrm{T}_{ij}).$$

Hence

$$\min_j \min_i(\mathrm{T}_{ij}) \le 1 - \prod_{j=1}^{n}\left(\prod_{i=1}^{m}(1 - \mathrm{T}_{ij})^{\mathrm{v}_i}\right)^{\mathrm{v}_j} \le \max_j \max_i(\mathrm{T}_{ij}) \quad (2)$$

Also

$$\min_j \min_i(\Psi_{ij}) \le \Psi_{ij} \le \max_j \max_i(\Psi_{ij}) \Rightarrow \left(\min_j \min_i(\Psi_{ij})\right)^{\sum_{i=1}^{m}\mathrm{v}_i} \le \prod_{i=1}^{m}(\Psi_{ij})^{\mathrm{v}_i} \le \left(\max_j \max_i(\Psi_{ij})\right)^{\sum_{i=1}^{m}\mathrm{v}_i}$$

$$\Leftrightarrow \min_j \min_i(\Psi_{ij}) \le \prod_{i=1}^{m}(\Psi_{ij})^{\mathrm{v}_i} \le \max_j \max_i(\Psi_{ij})$$

$$\Leftrightarrow \left(\min_j \min_i(\Psi_{ij})\right)^{\mathrm{u}_j} \le \left(\prod_{i=1}^{m}(\Psi_{ij})^{\mathrm{v}_i}\right)^{\mathrm{u}_j} \le \left(\max_j \max_i(\Psi_{ij})\right)^{\mathrm{u}_j}$$

$$\Leftrightarrow \left(\min_j \min_i(\Psi_{ij})\right)^{\sum_{j=1}^{m}\mathrm{u}_j} \le \prod_{i=1}^{n}\left(\prod_{i=1}^{m}(\hat{E}_{ij})^{\mathrm{v}_i}\right)^{\mathrm{u}_j} \le \left(\max_j \max_i(\Psi_{ij})\right)^{\sum_{j=1}^{m}\mathrm{u}_j}$$

Hence we get

$$\left(\min_j \min_i(\Psi_{ij})\right) \le \prod_{j=1}^{n}\left(\prod_{i=1}^{m}(\Psi_{ij})^{\mathrm{v}_i}\right)^{\mathrm{u}_j} \le \max_j \max_i(\Psi_{ij}) \quad (3)$$

Similarly

$$\min_j \min_i(\hat{E}_{ij}) \le \hat{E}_{ij} \le \max_j \max_i(\hat{E}_{ij}) \Rightarrow \left(\min_j \min_i(\hat{E}_{ij})\right)^{\sum_{i=1}^{m}\mathrm{v}_i} \le \prod_{i=1}^{m}(\hat{E}_{ij})^{\mathrm{v}_i} \le \left(\max_j \max_i(\hat{E}_{ij})\right)^{\sum_{i=1}^{m}\mathrm{v}_i} \Leftrightarrow \min_j \min_i(\hat{E}_{ij})$$

$$\le \prod_{i=1}^{m}(\hat{E}_{ij})^{\mathrm{v}_i} \le \max_j \max_i(\hat{E}_{ij}) \Leftrightarrow \left(\min_j \min_i(\hat{E}_{ij})\right)^{\mathrm{u}_j}$$

$$\le \left(\prod_{i=1}^{m}(\hat{E}_{ij})^{\mathrm{v}_i}\right)^{\mathrm{u}_j} \le \left(\max_j \max_i(\hat{E}_{ij})\right)^{\mathrm{u}_j} \Leftrightarrow \left(\min_j \min_i(\hat{E}_{ij})\right)^{\sum_{j=1}^{m}\mathrm{u}_j}$$

$$\le \prod_{j=1}^{n}\left(\prod_{i=1}^{m}(\hat{E}_{ij})^{\mathrm{v}_i}\right)^{\mathrm{u}_j} \le \left(\max_j \max_i(\hat{E}_{ij})\right)^{\sum_{j=1}^{m}\mathrm{u}_j},$$

Hence we get

$$\left(\min_j \min_i(\hat{E}_{ij})\right) \le \prod_{j=1}^{n}\left(\prod_{i=1}^{m}(\hat{E}_{ij})^{\mathrm{v}_i}\right)^{\mathrm{u}_j} \le \max_j \max_i(\hat{E}_{ij}) \quad (4)$$

Let $\wp = PFS_{ft}WA\ (\hat{H}_{S_{11}}), \hat{H}_{S_{12}}, \dots, \hat{H}_{S_{mn}} = (\mathrm{T}_{\wp}, \Psi_{\wp}, \hat{E}_{\wp})$, then by equations (2), (3), and (4),

$$\min_j \min_i(\mathrm{T}_{ij}) \le \mathrm{T}_{\wp} \le \max_j \max_i(\mathrm{T}_{ij}), \left(\min_j \min_i(\Psi_{ij})\right) \le \Psi_{\wp} \le \max_j \max_i(\Psi_{ij}), \left(\min_j \min_i(\hat{E}_{ij})\right) \le \hat{E}_{\wp} \le \max_j \max_i(\hat{E}_{ij}),$$

Now by using the SF definition

$$Scr.(\wp) = \mathrm{T}_{\wp} - \Psi_{\wp} - \hat{E}_{\wp} \le \max_j \max_i(\mathrm{T}_{ij}) - \min_j \min_i(\Psi_{ij}) - \min_j \min_i(\hat{E}_{ij}) = Scr.\left(\hat{H}^{+}{}_{S_{ij}}\right),$$

$$Scr.(\wp) = \mathrm{T}_{\wp} - \Psi_{\wp} - \hat{E}_{\wp} \ge \min_j \min_i(\mathrm{T}_{ij}) - \max_j \max_i(\Psi_{ij}) - \max_j \max_i(\hat{E}_{ij}) = Scr.\left(\hat{H}^{-}{}_{S_{ij}}\right).$$

Now we have three cases

Case 1: If $Scr.\ (\hat{H}_{S_{ij}}) < Scr.\ (\hat{H}^{+}{}_{S_{ij}})$ and $Scr.\ (\hat{H}_{S_{ij}}) > Scr.\ (\hat{H}^{-}{}_{S_{ij}})$, we have

$$\hat{H}^{-}{}_{S_{ij}} < PFS_{ft}WA\left(\hat{H}_{S_{11}}, \hat{H}_{S_{12}}, \dots, \hat{H}_{S_{mn}}\right) < \hat{H}^{+}{}_{S_{ij}}$$

Case 2: If $Scr.\ (\hat{H}_{S_{ij}}) = Scr.\ (\hat{H}^{+}{}_{S_{ij}})$, then by utilizing the above inequalities

$$\mathrm{T}_{\wp} = \max_j \max_i(\mathrm{T}_{ij}), \Psi_{\wp} = \min_j \min_i(\Psi_{ij}) \text{ and } \hat{E}_{\wp} = \min_j \min_i(\hat{E}_{ij}).$$

Thus

$$Acur.(\wp) = \mathrm{T}_{\wp} + \Psi_{\wp} + \dot{\hat{\mathrm{E}}}_{\wp} = \max_{\dot{\jmath}} \max_{\dot{\imath}}(\mathrm{T}_{\dot{\imath}\dot{\jmath}}) + \min_{\dot{\jmath}} \min(\Psi_{\dot{\imath}\dot{\jmath}}) + \min_{\dot{\jmath}} \min_{\dot{\imath}}(\hat{\mathrm{E}}_{\dot{\imath}\dot{\jmath}}) = Ac\left(\hat{\mathrm{H}}^{+}{}_{S_{\dot{\imath}\dot{\jmath}}}\right).$$

We get

$$PFS_{ft}WA\left(\hat{\mathrm{H}}_{S_{11}}, \hat{\mathrm{H}}_{S_{12}}, \ldots, \hat{\mathrm{H}}_{S_{\mathrm{M}\mathrm{n}}}\right) = \hat{\mathrm{H}}^{+}{}_{S_{\dot{\imath}\dot{\jmath}}}$$

Case 3: If *Scr.* $(\hat{\mathrm{H}}_{S_{\dot{\imath}\dot{\jmath}}}) = Scr.\ (\hat{\mathrm{H}}^{+}{}_{S_{\dot{\imath}\dot{\jmath}}})$ that is $\mathrm{T}_{\wp} - \Psi_{\wp} - \dot{\hat{\mathrm{E}}}_{\wp} = \min_{\dot{\jmath}} \min_{\dot{\imath}}(\mathrm{T}_{\dot{\imath}\dot{\jmath}}) - \max_{\dot{\jmath}} \max_{\dot{\imath}}(\Psi_{\dot{\imath}\dot{\jmath}}) - \max_{\dot{\jmath}} \max_{\dot{\imath}}(\dot{\hat{\mathrm{E}}}_{\dot{\imath}\dot{\jmath}})$, we get

$$\mathrm{T}_{\wp} = \min_{\dot{\jmath}} \min_{\dot{\imath}}(\mathrm{T}_{\dot{\imath}\dot{\jmath}}), \mathrm{T}_{\wp} = \max_{\dot{\jmath}} \max_{\dot{\imath}}(\Psi_{\dot{\imath}\dot{\jmath}}) \text{ and } \dot{\hat{\mathrm{E}}}_{\wp} = \max_{\dot{\jmath}} \max_{\dot{\imath}}(\dot{\hat{\mathrm{E}}}_{\dot{\imath}\dot{\jmath}}).$$

Thus

$$Acur.(\wp) = \mathrm{T}_{\wp} + \Psi_{\wp} + \dot{\hat{\mathrm{E}}}_{\wp} = \min_{\dot{\jmath}} \min_{\dot{\imath}}(\mathrm{T}_{\dot{\imath}\dot{\jmath}}) + \max_{\dot{\jmath}} \max_{\dot{\imath}}(\Psi_{\dot{\imath}\dot{\jmath}}) + \max_{\dot{\jmath}} \max_{\dot{\imath}}(\dot{\hat{\mathrm{E}}}_{\dot{\imath}\dot{\jmath}}) = Acur.\left(\hat{\mathrm{H}}^{-}{}_{S_{\dot{\imath}\dot{\jmath}}}\right).$$

Hence

$$PFS_{ft}WA\left(\hat{\mathrm{H}}_{S_{11}}, \hat{\mathrm{H}}_{S_{12}}, \ldots, \hat{\mathrm{H}}_{S_{\mathrm{M}\mathrm{n}}}\right) = \hat{\mathrm{H}}^{-}{}_{S_{\dot{\imath}\dot{\jmath}}}.$$

Proved.

3) (Shift-invariance): Let $\hat{\mathrm{H}}_{S} = (\mathrm{T}, \Psi, \dot{\hat{\mathrm{E}}})$ be another *PFS*$_{ft}$*N*, then

$$PFS_{ft}WA\left(\hat{\mathrm{H}}_{S_{11}} \oplus \hat{\mathrm{H}}_{S}, \hat{\mathrm{H}}_{S_{12}} \oplus \hat{\mathrm{H}}_{S}, \ldots, \hat{\mathrm{H}}_{S_{\mathrm{M}\mathrm{n}}} \oplus \hat{\mathrm{H}}_{S}\right) = PFS_{ft}WA\left(\hat{\mathrm{H}}_{S_{11}}, \hat{\mathrm{H}}_{S_{12}}, \ldots, \hat{\mathrm{H}}_{S_{\mathrm{M}\mathrm{n}}}\right) \oplus \hat{\mathrm{H}}_{S}$$

Proof: For two *PFS*$_{ft}$*N* $\hat{\mathrm{H}}_{S}$ and $\hat{\mathrm{H}}_{S_{\dot{\imath}\dot{\jmath}}}$

$$\hat{\mathrm{H}}_{S} \oplus \hat{\mathrm{H}}_{S_{\dot{\imath}\dot{\jmath}}} = \left(\left(1 - (1 - \mathrm{T})\left(1 - \mathrm{T}_{\dot{\imath}\dot{\jmath}}\right)\right), \Psi\Psi_{\dot{\imath}\dot{\jmath}}, \dot{\hat{\mathrm{E}}}\dot{\hat{\mathrm{E}}}_{\dot{\imath}\dot{\jmath}}\right).$$

Hence

$$PFS_{ft}WA\left(\hat{\mathrm{H}}_{S_{11}} \oplus \hat{\mathrm{H}}_{S}, \hat{\mathrm{H}}_{S_{12}} \oplus \hat{\mathrm{H}}_{S}, \ldots, \hat{\mathrm{H}}_{S_{\mathrm{M}\mathrm{n}}} \oplus \hat{\mathrm{H}}_{S}\right) = \oplus_{\dot{\jmath}=1}^{\mathrm{n}} \mathrm{Ч}_{\dot{\jmath}} \left(\oplus_{\dot{\imath}=1}^{\mathrm{M}} \mathrm{ъ}_{\dot{\imath}} \left(\hat{\mathrm{H}}_{S_{\dot{\imath}\dot{\jmath}}} \oplus \hat{\mathrm{H}}_{S}\right)\right)$$

$$= \begin{pmatrix} 1 - \prod_{\dot{\jmath}=1}^{\mathrm{n}} \left(\prod_{\dot{\imath}=1}^{\mathrm{M}} \left(1 - \mathrm{T}_{\dot{\imath}\dot{\jmath}}\right)^{\mathrm{ъ}_{\dot{\imath}}} (1 - \mathrm{T})^{\mathrm{ъ}_{\dot{\imath}}}\right)^{\mathrm{Ч}_{\dot{\jmath}}}, \prod_{\dot{\jmath}=1}^{\mathrm{n}} \left(\prod_{\dot{\imath}=1}^{\mathrm{M}} \left(\Psi_{\dot{\imath}\dot{\jmath}}\right)^{\mathrm{ъ}_{\dot{\imath}}} (\Psi)^{\mathrm{ъ}_{\dot{\imath}}}\right)^{\mathrm{Ч}_{\dot{\jmath}}}, \\ \prod_{\dot{\jmath}=1}^{\mathrm{n}} \left(\prod_{\dot{\imath}=1}^{\mathrm{M}} \left(\dot{\hat{\mathrm{E}}}\right)^{\mathrm{ъ}_{\dot{\imath}}} \left(\dot{\hat{\mathrm{E}}}_{\dot{\imath}\dot{\jmath}}\right)^{\mathrm{ъ}_{\dot{\imath}}}\right)^{\mathrm{Ч}_{\dot{\jmath}}} \end{pmatrix}$$

$$= \begin{pmatrix} 1 - (1 - \mathrm{T}) \prod_{\dot{\jmath}=1}^{\mathrm{n}} \left(\prod_{\dot{\imath}=1}^{\mathrm{M}} \left(1 - \mathrm{T}_{\dot{\imath}\dot{\jmath}}\right)^{\mathrm{ъ}_{\dot{\imath}}}\right)^{\mathrm{Ч}_{\dot{\jmath}}}, (\Psi) \prod_{\dot{\jmath}=1}^{\mathrm{n}} \left(\prod_{\dot{\imath}=1}^{\mathrm{M}} \left(\Psi_{\dot{\imath}\dot{\jmath}}\right)^{\mathrm{ъ}_{\dot{\imath}}}\right)^{\mathrm{Ч}_{\dot{\jmath}}}, \\ (\dot{\hat{\mathrm{E}}}) \prod_{\dot{\jmath}=1}^{\mathrm{n}} \left(\prod_{\dot{\imath}=1}^{\mathrm{M}} \left(\dot{\hat{\mathrm{E}}}_{\dot{\imath}\dot{\jmath}}\right)^{\mathrm{ъ}_{\dot{\imath}}}\right)^{\mathrm{Ч}_{\dot{\jmath}}} \end{pmatrix}$$

$$= \begin{pmatrix} 1 - \prod_{\dot{\jmath}=1}^{\mathrm{n}} \left(\prod_{\dot{\imath}=1}^{\mathrm{M}} \left(1 - \mathrm{T}_{\dot{\imath}\dot{\jmath}}\right)^{\mathrm{ъ}_{\dot{\imath}}}\right)^{\mathrm{Ч}_{\dot{\jmath}}}, \prod_{\dot{\jmath}=1}^{\mathrm{n}} \left(\prod_{\dot{\imath}=1}^{\mathrm{M}} \left(\Psi_{\dot{\imath}\dot{\jmath}}\right)^{\mathrm{ъ}_{\dot{\imath}}}\right)^{\mathrm{Ч}_{\dot{\jmath}}}, \\ \prod_{\dot{\jmath}=1}^{\mathrm{n}} \left(\prod_{\dot{\imath}=1}^{\mathrm{M}} \left(\dot{\hat{\mathrm{E}}}_{\dot{\imath}\dot{\jmath}}\right)^{\mathrm{ъ}_{\dot{\imath}}}\right)^{\mathrm{Ч}_{\dot{\jmath}}} \end{pmatrix} \oplus (\mathrm{T}, \Psi, \dot{\hat{\mathrm{E}}})$$

$$= PFS_{ft}WA\left(\hat{\mathrm{H}}_{S_{11}}, \hat{\mathrm{H}}_{S_{12}}, \ldots, \hat{\mathrm{H}}_{S_{\mathrm{M}\mathrm{n}}}\right) \oplus \hat{\mathrm{H}}_{S}$$

4) (Homogeneity): For $\mathrm{G}' > 0$ being the real number

$$PFS_{ft}WA\left(\mathrm{G}'\hat{\mathrm{H}}_{S_{11}}, \mathrm{G}'\hat{\mathrm{H}}_{S_{12}}, \ldots, \mathrm{G}'\hat{\mathrm{H}}_{S_{\mathrm{M}\mathrm{n}}}\right) = \mathrm{G}'PFS_{ft}WA\left(\hat{\mathrm{H}}_{S_{11}}, \hat{\mathrm{H}}_{S_{12}}, \ldots, \hat{\mathrm{H}}_{S_{\mathrm{M}\mathrm{n}}}\right)$$

Proof: For $\mathrm{G}' > 0$, $\mathrm{G}'\hat{\mathrm{H}}_{S_{\dot{\imath}\dot{\jmath}}} = \left(1 - \left(1 - \mathrm{T}_{\dot{\imath}\dot{\jmath}}\right)^{\mathrm{G}'}, \left(\Psi_{\dot{\imath}\dot{\jmath}}\right)^{\mathrm{G}'}, \left(\dot{\hat{\mathrm{E}}}_{\dot{\imath}\dot{\jmath}}\right)^{\mathrm{G}'}\right)$.

$$PFS_{ft}WA\left(\mathrm{G}'\hat{\mathrm{H}}_{S_{11}}, \mathrm{G}'\hat{\mathrm{H}}_{S_{12}}, \ldots, \mathrm{G}'\hat{\mathrm{H}}_{S_{\mathrm{M}\mathrm{n}}}\right)$$

$$= \begin{pmatrix} 1 - \prod_{\dot{\jmath}=1}^{\mathrm{n}} \left(\prod_{\dot{\imath}=1}^{\mathrm{M}} \left(1 - \mathrm{T}_{\dot{\imath}\dot{\jmath}}\right)^{\mathrm{G}'\mathrm{ъ}_{\dot{\imath}}}\right)^{\mathrm{Ч}_{\dot{\jmath}}}, \prod_{\dot{\jmath}=1}^{\mathrm{n}} \left(\prod_{\dot{\imath}=1}^{\mathrm{M}} \left(\Psi_{\dot{\imath}\dot{\jmath}}\right)^{\mathrm{G}'\mathrm{ъ}_{\dot{\imath}}}\right)^{\mathrm{Ч}_{\dot{\jmath}}}, \\ \prod_{\dot{\jmath}=1}^{\mathrm{n}} \left(\prod_{\dot{\imath}=1}^{\mathrm{M}} \left(\dot{\hat{\mathrm{E}}}_{\dot{\imath}\dot{\jmath}}\right)^{\mathrm{G}'\mathrm{ъ}_{\dot{\imath}}}\right)^{\mathrm{Ч}_{\dot{\jmath}}} \end{pmatrix}$$

$$= \begin{pmatrix} 1 - \left(\prod_{\dot{\jmath}=1}^{\mathrm{n}} \left(\prod_{\dot{\imath}=1}^{\mathrm{M}} \left(1 - \mathrm{T}_{\dot{\imath}\dot{\jmath}}\right)^{\mathrm{ъ}_{\dot{\imath}}}\right)^{\mathrm{Ч}_{\dot{\jmath}}}\right)^{\mathrm{G}'}, \left(\prod_{\dot{\jmath}=1}^{\mathrm{n}} \left(\prod_{\dot{\imath}=1}^{\mathrm{M}} \left(\Psi_{\dot{\imath}\dot{\jmath}}\right)^{\mathrm{ъ}_{\dot{\imath}}}\right)^{\mathrm{Ч}_{\dot{\jmath}}}\right)^{\mathrm{G}'}, \\ \left(\prod_{\dot{\jmath}=1}^{\mathrm{n}} \left(\prod_{\dot{\imath}=1}^{\mathrm{M}} \left(\dot{\hat{\mathrm{E}}}_{\dot{\imath}\dot{\jmath}}\right)^{\mathrm{ъ}_{\dot{\imath}}}\right)^{\mathrm{Ч}_{\dot{\jmath}}}\right)^{\mathrm{G}'} \end{pmatrix}$$

$$= \mathrm{G}'PFS_{ft}WA\left(\hat{\mathrm{H}}_{S_{11}}, \hat{\mathrm{H}}_{S_{12}}, \ldots, \hat{\mathrm{H}}_{S_{\mathrm{M}\mathrm{n}}}\right).$$

Definition 7: Assume that $\hat{\mathrm{H}}_{S_{\dot{\imath}\dot{\jmath}}} = (\mathrm{T}_{\dot{\imath}\dot{\jmath}}, \Psi_{\dot{\imath}\dot{\jmath}}, \dot{\hat{\mathrm{E}}}_{\dot{\imath}\dot{\jmath}})$ be the family of *PFS*$_{ft}$*Ns*; $\dot{\imath} = 1, 2, \ldots, \mathrm{M}$, $\dot{\jmath} = 1, 2, \ldots, \mathrm{n}$. Also let $\mathrm{Ч}_{\dot{\jmath}}$, $\mathrm{ъ}_{\dot{\imath}}$ represent the WVs for parameters $\mathrm{s}_{\dot{\jmath}}$ and experts $e_{\dot{\imath}}$ respectively with the constraint that $\mathrm{Ч}_{\dot{\jmath}} > 0$, $\mathrm{ъ}_{\dot{\imath}} > 0$ and $\sum_{\dot{\jmath}=1}^{\mathrm{n}} \mathrm{Ч}_{\dot{\jmath}} = 1, \sum_{\dot{\imath}=1}^{\mathrm{M}} \mathrm{ъ}_{\dot{\imath}} = 1$. $PFS_{ft}WG: \ddot{\Theta}^{\mathrm{M}} \to \ddot{\Theta}$ AO is given as

$$PFS_{ft}OWA\left(\hat{\mathrm{H}}_{S_{11}}, \hat{\mathrm{H}}_{S_{12}}, \ldots, \hat{\mathrm{H}}_{S_{\mathrm{M}\mathrm{n}}}\right) = \oplus_{\dot{\jmath}=1}^{\mathrm{n}} \mathrm{Ч}_{\dot{\jmath}} \left(\oplus_{\dot{\imath}=1}^{\mathrm{M}} \mathrm{ъ}_{\dot{\imath}} \hat{\mathrm{H}}_{S_{\alpha(\dot{\imath})\alpha(\dot{\jmath})}}\right)$$

$$= \begin{pmatrix} 1 - \prod_{\dot{\jmath}=1}^{\mathrm{n}} \left(\prod_{\dot{\imath}=1}^{\mathrm{M}} \left(1 - \mathrm{T}_{\dot{\imath}\dot{\jmath}}\right)^{\mathrm{ъ}_{\dot{\imath}}}\right)^{\mathrm{Ч}_{\dot{\jmath}}}, \prod_{\dot{\jmath}=1}^{\mathrm{n}} \left(\prod_{\dot{\imath}=1}^{\mathrm{M}} \left(\Psi_{\dot{\imath}\dot{\jmath}}\right)^{\mathrm{ъ}_{\dot{\imath}}}\right)^{\mathrm{Ч}_{\dot{\jmath}}}, \\ \prod_{\dot{\jmath}=1}^{\mathrm{n}} \left(\prod_{\dot{\imath}=1}^{\mathrm{M}} \left(\dot{\hat{\mathrm{E}}}_{\dot{\imath}\dot{\jmath}}\right)^{\mathrm{ъ}_{\dot{\imath}}}\right)^{\mathrm{Ч}_{\dot{\jmath}}} \end{pmatrix}$$

Noticed that $\alpha(\dot{\imath}), \alpha(\dot{\jmath}) \leq \alpha(\dot{\imath} - 1), \alpha(\dot{\jmath} - 1)$.

Definition 8: Assume that $\hat{\mathrm{H}}_{S_{\dot{\imath}\dot{\jmath}}} = (\mathrm{T}_{\dot{\imath}\dot{\jmath}}, \Psi_{\dot{\imath}\dot{\jmath}}, \dot{\hat{\mathrm{E}}}_{\dot{\imath}\dot{\jmath}})$ be the family of *PFS*$_{ft}$*Ns*; $\dot{\imath} = 1, 2, \ldots, \mathrm{M}$, $\dot{\jmath} = 1, 2, \ldots, \mathrm{n}$. Also let $\mathrm{Ч}_{\dot{\jmath}}$, $\mathrm{ъ}_{\dot{\imath}}$ represent the WVs for parameters $\mathrm{s}_{\dot{\jmath}}$ and experts $e_{\dot{\imath}}$respectively with the constraint that $\mathrm{Ч}_{\dot{\jmath}} > 0$, $\mathrm{ъ}_{\dot{\imath}} > 0$ and $\sum_{\dot{\jmath}=1}^{\mathrm{n}} \mathrm{Ч}_{\dot{\jmath}} = 1, \sum_{\dot{\imath}=1}^{\mathrm{M}} \mathrm{ъ}_{\dot{\imath}} = 1$. $PFS_{ft}WG: \ddot{\Theta}^{\mathrm{M}} \to \ddot{\Theta}$ AO is given as

$$PFS_{ft}WG\left(\hat{\mathrm{H}}_{S_{11}}, \hat{\mathrm{H}}_{S_{12}}, \ldots, \hat{\mathrm{H}}_{S_{\mathrm{M}\mathrm{n}}}\right) = \otimes_{\dot{\jmath}=1}^{\mathrm{n}} \left(\otimes_{\dot{\imath}=1}^{\mathrm{M}} \left(\hat{\mathrm{H}}_{S_{\dot{\imath}\dot{\jmath}}}\right)^{\mathrm{ъ}_{\dot{\imath}}}\right)^{\mathrm{Ч}_{\dot{\jmath}}}$$

Theorem 3: Assume that $\hat{\mathrm{H}}_{S_{\dot{\imath}\dot{\jmath}}} = (\mathrm{T}_{\dot{\imath}\dot{\jmath}}, \Psi_{\dot{\imath}\dot{\jmath}}, \dot{\hat{\mathrm{E}}}_{\dot{\imath}\dot{\jmath}})$ be the family of *PFS*$_{ft}$*Ns*; $\dot{\imath} = 1, 2, \ldots, \mathrm{M}$, $\dot{\jmath} = 1, 2, \ldots, \mathrm{n}$. Then aggregated result by using definition (8) is again *PFS*$_{ft}$*N* given by

$$PFS_{ft}WG\left(\hat{\mathrm{H}}_{S_{11}}, \hat{\mathrm{H}}_{S_{12}}, \ldots, \hat{\mathrm{H}}_{S_{\mathrm{M}\mathrm{n}}}\right) = \begin{pmatrix} \prod_{\dot{\jmath}=1}^{\mathrm{n}} \left(\prod_{\dot{\imath}=1}^{\mathrm{M}} \left(\mathrm{T}_{\dot{\imath}\dot{\jmath}}\right)^{\mathrm{ъ}_{\dot{\imath}}}\right)^{\mathrm{Ч}_{\dot{\jmath}}}, 1 - \prod_{\dot{\jmath}=1}^{\mathrm{n}} \left(\prod_{\dot{\imath}=1}^{\mathrm{M}} \left(1 - \Psi_{\dot{\imath}\dot{\jmath}}\right)^{\mathrm{ъ}_{\dot{\imath}}}\right)^{\mathrm{Ч}_{\dot{\jmath}}}, \\ 1 - \prod_{\dot{\jmath}=1}^{\mathrm{n}} \left(\prod_{\dot{\imath}=1}^{\mathrm{M}} \left(1 - \dot{\hat{\mathrm{E}}}_{\dot{\imath}\dot{\jmath}}\right)^{\mathrm{ъ}_{\dot{\imath}}}\right)^{\mathrm{Ч}_{\dot{\jmath}}} \end{pmatrix} \quad (5)$$

Proof: Assume that $\mathrm{M} = 1$ and $\mathrm{ъ}_1 = 1$

$$PFS_{ft}WG\left(\hat{H}_{S_{11}}, \hat{H}_{S_{12}}, \ldots, \hat{H}_{S_{m\mathfrak{n}}}\right) = \otimes_{j=1}^{\mathfrak{n}} \left(\hat{H}_{S_{ij}}\right)^{\mathfrak{q}_j}$$

$$= \left(\prod_{j=1}^{\mathfrak{n}} \left(\mathfrak{T}_{1j}\right)^{\mathfrak{q}_j}, 1 - \prod_{j=1}^{\mathfrak{n}} \left(1 - \Psi_{1j}\right)^{\mathfrak{q}_j}, 1 - \prod_{j=1}^{\mathfrak{n}} \left(1 - \hat{\mathfrak{E}}_{1j}\right)^{\mathfrak{q}_j}\right)$$

$$= \left(\begin{array}{c} \prod_{j=1}^{\mathfrak{n}} \left(\prod_{i=1}^{1} \left(\mathfrak{T}_{ij}\right)^{\mathfrak{v}_i}\right)^{\mathfrak{q}_j}, 1 - \prod_{j=1}^{\mathfrak{n}} \left(\prod_{i=1}^{1} \left(1 - \Psi_{ij}\right)^{\mathfrak{v}_i}\right)^{\mathfrak{q}_j}, \\ 1 - \prod_{j=1}^{\mathfrak{n}} \left(\prod_{i=1}^{1} \left(1 - \hat{\mathfrak{E}}_{ij}\right)^{\mathfrak{v}_i}\right)^{\mathfrak{q}_j} \end{array}\right)$$

For $\mathfrak{n} = 1$, we have $\mathfrak{q}_1 = 1$.

By using the definition (3)

$$PFS_{ft}WG\left(\hat{H}_{S_{11}}, \hat{H}_{S_{21}}, \ldots, \hat{H}_{S_{\mathfrak{m}1}}\right) = \otimes_{i=1}^{\mathfrak{m}} \left(\hat{H}_{S_{i1}}\right)^{\mathfrak{v}_i}$$

$$= \left(\prod_{i=1}^{\mathfrak{m}} \left(\mathfrak{T}_{i1}\right)^{\mathfrak{v}_i}, 1 - \prod_{i=1}^{\mathfrak{m}} \left(1 - \Psi_{i1}\right)^{\mathfrak{v}_i}, 1 - \prod_{i=1}^{\mathfrak{m}} \left(1 - \hat{\mathfrak{E}}_{i1}\right)^{\mathfrak{v}_i}\right)$$

$$= \left(\begin{array}{c} \prod_{j=1}^{1} \left(\prod_{i=1}^{\mathfrak{m}} \left(\mathfrak{T}_{ij}\right)^{\mathfrak{v}_i}\right)^{\mathfrak{q}_j}, 1 - \prod_{j=1}^{1} \left(\prod_{i=1}^{\mathfrak{m}} \left(1 - \Psi_{ij}\right)^{\mathfrak{v}_i}\right)^{\mathfrak{q}_j}, \\ 1 - \prod_{j=1}^{1} \left(\prod_{i=1}^{\mathfrak{m}} \left(1 - \hat{\mathfrak{E}}_{ij}\right)^{\mathfrak{v}_i}\right)^{\mathfrak{q}_j} \end{array}\right)$$

The result is true when $\mathfrak{m} = 1$, $\mathfrak{n} = 1$.

Let the result be true when $\mathfrak{n} = \mathfrak{c}_1 + 1$, $\mathfrak{m} = \mathfrak{c}_2$ and $\mathfrak{n} = \mathfrak{c}_1$, $\mathfrak{m} = \mathfrak{c}_2 + 1$.

$$\otimes_{j=1}^{\mathfrak{c}_1+1} \left(\otimes_{i=1}^{\mathfrak{c}_2} \hat{H}_{S_{ij}}^{\mathfrak{v}_i}\right)^{\mathfrak{q}_j}$$

$$= \left(\begin{array}{c} \prod_{j=1}^{\mathfrak{c}_1+1} \left(\prod_{i=1}^{\mathfrak{c}_2} \left(\mathfrak{T}_{ij}\right)^{\mathfrak{v}_i}\right)^{\mathfrak{q}_j}, 1 - \prod_{j=1}^{\mathfrak{c}_1+1} \left(\prod_{i=1}^{\mathfrak{c}_2} \left(1 - \Psi_{ij}\right)^{\mathfrak{v}_i}\right)^{\mathfrak{q}_j}, \\ 1 - \prod_{j=1}^{\mathfrak{c}_1+1} \left(\prod_{i=1}^{\mathfrak{c}_2} \left(1 - \hat{\mathfrak{E}}_{ij}\right)^{\mathfrak{v}_i}\right)^{\mathfrak{q}_j} \end{array}\right)$$

And

$$\otimes_{j=1}^{\mathfrak{c}_1} \left(\otimes_{i=1}^{\mathfrak{c}_2+1} \hat{H}_{S_{ij}}^{\mathfrak{v}_i}\right)^{\mathfrak{q}_j}$$

$$= \left(\begin{array}{c} \prod_{j=1}^{\mathfrak{c}_1} \left(\prod_{i=1}^{\mathfrak{c}_2+1} \left(\mathfrak{T}_{ij}\right)^{\mathfrak{v}_i}\right)^{\mathfrak{q}_j}, 1 - \prod_{j=1}^{\mathfrak{c}_1} \left(\prod_{i=1}^{\mathfrak{c}_2+1} \left(1 - \Psi_{ij}\right)^{\mathfrak{v}_i}\right)^{\mathfrak{q}_j}, \\ 1 - \prod_{j=1}^{\mathfrak{c}_1} \left(\prod_{i=1}^{\mathfrak{c}_2+1} \left(1 - \hat{\mathfrak{E}}_{ij}\right)^{\mathfrak{v}_i}\right)^{\mathfrak{q}_j} \end{array}\right).$$

Now for $\mathfrak{n} = \mathfrak{c}_1 + 1$, $\mathfrak{m} = \mathfrak{c}_2 + 1$

$$\otimes_{j=1}^{\mathfrak{c}_1+1} \left(\otimes_{i=1}^{\mathfrak{c}_2+1} \hat{H}_{S_{ij}}^{\mathfrak{v}_i}\right)^{\mathfrak{q}_j} = \otimes_{j=1}^{\mathfrak{c}_1+1} \left(\otimes_{i=1}^{\mathfrak{c}_2} \hat{H}_{S_{ij}}^{\mathfrak{v}_i} \otimes \left(\hat{H}_{S_{(\mathfrak{c}_2+1)j}}\right)^{\mathfrak{v}_{\mathfrak{c}_2+1}}\right)^{\mathfrak{q}_j}$$

$$= \otimes_{j=1}^{\mathfrak{c}_1+1} \left(\otimes_{i=1}^{\mathfrak{c}_2} \hat{H}_{S_{ij}}^{\mathfrak{v}_i}\right)^{\mathfrak{q}_j} \left(\otimes_{j=1}^{\mathfrak{c}_1+1} \left(\hat{H}_{S_{(\mathfrak{c}_2+1)j}}\right)^{\mathfrak{v}_{(\mathfrak{c}_2+1)}}\right)^{\mathfrak{q}_j}$$

$$= \left(\begin{array}{c} \prod_{j=1}^{\mathfrak{c}_1+1} \left(\prod_{i=1}^{\mathfrak{c}_2} \left(\mathfrak{T}_{ij}\right)^{\mathfrak{v}_i}\right)^{\mathfrak{q}_j} \otimes \prod_{j=1}^{\mathfrak{c}_1+1} \left(\left(\mathfrak{T}_{(\mathfrak{c}_2+1)j}\right)^{\mathfrak{v}_{(\mathfrak{c}_2+1)}}\right)^{\mathfrak{q}_j}, \\ 1 - \prod_{j=1}^{\mathfrak{c}_1+1} \left(\prod_{i=1}^{\mathfrak{c}_2} \left(1 - \Psi_{ij}\right)^{\mathfrak{v}_i}\right)^{\mathfrak{q}_j} \otimes 1 - \prod_{j=1}^{\mathfrak{c}_1+1} \left(\left(1 - \Psi_{(\mathfrak{c}_2+1)j}\right)^{\mathfrak{v}_{(\mathfrak{c}_2+1)}}\right)^{\mathfrak{q}_j}, \\ 1 - \prod_{j=1}^{\mathfrak{c}_1+1} \left(\prod_{i=1}^{\mathfrak{c}_2} \left(1 - \hat{\mathfrak{E}}_{ij}\right)^{\mathfrak{v}_i}\right)^{\mathfrak{q}_j} \otimes 1 - \prod_{j=1}^{\mathfrak{c}_1+1} \left(\left(1 - \hat{\mathfrak{E}}_{(\mathfrak{c}_2+1)j}\right)^{\mathfrak{v}_{(\mathfrak{c}_2+1)}}\right)^{\mathfrak{q}_j} \end{array}\right).$$

$$= \left(\begin{array}{c} \prod_{j=1}^{\mathfrak{c}_1+1} \left(\prod_{i=1}^{\mathfrak{c}_2+1} \left(\mathfrak{T}_{ij}\right)^{\mathfrak{v}_i}\right)^{\mathfrak{q}_j}, 1 - \prod_{j=1}^{\mathfrak{c}_1+1} \left(\prod_{i=1}^{\mathfrak{c}_2+1} \left(1 - \Psi_{ij}\right)^{\mathfrak{v}_i}\right)^{\mathfrak{q}_j}, \\ 1 - \prod_{j=1}^{\mathfrak{c}_1+1} \left(\prod_{i=1}^{\mathfrak{c}_2+1} \left(1 - \hat{\mathfrak{E}}_{ij}\right)^{\mathfrak{v}_i}\right)^{\mathfrak{q}_j} \end{array}\right).$$

Hence results are valid for $\mathfrak{n} = \mathfrak{c}_1 + 1$ and $\mathfrak{m} = \mathfrak{c}_2 + 1$. So the statement is valid for all $\mathfrak{n}, \mathfrak{m} \geq 1$.

Example 2: To illustrate how beautiful a house is, let $\hat{H} = \{f_1, f_2, f_3, f_4\}$ denote the set of experts and $S = \{s_1, s_2, s_3\}$ denote the set of parameters. Let the data of the decision analyst be described in the shape of $PFS_{ft}Ns$ (P,S)= $(\mathfrak{T}_{ij}, \Psi_{ij}, \hat{\mathfrak{E}}_{ij})$ against each parameter

$$(P,S) = \begin{bmatrix} (0.360, 0.340, 0.100) & (0.100, 0.660, 0.200) & (0.030, 0.880, 0.050) \\ (0.900, 0.070, 0.030) & (0.700, 0.100, 0.090) & (0.400, 0.330, 0.190) \\ (0.800, 0.070, 0.040) & (0.060, 0.810, 0.120) & (0.050, 0.830, 0.090) \\ (0.070, 0.820, 0.050) & (0.650, 0.250, 0.070) & (0.720, 0.140, 0.090) \end{bmatrix}$$

Let $\mathfrak{q} = (0.340, 0.410, 0.250)$ and $\mathfrak{v} = (0.300, 0.290, 0.220, 0.190)$ denote the WVs of parameters and experts respectively. By equation (5), we get

$$PFS_{ft}WG\left(\hat{H}_{S_{11}}, \hat{H}_{S_{12}}, \ldots, \hat{H}_{S_{43}}\right) = (0.2126, 0.2261, 0.3057).$$

In our further discussion in the application section, we will execute the formula of $PFS_{ft}WG$ AO in a similar fashion.

Now define the properties for the notion of $PFS_{ft}WG$ AO.

Theorem 4: Assume that $\hat{H}_{S_{ij}} = (\mathfrak{T}_{ij}, \Psi_{ij}, \hat{\mathfrak{E}}_{ij})$ be the family of $PFS_{ft}Ns$; $i = 1, 2, \ldots, \mathfrak{m}$, $j = 1, 2, \ldots, \mathfrak{n}$. Then $PFS_{ft}WG$ AO satisfies properties given by

1. (Idempotency): Assume that $\hat{H}_{S_{ij}} = (\mathfrak{T}_{ij}, \Psi_{ij}, \hat{\mathfrak{E}}_{ij})$ be the family of $PFS_{ft}Ns$; $i = 1, 2, \ldots, \mathfrak{m}$, $j = 1, 2, \ldots, \mathfrak{n}$ and $\hat{H}_S = (\mathfrak{T}, \Psi, \hat{\mathfrak{E}})$ then we get

$$PFS_{ft}WG\left(\hat{H}_{S_{11}}, \hat{H}_{S_{12}}, \ldots, \hat{H}_{S_{43}}\right) = \hat{H}_S$$

2. (Boundedness): Let **2)(Boundedness):** Let

$$\hat{H}^-_{S_{ij}} = \left(\min_j \min_i \left(\mathfrak{T}_{ij}\right), \max_j \max_i \left(\Psi_{ij}\right), \max_j \max_i \left(\hat{\mathfrak{E}}_{ij}\right)\right)$$

and

$$\hat{H}^+_{S_{ij}} = \left(\max_j \max_i \left(\mathfrak{T}_{ij}\right), \min_j \min_i \left(\Psi_{ij}\right), \min_j \min_i \left(\hat{\mathfrak{E}}_{ij}\right)\right),$$

then

$$\hat{H}^-_{S_{ij}} \leq PFS_{ft}WG\left(\hat{H}_{S_{11}}, \hat{H}_{S_{12}}, \ldots, \hat{H}_{S_{m\mathfrak{n}}}\right) \leq \hat{H}^+_{S_{ij}}$$

3. (Shift-invariance): Let $\hat{H}_S = (\mathfrak{T}, \Psi, \hat{\mathfrak{E}})$ be another $PFS_{ft}N$, then

$$PFS_{ft}WG\left(\hat{H}_{S_{11}} \oplus \hat{H}_S, \hat{H}_{S_{12}} \oplus \hat{H}_S, \ldots, \hat{H}_{S_{m\mathfrak{n}}} \oplus \hat{H}_S\right)$$
$$= PFS_{ft}WG\left(\hat{H}_{S_{11}}, \hat{H}_{S_{12}}, \ldots, \hat{H}_{S_{m\mathfrak{n}}}\right) \oplus \hat{H}_S$$

4. (Homogeneity): For any real number $\mathfrak{G} > 0$, we have

$$PFS_{ft}WG\left(\mathfrak{G}\hat{H}_{S_{11}}, \mathfrak{G}\hat{H}_{S_{12}}, \ldots, \mathfrak{G}\hat{H}_{S_{m\mathfrak{n}}}\right)$$
$$= \mathfrak{G}PFS_{ft}WG\left(\hat{H}_{S_{11}}, \hat{H}_{S_{12}}, \ldots, \hat{H}_{S_{m\mathfrak{n}}}\right)$$

Definition 9: Assume that $\hat{H}_{S_{ij}} = (\mathfrak{T}_{ij}, \Psi_{ij}, \hat{\mathfrak{E}}_{ij})$ be the family of $PFS_{ft}Ns$; $i = 1, 2, \ldots, \mathfrak{m}$, $j = 1, 2, \ldots, \mathfrak{n}$. Also let $\mathfrak{q}_j$, $\mathfrak{v}_i$ represent WVs for parameters s_j and experts e_i where $\mathfrak{q}_j > 0$, $\mathfrak{v}_i > 0$ and $\sum_{j=1}^{\mathfrak{n}} \mathfrak{q}_j = 1, \sum_{i=1}^{\mathfrak{m}} \mathfrak{v}_i = 1$. $PFS_{ft}OWG: \ddot{\Theta}^{\mathfrak{m}} \to \ddot{\Theta}$ AO is given as

$$PFS_{ft}OWG\left(\hat{H}_{S_{11}}, \hat{H}_{S_{12}}, \ldots, \hat{H}_{S_{Mn}}\right) = \otimes_{j=1}^{n}\left(\otimes_{i=1}^{M}\left(\hat{H}_{S_{\alpha(i)\alpha(j)}}\right)^{v_i}\right)^{q_j}$$

$$= \begin{pmatrix} \prod_{j=1}^{n}\left(\prod_{i=1}^{M}\left(T_{ij}\right)^{v_i}\right)^{q_j}, 1-\prod_{j=1}^{n}\left(\prod_{i=1}^{M}\left(1-\Psi_{ij}\right)^{v_i}\right)^{q_j}, \\ 1-\prod_{j=1}^{n}\left(\prod_{i=1}^{M}\left(1-\hat{E}_{ij}\right)^{v_i}\right)^{q_j} \end{pmatrix}$$

Noticed that $\alpha(i), \alpha(j) \leq \alpha(i-1), \alpha(j-1)$.

Algorithm

In this section of the paper, we will talk about an algorithm for the suggested employment and present an example to illustrate how well the given operators function.

Assume that the list of "t" alternatives that need to be considered is given by $\aleph = \{\aleph_1, \aleph_2, \ldots, \aleph_t\}$. Assume there exist, M experts, $e_1, e_2, \ldots, e_M$ and they will assess the provided choices against n parameters, $S = \{s_1, s_2, s_3\}$. Let $q = \{q_1, q_2, \ldots, q_n\}^T$ and $v = \{v_1, v_2, \ldots, v_M\}^T$ represents WVs for parameters s_j and experts e_i respectively with requirements that $q_j > 0$, $v_i > 0$ and $\sum_{j=1}^{n} q_j = 1$ and $\sum_{j=1}^{n} v_j = 1$. These experts share information on their preferences in the form of *PFS$_{ft}$Ns*. Consequently, the form of the collaborative decision matrix is $\mu = (\hat{H}S_{ij})_{M\times n}$. The aggregated *PFS$_{ft}$Ns* $\ddot{\Theta}_\gamma = (T_\gamma, \Psi_\gamma, \hat{E}_\gamma)$ $\aleph_\gamma$ ($\gamma = 1, 2, 3, \ldots, t$) are derived by utilizing the *PFS$_{ft}$WA* and *PFS$_{ft}$WG* AO. Finally, the alternatives are ranked using the SF formula used for *PFS$_{ft}$Ns*. The step-by-step explanation is provided below

Step 1: Compile the information related to every alternative within the various parameters and place them in the shape of *PFS$_{ft}$* matrix, $\mu = (T_{ij}, \Psi_{ij}, \hat{E}_{ij})_{M\times n}$

$$\mu_{M\times n} = \begin{bmatrix} (T_{ij}, \Psi_{ij}, \hat{E}_{ij}) & (T_{ij}, \Psi_{ij}, \hat{E}_{ij}) & \ldots & (T_{ij}, \Psi_{ij}, \hat{E}_{ij}) \\ (T_{ij}, \Psi_{ij}, \hat{E}_{ij}) & (T_{ij}, \Psi_{ij}, \hat{E}_{ij}) & \ldots & (T_{ij}, \Psi_{ij}, \hat{E}_{ij}) \\ \vdots & \vdots & \ddots & \vdots \\ (T_{ij}, \Psi_{ij}, \hat{E}_{ij}) & (T_{ij}, \Psi_{ij}, \hat{E}_{ij}) & \ldots & (T_{ij}, \Psi_{ij}, \hat{E}_{ij}) \end{bmatrix}$$

Step 2: Utilize the formula beneath to standardize the decision matrix for the gathered data.

$$N_{ij} = \begin{cases} \left(\hat{H}_{S_{ij}}\right)^c; \text{ for cost} - \text{type parameters} \\ \hat{H}_{S_{ij}}; \text{ for benefit} - \text{type parameters} \end{cases}$$

Where $(\hat{H}_{S_{ij}})^c = (\hat{E}_{ij}, \Psi_{ij}, T_{ij})$ is the complement of $\hat{H}_{S_{ij}} = (T_{ij}, \Psi_{ij}, \hat{E}_{ij})$.

Step 3: Utilize *PFS$_{ft}$WA* and *PFS$_{ft}$WG* operators to aggregate *PFS$_{ft}$Ns* for $\aleph_\gamma$ ($\gamma = 1, 2, 3, \ldots, t$) into a matrix of collaborative decisions $\ddot{\Theta}_\gamma = (T_\gamma, \Psi_\gamma, \hat{E}_\gamma)$.

Step 4: Utilizing definition (4), determine the score of $\ddot{\Theta}_\gamma$ for $\aleph_\gamma$ ($\gamma = 1, 2, 3, \ldots, t$).

Step 5: Select the best outcome by ranking the options.

Explanatory example

The field of education is being quickly revolutionized by artificial intelligence (AI). There are certain benefits to AI despite the frequently cited obstacles. It can be used, for instance, to support teachers as they create lessons and tests that accommodate the requirements of all the students in their classrooms. The following four techniques will help teachers use AI to generate fresh concepts and meet the various learning demands of their pupils. Assume that these strategies are given by

$\eth_1$ = Offer various concepts-teaching strategies.

$\eth_2$ = Discussing difficult and abstract skills

$\eth_3$ = Thinking about different and true evaluations

$\eth_4$ = Creating various formats of representations

The WVs for these alternatives are given by $v = \{0.26, 0.33, 0.23, 0.18\}^T$. Assume that there are four experts and determine which is best by considering the following four factors such as great learning environment, clear communication, critical thinking and great learning environment. The WVs of these parameters are $q = \{0.22, 0.28, 0.19, 0.31\}^T$. The utilization of the step-wise algorithm is given by

Utilization of PFS$_{ft}$WA AO

Step 1: Experts submit their evaluations in terms of *PFS$_{ft}$Ns* which are provided in Tables 3-6.

Step 2: The decision matrix does not need to be standardized because all of the parameters are of the same kind.

Step 3: The definition (6) is used to combine the various expert assessments for each alternative. We get

$$\ddot{\Theta}_1 = (0.3418, 0.1999, 0.2526), \ddot{\Theta}_2 = (0.3068, 0.2341, 0.2500)$$

$$\ddot{\Theta}_3 = (0.2697, 0.1817, 0.3069), \ddot{\Theta}_4 = (0.2868, 0.21650, 0.25610).$$

Step 4: Use definition (4) to get score results

$$Scr.(\ddot{\Theta}_1) = (0.79430), Scr.(\ddot{\Theta}_2) = (0.79090)$$

$$Scr.(\ddot{\Theta}_3) = (0.75830), Scr.(\ddot{\Theta}_4) = (0.75940).$$

Thus, their ranking result is *Scr.* $(\ddot{\Theta}_1) > Scr.$ $(\ddot{\Theta}_2) > Scr.$ $(\ddot{\Theta}_4) > Scr.$ $(\ddot{\Theta}_3)$.

Table 3. *PFS$_{ft}$* matrix for $\aleph_1$

	s_1	s_2	s_3	s_4
e_1	(.2, .3, .1)	(.6, .1, .2)	(.5, .1, .3)	(.2, .3, .1)
e_2	(.4, .2, .3)	(.5, .3, .2)	(.4, .3, .2)	(.2, .3, .4)
e_3	(.2, .5, .1)	(.5, .1, .2)	(.3, .1, .4)	(.1, .1, .6)
e_4	(.3, .2, .4)	(.1, .2, .6)	(.1, .6, .1)	(.4, .4, .4)

Table 4. PFS_{ft} matrix for ɮ_2

	s_1	s_2	s_3	s_4
e_1	(.5, .3, .2)	(.2, .3, .4)	(.2, .5, .1)	(.1, .6, .1)
e_2	(.1, .2, .6)	(.4, .4, .4)	(.3, .2, .4)	(.3, .1, .4)
e_3	(.6, .1, .2)	(.2, .3, .1)	(.4, .2, .3)	(.3, .3, .2)
e_4	(.5, .1, .2)	(.1, .1, .6)	(.2, .3, .1)	(.4, .3, .2)

Table 5. PFS_{ft} matrix for ɮ_3

	s_1	s_2	s_3	s_4
e_1	(.2, .1, .2)	(.1, .1, .6)	(.3, .3, .2)	(.1, .1, .6)
e_2	(.1, .3, .4)	(.6, .1, .1)	(.3, .2, .3)	(.3, .2, .4)
e_3	(.4, .1, .3)	(.3, .4, .2)	(.4, .3, .1)	(.2, .1, .5)
e_4	(.2, .2, .5)	(.2, .4, .3)	(.1, .2, .3)	(.1, .3, .5)

Table 6. PFS_{ft} matrix for ɮ_4

	s_1	s_2	s_3	s_4
e_1	(.7, .1, .1)	(.1, .1, .1)	(.3, .1, .2)	(.4, .3, .3)
e_2	(.2, .5, .1)	(.1, .3, .4)	(.5, .2, .1)	(.3, .4, .3)
e_3	(.3, .5, .2)	(.1, .2, .6)	(.1, .1, .7)	(.2, .2, .5)
e_4	(.2, .1, .6)	(.3, .2, .4)	(.3, .3, .4)	(.2, .5, .2)

Step 5: Hence "Offer various concepts-teaching strategies" is an important AI educational strategy.

Utilization of PFS_{ft}WG AO

Step 1: Same as above

Step 2: The decision matrix does not need to be standardized because all of the parameters are of the same kind.

Step 3: Here we use definition (8) to get aggregated results given by

$$\ddot{\theta}_1 = (0.2773, 0.2620, 0.3072), \ddot{\theta}_2 = (0.2522, 0.2936, 0.3177)$$

$$\ddot{\theta}_3 = (0.2125, 0.2099, 0.3740), \ddot{\theta}_4 = (0.2236, 0.27350, 0.34010).$$

Step 4: The score values are

$$Scr.(\ddot{\theta}_1) = (0.84650), Scr.(\ddot{\theta}_2) = (0.86350)$$

$$Scr.(\ddot{\theta}_3) = (0.79640), Scr.(\ddot{\theta}_4) = (0.83720).$$

Thus, their ranking result is $Scr.(\ddot{\theta}_2) > Scr.(\ddot{\theta}_1) > Scr.(\ddot{\theta}_4) > Scr.(\ddot{\theta}_3)$.

Step 5: Hence "Offer various concepts-teaching strategies" is an important AI educational strategy.

The WASPAS Approach

Using the concept of picture fuzzy soft numbers, we will describe an MCDM strategy for WASPAS approaches in this section of the study. WASPAS technique can combine weighted product and weighted sum model that keep this notion more accurate and valuable for MCDM approaches. The main algorithm for the execution of the WASPAS approach is given by

Algorithm

An algorithm for the WASPAS approach in the context of $PFS_{ft}Ns$ is described here for successfully addressing the MCDM problems.

Let signify the collection of "ʈ" alternatives by $\text{ɮ} = \{\text{ɮ}_1, \text{ɮ}_2, \ldots, \text{ɮ}_\text{ʈ}\}$. Assume there exist, ʍ experts, $e_1, e_2, \ldots, e_\text{ʍ}$ who will assess the provided alternatives against "ɲ" parameters $S = \{s_1, s_2, s_\text{ɲ}\}$. LetLet $\text{ɥ} = \{\text{ɥ}_1, \text{ɥ}_2, \ldots, \text{ɥ}_\text{ɲ}\}^T$ and $\text{ʊ} = \{\text{ʊ}_1, \text{ʊ}_2, \ldots, \text{ʊ}_\text{ʍ}\}^T$ represent the WVs for parameters s_j and experts e_i respectively and $\text{ɥ}_\text{j} > 0$, $\text{ʊ}_\text{i} > 0$ and $\sum_{\text{j}=1}^{\text{ɲ}} \text{ɥ}_\text{j} = 1$ and $\sum_{\text{j}=1}^{\text{ɲ}} \text{ʊ}_\text{j} = 1$.

The stepwise algorithm is now presented by

Step 1: Let the experts provide their opinions for each option that corresponds to each parameter in the manner of the PFS_{ft} matrix provided by

$$\mathfrak{m}_{m\times n}=\begin{bmatrix} (\mathrm{T}_{11},\Psi_{11},\hat{\mathrm{E}}_{11}) & (\mathrm{T}_{12},\Psi_{12},\hat{\mathrm{E}}_{12}) & \dots & (\mathrm{T}_{1n},\Psi_{1n},\hat{\mathrm{E}}_{1n}) \\ (\mathrm{T}_{21},\Psi_{21},\hat{\mathrm{E}}_{21}) & (\mathrm{T}_{22},\Psi_{22},\hat{\mathrm{E}}_{22}) & \dots & (\mathrm{T}_{2n},\Psi_{2n},\hat{\mathrm{E}}_{2n}) \\ \vdots & \vdots & \ddots & \vdots \\ (\mathrm{T}_{m1},\Psi_{m1},\hat{\mathrm{E}}_{m1}) & (\mathrm{T}_{m2},\Psi_{m2},\hat{\mathrm{E}}_{m2}) & \dots & (\mathrm{T}_{mn},\Psi_{mn},\hat{\mathrm{E}}_{mn}) \end{bmatrix}$$

Step 2: Afterward, normalize the provided decision-making matrix in Step 1 utilizing the formula as

$$\bar{\mathrm{G}}_{ij}=\begin{cases} \dfrac{\bar{\mathrm{G}}_{ij}}{\max\limits_{i}\bar{\mathrm{G}}_{ij}} & \text{for benefit}-\text{type criteria} \\ \dfrac{\min\limits_{i}\bar{\mathrm{G}}_{ij}}{\bar{\mathrm{G}}_{ij}} & \text{for cost}-\text{type criteria} \end{cases}$$

Where

$$\max_{i}\bar{\mathrm{G}}_{ij}=\left\{\max_{i}\mathrm{T}_{ij},\min_{i}\Psi_{ij},\min_{i}\hat{\mathrm{E}}_{ij}\right\}$$

And

$$\frac{\bar{\mathrm{G}}_{ij}}{\max\limits_{i}\bar{\mathrm{G}}_{ij}}=\left\{\min\left(\mathrm{T}_{ij},\max_{i}\mathrm{T}_{ij}\right),\max\left(\Psi_{ij},\min_{i}\Psi_{ij}\right),\max\left(\hat{\mathrm{E}}_{ij},\min_{i}\hat{\mathrm{E}}_{ij}\right)\right\}$$

Also,

$$\min_{i}\bar{\mathrm{G}}_{ij}=\left\{\min_{i}\mathrm{T}_{ij},\max_{i}\Psi_{ij},\max_{i}\hat{\mathrm{E}}_{ij}\right\}$$

And

$$\frac{\min\limits_{i}\bar{\mathrm{G}}_{ij}}{\bar{\mathrm{G}}_{ij}}=\left\{\min\left(\min_{i}\mathrm{T}_{ij},\mathrm{T}_{ij}\right),\max\left(\max_{i}\Psi_{ij},\Psi_{ij}\right),\max\left(\max_{i}\hat{\mathrm{E}}_{ij},\hat{\mathrm{E}}_{ij}\right)\right\}.$$

So we get

$$\mathrm{Z}=\begin{bmatrix} \bar{\mathrm{G}}_{11} & \bar{\mathrm{G}}_{12} & \dots & \bar{\mathrm{G}}_{1n} \\ \bar{\mathrm{G}}_{21} & \bar{\mathrm{G}}_{22} & \dots & \bar{\mathrm{G}}_{2n} \\ \vdots & \vdots & \ddots & \vdots \\ \bar{\mathrm{G}}_{m1} & \bar{\mathrm{G}}_{m2} & \dots & \bar{\mathrm{G}}_{mn} \end{bmatrix}$$

Step 3: Now relative importance of the alternative is calculated by

$$\mathfrak{G}_{i}^{WS}=\left(1-\prod_{j=1}^{n}\left(\prod_{i=1}^{m}\left(1-\mathrm{T}_{ij}\right)^{\mathfrak{v}_i}\right)^{\mathfrak{u}_j},\prod_{j=1}^{n}\left(\prod_{i=1}^{m}\left(\Psi_{ij}\right)^{\mathfrak{v}_i}\right)^{\mathfrak{u}_j},\prod_{j=1}^{n}\left(\prod_{i=1}^{m}\left(\hat{\mathrm{E}}_{ij}\right)^{\mathfrak{v}_i}\right)^{\mathfrak{u}_j}\right)$$

Step 4: Similarly, we have to find out

$$\mathfrak{G}_{i}^{WP}=\left(\prod_{j=1}^{n}\left(\prod_{i=1}^{m}\left(\mathrm{T}_{ij}\right)^{\mathfrak{v}_i}\right)^{\mathfrak{u}_j},1-\prod_{j=1}^{n}\left(\prod_{i=1}^{m}\left(1-\Psi_{ij}\right)^{\mathfrak{v}_i}\right)^{\mathfrak{u}_j},1-\prod_{j=1}^{n}\left(\prod_{i=1}^{m}\left(1-\hat{\mathrm{E}}_{ij}\right)^{\mathfrak{v}_i}\right)^{\mathfrak{u}_j}\right)$$

Step 5: Finally use WASPAS techniques for ordering alternatives given by

$$\mathfrak{G}_{i}=\frac{\mathfrak{G}_{i}^{WS}+\mathfrak{G}_{i}^{WP}}{2}$$

Step 6: Utilize definition (4) to get score values to access the best alternative.

We take a look at an illustrative example and attempt to evaluate the data above to validate the aforementioned theory.

Illustrative example

AI trading firms employ a variety of technologies within the AI toolbox to analyze the financial market, use data to compute price changes, pinpoint the causes of price variations, execute sales and trades, and keep an eye on the always-shifting market. However, any new technology that can enhance performance and reduce some of the effort involved in investing would certainly be embraced by investors, and artificial intelligence meets both of these requirements. While there will always be a human element to stock selection, portfolio management, and investing, artificial intelligence is likely to become more prevalent as technology advances.

There are several kinds of AI trading

Quantitative trading, algorithmic trading, high-frequency trading, and automated trading are some of the different types of AI trading.

1) Quantitative trading

The technique of spotting and making money from trading opportunities through the use of computer algorithms and programs based on simple or complex mathematical models is known as quantitative trading. To find profitable chances, quant trading frequently requires a study of historical data. Based on the generated trading earnings, small, medium, and large-sized trading firms may employ quant traders and earn a respectable income with significant incentive payouts. Quants use real-time data, which includes prices and quotes, to run their algorithms. A quant trader often carries out the following tasks (1) Create a trading plan (2) Create a workable algorithm based on a trading approach (3) Continued work on developing new tactics etc.

2) Algorithm trading

Algorithmic trading, sometimes referred to as automated trading or algo trading, is the process of executing a trade using a computer program that follows predefined rules. The transaction may theoretically generate profits faster and more frequently than a human trader could. Algorithmic trading uses a combination of financial markets and computer programming to execute trades at specific times. Alternatively, time-weighted average prices or volume-weighted average prices are used to execute algorithmic trading. There are following advantages of algorithms like

a) Best execution
b) No human error
c) Reduce transaction costs

3) High-frequency trading

High-frequency trading (HFT) is a style of trading in which several orders are processed in a small amount of

time by highly effective computer algorithms. It uses complex algorithms to assess many markets and execute orders based on market conditions. In general, traders who execute their trades faster than others tend to be more successful. HFT is a sophisticated form of algorithmic trading in which a lot of orders are filled quickly. HFT has increased market liquidity and eliminated bid-ask spreads that would have been excessively narrow in the past. This was put to the test by introducing fees for HFT, which increased bid-ask spreads. Trading securities in high volume and at high frequency enables investors to profit from even the smallest price changes. Institutions can profit significantly from bid-ask spreads thanks to it. Multiple markets and exchanges can be scanned by trading algorithms. High-frequency trading improves pricing efficiency, promotes and competitive market, and increases competition between trading venues.

4) Automated trading

By facilitating quicker strategy execution, automated trading can help you improve the efficiency of your trades. One of the main benefits of strategy automation is that if trades are done automatically when certain conditions are satisfied, it can help to reduce some of the emotions associated with trading. The majority of the time, automated trading systems need to be run on software connected to a direct access broker, and any particular rules must be developed in the platform's proprietary language. There are the following advantages of automated advantages (1) Backtesting uses past market data and trading rules to test an idea's viability. (2) Even in unstable markets, discipline is maintained since trading rules are created and transaction execution is done automatically.

Assume there is only one expert, four alternatives and four parameters given by

1) Execute the trade-in in a consistent and timely manner
2) Reduce the impact of human error
3) Monitor market condition
4) Allow the traders to set rules

Suppose the WVs for parameters are (0.230, 0.370, 0.260, 0.140). Let the expert provide his assessment in the form of PFS_{ft} matrix given in Table 7.

Step 1: The first step is about the collection of data. For this purpose assume that the expert presents his evaluation of each possibility about each parameter as a PFS_{ft} number is given in Table 7.

Step 2: For the normalization of the above given approach we will use the formula given by

$$\bar{\mathrm{G}}_{ij}=\frac{\bar{\mathrm{G}}_{ij}}{\max\limits_{i}\bar{\mathrm{G}}_{ij}}=\left\{min\left(\mathrm{T}_{ij},\max\limits_{i}\mathrm{T}_{ij}\right),\max\left(\Psi_{ij},\min\limits_{i}\Psi_{ij}\right),\max\left(\hat{\mathrm{E}}_{ij},\min\limits_{i}\hat{\mathrm{E}}_{ij}\right)\right\}$$

So Table 8 represents the normalized matrix. It can be observed that when criteria are benefit type then there is no change in data.

Step 3: Calculate the value for $\mathfrak{G}_i^{WS}$ as follows

$$\mathfrak{G}_i^{WS}=\left(\begin{array}{c}1-\prod_{j=1}^{n}\left(\prod_{i=1}^{m}\left(1-\mathrm{T}_{ij}\right)^{\tau_i}\right)^{\mu_j},\prod_{j=1}^{n}\left(\prod_{i=1}^{m}\left(\Psi_{ij}\right)^{\tau_i}\right)^{\mu_j},\\ \prod_{j=1}^{n}\left(\prod_{i=1}^{m}\left(\hat{\mathrm{E}}_{ij}\right)^{\tau_i}\right)^{\mu_j}\end{array}\right),$$

We will execute this formula based on the data of Table 8 as we have executed in example 1 and find out the result.

$$\mathfrak{G}_1^{WS}=(0.33820,0.18150,0.25470),\mathfrak{G}_2^{WS}=(0.29840,0.19860,0.29000)$$

$$\mathfrak{G}_3^{WS}=(0.28790,0.23390,0.20340),\mathfrak{G}_4^{WS}=(0.24830,0.23920,0.28770)$$

Step 4: Calculate the value for

$$\mathfrak{G}_i^{WP}=\left(\begin{array}{c}\prod_{j=1}^{n}\left(\prod_{i=1}^{m}\left(\mathrm{T}_{ij}\right)^{\tau_i}\right)^{\mu_j},1-\prod_{j=1}^{n}\left(\prod_{i=1}^{m}\left(1-\Psi_{ij}\right)^{\tau_i}\right)^{\mu_j},\\ 1-\prod_{j=1}^{n}\left(\prod_{i=1}^{m}\left(1-\hat{\mathrm{E}}_{ij}\right)^{\tau_i}\right)^{\mu_j}\end{array}\right).$$

Table 7. PFS_{ft} data

	s_1	s_2	s_3	s_4
$\mathfrak{z}_1$	(0.290, 0.260, 0.200)	(0.43, 0.15, 0.27)	(0.21, 0.16, 0.34)	(0.37, 0.21, 0.19)
$\mathfrak{z}_2$	(0.42, 0.16, 0.28)	(0.23, 0.23, 0.34)	(0.34, 0.20, 0.23)	(0.16, 0.19, 0.31)
$\mathfrak{z}_3$	(0.32, 0.23, 0.20)	(0.27, 0.27, 0.18)	(0.26, 0.23, 0.22)	(0.33, 0.17, 0.25)
$\mathfrak{z}_4$	(0.25, 0.26, 0.31)	(0.29, 0.25, 0.20)	(0.17, 0.17, 0.45)	(0.27, 0.35, 0.29)

Table 8. PFS_{ft} data

	s_1	s_2	s_3	s_4
$\mathfrak{z}_1$	(0.29, 0.26, 0.20)	(0.43, 0.15, 0.27)	(0.21, 0.16, 0.34)	(0.37, 0.21, 0.19)
$\mathfrak{z}_2$	(0.42, 0.16, 0.28)	(0.23, 0.23, 0.34)	(0.34, 0.20, 0.23)	(0.16, 0.19, 0.31)
$\mathfrak{z}_3$	(0.32, 0.23, 0.20)	(0.27, 0.27, 0.18)	(0.26, 0.23, 0.22)	(0.33, 0.17, 0.25)
$\mathfrak{z}_4$	(0.25, 0.26, 0.31)	(0.29, 0.25, 0.20)	(0.17, 0.17, 0.45)	(0.27, 0.35, 0.29)

We will execute this formula as we have done in example 2 and find out the result.

$$\mathbb{G}_1^{WP} = (0.31920, 0.18760, 0.26310), \mathbb{G}_2^{WP} = (0.27790, 0.20090, 0.29470)$$

$$\mathbb{G}_3^{WP} = (0.28590, 0.23710, 0.20520), \mathbb{G}_4^{WP} = (0.24150, 0.24760, 0.31020)$$

Step 5: Utilize the formula given below to determine the values of $\mathbb{G}_{\dot{1}}$

$\mathbb{G}_{\dot{1}} = \frac{\mathbb{G}_{\dot{1}}^{WS} + \mathbb{G}_{\dot{1}}^{WP}}{2}$, we get

$$\mathbb{G}_1 = \frac{\mathbb{G}_1^{WS} + \mathbb{G}_1^{WP}}{2}$$

$$\mathbb{G}_1 = \left\{\begin{matrix}\left(1-\left(1-\mathrm{T}_{11}^{WS}\right)^{0.5}\right), \left(\Psi_{11}^{WS}\right)^{0.5}, \\ \left(\hat{\mathrm{E}}_{11}^{WS}\right)^{0.5}\end{matrix}\right\} + \left\{\begin{matrix}\left(1-\left(1-\mathrm{T}_{11}^{WP}\right)^{0.5}\right), \left(\Psi_{11}^{WP}\right)^{0.5}, \\ \left(\hat{\mathrm{E}}_{11}^{WP}\right)^{0.5}\end{matrix}\right\}$$

$$\mathbb{G}_1 = \left\{\begin{matrix}(1-(1-0.3382)^{0.5}), (0.1815)^{0.5}, \\ (0.2547)^{0.5}\end{matrix}\right\} + \left\{\begin{matrix}(1-(1-0.3192)^{0.5}), (0.2371)^{0.5}, \\ (0.2052)^{0.5}\end{matrix}\right\}$$

$$\mathbb{G}_1 = \{(0.3287, 0.1845, 0.2589)\}$$

We clearly explain how we can find out the result of $\mathbb{G}_1$. Similarly, we can find out other values given by

$$\mathbb{G}_2 = \{(0.2883, 0.1998, 0.2923)\}$$

$$\mathbb{G}_3 = \{(0.2869, 0.2355, 0.2043)\}$$

$$\mathbb{G}_4 = \{(0.2449, 0.2434, 0.2987)\}$$

Step 6: Utilize definition (4) to get score values

$$Scr.(\mathbb{G}_1) = \mathrm{T}(\upsilon) - \Psi(\upsilon) - \hat{\mathrm{E}}(\upsilon) = -0.1150$$

$$Scr.(\mathbb{G}_2) = -0.2040,$$

$$Scr.(\mathbb{G}_3) - 0.1530$$

$$Scr.(\mathbb{G}_4) - 0.2970$$

Hence $Scr.(\mathbb{G}_1) > Scr.(\mathbb{G}_3) > Scr.(\mathbb{G}_2) > Scr.(\mathbb{G}_4)$. Hence "Quantitative trading" is the best alternative.

Hence we have executed the step-wise algorithm that shows that we can classify the AI Trading system through the defined noting of the WAPSAS technique under the development of $PFS_{ft}WA$ and $PFS_{ft}WG$ AOs.

RESULTS AND DISCUSSION

To demonstrate the validity and superiority of the established work, we will establish a comparative analysis of the delivered work with some other existing approaches in this section.

The Xu [8] technique, Xu and Yager [7] technique, Wang et al. [15] technique, and Arora [22] technique will be compared. To do this, we will make use of the data in Table 7.

1) We can observe that in the case of the Xu method [8] since it is based on IFS and IFS uses the condition that *sum* (*MG, NMG*) ∈ [0,1]. First of all, we can see that this introduced structure is limited because decision analysis cannot take advanced data. If the decision maker needs to utilize the AG in his structure then the idea of Xu [8] fails to handle such kind of information. It means that at the frost step the chance of data loss increases. Moreover, we can see that $PFS_{ft}S$ can discuss the AG and one more characteristic to discuss the parameterization tool as well. In the case of Xu [8], this structure cannot discuss the parameterization tool. Hence, the developed approach is more advanced.
2) Xu and Yager [7] proposed some geometric aggregation operators based on IFS but still this structure cannot deal with Ag and parameterization tools. When the data is available in the form of packets the only developed approach can handle such kind of information.
3) However, the nature of Arora's [22] method is more advanced than Xu and Yager's [7] technique because it can consider the parameterization tool. However, this approach is also limited in terms of condition its structure because the decision-makers provide their assessment as (0.6, 0.5) then we can observe that 0.6 + 0.5 ∉ [0,1] and the main condition for $IFS_{ft}S$ is violated. In

Table 9. Overall ranking results

Different Approaches	Score results	Ranking
Xu [8] approach	×××××××××××××	×××××××××××××
Xu and Yager [7] approach	×××××××××××××	×××××××××××××
Arora [22] approach	×××××××××××××	×××××××××××××
Wang et al. [15] approach	$Scr.(\ddot{\Theta}_1) = (0.76120)$, $Scr.(\ddot{\Theta}_2) = (0.7221)$	$\ddot{\Theta}_1 > \ddot{\Theta}_2 > \ddot{\Theta}_4 > \ddot{\Theta}_3$
	$Scr.(\ddot{\Theta}_3) = (0.7010)$, $Scr.(\ddot{\Theta}_4) = (0.7025)$	
PFS_{ft} *WA* (*delivered work*)	$Scr.(\ddot{\Theta}_1) = (0.8128)$, $Scr.(\ddot{\Theta}_2) = (0.7831)$	$\ddot{\Theta}_1 > \ddot{\Theta}_2 > \ddot{\Theta}_4 > \ddot{\Theta}_3$
	$Scr.(\ddot{\Theta}_3) = (0.7538)$, $Scr.(\ddot{\Theta}_4) = (0.7818)$	
PFS_{ft} *WG* (*delevired work*)	$Scr.(\ddot{\Theta}_1) = (0.8133)$, $Scr.(\ddot{\Theta}_2) = (0.7878)$	$\ddot{\Theta}_1 > \ddot{\Theta}_2 > \ddot{\Theta}_4 > \ddot{\Theta}_3$
	$Scr.(\ddot{\Theta}_3) = (0.7667)$, $Scr.(\ddot{\Theta}_4) = (0.7854)$	

Table 10. Characteristic analysis of the developed approach with existing notions

Methods	Utilization of fuzzy information	Utilization of parameterization tool
Xu [8] approach	✓	′
Xu and Yager [7] approach	✓	′
Arora [22] approach	✓	✓
Wang et al. [15] approach	✓	′
PFS_{fi} *WA* (*delivered work*)	✓	✓
PFS_{fi} *WG* (*delevired work*)	✓	✓

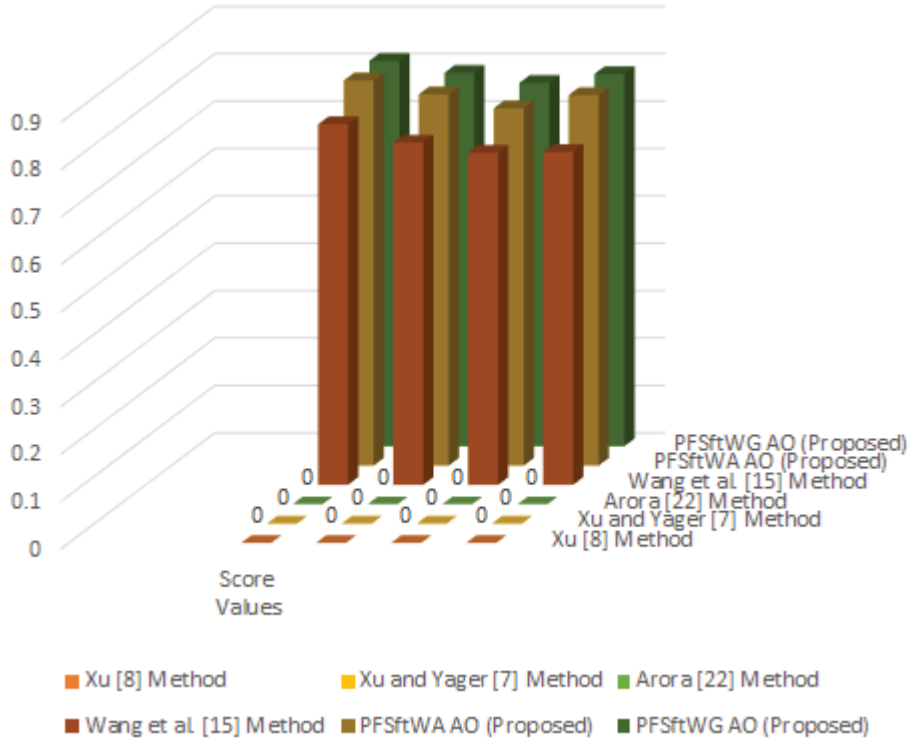


Figure 4. Graphical representation of score values given in Table 9.

many decision-making situations, we need to utilize such kind of structure which is free from all these kinds of complexities. The developed approach can cover all such kinds of issues in terms of the utilization of AG in its structure.

4) The proposed work in conjunction with the Wang et al. [15] method can address this problem more successfully. Additionally, the parameterization tool cannot be taken into account by the Xu technique [8], Xu and Yager method [7], or Wang et al. [15] while the introduced work is more general than the established work, which has a parameterized structure.
5) Additionally, the established works give decision-makers in real-world situations greater freedom. Consequently, established work is better. Table 9 also provides the score values and ranking outcomes.

The resulting theory is therefore very strong and trustworthy for handling ambiguous and unreliable data in practical circumstances.

Moreover, the characteristic analysis of the proposed work along with existing theory is given in Table 10.

Also, the graphical representation of the data given in Table 9 is given in Figure 4.

CONCLUSION

The aggregation operators are a beneficial tool to convert the overall information into a single value and accurate decisions can be made in decision-making problems.

Weighted average and geometric aggregation operators are the fundamental aggregation operators that are very easy to operate and the WASPAS approach can combine both of these notions into one structure which is the specialty of the WASPAS technique. Moreover, the notion of a picture fuzzy soft set can generalize the intuitionistic fuzzy soft set and it can discuss the membership grade, non-membership grade and abstinence grade in one structure. Hence keeping in mind all of these benefits, in this article, we have developed the idea of weighted averaging, ordered weighted averaging, weighted geometric, and ordered weighted averaging aggregation operators in this framework. Furthermore, we have provided the features of these developed concepts. We have implemented the WASPAS algorithm for picture fuzzy soft data and provided this technique for artificial intelligence trading categorization. Furthermore, we present several scenarios utilizing multiattribute decision-making to validate and illustrate the use of the previously described data and attempt to identify the optimal artificial intelligence trading system. We additionally compare the derived operators with a range of existing or already in-use techniques to raise the value of the evaluated information. The results in the discussion section show that the defined notions are beneficial in cases when decision-makers want to utilize more advanced data.

Limitations and Future Direction of the Proposed Work

The developed notions are also limited because if decision-makers provide their assessment as (0.3, 0.4, 0.5) then note that the necessary condition for $PFS_{ft}S$ that is $(0.3 + 0.4 + 0.5) \notin [0,1]$fail to hold. It means that in the future we can extend these notions to spherical fuzzy sets [42, 43] and T-spherical fuzzy sets given in [44-46]. The developed approach can be used in the future for supplier selection problems as proposed in [47, 48]. Also, some MCDM approaches can defined on defined work as given in [49]. This work can be extended to the existence of a fuzzy mild solution of the differential equation given in [50, 51].

AUTHORSHIP CONTRIBUTIONS

Authors equally contributed to this work.

DATA AVAILABILITY STATEMENT

The authors confirm that the data that supports the findings of this study are available within the article. Raw data that support the finding of this study are available from the corresponding author, upon reasonable request.

CONFLICT OF INTEREST

The author declared no potential conflicts of interest with respect to the research, authorship, and/or publication of this article.

ETHICS

There are no ethical issues with the publication of this manuscript.

STATEMENT ON THE USE OF ARTIFICIAL INTELLIGENCE

Artificial intelligence was not used in the preparation of the article.

REFERENCES

[1] Ferreira FG, Gandomi AH, Cardoso RT. Artificial intelligence applied to stock market trading: A review. IEEE Access 2021;9:30898–30917. [CrossRef]

[2] Luo S, Lin X, Zheng Z. A novel CNN-DDPG based AI-trader: Performance and roles in business operations. Transp Res Part E Logist Transp Rev 2019;131:68–79. [CrossRef]

[3] Yin S, Ai Q, Li J, Li D, Guo Q. Trading mode design for a virtual power plant based on main-side consortium blockchains. Appl Energy 2022;325:119932. [CrossRef]

[4] Azzutti A. AI trading and the limits of EU law enforcement in deterring market manipulation. Comput Law Secur Rev 2022;45:105690. [CrossRef]

[5] Zadeh LA. Fuzzy sets. Inf Control 1965;8:338–353. [CrossRef]

[6] Atanassov KT. Intuitionistic fuzzy sets. Fuzzy Sets Syst 1986;20:87–96. [CrossRef]

[7] Xu Z, Yager RR. Some geometric aggregation operators based on intuitionistic fuzzy sets. Int J Gen Syst 2006;35:417–433. [CrossRef]

[8] Xu Z. Intuitionistic fuzzy aggregation operators. IEEE Trans Fuzzy Syst 2007;15:1179–1187. [CrossRef]

[9] Yu D. Intuitionistic fuzzy geometric Heronian mean aggregation operators. Appl Soft Comput 2013;13:1235–1246. [CrossRef]

[10] Huang JY. Intuitionistic fuzzy Hamacher aggregation operators and their application to multiple attribute decision making. J Intell Fuzzy Syst 2014;27:505–513. [CrossRef]

[11] Zhou W, Xu Z. Score–hesitation trade–off and portfolio selection under intuitionistic fuzzy environment. Int J Intell Syst 2019;34:325–341. [CrossRef]

[12] Wang Y, Luo C. An intelligent quantitative trading system based on intuitionistic-GRU fuzzy neural networks. Appl Soft Comput 2021;108:107471. [CrossRef]

[13] Cuong BC. Picture fuzzy sets: First results, Part 1. Semin Neuro-Fuzzy Syst Appl 2013;4. [CrossRef]

[14] Dutta P, Ganju S. Some aspects of picture fuzzy set. Trans A Razmadze Math Inst 2018;172:164–175. [CrossRef]

[15] Wang C, Zhou X, Tu H, Tao S. Some geometric aggregation operators picture fuzzy aggregation operators and their applications to multicriteria decision-making. Arab J Sci Eng 2017;42:5275–5290. [CrossRef]
[16] Wei G. Picture fuzzy aggregation operators and their application to multiple attribute decision making. J Intell Fuzzy Syst 2017;33:713–724. [CrossRef]
[17] Garg H. Some picture fuzzy aggregation operators and their applications to multicriteria decision-making. Arab J Sci Eng 2017;42:5275–5290. [CrossRef]
[18] Molodtsov D. Soft set theory–First result. Comput Math Appl 1999;27:19–31. [CrossRef]
[19] Maji PK, Roy AR, Biswas R. Fuzzy soft sets. J Fuzzy Math 2001;9:589–602.
[20] Akram M, Adeel A, Alcantud JCR. Fuzzy N-soft sets: A novel model with applications. J Intell Fuzzy Syst 2018;35:4757–4771. [CrossRef]
[21] Maji PK, Roy AR, Biswas R. On intuitionistic fuzzy soft sets. J Fuzzy Math 2004;12:669–684.
[22] Arora R. Intuitionistic fuzzy soft aggregation operator based on Einstein norms and its applications in decision-making. In: Proc Int Conf Intell Syst Des Appl; 2018. p. 998–1008. [CrossRef]
[23] Albaity M, Mahmood T, Ali Z. Impact of machine learning and artificial intelligence in business based on intuitionistic fuzzy soft WASPAS method. Math 2023;11:1453. [CrossRef]
[24] Garg H, Arora R. Generalized Maclaurin symmetric mean aggregation operators based on Archimedean t-norm of the intuitionistic fuzzy soft set information. Artif Intell Rev 2021;54:3173–3213. [CrossRef]
[25] Garg H, Arora R. Novel scaled prioritized intuitionistic fuzzy soft interaction averaging aggregation operators and their application to multi criteria decision making. Eng Appl Artif Intell 2018;71:100–112. [CrossRef]
[26] Hayat K, Tariq Z, Lughofer E, Aslam MF. New aggregation operators on group-based generalized intuitionistic fuzzy soft sets. Soft Comput 2021;25:13353–13364. [CrossRef]
[27] Shahzadi S, Akram M. Intuitionistic fuzzy soft graphs with applications. J Appl Math Comput 2017;55:369–392. [CrossRef]
[28] Peng XD, Yang Y, Song J, Jiang Y. Pythagorean fuzzy soft set and its application. Comput Eng 2015;41:224–229.
[29] Hussain A, Ali MI, Mahmood T, Munir M. q-rung orthopair fuzzy soft average aggregation operators and their application in multicriteria decision-making. Int J Intell Syst 2020;35:571–599. [CrossRef]
[30] Yang Y, Liang C, Ji S, Liu T. Adjustable soft discernibility matrix based on picture fuzzy soft sets and its applications in decision making. J Intell Fuzzy Syst 2015;29:1711–1722. [CrossRef]
[31] Yang X, Mahmood T, Ahmmad J. Picture fuzzy soft Bonferroni mean aggregation operators and their applications. Heliyon 2023;9:e17278. [CrossRef]
[32] Mahmood T, Ahmmad J, Gwak J, Jan N. Prioritization of thermal energy techniques by employing picture fuzzy soft power average and geometric aggregation operators. Sci Rep 2023;13:1707. [CrossRef]
[33] Ahmmad J, Mahmood T. Picture fuzzy soft prioritized aggregation operators and their applications in medical diagnosis. Symmetry 2023;15:861. [CrossRef]
[34] Zavadskas EK, Turskis Z, Antucheviciene J, Zakarevicius A. Optimization of weighted aggregated sum product assessment. Elektron Elektrotech 2012;122:3–6. [CrossRef]
[35] Zavadskas EK, Turskis Z, Antucheviciene J. Selecting a contractor by using a novel method for multiple attribute analysis: Weighted aggregated sum product assessment with grey values (WASPAS-G). Stud Inform Control 2015;24:141–150. [CrossRef]
[36] Albaity M, Mahmood T, Ali Z. Impact of machine learning and artificial intelligence in business based on intuitionistic fuzzy soft WASPAS method. Math 2023;11:1453. [CrossRef]
[37] Lukić R. Evaluation of the performance trading companies in Serbia based on the FF-WASPAS and WASPAS methods. Eur J Appl Econ 2023;20:41–63. [CrossRef]
[38] Görçün ÖF, Pamucar D, Krishan Kumar R, Küçükönder H. The selection of appropriate Ro-Ro vessel in the second-hand market using the WASPAS' Bonferroni approach in type 2 neutrosophic fuzzy environment. Eng Appl Artif Intell 2023;117:105531. [CrossRef]
[39] Pamučar D, Sremac S, Stević Ž, Ćirović G, Tomić D. New multi-criteria LNN WASPAS model for evaluating the work of advisors in the transport of hazardous goods. Neural Comput Appl 2019;31:5045–5068. [CrossRef]
[40] Yontar E, Derse O. Prioritization of negative carbon strategies in the cargo industry with the SWARA/WASPAS method. J Adv Res Nat Appl Sci 2023;9:831–843. [CrossRef]
[41] Lukić R. Analysis of the trade performance of the European Union and Serbia on the base of FF-WASPAS and WASPAS methods. Rev Manag Comparat Int 2023;24:228–250.
[42] Hussain A, Bari M, Javed W. Performance of the multi attributed decision-making process with interval-valued spherical fuzzy Dombi aggregation operators. J Innov Res Math Comput Sci 2022;1:1–32.
[43] Zheng L, Mahmood T, Ahmmad J, Rehman UU, Zeng S. Spherical fuzzy soft rough average aggregation operators and their applications to multi-criteria decision making. IEEE Access 2022;10:27832–27852. [CrossRef]

[44] Mahmood T, Ullah K, Khan Q, Jan N. An approach toward decision-making and medical diagnosis problems using the concept of spherical fuzzy sets. Neural Comput Appl 2019;31:7041–7053. [CrossRef]

[45] Ali A, Božanić D, Akram M, Ijaz S. Heronian mean operators based multi-attribute decision making algorithm using T-spherical fuzzy information. J Innov Res Math Comput Sci 2022;1:55–82.

[46] Hussain M, Hussain A, Yin S, Abid MN. T-spherical fuzzy information and Shweizer-Sklar operations-based Maclaurin symmetric mean operator and their applications. J Innov Res Math Comput Sci 2023;2:52–64. [CrossRef]

[47] Çalık A. A comparative perspective in sustainable supplier selection by integrated MCDM techniques. Sigma J Eng Nat Sci 2020;38:835–852.

[48] Ayvaz B, Boltürk E, Kaçtıoğlu S. Supplier selection with TOPSIS method in fuzzy environment: An application in banking sector. Sigma J Eng Nat Sci 2015;33:351–362.

[49] Mutlu M, Tuzkaya G, Sennaroğlu B. Multi-criteria decision-making techniques for healthcare service quality evaluation: A literature review. Sigma J Eng Nat Sci 2017;35:501–512.

[50] Gunasekar T, Thiravidarani J, Mahdal M, Raghavendran P, Venkatesan A, Elangovan M. Study of non-linear impulsive neutral fuzzy delay differential equations with non-local conditions. Math 2023;11:3734. [CrossRef]

[51] Raghavendran P, Gunasekar T, Balasundaram H, Santra SS, Majumder D, Baleanu D. Solving fractional integro-differential equations by Aboodh transform. J Math Comput Sci 2023;32:229–240. [CrossRef]

Sigma J Eng Nat Sci, Vol. 44, No. 1, pp. 42–54, February, 2026

Sigma Journal of Engineering and Natural Sciences
Web page info: https://sigma.yildiz.edu.tr
DOI: 10.14744/sigma.2025.00000

Research Article

Commiphora myrrha-functionalized bacterial cellulose as a potential wound healing biomaterial

Seda GENÇ ŞİMŞEK[1], Cenk DENKTAŞ[2,*], Nelisa TÜRKOĞLU[3]

[1]*Department of Molecular Biology and Genetics, Yildiz Technical University, 34220, İstanbul, Türkiye*
[2]*Department of Physics, Yildiz Technical University, İstanbul, 34220, Türkiye*

ARTICLE INFO

Article history
Received: 07 June 2024
Revised: 21 August 2024
Accepted: 03 October 2024

Keywords:
Bacterial Cellulose; Commiphora Myrrha; Wound Healing

ABSTRACT

Bacterial cellulose (BC) is a valuable biomaterial for wound treatment due to its strong biocompatibility, porous structure, and mechanical strength. This study prepared BC membranes enriched with *myrrh* to enable them to contribute more effectively and rapidly to the wound healing process. *Commiphora myrrha*, a traditional medicinal plant known for its healing properties, was incorporated into the BC structure for the first time in this study; its physicochemical properties and cellular behavior were examined. Scanning electron microscopy (SEM) and atomic force microscopy (AFM) analyses conducted to examine morphological properties demonstrated that *myrrh* resin was successfully incorporated into the nanofiber network of BC. Fourier-transform infrared spectroscopy (FTIR), thermogravimetric analysis (TGA), and X-ray diffraction (XRD) analyses showed that increased *myrrh* content in BC films led to stronger intermolecular interactions within the membrane, which in turn supported enhanced thermal stability. According to the MTT test results performed using L929 mouse fibroblast cells, all biopolymers showed over 80% cell viability and were found to have no cytotoxic effect. Furthermore, it was noted that BC/mure composite films significantly increased cell adhesion and proliferation. Specifically, a 146.92% increase in cell adhesion was observed up to the 7th day in the BC membrane containing 2.5% mure. These findings indicate that the addition of mure improves the hydrogen bonding capacity, thermal properties, and cell compatibility of BC. The resulting natural composite structure can be considered a strong candidate for use in wound healing by supporting three-dimensional extracellular matrix formation and tissue regeneration.

Cite this article as: Genç Şimşek S, Denktaş C, Türkoğlu N. *Commiphora myrrha*-functionalized bacterial cellulose as a potential wound healing biomaterial. Sigma J Eng Nat Sci 2026;44(1):42–54.

INTODUCTION

The skin is the body's largest organ, covering its entirety and serving as both a physical and chemical barrier against pathogens, external substances, and dehydration [1]. Additionally, the skin fulfills many important functions such as protecting internal organs, providing sensory sensation, self-repair, and maintaining selective permeability

***Corresponding author.**
*E-mail address: cdenktas@yildiz.edu.tr

This paper was recommended for publication in revised form by Editor-in-Chief Ahmet Selim Dalkilic

Published by Yıldız Technical University Press, İstanbul, Turkey
© Author. This is an open access article under the CC BY-NC license (http://creativecommons.org/licenses/by-nc/4.0/).

[2]. The skin is structurally composed of three main layers: the epidermis, the dermis, and the hypodermis [3]: Wounds are generally classified according to the skin layers involved and the extent of the affected area. "Superficial wounds" involve only the outermost layer, the epidermis. "Partial-thickness wounds" affect both the epidermis and deeper dermal layers and may potentially involve blood vessels, sweat glands, and hair follicles. "Full-thickness wounds," on the other hand, result from injuries that extend from the epidermis and dermis to the subcutaneous fat tissue or deeper tissues [4,5].

A wound is any disruption in the skin's natural state caused by various medical factors, including mechanical, thermal, electrical, chemical, or physiological disturbances [6]. Wounds are generally categorized as either acute or chronic based on their healing process [7]. The primary goal of wound management is to facilitate rapid healing to prevent infection and reduce pain, discomfort, and scarring. Consequently, significant research has focused on developing wound dressings that support the healing process. These dressings can be produced in several forms, such as films, hydrocolloids, hydrogels, microneedles, and foams, using natural biomaterials like chitin, alginate, polyvinyl alcohol, cellulose, hyaluronic acid, starch, collagen, and gelatin [1,8].

An effective wound dressing should ideally [9]: i) enable quick and cost-effective healing, ii) create a suitable environment for epidermal regeneration, iii) offer mechanical support, iv) be biocompatible, v) maintain a moist environment conducive to healing, vi) possess anti-inflammatory and antimicrobial properties, and vii) be easy to manufacture and store. Wound healing is a complex biological process that involves a range of interactions between different cells and matrix components to restore the integrity of damaged tissue. This process unfolds through a series of stages that require the coordinated interplay of various biological systems to fully cover the wound [8]. The wound healing process involves a series of phases that collaborate to rebuild tissue integrity. It begins with hemostasis, where bleeding is stopped through clot formation [10]. This is followed by the inflammatory phase, which serves to protect against infection by employing immune cells to remove pathogens [11]. The next phase is proliferation, during which tissue repair and regeneration occur, marked by the formation of a new extracellular matrix and collagen synthesis [12]. Finally, the maturation and remodeling phase strengthens the newly formed tissue and matures the scar tissue, gradually returning the wound to a state similar to uninjured skin [13]. Each phase is crucial to achieving successful and complete healing.

Traditional wound dressings do not retain the necessary moisture at an adequate level and cannot fully support the healing process. Therefore, biomaterials such as BC have been proposed as a better alternative for use in tissue engineering. BC is a natural polymer formed by the linkage of glucose monomers via β(1→4) glycosidic bonds [14]. Its physicochemical and biological properties make it highly advantageous for wound dressing applications. BC, produced by non-pathogenic bacteria such as Gluconacetobacter xylinum, is notable for its high purity, durability, and lack of components found in plant cellulose, such as lignin, hemicellulose, and pectin [15,16]. This helps it provide a stronger, more porous, and purer structure.

BC's non-toxicity, moisture retention properties, lack of allergenicity, pain-reducing properties, and ease of removal without damaging tissues make it ideal for wound care. Studies in the literature have shown BC to be effective in burns [17], diabetic wounds [18], acute wounds [19], and infected wounds [20]. BC's three-dimensional nanofiber network supports cell adhesion, migration, and proliferation; it facilitates gas exchange by enabling the slow release of drugs. Its high water retention capacity helps control wound exudate, while its flexible structure allows for easy use even on irregular surfaces [21]. Furthermore, its semi-transparent appearance allows for better observation of the wound healing process [15]. BC can be combined with different biological agents or polymers to provide additional benefits to wound healing properties. In this study, *Commiphora myrrha* extract was added to the BC structure to increase fibroblast cell proliferation.

There is no study in the literature on the combined use of BC and *myrrh* resin. This resin, obtained from Commiphora species, has been used in wound care for many years due to its antimicrobial, antioxidant, and anti-inflammatory effects [22]. Adding this natural, economical, and biodegradable resin, known for its properties such as promoting wound dryness and supporting cleanliness, to BC is an approach that could enhance wound healing.

Although bacterial cellulose has been frequently studied in wound care, the combination of BC with *Commiphora myrrha* has not been previously addressed. The novelty of this study is that *myrrh*-enhanced BC membranes increase biocompatibility and promote fibroblast cell growth. This new approach offers an economical, sustainable, and biodegradable solution that can meet the biological requirements for wound healing. We believe our study will contribute to the literature on composite biomaterials and offer the healthcare sector a new alternative, particularly for the treatment of chronic and difficult-to-heal wounds.

MATERIAL AND METHOD

Materials

Gluconacetobacter xylinus (ATCC® 10245TM) was purchased from Formslab. *Commiphora myrrha* was obtained from Yaren Herbalist (Türkiye), a producer of organic and herbal products. All materials used in the bacterial cellulose synthesis were purchased from Sigma-Aldrich, USA. Peptone was of biotechnological grade, yeast extract was of molecular biology grade, glucose had a purity of 99.5% (GC), potassium phosphate monobasic (KH_2PO_4) was

an ACS reagent with 99.0% purity, and potassium phosphate dibasic K_2HPO_4 had a purity of 98%. For cell culture DMEM (high glucose, with glutamine), F-12 Nutrient Mixture (Ham's), Fetal Bovine Serum, and Trypsin EDTA (0.05%) procured from Capricorn Scientific (Germany) were utilized.

Production and Purification of Bacterial Cellulose

Bacterial cellulose (BC) membranes were synthesized using *Acetobacter xylinum* (ATCC® 10245TM). The bacteria were cultured in a static environment using Hestrin and Schramm (HS) liquid medium. The medium composition included 20 g/L glucose, 10 g/L bactopeptone, 10 g/L yeast extract, 4 mM KH_2PO_4, and 6 mM K_2HPO_4, with the pH adjusted to 5.0 by adding 1M HCl. Before use, the medium was sterilized at 120°C for 15 minutes. For inoculation, *A. xylinum* was pre-cultured for 2 days at 30°C using a rotary shaker. BC production occurred by transferring the inoculum to Petri dishes at a 1:10 ratio, where the culture was left undisturbed. Over a 7-day incubation period, BC nanofibers developed in a bacteriological incubator. Following incubation, the membranes were harvested and treated with 1% (w/v) NaOH at 80°C for 2 hours to remove residual bacteria [23]. Finally, the membranes were washed with distilled water to reach a pH of 7.0, then lyophilized and dried.

Preparation Of Bc/*Myrrh* Membranes

The powdered *myrrh* was dissolved in distilled water (1.5%, 2.5%, 5% by mass) at 400 rpm using a magnetic stirrer at 90°C for 4 h. The *myrrh* extract solution was then centrifuged at 10,000 rpm for 10 min and the supernatant was transferred to clean vials. Dried pure BC membranes were immersed in liquid *myrrh* extract solutions prepared at different ratios. Membranes were kept at room temperature for 24 hours. The next day the membranes were removed from the solutions and stored at +4 °C for analysis. Pure BC and BC membranes containing 1.5%, 2.5%, and 5% *myrrh* extract by mass were designated BC/M0, BC/M1, BC/M2, and BC/M3, respectively.

Characterization

Morphology of BC and BC/*Myrrh* membranes

The morphological properties of pure BC and composite BC/*Myrrh* membranes were determined by scanning electron microscope (SEM) (Zeiss Evo LS10) and atomic force microscope (AFM) (Shimadzu SPM 9600, Japan). For the analyses, the membranes were dried and then used. Before SEM analysis Au-Pd coating (Quorum SC-7620) was performed on samples for 1 min. The samples were examined at 20.00 KX magnification for SEM analysis and 2.5 nm magnification for AFM analysis.

Micro-structure of BC and BC/*Myrrh* membranes

The molecular structure and identification of intramolecular functional groups in all samples were examined using Fourier transform infrared (FTIR) spectroscopy (Perkin Elmer Inc., USA). The analysis was conducted over a wavenumber range of 4000–500 cm^{-1}. The spectra were collected with 32 scans at a resolution of 4 cm^{-1}.

Thermal analysis

The thermal stability of the produced membranes was assessed through thermogravimetric (TG) analysis using the SII6000 Exstar TG 6300. The average dry weight of the samples was around 1 mg, and all analyses were conducted under an inert nitrogen (N_2) atmosphere. A heating rate of 10 °C/min was used, with mass loss measured over 90 minutes, spanning a temperature range of 30 °C to 700 °C. The thermograms for each sample were then evaluated.

X-ray diffraction (XRD)

Crystallinity and amorphous of bacterial celluloses were determined using an X-ray diffractometer. The X-ray generator tension and current were 45 kV and 40 mA, respectively.

The swellıng analysıs of BC and BC/*Myrrh* membranes

The water retention degree of the membranes was determined by the swelling test [24]. Membranes (triplicates) were cut into 1 cm^2 square shapes and their dry weight was measured (W_0). Then, it was immersed in distilled water at room temperature (25 °C) for 24 h. The weights of the swollen membranes (W_s) were measured at regular intervals. The water retention rate of the samples was calculated using the following equation;

$$Swelling\ ratio = (W_S - W_{0)}/W_0 \quad (1)$$

W_0 represents the weight of the dry membrane and W_s represents the weight of the swollen membrane. The weight of the swollen membranes was measured after removing excess water from the surface using filter paper.

***In Vitro* Cytotoxicity Studies**

Cell viability

The in vitro cytotoxicity of the membranes on L929 mouse fibroblast cells (ATCC® CRL-6364™) was evaluated using the MTT assay [25]. The L929 cells were cultured in DMEM F-12 medium supplemented with 10% FBS and seeded in a 96-well plate at a density of 10^5 cells per well. The plate was incubated at 37 °C with 5% CO_2 for 24 hours. Following this incubation, the medium was removed, and the membranes, sterilized under UV light for 1 hour and cut into disk shapes, were placed in the wells with fresh medium. After another 24-hour incubation, the medium was replaced with 100 µL of MTT solution (5 mg/mL in medium), and the cells were incubated for 4 hours. The MTT solution was then removed, and 100 µL of dimethyl sulfoxide (DMSO) was added to dissolve the formazan crystals. The optical density was measured at 570 nm using an ELISA reader (Thermo Scientific Multiskan Go, USA).

Cell adhesion

Cell proliferation and adhesion properties on membranes were determined using the MTT assay [26]. In the study, L929 fibroblast cells cultured in DMEM F-12 medium supplemented with 10% FBS and 1% L-glutamine and maintained at 37°C in a 5% CO_2 environment were used. Membranes were cut into 1 cm x 1 cm pieces and placed in 24-well plates. 10^3 fibroblast cells were seeded onto each membrane and incubated for 24 hours. Cell adhesion and proliferation were tested on days 1, 3, and 7. After each time period, the membranes were placed in new 24-well plates, and 400 µL of MTT solution (5 mg/mL in the medium) was added to each well. After a 4-hour incubation, the medium was removed, and 400 µL of DMSO was added to dissolve the formazan crystals. Finally, cell viability was measured at an absorbance value of 570 nm.

Statıstical Analysis

Statistical comparisons were performed using *t*-test analysis. p values < 0.05 were considered statistically significant.

RESULTS AND DISCUSSION

Morphology of BC and BC/*Myrrh* Membranes

The surface morphological and topological properties of freeze-dried pure BC and BC/*Myrrh* membranes were determined by SEM and AFM analysis. The images of all membranes examined by SEM are shown in Figure 1. Pure BC is characterized by a three-dimensional (3D) nanofiber network structure. Thus, the BC matrix has a randomly arranged porous geometric structure [27]. BC makes it possible to impregnate various materials with different physical properties due to its unique morphology [28]. Pure BC membranes (Fig. 1a) exhibited a 3D network structure composed of interconnected fibrils. We found that the pure BC membrane morphology is compatible with the BC structure described in the literature.

Some changes in cellulose structure compared to pure BC were found when the *myrrh*-doped BC membrane was examined (Fig. 1b-d). The material surface is more irregular and complex. A thicker fiber network structure with the effect of *myrrh* and *myrrh*-induced spherical agglomerates appeared.

The formation of a flat surface due to the layer created by *myrrh* extract coating the BC is seen in Figure.1c. and the highest *myrrh* extract concentration leads to a thicker flat surface in Fig. 1d. Briefly, we can conclude depending on the increasing *myrrh* concentration, the porosity decreases in BC membranes, and a smooth layer is formed in BC/*Myrrh* membranes. Nevertheless, the 3D nanofiber network structure can still be observed in *myrrh*-doped membranes. According to the morphological findings

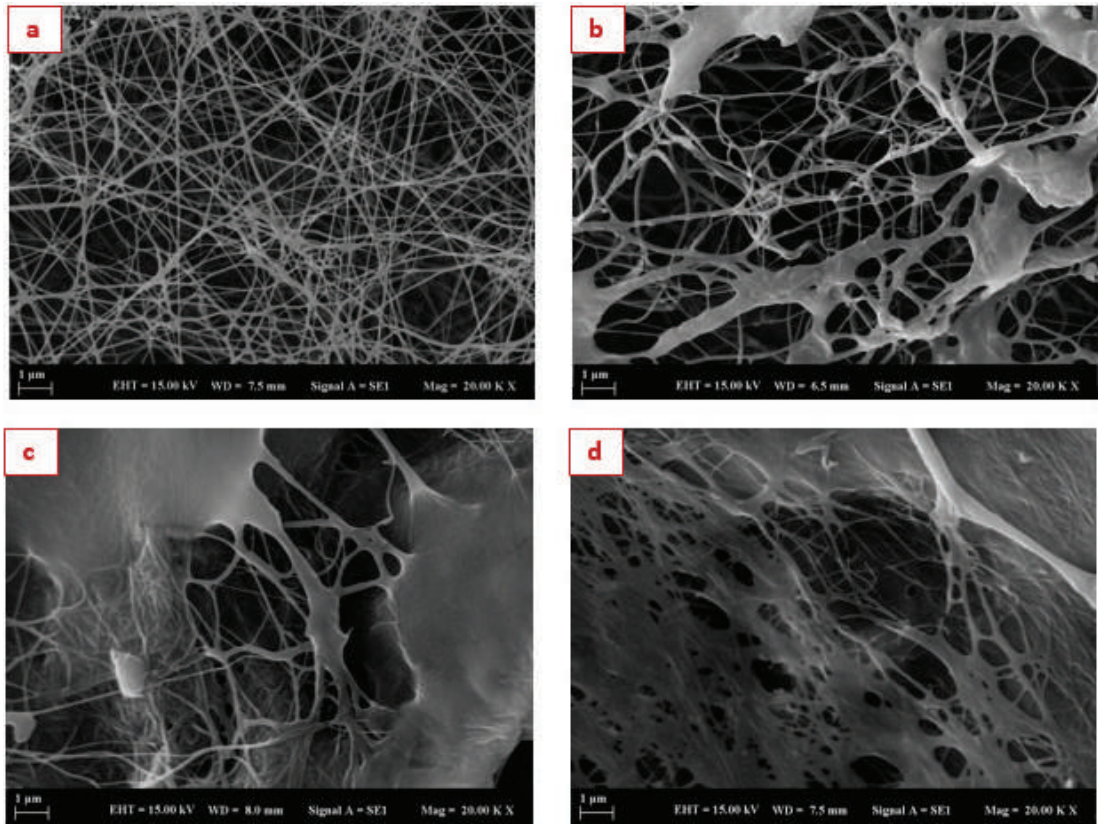


Figure 1. SEM images of all membranes: (a) BC/M0, (b) BC/M1, (c) BC/M2, (d) BC/M3 at 20.00 KX magnification.

of *myrrh*-doped BC membranes, a compact structure is observed in which *myrrh* can penetrate the BC surface and interact with microfibrils.

AFM images were obtained to visualize the surface topography of BC and BC/*Myrrh* membranes (Fig. 2). While pure BC membranes showed a clear nanofiber network structure, *myrrh*-added BC membranes exhibited unclear fibrous network structure. The findings obtained from AFM and SEM analyses confirm each other. Both analyses confirm that *myrrh*, a bioactive molecule, can be incorporated into BC membranes. When the morphologies of BC and BC/*Myrrh* membranes are examined, it is reported that interconnected fibers provide the necessary structure for cell adhesion and proliferation for tissue engineering applications [29]. Our results are consistent with the morphological characterization of the membranes obtained with pure BC and plant extract [30], vaccarin [26], lignin [31], and chitosan [32] doped BC composite materials in the literature.

ATR/FTIR Analysis of Membranes

The ATR/FTIR spectra of pure BC and *myrrh* extract doped celluloses are shown in Figure 3. The differences between the FTIR results of pure BC and BC/*Myrrh* composites indicate that there may be strong interactions between cellulose and *myrrh* molecules (see Fig.3). It is seen from Figure 3. that the peak at 3343 cm^{-1} in pure BC corresponds to the O-H stretching vibration in cellulose I and the peak at 3243 cm^{-1} corresponds to hydrogen-bound O-H [33,34]. As the *myrrh* extract content in BC increased, the OH-strain peak shifted to a higher wavenumber (from 3248 cm^{-1} to 3273 cm^{-1}). This result indicates that the OH groups in the *myrrh* molecule enhance the hydrogen bonding effect in the structure of the composites [35]. The range 3000-2750 cm^{-1} is also attributed to C-H stretching peaks. The intensity of the 1633 cm^{-1} peak [36], which is due to the H-O-H bending vibration of bound water molecules in cellulose, was found to change as a result of *myrrh* addition. In pure BC, a peak (1428 cm^{-1}) corresponding to CH_2 bending associated with the crystalline/amorphous ratio in some cellulose molecules was detected [37]. The interaction with *myrrh* resulted in a significant change in the peak intensity of the CH_2 bending. This change is an indication that it corresponds to a higher degree of crystallinity [37,38]. Although the peaks at 1161, 1108, 1056, and 1031 cm^{-1} in pure BC were evaluated by different authors [39-41] these peaks can be assigned to C-C stretching vibration, skeletal vibration, and ring vibration, respectively [42,43]. The peak at 898 cm^{-1} corresponding to crystallized cellulose-I in pure BC [36] was shifted to a higher wave number (926 cm^{-1}) upon interaction with *myrrh.* This result is evidence of the change in the crystal structure due to the presence of *myrrh* extract in BC. A new peak was also detected at 848 cm^{-1}. This peak is associated with *Commiphora* resin, commonly known as *myrrh*, one of the three major genera of the Burseraceae family [44,45]. As a result of the interaction between pure BC and *myrrh* extract, the peak at 663 cm^{-1} in pure BC disappeared.

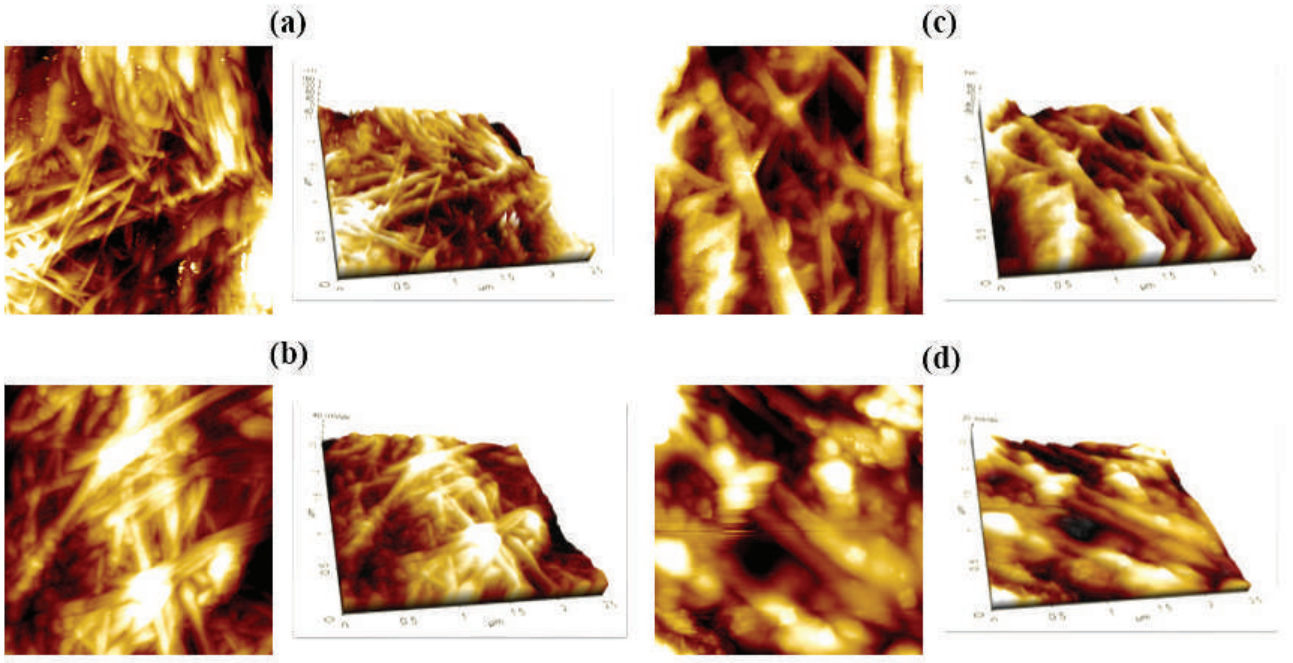


Figure 2. AFM images of all membranes: (a) BC/M0, (b) BC/M1, (c) BC/M2, (d) BC/M3.

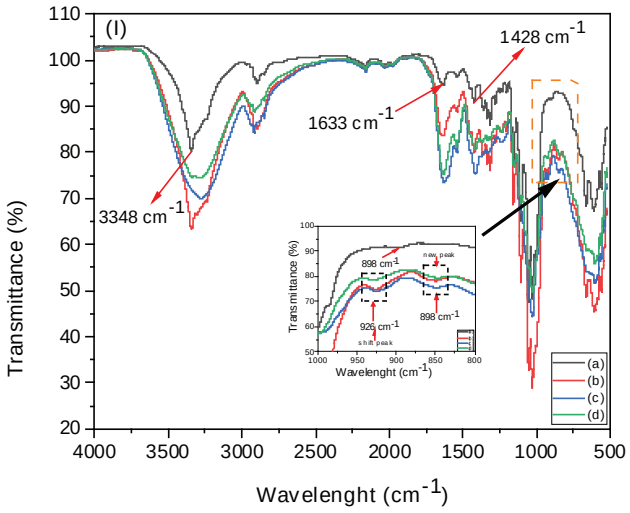


Figure 3. FTIR analysis of (I) All samples: (a) BC/M0, (b-d) BC/M1, BC/M2, BC/M3 composite BC membranes, respectively.

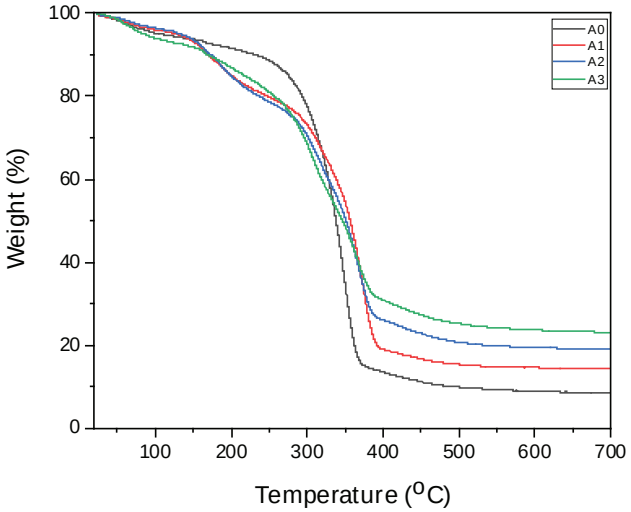


Figure 4. TGA curves of BC/M0, BC/M1, BC/M2 and BC/M3 membranes indicated by A0, A1, A2 and A3, respectively.

Thermal Analysis

The thermal properties of the samples were investigated by the TGA method. The TGA curves of the samples are shown in Figure 4. The samples indicated as A0, A1, A2, and A3 represent BC/M0, BC/M1, BC/M2, and BC/M3, respectively.

As seen in Figure 4. three degradation temperatures for pure BC exist. The first degradation temperature between 10-100 °C is associated with a slight weight loss (about 5%) of the broken inter and intra-molecular hydrogen bonds [46]. The largest mass loss (≈82 wt%), which is associated with depolymerization and pyrolytic decomposition in pure BC, was found to occur between 100-400 °C [47,48]. The mass loss of the BC/*Myrrh* composite after the addition of 5% *myrrh* by mass to pure BC was approximately 68%. This result can be attributed to the fact that the composite structure is more stable due to stronger hydrogen bonding and higher crystallinity. This result is supported by FTIR and XRD data.

X-Ray Diffraction (XRD) Analysis

Cellulose occurs naturally in two polymorphic forms, cellulose I and cellulose II [49]. Cellulose-I has a parallel chain structure and constitutes the natural form of cellulose [50]. The BC we produce also has the cellulose-I structure. The XRD patterns of all the samples were recorded, and the results are illustrated in Figure 5. As shown in Figure 5. centered at 2θ=14.56°, 17.07°, 19.68°, 22.74° and 25.52° indexed as (100), (010), (002), (110) and (114) [51,52] was observed in the XRD pattern of (pure BC), which is attributed to respectively in the triclinic unit cell of allomorph Iα [53], which are usually attributed to crystallographic planes of 100 (amorphous region), 010 (amorphous region), and 110 (crystalline region), respectively [54,55]. In addition, it can be seen from the X-ray diffraction image that the crystallization peak (110) is higher as a result of less amorphization during the production of pure BC. This result is an indication of hydrogen bond formation which is also supported by the FTIR result [34]. The relative crystal index (%CrI) and crystal lattice spacing (d-spacing) obtained from XRD patterns are critical factors affecting the properties of cellulose. The relative crystal index (% CrI) of all samples was found using peak height methods and the results are given in Table 1. The following equation was used for the Segal method [56].

$$\% \, CrI = \frac{I_{110} - I_{am.}}{I_{110}} \, x \, 100 \qquad (2)$$

Where I_{110} and $I_{am.}$ are the maximum intensities of both crystalline and amorphous regions, respectively. It can be seen from Table 1 when 5% *myrrh* was added to BC, the incorporation of *myrrh* into bacterial cellulose increased the crystal index of BC by 13%. This phenomenon can be explained by the increase in intramolecular and intermolecular hydrogen bonds formed as a result of the interaction of OH groups in the *myrrh* molecule with hydroxyl groups in the cellulose structure [57,58]. When these results are evaluated, it can be concluded that there are strong interactions between *myrrh* molecules and the cellulose structure.

The Swelling Analysis of BC and BC/*Myrrh* Membranes

The water holding capacity of Pure BC and BC/*Myrrh* composite membranes was determined by swelling test (Fig. 6). The hydrophilic nature of BC enables it to hold a high amount of water [59]. The water holding capacity of BC is related to its porous structure and surface area. The addition of secondary structures to cellulose influences its physicomechanical properties, thus resulting in differences

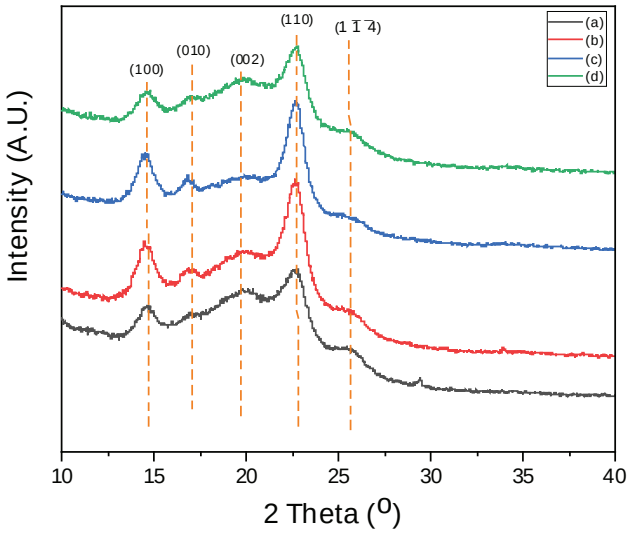


Figure 5. XRD pattern of (a) BC/M0, (b-d) BC/M1, BC/M2, BC/M3 composite BC membranes, respectively.

in the water holding capacity [60]. The swelling rates of the membranes in the first 30 min were about 5 times for pure BC and about 3 times for all BC/*Myrrh* membranes, relative to their dry weights. The swelling rate continued with a significant increase for pure BC and a slower increase for *myrrh* doped membranes. Pure BC had a higher water retention capacity. This is due to the presence of *myrrh* extract molecules penetrating the pure BC between the BC fibers [61]. After 24 h, the water holding capacity of BC/M0, BC/M1, BC/M2, and BC/M3 membranes were 1090.5%, 595.8%, 267.3%, and 137.8%, respectively. The t-test analysis reveals statistically significant differences in swelling behavior between the control membrane (BC/M0) and the *myrrh*-doped membranes (BC/M1, BC/M2, BC/M3) across the tested time intervals ($p < 0.05$). The water holding capacity of BC varies with the integration of substances such as drugs, nanoparticles, polymers, chemical agents, and plant extracts into the structure [62-64]. In the study, composite BC membranes retained a lower amount of water due to the closure of the existing pores of *myrrh*-doped BC. Accordingly, it can be concluded that the swelling test results are directly proportional to the SEM analysis. Providing a moist environment is one of the most critical issue for stimulated wound healing [22]. In this study, we evaluated that *myrrh-doped* cellulose membranes are wound dressings with sufficient swelling ratio because although swelling rates decrease with *myrrh* addition, the swelling analysis results are compatible with the other wound dressing materials reported in the literature [65].

Table 1. Relative crystal index (%CrI) and d-spacing (nm) due to *myrrh* effect on bacterial cellulose from XRD patterns: BC/M0, BC/M1, BC/M2, and BC/M3

Samples	BC/M0	BC/M1	BC/M2	BC/M3
% CrI	61.32	49.81	53.51	69.41
I_{110}	1238.97	1600.58	1172.71	1041.26
I_{100}	479.15	803.22	545.16	318.48

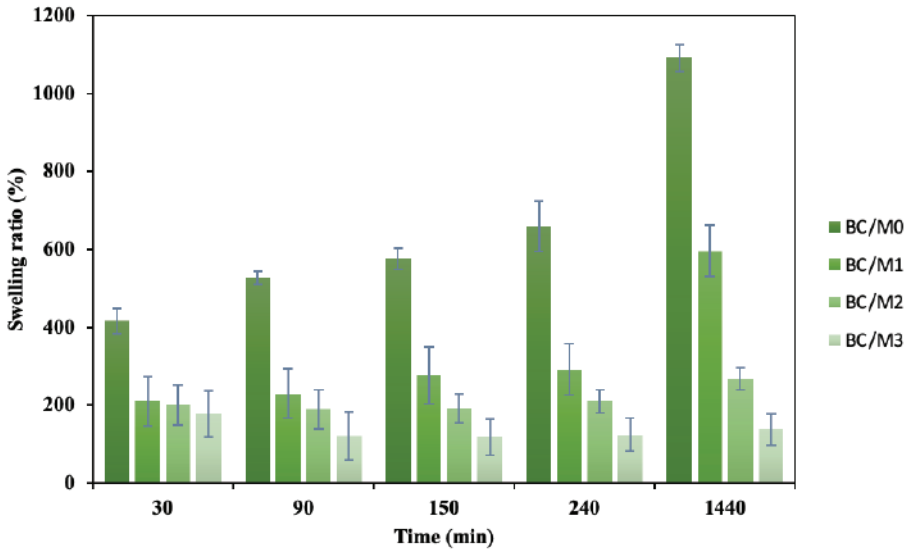


Figure 6. Water holding capacities of pure BC and BC/*Myrrh* membranes.

Cell Viability

The cytotoxicity assay of the membranes was determined by MTT assay on the L929 fibroblast cell line. The cytotoxic effects of *myrrh*-modified BC membranes on cell viability were assessed through t-test analysis at a significance level of $p<0.05$, as presented in Figure 7. The negative control in the graph represents living cells, while the positive control represents dead cells. Cell viability in pure BC membranes was measured as 85.87% (standard error ±3.17). In BC membranes with mixtures of myrrh, cell viability was found to be 88.92% (±2.32), 92.98% (±2.64), and 82.31% (±1.52), respectively. According to the MTT analysis, cell viability was over 80% in pure BC and all membranes containing different ratios of myrrh, and no significantly cytotoxicity was observed. In addition, the BC membrane containing 2.5% myrrh showed the highest cell viability at 92.98% (±2.64). This ratio indicates that the cells survived better without toxicity. The results are similar to previous studies in the literature [66]. Ajiteru et al. reported that *myrrh*-containing hydrocolloid wound dressing developed for wound healing stimulated cell proliferation in the CCK-8 cell line [67]. The fact that BC membranes are biocompatible [68] and positively support cell viability has been supported by studies on different cell lines such as glioblastoma [69], endothelium [70], fibroblast [61], and epithelium [71] with BC modified with different components.

Cell Adhesion

Fibroblast cell presence and proliferation are essential in wound healing since these cells migrate into the wound area and synthesize various collagen types that contribute to tissue repair [72]. For this reason, the L929 cell line was selected, and the adhesion and proliferation rates on the membranes were monitored on days 1, 3, and 7. The retention capacity of the cells is presented in Figure 8. In the graph, the negative control represents viable cells, while the positive control shows non-viable cells. After 24 hours, the adhesion rate on the pure BC membrane was 98.63% (±2.00). BC membranes containing 1.5%, 2.5%, and 5% myrrh showed adhesion rates of 107.65% (±2.38), 105.44% (±1.75), and 88.94% (±1.16), respectively. On day 3, adhesion on pure BC increased to 121.73% (±4.05), while BC/M1, BC/M2, and BC/M3 recorded 135.86% (± 3.76), 143.65% (± 2.92), and 118.84% (± 3.69). By day 7, adhesion on pure BC was 117.39% (±3.80), and the BC/M1, BC/M2, and BC/M3 composites showed 139.61% (±4.90), 146.92% (±3.18), and 124.56% (±2.48), respectively. Pure BC is known to provide an ECM-like environment that supports cell attachment and proliferation through its structural features [73]. Myrrh-added BC composites were also found to increase cell adhesion and proliferation.

According to the cell adhesion and proliferation analysis results, biofilms containing 2.5% mür were shown to provide higher levels of cell adhesion and proliferation compared to BC without mür and BC with 1.5% and 5% mür added. On the third day, the film structure containing 2.5% murex was the membrane with the highest cell adhesion rate at 143.65% (±2.92). This trend continued similarly on the seventh day, with the cell adhesion rate measured at 146.92% (±3.18). The increase in cell number on the third day was higher in membranes with added *myrrh,* while it was slightly lower in pure BC membranes. On the seventh day, the rate of increase in cell proliferation slowed down due to the increase in *myrrh* concentration. These results show that the addition of 2.5% *myrrh* significantly increases cell adhesion and promotes cell proliferation. This suggests that fibroblast activity, which is

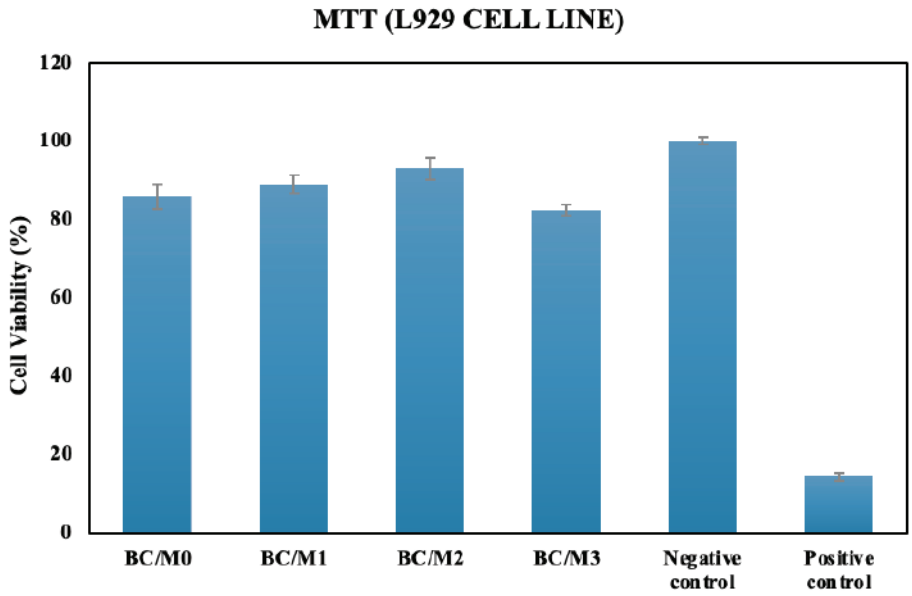


Figure 7. Cytotoxicity results of pure BC and composite BC/*Myrrh* membranes.

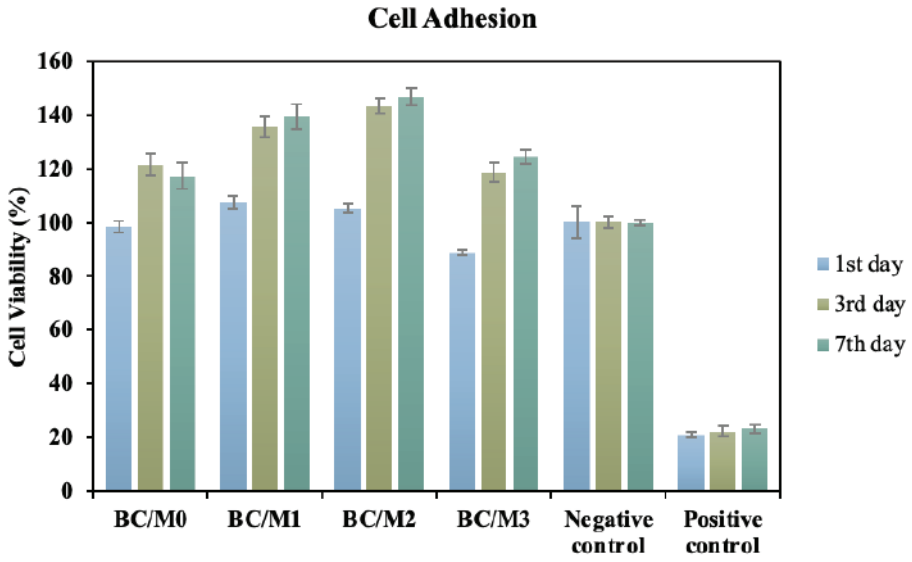


Figure 8. The L929 cell adhesion on membranes.

critical for wound healing, is better supported in this membrane. On the other hand, the lower cell proliferation in the membrane containing 5% *myrrh* may be due to restricted cell adhesion caused by the membrane having a softer surface and smaller pores. The data obtained show that cell adhesion in membranes with added *myrrh* is not statistically significant compared to the negative control ($p>0.05$) but is significantly higher than the positive control ($p<0.001$). Pure BC was found to support cell adhesion and proliferation, and these findings are consistent with previous studies in the literature [66, 74]. In the literature, among the BC hydrogels modified with 10%, 20%, and 30% dextran, materials containing 10% and 20% dextran were reported to have a better proliferation effect on NIH/3T3 mouse fibroblast cells [75]. Previous studies have reported that composite membranes developed by impregnating BC with different components such as aloe vera extract [76,77] alginate [78] and silk sericin [79] have no cytotoxic effect on different cell lines cultured and support cell proliferation. We can say that the results are similar to the literature.

CONCLUSION

This study demonstrated that *myrrh*-doped bacterial cellulose membranes hold strong potential as wound dressing materials by improving fibroblast adhesion, proliferation, and overall biocompatibility. Integrating *myrrh* recognized for its antimicrobial and anti-inflammatory activity into the bacterial cellulose matrix enhanced its biological performance, with the 2.5% *myrrh* formulation showing the most favorable results over the 7-day evaluation period. The in vitro findings indicate that these composite membranes may be effective candidates for advanced wound care, especially in cases where accelerated tissue regeneration is needed. Nevertheless, additional in vivo experiments and clinical studies are required to confirm their therapeutic benefits and to assess long-term behavior, including stability, degradation profile, and antimicrobial activity under physiological conditions. This study emphasize that combining biopolymers such as bacterial cellulose with natural bioactive compounds like m*yrrh* can produce sustainable and highly effective natural wound dressing materials. Future research may focus on integrating different bioactive molecules or complementary polymers to expand the functional properties of BC-based wound care dressings and support their use in regenerative medicine and biomedical fields.

ACKNOWLEDGMENT

We would like to thank Tanju Özer and the organic and herbal producer Yaren Herbalist for providing the *myrrh* extract.

AUTHORSHIP CONTRIBUTIONS

Seda Genç Şimşek: Investigation, Visualization, Writing-Original Draft, Preparation and characterization of BC membranes, Cell culture studies.

Cenk Denktaş: Investigation, Resources, Writing-Original Draft, Preparation and characterization of *Myrrh* doped-BC membranes.

Nelisa Türkoğlu: Resources, Writing-Original Draft, Cell culture studies.

DATA AVAILABILITY STATEMENT

The authors confirm that the data that supports the findings of this study are available within the article. Raw data that support the finding of this study are available from the corresponding author, upon reasonable request.

CONFLICT OF INTEREST

The author declared no potential conflicts of interest with respect to the research, authorship, and/or publication of this article. ETHICS There are no ethical issues with the publication of this manuscript.

STATEMENT ON THE USE OF ARTIFICIAL INTELLIGENCE

Artificial intelligence was not used in the preparation of the article.

REFERENCES

[1] Ijaola AO, Akamo DO, Damiri F, Akisin CJ, Bamidele EA, Ajiboye EG, Berrada M, Onyenokwe VO, Yang SY, Asmatulu E. Polymeric biomaterials for wound healing applications: a comprehensive review. J Biomater Sci Polym Ed 2022;33:1998–2050. [CrossRef]

[2] Takeo M, Lee W, Ito M. Wound healing and skin regeneration. Cold Spring Harb Perspect Med 2015;5:1. [CrossRef]

[3] Sorg H, Tilkorn DJ, Hager S, Hauser J, Mirastschijski U. Skin wound healing: An update on the current knowledge and concepts. Eur Surg Res 2017;58:81–94. [CrossRef]

[4] Tottoli EM, Dorati R, Genta I, Chiesa E, Pisani S, Conti B. Skin wound healing process and new emerging technologies for skin wound care and regeneration. Pharmaceutics 2020;12:80735. [CrossRef]

[5] Morton LM, Phillips TJ. Wound healing and treating wounds: Differential diagnosis and evaluation of chronic wounds. J Am Acad Dermatol 2016;74:589–605; quiz 605–6. [CrossRef]

[6] Yalman V, Laçin NT. Development of humic acid and alginate-based wound dressing and evaluation on inflammation. Mater Technol 2019;34:705–717. [CrossRef]

[7] Laçin NT, Demirbilek M, Yalman V. Tissue engineering and wound healing biomaterials. In book: Frontiers in Stem Cell and Regenerative Medicine Research. 8th ed. Saif Zone, Sharjah, U.A.E: Bentham Science Publisher; 2018. [CrossRef]

[8] Mir M, Ali MN, Barakullah A, Gulzar A, Arshad M, Fatima S, Asad M. Synthetic polymeric biomaterials for wound healing: a review. Prog Biomater 2018;7:1–21. [CrossRef]

[9] Ovington LG. Advances in wound dressings. Clin Dermatol 2007;25:33–38. [CrossRef]

[10] Velnar T, Bailey T, Smrkolj V. The wound healing process: an overview of the cellular and molecular mechanisms. J Int Med Res 2009;37:1528–1542. [CrossRef]

[11] Enoch S, Leaper JD. Basic science of wound healing. Reconstructive 2007;117:12S–34S. [CrossRef]

[12] Kaya S, Derman S. Production, characterization and antioxidant activity evaluation of quercetin loaded PLGA nanofibers. Sigma J Eng Nat Sci 2021;9:443–440.

[13] Das S, Baker AB. Biomaterials and nanotherapeutics for enhancing skin wound healing. Front Bioeng 2016;4:82. [CrossRef]

[14] Moon RJ, Martini A, Nairn J, Simonsen J, Youngblood J. Cellulose nanomaterials review: Structure, properties and nanocomposites. Chem Soc Rev 2011;40:3941–3994. [CrossRef]

[15] Ahmed J, Gultekinoglu M, Edirisinghe M. Bacterial cellulose micro-nano fibers for wound healing applications. Biotechnol Adv 2020;38:107549. [CrossRef]

[16] Chawla PR, Bajaj IB, Survase SA, Singhal RS. Microbial cellulose: Fermentative production and applications. Food Technol Biotechnol 2009;47:107–124.

[17] Mohamad N, Mohd Amin MCI, Pandey M, Ahmad N, Rajab NF. Bacterial cellulose/acrylic acid hydrogel synthesized via electron beam irradiation: Accelerated burn wound healing in an animal model. Carbohydr Polym 2014;114:312–320. [CrossRef]

[18] Khalid A, Madni A, Raza B, Islam MU, Hassan A, Ahmad F, et al. Multiwalled carbon nanotubes functionalized bacterial cellulose as an efficient healing material for diabetic wounds. Int J Biol Macromol 2022;203:256–267. [CrossRef]

[19] Foong CY, Hamzah MSA, Razak SIA, Saidin S, Nayan NHM. Influence of poly (lactic acid) layer on the physical and antibacterial properties of dry bacterial cellulose sheet for potential acute wound healing materials. Fibers Polym 2018;19:263–271. [CrossRef]

[20] Wang F, Sun M, Li D, Qin X, Liao Y, Liu X, et al. Multifunctional asymmetric bacterial cellulose membrane with enhanced anti-bacterial and anti-inflammatory activities for promoting infected wound healing. Small 2023;19:202303591. [CrossRef]

[21] Ul-Islam M, Khan S, Ullah MW, Park JK. Bacterial cellulose composites: Synthetic strategies and multiple applications in bio-medical and electro-conductive fields. Biotechnol J 2015;10:1847–1861. [CrossRef]

[22] Sulaeva I, Henniges U, Rosenau T, Potthast A. Bacterial cellulose as a material for wound treatment: Properties and modifications: A review. Biotechnol Adv 2015;33:1247–1261. [CrossRef]

[23] Cesur NP, Zad Ghaffari Vahdat K, Türkoğlu Laçin N. Fabrication of bacterial cellulose/PVP nanofiber composites by electrospinning. Biopolymers 2024;62:23606. [CrossRef]

[24] Jipa IM, Stoica-Guzun A, Stroescu M. Controlled release of sorbic acid from bacterial cellulose based mono and multilayer antimicrobial films. LWT 2012;47:400–406. [CrossRef]

[25] Erenler R, Çarlik ÜE, Aydin A. Antiproliferative activity and cytotoxic effect of essential oil and water extract from Origanum vulgare L. Sigma J Eng Nat Sci 2023;41:202–208. [CrossRef]
[26] Qiu Y, Qiu L, Cui J, Wei Q. Bacterial cellulose and bacterial cellulose-vaccarin membranes for wound healing. Mater Sci Eng C 2016;59:303–309. [CrossRef]
[27] Manan S, Ullah MW, Ul-Islam M, Shi Z, Gauthier M, Yang G. Bacterial cellulose: Molecular regulation of biosynthesis, supramolecular assembly, and tailored structural and functional properties. Prog Mater Sci 2022;47:100972. [CrossRef]
[28] Ul-Islam M, Alhajaim W, Fatima A, Yasir S, Kamal T, Abbas Y, et al. Development of low-cost bacterial cellulose-pomegranate peel extract-based antibacterial composite for potential biomedical applications. Int J Biol Macromol 2023 Mar 15;231:123269. [CrossRef]
[29] Zhijiang C, Guang Y. Bacterial cellulose/collagen composite: Characterization and first evaluation of cytocompatibility. J Appl Polym Sci 2011;120:2938–2944. [CrossRef]
[30] Fatima A, Yasir S, Khan MS, Manan S, Ullah MW, Ul-Islam M. Plant extract-loaded bacterial cellulose composite membrane for potential biomedical applications. J Bioresour Bioproducts 2021;6:26–32. [CrossRef]
[31] Zmejkoski D, Spasojević D, Orlovska I, Kozyrovska N, Soković M, Glamočlija J, et al. Bacterial cellulose-lignin composite hydrogel as a promising agent in chronic wound healing. Int J Biol Macromol 2018;118:494–503. [CrossRef]
[32] Lin WC, Lien CC, Yeh HJ, Yu CM, Hsu SH. Bacterial cellulose and bacterial cellulose-chitosan membranes for wound dressing applications. Carbohydr Polym 2013;94:603–611. [CrossRef]
[33] Tercjak A, Gutierrez J, Barud HS, Domeneguetti RR, Ribeiro SJL. Nano- and macroscale structural and mechanical properties of in situ synthesized bacterial cellulose/PEO-b-PPO-b-PEO biocomposites. ACS Appl Mater Interfaces 2015;7:4142–4150. [CrossRef]
[34] Ciolacu D, Ciolacu F, Popa VI. Amorphous cellulose—structure and characterization. Cellul Chem Technol 2011;45:13–21.
[35] Tian X, Chengcheng G, Yang Y, Shen X, Huang M, Shaowei LiuRetention and release properties of cinnamon essential oil in antimicrobial films based on chitosan and gum arabic. Food Hydrocoll 2018;84:84–92. [CrossRef]
[36] Rani MU, Udayasankar K, Appaiah KAA. Properties of bacterial cellulose produced in grape medium by native isolate Gluconacetobacter sp. J Appl Polym Sci 2011;120:2835–2841. [CrossRef]
[37] Schenzel K, Fischer S, Brendler E. New method for determining the degree of cellulose I crystallinity using FT Raman spectroscopy. Cellulose 2005;12:223–231. [CrossRef]
[38] Atykyan N, Revin V, Shutova V. Raman and FT-IR spectroscopy investigation the cellulose structural differences from bacteria Gluconacetobacter sucrofermentans during the different regimes of cultivation on a molasses media. AMB Express 2020;10:1. [CrossRef]
[39] Mohd Amin MCI, Ahmad N, Halib N, Ahmad I. Synthesis and characterization of thermo- and pH-responsive bacterial cellulose/acrylic acid hydrogels for drug delivery. Carbohydr Polym 2012;88:465–473. [CrossRef]
[40] Barud HS, Souza JL, Santos DB, Crespi MS, Ribeiro CA, Messaddeq Y, et al. Bacterial cellulose/poly(3-hydroxybutyrate) composite membranes. Carbohydr Polym 2011;83:1279–1284. [CrossRef]
[41] Sun D, Yang J, Wang X. Bacterial cellulose/TiO2 hybrid nanofibers prepared by the surface hydrolysis method with molecular precision. Nanoscale 2010;2:287–292. [CrossRef]
[42] Li D, Ao K, Wang Q, Lv P, Wei Q. Preparation of Pd/bacterial cellulose hybrid nanofibers for dopamine detection. Molecules 2016;21:618. [CrossRef]
[43] Wang SS, Han YH, Ye YX, Shi XX, Xiang P, Chen DL, et al. Physicochemical characterization of high-quality bacterial cellulose produced by Komagataeibacter sp. strain W1 and identification of the associated genes in bacterial cellulose production. RSC Adv 2017;7:45145–45155. [CrossRef]
[44] Gigliarelli G, Becerra JX, Curini M, Marcotullio MC, Forti L. Chemical composition and biological activities of fragrant Mexican copal (Bursera spp.). Molecules 2015;20:22383–22394. [CrossRef]
[45] Martín-Ramos P, Fernández-Coppel IA, Ruíz-Potosme NM, Martín-Gil J. Potential of ATR-FTIR spectroscopy for the classification of natural resins. Biol Eng Med Sci Rep 2018;4:3–6. [CrossRef]
[46] George J, Ramana KV, Sabapathy SN, Jagannath JH, Bawa AS. Characterization of chemically treated bacterial (Acetobacter xylinum) biopolymer: Some thermo-mechanical properties. Int J Biol Macromol 2005;37:189–194. [CrossRef]
[47] Surma-Ślusarska B, Presler S, Danielewicz D. Characteristics of bacterial cellulose obtained from Acetobacter xylinum culture for application in papermaking. Fibres Text East Eur 2008;16:108–111.
[48] Kumar V, Sharma DK, Sandhu PP, Jadaun JJ, Sangwan RS, Yadav SK. Sustainable process for the production of cellulose by an Acetobacter pasteurianus RSV-4 (MTCC 25117) on whey medium. Cellulose 2021;28:103–116. [CrossRef]
[49] Paul RA. Occurrence and functions of native cellulose. California, USA: CRC Press; 1991.
[50] Tsekos I. The sites of cellulose synthesis in algae: Diversity and evolution of cellulose-synthesizing enzyme complexes. J Phycol 1999;35:635–655. [CrossRef]

[51] Lopes TD, Riegel-Vidotti IC, Grein A, Tischer CA, Faria-Tischer PCS. Bacterial cellulose and hyaluronic acid hybrid membranes: Production and characterization. Int J Biol Macromol 2014;67:401–408. [CrossRef]
[52] Hult EL, Iversen T, Sugiyama J. Characterization of the supermolecular structure of cellulose in wood pulp fibres. Cellulose 2003;10:103–110. [CrossRef]
[53] Sugiyama J, Persson J, Chanzy H. Combined infrared and electron diffraction study of the polymorphism of native celluloses. Macromolecules 1991;24:2461–2466. [CrossRef]
[54] Wada M, Sugiyama J, Okano T. Native celluloses on the basis of two crystalline phase (Iα/Iβ) system. J Appl Polym Sci 1993;49:1491–1496. [CrossRef]
[55] Lee CM, Gu J, Kafle K, Catchmark J, Kim SH. Cellulose produced by Gluconacetobacter xylinus strains ATCC 53524 and ATCC 23768: Pellicle formation, post-synthesis aggregation and fiber density. Carbohydr Polym 2015;133:270–276. [CrossRef]
[56] Segal L, Creely JJ, Martin AE, Conrad CM. An empirical method for estimating the degree of crystallinity of native cellulose using the X-ray diffractometer. Textile Res J 1952;29:786–794. [CrossRef]
[57] Singh R, Mathur A, Goswami N, Mathur G. Effect of carbon sources on physicochemical properties of bacterial cellulose produced from Gluconacetobacter xylinus MTCC 7795. E-Polymers 2016;16:331–336. [CrossRef]
[58] Pogorelova N, Rogachev E, Digel I, Chernigova S, Nardin D. Bacterial cellulose nanocomposites: Morphology and mechanical properties. Materials (Basel) 2020;13:2249. [CrossRef]
[59] Gorgieva S, Trček J. Bacterial cellulose: Production, modification and perspectives in biomedical applications. Nanomaterials (Basel) 2019 Sep 20;9:1352. [CrossRef]
[60] Shezad O, Khan S, Khan T, Park JK. Physicochemical and mechanical characterization of bacterial cellulose produced with an excellent productivity in static conditions using a simple fed-batch cultivation strategy. Carbohydr Polym 2010;82:173–180. [CrossRef]
[61] Wang J, Wan YZ, Luo HL, Gao C, Huang Y. Immobilization of gelatin on bacterial cellulose nanofibers surface via crosslinking technique. Mater Sci Eng C 2012;32:536–541. [CrossRef]
[62] Lee KY, Quero F, Blaker JJ, Hill CAS, Eichhorn SJ, Bismarck A. Surface only modification of bacterial cellulose nanofibres with organic acids. Cellulose 2011;18:595–605. [CrossRef]
[63] Ybañez MG, Camacho DH. Designing hydrophobic bacterial cellulose film composites assisted by sound waves. RSC Adv 2021;11:32873–32883. [CrossRef]
[64] Kamal T, Ul-Islam M, Khan SB, Bakhsh EM, Chani MTS. Development of plant extract impregnated bacterial cellulose as a green antimicrobial composite for potential biomedical applications. Ind Crops Prod 2022;187:115337. [CrossRef]
[65] Ul-Islam M, Khan T, Park JK. Water holding and release properties of bacterial cellulose obtained by in situ and ex situ modification. Carbohydr Polym 2012;88:596–603. [CrossRef]
[66] Sanchavanakit N, Sangrungraungroj W, Kaomongkolgit R, Banaprasert T, Pavasant P, Phisalaphong M. Growth of human keratinocytes and fibroblasts on bacterial cellulose film. Biotechnol Prog 2006;22:1194–1199. [CrossRef]
[67] Ajiteru O, Lee OJ, Kim JH, Lee YJ, Lee JS, Lee H, et al. Fabrication and characterization of a myrrh hydrocolloid dressing for dermal wound healing. Colloids Interface Sci Commun 2022;48:100617. [CrossRef]
[68] Pértile RA, Moreira S, Gil da Costa RM, Correia A, Guãrdao L, Gartner F, et al. Bacterial cellulose: Long-term biocompatibility studies. J Biomater Sci Polym Ed 2012;23:1339–1354. [CrossRef]
[69] Unal S, Arslan S, Yilmaz BK, Oktar FN, Sengil AZ, Gunduz O. Production and characterization of bacterial cellulose scaffold and its modification with hyaluronic acid and gelatin for glioblastoma cell culture. Cellulose 2021;28:117–132. [CrossRef]
[70] Cesur NP, Laçin NT. Construction of vascular graft by 3D printing using bacterial cellulose formulation as bioink. Cellulose Chem Technol 2022;56:99–113. [CrossRef]
[71] Shao W, Wu J, Liu H, Ye S, Jiang L, Liu X. Novel bioactive surface functionalization of bacterial cellulose membrane. Carbohydr Polym 2017;178:270–276. [CrossRef]
[72] Ross R, Everett NB, Tyler R. Wound healing and collagen formation VI. The origin of the wound fibroblast studied in parabiosis. J Cell Biol 1970;44:645–654. [CrossRef]
[73] Halib N, Ahmad I, Grassi M, Grassi G. The remarkable three-dimensional network structure of bacterial cellulose for tissue engineering applications. Int J Pharm 2019;566:631–640. [CrossRef]
[74] Andrade FK, Alexandre N, Amorim I, Gartner F, Mauricio AC, Luis AL, et al. Studies on the biocompatibility of bacterial cellulose. J Bioact Compat Polym 2013;28:97–112. [CrossRef]
[75] Lin SP, Kung HN, Tsai YS, Tseng TN, Di Hsu K, Cheng KC. Novel dextran modified bacterial cellulose hydrogel accelerating cutaneous wound healing. Cellulose 2017;24:4927–4937. [CrossRef]
[76] Godinho JF, Berti FV, Müller D, Rambo CR, Porto LM. Incorporation of Aloe vera extracts into nanocellulose during biosynthesis. Cellulose 2016;23:545–555. [CrossRef]

[77] Ul-Islam M, Ahmad F, Fatima A, Shah N, Yasir S, Ahmad MW, et al. Ex situ synthesis and characterization of high strength multipurpose bacterial cellulose-Aloe vera hydrogels. Front Bioeng Biotechnol 2021;9:601988. [CrossRef]

[78] Chiaoprakobkij N, Sanchavanakit N, Subbalekha K, Pavasant P, Phisalaphong M. Characterization and biocompatibility of bacterial cellulose/alginate composite sponges with human keratinocytes and gingival fibroblasts. Carbohydr Polym 2011;85:548–553. [CrossRef]

[79] Lamboni L, Li Y, Liu J, Yang G. Silk sericin-functionalized bacterial cellulose as a potential wound-healing biomaterial. Biomacromolecules 2016;17:3076–3084. [CrossRef]

Sigma J Eng Nat Sci, Vol. 44, No. 1, pp. 55–73, February, 2026

Sigma Journal of Engineering and Natural Sciences
Web page info: https://sigma.yildiz.edu.tr
DOI: 10.14744/sigma.2025.00000

Research Article

Clustering business news for strategic insight: An unsupervised learning approach

Gaurav V. DAHAKE[1,*], M. S. ALI[1]

[1]*Department of Computer Science and Engineering, Prof. Ram Meghe College of Engineering and Management, Amravati, 01128, India*

ARTICLE INFO

Article history
Received: 03 April 2024
Revised: 18 July 2024
Accepted: 11 November 2024

Keywords:
BERT; Business News; Clustering Evaluation; Information Overload; K-Means; Text Clustering; Unsupervised Learning

ABSTRACT

Business news assists as an important tool which enables business leaders and marketers to create strategic plans through their decision-making process. The large number of news articles spread across different platforms creates difficulties when trying to find important information through efficient methods. The research presents an approach which employs unsupervised learning methods to cluster business news articles for solving information overload problems. The system uses K-Means and Agglomerative clustering algorithms together with Bag-of-Words and TF-IDF and BERT embeddings to identify articles with similar content. The research evaluates clustering performance through various assessment methods which include Elbow Score and Silhouette Score and Calinski-Harabasz Index and Davies-Bouldin Index to determine which approach works best. The combination of BERT with K-Means produces better results than TF-IDF because it reaches an accuracy level of 84.46%. The preprocessing stage required tokenization and stop word removal and stemming to solve the problems which occurred when dealing with noisy data and unimportant information. The results show that BERT achieves better clustering results because it understands deep semantic meanings in text data. The research investigates both scalability and practical implementation of the system through its proposed studies about real-time system flexibility and data bias ethical problems. The proposed solution improves users' ability to access business news which enables them to make better decisions.

Cite this article as: Dahake GV, Ali MS. Clustering business news for strategic insight: An unsupervised learning approach. Sigma J Eng Nat Sci 2026;44(1):55–73.

INTRODUCTION

The fast expansion of digital news platforms together with the large quantity of news content has created major difficulties for news organization and valuable information retrieval from this extensive information system. The process of grouping similar news articles has proven useful for solving these problems [1]. The system uses information retrieval and natural language processing to organize news articles through their semantic and thematic and contextual connections. The goal is to group articles with everyday topics, themes, or characteristics, enabling users to discover relevant content more efficiently [2,3]. The analysis of news

***Corresponding author.**
*E-mail address: gauravdahake.77@gmail.com

This paper was recommended for publication in revised form by Editor-in-Chief Ahmet Selim Dalkilic

Published by Yıldız Technical University Press, İstanbul, Turkey
© Author. This is an open access article under the CC BY-NC license (http://creativecommons.org/licenses/by-nc/4.0/).

article text content through information retrieval and natural language processing methods in clustering techniques helps researchers detect similar patterns in the data. Users can discover related content and hidden relationships and gain complete knowledge about various subjects through the process of clustering news articles [4]. The process of clustering news articles with similar content helps users organize information while recommending content and identifying trends which results in better news delivery and improved digital news access efficiency [5].

The process of clustering news articles which share similarities requires multiple solutions to achieve successful results. News articles contain language which remains ambiguous and subjective because this creates different ways for readers to understand what makes things similar. The process of article clustering becomes difficult because articles contain both background noise and unimportant data. The system needs to handle increasing news article numbers because its scalability becomes a problem which demands better algorithm performance [6]. The process of feature extraction and similarity measurement becomes more complicated because of different writing styles and language choices which appear in textual variations. News requires immediate processing because of its time-sensitive nature which makes temporal analysis essential for achieving proper clustering results [7]. The evaluation of clustering quality and determination of cluster numbers remains difficult while researchers face challenges when dealing with overlapping topics and multiple cluster assignments for articles [8]. The solution of these problems requires sophisticated methods for data preprocessing and feature extraction and similarity assessment and evaluation which produce better clustering results for news articles with similar content.

The current clustering methods lack sufficient power to detect semantic relationships between words because they use Bag-of-Words and TF-IDF approaches. The methods fail to handle high-dimensional data while their ability to process large datasets including continuously updated news articles remains limited. The current clustering methods fail to consider how news topics change over time which results in clusters that become irrelevant. The current methods fail to process news data which contains noisy information together with missing or unimportant content that appears in actual news datasets. Research studies depend on restricted evaluation criteria which produce restricted assessments of clustering performance. The current methods lack practical use in real-world settings which creates challenges for evaluating their performance in active operational environments. The research fills these knowledge gaps through its implementation of BERT embedding methods and its use of strong text processing techniques and its detailed assessment protocol which enhances its ability to work in practical scenarios.

The Paper contains its primary contribution which follows.

The system provides an organized framework to process large news datasets which enables users to find relevant information and discover important knowledge from their data. Clustering facilitates effective content organization and trend analysis by grouping similar articles together. It assists in identifying hidden patterns, emerging topics, and relationships within news articles, allowing users to navigate the news landscape more effectively.

- In order to develop clustering algorithms the following can be used: K-mean and Agglomerative, these integrated with Bag-Of-Words, Word2Vec, TF-IDF and BERT to generate data embeddings.
- The choice of evaluation metric such as Silhouette Score, Davies-Bouldin Index, Calinski Harabasz Index and Elbow method plays a crucial role in refining and improving clustering techniques for news articles that are similar.

The organization of the Paper is as follows: Section 2 presents the different approaches and techniques for clustering similar news articles. Section 3 presented the complete methodology for clustering identical news articles. The final section of this study presents both result analysis and establishes the research findings and future research possibilities.

Related Work

The field of text clustering involves various algorithms for grouping similar texts together. Among the most commonly used algorithms are the vector space model, k-means clustering plus its derivatives, techniques based on generation and on spectra, methods to reduce dimensionality and lastly, methods based on phrases [1]. This traditional approach, vector space model, is well suited to problems that have similar themes however the model assumes the number of clusters beforehand [2]. K-means clustering can be used for hierarchical clustering and partitioned clustering [3]. However, this kind of clustering has a few significant limitations. These include a high computational demand for large data sets, requirement for random initialisation and also the sensitivity to outliers present in the data. Another approach for clustering fake news based on the k-mean algorithm [9]. Advanced deep learning techniques such as CNN and BERT are being utilised for clustering based fake news detection [10]. The performance of generative algorithms decreases when working with different types of data and they need to know the number of clusters in advance [5]. The algorithm of spectral clustering achieves its best results when data exists as a bipartite graph because it lacks the need for cluster number specification [4-6]. The original computer vision methods for dimensionality reduction achieve high performance but they need random starting points which produce different results when analyzing the same data [7,8]. Phrase-based methods encode word order but don't guarantee higher accuracy than other clustering methods [9,10]. The Agglomerative were proposed for clustering short texts and news articles [11]. For instance,

discriminant topic models and social network analysis on Twitter [12,13]. Special kernel functions for semantic similarity and collective clustering methods have also shown promise in improving clustering accuracy for short texts and news [14,15]. RELEVANTNews, a web feed reader by Sonia Bergamaschi et al.[16], organizes news on similar topics from different newspapers based on syntactic and lexical similarities. However, many aggregators with similar functionalities are commercial products with proprietary systems [17]. Text clustering has become a crucial approach used to manage the enormous quantity of textual data that exists in the healthcare sector which holds important health-related information. In recent years, there has been a growing interest in the fields of natural language processing to the area of healthcare due to significant advancements in emerging deep learning approaches [18]. A combined optimal strategy utilizing K-means has been proposed that help doctors properly aggregate healthcare information connected to heart problems and discover the optimal remedy [18]. A cloud-edge computation architecture is the foundation for the C-means method established, allowing for the gathering of health information from several institutions [19]. Numerous techniques have been put out thus far for optimizing the cluster design [20]. These fall within the categories of neutral and biased techniques. Most approaches used to address the atomic framework optimization involve variations, namely, some methodologies, such as static lattice search [21]. These can make cluster optimization easier. However, their usefulness is severely limited because they work only with certain clusters and are hard to apply to other optimized feature situations. The Rock algorithm was used to optimizing the data cluster based on k-means [22,23]. In evaluating performance, hyperparameter optimization (HPO) acts as a valid process in and of itself. In contrast to the very substantial scientific work on the suitable assessment of supervised using, however, there is a lesser understanding regarding the appropriate assessment of cluster techniques in combination with HPO [24].

These clustering techniques fall into three broad categories, each with specific characteristics and applications.

1. Straightforward per user gives a graphical interface to imagining and gathering RSS channels from various papers. Essential capacities supporting the client in perusing are shown (for example, web crawler, distinctive requesting, a relationship of information to a guide);
2. News classifiers show the news arranged based on standards now and then chosen by the client. Straightforward characterizations might take advantage of the classes or potentially the watchwords given by the sites;
3. Progressed aggregators give extra elements to support the client in perusing, grouping, arranging, and putting away news.

Various studies have explored different approaches to organizing and presenting news. Velthune, introduced in [25], is a news search engine that uses a simple classifier to categorize information. In contrast, RELEVANTNews focuses on clustering similar information based on their content. This clustering method can create large newsgroups in the same category, making navigating harder for readers. RCS (RSS Clusgator device) proposed in [26] updates clusters of news over time, aiming to maintain the relevance of information. NewsInEssence [27], another aggregator, uses the TF*IDF clustering algorithm to group similar news and provide summarized content for readers. However, RELEVANTNews doesn't offer summaries but utilizes a customizable clustering algorithm based on syntax, words, and primary relationships to improve clustering accuracy.

The authors describe a system based on Matrix-based News Aggregation (MNA) which operates through a five-stage processing pipeline in their research [28]. The system starts by gathering data from web sources which gets stored before it moves to article classification and content reduction and visual presentation for user consumption. The main MNA methodology uses a structured matrix format to organize information where news entities serve as matrix rows and their attributes function as matrix columns. The system enables users to personalize their search preferences which become the starting point for the matrix. The process of summarization comprises several tasks such as summarization based on a topic and TF-IDF summarization of the content within each cell of the matrix.

These works illustrate various techniques used in clustering similar news articles, utilizing different techniques such as topic modeling, entity-based attributes, graph ranking, embedding techniques, and personal clustering. These works help in improving clustering techniques used in the task of clustering similar news articles, as they provide effective means of dealing with challenges of clustering news.

Proposed Methodology

This study employs a methodology to cluster similar news articles by combining text embedding techniques with K-Means and Agglomerative clustering. Initially, textual data is converted into numerical feature vectors using four representations: Bag-of-Words (BoW), which counts word frequencies; TF-IDF, which weights word importance; Word2Vec, which captures semantic relationships; and BERT, which generates context-aware embeddings. The embeddings provide a vector representation that captures the semantic meaning of each article. During the next stage the algorithm makes clusters by successively placing each story into the cluster whose centroid is closest according to a distance function such as Euclidean distance, thereby aiming to reduce the within cluster sum of squares. The iterations are continued until a stopping criterion is met. The hierarchical clustering algorithm employed is agglomerative clustering, where the procedure starts with each item of information as a separate cluster and then merges those clusters which are closest to each other according

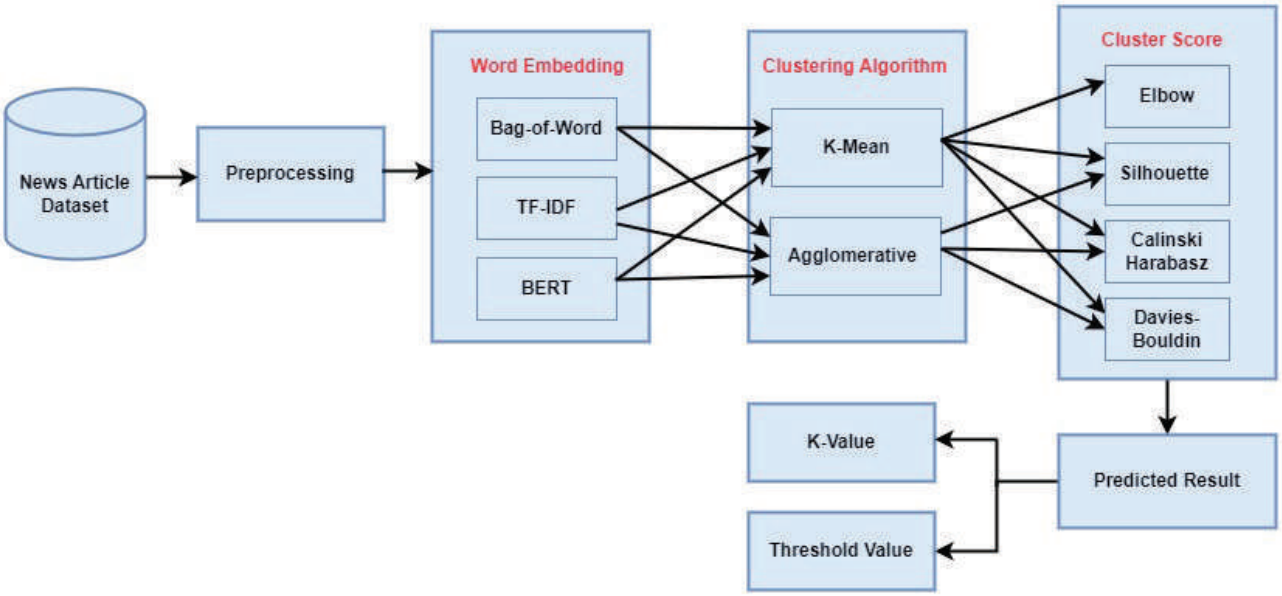


Figure 1. Proposed Architecture of clustering similar news articles.

to a defined similarity measure. The choice of appropriate clustering validation tool depends on data type. Techniques like silhouette, Calinski Harabasz, Davies-Bouldin index and elbow method can be used to decide on the optimal number of clusters. Through the use of these clustering algorithms and the appropriate application of embeddings, the proposed methodology seeks to efficiently cluster news articles based on content and facilitate an understanding of the relevant groupings of information.

Overview of Dataset

The dataset used in this study is the News Aggregator Dataset from Kaggle, a well-established resource for text analysis and machine learning research. This dataset encompasses many articles sourced from diverse publishers and covers a wide range of topics, including politics, technology, entertainment, and sports. The dataset contains 422,937 news stories or articles. Each item within the database includes detailed information, for instance publication date, news agency, the category the news story belongs to and title. This combination of large scale, topical variety, and rich metadata provides a robust foundation for developing and evaluating our clustering methodology, enabling rigorous testing of the algorithms' ability to organize and categorize real-world news content.

Data Preprocessing

At the beginning of the processing stage of a program which gathered news articles a number of problems were encountered. The presence of these elements, though, led to a loss of semantic coherence and a lessening of the semantic importance of the words used in the text, which resulted in a clustering accuracy that was lower than expected. In order to tackle these problems, various natural language processing techniques were utilised. The text was initially split into individual words by means of tokenisation, which at the same time removed punctuation from the text. By excluding articles such as 'the', 'a' and 'in', word filtering removes words which generally do not add much to the meaning of the document during the process of clustering. Stemming further reduced words to their root forms, minimizing variations of the same word, and Case Transformation standardized the text by converting all characters to lowercase. The NLTK tools were used to apply a series of text pre-processing steps which cleaned the data, improved its relevance and increased the accuracy of the clustering algorithms.

Embedding Techniques

This study employed three-word embedding techniques: Bag-of-Words, TF-IDF, and BERT. Each method was integrated with two clustering algorithms, namely K-means and Agglomerative, to cluster similar news articles.

Bag of words

A bag-of-words model is a method for extracting the relevant features from a similar news article dataset for modeling, such as with proposed classifiers. The approach is very simple and flexible and can be used in a myriad of ways [29].

To create a mathematical model using the Bag of Words (BoW) approach for clustering similar news articles,

Create a vocabulary V by collecting all unique terms from the preprocessed articles.

$$V = [n(w_{1,d})\ n(w_{2,d})\ n(w_{3,d})\ \ldots . n(w_{T,d})] \quad (1)$$

$N(.)$ is the number of news articles occurring in datasets

The similarity between the two articles is measure using distance based on cosine similarity

$$d(p_i, q_j) = \cos\theta \tag{2}$$

$$= \frac{p_i \cdot q_j}{||p_i||\,||q_j||} \tag{3}$$

Term Frequency-Inverse Document Frequency (TF-IDF)

Term frequency-ınverse document frequency (TF-IDF) is a commonly used statistical technique in natural language processing and information retrieval. It assesses the similarity of an article compared to a set of news articles. TF-IDF turns an article into a vector by multiplying its TF with the Inverse Document Frequency (IDF). This calculation helps determine how relevant a news article is to a dataset.

To establish a mathematical model using TF-IDF for clustering similar news articles

$$V = [n(w_{1,d})\; n(w_{2,d})\;\; n(w_{3,d})\;\; \ldots . n(w_{T,d})] \tag{4}$$

all the articles are not equally created

$$V_d = [(w_{1,d}) \propto_1 n(w_{2,d}) \propto_2 n(w_{3,d}) \propto_3 \ldots . n(w_{T,d}) \propto_T] \tag{5}$$

$$n(w_{i,d}) \propto_i = n(w_{i,d}) \log \left\{\frac{D}{\sum_{d'} 1[w_i \in d']}\right\} \tag{6}$$

Word2Vec

Word2Vec creates vectors of the article that are distributed numerical representations of news article features; these features could comprise articles that represent the context of the individual news articles present in datasets [30]. Word embeddings eventually help establish the association of news articles with other similar-meaning news articles through the created vectors.

To create a mathematical model using Word2Vec for clustering similar news articles, Measure the position x of each article and define the center news article at that position as c and the context article *o*. To recognize article, define window size *w*, denotes the proposed model will used as articles in position *t* - *w to t* + *w* as the context. Once the measure of all the context article at position *t*, to maximize the context article given the centroid article, measure the probability of the proposed model predicting the context news articlesbased on center article. The following equation shows to maximize the probability.

$$L(\emptyset) = \prod_{t=1}^{T} \prod_{\substack{-w \le j \le w \\ j \neq 0}} P(M_{t+j} | M_t; \emptyset) \tag{6}$$

Convert equation 6 into derivations and make it maximization problem, take the log and multiply by -1

$$J(\emptyset) = -\frac{1}{T} log L(\emptyset) = -\frac{1}{T} \sum_{t=1}^{T} \sum_{\substack{-w \le j \le w \\ j \neq 0}} \log P(M_{t+j} | M_t; \emptyset) \tag{7}$$

Measure the probability of context article. Denote each article by two sets of vectors, *Pm* and *Qm*. If m is context article, then use *Pm* and if *m* is centre article, then use *Qm*. according to this vector, probability equation for center article o and context article *c* as shown in equation 8

$$P\,(O = o | C = c) = \frac{\exp\,(p_o{}^T q_c)}{\sum_{m \in Dataset D} \exp\,(p_m{}^T q_c)} \tag{8}$$

Equation 8 retrieves the similarity of two vectors o and c. More similarity, more probability.

$$\emptyset = \begin{bmatrix} Qm1 \\ Qm2 \\ Qm3 \\ . \\ . \\ Qmn \\ Pm1 \\ Pm2 \\ Pm3 \\ . \\ . \\ Pmn \end{bmatrix} \in R^{2dV} \tag{9}$$

Equation 9 represents the vector that consists of both p and q vectors of d length for the articles.

BERT

This study uses BERT for word embedding to cluster similar articles. BERT embeddings capture contextual and semantic information of words and phrases, which highly benefits clustering similar news articles. By representing articles as vectors of BERT embeddings, measure the semantic similarity between articles. This enables the clustering of articles based on their content and context [31].

Figure 2 shows the representation of the BERT model to generate the context-based data embedding. This model is trained on a massive news article dataset of the English language. BERT's depth (12 layers), hidden size (512), and multi-head self-attention (12 heads) are vital components that allow it to capture rich contextual information from similar article data. In this research, information is taken from the output of the second-to-last layer of a transformer model, specifically the 11th layer. This information is turned into a form that looks like a tensor with measurements (n, 25, 511). Where 'n' stands for the number of articles in the dataset, '25' is how many words or parts are in each article, and '511' shows the size of the hidden information. Later, methods for extracting features and making the data consistent will be used on this information, leading to a matrix with measurements of (n, 511).

Utilizing BERT to cluster similar news articles involves the following mathematical model:

For the Articles *Ai* shows the sequence of words *w* = [*w*1, *w*2, *w*3.... *wn*], the article embedding *E*(*A*) can be computed as:

$$E(Ai) = BERT([w1, w2, w3 \ldots . wn]) \tag{10}$$

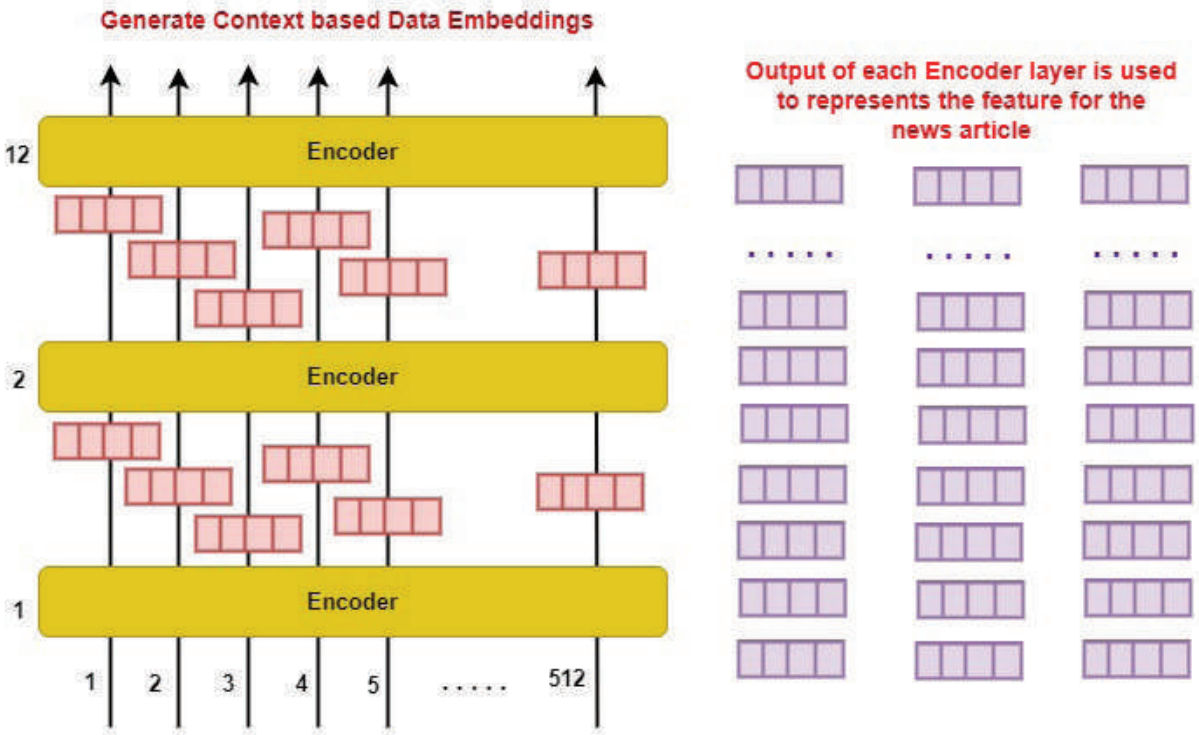


Figure 2. Representation of BERT for context-based data embedding.

The Max pooling layer cab be showed by further equation 11

$$a[k] = \max_{l=1,2....,n} w_{ik} \tag{11}$$

where, $w[k]$ is the *k-th* entry of similar articles data of vector w. The complete articles can represent all the contextual information vectors, and taking the mean of these vectors removes noise in the data, which is why mean pooling is considered. Equation 12 illustrates the mean pooling approach.

$$w[k] = \frac{\Sigma_{i=1}^{n} w_{ik}}{n} \tag{12}$$

$f(w) = w$ represents the identity normalization, which is used as an identity function. For the vector ai, standard normalization involves applying the function as described in the equation 13.

$$\overline{w} = \frac{w_i}{\|w_i\|} \tag{13}$$

Where, $\overline{w}$ represents the normalized vector. it converts vector into norm of 1. The layer normalization approach can minimize the covariate shift issue, during the training the model [31], equation shows the function in layer.

$$\overline{w} = \frac{w_i - \theta_i}{\sigma_i} \tag{14}$$

Where, θ_i and σ_i represents the mean and SD of the vector w_i. min-max normalization approach is used to maintain the primary distribution of the similar article data vectors. It utilizes the function described in the equation 15.

$$\overline{w} = \frac{w_i - min_d(w_{id})}{max_d(w_{id}) - min_d(w_{id})} \tag{15}$$

BERT processes the entire sequence and retrieves the contextual data and semantics of the articles. With article embedding obtained from BERT, similarity between articles is computed using various similarity measures based on Cosine similarity techniques. Example two articles embedding $E(Ai)$ and $E(Aj)$, the cosine similarity $S(Ai,Aj)$ is calculated as:

$$S(Ai, Aj) = \frac{E(Ai).E(Aj)}{||E(Ai)||.||E(Aj)||} \tag{16}$$

The dot (.) is used to measure the similarity the vectors, and the Euclidean norm (magnitude) is used to normalize the vectors.

Functioning of Clustering Techniques

Clustering methods used include K-Means and Agglomerative hierarchical clustering, due to their suitability for handling large numbers of features in each data point, such as those found in text vector representations. The K-means algorithm works well with very large collections and also performs well with techniques such as BERT and TF-IDF feature

extraction when the number of groups is known. In contrast, agglomerative clustering enables hierarchical cluster structuring which facilitates the identification of connections between documents that exhibit varying degrees of similarity. In such instances where these methods may not be optimal is when dealing with non-spherical cluster forms.

K-Means Clustering

Clustering analysis using the k-means method groups together a collection of data points, without prior knowledge, into K clusters. Randomly select k cluster centers from the data, which are often referred to as the centroids of the cluster. The centroids used are actually randomly chosen points from the given set of data. They are used to train a classifier with these centroids. This classifier then assigns data points to clusters, initially creating random clusters [33]. Afterward, each centroid is updated to the average position of the cluster it represents. This classification and centroid update process is repeated until the centroids' positions stop changing. As a result, the vectors lying in this space finally converge to stable centroids, which in turn classify the data points into groups or classes. This classification gives anonymous data points a particular identity and assigns them to specific clusters. In order to establish a mathematical model for K-means clustering for clustering similar news articles, we can define the equation 17 (Table 1):

$$A = \sum_{n=1}^{N} \sum_{k=1}^{K} r_{nk} ||x_n - \mu_k||^2 \quad (17)$$

r_{nk} is belongs to (0,1) represents the membership value of data x_n in cluster K. To minimizes the objective function A need to measure the specific value for r_{nk} and μ_k. The objective function A can be minimized by set the values of r_{nk} and μ_k based on the equation 18

$$r_{nk} = \begin{cases} 1 & k = arg\ min_k ||x_n - \mu_k||^2 \\ 0, Others \end{cases} \quad (18)$$

$$\mu_k = \frac{\sum_{n=1}^{N} r_{nk} x_n}{\sum_{n=1}^{N} r_{nk}} \quad (19)$$

Agglomerative Clustering

News articles are clustered based on their similarity in vector space, using agglomerative hierarchical clustering. This method uses a measure of distance such as the Euclidean distance. The program provides a comprehensive view of the way clusters are formed. Through this, it is possible to establish a detailed level of granularity in the clustering which the algorithm produces. This makes it easier to discover which news items are grouped together in the hierarchy created by the Table 2.

To create a mathematical model for Agglomerative Clustering to cluster similar news articles and define the following:

The agglomerative clustering techniques applied to non-vector data

Consider $A = x1, x2, ... xn$

A is the article dataset

Now updated the predefined threshold of distance. There are two cluster p and q are combined to each other and create new cluster r. Consider k represents the other existing cluster. If measured the distance between cluster q and cluster k. p and q are the existed, the distance between p and k and the distance between q and k. Represents the distance by $D(p, k)$ and $D(q, k)$

The cluster is the single link cluster

$$D(r, k) = min(D(r, k), D(q, k)) \quad (20)$$

$D(r, k)$ represents the minimum distance between the articles in cluster r and k resp. It can be denoted the equation 20 update the distance is similar to minimum distance between two articles over the two cluster.

Complete cluster is

$$D(r, k) = max(D(r, k), D(s, k)) \quad (21)$$

where, $D(r, k)$ represents the max distance between two articles in cluster r and k

The two distances, $D(p, k)$ and $D(q, k)$ are aggregated with the weighted sum

$$D(p, k) = \frac{1}{2} D(p, k) + \frac{1}{2} D(q, k) \quad (22)$$

The centroid measure for each cluster article and the distance between article clusters is represented as the distance between their centroids.

$$D(p, k) = \frac{1}{2} D(p, k) + \frac{1}{2} D(q, k) - \frac{1}{4} D(p, q) \quad (23)$$

Table 1. K-means clustering

Step 1: Initialize K cluster centroids, $\mu = \{\mu 1, \mu 2, .., \mu K\}$, randomly.

Step 2: Assign each news article xi in X to the nearest centroid:

$zi = argmin(||xn - \mu k||)$, for $k = 1$ to K, using a distance metric such as cosine similarity.

Step 3: Update the centroids by computing the mean of the vectors in each cluster:

$\mu k = (1/|Ck|) * \Sigma xi$, for xi in Ck.

Step 4: Repeat the assignment and update steps until convergence or a predefined stopping criterion is met. Convergence is achieved when the centroids no longer change significantly or when the maximum number of iterations is reached.

Table 2. Agglomerative clustering

Step 1: Initialize each news article *xi* as a separate cluster.

Step 2: While the number of clusters is greater than 1

- Find the pair of clusters with the minimum distance, i.e., the closest pair of clusters in the distance
- Matrix *D*.
- Combine the two neighbour clusters into a single cluster.
- Modify the distance *D* by recalculating the distances between the new cluster and the remaining clusters using a linkage criterion such as complete linkage.

Step 3: Assign each news article to its corresponding cluster based on the final clustering structure.

The following equation 24 can update the distance

$$D(r,k) = \frac{n_p+n_k}{n_p+n_q+n_k} D(p,k) + \frac{n_q+n_k}{n_p+n_q+n_k} D(q,k) - \frac{n_k}{n_p+n_q+n_k} D(p,q) \quad (24)$$

Hyperparameter Setting

When performing cluster analysis on similar news stories using K-means and agglomerative clustering, parameter tuning is required. The choice of the number of clusters, the way of initializing cluster centroids and the maximum number of iterations relate to the k-means clustering algorithm. Three metrics can be used to determine the number of clusters for k-means: the Silhouette method, the Davies-Bouldin method and the elbow method. The k-means algorithm can be enhanced by using the 'k-means++' algorithm for initialization to improve the clustering's stability and efficiency of convergence. The number of iterations (max_iter) should be set to 300, which ensures a sufficient number of iterations for convergence. Agglomerative clustering can be optimised by adjusting three parameters: the number of clusters, the average linkage method and the metric used to calculate the distance between clusters. In general, grid search with cross-validation was employed to find the best parameters of the algorithm so as to improve the cluster's accuracy and quality.

Parameter Evaluation

To obtain the most accurate cluster results in grouping similar news articles together, parameter settings need to be optimised. Some key parameters to consider when evaluating the effectiveness of clustering techniques:

Elbow Score: A heuristic to determine the optimal number of clusters. Generally, the cluster radius is obtained from the within cluster sum of squares, calculated as follows:

$$WCSS = \sum_{i=1}^{k} \sum_{j=1}^{n} (x_{ij} - c_j)^2 \quad (25)$$

Where, *K* represents the number of clusters to measure, n represents the number similar articles, x_{ij} denotes the *jth* similar articles in the ith cluster, c_j is the centroid of the *ith* cluster

Silhouette Score: The Silhouette Score is a tool that checks how healthy clusters created by a clustering method work. It determines how much an article matches its cluster compared to the other clusters. To find the Silhouette Score for a particular article, a specific formula is used:

$$S(i) = \frac{b(i) - a(i)}{max\{a(i),b(i)\}} \quad (26)$$

Where, $S(i)$ is the Silhouette Score for similar news articles point i, $a(i)$ represents the average distance of similar news articles i to all other articles in the similar cluster, $b(i)$ is the smallest average distance of similar news articles i to all news articles in other cluster

Calinski-Harabasz (CH): The Calinski-Harabasz (CH) score, also called the Variance Ratio Criterion, is used to judge how good clusters are when created by a clustering method. It calculates the ratio between how different clusters are from each other compared to how similar data points are within the clusters. A higher CH score means more apparent and more distinct clusters. The formula for the Calinski-Harabasz score is used to calculate this:

$$CH = \frac{B(K)}{W(K)} \times \frac{N-K}{K-1} \quad (27)$$

Where, *CH* is the Calinski-Harabasz score, *K* is the number of clusters, *N* is the total number of similar news articles. $B(K)$ is the between-cluster variance, which is calculated as the sum of squared distances between cluster centroids and the overall mean of the similar news articles, weighted by the number of articles in each cluster. $W(K)$ is the within-cluster variance, which is the sum of squared distances between similar news articles and their respective cluster centroids.

Davies-Bouldin: The Davies-Bouldin Index is a tool used to judge the quality of clusters made by a clustering method. It looks at how similar each cluster is to its most similar one while also considering the size of the clusters. The formula for calculating the Davies-Bouldin Index is utilized for this purpose:

$$DB = \frac{1}{K} \sum_{i=1}^{K} max_{j \neq i} \left(\frac{S_i+S_j}{a(c_i,c_j)} \right) \quad (28)$$

Each evaluation metric provides a different perspective on clustering quality. The Elbow method for determining the optimal number of clusters, while the Silhouette Score evaluates how well-separated the clusters are. Calinski-Harabasz and Davies-Bouldin indexes measure the internal structure of clusters, with the former focusing on the variance ratio and the latter assessing cluster compactness.

RESULT AND DISCUSSION

Clustering Result of K-Mean

In this phase, we employ various combinations of embedding techniques and clustering methods to group news articles. To assess these combinations, we used a collection of 3811 news articles. Techniques such as Bag-Of-Words, TF-IDF, Word2Vec, and BERT embeddings were applied to these articles. Subsequently, we employed K-means and Agglomerative clustering methods on the embedded news articles. The elbow method was utilized to determine the optimal value for K in K-means clustering.

Figure 3(a) shows the inertia of clusters from 15 to 30. The Bag-Of-Words technique was used to embed text into vectors. It can be observed from Figure 3 that there are considerable variations in inertia as try clusters from 15 to 25,

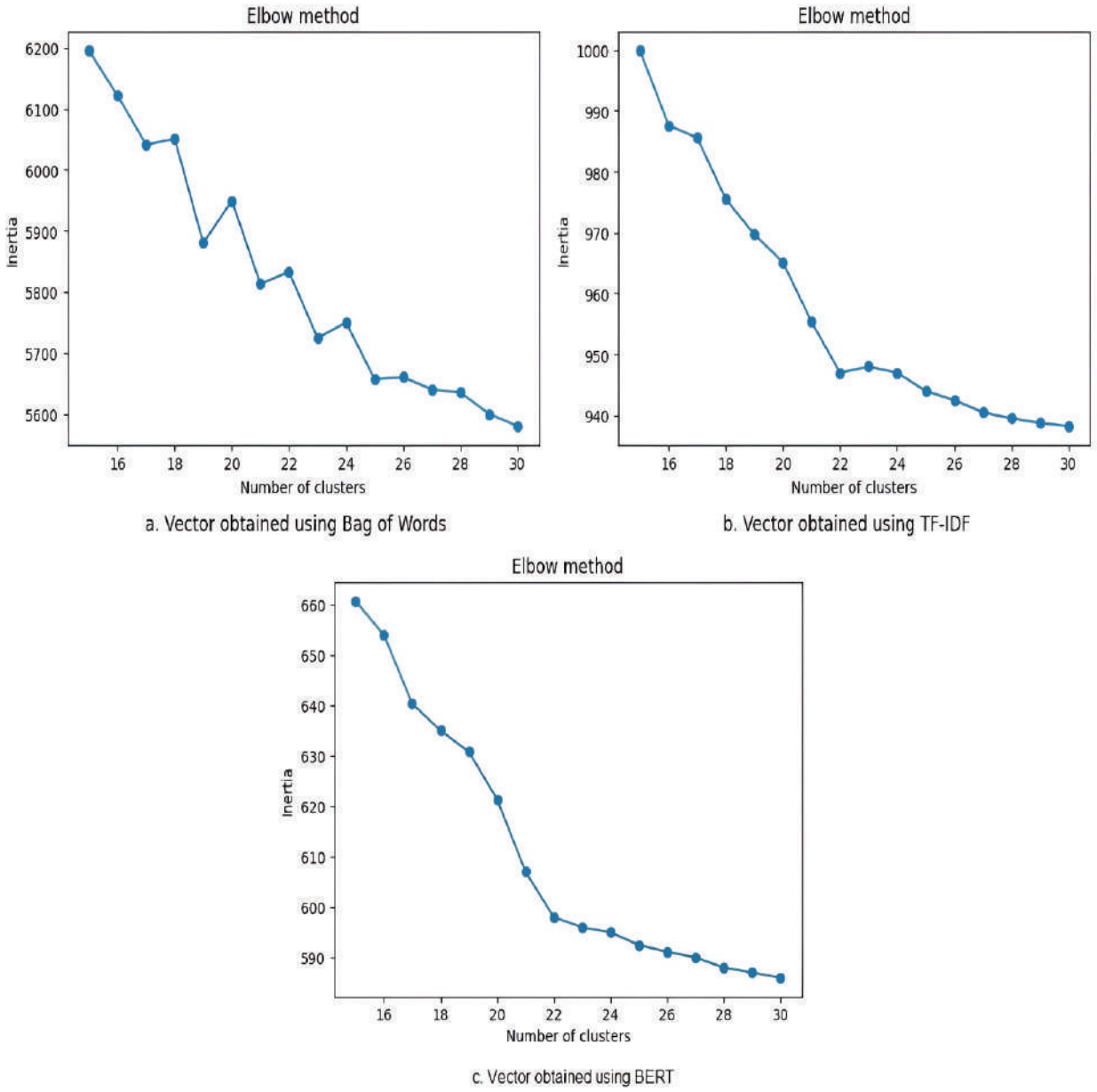


Figure 3. Vector obtained using Elbow method (a) Bag-Of-Words (b) TF-IDF (c) BERT of K-Mean.

and after 25 shows that inertia does not change much. So, according to Figure 3(a), the value of K can be taken as 25.

Figure 3(b) shows the inertia of clusters from 15 to 30. The TF-IDF technique was used to embed text into vectors. From Figure 3(b), the elbow shape is formed at 22 clusters. So, according to Figure 3(b), the value of K is 22.

Figure 3(c) shows the inertia of clusters from 15 to 30. The BERT technique was used to embed text into vectors. From Figure 3(c), it can be seen clearly that the elbow shape is formed at 22 clusters. According to Figure 3(c), the value of K is 22.

Figure 4 (a) shows the Silhouette Score of clusters from 15 to 30. The Bag-Of-Words technique was used to embed text into vectors. According to Figure 4 (a), the value of K is 22.

Figure 4 (b) shows the Silhouette Score of clusters from 15 to 30. The TF-IDF technique was used to embed text into vectors. According to Figure 4 (b), the value of K is 22.

Figure 4 (c) shows the Silhouette Score of clusters from 15 to 30. The BERT technique was used to embed text into vectors. According to Figure 4 (c), the value of K is 23.

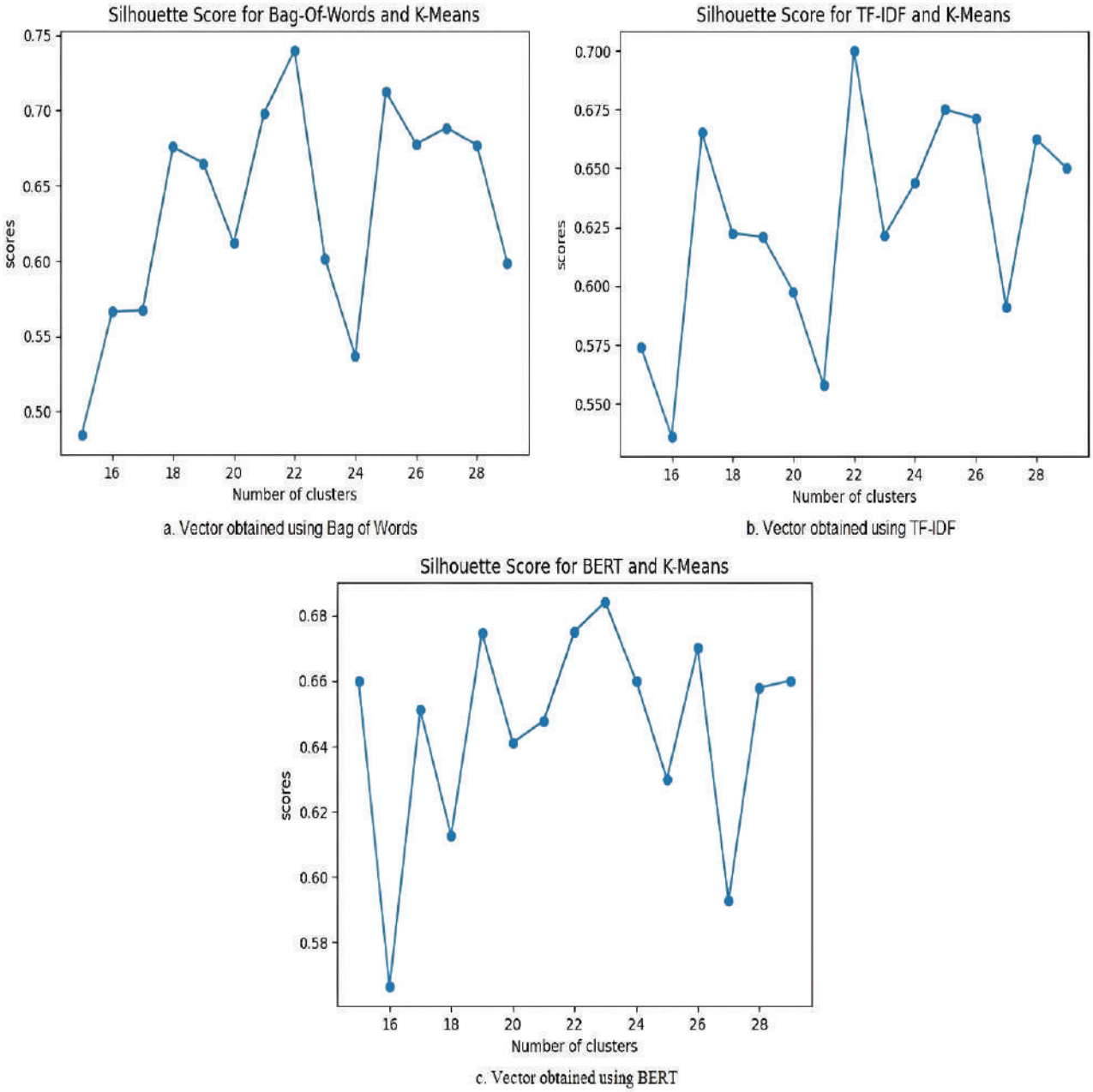


Figure 4. Vector obtained using Silhouette Score (a) Bag-Of-Words (b) TF_IDF (c) BERT of K-mean.

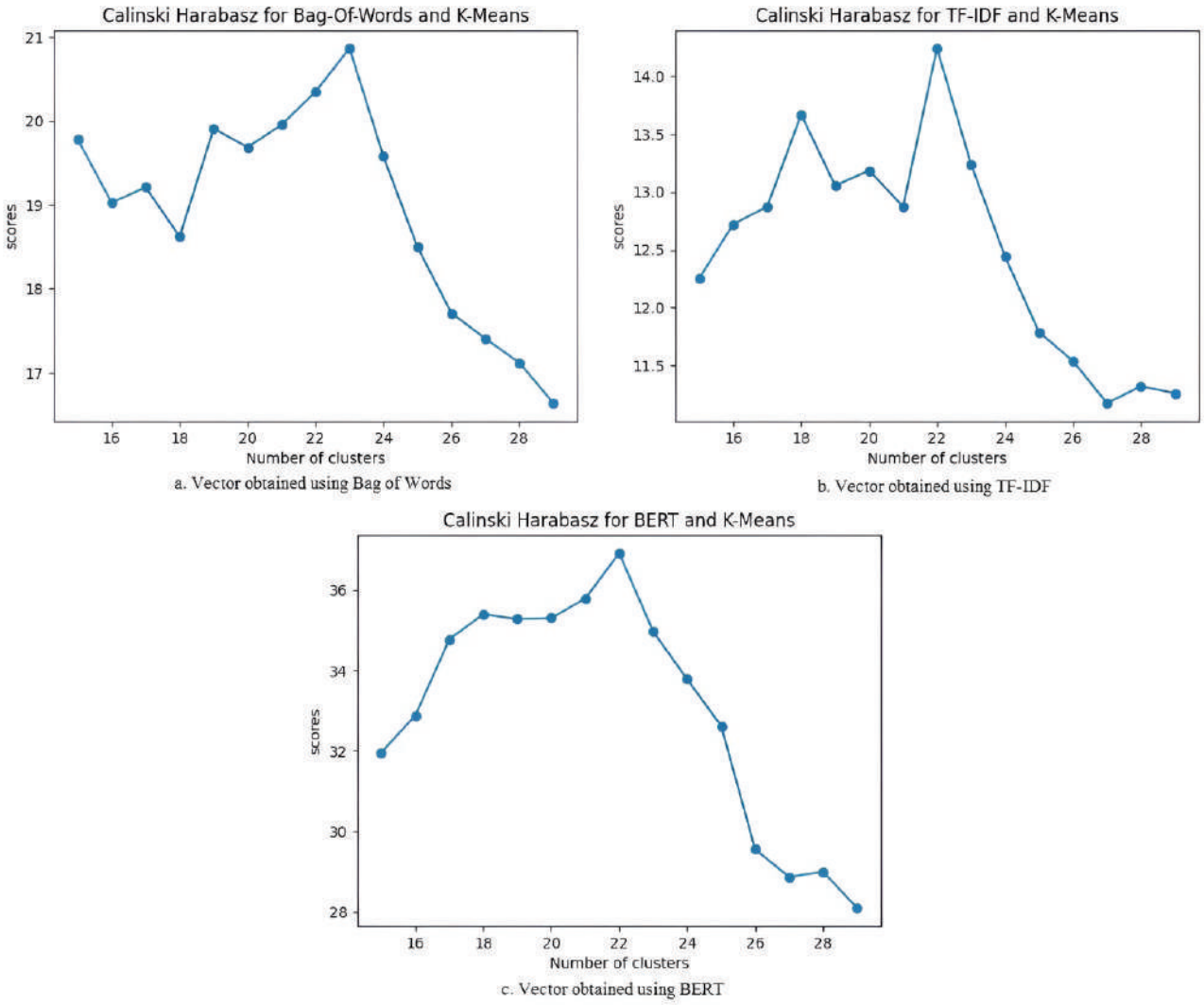


Figure 5. Vector obtained using Calinski Harabasz (a) Bag-Of-Words (b) TF-IDF (c) BERT of K-mean.

Figure 5 (a) shows the Calinski Harabasz Score of clusters from 15 to 30. The Bag-Of-Words technique was used to embed text into vectors. According to Figure 5 (a), the value of K is 23.

Figure 5 (b) shows the Calinski Harabasz of clusters from 15 to 30. The TF-IDF technique was used to embed text into vectors. According to Figure 5 (b), the value of K is 22.

Figure 5 (c) shows the Calinski Harabasz of clusters from 15 to 30. The BERT technique was used to embed text into vectors. According to Figure 5 (c), the value of K is 22.

Figure 6(a) shows the Davies-Bouldin Score of clusters from 15 to 30. The Bag-Of-Words technique was used to embed text into vectors. According to Figure 6(b), the value of K is 24.

Figure 6(b) shows the Davies-Bouldin of clusters from 15 to 30. The TF-IDF technique was used to embed text into vectors. According Figure 13, the value of K is 22.

Figure 6(c) shows the Davies-Bouldin of clusters from 15 to 30. The BERT technique was used to embed text into vectors. According to Figure 6(c), the value of K is 22.

Clustering Result of Agglomerative

A for loop is used to find the optimum threshold value, which starts from 0.75 to 0.85. In each iteration, this value is incremented by 0.0125. So, various scores, such as Silhouette, Calinski-Harabasz, Davies-Bouldin, etc., are evaluated for eight threshold values.

Figure 7(a) shows the Silhouette Score for threshold 0.75 to 0.85. The Bag-Of-Words technique was used to embed text into vectors. According to Figure 7(a), the value of threshold is 0.8.

Figure 7(b) shows the Silhouette Score for threshold 0.75 to 0.85. The TF-IDF technique was used to embed text into vectors. According to Figure 7(b), the value of threshold is 0.7875.

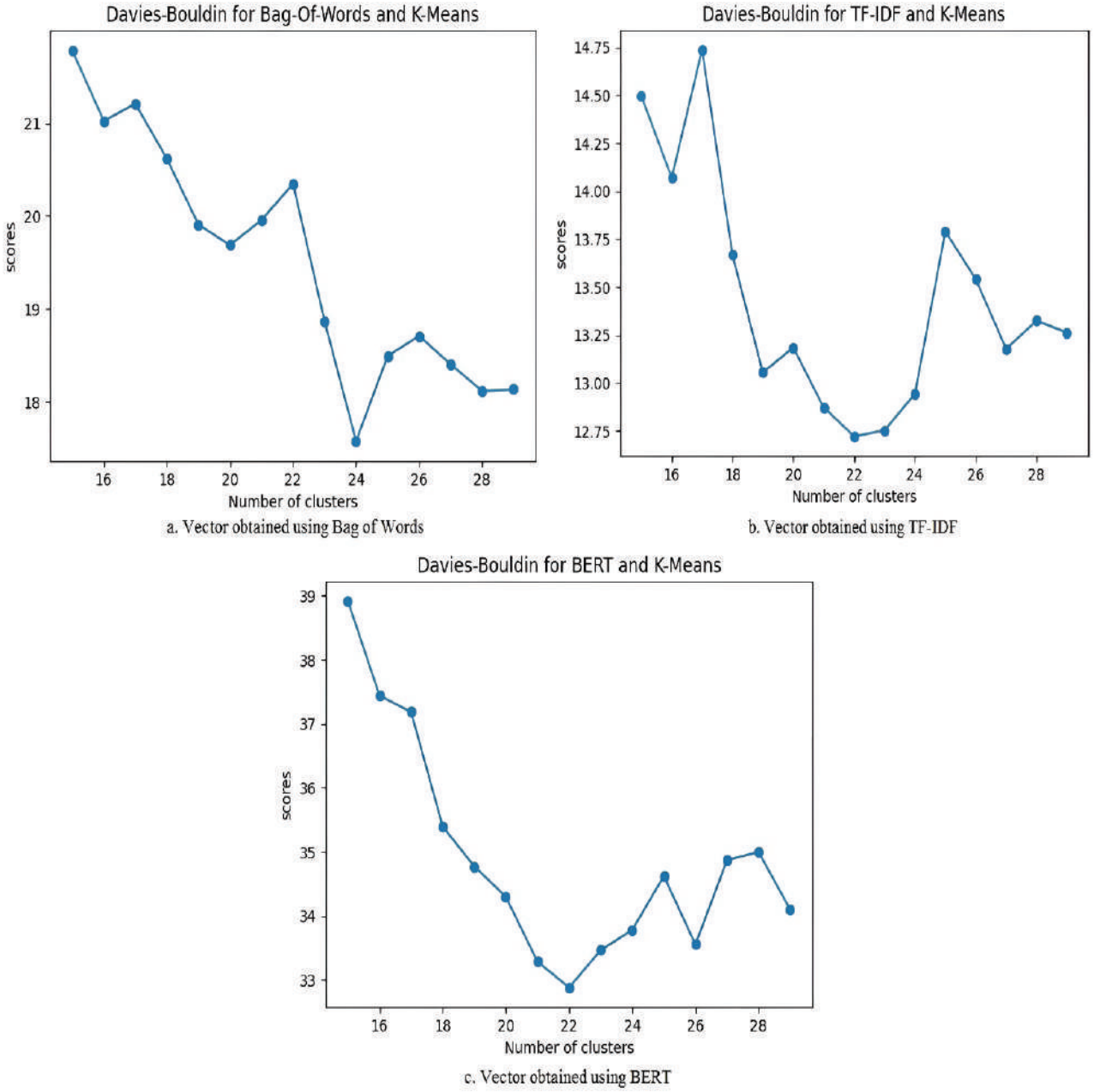


Figure 6. Vector obtained using Davies-Bouldin (a) Bag-Of-Words (b) TF-IDF (c) BERT of K-mean

Figure 7(c) shows the Silhouette Score for threshold 0.75 to 0.85. The BERT technique was used to embed text into vectors. According to Figure 7(c), the value of threshold is 0.7875.

Figure 8(a) shows the Calinski-Harabasz Score for threshold 0.75 to 0.85. The Bag-Of-Words technique was used to embed text into vectors. According to Figure 8(a), the value of threshold is 0.7875.

Figure 8(b) shows the Calinski-Harabasz Score for threshold 0.75 to 0.85. The TF-IDF technique was used to embed text into vectors. According to Figure 8(b), the value of threshold is 0.7875.

Figure 8(c) shows the Calinski-Harabasz Score for threshold 0.75 to 0.85. The BERT technique was used to embed text into vectors. According to Figure 8(c), the value of threshold is 0.7875.

Figure 9(a) shows the Davies-Bouldin score for thresholds 0.75 to 0.85. The Bag-Of-Words technique was used to embed text into vectors. According to Figure 9(a), the value of the threshold is 0.8.

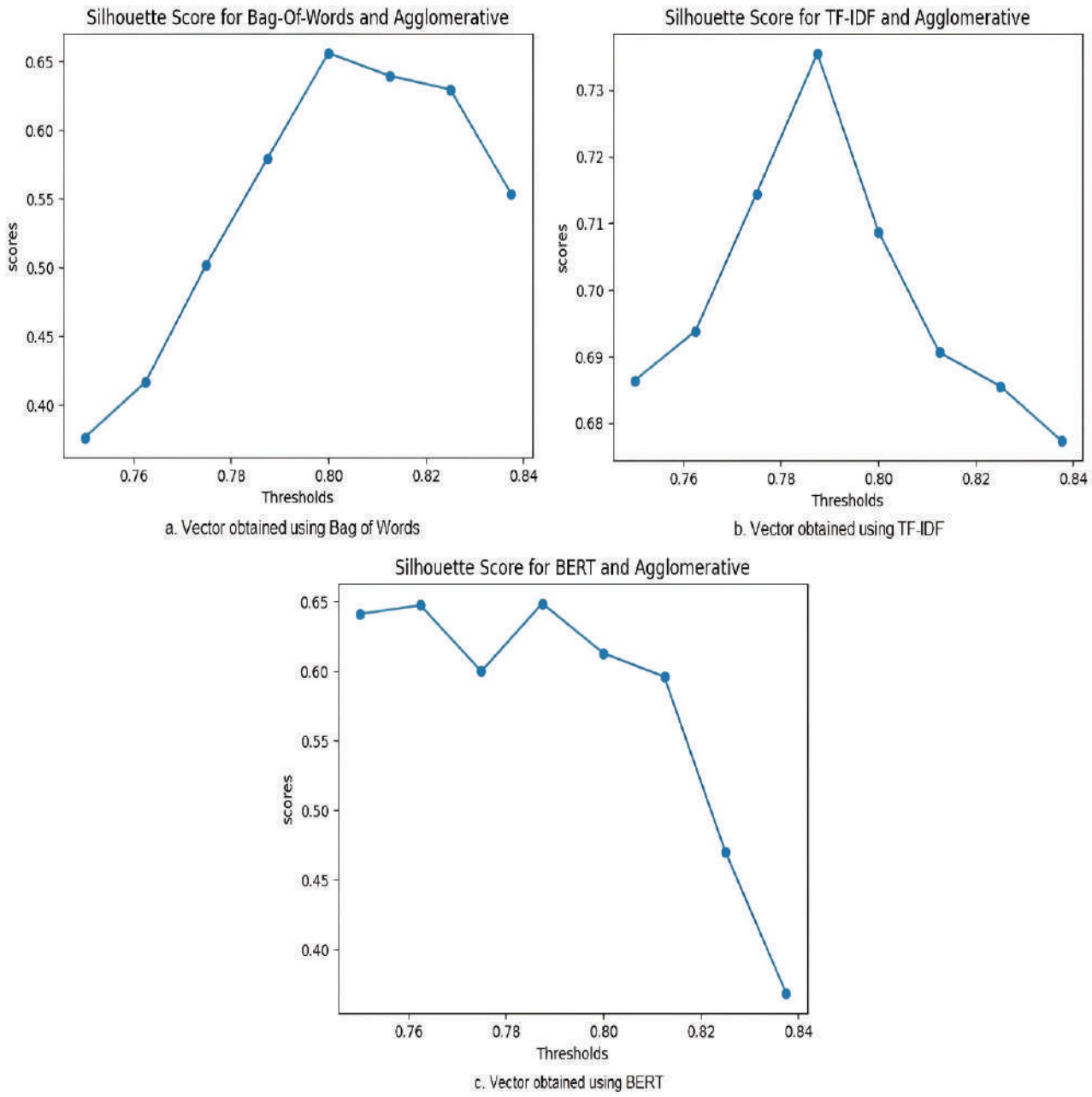


Figure 7. Vector obtained using Silhouette Score (a) Bag-Of-Words (b) TF-IDF (c) BERT of agglomerative.

Figure 9(b) shows the Davies-Bouldin score for threshold 0.75 to 0.85. The TF-IDF technique was used to embed text into vectors. According to Figure 9(b), the value of threshold is 0.7875.

Figure 9(c) shows the Davies-Bouldin score for thresholds 0.75 to 0.85. The BERT technique was used to embed text into vectors. The threshold value is 0.7875.

So, considering Figure 9(c), the value of K was set to 22. whereas for Agglomerative the threshold was set to 0.7875.

Once the clustering was done, the important task was to check the quality of the clusters, i.e., whether similar news was clustered in the same group or not. The proposed algorithm finds out the number of similar news articles correctly clustered in the same group. The accuracy was obtained by dividing this number by the total number of articles obtained, and finally, this ratio was multiplied by 100.

$$Accuracy = \frac{Total\ number\ of\ articles\ obtained}{Total\ Number\ of\ Articles} \times 100 \quad (29)$$

Tables 3 and 4 show the optimal and threshold values for tailoring the clustering process to the specific characteristics

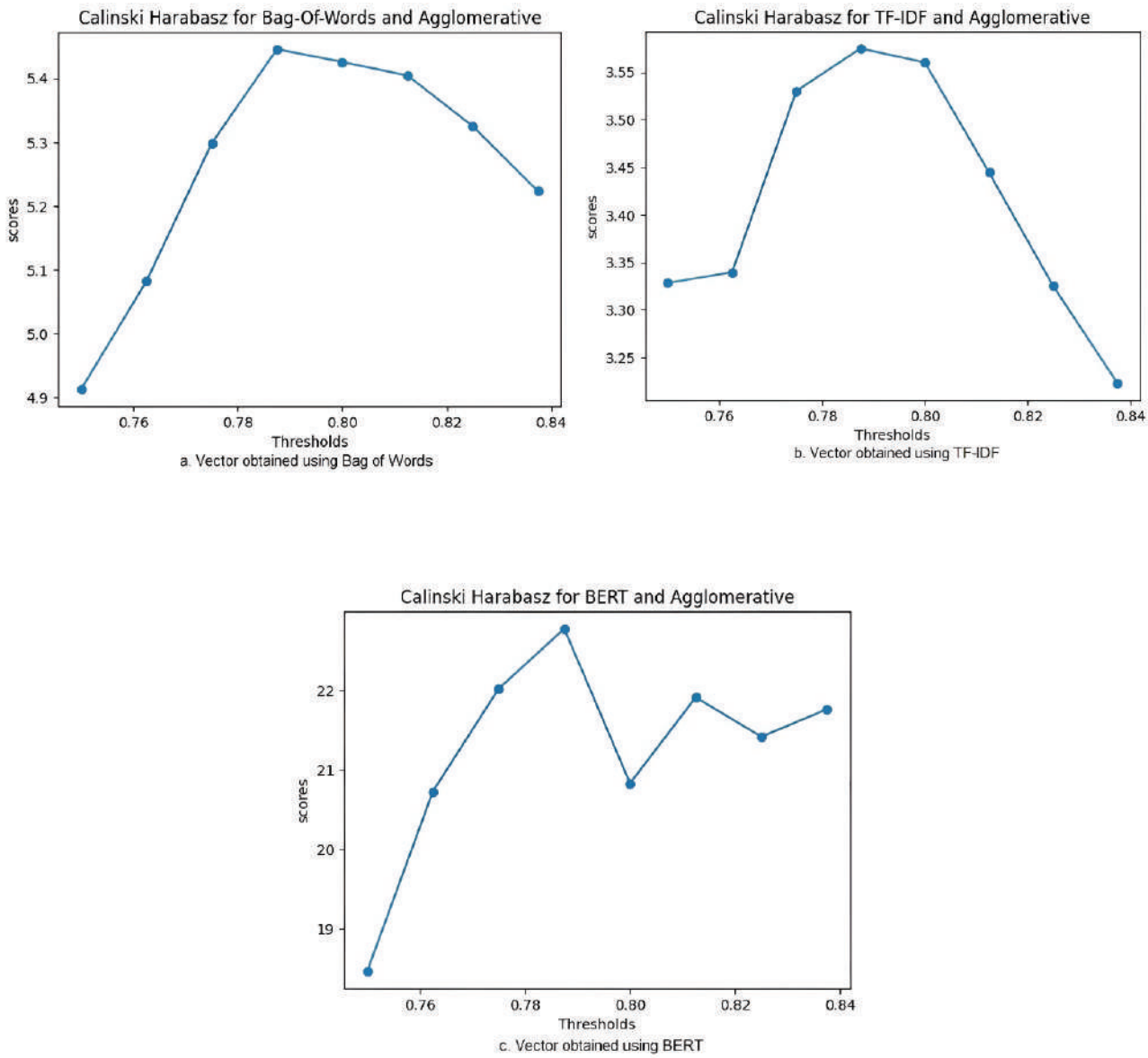


Figure 8. Vector obtained using Calinski-Harabasz (a) Bag-Of-Words (b) TF-IDF (c) BERT of agglomerative.

of the similar news article dataset and to ensure effective clustering of similar news articles.

Table 5 shows the accuracy of each embedding technique and clustering technique combination. It concludes that the combination of BERT and K-means algorithms was better than all other combinations.

A comparative analysis of the proposed BERT based clustering model is presented in Table 4 to the existing clustering algorithms that are used for clustering news articles. Malo et al. cite{malo} achieved an accuracy of 71% using the LPS approach, while Krishnamoorthy et al. cite{krishnamoorthy2} achieved 89% accuracy. The team's approach also reached an accuracy of 71% in the HSC assessment. Researchers achieved a score of 80.31% with a model they called "Ctrl-BERT". By combining K-means clustering with a pre-trained BERT language model, the study achieved a clustering accuracy of 84.46%, outperforming previously reported results in text-based classification tasks. This better performance is because BERT can understand the full context of a news article, including the relationships between the different pieces of information in it. This means it groups similar news stories more accurately. The proposed approach exhibits a notable edge over traditional methodologies as reflected in the data (Table 6).

When a technique that uses BERT to derive word embeddings and K-Means clustering was tested, it achieved higher accuracy than methods which use Bag-of-Words and Term

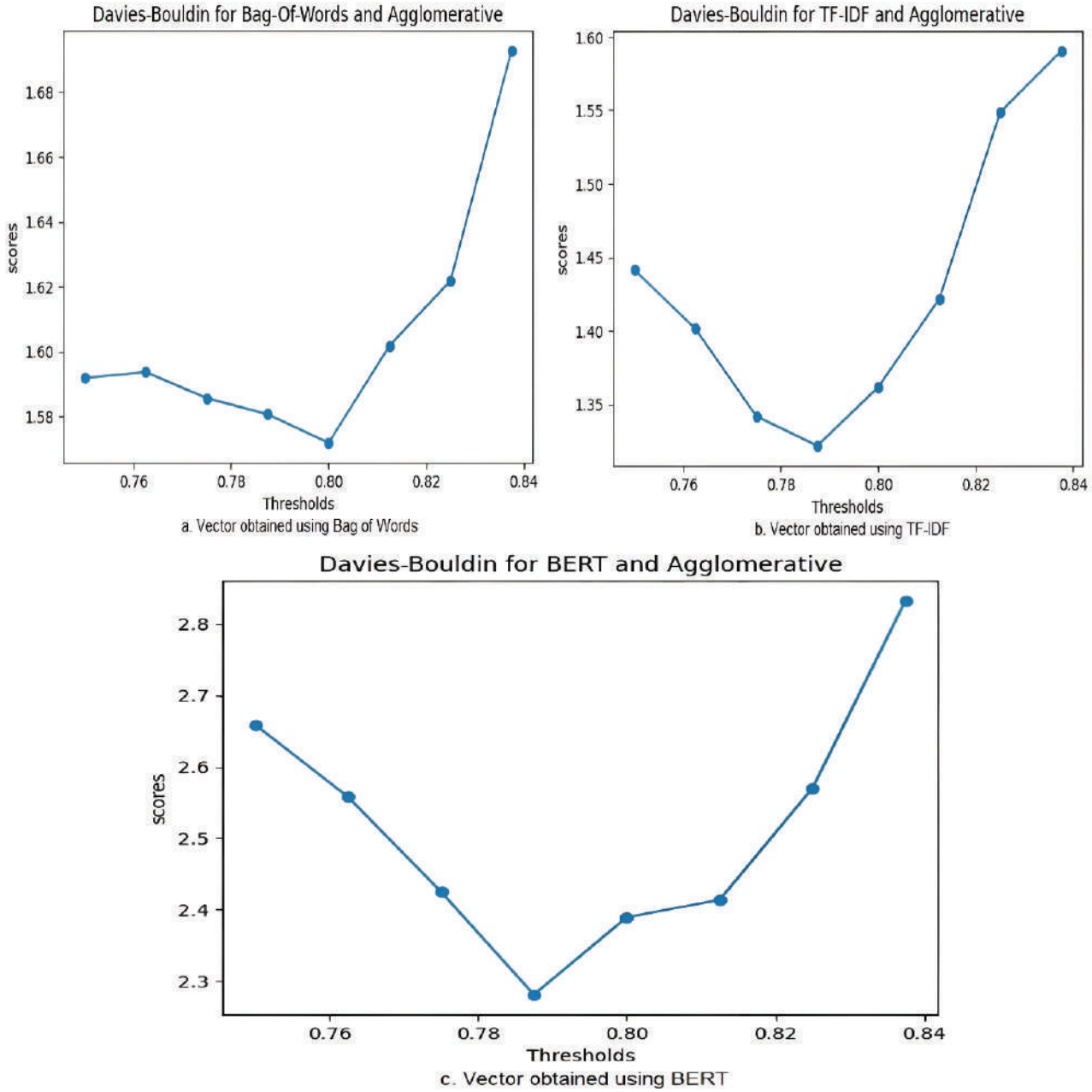


Figure 9. Vector obtained using Davies-Bouldin (a) Bag-Of-Words (b) TF-IDF (c) BERT of agglomerative.

Frequency-Inverse Document Frequency in experiments, 84.46% clustering accuracy was achieved. One of the main reasons BERT can improve upon traditional clustering methods is its ability to identify the deep relationships that exist between words. This relationship identification helps to improve the accuracy of the clustering results. In addition, several overall performance metrics were found to be useful. This includes the Davies-Bouldin Index, Calini ski - Harabasz statistic and the Silhouette Statistic, which are three methods that give cluster evaluation from multiple angles. Despite the effectiveness of BERT, one major drawback of BERT is the significant increase in computational power required for its operation, leading to difficulties when working with datasets of a considerable size. In order to minimize the effect of computational overhead, use of batch operations and the distribution of computational task were adopted. While BERT embeddings are effective to retain contextual and semantic information within text, which offers higher computational resources compared to Word2Vec and TF-IDF. This limitation becomes more

Table 3. Optimum value of 'K' using K-Mean algorithm

Methods	Embedding techniques	K-value
Elbow	Bag of Words	25
	TF-IDF	22
	BERT	22
Silhouette Score	Bag of Words	22
	TF-IDF	22
	BERT	23
Calinski-Harabsz Score	Bag of Words	23
	TF-IDF	22
	BERT	22
Davies-Bouldin Score	Bag of Words	24
	TF-IDF	22
	BERT	22

Table 4. Optimum value of threshold using agglomerative algorithm

Methods	Embedding Techniques	Threshold Value
Silhouette Score	Bag of Words	0.8
	TF-IDF	0.7875
	BERT	0.7875
Calinski-Harabsz Score	Bag of Words	0.7875
	TF-IDF	0.7875
	BERT	0.8
Davies-Bouldin Score	Bag of Words	0.7875
	TF-IDF	0.7875
	BERT	0.8

Table 5. Comparative result analysis of each embedding technique and clustering algorithm

Embedding Technique	Size of Each Vector	Clustering Algorithm	Accuracy (%)
Bag of words	1567	K-means clustering	63.89
		Agglomerative clustering	60.16
TF-IDF	1567	K-means clustering	74.96
		Agglomerative clustering	68.85
BERT	512	K-means clustering	84.46
		Agglomerative clustering	80.71

pronounced when working with large-scale datasets. In contrast, to ensure that the proposed method can be efficiently used with large datasets, the K-Means method was optimised. The linear computational complexity of K-Means makes it properly matched for handling large volume of datasets. An additional efficiency was achieved by employing BERT embeddings with the use of batch operations and distributed computing methodologies.

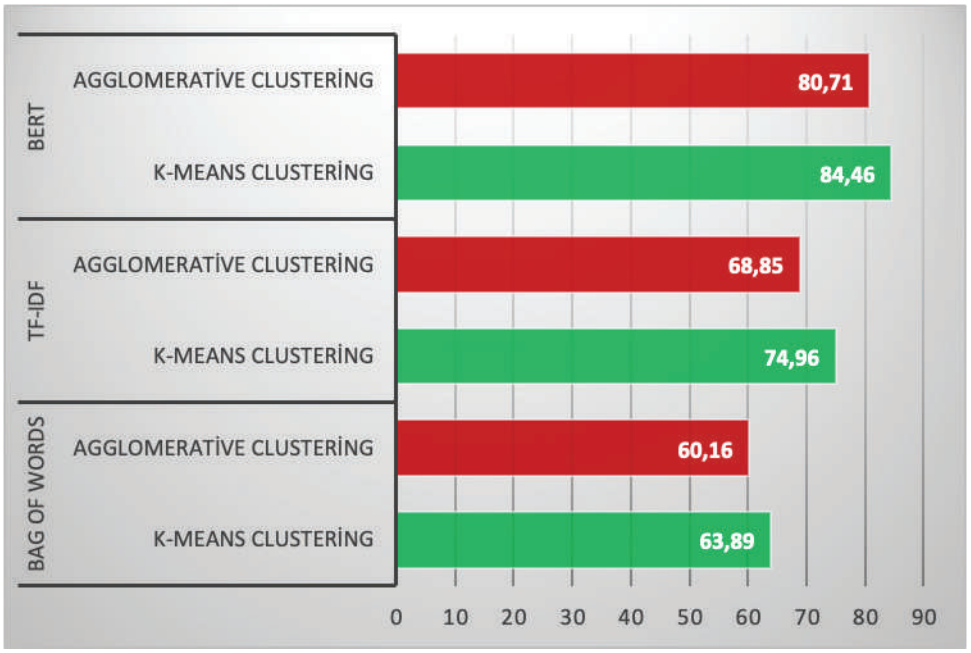


Figure 10. Bar represents the result analysis of each embedding technique and clustering algorithm.

Table 6. Comparative result analysis of cluster with existing methods

Authors	Methods	Accuracy in %
Malo et. al [35]	LPS	71.00
Krishnamoorthy et al. [36]	HSC	71.00
Raaci et al. [37]	ULMFit	83.00
Proposed	**BERT**	**84.46**

CONCLUSION

Large archives of similar news stories can be better understood and their key information identified through grouping news stories of a similar type together. News articles can be grouped based on their statistical properties by applying clustering algorithms such as K-means, hierarchical agglomerative clustering, Hierarchical or other techniques. The advantages of clustering data include the simplification of data retrieval, better structured data, the ability to more easily identify trends, the generation of tailored suggestions and the improvement of the process of exploring data. By facilitating browsing through news articles, it is possible to more easily discover trends and links. This also allows users to learn about topics which are becoming popular. This allows readers to gain greater insight into news and trends which are developing.

The number of clusters, K, which best categorizes news articles of a similar nature can differ based on the specific collection of articles and the degree of similarity desired. Since there is no single universally applicable value for the number of clusters (K) that works for all data sets, it is crucial to determine the ideal number of clusters by taking into account several factors. These include the nature of the data, the amount of data available, and the goals which the cluster analysis aims to achieve. Upon examination of all these algorithms and methods, it appears that the best outcome for this grouping of like news stories is obtained by setting k to 22 and a threshold of 0.7875. Presently the integration of real-time adaptability and deep learning into a news aggregator poses difficulties such as the maintenance of low computational costs, the processing of continuous streams of data and the adaptation to changing news topics. In future work, we anticipate the challenges identified in this research to be addressed by various methods including online learning and incremental clustering. Texts such as news websites can also use clustering to manage their content and offer readers with a news feed that is more tailored to their interests. Research into the grouping of similar newspaper articles is likely to be mainly based on deep learning techniques, the ability to process data in real time, clustering methods which use elements of other techniques, the incorporation of data in multiple formats,

understanding how decisions are made, tailoring the results to individual users, the detection of false information and large-scale applications. While the temporal effects of news articles were not studied here, their consideration is essential for further research. The evolving nature of news stories can be captured by the incorporation of techniques such as trend analysis or time-based clustering. In the rapidly changing news media environment, a goal of this research is to improve both the usability and the accuracy of cluster analysis tools.

AUTHOR CONTRIBUTION

Conceptualization, Gaurav V. Dahake and Dr. M. S. Ali; methodology, software, validation, formal analysis, Gaurav V. Dahake; investigation, Gaurav V. Dahake; resources, Gaurav V. Dahake; data curation, Gaurav V. Dahake; writing-original draft preparation, Gaurav V. Dahake; writing-review and editing, Gaurav V. Dahake; visualization, Gaurav V. Dahake; supervision, Dr. M. S. Ali; project administration, Dr. M. S. Ali.

DATA AVAILABILITY STATEMENT

The authors confirm that the data that supports the findings of this study are available within the article. Raw data that support the finding of this study are available from the corresponding author, upon reasonable request.

CONFLICT OF INTEREST

The author declared no potential conflicts of interest with respect to the research, authorship, and/or publication of this article. ETHICS There are no ethical issues with the publication of this manuscript.

STATEMENT ON THE USE OF ARTIFICIAL INTELLIGENCE

Artificial intelligence was not used in the preparation of the article.

REFERENCES

[1] Disayiram N, Rupasingha RA. A comparative study of clustering English news articles using clustering algorithms. In: Proc Int Res Conf Smart Comput Syst Eng; 2022; Colombo, Sri Lanka. p. 108–113. [CrossRef]

[2] Singh R, Singh S. Text similarity measures in news articles by vector space model using NLP. J Inst Eng India Ser B 2020;102. [CrossRef]

[3] Zhang Z, Liu X, Wang L. Spectral clustering algorithm based on improved Gaussian kernel function and beetle antennae search with damping factor. Comput Intell Neurosci 2020;2020. [CrossRef]

[4] Bianchi F, Grattarola D, Alippi C. Spectral clustering with graph neural networks for graph pooling. In: Proc Int Conf Mach Learn; 2020. p. 874–883.

[5] Hu Z, Nie F, Wang R, Li X. Multi-view spectral clustering via integrating nonnegative embedding and spectral embedding. Inf Fusion 2020;55:251–259. [CrossRef]

[6] Mirzal A. Statistical analysis of microarray data clustering using NMF spectral clustering k-means and GMM. 2020 2nd International Conference on Computer and Information Sciences (ICCIS) 13-15 Oct. 2020. [CrossRef]

[7] Viale L, Daga P, Fasana A, Garibaldi L. Dimensionality reduction methods of a clustered dataset for the diagnosis of a SCADA-equipped complex machine. Machines 2022;11:36. [CrossRef]

[8] Yujia S, Jan P. High-dimensional text clustering by dimensionality reduction and improved density peak. Wirel Commun Mob Comput 2020;2020:8881112.

[9] Zhang Z, Liu X, Wang L. Spectral clustering algorithm based on improved Gaussian kernel function and beetle antennae search with damping factor. Comput Intell Neurosci 2020;2020:1648573. [CrossRef]

[10] Izhar T, Mohammad U, Said MM, Ishak N, Dita A, Elly A. Clustering fake news with K-means and agglomerative clustering based on Word2Vec. Int J Math Comput Res 2024;12:3999–4007. [CrossRef]

[11] Hu Z, Nie F, Wang R, Li X. Multi-view spectral clustering via integrating nonnegative embedding and spectral embedding. Inf Fusion 2020;55:251–259. [CrossRef]

[12] Ravi J, Kulkarni S. Text embedding techniques for efficient clustering of Twitter data. Evol Intell 2023;16:1667–1677. [CrossRef]

[13] Shevendrakumar, Dubey. Clustering and retrieval of news articles using natural language processing. Int J Sci Res Eng Manag 2023;7:1–5. [CrossRef]

[14] Bhatnagar V, Ahuja S, Kaur S. Discriminant analysis-based cluster ensemble. Int J Data Min Model Manag 2015;7:83. [CrossRef]

[15] Bisandu B, Prasad R, Liman M. Clustering news articles using efficient similarity measure and N-grams. Int J Knowl Eng Data Min 2018;5:333–348. [CrossRef]

[16] Bergamaschi S, Guerra F, Orsini M, Sartori C, Vincini M. RELEVANTNews: A semantic news feed aggregator. 2007. Available at: https://ceur-ws.org/Vol-314/45.pdf Accessed on Jan 19, 2026.

[17] Gionis A, Mannila H, Tsaparas P. Clustering aggregation. ACM Trans Knowl Discov Data 2007;1:1217303. [CrossRef]

[18] Li I, Pan J, Goldwasser J, Verma N, Wong WP, Nuzumlalı MY, et al. Neural natural language processing for unstructured data in electronic health records: A review. Comput Sci Rev 2022;46:100511. [CrossRef]

[19] Bu F, Hu C, Zhang Q, Bai C, Yang LT, Baker T. A cloud-edge-aided incremental high-order possibilistic c-means algorithm for medical data clustering. IEEE Trans Fuzzy Syst 2021;29:148–155. [CrossRef]

[20] Jaya Mabel Rani A, Pravin A. Clustering by hybrid k-means-based rider sunflower optimization algorithm for medical data. Adv Fuzzy Syst 2022;2022:7783196. [CrossRef]

[21] Lynn N, Suganthan PNS. Ensemble particle swarm optimizer. Appl Soft Comput 2017;55:533–548. [CrossRef]

[22] Li HR, Tian XX, Luo XM, Yan M, Mu Y, Lu HG, Li SD. Heteroborospherene clusters Nin ∈ B40 (n = 1–4) and heteroborophene monolayers Ni2 ∈ B14 with planar heptacoordinate transition-metal centers in η7-B7 heptagons. Sci Rep 2017;7. [CrossRef]

[23] Ullmann T, Beer A, Hünemörder M, et al. Over-optimistic evaluation and reporting of novel cluster algorithms: An illustrative study. Adv Data Anal Classif 2023;17:211–238. [CrossRef]

[24] Bischl B, Binder M, Lang M, Pielok T, Richter J, Coors S, et al. Hyperparameter optimization: Foundations, algorithms, best practices and open challenges. arXiv 2021. Preprint. doi: 10.48550/arXiv.2107.05847

[25] Karwa R, Honmane V. Building search engine using machine learning technique. In: Proc Int Conf Comput Commun Syst; 2019. p. 1061–1064. [CrossRef]

[26] Messina A, Montagnuolo M. Content-based RSS and broadcast news streams aggregation and retrieval. In: Proc Int Conf Digit Inf Manag; 2008. p. 93–98. [CrossRef]

[27] Radev D, Blair-Goldensohn S, Zhang Z, Raghavan R. NewsInEssence: A system for domain-independent, real-time news clustering and multi-document summarization. In: Proc Int Conf Hum Lang Technol Res; 2001. [CrossRef]

[28] Felix H, Norman M, Bela G. Bias-aware news analysis using matrix-based news aggregation. Int J Digit Libr 2020;21:129–147. [CrossRef]

[29] Zhou B, Gao T. Automatic method for determining cluster number based on silhouette coefficient. Adv Mater Res 2014;951:227–230. [CrossRef]

[30] Mehta V, Bawa S, Singh J. WEClustering: Word embeddings-based text clustering technique for large datasets. Complex Intell Syst 2021;7:3211–3224. [CrossRef]

[31] Ba JL, Kiros JR, Hinton GE. Layer normalization. arXiv 2016. Preprint. doi: 10.48550/arXiv.1607.06450

[32] Wang H, Zhou C, Li L. Design and application of a text clustering algorithm based on parallelized k-means clustering. Rev Intell Artif 2019;33:453–460. [CrossRef]

[33] Thakare Y, Bagal S. Performance evaluation of k-means clustering algorithm with various distance metrics. Int J Comput Appl 2015;110:12–16. [CrossRef]

[34] Dubey D. Clustering and retrieval of news articles using natural language processing. Procedia Comput Sci 2022;207:3449–3458. [CrossRef]

[35] Malo P, Sinha A, Korhonen PJ, Wallenius J, Takala P. Good debt or bad debt: Detecting semantic orientations in economic texts. J Assoc Inf Sci Technol 2014;65:782–796. [CrossRef]

[36] Krishnamoorthy S. Sentiment analysis of financial news articles using performance indicators. Knowl Inf Syst 2018;56:373–394. [CrossRef]

[37] Raaci D. FinBERT: Financial sentiment analysis with pre-trained language models. arXiv 2019. Preprint. doi: 10.48550/arXiv.1908.10063

Sigma J Eng Nat Sci, Vol. 44, No. 1, pp. 74–82, February, 2026

Sigma Journal of Engineering and Natural Sciences
Web page info: https://sigma.yildiz.edu.tr
DOI: 10.14744/sigma.2025.00000

Research Article

Audio fingerprinting for song identification using discrete wavelet transform

Swati Mukesh DIXIT[1,*], Daulappa Guranna BHALKE[1]

[1]*Dr. D Y Patil Institute of Technology, Pimpri, Pune, 411018, India*

ARTICLE INFO

Article history
Received: 10 April 2024
Revised: 13 May 2024
Accepted: 08 December 2024

Keywords:
Audio Fingerprint; DWT; MFCC; Song Identification

ABSTRACT

This paper aims to enhance accuracy and robustness in audio recognition through the use of the Discrete Wavelet Transform (DWT) with Daubechies wavelets for song identification. This work is important because the actual song identity can be accurately matched based on small music fingerprints that are essential for applications such copyright detection and music identification apps. This method is based on decomposing the frames of a audio sample into sub-bands using Daubechies wavelets and extracting statistical features to form a 8-bit fingerprint. This fingerprint is much more compact than that yielded by other techniques such as FFT (256 bits) and FrFT (150 bits). By comparing these fingerprints to a database, the system can accurately identify songs from short snippets even in loud environments without needing song metadata. The results show that the accuracy of Daubechies wavelet method stands at 98% trailing behind existing wavelet based methods where they were reported to have accuracies of 86.7%, 97% and 90%. The high precision and reduced fingerprint size footprint makes the approach ideal for fast, accurate song matching. The novelty of the proposed work lies in its capability to generate very accurate as well as compact fingerprints which overcomes the limitations of previous techniques (e.g. FFT, FrFT etc.). The proposed approach outperforms previous works in the literature on audio fingerprinting for short audio content and noisy environments.

Cite this article as: Dixit SM, Bhalke DG. Audio fingerprinting for song identification using discrete wavelet transform. Sigma J Eng Nat Sci 2026;44(1):74–82.

INTRODUCTION

Music and song recognition has attracted sustained interest from both academic researchers and industry, owing to the technical complexity of the task and its significant commercial value [1]. Non-invasive techniques are widely utilized in applications such as retrieval, recognition, and authentication of digital content. These techniques work by analyzing the original signal without modifying it. Among these, fingerprinting stands out as a key application, offering a fast and reliable method for content identification [2]. An audio fingerprint is a compact digital representation used to identify and index short, unlabeled audio segments in a database [3]. Audio signals are often linked to metadata like song titles and artist names, stored in databases

*Corresponding author.
*E-mail address: swaatisutar@gmail.com

This paper was recommended for publication in revised form by Editor-in-Chief Ahmet Selim Dalkilic

Published by Yıldız Technical University Press, İstanbul, Turkey
© Author. This is an open access article under the CC BY-NC license (http://creativecommons.org/licenses/by-nc/4.0/).

via audio fingerprinting or content-based metadata [4]. Currently, the main audio fingerprinting methods incorporate the fingerprints of Shazam and Philips. Three methods are usually used in audio retrieval: key speaker identification, keyword detection, and key audio detection. While these technologies are fairly advanced, they still have several shortcomings. This paper mainly focuses on one thing to generate smaller size of fingerprint.

Audio fingerprinting extracts unique features from a piece of audio and stores them in a database. When an unidentified audio piece is presented, the system extracts its fingerprint and matches it against those in the database. For audio fingerprinting to be effective, the fingerprint must capture and describe the core attributes of the audio content [5]. This enables the system to recognize distorted versions of a recording as the same audio signal using fingerprints and matching algorithms [6,7]. Haitsma and Kalker proposed five main parameters for an audio fingerprinting system: [8,9]

Robustness: The system must be able to accurately recognize audio despite noise and distortion. It should consistently identify audio clips regardless of compression, with robustness measured by the bit error rate.

Reliability: This indicates the probability of incorrectly identifying an audio piece.

Fingerprint size: This pertains to the number of bits within a fingerprint.

Granularity: This indicates the minimal length of audio needed for identification.

Search speed and scalability: This measures how quickly a fingerprint can be found in a large database.

Database search efficiency: To maintain scalability, the fingerprint representation must allow for efficient database searches [10,11].

The different methods are used to generate audio fingerprint like FFT, FrFT, wavelet along with different feature extraction techniques like MFCC, LPCC, Receiver operating characteristics with different datasets like IRMAS and MTG-Jamendo . The summary of related previous work is arranged as follows-

Reise et al. [12] proposed a novel topological audio fingerprinting algorithm for efficient and accurate duplicate audio detection. This approach uses persistent homology on local spectral decomposition of audio signals, using filtered cubical complexes computed directly from mel-spectrograms. Using localized Betti curves to encode the audio signal, we get their guarantees that a time-shifted audio match can be accurately recovered. Experiments confirm the ability of our approach to find tracks having identical audio content even under obfuscations.This approach surpasses current methods, particularly in scenarios with topological distortions like time stretching and pitch shifting. Manjunath et al. [13] explained that audio fingerprinting technologies can monitor content without metadata or watermarks and have a wide range of applications. The algorithm is trained on a large set of short audio speech commands, where the efficiency is increased by including an audio feature extraction step at pre-processing. The accuracy of its generated model is up to 83.7%. Suhas [14] stated that over 90% of the audio signal processing domain is operated with Fourier based techniques, However, no new feature personally investigated. The present study addresses this problem by using the ROC curve to judge the performance of audio or acoustic features. Wavelet-based approaches have yielded results on par with the best-known fourier methods, therefore serving as potential alternatives for future audio processing research. Victoire Djimna Noyuma et al. [15] explained about listening to a song can inspire curiosity about the artist's biography and other works. This project centers on singer identification and includes three main phases: isolating the singer's voice from the background music, extracting vocal signal features, and using them for identification. Jaya Nameirakpam et al. [16] discussed the release of a singer recognition method, which uses DAMP-balanced dataset. It uses wavelet transform for pre-processing and MFCCs as audio features. A GMM is applied for classification. Comparison is analyzed between classification accuracy and computational time with and without use of wavelet transform in the study.

S. Preetha et al. [17] explained that the widely used Daubechies wavelet is fundamental to many modern techniques. Enhancing video copy detection can be achieved by optimizing the wavelet filter bank. This paper presents a wavelet design method using polyphase representation and the Gravitational Search Algorithm (GSA). Its effectiveness is supported by simulations as well appending. Sukanta Kumar Dash [18] The proposed system was evaluated on the IRMAS data set where n training is different from n testing . The DWT feature dimension was 250, which achieved the best performance. Aggregating micro and macro Precision, Recall, and F1scores the model reached 0.695 and 0.631. These results show gains of 12.28% and 23.0% above Han's benchmark CNN model. Mani Malekesmaeili et al. [19] introduced a novel fingerprinting scheme by extracting the local fingerprints feature from time-chroma images, which are robust against time/frequency scale transformation in audio content. This new approach outperforms significantly well known methods like SIFT. They propose also a finger-prints oriented song retrieval algorithm and display a copy error detection system which significantly outperforms state-of-the-art findings. In addition to detecting copied songs or partial copies, our system can correctly estimate pitch shift and/or tempo change into the song. Qiu-yu Zhang et al. [20] described how a feature matrix is created by combining the source speech such as the Mel-frequency cepstral coefficients (MFCC) and the linear prediction cepstrum coefficients (LPCC).Information entropy is used for columns, and an energy-based technique is used for rows, when applying dimension reduction. An audio fingerprint is formed by this reduced feature matrix. The normalized Hamming distance algorithm is used by retrieval for matching. According to experimental data, this technique

provides high recall and precision rates, produces smaller audio fingerprints, and is more robust for long speech segments. It also maintains better retrieval performance. Kamladas et al. [21] reported Fingerprint generation using DWT is robust with audio quality change for identification. This approach also yields a small number of fingerprints. Salvatore Serrano et al. [1] This paper compares a novel algorithm with various baseline methods for handling very short audio clips. Using a subset of the MTG-Jamendo dataset and a proprietary collection of 7000 songs, experimental findings indicate that the proposed algorithm outperforms others, especially for audio snippets shorter than 3 seconds. Rajnikumari et al. [4] The study presents a technique for minimizing background noise and distinguishing between voiced and unvoiced speech. This method is based on low and high-frequency subbands decomposition of voice data using the Maximal Overlap Discrete Wavelet Transform (MODWT). MODWT is robust across segments. Furthermore, in noisy conditions, PNCCs also provide much higher performance than Mel Cepstral Coefficients (MCC), resulting in a better SNR.

Although great progress has been made in many current work, limitations related to scalability, computational efficiency, the adaptability of a variety or complex dataset and need for further existence based method, explorations on reducing the fingerprint size. A new feature extraction approach, which is capable of generating a fingerprint that is robust and reliable for the audio fingerprinting system, is proposed in this paper. The proposed method tackles the challenge of minimizing audio fingerprint sizes, allowing for the storage of a large number of fingerprints in the database. As the database increases the search time increases. To overcome this, hash code of query fingerprint is generated and used to quickly locate matching entries in the hash table.

These measures help to maintain system performance as the database grows. It can recognize audio even if the speed and pitch have been changed [22,23].

Audio Fingerprint Requirements

Invariance to distortion

In the face of noise, distortion, and compression, an audio fingerprint should be able to distinguish an audio signal.

Compactness

The compact size of audio fingerprints enables the storage of a large number of them in the database.

Computational simplicity

It should take less time to extract a fingerprint.

Quicker identification

The speed of music identification through an audio fingerprint depends on the required duration of audio seconds for music recognition.

Audio Fingerprint Applications

Broadcast monitoring

This is the process of automatically creating a playlist for broadcasts on radio, television, or the internet in order to verify programs and advertisements collect royalties, and measure audience size. A central server that houses the fingerprint database and several monitoring locations make up a fingerprint-based wide-area broadcast monitoring system. At the monitoring stations, fingerprints were collected from each (local) broadcast channel. The fingerprints are gathered by the primary site from the monitoring sites. DWT is effective in identifying audio segments even when they have been slightly modified, such as those broadcasted by different radio stations using various compression formats.

Connected audio

This technology is utilized in consumer applications where audio is linked to supplementary and corroborated data. Speech coding, transmission across a cellular network, an acoustical channel between a mobile phone's loudspeaker and microphone, and FM/AM transmission can all cause an audio signal to deteriorate. Hence, this represents a challenging scenario.

Autonomous arrangement of music library

Numerous PC users possess hundreds or even thousands of tracks within their music collections. MP3 music files are compressed files. This music were downloaded from the internet, transferred via Bluetooth, and ripped from CDs, among other sources. Thus, the song library is disorganized. Since the metadata is constantly lacking and incorrect, the song library's metadata was properly organized using audio fingerprints [24].

Recommended Approach

Several techniques, including FFT, DCT, and Fractional Fourier transform or FrFT and Wavelet are used to generate audio fingerprints. Discrete wavelet transform is utilized in this paper to generate an audio fingerprint. This method uses wavelet transform as fingerprint extraction algorithm in time and frequency domain. After one and four layer wavelet decomposition of the audio signal, energy and band division are calculated. These values are then utilized as parameters to construct an 8-bit fingerprint block corresponding to each frame. Application of this algorithm reduces the amount of fingerprints datum per file, and consequently search time, system memory space. This in turn also allows for audio identification even where there is variation in the quality of audio waveforms [25].

The processes of fingerprint extraction and matching make up an audio fingerprint system. An audio signal in waveform is the system's input. The output plays back the song and contains its metadata. The suggested audio fingerprint system includes fingerprint matching and audio fingerprint extraction. Framing, overlapping, windowing, feature extraction, fingerprint modelling, and pre-processing are the

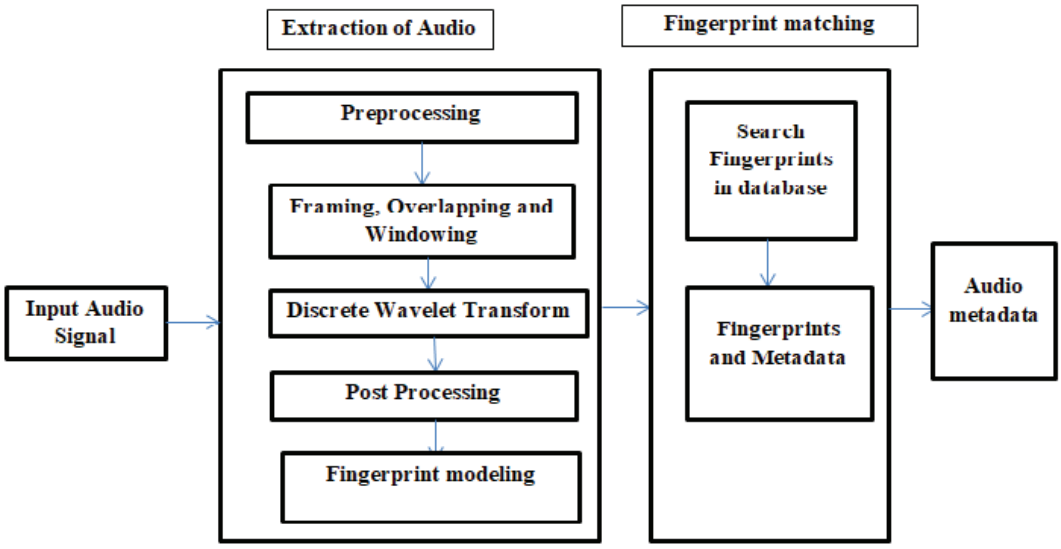


Figure 1. Recommended diagram for audio fingerprint extraction.

steps involved in audio fingerprint extraction. When two fingerprints match the best, the metadata is displayed and the song is played back. The matching process involves searching the fingerprint database [26]. Figure 1 shows the steps listed below are used to create an audio fingerprint.

Initial Preparation

This is useful to remove the silence part of an audio signal. To remove silent part, we make use of energy property of one component of the audio signal. 3. The first stage of the processing digitises the audio and converts it to a standard form (to 16-bit PCM, for example) monophonic with a sample rate varying between 5 kHz and 44.1 kHz. [27,28]. An audio fingerprinting system can usually work with various audio formats. Here, .mp3 files are converted into .wav file. It ensures that working with the original audio information without any loss due to compression. As all audio files converted into .wav, so sampling rate is same for all.

This signal is employed for down sampling to a standardized rate; in this case, 8 KHz is utilized as the down sampling rate to reduce the data rate, which is helpful for creating fingerprints.

Windowing, Framing, and Overlapping

Since audio signals are non-stationary, framing is crucial to maintaining signal stationary. For a few milliseconds, the signal is thought to be stationary; in this case, it is thought to be 20 ms. More overlap is thought to be necessary for resistance to shifting since it preserves statistical features. Overlap in this case is 90%. A Hamming window is applied to each frame to maintain coherence between its starting and ending points [29,30]. This window is chosen for its minimal sideband attenuation. Below is the representation of the Hamming window:

$$\mathrm{w(n)} = 0.54 - 0.46\cos\{\tfrac{2\pi n}{n-1}\},\ \ 0 \le n \le N-1 \qquad (1)$$

Discrete Wavelet Transform

An alternative to the short term fourier transform (STFT) in signal analysis is the Wavelet Transform (WT),which struggles with time and frequency resolution issues. The WT is effective for both stationary and non-stationary signals, with applications ranging from electrical noise reduction and sudden change detection to data compression. A specific type of WT, known as the Discrete Wavelet Transform (DWT), utilizes filters with different cutoff frequencies to analyze signals at various scales. Wavelet transforms offer a key advantage in their ability to localize signals effectively in both the time and frequency domains [31]. Wavelets break down the signal into its most basic components (detailed and approximation coefficient) and then accurately recreate it [32]. The Daubechies (db) wavelet makes audio signals more enjoyable by allowing for little degradation during de-noise and compression processes [33].

The DWT is given by the equation-

$$DWT(j,k) = \sum_j \sum_k x(k) 2^{-\frac{j}{2}} \qquad (2)$$

Since ψ(τ) is mother wavelet or transforming action.

The signal's high and low frequency components are examined using a variety of high-pass and low-pass filters. Upsampling and downsampling procedures alter the scale, while filtering refines the signal's resolution.

The processes used for filtering are by,

$$y_{\text{high}}\,[\mathrm{k}] = \sum_n X[n]\; g\;[2k-n] \qquad (3)$$

$$y_{\text{low}}\,[\mathrm{k}] = \sum_n X[n]\; h\;[2k-n] \qquad (4)$$

Thus, after being downsampled by 2, the high-pass (g) and low-pass (h) filtering yields the outputs yhigh [k] and ylow [k], respectively. Since the DWT is a decomposition method, coefficients as many as input points are produced. The decimation factor for the original signal is 2. It enables faster computing time by using DWT. In this case, the Daubechies 1 and 4 wavelet families of coefficients are used [16].

Energy Computation and Band Division

The power spectrum of the signal is increased in a range from 300 to 2000 Hz by the magnitude response of these 33 triangular band pass filters. Sub-bands are formed by the logarithmic spacing used. The bandpass filters are evenly spaced on an MEL frequency scale, which is defined as follows in terms of the standard linear frequency 'f':

$$Mel(f) = 2595 * \ln\left(1 + \frac{f}{700}\right) \quad (5)$$

Mel frequency, is directly proportional to the log-linear frequency transforming [18][25].

MFCC Sub Fingerprint Generation

Figure 2 illustrates number of steps included such as Preprocessing, framing, overlapping, windowing (cosine) frame, DWT and

Mel filter bank followed by log transformation and at the end it applies Discrete Cosine Transform (DCT). The mel-frequency cepstrum (MFC) is the representation and MFCCs are the coefficients. The DCT is then applied to the log power spectrum in order estimate the short-term audio spectrogram content across a non-linear Mel frequency scale**.**MFCCs have been widely recognized as the standard for representing acoustic features in audio processing tasks [20][33].

After obtaining MFCC coefficients discrete wavelet transform is applied to MFCC coefficients. This will decompose the MFCC values into approximation and detail coefficients at multiple levels. The statistical values has been calculated as follows-

Wavelet Decomposition

One should bear in mind that a Fourier transform produces frequency domain information and is not suitable for signals that are non-stationary (i.e., they change with time). Wavelet transform is applied since time- dependent information manifests in such signals. It decomposes signals into components that are both time and frequency localized. The signal is decomposed into wavelets through four levels, including one approximation and four details coefficients: CD1, CD2, CD3, and CD4. Features like variance, zero crossing rate, centroid, energy are also calculated once the signal is decomposed.

Variance

The variance describes how far the values in a dataset spread out from their mean. In the case of wavelet coefficients, their variance can be calculated using the following expression.

$$\sigma^2 = \frac{1}{N} \sum_i^N (c[i] - \bar{c})^2 \quad (6)$$

Since, $\bar{c}$ = Mean of the wavelet coefficients

c[i] = Wavelet coefficient at index i

N = Total number of wavelet coefficients

ii)Zero-crossing rate (ZCR)-

Another fundamental acoustic property that is simple to compute is the zero-crossing rate (ZCR). It is equivalent to the quantity of waveform zero crossings that occur inside a specific frame. For end-point identification, ZCR and volume are frequently combined. ZCR is specifically utilized to identify the beginning and ending locations of sounds that are not spoken.

$$\text{ZCR} = \frac{1}{N-1} \sum_{i=1}^{N-1} sgn(c[i]) \neq sgn(c[i+1]) \quad (7)$$

Since, sgn(x) = Sign function, which is 1 if x≥0 and −1 if x<0

iii) Centroid-

The center of energy distribution is used to represent the centroid of the wavelet domain. Since the audio signal's centroid varies over time in the wavelet domain, this property may indicate the audio signal's non-stationarity. The equation for determining the wavelet domain centroid is given as follows-

$$C = \frac{\sum_{i=1}^{N} |c[i].f[i]|}{\sum_{i=1}^{N} |c[i]|} \quad (8)$$

Since,

f[i] = Frequency associated with the coefficient c[i]

iv) Energy of wavelet domain-

An essential dynamic feature of the audio signal is its fluctuating amplitude, which can also represent variations in energy. The wavelet coefficients can capture the energy characteristics of an audio signal due to their correspondence with time-domain averages.

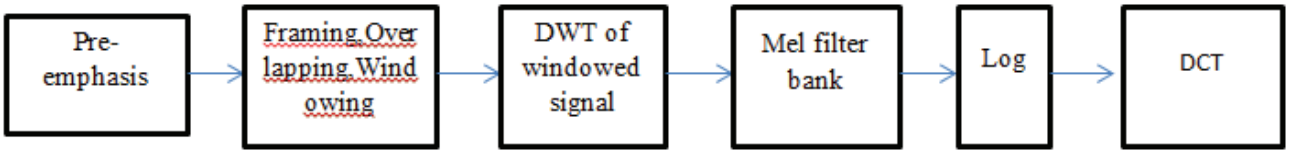


Figure 2. MFCC coefficient calculation.

$$E = \frac{1}{N}\sum_{i=1}^{N} |c[i]|^2 \quad (9)$$

Once the zero crossing rate, energy, variance and centroid were obtained for each frame of the audio stream they were used to create the fingerprints using equation (10). For each frame an 8-bit sub-fingerprint was generated. The variation of wavelet coefficients is employed to generate the final 5-bits of the 8-bit sub-fingerprints. The following equation is used to calculate hash bit values.

$$F(n,m)= \begin{cases} 1 & \text{if } E(n,m) - E(n,m+1) - (E(n-1,m) - E(n-1,m+1)) > 0 \\ 0 & \text{if } E(n,m) - E(n,m+1) - (E(n-1,m) - E(n-1,m+1)) \leq 0 \end{cases} \quad (10)$$

In this context, the m-th bit of the sub-fingerprint for frame n as F(n,m), whereas the energy of band m for frame n is denoted as E(n,m). The next 3-bits are generated by using zero crossing rate, centroid and energy of the wavelet coefficients. Therefore, for each frame, an 8-bit sub-fingerprint is generated. These bands are logarithmically in the range 300-2000 Hz. 150 additional fingerprints have been combined to form a fingerprint block. Again, slap-hand high-fives because this one has a metric shit ton of finger-pickage [21]. MFCCs are frequently utilized because they imitate human auditory perception and are less affected by noise and distortion.

Fingerprint Matching

To match fingerprints, first send a query signal to an audio fingerprint generation system. The fingerprints that were created and those that were kept in the database matched. When the best match is determined, the matching metadata is displayed and the song is played back. The matching process is based on the Hamming distance. AES256 (Advanced Encryption Standard) is a powerful encryption standard, used to protect the audio fingerprint itself and associated metadata. Once an audio fingerprint is generated, it's often sensitive data. AES256 can encrypt the fingerprint to prevent unauthorized access or modification. Audio fingerprint is a string of characters or numbers converted into a suitable format for AES256 encryption. Padding is essential to ensure data blocks align with the encryption block size because of its simplicity and effectiveness. All information stored in the database, including audio fingerprints, is protected with robust encryption methods advanced encryption standard AES-256. This ensures that even if unauthorized individuals gain access to the physical storage media, the data will remain indecipherable. AES is applied to fingerprint data before storing it. So it gives strong protection. As the key length is longer it gives strong protection.

RESULTS AND DISCUSSION

The audio files are. at 22050 Hz in.mp4 format for the input to this study. It includes three cases–i) without the wavelet db transformation, ii) applying on the transformed with the db1 db wavelets, and iii) using the db4. In each case, 9 MFCCs are computed for each audio signal. Noise is filtered by a low-pass filter. Feature extraction. The pre-processed signal is filtered and down-sampled to 8 kHz. It is then three-framed with overlap. Then each frame of the audio signal is windowed using a Hamming window. The Input signal, detail and approximation signals are shown in Figure 3.

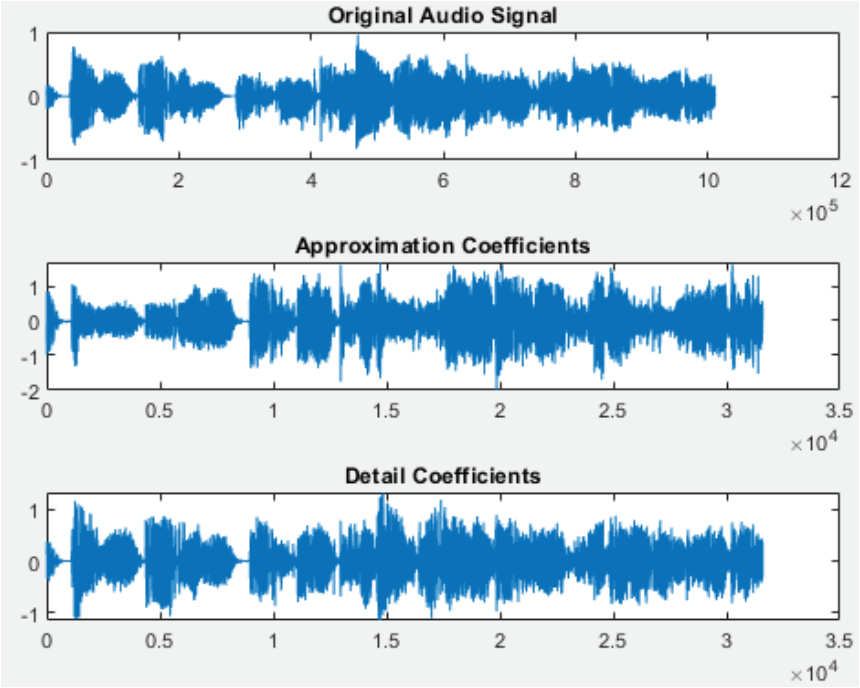


Figure 3. Original, approximation and detailed coefficient of an audio signal.

Table 1. Accuracy of song identification using different cases

Sr.No.	Cases	% Accuracy
1	Without using wavelet transform	97.2%
2	Using db1 wavelet	96%
3	Using db4 wavelet	98%

After feature extraction for MFCC coefficients, variance, zero-crossing rate, centroid and energy in the wavelet domain by using equations (6), (7), (8) and (9), an 8-bit fingerprint is obtained. The computed features are then mapped into bits: if the difference in variances between neighboring frames is positive, the bit value is 1; otherwise, it is 0. This process yields an 8-bit fingerprint for every frame in the audio signal.

While using db1 and db4, the db4 gives better accuracy i.e.98%. The comparison table of accuracy with 3 cases is shown in table1.

The proposed audio fingerprinting system using DWT (Daubechies) wavelets scales efficiently with larger databases due to the compact and robust nature of the wavelet-based fingerprints. However, as the database size increases, potential bottlenecks may arise in terms of computational resources and search speed. Here we generate a hash table, where each fingerprint is represented by a compact hash code derived from its features. These hash codes are then used as keys to store and retrieve the fingerprints efficiently. During a search, the hash code of a query fingerprint is computed and used to quickly locate matching entries in the hash table.

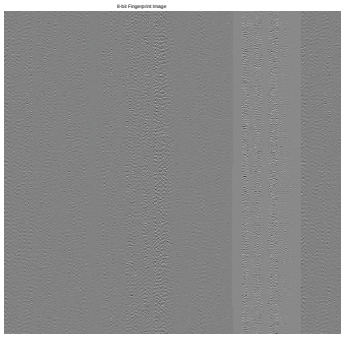


Figure 4. 8-bit fingerprint size.

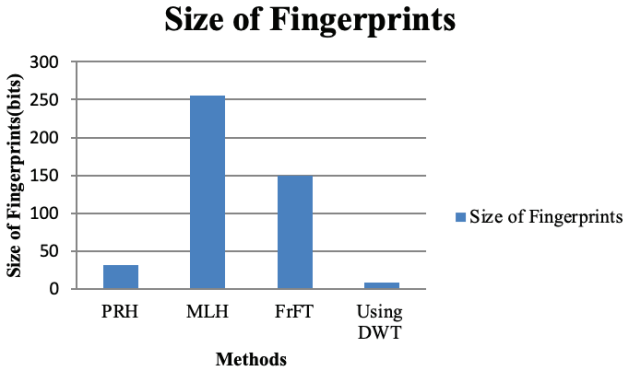


Figure 5. Comparison between different methods of fingerprint size.

Fig. 4] shows 8-bit fingerprint generated for song "Jeena Yahan marna yahan". Fig.5] shows graphical representation of the size of audio fingerprints generated by different methods like Philips Robust Hashing Method (PRH-32 bit), Multiple Hashing (MLH-256 bit) method, Fractional Fourier transform (150 bit) and proposed method (8 bit).

To better illustrate the compression potential, Table 2 presents the fingerprint size for each method. It includes the sizes for five comparison methods as well as the proposed method. Since all methods use frames of the same length and extract a fingerprint from each frame, the experiment only requires a comparison of the size of a single fingerprint

For robustness of the system this algorithm surpasses existing algorithms like PRH, MLH and FrFT when

Table 2. Fingerprint size per frame using different methods

Method	Fingerprint size (per frame)
Multiple Hashing Method	256 bits
Philips	32 bits
Shazam	32 bits
FFT	32 bits
FrFT	32 bits
DWT	8 bits

Table 3. Comparison between different methods for song identification in the presence of noise

SNR	PRH [32]	MLH[32]	FrFT[13]	MFCC+LPCC[27]	Proposed method
10	Misdetection occurred	Misdetection occurred	Misdetection occurred	Misdetection occurred	Song identified
25	Misdetection occurred	Song identified	Misdetection occurred	Song identified	Song identified
30	Song identified	Song identified	Song identified	Song identified	Song identified
40	Song identified	Song identified	Song identified	Song identified	Song identified

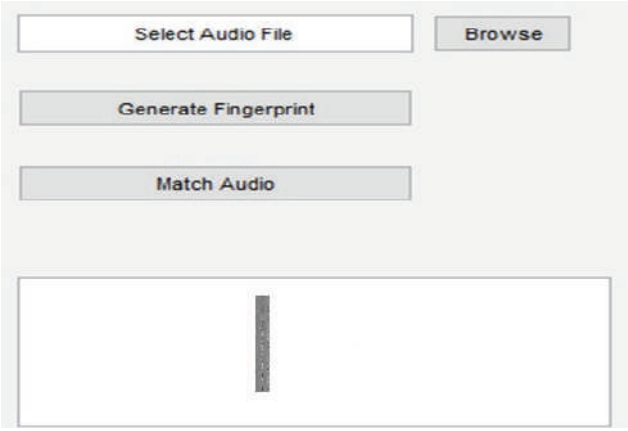


Figure 6. User interface for audio fingerprint.

handling AWGN noise at low signal-to-noise ratios (SNRs), PRH, MLH, and FrFT algorithms encounter challenges in identifying the song or may result in misdetections. Conversely, the proposed algorithm exhibits strong robustness against Additive White Gaussian Noise (AWGN), even when SNR levels are low.

Table 3 presents a comparison chart of the identification performance in the presence of AWGN noise for various algorithms, including the proposed one.

Figure 6 shows the user interface for audio fingerprint system.

As shown in fig.6] GUI is generated using MATLAB program. Select audio file field is likely where the user would input the audio file they want to process. There is a corresponding "Browse" link which can be clicked to locate and choose the file from your local computer. Create Fingerprint button simply means the action of creating the audio fingerprint for your selected audio file. The Match Audio button is used to match a new audio file to an existing fingerprint or database of fingerprints. After a match is found it shows the fingerprint.

CONCLUSION

The wavelet transform based audio fingerprinting scheme just now proposed is a milestone in audio technology. This new technique significantly limits the total number of fingerprints per file to 8 bits, quite novel from state-of-the-art wherein infinite number of fingerprints are generated. Such a reduction speeds up the search and reduces the storage of the database. With the availability of background noise in a significant amount, by involving db4 wavelet to aid fingerprints extracting process, the method improves accuracy and robustness. The Db4 wavelets are able to capture the significant features of single components with little noise interference, and it yields a comparable PF rate of 98%. This fine-grained precision is ideal for use cases that require a high-quality trigger in noisy acoustic environments, such as music recognition, audio surveillance and acoustic event detection applications. The key idea behind this work is reducing the size of fingerprint as well as improving accuracy. A smaller fingerprint size means faster fingerprints, and space for more songs in the database. The better processing of noise condition using db4 wavelets are approached over earlier methods, which makes this technique as a good number for high reliability sound recognition systems.

AUTHORSHIP CONTRIBUTIONS

Authors equally contributed to this work.

DATA AVAILABILITY STATEMENT

The authors confirm that the data that supports the findings of this study are available within the article. Raw data that support the finding of this study are available from the corresponding author, upon reasonable request.

CONFLICT OF INTEREST

The author declared no potential conflicts of interest with respect to the research, authorship, and/or publication of this article.

ETHICS

There are no ethical issues with the publication of this manuscript.

STATEMENT ON THE USE OF ARTIFICIAL INTELLIGENCE

Artificial intelligence was not used in the preparation of the article.

REFERENCES

[1] Serrano S, Scarpa M. Accuracy comparisons of fingerprint based song recognition approaches using very high granularity. Multimedia Tools Appl 2023;82:31591–31606. [CrossRef]

[2] Bhalke DG, Rao CBR, Bormane D. Hybridization of mel frequency cepstral coefficient and higher order spectral features for musical instruments classification. Arch Acoust 2016;41:427–436. [CrossRef]

[3] Lee S, Yook D, Chang S. An efficient audio fingerprint search algorithm for music retrieval. IEEE Trans Consum Electron 2013;59:739–745. [CrossRef]

[4] RajaniKumari, Babu K. Designing highly secured speaker identification with audio fingerprinting using MODWT and RBFNN. Int J Intell Syst Appl Eng 2024;12:25–30.

[5] Son HS, Byun SW, Lee SP. A robust audio fingerprinting using a new hashing method. IEEE Access 2020;8:168953–168963. [CrossRef]

[6] Liu Y, Cho K, Yun HS, Shin JW, Kim NS. DCT based multiple hashing technique for robust audio fingerprinting. IEEE Int Conf Acoust Speech Signal Process 2009:61–64. [CrossRef]
[7] Belletini C, Mazzini M. A framework for robust audio fingerprinting. J Commun 2010;5:401–408. [CrossRef]
[8] Haitsma J, Kalker T. A highly robust audio fingerprinting system. In: Proc Int Conf Music Inf Retrieval; 2002. p. 107–115.
[9] Unal E, Chew E, Georgiou PG, Narayanan SS. Challenging uncertainty in query by humming systems: a fingerprinting approach. IEEE Trans Audio Speech Lang Process 2008;16:359–371. [CrossRef]
[10] Doets P, Lagendijk R. Distortion estimation in compressed music using only audio fingerprints. IEEE Trans Audio Speech Lang Process 2008;16:275–286. [CrossRef]
[11] Singh A, Demuynck K, Arora V. Simultaneously learning robust audio embeddings and balanced hash codes for query-by-example. In: ICASSP 2023 - 2023 IEEE Int Conf Acoust Speech Signal Process; 2023. p. 1–5. [CrossRef]
[12] Reise W, Fernández X, Dominguez M, Harrington HA, Beguerisse-Díaz M. Topological fingerprints for audio identification. arXiv 2023;2309.03516. Preprint. doi: 10.48550/arXiv.2309.03516
[13] Arunakumar, BN, Shashidhar R, Sahana B, Jagadamba G, Manjunath AS, Roopa M. Fingerprint definition for song recognition using machine learning algorithm. In: 2023 Int Conf Smart Syst Appl Electr Sci (ICSSES); 2023. p. 1–6. [CrossRef]
[14] Suhas BN. Automatic bird sound detection in long-range field recordings using wavelets & mel filter bank features. In: 2020 IEEE Second Int Conf Cogn Mach Intell (CogMI); 2020. p. 978–1–7281-4144-2.
[15] Djimna Noyuma V, Perieukeu Mofenjoua Y, Feudjioa C, Göktugb A, Fokoué E. Boosting the predictive accuracy of singer identification using discrete wavelet transform for feature extraction. arXiv 2021;2102.00550v1. Preprint. doi: 10.48550/arXiv.2102.00550.
[16] Nameirakpam J, Biswas S, Bonjyostna A. Singer identification using wavelet transform. In: 2019 2nd Int Conf Innov Electr Signal Process Commun (IESC); 2019. p. 238–242. [CrossRef]
[17] Preetha S, Bindu VR. A wavelet optimized video copy detection using content fingerprinting. J Signal Process Syst 2023;95:363–377. [CrossRef]
[18] Dash SK, Solanki SS, Chakraborty S. Deep convolutional neural networks for predominant instrument recognition in polyphonic music using discrete wavelet transform. Circuits Syst Signal Process 2024;43:4239–4271. [CrossRef]
[19] Malekesmaeili M, Ward RK. A local fingerprinting approach for audio copy detection. Signal Process 2014;98:308–321. [CrossRef]
[20] Zhang QY, Xu FJ, Bai J. Audio fingerprint retrieval method based on feature dimension reduction and feature combination. KSII Trans Internet Inf Syst 2021;15:409–423. [CrossRef]
[21] Kamaladas M, Dialin M. Fingerprint extraction of audio signal using wavelet transform. In: 2013 Int Conf Signal Process Image Process Pattern Recognit (ICSIPR); 2013. p. 1–5. [CrossRef]
[22] Radha K, Bansal M, Pachori RB. Speech and speaker recognition using raw waveform modeling for adult and children's speech: A comprehensive review. Eng Appl Artif Intell 2024;131:107661. [CrossRef]
[23] Sutar SV, Bhalke DG. Audio fingerprinting using fractional fourier transform. IOSR J Electron Commun Eng 2015;10:30–34.
[24] Schreiber H, Muller M. Accelerating index based audio identification. IEEE Trans Multimedia 2014;16:1654–1664. [CrossRef]
[25] Bhalke DG, Rao CBR, Bormane DS. Hybridization of fractional fourier transform and acoustic features for musical instrument recognition. Int J Signal Process Image Process Pattern Recognit 2014;7:275–282. [CrossRef]
[26] Bhalke DG, Ramarao CB, Bormane DS. Automatic musical instrument classification using fractional fourier transform based-MFCC features and counter propagation neural network. J Intell Inf Syst 2015;46:425–446. [CrossRef]
[27] Son W, Cho H, Yoon K, Lee S. Sub-fingerprint masking for a robust audio fingerprinting system in real noise environment for portable consumer devices. IEEE Trans Consum Electron 2010;56:144–151. [CrossRef]
[28] Sharma G, Umapathy K, Krishnan S. Trends in audio signal feature extraction methods. Appl Acoust 2020;158:107020. [CrossRef]
[29] Hanifa RM, Isa K, Mohamad S. A review on speaker recognition: Technology and challenges. Comput Electr Eng 2021;90:107005. [CrossRef]
[30] Ravi ND, Bhalke DG. Musical instrument information retrieval using neural network. In: 2016 IEEE Int Conf Adv Electron Commun Comput Technol (ICAECCT); 2016. p. 418–422. [CrossRef]
[31] Jia M, Li T, Wang J. Audio fingerprint extraction based on locally linear embedding for audio retrieval system. Electronics 2020;9:1483. [CrossRef]
[32] Liu Y, Cho K, Yun HS, Shin JW, Kim NS. DCT based multiple hashing technique for robust audio fingerprinting. In: 2009 IEEE Int Conf Acoust Speech Signal Process; 2009. p. 61–64. [CrossRef]
[33] Osman MM, Büyük O. Parabolic filter mel frequency cepstral coefficient and fusion of features for speaker age classification. Sigma J Eng Nat Sci 2020;38:2177–2191.

Sigma Journal of Engineering and Natural Sciences
Web page info: https://sigma.yildiz.edu.tr
DOI: 10.14744/sigma.2025.00000

Research Article

The effect of eccentricity and asymmetry in the plan on the performance level in existing steel buildings with a medium bending frame

Kaveh NEZAMISAVOJBALAGHI[1,2,*]

[1]*Department of Civil Engineering, Mah.C., Islamic Azad University, Mahabad, Iran*
[2]*Department of Civil Engineering, Seismic Resilience Monitoring of Critical Infrastructure Research Center, Ur.C., Islamic Azad University, Urmia, Iran*

ARTICLE INFO

Article history
Received: 08 May 2024
Revised: 18 July 2024
Accepted: 11 November 2024

Keywords:
Non-linear Static Analysis, Accidental Torsion, Symmetric and Asymmetric Plan, Performance Level, Ductility

ABSTRACT

The evaluation of the torsional effects of earthquakes on the performance of steel buildings with medium-ductility moment frames, which are widely used in seismic regions, is critical because of their high flexibility and significant energy absorption capacity. Amplification of the seismic response of buildings owing to torsion and the precise and influential factors in its creation and amplification during an earthquake is essential. Design and seismic strengthening regulations should pay more attention to geometric asymmetry as a significant factor in amplifying building response. This study investigated the combined effect of geometric asymmetry in one direction with the effect of eccentricity in three states—accidental torsion, significant torsion, and severe torsion—as influencing factors on performance levels and vital parameters such as ductility changes. The selected models with five and nine stories have symmetric and asymmetric plans, at least in one direction, designed according to the Standard 2800 fourth edition and the National Steel Buildings Iran Regulations fifth edition. Then, by creating significant and severe torsional irregularities in the models of existing buildings using the guidelines for seismic rehabilitation of existing structures with nonlinear static analysis (pushover), the performance levels of the buildings were evaluated. The results indicate that the asymmetry in the plan in one direction compared to the symmetric plan reduces the performance level of 5-story models by more than 9-story models. In addition, changes in Ductility and seismic response due to torsion in 5-story buildings are more significant; therefore, asymmetry in one direction with severe torsion causes a 43% reduction in Ductility. These findings underscore the need for further research to fully understand the implications of asymmetry and torsion in seismic design and to incorporate these findings into future seismic codes and design practices.

Cite this article as: Nezamisavojbalaghi K. The effect of eccentricity and asymmetry in the plan on the performance level in existing steel buildings with a medium bending frame. Sigma J Eng Nat Sci 2026;44(1):83–92.

***Corresponding author.**
*E-mail address: Kaveh.Nezamisavojbolaghi@iau.ac.ir

This paper was recommended for publication in revised form by Editor-in-Chief Ahmet Selim Dalkilic

Published by Yıldız Technical University Press, İstanbul, Turkey
© Author. This is an open access article under the CC BY-NC license (http://creativecommons.org/licenses/by-nc/4.0/).

INTRODUCTION

One of the most common structural systems is steel frame buildings with moment frames. Due to their high flexibility and significant energy absorption capacity, steel moment frame buildings with medium Ductility are widely used in seismic regions. Past and recent earthquakes have shown that the presence of eccentricity in plans with varying percentages in existing buildings with symmetric and asymmetric plans has affected the performance of buildings due to torsion as a factor causing damage and destruction. Buildings undergo lateral and torsional movements due to earthquakes .[1]. Torsional effects are divided into two categories: inherent torsion and accidental torsion. Inherent torsion can be caused by predictable and measurable sources such as asymmetric building geometry and the uneven distribution of stiffness, member strength, and building mass. [2] Other factors that are difficult or impossible to quantify, and their direct consideration in design codes and evaluating existing buildings are problematic, are referred to as accidental torsion. Accidental torsion accounts for discrepancies between the distribution of mass, stiffness, and strength in analysis and the actual values at the time of an earthquake, torsion due to the earthquake's rotational component, and other sources of torsion. Building codes introduce an additional eccentricity to account for accidental torsion. In the "design accidental eccentricity," four additional load cases with changes in the center of mass along the x and y axes of all floors in both positive and negative directions must be considered [3]. Research by De la Llera and Chopra in the early 1990s, based on records of three buildings, indicated that the torsion rules based on 5% eccentricity were sufficient for the torsional movements observed in the studied buildings during recorded earthquakes .[4] However, these movements increased the member forces by up to 30% in one of the buildings. The results showed that accounting for accidental torsion was unnecessary in the design of two of the buildings for the recorded earthquakes. The study estimated that the rotational component of the earthquake contributed 25-40% of the total accidental torsion in the examined buildings. The accidental torsion rule in building codes, especially when significant approximations, such as typification in member design, are considered, has little impact on member sizing, detailing, and connections in these buildings. Buildings are rarely affected by the accidental design eccentricity rule .[5] Dimova et al. (2003) analytically estimated the dynamic effects on symmetric structures due to the displacement of the center of mass and its application in seismic design. The study results showed that even small eccentricities cause irregular behavior in symmetric structures, and using static application of torsional moments to account for accidental torsion effects is inappropriate. [6] A probabilistic study on short-height buildings, showing that the Ductility requirement for systems designed with and without accidental eccentricity was similar. Ramadan [7] (2008) conducted a probabilistic study on eight three-dimensional multi-story concrete buildings with symmetric plans under a single horizontal earthquake component, showing that accidental eccentricity significantly affects upper-story floors and is often less than the typical 5% value specified in building codes for floors with more than five upper stories.[8] Symmetric and biaxially eccentric reinforced concrete moment frame buildings. All buildings were designed for three different accidental eccentricities. Results showed that with the introduction of ±5% mass eccentricity, the Ductility requirement was similar in designed and non-designed buildings. Accidental mass eccentricity is insignificant when the building response is highly inelastic. [8] The effect of the number of upper floors, the dead-to-live load ratio, and the number of columns per floor on the amount of accidental eccentricity in rectangular and square plan buildings with 5 and 10 stories was investigated. [9] The results indicated that accidental eccentricity decreases with the number of lateral load-bearing members and increases with the number of upper floors. The dead-to-live load ratio has a minor effect on accidental eccentricity. The quality of the SEI/ASCE7 accidental torsion design requirements on building failure capacity was evaluated. [10] The results showed that the accidental eccentricity rule can be omitted in the seismic design of buildings without significant torsional or asymmetrical irregularities.[10] The importance of accidental eccentricity in symmetrically braced steel buildings with 10% and 20% biaxial eccentricities was studied.[11] First, the buildings were designed with accidental design eccentricities. Then, all these buildings were analyzed under a set of earthquakes that introduced accidental mass eccentricity. The results showed that the design of symmetrical plan buildings with biaxial eccentricities of 10% and 20% using accidental design eccentricity has little impact on the inelastic response of the structures.[11] An analytical and code review of torsional irregularities in low- to mid-rise structures using linear spectral analysis results and applying accidental torsion was conducted.[12] The building models were reinforced concrete with dual systems, and the position of shear walls, the number of floors, and the number of spans were considered to investigate torsional irregularity in one direction. The study results indicated that the maximum torsional irregularity coefficient increases with a decrease in the number of floors. Upper floors have lower torsional irregularity coefficients than lower floors. The results for floor rotations were opposite to those for torsional irregularity coefficients.[12] The effect of eccentricity and asymmetry in plans on performance levels and results in existing steel buildings with medium ductility moment frames could lead to significant discrepancies.[13] The study results indicated up to 18 times more rotation for structures with short-term natural periods. Additionally, the complex shapes of modern buildings often lead to irregular distribution of mass, stiffness, and strength, which can cause unwanted rotation and weaken the building during an earthquake. Based on last research,

geometric asymmetry in plans has been less considered in design and seismic strengthening codes as a significant factor in amplifying the seismic response of structures. This paper examines the simultaneous effect of eccentricity and symmetric and asymmetric plans in at least one direction in three states—Accidental torsion, significant torsion, and severe torsion—on performance levels and key parameters such as structural period and Ductility in these models.

CHARACTERISTICS OF THE STUDIED MODELS

This section introduces the structural system under study, the material properties, and the design method meticulously crafted in strict adherence to national codes and building regulations. The models are steel moment frame buildings with medium ductility considering eccentricity in three states: Accidental torsion, significant torsional irregularity, and severe torsional irregularity according to the standard 2800 fourth edition.[14] These models, with symmetric and asymmetric plans as shown in Figures 1 and 2, with 5 and 9 floors, totaling 12 models, have been designed.

Tables 1 and 2 introduce the names and dimensions of the spans in symmetric and asymmetric plans. The height of all floors in the models is 3 meters.

The construction of the models is considered in zoning with high relative risk (A = 0.30) and type II land with residential use (I = 1.0). The behavior coefficient is equal to 5 (R = 5), and the additional resistance coefficient is equal

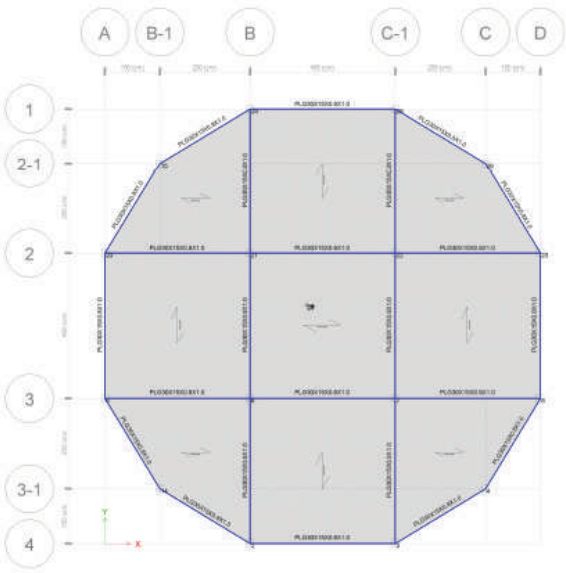


Figure 1. Symmetric plan of 5 and 9 floor models.



Figure 2. Asymmetric plan of 5 and 9 floor models.

Table 1. The name and size of openings in the symmetrical plan in centimeters in X and Y directions

The name of the opening in the X direction	A-(B-1)	(B-1)-B	B-(C-1)	(C-1)-C	C-D
Opening size (cm)	150	250	400	250	150
Name of opening in Y direction	**1-(2-1)**	**(2-1)-2**	**2-3**	**3-(3-1)**	**(3-1)-4**
Opening size (cm)	150	250	400	250	150

Table 2. The name and size of openings in the asymmetric plan in centimeters in X and Y directions

The name of the opening in the X direction	A-B	B-(C-1)	(C-1)-C	C-D	-
Opening size (cm)	400	400	250	150	-
The name of the opening in the Y direction	**1-(2-1)**	**(2-1)-2**	**2-3**	**3-(3-1)**	**(3-1)-4**
Opening size (cm)	150	250	400	250	150

to 3 (Ω = 3). The time of the prominent periodicity of the oscillation in 5-story models with symmetric and asymmetric plans, taking into account the effect of the interframe separator in seconds (Tx, Ty=0.488) with the base shear coefficient (Cx, Cy=0.15) and also the effect coefficient of higher modes (K=1) and the main period of oscillation in 9-story models with symmetric and asymmetric plans, taking into account the effect of the interframe separator in seconds (Tx, Ty=0.758) with the basic shear coefficient (Cx, Cy=0.1040) and also the effect coefficient of higher modes for 9-story models (K=1.129) has been calculated and considered, providing significant insights into the structural behavior of the models.

The specifications of the materials used for the steel frame and sections of the St-37 type have been selected. For loading and design, topic 6 of national regulations[15] and standard 2800, fourth edition[14], and topic 10 of national regulations, fifth edition [16] have been used.

The roof system is chosen as a single-sided slab, and the dimensions of the sections in the five and 9-story models with symmetric and asymmetric plans with random departure from the centrality are chosen to meet the design criteria based on national regulations for linear analysis from ETABS software. 2016 has been used. [17] For example, Figure 3 shows the three-dimensional view of the 9-story model with an asymmetrical plan. Figure 4 shows the three-dimensional view of the 5-story model with a symmetrical plan.

According to paragraph 1-7-1 of plan irregularity of clause B of standard 2800, high and severe torsion irregularity is defined in cases where the maximum relative displacement at one end of the building on each floor, including accidental torsion ing and assuming a magnification factor equal to 1 (Aj=0.1) should be more than 20% of the average relative displacement at both ends of the building on that floor. In these cases, the irregularity is "high," and in cases where this difference is more than 40%, it is described as "severe" torsional irregularity.[14] To create other models, assuming that the models are existing structures in the models designed based on national regulations and standard 2800, according to the criteria for defining high and severe torsional irregularity in standard 2800, the fourth edition, by making severe changes in the initial models and Creation of eccentricity along both axes in symmetric and asymmetric plans, other models have been created for investigation.

Analysis of Models

After modeling and performing linear analysis and design according to national regulations, to investigate the effect of distortion and asymmetry on the level of performance and plasticity of the models in three cases with departure from *accidental torsion*, extensive and severe torsional irregularity during an earthquake, Non-linear static analysis has been used to obtain the capacity curve of the structure. To check the performance level of the structure, it is necessary to find the target point on the capacity curve of the structure. At this point, the forces and deformations of the members for different performance levels should be checked. That point is called the change of target location, so in this research, the method of determining the coefficients of 360 publication was used for non-linear static analysis and obtaining the change of target location. The 360 revision publication of 2013, a significant resource in

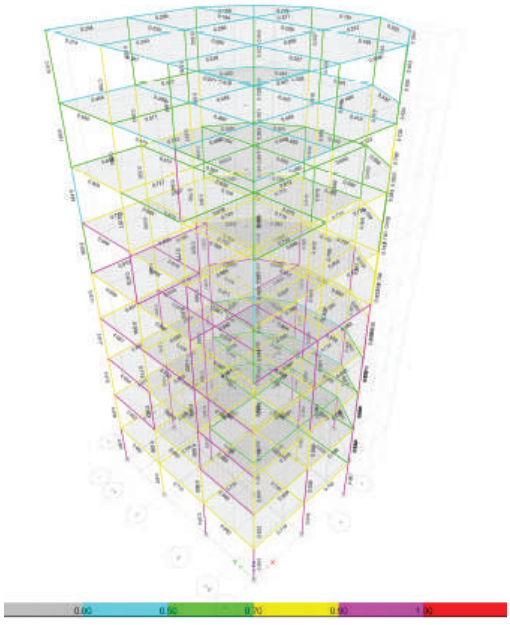


Figure 3. Designed model of 9 floors with asymmetric plan.

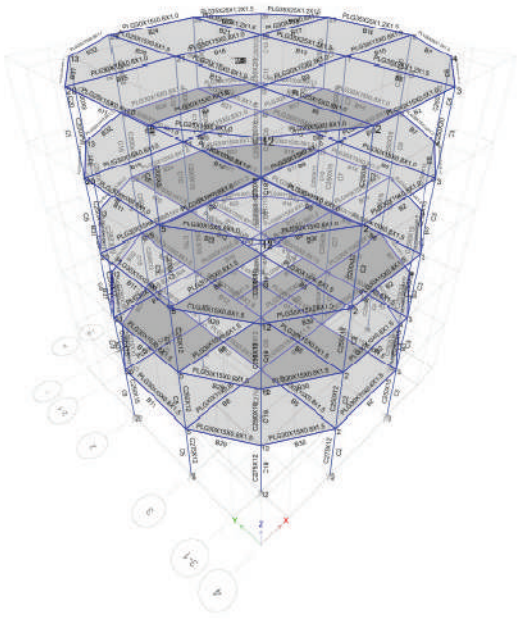


Figure 4. 3D model of 5 floors with symmetrical plan

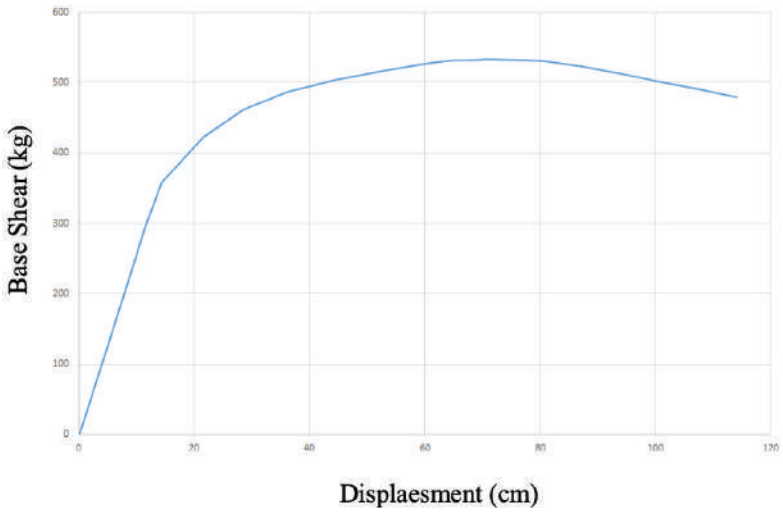


Figure 5. The capacity curve of the symmetrical 5-story structure with accidental torsion in the X direction irregularity.

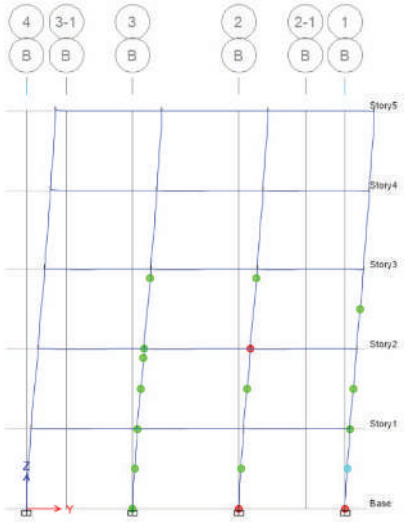


Figure 6. Distribution of plastic hinge in 5-story model with a symmetrical plan with high torsional irregularity.

structural engineering, was used for the non-linear specification of structural members.[18] The models' non-linear static analysis (incremental load) has been done with ETABS 2016, version 16.2.1 software.[16] After performing the non-linear static analysis, the performance level of the models can be observed according to the outputs. The performance level can be checked and observed according to the color of the joints formed at the place of the plastic joints. Also, the bearing curves can be used as an interpretable output to calculate the plasticity of the models and compare the results. For example, Figure 5 shows the capacity curve of a 5-story symmetrical structure with a deviation from the center to create an accidental torsion. Also, according to Figure 6, the distribution of plastic joints in the model with a symmetrical plan of 5 floors is shown with a departure from the centrality, which creates a severe torsion irregularity in the target location change in one of the frames. The formation of a plastic joint at the foot of the column in red indicates that the level of safety performance has been exceeded. Also, the formation of the green plastic joint on axis 3 indicates non-stop performance.

RESULTS AND DISCUSSION

Based on the analyses performed using the results of non-linear static analysis of the models, the role of symmetry and asymmetry in the plan with different percentages of departure from the centrality in three modes of accidental torsion, high and severe torsion irregularity on the structural capacity curve, ductility And the performance levels of the models in target displacement have been analyzed.

Based on the results of the analyses, the changes in the effective period of vibration of oscillation due to asymmetry in the Y direction are shown in Figure 7. The symbol 5-S-SY denotes the symmetric 5-story building, and the 5-story asymmetric building in the Y direction is denoted by 5-S-ASY. The symbol 9-S-SY denotes the symmetric 9-story building, and the 9-story asymmetric building in the Y direction is denoted by 9-S-ASY.

According to the analysis results shown in Figure 7, it is observed that the presence of asymmetry in one direction, along with accidental torsion, significantly increases the effective period of vibration of oscillation in all models.

As shown in Figure 7, in the 5-story model with a symmetric plan in the Y direction with accidental torsion, the effective period of vibration of oscillation was 0.72 seconds. The simultaneous effect of introducing asymmetry and accidental torsion increased the effective period of vibration to 0.75 seconds. In the 9-story models with a symmetric plan in the Y direction with accidental torsion, the effective period of vibration of oscillation was 1.03 seconds. The simultaneous effect of introducing asymmetry and accidental torsion increased the fundamental period to 1.07 seconds. In the 5-story model with a symmetric plan in the Y direction with significant torsion, the fundamental period of oscillation was 0.98 seconds. The simultaneous effect of introducing asymmetry and significant torsion increased the effective period of vibration to 1.13 seconds. In the 9-story model with a symmetric plan in the Y direction with significant torsion, the effective period of vibration of oscillation was 1.6 seconds. The simultaneous effect of introducing asymmetry and significant torsion increased the fundamental period to 1.9 seconds. In the case of severe torsion in the symmetric 5-story model, the effective period of vibration of oscillation was 0.88 seconds, and the introduction of asymmetry in that direction increased

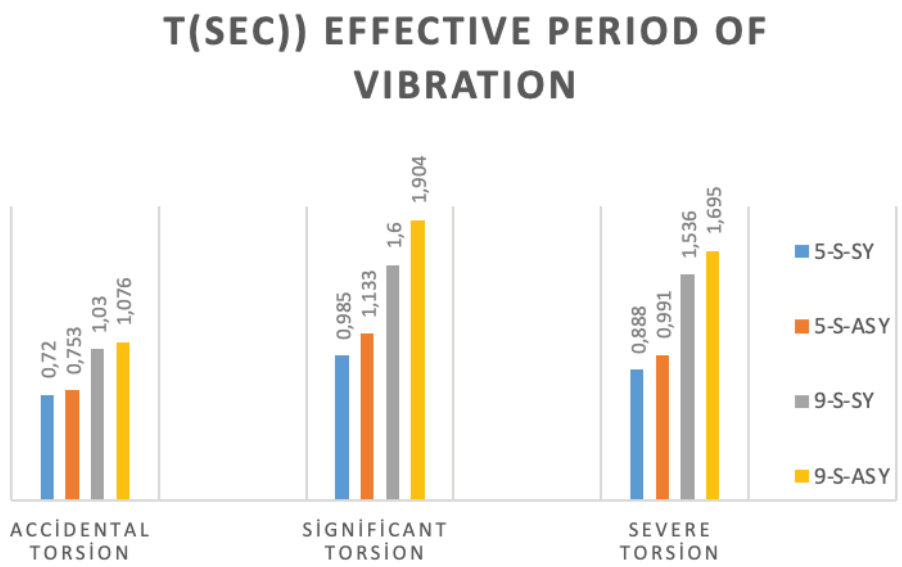


Figure 7. Changes in the effective period of vibration of oscillation due to asymmetry in the Y direction.

the period to 0.99 seconds. In the 9-story model with a symmetric plan in the Y direction with severe torsion, the fundamental period of oscillation was 1.53 seconds. The simultaneous effect of introducing asymmetry and significant torsion increased the effective period of vibration to 1.69 seconds. As illustrated in Figure 7, the slightest change in the effective period of vibration of oscillation due to asymmetry in the plan was observed in the 5-story model with accidental torsion. In contrast, the most significant change in the effective period of vibration was observed in the 9-story model with significant torsion.

As depicted in Figure 8, the changes in base shear due to the introduction of asymmetry in the plan in one direction are shown in three conditions: accidental, significant, and severe torsion across the models. The abbreviations for the models are used similarly to Figure 7 in Figure 8. In all models, it was observed that introducing asymmetry in the plan led to a reduction in base shear. The most negligible impact of asymmetry on base shear was in the 9-story model with accidental torsion, where the base shear for the symmetric model was 697,611 kg, which decreased to 690,829 kg due to the introduction of asymmetry—a reduction of 6,782 kg. The most significant impact of asymmetry on base shear changes was observed in the 5-story model under severe torsion. In the symmetric 5-story model, the base shear was 339,872 kg, and the introduction of asymmetry reduced the base shear to 294,767 kg—a decrease of 45,105 kg (equivalent to 45.1 tons).

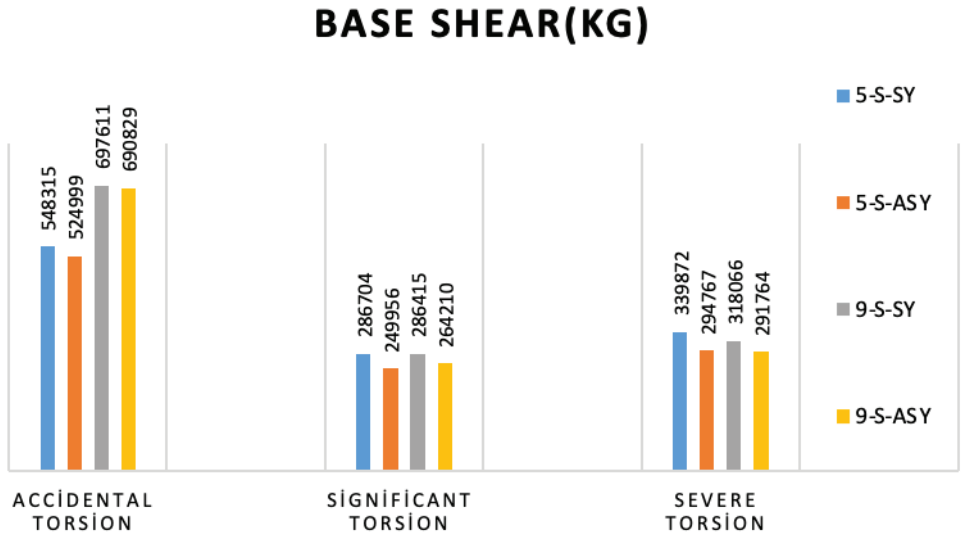


Figure 8. Changes in base shear due to asymmetry in the Y direction.

One of the most significant effects of asymmetry in one direction of the plan is the change in the ductility factor or simply ductility. A reduction in ductility indicates a decline in the building's performance level. Ductility is one of the most critical properties of structures in the nonlinear region. As shown in Figure 9, in the 5-story models, introducing asymmetry in the plan under all three conditions (accidental torsion, significant torsion, and severe torsion) reduced ductility. In the 5-story model with a symmetric plan and accidental torsion, the ductility factor was 5.21. Introducing asymmetry in the plan with accidental torsion reduced the ductility factor to 4.57, indicating a 1.13-fold decrease in ductility compared to the symmetric plan. This reduction ratio was 1.17 under significant torsion and 1.43 under severe torsion. In the 9-story model with a symmetric plan and accidental torsion, the ductility factor was 3.34. Introducing asymmetry in the plan with accidental torsion increased the ductility factor to 4.5, showing a 1.34-fold increase compared to the symmetric plan. However, under significant torsion, the ductility remained almost unchanged (about 2%), and under severe torsion, instead of increasing, it decreased by a factor of 1.38.

The summary of the results of the models related to 5-story structures with a symmetrical plan that are covered in the positive Y direction according to Table 3, and also, in this case, the results of the models related to the 5-story structures with an asymmetric plan that are covered in the positive Y direction and is summarized in Table 4.

By comparing Tables 3 and 4, It is possible to analyze the role of symmetry and asymmetry in the 5-story model in the positive Y direction of data overlay. The presence of asymmetry has caused an increase in the adequate rotation time; the highest percentage of increase was related to the mode of creating many twists with 15%. Also, asymmetry has caused a reduction in base cutting, such as changing the target location. The highest percentage of reduction related to severe torsion was about 16%. The increase in the target location change in high and severe torsion mode is significant, with an increase of 21 and 30%, respectively, due to asymmetry. There was no effect in the accidental torsion mode. A significant result is the reduction of ductility in all three modes: 25% in the accidental torsion mode, 31% for significant torsion, and 43% for severe torsion in models with an asymmetric plan.

According to Table 5, the results of models related to 9-story structures with symmetrical plans in all three cases, percentages of eccentricity that cause accidental, significant, and severe torsion and are covered in the negative direction of the Y axis, are written. In Table 6 of the results, the models related to the 9-story structures with asymmetric

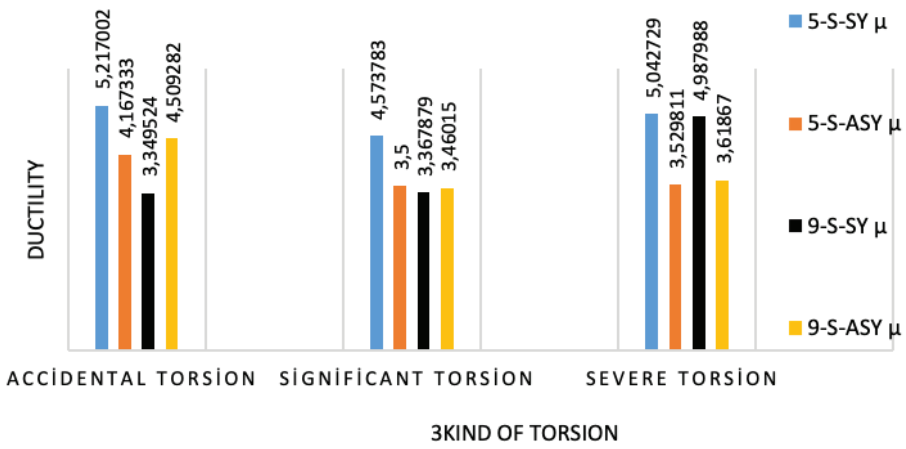


Figure 9. Changes in ductility due to asymmetry in the Y direction.

Table 3. Outputs of the 5-story model with a symmetrical plan with PUSH-YP

Torsion due to off-center modes	μ ductility	Δy Change of location of elastic limit	Δu Final relocation	V(kg) Base Shear	Δt(cm) Change target location	T(Sec) Effective period of vibration
accidental torsion (5)	5.217002	22.35	116.6	548315	10	0.72
significant torsion (1.2)	4.573783	13.35	61.06	286704	14	0.985
severe torsion (1.4)	5.042729	13.34	67.27	339872	13	0.888

Table 4. Outputs of the 5-story model with an asymmetric plan with PUSH-YP

Torsion due to off-center modes	μ ductility	Δy Change of location of elastic limit	Δu Final relocation	V(kg) Base Shear	Δt(cm) Change target location	T(Sec)) Effective period of vibration
accidental torsion (5)	4.167333	15	62.51	524999	10	0.753
significant torsion (1.2)	3.5	13.36	46.76	249956	17	1.133
severe torsion (1.4)	3.529811	13.25	46.77	294767	17	0.991

Table 5. Outputs of the 9-story symmetrical structure model with PUSH-YN

Torsion due to off-center modes	μ ductility	Δy Change of location of elastic limit	Δu Final relocation	V(kg) Base Shear	Δt(cm) Change target location	T(Sec)) Effective period of vibration
accidental torsion (5)	3.349524	19.97	66.89	697611	16	1.03
significant torsion (1.2)	3.367879	24.0098	80.8621	286415	27	1.6
severe torsion (1.4)	4.987988	19.98	99.66	318066	26	1.536

plans covered in the negative direction of the Y axis were collected for all three eccentricity cases.

By comparing Tables 5 and 6, It is possible to analyze the role of symmetry and asymmetry in the 9-story model, which is covered in the negative direction of Y. The existence of asymmetry has caused an increase in the Effective period of vibration; the highest percentage of increase was related to the mode of creating many twists, with 18%. Also, asymmetry has caused a reduction in base cutting, such as changing the target location. The highest percentage of reduction related to severe torsion was about 9%. The increase in the target location change in high and severe torsion mode is significant, with an increase of 22% and 12%, respectively, and with a lesser effect in the accidental torsional mode. The significant result is the reduction of ductility in both modes, 34% in the accidental torsion mode and 34% for severe torsion. 36% increase is less than 3% for significant torsion models with asymmetric plans.

Figure 10 shows capacity curves of 9-story models in four off-center states with symmetric and asymmetric plans, which significantly differ in performance, plasticity, and other parameters.

According to Figure 7, the capacity curves of the 9-story asymmetrical plan model with high torsional irregularity showed lower performance, ductility, and base shear compared to the 9-story symmetrical plan model with Accidental torsion. The impact of asymmetry in the plan is evident as an influential factor. The capacity curves of the 5-story models for all four eccentricity scenarios with symmetrical and asymmetrical plans, which showed significant differences in performance, ductility, etc., are illustrated in Figure 8, highlighting the contrast and its implications.

According to Figure 11, the capacity curves of the 5-story asymmetrical plan model with high torsional irregularity showed lower performance, ductility, and base shear than those of the 5-story symmetrical plan model with Accidental torsion. The impact of asymmetry in the plan as an influential factor in the non-linear behavior of the models is evident.

Table 6. Outputs of the 9-story asymmetric structure model with PUSH-YN

Torsion due to off-center modes	μ ductility	Δy Change of location of elastic limit	Δu Final relocation	V(kg) Base Shear	Δt(cm) Change target location	T(Sec)) Effective period of vibration
accidental torsion (5)	4.509282	19.93	89.87	690829	17	1.076
significant torsion (1.2)	3.46015	26.6	92.04	264210	33	1.904
severe torsion (1.4)	3.61867	19.9659	72.25	291764	29	1.695

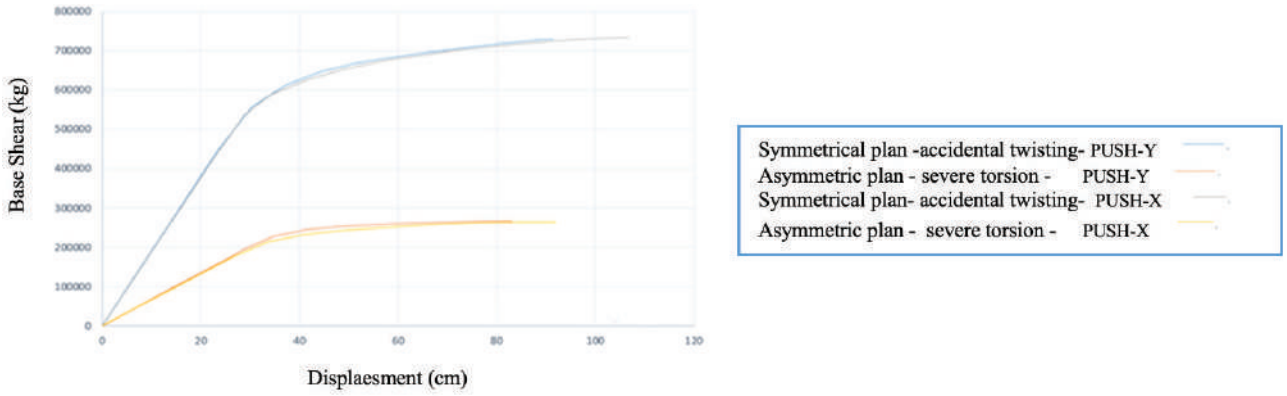


Figure 10. Selected capacity curves in 9 floor models.

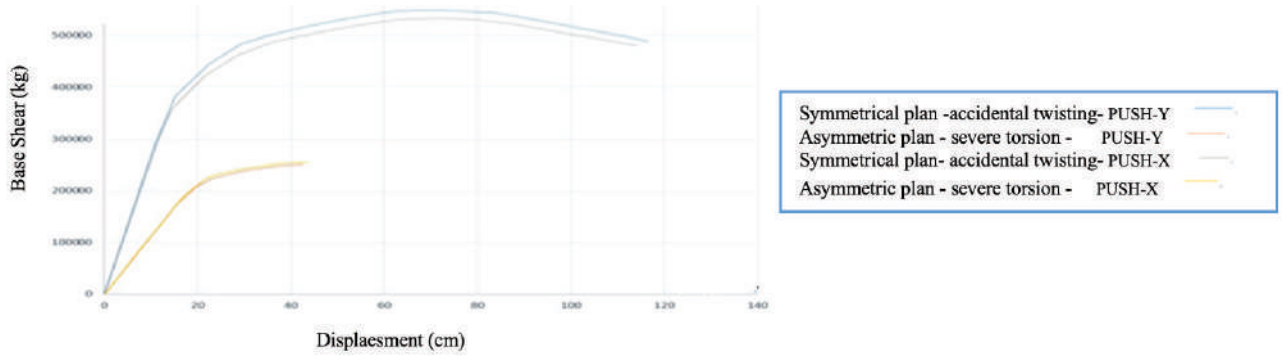


Figure 11. Selective capacity curves in 5-floor models.

CONCLUSION

This study, which is one of the first of its kind, investigated the combined effect of geometric asymmetry in one direction with the effect of eccentricity in three states—accidental torsion, significant torsion, and severe torsion—as influencing factors on performance levels and vital parameters such as ductility, effective period, and distribution of plastic hinges in existing medium steel moment frame buildings. The ductility was analyzed through a rigorous non-linear static analysis for 5-story and 9-story models with symmetrical and asymmetrical plans under three eccentricity scenarios (Accidental torsion, significant torsion irregularity, and severe torsional irregularity). The results showed that symmetry and asymmetry in the plan significantly affect the performance levels, ductility, and seismic response due to torsion, which is more pronounced in 5-story buildings. A notable 43% reduction in ductility was observed due to asymmetry in the severe torsional irregularity scenario compared to the symmetrical scenario. Additionally, the reduction in damage control range in the performance of these models is significant.

Urgent further studies on models with asymmetry in two directions are strongly recommended. Moreover, other steel and concrete buildings with different ductility levels and heights should be examined. Based on the research findings, an influential parameter called the asymmetry coefficient should be incorporated into the seismic design and retrofitting guidelines to reduce structural performance and non-linear analysis results. This study serves as the initial research in this area, and future studies on systems with two-directional asymmetry will be presented in upcoming publications.

AUTHORSHIP CONTRIBUTIONS

Authors equally contributed to this work.

DATA AVAILABILITY STATEMENT

The authors confirm that the data that supports the findings of this study are available within the article. Raw data that support the finding of this study are available from the corresponding author, upon reasonable request.

CONFLICT OF INTEREST

The author declared no potential conflicts of interest with respect to the research, authorship, and/or publication of this article. ETHICS There are no ethical issues with the publication of this manuscript.

STATEMENT ON THE USE OF ARTIFICIAL INTELLIGENCE

Artificial intelligence was not used in the preparation of the article.

REFERENCES

[1] De la Llera JC, Chopra AK. Evaluation of code accidental-torsion provisions using earthquake records from three nominally symmetric-plan buildings. Earthq Eng Res Cent Rep UCB EERC-93/09. Berkeley (CA): Univ California; 1993.

[2] De la Llera JC, Chopra AK. Evaluation of code accidental-torsion provisions from building records. J Struct Eng 1994;120:597–616. [CrossRef]

[3] CEN. Eurocode 8: Design of structures for earthquake resistance. Part 1: General rules, seismic actions and rules for buildings. EN 1998-1:2004. Brussels: Eur Comm Stand; 2004.

[4] Chopra AK, De la Llera JC. Accidental torsion in earthquake response and design of buildings. In: Proc 11th World Conf Earthq Eng; Acapulco, Mexico. Paper No. 580; 1996.

[5] Dimova SL, Alashki I. Seismic design of symmetric structures for accidental torsion. Bull Earthq Eng 2003;1:303–320. [CrossRef]

[6] De la Colina J, Almeida C. Probabilistic study on accidental torsion of low-rise buildings. Earthq Spectra 2004;20:25–41. [CrossRef]

[7] Ramadan OMO, Mehanny SSF, Mostafa A. Revisiting the 5% accidental eccentricity provision in seismic design codes for multi-story buildings. In: Proc 14th World Conf Earthq Eng; Beijing, China. Paper No. S10-038; 2008.

[8] Stathopoulos KG, Anagnostopoulos SA. Accidental design eccentricity: Is it important for the inelastic response of buildings to strong earthquakes? Soil Dyn Earthq Eng 2010;30:782–797. [CrossRef]

[9] De la Colina J, Valdes J, Velazquez M. Effect of the number of upper floors, dead-to-live load ratio and number of columns per floor on accidental eccentricity. Earthq Eng Struct Dyn 2011;40:123–140.

[10] DeBock DJ, Liel AB, Haselton CB, Hooper JD, Henige RA Jr. Importance of seismic design accidental torsion requirements for building collapse capacity. Earthq Eng Struct Dyn 2014;43:831–850. [CrossRef]

[11] Anagnostopoulos SA, Kyrkos MT, Stathopoulos KG. Earthquake induced torsion in buildings: Critical review and state of the art. Earthq Struct 2015;8:305–377. [CrossRef]

[12] Sannati B, Ahmadi J. Analytical and regulatory review of torsional irregularities in short to tall structures. Anal Struct Earthq 2017;13:39–49.

[13] Rezaei MR. Evaluation of rotation effects in steel structures with irregular plan under earthquake in project management. Int J Supply Chain Manag 2020;9:945.

[14] Standard 2800. Iranian code of practice for seismic resistant design of buildings. 4th ed. Tehran: Hous Urban Dev Res Cent; 2013.

[15] Natl Build Regul Iran. Loads for buildings. Chapter 6. 4th ed. Tehran: Build Hous Res Cent; 2018.

[16] Comput Struct Inc. ETABS: Integrated building design software. Version 16.2.1. Berkeley (CA): CSI; 2016.

[17] Irans Natl Constr Regul. Steel structures. Chapter 10. 5th ed. Tehran: Build Hous Res Cent, Min Hous Urban Dev; 2021.

[18] Instruction 360. Guidelines for seismic rehabilitation of existing structures. 2nd rev. Tehran: Hous Urban Dev Res Cent; 2013.

Sigma Journal of Engineering and Natural Sciences
Web page info: https://sigma.yildiz.edu.tr
DOI: 10.14744/sigma.2025.00000

Research Article

Multiclass anemia classification based on multivariate adaptive regression spline method: Developing a decision support system for doctors

Nagihan YAĞMUR[1,*], Idiris DAĞ[2]

[1]*Department of Computer Engineering, Kutahya Dumlupinar University, Kutahya, 43100, Türkiye*
[2]*Department of Computer Engineering, Eskisehir Osmangazi University, Eskisehir, 26040, Türkiye*

ARTICLE INFO

Article history
Received: 05 March 2024
Revised: 13 May 2024
Accepted: 15 October 2024

Keywords:
Anemia Classification; Decision-Support Systems; Machine Learning; Multivariate Adaptive Regression Spline Method

ABSTRACT

Artificial intelligence and machine learning have the potential to forecast emerging diseases by analyzing patient medical data, offering decision-support systems for healthcare practitioners. These approaches are pivotal in minimizing diagnostic inaccuracies for physicians and hold significant value for patients and healthcare organizations in scrutinizing medical records. Nevertheless, the effectiveness of algorithms fluctuates based on various attributes of datasets, fluctuations in the size of datasets, diverse parameters and their characteristics, and varying quantities of patient records. In this research, two distinct models have been suggested for categorizing five types of anemia diseases using the multivariate adaptive regression spline method: a 1st-degree multiclass multivariate adaptive regression spline model and a 2nd-degree multiclass multivariate adaptive regression spline model. These models were employed to classify entries into non-anemia, folate deficiency anemia, Hgb-anemia, B12 deficiency anemia, and iron deficiency anemia. When the results were analyzed, 98.30% accuracy, 92.91% precision, 92.76% recall, and 92.74% F1-score were obtained with the 2nd order multiclass multivariate adaptive regression spline model. The outcomes obtained aim to offer valuable insights to medical students and physicians engaged in addressing the anemia classification challenge. The application of these models holds significant promise in enhancing diagnostic procedures, minimizing error rates, and devising more efficient treatment strategies. At the same time, in addition to the studies using the same data set in the literature, it has been shown that the adaptive spline method also shows successful results.

Cite this article as: Yağmur N, Dağ I. Multiclass anemia classification based on multivariate adaptive regression spline method: Developing a decision support system for doctors. Sigma J Eng Nat Sci 2026;44(1):93–104.

***Corresponding author.**
*E-mail address: nagihan.yagmur@dpu.edu.tr

This paper was recommended for publication in revised form by Editor-in-Chief Ahmet Selim Dalkilic

Published by Yıldız Technical University Press, İstanbul, Turkey
© Author. This is an open access article under the CC BY-NC license (http://creativecommons.org/licenses/by-nc/4.0/).

INTRODUCTION

Thanks to advances in science and technology, diagnoses in the medical world have greatly benefited from the measurement of data such as patients' blood values, medical images, and medical signals [1]. Making these measurements in detail facilitates the detection of patterns and hidden connections in datasets thanks to machine learning methods, a sub-branch of artificial intelligence that can make connections between complex data. Artificial intelligence and machine learning methods lead to the rapid and accurate resolution and diagnosis of diseases [1–3].

Artificial intelligence and machine learning methods are often used in various studies such as heart failure disease prediction, Diabetes classification, and heart failure disease prediction, which are frequently researched in the literature [4-9]. These studies aim to train processes to speed up the decision-making process of specialist doctors when a new case comes in. That is, the aim is to ensure that when specialists are faced with new cases, the system can similarly make decisions for them.

Modeling data and disease is a major component of medicine today. One of the two processes that enhance this is the determination of model parameters by machine learning methods. The terms Data, Disease, and Modeling are used in the determination of model parameters and machine learning methods help this process to be performed faster and more accurately. In a study using deep learning architectures Alexnet and Resnet50 for automatic detection of lung cancer using computed tomography images, the performances of the model parameters were compared and the highest accuracy value was obtained with the AlexNet architecture [10]. In the study where the success of the k-means algorithm was improved with machine learning methods using various cancer data, the death game optimization algorithm was combined with the k-means method. As a result, the success of the proposed clustering method was increased [11]. In a study on brain tumor classification using two-dimensional MRI images, promising results were obtained for complex classification problems by optimizing the vision transformer (ViT) network [12]. A hybrid k-means method is presented to assign weights to input parameters in a study conducted to correctly diagnose diseases in four different medical datasets. It is emphasized that the results obtained will reduce staff workload and test costs. [13]. In a study to reduce the effects of COVID-19 on the education system, an IoT and deep learning-based system was proposed [14]. The proposed system aims to protect students and staff against infectious diseases and improve students' performance in classes by monitoring environmental conditions through an IoT-based sensor network to ensure the use of masks in closed areas during the current pandemic. In the study conducted on the Face Mask Detection Dataset containing a total of 7553 masked and unmasked images, the best results were obtained as 99.5% for F1 Score and 99% for MCC with the model trained on the InceptionV3 network. In a study using Machine Learning classification methods such as K-Nearest Neighbors (KNN), Random Forest (RF), Support Vector Machine (SVM), Artificial Neural Network (ANN), and Decision Tree (DT) for diabetes prediction by taking different attributes related to diabetes disease, random forest achieved high success in predicting diabetes compared to other machine learning methods [15]. In a study of brain tumor detection using YOLOv5, YOLOv7, and YOLOv8, it was concluded that brain tumors were better detected with YOLOv8 [16]. The images were first preprocessed by applying color transformation, histogram equalization, and filter operations. As a result, a high success rate of 87% was achieved. In a study using Computed Tomography (CT) images for the detection of brain hemorrhages (ResNet), Visual Geometry Group (VGG), and EfficientNet architectures, it was emphasized that it is important to choose the most appropriate model for the dataset [17]. As a result, it was emphasized that the success of the EfficientNet-B2 model was higher than the other models in the literature.

Thanks to scientific and technological developments, artificial intelligence system applications used to support many areas are widely used. Thus, the health sector is now in need of experts in the evaluation of data due to technological advances. Doctors' busy working hours, difficulties in accessing various specialists, and the vital importance of early diagnosis of urgent pathologies contribute to the growing need for apps that support healthcare professionals.

The diagnosis of anemia is crucial for physicians, and anemia signifies a condition where oxygen is not adequately transported; in this case, red blood cells fail to fulfill their function completely. It occurs as a result of low hemoglobin, indicating values below 13 g/dl in men and 12 g/dl in women. Iron deficiency anemia is the most common form of anemia. It is caused by insufficient intake or reduced absorption of the iron the body needs. Most iron is found in red blood cells, and women can develop iron deficiency and anemia due to blood loss. The main causes of anemia are bleeding, destruction of red blood cells (hemolysis), insufficient production of red blood cells, and low hemoglobin production. Women are at higher risk of anemia due to menstrual bleeding [18]. Children may develop anemia due to stomach bleeding caused by the frequent use of aspirin and antipyretics [19]. Hemolytic anemia, B12 deficiency anemia, iron deficiency anemia, thalassemia, Fanconi anemia, etc. The main causes of anemia, which has varieties such as can be examined under 3 headings: 1. blood loss 2. insufficiency of red blood cells 3. high rate of red blood cell destruction [19].

The World Health Organization (WHO) has characterized anemia as a state where the red blood cells or their capability to carry oxygen are inadequate [16]. This condition has been highlighted to predominantly impact women and young children, leading to a considerable decline in quality of life and potential association with severe illnesses.

There are also studies on the classification of anemia disease, which aim to provide decision support to physicians. When the studies were examined, it was seen that they were divided into two groups as binary class (anemia / no anemia) studies and multi-class (iron deficiency anemia, B12 vitamin deficiency anemia, etc.). In an analysis of binary class studies, a research effort utilized MARS and the Harris hawks algorithm (HHO) to process data from 1732 patients categorized as anemic or non-anemic, sourced from the Kaggle database [20]. In the study, six different algorithms including multiple linear form HHO, multiple quadratic form HHO, multiple exponential form HHO, 1st order MARS model, 2nd order MARS model, and the strongest MARS model were proposed. At the end of the study, the performance evaluations of the six proposed methods were found to be higher than other studies in the literature. In a study to detect the anemia status of a patient, a model based on classification with support vector machine (SVM) and RF was developed [21]. In a study conducted using blood data from Kanti children's hospital, a model was designed to predict anemia in children under 5 years of age [22]. The dataset consisting of 700 records was first normalized and data balanced. As a result, the RF method demonstrated the most successful performance with an accuracy rate of 98.4%. Finally, it aims to increase the performance of the algorithms by using methods such as feature selection and Ensemble Learning methods, Voting, Stacking, Bagging, and Boosting. Machine learning methods such as CNN, k-NN, Decision Tree (DT), NB and SVM have been used to propose using palm images for anemia detection as an effective, cost- and time-saving solution as an alternative to invasive methods [23]. In a study focused on predicting anemia in children, various machine-learning methods were used to find factors associated with anemia [24]. While MLP showed the highest success with 81.67%, the highest success (82.5%) was achieved when the DT feature selection method was applied. In a study where 1732 blood data taken from the Kaggle database were classified using the Crow Search Optimization Algorithm (CSO), CSO was analyzed in 2 different scenarios. Multilinear form CSO and quadratic linear form CSO [25].

Again, in a study in which various machine learning algorithms such as DT, SVM, RF, LR and k-NN were tested to predict anemia in children, a powerful prediction model was created by improving classifiers with learning techniques such as bagging, boosting, and stacking [26]. In another study, the process of diagnosing anemia and anemia-related diseases was performed with machine-learning methods [27]. In this context, a machine learning architecture that can diagnose 12 different types of anemia was developed. The data were obtained from Düzce University Research and Application Hospital with ethics committee permission. Then, the weights of the data were calculated using techniques such as Information Gain, Information Gain Ratio, Correlation, and Principal Component Analysis. After the calculations, machine learning techniques such as Support Vector Machines, Decision Trees, Naive Bayes, and Artificial Neural Networks were applied to the original dataset and the datasets created using the new attributes. The results obtained by using cross-validation method in all models were evaluated with performance indicators such as accuracy, classification error, sensitivity, precision, and f1-score. In a study where anemia was predicted using various methods such as XGBoost, LightGBM, Lasso, Rigde and Elastic-net, the SMOTE technique, which attempts to balance the distribution of classes by randomly increasing and replicating minority class instances, and Pearson correlation to identify strongly correlated points that are thresholds for feature selection [28]. As a result, the Light GBM algorithm outperformed the others in terms of accuracy. Some recent studies have proposed a robust and efficient classification algorithm using SVM, k-NN, LR, DT, RF algorithm to overcome the weaknesses of manual evaluation and thus classify Sickle Cell Anemia (SCA) case into 3 different classes [29]. Also, in a different study to solve the 5-class anemia classification problem like this study, it was proposed to use fuzzy logic-based parameter optimization and achieve class-based and overall accuracy improvement within the dataset [30]. Six new models are introduced with the integration of TreeBagger, Chicken Swarm Optimization Algorithm (CSA), CSO and JAYA method.

In this study, 15.300 patient hematology data obtained from the study titled "Nutritional Anemia Disease Classification Based on Genetic Algorithm and Deep Learning Algorithms" by Kilicarslan et al. at Tokat Gaziosmanpaşa University Faculty of Medicine [31,32]. The dataset encompasses records of individuals with Hgb-anemia, iron deficiency anemia, B12 vitamin deficiency anemia, folate deficiency anemia, and non-anemia. The primary objective of this study is to develop a system useful in diagnosing anemia in general healthcare services, particularly in situations where access to specialist physicians is becoming challenging due to the rising number of patients and hospital density. It is anticipated that this study can make substantial contributions not only to non-specialized healthcare professionals but also to the existing literature.

It is possible to note that, the MARS method is a mathematical modeling approach preferred in general for analyzing complex data sets and often used in various studies such as prediction, analysis, and classification [20,33,34]. Different mathematical modeling approaches have been studied in detail by mathematicians in the literature [37–39]. The behavior of MARS can also be seen in many studies in the literature. When the studies examined, it is understood from the values of different performance criteria that this machine learning based method can be used to develop effective prediction models, especially for engineering datasets [20,40].

In this study, it is determined that the MARS method, which mathematically models complex data and is frequently used in prediction and classification problems, has not been used in the anemia classification problem as far as

it is known and examined under two scenarios. 1st order multiclass MARS model and 2nd order multiclass MARS model. As a result, it aims to reveal complex models by examining the pruning parameters and degree values that significantly affect the performance of the MARS method.

MATERIALS AND METHODS

Preprocessing

The data set used in the study is Kılıçarslan et al. It includes the blood count results of 15300 patients taken from Tokat Gaziosmanpaşa University Faculty of Medicine [32]. Data of pregnant women, cancer patients, and children and irrelevant and missing parameters were published by Kılıçarslan et al. It was removed from the data set by. The dataset used in the study includes 24 parameters and 5 different classes. Due to numerical value differences in the data set, blood values were normalized by scaling them between 0.1 and 0.9.

MARS Method

MARS method has a nonlinear and nonparametric structure and it is a method introduced to the literature by Friedman (1991) [41]. With its ability to make reliable predictions, it finds itself used in many fields thanks to its success. Also, it produces strong predictions compared to other models and gives robust results. Therefore, despite the fact that the models include especially large number of terms, it is frequently preferred. MARS method is composed of 2 stages. And the first of these stages is the stage of "step-forward algorithm". In this stage, the aim is to maximize the basic functions under the forward step algorithm which forms complex model. And as it is a result of this, the models that include incorrect terms often come out. In this step, an iterative process is carried out with the aim of obtaining an optimal model by reducing complexity. Thanks to the iterative process, it is aimed to achieve a balance between accuracy and model complexity until the number of basic functions is maximum.

Thanks to the backward step algorithm, the complexity of the models produced in the forward step phase is reduced and the functions that contribute the least to the increase in total squares are determined and removed from the model. Improvement is achieved in this way and helps to expand and simplify the model. This process is called "pruning" and is managed by a hyperparameter called "nprune". As a result, the optimal prediction model is created with the pruning parameter [42]. In the MARS method, which provides good modeling in high dimensional and complex data, the degree of pruning affects this performance, as does the selection of interactions or functions to be extracted. There is another important hyperparameter in the MARS, where it creates piecewise basis functions. This is "degree". This parameter contributes an ability that has already learned by the model, to understand the different relationships. Therefore it can learn complex relationships. Reducing the degree, it may also capture simpler relationships. Choosing the right degree is very essential for the model that best fits with the data and learns, and for not facing with simplification problem. In short, degree and pruning parameters are very important for this method's performance.

The general MARS model is expressed as [43]

$$Y = \beta_0 + \sum_{k=1}^{K} a_k \beta_k(X_t) + \varepsilon_t \quad (1)$$

In this context, X represents the independent variable, while K denotes the number of basis functions, and k stands for the number of nodes. The coefficients of the kth basis function are represented by a_k, B_0 signifies the constant term, and $B_k(X_t)$ denotes the k. independent variable for the k. basis function. The basis function is expressed as $k=1,2,..K$ has the following form [43].

$$B_m(x) = \prod_{t=1}^{L_m} \left[S_{l,m}\left(x_{v(1,m)} - k_{l,m}\right)\right] \quad (2)$$

According to Equation 2, L_m is the degree of interaction, $S_{l,m} \in [\pm 1]$, $k_{l,m}$ is the node value, $x_{v(1,m)}$ is the argument value.

Adaptation of the Mars Method to Multiple Anemia Classification Problem

Table 1. Types of models utilizing the MARS method

Models	Model characteristics
MARS_model-1	*Degree = 1 nprune = 20*
MARS_model-2	*Degree = 1 nprune = 20*

In order to evaluate the performance of the MARS method, analyzes were carried out on 2 separate models using different combination of hyperparameters. These analyzes were carried out on very different set of hyperparameters. The aim of this analyzes is to find out the prediction performance of the model and / or find out the combination of hyperparameters when the model is at peak level. This really creates a comprehensive understanding of the MARS method applied to the data – how it hinges on making elaborate predictions and still maintains reasonable ability to generalize. Experimentally, MARS_Model-1 was configured with degree 1 and nprune 20 and MARS_Model-2 was configured with degree 2 and NPRUNE 20.

For MARS_Model-1, a 10-fold cross-validation method was employed, and the accuracy values along with the average accuracy obtained at each fold are presented in Table 2.

Table 2. Accuray values obtained as a result of each fold by MARS_model-1.

Resample	Accuracy
Fold-1	%97.98
Fold-2	%97.97
Fold-3	%98.50
Fold-4	%97.91
Fold-5	%98.43
Fold-6	%97.84
Fold-7	%97.65
Fold-8	%97.71
Fold-9	%98.24
Fold-10	%97.97
Avg Acc =	%98.02

The high accuracy values signify that the model is robust even in the presence of an imbalanced dataset.

Prior to pruning, 7 basis functions with low success rates were produced and subsequently eliminated from MARS_Model-1. Subsequently, the 20 basis functions generated through the MARS method for MARS_Model-1, along with the corresponding weights, are detailed in Table 3.

As indicated in Table 3, j represents the number of basis functions, and the BFj values denote the basis functions defined for the model. Based on the details provided in Table 3, the mathematical equation for MARS_Model-1 can be expressed as follows:

$$\begin{aligned} Model-1_{class1} = &-125.71 - 363.02xBF1 - 344.7xBF2 \\ &- 238023.15xBF3 - 408104.61xBF4 - 173907xBF5 \\ &+ 71438.5xBF6 - 71404.2xBF7 + 112.9xBF8 \\ &+ 4258.14xBF9 - 37.93xBF10 + 345.57xBF11 \\ &- 46.38xBF12 + 175.68xBF13 - 498.41xBF14 \\ &- 317.83xBF15 + 435.40xBF16 - 562.54xBF17 \\ &+ 2909.55xBF18 + 308.51xBF19 \end{aligned} \quad (3)$$

$$\begin{aligned} Model-1_{class2} = &-4.3 + 3.37xBF1 + 10.01xBF2 \\ &+ 270.13xBF3 - 863.32xBF4 + 576.51xBF5 \\ &- 916.55xBF6 - 12198.40xBF7 - 7.69xBF8 \\ &+ 14577.59xBF9 + 30.70xBF10 - 4.91xBF11 \\ &- 40.22xBF12 - 16.44xBF13 - 14.40xBF14 \\ &- 112.42xBF15 - 110.40xBF16 - 276.26xBF17 \\ &- 3255.93xBF18 + 14.83xBF19 \end{aligned} \quad (4)$$

Table 3. The prediction results of MARS_model-1

Basic Functions		Weights				
		1	2	3	4	5
	Constant	-125.71	-4.3	3.27	-15.13	-6.5
*BF*1	*GENDER*	-363.02	3.37	4.2	1.79	2.1
*BF*2	*max (0,0.51 – RBC)*	-344.7	10.01	-18.46	8.70	4.3
*BF*3	*max (0, HBG – 0.45)*	-238023.15	270.13	637.28	332.25	376.8
*BF*4	*max (0, HBG – 0.46)*	408104.61	-863.32	-1991.35	-1081.53	-907.4
*BF*5	*max (0, HBG – 0.47)*	-173907.0	576.51	1375.29	775.40	544.1
*BF*6	*max (0, HBG – 0.51)*	71438.5	-916.55	-644.43	-814.26	-416.6
*BF*7	*max (0, HBG – 0.52)*	-71404.2	-12198.40	-20551.91	-6425.84	-27267.2
*BF*8	*max (0,0.57 – HBG)*	112.9	-7.69	11.09	-9.82	-2.1
*BF*9	*max (0, HBG – 0.57)*	4258.14	14577.59	23525.97	7988.08	31474.9
*BF*10	*max (0,0.07 – MCH)*	-37.93	30.70	-37.38	-57.23	-33.7
*BF*11	*max (0, MCH – 0.07)*	345.57	-4.91	4.41	-29.11	6.1
*BF*12	*max (0,0.11 – SD)*	-46.38	-40.22	11.97	-15.25	-22.8
*BF*13	*max (0, SD – 0.11)*	175.68	-16.44	42.29	-8.98	-9.7
*BF*14	*max (0, SD – 0.29)*	-498.41	14.40	-27.40	10.86	10
*BF*15	*max (0, TSD – 0.16)*	-317.83	112.42	-147.25	174.98	77.9
*BF*16	*max (0, TSD – 0.23)*	435.40	-110.40	130.38	-174.64	-77.1
*BF*17	*max (0,0.08 – FOLATE)*	-562.54	-276.26	-5.99	238.40	-174.7
*BF*18	*max (0,0.006 – B12)*	2909.55	-3255.93	-61.46	251.27	784.4
*BF*19	*max (0, B12 – 0.006)*	308.51	14.83	-11.04	16.43	-4127036.3

$$\begin{aligned} Model-1_{class3} &= 3.27 + 4.2xBF1 - 18.46xBF2 \\ &+ 637.28xBF3 - 1991.35xBF4 + 1375.29xBF5 \\ &- 644.43xBF6 - 20551.91xBF7 - 11.09xBF8 \\ &+ 23525.97xBF9 - 37.38xBF10 + 4.41xBF11 \\ &+ 11.97xBF12 + 42.29xBF13 - 27.40xBF14 \\ &- 147.25xBF15 + 130.38xBF16 - 5.99xBF17 \\ &- 61.46xBF18 - 11.04xBF19 \end{aligned} \quad (5)$$

$$\begin{aligned} Model-1_{class4} &= -15.13 + 1.79xBF1 + 8.70xBF2 \\ &+ 332.25xBF3 - 1081.53xBF4 + 775.40xBF5 \\ &- 814.26xBF6 - 6425.84xBF7 - 9.82xBF8 \\ &+ 7988.08xBF9 - 57.23xBF10 - 29.11xBF11 \\ &- 15.25xBF12 - 8.98xBF13 + 10.86xBF14 \\ &+ 174.98xBF15 - 174.64xBF16 + 238.40xBF17 \\ &+ 251.27xBF18 + 16.43xBF19 \end{aligned} \quad (6)$$

$$\begin{aligned} Model-1_{class5} &= -6.5 + 2.1xBF1 + 4.3xBF2 + 376.8xBF3 \\ &- 907.4xBF4 + 544.1xBF5 - 416.6xBF6 - 27267.2xBF7 \\ &- 2.1xBF8 + 31474.9xBF9 - 33.7xBF10 + 6.1xBF11 \\ &- 22.8xBF12 - 9.7xBF13 + 10xBF14 + 77.9xBF15 \\ &- 77.1xBF16 - 174.7xBF17 + 784.4xBF18 \\ &- 4127036.3xBF19 \end{aligned} \quad (7)$$

According to the information provided in Table 3 and Equations 3-7, the MARS method pruned and eliminated 16 out of the 24 parameters from the model as they made minimal contributions to the model's performance. Consequently, the model was constructed with parameters such as GENDER, RBC, HBG, MCH, SD, TSD, FOLATE, and B12, which have a high contribution to the model performance. Upon reviewing Equations 3-7, it is evident that with a degree of 1, the formation of simple linear functions occurs, without any interaction among the basis functions. As stated in the equations, the dataset was subjected to class-based modeling with the MARS method, and the prediction result with a high success rate was taken as a reference. Classification was performed in this way.

Table 4. Accuray values obtained as a result of each fold by MARS_model-2.

Resample	Accuracy
Fold-1	%98.17
Fold-2	%97.97
Fold-3	%98.36
Fold-4	%97.84
Fold-5	%98.63
Fold-6	%98.24
Fold-7	%98.24
Fold-8	%98.10
Fold-9	%98.69
Fold-10	%98.23
Avg Acc =	%98.25

For MARS_Model-2, 10-fold cross-validation was applied and the accuracy and average accuracy values obtained at each folding step are presented in Table 4. High accuracy values indicate that the model is not affected by the unbalanced data set.

Before the pruning process for MARS_Model-2, a collection of 32 basis functions was initially created, following which 12 functions with lower success rates were omitted from the model. Subsequently, Table 5 presents the 20 basis functions derived using the MARS method for MARS_Model-2, inclusive of their corresponding weights.

$$\begin{aligned} Model-2_{class1} &= -980.82 + 114.02xBF1 + 101764.59xBF2 \\ &- 134629.02xBF3 + 34290.32xBF4 + 1682.25xBF5 \\ &- 103544.43xBF6 + 91825.56xBF7 + 20620.6xBF8 \\ &- 52302.795xBF9 + 41493.423xBF10 + 8.29xBF11 \\ &- 31.94xBF12 + 37.45xBF13 - 70.35xBF14 \\ &- 141.35xBF15 + 718.07xBF16 - 645.69xBF17 \\ &+ 859.32xBF18 + 5601.58xBF19 \end{aligned} \quad (8)$$

$$\begin{aligned} Model-2_{class2} &= -0.64 + 1.18xBF1 - 227.76xBF2 \\ &- 173.04xBF3 + 319.64xBF4 + 242251.42xBF5 \\ &- 12420.24xBF6 - 1776.51xBF7 - 32.58xBF8 \\ &+ 182.65xBF9 - 54.8xBF10 - 28.69xBF11 \\ &+ 145.03xBF12 + 1440497.07xBF13 \\ &- 1440545.22xBF14 + 194.93xBF15 - 1330.09xBF16 \\ &- 1439373.27xBF17 - 1358.75xBF18 - 20917.73xBF19 \end{aligned} \quad (9)$$

$$\begin{aligned} Model-2_{class3} &= +1.13 - 3.15xBF1 - 594.10xBF2 \\ &+ 362.84xBF3 + 10.65xBF4 - 12.37xBF5 \\ &- 3779.46xBF6 - 2504.97xBF7 - 134.71xBF8 \\ &+ 397.15xBF9 + 4.44xBF10 + 80.66xBF11 \\ &- 542.99xBF12 - 176.54xBF13 + 210.18xBF14 \\ &- 363.42xBF15 + 2035.7xBF16 - 1487.89xBF17 \\ &- 233.22xBF18 + 96.33xBF19 \end{aligned} \quad (10)$$

$$\begin{aligned} Model-2_{class4} &= +0.53 + 0.77xBF1 - 762.61xBF2 \\ &+ 847.54xBF3 - 399.29xBF4 + 15652.09xBF5 \\ &- 17315.68xBF6 - 869.46xBF7 - 137.27xBF8 \\ &+ 383.62xBF9 + 103.92xBF10 + 176.29xBF11 \\ &- 3008.09xBF12 + 94423.9xBF13 - 94344.426xBF14 \\ &- 175.84xBF15 - 5330.8xBF16 - 88906.14xBF17 \\ &+ 3485.53xBF18 - 256.41xBF19 \end{aligned} \quad (11)$$

$$\begin{aligned} Model-2_{class5} &= -1.71 + 0.41xBF1 - 271.61xBF2 \\ &+ 139.7xBF3 + 4.3xBF4 + 261731.73xBF5 \\ &- 24207.21xBF6 - 690.03xBF7 - 27.48xBF8 \\ &+ 145.52xBF9 + 36.53xBF10 - 10.48xBF11 \\ &- 19.02xBF12 + 15566.1xBF13 - 1556574.2xBF14 \\ &+ 183.53xBF15 - 1116.8xBF16 - 15555652.35xBF17 \\ &- 1838.8xBF18 + 14763.27xBF19 \end{aligned} \quad (12)$$

Table 5. The prediction results of MARS_model-2

Basic Function		Weights				
		1	**2**	**3**	**4**	**5**
	Constant	-980.82	-0.64	1.13	0.53	-1.71
*BF*1	*GENDER*	114.02	1.18	-3.15	0.77	0.41
*BF*2	*max* (0, *HBG* – 0.45)	101764.59	-227.76	-594.10	-762.61	-271.61
*BF*3	*max* (0, *HBG* – 0.47)	-134629.02	-173.04	362.8	847.54	139.7
*BF*4	*max* (0, *HBG* – 0.49)	34290.32	319.64	10.65	-399.29	4.3
*BF*5	*max* (0,0.57 – *HBG*)	1682.25	242251.42	-12.37	15652.09	261731.73
*BF*6	*GENDER** *max* (0, *HBG* – 0.52)	-103544.43	-12420.24	-3779.46	-17315.68	-24207.21
*BF*7	*GENDER** *max* (0, *HBG* – 0.51)	91825.56	-1776.51	-2504.97	-869.46	-690.03
*BF*8	*GENDER** *max* (0, *HBG* – 0.4)	20620.6	-32.58	-134.71	-137.27	-27.48
*BF*9	*GENDER** *max* (0, *HBG* – 0.43)	-52302.795	182.65	397.15	383.62	145.52
*BF*10	*GENDER** *max* (0, *HBG* – 0.48)	41493.423	-54.8	4.44	103.92	36.53
*BF*11	*GENDER** *max* (0,0.24 – *TSD*)	8.29	-28.69	80.66	176.29	-10.48
*BF*12	*max* (0, *HBG* – 0.44)* *max* (0,0.24 – *TSD*)	-31.94	145.03	-542.99	-3008.09	-19.02
*BF*13	*max* (0,0.57 – *HBG*)* *max* (0, *TSD* – 0.35)	37.45	1440497.07	-176.54	94423.9	1556592.1
*BF*14	*max* (0,0.57 – *HBG*)* *max* (0,0.35 – *TSD*)	-70.35	-1440545.22	210.18	-94344.426	-1556574.25
*BF*15	*max* (0,0.57 – *HBG*)* *max* (0, *TSD* – 0.25)	-141.35	194.93	-363.42	-175.84	183.53
*BF*16	*max* (0,0.57 – *HBG*)* *max* (0, *TSD* – 0.21)	718.07	-1330.09	2035.7	-5330.8	-1116.8
*BF*17	*max* (0,0.57 – *HBG*)* *max* (0, *TSD* – 0.18)	-645.69	-1439373.27	-1487.89	-88906.14	-15555652.35
*BF*18	*max* (0,0.57 – *HBG*)* *max* (0,0.83 – *FOLAT*)	859.32	-1358.75	-233.22	3485.53	-1838.8
*BF*19	*max* (0,0.57 – *HBG*)* *max* (0,0.006 – *B*12)	5601.58	-20917.73	96.33	-256.41	14763.27

Upon examination of Table 5 and Equations 8-12, it is evident that the highest interaction level of the basis functions is 2, established by setting the degree to 2. This signifies that the model's basis functions consist of both linear and quadratic functions, as depicted in Table 5.

With the MARS method, it was observed that *BF1*, *BF2*, *BF3*, *BF4*, and *BF5* represent linear functions, while the remaining basis functions are quadratic functions resulting from the product of two basis functions. Additionally, 19 out of 24 parameters were pruned and eliminated from the model due to their minimal contribution to the model's performance, resulting in the model being created with GENDER, HBG, TSD, FOLATE, and B12 parameters, which exhibited high contribution to the model performance.

Upon reviewing Equations 8-12, it is evident that the dataset is modeled based on a class basis using the MARS method, with the prediction result showing a high success rate serving as the benchmark for classification. Classification was carried out in this manner. Consequently, when evaluating new patient data using Equations 3-12, classification can be accomplished by inputting the required information into the *BFj* basis functions.

Evaluation

In this study, a 10-fold cross-validation method is used to evaluate the performance of the proposed models for

classifying the five-class anemli problem. The strategy of dividing the dataset into 10 different subsets and testing one subset at a time involves using the remaining subsets for training purposes. In this way, problems due to class imbalance were minimized. Performances were measured with ROC analysis metrics. ROC analysis is a performance evaluation metric. The results obtained showed that the proposed models were effective in correctly classifying the anemia class.

In equations 13-16, macro metric formulas representing unweighted average calculations for each class are presented.

$$Accuracy = \frac{TP + TN}{TP + TN + FP + FN} \tag{13}$$

$$Recall_m = \frac{TP_c}{TP_c + FN_c} \tag{14}$$

$$Precision_m = \sum_c \frac{TP_c}{TP_c + FP_c}, c \in classes \tag{15}$$

$$F1 - Score_m = \frac{2xPrecision_m xRecall_m}{Precision_m + Recall_m} \tag{16}$$

Within the equations, when considering the macro metric m and the *classes = {non-disease records, HGB-anemia, iron deficiency anemia, B12 deficiency anemia, folic acid deficiency anemia}*, the term TP_c denotes the count of samples accurately categorized as *c*.

The objective of ROC analysis is to assess the efficacy of outcomes derived from different methods and to compare them using metrics like Accuracy, Specificity, Sensitivity, F1-Score, Precision, and AUC [44]. The fundamental ROC parameters utilized in the analysis, namely *FN (False Negative)*, *TN (True Negative)*, *FP (False Positive)*, and *TP (True Positive)* serve to indicate the accuracy of the classification results through true and false predictions.

To evaluate model performance, it is important to select appropriate metrics such as Accuracy, AUC and F1-Score. Accuracy measures the proportion of correct predictions, while AUC evaluates the balance between True Positive Rate (TPR) and False Positive Rate (FPR) at different thresholds, targeting high TPR and low FPR (Yagmur et al., 2024). In unbalanced datasets, relying on Accuracy alone is insufficient. Sensitivity and recall-based F1-Score are commonly used for imbalanced datasets. A high F1-Score indicates the minimal difference between two values. In particular, a high recall implies low sensitivity and vice versa. Moreover, a high recall value implies that a significant proportion of samples in the minority class are correctly predicted, while high precision indicates that the predicted minority samples most likely belong to the minority class. Increasing precision and recall values lead to a higher F1-Score, indicative of the difference between minimal precision and recall values.

Although AUC is widely used to address imbalanced data issues, the F-measure is considered more appropriate for imbalanced data sets. This is because the minority class usually has a higher weight than the majority class and the F-measure is capable of classifying samples in the minority class with better accuracy and less misclassification. The F-measure focuses only on the accuracy of the classifier on the minority class. The AUC measure evaluates the overall accuracy of the classifier on both the majority and minority classes. Given the imbalanced nature of the dataset used in this study, the next section compares the performance of AUC and F1-Score. However, other studies in the literature often prioritize accuracy metrics, so additional ROC metrics are also presented.

RESULTS AND DISCUSSION

This study encompassed the execution of a classification analysis on the blood metrics and results of patients diagnosed with anemia. Patients were sorted using the MARS method, with the effectiveness of the method evaluated across two separate models.

For MARS_Model-1, 1st order models with a pruning coefficient of 20 and for MARS_Model-2, 2nd order models with a pruning coefficient of 20 were used.

In this part, we display ROC performance analyses and confusion matrices and obtained for two separate models. Figure 1, 2 exhibits the confusion matrices for MARS_Model-1 and MARS_Model-2, alongside the computed ROC performance values derived from these matrices.

These analyses visually present the classification performance of each model and evaluate the sensitivity, specificity and performance of the algorithms through the ROC curves given in Figure 3, 4. The results obtained reveal that Model-1 and Model-2 have successful classification performance. These graphs allow us to evaluate in more detail the ability of each algorithm to detect the disease.

The evaluation of confusion matrices in Figure 1 and Figure 2 reveals that, as a result, 282 patients were misclassified by Model-1, and 260 patients were misclassified by Model-2 out of the total cases.

Table 6 encompasses ROC performance analyses obtained from testing two different models. This table provides a detailed overview of the sensitivity, specificity, and overall performance of each model through ROC curves. ROC performance analyses assess the ability of Model-1 and Model-2 to detect the disease, offering a comprehensive view of the classification performance of each algorithm.

The results of evaluation on MARS method performances are given in Table 6. The accuracy measures are quite successful in both tables and the proposed methods exhibit high precision through the datasets.Creation of

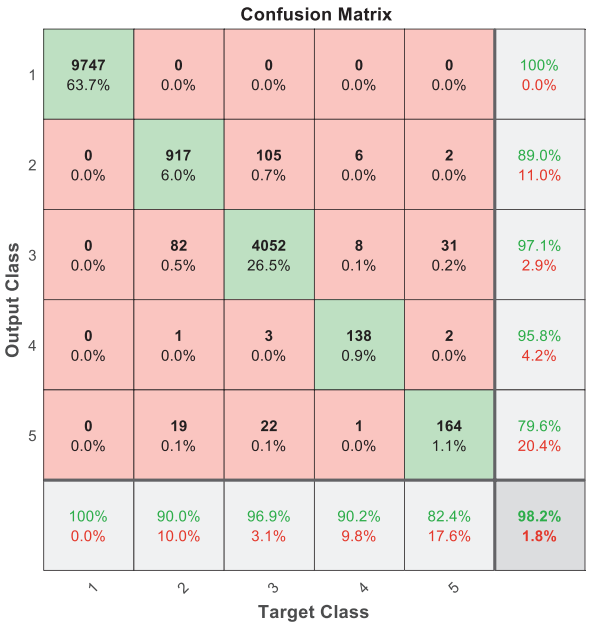


Figure 1. Confussion matrix of model-1.

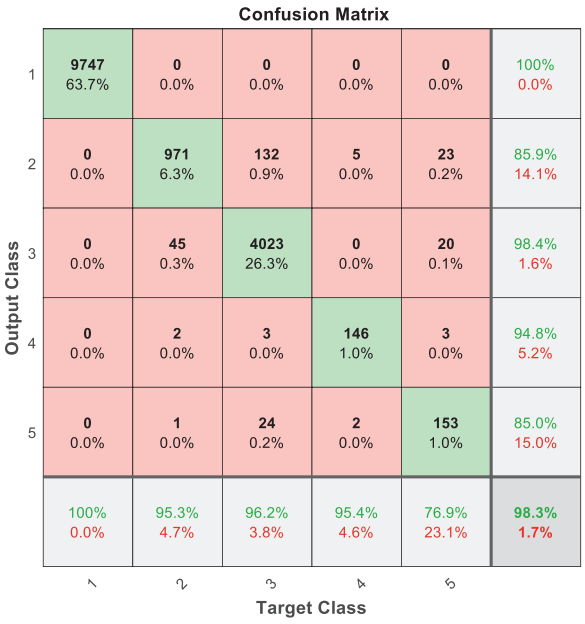


Figure 2. Confussion matrix of model-2

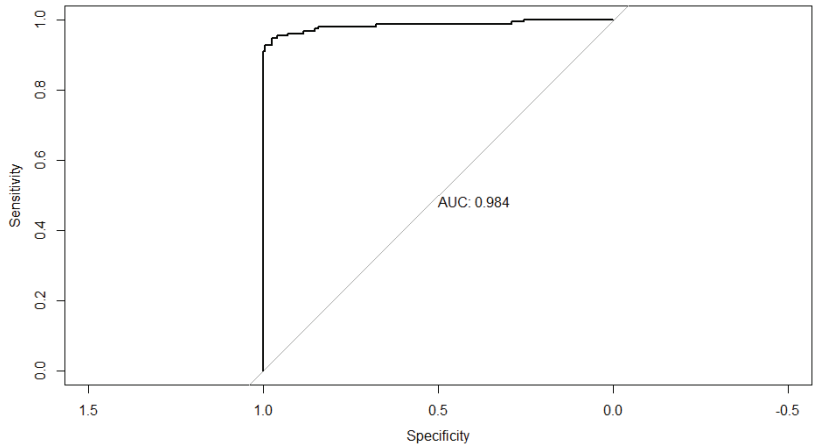


Figure 3. ROC of model-1.

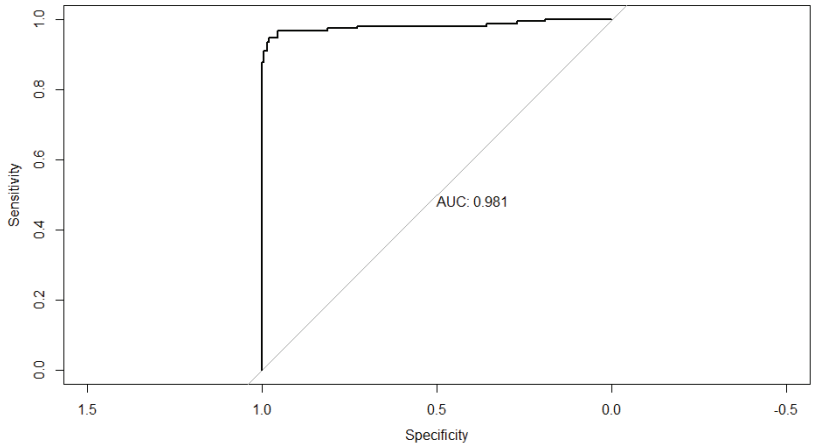


Figure 4. ROC of model-2.

Table 6. ROC analyzes

Model name	Accuracy	Recall	Precision	F1-Score	AUC
MARS_Model-1	98.1569	0.9190	0.9231	0.9208	0.984
MARS_Model-2	98.3007	0.9276	0.9291	0.9274	0.981

effective classification on such an imbalanced dataset is quite striking across ten different subsets. In our study on discrimination of anemia disease through the same levels of different parameters, we applied the two tests which are capable of successfully modeling and interpreting interaction among anemia parameters in different levels. The high efficacy of MARS method was revealed in the classification of anemia disease. The F1-Score values of 92.08% and 92.74% signify a higher percentage of accurately classified instances within the minority class and a decreased misclassification rate. This metric provides an overall assessment of model performance by balancing precision and recall. The research demonstrates positive outcomes in the classification of diverse types of anemia diseases using MARS methods, specifically highlighting their effectiveness in addressing issues arising from dataset imbalance.

CONCLUSION

The dataset used in the study consists of complete blood count results obtained from studies conducted at Gaziosmanpaşa University Faculty of Medicine. This data set includes information on 15.300 patients between 2013-2018. In the study conducted by Kılıçarslan and colleagues, data from pregnant women, cancer patients and children were excluded and the dataset was subjected to a noise removal process to eliminate insignificant and missing parameter records. The parameter values of the dataset, which was made publicly available in the Kaggle database, were normalized by scaling them between 0.1 and 0.9. This normalization aimed to compensate for significant numerical differences between parameter values.

Tests were conducted on two different models (Model-1 and Model-2). The tests performed on two different models with parameters set as multivariate adaptive regression spline method 1st order and pruning coefficient 20 for Model-1 and 2nd order and pruning coefficient 20 for Model-2 gave successful results. For Model-1, 98.1569% accuracy, 92.31% precision, 91.90% recall, 92.08% F1-score were obtained. Model-2 showed 98.30% accuracy, 92.91% precision, 92.76% recall and 92.74% F1-score. As a result, Model-1 misclassified a total of 282 patients, while Model-2 misclassified a total of 260 patients.

The findings from this study are expected to provide valuable information for medical students and practitioners in predicting five different types of anemia. We are confident that the classification performance of our proposed models will contribute positively to the existing literature. In future studies, more parameters and patient datasets can be used and success can be compared using different degrees and pruning coefficients.

AUTHORSHIP CONTRIBUTIONS

Authors equally contributed to this work.

DATA AVAILABILITY STATEMENT

The data that support the findings of this study are openly available in Anemia Disease Dataset at https://www.kaggle.com/code/serhathoca/anemia-disease-dataset/notebook.

CONFLICT OF INTEREST

The author declared no potential conflicts of interest with respect to the research, authorship, and/or publication of this article.

ETHICS

There are no ethical issues with the publication of this manuscript.

STATEMENT ON THE USE OF ARTIFICIAL INTELLIGENCE

Artificial intelligence was not used in the preparation of the article.

REFERENCES

[1] Yılmaz H, Buldu A, Yılmaz K, Kuncan F. Early stage diabetes risk prediction with artificial intteligence methods. J Sci Rep B 2023:7:59–71.

[2] Dursun MA, Serttaş S. A Multi-Metric Model for analyzing and comparing extractive text summarization approaches and algorithms on scientific papers. Dicle Univ J Eng 2024;15:31–48. [CrossRef]

[3] Dursun MA, Yavuz G. L-PFO: Enhancing polar fox optimization with linear population size reduction for complex Benchmark problems. Artif Intell Stud 2025;8:100–115.

[4] Badik ŞT, Mutlu A. Machine learning classification models for the patients who have heart failure. Sigma J Eng Nat Sci 2024;42:235–44. [CrossRef]

[5] Bolukbasi IB. Dengesiz bir diyabet veri setinde makine öğrenmesi yöntemlerini kullanarak diyabet hastalığının teşhisi [Doctoral dissertation]. Bursa: Uludag University; 2023.
[6] Cihan M, Uzbaş B, Ceylan M. Fusion and CNN based classification of liver focal lesions using magnetic resonance imaging phases. Sigma J Eng Nat Sci 2023;41:135–45. [CrossRef]
[7] Dörterler S, Dumlu H, Özdemir D, Temurtas H. Hybridization of k-means and meta-heuristics algorithms for heart disease diagnosis. In book: New Trends in Engineering and Applied Natural Sciences. 1st ed. Chapter: 5 Publisher: İzmir: Duvar Publishing; 2022. p. 55.
[8] Yağmur N. A hybrid approach to obesity level determination with decision tree and pelican optimization algorithm. J Sci Rep A 2024;57:97–109. [CrossRef]
[9] Yağmur N, Temurtaş H, Dağ İ. Classification of anemia disease using artificial neural networks methods. J Sci Rep 2023;8:20–34.
[10] Narin D, Onur TÖ. The effect of hyper parameters on the classification of lung cancer images using deep learning methods. Erzincan Univ J Sci Technol 2022;15:258–68. [CrossRef]
[11] Dörterler S. Kanser hastalığı teşhisinde ölüm oyunu optimizasyon algoritmasinin etkisi. In: Genç N, Mühendislik Alanında Uluslararası Araştırmalar VIII. Konya: Eğitim Yayınevi; 2023. p. 15.
[12] Şahin E, Özdemir D, Temurtaş H. Multi-objective optimization of ViT architecture for efficient brain tumor classification. Biomed Signal Process Control 2024;91:105938. [CrossRef]
[13] Dörterler S, Dumlu H, Özdemir D, Temurtaş H. Hybridization of meta-heuristic algorithms with K-means for clustering analysis: Case of medical datasets. Gazi J Eng Sci 2024;10:1–11. [CrossRef]
[14] Aydemir F, Arslan S. A system design with deep learning and IoT to ensure education continuity for Post-COVID. IEEE Trans Consum Electron 2023;69:217–255. [CrossRef]
[15] Nahzat S, Yağanoğlu M. Diabetes prediction using machine learning classification algorithms. Eur J Sci Technol 2021;24:53–9.
[16] Özcan B, Bakır H. Yapay zeka destekli beyin görüntüleri üzerinde tümör tespiti. Int Conf Pioneer Innov Stud 2023;1:297–306. [CrossRef]
[17] Gençtürk TH, Gülağız FK, İsmail K. A Comparative analysis of brain hemorrhage diagnosis on CT scans using deep learning methods. J Intell Syst Theory Appl 2023;6:75–84. [CrossRef]
[18] WHO. Anaemia. World Health Organization. Available at: https://www.who.int/healthtopics/anaemia#tab=tab_1 Accessed on Oct 4, 2023.
[19] Salman ME, Arı S. Bulanık mantık tekniği kullanılarak anemi hastalığı teşhisi. Sakarya: Sakarya Üniversitesi Fen Bilimleri Enstitüsü; 2016. p. 61.
[20] Yagmur N, Dag I, Temurtas H. Classification of anemia using Harris Hawks optimization method and multivariate adaptive regression spline. Neural Comput Appl 2024;36:1–20. [CrossRef]
[21] Dixit A, Jha R, Mishra R, Vhatkar S. Prediction of anemia disease using machine learning algorithms. Intelligent Computing and Networking: Proceedings of IC-ICN 2022, Springer; 2023, p. 229–238. [CrossRef]
[22] Dhakal P, Khanal S, Bista R. Prediction of anemia using machine learning algorithms. AIRCC's Int J Comput Sci InformTechnol 2023;15:15–30. [CrossRef]
[23] Appiahene P, Asare JW, Donkoh ET, Dimauro G, Maglietta R. Detection of iron deficiency anemia by medical images: a comparative study of machine learning algorithms. BioData Min 2023;16:1–20. [CrossRef]
[24] Saihood Q, Sonuç E. The efficiency of classification techniques in predicting anemia among children: A comparative study. International Conference on Emerging Technology Trends in Internet of Things and Computing, New York: Springer; 2021, p. 167–81. [CrossRef]
[25] Yağmur N. Anemi hastalığı sınıflandırmasında karga arama optimizasyon algoritması. Mühendislik Alanında Akademik Araştırma ve Derlemeler 2023;291–307.
[26] Farzaliyev E, Saihood Q, Sonuç E. Çocuklarda anemi hastalığının teşhisinde topluluk öğrenme yöntemlerinin kullanılması. Int Conf Recent Acad Stud 2023;1:129–135. [CrossRef]
[27] Karagül Yıldız T. Performance comparison of artificial intelligence techniques in the diagnosis of hematological diseases (Doctorial thesis). Sakarya: Sakarya Üniversitesi Fen Bilimleri Enstitüsü; 2021.
[28] Aishwarya K. Threshold based feature selection for anemia prediction. 2023 International Conference on Computer Communication and Informatics (ICCCI), IEEE; 2023, p. 1–5. [CrossRef]
[29] Yeruva S, Gowtham BP, Chandana YH, Varalakshmi MS, Jain S. Prediction of Anemia Disease Using Classification Methods. Machine Learning Technologies and Applications: Proceedings of ICACECS 2020. New York: Springer; 2021, p. 1–11. [CrossRef]
[30] Yagmur N, Dag I, Temurtas H. A new computer-aided diagnostic method for classifying anaemia disease: Hybrid use of Tree Bagger and metaheuristics. Expert Syst 2023;41:e13528. [CrossRef]
[31] Kilicarslan S, Celik M, Sahin Ş. Hybrid models based on genetic algorithm and deep learning algorithms for nutritional Anemia disease classification. Biomed Signal Process Control 2021;63:102231. [CrossRef]
[32] Kilicarslan S. Anemia disease dataset. Available at: https://www.kaggle.com/code/serhathoca/anemia-disease-dataset. Accessed on Jul 3, 2023.

[33] Celik S, Yilmaz O. Prediction of body weight of Turkish tazi dogs using data mining Techniques: Classification and Regression Tree (CART) and multivariate adaptive regression splines (MARS). Pak J Zool 2018;50:575–583. [CrossRef]

[34] Ture M, Kurt I, Kurum AT, Ozdamar K. Comparing classification techniques for predicting essential hypertension. Expert Syst Appl 2005;29:583–588. [CrossRef]

[35] Rajawat RS, Singh KK, Mishra VN. Approximation by modified Bernstein polynomials based on real parameters. Mathematical Foundations of Computing 2024;7:297-309. [CrossRef]

[36] Mishra VN, Rajawat RS, Sharma V. On generalized quantum Bernstein polynomials. Advances in Pure and Applied Algebra: Proceedings of the CONIAPS XXVII International Conference 2021, Walter de Gruyter GmbH & Co KG; 2023, p. 149. [CrossRef]

[37] Raiz M, Rajawat RS, Mishra VN. α-Schurer Durrmeyer operators and their approximation properties. Ann Univ Craiova Math Comput Sci Ser 2023;50:189–204. [CrossRef]

[38] Pandey S, Rajawat RS, Mishra VN. Approximation properties of modified Jain-Gamma operators preserving linear function. Palestine J Math 2023;12:169–182.

[39] Raiz M, Rajawat RS, Mishra LN, Mishra VN. Approximation on bivariate of Durrmeyer operators based on beta function. J Anal 2024;32:311–333. [CrossRef]

[40] Agwu OE, Elraies KA, Alkouh A, Alatefi S. Mathematical modelling of drilling mud plastic viscosity at downhole conditions using multivariate adaptive regression splines. Geoenergy Sci Eng 2024;233:212584. [CrossRef]

[41] Friedman JH. Multivariate adaptive regression splines. Ann Stat 1991;19:1–67. [CrossRef]

[42] Kuter S. Atmospheric correction and image classification on MODIS images by nonparametric regression splines (Doctorial Thesis). Ankara: Middle East Technical University; 2014.

[43] Özfalcı Y. Multivariate adaptive regression splines (Master thesis). Ankara: Gazi Üniversitesi; 2008.

[44] Dursun MA, Kavas PÖ. Beyond diagnosis: Cross-dataset evaluation of risk factors for thyroid cancer recurrence. Artif Intell Stud 2025;8:38–69. [CrossRef]

Sigma Journal of Engineering and Natural Sciences
Web page info: https://sigma.yildiz.edu.tr
DOI: 10.14744/sigma.2025.00000

Research Article

Properties of N, acetylamide-rich biopolymers from five different aquatic invertebrates

Oluwashina Philips GBENEBOR[1,2,*], Abimbola Patricia POPOOLA[2]

[1]*Department of Metallurgical and Materials Engineering, University of Lagos, Lagos, Nigeria*
[2]*Department of Chemical, Metallurgical and Materials Engineering, Tshwane University of Technology, Pretoria, South Africa*

ARTICLE INFO

Article history
Received: 15 July 2024
Revised: 22 August 2024
Accepted: 19 December 2024

Keywords:
Acetylation; Biopolymers; Calcite; Chitin; Crab

ABSTRACT

There have been huge demands for aquaculture products over the years owing to continuous population growth the globe consistently witnesses. Marine invertebrates such as the molluscs and crustaceans are affirmed to be good source of protein. The shells of these animals however are often discarded after the edible parts are consumed; this ends up polluting the environment. A useful material that can be sourced from these shells is a natural polymer – chitin. In this study, chitin was chemically extracted from ground snail, periwinkle, crab, shrimp and prawn shells under similar isolation conditions using 1 M hydrochloric acid and sodium hydroxide. This was done to investigate the influence of each shell on the ease of chitin isolation and eventually, its properties. It was observed that property of chitin depended on features of each shell. The harder the shell, the longer it was to achieve complete demineralization as more acid volumes were consumed. A maximum volume of 2490 ml was needed for total demineralization of 150 g periwinkle while the least (1498 ml) was required for shrimp shell of the same quantity. This implied that snail and periwinkle shells contain more inorganic minerals other than the dominant calcium carbonate. Degree of acetylation, calculated from Energy Dispersion Spectroscopy results, was the maximum for shrimp chitin (79.9 %) while the least (61.6 %) was calculated for periwinkle chitin. Thermogravimetry Analysis showed that 47.8, 15, 60.8, 78.4 and 63.7 % chitin was yielded from periwinkle, crab, prawn and shrimp shells respectively. The highest value of degree of acetylation possessed by shrimp chitin was responsible for its superlative thermal stability (324.6 kJ). Average intra and intermolecular OH bonds in shrimp chitin was calculated to be 5.461 kCal, which was the highest magnitude; 4.642, 4.543, 4.696 and 4.952 kCal were calculated for snail, periwinkle, crab and prawn chitin respectively.

Cite this article as: Gbenebor OP, Popoola AP. Properties of N, acetylamide-rich biopolymers from five different aquatic invertebrates. Sigma J Eng Nat Sci 2026;44(1):105–114.

INTRODUCTION

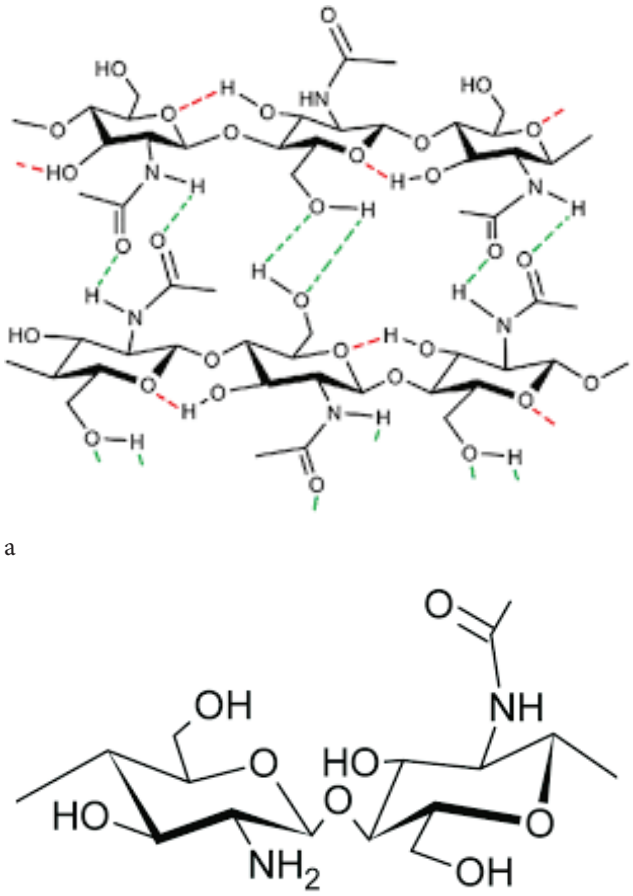
Majority of the wastes in the food industry comprise high amount of biochemical oxygen demand (BOD) components; these wastes are recoverable as they are organic in nature containing vitamins, carbohydrates, fats and proteins [1]. Continuous demands in sea foods' edible

*Corresponding author.
*E-mail address: philipsogbenebor@gmail.com

This paper was recommended for publication in revised form by Editor-in-Chief Ahmet Selim Dalkilic

Published by Yıldız Technical University Press, İstanbul, Turkey
© Author. This is an open access article under the CC BY-NC license (http://creativecommons.org/licenses/by-nc/4.0/).

products for consumption have greatly influenced activities in aquaculture globally over the years owing to speedy population growth. In the tropical and subtropical oceans (Pacific, Atlantic and Indian), lobsters, prawns, crabs and shrimps have been of great commercial importance; their shells have been a major source of chitin. Prawns, although look like shrimps, they are usually bigger in terms of size while both crustaceans find their habitats in salt and fresh water [2,3], According to Soundhar and Kandasamy [4], the crab shell is the second most common natural composite in the world; it prevents the entire body from damage through external loads, harsh temperatures and chemicals. This can also be said about shells of molluscs such as snail and periwinkle, which play key role in protecting their living tissues. Farming of molluscs in recent times has been proven to be a sustainable food source and it is affirmed to be a potential operation for food security in the future [5]. The shells which were earlier reported to pollute the environment have been a huge raw material for cement [6], hydroxyapatite [7] and farming [5] owing to the large content of calcium carbonate /calcite/lime stone ($CaCO_3$) present in them. In many countries, snails are regarded as an epicurean delicacy and it is being assessed as a good source of protein [8]. The shell of snail has been proven to contain 95 wt. % $CaCO_3$ and 5 wt. % organic constituents [9] but earlier studies have reported that the 95 wt. % comprises P, Mn, Fe, Cu, Zn, Na and K – containing minerals [10]. Potortì et al. [11] reported that snail shell wastes are a good source of chitin, chitosan and $CaCO_3$. Same have been affirmed about periwinkle shell – it contains $CaCO_3$ as a major inorganic mineral [12,13]. In the findings of Aranaz et al. [14], it was confirmed that crustacean exoskeletons are made of inorganic mineral - $CaCO_3$, (30–50 %), protein (30-40 %) and chitin (20–30 %). Chitin is a natural polymer second to cellulose in terms of abundance and it has also been reported to exist in the shells of molluscs [15]. It can thus be said that the shells of molluscs and crustaceans are composites comprising $CaCO_3$, protein and chitin. This natural polymer is a polysaccharide whose chains are strongly gripped by hydrogen bonds (Figure 1a). This tight network is linked by the strong carbonyl (C=O) and amine (H-N) groups, which are responsible for its thermal, mechanical and chemical properties. The combination of these groups makes up the amide ($CONH_2$) group that basically defines the structure of chitin. This natural polymer has found its applications in medicine [16], food packaging [17], water treatment [18], adhesives and tissue engineering [19]. Isolating chitin from these shells is often done conventionally using acid and alkali solutions of different concentrations [20,21]. The former eliminates $CaCO_3$ (demineralization) while the latter separates protein from the organic matrix (deproteinization) [20,22-24], leaving chitin to be directly used for its desired applications or for further processing such as depigmentation [22, 25] and deacetylation to chitosan (a derivative of chitin) [19]. Here, C=O is eliminated leaving H-N in is structure (Fig. 1b) [26,27].



a

b

Figure 1. (a) Chitin structure and its layers connected by inter and intra molecular hydrogen bonds (b) structure of chitosan.

In some cases, deproteinization may precede demineralization during the process of chitin isolation. This was executed by Adekanmi et al. [28] where dry snail shell particles were first deproteinized using 2 % (wt. /v) NaOH at 90 °C for 2 h. Mineral contents removal was later achieved by reacting deproteinized shells with 2.5 % (v /v) HCl at room temperature for 6 h. This method was contrary to that practised by Rajathy et al. [29] who first demineralized telescope snail shells with 5 % (v /v) HCl at room temperature for 48 h. For the same period, protein was later removed using 3 % (wt. /v) NaOH at 70 °C. Within 1 h, Ayorinde and Edema [30] refluxed ground periwinkle shells in 1 M HCl at 100 °C for demineralization. This was followed by deproteinization where 1 M NaOH was used at 80 °C for 1 h. The first stage of chitin production from shrimp shell as engaged by Fonseca et al. [31] was depigmentation which entailed the use of 80 % (v/v) ethanol/water solution. Shrimp shells have been confirmed to contain pigments such as carotenoproteins and carotenoid [32], which is believed to influence chitin's colour and its properties. At room temperature and 50 min steady agitation, the researchers [31] demineralized shrimp

shells with 5.2 % (v /v) HCl, followed by reaction with 4 % (wt. /v) NaOH for protein separation. A reagent commonly used for depigmentation/ decolouration is hydrogen peroxide (H_2O_2) which has been used by Zhang et al. [33]. Unlike Fonseca et al. [31], Zhang et al. [33] performed depigmentation after ground shrimp shells with Natural deep eutectic solvent (NADES). The solvent comprised choline chloride and organic acids; it was used as an alternative to demineralization and deproteinization process. Chitin has been sourced from ground crab shells following three stages – deproteinization, depigmentation and demineralization [34]. Protein was removed from the shells using 5 % (wt. /v) NaOH for 10 h at 80 °C. Soaking the protein-free shells in acetone for 24 h removed the pigments while treatment with 1 % (v/v) HCl for 24 h was carried out to eliminate $CaCO_3$. Mohan et al. [35] successfully isolated chitin from crab shell by following the sequence, demineralization (2.5 M HCl at 60 °C and 2.5 h), deproteinization (3 M NaOH at 80 °C and 2 h) and depigmentation (chloroform/methanol/ distilled water solution). In the works of Novikov et al. [36], chitin was processed from king crab shell without depigmentation. The first step involved reaction with 4 % (wt. /v) NaOH at 95 °C for deproteinization while demineralization was achieved at room temperature with 3.6 % (v/v) HCl for 30 min. Sreeja et al. [37] also sourced chitin from powdered crab shells without depigmentation. Unlike Novikov et al. [36], demineralization was performed first by treating the powder with 2 N HCl for 24 h; with the same period, 2 N NaOH at 80 °C dissolved the protein present.

Studies however have shown that irrespective of the processing sequence followed, chitin can be successfully extracted from shells of crustaceans and molluscs, [15,20,22], where different acid and alkali solutions (with varying concentrations and temperatures) have been employed. The diverse conditions of chitin isolation from these different sources have made it difficult to decipher how the nature of each shell influences the ease of chitin isolation with its properties. This can only be possible if shells of crustaceans and molluscs are chemically treated under similar conditions. In this study, we have decided to chemically isolate chitin from shells of five different marine invertebrates – snail, periwinkle, crab, shrimp and prawn under same experimental conditions. With this, the role of each shell nature on the ease of chitin isolation is deciphered; properties of each isolated chitin are investigated and comparisons are made.

MATERIALS AND METHODS

Isolatıon of Chitin From Different Shells

Snail, periwinkle, crab, prawn and shrimp shells were thoroughly washed with distilled water to remove other tissues after edible parts were removed. Shells of each invertebrate were sun-dried, ground and milled to 250 µm particles. In other to remove the inorganic mineral(s) present in each shell, volumes of 1 M HCl at room temperature were made to react with each shell (150 g) until the emission of carbon (IV) oxide, CO_2 cased. The mineral-free particles (from each source) were separately washed with distilled water and oven-dried at 75 °C for 5 h after filtering. Protein removal (deproteinization) was achieved by refluxing mineral-free particles with 1 M NaOH at 100 °C for 1 h. At the end of this process, particles were washed, filtered and completely dried in an oven as earlier done. Processed chitin samples were stored in moisture-free covered containers prior to characterizations. For clarity purpose, the following designations, S, P, C, Pr and Sh are used to represent snail, periwinkle, crab, prawn and shrimp respectively in this study.

CHARACTERIZATIONS

Elemental Constituents

Constituents of shells with their corresponding chitin produce were studied with the use of an energy dispersion spectrometer (EDS). This device determined the extent of isolation by detecting elements present before and after chemical treatments.

Thermogravimetric Analysis (TGA)

Temporaries at which chitin began and completed its decomposition including the dominant mineral contents were measured using PerkinElmer TGA 4000 equipment. Each powdered sample of 2 mg (from both shells and chitin) was heated from 0 - 750 °C at a heating rate of at10 °C/ min.

Fourier Transform Infrared Spectroscopy (FTIR)

Functional groups present in both shells and isolated chitin was detected with a spectrometer (PerkinElmer Spectrum Two) in a transmittance mode between 500–4000 cm^{-1} and 4 cm^{-1} resolution.

RESULTS AND DISCUSSION

Volume of Acid Consumed

The total volume of HCl used to completely demineralize each shell is given in Table 1. Periwinkle and snail shells require much of the acid compared to other shells. It can be concluded here that the harder the shell, the more volume of HCl that will be required for complete demineralization. It may also be inferred that more minerals are present in the shells of periwinkle and snail which may be strongly bonded to chitin embedded in them. Shrimp and prawn shells, whose HCl demineralization volume is in the difference of 0.8 %, can be easily demineralized compared to crab shells. It should be noted here that the volume of HCl used just indicates the ease of mineral removal from each shell. Values may differ for other experiments based on parameters such as type and concentration of acid used, particle

Table 1. Total volume of HCl consumed

Shell	HCl volume (ml)
S	2476
P	2490
C	1796
Pr	1510
Sh	1498

size and specie of shells, temperature of demineralization, etc. This study just establishes that under same conditions, chitin can be easily extracted from prawn and shrimp shells rather than from periwinkle and snail shells.

Elemental Constituents

The EDS results show that periwinkle shell contains the highest content of silica (SiO_2) as indicated by Si (14.5 %) followed by snail shell, containing 12.3 % (see Table 2). This (coupled with the presence of $CaCO_3$) may be responsible for the high volumes of HCl required for their complete demineralization. All virgin shells contain calcium (Ca), which maintains the highest amount for each shell, indicating that $CaCO_3$ is a dominating mineral in the exoskeletons of these marine invertebrates. Demineralization and deproteinization of these shells have imparted significant reductions in these minerals with increase in carbon (C) contents implying chitin formation. In this study, the acetylation degree (DA), which is a measure of acetyl group (RC=O) present in the whole chitin chain is calculated using C/N ratio in equation (1) as employed by Abdou et al. [38].

$$D.A = \frac{C/N - 5.14}{1.72} x\ 100 \quad (1)$$

Carbon and nitrogen are represented by C and N respectively. The ratio is got from the elemental content as determined via EDS. Calculation shows that DA of 65.3, 61.6, 72.2, 79.9 and 79.8 % is possessed by snail, periwinkle, crab, shrimp and prawn chitin. This implies that shrimp and prawn chitins have the highest C=O amount (approximately 80 %) in their chains. Young's Modulus of chitin has been reported to be directly linked with its DA [39]; this implies that the higher chitin's DA, the stiffer it becomes. Also, when chitin has more of C=O units in its structure, it becomes less prone to aqueous solution attacks – it becomes more hydrophobic [40]. The enhanced elastic modulus qualifies chitin to be used as a temporary supporting device in tissue engineering [41]. Balancing high chitin's stiffness with improved hydrophilicity can be achieved by controlling its C=O units with hydrophilic polymers such as cellulose chitosan and polyvinyl alcohol (PVA) [42,43].

Thermal Stability and Yield of Chitin

Thermogravimetric analysis results of each shell and its corresponding isolated chitin are illustrated in Tables 3 and 4. Each stage of decomposition depicts the existence of moisture, chitin or $CaCO_3$. t Each virgin shell is characterized with three decomposition stages while each isolated chitin TGA possesses two. Decomposition stage between 90 – 110 °C represents the elimination of moisture content existing in each sample and this ranges between 0.5 – 10.1 wt. %. The TGA has been able to identify the occurrence of $CaCO_3$ in each untreated shell which justifies the prevalence of this mineral. Temperatures of commencement (T_{onset}) and end of decomposition (T_{finish}) of chitin and $CaCO_3$ with their contents are also illustrated in Table 3. High amount of residue present in the TGA of untreated snail and periwinkle shells imply the existence of minerals other than SiO_2 and $CaCO_3$ that is not identified via this analysis owing to the temperature range employed. Treatment of each shell with acid and alkali solutions further increases chitin content with reduced residue which shows that there exist some compounds present (in the residue) which is not identified via TGA. The incomplete (majorly from snail and periwinkle shells) and/or non-isolation of other unidentified minerals existing in these shells may be responsible for incomplete chitin isolation. The highest content of chitin can be realized from shrimp shell; this is followed by prawn shell. This study shows that the harder the shell, the lower the amount of chitin that can be yielded (Table 4). Thermal stability of chitin explains the energy required to break its glycosidic linkage. Nam et al. [44] explained that the N- acetyl groups (C=O) in chitin plays a key role in its thermal stability. This implies that chitin with a high DA (more of C=O units) is expected to be stable. In this study, thermal stability of each isolated chitin is quantified from activation energy calculations from the TGA results according to equation (2) [45].

$$Ln\ (-Ln\ (1-X)) = -Ea/RT + Const. \quad (2)$$

The absolute decomposition temperature is designated as T (K) while the activation energy of the decomposition is Ea (kJ/mol); R has a value of 8.314 J/mol·K (universal gas constant). Decomposition degree, X is obtained using equation (3):

$$X = [(W_o - W_i) / (W_o - W_f)] \quad (3)$$

Shrimp chitin possesses the highest thermal stability while periwinkle chitin is the least thermally stable (Table 4). This further justifies the findings of Nam et al. [44] as increasing trend of DA for each isolated chitin sample corresponds with the trend of Ea. In addition, the existence of impurities could be responsible for chitin's thermal stability; the more the impurities in the shell, the lower the thermal stability of isolated chitin. All chitin samples have

Table 2. Elemental composition results of shell and chitin from snail, periwinkle, crab, shrimp and prawn via EDS

Elements (%)	S. shell	S. chitin	P. shell	P. chitin	C. shell	C. chitin	Sh. shell	Sh. chitin	Pr. shell	Pr. chitin
O	50.1	69.8	44.3	69	71.5	74.6	77.2	73.2	75.1	70.2
Si	12.3	1.2	14.5	1.2	0.8	--	0.4	--	--	--
C	3.7	23.8	8.1	24.8	10.2	21.7	5.9	22.8	7.7	25.4
N	5.1	3.8	4.7	4	5.4	3.4	6.6	3.5	6.1	3.9
Ca	28.8	1.4	28.4	1	10.8	0.3	9.9	0.5	11.1	0.5
Mg	--	--	--	--	1.3	--	--	--	--	--

Table 3. TGA results for untreated snail, periwinkle, crab, shrimp and prawn shells

Chitin				$CaCO_3$			Residue (%)
Shell	T_{onset} (°C)	T_{finish} (°C)	Amount (%)	T_{onset} (°C)	T_{finish} (°C)	Amount (%)	
S	234	490	2.9	636	782	41.4	54.5
P	232	490	2.7	632	748	20.3	76.5
C	285	474	11.1	640	721	28.7	54.7
Sh	282	407	37.2	646	712	15.2	38.9
Pr	275	407	47.2	669	735	9.4	33.3

Table 4. TGA results for isolated chitin from snail, periwinkle, crab, shrimp and prawn shells

Shell source	T_{onset} (°C)	T_{finish} (°C)	Amount (%)	Residue (%)	Ea (kJ)
S	260	399	47.8	45.7	59.0
P	277	419	15	81.7	57.4
C	290	420	60.8	29.1	99.8
Sh	298	427	78.4	13.9	324.6
Pr	283	407	63.7	30.7	270.2

high T_{onsent} (beyond 250 °C) and this implies that they can find a potential use within this temperature range in areas such as food packaging and medical devices including dialyzers, sterilizing boxes, etc. Majority of the polymers used for these applications are fossil fuel based.

Functional Groups and OH Bonding

The functional groups present in each shell and their associated isolated chitin is presented in Figure 2a and b. Each shell spectrum justifies the existence of $CaCO_3$ as a dominant inorganic mineral, which is more on snail and periwinkle shells. This mineral is formed on 866 and 668 cm^{-1} in both shells (Figure 2a) while it forms as one peak in crab, shrimp and prawn shells Major conventional chitin functional groups (Amides I, III and III) are formed after isolation (Figure 2b) with their OH regions stretching wider. Chitin spectra are similar to that investigated by Algethami et al. [34].Tables 5 and 6 identify the functional groups in untreated shells and isolated chitin respectively.

The intra and intermolecular hydrogen bonds in each chitin sample was obtained from FTIR fitting via Gaussian deconvolution between 3600 and 3000 cm^{-1} (Figure 3a - e).The intra molecular bonds (OH(6)…OC and OH(3)…O(5)) exist between 3461- 3521 cm^{-1} and 3269 - 3497 cm^{-1}. In addition, between 3257 - 3281 cm^{-1} lie intermolecular CO…HN bond is formed; another intermolecular bond (OH…OC) exists between 3052 and 3098 cm^{-1}. The hydrogen bond energy E_H for each chitin sample between 3600 and 3000 cm^{-1} was determined by applying equation (4) [46]:

$$E_H\,(kCal) = \frac{1}{K}\,x\,\frac{Vo - V}{Vo} \qquad (4)$$

K is a constant (1.68 × 10−2 $kcal^{-1}$); Vo takes the value of 3600 cm^{-1} (standard wavenumber of OH) and V is the corresponding wavenumber of bonded OH

The hydrogen bond energy E_H magnitude for each chitin variant increases as the wavenumber is towards 3000

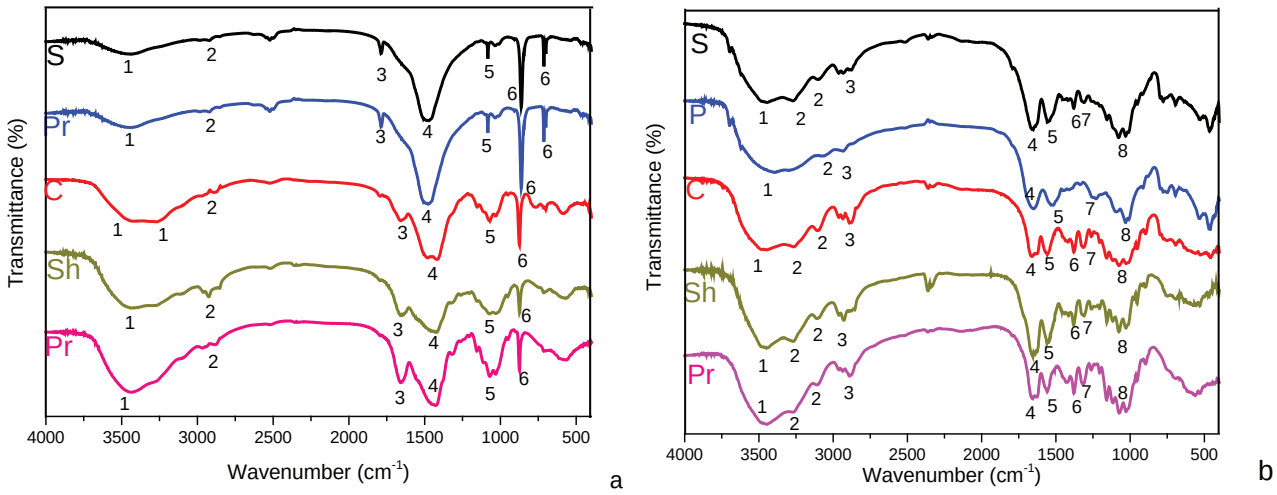


Figure 2. FTIR spectrum of snail, periwinkle, crab, shrimp and prawn (a) shells and (b) chitin.

Table 5. Functional groups of untreated snail, periwinkle, crab, shrimp and prawn shells

		Wavenumber (cm^{-1})				
	Functional groups	**S**	**P**	**C**	**Sh**	**Pr**
1	OH stretching	3443	3456	3456, 3266	3449	3436
2	Ch_3 (symmetric) and CH_2 (asymmetric) stretching	2903	2903	2910	2942	2872
3	C=O (amide I)	1768	1799	1659	1653	1672
4	CH_2 (bending) and CH_3 (deformation)	1488	1481	1481	1437	11418
5	C-O-C	1082	1082	1075	1056	1069
6	$CaCO_3$	866, 668	866, 668	877	859	859

Table 6. Functional groups of isolated chitin from snail, periwinkle, crab, shrimp and prawn shells

		Wavenumber (cm^{-1})				
	Functional groups	**S**	**P**	**C**	**Sh**	**Pr**
1	OH stretching	3494	3374	3469	3469	3456
2	NH stretching	3240, 3094	3008	3253,3008	3259,3101	3240,3101
3	Ch_3 (symmetric) and CH_2 (asymmetric) stretching	2922	2903	2910	2916	2903
4	C=O (amide I)	1666	1659	1659	1653	1659
5	NH and CN (amide II)	1520	1520	1545	1538	1551
6	CH2 wagging (amide III)	1355	--	1367	1367	1361
7	Asymmetric bridge oxygen stretching	1285	1253	1298	1285	1291
8	C-O-C	1049	1031	1043	1043	1049

cm^{-1} implying that each intermolecular bond in chitin is stronger than intra molecular bond (Table 7). The average E_H is of the highest magnitude in shrimp chitin while periwinkle chitin maintains the least. Results from this study show that increasing contents of $CaCO_3$ (with other inorganic minerals) present in the shell of each marine invertebrate lowers the average E_H of each isolated chitin. This could be as a result of more volumes of HCl required to demineralize harder shells.

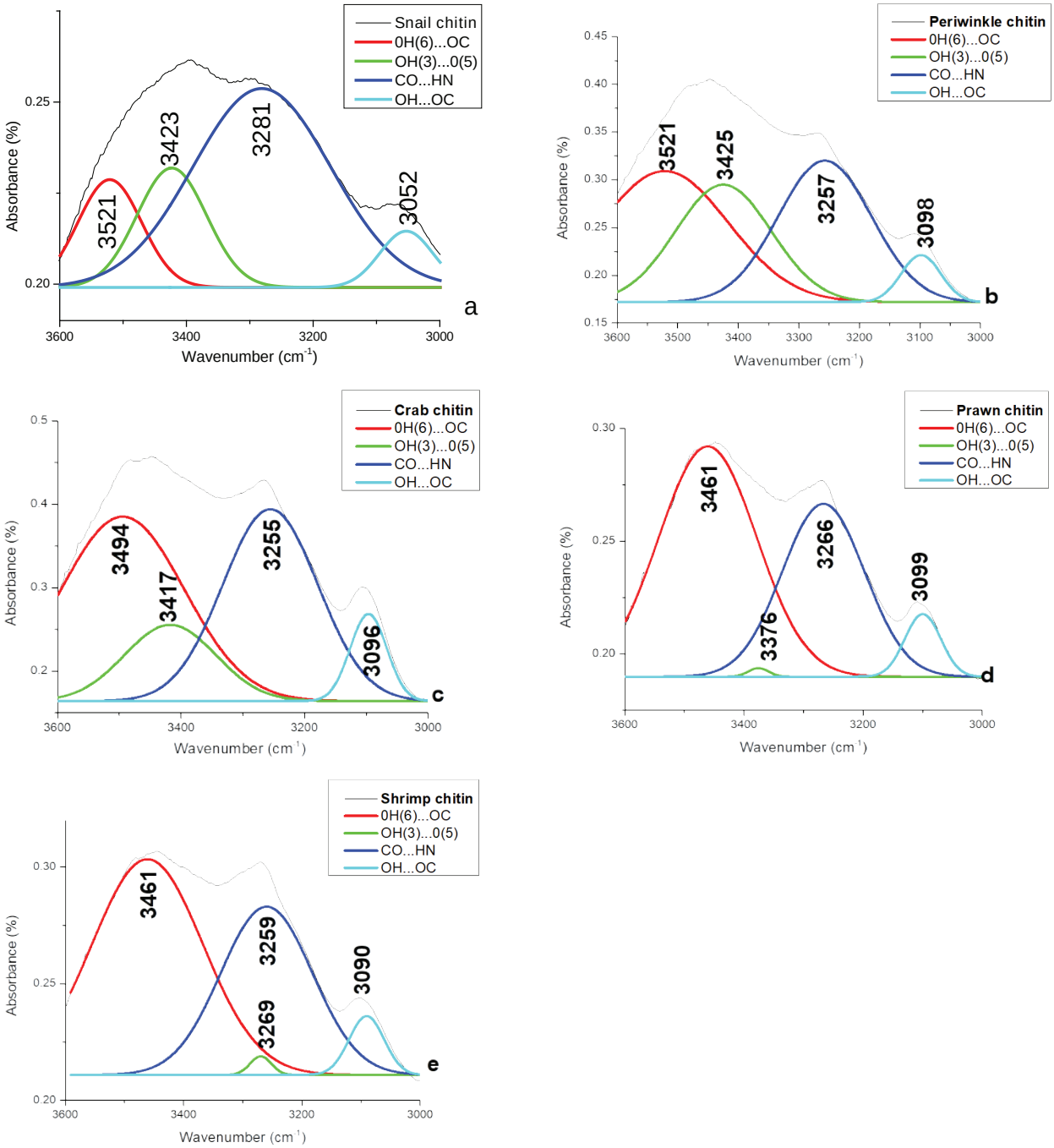


Figure 3. Spectra fitting of OH of (a) snail (b) periwinkle (c) crab (d) prawn and (e) shrimp chitin.

Table 7. Hydrogen bond energies of isolated chitin from snail, periwinkle, crab, prawn and shrimp shells

H-Bond energy, E_H (kCal)					Average E_H (kCal)
Chitin	**OH(6)…OC**	**OH(3)…O(5)**	**CO…HN**	**OH…OC**	
S	1.306	2.927	5.274	9.061	4.642
P	1.306	2.894	5.671	8.3	4.543
C	1.753	2.993	5.704	8.333	4.696
Pr	2.298	5.473	5.638	8.433	4.952
Sh	2.298	3.704	5.522	8.284	5.461

CONCLUSION

Chitin has been successfully isolated chemically from shells of snail, periwinkle, crab, shrimp and prawn using 1 M hydrochloric acid and sodium hydroxide. Comparing these shells (and their corresponding isolated chitin) with one another, this study has shown that under similar extraction conditions, it is difficult to isolate chitin from snail and periwinkle shells compared to other shells (crab, shrimp and prawn) as evidenced in the total volume of acid solution consumed. This could be attributed to a strong calcium carbonate – chitin bond and/or presence of other inorganic minerals existing in these molluscs' shells. The reduced inorganic minerals and weak mineral-polymer bond in shrimp and prawn shells culminates in a comparable repeating C=O units of 79.9 and 79.8 % respectively while crab chitin possesses 72.2 %; this is greater than that of snail (65.3 %) and periwinkle (61.6 %) chitins. It is expected that chitin with the highest C=O units (by virtue of acetylation degree value) should display the maximum mechanical properties when in use. This is also related to the average hydrogen bond energy which ranges in the order: shrimp chitin > prawn chitin > crab chitin > snail chitin > periwinkle chitin. The intra and intermolecular bonds (coupled with C=O repeating units) is also responsible for chitin's thermal stability in the same order as earlier stated. Considering similar extracting conditions as devised in this study, maximum amount of chitin can be realized from shrimp shell and the least, from shell of periwinkle. Thermal result from thermogravimetric analysis shows that all virgin shells with their isolated chitins contain some residues which is very high for periwinkle chitin. The decomposition temperature range (0 – 750 °C) employed for the analysis was not sufficient to detect other inorganic materials present. To achieve improved chitin yield from these shells (most especially snail and periwinkle), more studies need to be carried out to identify these minerals and effective methods to isolate them needs to be devised. We are undertaking further studies to achieve this.

AUTHOR CONTRIBUTIONS

GBENEBOR O.P.: conceptualization, investigation, methodology, data analysis, writing an original draft, and reviewing; POPOOLA A.P.I.: investigation, methodology, editing and funding acquisition. Authors have read and agreed to the published version of the manuscript.

DATA AVAILABILITY STATEMENT

The authors confirm that the data that supports the findings of this study are available within the article. Raw data that support the finding of this study are available from the corresponding author, upon reasonable request.

CONFLICT OF INTEREST

The author declared no potential conflicts of interest with respect to the research, authorship, and/or publication of this article.

ETHICS

There are no ethical issues with the publication of this manuscript.

STATEMENT ON THE USE OF ARTIFICIAL INTELLIGENCE

Artificial intelligence was not used in the preparation of the article.

REFERENCES

[1] Tarafdar A, Biswas G. Extraction of chitosan from prawn shell wastes and examination of its viable commercial applications. Int J Technol Adv Res Mech Eng 2013;2:18–24.

[2] New MB, Nair CM. Global scale of freshwater prawn farming. Aquac Res 2012;43:960–969. [CrossRef]

[3] Hou Y, Yang J, Russoniello CJ, Zheng T, Wu M, Yu X. Impacts of coastal shrimp ponds on saltwater intrusion and submarine groundwater discharge. Water Resour Res 2022:1–17. [CrossRef]

[4] Soundhar A, Kandasamy J. Mechanical, chemical and morphological analysis of crab shell/Sisal natural fiber hybrid composites. J Nat Fibers 2021;18:1–18. [CrossRef]

[5] Morris JP, Backeljau T, Chapelle C. Shells from aquaculture: A valuable biomaterial, not a nuisance waste product. Rev Aquacult 2019;11:42–57. [CrossRef]

[6] Alla S, Asadi SS. Experimental investigation and microstructural behavior of un-calcined and calcined snail shell powder cement mortar. J Build Rehabil 2022;7:1–14. [CrossRef]

[7] Zuliantoni Z, Suprapto W, Setyarini PH, Gapsari F. Extraction and characterization of snail shell waste hydroxyapatite. Results Eng 2022;14:1–7. [CrossRef]

[8] Yastrebova MA, Khamidullina AI, Tatarskiy VV, Scherbakov AM. Snail family proteins: Role in carcenogenesis and prospects for antitumour therapy. Acta Naturae 2021;13:76–90. [CrossRef]

[9] Wang H, Yan K, Chen J. Preparation of hydroxyapatite microspheres by hydrothermal self-assembly of marine shell for effective adsorption of Congo Red. Mater Lett 2021;304:1–4. [CrossRef]

[10] Checa AG. Physical and biological determinants of the fabrication of molluscan shell microstructures. Front Mar Sci 2018;5:1–21. [CrossRef]

[11] Potortì AG, Messina L, Licata P, Gugliandolo E, Santini A, Bella GD. Snail shell waste threat to sustainability and circular economy: Novel application in food industries. Sustainability 2024;16:1–17. [CrossRef]

[12] Eddy NO, Garg R, Ukpe RA, Ameh PO, Garg R, Runde M, et al. Application of periwinkle shell for the synthesis of calcium oxide nanoparticles and in the remediation of Pb2+-contaminated water. Biomass Convers Biorefin 2024:1–19. [CrossRef]

[13] Aremo B, Isadare DA, Akinduro OE, Bello OE, Adeoye MO, Ayodeji SA, et al. Production of glass ceramic from rice husk and periwinkle shells. Discov Mater 2024:1–13. [CrossRef]

[14] Aranaz I, Mengíbar M, Harris R, Paños I, Miralles B, Acosta N, et al. Functional characterization of chitin and chitosan. Curr Chem Biol 2009;3:203–230. [CrossRef]

[15] Akpan EI, Gbenebor OP, Adeosun SO. Synthesis and characterisation of chitin from periwinkle (Tympanotonus fusatus (L.)) and snail (Lissachatina fulica (Bowdich)) shell. Int J Biol Macromol 2018;106:1080–1088. [CrossRef]

[16] Dave U, Somanader E, Baharlouei P, Pham L, Rahman MA. Applications of chitin in medical, environmental, and agricultural industries. J Mar Sci Eng 2021;9:1–18. [CrossRef]

[17] Srinivasa PC, Tharanathan RN. Chitin/chitosan-safe, ecofriendly packaging materials with multiple potential uses. Food Rev Int 2007;23:53–71. [CrossRef]

[18] Gbenebor OP, Popoola API. Dendrobranchiata chitin deacetylation degree and its potency as iron (III) ion adsorbent from aqueous solution. Int J Eng Appl Sci 2023;15:150–162. [CrossRef]

[19] Odili CC, Ilomuanya MO, Sekunowo OI, Gbenebor OP, Adeosun SO. Knot strength and antimicrobial evaluations of partially absorbable suture. Prog Biomater 2023;12:51–59. [CrossRef]

[20] Gbenebor OP, Adeosun SO, Adegbite AA, Akinwande C. Organic and mineral acid demineralizations: Effects on crangon and liocarcinus vernalis –sourced biopolymer yield and properties. J Taibah Univ Med Sci 2018;12:837–845. [CrossRef]

[21] Zamani A, Edebo L, Sjöström B, Taherzadeh MJ. Extraction and precipitation of chitosan from cell wall of zygomycetes fungi by dilute sulfuric acid. Biomacromolecules 2007;8:3786–3790. [CrossRef]

[22] Gbenebor OP, Adeosun SO, Lawal GI, Jun S. Role of CaCO3 in the physicochemical properties of crustacean-sourced structural polysaccharides. Mater Chem Phys 2016;184:203–209. [CrossRef]

[23] Greene BHC, Robertson KN, Young JCOC, Clyburne JAC. Lactic acid demineralization of green crab (Carcinus maenas) shells: Effect of reaction conditions and isolation of an unusual calcium complex. Green Chem Lett Rev 2016;9:1–11. [CrossRef]

[24] Pohling J, Dave D, Liu Y, Murphy W, Trenholm S. Two-step demineralization of shrimp (Pandalus borealis) shells using citric acid: An environmentally friendly, safe and cost-effective alternative to the traditional approach. Green Chem 2022;24:1141–1151. [CrossRef]

[25] Mirwandhono E, Nasution MIA, Yunilas. Extraction of chitin and chitosan black soldier fly (Hermetia illucens) prepupa phase on characterization and yield. IOP Conf Ser Earth Environ Sci 2019:1–4.

[26] Cao S, Liu Y, Shi L, Zhu W, Wang H. N-acetylglucosamine as a platform chemical produced from renewable resources: Opportunity, challenge, and future prospects. Green Chem 2022;24:493–509. [CrossRef]

[27] Costa BET, Andrade CT. Chitosan as a valuable biomolecule from seafood industry waste in the design of green food packaging. Biomolecules 2021;11:1–19. [CrossRef]

[28] Adekanm AA, Adekanmi UT, Adekanm AS, Ahmad LK, Emmanue OO. Production and characterisation of chitosan from chitin of snail shells by sequential modification process. Afr J Biotechnol 2023;22:39–53. [CrossRef]

[29] Rajathy TJ, Srinivasan M, Mohanraj T. Physicochemical and functional characterization of chitosan from horn snail gastropod Telescopium. J Appl Pharm Sci 2021;11:052–058.

[30] Ayorinde JO, Edema OG. Adsorption of colour pigments from palm kernel oil onto biopolymer prepared from periwinkle shell waste. Int J Biochem Res Rev 2021;30:51–62. [CrossRef]

[31] Fonseca ACM, Santoro BF, Fernández OJG, Santos MT. A conceptual design and economic assessment of a chitin biorefinery based on shrimp processing wastes. Comput Aided Chem Eng 2024;53:2551–2556. [CrossRef]

[32] Nekvapil F, Glamuzina B, Tudoran LB, Suciu M, Tămaş T, Pinzaru SC. Promoting hidden natural design templates in wasted shells of the mantis shrimp into valuable biogenic composite. Spectrochim Acta A Mol Biomol Spectrosc 2021;250:1–11. [CrossRef]

[33] Lei J, Zhang J, Li K, Qin H, Liu H, Li P, et al. Pretreatment of shrimp shells with an acidic deep eutectic solvent system for chitin extraction and its enhanced performance as a carrier for immobilized lipase. Int J Biol Macromol 2024;264:1–10. [CrossRef]

[34] Algethami JS, Jugade R, El Kaim RB, Bahsis L, Achak M, Majdoubi H, et al. Chitin extraction from crab shells and synthesis of chitin@metakaolin composite for efficient amputation of Cr (VI) ions. Environ Res 2024;252:1–13. [CrossRef]

[35] Mohan K, Muralisankar T, Jayakumar R, Rajeevgandhi C. A study on structural comparisons of α-chitin extracted from marine crustacean shell waste. Carbohydr Polym Technol Appl 2021;2:1–9. [CrossRef]

[36] Novikov VY, Rysakova KS, Shumskaya NV, Mukhortova AM, Kesarev KA. King crab gills as a new source of chitin/chitosan and protein hydrolysates. Int J Biol Macromol 2023;232:1–12. [CrossRef]

[37] Sreeja SJ, Tamilarutselvi K, Tamilselvi A, Sarojini KP, Jasmin KJ, Malin MM. Production of chitin and conversion into chitosan from crab (Scylla tranquebarica) shells and evaluation of its antioxidant activities. Biomass Convers Biorefin 2024;41:17193–17199. [CrossRef]

[38] Abdou ES, Nagy KSA, Elsabee MZ. Extraction and characterization of chitin and chitosan from local sources. Bioresour Technol 2008;99:1359–1367. [CrossRef]

[39] Krumme A, Mendez JD. Electrospinning polyvinyl alcohol reinforced with chitin: The effect of the degree of acetylation. Polymers 2021;16:1–11. [CrossRef]

[40] Yu S, Peng G, Wu D. Effect of surface acetylation of chitin nanocrystals on the preparation and viscoelasticity of sunflower seed oil-in-water Pickering emulsions. Int J Biol Macromol 2024;254:1–9. [CrossRef]

[41] Basak T, Shamshina JL. Design of chitin cell culture matrices for 3d tissue engineering: The importance of chitin types, solvents, cross-linkers, and fabrication techniques. Pharmaceutics 2024;16:1–26. [CrossRef]

[42] Zhou D, Wang H, Guo S. Preparation of cellulose/chitin blend materials and influence of their properties on sorption of heavy metals. Sustainability 2021;13:1–11. [CrossRef]

[43] Eze FN, Jayeoye TJ, Eze RC, Ovatlarnporn C. Construction of carboxymethyl chitosan/pva/chitin nanowhiskers multicomponent film activated with Cotylelobium lanceolatum phenolics and in situ senp for enhanced packaging application. Int J Biol Macromol 2023;255:1–16. [CrossRef]

[44] Nam YS, Park WH, Ihm D, Hudson SM. Effect of the degree of deacetylation on the thermal decomposition of chitin and chitosan nanofibers. Carbohydr Polym 2010;80:291–295. [CrossRef]

[45] Broido A. Simple, sensitive graphical method of treating thermogravimetric analysis data. J Polym Sci Part A Polym Phys 1969;27:1761–1774. [CrossRef]

[46] Ciolacu D, Kovac J, Kokol V. The effect of the cellulose-binding domain from Clostridium cellulovorans on the supramolecular structure of cellulose fibres. Carbohydr Res 2010;345:621–630. [CrossRef]

Sigma J Eng Nat Sci, Vol. 44, No. 1, pp. 115–126, February, 2026

Sigma Journal of Engineering and Natural Sciences
Web page info: https://sigma.yildiz.edu.tr
DOI: 10.14744/sigma.2025.00000

Research Article

Study of improved quantum particle swarm optimization for modeling of wasted surgical mask

Subhojit CHATTARAJ[1,*], Sk Tanbir ISLAM[2], Pijush DUTTA[3], Mahuya DAS[4]

[1]Department of Civil Engineering, Greater Kolkata College of Engineering and Management, Kolkata, 743387, India
[2]Department of Mechanical Engineering, Greater Kolkata College of Engineering and Management, Kolkata, 743387, India
[3]Department of Computer Science Engineering, Greater Kolkata College of Engineering and Management, Kolkata, 743387, India
[4]Department of Chemistry, Bankura Zilla Saradamani Mahila Mahabivyapith Nutanchati, West Bengal, 722101, India

ARTICLE INFO

Article history
Received: 16 June 2024
Revised: 21 August 2024
Accepted: 13 January 2025

Keywords:
Artificial Neural Network (ANN); Improved Particle Swarm Optimization; Parametric Optimization; Plastic Board

ABSTRACT

The complexity of real-world optimization problems has been steadily driving computer science researchers to come up with new and efficient optimization techniques. Precise modeling of the plastic boards by use of experimental data, in which discarded surgical masks are used, is a major challenge to engineering professionals. In this article, a Modified Gaussian Quantum Particle Swarm Optimization (GQPSO) is proposed for the efficient and accurate estimation of manufacturing plastic board characteristics. The algorithm was initially tested using two benchmark functions, which included Elongation at fracture (EF) and Percentage of total elongation at maximum force (MF), using material compositions including those of polypropylene (PP), Maleic anhydride Grafted Polypropylenes (MA), Titanium dioxide (TiO2), and Tensile Strength (TS). Experiment findings and comparisons with other optimization techniques clearly show that this suggested method is successful in terms of final solution correctness, success rate, convergence speed, and stability. The suggested GQPSO optimization approach was then evaluated against the manufacturer's datasheet of the optimal outcome of both elongations at fracture and the percentage of total elongation at maximum force are 29.678%, 11.082%, 0.4412%, and 26.712, respectively for polypropylene (PP), Maleic anhydrite Grafted polypropylene (MA), Titanium dioxide (TiO2), and Tensile Strength (TS) during waste surgical mask design. The findings prove the efficiency of the Gaussian Quantum-behaved Particle swarm optimization (GQPSO) algorithm in different working conditions.

Cite this article as: Chattaraj S, Islam ST, Dutta P, Mahuya DASM. Study of improved quantum particle swarm optimization for modeling of wasted surgical mask. Sigma J Eng Nat Sci 2026;44(1):115–126.

***Corresponding author.**
*E-mail address: subhojitchattaraj@gmail.com

This paper was recommended for publication in revised form by Editor-in-Chief Ahmet Selim Dalkilic

Published by Yıldız Technical University Press, İstanbul, Turkey
© Author. This is an open access article under the CC BY-NC license (http://creativecommons.org/licenses/by-nc/4.0/).

INTRODUCTION

The daily applications of plastic polymers have a number of good effects in society, but the microplastic (MP) particles linked with the plastic era have health and environmental issues [1]. Multiples of the research on plastic polymers have been carried out, some of which are highlighted in this section. In late 2019, the outbreak of the COVID-19 pandemic resulted in a surge in the use of using single-use personal protective equipment (PPE), in particular surgical masks [2,3]. Consequently, there is increasing concern about the manner in which these masks are to be disposed of since they are disposed of in improper ways, a factor that will lead to environmental degradation. Surgical masks are usually crafted in the form of non-woven polypropylene, and their property may come in handy during waste sorting and management. [4,5]. Numerous works were devoted to measuring the effectiveness of various ways of using surgical masks in an environmentally friendly way. Such practices involved burning, landfill dumping, as well as sterilization before disposal in an effort to reduce the possible risks [6]. Other scholars investigated the possibility of recycling surgical masks to extract useful resources from them, e.g., polypropylene. The building materials and textiles, among other items, were made using the materials of masks. The research into the ways of reclaiming and reusing those materials may help to save resources and lower the volume of waste [7,8]. Researchers investigated the biodegradability of surgical mask materials in light of the trend toward more sustainable waste management practices. Some studies have assessed the potential for incorporating surgical mask components into composting processes, considering their biodegradable properties under specific conditions. Few studies investigated the potential of developing biodegradable surgical masks using sustainable materials. These masks could help alleviate the environmental impact associated with traditional single-use masks [9,10]. Other new avenues that have been researched are novel technologies of transforming used surgical masks into energy or other useful products via things such as pyrolysis or gasification. The polypropylene has a high percentage of energy content which in turn could be utilized by controlled incineration which may serve as an extra energy source to the waste-to-energy facility [11,12]. Although surgical masks are traditionally used in health care facilities to prevent infections, uses in waste management are also discussed in the context of sustainability as a whole. Whiteboards, writing boards, chalkboards or marker boards are typical learning tools that are used in brainstorming, presentations and creativity. The choice of the right writing board material is important so that it needs to be long-lasting and functional. Writing boards WBs are available in different materials so that each has different characteristics. Melamine boards: This type is composed of a paper surface infused with resin on a fiberboard and consists of a core; the boards are cheap yet tend to be stained and ghosted; the durability of the boards is decent and good enough to use in mild and moderate activities [13,14]. Porcelain steel boards or ceramic steel boards are created by gluing porcelain enamel on a metal surface, making it highly strong, hard, and removable. And, they do not get scratched or soiled, and can be used in heavy-duty and strenuous environments like schools [15,16]. Toughened safety glass in the form of tempered glass boards has a smooth appearance, excellent erasability, and great durability, albeit being likely to break when hit [17]. Acrylic boards are lightweight and a low-cost alternative that has proper erasability and average durability, but can be easily scratched and stained. The mechanical properties of these materials play a significant role in their performance. Hardness influences scratch resistance, with porcelain and glass being highly resistant, while melamine and acrylic are more vulnerable. Durability is best in porcelain and glass due to their robust nature, with melamine and acrylic being less so. Erasability is better in porcelain and glass; however, melamine and acrylic boards can stain and ghost. Impact resistance varies, with glass being the weakest and porcelain and melamine being the strongest [13-16]. An NP-complete problem is the modeling of plastic boards employing waste surgical masks as the key concern for minimizing plastic waste as part of solid waste power consumption [18].

The transmission of thermal energy is also associated with the other dimension of the research on nanofluids. Ahmed et al. [19] examined the dynamics and behaviour of gyrotactic microorganisms in magnetohydrodynamic (MHD) Eyring-Powell nanofluid flow with a focus on the influences of thermal radiation and Darcy-Forchheimer relation. The study will add to the knowledge of bioconvection in the behavior of fluids in different applications. Faizan Ahmed et al. [20] indicated the importance of the flow of bioconvection in tangent hyperbolic nanofluids, especially on the minimisation of entropy. The study is critical in the use of this in biomedical engineering and thermal management systems. Faizan Ahmed et al. [21] highlight the importance of the bioconvection flow in the tangent hyperbolic nanofluids, especially in the entropy minimization. The study is critical in the use of this in biomedical engineering and thermal management systems. Ali et al. [22] investigate the role of bioconvective studies in tangent hyperbolic nanoliquids and highlight the possibilities of improving energy systems with the mentioned property. The study is critical in explaining how nanofluids may enhance the thermal management of different processes. In bioconvection on a stretching sheet, Puneeth et al. study the thermal properties of Ree–Eyring nanofluid [23]. The study is notable because it is based on prior literature on non-Newtonian fluids and bioconvection, offering information on the heat transfer. Ali and Zaib [24] analyse the erratic flow of Eyring-Powell nanofluid near a stagnation point following a stretched sheet that has gone through convective heating. This study plays an important role in determining how the non-dynamism of nanofluids is in thermal use [24]. Ali

and Summayya [25] investigate numerical simulation of the Cattaneo -Christov theory of double-diffusion in MHD Eyring-Powell nanofluid with the emphasis on the effects of thermal radiation at a stagnation point. This research is significant in understanding fluid dynamics under complex thermal and magnetic influences.

Back propagation neural network (BP) is a form of artificial neural network that can, however, without any knowledge of the relationship between the input and the output data, simulate any non-linear or linear functional link [18, 26]. Nonetheless, BP has many drawbacks, such as long time calculation, slow convergence, and the risk of local minima. As a result, a range of hybrid optimization approaches based on global optimization algorithms were developed to increase the generalization ability of artificial neural networks [27,28]. However, because PSO is limited in its search power, it may become imprisoned in the local optima of the objective function when used to pick ANN parameters [29-31].

In 2004, a new variant of particle swarm optimization under the name quantum-behaved particle swarm optimization method was proposed [32]. Furthermore, simulation results of a variety of complicated benchmark functions revealed that QPSO outperforms the standard PSO in terms of global searching capabilities [33,34]. As a result, QPSOs are commonly utilized to tackle difficult optimization issues such as hydrothermal scheduling and economic dispatch [35,36]. However, there have been a few reports regarding employing QPSO for artificial neural network parameter calibration. To enhance the capacity for generalization and computational effectiveness of artificial neural networks, this study develops a hybrid approach for daily reservoir runoff forecasting. The QPSO algorithm is selected as the neural network's training algorithm to improve the accuracy of hydrologic forecasts. The use of Gaussian and differential sequences in GQPSO and DQPSO improves premature convergence to local optima observed in QPSO performance. However, the objective of this paper is to find out the optimum, efficient, and accurate estimate of manufacturing plastic board parameters such that two different benchmark functions, namely Elongation at fracture (EF) and Percentage of total elongation at maximum force (MF) are minimized. For this purpose, we have used an artificial neural network (ANN) based linear equation that was optimized by using Particle swarm optimization and its different improved versions of PSO. Briefly, the contributions of this research are as follows:

- Implement the linear model using an artificial neural network with input-output parameters of the plastic board using a waste surgical mask.
- To optimize material composition using ANN via comprehensive fractional design based on process modeling.
- Using PSO and its three upgraded PSO approaches, the impacts of the input variables (polypropylene (PP), Maleic anhydrite Grafted polypropylene (MA), Titanium dioxide (TiO2), and Tensile Strength (TS)) on two responses (Elongation at fracture (EF) and Percentage of total elongation at maximum force (MF)) were explored and optimized.

The remainder of the paper is organized as follows: Section 2 discusses the materials and techniques of the current study, followed by Section 3, which describes Neural network modeling and characteristics of various advanced PSO for continuous optimization. Section 4 discusses nonlinear model optimization strategies. Section 5 presents the results of the optimization and compares the methods of solving case studies of engineering troubles. Lastly, Section 6 will provide a conclusion to the paper.

MATERIALS AND METHOD

Initially, discarded surgical masks undergo a cleaning process and are subsequently shredded into small fibrous components. The masks, PP, and TiO2 are then blended using various mixing ratios utilizing a Sigma blade mixer from Brabender, Germany. This blending operation lasts 5 minutes at a temperature of 180°C, with MA-g-PP acting as the compatibilizer. Subsequently, the composite material undergoes compression molding at a temperature of 160°C and is maintained for 5 minutes to achieve the intended thickness. Finally, tensile testing samples are taken from the molded sheet having a 30mm gauge length, 4.31mm width, and a thickness of 1.85mm (approx.). Tensile tests are carried out with a tensile testing instrumentfollowing ASTM D638and three specimens for each different composition. Throughout all scenarios, the strain rate is kept constant at 50mm/min. Figure 1 depicts the experimental approach of the current study, whereas Figures 2 and 3 depict the results of the process. Table 1 shows the input parameters and their ranges.

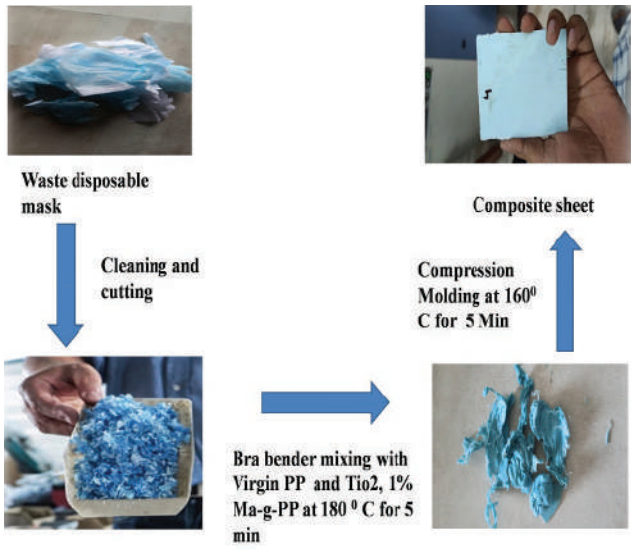


Figure 1. The methodology used in the present research.

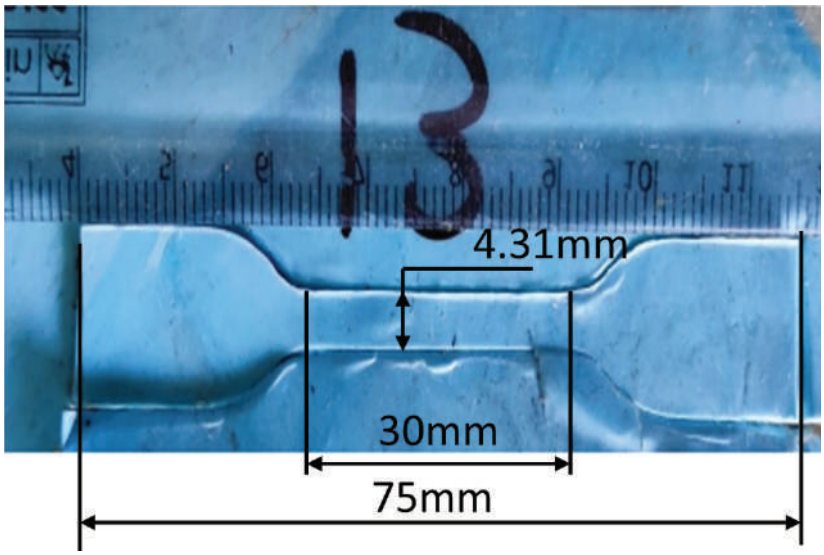
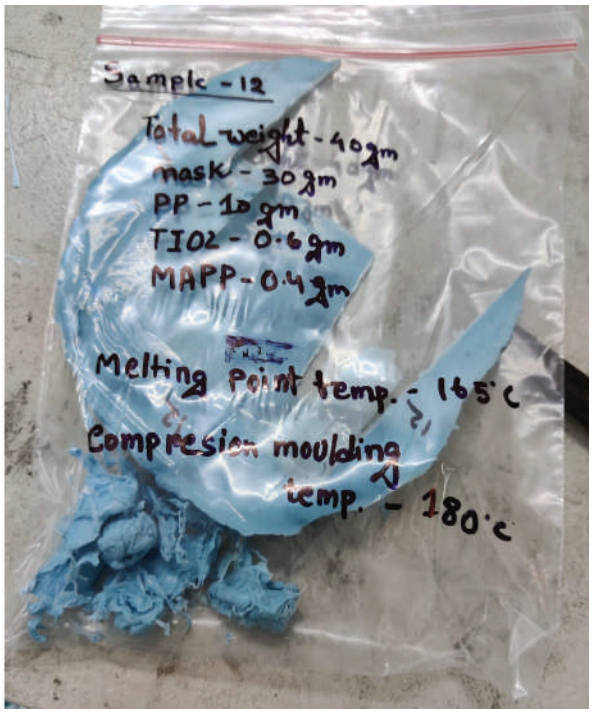


Figure 2. Tensile testing sample made of the composite.



(a)



(b)

Figure 3. (a) Sigma blade mixer &(b) plastic board.

Table 1. Range of input parameters

Process Parameters (Variables)	Range	
	LB	UB
PP (%)	10	30
MA (%)	3	28
TiO_2 (%)	0	0.6
TS (%)	10.229	27.98

MATHEMATICAL MODELLING

Neural Network Model for Elongation at Fracture (EF) and Percentage of Total Elongation at Maximum Force (MF)

From the experimental work, it has been observed that there is a certain linear relationship between process input variables, Polypropylene (PP), Maleic anhydride Grafted Polypropylene (MA), Titanium dioxide (TI), and Tensile Strength (TS), with output variables Elongation at Fracture

(EF) and Percentage of Total Elongation at Maximum Force (MF). Now, the fitness function (FF) of improved versions of PSO for this work is the obtained regression equation of Elongation at Fracture (EF), and Maximum Force (MF), which is a function of Polypropylene (PP), Maleic anhydride Grafted Polypropylene (MA), Titanium dioxide (TiO2), and Tensile Strength (TS). A simple Neuron with no buried layers represents a linear function. As a consequence, it is possible to write it as

$$FF = EF = f_1 (PP, MA, TI, TS) \quad (1)$$

$$FF = MF = f_2 (PP, MA, TI, TS) \quad (2)$$

The objective is to determine the best condition (optimal values of PP, MA, TiO2, and TS) to minimize the value of EF and MF. During the mathematical formulation of the ANN model using input and output variables, Polypropylene (PP), metal removal rate (MA), Titanium oxide (TiO2), and TS are kept in input nodes, whereas Elongation at fracture (EF) and Percentage of total elongation at maximum force (MF) are output layer nodes of the ANN model. Therefore, the dimension of the search for an improved version of PSO is 5. The weights w_1,w_2, w_3, w_4 re-applied to the three inputs, while the bias term β is assigned to the output node. The absence of an activation function is not a classification issue in this circumstance. As a consequence, using a neural network model, Elongation at fracture (EF) and Percentage of total elongation at maximum force may be stated as follows

$$EF = PP * w_{1,E} + MA * w_{2E} + TI * w_{3,E} + TS * w_{4,E} + \beta_E \quad (3)$$

$$MF = PP * w_{1,M} + MA * w_{2,M} + TI * w_{3,M} + TS * w_{4,M} + \beta_M \quad (4)$$

Now we have to determine the most optimal values for the weights and bias parameters in equations 3 and 4. We employed particle swarm optimization and its improved version to optimize the ANN model implemented for two response variables, EF and MF, respectively. The proposed NN model was created using training datasets gathered through experiments. Proposed algorithms are used to find the coefficient of w_1,w_2, w_3, w and β So that squared error should be minimum [37-39].

$$E = \sum_{i=1}^{m} (t_i - c_i)^2 \quad (5)$$

Where t and c are the targets and estimated outputs from the training data, and E is the objective function.

Quantum Particle Swarm Optimization (QPSO) Evolutionary Strategy in Process Modelling

In classical mechanics, a particle is represented by its location vector x_i and velocity vector v_i, which defines the particle's journey. In Newtonian mechanics, the particle proceeds following a predetermined course, but this is not the case in quantum mechanics. The word trajectory has no significance in the quantum realm since x_i and v_i, of a particle, following the uncertainty, exhibits quantum behavior, the PSO algorithm is bound to behave differently [26]. Instead of position and velocity, the state of a particle is expressed by wave function ψ(x, t) (Schrödinger equation) [27] in the quantum form of a PSO termed QPSO. The probability of the particle occurring in location xi from the probability density function $\|\psi(x,t)\|^2$ [28]. When applying the Monte Carlo technique, the particles move in accordance with the iterative equation [28-30]. Its position $x_i(t + 1)$ may now be computed using the following equation:

$$\begin{aligned} x_i(t+1) &= p + \beta \, \|Mbest_i - x_i(t)\| . \ln\left(\frac{1}{u}\right) \text{ if } k \geq 0.5 \\ x_i(t+1) &= p - \beta \, \|Mbest_i - x_i(t)\| . \ln\left(\frac{1}{u}\right) \text{ if } k < 0.5 \end{aligned} \quad (6)$$

where b is a contraction-expansion coefficient, u is a design parameter, and k [38] are values created using uniform probability distribution functions in the range [0, 1]. Mean Best (M_{best}) The population's global point is defined as the mean of P_{best} locations of all particles

$$Mbest_i = \frac{1}{N} \sum_{i=1}^{N} p_{gd}(t) \quad (7)$$

The best particle index by "g" among all the particles and a local attractor of PSO convergence has the following coordinates:

$$p = \frac{(c_1 p_{id} + c_1 p_{gd})}{c_1 + c_2} \quad (8)$$

Quantum-Behaved Particle Swarm Optimization Using Gaussian Mutation (GQPSO)

Uniform probability distribution is a method that most commonly produces random numbers. However, another new technique can be used to update the PSO velocity by the use of Gaussian, Cauchy, and exponential probability distributions [35]. In GQPSO, we offer a mutation operator in QPSO using a Gaussian probability distribution. For the stochastic coefficients of GQPSO, generating Gaussian distribution sequences with zero mean and unit variance abs [N(0,1)] may provide a good compromise to move away from the current point and escape from local minima (Table 2). These novel QPSO techniques in conjunction with the mutation operator are as follows:

Approach 1: Update the positional vector with the following equation:

$$\begin{aligned} x_i(t+1) &= p + \beta \, \|Mbest_i - x_i(t)\| . \ln\left(\frac{1}{G}\right) \text{ if } k \geq 0.5 \\ x_i(t+1) &= p - \beta \, \|Mbest_i - x_i(t)\| . \ln\left(\frac{1}{G}\right) \text{ if } k < 0.5 \end{aligned} \quad (9)$$

where G = abs (N(0,1)).

Approach 2: Update the parameters c_1 and c_2 by the following equation:

$$p = \frac{(G.p_{id}+g.p_{gd})}{c_1+c_2} \quad (10)$$

Where, g =abs [N(0,1)]. Approach 3: This approach uses Eqn. (9) and (10)

OPTIMIZATION OF MATHEMATICAL MODEL

Table 3 represents the basic parameters of PSO and quantum-inspired PSO. In this section, three linear NN model response variable equations (Eqn. 11- Eqn. 18) optimized by PSO, QPSO, DQPSO, and GQPSO& finally obtained the co-efficient (shown in Table 3) & their response variable equations respectively. To execute this algorithm, we used MATLAB 2013A with processor specification 11th Gen Intel(R) Core (TM) i5-1155G7 @ 2.50GHz 2.50 GHz. As the algorithms are heuristics so there is a chance that in every iteration it produces a different fitness value, for this reason, we run each algorithm 10 times with several iterations taken 1000, 2000, 3000,4000 & 5000 respectively, and all values are taken as average from the outcomes.

Model Validation on Testing Dataset

Table 5 & Table 6 represent the average computational time for all the algorithms during cross-validation & RMSE. Where, accuracy in % = (100-RMSE) in %.

Response variable equation obtained after the optimization of NN model representing by the following equations:

$$(EF)_{DQPSO\text{-}ANN} = -0.3792*PP - 0.3391*M + 7.0282*TI - 0.0381*TS + 15 \quad (13)$$

$$(EF)_{GQPSO\text{-}ANN} = -0.42166*PP - 0.4109*M + 15*TI - 0.02200*TS + 12.832 \quad (14)$$

Table 2. Flow chart of the proposed ANN-GQPSO-based method

Preparation	Step 1	Set the GQPSO to maximize iterations and population size
		Divide the total data into training and validation sets
		Define the transfer function of neurons
		Both the training and validation datasets are normalized
		Encode each particle by the initial connection weights vector and the thresholds vector of the ANN
Initialization	Step 2	Start the evolution from the 1st generation
		Randomize a fixed population of different individual networks (weights of all connections & initial threshold)
Evolution	Step 3	Construct a network with the corresponding particles one by one.
		Input the training & testing data into each constructed network
		Compute the values of the objective function for all networks
		Update the best-known position of each and the whole population
		Calculate the mean best position of the whole population
		Calculate the contraction-expansion coefficient
		Reproduce the subpopulation by updating the particle swarm position
Prediction	Step 4	Maximum iteration reached if yes go to Step 3
		Otherwise, increase the maximum iteration by 1 & go to the next Step
		The optimal model is obtained
		The forecast value is obtained
		Stop

Table 3. Parameters of PSO and QPSO

Parameters of PSO	Parameters of QPSO
Inertia Weight, w=1	Inertia weight, w_1 = 0.5; w_2 = 1.0;
Inertia Weight Damping Ratio, W_{damp} =0.99	Personal Learning Coefficient, c_1 = 1.5; c_2 = 1.5;
Personal Learning Coefficient, c_1=1.5;	No. of Populations: n_{pop}=100
Global Learning Coefficient, c_2 =2.0;	
No. of Populations: n_{pop}=100	

Table 4. Coefficient of NN model of response variable

Name of the algorithms	Coefficients of the NN model after Elongation at Fabrication (EF) Optimizations				
	w_1	w_2	w_3	w_4	$ß$
PSO	0.02781	0.00458	1.0148	0.1830	-1.5222
QPSO	0.359707	0.2848	-3.882	0.3584	-15
DQPSO	-0.3792	-0.3391	7.0282	-0.0381	15
GQPSO	-0.42166	-0.4109	15	-0.02200	12.832
Name of the algorithms	**NN model coefficients after optimization of Percentage of total elongation at maximum force (MF)**				
	w_1	w_2	w_3	w_4	$ß$
PSO	-0.0069	-0.0109	0.4213	0.0411	0.3216
QPSO	-1.1755	-1.5437	0.2425	-1.1315	3.1451
DQPSO	-0.3685	-0.3163	5.7625	-0.1528	15
GQPSO	0.37045	0.3077	-5.1539	0.2437	-15

Table 5. Time required to compute both objective functions maximum force elongation facture and percentage of total elongation

Name of algorithm	Computation time in Sec.	
	Elongation at Facture (EF)	Elongation at maximum Force (MF)
PSO	70.535	108.412
QPSO	25.48	29.76530.25
DQPSO	64.77	30.826
GQPSO	32.76	24.952

Table 6. Model accuracy of testing dataset

Name of algorithm	RMSE in %	
	Elongation at facture (EF)	Elongation at maximum force (MF)
PSO	4.35826	5.89261
QPSO	3.05068	4.66867
DQPSO	2.74599	4.62517
GQPSO	2.37064	2.58097

$$(MF)_{PSO\text{-}ANN} = -0.0069*PP - 0.0109*M + 0.4213*TI + 0.0411*TS + 0.3216 \quad (15)$$

$$(MF)_{QPSO\text{-}ANN} = -1.1755*PP - 1.5437*MA + 0.2425*TI - 1.1315*TS + 3.1451 \quad (16)$$

$$(MF)_{DQPSO\text{-}ANN} = -0.3865*PP - 0.3163*M + 5.7625*TI - 0.1528*TS + 15 \quad (17)$$

$$(MF)_{GQPSO\text{-}ANN} = 0.3705*PP + 0.3077*MA - 5.1539*TI + 0.2437*TS - 15 \quad (18)$$

Figure 4 and Figure 5 shows the deviation characteristics of PSO-ANN, QPSO-ANN, DQPSO-ANN & GQPSO-ANN algorithms for both the response variables Elongation at fracture (EF) and Percentage of total elongation at maximum force (MF). Figure 6 represents the objective function of all the algorithms during model validation.

RESULT AND DISCUSSION

All the techniques are simulated using MATLAB 2015a in a computer with 16 GB RAM, Processor11th Gen Intel(R) Core (TM) i5-1155G7 @ 2.50GHz, 2496 Mhz, 4 Core(s), 8 Logical Processor(s) and Windows11 Operating System.

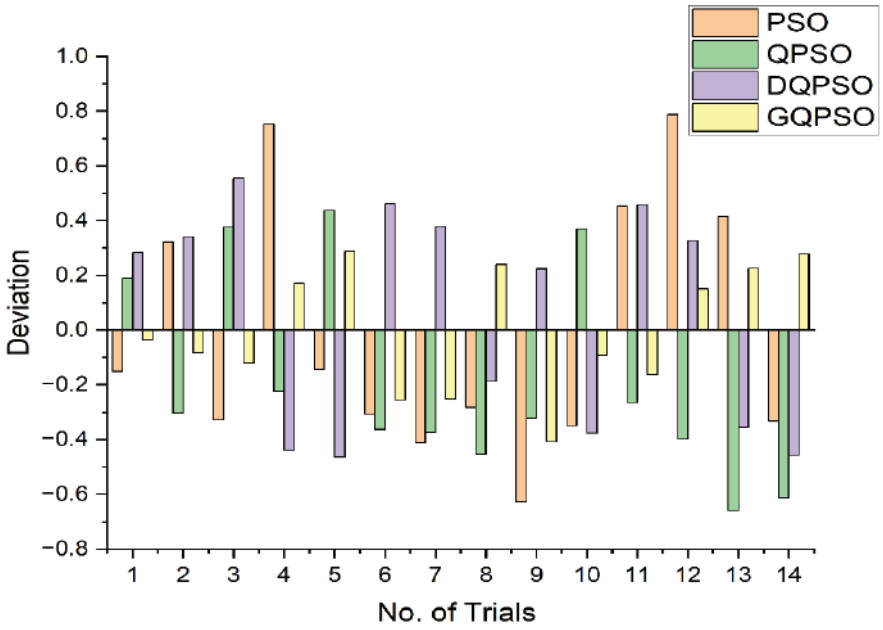


Figure 4. A comparative study based on Elongation at fracture (EF).

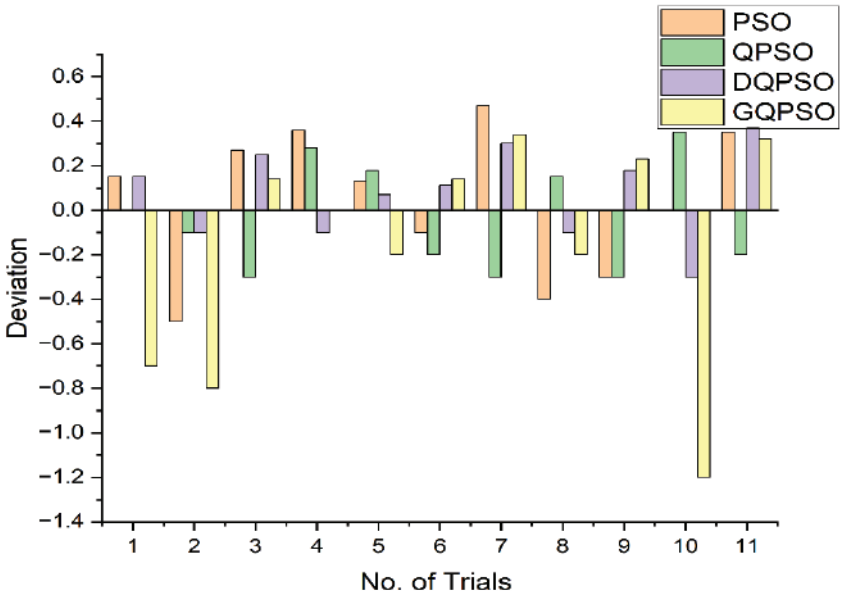


Figure 5. Comparative study based on and percentage of total elongation at maximum force (MF).

Cross-validation of Model

This part compares four computational models, PSO-ANN, QPSO-ANN, DQPSO-ANN, and GQPSO-ANN to determine the best-fitting model based on 16 experimental datasets. To do this, each set of input variables is entered into Eqn. 11-14 to determine the response variables of Elongation at fracture (EF) and Percentage of total elongation at maximum force (MF). The cross-validation comparison research for EF and MF is given in Figures 1 and 2. Table 6 depiction clearly shows that the GQPSO-ANN model outperformed other upgraded PSO-ANN models. Another significant aspect of determining the optimum optimization model is computational time.

Model Prediction Based on Improved PSO-ANN

Model validation is done in this portion for 10% of the experimental dataset (2 experimental data). Table 5 compares model validation between PSO-ANN and three

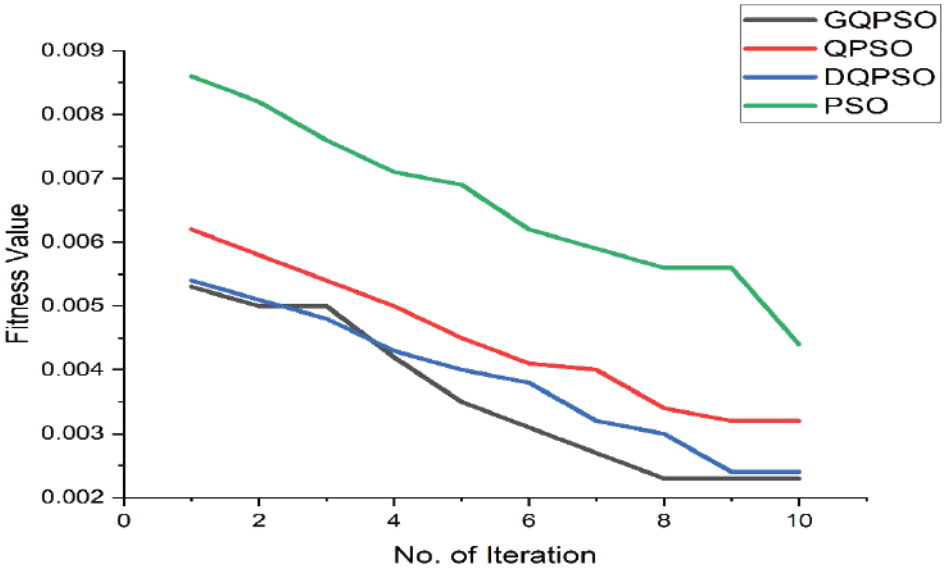


Figure 6. A comparative study based on Fitness value.

Table 7. Model accuracy of cross-validation dataset

s	RMSE in %	
	Elongation at facture (EF)	**Elongation at maximum force (MF)**
PSO	8.562	7.2916
QPSO	6.8605	7.7686
DQPSO	5.9747	4.7612
GQPSO	4.4670	3.9708

upgraded PSO-ANN procedures (QPSO-ANN, DQPSO-ANN, and GQPSO-ANN). According to the results, the average RMSE for GQPSO-ANN in response variables EF& MF is much lower.

Optimal Condition for ANN Based Model

According to the preceding section, GQPSO-based ANN beat the other three optimization models in cross-validation and model prediction. In this phase, the best conditions for proper modeling of manufactured plastic boards are determined by searching for optimal values of polypropylene (PP), Maleic anhydrite grafted polypropylene (MA), Titanium dioxide (TiO_2), and tensile strength (TS), such that elongation at fracture (EF) and percentage of total elongation at maximum force (MF) ismaximized. A new fitness function (OF) is defined as a combination of EF and MF by their numerical values.

$$OF = (EF)_{GQPSO\text{-}ANN} + (MF)_{GQPSO\text{-}ANN}$$

$$\begin{aligned} OF = {} & (-0.0069*PP - 0.0109*MA + 0.4213*TI \\ & + 0.0411*TS + 0.3216) + (0.3705*PP \\ & + 0.3077*MA - 5.1539*TI + 0.2437*TS - 15) \end{aligned} \quad (19)$$

Maximum polypropylene (PP) concentration is 29.678%, minimum Maleic anhydrite Grafted polypropylene (MA) concentration is 11.082%, maximum Titanium dioxide (TiO2) concentration is 0.4412%, and maximum Tensile Strength (TS) is 26.712. GQPSO is the best evolutionary algorithm to minimize the combined objective function (OF) of the developed neural models for EF and MF. OF will have the highest value when PP, TiO2, and TS have the highest values and MA has the lowest value. This determined optimal value has been confirmed by experimental data, indicating that the output of this procedure is extremely excellent. The GQPSO-NN model takes 23.931 seconds to achieve the optimal condition.

CONCLUSION

The parametric analysis of plastic boards employing waste surgical maskswas performed in our current study. The efficient and accurate estimate of manufacturing plastic board characteristics depends on two potential functions, Elongation at fracture (EF) and Percentage of total elongation at maximum force (MF). To achieve the optimal

estimate of plastic board characteristics we performed three improved particle swarm optimization techniques. The outcomes of the present research are drawnout below:

1. Elongation at fracture (EF) and Percentage of total elongation at maximum force (MF) increased by increasing the concentration of independent variables such as material compositions of material composition of polypropylene (PP), Titanium dioxide (TiO2), and Tensile Strength (TS), while keeping Maleic anhydrite Grafted Polypropylenes (MA) as minimum value.
2. Overall dataset split into 9:1 ratio for perform cross-validation and model validation. During cross-validation, it has been observed that proposed all ANN-based improved PSO techniques obtained better accuracy but ANN-based GQPSO achieved the maximum accuracy in both the response variables Elongation at fracture (EF) and Maximum force (MF) about 95.533% and 96.0292% respectively.
3. For multi-response optimization, the optimal parametric conditions for polypropylene (PP), Maleic anhydrite Grafted polypropylene (MA), Titanium dioxide (TiO2), and Tensile Strength (TS) during waste surgical mask design are 29.678%, 11.082%, 0.4412%, and 26.712, respectively.
4. The Gaussian Quantum behaved Particle Swam Optimization (GQPSO)-based artificial neural network (ANN) optimization technique is more suitable than artificial neural network (ANN) optimized Particle Swam Optimization (PSO), Quantum behaved Particle Swam Optimization (QPSO), and Differential Quantum behaved Particle Swam Optimization (DQPSO) using computation time, better cross-validation, and best-fitted model for testing dataset.
5. The model's accuracy may be increased further by increasing the number of experimental datasets and employing various mathematical models (Response Surface Methodology & Analysis of variance) optimized heuristic optimization approaches.

AUTHORSHIP CONTRIBUTIONS

Authors equally contributed to this work.

DATA AVAILABILITY STATEMENT

The authors confirm that the data that supports the findings of this study are available within the article. Raw data that support the finding of this study are available from the corresponding author, upon reasonable request.

CONFLICT OF INTEREST

The author declared no potential conflicts of interest with respect to the research, authorship, and/or publication of this article.

ETHICS

There are no ethical issues with the publication of this manuscript.

STATEMENT ON THE USE OF ARTIFICIAL INTELLIGENCE

Artificial intelligence was not used in the preparation of the article.

REFERENCES

[1] Derman S, Kızılbey K, Akdeste ZM. Polymeric nanoparticles. Sigma J Eng Nat Sci 2013;31:107–120.

[2] Şahin Fİ, Acaralı N. Evaluation of properties for synthetic polymers in medicine. Sigma J Eng Nat Sci 2014;42:1315–1324.

[3] Aragaw TA. Surgical face masks as a potential source for microplastic pollution in the COVID-19 scenario. Mar Pollut Bull 2020;159:111517. [CrossRef]

[4] Rowan NJ, Laffey JG. Unlocking the surge in demand for personal and protective equipment (PPE) and improvised face coverings arising from coronavirus disease (COVID-19) pandemic: Implications for efficacy, re-use and sustainable waste management. Sci Total Environ 2021;752:142259. [CrossRef]

[5] Mondal R, Mishra RS, Pillai JK, Sahoo M. COVID-19 pandemic and biomedical waste management practices in healthcare system. J Fam Med Prim Care 2022;11:439. [CrossRef]

[6] Selvaranjan K, Navaratnam S, Rajeev P, Navintherakumaran N. Environmental challenges induced by extensive use of face masks during COVID-19: A review and potential solutions. Environ Chall 2021;3:100039. [CrossRef]

[7] Maderuelo-Sanz R, Acedo-Fuentes P, García-Cobos FJ, Sánchez-Delgado FJ, Mota-López I, Meneses-Rodríguez JM. The recycling of surgical face masks as sound porous absorbers: Preliminary evaluation. 2021;786:147461. [CrossRef]

[8] Occasi G, De Angelis D, Scarsella M, Tammaro M, Tuccinardi L, Tuffi R. Recovery material from a new designed surgical face mask: A complementary approach based on mechanical and thermo-chemical recycling. J Environ Manag 2022;324:116341. [CrossRef]

[9] Ray SS, Lee HK, Huyen DTT, Chen SS, Kwon YN. Microplastics waste in environment: A perspective on recycling issues from PPE kits and face masks during the COVID-19 pandemic. Environ Technol Innov 2022;26:102290. [CrossRef]

[10] Hasija V, Patial S, Kumar A, Singh P, Ahamad T, Khan AAP, et al. Environmental impact of COVID-19 vaccine waste: A perspective on potential role of natural and biodegradable materials. J Environ Chem Eng 2022;10:107894. [CrossRef]

[11] Dharmaraj S, Ashokkumar V, Chew KW, Chia SR, Show PL, Ngamcharussrivichai C. Novel strategy in biohydrogen energy production from COVID-19 plastic waste: A critical review. Int J Hydrogen Energy 2022;47:42051–42074. [CrossRef]

[12] Yousef S, Eimontas J, Zakarauskas K, Jančauskas A, Striūgas N. An eco-friendly strategy for recovery of H2-CH4-rich syngas, benzene-rich tar, and carbon nanoparticles from surgical mask waste using an updraft gasifier system. 2023;45:5063–5080. [CrossRef]

[13] Mili M, Hashmi SAR, Ather M, Hada V, Markandeya N, Kamble S, et al. Novel lignin as natural-biodegradable binder for various sectors—A review. J Appl Polym Sci 2022;139:51951. [CrossRef]

[14] Mullins MJ, Liu D, Sue HJ. Mechanical properties of thermosets. In: Thermosets: Structure, Properties, and Applications. 2nd ed. Amsterdam: Elsevier; 2018. p. 35–68. [CrossRef]

[15] Franzoni E, Pigino B, Graziani G, Lucchese C, Fregni A. A new prefabricated external thermal insulation composite board with ceramic finishing for buildings retrofitting. Mater Struct 2016;49:1527–1542. [CrossRef]

[16] Spector M, Johnson C. Porcelain coated steel printed wiring boards. In: 1979 EIC 14th Electrical/Electronics Insulation Conference. 1979;339–343. [CrossRef]

[17] Stull AT, Fiorella L, Gainer MJ, Mayer RE. Using transparent whiteboards to boost learning from online STEM lectures. Comput Educ 2018;120:146–159. [CrossRef]

[18] Pekel E, Kara SS. A comprehensive review for artificial neural network application to public transportation. Sigma J Eng Nat Sci 2017;35:157–179.

[19] Ahmed MF, Zaib A, Ali F, Bafakeeh OT, Tag-ElDin ESM, Guedri K, et al. Numerical computation for gyrotactic microorganisms in MHD radiative Eyring–Powell nanomaterial flow by a static/moving wedge with Darcy–Forchheimer relation. Micromachines 2022;13:1768. [CrossRef]

[20] Ahmed FM, Khalid M, Ali F, Al-Bossly A, Alduais FS, Eldin SM, Saeed A. Importance of bioconvection flow on tangent hyperbolic nanofluid with entropy minimization. Front Phys 2023;11:1154478. [CrossRef]

[21] Ali F, Loganathan K, Eswaramoorthi S, Faizan M, Prabu E, Zaib A. Bioconvective applications of unsteady slip flow over a tangent hyperbolic nanoliquid with surface heating: Improving energy system performance. Int J Appl Comput Math 2022;8:276. [CrossRef]

[22] Ali F, Padmavathi T, Hemalatha B. Entropy minimization in darcy forchheimer on sutterby nanofluid past a stretching surface with swimming of gyrotactic microorganisms. Waves Rand Complex Media 2022;35:10333–10356. [CrossRef]

[23] Puneeth V, Ali F, Khan MR, Anwar MS, Ahammad NA. Theoretical analysis of the thermal characteristics of Ree–Eyring nanofluid flowing past a stretching sheet due to bioconvection. Biomass Convers Biorefinery 2024;14:8649–8660. [CrossRef]

[24] Ali F, Zaib A. Unsteady flow of an Eyring-Powell nanofluid near stagnation point past a convectively heated stretching sheet. Arab J Basic Appl Sci 2019;26:215–224. [CrossRef]

[25] Ali F, Summayya N. Numerical simulation of Cattaneo–Christov double-diffusion theory with thermal radiation on MHD Eyring–Powell nanofluid towards a stagnation point. Int J Ambient Energy 2022;43:4939–4949. [CrossRef]

[26] Demir S. Artificial neural network simulation of advanced biological wastewater treatment plant performance. Sigma J Eng Nat Sci 2020;38:1713–1728.

[27] Chau KW. Particle swarm optimization training algorithm for ANNs in stage prediction of Shing Mun River. J Hydrol 2006;329:363–367. [CrossRef]

[28] Asadnia M, Chua LHC, Qin XS, Talei A. Improved particle swarm optimization based artificial neural network for rainfall-runoff modeling. J Hydrol Eng 2014;19:1320–1329. [CrossRef]

[29] Liu WC, Chung CE. Enhancing the predicting accuracy of the water stage using a physical-based model and an artificial neural network-genetic algorithm in a river system. Water 2014;6:1642–1661. [CrossRef]

[30] Dutta P, Cengiz K, Kumar A. Study of bio-inspired neural networks for the prediction of liquid flow in a process control system. In: Cognitive Big Data Intelligence with a Metaheuristic Approach. New York: Academic Press; 2022. p. 173–191. [CrossRef]

[31] Jeong DI, Kim YO. Combining single-value streamflow forecasts—A review and guidelines for selecting techniques. J Hydrol 2009;377:284–299. [CrossRef]

[32] Sun J, Feng B, Xu WB. Particle swarm optimization with particles having quantum behavior. In: Proceedings of the 2004 Congress on Evolutionary Computation, CEC2004. Portland, OR, USA; 2004. p. 325–331.

[33] Fang W, Sun J, Ding Y, Wu X, Xu W. A review of quantum-behaved particle swarm optimization. IETE Tech Rev 2010;27:336–348. [CrossRef]

[34] Xi M, Sun J, Xu W. An improved quantum-behaved particle swarm optimization algorithm with weighted mean best position. Appl Math Comput 2008;205:751–759. [CrossRef]

[35] Mondal K, Mallick B, Hameed AS, Sarkar A, Mahato J, Dutta P. Experimental analysis and hybrid-optimization of micro-ECDM process parameters to enhance micro-machining performances of silica by Gaussian-Quantum-PSO. J Adv Manuf Syst 2024;241:125–141. [CrossRef]

[36] Sun C, Lu S. Short-term combined economic emission hydrothermal scheduling using improved quantum-behaved particle swarm optimization. Expert Syst Appl 2010;37:4232–4241. [CrossRef]

[37] Dutta P, Kumar A. Design an intelligent calibration technique using optimized GA-ANN for liquid flow control system. J Eur Syst Autom 2017;50:449. [CrossRef]

[38] Dutta P, Kumar A. Modeling and optimization of a liquid flow process using an artificial neural network-based flower pollination algorithm. J Intell Syst 2018;29:787–798. [CrossRef]

[39] Bellubbi S, Mallick B, Hameed AS, Dutta P, Sarkar MK, Nanjundaswamy S. Neural network (NN)-based RSM-PSO multiresponse parametric optimization of the electro chemical discharge micromachining process during microchannel cutting on silica glass. J Adv Manuf Syst 2022;21:869–897. [CrossRef]

Sigma J Eng Nat Sci, Vol. 44, No. 1, pp. 127–139, February, 2026

Sigma Journal of Engineering and Natural Sciences
Web page info: https://sigma.yildiz.edu.tr
DOI: 10.14744/sigma.2025.00000

Research Article

Metaheuristic and cryptographic approaches with upgraded discrete and lifting wavelet transform for effective data security in steganography

S. SARATHA[1,*], V. MURUGAN[2], P. Arockia Jansi RANI[1]

[1]Manonmaniam Sundaranar University, Tirunelveli, 627012, India
[2]Goverment Arts and Science College, 673018, India

ARTICLE INFO

Article history
Received: 20 July 2024
Revised: 09 September 2024
Accepted: 02 December 2024

Keywords:
Discrete Wavelet Transform; Genetic Algorithm; Lifting Wavelet Transform; Rivest – Shamir- Adleman; Steganography

ABSTRACT

In recent years, digital communication captured massive attention among people, and it plays a significant role in various streams such as banking, healthcare departments, industries, information technologies, and more. At present, all data transfers are transmitted through the internet, which requires a high level of security to transfer the original message until it reaches the destination. Cryptography and Steganography are the two important functionalities that ensure data security over open internet sources. Steganography is the procedure that deals with hiding secret text, audio, and video within massive data. It is found to be a useful source as well as it paves the way for secured communication between two groups to hide the information. However, existing methods are not capable enough to provide efficient results and key creation frequently depend on predictable, deterministic techniques, which might not fully account for anomalies or inefficiencies in the key selection procedure. Hence, proposed method introduces effective key generation using an Optimized Genetic Algorithm (OGA) as it produces complex keys along with Enhanced Rivest – Shamir- Adleman (RSA) encryption and Enhanced RSA decryption algorithm. Enhanced Discrete Wavelet Transform (E-DWT) is employed for the compression and decompression process, and Improvised Lifting Wavelet Transform (I-LWT) is used for the data embedding process. The Genetic algorithm with the Rabin Miller Primality test (RMPT) is mainly proposed for the complex key generation process with secured communication. The private and public keys are generated using an optimized genetic algorithm. Performance metrics are employed to evaluate and analyse the capability of the proposed method considering the Peak signal noise ratio (PSNR), Single to noise ratio (SNR), and Mean Squared Error (MSE) metrics. The proposed model resulted in of MSE rate of 0.00000000042036 and an SNR value of 99.98 %.

Cite this article as: Saratha S, Murugan V, Rani PAJ. Metaheuristic and cryptographic approaches with upgraded discrete and lifting wavelet transform for effective data security in steganography. Sigma J Eng Nat Sci 2026;44(1):127–139.

*Corresponding author.
*E-mail address: journalpub23@gmail.com

This paper was recommended for publication in revised form by Editor-in-Chief Ahmet Selim Dalkilic

Published by Yıldız Technical University Press, İstanbul, Turkey
© Author. This is an open access article under the CC BY-NC license (http://creativecommons.org/licenses/by-nc/4.0/).

INTRODUCTION

In recent years, breach of data privacy has become one of the common threats to people since these data contain sensitive or personal information, and this information is stored and transmitted over the internet, which requires a high level of protection. Therefore, more reliable methods should be implemented to secure information, such as cryptography and steganography. Cryptography [1] protects communication and information via the implementation of codes so that only those for whom the information is anticipated can read and process it. It is a process of encrypting sensitive and secretive information into scrambled or jumbled messages [2]. In cryptography encryption and decryption algorithm are employed, encryption algorithms are used to convert plain texts into incomprehensible and inexplicable format whereas decryption algorithm is the reverse process of encryption algorithm, which convert cipher text back into plaintext.

Along with cryptography, steganography can also be employed. Steganography is a technique that hides data or information in an image form, audio form, or video form, and the data will be transformed from sender to receiver. There are several types of steganography deals with the methods of audio, video and text. Text steganography involves making modifications to the text which previously exists to conceal the stenographic information. In audio steganography, a psychoacoustical masking technique of HAS (human auditory system) is usually employed to conceal information [3].

Stenography, which uses the image to hide information is called image steganography and it is the most widely used steganography [4]. Some of the significant factors of employing steganography are that, steganography allows users to conceal a large amount of information with audio, image, and video format. Steganography and cryptography are employed in the existing study for data security techniques [5], suggested study employed cryptography and steganography, which used AES for cryptography and LSB for steganography, suggested paper revealed that combining these 2 algorithms can enhance the integrity, confidentiality, and flexibility of the data. Similarly, the suggested study employed cryptography and steganography to hide and unhide the text file into an image file. LSB (Least Significant Bit) is implemented for the insertion technique in steganography along with it, the LZ algorithm is executed for the data compression process. The algorithm utilized in the suggested study is the RSA algorithm for cryptography. Besides conventional steganography, hybrid steganography is employed in the suggested study [6] along with RSA (Rivest – Shamir- Adleman) cryptosystem employed to encrypt the plain text with the image file. The suggested paper divided the algorithms into cryptosystem and steganography, and MATLAB environment is used to run the code. The concept of the RSA algorithm is utilized in the suggested study since they are ideally used in various mathematical problems. The computational time has to be considered as it is a crucial factor when developing a steganographic algorithm [7].

Correspondingly, the conventional paper has presented 6 spiral functions and 2 hybrid functions (SEB-ChOA) for rectifying deficiencies. The performance is evaluated on 20 benchmarks of IEEE CEC-2005, 12 constrained real-world engineering problems of IEEE CEC-2020 and 23 standard benchmarks. Statisical evidence have shown that the prevailing SEB-ChOA has attained better results [8]. Likely, the prevailing method has developed a modified ChOA to enhance the exploitation and exploration abilities of ChOA. It has used 23 standard benchmarks, randomly created landscape, 10 suit tests and 12 real-world constrained optimisation issues from different engineering fields. Such as power system, mechanical design, chemical producer, power-electronic, process synthesis and design nad livestock feed ration. The prevailing model has attained high rank results [9]. Likely, the prevailing model utilised Opposition-Based Learning (OBL) and Greedy Search (GS) increases the ChOA [10]. A memory structure has exploited to save dominated solutions a grid mechanism and leader strategy to study on Multi-Objective version namely (MOChOA). It could be applied in various engineering fields and attained better results [11].

Though existing studies have provided better results, they lack in [12] image compression technique which is yet to be performed, the accuracy of the results, etc. These drawbacks can be overcome by utilizing a optimized genetic algorithm for the key generation process and Enhanced DWT for the compression and decompression process using the Enhanced RSA algorithm for the process of decryption and encryption. The GA can enhance the key generation process by optimizing key parameters, thereby increasing efficiency and reducing irregularities in the RSA algorithm. This optimization leads to faster computation times compared to traditional methods. RSA is favored for its strong confidentiality and integrity, rooted in complex mathematical principles that make it challenging to crack. By integrating GA with RSA, the proposed method not only improves key generation but also leverages the robust security features of RSA, ensuring that the encryption remains resilient against attacks while maintaining efficient performance in real-world applications. The security of the RSA mainly depends on the difficulty of factoring huge integers. Due to these remarkable advantages, the proposed method utilized OGA for key generation, EDWT, and ERSA algorithm.

Aim and Objectives

- To perform key generation of the private and public keys with the help of an Optimized Genetic Algorithm (OGA).
- To perform the operation of encryption and decryption, ERSA algorithm is performed.

- To perform compression and decompression of the image by using Enhanced Discrete Wavelet Transform (E-DWT).
- To embed the data, an Improvised Lifting Wavelet Transform (I-LWT) is proposed.
- To assess the efficiency of the proposed model using performance metrics to confirm the efficiency of the proposed method.

Paper Organization

The study is being organised in a manner like section I deals with the introduction part and Section II discusses the reviews of various existing works that pertain to this context. Then, section III explores the overall proposed method to encrypt and decrypt the data in steganography efficiently. Subsequently, section IV discusses the results obtained from the implementation of the proposed study. At the final point, the overall research is summarised in section V.

Review of Existing Works

Steganography is the approach or a main discipline to hide information in digital mediums, either audio, video, or text formats. The hided information will not be visible to the naked eye. The research paper incorporated with RSA algorithm for the encryption process to convert the information into secret information. The segmentation process of the cover image is divided into non-edge and edge pixels by employing the technique of the Canny edge detector. The bits of the secret messages that are comprised in the technique such as N1 and N2 are buried into the non-edge and edge pixel areas by utilizing the LSB approach. The implantation of the essential parameters such as N1 and N2 is prepared in the four pixels. The hidden data is extracted at the recipient's side from the stego image before the extraction of N1 and N2 length. The reversible process occurs by incorporating the RSA algorithm for decryption by employing two keys. The performance metrics such as MSE, PSNR, and Histogram are evaluated. The method employed in the paper has attained better efficiency in hiding the information [13].

The private and confidential information or data are secured by utilizing the approach of steganography. This technique has been emerging as a trend that assists in locking up the secret message. LSB is considered to be a profound method and an effective strategy that is practiced in Image Steganography. The method of encryption in this specific paper is practiced by LSB, RSA, and DWT algorithms. The time consumed for the encryption process is reduced in this specific study in contrast to the traditional or conventional methods. These methods can better protect the message from brutal attack forces [14]. Likewise, LSB is considered the effectual process for image steganography, mainly incorporated in entrenching the communication, i.e., undisclosed. The LSB is employed in the study that relies upon the hash function. The main purpose of employing this technique lies in deciding the position to conceal the secret data by utilizing the hash function. The algorithm is proposed in the study to conceal the text which is constituted in the text file or file of a cover image. The two main stages are involved in the study: the encryption process being practiced by applying the RSA algorithm. Then the insertion of encrypted text into the cover image is practiced by operating the LSB approach. The implementation process and assessment of the algorithm are practiced by C#.net. The proposed results have shown that the model has better efficiency in hiding and retrieving the text in the image [15].

The high level of the stenographic method is employed to protect the data and the data integration. CICS cryptography is practiced in this particular study. Dual RSA is employed in the study, and the encrypted images are covered under the stego images. When the Dual RSA is utilized in the study, it enables less memory utilization, and the process is robust. Certain performance metrics are considered to evaluate the model's ability, such as calculating the value of SSIM and PSNR that ensures the efficacy of the CICS in contrast to conventional Steganography [16]. Congruently, the existing research has employed a Radial Basis Function Neural Network (RBF-NN), an automatic sonar target recognition model. For the prevailing RBF-NN, a Whale Optimisation Algorithm with fuzzy system has been utilised for training. Simulation result has shown with 97.49% of accuracy on sonar data [17]. Insertion of the LSB method is an efficient technique for embedding the data. LSB embedding approach has the greater capacity to conceal the information from the naked eye. The information or a message cannot be figured out from the cover file of LSB. This specific study incorporates steganography and cryptography to send the compressed message along with the process of decryption and decompression originating from the stego image. The two combinations are constituted in the study such as steganography by utilizing DWT and Huffman coding whereas cryptography by utilizing the correlation of RSA would be an effective method. LSB is applied to implant the encrypted data in the compact cover image. This model has shown better performance than other traditional approaches by considering the performance metrics [18]. Systems can be hacked in many different ways, and it can cause risky thing and threats to the confidential files that are comprised in the system. Hence it is important to save data as much as possible irrespective to the data type, which can be in any form like text, audio, video, or images, however, the suggested paper mainly depended on the basic image which can be protected in another image after modifying its formal to composites by utilizing DWT (Discrete wavelet transform). The strategy employed in the suggested study is to hide the 2D and 3D images on other images to produce a single encrypted image with tall efficacy [19].

Like any other financial sector, the intelligence sector must protect the data. However, brute force attacks are common and highly frequent, so the suggested study [20]

employed the Playfair algorithm, considered one of the most powerful cryptographic algorithms. The suggested Playfair algorithm enhances the performance of the conventional Playfair cipher. It assists keyless transposition, and an additional layer of security between the sender and receiver is improved by employing steganography and the RSA algorithm. Sometimes there is a possibility, that the decryption process can be slow, hence suggested study used the Chinese remainder theorem, which mainly concentrated on modulus calculation. It also emphasized improving the sturdiness of the system with the help of steganography. CRT speeds up the operation of the private key. In cryptography, CRT is used in sharing via error-correcting code. In addition to the theorem, a faster RSA-CRT algorithm for the decryption of data is also employed. More protection can be offered by 2 algorithms, the LSB-RSA algorithm. Even Steganalyis is not feasible enough to recover the data from attackers when RSA-CRT is implemented [21]. Most of the existing studies either use steganography or cryptography however suggested paper employed both methods, which ensured added security for the user from unauthorized access. It used MSB (Most Significant Bit) for steganography and RSA for cryptography. RSA-MSB provided better capacity and memory consumption results than existing methods [22].

Apart from RSA, several other algorithms provided many solutions to avoid the theft of data. One of the common algorithms employed to avoid data theft is AES (Advanced Encryption Standard). The suggested study employed AES and steganography, in which input data used to protect from threats are images. These images are secured by employing watermarking with BS (bit shifting). AES encryption method is employed with watermarked images and AES decryption is employed to retrieve the original image. Performances metrics such as MSE and PSNR were implemented to compare the image in terms of compression quality and image similarity can be demonstrated using SSIM (structural similarity index) [23].

In general, data are in different forms, which include images, audio, video, and text however, specifically while protecting the data in audio format, degradation of the quality of data is possible hence suggested study employed a technique that provided an enhanced quality of PSNR and SNR when steganography is applied. The suggested study revealed that there was no significant distortion of audio after the encrypted text was hidden in the audio file. The algorithm employed to encrypt the text is AES, later, two inputs were needed for the DWT algorithm since one input was used to cipher the text and the other was used to cover the audio. Finally, the quality of the audio file was evaluated using various metrics: PSNR, SNR, and MSE. Higher PSNR value resulted in a better quality of compression. Finally, SNR was evaluated to compare the different levels of preferred signal to the background noise level [24]. Various types of steganography and specific steganography, known as image steganography, are evaluated in the suggested study. Image steganography deals with concealing confidential data within an image. However, one of the disadvantages of employing image steganography is that a lot of information cannot be hidden in an image since it may lead to irrelevant results [25].

Problem Identification

From the existing studies, various problems are identified in the field of steganography. Among the several problems, the significant problems are addressed in this section.

- The accuracy is less in existing steganography models, which needs attention in the future to enhance efficiency [24]
- Excellent steganography approaches can be employed in the future with the presence of hybrid cryptography that enhances security [14].

MATERIALS AND METHODS

The study aims to encrypt and decrypt the data such as Images, Audio, and text in steganography. For this purpose, the four main techniques are involved in the study. The complex keys (public and private keys) are generated using an optimized genetic algorithm (OGA). The encryption and decryption are carried out by the RSA algorithm. The compression and the decompression process is proceeded by enhanced discrete wavelet transform (E-DWT) and the process of decomposition and extraction of the compressed image is by Improvised Lifting Wavelet Transform for decomposition (I-LWT). OGA is used for effective key generation, producing complex keys for encryption. An improved version of the RSA algorithm for encryption and decryption. E-DWT Used for data compression and decompression. Improvised Lifting Wavelet Transform (I-LWT) is utilized for embedding data securely. The overall flow of the proposed methodology is been depicted in the Figure 1.

Figure 1 shows the overall flow of the proposed method. Initially, the message is given as input (Audio, video, or text). The public key and the private key are generated by employing a genetic algorithm. The public and the private key is responsible for the encryption and the decryption method. The function of encryption is processed using the ERSA algorithm. The encrypted result is obtained. Subsequently, the compression procedure, along with the pre-processing, is carried out by applying the Enhanced Discrete Wavelet Transform (E-DWT) method. From that procedure, the compressed image is gained as an outcome. The compressed image before the pre-processing method is given as the cover input. The cover input is concealed by Improvised Lifting Wavelet Transform for decomposition (I-LWT) in steganography. The embedded result is attained through this procedure. Eventually, a reversible process is carried out to extract the data. The cover image is extracted by employing the ILWT. Thus, the cover output is obtained. The decompression process is undergone by Enhanced Discrete Wavelet Transform (E-DWT). The decompressed result is gained. Again ERSA proceeded with

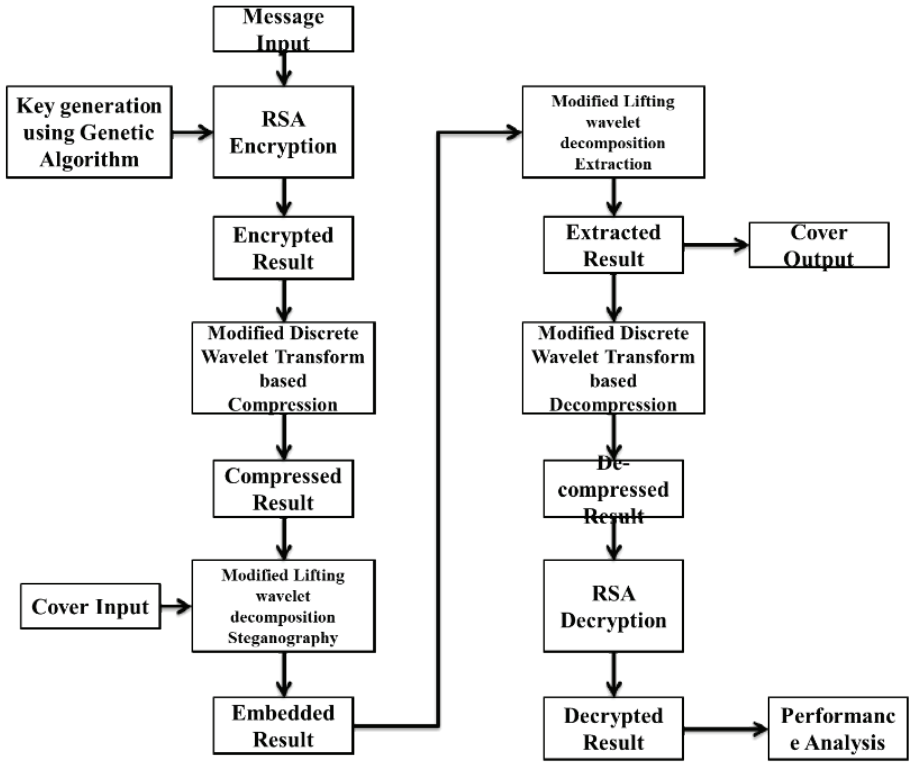


Figure 1. Overall view of the proposed method.

the decryption method. Therefore, the decrypted result is accomplished. The performance of the respective method is assessed to determine the efficacy.

KEY GENERATION USING OPTIMIZED GENETIC ALGORITHM (OGA)

Asymmetric cryptography is carried out in the study, which involves two keys, such as private and public. Public key is utilised for an encryption process, and then private key is utilised for a decryption process. There will be many brute-force attacks that occur to evaluate the strength of the algorithm. The effect of the attacks is based upon the parameters that rely on the key's length and the key's complexity from where it is generated. When the key generation process is more complex, it would be challenging for a cryptanalyst. The OGA is proposed in the study since it is a highly adaptive and heuristic algorithm. It is significantly practiced in optimizing and searching processes, making the key more complex. The principle of the genetic algorithm relies upon natural genetics and natural selection. Numerous advantages exist in the genetic algorithm like reliability, efficiency and parallelism and it can be modified to solve varied problems. It possesses a huge extension solution space in searching ability. The existence of the fitness function in the Genetic algorithm is practiced for the evaluation. It is latent to operate as a multi-objective optimizer. Thus, the Genetic algorithm with the Rabin Miller Primality test (RMPT) is mainly proposed for the complex key generation process with secured communication. The private and public keys are generated using an OGA. Three main processes are involved in the Genetic algorithm namely selection, crossover, and mutation process until it reaches the destination criteria. The crossover and the reproduction process enable better searching for the genetic algorithm.

The process involved in OGA is that, fitness value obtained from the genetic algorithm is fed to public key, and the value obtained by the public key is multiplied with the fitness value obtained by the genetic algorithm. However, in the proposed OGA model, the fitness value is iterated again by employing in crossover and mutation in order to secure the key in a more protective way. Pseudo code of the OGA is listed (Algorithm 1).

Firstly, parameters are initialized after initialization, initial chromosomes and genes are created. Here, the crossover probability Pc_{val} = 100 where, each time a pair of parents is selected and there is an occurrence of crossover. When it reaches the maximum recombination of genetic material, it leads to the convergence of algorithm quickly and it is potentially held at the local optimum without adequate consideration of further possible solutions. Besides, Mutation probability m_{val} = 100, then each gene of individual in the population is mutated in every generation. It can extremely modify the genetic population in every iteration. This makes the algorithm to perform like

Algorithm 1. Optimized genetic algorithm

INPUT: msg_{sig}

OUTPUT: key_{val}

Step 1: Initialize the parameter

$$chro_{num} \rightarrow 20$$
$$genes_{num} \rightarrow 20$$
$$max_{gen} \rightarrow 100$$
$$Pc_{val} \rightarrow 100$$
$$Pm_{val} \rightarrow 100$$
$$Er_{val} \rightarrow 100$$

Step 2: *Chromosomes*

Create initial Chromosomes $chro_{val}$ *and genes* $genes_{val} \rightarrow msg_{sig}$;

Step 3: *Compute the fitness function*

$fitness_{val}$ *by using the sphere function*

Step 4: $t \rightarrow 1$

Step 5: *Sort the* $fitness_{val}$ *in descending order*

Step 6: $con_{curve} \rightarrow$ *compute the highest index fitness value*

Step 7: *For* $t \rightarrow 2$ *to* max_{gen}

calculate the fitness value By using population do the selection operation find 2 *parent*

By using parent do the crossover operation find 2 *child*

By using child 1 *and* Pm_{val} *do the mutation operation find child* 1

By using child 2 *and* Pm_{val} *do the mutation operation find child* 2

Compute the update population by using child

$new_{pop} \rightarrow$ *By using old populaion and updated population, compute the new population by using elisism operation*

$con_{curve}(t) \rightarrow$ *Assign* new_{pop} *first fitness value*

end

Step 8: $key_{val} \rightarrow$ *Compute the* 2 *best prime fitness values*

Step 9: end

Step 10: end

a random search compared with GA. Hence, the constant destruction of collected individuals can prevent the algorithm against an effective preservation and propagation of good solutions. Moreover, the sphere function is given by $(x) = \sum_{i=1}^{n} x_i^2$, where x = (x1, x2,…xn) signifies the vector of the decision variables (genes in the chromosomes), n is the variable numbers (genes), xi denotes the value of the 3rd variable (gene).Then the fitness function is computed and the fitness values generated are sorted in descending order, the highest index fitness value is computed, and finally, 2 best prime fitness values are generated.

Enhanced RSA Encryption

The proposed study has utilized the ERSA method for the process encryption and as well as the decryption. This method is employed with two keys such as public and private to perform the operation. In ERSA, the public key required to encode the sensitive information, whereas the matching private key is required to decode the encrypted message. RSA algorithm is an easy algorithm to implement, confidential and personal data can be transmitted carefully and firmly via the ERSA algorithm. ERSA offers a high level of security. ERSA is a public key encryption algorithm that employs an asymmetric algorithm for data encryption. ERSA is the most frequently used public key algorithm. 2 big prime numbers, p, and q are made utilising the Rabin-miller algorithm. The Pseudo code of the corresponding Algorithm 2 is listed.

Algorithm 2. Enchanced RSA encryption algorithm

Step 1: Initialization

$$p_{val} \rightarrow key_{val}(1)$$
$$q_{val} \rightarrow key_{val}(2)$$
$$pk_{val} \rightarrow p_{val} * q_{val}$$
$$phi_{val} \rightarrow (p_{val} - 1) * (q_{val} - 1)$$

Step 2: Compute the public key

$$x = 2, PU_{key} = 1$$
$$Whilex > 1$$
$$PU_{key} = PU_{key} + 1$$
$$x = gcd\ gcd\ (phi_{val}, PU_{key})$$
$$end$$

Step 3: Compute the Private key

$$i = 1, r = 1$$
$$While\ \ r > 1$$
$$k = phi_{val} * i + 1$$
$$r = remainder(k, PU_{key})$$
$$i = i + 1$$
$$End$$

Step 4: $PR_{key} = k / PU_{key}$

Step 5: $msg_{len} \rightarrow$ *compute the length of the* msg_{sig}

Step 6: *for* $j \rightarrow 1$ *to* msg_{len}

$encry_{sig}(j) \rightarrow crypt(msg_{sig}, pk_{val}, PU_{key})$

End

The existing approaches to key creation frequently depend on predictable, deterministic techniques, which might not fully account for anomalies or inefficiencies in the key selection procedure. These techniques usually involve fixed algorithms that produce keys by applying common mathematical operations, which might result in weaknesses if the patterns of the keys are identified. GA presents an adaptive and stochastic method for generating keys. GA can explore a larger solution space and dynamically optimize important parameters by mimicking natural selection processes. Because GAs can successfully eliminate anomalies and enhance computational efficiency, the outcome is a less predictable and more secure key. All things considered, even though current techniques might offer a minimum degree of protection, the incorporation of GA amplifies the resilience and versatility.

Enhanced - DWT Compression (E-DWT Compression)

DWT is a recently developed compression method that is used for image compression. DWT image compression comprises the decomposition process, entropy encoding, and detail co-efficient thresholding process. The suggested method›s use of the LWT and DWT supported by pointing out its unique benefits for steganography. DWT is renowned for its capacity to offer multi-resolution analysis, enabling efficient data embedding at different sizes without appreciably lowering the cover medium›s quality. This characteristic increases imperceptibility, reducing the ability to identify hidden information. However, compared to conventional wavelet transformations, LWT allows for in-place computations and faster processing times, making it more computationally efficient and simpler to implement. Furthermore, LWT›s capacity to adaptively change coefficients makes it especially well-suited for safely embedding data, improving data security in general. The report can illustrate why these transformations were chosen over alternative solutions by outlining these benefits. The following methodology involves transforming an image using the DWT and thresholding techniques. DWT is predominantly implemented for image pre-processing, especially for lossless image compression. DWT is majorly employed for lossy compression. In most cases, the threshold values are constant in addition to, high encryption time and quality of reconstructed image will be affected, however, in the proposed work value of the threshold is set which diminishes the time taken for encryption and retain a better quality reconstructed image. Due to these enhancements, Enhanced DWT is implemented to minimize the distortion of the cover image, it also provides better security, quality, and imperceptibility. In general, the existing model utilizes low pass filter only, however, in the proposed E-DWT, the model is enhanced by using both low pass filter and high pass filter.The process involved in E-DWT is that, size of the input data which includes size of image, audio or text is multiplied with the value of the Quantizer - 0.255 (constant value). This E-DWT helps in providing lossless image compression. The pseudo-code of algorithm III is listed (Algorithm 3).

Algorithm 3. E-DWT compression

Input: $encry_{sig}$

Output: $comp_{data}$

Step 1: $[m,n] = size(encry_{sig})$

Step 2: $d_val(i,j) \rightarrow \sum_{i\rightarrow 1}^{m} \sum_{j\rightarrow 1}^{n} \sqrt{\left(i-\frac{m}{2}\right)^2+\left(j-\frac{n}{2}\right)^2}$

Step 3: $h_val(i,j) \rightarrow \sum_{i\rightarrow 1}^{m} \sum_{j\rightarrow 1}^{n} e^{-\frac{\left(d_{val(i,j)}\right)^2}{2*10^2}}$

Step 4: $low_{pass}(i,j) \rightarrow \sum_{i\rightarrow 1}^{m} \sum_{j\rightarrow 1}^{n} h_{val(i,j)} * encry_{sig}(i,j)$

Step 5: $h_val(i,j) \rightarrow \sum_{i\rightarrow 1}^{m} \sum_{j\rightarrow 1}^{n} 1-e^{-\frac{\left(d_{val(i,j)}\right)^2}{2*10^2}}$

Step 6: $high_{pass}(i,j) \rightarrow \sum_{i\rightarrow 1}^{m} \sum_{j\rightarrow 1}^{n} h_{val(i,j)} * encry_{sig}(i,j)$

Step 7: $comp_{data}$ → Do discrete wavelet transform for $encry_{sig}$ by using low_{pass} and $high_{pass}$

Improvised Lifting Wavelet Transform for Decomposition (I-LWT)

LWT is a method that substitutes the standard DWT is employed for the computation process of the wavelet co-efficient. The methodology of lifting originates from the lifting scheme. A lifting scheme is an approach employed in the design of wavelet. The LWT relies on the convolutional of the original signal with FIR comprised with the structure of FIR. The original filter is broken into a sequence of tiny structures that enables a versatile and a sophisticated algorithm that is 50% quicker and faster than conventional ones. Traditional lifting wavelet decomposition employs the 1D method however, the proposed I-LWT for decomposition employs the 2D method. One of the advantages of implementing the 2D method over 1D method is that, resolution of the image is increased when compared to the conventional one. In addition to, I-LWT provides excellent ability of resistance to attack, large key space and high key sensitivity. Instead of opting for ReLU activation function, proposed study has implemented Adam activation function since Adam function has the potential to reduce the loss function and deliver high accuracy rate. In addition to that, proposed framework has the ability to incorporate 1D and 2D models as input like audio, image due to the implementation of Adam activation function. In most existing

Algorithm 4. (I-LWT)

Step 1: *text* → $comp_{data}$ Convert to unsigned 32-bit integer.

Step 2: bin_{text} → *convet decimal to binary in* 32 *bit*

Step 3: ch_{num} → *compute length of the* bin_{text}

Step 4: *Perform Lifting wavelet decomposition for* $comp_{data}$ *compute approximation coefficients vector* Ca_{vec} and *detail coefficients vector* Cd_{vec}

Step 5: $zero_{val}$ → (Cd_{vec} (Cd_{vec} > -2 *AND* Cd_{vec} < 0))

Step 6: one_{val} → (Cd_{vec} (Cd_{vec} > 0 *AND* Cd_{vec} < 2))

Step 7: out_{CDvec} → Cd_{vec}

Step 8: out_{CDvec} (1) → $zero_{val}$

Step 9: out_{CDvec} (2) → $zero_{val}$

Step 10: $char_{enc}$ → *decimal to binary convertion for* ch_{num} *in* 64 *bit format*

Step 11: $char_{enc}$ → {$zero_{val}$ $char_{enc}$ == 0 one_{val} $char_{enc}$ == 1

Step 12: out_{CDvec} (3 *to* 66) → $char_{enc}$

Step 13: *For* i → 1 *to size of* bin_{text}

idx_{val} → [(i - 1 * 32 + 1) *to* i * 32] * 2 + 66

$text_{byte} = bin_{text_{i,:}}$

$text_{byte}$ → {$zero_{val}$ $text_{byte}$ == 0 one_{val} $text_{byte}$ == 1

out_{CDvec} (idx_{val}) = $text_{byte}$

Step 14: *end*

Step 15: *Perform inverse Lifting wavelet decomposition*

methods maximum 8 bits are used whereas the proposed method can use upto 32 bits which makes the proposed model more efficient other models. The pseudo-code of Algorithm IV is presented.

RESULTS AND DISCUSSION

The study proposed an Optimized Genetic Algorithm for key generation, an Enhanced RSA algorithm for encryption and decryption, Enhanced DWT for compression-decompression, and I-LWT for decomposition extraction to encrypt and decrypt the data efficiently.

Performance Metrics

Various valuation metrics like peak signal noise to ratio (PSNR), average difference (AD), root mean square error (RMSE), structural content (SC), universal quality index (UQI), normalised cross correlation (NCC), multi scale structural similarity index method (MS-SSMI), contrast to noise ratio (CNR), ENL, GAE, LMSE, NAE, MD are employed to evaluate the efficiency of the proposed model.

Root mean square error (RMSE)

RMSE assess the average difference between a statistical model's predicted values and the actual values.

$$RMSE = \sqrt{\frac{\sum_{i=1}^{n} (\widehat{y_i} - y_i)\text{^}2}{n}} \quad (1)$$

Peak signal noise to ratio (PSNR)

PSNR is defined as the ratio between a signal›s maximum power and the power of the signal›s noise. The PSNR mathematical depiction is defined in Equation 2.

$$PSNR = 10 \log_{10} \left(\frac{MAX^2}{MSE}\right) \quad (2)$$

Here, MAX is denoted as the maximum possible pixel value of the image or signal.

Structural content (SC)

SC helps in find the similarity between original image and denoised image.

$$SC = \frac{\sum_{j=1}^{M} \sum_{k=1}^{M} x_j^2 \, ,k}{\sum_{j=1}^{M} \sum_{k=1}^{M} (x_{j,k})^2} \quad (3)$$

Mean squared error (MSE)

MSE assess the mean value of the average square of the difference between expected and actual values. Where H is the cover medium and stego data is S and it is expressed as: The MSE formula with is presented in the equation 4.

$$MSE = \frac{1}{N} \sum_{i=1}^{N} (H_i - S_i)^2 \quad (4)$$

Signal noise ratio (SNR)

SNR is used to compare the level of a preferred signal to the level of background noise. SNR is examined as the ratio of signal power to the noise power, and NR is frequently expressed in db (decibels). A mathematical depiction of SNR is defined in Equation 5.

$$SNR = 10 \log_{10} \left(\frac{\sum_{i=1}^{N} S_i^2}{\sum_{i=1}^{N} (S_i - H_i)^2}\right) \quad (5)$$

Performance Analysis

Various file formats are employed in order to evaluate the performance of the proposed study

Image file

The file format which has been taken into consideration is audio format. Figure 2 shows the process of Input image to decrypted image

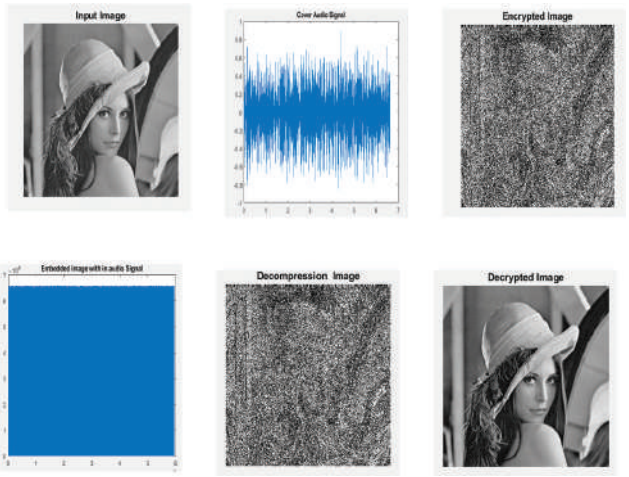


Figure 2. Input image to decrypted image.

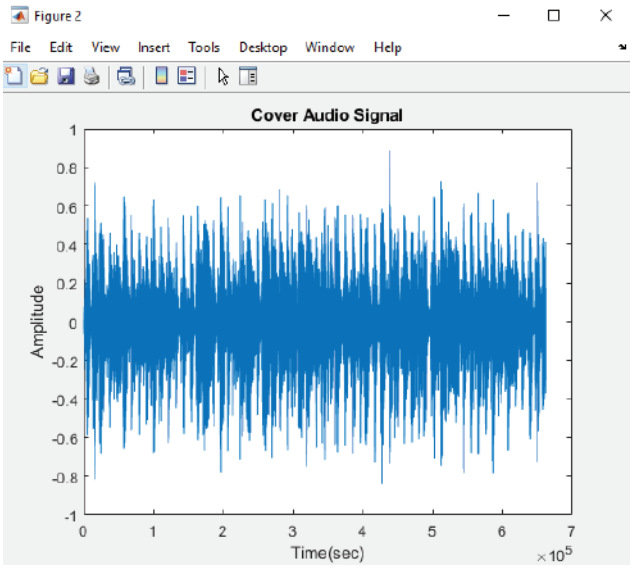


Figure 3. Audio file.

Audio file

Next file format which has been taken into consideration is audio format. Figure 3 shows the audio file which is considered as the input. Figure 4. shows the embedded image of the audio file.

And finally original file has been retrieved using decryption method in Figure 5.

Text file

Finally, text file has been taken into account. Initially, an input text has been embedded into audio file, after encryption process, text will be recovered from the safely and securely. Figure 6. depicts that text has been recovered successfully.

Table 1 shows the analysis of steganography file size. 3 different file formats such as audio, image and text files are taken into consideration. In audio, SA1.wav file has been taken into consideration. The size of the file utilized for the proposed model is 0.6388 MB. Once the file is compressed, the size of the file obtained after compression is 2.031 MB. After encryption, the size of the audio file is 5.079 MB. Further, the size of the cover file is 42.35 MB and the size of the file after steganography is 381.19 MB.

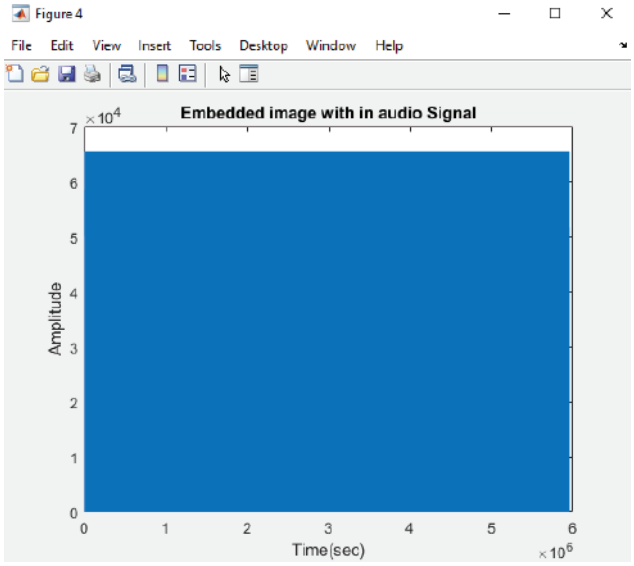


Figure 4. Embedded image with in audio signal.

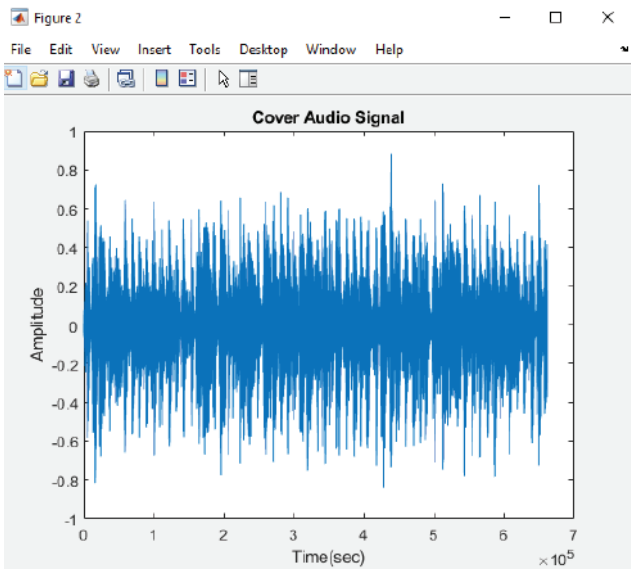


Figure 5. Decrypted image of the audio file.

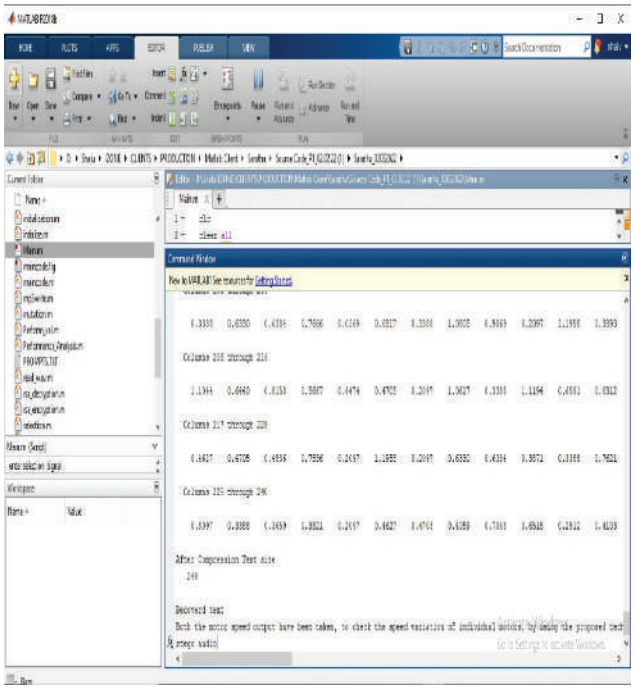


Figure 6. Decrypted text.

Table 1. Analysis of steganography file size

Name of the file to be secured	SA1.wav	Cameraman.tiff	Textinput.txt
File size	0.6388 MB	4.19 MB	7.68 KB
File size after compression	2.031 MB	2.09 MB	15.36 MB
File size after encryption	5.079 MB	4.19 MB	30.72 KB
Size of the cover file (audio file)	42.35 MB	42.35 MB	42.35 MB
Size of the file after steganography	381.19 MB	224.15 MB	158.09 MB

Table 2. Performance metrics of the different files

Performance Metrics	Audio	Image	Text
PSNR (Peak Signal to Noise Ratio)	69.1680	69.3059	47.9535
NAE (Normalized Absolute Error)	-1	1.2896e-05	0.0022
Structural Content	0	1.0000	0.9961
LMSE (Laplacian Mean Square Error)	1	2.5350e-06	1.7024e-05
UQI (Universal Quality Index)	0	0.7500	0.7510
NCC (Normalized Cross-correlation)	0	1.0000	1.0019
RMSE (Root Mean Square Error)	0.0178	0	0.2554
FSIM (Feature Similarity Index Metrics)	0.0887	0.0873	1.0206
MSSIM (Multiscale Structural Similarity Index Metric)	0.9996	1.0000	0.9999
ENL (Equivalent Number of Looks)	1.0000e-04	6.0127e+05	20.4403
GAE (Geometric Average Error)	1.0001	1.0001	1.0079
MD (Maximum Difference)	5	5	5
Average Difference	0.0016	0.0015	0.2083

For image format, the size of the file taken is 4.19 MB, after compression the size of the file is 2.09 MB. After compression, the file is encrypted, the size of the file after encryption is 4.19 MB. Further the size of the cover file is 42.3 MB and eventually, the size of the file after steganography is 381.19 MB.

Size of the text file, which is taken as input is 7.68 KB. The file size after compression is 15.36 MB. After compression, file size after encryption is 30.72 KB. Moreover, the size of the cover file is 42.35 MB. Eventually, the size of the file obtained after steganography is 381.19 MB.

Table 2 represents the performance metrics of different files. Different format of files are considered, which includes audio, images and text files. Different metrics such as PSNR, NAE, Structural content, LMSE, UQI, NCC, RMSE, FSIM, MMSIM, ENL, GAE, maximum difference and average difference are depicted in the table.

Comparative Analysis

In comparative analysis, different existing methods are compared with the proposed methods for detecting MSE and SNR values.

Image files are considered as input in Table 3 [26]. From Table 3, existing studies used velocity-updated grey wolf optimization, however, the MSE obtained by the existing model is 0.327645, and SNR obtained was 28.402, similarly, the existing study employed AES encryption, and MSE obtained was 0.47686, and SNR obtained was 25.767, backward movement oriented shark smell optimization technique was also employed in the existing studies in which the MSE attained was 0.16641 and SNR attained was 29.202 and LSB-BMSE acquired MSE of 0.001995 and SNR of 99.8, however, the proposed model has outperformed rather than the existing approaches. The proposed model resulted in of MSE rate of 0.00000000042036 and an SNR value of 99.98 percent. Table 4 shows the performance comparison of the present model.

From Table 4 [30] and Figure 7, it clears that the proposed LSTM model attained better results. Similarly, Figure

Table 4. Comparison performance

Algorithm	Accuracy
Existing LSTM	90
LSTM Proposed	**99.12**

Table 3. Comparative analysis using existing methods

Method	MSE	SNR
Velocity-updated grey wolf optimisation [27]	0.27645	28.402
AES encryption [28]	4.77E-01	25.767
Backward movement-oriented shark smell optimization [29]	0.16641	29.202
Existing - LSB-BMSE [26]	0.001995	99.8
Proposed model	**4.20E-10**	**99.98**

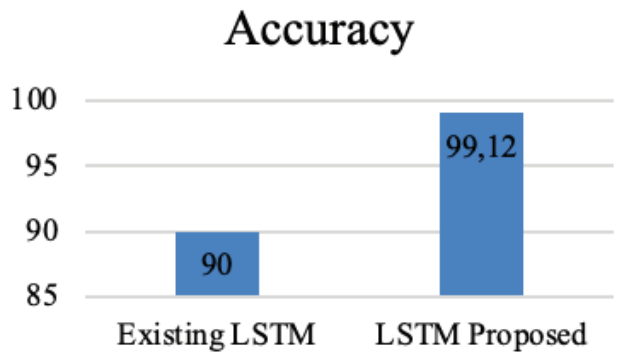


Figure 7. Comparison.

Table 5. Comparison performance

Metrics	RF	XGBoost	Proposed
Accu	97.07%	98.53%	99.12%
Prec	97%	98%	99%
Rec	97%	99%	99%
F1	97%	98%	99%

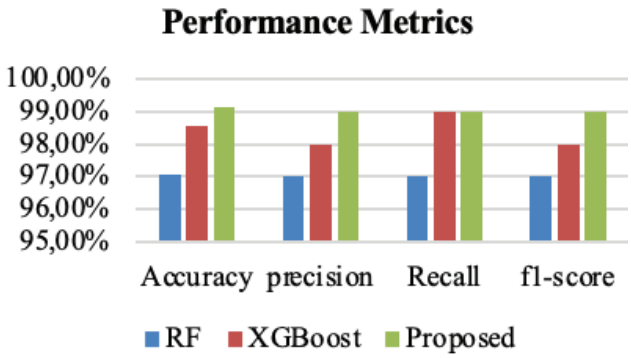


Figure 8. Proposed comparison.

8 and Table 5 describes comparison performance with existing model.

From above Table 5 [31] and Figure 4, the proposed model achieved high results than prevailing RF and XG Boost models.

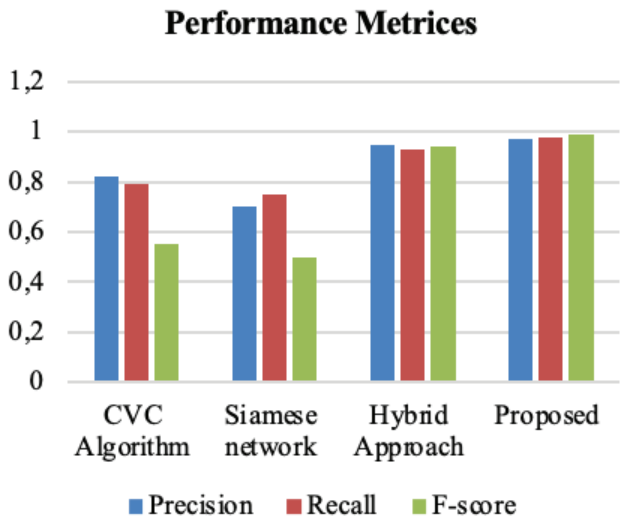


Figure. 9 Metrics comparison.

From Table 6 [32] and Figure 9, it shows that the proposed model achieved better values in terms of metrics. It attained 0.97, 0.98, 0.99 and 0.99 of Precision, Recall, F-score and Accuracy respectively. In terms of limitations, there are few limitations which should be taken into consideration, the size of the images should ranges from 0 – 512 Mb, the size of the text file should range from 0 – 250 Mb and audio file must range form 0 – 128 Mb.

CONCLUSION

Encryption and decryption using the Enhanced Rivest – Shamir- Adleman (RSA) algorithm were obtained since Enhanced RSA offers a high level of security. Key generation of private and public keys with the help of an optimized genetic algorithm was achieved since the genetic algorithm can produce more complex keys by employing the genetic algorithm principle. Compression and decompression of the image using Enhanced Discrete Wavelet Transform (E-DWT) were attained by setting a threshold instead of utilizing the constant value. Improvised Lifting Wavelet Transform (I-LWT) provided better results than LWT since the proposed method utilized the 2D method instead 1D method. Finally, the performance of the proposed model was evaluated using performance metrics and performance are analyzed using three different file formats

Table 6. Comparison analysis

Algorithm	Precision metric	Recall metric	F-score metric	Accuracy metric
CVC Algorithm	82	79	55	67
Siamese network	7	75	5	69
Hybrid Model	95	93	94	93
Proposed	**97**	**98**	**99**	**99**

which includes audio, video and text file. This study may assist security professionals to send sensitive information, allowing communication between different parties to avoid brute force attacks by unauthorized parties. Enhanced RSA algorithm is employed in the study for the process of encrypting the public key, which enhances data security. In the future, as an enhancement, the Enhanced RSA algorithm can be replaced with robust algorithms to avoid inevitable threats.

AUTHORSHIP CONTRIBUTIONS

Authors equally contributed to this work.

DATA AVAILABILITY STATEMENT

The authors confirm that the data that supports the findings of this study are available within the article. Raw data that support the finding of this study are available from the corresponding author, upon reasonable request.

CONFLICT OF INTEREST

The author declared no potential conflicts of interest with respect to the research, authorship, and/or publication of this article.

ETHICS

There are no ethical issues with the publication of this manuscript.

STATEMENT ON THE USE OF ARTIFICIAL INTELLIGENCE

Artificial intelligence was not used in the preparation of the article.

REFERENCES

[1] Varghese F, Sasikala P. A detailed review based on secure data transmission using cryptography and steganography. Wirel Pers Commun 2023;129:2291–2318. [CrossRef]

[2] Antonio H, Prasad P, Alsadoon A. Implementation of cryptography in steganography for enhanced security. Multimed Tools Appl 2019;78:32721–32734. [CrossRef]

[3] Azzam ESNA, Algamdi A. Survey steganography applications. Al-Salam J Eng Technol 2023;2:69–75. [CrossRef]

[4] Dhivya MN, Banupriya MS. Network security with cryptography and steganography. Int J Eng Res Technol 2020;8:1–4.

[5] Yahaya MM, Ajibola A. Cryptosystem for secure data transmission using Advance Encryption Standard (AES) and Steganography. Int J Sci Res Comput Sci Eng Inf Technol 2019;5:317–322. [CrossRef]

[6] Al Saffar NFH. Steganography algorithm based RSA cryptosystem. J Eng Appl Sci 2019;14:2240–2243. [CrossRef]

[7] Sarmah DK, Kulkarni AJ. Improved cohort intelligence—A high capacity, swift and secure approach on JPEG image steganography. J Inf Secur Appl 2019;45:90–106. [CrossRef]

[8] Qian L, Khishe M, Huang Y, Mirjalili S. SEB-ChOA: an improved chimp optimization algorithm using spiral exploitation behavior. Neural Comput Appl 2024;36:4763–4786. [CrossRef]

[9] Khishe M. Greedy opposition-based learning for chimp optimization algorithm. Artif Intell Rev 2023;56:7633–7663. [CrossRef]

[10] Bo Q, Cheng W, Khishe M. Evolving chimp optimization algorithm by weighted opposition-based technique and greedy search for multimodal engineering problems. Appl Soft Comput 2023;132:109869. [CrossRef]

[11] Khishe M, Orouji N, Mosavi MR. Multi-objective chimp optimizer: an innovative algorithm for multi-objective problems. Expert Syst Appl 2023;211:118734. [CrossRef]

[12] Ardiansyah G, Sari CA, Rachmawanto EH. Hybrid method using 3-DES, DWT and LSB for secure image steganography algorithm. In: 2017 2nd International Conferences on Information Technology, Information Systems and Electrical Engineering (ICITISEE); 2017; IEEE. p. 249–254. [CrossRef]

[13] Kalaichelvi V, Meenakshi P, Devi PV, Manikandan H, Venkateswari P, Swaminathan S, et al. A stable image steganography: a novel approach based on modified RSA algorithm and 2–4 least significant bit (LSB) technique. J Ambient Intell Humaniz Comput 2021;12:7235–7243. [CrossRef]

[14] Bhargava S, Mukhija M. Hide image and text using LSB, DWT and RSA based on image steganography. ICTACT J Image Video Process 2019;9. [CrossRef]

[15] Manral N. Secure data transfer using image steganography. Int J Res Appl Sci Eng 2021;9:175–180.

[16] Vinothkanna R. A secure steganography creation algorithm for multiple file formats. J Innov Image Process 2019;1:20–30. [CrossRef]

[17] Saffari A, Zahiri SH, Khishe M. Fuzzy whale optimisation algorithm: a new hybrid approach for automatic sonar target recognition. J Exp Theor Artif Intell 2023;35:309–325. [CrossRef]

[18] Wahab OFA, Khalaf AA, Hussein AI, Hamed HF. Hiding data using efficient combination of RSA cryptography, and compression steganography techniques. IEEE Access 2021;9:31805–31815. [CrossRef]

[19] Al Rikabi H, Hazim HT. Enhanced data security of communication system using combined encryption and steganography. Int J Interact Mob Technol 2021;15:145. [CrossRef]

[20] Patil R, Bang S, Bangar R. Improved cryptography by applying transposition on modified playfair algorithm followed by steganography. Int J Innov Sci Res Technol 2021;6:616–620.
[21] Eseyin JB, Gbolagade KA. A residue number system based data hiding using steganography and cryptography. NIU J Soc Sci 2019;5:345–351.
[22] Adebayo OS, Ganiyu SO, Osang FB, Salawu SA, Mustapha K, Abdulazeez L. Data privacy system using steganography and cryptography. 2022. [Eksik Bilgi - Yayın Yeri Yok].
[23] Arsha P, Venugopal N. Data security with RSA and steganography. Heritage Res J 2022;70:1–7.
[24] Patil AP. AES hybridization with DWT audio steganography [Master's thesis]. Dublin: National College of Ireland; 2019.
[25] Khalid I, Naeem M, Shahzad A, Muhammed I, Khan M, Zeeshan M, et al. A comprehensive analysis of image steganography and its techniques. Webology 2021;18:2523-2532.
[26] Mahmoud MM, Elshoush HT. Enhancing LSB using binary message size encoding for high capacity, transparent and secure audio steganography–an innovative approach. IEEE Access 2022;10:29954–29971. [CrossRef]
[27] Vhatkar KN, Bhole GP. Particle swarm optimisation with grey wolf optimisation for optimal container resource allocation in cloud. IET Netw 2020;9:189–199. [CrossRef]
[28] Manjunath K, Ramaiah GK, Rasad D. An efficient audio steganography technique using hybridization of compression and cryptography algorithm. J Adv Res Dyn Control Syst 2019;11:132–147. [CrossRef]
[29] Manjunath K, Ramaiah GK, GiriPrasad M. Backward movement oriented shark smell optimization-based audio steganography using encryption and compression strategies. Digit Signal Process 2022;122:103335. [CrossRef]
[30] Liu L, Gao M, Zhang Y, Wang Y. Application of machine learning in intelligent encryption for digital information of real-time image text under big data. EURASIP J Wirel Commun Netw 2022;2022:21. [CrossRef]
[31] Higuchi M, Emori A, Kawasaki S, Gamba J, Koike A, Murakami H. Performance evaluation of visual cryptography schemes with intensity transformations for gray-scale images. In: Proceedings of the 3rd WSEAS International Conference on Visualization, Imaging and Simulation; 2010; p. 111–117.
[32] Mohan J, Rajesh R. Enhancing home security through visual cryptography. Microprocess Microsyst 2021;80:103355. [CrossRef]

Sigma J Eng Nat Sci, Vol. 44, No. 1, pp. 140–152, February, 2026

Sigma Journal of Engineering and Natural Sciences
Web page info: https://sigma.yildiz.edu.tr
DOI: 10.14744/sigma.2025.00000

Research Article

Metaheuristic algorithms for multi objective vehicle routing problem

İlknur TÜKENMEZ[1,*], Onur KAYA[2]

[1]*Department of Industrial Engineering, Bursa Technical University, Bursa, 16310, Türkiye*
[2]*Department of Industrial Engineering, Eskisehir Technical University, Eskisehir, 26555, Türkiye*

ARTICLE INFO

Article history
Received: 13 June 2024
Revised: 21 August 2024
Accepted: 26 December 2024

Keywords:
Alternative Links; Adaptive Large Neighborhood Search Algorithm; Simulated Annealing Algorithm; Sustainability; Vehicle Routing Problem

ABSTRACT

Besides its economic purpose, the vehicle routing problem has also garnered attention due to its social and environmental objectives in recent years. In terms of ensuring sustainability, it is beneficial to consider these three objectives together. CO_2 emissions, which is one of the causes of global warming, which we have felt more prominently in the past few years, has also affected the policies of logistics companies. Organizing working hours and ensuring fairness among employees are also one of our motivations in this study. Financial objectives has always taken into account. Simulated annealing algorithm and adaptive large neighborhood search algorithm are developed for the solution of the multi-objective mix integer mathematical model, in which financial, environmental, and social objective functions, which include alternative ways with different properties between nodes and different speed options. Small problems can be solved with exact solution method in literature, but to solve medium and larger samples heuristic algorithms are needed. When comparing algorithms, Simulated Annealing also gives better results than Adaptive Large Neighborhood Search in a shorter time.

Cite this article as: Tükenmez İ, Kaya O. Metaheuristic algorithms for multi objective vehicle routing problem. Sigma J Eng Nat Sci 2026;44(1):140–152.

INTRODUCTION

Although vehicle routing problem (VRP) is an old problem, it is still studied by researchers. VRP still has a wide range of applications in different industries. Reducing CO_2 emissions, one of the main factors of global warming, has also become an important issue for companies. In addition, transporters are bound by the legislation enforcing driver working hours. Also, unbalanced working hours might create problems among the workers and it may cause a trust problem towards the firm [1-3]. With the increasing sensitivity to environmental and social issues in recent years, these objectives are considered together with financial objectives [4-6]. Motivated by these issues, vehicle routing problem considering financial, environmental, and social objectives are considered.

In general VRP studies in the literature, it is assumed that there is only one direct link between each pair of nodes in the network [7]. However, in reality, there may be more than one direct connection between two nodes. In Figure 1, the first value on each link denotes the length of the link (in km) and the two values inside the parentheses denote two different speed levels (in km/hour) that the vehicles can choose to go on that link. Besides, these alternative

***Corresponding author.**
*E-mail address: ilknur.tukenmez@btu.edu.tr

This paper was recommended for publication in revised form by Editor-in-Chief Ahmet Selim Dalkilic

Published by Yıldız Technical University Press, İstanbul, Turkey
© Author. This is an open access article under the CC BY-NC license (http://creativecommons.org/licenses/by-nc/4.0/).

links might have different features as lengths, durations, and costs. For example, a short road might require a longer time due to traffic. Similarly, some roads require additional payments, leading to higher costs, or some roads may cause more CO_2 emissions due to speed limits.

In literature, even though the existence of alternative roads between different points is acknowledged, the shortest or the fastest of these roads is taken as a single link in the model, and the other alternatives are omitted, assuming that longer or slower roads will never be chosen based on the model objectives [8]. However, alternative links between nodes are studied by [9-11].

However, in real life, the shortest roads are not always the best ones due to speed limits, traffic jams, or toll roads. Depending on the objective function and constraints of the model, a faster but longer road might be chosen to go from one node to another node, even if a shorter road may be in the same network.

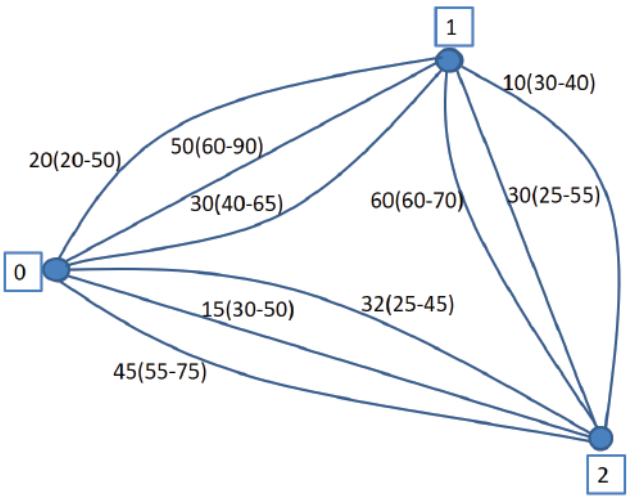


Figure 1. Sample of alternative links and speed choices between nodes.

As it is seen in Figure 2, 0 represents depot, 1 and 2 are customers. When there is no time window restriction in Figure 2 part of A, route is 0-1-2-0, and the length of selected alternative links are 20, 10 and 15, and selected speed levels are 50, 40, and 50. However, if there is time window restriction for node 1, the route is still the same, but, the selected alternative link is changed. In Figure 2 part of B, the selected length between the node of 0 and 1 is 50, and the selected speed level is 90. If the time window restriction is relaxed a little, the selected speed level between 0-1 could be 60 while the route and alternative links remain the same.

In the literature, according to the objective functions and constraints, different types of VRP are found. However, the mostly papers that are related to our study are analyzed [6,12,13] review different types of VRP literature [14-16]. Also review the literature about green vehicle routing problem (G-VRP).

The aim of G-VRP is minimizing CO_2 emissions or fuel consumption [17]. Solve multi-objective G-VRP with the iterated local search algorithm. Cost, fuel consumption, and distance equity are considered as an objectives [18] add different carbon emission policies into the inventory routing problem with minimizing inventory holding cost, transportation cost, and fuel consumption cost [19]. Minimize operational and environmental costs for the green capacitated location-routing problem [20]. Study the time-dependent vehicle routing and scheduling problem to minimize CO_2 emissions and develop an exact dynamic programming algorithm [21] are also interested in carbon emission. Speed of vehicle is separated into ranges, and so model linearized [22]. Compares metaheuristic algorithms for time window G-VRP. When looking the results, greedy randomized adaptive search procedure (GRASP) and ant colony optimization (ACO) gives better results than tabu search (TS) and variable neighborhood search (VNS) [23]

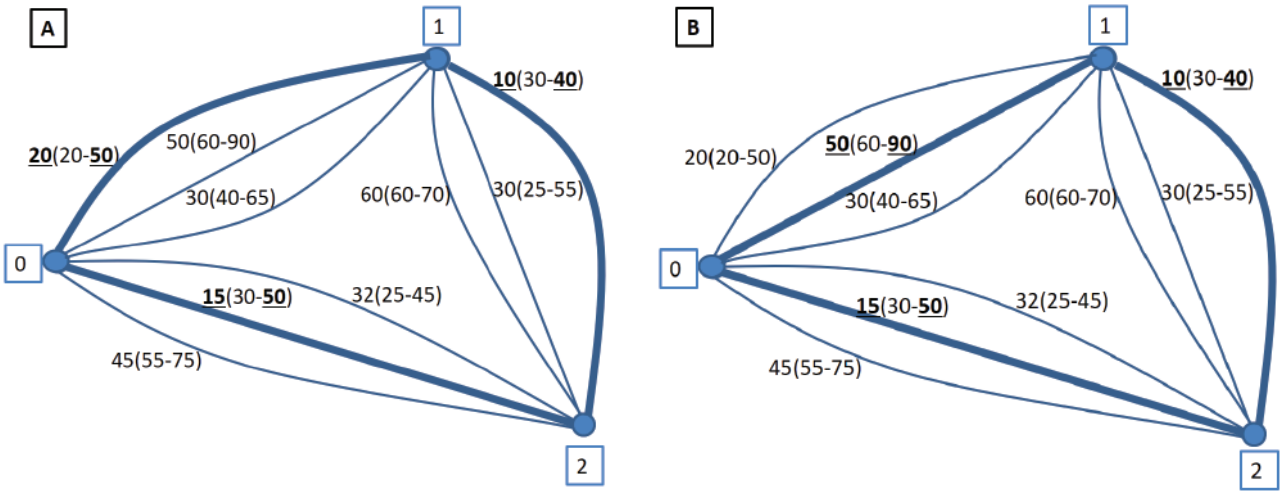


Figure 2. Selection of different links and speed levels.

measured releasing CO_2, NO_x, CO with time-dependent Open-VRP [24]. Minimize total fuel cost and driver cost with a heterogeneous vehicle fleet [5] analyze the relationship between load and CO_2 emissions using a heterogeneous fleet of vehicles. They show that, the used vehicle type, curb weight, and carried weight affect the fuel consumption used genetic algorithm and weighted superposition attraction algorithm to solve green VRP [25,26]. State that the vehicle type, speed, and load capacity affect the objective functions composed of distribution cost, customer satisfaction, and environmental pollution with adding time windows and heterogeneous vehicle fleet [27]. Also analyze the effect of different speed choices on fuel consumption and route times [28]. Study the time-dependent pollution routing problem to minimize total fuel cost and driver wages. They attract attention to rising driver wages because of low speeds in congested traffic at certain hours consider the green open vehicle routing problem with time windows [29].

Since the classical VRP is NP-Hard, heuristic and meta-heuristic methods are generally used in the literature to solve these problems [30]. States that the optimal solution is difficult to find with more than 10 nodes and thus presents an approximation algorithm for the solution of his models [31]. Develop an adaptive large neighborhood search (ALNS) heuristic for the pollution routing problem, and they offer a speed optimization algorithm to minimize fuel and driver costs [32]. Also employ an ALNS algorithm to solve a bi-objective pollution routing model that minimizes fuel consumption and delivery time [33]. Consider fuel emission cost and driver cost as an objective function of (G-VRP) with stochastic demands [34]. Hybridized genetic algorithm (GA) and VNS to cope with time-dependent GVRP with multiple depots and time windows [35]. Solves multi-objective GVRP fuzzy distances and split-delivery by using GA [36]. Solved multi depot green VRP with using ALNS. Two speeding up methods are used, and results are better than classic algorithm. As different perspective, [37] used multiple-depot to decrease carbon emission [38]. Combined GVRP with disassembly line problem. Several multi criteria decision making methods are used to determine best pareto optimal solutions [39]. Minimizes total cost and fuel consumption, and problem solves with strength pareto evolutionary algorithm (SPEA2) and Non-dominated Sorting-based Genetic Algorithm (NSGA-II). When comparing results, NSGA-II gives better results. As a different perspective, [40] considered the cost of perishable products along with the financial cost. To solve time-dependent GVRP, VNS and GA is hybridized [41]. Considered energy consumption, partial re-charging policy and carbon emissions simultaneously for Electric VRP, and ALNS and Cplex are used to solve the problem [42]. Used two construction algorithm and SA algorith to solve VRP with simultaneous linehauls and backhauls used GA and ACO to solve multi depot VRP [43].

In the literature, generally financial and environmental objectives are considered, and social considerations are studied less than others [44]. Considered economic, environmental, and social objectives simultaneously in facility location problem focus on environmental and social issues in multi-objective VRP [4]. Present an integer linear program for the balanced VRP and a rank-based ant system algorithm for the solution of their model [45,46]. Analyze a multi-depot vehicle routing problem with simultaneous pickup and delivery with the aim to have a balanced distribution of travels. They include the total routing cost, penalty cost for overworking of drivers, and fix costs of drivers' employment in their objective function [47]. Study a bi-objective capacitated general routing problem solved VRP with using Particle Swarm Optimization (PSO) and ACO that takes into account route balancing handeled fresh cut flowers delivering problem [48-50]. Initial solution is obtained with the path cheapest arc heuristic, after solution is improved with guided local earch algorithm. Different from classical algorithms, [50] used conditional neural heuristic algorithm to solve multi objective VRP. In addition, [51] used deep reinforcement learning based algorithm to solve green VRP.

Companies should regulate and comply with the laws of working and resting hours [52]. Notes that while regulations on drivers' working hours significantly affect total travel times, the vehicle routing literature has largely overlooked these restrictions. They describe the regulations for drivers' working hours in the European Union and present the vehicle routing problem considering these regulations [1]. Presents a model showing how driving periods, breaks, resting periods, and processing activities can be scheduled, and proposes a large neighbourhood search algorithm to create vehicle tours complying with the new regulations released by the European Union in 2007 [3]. And [2] also consider social legislations. [53] also study multi-objective GVRP as a financial, environmental and social objectives, and biased-randomized iterated greedy algorithm used to solve the problem. Financial cost consist of fixed vehicle costs, driver wages and fuel cost, the environmental cost is correlated with fuel consumption, and finally, social cost is accident risk cost.

In this study, like [10], and [11], minimizing the fuel cost, drivers cost, and fixed vehicle cost are considered as the financial objective for the company, minimizing the CO_2 emissions and oil usage are considered as the environmental objective, and the balancing drivers' working hours and adjusting route times are considered as the social objectives. Which routes, which alternative links, and which speed choices will be selected are determined by considering the financial, environmental, and social objectives. Although the problem is discussed in this study is the same as [11], unlikely, to solve middle and large data sets, and different scenarios, heuristic algorithms are used in this study.

In the next section, the problem is defined and model is explained. Then, in section 3, the Simulated Annealing (SA), and ALNS heuristic methods are presented to solve the problem. In section 4, numerical experiments with a discussion of the results are presented, and finally conclude our study in section 5.

PROBLEM DEFINITION AND MODEL

For a given set of n demand nodes and a depot, a directed graph is defined on these nodes. In the classical VRP problems, a single arc *(i, j)* is defined between a pair of nodes *i* and *j*. However, in our study, for more than one arc between each pair of nodes *i* and *j* is allowed, thus the notation (*i, j, k)* is used, where *k* denotes one of the alternative links between nodes *i* and *j*. Each link is assumed to have a distance denoted by d_{ijk}, and x_{ijk} denote the binary variable that is equal to 1 if a vehicle goes from *i* to *j* through link *k*. In addition, each vehicle can choose a different speed on each link and v_{ijkn} denotes the binary variable that is equal to 1 if a vehicle goes from *i* to *j* through link *k* at speed level *n*, and 0 otherwise. The possible speed levels that can be chosen at each arc are different from each other depending on the type of the arc. While vehicles can go at higher speeds on some arcs (i.e. highways), they need to choose slower speeds at others (i.e. inside the city). However, since faster roads might also be longer or more costly, the choice of the link depends on the parameters, constraints and the objectives of the problem. Even though different links have different characteristics, it is assumed that these characteristics are not time-dependent. Time-dependent speed choices and durations can be incorporated into the model, however since our focus is not on time-dependency, it is leaved for future studies as it makes the problem much more complicated and the solutions much harder to obtain.

In this model, each demand node *i* has a demand quantity, denoted by q_i, and if a demand node is visited, all of its demand needs to be delivered. In other words, partial delivery is not allowed. It is assumed a homogeneous fleet of vehicles and each vehicle is assumed to have a fixed capacity *Q*. In addition, time windows are considered in our problem, such that a delivery to a node *i* can only be made between times a_i and b_i, the earliest and latest service times for node *i*, respectively. If a truck arrives to a node before time a_i, it needs to wait there until time a_i, and it is not allowed to arrive a node *i* after time b_i. t_i is denoted the delivery service time at node *i,* such that each truck spends t_i time units at node *i* to make the deliveries. *RT* denotes the allowed regular time for a route and if the total duration of a route exceeds the value of *RT*, the drivers need to make overtime and an overtime cost is applied. The indices, parameters, decision variables of the model are defined in the [11] as follows:

Indices:

i, j: Indices used for demand nodes
k: Index used to denote alternative links between nodes
n: Index used to denote the speed level

Clusters:

N=(0,…*N*) Set of nodes, 0 denoting the depot
*N*0 = *N*/{0} Set of customers
Nh = Set of speed levels
K = Set of arcs
$\mathcal{A}$ =((i,j) : *i,j* ϵℕ and *i*≠*j*) Set of links between nodes

Parameters:

q_i: Quantity of demand at node *i*
a_i: the earliest service start time for node *i*
b_i: the latest service start time for node *i*
Q: Vehicle capacity
t_i: Service time for node *i*
m: Number of available vehicles
M: A large number used in modeling
f_v: Cost per vehicle used
f_d: Cost of overtime for drivers on a route per unit time
f_s: Cost of drivers/vehicles per unit time
f_e: Social cost of unbalanced routes per unit difference
f_a: Social cost of overtime per unit time
f_b: CO_2 emission(kg/lt)
d_{ijk}: Distance between node *i* and *j* through link *k*
S_{ijkn}: Speed level *n* at link k between nodes *i* and *j*
RT= Allowed regular time per route

Decision Variables:

$x_{ijk.}$ Binary variable equal to 1 if a vehicle goes from *i* to *j* through link *k*; 0 otherwise
v_{ijkn}: Binary variable equal to 1, if a vehicle goes from *i* to *j* through link *k* at speed level *n*; 0 otherwise
f_{ijk}: Flow carried from *i* to *j* through link *k*
y_i: Start time of service at node *i*
s_j: Total time of a route when *j* is the last node of the route
o_j: Amount of overtime on a route
e_{ij}: Difference between route times, when *i* and *j* are last nodes in two different routes
Z: Objective function.

It is known that the amount of fuel consumption depends on the speed of the vehicle, as well as the load of the vehicle, among others. Emissions and fuel consumption is computed using comprehensive modal emissions modelling (CMEM) developed by [54]. CMEM assumes that the vehicle is in a steady state between two consecutive locations and thus the vehicle's speed is assumed to be constant [55]. Examine the precision of carbon emission and fuel consumption calculations in green vehicle routing. Even though speed fluctuations and real life driving conditions are seen to have an impact on the results, CMEM computations are widely used in literature and generally thought to provide a good estimation of fuel consumption under realistic driving conditions. Thus, assuming that the vehicles maintain a constant speed between any two nodes, the average speed is used in our model as an approximation to the exact consumption values, which is a common approach in the literature [31]. Use CMEM and present the relationship between fuel consumption, speed and load. They calculate the amount of fuel consumption depending on the speed, load, and other factors as below:

$$f(v) = \lambda(\text{kNV+w}\gamma\alpha v + \gamma\alpha f v + \beta\gamma v^3)\frac{d}{v}$$

In the above relation, v denotes the speed, d denotes the distance, f denotes the load. In addition, $\lambda = \xi/\kappa\psi$, $\lambda = 1/1000\ n_{tf}\eta$, $\alpha = \tau + g\sin\theta + gC_r\cos\theta$, $\beta = 0.5\ C_d\rho A$ are the values calculated using the constants given in Table 1. Most of the data provided in Table 1 are obtained from [31]. It is assumed that the acceleration and the angle of the road denoted as τ and θ, respectively, are assumed to be 0.

Using the notation above and the decision variables in our model, the amount of fuel consumption is written as below:

$$\begin{aligned}\text{Fuel Consumption } (FC) = & \sum_{i,j,k,n} kNVd_{ijk}\frac{v_{ijkn}}{s_{ijkn}} \\ & + \sum_{ijk} w\gamma\alpha_{ijk}d_{ijk}x_{ijk} \\ & + \sum_{i,j,k} \gamma\lambda\alpha_{ijk}d_{ijk}f_{ijk} \\ & + \sum_{ijkn} \beta\gamma\lambda d_{ijk}v_{ijkn}(S_{ijkn})^2\end{aligned} \quad (1)$$

For the objective functions, financial, environmental, and social costs are considered in our model. The economic cost of fuel consumption (f_cFC), the cost for regular time, and overtime costs of drivers/vehicles ($f_s\Sigma_j s_j + f_d\Sigma_j o_j$), and the fixed cost for the number of drivers/vehicles used ($f_v\Sigma_{j\,\epsilon\,N0}\,x_{0jk}$) are considered as the financial cost. Since the amount of fuel consumption defines the CO_2 emissions, the environmental effect is calculated by multiplying FC with the emission factor, f_b. Thus, f_bFC is considered as the environmental cost.

For the social cost, the overtime of drivers is considred firstly, which is socially undesirable. As the working hours of the drivers' increase, they become more tired on the road and this will increase the risk of accidents. In addition, driving hour regulations in some countries enforce certain constraints on the tour durations. Even though tour durations are not considered as hard constraints in our model, as soft constraints such that any additional time over the regular working hours is penalized in the objective function is used. Thus, have as little overtime for the drivers as possible is aimed firstly. In addition, balanced route times between different drivers are desired. Unbalanced working hours lead to discussions between drivers and the company, and result in an unpleasant working environment. Sometimes drivers are paid by the duration of their services and the drivers who are assigned fewer driving hours than others tend to complain about the fairness of the managers. On the other hand, sometimes drivers who are assigned more driving hours also complain about the long working hours, especially when the additional payments they get do

Table 1. Definition of parameters and their values from real life data

Notation	Definition	Value
W	Curb-Weight (kg)	6350
Ξ	Fuel to air mass ratio	1
K	Engine friction factor (kilojoule/rev/litre)	0.2
N	Engine speed(rev/sn)	33
V	Engine displacement(liters)	5
G	Gravitational constant(meter/second^2)	9.81
C_d	Coefficient of aerodynamic drag	0.7
P	Air density (kg/m^3)	1.2041
A	Frontal surface area(m^2)	3.912
C_r	Coefficient of rolling distance	0.01
n_{tf}	Vehicle drive train efficiency	0.4
H	Efficiency parameter for diesel engines	0.9
f_b	CO_2 emissions per liter fuel used (kg	2.67
f_c	Fuel emissions cost per liter(TL)	5.81
f_a	Social cost of overtime per unit time(per second)	0.025
f_d	Overtime cost for drivers (TL per second)	0.0124
f_s	Regular time driver cost (TL per second)	0.0062
f_v	Fixed Vehicle Cost (TL)	200
Q	Vehicle Capacity (kg)	5500
K	Heating value of a typical diesel fuel(kilojoule/gr)	44
Ψ	Conversion factor(gram/second to liter/second)	737
T	Acceleration	0
θ	Road angle	0

not justify the additional working hours. Thus, have balanced durations between routes are aimed. The differences between the durations of the routes, denoted as e_{ij} where i and j are the last two nodes in two different routes are calculated, and s_i and s_j are the total time of a route. Include these values as social cost factors in the objective function in order to obtain more balanced routes. As a result, the social cost of overtime for drivers with the social cost of unbalanced routes ($f_a\Sigma_j o_j + f_e\Sigma_{i,j} e_{i,j}$) are considered as the social objectives to be minimized. Thus, the model is developed in a multi-objective setting as follows.

Objective functions:

$$\text{Min } Z_f = f_c FC + f_s \sum_j s_j + f_d \sum_j o_j + f_v \sum_{j \in N0} x_{0jk} \quad (2)$$

$$\text{Min } Z_e = f_b FC \quad (3)$$

$$\text{Min } Z_s = f_a \sum_j o_j + f_e \sum_{i,j} e_{ij} \quad (4)$$

Constraints:

$$\sum_{j \in N, k \in K} x_{0jk} \leq m \quad (5)$$

$$\sum_{j \in N, k \in K} x_{j0k} \leq m \quad (6)$$

$$\sum_{j \in N, k \in K} x_{ijk} = 1, \forall i \in N0 \quad (7)$$

$$\sum_{i \in N, k \in K} x_{ijk} = 1, \forall j \in N0 \quad (8)$$

$$\sum_{j \in N, k \in K} f_{jik} - \sum_{j \in N, k \in K} f_{ijk} = q_i, \forall i \in N0 \quad (9)$$

$$q_j x_{ijk} \leq f_{ijk} \leq (Q - q_i) x_{ijk}, \forall (i,j) \in \mathcal{A}, k \in K \quad (10)$$

$$y_i - y_j + t_i + \sum_{n \in Nh} d_{ijk} v_{ijkn} / S_{ijkn} \leq M(1 - x_{ijk}), \quad \forall i \in N, \forall j \in N0, i \neq j \quad (11)$$

$$y_j + t_j - s_j + \sum_{n \in Nh} d_{j0k} v_{j0kn} / S_{j0kn} \leq M(1 - x_{j0k}), \forall j \in N0 \quad (12)$$

$$a_i \leq y_i \leq b_i, \forall i \in N0 \quad (13)$$

$$\sum_{n \in Nh} v_{ijkn} = x_{ijk}, \forall (i,j) \in \mathcal{A} \quad (14)$$

$$o_j \geq (s_j - RT), \forall j \in N \quad (15)$$

$$s_i - s_j \leq e_{i,j} + M(1 - \sum_k x_{j0k}), \forall (i,j) \in N0 \quad (16)$$

$$s_j - s_i \leq e_{i,j} + M(1 - \sum_k x_{i0k}), \forall (i,j) \in N0 \quad (17)$$

$$f_{ijk} \geq 0, \forall (i,j) \in \mathcal{A}, k \in K \quad (18)$$

$$y_i \geq 0, \forall i \in N \quad (19)$$

$$o_j \geq 0, \forall j \in N0 \quad (20)$$

The objective function contains financial, environmental and social objectives. (2) represents the fuel cost, regular and overtime costs for routes and fixed vehicle costs as the financial cost, (3) represents emissions associated with the fuel consumption amount as the environmental cost, and (4) represents the overtime cost of drivers, and the penalty cost for imbalances between route times as the social cost.

Constraints (5-7) and (8) ensure that all vehicles leave from and return back to the depot, visiting each customer only once. (9) and (10) calculate the carried load at each node and make sure that each customer's demand is satisfied. They also eliminate sub-tour formations in the solution. (11) and (12) calculate the service time and total route time, respectively. (13) ensures time window constraints. (14) guarantees that one-speed level is selected for each arc. (15) calculates the overtime for each route. (16) and (17) calculate the differences between route times. Finally, (18-20) are nonnegativity constraints.

METAHEURISTIC ALGORITHM FOR VRP WITH ALTERNATIVE LINKS

Showed that middle VRP can not be solved for exact methods. Because of that, it is needed to heuristic methods. In literature, there are many heuristic methods for VRP [56-63], used SA for different kind of routing problems [36,41,64-66], used ALNS algorithm to solve VRP. In this study, because of giving good solution for combinatorial optimization problems, and remarkable success of ALNS and SA algorithms in routing problems, both of them are used to solve the problems. SA is a stochastic search method. It is inspired by the annealing process of solids. Solids heat until a definite temperature, it is kept this temperature for a while, and it cools slowly. Different temperatures and cooling rate can be used. SA is introduced by [67,68] modified LNS by using different searching methods, and named ALNS. In ALNS algorithm, probability of selecting a neighborhood changes according to past performance in the searching process. The detailed structure of ALNS is explained in the algorithm.

A mathematical model is used to solve this problem. For 20, 50, 75 and 100 nodes, and different scenarios are tried to

solve. But, the best solution can not be found within a time limit (3 hours). In our study, SA, and ALNS does not have start with a feasible solution. If a solution does not ensure constraints, penalty cost is incorporated into the objective function for each instance of infeasibility. Therefore, with every iteration, the result is close to a feasible solution. Initial solutions are generated using the Cheapest Insertion algorithm.

The Cheapest Insertion Algorithm

To find initial solution The Cheapest Insertion Algorithm (TCIA) is used. When starting with a better solution than a random solution, a better solution can be obtained with fewer iteration numbers. In addition, in most of the scenarios covered in this problem, there are time window constraints. In addition, a good solution based on a fit-only objective function may be far from a solution with time window constraints. With TCIA, compliance with time window constraints is also ensured. Initially, the vehicle starts the route from depot, and ends at the depot. Randomly a node is selected, and inserted to the route, and the best alternative link and speed is selected in accordance with the objective function. Until all nodes are inserted to the routes, every node is inserted between node *i* and *j*, and the objective function is calculated for every *i-j* position, and the best position is selected. This obtained solution is the initial solution of SA and ALNS.

Simulated Annealing Algorithm

Input: Demand, speed, distance, time windows, service time, initial temperature (T), cooling rate (t), iteration number (Y), and initial route values.

$X_{best} \leftarrow X_{now} \leftarrow X_{initial}$;
T=T;
While T<1
y=1;
for y=1 to Y
Generate X_{new}
If $X_{new} < X_{now}$;
$X_{now} \leftarrow X_{new}$;
Else if
$v = e^{-(X_{new} - X_{now})/T}$;
Generate a random value(a) $a \in [0,1]$;
If a<v;
$X_{now} \leftarrow X_{new}$;
End If
End If;
If $X_{now} < X_{best}$;
$X_{best} \leftarrow X_{now}$;
End If
y=y+1;
*T=T*t;*
Output: X_{best}

Adaptive Large Neighborhood Search

The ALNS algorithm has four main components in [69,70] and same format is followed.

Large neighborhoods: The current solution is changed by using seven neighborhood search procedures. These procedures are given in section 3.1. After modifying, the best link and speed levels are identified according to multi-objective functions. If there is any infeasibility due to capacity or time constraints, penalty cost is added to the objective function.

Adaptive search engine: In each iteration of the algorithm, the neighborhood search procedure is chosen using a roulette-wheel mechanism. Each neighborhood is assigned a weight, determining its probability of selection. After a certain iteration, the weight of neighborhood is changed according to past performance of the neighborhoods in selecting new current solutions. Let w_v be the weight of neighborhood v depending on its past performance. The neighborhood is selected with probability $w_v / \sum_{k=1}^{NoN} w_k$ (*NoN*: Number of Neighborhoods defined in algorithm).

Adaptive weight adjustment: Initially, each neighborhood has equal weight, and same probability of being selected. The iteration number of algorithm is divided into several phases that contains the same number of iterations named Ω. After finishing each phase, the weights of the neighborhoods w_v are updated as reported by their performance of the current phase. The performance of each neighborhood is represented by π_v, for neighborhood v. After finishing each iteration, the mark of the neighborhood selected at that iteration is updated as below, where α_1, α_2, α_3 are integer numbers that $\alpha_1 > \alpha_2 > \alpha_3$, x_{new} is the new solution, x_{best} is the best solution, x_{now} is the current solution, and z is the objective function to be minimized. Generally ALNS is used SA based algorithm.

if $z_{new} < z_{best}$:
π_v: $\pi_v + \alpha_1$
else if $z_{new} < z_{now}$:
π_v: $\pi_v + \alpha_2$
else if z_{new} is accepted as the next current solution by the SA criterion:
π_v: $\pi_v + \alpha_3$
else:
π_v: π_v
end if

The aim of this process is enhancing probability of selecting the neighborhood v with better solution. After finishing each phase the weights are updated as follows:

$$w_{v+1} = \begin{cases} w_{vj} & if\ o_{vj} = 0 \\ (1-\eta) w_{vj} + \frac{\eta \pi v}{o_{vj}} & otherwise \end{cases}$$

o_{vj} is the number of times neighborhood v is selected in the current phase j, and η is a controlling factor that affects the current weights. In our algorithm, the lenght of phase is 200, 300, 400 and 500 for 20, 50, 75 and 100 nodes respectively. The update score α_1, α_2, α_3 is 6, 4 and 2 respectively. The controlling factor η is 0.3. When η is greater than 0.3,

results are not of good quality. If η is less than 0.3, there will not be much difference between SA and ALNS.

Stopping criteria: Stopping criteria is defined as an cooling temperature.

Neighborhood Search Procedures

Different neighborhood structures are used in VRP to enhance the quality of the solution, [70] are used some destroy and repair procedures. Some of them are used in accordance with the problem.

Link-Speed Change: One route is selected, and one node is selected in that route. The best links and speed levels according to objective function between previous and next nodes are found and selected.

Interroute 1-0 move*:* As seen in Figure 3-A, different two routes are chosen, and two nodes are chosen each selected route. A node at the first route is taken out, and this node is added at the second route after the selected node.

Interroute 1-1 exchange: As seen in Figure 3-B, different two routes are chosen, and two nodes are chosen for each selected route. These nodes are swapped.

Interrote 1-1-1 rotation: As seen in Figure 3-C, different three routes are chosen, and three nodes are chosen for each selected route. These nodes are swapped.

Swap: As seen in Figure 3-D, one route is selected, and one node is selected in that route. Swap two nodes (before and after node of the selected node).

Interroute 2-opt move: Two different routes are selected, and two nodes are chosen from each route. All the nodes following the chosen nodes are then swapped between the routes. A new objective function(X_{new}) value is calculated. For example, routes are: 0-1-2-3-4-0, and, 0-5-6-7-8-0, after procedure new routes are: 0-1-2-7-8-0, 0-5-6-3-4-0.

Intraroute 2-Opt: As seen in Figure 3-E, one route is selected, and two-node is selected in that route. Those nodes between two nodes are reversed, ann connected again. For example, the route is: 0-1-2-3-4-5-6-0. 2 and 5 are selected. 2-3-4-5 is reversed, turned to 5-4-3-2, and connected again. Finally, route is 0-1-5-4-3-2-6-0.

After implied neighborhood searching procedures, at new routes, the best link and speed levels between previous and next nodes are calculated and selected according to the multi-objective functions. According to link and speed values, the earliest starting service time is specified. If the starting service time exceeds the latest starting service time, the penalty cost is added to the objective function. Also, the new total demand of routes is calculated. If total demand exceeds the vehicle capacity the penalty cost is added to the objective function.

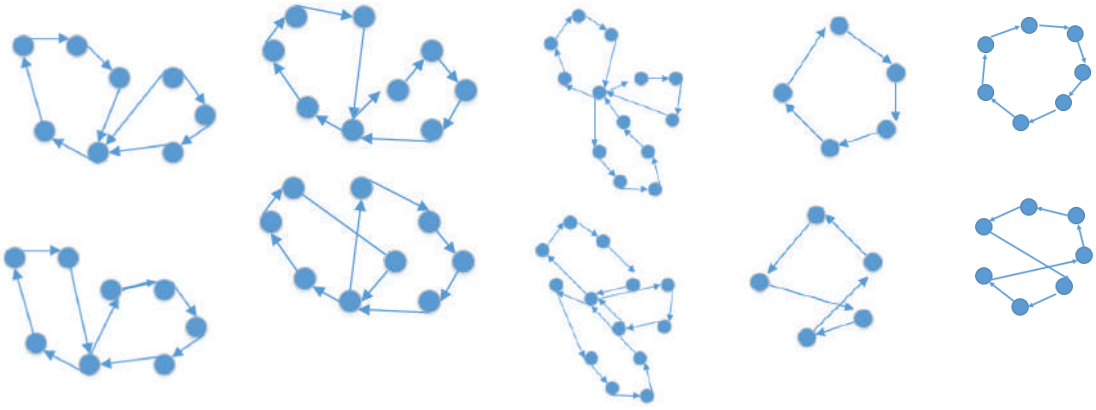
NUMERICAL RESULTS AND DISCUSSION

In this section, the computational results of the models are presented and explained above under different parameter settings. All the results in this section are obtained by solving the models using GAMS with the solver Cplex on a workstation with an Intel(R) Xeon(R) CPU E5-1650 v2 @ 3.50GHz, and 16 GB of RAM.

[11], find optimal solution of 10 nodes. But, for larger problems, optimal solutions can not be found within a reasonable time limit by using GAMS, Cplex solver. Because of that, in this study, 20, 50, 75 and 100 nodes are tried to solve using SA and ALNS.

In this case studies, a logistics company that serves different customers in Turkey at various locations and needs to deliver the products in the required time windows is considered. In all of models in this study, the same parameters are used as in the previous section and the data given in Table 1.

In addition to the real-life data given in Table 1, it is assumed that RT=9 hours, t_i=20 minutes for all nodes i, and f_a=1.5 Turkish Lira (TL) per minute. Different scenarios are considered as explained below and the results of each



A. 1-0 Move | **B**. Interroute 1-1 exchange | **C.** Interroute 1-1-1 rotation | **D**. Swap | **E.** Intraroute 2-Opt move

Figure 3. Neighborhood structures.

scenario for 20, 50, 75 and 100 nodes respectively are presented in Table 2, Table 3, Table 4 and Table 5.

The flexible time window is between 0 and 10 hours for all customers. For base case time windows there are 3-4 hours between early and late starting service times for these customers. In strict time windows, there are 2-3 hours between early and late starting time windows.

For SA, T is used as a 300, t is 0.9, and y depends on the customer dimension, 1200, 1400, 1500 and 1800, is used for 20, 50, 75 and 100 nodes respectively. For each sample, SA was run 10 times and the best result is given. One cycle for 20 nodes is completed in an average of 180 seconds. For 50,75 and 100 nodes, this time averages 310, 500, and 620 seconds, respectively.

For ALNS algorithm, T is used 900, t is 0.98, and y 200, 300, 400 and 500 for 20, 50, 75 and 100 nodes respectively. Since the weights of the neighborhood structures change after each phase, the number of iterations at each temperature is not increased much, the starting temperature of the algorithm is increased when comparing SA. When ALNS and SA are runned at the same iteration ALNS does not give close results to SA. Therefore, cooling temperature to stop is decreased, and iteration number is increased. When results does not change, it is stopped. Solution times of ALNS are 200, 320, 600, 800 seconds for 20, 50, 75 and 100 nodes respectively.

When number of nodes increases, problem can not be solved with exact methods, and GAP becomes so large. In addition, increasing the cost multiplier greatly increases the value of GAP. For exact method, 3 hours time limit is used. GAP values obtained with GAMS-Cplex solver are 12.8%, 17.5%, 7.36%, 15.8%, 32%, 94.6%, 97%, 90% for scenarios of 20 nodes respectively. As the number of nodes increases, larger GAP values appear. In this situation, the quality of metaheuristic algorithms are not compared with these GAP values. All of the samples the best results are obtained with SA. Therefore, Relative GAP is calculated, and results are compared according to SA. Result of SA is expressed by z_1, and to calculate relative gap of ALNS z_2 is expressed the result of ALNS, and to calculate GAP of CPLEX, z_2 is expressed the result of CPLEX. Relative GAP is given in equation 4.1.

$$Relative\ gap = \frac{z_2 - z_1}{z_1}.100 \tag{4.1}$$

A larger number of customers and present the results for N=20, N=50, N=75, and N=100 customers, results of SA, relative gap of SA, results of ALNS, relative gap of ALNS, results of Cplex, and relative gap of Cplex are given in Table 2, respectively.

Table 2. Results of 20 nodes

Scenarios	Results of SA	Relative Gap of SA (%)	Results of ALNS	Relative Gap of ALNS (%)	Results of Cplex	Relative Gap of Cplex (%)
Base case	**2135**	0%	2143	0.37%	2140	0.23%
Flexible time windows	**1937**	0%	1940	0.15%	1945	0.41%
Strict Time windows (STW)	**2281**	0%	2351	3.05%	2287	0.26%
Base case, and RT=8	**2145**	0%	2152	0.32%	2153	0.37%
Base case, and RT=6	**2650**	0%	2698	1.81%	2704	2.03%
Base case, RT=6 and f_d=3	**33404**	0%	34057	1.95%	33460	0.16%
Base case, RT=6 and f_d=6	**63967**	0%	65562	2.49%	63987	0.03%
Base case, RT=6, f_d=6 and f_s=0.744	**118910**	0%	119180	0.22%	127843	7.51%

Table 3. Results of 50 nodes

Scenarios	Results of SA	Relative Gap of SA (%)	Results of ALNS	Relative Gap of ALNS (%)	Results of Cplex	Relative Gap of Cplex (%)
Base Case	**4065**	0%	4642	14.2%	4170	2.58%
Flexible time windows	**3616**	0%	3765	4.13%	3675	1.62%
Strict time windows	**4492**	0%	4953	10.26%	4515	0.51%
Base case, and RT=8	**4316**	0%	4844	12.21%	4585	6.23%
Base case, and RT=6	**5582**	0%	6387	14.42%	5673	1.63%
Base case, RT=6 and f_d=3	**107997**	0%	118556	9.77%	118209	9.45%
Base case, RT=6 and f_d=6	**202765**	0%	222827	9.89%	211385	4.25%
Base case, RT=6, f_d=6 and f_s=0.744	**329996**	0%	355591	7.75%	390714	18.39%

Table 4. Results of 75 nodes

Scenarios	Results of SA	Relative Gap of SA (%)	Results of ALNS	Relative Gap of ALNS (%)	Results of Cplex	Relative Gap of Cplex (%)
Base case	**5288**	0%	5827	10.2%	5937	12.28%
Flexible time windows	**5336**	0%	5776	8.22%	5510	3.24%
Strict time windows	**5993**	0%	7040	17.4%	6088	1.58%
Base case, and RT=8	**5896**	0%	6692	13.4%	5989	1.57%
Base case, and RT=6	**7002**	0%	8542	21.9%	8701	24.2%
Base case, RT=6 and f_d=3	**60462**	0%	78181	29.3%	93449	54.5%
Base case, RT=6 and f_d=6	**108752**	0%	142316	30.8%	151305	39.1%
Base case, RT=6, f_d=6 and f_s=0.744	**274577**	0%	360975	31.1%	347961	26.7%

Table 5. Results of 100 nodes

Scenarios	Results of SA	Relative Gap of SA (%)	Results of ALNS	Relative Gap of ALNS (%)	Results of Cplex	Relative Gap of Cplex (%)
Base case	**7450**	0%	8599	15.42%	10285	38.05%
Flexible time windows	**6982**	0%	7797	11.6%	7859	12.56%
Strict time windows	**7706**	0%	9291	20.57%	10608	37.65%
Base case, and RT=8	**7488**	0%	8901	18.86%	9080	21.25%
Base case, and RT=6	**8719**	0%	11203	28.48%	12172	39.59%
Base case, RT=6 and f_d=3	**80447**	0%	107086	33.11%	182031	126.44%
Base case, RT=6 and f_d=6	**132517**	0%	191183	44.26%	343189	158.97%
Base case, RT=6, f_d=6 and f_s=0.744	**329535**	0%	425075	28.99%	601155	82.42%

When the exact solution method is compared with the heuristic methods, it is seen that the heuristic methods achieve better results in a shorter time than the exact solution method in every sample and scenario. In addition, all of the samples SA gives better results than ALNS. Solution time of ALNS and SA are close to each other. As seen in Table 2, relative gap of ALNS are close to results of SA. When looking at the results obtained with ALNS and Cplex for larger samples, it is seen that the relative gap value increases. Looking at the results in Tables 2-5, it is observed that the gap value obtained in scenarios with flexible time windows is lower than in other scenarios. The increase in cost parameters also increased the gap value. Generally, the best solutions found are obtained by SA. When the results obtained with ALNS and the exact solution method are compared, in some examples the ALNS, and in some examples the exact solution method give better results than other.

CONCLUSION

The vehicle routing problem on a network with multiple alternative links between nodes, considering the three main pillars of sustainability; financial, environmental and social are analyzed. The optimal routes are determined to deliver the goods to a set of customers in order to minimize the delivery cost for the company, minimize the gas emissions to decrease environmental effects and improve the working conditions for drivers. A multi objective mixed integer linear model for this problem is solved with simulated annealing and adaptive large neighborhood solutions algorithms.

The shortest path or the fastest path may not always be chosen according to the objective functions and constraints discussed in the problem. When the financial, environmental and social objectives are considered together, it is seen that alternative links and speed levels are also chosen. Even though the optimal solution is obtained for small sized problems, as the problem size increases, the optimal solution could not be obtained in a reasonable time limit. Therefore, heuristic methods are used to solve problem in resonable time limit. Simulated annealing is easily implemented, and in a short time, good solution can be attained. To compare quality of results, adaptive large neighborhood solutions is used to solve same problem. Examples of 20, 50, 75 and 100 node sizes are prepared and 8 scenarios are created using different parameters for each size. Different problem sizes and scenarios are solved, and for all of the samples, Simualted Annealing gives better results in a

shorter time than adaptive large neighborhood solutions. It is seen that as the problem size increases, the gap values increase in the results obtained with the exact solution method.

Time-dependent speed choices and durations can be incorporated into the model in the future. In addition, stochastic versions of this problem in which the durations or speeds are random due to unknown traffic conditions, can be analyzed. In recent years, algorithms using artificial intelligence have begun to be used to solve vehicle routing problems. Algorithms using artificial intelligence can also be used to solve this problem. The production and use of electric vehicles has increased in recent years. The energy consumption of these vehicles can be handled with the same objectives and constraints. Finally, several extensions of this vehicle routing problem such as using heterogeneous fleet of vehicles, multiple depots etc. can be analyzed in future studies.

AUTHORSHIP CONTRIBUTIONS

Authors equally contributed to this work.

DATA AVAILABILITY STATEMENT

The authors confirm that the data that supports the findings of this study are available within the article. Raw data that support the finding of this study are available from the corresponding author, upon reasonable request.

CONFLICT OF INTEREST

The author declared no potential conflicts of interest with respect to the research, authorship, and/or publication of this article.

ETHICS

There are no ethical issues with the publication of this manuscript.

STATEMENT ON THE USE OF ARTIFICIAL INTELLIGENCE

Artificial intelligence was not used in the preparation of the article.

REFERENCES

[1] Goel A. Vehicle scheduling and routing with drivers' working hours. Transp Sci 2009;43:17–26. [CrossRef]

[2] Kok AL, Meyer CM, Kopfer H, Schutten JMJ. A dynamic programming heuristic for the vehicle routing problem with time windows and European Community social legislation. Transp Sci 2010;44:442–454. [CrossRef]

[3] Gagnon EP, Desaulniers G, Drexl M, Rousseau LM. European driver rules in vehicle routing with time windows. Transp Sci 2010;44:455–473. [CrossRef]

[4] Eguia I, Racero J, Molina JC, Guerrero F. Environmental issues in vehicle routing problems. In: Erechtchoukova MG, et al., editors. Sustainability Appraisal: Quantitative Methods and Mathematical Techniques for Environmental Performance Evaluation. Berlin: Springer-Verlag; 2013. [CrossRef]

[5] Kopfer HW, Schönberger J, Kopfer H. Reducing greenhouse gas emissions of a heterogeneous vehicle fleet. Flex Serv Manuf J 2013;26:221–248. [CrossRef]

[6] Lin C, Choy KL, Ho GTS, Chung SH, Lam HY. Survey of green vehicle routing problem: Past and future trends. Expert Syst Appl 2014;41:1118–1138. [CrossRef]

[7] Toth P, Vigo D, editors. The Vehicle Routing Problem. Society for Industrial and Applied Mathematics; 2002. [CrossRef]

[8] Fisher M. Vehicle routing. In: Ball MO, Magnanti T, Monma C, Nemhauser G, editors. Handbooks in Operations Research and Management Science. Vol. 8. Elsevier; 1995. p. 1–33.

[9] Garaix T, Artigues C, Feillet D, Josselin D. Vehicle routing problem with alternative paths, an application to on-demand transportation. Eur J Oper Res 2010;204:62–75. [CrossRef]

[10] Tukenmez I. Vehicle routing problem with alternative links from the triple bottom line accounting perspective [Master's thesis]. Eskişehir: Anadolu University; 2017.

[11] Tukenmez I, Kaya O. A sustainable vehicle routing problem with alternative road and speed options. J Fac Eng Archit Gazi Univ 2021;36:2037–2051. [CrossRef]

[12] Kim G, Ong YS, Heng CK, Tan PS, Zhang NA. City vehicle routing problem. IEEE Trans Intell Transp Syst 2015;16:1654–1666. [CrossRef]

[13] Mor A, Speranza MG. Vehicle routing problems over time: A survey. Ann Oper Res 2022;314:255–275. [CrossRef]

[14] Asghari M, Al-e-hashel SMJM. Green vehicle routing problem: A state of the art review. Int J Prod Econ 2021;231:107899. [CrossRef]

[15] Moghdani R, Salimifard K, Demir E, Benyettou A. The green vehicle routing problem: A systematic literature review. J Clean Prod 2021;279:123691. [CrossRef]

[16] Sabet A, Farooq B. Green vehicle routing problem: State of the art and future directions. IEEE Access 2022;10:8544–8569. [CrossRef]

[17] Londono JFC, Rendon RAG, Ocampo T. Iterated local search multi-objective methodology for the green vehicle routing problem considering workload equity with a private fleet and a common carrier. Int J Ind Eng Comput 2021;12:115–130. [CrossRef]

[18] Cheng C, Qi M, Wang X, Zhang Y. Multi-period inventory routing problem under carbon emission regulations. Int J Prod Econ 2016;182:263–275. [CrossRef]

[19] Toro EM, Franco JF, Echeverri MG, Guimaraes FG. A multi-objective model for the green capacitated location-routing problem considering environmental impact. Comput Ind Eng 2017;110:114–125. [CrossRef]

[20] Xiao Y, Konak A. A genetic algorithm with exact dynamic programming for the green vehicle routing & scheduling problem. J Clean Prod 2017;167:1450–1463. [CrossRef]

[21] Cai L, Lv W, Xiao L, Xu Z. Total carbon emissions minimization in connected and automated vehicle routing problem with speed variables. Expert Syst Appl 2021;165:113910. [CrossRef]

[22] Prakash R, Pushkar S. Green vehicle routing problem: Metaheuristic solution with time window. Expert Syst 2022;39:e13007. [CrossRef]

[23] Naderipour M, Alinaghian M. Measurement, evaluation and minimization of CO2, NOx and CO emission in the open time dependent vehicle routing problem. Measurement 2016;90:443–452. [CrossRef]

[24] Koç Ç, Bektaş T, Jabali O, Laporte G. The fleet size and mix pollution-routing problem. Transp Res Part B Methodol 2014;70:239–254. [CrossRef]

[25] Boz E, Çalık A, Şahin Y. Solution approaches for the green vehicle routing problem with time window and simultaneous pickup and delivery. J Fac Eng Archit Gazi Univ 2024;39:757–770. [CrossRef]

[26] Yang B, Hu ZH, Wei C, Li SQ, Zhao L, Jia S. Routing with time-windows for multiple environmental vehicle types. Comput Ind Eng 2015;89:150–161. [CrossRef]

[27] Maden W, Eglese R, Black D. Vehicle routing and scheduling with time-varying data: A case study. J Oper Res Soc 2010;61:515–522. [CrossRef]

[28] Franceschetti A, Honhon D, Van Woensel T, Bektaş T, Laporte G. The time dependent pollution-routing problem. Transp Res Part B Methodol 2013;56:265–293. [CrossRef]

[29] Niu Y, Yang Z, Chen P, Xiao J. Optimizing the green open vehicle routing problem with time windows by minimizing comprehensive routing cost. J Clean Prod 2018;171:962–971. [CrossRef]

[30] Suzuki Y. A new truck-routing approach for reducing fuel consumption and pollutants emission. Transp Res Part D Transp Environ 2011;16:73–77. [CrossRef]

[31] Demir E, Bektaş T, Laporte G. An adaptive large neighborhood search heuristic for the pollution-routing problem. Eur J Oper Res 2012;223:346–359. [CrossRef]

[32] Demir E, Bektaş T, Laporte G. The bi-objective pollution routing problem. Eur J Oper Res 2014;232:464–478. [CrossRef]

[33] Niu Y, Zhang Y, Cao Z, Gao K, Xiao J, Song W, et al. MIMOA: A membrane-inspired multi-objective algorithm for green vehicle routing problem with stochastic demands. Swarm Evol Comput 2021;60:100767. [CrossRef]

[34] Fan H, Zhang Y, Tian P, Lv Y, Fan H. Time-dependent multi-depot green vehicle routing problem with time windows considering temporal-spatial distance. Comput Oper Res 2021;129:105211. [CrossRef]

[35] Gupta P, Govindan K, Mehlawat MK, Khaitan A. Multiobjective capacitated green vehicle routing problem with fuzzy time-distances and demands split into bags. Int J Prod Res 2021. doi: 10.1080/00207543.2021.1888392. [Epub ahead of print].

[36] Wen M, Sun W, Yu Y, Tang J, Ikou K. An adaptive large neighborhood search for the larger-scale multi depot green vehicle routing problem with time windows. J Clean Prod 2022;374:133916. [CrossRef]

[37] Wang S, Han C, Yu Y, Huang M, Sun W, Kaku I. Reducing carbon emissions for the vehicle routing problem by utilizing multiple depots. Sustainability 2022;14:1264. [CrossRef]

[38] Durmaz N, Budak A. An integrated bi-objective green vehicle routing and partial disassembly line problem for electronic waste: An industrial case study. Int J Comput Integr Manuf 2024. doi: 10.1080/0951192X.2023.2285188. [Epub ahead of print].

[39] Dutta J, Barma PS, Mukherjee A, Kar S, De T. A hybrid multi-objective evolutionary algorithm for open vehicle routing problem through cluster primary-route secondary approach. Int J Manag Sci Eng Manag 2021;17:34-47. [CrossRef]

[40] Wu D, Wu C. TDGVRPSTW of fresh agricultural products distribution: Considering both economic cost and environmental cost. Appl Sci 2021;11:10579. [CrossRef]

[41] Yu VF, Jodiawan P, Gunawan A. An adaptive large neighborhood search for the green mixed fleet vehicle routing problem with realistic energy consumption and partial recharges. Appl Soft Comput 2021;105:107251. [CrossRef]

[42] Demirbilek M. A metaheuristic solution approach with two construction heuristics for vehicle routing problem with simultaneous linehauls and backhauls. Sigma J Eng Nat Sci 2021;39:226–236. [CrossRef]

[43] Yücenur GN, Çetin Demirel N. A hybrid algorithm with genetic algorithm and ant colony optimization for solving multi-depot vehicle routing problem. J Eng Nat Sci Sigma 2011;29:340–350.

[44] Anvari S, Turkay M. The facility location problem from the perspective of triple bottom line accounting of sustainability. Int J Prod Res 2017;55:6266–6287. [CrossRef]

[45] Yousefikhoshbakht M, Didehvar F, Rahmati F. An effective rank based ant system algorithm for solving the balanced vehicle routing problem. Int J Ind Eng 2016;23.

[46] Koulaeian M, Seidgar H, Kiani M, Fazlollahtabar H. A multi depot simultaneous pickup and delivery problem with balanced allocation of routes to drivers. Int J Ind Eng 2015;22:223–242.
[47] Halvorsen-Weare EE, Savelsbergh MWP. The bi-objective mixed capacitated general routing problem with different route balance criteria. Eur J Oper Res 2016;251:451–465. [CrossRef]
[48] Huang SH, Huang YH, Lee HC, Tong YY. A new hybrid algorithm for solving the vehicle routing problem with route balancing. Int J Ind Eng Manag 2023;14:51–62. [CrossRef]
[49] Rodrigo S, Kosgoda D, Fernando WM, Nielsen P, Thibbotuwawa A. Optimizing fresh-cut flower distribution using the vehicle routing problem for perishable goods. Sci J Logist 2024;20:23–37. [CrossRef]
[50] Fan M, Wu Y, Cao Z, Song W, Sartoretti G, Liu H, et al. Conditional neural heuristic for multiobjective vehicle routing problem. IEEE Trans Neural Netw Learn Syst 2024. doi: 10.1109/TNNLS.2023.3343467. [Epub ahead of print].
[51] Yue B, Ma J, Shi J, Yang J. A deep reinforcement learning-based adaptive search for solving time-dependent green vehicle routing problem. IEEE Access 2024;12:2855–2867. [CrossRef]
[52] Goel A, Gruhn V. Drivers' working hours in vehicle routing and scheduling. In: Proceedings of the 2006 IEEE Intelligent Transportation Systems Conference; 2006 Sep 17-20; Toronto, Canada. IEEE; 2006. [CrossRef]
[53] Abdullahi H, Reyes-Rubiano L, Ouelhadj D, Faulin J, Juan AA. Modelling and multi-criteria analysis of the sustainability dimensions for the green vehicle routing problem. Eur J Oper Res 2021;292:143–154. [CrossRef]
[54] Barth M, Younglove T, Scora G. Development of a heavy-duty diesel modal emissions and fuel consumption model. Technical report. California Partners for Advanced Transit and Highways (PATH); 2005. Available at: http://escholarship.org/uc/item/67f0v3zf. Accessed on January 22, 2026.
[55] Turkensteen M. The accuracy of carbon emission and fuel consumption computations in green vehicle routing. Eur J Oper Res 2017;262:647–659. [CrossRef]
[56] Bektaş T, Laporte G. The pollution-routing problem. Transp Res Part B Methodol 2011;45:1232–1250. [CrossRef]
[57] Ferreira KM, Queiroz TA. A simulated annealing based heuristic for a location-routing problem with two-dimensional loading constraints. Appl Soft Comput 2022;118:108443. [CrossRef]
[58] İlhan İ. An improved simulated annealing algorithm with crossover operator for capacitated vehicle routing problem. Swarm Evol Comput 2021;64:100991. [CrossRef]
[59] Kancharla SR, Ramadurai G. Simulated annealing algorithm for multi depot two-echelon capacitated vehicle routing problem. Eur Transp 2020;78. [CrossRef]
[60] Rabbouch B, Saadaoui F, Mraihi R. Empirical-type simulated annealing for solving the capacitated vehicle routing problem. J Exp Theor Artif Intell 2021;33:179-197.
[61] Yu VF, Redi AANP, Hidayat YA, Wibowo OJ. A simulated annealing heuristic for the hybrid vehicle routing problem. Appl Soft Comput 2017;53:119–132. [CrossRef]
[62] Chiang W, Russell RA. Simulated annealing metaheuristic for the vehicle routing problem with time windows. Ann Oper Res 1996;63:3–27. [CrossRef]
[63] Kesen SE, Alim M. Solution approaches for mixed pallet collection problem: A case study in a logistics company. Sigma J Eng Nat Sci 2019;37:827–840.
[64] Alinaghian M, Shokouhi N. Multi-depot multi-compartment vehicle routing problem, solved by a hybrid adaptive large neighborhood search. Omega 2018;76:85–99. [CrossRef]
[65] Azi N, Gendreau M, Potvin JY. An adaptive large neighborhood search for a vehicle routing problem with multiple routes. Comput Oper Res 2014;41:167–173. [CrossRef]
[66] Alinaghian M, Jamshidian M, Tirkolaee EB. The time dependent multi-depot fleet size and mix green vehicle routing problem: Improved adaptive large neighborhood search. Optimization 2022;71:3165–3193. [CrossRef]
[67] Kirkpatrick S, Gelatt CD, Vecchi MP. Optimization by simulated annealing. Science 1983;220:671–680. [CrossRef]
[68] Ropke S, Pisinger D. An adaptive large neighborhood search heuristic for the pickup and delivery problem with time windows. Transp Sci 2006;40:455–472. [CrossRef]
[69] Coelho LC, Cordeau JF, Laporte G. The inventory-routing problem with transshipment. Comput Oper Res 2012;39:2537–2548. [CrossRef]
[70] Aksen D, Kaya O, Salman FS, Tüncel Ö. An adaptive large neighborhood search algorithm for a selective and periodic inventory routing problem. Eur J Oper Res 2014;239:413–426. [CrossRef]

Sigma J Eng Nat Sci, Vol. 44, No. 1, pp. 153–161, February, 2026

Sigma Journal of Engineering and Natural Sciences
Web page info: https://sigma.yildiz.edu.tr
DOI: 10.14744/sigma.2025.00056

Research Article

Electricity energy consumption forecasting using LSTM and NAR

Parastou BEHGOUY[1,*], Abbas UĞURENVER[2]

[1]Institute of Graduate Studies, Department of Electrical and Electronic Engineering, Istanbul Aydın University, Istanbul, 34295, Türkiye

ARTICLE INFO

Article history
Received: 21 July 2024
Revised: 18 September 2024
Accepted: 13 January 2025

Keywords:
Deep Neural Network; Energy Consumption; Forecasting; Energy Efficiency; Long Short-term Memory; LSTM; NAR Neural Network; Nonlinear Autoregressive; Time Series Analysis

ABSTRACT

Energy management systems (EMS) have gained importance in reducing energy waste and overconsumption. One critical component of effective EMS is long-term electricity consumption forecasting, which helps estimate energy demand and provides a general view of the future for macro-level planning. To achieve this, accurate predictions are essential for developing efficient energy plans. Consequently, machine learning models have garnered significant attention in recent decades due to their ability to address these challenges. These models, artificial neural networks with deep structures, are particularly effective, as they can analyze large volumes of data and provide accurate forecasts, even when the data exhibits complex, non-linear patterns. In this study, long-term electrical energy consumption has been forecasted using MATLAB software according to the past trend of consumption with long short-term memory (LSTM) and nonlinear autoregressive (NAR) neural networks. Monthly energy consumption data between 1973-2022 in USA was used as the data set.

The assessment metrics used for both networks included Mean Absolute Percentage Error (MAPE), Symmetric Mean Absolute Percentage Error (SMAPE), Root Mean Square Error (RMSE), Mean Absolute Error (MAE), Mean Bias Error (MBE), and the Coefficient of Determination (R^2). These metrics were calculated to evaluate the performance and accuracy of the networks. The fewer error values and the higher value of Coefficient of determination (R^2 =0.9318) in LSTM show more accuracy in this network when it's compared with NAR (R^2 =0.6387). The same situation with the Root Mean Square Error witch it shows that the LSTM gives better results (RMSE =8.8033) than the NAR (RMSE =20.1971).

The results show LSTM network has better performance and can produce more accurate output because of its structure which has short-term and long-term memories that make it able to remember information for long periods and has feedback connections. In fact, LSTM is a high-performance nonlinear predictor.

Cite this article as: Behgouy P, Uğurenver A. Electricity energy consumption forecasting using LSTM and NAR. Sigma J Eng Nat Sci 2026;44(1):153–161.

***Corresponding author.**
*E-mail address: parastoubehgouy@stu.aydin.edu.tr

This paper was recommended for publication in revised form by Editor-in-Chief Ahmet Selim Dalkilic

Published by Yıldız Technical University Press, İstanbul, Turkey
© Author. This is an open access article under the CC BY-NC license (http://creativecommons.org/licenses/by-nc/4.0/).

INTRODUCTION

Global electricity consumption has been raised rapidly because of population growth and technology development [1], the energy management system (EMS) has gained importance to reduce waste of energy and energy overconsumption. Energy consumption forecasting has an important role in EMS [2,3] and accurate prediction is essential to achieve energy efficiency.

So far different type of techniques have been proposed as predictive model to forecast the future behavior of the system, Statistical approach such as SARIMA, ARMA, DLM, Holt–Winters, artificial neural networks including multilayer perceptron [4], physical models and also hybrid techniques. Machine learning (ML) as data-driven models has been realized the most accurate technique to obtain acceptable output in forecasting [5-7]. expresses artificial neural networks have perfect performance if there is sufficient data to train the models.

Recently, researchers have been attracted to deep learning networks because of their ability to receive and analyze data when they follow complex non-linear patterns and have a large volume [8,9]. Deep learning has provided significant progress in energy forecasting. These networks have created more innovative research opportunities that increase prediction accuracy [10].

Convolutional neural network with deep structure is presented in [11], which has been able to improve the electricity consumption estimation compared to the seasonal ARIMAX method. The results show that the accuracy of the deep neural network is higher than the ARIMAX. Another study shows the Solar radiation forecasting by using deep neural networks (ARIMAX method) in Eskisehir, Türkiye [12]. A hybrid LSTM model integrated with a stationary wavelet transform (SWT) has demonstrated efficacy in rectifying abnormalities in home energy use, hence enhancing forecast precision in both the short and long term [13]. Another study comparing LSTM, GRU, and Drop-GRU models revealed that LSTM excels above the other models in handling long-term dependencies and nonlinearities in energy data [14]. The integration of CNN with LSTM improves prediction by effectively capturing both geographical and temporal data, as evidenced in a study on multivariate energy use [15]. The efficacy of LSTM in time series analysis was demonstrated in a study that investigated data quality and hyperparameter optimization, highlighting the significance of preprocessing for precision [16,17] Indicates comparison of LSTM neural network and ARIMA for energy consumption forecasting. The result expresses this network is more accurate than statistical estimation methods such as ARIMA. Also, LSTM neural networks are more accurate than non-deep artificial neural networks for prediction. Overfitting may occur during the training process by adding layers in LSTM neural networks. This problem is a challenge in deep neural networks. In fact, if the number of layers increases regardless of the evaluation step error, the prediction error will increase. The over-fitting issue could be solved by increasing data diversity and volume [18]. In conclusion, LSTM and its derivatives exhibit significant adaptability to various prediction tasks, offering solid solutions for dynamic energy systems. The results illustrate the capability of sophisticated machine learning algorithms to tackle issues in energy consumption predictions with significant accuracy and generalizability.

In this research, long-term electrical energy consumption is forecasted by LSTM and NAR neural networks using MATLAB software. Monthly energy consumption data from 1973-2022 in USA was used as the data set and the accuracy of the implemented networks was compared. There were different types of studies like the work of this paper. For example, in [19] the LSTM and NAR were used to forecast monthly smoothed sunspot number time series. In [20], The LSTM and NAR have been used to predict the wind turbine's generated power. Also, in [21] the LSTM and NAR are designed and compared to find the most accurate solution to forecast daily water consumption.

This paper consists of the following sections:

The predictive models were presented in Section 2. In Section 3, the data set and experimental results were expressed, evaluation metrics are proposed and calculated in Section 4 and finally, there is the conclusion in Section 5.

PREDICTIVE MODELS

In this paper, two neural networks with different structures (LSTM and NAR) were implemented as multi-step predictive models which are accurate models for analyzing time series data and forecasting future values.

LSTM Neural Network

LSTM is a type of Recurrent Neural Network (RNN) which could solve RNN's long-term memory problem. The gates of LSTM control the flow of information and data and indicate which data is unimportant and must be deleted and which ones should be kept, so this network allows to passe only the important data to achieve the accurate output [22,23]. Figure 1 shows LSTM cell structure [24].

LSTM includes 3 gates, input, output and forget gates. Every cell has two inputs, x_t and h_{t-1} also h_t and c_t as output. c_{t-1} is connected to c_t directly which is possible to add or delete some data, in fact, unnecessary data is deleted by forget gate. c is the short form of cell state which is long-term memory. The data is always between -1 and 1 by using the tanh. The below equations make up LSTM network, where W_o, W_g, W_i and W_f are the weight matrices. b_o, b_g, b_i and b_f are bias vectors and σ indicates sigmoid activation functions. [24,25]

$$f_t = \sigma\left(W_f \times [x_t, h_{t-1}] + b_f\right) \quad (1)$$

$$i_t = \sigma\left(W_i \times [x_t, h_{t-1}] + b_i\right) \quad (2)$$

$$g_t = \tanh\left(W_g \times [x_t, h_{t-1}] + b_g\right) \quad (3)$$

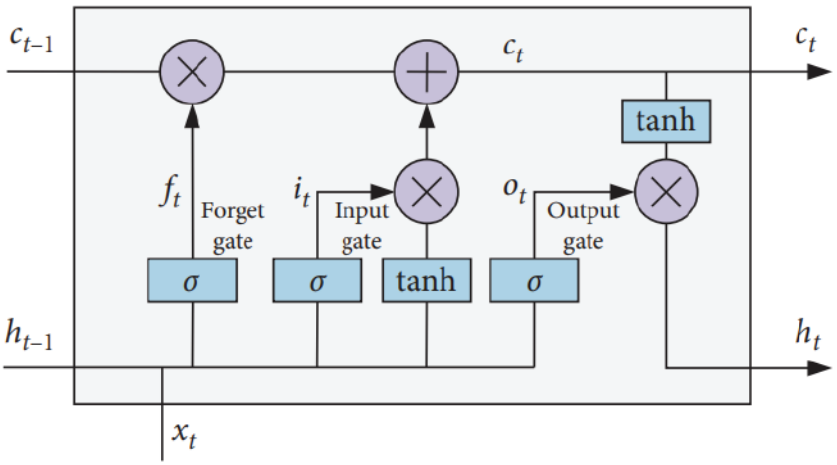


Figure 1. LSTM structure.

$$c_t = f_t \times c_{t-1} + f_t \times g_t \quad (4)$$

$$o_t = \sigma\,(W_o \times [x_t, h_{t-1}] + b_o) \quad (5)$$

$$h_t = o_t \times \tanh(c_t) \quad (6)$$

The training process is maintained until the minimum error or maximum epoch is achieved. According to the obtained results, the LSTM neural network is a successful deep learning approach based on a sophisticated network structure. It uses memory units in the model to capture time-series correlations.

NAR (Nonlinear Auto-Regressive) Neural Network LSTM

NAR neural network is an effective model to recognize time series patterns and nonlinear trends. In fact, it's a dynamic network where the future values are forecasted only from past values. This network can be implemented as a time series forecasting model [26,27]. Figure 2 shows the NAR neural network structure [28].

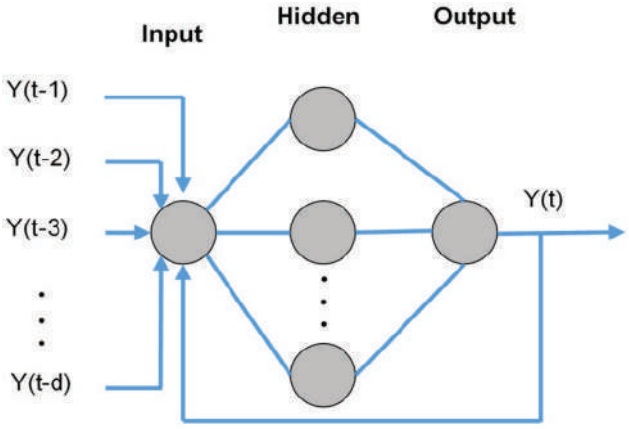


Figure 2. NAR Neural Network Structure [28].

This network can be expressed by the below function [28] where y(t), f are forecasted value and nonlinear approximation function which is determined by NAR network during training and ϵ (t) is the error.

$$y(t) = f(y(t-1), y(t-2), y(t-3), \ldots . y(t-n)) + \epsilon(t) \quad (7)$$

EXPERIMENTAL RESULTS

Monthly electricity consumption data from 1973-2022 in USA was used as the data set and input of the models which is shown in Figure 3.

The data set is normalized by the following equation in order to achieve a similar scale by the min-max method, where X *and* X_n are actual and normalized values, X_{MIN} *and* X_{MAX} refer to minimum and maximum data's values [29].

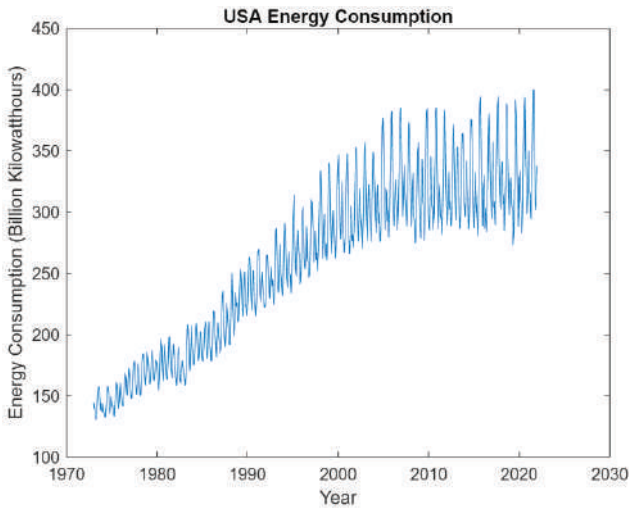


Figure 3. Monthly electricity energy consumption.

$$X_N = \frac{X - X_{MIN}}{X_{MAX} - X_{MIN}} \quad (8)$$

In LSTM, the time series data is divided into two parts for training (90%) and testing (10%) and in NAR into three parts, train (80%), Validation (10%) and test (10%). ANN parameters are usually set by previous experience in trial-and-error procedure, and we found that the best value for the hidden units is 300 in both networks. We trained our model depending on the dataset number that we have. At the first we divide our training to three parts. In the first part we chose a small number of hidden units which is between 100-150 and we got underfitting in our model. And then we tried to increase our hidden units to 450 units and then we got overfitting situation. So, the best situation was to choose 300 hidden units.

Figure 4 shows the proposed layers structure for models. Table 1 represents the training details for the LSTM network, where the Gradient Decay Factor is equal to 0.9, as it is the optimum value between 0.9 and 0.99. The Initial Learning Rate falls within the range of 0.001 to 0.01, the Learning Rate Schedule specifies the temporal variations of the learning rate throughout the training process, and the Learning Rate Drop Factor is usually set to a value between 0.1 and 0.5. The Learning Rate Drop Period specifies the frequency of learning rate updates, often adjusted by the drop factor. It indicates the number of epochs or training iterations after which the learning rate should decrease. The Max Epochs parameter is set to 250, considering the specific requirements of the LSTM modeling process. The Mini Batch Size, which denotes the amount of training data utilized in each gradient descent update, is set to 128 to provide more stable gradients and faster convergence. The Verbose Frequency is set to 50, meaning the training progress will be displayed after every 50 epochs. The Validation Frequency specifies how often the model's performance is assessed on a validation dataset throughout the training process.

In Table 2, For NAR, 80 percent of the data used for training and 10 percent for testing and 10 percent for validation. The epoch number is decided by using empirical testing and chosen to be 1000 epoch to capture the intricate patterns and dependencies in the data. As can be shown from the results in NAR the Gradient is too small and the model uncertainty (MU) is too big, and this indicates that the LSTM performance is better than NAR in this research.

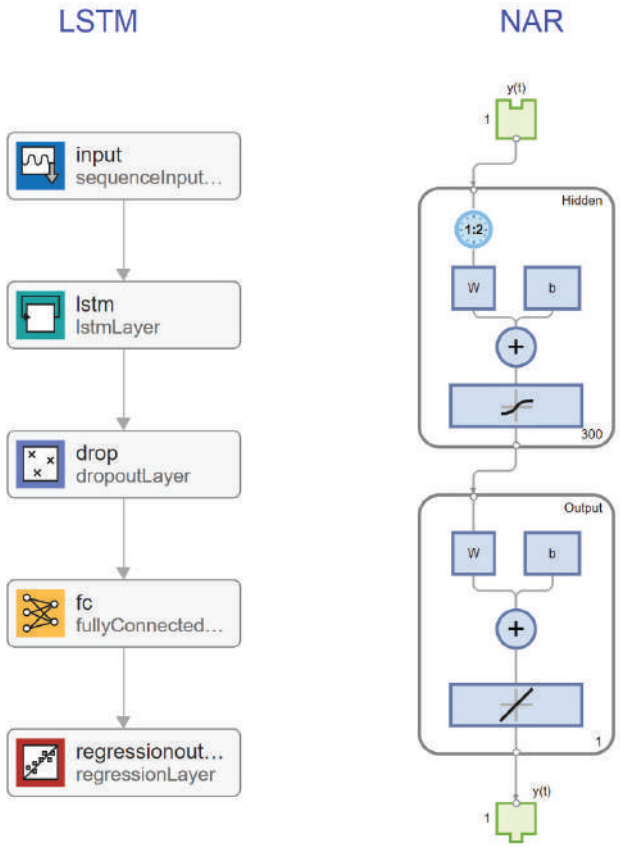


Figure 4. Proposed layers structure for LSTM and NAR networks.

Table 1. LSTM Training

Parameters	Value
Gradient Decay Factor	0.9000
Initial Learn Rate	0.0050
Learn Rate Schedule	Piecewise
Learn Rate Drop Factor	0.2000
Learn Rate Drop Period	125
Gradient Threshold Method	l2norm
Gradient Threshold	1
Max Epochs	250
Mini Batch Size	128
Verbose Frequency	50
Validation Frequency	50

Table 2. NAR Training

Parameters	Value
Training	%80
Validation	%10
Testing	%10
Epoch	1000
Time	03:14
Performance	260.7
Gradient	1e-7
MU	1e+10
Validation Check	6

Figure 5 shows how the RMSE changes across iterations during the training phase in LSTM. It starts high, and at the 100th iteration, it stabilizes, indicating that the model has reached convergence. By the 250th iteration, it fits all the trained data.

Figure 6 shows the performance of NAR in training. The Mu is almost stable at 0.05 throughout the training, indicating no adjustment was needed to facilitate learning stability. Also, the gradient is declining from 4.34×106 to 2.59 which means that the NAR model is near to local or global minimum.

In the first experiment, energy forecasting was done with LSTM network. Figure 7 shows a comparison of actual data and forecast, also the error which is the difference between these two values. In figure 7, the blue line represents the real data, and the red line shows the estimated data. According

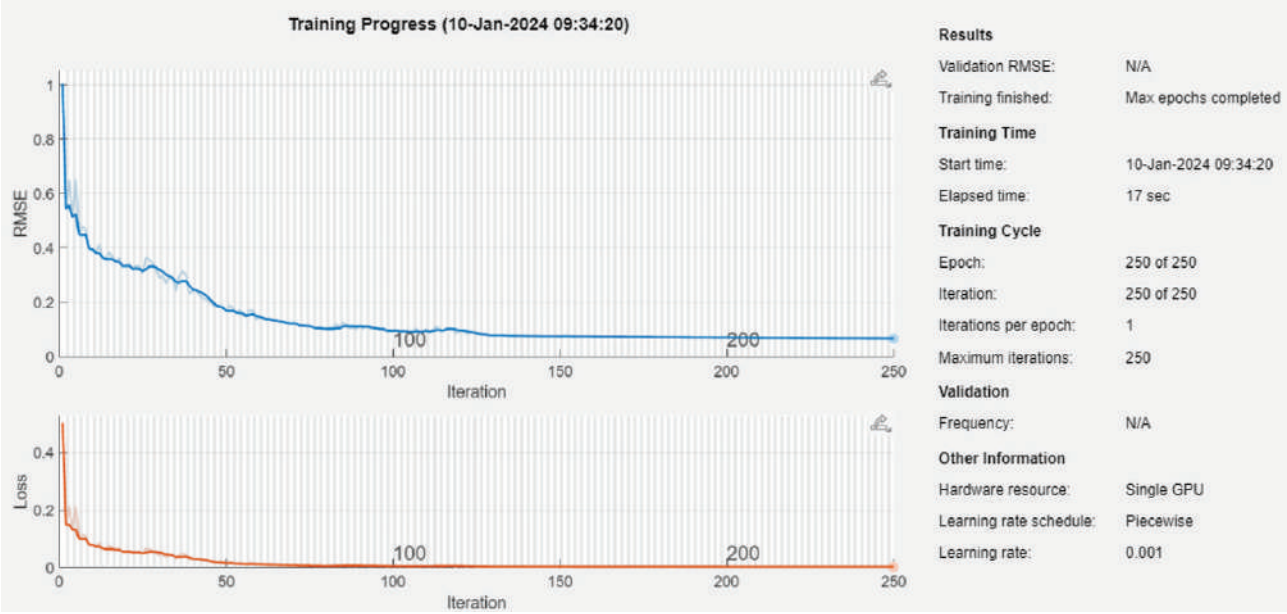


Figure 5. LSTM Training Progress.

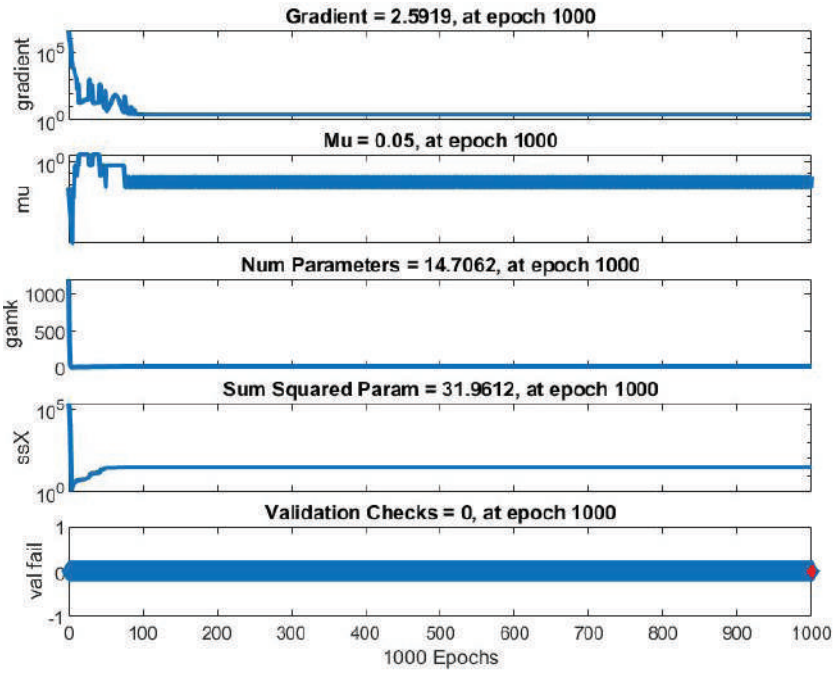


Figure 6. NAR training progress.

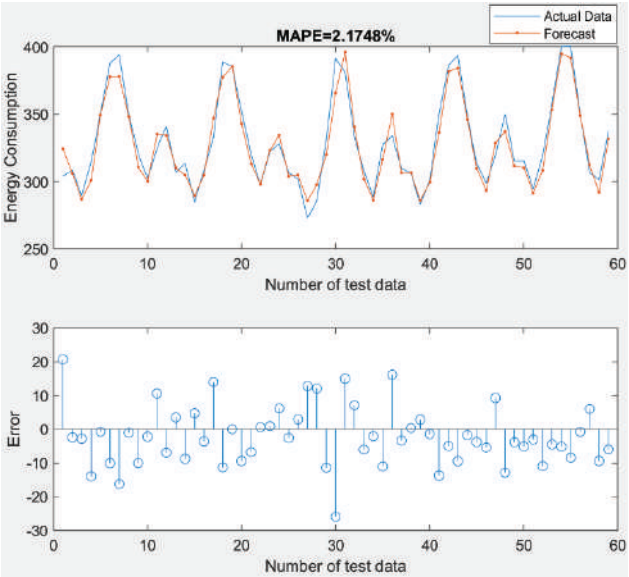


Figure 7. Forecasting, error (LSTM).

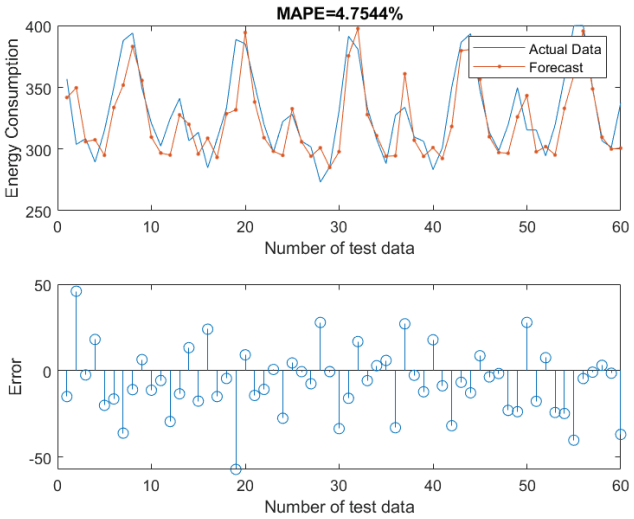


Figure 8. Forecasting, error (NAR).

to the result, MAPE is about 2.1748% which shows high accuracy of the model. The second graph shows the amount of errors in each test data point.

As the second method, NAR neural network was used, and the performance of the model and error graphs are shown in Figure 8, although the MAPE is low which is around 4.7544% and the deviations are minimal, still the LSTM method shows better results than NAR.

EVALUATION METRICS

The assessment of the presented networks was done by calculating 6 errors: MAPE, SMAPE, RMSE, MAE, MBE and R^2 which are expressed by the below formulas [30,31].

$$MAPE = \frac{1}{m}\sum_{i=1}^{m}\left|\frac{Y_i - X_i}{Y_i}\right| \quad (9)$$

$$SMAPE = \frac{1}{m}\sum_{i=1}^{m}\left|\frac{|X_i - Y_i|}{\frac{|X_i| + |Y_i|}{2}}\right| \quad (10)$$

$$MSE = \frac{1}{m}\sum_{i=1}^{m}(X_i - Y_i)^2 \quad (11)$$

$$RMSE = \sqrt{\frac{1}{m}\sum_{i=1}^{m}(X_i - Y_i)^2} \quad (12)$$

$$MAE = \frac{1}{m}\sum_{i=1}^{m}|X_i - Y_i| \quad (13)$$

$$MBE = \frac{1}{m}\sum_{i=1}^{m}X_i - Y_i \quad (14)$$

$$R^2 = 1 - \frac{\sum_{i=1}^{m}(X_i - Y_i)^2}{\sum_{i=1}^{m}(\bar{Y} - Y_i)^2} \quad (15)$$

Where Xi, Yi and m are the actual value, forecasted value and the number of test data respectively.The results are expressed in Table 3. The fewer errors and the higher value of R^2 in LSTM show this model is more accurate.

In this study, the number of hidden units which were used in the networks for achieving optimal accuracy was 300. LSTM can produce more accurate output because of feedback connections and having short-term and long-term memories. The accuracy that we can see by using LSTM and NAR shows to us clearly that the proposed LSTM model achieves better

Table 3. Results

Neural Network	MAPE	SMAPE	RMSE	MAE	MBE	R2
LSTM NN	2.1748	2.1265	8.8033	7.0646	-2.3907	0.9318
NAR NN	4.7544	4.8278	20.1971	15.8327	-6.9090	0.6387

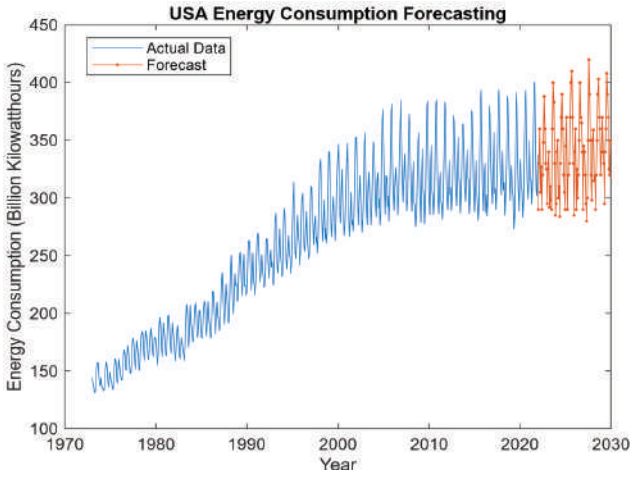


Figure 9. Forecasting with LSTM.

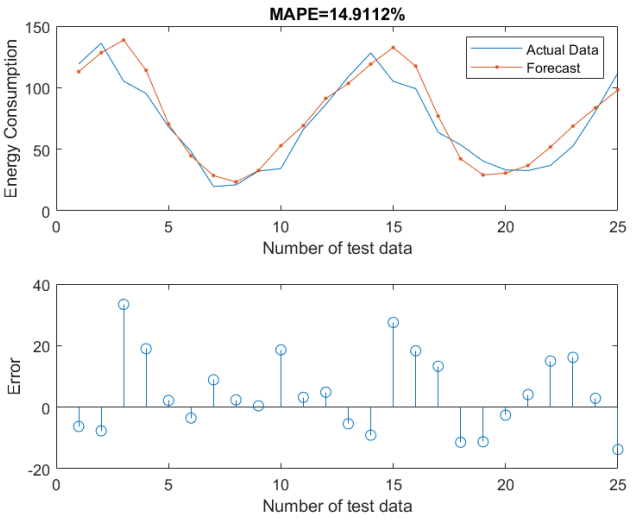


Figure 10. Forecasting with LSTM.

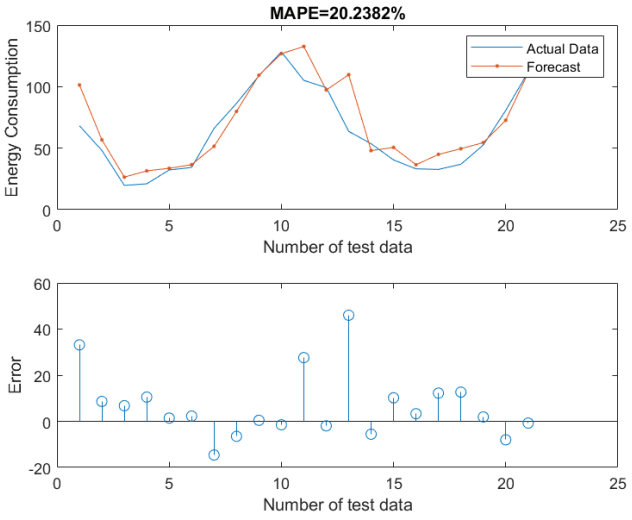


Figure 11. Forecasting with NAR.

performance in terms of estimating a long data when compared with the non-linear auto regressive (NAR). The evaluation was based on the coefficient of determination (R^2) which is a number between 0 and 1 that measures how well a statistical model predicts an outcome and its shows that LSTM have a better performance (0.9318) than NAR (0.6387). Also, by looking at table 3 we can see that the MAPE, SMAPE, RMSE, MAE, MBE all these values indicate that LSTM is better than NAR. Figure 9 shows forecasting with LSTM till 2030 which can give a general view for planning.

For this study LSTM and NAR were tested also with different datasets and different periods. The data were taken from Danish energy agency For Use of Electrical Energy Consumption from 2000 to 2020 and the results indicate that LSTM have a better Coefficient of determination (R^2) = 0.8591 and better Mean Absolute Percentage Error MAPE=14.9 than NAR which it has a Coefficient of determination (R^2) = 0.7683 and MAPE=20.23 as we can see from figures 10 and 11.

CONCLUSION

In this research, long-term electricity energy consumption was forecasted using MATLAB software with two predictive models, LSTM which is a kind of RNN and NAR (nonlinear autoregressive) neural network. The monthly energy consumption data from 1973-2022 in USA was used as a time series data set and input of the networks.The experimental results of both networks were compared and evaluation metrics in this study were different errors such as MAPE, SMAPE, RMSE, MAE, MBE and R^2 for measuring forecasting accuracy. The lower value of the errors and the higher value of R^2 in LSTM (0.9318) shows this model is more accurate than NAR (0.6387). Also, if we compared the Symmetric Mean Absolute Percentage Error in LSTM (2.1265) which gives better performance than the NAR (4.8278) and here also the lower value means the better performance. These results indicate that LSTM method is more efficient than NAR because LSTM has short-term and long-term memories which can keep information for long periods and has feedback connections. In fact, this network has shown better performance.

For the future work, we will use the same data with different NN estimation methods like, for example NARX. Also, this work can be used to estimate the stock market. Also, to increase the accuracy of the model optimization algorithms like particle swarm optimization algorithm hyperparameters of LSTM can be used.

AUTHORSHIP CONTRIBUTIONS

Authors equally contributed to this work.

DATA AVAILABILITY STATEMENT

The authors confirm that the data that supports the findings of this study are available within the article. Raw

data that support the finding of this study are available from the corresponding author, upon reasonable request.

CONFLICT OF INTEREST

The author declared no potential conflicts of interest with respect to the research, authorship, and/or publication of this article.

ETHICS

There are no ethical issues with the publication of this manuscript.

STATEMENT ON THE USE OF ARTIFICIAL INTELLIGENCE

Artificial intelligence was not used in the preparation of the article.

REFERENCES

[1] Kim TY, Cho SB. 2019. Predicting residential energy consumption using CNN-LSTM neural networks. Energy 2019;182:72–81. [CrossRef]

[2] Kim JY, Cho SB. Electric Energy Consumption Prediction by Deep Learning with State Explainable Autoencoder. Energies 2019;12:739. [CrossRef]

[3] Djenouri D, Laidi R, Djenouri Y, Balasingham I. Machine learning for smart building applications: Review and taxonomy. ACM Comput Surv 2019;52:1–36. [CrossRef]

[4] Silva FLC, Costa K, Rodrigues PC, Salas R, Gonzales JLL. Statistical and artificial neural networks models for electricity consumption forecasting in the Brazilian industrial sector. Energies, 2022;15:588. [CrossRef]

[5] Ajayi RO, Alaka H, Sulaimon I, Sunmola F, Ajayi S. Building energy consumption prediction for residential buildings using deep learning and other machine learning techniques. J Build Eng 2022;45:103406. [CrossRef]

[6] Fathi S, Srinivasan R, Fenner A, Fathi S. Machine learning applications in urban building energy performance forecasting: A systematic review. Renew Sustain Energy Rev 2020;133:110287. [CrossRef]

[7] Bourhnane S, Abid MR, Lghoul R, Dine KZ, Elkamoun N, Benhaddou D. Machine learning for energy consumption prediction and scheduling in smart buildings. SN Appl Sci 2020;2:1–10. [CrossRef]

[8] Donmez I, Aslan Z. Role of air pollution on COVID-19 in Istanbul. Sigma J Eng Nat Sci 2023;4:793–806. [CrossRef]

[9] Gozzoglu A, Ozgonenel O, Gezegin C. Modeling and implementation of demand-side energy management system. Sigma J Eng Nat Sci 2024;42:1628–1645. [CrossRef]

[10] Wang H, Lei Z, Zhang X, Zhou B, Peng J. A review of deep learning for renewable energy forecasting. Energy Convers Manage 2019;198:111799. [CrossRef]

[11] Cai M, Pipattanasomporn M, Rahman S. Day-ahead building-level load forecasts using deep learning vs. traditional time-series techniques. Appl Energy 2019;236:1078–1088. [CrossRef]

[12] Qasem M, Başaran Filik Ü. Solar radiation forecasting by using deep neural networks in Eskişehir. Sigma J Eng Nat Sci 2021;39:159–169. [CrossRef]

[13] Yan K, Li W, Ji Z, Qi M, Du Y. A Hybrid LSTM Neural Network for Energy Consumption Forecasting of Individual Households. IEEE Access 2019;7:157633–157642. [CrossRef]

[14] Mahjoub S, Alaoui LC, Marhic B, Delahoche L. Predicting Energy Consumption Using LSTM, Multi-Layer GRU and Drop-GRU Neural Networks. Sensors 2022;22:4062. [CrossRef]

[15] Chung J, Jang B. Accurate prediction of electricity consumption using a hybrid CNN-LSTM model based on multivariable data. PLoS One 2022;17:e0278071. [CrossRef]

[16] Durand D, Aguilar J, R-Moreno MD. An Analysis of the Energy Consumption Forecasting Problem in Smart Buildings Using LSTM. Sustainability 2022;14:13358. [CrossRef]

[17] Mpawenimana I, Pegatoquet A, Roy V, Rodriguez L, Belleudy C. A comparative study of LSTM and ARIMA for energy load prediction with enhanced data preprocessing. IEEE Sens Appl Symp 2020;1–6. [CrossRef]

[18] Shi H, Xu M, Li R. Deep learning for household load forecasting—A novel pooling deep RNN. IEEE Trans Smart Grid 2017;9:5271–5280. [CrossRef]

[19] Ramadevi B, Bingi. Time Series Forecasting Model for Sunspot Number. IEEE Xplore 2022;1-6. [CrossRef]

[20] Sunder M, Abishek R, Maiti M, Bingi K, Devan PAM, Assaad M. Forecasting of Wind Turbines Generated Power with Missing Input Variables. 2022 International Conference on Future Trends in Smart Communities (ICFTSC), Kuching, Sarawak, Malaysia, 2022, pp. 98-103. [CrossRef]

[21] Boudhaouia A, Wira P. Comparison of machine learning algorithms to predict daily water consumptions. IEEE Xplore 2021;1–6. [CrossRef]

[22] Torres JF, Álvarez FM, Troncoso A. A deep LSTM network for the Spanish electricity consumption forecasting. Neural Comput Appl 2022;34:10533–10545. [CrossRef]

[23] Jang J, Han J, Leigh SB. Prediction of heating energy consumption with operation pattern variables for non-residential buildings using LSTM networks. Energy Build 2022;255:111647. [CrossRef]

[24] Wang B, Zhang L, Ma H, Wang H, Wan S. Parallel LSTM-based regional integrated energy system multienergy source-load information interactive energy prediction. Complexity 2019;1–13. [CrossRef]

[25] Jang G, Kim N, Ha T, Lee C, Cho S. Base station switching and sleep mode optimization with LSTM-based user prediction. IEEE Access 2020;8:222711–222723. [CrossRef]

[26] Sarkar R, Julai S, Hossain S, Chong WT, Rahman M. A comparative study of activation functions of NAR and NARX neural network for long-term wind speed forecasting in Malaysia. Math Probl Eng 2019:3:1–14. [CrossRef]

[27] Khaleghi S, Karimi D, Beheshti SH, Hosen S, Behi H, Berecibar M, et al. Online health diagnosis of lithium-ion batteries based on nonlinear autoregressive neural network. Appl Energy 2021;282:116159. [CrossRef]

[28] Taherdangkoo R, Tatomir A, Taherdangkoo M, Qiu P, Sauter M. Nonlinear autoregressive neural networks to predict hydraulic fracturing fluid leakage into shallow groundwater. Water 2020;12:841. [CrossRef]

[29] Ghimire S, Huy TN, Prasad R, Deo RC, Perez DC, Sanz SS, Bhandari B. Hybrid convolutional neural network-multilayer perceptron model for solar radiation prediction. Cogn Comput 2023;15:645–671. [CrossRef]

[30] Chicco D, Warrens MJ, Jurman G. The coefficient of determination R-squared is more informative than SMAPE, MAE, MAPE, MSE and RMSE in regression analysis evaluation. PeerJ Comput Sci 2021;7:e623. [CrossRef]

[31] Jiménez JAB, Estévez J, Marín APG. New machine learning approaches to improve reference evapotranspiration estimates using intra-daily temperature-based variables in a semi-arid region of Spain. Agric Water Manag 2021;245:106558. [CrossRef]

Sigma Journal of Engineering and Natural Sciences
Web page info: https://sigma.yildiz.edu.tr
DOI: 10.14744/sigma.2025.00000

Research Article

Screening of *Trichoderma* spp. for biofertilizer and biocontrol potential in vitro

Kemal KARACA[1,*], Rengin ELTEM[2]

[1]*Department of Bioengineering, Graduate School of Natural and Applied Sciences, Ege University, Izmir, 35100, Türkiye*
[2]*Department of Bioengineering, Faculty of Engineering, Ege University, Izmir, 35100, Türkiye*

ARTICLE INFO

Article history
Received: 14 March 2025
Revised: 01 June 2025
Accepted: 23 August 2025

Keywords:
Biological Control; Microbial Fertilizer; PGPF; Trichoderma

ABSTRACT

Agricultural yields can be significantly increased by using Plant Growth Promoting Microorganism (PGPMs). *Trichoderma* spp., which support plant growth, have been studied as soil microorganisms for many years. This study investigated the PGPM properties of 62 *Trichoderma* species. The properties examined included antagonistic effects against phytopathogens; lytic enzyme activities (β-1,3-glucanase, chitinase, protease, and cellulase); siderophore and indole-3-acetic acid (IAA) production; and phosphate solubility and potassium mobilization capabilities. Therefore, this study aimed to specify the biofertilizer and biocontrol properties of *Trichoderma* spp. that are candidates for use in agriculture. Out of the 62 *Trichoderma* spp. examined, 62.90% exhibited chitinase activity, 83.87% β-1,3-glucanase activity, and all of the strains showed cellulase and protease production. Furthermore, 40 strains produced siderophores, all tested positive for IAA production, and 30 strains were able to solubilize potassium and 58 strains were similarly effective in phosphate solubilization. *Trichoderma* species exhibited inhibition rates ranging from 0-87.92% against *Botrytis cinerea,* 21.75-86.25% against *Fusarium solani,* and 17.64-91.17% against *Rhizoctonia solani*. Two *Trichoderma koningiopsis* species and one *Trichoderma harzianum* species exhibiting high PGPF activity were identified. The microbial fertilizer and biological control properties of *Trichoderma* species molecularly identified in this study show promise for biotechnological applications to reduce chemical inputs in agricultural production.

Cite this article as: Karaca K, Eltem R. Screening of *Trichoderma* spp. for biofertilizer and biocontrol potential in vitro. Sigma J Eng Nat Sci 2026;44(1):162–173.

INTRODUCTION

Plant Growth Promoting Microorganisms (PGPMs) are defined as microorganisms that promote plant growth by increasing the production of various hormones and nutrient uptake, and that can exhibit antagonistic activity against many plant pathogens. Plant growth promoting fungi (PGPFs) are an important group of microorganisms for their ability to stimulate plant growth and activate plant defense mechanisms [1–4].

Trichoderma are attracting great interest due to their multifaceted roles in promoting plant growth and protect

***Corresponding author.**
*E-mail address: kemalkaraca1@gmail.com

This paper was recommended for publication in revised form by Editor-in-Chief Ahmet Selim Dalkilic

Published by Yıldız Technical University Press, İstanbul, Turkey
© Author. This is an open access article under the CC BY-NC license (http://creativecommons.org/licenses/by-nc/4.0/).

plant diseases. The use of chemicals in agriculture leads to a decrease in biodiversity. By supporting plant nutrition, *Trichoderma* spp. increases soil fertility and contributes to the long term maintenance of soil health [5–7]. *Trichoderma* spp. reduce plant pathogen populations through competition for nutrients and habitat, secondary metabolite production, and mycoparasitism. They also strengthen plant resistance to diseases by enhancing antioxidant defense systems and systemic resistance. Furthermore, they promote plant growth through the release of growth-promoting molecules. *Trichoderma* species produce hydrolytic enzymes that help convert large substrates into smaller, more accessible forms for plant use. Studies on *Trichoderma* spp. have shown that they are extremely resistant to chemical fungicides, as their ability to metabolize different types of pesticides has been proven [5,7,8]. These characteristics allow *Trichoderma* species to be widely used in agriculture as microbial fertilizers and biocontrol agents. *Trichoderma* species have been attracting increasing attention in recent years due to their various functions in sustainable agriculture. By producing lytic enzymes and secondary metabolites, these fungi not only support plant growth through processes like phytohormone synthesis, nutrient solubilization, and siderophore secretion, but they also effectively biocontrol a variety of phytopathogens. Moreover, many recent research have highlighted their capacity to enhance soil health and plant stress tolerance. These characteristics make *Trichoderma* spp. attractive options for biofertilizer formulations and integrated pest management in a range of agroecological environments [9–11]

In this study, the important PGPM properties of *Trichoderma* spp. isolated isolated from different locations were determined. These properties include antagonistic effects against plant pathogens, siderophore and IAA production, lytic enzyme activities, phosphate solubility, and potassium mobilization. This study aimed to contribute to the literature by identifying *Trichoderma* strains with high potential for use in agricultural production.

Therefore, the aim of this study is to evaluate the PGPM potential of *Trichoderma* spp. and to identify promising strains that can be used as biofertilizers and biological control agents in agriculture. Few research have combined molecular identification with a wide range of biofertilizer and biocontrol activities, despite the fact that numerous studies have examined specific plant growth-promoting features of *Trichoderma* spp. By analyzing several PGPM characteristics and linking them to strains that have been genetically identified, this study fills this knowledge gap.

MATERIALS AND METHODS

Microorganisms Used

Sixty of the *Trichoderma* spp. (n=62) used in this study were strains obtained from soil and mushroom compost samples collected from different regions in previous studies [12–15], while two *Trichoderma harzianum* strains were obtained from the Bioengineering Department culture collection. The details of these strains are presented in Table 1. Microscopic structures of the *Trichoderma* spp. were examined using a light microscope at 40× magnifications after staining with 0.05% lactophenol cotton blue. Morphological features such as hyphal structure, conidiophores, and conidia formation were observed and recorded. All of the *Trichoderma* spp. were stored on agar slant at 4 °C and in soil at room temperature.

Phytopathogenic fungi such as *Botrytis cinerea*, *Fusarium solani*, and *Rhizoctonia solani*, found in the Industrial Microbiology culture collection of the Department of Bioengineering, Ege University, were used to determine the antagonistic activity of *Trichoderma* species [16].

Assessment of Antagonıstıc Effect of *Trichoderma* Spp. Against Phytopathogenıc Fungi

The antagonistic effect of *Trichoderma* species against *Rhizoctonia solani*, *Botrytis cinerea*, and *Fusarium solani* was determined by dual culture testing. Under aseptic conditions, *Trichoderma* spp. and phytopathogenic discs were placed on sterile Potato Dextrose Agar (PDA). Petri plates containing only phytopathogenic fungi, not *Trichoderma* spp., were used as a control group. After incubating the Petri dishes at 28 °C for 5 days, the inhibition percentages were determined [17–21].

The formula was used to calculate the growth inhibition:

$$\text{Growth inhibition (\%)} = \frac{(C-T)}{C} x100$$

C: Colony diameter (cm) of the phytopathogenic fungi on the control plate.

Table 1. Sources of *Trichoderma* spp. from different samples

Sampling codes	Sampling types	Sampling places
3, 4	*Pleurotus ostreatus* compost	Izmır, Türkiye
7, 11	*Agaricus bisporus* compost	Kocaeli, Türkiye
6, 8, 12	*Agaricus bisporus* casing soil	Kocaeli, Türkiye
13, 14, 15, 16, 17, 18, 19, 20	Heavy metal contamination soil samples	Trabzon, Türkiye
EGE-K-38, EGE-K-49	Soil samples	Izmir, Türkiye

T: Colony diameter (cm) of the phytopathogenic fungi on the plate where the antifungal activity was tested.

Evaluation of Lytic Enzyme Activities

Spore suspensions were prepared from activated *Trichoderma* species at a concentration of 10^8 spores/mL using a 0.1% Tween 80 solution. These suspensions were inoculated 2% (v/v) rate into *Trichoderma* Liquid Enzyme (TLE) Medium, which was modified by the addition of 0.5% colloidal chitin, (14.3 g/L corn step solid, 10 g/L soy peptone, 2 g/L monopotassium phosphate, 0.3 g/L magnesium sulfate heptahydrate, 0.3 g/L glucose, 5 g/L colloidal chitin, 1 mL/L stock salt solution; Stock salt solution: 0.002 g/L $CoCl_2.6H_2O$, 0.0016 g/L $MnSO_4.4H_2O$, 0.005 g/L $FeSO_4.7H_2O$, 0.0014 g/L $ZnSO_4.7H_2O$) for the production of β-1,3 glucanase, chitinase, and protease, and into *Trichoderma* Cellulase Production Medium (20 g/L carboxymethtl cellulose (CMC), 15 g/L KH_2PO_4, 5 g/L $(NH_4)_2SO_4$, 0.6 g/L $CaCl_2.2H_2O$, 0.5 g/L $MgSO_4.7H_2O$) for cellulase production. *Trichoderma* spp. were incubated at 180 rpm for 5 days at 30 °C [18,22,23]. Inoculum-free production medium was used as a negative control.

The 3,5-dinitrosalicylic acid (DNS) method described by Miller (1959) was used to determine β-1,3-glucanase, chitinase, and cellulase activities [24,25]. To determine chitinase activity, 0.6 mL of supernatant was mixed with 1 mL of 0.1 M acetate buffer (colloidal chitin, 1% (w/v)), and the mixture was incubated at 45 °C for 1 h. For β-1,3-glucanase activity, 50 µL of supernatant was mixed with 100 µL of 0.05 M acetate buffer (laminarin, 1% (w/v)), and incubated for 30 min at 40 °C. To determine cellulase activity, 200 µL of supernatant was mixed with 0.1 M acetate buffer containing 500 µL of 1% carboxymethyl cellulose (CMC) and incubated for 15 min at 50 °C. Following the incubation periods, 0.75 mL of DNS reagent was added, and the mixtures were boiled at 100 °C for 10 min. Then, all samples were centrifuged at 10,000 rpm for 5 min, and the absorbances of the supernatants were measured at 530 nm for chitinase and at 540 nm for cellulase and β-1,3-glucanase. Standard curves establish using N-acetylglucosamine for chitinase and glucose for β-1,3-glucanase and cellulase were used to calculate enzyme activities [18,22,25,26].

To determine protease activity, 50 µL of supernatant was mixed with 450 µL of 0.1 M phosphate buffer (azokazein, 1% (w/v)) and the mixture was incubated for 30 min at 50 °C. The reaction was stopped by adding 250 µL of 25% (w/v) TCA. The absorbance of the samples was measured at 440 nm after mixing the supernatant and 1 N NaOH in a 1:1 ratio. One unit (U) of protease activity was defined as the amount of enzyme that produces 1 µmol of free amino acids in 1 minute, and results were expressed in U/mL [18].

To determine the amount of protein produced by *Trichoderma* species, 100 µL of supernatant and 1 mL of Bradford reagent were mixed, and the mixture was incubated for 5 min. Absorbance values at a wavelength of 595 nm were determined by spectrophotometer. Protein concentration was calculated from a standard curve prepared using bovine serum albumin (BSA) [23]. The specific activity (U/mg) was determined by dividing the enzyme activity (U/mL) by the protein concentration (mg/mL).

Evaluation of Siderophore Production

Activated *Trichoderma* spp. were inoculated into the center of Chromium Azurol S (CAS) agar plates. After incubating *Trichoderma* spp. for 10 days, strains showing zone/orange zone formation were evaluated as positive for siderophore production [27]. The siderophore production index was determined using the following formula: Siderophore Production Index = (Zone Diameter (cm) / Colony Diameter (cm)).

Evaluation of Indole-3-Acetic Acid (IAA) Production

Agar discs taken from each activated *Trichoderma* spp. were inoculated into half-concentration Tryptic Soy Broth (TSB) enriched with 0.5% (w/w) L-tryptophan and incubated for 7 days at 30 °C and 180 rpm. After incubation, the biomass and culture medium were separated by centrifugation. 2 mL of Salkowski reagent was mixed with 1 mL of supernatant and incubated for 20 min. The absorbances of the samples were then measured at 530 nm. The standard curve was prepared with different concentrations of IAA. TSB medium without inoculum was used as a negative control. [18,28].

Evaluation of Phosphate Solubility

1 mL of 10^8 spores/mL *Trichoderma* spore suspension was inoculated into National Botanical Research Institute's Phosphate (NBRIP) medium (10 g/L glucose, 5 g/L tricalcium phosphate, 5 g/L $MgCl_2{\cdot}6H_2O$, 0.25 g/L $MgSO_4{\cdot}7H_2O$, 0.2 g/L KCl, 0.1 g/L ammonium sulfate). After incubation at 30 °C for 7 days at 180 rpm, the samples were centrifuged at 9000 rpm for 10 min. 0.8 mL of ascorbic acid and 4 mL of supernatant were mixed and incubated for 10 min. The absorbance of the samples was measured at 700 nm. A standard curve was constructed using different dissolved phosphate concentrations [18,29].

Evaluation of Potassium Mobility

Activated *Trichoderma* spp. were inoculated spot method onto Modified Alexandrov Agar (10 g/L glucose, 0.5 g/L $MgSO_4{\cdot}7H_2O$, 0.005 g/L $FeCl_3$, 0.1 g/L calcium carbonate, 2 g/L calcium orthophosphates, 5 g/L potassium silicate and, 0.025% bromotymmol blue). The potassium mobilization of *Trichoderma* species after 10 days of incubation at 27°C was determined by the diameter of the zone formation and the appearance of an orange color [30].

Identification of Microorganisms

ITS species identification of *Trichoderma* spp. (n=3) was performed through external analysis obtained from BM Software Consulting and Lab. Systems Ltd. MEGA software (v11) was used to generate the phylogenetic tree.

Statistical Analysis

All experiments were conducted in triplicate, and standard deviations were calculated. In this study, normality tests were not performed; therefore, the data were analyzed using one-way ANOVA followed by Tukey's post hoc test at a significance level of $p<0.05$, under the assumption of normal distribution. PASW Statistics software (v18) was used for statistical analyses. Means followed by the same letter in parentheses belong to the same statistical group. Letter combinations in parentheses (e.g., (ab)) represent a distinct group and should not be interpreted as equivalent to either 'a' or 'b' groups alone.

RESULTS AND DISCUSSION

A total of 62 *Trichoderma* spp. were used in this study. *T. pleuroticola* 3-2, *T. pleuroticola* 4-2, *T. harzianum* 6-2, *T. pleuroticola* 6-5, *T. virens* 7-2, *T. afroharzianum* 7-4, *T. pleuroticola* 8-3, *T. pleuroticola* 8-7, *T. pleuroticola* 11-2, and *T. harzianum* EGE-K-38 are *Trichoderma* strains that have been identified in previous studies [13,31]. The strains were examined under a microscope. Figure 1 presents the growth of the *Trichoderma harzianum* EGE-K-16-3 strain on PDA plates and its distinct morphological structures observed under the light microscope.

Controlling plant diseases through chemical methods carries many undesirable risks in terms of health, safety, and the environment. Therefore, biological control is considered a powerful and environmentally friendly approach to reducing damage caused by plant pathogens. Evaluation the antagonistic effects of *Trichoderma* species against various phytopathogens is considered important in studies [32]. The inhibition rate results against phytopathogenic fungi are shown in Table 2 and Figure 2.

Based on a review of various studies, it is believed that this research will make significant contributions to the existing literature. In particular, the evaluation of the *Trichoderma* strains identified in this study in different research studies is of great importance. In our study, the *T. harzianum* EGE-K-49 showed the highest antagonistic activity against *F. solani* with an inhibition rate of 86.25%. Zhan et al. (2023), Savaş et al. (2021), and Stracquadanio et al. (2020) reported the effects of *Trichoderma* strains against various pathogens such as *Lasiodiplodia theobromae, B. cinerea,* and *Fusarium* in their studies [33-35].

Table 2. Percentage inhibition values of *Trichoderma* species against phytopathogenic fungi (*B. cineria*, BC; *F. solani*, FS and *R. solani*, RS)

Inhibition percent range	BC	FS	RS
	Number of *Trichoderma* spp.		
0-40	1	1	1
41-60	9	7	0
61-80	41	40	34
81-99	11	14	27

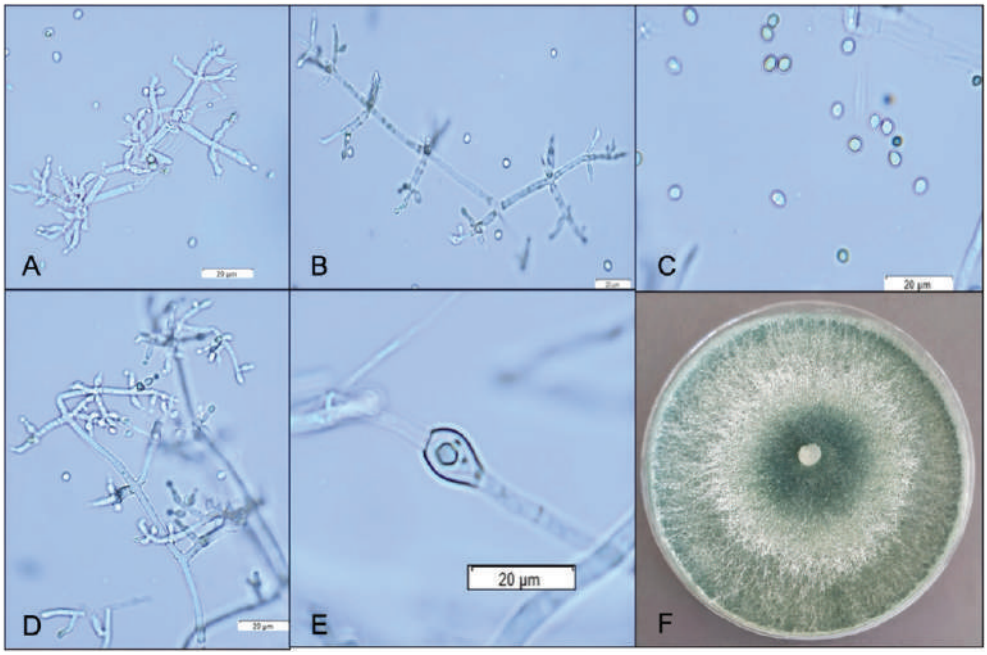


Figure 1. Light microscopic observation at 40x magnifications and PDA plates cultures of *Trichoderma harzianum* EGE-K-16-3. **A, B, D)** Conidiophores, **C)** Conidia, **E)** Chlamydospores, **F)** Cultures on PDA plates.

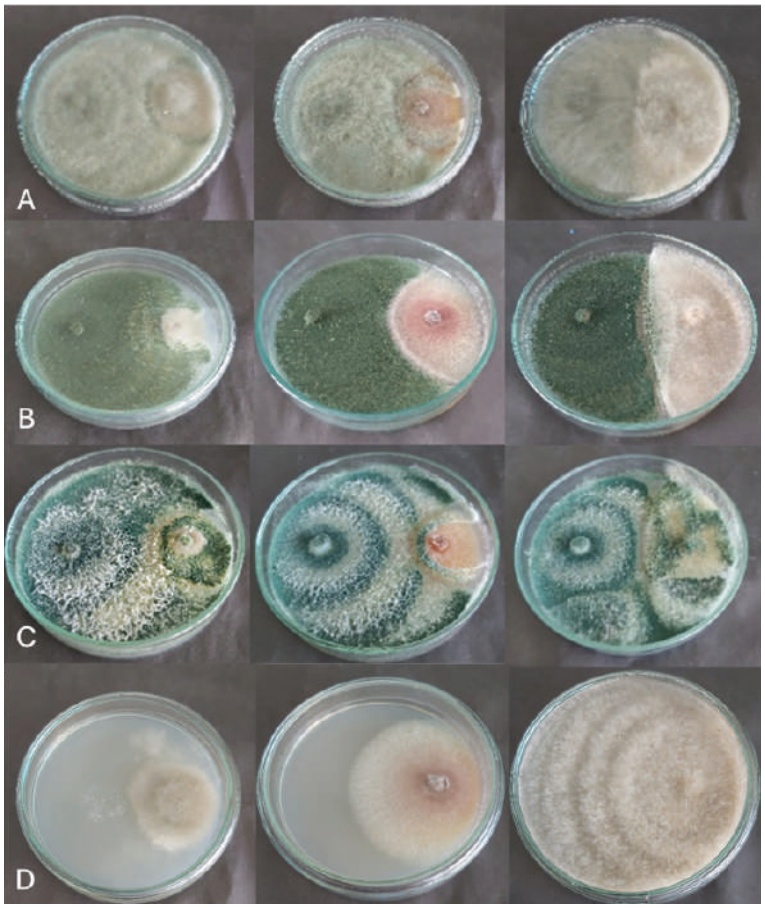


Figure 2. In the dual culture test, *Trichoderma* spp. showed antagonistic activity against phytopathogenic fungi. **A)** *Trichoderma pleuroticola* 4-2, **B)** *Trichoderma harzianum* EGE-K-49, **C)** *Trichoderma harzianum* EGE-K-38, **D)** Control group of phytopathogenic fungi (The phytopathogenic fungi are *B. cinerea*, *F. solani*, and *R. solani*, from left to right).

In this study, the highest inhibition rate against *B. cinerea* was obtained with the *Trichoderma* sp. 19-4 strain, at 87.92%. *Trichoderma* strains are also included in studies aimed at reducing pesticide use within the scope of Integrated Pest Management (IPM). The high antagonistic activities obtained against phytopathogenic fungi in this study contribute to the literature. If field studies are carried out with the *Trichoderma* spp. to be determined, the results to be obtained are very important in this respect. [36,37]. In a study conducted in the literature, the antifungal effects of *Trichoderma* strains on *Fusarium* spp. were investigated in vitro and in vivo. They found an inhibition rate of 71 to 80% in the dual test. In vivo, they reached an inhibition rate of 47 to 51% in chickpea plants. In the literature, differences between in vivo and in vitro are seen as an expected situation [38].

Among the 62 *Trichoderma* spp. examined, strains 52, 39, 62, and 62, respectively, were found to be positive for β-1,3-glucanase, chitinase, protease, and cellulase enzyme production. Chitinase activity ranged from 0.01–0.40 U/mL (0.15–30.66 U/mg), with the highest production observed in *Trichoderma* sp. 13-15. Cellulase activity varied between 1.40–31.43 U/mL (45.99–1231.89 U/mg), with the highest specific activity observed in *Trichoderma* sp. 13-4. β-1,3-glucanase activity was found to be between 0.58–3.38 U/mL (7.69–103.64 U/mg), with the highest production belonging to the *T. afroharzianum* 7-4. Protease activity ranged from 8.00–261.33 U/mL (123.30–7610.18 U/mg), with the highest specific activity determined in the *Trichoderma* sp. 19-3. As seen in Figure 3, the numerical values for β-1,3-glucanase and chitinase activities are relatively low, showing a narrow range of variation. In contrast, cellulase and protease activities have higher numerical values and exhibit a wide range of variation.

When the results in the literature are examined, the enzyme activities determined as a result of this study are similar to previous studies [18,22,39-41]. Chitinase activity results in *Trichoderma* isolates ranged from 0.1-4.5 U/mL. These studies indicated differences in activity among different *Trichoderma* species and incubation periods. [18,39,40]. In this study, enzyme activity was determined only for screening purposes. Similar results to the optimization

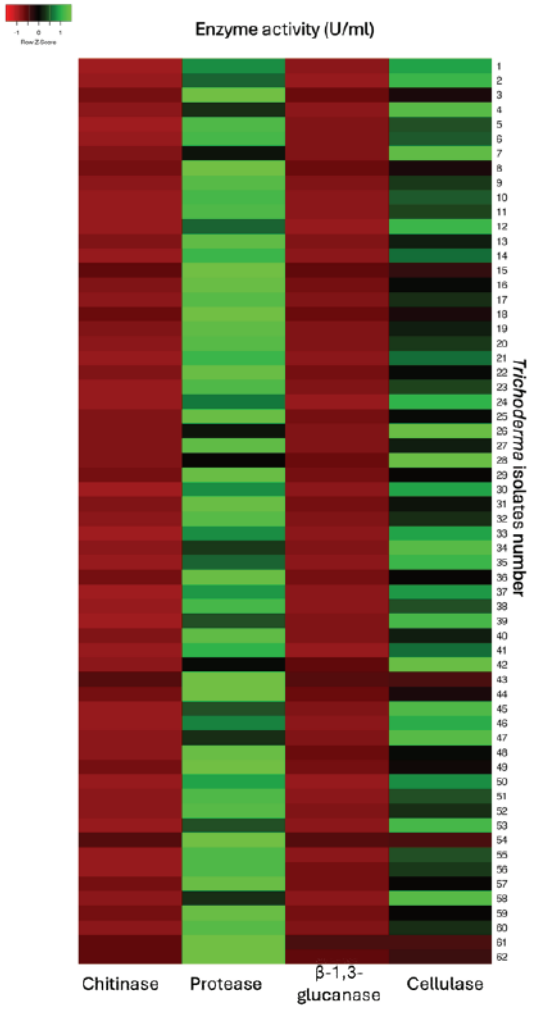


Figure 3. Heatmap including chitinase, protease, β-1,3-glucanase, and cellulase enzyme activity results of *Trichoderma* spp.

studies in the literature indicate that the *Trichoderma* spp. in this study are good enzyme producer candidates. In this regard, it is important to conduct enzyme production optimization studies with the selected *Trichoderma* strains. The fact that different *Trichoderma* spp. showed different results indicates that microorganisms have different characteristics depending on the strain. Even different strains of the same species showed different results. This shows us the importance of screening in a specific study. For example, in our study, *T. pleuroticola* 3-2 exhibited 16.32 U/mg β-1,3-glucanase activity, whereas *T. pleuroticola* 4-2 did not exhibit β-1,3-glucanase activity. Despite belonging to the same species, different results were obtained. Parameters such as the type of sample from which *Trichoderma* spp. was isolated and the location also affect these results.

Although all strains were able to grow on CAS agar medium, zone formation was observed in 40 *Trichoderma* spp. The top row of images in Figure 4 shows the zones formed by *Trichoderma* spp. due to siderophore production. Siderophores produced by microorganisms facilitate iron uptake and can be detected on CAS agar medium thanks to the zones formed as a result of the chelation of Fe from the dye [42,43]. Although studies have shown that hexadecyltrimethylammonium bromide (HDTMA) found in CAS agar causes toxicity in fungi and Gram-positive bacteria, it is thought that *Trichoderma* species may also show high tolerance to the toxic effects caused by HDTMA [42,44,45]. In addition, since siderophores are known to cause biosorption and biological degradation of azo dyes, the transparent zones observed in our study are thought to be degradation [46,47].

In our study, where all strains gave positive results in terms of IAA production, *Trichoderma* sp. 18-13 was determined as the highest IAA producer (111.92 mg/mL). There are limited

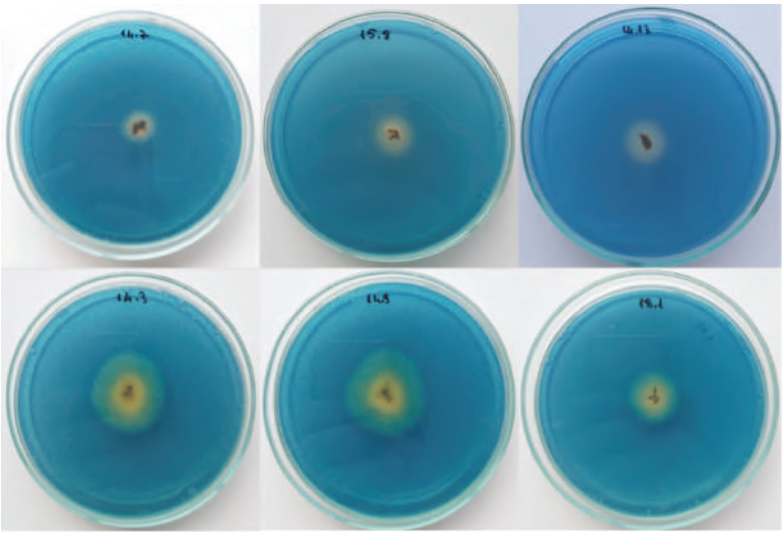


Figure 4. Siderophore results on CAS agar plates. The top row shows clear zone formation indicating siderophore production; the bottom row shows without zone formation.

studies on IAA production by fungi, so it is thought that the results in our study will make a great contribution to the literature [18, 42]. The study results reveal that *Trichoderma* strains are effective microorganisms in terms of IAA production. These characteristics make them promising candidates that can be used in microbial biofertilizer formulations.

In this study, 58 out of 62 *Trichoderma* spp. strains showed positive results in terms of phosphate solubility, with soluble phosphate levels ranging from 0.31 to 4.72 mg/L. *Trichoderma* sp. 13-16 was identified as the strain with the highest phosphate solubility, at 4.72 mg/L. In studies in the literature, *Trichoderma* strains helped dissolve an average of 0.1-20 mg/L of phosphate [18, 48]. When the data obtained from this study are compared with the literature, it is seen that similar phosphate solubility ranges were obtained, but strains showing higher phosphate solubility have also been reported in the literature.

Potassium mobility of *Trichoderma* spp. was evaluated based on zone formation and orange color development in solid medium (Fig. 5). Positive results for potassium mobility between 0.8–5.45 cm were observed in thirty of

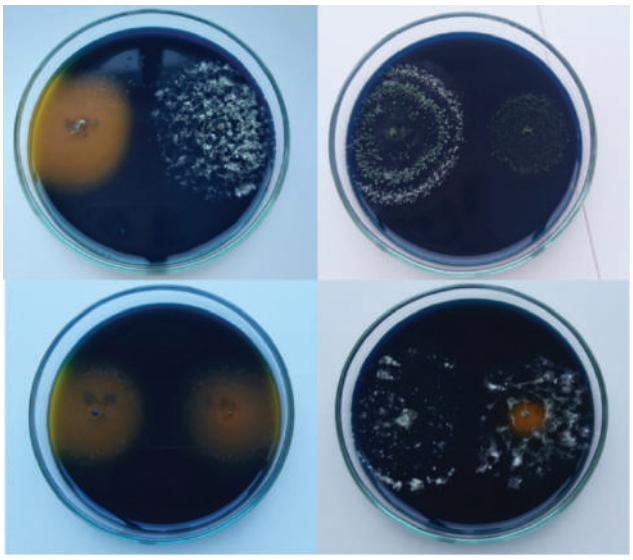


Figure 5. Orange zones formed by *Trichoderma* strains dissolving potassium.

Table 3. *Trichoderma* spp. exhibiting strong antagonistic activity and lytic enzyme production as part of their PGPM potential

Trichoderma spp.	Antagonictic Activity (% Inhibition rate)			Lytic Enzyme Spesific Activity (U/mg)			
	BC	FS	RS	Chitinase	β-1,3-glucanase	Cellulase	Protease
7-2	87.87±0.01 ^{ab}	76.62±1.87 $^{h-k}$	75.92±1.67 ^{ijk}	4.71±3.06 $^{d-i}$	98.5±15.99 ^{ab}	903.37±121.58 ^{bc}	1204.30±560.47 $^{d-h}$
7-4	88.33±0.15 ^{a}	79.22±2.35 ^{fgh}	75.0±1.0 ^{jkl}	3.9±0.13 $^{e-i}$	103.64±12.99 ^{a}	923.73±61.57 ^{b}	1751.14±82.77 $^{d-h}$
8-3	75.75±0.14 $^{i-n}$	75.32±4.56 $^{i-l}$	80.55±0.55 ^{fgh}	1.24±0.18 ^{hi}	12.69±0.42 ^{ijk}	548.99±23.71 $^{d-j}$	232.78±12.45 ^{fgh}
13-2	ND	50.0±1.0 ^{v}	66.66±1.87 ^{o}	11.26±4.0 $^{b-f}$	60.89±35.59 $^{a-h}$	372.73±5.42 $^{h-n}$	3157.68±207.01 $^{c-g}$
13-4	74.44±1.46 $^{k-q}$	80.48±2.35 $^{d-g}$	87.05±11.34 ^{b}	7.23±3.53 $^{c-i}$	45.18±3.82 $^{d-j}$	1231.89±81.21 ^{a}	1822.60±475.60 $^{d-h}$
13-5	75.94±2.67 $^{i-n}$	69.49±11.09 ^{op}	85.88±2.88 ^{bc}	3.05±0.86 $^{f-i}$	24.02±1.29 $^{g-k}$	404.66±16.41 $^{g-m}$	6157.63±113.40 ^{ab}
13-7	72.22±8.76 ^{os}	75.60±8.97 ^{ijk}	86.47±8.75 ^{b}	15.58±8.46 ^{bc}	48.11±6.61 $^{d-j}$	369.81±80.23 $^{h-n}$	2983.79±591.17 $^{c-h}$
13-13	58.0±1.50 $^{z-(aa)}$	80.58±5.60 $^{d-g}$	75.89±1.45 ^{ijk}	0.70±0.34 ^{i}	19.25±1.17 $^{g-k}$	776.35±9.39 $^{b-e}$	1454.22±86.66 $^{d-h}$
13-15	74.0±0.10 $^{l-q}$	81.55±2.0 $^{c-f}$	75.89±0.01 ^{ijk}	30.66±4.47 ^{a}	89.72±17.84 $^{a-d}$	355.35±51.18 $^{i-n}$	5229.08±115.86 ^{abc}
13-16	70.0±1.0 $^{r-u}$	80.58±1.45 $^{d-g}$	75.89±0.45 ^{ijk}	5.96±0.46 $^{d-i}$	40.0±14.89 $^{e-k}$	441.82±0.11 $^{g-l}$	1097.24±189.81 $^{d-h}$
14-1	72.0±2.50 $^{p-s}$	86.46±6.78 ^{a}	77.67±1.37 ^{hij}	4.16±2.43 $^{d-i}$	24.49±12.28 $^{g-k}$	431.12±49.93 $^{g-m}$	1010.19±79.86 $^{d-h}$
14-7	80.0±1.0 ^{fgh}	82.52±5.65 $^{c-f}$	74.6±1.84 $^{j-m}$	2.69±0.35 $^{f-i}$	10.83±0.76 ^{ijk}	407.37±23.67 $^{g-m}$	466.83±33.69 ^{fgh}
14-10	52.0±1.50 $^{(ab)}$	84.46±4.58 ^{abc}	75.89±0.01 ^{ijk}	3.91±2.53 $^{e-i}$	41.82±2.37 $^{e-k}$	601.64±81.87 $^{c-j}$	892.30±71.05 $^{e-h}$
14-13	68.0±0.50 ^{tuv}	82.52±0.20 $^{c-f}$	77.60±0.60 ^{hij}	0.15±0.02 ^{i}	13.23±0.05 ^{ijk}	510.45±105.31 $^{e-k}$	256.42±53.49 ^{fgh}
15-1	84.21±1.26 ^{cde}	69.23±0.45 ^{op}	71.92±2.35 ^{lm}	3.94±0.81 $^{e-i}$	14.35±2.09 ^{ijk}	403.53±37.74 $^{g-m}$	852.71± 146.76^{e-h}
15-8	78.0±20.54 ^{ghi}	71.18±2.34 $^{m-p}$	87.05±5.40 ^{b}	1.96±0.46 ^{ghi}	13.39±5.68 ^{ijk}	444.10±66.74 $^{g-l}$	547.12±30.21 ^{fgh}
16-3	74.44±12.0 $^{k-q}$	76.82±0.78 $^{h-k}$	85.88±4.55 ^{bc}	3.59±0.45 $^{f-i}$	20.85±1.23 $^{g-k}$	664.04±5.64 $^{b-h}$	2371.32±92.38 $^{c-h}$
16-4	81.01±0.01 ^{efg}	74.57±1.97 $^{j-m}$	91.17±1.17 ^{a}	1.81±0.59 ^{ghi}	51.18±18.32 $^{c-j}$	484.99±29.81 $^{e-k}$	515.50±36.98 ^{fgh}
17-2	74.44±4.87 $^{k-q}$	75.6±4.56 ^{ijk}	86.47±2.56 ^{b}	ND	8.34±1.19 ^{jk}	393.37±38.94 $^{g-m}$	248.18±22.56 ^{fgh}
18-1	74.44±1.23 $^{k-q}$	68.29±0.01 ^{pq}	87.67±7.88 ^{b}	2.8±0.47 $^{f-i}$	34.98±3.14 $^{f-k}$	465.39±12.14 $^{f-l}$	2734.75±280.88 $^{c-h}$
18-13	86.36±6.79 ^{abc}	77.92±4.67 $^{g-j}$	75.92±3.45 ^{ijk}	ND	102.08±5.53 ^{a}	418.65±24.04 $^{g-m}$	1564.02±134.56 $^{d-h}$
K-38	55.60±1.60 $^{(aa)}$	84.90±3.27 ^{abc}	72.6±15.40 ^{klm}	2.01±1.51 ^{ghi}	28.20±3.64 $^{g-k}$	421.78±18.11 $^{g-m}$	3081.97±170.89 $^{c-h}$

Each value is the mean ± SD of three replicates. Values with the same letter in a column are not significantly different (Tukey's test, $P > 0.05$).
BC, *Botrytis cinerea*; FS, *Fusarium solani*, and RS, *Rhizoctonia solani.*
ND, not detected

Table 4. *Trichoderma* spp. exhibiting phosphate solubilization, IAA production, siderophore production, and potassium mobilization.

Trichoderma spp.	Phosphate Solubilization (mg/L)	IAA Production (mg/L)	Siderophore Production Indeks	Potassium Mobilization (Zone diameter, cm)
7-2	2.63±0.07 $^{h-t}$	80.18±1.25 $^{a-e}$	1.06±0.01 ^{op}	ND
7-4	4.61±0.16 ^{ab}	43.10±3.62 $^{e-m}$	1.13±0.01 ^{nop}	ND
8-3	4.15±0.04 $^{a-f}$	67.24±44.68 $^{a-g}$	1.33±0.23 $^{i-p}$	ND
13-2	3.00±0.52 $^{f-r}$	36.34±6.25 $^{e-m}$	1.55±0.05 $^{f-o}$	4.15±0.05 $^{e-h}$
13-4	2.15±0.51 $^{p-v}$	23.10±0.32 $^{g-m}$	1.88±0.38 $^{c-h}$	4.60±0.01 ^{bcd}
13-5	2.95±0.19 $^{g-s}$	17.07±1.89 $^{i-m}$	2.0±0.18 $^{c-g}$	3.85±0.05 ^{hi}
13-7	3.05±0.09 $^{e-q}$	55.29±11.61 $^{c-m}$	2.30±0.38 ^{bc}	4.15±0.15 $^{e-h}$
13-13	2.60±0.01 $^{i-t}$	95.97±14.94 ^{abc}	1.50±0.15 $^{f-p}$	3.90±0.40 ^{hi}
13-15	2.28±0.36 $^{n-t}$	109.98±0.16 ^{a}	1.75±0.22 $^{d-i}$	4.55±0.15 ^{cde}
13-16	4.72±0.20 ^{a}	36.04±4.16 $^{e-m}$	1.43±0.14 $^{h-p}$	4.0±0.01 ^{ghi}
14-1	3.48±0.01 $^{b-m}$	60.95±5.65 $^{b-k}$	ND	1.10±0.30 ^{jkl}
14-7	2.49±0.01 $^{l-t}$	33.63±8.48 $^{f-m}$	1.77±0.08 $^{d-i}$	3.65±0.15 ^{i}
14-10	2.57±0.04 $^{j-t}$	51.28±0.60 $^{c-m}$	2.0±0.01 $^{c-g}$	4.65±0.25 ^{bcd}
14-13	1.86±0.04 $^{r-w}$	34.92±10.97 $^{e-m}$	2.36±0.07 ^{bc}	4.10±0.10 ^{fgh}
15-1	2.27±0.19 $^{n-t}$	47.78±11.23 $^{d-m}$	1.80±0.20 $^{d-i}$	4.40±0.10 $^{d-g}$
15-8	2.19±0.65 $^{o-u}$	92.69±0.06 $^{a-d}$	2.36±0.22 ^{bc}	4.45±0.05 ^{def}
16-3	3.69±0.09 $^{a-k}$	37.16±2.75 $^{e-m}$	4.69±0.13 ^{a}	ND
16-4	0.74±0.06 ^{vwx}	68.12±5.97 $^{a-g}$	2.0±0.37 $^{c-f}$	4.45±0.05 ^{def}
17-2	3.07±0.20 $^{d-q}$	60.65±9.96 $^{b-l}$	1.60±1.50 $^{f-n}$	5.45±0.05 ^{a}
18-1	0.52±0.48 ^{x}	14.64±0.43 ^{klm}	ND	1.25±0.35 ^{jk}
18-13	3.52±0.15 $^{b-m}$	111.92±0.35 ^{a}	1.11±0.04 ^{nop}	ND
K-38	3.87±0.27 $^{a-g}$	63.01±0.19 $^{b-i}$	1.25±0.05 $^{j-p}$	ND

ND, not detected

Each value is the mean ± SD of three replicates. Values with the same letter in a column are not significantly different (Tukey's test, $P > 0.05$).

the 62 *Trichoderma* spp. Mycelial growth was detected in some petri dishes even without zone formation. It is known that *Trichoderma* strains provide potassium solubility by producing various organic acids (citric, lactic, acetic etc.) [49]. The potassium solubilities of *Trichoderma* spp., which are not widely available in the literature, were also determined within the scope of our study. By determining the properties such as IAA production, phosphate solubility and potassium mobility, it was observed that *Trichoderma* strains were also strong in microbial fertilizer properties. From now on, it is thought that microbial fertilizer studies should be used frequently in addition to biocontrol studies.

Analyses identified 22 *Trichoderma* spp. with the highest performance from a total of 62 strains. Table 3 and Table 4 present the quantitative results of the PGPF characteristics exhibited by these strains and their statistical comparisons. Among these, strains 13-15, 14-13, and 16-3, which exhibited superior performance across multiple PGPM assays, were chosen for molecular identification.

The selection of isolates for molecular identification was based on their PGPM traits, considering spectrophotometric quantitative results (lytic enzymes, IAA, phosphate solubilization), percent inhibition in dual culture tests, and semi-quantitative traits such as siderophore and potassium solubilization. *Trichoderma* sp. 13-15 was selected because it showed positive results for all PGPM characteristics, exhibited the highest IAA production, and demonstrated strong antagonistic activity (>70%) against phytopathogens. *Trichoderma* sp. 14-13 was selected for its overall positive PGPM profile and notably high antagonistic activity against *F. solani* (82.52%). Finally, *Trichoderma* sp. 16-3 was chosen due to its high antagonistic effect (>70%), statistically significant siderophore production, and high activity in all four lytic enzymes.

Molecular identification of three *Trichoderma* spp. exhibiting high PGPM activity revealed that two strains were *T. koningiopsis* and one strain was *T. harzianum* (Table 5). Molecular identification has revealed two different strains of *T. koningiopsis*. The fact that the strains showing high PGPM activity gave similar results confirms the relationship between them. One strain was also identified as *Trichoderma harzianum*. This species is one of the most known and studied species among *Trichoderma*. This result supports the literature that it is an important species in terms of PGPM properties. Figure 6 shows the phylogenetic tree.

Table 5. ITS species identification of three *Trichoderma* spp.

Trichoderma spp. No	Accession number	*Trichoderma* strain No	Similarity ratio
13-15	PP127882	*T. koningiopsis* EGE-K-13-15	99.77%
14-13	PP127885	*T. koningiopsis* EGE-K-14-13	99.83%
16-3	PP127886	*T. harzianum* EGE-K-16-3	100%

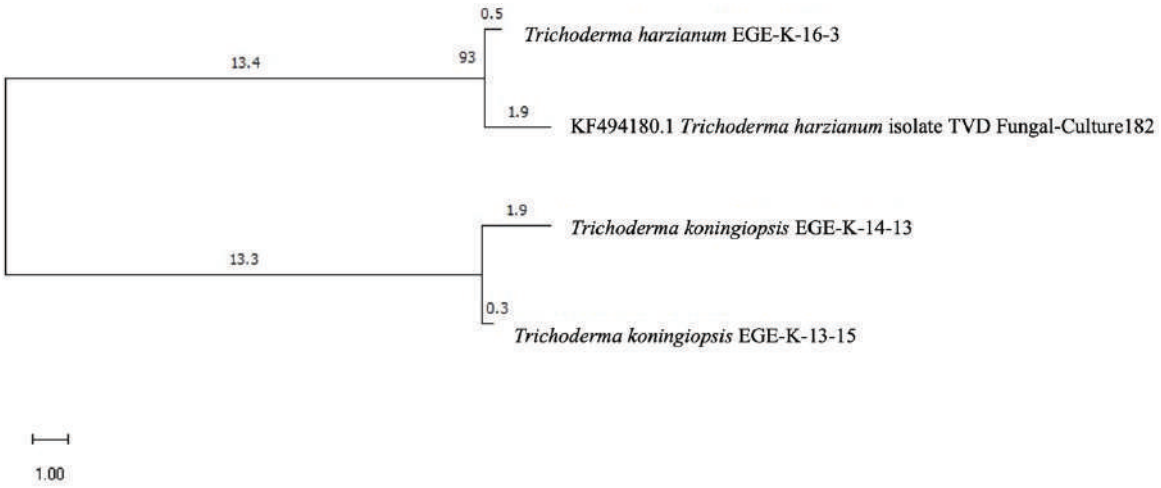


Figure 6. Phylogenetic tree of selected *Trichoderma* strains.

Our study has shown that *Trichoderma* spp. have significant potential as both biocontrol agents and plant growth-promoting microorganisms. In particular, strains *T. koningiopsis* EGE-K-13-15, *T. koningiopsis* EGE-K-14-13, and *T. harzianum* EGE-K-16-3 exhibited high levels of biological activity, demonstrating the high ecological adaptability of *Trichoderma* spp. and highlighting their promising potential as multifunctional bioinoculants for sustainable and integrated agricultural practices.

In addition to the characterization and molecular identification of *Trichoderma* strains for commercialization, effective bioprocessing should also be developed. Developing the production process of *Trichoderma* strains, determining appropriate production conditions and post-production formulation studies are important for commercialization. These parameters, which affect the product's shelf life, must be considered in terms of both application and the continuity of PGPM effectiveness [50,51].

CONCLUSION

Trichoderma species are important in agriculture due to their plant growth-promoting and biological control properties. This study highlights the importance of *Trichoderma* species as plant growth promoters in agricultural applications. Our in vitro results show that *Trichoderma* spp. have remarkable potential in promoting plant growth.

Future studies are recommended to conduct field trials to validate the efficacy of promising *Trichoderma* strains under realistic agricultural conditions. The objectives of this study should be to evaluate their effects on disease control, plant growth promotion, and crop yield under different soil types and climatic conditions. Furthermore, examining the formulation structure and resistance of bio-inoculants developed from these strains is of great importance for their commercial use. In vitro screening studies, however, remain critical as a rapid and cost-effective preliminary evaluation stage that allows for the identification of promising strains based on their functional properties under controlled conditions. Co-inoculation studies with other PGPMs and evaluation of compatibility with chemical pesticides and fertilizers will also make significant contributions to integrated management strategies in sustainable agriculture.

In industrial production, optimizing the production environment contents and physical production parameters should be the next step. It will be a great contribution to the literature to carry out the mentioned studies with three *Trichoderma* strains whose biofertilizer and biological control properties have been determined and molecular identification has been made.

ACKNOWLEDGEMENTS

We would like to thank TUBITAK (The Scientific And Technological Research Council Of Türkiye) for their

financial support to project number 122Z711 under the 1002 - Short-Term Support Module.

AUTHORSHIP CONTRIBUTIONS

Authors equally contributed to this work.

DATA AVAILABILITY STATEMENT

The authors confirm that the data that supports the findings of this study are available within the article. Raw data that support the finding of this study are available from the corresponding author, upon reasonable request.

CONFLICT OF INTEREST

The author declared no potential conflicts of interest with respect to the research, authorship, and/or publication of this article.

ETHICS

There are no ethical issues with the publication of this manuscript.

STATEMENT ON THE USE OF ARTIFICIAL INTELLIGENCE

Artificial intelligence was not used in the preparation of the article.

REFERENCES

[1] Bent E. Induced Systemic Resistance Mediated by Plant Growth-Promoting Rhizobacteria (PGPR) and Fungi (PGPF). Springer US 2006;225–58. [CrossRef]

[2] Kumar A, Prakash A, Johri BN. Bacillus as PGPR in Crop Ecosystem. Springer Berlin 2011;37–59. [CrossRef]

[3] Lopes MJS, Dias-Filho MB, Gurgel ESC. Successful Plant Growth-Promoting Microbes: Inoculation Methods and Abiotic Factors. Front Sustain Food Syst 2021;5. [CrossRef]

[4] Karaca K, Bora S, Eltem R. Determination of the synergistic effect of some plant growth promoting rhizobacteria (PGPR) on the development of wheat and maize seeds in vitro conditions. J BAUN Inst Sci Technol 2025;27:370–383. [Turkish][CrossRef]

[5] Bhandari S, Pandey KR, Joshi YR, Lamichhane SK. An overview of multifaceted role of Trichoderma spp. for sustainable agriculture. Arch Agric Environ Sci 2021;6:72–79. [CrossRef]

[6] Gangwar M, Saini P, Nikhanj P, Kaur S. Plant Growth-Promoting Microbes (PGPM) as Potential Microbial Bio-Agents for Eco-Friendly Agriculture. New York: Springer; 2017. p. 37–55. [CrossRef]

[7] Malgioglio G, Rizzo GF, Nigro S, du Prey VL, Herforth-Rahmé J, Catara V, et al. Plant-microbe ınteraction in sustainable agriculture: The factors that may ınfluence the efficacy of PGPM application. Sustainability 2022;14:2253. [CrossRef]

[8] Karuppiah V, Sun J, Li T, Vallikkannu M, Chen J. Co-cultivation of trichoderma asperellum GDFS1009 and bacillus amyloliquefaciens 1841 causes differential gene expression and ımprovement in the wheat growth and biocontrol activity. Front Microbiol 2019;10:01068. [CrossRef]

[9] Asghar W, Craven KD, Kataoka R, Mahmood A, Asghar N, Raza T, et al. The application of Trichoderma spp., an old but new useful fungus, in sustainable soil health intensification: A comprehensive strategy for addressing challenges. Plant Stress 2024;12:100455. [CrossRef]

[10] Shao Y, Gu S, Peng H, Zhang L, Li S, Berendsen RL, et al. Synergic interactions between Trichoderma and the soil microbiomes improve plant iron availability and growth. NPJ Biofilms Microbiomes 2025;11:56. [CrossRef]

[11] Santoyo G, Orozco-Mosqueda MC, Afridi MS, Mitra D, Valencia-Cantero E, Macías-Rodríguez L. Trichoderma and Bacillus multifunctional allies for plant growth and health in saline soils: recent advances and future challenges. Front Microbiol 2024;15:1423980. [CrossRef]

[12] Pehlivan N, Gedik K, Eltem R, Terzi E. Dynamic interactions of Trichoderma harzianum TS 143 from an old mining site in Turkey for potent metal(oid) s phytoextraction and bioenergy crop farming. J Hazard Mater 2021;403:123609. [CrossRef]

[13] Turgay G, Eren E, Eltem R, Cakır D, Aydemir BC. Molecular characterization of Trichoderma spp. isolates in growing farms in Turkey and their effects on Agaricus bisporus production. Plant Pathol 2023;72:1272-1282. [CrossRef]

[14] Gul DM, Eltem R. In vitro investigation of the effects of some fertilizers and fungicides on the growth of trichoderma species. Anadolu J AARI 2022;0225:167–181. [Turkish] [CrossRef]

[15] Karaca K, İphar M, Eltem R. Screening of antibacterial effects of various trichoderma isolates on some human and plant pathogenic bacteria under in vitro conditions. J Fungus 2025;16:34–41. [Turkish]

[16] Gul DM, Eltem R. Evaluation of bacillus isolates as a biological control agents against soilborne phytopathogenic fungi. Int Microbiol 2024;28:75–89. [CrossRef]

[17] Bader AN, Salerno GL, Covacevich F, Consolo VF. Native Trichoderma harzianum strains from Argentina produce indole-3 acetic acid and phosphorus solubilization, promote growth and control wilt disease on tomato (Solanum lycopersicum L.). J King Saud Univ Sci 2020;32:867–873. [CrossRef]

[18] Gezgin Y, Gul DM, Sensatar SS, Kara CU, Sargın S, Sukan FV, et al. Evaluation of Trichoderma atroviride and Trichoderma citrinoviride growth profiles and their potentials as biocontrol agent and biofertilizer. Turk Journal of Biochemistry 2020;45:1–13. [CrossRef]

[19] Khaledi N, Taheri P. Biocontrol mechanisms of Trichoderma harzianum against soybean charcoal rot caused by Macrophomina phaseolina. J Apll Res Plant Protect 2016;56. [CrossRef]

[20] Kumar NV, Rajam KS, Rani ME. Plant growth promotion efficacy of ındole acetic acid (IAA) produced by a mangrove associated fungi-trichoderma viride VKF3. Int J Curr Microbiol Appl Sci 2017;6:2692–701. [CrossRef]

[21] Mis B, Karaca K, Eltem R. In vitro antagonistic activity of plant growth promoting rhizobacteria against aggressive biotypes of the green mold. J Basic Microbiol 2024;64:e2400422. [CrossRef]

[22] Qian Y, Zhong L, Sun Y, Sun N, Zhang L, Liu W, et al. Enhancement of Cellulase Production in Trichoderma reesei via Disruption of Multiple Protease Genes Identified by Comparative Secretomics. Front Microbiol 2019;10:1–12. [CrossRef]

[23] Bradford MM. A Rapid and Sensitive Method for the Quantitation of Microgram Quantities of Protein Utilizing the Principle of Protein-Dye Binding. Anal Biochem 1976;72:248–254. [CrossRef]

[24] Miller GL. Use of Dinitrosalicylic Acid Reagent for Determination of Reducing Sugar. Anal Chem 1959;31:426–468. [CrossRef]

[25] Gajera HP, Vakharia DN. Production of lytic enzymes by Trichoderma isolates during in vitro antagonism with Aspergillus niger, the causal agent of collar rot of peanut. Brazilian J Microbio 2012;43:33–52. [CrossRef]

[26] Zarei M, Aminzadeh S, Zolgharnein H, Safahieh A, Daliri M, Noghabi KA, et al. Characterization Of A Chitinase Wıth Antifungal Actıvıty From A Native Serratia marcescens B4a. Brazilian J Microbio 2011;42:1017–1029. [CrossRef]

[27] Schwyn B, Neilands JB. Universal chemical assay for the detection and determination of siderophores. Anal Biochem 1987;160:47–56. [CrossRef]

[28] Gravel V, Antoun H, Tweddell RJ. Growth stimulation and fruit yield improvement of greenhouse tomato plants by inoculation with Pseudomonas putida or Trichoderma atroviride: Possible role of indole acetic acid (IAA). Soil Biol Biochem 2007;39:1968–1977. [CrossRef]

[29] Murphy J, Riley JP. A modified single solution method for the determination of phosphate in natural waters. Anal Chim Acta 1962;27:31–36. [CrossRef]

[30] Prajapati K, Ssharma MC, Modi HA. Isolation of two potassium solubilizing fungi from ceramic industry soils. Life Sci Leaf 2012;27:71-75.

[31] Sargin S, Gezgin Y, Eltem R, Vardar F. Micropropagule production from Trichoderma harzianum EGE-K38 using solid-state fermentation and a comparative study for drying methods. Turkish J Bio 2013;37:139–46. [CrossRef]

[32] Mukhopadhyay R, Kumar D. Trichoderma: a beneficial antifungal agent and insights into its mechanism of biocontrol potential. Egypt J Biol Pest Control 2020;30:133. [CrossRef]

[33] Stracquadanio C, Quiles JM, Meca G, Cacciola SO. Antifungal activity of bioactive metabolites produced by Trichoderma asperellum and Trichoderma atroviride in liquid medium. J Fungi 2020;6:1–18. [CrossRef]

[34] Zhan X, Khan RAA, Zhang J, Chen J, Yin Y, Tang Z, et al. Control of postharvest stem-end rot on mango by antifungal metabolites of Trichoderma pinnatum LS029-3. Sci Hortic 2023;310:111696. [CrossRef]

[35] Savas NG, Yildiz M, Eltem R, Ozkale E. Determination of antifungal efficiency of some fungicides and secondary metabolites of Trichoderma species against Botrytis cinerea. J Environ Biol 2021;42:705–713. [CrossRef]

[36] Thangaraj P, Balamurali AS, Muthusamy N. Biological control of Trichoderma spp.: Mechanisms of action against phytopathogens, insect pests, and its multifaceted roles in agro-ecosystems. Environ Conserv J 2025;26:302–314. [CrossRef]

[37] Monte E. Understanding Trichoderma: between biotechnology and microbial ecology. Int Microbiol 2001;4:1–4.

[38] Adnani M, El Hazzat N, El Alaoui MA, Selmaoui K, Benkirane R, Ouazzani Touhami A, et al. In vitro and in vivo study of the antagonistic effects of a Trichoderma strain against four isolates of Fusarium that are pathogenic to chickpea. 3 Biotech 2024;14:271. [CrossRef]

[39] Liu H, Hao D, Li Y, Wang X. Approaches for the establishment of optimized co-culture system of multiple Trichoderma strains for culture metabolites highly effective in cucumber growth promotion 2022;13:1020077. [CrossRef]

[40] Kucuk C. In vitro Antagonistic Activity against Fusarium Species of Local Trichoderma spp. Isolates. J Biol Environ Sci 2017;11:67–74.

[41] Nathan VK, Rani ME, Rathinasamy G, Dhiraviam KN, Jayavel S. Process optimization and production kinetics for cellulase production by Trichoderma viride VKF3. Springerplus 2014;3:92. [CrossRef]

[42] Bogumił A, Paszt LS, Lisek A, Trzciński P, Harbuzov A. Identification of new Trichoderma strains with antagonistic activity against Botrytis cinerea. Folia Horticulturae 2013;25:123–132. [CrossRef]

[43] Sivasakthi S, Usharani G, Saranraj P. African Journal of Agricultural Research Biocontrol potentiality of plant growth promoting bacteria (PGPR)-Pseudomonas fluorescens and Bacillus subtilis: A review 2014;9:1265–1277.

[44] Milagres AMF, Machuca A, Napoleão D. Detection of siderophore production from several fungi and bacteria by a modification of chrome azurol S (CAS) agar plate assay. J Microbiol Methods 1999;37:1–6. [CrossRef]

[45] Yadav G, Sharma N, Goel A, Varma A, Mishra A, Choudhary SLKDK. Trichoderma Mediated Metal Chelator and Its Role in Solanum melongena Growth Under Heavy Metals. J Plant Growth Regul 2023;43:178-200. [CrossRef]

[46] Win TT, Swe TM, Ei HH, Win NN, Swe KK, Nandar W, et al. An evaluation into the biosorption and biodegradation of azo dyes by indigenous siderophores-producing bacteria immobilized in chitosan. Biodegradation 2021;32:697–710. [CrossRef]

[47] L Ghosh SK, Banerjee S, Sengupta C. Siderophore production by antagonistic fungi. J Biopest 2017;10(2):105-112. [CrossRef]

[48] Tandon A, Fatima T, Anshu, Shukla D, Tripathi P, Srivastava S, et al. Phosphate solubilization by Trichoderma koningiopsis (NBRI-PR5) under abiotic stress conditions. J King Saud Univ Sci 2020;32:791–798. [CrossRef]

[49] Bashir Z, Zargar MY, Vishwakarma DK. Potassium-Solubilizing Microorganisms for Sustainable Agriculture. Applied Agricultural Practices for Mitigating Climate Change. 1st ed. Boca Raton, Florida: CRC Press; 2020. p. 17–28. [CrossRef]

[50] Kumar V, Koul B, Taak P, Yadav D, Song M. Journey of trichoderma from pilot scale to mass production: A review. Agriculture 2023;13:2022. [CrossRef]

[51] Martinez Y, Ribera J, Schwarze FWMR, De France K. Biotechnological development of Trichoderma-based formulations for biological control. Appl Microbiol Biotechnol 2023;107:5595–5612. [CrossRef]

Sigma J Eng Nat Sci, Vol. 44, No. 1, pp. 174–183, February, 2026

Sigma Journal of Engineering and Natural Sciences
Web page info: https://sigma.yildiz.edu.tr
DOI: 10.14744/sigma.2025.00000

Research Article

Structural, thermal, morphological, and rheological properties of yeast extracts obtained from *Saccharomyces cerevisiae, Saccharomyces boulardii,* and *Kluyveromyces marxianus*

Furkan DEMİRGÜL[1,*], Ömer ŞİMŞEK[2], Enes DERTLİ[3], Osman SAĞDIÇ[2]

[1]*Department of Gastronomy and Culinary Arts, Faculty of Fine Arts and Design, Doğuş University, İstanbul, 34775, Türkiye*
[2]*Department of Food Engineering, Faculty of Chemical and Metallurgical Engineering, Yıldız Technical University, 34220, İstanbul, Türkiye*
[3]*Department of Food Engineering, Faculty of Chemical and Metallurgical Engineering, Istanbul Technical University, 34467, İstanbul, Türkiye*

ARTICLE INFO

Article history
Received: 05 August 2024
Revised: 03 October 2024
Accepted: 07 December 2024

Keywords:
DSC; FTIR; Rheological Properties; SEM; Yeast Extract

ABSTRACT

Yeast extracts, which are mostly used as flavor enhancers in foods, also give to the nutritional value of foods, especially due to their amino acid profiles. In addition to all these properties, yeast extracts have the possibility to supply added technological advantages to the foods they are used in due to their physicochemical properties. However, there are not enough studies investigating the structural, thermal, morphological, and rheological properties of yeast extract powders. To fill this gap and investigate the potential of yeast extracts to supply added benefits to foods, in this study, yeast extract powders obtained from *Saccharomyces cerevisiae* TGM10, *Saccharomyces boulardii* S11, and *Kluyveromyces marxianus* TGM66 structural properties were investigated using Fourier Transform Infrared Spectroscopy, thermal properties using Differential Scanning Calorimetry, morphological properties using Scanning Electron Microscopy and rheological properties using rheometer. The melting points of *Saccharomyces cerevisiae* TGM10, *Saccharomyces boulardii* S11, and *Kluyveromyces marxianus* TGM66 extracts were 129 °C, 128 °C and 132 °C, respectively. It is believed that the Fourier Transform Infrared spectra obtained in the study will contribute to the literature in terms of the production and identification of yeast extracts, and the morphological properties will contribute to the determination of the drying method to be applied to the extracts. It was determined that all three yeast extracts used in the study had the potential to increase the viscosity of the soup, and the yeast extract obtained from *Kluyveromyces marxianus* TGM66 was the most successful sample in this respect. It is thought that this may be related to the fact that this extract has a different carbohydrate and/or amino acid profile than others. Considering the data obtained in the study, it is thought that with a better understanding of the structural, thermal, morphological, and rheological properties of yeast extracts, the possibility of using these additives in foods will expand.

Cite this article as: Demirgül F, Şimşek Ö, Dertli E, Sağdıç O. Structural, thermal, morphological, and rheological properties of yeast extracts obtained from *Saccharomyces cerevisiae*, *Saccharomyces boulardii*, and *Kluyveromyces marxianus*. Sigma J Eng Nat Sci 2026;44(1):174–183.

***Corresponding author.**
*E-mail address: fdemirgul@edu.tr

This paper was recommended for publication in revised form by Editor-in-Chief Ahmet Selim Dalkilic

Published by Yıldız Technical University Press, İstanbul, Turkey
© Author. This is an open access article under the CC BY-NC license (http://creativecommons.org/licenses/by-nc/4.0/).

INTRODUCTION

The product obtained by breaking down and removing the yeast cell wall in various ways (such as autolysis, plasmolysis, enzymatic hydrolysis, thermolysis, and mechanical disruption) and consisting of water-soluble constituents of the yeast cell is called yeast extract [1]. The major constituent of yeast extracts is hydrolyzed protein [2], and the protein quantity of yeast extract generally varies between approximately 46% [3] and 74% [4] by dry weight (dw). The fat content of yeast extracts is approximately 1% [5]. Yeast extracts, which are also rich in essential amino acids, are a good source of taking these amino acids into the body [6]. Moreover, yeast extracts contain B group vitamins [4], minerals like magnesium, calcium, iron, and zinc, and phenolic compounds like (±)-catechin, gallic acid, protocatechuic acid, ferulic acid, and *p*-coumaric acid [7]. Due to their rich nutritional composition, yeast extracts are used in the nutrition of both humans and various animals. In addition to their nutritional properties, yeast extracts have begun to be utilized in various foods as a natural flavor enhancer another option to monosodium glutamate in recent years, as it has been understood that they cause meat-like flavor and umami taste due to the high amounts of glutamic acid [8], 5'-monophosphate nucleotides [9], and peptide profiles [10] they contain.

In addition to their nutritional and flavor-enhancing properties, yeast extracts may also contribute technologically to the foods they are used in, especially due to the carbohydrates and proteins they contain. As a matter of fact, in a previous study [5] we conducted, we determined that yeast extracts can supply technological benefits to foods due to their water-holding capacity, oil-binding capacity, and emulsion stability. In fact, the yeast cell wall, which is removed in the production of yeast extract, has thickening properties due to its carbohydrate (especially β-glucans) profile [11]. However, there is the potential for slight losses in flavor when yeast cell walls are used in foods [12]. Although there are some studies examining the rheological properties of yeast protein extracts [13, 14] and yeast extract pastes (Marmite™) [15], to our knowledge, there is no study examining the effects of yeast extract powders used as additives in some foods in recent years on the rheological properties of foods such as soup. However, yeast extracts contain approximately 12.9% carbohydrates [7], and due to their rich protein and carbohydrate content, yeast extracts have the potential to contribute to the rheological properties of foods if used in appropriate foods. In addition, there are not enough studies investigating the structural, thermal, and morphological properties of yeast extracts. However, with a better understanding of their structural and morphological properties, more effective yeast extract powder production can be achieved, and with a better understanding of their thermal properties, the possibilities of using yeast extracts in suitable food systems can be increased. In this context, this study aims to investigate the structural, thermal, morphological, and rheological features of yeast extracts obtained from *S. cerevisiae* TGM10, *S. cerevisiae* var. *boulardii* S11, and *K. marxianus* TGM66 yeasts and define their characteristic properties. Thus, it is targeted to determine whether yeast extracts, which are mostly used in various foods due to their flavor-enhancing and nutritional features, have the potential to provide added benefits to the foods in which they are used.

MATERIALS AND METHODS

Materials

In this study, lyophilized yeast extract powders obtained from *S. cerevisiae* TGM10, *S. boulardii* S11, and *K. marxianus* TGM66 strains in our previous study [5] were used. The chemical compositions of the yeast extracts used in the study are summarized in Table 1 [5].

Methods

The experimental framework of the study using three different yeast extracts is summarized in Figure 1.

Structural Properties

Structural properties of yeast extracts were examined using Fourier Transform Infrared (FTIR) spectroscopy (Bruker Tensor 27, Germany). Measurements were done by dissolving yeast extract powders in distilled water and preparing 10% solutions. Before measurement, distilled water was used to ensure that the spectroscopy accepted distilled water as a reference. Measurements of the samples were carried out at room temperature and in the mid-infrared region (in the wavelength range of 500-3500 cm^{-1}).

Table 1. Chemical compositions of yeast extract powders obtained from *S. cerevisiae* TGM10, *S. boulardii* S11, and *K. marxianus* TGM66 strains used in the study

Chemical composition (g/100 g dw)	TGM10	S11	TGM66
Moisture (%)	13.93	14.20	15.37
Ash	11.77	12.82	11.15
Protein	69.17	66.16	62.42
Fat	1.36	1.09	1.33
Carbohydrates and other compounds	17.69	19.93	25.10

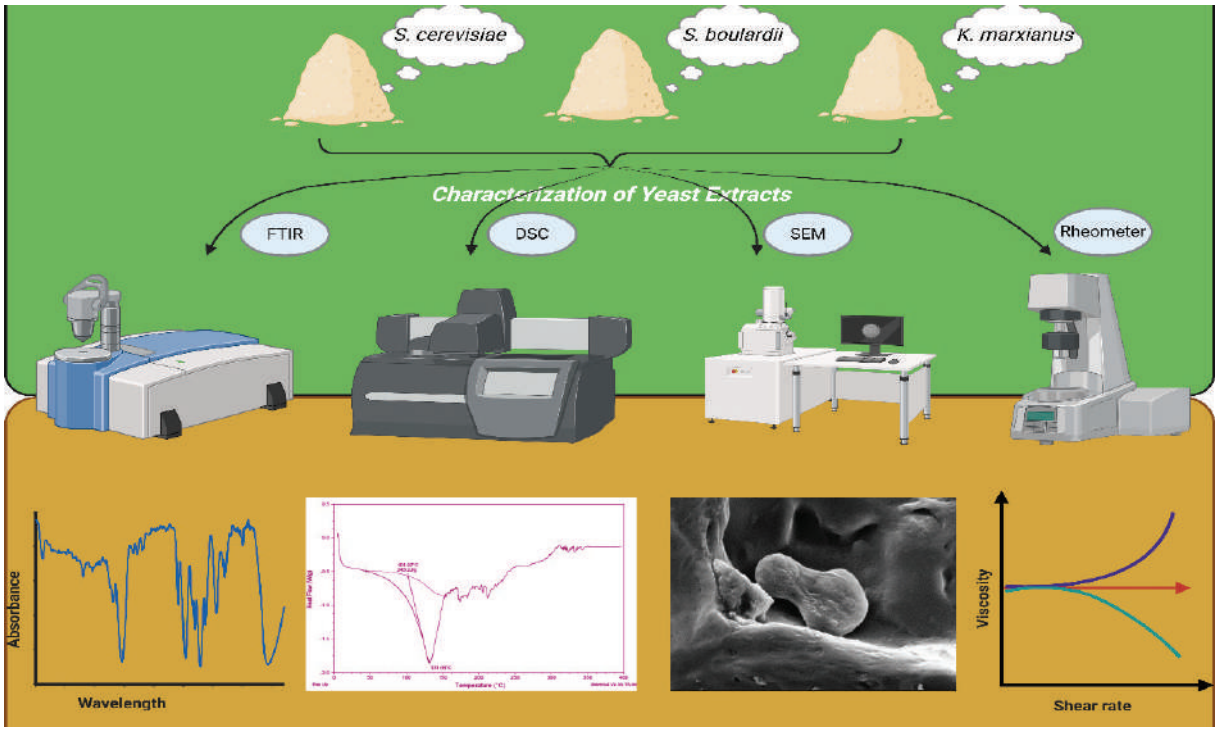


Figure 1. Experimental framework of the study [Figure 1 was figured out by the author (F.D.) using BioRender.com.]

Thermal Properties

Thermal properties of yeast extracts were examined by a Differential Scanning Calorimeter (DSC, Q20, TA Instruments Inc., USA) with some modifications to the method proposed by Kavosi et al. [16]. The samples were weighed as 10-15 mg onto aluminum DSC pans and kept in a desiccator for 20-30 minutes. Then, the hermetically sealed pans were loaded into the DSC calorimeter and heated to 400 °C under high-purity nitrogen gas (20 mL/min) with a heating rate of 10 °C/min. An identical blank pan was used as a control. Melting temperatures of yeast extracts were calculated from the DSC thermograms obtained.

Morphological Properties

Surface morphological properties of yeast extracts were determined by Scanning Electron Microscopy (SEM, Zeiss Evo LS 10, Germany) by slightly modifying the method proposed by İşçi and Hayta [17]. Before analysis, samples were coated with gold-palladium in a gold-plating device (Quorum SC7620, UK) for 120 seconds. Examination of the samples with SEM was carried out at 10 kV.

Rheological Properties

Rheological properties of yeast extracts were examined by making some modifications to the procedure suggested by Zehir-Şentürk et al. [18]. Yeast extracts were dissolved in vegetable soup (Penelope Gurme, Türkiye; consists of semolina, dried broccoli, dried spinach, and dried celery) at two different concentrations (0.5% and 1%) and shear stress (Pa) values against shear rate (s^{-1}) were obtained by measuring 100 points on the rheometer (Anton Paar, MCR-302, Austria) at two different temperatures (25 °C and 50 °C) and the flow behavior of the samples was examined. The obtained data were adapted to the Ostwald de Waele (Power Law) rheological model with the help of the following equation:

$$\tau = K(\gamma)^n$$

Here, τ represents the shear stress (Pa), γ is the shear rate (s^{-1}), K is the consistency coefficient ($Pa \cdot s^n$), and n is the flow behavior index.

Statistical Analysis

Statistical analyses were made with the SPSS (PASW 18.0) program, all experiments were made in triplicate. Data were subjected to one-way analysis of variance (ANOVA) and post hoc comparisons were made using the Tukey test. Differences between data were considered statistically significant at the 95% ($p \leq 0.05$) confidence interval. Statistica 14.0 (TIBCO, USA) software was used to evaluate rheological analyses.

RESULTS AND DISCUSSION

Structural Properties

FTIR spectroscopy, a type of vibration spectroscopy, is a technique that can provide easy and fast results that reflect both the molecular structure and the molecular environment, and the fact that each chemical bond has a separate vibration frequency in infrared spectroscopy allows the

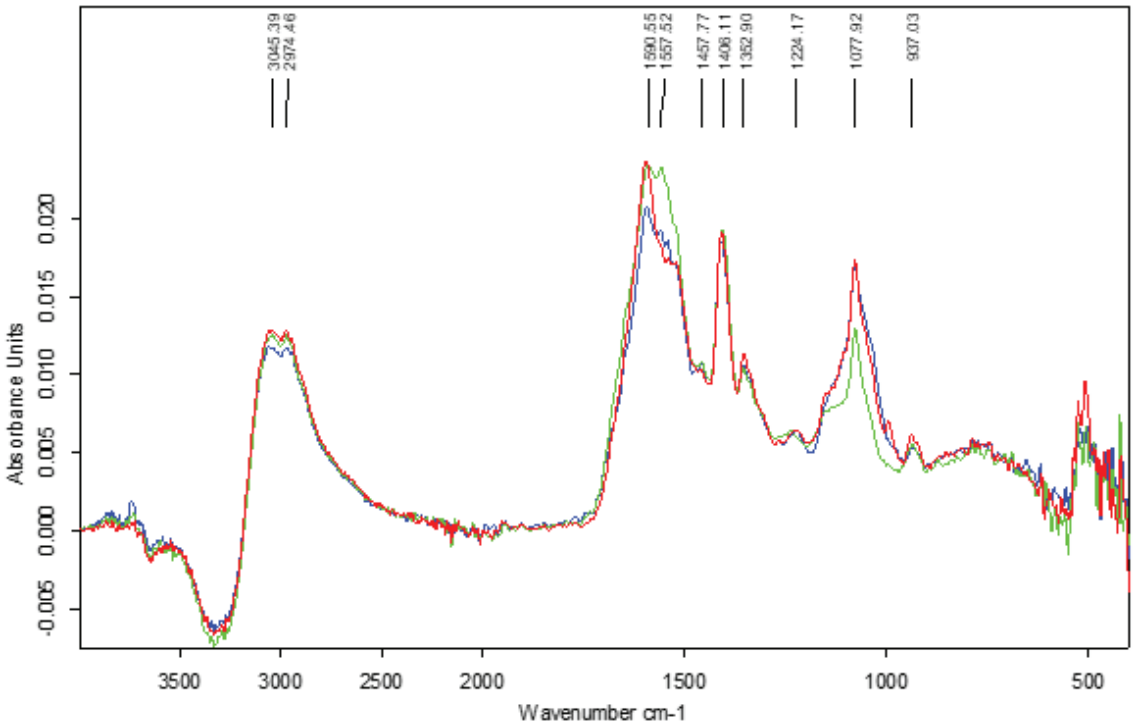


Figure 2. FTIR spectra of three different yeast extracts (the green spectrum belongs to the *S. cerevisiae* TGM10 extract, the red spectrum to the *S. boulardii* S11 extract, and the blue spectrum to the *K. marxianus* TGM66 extract).

identification of chemical groups [19]. For this reason, FTIR spectroscopy was used to perform the structural properties of yeast extracts in this study, and the FTIR spectra of *S. cerevisiae* TGM10, *S. boulardii* S11, and *K. marxianus* TGM66 extracts are shown in Figure 2.

Distinct peaks in the FTIR spectra of the yeast extracts were examined, and it was observed that all three yeast extracts gave peaks at similar wavelengths. Yeast extracts are mainly composed of proteins, peptides, amino acids, nucleic acids, carbohydrates, fats, vitamins, minerals and phenolic compounds [8], and the vibrational peaks in the FTIR spectrum of yeast extracts are thought to be associated with these compounds, especially proteins and amino acids. Since there are many overlapping bands in the infrared spectrum, the chemical structure of a protein cannot be inferred from it, but changes in chemical structure can be understood [20].

The bands at approximately 3000 cm^{-1} are generally associated with C-H bonds, and more specifically, the bands to the left of 3000 cm^{-1} (between 3150 cm^{-1} and 3000 cm^{-1}) are attributed to aromatic (between 3010 cm^{-1} and 3050 cm^{-1}) and vinyl CH, while the bands to the right are attributed to aliphatic C-H stretching [21]. Considering this information, the bands at approximately 3039 cm^{-1} and 2975 cm^{-1}; 3045 cm^{-1} and 2974 cm^{-1}; 3042 cm^{-1} and 2976 cm^{-1} in *S. cerevisiae* TGM10, *S. boulardii* S11, and *K. marxianus* TGM66 extracts, respectively, may be due to the vibration of aromatic and aliphatic C-H bonds. The bands between 1595 cm^{-1} and 1541 cm^{-1} in the spectrum are thought to be related to amino acids and arise from antisymmetric NH_3^+ deformation or antisymmetric COO– stretching [22]. The bands at approximately 1457 cm^{-1}, 1459 cm^{-1}, and 1457 cm^{-1} in *S. cerevisiae* TGM10, *S. boulardii* S11, and *K. marxianus* TGM66 extracts, respectively, may be due to different CH_2/CH_3 bending vibrations in the proteins. The bands at 1406 cm^{-1} (*S. cerevisiae* TGM10), 1407 cm^{-1} (*S. boulardii* S11), and 1408 cm^{-1} (*K. marxianus* TGM66) in the samples are probably related to the $C(CH_3)_2$ stretching that generally occurs in proteins. The bands at approximately 1353 cm^{-1} (*S. cerevisiae* TGM10), 1352 cm^{-1} (*S. boulardii* S11), and 1353 cm^{-1} (*K. marxianus* TGM66) may be due to CH_2 deformation in lipids. It is thought that the bands at approximately 1236 cm^{-1} (*S. cerevisiae* TGM10), 1224 cm^{-1} (*S. boulardii* S11), and 1224 cm^{-1} (*K. marxianus* TGM66) may be related to C-O stretching in free nucleotides [23, 24]. The bands at approximately 1076 cm^{-1} (*S. cerevisiae* TGM10), 1077 cm^{-1} (*S. boulardii* S11), and 1077 cm^{-1} (*K. marxianus* TGM66) are probably related to the symmetric stretching of $PO2^-$ in the RNA [23, 25]. The bands around 900 cm^{-1} and 1000 cm^{-1} are generally associated with carbohydrates, and the bands at approximately 936 cm^{-1} (*S. cerevisiae* TGM10), 994 and 937 cm^{-1} (*S. boulardii* S11), and 933 cm^{-1} (*K. marxianus* TGM66) are thought to be related to vibrations in glycosidic bonds [23, 26].

In recent years, FTIR spectroscopy has become widespread because it is a sensitive, fast, easy, and relatively

inexpensive method for estimating the structural properties of foods. FTIR spectroscopy can be used to estimate the structural properties of yeast extracts, monitor cell growth in yeast biomass production, and monitor the effectiveness of autolysis or other cell lysis methods, which is one of the most important levels of yeast extract production [24].

Thermal Properties

DSC is a useful thermoanalytical approach in which the heat difference required to increase the temperature of a sample, and a reference is measured as a function of temperature, allowing to quickly analyze phase changes caused by some chemical reactions such as water crystallization (melting and freezing), water evaporation, and protein denaturation [27]. In this context, DSC analysis was made to determine the melting temperatures of yeast extracts, and the DSC thermograms of *S. cerevisiae* TGM10, *S. boulardii* S11, and *K. marxianus* TGM66 extracts are shown in Figure 3.

When DSC thermograms are examined, endothermic peaks are observed at approximately 129 °C, 128 °C and 132 °C, corresponding to the melting points of *S. cerevisiae* TGM10, *S. boulardii* S11 and *K. marxianus* TGM66 extracts, respectively. It was observed that the thermal stability of *S. cerevisiae* TGM10 and *S. boulardii* S11 extracts were similar to each other, while the thermal stability of *K. marxianus* TGM66 extracts was slightly higher than the other samples.

There are not sufficient studies in literature examining the thermal properties of yeast extracts. However, DSC analysis has a high potential for determining stability parameters in complex systems such as yeast extracts and can be utilized as an easy, rapid, and reliable technique to examine the stability of proteins and fatty acids in particular.

Morphological Properties

With SEM, information can be obtained about the microstructural surface morphologies and chemical compositions of the samples [28]. SEM was used to observe the morphologies of yeast extract powders. Micrographs of *S. cerevisiae* TGM10, *S. boulardii* S11, and *K. marxianus* TGM66 extracts examined by SEM are shown in Figure 4.

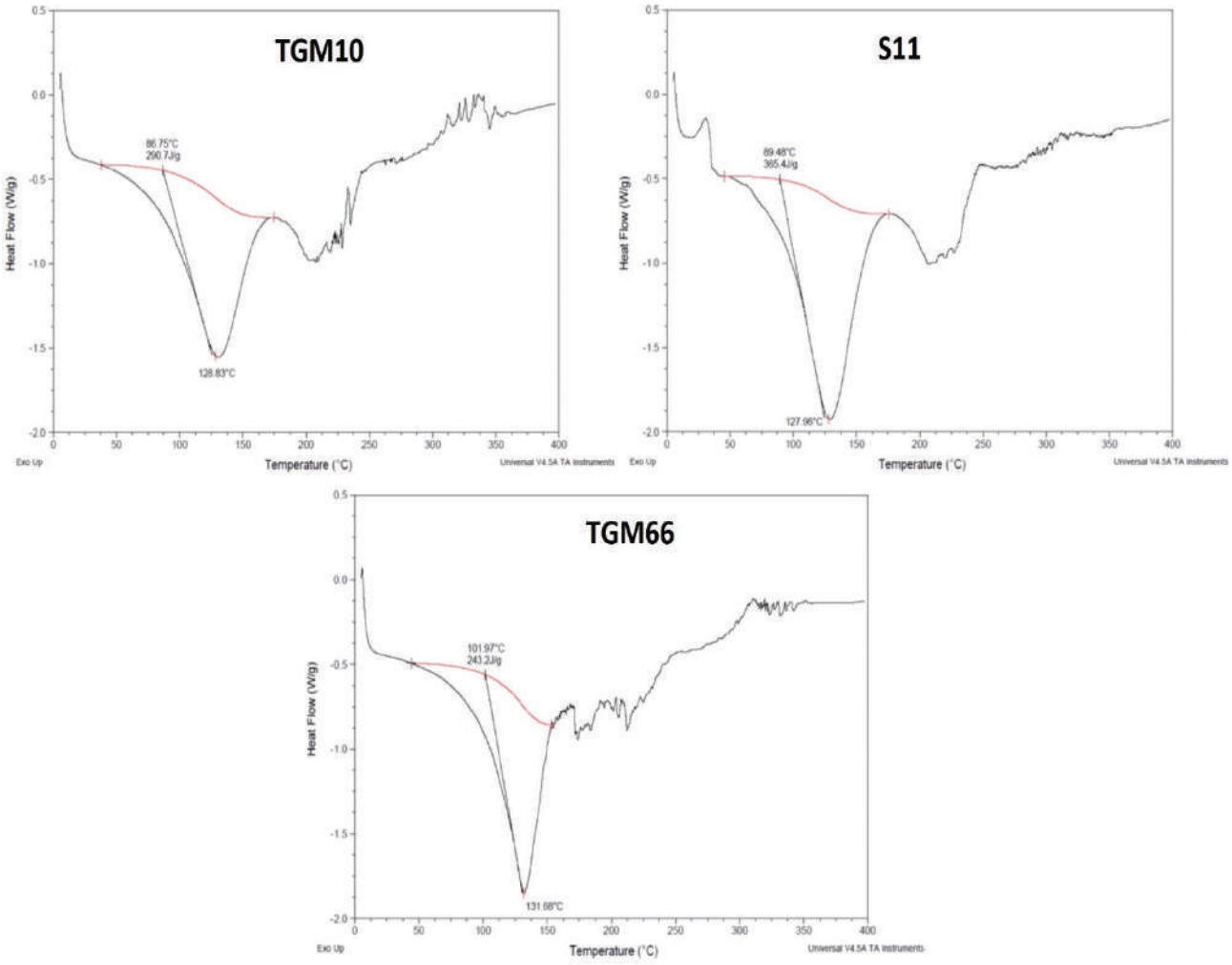


Figure 3. DSC thermograms of *S. cerevisiae* TGM10, *S. boulardii* S11, and *K. marxianus* TGM66 extracts, respectively.

The drying process (such as freeze drying and spray drying) applied to liquid samples affects the particle size of the resulting powder particles [29]. In the freeze drying (lyophilization) process, liquid samples are first frozen and then water is removed from the frozen sample by sublimation. Therefore, lyophilized particles break down and become compressed into sheet-like layers with a porous surface [29]. When micrographs of lyophilized yeast extract powders are examined, it is seen that the samples have a porous surface similar to each other and are irregularly distributed. In their study where they examined freeze- and spray-dried samples of yeast β-glucan, Petravić-Tominac et al. [29] reported that elliptical and oval shapes were observed in spray-dried samples with better preservation of the original structure.

Rheological Properties

The consistency coefficients, flow behavior indices, and R^2 values of yeast extracts dissolved in vegetable soup at two different concentrations (0.5% and 1%) at 25 °C and 50 °C, determined using the Ostwald de Waele model, are shown in Tables 2 and 3, respectively.

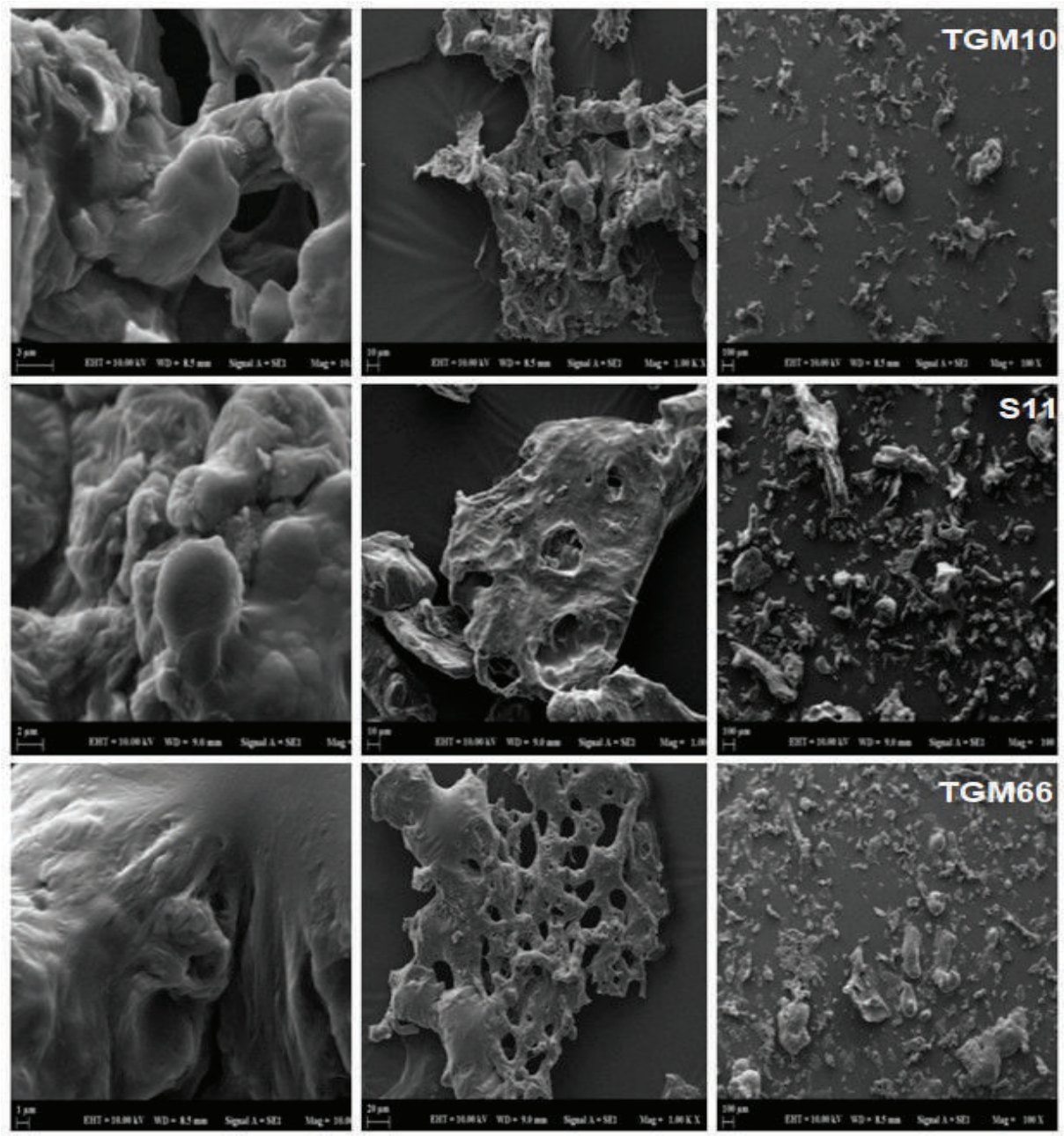


Figure 4. Micrographs of extracts of *S. cerevisiae* TGM10, *S. boulardii* S11, and *K. marxianus* TGM66, respectively.

Table 2. Rheological properties of vegetable soup samples, in which yeast extracts obtained from *S. cerevisiae* TGM10, *S. boulardii* S11, and *K. marxianus* TGM66 strains were mixed at two different concentrations (0.5% and 1%), at 25 °C

Samples	Consistency coefficient (Pa.s^n)	Flow behavior index (n)	R^2
TGM10 (0.5%)	2.22 ± 0.14^{b}	0.819 ± 0.056^{ab}	0.9923
S11 (0.5%)	2.35 ± 0.46^{b}	0.793 ± 0.023^{ab}	0.9893
TGM66 (0.5%)	2.41 ± 0.18^{b}	0.777 ± 0.044^{ab}	0.9883
TGM10 (1%)	2.54 ± 0.39^{ab}	0.787 ± 0.081^{ab}	0.9938
S11 (1%)	3.00 ± 0.51^{ab}	0.754 ± 0.034^{b}	0.9884
TGM66 (1%)	3.43 ± 0.44^{a}	0.746 ± 0.035^{b}	0.9899
C-1 (Plain soup)	2.08 ± 0.14^{b}	0.905 ± 0.044^{a}	0.9953

Results are expressed as mean values (n = 3) ± Standard Deviation (SD). Different letters in the same column specify that the difference between the two values is statistically significant ($p \leq 0.05$).

In the measurements, the flow behavior indices of all samples were below 1, but close to 1 (between 0.746-0.969) (Table 2 and 3). The flow behavior index being below 1 is classified as pseudoplastic flow behavior [30]. However, since the flow behavior indices are close to 1, it can be said that the flow behavior of all samples shows a weak pseudoplastic characteristic. In a study by Pacheco and Sgarbieri [13] on brewer's yeast protein concentrates prepared by three different procedures, it was reported that all yeast protein concentrates showed pseudoplastic behavior. In a study [14] investigating the possibility of using yeast protein extracts obtained from *S. cerevisiae* and *Schizosaccharomyces pombe* as an alternative to egg lecithin in mayonnaise sauce production, it was determined that both samples showed similar viscoelastic behavior when compared to mayonnaise containing egg powder. In the study conducted by White et al. [15], according to steady-state shear tests, yeast extract paste (Marmite™) exhibits thixotropic behavior at ambient temperature, while at higher temperatures the extent of thixotropy decreases and approaches Newtonian behavior. The differences between the results are thought to be mainly related to the form, composition, and production methodology of the products. More research is needed to shed light on the issue.

In addition to the flow behavior index, consistency coefficients are also important for yeast extracts. The consistency coefficient of a fluid gives an idea about the viscosity, and a high consistency coefficient indicates that the viscosity is also high [30]. In measurements made at 25 °C, all samples with added yeast extract increased the consistency coefficient of plain vegetable soup (Table 2), and the most successful sample in this respect was *K. marxianus* TGM66 (1%) ($p \leq 0.05$). In addition, all yeast extracts increased the consistency coefficient of vegetable soup by similar ($p > 0.05$) amounts if used at the same concentration. Although the effect of samples other than *K. marxianus* TGM66 (%1) on the consistency coefficient was statistically insignificant ($p > 0.05$), it can be said that yeast extracts will have a positive contribution to the viscosity of foods such as soup at room temperature.

The consistency coefficients of both plain vegetable soup (control) and vegetable soups with yeast extract added at the same concentration decreased significantly ($p \leq 0.05$) as the temperature increased from 25 °C to 50 °C. However, the consistency coefficients of all samples with added yeast

Table 3. Rheological properties of vegetable soup samples, in which yeast extracts obtained from *S. cerevisiae* TGM10, *S. boulardii* S11, and *K. marxianus* TGM66 strains were mixed at two different concentrations (0.5% and 1%), at 50 °C

Samples	Consistency coefficient (Pa.s^n)	Flow behavior index (n)	R^2
TGM10 (0.5%)	1.17 ± 0.11^{cd}	0.944 ± 0.014^{a}	0.9821
S11 (0.5%)	1.34 ± 0.23^{bcd}	0.924 ± 0.029^{ab}	0.9795
TGM66 (0.5%)	1.40 ± 0.13^{bc}	0.932 ± 0.015^{a}	0.9823
TGM10 (1%)	1.56 ± 0.08^{abc}	0.863 ± 0.030^{bc}	0.9819
S11 (1%)	1.81 ± 0.21^{ab}	0.815 ± 0.011^{cd}	0.9761
TGM66 (1%)	1.97 ± 0.14^{a}	0.792 ± 0.032^{d}	0.9797
C-2 (Plain soup)	0.88 ± 0.21^{d}	0.969 ± 0.012^{a}	0.9877

Results are expressed as mean values (n=3) ± SD. Different letters in the same column specify that the difference between the two values is statistically significant ($p \leq 0.05$).

extract were higher compared to the control. Similar to measurements performed at 25 °C, all yeast extracts increased the consistency coefficient of vegetable soup by similar ($p>0.05$) amounts when used at the same concentrations. The effect of all samples containing yeast extract at 1% concentration on the consistency coefficient of plain soup was statistically significant ($p\leq0.05$). However, *K. marxianus* TGM66 sample significantly ($p\leq0.05$) increased the consistency coefficient of plain soup even when used at 0.5% concentration. In measurements performed at both 25 °C and 50 °C, *K. marxianus* TGM66 extract stands out among all extracts. It is thought that the reason for this situation may be related to the carbohydrate structure and amount and/or amino acid profile of the *K. marxianus* TGM66 extract.

To our knowledge, apart from the present study, there is no study in the literature examining the effects of distinct yeast extract powders on the rheological properties of foods such as soup. Whereas, with a better understanding of the effects of ingredients like yeast extracts and yeast protein extracts on the rheology of different food systems, the possibility of using yeast extract-based products, especially in vegan foods, may increase, as they are generally cheaper than their counterparts and are not animal-based.

CONCLUSION

Although numerous studies have been conducted on the flavor and nutritional properties of yeast extracts, there are not sufficient studies in the literature examining the structural, thermal, morphological, and rheological properties of different yeast extract powders. To fill this gap in the literature, this study investigated whether three different yeast extracts obtained from *Saccharomyces cerevisiae* TGM10, *Saccharomyces boulardii* S11, and *Kluyveromyces marxianus* TGM66 had additional benefits other than their flavor-enhancing and nutritional value-enhancing effects in foods. In this context, structural properties of yeast extracts were examined by Fourier Transform Infrared spectroscopy, and their thermal stability was determined by Differential Scanning Calorimeter. Additionally, surface morphologies of lyophilized yeast extract powders were examined through Scanning Electron Microscopy micrographs. As a result of these investigations, characterizations of three different yeast extracts were provided. It is thought that the Fourier Transform Infrared spectra of yeast extracts obtained from three different yeasts will contribute to the existing literature in terms of the widespread use of Fourier Transform Infrared spectroscopy in the production and identification of yeast extracts, considering that this method is easy, fast, and inexpensive. In addition, it is expected that the determination of the thermal stability of yeast extracts will contribute to the use strategies of yeast extracts in food systems. It is thought that determining the surface morphology of yeast extracts will contribute to the choice of method to be used in drying yeast extracts. In addition, in this study, the effects of extracts obtained from three different yeasts on the rheological properties of vegetable soup, which was preferred as a model food, were investigated. The findings showed that all yeast extracts slightly increased the viscosity of the soup, but *Kluyveromyces marxianus* TGM66, especially at 50 °C, significantly increased the viscosity of the plain soup at both different concentrations. In light of all these findings, it can be said that the use of yeast extracts in appropriate concentrations, especially in foods that are generally consumed hot, such as soup, and where consistency is an important quality criterion, has the potential to contribute to the sensory properties of foods, such as viscosity. This situation, when considered together with the umami taste and meat-like flavoring properties of yeast extracts, may allow the production of more sensory successful foods by using yeast extracts in appropriate foods and at appropriate concentrations. However, in order to better understand the effects of yeast extracts on viscosity, the chemical profiles of yeast extracts, especially their carbohydrate profiles, need to be elucidated. Further studies to elucidate the effects of yeast extracts on viscosity in different food systems such as sauces as well as different types of soups may pave the way for the increased use of these nutritive additives in foods. In conclusion, with a better understanding of the structural, thermal, morphological, and rheological properties of yeast extracts, the production efficiency of the extracts can be increased and it may be possible to obtain more successful results by using these extracts in food systems for which they are suitable.

AUTHORSHIP CONTRIBUTIONS

F.D.: Conceptualization, Investigation, Methodology, Writing - Original Draft, Writing - Review & Editing. Ö.Ş.: Conceptualization, Investigation, Methodology, Writing - Review & Editing, Supervision. E.D.: Conceptualization, Writing - Review & Editing, Supervision. O.S.: Conceptualization, Writing - Review & Editing, Supervision.

DATA AVAILABILITY STATEMENT

The authors of the manuscript confirm that the data supporting the findings of this study are available in the manuscript. The raw data for the findings obtained in this study can be obtained from the corresponding author upon request.

CONFLICT OF INTEREST

All authors of the manuscript declare that they have no conflicts of interest resulting from the contents of this manuscript.

ETHICS

There is no ethical problem in publishing this manuscript.

STATEMENT ON THE USE OF ARTIFICIAL INTELLIGENCE

Artificial intelligence was not used in the preparation of the article.

REFERENCES

[1] Jacob FF, Michel M, Zarnkow M, Hutzler M, Methner FJ. The complexity of yeast extracts and its consequences on the utility in brewing: a review. Brewing Sci 2019;72:50–62.

[2] Rakowska R, Sadowska A, Dybkowska E, Świderski F. Spent yeasts as natural source of functional food additives. Rocz Panstw Zakl Hig 2017;68:115–121.

[3] Tanguler H, Erten H. Utilisation of spent brewer's yeast for yeast extract production by autolysis: The effect of temperature. Food Bioprod Process 2008;86:317–321. [CrossRef]

[4] Jacob FF, Striegel L, Rychlik M, Hutzler M, Methner FJ. Yeast extract production using spent yeast from beer manufacture: Influence of industrially applicable disruption methods on selected substance groups with biotechnological relevance. Eur Food Res Technol 2019;245:1169–1182. [CrossRef]

[5] Demirgül F, Şimşek Ö, Bozkurt F, Dertli E, Sağdıç O. Production and characterization of yeast extracts produced by *Saccharomyces cerevisiae, Saccharomyces boulardii* and *Kluyveromyces marxianus*. Prep Biochem Biotech 2022;52:657–667. [CrossRef]

[6] Vieira E, Cunha SC, Ferreira IMPLVO. Characterization of a potential bioactive food ingredient from inner cellular content of brewer's spent yeast. Waste and Biomass Valorization 2019;10:3235–3242. [CrossRef]

[7] Vieira EF, Carvalho J, Pinto E, Cunha S, Almeida AA, Ferreira IMPLVO. Nutritive value, antioxidant activity and phenolic compounds profile of brewer's spent yeast extract. J Food Compos Anal 2016;52:44–51. [CrossRef]

[8] Demirgül F, Şimşek Ö, Sağdıç O. Amino acid, mineral, vitamin B contents and bioactivities of extracts of yeasts isolated from sourdough. Food Biosci 2022;50:102040. [CrossRef]

[9] Vieira E, Brandão T, Ferreira IMPLVO. Evaluation of brewer's spent yeast to produce flavor enhancer nucleotides: Influence of serial repitching. J Agric Food Chem 2013;61:8724–8729. [CrossRef]

[10] Alim A, Yang C, Song H, Liu Y, Zou T, Zhang Y, Zhang S. The behavior of umami components in thermally treated yeast extract. Food Research International 2019;120:534–543. [CrossRef]

[11] Caruso MA, Piermaria JA, Abraham AG, Medrano M. β-glucans obtained from beer spent yeasts as functional food grade additive: Focus on biological activity. Food Hydrocoll 2022;133:107963. [CrossRef]

[12] Raikos V, Grant SB, Hayes H, Ranawana V. Use of β-glucan from spent brewer's yeast as a thickener in skimmed yogurt: Physicochemical, textural, and structural properties related to sensory perception. J Dairy Sci 2018;101:5821–5831. [CrossRef]

[13] Pacheco MTB, Sgarbieri VC. Hydrophilic and rheological properties of brewer's yeast protein concentrates. J Food Sci 1998;63:238–243. [CrossRef]

[14] Coelho P, Komora N, Xavier A, Centeno F, Raymundo A. New formulas in mayonnaise production - A new rheological perspective for systems with yeast protein extract (YPE). Proceedings of the Iberian meeting on rheology. Springer Proc Mater 2024;56:181–184. [CrossRef]

[15] White DE, Moggridge GD, Wilson DI. Solid–liquid transitions in the rheology of a structured yeast extract paste, Marmite™. J Food Eng 2008;88:353–363. [CrossRef]

[16] Kavosi M, Mohammadi A, Shojaee-Aliabadi S, Khaksar R, Hosseini SM. Characterization and oxidative stability of purslane seed oil microencapsulated in yeast cells biocapsules. J Sci Food Agric 2018;98:2490–2497. [CrossRef]

[17] Iscimen EM, Hayta M. Optimization of ultrasound-assisted extraction of protein from the by-product of the hazelnut oil industry using reverse micelles. Sigma J Eng Nat Sci 2024;42:1202–1213.

[18] Zehir Senturk D, Dertli E, Erten H, Simsek O. Structural and technological characterization of ropy exopolysaccharides produced by *Lactobacillus plantarum* strains isolated from Tarhana. Food Sci Biotechnol 2020;29:121–129. [CrossRef]

[19] Duygu D, Baykal T, Acıkgoz I, Yıldız K. Fourier transform infrared (FT-IR) spectroscopy for biological studies. Gazi Univ J Sci 2010;22:117–121.

[20] Barth A. Infrared spectroscopy of proteins. Biochimica Biophysica Acta 2007;1767:1073–1101. [CrossRef]

[21] Pavia DL, Lampman GM, Kriz GS. Introduction to spectroscopy. 3rd ed. Washington, USA: Thomson Learning; 2001.

[22] Wolpert M, Hellwig P. Infrared spectra and molar absorption coefficients of the 20 alpha amino acids in aqueous solutions in the spectral range from 1800 to 500 cm^{-1}. Spectrochimica Acta Part A 2006;64:987–1001. [CrossRef]

[23] Burattini E, Cavagna M, Dell'Anna R, Campeggi FM, Monti F, Rossi F, Torriani S. A FTIR microspectroscopy study of autolysis in cells of the wine yeast Saccharomyces cerevisiae. Vib Spectrosc 2008;47:139–147. [CrossRef]

[24] Cavagna M, Dell'anna R, Monti F, Rossi F, Torriani S. Use of ATR-FTIR microspectroscopy to monitor autolysis of *Saccharomyces cerevisiae* cells in a base wine. J Agric Food Chem 2010;58:39–45. [CrossRef]

[25] Barja BC, Afonso MDS. An ATR-FTIR study of glyphosate and its Fe(III) complex in aqueous solution. Environ Sci Technol 1998;32:3331–3335. [CrossRef]
[26] Dziuba B, Babuchowski A, Nałęcz D, Niklewicz M. Identification of lactic acid bacteria using FTIR spectroscopy and cluster analysis. Int Dairy J 2007;17:183–189. [CrossRef]
[27] Karoui R. Food authenticity and fraud. In: Chemical Analysis of Food Techniques and Applications. 2nd ed. London: Academic Press; 2020. [CrossRef]
[28] Zhou W, Apkarian RP, Wang ZL, Joy D. Fundamentals of scanning electron microscopy (SEM). In: Scanning Microscopy for Nanotechnology. New York, USA: Springer; 2006. p. 1–40. [CrossRef]
[29] Petravić-Tominac V, Zechner-Krpan V, Berković K, Galović P, Herceg Z, Srečec S, Špoljarić I. Rheological properties, water-holding and oil-binding capacities of particulate β-glucans isolated from spent brewer's yeast by three different procedures. Food Technol Biotech 2011;49:56–64.
[30] Björn A, de La Monja PS, Karlsson A, Ejlertsson J, Svensson BH. Rheological characterization. In: Kumar S, (editor). Biogas. London: InTech Open; 2012. [CrossRef]

Sigma J Eng Nat Sci, Vol. 44, No. 1, pp. 184–199, February, 2026

Sigma Journal of Engineering and Natural Sciences
Web page info: https://sigma.yildiz.edu.tr
DOI: 10.14744/sigma.2025.00000

Research Article

Technological developments and sustainable construction in Iraqi architecture

Osamah A AL-TAMEEMI[1,*]

[1]*Department of Architecture, College of Engineering, University of Baghdad, 10071, Iraq*

ARTICLE INFO

Article history
Received: 17 July 2024
Revised: 16 October 2024
Accepted: 30 December 2024

Keywords:
Contemporary Architecture; Local Architecture; Structural Systems; Sustainability; Technological Development

ABSTRACT

The current paper addresses the issue of how the use of technology may influence sustainable construction in Iraq with the focus on the balance between environmental and economic sustainability, local contextual issues, and the maintenance of architectural heritage. Taking into consideration the climatic and economic limitations of Iraq, sustainable construction as the way of increasing energy saving and decreasing environmental destruction becomes a very important direction. The environmental performance and energy efficiency of three major public buildings such as the Ministry of Industry and Minerals, the Ministry of Housing and the Central Bank of Iraq were tested using a quantitative, comparative methodology. Through the analysis of the sustainability indicators of each project, it was shown that the combination of high-efficiency glass and the optimization of building orientation reduced energy consumption by up to 20% and thus enhanced the environmental performance of the projects and reduced the reliance on industrial cooling. The study provides a unique contribution to the field, as modern technologies are combined with the traditional architecture components, which consequently offer a model that could be implemented in similar contexts at the global level. The results indicate that sustainable policies in constructing buildings in Iraq have the potential of increasing the use of local materials, which will assist communities in overcoming the environmental and economic problems in Iraq and simultaneously preserve the cultural heritage. This paper will present a new model which combines new technologies with the old ones in the sustainable construction industry in Iraq, providing a practical framework that would be flexible to similar conditions in other parts of the world.

Cite this article as: Al-Tameemi OA. Technological developments and sustainable construction in Iraqi architecture. Sigma J Eng Nat Sci 2026;44(1):184–199.

INTRODUCTION

The world construction industry is facing a radical shift that is being influenced by the increasing environmental demands and highly budgetary provisions. Sustainable building has become a crucial concept, which allows creating buildings that are less harmful to the environment and at the same time more resource-efficient and safe in financial terms. This aspect has particularly relevant implications

***Corresponding author.**
*E-mail address: osamah.al-tameemi@coeng.uobaghdad.edu.iq

This paper was recommended for publication in revised form by Editor-in-Chief Ahmet Selim Dalkilic

Published by Yıldız Technical University Press, İstanbul, Turkey
© Author. This is an open access article under the CC BY-NC license (http://creativecommons.org/licenses/by-nc/4.0/).

to Iraq since it is unique in terms of climatic conditions, economic realities, and socio-politics. The necessity of the context-specific solutions that combine the environmental health, financial stability, and cultural heritage is more than ever.

The paper will explore how technological innovations have impacted some of the practices that are sustainable in Iraq as regards construction. The paper critically examines modern technologies in the context of modern architecture and the ways of implementing them in the buildings with traditional architectural features to create the model of buildings that are environmentally and financially viable. The study will help in developing a holistic framework that could be used in similar areas that face similar challenges through the connection of current practice with the findings that will be based on the traditional knowledge system.

The essence of this study is the utilization of quantitative and comparative study. The chosen case studies that will be discussed applying certain sustainability indicators include the case of the Ministry of Industry and Minerals, the Ministry of Housing, and the Central Bank of Iraq. The study looks at the environmental impact and energy efficiency of the performance of these projects. The results highlight how the introduction of modern technologies, especially high-efficiency glass and orientation of the building strategy can help reduce energy use and increase the level of sustainability.

These outcomes range between meeting local demand to offering a case study on sustainable construction in most of the hot-arid environments of the world whereby resources are limited.

The proposed research aims to bridge an existing research gap by coming up with a new model that combines the new technological development with the vintage aspect of the sustainable construction industry. This contribution will drive additional studies and execution of sustainable measures that regarding cultural history and thus promote environmental as well as economic goals.

MATERIALS AND METHODS

The current study will use an integrative methodology, which is a combination of descriptive and quantitative analysis, and the aim of investigating the influence of sustainable technologies in the Iraqi environment. Therefore, the study design is a comparative analysis to be conducted using economic and environmental indicators to determine the gaps and the success of the solutions in place. The instruments and techniques to be used in the study include:

- **Quantitative Analysis**

The research evaluates energy utilization patterns using quantitative methods and evaluates the environmental performance of sustainable buildings thus giving a more accurate analysis of the effectiveness of sustainability measures that have been implemented.

- **Comparative Case Study Analysis**

The research process will involve the local examples of sustainable building, that is, the projects of the Ministry of Industry and Minerals, the Ministry of Housing, and the Central Bank of Iraq. To determine the operational results of these initiatives, the measures will be compared using the determination of comparative indicators, such as material sustainability, energy performance, and environmental integration.

- **Descriptive Analysis Backed with Statistical Data**

Quantitative data shall be used to support the descriptive analysis in order to reveal the major trends and gaps by using statistical analysis and mathematical modeling. Such a mixed-methods strategy allows making a subtle definition of environmental issues and sustainable working practices.

- **Analytical Approach**

The following analytical method will be used to analyze the chosen projects based on the environmental, economic, and social indicators: An integrative analytical methodology comprising both quantitative and descriptive methods. Information will be gathered by reviewing architectural projects, formal environmental assessment and through information that is available in the relevant institutions.

- **Analytical Tools**

Building data analysis software and statistical modelling were used in the evaluation to measure the efficiency of energy and water use. Additionally, project design documents were examined to determine the materials and sustainable construction techniques that were used in specific projects.

LITERATURE REVIEW

Even though the possibilities regarding combating the environmental issues and resource limitation have also become a point of great international interest, there has been very little in terms of investigating the idea of sustainable practices in the context of Iraq, especially as far as the incorporation of local materials with modern technologies is concerned. The literature review will consider the applicable studies with the aim of offering a thorough view of the technologies availed in sustainable construction and how they apply to Iraq.

Major Technological Developments in Sustainable Building

Al-Zubaidi & Shahin [1] assumed that the use of local materials could make construction more sustainable. They found clay bricks to be cost efficient and environmentally friendly not to mention that they are acceptable in the climate of Iraq. Similarly, Al-Saffar & Al-Tameemi [2] have mentioned recycled concrete blocks, which could help minimize construction waste, reuse materials, thus they should be utilized.

Comparative Studies in Practices of Sustainability

In the comparison of sustainability practices, there is also a significant disparity in the sustainability principles implementation in the projects, according to comparative research. For example, Kibert [3] offers approaches to evaluating energy efficiency and material sustainability, and they can be used to apply them to local Iraqi projects. These frameworks are useful as a reflection of the compromise between the new technological age and the old traditions.

Identified Research Gaps

Sustainable construction is still in its early stages in the world, but Iraq has more issues, such as the regulatory barriers, lack of awareness among the stakeholders, and high start-up expenses. To overcome these obstacles, there should be a strategy that is neither in opposition to the socio-economic, climatic, and cultural reality of Iraq. The following section aims at closing these gaps by providing a more detailed literature review uniting both quantitative and qualitative findings, thus providing a roadmap towards introducing sustainable construction practices that would be specific to the conditions of Iraq.

SUSTAINABLE DEVELOPMENT IN LOCAL ARCHITECTURE

Brian Edwards, who is one of the most important specialists in sustainability and green architecture, emphasizes the foundations of sustainability in traditional architecture. He said: "Traditional architecture has been able to combine the dimensions of social sustainability with environmental requirements to form a sustainable architecture compatible with the environment" [1].

In addition, the physical phenomena represented by the forces of nature helped in self-adaptation of the traditional urban environment by integrating the part with the urban fabric, which affected the process of adapting the environment. The urban environment, which helped increase adaptation by using appropriate building materials characterized by slow heat gain and loss, and the use of systems. which gave the traditional environment a high environmental efficiency and comprehensiveness that the urban designer and planner can adopt to reach a contemporary urban environment based on the principles of traditional environment [4,5].

SUSTAINABLE CONSTRUCTION

Sustainable construction presents the idea to build an environmentally friendly management system, with the focus on the efficient use of resources and the tendency to follow the principles that contribute to the identity with the natural environment. The idea of sustainable design is aimed at reducing the adverse environmental effects of construction through improvement of energy and resource efficiency especially in a construction perspective and focus on utilization of natural, renewable and environmentally friendly sources of energy.

When considering sustainable construction, one will notice that the concept has been based on the considerations of the environment and human beings as well. Sustainable construction was defined at the 21st Century Conference on Sustainable Building in Developing Countries as a central part of sustainable development and was defined as a whole effort that seeks to restore a balance between the natural and built environment as well as fostering human dignity and economic fairness.

Similarly, "Kent" Kent referred to sustainable construction as a conglomerate of construction procedures that are meant to help communities improve on the infrastructure they have and use not to mention the fact that it ensures conservation of the environment. This involves setting up of construction practices that are environmentally guardian, increasing community consciousness and ensuring that economic viability is achieved in the long term [6].

Practical Objectives for Sustainable Construction

Sustainable construction aims to achieve multiple objectives, as outlined below:

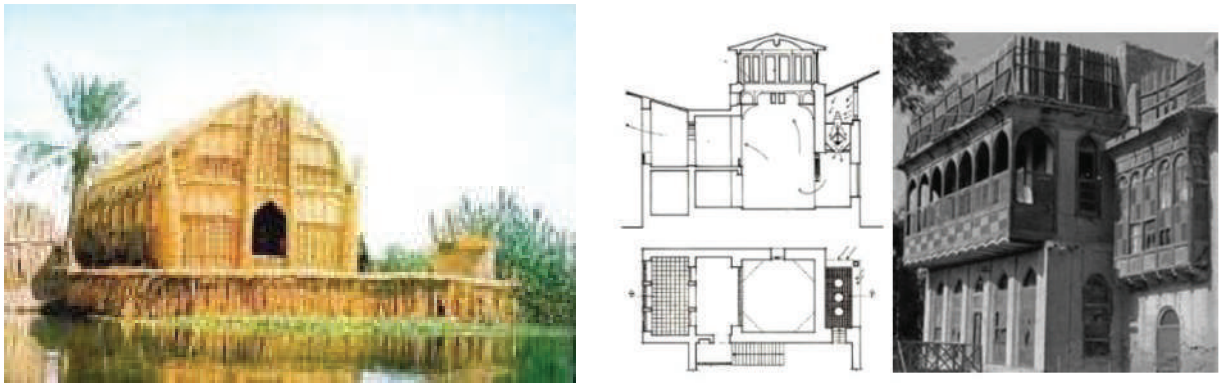


Figure 1. Utilizing renewable energy using air stacks and chanshes [29] reproduced with permission from the author.

Aim

- Evaluate the impact of technological advancements on sustainability in Iraq's construction industry [3].
- Propose an integrated model that combines modern technologies with traditional architectural elements for sustainable development [2].

Objectives

- Analyze the role of local materials in enhancing sustainability.
- Assess the effectiveness of modern technologies in improving energy efficiency and reducing environmental impact [7].
- Develop a framework that integrates traditional and modern practices in sustainable construction.
- Address specific challenges to implementing sustainable construction in Iraq's socio-economic context.

Scope

- Focuses on sustainable construction within the context of Iraq.
- Includes case studies of three buildings: the Ministry of Industry and Minerals, the Ministry of Housing, and the Central Bank of Iraq [8,9].
- Evaluates environmental, economic, and social indicators related to sustainable construction.
- Highlights the potential application of findings to regions with similar hot-arid climates.

Limitations

- Limited to selected case studies that may not fully represent all construction practices in Iraq [10].
- Relies on available data, which might not cover all sustainability indicators [10]
- Primarily focuses on environmental and economic sustainability [11], with less emphasis on social and cultural dimensions beyond the studied cases [12].

Challenges in Sustainable Construction

When thinking about the main issues of sustainable construction, one cannot help mention the complications associated with the practices of incorporating the environment-conscious and resource-efficient procedures into the construction life cycle. The key identified challenges would be summarised below with appropriate citations shown to bring out the issues in brief:

- **High initial costs**

High initial costs of sustainable projects are the major challenge as they require high quality materials, as well as high level of technology. This cost restricts its acceptance by local developer [13].

- **Awareness and knowledge gaps**

Lack of awareness among professionals and the general population in terms of sustainable practices and their advantages is a significant issue in the spread of sustainable construction methods [14].

- **Regulatory and policy barriers**

This is often complicated by the lack of an effective policy and regulatory framework to help with sustainable building practices. To reinforce these practices, it is necessary to have extensive guidelines and incentives to develop an environment that supports adoption [11].

INTEGRATION INDICATORS

- **Environmental Efficiency**

Environmental indicators are concerned with water conservation and waste management, and energy efficiency. Environmental performance of buildings is evaluated on the strategies as rainwater harvesting and energy saving lighting systems [2].

- **Economic Contribution**

Local materials should be used, and this will help to minimize carbon footprint and help support the local economy. Local materials, including clay bricks have become environmentally and economically viable in Iraq [14].

- **Social Impact and Community Engagement**

Social sustainability metrics, such as community engagement via educational programs on sustainability, will make sure sustainability construction projects have an impact on the long-term community well-being Figure 2 [12,15].



Figure 2. Sustainable construction methods [13] reproduced with permission from the page owner.

CONSTRUCTIONAL PRACTICE IN SUSTAINABLE ARCHITECTURE

This includes the strategies and methods that relate to building and will minimize the impact caused on the environment, hence improving building efficiency and performance and making the building fit for the health of the occupants. They are very critical and important, for that is the way through which the objectives that sustain the construction and operation of the building can be achieved [16] This paper outlines the major constructional practices in sustainable architecture, supported by authoritative source citations.

Energy Efficiency

Construction and design principles bring down to a very low degree the energy that could be used. Notably, they would include things like insulation, high-efficiency windows, energy-efficient lighting, and energy-efficient HVAC systems. They involve, where possible, passive solar design principles to maximize natural heating, cooling, and lighting.

Sustainable Material Use

Selecting the material for its use in construction according to the effect on the environment. They include recycled, renewable, local, and low-embodied-energy material. The aim is at the reduction of the carbon footprint and environmental impact of building materials [17].

Water Saving

The systems or practices in water sustainability that intend to bring down the quantity of water involved in their integration. Examples are water harvesting from rain, water-efficient irrigation systems, and water-efficient fixtures [18].

Improved Indoor Environmental Quality (IEQ)

Improved IEQ with enhanced comfort, health, and well-being of the building occupants is well ensured by good ventilation and the use of non-toxic materials to make sure indoor air pollution is at a minimum, 100% maximization of natural light [9,19].

Reuse and Waste Management

The practice reduces the waste produced during the construction period and while the building is in use. It includes recycling construction waste, designing for disassembly, and the use of pre-assembled components [20].

Environment Integration: In building design, it is important to integrate with the environment, considering the ecosystem, climate, and natural features of the site. The design practice aims at reducing adverse impacts both on the environment and human health while efficiently using the local environmental condition to obtain better performance [14,21].

Energy Use of Renewable Nature

The energy requirement for buildings is to be satisfied with renewable sources such as solar panels, windmills, and geothermal systems to meet the sustainability aspects [22,23].

SUSTAINABLE CONSTRUCTION APPLICATIONS IN IRAQI ARCHITECTURE

Sustainable construction applications of the Iraqi architecture include a huge range of practices, techniques, with enhanced sustainability and environmental efficiency in buildings and urban projects. What follows is a showcase of such applications that are locally environmental- and economic-challenge-compatible:

The use of local and sustainable building materials, such as clay bricks and plasters, has a lower environmental impact compared to imported counterparts. This usage will help in strengthening the local economy and also reduce the carbon footprint of the project [24].

Architectural Design Compatible with Local Environment Conditions

Prepare the architectural design compatible with environmental conditions of the place, such as high temperature; make sure that there is proper natural lighting in the building that requires minimal use of electrical energy for cooling and lighting. Few of them include the use of shading techniques, natural ventilation, and building orientation to harness the maximum from prevailing natural conditions [25].

Energy and Water Efficiency

The evolving technologies and systems will make the buildings highly energy and water-efficient, hence reducing the cost. This includes the use of solar energy systems, rainwater collection and use systems, sanitary equipment, and water-consuming fixtures [26].

Green Roofs and Vertical Gardens: Natural environment re-establishment in urban areas includes green roofs and vertical gardens as one of the main instruments in use to improve thermal insulation, cool urban heat islands, and improve air quality. Re-creation of the natural environment in the city includes such elements as green roofs and vertical gardens in the list of the main means of practice.

Urban Sustainable Planning: elaboration of urban layouts according to sustainability and eco-friendly transport that reduce the dependency on private cars, bringing forward public transportation and public green spaces. This will also include the development of integrated communities, which will reduce the need for long commutes and increase quality of life in such communities [27,28].

These applications reflect an effort aimed at integrating sustainability principles within architecture and urban planning in Iraq, with a view to character trials experienced by the environment and the economy. In practice, the goals assure the maintenance of development in urban centers, natural resources, and quality life for future and current generations [29].

CRITERIA FOR MEASURING THE DEGREE OF APPLICATION OF LOCAL SUSTAINABILITY HUBS

The research emphasizes the need for specific criteria and values that contribute to the promotion of sustainable construction experience through a set of main and sub-values that relate to conceptual or practical aspects through which any local experience or architectural model can be assessed to demonstrate its achievement of sustainable construction aspects and achieve its desired objectives. As shown in the following. Figure 3, Table 1.

Where these axes can be applied in contemporary local architectural experiences shared as administrative buildings are elected in a sequence of time to show the extent to which they achieve structural sustainability in all its various aspects. Therefore, three projects were selected in Baghdad in Table 2.

CASE STUDY PROJECTS (SAMPLES)

1. **Sample 1: Ministry of Industry and Minerals (1978). Figure 4.**
2. **Sample 2: Ministry of Housing Building (2012). Figure 5.**
3. **Sample 3: The Central Bank of Iraq (under construction). Figure 6.**

ANALYSIS OF CASE STUDIES

Case Study 1: Ministry of Industry and Minerals Project (1978)

Environmental results

The empirical study of the environmental factors shows that the use of traditional Iraqi brick in this building offers good natural insulation thus lessening reliance on artificial cooling systems. Natural ventilation is achieved through large fenestration, and this reduces the overall energy consumption.

Economic results

The project had comparatively small upfront costs due to the use of locally acquired materials. However, the discussion reveals that its efficiency in the long run is rather limited compared to the modern buildings that are equipped with sophisticated thermal and energy-saving methods.

Social results

The design uses the features typical of the traditional Iraqi architecture which allow developing a feeling of cultural belonging and group pride; one feels that the building is a part of the local culture.

Case Study 2: Ministry of Housing Project (2012)

Environmental results

The environmental analysis shows that there are significant improvements in efficiency due to the use of thermal insulation and water-saving systems, such as rainwater harvesting. The level of energy efficiency is higher than the one of the Ministry of Industry and Minerals building.

Economic results

First of all, despite the fact that the launch of new technologies increased the initial costs, the savings made in the long term both in terms of energy and water spending make the project cost-effective.

Social results

The building improves thermal comfort and quality of life and is combined with modern technologies to create a health-oriented and comfortable environment in which the occupants will live.

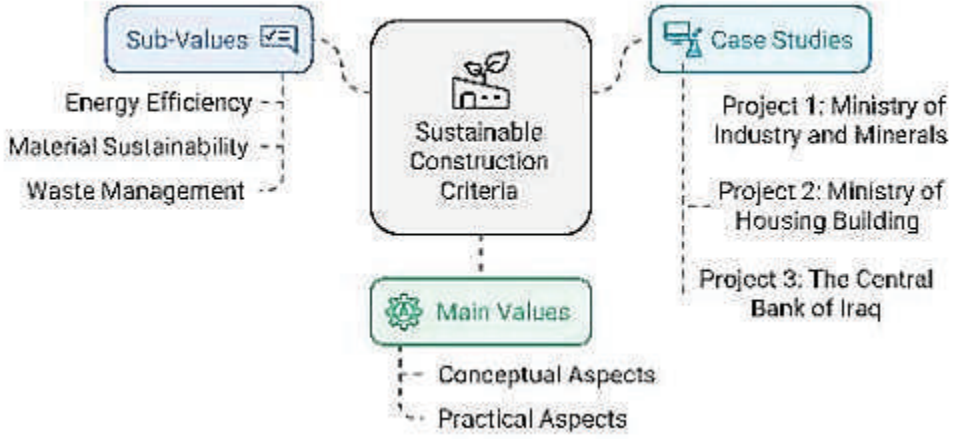


Figure 3. Criteria for measuring the degree of application. Source: Author.

Table 1. Indicators of the application of local sustainability hubs. Source: Author

	Indicators	Main Values	Sub-values	Application values
Sustainable Construction	Environmental sustainability	Materials	Contemporary local	Local materials with new treatments
			Traditional local	Local materials with the same treatments
			Ancient heritage	Traditional materials of the same architectural value
		Technologies	Lighting	The degree of maneuverability in the design of natural and industrial lighting
			Means of implementation	The use of advanced operational techniques in building a sustainable building
	Economic Sustainability	Resource development and capacity development	Economic planning	Degree of clear implementation strategies for sustainable construction
			Employment of local workers	Effectiveness of local employment in sustainable construction
			Providing tourist facilities	The feasibility of tourism for sustainable buildings
		Finance	Government sector	The extent of funding and government interest in the sustainable construction sector
			Private Investment Sector	The degree of investment in constructional sustainability
			NGO	The effectiveness of organizations in support and encouragement
	Social sustainability	Social participation	Community awareness	The degree of community awareness that contributes to the promotion of sustainable reality
			Exchange of experiences	The degree of influence of external expertise in the local experience



Figure 4. Ministry of industry and minerals**.** Source: Author.



Figure 5. Ministry of housing building**.** Source: Author.



Figure 6. The Central Bank of Iraq. Source: Author.

Table 2. Application of the theoretical framework Source: Author

		Sample 1			**Sample 2**			**Sample 3**		
		Ministry of Industry and Minerals			Ministry of Housing Building			The Central Bank of Iraq		
		Designed by Fadhil Ajina, located in Tayaran Square - Baghdad, Year of Construction 1978, The building consists of about 10 administrative floors and packaging was brick screens out of the traditional designs of traditional bricks			Government administrative building located in the museum square, Baghdad; the year of project accomplishment was 2012. The building consists of 10 floors and 43 meters in height. It is environmentally friendly due to the adoption of many environmental treatments.			Designed by Zaha Hadid, the project is located on the Tigris River, The building consists of a horizontal part (Podium) and vertical part (Tower), which is about 170 meters above the street level		
										
Environmental sustainability	Materials	Contemporary	Traditional local	Mixed	Contemporary	Traditional local	Mixed	Contemporary	Traditional local	Mixed
				●	●			●		
	Technologies	Natural Lighting	Artificial Lighting	Mixed	Natural Lighting	Artificial Lighting	Mixed	Natural Lighting	Artificial Lighting	Mixed
				●		●				●
		High- tech	Traditional	Sustainable	High- tech	Traditional	Sustainable	High- tech	Traditional	Sustainable
			●		●					●
Economic Sustainability	Resource development and capacity development	Economic planning	Employment of local workers	Providing tourist facilities	Economic planning	Employment of local workers	Providing tourist facilities	Economic planning	Employment of local workers	Providing tourist facilities
		●	●		●					●
	Finance	Government sector	Private Investment Sector	NGO	Government sector	Private Investment Sector	NGO	Government sector	Private Investment Sector	NGO
		●			●			●		●
Social sustainability	Social participation	Sustainable Knowledge and Awareness	Sustainable Awareness	Sustainable Knowledge	Sustainable Knowledge and Awareness	Sustainable Awareness	Sustainable Knowledge	Sustainable Knowledge and Awareness	Sustainable Awareness	Sustainable Knowledge
				●		●		●		
		Local experiences	Foreign experiences	Mixed experiences	Local experiences	Foreign experiences	Mixed experiences	Local experiences	Foreign experiences	Mixed experiences
			●		●					●

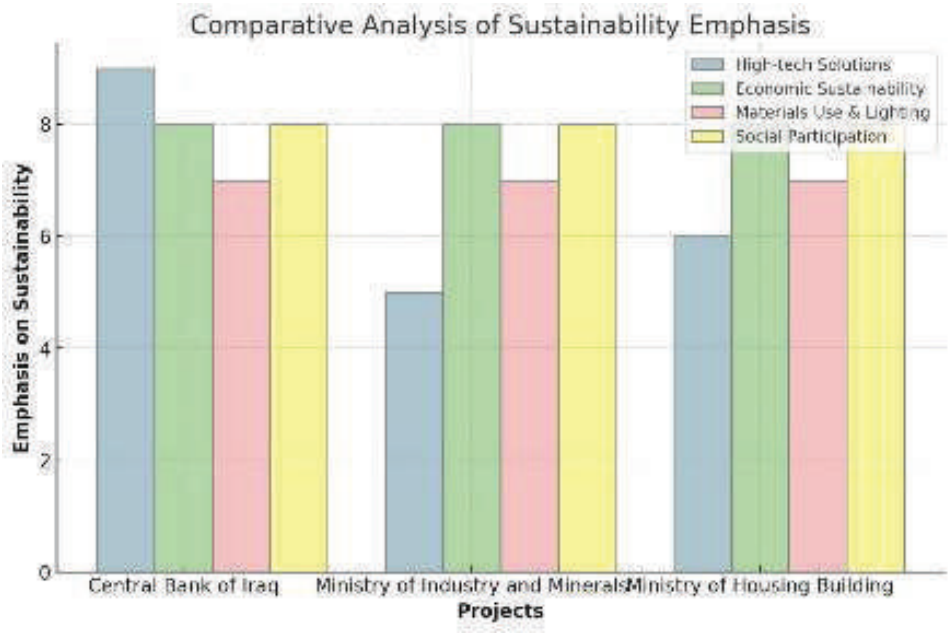


Figure 7. Comparative analysis of sustainable emphasis (Author).

Case Study 3: Central Bank of Iraq (Under Construction)

Environmental results

The architectural design includes high-efficiency glass fronts and has a good orientation to reduce solar heating that would substantially increase energy efficiency. The design takes the best use of natural lighting and uses natural cooling strategies.

Economic results

The initial budget of the project will be high given the high level of materials and technologies used, but the long-term savings made by the project owing to energy efficiencies will make it a good financial investment.

Social results

The building is expected to give contemporary environmental experience, and it aims at raising the status of the building in the field of sustainable architecture as a model of innovation in the key projects, Figure 7.

COMPARISON OF CASE STUDIES

Such case studies are indicative of different priorities on sustainable construction practices, where better local architecture is adopted via the use of technology, material replacement, and environmental adjustment.

Ministry of Industry and Minerals Project (1978)

A governmental building that represents the most progressive application of local classical material technology: Iraqi clay bricks.

Housing Ministry Project (2012)

A sort of short-term construction that entails a combination of local materials and new sustainable thinking. It also integrates thermal insulation and water-saving mechanisms that strike a balance between adaptation to the climate and the latest technologies that are resource-efficient such as natural shading, air conditioning systems, and rainwater collection.

The combination of these traditional materials and modern high-tech details indicates the eco-friendly reaction to the climatic crises on the optimistic note, which means that the construction should be stable in the face of local ecological factors.

Central Bank of Iraq (Under Construction)

Another building designed by Zaha Hadid, the new Central bank represents an extended version regarding high-tech sustainable construction in Iraq. Its high-efficiency glass façades are strategically oriented for maximum natural light and solar heat gain reduction. High efficiency lighting and advanced HVAC systems also add to the power conservation efforts. It is a vision of the future regarding sustainable high-rise design and technology for Iraq, resulting from an efficient blend between sustainability with automated features in Central Bank structure Figure 8.

COMPARATIVE STATISTICAL ANALYSIS

The numbers used in the bar chart are purely subjective information meant to visualize the comparative weight or emphasis of different elements of sustainability in the Central Bank of Iraq, Ministry of Industry and Minerals,

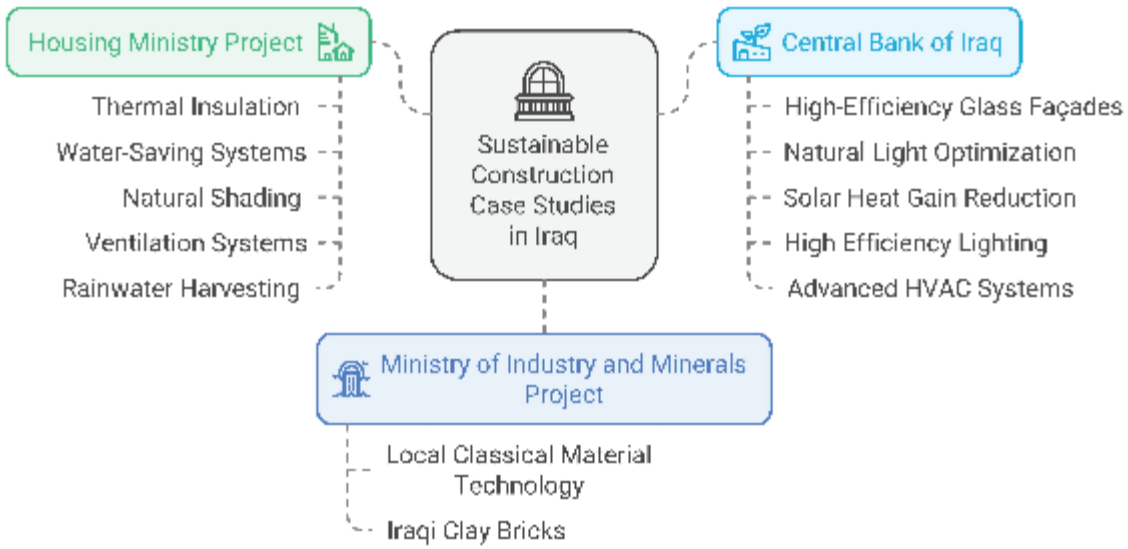


Figure 8. Comparison of case studies. Source: Author.

and Ministry of Housing Building, based on the descriptive analysis provided. However, as the former information never held quantitative data to compare directly, some values had to be assigned to quantify them in order to present narration pictorially. Here is a breakdown of the reasoning:

High-tech Solutions for Sustainability

Central Bank of Iraq: Assigned a 9 to really point out that the bank is very progressive and forward in adopting high-tech solutions for sustainability, as mentioned due to the recent development and design by Zaha Hadid.

Ministry of Industry and Minerals: 5, Moderate emphasis for putting the solutions in place with high technologies.

It gives an impression of balanced approach—most probably, there are some high techs but much greater emphasis is given to traditional practices.

Ministry of Housing Building: 6, Slightly Higher These results, while insinuating a slightly greater, yet moderate, focus on the integration of high-tech sustainable solutions within its projects, can be taken to indicate.

Economic Sustainability & Local Employment

All projects were, in other words, assigned a strong and uniform value of 8, which told about a strong and uniform commitment to economic sustainability and local employment among all projects. This reflects the analysis of the fact that strong support for economic sustainability and local employment is essential for the long-term growth and stability of a region.

Mixed Materials Use & Lighting Strategies

The mean score of all the reviewed projects was very high (7) which means that the combination of mixed material systems and proper lighting strategies has been taken into account. This highlights the comprehensive approach to the sustainability that cuts across tradition and modernity.

Social Participation & Sustainable Knowledge

Once more, an 8 was assigned, showing serious concern for community involvement and assurance that the developed knowledge is sustainable. The relevance that social participation and education gain in sustainability effort is precisely referred to in the analysis. These are illustrative and based on certain crafted values that could give a clear visual comparison according to the qualitative insights from the comparative analysis; they are not exactly from data points but meant to put forward a general feel of the story as narrated through visualization.

RESULTS AND DISCUSSION

The findings which are presented in this study are congruent with the goals stated in the abstract and the introduction. Combining modern technologies with the tried-and-test practices, the case studies considered show that there has been a significant improvement in the sustainability indicators through the simultaneous implementation of modern innovations and traditional applications. The key results of each case study are outlined below:

Case Study 1: Ministry of Industry and Minerals

Energy efficiency

The use of traditional clay bricks reduced the need to have artificial cooling system. The thermal insulating quality of clay bricks enabled 15% lessening of energy usage of

the houses during the peak summer seasons and regulated temperatures of the houses during winter seasons.

Material sustainability

The use of local materials reduced the cost of transportation and carbon emissions and thus compatible with the economic and environmental limitation common in Iraq.

Social impact

The design of the architecture remained and mirrored the traditional features of the Iraqi architecture thus strengthening the cultural identity and promotion of the community acceptance.

Case Study 2: Ministry of Housing

Energy efficiency

New insulation systems with shading systems produced an energy reduction of 18%, especially in cooling conditions.

Water management

Water-conserving plumbing and rainwater collection systems generated 15% cut in the water usage. These systems were incorporated in the building design without any hustle and bustle, which is an example of some of the possible practices of sustainability.

Economic viability

Although the initial cost of construction was increased by modern technologies, the pay-back period in the long term saved the money.

Case Study 3: Central Bank of Iraq

High-tech integration

Contemporary exterior and building alignment creating the maximum reduction in using energy in the outdoor lightings and air conditioning by 20%.

Material innovation

The mixes of classic and modern materials increased structural resilience and energy efficiency.

Global impact

This project, created by Zaha Hadid, has taken into consideration high-tech devices and environmentally friendly structures and provides a model of how a sustainable project can be built in Iraq, as well as in other areas.

Data Visualization and Validation

The findings were supported with the following graphical analyses:

Energy consumption trends

Line graphs show that there is a decrease in energy demand within the case studies and thus it can be seen how sustainable design solutions are effective.

Material efficiency comparisons

Bar graphs are used to analyze the sustainability performance of imported and local materials highlighting the local sourcing and the associated benefits to the environment and cost.

Water management metrics

Pie charts are used to show the ratio of water saved by using effective plumbing systems and rainwater harvesting.

Cross-Case Comparative Analysis

When compared, these projects reveal that the contribution of modern technologies to traditional practices has enormous benefits in terms of environmental, economic and social aspects. These findings prove that the model introduced in the abstract can be replicated in order to build sustainably in hot-arid areas like that of Iraq, and the findings are further supported by the consistency of the abstract and introduction with the results, which, in turn, confirms that sustainable construction has potential to help resolve the issues in the region and still manage to preserve

Table 3. Sustainability analysis in three architectural projects in Iraq (Author)

Indicator	Ministry of Industry and Minerals	Ministry of Housing	Central Bank of Iraq
Environmental Sustainability	Use of local clay bricks for thermal insulation	Thermal insulation techniques and rainwater harvesting	High-efficiency glass facades and strategic orientation
Initial Cost	Low due to use of local materials	Moderate due to modern technologies	High due to advanced technology costs
Economic Impact	Boosts local economy through local employment	Improves energy efficiency and reduces operational costs	Long-term investment in energy efficiency
Social Participation	Cultural connection with local heritage	Improves quality of life with comfortable environment	Architectural model enhancing Iraq's image
Technology Used	Simple techniques with local materials	Moderate techniques with advanced local materials	Advanced technology like high-efficiency glass and sustainable cooling

cultural heritage and address the global requirements of sustainability. Table 3.

Comparison of the current results with the previous literature reveals the presence of a distinct correspondence in the terms of practicality of indigenous resources and sustainable design approaches to the improvement of energy efficiency in Iraq. For instance, Al-Obaidi & Al-Tameemi [12] presented facts that local resources like clay bricks can alleviate the situation on the environment and increase the financial sustainability, and that is why, in our case, high-efficiency glazing and architectural designs that correspond to the conditions of the country can decrease the usage of energy by almost 20%. Similarly, Al-Saffar & Al-Tameemi [2] have found that the use of modern technology combined with traditional resources enhances the performance of the environment, and our study builds on this idea by proposing a feasible model based on the harsh weather conditions in Iraq.

Nevertheless, this research offers a fresh angle because it puts an emphasis on the central role of strategic-oriented architectural constructions that respond to the local climatic parameters which have not been given enough consideration on earlier studies. We have empirical evidence to indicate that synthesizing technology using traditional elements can positively maintain the cultural heritage and achieve the goals of environmental sustainability. Moreover, the comparative analysis of three major Iraqi architectural tasks, namely the Ministry of Industry and Minerals, the Ministry of Housing and Building, the Central Bank of Iraq, shows that the approaches to sustainability are divergent.

Environmental sustainability across architectural projects

Unlike the Ministry of Housing and Building and the Ministry of Industry and Minerals, which prefer to use traditional and locally available mixed materials, these projects focus on the maximization of the utilization of local resources that are available, and thus environmental sustainability is strengthened. The Central Bank of Iraq, the work of the great architect Zaha Hadid, is the example of the combination of the traditional, local, and the advanced design, which is supported by the latest technologies, and reflects the new meaning of sustainability, which is based on the technological dependence.

Economic impact and sustainability considerations

The three projects have a combined effect on the economic sustainability impact: the projects contribute to economic sustainability in such aspects as local employment, the boost of tourism, the involvement of more investors (both private and non-governmental). The general plan goes beyond the creation of architectural landmarks; it will aim at reviving the local economies, creating jobs, and encouraging the tourism industry hence, enhancing economic sustainability

Social sustainability and community engagement

The importance of social participation and the introduction of local and international knowledge are stressed in all the projects. The design practice is community-based involving cultural attitudes based on the local practices, and thus enhancing efforts that engage and inform the community as the requisite attributes of attaining sustainability.

Technological innovation and resource optimization

The combination of high-technology and the old-fashioned sustainable technologies into the building constructions is associated with the complex approach toward managing the resources, the attempt to achieve the balance to meet the modern demands and reduce the harmful influence on the environment. Innovative technology is also used in buildings to the extent of integrating daylight-optimal lighting systems. The Ministry of Housing and Building and Central Bank of Iraq can be viewed as examples of the ways the country uses solar radiation to improve efficiency and sustainability of resources.

Global significance of research

This study will be global meaning that it will enable the analysis of the financial implications in the international financial markets in the current era. It offers the generalized information which aims at building ecologically friendly practice that can be applied to hot-arid regions and economic conditions that are similar to those found in the Iraq country.

The results prove that the combination of local and innovative technologies may lead to environmental and economic sustainability; it provides the viable framework that can be implemented in other countries to reduce the environmental footprint and at the same time maintain cultural identity. This study will spur future research that can help conduct comparative studies on the sustainable building projects in the different settings, which may provide more streamlined advices that will be applicable to other climatic and cultural contexts.

The ability to investigate spots similar to Iraq will also allow further studies to increase the efficacy and applicability of sustainable construction techniques on a global scale.

The originality of the given research is supported by quantitative data that demonstrates that the use of modern technologies such as high-efficiency glazing and the creation of the building structure can help to achieve more efficient energy usage, reducing the consumption by almost 20%. This supports the contribution of the research in the form of giving viable solutions to sustainable architecture in Iraq.

CONCLUSION

- The research will add to the existing literature as it has a pragmatic model that combines the newest technology with traditional materials. It shows how the principles

of sustainable construction may be implemented in the local context with the aim of realizing the long-term environmental and economic sustainability, which can be duplicated in other similar localities with similar challenges.

- Comparative studies of these two architectural projects then illustrate diverse though complementary approaches that are made to sustainability, combining the environmental, economic, and social considerations with technological advancement. This perspective of sustainability in architecture has hence viewed the designing of the future city as an all-embracing concept, dynamic in its involvement of adaptability, community engagement, and technological integration with a view to obtaining outputs that will be regarded as sustainable.
- The Iraqi local architecture was indeed adapted to the local environmental condition. It was mostly using natural materials, like mud bricks offering thermal insulation, and designs examining the best natural potential for ventilation in the area. Global architecture, on the other hand, uses high technology in smart façades and renewable energy systems to be sustainable. Iraqi architecture is strongly attached to local heritage and the environment, whereas the architecture of the global approach tends to be more inclined toward the global attitude, giving more emphasis to the latest technologies and efficiency.
- According to the concepts of sustainability, the origin must achieve the minimum constructional cost required to complete the necessary specifications.
- Sustainable development focuses on two aspects: human and environmental, as it is one of the integral processes of sustainable development, which is seen as a comprehensive process aimed at restoring harmony between the natural environment and the built environment on the one hand, and the construction of buildings on the other, Human rights as well as economic justice.
- Sustainable construction is a set of design, construction and operational processes that help communities improve the infrastructure used while providing environmental protection. As well as building methods that protect the environment, raise public awareness and achieve long-term economic profitability.
- Sustainable construction in practice aims at finding constructional aspects and systems that achieve the highest possible structural, environmental efficiency.
- Constructional efficiency and sustainable environmental performance depend largely on the nature of the selected constructional material and its characteristics, especially regarding its constructional and environmental performance. This nature and the physical properties of constructional materials have played a major role in the selection of suitable constructional systems.
- Balancing objectives and means to achieve and achieve the best origin and architecture more satisfactory, the effect of origin is on architecture and the environment in general, and on the expressive side in particular.
- Sustainable construction seeks to optimize the utilization of construction technology at the level of technologies and materials through design, implementation and use processes while achieving comfort, safety and cost reduction.
- Taking advantage of the architectural elements and the traditional and traditional architectural materials and others that are still able to give our modern buildings as they are or after their development in line with the requirements and technologies of the era and the degree of progress to obtain a design can be called comprehensive design.
- **Ministry of Industry and Minerals Project**: This project underscores how using traditional materials can balance low initial costs with environmental sustainability in government infrastructure.
- **Ministry of Housing Project:** It exemplifies how combining modern technology with local materials can achieve strong environmental and economic sustainability.
- **Central Bank of Iraq:** This high-tech, sustainable construction aligns with global standards, establishing a benchmark for future projects in Iraq.

Recommendations

1. Encourage Local Material Use and Innovation: The use of local material, which is durable and locally sourced, and environmentally friendly would reduce carbon emissions and enhance the local economy. When using traditional materials like clay and limestone, it is recommended to seek alternative methods of improving their resilience and applicability in sustainable, modern construction.
2. Enhance Technological Integration for Sustainability: The increase in the use of the latest technologies, including water management, improved thermal insulation, and the use of green energy sources (e.g., solar, wind), should be a top priority. Passive design strategies that should also be emphasized to supplement natural lighting and ventilation and help reduce the energy use of buildings should also be promoted. These technologies are quite favorable to the climate of Iraq, and they will maximize the efficiency of buildings, and save the resources.
3. Boost Awareness and Develop Supportive Policies: There is a need to teach the architects, developers and people about the advantages of sustainable architecture. Moreover, by establishing friendly policies and incentives, including tax cuts, grants or fast track support in processing of sustainable projects, then this will create a more favorable climate in green development.
4. The work promotes national and regional policies to promote sustainable construction, which would recommend the promotion of local sustainable materials

and introducing the financial incentives or tax breaks to environmentally friendly projects. It also proposes simplification of certification and regulatory systems of sustainable building solutions to facilitate more evaluation.

AUTHORSHIP CONTRIBUTIONS

Authors equally contributed to this work.

DATA AVAILABILITY STATEMENT

The authors confirm that the data that supports the findings of this study are available within the article. Raw data that support the finding of this study are available from the corresponding author, upon reasonable request.

CONFLICT OF INTEREST

The author declared no potential conflicts of interest with respect to the research, authorship, and/or publication of this article.

ETHICS

There are no ethical issues with the publication of this manuscript.

STATEMENT ON THE USE OF ARTIFICIAL INTELLIGENCE

Artificial intelligence was not used in the preparation of the article.

REFERENCES

[1] AlZubaidi M, Shahin B. Sustainability Principals of Traditional Architecture in the Islamic Perception. Iraqi J Archit Plan 2007:74-91.

[2] Al-Saffar IM, Al-Tameemi OA. Technological strategies for recycling concrete block in Iraq. in J Phys Conf Ser 2021;1973:12090. [CrossRef]

[3] Kibert CJ. Sustainable construction: green building design and delivery. New York: John Wiley & Sons; 2016.

[4] Al-Nadawi T. The ecology phenomenon and sustainable architecture. Baghdad: University of Baghdad; 2003.

[5] Al-Tameemi OA, Toma TA. Automation in architecture and its effect on the regeneration of traditional buildings: Al-Shawi House as a case study. Mater Sci Eng 2020;012027. [CrossRef]

[6] Hillier T. The Kent Design Guide. Maidstone, UK: Kent Design Guide; 2000.

[7] Energy Efficiency & Renewable Energy. U.S. Department of Energy. Available at: https://www.energy.gov/eere/office-energy-efficiency-renewable-energy. Accessed on Feb 03, 2026.

[8] Ertunç HM. A combined decision algorithm for diagnosing bearing faults using artificial intelligent techniques. Sigma J Eng Nat Sci 2018;36:1235–1253.

[9] WHO guidelines for indoor air quality: selected pollutants. World Health Orgazination, 2010. Available at: https://www.who.int/publications/i/item/9789289002134 Accessed on Feb 03, 2026.

[10] U.S. Green Building Council. Available at: https://www.usgbc.org/ Accessed on Feb 03, 2026.

[11] Guidelines for a just transition towards environmentally sustainable economies and societies for all. IL Orgazination. 2017. Available at: https://www.ilo.org/global/topics/green-jobs/publications/WCMS_432859/lang--en/index.htm Accessed on Feb 03, 2026.

[12] Al-Obaidi HAA, Al-Tameemi OA. Built Heritage Attractions in Cultural Tourism: the case of Al-Mustansiriya Madrassa, Baghdad. Al-Nahrain J Eng Sci 2019;22:37–43. [CrossRef]

[13] Al-Saffar MH, Al-Tameemi OA. The effect of applying new facade technologies on the effective response of the building. Melville, NY: AIP Publishing; 2023;2977:020110. [CrossRef]

[14] Marichova A. Role of the Government for Development of Sustainable Construction. Ovidius Univ Ann Constanta-Series Civ Eng 2020;22:53–62. [CrossRef]

[15] Karakurt AS, Sahin B. A new method for the size and performance analyses and optimization of thermal systems: The exergy density. Sigma J Eng Nat Sci 2019;37:571–583.

[16] Tokatlı C. Application of water quality index for drinking purposes in dam lakes: A case study of thrace region. Sigma J Eng Nat Sci 2020;38:393–402.

[17] Al-Ahbabi SA, Al-Alwan HAS. Enhancing the Continuity of Utilization of External Spaces at the Campus: Insights from the University of Baghdad Campus in Jadriya. Assoc Arab Univ J Eng Sci 2023;30:32–41.

[18] Swilling M, Hajer M, Suh S, Bergesen J, Salat S, Robinson B, et al. The weight of cities: Resource requirements of future urbanization. Washington: UN Environment International Resource Panel; 2018.

[19] Shaheen BR. Al-Ethari AM, Abdul-Munʾemt U. The effect of services system in architectural form developments. J Eng 2014;20:1–20. [CrossRef]

[20] Lay C, Dharmaraja J, Shobana S, Priya RK, Jeyakumar RB, Kumar G, et al. Lignocellulose biohydrogen towards net zero emission: A review on recent developments. Bioresour Technol 2022;364:128084. [CrossRef]

[21] McLennan JF. The philosophy of sustainable design: The future of architecture. Ecotone publishing. 2004.

[22] D'Odorico P, Davis KF, Rosa L, Carr JA, Chiarelli D, Gephart J, et al. The global food-energy-water nexus. Rev Geophys 2018;56:456–531. [CrossRef]

[23] Santos P, Martins C, Silva LS. Thermal performance of lightweight steel-framed construction systems. Metall Res Technol 2014;111:329–338. [CrossRef]

[24] Sirryeh SA. Sustainability Principles in Traditional Islamic Architecture. EcoMENA 2021. Available at: https://www.ecomena.org/sustainability-islamic-architecture/ Accessed on Feb 03, 2026.

[25] Khuraibet UA. Constructional Efficiency in Al_ Ahwaar Traditional Architecture. J Eng 2016;22:1–19. [CrossRef]

[26] Al-Assadi FI, Najah FT, Al-Saffar IMA. Alienation in Contemporary Iraqi Architecture: The Questions of Space-Time Communication and Style. J Int Soc Stud Vernac Settl 2022;9:387-407.

[27] Langston C. Sustainable practices in the built environment. London: Routledge; 2008. [CrossRef]

[28] Calkins M. Materials for sustainable sites: a complete guide to the evaluation, selection, and use of sustainable construction materials. New York: John Wiley & Sons; 2008.

[29] Salman N. Towards optimal design strategies in hot-arid climate: A comparative study of environmental and socio-cultural performance of the traditional and modern housing in Baghdad, Iraq (Master theis). Cardiff, UK: Cardiff University; 2017.

Sigma J Eng Nat Sci, Vol. 44, No. 1, pp. 200–209, February, 2026

Sigma Journal of Engineering and Natural Sciences
Web page info: https://sigma.yildiz.edu.tr
DOI: 10.14744/sigma.2025.00093

Research Article

Evaluation of the effects of sustainable development goals on improvement of air quality in cities

Şahin KORKMAZ[1], Damla MUSTAFAOĞLU[1,*], Zeynep CEYLAN[1]

[1]*Department of Environmental Engineering, Atatürk University, Erzurum, 25240, Türkiye*

ARTICLE INFO

Article history
Received: 01 October 2024
Revised: 12 November 2024
Accepted: 19 December 2024

Keywords:
Air Quality; Air Pollution; Sustainable Environment; Sustainable Development; Sustainability

ABSTRACT

In parallel with the rapid population growth, air pollution has become one of the most important problems in cities, along with water pollution, soil pollution, nuclear pollution and other pollution (noise-light pollution). Pollution elements, which have many negative effects on the natural environment and human health, and which have increased in recent years and cause serious air pollution, need to be reduced in the urban atmosphere and even eliminated at the source. With effective air quality policies to be implemented in the city, the amount of emissions of these pollutants to the atmosphere can be reduced and the emissions of these emissions can be solved at their sources thanks to clean technologies. In this context; effective implementation of the sustainable development goals will improve air quality by aiming to reduce pollutant emissions in cities. This study reveals which of the sustainable development goals can be used to minimize air pollutants in cities within the scope of sustainable environment in line with sustainable development goals and how these goals can have a positive impact on air quality. In order to investigate the impact of Sustainable Development Goals on air quality in cities, one-on-one interviews were conducted with expert academic staff from the environmental engineering department of our university and the collected data were presented.

Cite this article as: Korkmaz Ş, Mustafaoğlu D, Ceylan Z. Evaluation of the effects of sustainable development goals on improvement of air quality in cities. Sigma J Eng Nat Sci 2026;44(1):200–209.

INTRODUCTION

Globally, air pollution is one of the most important environmental problems in cities. Worldwide, emissions from production, consumption processes and logistics activities degrade urban air quality. In order to solve this problem, it is necessary to identify air pollutants, investigate emission sources and reduce or even eliminate pollutants released into the atmosphere at the source [1].

Problems of global dimension emerged especially after the industrial revolution in the 19th century when fossil fuels such as coal and oil started to be used in energy production. Concentrations of pollutants such as Carbon dioxide (CO_2), sulfur dioxide (SO_2) and Particulate Matter (PM) gradually increased in the atmosphere, and this increase, together with the increase in greenhouse gases (methane, chlorofluorocarbons, etc.) after the second half of the 20th

***Corresponding author.**
*E-mail address: damlamustafaoglu83@gmail.com

This paper was recommended for publication in revised form by Editor-in-Chief Ahmet Selim Dalkilic

Published by Yıldız Technical University Press, İstanbul, Turkey
© Author. This is an open access article under the CC BY-NC license (http://creativecommons.org/licenses/by-nc/4.0/).

century, caused problems such as global warming and ozone depletion on a global scale. This worldwide problem has caused problems such as acid rain in various parts of the world on a regional scale, while on a local (urban) scale, it has caused serious air pollution in large residential areas and industrial zones [2].

If we consider air pollution as a system with three basic components; (Fig. 1) these components are; Pollutant Source, Carrier Environment and Receiving Environment. The urban atmosphere is the environment where these three components are together. Air pollutant emissions generated as a result of production processes in industrial areas of cities affect other parts of the city, especially these areas. In addition, other pollutants from traffic and residential heating also participate in this process and negatively affect urban air quality.

The most important air pollutants in the urban atmosphere are inorganic in origin; carbon oxides (CO/CO_2), sulfur oxides ($SO/SO_2/SO_X$), nitrogen oxides ($NO/NO_2/NO_X$), ozone (O_3), heavy metals and particulate matter (especially $PM_{2.5}$ and PM_{10}), and organic ones, volatile organic compounds (BTX/VOCs), polyaromatic hydrocarbons (PAHs), dioxin and dibenzo-p-dioxin derivatives, hydrocarbon (HC) and chlorofluorocarbons (CFCs), etc.

Substances released into the atmosphere in cities and affecting air quality may undergo transformation through chemical/photochemical reactions and meteorological factors such as wind vector, relative humidity, temperature, temperature variation with height, pressure, precipitation may affect horizontal/vertical transport (advection/convection), dispersion and deposition (Fig. 2). Control methods should be used effectively in all of the main topics of source, urban atmosphere and impacts [3-4].

Air pollutants in the urban atmosphere have adverse effects on visibility, materials, plants and animal health, especially human health. Aerosols, a gaseous mixture of

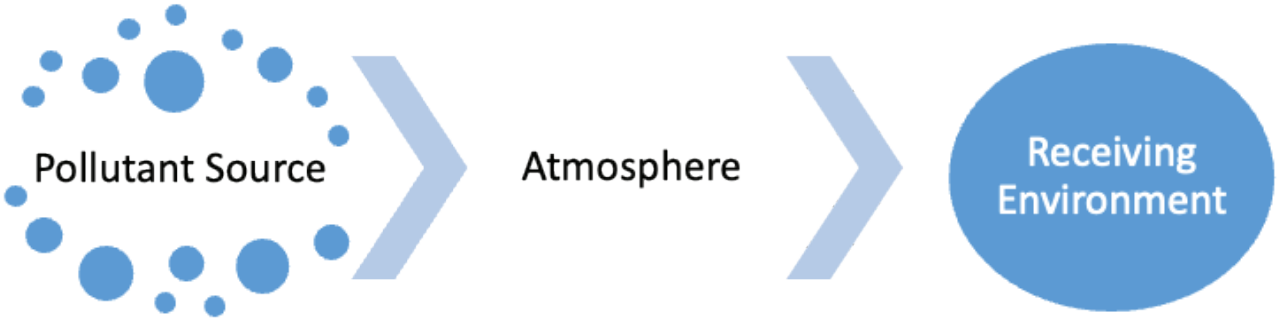


Figure 1. Components of air pollution.



Figure 2. Processes in air pollution.

Table 1. Common air pollutants and greenhouse gases and their impacts on climate, human- environmental health and ecosystems.

Air pollutant	Life time	Domain	Effect on global warming	Environmental ımpacts
Carbon dioxide (CO_2)				
Sulfur dioxide (SO_2)				
Methane (CH_4)				
Nitrogen oxide (NO_X)				
Nitrous oxide (N_2O)				
Tropospheric ozone (O_3)				
Volatile organic Compounds (VOC)				
Carbon monoxide (CO)				
Chloro fluoro carbons (CFC)				
Particulate matter (pm_{10})				
Particulate matter ($pm_{2.5}$)				
Impact indicators		Local		
		Global		
		Increase in global temperature		
		Decrease in global temperature		
		Effective on human health		
		Effective on ecosystems		
		It has no direct impact on human, environmental health and ecosystems.		

solid and liquid particles resulting from incomplete combustion of carbonaceous materials such as solid fuels and fuel oil, are a form of air pollution and have a visibility-reducing effect. Air pollution has a destructive and deforming effect on artistic and architectural structures (especially historical monuments). In plants, it can kill and inhibit growth by closing leaf stomata. The effects of air pollution on human health are caused by inhalation of high amounts of harmful substances in the atmosphere. These pollutants are known to have both acute and chronic effects on human health in urban areas and affect many organs, especially the respiratory tract. It causes many health problems such as upper respiratory tract irritation, chronic respiratory and heart disease, lung cancer, acute respiratory infections in children, chronic bronchitis in adults, adverse effects on pre-existing heart and lung diseases and asthma attacks. In a statement made at the United Nations Climate Change Conference (COP26) held in Glasgow, England, between October 31 and November 12, 2021, it was emphasized that 7.8 million people a year suffer from different types of cancer due to air pollution [5-8].

Urban air pollutants should be measured and controlled by developing effective urban policies, pollutant emissions should be reduced, health effects should be determined and their effects should be eliminated with regulations and objectives (SDGs). Reducing all the negative effects of these pollutants on the environment and human health is directly and indirectly linked to the effective implementation of SDG targets in cities (Table 1).

The concept of sustainability, which is frequently used in many fields, is defined as a participatory process [9-10] that ensures the careful use of all of society's social, cultural, scientific, natural and human resources and creates a social perspective based on respect for them. It can be said that sustainability began to manifest itself concretely in the literature in the early 19th century and emerged as a specific notion in renewable resources such as agriculture, forests and fisheries. The main feature of the concept, which is used in different fields, is that it deals with the human future and includes the protection of the resources of the area in which it is used. When the concept is viewed from this perspective, it is seen as a concept that combines economics, social justice, environmental science and management, business management, politics and law [11-14].

"Sustainable Development (SD)", which is the translation of the English concept of "Sustainable Development" into Turkish, is defined in the dictionary as "ensuring economic development without sacrificing the principle of using environmental values and natural resources in a rational way that does not lead to wastefulness, taking into account the rights and benefits of present and future generations." [15-16]. Almost all of the economic development models adopted today are models developed without taking into account environmental quality and the deformation of natural resources. "Sustainable development", which is seen as the only long-term development model that takes into account environmental quality and human capital and aims at the optimum use of resources, has been frequently used in the economic literature in recent years [17]. The transformation of SD into a globally active policy was realized with the "United Nations Conference on Environment and Development" (1992 Rio Conference) held in Rio de Janeiro, Brazil on June 3-4, 1992 with the participation of 178 heads of state or government of 178 countries. At the conference,



Figure 3. Sustainable development goals (UNDP 2024).

it was accepted that humans beings are at the center of SD and have the right to a healthy, harmonious and productive life with nature. The conference adopted two fundamental documents, the Rio Declaration and Agenda 21. With this conference, the content of the concept of SD has expanded considerably and has started to be used frequently in many disciplines [14,18-22].

A total of 17 Sustainable Development Goals (SDGs) have been defined under the 2030 Agenda, which envisages shifting the direction of global development to a more sustainable course (Fig. 3). With a total of 169 targets, sustainable development covers all economic, social and environmental dimensions [23-26]. Sustainable development goals are defined below:

Goal 1. No Poverty

It aims to end extreme poverty in all its forms (income below USD 1.90 per capita per day), achieve income justice for all and improve access to economic resources.

Goal 2. Zero Hunger

The goal of ending global hunger and malnutrition and ensuring access to safe, nutritious and sufficient food for all by promoting sustainable agricultural methods and food systems.

Goal 3. Good Health and Well-being

It aims to make global progress on issues such as infectious diseases, maternal and child health and mental health by promoting a healthy life for people of all ages and improving health systems.

Goal 4. Quality Education

Efforts are made to promote lifelong learning opportunities by providing inclusive, equitable and quality education opportunities for all.

Goal 5. Gender Equality

It targets the transformations necessary to end all forms of discrimination against women and girls and to ensure their equal participation in society, economy and politics.

Goal 6. Clean Water and Sanitation

Promotes the efficient use of water resources to ensure access to clean and safe water for all and sustainable sanitation practices.

Goal 7. Affordable and Clean Energy

It aims to guarantee access to modern, secure, sustainable and affordable energy sources for all.

Goal 8. Decent Work and Economic Growth

It promotes inclusive and sustainable economic growth, full employment and the creation of decent work opportunities.

Goal 9. Industry, Innovation and Infrastructure

It aims to create a global system that promotes sustainable industrialization, supports innovative solutions and builds resilient infrastructures.

Goal 10. Reduced Inequalities

It aims to reduce inequalities in income and opportunity between and within countries.

Goal 11. Sustainable Cities and Communities

It works to create inclusive, safe, resilient and sustainable cities and to improve the quality of urban life.

Goal 12. Responsible Consumption and Production

It supports responsible production and consumption through the efficient use of natural resources, waste management and the promotion of sustainable consumption patterns.

Goal 13. Climate Action

It aims to strengthen action to reduce carbon emissions and limit global temperature rise by taking urgent measures to combat climate change.

Goal 14. Life Below Water

It aims to protect underwater ecosystems by promoting the sustainable use of oceans, seas and marine resources.

Goal 15. Life on Land

It aims to protect forests, combat desertification, conserve biodiversity and ensure sustainable management of terrestrial ecosystems.

Goal 16. Peace, Justice and Strong Institutions

It promotes access to justice for all, building peaceful and inclusive societies, and building effective, accountable institutions.

Goal 17. Partnerships for the Goals

It aims to strengthen global cooperation, increase financial resources and facilitate information sharing to achieve sustainable development goals.

In Türkiye, the "Türkiye's Current Situation Analysis Project on Sustainable Development Goals" supports the development of policy, legislation, institutional framework and project development for Türkiye in the context of sustainable development goals. Within the scope of the project, Türkiye's current situation was assessed for each SDG, and gaps and areas in need of improvement were identified in line with the findings and determinations made (Sustainable Development Goals Assessment report 2019).

There are three important factors affecting environmental sustainability. These are industrialization, urbanization and rapid population growth. The rapid increase in population started in the 18th century and today, urbanization has brought environmental problems in cities with unpreventable migration. With the development of technology, the use of natural resources has increased. Natural resources, which were previously considered unlimited and free, have turned into a limited capital with increasing production activities in contemporary societies [27].

The environment has been greatly affected by exploitation, which is referred to as an economic- based attack, especially after the Industrial Revolution. From this period until the 1960s, the damage to the natural environment was seriously ignored [28]. However, after the 1970s, it is seen that this situation will not continue, there is no sustainability and environmental problems have started to emerge on a global scale. In terms of the sustainability of the environment and the ecosystem, within the framework of renewable resources; the level of use of resources should never exceed the level of regeneration of resources [18,29].

Especially developing countries have to develop and use their natural resources while doing so. Intensive use of natural resources creates the risk of destroying these resources and destroying environmental values. At the time, this was considered an inevitable consequence of development. Since the 20th century, rapidly developing countries have achieved social welfare, completed their economic development and developed an environmentally sensitive development policy. However, the infinity of human needs has necessitated the infinity of demands, and new demands and unstoppable consumption frenzy continue to harm the environment. In response to the limited natural resources and the rapid increase in the world population, natural resources have started to decrease and environmental pollution has started to increase. Rapid industrialization, urbanization, modernization of agriculture, developments in technology and economy have disrupted the resource-need balance, and efforts to achieve social welfare have begun to threaten the future of humanity. Thus, the concept of SDGs was developed in order to develop socio-economically, protect environmental values and stop the rapidly approaching global climate crisis [30-31].

Among the SDGs, which take measures on many issues and call for global action, there are some goals directly related to the environment. Goal 6 (Clean Water and Sanitation), Goal 7 (Affordable and Clean Energy), Goal 9 (Industrial Innovation and Infrastructure), Goal 11 (Sustainable Cities and Communities), Goal 12 (Responsible Production and Consumption), Goal 13 (Climate Action), Goal 14 (Life in Water) and Goal 15 (Life on Land) directly contribute to solving environmental problems, mitigating the impacts of climate change and creating a sustainable world ecosystem. Within these goals, some goals and sub-goals directly address air quality in cities and reduce the negative impacts of air pollutants on the environment and human health.

MATERIALS AND METHODS

In this study, the effects of sustainable development goals on the improvement of air quality in cities were evaluated by our expert team by examining the SDGs in detail through literature reviews. The study was developed in two steps. In the first step, SDGs directly related to the environment were identified. Following this identification, in the second step, it was examined which SDGs and sub-goals can improve air quality in cities. While performing these two steps, academic databases were scanned in detail. In this study, one-on-one interviews are conducted with 19 academic staff from the environmental engineering department of our university in order to investigate the impact of SDGs on air quality in cities. The data collected as a result of these interviews are presented in the Results and Discussion section.

RESULTS AND DISCUSSION

The effects of SDGs and their sub-objectives on air quality in cities have been revealed as a result of the studies. The relationship between SDGs and air quality is interpreted through the effects of these objectives on air quality components. Afterward, it is discussed which SDGs and sub-objectives can be used to improve air quality in cities.

Relationship Between Scalars and Urban Air Quality

Improving air quality in cities is linked to the effective implementation of the SDGs and has received considerable attention in recent years (Fig. 4). Understanding the extent to which air pollution also affects the process of achieving the SDGs can help to estimate the benefit of reducing air pollution to improve sustainable development and assess the necessity and urgency of reducing air pollutants and improving air quality [32]. Clearly, air pollution, urban air quality and SDGs mutually influence each other [33,34].

Reducing air pollution can improve the progress of sustainable development in several ways. First and foremost, air pollution changes the composition of the atmosphere, causing global warming by affecting greenhouse gas emissions and generating significant amounts of potentially health-threatening carbon monoxide (CO), sulphur dioxide (SO_2), nitrogen oxides (NOx) and particulate matter. Second, air pollutants can enter water and soil and be taken up by plants and grazing animals, thus affecting the entire ecosystem [29, 35-38].

Air pollution causes adverse health effects that have been widely researched in recent years. These health impacts include increased mortality and hospitalization



Figure 4. Relationship between air pollution and urban air quality and SDGs.

Table 2. Relationship between Air Pollution and SDGs

SDG	Effect on air pollutants sources	Air quality	Effects on human and environmental health
SDG 1	Neutral	Neutral	Ineffective
SDG 2	Neutral	Neutral	Ineffective
SDG 3	Reduces	Increases	Positive Impact
SDG 4	Neutral	Neutral	Ineffective
SDG 5	Neutral	Neutral	Ineffective
SDG 6	Neutral	Neutral	Ineffective
SDG 7	Reduces	Increases	Positive Impact
SDG 8	Neutral	Neutral	Ineffective
SDG 9	Neutral	Neutral	Ineffective
SDG 10	Neutral	Neutral	Ineffective
SDG 11	Reduces	Increases	Positive Impact
SDG 12	Neutral	Neutral	Ineffective
SDG 13	Reduces	Increases	Positive Impact
SDG 14	Reduces	Increases	Positive Impact
SDG 15	Reduces	Increases	Positive Impact
SDG 16	Neutral	Neutral	Ineffective
SDG 17	Neutral	Neutral	Ineffective

Indicators
Effect on Air Pollutants Sources: Increases-Neutral-Reduces
Air Quality: Increases-Neutral-Reduces
Effects on Human and Environmental Health: Positive Effect- Ineffective-Negative Effect

more chronic and respiratory diseases such as diseases of the nervous system, heart, brain, vascular diseases, reduced lung function and exacerbation of asthma and exercise-induced bronchoconstriction, chronic obstructive pulmonary disease and acute lower respiratory tract infections. Efforts to reduce air pollution can improve these conditions and thus benefit the achievement of the SDGs (Table 2). However, as a product of human activities, air pollution is associated with major social economic sectors, such as agriculture, industry, housing, and transportation sectors, which increase a country's Gross Domestic Product (GDP).

SDGS Effective in Improving Air Quality

Reducing urban air pollution and improving air quality is possible through the effective implementation of environmental SDG targets 3-7-11-13-14-15. Improving air quality will also positively affect SDG achievement as a positive feedback.

Among the SDGs, there are 13 targets under SDG 3 (Ensure a healthy and quality life at all ages).

These objectives are:

Sub-target 3.9 "By 2030, significantly reduce deaths and illnesses caused by hazardous chemicals and air, water and soil pollution and contamination with hazardous chemicals" and sub-target 3.d "Strengthen early warning, mitigation and risk management capacities of all countries, in particular developing countries, against national and global health risks" directly contribute to reducing air pollution.

SDG 7 (Ensure access to affordable, reliable, sustainable and modern energy for all) includes five targets, including;

Sub-target 7.1 "By 2030, ensure universal access to affordable, reliable and modern energy services", sub-target 7.2 "By 2030, significantly increase the share of renewable energy in the global energy mix", sub-target 7.3 "By 2030, double the global rate of improvement in energy efficiency", sub-target 7.a "By 2030, scale up international cooperation to facilitate access to clean energy research and technologies, including renewable energy, energy efficiency, advanced and cleaner fossil fuel technologies, and support investments in energy infrastructure and clean energy technologies" sub-target 7.b "By 2030, expand infrastructure and upgrade technologies in all developing countries, especially in the least developed countries, small island developing States and landlocked developing countries, to provide modern and sustainable energy services for all", the use of renewable and clean energy and the reduction of fossil air pollutants can be achieved.

SDG 11 (Making cities and human settlements inclusive, safe, resilient and sustainable) has 10 targets. These targets include;

Sub-target 11.2 "By 2030, ensure access to safe, affordable, accessible and sustainable transport systems for all,

with particular attention to the needs of vulnerable people, women, children, persons with disabilities and the elderly, by improving road safety and improving public transport systems in particular" and sub-target 11.4 "Strengthen efforts to protect and preserve the world's cultural and natural heritage" will reduce traffic-related emissions in cities and improve air quality around historical monuments through sustainable transport systems. In addition, sub-target 11.6 "By 2030, reduce negative environmental impacts per capita in cities, with particular attention to the management of municipal and other waste and air quality", sub- target 11.7 "By 2030, ensure universal access to safe, inclusive and accessible green and public spaces, especially for women, children, older people and persons with disabilities" and sub- target 11.7 "By 2030, ensure universal access to safe, inclusive and accessible green and public spaces, especially for women, children, older people and persons with disabilities", and sub- target 11.7.a "Promote positive economic, social and environmental relations between urban, peri-urban and rural areas through strengthening national and regional development planning", air quality can be given special attention, air pollutants can be reduced and positive environmental relations can be increased by increasing green areas within the city.

There are 5 targets under SDG 13 (Taking urgent action to combat climate change and its impacts). Among these; sub-target 13.1 "Strengthen resilience and adaptive capacity to climate change-related hazards and natural disasters in all countries", sub-target 13.2 "Incorporate climate change measures into national policies, strategies and planning processes", sub-target 13.3 "Develop training, awareness, individual and institutional capacity on climate change prevention and mitigation, climate change adaptation and early warning", sub-target 13.a "In order to meet the needs of developing countries in the context of meaningful mitigation actions and transparency in implementation, to ensure that developed countries that are parties to the United Nations Framework Convention on Climate Change realize their commitments to jointly mobilize USD 100 billion annually from all sources by 2020 and to operationalize the Green Climate Fund by completing the capital formation as soon as possible" sub-target 13.b "Promote mechanisms to increase planning and management capacity for climate change, including a focus on women, youth and local and marginalized communities in least developed countries and small island developing States".

SDG 14 (Protecting and sustainably using the oceans, seas and marine resources for sustainable development) has 10 targets. These include;

14.1 "By 2025, prevent and significantly reduce all forms of marine pollution, particularly from land-based activities, including marine litter and nutrient pollution", sub-target 14.2 Sub-target

14.1 "By 2020, manage and protect marine and coastal ecosystems sustainably, including by increasing their resilience, to avoid significant adverse impacts, and take action to restore ecosystems for healthy and productive oceans", sub-target 14.3 "Address and, as far as possible, reduce the impacts of ocean acidification, including through enhanced scientific cooperation at all levels", sub-target 14.a "Increase scientific knowledge, strengthen research capacity and transfer marine technologies to improve ocean health and enhance the contribution of marine biodiversity to the development of developing countries, in particular small island states and least developed countries, in line with the Criteria and Guidelines of the Intergovernmental Oceanographic Commission on the Transfer of Marine Technology", sub-goal 14.a; and sub- goal 14.c "As stated in paragraph 158 of "The Future We Want" The sub-objective 14.c "Improve the conservation and sustainable use of oceans and ocean resources by applying international law as enshrined in the United Nations Convention on the Law of the Sea, which sets out the legal framework for the conservation and sustainable use of oceans and ocean resources, as set out in paragraph 158 of the "The Future We Want" document" will enhance marine and ocean health and improve air quality globally.

There are 12 targets under SDG 15 (Protect, restore and promote sustainable use of terrestrial ecosystems; ensure sustainable forest management; combat desertification; halt and reverse land degradation; prevent biodiversity loss). Among these targets; sub-target 15.1 "By 2020, in line with obligations under international agreements, ensure the protection, restoration and sustainable use of terrestrial and inland freshwater ecosystems and their services, in particular forests, wetlands, mountains and drylands" will reduce air pollutants from acid rain and forest fires. 15.2 The sub-target 15.2 "By 2020, promote the practice of sustainable management for all forest types, halt deforestation, restore degraded forests, and substantially increase reforestation and reforestation globally" is to reduce greenhouse gas emissions by preventing climate change. Sub-target 15.3 "By 2020, combat desertification, restore degraded lands and soils, including lands affected by desertification, droughts and floods, and strive to achieve a world free from soil degradation" and sub-target 15.b "mobilize all resources at all levels to a significant extent to finance sustainable forest management and provide adequate incentives for developing countries to further sustainable forest management, including conservation and reforestation" improve air quality by protecting forest areas.

CONCLUSION

With the industrial revolution in the twentieth century, there has been an increase in human interaction with the environment and ecosystems. The desire of human beings to meet their unlimited needs has caused them to utilize nature, which they see as an unlimited resource, to misuse it and to pollute the environment as a result of this relationship. The fact that environmental pollution has reached great dimensions especially after the 1970s has brought to the agenda the sustainable development policy, which,

instead of growing no matter what, attaches importance to human beings, considers the interests of current and future generations, envisages the optimum use of natural and cultural resources, and advocates the harmony of economic and social policies with environmental policies at every stage of development. With this policy, economic and environmental problems have moved to an international dimension. Following the SDG policy, which brings a new dimension to the relationship between economic development and the environment, will ensure the establishment of a sustainable relationship with the environment.

In recent years, many studies have been conducted and published on air pollution, which causes significant health and environmental problems throughout our country. By increasing the number of studies, pollutant sources can be better identified, emission sources can be monitored, and their effects on the environment and human health can be better investigated. Identifying the sources of pollutants is possible by implementing the necessary measures and Sustainable Development Goals to eliminate pollutants at the source and in the urban atmosphere. Reducing pollution with a mechanism that affects each other will ensure that these goals are fulfilled more healthily.

As a result; full implementation of SDGs that are directly and indirectly related to air quality will contribute to the reduction of pollutants in the urban atmosphere and indirectly improve urban air quality. It should be noted that all stakeholders who are trying to implement relevant SDGs effectively in improving air quality within the city contribute to the process.

AUTHORSHIP CONTRIBUTIONS

Authors equally contributed to this work.

DATA AVAILABILITY STATEMENT

The authors confirm that the data that supports the findings of this study are available within the article. Raw data that support the finding of this study are available from the corresponding author, upon reasonable request.

CONFLICT OF INTEREST

The author declared no potential conflicts of interest with respect to the research, authorship, and/or publication of this article.

ETHICS

There are no ethical issues with the publication of this manuscript.

STATEMENT ON THE USE OF ARTIFICIAL INTELLIGENCE

Artificial intelligence was not used in the preparation of the article.

REFERENCES

[1] Gkatzelis GI, Gilman JB, Brown SS, Eskes H, Gomes AR, Lange AC, Kiendler-Scharr A. The global impacts of COVID-19 lockdowns on urban air pollution: A critical review and recommendations. Elem Sci Anth 2021;9:00176. [CrossRef]

[2] Fowler D, Brimblecombe P, Burrows J, Heal MR, Grennfelt P, Stevenson DS, Vieno M. A chronology of global air quality. Philos Trans R Soc A 2020;378:20190314. [CrossRef]

[3] Molina LT, Zhu T, Wan W, Gurjar BR. Impacts of megacities on air quality: Challenges and opportunities. Oxford Research Encyclopedia of Environmental Science. Oxford: Oxford University Press; 2020. [CrossRef]

[4] Goodsite ME, Hertel O, Johnson MS, Jørgensen NR. Urban air quality: Sources and concentrations. In: Air Pollution: Sources, Statistics and Health Effects. New York: Springer; 2021. p. 193–214. [CrossRef]

[5] Bernstein JA, Alexis N, Barnes C, Bernstein IL, Nel A, Peden D, Williams PB. Health effects of air pollution. J Allergy Clin Immunol 2004;114:1116–1123. [CrossRef]

[6] Folinsbee LJ. Human health effects of air pollution. Environ Health Perspect 1993;100:45–56. [CrossRef]

[7] Dominski FH, Branco JHL, Buonanno G, Stabile L, da Silva MG, Andrade A. Effects of air pollution on health: A mapping review of systematic reviews and meta-analyses. Environ Res 2021;201:111487. [CrossRef]

[8] Glencross DA, Ho TR, Camina N, Hawrylowicz CM, Pfeffer PE. Air pollution and its effects on the immune system. Free Radic Biol Med 2020;151:56–68. [CrossRef]

[9] Gladwin TN, Kennelly JJ, Krause TS. Shifting paradigms for sustainable development: Implications for management theory and research. Acad Manag Rev 1995;20:874–907. [CrossRef]

[10] Çapan Mustafaoğlu D, Korkmaz Ş, Ceylan Z. Recycling domestic sewage sludge to agricultural and farming areas in line with Sustainable Development Goals (SDG). Environ Res Technol 2023;6:159–171. [CrossRef]

[11] Wilson M. Corporate sustainability: What is it and where does it come from. Ivey Bus J 2003;67:1–5.

[12] SDG. Sustainable development goals: The energy progress report. Tracking SDG 7. 2019;805–814.

[13] Klopp JM, Petretta DL. The urban sustainable development goal: Indicators, complexity and the politics of measuring cities. Cities 2017;63:92–97. [CrossRef]

[14] Pradhan P, Costa L, Rybski D, Lucht W, Kropp JP. A systematic study of sustainable development goal (SDG) interactions. Earth's Future 2017;5:1169–1179. [CrossRef]

[15] Fund S. Sustainable development goals. United Nations. 2024 Available at: https://www.un.org/sustainabledevelopment/inequality Accessed on Jan 29, 2026.
[16] Altan R. Transformation from the Millennium Development Goals to the Sustainable Development Goals in Turkey and the World. Int J Econ Admin Soc Sci 2021;4:1–19.
[17] Şapaloğlu I. Text mining on sustainability reports of top 40 airlines and bibliometric analysis of airline's sustainability. Environ Res Technol 2024;7:186–193. [CrossRef]
[18] Tıraş H. Sustainable development and environment: An examine in theory. KSÜ İİBF Derg 2012;2:57–73. [Turkish]
[19] Visseren-Hamakers IJ. The 18th sustainable development goal. Earth Syst Gov 2020;3:100047. [CrossRef]
[20] Yücel Karamustafa E, Arsan B, Beşoğul K. The impact of circular economy and industry 4.0 on achievement of sustainable development goals: A systematic literature review. J Soc Sci 2022;24:294–323. [Turkish] [CrossRef]
[21] Köse HÖ. Audit of environmental sustainable development goals (SDGs) and intosai guidance. J Turk Court Accounts 2022;33:501–516. [Turkish] [CrossRef]
[22] Tohumcu Kaya T, Çakmaklı AB. Climate change and the built environment: Sustainable development goals and evaulation of the net zero carbon building (NZCB) design approach. İdealkent 2024;16:460–484. [Turkish] [CrossRef]
[23] The UNDP website. 2024. Available at: https://www.undp.org/sustainable-development-goals Accessed on Jan 29, 2026.
[24] Katila P, Colfer CJP, De Jong W, Galloway G, Pacheco P, Winkel G. Sustainable development goals. Cambridge: Cambridge University Press; 2019.
[25] Bengü E, Aslantaş Ateş B. Wellbeing in higher education in context of UN sustainable development goals. J Theory Pract Educ 2023;19:1–13. [Turkish] [CrossRef]
[26] Mızık ET, Yiğit Avdan Z. The cornerstone of sustainability: Ecological footprint. J Nat Hazards Environ 2020;6:451–467. [Turkish] [CrossRef]
[27] Zhang X, Han L, Wei H, Tan X, Zhou W, Li W, et al. Linking urbanization and air quality together: A review and a perspective on the future sustainable urban development. J Clean Prod 2022;346:130988. [CrossRef]
[28] Yaylı H. Development, environment and population in the context of environmental ethics. J Süleyman Demirel Univ Inst Soc Sci 2012;15:151–169. [Turkish]
[29] Longhurst J, Barnes J, Chatterton T, De Vito L, Everard M, Hayes E, et al. Analysing air pollution and its management through the lens of the UN sustainable development goals: A review and assessment. WIT Trans Ecol Environ 2018;230:3–14. [CrossRef]
[30] Elder M, Olsen SH. The design of environmental priorities in the SDGs. Glob Policy 2019;10:70–82. [CrossRef]
[31] Li L, Xia XH, Chen B, Sun L. Public participation in achieving sustainable development goals in China: Evidence from the practice of air pollution control. J Clean Prod 2018;201:499–506. [CrossRef]
[32] Amann M, Kiesewetter G, Schöpp W, Klimont Z, Winiwarter W, Cofala J, Pavarini C. Reducing global air pollution: The scope for further policy interventions. Philos Trans R Soc A 2020;378:20190331. [CrossRef]
[33] Zhu J, Zhai Y, Feng S, Tan Y, Wei W. Trade-offs and synergies among air-pollution-related SDGs as well as interactions between air-pollution-related SDGs and other SDGs. J Clean Prod 2022;331:129890. [CrossRef]
[34] Paramitha VN. Law enforcement over air pollution to bring about Sustainable Development Goals (SDGs) (A case study on air pollution in Palangkaraya, Central Kalimantan). Al-Daulah: J Hukum Perundang Islam 2021;11:297–315. [CrossRef]
[35] Vardoulakis S, Salmond J, Krafft T, Morawska L. Urban environmental health interventions towards the sustainable development goals. Sci Total Environ 2020;748:141530. [CrossRef]
[36] Rastgeldi Doğan T, Yeşilnacar Mİ, Çullu MA. Seasonal investigation of atmospheric desert dust affecting Şanlıurfa using MODIS satellite and HYSPLIT model data. Sigma J Eng Nat Sci 2018;36:905–916.
[37] Dinçer AR, Aral IF. Carbon dioxide emission in Thrace Region and neighboring countries as a result of aerobic stabilization of urban treatment sludges. Sigma J Eng Nat Sci 2021;38:1729–1733.
[38] Pekmezci A, Yalçın MO. Vector autoregressive clustering for redundancy analysis in air pollution monitoring networks in Türkiye. Sigma J Eng Nat Sci 2024;42:399–406. [CrossRef]

Sigma J Eng Nat Sci, Vol. 44, No. 1, pp. 210–221, February, 2026

Sigma Journal of Engineering and Natural Sciences
Web page info: https://sigma.yildiz.edu.tr
DOI: 10.14744/sigma.2025.00000

Research Article

An innovative group decision-making approach utilizing picture fuzzy hypersoft expert set

Muhammad IHSAN[1,*], Muhammad SAEED[1], Muhammad Yasir HAYAT MALIK[2]

[1]*Department of Mathematics, University of Management and Technology, Lahore, 54000, Pakistan*
[2]*Department of Mathematics, Division of Science and Technology, University of Education, Lahore, 54000, Pakistan*

ARTICLE INFO

Article history
Received: 27 July 2024
Revised: 03 October 2024
Accepted: 17 December 2024

Keywords:
Algorithm; Decision-Making; Fuzzy Set; Fuzzy Soft Set; Hypersoft Expert Set

ABSTRACT

The goal of this study is to propose a novel hybrid model called picture fuzzy hypersoft expert sets. This hybrid model is a combination of picture fuzzy sets with hypersoft expert sets for dealing with uncertainties in various real-world group decision-making problems. Picture fuzzy sets are an extension of intuitionistic fuzzy sets, and their theory takes into account the degree of refusal during a decision-making process in addition to the degrees of acceptance and rejection. A more comprehensive version of intuitionistic fuzzy hypersoft expert sets is the hybrid model that has been suggested. Along with matching examples, certain novel desirable features of the proposed model namely, subset, equality, complement, union, and intersection are examined. For the constructed model, two renowned operations AND and OR are also examined. Additionally, a decision-making process under the suggested strategy is described, supported by an algorithmic framework. Additionally, an example application is offered for a more thorough explanation; however, it is contingent upon the choice of an appropriate virtual reality device provider. Lastly, the contrast between the started approach and a few current models such as intuitionistic fuzzy hypersoft expert sets is investigated.

Cite this article as: Ihsan M, Saeed M, Hayat Malik MY. An innovative group decision-making approach utilizing picture fuzzy hypersoft expert set. Sigma J Eng Nat Sci 2026;44(1):210–221.

INTRODUCTION

An effective process that may produce rankings for a finite group of items according to several criteria related to these items is multi-attribute group decision making, or MAGDM. How to more precisely and effectively assign a numerical value to a given choice is a major issue in real-world decision-making procedures. It was impossible to characterise items with precise values since fuzziness existed in many difficult practical decision-making situations. Zadeh [1] was the first to introduce the idea of a fuzzy set (FS). This set is a superset of the classical set, as a solution to this problem. The idea of partial truth between ”absolute true” and ”absolute false” is what FS genuinely addresses. It is crucial that the membership function provide objects from closed unit intervals with their membership values. In certain real-world scenarios, the notion of FSs is inapplicable. If a specialist renders a decision regarding the non-membership degree of an item, for example.

***Corresponding author.**
*E-mail address: mihkhb@gmail.com

This paper was recommended for publication in revised form by Regional Editor Ahmet Selim Dalkilic

Published by Yıldız Technical University Press, İstanbul, Turkey
© Author. This is an open access article under the CC BY-NC license (http://creativecommons.org/licenses/by-nc/4.0/).

Then the non-membership degree is derived by taking into account the standard negation of the membership degree. As a generalisation of fuzzy sets (FSs), Atanassov [2] introduced the theory of intuitionistic fuzzy sets (IFSs) to address these kinds of issues. The description of FSs was altered by the addition of a new element (which determines the non-membership grade). As a result, an IFS includes two ambiguous components: membership grade and non-membership grade. This is a crucial point to demonstrate the IFS's expanding range of practical uses. There is a restriction on membership and non-membership grades in an IFS setting; that is, the total of the two grades is constrained by one. Many academics have focused on the aforementioned ideas during the past 20 years. Their efforts have produced a lot of successful outcomes in a variety of fields, such as taking decisions, health care diagnosis, and analysis of clustering [3–6]. While the aforementioned theories have proven useful in various real-world contexts, there are certain circumstances that IFSs are unable to fully explain. For instance, in a voting scenario when there are human viewpoints with more than two possible responses yes, no, abstain, or refusal. In these situations, IFSs are unable to appropriately represent the circumstance. Furthermore, an expert can provide their assessment of an object belonging to a universal set concerning a specific attribute. For example, an object's membership value with regard to a given property could be 0.5, its non-membership value could be 0.2, and its neutral behaviour could be 0.3, which indicates that the expert is unsure about the value. Since the current FSs and IFSs are unable to address this issue, Cuong [7] introduced the concept of picture fuzzy sets (PFSs). This structure is a direct generalisation of FS and IFS that incorporates the notion of positive, negative, and neutral membership degrees of an alternative. In contrast to FSs and IFSs, a PFS includes membership, neutral, and non-membership values. Due to these things, it is much better suited to illustrate ambiguous information. Numerous research have been proposed to date to address various everyday issues within the helpful framework of PFSs. Zhu et al. [8] introduced new distance measure for PFSs with applications. Singh [9], for instance, developed a correlation coefficient method for the PFSs. Son [10] developed a generalised distance measure for PFSs and used it to apply the solution to the clustering issue. Garg [11] constructed a few picture fuzzy aggregation operations employing t-norm and t-conorm. Then he applied them to multi-criteria decision making (MCDM). Following that, Wei [12] presented the TODIM approach for MCDM in a PFS setting. Some MAGDM techniques were developed by Ashraf et al. [13] and their applications to group decision-making were investigated. From an alternative angle, Sahu et al. [14] employed a hybridised distance measure for students' job choosing that was based on the theories of PFSs and rough sets. For other key terms pertaining to PFSs, readers should consult [15–24]. Following the development of fuzzy sets, Pawlak [25] developed the rough set model in 1982. This model proved very helpful tool for handling imprecise information. Due to their inability to accept parameterized values, the fuzzy and the rough sets theories are both ineffective when evaluating opinions based on disparate parameters. Verma, and Rohtagi [26] developed the similarity measures by using picture fuzzy sets for the different applications. Khan et al. [27] gave the idea of generalised picture fuzzy set with applications in different areas. Molodtsov [28] in troduced the idea of soft sets (SSs) to close this gap. The SS model functions as a powerful parameterization tool when handling uncertainties. This model is composed of the parameterized families of a universal set. Ali et al. [29] expanded on the work by introducing a few new SS concepts and features. An application of SSs for decision-making was presented by Maji et al. [30]. In order to integrate the advantages and capacities of current models, more effective models are required as uncertain circumstances get more complicated. Hybrid designs, which are merely mixtures of current models, effectively accomplish the goal. Many hybrid models have been developed in the past to address MAGDM scenarios that are unclear [31,32]. For example, Yang et al. [33] introduced picture fuzzy SSs (PFSSs) and their decision-making applications by combining SSs with PFSs. Asgher et al. [34] used the structure of complex picture fuzzy soft set in MADM methods. Asgher et al. [35] again used this structure to give example of MADM. Mutlu et al. [36] developed MADM methods for health systems. Yolcu [37] gave MCDM methods by using intuitionistic fuzzy soft sets. In relation to hesitating, Akram et al. [38] examined N-soft sets and their uses in MAGDM. Additionally, Alcantud and Giarlotta [39] provided possible fuzzy sets that are both necessary and feasible for group decision making. Alkhazalah and Salleh [40] developed the idea of soft expert sets (SESs), which can handle several expert opinions on a single platform, to get over this restriction. Subsequently, fuzzy SESs were introduced by Alkhazalah and Salleh [41] by extending the notions of SESs by their combination with fuzzy theory. Numerous scholars have used the powerful notion of SESs to solve a variety of group making choices difficulties, as seen in [42-45]. For example, intuitionistic fuzzy SESs (IFSESs) were introduced and their applications were examined by Broumi and Smarandache [46]. The bipolar fuzzy SES model was presented by Qudah and Hassan [47] along with certain applications. To describe the certain important characteristics of convexity, Ihsan et al. [48,49] made use of SES and FSES in the convexity. Ali et al. [50] have recently introduced a new hybrid model known as fuzzy bipolar SESs and examined its use in different fields. Soft set like models have been introduced only for the one expert opinion and have no idea about the partitioning of attributes. To solve the problem of partitioning of parameters, Smarandache [51] made extension in the soft set to established the hypersoft set (HS). He also made the combination of this model with other fuzzy set like structures to form fuzzy, intuitionistic fuzzy hypersoft sets.

Rah- man et al. [52] made use of HS with the concept of mappings in supply chain management. Saeed et al. [53] made use of the fuzzy hypersoft set for renewable energy resources with the help of an example. After this Saeed et al. [54] introduced the fundamentals of picture fuzzy hypersoft sets. To handle the situation of multi-opinions of multi-experts having in a single, Ihsan et al. [55] gave the structure of hypersoft expert set(HSES). Ihsan et al. [56] also made combination of this model with fuzzy environment to form fuzzy [57] and intuitionistic fuzzy hypersoft expert sets (IFHSES) [58]. According to the aforementioned research, a number of models, such as PFSs or IFHSESs, have been put forth to efficiently synthesise picture fuzzy information; yet, there hasn't been any attention paid to the development of an effective hybrid model that combines PFSs and HESs [59-61].

Research Gap, Motivation and Novelty

The following is a summary of the primary motivations and novelty for this construction:

(1) In reality, the combination of models, known as IFSESs [46], deals with two dimensional data. Such kind of a data has been assessed by several specialists in relation to various parameters. This approach falls short in addressing the crucial concept of neutrality degree. This degree is evident in a number of real-world scenarios. In such scenarios, we are presented with expert judgements in the form of yes, no, abstain, and refusal. For example, the neutrality degree can be taken into account while diagnosing medical conditions. Certain illnesses (such as chest or heart problems) may not present with symptoms like fever and headache. Similarly, the symptoms of stomach and chest pain are inert against a variety of illnesses, such as viral fever, typhoid, and malaria.

(2) Yang et al. [33] integrated the ideas of PFS and SES to develop an innovative hybrid approach called PFSESs. Yet this model is unable to appropriately handle the partitioning of parameters into sub-parameters with non-overlapping parametric set values. To effectively handle many experts, we combine PFSESs with HSs to develop a novel hybrid model we call picture fuzzy PFHSESs.

The developed picture fuzzy HSES (PFHSES) model has the following main contributions:

1. Motivated by PFSs' ability to handle ambiguous and uncertain data in practical situations, this work aims to introduce a novel hybrid model PFHSESs that combines PFSEs with HSs.
2. Corresponding examples are used to examine some of its desired qualities, including subset complement, union, intersection, OR operation, and AND operation.
3. Based on PFHSESs, a decision-making algorithm is developed.
4. To better illustrate the suggested methodology, an illustrative application is included.
5. In addition, the advantages and a comparison of the suggested hybrid model with a few other modelsincluding intuitionistic fuzzy SESs are examined in order to demonstrate the effectiveness and dependability of the model.

This paper's remaining sections are organised as follows: A thorough explanation of several basic concepts, such as SES, PFS, scoring function, and accuracy function for PFSs and PFSSs, is given in Section 2. An effective expansion of PFSSs or IFSESs, the new hybrid model known as PFHSESs is presented in Section 2. Through illustrative numerical examples, various fundamental features and operations, including subset, complement, union, intersection,

OR operation, and AND operation, are also examined for PFHSESs. For a more thorough explanation of the suggested method, Section 4 offers an application in real life. In order to demonstrate the effectiveness and dependability of our developed model, Section 5 examines the advantages and contrasts the model with others already in use, including IFSESs. The paper's conclusion and recommendations for future research are provided in Section 6.

PRELIMINARY KNOWLEDGE

This part goes over a few fundamental ideas, such as PFSES, and their basic operations, this will come in handy for the paper's remaining sections.

Definition 2.1. [62] Suppose there are sets Υ, Δ, Ω and Γ which are named as a universe of discourse, collection of parameters, experts and opinions respectively. Take $R = \Delta \times \Omega \times \Gamma$, then picture fuzzy soft expert can be considered as a pair (ζ, R) such that: $\zeta : R \to P^{F(Y)}$.

In set form it can be shown as $(\zeta, R) = \{\langle b, \zeta(b)\rangle : b \in R\}$, where $\zeta(b) = \{y, \langle \eta_R(b), \beta_R(b), \theta_R(b)\rangle : y \in \Upsilon\}$ fulfilling the condition that their sum lies between 0 and 1. While $\eta_R(b)$, $\beta_R(b)$ and $\theta_R(b)$ are used here for truth, neutrality and falsity degrees respectively and each of which lies between 0 and 1.

Definition 2.2 [62] The subset relation between two PFSESs (ζ, R) and (α, P) can be seen as: (1) $R \subseteq P$, (2) $\zeta(b) \subseteq \alpha(b)$, whenever $\eta R(b) \leq \eta P(b)$, $\beta R(b) \leq \beta P(b)$ and $\theta R(b) \geq \theta P(b)$.

Definition 2.3 [62] The equality of two PFSESs (ζ, R) and (α, P) i. e., $(\zeta, R) = (\alpha, P)$ can be seen iff $(\zeta, R) \subseteq (\zeta, P)$ and $(\zeta, P) \subseteq (\zeta, R)$.

Definition 2.4 [62] The union operation between two PFSESs (ζ, R) and (α, P) defines an- other PFSESs $(\beta, Q) = (\zeta, R) \cup (\alpha, P)$ with $Q = R \cup P$ and for all $b \in Q$,

$$\beta(b) = \begin{cases} \zeta(b) & ; \ b \in R - P \\ \alpha(b) & ; \ b \in P - R \\ \cup(\zeta(b), \alpha(b)) & ; \ b \in R \cap P, \end{cases},$$

where $\cup(\zeta(b), \alpha(b)) = \{< u, \max\{\mu1(b), \mu2(b)\}, \min\{\nu1(b), \nu2(b)\}, \min\{\omega1(b), \omega2(b)\} >: u \in \Upsilon\}$.

Definition. 2.5. [62] The operation intersection between two PFSESs (ζ, R) and (α, P) defines another PFSESs (β, Q) = (ζ, R) ∩ (α, P) with Q = R ∩ P and for all b ∈ Q,

$$\beta(b) = \begin{Bmatrix} \zeta(b) & ; \ b \in R-P \\ \alpha(b) & ; \ b \in P-R \\ \cap(\zeta(b), \alpha(b)) & ; \ b \in R \cap P, \end{Bmatrix},$$

where ∩(ζ(b), α(b)) = {< u, min {μ1(b), μ2(b)}, min {ν1(b), ν2(b)}, max {ω1(b), ω2(b)} >: u ∈ ϒ}.

PICTURE FUZZY HYPERSOFT EXPERT SETS

This part presents the central idea of the study, which is PFHSESs, along with a few basic model characteristics that are clarified through examples of illustration.

Definition.3.1. Let $\hat{W} = \{\bar{S}_1, \bar{S}_2, \bar{S}_3 \ldots \bar{S}_n\}$ be the set of different sub-classes corresponds to distinct attributes $\bar{s}_1$, $\bar{s}_2$, $\bar{s}_3 \ldots \bar{s}_n$, and $\hat{B} = \hat{W} \times \Omega \times \Gamma$, then picture fuzzy hypersoft expert set can be defined by a mapping $\chi : \hat{B} \to P^{F(\Upsilon)}$. In set form it can be written as: $(\chi, \hat{B}) = \{\langle b, \chi(b)\rangle : b \in \hat{B}\}$ where $\chi(b) = \{\langle g, \eta\hat{B}(g), \beta\hat{B}(g), \theta\hat{B}(g)\rangle : g \in \Upsilon\}$ having the condition $0 \le \eta\hat{B}(g) + \beta\hat{B}(g) + \theta\hat{B}(g) \le 1$. Some hesitancy degree can also be calculated as $1 - (\eta\hat{B}(g) + \beta\hat{B}(g) + \theta\hat{B}(g))$. While $\eta\hat{B}(g)$, $\beta\hat{B}(g)$, and $\theta\hat{B}(g) \in [0, 1]$ represent the satisfying, neutral, and non-satisfying degrees respectively.

Example.3.2. Considering the three alternatives ϒ = {KIA = δ_1, City Honda = δ_2, PASSO Japan = δ_3} available to an organization looking to purchase electric automobiles, the global market for commercial electric vehicles is growing at a rapid pace. The company must consider the advice of two experts $\Omega = \{\hat{p}_1, \hat{p}_2\}$ in the field to determine which electric vehicle is ideal. Let Δ = {s_1=milage capacity, s_2 = price } be a helpful set of guidelines supplied by the business to assist professionals in the assessment process so they can appropriately meet their needs. Let S_{11} = 15 km, S_{12} = 20 km and S_{21} = 50, 000 Dollar, S_{22} = 60, 000 Dollar, be the different sub-classes corresponding to the attributes {s_1= milage capacity, s_2= price. $\hat{W} = s_1 \times s_2 = \{\partial_1, \partial_2, \partial_3, \partial_4\}$. we get 4 pairs and now $\hat{W} \times \Omega \times \Gamma = \{\xi_1, \xi_2, \xi_3, ..., \xi_{16}\} = \{\xi_i = (\partial_i, \hat{p}_i, 1 \text{ or } 0)\}$. We get 16 pairs and each pair is a 3-triplet. The PFHSES can be established on the basis of. the experts judgements which is given in Table 1.

In this Table 1, ⟨0.33, 0.23, 0.32⟩ the values 0.33, 0.23, 0.32 represent the satisfaction, neutral and non-satisfaction degrees respectively.

Definition 3.3. Consider two PFHSESs $(\chi_1, \hat{B}_1)$ and $(\chi_2, \hat{B}_2)$. The subset relation between two these sets can be seen as if

1. $\hat{B}1 \subseteq \hat{B}_2$,
2. $\chi_1(b) \subseteq \chi_1(b)$ for all $b \in \hat{B}_1 \Longleftrightarrow \eta\hat{B}_1 \le \eta\hat{B}_2$, $\beta\hat{B}_1 \le \beta\hat{B}_2$ and $\theta\hat{B}_1 \ge \theta\hat{B}_2$.

The representation for the subset relation is $(\chi_1, \hat{B}_1) \subseteq (\chi_2, \hat{B}_2)$.

Here is a mathematical illustration of an picture fuzzy soft expert subset relation to help understand it:

Example 3.4. Let $(\chi_1, \hat{B}_1)$ and $(\chi_2, \hat{B}_2)$ be two PFHSESs over ϒ. These two sets have been shown in Tables 2, and 3, respectively such that χ_1 and χ_2 have been below: $\chi_1 = \{(\partial_1, \hat{p}_1, 1)(\partial_1, \hat{p}_1, 0)\}$ and $\chi_2 = \{(\partial_1, \hat{p}_1, 1)(\partial_1, \hat{p}_1, 0)(\partial_1, \hat{p}_2, 1)\}$.

Table 1. Tabular form of PFHSES

$(\partial_i, \hat{p}_i, 1)$	δ_1	δ_2	δ_3
$(\partial_1, \hat{p}_1, 1)$	⟨0.33, 0.23, 0.32⟩	⟨0.22, 0.31, 0.30⟩	⟨0.32, 0.31, 0.31⟩
$(\partial_1, \hat{p}_2, 1)$	⟨0.35, 0.21, 0.15⟩	⟨0.33, 0.22, 0.13⟩	⟨0.30, 0.21, 0.11⟩
$(\partial_2, \hat{p}_1, 1)$	⟨0.15, 0.37, 0.24⟩	⟨0.15, 0.31, 0.25⟩	⟨0.23, 0.33, 0.25⟩
$(\partial_2, \hat{p}_2, 1)$	⟨0.42, 0.15, 0.35⟩	⟨0.43, 0.17, 0.32⟩	⟨0.42, 0.11, 0.32⟩
$(\partial_3, \hat{p}_1, 1)$	⟨0.25, 0.32, 0.32⟩	⟨0.21, 0.35, 0.30⟩	⟨0.32, 0.32, 0.21⟩
$(\partial_3, \hat{p}_2, 1)$	⟨0.25, 0.15, 0.15⟩	⟨0.23, 0.13, 0.13⟩	⟨0.30, 0.12, 0.21⟩
$(\partial_4, \hat{p}_1, 1)$	⟨0.27, 0.17, 0.37⟩	⟨0.25, 0.35, 0.15⟩	⟨0.13, 0.23, 0.03⟩
$(\partial_4, \hat{p}_2, 1)$	⟨0.32, 0.04, 0.35⟩	⟨0.42, 0.02, 0.42⟩	⟨0.32, 0.21, 0.42⟩
$(\partial_1, \hat{p}_1, 0)$	⟨0.23, 0.43, 0.32⟩	⟨0.11, 0.31, 0.40⟩	⟨0.32, 0.32, 0.41⟩
$(\partial_1, \hat{p}_2, 0)$	⟨0.45, 0.25, 0.25⟩	⟨0.42, 0.43, 0.13⟩	⟨0.40, 0.32, 0.11⟩
$(\partial_2, \hat{p}_1, 0)$	⟨0.27, 0.17, 0.27⟩	⟨0.25, 0.35, 0.15⟩	⟨0.13, 0.23, 0.43⟩
$(\partial_2, \hat{p}_2, 0)$	⟨0.43, 0.16, 0.31⟩	⟨0.42, 0.32, 0.12⟩	⟨0.42, 0.21, 0.13⟩
$(\partial_3, \hat{p}_1, 0)$	⟨0.24, 0.36, 0.38⟩	⟨0.22, 0.34, 0.31⟩	⟨0.23, 0.33, 0.30⟩
$(\partial_3, \hat{p}_2, 0)$	⟨0.36, 0.23, 0.17⟩	⟨0.33, 0.26, 0.12⟩	⟨0.31, 0.23, 0.11⟩
$(\partial_4, \hat{p}_1, 0)$	⟨0.13, 0.37, 0.29⟩	⟨0.16, 0.38, 0.21⟩	⟨0.13, 0.36, 0.22⟩
$(\partial_4, \hat{p}_2, 0)$	⟨0.43, 0.15, 0.35⟩	⟨0.44, 0.18, 0.32⟩	⟨0.43, 0.13, 0.32⟩

Table 2. Tabular form of PFHSES $(\chi_1, \hat{B}1)$

$(\partial_i, \hat{p}_i, 1)$	δ_1	δ_2	δ_3
$(\partial_1, \hat{p}_1, 1)$	⟨0.33, 0.23, 0.32⟩	⟨0.22, 0.31, 0.30⟩	⟨0.32, 0.31, 0.31⟩
$(\partial_1, \hat{p}_1, 0)$	⟨0.23, 0.43, 0.32⟩	⟨0.11, 0.31, 0.40⟩	⟨0.32, 0.32, 0.41⟩

Table 3. Tabular form of PFHSES $(\chi_2, \hat{B}_2)$

$(\partial_i, \hat{p}_i, 1)$	δ_1	δ_2	δ_3
$(\partial_1, \hat{p}_1, 1)$	⟨0.33, 0.23, 0.32⟩	⟨0.21, 0.30, 0.30⟩	⟨0.32, 0.31, 0.31⟩
$(\partial_1, \hat{p}_1, 0)$	⟨0.23, 0.43, 0.32⟩	⟨0.11, 0.31, 0.40⟩	⟨0.32, 0.32, 0.41⟩
$(\partial_1, \hat{p}_2, 1)$	⟨0.35, 0.21, 0.15⟩	⟨0.33, 0.22, 0.13⟩	⟨0.30, 0.21, 0.11⟩

From above two tables, it is clear that $(\chi_1, \hat{B}_1) \sqsubseteq (\chi_2, \hat{B}_2)$.

Definition 3.5. Two PFHSESS $(\chi_1, \hat{B}_1)$ and $(\chi_2, \hat{B}_2)$ are said to be equal iff $(\chi_1, \hat{B}_1) \subseteq (\chi_2, \hat{B}_2)$ and $(\chi_2, \hat{B}_2) \subseteq (\chi_1, \hat{B}_1)$.

Definition 3.6. Another subset relation called agree-PFHSES $(\chi, \hat{B})_1$ which can be stated as: $(\chi, \hat{B})_1 = \{\chi(b) : b \in \hat{W} \times \Omega \times \{1\}\}$.

Retaking the PFHSES $(\chi, \hat{B})$ in Example 3.2. Then, we can find the agree-PFHSES as shown in Table 4.

Table 4. Tabular form of agree-PFHSES

$(\partial_i, \hat{p}_i, 1)$	δ_1	δ_2	δ_3
$(\partial_1, \hat{p}_1, 1)$	⟨0.33, 0.23, 0.32⟩	⟨0.22, 0.31, 0.30⟩	⟨0.32, 0.31, 0.31⟩
$(\partial_1, \hat{p}_2, 1)$	⟨0.35, 0.21, 0.15⟩	⟨0.33, 0.22, 0.13⟩	⟨0.30, 0.21, 0.11⟩
$(\partial_2, \hat{p}_1, 1)$	⟨0.15, 0.37, 0.24⟩	⟨0.15, 0.31, 0.25⟩	⟨0.23, 0.33, 0.25⟩
$(\partial_2, \hat{p}_2, 1)$	⟨0.42, 0.15, 0.35⟩	⟨0.43, 0.17, 0.32⟩	⟨0.42, 0.11, 0.32⟩
$(\partial_3, \hat{p}_1, 1)$	⟨0.25, 0.32, 0.32⟩	⟨0.21, 0.35, 0.30⟩	⟨0.32, 0.32, 0.21⟩
$(\partial_3, \hat{p}_2, 1)$	⟨0.25, 0.15, 0.15⟩	⟨0.23, 0.13, 0.13⟩	⟨0.30, 0.12, 0.21⟩
$(\partial_4, \hat{p}_1, 1)$	⟨0.27, 0.17, 0.37⟩	⟨0.25, 0.35, 0.15⟩	⟨0.13, 0.23, 0.03⟩
$(\partial_4, \hat{p}_2, 1)$	⟨0.32, 0.04, 0.35⟩	⟨0.53, 0.02, 0.42⟩	⟨0.32, 0.21, 0.42⟩

Definition 3.7. Another subset relation called disagree-PFHSES $(\chi, \hat{B})_0$ which can be stated as: $(\chi, \hat{B})_0 = \{\chi(b) : b \in \hat{W} \times \Omega \times \{0\}\}$.

Retaking the PFHSES $(\chi, \hat{B})$ in Example 3.2. Then, we can find the disagree-PFHSES as shown in Table 5.

Table 5. Tabular form of disagree-PFHSES

$(\partial_i, \hat{p}_i, 0)$	δ_1	δ_2	δ_3
$(\partial_1, \hat{p}_1, 0)$	⟨0.23, 0.43, 0.32⟩	⟨0.11, 0.31, 0.40⟩	⟨0.32, 0.32, 0.41⟩
$(\partial_1, \hat{p}_2, 0)$	⟨0.45, 0.25, 0.25⟩	⟨0.42, 0.43, 0.13⟩	⟨0.40, 0.32, 0.11⟩
$(\partial_2, \hat{p}_1, 0)$	⟨0.27, 0.17, 0.27⟩	⟨0.25, 0.35, 0.15⟩	⟨0.13, 0.23, 0.43⟩
$(\partial_2, \hat{p}_2, 0)$	⟨0.43, 0.16, 0.31⟩	⟨0.42, 0.32, 0.12⟩	⟨0.42, 0.21, 0.13⟩
$(\partial_3, \hat{p}_1, 0)$	⟨0.24, 0.36, 0.38⟩	⟨0.22, 0.34, 0.31⟩	⟨0.23, 0.33, 0.30⟩
$(\partial_3, \hat{p}_2, 0)$	⟨0.36, 0.23, 0.17⟩	⟨0.33, 0.26, 0.12⟩	⟨0.31, 0.23, 0.11⟩
$(\partial_4, \hat{p}_1, 0)$	⟨0.13, 0.37, 0.29⟩	⟨0.16, 0.38, 0.21⟩	⟨0.13, 0.36, 0.22⟩
$(\partial_4, \hat{p}_2, 0)$	⟨0.43, 0.15, 0.35⟩	⟨0.44, 0.18, 0.32⟩	⟨0.43, 0.13, 0.32⟩

Definition 3.8. Here we define the union operation between two PFHSESs $(\chi_1, \hat{B}_1)$ and $(\chi_2, \hat{B}_2)$, which is again PFHSES $(\chi_1, \hat{B}_1) \cup (\chi_2, \hat{B}_2) = (\chi_3, \hat{B}_3)$, such that $\hat{B}_3 = \hat{B}_1 \cap \hat{B}_2$

$$\hat{B}_3(b) = \begin{cases} \hat{B}_1(b) & ; \ b \in \chi_1 - \chi_2 \\ \hat{B}_2(b) & ; \ b \in \chi_2 - \chi_1 \\ \cup(\hat{B}_1(b), \hat{B}_2(b)) & ; \ b \in \chi_1 \cap \chi_2, \end{cases}$$

Where

$\cup(\hat{B}_1(b), \hat{B}_2(b)) = \{< u, max\{\mu_1(b), \mu_2(b)\}, min\{v_1(b), v_2(b)\}, min\{\omega_1(b), \omega_2(b)\} >: u \in \Upsilon\}$.

Example 3.9. Consider two two PFHSESs $(\chi_1, \hat{B}_1)$ and $(\chi_2, \hat{B}2)$ in example 3.2 such that $\hat{B}_1 = (\partial_1, \hat{p}_1, 1), (\partial_1, \hat{p}_1, 0), (\partial_1, \hat{p}_2, 1)$ and $\hat{B}_2 = (\partial_1, \hat{p}_1, 1), (\partial_1, \hat{p}_1, 0)$.

Now we see the tabular form of these two sets given by as:

Table 6. Tabular form of PFHSES

$(\partial_i, \hat{p}_i, 1)$	δ_1	δ_2	δ_3
$(\partial_1, \hat{p}_1, 1)$	⟨0.33, 0.23, 0.32⟩	⟨0.22, 0.31, 0.30⟩	⟨0.32, 0.31, 0.31⟩
$(\partial_1, \hat{p}_2, 1)$	⟨0.35, 0.21, 0.15⟩	⟨0.33, 0.22, 0.13⟩	⟨0.30, 0.21, 0.11⟩
$(\partial_1, \hat{p}_1, 0)$	⟨0.23, 0.43, 0.32⟩	⟨0.11, 0.31, 0.40⟩	⟨0.32, 0.32, 0.41⟩

Table 7. Tabular form of PFHSES

$(\partial_i, \hat{p}_i, 1)$	δ_1	δ_2	δ_3
$(\partial_1, \hat{p}_1, 1)$	⟨0.33, 0.23, 0.32⟩	⟨0.22, 0.31, 0.30⟩	⟨0.32, 0.31, 0.31⟩
$(\partial_1, \hat{p}_2, 1)$	⟨0.35, 0.21, 0.15⟩	⟨0.33, 0.22, 0.13⟩	⟨0.30, 0.21, 0.11⟩

Now tabular form of their union is given by in a table 8.

Table 8. Tabular form of union of two PFHSES sets

$(\partial_i, \hat{p}_i, 1)$	δ_1	δ_2	δ_3
$(\partial_1, \hat{p}_1, 1)$	⟨0.33, 0.23, 0.32⟩	⟨0.22, 0.31, 0.30⟩	⟨0.32, 0.31, 0.31⟩
$(\partial_1, \hat{p}_2, 1)$	⟨0.35, 0.21, 0.15⟩	⟨0.33, 0.22, 0.13⟩	⟨0.30, 0.21, 0.11⟩
$(\partial_1, \hat{p}_1, 0)$	⟨0.23, 0.43, 0.32⟩	⟨0.11, 0.31, 0.40⟩	⟨0.32, 0.32, 0.41⟩

Definition S.10. Here we define the intersection operation between two PFHSESs $(\chi_1, \hat{B}_1)$

and $(\chi_2, \hat{B}_2)$, which is again PFHSES $(\chi_1, \hat{B}_1) \cap (\chi_2, \hat{B}_2) = (\chi_3, \hat{B}_3)$, such that $\hat{B}_3 = \hat{B}_1 \cap \hat{B}_2$ with b $\in \chi_3$,

$$\hat{B}_3(b) = \begin{cases} \hat{B}_1(b) & ; \ b \in \chi_1 - \chi_2 \\ \hat{B}_2(b) & ; \ b \in \chi_2 - \chi_1 \\ \bigcap(\hat{B}_1(b), \hat{B}_2(b)) & ; \ b \in \chi_1 \bigcap \chi_2, \end{cases}$$

Where

$\bigcap(\hat{B}_1(b), \hat{B}_2(b)) = \{< u, max\{\mu_1(b), \mu_2(b)\}, min\{v_1(b), v_2(b)\}, min\{\omega_1(b), \omega_2(b)\} >: u \in \Upsilon\}$.

Example 3.11. Consider two PFHSESs $(\chi_1, \hat{B}_1)$ and $(\chi_2, \hat{B}_2)$ in example 3.9, then the tabular form of their intersection is given by in a table 9.

Table 9. Tabular form of intersection of two PFHSES

$(\partial_i, \hat{p}_i, 1)$	δ_1	δ_2	δ_3
$(\partial_1, \hat{p}_1, 1)$	⟨0.33, 0.23, 0.32⟩	⟨0.22, 0.31, 0.30⟩	⟨0.32, 0.31, 0.31⟩
$(\partial_1, \hat{p}_2, 1)$	⟨0.35, 0.21, 0.15⟩	⟨0.33, 0.22, 0.13⟩	⟨0.30, 0.21, 0.11⟩

Definition 3.12. Here we define the AND operation between two PFHSESs $(\chi_1, \hat{B}_1)$ and $(\chi_2, \hat{B}_2)$, which is shown

as $(\chi_1, \hat{B}_1) \Lambda (\chi_2, \hat{B}_2) = (\chi_3, \hat{B}_3)$, such that $\hat{B}_3 = \hat{B}_1 \infty \hat{B}_2$ with $\chi_3 = \chi_1(b_1) \cap \chi_2(b_2)$ and, $\chi_3(b_1, b_2)(u) = \{< u, min\{\mu_1(u), \mu_2(u)\}, min\{v_1(u), v_2(u)\}, max\{\omega_1(u), \omega_2(u)\} >: u \in \Upsilon\}$, $\forall(b_1, b_2) \in \hat{B}_1 \infty \hat{B}_2$.

Definition 3.13. Here we define the OR operation between two PFHSESs $(\chi_1, \hat{B}1)$ and $(\chi_2, \hat{B}_2)$, which is shown as $(\chi_1, \hat{B}_1)$ V $(\chi_2, \hat{B}_2) = (\chi_3, \hat{B}_3)$, such that $\hat{B}_3 = \hat{B}_1 \infty \hat{B}_2$ with $\chi_3 = \chi_1(b_1) \cup \chi_2(b_2)$ and, $\chi_3(b_1, b_2)(u) = \{< u, max\{\mu_1(u), \mu_2(u)\}, min\{v_1(u), v_2(u)\}, min\{\omega_1(u), \omega_2(u)\} >: u \in \Upsilon\}$, $\forall(b_1, b_2) \in \hat{B}_1 \infty \hat{B}_2$.

DECISION SUPPORT SYSTEM

Algorithm: Different parts of the algorithm have been shown here.

1. First part: Input

1.1 Group of renowned business VR devices as a set of alternatives.

1.2 Group of parameters used for the evaluation of devices.

1.3 Sub-classes having different parametric valued sets.

1.4 Group of experts for the evaluation of parameters and group of opinions {0, 1} of experts.

2. Second part: Construction and computations

2.1 Construction of FPHSESs by the use of input data.

2.2 Separation of agree and disagree-FPHSESs.

2.3 Find the score values for the both agree and disagree-FPHSESs by formula $(\eta - \beta - \theta)$.

2.4 Calculate the difference of scores values of agree and disagree-FPHSESs.

2.5 Calculation of maximum score value.

3. Third part: Output

3.1 Selection of best alternative based on the maximum value.

The pictorial version of the algorithm have been shown in the Figure 1.

Validation of Algorithm

The steps of the algorithm that is suggested here are detailed in the example that follows.

Example 3.14. Morton Heilig invented virtual reality (VR) in 1957. His VR system, the Sen- sorama, is considered to be among the best entertainment devices. In actuality, analyst Jaron Lanier coined the word ”virtual reality” (VR) in 1987. His research and analysis helped to ad- vance a number of VR-related sectors. Virtual reality technology mostly relies on computer engineering to develop a virtual environment. Instead of having a screen in front of them, users are able to interact and become fully engaged in a three-dimensional (3D) world. The computer is transformed into a doorkeeper to this strange world by mimicking as many per- ceptions as possible, including listening, feel good, gaze, and even taste. The most recognis- able component of virtual reality is the head-mounted display. Virtual reality (VR) is making significant contributions to several major scientific sectors, including medical care, schooling, and the armed forces. Virtual reality is used in several health-care domains. With virtual reality (VR), any kind of medical situation may be replicated, allowing students to handle it just like in real life. VR can be used to enhance students' capacity for learning. Virtual reality education has the potential to significantly alter the way that educational content is delivered; it works by developing a virtual reality that users may engage with in addition

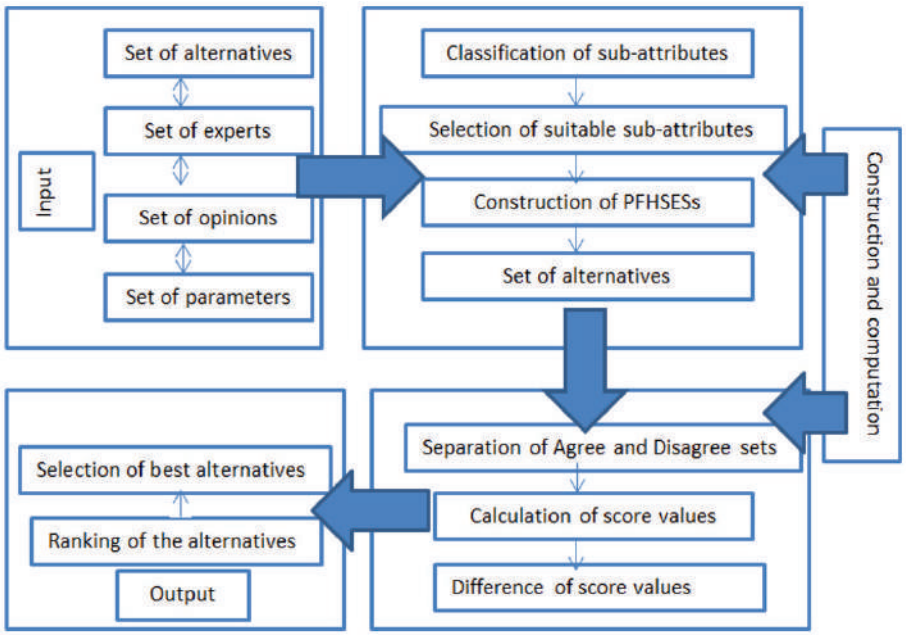


Figure 1. Flow chart of the suggested algorithm.

to viewing. The Link Company's flight instructors were the first to use simulators in a military setting in the late 1920s and early 1930s. The army, navy, and air force are among the armed forces branches that have utilised virtual reality (VR) for instructional reasons. Moreover, one of the applications for VR that is most passionate about VR is the tourism sector. Beginning in 2017, the British Museum unveiled a virtual reality (VR) experience that allowed visitors to fully in teract with a VR headset and have an unmatched digital experience on a computer or mobile device. The discussion above highlights a crucial point: because VR systems have a variety of features, or parameters, choosing the optimal manufacturer is an unpredictable process. Selecting the optimal solution is therefore a crucial task for the consumers. The assessment of various experts about VR systems in accordance with the advantageous characteristics of buyers (wholesale dealers) can assist in the selection of a suitable company producing VR sys- tems. Assume that the group of renowned businesses producing VR equipment is denoted by $\Upsilon = \{\delta_1 = Unity, \delta_2 = Meta, \delta_3 = Apple, \delta_4 = Talespin\}$. To find the top firm that produces VR systems, Think about $\Delta = \{s_1 = PriceValue, s_2 = Warrantytime, s_3 = Ref reshrate, s_4 = Headsetweight, s_5 = Fieldo f viewrange\}$ is the collection of criteria that a dealer uses to deter- mine which manufacturer is most suited to produce VR equipment. The sub-classes having different values sets are $s_1 = \{s_{11} = §400, s_{12} = §500\}$, $s_2 = \{s_{21} = 2years, s_{22} = 3years\}$, $s_3 = \{s_{31} = 90Hz, s_{32} = 120Hz\}$, $s_4 = \{s_{41} = 500\ gram, s\ s_{42} = 600grmas\}$, $s_5 = \{s_{51} = -90degree\ and s_{52} = 120degree\}$.

pairs and each pair is a 5-tuple element. Again $\Psi_{CP} \times \Omega \times \Gamma =$ We will get 40 pairs and each one is a triplet. On preferential basis, we select any 16 pairs. The PFHSES can be established on the basis of the experts judgements which is given in table 10 by as:

Table 10. Tabular form of PFHSES

$(\partial_i, \hat{p}_i, 1)$	δ_1	δ_2	δ_3	δ_4
$(\partial_1, \hat{p}_1, 1)$	⟨0.33, 0.21, 0.12⟩	⟨0.22, 0.31, 0.10⟩	⟨0.32, 0.31, 0.31⟩	⟨0.12, 0.31, 0.21⟩
$(\partial_1, \hat{p}_2, 1)$	⟨0.35, 0.21, 0.15⟩	⟨0.33, 0.22, 0.13⟩	⟨0.30, 0.21, 0.11⟩	⟨0.22, 0.31, 0.11⟩
$(\partial_2, \hat{p}_1, 1)$	⟨0.15, 0.37, 0.24⟩	⟨0.15, 0.31, 0.25⟩	⟨0.23, 0.33, 0.25⟩	⟨0.12, 0.31, 0.01⟩
$(\partial_2, \hat{p}_2, 1)$	⟨0.42, 0.15, 0.35⟩	⟨0.43, 0.17, 0.32⟩	⟨0.42, 0.11, 0.32⟩	⟨0.02, 0.31, 0.11⟩
$(\partial_3, \hat{p}_1, 1)$	⟨0.25, 0.32, 0.32⟩	⟨0.21, 0.35, 0.30⟩	⟨0.32, 0.32, 0.21⟩	⟨0.32, 0.01, 0.31⟩
$(\partial_3, \hat{p}_2, 1)$	⟨0.25, 0.10, 0.05⟩	⟨0.23, 0.13, 0.13⟩	⟨0.30, 0.12, 0.21⟩	⟨0.02, 0.31, 0.01⟩
$(\partial_4, \hat{p}_1, 1)$	⟨0.27, 0.17, 0.37⟩	⟨0.25, 0.35, 0.15⟩	⟨0.13, 0.23, 0.03⟩	⟨0.30, 0.01, 0.31⟩
$(\partial_4, \hat{p}_2, 1)$	⟨0.32, 0.04, 0.35⟩	⟨0.53, 0.02, 0.42⟩	⟨0.32, 0.21, 0.42⟩	⟨0.32, 0.11, 0.31⟩
$(\partial_1, \hat{p}_1, 0)$	⟨0.23, 0.43, 0.32⟩	⟨0.11, 0.31, 0.40⟩	⟨0.32, 0.32, 0.41⟩	⟨0.32, 0.21, 0.31⟩
$(\partial_1, \hat{p}_2, 0)$	⟨0.45, 0.25, 0.25⟩	⟨0.53, 0.43, 0.13⟩	⟨0.40, 0.32, 0.11⟩	⟨0.02, 0.31, 0.31⟩
$(\partial_2, \hat{p}_1, 0)$	⟨0.27, 0.17, 0.27⟩	⟨0.25, 0.35, 0.15⟩	⟨0.13, 0.23, 0.43⟩	⟨0.32, 0.31, 0.11⟩
$(\partial_2, \hat{p}_2, 0)$	⟨0.43, 0.16, 0.31⟩	⟨0.42, 0.32, 0.12⟩	⟨0.42, 0.21, 0.13⟩	⟨0.21, 0.11, 0.31⟩
$(\partial_3, \hat{p}_1, 0)$	⟨0.24, 0.36, 0.38⟩	⟨0.22, 0.34, 0.31⟩	⟨0.23, 0.33, 0.30⟩	⟨0.32, 0.21, 0.31⟩
$(\partial_3, \hat{p}_2, 0)$	⟨0.36, 0.23, 0.17⟩	⟨0.33, 0.26, 0.12⟩	⟨0.31, 0.23, 0.11⟩	⟨0.32, 0.11, 0.52⟩
$(\partial_4, \hat{p}_1, 0)$	⟨0.13, 0.37, 0.29⟩	⟨0.16, 0.38, 0.21⟩	⟨0.13, 0.36, 0.22⟩	⟨0.02, 0.11, 0.71⟩
$(\partial_4, \hat{p}_2, 0)$	⟨0.43, 0.15, 0.35⟩	⟨0.44, 0.18, 0.32⟩	⟨0.43, 0.13, 0.32⟩	⟨0.02, 0.91, 0.01⟩

Table 11. Tabular form of agree-PFHSES

$(\partial_i, \hat{p}_i, 1)$	δ_1	δ_2	δ_3	δ_4
$(\partial_1, \hat{p}_1, 1)$	⟨0.33, 0.21, 0.12⟩	⟨0.22, 0.31, 0.10⟩	⟨0.32, 0.31, 0.31⟩	⟨0.12, 0.31, 0.21⟩
$(\partial_1, \hat{p}_2, 1)$	⟨0.35, 0.21, 0.15⟩	⟨0.33, 0.22, 0.13⟩	⟨0.30, 0.21, 0.11⟩	⟨0.22, 0.31, 0.11⟩
$(\partial_2, \hat{p}_1, 1)$	⟨0.15, 0.37, 0.24⟩	⟨0.15, 0.31, 0.25⟩	⟨0.23, 0.33, 0.25⟩	⟨0.12, 0.31, 0.01⟩
$(\partial_2, \hat{p}_2, 1)$	⟨0.42, 0.15, 0.35⟩	⟨0.43, 0.17, 0.32⟩	⟨0.42, 0.11, 0.32⟩	⟨0.02, 0.31, 0.11⟩
$(\partial_3, \hat{p}_1, 1)$	⟨0.25, 0.32, 0.32⟩	⟨0.21, 0.35, 0.30⟩	⟨0.32, 0.32, 0.21⟩	⟨0.32, 0.01, 0.31⟩
$(\partial_3, \hat{p}_2, 1)$	⟨0.25, 0.10, 0.05⟩	⟨0.23, 0.13, 0.13⟩	⟨0.30, 0.12, 0.21⟩	⟨0.02, 0.31, 0.01⟩
$(\partial_4, \hat{p}_1, 1)$	⟨0.27, 0.17, 0.37⟩	⟨0.25, 0.35, 0.15⟩	⟨0.13, 0.23, 0.03⟩	⟨0.30, 0.01, 0.31⟩
$(\partial_4, \hat{p}_2, 1)$	⟨0.32, 0.04, 0.35⟩	⟨0.53, 0.02, 0.42⟩	⟨0.32, 0.21, 0.42⟩	⟨0.32, 0.11, 0.31⟩

Table 12. Tabular form of disagree-PFHSES

$(\partial_i, \hat{p}_i, 1)$	δ_1	δ_2	δ_3	δ_4
$(\partial_1, \hat{p}_1, 0)$	⟨0.23, 0.43, 0.32⟩	⟨0.11, 0.31, 0.40⟩	⟨0.32, 0.32, 0.41⟩	⟨0.32, 0.21, 0.31⟩
$(\partial_1, \hat{p}_2, 0)$	⟨0.45, 0.25, 0.25⟩	⟨0.53, 0.43, 0.13⟩	⟨0.40, 0.32, 0.11⟩	⟨0.02, 0.31, 0.31⟩
$(\partial_2, \hat{p}_1, 0)$	⟨0.27, 0.17, 0.27⟩	⟨0.25, 0.35, 0.15⟩	⟨0.13, 0.23, 0.43⟩	⟨0.32, 0.31, 0.11⟩
$(\partial_2, \hat{p}_2, 0)$	⟨0.43, 0.16, 0.31⟩	⟨0.42, 0.32, 0.12⟩	⟨0.42, 0.21, 0.13⟩	⟨0.21, 0.11, 0.31⟩
$(\partial_3, \hat{p}_1, 0)$	⟨0.24, 0.36, 0.38⟩	⟨0.22, 0.34, 0.31⟩	⟨0.23, 0.33, 0.30⟩	⟨0.32, 0.21, 0.31⟩
$(\partial_3, \hat{p}_2, 0)$	⟨0.36, 0.23, 0.17⟩	⟨0.33, 0.26, 0.12⟩	⟨0.31, 0.23, 0.11⟩	⟨0.32, 0.11, 0.52⟩
$(\partial_4, \hat{p}_1, 0)$	⟨0.13, 0.37, 0.29⟩	⟨0.16, 0.38, 0.21⟩	⟨0.13, 0.36, 0.22⟩	⟨0.02, 0.11, 0.71⟩
$(\partial_4, \hat{p}_2, 0)$	⟨0.43, 0.15, 0.35⟩	⟨0.44, 0.18, 0.32⟩	⟨0.43, 0.13, 0.32⟩	⟨0.02, 0.91, 0.01⟩

Table 13. Score values of agree-PFHSES

Pairs	δ_1	δ_2	δ_3	δ_4
$(\partial_1, \hat{p}_1, 1)$	0.0	-0.19	-0.30	-0.30
$(\partial_1, \hat{p}_2, 1)$	-0.01	-0.02	-0.02	-0.20
$(\partial_2, \hat{p}_1, 1)$	-0.46	-0.41	-0.35	-0.20
$(\partial_2, \hat{p}_2, 1)$	-0.08	-0.06	-0.01	-0.40
$(\partial_3, \hat{p}_1, 1)$	-0.39	-0.34	-0.21	0.00
$(\partial_3, \hat{p}_2, 1)$	-0.10	-0.03	-0.03	-0.30
$(\partial_4, \hat{p}_1, 1)$	-0.27	-0.25	-0.13	-0.02
$(\partial_4, \hat{p}_2, 1)$	-0.07	0.09	-0.31	-0.1
$t_{ij} = \Sigma\, \hat{p}_{ij}$	$t_1 = -1.38$	$t_2 = -0.98$	$t_3 = -1.36$	$t_4 = -1.52$

Table 14. Score values of disagree-PFHSES

Pairs	δ_1	δ_2	δ_3	δ_4
$(\partial_1, \hat{p}_1, 0)$	-0.32	-0.60	-0.41	-0.20
$(\partial_1, \hat{p}_2, 0)$	-0.25	-0.03	-0.19	-0.60
$(\partial_2, \hat{p}_1, 0)$	-0.17	-0.25	-0.53	-0.11
$(\partial_2, \hat{p}_2, 0)$	-0.04	0.02	0.08	-0.21
$(\partial_3, \hat{p}_1, 0)$	-0.50	-0.43	-0.40	-0.42
$(\partial_3, \hat{p}_2, 0)$	-0.04	-0.05	-0.03	-0.31
$(\partial_4, \hat{p}_1, 0)$	-0.53	-0.43	-0.45	-0.08
$(\partial_4, \hat{p}_2, 0)$	-0.07	-0.06	-0.02	-0.9
$y_{ij} = \Sigma\, \hat{p}_{ij}$	$y_1 = -1.92$	$y_2 = -1.83$	$y_3 = -1.31$	$y_4 = -2.83$

Table 15. Final score values

$t_{ij} = \Sigma\, \hat{p}_{ij}$	$y_{ij} = \Sigma\, \hat{p}_{ij}$	$\delta_{ij} = \lvert t_{ij} - y_{ij} \rvert$
$t_1 = -1.38$	$y_1 = -1.92$	3.3
$t_2 = -0.98$	$y_2 = -1.83$	2.81
$t_3 = -1.36$	$y_3 = -1.31$	2.67
$t_4 = -1.52$	$y_4 = -2.83$	4.35

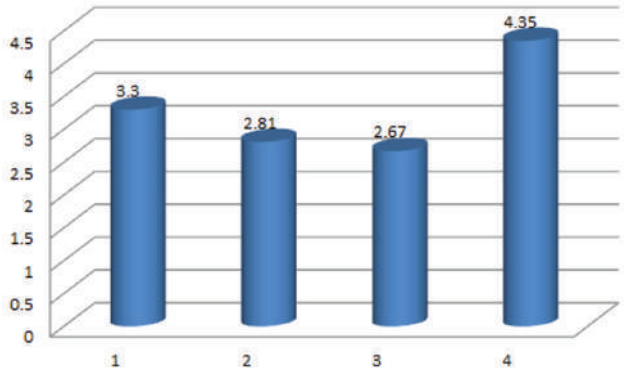


Figure 2. Representation of alternatives's rankings.

This PFHSESs has been partitioned into two parts, i. e., agree and disagree-PFHSESs. These two sets have been shown in two different Tables 11 and 12 respectively.

Tables 13 and 14 respectively are created to find the score values of agree and disagree- PFHSESs by using the formula $(\eta - \beta - \theta)$.

Table 15 is created to find the final score values of alternatives using values obtained from the above two tables 13 and 14 respectively and the results obtained from the 15 are shown in Figure 2.

RESULTS AND DISCUSSION

When we examine the past few decades, from the development of FS theory to the present, we can see that numerous researchers from practically every field of study have engaged in a race to produce various natural generalizations of FSs, including complex FSs, generalized FSs, IFSs, PFSs, and so on, or structures combining these extensions with other known un- certainty theories, such rough sets, SESs, and soft sets. It is evident that hybrid models of PFS with SES are still unable to manage multi-expert picture fuzzy soft information more effectively.

Table 16. Computational comparison

Samples	$\delta_1, \delta_2, \delta_3, \delta_4$	Ranking	Best option
IFSESs [46]	4.33, 0.19, 3.21, 7.21	$\delta_4 > \delta_1 > \delta_3 > \delta_2$	δ_4
PFSESs [62]	4.85, -0.26, 5.15, 11.0	$\delta_4 > \delta_3 > \delta_1 > \delta_2$	δ_4
Suggested App.	3.3, 2.81, 2.67, 4.35	$\delta_4 > \delta_1 > \delta_2 > \delta_3$	δ_4

This feature served as the impetus for this work, which combined the previously described existing theories to develop a novel hybrid model known as PFHSESs. Several experts' assessments of each alternative in relation to each parameter under consideration can be handled by our established model. The suggested method works really well and is work- able for handling soft expert information that is ambiguous and imprecise. Especially when the issue being considered is founded on soft, fuzzy picture data that has been gathered using the opinions of various experts. As an extension of PFSs, such as PFSSs, several successful outcomes have been generated to address various issues of multiple scientific domains, including artificial intelligence. We developed our suggested model as an effective generalisation of SESs, FSESs, IFSESs, or PFSSs as PFSS is a soft extension of the PFS model but cannot handle the individual evaluation of multiple experts in a group decision-making scenario. By using the suggested method and the current IFSES model to solve the application in Section 4, we were able to evaluate the efficacy of our proposed model. Although it is obvious that we get the best results, the order in which the sub-optimal decision objects are ranked has changed slightly. Table 16 presents the comparative analysis of the established PFHSES model in both qualitative and quantitative modes. We see that, in the picture fuzzy hypersoft expert environment, the initial strategy is more coherent and feasible to handle various real-world problems. Table 16 shows the values of alternatives obtain through the suggested approach are smaller than the values obtained in [46] and [62] respectively.

Limitations of the Study

The use of uncertainty theories to mathematical modeling-based real-world systems has grown significantly over the last 20 years. Experts can utilise a hybrid model, which combines two or more ideas, to help them make decisions. No matter how good a hybrid model is, models will nearly always have limitations. A good hybrid model can solve some of the problems with existing theories and produce more accurate findings than existing ones. The following talks about the initiated approach's shortcomings that we saw when it was being built.

- Since assessments and input data are the primary sources of information for mathematical modelling. In the case of a big data set, the computational speed of the suggested hybrid model may be slow. This shortcoming exists in nearly all models tha are now in use, but it may be fixed with the aid of tools, such as MATLAB, and the proper coding technique.
- When new parameters or alternatives are added to an existing set in a group decision- making situation, our initial model faces additional challenges related to the ranking of alternatives. The autonomous behaviour of parameters and objects is the primary cause of these issues.

Benefits of the Proposed Study

The described study has the following benefits over the existing structures:

- Multiple levels of uncertainty are incorporated into the PFHSE-set framework through image fuzzy sets, which support refusal degrees in addition to positive, neu- tral, and negative membership degrees. In comparison with intuitionistic fuzzy sets or ordinary fuzzy sets, which can only accommodate two or three degrees of membership, respectively, this offers more versatility.
- The method enables the more structured capturing of expert information by including the expert set element into the PFHSE framework. Experts can indicate their levels of confidence or lack thereof (refusal degree), which enhances decision-making models that depend heavily on expert judgment.
- When dealing with multidimensional characteristics, the PFHSE-set may handle dis- junct sets of parameters thanks to the hypersoft framework. This helps with complex, subtle, or connected features in particular. It provides a more in-depth comprehension of real-world situations, including medical diagnosis or industrial operations, which frequently call for this level of specificity.

CONCLUSION

In this study, a novel hybrid model PFHSESs that is an expansion of PFSSs, FSESs, FH- SESs or IFSESs is structured. This new structure has been used more broadly and effectively to characterise its properties. Specifically, a number of fundamental operations are built and examined with corresponding numerical examples. These include subset, equality, union, intersection, complement, OR operation, AND operation, and agree and disagree-PFHSESs. Additionally, the AND and OR operations confirm several of De Morgan's laws for PFHSESs. Additionally, a PFHSES-based approach to solving the

MAGDM difficulties is described. To describe the validity and cogency of the developed hybrid model that is, a choice of the top VR system manufacturing company, we tested our proposed technique on a real-world application. Lastly, a comparison between the technique that has been offered and a few models that already exist, is given. Then its certain limitations have been discussed. In order to address decision-making under uncertainty, this research may go in other directions in the future by implementing the picture fuzzy hypersoft expert model in a variety of industries, including healthcare, finance, and environmental management. Furthermore, this model's practical applicability could be increased by integrating it with other decision-making approaches, building software tools, and optimizing algorithms. Its performance could also be benchmarked through comparative research with other fuzzy and soft set-based models; additionally, adding feedback mechanisms and expanding the model to dynamic contexts could improve its practicality.

AUTHORSHIP CONTRIBUTIONS

Authors equally contributed to this work.

DATA AVAILABILITY STATEMENT

The authors confirm that the data that supports the findings of this study are available within the article. Raw data that support the finding of this study are available from the corresponding author, upon reasonable request.

CONFLICT OF INTEREST

The author declared no potential conflicts of interest with respect to the research, authorship, and/or publication of this article.

ETHICS

There are no ethical issues with the publication of this manuscript.

STATEMENT ON THE USE OF ARTIFICIAL INTELLIGENCE

Artificial intelligence was not used in the preparation of the article.

REFERENCES

[1] Zadeh LA. Fuzzy sets. Inf Control 1965;8:338–353. [CrossRef]

[2] Abu Arqub O. Adaptation of reproducing kernel algorithm for solving fuzzy Fredholm-Volterra integrodifferential equations. Neural Comput Appl 2017;28:1591–1610. [CrossRef]

[3] Božanić D, Milić A, Tešić D, Salabun W, Pamučar D. D numbers–FUCOM–fuzzy RAFSI model for selecting the group of construction machines for enabling mobility. Facta Univ Ser Mech Eng 2021;19:447–471. [CrossRef]

[4] Chen CH. A novel multi-criteria decision-making model for building material supplier selection based on entropy-AHP weighted TOPSIS. Entropy 2020;22:259. [CrossRef]

[5] Dymova L, Kaczmarek K, Sevastjanov P, Kulawik J. A fuzzy multiple criteria decision making approach with a complete user friendly computer implementation. Entropy 2021;23:203. [CrossRef]

[6] Pamucar D, Yazdani M, Montero-Simo MJ, Araque-Padilla RA, Mohammed A. Multi-criteria decision analysis towards robust service quality measurement. Expert Syst Appl 2021;170:114508. [CrossRef]

[7] Cuong BC. Picture fuzzy sets-first results. Comput Sci Cybern 2014;30:409–420.

[8] Zhu S, Liu Z, Ur Rahman A. Novel distance measures of picture fuzzy sets and their applications. Arab J Sci Eng 2024;49:12975–12988. [CrossRef]

[9] Singh P. Correlation coefficients for picture fuzzy sets. J Intell Fuzzy Syst 2015;28:591–604. [CrossRef]

[10] Son LH. Generalized picture distance measure and applications to picture fuzzy clustering. Appl Soft Comput 2016;46:284–295. [CrossRef]

[11] Garg H. Some picture fuzzy aggregation operators and their applications to multicriteria decision-making. Arab J Sci Eng 2017;42:5275–5290. [CrossRef]

[12] Wei G. TODIM method for picture fuzzy multiple attribute decision making. Informatica 2018;29:555–566. [CrossRef]

[13] Ashraf S, Mahmood T, Abdullah S, Khan Q. Different approaches to multi-criteria group decision making problems for picture fuzzy environment. Bull Braz Math Soc New Ser 2019;50:373–397. [CrossRef]

[14] Sahu R, Dash SR, Das S. Career selection of students using hybridized distance measure based on picture fuzzy set and rough set theory. Decis Mak Appl Manag Eng 2021;4:104–126. [CrossRef]

[15] Wei GW. Some similarity measures for picture fuzzy sets and their applications. Iranian J Fuzzy Syst 2018;15:77–89.

[16] Jiang Z, Wei G, Wu J, Chen X. CPT-TODIM method for picture fuzzy multiple attribute group decision making and its application to food enterprise quality credit evaluation. J Intell Fuzzy Syst 2021;40:10115–10128. [CrossRef]

[17] Akram M, Habib A, Alcantud JCR. An optimization study based on Dijkstra algorithm for a network with trapezoidal picture fuzzy numbers. Neural Comput Appl 2021;33:1329–1342. [CrossRef]

[18] Khalil AM, Li SG, Garg H, Li H, Ma S. New operations on interval-valued picture fuzzy set, interval-valued picture fuzzy soft set and their applications. IEEE Access 2019;7:51236–51253. [CrossRef]

[19] Khan MJ, Kumam P, Liu P, Kumam W. An adjustable weighted soft discernibility matrix based on generalized picture fuzzy soft set and its applications in decision making. J Intell Fuzzy Syst 2020;38:2103–2118. [CrossRef]
[20] Lin M, Huang C, Xu Z. MULTIMOORA based MCDM model for site selection of car sharing station under picture fuzzy environment. Sustain Cities Soc 2020;53:101873. [CrossRef]
[21] Liu M, Zeng S, Balezentis T, Streimikiene D. Picture fuzzy weighted distance measures and their application to investment selection. Amfiteatru Econ 2019;21:682–695. [CrossRef]
[22] Liu D, Luo Y, Liu Z. The linguistic picture fuzzy set and its application in multi-criteria decision-making: An illustration to the TOPSIS and TODIM methods based on entropy weight. Symmetry 2020;12:1170. [CrossRef]
[23] Simic V, Karagoz S, Deveci M, Aydin N. Picture fuzzy extension of the CODAS method for multi-criteria vehicle shredding facility location. Expert Syst Appl 2021;175:114644. [CrossRef]
[24] Zhao R, Luo M, Li S. A dynamic distance measure of picture fuzzy sets and its application. Symmetry 2021;13:436. [CrossRef]
[25] Pawlak Z. Rough sets. Int J Comput Inf Sci 1982;11:341–356. [CrossRef]
[26] Verma R, Rohtagi B. Novel similarity measures between picture fuzzy sets and their applications to pattern recognition and medical diagnosis. Granul Comput 2022;7:761–777. [CrossRef]
[27] Khan MJ, Phiangsungnoen S, Kumam W. Applications of generalized picture fuzzy soft set in concept selection. Thai J Math 2020;18:296–314.
[28] Molodtsov D. Soft set theory—first results. Comput Math Appl 1999;37:19–31. [CrossRef]
[29] Ali MI, Feng F, Liu X, Min WK, Shabir M. On some new operations in soft set theory. Comput Math Appl 2009;57:1547–1553. [CrossRef]
[30] Maji PK, Roy AR, Biswas R. An application of soft sets in a decision making problem. Comput Math Appl 2002;44:1077–1083. [CrossRef]
[31] Rahman AU, Saeed M, Ihsan M, Arshad M, Ayaz S. A conceptual framework of m-convex and m-concave sets under soft set environment with properties. Trans Math Comput Sci 2021;1:40–60.
[32] Rahman AU, Saeed M, Arshad M, Ihsan M, Ahmad MR. (m; n)-convexity-cum-concavity on fuzzy soft set with applications in first and second sense. Punjab Univ J Math 2021;53:19–33. [CrossRef]
[33] Yang Y, Liang C, Ji S, Liu T. Adjustable soft discernibility matrix based on picture fuzzy soft sets and its applications in decision making. J Intell Fuzzy Syst 2015;29:1711–1722. [CrossRef]
[34] Asghar A, Khan KA, Rahman AU. A multi-attribute decision-making context for hospital site evaluation using distance measures under complex picture fuzzy soft set environment. Yugoslav J Oper Res 2024;34:795–812. [CrossRef]
[35] Asghar A, Khan KA, Albahar MA, Alammari A. An optimized multi-attribute decision-making approach to construction supply chain management by using complex picture fuzzy soft set. PeerJ Comput Sci 2023;9:e1540. [CrossRef]
[36] Mutlu M, Tuzkaya G, Sennaroğlu B. Multi-criteria decision making techniques for healthcare service quality evaluation: a literature review. Sigma J Eng Nat Sci 2017;35:501–512.
[37] Yolcu A. Intuitionistic fuzzy hypersoft topology and its applications to multi-criteria decision-making. Sigma J Eng Nat Sci 2023;41:106–118. [CrossRef]
[38] Akram M, Adeel A, Alcantud JCR. Group decision-making methods based on hesitant N-soft sets. Expert Syst Appl 2019;115:95–105. [CrossRef]
[39] Alcantud JCR, Giarlotta A. Necessary and possible hesitant fuzzy sets: A novel model for group decision making. Inf Fusion 2019;46:63–76. [CrossRef]
[40] Alkhazaleh S, Salleh AR. Soft expert sets. Adv Decis Sci 2011;2011:757868. [CrossRef]
[41] Alkhazaleh S, Salleh AR. Fuzzy soft expert set and its application. Appl Math 2014;5:1349–1368. [CrossRef]
[42] Arockiarani I, Lancy AA. Multi criteria decision making problem with soft expert set. Int J Comput Appl 2013;78:1–4. [CrossRef]
[43] Ihsan M, Saeed M, Rahman AU. Optimizing hard disk selection via a fuzzy parameterized single-valued neutrosophic soft set approach. J Oper Strat Anal 2023;1:62–69. [CrossRef]
[44] Bashir M, Salleh AR. Possibility fuzzy soft expert set. Open J Appl Sci 2012;12:208–211. [CrossRef]
[45] Qayyum A, Abdullah S, Aslam M. Cubic soft expert sets and their application in decision making. J Intell Fuzzy Syst 2016;31:1585–1596. [CrossRef]
[46] Broumi S, Smarandache F. Intuitionistic fuzzy soft expert sets and its application in decision making. J New Theory 2015;1:89–105. [CrossRef]
[47] Al-Qudah Y, Hassan N. Bipolar fuzzy soft expert set and its application in decision making. Int J Appl Decis Sci 2017;10:175–191. [CrossRef]
[48] Ihsan M, Saeed M, Rahman AU, Khalifa HAEW. A rudimentary approach to develop context for convexity cum concavity on soft expert set with some generalized results. Punjab Univ J Math 2021;53:621–629. [CrossRef]
[49] Ihsan M, Rahman AU, Saeed M, Khalifa HAEW. Convexity-cum-concavity on fuzzy soft expert set with certain properties. Int J Fuzzy Logic Intell Syst 2021;21:233–242. [CrossRef]
[50] Ali G, Muhiuddin G, Adeel A, Zain Ul Abidin M. Ranking effectiveness of COVID-19 tests using fuzzy bipolar soft expert sets. Math Prob Eng 2021;2021:5874216. [CrossRef]

[51] Smarandache F. Extension of soft set to hypersoft set, and then to plithogenic hypersoft set. Neutrosophic Sets Syst 2018;22:168–170.
[52] Rahman AU, Razaq A, Saeed M, Bajri SA, Alhabeeb SA, Khalifa HAEW. A risk analysis based multi-attribute decision-making framework for supply chain management using hypersoft mappings. IEEE Access 2024;12:112261–112277. [CrossRef]
[53] Saeed MH, Saeed M, Rahman AU, Ahsan M, Mohammed MA, Marhoon HA, et al. Renewable energy resource management using an integrated robust decision making model under entropy and similarity measures of fuzzy hypersoft set. Heliyon 2024;10:e33464. [CrossRef]
[54] Saeed M, Harl MI. Fundamentals of picture fuzzy hypersoft set with application. Neutrosophic Sets Syst 2023;53:382–400.
[55] Ihsan M, Rahman AU, Saeed M. Hypersoft expert set with application in decision making for recruitment process. Neutrosophic Sets Syst 2021;42:191–207.
[56] Ihsan M, Saeed M, Rahman AU, Smarandache F. An inclusive study on fundamentals of hypersoft expert set with application. Collected Papers. Volume XIII: On various scientific topics 2022;54:304.
[57] Ihsan M, Rahman AU, Saeed M. Fuzzy hypersoft expert set with application in decision making for the best selection of product. Neutrosophic Sets Syst 2021;46:318–336.
[58] Ihsan M, Saeed M, Rahman AU. An intuitionistic fuzzy hypersoft expert set-based robust decision-support framework for human resource management integrated with modified TOPSIS and correlation coefficient. Neural Comput Appl 2024;36:1123–1147. [CrossRef]
[59] Pamucar D, Ecer F. Prioritizing the weights of the evaluation criteria under fuzziness: The fuzzy full consistency method–FUCOM-F. Facta Univ Ser Mech Eng 2020;18:419–437. [CrossRef]
[60] Cuong BC, Kreinovich V. Picture fuzzy sets. J Comput Sci 2014;30:409–420.
[61] Biocca F. Virtual reality technology. A tutorial. J Commun 1992;42:23–72. [CrossRef]
[62] Tchier F, Ali G, Gulzar M, Pamučar D, Ghorai G. A new group decision-making technique under picture fuzzy soft expert information. Entropy 2021;23:1176. [CrossRef]

Sigma J Eng Nat Sci, Vol. 44, No. 1, pp. 222–233, February, 2026

Sigma Journal of Engineering and Natural Sciences
Web page info: https://sigma.yildiz.edu.tr
DOI: 10.14744/sigma.2025.00000

Research Article

Investigation of civil engineering students' general disaster preparedness beliefs

Esra Zehra BİÇER ÖZDEMİR[1,*], Özlenur CESUR AKIN[1], Egemen ÜNAL[1], Salih MOLLAHALİLOĞLU[1]

[1]*Department of Public Health, Faculty of Medicine, Ankara Yıldırım Beyazit University, Ankara, 06760, Türkiye*

ARTICLE INFO

Article history
Received: 16 July 2024
Revised: 04 September 2024
Accepted: 07 December 2024

Keywords:
Civil Engineering Students; Disaster Preparedness; Health Belief Model

ABSTRACT

In response to the increasing number of natural disasters worldwide, understanding the disaster preparedness of civil engineering students becomes essential for societal resilience. This study investigates the relationships between socio-demographic factors, disaster awareness and preparedness levels among civil engineering students. It also aims to provide insights that could potentially inform and improve disaster response strategies, thereby contributing to the development of a more resilient society. This cross-sectional study, conducted from September 25, 2023, to January 5, 2024, involved civil engineering students at Ankara Yildirim Beyazit University. Data were collected via an online survey on Google Forms, which included socio-demographic questions and the General Disaster Preparedness Belief Scale. The collected data were analyzed to assess students' socio-demographic characteristics, their disaster preparedness levels, and the relationships between these variables. Lastly, a linear regression model was applied to evaluate the effect of independent variables on the General Disaster Preparedness score. The study included 220 participants, with 77.7% male and 22.3% female, and an average age of 22 years. Notably, 37.3% of participants reported prior experience with disasters. The participants exhibited an average total score of 110.59 (±15.38), with scores ranging from 67 to 151. The key factors affecting disaster preparedness score were found to be gender ($p<0.001$), maternal education level ($p=0.026$), type of residence ($p=0.007$), prior disaster experience ($p=0.007$), experiencing the 6 February 2023 Kahramanmaraş earthquakes ($p=0.020$), feeling prepared for a disaster ($p=0.033$), having a disaster/emergency kit ($p<0.001$), receiving emergency/disaster education ($p=0.046$), and knowledge of the emergency assembly points in the participants' area ($p=0.005$). This study represents the first comprehensive investigation into the general disaster preparedness beliefs of civil engineering students, specifically examining the impact of socio-demographic factors and prior disaster experiences on their preparedness perceptions. The results of the study reveal that, despite being above average, the students' General Disaster Preparedness Belief level is still considered inadequate. These results underscore the importance of targeted educational interventions for disaster preparedness, particularly in university settings, and the critical role of students in disaster preparedness and mitigation strategies, which is crucial for building future resilience.

Cite this article as: Biçer Özdemir EZ, Cesur Akın Ö, Ünal E, Mollahalıloğlu S. Investigation of civil engineering students' general disaster preparedness beliefs. Sigma J Eng Nat Sci 2026;44(1):222–233.

***Corresponding author.**
*E-mail address: esrazehrabicer@aybu.edu.tr

This paper was recommended for publication in revised form by Editor-in-Chief Ahmet Selim Dalkilic

Published by Yıldız Technical University Press, İstanbul, Turkey
© Author. This is an open access article under the CC BY-NC license (http://creativecommons.org/licenses/by-nc/4.0/).

INTRODUCTION

Disasters are defined as events that can occur naturally, technologically, or be caused by human actions. Throughout history, the world and humanity have encountered various disasters and a range of challenges caused by these events. Nonetheless, the capacity of societies to adequately manage and mitigate the repercussions of such events frequently proves inadequate [1].

Pre-disaster strategies encompass the phases of mitigation and preparedness, which are executed through proactive assessments of anticipated impacts associated with a potential disaster. Strategic decisions taken during the mitigation and preparedness phases determine the timing and effectiveness of the response and recovery processes. Therefore, holistic disaster management can only be successful if actions taken at each stage are planned and implemented in a coordinated manner [2–4].

Disaster preparedness encompasses all action plans and efforts designed before a disaster occurs, as well as activities carried out to establish a disaster response system [5]. As a crucial component, disaster preparedness mitigates the adverse impacts of disasters [6,7]. Additionally, it is well-documented that individuals unprepared for emergencies are more likely to experience severe harm or fatality.[8].

A review of the literature identifies various factors that account for differences in disaster preparedness. It has been demonstrated that socio-demographic factors, including age, education and income [9–11] significantly influence preparedness, as well as behavioural factors such as individuals' awareness of disasters [12], risk perceptions [13], feeling prepared for disaster [14], past disaster experiences [15,16] and disaster/first aid training [17,18].

A number of behavioural change models in the literature that can be used to examine how perception can influence behavioural responses regarding health risks [19–21]. Disasters are recognized as significant public health threats, and theoretical frameworks such as the Health Belief Model (HBM) can be effectively employed to predict individuals' behaviours regarding disaster preparedness. HBM is a widely used theoretical framework to predict whether individuals will engage in risk reduction/disease prevention [22]. In addition, the model is based on a value expectancy framework, which suggests that human behaviour is largely driven by the value an individual places on a desired outcome and their assessment of the likelihood that a particular action will achieve that outcome [20,23].

Previous studies utilizing the HBM in assessing disaster preparedness behaviours have highlighted factors such as age, gender, monthly income, occupational status, home ownership, marital status, educational status, and disaster experience as key factors influencing preparedness behaviours. In addition, these studies have found that over half of the participants had not received disaster/emergency and basic first aid training [24–26].

As the incidence of disasters has increased recently, awareness of these catastrophic events has heightened across societies. Nonetheless, the strategies for disaster preparedness, response, and mitigation in educational institutions such as universities and schools remain inadequate [26]. Tanner and Doberstein have highlighted that students are often the least considered group in the development of emergency preparedness plans [27]. In addition, studies have shown that they are more vulnerable to disasters than the general public [28–30].

Although extensive research has addressed the broader aspects of disaster preparedness, the specific role of civil engineering education in fostering disaster response capabilities remains largely unexplored. This study seeks to bridge this gap by applying the HBM to assess how civil engineering students perceive and prepare for disasters. Since the HBM's basic constructs of risk and threat perceptions are well-suited for measuring individuals' levels of disaster preparedness and their perceptions of disasters, this study used the General Disaster Belief Preparedness Scale. Developed on the Health Belief Model and subsequently adapted by Inal, Altintas, and Dogan, this scale is suitable for assessing the preparedness beliefs of individuals [18]. The findings from this study are expected to not only fill a critical gap in current literature but also contribute substantially to enhancing both educational and disaster readiness strategies, thereby improving the overall efficacy of disaster response and mitigation efforts among future engineers.

MATERIAL AND METHODS

Study Design, Data Collection and Sample Size

This cross-sectional study was conducted between 25.09.2023 and 05.01.2024 involving 1st, 2nd, 3rd and 4th grade students who were actively studying at Ankara Yildirim Beyazit University, Faculty of Engineering and Natural Sciences, Department of Civil Engineering. The population of the study consisted of 397 students. The minimum sample size was determined using the OpenEpi software, based on a projected 50% prevalence rate of disaster preparedness behaviours, a 5% margin of error, and a design effect of 1.0. This calculation indicated that a sample size of 196 was necessary to achieve statistically reliable results [31,32].

The research data were collected using an online survey method via Google Forms. Participation in the study was voluntary, emphasizing ethical considerations, and anonymity was strictly maintained as no personal identifiers were collected. Eligibility for the study required participants to be an active undergraduate students enrolled in Ankara Yildirim Beyazit University, Faculty Engineering and Natural Sciences, of Department of Civil Engineering. Exclusion criteria were not being in target undergraduate groups (e.g., graduate or preparatory year students) or not completing the survey fully.

Questionnaire

The General Disaster Preparedness Belief (GDPB) scale, developed by Inal et al. in 2018, is utilized to assess participants' beliefs regarding their disaster preparedness. Additionally, the model proposes that the likelihood of individuals engaging in protective health behaviours is determined by their perceptions regarding: (a) their susceptibility to a particular threat, (b) the severity of the potential consequences of the threat, (c) the availability of preventative measures, and (d) the perceived benefits of these measures outweighing the associated costs.

Within the framework of the HBM, disaster preparedness is determined by a set of critical factors: perceived susceptibility to a disaster, perceived severity of potential disaster impacts, perceived benefits of taking preparedness measures, perceived barriers to implementing these measures, cues to action for preparedness actions, and self-efficacy regarding one's capability to handle disaster scenarios [18]. The cronbach alpha coefficient of the scale is 0.93. The scale has no cut-off point.

The survey is structured into two sections. The first section consists of 19 questions that collect socio-demographic data and information related to disaster experiences of the participants. The second section employs the GDPB scale, which is derived from the Health Belief Model. This scale is divided into six dimensions with a total of 31 items: Self-efficacy (8 items), Cues to action (5 items), Perceived susceptibility (6 items), Perceived barriers (6 items), Perceived benefits (3 items), and Perceived severity (3 items).

In this study, the dependent variable is the GDPB score. Explanatory variables include age, gender, class, parental education level, family income, type of residence, previous experience with any disaster, experience of the 06.02.2024 Kahramanmaraş Earthquake, participation in any emergency/disaster education, possession of an emergency/disaster kit, and knowledge of the emergency assembly point at both the university and the residence.

The GDPB score is measured using a 5-point Likert scale. Evaluation for positive statements; (1) Strongly disagree, (2) Disagree, (3) Neutral, (4) Agree, (5) Strongly agree. In negative expressions; (5) Strongly Disagree, (4) Disagree, (3) Undecided, (2) Agree, (1) Strongly Agree. This scoring system allows for a comprehensive evaluation of participants' disaster preparedness beliefs, with scores ranging from a minimum of 31 to a maximum of 155.

Statistical Analysis

The research data were initially collected and organized in Microsoft Excel, after which the necessary corrections were made. The data were then transferred to the SPSS 21.0 software package for analysis. The total GDPB score was found to follow a normal distribution based on the mean, median, percentage, standard deviation, and the Kolmogorov-Smirnov test. However, the sub-dimensions of the scale did not show a normal distribution. To examine the relationships between variables, the independent groups t-test and one-way ANOVA were applied to data with normal distribution, whereas the Mann Whitney U and Kruskal-Wallis tests were utilized for data that were not normally distributed. A linear regression model was applied to evaluate the effect of independent variables on the GDPB score. The statistical significance limit was set as $p<0.05$.

RESULTS

The study included 220 participants, consisting of 171 (77.7%) males and 49 (22.3%) females, with an average age of 22 years (min=18, max=32). Regarding the educational backgrounds of the participants' parents, 30.9% of mothers were high school graduates, while 39.1% held university degrees or higher. For fathers, 56.4% were university graduates. The majority of participants were mostly grade student (35%). Most of the participants live in a flat (77.3%) and more than half of them live with their families (62.3%). Family income levels were reported as below expenses by 25 participants (11.4%), equal to expenses by 109 (49.5%), and above expenses by 86 (39.1%) (Table 1).

Disaster experience was reported by 82 participants (37.3%), with 36 having experienced the recent Kahramanmaraş earthquakes (16.4%) and 9 the 1999 Marmara earthquake (4.1%). While 17.7% of the individuals feel adequately prepared for emergencies or disasters, 12.7% of them have an individual emergency or disaster kit. Of the sample, 91 participants (41.4%) had received training on emergencies and disasters, yet only 14 (6.4%) were aware of their university's emergency plan. Knowledge of emergency assembly locations was also limited, with only 33 participants (15%) familiar with the location at their school and 91 (41.4%) at their place of residence (Table 1).

Figure 1 illustrates the maximum, minimum, mean and standard deviation values of the scores obtained from the subcategories of the GDPB scale. The participants achieved a mean total score of 110.59 (±15.38), with a range of scores between 67 and 151 (Fig. 1).

The total score of the GDPB scale was affected by gender ($p=0.038$), with females exhibiting a higher mean total score. The relationship between the educational level of participants' mothers and the total score was statistically significant ($p=0.026$), with the highest scores observed in children of mothers who had graduated from secondary school. Additionally, the type of residence significantly impacted the total scores ($p=0.007$); participants residing in state dormitories demonstrated higher mean total scores. Besides, prior disaster experience ($p=0.007$) and experiencing the Kahramanmaraş earthquakes ($p=0.020$) also had higher total scores. Participants who felt adequately prepared for a disaster ($p=0.033$), have a disaster kit ($p<0.001$), or had received emergency/disaster education ($p=0.046$) have statistically impacted the total score. Additionally, awareness of the emergency assembly location in both university and residency had a higher mean total score (Table 2).

Table 1. Sociodemographic characteristics of participants and distribution of disaster-related variables (n=220)

		n	(%)
Sex	Female	49	22.3
	Male	171	77.7
Mother's Educational Level	Uneducated	5	2.3
	Primary School	35	15.9
	Secondary School	26	11.8
	High School	68	30.9
	Higher Education	86	39.1
Father's Educational Level	Uneducated	0	0.0
	Primary School	20	9.1
	Secondary School	22	10.0
	High School	54	24.5
	Higher Education	124	56.4
Year of Study	1st Year	43	19.6
	2nd Year	57	25.9
	3rd Year	43	19.5
	4th Year	77	35.0
Type of Residence	Flat	170	77.3
	Public Dorm	26	11.8
	Private Dorm	24	10.9
The people live with	Single	30	13.6
	Friend/Friends	48	21.8
	Family	137	62.3
	Relative	5	2.3
Family income status	Income<Expense	25	11.4
	Income=Expense	109	49.5
	Income>Expense	86	39.1
Have you ever experienced a disaster (earthquake, flood, avalanche, landslide, etc.)?	Yes	82	37.3
	No	138	62.7
Have you experienced the Kahramanmaras Earthquakes on February 6, 2023?	Yes	36	16.4
	No	184	83.6
Have you experienced the Marmara Earthquake of 17 August 1999?	Yes	9	4.1
	No	211	95.9
Are you adequately prepared for emergencies/disasters?	Yes	39	17.7
	No	181	82.3
Do you have an individual emergency/disaster kit?	Yes	28	12.7
	No	192	87.3
Have you received any training on emergencies/disasters?	Yes	91	41.4
	No	129	58.6
What educations have you received on emergencies/ disasters?	First Aid	54	24.5
	Community Disaster Volunteer	2	0.9
	Basic Disaster Awareness	33	15.0
	Other	2	0.9
Are you aware of your university's emergency/disaster preparedness plan?	Yes	14	6.4
	No	206	93.6
Do you know the emergency/disaster assembly location in your school?	Yes	33	15.0
	No	187	85.0
Do you know the emergency/disaster assembly location where you live?	Yes	91	41.4
	No	129	58.6

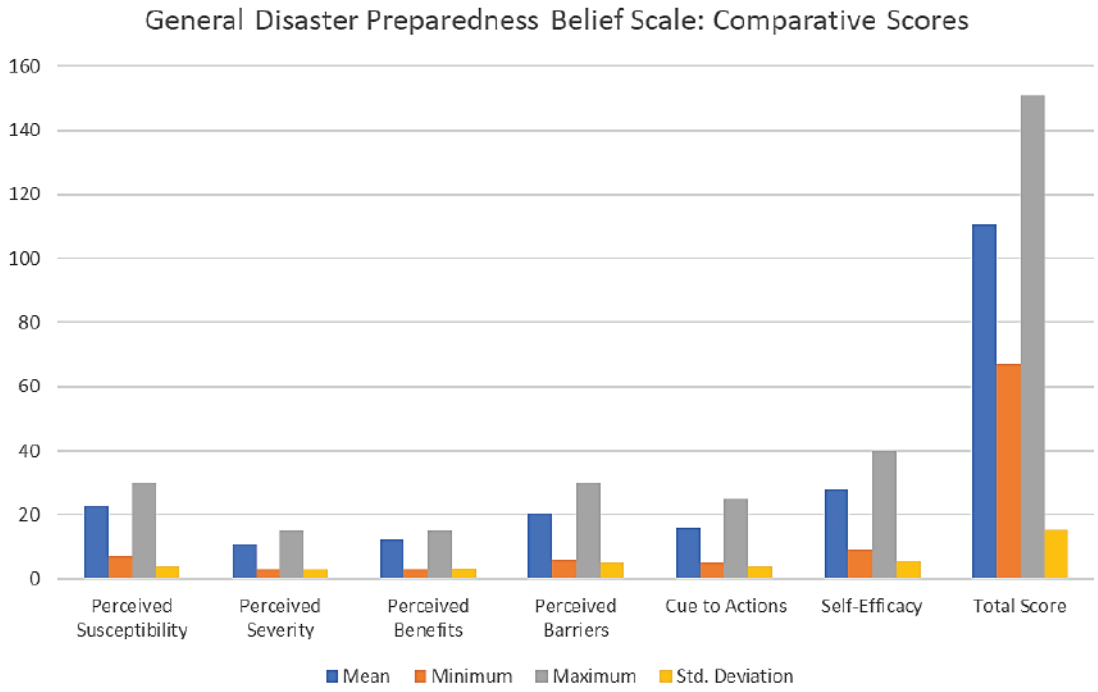


Figure 1. Comparative scores of the general disaster preparedness belief scale factors.

The relationship between "perceived susceptibility", one of the subcategories of the GDPB scale, and the participants' type of residence (p=0.008), previous disaster history (p=0.005), experience of the Kahramanmaraş earthquakes (p=0.002), having a disaster/emergency kit (p=0.004), and knowledge of the emergency assembly point in the region where they live (p=0.046) is statistically significant. The perceived susceptibility scores of those who lived in a state dormitory, had a previous disaster history, had a history of the 6 February 2023 Kahramanmaraş earthquake, had a disaster bag, and knew the emergency assembly point in their region were higher (Table 3).

Gender (p<0.001), experiencing the Kahramanmaraş earthquakes (p=0.009) and feeling adequately prepared for disasters (p=0.021) affect the scores of "perceived severity", one of the subcategories of the GDPB scale. The female gender, having experienced the Kahramanmaraş earthquakes, and participants who felt inadequately prepared for disasters exhibited higher perceived severity medians (Table 3).

There was a statistically significant difference between the self-efficacy subcategory and disaster experience (p=0.001), feeling prepared for a disaster (p<0.001), having a disaster/emergency kit (p=0.001), having received disaster/emergency (p<0.001) and having knowledge of the emergency assembly point in the region where they live (p=0.005) (Table 3).

The independent variables included in the model during the linear regression analysis were gender, mother's education level, type of residence, disaster history, experiencing the Kahramanmaraş earthquakes, disaster preparedness, receiving disaster/emergency education, and knowledge of the emergency assembly point in the region of residence, which had a statistically significant relationship with the total score. The correlation between the independent variables included in the model was examined: gender and experiencing the Kahramanmaraş earthquakes (p=0.041 and r=0.118), gender and disaster preparedness status (p=0.024 and r=-0.134), mother's education level and types of residence (p<0.001 and r=-0.222), mother's education status and disaster preparedness status (p=0.014 and r=-0.149), type of residence and disaster history (p<0.001 and r=-0.149), 346), type of residence and experiencing the Kahramanmaraş earthquakes (p<0.001 and r=-0.238), disaster experience and experiencing the Kahramanmaraş earthquakes (p<0.001 and r=0.447), experiencing the Kahramanmaraş earthquakes earthquakes and receiving disaster/emergency education (p=0.035 and r=-0.122), disaster preparedness status and receiving disaster/emergency education (p=0.001 and r=0.214) were found to be statistically significant.

While the total scores of the participants' GDPB were found to be significant in single analyses with mother's education level, knowledge of the emergency assembly point in residence, past disaster experience, experiencing Kahramanmaraş earthquakes and feeling prepared for a disaster/emergency, they were found not significant in linear regression analyses. The results of multiple analyses of total scores and related factors are given in Table 4.

Table 2. The relationship between the total score of the general disaster belief scale and independent variables

		Mean	Std. Deviation	p-value
Sex**	Female	114.61	17.80	**0.038***
	Male	109.44	14.47	
Mother's Educational Level * **	Uneducated	100.20	8.29	**0.026***
	Primary School	105.14	14.16	
	Secondary School	116.46	15.77	
	High School	111.92	15.39	
	Higher Education	110.58	15.36	
Father's Educational Level * **	Uneducated			0.340
	Primary School	107.25	11.29	
	Secondary School	107.32	17.21	
	High School	113.09	16.96	
	Higher Education	110.62	14.86	
Year of Study***	1st Year	111.55	14.48	0.156
	2nd Year	113.02	15.54	
	3rd Year	111.39	16.25	
	4th Year	107.80	14.97	
Type of Residence***	Flat	109.94	15.03	**0.007***
	Public Dorm	118.88	17.65	
	Private Dorm	106.20	12.38	
People live with***	Single	109.70	20.57	0.851
	Friend/Friends	109.70	14.66	
	Family	111.23	14.35	
	Relative	106.80	17.56	
Family Income Status***	Income<Expense	115.24	19.60	0.232
	Income=Expense	109.41	14.55	
	Income>Expense	110.73	14.96	
Ever experienced any Disaster**	Yes	114.20	15.43	**0.007***
	No	108.44	15.00	
Experienced 6 February 2023 Kahramanmaras Earthquakes**	Yes	116.02	16.96	**0.020***
	No	109.52	14.87	
Experienced 17 August 1999 Earthquake**	Yes	111.77	15.24	0.814
	No	110.54	15.42	
Feeling prepared for a disaster/emergency**	Yes	115.35	16.14	**0.033***
	No	109.56	15.06	
Having disaster/emergency kit**	Yes	120.35	13.10	**<0.001***
	No	109.16	15.20	
Had any emergency/disaster education**	Yes	113.05	16.47	**0.046***
	No	108.85	14.38	
Has knowledge of the University's Disaster Plan**	Yes	114.71	14.32	0.301
	No	110.31	15.44	
Has knowledge of the university's emergency assembly point**	Yes	113.69	12.10	0.209
	No	110.04	15.85	
Has knowledge of the emergency assembly point in the residence**	Yes	114.24	12.56	**0.002***
	No	108.01	16.67	

*p<0,05. **Two-sample t-test was performed. ***One-way ANOVA test was performed.

Table 3. The relationship between general disaster preparedness belief scale subcategories and independent variables

		Perceived susceptibility		Perceived severity		Perceived benefits		Perceived barriers		Cue to actions		Self-efficacy	
		Med. (max-min)	p	Med. (max-min)	p	Med. (max-min)	p	Med. (max-min)	p	Med. (max-min)	p	Med. (max-min)	p
Sex**	Female	24 (13-30)	0,348	13 (5-15)	**<0.001***	14 (3-15)	0,280	23 (12-30)	**0.005***	17 (7-25)	**0,034***	27 (12-40)	0.121
	Male	23 (7-30)		11 (3-15)		13 (3-15)		20 (6-30)		16 (5-25)		29 (9-39)	
Mother's Educational Level ***	Uneducated	22 (13-24)	0.200	10 (6-12)	0.180	11 (7-12)	0.074	18 (12-21)	**0.009***	16 (15-18)	0.387	25 (25-30)	0.821
	Primary School	22 (13-28)		11 (3-15)		12 (3-15)		18 (6-26)		15 (5-25)		28 (18-39)	
	Secondary School	23 (14-30)		13 (6-15)		14 (3-15)		22,5 (12-30)		17 (10-25)		29 (11-40)	
	High School	24 (7-30)		11,5 (3-15)		14 (3-15)		21 (11-30)		16 (7-25)		29 (9-39)	
	Higher Education	23 (13-30)		11 (5-15)		14 (3-15)		22 (6-30)		16,5 (6-25)		28 (14-38)	
Father's Educational Level ***	Uneducated		0.784		0.557		0.707		0.187		0.366		0.245
	Primary School	23 (17-28)		10,5 (6-15)		12,5 (8-15)		19 (6-27)		15,5 (9-21)		28 (17-39)	
	Secondary School	23 (13-30)		12 (5-15)		14 (3-15)		18.5 (10-30)		14 (7-25)		27 (11-40)	
	High School	23 (12-30)		12 (3-15)		13.5 (3-15)		21.5 (13-30)		16.5 (5-25)		28.5 (17-40)	
	Higher Education	23.5 (7-30)		11 (3-15)		13 (3-15)		21 (6-30)		16 (6-25)		29 (9-39)	
Year of Study***	1st Year	24 (13-30)	0.213	12 (3-15)	0.590	12.5 (3-15)	0.528	22 (6-30)	0,687	16 (5-25)	0,214	28.5 (12-38)	0.755
	2nd Year	24 (15-30)		12 (3-15)		14 (3-15)		22 (6-30)		17 (7-25)		29 (17-40)	
	3rd Year	23 (13-30)		11 (4-15)		14 (3-15)		20 (6-30)		17 (10-25)		28 (14-39)	
	4th Year	23 (7-29)		11 (5-15)		13 (3-15)		19 (6-30)		15 (7-24)		28 (9-37)	
Residency***	Flat	23 (7-30)	**0.008***	11 (3-15)	0.293	14 (3-15)	0.398	21 (6-30)	0.075	16 (5-25)	**0.042***	28 (9-39)	0.134
	Public Dorm	25 (16-30)		12 (6-15)		13 (6-15)		20,5 (6-30)		18,5 (6-25)		30 (20-40)	
	Private Dorm	23 (13-28)		11 (6-15)		13 (3-15)		18 (6-30)		15,5 (9-25)		28 (17-37)	
People live with***	Single	23 (7-30)	0.481	12.5 (6-15)	0.619	14 (3-15)	0.584	20 (6-30)	0.088	16 (6-25)	0.831	29 (9-40)	0.543
	Friend/Friends	24 (14-30)		12 (6-15)		13 (3-15)		19 (6-30)		16 (9-22)		28.5(14-39)	
	Family	23 (12-30)		11 (3-15)		14 (3-15)		21 (6-30)		16 (5-25)		28 (11-39)	
	Relative	21 (14-30)		12 (9-12)		12 (3-15)		24 (12-26)		18 (12-19)		26 (19-28)	
Family income status***	Income<Expense	24 (13-30)	0.841	12 (6-15)	0.843	15 (3-15)	0.557	22 (6-30)	0.729	18 (7-25)	0.226	31 (14-40)	0.085
	Income=Expense	23 (13-30)		12 (3-15)		13 (3-15)		20 (6-30)		16 (7-25)		28 (11-39)	
	Income>Expense	23 (7-30)		11 (3-15)		13 (3-15)		21 (6-30)		16 (5-25)		29 (9-39)	

Table 3. The relationship between general disaster preparedness belief scale subcategories and independent variables (continued)

		Perceived susceptibility		Perceived severity		Perceived benefits		Perceived barriers		Cue to actions		Self-efficacy	
		Med. (max-min)	p	Med. (max-min)	p	Med. (max-min)	p	Med. (max-min)	p	Med. (max-min)	p	Med. (max-min)	p
Ever experienced any Disaster**	Yes	24 (13-30)	**0.005***	11 (5-15)	0.174	14 (3-15)	0.066	20 (6-30)	0.520	15,5 (6-25)	0.692	29 (17-40)	**0.001***
	No	23 (7-30)		11 (3-15)		13 (3-15)		21 (6-30)		16 (5-25)		28 (9-38)	
Experienced 6 February 2023 Kahramanmaras Earthquakes**	Yes	25 (13-30)	**0.002***	13 (6-15)	**0.009***	14 (3-15)	0.586	22 (6-30)	0.105	15 (6-25)	0.989	29 (11-40)	0.291
	No	23 (7-30)		11 (3-15)		13 (3-15)		20 (6-30)		16 (5-25)		28 (9-39)	
Experienced 17 August 1999 Earthquake**	Yes	23 (13-25)	0.293	10 (5-15)	0.378	13 (7-15)	0.864	24 (6-28)	0.162	16 (12-22)	0.544	31 (25-36)	0.248
	No	23 (7-30)		11 (3-15)		13 (3-15)		20 (6-30)		16 (5-25)		28 (9-40)	
Feeling prepared for a disaster/ emergency**	Yes	24 (7-30)	0.300	11 (5-15)	**0.021***	14 (3-15)	0.610	23 (6-30)	**0.024***	17 (6-25)	0.056	31 (9-40)	**<0.001***
	No	23 (12-30)		12 (3-15)		13 (3-15)		20 (6-30)		16 (5-25)		28 (11-40)	
Having a disaster/ emergency kit**	Yes	25 (15-30)	**0.004***	11.5 (6-15)	0.883	13.5 (3-15)	0.722	23 (6-30)	**0.005***	18 (12-25)	**0.002***	31 (19-40)	**0.002***
	No	23 (7-30)		11 (3-15)		13 (3-15)		20 (6-30)		16 (5-25)		28 (9-40)	
Had any emergency/disaster education**	Yes	23 (7-30)	0.652	11 (3-15)	0.831	14 (3-15)	0.085	21 (6-30)	0.382	16 (6-25)	0.496	30 (9-40)	**<0.001***
	No	24 (13-30)		12 (3-15)		13 (3-15)		20 (6-30)		16 (5-25)		28 (11-40)	
Has knowledge of the University's Disaster Plan**	Yes	23.5 (15-27)	0.860	10 (7-15)	0.272	12.5 (3-15)	0.483	21 (10-30)	0.456	18 (15-25)	**0.002***	29 (22-39)	0.544
	No	23 (7-30)		11 (3-15)		13 (3-15)		20 (6-30)		16 (5-25)		28 (9-40)	
Has knowledge of the university's emergency assembly point**	Yes	24 (15-29)	0.452	11 (4-15)	0.192	14 (3-15)	0.794	21 (11-30)	0.331	17 (10-24)	0.297	30 (11-39)	0.063
	No	23 (7-30)		12 (3-15)		13 (3-15)		20 (6-30)		16 (5-25)		28 (9-40)	
Has knowledge of the emergency assembly point in the residence**	Yes	24 (14-30)	**0.046***	11 (3-15)	0.748	13 (3-15)	0.876	22 (11-30)	**0.002***	17 (5-25)	0.066	30 (11-39)	**0.005***
	No	23 (7-30)		11 (3-15)		13 (3-15)		19 (6-30)		15 (6-25)		28 (9-40)	

*p<0.05. **Mann-Whitney U test was performed. ***Kruskal-Wallis test was performed.

Table 4. Multiple Regression Analysis for the Factors Affecting the Total Score of the Participants on the General Disaster Preparedness Belief Scale

Variable	B	Std. Error	Beta	95% CI		p
				Lower	Upper	
Constant	155.506	10.796	-	134.223	176.789	<0.001*
Sex	-5.590	2.421	-0.152	-10.362	-0.818	0.022*
Type of residence	-0.843	1.648	-0.036	-4.092	2.406	0.609
Disaster experience	-4.496	2.407	-0.142	-9.241	0.250	0.063
Experience of the February 6 Kahramanmaraş earthquake	-3.778	3.073	-0.091	-9.836	2.280	0.220
Feeling prepared for a disaster	-3.654	2.723	-0.091	-9.022	1.715	0.181
Disaster/emergency training	-4.420	2.103	-0.142	-8.566	-0.274	0.037*
Knowledge of the emergency Assembly point (residential)	-6.066	2.021	-0.195	-10.051	-2.082	0.003*

*p<0.05

(Reference categories: Sex = Female; Type of residence = Home; Disaster experience = Yes; Experience of the February 6 Kahramanmaraş earthquake = Yes; Feeling prepared for a disaster = Yes; Disaster/emergency training = Yes; Knowledge of the emergency assembly point in the residential area = Yes)

DISCUSSION

In this study, the effects of socio-demographic characteristics and disaster-related factors on disaster preparedness beliefs of civil engineering students were investigated using the Health Belief Model.

In general, the disaster preparedness of the participants was above average. In comparison with other studies conducted to determine the level of belief in disaster preparedness, similar results were found in the studies by Inal et al., Ertugrul and Unal, and Arslanoglu et al. [24,25,32].

The results of the study showed that gender, mother's education level, previous disaster experience, type of residence, feeling of being prepared for a disaster/emergency, having a disaster kit, having received disaster/emergency education, and knowledge of the disaster/emergency assembly point had a statistically significant effect on the level of disaster preparedness beliefs.

The results indicate that gender has a significant impact on students' GDPB. In this study, the level of GDPB of female participants exhibited higher levels of GDPB than male participants. Our results align with many studies in the literature [24,32]. However, Inal et al. found no significant effect of gender in their study [25]. The higher scores of females in the perceived severity subcategory may suggest that women perceive disasters more seriously and are more sensitive to potential risks.

In this study, a statistically significant relationship was found between past disaster experience and disaster preparedness belief. Similarly, there are many studies in the literature demonstrating the effect of past disaster experience on disaster preparedness beliefs [24–26]. However, Ertugrul and Unal concluded in their study that past disaster experience had no statistical effect on disaster preparedness [32]. We believe that people with past disaster experience are more likely to be prepared than those without.

Besides, it was found that there was a statistically significant effect on the level of disaster preparedness belief among participants who had experienced the recent 6 February 2023 Kahramanmaraş Earthquakes. Additionally, a statistically significant effect of having experienced these earthquakes on perceived susceptibility and severity was observed. It is thought that the recent nature of the earthquake, the significant casualties and the devastating effect of the earthquake contributed to the high level of disaster awareness and belief in disaster preparedness among participants who had experienced these earthquakes.

Feeling adequately prepared for a disaster/emergency has a significant difference in the disaster preparedness belief level of participants. The disaster preparedness belief level of those who feel prepared was found to be higher in this study. A study conducted among students, demonstrated a significant effect of believing that one is prepared for a disaster/emergency was demonstrated at the level of disaster preparedness beliefs [32]. Additionally, in the Nafaji et al. study, participants were asked if they felt prepared for a disaster, and about four out of five individuals indicated that they did not feel prepared [33]. A similar result was obtained in this study.

The present study revealed a statistically significant correlation between the possession of a disaster/emergency kit and the level of disaster preparedness belief. Participants who had a disaster/emergency kit exhibited a higher level of disaster preparedness belief compared to those who do not. These findings are consistent with those reported in the studies conducted by Arslanoglu et al. and Ertugrul and Unal, which investigated the level of disaster preparedness beliefs [24,32]. It may be posited that individuals who have

a disaster kit are inherently more aware of the potential for disasters.

Furthermore, when the relationship between having a disaster kit and the subgroups of the scale was examined, a statistically significant correlation was found with perceived susceptibility, perceived barriers, cues of action and self-efficacy. Similarly, Arslanoglu et al. have identified the same relationships in their study [24].

The results demostrated a statistically significant effect of receiving basic disaster/emergency education on disaster preparedness belief level, and the disaster preparedness levels of those who received these educations were higher than those who did not receive these educations. This finding is consistent with many studies shows that receiving disaster education increases belief in disaster preparedness [25,32]. In addition, the self-efficacy scores of the participants who received the education were higher than those of the control group. In a study investigating the level of disaster preparedness beliefs of women in the city of Hamadan, Iran, before and after disaster education, it was concluded that the level of disaster preparedness beliefs and self-efficacy increased after the participants were educated [34]. In light of the aforementioned evidence, it can be posited that the provision of fundamental disaster and emergency training has a discernible effect on the levels of disaster preparedness belief and self-efficacy exhibited by those who have undergone such training.

The findings indicated a significant relationship between the level of disaster preparedness beliefs and the state of knowing the emergency assembly point in the region where the participants lived. It was observed that less than half of the students did not know the emergency assembly point in their neighbourhood, and the level of disaster preparedness beliefs of those who knew was higher than those who did not know. Ertugrul and Unal reached a similar result in their study [32].

In the last stage of this study, a regression model was constructed with the factors having a statistically significant relationship with the level of GDPB, which were gender, mother's education level, accommodation type, disaster history, experiencing the Kahramanmaraş Earthquakes, feeling prepared for disaster, disaster/emergency education and knowing the disaster assembly point in the region where they lived, and its relationship with the level of disaster preparedness belief was examined. The findings showed that there was a statistically significant relationship between the level of disaster preparedness beliefs and only gender, receiving disaster/emergency education and knowing the disaster assembly point in the region where they lived. The discrepancies between the initial correlations and the final regression model outcomes suggest that while certain factors appeared to be influential in isolation, their effects may be moderated by interactions with other variables not captured in the model. This could indicate that the direct impact of these factors on disaster preparedness beliefs is less significant when considered in the broader context of interrelated influences.

Limitations

This study is cross-sectional, and its results are specifically generalizable only to civil engineering students at the university where the research was conducted, not to civil engineering students at other institutions. Further studies may focus on a larger sample including different universities. Although we reached the minimum sample size in this study, a total of 55% of civil engineering students responded to the survey. Despite these limitations, measuring the level of disaster preparedness beliefs of civil engineering students, who will play an active role in the creation of disaster resilient cities and disaster preparedness strategies in the future, will contribute to the limited literature in this area.

CONCLUSION

This study investigated the General Disaster Preparedness Belief level of undergraduate students in the Department of Civil Engineering, Faculty of Engineering and Natural Sciences, Ankara Yildirim Beyazit University. This study is the first comprehensive exploration of disaster preparedness beliefs among civil engineering students, revealing how socio-demographic factors and prior disaster experiences shape their perceptions of preparedness. In general, the students' General Disaster Preparedness Belief level is above average but is considered to be inadequate.

The results of this study showed that the level of disaster preparedness beliefs was related to gender, mother's education level, previous disaster experience, type of residence, believing to be prepared for a disaster/emergency, having a disaster/emergency kit, being trained for a disaster/emergency and knowing the emergency assembly point in the region where they lived. These indicators can be the focus of further studies on the general disaster preparedness of civil engineering students.

Insufficient disaster preparedness, which is one of the pre-disaster processes, may cause great loss of life and property during a disaster. Therefore, universities and schools should take a more active role in raising disaster awareness among students and developing effective educational strategies on disaster preparedness. These actions can increase students' awareness of disasters and contribute to society's overall belief in disaster preparedness. In this context, it is important to more effectively direct awareness-raising policies, create unique and effective educational curricula, and develop more effective strategies to enhance students' disaster preparedness capacities.

The findings of this study offer valuable insights into integrating disaster preparedness training among civil engineering students. Future research should investigate how these training programs can be scaled and adapted across different educational levels and engineering disciplines. Additionally, longitudinal studies assessing the impact

of such trainings on students' abilities to respond to real-world disasters would be instrumental. This would provide a clearer understanding of the effectiveness of educational curricula in practical applications. Another significant area for future investigation could involve examining the psychological impacts of disaster preparedness training on students. Determining whether these trainings positively affect students' mental health could inform the development of educational strategies that consider psychological well-being alongside technical skills.

AUTHORSHIP CONTRIBUTIONS

Authors equally contributed to this work.

DATA AVAILABILITY STATEMENT

The authors confirm that the data that supports the findings of this study are available within the article. Raw data that support the finding of this study are available from the corresponding author, upon reasonable request.

CONFLICT OF INTEREST

The author(s) declared no potential conflicts of interest with respect to the research, authorship, and/or publication of this article.

ETHICS

The necessary permission and ethical approval to conduct the study was obtained from Ankara Yıldırım Beyazıt University Health Sciences Ethics Committee (14.06.2023, decision number: 06-283). The purpose of the study was communicated to all students. Prior to commencing the study, both verbal and written consent were obtained from all willing students involved. No identifiers were recorded to maintain confidentiality.

STATEMENT ON THE USE OF ARTIFICIAL INTELLIGENCE

Artificial intelligence was not used in the preparation of the article.

REFERENCES

[1] Republic of Turkey Ministry of Internal Affairs Disaster and Emergency Management Presidency. Annotated Dictionary of Disaster Management Terms. Available at: https://www.afad.gov.tr/aciklamali-afet-yonetimi-terimleri-sozlugu. Accessed on May 30, 2023.

[2] Sawalha IH. A contemporary perspective on the disaster management cycle. Foresight 2020;22:469–482. [CrossRef]

[3] D'Andrea A, Grifoni P, Ferri F. FADM: A feasible approach to disaster management. Dev Policy Rev 2023;41:e12633. [CrossRef]

[4] Nipa TJ, Kermanshachi S, Pamidimukkala A. Identification of resilience dimensions in critical transportation infrastructure networks. J Leg Aff Dispute Resolut Eng Constr 2023;15:3122001. [CrossRef]

[5] Choi WS, Hyun SY, Oh H. Perceived disaster preparedness and willingness to respond among emergency nurses in South Korea: A cross-sectional study. Int J Environ Res Public Health 2022;19. [CrossRef]

[6] Tkachuck MA, Schulenberg SE, Lair EC. Natural disaster preparedness in college students: Implications for institutions of higher learning. J Am Coll Health 2018;66:269–279. [CrossRef]

[7] McEntire DA, Myers A. Preparing communities for disasters: Issues and processes for government readiness. Disaster Prev Manag 2004;13. [CrossRef]

[8] Levac J, Toal-Sullivan D, O'Sullivan TL. Household emergency preparedness: A literature review. J Community Health 2012;37:725–733. [CrossRef]

[9] Sattler D, Kaiser C, Hittner J. Disaster preparedness: Relationships among prior experience, personal characteristics and distress. J Appl Soc Psychol 2006;30:1396–1420. [CrossRef]

[10] Kasapoğlu A, Ecevit M. Impact of the 1999 East Marmara Earthquake in Turkey. Popul Environ 2003;24:339–358. [CrossRef]

[11] Alkalash SH, Alhashmi Alamer EH, Allihyani AM, Alhazmi AS, Alharthi RM, Bugis AM. Knowledge of and attitude toward disaster preparedness among secondary school students in the Western Region of Saudi Arabia. Cureus 2023;15:e33926. [CrossRef]

[12] Paton D. Disaster preparedness: A social-cognitive perspective. Disaster Prev Manag 2003;12:210–216. [CrossRef]

[13] Miceli R, Sotgiu I, Settanni M. Disaster preparedness and perception of flood risk: A study in an Alpine Valley in Italy. J Environ Psychol 2008;28:164–173. [CrossRef]

[14] Mulilis JP, Duval T. Negative threat appeals and earthquake preparedness: A person-relative-to-event (PrE) model of coping with threat. J Appl Soc Psychol 2006;25:1319–1339. [CrossRef]

[15] Dooley D, Catalano R, Mishra S, Serxner S. Earthquake preparedness: Predictors in a community survey. J Appl Soc Psychol 2006;22:451–470. [CrossRef]

[16] Rincon E, Linares MYR, Greenberg B. Effect of previous experience of a hurricane on preparedness for future hurricanes. Am J Emerg Med 2001;19:276–279. [CrossRef]

[17] Sorensen JH. Knowing how to behave under the threat of disaster: Can it be explained? Environ Behav 1983;15:438–457. [CrossRef]

[18] İnal E, Altıntaş K, Doğan N. The development of a general disaster preparedness belief scale using the health belief model as a theoretical framework. Int J Assess Tools Educ 2018;5:146–158. [CrossRef]
[19] Montano D, Kasprzyk D. Theory of reasoned action, theory of planned behavior, and the integrated behavioral model. In: Glanz K, Rimer BK, Viswanath K, editors. Health Behavior and Health Education: Theory, Research, and Practice. 4th ed. San Francisco, CA: Jossey-Bass Press; 2008. p. 67–92.
[20] Akompab DA, Bi P, Williams S, Grant J, Walker IA, Augoustinos M. Heat waves and climate change: Applying the health belief model to identify predictors of risk perception and adaptive behaviours in Adelaide, Australia. Int J Environ Res Public Health 2013;10:2164–2184. [CrossRef]
[21] Shitu K, Adugna A, Kassie A, Handebo S. Application of health belief model for the assessment of COVID-19 preventive behavior and its determinants among students: A structural equation modeling analysis. PLoS One 2022;17:e0263568. [CrossRef]
[22] Rosenstock IM. Health belief model. In: Kazdin AE, editor. Encyclopedia of Psychology. Vol. 4. Oxford University Press; 2000. p. 78–80. [CrossRef]
[23] Bartholomew Eldredge LK, Markham CM, Ruiter RAC, Fernández ME, Kok G, Parcel GS. Planning Health Promotion Programs: An Intervention Mapping Approach. 4th ed. Jossey-Bass; 2016.
[24] Arslanoğlu A, Erdogan M, Düdükcü Y, Keceli S. Individual preparedness for emergency disasters based on the health belief model and factors affecting these. J Disaster Risk 2023;6:367–390. [CrossRef]
[25] Inal E, Altintas KH, Dogan N. General disaster preparedness beliefs and related sociodemographic characteristics: The example of Yalova University, Türkiye. Turk J Public Health 2019;17:1–15. [CrossRef]
[26] Rostami-Moez M, Rabiee-Yeganeh M, Shokouhi M, Dosti-Irani A, Rezapur-Shahkolai F. Earthquake preparedness of households and its predictors based on health belief model. BMC Public Health 2020;20:1–8. [CrossRef]
[27] Tanner A, Doberstein B. Emergency preparedness amongst university students. Int J Disaster Risk Reduct 2015;13:409–413. [CrossRef]
[28] Su T, Han X, Chen F, Du Y, Zhang H, Yin J, et al. Knowledge levels and training needs of disaster medicine among health professionals, medical students and local residents in Shanghai, China. PLoS One 2013;8:e67041. [CrossRef]
[29] Tan Y, Liao X, Su H, Li C, Xiang J, Dong Z. Disaster preparedness among university students in Guangzhou, China: Assessment of status and demand for disaster education. Disaster Med Public Health Prep 2017;11:310–317. [CrossRef]
[30] Li Q, Hao Y, Wu Q. Status of emergency preparedness and its influencing factors among residents in Harbin City. Chin J Public Health 2015;31:97–101.
[31] Dean AG, Sullivan KM, Soe MM. OpenEpi: Open Source Epidemiologic Statistics for Public Health, Version 3.01. Available at: https://www.OpenEpi.com. Accessed on May 10, 2023.
[32] Ertugrul B, Ünal SD. Determination of general disaster preparedness beliefs of students studying at a foundation university health services vocational school. J Disaster Risk 2020;3:31–45. [CrossRef]
[33] Najafi M, Khankeh HR, Elmi H, Pourvakhshoori N. Behavioral, normative and control beliefs about earthquake preparedness: A deductive content analysis study. PLoS Curr 2018;10. [CrossRef]
[34] Amini R, Biglari F, Khodaveisi M, Tapak L. Effect of education based on the health belief model on earthquake preparedness in women. Int J Disaster Risk Reduct 2021;52:101954. [CrossRef]

Sigma J Eng Nat Sci, Vol. 44, No. 1, pp. 234–251, February, 2026

Sigma Journal of Engineering and Natural Sciences
Web page info: https://sigma.yildiz.edu.tr
DOI: 10.14744/sigma.2025.00000

Research Article

Impact of halloysite clay on the thermal degradation behaviour, kinetics analysis, and pyrolysis product distribution during catalytic pyrolysis of bakelite

Chinmaya KAR[1], Achyut KUMAR PANDA[1], Pabitra MOHAN MAHAPATRA[2,*]

[1]*Veer Surendra Sai University of Technology, Burla, India*
[2]*Department of Chemistry, Veer Surendra Sai University of Technology, Burla, Odisha, India*

ARTICLE INFO

Article history
Received: 04 September 2024
Revised: 25 October 2024
Accepted: 08 December 2024

Keywords:
Batch Pyrolysis; Catalytic Pyrolysis; Coats-Redfern Integral Method; Discarded Bakelite; Halloysite Clay

ABSTRACT

This study is used to explore the effect of a clay catalyst, like Halloysite, on the pyrolysis of Bakelite, showing the different issues of waste bakelite and providing an eco-friendly thermal process to convert the discarded Bakelite into valuable products. In this study, the pyrolysis of Bakelite is conducted to set the backbone of the study. Then, based on the pyrolysis of Bakelite, the catalytic pyrolysis of Bakelite with Halloysite clay is conducted to compare the pyrolysis kinetics and product yields for reactor design. The kinetic analysis is completed by using TGA data and Coats–Redfern modeling from 150–450 °C. The thermodynamic parameters are calculated by the Eyring equation from the TGA data. The TGA data of Bakelite and its blend with the different concentrations (2.5, 5, 7.5, and 10 wt%) of Halloysite clay were obtained at a heating rate of 20 °C/min over the temperature range of 30 to 1000 °C. The batch pyrolysis of the Bakelite in the presence of Halloysite clay is conducted at the optimum pyrolysis temperature for the pyrolysis of Bakelite. The pyrolytic oils produced are analyzed by Fourier transform infrared spectroscopy (FTIR) and gas chromatography–mass spectrometry (GC-MS). The weight loss at a heating rate of 20 °C/min increases from 56.49% to 62.57% with the addition of 5 wt% Halloysite clay. The degradation of Bakelite without Halloysite clay follows a 1.5th-order kinetic mechanism with an activation energy of 81.088 kJ/mol and an Arrhenius constant of 4.39×10^{12} min^{-1}. However, with 5 wt% Halloysite clay, the activation energy decreases to 77.883 kJ/mol and the Arrhenius constant drops to 2.08×10^{12} min^{-1}, without changing the kinetic mechanism. The thermodynamic parameters, such as the changes in enthalpy and Gibbs free energy for the thermal degradation of Bakelite, decrease with the addition of Halloysite clay. The addition of 5% Halloysite clay to Bakelite increases the condensable products from 39.12% to 41.25%, while the gas fraction decreases from 30.36% to 29.51% and the residue from 30.52% to 29.24%. FTIR and GC-MS support the presence of alkanes, cycloalkanes, alkenes, cycloalkenes, aromatics, and oxygenated species in the pyrolytic oils. These results highlight that the addition of Halloysite clay with Bakelite during thermal conversion alters the kinetic analysis, improves the product yields, and varies the composition of the pyrolytic oil. The novelty of this study lies in demonstrating the catalytic effect of Halloysite clay on thermal degradation, kinetics, and product distribution for optimal reactor design.

Cite this article as: Kar C, Kumar Panda A, Mohan Mahapatra P. Impact of halloysite clay on the thermal degradation behaviour, kinetics analysis, and pyrolysis product distribution during catalytic pyrolysis of bakelite. Sigma J Eng Nat Sci 2026;44(1):234–251.

***Corresponding author.**
*E-mail address: pabitra.mahapatra3@gmail.com; pmmahapatra_phdchem@vssut.ac.in

This paper was recommended for publication in revised form by Regional Editor Ahmet Selim Dalkilic

Published by Yıldız Technical University Press, İstanbul, Turkey
© Author. This is an open access article under the CC BY-NC license (http://creativecommons.org/licenses/by-nc/4.0/).

INTRODUCTION

The polymer and its composite-based materials are widely used for manufacturing heat-resistant components in the automotive and aerospace industries [1]. The use of polymers has grown due to their low density, poor heat and electrical conductivity, high strength, flexibility, and low cost [2]. About 1.75×10^5 tons/annual of Bakelite are used in over 15,000 products [3]. The synthetic Bakelite is used widely in the manufacture of electronics, glassware, chemicals, metals, polymers, mobile cases, kitchenware, containers, and pipe stems [4]. The global Bakelite market is expected to increase from USD 3.51 billion in 2024 to USD 4.22 billion by 2029, with a CAGR of over 3.5% [5]. The widespread use of Bakelite increases the volume of discarded Bakelite. The Bakelite waste production in India was 8×10^4 tons in 2020, and it is expected to increase to 7 million tons by 2050 [6]. The vast waste of Bakelite causes a negative impact on the environment and human beings. So, bakelite waste is essential to reduce. The microplastics produced from waste plastic cause a major threat to aquatic life [7]. The disposal of waste Bakelite in landfills or the burning of waste Bakelite contaminates water, soil, and air with harmful substances such as methanol, formaldehyde, and asbestos. The cross-linked structure of thermosetting plastic Bakelite provides heat resistance, which complicates recycling [3]. So, developing eco-friendly disposal methods for waste bakelite remains challenging for valorisation, including plastic fuel production in the ongoing research.

To date, researchers are working on new technologies and methods to mitigate Bakelite waste. Mohan et al. used discarded bakelite as a reusable component in concrete beam fabrication [4]. Murali and Sambath mixed waste Bakelite into concrete and used it for solid block manufacturing [3]. Surendranath and Ramana used discarded bakelite as an alternative to conventional aggregates in concrete [6]. Nowadays, many researchers are working on alternative recycling technologies such as thermal and catalytic pyrolysis, gasification, and plasma arc gasification [8]. Dhunna et al. used the waste bakelite as a carbon source in ironmaking [9]. Horikawa et al. carbonised the phenol-formaldehyde resin by using ethylene glycol, 1,6-hexanediol, and polyethylene glycol [10]. Chen et al. synthesized nitrogen-doped mesoporous carbon with 11.64% nitrogen and a 2D hexagonal structure by carbonizing phenolic resin with melamine [11].

Pyrolysis is an efficient, cost-effective method for converting carbon-rich waste into fuels and energy [12]. Pyrolysis is a tertiary recycling process that reduces high molecular weight polymers into smaller molecules in an oxygen-free atmosphere, according to ASTM D5033-00 [13]. This method operates at 300–900°C, converting plastic waste into liquid hydrocarbons, char, and gas. By generating higher-quality liquid hydrocarbons at lower temperatures and with shorter reaction periods, catalytic pyrolysis performs better than thermal pyrolysis and copyrolysis [8]. Xu et al. synthesized carbon aerogels by pyrolyzing phenolic resin gels with $ZnCl_2$ [14]. Wang et al. obtained char residues of 62.9% and 60.5% from pure phenol-formaldehyde resin, and 71.9% and 68.4% from boron carbide-modified PF resin at 700°C and 1000°C, respectively [15].

Research has produced phenolic-rich oils and chemicals from PF resins via pyrolysis, co-pyrolysis, and catalytic pyrolysis [12]. Bennett and Payne examined the volatile organic compounds released during the thermal disintegration of phenolic resin under varied pyrolysis conditions, identifying phenol as the primary product, along with benzene, methylbenzene, 1,4-dimethylbenzene, 1,2-dimethylbenzene, 1,3,5-trimethylbenzene, 2-methylphenol, 4-methylphenol, 2,6-dimethylphenol, 2,4-dimethylphenol, 2,4,6-trimethylphenol, 9H-xanthene, and phenanthrene. They also quantified permanent gases like CO, CO_2, CH_4, and H_2O, excluding hydrogen. Lower heating rates led to more complete decomposition with fewer secondary reactions, while higher rates preserved larger VOC fragments. Faster heating at 20,000°C per second produced more volatile organic compounds and less CO_2 than slower heating at 20°C per minute, though the residue composition remained consistent [16]. Xu et al. synthesized aromatic amines with 14.2% carbon content and 57.6% selectivity from phenol-formaldehyde resins using an HZSM-5-3 zeolite catalyst at 650°C. Adding lignin increased the yield of aromatic amines by 32.2% and achieved 11.8% carbon content at a 1:1 lignin-to-PF resin ratio [17]. Wong et al. performed batch pyrolysis of resole-type phenol-formaldehyde resin from 320 K to 1290 K, resulting in a 39.2% mass loss. They produced three product types: water below 800 K, phenolic derivatives from 500 to 850 K, and permanent gases (H_2, CH_4, CO, CO_2) above 800 K. Aromatics formed between 700 and 850 K, while C_2–C_4 hydrocarbons peaked at 1000 K [18]. Xu et al. showed that pyrolyzing PF resin with calcium hydroxide enhanced thermal decomposition and cracking, increasing monophenol yield. At 650°C and 5% calcium hydroxide, the process produced a phenolic-rich oil with 9.1% aromatic hydrocarbons, 82.8% phenols, and a 33.7% carbon yield. Pyrolyzing the residue at 800°C produced a CaO/char catalyst that reduced bio-oil oxygen content from 14.4% to 2.4% during soybean oil pyrolysis [19]. However, to improve the quality and yield of phenolic-rich oil from waste Bakelite using an optimized reactor, it is need to study the thermal degradation with and without a catalyst, various co-feedstocks, pyrolysis kinetics, and product analysis.

Many studies have been proposed by many researchers regarding the kinetics and mechanisms of bakelite.

Jiang et al. explore the kinetics of the pyrolysis of PF using non-isothermal thermogravimetry at heating rates of 5–20 K/min from 363 to 1100 K. They suggested that the thermal degradation of Bakelite is conducted in three stages. The activation energy, Arrhenius factor, and integral form for the first stage are 222.73 kJ/mol, 1.19×10^9 min^{-1}, and $g(\alpha) = (1-\alpha)^{-3}$; for the second stage they are 271.70 kJ/mol, 4.02×10^6 min^{-1}, and $g(\alpha) = (1-\alpha)^{-1}$; and for the third

stage they are 305.14 kJ/mol, 3.60×10^7 min^{-1}, and $g(\alpha) = 1 + (2/3)\alpha - (1+\alpha)^2/^3$, respectively [20]. Jiang et al. conducted infrared spectroscopy of PF resin pyrolysis from 450 to 750°C. Their research showed that CO and CO_2 arise from methylene group oxidation, with PF resin decomposition driven by methylene scission. However, methylene radicals react with smaller molecules to form volatile compounds like ethylene and methanol. PF resin gradually converts into amorphous carbon as temperature increases through pyrolysis and polycyclic reactions [21].

Catalytic pyrolysis technology progress is limited by the lack of effective, affordable catalysts. Therefore, research on improved catalysts is important to increase the catalytic efficiency and reduce the cost of the catalyst, for commercially producing renewable fuels and chemicals through catalytic pyrolysis [12]. The effective catalytic pyrolysis of waste plastic depends upon the selection of a suitable catalyst [8]. The clay catalysts are widely used due to strong adsorption and surface activity [12]. Clay catalysts have a layered structure, with silica tetrahedra and hydrated alumina octahedra linked by covalent and van der Waals forces [22]. Halloysite (Hal) clay, a cost-effective dioctahedral 1:1 alumosilicate ($Al_2Si_2O_5(OH)_4{\cdot}nH_2O$), is chemically similar to kaolinite. This clay contains internal gibbsite (Al-OH) sheets, external siloxane (Si-O-Si) groups, and a monolayer of water between layers. The hydrated halloysite-(10 Å) has a single water layer between its layers, while dehydrated halloysite-(7 Å) forms by removing interlayer water through mild heating or vacuum.

The spherical or plate-like shape of Halloysite clay depends on its origin [23]. The researcher explores the use of different clay catalysts like bentonite, montmorillonite, kaolin, and synthetic hydrotalcite. However, little research has been completed on the use of Halloysite clay. Cai et al. evaluated the catalytic performance of bentonite, montmorillonite, kaolin, and synthetic hydrotalcite in pyrolyzing mixed plastics (PE: PP: PS = 40:20:20:20) for fuel and energy recovery at a 1:10 ratio. The catalyst, like hydrotalcite, increased oil yield and reduced wax. Bentonite increased the gas production, montmorillonite increased the oil production, and kaolin promoted wax generation. Montmorillonite achieved the highest oil yield (71.0%), kaolin produced the most gasoline-range hydrocarbons, and bentonite nanoclay yielded the most diesel-range hydrocarbons. Clay catalysts increased hydrocarbons (methane, ethane, ethene, propene, butane) and reduced CO_2 levels. The study shows that during the catalytic pyrolysis of mixed plastic waste, the moderate acidity of clay catalysts is essential for increasing oil production and gasoline and diesel range fuels. Mechanistic analysis revealed that radicals from plastic breakdown strongly influence the pyrolysis process [12]. Panda and Singh used a batch reactor to fracture waste polypropylene thermally and catalytically at 400–550°C. At 500°C, they obtained the maximum liquid yield (82.85%). Adding kaolin catalyst reduced reaction time and increased production, achieving an 87.5% oil yield at a 1:3 kaolin-to-plastic ratio and 500°C, with oil resembling petroleum fuels [24].

Kanattukara et al. investigated the effect of HNT on the production of pyrolytic oil from HDPE, LLDPE, and PP through catalytic pyrolysis. The HNT catalyst reduced the pyrolysis temperature from 470°C to 450°C and enhanced the yield of liquid. The liquid and gas yields for PP are 66.8% and 32.4%, for HDPE are 51.5% and 37.5%, and for LLDPE are 66.5% and 32.3%, respectively. The HNT catalyst produced a liquid rich in paraffins, naphthenes, olefins, and aromatics, shifting the product distribution toward lighter C_6-C_{10} hydrocarbons, similar to gasoline. The pyrolysis oil with the HNT catalyst contained lighter liquid fractions: 34.2% for PP, 16.0% for LLDPE, and 18.9% for HDPE [13]. Li et al. investigated how poly (butylene adipate-co-terephthalate) (PBAT) is thermally degraded by halloysite nanotubes. Both PBAT and its Halloysite nanotube nanocomposite showed a single-step degradation process. The residual char from PBAT was 0.88%, while the halloysite nanotube/PBAT nanocomposite produced 7.63%, nearly eight times higher. The degradation of both materials released water, alcohols, acids, CO_2, CO, esters, and alkenes [25].

Understanding the chemical kinetics of degradation is crucial for evaluating, designing, and scaling up industrial waste polymer conversion units. The most used technique for examining the kinetics of thermal degradation is thermogravimetric analysis.

There are considerable work has been done to calculate kinetic parameters using the Coats-Redfern model (CR). Ganesha et al. use thermogravimetric analysis and the Coats–Redfern method to investigate the pyrolysis and co-pyrolysis kinetics of mango seed kernel (MSK), mango seed shell (MSS), and PET at heating speeds of 15, 20, and 25°C/min. MSS degraded at higher temperatures than MSK due to its higher cellulose content. The degradation rate depends upon the type of biomass and the PET-to-biomass ratio. Although the reaction order may change depending on the material composition, co-pyrolysis of PET with MSK and MSS increased thermal degradation rates and activation energy. The initial degradation stage has a higher order and lower activation energy than the secondary and tertiary stages. The reaction order varies with raw material composition, ranging from 0.1 to 3 [26]. Arias et al. used thermogravimetric analysis using models such as Friedman, Coats-Redfern, and ASTM E1641 to investigate the effects of particle size (0.3 and 5.0 mm) on waste tire pyrolysis kinetics. Waste tire pyrolysis occurs in two stages between 200 and 520°C, involving plasticizer volatilization and rubber degradation. The larger sizes cause higher kinetic parameters due to heat and mass transfer processes. The activation energy in the Friedman model varied between 40 and 117 kJ/mol for particles of 0.3 mm and between 23 and 119 kJ/mol for particles of 5.0 mm. The activation energy in the Coats-Redfern model varied between 46 and 87 kJ/mol for 0.3 mm and 43 and 124 kJ/mol for 5.0 mm. According

to ASTM E1641, activation energy was 56-60 kJ/mol for both 0.3- and 5.0-mm particles. The reaction order was approximately one in both decomposition zones [27]. Uzun et al. investigated the co-pyrolysis behavior and kinetics of blends of walnut shell, polypropylene, and low-density polyethylene (1:2, 1:1, and 2:1 ratios) using the Arrhenius and Coats–Redfern models and thermogravimetric analysis data at heating rates of 5–50 °C/min. Walnut shell had three devolatilization stages: water removal, hemicellulose/cellulose decomposition, and lignin degradation. Polypropylene and low-density polyethylene decomposed in a single stage with a weight loss of 45% in the active pyrolysis zone. As pyrolysis progressed, activation energy and the Arrhenius factor changed concurrently, indicating a compensating effect. The Arrhenius method gave activation energies of 69.32 kJ/mol for walnut shell, 295.65 kJ/mol for polypropylene, and 254.55 kJ/mol for LDPE, while the Coats-Redfern method yielded 101.58, 333.53, and 316.77 kJ/mol for WS, PP, and LDPE, respectively [28].

Numerous studies have been conducted for converting waste bakelite into valuable products like char, phenolic-rich oils, and chemicals via pyrolysis. However, limited research has focused on the kinetic study and pyrolytic mechanism of bakelite. Several studies have been proposed about the catalytic pyrolysis by using catalysts like kaolin, montmorillonite, bentonite, and halloysite nanotubes to improve yields and efficiency. A lot of work is also completed by using the Coats-Redfern model for the accurate calculation of kinetic parameters. From the above literature review, a research gap is identified, namely, the catalytic batch pyrolysis of Bakelite by using Halloysite clay. This study aims to address these gaps by examining the pyrolytic degradation, kinetic studies using the Coats–Redfern method and thermogravimetry analysis data, thermodynamics analysis by the Eyring equation, and catalytic batch pyrolysis of Bakelite using different concentrations of Halloysite clay. The goal of this study is to improve the valorisation of the waste bakelite by using a suitable clay catalyst. This study offers a novel approach by investigating the catalytic pyrolysis of bakelite using Halloysite clay, a cost-effective material rarely explored for waste management.

MATERIALS AND METHODS

Materials

The discarded electric switches, plugs, and holders collected from the VSSUT electrical maintenance department were used as a source of materials for producing bakelite. The discarded electrical components were first manually broken down into small fragments. These bakelite pieces were then ground into powder using a Philips domestic grinder (model HL7756/00, 750 watts). The ground powder is passed through a No. 18 sieve (Gilson Company, Inc, Model: V8SF#18, ASTM E11 standard) to get a uniform particle size of 1mm. The Hal clay, sourced from Vedayukt India Private Limited, India, has a purity of 98-99% (with Al_2O_3 = 37.079% and SiO_2 = 55.056%). The Halloysite clay sample has the following features: a BET surface area of 7.672 m^2/g, an average pore radius of 7.065 nm, a total pore volume of 0.026 cc/g, and a density ranging from 1.8 to 2.6 g/cm^3. The clay features an irregular plateau shape and a rough surface texture and is utilized as a catalyst.

Methods

Characterization of Bakelite

The proximate analysis is performed by using the different ASTM methods: moisture content (ASTM D 4442), volatile matter (ASTM D 3172), fixed carbon (ASTM D 3177), and ash content (ASTM D 3175). The CHNS elemental analyzer is used for ultimate analysis. The bomb calorimetry is used to calculate the calorific value.

Thermogravimetric Analysis

The study employed a pyrolysis simultaneous thermal analyzer 8000 for Thermogravimetric and Derivative Thermogravimetry evaluation of discarded bakelite and its blends with Hal clay. Samples, each weighing about 9.6 ± 0.25 milligrams, included bakelite and blends with Hal clay at concentrations of 2.5, 5, 7.5, and 10 wt/wt%. The samples are taken in a crucible, and the crucible is subjected to heating under nitrogen flow at 20 ml/min, with temperatures from 30°C to 1000°C and a consistent heating rate of 20°C/min. The thermogravimetry analysis is performed in triplicate to ensure result accuracy.

Batch Pyrolysis and Pyrolysis Oil Analysis

The pyrolysis and catalytic pyrolysis of Bakelite using different concentrations (2.5, 5, 7.5, and 10 wt/wt%) of Halloysite clay are performed in a stainless-steel tube batch reactor with an internal diameter of 37 mm, an exterior diameter of 41 mm, and a length of 145 mm. The reactor, which features a top opening, was filled with 30 grams of sample and securely sealed with nuts and bolts. The batch reactor is heated using an external electric furnace at a heating rate of 20 °C per minute. The reactor temperature was monitored using a Cr-Al: K thermocouple, and the temperature is regulated with an accuracy of ±3.6 °C by a PID controller. The pyrolysis temperature ranges from 300 to 500 °C, revealing that 450 °C is the optimal temperature for bakelite pyrolysis, maximizing the yield of condensable fractions. Therefore, catalytic pyrolysis of the bakelite-Hal clay blend is also performed at 450 °C. The vapors formed are passed through a condenser to condense into liquid and wax. The non-condensable gases are away from the system. The residual solid is collected from the reactor. By comparing the mass of the collected materials to the initial mass of the reactant, the yield of liquid and wax products was evaluated. The percentage yield of the pyrolytic products, including condensable substances and residue, is calculated, and the non-condensable gases are calculated by subtracting from 100%. The batch pyrolysis experiment is

conducted three times for each sample to maintain accuracy and reliability. The FTIR analysis of the pyrolytic oils is performed by using a Bruker Alpha FTIR spectrophotometer (Resolution = 2 cm^{-1} and Spectrum range = 500–4000 cm^{-1}). For GC-MS analysis, a Shimadzu GC-MS QP 2020 NX system with an SH-Rxi-5ms capillary non-polar column (30 m × 0.25 mm ID × 0.25 μm film thickness) was utilized.

The GC-MS analysis is conducted by including the experimental condition: Carrier gas (He): 1.0 mL/min, Injection volume: 1 μL, Temperature program: 35–280 °C at 5 °C/min, and Mass range: 35–650 m/z (NIST 20 library.

Pyrolysis Kinetic Theory

The complexity of pyrolysis makes it difficult to create kinetic models that fully explain the principles underlying thermal breakdown. However, instead of a complete kinetic analysis, average kinetic values can still be used [29]. The thermogravimetry analysis data are used in the Coats-Redfern integral method to calculate the kinetic parameters [30].

The overall rate of pyrolytic degradation of bakelite in the absence and presence of Hal clay (dα/dt) is defined by equation 1.

$$\frac{d\alpha}{dt} = kf(\alpha) \tag{1}$$

Here, f(α) is a function of α, and the value of f(α) varies from model to model, and k is the rate constant [31].

The earlier work suggests that the thermal degradation of Bakelite follows the F_5 order mechanism [32]. Catalysts influence cracking rates [33], allowing variations in reaction order without altering the overall model with the Hal catalyst. Therefore, this study employed the order-based Coats-Redfern model for clarity, as adding other models could complicate the analysis without significant benefits. Equation 2 defines the value of f(α) for the nth-order decomposition reaction.

$$f(\alpha) = (1-\alpha)^n \tag{2} [34]$$

The reaction order (n) is used to describe the pyrolysis model.

The value of the extent of pyrolysis of the sample (α) derived from thermo-gravimetric analysis, and is expressed as: [29]

$$\alpha = \frac{W_i - W_t}{W_i - W_f} \tag{3}$$

Here, W_i = Initial weight of the sample at time t = 0, W_t = Weight of the sample at an intermediate time t, and W_f = Final weight of the sample as time approaches infinity

The relationship between temperature and the rate constant k is described by the Arrhenius equation, provided as:

$$k = A \exp\left(-\frac{Ea}{RT}\right) \tag{4} [35]$$

Ea stands for activation energy, R for universal gas constant, T for absolute temperature, and A for pre-exponential component in equation 4.

From equation (1) and (4)

$$\frac{d\alpha}{dt} = A \exp\left(-\frac{Ea}{RT}\right) f(\alpha)$$
$$\Rightarrow \frac{d\alpha}{f(\alpha)} = A \exp\left(-\frac{Ea}{RT}\right) dt \tag{5}$$

Now integrate the equation (5)

$$g(\alpha) = \int_0^\alpha \frac{d\alpha}{f(\alpha)} = A \int_0^t \exp\left(-\frac{Ea}{RT}\right) dt \tag{6}$$

Now multiply and divide dT with the right side of equation (6)

$$\int_0^\alpha \frac{d\alpha}{f(\alpha)} = A \int_0^t \exp\left(-\frac{Ea}{RT}\right) dt \times \frac{dT}{dT}$$
$$\Rightarrow \int_0^\alpha \frac{d\alpha}{f(\alpha)} = A \int_0^t \exp\left(-\frac{Ea}{RT}\right) \frac{dt}{dT} \times dT \tag{7}$$

For the linear heating program,

Heating rate (β) = dT/dt (8) [36]

From equation (7) and (8)

$$\int_0^\alpha \frac{d\alpha}{f(\alpha)} = A \int_0^T \exp\left(-\frac{Ea}{RT}\right) \frac{1}{\beta} \times dT$$
$$\Rightarrow \int_0^\alpha \frac{d\alpha}{f(\alpha)} = \frac{A}{\beta} \int_0^T \exp\left(-\frac{Ea}{RT}\right) dT \tag{9} [31]$$

The right-hand side of equation (9), though obtaining a precise analytical solution is not possible.

By using Cauchy's rule, the equation (9) becomes

$$\frac{A}{\beta} \int_0^T \exp\left(-\frac{Ea}{RT}\right) dT \cong \frac{ART^2}{\beta Ea}\left(1-\frac{2RT}{Ea}\right)\exp\left(-\frac{Ea}{RT}\right) \tag{10}$$

From equation (9) and (10)

$$\int_0^\alpha \frac{d\alpha}{f(\alpha)} = \frac{ART^2}{\beta Ea}\left(1-\frac{2RT}{Ea}\right)\exp\left(-\frac{Ea}{RT}\right) \tag{11}$$

From equation (2) and (11)

$$\int_0^\alpha \frac{d\alpha}{(1-\alpha)^n} = \frac{ART^2}{\beta Ea}\left(1-\frac{2RT}{Ea}\right)\exp\left(-\frac{Ea}{RT}\right) \tag{12}$$

Since, (2RT/Ea) <<< 1, So, the value of (2RT/Ea) is neglected, and equation (12) becomes

$$\int_0^{\alpha}\frac{d\alpha}{(1-\alpha)^n}\cong\frac{ART^2}{\beta Ea}\exp\left(\frac{-Ea}{RT}\right)$$
$$\Rightarrow\int_0^{\alpha}(1-\alpha)^{(-n)}d\alpha=\frac{ART^2}{\beta Ea}\exp\left(\frac{-Ea}{RT}\right)$$
$$\Rightarrow\left[\frac{(1-\alpha)^{(-n+1)}}{(-n+1)}\times(-1)\right]_0^{\alpha}=\frac{ART^2}{\beta Ea}\exp\left(\frac{-Ea}{RT}\right)$$
$$\Rightarrow\left(\frac{(1-\alpha)^{(-n+1)}}{(-n+1)}\times(-1)\right)-\left(\frac{(1)^{(-n+1)}}{(-n+1)}\times(-1)\right)=\frac{ART^2}{\beta Ea}\exp\left(\frac{-Ea}{RT}\right)$$
$$\Rightarrow\frac{(1-\alpha)^{(1-n)}}{(1-n)}\times(-1)-\frac{(1)^{(1-n)}}{(1-n)}\times(-1)=\frac{ART^2}{\beta Ea}\exp\left(\frac{-Ea}{RT}\right)$$
$$\Rightarrow\frac{(1-\alpha)^{(1-n)}}{(1-n)}\times(-1)+\frac{1}{(1-n)}=\frac{ART^2}{\beta Ea}\exp\left(\frac{-Ea}{RT}\right)$$
$$\Rightarrow\frac{1}{(1-n)}-\frac{(1-\alpha)^{(1-n)}}{(1-n)}=\frac{ART^2}{\beta Ea}\exp\left(\frac{-Ea}{RT}\right)$$
$$\Rightarrow\frac{1-(1-\alpha)^{(1-n)}}{(1-n)}=\frac{ART^2}{\beta Ea}\exp\left(\frac{-Ea}{RT}\right)\quad(13)\ [30]$$

Now divide T^2 and apply logarithm on both sides

$$\ln\left\{\frac{1-(1-\alpha)^{(1-n)}}{T^2(1-n)}\right\}=\ln\left\{\frac{AR}{\beta Ea}\exp\left(\frac{-Ea}{RT}\right)\right\}$$
$$\Rightarrow\ln\left\{\frac{1-(1-\alpha)^{(1-n)}}{T^2(1-n)}\right\}=\ln\left(\frac{AR}{\beta Ea}\right)-\frac{Ea}{RT}\quad(14)$$

The equation (14) is validated for n≠1

If n=1, then equation (13) becomes,

$$\int_0^{\alpha}\frac{d\alpha}{(1-\alpha)}=\frac{ART^2}{\beta Ea}\exp\left(\frac{-Ea}{RT}\right)$$
$$\Rightarrow\left[-\ln(1-\alpha)\right]_0^{\alpha}=\frac{ART^2}{\beta Ea}\exp\left(\frac{-Ea}{RT}\right)$$
$$\Rightarrow-\ln(1-\alpha)-(-\ln 1)=\frac{ART^2}{\beta Ea}\exp\left(\frac{-Ea}{RT}\right)\quad(15)$$
$$\Rightarrow-\ln(1-\alpha)=\frac{ART^2}{\beta Ea}\exp\left(\frac{-Ea}{RT}\right)$$

Now divide by T^2 and apply logarithm on both sides of equation (15)

$$\ln\left(\frac{-\ln(1-\alpha)}{T^2}\right)=\ln\left(\frac{AR}{\beta Ea}\right)-\frac{Ea}{RT}\quad(16)$$

The Coats-Redfern model equations, given as equations (14) and (16), are employed for calculating kinetic parameters [34]. The Coats-Redfern model kinetic equations used in model-fitting methods are tabulated in Table 1.

By plotting ln [g(α)/T^2] versus 1/T graph, the Y-intercept will be ln [(AR)/(βEa)] and the slope will be – (Ea/R) allowing to determine the values Ea and A respectively [37]. The reaction order for the thermal degradation of bakelite with

Table 1. Coats-Redfern kinetic equation used in model-fitting methods

Method	Kinetic Equations	Plot
CR	(i) $n\neq1$, $\ln\left[\frac{1-(1-\alpha)^{1-n}}{T^2(1-n)}\right]=\ln\left(\frac{AR}{\beta Ea}\right)-\frac{Ea}{RT}$	$\ln\left[\frac{g(\alpha)}{T^2}\right]$ Versus $\frac{1}{T}$
	(ii) $n=1$, $\ln\left[\frac{-\ln(1-\alpha)}{T^2}\right]=\ln\left(\frac{AR}{\beta Ea}\right)-\frac{Ea}{RT}$	

Table 2. Value of f(α) and g(α)

Reaction mechanism	Symbols	f(α)	g(α)
One-half order	$F_{0.5}$	$(1-\alpha)^{1/2}$	$2(1-\alpha)^{1/2}$
First order	F_1	$(1-\alpha)$	$-\ln(1-\alpha)$
Three-halves order	$F_{1.5}$	$(1-\alpha)^{3/2}$	$-2[1-(1-\alpha)^{-(1/2)}]$
Second order	F_2	$(1-\alpha)^2$	$-[1-(1-\alpha)^{-1}]$
Five-halves order	$F_{2.5}$	$(1-\alpha)^{5/2}$	$-(2/3)[1-(1-\alpha)^{-(3/2)}]$
Third order	F_3	$(1-\alpha)^3$	$-(1/2)[1-(1-\alpha)^{-2}]$
Seven-halves order	$F_{3.5}$	$(1-\alpha)^{7/2}$	$-(2/5)[1-(1-\alpha)^{-(5/2)}]$
Fourth-order	F_4	$(1-\alpha)^4$	$-(1/3)[1-(1-\alpha)^{-3}]$
Nine-halves order	$F_{4.5}$	$(1-\alpha)^{9/2}$	$-(2/7)[1-(1-\alpha)^{-(7/2)}]$
Fifth order	F_5	$(1-\alpha)^5$	$-(1/4)[1-(1-\alpha)^{-4}]$
Eleven-halves order	$F_{5.5}$	$(1-\alpha)^{11/2}$	$-(2/9)[1-(1-\alpha)^{-(9/2)}]$
Sixth order	F_6	$(1-\alpha)^6$	$-(1/5)[1-(1-\alpha)^{-5}]$

or without Hal is shown by the plot with the R^2 value closest to 1. The values of g(α) and f(α) are displayed in Table 2 [31, 35].

The activated complex theory and the Eyring equation are employed to calculate further kinetic parameters of the process, as given by:

$$k = \frac{e\chi k_B T_m}{h} \exp\left(\frac{\Delta S}{R}\right) \exp\left(-\frac{Ea}{RT_m}\right) \quad (17)$$

Where, e = Neper number (2.7183)

χ = Transmission factor which is unity for monomolecular reactions

k_B = Boltzmann constant

T_m = Peak temperature which can be obtained from the DTG plot

h = Planck's constant

ΔS = Change in entropy

From equation (4) and (17)

$$A = \left(\frac{e\chi K_B T_m}{h}\right) \exp\left(\frac{\Delta S}{R}\right) \quad (18)$$

$$\Rightarrow \Delta S = R\ln\left(\frac{Ah}{e\chi K_B T_m}\right) \quad (19)\ [35]$$

We know,

$Ea = \Delta H + RT_m$, Where, ΔH = Change in enthalpy

$$\Rightarrow \Delta H = Ea - RT_m \quad (20)$$

According to the Gibbs–Helmholtz equation

$$\Delta G = \Delta H - T_m \Delta S \quad (21)\ [30]$$

Where, ΔG = Change in Free energy

RESULTS AND DISCUSSION

Characterization of Bakelite

The proximate analysis of bakelite shows volatile compounds at 68.22%, moisture at 3.24%, ash at 6.82%, and fixed carbon at 21.72%. Discarded bakelite can be used as a possible feedstock for pyrolysis because of its high volatile content, and its high fixed carbon content increases the possibility that it will be converted into useful carbonaceous products [32]. However, the moisture content necessitates additional energy for drying, and the relatively high ash content increases both handling and processing costs [38].

The ultimate analysis of bakelite reveals a carbon content of 68.04%, oxygen at 14.78%, and hydrogen at 5.09%. Pyrolytic degradation of Bakelite produces more oxygenated compounds due to the presence of oxygen. Bakelite has zero nitrogen and sulfur content, so no nitrogen- or sulfur-containing compounds are produced [38]. A high amount of carbon and hydrogen produces a higher number of aromatic compounds. This high carbon and hydrogen content causes a higher heating value of Bakelite. With a calorific value of 6610 Cal/g, bakelite is an efficient fuel that can be utilized to maximize combustion temperature in operations involving the use of raw materials [39].

TG-DTG Analysis

In earlier research, the thermal study was conducted at various heating rates (5, 10, 20, 30, and 50°C/min) [32]. According to the ICTAC guidelines [40], heating rates in the 1–20°C/min range are commonly used, as this range provides reliable and reproducible results for TGA/DTG analysis. The moderate heating rate of 20 °C/min is selected for the TG–DTG analysis of the impact of Halloysite clay on the thermal degradation of Bakelite to ensure continuity and comparability with earlier findings at heating rates ranging from 5 to 50 °C/min. Figure 1 presents the TG–DTG curve for the thermal degradation of Bakelite in the absence and presence

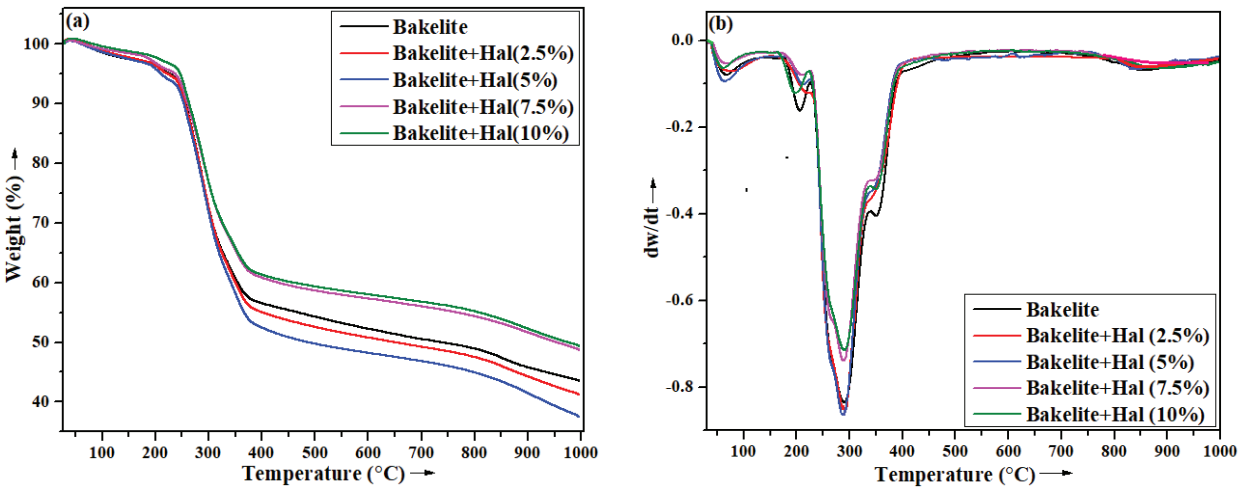


Figure 1. (a) TGA, (b) DTG of bakelite and its blends with Hal clay.

of different concentrations (2.5%, 5%, 7.5%, and 10%) of Hal clay at a heating rate of 20 °C/min.

The temperature affects the extent of the pyrolytic cracking reaction, which changes the quantities of condensable gases, non-condensable gases, and char yield. At a lower temperature, long-chain hydrocarbons are formed, but at higher temperatures, these long hydrocarbons undergo C-C bond cracking to form shorter hydrocarbons. Secondary reactions, which lead to the formation of aromatic compounds, are more prominent at elevated temperatures. Catalytic conditions further enhance the conversion rate at lower temperatures than thermal pyrolysis [8]. The Hal clay catalyst enhances the reaction rate of thermal degradation of Bakelite, resulting in a lower activation energy. The presence of the Hal clay catalyst promotes phenolation, transalkylation, and oxidative coupling, which leads to the formation of a broader range of degradation products [41]. The pyrolysis of Bakelite follows free radical-initiated chain scission, whereas catalytic pyrolysis of Bakelite occurs via a carbocation mechanism. Therefore, the presence of the Halloysite clay catalyst changes the product distribution and composition [12]. The larger compounds begin degrading on the outer surface of the catalyst, but with further degradation, the process occurs in the internal pores, influencing product selectivity. Adding 5% Hal clay catalyst promotes bakelite degradation; however, a higher catalyst/polymer ratio leads to more char formation. Therefore, as Hal clay concentration is increased from 5% to 7.5% and 10%, weight loss decreases, resulting in more residue [8]. However, compared to pyrolysis without the catalyst, weight loss increases when the concentration of Hal clay is decreased from 5% to 2.5%, although it stays lower than when the concentration of Hal clay is 5%. This could be due to an inadequate amount of catalyst for effective degradation. Table 3 shows the initial temperature (T_i), peak temperature (T_m), final temperature (T_f), and percentage weight loss (W) at different stages from Figure 1.

According to Table 3, bakelite loses 56.95% of its total weight when heated at a heating rate of 20°C per minute. When blended with Hal clay at concentrations of 2.5%, 5%, 7.5%, and 10% wt/wt, the weight losses change to 58.9%, 62.57%, 51.45%, and 50.71%, respectively. The 5% concentration proves to be the most effective, leading to the highest weight loss. At a heating rate of 20°C/min, the thermal degradation of discarded bakelite and its blend with Hal clay of varying concentrations takes place in four stages over a temperature range of 30 to 1,000°C, both with and without the Hal clay catalyst. The addition of a 5% Hal clay catalyst accelerates all stages of thermal degradation of Bakelite. Bakelite loses 3.01% in the first stage (30–185°C), while Bakelite with 5% Hal catalyst loses 3.38% in the first stage (30–186°C), mainly due to the loss of adsorbed water and volatile substances. Bakelite loses 2.49% in the second stage (185–231°C), while Bakelite with 5% Hal catalyst loses 2.77% in the second stage (186–230°C), primarily due to phenol derivatives, heavier aromatic species, and water

Table 3. Thermal weight loss profile of bakelite with halloysite clay at different concentrations as a catalyst at various stages

Sample	First stage				Second stage				Third stage				Four stage				Total weight loss (%)
	Ti	Tm	Tf	W	Ti	Tm	Tf	W	Ti	Tm	Tf	W	Ti	Tm	Tf	W	
Bakelite	30	65	185	3.01	185	212	231	2.49	231	290	392	37.70	392	852	1000	13.75	56.95
Bakelite + Hal (2.5%)	30	77	184	2.88	184	220	232	2.60	232	290	395	40.16	395	854	1000	13.26	58.90
Bakelite + Hal (5%)	30	64	186	3.38	186	215	230	2.77	230	289	391	40.89	391	845	1000	15.53	62.57
Bakelite + Hal (7.5%)	30	67	180	2.09	180	214	227	2.31	227	289	390	34.35	390	875	1000	12.70	51.45
Bakelite + Hal (10%)	30	62	172	1.60	172	198	226	1.74	226	289	393	35.12	393	878	1000	12.25	50.71

released during degradation and cross-linking. Bakelite loses 37.70% in the third stage (231–392°C), while Bakelite with 5% Hal catalyst loses 40.89% in the second stage (230–391°C), mainly due to the release of volatiles, water, and unreacted oligomers. Bakelite loses 13.75% in the fourth stage (392–1000°C), while Bakelite with 5% Hal catalyst loses 15.53% in the second stage (391–1000°C), mainly due to the release of volatiles, water, and unreacted oligomers. The weight loss in this stage is primarily due to the release of CO, CO_2, CH_4, methanol, Tar, aromatic hydrogen, benzene, toluene, xylene, phenol, 2,6-xylenol, 2,4-xylenol, and 2,4,6-Trimethylphenol, naphthalene, biphenyl, dibenzofurans, fluorene, phenanthrene, and anthracene. The residue obtained at the end of the thermal degradation process is a mixture of char and major fillers, including SiO_2, Al_2O_3, BaO, CaO, and ZnO [32].

There is no consistent trend in the variation of peak temperature with the addition of different concentrations of Hal clay catalyst to bakelite. Figure 1(b) confirms that the addition of 5% Hal clay results in a decrease in peak temperatures in the first stage (65–64°C), third stage (289–290°C), and fourth stage (852–845°C), while the second stage shows a slight growth in peak temperature from 212°C to 215°C.

Kinetic Analysis Through Model Fitting

Kinetic graphs for the thermal degradation of bakelite, and its blend with Hal clay at 2.5%, 5%, 7.5%, and 10% wt/wt concentrations, were produced using non-isothermal thermogravimetric data and the Coats-Redfern model equations. The kinetic graphs are shown in Figure 2 at a heating rate of 20°C/min.

The activation energy and Arrhenius factor for the thermal degradation of bakelite in the absence and presence of Hal clay catalyst at several concentrations (2.5, 5, 7.5, and 10% wt/wt) are calculated by slope and Y-intercept of kinetic graphs, respectively. Table 4 shows the values of activation energy, Arrhenius factor, and regression factor for several order-based reaction models. The different values of f(α) for various order-based models result in variations in both the slope and the Y-intercept of the kinetic plots. This is because each reaction order model assumes a distinct relationship between conversion (α) and time or temperature, leading to different mathematical expressions f(α). Therefore, the activation energy and Arrhenius factor were calculated from the slope and Y-intercept of these plots and vary depending on the order of the reaction being modeled. The variation of activation energy and Arrhenius factor values proves the need to select the appropriate reaction order for accurately analyzing the thermal degradation kinetics. The best-fit kinetic model provides more reliable kinetic parameters and improves understanding of the degradation mechanisms. The results of activation energy, pre-exponential factor, and correlation coefficient for the thermal degradation of Bakelite in the absence and presence of Hal clay catalyst at different concentrations (2.5, 5, 7.5, and 10 wt%) are listed in Table 4.

Using a variety of kinetic models, including model fitting and model-free (KAS, FWO, STR, FRM, LTA, VYZ, and Kissinger), the non-isothermal degradation of bakelite was investigated in a previous study at heating rates of 5, 10, 20, 30, and 50°C/min in a nitrogen atmosphere. It was discovered to follow an F_5 order-based mechanism with an activation energy of 213 kJ/mol and an Arrhenius factor of 4×10^{16} min.$^{-1}$ [32]. To elaborate, the present study examines how the Coats-Refern method and varying concentrations of Hal clay catalyst affect the kinetic triplets (activation energy, Arrhenius factor, and mechanism) of the thermal degradation of bakelite. From Table 4, it is seen that the value of Ea generally increases with the reaction order for all samples [26]. The pre-exponential factor (A) also rises exponentially with the reaction order, indicating increased reaction complexity at higher orders [31]. Additionally, the R^2 values, which indicate the goodness of fit for the kinetic models, generally increase up to the 1.5th order and then decrease with increasing reaction order, reflecting a decline in model accuracy at higher orders. The value of R^2 for all samples is maximum at the 1.5th order as compared to the other orders. Therefore, the thermal degradation of bakelite with Hal clay catalyst or without Hal clay catalyst of different concentrations follows a 1.5th order mechanism. However, the thermal degradation characteristics of bakelite change with Hal clay concentration, affecting activation energy and Arrhenius factor. The activation energy and Arrhenius factor for the thermal degradation of Bakelite are 81.088 kJ/mol and 4.39×10^{12} min^{-1}, respectively. With 2.5% Hal clay, the activation energy is 79.524 kJ/mol, and the Arrhenius factor is 3.01×10^{12} min^{-1}. With 5% Hal clay, these values are 77.883 kJ/mol and 2.08×10^{12} min^{-1}, respectively. At 7.5% Hal clay, activation energy is 78.471 kJ/mol, and the Arrhenius factor is 2.41×10^{12} min^{-1}. The activation energy increases to 81.732 kJ/mol and the Arrhenius factor to 4.74×10^{12} min^{-1} for the thermal degradation of Bakelite using 10% Hal clay. So, the optimized catalyst for the thermal degradation of Bakelite is 5% Hal clay.

Thermodynamic Parameters

The evaluation of thermodynamic parameters helps determine the energy analysis and feasibility of the pyrolytic process [42]. During forming the activated complex, higher free energy means the reaction is less favorable. Negative change in free energy indicates the reaction is spontaneous, while positive change in free energy indicates it is non-spontaneous and requires extra energy [37]. The enthalpy is the energy required to increase the temperature of a feedstock for pyrolysis until it converts into a product [42]. The positive change in enthalpy confirms an endothermic reaction requiring energy, while a negative change confirms an exothermic reaction that releases energy [37]. The change in free energy shows the amount of heat energy necessary to convert various products, whereas the change

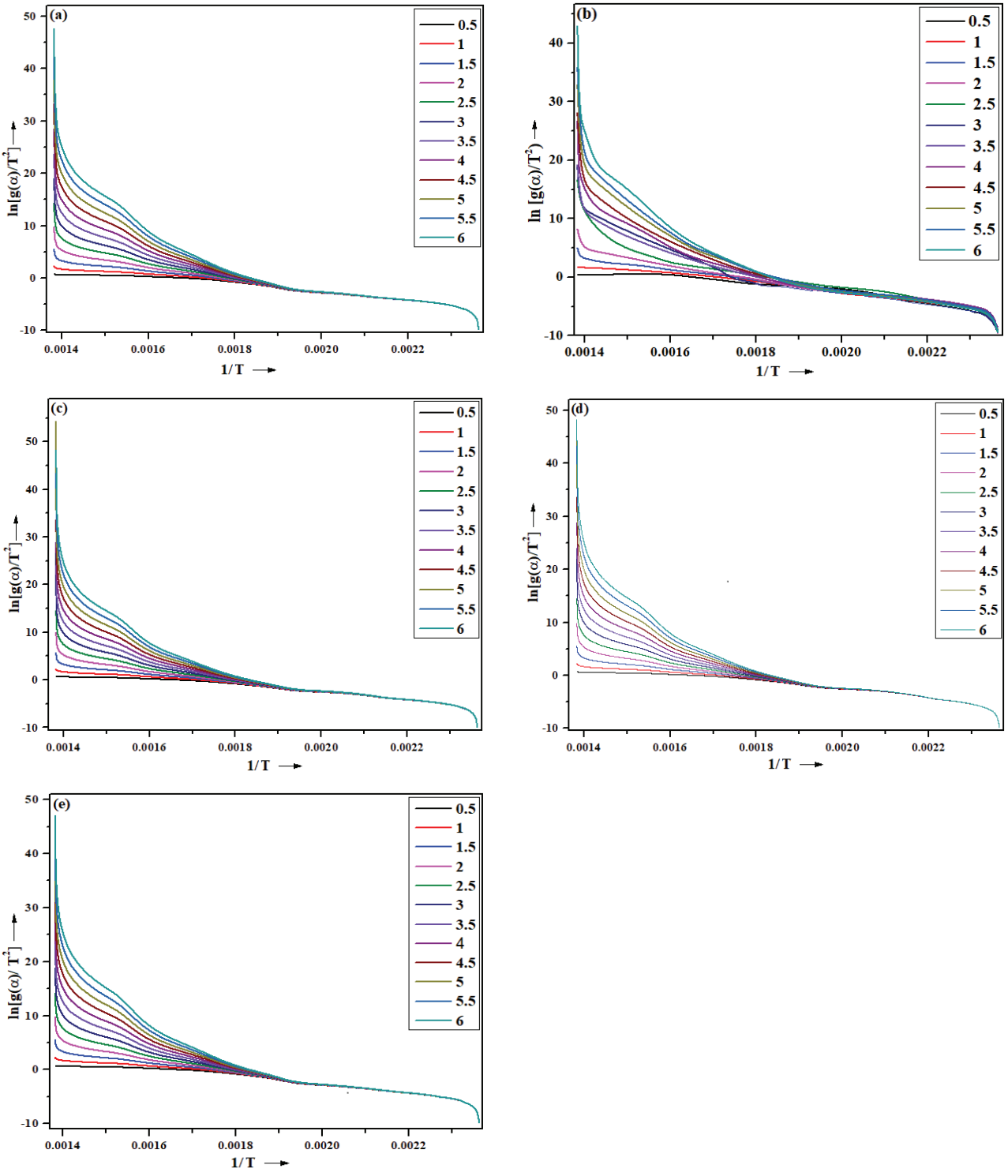


Figure 2. Kinetic plot for pyrolysis of (a) bakelite, (b) bakelite-Hal (2.5%) (c) bakelite-Hal (5%) (d) bakelite-Hal (7.5%), and (e) bakelite-Hal (10%).

in enthalpy value represents the overall energy absorbed by the feedstocks [31]. The entropy change that occurs during thermochemical conversion or combustion defines the thermodynamic complex. A positive change in entropy means the feedstock is more reactive and forms an activated complex faster. In contrast, a negative change indicates the reaction reaches equilibrium quickly and forms a more ordered complex [42]. The values of ΔS, ΔH, and ΔG for bakelite and its mixes with Hal clay at various concentrations (2.5%, 5%, 7.5%, and 10% wt/wt) were computed

Table 4. Outcomes of kinetics analysis of bakelite, and its blends

Order	Bakelite			Bakelite + Hal (2.5%)		
	Ea	A	R2	Ea	A	R2
0.5	58.362	1.08×10^{10}	0.940	59.077	1.20×10^{10}	0.907
1	67.833	1.36×10^{11}	0.974	67.254	1.16×10^{11}	0.977
1.5	81.088	4.39×10^{12}	0.990	79.524	3.01×10^{12}	0.990
2	97.398	3.02×10^{14}	0.979	94.955	1.71×10^{14}	0.977
2.5	115.602	3.26×10^{16}	0.954	124.578	4.68×10^{17}	0.909
3	134.939	4.61×10^{18}	0.928	147.163	1.11×10^{20}	0.909
3.5	154.991	7.66×10^{20}	0.905	168.590	8.58×10^{21}	0.877
4	175.523	1.42×10^{23}	0.885	169.852	4.24×10^{22}	0.874
4.5	196.398	2.83×10^{25}	0.869	188.649	4.71×10^{24}	0.871
5	217.528	5.96×10^{27}	0.855	212.735	2.08×10^{27}	0.860
5.5	238.855	1.31×10^{30}	0.844	226.227	7.09×10^{28}	0.841
6	260.337	2.97×10^{32}	0.835	252.738	4.18×10^{31}	0.834
Order	**Bakelite + Hal (5%)**			**Bakelite + Hal (7.5%)**			**Bakelite + Hal (10%)**		
	Ea	**A**	**R2**	**Ea**	**A**	**R2**	**Ea**	**A**	**R2**
0.5	56.360	$7.02\times1^{0}9$	0.941	56.727	7.66×10^{9}	0.935	59.347	1.30×10^{10}	0.942
1	65.378	7.78×10^{10}	0.976	65.816	8.67×10^{10}	0.972	68.682	1.56×10^{11}	0.976
1.5	77.883	2.08×10^{12}	0.990	78.471	2.41×10^{12}	0.988	81.732	4.74×10^{12}	0.990
2	93.219	1.11×10^{14}	0.975	94.003	1.35×10^{14}	0.975	97.777	3.02×10^{14}	0.977
2.5	110.332	9.12×10^{15}	0.947	111.335	1.18×10^{16}	0.948	115.672	3.00×10^{16}	0.950
3	128.647	9.92×10^{17}	0.915	130.024	1.41×10^{18}	0.915	134.677	3.86×10^{18}	0.922
3.5	147.414	1.19×10^{20}	0.892	148.874	1.73×10^{20}	0.893	154.385	5.83×10^{20}	0.897
4	166.770	1.63×10^{22}	0.870	168.462	2.51×10^{22}	0.872	174.567	9.79×10^{22}	0.876
4.5	186.463	2.41×10^{24}	0.853	188.388	3.93×10^{24}	0.854	195.089	1.77×10^{25}	0.859
5	206.654	3.99×10^{26}	0.835	209.110	7.44×10^{26}	0.835	215.864	3.38×10^{27}	0.844
5.5	226.547	6.11×10^{28}	0.826	228.938	1.12×10^{29}	0.828	236.834	6.74×10^{29}	0.832
6	246.842	$1.02\times1^{03}1$	0.816	249.466	2.00×10^{31}	0.818	257.961	1.39×10^{32}	0.822

using equations 19-21 at a heating rate of 20°C/min. The results of thermodynamic parameters are shown in Table 5.

From Table 5, it is seen that the value of ΔS and ΔH increase, but ΔG decreases as order increases. The non-spontaneity of the reactions across all temperatures is demonstrated by positive ΔG and ΔH values and a negative ΔS [32]. Therefore, the 0.5th, 1st order, 1.5th, and 2nd order based thermal degradation reaction of bakelite and its blends with different concentrations (2.5, 5, 7.5, and 10 %wt/wt) show a non-spontaneous reaction, while others are not. The thermal degradation reactions, which all have a positive ΔH, are endothermic, and this is consistent across reactions of all orders. The thermal degradation reactions of bakelite and its blends (2.5%, 5%, 7.5%, and 10% wt/wt) for 0.5th, 1st, 1.5th, and 2nd orders show a negative entropy change, indicating the formation of a more ordered system. These reactions reach equilibrium quickly and form a stable complex. In contrast, reactions of other orders are more reactive, forming the activated complex faster and resulting in a less ordered system. For the 1.5th order-based thermal degradation, bakelite shows ΔS, ΔH, and ΔG values of -0.050 $kJK^{-1}mol^{-1}$, 76.415 kJ/mol, and 104.803 kJ/mol, respectively, while for bakelite blended with Hal clay, the values are -0.054 $kJK^{-1}mol^{-1}$, 74.844 kJ/mol, and 105.050 kJ/mol for 2.5% Hal clay; -0.057 $kJK^{-1}mol^{-1}$, 73.210 kJ/mol, and 105.095 kJ/mol for 5% Hal clay; -0.055 $kJK^{-1}mol^{-1}$, 73.873 kJ/mol, and 104.492 kJ/mol for 7.5% Hal clay; and -0.050 $kJK^{-1}mol^{-1}$, 77.059 kJ/mol, and 105.088 kJ/mol for 10% Hal clay, respectively. Among the others, the 5% Hal clay catalyst blend for bakelite's 1.5th order-based thermal degradation offers the benefit of the lowest entropy and enthalpy among the blends, suggesting a more controlled degradation process with less disorder and lower heat absorption. These results are useful to confirm a more stable and efficient thermal degradation process. The change in entropy for the thermal degradation of Bakelite in the presence of Hal clay (5%) is slightly greater, creating more disorder during the process. The lower change in enthalpy leads to more energy-efficient degradation. The

Table 5. Outcomes of thermodynamic parameters of bakelite and its blends

Order	Bakelite			Bakelite +Hal (2.5%)		
	ΔS	ΔH	ΔG	ΔS	ΔH	ΔG
0.5	-0.100	53.681	110.220	-0.099	54.396	110.461
1	-0.079	63.152	107.873	-0.081	62.573	108.009
1.5	-0.050	76.407	104.853	-0.054	74.844	105.050
2	-0.015	92.717	101.365	-0.020	90.274	101.589
2.5	0.024	110.921	97.638	0.046	119.897	94.153
3	0.065	130.258	93.804	0.127	163.909	92.215
3.5	0.107	150.310	89.922	0.091	142.482	91.168
4	0.151	170.842	86.018	0.141	165.172	85.997
4.5	0.195	191.717	82.106	0.180	183.969	82.754
5	0.239	212.847	78.193	0.230	208.054	78.332
5.5	0.284	234.174	74.280	0.260	221.546	75.301
6	0.329	255.656	70.370	0.313	248.057	71.955

Order	Bakelite +Hal (5%)			Bakelite +Hal (7.5%)			Bakelite +Hal (10%)		
	ΔS	ΔH	ΔG	ΔS	ΔH	ΔG	ΔS	ΔH	ΔG
0.5	-0.104	51.697	110.165	-0.103	52.054	110.112	-0.099	54.674	110.264
1	-0.084	60.706	107.935	-0.083	61.144	107.864	-0.078	64.010	107.999
1.5	-0.057	73.210	105.095	-0.055	73.798	104.992	-0.050	77.059	105.088
2	-0.024	88.546	101.830	-0.022	89.331	101.689	-0.015	93.104	101.725
2.5	0.013	105.660	98.351	0.015	106.662	98.167	0.023	111.001	98.136
3	0.052	123.975	94.757	0.055	125.352	94.507	0.063	130.005	94.443
3.5	0.092	142.741	91.154	0.095	144.201	90.882	0.105	149.712	90.705
4	0.133	162.098	87.515	0.136	163.790	87.199	0.148	169.895	86.947
4.5	0.174	181.791	83.870	0.178	183.715	83.510	0.191	190.416	83.181
5	0.217	201.981	80.191	0.222	204.448	79.745	0.235	211.191	79.413
5.5	0.258	221.874	76.579	0.264	224.266	76.130	0.279	232.162	75.647
6	0.301	242.169	72.937	0.307	244.793	72.444	0.323	253.288	71.883

*ΔS = $kJK^{-1}mol^{-1}$, ΔH = kJ/mol, ΔG = kJ/mol

greater change in Gibbs free energy makes the process less spontaneous than pure Bakelite.

Batch Pyrolysis Outcomes and Oil Characterization

The conditions of the process and the type of plastic significantly affect the yields and compositions of the final products [43]. Catalysts also influence product distribution by promoting further cracking of initial fragments into smaller hydrocarbons at their active sites [13]. In the batch pyrolysis of bakelite and its Hal clay-catalyzed variant at 450°C, products such as waxy oil, pure wax, residue, and non-condensable gas were classified. Figures 3 (a) and (b) present the yield versus products and feedstock type versus reaction time, respectively.

Figure 3a shows that the yields of waxy oil, pure wax, gas, and residue during batch pyrolysis of bakelite are 11.73%, 27.39%, 30.52%, and 30.36%, respectively, while during Hal clay (5%) catalyzed pyrolysis, the yields are 16.42%, 24.83%, 29.24%, and 29.24%, respectively. Cai et al. found that using a clay catalyst notably enhances the production of liquid products while decreasing the yields of wax and gas. Additionally, the catalyst effectively inhibits the further conversion of liquid oil into gas [12]. Pyrolysis causes the development of solid residue (char) through condensation. A catalyst increases the ash concentration and H/C ratio of the char without changing its elemental composition. Nevertheless, the buildup of char on the catalyst can lower its active sites, thereby diminishing catalytic performance. The catalyst also enhances the quality and amount of the resultant liquid oil [8]. Viscous and waxy products result from inadequate cracking of plastics into high molecular weight hydrocarbons. Therefore, waxy oil forms rather than pure oil, and pure wax is produced in larger quantities than waxy oil. Catalysts promote polymer cracking by providing a solid surface for the reaction to occur [44]. The external surface of a catalyst is where primary plastic cracking

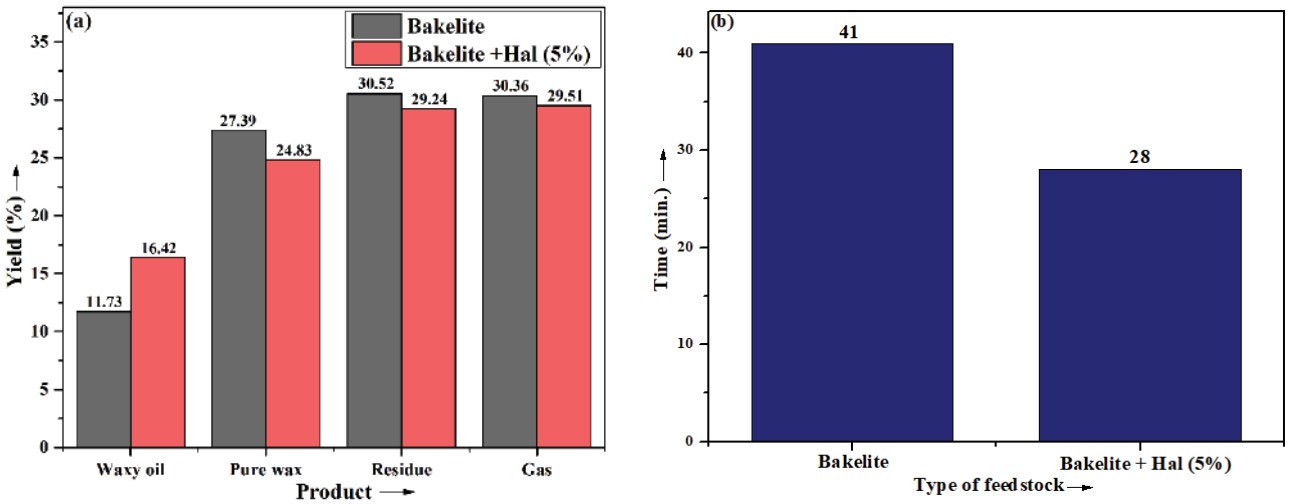


Figure 3. (a) Product versus Yield (b) Types of feedstocks versus Reaction time.

occurs, with subsequent cracking happening inside the pores of the catalyst. So, the surface area and pore volume of the Halloysite clay catalyst have a significant impact on the thermal conversion process, such as pyrolysis. The more the surface area and pore volume, the more the production of gaseous products, and the lower the liquid amount [13]. The thermal degradation of bakelite using Hal clay, which has a smaller surface area and pore volume, produces lower gas and larger liquid yields. Therefore, introducing 5% Hal clay in the pyrolysis of bakelite lowers the formation of pure wax and gas, while enhancing pure oil yields and reducing residue. Figure 3b shows a reduction in the reaction time for bakelite pyrolysis from 41 minutes to 28 minutes with the addition of Hal clay catalyst, as the catalyst accelerates the cracking reactions [8].

The chemical composition of the oils is determined by FTIR and GC-MS analysis. The outcomes of the FTIR analysis for bakelite pyrolysis oils, in the presence and absence of Hal clay, are presented in Figure 4. The FTIR results of the pyrolytic oils have similar functional groups, which confirms that both pyrolytic oils have nearly the same chemical composition. Peaks located at 1015, 1050, and 1106 cm^{-1} suggest the presence of C-C stretching in alkanes. At 2871 and 2968 cm^{-1}, peaks signify the asymmetrical and symmetrical stretching of methyl C-H in alkanes, while the 1453 cm^{-1} peak denotes the bending of both methyl and methylene C-H. The C-H stretching of cycloalkanes is noted at 2968 cm^{-1}. A characteristic peak for C=C stretching in alkenes appears at 1607 cm^{-1}. A peak at 1050 cm^{-1} identifies C-O stretching in alcohols. The two peaks appear at 3209 and 3338 cm^{-1} related to O-H stretching. The peak obtained at 1393 cm^{-1} shows both O-H and C-O bending. The C-O stretch at 1106 cm^{-1} signifies the presence of ether. The peak obtained at 1539 cm^{-1} C=C stretching of aromatic hydrocarbons. The peak obtained at 3665 cm^{-1} indicates O-H stretching of alcohol. The typical peaks at 3549 cm^{-1} and 1393 cm^{-1}, respectively, correspond to O–H and C–O stretching in phenols found in the pyrolytic oil obtained from Bakelite in the presence of the Hal clay (5%) catalyst [45]. These results confirm that both oils have quite similar chemical composition, except for the presence of phenolic content in the pyrolysis oil obtained from Bakelite in the presence of Halloysite clay catalyst. The presence of Phenol as a major compound in the pyrolytic oil is also supported by Bennett and Payne [16]. Wong et al. also reported that phenol derivatives are formed during the batch pyrolysis of resole-type phenol-formaldehyde resin at 500-850K [18]. Xu et al. showed that at 650°C and 5% calcium hydroxide, the pyrolysis of PF produced 82.8% phenols [19]. The FTIR analysis confirmed the presence of alkanes, cycloalkanes, alkenes, alcohols, ethers, and aromatic compounds, and the results are also supported by GC-MS analysis.

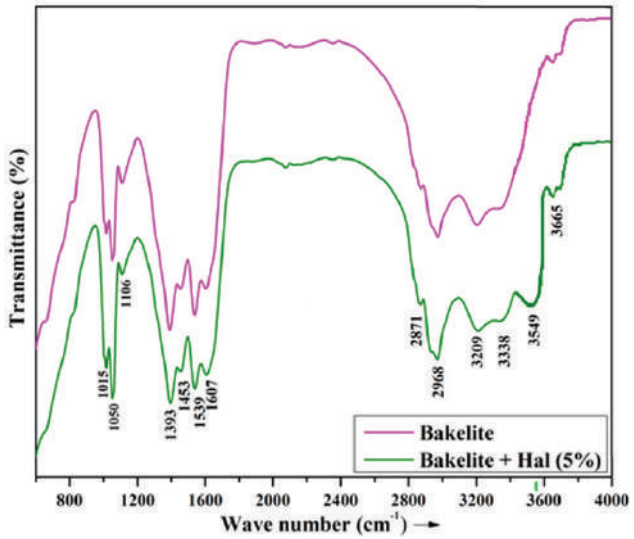


Figure 4. FTIR curve of pyrolytic oils.

The previous work [46] reported that the pyrolytic oil from Bakelite contained compound-like alkane, cycloalkane, alkene, cycloalkene, oxygenated compounds like ester, ketone, alcohol, ether, alcohol, ether, and aromatic compounds. In this work, the oil obtained from Bakelite in the presence of 5% Hal clay catalyst confirms the presence of alkanes, cycloalkanes, alkenes, cycloalkenes, aromatic hydrocarbons, and oxygenated compounds. Wong et al. support the formation of aromatic compounds between 700 and 850 K, while C_2–C_4 hydrocarbons peaked at 1000 K [18]. Xu et al. showed that pyrolyzing PF at 650°C and 5% calcium hydroxide produced 9.1% aromatic hydrocarbons [19]. Table 6 lists different types of compounds present in the pyrolytic oils obtained from the Bakelite in the absence and presence of Halloysite clay (5%).

Research by Ates et al. confirms that catalysts efficiently convert long-chain aliphatic compounds to aromatic ones [47]. Syamsiroa et al., on the other hand, reported that while thermal pyrolysis yields compounds with carbon chains ranging from C_5 to C_{28}, catalysts lead to a higher proportion of lighter oil fractions (C_5-C_{12}) [48]. The GC-MS results (Table 6) show that the presence of Hal clay promotes the production of hydrocarbons, including alkanes, alkenes, cycloalkenes, and aromatic compounds, while reducing the formation of cycloalkane and oxygenated compounds. This shift towards hydrocarbon-rich products results in a more liquid, oil-like consistency, as these hydrocarbons are typically found in the oil fraction of pyrolysis products. On the other hand, the reduction in oxygenated compounds, which often contribute to the formation of solid or

Table 6. GC-MS results of bakelite and bakelite-Hal clay (5%) pyrolysis oils

Compound	Formula	Area (%)	
		Bakelite	Bakelite + Hal (5%)
(i) Alkane		**11.92**	**12.11**
2,3,5-trimethyl hexane	C_9H_{20}	0.20	0.55
3-Ethyl-3-methyl heptane	$C_{10}H_{22}$	0.46	0.85
2,2-Dimethylnonane	$C_{11}H_{24}$	-----	0.78
2,3-Dimethylnonane	$C_{11}H_{24}$	-----	0.81
3,7-dimethyl decane	$C_{12}H_{26}$	0.10	0.25
3-Ethylundecane	$C_{12}H_{26}$	-----	3.15
5-Butyl nonane	$C_{13}H_{28}$	3.40	-----
Tridecane	$C_{13}H_{28}$	-----	0.97
5,5-Diethylpentadecane	$C_{19}H_{40}$	0.82	-----
2-Methylnonadecane	$C_{20}H_{42}$	-----	2.80
2,3-Dimethylnonadecane	$C_{21}H_{44}$	-----	1.95
2,6,10,14,18-Pentamethyl nonadecane	$C_{24}H_{50}$	2.90	-----
Tetracosane	$C_{24}H_{50}$	1.01	-----
11-Methyltricosane	$C_{24}H_{50}$	0.97	-----
2-Methylhentriacontane	$C_{32}H_{66}$	2.06	-----
(ii) Cycloalkane		**2.13**	**1.85**
1,2-Dimethylcyclohexane	$C_{10}H_{18}$	-----	1.30
1,2,3-Trimethylcyclododecane	$C_{12}H_{24}$	-----	0.40
ϒ-Elemene	$C_{15}H_{24}$	1.01	0.15
1,3,5-Triphenyl cyclohexane	$C_{24}H_{24}$	1.12	-----
(iii) Alkene		**7.65**	**7.82**
1,4-Nonadiene	C_9H_{14}	-----	0.45
2,3-Nonadiene	C_9H_{14}	-----	2.50
2,5,6-Trimethyl-1,3,6-heptatriene	$C_{10}H_{16}$	1.30	1.42
2,5-Dimethyl-3-methylene-1,5-heptadiene	$C_{10}H_{16}$	0.62	0.75
2,6-Dimethyl-1,6-octadiene	$C_{10}H_{18}$	2.42	-----
2,3,6-Trimethyl-1,5-heptadiene	$C_{10}H_{18}$	1.36	1.40
2,6-Dimethyl-2,6-octadiene	$C_{10}H_{18}$	0.89	-----
1,3-Undecadiene	$C_{11}H_{20}$	-----	0.95

Table 6. GC-MS results of bakelite and bakelite-Hal clay (5%) pyrolysis oils (continued)

Compound	Formula	Area (%)	
		Bakelite	**Bakelite + Hal (5%)**
1,3-Tridecadiene	$C_{13}H_{24}$	-----	0.35
3-Octadecene	$C_{18}H_{36}$	0.50	-----
Squalene	$C_{30}H_{50}$	0.56	-----
(iv) Cycloalkene		**54.26**	**54.64**
Bicyclo [4.2.0] octa-1,3,5-triene	C_8H_8	6.30	6.51
2,4-Cyclooctadiene	C_8H_{12}	-----	1.23
1,5-Cyclooctadiene	C_8H_{12}	-----	2.50
2,5-Cyclononadiene	C_9H_{12}	-----	1.29
1,3-Cyclononadiene	C_9H_{12}	-----	1.32
D-Limonene	$C_{10}H_{16}$	47.84	41.79
1-Methyl-4-(1-methylethyl) 1,3-cyclohexadiene	$C_{10}H_{16}$	0.12	-----
(v) Aromatic hydrocarbon		**14.74**	**16.76**
Toluene	C_7H_8	1.92	2.1
o-Xylene	C_8H_{10}	-----	2.85
1,2-Dimethylbenzene	C_8H_{10}	-----	2.85
p-Xylene	C_8H_{10}	1.75	1.99
1,3-Dimethylbenzene	C_8H_{10}	-----	1.34
Ethylbenzene	C_8H_{10}	2.83	3.01
α-Methyl Styrene	C_9H_{10}	2.75	-----
Mesitylene	C_9H_{12}	0.84	-----
Propyl benzene	C_9H_{12}	0.80	0.95
Benzene, 1,2,4-trimethyl	C_9H_{12}	-----	0.62
1-Methyl-4-(1-methylethenyl) benzene	$C_{10}H_{12}$	0.91	-----
p-Cymene	$C_{10}H_{14}$	2.51	-----
Biphenyl	$C_{12}H_{10}$	-----	1.05
1,2,3-Trimethylindene	$C_{12}H_{14}$	0.43	-----
(vi) Oxygenate compound		**9.30**	**6.82**
Phenol	C_6H_6O	-----	1.15
2-Methyl phenol	C_7H_8O	-----	1.02
p-Cresol	C_7H_8O	-----	0.55
Benzofuran	C_8H_6O	-----	0.62
2,4-Dimethyl phenol	$C_8H_{10}O$	-----	1.15
1,9-Nonanediol	$C_9H_{20}O_2$	1.00	0.22
Dibenzofuran	$C_{12}H_8O$	-----	0.35
1-Acetoxymethyl-3-isopropenyl-2-methyl cyclopentane	$C_{12}H_{20}O_2$	0.49	0.68
3-(1-Methylhept-1-enyl)-5-methyl-2,5-dihydrofuran-2-one	$C_{13}H_{20}O_2$	0.36	0.15
11-Methyldodecanol	$C_{13}H_{28}O$	0.30	0.11
2-Benzyl-p-cresol	$C_{14}H_{14}O$	-----	0.38
Valeric acid, 2,7-dimethyl oct-7-en-5-yn-4-yl ester	$C_{15}H_{24}O_2$	1.24	-----
2-Ethyl-2-methyl-tri decanol	$C_{16}H_{34}O$	0.53	-----
5,9,13-Trimethyl-4,8,12-tetradecatrien-1-ol	$C_{17}H_{30}O$	0.69	0.32
Methyl palmitate	$C_{17}H_{34}O_2$	1.50	-----
6,9-Octadecadiynoic acid, methyl ester	$C_{19}H_{30}O_2$	0.23	0.12
3-Tridecanoyl cyclo hexen-4-ol-1-one	$C_{19}H_{32}O_3$	1.01	-----
11,14-Eicosadienoic acid, methyl ester	$C_{21}H_{38}O_2$	0.58	-----
Methyl 13,16-docosadienoate	$C_{23}H_{42}O_2$	0.50	-----
1,3-Propanediol, docosyl ethyl ether	$C_{27}H_{56}O_2$	0.87	-----

semi-solid residues like wax, leads to a decrease in the wax content. These results also suggest that Hal clay acts as a catalyst, enhancing the conversion of bakelite into lighter, more volatile hydrocarbon molecules that remain in the oil phase, thereby producing a higher yield of pure oil and a lower yield of wax.

CONCLUSION

This study explores the catalytic pyrolysis of bakelite with varying concentrations of Halloysite clay, demonstrating its significant impact on enhancing pyrolysis kinetics, thermodynamic parameters, product yields, and selectivity toward valuable chemical compounds. The maximum weight loss (62.57%) of bakelite takes place due to the addition of 5 wt/wt % halloysite clay. The degradation process of bakelite using 5 wt/wt % halloysite clay is characterized by a 1.5th order mechanism, with an activation energy of 77.883 kJ/mol and an Arrhenius factor of 2.08×10^{12} min^{-1}. The change in entropy, change in enthalpy, and change in energy values for 1.5th order based thermal degradation of blended bakelite with halloysite clay (5%) are -0.057kJ$K^{-1}mol^{-1}$,73.210kJ/mol, and 105.095 kJ/mol, respectively. In the halloysite clay (5%) catalyzed pyrolysis of bakelite, the yields of condensable products (oil + wax), gas, and residue are 41.25%, 29.51%, and 29.24%, respectively. Fourier transform infrared spectroscopy and gas chromatography-mass spectrometry analysis confirmed that the pyrolysis oil from bakelite with a 5% halloysite clay blend contains alkanes, cycloalkanes, alkenes, alcohols, ethers, phenols, and aromatic chemicals. These results signify the impact of Halloysite clay during the catalytic pyrolysis of Bakelite on reducing activation energy and enhancing yields and quality of valuable products. This study shows that using Halloysite clay in the catalytic pyrolysis of Bakelite improves the kinetics, product yields, and chemical composition for sustainable and scalable industrial applications.

ACKNOWLEDGEMENTS

We express our acknowledgement to TEQIP-III, VSSUT, Burla, for allowing us to use the instrumental facilities available for this research work.

AUTHORSHIP CONTRIBUTIONS

Authors equally contributed to this work.

DATA AVAILABILITY STATEMENT

The authors confirm that the data that supports the findings of this study are available within the article. Raw data that support the finding of this study are available from the corresponding author, upon reasonable request.

CONFLICT OF INTEREST

The author declared no potential conflicts of interest with respect to the research, authorship, and/or publication of this article.

ETHICS

There are no ethical issues with the publication of this manuscript.

STATEMENT ON THE USE OF ARTIFICIAL INTELLIGENCE

Artificial intelligence was not used in the preparation of the article.

REFERENCES

[1] Colak OU, Cakır Y. Genetic algorithm optimization method for parameter estimation in the modeling of storage modulus of thermoplastics. Sigma J Eng Nat Sci 2019;37:981–988.

[2] Cankaya N. Synthesis, characterization, and thermal properties of new oxoethyl acrylate-containing polymer. Sigma J Eng Nat Sci 2020;38:281–288.

[3] Murali K, Sambath K. Transformation of waste bakelite into concrete and solid blocks. IOSR J Mech Civ Eng 2020;17:31–34.

[4] Chakrawarthi RM, Nagaraju TV, Avudaiappan S, Awolusi T, Roco-Videla Á, Azab M, et al. Performance of recycled bakelite plastic waste as eco-friendly aggregate in the concrete beams. Case Stud Constr Mater 2023;18:e02200. [CrossRef]

[5] Bakelite market size. Mordor Intelligence. Available at: https://www.mordorintelligence.com/industry-reports/bakelite-market. Accessed Sep 3, 2024.

[6] Surendranath A, Ramana P. Valorization of bakelite plastic waste aimed at auxiliary comprehensive concrete. Constr Build Mater 2022;325:126851. [CrossRef]

[7] Klun B, Rozman U, Ogrizek M, Kalcikova G. The first plastic produced, but the latest studied in microplastics research. The assessment of leaching, ecotoxicity and bioadhesion of bakelite microplastics. Environ Pollut 2022;307:119454. [CrossRef]

[8] Miandad R, Barakat M, Aburiazaiza AS, Rehan M, Nizami A. Catalytic pyrolysis of plastic waste. A review. Process Saf Environ Prot 2016;102:822–838. [CrossRef]

[9] Dhunna R, Khanna R, Mansuri I, Sahajwalla V. Recycling waste bakelite as an alternative carbon resource for ironmaking applications. ISIJ Int 2014;54:613–619. [CrossRef]

[10] Horikawa T, Ogawa K, Mizuno K, Hayashi J, Muroyama K. Preparation and characterization of the carbonized material of phenol–formaldehyde resin with addition of various organic substances. Carbon 2003;41:465–472. [CrossRef]

[11] Chen H, Zhou M, Wang Z, Zhao S, Guan S. Rich nitrogen-doped ordered mesoporous phenolic resin-based carbon for supercapacitors. Electrochim Acta 2014;148:187–194. [CrossRef]

[12] Cai W, Kumar R, Zheng Y, Zhu Z, Wong JW, Zhao J. Exploring the potential of clay catalysts in catalytic pyrolysis of mixed plastic waste for fuel and energy recovery. Heliyon 2023;9:e23140. [CrossRef]

[13] Kanattukara BV, Singh G, Sarkar P, Chopra A, Singh D, Mondal S, et al, Ramakumar SSV. Catalyst-mediated pyrolysis of waste plastics. Tuning yield, composition, and nature of pyrolysis oil. Environ Sci Pollut Res 2023;30:64994–65010. [CrossRef]

[14] Xu Z, Wang J, Hu Z, Geng R, Gan L. Structure evolutions and high electrochemical performances of carbon aerogels prepared from the pyrolysis of phenolic resin gels containing ZnCl2. Electrochim Acta 2016;231:601–608. [CrossRef]

[15] Wang J, Jiang H, Jiang N. Study on the pyrolysis of phenol-formaldehyde (PF) resin and modified PF resin. Environ Sci Pollut Res 2009;496:136–142. [CrossRef]

[16] Bennett A, Payne D, Court R. Quantitative pyrolytic and elemental analysis of a phenolic resin. 51st AIAA Aerospace Sciences Meeting Including the New Horizons Forum and Aerospace Exposition 2013. 51st AIAA Aerospace Sciences Meeting including the New Horizons Forum and Aerospace Exposition.

[17] Xu L, He Z, Zhang H, Wu S, Dong C, Fang Z. Production of aromatic amines via catalytic co-pyrolysis of lignin and phenol-formaldehyde resins with ammonia over commercial HZSM-5 zeolites. Bioresour Technol 2020;320:124252. [CrossRef]

[18] Wong HW, Peck J, Bonomi RE, Assif J, Panerai F, Reinisch G, Lachaud J, Mansour NN. Quantitative determination of species production from phenol-formaldehyde resin pyrolysis. Polym Degrad Stab 2015;112:122–131. [CrossRef]

[19] Xu L, Zhong Q, Dong Q, Zhang L, Fang Z. Co-production of phenolic oil and CaO/char deoxidation catalyst via catalytic fast pyrolysis of phenol-formaldehyde resin with Ca(OH)2. J Anal Appl Pyrolysis 2019;142:104663. [CrossRef]

[20] Jiang H, Wang J, Wu S, Wang B, Wang Z. Pyrolysis kinetics of phenol–formaldehyde resin by non-isothermal thermogravimetry. Carbon 2009;48:352–358. [CrossRef]

[21] Jiang H, Wang J, Wu S, Yuan Z, Hu Z, Wu R, Liu Q. The pyrolysis mechanism of phenol formaldehyde resin. Polym Degrad Stab 2012;97:1527–1533. [CrossRef]

[22] Parida S, Panda AK. Surface activation of calcium bentonite by acid treatment. Int J Res Chem Environ 2017;54–60.

[23] Sadjadi S. Halloysite nanoclay for the development of heterogeneous catalysts. New York: Elsevier; 2020. p. 275–303. [CrossRef]

[24] Panda AK, Singh RK. Experimental optimization of process for the thermo-catalytic degradation of waste polypropylene to liquid fuel. Adv Energy Eng 2013;1:74–84. [CrossRef]

[25] Li X, Cai Z, Wang X, Zhang Z, Tan D, Xie L, Suna H, Zhong G. The combined effect of absorption and catalysis of halloysite nanotubes during the thermal degradation of PBAT nanocomposites. Appl Clay Sci 2020;196:105762. [CrossRef]

[26] Ganeshan G, Shadangi KP, Mohanty K. Degradation kinetic study of pyrolysis and co-pyrolysis of biomass with polyethylene terephthalate (PET) using Coats–Redfern method. J Therm Anal Calorim 2017;131:1803–1816. [CrossRef]

[27] Arias AMR, Moreno-Pirajan JC, Giraldo L. Kinetic study of waste tire pyrolysis using thermogravimetric analysis. ACS Omega 2022;7:16298–16305. [CrossRef]

[28] Uzun BB, Yaman E. Pyrolysis kinetics of walnut shell and waste polyolefins using thermogravimetric analysis. J Energy Inst 2016;90:825–837. [CrossRef]

[29] Kantarelis E, Yang W, Blasiak W, Forsgren C, Zabaniotou A. Thermochemical treatment of E-waste from small household appliances using highly pre-heated nitrogen. Thermogravimetric investigation and pyrolysis kinetics. Appl Energy 2010;88:922–929. [CrossRef]

[30] Vlaev LT, Markovska I, Lyubchev L. Non-isothermal kinetics of pyrolysis of rice husk. Thermochim Acta 2003;406:1–7. [CrossRef]

[31] Mahapatra PM, Kumar S, Panda AK. Synergy, kinetics, and thermodynamics analysis in the valorization of waste bakelite through co-pyrolysis with HDPE. Cleaner Eng Technol 2023;13:100601. [CrossRef]

[32] Mahapatra PM, Panda AK, Ahmed S, Kumar S. Pyrolysis kinetics and thermodynamics of discarded bakelite. Korean J Chem Eng 2023;40:1380–1388. [CrossRef]

[33] Gebre SH, Sendeku MG, Bahri M. Recent trends in the pyrolysis of non-degradable waste plastics. Chem Open 2021;10:1202–1226. [CrossRef]

[34] Sun J, Wang W, Liu Z, Ma Q, Zhao C, Ma C. Kinetic study of the pyrolysis of waste printed circuit boards subject to conventional and microwave heating. Energies 2012;5:3295–3306. [CrossRef]

[35] Vlaev LT, Nikolova MM, Gospodinov GG. Study on the kinetics of non-isothermal dehydration of alkaline earth metal selenites. Monatshefte Für Chemie Chem Mon 2005;136:1553–1566. [CrossRef]

[36] Coats AW, Redfern JP. Kinetic parameters from thermogravimetric data. Nature 1964;201:68–69. [CrossRef]

[37] Ferfari O, Belaadi A, Bourchak M, Ghernaout D, Ajaj RM, Chai BX. Thermal decomposition of Syagrus romanzoffiana palm fibers. Thermodynamic and kinetic studies using the Coats-Redfern method. Renew Energy 2024;231. [CrossRef]

[38] Mahapatra PM, Panda AK. Co-pyrolytic recycling of bakelite and polymethyl methacrylate. Kinetic, synergistic, and thermodynamic analysis. Chem Select 2024;9. [CrossRef]

[39] Mahapatra PM, Kumar S, Mishra P, Panda AK. Effect of different thermoplastics on the thermal degradation behavior, kinetics, and thermodynamics of discarded bakelite. Environ Sci Pollut Res 2023;31:38788–38800. [CrossRef]

[40] Vyazovkin S, Chrissafis K, Di Lorenzo ML, Koga N, Pijolat M, Roduit B, Sbirrazzuoli N, Sunol JJ. ICTAC kinetics committee recommendations for collecting experimental thermal analysis data for kinetic computations. Thermochim Acta 2014;590:1–23. [CrossRef]

[41] Kasar P, Ahmaruzzaman M. Studies on catalytic co-pyrolysis of bakelite and refineries residual fuel oil using ZSM-5 catalyst to produce lighter fuel oil. J Sci Ind Res Preprint. Available at: https://www.academia.edu/116926541/Studies_on_catalytic_co_pyrolysis_of_bakelite_and_refineries_residual_fuel_oil_using_ZSM_5_catalyst_to_produce_lighter_fuel_oil Accessed on Jan 26, 2025.

[42] Mahapatra PM, Mishra PC, Kumar S, Mishra P, Panda AK. Investigation of synergetic, kinetics, thermodynamics, and batch pyrolysis of polypropylene-bakelite co-pyrolysis. Results Eng 2023;21:101720. [CrossRef]

[43] Colantonio S, Cafiero L, De Angelis D, Ippolito NM, Tuffi R, Ciprioti SV. Thermal and catalytic pyrolysis of a synthetic mixture representative of packaging plastics residue. Front Chem Sci Eng 2019;14:288–303. [CrossRef]

[44] Panda AK, Singh RK. Catalytic performances of kaoline and silica-alumina in the thermal degradation of polypropylene. J Fuel Chem Technol 2011;39:198–202. [CrossRef]

[45] Sharma YR. Elementary organic spectroscopy. Ram Namgar, New Delhi: S Chand Publishing; 2007.

[46] Mahapatra PM, Pradhan D, Kumar S, Panda AK. Isothermal pyrolysis of discarded bakelite. Kinetics analysis and batch pyrolysis studies. Circul Econ 2024;100102. [CrossRef]

[47] Ateş F, Miskolczi N, Borsodi N. Comparision of real waste (MSW and MPW) pyrolysis in batch reactor over different catalysts. Part I: Product yields, gas and pyrolysis oil properties. Bioresour Technol 2013;133:443–454. [CrossRef]

[48] Syamsiro M, Saptoadi H, Norsujianto T, Noviasri P, Cheng S, Alimuddin Z, Yoshikawa K. Fuel oil production from municipal plastic wastes in sequential pyrolysis and catalytic reforming reactors. Energy Proced 2014;47:180–188. [CrossRef]

Sigma Journal of Engineering and Natural Sciences
Web page info: https://sigma.yildiz.edu.tr
DOI: 10.14744/sigma.2025.00000

Research Article

Simultaneous electricity generation and removal of Sars-Cov-2 from wastewater in microbial fuel cells

Sıla ARSLAN[1], Tunç ÇATAL[1,*]

[1]*Department of Molecular Biology and Genetics, Uskudar University, İstanbul, 34662, Türkiye*

ARTICLE INFO

Article history
Received: 02 August 2024
Revised: 03 October 2024
Accepted: 18 November 2024

Keywords:
SARS-CoV-2; Wastewater; Microbial Fuel Cells; S1 Protein; Bioremediation

ABSTRACT

In this study, whether wastewater contaminated with SARS-CoV2 virus can be disinfected using microbial fuel cells was modeled using the S1 anchor protein of the virus. The disinfection potential and simultaneous electricity production of wastewater contaminated with SARS-CoV-2 mixed with wastewater using microbial fuel cells, an innovative technology, were investigated. Bioremediation of SARS-CoV-2 contaminated wastewater was modeled using SARS-CoV-2 surface antigen (S1) and studied in microbial fuel cells at different temperatures (30 °C vs. 25 °C). Our results show that microbial fuel cells gradually reduced the SARS-CoV-2 viral concentration from 213 ng/mL, especially at ambient temperature, and simultaneously achieved a power density of 184.19±21.31 mW/m^2 at a current density of 0.073±0.029 mA/cm^2. The log reduction rates of closed-circuit microbial fuel cells increased steadily from 0.005 to 0.163. In conclusion, microbial fuel cells can be used to simultaneously generate electricity to enable biological treatment of wastewater contaminated by SARS-CoV-2.

Cite this article as: Arslan S, Çatal T. Simultaneous electricity generation and removal of Sars-Cov-2 from wastewater in microbial fuel cells. Sigma J Eng Nat Sci 2026;44(1):252–261.

INTRODUCTION

Due to the world's ever-increasing population and industrialization trend, global water availability and energy consumption have become important topics of discussion. The world population is growing rapidly and is expected to increase by another 21% by 2040. As a result, both the need for clean water and the need for energy are increasing. Fossil fuels are widely used to meet energy needs but are becoming increasingly depleted, so alternative energy sources are needed [1]. Similarly, water scarcity remains a major problem worldwide, and the Earth's freshwater resources may decrease by 40% in the next decade [2]. Since organic waste is a viable energy source, wastewater has become a renewable energy source with minimal environmental impact. Microbial fuel cell (MFC) technology, which has versatile features, is a technology on which intensive research has been carried out in recent years, as it enables the production of electricity from organic waste and contributes to the simultaneous production of clean water [3-5]. In microbial fuel cells, microorganisms called exoelectrogens release electrons and protons while breaking down carbon sources in organic waste materials as substrates [6-7-8]. These released electrons are taken by an anode and transferred to

*Corresponding author.
*E-mail address: tunc.catal@uskudar.edu.tr

This paper was recommended for publication in revised form by Editor-in-Chief Ahmet Selim Dalkilic

Published by Yıldız Technical University Press, İstanbul, Turkey
© Author. This is an open access article under the CC BY-NC license (http://creativecommons.org/licenses/by-nc/4.0/).

the cathode through the external circuit. Protons also reach the cathode through the medium solution and react with electrons in the presence of oxygen to form water. Electrical energy is generated as electrons flow through the external circuit. In addition, the breakdown of organic waste and the formation of water by cathodic reaction allows wastewater treatment. Thanks to these versatile features, microbial fuel cells have the potential to support operating costs by being integrated into wastewater treatment plants. By using microbial fuel cells, which are a clean technology, antibiotics, heavy metals, drug metabolites, or various environmental pollutants mixed into wastewater, the ecosystem can be cleaned [9–11]. As a recent contaminant, the detection and disinfection of SARS-CoV-2 viruses, a significant risk, in wastewater has drawn attention to this issue.

After infection by the SARS-CoV-2 virus [12], which has affected all humanity and emerged with life-threatening effects in recent years, viral proteins in gastrointestinal epithelial biopsy samples and virus detection in stool samples have been reported [13]. The effects of COVID-19 on various patients are still being investigated [14], and using actual data, deterministic COVID-19 models were examined to assess the effects of COVID-19 and dynamic transmission [15]. Viral RNA can be found in the feces of approximately 40% of infected individuals [16]. SARS-CoV-2 can be detected in stool samples for longer periods than the virus can be detected in nasal swab samples [16]. Some studies have reported that SARS-CoV-2 survives longer in the urine of infected individuals than in their feces [17]. Accordingly, the SARS-CoV-2 virus in wastewater was investigated [18]. The first detection of SARS-CoV-2 in wastewater was achieved by qRT-PCR testing, isolating it from municipal wastewater in six different cities in the Netherlands. Viral load in wastewater varies by region. In settlements close to sampling sites, the number of viral genomes detected in wastewater has been reported to increase at the regional level due to COVID-19-related hospitalizations [19]. A study by Škulcová et al. [20] reported that the SARS-CoV-2 virus was detected in hospital wastewater, and the relevant virus was detected in the feces of 40% to 89% of COVID-19 patients. Samples taken over six-day periods from a wastewater plant in Australia resulted in two positive results for the presence of SARS-CoV-2 [21]. Additionally, Guerrero-Esteban et al. [22] state that the detection of S1 protein in rivers and wastewater is possible. The immunosensor detects spike protein at the pg/ml level. Miyani et al. [23] investigated the amount of SARS-CoV-2 with concentrations of 10^4–10^5 genomic copies/L in wastewater. An average of 3.10^6 genome units per liter were detected in SARS-COV-2 samples from various wastewater treatment plants [24]. Wurtzer et al. [24] reported that the concentration of SARS-CoV-2 increased from 5×10^4 copies/L to 3×10^6 genome units per liter in a wastewater treatment plant.

In another wastewater treatment plant, SARS-CoV-2 viral RNA N1 and N2 gene regions are quantified in wastewater solids in water resource recovery facilities [25]. The presence of SARS-CoV-2 in sewers has been identified as an indicator of the potential for the virus to transmit to humans [26]. The Omicron variant was detected in aircraft wastewater [27]. According to a study conducted in 2022, the Omicron variant was found in a wastewater treatment plant [28]. Another study reported an adaptable protocol to monitor SARS-CoV-2 variants in wastewater with high sensitivity and specificity [29]. Various techniques have been proposed to eliminate SARS-CoV-2 from wastewater because it poses a risk to the environment and human health. For example, techniques such as chlorine dioxide, liquid chlorine, sodium hypochlorite, ozone, ultraviolet, and ultrafiltration have been proposed to purify wastewater from SARS-CoV-2 viral load [19]. However, retardation, dispersion, inactivation, and degradation can all have an impact on the destiny of viruses in wastewater. Temperature is the primary factor influencing influencing virus survival [30]. A shorter viral lifespan in the sewage is caused by an increase in the inactivation rate coefficient with temperature [30]. As a disinfection method, microbial fuel cell technology has been proposed to disinfect human urine contaminated with viral load [31]. However, this study is the first in the literature, as there has been no research on SARS-CoV-2 disinfection and simultaneous electricity production using microbial fuel cells. In this regard, this study is novel in that it suggests, for the first time, that SARS-CoV2-contaminated wastewater can be disinfected and electricity generated using MFCs.

This study used the S1 protein, the protein's surface antigen of the SARS-CoV-2 virus, to model wastewater contaminated with SARS-CoV-2. The electrical performances of MFCs were evaluated at different temperatures simultaneously with the biological treatment of modeled polluted wastewater. ELISA testing was used to measure the concentration of SARS-CoV-2 viral proteins during operation in MFCs.

MATERIALS AND METHODS

Materials

Inoculation of microbial fuel cells (MFCs)

The single-chamber MFC was prepared per the research procedure published in a previous report [3]. Plexiglass, a plastic glass material, was utilized to construct the MFC. The plexi cube had a total volume of 12 mL. The anode's plexi cover was entirely closed and designed so it would not come into contact with oxygen. This procedure was carried out to prevent oxygen from leaking into the anode region. Carbon cloth was cut to 7 cm^2 for it to operate as an anode and a cathode. The anode was made of carbon fabric (Cat. no: 14032102, FuelCells, Texas, USA). The cathode material consisted of coarse carbon cloth (Cat. no: CTO32414, FuelCells, Texas, USA) covered with Nafion

(5%, Sigma–Aldrich, 7 mL per mg of Pt/C catalyst) and platinum (Pt) (20 wt% Pt/C Vulcan XC-72, FuelCell Store, USA) [32,33]. A synthetic wastewater consisting of sodium phosphate buffer (100 mM strength at pH 7.4) and sodium acetate trihydrate (20 mM) ($C_2H_3NaO_2.3H_2O$, VWR Chemicals, Product No: 27652.298, Batch: 15D140018, Geldenaaksebaan, Leuven, Belgium) was prepared [34]. Activated sludge was obtained from a local domestic wastewater treatment plant (Pasakoy, Advanced Biological Wastewater Treatment Plant, Istanbul, Türkiye) [35]. The computer-aided data acquisition system (Keithley KickStart Software, Version 1.9.8.21, Tektronix Company, Beaverton, Oregon, USA) recorded voltage data. The KickStart program was designed to collect data every 11 minutes. MFCs (n=2) operated at 37 °C and 25 °C.

Modeling of contaminated wastewater with SARS-CoV-2

SARS-CoV-2 S1 protein (Nepenthe Research Technologies, Ref No: E91011) was used to model the SARS-CoV-2 contaminated wastewater in synthetic wastewater. 23 µL of S1 protein at 1.13 g/mL concentration was kept at -20 °C until use. To detect the wastewater contaminated with SARS-CoV-2, an enzyme-linked immunosorbent assay (ELISA) kit (Nepenthe Research Technologies, 96 tests, Ref No: NE0000211101) research was carried out.

The concentration of S1 protein to be used for SARS-CoV-2 contaminated wastewater modeling was 213 ng/mL [36].

Operation of MFCs

MFCs were operated at 30 °C and 25 °C temperatures using an external resistance of 985Ω in a batch mode. Three and a half hours of operation were completed by sampling 100 µL samples from the reactors at half-hour intervals [31]. All MFCs were examined to monitor the disinfection. The entire operational time was judged to be 40 minutes. Every 10 minutes, 100 µL of the sample was collected. Current (I= V/R) and power (P= I.V.) densities were calculated using voltage (V) data according to Ohm's law and normalized to the electrode surface area at different external resistances (R) [37].

ELISA Application

After the microbial operations were performed, eight different concentrations of S1 standard were prepared by serial dilution technique using the S1 antigen standard solution and blocking solution included in the ELISA kit to determine the concentrations of the samples by creating a standard graph other than the collected samples.
ELISA was performed following the kit protocol (Nepenthe Co., Istanbul). Absorbance was measured at 450 nm with a microplate reader (Thermo Scientific, Multiskan Go, Microplate Spectrophotometer). The GraphPad Prism 7.0.0 program was used to calculate the concentration of absorbance data for each sample. The concentration of each sample was determined using the obtained absorbance values. The log reduction was calculated using the pre-operative and post-operative concentrations. The log reduction formula was used as outlined in the study by Pasternak et al. [31]:

$$LR = Log_{10}.(A/B)$$

A equals the antigen concentration of the sample before the operation, and B equals the antigen concentration of the sample after the procedure.

Calculation of Statistical Data

The t-test p-values were computed using n-Whitney test on the MFCs run using the GraphPad Prism 7.0.0 software. A p-value less than 0.05 indicates that the result iswere determined. In contrast, the t-test reveals whether the findings are substantially different. The time-dependent SARS-CoV-2 concentration and the t-test p-value of the SARS-CoV-2 virus's log reduction rate was determined as a result.

RESULTS AND DISCUSSION

MFC Performances and Effects of SARS-CoV-2 Proteins on Electricity Generation

Only 20 mM sodium acetate as the sole carbon source was inoculated into MFC until stable, and consistent voltage data was obtained (for 134 days). During this period, up to 0.394 V of electricity was produced at 30 °C (Fig. 1A). At ambient temperature (25 °C), the outcome of the produced voltage was tracked. The maximum voltage at 25 °C was 0.3810 V (Fig. 1B) at 985 Ohm external resistance. To assess the current and power density, external resistances with varied Ohm values (1204Ω, 985Ω, 646Ω, 325Ω, and 215Ω) were examined. The maximum power density was 145 mW/m^2 at the current density level of 0.05 mA/cm^2 at 30 °C, where the power density increased when the temperature decreased to 25 °C (210 mW/m^2) (Fig. 2B).

These results indicate that temperature has an effect on voltage generation and power generation in microbial fuel cells. Synthetic wastewater contaminated with SARS-CoV-2 protein was fed to the MFC at 30 °C, and the voltage data was monitored. Under the 30 °C temperature condition, no significant change in voltage production was observed when SARS-CoV-2 protein was introduced into MFCs. Voltage production levels remained at 0.36 V under 30 °C temperature conditions. The maximum voltage produced was 0.36 V. SARS-CoV-2 polluted wastewater modeling at ambient temperature and ambient temperature was performed in the MFC with a 20 mM acetate inoculation solution. However, an instantaneous increase in voltage production was detected when the SARS-CoV-2 viral protein was added to synthetic wastewater at 25 °C (Fig. 3). These findings suggested whether microbial fuel cells could be used as biosensors for the presence of SARS-CoV-2 in wastewaters.

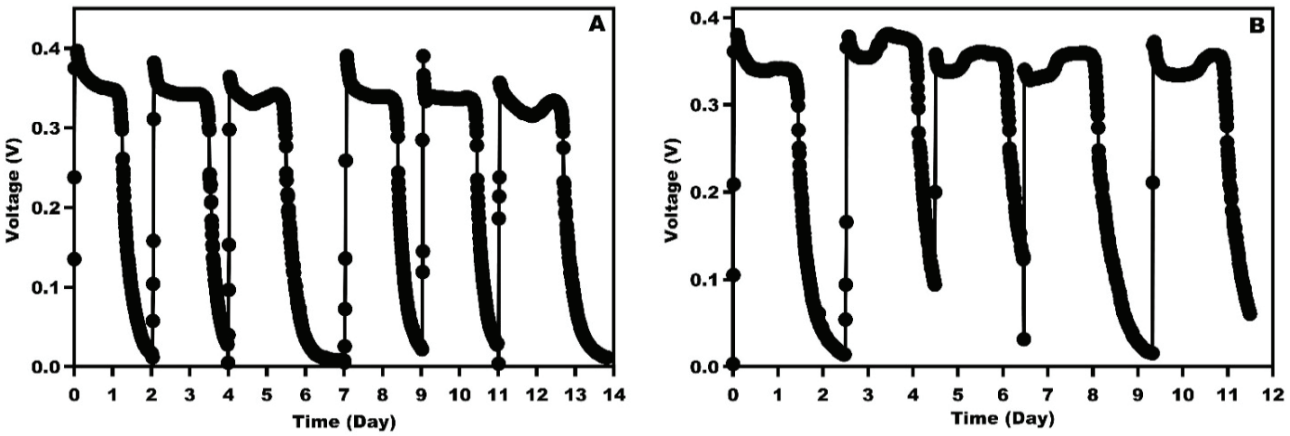


Figure 1. Voltage versus time data of MFC with 985 Ω external resistance at controlled temperature (A), Voltage versus time data of MFC with 985 Ω external resistance at ambient temperature.

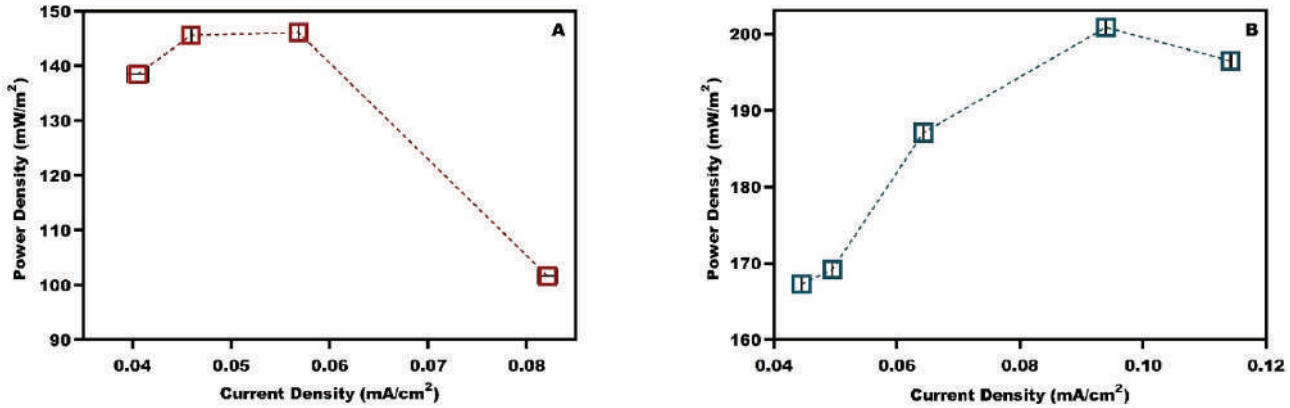


Figure. 2. MFC performances at 30 °C (A), and at 25 °C (B).

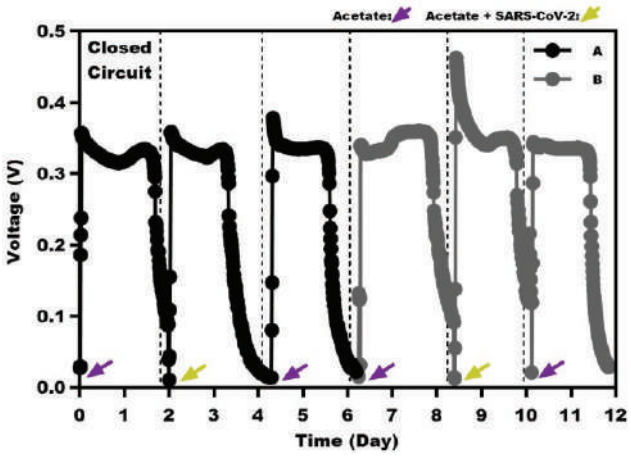


Figure 3. Voltage during the operation plot of SARS-CoV-2 contaminated wastewater modeling at 30 °C temperature (A) and 25 °C (B). Yellow arrow indicates the addition of SARS-CoV-2 S1 protein.

Removal of SARS-CoV-2 Viral Protein in MFCs

Following ELISA, a standard curve was produced based on the absorbance of S1 antigen concentrations at 450 nm (OD_{450}). A total of eight S1 antigen concentrations were used. The created standard curve had an R^2 value of 0.9967. Figure 4 shows the standard curve plot of the S1 antigen.

At 30 minutes, the concentration of SARS-CoV-2 in the MFC decreased to 47 ng/mL. Under the 30 C temperature condition, S1 protein concentration rapidly decreased (47 ng/L). Concentration levels remained at this level for the 210th minute. However, when the operating temperature was reduced to 25 °C, the decrease in S1 concentration slowed down. At a temperature of 25 °C, S1 concentration reached 180 ng/L. These findings showed that operating temperature is an important parameter in the disinfection of wastewater contaminated with SARS-CoV-2. MFC log reduction rates were computed on an hourly basis. The substantial log reduction rate implied that the SARS-CoV-2 virus was successfully removed. The log reduction rate of

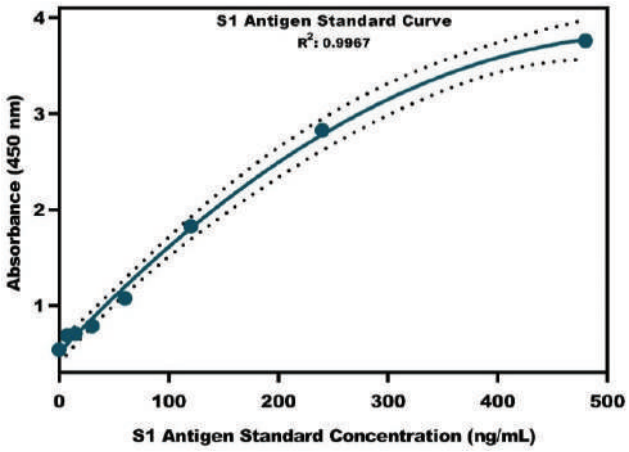


Figure 4. The standard curve plot of S1 antigen.

the MFC after half an hour at 30 °C temperature was 1.40. After three and a half hours, it was measured as 0.17. The rate of log reduction steadily reduced (Fig. 5). These results suggest that SARS-CoV-2 viral proteins are removed in MFCs.

At 30 minutes, the concentration of SARS-CoV-2 in the closed circuit MFC decreased to 47 ng/mL, while the virus concentration in the abiotic control MFC decreased to 21 ng/mL. At the end of one hour, the SARS-CoV-2 concentration in the closed circuit had risen to 49 ng/mL, whereas the abiotic control had a concentration of 23 ng/mL. After an hour and a half, the SARS-CoV-2 concentration in the closed-circuit MFC sample was 64 nanograms per milliliter. The abiotic control sample obtained simultaneously had a concentration of 36 ng/mL. The fifth sample was obtained from both MFCs after two hours. The concentration of MFC' in these samples was reduced to 58 ng/mL for the closed circuit MFC' and 15 ng/mL for the abiotic control MFC. The fifth sample was obtained from both MFCs after two hours. The concentration of MFC' in these samples was reduced to 58 ng/mL for the closed circuit MFC' and 15 ng/mL for the abiotic control MFC. The concentration of SARS-CoV-2 contaminated wastewater in the closed circuit MFC was 61 ng/mL after two and a half hours. The concentration of SARS-CoV-2 in the abiotic circuit was 12 ng/mL. Three hours later, the viral concentration in the closed circuit MFC was 65 ng/mL. The appropriate concentration for the abiotic control MFC was 25 ng/mL. The operation of the simulated slater concluded three and a half hours later, with the collection of the final sample. The ultimate sample concentration of MFC in the closed circuit was 59 ng/mL. SARS-CoV-2 was found at a concentration of 43 ng/mL in the final sample of abiotic control MFC (Fig. 6).

A novel approach was established for MFCs at ambient temperature based on the operation ELISA findings of MFCs at controlled temperature. The entire operating time in this newly created approach was lowered to forty

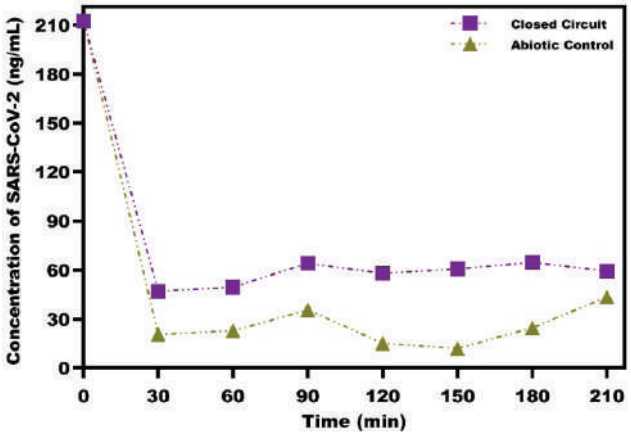


Figure 6. Time-dependent concentration graph of MFC at controlled temperature throughout the operation.

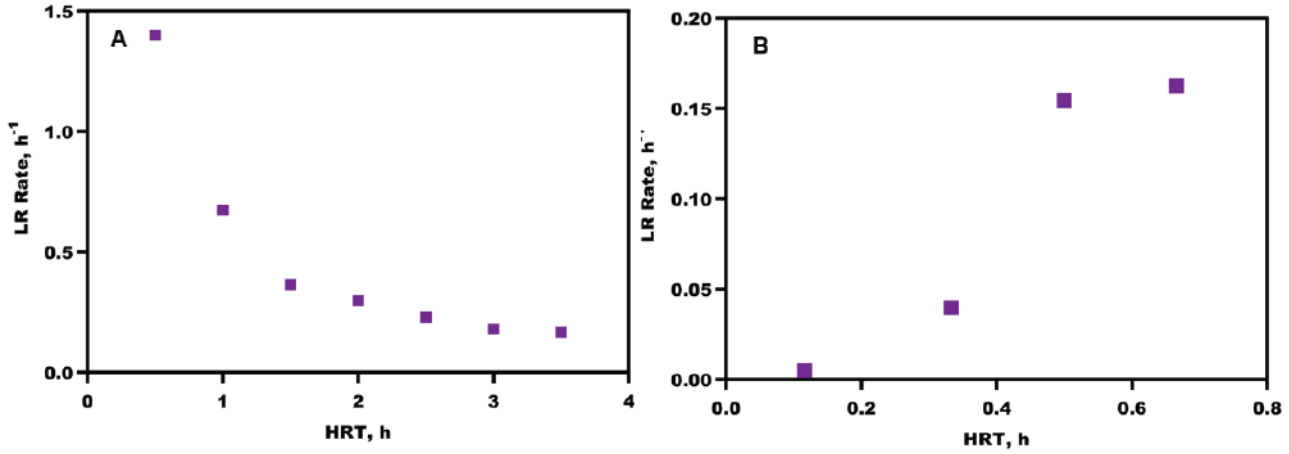


Figure 5. Graph of log reduction of MFCs at 30 °C temperature (A). Graph of log reduction of MFCs at 25 °C.

minutes, and sample periods were updated to every ten minutes. Given the findings at controlled temperature, it was decided to install an additional circuit (open circuit MFC). The SARS-CoV-2 concentration at which each MFC began functioning was 213 ng/mL. Within the first 10 minutes, the concentration of open-circuit MFC dropped to 65 ng/mL, the closed-circuit open-circuit MFC dropped to 65 ng/mL, the closed-circuit MFC to 213 ng/mL, and the abiotic control MFC to 133 ng/mL. The SARS-CoV-2 concentration of open circuit and abiotic control MFCs rose 20 minutes after the surgery, but the concentration of closed MFCs continued to drop. At 20 minutes, the open circuit MFC concentration was 80 ng/mL. The SARS-CoV-2 concentration in the closed circuit MFC was 206 nanograms per milliliter, whereas it was 138 ng/mL in the abiotic control. Thirty minutes later, the open circuit MFC concentration was determined to be 82 ng/mL. The concentrate circuit closed-circuit MFC steadily decreased, and the SARS-CoV-2 concentration was 178 ng/mL at the end of half an hour. After thirty minutes, the abiotic control MFC had a deadly viral concentration of 108 ng/mL. The concentration of open circuit and abiotic control MFCs continued to grow during the forty-first minute of the operation, whereas it continued to drop in the closed circuit MFCs. In the fortieth minute of the open circuit MFC, the SARS-CoV-2 concentration climbed to 92 ng/mL. In a closed circuit MFC, the SARS-CoV-2 concentration was determined to be 116 ng/mL. In the last ten minutes, the concentration of SARS-CoV-2 in the abiotic control MFC reached 156 ng/mL. This rate represents an exceptional rise in past operations' outcomes. At the end of the forty-first minute, the abiotic control MFC's SARS-CoV-2 concentration was nearly equivalent to the closed circuit MFC, which declined gradually and methodically (Fig. 7).

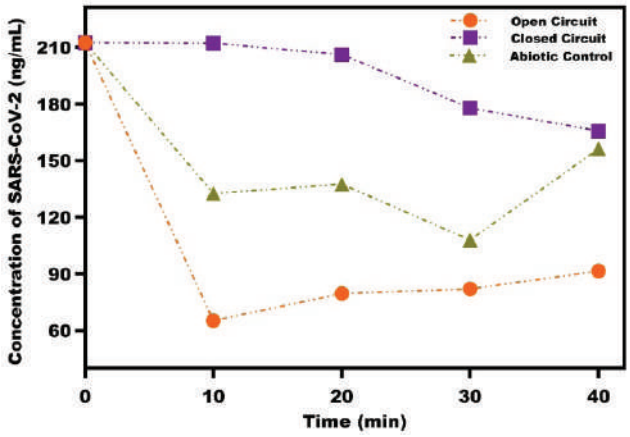


Figure 7. Time-dependent concentration graph of MFC at ambient temperature throughout the operation.

The detection of SARS-CoV-2 in wastewater has been reported previously, and the presence of SARS-CoV-2 in wastewater increases the potential spread. However, the need for SARS-COV-2 removal from wastewater has arisen. Within the scope of the large-scale study by Acosta et al. (2021), wastewater samples were collected twice a week from three different hospitals for four months [38]. It has been reported that the amount of SARS-CoV-2 in wastewater is directly proportional to hospitalizations due to COVID-19 cases [38]. The presence and amount of SARS-CoV-2 in the wastewater where the treated water from the wastewater treatment plant mixes into the river, depending on the number of hospitalizations of COVID-19-related cases in the hospital [39], and the SARS-CoV-2 virus was also found in river water and with a high detection frequency. Thus, it has been reported that treating treated wastewater mixed with river water may not be sufficient [39]. The effects of currently used wastewater treatment methods on SAR, such as chlorination of wastewater, ultraviolet (U.V.) irradiation, membrane technology, and advanced oxidation processes the effect of temperature on voltage production in MFCs, were the effect of temperature on voltage production in MFCs was the effect of temperature on voltage production in MFCs was the effect of temperature on voltage production in MFCs was reported and showed that it has an impact on power production [40]. Pasternak et al. [31], a deadly pathogen and biological contaminant, succeeded in separating the hepatitis B virus from human urine and generating electricity using MFCs [31]. Enough removal of hepatitis B viruses by microbial fuel cells was reported to reduce the risk of viral spread. However, they stated that they needed to apply the method they developed to different kinds of viruses to make the results more explainable. The log reduction rate calculated by Pasternak et al. [31] for the surface antigen started from almost 5 for the closed

Table 1. Comparison of MFC performances for disinfection of various contaminants

Disinfected material	MFC Type	Power density	Current density	Removal efficiency	References
SARS-CoV2	Single chamber air-cathode MFCs	184.19±21.31	0.073±0.029	78%	This study
Hepatitis virus	Single chamber air-cathode MFCs	n.a.	n.a.	99.99%	[31]
Ammonia/nitrate/nitrite	Sediment MFC	1794	1.1	~100%/ 65%/~90%	[41]

n.a.: not available

Table 2. The statistical significance of the difference between time-dependent concentration values of S1 antigen of MFCs (*). The statistical significance of the difference between SARS-COV-2 log reduction values of MFCs (**)

	Controlled Temp.		Ambient Temp.	
	Closed Circuit vs. Abiotic Control	Open Circuit vs. Closed Circuit	Closed Circuit vs. Abiotic Control	Open Circuit vs. Abiotic Control
t-test p-value*	0.007	0.01	0.05	0.22
t-test p-value**	0.0012	0.03	0.03	0.03

circuit MFC. The log reduction rates of hepatitis B virus surface antigen gradually decreased for both MFCs [31]. In our study, the first log reduction rate of the closed circuit MFC in a temperature environment of 30±2°C was 1.40. While the initial SARS-CoV-2 log reduction rate calculated for the closed circuit MFC at room temperature was 0.005, this rate increased gradually throughout the operation period. It reached 0.163 at the end of forty minutes. The difference in log reduction between the study of Pasternak et al. [31] and our study at room temperature is thought to be due to the different biofilm structures of MFCs or the difference in the viruses used [31–41].

These results suggest that external factors such as temperature and MFC configuration may affect the disinfection of SARS-CoV-2, where simultaneous electricity can be generated.

The t-test p-value of the closed circuit MFC and abiotic control reactor in a controlled temperature environment was 0.007, and the time-dependent SARS-CoV-2 concentration data of the two bioreactors differed considerably. Three distinct MFC time-dependent SARS-CoV-2 concentration values at ambient temperature were statistically compared. The t-test p-value for closed-circuit MFC and open-circuit MFC was 0.01, suggesting that they varied substantially. Again, at ambient temperature, the t-test p-value of the closed circuit MFC and abiotic control bioreactors was 0.05, and the time-dependent concentration values were not substantially different. Finally, the t-test p-value of 0.22 showed that the time-dependent SARS-CoV-2 concentration data from open MFC and abiotic control bioreactor were not significantly different (Table 1).

The t-test p-value for SARS-CoV-2 log reduction values of the closed circuit MFC and abiotic control bioreactors in a controlled temperature environment was 0.0012, showing a significant difference between the two bioreactors. In an ambient temperature setting, the t-test p-value findings of the SARS-CoV-2 log reduction values of three distinct MFCs were comp circuit circuit open-circuit MFC and closed-circuit MFC was 0.03, and the log reduction difference was significant. Closed circuit MFC and abiotic control had a t-test p-value of 0.03, indicating a significant difference between these two bioreactors. Lastly, at ambient temperature, the t-test p-value of the open circuit MFC and abiotic control was determined to be 0.03. This finding indicates that the log reduction value of the SARS-CoV-2 virus differs significantly across the two MFCs (Table 1). Not only viruses but also other contaminants can be treated in MFCs. The efficiency and efficacy of heavy metal removal from wastewater are anticipated to be substantially improved by current research endeavors and advancements in MFC technology [42]. It is highly conceivable that autonomous wastewater treatment plants and MFCs—capable of remotely detecting —will be used in the future [43]. For this purpose, MFC technology can support the development of biosensors that can perform target-oriented detection. Our findings on eliminating SARS-CoV-2 from wastewater represent a substantial improvement in public health protection and environmental sustainability. By incorporating MFCs into wastewater treatment facilities, we can improve disinfection while decreasing virus loads and creating renewable energy. These findings have far-reaching ramifications, advising policymakers about new policies prioritizing pathogen elimination in wastewater management. Furthermore, MFC technology may be used to remove different types of organisms.

CONCLUSION

In conclusion, the concentration of SARS-CoV-2 protein declined progressively over the operation duration of the microbial fuel cells, which were operated in a 25 °C temperature environment. It did not rise during the operating period of the other examined reactors. Simultaneously, the log decrease rate progressively and steadily increased. In addition to all of this, the power generation efficiency was fairly great. As a result, it was determined that microbial fuel cells, running at a temperature of 25 °C ambient temperature, executed the treatment of SARS-CoV-2 contaminated wastewater in a steady and circulatory manner, the bio removal of SARS-CoV-2 was accomplished, and there was considerable power production. Various parameters are needed for our promising work to be developed and extensively used. It is hoped that researching how diseases are removed at the molecular level may pave the way for more effective removal and eradication of additional pathogens. This study gives information on the real investigation of

SARS-CoV-2 polluted wastewater in advance. Furthermore, bioremediation of SARS-CoV-2 polluted wastewater using microbial fuel cells is expected to limit the production of new variants. Our findings suggest that novel microbial biosensors could be developed to detect the SARS-CoV-2 virus in wastewater.

AUTHORSHIP CONTRIBUTIONS

Authors equally contributed to this work.

DATA AVAILABILITY STATEMENT

The authors confirm that the data that supports the findings of this study are available within the article. Raw data that support the finding of this study are available from the corresponding author, upon reasonable request.

CONFLICT OF INTEREST

The author declared no potential conflicts of interest with respect to the research, authorship, and/or publication of this article.

ETHICS

There are no ethical issues with the publication of this manuscript.

STATEMENT ON THE USE OF ARTIFICIAL INTELLIGENCE

Artificial intelligence was not used in the preparation of the article.

REFERENCES

[1] Naseer MN, Zaidi AA, Khan H, Kumar S, Owais MT, Jaafar J, et al. Mapping the field of microbial fuel cell: A quantitative literature review (1970-2020). Energy Rep 2021;4126–4138. [CrossRef]

[2] Gupta S, Srivastava P, Patil SA, Yadav AK. A comprehensive review on emerging constructed wetland coupled microbial fuel cell technology: Potential applications and challenges. Bioresource Technol 2021;124376. [CrossRef]

[3] Catal T, Liu H, Kilinc B, Yilancioglu K. Extracellular polymeric substances in electroactive biofilms play a crucial role in improving the efficiency of microbial fuel and electrolysis cells. Appl Microbiol 2024;77. [CrossRef]

[4] Durna Piskin E, Genc N. Microbial fuel cells in electricity generation with waste treatment: Alternative electron acceptors. Sigma J Eng Nat Sci 2024;42:273–288. [CrossRef]

[5] Sukkasem C. Exploring biofilm-forming bacteria for integration into BioCircuit wastewater treatment. Eur Chem Biotechnol J 2024;2:39–52. [CrossRef]

[6] Liu H, Cheng S, Logan BE. Production of electricity from acetate or butyrate using a single-chamber microbial fuel cell. Environ Sci Technol 2005;39:658–662. [CrossRef]

[7] Sonmez E, Avci B, Mohamed N, Bermek H. Investigation of performance losses in microbial fuel cells with low platinum loadings on air-cathodes. Eur Chem Biotechnol J 2024;1:11–26. [CrossRef]

[8] Sukkasem C. Exploring biofilm-forming bacteria for integration into BioCircuit wastewater treatment. Eur Chem Biotechnol J 2024;2:39–52. [CrossRef]

[9] Catal T, Yavaser S, Enisoglu-Atalay V, Bermek H, Ozilhan S. Monitoring of neomycin sulfate antibiotic in microbial fuel cells. Bioresource Technol 2018;268:116–120. [CrossRef]

[10] Catal T, Kul A, Atalay VE, Bermek H, Ozilhan S, Tarhan N. Efficacy of microbial fuel cells for sensing of cocaine metabolites in urine-based wastewater. J Power Sources 2019;414:1–7. [CrossRef]

[11] Fan Y, Janicek A, Liu H. Stable and high voltage and power output of CEA-MFCs internally connected in series (iCiS-MFC). Eur Chem Biotechnol J 2024;1:47–57. [CrossRef]

[12] Berg KS, Palm P, Nielsen SD, Nygaard U, Bundgaard H, Rotvig C, Christensen AV. Acute symptoms in SARS-CoV-2 positive adolescents aged 15-18 years Results from a Danish national cross-sectional survey study. Lancet Reg 2022;100354. [CrossRef]

[13] Fumian TM, Malta FC, Dos Santos DRL, Pauvolid-Corrêa A, Fialho AM, Leite JPG, et al. SARS-CoV-2 RNA detection in stool samples from acute gastroenteritis cases, Brazil. J Med Virol 2021;93:2543–2547. [CrossRef]

[14] Farman M, Akgul A, Sultan MRS, Asif H, Agarwal P, Hassani MK. Numerical study and dynamics analysis of diabetes mellitus with co-infection of COVID-19 virus by using fractal fractional operator. Scientific Reports 2024;14:16489. [CrossRef]

[15] Jamil S, Naik PA, Farman M, Saleem MU, Ganie AH. Stability and complex dynamical analysis of COVID-19 epidemic model with non-singular kernel of Mittag-Leffler law. J Appl Mat Comput 2024;70:3441–3476. [CrossRef]

[16] Izquierdo-Lara R, Elsinga G, Heijnen L, Munnink BBO, Schapendonk CME, Nieuwenhuijse D, et al. Monitoring SARS-CoV-2 Circulation and Diversity through Community Wastewater Sequencing, the Netherlands and Belgium. Emerg Infect Dis 2021;27:1405–1415. [CrossRef]

[17] Zamhuri SA, Soon CF, Nordin AN, Rahim RA, Sultana N, Khan MA, et al. A review on the contamination of SARS-CoV-2 in water bodies: Transmission route, virus recovery and recent biosensor detection techniques. Sens Bio-Sens Res 2022;100482. [CrossRef]

[18] Reynolds LJ, Gonzalez G, Sala-Comorera L, Martin NA, Byrne A, Fennema S, et al. SARS-CoV-2 variant trends in Ireland: Wastewater-based epidemiology and clinical surveillance. Sci Total Environ 2022;155828. [CrossRef]

[19] Zahmatkesh S, Amesho KT, Sillanpää M. A critical review on diverse technologies for advanced wastewater treatment during SARS-CoV-2 pandemic: What do we know? J Hazardous Mater Adv 2022;7:100121. [CrossRef]

[20] Škulcová AB, Tamášová K, Staňová AV, Bírošová L, Krahulcová M, Gál M, et al. Effervescent ferrate(VI)-based tablets as an effective means for removal SARS-CoV-2 RNA, pharmaceuticals and resistant bacteria from wastewater. J Water Proc Eng 2021;43:102223. [CrossRef]

[21] Ahmed W, Angel N, Edson J, Bibby K, Bivins A, O'Brien JW, et al. First confirmed detection of SARS-CoV-2 in untreated wastewater in Australia: A proof of concept for the wastewater surveillance of COVID-19 in the community. Sci Total Environ 2020;728:138764. [CrossRef]

[22] Guerrero-Esteban T, Gutiérrez-Sánchez C, Villa-Manso AM, Revenga-Parra M, Pariente F, Lorenzo E. Sensitive SARS-CoV-2 detection in wastewaters using a carbon nanodot-amplified electrochemiluminescence immunosensor. Talanta 2022;247:123543. [CrossRef]

[23] Miyani B, Fonoll X, Nortan F, Mehrotra A, Xagoraraki I. SARS-CoV-2 in Detroit Wastewater. J Environ Manage 2020;146:06020004. [CrossRef]

[24] Wurtzer S, Marechal V, Mouchel JM, Maday Y, Teyssou R, Richard E, et al. Evaluation of lockdown effect on SARS-CoV-2 dynamics through viral genome quantification in waste water. Euro Surveill 2020;25:pii=2000776. [CrossRef]

[25] D'Aoust PM, Mercier E, Montpetit D, Jia JJ, Alexandrov I, Neault N, et al. Quantitative analysis of SARS-CoV-2 RNA from wastewater solids in communities with low COVID-19 incidence and prevalence. Water Res 2021;188:116560. [CrossRef]

[26] Al-Gheethi A, Al-Sahari M, Malek MA, Noman E, Al-Maqtari Q, Mohamed R, et al. Disinfection Methods and Survival of SARS-CoV-2 in the Environment and Contaminated Materials: A Bibliometric Analysis. Sustainabilty 2020;12:7378. [CrossRef]

[27] Ahmed W, Bivins A, Smith WJM, Metcalfe S, Stephens M, Jennison AV, et al. Detection of the Omicron (B.1.1.529) variant of SARS-CoV-2 in aircraft wastewater. Sci Total Environ 2022;820:153171. [CrossRef]

[28] Wilhelm A, Schoth J, Meinert-Berning C, Agrawal S, Bastian D, Orschler L, et al. Wastewater surveillance allows early detection of SARS-CoV-2 omicron in North Rhine-Westphalia, Germany. Sci Total Environ 2022;846:157375. [CrossRef]

[29] Van Poelvoorde LAE, Gobbo A, Nauwelaerts SJD, Verhaegen B, Lesenfants M, Janssens R, et al. Development of a reverse transcriptase digital droplet polymerase chain reaction-based approach for SARS-CoV-2 variant surveillance in wastewater. Water Environment research: a research publication of the Water Environment Federation 2024;96:e10999. [CrossRef]

[30] Kallem P, Hegab H, Alsafar H, Hasan SW, Banat F. SARS-CoV-2 detection and inactivation in water and wastewater: review on analytical methods, limitations and future research recommendations. Emerg Microbes Infect 2023;12:2222850. [CrossRef]

[31] Pasternak G, Greenman J, Ieropoulos I. Removal of Hepatitis B virus surface HBsAg and core HBcAg antigens using microbial fuel cells producing electricity from human urine. Sci Rep 2019;9:11787. [CrossRef]

[32] Cheng S, Liu H, Logan BE. Increased performance of single-chamber microbial fuel cells using an improved cathode structure. Electrochem Commun 2006;8:489–494. [CrossRef]

[33] Catal T, Li K, Bermek H, Liu H. Electricity production from twelve monosaccharides using microbial fuel cells. J Power Sources 2008;175:196–200. [CrossRef]

[34] Lovley DR, Phillips EP. Novel mode of microbial energy metabolism: organic carbon oxidation coupled to dissimilatory reduction of iron or manganese. App Environ Microbiol 1988;54:1472–1480. [CrossRef]

[35] Catal T, Lesnik KL, Liu H. Suppression of methanogenesis for hydrogen production in single-chamber microbial electrolysis cells using various antibiotics. Bioresour Technol 2015;187:77–83. [CrossRef]

[36] Bar-Or I, Indenbaum V, Weil M, Elul M, Levi N, Aguvaev I, et al. National Scale Real-Time Surveillance of SARS-CoV-2 Variants Dynamics by Wastewater Monitoring in Israel. Viruses 2022;14:1229. [CrossRef]

[37] Sonmez E, Avci B, Mohamed N, Bermek H. Investigation of performance losses in microbial fuel cells with low platinum loadings on air-cathodes. Eur Chem Biotechnol J 2024;1:11–26. [CrossRef]

[38] Acosta N, Bautista MA, Hollman J, McCalder J, Beaudet AB, Man L, et al. A multicenter study investigating SARS-CoV-2 in tertiary-care hospital wastewater. viral burden correlates with increasing hospitalized cases as well as hospital-associated transmissions and outbreaks. Water Research 2021;201:117369. [CrossRef]

[39] Tandukar S, Sthapit N, Thakali O, Malla B, Sherchan SP, Shakya BM, et al. Detection of SARS-CoV-2 RNA in wastewater, river water, and hospital wastewater of Nepal. Sci Total Environ 2022;824:153816. [CrossRef]

[40] Catal T, Kavanagh P, O'Flaherty V, Leech D. Generation of electricity in microbial fuel cells at sub-ambient temperatures. J Power Sour 2011;196:2676–2681. [CrossRef]

[41] Emalya N, Tarmizi S, Munawar E, Fellner J, Yunardi. Coupling electrochemical energy generation with leachate bioremediation in sediment microbial fuel cell reactors. Case Stud Chem Environ Eng 2024;10:100896. [CrossRef]

[42] Akagunduz D, Aydin O, Tuncay E, Bermek H. Microbial fuel cells: A potent and sustainable solution for heavy metal removal. Eur Chem Biotechnol J 2025;1:45–69. [CrossRef]

[43] Catal T, Liu H. Microbial fuel cell technology: Novelties for a clean future. Eur Chem Biotechnol J 2025;1:1–20. [CrossRef]

Sigma Journal of Engineering and Natural Sciences
Web page info: https://sigma.yildiz.edu.tr
DOI: 10.14744/sigma.2025.00060

Research Article

An exact analysis of chemical reaction and porosity effects for mixed convective magnetohydrodynamics Casson fluid

Nur Fatihah MOD OMAR[1], Zulkhibri ISMAIL[1,*], Rahimah JUSOH[1], Muhammad Azrin AHMAD[1], Ahmad Qushairi MOHAMAD[2]

[1]Centre for Mathematical Sciences, Universiti Malaysia Pahang Al-Sultan Abdullah, Lebuhraya Persiaran Tun Khalil Yaakob, Gambang, Pahang, 26300, Malaysia
[2]Department of Mathematical Sciences, Faculty of Science, Universiti Teknologi Malaysia, Johor Bahru, Johor, 81310, Malaysia

ARTICLE INFO

Article history
Received: 04 August 2024
Revised: 17 October 2024
Accepted: 13 January 2025

Keywords:
Accelerated Plate; Casson Fluid; Chemical Reaction; Magnetohydrodynamic; Radiation

ABSTRACT

In this research, we explore the Casson fluid flow under mixed convection in a plate undergoing acceleration within a porous medium, considering the effects of chemical reaction and magnetisation. The investigation encompasses heat and mass transfer characteristics, incorporating thermal radiation and chemical reactions. Inspired by the previous studies of the chemical reaction and porosity of magnetohydrodynamic Casson fluid, the focus of this research revolves around the Casson parameter with convective double diffusion flows with magnetohydrodynamics (MHD) over a plate undergoing acceleration within a porous medium, considering the occurrence of a radiative chemical reaction. Ordinary differential equations are transformed from the governing partial differential equations through appropriate non-dimensional variables to facilitate mathematical analysis. Subsequently, the Laplace transform method is utilised to get the solution for the resulting non-dimensional ordinary differential equations system. The study provides graphical representations illustrating the behaviour of various physical parameters. The trend reveals that the rising Casson parameter will descend the fluid velocity, primarily attributed to the elevated fluid viscosity. Notably, the Casson parameter has no impact as the fluid approaches the centre between the bounding surfaces. Additionally, it is seen that a higher Casson parameter results in behaviour resembling that of a Newtonian fluid. On top of that, the velocity increases significantly for larger chemical reaction coefficient values. Finally, it is noticed that velocity tends to decrease as the porosity parameter decreases and the magnetic field strength increases.

Cite this article as: Mod Omar NF, İsmail Z, Jusoh R, Ahmad MA, Mohamad AQ. An exact analysis of chemical reaction and porosity effects for mixed convective magnetohydrodynamics Casson fluid. Sigma J Eng Nat Sci 2026;44(1):262–272.

***Corresponding author.**
*E-mail address: zulkhibri@umpsa.edu.my

This paper was recommended for publication in revised form by Editor-in-Chief Ahmet Selim Dalkilic

Published by Yıldız Technical University Press, İstanbul, Turkey
© Author. This is an open access article under the CC BY-NC license (http://creativecommons.org/licenses/by-nc/4.0/).

INTRODUCTION

A chemical reaction is a transformative process in which one group of chemical substances changes into another. Additionally, chemical reactions often occur between a fluid and a foreign mass. Typically, these categories are divided into two primary categories; homogeneous and heterogeneous chemical reactions, contingent on whether they transpire at an interface or within a volume comprising a single phase. The scrutiny of flows of mass transfer involving chemical reactions has proven highly valuable in various chemical and hydrometallurgical industries. This encompasses applications like catalytic chemical reactors, food processing, processes involving either endothermic or exothermic chemical reactions, and the manufacturing of glassware and ceramics [1]. The extensive application of mass transport with activation energy, as necessitated by the above, has captured the interest of researchers. The concept of activation energy was introduced by Arrhenius in 1889, representing the least amount of energy needed for particles to engage in a chemical reaction. They conferred that this energy could manifest as kinetic or potential energy, and without it, the transformation of reactants into products cannot occur [2]. Research has been carried out to examine double diffusions in the context of the Casson fluid flow, with magnetohydrodynamic over a wedge with the inclusion of thermal radiation and chemical reaction. The concentration of Casson fluid decreases due to the chemical reaction parameter actively rising. This is because the chemical reaction hinders the fluid's momentum [3]. Recently, Sene [4] discussed a solution method for the model of fractional Casson fluid, adapting the chemical reaction and heat generation impact. It shows that the Casson fluid parameter influences the boundary layer thickness and induces the velocity to rise.

Casson fluid stands out as one of the ultimate renowned non-Newtonian fluids. Casson introduced this substance as a crucial element of pseudoplastic fluids in 1959. The Casson fluid model offers two significant strengths; firstly, the derivation is from liquid kinetic theory rather than an empirical correlation, and secondly, it transforms to a Newtonian nature at certain shear rates [5]. Casson fluid behaves like a solid when the yield stress exceeds the shear stress, but it flows like a liquid when the yield stress is lower than the shear stress [6]. Moreover, it is also appropriate for heating and cooling processes due to their effective influence on the rate of energy transfer [7]. In 2018, Hussanan et al. [8] considered unsteady natural convection of a nanofluid flow based on sodium alginate viscoplastic Casson fluid over a vertical plate. By implying uniform free stream velocity as well as temperature, it is resolved by applying the Runge–Kutta numerical method in combination with a shooting technique. The conclusion discloses that the velocity field diminishes when the Casson parameter elevates. Aman et al. [9] explored using Caputo time-fractional models towards MHD Casson fluid flow. Fractional calculus is an intriguing subject due to its applications in Mathematics, Applied Mathematics, and Fluid Dynamics. Moreover, Akhil and Patel [10] enticed the influence of heat generation and non-linear radiation on the mixed convection MHD Casson fluid flow. It can be inferred that the Casson fluid parameter tends to lower both skin friction and concentration profiles. Subsequently, by means of an accelerated plate, Shahrim et al. [11] investigated a fractional convection problem involving Casson fluid. As a point of reference, the use of fractional derivatives to characterise the physical properties of non-Newtonian fluid flow over accelerated plate remains uncommon. Their findings indicated that the velocity would escalate by ascending values of time, t and Grashof number, Gr. Conversely, a decrease in the Prandtl number, Pr and Casson fluid parameter reduced velocity.

Magnetohydrodynamics (MHD) illustrates the behaviour of fluids with high conductivity in the occurrence of magnetisation. These MHD flows play a crucial role in diverse applications, including MHD energy generators, cancer treatment, biomedical flow control, magneto-fluid rotary blood pumping, drug targeting through MHD, materials processing, separation devices, and bio-micro-fluidic devices utilizing MHD [12]. The core principle of magnetohydrodynamics (MHD) is that a magnetic field can generate flows in a conductive fluid in motion, resulting in fluid polarization and altering the magnetic field. The equations governing MHD combine the Navier–Stokes equations of fluid dynamics with Maxwell's equations of electromagnetism. Examples of such magneto-fluids include plasmas, liquid metals, salt water, and electrolytes [13]. Given its diverse technological and engineering applications, a comprehensive understanding and exploration of Magnetohydrodynamics (MHD) flow is crucial. The major goal of MHD fundamentals is to steer the flow field in a predetermined specific direction by changing the boundary layer development. Consequently, the implementation of MHD appears to be a further adaptable and dependable approach for modifying flow kinematics. In the realms of pharmaceuticals and environmental science, MHD plays a pivotal part in biomedical engineering and fluid dynamics applications. Chemical engineering employs MHD for both purification and filtration objectives [14]. Ismail et al. [15] undertook a study to investigate the impact of magnetohydrodynamics (MHD) along with radiation under ramped wall temperature conditions on natural convection through a porous medium past an infinitely inclined plate. They employed the Laplace transform method in their analysis. Furthermore, Prasad [16] discussed the thermal and species concentration characteristics of MHD Casson fluid along a vertical sheet. On top of that, Jagadesh et al. [17] have performed an analysis of dissipative heat transfer and peristaltic pumping in the context of MHD Casson fluid flow within an inclined channel. Their findings indicated that incremental in both magnetisation and Casson parameter led to an elevation in the heat transfer rate. Recently, J

Raza et al. studied Casson nanofluid past a stretching sheet and discovered that an increase in the magnetic parameter amplifies the Brownian motion of fluid particles, leading to a gradual rise in the fluid's temperature [18].

Presently, numerous researchers have examined the effects of fluid thermal radiation on the properties of heat transport over extended surfaces. The process of heat transfer is significant in the implementation of photochemical reactors and solar power technology. The term thermal radiation refers to the emission of electromagnetic waves by a substance, leading to an increase in its internal energy and resulting in warming [19]. Kataria and Patel [20] successfully derived the solution analytically for the flow of an oscillating plate through an MHD Casson fluid, in addition to radiative chemical reaction parameters. [21] examines heat and mass transfer in a magnetohydrodynamic flow over a moving vertical plate with convective boundary conditions under the influence of thermal radiation. Increased values of the radiation parameter promote conduction over radiation, thereby reducing the thermal boundary layer thickness. Besides, Omar et al. [22] studied the influence of radiation and Magnetohydrodynamic of Casson Fluid over a plate undergoing acceleration. It was discovered that thermal radiation increases with a temperature rise.

Khan [23] investigated the unsteady squeezing flow of MHD Casson fluid flowing via a porous medium. The term porous medium is recognised as a substance containing fluid-filled pores and is consistently defined by attributes like porosity and permeability. Porosity determines the volume of fluid the material can retain, while permeability quantifies the fluid's ability to traverse through it. Diverse applications encompass chemical reactors, groundwater hydrology, drainage, seepage, irrigation, and the extraction of crude oil from reservoir rock pores. Several intriguing findings are present within [24–26].

Inspired by the aforementioned research, the focus of this research revolves around the Casson parameter with convective double diffusion flows with magnetohydrodynamics over a plate undergoing acceleration within a porous medium, considering the occurrence of the radiative chemical reaction. Limiting cases are conducted to verify consistency with previous findings. These analytical solutions can help scientists and engineers verify the accuracy of complex model solutions derived from numerical schemes. This research work can later be extended by using different fluids. Additionally, the proposed mathematical model is anticipated to serve as a reference for researchers in academia, engineering, and industry, facilitating further analysis of flow characteristics, heat transfer, and mass transfer performance of such fluids.

MATHEMATICAL FORMULATION

The research intends to obtain solutions in the presence of porous medium, magnetohydrodynamics and chemical reaction as well as radiation. The focus is on the context of an unsteady Casson fluid flowing in a state of the accelerated plate, positioned at the flow being restrained to $x > 0$, where x denotes the coordinate measurement in the direction perpendicular to the surface. At the start, at the time $t = 0$ the plate and fluid are at rest, exhibiting a uniform concentration and temperature. Then, as $t > 0$, the plate undergoes acceleration with a velocity $u' = At$ and concurrently, the temperature of the plate is increased to T'_w while the concentration is elevated to T'_w.

The dimensional momentum, energy, and concentration equations that govern the flow are as follows:

$$\rho \frac{\partial u'}{\partial t'} = \mu \left(1+\frac{1}{\gamma}\right)\frac{\partial^2 u'}{\partial x'^2} + \rho g \beta_T \left(T'-T'_\infty\right) + \rho g \beta_C \left(C-C'_\infty\right) - \sigma B_0^2 u' - \frac{\mu \varphi}{K} u' \tag{1}$$

$$\rho c_p \frac{\partial T'}{\partial t'} = k \frac{\partial^2 T'}{\partial x'^2} - \frac{\partial q'_r}{\partial x'} \tag{2}$$

$$\rho c_p \frac{\partial C'}{\partial t'} = D \frac{\partial^2 C'}{\partial x'^2} - Kr'(C'-C'_\infty) \tag{3}$$

In the given context, γ represents the parameter of Casson fluid, u' denotes fluid in the x- direction, t depicts the variable of time, T' corresponds to the temperature of the fluid near the plate, whereas T'_∞ signifies the plate temperature, C' represents concentration, ρ stands for fluid density, μ represents dynamic viscosity, g signifies acceleration due to gravity, β represents the thermal expansion coefficient, B_0 indicates external magnetic field, σ is the electrical conductivity, φ refers to the porosity, k represents thermal conductivity, K denotes permeability, c_p refers to specific heat at constant pressure, q_r signifies radiative heat flux, D refers to mass diffusion and Kr indicates chemical reaction alongside the initial value and boundary conditions:

$$\begin{aligned} &u'(x',0) = 0; \quad u'(0,t') = At; \quad u'(\infty,t') = 0; \\ &T'(x',0) = T'_\infty; \quad T'(0,t) = T'_w; \quad T'(\infty,t) = T'_\infty, \\ &C'(x',0) = C'_\infty; \quad C'(0,t) = C'_w; \quad C'(\infty,t) = C'_\infty, \end{aligned} \tag{4}$$

MATHEMATICAL SOLUTION

Through the introduction of dimensionless variables:

$$u = \frac{u'}{(\nu A)^{\frac{1}{3}}}; \; t = \frac{t' A^{\frac{2}{3}}}{\nu^{\frac{1}{3}}}; \; x = \frac{x' A^{\frac{1}{3}}}{\nu^{\frac{2}{3}}}; \; T = \frac{T'-T'_\infty}{T'_w - T'_\infty}; \; C = \frac{C'-C'_\infty}{C'_w - C'_\infty} \tag{5}$$

The dimensionless representation of equations (1) - (3),

$$\frac{\partial u}{\partial t} = A\frac{\partial^2 u}{\partial x^2} + GrT - Bu + GcC \tag{6}$$

$$\lambda \frac{\partial T}{\partial t} = \frac{\partial^2 T}{\partial x^2} \tag{7}$$

$$\frac{\partial C}{\partial t} = \frac{1}{Sc}\frac{\partial^2 C}{\partial x^2} - KrC \tag{8}$$

The method of Laplace transform is employed for equations (6) - (8),

$$\frac{d^2\overline{U}}{dx^2} - \frac{(s+B)}{A}\overline{U} = -P\overline{T} - Q\overline{C} \tag{9}$$

$$\frac{d^2\overline{T}}{dx^2} - \lambda s\overline{T} = 0 \tag{10}$$

$$\frac{d^2\overline{C}}{dx^2} - \overline{C}(ScKr + Scs) = 0 \tag{11}$$

The transformed equations are,

$$\overline{U} = \left(\frac{1-e^{-s}}{s^2} - \frac{a1}{s(s-a2)} - \frac{a3}{s(s-a4)}\right)e^{-x\sqrt{\frac{(s+B)}{A}}} + \frac{a1}{s(s-a2)}e^{-x\sqrt{\lambda s}} + \frac{a3}{s(s-a4)}e^{-x\sqrt{Sc}\sqrt{s+Kr}} \tag{12}$$

$$\overline{T} = \frac{1}{s}e^{-x\sqrt{\lambda s}} \tag{13}$$

$$\overline{C} = \frac{1}{s}e^{-x\sqrt{Sc}\sqrt{(s+Kr)}} \tag{14}$$

and the parameters utilised in this study are as follows:

$$Gr = \frac{g\beta(T_w - T_\infty)}{A};\quad A = 1 + \frac{1}{\gamma};\quad B = M + \frac{1}{K};\quad \lambda = \frac{\Pr}{1+N};\quad P = \frac{Gr}{A};$$

$$Gc = \frac{g\beta(C_w - C_\infty)}{A};\quad Q = \frac{Gc}{A};\quad M = \frac{\sigma B_0^{2*} v^{\frac{1}{3}}}{\rho A^{\frac{2}{3}}};\quad N = \frac{16\sigma^* T_\infty'^3}{3kk^*};\quad \Pr = \frac{\mu c_p}{k}.$$

Solutions for equations (12), (13), and (14) are subsequently obtained by inversing the method of Laplace transform:

$$T(x,t) = erfc\frac{x\sqrt{\lambda}}{2\sqrt{t}}$$

$$C(x,t) = \begin{pmatrix} \frac{1}{2}((e^{x\sqrt{ScKr}}\, erfc\frac{x\sqrt{Sc}}{2\sqrt{t}} + \sqrt{Krt}) \\ +(e^{-x\sqrt{ScKr}}\, erfc\frac{x\sqrt{Sc}}{2\sqrt{t}} - \sqrt{Krt})) \end{pmatrix}$$

$$U0(x,t) = \begin{pmatrix} (\frac{t}{2} + \frac{x}{4}\sqrt{\frac{1}{AB}})e^{x\sqrt{\frac{B}{A}}}erfc((\frac{x}{2\sqrt{At}}) + \sqrt{Bt}) \\ +(\frac{t}{2} - \frac{x}{4}\sqrt{\frac{1}{AB}})e^{-x\sqrt{\frac{B}{A}}}erfc((\frac{x}{2\sqrt{At}}) - \sqrt{Bt}) \end{pmatrix}$$

$$U1(x,t) = \begin{pmatrix} (-\frac{a1}{a2}erfc(\frac{x\sqrt{\lambda}}{2\sqrt{t}})) + (\frac{a1}{a2}\frac{e^{a2t}}{2})((e^{x\sqrt{\lambda a2}}erfc((\frac{x\sqrt{\lambda}}{2\sqrt{t}}) + \sqrt{a2t})) \\ +(e^{-x\sqrt{\lambda a2}}erfc((\frac{x\sqrt{\lambda}}{2\sqrt{t}}) - \sqrt{a2t}) \end{pmatrix}$$

$$U2(x,t) = \begin{pmatrix} -\frac{a3}{2a4}(e^{x\sqrt{ScKr}}erfc(\frac{x\sqrt{Sc}}{2\sqrt{t}}) + \sqrt{Krt} + e^{-x\sqrt{ScKr}}erfc(\frac{x\sqrt{Sc}}{2\sqrt{t}}) \\ -\sqrt{Krt}) + \frac{a3}{a4}\frac{e^{a4t}}{2}(e^{x\sqrt{Sc(Kr+a4)}}erfc(\frac{x\sqrt{Sc}}{2\sqrt{t}}) + \sqrt{(Kr+a4)t} \\ +e^{-x\sqrt{Sc(Kr+a4)}}erfc(\frac{x\sqrt{Sc}}{2\sqrt{t}}) - \sqrt{(Kr+a4)t}) \end{pmatrix}$$

$$U3(x,t) = \begin{pmatrix} \frac{a1}{2a2}e^{x\sqrt{\frac{B}{A}}}erfc[(\frac{x}{2\sqrt{At}}) + \sqrt{Bt} + e^{-x\sqrt{\frac{B}{A}}}erfc((\frac{x}{2\sqrt{At}}) - \sqrt{Bt}) \\ -(\frac{a1}{a2}\frac{e^{a2t}}{2})((e^{x\sqrt{\frac{1}{A}(B+a2)}}erfc((\frac{x}{2\sqrt{At}}) + \sqrt{(B+a2)t}) \\ +(e^{-x\sqrt{\frac{1}{A}(B+a2)}}erfc((\frac{x}{2\sqrt{At}}) - \sqrt{(B+a2)t}) \end{pmatrix}$$

$$U4(x,t) = \begin{pmatrix} \frac{a3}{2a4}e^{x\sqrt{\frac{B}{A}}}erfc[(\frac{x}{2\sqrt{At}}) + \sqrt{Bt} + e^{-x\sqrt{\frac{B}{A}}}erfc((\frac{x}{2\sqrt{At}}) - \sqrt{Bt}) \\ -(\frac{a3}{a4}\frac{e^{a4t}}{2})((e^{x\sqrt{\frac{1}{A}(B+a4)}}erfc((\frac{x}{2\sqrt{At}}) + \sqrt{(B+a4)t}) \\ +(e^{-x\sqrt{\frac{1}{A}(B+a4)}}erfc((\frac{x}{2\sqrt{At}}) - \sqrt{(B+a4)t}) \end{pmatrix}$$

$$U(x,t) = U0(x,t) + U1(x,t) + U2(x,t) + U3(x,t) + U4(x,t)$$

with

$$a1 = \frac{aP}{A\lambda - 1};\quad a2 = \frac{B}{A\lambda - 1};\quad a3 = \frac{AQ}{ASc - 1};\quad a4 = \frac{AScKr - B}{ASc - 1}.$$

RESULTS AND DISCUSSION

This research employs an analytical approach to investigate the flow of Casson fluid under mixed convection within a porous medium, around an accelerated plate, incorporating the effects of magnetisation and chemical reactions. The analytical techniques include the Laplace transform [14,21], Fourier series [27], Homotopy Analysis Method (HAM) [20], and fractional derivative method [8,10].

The Laplace transform has certain limitations, requiring the governing equations to be linear for effective

application. While it can handle complex equations, solving them becomes challenging without computational software.

The Laplace transform belongs to a class of operations known as integral transforms. It converts a function $f(t)$ of a single variable t (interpreted as time) into a new function $F(s)$ defined in terms of another variable s, the complex frequency. The appeal of the Laplace transform lies in its ability to transform differential equations in the t, time domain into algebraic equations in the frequency domain. This simplifies the process of solving differential equations, reducing it to solving algebraic equations in the s domain. Another significant advantage is that the Laplace transform inherently incorporates initial conditions into the solution, making it especially useful for solving initial-value problems commonly encountered in studies of electrical circuits and mechanical vibrations [28 - 33]. The core idea involves transforming a constant-coefficient differential equation in $f(t)$ into a simpler algebraic equation for the Laplace-transformed function, $F(s)$ solving this algebraic equation, and then using the inverse Laplace transform to return to the original time-domain solution, $f(t)$ The precise definition of the Laplace transform and the specific properties it satisfies make this process feasible [33].

Analytical solutions offer numerous advantages. They are benchmarks for validating numerical methods and provide insights into underlying physical phenomena [34]. Additionally, they are valuable for addressing large-scale problems, such as modelling hydrocarbon reservoirs, by enabling dimensional analysis [35]. In heat conduction problems, analytical solutions act as foundational components for constructing solutions through superposition [36]. They also allow the efficient computation of exact results using concise representations for short- and large-time behaviour [37]. Furthermore, analytical solutions are essential for verifying numerical results generated by computational methods. Besides, Computational Physicists play a crucial role in resolving inconsistencies between numerical simulations and experimental data, facilitating comparisons between theory, simulations, and experimental observations [38].

It is necessitated to establish comprehensive insight into the employed model, especially when compared to previous studies. Before delving into more detailed discussions, it is essential to verify this research against previous research to confirm, its correct execution. Figure 1a provides a comparison with Shahrim et al. [11] for different Grashof numbers, Gr and Figure 1b presents the comparison for different time, t values. The results demonstrate a strong agreement between the current study and the previous one, as demonstrated by the plotted graph comparing the two. Furthermore, it has been confirmed that all the plotted graphs comply with the specified boundary conditions. Validation demonstrates a strong agreement with the studied problem. Consequently, we have confidence that the solutions obtained are accurate. The graphical interpretation and physical insight are also discussed using fixed values of $\gamma = 0.1$, $t = 1$, $N = 5$, $Pr = 7$, $M = 1$, $K = 0.2$, $Kr = 1$, $Gr = 1$, $Gc = 1$ and $Sc = 0.6$ respectively.

In Figure 2a, a concentration profile exhibits a pronounced impact from the Schmidt number. Observably, by increasing the Schmidt number, there is a deterioration in the concentration profile. This trend is attributed to the reciprocal correlation of the Schmidt number and mass diffusivity. As the value of the Schmidt number climbs, the flow of the fluid regime demonstrates lower values of mass diffusion, leading to a decrease in the distribution of concentration. In applications involving biofluid dynamics, such as blood flow, where Casson fluid models

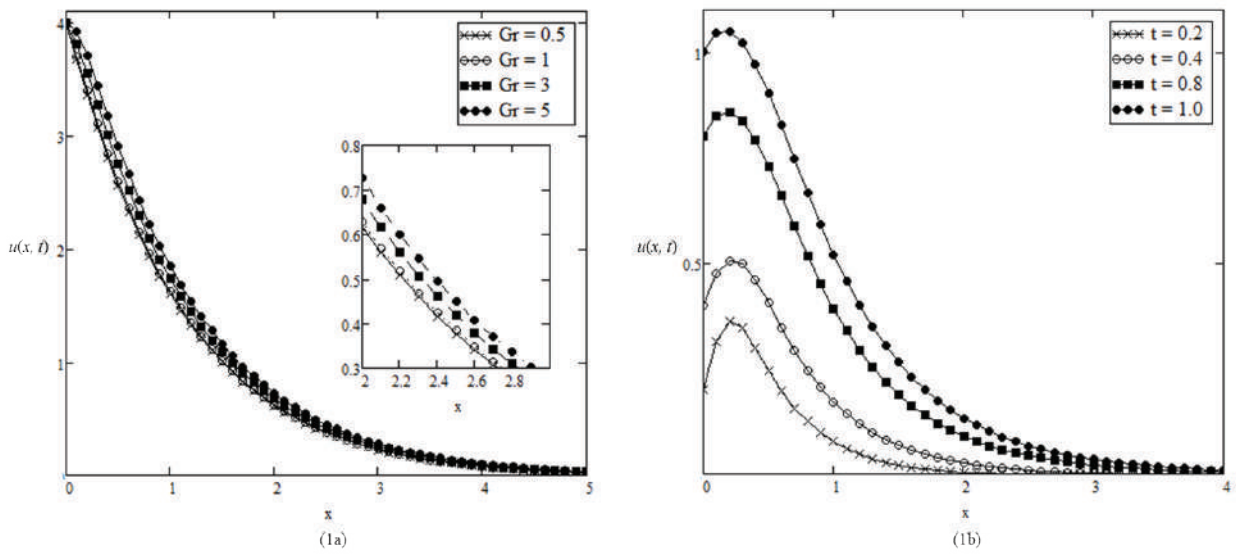


Figure 1. Validation results of Fig. 1a for different Grashof number, Gr and Fig. 1b for different time, t.

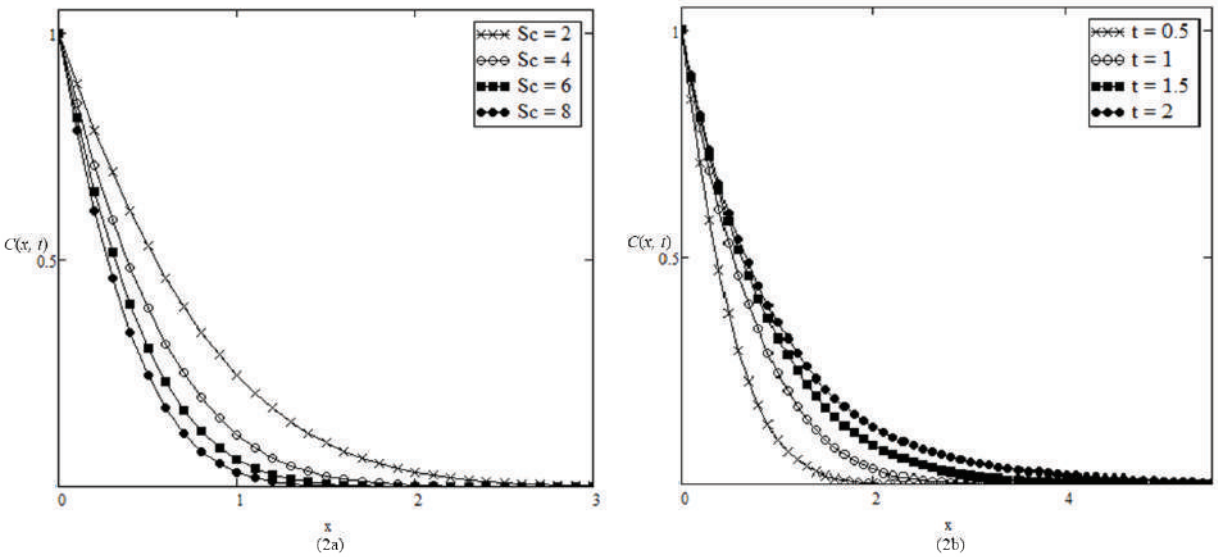


Figure 2. Concentration profiles of different Schmidt number, *Sc* (2a) and time, *t* (2b).

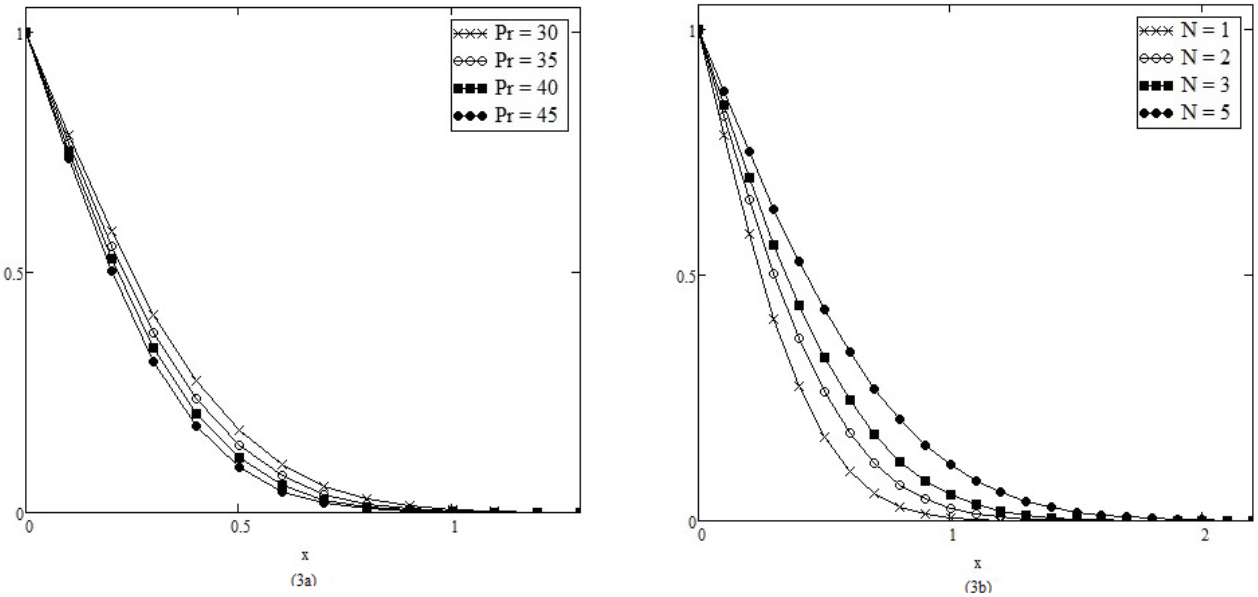


Figure 3. Temperature profiles of different Prantl number, *Pr* (3a) and radiation, *N* (3b).

are commonly employed, for example, when the Schmidt number *Sc* is high, the transport of nutrients or solutes (e.g., oxygen, pharmaceuticals) becomes less efficient due to the reduced thickness of the concentration boundary layer. This can influence the effective delivery of solutes to targeted regions in industrial or biological systems. Figure 2b illustrates the influence of time on the concentration profile, with temperature gradually increasing as time rises.

An elevation of *Pr* results in a decrement in temperature as depicted in Figure 3a. It arises from the thickness of the thermal boundary layer decreasing while the *Pr* number ascends. Figure 3b demonstrates the radiation parameter effect on the elevated temperature profile. When the radiation constraint surges, there is a rise in the thermal boundary layer thickness and temperature profile. Radiation-induced heating lowers viscosity and yield stress, enhancing fluid mobility and convective heat transfer. Increased radiation initiates steeper temperature gradients near the surface, penetrating the fluid through thermal diffusion. For instance, undertaking polymer processing in

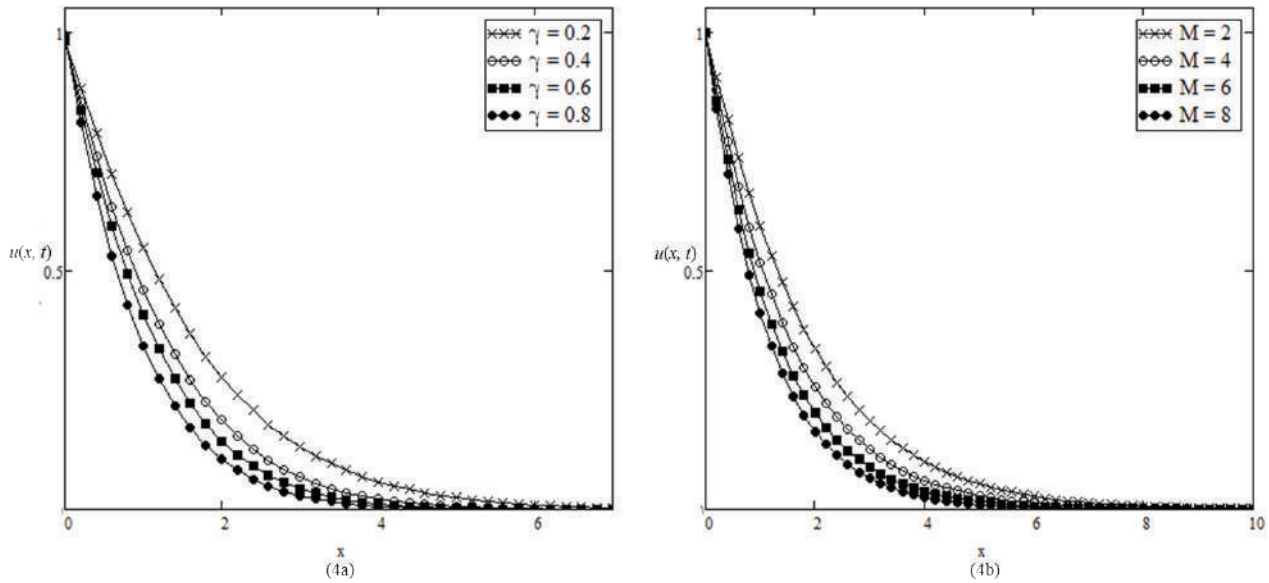


Figure 4. Velocity profiles of different Casson parameter, γ (4a) and magnetic parameter, M (4b).

industrial processes or molten metals modelled as Casson fluids, increased radiation enhances heat distribution which is essential for achieving uniform material properties. On top of that, from biomedical applications, radiative heating in capillary blood flow can lead to elevated temperatures, influencing metabolic reactions.

In Figure 4a, velocity profiles are exhibited for various Casson parameter values. The trend reveals that the rising Casson parameter will descend the fluid velocity, primarily attributed to the elevated fluid viscosity. An increased Casson parameter indicates a lower yield stress, allowing the fluid to transition to a flowing state more readily. This enhances resistance to flow and restricts the momentum transfer into the fluid, resulting in a steeper velocity gradient from the boundary to the bulk flow and a thinner boundary layer. With an increased Casson parameter, more energy is required to sustain the flow as the fluid dissipates additional energy to overcome the heightened viscous resistance. It decreases momentum transfer efficiency, confining it to a smaller region near the boundary. Notably, the Casson parameter has no impact as the fluid approaches the centre between the bounding surfaces. Additionally, it is seen that a higher Casson parameter results in behaviour resembling that of a Newtonian fluid. Consequently, boundary layer thickness velocity is higher than observed for a Newtonian fluid owing to the plasticity inherent in Casson fluid. Conversely, a decrease in the Casson parameter, associated with a rise in plasticity, results in the thickness of the boundary layer, which increases due to a simultaneous rise in the momentum boundary layer. Diving into engineering applications, in processes involving Casson fluids, such as blood flow, molten polymers, or slurries, an increase in γ results in lower flow rates and thinner boundary layers, affecting heat transfer, mixing efficiency, and pressure drop requirements. For fluids such as blood in biological systems, commonly modelled as a Casson fluid, a higher γ can indicate pathological conditions (e.g., decreased shear sensitivity due to increased plasma viscosity). This results in slower flow velocity near vessel walls and may lead to flow stagnation.

Figure 4b illustrates the impact of the magnetic field parameter M on velocity profiles. It is observed that the velocity diminishes as the magnetic field strength increases. Applying a magnetic field to a flowing, electrically conductive fluid induces an electric current in the fluid. The correlation of the induced currents and the magnetic field produces Lorentz force; referred to as a resistive force. This force acts externally in the opposite direction to the fluid flow, impeding its motion, analogous to the effect of drag force. Moreover, a rise in the magnetic parameter M will result in resistive forces, hindering the flow of the fluid, and consequently declining the velocity of the fluid.

In Figure 5a, the upshot of the chemical reaction on velocity distribution is demonstrated. It is evident that the velocity increases significantly for larger chemical reaction coefficient, Kr values. Consequently, it is established that the magnitude of the Kr coefficient plays a crucial role in shaping the velocity distribution.

Figure 5b showcases values of the porosity parameters, K for various velocity profiles, while other flow parameters are held constant. In practical terms, there is a decrease in velocity with a reduction in the porosity parameter, K. This outcome aligns with Darcy's law, which states that the presence of a porous medium descends the flow resistance, thus enhancing fluid motion. Hence, the graphical

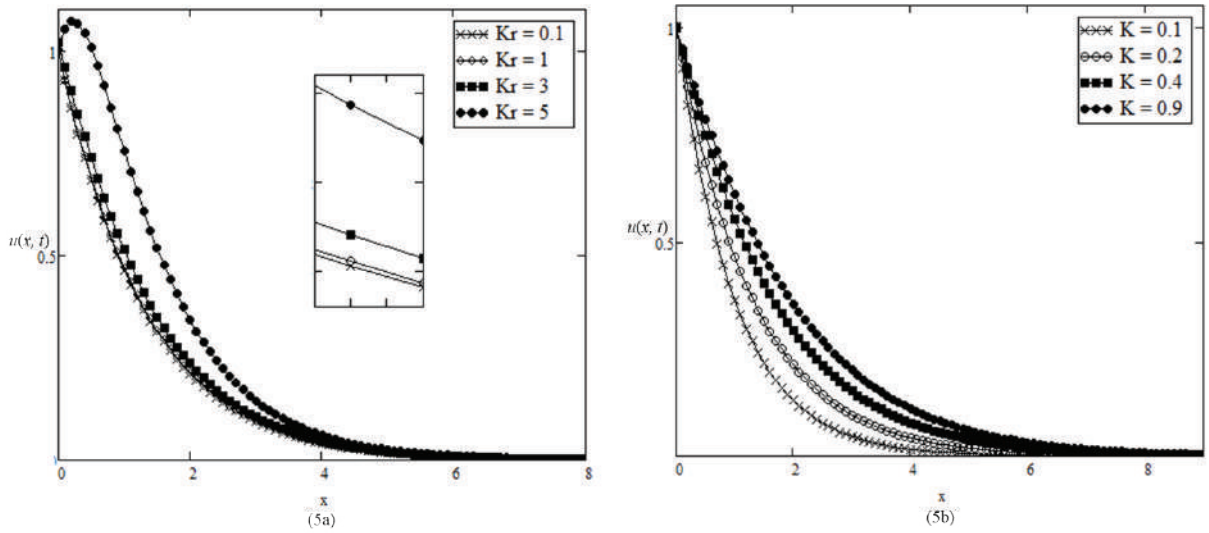


Figure 5. Velocity profiles of different chemical species parameter, *Kr* (5a) and porosity parameter, *K* (5b).

representation confirms that porosity is a pivotal factor in the current research.

Figure 6a displays the velocity profiles of the fluid for different thermal radiation values, *N*. The velocity reduces the existence of thermal radiation. This is anticipated since lower temperatures correspond to reduced radiation, leading to a decline in velocity. The fluid velocity will elevate with time, as illustrated in Figure 6b.

Figure 7a delineates the effect of the Grashof number, *Gr* on the velocity profile, symbolising the proportional thermal buoyant force's influence compared to the hydrodynamic viscous force. A steady elevation in velocity is noticed with the increasing Grashof number. This occurrence is ascribed to the intensified buoyancy force within the flow, resulting in all-in-all enhancement of fluid velocity. Figure 7b reveals the implication of the Grashof concentration number, *Gc* on the velocity profile, where the number is characterised as the ratio of species buoyant force to viscous hydrodynamic force. A rise in the *Gc* number implies the dominance of species buoyancy force relative to the force of viscous hydrodynamic, leading to a significant rise in velocity for both Casson as well as Newtonian fluids. The value of the positive Grashof number corresponds to the physical cooling of the plates. Essentially, buoyant force

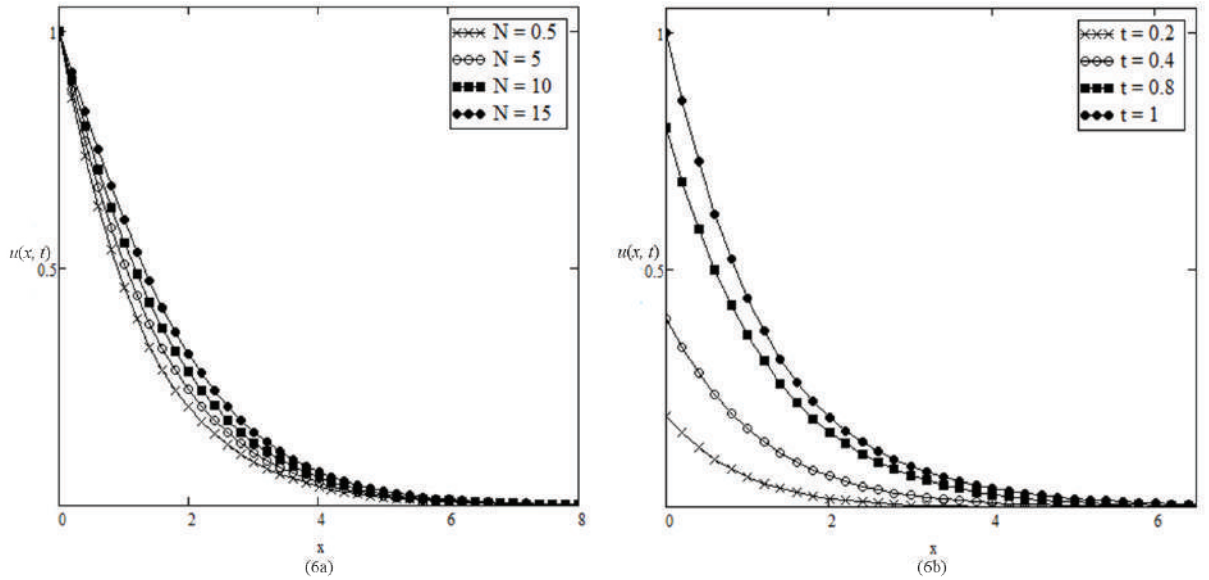


Figure 6. Velocity profiles of different radiation parameter, *N* (6a) and time, *t* (6b).

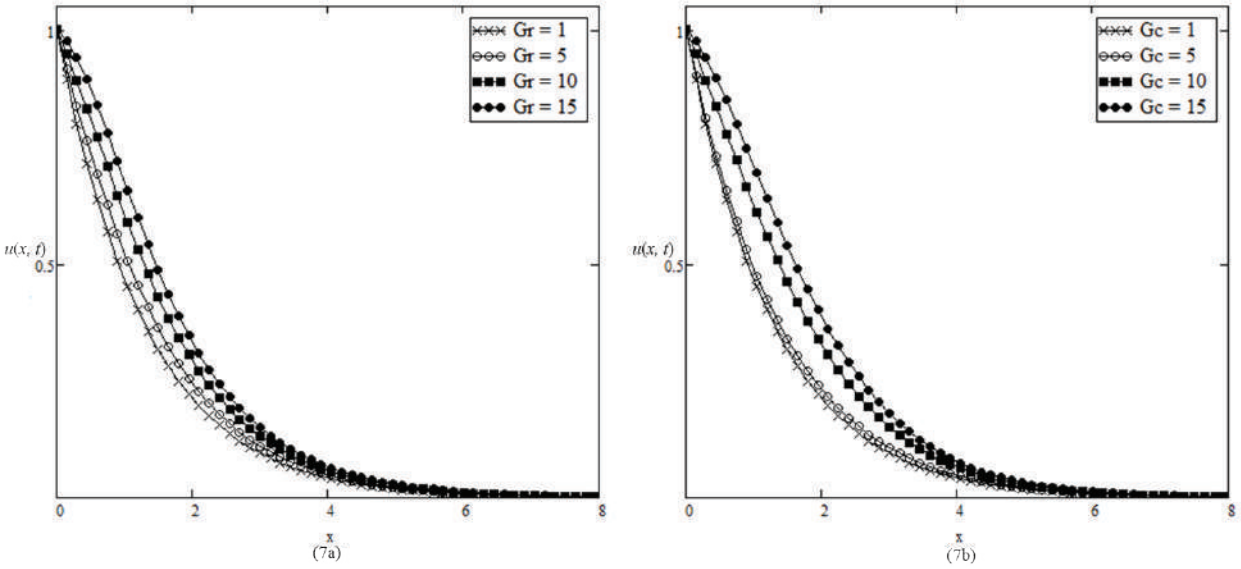


Figure 7. Velocity profiles of different Grashof number, *Gr* (7a) and Grashof concentration number, *Gc* (7b).

prevails over viscous force, complicating the flow dynamics due to its coupling with mass and thermal aspects.

CONCLUSION

The study establishes a mathematical solution for the influence of the Casson fluid parameter on MHD convective heat and mass transfer over an accelerating plate in a porous medium. Important considerations, such as the impact of chemical reactions and radiation, are analysed. The results, obtained through Laplace transform techniques, are acceptable and provide insights into fluid behaviour under the considered conditions. The study's findings have practical implications for applications within engineering and technology fields. In summary, we observed that:

- It is observed that increasing the *Sc* number leads to a reduction in the concentration profile.
- Temperature progressively increases with rising time, *t*.
- An increase in the *Pr* number leads to a decrease in temperature.
- An increase in the radiation constraint, *N* results in a reduction in both the thermal boundary layer thickness and the temperature profile.
- The trend indicates that an increase in the Casson parameter, γ reduces the fluid velocity.
- The velocity is observed to decrease with an increase in magnetic field strength, *M*.
- The velocity increases notably with higher values of the chemical reaction coefficient, *Kr*.
- The velocity decreases in the presence of thermal radiation, *N*.
- The fluid velocity increases over time, *t*.
- A steady elevation in velocity is noticed with the increasing Grashof number, *Gr*.
- An increase in the *Gc* number indicates that species buoyancy force dominates over the viscous hydrodynamic force, resulting in a substantial increase in velocity for Casson fluid.

NOMENCLATURE, SYMBOL AND SUBSCRIPT

γ	Casson parameter fluid in the x – direction
x	fluid in the x – direction
t	Time (s)
u'	velocity (ms^{-1})
T'	temperature (K)
C'	concentration ($molL^{-1}$)
ρ	fluid density (kgm^{-3})
μ	Dynamic viscosity ($kgm^{-1}\,s^{-1}$)
g	acceleration due to gravity (ms^{-2})
β	thermal expansion ($1\,/\,K$)
σ	electrical conductivity ($S\,/\,m$)
B_0	Magnetic field ($Nm^{-1}A^{-1}$)
k	thermal conductivity ($Wm^{-1}K^{-1}$)
φ	porosity of medium
K	permeability of medium (m^2)
c_p	specific heat at constant pressure ($Jkg^{-1}K^{-1}$)
q_r	radiative heat flux (Wm^{-2})
D	mass diffusion (m^{-3})
Kr	chemical reaction parameter (s^{-1})
Pr	Prantl number
Sc	Schmidt number
Gr	Grashof number
Gc	Grashof concentration number

ACKNOWLEDGEMENT

The authors express their gratitude to Ministry of Higher Education Malaysia for supporting this work through the Fundamental Research Grant Scheme, referenced as FRGS/1/2024/STG06/UMP/02/9 (Universiti Malaysia Pahang Al-Sultan Abdullah reference: RDU240132).

AUTHORSHIP CONTRIBUTIONS

Authors equally contributed to this work.

DATA AVAILABILITY STATEMENT

The authors confirm that the data that supports the findings of this study are available within the article. Raw data that support the finding of this study are available from the corresponding author, upon reasonable request.

CONFLICT OF INTEREST

The author declared no potential conflicts of interest with respect to the research, authorship, and/or publication of this article.

ETHICS

There are no ethical issues with the publication of this manuscript.

STATEMENT ON THE USE OF ARTIFICIAL INTELLIGENCE

Artificial intelligence was not used in the preparation of the article.

REFERENCES

[1] Kodi R, Mopuri O, Sree S, Konduru V. Investigation of MHD Casson fluid flow past a vertical porous plate under the influence of thermal diffusion and chemical reaction. Heat Transf 2022;51:377–394. [CrossRef]

[2] Li S, Raghunath K, Alfaleh A, Ali F, Zaib A, Khan MI, et al. Effects of activation energy and chemical reaction on unsteady MHD dissipative Darcy–Forchheimer squeezed flow of Casson fluid over horizontal channel. Sci Rep 2023;13:2666. [CrossRef]

[3] Sulochana C, Aparna SR, Sandeep N. Heat and mass transfer of magnetohydrodynamic Casson fluid flow over a wedge with thermal radiation and chemical reaction. Heat Transf 2021;50:3704–3721. [CrossRef]

[4] Sene N. Solution procedure for fractional Casson fluid model considered with heat generation and chemical Reaction. Sustainability 2023;15:5306. [CrossRef]

[5] Kumar MA, Reddy YD, Goud BS, Rao VS. An impact on non-Newtonian free convective MHD Casson fluid flow past a vertical porous plate the existence of Soret, Dufour, and chemical reaction. Int J Ambient Energy 2022;43:7410–7418. [CrossRef]

[6] Akaje TW, Olajuwon BI, Raj MT. Computational analysis of the heat and mass transfer in a casson nanofluid with a variable inclined magnetic field. Sigma J Eng Nat Sci 2023;41:512–523. [CrossRef]

[7] Osman HI, Vieru D, Ismail Z. Transient Axisymmetric Flows of Casson Fluids with Generalized Cattaneo's Law over a Vertical Cylinder. Symmetry 2022;14:1–14. [CrossRef]

[8] Hussanan A, Aman S, Ismail Z, Salleh MZ, Widodo B. Unsteady natural convection of sodium alginate viscoplastic casson based based nanofluid flow over a vertical plate with leading edge accretion/ablation. J Adv Res Fluid Mech Therm Sci 2018;45:92–98.

[9] Aman S, Zokri SM, Ismail Z, Salleh MZ, Khan I. Casson model of MHD flow of SA-based hybrid nanofluid using Caputo time-fractional models. Defect Diffus Forum 2019;390:83–90. [CrossRef]

[10] Mittal AS, Patel HR. Influence of thermophoresis and Brownian motion on mixed convection two dimensional MHD Casson fluid flow with non-linear radiation and heat generation. Physica A Stat Mech Appl 2020;537:122710. [CrossRef]

[11] Shahrim MN, Mohamad AQ, Jiann LY, Zakaria MN, Shafie S, Ismail Z, et al. Exact solution of fractional convective Casson fluid through an accelerated plate. CFD Letters 2021;13:15–25. [CrossRef]

[12] Hafez NM, Abd-Alla AM, Metwaly TMN. Influences of rotation and mass and heat transfer on MHD peristaltic transport of Casson fluid through inclined plane. Alex Eng J 2023;68:665–692. [CrossRef]

[13] Gholinia M, Javadi H, Gatabi A, Khodabakhshi A, Ganji DD. Analytical study of a two-phase revolving system of nanofluid flow in the presence of a magnetic field to improve heat transfer. Sigma J Eng Nat Sci 2019;37:341–360.

[14] Kodi R, Mopuri O. Unsteady MHD oscillatory Casson fluid flow past an inclined vertical Porous plate in the presence of chemical reaction with heat absorption and Soret effects. Heat Transf 2022;51733–752. [CrossRef]

[15] Ismail Z, Hussanan A, Khan I, Shafie S. MHD and radiation effects on natural convection flow in a porous medium past an infinite inclined plate with ramped wall temperature: An exact analysis. Int J Appl Math and Stat 2013;45:77–86.

[16] Prasad KV, Vajravelu K, Vaidya H, Basha NZ, Umesh V. Thermal and species concentration of MHD Casson fluid at a vertical sheet in the presence variable fluid properties. Ain Shams Eng J 2018;9:1763–1779. [CrossRef]

[17] Jagadesh V, Sreenadh S, Ajithkumar M, Lakshminarayana P, Lakshminarayana P, Sucharitha G. Investigation of dissipative heat transfer and peristaltic pumping on MHD Casson fluid flow in an inclined channel filled with porous medium. Numer Heat Trans B Fund 2023;85:1654–1672. [CrossRef]

[18] Raza J, Oudina FM, Ali H, Sarris IE. Slip effects on Casson nanofluid over a stretching sheet with activation energy: RSM analysis. Front Heat Mass Transf 2024;22:1017–1041. [CrossRef]

[19] Dharmaiah G, Oudina FM, Balamurugan KS, Vedavathi N. Numerical analysis of the magnetic dipole effect on a radiative ferromagnetic liquid flowing over a porous stretched sheet. Fluid Dyn Mater Process 2023;20:293–310. [CrossRef]

[20] Kataria HR, Patel HR. Radiation and chemical reaction effects on MHD Casson fluid flow past an oscillating vertical plate embedded in porous medium. Alex Eng J 2016;55:583–595. [CrossRef]

[21] Akinbo BJ, Olajuwon BI. Heat and mass transfer in Magnetohydrodynamics (MHD) flow over a moving vertical plate with convective boundary condition in the presence of thermal radiation. Sigma J Eng Nat Sci 2019;37:1031–1053.

[22] Omar NFM, Osman HI, Mohamad AQ, Jusoh R, Ismail Z. Effects of Radiation and Magnetohydrodynamic on Unsteady Casson Fluid Over Accelerated Plate. J Adv Res Fluid Mech Therm Sci 2021;85:93–100. [CrossRef]

[23] Khan H, Qayyum M, Khan O, Ali M. Unsteady squeezing flow of Casson fluid with magnetohydrodynamic effect and passing through porous medium. Math Probl Eng 2016;2016:4293721. [CrossRef]

[24] Khan D, Khan A, Khan I, Ali F, Karim F, Tlili I. Effects of relative magnetic field, chemical reaction, heat generation and Newtonian heating on convection flow of Casson fluid over a moving vertical plate embedded in a porous medium. Sci Rep 2019;9:400. [CrossRef]

[25] Goud BS, Kumar PP, Malga BS. Effect of heat source on an unsteady MHD free convection flow of Casson fluid past a vertical oscillating plate in porous medium using finite element analysis. Partial Differ Equ Appl Math 2020;2:100015. [CrossRef]

[26] Jalili P, Azar AA, Jalili B, Ganji DD. Study of nonlinear radiative heat transfer with magnetic field for non-Newtonian Casson fluid flow in a porous medium. Results Phys 2023;48:106371. [CrossRef]

[27] Vera MR, Niño Y, Valencia A. On the application of the fourier series solution to the hydromagnetic buoyant two-dimensional laminar vertical jet. Math Probl Eng 2012;2012:986834. [CrossRef]

[28] Kumar KL. Engineering Fluid Mechanics. 8th Ed. New Delhi: S. Chand; 2014.

[29] Kumar DS. Fluid Mechanics and Fluid Power Engineering. 8th ed. New Delhi: Katson Books; 2013.

[30] Modi PN, Seth SM. Hydraulics & Fluid Mechanics Including Hydraulics Machines. 19th ed. New Delhi: Standard Book House; 2017.

[31] Manshoor B, Khalid A, Sapit A, Zaman I, Mohammad AN. Numerical solution of Burger's equation based on Lax-Friedrichs and Lax-Wendroff schemes. AIP Conf Proc 2017;1831. [CrossRef]

[32] Egbako UA, Adeboye KR. One-Step, Sixth Order Numerical Method via Pade Approximations for the Solutions of Stiff Differential Equations. Am J Comput Appl Math 2012;2:10–13. [CrossRef]

[33] Nazri NN, Manshoor B, Zaman I, Didane DH, Abdelaal MAS, Ibrahim MN. Velocity and shear stress distribution of laminar flow between parallel plate by laplace transform approach. J Complex Flow 2022;4:19–23.

[34] Seilabi SE. Dimensional analysis and analytical solutions. In: El-Amin MF, editors. Numerical Modeling of Nanoparticle Transport in Porous Media. 1st ed. Amsterdam: Elsevier; 2023. p. 33–56.

[35] Woodbury KA, Najafi H, Monte F, Beck JV. Inverse Heat Conduction: Ill-Posed Problems. 2nd ed. New Jerjey: Wiley; 2023.

[36] Kucheva NA. Analytical solution of the problem of thermoelasticity for a plate heated by a source with a constant heat supply on one surface. Turk J Comput Math Educ 2021;12:1622–1633.

[37] Kato S, Matsuda S. Analytical solution for the problem of one-dimensional quasi-steady non-charring ablation in a semi-infinite solid with temperature-dependent thermo-physical properties. Therm Sci Eng Prog 2022;3:101181. [CrossRef]

[38] Noranuar WNN, Mohamad AQ, Lim YJ, Shafie S. Analytical Simulation of Magnetohydrodynamics Casson Blood Flow using Carbon Nanotubes in a Channel with Atherosclerosis Condition. Semarak Current Biomedical Res J 2024;1:1–17. [CrossRef]

Sigma J Eng Nat Sci, Vol. 44, No. 1, pp. 273–291, February, 2026

Sigma Journal of Engineering and Natural Sciences
Web page info: https://sigma.yildiz.edu.tr
DOI: 10.14744/sigma.2025.00000

Research Article

Image segmentation for semi-supervised fuzzy clustering with KL-divergence using Kernel method

Muthulakshmi K[1], Jayalakshmi M[1,*]

[1]*Department of Mathematics, Vellore Institute of Technology, Vellore, Tamil Nadu, 632014, India*

ARTICLE INFO

Article history
Received: 10 September 2024
Revised: 17 October 2024
Accepted: 08 December 2024

Keywords:
Fuzzy Cluster; Kernel Distance Measures; Robustness; Semi-Supervised; Uncertainty

ABSTRACT

Image segmentation is computer vision and analysis of images. However, several segmentations couldn't be manageable due to high noise levels. It is tough to deal with semi-supervised fuzzy clustering since it is not robust, and reduction needs to be improved. Many researchers have developed in this cluster. Our research focuses on adding noise, reducing noise, and applying our techniques to get detailed, clear images. Now, we introduce the robust approach kernel method based on semi-supervised fuzzy clustering with Kullback-Leibler divergence. It incorporates Kullback-Leibler divergence, and semi-supervised clustering is of essential significance. The primary benefit of robust semi-supervised fuzzy clustering is that it manages uncertainty data and kernel distance measures to capture the similarity between data points, enhancing segmentation performance. We use various strategies to introduce noise and minimise it compared to kernel robustness semi-supervised fuzzy clustering with Kullback-Leibler divergence. The effectiveness of the recommended technique was evaluated using synthetic datasets, the publicly accessible simulated human brain Magnetic Resonance Imaging dataset, and the BraTS2020 medical imaging and lung computed tomography scans. The experimental findings show that the suggested method outperforms existing algorithms in peak signal noise ratio, accuracy, precision, F1 score, and Jaccard index.

Cite this article as: K M, M J. Image segmentation for semi-supervised fuzzy clustering with KL-divergence using Kernel method. Sigma J Eng Nat Sci 2026;44(1):273–291.

INTRODUCTION

Image segmentation is the most essential need; day by day, they can quickly analyse something early. However, traditional approaches often break down when dealing with complex images with a lot of noise. The noise reduction achieved by traditional fuzzy clustering approaches needs to improve due to their lack of robustness. Because it produces precise images without ionising radiation, Magnetic Resonance Imaging (MRI) is crucial to modern medicine and ensures patient safety. Because MRI can produce multidimensional, high-contrast images, it is beneficial in the research of more delicate brain regions, such as the white matter (WM), grey matter (GM), and cerebrospinal fluid (CSF). It is essential for target detection and pattern recognition tasks in medical image processing. Many segmentation algorithms have developed, such as spectral clustering

***Corresponding author.**
*E-mail address: m.jayalakshmi@vit.ac.in

This paper was recommended for publication in revised form by Editor-in-Chief Ahmet Selim Dalkilic

Published by Yıldız Technical University Press, İstanbul, Turkey
© Author. This is an open access article under the CC BY-NC license (http://creativecommons.org/licenses/by-nc/4.0/).

approaches [1], density clustering [2], threshold-based methods [3], and level set methods [4].

With a large amount of MRI data generated daily, faster and more accurate analysis of this data is desired, which requires skilled radiologists. However, radiologists manually analyse these images, which is time-consuming. Further, the varying knowledge level of radiologists makes analysing these images inconsistent. All these factors require automated algorithms to support radiologists in providing quicker and more efficient analysis of these images. Supervised learning is completely labeled data. Unsupervised learning is completely unlabeled samples [5]. It is used for assigning data points to clusters when there is no available information about the correct clustering. Semi-supervised and unsupervised learning are more favorable than supervised learning since they are time-consuming and most practical real-world situations do not require previous knowledge. In this literature introduces many automated medical image segmentation methodologies, including clustering algorithms. Clustering belongs to the class of unsupervised learning methods in which there is no given information about the labels of the data elements, dissimilar to classification methods. It is most successful because it provides a decent trade-off between time complexity and segmentation quality, a key shortcoming of most other approaches. One of the popular techniques is fuzzy set theory, especially in medical image segmentation, because of the inherent ambiguity of images and the complexity of human vision. Fuzzy theory and clustering technologies have generated a lot of academic interest. Deep learning is frequently used to assess comparable performance indicators like accuracy (Acc), precision (Pre), recall (RC), and F1 scores have been evaluated [6]. Many clustering algorithms are available in the literature, broadly categorised into hard clustering [7] and soft clustering [8,9] strategies. Methods like kernel-based algorithms [10], SVM [11], and K-means clustering have garnered significant attention, leading to several extensions such as fuzzy ISODATA [1], kernel principal component analysis, KFDA [12], neutrosophic set [13], kernel-based algorithms, and Grey Wolf Optimizer [14]. RBF networks [1] using segment regions of clusters have shown to be particularly advantageous and may have been applied to overcome issues in numerous communication systems.

Bezdek et al. created the fuzzy c-means (FCM) clustering, a soft clustering method inspired by Zadeh's fuzzy set theory [15,16]. Pixels can be assigned to many clusters at once by changing their degree of membership. FCM is a center-based clustering algorithm that modifies the degree of membership inversely based on a pixel's distance from the cluster centers [17,18]. Many researchers have been attempting to improve the FCM algorithm for medical image segmentation, addressing difficulties including low sharpness and poor understanding, which need clarification. However, research has found problems with FCM-based clustering algorithms due to reluctance when allocating membership functions. As a result, several researchers have developed the intuitionistic fuzzy c-means (IFCM) based on an intuitionistic fuzzy set (IFS) expanded by Atanassov [19], which considers membership, non-membership and hesitation degrees, hence enhancing clustering outcomes for imprecise data. FCM uses Euclidean distance in the original feature space, making it a less noisy environment, whereas kernel-based fuzzy clustering transforms data into a higher-dimensional space, improving cluster [20]. Lavanya [21] developed the modified quick kernel-induced intuitionistic fuzzy generator to enhance input images by minimising uncertainty. The grey-level histogram of the morphologically reconstructed IFS picture is subsequently examined utilising the kernel distance of IFCM clustering [14]. Additionally, Bui Cong Cuong [22] published image fuzzy sets in 2014, paving the way for the development of picture fuzzy clustering (PFCM) for tumor segmentation, which accounts for degrees of rejection, membership, neutrality, and non-membership. Chengmao Wu [23] enhanced the robustness of prior PFCM algorithms by resolving issues related to the selection of spatial constraint parameters, leading to the development of a novel PFCM, the resilient dynamic semi-supervised symmetric regularised PFCM [24], which incorporates Kullback-Leibler (KL) divergence [25] and spatial information prerequisites. Inder Khatri also kernel fuzzy clustering, which can explore non-linear relations of pixels in an image [26]; its basic idea is to implicitly transform the input data into a higher dimensional feature space via a nonlinear map, which greatly increases the possibility of linear separability of the patterns in the feature space, then perform FCM in the feature space, which enhances boundary detection and adapts to complex shapes [9]. This method calculates fuzzy memberships with greater precision, mitigating boundary leakage and enhancing contour accuracy despite noise, as an extension of image fuzzy set-based clustering techniques that employ picture fuzzy sets and the KL divergence metric. In 2015, R. R. Gharieb [26] proposed a method for integrating local membership data into conventional FCM clustering via regularisation using KL divergence. Kamil Kmita [12] developed a scaling factor α that affects partial supervision as a nonlinear function in fuzzy clustering. Then developed semi-supervised clustering improves unsupervised clustering algorithms, and labeled data is highly scarce. Acquiring labeled samples is difficult and laborious. The labelling of all data is a labour-intensive endeavour because to the substantial volume of real-world data and the rapid pace of data generation, particularly in a streaming data context. Semi-supervised fuzzy clustering analysis of scaling factor descriptions validate their similarity and corroborate the interpretation by Pedrycz and Waletzky [9]. Kernel-based semi-supervised clustering [27] has been proposed and applied in many fields. According to the scaling factor, optimization requires balancing supervised and unsupervised components, which results in improved image feature interpretation and the ability to do further clustering. It improves the algorithm using KL-divergence, which helps maintain the two-probability distribution. It also helps

measure spatial data distribution, ensuring that the clustering process remains sensitive to noise and uncertainty while preserving the structure of the segmented regions. In my research case, modifying the algorithm improves the clustering accuracy. It has been successfully used in classification and clustering problems. Morphological reconstruction has been smoothing out excess connected pixels while retaining contour information to understand the clustering process better. It addresses the problem of balancing the number of segmented regions with the contour accuracy. Clustering methods are applied after the image's grey-level histogram to save processing time. Finally, the Gaussian kernel distance measure is utilized to compute the distance measure in higher dimensional feature space. Due to the transformation of data points in higher dimensional feature space, the Gaussian kernel can solve the problem of inherent non-linearity in data without increasing the computational complexity. We incorporate this method by implementing Kernel based on semi-supervised fuzzy clustering with KL-divergence (KSSFKL) on the histogram of morphologically rebuilt images and a unique FCM that clusters complicated data without hesitation and in less time, which gives a better tradeoff between robustness to noise and shape preservation.

In summary of major contribution:

1. The clustering optimization problem is formulated within a semi-supervised theoretical framework, effectively addressing noise and non-linearity. A unique semi-supervised FCM method is being developed to improve cluster representation capabilities and decision-making.
2. The proposed method reduces noise in segmentation by incorporating KL divergence metrics. In addition, kernel distance aims to handle non-linear systems effectively.
3. As a result, the proposed clustering approach mitigates noise and non-linear structures found in images and substantially enhances segmentation tasks, providing a promising prospect for future applications.

The remainder of the article is structured into five sections, each building upon the previous one. Section 2 delineates the preparatory measures necessary for the proposed methodology, establishing the foundation for our research. Section 3 comprehensively elucidates the clustering process, which constitutes the essence of our methodology. Section 4 subsequently concentrates on parameter selection and experimental analysis, utilising the techniques from preceding parts. Section 5 presents and elucidates the calculated results derived from our experimental endeavours. Finally, sections 6 and 7 discuss the suggested technique and the conclusion of our study.

PRELIMINARIES

This section comprises definitions and explanations of the fundamental concepts utilized in this study. It delineates the fundamental principles and approaches utilised, together with the corresponding notations employed throughout the work.

Fuzzy C-means Clustering

The incorporation of fuzzy logic into the FCM technique represents an extension of the widely-used K-means algorithm for clustering. The FCM algorithm, like K-means, is iterative, with a preset beginning grouping and several clusters (C). Let $T = (y_1, y_2, \ldots, y_N)$ denote the collection of data points, and $V = \{v_1, v_2, \ldots, v_C\}$ represent the center of cluster. FCM algorithm aims to minimize the following objective function to divide N data points into C clusters.

$$J = \sum_{j=1}^{N}\sum_{i=1}^{C} u_{ij}^{m} \left\|y_j - v_i\right\|^2, \quad 1 < m < \infty, \tag{1}$$

The fuzzy partition matrix $U = (u_{ij})_{C*N}$ meets the following conditions, with m representing the weighting exponent:

$$u_{ij} \in [0,1], \quad \sum_{i=1}^{C} u_{ij} = 1, 1 \le i \le C, 1 \le j \le N \tag{2}$$

where the value of membership u_{ij} for the jth pixel in the ith cluster, denoted by v_i, is determined by the square Euclidean distance $\|y_j - v_i\|^2$. Here, $m \in [1,\infty]$ is an integer that regulates the fuzziness exponent. The membership degree u_{ij} and the cluster center v_i can be expressed using the Lagrange multiplier method as follows:

$$u_{ij} = \frac{\left(\left\|y_j - v_i\right\|^2\right)^{\frac{-1}{m-1}}}{\sum_{k=1}^{C}\left(\left\|y_j - v_k\right\|^2\right)^{\frac{-1}{m-1}}} \tag{3}$$

$$v_i = \frac{\sum_{j=1}^{N} u_{ij}^{m}\, y_j}{\sum_{j=1}^{N} u_{ij}^{m}}, \quad 1 \le i \le C \tag{4}$$

Semi-supervised Clustering

Traditional fuzzy clustering methods treat pixels independently, which is not optimal for pixel clustering. Pedrycz et al. [12] proposed an SSFCM to improve FCM clustering performance. The optimization models for the SSFCM algorithm are delineated as follows [24]:

$$\begin{aligned} J = &\sum_{j=1}^{N}\sum_{i=1}^{C} u_{ij}^{m} \left\|y_j - v_i\right\|^2 \\ &+ \rho \sum_{j=1}^{N}\sum_{i=1}^{C} \left(u_{ij} - f_{ij} b_i\right)^m \left\|y_j - v_i\right\|^2 \end{aligned} \tag{5}$$

where $\sum_{j=1}^{N} u_{ij}, i = 1, 2, \ldots, N$. Ref. [1] provides a detailed description of the parameters ρ, b_i, and supervised information f_{ij}. The membership degree u_{ij} and cluster center v_i can be expressed as follows.

$$u_{ij} = \frac{1}{1+\rho}\left[\frac{1+\rho\left(1-b_i\sum_{k=1}^{C} f_{ij}\right)}{\sum_{k=1}^{C}\frac{\|y_j - v_i\|^2}{\|y_j - v_k\|^2} + \rho f_{ij} b_i}\right] \quad (6)$$

$$v_i = \frac{\sum_{j=1}^{N} u_{ij}^m y_j + \rho\sum_{j=1}^{N}\left(u_{ij} - f_{ij}b_i\right)^2 y_j}{\sum_{j=1}^{N} u_{ij}^m + \rho\sum_{j=1}^{N}\left(u_{ij} - f_{ij}b_i\right)^2} \quad (7)$$

If $\rho = 0$, the SSFCM method transforms into the standard FCM algorithm. Thus, the FCM algorithm is an upgraded version of the SSFCM technique.

Fuzzy c means with KL-Divergence

In Ref. [14], the FCM algorithm's objective function updates a regularisation technique that includes an entropy term. This approach [24] is defined as:

$$J = \sum_{j=1}^{N}\sum_{i=1}^{C} u_{ij}^m \|y_j - v_i\|^2 + \lambda\sum_{j=1}^{N} u_{ij}\log\frac{u_{ij}}{\pi_{ij}} \quad (8)$$

Where π_{ij} is represented as the average local membership function.

$$\pi_j = \frac{1}{N_k}\sum_{j=1}^{N} u_{ij}$$

As a result, the KL divergence [26] is minimized, guiding u_{ij} towards the membership value, and the average pixel π_{ij} consider as an adjacent neighbourhood. This strategy produces piecewise homogenous labeling and can be used to smooth noise. The equation (8) is minimized by:

$$u_{ij} = \frac{\pi_j \exp\left(-\frac{\|y_j - v_i\|^2}{\lambda}\right)}{\sum_{k=1}^{C}\pi_k \exp\left(-\frac{\|y_j - v_k\|^2}{\lambda}\right)} \quad (9)$$

$$v_i = \frac{\sum_{j=1}^{N} u_{ij}^m\, y_j}{\sum_{j=1}^{N} u_{ij}^m}, \quad 1 \le i \le C \quad (10)$$

PFCM

Cuong [22] developed the Picture Fuzzy Set (PFS) concept, which extends the traditional fuzzy set and IFS. A PFS defined on a non-empty set *X* and a positive degree in FCM represents the probability that a sample belongs to a particular cluster. As a result, the literature proposes a novel PFS with a clustering approach [28], with an optimization model described as:

$$J = \sum_{j=1}^{N}\sum_{i=1}^{C}\left(\frac{u_{ij}}{1-\zeta_{ij}-\varrho_{ij}}\right)^m \|y_j - v_i\|^2 \quad (11)$$

The following conditions are satisfied by the constraints:

$$0 \le u_{ij}, \zeta_{ij}, \varrho_{ij} \le 1, 0 \le u_{ij} + \zeta_{ij} + \varrho_{ij} \le 1, , i = 1,2,\dots,N.$$

$$\sum_{j=1}^{N}\left(\frac{u_{ij}}{1-\zeta_{ij}-\varrho_{ij}}\right)^m = 1\ , i = 1,2,\dots.,N$$

$$\sum_{j=1}^{N}\left(\zeta_{ij} + \varrho_{ij}/C\right) = 1\ , i = 1,2,\dots.,N.$$

Which as *N*, *C*, y_j and v_i represent the no. of samples, the no. of clusters, the ith sample in the dataset y_j, and the center of cluster of the jth cluster, respectively. Additionally, u_{ij}, ζ_{ij} and ϱ_{ij} denote the positive, neutral, and refusal degree of sample y_j belongs to the ith cluster.

$$u_{ij} = \frac{1-\zeta_{ij}-\varrho_{ij}}{\sum_{k=1}^{C}\left(\frac{\|y_j - v_i\|^2}{\|y_j - v_k\|^2}\right)^{\frac{1}{m-1}}} \quad (12)$$

$$v_i = \frac{\sum_{j=1}^{N}\left(\frac{u_{ij}}{1-\zeta_{ij}-\varrho_{ij}}\right)^m y_j}{\sum_{j=1}^{N}\left(\frac{u_{ij}}{1-\zeta_{ij}-\varrho_{ij}}\right)^m} \quad (13)$$

$$\zeta_{ij} = 1 - \varrho_{ij} - \frac{\frac{C-1}{C}}{\sum_{k=1}^{C}\frac{u_{ij}}{u_{ik}}\left(-\frac{\|y_j - v_i\|^2}{\|y_j - v_k\|^2}\right)^{\frac{1}{m-1}}} \quad (14)$$

$$\varrho_{ij} = 1 - \left(u_{ij} + \zeta_{ij}\right) - \left(1 - \left(u_{ij} + \zeta_{ij}\right)^{\alpha}\right)^{\frac{1}{\alpha}} \quad (15)$$

Kernel Method

Kernel-based machine learning techniques, such as SVM [29], Kernel Principal Component Analysis (KPCA) [11], and Kernel Fisher Discriminant (KFD) [30], have demonstrated efficiency in various classification and feature extraction tasks. The based-on-kernel approach facilitates [21] the feature mapping space from its original dimensionality to a kernel equation, transforming a higher-dimensional space and allowing for arbitrary nonlinearity. This characteristic enhances the linear machine's expressiveness, and its integration into clustering algorithms can improve their clustering power and accuracy. The main advantage of

kernel methods lies in the fact that the dot product in the kernel space is such that,

$$K(y_i, y_j) = \phi(y_i)^T \phi(y_j) \tag{16}$$

where y_i represents the data in the original space while $\phi(y_j)$ represent as the data in higher-dimensional space. Kernel equations that are frequently employed [24] include there are four kernel functions: linear, polynomial of degree p, Sigmoid and Gaussian radial basis function [31] (RBF). These are provided as follows:

$$\begin{aligned} K(y_i, y_j) &= y_j^T y_i \\ K(y_i, y_j) &= (1 + y_j^T y_i)^p \\ K(y_i, y_j) &= \tanh(\rho(y_j^T y_i) + \beta) \\ K(y_i, y_j) &= exp\left(-\frac{\|y_i - y_j\|^2}{\sigma^2}\right) \end{aligned}$$

Equation (16) allows the preceding equation to be represented as:

$$\|\phi(y_i) - \phi(y_j)\|^2 = K(y_i, y_i) + K(y_j, y_j) - 2K(y_i, y_j) \tag{17}$$

The Gaussian RBF kernel can be represented as:

$$\|\phi(y_i) - \phi(y_j)\|^2 = 2\left(1 - K(y_i, y_j)\right) \tag{18}$$

Similarly, the Euclidean distance between extra kernel spaces by applying a suitable kernel function in equation (17).

Kernel-based on picture fuzzy clustering with KL-divergence

Optimize PFS using kernel fuzzy clustering and KL-divergence metric, as described in [32-35].

$$\begin{aligned} J = &\sum_{j=1}^{N}\sum_{i=1}^{C}\left(u_{ij}(2 - \varrho_{ij})\right)\left(1 - k(y_j, v_i)\right) \\ &+ \gamma \sum_{j=1}^{N}\sum_{i=1}^{C} u_{ij}(2 - \varrho_{ij}) \log\frac{u_{ij}(2 - \varrho_{ij})}{\pi_{ij}} \\ &+ \sum_{j=1}^{N}\sum_{i=1}^{C}\left(\zeta_{ij}(\log\zeta_{ij} + \varrho_{ij})\right) \end{aligned} \tag{19}$$

Where $\pi_{ij} = \frac{1}{N}\sum_{j=1}^{N} u_{ij}(2 - \varrho_{ij})$

The following satisfied constraints:

$$\begin{aligned} &0 \le u_{ij}, \zeta_{ij}, \varrho_{ij} \le 1, \\ &0 \le u_{ij} + \zeta_{ij} + \varrho_{ij} \le 1, 1 \le i \le C, 1 \le j \le N \\ &\textstyle\sum_{i=1}^{C} u_{ij}(2 - \varrho_{ij}) = 1, 1 \le j \le N \\ &\textstyle\sum_{i=1}^{C}(\zeta_{ij} + \varrho_{ij}/C) = 1, 1 \le j \le N, \end{aligned}$$

Where $k(y_j, v_i) = \exp\left(-\frac{\|y_j - v_i\|^2}{\sigma^2}\right)$ is defined by kernel distance measure and where γ is the regularization parameter. Here, v_i for all $i = 1, 2, ..., C$ and $j = 1, 2, ..., N$, y_j represents the cluster centers and data point centroids. After solving the equation (19) is an optimization problem, the degree of membership values u_{ij}, center of cluster v_i, neutrality degree ζ_{ij}, and refusal degree ϱ_{ij} may be Langrage's indetermined multipliers method derived from the following condition:

$$u_{ij} = \frac{\pi_{ij}\exp\left(\frac{-(1 - y_j - v_i)}{\gamma}\right)}{\sum_{l=1}^{C}\pi_{lj}\exp\left(\frac{-(1 - y_j - v_i)}{\gamma}\right)}\frac{1}{(2 - \varrho_{ij})} \tag{20}$$

$$v_i = \frac{\sum_{j=1}^{N}\left(u_{ij}(2 - \varrho_{ij})\right)\left(k(y_j, v_i)\right)y_j}{\sum_{j=1}^{N}\left(u_{ij}(2 - \varrho_{ij})\right)\left(k(y_j, v_i)\right)} \tag{21}$$

$$\zeta_{ij} = \frac{\exp(-\varrho_{ij})}{\sum_{l=1}^{C}\exp(-\varrho_{ij})}\left(1 - \sum_{l=1}^{C}\frac{\varrho_{lj}}{C}\right) \tag{22}$$

$$\varrho_{ij} = 1 - (u_{ij} + \zeta_{ij}) - \left(1 - (u_{ij} + \zeta_{ij})^{\alpha}\right)^{\frac{1}{\alpha}} \tag{23}$$

MATERIALS AND METHODS

As previously mentioned, non-linear features and image noise present significant challenges for image segmentation. In this literature has proposed various fuzzy set theory-based techniques to address these difficulties. The main objective of this correct selection of regularization parameter values substantially impacts segmentation performance in noisy pictures. Figure 1 displays the main framework of the proposed approach.

Image segmentation in noisy and uncertain environments, especially medical images, poses significant challenges. This research presents a semi-supervised clustering strategy for image segmentation. It is one of the techniques that addresses the challenges of improving clustering accuracy under the supervision of a limited amount of data. In this case, the optimization using robust kernel-based semi-supervised fuzzy clustering optimization problem using the KL-divergence. This optimization issue consists of three words that attempt to overcome the constraints of present approaches. The first term uses kernel distance metrics to deal with non-Euclidean distance. The second term attempts to reduce noise during segmentation by using the KL divergence metric, adding neighbourhood information to assign pixel cluster labels appropriately by introducing model fuzziness. The third term improves clustering quality by minimizing the information required for

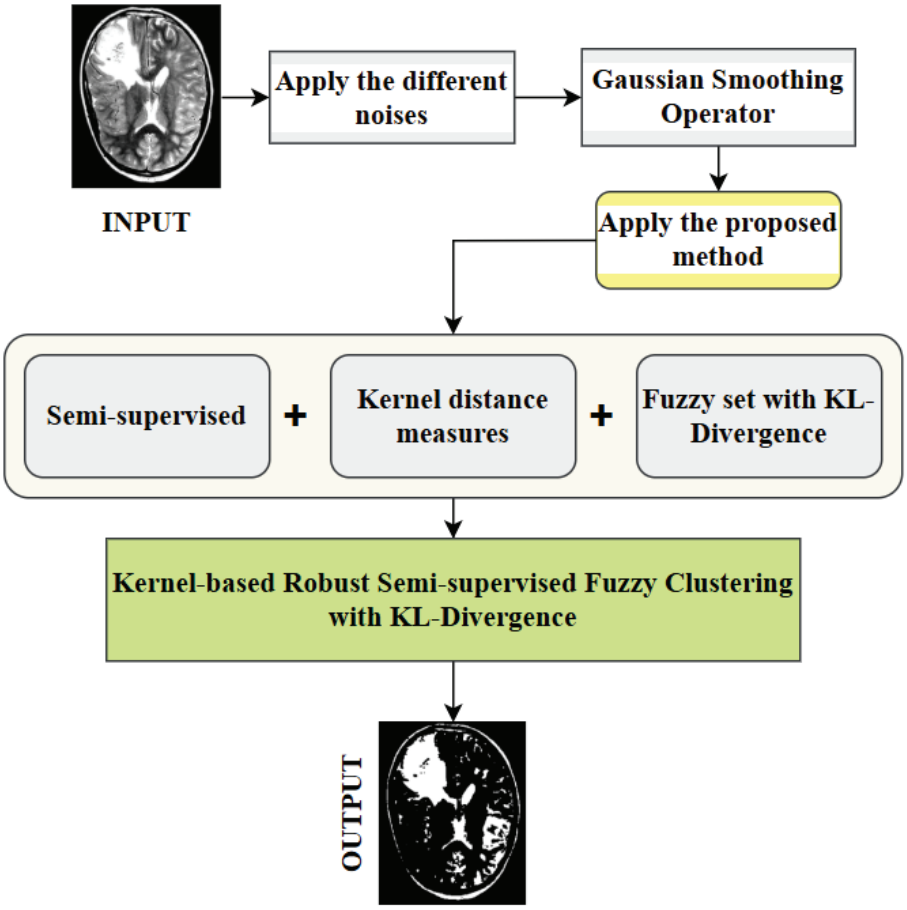


Figure 1. Flow chart of the proposed work

semi-supervised algorithms to acquire optimal cluster locations. This approach is defined as:

$$J = \sum_{j=1}^{N}\sum_{i=1}^{C} u_{ij}^{m}\left(1 - k(y_j, v_i)\right) + \rho \sum_{j=1}^{N}\sum_{i=1}^{C}\left(u_{ij} - f_{ij}b_i\right)^{m}\left(1 - k(y_j, v_i)\right) + \lambda \sum_{j=1}^{N}\sum_{i=1}^{C}\left(u_{ij}(\log u_{ij})\right) \quad (24)$$

$\rho \geq 0$ is a scaling factor that controls the ratio of supervised and unsupervised components in the optimization method. We employ a two-value boolean indicator $b = [b_k]$, with $k = 1, 2, ..., N$ with either 0 or 1 entries to discriminate between labeled and unlabeled structures. Similarly, $F = [f_{ik}]$ is the labeled patterns of the membership function recognized in matrix form, denoted as where $i = 1, 2, ..., C$, $K = 1, 2, ..., N$. Using the kernel distance metric, we use Gaussian representations for cluster centroids and data points. It deals with the non-linear structure present in data. Due to the transformation of data points in higher dimensional feature space, the kernel trick can solve the problem of inherent non-linearity present in data without increasing the computational complexity. After addressing the optimization issue, the value of membership function u_{ij} and center of cluster v_i and using calculating Lagrange's approach using indeterminate multipliers, as follows:

$$u_{ij} = \frac{\exp\left(\frac{-\lambda + 2(1+\rho)\left(1 - k(y_j, v_i)\right)\left[\rho\sum_{i=1}^{c} f_{ij}b_j - u_{ij}\right]}{\lambda}\right)}{\sum_{k=1}^{c}\exp\left(\frac{-\lambda + 2(1+\rho)\left(1 - k(y_j, v_k)\right)\left[\rho\sum_{i=1}^{c} f_{ij}b_j - u_{ij}\right]}{\lambda}\right)} \quad (25)$$

$$v_i = \frac{\sum_{j=1}^{N} u_{ij}k(y_j, v_i)y_j + \rho\sum_{j=1}^{N}\left(u_{ij} - f_{ij}b_i\right)^2 y_j}{\sum_{j=1}^{N} u_{ij}k(y_j, v_i)y_j + \rho\sum_{j=1}^{N}\left(u_{ij} - f_{ij}b_i\right)^2} \quad (26)$$

The primary purpose of this strategy is to reduce the weighted sum of squared distances between data points and their cluster centers while also integrating robust constraints and a regularisation term to encourage smooth cluster memberships. This iterative approach is intended to reduce the effect of noise and properly locate cluster

centers in noisy image environments (Appendix A). These are ensured that the following steps improves the clustering and decision-making is more reliable, even when faced with noise and uncertainty (Algorithm 1).

Algorithm 1. KKSFKL Algorithm
1: Step 1: Given the number of clusters C, parameters b and f choose the distance function and initialize the partition matrix including membership values.
2: Step 2: Calculate the cluster centers v_i using equation 26 and the distances between data points and cluster centers.
3: Step 3: Update the membership values u_{ij} in accordance with equation 25.
4: Step 4: If U - $U' < \delta$ then
5: Stop
6: Else
7: Set $U = U'$ and go to Step 2

Advantage
- ✓ The proposed semi-supervised clustering approach produces strong segmentation results by reducing the effects of noise and nonlinearity.
- ✓ Using KL-divergence together with kernel-based distance measures improves cluster descriptions and supports reliable segmentation, even under challenging conditions.

Disadvantage
- ✓ Our performance in achieving segmentation results is generally good, but we struggle with maintaining accuracy in the presence of noise.

PARAMETER SELECTION

In order to validate the efficacy of the proposed KSSFKL method, we have performed experiments on five open-access and synthetic datasets, two open brain tumor datasets and a computed tomography (CT) scan image. The experiment aims to show the effectiveness of the proposed KSSFKL clustering approach for image segmentation tasks for different kinds of images, including natural and medical images. Experiments are designed to check the proposed method's efficacy compared to other related methods such as FCM, FCMKL, PFCM, and KFPKL. The list of parameters is presented in Table 1. Quantitative and qualitative results are obtained on several images for comparison purposes. Evaluating PSNR, Acc, Pre, F1, and JI are used to measure the segmentation quality by comparing the predicted clusters against GT, mainly focusing on boundary accuracy and region overlap. They are used as quantitative measurements to assess the resilience of different clustering from segmentation approaches against noise. These metrics thoroughly assess the method's proficiency in precisely segmenting regions of interest while reducing noise and border inaccuracies. PSNR measures the image quality after segmentation, while accuracy, Jaccard index, and Dice coefficient evaluate how well the segmented regions match the GT. This research evaluates the algorithm's efficiency, which is described as several types of noise, and introduces it to different grayscale images for segmentation tests in Python. FCM, FCMKL, PFCM, KFPKL, and KSSFKL are suggested algorithms used in segmentation testing. PSNR, Acc, Pre, F1, and JI are used as quantitative measurements to assess the resilience of different clustering from segmentation approaches against noise. $\in = 0.0001$ is the iteration error, and then the maximum iteration is $t_{max} = 1000$.The statement KSSFKL gives better results compared to other algorithms implies that in experimental or empirical evaluations, KSSFKL in this performance metric is greater than the other performance.

Table 1. List of parameter values associated with each method

Method	Input Parameters & Value
FCM	m = 2, n = 5
FCMKL	m = 2, n = 4, λ = 1.0, h = 0.1
PFCMPFCM	m = 2, n = 5, α = 10
KFPKL	m = 3, n = 2, α = 1, γ = 1, σ = 10
KSSFKL	m = 2, n = 2, α = 10, λ = 10, σ = 70

Evaluations

To compare the performance of several clustering techniques honestly using segmentation, the improved peak signal noise ratio (PSNR) is used as a crucial assessment metric and to analyze the suggested algorithm's resilience to noise. The improved PSNR is as follows:

$$PSNR = 10log_{10}\left(\frac{255^2}{\text{MSE}}\right)$$

Here, mean square error (MSE) [20] measures the discrepancy between the segmentation results and the GT image achieved by the method. A higher PSNR value indicates the method's robustness against noise and provides reassurance that the model is less sensitive to noise during the segmentation process.

Furthermore, to completely evaluate the proposed algorithm's segmentation and clustering performance, we must use [24] pixel Acc, Pre, F1, and JI as metrics. These measures are described as follows:

The ratio of correctly identified total number of samples is used to calculate accuracy.

$$Acc = \frac{TP + TN}{TP + TN + FP + TN} \quad (27)$$

where *TP, TN, FP* and *FN* denote true positives, true negatives, false positives, and false negatives, respectively.

Pre quantifies the accuracy of positive predictions and is computed as:

$$Pre = \frac{TP}{TP + TN} \tag{28}$$

F1 balances Pre and RC, defined as

$$F1 = \frac{2\,Pre.RC}{Pre + RC} \tag{29}$$

where RC, also known as sensitivity, represents the fraction of *TP* cases properly detected by the model and is given as

$$RC = \frac{TP}{TP + FN} \tag{30}$$

The formula of JI can be expressed as

$$\text{JI} = \frac{\sum_{i=1}^{C} A_i \cap B_i}{\sum_{i=1}^{C} A_i \cup B_i} \tag{31}$$

A_i represents the number of pixels categorised into the ith class, B_i denotes the number of pixels in the ith class in the GT image, and C represents the overall number of clusters. The JI emphasises the agreement of overlapping areas in segmentation masks. These measurements provide vital insights into the performance and quality of image-processing algorithms, allowing academics and practitioners to evaluate the efficiency of different comparison methods. Higher pixel Acc, Pre, F1, and JI values imply better algorithm performance and segmentation outcomes.

EXPERIMENTAL RESULT

To further illustrate the variety of images from numerous standard datasets to demonstrate the approached method's robust anti-noise capabilities and excellent segmentation performance. These datasets include brain tumor images from Kaggle (https://www.kaggle.com/datasets/navoneel/brain-mri-images-for-brain-tumor-detection), chest CT scan images (https://www.kaggle.com/datasets/mohamed-hanyyy/chest-ctscan-images), authorised medical datasets of brain tumors (https://www.med.upenn.edu/cbica/brats2020/data.html), and synthetic images from open web sources. These distinct images are exposed to varying noise levels and tested to validate the suggested algorithm's performance. The testing results for analysing the noise images were clarified with parameter measurement tables for

Table 2. Comparison of image denoising methods under various noise types and evaluation metric

Noise	Index	FCM	FCMKL	PFCM	KFPKL	KSSFKL
Gaussian (0, 0.7)	PSNR	10.5304	10.5310	10.5310	**10.5311**	10.5003
	Acc	**0.9070**	0.8018	0.7620	0.8303	0.9011
	Pre	0.9088	**0.9107**	**0.9107**	**0.9107**	0.8360
	F1	**0.9079**	0.8528	0.8298	0.8687	0.8673
	JI	0.8654	0.4498	0.3746	0.5254	**0.9390**
S & P (5%)	PSNR	6.6477	**6.6733**	6.6420	6.6501	6.6178
	Acc	0.3385	0.5936	0.5817	**0.7377**	0.7268
	Pre	**0.7727**	0.7604	0.7614	0.7288	0.6331
	F1	0.4708	0.6667	0.6595	**0.7332**	0.6768
	JI	0.3240	0.4961	0.4847	0.5282	**0.6280**
Impulse (15)	PSNR	**4.5244**	4.4451	4.4111	4.4562	4.4452
	Acc	0.1815	0.2211	0.2349	0.2753	**0.2774**
	Pre	0.2750	0.2733	0.2769	0.2321	**0.2777**
	F1	0.2194	0.2444	0.2205	**0.2518**	0.2413
	JI	0.8828	0.9234	0.9144	**0.9229**	0.9180
Speckle (0.5)	PSNR	**5.9101**	5.8744	5.8744	5.8975	5.8431
	Acc	0.6145	0.5834	0.6949	0.7251	**0.7284**
	Pre	**0.7394**	**0.7394**	0.7386	0.7351	0.5564
	F1	0.6712	0.6522	0.7160	0.7301	**0.9329**
	JI	0.6761	0.6255	0.8517	0.8722	**0.9329**
Rician (30)	PSNR	6.6587	6.6269	6.6587	6.6354	**6.7245**
	Acc	0.7808	0.7825	0.7808	0.7828	**0.7845**
	Pre	0.7678	0.6124	**0.7678**	0.6255	0.7296
	F1	0.7742	0.6871	0.7742	**0.7928**	0.7845
	JI	0.9236	0.8154	0.9236	0.8154	**0.9378**

different noise levels. Experimental data indicate that the proposed method gets a good result analysis of the parameter evaluation.

Testing and analysis of images

To ensure that this suggested approach is comparable to other algorithms such as FCM, FCMKL, PFCM, and KFPKL. Figure 2 shows that the result of the performance of algorithms that present different noises during the segmentation extraction successfully exhibits smaller inhomogeneity and indicates superior segmentation performance and robustness. The denoising process is applied to various noise types in the original image (OI). Each row corresponding to different noise applies the level range of Gaussian noise (normalized variance of 0.7), salt and pepper noise (intensity of 0.4), impulse noise (rate of 0.5), speckle noise (normalized variance of 0.5), and Rician noise (standard deviation of 30). Then, noise reduction would be applied using Gaussian blur. This noise level enables a clear comparison of each algorithm, implying denoising performance under specific noise conditions. This assessment measures PSNR, accuracy, precision, F1 score, and Jaccard index on synthetic datasets.

Furthermore, the segmentation results are presented in Table 2, which crossovers the different segmentation results compared to the GT image. The bold values indicate the outperformance of other denoising techniques. Although these values, due to running time, create random variability, the more consistent yielding better segmentation results trend of this proposed method than various algorithms are significant. Our methodology: This technique is typically appropriate and attains greater segmentation accuracy, improving noise reduction and overall image clarity.

Figures 3-7 present bar graphs comparing the performance of various algorithms under different noise levels. These graphs are present in Figure 2, which illustrates the metrics evaluated across various noise intensities at the level of Gaussian; mean values of 0 and normalized variances

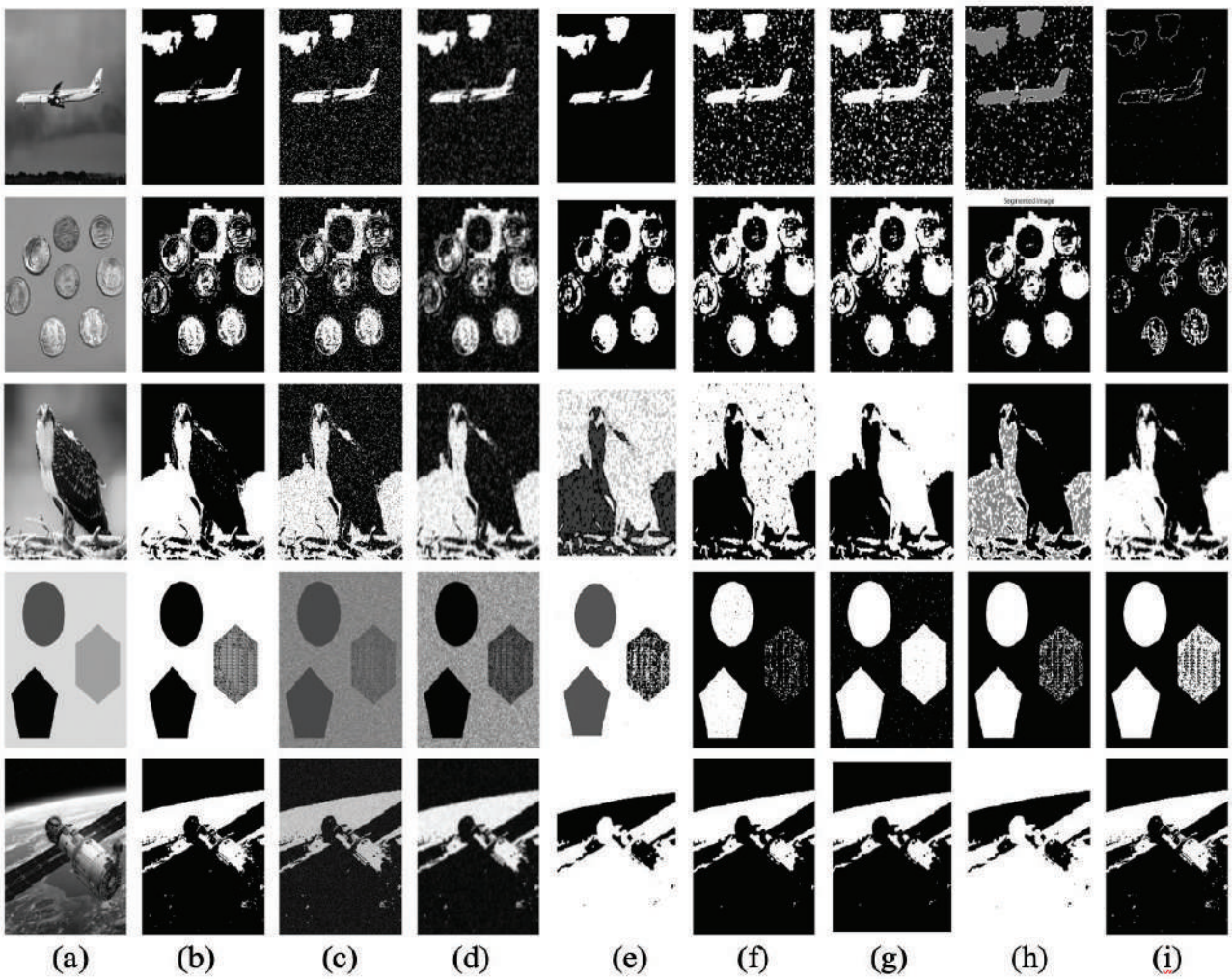


Figure 2. (a) OI; (b) Ground Truth; (c) Noise Image; (d) Denoise image; (e) FCM; (f) FCMKL; (g) PFCM; (h) KFPKL; (i) Proposed (KSSFKL).

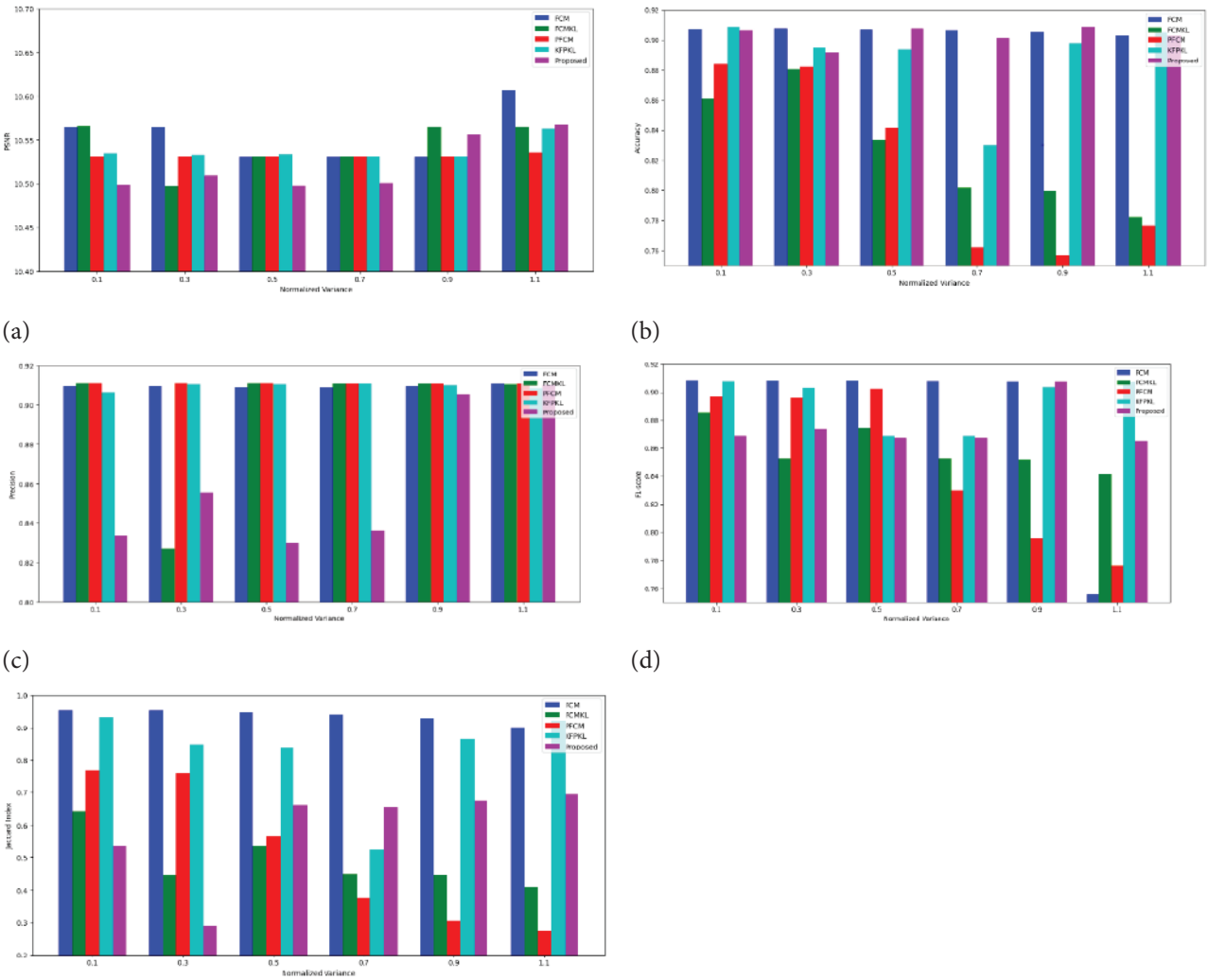


Figure 3. Figure 2 shows the performance curves of multiple techniques applied to the first-row image affected by Gaussian noise. a) PSNR; b) Acc; c) Pre; d) F1; e) JI.

from 0.1 to 1.1 are considered. Salt and pepper noise is intensities from 1% to 6%. Impulse noise is applied at a rate ranging from 5% to 30%. Speckle noise shows normalized variances from 0.1 to 1.1, and Rician noise has standard deviations increasing from 10 to 60. It is easy to handle. It is one of the statistical methods randomly added to the image function to generate this noise.

Medical Image Segmentation

Evaluating the method on both synthetic and real datasets ensures robustness, as synthetic data helps test theoretical aspects of the model, while real data validates its practical effectiveness in real-world scenarios like brain MRI or lung CT scans. Synthetic data are crucial in this interplay since they can provide large and diverse data. However, privacy is an important factor which is not guaranteed by data fidelity. To this end, best practices should be adopted for data protection, clearer standards for assessing identifiability, and proportionate regulatory approaches to facilitate innovation while ensuring privacy. Consequently, the accessibility of superior synthetic data can facilitate researchers in the development of multimodal AI models. Furthermore, synthetic data can enable the simulation of complex patient scenarios that might not be frequently encountered in real datasets, thereby enhancing the robustness of healthcare systems against rare but critical conditions. Moreover, by utilizing synthetic data, researchers can bypass many logistical and ethical hurdles that occur during the aggregation and analysis of multimodal data, thus accelerating the pace of research. Ultimately, the use of medical data can significantly advance personalised medicine, improving

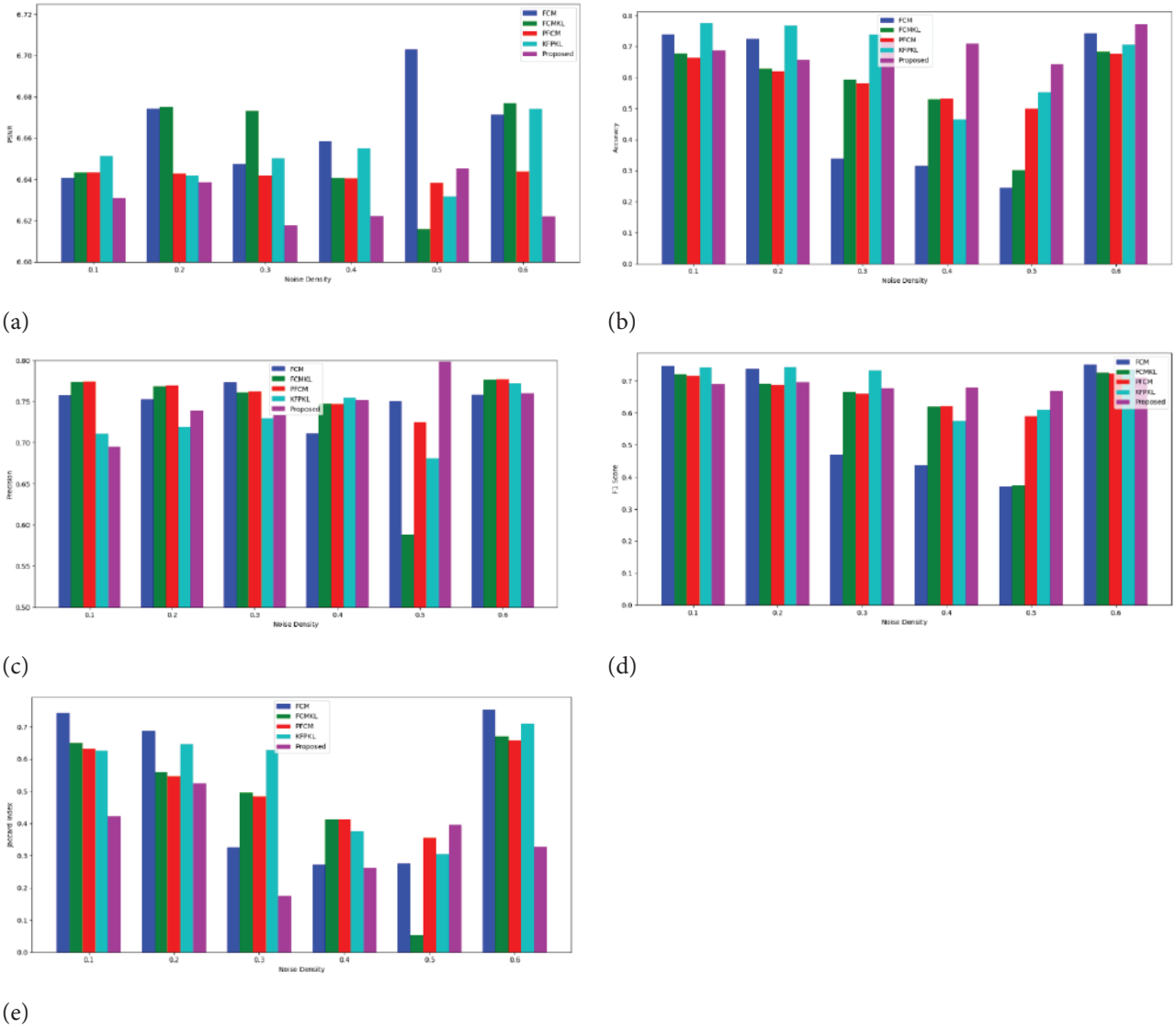


Figure 4. Figure 2 shows the performance curves of multiple techniques applied to the second-row image affected by salt noise. a) PSNR; b) Acc; c) Pre; d) F1; e) JI.

treatment efficacy and patient outcomes while upholding stringent data privacy standards. Now, we discuss the medical image segmentation of Brain MRI images and lung CT scan images. Image segmentation was formulated to segment different tissue types: WM, GM, and CSF—additionally, the Gaussian noise level range at 0.7 and salt and pepper noise (0.4). Then, denoise techniques applying Gaussian blur detail segmentation results are shown in Figure 8, which implies the FCM, FCMKL, PFCM, KFPKL, and proposed method. KSSFKL, better than other methods, reduces noise reduction through kernel approach and KL-divergence, which allows the clustering process to focus on relevant image features while suppressing the influence of noise. This results in more stable and accurate segmentation, especially in medical image analysis, where noise can obscure critical details. Each clustering method resulted in the segmentation of different noise types; the extraction result is shown in Figure 9. We get more accurate segmentation results compared to other cluster techniques to evaluate the similarity measurement compared to the GT image to existing output image to draw the bar graph presented in Figure 10 of accurate performance in MRI and CT scan images.

Visualize the Approach Method of Brats2020 without Noise

The Brats2020 dataset, known for its diverse and challenging brain tumor cases, was employed to test rigorously. Figure 11 illustrates the range defined by the parameter rho (ρ)= 5,10,15 and lambda (λ)= 5,10,15 with the call as

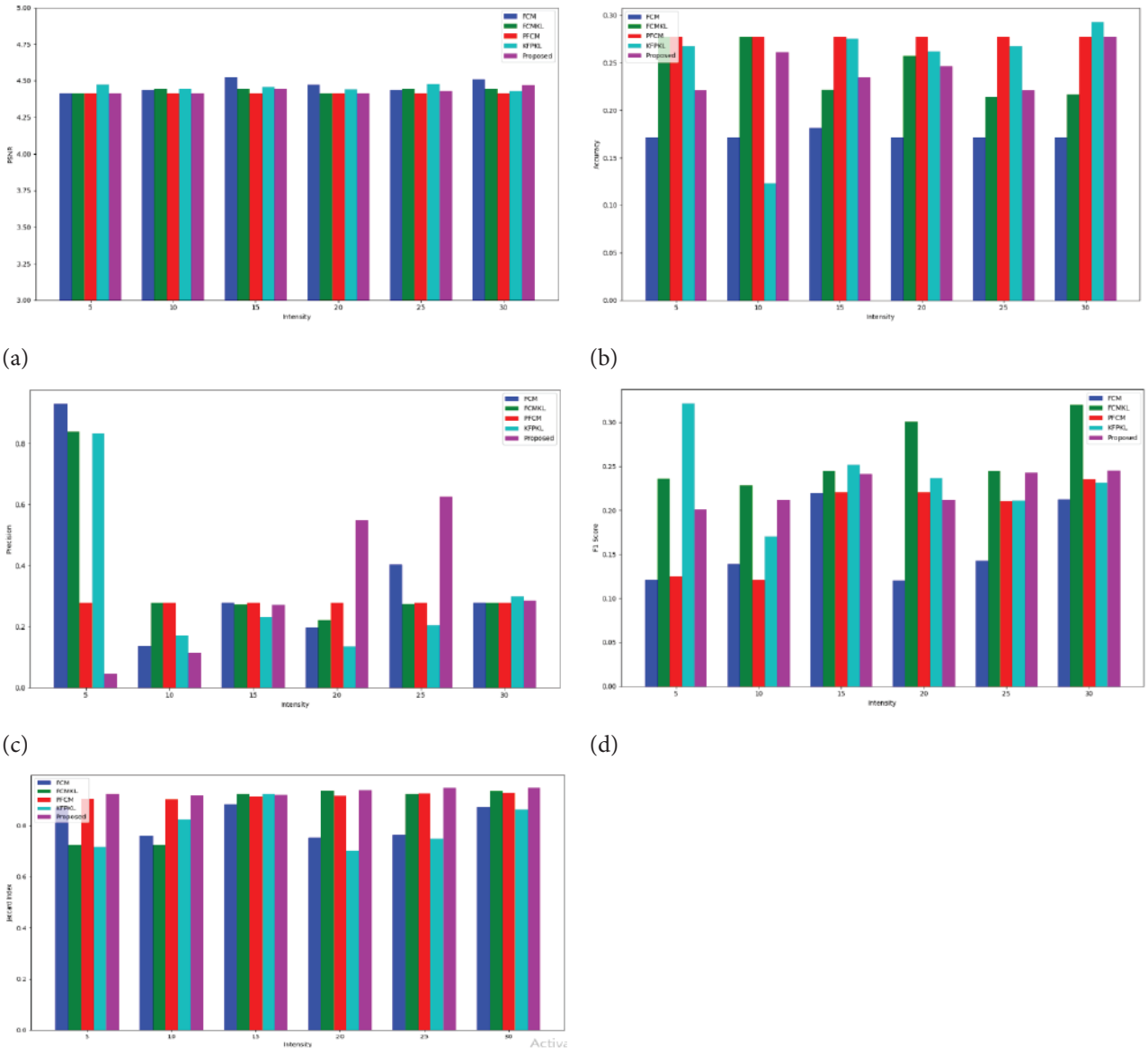


Figure 5. Figure 2 shows the performance curves of various algorithms for the third-row image that has been contaminated by impulse noise. a) PSNR; b) Acc; c) Pre; d) F1; e) JI.

various segmentation approaches to test different cluster configurations. It performs the KSSFKL for each combination of parameter values. The parameter values affect overall clustering performance. Different datasets may require different data balance parameters. Sometimes, the performance level exists.

Our proposed method obtained good segmentation and accurate segmentation results. Aggregating the noise pixels of an image produces more accurate clustering by distinguishing relevant features from noise. The proposed method shows that the optimization algorithm can obtain better detection results when processing noise images.

RESULTS AND DISCUSSION

In our research, we employed a blend of synthetic and authentic datasets to validate the robustness of our suggested model. Synthetic data enabled us to systematically evaluate theoretical components, offering a controlled setting for replicating intricate patient scenarios that are infrequent in actual datasets yet crucial to examine. The system enabled the simulation of various abnormal conditions,

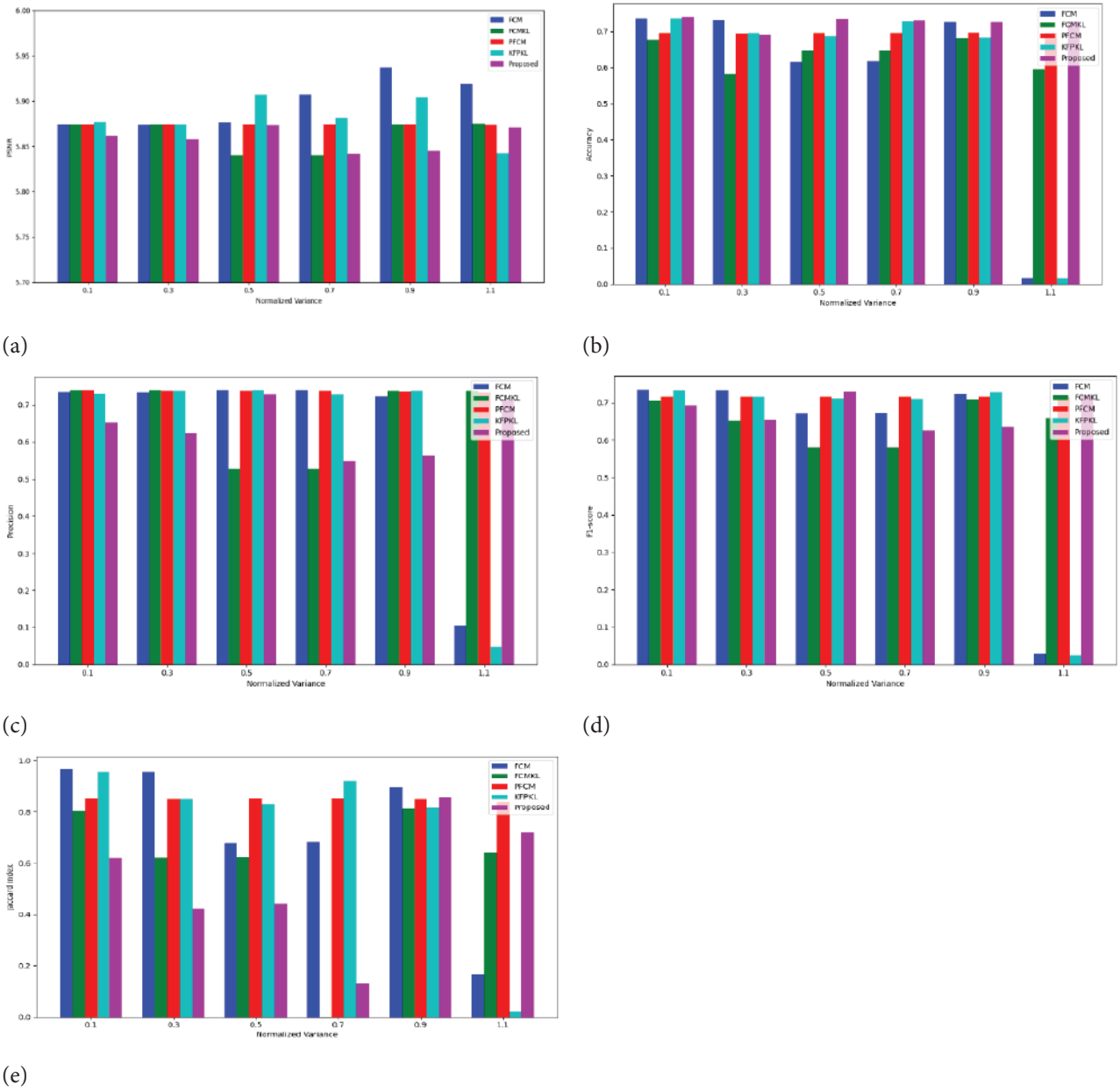


Figure 6. Figure 2 shows the performance curves of various algorithms for the fourth-row image contaminated by speckle noise. a) PSNR; b) Acc; c) Pre; d) F1; e) JI.

improving the model's adaptability to various healthcare challenges such as brain MRI and lung CT scan analysis. Meanwhile, real data confirmed the practical performance of our model in real-world applications, ensuring that it is highly applicable to real clinical situations. Our analysis showed that many current methods are unable to effectively reduce noise interference. In contrast, our proposed KSSFKL method significantly reduces noise's impact, achieving more accurate segmentation results. For subjective analysis, the clustering effect generated by our method was beneficial for analysing tumor shape, size, and texture. By implementing morphological reconstruction, we can define precise edges and boundaries, enabling a more accurate and detailed segmentation of internal regions without ambiguity. Following this, our objective analysis further demonstrated the benefits of our approach. As seen in Table 3, our methods outperformed more advanced techniques. This performance was achieved within a short processing time, raising the potential of this method as a reliable and time-efficient solution for real-world medical imaging applications.

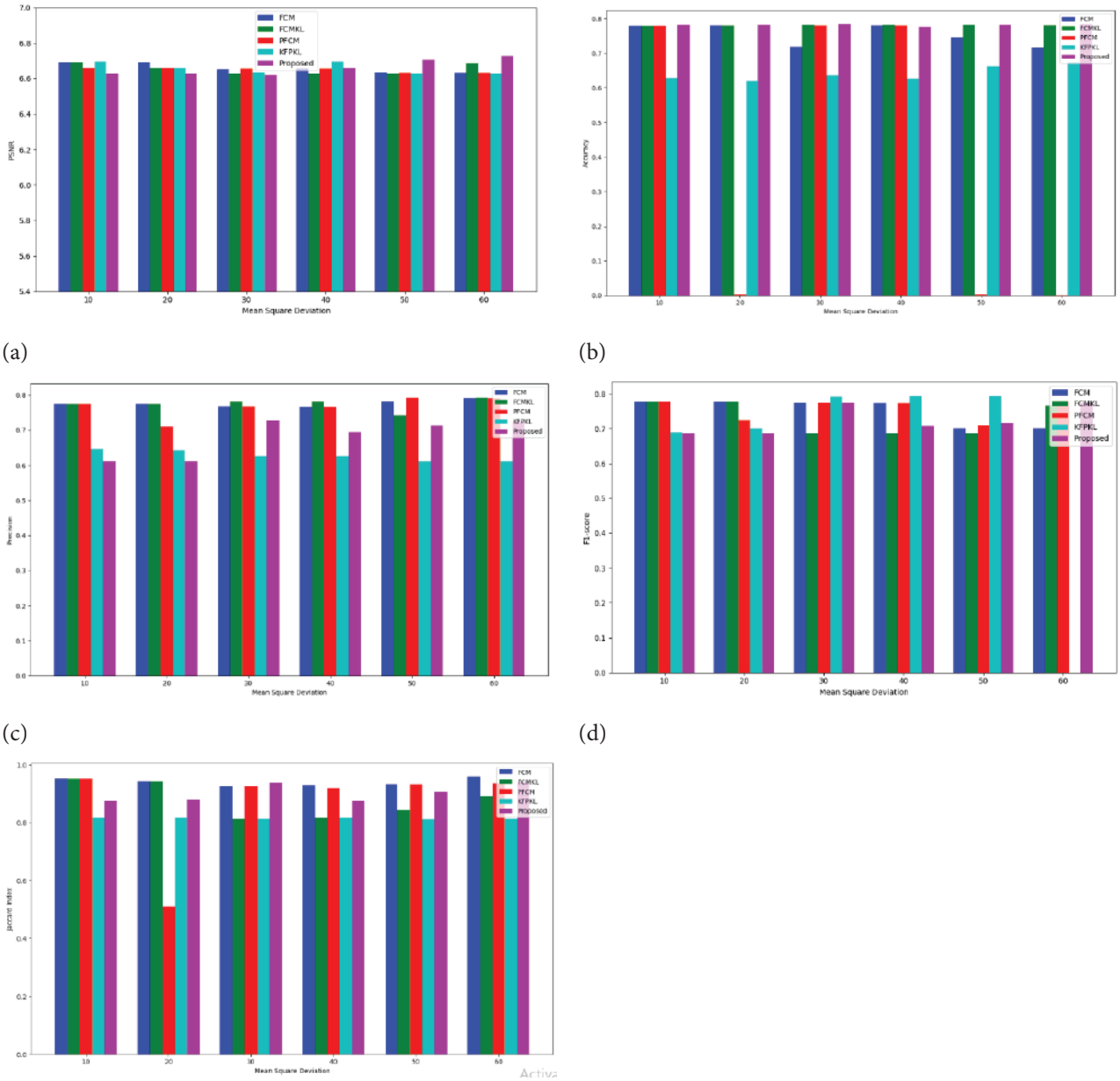


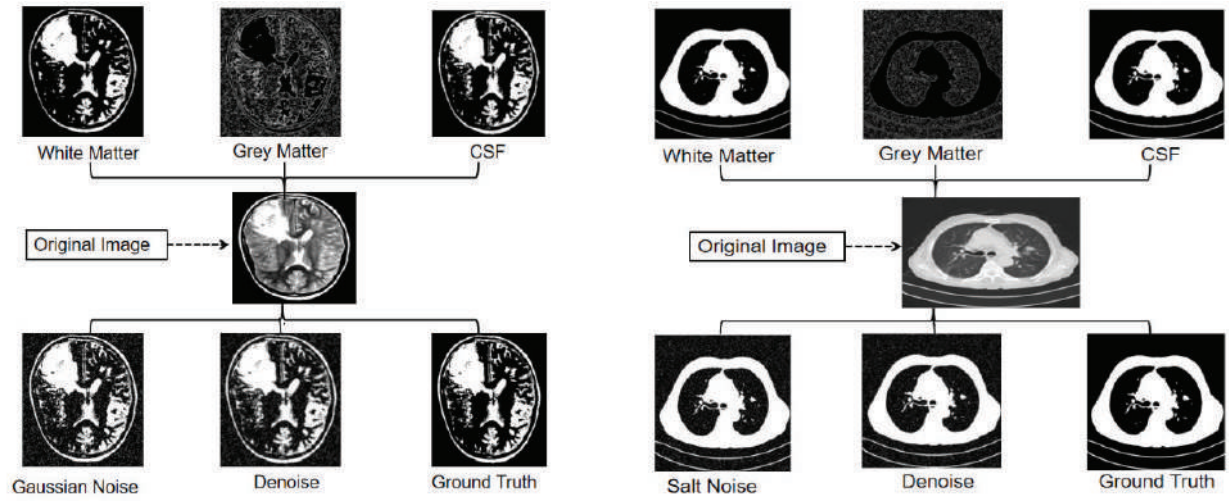
Figure 7. Figure 2 shows the performance curves of various algorithms for the fifth-row image that has been contaminated by rician noise. a) PSNR; b) Acc; c) Pre; d) F1; e) JI.

Table 3. The statement contrasts the runtimes of several clustering techniques, highlighting the computational efficiency of each

Clustering methods	Running time (s)
FCM	0.7 min
FCMKL	1.2 min
PFCM	2 min
KFPKL	4.9 min
KSSFKL	2.8 min

CONCLUSION

This study introduces a kernel-based semi-supervised fuzzy clustering method that integrates Kullback–Leibler divergence to tackle common image clustering problems such as noise, uncertainty, and non-linear patterns. A Gaussian kernel is used to better manage noise and complex structures within the semi-supervised fuzzy clustering framework. An extensive evaluation across multiple datasets, including computed tomography scans, brain magnetic resonance imaging data, the BraTS2020 Dataset, and synthetic



(a) (b)

Figure 8. a) represent the Brain MRI image and b) represent the lung CT scan image.

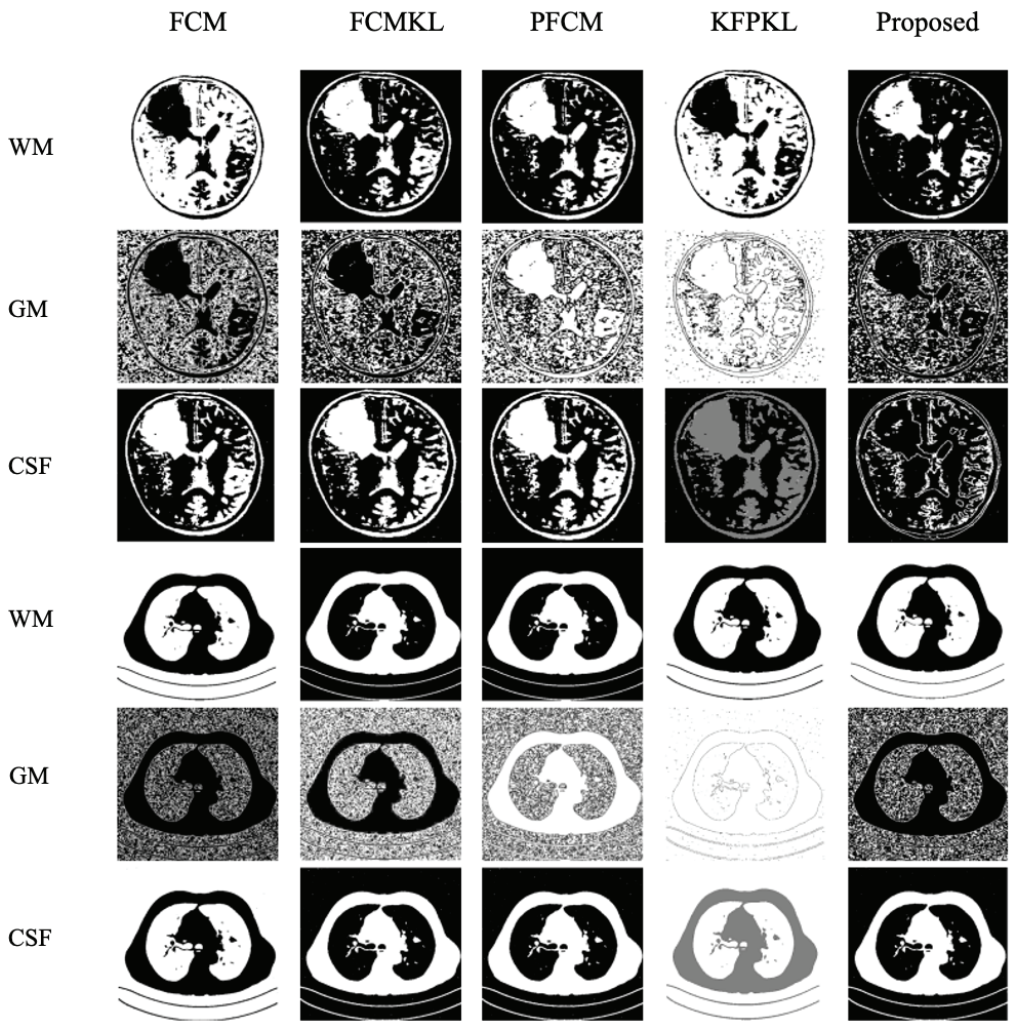
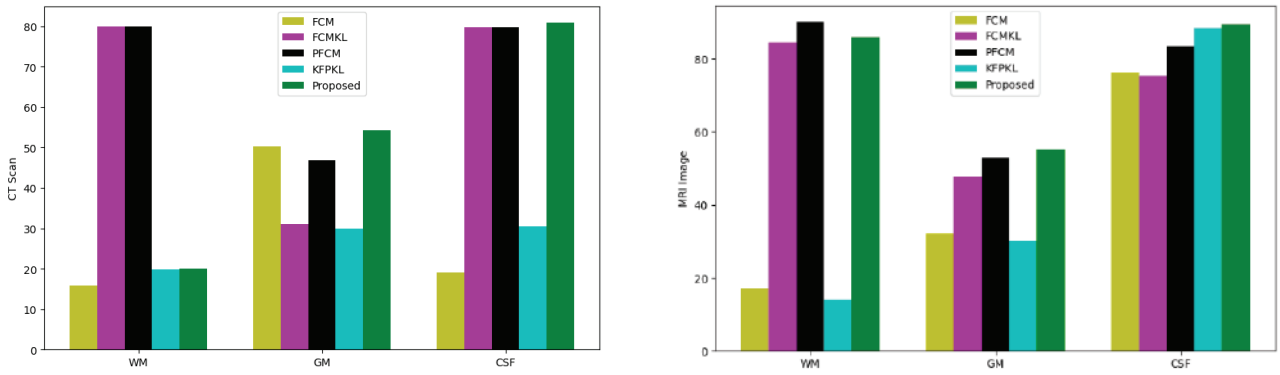


Figure 9. Comparison of segmentation results using different clustering algorithms. The columns correspond to segmentation results obtained using FCM, FCMKL, PFCM, KFPKL, and the proposed method. Rows denote the segmentation of WM, GM, and CSF.



(a) (b)

Figure 10. (a) and (b) denote the precision of the CT scan and MRI imaging efficacy.

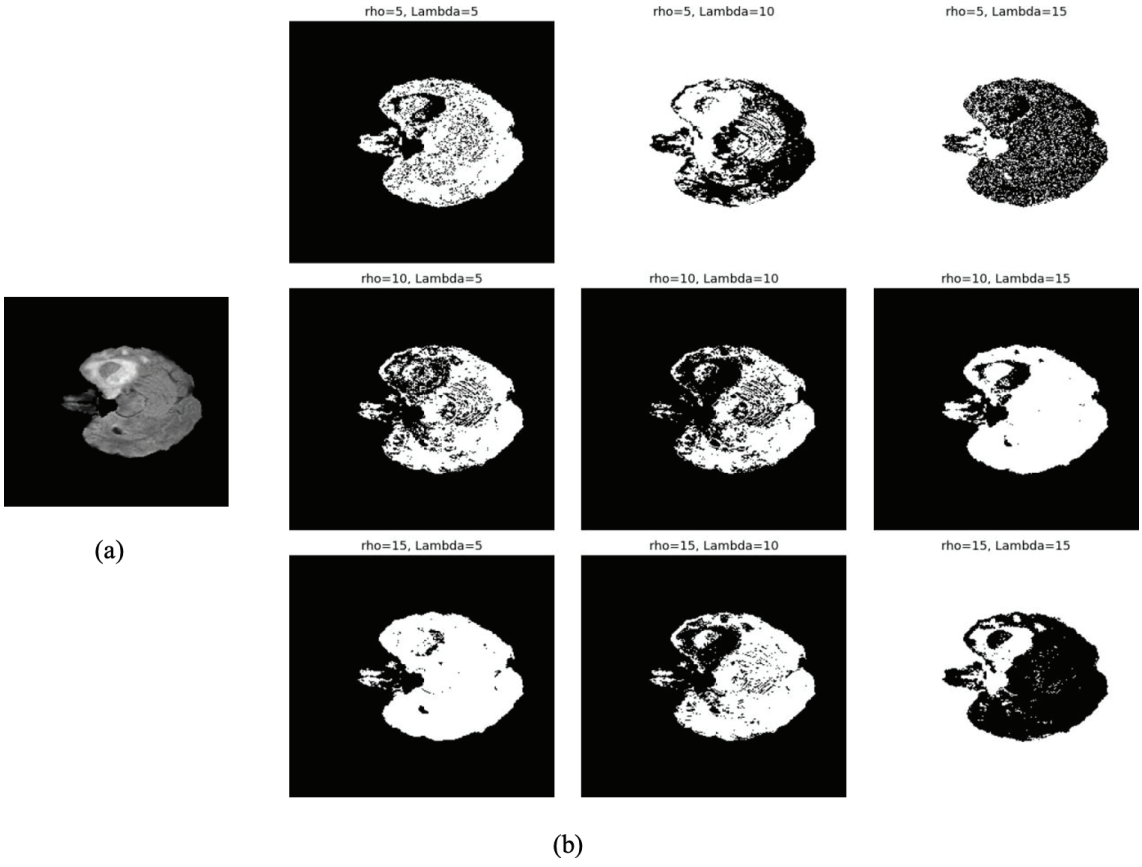


Figure 11. Result of KSSFKL applying different rho and lambda values.

images, unequivocally demonstrates the efficacy of our strategy. The segmentation accuracy has significantly improved compared to current state-of-the-art methods. Both subjective and objective evaluations confirm the advantages of clustering precision, artefact reduction, convergence efficiency, and computational speed. Comparative results show that the proposed method is also faster than several existing approaches, which supports its practical use. Overall, the method improves image segmentation by strengthening feature representation and improving clustering quality. Future work will focus on automatically estimating the number of clusters and incorporating more image-specific prior knowledge. It is crucial to acknowledge that each algorithm is constrained to 1000 iterations. The potential applications of our

approach extend beyond medical imaging. Its noise resistance renders it advantageous for several applications requiring precise segmentation, including remote sensing, satellite imagery, and industrial inspection, where uncertainty and noise present inherent challenges.

AUTHORSHIP CONTRIBUTIONS

Muthulakshmi K: Methodology, conceptualization, Formal analysis, Writing Original draft preparation, and editing. Jayalakshmi M: Supervision, conceptualization, Editing and Validation.

DATA AVAILABILITY STATEMENT

The authors confirm that the data that supports the findings of this study are available within the article. Raw data that support the finding of this study are available from the corresponding author, upon reasonable request.

CONFLICT OF INTEREST

The author declared no potential conflicts of interest with respect to the research, authorship, and/or publication of this article.

ETHICS

There are no ethical issues with the publication of this manuscript.

STATEMENT ON THE USE OF ARTIFICIAL INTELLIGENCE

Artificial intelligence was not used in the preparation of the article.

REFERENCES

[1] Pedrycz W, Waletzky J. Fuzzy clustering with partial supervision. IEEE Trans Syst Man Cybern B Cybern 1997;27:787–795. [CrossRef]

[2] Goyal S, Kumar S, Zaveri MA, Shukla AK. Fuzzy similarity measure based spectral clustering framework for noisy image segmentation. Int J Uncertain Fuzziness Knowl Based Syst 2017;25:649–673. [CrossRef]

[3] Du M, Ding S, Xue Y. A robust density peaks clustering algorithm using fuzzy neighborhood. Int J Mach Learn Cybern 2018;9:1131–1140. [CrossRef]

[4] Cuevas E, Fausto F, González A. Locust search algorithm applied to multi-threshold segmentation. In: New Advancements in Swarm Algorithms: Operators and Applications. 2020:211–240. [CrossRef]

[5] Oskouei AG, Samadi N, Tanha J. Feature-weight and cluster-weight learning in fuzzy c-means method for semi-supervised clustering. Appl Soft Comput 2024;161:111712. [CrossRef]

[6] Pan H, Liu W, Li L, Zhou G. A novel level set approach for image segmentation with landmark constraints. Optik 2019;182:257–268. [CrossRef]

[7] Atanassov K. Review and new results on intuitionistic fuzzy sets. Preprint IM-MFaIS-1-88, Soa 1988:1–8.

[8] Bora DJ, Gupta DA. A comparative study between fuzzy clustering algorithm and hard clustering algorithm. arXiv Prepr arXiv:1404.6059. 2014 Apr 24.

[9] Ferraro MB, Giordani P. Soft clustering. Wiley Interdiscip Rev Comput Stat 2020;12:e1480. [CrossRef]

[10] Pitchai R, Supraja P, Victoria AH, Madhavi MJ. Retracted article: Brain tumor segmentation using deep learning and fuzzy k-means clustering for magnetic resonance images. Neural Process Lett 2021;53:2519–2532. [CrossRef]

[11] Schölkopf B, Smola A, Müller KR. Kernel principal component analysis. In: Int Conf Artif Neural Netw 1997:583–588. [CrossRef]

[12] Kmita K, Kaczmarek-Majer K, Hryniewicz O. Explainable impact of partial supervision in semi-supervised fuzzy clustering. IEEE Trans Fuzzy Syst 2024 Feb 27. [CrossRef]

[13] Guo Y, Sengur A. A novel color image segmentation approach based on neutrosophic set and modified fuzzy c-means. Circuits Syst Signal Process 2013;32:1699–1723. [CrossRef]

[14] Miyamoto S, Ichihashi H, Honda K. Algorithms for fuzzy clustering. Heidelberg: Springer; 2008.

[15] Klir G, Yuan B. Fuzzy sets and fuzzy logic. New Jersey: Prentice Hall; 1995. [CrossRef]

[16] Zadeh LA. Fuzzy sets. University of California Electronic Research Laboratory. California: University of California;1965. [CrossRef]

[17] Zhao F, Yang Y, Liu H, Wang C. A robust multi-view knowledge transfer-based rough fuzzy c-means clustering algorithm. Complex Intell Syst 2024 Apr 25:1–28.

[18] Dattoli G, Ricci PE, Cesarano C. The Lagrange polynomials, the associated generalizations, and the umbral calculus. Integral Transf Spec Funct 2003;14:181–186. [CrossRef]

[19] Graves D, Pedrycz W. Kernel-based fuzzy clustering and fuzzy clustering: A comparative experimental study. Fuzzy Sets Syst 2010;161:522–543. [CrossRef]

[20] Zhu H, Xie W, Mu Y, Xu J, Wang FL, Qu Y, et al. A new semi-supervised fuzzy k-means clustering method with dynamic adjustment and label discrimination. Neural Comput Appl 2024;36:4709–4725. [CrossRef]

[21] Lavanya KG, Dhanalakshmi P, Nandhini M. A novel enhancement-based rapid kernel-induced intuitionistic fuzzy c-means clustering for brain tumor image. Soft Comput 2024;28:6657–6670. [CrossRef]

[22] Cuong BC, Kreinovich V. Picture fuzzy sets. J Comput Sci Cybern 2014;30:409–420.

[23] Wu C, Chen Y. Adaptive entropy weighted picture fuzzy clustering algorithm with spatial information for image segmentation. Appl Soft Comput 2020;86:105888. [CrossRef]
[24] Wu C, Zhang J. Robust semi-supervised spatial picture fuzzy clustering with local membership and KL-divergence for image segmentation. Int J Mach Learn Cybern 2022;13:963–987. [CrossRef]
[25] Shlens J. Notes on Kullback-Leibler divergence and likelihood. arXiv Prepr arXiv:1404.2000. 2014 Apr 8.
[26] Gharieb RR, Gendy G. Fuzzy c-means with local membership based weighted pixel distance and KL divergence for image segmentation. J Pattern Recognit Res 2015;10:53–60. [CrossRef]
[27] Halder A, Talukdar NA. Kernel induced semi-supervised spatial clustering: A novel brain MRI segmentation technique. Multimed Tools Appl 2024;83:49213–49241. [CrossRef]
[28] Thong PH, Son LH. Picture fuzzy clustering: A new computational intelligence method. Soft Comput 2016;20:3549–3562. [CrossRef]
[29] Cristianini N. An introduction to support vector machines and other kernel-based learning methods. Cambridge: Cambridge Univ Press; 2000. [CrossRef]
[30] Liu Q, Lu H, Ma S. Improving kernel Fisher discriminant analysis for face recognition. IEEE Trans Circuits Syst Video Technol 2004;14:42–49. [CrossRef]
[31] Antolìn AG, Garcìa JP, Gòmez JL. Radial basis function networks and their application in communication systems. In: Comput Intell Eng Manuf 2007:109–130. [CrossRef]
[32] Taha K. Semi-supervised and un-supervised clustering: A review and experimental evaluation. Inf Syst 2023;114:102178. [CrossRef]
[33] Khatri I, Kumar D, Gupta A. A noise robust kernel fuzzy clustering based on picture fuzzy sets and KL divergence measure for MRI image segmentation. Appl Intell 2023;53:16487–16518. [CrossRef]
[34] Kumar SA, Harish BS, Aradhya VM. A picture fuzzy clustering approach for brain tumor segmentation. In: Int Conf Cogn Comput Inf Process 2016:1–6. [CrossRef]
[35] Chen DZ. Fuzzy clustering using kernel method. IEEE, Nanjing, China. 2002.

APPENDIX

The derivation method for equations (25–26) in the suggested algorithm is as follows. KL divergence clustering is used in the resilient semi-supervised fuzzy clustering optimization model.

$$J = \sum_{j=1}^{N}\sum_{\mathrm{i}=1}^{C} u_{ij}^{m} d_{ij}^{2} + \rho \sum_{j=1}^{N}\sum_{\mathrm{i}=1}^{C} \left(u_{ij} - f_{ij} b_i\right)^{m} d_{ij}^{2} + \lambda \sum_{j=1}^{N}\sum_{\mathrm{i}=1}^{C} \left(u_{ij}\left(\log u_{ij}\right)\right) \tag{32}$$

Where,

$$\begin{aligned} d^2 &= \left\|\phi(y_i) - \phi(y_j)\right\|^2 \\ &= \left\|\phi(y_i) - \phi(y_j)\right\|^T \left\|\phi(y_i) - \phi(y_j)\right\|^2 \\ &= \phi(y_i)^T\phi(y_i) - \phi(y_i)^T\phi\left(y_j\right) - \phi\left(y_j\right)^T\phi(y_i) + \phi\left(y_j\right)^T\phi\left(y_j\right) \\ &= \phi(y_i)^T\phi(y_i) + \phi\left(y_j\right)^T\phi\left(y_j\right) - 2\phi(y_i)^T\phi(y_j) \end{aligned}$$

The mapping utilized for the transformation of samples to higher dimensional space is represented by ϕ. The optimization problem equation (16) for the RBF kernel function using equation (17) can be rewritten as

$$\begin{aligned} d^2 &= k(y_i, y_i) + k\left(y_j, y_j\right) - 2k\left(y_i, y_j\right) \\ &= 2 - 2k\left(y_i, y_j\right) = 2\left(1 - k\left(y_i, y_j\right)\right) \end{aligned}$$

To determine the partial derivatives of $\lambda, u = 0$, by using equation (24):

$$\frac{\partial J}{\partial \lambda} = \sum_{j=1}^{N}\sum_{\mathrm{i}=1}^{C} \left(u_{ij}(\log u_{ij})\right) = 0 \tag{33}$$

$$\frac{\partial J}{\partial u_{ij}} = \sum_{j=1}^{N}\sum_{\mathrm{i}=1}^{C} m\, u_{ij}^{m-1}\left(1 - k(y_i, y_j)\right) + \rho \sum_{j=1}^{N}\sum_{\mathrm{i}=1}^{C} m\left(u_{ij} - f_{ij} b_i\right)^{m-1}\left(1 - k(y_i, y_j)\right) + \lambda \sum_{j=1}^{N}\sum_{\mathrm{i}=1}^{C}\left(1 + \log u_{ij}\right) = 0 \tag{34}$$

Simplify the equation (34), we obtained u_{ij}:

$$2u_{ij}\left(1 - k\left(y_i, y_j\right)\right) + 2\rho\left(u_{ij} - f_{ij} b_i\right)\left(1 - k\left(y_i, y_j\right)\right) + \lambda + \lambda \log u_{ij} = 0.$$

Derive the above equation to get the derivation of

$$u_{ij} = \frac{1}{1+\rho}\left[-\frac{\lambda - \lambda \log u_{ij}}{2\left(1 - k\left(y_i, y_j\right)\right)} + \rho f_{ij} b_i\right]$$

and then,

$$\log u_{ij} = \frac{-\lambda + 2(1+\rho)\left(1 - k\left(y_i, y_j\right)\right)[\rho f_{ij} b_i - u_{ij}]}{\lambda}$$

$$u_{ij} = e^{\frac{-\lambda + 2(1+\rho)\left(1 - k\left(y_i, y_j\right)\right)[\rho f_{ij} b_i - u_{ij}]}{\lambda}}$$

Furthermore, obtain

$$u_{ij} = \frac{\exp\left(\dfrac{-\lambda + 2(1+\rho)(1 - k\left(y_j, v_i\right)[\rho \sum_{\mathrm{i}=1}^{C} f_{ij} b_j - u_{ij}]}{\lambda}\right)}{\sum_{k=1}^{C} \exp\left(\dfrac{-\lambda + 2(1+\rho)(1 - k\left(y_j, v_k\right)[\rho \sum_{\mathrm{i}=1}^{C} f_{ij} b_j - u_{ij}]}{\lambda}\right)} \tag{35}$$

and

$$v_i = \frac{\sum_{j=1}^{N} u_{ij} k\left(y_j, v_i\right) y_j + \rho \sum_{j=1}^{N}\left(u_{ij} - f_{ij} b_i\right)^2 y_j}{\sum_{j=1}^{N} u_{ij} k\left(y_j, v_i\right) y_j + \rho \sum_{j=1}^{N}\left(u_{ij} - f_{ij} b_i\right)^2} \tag{36}$$

Finally, using these equations, we obtained the membership value u_{ij} and the cluster center v_i for the proposed image segmentation approach.

Sigma Journal of Engineering and Natural Sciences
Web page info: https://sigma.yildiz.edu.tr
DOI: 10.14744/sigma.2025.00101

Research Article

Optimization of precision machine part manufacturing by integration of Grey-Taguchi method with principal component analysis

Kübra EROL[1,*], Selda KAPAN ULUSOY[2], Ercan ŞENYİĞİT[2]

[1]*Department of Quality Coordination, Abdullah Gul University, Kayseri, 38080, Türkiye*
[2]*Department of Industrial Engineering, Erciyes University, Kayseri 38039, Türkiye*

ARTICLE INFO

Article history
Received: 05 September 2024
Revised: 18 November 2024
Accepted: 14 January 2025

Keywords:
Confirmation Test; Grey Relational Analysis; Precision Machine Part Manufacturing; Principal Component Analysis; Sensitivity Analysis; Taguchi Method

ABSTRACT

Determining and optimizing the process parameters impacting the outputs at each production stage is necessary to reduce production costs. The Taguchi Method (TM) and the Grey Relational Analysis (GRA) are commonly utilized two techniques for process parameter optimization. In precision machine part manufacturing, Computer Numerical Control (CNC) production is the most critical process. In this study, the objective is to optimize CNC manufacturing parameters using TM, GRA and Principal Component Analysis (PCA) in metal sector. Process parameters like operator experience level (in years), CNC machine brand, CNC machine age, and CNC machine size were determined and optimized based on their degree of impact on the outputs. The experiments were carried out using a four-factor, four-level Taguchi orthogonal array (L16), and Analysis of Variance (ANOVA) was conducted aiming to determine the effects of these process parameters on production time, dimension conformity, and surface roughness performance factors. Selection of these input parameters and performance factors in the study is to provide a solution to a problem in the company from which the data are obtained with scientific methods and to contribute to the literature. Utilizing TM, the optimal values of process parameters are determined as ten years for operator experience, as Mazak for CNC machine brand, as two years for machine age, and as 500x550x550 for machine size. Utilizing the combination of GRA and PCA optimal parameter values are determined as ten years for operator experience, as Yuntes for CNC machine brand, as two years for machine age, and as 700x450x500 for machine size. A sensitivity analysis was performed using 21 different weight sets for performance factors (production time, dimension conformity, and surface roughness). Compared to the initial CNC production process parameters, 45%, 95%, and 504% improvements were obtained in production time, dimension conformity, and surface roughness process parameters. Companies, especially operating in the metal sector, can benefit from managerial practices by considering the ranking of parameters affecting CNC production according to the results obtained from this study.

Cite this article as: Erol K, Kapan Ulusoy S, Şenyiğit E. Optimization of precision machine part manufacturing by integration of Grey-Taguchi method with principal component analysis. Sigma J Eng Nat Sci 2026;44(1):292–308.

***Corresponding author.**
*E-mail address: kubra.isik@agu.edu.tr

This paper was recommended for publication in revised form by Editor-in-Chief Ahmet Selim Dalkilic

Published by Yıldız Technical University Press, İstanbul, Turkey
© Author. This is an open access article under the CC BY-NC license (http://creativecommons.org/licenses/by-nc/4.0/).

INTRODUCTION

Precision machine part manufacturing aims to produce machine parts that precisely fit the specified shapes and dimensions [1]. Computer Numerical Control (CNC) machines are often utilized for manufacturing precision parts. CNC is a machining process in which the machining tools are automatically controlled by a computer and operated on the workpiece to be shaped. It is the most critical process of an organization operating in the metal sector. A CNC machine follows the instructions programmed with codes to precisely machine a workpiece of a specific type of material (such as metal, plastic, ceramics, or composites) until the workpiece has the desired dimensions and shape [2]. To enhance quality and efficiency in CNC production, minimizing the variability caused by the uncontrollable process parameters is necessary. This may be achieved by optimizing the controllable process parameters of the CNC process. For this purpose, both Taguchi Method (TM) and the Grey Relational Analysis (GRA) methods are used commonly in the literature.

TM is a statistical experimental design technique that is utilized to make the products or processes more robust. Uncontrollable process parameters cause variation in the performance factors. TM minimizes this variation by optimizing the controllable process parameters [3]. In factorial or fractional experimental designs, as the quantity of independent variables and their levels increase, the quantity of experiments to be performed rises significantly. TM employs orthogonal arrays to decrease the quantity of experiments thus it provides more efficient experimentation for robust design [4]. The downside of the TM is that it can only optimize a product or a process for a single performance factor. When there are multiple performance factors TM can only find sub-optimal solutions. In such cases, TM in combination with GRA can be utilized to find the optimal solutions.

GRA is an approach to measure the degree of convergence between arrays using the grey relational degree [5]. GRA can transform a multi-objective problem into a single-objective problem through determining a Grey Relational Grade (GRG). The GRG estimates the impacts of parameters on the overall performance [6]. In the experimental design case, GRA is utilized to decrease multiple performance factors to an individual performance factor by combining them. Then using the combined performance factor TM is utilized to discover the optimal levels of process parameters.

Principal Component Analysis (PCA) is a statistical technique used for decreasing the dimensionality of a problem. This method considerably decreases the complexity of the solution by decreasing inter-related variables to independent principal components preserving the primary data with linear combinations [13]. PCA can be used to calculate the combination weights in GRA according to the relative importance of the factors. The literature review indicated that various studies have been carried out to optimize CNC process parameters utilized the Grey-Taguchi method. However, no studies use the Grey-Taguchi method in combination with PCA for the optimization of CNC manufacturing parameters [7]. PCA can be used to calculate the combination weights in GRA according to the relative importance of the factors.

Literature Review

TM in combination with GRA (Grey-Taguchi) has been used in many studies for multiple performance optimization in CNC manufacturing. E.g. Rao et al. [8] applied the Taguchi method to investigate the parameters sliding speed, load and sliding distance using the minimum number of tests possible. Kasman et al. [9] utilized the Taguchi method to establish an experimental installation to analyse the impacts of laser engraving on engraving depth and surface roughness. Swapna et al. [10] utilized the integration of PCA with GRA for optimizing the process parameters in sheet forming of Al6061-T6. Adar [11] used Taguchi method to analyse the influence of temperature, substrate/inoculation ratio and mixing speed parameters on the anaerobic digestion of cattle manure liquid fraction. Mola et al. [12] utilised the TM, and optimal levels of parameters were identified for flexural strength, toughness and strength. Singh et al. [13] intended to evaluate the impact of the parameters while milling on the material removal rate and surface roughness of AISI H11. Kumar et al. [14] employed Taguchi-based GRA to optimize corrosion rate, material removal rate and surface roughness for CNC milling of ZE41A Mg alloy. Esangbedo & Abifarin [15] used statistical approaches and GRA to optimize the surface roughness and cutting force of CNC machine to produce halloysite nanotube hybrid composite. Suresh Kumar et al. [16] used TM and GRA to measure the effect on the surface quality of Al-6063 regarding material removal rate and surface integrity. Prakash et al. [17] dealt with the optimization of machining parameters such as surface finish and material removal rate during production of Aluminium/Rock dust composite via Taguchi and GRA. Kouahla et al. [18] aimed to optimize the cutting force, tool vibration, material removal rate, power consumption and surface roughness under different cutting conditions such as feed rate, cutting speed, tool nose radius and depth of cut. Teja et al. [19] deals with on their study to optimize tool temperature, work temperature and surface roughness while producing Ti alloy CNC machining parameters like cutting depth, spindle speed and feed utilized TM. Raguraman et al. [20] analysed the CNC turning machining parameters of AA6061 alloy using TM, ANOVA and GRA. Zhujani et al. [21] aimed to utilized TM based GRA approach to optimize the parameters such as tool wear, surface roughness and machining time of Inconel 718 alloy. Zeydan [22] intended to optimize process factors of flexible polyurethane foam by TM. Sahare et al. [23] used GRA with Taguchi to propose an optimum milling process parameter set-up for multi

performance factors. Mastan Rao et al. [24] examined the exploit of Taguchi and GRA to optimize the turning process parameters of a nickel-based alloy, taking into account surface roughness, tool wear rate and material removal rate. Summary of literature review that used TM-GRA for CNC parameter design is given in Table 1. The literature in Table 1 is also detailed by adding the input parameters and performance factors used in the papers.

This study focuses on applying Grey-Taguchi method in combination with PCA techniques to optimize selected

Table 1. Summary of literature review

Author(s)	Input Parameters	Performance factors	Author(s)	Input Parameters	Performance factors
Ficko et al. [36]	Feed rate, cutting speed and cutting depth	Material removal rate and surface roughness	Rao et al. [8]	Sliding speed, load, distance	Wear, coefficient of friction
Mola et al. [12]	Water/binder ratio, silica fume, kevlar fiber and steel fiber	Compressive strength, flexural strength, and toughness	Swapna et al. [10]	Die speed, temperature, type of lubricant and sheet thickness	Punch force, thickness variation
Singh et al. [13]	Feed rate, cutting speed and cutting depth	Material removal rate and surface roughness	Zeydan [22]	TDI (Toluene Diisocyanate) index, polyol, water, air amount	Hardness
Adar [11]	Temperature, Mixing speed and substrate/ inoculation ratio	Methane yield	Kumar et al. [14]	Tool rotation, feed rate, cutting speed and cutting depth	Metal removal rate, corrosion rate and surface roughness
Esangbedo & Abifarin [15]	Spindle speed, cutting depth and feed rate	Cutting force and surface roughness	Zade & Meshram [37]	Feed load, cutting speed and reduction depth	Roundness and surface roughness
Suresh Kumar & Senthil Kumar [16]	Feed rate, spindle speed, cutting depth	Metal removal rate and surface roughness	Dhanalakshmi & Rameshbabu [34]	Feed rate, cutting speed, depth of cut, and cutting fluid flow rate	Metal removal rate, cost analysis and surface roughness
Prakash et al. [17]	Particle size, particle weight, feed, speed and cutting depth	Surface roughness and metal removal rate	Sundara Bharathi et al. [38]	Feed rate, cutting speed and cutting depth	Metal removal rate and surface
Kouahla et al. [18]	Feed rate, cutting speed, tool nose radius and cutting depth	Surface roughness, tool vibration, power consumption, cutting force, and material removal rate	Azim et al. [35]	Spindle speed, depth of cut, feed rate	Surface roughness
Teja et al. [19]	Spindle speed, feed, cutting depth	Tool temperature, surface roughness and work temperature	Sahare et al. [23]	Feed, spindle speed, tool diameter, and tool type	Material removal rate, surface roughness, cutting force and tool wear
Kumar Yadav et al. [39]	Spindle speed, depth of cut, tool diameter and feed rate	Surface roughness and material removal rate	Mastan Rao et al. [24]	Speed, feed rate, cutting depth	Tool wear rate, surface roughness and material removal rate
Raguraman et al. [20]	Rotational speed, feed, depth of cut	Metal removal rate and surface roughness	Rathod et al. [33]	Cutting speed, cutting depth and feed rate	Tool life, surface roughness, and production time
Zhujani et al. [21]	Cutting speed, feed rate and cutting depth	Maximum roughness, average roughness and roundness	Kasman et al. [9]	Scan speed, scan direction, and fill spacing	Surface roughness and engraving depth

Table 2. Process parameters and levels for CNC production

Parameters	Symbol	Level 1	Level 2	Level 3	Level 4
Operator Experience Year	A	2.00	3.00	10.00	14.00
CNC Machine Brand	B	Mazak	Okuma	Taksan	Yuntes
CNC Machine Age	C	2.00	11.00	15.00	17.00
Workbench Size (mm)	D	500x550x550	700x450x500	1000x500x500	1600x3000x800

parameters in CNC manufacturing considering multiple performance factors. The proposed TM-GRA-PCA method is applied to the CNC process of a metal industry company. Input parameters and performance factors chosen for this study were determined in line with the opinions of expert engineers in the company. Firstly, TM is used to optimize selected CNC input parameters for each performance factor separately. The experiments used a Taguchi orthogonal array (L16) with four factors and four levels. This analysis could result in only a sub-optimal solution since for each performance factor different levels of input parameters were optimal. Secondly, a TM-GRA approach is utilized in which the combination weights of the performance factors are taken equally. Again this analysis is sub-optimal since it is not considered the relative importance of the performance factors. As the final method, a TM-GRA-PCA technique is used in which the combination weights of the performance factors are calculated using PCA reflecting the relative importance of the performance factors. A sensitivity analysis was performed as risks, and uncertainties could potentially affect the study. As a result of the confirmation experiments conducted in the study, the compatibility of the estimated S/N values of the CNC manufacturing parameters with the actual S/N values was determined and an improvement level was obtained compared to the initial CNC manufacturing process parameters.

When the open literature on TM and GRA for multiple performance optimization of CNC production in the metal sector is reviewed, it is seen that primarily input parameters such as cutting speed, depth of cut and feed rate and their short-term impacts on production results [13,15–17,19–21] are studied and it is noted that the input parameters and dimension conformity performance factors used in this study have yet to be researched. Selection of these input parameters and performance factors in the study is to provide a solution to a problem in the company from which the data are obtained with scientific methods and to contribute to the literature. Moreover, in this study, besides the TM and GRA, PCA was conducted to weigh the performance factors, and sensitivity analysis was carried out to identify the risks or uncertainties that may potentially affect the study. In these aspects, this study is unique and contributes to the literature.

MATERIALS AND METHODS

The data used in the study were obtained from a company operating in the metal sector in Kayseri, Turkey. Production engineers have identified the CNC production process parameters and their levels and this information is shown in Table 2.

In the study, TM, GRA, and PCA are used to optimize the process parameters that affect CNC production outputs, such as operator experience level (in years), CNC machine brand, CNC machine age, and CNC machine size. To determine the influences of process parameters on production time, dimension conformity, and surface roughness performance factors, sensitivity analysis and Analysis of Variance (ANOVA) were also conducted. Last but not least, confirmation experiments were conducted to verify if predicted S/N ratios are consistent with the actual values. Details of the analysis are given below.

Taguchi Method

TM was used as the initial method to optimize the process parameters. A four-factor and four-level orthogonal design L16 was selected for the study. Operator experience year, CNC machine brand, CNC machine age, and workbench size were used as control parameters. The TM, based on the orthogonal array, facilitates the design of experiments and evaluates process performance using the signal-to-noise (S/N) ratio, which is resistant to the effects of noise factors and acts as an objective function for optimization, guiding the selection of control levels that best compensate for the impact of noise factors on performance [10], [22]. Noise factors are uncontrollable variables that can impact the product or process. The highest S/N ratio was taken into account to identify the optimum levels for each parameter. The S/N ratio for each response variable (output factor) was identified by transforming the response variable into a fixed value (decibels, dB) utilizing the "Smaller the better" or "Larger the better" criteria. S/N ratios for the response of production time, dimension conformity, and surface roughness were calculated utilizing the "Smaller the better," "Larger the better," and "Smaller the better" criteria, respectively. The smaller the better, and larger the better, calculations for input parameters were performed successively according to Equation 1 and Equation 2 [25].

$$\frac{S}{N} = -10\,log\left[\frac{1}{n}\sum_{i=1}^{n} y_i^2\right] \quad (1)$$

$$\frac{S}{N} = -10\,log\left[\frac{1}{n}\sum_{i=1}^{n} \frac{1}{y_i^2}\right] \quad (2)$$

where i is the experiment order, y_i is the experimental result, and n is the total number of experiments.

Grey Relational Analysis- Principal Component Analysis

GRA-PCA was utilized to optimize the process parameter levels corresponding to each output factor, considering their weighting in CNC machining. GRA was applied to analyse the relations in a multi-factor system. At the same time, PCA was performed to identify the corresponding weight value indicating the relative significance of each response in GRA. In this context, the following steps of GRA in combined with PCA were applied to optimize multiple responses:

1. Normalization of S/N results for each response: Normalization of the S/N values obtained from Taguchi analysis, the "Smaller the Better", and "Larger the Better" calculations were performed using Equation 3 and Equation 4, respectively.

$$N_{rp} = \frac{\left[maxe_{rp} - e_{rp}\right]}{\left[maxe_{rp} - mine_{rp}\right]} \quad (3)$$

$$N_{rp} = \frac{\left[e_{rp} - mine_{rp}\right]}{\left[maxe_{rp} - mine_{rp}\right]} \quad (4)$$

N_{rp} represents the normalized experimental data of e_{rp}, which is the experimental result of the rth response variable before the normalization process is applied. Min_{erp} is the smallest value of e_{rp}, while max_{erp} is the largest value of e_{rp} [26].

2. Identification of grey correlation coefficient (GRC) and GRG: GRCs are calculated using Equation 5 to states the relationship between optimal and actual test results. The coefficient value (φ) is taken as 0.5 in this equation. In the literature, it has been found that this coefficient does not efficiently change the grey relational ranking [25]. Δ_{0i} is the difference between the reference ($y_0(k)$) and comparison ($y_i(k)$) values (Equation 6). Δ_{min} (Equation 7) and Δ_{max} (Equation 8) indicate the min and max values of Δ_{0i}, respectively.

$$GRC\left(X_0(k)X_i(k)\right) = \frac{\Delta_{min} + \varphi\Delta_{max}}{\Delta_{0i} + \varphi\Delta_{max}} \quad (5)$$

$$\Delta_{0i}(k) = \left|X_0(k) - X_j(k)\right| \quad (6)$$

$$\Delta_{min} = min_j min_k \left|X_0(k) - X_j(k)\right| \quad (7)$$

$$\Delta_{max} = max_j max_k \left|X_0(k) - X_j(k)\right| \quad (8)$$

The weighted PCA-GRG was identified using the different weighted factors in Equation 9.

$$GRG(X_0X_i) = \frac{1}{n}\sum_{k=1}^{n} w_k\varphi_i(k) \quad (9)$$

where n is the quantity of experiments and w_k is the weight for the kth performance [26]. The w_k value of each response was identified by PCA. PCA method was performed using MINITAB, in this study.

3. PCA: In GRA, weighting values for multiple responses are objectively defined utilizing PCA [27]. This multi-variate data analysis aims to decrease the dimensionality of the study as much as practicable [28]. PCA is an orthogonal transformation method that transforms observations of potentially correlated factors into uncorrelated factor (PCs) values [29]. The following equation was utilized to assess the targeted PCs.
   (i) The variance-covariance sequence X is formulated by GRCs, as given in Equation 10.

$$X = \begin{bmatrix} X_1(1) & \cdots & X_1(n) \\ \vdots & \ddots & \vdots \\ X_m(1) & \cdots & X_m(n) \end{bmatrix} \quad (10)$$

where X is the GRC for each response, m is the quantity of experiments, and n is the quantity of responses.

   (ii) The set of correlation coefficients was predicted utilizing Equation 11.

$$R_{jl}\left(\frac{cov\left(x_i(j)x_i(l)\right)}{\sigma_{xi}(j)\sigma_{xi}(l)}\right), j = 1,2,3,\ldots,n\ l = 1,2,3,\ldots,n \quad (11)$$

$cov(x_i(j)\ x_i(l))$ is the covariance of $x_i(j)$ and $x_i(l)$; $\sigma_{xi}(j)$ and $\sigma_{xi}(l)$ are the standard deviation of $x_i(j)$ and $x_i(l)$, respectively.

   (iii) The eigenvectors and eigenvalues attained by employing the correlation coefficient array are given in Equation 12.

$$(R - \lambda_k\ l_m)V_{ik} = 0 \quad (12)$$

where λ_k are the eigenvalues; $V_{ik} = [\alpha_{k1}\alpha_{k2}...\alpha_{km}]^T$ are the eigenvectors related to the eigenvalues λ_k and $\sum_{k=1}^{n}\lambda_k = n, k = 1,2,\ldots,n$.

   (iv) The PCs of the model responses are predicted using Equation 13.

$$Y_{mk} = \sum_{i=1}^{n} Y_m(i)V_{ik} \quad (13)$$

where Y_{m1}, Y_{m2}, ..., Y_{mn} are referred to as the first PC, second PC, etc. (decreasing order of variance).

Sensitivity Analysis

A sensitivity analysis was applied to analyse the potential effect of risks and uncertainties on the study. In this study, twenty-one different importance (weight) levels were determined for the responses besides TM, GRA, and GRA-PCA methods, and it was researched to which extent the weights affect the results obtained.

Analysis of Variance (ANOVA)

ANOVA is an effective statistical tool for evaluating the relative influence of different process parameters and for evaluating experimental errors. ANOVA ensures a countable measure of the contribution of each factor, providing a better understanding of the comparative impacts on output variables. This technique is crucial for identifying any error variability in factor impact and the disparity in estimation errors. The main objective of ANOVA is to determine which design parameters substantially affect quality characteristics [30]. ANOVA determined the influence ratio of input parameters on performance factors. With this statistical approach, differences in input parameters can be demonstrated in terms of output values, in this study. The most efficient parameter for the process characteristics can be identified, and that factor can be controlled to improve the process [31].

Confirmation Experiment

The final stage of optimization is to confirm the outcomes. After the optimum process parameters have been defined, the predicted values of the optimal factor levels obtained from the S/N ratios and the experimental values are utilized to confirm the accuracy of the optimization process. The experimental findings under optimum conditions were used to determine the progress in performance factors. The estimated S/N ratios and the optimum levels of the process parameters were calculated using Equation 14.

$$n_o = n_m + \sum_{i=1}^{j} (n_i - n_m) \tag{14}$$

where η_m is the overall average of the S/N ratio, η_i is the average of the S/N ratio corresponds to the optimal levels, and j is the number of process parameters.

RESULTS AND DISCUSSION

Taguchi Optimization

In the study, as an initial method, TM was conducted to determine the optimum process parameters for each performance factor separately since TM could handle only one performance factor at a time. The findings of the TM are shown in Table 3 and Table 4.

Table 3 shows the L16 orthogonal array, the average values, and the S/N ratios of the performance factors. Table 4 shows the S/N ratios of each process parameter for performance factors. As can be seen in Table 4, S/N ratios for production time, dimension conformity, and surface roughness

Table 3. Taguchi L16 orthogonal array for CNC manufacturing, average values, and S/N ratios

	Process Parameters				Average Values			S/N Ratios, dB		
No.	A	B	C	D	Production Time (min)	Dimension Conformity (ratio)	Surface Roughness (μm)	Production Time (min)	Dimension Conformity (ratio)	Surface Roughness (μm)
1	1	1	1	1	282.00	0.36	1.49	-49.00	-8.87	-3.46
2	1	2	2	2	220.00	0.50	0.28	-46.85	-5.98	10.91
3	1	3	3	3	377.00	0.35	1.22	-51.53	-9.16	-1.73
4	1	4	4	4	464.00	0.07	0.37	-53.33	-23.53	8.70
5	2	1	2	3	265.00	0.82	0.21	-48.46	-1.68	13.62
6	2	2	1	4	48.00	0.42	0.68	-33.62	-7.52	3.41
7	2	3	4	1	223.00	0.10	1.34	-46.97	-19.96	-2.54
8	2	4	3	2	257.00	0.97	1.41	-48.20	-0.26	-2.98
9	3	1	3	4	434.00	0.86	0.80	-52.75	-1.27	1.94
10	3	2	4	3	349.00	0.72	1.37	-50.86	-2.85	-2.73
11	3	3	1	2	106.00	1.00	0.25	-40.51	0.00	12.02
12	3	4	2	1	37.00	0.40	1.19	-31.36	-7.93	-1.51
13	4	1	4	2	255.00	0.87	0.17	-48.13	-1.18	15.28
14	4	2	3	1	272.00	0.19	0.45	-48.69	-14.43	7.03
15	4	3	2	4	527.00	0.14	1.09	-54.44	-16.88	-0.75
16	4	4	1	3	388.00	0.95	0.10	-51.78	-0.43	20.12

Table 4. S/N for production time, dimension conformity, and surface roughness responses*

	Production Time (min)				Dimension Conformity (ratio)				Surface Roughness (μm)			
Levels	**A**	**B**	**C**	**D**	**A**	**B**	**C**	**D**	**A**	**B**	**C**	**D**
1	-50.18	-49.59	**-43.73**	**-44.01**	- 11.89	**-3.25**	**-4.20**	-12.80	3.60	**6.84**	**8.02**	-0.12
2	-44.31	**-45.01**	-45.28	-45.92	- 7.35	-7.69	-8.12	**-1.85**	2.88	4.65	5.57	**8.81**
3	**-43.87**	-48.36	-50.29	-50.66	**- 3.01**	-11.50	-6.28	-3.53	2.43	1.75	1.06	7.32
4	-50.76	-46.17	-49.82	-48.54	- 8.23	-8.04	- 11.88	-12.30	**10.42**	6.08	4.68	3.32
Delta**	6.89	4.58	6.56	6.65	8.87	8.25	7.67	10.94	7.99	5.09	6.96	8.93
Rank***	1	4	3	2	2	3	4	1	2	4	3	1

*Optimum values of the process parameters are given in bold, ** Delta represents the absolute value of the difference between the max and min S/N ratio [40], *** Rank is determined by the order of the delta value and indicates the relative importance of the parameters according to their influence [40].

responses vary between -43.73-50.76, -1.85-12.80, and -0.12-10.42 dB, respectively. According to the Delta results, the process parameters affecting the production time are operator experience level (Δ=6.89), machine size (Δ=6.65), CNC machine age (Δ=6.56), and CNC machine brand (Δ=4.58). The parameters influencing the dimension conformity factor are machine size (Δ=10.94), operator experience level (Δ=8.87), CNC machine brand (Δ=8.25), and CNC machine age (Δ=7.67). The responses affecting surface roughness are machine size (Δ=8,93), operator experience level (Δ=7,99), CNC machine age (Δ=6,96), and CNC machine brand (Δ=5,09), respectively.

Fig. 1, Fig. 2, Fig. 3, and Table 5 present the optimum values of the process parameters for S/N ratios.

As seen in Figure 1, the best value of the parameter operator experience level is obtained as level 3 (10,00),

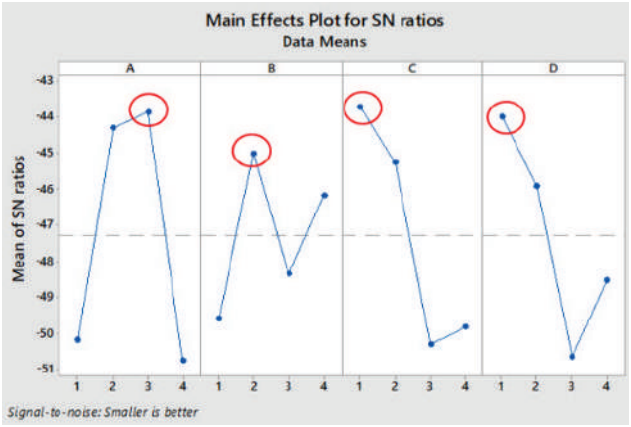


Figure 1. Mean effects plot of production time for S/N ratios.

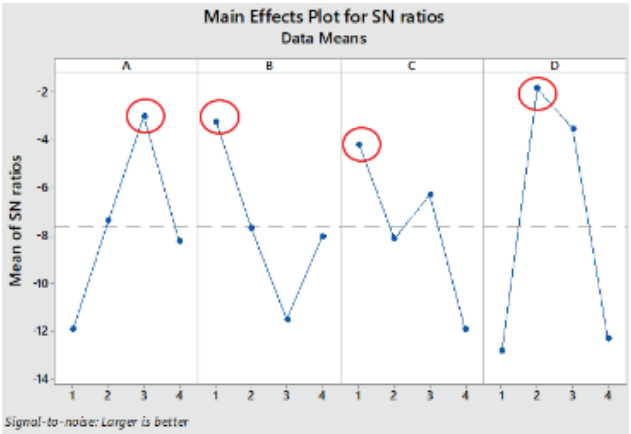


Figure 2. Mean effects plot of dimension conformity for S/N ratios.

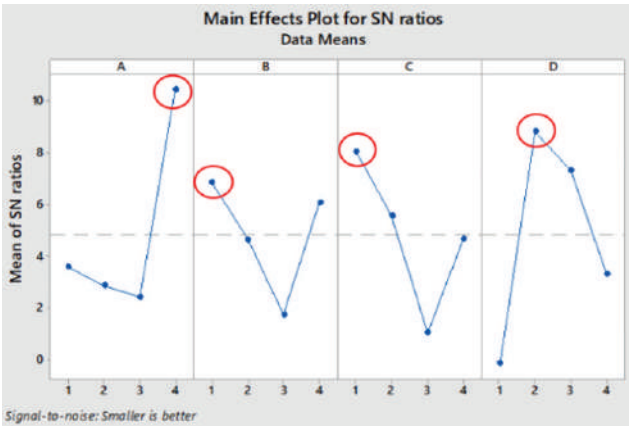


Figure 3. Mean effects plot of surface roughness for S/N ratios.

Table 5. Optimum values of the process parameters according to S/N ratios

Performance factors	**A**	**B**	**C**	**D**
Production Time (min)	3	2	1	1
Dimension Conformity (ratio)	3	1	1	2
Surface Roughness (μm)	4	1	1	2
Combination	3	1	1	2

the best value of the CNC machine brand is obtained as level 2 (Okuma), the best value of the CNC machine age is obtained as level 1 (2,00) and the best value of machine size is obtained as level 1 (500x550x550) for production time. As can be seen in Figure 2, the best value of the operator experience level parameter was found as level 3 (10,00), the best value of the CNC machine brand was found as level 1 (Mazak), the best value of the CNC machine age was found as level 1 (2,00) and the best value of machine size was found as level 2 (700x450x500) for dimension conformity. Lastly, as seen in Figure 3, the best value of the operator experience level parameter was found as level 4 (14,00), the best value of the CNC machine brand was found as level 1 (Mazak), the best value of CNC machine age was found as level 1 (2,00) and the best value of machine size was found as level 2 (700x450x500) for surface roughness. When the responses are combined according to the levels' frequency of occurrence, the best value of the operator experience level parameter is level 3 (10,00), the best value of the CNC machine brand is level 1 (Mazak), the best value of the CNC machine age is level 1 (2,00) and the best value of machine size is level 2 (700x450x500).

When the optimal input levels of performance factors are compared in light of the results obtained with TM, it is concluded that TM is insufficient for the simultaneous optimization of multiple performances for CNC production. The GRA method was utilized following TM, and the resulting data was analysed.

Grey Relational Analysis Optimization

As a second method GRA with equal weights are utilized in combination with TM. Table 6 shows the results obtained with GRA for the responses. S/N ratio values were first normalized and then converted to normalization values. The distance matrix and weightings of the test samples were calculated, and then GRGs were estimated using GRA.

The average GRG values and the optimal values of the input parameters according to the parameters and GRGs are given in Table 7 and Table 8, respectively.

Table 7. Average GRG values and parameters

Levels	A	B	C	D
1	0.48	0.60	0.68	0.49
2	0.60	0.56	0.57	0.71
3	0.63	0.52	0.52	0.59
4	0.60	0.61	0.53	0.51
Delta	0.15	0.10	0.16	0.22
Rank	3	4	2	1

Table 8. Optimum values of input parameters by GRGs

Method	A	B	C	D
GRA	3	4	1	2

Table 6. GRA results for CNC production

	Normalization			Distance Matrix			Weighting				
No.	Production Time (min)	Dimension Conformity (ratio)	Surface Roughness (μm)	Production Time (min)	Dimension Conformity (ratio)	Surface Roughness (μm)	Production Time (min)	Dimension Conformity (ratio)	Surface Roughness (μm)	GRG	Rank
1	0.50	0.29	-0.06	0.50	0.71	1.06	0.50	0.41	0.32	0.41	14
2	0.63	0.45	0.86	0.37	0.55	0.14	0.57	0.47	0.78	0.61	6
3	0.31	0.28	0.14	0.69	0.72	0.86	0.42	0.41	0.37	0.40	15
4	0.13	-0.04	0.80	0.87	1.04	0.20	0.36	0.33	0.71	0.47	11
5	0.53	0.80	0.92	0.47	0.20	0.08	0.52	0.72	0.86	0.70	3
6	0.98	0.36	0.56	0.02	0.64	0.44	0.96	0.44	0.53	0.64	5
7	0.62	0.00	0.05	0.38	1.00	0.95	0.57	0.33	0.35	0.42	13
8	0.55	0.97	0.00	0.45	0.03	1.00	0.53	0.94	0.33	0.60	8
9	0.19	0.85	0.46	0.81	0.15	0.54	0.38	0.77	0.48	0.54	9
10	0.36	0.69	0.03	0.64	0.31	0.97	0.44	0.62	0.34	0.47	12
11	0.86	1.00	0.88	0.14	0.00	0.12	0.78	1.00	0.81	0.86	1
12	1.00	0.33	0.17	0.00	0.67	0.83	1.00	0.43	0.38	0.60	7
13	0.56	0.86	0.94	0.44	0.14	0.06	0.53	0.78	0.90	0.74	3
14	0.52	0.10	0.74	0.48	0.90	0.26	0.51	0.36	0.65	0.51	10
15	0.00	0.05	0.24	1.00	0.95	0.76	0.33	0.34	0.40	0.36	16
16	0.28	0.95	1.00	0.72	0.05	0.00	0.41	0.90	1.00	0.77	2

The optimal values of the input parameters for the responses with the GRA method are as follows: operator experience level is level 3 (10,00), CNC machine brand is level 4 (Yuntes), CNC machine age is level 1 (2,00), and machine size is level 2 (700x450x500).

The results show that the optimum values of input parameters according to TM and GRA are slightly different. This reveals this study's inadequate use of TM and GRA for multiple performance optimization of CNC machining. Hence, GRGs are computed using GRA-PCA in the following subsection of this study.

Grey Relational Analysis- Principal Component Analysis Optimization

The GRA-PCA method was applied after the GRA method for multiple performance optimization. The correlation coefficient matrix generated utilizing the variance-covariance matrix was also utilized to identify the eigenvalues and associated eigenvectors for each response of the model. The eigenvectors corresponding to the PCs and the weight contribution of each process parameter predicted for the first PC are represented in Table 9.

As seen in Table 9, the weight contribution of production time, dimension conformity, and surface roughness responses are 45.3%, 32.3%, and 22.4%, respectively. Based on this, it is seen that the weight contribution of production time is the most significant for CNC production.

After conducting GRA-PCA, GRCs for responses were recalculated based on the weighted factors. Lastly, each response was combined into a single response as a GRG value (Table 10).

According to GRG values obtained with GRA-PCA, the optimal values of the input parameters are as follows: operator experience level is level 3 (10,00), CNC machine brand is level 4 (Yuntes), CNC machine age is level 1 (2,00) and machine size is level 2 (700x450x500). While the most significant parameter for CNC production is machine size, the least effective parameter for CNC production is the CNC machine brand. The efficiency levels of the parameters are as follows in order from highest to lowest: machine size, operator experience level, CNC machine age, and CNC machine brand. After the GRA-PCA method was applied, sensitivity analysis was applied, and twenty-one different alternatives were analysed according to the weight levels that the perfomance factors could be weighted.

Sensitivity Analysis

At this subsection of this study, a sensitivity analysis was performed as it was expected that the risks and uncertainties that may arise from the results obtained with the previously applied methods could potentially affect the study. Twenty-one alternative weight levels were defined for the responses of production time, dimension conformity, and surface roughness. The weight values are shown in Table 11. The weighted GRG values and parameters for the alternatives are shown in Table 12 - Table 32.

The results attained in the sensitivity analysis performed are as follows: In the seven different alternatives (alternative no. 4, 5, 6, 7, 8, 9, and 15), level 3 of parameter A (10.00), the level 4 of parameter B (Yuntes); the level 1 of parameter C (2.00) and the level 2 of parameter D (700x450x500) are optimum. In the six different alternatives (alternative no. 16, 17, 18, 19, 20, and 21), level 4 of parameter A (14.00), level 1 of parameter B (Mazak), level 1 of parameter C (2.00) and level 2 of parameter D (700x450x500) are optimum. In the five different alternatives (alternative no. 10, 11, 12, 13, and 14), level 3 of parameter A (10.00); level 1 of parameter B (Mazak); level 1 of parameter C (2.00), and level 2 of parameter D (700x450x500) are optimum. In the two different alternatives (alternative no. 2 and 3), level 3 of parameter A (10.00), level 2 of parameter B (Okuma), level 1 of parameter C (2.00), and level 2 of parameter D (700x450x500) are obtained as optimum. Finally, among the twenty-one different alternatives, in the one alternative (alternative no. 1), level 3 of parameter A (10.00); level 2 of parameter B (Okuma); level 1 of parameter C (2.00); and level 1 of parameter D (500x550x550), are determined as optimum.

Table 10. Weighted GRG values and parameters according to GRA-PCA

Levels	A	B	C	D
1	0.469	0.583	**0.675**	0.517
2	0.608	0.568	0.574	**0.692**
3	**0.639**	0.519	0.516	0.564
4	0.564	**0.610**	0.515	0.507
Delta	0.17	0.09	0.16	0.19
Rank	2	4	3	1

Table 9. Eigenvectors for PCs and the contribution of each response

Responses	PC1	PC2	PC3	Weight contribution
Production Time (min)	0.361	0.895	-0.261	0.453
Dimension Conformity (ratio)	-0.69	0.068	-0.721	0.323
Surface Roughness (μm)	0.628	-0.44	-0.642	0.224

Table 11. Weight values of performance factors in sensitivity analysis

Alternative No.	Production Time (min)	Dimension Conformity (ratio)	Surface Roughness (μm)
1	1.00	0.00	0.00
2	0.90	0.10	0.00
3	0.80	0.10	0.10
4	0.70	0.20	0.10
5	0.60	0.20	0.20
6	0.50	0.30	0.20
7	0.40	0.30	0.30
8	0.30	0.40	0.30
9	0.20	0.50	0.30
10	0.10	0.60	0.30
11	0.10	0.70	0.20
12	0.10	0.80	0.10
13	0.00	0.90	0.10
14	0.00	1.00	0.00
15	0.30	0.30	0.40
16	0.20	0.30	0.50
17	0.20	0.20	0.60
18	0.10	0.20	0.70
19	0.10	0.10	0.80
20	0.00	0.10	0.90
21	0.00	0.00	1.00

Table 12. Weighted GRG values and parameters for Alternative-1

Levels	A	B	C	D
1	0.464	0.482	**0.662**	**0.645**
2	0.643	**0.620**	0.606	0.602
3	**0.650**	0.525	0.459	0.447
4	0.446	0.576	0.476	0.509
Delta	0.204	0.138	0.203	0.198
Rank	1	4	2	3

Table 13. Weighted GRG values and parameters for Alternative-2

Levels	A	B	C	D
1	0.459	0.502	**0.665**	0.619
2	0.640	**0.606**	0.595	**0.622**
3	**0.656**	0.525	0.476	0.469
4	0.462	0.584	0.480	0.506
Delta	0.197	0.104	0.189	0.153
Rank	1	4	2	3

Table 14. Weighted GRG values and parameters for Alternative-3

Levels	A	B	C	D
1	0.468	0.518	**0.667**	0.599
2	0.628	**0.603**	0.596	**0.634**
3	**0.643**	0.522	0.477	0.489
4	0.492	0.587	0.491	0.509
Delta	0.175	0.084	0.189	0.144
Rank	2	4	1	3

Table 15. Weighted GRG values and parameters for Alternative-4

Levels	A	B	C	D
1	0.463	0.538	**0.670**	0.573
2	0.625	0.589	0.586	**0.654**
3	**0.649**	0.523	0.494	0.512
4	0.507	**0.595**	0.496	0.506
Delta	0.185	0.073	0.176	0.147
Rank	1	4	2	3

Table 16. Weighted GRG values and parameters for Alternative-5

Levels	A	B	C	D
1	0.473	0.555	**0.671**	0.553
2	0.614	0.586	0.586	**0.665**
3	**0.635**	0.519	0.495	0.532
4	0.537	**0.599**	0.507	0.510
Delta	0.163	0.080	0.176	0.155
Rank	2	4	1	3

Table 17. Weighted GRG values and parameters for Alternative-6

Levels	A	B	C	D
1	0.468	0.574	**0.674**	0.527
2	0.611	0.572	0.576	**0.685**
3	**0.641**	0.520	0.512	0.554
4	0.553	**0.607**	0.511	0.506
Delta	0.174	0.087	0.163	0.178
Rank	2	4	3	1

Table 18. Weighted GRG values and parameters for Alternative-7

Levels	A	B	C	D
1	0.477	0.591	**0.676**	0.507
2	0.600	0.569	0.577	**0.696**
3	**0.628**	0.517	0.513	0.574
4	0.583	**0.611**	0.522	0.510
Delta	0.151	0.094	0.162	0.190
Rank	3	4	2	1

Table 19. Weighted GRG values and parameters for Alternative-8

Levels	A	B	C	D
1	0.472	0.610	**0.679**	0.481
2	0.597	0.555	0.566	**0.716**
3	**0.633**	0.517	0.530	0.597
4	0.599	**0.619**	0.527	0.507
Delta	0.162	0.102	0.152	0.235
Rank	2	4	3	1

Table 20. Weighted GRG values and parameters for Alternative-9

Levels	A	B	C	D
1	0.467	**0.630**	**0.682**	0.456
2	0.594	0.541	0.555	**0.736**
3	**0.639**	0.517	0.546	0.619
4	0.614	0.627	0.531	0.503
Delta	0.173	0.113	0.151	0.280
Rank	2	4	3	1

Table 21. Weighted GRG values and parameters for Alternative-10

Levels	A	B	C	D
1	0.462	**0.649**	**0.685**	0.431
2	0.591	0.527	0.545	**0.756**
3	**0.645**	0.517	0.563	0.641
4	0.630	0.635	0.536	0.500
Delta	0.183	0.132	0.149	0.326
Rank	2	4	3	1

Table 22. Weighted GRG values and parameters for Alternative-11

Levels	A	B	C	D
1	0.448	**0.652**	**0.687**	0.426
2	0.600	0.516	0.533	**0.765**
3	**0.665**	0.521	0.578	0.643
4	0.616	0.639	0.530	0.493
Delta	0.217	0.136	0.157	0.339
Rank	2	4	3	1

Table 23. Weighted GRG values and parameters for Alternative-12

Levels	A	B	C	D
1	0.433	**0.655**	**0.689**	0.422
2	0.608	0.505	0.522	**0.774**
3	**0.684**	0.524	0.593	0.645
4	0.601	0.643	0.523	0.487
Delta	0.251	0.150	0.167	0.352
Rank	2	4	3	1

Table 24. Weighted GRG values and parameters for Alternative-13

Levels	A	B	C	D
1	0.428	**0.674**	**0.692**	0.396
2	0.605	0.491	0.512	**0.794**
3	**0.690**	0.524	0.609	0.667
4	0.617	0.651	0.528	0.483
Delta	0.262	0.183	0.180	0.398
Rank	2	3	4	1

Table 25. Weighted GRG values and parameters for Alternative-14

Levels	A	B	C	D
1	0.414	**0.677**	**0.694**	0.392
2	0.614	0.480	0.500	**0.803**
3	**0.709**	0.528	0.624	0.669
4	0.603	0.655	0.522	0.476
Delta	0.295	0.197	0.194	0.411
Rank	2	3	4	1

Table 26. Weighted GRG values and parameters for Alternative-15

Levels	A	B	C	D
1	0.486	0.608	**0.677**	0.486
2	0.588	0.566	0.577	**0.707**
3	**0.614**	0.513	0.515	0.595
4	0.613	**0.615**	0.533	0.514
Delta	0.128	0.101	0.162	0.222
Rank	3	4	2	1

Table 27. Weighted GRG values and parameters for Alternative-16

Levels	A	B	C	D
1	0.495	**0.624**	**0.678**	0.465
2	0.577	0.563	0.578	**0.719**
3	**0.601**	0.510	0.516	0.615
4	0.643	0.619	0.544	0.517
Delta	0.148	0.114	0.162	0.254
Rank	3	4	2	1

Table 28. Weighted GRG values and parameters for Alternative-17

Levels	A	B	C	D
1	0.510	**0.622**	**0.676**	0.470
2	0.569	0.574	0.589	**0.710**
3	0.581	0.507	0.501	0.613
4	**0.657**	0.615	0.550	0.524
Delta	0.148	0.115	0.175	0.240
Rank	3	4	2	1

Table 29. Weighted GRG values and parameters for Alternative-18

Levels	A	B	C	D
1	0.519	**0.638**	**0.678**	0.449
2	0.557	0.570	0.590	**0.721**
3	0.568	0.504	0.502	0.634
4	**0.687**	0.619	0.561	0.527
Delta	0.169	0.135	0.175	0.272
Rank	3	4	2	1

Table 30. Weighted GRG values and parameters for Alternative-19

Levels	A	B	C	D
1	0.533	0.636	0.676	0.453
2	0.549	0.581	0.601	0.713
3	0.548	0.500	0.487	0.632
4	0.702	0.615	0.567	0.534
Delta	0.169	0.135	0.188	0.259
Rank	3	4	2	1

Table 31. Weighted GRG values and parameters for Alternative-20

Levels	A	B	C	D
1	0.542	0.653	0.677	0.433
2	0.537	0.578	0.602	0.724
3	0.535	0.497	0.489	0.652
4	0.732	0.618	0.578	0.538
Delta	0.197	0.155	0.188	0.291
Rank	2	4	3	1

Table 32. Weighted GRG values and parameters for Alternative-21

Levels	A	B	C	D
1	0.557	0.650	0.675	0.437
2	0.529	0.589	0.614	0.715
3	0.515	0.494	0.474	0.650
4	0.746	0.614	0.585	0.545
Delta	0.231	0.156	0.201	0.278
Rank	2	4	3	1

The ranking of parameters in terms of their influence on the performance factors (responses) is as follows:

- In the eight different alternatives (alternative no. 6, 8, 9, 10, 11, 12, 20, and 21): D > A > C > B,
- In the six different alternatives (alternative no. 7, 15, 16, 17, 18, and 19): D > C > A > B,
- In the three different alternatives (alternative no. 1, 2, and 4): A > C > D > B,
- In the two different alternatives (Alternative No. 3 and 5): C > A > D > B,
- In the two different alternatives (Alternative No. 13 and 14): D > A > B > C.

Based on the results obtained, it has been observed that the impact ranking of parameters on responses has converged into five different clusters for the various alternatives. Table 33 shows the optimal levels of input parameters for all problem solutions.

From the 24 different solutions, in 18 of them, the best level of parameter A was 3 (10,00), and in 6 of them, the best level was 4 (14,00). In 12 solutions, the best level of parameter B was 1 (Mazak); in 9 solutions, the best level was 4 (Yuntes), and in 3 solutions, the best level was 2 (Okuma). The best level of parameter C was found to be 1 (2.00) in all solutions. Lastly, the best level of parameter D was 2 (700x450x500) in 23 solutions and level 1 (500x550x550) in 1 solution. After the obtained results, the ANOVA method was applied based on the S/N ratios of CNC production in the next stage of this study.

Analysis of Variance

ANOVA, which is a statistical approach was applied according to the S/N ratios; the obtained results are given in Table 34.

SS represents the total variability between and within groups, while MS is the value obtained by dividing SS by the degrees of freedom (df). The F-value is the ratio of the variance between groups to the variance within groups. This value is used to test whether there is a significant difference between groups. The p-value indicates the probability that the observed difference between groups occurred by chance based on the calculated F-value. If $p<0.05$, the difference between groups is statistically significant, whereas if $p\geq0.05$, the difference is not statistically significant [32].

Table 33. Optimum values according to all applied methods

Methods	A	B	C	D
TM	3	1	1	2
GRA	3	4	1	2
GRA-PCA	3	4	1	2
Alt. 1	3	2	1	2
Alt. 2	3	2	1	2
Alt. 3	3	2	1	2
Alt. 4	3	4	1	2
Alt. 5	3	4	1	2
Alt. 6	3	4	1	2
Alt. 7	3	4	1	2
Alt. 8	3	4	1	2
Alt. 9	3	4	1	2
Alt. 10	3	1	1	2
Alt. 11	3	1	1	2
Alt. 12	3	1	1	2
Alt. 13	3	1	1	2
Alt. 14	3	1	1	2
Alt. 15	3	4	1	2
Alt. 16	4	1	1	2
Alt. 17	4	1	1	2
Alt. 18	4	1	1	2
Alt. 19	4	1	1	2
Alt. 20	4	1	1	2
Alt. 21	4	1	1	2

According to the ANOVA, the contributions of the process parameters and their influence ranking on the performance factors according to the F-values are given below.

i) For production time: A (24.71%) > C (19.40%) > D (15.41%) > B (7.79%).
ii) For dimension conformity: D (46.56%) > A (18.80%) > B (16.18%) > C (15.02%).
iii) For surface roughness response is as follows: D (18.11%) > A (14.31%) > C (6.71%) > B (5.82%).

For input parameter production time, the ranking of the input parameters by applying Taguchi method was found as *A* (Δ=6.89) > *D* (Δ=6.65) > *C* (Δ=6.56) > *B* (Δ=4.58) (see Table 4), while the ranking in ANOVA was obtained as A (24.71%) > C (19.40%) > D (15.41%) > B (7.79%) (see Table 34). It is seen that the difference between the delta values of C (CNC Machine Age) and D (Workbench Size (mm)) parameters is quite low, while the percentage differences obtained by ANOVA are rather high. Additionally, with the expert feedback from the manufacturing company, it can be said that C is more important than D parameter in CNC production. When the results are observed, it can be

Table 34. ANOVA table for S/N ratios of CNC production

Responses	Parameters	df	SS	MS	F-value	P-value	Contribution (%)
Production Time (min)	A	3	163.7	54.58	1.31	0.316	24.71
	B	3	51.6	17.2	0.34	0.798	7.79
	C	3	128.6	42.86	0.96	0.442	19.4
	D	3	102.1	34.05	0.73	0.554	15.41
Dimension Conformity (ratio)	A	3	159.4	53.14	0.93	0.457	18.8
	B	3	137.2	45.74	0.77	0.531	16.18
	C	3	127.4	42.45	0.71	0.566	15.02
	D	3	394.8	131.59	3.48	0.05	46.56
Surface Roughness (μm)	A	3	0.5723	0.1908	0.67	0.588	14.31
	B	3	0.2329	0.07763	0.23	0.862	5.82
	C	3	0.2682	0.08941	0.29	0.834	6.71
	D	3	0.7245	0.2415	0.88	0.477	18.11

Abbreviations: df; degrees of freedom, SS; the sum of squares of errors, MS; the mean sum of squares of errors

concluded that the results of the ANOVA support the findings obtained in the other methods.

Confirmation Tests

Confirmation tests were carried out to verify the optimality of CNC process parameter levels found by the GRA-PCA-TM method and to confirm the improvement in the performance factors. The results are shown in Table 35. The experimental results of production time, dimension conformity, and surface roughness responses at the optimal parameter levels were utilized to predict the actual S/N ratio.

In the confirmation tests, it was observed that the estimated S/N values and the real S/N values were consistent. As a result, the actual S/N ratio for production time (-28.79) improved by 45% compared to the initial process parameter (-49.00), the actual S/N ratio for dimension conformity (-0.45) improved by 95% compared to the initial process parameter (-8.87) and lastly, the actual S/N ratio for surface roughness (13.98) improved by 504% compared to the initial process parameter (-3.46).

As previously stated in the study, no study using the input parameters used in this study has been found in the literature. While many studies in the literature have used surface roughness as a performance factor, one study has been encountered in which production time has been used [33], while no study has been found in which dimension conformity has been used. Although TM, GRA and PCA methods were used in this study, there is no other study in

Table 35. Results of confirmation tests for production time, dimension conformity, and surface roughness responses

			Optimum CNC production parameters	
Responses		**Initial CNC production parameters**	**Prediction**	**Experiment**
Production Time (min)	Levels	A1B1C1D1	A3B2C1D1	A3B2C1D1
	Average values	282.00		27.50
	S/N ratios	-49.00	-34.77	-28.79
	Improvement in S/N ratios			20.21 (%45)
Dimension Conformity (ratio)	Levels	A1B1C1D1	A3B1C1D2	
	Average values	0.36		
	S/N ratios	-8.87	10.54	-0.45
	Improvement in S/N ratios			8.42 (%95)
Surface Roughness (μm)	Levels	A1B1C1D1	A4B1C1D2	
	Average values	1.49		
	S/N ratios	-3.46	19.59	13.98
	Improvement in S/N ratios			17.44 (%504)

the literature that hybridises these methods. In this study, 45%, 95%, and 504% improvements were obtained in production time, dimension conformity and surface roughness, respectively, while it was observed that this level of improvement was not acquired earlier studies in the literature [14,17,21,24,34,35]. Since the input parameters used in the previous studies in the literature differ from those used in this study, it was not feasible to compare the findings obtained in terms of the parameters affecting CNC production with the appropriate studies in the literature.

CONCLUSION

This study focuses on multiple performance factor optimization of the process parameters of CNC production in metal sector, which is the most significant process of an organization operating in this sector, using TM, GRA, and GRA-PCA and performing sensitivity analysis. In this scope, the impacts of CNC production process parameters, which are operator experience level, CNC machine brand, CNC machine age, and machine size, on the performance factors of production time, dimension conformity, and surface roughness were searched and multiple performance optimization was conducted. The study revealed that the most influential parameter for CNC production was the machine size in TM, GRA, GRA-PCA, and sensitivity analysis in sixteen alternatives. The least affecting parameter for CNC production is the CNC machine brand in TM, GRA, GRA-PCA, and nineteen different alternative weightings made in the sensitivity analysis. The ANOVA application has supported these results and has been confirmed by the subsequent confirmation tests.

As a result of the confirmation tests, it was concluded that the estimated S/N values and the real S/N values are compatible. For production time, the actual S/N ratio (-28.79) improved by 45% compared to the initial process parameter (-49.00); for dimension conformity, the actual S/N ratio (-0.45) improved by 95% compared to the initial process parameter (-8.87) and finally for surface roughness the actual S/N ratio (13.98) improved by 504% in comparison to the initial process parameter (-3.46).

The optimum combination of CNC production parameters based on multiple response variables was obtained as A3B1C1D2, so the optimum values were determined as 10.00 for operator experience level, Mazak for CNC machine brand, 2.00 for CNC machine age and 700x450x500 for machine size.

From all the results obtained, this study has limitations that open a field of study for future research since the findings obtained from the data set received from the company operating in the metal sector are focused on a particular sector. Besides the TM and GRA, PCA was conducted to weigh the performance factors, and sensitivity analysis was performed to determine the risks or uncertainties that may potentially affect this study. In these aspects, this study is unique and contributes to the literature. Moreover, companies can benefit from managerial practices by considering the ranking of parameters affecting CNC production according to the results obtained from the study. For instance, companies can assign CNC operators to the appropriate machine especially in critical parts. In addition, in critical material production, the part can be assigned to the most proper machine. Additionally, the obtained results in this study provide managers a strategic perspective for future recruitment, machine investment decisions or long-term process planning.

In future studies, it is concluded that different multi-criteria decision-making methods can be used for multiple optimization of process parameters and the diversity of process parameters and response factors can be increased in CNC production.

AUTHORSHIP CONTRIBUTIONS

Authors equally contributed to this work.

DATA AVAILABILITY STATEMENT

The authors confirm that the data that supports the findings of this study are available within the article. Raw data that support the finding of this study are available from the corresponding author, upon reasonable request.

CONFLICT OF INTEREST

The author declared no potential conflicts of interest with respect to the research, authorship, and/or publication of this article.

ETHICS

There are no ethical issues with the publication of this manuscript.

STATEMENT ON THE USE OF ARTIFICIAL INTELLIGENCE

Artificial intelligence was not used in the preparation of the article.

REFERENCES

[1] Molotnikov V, Molotnikova A. Precision Manufacturing of Machine Parts. In Theoretical and Applied Mechanics. New York: Springer; 2023. p. 497–507. [CrossRef]

[2] de Lacalle LNL, Lamikiz A. Machine Tools for High Performance Machining. Springer; 2009.

[3] Taguchi G, Don C. Robust quality. Harv Bus Rev 1990;68:65–75. [CrossRef]

[4] Dimou M, Marnasidis S, Antoniadou I, Pliatsika M, Besseris GJ. The application of Taguchi method to determine the optimum blend of unifloral honeys to most closely match thyme honey quality. Int J Food Sci Technol 2009;44:1877–1886. [CrossRef]

[5] Julong D. Introduction to grey system theory. J Grey Syst 1989;1:1–24.
[6] Sankar B, Umamaheswarrao P, Srinivasulu V, Chowdari GK. Optimization of milling process on jute polyester composite using Taguchi based grey relational analysis coupled with principle component analysis. Mater Today Proc 2015;2:2522–2531. [CrossRef]
[7] Raju BS, Chandra Sekhar U, Drakshayani DN. Grey relational analysis coupled with principal component analysis for optimization of stereolithography process to enhance part quality. IOP Conf Ser Mater Sci Eng 2017;191:012228. [CrossRef]
[8] Rao PM, Vijaya M, Srinivas K, Chilakala DR, Chaitanya KL, Chowdary JR, et al. Optimization of wear parameters & coefficient of friction of SiC and graphite reinforced hybrid aluminium composites. Sigma J Eng Nat Sci 2023;41:1019–1028.
[9] Kasman Ş, Büyüker B, Ozan S. Machining of Ti–6Al–4V alloy by fiber laser: Determining the effects of parameters on surface roughness. Sigma J Eng Nat Sci 2023;41:770–780. [CrossRef]
[10] Swapna D, Srinivasa Rao C, Sameer Kumar D, Radhika S. Taguchi based GRA-PCA hybrid optimization for the forming of AL6061 alloy in automotive applications. Sigma J Eng Nat Sci 2022;40:742–754. [CrossRef]
[11] Adar E. Optimization of cattle manure liquid fraction anaerobic digestion at different temperatures: Modelling by Taguchi method. Sigma J Eng Nat Sci 2021;38:1753–1766.
[12] Mola E, Bayrak OÜ, Baş Fİ, Bayata HF. Investigating the usability of Kevlar and steel fibers as a hybrid in concrete pavements. Sigma J Eng Nat Sci 2024;42:344–355. [CrossRef]
[13] Singh PK, Saini P, Kumar D. Multi response optimization of CNC end milling of AISI H11 alloy steel for rough and finish machining using TGRA. Mater Today Proc 2020;26:2564–2573. [CrossRef]
[14] Kumar R, Katyal P, Kumar K. Effect of end milling process parameters and corrosion behaviour of ZE41A magnesium alloy using Taguchi based GRA. Biointerface Res Appl Chem 2023;13. [CrossRef]
[15] Esangbedo MO, Abifarin JK. Cost and quality optimization Taguchi design with grey relational analysis of halloysite nanotube hybrid composite: CNC machine manufacturing. Materials 2022;15:8154. [CrossRef]
[16] Suresh Kumar R, Senthil Kumar S. Green machining characteristics study of Al-6063 in CNC milling using Taguchi method and grey relational analysis. Adv Mater Sci Eng 2021;2021:1–12. [CrossRef]
[17] Prakash KS, Gopal PM, Karthik S. Multi-objective optimization using Taguchi based grey relational analysis in turning of Rock dust reinforced Aluminum MMC. Measurement 2020;157:107664. [CrossRef]
[18] Kouahla I, Yallese MA, Belhadi S, Safi K, Nouioua M. Tool vibration, surface roughness, cutting power, and productivity assessment using RSM and GRA approach during machining of Inconel 718 with PVD-coated carbide tool. Int J Adv Manuf Technol 2022;122:1835–1856. [CrossRef]
[19] Teja BVR, Sai NP, Prasad JSD, Chandu MSS, Rao V. Design and optimization of process parameters during turn-milling process of titanium alloy using GRA method. Int J Mod Trends Sci Technol 2022;8:95–101.
[20] Raguraman D, Balu P, Manavalan S, Raja E. Multilinear optimization of machining parameters of CNC turning of AA6061alloy using GRA method. Mater Today Proc 2023. [CrossRef]
[21] Zhujani F, Abdullahu F, Todorov G, Kamberov K. Optimization of multiple performance characteristics for CNC turning of Inconel 718 using Taguchi–Grey relational approach and analysis of variance. Metals 2024;14:186. [CrossRef]
[22] Zeydan M. Optimization of flexible polyurethane foam hardness by reducing process variance. Sigma J Eng Nat Sci 2021;38:1851–1867.
[23] Sahare S, Kamble P, Giri J, Sunheriya N, Sathish T, Chadge R, et al. Multi objective optimization of cutting parameters of end milling operation by Taguchi Grey: Relational analysis (TGRA). Interact 2024;245:1–18. [CrossRef]
[24] Mastan Rao P, Deva Raj C, Dhoria SH, Vijaya M, Chowdary JRR, et al. Multi-objective optimization of turning for nickel-based alloys using Taguchi-GRA and TOPSIS approaches. J Inst Eng India Ser D 2023;105:1473–1484. [CrossRef]
[25] Üstüntağ S, Şenyiğit E, Mezarcıöz S, Türksoy HG. Optimization of coating process conditions for denim fabrics by Taguchi method and grey relational analysis. J Nat Fibers 2020;19:685–699. [CrossRef]
[26] Arce ME, Saavedra Á, Míguez JL, Granada E. The use of grey-based methods in multi-criteria decision analysis for the evaluation of sustainable energy systems: A review. Renew Sustain Energy Rev 2015;47:924–932. [CrossRef]
[27] Oliver Nesa Raj S, Prabhu S. Modeling and analysis of titanium alloy in wire-cut EDM using Grey relation coupled with principle component analysis. Aust J Mech Eng 2017;15:198–209. [CrossRef]
[28] Sehgal AK. Grey relational analysis coupled with principal component analysis to optimize the machining process of ductile iron. Mater Today Proc 2018;5:1518–1529. [CrossRef]
[29] Vasudevan H, Rajguru R, Tank K, Shetty N. Optimization of multi-performance characteristics in the turning of GFRP (E) composites using principle component analysis combined with grey relational analysis. Mater Today Proc 2018;5:5955–5967. [CrossRef]

[30] Rojas H, Vargas Z, Valdez S, Serrano M, del Pozo A, Alcántara M. Taguchi, Grey Relational Analysis, and ANOVA optimization of TIG welding parameters to maximize mechanical performance of Al-6061 T6 alloy. J Manuf Mater Process 2024;8:246. [CrossRef]

[31] Deepanraj B, Sivasubramanian V, Jayaraj S. Multi-response optimization of process parameters in biogas production from food waste using Taguchi–Grey relational analysis. Energy Convers Manag 2017;141:429–438. [CrossRef]

[32] Kao LS, Green CE. Analysis of variance: Is there a difference in means and what does it mean? J Surg Res 2008;144:158–170. [CrossRef]

[33] Rathod NJ, Chopra MK, Chaurasiya PK, Vidhate US. Optimization of tool life, surface roughness and production time in CNC turning process using Taguchi method and ANOVA. Ann Data Sci 2023;10:1179–1197. [CrossRef]

[34] Dhanalakshmi S, Rameshbabu T. Multi-Aspects optimization of process parameters in CNC turning of LM 25 alloy using the Taguchi-Grey approach. Metals 2020;10:453. [CrossRef]

[35] Azim S, Noor S, Khalid QS, Khan AM, Pimenov DY, Ahmad I, et al. Sustainable manufacturing and parametric analysis of mild steel grade 60 by deploying CNC milling machine and Taguchi method. Metals 2020;10:1303. [CrossRef]

[36] Ficko M, Begic-Hajdarevic D, Hadziabdic V, Klancnik S. Multi-response optimisation of turning process parameters with GRA and topsis methods. Int J Simul Model 2020;19:547–558. [CrossRef]

[37] Zade MH, Meshram S. Optimization of CNC boring process by Taguchi's-Grey relational evaluation. Int Res J Mod Eng Technol Sci 2022;4:1585–1589.

[38] Sundara Bharathi SR, Ravindran D, Moshi AAM. Multi-response optimization of CNC turning parameters of austenitic stainless steel 303 using Taguchi-based grey relational analysis. Trans Can Soc Mech Eng 2020;44:592–601. [CrossRef]

[39] Kumar Yadav D, Kumar Dixit N, Agarwal D, Kumar Khare S. Optimization of machining parameters in CNC milling of Ti-6Al-4 V alloy using multiple methodology. Mater Today Proc 2022;59:138–143. [CrossRef]

[40] Guldane M, Dogan M. Multi-response optimization of process parameters of saponin-based model foam using Taguchi method and gray relational analysis coupled with principal component analysis. J Food Process Preserv 2022;46:e16553. [CrossRef]

Sigma J Eng Nat Sci, Vol. 44, No. 1, pp. 309–317, February, 2026

Sigma Journal of Engineering and Natural Sciences
Web page info: https://sigma.yildiz.edu.tr
DOI: 10.14744/sigma.2025.00000

Research Article

Improved error limits for numerical integration via some perturbed trapezoidal inequalities

Duygu DÖNMEZ DEMİR[1,*], Gülsüm ŞANAL[2]

[1]*Department of Mathematics, Faculty of Engineering and Natural Sciences, Manisa Celal Bayar University, 45140, Manisa, Türkiye*
[2]*Administrative and Social Sciences, İstanbul Nişantaşı University, Department of Management Information Systems, Faculty of Economics, Istanbul, 34481742, Türkiye*

ARTICLE INFO

Article history
Received: 05 June 2024
Revised: 21 August 2024
Accepted: 19 December 2024

Keywords:
Numerical Integration; Perturbed Trapezoid Inequality; *s*-convex; *tgs*-convex

ABSTRACT

Integral inequalities prove extremely effective in obtaining error bounds for numerical integration formulas, which are particularly useful in optimization problems. This study presents reduced results of perturbed trapezoidal inequalities derived using the triangle inequality, Hölder's inequality, and power mean inequalities for previously constructed n^{th}-order differentiable *s*-convex and *tgs*-convex functions. These results help determine error limits for the trapezoidal rule and the remaining term of the midpoint formula in numerical integration. The study shows that these reduced inequalities yield better error limits. Additionally, an example involving a *tgs*-convex function defined under certain conditions demonstrates the practical application of these theoretical results.

Cite this article as: Dönmez Demir D, Şanal G. Improved error limits for numerical integration via some perturbed trapezoidal inequalities. Sigma J Eng Nat Sci 2026;44(1):309–317.

INTRODUCTION

Convex functions and trapezoidal inequalities are of great importance in mathematics and optimization theory, as well as many other disciplines. The special structure of convex functions allows for the production of unique and stable solutions, especially in optimization problems. Therefore, these functions are considered a mathematical guarantee of model reliability in machine learning, economic equilibrium models, risk analysis, and engineering design processes. In numerical analysis, they guarantee stability, convergence, and physical significance in the solution of differential equations. In this context, the trapezoidal inequality is an important tool in the constraint of integrals and error analysis of numerical integration methods. When a function is convex, the trapezoidal inequality provides precise lower and upper bounds on the true value of the integral, and is used both in the accuracy evaluation of numerical methods and in the derivation of mean value inequalities. Convex optimization also finds applications in signal processing, game theory, control theory, economic models, statistics, telecommunications, geometry, topology, energy systems, operations research, and computer vision.

The development of inequality theory is significantly influenced by convex functions. Various types of convex functions have been defined as α-convex, *m*-convex,

***Corresponding author.**
*E-mail address: duygu.donmez@cbu.edu.tr

This paper was recommended for publication in revised form by Editor-in-Chief Ahmet Selim Dalkilic

Published by Yıldız Technical University Press, İstanbul, Turkey
© Author. This is an open access article under the CC BY-NC license (http://creativecommons.org/licenses/by-nc/4.0/).

h-convex, (*α, m*)-convex, (*h, m*)-convex, *s*-convex, (*s, m*)-convex, *φ*-convex, quasi-convex, *φ*-quasi-convex and *tgs*-convex. [1]. Tunç and Şanal [2] introduced some perturbed trapezoid inequalities for *s*-convex and *tgs*-convex functions in 2015. Dönmez Demir and Şanal [3] extended the trapezoidal inequalities given for second-order differentiable *s*-convepx and v-convex functions to n^{th} order differentiable functions. Mehreen and Anwar [4] established some Hermite-Hadamard type inequalities for *tgs*-convex functions with generalized fractional integrals. Ge-JiLe et. al. [5] presented new Hermite-Hadamard inequalities for exponentially *tgs*-convex functions with conformable fractional integrals. Tariq et. al. [6] suggested a new convex mapping regarding exponentially *s*-convexity. Barsam et. al. [7] derived a type of the Jensen's inequality for *tgs*-convex functions with specific examples. Huang and Xu [8] obtained the generalizations of some Hermite-Hadamard inequalities for *tgs*-convex functions. Maden et. al. [9] introduced a new identity for $M_f A$ - *P*-function using the Hermite-Hadamard integral inequality. Demir [10] investigated a new class of convex functions that is called exponential trigonometric convex functions. İşcan et. al. [11] obtained several new inequalities for *n*-time differentiable quasi-convex functions via the Hölder and the Power mean integral identities. Khan et. al. [12] presented the class of *LR* - (*p, h*)-convex interval-valued functions (IVFs) and constituted inequalities of Jensen, Schur, Hermite-Hadamard (HH) and HH-Fejer type for *LR* - (*p, h*)-convex IVSs by means of Pseudo-order relations via Riemann integrals.

In recent years, applications of convex functions to fractional integral inequalities have attracted considerable attention. Rehman et. al. [13] generalized Petrovic inequality for *h*-convex functions. Farid et. al. [14] introduced the Hadamard and Fejer-Hadamard type integral inequalities for convex and relative convex functions. They [15] consider a generalized fractional integral operator involving the generalized Mittag-Leffler function to construct some new integral inequalities of Grüss type. They [16] suggested Hadamard inqualities for strongly *m*-convex functions using the Riemann-Louville fractional integral. Farid and Mishra [17] introduced some new Caputo fractional integral inequalities for (*h - m*)-convex functions. Farid et. al. [18] constructed the Hadamard inequality for strongly (*s, m*)-convex functions via Caputo fractional derivatives. Besides, they [19] introduced the fractional Hadamard and the Fejer-Hadamard inequalities for exp. (*α, H - M*)-convex functions. Rathour et al. [20] suggested Hadamard type fractional integral inequalities by using k-analogue of Riemann Liouville fractional integrals for strongly exponentially (*α, H - M*)-convex functions. Şanlı et. al. [21] presented new Katugampola fractional Hermite-Hadamard type inequalities for convex functions. Convex functions have a wide range of applications and can be applied to even more diverse areas. [22-26].

Considering the application areas of trapezoidal inequalities, the analysis and error estimation of numerical methods stand out in particular. They are also frequently used in the analysis of trapezoidal, rectangular, and Simpson's rules, which are commonly used numerical integration methods in practice. These inequalities allow for the estimation of the error between the exact integral and the approximate integral obtained through numerical integration. On the other hand, in numerical interpolation and approximate solution methods, trapezoidal inequalities are used to estimate the error between interpolated or approximate values and the true value of a function. They play a important role in the error analysis of various numerical methods, including finite difference methods, numerical solutions of differential equations, and other numerical approximations. Besides, they are used in function approximation, control of numerical errors, complex analysis, probability theory and statistics.

Dönmez Demir and Şanal [27] started their studies by extending second order differentiable convex functions to n^{th} order differentiable convex functions via perturbed trapezoid inequalities. They [28] presented some inequalities for *n*-times differentiable strongly convex functions. They introduced some perturbed trapezoid inequalities for *n*-times differentiable strongly *log*-convex functions [29]. They considered *n*-times differentiable strongly *s*-convex functions [30]. Besides, the authors introduced the various applications related to *n*-times differentiable strongly l*og*-convex functions [31].

It is possible to obtain improved error bounds for numerical integration formulas via integral inequalities such as the triangle inequality, Hölder inequality, and power mean inequalities. This study is significant as it provides more precise estimates of the errors in trapezoidal and midpoint integration methods. It can be seen that the improved error limits are applicable to *s*-convex and *tgs*-convex functions based on the results obtained. For improving the accuracy of numerical solutions, theoretical results can be directly applied to real-world problems such as machine learning, finance, control systems, engineering simulations, and statistical analysis. The defined error limits lead to more reliable and efficient numerical solutions, which can have a significant impact across various fields.

PRELIMINARIES

Definition 2.1 [32]: A function $\varphi: I^{\circ} \subseteq \mathbb{R} \to \mathbb{R}$ is convex on *I*, if the inequality

$$\varphi(rx + (1-r)y) \leq r\varphi(x) + (1-r)\varphi(y) \qquad (1)$$

holds for all $x, y \in I$ and $r \in (0,1]$. It is said that φ is concave if $(-\varphi)$ is convex. For numerical integration, trapezoidal inequality is introduced as

$$\left| \int_x^y \varphi(u)du - \frac{1}{2}(y-x)(\varphi(x)+\varphi(y)) \right| \leq \frac{1}{12} M_2 (y-x)^3 \quad (2)$$

where φ: $[x, y] \to \mathbb{R}$ is assumed to be twice differentiable on (x, y) with the second derivative bounded on (x, y) by $M_2 = sup_{u\in(x,y)} |\varphi''(u)| < +\infty$.

Definition 2.2 [33]: Let be $s \in (0,1]$. Then, a real valued function on an interval $I \subset \mathbb{R}$, Φ: $I \to \mathbb{R}$ is s-convex in the second sence provided

$$\phi(nx + my) \le n^s\phi(x) + m^s\phi(y) \tag{3}$$

for $x, y \in I$ and $n, m \ge 0$ with $n + m = 1$. This is denoted by $\phi \in K_s^2$ [33].

Definition 2.3 [34]: A function $I \subset \mathbb{R}$, Φ: $I \to \mathbb{R}$ is said to be *tgs*-convex on I, if inequality

$$\phi(rx + (1-r)y) \le r(1-r)[\phi(x) + \phi(y)] \tag{4}$$

holds for all $x, y \in I$ and $r \in (0,1)$. We say that ϕ is *tgs*-concave if $(-\phi)$ is *tgs*-convex.

Theorem 2.1 [35]: Let ϕ: $(x, y) \to \mathbb{R}$ be continuous and twice differentiable on (x, y) and assume that the second derivative φ'': $(x, y) \to \mathbb{R}$ satisfies the condition:

$$\upsilon \le \phi'' \le \varphi \tag{5}$$

for all $u \in (x, y)$. Then, we have the inequality

$$\begin{aligned}&\left|\phi(u) - \left(u - \tfrac{x+y}{2}\right)\phi'(u)\right.\\&\left. + \left[\tfrac{(y-x)^2}{24} + \tfrac{1}{2}\left(u - \tfrac{x+y}{2}\right)^2\right]\tfrac{\phi'(y)-\phi'(x)}{y-x} - \tfrac{1}{y-x}\int_x^y \phi(t)dt\right| \\&\le \tfrac{1}{8}(\varphi - \upsilon)\left[\tfrac{1}{2}(y-x) + \left|u - \tfrac{x+y}{2}\right|\right]^2\end{aligned} \tag{6}$$

for all $u \in (x, y)$. Then, the perturbed midpoint inequality is presented as

$$\begin{aligned}&\left|\phi\left(\tfrac{x+y}{2}\right) + \tfrac{1}{24}(y-x)\left(\phi'(y) - \phi'(x)\right) - \tfrac{1}{y-x}\int_x^y \phi(t)dt\right| \\&\le \tfrac{1}{32}(\varphi - \upsilon)(y-x)^2 .\end{aligned} \tag{7}$$

Then, we have the following perturbed trapezoidal inequality:

$$\begin{aligned}&\left|\tfrac{\phi(x)+\phi(y)}{2} - \tfrac{1}{12}(y-x)\left(\phi'(y) - \phi'(x)\right) - \tfrac{1}{y-x}\int_x^y \phi(t)dt\right| \\&\le \tfrac{1}{8}(\varphi - \upsilon)(y-x)^2 .\end{aligned} \tag{8}$$

Application to the Midpoint and Trapezoidal Formula

Let d be a division of the interval $[x, y]$, i.e. $x = u_0 < u_1 < ... < u_{n-1} < u_n = y$, $i = 0, 1, 2, ..., n - 1$ and consider the quadrature formula

$$\int_x^y \phi(u)du = T(\phi, d) + E(\phi, d) \tag{9}$$

and

$$\int_x^y \phi(u)du = T'(\phi, d) + E'(\phi, d) \tag{10}$$

where

$$T(\phi, d) = \sum_{i=0}^{n-1}(u_{i+1} - u_i)\phi\left(\tfrac{u_i+u_{i+1}}{2}\right) \tag{11}$$

and

$$T'(\phi, d) = \sum_{i=0}^{n-1}(u_{i+1} - u_i)\phi\left(\tfrac{u_i+u_{i+1}}{2}\right) \tag{12}$$

are the midpoint and trapezoidal versions and $E(\phi, d)$ and $E'(\phi, d)$ are the associated errors, respectively. Here, we derive some error estimates for the sum of midpoint and trapezoidal formula [36].

Proposition 2.5. [36]: Let ϕ: $I \subseteq \mathbb{R} \to \mathbb{R}$ be a differentiable function on I° such that $\phi' \in L([x,y])$ where $x, y \in I^\circ$ with $x < y$. If $|\phi'|$ is convex on $[x, y]$, then one obtains

$$\begin{aligned}|E(\phi, d)| + |E'(\phi, d)| \le \tfrac{1}{8}\sum_{i=0}^{n-1}(u_{i+1} - u_i)^2[|\phi'(u_i)| \\ + |\phi'(u_{i+1})|]\end{aligned} \tag{13}$$

for every division d of $[x, y]$.

Theorem 2.6 [35]: Let ϕ: $I \subseteq \mathbb{R} \to \mathbb{R}$ be a differentiable function on I° such that $\phi' \in L([x,y])$where $x, y \in I^\circ$ with $[x, y]$. If $|\varphi''|^q$ is s-convex on $[x, y]$ for $q \ge 1$, then we have

$$\begin{aligned}|E'(\phi, d)| \le \tfrac{1}{2^{4+\frac{s}{q}}}\left(\tfrac{2}{3}\right)^{1-\frac{1}{q}}\sum_{i=0}^{n-1}\left\{\left(\tfrac{(s+4)}{(s+2)(s+3)}|\phi''(u_i)|^q\right.\right. \\ \left. + \left(\tfrac{2}{3} + \tfrac{2}{(s+1)(s+3)}B(s+1,n)\right)|\phi''(u_{i+1})|^q\right)^{\frac{1}{q}} \\ + \left(\tfrac{(s+4)}{(s+2)(s+3)}|\phi''(u_{i+1})|^q\right. \\ \left.\left. + \left(\tfrac{2}{3} + \tfrac{2}{(s+1)(s+3)}B(s+1,n)\right)|\phi''(u_i)|^q\right)^{\frac{1}{q}}\right\}\end{aligned} \tag{14}$$

for every division d of $[x, y]$.

Theorem 2.7. [37]: Let l^n: $x = u_0 < u_1 < ... < u_{n-1} < u_n = y$, be a division of the interval $[x, y]$, and let $\xi_i \in \left[u_i + \delta\tfrac{h_i}{2}, u_{i+1} - \delta\tfrac{h_i}{2}\right]$, $i = 0, 1, ..., n - 1$ be a sequence of intermediate points and $h_i = u_{i+1} - u_i$, $i = 0, 1, ..., n - 1$, then we have the following quadrature rule:

Let ϕ: $I \subseteq \mathbb{R} \to \mathbb{R}$ be a twice differentiable on (x, y) whose second derivative and I° belongs to $L_1(x,y)$ i.e. $\|\phi''\|_1 := \int_x^y \|\phi''\|dt < \infty$. Then, the perturbed Riemann's quadrature formula holds:

$$\int_x^y \phi(t)dt = A(\phi, \phi', I_n, \xi, \delta) + R(\phi, \phi', I_n, \xi, \delta) \tag{15}$$

where

$$A(\phi,\phi',I_n,\xi,\delta)=(1-\delta)\sum_{i=0}^{n-1}h_i\left(\xi_i-\frac{u_i+u_{i+1}}{2}\right)\phi'(\xi_i)+\frac{\delta}{2}\sum_{i=0}^{n-1}h_i\big(\phi(u_i)+\phi(u_{i+1})\big)-\frac{\delta^2}{8}\sum_{i=0}^{n-1}{h_i}^2\big(\phi'(u_{i+1})-\phi'(u_i)\big)$$

and the remainder term, $R(\phi,\ \phi',\ I_n,\xi,\delta)$ satisfies the estimation:

$$R(\phi,\phi',I_n,\xi,\delta)\le\frac{1}{2}\sum_{i=0}^{n-1}\left[\frac{h_i(1-\delta)}{2}+\left|\xi_i-\frac{u_i+u_{i+1}}{2}\right|\right]^2\|\phi"\|_1\le\left(1-\frac{\delta}{2}\right)^2\sum_{i=0}^{n-1}\frac{{h_i}^2}{2}\|\phi"\|_1$$

such as $\delta\in[0,1]$ and $u_i+\delta\frac{h_i}{2}\le\xi_i\le u_{i+1}-\delta\frac{h_i}{2}$. The following perturbed midpoint rule holds:

$$\int_x^y\phi(t)dt=M(\phi,\phi',I_n)+R_M(\phi,\phi',I_n)\tag{16}$$

where

$$M(\phi,\phi',I_n)=\textstyle\sum_{i=0}^{n-1}h_i\phi\left(\frac{u_i+u_{i+1}}{2}\right),\tag{17}$$

and the remainder term $R_M(\phi,\phi',I_n)$ satisfies the estimation:

$$|R_M(\phi,\phi',I_n)|\le\|\phi"\|_1\textstyle\sum_{i=0}^{n-1}\frac{{h_i}^2}{8}\tag{18}$$

The following perturbed trapezoidal rule holds:

$$\int_x^y\phi(t)dt=T(\phi,\phi',I_n)+R_T(\phi,\phi',I_n)\tag{19}$$

where

$$T(\phi,\phi',I_n)=\tfrac{1}{2}\textstyle\sum_{i=0}^{n-1}h_i\big(\phi(u_i)+\phi(u_{i+1})\big)-\frac{1}{8}\sum_{i=0}^{n-1}{h_i}^2\left(\phi'^{(u_{i+1})}-\phi'(u_i)\right)\tag{20}$$

and the residual term

$$|R_T(\phi,\phi',I_n)|\le\textstyle\sum_{i=0}^{n-1}\frac{{h_i}^2}{2}\|\phi\|_1.\tag{21}$$

Theorem 2.8 [3]: Let $s\in(0,1]$ and $\phi: I\subseteq\mathbb{R}_+\to\mathbb{R}$ be n times differentiable mapping on I°, $x, y\in I^\circ$ with $x<y$ where n is even number. If $|\phi^{(n)}|$ is s -convex on $[x, y]$, then the inequality in the following holds:

$$\left|\frac{1}{y-x}\int_x^y\phi(u)du-\frac{\phi(x)+\phi(y)}{2}+\cdots-\frac{(y-x)^{n-4}[n.(n-1).(n-2).a_n+\cdots+4.3.2.a_4]}{2.n!.a_n}\left[\phi^{(n-4)}(x)+\phi^{(n-4)}(y)\right]+\frac{(y-x)^{n-3}[n.(n-1).a_n+\cdots+4.3.a_4+3.2.a_3+4a_2]}{2.n!.a_n}\left[\phi^{(n-3)}(y)-\phi^{(n-3)}(x)\right]-\frac{(y-x)^{n-2}[n.a_n+\cdots+2.a_2]}{2.n!.a_n}\left[\phi^{(n-2)}(x)+\phi^{(n-2)}(y)\right]+\frac{(y-x)^{n-1}[a_n+\cdots+a_1+2a_0]}{2.n!.a_n}\left[\phi^{(n-1)}(y)-\phi^{(n-1)}(x)\right]\right|\le\frac{(y-x)^n}{2.n!.|a_n|}\left[|\phi^{(n)}(x)|+|\phi^{(n)}(y)|\right]\left[\textstyle\sum_{i=0}^n\frac{|a_i|}{i+s+1}+\sum_{i=0}^n\frac{|a_i|\Gamma(i+1)\Gamma(s+1)}{i+s+2}\right].$$

Theorem 2.9 [3]: Let $s\in(0,1]$ and $\phi: I\subseteq\mathbb{R}_+\to\mathbb{R}$ be n times differentiable mapping on I°, $x, y\in I^\circ$ with $x<y$ and $p>1, \frac{1}{p}+\frac{1}{q}=1$ where n is even number. If the mapping $|\phi^{(n)}|^q$ is s -convex on the interval $[x, y]$, thus one obtains

$$\left|\frac{1}{y-x}\int_x^y\phi(u)du-\frac{\phi(x)+\phi(y)}{2}+\cdots-\frac{(y-x)^{n-4}[n.(n-1).(n-2).a_n+\cdots+4.3.2.a_4]}{2.n!.a_n}\left[\phi^{(n-4)}(x)+\phi^{(n-4)}(y)\right]+\frac{(y-x)^{n-3}[n.(n-1).a_n+\cdots+4.3.a_4+3.2.a_3+4a_2]}{2.n!.a_n}\left[\phi^{(n-3)}(y)-\phi^{(n-3)}(x)\right]-\frac{(y-x)^{n-2}[n.a_n+\cdots+2.a_2]}{2.n!.a_n}\left[\phi^{(n-2)}(x)+\phi^{(n-2)}(y)\right]+\frac{(y-x)^{n-1}[a_n+\cdots+a_1+2a_0]}{2.n!.a_n}\left[\phi^{(n-1)}(y)-\phi^{(n-1)}(x)\right]\right|\le\frac{(y-x)^n}{n!.|a_n|}\left[\textstyle\sum_{i=0}^n\frac{|a_i|}{(ip+1)^{\frac{1}{p}}}\right]\left\{\left[\frac{|\phi^{(n)}(x)|^q}{s+1}+\frac{|\phi^{(n)}(y)|^q\Gamma(s+1)}{\Gamma(s+2)}\right]^{\frac{1}{q}}+\left[\frac{|\phi^{(n)}(y)|^q}{s+1}+\frac{|\phi^{(n)}(x)|^q\Gamma(s+1)}{\Gamma(s+2)}\right]^{\frac{1}{q}}\right\}$$

Theorem 2.10. [3]: Let $s\in(0,1]$ and $\phi: I\subseteq\mathbb{R}_+\to\mathbb{R}$ be n times differentiable mapping on I°, $x, y\in I^\circ$ with $x<y$ and $p>1, \frac{1}{p}+\frac{1}{q}=1$ where n is even number. If the mapping $|\phi^{(n)}|^p$ is s -convex on $[x, y]$, then the inequality in the following holds:

$$\left|\frac{1}{y-x}\int_x^y\phi(u)du-\frac{\phi(x)+\phi(y)}{2}+\cdots-\frac{(y-x)^{n-4}[n.(n-1).(n-2).a_n+\cdots+4.3.2.a_4]}{2.n!.a_n}\left[\phi^{(n-4)}(x)+\phi^{(n-4)}(y)\right]+\frac{(y-x)^{n-3}[n.(n-1).a_n+\cdots+4.3.a_4+3.2.a_3+4a_2]}{2.n!.a_n}\left[\phi^{(n-3)}(y)-\phi^{(n-3)}(x)\right]-\frac{(y-x)^{n-2}[n.a_n+\cdots+2.a_2]}{2.n!.a_n}\left[\phi^{(n-2)}(x)+\phi^{(n-2)}(y)\right]+\frac{(y-x)^{n-1}[a_n+\cdots+a_1+2a_0]}{2.n!.a_n}\left[\phi^{(n-1)}(y)-\phi^{(n-1)}(x)\right]\right|\le\frac{(y-x)^n}{2.n!.|a_n|}\left[\textstyle\sum_{i=0}^n\frac{|a_i|}{i+1}\right]^{1-\frac{1}{p}}\left\{\left[\left(\sum_{i=0}^n\frac{|a_i|}{i+s+1}\right)|\phi^{(n)}(x)|^p+\left(\sum_{i=0}^n\frac{|a_i|\Gamma(s+1)\Gamma(i+1)}{\Gamma(i+s+2)}\right)|\phi^{(n)}(y)|^p\right]^{\frac{1}{p}}+\left[\left(\sum_{i=0}^n\frac{|a_i|}{i+s+1}\right)|\phi^{(n)}(y)|^p+\left(\sum_{i=0}^n\frac{|a_i|\Gamma(s+1)\Gamma(i+1)}{\Gamma(i+s+2)}\right)|\phi^{(n)}(y)|^p\right]^{\frac{1}{p}}\right\}.$$

Theorem 2.11. [3]: Let $\phi: I\subseteq\mathbb{R}\to\mathbb{R}$ be n times differentiable mapping on I°, $x, y\in I^\circ$ with $x<y$ where n is even number. If $|\phi^{(n)}|$ is *tgs*-convex on $[x, y]$, then the inequality in the following holds:

$$\left|\frac{1}{y-x}\int_x^y \phi(u)du - \frac{\phi(x)+\phi(y)}{2} + \cdots \right.$$
$$-\frac{(y-x)^{n-4}[n.(n-1).(n-2).a_n + \cdots + 4.3.2.a_4]}{2.n!.a_n}\left[\phi^{(n-4)}(x)+\phi^{(n-4)}(y)\right]$$
$$+\frac{(y-x)^{n-3}[n.(n-1).a_n + \cdots + 4.3.a_4 + 3.2.a_3 + 4a_2]}{2.n!.a_n}\left[\phi^{(n-3)}(y)-\phi^{(n-3)}(x)\right]$$
$$-\frac{(y-x)^{n-2}[n.a_n + \cdots + 2.a_2]}{2.n!.a_n}\left[\phi^{(n-2)}(x)+\phi^{(n-2)}(y)\right]$$
$$\left.+\frac{(y-x)^{n-1}[a_n + \cdots + a_1 + 2a_0]}{2.n!.a_n}\left[\phi^{(n-1)}(y)-\phi^{(n-1)}(x)\right]\right|$$
$$\leq \frac{(y-x)^n}{n!.|a_n|}\left[\phi^{(n)}(x)+\phi^{(n)}(y)\right]\left[\sum_{i=0}^{n}\frac{|a_i|}{(i+2)(i+3)}\right].$$

Theorem 2.12. [3]: Let $\phi: I \subseteq \mathbb{R} \to \mathbb{R}$ be n times differentiable mapping on I°, $x, y \in I^\circ$ with $x < y$ and $p > 1$, $\frac{1}{p}+\frac{1}{q}=1$ where n is even number. If the mapping $|\phi^{(n)}|^q$ is *tgs*-convex on the interval $[x, y]$, thus one obtains

$$\left|\frac{1}{y-x}\int_x^y \phi(u)du - \frac{\phi(x)+\phi(y)}{2} + \cdots \right.$$
$$-\frac{(y-x)^{n-4}[n.(n-1).(n-2).a_n + \cdots + 4.3.2.a_4]}{2.n!.a_n}\left[\phi^{(n-4)}(x)+\phi^{(n-4)}(y)\right]$$
$$+\frac{(y-x)^{n-3}[n.(n-1).a_n + \cdots + 4.3.a_4 + 3.2.a_3 + 4a_2]}{2.n!.a_n}\left[\phi^{(n-3)}(y)-\phi^{(n-3)}(x)\right]$$
$$-\frac{(y-x)^{n-2}[n.a_n + \cdots + 2.a_2]}{2.n!.a_n}\left[\phi^{(n-2)}(x)+\phi^{(n-2)}(y)\right]$$
$$\left.+\frac{(y-x)^{n-1}[a_n + \cdots + a_1 + 2a_0]}{2.n!.a_n}\left[\phi^{(n-1)}(y)-\phi^{(n-1)}(x)\right]\right|$$
$$\leq \frac{(y-x)^n}{n!.|a_n|}\left[\sum_{i=0}^{n}\frac{|a_i|}{(ip+1)^{\frac{1}{p}}}\right]\left[\frac{|\phi^{(n)}(x)|^q+|\phi^{(n)}(y)|^q}{6}\right]^{\frac{1}{q}}.$$

Theorem 2.13. [3]: Let $\phi: I \subseteq \mathbb{R} \to \mathbb{R}$ be n times differentiable mapping on I°, $x, y \in I^\circ$ with $x < y$ and $p > 1$, $\frac{1}{p}+\frac{1}{q}=1$ where n is even number. If the mapping $|\phi^{(n)}|^p$ is *tgs*-convex on $[x, y]$, thus the inequality in the following holds:

$$\left|\frac{1}{y-x}\int_x^y \phi(u)du - \frac{\phi(x)+\phi(y)}{2} + \cdots \right.$$
$$-\frac{(y-x)^{n-4}[n.(n-1).(n-2).a_n + \cdots + 4.3.2.a_4]}{2.n!.a_n}\left[\phi^{(n-4)}(x)+\phi^{(n-4)}(y)\right]$$
$$+\frac{(y-x)^{n-3}[n.(n-1).a_n + \cdots + 4.3.a_4 + 3.2.a_3 + 4a_2]}{2.n!.a_n}\left[\phi^{(n-3)}(y)-\phi^{(n-3)}(x)\right]$$
$$-\frac{(y-x)^{n-2}[n.a_n + \cdots + 2.a_2]}{2.n!.a_n}\left[\phi^{(n-2)}(x)+\phi^{(n-2)}(y)\right]$$
$$\left.+\frac{(y-x)^{n-1}[a_n + \cdots + a_1 + 2a_0]}{2.n!.a_n}\left[\phi^{(n-1)}(y)-\phi^{(n-1)}(x)\right]\right|$$
$$\leq \frac{(y-x)^n}{2.n!.|a_n|}\left[\sum_{i=0}^{n}\frac{|a_i|}{i+1}\right]^{1-\frac{1}{p}}\left[\left|\phi^{(n)}(x)\right|^q+\left|\phi^{(n)}(y)\right|^p\right]^{\frac{1}{p}}\left[\sum_{i=0}^{n}\frac{|a_i|}{(i+2)(i+3)}\right]^{\frac{1}{p}}.$$

RESULTS AND DISCUSSION

Corollary 3.1: Under the assumptions of Theorem 2.8 and $n = 2$, we have the following inequality:

$$\left|\frac{1}{y-x}\int_x^y \phi(u)du - \big(\phi(x)+\phi(y)\big) + \frac{(y-x)[a_2+a_1+2a_0]}{4.a_2}[\phi'(y)-\phi'(x)]\right|$$
$$\leq \frac{(y-x)^2}{4.|a_2|}\left[|\phi''(x)|+|\phi''(y)|\right]\left[\sum_{i=0}^{2}\frac{|a_i|}{i+s+1}+\sum_{i=0}^{2}\frac{|a_i|\Gamma(i+1)\Gamma(s+1)}{i+s+2}\right].$$

Corollary 3.2: Under the assumptions of Theorem 2.9 and $n = 2$, the following inequality is obtained

$$\left|\frac{1}{y-x}\int_x^y \phi(u)du - \big(\phi(x)+\phi(y)\big) + \frac{(y-x)[a_2+a_1+2a_0]}{4.a_2}[\phi'(y)-\phi'(x)]\right|$$
$$\leq \frac{(y-x)^2}{2.|a_2|}\left[\sum_{i=0}^{2}\frac{|a_i|}{(ip+1)^{\frac{1}{p}}}\right]\left\{\left[\frac{|\phi''(x)|^q}{s+1}+\frac{|\phi''(y)|^q\Gamma(s+1)}{\Gamma(s+2)}\right]^{\frac{1}{q}}+\left[\frac{|\phi''(y)|^q}{s+1}+\frac{|\phi''(x)|^q\Gamma(s+1)}{\Gamma(s+2)}\right]^{\frac{1}{q}}\right\}.$$

Corollary 3.3: The assumptions of Theorem 2.10 and $n = 2$ yields

$$\left|\frac{1}{y-x}\int_x^y \phi(u)du - \big(\phi(x)+\phi(y)\big) + \frac{(y-x)[a_2+a_1+2a_0]}{4.a_2}[\phi'(y)-\phi'(x)]\right|$$
$$\leq \frac{(y-x)^2}{4.|a_2|}\left[\sum_{i=0}^{2}\frac{|a_i|}{i+1}\right]^{1-\frac{1}{p}}\left\{\left[\left(\sum_{i=0}^{2}\frac{|a_i|}{i+s+1}\right)|\phi''(x)|^p+\left(\sum_{i=0}^{2}\frac{|a_i|\Gamma(s+1)\Gamma(i+1)}{\Gamma(i+s+2)}\right)|\phi''(y)|^p\right]^{\frac{1}{p}}\right.$$
$$\left.+\left[\left(\sum_{i=0}^{2}\frac{|a_i|}{i+s+1}\right)|\phi''(y)|^p+\left(\sum_{i=0}^{2}\frac{|a_i|\Gamma(s+1)\Gamma(i+1)}{\Gamma(i+s+2)}\right)|\phi''(y)|^p\right]^{\frac{1}{p}}\right\}.$$

Corollary 3.4: Under the assumptions of Theorem 2.11 and $n = 2$, the following inequality holds

$$\left|\frac{1}{y-x}\int_x^y \phi(u)du - \big(\phi(x)+\phi(y)\big) + \frac{(y-x)[a_2+a_1+2a_0]}{4.a_2}[\phi'(y)-\phi'(x)]\right|$$
$$\leq \frac{(y-x)^2}{2.|a_2|}[\phi''(x)+\phi''(y)]\left[\sum_{i=0}^{2}\frac{|a_i|}{(i+2)(i+3)}\right].$$

Corollary 3.5: Under the assumptions of Theorem 2.12 and $n = 2$, we have the following inequality:

$$\left|\frac{1}{y-x}\int_x^y \phi(u)du - \big(\phi(x)+\phi(y)\big) + \frac{(y-x)[a_2+a_1+2a_0]}{4.a_2}[\phi'(y)-\phi'(x)]\right|$$
$$\leq \frac{(y-x)^2}{2.|a_2|}\left[\sum_{i=0}^{2}\frac{|a_i|}{(ip+1)^{\frac{1}{p}}}\right]\left[\frac{|\phi''(x)|^q+|\phi''(y)|^q}{6}\right]^{\frac{1}{q}}.$$

Corollary 3.6: The assumptions of Theorem 2.13 and $n = 2$ yields

$$\left|\frac{1}{y-x}\int_x^y \phi(u)du - \big(\phi(x)+\phi(y)\big) + \frac{(y-x)[a_2+a_1+2a_0]}{4.a_2}[\phi'(y)-\phi'(x)]\right|$$
$$\leq \frac{(y-x)^2}{4.|a_2|}\left[\sum_{i=0}^{2}\frac{|a_i|}{i+1}\right]^{1-\frac{1}{p}}\left[|\phi''(x)|^q+|\phi''(y)|^p\right]^{\frac{1}{p}}\left[\sum_{i=0}^{2}\frac{|a_i|}{(i+2)(i+3)}\right]^{\frac{1}{p}}.$$

Applications in Numerical Integration

Numerical integration is a technique used to approximately calculate the definite integral of functions that are integrable or difficult to integrate, using numerical methods. This technique is widely used in applications arised many fields such as engineering, physics, data science, statistics, and medicine. For approximating the integral of a function over a definite interval, trapezoidal and midpoint integration methods are used for n -times differentiable convex functions. In this section, we introduce some error estimations for the trapezoidal formula in terms of absolute values of the second derivative of ϕ which may be better than those already existing in the literature.

Let d be a division of the interval $[x, y]$, i.e. $x = u_0 < u_1 < \ldots < u_{n-1} < u_n = y$, $h_i = u_{i+1} - u_i$, $i = 1, 2, 3, \ldots, n-1$ and consider perturbed trapezoidal rule

$$\int_x^y \phi(t)dt = T(\phi, \phi', I_h) + \tilde{R}_T(\phi, \phi', I_h) \tag{21}$$

where

$$T(\phi, \phi', I_h) = \sum_{i=0}^{n-1} |\phi(u_i) + \phi(u_{i+1})| h_i + \frac{[a_2 + a_1 + 2a_0]}{4.a_2} \sum_{i=0}^{n-1} [\phi'(u_{i+1}) - \phi'(u_i)] {h_i}^2 \tag{22}$$

is the trapezoidal variants and $\tilde{R}_T(\phi, \phi', I_h)$ is the associated error.

Theorem 4.1: Let's assume that $s \in (0,1]$ and $\phi: I \subseteq \mathbb{R}_+ \to \mathbb{R}$ is a function with second-order derivatives on I° such that $\varphi'' L([x,y])$ where $x, y \in I^\circ$ with $x < y$. If $|\varphi''|$ is s-convex on $[x, y]$, then we have

$$\left|\tilde{R}_T(\phi, \phi', I_h)\right| \leq \frac{1}{4.|a_2|}\left[\sum_{j=0}^{2} \frac{|a_j|}{j+s+1} + \sum_{j=0}^{2} \frac{|a_j|\Gamma(j+1)\Gamma(s+1)}{j+s+2}\right] \times \sum_{i=0}^{2} [|\phi''(u_i)| + |\phi''(u_{i+1})|] {h_i}^3 \tag{23}$$

for every division d of $[x, y]$, $x = u_0 < u_1 < \ldots < u_{n-1} < u_n = y$ i. e.

Proof 4.1: Applying Corollary (3.1) on the subinterval $[u_i, u_{i+1}]$; $(i = 1, 2, 3, \ldots, n-1)$ of the division d yields

$$\left|\tilde{R}_T(\phi, \phi', I_h)\right| = \left|\sum_{i=0}^{n-1} [\phi(u_i) + \phi(u_{i+1})] h_i - \frac{a_2 + a_1 + 2a_0}{4a_2} \sum_{i=0}^{n-1} [\phi'(u_i) + \phi'(u_{i+1})] {h_i}^2 - \int_{u_i}^{u_{i+1}} \phi(t)dt\right|$$

$$\leq \sum_{i=0}^{n-1} h_i \left|[\phi(u_i) + \phi(u_{i+1})] - \frac{a_2 + a_1 + 2a_0}{4a_2} [\phi'(u_i) + \phi'(u_{i+1})] h_i - \frac{1}{h_i} \int_{u_i}^{u_{i+1}} \phi(t)dt\right|$$

$$\leq \frac{1}{4.|a_2|}\left[\sum_{j=0}^{2} \frac{|a_j|}{j+s+1} + \sum_{j=0}^{2} \frac{|a_j|\Gamma(j+1)\Gamma(s+1)}{j+s+2}\right] \sum_{i=0}^{2} [|\phi''(u_i)| + |\phi''(u_{i+1})|] {h_i}^3.$$

Theorem 4.2: Let's assume that $s \in (0,1]$ and $\phi: I \subseteq \mathbb{R}_+ \to \mathbb{R}$ is a function with second-order derivatives on I° such that $\varphi'' L([x,y])$ where $x, y \in I^\circ$ with $x < y$, $p, q > 1$ and $\frac{1}{p} + \frac{1}{q} = 1$. If $|\varphi''|^q$ is s-convex on $[x, y]$, then one obtains

$$\left|\tilde{R}_T(\phi, \phi', I_h)\right| \leq \frac{(y-x)^2}{2.|a_2|}\left[\sum_{j=0}^{2} \frac{|a_j|}{(jp+1)^{\frac{1}{p}}}\right] \sum_{i=0}^{n-1} \left\{\left[\frac{|\phi''(u_i)|^q}{s+1} + \frac{|\phi''(u_{i+1})|^q \Gamma(s+1)}{\Gamma(s+2)}\right]^{\frac{1}{q}} + \left[\frac{|\phi''(u_{i+1})|^q}{s+1} + \frac{|\phi''(u_i)|^q \Gamma(s+1)}{\Gamma(s+2)}\right]^{\frac{1}{q}}\right\} {h_i}^3 \tag{24}$$

for every division d of $[x, y]$, i.e. $x = u_0 < u_1 < \ldots < u_{n-1} < u_n = y$

Proof 4.2: Applying Corollary (3.2) on the subinterval $[u_i, u_{i+1}]$; $(i = 1, 2, 3, \ldots, n-1)$ of the division d yields

$$\left|\tilde{R}_T(\phi, \phi', I_h)\right| = \left|\sum_{i=0}^{n-1} [\phi(u_i) + \phi(u_{i+1})] h_i - \frac{a_2 + a_1 + 2a_0}{4a_2} \sum_{i=0}^{n-1} [\phi'(u_i) + \phi'(u_{i+1})] {h_i}^2 - \int_{u_i}^{u_{i+1}} \phi(t)dt\right|$$

$$\leq \sum_{i=0}^{n-1} h_i \left|[\phi(u_i) + \phi(u_{i+1})] - \frac{a_2 + a_1 + 2a_0}{4a_2} [\phi'(u_i) + \phi'(u_{i+1})] h_i - \frac{1}{h_i} \int_{u_i}^{u_{i+1}} \phi(t)dt\right|$$

$$\leq \frac{(y-x)^2}{2.|a_2|}\left[\sum_{j=0}^{2} \frac{|a_j|}{(jp+1)^{\frac{1}{p}}}\right] \sum_{i=0}^{n-1} \left\{\left[\frac{|\phi''(u_i)|^q}{s+1} + \frac{|\phi''(u_{i+1})|^q \Gamma(s+1)}{\Gamma(s+2)}\right]^{\frac{1}{q}} + \left[\frac{|\phi''(u_{i+1})|^q}{s+1} + \frac{|\phi''(u_i)|^q \Gamma(s+1)}{\Gamma(s+2)}\right]^{\frac{1}{q}}\right\} {h_i}^3.$$

Theorem 4.3: Let's assume that $s \in (0,1]$ and $\phi: I \subseteq \mathbb{R}_+ \to \mathbb{R}$ is a function with second-order derivatives on I° such that $\varphi'' L([x,y])$ where $x, y \in I^\circ$ and $\frac{1}{p} + \frac{1}{q} = 1$ with $x < y$, $p, q > 1$. If $|\varphi''|^p$ is s-convex on $[x, y]$, then the inequality is obtained as

$$\left|\tilde{R}_T(\phi, \phi', I_h)\right| \leq \frac{1}{4.|a_2|}\left[\sum_{j=0}^{2} \frac{|j|}{j+1}\right]^{1-\frac{1}{p}} \sum_{i=0}^{n-1} \left\{\left[\left(\sum_{j=0}^{2} \frac{|a_j|}{j+s+1}\right) |\phi''(u_i)|^p + \left(\sum_{j=0}^{2} \frac{|a_j|\Gamma(s+1)\Gamma(i+1)}{\Gamma(j+s+2)}\right) |\phi''(u_{i+1})|^p\right]^{\frac{1}{p}} + \left[\left(\sum_{j=0}^{2} \frac{|a_j|}{j+s+1}\right) |\phi''(u_{i+1})|^p + \left(\sum_{j=0}^{2} \frac{|a_j|\Gamma(s+1)\Gamma(i+1)}{\Gamma(j+s+2)}\right) |\phi''(u_i)|^p\right]^{\frac{1}{p}}\right\} {h_i}^3 \tag{25}$$

for every division d of $[x, y]$, i. e. $x = u_0 < u_1 < \ldots < u_{n-1} < u_n = y$.

Proof 4.3: Applying Corollary (3.3) on the subinterval $[u_i, u_{i+1}]$; $(i = 1, 2, 3, \ldots, n-1)$ of the division d yields

$$\left|\tilde{R}_T(\phi, \phi', I_h)\right| = \left|\sum_{i=0}^{n-1} [\phi(u_i) + \phi(u_{i+1})] h_i - \frac{a_2 + a_1 + 2a_0}{4a_2} \sum_{i=0}^{n-1} [\phi'(u_i) + \phi'(u_{i+1})] {h_i}^2 - \int_{u_i}^{u_{i+1}} \phi(t)dt\right|$$

$$\leq \sum_{i=0}^{n-1} h_i \left|[\phi(u_i) + \phi(u_{i+1})] - \frac{a_2 + a_1 + 2a_0}{4a_2} [\phi'(u_i) + \phi'(u_{i+1})] h_i - \frac{1}{h_i} \int_{u_i}^{u_{i+1}} \phi(t)dt\right|$$

$$\leq \frac{1}{4.|a_2|}\left[\sum_{j=0}^{2} \frac{|j|}{j+1}\right]^{1-\frac{1}{p}} \sum_{i=0}^{n-1} \left\{\left[\left(\sum_{j=0}^{2} \frac{|a_j|}{j+s+1}\right) |\phi''(u_i)|^p + \left(\sum_{j=0}^{2} \frac{|a_j|\Gamma(s+1)\Gamma(i+1)}{\Gamma(j+s+2)}\right) |\phi''(u_{i+1})|^p\right]^{\frac{1}{p}} + \left[\left(\sum_{j=0}^{2} \frac{|a_j|}{j+s+1}\right) |\phi''(u_{i+1})|^p + \left(\sum_{j=0}^{2} \frac{|a_j|\Gamma(s+1)\Gamma(i+1)}{\Gamma(j+s+2)}\right) |\phi''(u_i)|^p\right]^{\frac{1}{p}}\right\} {h_i}^3$$

Theorem 4.4: Let's assume that $\phi: I \subseteq \mathbb{R} \to \mathbb{R}$ is a function with second-order derivatives on I° such that $\varphi'' L([x,y])$ where $x, y \in I^\circ$ with $x < y$. If $|\varphi''|$ is tgs-convex on $[x, y]$, then for every division d of $[x, y]$, i. e. $x = u_0 < u_1 < \ldots < u_{n-1} < u_n = y$, we have

$$\left|\tilde{R}_T(\phi, \phi', I_h)\right| \leq \frac{1}{2.|a_2|}\left[\sum_{j=0}^{2} \frac{|a_j|}{(j+2)(j+3)}\right] \sum_{i=0}^{n-1} [\phi''(u_i) + \phi''(u_{i+1})] {h_i}^3 \tag{26}$$

Proof 4.4: Applying Corollary (3.4) on the subinterval $[u_i, u_{i+1}]$; $(i = 1, 2, 3, \ldots, n-1)$ of the division yields

$$\left|\tilde{R}_T(\phi, \phi', I_h)\right| = \left|\sum_{i=0}^{n-1} [\phi(u_i) + \phi(u_{i+1})] h_i - \frac{a_2 + a_1 + 2a_0}{4a_2} \sum_{i=0}^{n-1} [\phi'(u_i) + \phi'(u_{i+1})] {h_i}^2 - \int_{u_i}^{u_{i+1}} \phi(t)dt\right|$$

$$\leq \sum_{i=0}^{n-1} h_i \left|[\phi(u_i) + \phi(u_{i+1})] - \frac{a_2 + a_1 + 2a_0}{4a_2} [\phi'(u_i) + \phi'(u_{i+1})] h_i - \frac{1}{h_i} \int_{u_i}^{u_{i+1}} \phi(t)dt\right|$$

$$\leq \frac{1}{2.|a_2|}\left[\sum_{j=0}^{2} \frac{|a_j|}{(j+2)(j+3)}\right] \sum_{i=0}^{n-1} [\phi''(u_i) + \phi''(u_{i+1})] {h_i}^3$$

Theorem 4.5: Let's assume that $\phi: I \subseteq \mathbb{R} \to \mathbb{R}$ is a function with second-order derivatives on I° such that $\varphi'' L([x,y])$ where $x, y \in I^\circ$ with $x < y$, $p, q > 1$, $\frac{1}{p} + \frac{1}{q} = 1$. If $|\varphi''|^q$ is tgs-convex on $[x, y]$, then one obtains

$$\left|\tilde{R}_T(\phi, \phi', I_h)\right| \leq \frac{1}{2.|a_2|}\left[\sum_{j=0}^{2} \frac{|a_j|}{(jp+1)^{\frac{1}{p}}}\right] \sum_{i=0}^{n-1} \left[\frac{|\phi''(x)|^q + |\phi''(y)|^q}{6}\right]^{\frac{1}{q}} {h_i}^3 \tag{27}$$

for every division d of $[x, y]$, i. e. $x = u_0 < u_1 < \ldots < u_{n-1} < u_n = y$.

Proof 4.5: Applying Corollary (3.5) on the subinterval $[u_i, u_{i+1}]$; (i = 1, 2, 3,..., n - 1) of the division d yields

$$|\tilde{R}_T(\phi,\phi',I_h)| = \left|\sum_{i=0}^{n-1}[\phi(u_i)+\phi(u_{i+1})]h_i - \frac{a_2+a_1+2a_0}{4a_2}\sum_{i=0}^{n-1}[\phi'(u_i)+\phi'(u_{i+1})]{h_i}^2 - \int_{u_i}^{u_{i+1}}\phi(t)dt\right|$$

$$\leq \sum_{i=0}^{n-1} h_i\left|[\phi(u_i)+\phi(u_{i+1})] - \frac{a_2+a_1+2a_0}{4a_2}[\phi'(u_i)+\phi'(u_{i+1})]h_i - \frac{1}{h_i}\int_{u_i}^{u_{i+1}}\phi(t)dt\right|$$

$$\leq \frac{1}{2|a_2|}\left[\sum_{j=0}^{2}\frac{|a_j|}{(jp+1)^{\frac{1}{p}}}\right]\sum_{i=0}^{n-1}\left[\frac{|\phi^*(x)|^q+|\phi^*(y)|^q}{6}\right]^{\frac{1}{q}}{h_i}^3.$$

Theorem 4.6: Let's assume that ϕ: $I \subseteq \mathbb{R} \to \mathbb{R}$ is a function with second-order derivatives on I° such that $\varphi'' L([x,y])$ where $x, y \in I^\circ$ with $x < y$, $p, q > 1$, $\frac{1}{p}+\frac{1}{q}=1$. If $|\varphi''|^p$ is *tgs*-convex on $[x, y]$, then the inequality in the following is obtained

$$|\tilde{R}_T(\phi,\phi',I_h)| \leq \frac{1}{4.|a_2|}\left[\sum_{j=0}^{2}\frac{|a_j|}{j+1}\right]^{1-\frac{1}{p}}\left[\sum_{j=0}^{2}\frac{|a_j|}{(j+2)(j+3)}\right]^{\frac{1}{p}}\sum_{i}^{n-1}[|\phi''(u_i)|^q+|\phi''(u_{i+1})|^p]^{\frac{1}{p}}{h_i}^3 \quad (28)$$

for every division d of $[x, y]$, i. e. $x = u_0 < u_1 < ... < u_{n-1} < u_n = y$.

Proof 4.6: Applying Corollary (3.6) on the subinterval $[u_i, u_{i+1}]$; (i = 1, 2, 3,..., n - 1) of the division d yields

$$|\tilde{R}_T(\phi,\phi',I_h)| = \left|\sum_{i=0}^{n-1}[\phi(u_i)+\phi(u_{i+1})]h_i - \frac{a_2+a_1+2a_0}{4a_2}\sum_{i=0}^{n-1}[\phi'(u_i)+\phi'(u_{i+1})]{h_i}^2 - \int_{u_i}^{u_{i+1}}\phi(t)dt\right|$$

$$\leq \sum_{i=0}^{n-1} h_i\left|[\phi(u_i)+\phi(u_{i+1})] - \frac{a_2+a_1+2a_0}{4a_2}[\phi'(u_i)+\phi'(u_{i+1})]h_i - \frac{1}{h_i}\int_{u_i}^{u_{i+1}}\phi(t)dt\right|$$

$$\leq \frac{1}{4.|a_2|}\left[\sum_{j=0}^{2}\frac{|a_j|}{j+1}\right]^{1-\frac{1}{p}}\left[\sum_{j=0}^{2}\frac{|a_j|}{(j+2)(j+3)}\right]^{\frac{1}{p}}\sum_{i}^{n-1}[|\phi''(u_i)|^q+|\phi''(u_{i+1})|^p]^{\frac{1}{p}}{h_i}^3.$$

SOME APPLICATIONS IN SPECIAL MEANS

In this section, we will apply the inequalities which we found using the *tgs*-convex functions in Ref. [3], by considering the *tgs*-convex function example.

Proposition 5.1: Let be $x, y \in \mathbb{R}$, $0 < x < y$, $n \in \mathbb{N}$, $n > 2$ where n is even number. Then, the inequality in the following holds:

$$\begin{aligned}&\left|ne^{eI(x,y)+1} - A(xn,yn) + \ln\big(G(y^{ny},x^{nx})\big) + \cdots\right.\\ &+\frac{(y-x)^{n-4}[n.(n-1).(n-2).a_n+\cdots+4.3.2.a_4]}{2.(n-1).(n-2).(n-3)(n-4).a_n}\left[\frac{(-1)^{n-3}}{H(x^{n-4},y^{n-4})}\right]\\ &+\frac{(y-x)^{n-3}[n.(n-1).a_n+\cdots+4.3.a_4+3.2.a_3+4a_2]}{2.(n-1).(n-2).(n-3).a_n}\left[\frac{(-1)^{n-2}}{H(x^{n-3},y^{n-3})}\right]\\ &+\frac{(y-x)^{n-2}[n.a_n+\cdots+2.a_2]}{2.(n-1).(n-2).a_n}\left[\frac{(-1)^{n-1}}{H(x^{n-2},y^{n-2})}\right]\\ &\left.+\frac{(y-x)^{n-1}[a_n+\cdots+a_1+2.a_0]}{2.(n-1).a_n}\left[\frac{(-1)^{n}}{H(x^{n-1},y^{n-1})}\right]\right|\\ &\leq \frac{(y-x)^n}{|a_n|}\left[\frac{1}{H(x^n,y^n)}\right]\left[\sum_{i=0}^{n}\frac{|a_i|}{(i+2)(i+3)}\right].\end{aligned} \quad (29)$$

Proof 5.1: The proof is obtained from Theorem 2.11 [3] such that $\phi(u) = -\ln u^n$, $u \in (2, \infty)$.

Proposition 5.2: Let be $x, y \in \mathbb{R}$, $0 < x < y$, $\forall$ $p, q > 1$, $\frac{1}{p}+\frac{1}{q}=1$, $n \in \mathbb{N}$, $n > 2$ where n is even number.

$$\begin{aligned}&\left|ne^{eI(x,y)+1} - A(xn,yn) + \ln\big(G(y^{ny},x^{nx})\big) + \cdots\right.\\ &+\frac{(y-x)^{n-4}[n.(n-1).(n-2).a_n+\cdots+4.3.2.a_4]}{2.(n-1).(n-2).(n-3)(n-4).a_n}\left[\frac{(-1)^{n-3}}{H(x^{n-4},y^{n-4})}\right]\\ &+\frac{(y-x)^{n-3}[n.(n-1).a_n+\cdots+4.3.a_4+3.2.a_3+4a_2]}{2.(n-1).(n-2).(n-3).a_n}\left[\frac{(-1)^{n-2}}{H(x^{n-3},y^{n-3})}\right]\\ &+\frac{(y-x)^{n-2}[n.a_n+\cdots+2.a_2]}{2.(n-1).(n-2).a_n}\left[\frac{(-1)^{n-1}}{H(x^{n-2},y^{n-2})}\right]\\ &\left.+\frac{(y-x)^{n-1}[a_n+\cdots+a_1+2.a_0]}{2.(n-1).a_n}\left[\frac{(-1)^{n}}{H(x^{n-1},y^{n-1})}\right]\right|\\ &\leq \frac{(y-x)^n}{6^{\frac{q+1}{q}}|a_n|}\left[\sum_{i=0}^{n}\frac{|a_i|}{(ip+1)^{\frac{1}{p}}}\right]\left[\frac{1}{H(x^{nq},y^{nq})}\right].\end{aligned} \quad (30)$$

Proof 5.2: The proof is obtained from Theorem 2.12 [3] such that $\phi(u) = -\ln u^n$, $u \in (2, \infty)$.

Proposition 5.3: Let be $x, y \in \mathbb{R}$, $0 < x < y$, $\forall$ $p, q > 1$, $\frac{1}{p}+\frac{1}{q}=1$, $n \in \mathbb{N}$, $n > 2$ where n is even number. Then, the inequality in the following holds:

$$\begin{aligned}&\left|ne^{eI(x,y)+1} - A(xn,yn) + \ln\big(G(y^{ny},x^{nx})\big) + \cdots\right.\\ &+\frac{(y-x)^{n-4}[n.(n-1).(n-2).a_n+\cdots+4.3.2.a_4]}{2.(n-1).(n-2).(n-3)(n-4).a_n}\left[\frac{(-1)^{n-3}}{H(x^{n-4},y^{n-4})}\right]\\ &+\frac{(y-x)^{n-3}[n.(n-1).a_n+\cdots+4.3.a_4+3.2.a_3+4a_2]}{2.(n-1).(n-2).(n-3).a_n}\left[\frac{(-1)^{n-2}}{H(x^{n-3},y^{n-3})}\right]\\ &+\frac{(y-x)^{n-2}[n.a_n+\cdots+2.a_2]}{2.(n-1).(n-2).a_n}\left[\frac{(-1)^{n-1}}{H(x^{n-2},y^{n-2})}\right]\\ &\left.+\frac{(y-x)^{n-1}[a_n+\cdots+a_1+2.a_0]}{2.(n-1).a_n}\left[\frac{(-1)^{n}}{H(x^{n-1},y^{n-1})}\right]\right|\\ &\leq \frac{(y-x)^n}{2|a_n|}\left[\sum_{i=0}^{n}\frac{|a_i|}{i+1}\right]^{1-\frac{1}{p}}\left[\frac{1}{H(x^{np},y^{np})}\right]^{\frac{1}{p}}\left[\sum_{i=0}^{n}\frac{|a_i|}{(i+2)(i+3)}\right]^{\frac{1}{p}}.\end{aligned} \quad (31)$$

Proof 5.3: The proof is obtained from Theorem 2.13 [3] such that $\phi(u) = -\ln u^n$, $u \in (2, \infty)$.

CONCLUSION

This study focuses on trapezoidal inequalities, triangle inequality, Hölder inequality, and power mean inequality to improve error bounds. These inequalities are applied to s -convex and *tgs*-convex functions. The results show that better error bounds have been reached for the trapezoid and midpoint formulas. This shows an improvement in the accuracy of numerical integration methods. Theoretical studies on *tgs*-convex functions provide an example of how they can be applied in practice. This strengthens the relationship between theory and practice. Consequently, this study demonstrates how to effectively apply and improve mathematical tools used to increase the accuracy of numerical integration techniques and improve error analysis. These findings may be useful to obtain more reliable results, especially in optimization problems.

NOMENCLATURE

I	Identric mean
A	Aritmetic mean
G	Geometric mean
H	Harmonic mean

AUTHORSHIP CONTRIBUTIONS

Authors equally contributed to this work.

DATA AVAILABILITY STATEMENT

The authors confirm that the data that supports the findings of this study are available within the article. Raw data that support the finding of this study are available from the corresponding author, upon reasonable request.

CONFLICT OF INTEREST

The author declared no potential conflicts of interest with respect to the research, authorship, and/or publication of this article.

ETHICS

There are no ethical issues with the publication of this manuscript.

STATEMENT ON THE USE OF ARTIFICIAL INTELLIGENCE

Artificial intelligence was not used in the preparation of the article.

REFERENCES

[1] Farid G, Zahra M. Some integral inequalities involving Mittag-Leffler functions for tgs-convex functions. Comput Math 2021;3:1–11. [CrossRef]

[2] Tunç M, Şanal Ü. Some perturbed trapezoid inequalities for convex, *s* -convex and tgs-convex functions. Tbilisi Math J 2015;8:103–118. [CrossRef]

[3] Dönmez Demir D, Şanal G. Some inequalities for n-times differentiable *s* -convex and tgs-convex functions. Univ J Appl Math 2020;8:1–12. [CrossRef]

[4] Mehreen N, Anwar M. On some Hermite–Hadamard type inequalities for *tgs*-convex functions via generalized fractional integrals. Adv Differ Equ 2020;6:1–17. [CrossRef]

[5] Ge-JiLe HB, Rashid S, Noor MA, Suhail A, Chu YM. Some unified bounds for exponentially tgs-convex functions governed by conformable fractional operators. AIMS Math 2020;5:6108–6123. [CrossRef]

[6] Tariq M, Sahoo SK, Nasir J, Aydi H, Alsamir H. Some Ostrowski type inequalities via *n* -polynomial exponentially *s* -convex functions and their applications. AIMS Math 2021;6:13272–13290. [CrossRef]

[7] Barsam H, Sayyari Y, Mirzadeh S. Jensen's inequality and *tgs*-convex functions with applications. J Mahani Math Res Cent 2023;12:459–469.

[8] Huang H, Xu G. The new inequalities for *tgs*-convex functions. Kragujevac J Math 2024;48:689–695. [CrossRef]

[9] Maden S, Demirel AK, Turhan S, İşcan İ. Some integral inequalities for the new convex functions. Sigma J Eng Nat Sci 2018;9:319–326.

[10] Demir Ş. New inequalities of Hermite–Hadamard type for functions whose second derivatives absolute values are exponential trigonometric convex. Sigma J Eng Nat Sci 2023;41:451–456. [CrossRef]

[11] İşcan İ, Kadakal H, Kadakal M. Some new integral inequalities for *n* -times differentiable quasi-convex functions. Sigma J Eng Nat Sci 2017;35:363–368. [CrossRef]

[12] Khan MB, Noor MA, Noor KI, Çetkin V. Some new inequalities for *LR* - *(p, h)*(-convex interval-valued functions by means of pseudo order relation. Sigma J Eng Nat Sci 2023;41:524–537. [CrossRef]

[13] Rehman AU, Farid G, Mishra VN. Generalized convex function and associated Petrovic's inequality. Int J Anal Appl 2019;17:122–131.

[14] Farid G, Mishra VN, Mehmood S. Hadamard and Fejér–Hadamard type inequalities for convex and relative convex functions via an extended generalized Mittag-Leffler function. Int J Anal Appl 2019;17:892–903.

[15] Farid G, Rehman AU, Mishra VN, Mehmood S. Fractional integral inequalities of Grüss type via generalized Mittag-Leffler function. Int J Anal Appl 2019;17:548–558.

[16] Farid G, Akbar SB, Rathour L, Mishra LN, Mishra VN. Riemann–Liouville fractional versions of Hadamard inequality for strongly m-convex functions. Int J Anal Appl 2022;20:1–12. [CrossRef]

[17] Farid G, Mishra VN. Caputo fractional derivative inequalities via (*h* - *m*) -convexity. J Math Ext 2022;16:1–15.

[18] Farid G, Bibi S, Rathour L, Mishra LN, Mishra VN. Fractional versions of Hadamard inequalities for strongly (*s* - *m*) -convex functions via Caputo fractional derivatives. Korean J Math 2023;31:75–94.

[19] Farid G, Mehmood S, Rathour L, Mishra LN, Mishra VN. Fractional Hadamard and Fejér–Hadamard inequalities associated with exp. (*α, H* - *M*) -convexity. Dyn Contin Discrete Impuls Syst Ser A Math Anal 2023;30:353–367.

[20] Rathour L, Rehman AU, Bibi S, Farid G. *k* -fractional integral inequalities of Hadamard type for strongly exponentially (α,h–m)-convex functions. Appl Math E-Notes 2023;23:393–411.

[21] Şanlı Z, Kunt M, Köroğlu T. Improved Hermite–Hadamard type inequalities for convex functions via Katugampola fractional integrals. Sigma J Eng Nat Sci 2019;37:461–474. [CrossRef]

[22] Rathour L, Singh V, Yadav H, Sharma MK, Mishra VN. A dual hesitant fuzzy set theoretic approach in fuzzy reliability analysis of a fuzzy system. Inf Sci Lett 2024;13:433–440. [CrossRef]

[23] Sharma MK, Chaudhary S, Rathour L, Mishra VN. Modified genetic algorithm with novel crossover and mutation operator in travelling salesman problem. Sigma J Eng Nat Sci 2024;42:1–8. [CrossRef]

[24] Negero NT, Duressa GF, Rathour L, Mishra VN. A novel fitted numerical scheme for singularly perturbed delay parabolic problems with two small parameters. Partial Differ Equ Appl Math 2023;8:100546. [CrossRef]

[25] Hogeme MS, Woldaregay MM, Rathour L, Mishra VN. A stable numerical method for singularly perturbed Fredholm integro-differential equation using exponentially fitted difference method. J Comput Appl Math 2024;441:115709. [CrossRef]

[26] Younus A, Dastgeer Z, Rathour L, Mishra LN, Mishra VN, Pandey S. Distinguishability criteria of conformable hybrid linear systems. Nonlinear Eng 2022;11:420–427. [CrossRef]

[27] Dönmez Demir D, Şanal G. Perturbed trapezoid inequalities for nth order differentiable convex functions and their applications. AIMS Math 2020;5:5495–5509. [CrossRef]

[28] Dönmez Demir D, Şanal G. Some inequalities for n-times differentiable strongly convex functions. Math Stat 2022;10:390–396. [CrossRef]

[29] Dönmez Demir D, Şanal G. Some perturbed trapezoid inequalities for n-times differentiable strongly log-convex functions. Celal Bayar Univ J Sci 2022;18:355–363. [CrossRef]

[30] Dönmez Demir D, Şanal G. On n-times differentiable strongly convex functions. Int J Math Comput Eng 2023;1:201–210. [CrossRef]

[31] Dönmez Demir D, Şanal G. Some inequalities and applications for n-times differentiable strongly tgs-convex functions. In: Int Res Math Sci III. New York: Eğitim Publishing; 2022. p. 37–54.

[32] Hermite C. Sur deux limites d'une intégrale définie. Mathesis 1883;82.

[33] Breckner WW. Stetigkeitsaussagen für eine Klasse verallgemeinerter konvexer Funktionen in topologischen linearen Räumen. Publ Inst Math Beograd 1978;23:13–20.

[34] Tunç M, Göv E, Şanal Ü. On tgs-convex function and their inequalities. Facta Univ Ser Math Inform 2015;30:679–691.

[35] Cerone P, Dragomir SS, Roumeliotis J. An inequality of Ostrowski–Grüss type for twice differentiable mappings and applications in numerical integration. RGMIA Res Rep Collect 1998;1. [CrossRef]

[36] Cerone P, Dragomir SS. Trapezoidal-type rules from an inequalities point of view. In: Handbook of analytic computational methods in applied mathematics. Melbourne, Australia: Victoria University; 2000. p. 70. [CrossRef]

[37] Qayyum A, Faye I, Shoaib MM, Latif AA. Generalization of Ostrowski type inequality for mappings whose second derivatives belong to and applications. Int J Pure Appl Math 2015;98:169–180. [CrossRef]

Sigma Journal of Engineering and Natural Sciences
Web page info: https://sigma.yildiz.edu.tr
DOI: 10.14744/sigma.2025.00000

Research Article

Hall current's effect on MHD boundary layer compressible flow of fluid past a stretching sheet with viscous dissipation

Bandita DAS[1], Sunmoni MUDOI[2,*], Dipak SARMA[2]

[1]*Department of Mathematics, Guwahati College, Guwahati, 781021, India*
[2]*Department of Mathematics, Cotton University, Guwahati, 781001, India*

ARTICLE INFO

Article history
Received: 21 July 2024
Revised: 18 September 2024
Accepted: 28 November 2024

Keywords:
bvp4c; Hall Current; Heat Transfer; MHD; Viscous – Dissipation

ABSTRACT

This work investigates the consequence of hall current on the boundary layer along a stretching sheet in the occurrence of magnetohydrodynamics, heat transfer and viscous dissipation. In the direction of the flow, a uniform transverse magnetic field is applied. Here, the controlling equations are modified into nonlinear ordinary expressions, implementing the similarity transformation. Validation is accomplished by applying the MATLAB bvp4c skill. We then visually display the impact of varied parameters by introducing temperature and non-dimensional velocity into the problem. Moreover, it is found that the relevant parameters significantly affect the flow patterns and other important physical quantities by organizing and categorizing their effects on the coefficients of skin-friction and heat transfer rate using the Nusselt number, which are of concrete relevance. Our study shows that increasing the Hall current parameter results in an enhanced primary velocity flow pattern, accompanied by a reduction in secondary velocity and temperature flow patterns.

Cite this article as: Das B, Mudoi S, Sarma D. Hall current's effect on MHD boundary layer compressible flow of fluid past a stretching sheet with viscous dissipation. Sigma J Eng Nat Sci 2026;44(1):318–328.

INTRODUCTION

A basic idea in fluid dynamics, laminar boundary layer flow specifies how a fluid behaves when it passes over a solid surface with layers that are smooth and organized. Every layer of the fluid slides easily over the layer below it in this kind of flow, which is composed of parallel layers. Laminar boundary layer flow is very important to engineers working on heat transfer surfaces, pipes, and airplane wings and laminar boundary layer flows have been comprehensively reviewed by various researchers, offering a deep understanding of a key aspect of fluid mechanics to the research community [1–4]. Boundary layer flows over a continuous surface of a solid body have been comprehensively reviewed by a variety of researchers, each contributing to our knowledge base in different aspects, including fundamental theories, mechanisms and theories of stability and transition, control techniques, effects of surface conditions, numerical analysis, experimental techniques, and inter/multidisciplinary studies, among others, of boundary

***Corresponding author.**
*E-mail address: sunmoni77.mudoi@gmail.com

This paper was recommended for publication in revised form by Editor-in-Chief Ahmet Selim Dalkilic

Published by Yıldız Technical University Press, İstanbul, Turkey
© Author. This is an open access article under the CC BY-NC license (http://creativecommons.org/licenses/by-nc/4.0/).

layer flows associated with or involving boundary layer flows on continuous surfaces of solid bodies, like the body of an airplane, the fuselage of an airplane, or airplane wings, among other aerospace surface structures and other bodies like tanks and buses, among other applications [5,6]. The effects of heat radiation on gray fluids that absorb and emit near a black vertical plate were studied by cess [7].

Unsteady free convective transport accompanied by MHD mass transfer along a vertical porous plate is an interesting phenomenon to explore and has numerous applications in environmental sciences, engineering, and physics. To understand phenomena of plasmas, core dynamics of the Earth, and metal liquids in industries, it is necessary to understand the nature of the magnetohydrodynamic fluids or MHD. It leads to more complex fluid dynamics and is used in heat transfer systems and cooling systems accompanied by free convection currents and is induced by density differences caused by fluid temperatures. Taking into account the diffusion of chemicals within the fluid leads to more complex dynamics because of the inclusion of mass transfer. It is necessary to understand the dynamics of mass transfer because of its applications in environmental pollution and other different applications in the field of chemical engineering. In general, exploring magnetohydrodynamic unsteady free convection transport together along with a vertical porous plate increases our understanding of fluid dynamics and is used in different applications in the field of technology. Numerous researchers [8–11] have investigated the dynamics of forced and natural convection present in magnetohydrodynamic transport. Similarity analysis on the boundary layer forced and natural convection of incompressible fluid was first proposed by Ferdows [12]. The study focused on the flow process in a non-conducting porous plate.

Stretching sheets are prepared by elongating a film of a polymeric material. This is a widely relevant topic in a polymeric industrial setup. Some of the applications of this technology involve preparation of films, packing, or even textiles. This operation of sheet stretching is a widely important aspect of tailoring materials for a specific application, and it helps a great deal in altering the properties of a particular material considerably. Stretching sheets are used within the polymeric industry for making a number of products such as shrink wraps, tapes, food packing plastic films, or synthetic fibers for textiles [13–16].

Quality of product can be largely affected if there is variation in the rate of cooling. Moreover, through the application of electrically conductive fluids within a magnetic field, control over the rate of cooling can be easily exercised. This will make it relatively simpler to provide the desired properties to the product. In order to study and ensure the desired product quality, one requires complete knowledge about heat transfer. In case of radiative heat transfer of a complex nature inside a medium located around specular reflectors, the medium interacts with the radiation in different manners such as scattering, emission, and absorption. The heat transfer rate can be enhanced through the confinement of radiation within the medium using spherical reflectors. In order to provide better thermal performance for an efficient rate of heat transfer as observed in practical applications such as solar energy collection systems as well as thermal insulation systems, it is essential to make proper modifications in the design of specular reflectors and control the properties of the medium involved [17–21].

Hall currents affect fluid flow immensely in various applications, but their importance is most prominent in magnetohydrodynamics (MHD) applications, where magnetic fields are applied to electrically conductive fluids. There will be additional forces acting on the fluids when the Hall current is also taken into consideration, as it depends upon the combined effects of the electric current and the magnetic field applied. Various applications of engineering, such as the production of power using MHD, semiconductor devices, plasma research, and microfluidics, all involve knowing the effects of Hall currents on the flow of fluids. The effect of the Hall current on an unsteady natural convection flow is explained by Sattar and Hossain [22]. They took into account the concentration and plate temperature as time-dependent variables. The properties of mass transfer and stable double-diffusive free convective heat in a chemically-reacting micropolar fluid were investigated by beg [23].

A stretching sheet is a flat surface that expands or stretches in a single direction at a speed proportional to its distance from the origin. If a fluid flows through a stretched sheet in a continuous two-dimensional hydromagnetic flow, things like the effect of magnetic fields, fluid dynamics, and behavior of boundary layer become very important to the study. Recent research has investigated the constant two-dimensional hydromagnetic flow of a fluid past a stretching sheet. The effects of viscous and Joule dissipations on the flow characteristics were the focus of the enquiry [24]. The work introduced the aspects of Brownian motion in the transport equations. The repercussions of diffusion-thermo and thermal-diffusion on the axisymmetric magnetohydrodynamic flow were studied by Hayat and Hendi [25]. They used the HAM method to inspect the implications of viscous dissipation, Joule heating, Hall and ion-slip currents, and a first order chemical process. The problem was scrutinized by running the Chebyshev collocation method jointly with the successive linearization method (SLM) considering variable thermal diffusivity, Hall and ion-slip currents, and chemical reaction. Marin [26–28] has reviewed a great deal on materials' thermoelectricity and micropolar bodies. Ferdows et al. [29] have investigated the impact of Hall current and viscous dissipation on boundary layer flow.

This study investigates the effect of various parameters in natural convection in the presence of a strongly magnetic field on a stretching sheet. It focuses on the aspects of heat transfer and boundary layer flow. This study aims to integrate the dynamic effect of hall currents and viscous

dissipation. The equations, numerical method, and mathematical modeling required for simulation are described later on.

MATHEMATICAL DESCRIPTION

We study the behavior of an electrically conducting, incompressible, viscous, and stable fluid moving in the x-direction down a vertical surface while taking heat transfer into account. As illustrated in Figure 1, the flow is further influenced by a strong magnetic field B_0 of constant intensity oriented along the y-axis. As a stretching sheet gets farther from the leading edge, its velocity component $\bar{u}$, changes proportionally. Here, the velocity components in the *x*, *y* and *z* direction are, respectively, $\bar{u}$, $\bar{v}$, and $\bar{w}$.

An electrically conducting fluid is typically affected by Hall current when a magnetic field is present. Because of the Hall current effect, there is a force in the z-direction, which causes a cross-flow and makes the flow three-dimensional.J_y = constant is the result of the conservation of charge equation $\nabla.\bar{J} = 0$, where the current density is $\bar{J} = (J_x, J_y, J_z)$. $J_y = 0$ at the plate and hence everywhere since this constant is zero because the plate is non-conducting.

To simplify the problem, we assume that the amounts of heat transfer and flow in the z-direction are constant. By using the standard boundary layer theory, Boussinesq approximations and the previously indicated assumptions, the governing boundary layer equations can be formulated as follows:

$$\bar{u}_x + \bar{v}_x = 0 \tag{1}$$

$$\bar{u}\bar{u}_x + \bar{v}\bar{u}_y = v\bar{u}_{yy} + \overline{ue}\,\overline{ue}_x + g^*\beta^*(\bar{T} - \bar{T}_\infty) - \frac{\bar{B}_0}{\rho}J_z \tag{2}$$

$$\bar{u}\bar{w}_x + \bar{v}\bar{w}_y = v\bar{w}_{yy} + \frac{\bar{B}_0}{\rho}J_x \tag{3}$$

$$\bar{u}\bar{T}_x + \bar{v}\bar{T}_y = \frac{k}{\rho C_p}\bar{T}_{yy} + \frac{v}{C_p}\left((\bar{u}_y)^2 + (\bar{w}_y)^2\right) + \frac{\sigma\mu_e\bar{B}_0^2\lambda}{\rho C_p(1+m^2\lambda^2)}(u^2 + w^2) \tag{4}$$

Physical Boundary Conditions

$$\text{At } y=0,\ \bar{u}=u_0=Bx,\ \bar{v}=0,\ \bar{w}=0,\ \bar{T}=\bar{T}_w=\bar{T}_\infty+A\left(\frac{x}{l}\right)$$

$$As\ y\to\infty,\quad \bar{u}=\overline{ue}(x)=Cx, w\to 0, \bar{T}\to\bar{T}_\infty \tag{5}$$

Similarity Analysis

$$\eta = y\left(\frac{B}{v}\right)^{\frac{1}{2}},\ \bar{u} = Bxf'(\eta),\ \bar{v} = -(Bv)^{\frac{1}{2}}f(\eta),\ \bar{w} = Bxg(\eta)\ and\ \theta(\eta) = \frac{\bar{T}-\bar{T}_\infty}{\bar{T}_w-\bar{T}_\infty} \tag{6}$$

Transformed equations

$$f''' + ff'' - f'^2 + \delta^2 + Gr^*\theta - \frac{M\lambda}{m^2\lambda^2+1}(f' + mg\lambda) = 0 \tag{7}$$

$$g'' + g'f + gf' + \frac{M\lambda}{m^2\lambda^2+1}(mf'\lambda - g) = 0 \tag{8}$$

$$\theta'' + \theta' fPr - \theta f'Pr + \frac{M\lambda}{m^2\lambda^2+1}Ec.\Pr(g^2 + f'^2) = 0 \tag{9}$$

The modified boundary conditions are as follows:

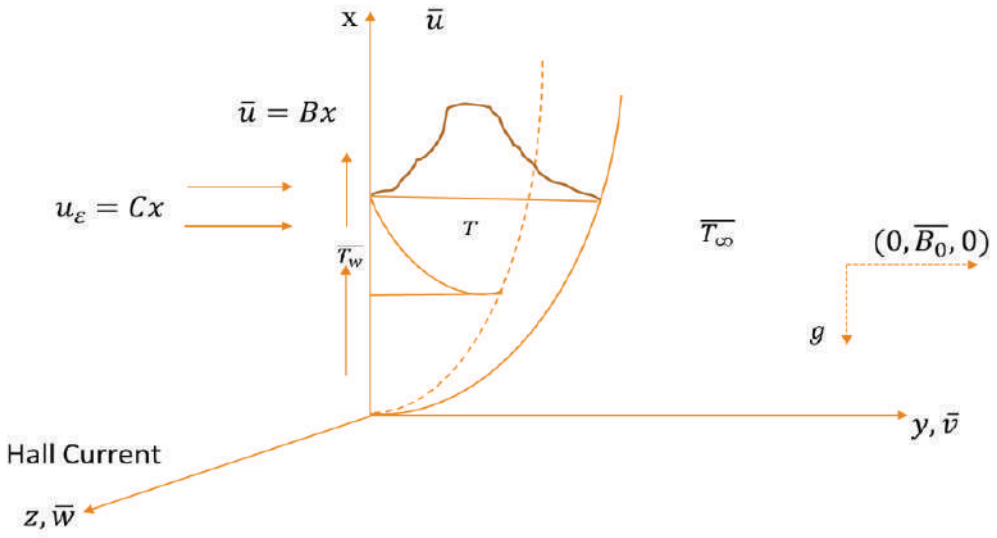


Figure 1. Geometrical model.

$$f(0) = 0, f'(0) = 1, g(0) = 0, \text{and } \theta(0) = 1$$

$$f' \to \delta, g \to 0, \theta \to 0 \qquad as \ \ \eta \to \infty \qquad (10)$$

MATERIALS AND METHODS

To solve equations (7), (8), and (9) while adhering to the restriction outlined in condition (10), we will now utilise the bvp4c approach. It is a mathematical method that MATLAB has built-in. For the various parameters, the temperature coefficient and velocity graph findings are explained in detail.

To apply finite difference-based solver bvp4c the dimensionless equations (7)- (9) respectively transformed as:

$$f = y1; f' = y1' = y2; f'' = y2' = y3$$

$$g = y4; \ \ g' = y4' = y5; \ \ \theta = y6, \qquad \theta' = y6' = y7$$

$$y3' = -y1 * y3 + 2 * y2^2 - \delta^2 - Gr * y6 + \left(\frac{m\lambda}{m^2 * \lambda^2 + 1}\right) * (y2 + m * y4 * \lambda)$$

$$y5' = -y5 * y1 - y4 * y2 - \left(\frac{m\lambda}{m^2 * \lambda^2 + 1}\right) * (m * y2 * \lambda - y4)$$

$$y7' = -Pr * \left(y1 * y7 - y6 * y2 + \left(\frac{m\lambda}{m^2 * \lambda^2 + 1}\right) * Ec * (y4^2 + y2^2)\right)$$

Also, initial and boundary conditions (10) are transformed:

$$y1(0) = 0; y2(0) = 1; y4(0) = 0; y6(0) = 1$$

$$y2(\infty) = \delta; \ \ y4(\infty) = 0; \ \ y6(\infty) = 0$$

These transformed results are used in MATLAB to perform the numerical computation of the solution.

RESULTS AND DISCUSSION

We explore the physical consequence of several critical parameters on the temperature distribution, secondary flow distribution, and primary flow distribution in this section. Magnetic parameter (M), Grashof number (Gr), Hall current (m), Prandtl number (Pr) are the parameters of interest. Figures 2-16 shows the graphical depictions of these impacts.

Effects of Prandtl Number

The temperature and momentum boundary layers proportional thickness are described by a dimensionless number called the Prandtl number. The ratio of momentum diffusivity to heat diffusivity can be used to express it.

Comparing thermal diffusivity with momentum diffusivity, the former is smaller for high values of Pr. Consequently, there is a higher momentum boundary layer compared to a lower temperature boundary layer. Lower primary flow velocity ensues from the fluid experiencing higher resistance to motion. The motion of fluid is slower nearer the boundary; this is evidenced by a steeper velocity gradient which approaches the wall. On the contrary, when Pr is smaller, thermal diffusivity is higher than the momentum diffusivity. In this case, the fluid can move more freely because the momentum boundary layer is thinner than the temperature boundary layer. This leads to a less steep velocity gradient near the wall and thus a higher primary flow velocity. Globally, the secondary flow is less influenced by Pr than the primary flow is influenced by it. However, there may still be an effect from the differences in Prandtl number on the global stability and structure of flow. Due to higher viscosities, a large Pr number could dampen secondary flow or a small Pr number could enhance secondary flow through reduced viscous resistance. Higher Pr number: Sharp velocity gradient near the wall, small momentum boundary layer, and localized fluid flow. Smaller Pr, faster fluid flow, a large momentum boundary layer, and a gradual velocity gradient region close to the wall. More severe temperature gradient close to the wall, small thermal boundary layer, smaller temperature gradient for higher Pr, and localized conduction. Less severe temperature gradient close to the wall, large thermal boundary layer, and diffused conduction. Figures 2-4 describe Prandtl number effects on primary, secondary, and temperature profiles.

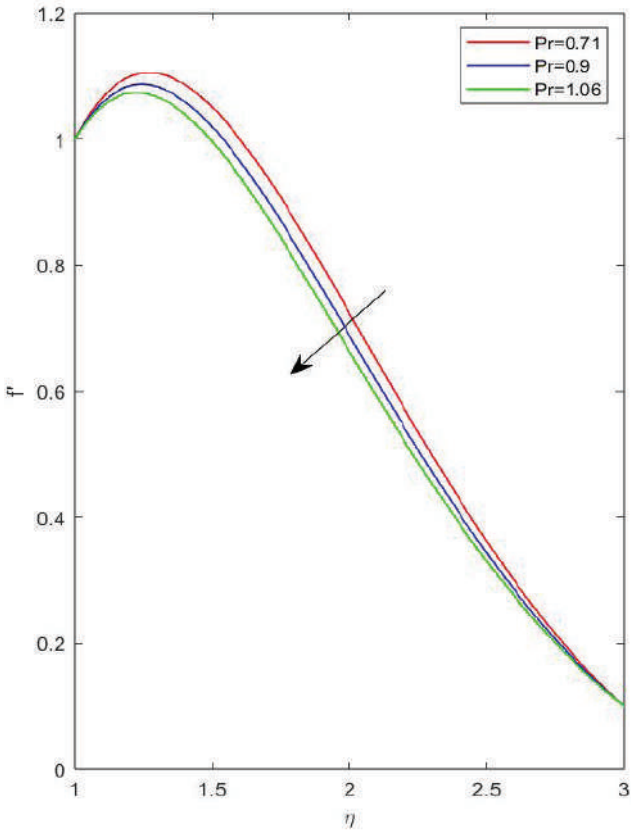


Figure 2. Primary velocity flow patterns for Pr.

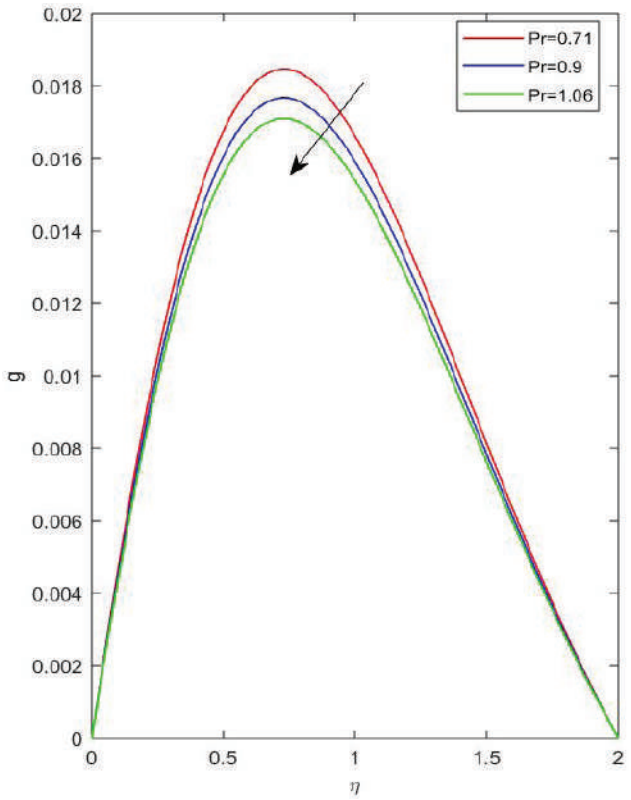


Figure 3. Secondary velocity flow patterns for Pr.

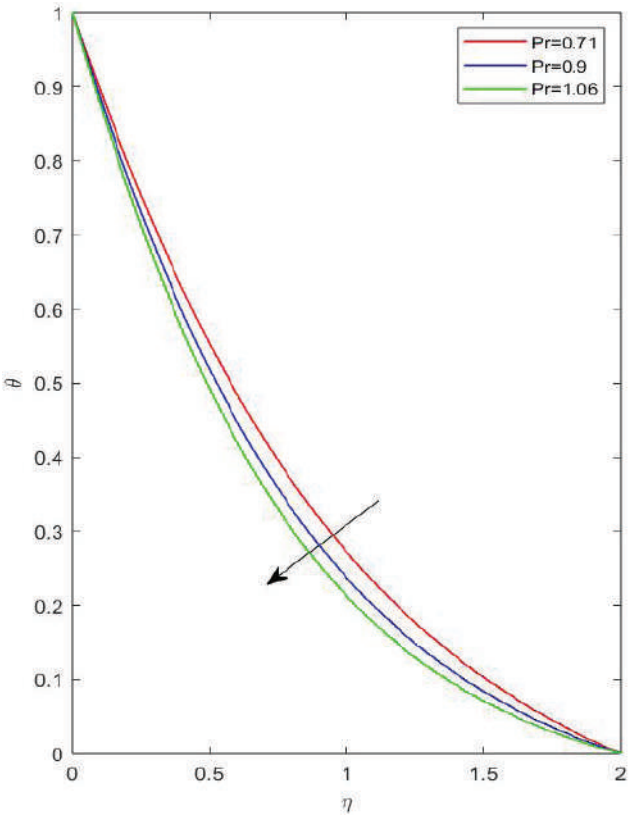


Figure 4. Temperature variations for Pr.

Effect of Magnetic Parameter

One of the significant aspects of fluid dynamics, especially in the context of magnetohydrodynamics, is the effect of the magnetic parameter on the velocity profile.

The main velocity in MHD fluids is considerably affected by the presence of the magnetic parameter, which is named the Hartmann number. The increase in the magnetic damping corresponding to a larger value of the parameter M, results in a homogeneous velocity profile and a reduced boundary layer. This similarity in the velocity profile, from a parabolic to a flat profile, highlights the significance of the magnetic field in the control of fluid velocity in MHD processes. The velocity perpendicular to the principal direction of the principal velocity, normally because of the emergence of the magnetic field, is named the velocity profile of the second kind in MHD. For the use of MHD pumps, generators, and the control of the fluid process in various engineering systems, it is necessary to understand the penetration of the magnetic parameter in the second velocity profile of the MHD process. The second velocity profile of the MHD process is immensely influenced by the magnetic parameter. A flat velocity profile occurs in the middle region of the process, and a high velocity gradient occurs in the boundary layer as the magnetic parameter, m,

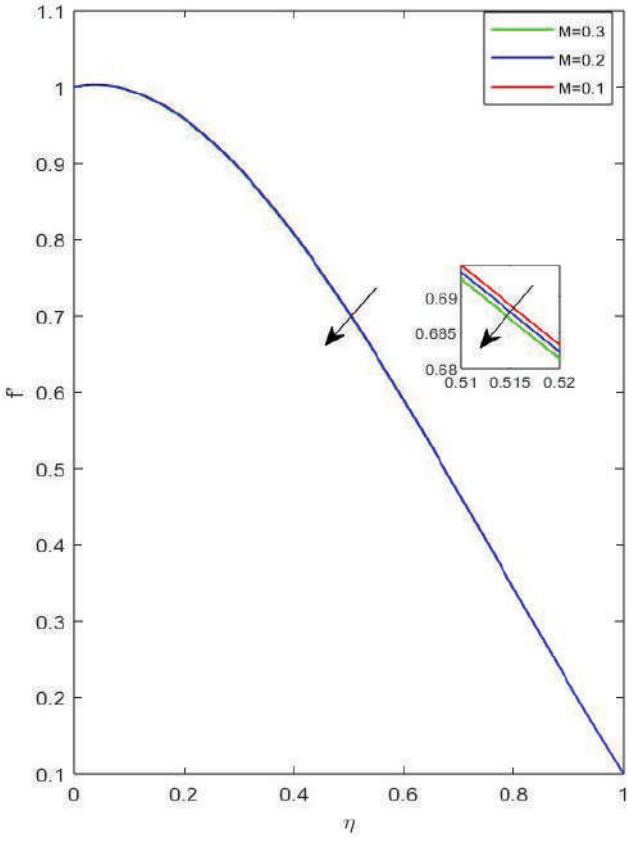


Figure 5. Primary velocity flow patterns for Magnetic parameter (M).

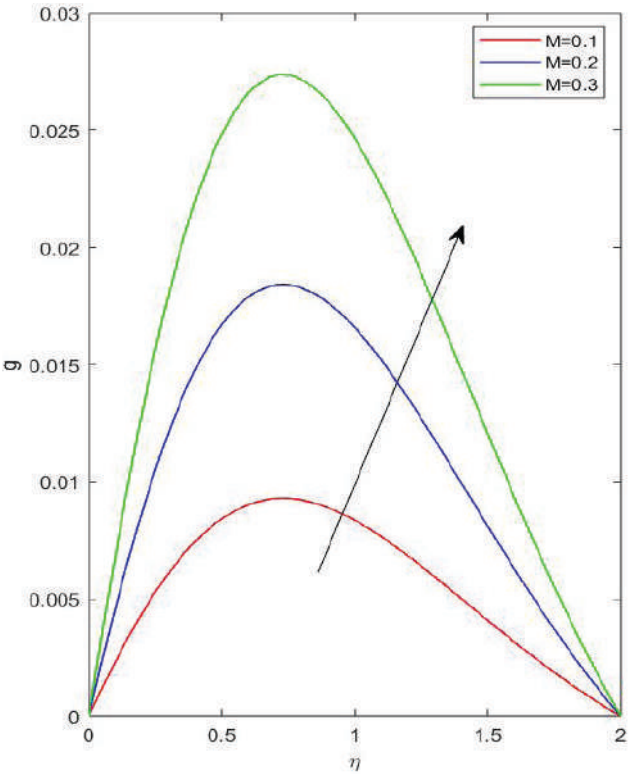


Figure 6. Secondary velocity flow patterns for magnetic parameter.

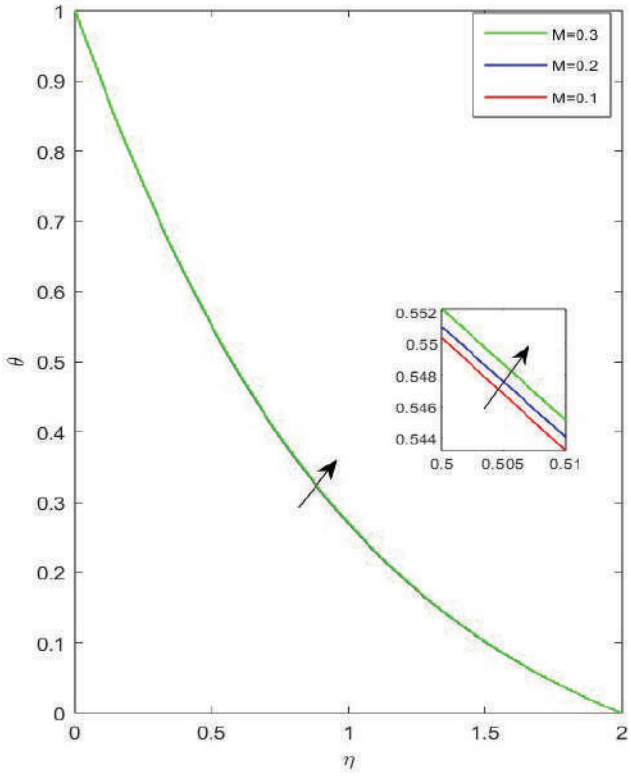


Figure 7. Temperature variations for magnetic parameter.

increments due to intensified magnetic damping, accompanied by a decrement in the second velocity.

In many technical and commercial applications, the impact of the magnetic parameter on the temperature flow patterns in MHD flows is crucial to take into account. Due to variations in flow dynamics and heat transfer properties, the existence of a magnetic field affects both the velocity and the temperature flow patterns.

The effects of the magnetic parameter on the primary velocity flow patterns, secondary velocity flow patterns, and temperature distribution are shown, respectively, in Figures 5-7.

Effects of Hall Current

The behavior of the primary, secondary, and temperature distribution in MHD is further complicated by the Hall effect, which arises when a magnetic field is applied at right angled to the flow of an electrically conducting fluid. Because of the way the magnetic field and fluid motion interact, the Hall current can drastically change these characteristics.

In Magnetohydrodynamic flows, the main velocity, secondary velocity, and temperatures are strongly affected by the Hall current given by the following equations:

The main velocity is impacted by the inclusion of potential asymmetries and the change of the Lorentz force because of the Hall current. Because of the induced currents that are opposite to the magnetic field and the main flow, the secondary velocity is amplified and could possibly have more complexity. Because of the induced currents that are opposite to the magnetic field and the main flow, the secondary velocity is amplified and could possibly have more complexity. There could be effects of raised local temperatures and differences in the thermal boundary layers because of changes in the temperature profile owing to differences in the convective heat transfer and Joule heating.

The effects of the Hall parameter on the primary velocity flow patterns, secondary velocity flow patterns, and temperature distribution are shown, respectively, in Figures 8-10.

Effect of Grashof Number

A dimensionless integer called Grashof number, Gr, denotes the relative significance of buoyancy force to viscous force in fluid mechanics and conduction of heat. The following description illustrates the significance of the Grashof number in different ways, concerning the phenomenon of natural convection, a type of fluid motion driven by buoyancy force:

Main Velocity Profile: The main velocity profile would show the fluid moving upwards in the vicinity of the heated surface and subsequently moving downwards in the opposite direction. The Grashof number depends on this. The buoyant force will be large when there is a higher velocity, which is expressed through the Grashof number.

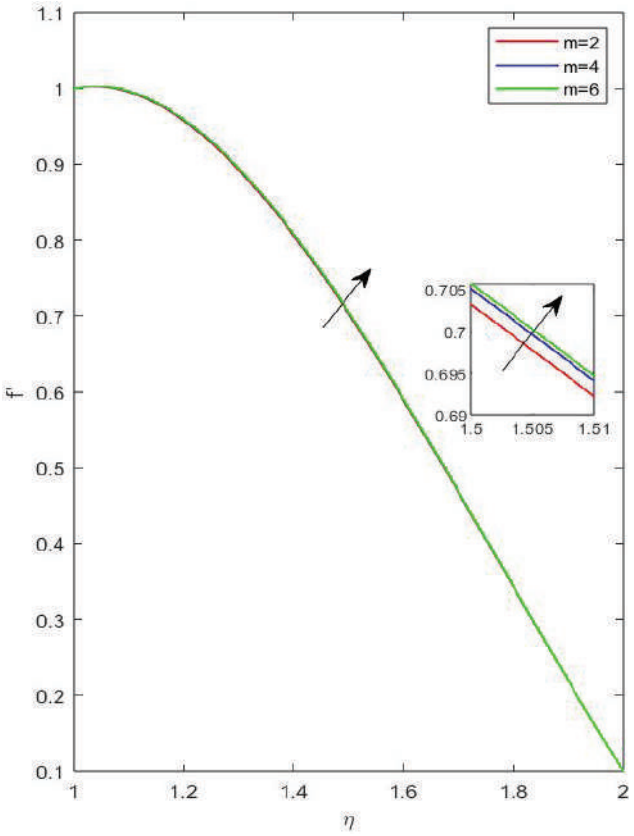


Figure 8. Primary velocity flow patterns for hall current (m).

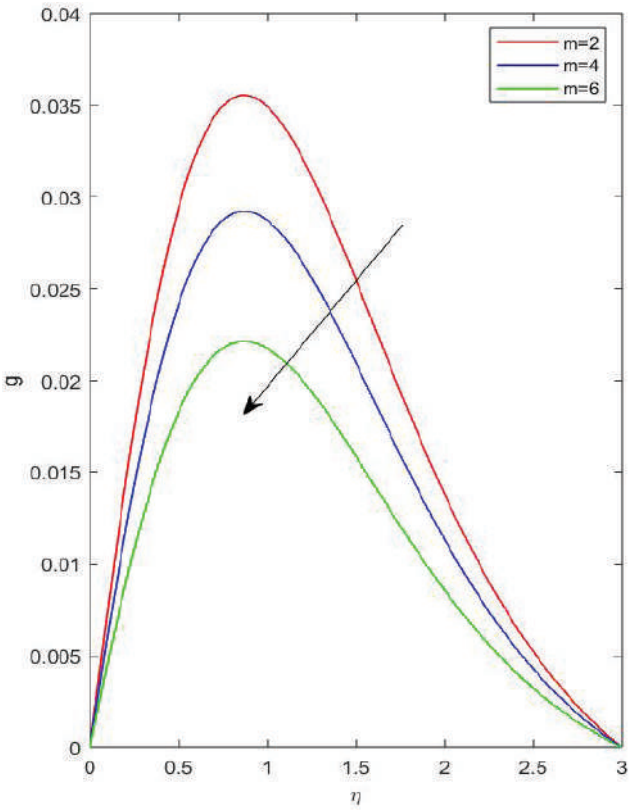


Figure 9. Secondary velocity flow patterns for hall current (m).

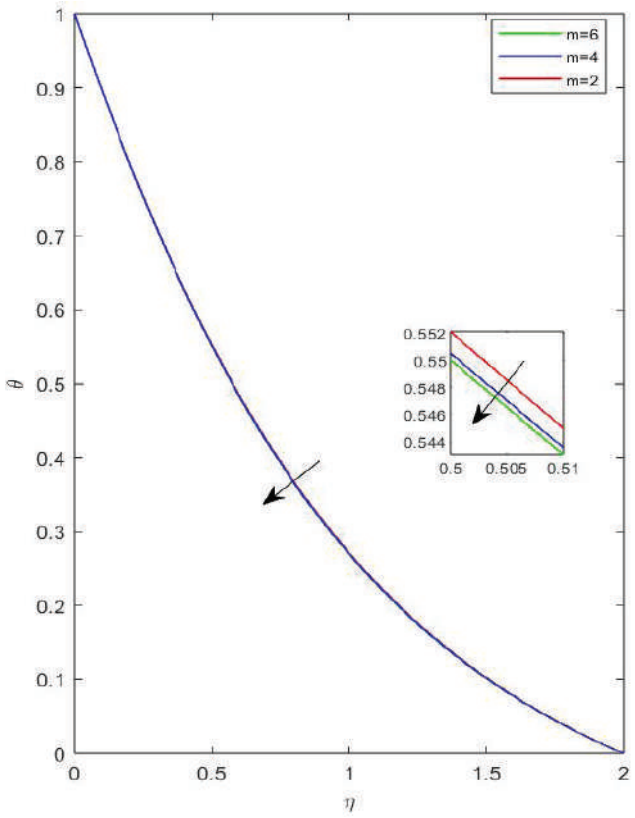


Figure 10. Temperature variations for hall current (m).

Secondary Velocity Profile: The presence of any obstruction to the flow direction, such as walls or other obstructions, may produce a couple with the principal buoyancy-driven flow, giving rise to secondary flows, swirls, and vortices. The intensity and nature of the secondary flows are functions of the Grashof number.

Temperature Profile: The Gr, or Grashof number, too has its say in the temperature profile for free convection. Since more fluid is moved due to buoyancy forces, a higher Grashof number leads to a more apparent temperature gradient and results in a higher heat transfer rate. Therefore, the temperature of the fluid will distribute more uniformly far away from the heated surface and steeper near it.

As one can conclude, the Grashof number affects both the temperature profile and the primary and secondary velocity flow patterns in fluid movement due to natural convection. Larger buoyancy effects would lead to more energetic fluid motion and, therefore, enhanced heat transmission, which can be demonstrated by higher Grashof values. Figures 1-13 present both the primary and secondary velocity profiles and the temperature distribution for different Gr values.

Table 1 demonstrates the validity of our work in comparison to some previously published research. Here, we compare the heat transfer rate values for various parameters with those from published papers. We see that our work is valid with some previously published

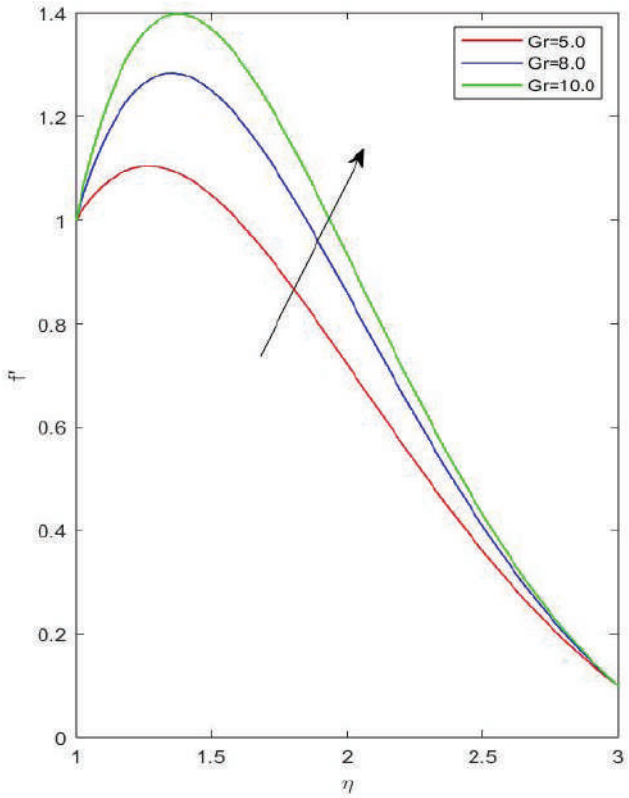


Figure 11. Primary velocity flow patterns for grashof number.

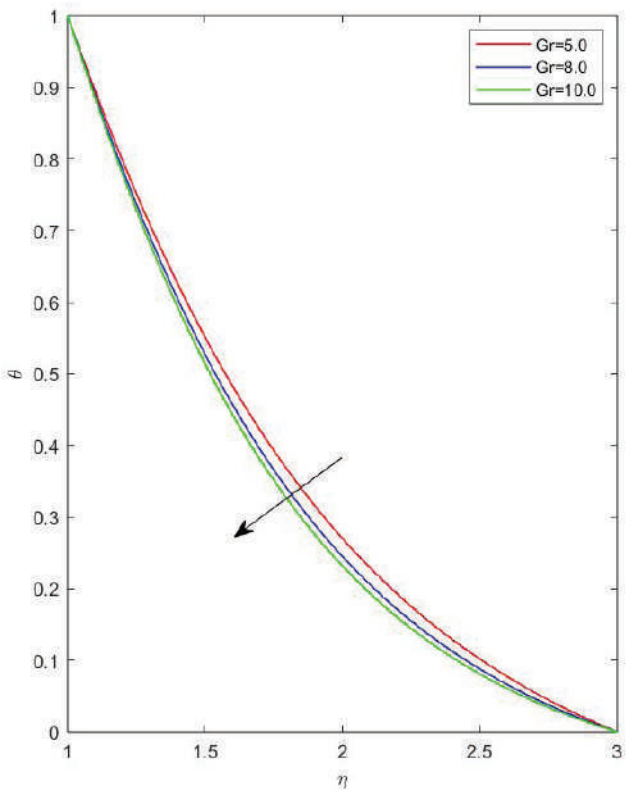


Figure 13. Temperature variation for grashof number.

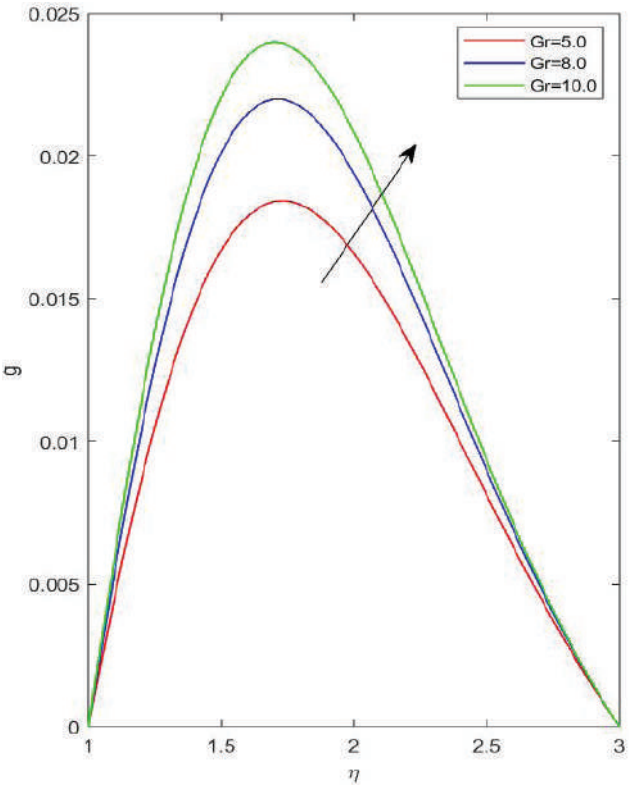


Figure 12. Secondary velocity flow patterns for grashof number.

papers. Lastly, Table 2. shows the consequences of several scientific parameters that arose at the plate surface in the problem, including skin frictions caused by primary and secondary velocity ($C_{fx} \propto f''(0)$ and $C_{fz} \propto g'(0)$) and the Nusselt number ($Nu_x \propto -\theta'(0)$). Skin friction is increased with increasing *m, Ec, Gr,* and δ and decreased with increasing *M* and *Pr*. Raising the skin friction coefficient causes the surface to experience more shear stress, higher drag force, and improved fluid-surface momentum transfer. It causes a greater pressure drop, a lower flow rate, more drag, less lift, improved heat transfer, and faster reaction times. With increasing *M, Gr,* and δ the Nusselt number increases, but it decreases with growing *M* and *Pr.* Increases in the Nusselt number indicate changes in the convective heat transfer coefficient, variations in the thickness of the thermal boundary layer, and augmentation or decrease of heat transmission. The repercussions include variations in surface temperature and an increase or reduction in the rate of heat transfer. The Sherwood number coefficient increases with growing *m, Pr, Gr,* and δ, but it decreases with increasing *M* and *Ec*. A greater convective mass transfer coefficient and a thinner concentration boundary layer are implied by an increase in Sherwood number. Faster response speeds and increased absorption efficiency are among the effects' after effects.

Table 1. Comparision of results of heat transfer rate

Pr	Yih [30]	Ali [31]	Reddy [32]	Present study
0.71	0.8086	0.8086	0.8086	0.8085
1	1	1	1.0001	1.0002
3	1.9237	1.9237	1.9230	1.9239

Table 2. Variations of physical parameters

m	M	Pr	Ec	δ	Gr	$f''(0)$	$g'(0)$	$-\theta'(0)$
2						0.1402	0.0215	1.3041
4	0.2	0.72	3	0.5	8	0.1504	0.0173	1.3062
6						0.1538	0.0130	1.3068
	0.1					0.1520	0.0100	1.3065
	0.2					0.1467	0.0199	1.3054
	0.3					0.1414	0.0298	1.3044
		0.5				0.1749	0.0200	1.2158
		0.72				0.1467	0.0199	1.3054
		2				0.0074	0.0192	1.7761
			0.3			0.1469	0.0199	1.3048
			3			0.1522	0.0199	1.2821
			6			0.1582	0.0199	1.2621
					5	0.1467	0.0199	1.3054
					8	0.9525	0.0223	1.3335
					10	1.4777	0.0239	1.3513
				0.1		0.1467	0.0199	1.3054
				0.5		0.2493	0.0203	1.3100
				1		0.5682	0.0216	1.3242

CONCLUSION

In this study, we explore the impact of the Hall current on the MHD boundary layer flow of a compressible viscous fluid over a stretching sheet, considering the effects of viscous dissipation.

The investigation yields the following findings:

- The temperature flow patterns, along with the primary and secondary velocity flow patterns, decreases as the Prandtl number rises.
- The temperature distribution and secondary velocity flow patterns both rise when the magnetic parameter increases, whereas the primary velocity flow patterns falls.
- Higher primary velocity flow pattern is achieved at the expense of decreased secondary velocity and temperature flow patterns when the Hall current parameter is increased.
- The primary and secondary velocity flow patterns rise with an increase in Grashof number, but the temperature gradients fall.
- As m, Ec, Gr, and δ increase, skin friction increases; as M and Pr increase, skin friction decreases.
- The Nusselt number rises as M, Gr, and δ increase but falls when m and Pr increase.
- As m, Pr, Gr, and δ increase, the Sherwood number coefficient rises; however, as M and Ec increase, it falls.

These studies have far too many potential applications. They include; examining how Hall currents affect MHD boundary layer flow of non-Newtonian fluids; analyzing how hall currents affect MHD boundary layer flow of nanofluids with viscous dissipation; examining how hall currents affect MHD boundary layer flow through porous media with a stretching sheet; examining unsteady MHD boundary layer flow with Hall currents, viscous dissipation, and a stretching sheet; and developing and comparing effective numerical methods.

AUTHORSHIP CONTRIBUTIONS

Authors equally contributed to this work.

DATA AVAILABILITY STATEMENT

The authors confirm that the data that supports the findings of this study are available within the article. Raw data that support the finding of this study are available from the corresponding author, upon reasonable request.

CONFLICT OF INTEREST

The author declared no potential conflicts of interest with respect to the research, authorship, and/or publication of this article.

ETHICS

There are no ethical issues with the publication of this manuscript.

STATEMENT ON THE USE OF ARTIFICIAL INTELLIGENCE

Artificial intelligence was not used in the preparation of the article.

NOMENCLATURE

$Gr^* = \frac{g^*\beta^*(T_w - T_\infty)}{u_0^2}$ = Grashof Number

$M = \frac{\mu_e \sigma B_0^2 x}{u_0 \rho}$ = Magnetic parameter

σ = Electrical conductivity

μe = Viscosity of the fluid

m = ωe τe Hall parameter

δ = C/B = Velocity Parameter

λ= cos α

E = Intensity of electric field

ne = Electron number density

E = Intensity of electric field

v = Kinematic Viscosity

k = Thermal conductivity

u_e= External velocity

$\bar{B}_0 = \frac{B}{\sqrt{x}}$ = Magnetic field parameter

$Ec = \frac{u_0^2}{c_p(\bar{T}_w - \bar{T}_\infty)}$ = Eckert number

Nu = Nusselt number

ρ = Density of fluid

β = Volumetric coefficient of thermal expansion

Cp = Specific heat capacity at constant pressure

A = constant

l = length

$C_{fx} = \frac{\tau_{wx}}{\frac{1}{2}\rho u_0^2}$ = Shear stress component due to primary velocity

$C_{fz} = \frac{\tau_{wz}}{\frac{1}{2}\rho u_0^2}$ = Shear stress component due to secondary velocity

$\tau_{wx} = \mu \frac{\partial u}{\partial y}\Big|_{y=0} = \mu u_0 \left(\frac{B}{\upsilon}\right)^{\frac{1}{2}} f''(0)$ = Skin friction due to primary velocity

$\tau_{wz} = \mu \frac{\partial w}{\partial y}\Big|_{y=0} = \mu u_0 \left(\frac{B}{\upsilon}\right)^{\frac{1}{2}} g'(0)$ = Skin friction due to secondary velocity

$Nu_x = \frac{x q_w}{k((\bar{T}_w - \bar{T}_\infty))}$ = Nusselt number

REFERENCES

[1] Yang KT, Jerger EW. First-order perturbations of laminar free-convection boundary layers on a vertical plate. J Heat Transf 1964;86:107–114. [CrossRef]

[2] Ostrach S. An analysis of laminar free-convection flow and heat transfer about a flat plate parallel to the direction of the generating body force. In: Radiation Heat Transfer, Augmented Edition. London: Routledge; 2018.

[3] Henkes RAWM, Hoogendoorn CJ. Laminar natural convection boundary-layer flow along a heated vertical plate in a stratified environment. Int J Heat Mass Transf 1989;32:147–155. [CrossRef]

[4] Elbashbeshy EMA. Laminar boundary layer flow along a stretching cylinder embedded in a porous medium. Int J Phys Sci 2012;7. [CrossRef]

[5] Sakiadis BC. Boundary-layer behavior on continuous solid surfaces: I. Boundary-layer equations for two-dimensional and axisymmetric flow. AIChE J 1961;7:26–28. [CrossRef]

[6] Jha BK, Samaila G. Variable viscosity effect on boundary layer flow along continuously moving plate with the thermal boundary condition of the third kind. Int J Appl Comput Math 2021;7. [CrossRef]

[7] Cess RD. The interaction of thermal radiation with free convection heat transfer. Int J Heat Mass Transf 1966;9:1269–1277. [CrossRef]

[8] Soundalgekar VM, Vighnesam NV, Pop I. Combined free and forced convection flow past a vertical porous plate. Int J Energy Res 1981;5:215–226. [CrossRef]

[9] Singh AK. MHD free-convection flow past an accelerated vertical porous plate in a rotating fluid. Astrophys Space Sci 1984;103:155–163. [CrossRef]

[10] Kim YJ. Unsteady MHD convective heat transfer past a semi-infinite vertical porous moving plate with variable suction. Int J Eng Sci 2000;38:833–845. [CrossRef]

[11] Bhavana M, Kesavaiah DC, Sudhakaraiah A. The Soret effect on free convective unsteady MHD flow over a vertical plate with heatsource. Int J Innov Res Sci Eng Technol 2013;2:1617–1628.

[12] Ferdows M, Ota M. Similarity solution for MHD flow through vertical porous plate with suction. J Comput Appl Mech 2005;6:15–25.

[13] Crane LR. Flow past a stretching plate. Z Angew Math Phys 1970;21:645–647. [CrossRef]

[14] Subhashini SV, Sumathi R, Pop I. Dual solutions in a thermal diffusive flow over a stretching sheet with variable thickness. Int Commun Heat Mass Transf 2013;48:61–66. [CrossRef]
[15] Wang CY. Analysis of viscous flow due to a stretching sheet with surface slip and suction. Nonlinear Anal Real World Appl 2009;10:375–380. [CrossRef]
[16] Wang CY. Flow due to a stretching boundary with partial slip—an exact solution of the Navier–Stokes equations. Chem Eng Sci 2002;57:3745–3747. [CrossRef]
[17] Sparrow EM. Radiation Heat Transfer. Augmented Edition. Taylor & Francis; 2017.
[18] Hady FM, Mohamed RA. Mixed convection-radiation interaction heat transfer in boundary-layer over a semi-infinite flat plate embedded in porous medium with a transfer magnetic field. Appl Math Comput 1994;66:103–128. [CrossRef]
[19] Krishnaprakas CK. Radiation heat transfer in a participating medium bounded by specular reflectors. Int Commun Heat Mass Transf 1998;25:1181–1188. [CrossRef]
[20] Soundalgekar VM, Patil MR, Takhar HS. MHD flow past a vertical oscillating plate. Nucl Eng Des 1981;64:43–48. [CrossRef]
[21] Samad MA, Karim ME, Mohammad D. Free convection flow through a porous medium with thermal radiation, viscous dissipation and variable suction in presence of magnetic field. Bangladesh J Sci Res 2010;23.
[22] Sattar A, Hossain M. Unsteady hydromagnetic free convection flow with Hall current and mass transfer along an accelerated porous plate with time-dependent temperature and concentration. Can J Phys 1992;70:369–374. [CrossRef]
[23] Beg OA, Bhargava R, Rawat S, Takhar HS, Beg TA. A study of steady buoyancy driven dissipative micro polar free convection heat and mass transfer in a darcian porous regime with chemical reaction. Nonlinear Anal Model Control 2007;12:157–180. [CrossRef]
[24] Mahatha BK, Nandkeolyar R, Mahato GK, Sibanda P. Dissipative effects in hydromagnetic boundary layer nanofluid flow past a stretching sheet with Newtonian heating. J Appl Fluid Mech 2016;9:1977–1989. [CrossRef]
[25] Hayat T, Hendi FA. Thermal-diffusion and diffusion-thermo effects on MHD three-dimensional axisymmetric flow with Hall and ion-slip currents. J Am Sci 2012;8:284–294.
[26] Marin M. On existence and uniqueness in thermoelasticity of micropolar bodies. C R Acad Sci Paris Ser II 1995;321:475–480.
[27] Marin M. Some estimates on vibrations in thermoelasticity of dipolar bodies. J Vib Control 2010;16:33–47. [CrossRef]
[28] Marin M. Lagrange identity method for microstretch thermoelastic materials. J Math Anal Appl 2010;363:275–286. [CrossRef]
[29] Ferdows M, Ahmed AA, Tzirtzilakis E. Hall current and viscous dissipation effects on boundary layer flow of heat transfer past a stretching sheet. Int J Appl Comput Math 2017;3:3471–3487. [CrossRef]
[30] Yih KA. Free convection effect on MHD coupled heat and mass transfer of a moving permeable vertical surface. Int Commun Heat Mass Transf 1999;26:95–104. [CrossRef]
[31] Ali FM, Nazar R, Arifin NM, Pop I. Effect of Hall current on MHD mixed convection boundary layer flow over a stretched vertical flat plate. Meccanica 2011;46:1103–1112. [CrossRef]
[32] Reddy MV. Influence of thermal radiation, viscous dissipation and Hall current on MHD convection flow over a stretched vertical flat plate. Ain Shams Eng J 2014;5:169–175. [CrossRef]

Sigma Journal of Engineering and Natural Sciences
Web page info: https://sigma.yildiz.edu.tr
DOI: 10.14744/sigma.2025.00000

Research Article

Classification of cluster analysis techniques by using hesitant bipolar complex fuzzy multi-attribute decision-making approach based on dombi prioritized aggregation operators

Hafiz Muhammad WAQAS[1], Tahir MAHMOOD[1,*], Ubaid ur REHMAN[2]

[1]*Department of Mathematics and Statistics, International Islamic University Islamabad, 44000, Pakistan*
[2]*Department of Mathematics, University of Management and Technology, C-II, Johar Town, Lahore, 54700, Pakistan*

ARTICLE INFO

Article history
Received: 09 July 2024
Revised: 21 August 2024
Accepted: 17 January 2025

Keywords:
Cluster Analysis; Hesitant Bipolar Complex Fuzzy Set; Multiattribute Decision-Making Technique

ABSTRACT

Cluster analysis is a dynamic technique used to uncover natural groupings within data, making complex relationships easier to understand. By identifying similarities and patterns, it helps reveal insights that might otherwise go unnoticed. Methods like K-means, hierarchical clustering, mean shift clustering, spectral clustering, and fuzzy c-means clustering are widely embraced for their ability to transform raw data into clear, actionable clusters, simplifying decision-making and enhancing data analysis. Classification of things is very important in our daily life because when we do classification, it makes the importance of things clear and their characteristics are known, and later, we can use them easily. We have classified cluster analysis techniques in this manuscript, and maybe someone else before us has classified cluster analysis techniques by applying some other fuzzy structure, but our approach is different and generalized from all of them. We develop a strong mathematical framework by employing the theory of hesitant bipolar complex fuzzy sets. The proposed framework of Dombi Prioritized aggregation operators has various facts and features to solve multiple tasks in one frame. The proposed framework effectively handles both the positive and negative aspects of any object simultaneously. Additionally, it is designed to address the inherent hesitancy associated with objects, offering a comprehensive and adaptable solution. This framework also provides an extra step for the collection of some extra fuzzy information. Keeping in mind all these characteristics, we have classified cluster analysis techniques using this framework. Moreover, we used the multi-attribute decision methodology with a hesitant bipolar complex fuzzy Dombi Prioritized framework for the classification of the best cluster analysis technique. The key findings and results are the development of some aggregation operators, such as hesitant bipolar complex fuzzy Dombi prioritized arithmetic aggregation operators; hesitant bipolar complex fuzzy Dombi prioritized weighted arithmetic aggregation operators; hesitant bipolar complex fuzzy Dombi prioritized geometric aggregation operators, and hesitant bipolar complex fuzzy Dombi prioritized weighted geometric aggregation operators. At the end of the manuscript, we make a valuable comparison between the proposed theory and existing theories.

Cite this article as: Waqas HM, Mahmood T, Rehman U. Classification of cluster analysis techniques by using hesitant bipolar complex fuzzy multi-attribute decision-making approach based on dombi prioritized aggregation operators. Sigma J Eng Nat Sci 2026;44(1):329–350.

***Corresponding author.**
*E-mail address: tahirbakhat@iiu.edu.pk

This paper was recommended for publication in revised form by Editor-in-Chief Ahmet Selim Dalkilic

Published by Yıldız Technical University Press, İstanbul, Turkey
© Author. This is an open access article under the CC BY-NC license (http://creativecommons.org/licenses/by-nc/4.0/).

INTRODUCTION

Cluster analysis (CA) or clustering is a method important to data mining, machine learning, and statistics to derive concealed patterns or structures in data. It operates through clustering of the points of data according to similarity. It is relevant because it possesses the ability to categorize complex, unlabeled data into meaningful categories, which helps companies and researchers to make sense of large datasets without preconception. K-means clustering, which is one of the most popular, is characterized by simplicity of use and efficiency. It breaks down the set of data into k clusters by reducing the variation within each cluster. K-means is easy to apply; however, it also possesses some disadvantages. To illustrate, it is less effective with complicated data since it presupposes an understanding of the number of clusters and is vulnerable to outliers and shape of clusters. Hierarchical clustering is based on any agglomerative method to form a tree-like form of clusters, which is more flexible. This method is particularly useful when the quantity of clusters is unknown, as it makes it possible to check the structure at the granularity level. However, it cannot be considered so suitable for truly large datasets due to its calculation expense.

On the other hand, density-based spatial clustering can be considered a good alternative in a real-life scenario where data can be noisy or have anomalies because it can effectively deal with noise and identify clusters of any form. Gaussian mixture models (GMM) provide a probabilistic approach in which the points of data are assumed to be a result of a mixture of Gaussians. This can be more flexible than K-means with certain kinds of data, allowing more complex, elliptical cluster geometry, and allowing a measurement of the uncertainty of cluster assignments. The probabilistic nature of the GMMs is essential in fields of data interpretation where uncertainty is a significant issue, such as finance and biology. Fuzzy clustering introduces a further level of complexity by allowing data points to be members of many clusters with varying degrees of membership, and gives the often blurred lines between categories in real-life data. CA will continue to gain importance in the future due to the ever-growing exponential increase in the amount of data being generated in fields like social media, finance, and healthcare. The Internet of Things and big data will require clustering techniques to make sense of such huge and complicated data. As an example, in the healthcare field, clustering has already been applied in patient segmentation and sickness prediction, and its implementation will likely increase with the development of personalized medicine. Clustering can be used by marketing firms to better target some sections of the customer base with their products. This trend is expected to continue as customer-focused business models develop. The current trends of clustering will continue to push the envelope in the future due to approaches such as spectral clustering and clustering with deep learning. These methods deal with highly non-linear, complex relationships in data, exploiting the powers of neural networks and graph-based approaches. This paves a new path of addressing clustering problems that were impossible to address before. Figure 1 covers the graphical representation of the cluster analysis process.

Significance of CA Technique Across Different Fields

CA is an analytic method that uses similarities to categorize items, information, or variables. It reduces large volumes of data, identifies trends in the data, and unearths structure without previous labeling. The reason is that this technique plays a key role in numerous applications, which might result in more effective allocation of resources, enhanced DM, and problem-solving. CA aids in offering tailor-made solutions to anything, as well as grouping genes in biology to marketing customer targeting. This is because it enhances predictive analytics data through its combination in a manner that is relevant and provides the possibility of exploring the study. It promotes innovation and effectiveness and can be applied in many industries. It is also good at increasing automation and large data analysis capabilities as

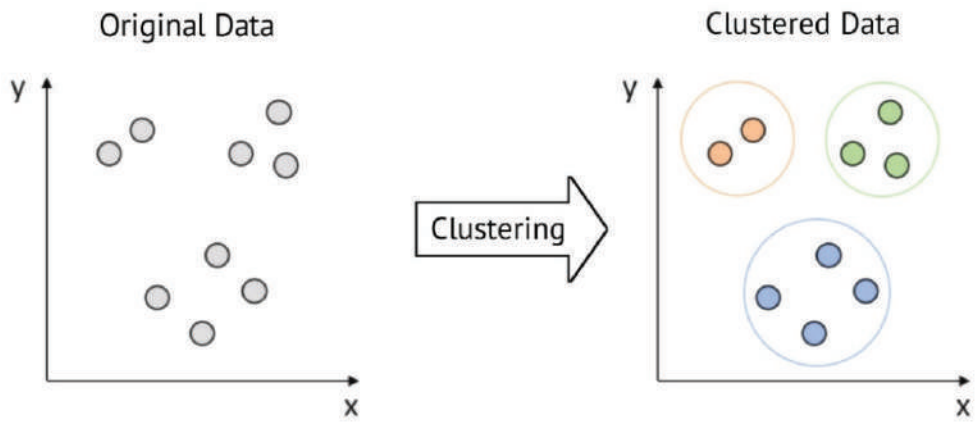


Figure 1. Working of CA techniques.

Table 1. Applications of CA techniques in different fields

Fields	Application/explanation
Healthcare and medicine	CA in healthcare helps to differentiate subgroups of patients either by the symptoms they show or their responses to treatment. It is also very useful in classifying diseases and understanding genetic profiles. It is used in other ways, namely during research on patient demographics, risk factors, and health outcomes. For instance, it can form the backbone of research into cancer, grouping tumor genetics to target therapies. The technique also fits public health since it helps identify outbreaks and risk populations.
Marketing and customer segmentation	CA assists in the division of customers using marketing based on behaviors, preferences, and demographics. Businesses use the information to enhance advertising campaigns, improve customer satisfaction, and enhance product offerings. It identifies the profitable customer group and predicts future purchase trends. E-commerce companies use clustering in recommending products based on user behavior. This way, a company can attain maximum return on investment while building a stronger relationship with customers.
Biology and genetics	CA is common in biology to cluster together genes, proteins, or species using common features. It supports taxonomy, where organisms can be classified, and helps find evolutionary relationships. In genetics, it picks up patterns of gene expression related to certain characteristics or diseases. Researchers employ clustering to study the DNA sequence and discover genetic markers. The technique also holds great importance in proteomics, that is, studying how proteins interact and what proteins do.
Information technology and machine learning	CA is a very core technique in machine learning and IT for pattern recognition and anomaly detection. It is used during unsupervised learning of group unlabeled data, with a high accuracy of the algorithm. Its applications come in image and speech recognition, cybersecurity, and network analysis. For instance, grouping will help detect fraudulent transactions or group similar documents within text mining. This thus makes IT systems more efficient and secure.
Economics and finance	CA is employed in economics and finance for market segmentation, grouping of economies, or identifying financial risk. It aids in classifying countries or regions based on economic indicators or patterns of consumer expenditure. Analysts use clustering to find patterns in the stock market as well as to classify similar investment portfolios. This technique helps credit analysts in classifying borrowers by risk profile. The better a decision is made for investments and policy, the higher the chances of good decision-making.
Education and learning analytics	CA is a process of grouping learners according to their learning styles, performance, or their levels of engagement in learning exercises. It helps to create individualistic teaching strategies and improves academic outcomes. The method is used to study the rates of dropouts, identify students at risk, and evaluate the teaching methods. The method can support adaptive learning systems because it shapes the content based on the needs of an individual. It also provides an understanding of the trends in the education systems and performance of institutions.

it works well with machine learning. On the whole, cluster analysis can be used to bridge the gap between employable findings and data complexity. Table 1 discusses some of the applications of CA techniques in other areas.

LITERATURE REVIEW

In this section of the manuscript, we discuss the detailed literature review of cluster analysis techniques and decision-making (DM) in different fuzzy frameworks.

Literature Exploration of Cluster Analysis Methodologies

A statistical method related to data analysis and machine learning is known as CA and is used to group similar data into segments or clusters depending on traits or properties. The primary objective of cluster analysis is to find patterns and relationships that help in determining the underlying structures or groupings in the data. This method proves particularly useful in cases when the data is difficult to grasp by its visible patterns or when you have to look at the underlying pattern in the data that is not readily evident. Since CA can provide a professional point of view regarding the layout and content of complex information, it is a priceless tool. By clustering the data points that share a common type, CA can discover the data set patterns and interrelationships that exist within the data. It finds application in diverse fields, such as biology, marketing, finance, and the social sciences. As an example, the application of CA in marketing can help the business to divide its customers according to buying patterns, demographics, and any other relevant variables. Moreover, this data can be used to customize the customer segmentation and marketing strategy. Homologous genetic characteristics in individuals or species in biology. A comparative genetic analysis can be used to find homologous genetic characteristics in individuals or species, and to assist in classifying and understanding

biological variation. The ability to work with large and complex datasets is one of the best features of CA, and this is why the method is the most effective in the era of big data. This is accomplished by organizing the data into logical clusters and placing them in a logical sequence, which facilitates the researcher and analyst's analysis of massive amounts of data. There are several CAs approaches, such as k-means clustering and hierarchical clustering, that differ in their efficacy and drawbacks. The ideal approach for the study is determined by the specific use case and the type of data. For all researchers, analysts, and decision-makers in a variety of professions, CA is an essential tool. This tool helps to discover patterns, correlations, and structures in the data sets. CA, especially in fuzzy environments, has emerged as an effective tool to deal with data uncertainty and imprecision across various fields. Since fuzzy clustering allows for data points to be grouped and the boundaries to overlap, it has been successful in solving real-world problems for which traditional clustering methods usually fail. This review summarizes contributions from key studies concerning the evolution of comparison and application of fuzzy clustering techniques. Liang et al. [1] suggested a CA framework based on fuzzy equivalence relations, which is a mathematical model developed for managing the vagueness involved in data classification. In the paper, the benefits of FS usage in the absence of perfect binary classification methods inherent within traditional clustering approaches were recognized. Thus, it led to establishing the base foundation for incorporating fuzzy logic into the operational research domain to aid in more precise modeling when applied to ambiguous relationships within the data. Azad and Sharma [2] discussed the applications of fuzzy logic in wireless sensor networks, where cluster head selection has been focused. The result indicated how fuzzy clustering improves hierarchical structure in sensor networks by offering increased energy efficiency, better aggregation of data, and enhanced lifespan of the network. Doring et al. [3] carried out an in-depth review of the fuzzy clustering technique of analysis. They highlighted the malleability of fuzzy methods in overlapping clusters and tolerance to noisy data. This study well elucidates the flexibility of fuzzy algorithms in complex problems, where image processing customer segmentations, for example, cannot be taken care of by traditional hard clustering methodologies. Zhao et al. [4] conducted a comparative study of self-organizing feature maps, fuzzy c-means, and k-means clustering algorithms for regionalizing natural soil environments in China. Their findings demonstrated the better ability of fuzzy c-means to capture complex, nonlinear relationships in environmental data. Zhou et al. [5] presented a collaborative fuzzy clustering algorithm suitable for distributed network environments. Their work focused on the issue of decentralized clustering of data and proposed an approach that guarantees consistency in efficiency at network nodes. Budayan et al. [6] compared traditional CA approach, self-organizing maps, and fuzzy c-means for strategic groupings in management scenarios and concluded that fuzzy c-means outperformed others because they could handle ambiguity very well and reveal meaningful information based on imprecise data. Lange et al. [7] discussed fuzzy clustering applied to biomedical images for the analysis of functional MRI. They compared with neural clustering techniques and observed the superiority of fuzzy clustering over these methods in the handling of high-dimensional, noisy data. Rajkumar et al. [8] used fuzzy clustering and fuzzy c-means for the analysis of bibliometric data, based on the cite score dataset. Overall, their study confirmed the strength of fuzzy clustering in classifying scholarly metrics, thus exhibiting subtle patterns and trends within academic publishing. All of these studies highlight the flexibility and capability of fuzzy clustering to overcome traditional methods' limitations. As it tolerates uncertainty, provides nuanced interpretation, and offers scalability, fuzzy clustering has emerged as a highly versatile tool in all sorts of applications, including operations research, environmental science, wireless networks, biomedical imaging, and bibliometric analysis. Integration with other novel technologies like machine learning and distributed systems further enhances its promise to solve complex real-world problems.

MCDM with Different Fuzzy Environments

DM is a critical mental process that we unconsciously do daily. It is considering and making decisions on what would be the most appropriate step to take on a range of considerations, such as judgment, knowledge, values, and preferences. Not always easy since effective DM may presuppose the analysis of the benefits and harms, possible consequences, and treatment of ambiguity. We can never do without a few methods and problem-solving tools to deal with ambiguity and uncertainty. These tricks and methods may be simple or mathematical. Due to the mathematical tools, we have a good path and determination to achieve the required result and end in a practical way. DM becomes quite simple when you have only choices. Yes or no, but we need another mathematical system in case of a large amount of information, uncertainty, and ambiguity. The original idea of FS theory was given by Zadeh [9], and he met the following preconditions. The fuzzy framework can manage or solve all DM situations that cannot be solved using formal mathematics. FS only manages the membership degree (MD) of every element of a universal set. The FS theory was developed, and it was happy to provide decision-makers who began applying it to guide their decisions making their lives much easier. The decision-making process entails the use of FS theory in diverse settings. Continuing on the concept of FS theory introduced by Ezghari et al. [10], a new nearest-neighbor classification method is an FS theory and aggregation operators (AOs) based one. In transportation problems that are intuitionistic fuzzy, Sharma et al. [11] propose the fuzzy ranking Fermatean function in the optimization process. Sharma et al. [12] also established a neutrosophic Monte Carlo

simulation method of DM in the medical diagnostic process in case of uncertain environments. On type-2 fuzzy sets, the concept of AOs was defined by Torres et al. [13]. Hadi et al. [14] provided a mathematical fuzzy environment in a special solution of MADM problems in Fermatean fuzzy Hamacher AOs. Merigo et al. [15] introduced the concept of fuzzy generalized hybrid AOs and how they are applied in fuzzy DM. Besides, it is worth remembering that Zimmermann [16] brought the generally recognized concept of FS applications to mathematical programming. We can say that FS is inadequate with multivalued opinions when a DM possesses a vast number of opinions, as he cannot process them by using FS. The new generalization of DMs was therefore the Hesitant fuzzy sets (HFSs). The HF ideas presented by Torra [17] can enable HFS to handle a variety of information or opinions. Besides, generalized HFS and its application to decision-support systems were introduced by Qian et al. [18]. Xu and Xia [19] provide the background of the distance and similarity measures of HFS. Chen et al. [20] present the history of HFS correlation coefficients and recommend their application in clustering research. AOs are also needed to transform a combination of values into one value. Xia and others [21] demonstrate some of the HF AOs and how they are used in group decision-making (GDM) because of aggregation requirements. Rathour et al. [22] refer to the dual HF set-theoretic approach of fuzzy reliability analysis of a fuzzy system. The concept of HF power AOs is also addressed by Zhang [23], and this is used as the concept of multi-attribute group decision-making (MAGDM). Similarly, many scholars discuss their theories. Tan et al. present the idea of HF Hamacher AOs used in multicriteria decision-making (MCDM) [24]. The majority of the problems that we face in real life are the consequence of a poor choice. One can use the example of an inefficient drug that cannot possibly have any side effects. Hence, bipolarity plays a role in human DM. The second significant factor in human DM is the rating and ranking of various possibilities that are generated in the process of focused inquiry. There are various bipolar fuzzy (BF) DM solutions with varying approaches in the literature. First of all, Zhang [25] proposed the idea of the bipolar fuzzy set (BFS) in 1998. The concept of BFS was a monumental achievement in the development of the FS theory with positive and negative grades. The concept of BFS has been applied by many scholars in numerous disciplines of science and technology since its inception. A few of them are talked about. Jana et al. [26] introduce the notion of BF Dombi AOs and the role of the latter in the MADM process. Moreover, a strong AO of the MCDM technique with a BF soft environment was also resolved by Jana et al. [27]. Lathamaheswari et al. [28] proposed that the use of bipolar neutrosophic Frank AOs in MCDM was feasible. Riaz et al. [29] establish innovative BF sine trigonometric AOs and SIR approach to the medical tourism supply chain. Wei et al. [30] introduced a very attractive concept of BF Hamacher AO in MADM. Furthermore, Jana et al. [26] gave the BF Dombi the priority of AOs in MADM. Riaz and Tehrim [31] studied a strong extension of the VIKOR method of BFS that makes use of connection numbers of the metric spaces of the SPA theory. Jamil et al. [32] discuss the Einstein AOs in a bipolar neutrosophic environment and their use in MCDM. BFS suffices well in the case of only one element and all of the good and bad qualities of the element; however, it does not work when one needs to address an item with many values against many elements, as it can only deal with an element of value and is not able to deal with a set of values against an element. Considering the above factors as well as the situation, Mandal and Ranadive [33] developed a concept of a hesitant bipolar fuzzy set (HBFS) named HB-valued FS and bipolar-valued HBFS and their applications in MAGDM. Debates on HBfs continue to accumulate later, and some of them are mentioned here. Wei et al. [34] discuss the HBF AOs in MADM. Gao et al. [35] cover AOs that are dual HBF Hamacher prioritized in MADM. Gao et al. [36] designed dual HBF Hamacher AOs, which were tested on MADM. Recently, Ali [37] proposed a probability-based HBF Hamacher that prioritized AOs and their best use in MCGDM. Ullah et al. [38] present quite a concise summary of the HBFSs and elaborate on the idea of BHFS in the title of HFS and its applications in MADM. It later became clear to decision-makers that the data provided by HBFSs and BFSs were not enough to be used to discuss the data about two-dimensional areas. Based on this, Mahmood Rehman [39] proposed the bipolar complex fuzzy sets (BCFSs). Given that the BCFS theory addresses both the two-dimensional information of an item and all the attributes and counter properties of an item, it is highly significant in the real life and everyday DM issues. Further discussion of BCFSs can be discovered in the works of the following scholars. Mahmood et al. [40] developed the concept of BCF Hamacher AOs and their usage in MADM. Moreover, Rehman et al. [41] provide aggregation tools that they refer to as Identifying and prioritizing DevOps success factors using BCF setting with Frank AOs and analytical hierarchy technique to generate values with the least effort. Mahmood and Rehman [42] also introduced the method of dombi AOs under the control of BCF information to make the MADM technique more successful. Gulistan et al. [43] present a complex set of bipolar fuzzy and its implementation in a company with transportation. The investigation and application of Aczel-Alsina AOs on the basis of BCF data in MADM are discussed by Mahmood et al. [44]. The fundamental concept of identification and classification of AOs using the bipolar complex fuzzy settings and their use in the decision support system is also presented by Mahmood et al. [45,46]. Still remembering the concept of BCFSs and the issue of their hesitancy, Aslam et al. [47] introduce the main concept of HBCFSs and their use in DM, which became our main source of inspiration. Based on this concept, we came up with a new theory of AOs.

MOTIVATION AND CONTRIBUTION

In this section of the manuscript, we discuss the motivation and main contribution of the proposed work.

Motivation

The structures of FSs, HFSs, BFSs, HBFSs, and BCFSs have some limitations and situations, as we have seen during the study of the literature. Some of the points that outline the terms and circumstances of different structures are given below. The inappropriateness of these concepts with other constructs was also studied. We also discussed the problems of the existing theories, besides the discussion of why and where our theory works.

- Zadeh [9] gave a summary of the basic concepts of FS theory. FS is restricted by the terms and conditions. All the membership values of all the elements in the universal set should be within the unit interval [0, 1] since FS will only accept membership values. Any verdict made with a fuzzy framework cannot work when the membership values do not take singletons, but instead a finite set. More so, bipolar or two-dimensional structures cannot be solved using simple fuzzy structures. Thus, a simple fuzzy system is not adequate in case any decision-maker desires to make a judgment that considers bipolar elements.
- Torra [17], in order to address the reluctance and inability to handle any information, increased FSs to HFSs. HFS gives every member of the universal set a membership grade in the form of a finite subset of the unit interval [0, 1]. Thus, a decision maker can use the HF framework to develop decisions that have hesitation attributes using fuzzy information. The risk of not concluding on the important information is vast because opting to use bipolarity and two-dimensional characteristics of the choice would not be solvable through the HF framework.
- The idea of BFSs as a means of addressing the bipolarity problems of any material was introduced by Zhang [25]. BFS is a significant equation that offers judgment-makers an effective network that aids them in making choices and taking into account the strengths and weaknesses of each specific item. BFS can easily manage bipolarity, but cannot concurrently manage the hesitancy nature of any object. We may not assume that the BF framework is a correct format of responding to all attributes within a single frame, such as bipolarity, hesitancy, and complexity.
- The aspects of hesitancy of bipolarity have been characterized by Mandal and Ranadive [33]. With the establishment of HBFSs, bipolarity and hesitation become less trouble to handle in any decision.
- Besides, the BCFSs were also given by Mahmood et al. [39]. The BCFSs are more acceptable than other theories because they provide the decision-makers with bipolarity and a little bit of complex information simultaneously. Nonetheless, the hesitant expressions of the BCF information are yet to be incorporated, and this is the reason why the creation of HBCFSs took place.
- We developed a few more AOs based on the HBCFSs architecture of Aslam et al. [47] because of this reason. HBCFSs are the driving force behind our discussion of the different AOs, as the HBCF framework is a useful tool for decision-makers. HBCFSs possess numerous traits and characteristics within one frame. HBCFSs can deal with bipolarity, hesitation, and protest of more fuzzy information in the form of iota. Accordingly, this framework can not lose any data, information, or any other important informative elements.
- The classification of the cluster analysis approach is very critical in this age of technology, data science, and machine learning. In this paper, we discuss the classification of cluster analysis methodologies using the formulation of HBCFSs. The cluster analysis methods can certainly be divided into groups of fuzzy frameworks, yet the newly introduced method is especially interesting and helpful, because they cover the merits and demerits of the object. There is also some additional fuzzy data saved, and a problem of hesitating is resolved in the new approach. In this way, we can say that it is a new method and approach.

Contributions

As the above motivations reveal, all the theories mentioned above have several research gaps and limitations that do not allow them to process all the data required to categorize cluster analysis approaches. We therefore give the HBCF Dombi Prioritized AOs with all the shortcomings considered. To start with, we proposed HBCFDPWA, HBCFDPA, HBCFDPG, and HBCFDPWG AOs to this publication. We then offer the MADM method of selecting the best cluster analysis method using these recommended AOs. We also discussed the case study of the cluster analysis methods in this section. Also, we discussed the comparison of the proposed work with other existing works. Finally, we read through the conclusion of the whole text.

AIM AND OBJECTIVES

This study aimed to develop the new theory of Dombi Prioritized AOs by using the prevailing concept of HBCFSs for the mathematical classification of CA techniques. The environment of the proposed theory is different compared to other existing theories.

Now the specific objectives for this development are:

- To define some basic notions of HFSs, BCFSs, and HBCFSs for a better understanding of the proposed work.
- To define and develop some operations related to the above notions for basic addition and multiplication.
- To develop some new AOs, such as HBCFDPWA, HBCFDPA, HBCFDPG, and HBCFDPWG AOs, using the framework of HBCFSs.

- To select a suitable MADM method based on the problem characteristics and data availability.
- To choose an appropriate MADM approach depending on the features of the issue and the accessibility of the data.
- To define the MADM algorithm using the defined AOs and their related properties to aggregate the final results of CA techniques into the singleton form.
- To discuss the case study of supposed CA techniques, and then apply all the data and AOs for finding the final results.
- To investigate the comparative analysis between the suggested approaches and current ideas to demonstrate the superiority and effectiveness of the existing work. By fulfilling these goals, this research will aid in the creation of a methodical and trustworthy process for choosing the optimal CA methodology to facilitate work across many scientific and technological domains.

Layout of the Article

For easy and clear understanding, the paper is structured into several sections. Section 1 introduces the topic. Section 2 presents a comprehensive literature review. Section 3 states the motivation for the study and describes the main contributions of the proposed work. Finally, in Section 4, we give foundational notions regarding HFSs, BCFSs, and HBCFSs. Here, we describe the Dombi prioritized operator, t-norm, and t-conorm. Section 5 brings on a set of AOs named HBCFDPWA, HBCFDPA, HBCFDPG, and HBCFDPWG, and all are derived on top of these concepts. Section 6 proposes the MADM method via HBCF Dombi prioritized AOs, and demonstrates its practical illustration via case study and numerical example, respectively. Finally, a comparative analysis with available methodologies has been carried out in Section 7. Then we concluded this manuscript in Section 8. The overall structure of the manuscript is shown in Figure 2.

Fundamentals

We discuss the fundamental notions of HFSs, BCFSs and HBCFSs in this section of the manuscript. Moreover, we discuss their related operational laws and characteristics.

Definition 1: [9] A HFS $\hat{\mathrm{F}}$ over the fixed set $\widehat{\mathrm{G}}$ is defined by;

$$\hat{\mathrm{F}} = \left\{< \dot{s}, G_{\hat{f}}(\dot{s}) > \mid \dot{s} \in \widehat{G}\right\} \tag{1}$$

Where $G_{\hat{f}}(\dot{s}) \in [0,1]$ is the set of finite values which shows the MD of each $\dot{s} \in \widehat{G}$. For easiness $\bar{F} = G_{\hat{f}}(\dot{s})$ represents a hesitant fuzzy number (HFN).

Definition 2: [9] For three HFNs $\bar{F}_1, \bar{F}_2$ and $\bar{F}_3$ and $\lambda > 0$, then the following holds;

$$1.\ \bar{F}_1 \cup \bar{F}_2 = \bigcup_{\check{\kappa}_1 \in \bar{F}_1, \check{\kappa}_2 \in \bar{F}_2} \max\{\check{\kappa}_1, \check{\kappa}_2\},$$

$$2.\ \bar{F}_1 \cap \bar{F}_2 = \bigcup_{\check{\kappa}_1 \in \bar{F}_1, \check{\kappa}_2 \in \bar{F}_2} \min\{\check{\kappa}_1, \check{\kappa}_2\}.$$

$$3.\ \bar{F}_1 \oplus \bar{F}_2 = \bigcup_{\check{\kappa}_1 \in \bar{F}_1, \check{\kappa}_2 \in \bar{F}_2} \{\check{\kappa}_1 + \check{\kappa}_2 - \check{\kappa}_1 \check{\kappa}_2\},$$

$$4.\ \bar{F}_1 \otimes \bar{F}_2 = \bigcup_{\check{\kappa}_1 \in \bar{F}_1, \check{\kappa}_2 \in \bar{F}_2} \{\check{\kappa}_1 \check{\kappa}_2\}.$$

Definition 3: [39] Let $\hat{\mathrm{F}}$ be a BCFS over the fixed set $\widehat{\mathrm{G}}$ then;

$$\hat{\mathrm{F}} = \left\{< \dot{s}, \left(G_{\hat{f}}^{+}(\dot{s}), G_{\hat{f}}^{-}(\dot{s})\right) > \mid \dot{s} \in \widehat{G}\right\} \tag{2}$$

Where $G_{\hat{f}}^{+}(\dot{s}) = \check{\kappa}_{\hat{f}}^{+R}(\dot{s}) + \iota\check{\kappa}_{\hat{f}}^{+\bar{I}}(\dot{s})$ denotes the PMG and $G_{\hat{f}}^{-}(\dot{s}) = \check{\kappa}_{\hat{f}}^{-R}(\dot{s}) + \iota\check{\kappa}_{\hat{f}}^{-\bar{I}}(\dot{s})$ denotes the NMG for each

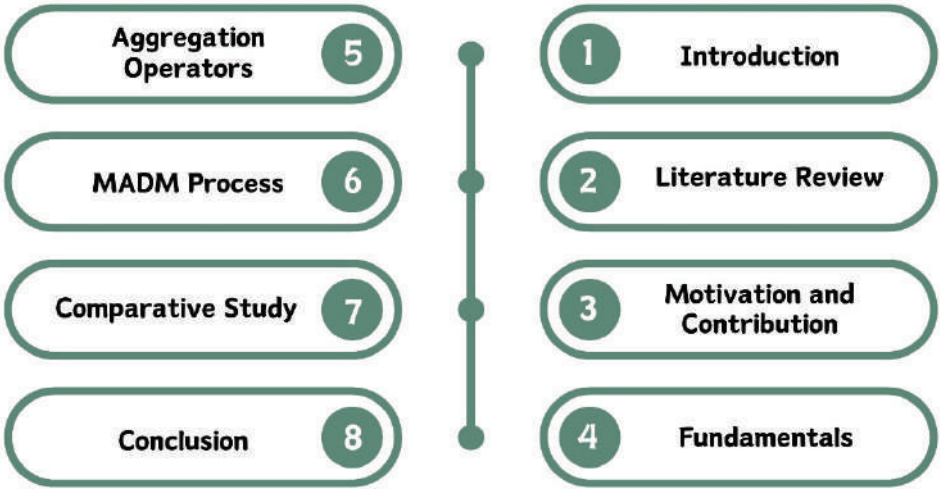


Figure 2. Graphical representation of the proposed work.

$\dot{s} \in \widehat{G}$. All values of PMG and NMG are from the unit square of a complex plane. Where $\breve{\kappa}_{\hat{F}}^{+R}(\dot{s}), \breve{\kappa}_{\hat{F}}^{+\bar{I}}(\dot{s}) \in [0,1]$ and $\breve{\kappa}_{\hat{F}}^{-R}(\dot{s}), \breve{\kappa}_{\hat{F}}^{-\bar{I}}(\dot{s}) \in [-1,0]$. For simplicity, the bipolar complex fuzzy number is symbolized by $\overline{F} = (G^+, G^-) = \left(\breve{\kappa}^{+R} + \iota\breve{\kappa}^{+\bar{I}}, \breve{\kappa}^{-R} + \iota\breve{\kappa}^{-\bar{I}}\right)$.

Definition 4: [**40**] Let $\hat{F}$, $\overline{F}_1$ and $\overline{F}_2$ be three BCFNs and $\lambda > 0$ then the following holds;

$$1.\ \overline{F}_1 \cup \overline{F}_2 = \left\{\left(\begin{matrix}\left(\max\left(\breve{\kappa}_1^{+R}, \breve{\kappa}_2^{+R}\right) + \iota\max\left(\breve{\kappa}_1^{+\bar{I}}, \breve{\kappa}_2^{+\bar{I}}\right)\right), \\ \left(\min\left(\breve{\kappa}_1^{-R}, \breve{\kappa}_2^{-R}\right) + \iota\min\left(\breve{\kappa}_1^{-\bar{I}}, \breve{\kappa}_2^{-\bar{I}}\right)\right)\end{matrix}\right)\right\},$$

$$2.\ \overline{F}_1 \cap \overline{F}_2 = \left\{\left(\begin{matrix}\left(\min\left(\breve{\kappa}_1^{+R}, \breve{\kappa}_2^{+R}\right) + \iota\min\left(\breve{\kappa}_1^{+\bar{I}}, \breve{\kappa}_2^{+\bar{I}}\right)\right), \\ \left(\max\left(\breve{\kappa}_1^{-R}, \breve{\kappa}_2^{-R}\right) + \iota\max\left(\breve{\kappa}_1^{-\bar{I}}, \breve{\kappa}_2^{-\bar{I}}\right)\right)\end{matrix}\right)\right\}.$$

$$3.\ \overline{F}_1 \oplus \overline{F}_2 = \left(\begin{matrix}\left(\left(\breve{\kappa}_1^{+R} + \breve{\kappa}_2^{+R} - \breve{\kappa}_1^{+R}\breve{\kappa}_2^{+R}\right) + \iota\left(\breve{\kappa}_1^{+\bar{I}} + \breve{\kappa}_2^{+\bar{I}} - \breve{\kappa}_1^{+\bar{I}}\breve{\kappa}_2^{+\bar{I}}\right)\right), \\ \left(\left(-\left(\breve{\kappa}_1^{-R}\breve{\kappa}_2^{-R}\right)\right) + \iota\left(-\left(\breve{\kappa}_1^{-\bar{I}}\breve{\kappa}_2^{-\bar{I}}\right)\right)\right)\end{matrix}\right),$$

$$4.\ \overline{F}_1 \otimes \overline{F}_2 = \left(\begin{matrix}\left(\left(\breve{\kappa}_1^{+R}\breve{\kappa}_2^{+R}\right) + \iota\left(\breve{\kappa}_1^{+\bar{I}}\breve{\kappa}_2^{+\bar{I}}\right)\right), \\ \left(\left(\breve{\kappa}_1^{-R} + \breve{\kappa}_2^{-R} + \breve{\kappa}_1^{-R}\breve{\kappa}_2^{-R}\right) + \iota\left(\breve{\kappa}_1^{-\bar{I}} + \breve{\kappa}_2^{-\bar{I}} + \breve{\kappa}_1^{-\bar{I}}\breve{\kappa}_2^{-\bar{I}}\right)\right)\end{matrix}\right),$$

Definition 5: [**49**] Let $ß_1$ and $ß_2$ be two real numbers then the Dombi t-norm and t-conorm are defined as;

$$\mathrm{Dom}(ß_1, ß_2) = \frac{1}{1+\left\{\left(\frac{1-ß_1}{ß_1}\right)^{ϟ} + \left(\frac{1-ß_2}{ß_2}\right)^{ϟ}\right\}^{\frac{1}{ϟ}}} \tag{3}$$

$$\mathrm{Dom}*\ (ß_1, ß_2) = 1 - \frac{1}{1+\left\{\left(\frac{ß_1}{1-ß_1}\right)^{ϟ} + \left(\frac{ß_2}{1-ß_2}\right)^{ϟ}\right\}^{\frac{1}{ϟ}}} \tag{4}$$

Where $ϟ \geq 1$ and $(ß_1, ß_2) \in [0,1] \times [0,1]$.

Definition 6: [**50**] Let us assume that $Ω = \{Ω_1, Ω_2, Ω_3, \ldots, Ω_z\}$ be a set of attributes and have a Prioritization between the attributes by the following linear order $Ω_1 \succ Ω_2 \succ Ω_3 \succ, \ldots, \succ Ω_z$, which indicates that $Ω_ţ$ has a greater significance than $Ω_ţ$, if $ţ < ç$. The value of $Ω_ç(\dot{s})$ is the performance of any alternative $\dot{s}$ under the attribute $Ω_ţ$ which satisfy $Ω_ţ \in [0,1]$. If

$$\mathrm{PA}\left(Ω_ţ(\dot{s})\right) = \sum_{ç=1}^{z} ϑ_ç Ω_ţ(\dot{s}) \tag{5}$$

Where $ϑ_ç = \frac{₣_ç}{\sum_{ç=1}^{z} ₣_ç}$, $₣_ç = \prod_{ļ=1}^{ç-1} Ω_ļ(\dot{s})\ (ļ = 1,2,3, \ldots, z)$, $₣_1 = 1$.

Definition 7: [**48**] A HBCFS $\hat{F}$ over fixed $\widehat{G}$ is noted as;

$$\hat{F} = \left\{< \dot{s}, \overline{F}_{\hat{F}}(\dot{s}) > | \dot{s} \in \widehat{G}\right\} = \left\{< \dot{s}, \left(G_{\hat{F}}^{+}(\dot{s}), G_{\hat{F}}^{-}(\dot{s})\right) > | \dot{s} \in \widehat{G}\right\} \tag{6}$$

Where

$G_{\hat{F}}^{+}(\dot{s}) = \left\{\breve{\kappa}_{\hat{F}_j}^{+R}(\dot{s}) + \iota\breve{\kappa}_{\hat{F}_j}^{+\bar{I}}(\dot{s}),\ j = 1,2,\ldots m\right\} \in [0,1]$ and $G_{\hat{F}}^{-}(\dot{s}) = \left\{\breve{\kappa}_{\hat{F}_k}^{-R}(\dot{s}) + \iota\breve{\kappa}_{\hat{F}_k}^{-\bar{I}}(\dot{s}),\ k = 1,2,\ldots n\right\} \in [-1,0]$ are the set of finite values that lie in the unit square of a complex plane and denote the positive and negative parts of the membership grade for each $\dot{s} \in \widehat{G}$. For easiness, the HBCFN is identified by $\overline{F} = (G^+, G^-) = \left(\breve{\kappa}^{+R} + \iota\breve{\kappa}^{+\bar{I}}, \breve{\kappa}^{-R} + \iota\breve{\kappa}^{-\bar{I}}\right)$.

Definition 8: [**47**] Let us assume that the $\overline{F} = (G^+, G^-) = \left(\breve{\kappa}^{+R} + \iota\breve{\kappa}^{+\bar{I}}, \breve{\kappa}^{-R} + \iota\breve{\kappa}^{-\bar{I}}\right)$, $\overline{F}_1 = (G_1^+, G_1^-) = \left(\breve{\kappa}_1^{+R} + \iota\breve{\kappa}_1^{+\bar{I}}, \breve{\kappa}_1^{-R} + \iota\breve{\kappa}_1^{-\bar{I}}\right)$ and $\overline{F}_2 = (G_2^+, G_2^-) = \left(\breve{\kappa}_2^{+R} + \iota\breve{\kappa}_2^{+\bar{I}}, \breve{\kappa}_2^{-R} + \iota\breve{\kappa}_2^{-\bar{I}}\right)$ be three HBCFNs, then

$$1.\ \overline{F}^c = \left(\bigcup_{\breve{\kappa}^+ \in G^+} \left\{(1 - \breve{\kappa}^{+R}) + \iota\left(1 - \breve{\kappa}^{+\bar{I}}\right)\right\}, \bigcup_{\breve{\kappa}^- \in G^-} \left\{(-1 - \breve{\kappa}^{-R}) + \iota\left(-1 - \breve{\kappa}^{-\bar{I}}\right)\right\}\right),$$

$$2.\ \overline{F}_1 \cup \overline{F}_2 = \left(\begin{matrix}\bigcup_{\breve{\kappa}_1^+ \in G_1^+, \breve{\kappa}_2^+ \in G_2^+} \left\{\max\left(\breve{\kappa}_1^{+R}, \breve{\kappa}_2^{+R}\right) + \iota\max\left(\breve{\kappa}_1^{+\bar{I}}, \breve{\kappa}_2^{+\bar{I}}\right)\right\}, \\ \bigcup_{\breve{\kappa}_1^- \in G_1^-, \breve{\kappa}_2^- \in G_2^-} \left\{\min\left(\breve{\kappa}_1^{-R}, \breve{\kappa}_2^{-R}\right) + \iota\min\left(\breve{\kappa}_1^{-\bar{I}}, \breve{\kappa}_2^{-\bar{I}}\right)\right\}\end{matrix}\right),$$

$$3.\ \overline{F}_1 \cap \overline{F}_2 = \left(\begin{matrix}\bigcup_{\breve{\kappa}_1^+ \in G_1^+, \breve{\kappa}_2^+ \in G_2^+} \left\{\min\left(\breve{\kappa}_1^{+R}, \breve{\kappa}_2^{+R}\right) + \iota\min\left(\breve{\kappa}_1^{+\bar{I}}, \breve{\kappa}_2^{+\bar{I}}\right)\right\}, \\ \bigcup_{\breve{\kappa}_1^- \in G_1^-, \breve{\kappa}_2^- \in G_2^-} \left\{\max\left(\breve{\kappa}_1^{-R}, \breve{\kappa}_2^{-R}\right) + \iota\max\left(\breve{\kappa}_1^{-\bar{I}}, \breve{\kappa}_2^{-\bar{I}}\right)\right\}\end{matrix}\right).$$

Definition 9: [**48**] Let $\overline{F}_1$ and $\overline{F}_2$ be two HBCFNs, then

$$1.\ \overline{F}_1 \oplus \overline{F}_2 = \left(\begin{matrix}\bigcup_{\breve{\kappa}_1^+ \in G_1^+, \breve{\kappa}_2^+ \in G_2^+} \left\{\begin{matrix}\left(\breve{\kappa}_1^{+R} + \breve{\kappa}_2^{+R} - \breve{\kappa}_1^{+R}\breve{\kappa}_2^{+R}\right) + \\ \iota\left(\breve{\kappa}_1^{+\bar{I}} + \breve{\kappa}_2^{+\bar{I}} - \breve{\kappa}_1^{+\bar{I}}\breve{\kappa}_2^{+\bar{I}}\right)\end{matrix}\right\}, \\ \bigcup_{\breve{\kappa}_1^- \in G_1^-, \breve{\kappa}_2^- \in G_2^-} \left\{\left(-\breve{\kappa}_1^{-R}\breve{\kappa}_2^{-R}\right) + \iota\left(-\breve{\kappa}_1^{-\bar{I}}\breve{\kappa}_2^{-\bar{I}}\right)\right\}\end{matrix}\right),$$

$$2.\ \overline{F}_1 \otimes \overline{F}_2 = \left(\begin{matrix}\bigcup_{\breve{\kappa}_1^+ \in G_1^+, \breve{\kappa}_2^+ \in G_2^+} \left\{\left(\breve{\kappa}_1^{+R}\breve{\kappa}_2^{+R}\right) + \iota\left(\breve{\kappa}_1^{+\bar{I}}\breve{\kappa}_2^{+\bar{I}}\right)\right\}, \\ \bigcup_{\breve{\kappa}_1^- \in G_1^-, \breve{\kappa}_2^- \in G_2^-} \left\{\begin{matrix}\left(\breve{\kappa}_1^{-R} + \breve{\kappa}_2^{-R} + \breve{\kappa}_1^{-R}\breve{\kappa}_2^{-R}\right) + \\ \iota\left(\breve{\kappa}_1^{-\bar{I}} + \breve{\kappa}_2^{-\bar{I}} + \breve{\kappa}_1^{-\bar{I}}\breve{\kappa}_2^{-\bar{I}}\right)\end{matrix}\right\}\end{matrix}\right).$$

Definition 10: [**48**] Let $\overline{F} = (G^+, G^-) = \left(\breve{\kappa}^{+R} + \iota\breve{\kappa}^{+\bar{I}}, \breve{\kappa}^{-R} + \iota\breve{\kappa}^{-\bar{I}}\right)$ be an HBCFN and $\lambda > 0$, then.

$$1.\ \overline{F}^{\lambda} = \left(\bigcup_{\breve{\kappa}^+ \in G^+} \left\{\left(\breve{\kappa}^{+R}\right)^{\lambda} + \iota\left(\breve{\kappa}^{+\bar{I}}\right)^{\lambda}\right\}, \bigcup_{\breve{\kappa}^- \in G^-} \left\{\left(-1 + \left(1 + \breve{\kappa}^{-R}\right)^{\lambda}\right) + \iota\left(-1 + \left(1 + \breve{\kappa}^{-\bar{I}}\right)^{\lambda}\right)\right\}\right),$$

$$2.\ \lambda\overline{F} = \left(\bigcup_{\breve{\kappa}^+ \in G^+} \left\{\left(1 - \left(1 - \breve{\kappa}^{+R}\right)^{\lambda}\right) + \iota\left(1 - \left(1 - \breve{\kappa}^{+\bar{I}}\right)^{\lambda}\right)\right\}, \bigcup_{\breve{\kappa}^- \in G^-} \left\{\left(-\left|\breve{\kappa}^{-R}\right|^{\lambda}\right) + \iota\left(-\left|\breve{\kappa}^{-\bar{I}}\right|^{\lambda}\right)\right\}\right).$$

Definition 11: [**48**] Let $\overline{F} = (G^+, G^-) = \left(\breve{\kappa}^{+R} + \iota\breve{\kappa}^{+\bar{I}}, \breve{\kappa}^{-R} + \iota\breve{\kappa}^{-\bar{I}}\right)$ be an HBCFN then the score and accuracy function are originated by:

$$\mathbb{S}(\overline{F}) = \frac{1}{4}\left(2 + \frac{1}{\left|\breve{\kappa}^{+R}\right|}\sum_{\breve{\kappa}^+ \in G^+} \breve{\kappa}^{+R} + \frac{1}{\left|\breve{\kappa}^{+\bar{I}}\right|}\sum_{\breve{\kappa}^+ \in G^+} \breve{\kappa}^{+\bar{I}} + \frac{1}{\left|\breve{\kappa}^{-R}\right|}\sum_{\breve{\kappa}^- \in G^-} \breve{\kappa}^{-R} + \frac{1}{\left|\breve{\kappa}^{-\bar{I}}\right|}\sum_{\breve{\kappa}^- \in G^-} \breve{\kappa}^{-\bar{I}}\right),$$

$\mathbb{S}(\overline{F}) \in [0,1]$

$$\mathbb{A}(\overline{F}) = \frac{1}{4}\left(\frac{1}{\left|\breve{\kappa}^{+R}\right|}\sum_{\breve{\kappa}^+ \in G^+} \breve{\kappa}^{+R} + \frac{1}{\left|\breve{\kappa}^{+\bar{I}}\right|}\sum_{\breve{\kappa}^+ \in G^+} \breve{\kappa}^{+\bar{I}} - \frac{1}{\left|\breve{\kappa}^{-R}\right|}\sum_{\breve{\kappa}^- \in G^-} \breve{\kappa}^{-R} - \frac{1}{\left|\breve{\kappa}^{-\bar{I}}\right|}\sum_{\breve{\kappa}^- \in G^-} \breve{\kappa}^{-\bar{I}}\right),$$

$\mathbb{A}(\overline{F}) \in [0,1]$

Theorem 1: Let us assume that $\overline{\mathrm{F}}$, $\overline{\mathrm{F}}_1$ and $\overline{\mathrm{F}}_2$ be three HBCFNs and $\lambda > 0$, then the following holds;

1. $(\overline{\mathrm{F}}^{c})^{\lambda} = (\lambda\overline{\mathrm{F}})^{c}$,
2. $\lambda\overline{\mathrm{F}}^{c} = \left(\overline{\mathrm{F}}^{\lambda}\right)^{c}$,
3. $\overline{\mathrm{F}}_1^{c} \cup \overline{\mathrm{F}}_2^{c} = (\overline{\mathrm{F}}_1 \cap \overline{\mathrm{F}}_2)^{c}$,
4. $\overline{\mathrm{F}}_1^{c} \cap \overline{\mathrm{F}}_2^{c} = (\overline{\mathrm{F}}_1 \cup \overline{\mathrm{F}}_2)^{c}$,
5. $\overline{\mathrm{F}}_1^{c} \oplus \overline{\mathrm{F}}_2^{c} = (\overline{\mathrm{F}}_1 \otimes \overline{\mathrm{F}}_2)^{c}$.

HBCF Dombi Operational Laws

In this subsection, we develop new Dombi operations for HBCFNs.

Definition 12: [**48**] Let $\overline{\mathrm{F}}$, $\overline{\mathrm{F}}_1$ and $\overline{\mathrm{F}}_2$ be three HBCFNs and $\lambda > 0$ then

$$1.\ \overline{\mathrm{F}}_1 \oplus \overline{\mathrm{F}}_2 = \left(\bigcup_{\breve{\kappa}_1^{+} \in G_1^{+}, \breve{\kappa}_2^{+} \in G_2^{+}} \left\{ \left(1 - \frac{1}{1 + \left\{ \left(\frac{\breve{\kappa}_1^{+\mathrm{R}}}{1 - \breve{\kappa}_1^{+\mathrm{R}}} \right)^{\mathfrak{h}} + \left(\frac{\breve{\kappa}_2^{+\mathrm{R}}}{1 - \breve{\kappa}_2^{+\mathrm{R}}} \right)^{\mathfrak{h}} \right\}^{\frac{1}{\mathfrak{h}}}} \right) + \iota \left(1 - \frac{1}{1 + \left\{ \left(\frac{\breve{\kappa}_1^{+\mathrm{I}}}{1 - \breve{\kappa}_1^{+\mathrm{I}}} \right)^{\mathfrak{h}} + \left(\frac{\breve{\kappa}_2^{+\mathrm{I}}}{1 - \breve{\kappa}_2^{+\mathrm{I}}} \right)^{\mathfrak{h}} \right\}^{\frac{1}{\mathfrak{h}}}} \right) \right\}, \right.$$
$$\left. \bigcup_{\breve{\kappa}_1^{-} \in G_1^{-}, \breve{\kappa}_2^{-} \in G_2^{-}} \left\{ \left(\frac{-1}{1 + \left\{ \left(\frac{1 + \breve{\kappa}_1^{-\mathrm{R}}}{|\breve{\kappa}_1^{-\mathrm{R}}|} \right)^{\mathfrak{h}} + \left(\frac{1 + \breve{\kappa}_2^{-\mathrm{R}}}{|\breve{\kappa}_2^{-\mathrm{R}}|} \right)^{\mathfrak{h}} \right\}^{\frac{1}{\mathfrak{h}}}} \right) + \iota \left(\frac{-1}{1 + \left\{ \left(\frac{1 + \breve{\kappa}_1^{-\mathrm{I}}}{|\breve{\kappa}_1^{-\mathrm{I}}|} \right)^{\mathfrak{h}} + \left(\frac{1 + \breve{\kappa}_2^{-\mathrm{I}}}{|\breve{\kappa}_2^{-\mathrm{I}}|} \right)^{\mathfrak{h}} \right\}^{\frac{1}{\mathfrak{h}}}} \right) \right\} \right),$$

$$2.\ \overline{\mathrm{F}}_1 \otimes \overline{\mathrm{F}}_2 = \left(\bigcup_{\breve{\kappa}_1^{+} \in G_1^{+}, \breve{\kappa}_2^{+} \in G_2^{+}} \left\{ \left(\frac{1}{1 + \left\{ \left(\frac{1 - \breve{\kappa}_1^{+\mathrm{R}}}{\breve{\kappa}_1^{+\mathrm{R}}} \right)^{\mathfrak{h}} + \left(\frac{1 - \breve{\kappa}_2^{+\mathrm{R}}}{\breve{\kappa}_2^{+\mathrm{R}}} \right)^{\mathfrak{h}} \right\}^{\frac{1}{\mathfrak{h}}}} \right) + \iota \left(\frac{1}{1 + \left\{ \left(\frac{1 - \breve{\kappa}_1^{+\mathrm{I}}}{\breve{\kappa}_1^{+\mathrm{I}}} \right)^{\mathfrak{h}} + \left(\frac{1 - \breve{\kappa}_2^{+\mathrm{I}}}{\breve{\kappa}_2^{+\mathrm{I}}} \right)^{\mathfrak{h}} \right\}^{\frac{1}{\mathfrak{h}}}} \right) \right\}, \right.$$
$$\left. \bigcup_{\breve{\kappa}_1^{-} \in G_1^{-}, \breve{\kappa}_2^{-} \in G_2^{-}} \left\{ \left(-1 + \frac{1}{1 + \left\{ \left(\frac{|\breve{\kappa}_1^{-\mathrm{R}}|}{1 + \breve{\kappa}_1^{-\mathrm{R}}} \right)^{\mathfrak{h}} + \left(\frac{|\breve{\kappa}_2^{-\mathrm{R}}|}{1 + \breve{\kappa}_2^{-\mathrm{R}}} \right)^{\mathfrak{h}} \right\}^{\frac{1}{\mathfrak{h}}}} \right) + \iota \left(-1 + \frac{1}{1 + \left\{ \left(\frac{|\breve{\kappa}_1^{-\mathrm{I}}|}{1 + \breve{\kappa}_1^{-\mathrm{I}}} \right)^{\mathfrak{h}} + \left(\frac{|\breve{\kappa}_2^{-\mathrm{I}}|}{1 + \breve{\kappa}_2^{-\mathrm{I}}} \right)^{\mathfrak{h}} \right\}^{\frac{1}{\mathfrak{h}}}} \right) \right\} \right),$$

$$3.\ \lambda\overline{\mathrm{F}} = \left(\bigcup_{\breve{\kappa}^{+} \in G^{+}} \left\{ \left(1 - \frac{1}{1 + \left\{ \lambda \left(\frac{\breve{\kappa}^{+\mathrm{R}}}{1 - \breve{\kappa}^{+\mathrm{R}}} \right)^{\mathfrak{h}} \right\}^{\frac{1}{\mathfrak{h}}}} \right) + \iota \left(1 - \frac{1}{1 + \left\{ \lambda \left(\frac{\breve{\kappa}^{+\mathrm{I}}}{1 - \breve{\kappa}^{+\mathrm{I}}} \right)^{\mathfrak{h}} \right\}^{\frac{1}{\mathfrak{h}}}} \right) \right\}, \right.$$
$$\left. \bigcup_{\breve{\kappa}^{-} \in G^{-}} \left\{ \left(\frac{-1}{1 + \left\{ \lambda \left(\frac{1 + \breve{\kappa}^{-\mathrm{R}}}{|\breve{\kappa}^{-\mathrm{R}}|} \right)^{\mathfrak{h}} \right\}^{\frac{1}{\mathfrak{h}}}} \right) + \iota \left(\frac{-1}{1 + \left\{ \lambda \left(\frac{1 + \breve{\kappa}^{-\mathrm{I}}}{|\breve{\kappa}^{-\mathrm{I}}|} \right)^{\mathfrak{h}} \right\}^{\frac{1}{\mathfrak{h}}}} \right) \right\} \right),$$

$$4.\ \overline{\mathrm{F}}^{\lambda} = \left(\bigcup_{\breve{\kappa}^{+} \in G^{+}} \left\{ \left(\frac{1}{1 + \left\{ \lambda \left(\frac{1 - \breve{\kappa}^{+\mathrm{R}}}{\breve{\kappa}^{+\mathrm{R}}} \right)^{\mathfrak{h}} \right\}^{\frac{1}{\mathfrak{h}}}} \right) + \iota \left(\frac{1}{1 + \left\{ \lambda \left(\frac{1 - \breve{\kappa}^{+\mathrm{I}}}{\breve{\kappa}^{+\mathrm{I}}} \right)^{\mathfrak{h}} \right\}^{\frac{1}{\mathfrak{h}}}} \right) \right\}, \right.$$
$$\left. \bigcup_{\breve{\kappa}^{-} \in G^{-}} \left\{ \left(-1 + \frac{1}{1 + \left\{ \lambda \left(\frac{|\breve{\kappa}^{-\mathrm{R}}|}{1 + \breve{\kappa}^{-\mathrm{R}}} \right)^{\mathfrak{h}} \right\}^{\frac{1}{\mathfrak{h}}}} \right) + \iota \left(-1 + \frac{1}{1 + \left\{ \lambda \left(\frac{|\breve{\kappa}^{-\mathrm{I}}|}{1 + \breve{\kappa}^{-\mathrm{I}}} \right)^{\mathfrak{h}} \right\}^{\frac{1}{\mathfrak{h}}}} \right) \right\} \right).$$

Example-1: Let $\overline{\mathrm{F}} = \left(\begin{Bmatrix} (0.2 + \iota 0.4), \\ (0.5 + \iota 0.7) \end{Bmatrix}, \begin{Bmatrix} (-0.3 - \iota 0.6), \\ (-0.4 - \iota 0.3) \end{Bmatrix} \right)$, $\overline{\mathrm{F}}_1 = \left(\begin{Bmatrix} \{(0.6 + \iota 0.3)\}, \\ (-0.1 - \iota 0.9), \\ (-0.6 - \iota 0.3) \end{Bmatrix} \right)$ and $\overline{\mathrm{F}}_2 = \left(\begin{Bmatrix} (0.2 + \iota 0.7), \\ (0.4 + \iota 0.6) \end{Bmatrix}, \begin{Bmatrix} (-0.5 - \iota 0.8), \\ (-0.4 - \iota 0.1) \end{Bmatrix} \right)$ be three HBCFNs and if $\lambda = 3$, $\mathfrak{h} = 4$ then the above Dombi operations can be calculated as follows;

$$1.\ \overline{\mathrm{F}}_1 \oplus \overline{\mathrm{F}}_2 = \left(\begin{Bmatrix} \left(1 - \frac{1}{1 + \left(\left(\frac{0.6}{1 - 0.6} \right)^4 + \left(\frac{0.2}{1 - 0.2} \right)^4 \right)^{\frac{1}{4}}} \right) + \iota \left(1 - \frac{1}{1 + \left(\left(\frac{0.3}{1 - 0.3} \right)^4 + \left(\frac{0.7}{1 - 0.7} \right)^4 \right)^{\frac{1}{4}}} \right), \\ \left(1 - \frac{1}{1 + \left(\left(\frac{0.6}{1 - 0.6} \right)^4 + \left(\frac{0.4}{1 - 0.4} \right)^4 \right)^{\frac{1}{4}}} \right) + \iota \left(1 - \frac{1}{1 + \left(\left(\frac{0.3}{1 - 0.3} \right)^4 + \left(\frac{0.6}{1 - 0.7} \right)^4 \right)^{\frac{1}{4}}} \right) \end{Bmatrix}, \right.$$
$$\left. \begin{Bmatrix} \left(\frac{-1}{1 + \left(\left(\frac{1 - 0.1}{|-0.1|} \right)^4 + \left(\frac{1 - 0.5}{|-0.5|} \right)^4 \right)^{\frac{1}{4}}} \right) + \iota \left(\frac{-1}{1 + \left(\left(\frac{1 - 0.9}{|-0.9|} \right)^4 + \left(\frac{1 - 0.8}{|-0.8|} \right)^4 \right)^{\frac{1}{4}}} \right), \\ \left(\frac{-1}{1 + \left(\left(\frac{1 - 0.1}{|-0.1|} \right)^4 + \left(\frac{1 - 0.4}{|-0.4|} \right)^4 \right)^{\frac{1}{4}}} \right) + \iota \left(\frac{-1}{1 + \left(\left(\frac{1 - 0.9}{|-0.9|} \right)^4 + \left(\frac{1 - 0.1}{|-0.1|} \right)^4 \right)^{\frac{1}{4}}} \right), \\ \left(\frac{-1}{1 + \left(\left(\frac{1 - 0.6}{|-0.6|} \right)^4 + \left(\frac{1 - 0.5}{|-0.5|} \right)^4 \right)^{\frac{1}{4}}} \right) + \iota \left(\frac{-1}{1 + \left(\left(\frac{1 - 0.3}{|-0.3|} \right)^4 + \left(\frac{1 - 0.8}{|-0.8|} \right)^4 \right)^{\frac{1}{4}}} \right), \\ \left(\frac{-1}{1 + \left(\left(\frac{1 - 0.6}{|-0.6|} \right)^4 + \left(\frac{1 - 0.4}{|-0.4|} \right)^4 \right)^{\frac{1}{4}}} \right) + \iota \left(\frac{-1}{1 + \left(\left(\frac{1 - 0.3}{|-0.3|} \right)^4 + \left(\frac{1 - 0.1}{|-0.1|} \right)^4 \right)^{\frac{1}{4}}} \right) \end{Bmatrix} \right)$$
$$= \left(\begin{Bmatrix} (0.36281267 + \iota 0.70005971), \\ (0.36779797 + \iota 0.66678367) \end{Bmatrix}, \begin{Bmatrix} (-0.11110264 - \iota 0.99898789), \\ (-0.11108545 - \iota 0.11110687), \\ (-0.82132729 - \iota 0.42501765), \\ (-0.63220202 - \iota 0.11098175) \end{Bmatrix} \right)$$

$$2.\ \bar{F}_1 \otimes \bar{F}_2 = \left(\begin{array}{l}\left\{\left(\frac{1}{1+\left(\left(\frac{1-0.6}{0.6}\right)^4+\left(\frac{1-0.2}{0.2}\right)^4\right)^{\frac{1}{4}}}\right)+\iota\left(\frac{1}{1+\left(\left(\frac{1-0.3}{0.3}\right)^4+\left(\frac{1-0.7}{0.7}\right)^4\right)^{\frac{1}{4}}}\right),\right.\\ \left.\left(\frac{1}{1+\left(\left(\frac{1-0.6}{0.6}\right)^4+\left(\frac{1-0.4}{0.4}\right)^4\right)^{\frac{1}{4}}}\right)+\iota\left(\frac{1}{1+\left(\left(\frac{1-0.3}{0.3}\right)^4+\left(\frac{1-0.6}{0.7}\right)^4\right)^{\frac{1}{4}}}\right)\right\},\\ \left\{\left(-1+\frac{1}{1+\left(\left(\frac{|-0.1|}{1-0.1}\right)^4+\left(\frac{|-0.5|}{1-0.5}\right)^4\right)^{\frac{1}{4}}}\right)+\iota\left(-1+\frac{1}{1+\left(\left(\frac{|-0.9|}{1-0.9}\right)^4+\left(\frac{|-0.8|}{1-0.8}\right)^4\right)^{\frac{1}{4}}}\right),\right.\\ \left.\left(-1+\frac{1}{1+\left(\left(\frac{|-0.1|}{1-0.1}\right)^4+\left(\frac{|-0.4|}{1-0.4}\right)^4\right)^{\frac{1}{4}}}\right)+\iota\left(-1+\frac{1}{1+\left(\left(\frac{|-0.9|}{1-0.9}\right)^4+\left(\frac{|-0.1|}{1-0.1}\right)^4\right)^{\frac{1}{4}}}\right)\right\},\\ \left\{\left(-1+\frac{1}{1+\left(\left(\frac{|-0.6|}{1-0.6}\right)^4+\left(\frac{|-0.5|}{1-0.5}\right)^4\right)^{\frac{1}{4}}}\right)+\iota\left(-1+\frac{1}{1+\left(\left(\frac{|-0.3|}{1-0.3}\right)^4+\left(\frac{|-0.8|}{1-0.8}\right)^4\right)^{\frac{1}{4}}}\right),\right.\\ \left.\left(-1+\frac{1}{1+\left(\left(\frac{|-0.6|}{1-0.6}\right)^4+\left(\frac{|-0.4|}{1-0.4}\right)^4\right)^{\frac{1}{4}}}\right)+\iota\left(-1+\frac{1}{1+\left(\left(\frac{|-0.3|}{1-0.3}\right)^4+\left(\frac{|-0.1|}{1-0.1}\right)^4\right)^{\frac{1}{4}}}\right)\right\}\end{array}\right)$$

$$=\left(\begin{Bmatrix}(0.24970848+\iota 0.29994028),\\(0.63220202+\iota 0.29981153)\end{Bmatrix},\begin{Bmatrix}(-0.1591196-\iota 0.88995108),\\(-0.0440955-\iota 0.88889312),\\(-0.38657653-\iota 0.75025174),\\(-0.36779797-\iota 0.00829708)\end{Bmatrix}\right)$$

$$3.\ \lambda\bar{F} = \left(\begin{array}{l}\left\{\left(1-\frac{1}{1+\left(3\left(\frac{0.2}{1-0.2}\right)^4\right)^{\frac{1}{4}}}\right)+\iota\left(1-\frac{1}{1+\left(3\left(\frac{0.4}{1-0.4}\right)^4\right)^{\frac{1}{4}}}\right),\right.\\ \left.\left(1-\frac{1}{1+\left(3\left(\frac{0.5}{1-0.5}\right)^4\right)^{\frac{1}{4}}}\right)+\iota\left(1-\frac{1}{1+\left(3\left(\frac{0.7}{1-0.7}\right)^4\right)^{\frac{1}{4}}}\right)\right\},\\ \left\{\left(\frac{-1}{1+\left(3\left(\frac{1-0.3}{|-0.3|}\right)^4\right)^{\frac{1}{4}}}\right)+\iota\left(\frac{1}{1+\left(3\left(\frac{1-0.6}{|-0.6|}\right)^4\right)^{\frac{1}{4}}}\right),\right.\\ \left.\left(\frac{1}{1+\left(3\left(\frac{1-0.4}{|-0.4|}\right)^4\right)^{\frac{1}{4}}}\right)+\iota\left(\frac{1}{1+\left(3\left(\frac{1-0.3}{|-0.3|}\right)^4\right)^{\frac{1}{4}}}\right)\right\}\end{array}\right)$$

$$=\left(\begin{Bmatrix}(0.00290841+\iota 0.46734354),\\(0.66768760+\iota 0.75435041)\end{Bmatrix},\begin{Bmatrix}(-0.14284227-\iota 0.49247906),\\(-0.49854579-\iota 0.32473475)\end{Bmatrix}\right)$$

$$4.\ \bar{F}^{\lambda} = \left(\begin{array}{l}\left\{\left(\frac{1}{1+\left(3\left(\frac{1-0.2}{0.2}\right)^4\right)^{\frac{1}{4}}}\right)+\iota\left(\frac{1}{1+\left(3\left(\frac{1-0.4}{0.4}\right)^4\right)^{\frac{1}{4}}}\right),\right.\\ \left.\left(\frac{1}{1+\left(3\left(\frac{1-0.5}{0.5}\right)^4\right)^{\frac{1}{4}}}\right)+\iota\left(\frac{1}{1+\left(3\left(\frac{1-0.7}{0.7}\right)^4\right)^{\frac{1}{4}}}\right)\right\},\\ \left\{\left(-1+\frac{1}{1+\left(3\left(\frac{|-0.3|}{1-0.3}\right)^4\right)^{\frac{1}{4}}}\right)+\iota\left(-1+\frac{1}{1+\left(3\left(\frac{|-0.6|}{1-0.6}\right)^4\right)^{\frac{1}{4}}}\right),\right.\\ \left.\left(-1+\frac{1}{1+\left(3\left(\frac{|-0.4|}{1-0.4}\right)^4\right)^{\frac{1}{4}}}\right)+\iota\left(-1+\frac{1}{1+\left(3\left(\frac{|-0.3|}{1-0.3}\right)^4\right)^{\frac{1}{4}}}\right)\right\}\end{array}\right)$$

$$=\left(\begin{Bmatrix}(0.18989713+\iota 0.33623492),\\(0.33231239+\iota 0.63937322)\end{Bmatrix},\begin{Bmatrix}(-0.28055631-\iota 0.77791305),\\(-0.10982821-\iota 0.02381376)\end{Bmatrix}\right)$$

HBCF Dombi Prioritized AOS

We built the Dombi Prioritized geometric and arithmetic AOs in the context of HBCFNs in this portion of the article.

HBCF Dombi Prioritized Arithmetic AOS

We introduce HBCF Dombi Prioritized weighted arithmetic (HBCFDPWA) and HBCF Dombi Prioritized arithmetic (HBCFDPA) AOs in this subsection.

Definition 13: Let $\bar{F}_ç=\left(G_ç^+,G_ç^-\right)=\left(\breve{\kappa}_ç^{+R}+\iota\breve{\kappa}_ç^{+\bar{I}},\breve{\kappa}_ç^{-R}+\iota\breve{\kappa}_ç^{-\bar{I}}\right),\ (ç=1,2,3,\ldots,z)$ be a collection of HBCFNs, then the HBCFDPA operator is a function of $\text{HBCFDPA}:\bar{F}^z\longrightarrow\bar{F}$ such that.

$$\text{HBCFDPA}(\bar{F}_1,\bar{F}_2,\ldots,\bar{F}_z)=\bigoplus_{ç=1}^{z}\left(\frac{₣_ç}{\sum_{ç=1}^{z}₣_ç}\bar{F}_ç\right) \tag{7}$$

Where $₣_ç=\prod_{l=1}^{ç-1}\mathbb{S}\left(\bar{F}_l\right)\ (l=1,2,3,\ldots,z),\ ₣_1=1$ and $\mathbb{S}\left(\bar{F}_l\right)$ denotes the score value. It is possible to convert the HBCFDPA operators to the following theorem with the use of HBCF operational rules.

Theorem 2: Let $\bar{F}_ç=\left(G_ç^+,G_ç^-\right),\ (ç=1,2,3,\ldots,z)$ be a collection of HBCFNs, then by employing the above eq. (7), we get an HBCFN and

$$\text{HBCFDPA}(\bar{F}_1,\bar{F}_2,\ldots,\bar{F}_z)=\bigoplus_{ç=1}^{z}\left(\frac{₣_ç}{\sum_{ç=1}^{z}₣_ç}\bar{F}_ç\right)=\frac{₣_1}{\sum_{ç=1}^{z}₣_ç}\bar{F}_1\oplus\ldots\oplus\frac{₣_z}{\sum_{ç=1}^{z}₣_ç}\bar{F}_z$$

$$=\left(\begin{array}{l}\bigcup_{\breve{\kappa}_1^+\in G_1^+,\ldots,\breve{\kappa}_z^+\in G_z^+}\left\{\left(1-\frac{1}{1+\left\{\sum_{ç=1}^{z}\frac{₣_ç}{\sum_{ç=1}^{z}₣_ç}\left(\frac{\breve{\kappa}_ç^{+R}}{1-\breve{\kappa}_ç^{+R}}\right)^{\eta}\right\}^{\frac{1}{\eta}}}\right)+\right.\\ \left.\iota\left(1-\frac{1}{1+\left\{\sum_{ç=1}^{z}\frac{₣_ç}{\sum_{ç=1}^{z}₣_ç}\left(\frac{\breve{\kappa}_ç^{+\bar{I}}}{1-\breve{\kappa}_ç^{+\bar{I}}}\right)^{\eta}\right\}^{\frac{1}{\eta}}}\right)\right\},\\ \bigcup_{\breve{\kappa}_1^-\in G_1^-,\ldots,\breve{\kappa}_z^-\in G_z^-}\left\{\left(\frac{-1}{1+\left\{\sum_{ç=1}^{z}\frac{₣_ç}{\sum_{ç=1}^{z}₣_ç}\left(\frac{1+\breve{\kappa}_ç^{-R}}{|\breve{\kappa}_ç^{-R}|}\right)^{\eta}\right\}^{\frac{1}{\eta}}}\right)+\right.\\ \left.\iota\left(\frac{-1}{1+\left\{\sum_{ç=1}^{z}\frac{₣_ç}{\sum_{ç=1}^{z}₣_ç}\left(\frac{1+\breve{\kappa}_ç^{-\bar{I}}}{|\breve{\kappa}_ç^{-\bar{I}}|}\right)^{\eta}\right\}^{\frac{1}{\eta}}}\right)\right\}\end{array}\right) \tag{8}$$

Where $₣_ç=\prod_{l=1}^{ç-1}\mathbb{S}\left(\bar{F}_l\right)\ (l=1,2,3,\ldots,z),\ ₣_1=1$ and $\mathbb{S}\left(\bar{F}_l\right)$ denotes the score value.

Proof: By mathematical induction to prove the above statement.

Let $\mathfrak{z} = 2$, the left side of (8) becomes

$$\mathrm{HBCFDPA}(\bar{\mathrm{F}}_1, \bar{\mathrm{F}}_2) = \bar{\mathrm{F}}_1 \oplus \bar{\mathrm{F}}_2$$

And the Right side of (8) becomes

$$= \left(\bigcup_{\breve{\kappa}_1^+ \in G_1^+, \breve{\kappa}_2^+ \in G_2^+} \left\{ \left(1 - \frac{1}{1 + \left\{ \frac{\mathrm{F}_1}{\sum_{\varsigma=1}^{2} \mathrm{F}_\varsigma} \left(\frac{\breve{\kappa}_1^{+\mathrm{R}}}{1 - \breve{\kappa}_1^{+\mathrm{R}}} \right)^{\iota} + \frac{\mathrm{F}_2}{\sum_{\varsigma=1}^{2} \mathrm{F}_\varsigma} \left(\frac{\breve{\kappa}_2^{+\mathrm{R}}}{1 - \breve{\kappa}_2^{+\mathrm{R}}} \right)^{\iota} \right\}^{\frac{1}{\iota}}} \right) + \iota \left(1 - \frac{1}{1 + \left\{ \frac{\mathrm{F}_1}{\sum_{\varsigma=1}^{2} \mathrm{F}_\varsigma} \left(\frac{\breve{\kappa}_1^{+\mathrm{I}}}{1 - \breve{\kappa}_1^{+\mathrm{I}}} \right)^{\iota} + \frac{\mathrm{F}_2}{\sum_{\varsigma=1}^{2} \mathrm{F}_\varsigma} \left(\frac{\breve{\kappa}_1^{+\mathrm{I}}}{1 - \breve{\kappa}_1^{+\mathrm{I}}} \right)^{\iota} \right\}^{\frac{1}{\iota}}} \right) \right\}, \right.$$

$$\left. \bigcup_{\breve{\kappa}_1^- \in G_1^-, \breve{\kappa}_2^- \in G_2^-} \left\{ \left(\frac{-1}{1 + \left\{ \frac{\mathrm{F}_1}{\sum_{\varsigma=1}^{2} \mathrm{F}_\varsigma} \left(\frac{1 + \breve{\kappa}_1^{-\mathrm{R}}}{\left| \breve{\kappa}_1^{-\mathrm{R}} \right|} \right)^{\iota} + \frac{\mathrm{F}_2}{\sum_{\varsigma=1}^{2} \mathrm{F}_\varsigma} \left(\frac{1 + \breve{\kappa}_2^{-\mathrm{R}}}{\left| \breve{\kappa}_2^{-\mathrm{R}} \right|} \right)^{\iota} \right\}^{\frac{1}{\iota}}} \right) + \iota \left(\frac{-1}{1 + \left\{ \frac{\mathrm{F}_1}{\sum_{\varsigma=1}^{2} \mathrm{F}_\varsigma} \left(\frac{1 + \breve{\kappa}_2^{-\mathrm{I}}}{\left| \breve{\kappa}_2^{-\mathrm{I}} \right|} \right)^{\iota} + \frac{\mathrm{F}_2}{\sum_{\varsigma=1}^{2} \mathrm{F}_\varsigma} \left(\frac{1 + \breve{\kappa}_2^{-\mathrm{I}}}{\left| \breve{\kappa}_2^{-\mathrm{I}} \right|} \right)^{\iota} \right\}^{\frac{1}{\iota}}} \right) \right\} \right)$$

$$= \left(\bigcup_{\breve{\kappa}_1^+ \in G_1^+, \breve{\kappa}_2^+ \in G_2^+} \left\{ \left(1 - \frac{1}{1 + \left\{ \sum_{\varsigma=1}^{2} \frac{\mathrm{F}_\varsigma}{\sum_{\varsigma=1}^{2} \mathrm{F}_\varsigma} \left(\frac{\breve{\kappa}_\varsigma^{+\mathrm{R}}}{1 - \breve{\kappa}_\varsigma^{+\mathrm{R}}} \right)^{\iota} \right\}^{\frac{1}{\iota}}} \right) + \iota \left(1 - \frac{1}{1 + \left\{ \sum_{\varsigma=1}^{2} \frac{\mathrm{F}_\varsigma}{\sum_{\varsigma=1}^{2} \mathrm{F}_\varsigma} \left(\frac{\breve{\kappa}_\varsigma^{+\mathrm{I}}}{1 - \breve{\kappa}_\varsigma^{+\mathrm{I}}} \right)^{\iota} \right\}^{\frac{1}{\iota}}} \right) \right\}, \right.$$

$$\left. \bigcup_{\breve{\kappa}_1^- \in G_1^-, \breve{\kappa}_2^- \in G_2^-} \left\{ \left(\frac{-1}{1 + \left\{ \sum_{\varsigma=1}^{2} \frac{\mathrm{F}_\varsigma}{\sum_{\varsigma=1}^{2} \mathrm{F}_\varsigma} \left(\frac{1 + \breve{\kappa}_\varsigma^{-\mathrm{R}}}{\left| \breve{\kappa}_\varsigma^{-\mathrm{R}} \right|} \right)^{\iota} \right\}^{\frac{1}{\iota}}} \right) + \iota \left(\frac{-1}{1 + \left\{ \sum_{\varsigma=1}^{2} \frac{\mathrm{F}_\varsigma}{\sum_{\varsigma=1}^{2} \mathrm{F}_\varsigma} \left(\frac{1 + \breve{\kappa}_\varsigma^{-\mathrm{I}}}{\left| \breve{\kappa}_\varsigma^{-\mathrm{I}} \right|} \right)^{\iota} \right\}^{\frac{1}{\iota}}} \right) \right\} \right)$$

This shows that (8) holds for $\mathfrak{z} = 2$.

Now assume that (8) holds for $\mathfrak{z} = \acute{\mathrm{g}}$

$$\mathrm{HBCFDPA}\left(\bar{\mathrm{F}}_1, \bar{\mathrm{F}}_2, \ldots, \bar{\mathrm{F}}_{\acute{\mathrm{g}}}\right) = \bigoplus_{\varsigma=1}^{\acute{\mathrm{g}}} \left(\frac{\mathrm{F}_\varsigma}{\sum_{\varsigma=1}^{\mathfrak{z}} \mathrm{F}_\varsigma} \bar{\mathrm{F}}_\varsigma \right)$$

$$= \left(\bigcup_{\breve{\kappa}_1^+ \in G_1^+, \ldots, \breve{\kappa}_{\acute{\mathrm{g}}}^+ \in G_{\acute{\mathrm{g}}}^+} \left\{ \left(1 - \frac{1}{1 + \left\{ \sum_{\varsigma=1}^{\acute{\mathrm{g}}} \frac{\mathrm{F}_\varsigma}{\sum_{\varsigma=1}^{\mathfrak{z}} \mathrm{F}_\varsigma} \left(\frac{\breve{\kappa}_\varsigma^{+\mathrm{R}}}{1 - \breve{\kappa}_\varsigma^{+\mathrm{R}}} \right)^{\iota} \right\}^{\frac{1}{\iota}}} \right) + \iota \left(1 - \frac{1}{1 + \left\{ \sum_{\varsigma=1}^{\acute{\mathrm{g}}} \frac{\mathrm{F}_\varsigma}{\sum_{\varsigma=1}^{\mathfrak{z}} \mathrm{F}_\varsigma} \left(\frac{\breve{\kappa}_\varsigma^{+\mathrm{I}}}{1 - \breve{\kappa}_\varsigma^{+\mathrm{I}}} \right)^{\iota} \right\}^{\frac{1}{\iota}}} \right) \right\}, \right.$$

$$\left. \bigcup_{\breve{\kappa}_1^- \in G_1^-, \ldots, \breve{\kappa}_{\mathfrak{z}}^- \in G_{\mathfrak{z}}^-} \left\{ \left(\frac{-1}{1 + \left\{ \sum_{\varsigma=1}^{\acute{\mathrm{g}}} \frac{\mathrm{F}_\varsigma}{\sum_{\varsigma=1}^{\mathfrak{z}} \mathrm{F}_\varsigma} \left(\frac{1 + \breve{\kappa}_\varsigma^{-\mathrm{R}}}{\left| \breve{\kappa}_\varsigma^{-\mathrm{R}} \right|} \right)^{\iota} \right\}^{\frac{1}{\iota}}} \right) + \iota \left(\frac{-1}{1 + \left\{ \sum_{\varsigma=1}^{\acute{\mathrm{g}}} \frac{\mathrm{F}_\varsigma}{\sum_{\varsigma=1}^{\mathfrak{z}} \mathrm{F}_\varsigma} \left(\frac{1 + \breve{\kappa}_\varsigma^{-\mathrm{I}}}{\left| \breve{\kappa}_\varsigma^{-\mathrm{I}} \right|} \right)^{\iota} \right\}^{\frac{1}{\iota}}} \right) \right\} \right)$$

Next, we show that (8) holds for $\mathfrak{z} = \acute{\mathrm{g}} + 1$.

$$\mathrm{HBCFDPA}\left(\bar{\mathrm{F}}_1, \bar{\mathrm{F}}_2, \ldots, \bar{\mathrm{F}}_{\acute{\mathrm{g}}}, \bar{\mathrm{F}}_{\acute{\mathrm{g}}+1}\right) = \bigoplus_{\varsigma=1}^{\acute{\mathrm{g}}} \left(\frac{\mathrm{F}_\varsigma}{\sum_{\varsigma=1}^{\mathfrak{z}} \mathrm{F}_\varsigma} \bar{\mathrm{F}}_\varsigma \right) \oplus \left(\frac{\mathrm{F}_{\acute{\mathrm{g}}+1}}{\sum_{\varsigma=1}^{\mathfrak{z}} \mathrm{F}_\varsigma} \bar{\mathrm{F}}_{\acute{\mathrm{g}}+1} \right)$$

$$= \left(\bigcup_{\breve{\kappa}_1^+ \in G_1^+, \ldots, \breve{\kappa}_{\acute{\mathrm{g}}}^+ \in G_{\acute{\mathrm{g}}}^+} \left\{ \left(1 - \frac{1}{1 + \left\{ \sum_{\varsigma=1}^{\acute{\mathrm{g}}} \frac{\mathrm{F}_\varsigma}{\sum_{\varsigma=1}^{\mathfrak{z}} \mathrm{F}_\varsigma} \left(\frac{\breve{\kappa}_\varsigma^{+\mathrm{R}}}{1 - \breve{\kappa}_\varsigma^{+\mathrm{R}}} \right)^{\iota} \right\}^{\frac{1}{\iota}}} \right) + \iota \left(1 - \frac{1}{1 + \left\{ \sum_{\varsigma=1}^{\acute{\mathrm{g}}} \frac{\mathrm{F}_\varsigma}{\sum_{\varsigma=1}^{\mathfrak{z}} \mathrm{F}_\varsigma} \left(\frac{\breve{\kappa}_\varsigma^{+\mathrm{I}}}{1 - \breve{\kappa}_\varsigma^{+\mathrm{I}}} \right)^{\iota} \right\}^{\frac{1}{\iota}}} \right) \right\}, \right.$$

$$\left. \bigcup_{\breve{\kappa}_1^- \in G_1^-, \ldots, \breve{\kappa}_{\mathfrak{z}}^- \in G_{\mathfrak{z}}^-} \left\{ \left(\frac{-1}{1 + \left\{ \sum_{\varsigma=1}^{\acute{\mathrm{g}}} \frac{\mathrm{F}_\varsigma}{\sum_{\varsigma=1}^{\mathfrak{z}} \mathrm{F}_\varsigma} \left(\frac{1 + \breve{\kappa}_\varsigma^{-\mathrm{R}}}{\left| \breve{\kappa}_\varsigma^{-\mathrm{R}} \right|} \right)^{\iota} \right\}^{\frac{1}{\iota}}} \right) + \iota \left(\frac{-1}{1 + \left\{ \sum_{\varsigma=1}^{\acute{\mathrm{g}}} \frac{\mathrm{F}_\varsigma}{\sum_{\varsigma=1}^{\mathfrak{z}} \mathrm{F}_\varsigma} \left(\frac{1 + \breve{\kappa}_\varsigma^{-\mathrm{I}}}{\left| \breve{\kappa}_\varsigma^{-\mathrm{I}} \right|} \right)^{\iota} \right\}^{\frac{1}{\iota}}} \right) \right\} \right)$$

$$\oplus$$

$$\left(\bigcup_{\breve{\kappa}_1^+ \in G_1^+, \ldots, \breve{\kappa}_{\acute{\mathrm{g}}}^+ \in G_{\acute{\mathrm{g}}}^+, \breve{\kappa}_{\acute{\mathrm{g}}+1}^+ \in G_{\acute{\mathrm{g}}+1}^+} \left\{ \left(1 - \frac{1}{1 + \left\{ \frac{\mathrm{F}_{\acute{\mathrm{g}}+1}}{\sum_{\varsigma=1}^{\mathfrak{z}} \mathrm{F}_\varsigma} \left(\frac{\breve{\kappa}_{\acute{\mathrm{g}}+1}^{+\mathrm{R}}}{1 - \breve{\kappa}_{\acute{\mathrm{g}}+1}^{+\mathrm{R}}} \right)^{\iota} \right\}^{\frac{1}{\iota}}} \right) + \iota \left(1 - \frac{1}{1 + \left\{ \frac{\mathrm{F}_{\acute{\mathrm{g}}+1}}{\sum_{\varsigma=1}^{\mathfrak{z}} \mathrm{F}_\varsigma} \left(\frac{\breve{\kappa}_{\acute{\mathrm{g}}+1}^{+\mathrm{I}}}{1 - \breve{\kappa}_{\acute{\mathrm{g}}+1}^{+\mathrm{I}}} \right)^{\iota} \right\}^{\frac{1}{\iota}}} \right) \right\}, \right.$$

$$\left. \bigcup_{\breve{\kappa}_1^- \in G_1^-, \ldots, \breve{\kappa}_{\mathfrak{z}}^- \in G_{\mathfrak{z}}^-, \breve{\kappa}_{\acute{\mathrm{g}}+1}^- \in G_{\acute{\mathrm{g}}+1}^-} \left\{ \left(\frac{-1}{1 + \left\{ \frac{\mathrm{F}_{\acute{\mathrm{g}}+1}}{\sum_{\varsigma=1}^{\mathfrak{z}} \mathrm{F}_\varsigma} \left(\frac{1 + \breve{\kappa}_{\acute{\mathrm{g}}+1}^{-\mathrm{R}}}{\left| \breve{\kappa}_{\acute{\mathrm{g}}+1}^{-\mathrm{R}} \right|} \right)^{\iota} \right\}^{\frac{1}{\iota}}} \right) + \iota \left(\frac{-1}{1 + \left\{ \frac{\mathrm{F}_{\acute{\mathrm{g}}+1}}{\sum_{\varsigma=1}^{\mathfrak{z}} \mathrm{F}_\varsigma} \left(\frac{1 + \breve{\kappa}_{\acute{\mathrm{g}}+1}^{-\mathrm{I}}}{\left| \breve{\kappa}_{\acute{\mathrm{g}}+1}^{-\mathrm{I}} \right|} \right)^{\iota} \right\}^{\frac{1}{\iota}}} \right) \right\} \right)$$

$$= \left(\bigcup_{\breve{\kappa}_1^+ \in G_1^+, \ldots, \breve{\kappa}_{\acute{\mathrm{g}}}^+ \in G_{\acute{\mathrm{g}}}^+, \breve{\kappa}_{\acute{\mathrm{g}}+1}^+ \in G_{\acute{\mathrm{g}}+1}^+} \left\{ \left(1 - \frac{1}{1 + \left\{ \sum_{\varsigma=1}^{\acute{\mathrm{g}}+1} \frac{\mathrm{F}_\varsigma}{\sum_{\varsigma=1}^{\mathfrak{z}} \mathrm{F}_\varsigma} \left(\frac{\breve{\kappa}_\varsigma^{+\mathrm{R}}}{1 - \breve{\kappa}_\varsigma^{+\mathrm{R}}} \right)^{\iota} \right\}^{\frac{1}{\iota}}} \right) + \iota \left(1 - \frac{1}{1 + \left\{ \sum_{\varsigma=1}^{\acute{\mathrm{g}}+1} \frac{\mathrm{F}_\varsigma}{\sum_{\varsigma=1}^{\mathfrak{z}} \mathrm{F}_\varsigma} \left(\frac{\breve{\kappa}_\varsigma^{+\mathrm{I}}}{1 - \breve{\kappa}_\varsigma^{+\mathrm{I}}} \right)^{\iota} \right\}^{\frac{1}{\iota}}} \right) \right\}, \right.$$

$$\left. \bigcup_{\breve{\kappa}_1^- \in G_1^-, \ldots, \breve{\kappa}_{\mathfrak{z}}^- \in G_{\mathfrak{z}}^-, \breve{\kappa}_{\acute{\mathrm{g}}+1}^- \in G_{\acute{\mathrm{g}}+1}^-} \left\{ \left(\frac{-1}{1 + \left\{ \sum_{\varsigma=1}^{\acute{\mathrm{g}}+1} \frac{\mathrm{F}_\varsigma}{\sum_{\varsigma=1}^{\mathfrak{z}} \mathrm{F}_\varsigma} \left(\frac{1 + \breve{\kappa}_\varsigma^{-\mathrm{R}}}{\left| \breve{\kappa}_\varsigma^{-\mathrm{R}} \right|} \right)^{\iota} \right\}^{\frac{1}{\iota}}} \right) + \iota \left(\frac{-1}{1 + \left\{ \sum_{\varsigma=1}^{\acute{\mathrm{g}}+1} \frac{\mathrm{F}_\varsigma}{\sum_{\varsigma=1}^{\mathfrak{z}} \mathrm{F}_\varsigma} \left(\frac{1 + \breve{\kappa}_\varsigma^{-\mathrm{I}}}{\left| \breve{\kappa}_\varsigma^{-\mathrm{I}} \right|} \right)^{\iota} \right\}^{\frac{1}{\iota}}} \right) \right\} \right)$$

This shows that (8) holds for $\mathfrak{z} = \acute{\mathrm{g}} + 1$. This implies that (8) holds for every $\mathfrak{z}$.

Given below properties can be proved in the simplest way

Theorem 3: (Idempotency) Let $\bar{\mathrm{F}}_\varsigma = \left(\mathrm{G}_\varsigma^+, \mathrm{G}_\varsigma^-\right)$, $(\varsigma = 1,2,3,\ldots,\mathfrak{z})$ be a collection of HBCFNs. If all $\bar{\mathrm{F}}_\varsigma$ are equal i.e., $\mathrm{F}_\varsigma = \mathrm{F}\ \forall \varsigma$, then

$$\mathrm{HBCFDPA}(\bar{\mathrm{F}}_1, \bar{\mathrm{F}}_2, \ldots, \bar{\mathrm{F}}_{\mathfrak{z}}) = \bar{\mathrm{F}}$$

Theorem 4: (Boundedness) Let $\overline{\mathrm{F}}_{\varsigma}=\left(\mathrm{G}_{\varsigma}^{+},\mathrm{G}_{\varsigma}^{-}\right)$, $(\varsigma=1,2,3,\ldots,\mathrm{z})$ be a collection of HBCFNs, and $\overline{\mathrm{F}}^{-}=\min(\overline{\mathrm{F}}_1,\overline{\mathrm{F}}_2,\overline{\mathrm{F}}_3,\ldots,\overline{\mathrm{F}}_{\mathrm{z}})$, $\overline{\mathrm{F}}^{+}=\max(\overline{\mathrm{F}}_1,\overline{\mathrm{F}}_2,\overline{\mathrm{F}}_3,\ldots,\overline{\mathrm{F}}_{\mathrm{z}})$ then

$$\overline{\mathrm{F}}^{-}\leq \mathrm{HBCFDPA}(\overline{\mathrm{F}}_1,\overline{\mathrm{F}}_2,\ldots,\overline{\mathrm{F}}_{\mathrm{z}})\leq \overline{\mathrm{F}}^{+}$$

Theorem 5: (Monotonicity) Let $\overline{\mathrm{F}}_{\varsigma}=\left(\mathrm{G}_{\varsigma}^{+},\mathrm{G}_{\varsigma}^{-}\right)$, $(\varsigma=1,2,3,\ldots,\mathrm{z})$ and

$\overline{\mathrm{F}}'_{\varsigma}=\left(\mathrm{G}'^{+}_{\varsigma},\mathrm{G}'^{-}_{\varsigma}\right)=\left(\breve{\kappa}'^{+[\mathrm{R}]}_{\varsigma}+\iota\breve{\kappa}'^{+[\bar{\mathrm{I}}]}_{\varsigma},\breve{\kappa}'^{-[\mathrm{R}]}_{\varsigma}+\iota\breve{\kappa}'^{-[\bar{\mathrm{I}}]}_{\varsigma}\right)$ $(\varsigma=1,2,3,\ldots,\mathrm{z})$ be a collection of two HBCFNs, then

$$\mathrm{HBCFDPA}(\overline{\mathrm{F}}_1,\overline{\mathrm{F}}_2,\ldots,\overline{\mathrm{F}}_{\mathrm{z}})\leq \mathrm{HBCFDPA}(\overline{\mathrm{F}}'_1,\overline{\mathrm{F}}'_2,\ldots,\overline{\mathrm{F}}'_{\mathrm{z}})$$

If $\overline{\mathrm{F}}_{\varsigma}\leq\overline{\mathrm{F}}'_{\varsigma}\ \forall\varsigma$.

If we suppose the weights of $\overline{\mathrm{F}}_{\varsigma}$ $(\varsigma=1,2,3,\ldots,\mathrm{z})$ is $\varpi=(\varpi_1,\varpi_2,\varpi_3,\ldots,\varpi_{\mathrm{z}})^{\mathrm{T}}$ such as $\varpi_{\varsigma}>0$ and $\sum_{\varsigma=1}^{\mathrm{z}}\varpi_{\varsigma}=1$, then we define the HBCFDPWA operator as follows:

Definition 14: Let $\overline{\mathrm{F}}_{\varsigma}=\left(\mathrm{G}_{\varsigma}^{+},\mathrm{G}_{\varsigma}^{-}\right)$, $(\varsigma=1,2,3,\ldots,\mathrm{z})$ be a collection of HBCFNs, then the HBCFDPWA operator is a function of $\mathrm{HBCFDPWA}:\overline{\mathrm{F}}^{\mathrm{z}}\longrightarrow\overline{\mathrm{F}}$ such that.

$$\mathrm{HBCFDPWA}_{\varpi}(\overline{\mathrm{F}}_1,\overline{\mathrm{F}}_2,\ldots,\overline{\mathrm{F}}_{\mathrm{z}})=\bigoplus_{\varsigma=1}^{\mathrm{z}}\left(\frac{\varpi_{\varsigma}\mathrm{F}_{\varsigma}}{\sum_{\varsigma=1}^{\mathrm{z}}\varpi_{\varsigma}\mathrm{F}_{\varsigma}}\overline{\mathrm{F}}_{\varsigma}\right)\quad(9)$$

Where $\mathrm{F}_{\varsigma}=\prod_{\mathrm{l}=1}^{\varsigma-1}\mathbb{S}\left(\overline{\mathrm{F}}_{\mathrm{l}}\right)$ $(\mathrm{l}=1,2,3,\ldots,\mathrm{z})$, $\mathrm{F}_1=1$ and $\mathbb{S}\left(\overline{\mathrm{F}}_{\mathrm{l}}\right)$ denotes the score value. It is possible to convert the HBCFDPWA operators to the below theorem with the aid of HBCF operational rules.

Theorem 6: Let $\overline{\mathrm{F}}_{\varsigma}=\left(\mathrm{G}_{\varsigma}^{+},\mathrm{G}_{\varsigma}^{-}\right)$, $(\varsigma=1,2,3,\ldots,\mathrm{z})$ be a collection of HBCFNs, then by employing the above eq. (9), we get a HBCFN and

$$\mathrm{HBCFDPWA}_{\varpi}(\overline{\mathrm{F}}_1,\overline{\mathrm{F}}_2,\ldots,\overline{\mathrm{F}}_{\mathrm{z}})=\bigoplus_{\varsigma=1}^{\mathrm{z}}\left(\frac{\varpi_{\varsigma}\mathrm{F}_{\varsigma}}{\sum_{\varsigma=1}^{\mathrm{z}}\varpi_{\varsigma}\mathrm{F}_{\varsigma}}\overline{\mathrm{F}}_{\varsigma}\right)=\frac{\varpi_1\mathrm{F}_1}{\sum_{\varsigma=1}^{\mathrm{z}}\varpi_{\varsigma}\mathrm{F}_{\varsigma}}\overline{\mathrm{F}}_1\oplus\ldots\oplus\frac{\varpi_{\mathrm{z}}\mathrm{F}_{\mathrm{z}}}{\sum_{\varsigma=1}^{\mathrm{z}}\varpi_{\varsigma}\mathrm{F}_{\varsigma}}\overline{\mathrm{F}}_{\mathrm{z}}$$

$$=\left(\begin{array}{c}\bigcup\limits_{\breve{\kappa}_1^{+}\in\mathrm{G}_1^{+},\ldots,\breve{\kappa}_{\mathrm{z}}^{+}\in\mathrm{G}_{\mathrm{z}}^{+}}\left\{\begin{array}{l}\left(1-\dfrac{1}{1+\left\{\sum_{\varsigma=1}^{\mathrm{z}}\dfrac{\varpi_{\varsigma}\mathrm{F}_{\varsigma}}{\sum_{\varsigma=1}^{\mathrm{z}}\varpi_{\varsigma}\mathrm{F}_{\varsigma}}\left(\dfrac{\breve{\kappa}_{\varsigma}^{+\mathrm{R}}}{1-\breve{\kappa}_{\varsigma}^{+\mathrm{R}}}\right)^{\mathfrak{h}}\right\}^{\frac{1}{\mathfrak{h}}}}\right)+\\ \iota\left(1-\dfrac{1}{1+\left\{\sum_{\varsigma=1}^{\mathrm{z}}\dfrac{\varpi_{\varsigma}\mathrm{F}_{\varsigma}}{\sum_{\varsigma=1}^{\mathrm{z}}\varpi_{\varsigma}\mathrm{F}_{\varsigma}}\left(\dfrac{\breve{\kappa}_{\varsigma}^{+\bar{\mathrm{I}}}}{1-\breve{\kappa}_{\varsigma}^{+\bar{\mathrm{I}}}}\right)^{\mathfrak{h}}\right\}^{\frac{1}{\mathfrak{h}}}}\right)\end{array}\right\},\\ \bigcup\limits_{\breve{\kappa}_1^{-}\in\mathrm{G}_1^{-},\ldots,\breve{\kappa}_{\mathrm{z}}^{-}\in\mathrm{G}_{\mathrm{z}}^{-}}\left\{\begin{array}{l}\left(\dfrac{-1}{1+\left\{\sum_{\varsigma=1}^{\mathrm{z}}\dfrac{\varpi_{\varsigma}\mathrm{F}_{\varsigma}}{\sum_{\varsigma=1}^{\mathrm{z}}\varpi_{\varsigma}\mathrm{F}_{\varsigma}}\left(\dfrac{1+\breve{\kappa}_{\varsigma}^{-\mathrm{R}}}{\left|\breve{\kappa}_{\varsigma}^{-\mathrm{R}}\right|}\right)^{\mathfrak{h}}\right\}^{\frac{1}{\mathfrak{h}}}}\right)+\\ \iota\left(\dfrac{-1}{1+\left\{\sum_{\varsigma=1}^{\mathrm{z}}\dfrac{\varpi_{\varsigma}\mathrm{F}_{\varsigma}}{\sum_{\varsigma=1}^{\mathrm{z}}\varpi_{\varsigma}\mathrm{F}_{\varsigma}}\left(\dfrac{1+\breve{\kappa}_{\varsigma}^{-\bar{\mathrm{I}}}}{\left|\breve{\kappa}_{\varsigma}^{-\bar{\mathrm{I}}}\right|}\right)^{\mathfrak{h}}\right\}^{\frac{1}{\mathfrak{h}}}}\right)\end{array}\right\}\end{array}\right)\quad(10)$$

Where $\mathrm{F}_{\varsigma}=\prod_{\mathrm{l}=1}^{\varsigma-1}\mathbb{S}\left(\overline{\mathrm{F}}_{\mathrm{l}}\right)$ $(\mathrm{l}=1,2,3,\ldots,\mathrm{z})$, $\mathrm{F}_1=1$ and $\mathbb{S}\left(\overline{\mathrm{F}}_{\mathrm{l}}\right)$ shows the value of the score.

The HBCFDPWA operators hold the property of idempotent, monotonicity, and boundedness.

HBCF Dombi Prioritized Geometric AOS

This section consists of the following AOs in the environment of HBCFNs. The HBCFDPG operators and HBCFDPWG operators.

Definition 15: Let $\overline{\mathrm{F}}_{\varsigma}=\left(\mathrm{G}_{\varsigma}^{+},\mathrm{G}_{\varsigma}^{-}\right)$, $(\varsigma=1,2,3,\ldots,\mathrm{z})$ be a collection of HBCFNs, then the HBCFDPG operator is a function of $\mathrm{HBCFDPG}:\overline{\mathrm{F}}^{\mathrm{z}}\longrightarrow\overline{\mathrm{F}}$ such that.

$$\mathrm{HBCFDPG}(\overline{\mathrm{F}}_1,\overline{\mathrm{F}}_2,\ldots,\overline{\mathrm{F}}_{\mathrm{z}})=\bigotimes_{\varsigma=1}^{\mathrm{z}}\left(\overline{\mathrm{F}}_{\varsigma}\right)^{\frac{\mathrm{F}_{\varsigma}}{\sum_{\varsigma=1}^{\mathrm{z}}\mathrm{F}_{\varsigma}}}=\left(\overline{\mathrm{F}}_1\right)^{\frac{\mathrm{F}_1}{\sum_{\varsigma=1}^{\mathrm{z}}\mathrm{F}_{\varsigma}}}\otimes\ldots\otimes\left(\overline{\mathrm{F}}_{\mathrm{z}}\right)^{\frac{\mathrm{F}_{\mathrm{z}}}{\sum_{\varsigma=1}^{\mathrm{z}}\mathrm{F}_{\varsigma}}}\quad(11)$$

Where $\mathrm{F}_{\varsigma}=\prod_{\mathrm{l}=1}^{\varsigma-1}\mathbb{S}\left(\overline{\mathrm{F}}_{\mathrm{l}}\right)$ $(\varsigma=2,3,\ldots,\mathrm{z})$, $\mathrm{F}_1=1$ and $\mathbb{S}\left(\overline{\mathrm{F}}_{\mathrm{l}}\right)$ denotes the score value.

Theorem 7: Let $\overline{\mathrm{F}}_{\varsigma}=\left(\mathrm{G}_{\varsigma}^{+},\mathrm{G}_{\varsigma}^{-}\right)$, $(\varsigma=1,2,3,\ldots,\mathrm{z})$ be a collection of HBCFNs, then by employing the above eq. (11), we get the HBCFN and

$$\mathrm{HBCFDPG}(\overline{\mathrm{F}}_1,\overline{\mathrm{F}}_2,\ldots,\overline{\mathrm{F}}_{\mathrm{z}})=\bigotimes_{\varsigma=1}^{\mathrm{z}}\left(\overline{\mathrm{F}}_{\varsigma}\right)^{\frac{\mathrm{F}_{\varsigma}}{\sum_{\varsigma=1}^{\mathrm{z}}\mathrm{F}_{\varsigma}}}$$

$$=\left(\begin{array}{c}\bigcup\limits_{\breve{\kappa}_1^{+}\in\mathrm{G}_1^{+},\ldots,\breve{\kappa}_{\mathrm{z}}^{+}\in\mathrm{G}_{\mathrm{z}}^{+}}\left\{\left(\dfrac{1}{1+\left\{\sum_{\varsigma=1}^{\mathrm{z}}\frac{\mathrm{F}_{\varsigma}}{\sum_{\varsigma=1}^{\mathrm{z}}\mathrm{F}_{\varsigma}}\left(\frac{1-\breve{\kappa}_{\varsigma}^{+\mathrm{R}}}{\breve{\kappa}_{\varsigma}^{+\mathrm{R}}}\right)^{\mathfrak{h}}\right\}^{\frac{1}{\mathfrak{h}}}}\right)+\iota\left(\dfrac{1}{1+\left\{\sum_{\varsigma=1}^{\mathrm{z}}\frac{\mathrm{F}_{\varsigma}}{\sum_{\varsigma=1}^{\mathrm{z}}\mathrm{F}_{\varsigma}}\left(\frac{1-\breve{\kappa}_{\varsigma}^{+\bar{\mathrm{I}}}}{\breve{\kappa}_{\varsigma}^{+\bar{\mathrm{I}}}}\right)^{\mathfrak{h}}\right\}^{\frac{1}{\mathfrak{h}}}}\right)\right\},\\ \bigcup\limits_{\breve{\kappa}_1^{-}\in\mathrm{G}_1^{-},\ldots,\breve{\kappa}_{\mathrm{z}}^{-}\in\mathrm{G}_{\mathrm{z}}^{-}}\left\{\begin{array}{l}\left(-1+\dfrac{1}{1+\left\{\sum_{\varsigma=1}^{\mathrm{z}}\frac{\mathrm{F}_{\varsigma}}{\sum_{\varsigma=1}^{\mathrm{z}}\mathrm{F}_{\varsigma}}\left(\frac{\left|\breve{\kappa}_{\varsigma}^{-\mathrm{R}}\right|}{1+\breve{\kappa}_{\varsigma}^{-\mathrm{R}}}\right)^{\mathfrak{h}}\right\}^{\frac{1}{\mathfrak{h}}}}\right)+\\ \iota\left(-1+\dfrac{1}{1+\left\{\sum_{\varsigma=1}^{\mathrm{z}}\frac{\mathrm{F}_{\varsigma}}{\sum_{\varsigma=1}^{\mathrm{z}}\mathrm{F}_{\varsigma}}\left(\frac{\left|\breve{\kappa}_{\varsigma}^{-\bar{\mathrm{I}}}\right|}{1+\breve{\kappa}_{\varsigma}^{-\bar{\mathrm{I}}}}\right)^{\mathfrak{h}}\right\}^{\frac{1}{\mathfrak{h}}}}\right)\end{array}\right\}\end{array}\right)\quad(12)$$

Where $\mathrm{F}_{\varsigma}=\prod_{\mathrm{l}=1}^{\varsigma-1}\mathbb{S}\left(\overline{\mathrm{F}}_{\mathrm{l}}\right)$ $(\varsigma=2,3,\ldots,\mathrm{z})$, $\mathrm{F}_1=1$ and $\mathbb{S}\left(\overline{\mathrm{F}}_{\mathrm{l}}\right)$ denotes the score value.

Proof: To support the aforementioned claim, we shall employ mathematical induction.

Suppose $\mathrm{z}=2$, the left side of (12) becomes

$$\mathrm{HBCFDPG}(\overline{\mathrm{F}}_1,\overline{\mathrm{F}}_2)=\overline{\mathrm{F}}_1\otimes\overline{\mathrm{F}}_2$$

and the right side of (12) becomes

$$=\left(\begin{array}{l}\bigcup\limits_{\breve{\kappa}_1^{+}\in G_1^{+},\breve{\kappa}_2^{+}\in G_2^{+}}\left\{\left(\dfrac{1}{1+\left\{\dfrac{F_1}{\sum_{\varsigma=1}^{z}F_\varsigma}\left(\dfrac{1-\breve{\kappa}_1^{+R}}{\breve{\kappa}_1^{+R}}\right)^{\mathfrak{h}}+\dfrac{F_2}{\sum_{\varsigma=1}^{z}F_\varsigma}\left(\dfrac{1-\breve{\kappa}_2^{+R}}{\breve{\kappa}_2^{+R}}\right)^{\mathfrak{h}}\right\}^{\frac{1}{\mathfrak{h}}}}\right)+\iota\left(\dfrac{1}{1+\left\{\dfrac{F_1}{\sum_{\varsigma=1}^{z}F_\varsigma}\left(\dfrac{1-\breve{\kappa}_1^{+\bar{I}}}{\breve{\kappa}_1^{+\bar{I}}}\right)^{\mathfrak{h}}+\dfrac{F_2}{\sum_{\varsigma=1}^{z}F_\varsigma}\left(\dfrac{1-\breve{\kappa}_2^{+\bar{I}}}{\breve{\kappa}_1^{+\bar{I}}}\right)^{\mathfrak{h}}\right\}^{\frac{1}{\mathfrak{h}}}}\right)\right\},\\ \bigcup\limits_{\breve{\kappa}_1^{-}\in G_1^{-},\breve{\kappa}_2^{-}\in G_2^{-}}\left\{\left(-1+\dfrac{1}{1+\left\{\dfrac{F_1}{\sum_{\varsigma=1}^{z}F_\varsigma}\left(\dfrac{\left|\breve{\kappa}_1^{-R}\right|}{1+\breve{\kappa}_1^{-R}}\right)^{\mathfrak{h}}+\dfrac{F_2}{\sum_{\varsigma=1}^{z}F_\varsigma}\left(\dfrac{\left|\breve{\kappa}_2^{-R}\right|}{1+\breve{\kappa}_2^{-R}}\right)^{\mathfrak{h}}\right\}^{\frac{1}{\mathfrak{h}}}}\right)+\iota\left(-1+\dfrac{1}{1+\left\{\dfrac{F_1}{\sum_{\varsigma=1}^{z}F_\varsigma}\left(\dfrac{\left|\breve{\kappa}_2^{-\bar{I}}\right|}{1+\breve{\kappa}_2^{-\bar{I}}}\right)^{\mathfrak{h}}+\dfrac{F_2}{\sum_{\varsigma=1}^{z}F_\varsigma}\left(\dfrac{\left|\breve{\kappa}_2^{-\bar{I}}\right|}{1+\breve{\kappa}_2^{-\bar{I}}}\right)^{\mathfrak{h}}\right\}^{\frac{1}{\mathfrak{h}}}}\right)\right\}\end{array}\right)$$

$$=\left(\begin{array}{l}\bigcup\limits_{\breve{\kappa}_1^{+}\in G_1^{+},\breve{\kappa}_2^{+}\in G_2^{+}}\left\{\left(\dfrac{1}{1+\left\{\sum_{\varsigma=1}^{2}\dfrac{F_\varsigma}{\sum_{\varsigma=1}^{z}F_\varsigma}\left(\dfrac{1-\breve{\kappa}_\varsigma^{+R}}{\breve{\kappa}_\varsigma^{+R}}\right)^{\mathfrak{h}}\right\}^{\frac{1}{\mathfrak{h}}}}\right)+\iota\left(\dfrac{1}{1+\left\{\sum_{\varsigma=1}^{2}\dfrac{F_\varsigma}{\sum_{\varsigma=1}^{z}F_\varsigma}\left(\dfrac{1-\breve{\kappa}_\varsigma^{+\bar{I}}}{\breve{\kappa}_\varsigma^{+\bar{I}}}\right)^{\mathfrak{h}}\right\}^{\frac{1}{\mathfrak{h}}}}\right)\right\},\\ \bigcup\limits_{\breve{\kappa}_1^{-}\in G_1^{-},\breve{\kappa}_2^{-}\in G_2^{-}}\left\{\left(-1+\dfrac{1}{1+\left\{\sum_{\varsigma=1}^{2}\dfrac{F_\varsigma}{\sum_{\varsigma=1}^{z}F_\varsigma}\left(\dfrac{\left|\breve{\kappa}_\varsigma^{-R}\right|}{1+\breve{\kappa}_\varsigma^{-R}}\right)^{\mathfrak{h}}\right\}^{\frac{1}{\mathfrak{h}}}}\right)+\iota\left(-1+\dfrac{1}{1+\left\{\sum_{\varsigma=1}^{2}\dfrac{F_\varsigma}{\sum_{\varsigma=1}^{z}F_\varsigma}\left(\dfrac{\left|\breve{\kappa}_\varsigma^{-\bar{I}}\right|}{1+\breve{\kappa}_\varsigma^{-\bar{I}}}\right)^{\mathfrak{h}}\right\}^{\frac{1}{\mathfrak{h}}}}\right)\right\}\end{array}\right)$$

This shows that (12) holds for $z = 2$.

Now assume that (12) holds for $z = \dot{g}$

$$\mathrm{HBCFDWG}_{\omega}\left(\bar{F}_1,\bar{F}_2,\ldots,\bar{F}_{\dot{g}}\right)=\bigotimes_{\varsigma=1}^{\dot{g}}\left(\bar{F}_\varsigma\right)^{\frac{F_\varsigma}{\sum_{\varsigma=1}^{z}F_\varsigma}}$$

$$=\left(\begin{array}{l}\bigcup\limits_{\breve{\kappa}_1^{+}\in G_1^{+},\ldots,\breve{\kappa}_{\dot{g}}^{+}\in G_{\dot{g}}^{+}}\left\{\left(\dfrac{1}{1+\left\{\sum_{\varsigma=1}^{\dot{g}}\dfrac{F_\varsigma}{\sum_{\varsigma=1}^{z}F_\varsigma}\left(\dfrac{1-\breve{\kappa}_\varsigma^{+R}}{\breve{\kappa}_\varsigma^{+R}}\right)^{\mathfrak{h}}\right\}^{\frac{1}{\mathfrak{h}}}}\right)+\iota\left(\dfrac{1}{1+\left\{\sum_{\varsigma=1}^{\dot{g}}\dfrac{F_\varsigma}{\sum_{\varsigma=1}^{z}F_\varsigma}\left(\dfrac{1-\breve{\kappa}_\varsigma^{+\bar{I}}}{\breve{\kappa}_\varsigma^{+\bar{I}}}\right)^{\mathfrak{h}}\right\}^{\frac{1}{\mathfrak{h}}}}\right)\right\},\\ \bigcup\limits_{\breve{\kappa}_1^{-}\in G_1^{-},\ldots,\breve{\kappa}_z^{-}\in G_z^{-}}\left\{\left(-1+\dfrac{1}{1+\left\{\sum_{\varsigma=1}^{\dot{g}}\dfrac{F_\varsigma}{\sum_{\varsigma=1}^{z}F_\varsigma}\left(\dfrac{\left|\breve{\kappa}_\varsigma^{-R}\right|}{1+\breve{\kappa}_\varsigma^{-R}}\right)^{\mathfrak{h}}\right\}^{\frac{1}{\mathfrak{h}}}}\right)+\iota\left(-1+\dfrac{1}{1+\left\{\sum_{\varsigma=1}^{\dot{g}}\dfrac{F_\varsigma}{\sum_{\varsigma=1}^{z}F_\varsigma}\left(\dfrac{\left|\breve{\kappa}_\varsigma^{-\bar{I}}\right|}{1+\breve{\kappa}_\varsigma^{-\bar{I}}}\right)^{\mathfrak{h}}\right\}^{\frac{1}{\mathfrak{h}}}}\right)\right\}\end{array}\right)$$

Next, we show that (12) holds for $z = \dot{g} + 1$

$$\mathrm{HBCFDPG}\left(\bar{F}_1,\bar{F}_2,\ldots,\bar{F}_{\dot{g}},\bar{F}_{\dot{g}+1}\right)=\bigotimes_{\varsigma=1}^{\dot{g}}\left(\bar{F}_\varsigma\right)^{\frac{F_\varsigma}{\sum_{\varsigma=1}^{z}F_\varsigma}}\otimes\left(\bar{F}_{\dot{g}+1}\right)^{\frac{F_{\dot{g}+1}}{\sum_{\varsigma=1}^{z}F_\varsigma}}$$

$$=\left(\begin{array}{l}\bigcup\limits_{\breve{\kappa}_1^{+}\in G_1^{+},\ldots,\breve{\kappa}_{\dot{g}}^{+}\in G_{\dot{g}}^{+}}\left\{\left(\dfrac{1}{1+\left\{\sum_{\varsigma=1}^{\dot{g}}\dfrac{F_\varsigma}{\sum_{\varsigma=1}^{z}F_\varsigma}\left(\dfrac{1-\breve{\kappa}_\varsigma^{+R}}{\breve{\kappa}_\varsigma^{+R}}\right)^{\mathfrak{h}}\right\}^{\frac{1}{\mathfrak{h}}}}\right)+\iota\left(\dfrac{1}{1+\left\{\sum_{\varsigma=1}^{\dot{g}}\dfrac{F_\varsigma}{\sum_{\varsigma=1}^{z}F_\varsigma}\left(\dfrac{1-\breve{\kappa}_\varsigma^{+\bar{I}}}{\breve{\kappa}_\varsigma^{+\bar{I}}}\right)^{\mathfrak{h}}\right\}^{\frac{1}{\mathfrak{h}}}}\right)\right\},\\ \bigcup\limits_{\breve{\kappa}_1^{-}\in G_1^{-},\ldots,\breve{\kappa}_z^{-}\in G_z^{-}}\left\{\left(-1+\dfrac{1}{1+\left\{\sum_{\varsigma=1}^{\dot{g}}\dfrac{F_\varsigma}{\sum_{\varsigma=1}^{z}F_\varsigma}\left(\dfrac{\left|\breve{\kappa}_\varsigma^{-R}\right|}{1+\breve{\kappa}_\varsigma^{-R}}\right)^{\mathfrak{h}}\right\}^{\frac{1}{\mathfrak{h}}}}\right)+\iota\left(-1+\dfrac{1}{1+\left\{\sum_{\varsigma=1}^{\dot{g}}\dfrac{F_\varsigma}{\sum_{\varsigma=1}^{z}F_\varsigma}\left(\dfrac{\left|\breve{\kappa}_\varsigma^{-\bar{I}}\right|}{1+\breve{\kappa}_\varsigma^{-\bar{I}}}\right)^{\mathfrak{h}}\right\}^{\frac{1}{\mathfrak{h}}}}\right)\right\}\end{array}\right)$$

$\otimes$

$$\left(\bigcup_{\breve{\kappa}_1^+\in G_1^+,\ldots,\breve{\kappa}_{\acute{g}}^+\in G_{\acute{g}}^+,\breve{\kappa}_{\acute{g}+1}^+\in G_{\acute{g}+1}^+}\left\{\left(\frac{1}{1+\left\{\frac{\mathrm{F}_{\acute{g}+1}}{\sum_{\varsigma=1}^{z}\mathrm{F}_\varsigma}\left(\frac{1-\breve{\kappa}_{\acute{g}+1}^{+\mathrm{R}}}{\breve{\kappa}_{\acute{g}+1}^{+\mathrm{R}}}\right)^{\mathfrak{h}}\right\}^{\frac{1}{\mathfrak{h}}}}\right)+\iota\left(\frac{1}{1+\left\{\frac{\mathrm{F}_{\acute{g}+1}}{\sum_{\varsigma=1}^{z}\mathrm{F}_\varsigma}\left(\frac{1-\breve{\kappa}_{\acute{g}+1}^{+\bar{\mathrm{I}}}}{\breve{\kappa}_{\acute{g}+1}^{+\bar{\mathrm{I}}}}\right)^{\mathfrak{h}}\right\}^{\frac{1}{\mathfrak{h}}}}\right)\right\},\right.$$

$$\left.\bigcup_{\breve{\kappa}_1^-\in G_1^-,\ldots,\breve{\kappa}_{\acute{g}}^-\in G_{\acute{g}}^-,\breve{\kappa}_{\acute{g}+1}^-\in G_{\acute{g}+1}^-}\left\{\left(-1+\frac{1}{1+\left\{\frac{\mathrm{F}_{\acute{g}+1}}{\sum_{\varsigma=1}^{z}\mathrm{F}_\varsigma}\left(\frac{\left|\breve{\kappa}_{\acute{g}+1}^{-\mathrm{R}}\right|}{1+\breve{\kappa}_{\acute{g}+1}^{-\mathrm{R}}}\right)^{\mathfrak{h}}\right\}^{\frac{1}{\mathfrak{h}}}}\right)+\iota\left(-1+\frac{1}{1+\left\{\frac{\mathrm{F}_{\acute{g}+1}}{\sum_{\varsigma=1}^{z}\mathrm{F}_\varsigma}\left(\frac{\left|\breve{\kappa}_{\acute{g}+1}^{-\bar{\mathrm{I}}}\right|}{1+\breve{\kappa}_{\acute{g}+1}^{-\bar{\mathrm{I}}}}\right)^{\mathfrak{h}}\right\}^{\frac{1}{\mathfrak{h}}}}\right)\right\}\right)$$

$$=\left(\bigcup_{\breve{\kappa}_1^+\in G_1^+,\ldots,\breve{\kappa}_{\acute{g}}^+\in G_{\acute{g}}^+,\breve{\kappa}_{\acute{g}+1}^+\in G_{\acute{g}+1}^+}\left\{\left(\frac{1}{1+\left\{\sum_{\varsigma=1}^{\acute{g}+1}\frac{\mathrm{F}_\varsigma}{\sum_{\varsigma=1}^{z}\mathrm{F}_\varsigma}\left(\frac{1-\breve{\kappa}_\varsigma^{+\mathrm{R}}}{\breve{\kappa}_\varsigma^{+\mathrm{R}}}\right)^{\mathfrak{h}}\right\}^{\frac{1}{\mathfrak{h}}}}\right)+\iota\left(\frac{1}{1+\left\{\sum_{\varsigma=1}^{\acute{g}+1}\frac{\mathrm{F}_\varsigma}{\sum_{\varsigma=1}^{z}\mathrm{F}_\varsigma}\left(\frac{1-\breve{\kappa}_\varsigma^{+\bar{\mathrm{I}}}}{\breve{\kappa}_\varsigma^{+\bar{\mathrm{I}}}}\right)^{\mathfrak{h}}\right\}^{\frac{1}{\mathfrak{h}}}}\right)\right\},\right.$$

$$\left.\bigcup_{\breve{\kappa}_1^-\in G_1^-,\ldots,\breve{\kappa}_{\acute{g}}^-\in G_{\acute{g}}^-,\breve{\kappa}_{\acute{g}+1}^-\in G_{\acute{g}+1}^-}\left\{\left(-1+\frac{1}{1+\left\{\sum_{\varsigma=1}^{\acute{g}+1}\frac{\mathrm{F}_\varsigma}{\sum_{\varsigma=1}^{z}\mathrm{F}_\varsigma}\left(\frac{\left|\breve{\kappa}_\varsigma^{-\mathrm{R}}\right|}{1+\breve{\kappa}_\varsigma^{-\mathrm{R}}}\right)^{\mathfrak{h}}\right\}^{\frac{1}{\mathfrak{h}}}}\right)+\iota\left(-1+\frac{1}{1+\left\{\sum_{\varsigma=1}^{\acute{g}+1}\frac{\mathrm{F}_\varsigma}{\sum_{\varsigma=1}^{z}\mathrm{F}_\varsigma}\left(\frac{\left|\breve{\kappa}_\varsigma^{-\bar{\mathrm{I}}}\right|}{1+\breve{\kappa}_\varsigma^{-\bar{\mathrm{I}}}}\right)^{\mathfrak{h}}\right\}^{\frac{1}{\mathfrak{h}}}}\right)\right\}\right)$$

This shows that (12) holds for $z = \acute{g} + 1$. This implies that (12) holds for every z.

If we suppose the weights of $\bar{\mathrm{F}}_\varsigma$ $(\varsigma = 1,2,3,\ldots,z)$ is $\varpi = (\varpi_1, \varpi_2, \varpi_3, \ldots, \varpi_z)^{\mathrm{T}}$ such as $\varpi_\varsigma > 0$ and $\sum_{\varsigma=1}^{z}\varpi_\varsigma = 1$, then we define the HBCFDPWG operator as follows.

Definition 16: Let $\bar{\mathrm{F}}_\varsigma = \left(\mathrm{G}_\varsigma^+, \mathrm{G}_\varsigma^-\right)$, $(\varsigma = 1,2,3,\ldots,z)$ be a collection of HBCFNs, then the HBCFDPWG operator is a function of HBCFDPWG: $\mathrm{F}^z \longrightarrow \mathrm{F}$ such that.

$$\mathrm{HBCFDPWG}_\varpi(\bar{\mathrm{F}}_1, \bar{\mathrm{F}}_2, \ldots, \bar{\mathrm{F}}_z) = \bigotimes_{\varsigma=1}^{z}\left(\bar{\mathrm{F}}_\varsigma\right)^{\left(\frac{\varpi_\varsigma \mathrm{F}_\varsigma}{\sum_{\varsigma=1}^{z}\varpi_\varsigma \mathrm{F}_\varsigma}\right)} \quad (13)$$

Where $\mathrm{F}_\varsigma = \prod_{\mathfrak{l}=1}^{\varsigma-1}\mathbb{S}\left(\bar{\mathrm{F}}_\mathfrak{l}\right)$ $(\mathfrak{l} = 1,2,3,\ldots,z)$, $\mathrm{F}_1 = 1$ and $\mathbb{S}\left(\bar{\mathrm{F}}_\mathfrak{l}\right)$ denotes the score value. The HBCFDPWG operators may be transformed into the below theorem with the use of HBCF operational rules.

Theorem 8: Let $\bar{\mathrm{F}}_\varsigma = \left(\mathrm{G}_\varsigma^+, \mathrm{G}_\varsigma^-\right)$, $(\varsigma = 1,2,3,\ldots,z)$ be a collection of HBCFNs, then by employing the above eq. (13), we get a HBCFN and

$$\mathrm{HBCFDPWG}_\varpi(\bar{\mathrm{F}}_1, \bar{\mathrm{F}}_2, \ldots, \bar{\mathrm{F}}_z) = \bigotimes_{\varsigma=1}^{z}\left(\bar{\mathrm{F}}_\varsigma\right)^{\frac{\varpi_\varsigma \mathrm{F}_\varsigma}{\sum_{\varsigma=1}^{z}\varpi_\varsigma \mathrm{F}_\varsigma}} = \frac{\varpi_1 \mathrm{F}_1}{\sum_{\varsigma=1}^{z}\varpi_\varsigma \mathrm{F}_\varsigma}\bar{\mathrm{F}}_1 \otimes \ldots \otimes \frac{\varpi_z \mathrm{F}_z}{\sum_{\varsigma=1}^{z}\varpi_\varsigma \mathrm{F}_\varsigma}\bar{\mathrm{F}}_z$$

$$=\left(\bigcup_{\breve{\kappa}_1^+\in G_1^+,\ldots,\breve{\kappa}_z^+\in G_z^+}\left\{\left(\frac{1}{1+\left\{\sum_{\varsigma=1}^{z}\frac{\varpi_\varsigma \mathrm{F}_\varsigma}{\sum_{\varsigma=1}^{z}\varpi_\varsigma \mathrm{F}_\varsigma}\left(\frac{1-\breve{\kappa}_\varsigma^{+\mathrm{R}}}{\breve{\kappa}_\varsigma^{+\mathrm{R}}}\right)^{\mathfrak{h}}\right\}^{\frac{1}{\mathfrak{h}}}}\right)+\iota\left(\frac{1}{1+\left\{\sum_{\varsigma=1}^{z}\frac{\varpi_\varsigma \mathrm{F}_\varsigma}{\sum_{\varsigma=1}^{z}\varpi_\varsigma \mathrm{F}_\varsigma}\left(\frac{1-\breve{\kappa}_\varsigma^{+\bar{\mathrm{I}}}}{\breve{\kappa}_\varsigma^{+\bar{\mathrm{I}}}}\right)^{\mathfrak{h}}\right\}^{\frac{1}{\mathfrak{h}}}}\right)\right\},\right.$$

$$\left.\bigcup_{\breve{\kappa}_1^-\in G_1^-,\ldots,\breve{\kappa}_z^-\in G_z^-}\left\{\left(-1+\frac{1}{1+\left\{\sum_{\varsigma=1}^{z}\frac{\varpi_\varsigma \mathrm{F}_\varsigma}{\sum_{\varsigma=1}^{z}\varpi_\varsigma \mathrm{F}_\varsigma}\left(\frac{\left|\breve{\kappa}_\varsigma^{-\mathrm{R}}\right|}{1+\breve{\kappa}_\varsigma^{-\mathrm{R}}}\right)^{\mathfrak{h}}\right\}^{\frac{1}{\mathfrak{h}}}}\right)+\iota\left(-1+\frac{1}{1+\left\{\sum_{\varsigma=1}^{z}\frac{\varpi_\varsigma \mathrm{F}_\varsigma}{\sum_{\varsigma=1}^{z}\varpi_\varsigma \mathrm{F}_\varsigma}\left(\frac{\left|\breve{\kappa}_\varsigma^{-\bar{\mathrm{I}}}\right|}{1+\breve{\kappa}_\varsigma^{-\bar{\mathrm{I}}}}\right)^{\mathfrak{h}}\right\}^{\frac{1}{\mathfrak{h}}}}\right)\right\}\right) \quad (14)$$

Where $\mathrm{F}_\varsigma = \prod_{\mathfrak{l}=1}^{\varsigma-1}\mathbb{S}\left(\bar{\mathrm{F}}_\mathfrak{l}\right)$ $(\mathfrak{l} = 1,2,3,\ldots,z)$, $\mathrm{F}_1 = 1$ and $\mathbb{S}\left(\bar{\mathrm{F}}_\mathfrak{l}\right)$ denotes the score value.

The HBCFDPWG operators possess boundedness, monotonicity, and idempotence.

HBCF-MADM

In this section, we propose a MADM approach based on the proposed operators and in the environment of HBCFNs.

Let us assume that there are $\dot{\mathrm{Y}}$ alternatives signified by $\grave{\mathrm{A}} = \left\{\grave{\mathrm{A}}_1, \grave{\mathrm{A}}_2, \ldots \grave{\mathrm{A}}_{\dot{\mathrm{Y}}}\right\}$ and $\acute{\mathrm{Y}}$ attributes signified by $\mathcal{S} = \left\{\mathcal{S}_1, \mathcal{S}_2, \mathcal{S}_2, \ldots, \mathcal{S}_{\acute{\mathrm{Y}}}\right\}$. Let $\varpi = (\varpi_1, \varpi_2, \varpi_3, \ldots, \varpi_{\acute{\mathrm{Y}}})$ be the weight vector of attributes with $\varpi_\varsigma \in [0,1], \varsigma = \left(1,2,3,\ldots,\acute{\mathrm{Y}}\right)$ and $\sum_{\varsigma=1}^{\acute{\mathrm{Y}}}\varpi_\varsigma = 1$. Now let $\mathcal{M} = \left(\bar{\mathrm{F}}_{\mathrm{P}\varsigma}\right)_{\dot{\mathrm{Y}}\times\acute{\mathrm{Y}}} = \left(\mathrm{G}_{\mathrm{P}\varsigma}^+, \mathrm{G}_{\mathrm{P}\varsigma}^-\right)_{\dot{\mathrm{Y}}\times\acute{\mathrm{Y}}} = \left(\breve{\kappa}_{\mathrm{P}\varsigma}^{+\mathrm{R}} + \iota\breve{\kappa}_{\mathrm{P}\varsigma}^{+\bar{\mathrm{I}}}, \breve{\kappa}_{\mathrm{P}\varsigma}^{-\mathrm{R}} + \iota\breve{\kappa}_{\mathrm{P}\varsigma}^{-\bar{\mathrm{I}}}\right)_{\dot{\mathrm{Y}}\times\acute{\mathrm{Y}}}$ be an HBCF decision matrix, Where $\mathrm{F}_{\mathrm{P}\varsigma}$ is a fondness value, which is in the shape of HBCFN as prearranged by the decision analysis for the alternative $\grave{\mathrm{A}}_\mathrm{P} \in \grave{\mathrm{A}}$ concerning the attribute $\mathcal{S}_\mathrm{P} \in \mathcal{S}$. The MADM issue aims to rank the alternative. To solve the MADM issue, we have the following approach using the HBCFDPA and HBCFDPG operators.

Step 1: In each MADM process, the attribute may be in two types, one is benefit type and the second is cost type. If attributes are in cost type, then we use the following formula to make it benefit type:

$$\bar{\mathrm{F}}_{\mathrm{P}\varsigma} = \begin{cases} \left(\breve{\kappa}_{\mathrm{P}\varsigma}^{+\mathrm{R}} + \iota\breve{\kappa}_{\mathrm{P}\varsigma}^{+\bar{\mathrm{I}}}, \breve{\kappa}_{\mathrm{P}\varsigma}^{-\mathrm{R}} + \iota\breve{\kappa}_{\mathrm{P}\varsigma}^{-\bar{\mathrm{I}}}\right) & for\ benefit\ type\ of\ attribute \\ \left(\breve{\kappa}_{\mathrm{P}\varsigma}^{+\mathrm{R}} + \iota\breve{\kappa}_{\mathrm{P}\varsigma}^{+\bar{\mathrm{I}}}, \breve{\kappa}_{\mathrm{P}\varsigma}^{-\mathrm{R}} + \iota\breve{\kappa}_{\mathrm{P}\varsigma}^{-\bar{\mathrm{I}}}\right)^{\mathrm{C}} & for\ cost\ type\ of\ attribute \end{cases}$$

Step 2: In this step, we first discover the values of $\mathrm{F}_{\mathrm{P}\varsigma}(\mathrm{P} = 1, 2, 3, \ldots, \bar{\mathrm{Y}};\ \varsigma = 1, 2, 3, \ldots, \hat{\mathrm{Y}})$ as

$$\mathrm{F}_{\mathrm{P}\varsigma} = \prod_{a=1}^{\varsigma-1} \mathbb{S}(\bar{\mathrm{F}}_{\mathrm{P}a})(\mathrm{P} = 1, 2, 3, \ldots, \bar{\mathrm{Y}};\ \varsigma = 1, 2, 3, \ldots, \hat{\mathrm{Y}}) \quad (15)$$

Also,

$$\mathrm{F}_{\mathrm{P}1} = 1, (\mathrm{P} = 1, 2, 3, \ldots, \bar{\mathrm{Y}}) \quad (16)$$

Step-3: Using the HBCFDPWA and HBCFDPWG operators to aggregate the data given in the decision matrix.

Step 3: Compute the score values $\mathbb{S}(\bar{\mathrm{F}}_{\mathrm{P}})(\mathrm{P} = 1, 2, 3, \ldots, \bar{\mathrm{Y}})$ to rank the alternatives $\breve{\mathrm{A}}_{\mathrm{P}}(\mathrm{P} = 1, 2, 3, \ldots, \bar{\mathrm{Y}})$ for selecting the best one.

Step-4: By way of ascending and descending order we rank all the alternatives $\breve{\mathrm{A}}_{\mathrm{P}}(\mathrm{P} = 1,2, \ldots, \bar{\mathrm{Y}})$ to find the best alternative with $\mathbb{S}(\bar{\mathrm{F}}_{\mathrm{P}})(\mathrm{P} = 1, 2, 3, \ldots, \bar{\mathrm{Y}})$.

Step 5: Choose the best alternative.

Case Study

Suppose XYZ Mart, a retail business, is looking to enhance its client segmentation strategy. To do this, they need to select the most suitable CA technique from a range of options. After a thorough evaluation, they have identified four key CA techniques as an alternative in Table 2 and also discussed their criteria in Table 3.

Table 2. CA techniques and their explanations

Notions	Alternatives	Detail/Explanation
$\grave{\mathrm{A}}_1$	K-Means clustering	K-means clustering is a partitioning technique that may be used to classify data points into distinct groups or clusters. To minimize the within-cluster sum of squares, each data point is assigned to the cluster with the closest centroid. K is a user-defined number, and the first K initial cluster centroids are selected at random. Next, by repeatedly allocating data points to the nearest centroid, the algorithm modifies the centroids by taking the average of the points in each cluster into account. This process is repeated until convergence produces K clusters as the result.
$\grave{\mathrm{A}}_2$	Hierarchical clustering	Hierarchical clustering is simply an orderly process of grouping data into clusters. It has two types: agglomerative, where every point starts as its cluster and similar ones get merged at each step, or divisive, where everything starts in one large group and then gets split. In agglomerative clustering, clusters merge based on their proximity to each other, creating a tree-like diagram known as a dendrogram that indicates how closely clusters are related to each other. However, to decide which clusters should be combined, several linkage criteria are used. Some common ones are: Ward's linkage minimizes the difference between clusters, complete linkage, which uses the farthest points in the join between the clusters, and average linkage, which merges based on the average distance between points in different clusters. All these help put patterns and relationships in the data.
$\grave{\mathrm{A}}_3$	DBSCAN	Density-Based Spatial Clustering of Applications with Noise is one of the more popular cluster algorithms that groups points based on density in space. Unlike other classic approaches, the number of clusters need not be known a priori for DBSCAN. Instead, the DBSCAN algorithm finds clusters by selecting areas with densely packed points together and treating points in low-density areas as noise or outliers. It works by exploring each point's neighborhood, which is determined by the following two parameters: eps (the maximum distance between two points to be considered neighbors) and minutes (the minimum number of neighboring points required to form a dense region or cluster). DBSCAN initiates with an arbitrary point. Then the cluster is expanded, including more and more neighboring points satisfying the density criteria. If the point does not qualify, it is marked as noise, although it may come under another cluster later on. One of the strongest features of DBSCAN is the capability to find clusters of arbitrary shape and the ability to handle noisy data.
$\grave{\mathrm{A}}_4$	Gaussian mixture model (GMM)	GMM is an acronym that means Gaussian Mixture Model. It is a probabilistic algorithm that is based on the data where the points are created as a combination of two or more Gaussian distributions, and therefore, each of the distributions is a cluster. It works when the clusters overlap or with such data of complex structures. GMM is also referred to as soft clustering, and this is very unlike other hard clustering methods since it has probabilities. Each point may be a part of more than one cluster with varying probability. The expectation-maximization algorithm is applied to utilize GMMs on data; the algorithm generates estimates of group membership probability and model parameters. This enables it to be flexible to complex relationships among clusters. GMMs are widely used in applications that are related to customer segmentation, image processing, and anomaly detection models, where the boundaries of clusters are overlapping or fuzzy. But to be able to depict the structure of data properly, model parameters should be tuned properly, and the issue of overfitting should be taken into account.

Table 3. Criteria or attributes of CA techniques

Notions	Attributes	Explanations/ details
$\mathcal{S}_1$	Accuracy	This measure is used to assess the extent to which similar consumers are matched and clustered with the help of cluster analysis. The measure can be measured, e.g. the silhouette or purity score.
$\mathcal{S}_2$	Interpretability	The extent to which the findings of the cluster analysis can be understood and consistent is called interpretability. Although certain of these methods may create clusters that are more easily labeled, others may create clusters that may not be immediately apparent.
$\mathcal{S}_3$	Robustness	The strength of the CA approach measures the fact that it can withstand variations in the data. They should be able to give consistent results with a robust methodology, regardless of the data set or when the input parameters have been significantly altered.
$\mathcal{S}_4$	Computational efficiency	This feature shows the processing power requirements of each clustering technique of clustering. It takes into account such aspects as processing time and resource requirements that are necessary in large datasets or applications that are time-sensitive.

These four criteria are the standards by which these approaches are being assessed.

The business must evaluate these qualities in light of its demands. To choose the best CA technique for maximizing its customer segmentation strategy, the business must carefully consider these factors. Let's now examine four prospective CA techniques and assess them in light of the aforementioned attributes. The examined values in the HBCF framework are demonstrated in Table 4 as:

Table 4. Expert decision matrix based on HBCFNSs

	$\mathcal{S}_1$	$\mathcal{S}_2$	$\mathcal{S}_3$	$\mathcal{S}_4$
$\tilde{\mathbf{A}}_1$	$\left(\begin{Bmatrix}(0.1124+\\ \iota 0.1333)\end{Bmatrix}, \begin{Bmatrix}(0.9809+\\ \iota 0.3657)\end{Bmatrix}, \begin{Bmatrix}(-0.1172-\\ \iota 0.2317)\end{Bmatrix}\right)$	$\left(\begin{Bmatrix}(0.0914+\\ \iota 0.3983)\end{Bmatrix}, \begin{Bmatrix}(0.0879+\\ \iota 0.2416)\end{Bmatrix}, \begin{Bmatrix}(-0.2697-\\ \iota 0.0976)\end{Bmatrix}, \begin{Bmatrix}(-0.9985-\\ \iota 0.1119)\end{Bmatrix}\right)$	$\left(\begin{Bmatrix}(0.1004+\\ \iota 0.1149)\end{Bmatrix}, \begin{Bmatrix}(0.1002+\\ \iota 0.9189)\end{Bmatrix}, \begin{Bmatrix}(-0.6787-\\ \iota 0.2303)\end{Bmatrix}, \begin{Bmatrix}(-0.0907-\\ \iota 0.1902)\end{Bmatrix}\right)$	$\left(\begin{Bmatrix}(0.8901+\\ \iota 0.4979)\end{Bmatrix}, \begin{Bmatrix}(0.3481+\\ \iota 0.7613)\end{Bmatrix}, \begin{Bmatrix}(-0.1984-\\ \iota 0.1119)\end{Bmatrix}, \begin{Bmatrix}(-0.7971-\\ \iota 0.4975)\end{Bmatrix}\right)$
$\tilde{\mathbf{A}}_2$	$\left(\begin{Bmatrix}(0.3261+\\ \iota 0.7745)\end{Bmatrix}, \begin{Bmatrix}(0.7663+\\ \iota 0.1241)\end{Bmatrix}, \begin{Bmatrix}(-0.9983-\\ \iota 0.3199)\end{Bmatrix}, \begin{Bmatrix}(-0.8387-\\ \iota 0.1431)\end{Bmatrix}\right)$	$\left(\begin{Bmatrix}(0.1915+\\ \iota 0.3902)\end{Bmatrix}, \begin{Bmatrix}(-0.1443-\\ \iota 0.2744)\end{Bmatrix}\right)$	$\left(\begin{Bmatrix}(0.1127+\\ \iota 0.2995)\end{Bmatrix}, \begin{Bmatrix}(0.6987+\\ \iota 0.9806)\end{Bmatrix}, \begin{Bmatrix}(-0.3095-\\ \iota 0.5878)\end{Bmatrix}, \begin{Bmatrix}(-0.1985-\\ \iota 0.1209)\end{Bmatrix}\right)$	$\left(\begin{Bmatrix}(0.3761+\\ \iota 0.1085)\end{Bmatrix}, \begin{Bmatrix}(0.8909+\\ \iota 0.2093)\end{Bmatrix}, \begin{Bmatrix}(-0.4908-\\ \iota 0.9879)\end{Bmatrix}, \begin{Bmatrix}(-0.4569-\\ \iota 0.4564)\end{Bmatrix}\right)$
$\tilde{\mathbf{A}}_3$	$\left(\begin{Bmatrix}(0.1005+\\ \iota 0.3172)\end{Bmatrix}, \begin{Bmatrix}(0.4321+\\ \iota 0.8799)\end{Bmatrix}, \begin{Bmatrix}(-0.3452-\\ \iota 0.1390)\end{Bmatrix}, \begin{Bmatrix}(-0.9908-\\ \iota 0.2476)\end{Bmatrix}\right)$	$\left(\begin{Bmatrix}(0.5987+\\ \iota 0.6784)\end{Bmatrix}, \begin{Bmatrix}(0.7869+\\ \iota 0.2986)\end{Bmatrix}, \begin{Bmatrix}(-0.4876-\\ \iota 0.6143)\end{Bmatrix}\right)$	$\left(\begin{Bmatrix}(0.1005+\\ \iota 0.0986)\end{Bmatrix}, \begin{Bmatrix}(0.6791+\\ \iota 0.0978)\end{Bmatrix}, \begin{Bmatrix}(-0.5904-\\ \iota 0.3433)\end{Bmatrix}\right)$	$\left(\begin{Bmatrix}(0.2081+\\ \iota 0.3761)\end{Bmatrix}, \begin{Bmatrix}(-0.1308-\\ \iota 0.0978)\end{Bmatrix}, \begin{Bmatrix}(-0.9909-\\ \iota 0.1976)\end{Bmatrix}\right)$
$\tilde{\mathbf{A}}_4$	$\left(\begin{Bmatrix}(0.9531+\\ \iota 0.1991)\end{Bmatrix}, \begin{Bmatrix}(0.8769+\\ \iota 0.9742)\end{Bmatrix}, \begin{Bmatrix}(-0.9881-\\ \iota 0.0998)\end{Bmatrix}, \begin{Bmatrix}(-0.0976-\\ \iota 0.1209)\end{Bmatrix}\right)$	$\left(\begin{Bmatrix}(0.8719+\\ \iota 0.9082)\end{Bmatrix}, \begin{Bmatrix}(-0.2651-\\ \iota 0.8909)\end{Bmatrix}, \begin{Bmatrix}(-0.9111-\\ \iota 0.0987)\end{Bmatrix}\right)$	$\left(\begin{Bmatrix}(0.9711+\\ \iota 0.1192)\end{Bmatrix}, \begin{Bmatrix}(0.8989+\\ \iota 0.8982)\end{Bmatrix}, \begin{Bmatrix}(-0.7619-\\ \iota 0.9448)\end{Bmatrix}, \begin{Bmatrix}(-0.4593-\\ \iota 0.1765)\end{Bmatrix}\right)$	$\left(\begin{Bmatrix}(0.4581+\\ \iota 0.9979)\end{Bmatrix}, \begin{Bmatrix}(-0.0154-\\ \iota 0.0989)\end{Bmatrix}, \begin{Bmatrix}(-0.1097-\\ \iota 0.0893)\end{Bmatrix}\right)$

Step 1: The given data in Table 1 is benefit type so there is no need to normalize it.

Step 2: By using eq (15) and (16) to determine the values of $\mathbb{F}_{\mathbb{P}\mathbb{ç}}$ $(\mathbb{P} = 1, 2, 3, \ldots, \bar{\mathbb{Y}})$; $(\mathbb{ç} = 1, 2, 3, \ldots, \hat{\mathbb{Y}})$ as

$$\mathbb{F}_{\mathbb{P}\mathbb{ç}} = \begin{bmatrix} 1 & 0.626125 & 0.261525 & 0.132217 \\ 1 & 0.461375 & 0.268451 & 0.163581 \\ 1 & 0.500888 & 0.268319 & 0.11255 \\ 1 & 0.712113 & 0.483409 & 0.274631 \end{bmatrix}$$

Step 2: For $\mathbb{h} = 2$ use the HBCFDPWA operators to determine all the preferences values $\mathbb{F}_{\mathbb{P}}$ of the cluster analysis technique $\ddot{\mathbb{A}}_{\mathbb{P}}$ $(\mathbb{P} = 1, 2, 3, 4)$.

$$\bar{\mathbb{F}}_1 = \left(\begin{Bmatrix} (0.415378 + \iota 0.095932), \\ (0.998445 + \iota 0.84988) \end{Bmatrix}, \begin{Bmatrix} (-0.06129 - \iota 0.04503), \\ (-0.0524 - \iota 0.03521) \end{Bmatrix} \right), \bar{\mathbb{F}}_2 = \left(\begin{Bmatrix} (0.07305 + \iota 0.765683), \\ (0.808422 + \iota 0.991984) \end{Bmatrix}, \begin{Bmatrix} (-0.14069 - \iota 0.29328), \\ (-0.13036 - \iota 0.05228) \end{Bmatrix} \right)$$

$$\bar{\mathbb{F}}_3 = \left(\begin{Bmatrix} (0.285225 + \iota 0.459472), \\ (0.73589 + \iota 0.934554) \end{Bmatrix}, \begin{Bmatrix} (-0.38271 - \iota 0.8149), \\ (-0.73024 - \iota 0.25101) \end{Bmatrix} \right), \bar{\mathbb{F}}_4 = \left(\begin{Bmatrix} (0.994275 + \iota 0.999772), \\ (0.999773 + \iota 0.999787) \end{Bmatrix}, \begin{Bmatrix} (-0.01224 - \iota 0.05044), \\ (-0.04888 - \iota 0.03083) \end{Bmatrix} \right)$$

Step 3: The obtained score values of $\mathbb{S}(\bar{\mathbb{F}}_{\mathbb{P}})(\mathbb{P} = 1, 2, 3, 4)$ of the overall HBCFNs are

$$\mathbb{S}(\bar{\mathbb{F}}_1) = 0.770714, \mathbb{S}(\bar{\mathbb{F}}_2) = 0.752815,$$
$$\mathbb{S}(\bar{\mathbb{F}}_3) = 0.621213, \mathbb{S}(\bar{\mathbb{F}}_4) = 0.981402$$

Step 4: Rank all the cluster analysis techniques $\ddot{\mathbb{A}}_{\mathbb{P}}$ $(\mathbb{P} = 1, 2, 3, 4)$ with the following score values $\mathbb{S}(\bar{\mathbb{F}}_{\mathbb{P}})(\mathbb{P} = 1, 2, 3, 4)$ of the overall HBCFNs.

$$\ddot{\mathbb{A}}_4 > \ddot{\mathbb{A}}_1 > \ddot{\mathbb{A}}_2 > \ddot{\mathbb{A}}_3.$$

Step 5: $\ddot{\mathbb{A}}_4$ is selected as the best cluster analysis technique.

The graphical representation of the best CA technique is discussed in Figures 3 and 4.

If we use the HBCFDPWG operator to determine the best alternative.

Step 1: The given data in Table 1 is benefit type so there is no need to normalize it.

Step 2: For $\mathbb{h} = 2$ use the HBCFDPWA operators to determine all the preferences values $\mathbb{F}_{\mathbb{P}}$ of the cluster analysis techniques $\ddot{\mathbb{A}}_{\mathbb{P}}$ $(\mathbb{P} = 1, 2, 3, 4)$.

$$\bar{\mathbb{F}}_1 = \left(\begin{Bmatrix} (0.025199 + \iota 0.069985), \\ (0.037949 + \iota 0.267579) \end{Bmatrix}, \begin{Bmatrix} (-0.48065 - \iota 0.02771), \\ (-0.99999 - \iota 0.01997) \end{Bmatrix} \right), \bar{\mathbb{F}}_2 = \left(\begin{Bmatrix} (0.122523 + \iota 0.371787), \\ (0.694091 + \iota 0.066268) \end{Bmatrix}, \begin{Bmatrix} (-0.99999 - \iota 0.98995), \\ (-0.87996 - \iota 0.02304) \end{Bmatrix} \right)$$

$$\bar{\mathbb{F}}_3 = \left(\begin{Bmatrix} (0.038047 + \iota 0.159645), \\ (0.662536 + \iota 0.16530) \end{Bmatrix}, \begin{Bmatrix} (-0.24985 - \iota 0.31952), \\ (-0.99969 - \iota 0.1686) \end{Bmatrix} \right), \bar{\mathbb{F}}_4 = \left(\begin{Bmatrix} (0.968981 + \iota 0.122724), \\ (0.992966 + \iota 0.996933) \end{Bmatrix}, \begin{Bmatrix} (-0.99932 - \iota 0.97091), \\ (-0.95486 - \iota 0.00964) \end{Bmatrix} \right)$$

Step 3: The obtained score values of $\mathbb{S}(\bar{\mathbb{F}}_{\mathbb{P}})(\mathbb{P} = 1, 2, 3, 4)$ of the overall HBCFNs are

$$\mathbb{S}(\bar{\mathbb{F}}_1) = 0.359049, \mathbb{S}(\bar{\mathbb{F}}_2) = 0.295216,$$
$$\mathbb{S}(\bar{\mathbb{F}}_3) = 0.410983, \mathbb{S}(\bar{\mathbb{F}}_4) = 0.518361$$

Step 4: Rank all of the cluster analysis techniques $\ddot{\mathbb{A}}_{\mathbb{P}}$ $(\mathbb{P} = 1, 2, 3, 4)$ with the following score values $\mathbb{S}(\bar{\mathbb{F}}_{\mathbb{P}})(\mathbb{P} = 1, 2, 3, 4)$ of the overall HBCFNs.

$$\ddot{\mathbb{A}}_4 > \ddot{\mathbb{A}}_3 > \ddot{\mathbb{A}}_1 > \ddot{\mathbb{A}}_2.$$

Step 5: Hence $\ddot{\mathbb{A}}_4$ is selected as the best cluster analysis technique.

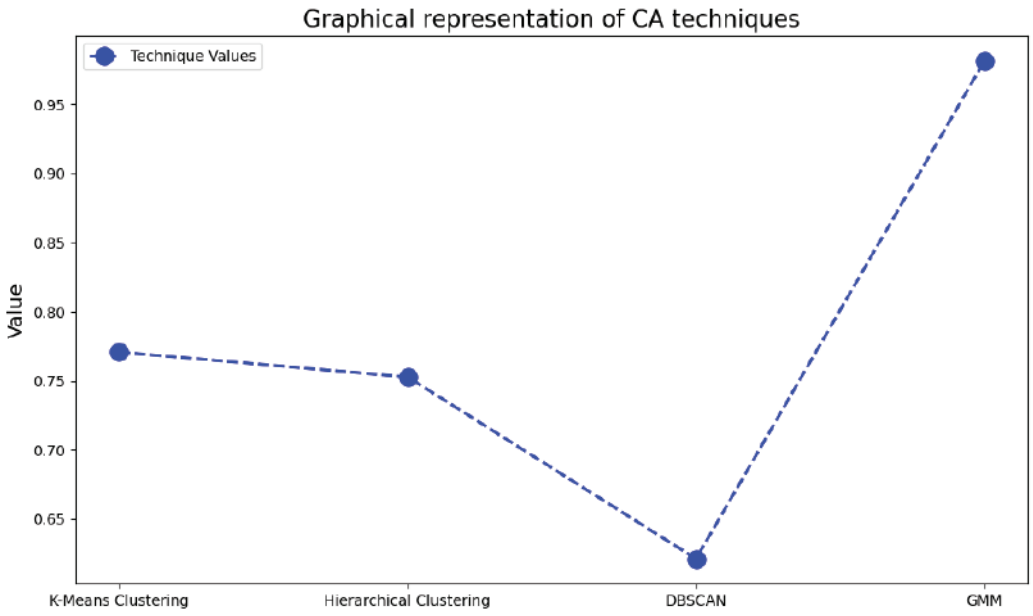


Figure 3. Ranking CA techniques based on HBCFDPWA operators.

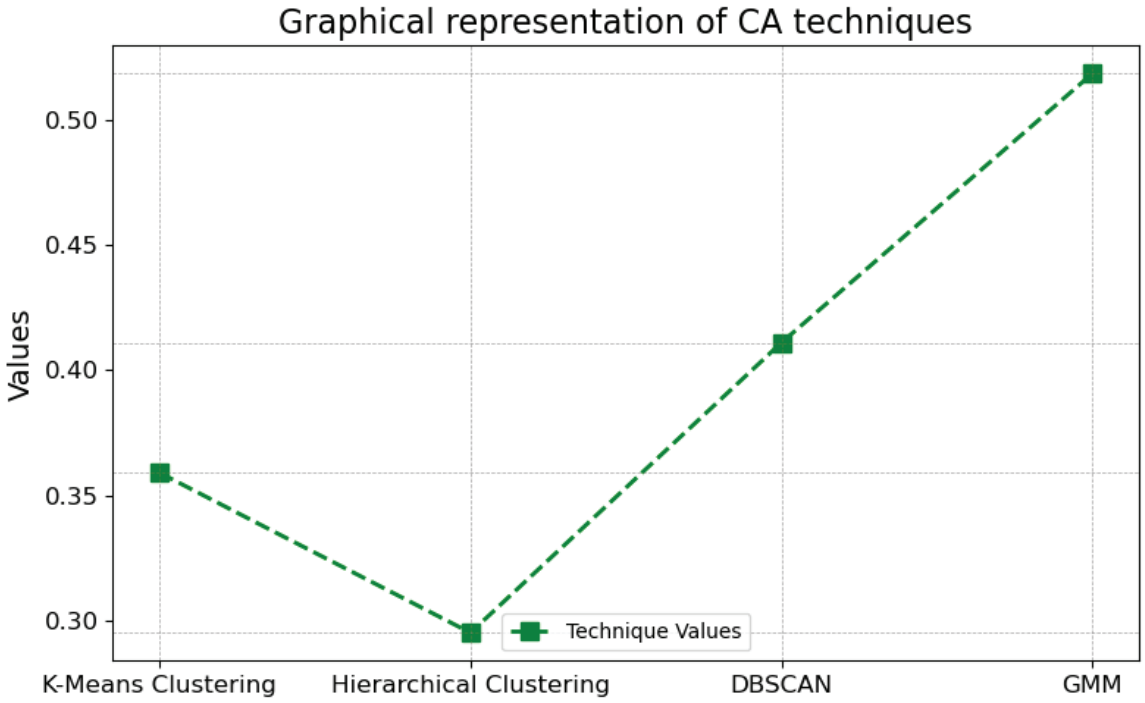


Figure 4. Ranking CA techniques based on HBCFDPWG operators.

Comparative Analysis

In order to demonstrate the advantages and tenets of the diagnosed theory, we compare the findings of the diagnosed work with the findings of the prior studies. The reason is in the fact that every newly developed work should be regarded and compared to understand its relevance and efficiency. We are unable to draw the line between the superior and inferior without making a comparison. To ensure this, we use some of the concepts that have already been published (discussed in Table 5). Then we will apply all these concepts to the suggested theory and will examine the findings, which are presented in Table 2. We give some of the selected theories first:

Most of the theories mentioned above are associated with the concept of aggregation and involve HF AOs, HF power AOs, BFDAOs, HFPAOs, ROAOs, HBFAOs, and BCFFPAOs. We make a comparison with our proposed Dombi Prioritized AOs idea. The first stage of calculating the value of the score of HBCFNs was performed with the Dombi Prioritized AOs. Once these values in the form of scores have been determined by the above operations, we attempt to draw a comparison of all the values in Table 6 as follows.

The conclusion that we draw from the table above is very curious. We find various experiences and results in comparing our suggested theory with all the past hypotheses. At first, we are trying to find the solution to the HBCF information with the theory of FGHAOs by Merigo and Casanovas [15]. Considering that this hypothesis can explain half of the information, we can conclude that this theory can not solve all of our information. As in the case

Table 5. A few selected theories for comparative analysis

• The theory of fuzzy generalized hybrid AOs (FGHAOs) and its application in fuzzy DM by Merigo and Casanovas [15].
• The theory of some HF AOs with their application in GDM by Xia et al. [21].
• The theory of some HF AOs with their application in GDM by Xia et al. [21].
• The theory of bipolar fuzzy Dombi AOs (BFDAOs) and its application in MADM by Jana et al. [26].
• The theory of robust AOs (ROAOs) for MCDM with BF soft environment by Jana et al. [27].
• The theory of HBFAOs in MADM by Wei et al. [30].
• The theory of classification of renewable energy and its sources with DM approach based on BCF frank power AOs (BCFFPAOs) by Eem et al. [45].

Table 6. Comparison between existing and proposed theories

Theories	Methods	Score values	Ranking
Merigo and Casanovas [15]	FGHAOs	$\mathbb{S}(\bar{\mathrm{F}}_1) = \text{No Result}, \mathbb{S}(\bar{\mathrm{F}}_2) = \text{No Result}$ $\mathbb{S}(\bar{\mathrm{F}}_3) = \text{No Result}, \mathbb{S}(\bar{\mathrm{F}}_4) = \text{No Result}$	No ranking
Xia et al. [21]	HFPAOs	$\mathbb{S}(\bar{\mathrm{F}}_1) = \text{No Result}, \mathbb{S}(\bar{\mathrm{F}}_2) = \text{No Result}$ $\mathbb{S}(\bar{\mathrm{F}}_3) = \text{No Result}, \mathbb{S}(\bar{\mathrm{F}}_4) = \text{No Result}$	No ranking
Zhang [23]	BFDAOs	$\mathbb{S}(\bar{\mathrm{F}}_1) = \text{No Result}, \mathbb{S}(\bar{\mathrm{F}}_2) = \text{No Result}$ $\mathbb{S}(\bar{\mathrm{F}}_3) = \text{No Result}, \mathbb{S}(\bar{\mathrm{F}}_4) = \text{No Result}$	No ranking
Jana et al. [26]	BFDAOs	$\mathbb{S}(\bar{\mathrm{F}}_1) = \text{No Result}, \mathbb{S}(\bar{\mathrm{F}}_2) = \text{No Result}$ $\mathbb{S}(\bar{\mathrm{F}}_3) = \text{No Result}, \mathbb{S}(\bar{\mathrm{F}}_4) = \text{No Result}$	No ranking
Jana et al. [27]	ROAOs	$\mathbb{S}(\bar{\mathrm{F}}_1) = \text{No Result}, \mathbb{S}(\bar{\mathrm{F}}_2) = \text{No Result}$ $\mathbb{S}(\bar{\mathrm{F}}_3) = \text{No Result}, \mathbb{S}(\bar{\mathrm{F}}_4) = \text{No Result}$	No ranking
Wei et al. [30]	HBFAOs	$\mathbb{S}(\bar{\mathrm{F}}_1) = \text{No Result}, \mathbb{S}(\bar{\mathrm{F}}_2) = \text{No Result}$ $\mathbb{S}(\bar{\mathrm{F}}_3) = \text{No Result}, \mathbb{S}(\bar{\mathrm{F}}_4) = \text{No Result}$	No ranking
Mahmood et al. [46]	BCFFPAOs	$\mathbb{S}(\bar{\mathrm{F}}_1) = \text{No Result}, \mathbb{S}(\bar{\mathrm{F}}_2) = \text{No Result}$ $\mathbb{S}(\bar{\mathrm{F}}_3) = \text{No Result}, \mathbb{S}(\bar{\mathrm{F}}_4) = \text{No Result}$	No ranking
Proposed work	HBCFDPWA AOs	$\mathbb{S}(\bar{\mathrm{F}}_1) = 0.770714, \mathbb{S}(\bar{\mathrm{F}}_2) = 0.752815,$ $\mathbb{S}(\bar{\mathrm{F}}_3) = 0.621213, \mathbb{S}(\bar{\mathrm{F}}_4) = 0.981402$	$\grave{\mathrm{A}}_4 > \grave{\mathrm{A}}_1 > \grave{\mathrm{A}}_2 > \grave{\mathrm{A}}_3.$
Proposed work	HBCFDPWG AOs	$\mathbb{S}(\bar{\mathrm{F}}_1) = 0.359049, \quad \mathbb{S}(\bar{\mathrm{F}}_2) = 0.295216,$ $\mathbb{S}(\bar{\mathrm{F}}_3) = 0.410983, \mathbb{S}(\bar{\mathrm{F}}_4) = 0.518361$	$\grave{\mathrm{A}}_4 > \grave{\mathrm{A}}_3 > \grave{\mathrm{A}}_1 > \grave{\mathrm{A}}_2.$

of Xia et al. [21] and Zhang's theory of HF AOs and application to GDM, which is incapable of accommodating our terms and conditions, we find that HFS and their AOs are only able to deal with the set of possible membership values and not with two-dimensional information, such as bipolarity with complexity. Then, we suppose that the MCDM technique with a BF soft environment can concurrently address both the positive and negative aspects associated with each item using the Jana et al. [26] theory of BFDAOs and Jana et al. [27] theory of ROAOs. Nonetheless, BF theories of [26] and [27] can process only one element of bipolarity simultaneously and cannot work out the remaining two elements of HBCF information, which entails three different aspects: bipolarity, complex form, and hesitation. Consequently, they cannot process HBCF information. Moreover, the theory of HBFAOs in MADM by Wei et al. [30] is similar to [26] and [27]. The only difference is that the theory of HBFAOs in MADM by Wei et al. [30] can also address the bipolar information in a set form. To conclude, we assume that the theory of BCFFPAOs by Mahmood et al. [45] is highly similar and relative to our theory, but it also cannot explain all the available data. It can solve both complex numbers and bipolarity, but not set-level information. Thus, all the above-mentioned concepts cannot describe our facts and information. This is the manifestation of the power and importance of our proposed theory.

CONCLUSION

Techniques of cluster analysis play a significant role in revealing the hidden trends in diverse data sets and increasing the knowledge of the data structure. They allow the incorporation of the points of data that are relevant, which could result in more specific strategic planning and decision-making. These methods help to evaluate data and form insights and ideas that would have been neglected otherwise by seeing patterns in the data. The areas where they play a significant role are very numerous, such as consumer profiling and market segmentation in genetic studies. The outcome of a cluster analysis is a more deeply explored connection in data and better decisions that are informed and data-driven. In order to explore the most effective cluster analysis approaches, we present the theory of hesitant bipolar complex fuzzy Dombi Prioritized aggregation operators in this paper. The current ideas and findings cannot deal with hesitant bipolar complex fuzzy data. Thus, we seek to apply the hesitant bipolar complex fuzzy framework in developing a tool that can be effective in handling the two-dimensional data, which has bipolar characteristics. Through this framework, decision-makers can solve the prevalent problems realistically. We also come up with operational instructions of hesitant bipolar complex fuzzy sets that can be used to solve various issues.

The primary results of our research are the creation of various types of aggregation operators, like the hesitant bipolar complex fuzzy Dombi prioritized arithmetic and geometric aggregation operators, that are used to find the solution to the multi-attribute decision-making problem in terms of a structured algorithm. In addition, we apply the multi-attribute decision-making to provide numbers to visualize the concept. In the case of two-dimensional circumstances that have complexities, bipolarity, and hesitation features our theory proves to be a useful tool. We are intending to map the fuzzy concept of the hesitant bipolar complex in the future over a couple of additional structures, such as bipolar graphs, rough sets, and soft sets. We also opt to transform them into other concepts [50-59] in the future, bearing in mind the relevance of hesitant bipolar complex fuzzy sets.

Limitations

HBCFSs are powerful tools for managing uncertain and complex information, but they do come with some limitations. One major challenge is the complexity of their mathematical operations, which can make computations time-consuming, especially for large datasets or real-time applications. Moreover, the structure of HBCFSs is only applicable to hesitancy, bipolarity, and imaginary aspects associated with any object. All other structures are not solved by using the framework of HBCFSs because every structure has its own domain and limitations.

Advantages and Disadvantages of the Proposed Theory

In this subsection, we discuss the advantages and disadvantages of the main discussed theory.

Advantages of the Proposed Theory

- HBCFSs manage circumstances with hesitation and complex-valued membership, and they can capture both positive and negative information (bipolarity). They are therefore very good at expressing uncertainty in complicated DM circumstances.
- The hesitant aspect allows for expressing multiple possible membership values when uncertainty or indecision exists, providing more flexibility and precision in modeling real-world problems.
- By using complex numbers to represent membership degrees, HBCFSs provide an extra dimension for modeling the amplitude and phase of data, enriching the analysis of complex relationships.
- HBCFSs are particularly useful in MCDM applications due to their ability to model both conflicting information and varying levels of hesitation, which are common in human decision processes.
- Since human choice processes sometimes involve contradictory information and variable degrees of hesitation, HBCFSs are very helpful in MCDM applications.

Disadvantages of the Proposed Theory

- The use of hesitation, bipolarity, and complex-valued membership adds additional complexity to the computation, so it is difficult to use HBCFSs to solve large problems or even to process in real-time.
- This is because the output of HBCFSs may be hard to decipher because it is based on complex numbers, bipolarity, and hesitations. This complication can be a problem for decision-makers who are not conversant with fuzzy set theories.
- HBCFSs are also based on various parameters, including complex-valued membership levels, the degree of hesitation, and bipolarity. These parameters are sensitive to the outcomes and improper selection can influence the accuracy and strength of the outcomes.

AUTHORSHIP CONTRIBUTIONS

Authors equally contributed to this work.

DATA AVAILABILITY STATEMENT

The authors confirm that the data that supports the findings of this study are available within the article. Raw data that support the finding of this study are available from the corresponding author, upon reasonable request.

CONFLICT OF INTEREST

The author declared no potential conflicts of interest with respect to the research, authorship, and/or publication of this article.

ETHICS

There are no ethical issues with the publication of this manuscript.

STATEMENT ON THE USE OF ARTIFICIAL INTELLIGENCE

Artificial intelligence was not used in the preparation of the article.

REFERENCES

[1] Liang GS, Chou TY, Han TC. Cluster analysis based on fuzzy equivalence relation. Eur J Oper Res 2005;166:160–171. [CrossRef]

[2] Azad P, Sharma V. Cluster head selection in wireless sensor networks under fuzzy environment. Int Scholarly Res Notices 2013;2013:909086. [CrossRef]

[3] Doring C, Lesot MJ, Kruse R. Data analysis with fuzzy clustering methods. Comput Stat Data Anal 2006;51:192–214. [CrossRef]

[4] Zhao W, Ma J, Liu Q, Song J, Tysklind M, Liu C, et al. Comparison and application of SOFM, fuzzy c-means, and k-means clustering algorithms for natural soil environment regionalization in China. Environ Res 2023;216:114519. [CrossRef]

[5] Zhou J, Chen CP, Chen L, Li HX. A collaborative fuzzy clustering algorithm in distributed network environments. IEEE Trans Fuzzy Syst 2013;22:1443–1456. [CrossRef]
[6] Budayan C, Dikmen I, Birgonul MT. Comparing the performance of traditional cluster analysis, self-organizing maps and fuzzy C-means method for strategic grouping. Expert Syst Appl 2009;36:11772–11781. [CrossRef]
[7] Lange O, Meyer-Bäse A, Hurdal M, Foo S. A comparison between neural and fuzzy cluster analysis techniques for functional MRI. Biomed Signal Process Control 2006;1:243–252. [CrossRef]
[8] Rajkumar KV, Yesubabu A, Subrahmanyam K. Fuzzy clustering and fuzzy C-means partition cluster analysis and validation studies on a subset of CiteScore dataset. Int J Electr Comput Eng 2019;9:2760–2767. [CrossRef]
[9] Zadeh LA. Fuzzy sets. Inf Control 1965;8:338–353. [CrossRef]
[10] Ezghari S, Zahi A, Zenkouar K. A new nearest neighbor classification method based on fuzzy set theory and aggregation operators. Expert Syst Appl 2017;80:58–74. [CrossRef]
[11] Sharma MK, Sadhna, Bhargava AK, Kumar S, Rathour L, Mishra LN, Pandey S. A Fermatean fuzzy ranking function in optimization of intuitionistic fuzzy transportation problems. Adv Math Models Appl 2022;7:191–204.
[12] Sharma MK, Dhiman N, Kumar S, Rathour L, Mishra VN. Neutrosophic Monte Carlo simulation approach for decision making in medical diagnostic process under uncertain environment. Int J Neutrosophic Sci 2023;22:8–16. [CrossRef]
[13] Torres-Blanc C, Cubillo S, Hernández P. Aggregation operators on type-2 fuzzy sets. Fuzzy Sets Syst 2017;324:74–90. [CrossRef]
[14] Hadi A, Khan W, Khan A. A novel approach to MADM problems using Fermatean fuzzy Hamacher aggregation operators. Int J Intell Syst 2021;36:3464–3499. [CrossRef]
[15] Merigó JM, Casanovas M. Fuzzy generalized hybrid aggregation operators and its application in fuzzy decision making. Int J Fuzzy Syst 2010;12:15–24. [CrossRef]
[16] Zimmermann HJ. Applications of fuzzy set theory to mathematical programming. Inf Sci 1985;36:29-58. [CrossRef]
[17] Torra V. Hesitant fuzzy sets. Int J Intell Syst 2010;25:529–539. [CrossRef]
[18] Qian G, Wang H, Feng X. Generalized hesitant fuzzy sets and their application in decision support system. Knowl-Based Syst 2013;37:357–365. [CrossRef]
[19] Xu Z, Xia M. Distance and similarity measures for hesitant fuzzy sets. Inf Sci 2011;181:2128–2138. [CrossRef]
[20] Chen N, Xu Z, Xia M. Correlation coefficients of hesitant fuzzy sets and their applications to clustering analysis. Appl Math Model 2013;37:2197–2211. [CrossRef]
[21] Xia M, Xu Z, Chen N. Some hesitant fuzzy aggregation operators with their application in group decision-making. Group Decis Negot 2013;22:259–279. [CrossRef]
[22] Rathour L, Singh V, Yadav H, Sharma MK, Mishra VN. A dual hesitant fuzzy set theoretic approach in fuzzy reliability analysis of a fuzzy system. Inf Sci Lett 2024;13:433–440. [CrossRef]
[23] Zhang Z. Hesitant fuzzy power aggregation operators and their application to multiple attribute group decision making. Inf Sci 2013;234:150–181. [CrossRef]
[24] Tan C, Yi W, Chen X. Hesitant fuzzy Hamacher aggregation operators for multicriteria decision-making. Appl Soft Comput 2015;26:325–349. [CrossRef]
[25] Zhang WR. Yin-Yang bipolar fuzzy sets. In: Proc IEEE Int Conf Fuzzy Syst 1998;1:835–840. [CrossRef]
[26] Jana C, Pal M, Wang JQ. Bipolar fuzzy Dombi aggregation operators and its application in the multiple-attribute decision-making process. J Ambient Intell Humaniz Comput 2019;10:3533–3549. [CrossRef]
[27] Jana C, Pal M, Wang JQ. A robust aggregation operator for multi-criteria decision-making method with bipolar fuzzy soft environment. Iran J Fuzzy Syst 2019;16:1–16.
[28] Lathamaheswari M, Sudha S, Broumi S, Smarandache F. Bipolar neutrosophic Frank aggregation operator and its application in multi-criteria decision making. Neutrosophic Sets Syst 2022;51:27–39.
[29] Riaz M, Pamucar D, Habib A, Jamil N. Innovative bipolar fuzzy sine trigonometric aggregation operators and SIR method for medical tourism supply chain. Math Probl Eng 2022;2022:4182740. [CrossRef]
[30] Wei G, Alsaadi FE, Hayat T, Alsaedi A. Bipolar fuzzy hamacher aggregation operators in multiple attribute decision making. Int J Fuzzy Syst 2018;20:1–12. [CrossRef]
[31] Riaz M, Tehrim ST. A robust extension of the VIKOR method for bipolar fuzzy sets using connection numbers of SPA theory-based metric spaces. Artif Intell Rev 2021;54:561–591. [CrossRef]
[32] Jamil M, Afzal F, Akgül A, Abdullah S, Maqbool A, Razzaque A, et al. Einstein aggregation operators under bipolar neutrosophic environment with applications in multi-criteria decision-making. Appl Sci 2022;12:10045. [CrossRef]
[33] Mandal P, Ranadive AS. Hesitant bipolar-valued fuzzy sets and bipolar-valued hesitant fuzzy sets and their applications in multi-attribute group decision making. Granul Comput 2019;4:559–583. [CrossRef]

[34] Wei G, Alsaadi FE, Hayat T, Alsaedi A. Hesitant bipolar fuzzy aggregation operators in multiple attribute decision making. J Intell Fuzzy Syst 2017;33:1119–1128. [CrossRef]
[35] Gao H, Wei G, Huang Y. Dual hesitant bipolar fuzzy hamacher prioritized aggregation operators in multiple attribute decision-making. IEEE Access 2017;6:11508–11522. [CrossRef]
[36] Gao H, Lu M, Wei Y. Dual hesitant bipolar fuzzy Hamacher aggregation operators and their applications to multiple attribute decision making. J Intell Fuzzy Syst 2019;37:5755–5766. [CrossRef]
[37] Ali J. Probabilistic hesitant bipolar fuzzy Hamacher prioritized aggregation operators and their application in multi-criteria group decision-making. Comput Appl Math 2023;42:260. [CrossRef]
[38] Ullah K, Mahmood T, Jan N, Broumi S, Khan Q. On bipolar-valued hesitant fuzzy sets and their applications in multi-attribute decision making. Nucleus 2018;55:93–101. [CrossRef]
[39] Mahmood T, Rehman UU. A novel approach towards bipolar complex fuzzy sets and their applications in generalized similarity measures. Int J Intell Syst 2022;37:535–567. [CrossRef]
[40] Mahmood T, Rehman UU, Ahmmad J, Santos-García G. Bipolar complex fuzzy Hamacher aggregation operators and their applications in multi-attribute decision making. Mathematics 2021;10:23. [CrossRef]
[41] Rehman UU, Mahmood T, Albaity M, Hayat K, Ali Z. Identification and prioritization of DevOps success factors using the bipolar complex fuzzy setting with Frank aggregation operators and analytical hierarchy process. IEEE Access 2022;10:74702–74721. [CrossRef]
[42] Mahmood T, Rehman UU. A method to multi-attribute decision-making technique based on Dombi aggregation operators under bipolar complex fuzzy information. Comput Appl Math 2022;41:47. [CrossRef]
[43] Gulistan M, Yaqoob N, Elmoasry A, Alebraheem J. Complex bipolar fuzzy sets: An application in a transport's company. J Intell Fuzzy Syst 2021;40:3981–3997. [CrossRef]
[44] Mahmood T, Rehman U, Ali Z. Analysis and application of Aczel–Alsina aggregation operators based on bipolar complex fuzzy information in multiple attribute decision-making. Inf Sci 2023;619:817–833. [CrossRef]
[45] Eem M, Mahmood T, Rehman U, Mehmood F. Classification of renewable energy and its sources with a decision-making approach based on bipolar complex fuzzy Frank power aggregation operators. Energy Strategy Rev 2023;49:101162. [CrossRef]
[46] Mahmood T, Rehman UU, Ali Z, Aslam M, Chinram R. Identification and classification of aggregation operators using bipolar complex fuzzy settings and their application in decision support systems. Mathematics 2022;10:1726. [CrossRef]
[47] Aslam M, Waqas HM, Rehman UU, Mahmood T. Selection of cloud services provider by utilizing multi-attribute decision-making based on hesitant bipolar complex fuzzy Dombi aggregation operators. IEEE Access 2024;12:35417–35447. [CrossRef]
[48] Dombi J. A general class of fuzzy operators, the De Morgan class of fuzzy operators, and fuzziness measures induced by fuzzy operators. Fuzzy Sets Syst 1982;8:149–163. [CrossRef]
[49] Yager RR. Prioritized aggregation operators. Int J Approx Reason 2008;48:263–274. [CrossRef]
[50] Sharma MK, Chaudhary S, Rathour L, Mishra VN. Modified genetic algorithm with novel crossover and mutation operator in travelling salesman problem. Sigma J Eng Nat Sci 2024;42:6. [CrossRef]
[51] Negero NT, Duressa GF, Rathour L, Mishra VN. A novel fitted numerical scheme for singularly perturbed delay parabolic problems with two small parameters. Partial Differ Equ Appl Math 2023;8:100–115. [CrossRef]
[52] Hogeme MS, Woldaregay MM, Rathour L, Mishra VN. A stable numerical method for singularly perturbed Fredholm integro differential equation using exponentially fitted difference method. J Comput Appl Math 2024;441:115709. [CrossRef]
[53] Naik PA, Yeolekar BM, Qureshi S, Yeolekar M, Madzvamuse A. Modeling and analysis of the fractional-order epidemic model to investigate mutual influence in HIV/HCV co-infection. Nonlinear Dyn 2024;112:11679–11710. [CrossRef]
[54] Naik PA, Yavuz M, Qureshi S, Owolabi KM, Soomro A, Ganie AH. Memory impacts in hepatitis C: A global analysis of a fractional-order model with an effective treatment. Comput Methods Programs Biomed 2024;254:108306. [CrossRef]
[55] Naik PA, Farman M, Zehra A, Nisar KS, Hincal E. Analysis and modeling with fractal–fractional operator for an epidemic model with reference to COVID-19 modeling. Partial Differ Equ Appl Math 2024;10:100663. [CrossRef]
[56] Jaleel A. WASPAS technique utilized for agricultural robotics system based on Dombi aggregation operators under bipolar complex fuzzy soft information. J Innov Res Math Comput Sci 2022;1:67–95.
[57] Rehman UU. Selection of database management system by using multi-attribute decision-making approach based on probability complex fuzzy aggregation operators. J Innov Res Math Comput Sci 2023;2:1–16.
[58] Hussain A, Ullah K, Pamucar D, Haleemzai I, Tatić D. Assessment of solar panel using multiattribute decision-making approach based on intuitionistic fuzzy Aczel–Alsina Heronian mean operator. Int J Intell Syst 2023;2023:6268613. [CrossRef]
[59] Ullah K, Naeem M, Hussain A, Waqas M, Haleemzai I. Evaluation of electric motor cars based on Frank power aggregation operators under picture fuzzy information and a multi-attribute group decision-making process. IEEE Access 2023;11:67201–67219. [CrossRef]

Sigma Journal of Engineering and Natural Sciences
Web page info: https://sigma.yildiz.edu.tr
DOI: 10.14744/sigma.2025.00000

Research Article

Harnessing AI for real-time detection and mitigation of technostress in digital epoch

Rachana PARIKH[1,*], Vishal DAHIYA[1]

[1]*Sardar Vallabhbhai Global University, Ahmedabad, Gujarat, 380015, India*

ARTICLE INFO

Article history
Received: 17 December 2024
Revised: 20 February 2025
Accepted: 17 March 2025

Keywords:
Artificial Intelligence; ICT; Technostress, Machine Learning; Techno-complexity; Technostress Creators

ABSTRACT

Technology is now part of nearly everyone's daily routine — office workers, students, gamers, remote employees, teachers, doctors, parents, influencers, call-centre agents, entrepreneurs… the list keeps growing. When people can't quite keep up with it, they end up feeling genuinely distressed. Researchers call this technostress. Studies show it usually shows up in two main ways: some struggle to get their heads around new tools and feel anxious (techno-anxiety), while others get far too attached and can't switch off (techno-addiction). You'll also hear terms like techno-invasion, techno-unreliability, techno-complexity, and techno-insecurity — all different flavours of the same problem. ICT has been a massive help in computing, managing data, and connecting the world throughout the 21st century. Then COVID-19 hit and suddenly forced almost everyone into remote setups overnight, making digital tools non-negotiable. Too much information and constant pings from devices and apps are the real culprits behind rising technostress levels. Meanwhile, Artificial Intelligence and Machine Learning have delivered impressive results across education, healthcare, agriculture, and countless other fields. Because technostress now touches so many areas of life, this paper explores how ML-based approaches can spot it early and give people practical ways to cope.

Cite this article as: Parikh R, Dahiya V. Harnessing AI for real-time detection and mitigation of technostress in digital epoch. Sigma J Eng Nat Sci 2026;44(1):351–359.

INTRODUCTION

In the last few years, researchers have paid growing attention to a modern kind of strain that comes directly from using technology — especially at work. We call it technostress: the mental friction, frustration, and exhaustion that appear when people struggle to adapt to digital tools [1, 2].

It takes several shapes. Some feel buried under endless emails and notifications (techno-overload). Others can't switch off because colleagues expect instant replies even at night (techno-invasion). Many find new software confusing (techno-complexity), worry that AI will replace them (techno-insecurity), or get tired of systems that change every few months (techno-uncertainty) [3]. The numbers are worrying. People who score high on technostress measures are 2.3 times more likely to burn out and 30 % less productive [4]. In one survey of 1,500 remote workers, 68 % said they could no longer separate work from the rest of their lives because

*Corresponding author.
*E-mail address: phd.rachana2023@gmail.com

This paper was recommended for publication in revised form by Editor-in-Chief Ahmet Selim Dalkilic

Published by Yıldız Technical University Press, İstanbul, Turkey
© Author. This is an open access article under the CC BY-NC license (http://creativecommons.org/licenses/by-nc/4.0/).

of digital demands [5]. Beyond lower output, technostress is linked to higher absenteeism, emotional exhaustion, and even quiet quitting [3, 6–8]. The COVID pandemic poured fuel on the fire: millions were forced online overnight, and levels of anxiety, loneliness, and fatigue shot up [5].

Figuring out the relationship between technostress and its effects is important to create effective coping mechanisms and interventions to reduce the negative effects of stress [9]. What makes someone more vulnerable? Personality plays a role — self-esteem, conscientiousness, and overall psychological capital all act as buffers [2, 10]. So do simple things like mindfulness practice and genuine support from managers [11–13]. Training and a sense of control over technology matter too [14,15].

Figure 1 sketches the big picture: When companies offer training, encourage mindful breaks, and build a supportive culture, job satisfaction tends to rise even when digital pressure is high [12, 14].

Practicing mindfulness techniques offers a practical way to ease technostress and enhance how we approach daily tasks [11, 12]. Beyond that, a range of coping mechanisms—such as proactive planning or reactive adjustments—can empower individuals to handle tech-related pressures without slipping into burnout [13]. The pandemic laid bare just how much technostress hampers productivity; it was impossible to ignore its toll on focus and output during those chaotic shifts to remote setups [14]. What stands out in recent findings is how factors like targeted training, a spark of creative confidence, and solid tech savvy act as buffers, dialing down the downsides and lifting overall performance [14, 15]. On top of that, organizational support, sensible leadership practices, and access to these tools play a crucial role in curbing technostress and fostering a healthier workforce [8, 9].

Current scholarship shines a light on how technostress erodes not just productivity and job satisfaction, but broader well-being too. Yet, there's a glaring shortfall in studies tackling machine learning (ML) for spotting and addressing it on the fly. In what follows, I'll break down key areas like sentiment tracking, physiological monitoring, behavioral pattern analysis, and quantitative stress modeling as cornerstones for intervention. I'll also touch on how natural language processing (NLP) shines in sifting stress signals from chats, emails, or even vocal inflections. At its core, technostress stems from the relentless push of digital ecosystems into every corner of work life, chipping away at mental resilience and efficiency. Drawing from this, my review here spotlights ML approaches that deliver sharper detection and tailored relief, all while navigating the real-world messiness of tech overload. It's no surprise that this surge in digital demands has left teams drained—sparking anxiety, exhaustion, and slip-ups from folks ill-equipped for the constant upgrades. And here's the kicker: since it hits both bottom lines (personal health and company results), ignoring it isn't an option anymore.

We're seeing ML step up more and more as a frontline defense against technostress, paving the way for proactive nudges via real-time alerts and forward-looking forecasts. Algorithms like support vector machines (SVM), Random Forest ensembles, and Gradient Boosting classifiers stand out for their balance of accuracy and speed. What I appreciate about them is how they nail down subtle stress triggers with impressive reliability, all while crunching data fast enough for on-the-spot interventions in busy offices. In light of technostress's growing drag on morale and metrics, it's clear we need more targeted research into actionable safeguards.

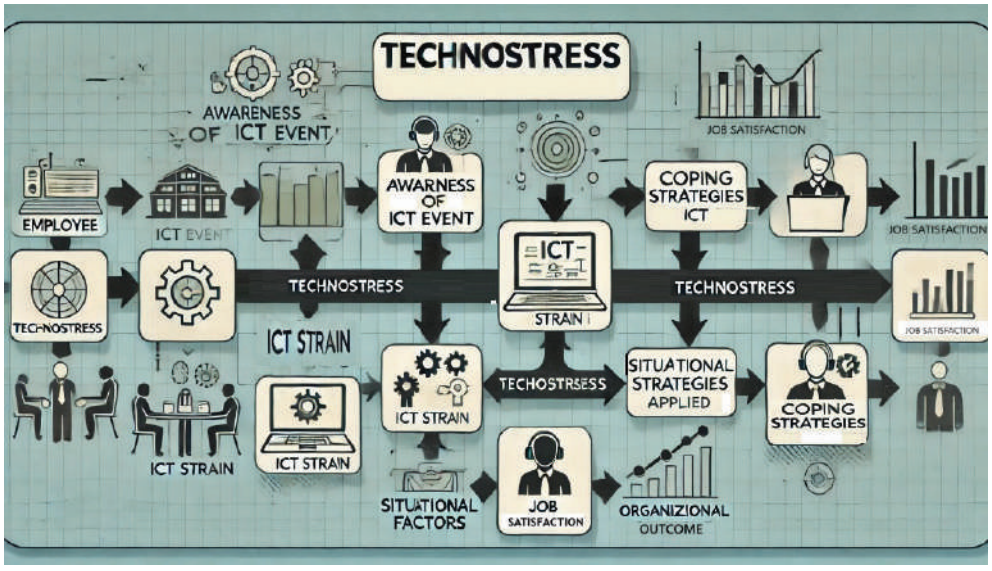


Figure 1. Conceptual model for job satisfaction related to technostress in working environment.

Sure, the bulk of today's literature maps out the problem convincingly—its symptoms, its spread—but it rarely dives into live, analytics-fueled fixes. That's precisely why ML feels like such a game-changer. Picture this: models quietly scanning your keystroke rhythms, pulse fluctuations, message vibes, or endless tab switches, then piping up early with a gentle redirect—a five-minute breather, maybe, or a workload tweak—before the whole system crashes into fatigue. In my experience reviewing these tools, that kind of foresight isn't just helpful; it's transformative for keeping teams steady.

The Impact of Technological Stress on the Workplace

The last decade, and especially the pandemic, turned technostress from an annoyance into a serious workplace issue [1–3].

It hits productivity hard. Studies consistently link it to lower job satisfaction, higher turnover intentions, and weaker organizational commitment [4–6]. In consulting firms, for example, technostress translates directly into job strain and lost performance [5].

The human cost is even clearer. Persistent digital pressure has been tied to a 40 % jump in emotional exhaustion and a 35 % rise in stress-related sick days [7]. One large study of 2,000 corporate employees found 72 % struggling with anxiety from digital complexity and 48 % overwhelmed by constant connectivity [8]. Brain-wave and heart-rate research confirms the same story: chronic technostress keeps the sympathetic nervous system in overdrive — a textbook marker of long-term stress [9].

Left unchecked, the fallout shows up as disengagement, cynicism, and burnout. The fix isn't just individual resilience; organizations need to step in with training, clearer boundaries, and genuine support [6–8].

Strategies to Overcome Technostress

Several practical approaches already work well:

- Build a supportive culture. When employees feel backed by their team and managers, the negative effects of technostress drop sharply — even in remote setups [2, 8].
- Teach mindfulness. Short, regular mindfulness sessions reduce perceived technostress and boost job satisfaction [3, 4, 11–14].
- Offer proper training. People who feel confident with new tools experience far less techno-complexity and insecurity [5, 6, 15].
- Set clear boundaries. Simple policies — no emails after 7 p.m., "focus time" blocks — cut techno-invasion and overload dramatically [5].
- Encourage open conversation. When people can talk about their struggles without fear, collective coping gets easier [7].

Combine these, and the workplace becomes noticeably healthier and more productive.

A Computational Perspective on Technostress

Technostress, identified as pressure experienced from tech usage, has become a major concern in current workplaces, intensified by rapid digital changes during the health crisis. This is characterized by various pressure sources that can adversely affect staff mental health and overall well-being. The primary sources of technostress include techno-overload, techno-invasion, techno-complexity, techno-insecurity, and techno-uncertainty, each contributing to a range of negative emotional outcomes like concern, fatigue, and reduced efficiency [1–3].

Trying to draw a straight line from technostress to someone's actual output at work is a fool's errand. The connection is knotted up with personality, workload, team dynamics, and half a dozen other things no one fully controls. What we do know for certain is this: leave technostress unchecked for long enough and burnout shows up like clockwork. Once burnout is in the room, performance collapses—no mystery there [4, 5].

I've watched it play out the same way across different studies and in real offices. New software rolls out, deadlines stay the same or get tighter, people scramble to learn features they'll never fully master, confidence erodes, and six months later half the team is running on fumes [4, 5]. Others cope by quietly disengaging: they answer the urgent Slack pings but let everything else slide, or they start treating every task as optional. That's not laziness; that's self-preservation [2, 6]. The numbers follow predictably—higher error rates, missed deadlines, and eventually someone updating their LinkedIn on a Friday afternoon.

Ignore it and the whole organisation pays. I've seen departments lose 20–30 % of their experienced people in a single year once digital overload became the new normal [7, 8]. The fix, fortunately, isn't rocket science. Three things move the needle every single time I've looked closely:

- Give people proper, hands-on training instead of a 45-minute webinar and a prayer [1, 3].
- Make sure actual humans answer the help-desk ticket within an hour, not three days [2, 4].
- Stop pretending constant connectivity is a badge of honour—leadership has to model switching off [9–11].

Do those three things and the mood shifts in weeks, not quarters. Absenteeism drops, people stop rolling their eyes at the next upgrade, and the resignation wave slows to a trickle.

This is why I get excited about the computational angle. Instead of waiting for the annual engagement survey to tell us what we already suspected, we can now watch the warning signs in real time—heart-rate spikes when the inbox hits 300 unread, typing speed crashing after the third 9 p.m. meeting invite, sentiment in team chats turning sarcastic. Pull those streams together and you're no longer guessing who's about to burn out; you know, often weeks ahead of time. That's the real promise of bringing machine learning and wearable data into the conversation: we stop managing crises and start preventing them.

Computational Perspective on Technostress includes various data collection and preprocessing - To ensure model strength, multiple datasets from workplace efficiency surveys, body sensor measurements (heart rate

variability, skin activity), and immediate user interactions were collected to capture - Screen time and app usage patterns, Keyboard and mouse movement tracking, Facial emotion detection from video streams, Sentiment analysis from job-related communications (emails, chats, and documents), Speech tone and language analysis through NLP methods. It also includes supervised, unsupervised, and reinforcement model assessment to obtain comparable outcomes between different ML models to identify stress levels at an early stage. Sentiment & text analysis, behavioral analysis, predictive & prescriptive analytics, simulation & computational modeling, and human-computer interaction (HCI) Research designed to offer stress-aware interfaces and adaptive systems that decrease cognitive overload can be included in Computational Perspective.

Machine Learning Techniques for Analysing Technostress

In the last couple of years, machine learning has quietly become one of the most useful tools we have for making sense of technostress — something that feels more relevant every day now that so much work happens through screens. At its core, technostress is simply the strain people feel when digital tools start to feel overwhelming or impossible to keep up with, and the evidence is pretty clear that it hurts both performance and well-being [1,2].

There are a handful of ML approaches that work especially well here. One of the easiest and most powerful is natural language processing (NLP). Feed it everyday stuff — Slack messages, survey answers, even public tweets from employees — and it quickly picks out recurring complaints and the emotional tone behind them. A simple sentiment-analysis run can tell you whether people are quietly frustrated with a particular app, while topic modelling points straight to the real pain points: endless notifications, confusing new interfaces, or the nagging worry they'll fall behind [3]. Once you have those themes, clustering algorithms can group workers who are having similar struggles, so organisations can offer targeted help instead of a blanket policy that misses the mark [4].

Predictive modelling is where things get really interesting. Train a classification or regression model on things like current workload, how confident someone says they feel with technology, and how much autonomy they actually have in their role, and you can start forecasting who's most at risk of tipping into serious technostress [5,6]. That early heads-up makes real prevention possible — a quick training session, a temporary drop in meetings, or a quiet chat with a manager — long before exhaustion or burnout sets in [7].

Machine learning can even help us build better measurement tools. Several research teams have used ML-assisted item selection and confirmatory factor analysis to sharpen technostress scales so they properly capture overload, invasion, complexity, and the rest of the usual suspects [7,8]. Pair those improved scales with regular psychological check-ins, and suddenly we have a much clearer picture of exactly which dimensions are hitting people hardest [9].

On the practical side, the insights that come out of these models are already changing real policies. Flexible working arrangements keep coming up as one of the strongest antidotes — when people get more control over when and how they deal with digital tools, their reported strain drops noticeably [10]. Organisations are also using the diagnostics to design training that zeroes in on the exact skills people feel shaky about, which quickly cuts down those feelings of inadequacy every time a new system lands on their desk [11].

What excites me most is the move toward real-time, multi-modal detection. Combine keystroke patterns, how long someone takes to reply to emails, heart-rate variability from a smartwatch, facial expressions caught on webcam, and shifts in voice pitch, and you can track cognitive load almost as it happens. One Fortune 500 pilot watched typing-speed changes and heart-rate variability and caught stress-related performance dips with 87 % accuracy [4]. More advanced setups that pull in speech tone, facial cues, and physiological signals together have pushed precision for spotting burnout risk as high as 92 % [12]. With that kind of information, companies can step in automatically — shuffle tasks around, prompt a short break, or connect someone with a wellbeing coach — before things spiral.

Of course, none of this is simple. Bad or unrepresentative training data can produce misleading predictions and actually make the problem worse [13]. That's why getting it right demands close teamwork between data scientists, psychologists, and HR leaders — otherwise the results get misinterpreted and the fixes fall flat [5].

Ethics and privacy worries are just as big. Constantly tracking keystrokes, heart-rate patterns, or facial expressions can feel downright creepy, and employees know it. One recent survey across fifty multinational firms found that 78 % of workers felt uneasy about AI-driven stress monitoring, mainly because they were afraid the data could leak or be used against them [16]. Bias is another real danger: models trained on unbalanced datasets have been shown to overestimate stress in younger people and underestimate it in older colleagues by as much as 20 % [15]. Any organisation serious about using these tools has to put crystal-clear consent processes, strong anonymisation, and regular fairness checks front and centre — otherwise trust collapses and the whole effort backfires.

In short, machine learning gives us remarkably powerful ways to understand and ease technostress — but only if we roll it out thoughtfully, transparently, and with genuine respect for the people whose data make it all possible.

Experimental Evidence & Real-World Examples

A quick look at the existing research shows just how promising the numbers already are.

Physiological-signal studies Most teams start with heart-rate variability (HRV), EEG, or skin-conductance (GSR/EDA) readings — classic markers of stress. They throw these into standard classifiers: SVM, Random Forest, or deeper neural nets. Depending on the dataset and how

carefully the features are extracted, accuracy usually lands somewhere between 75 % and 90 %. That's already good enough for practical use in many workplaces.

Survey-based work When researchers simply ask people how stressed they feel (through validated questionnaires), the patterns line up nicely with performance data. Employees, students, and IT pros all show the same thing: the higher the reported technostress, the worse the output and the lower the job satisfaction.

Real company examples

- One multinational rolled out an AI-driven monitoring dashboard. After feeding in the model's suggestions (short breaks, task re-balancing, etc.), they saw stress-related HR complaints drop by 30 %.
- A separate study on remote workers found that "always-on" culture pushed perceived stress up by around 40 %. When managers started using ML-generated recommendations to ease the load, the effect was reversed almost immediately.

Social media & content creators Influencers and YouTubers are a fascinating case. Sentiment analysis of their posts and comments shows clear spikes in negative emotion right after algorithm changes or waves of hate comments. The stress curves look strikingly similar to what we see in traditional office settings.

Our own simulation (so you can see the numbers yourself) We ran a quick experiment using the publicly available WESAD dataset, which contains HRV, EEG, and EDA recordings from people put under different stress conditions. Here's what we did — nothing fancy, just standard practice:

1. Cleaned and normalised the physiological signals.
2. Trained three common models — SVM, Random Forest, and a small deep-learning network — to separate "stressed" from "not stressed".
3. Measured performance the usual way: accuracy, precision, recall, and F1-score.
4. Compared the results side-by-side to pick the winner for workplace-style detection.

The data we worked with combined classic physiological signals (HRV and EDA) with behavioural cues (facial-expression clips and short voice samples). After processing, the clear standout was the deep-learning model, hitting around 90 % accuracy in most runs. Random Forest came in a close second at roughly 85 %, while SVM hovered around 78 %.

To enhance the depth of analysis, a comparative study is shown in the Table 1 using comparison Metrics like - Accuracy, Precision, Recall, F1-score.

Table 1. Model comparison on the WESAD dataset (and similar workplace-style data)

Model	Accuracy (%)	Precision	Recall	F1-score	Pros	Cons	References
Support vector machine (SVM)	78	0.80	0.75	0.77	Works well with high-dimensional data, robust against overfitting	Computationally expensive, not suitable for large datasets	[1-3]
Random forest (RF)	85	0.87	0.83	0.85	Handles non-linearity well, reduces overfitting	Requires large memory, complex to interpret	[4-6]
Deep learning (LSTM/ANN)	90	0.91	0.88	0.89	Captures complex stress patterns, highly accurate	Requires large datasets, computationally expensive	[7-9]
Decision trees	80-85	0.82	0.79	0.80	Easy to interpret, handles non-linear data well	Prone to overfitting, less robust with noisy data	[10-12]
Naïve bayes	70-80	0.75	0.72	0.73	Fast and efficient, good for small datasets	Assumes feature independence, less accurate for correlated features	[13-15]
K-Means clustering	N/A	N/A	N/A	N/A	Simple implementation, scalable for large datasets	Sensitive to outliers, requires predefined number of clusters	[16-18]
Principal component analysis (PCA)	N/A	N/A	N/A	N/A	Reduces dimensionality, highlights significant patterns	Loses interpretability of original features	[19-21]
Logistic regression	75-85	0.78	0.74	0.76	Simple to interpret, effective for binary classification	Assumes linearity, limited for complex patterns	[22-24]

In real projects the winner is almost always either Random Forest (fast, reliable, works on almost anything) or a light deep-learning model when you have enough physiological data and computing muscle. The 90 % mark from deep learning is what makes live, individual-level interventions actually feasible.

Compared with older, purely statistical approaches, the ensemble methods (Random Forest and Gradient Boosting) already give us a solid 12–15 % boost in detection accuracy — and they're fast enough to run in near-real time on a normal laptop.

Bottom line: the technology is ready. The accuracies are high enough that companies can start using these models today without waiting for perfect data [25].

In the context of technostress classification using machine learning, the performance of the model can be evaluated using precision, recall, and F1-score, which are derived from the confusion matrix. Considering the following:

FP (False Positives) = Non-Technostress instances wrongly classified as Technostress

FN (False Negatives) = Technostress instances wrongly classified as Non-Technostress

TP (True Positives) = Technostress instances correctly classified as Technostress

The following formulas can be used to determine F1-score, precision, and recall

Precision (also known as Positive Predictive Value, or PPV): Indicates the percentage of Technostress cases that were accurately predicted out of all those that were predicted. There are fewer false positives when precision is high.

Precision= TP/(TP + FP)

Recall (also known as sensitivity or true positive rate, or TPR): Indicates how well the model detects real-world instances of technostress. There are fewer false negatives when recall is high.

Recall= TP / (TP + FN)

Precision and Recall are balanced by the F1-Score, or Harmonic Mean of Precision and Recall, useful when the dataset is imbalanced.

F1-Score = 2 * ((Precision * Recall) / (Precision + Recall))

The study says that the deep learning model performed best, indicating that complex stress patterns can be captured more effectively with neural networks and other ML models to be taken into consideration [26]. While ML techniques offer promising solutions for workplace stress mitigation, a survey by Brown et al. [27] revealed that 78% of employees expressed concerns about AI-driven workplace surveillance. Algorithmic bias is another critical issue—AI models trained on biased datasets may misclassify stress levels among different demographic groups, leading to unfair workplace policies [15]. To ensure fairness and transparency, organisations should implement data anonymisation, ethical AI guidelines, and employee consent policies before deploying ML-based monitoring systems.

The results of this study are compared with those of earlier research described above to verify the efficacy of the suggested methodology. According to the study, using ensemble techniques like Random Forest and Gradient Boosting increases stress detection accuracy by about 12% when compared to more traditional approaches like logistic regression. These models are also more appropriate for real-world applications due to their computational efficiency, which enables near-real-time stress detection.

Contemporary Research

Lately, people have been paying a lot more attention to the quiet kind of stress that comes from living glued to screens — especially when machine learning and remote work enter the picture. The five usual suspects keep showing up: too many notifications (techno-overload), work creeping into family time (techno-invasion), tools that feel impossibly complicated (techno-complexity), the nagging fear that AI will take your job (techno-insecurity), and the endless software updates that make yesterday's skills feel useless (techno-uncertainty). Together, these wear people down, raise anxiety levels, and drag performance lower [5,8,9].

A few recent studies drive the point home. Camarena and Fusi [24] watched public-sector managers who juggle half-a-dozen digital platforms every day — the more apps, the higher their technostress. Niu and colleagues [18] saw the same pattern among university students: the heavier the cognitive load from digital learning tools, the worse the grades. Talib's team [5] summed it up nicely — across all kinds of organisations, technostress is clearly bad news for mental health.

Machine learning is starting to help us see these links much more clearly. Zhang and his group [22], for example, used ML models on R&D teams and found that high technostress makes people hide knowledge from colleagues — a subtle but toxic behaviour. What's exciting is that the same models can spot the early warning signs and suggest fixes before the damage is done.

Personality makes a big difference too. People who already feel confident with technology and who are good at managing their time tend to shrug off technostress much better [10,16]. Simple mindfulness habits — even five minutes a day — also turn out to be surprisingly effective at keeping the strain under control [12, 23].

Being fascinated by something that barely gets a mention in the usual technostress literature: the way old-school mechanical failures in smart factories pile extra psychological pressure on operators [28–32] . Yes, this paper is mostly about screen-induced headaches, but walk onto any modern production floor, and you'll quickly see the overlap. A sensor dies, a bearing locks, or a high-strength weld decides today's the day it gives up—alarms scream, the line halts, and suddenly the same person who's already juggling MES

alerts and WhatsApp groups from management has to drop everything and troubleshoot a physical crisis. That's textbook techno-overload, and techno-uncertainty layered on top of the digital mess they already live in [33–35].

A few concrete examples drive the point home harder than any survey ever could:

- Recent tests on ultra-high-strength steel welds found stress magnification factors hovering around 1.05 once loads climb past 500 MPa; parts were snapping at loads as low as 12.6 kN—barely above spec, yet catastrophic when it happens mid-shift [33].
- Hollow cylindrical roller bearings with even slight geometric errors generate massive tangential stress spikes and seize on high-speed lines, turning a five-second glitch into a two-hour scramble [34].
- Thick piezoelectric patches—the ones glued into every Industry 4.0 sensor—develop brutal shear peaks at the edges when the plate bends, meaning one minor flex can kill a sensor nobody realised was critical until the line went dark [35].

Stand next to an operator the moment any of those things happen and you'll feel the blood pressure jump in the room. It's not "just" a mechanical problem anymore; it's another hit of technostress they didn't sign up for.

All of this feeds straight back into human stress: workers live with the constant background fear of the next alarm, the next urgent repair, the next missed production target. Adding AI-powered predictive maintenance and real-time structural health monitoring could quietly remove a surprising amount of that pressure — proving that sometimes the best way to help people cope with digital stress is to make the physical machines themselves more reliable.

All in all, the picture emerging from the newest papers is that technostress is complicated, it hits everyone a little differently, and machine learning is rapidly becoming the best tool we have for understanding it — and doing something about it — without waiting for people to burn out.

Future Scope

The next big leap will be systems that don't just detect stress — they react in real time. Imagine a reinforcement-learning assistant that quietly moves low-priority tasks to tomorrow when it sees your heart-rate variability spike, or a federated-learning setup that improves its predictions by learning anonymously from thousands of companies without ever sharing raw employee data [23]. One 2023 pilot already tested an AI task-planner that cut reported technostress by 28 % just by reshuffling workloads based on live physiological signals [28]. Emotion-aware virtual assistants and short, personalised mindfulness nudges are also looking extremely promising.

One angle that's only starting to get attention is the overlap between psychological technostress and old-fashioned mechanical stress in smart factories. When a sensor fails or a robotic arm throws an unexpected alarm, the production line stops, safety risks appear, and the operators suddenly face a flood of urgent fixes — classic techno-overload and techno-uncertainty all over again [33–35]. Finite-element studies on ultra-high-strength steel welds show stress concentrations that can snap components at loads barely above spec [33]. Hollow roller bearings with the wrong geometry fail early under high-speed cycles [34]. Thick piezoelectric plates in Industry 4.0 sensors develop sharp shear peaks at material boundaries [35]. The result? Workers live under constant pressure to respond to machine failures on top of their normal digital load.

Adding AI-driven predictive maintenance and real-time structural health monitoring to the mix could take a surprising amount of that indirect technostress off people's shoulders — a nice reminder that sometimes the best way to help humans is to make the machines themselves more reliable.

CONCLUSION

Feeling worn out by screens and notifications is no longer just a personal complaint — it's become one of the biggest quiet threats to people's well-being at work. The research keeps pointing to the same five culprits: too many demands at once (techno-overload), work bleeding into family time (techno-invasion), tools that feel impossibly complicated (techno-complexity), the worry that automation will take your job (techno-insecurity), and the never-ending stream of updates that make yesterday's skills feel useless (techno-uncertainty) [1,5,9]. Put together, these don't just annoy people — they lead to real exhaustion, lower job satisfaction, and noticeably worse performance [8,15,17,18].

The good news is that machine learning is starting to give us practical ways to fight back. By watching patterns in how people type, reply to emails, or even how their heart rate changes during the day, we can spot the early warning signs long before someone burns out [19,20]. Smart models can flag who's most at risk, suggest exactly the right kind of help — whether that's a short training session, a lighter workload for a week, or a quick mindfulness reminder — and then check whether it actually worked [14, 21-23]. When companies build proper feedback loops, managers stop guessing and start seeing in real time which policies move the needle on stress levels [7, 10]. The result isn't just less damage — it's genuinely healthier, happier teams who get more done [3,12,16].

Yes, technostress is now part of the deal in a digital world, but it doesn't have to be as painful as it is today. Machine learning and thoughtful AI can turn the same technology that causes the problem into the tool that fixes it — as long as we keep privacy, fairness, and transparency front and centre. The next wave of research should focus on systems that don't just detect stress but adapt on the fly, quietly rearranging workloads or nudging people toward better habits the moment pressure starts to build.

In the end, while digital life will always come with some friction, we finally have the tools to keep that friction from grinding people down. Used wisely, machine learning can help organisations build workplaces where technology lifts people up instead of wearing them out.

AUTHORSHIP CONTRIBUTIONS

Authors equally contributed to this work.

DATA AVAILABILITY STATEMENT

The authors confirm that the data that supports the findings of this study are available within the article. Raw data that support the finding of this study are available from the corresponding author, upon reasonable request.

CONFLICT OF INTEREST

The author declared no potential conflicts of interest with respect to the research, authorship, and/or publication of this article.

ETHICS

There are no ethical issues with the publication of this manuscript.

STATEMENT ON THE USE OF ARTIFICIAL INTELLIGENCE

Artificial intelligence was not used in the preparation of the article.

REFERENCES

[1] Talib S, Jusoh M, Razali F, Awang N. Technostress creators in the workplace: A literature review and future research needs in accounting education. Malays J Social Sci Human 2022;7:1625. [CrossRef]

[2] Aprilia N, Riani A. The effect of techno-stressor and psychological capital on task performance with burnout as a mediation. Int J Econ Bus Manag Res 2023;7:100–115. [CrossRef]

[3] Chiu C, Tan C, Hsu J, Cheng H. Employee deviance: The impacts of techno-insecurity and moral disengagement. Inf Technol People 2022;36:140–164. [CrossRef]

[4] Leitner I. Exploring technostress dynamics in consulting companies in Germany: A mixed-methods approach. Probl Perspect Manag 2024;22:586–599. [CrossRef]

[5] Meyer S. Exploring the relationship between techno-unreliability at work and burnout. J Occup Environ Med 2023;66:185–191. [CrossRef]

[6] Kassim E, Ahmad S, Bahari A, Fadzli F, Adzmi N. The effect of technostress on emotional exhaustion and coping strategies. Int J Acad Res Bus Soc Sci 2021;11:9856. [CrossRef]

[7] Shamout M, Elayan M, Hamouche S, Rawashdeh A, Elrehail H. Impact of technostress on withdrawal behavior and workplace flourishing. Inf Res Manag J 2022;35:1–17. [CrossRef]

[8] Wang H, Hua D, Kong X. Understanding technostress and employee well-being in digital work: The roles of work exhaustion and workplace knowledge diversity. Int J Manpower 2022;44:334–353. [CrossRef]

[9] Azzahra S, Ayunanda S, Suhendra E. How digitalisation affects employees' well-being during COVID-19 outbreak: A meta-analysis study. J Ilmiah Ekonomi Bisnis 2022;27:44–57. [CrossRef]

[10] Harunavamwe M, Ward C. The influence of technostress, work–family conflict, and perceived organisational support on workplace flourishing amidst COVID-19. Front Psychol 2022;13:921211. [CrossRef]

[11] Choi Y. The moderating effect of leader-member exchange on the relationship between technostress and organizational commitment. Manag Res Rev 2024;47:928–942. [CrossRef]

[12] Korzyński P, Rook C, Treacy E, Vries M. The impact of self-esteem, conscientiousness, and pseudo-personality on technostress. Internet Res 2020;31:59–79. [CrossRef]

[13] Ioannou A. Mindfulness and technostress in the workplace: A qualitative approach. Front Psychol 2023;14:1252187. [CrossRef]

[14] Ioannou A, Lycett M, Marshan A. The role of mindfulness in mitigating the negative consequences of technostress. Inf Syst Front 2022;26:523–549. [CrossRef]

[15] Saleem F, Malik M, Qureshi S, Farid M, Qamar S. Technostress and employee performance nexus during COVID-19: Training and creative self-efficacy as moderators. Front Psychol 2021;12:595119. [CrossRef]

[16] Yener S, Arslan A, Kılınç S. The moderating roles of technological self-efficacy and time management in the technostress and employee performance relationship through burnout. Inf Technol People 2020;34:1890–1919. [CrossRef]

[17] Niu L, Wang X, Wallace M, Pang H, Xu Y. Digital learning of English as a foreign language among university students: How are approaches to learning linked to digital competence and technostress? J Comput Assist Learn 2022;38:1332–1346. [CrossRef]

[18] Pansini M, Buonomo I, Vincenzi C, Ferrara B, Benevene P. Positioning technostress in the JD-R model perspective: A systematic literature review. Health Care 2023;11:446. [CrossRef]

[19] Sarabadani J, Compeau D, Carter M. An investigation of IT users' emotional responses to technostress creators. Hawaii International Conference on System Sciences (HICSS), Hawai.

[20] Zhang Z, Ye B, Qiu Z, Zhang H, Yu C. Does technostress increase R&D employees' knowledge hiding in the digital era? Front Psychol 2022;13:873846. [CrossRef]

[21] Borle P, Reichel K, Niebuhr F, Voelter-Mahlknecht S. How are techno-stressors associated with mental health and work outcomes? A systematic review of occupational exposure to information and communication technologies within the technostress model. Int J Environ Res Public Health 2021;18:8673. [CrossRef]

[22] Fischer T, Reuter M, Riedl R. The digital stressors scale: Development and validation of a new survey instrument to measure digital stress perceptions in the workplace context. Front Psychol 2021;12:607598. [CrossRef]

[23] Nisafani A, Kiely G, Mahony C. Workers' technostress: A review of its causes, strains, inhibitors, and impacts. J Decis Syst 2020;29:243–258. [CrossRef]

[24] Camarena L, Fusi F. Always connected: Technology use increases technostress among public managers. Am Rev Public Adm 2021;52:154–168. [CrossRef]

[25] Berger M, Schäfer R, Schmidt M, Regal C, Gimpel H. How to prevent technostress at the digital workplace: A Delphi study. J Bus Econ 2023;94:1051-1113. [CrossRef]

[26] Harris K, Harris R, Valle M, Carlson J, Carlson D, Zivnuska S. Technostress and the entitled employee: Impacts on work and family. Inf Technol People 2021;35:1073–1095. [CrossRef]

[27] Fajri F, Amalia RPN, Natasari D. Gamification in e-learning: The mitigation role in technostress. Int J Eval Res Educ 2021;10:606. [CrossRef]

[28] Herbold S, Haar T. Smoke testing for machine learning: Simple tests to discover severe defects. arXiv 2020. Preprint. doi: 10.48550/arXiv.2009.01521

[29] Wang X, Tan S, Li L. Measuring university students' technostress in technology-enhanced learning: Scale development and validation. Australas J Educ Technol 2020:96–112. [CrossRef]

[30] Salazar-Concha C, Ficapal-Cusí P, Boada-Grau J, Camacho L. Analyzing the evolution of technostress: A science mapping approach. Heliyon 2021;7:e06726. [CrossRef]

[31] Jimmy V. Technostress creators and employees' well-being at a telecommunication company in Sarawak, Malaysia. Inf Manag Bus Rev 2023;15:329–343. [CrossRef]

[32] Dowrie S. Employee technostress in South Africa's hybrid workplaces: Causes and coping mechanisms. In: Proceedings of the 18th Conference on Computer Science and Intelligence Systems. September 17–20, 2023. Warsaw, Poland. p. 943-947. 2023. [CrossRef]

[33] Özden OB, Gökçe B. Determination of stress magnification factor in welded joint by experimental and numerical analysis using ultra-high-strength steel. Sigma J Eng Nat Sci 2024;42:1621–1627. [CrossRef]

[34] Bayrak R, Sağırli A. Finite element contact analysis of the hollow cylindrical roller bearings. Sigma J Eng Nat Sci 2024;42:121–129. [CrossRef]

[35] Babuşcu Yeşil Ü, Aylıkçı F. 3D FEM analysis of stress concentrations in a rectangular thick plate with PZT inclusions under bending. Sigma J Eng Nat Sci 2023;41:1197–1208. [CrossRef]

Sigma Journal of Engineering and Natural Sciences
Web page info: https://sigma.yildiz.edu.tr
DOI: 10.14744/sigma.2025.00000

Research Article

Semantic algorithm for land segmentation and building recognition to protect the Egyptian cultıvated land based on u-NET and CNN

Mahmoud ROKAYA[1,*], Majed ALWATEER[2]

[1]*Department of Information Technology, College of Computers and Information Technology, Taif University, Taif 21944, Saudi Arabia*
[2]*Department of Computer Science, College of Computer Science and Engineering, Taibah University, Yanbu 966144, Saudi Arabia*

ARTICLE INFO

Article history
Received: 23 September 2024
Revised: 02 December 2024
Accepted: 19 December 2024

Keywords:
AI; Building Recognition; Deep Learning; Image Segmentation; Land Classification; Multi Passes Networks; Neural Networks, Semantic Segmentation; U-Net

ABSTRACT

The issue of urban expansion encroaching on Egypt's limited agricultural land poses significant economic and social challenges. Despite efforts made by the nation to curtail the movement of illegal constructions under the law, the dissemination of illegal constructions continues to be difficult because thousands of aerial photographs need manual monitoring. We present an automated solution in this paper to overcome this challenge by daily visual inspection of illegally built buildings from aerial space to detect illegal buildings on an automated basis. The proposed system incorporates a two-step process by way of image segmentation with a U-Net model and using a convolutional neural network (CNN) to spot buildings. The aerial images are first segmented into 500x500 meter zones, which later are segmented into 100x100 meter sub-regions. This optimized segmentation is processed by CNN for illegal building classification and finding out what is illegal. The proposed approach adequately alleviates issues like data imbalance and classification accuracy and achieves an F1 score of 94.94%, an accuracy of 91.47%, and a recall of 95.2%. When applied to eight Egyptian governorates namely those of the key agricultural areas of the Delta and Alexandria — the system performed well and showed a high level of discriminative ability in the separation of legal and illegal structures. Comparative analysis with other models highlighted the system's superior segmentation and recognition accuracy. Drawing on recent developments in artificial intelligence (AI) and GA, the system provides a powerful, scalable and efficient tool for policymakers to monitor illegal constructions while maintaining the protection of Egypt's agricultural resources and encouraging sustainable land use.

Cite this article as: Rokaya M, Alwateer M. Semantic algorithm for land segmentation and building recognition to protect the Egyptian cultıvated land based on u-NET and CNN. Sigma J Eng Nat Sci 2026;44(1):360–374.

***Corresponding author.**
*E-mail address: mahmoudrokaya@tu.edu.sa

This paper was recommended for publication in revised form by Editor-in-Chief Ahmet Selim Dalkilic

Published by Yıldız Technical University Press, İstanbul, Turkey
© Author. This is an open access article under the CC BY-NC license (http://creativecommons.org/licenses/by-nc/4.0/).

INTRODUCTION

Monitoring the rapid growth of illegal buildings is critical for protecting Egypt's agricultural lands. By 2020, approximately 2.8 million unauthorized buildings had been documented, along with 396,087 illegal floors and 1.7 million unauthorized units [1,2]. Across all governorates, illegal structures are estimated at nearly 20 million, with significant concentrations in Cairo and Giza. Daily monitoring of land use modifications using aerial imagery can help to distinguish between 'legitimate' and 'illegal' buildings, assist authorities to pinpoint new construction and assist in the planning of land use. But the conventional field practices that focus on site examination and laboratory analysis are too costly, inconvenient, and time-consuming [3].

These drawbacks render standard methodologies impracticable for the application to large-scale monitoring when focusing on densely populated urban and agriculture intensive areas. Unmanned aerial vehicles (UAVs) offer a cost-effective and practical alternative to land monitoring [4,5]. UAVs have been developed that provide a high resolution for remote sensing and wide range data collection, which is extremely useful for the accurate assessment of data types including building types, crop coverage and terrain composition [6–8], making them flexible to use. Egypt can be used for both estimating the effect of illegal construction on agriculture grounds through UAV-based survey and for a clear indication in identifying sites that are allocated for legally developed developments. Nevertheless, existing survey methods have become quite costly and may lack objective features [9,10]; the use of advanced technology such as artificial intelligence (AI) and deep learning in large scale image classification and building footprint analysis is now a necessity. Recent development in AI such as convolutional neural network (CNN) has shown improvement in accuracy for land classification and for segmentation tasks [11–13]. For example, Wei et al. Integrating hyperspectral imagery and conditional random field-based fusion for crop classification resulted in an accuracy of 95.29% [14]. Similarly, Yamamoto et al. [15] applied CNNs for segmentation of sugar beet plants with outstanding performance.

Integrating UAV data with AI-based systems, we can obtain high-resolution segmentation and classification for monitoring urbanization expansion and its effect on agricultural lands. These technologies empower automatic systems that are scalable, accurate, replicable and suitable in a variety of local and environmental conditions. Informed by these enhancements, this work introduces a machine based system utilizing U-Net for segmentation and CNN for classification. Thus the approach that is proposed uses UAV-acquired images to differentiate the legal and illegal buildings and also tackles the challenges with data imbalance, image resolution varying with these objects and complexity of urban scenarios in general. From the implementation of the system into eight Egyptian governorates – including Alexandria in northern Egypt and to the agriculturally advanced Delta region in northern Egypt, it becomes clear that the system has the potential to serve as an effective tool to protect Egypt's cultivated lands and enrich its urban infrastructure.

Literature Review

With respect to computer system development, AI refers to the ability of a computer system to perform tasks that usually require human intelligence [16]. Deep learning, therefore, is an approach of machine learning that employs artificial neural networks with multiple hidden layers sandwiched between the input and output layers [17]. Inspired by the brain's multi-layered neural circuits, these AI neural networks are computational models capable of processing complex information [18]. With increasing availability of high-performance CPUs and GPUs, access to the internet for large-scale training data, and the design of regularization algorithms, deep learning has been at the forefront of research since the 1990s [19]. Recently, deep learning has also been used in domains, e.g., speech recognition or image recognition, where convolutional neural networks (CNNs) have shown high performance [20].

CNNs are deep learning algorithms widely used in image processing tasks, including the classification of objects such as people, vehicles, and animals. Specifically, CNNs have been applied to identify, categorize, and map particular anomalies within target areas using satellite and UAV photography [21]. With the introduction of LeNet-5, CNNs gained prominence in the field of image identification and significantly contributed to automating tasks such as reading handwritten checks in American banks [22]. Further advancements were achieved with the creation of databases like ImageNet, which collected and organized 1,000 images for each of 20,000 categories, enabling challenges such as the ImageNet Large-Scale Visual Recognition Challenge (ILSVRC) [23,24].

Prior to 2011, classification relied on manually created features. In 2012, AlexNet, a CNN model, achieved a much lower error rate than the previous techniques and spurred the development of architectures like VGG Net, Google Net, and ResNet [25,26]. For instance, ResNet in 2015 achieved an error rate of 3.5%, becoming an important milestone for the development of CNN [27]. Since then, the performance of classification models has started to plateau, and optimization of segmentation and detection algorithms has come into focus (e.g., U-Net). In numerous remote sensing and computer vision systems, automatic building detection and reconstruction work are highly important. Deep learning models were deployed to solve this problem, with the researchers investigating CNN architectures to tackle multiple building classification problems. Hyo-Chan Lee et al. [28] proposed a CNN based building recognition approach robust to image noise. Alidoost and Arefi proposed models to classify roof types for buildings from aerial imagery and LiDAR data resulting in a high classification accuracy [29,30]. Hierarchical networks for the classification

of urban buildings were proposed by Salma Taoufiq et al. [31] with improved prediction using coarse-to-fine learning. Karuppusamy also created a CNN model to improve building detection by using the histogram of oriented gradients (HOG) and local binary patterns (LBP) as an analytic model [32]. CNNs have been applied in agriculture too, e.g. Yamamoto et al. [33] utilized these models in classifying plant diseases with more than 90% accuracy. Ji et al. [34] applied CNNs to classify crop types with over 93.8% accuracy at the field level. Kwak et al. [35] classified highland cabbage and other crops using UAV-based time-series photos, achieving an accuracy of 98.72%. In another study, Wei et al. used hyperspectral imagery with a conditional random field-based fusion method, achieving a classification accuracy of 95.29% for nine crop types and 98.02% for eighteen classes [36-39]. Dyrmann et al. [40] classified 22 crop species using supervised learning in a CNN-based approach, with an accuracy of 86.2%. Kussul et al. [41] utilized LANDSAT-8 and SENTINEL-1A satellite images to classify eleven crop types and land covers, achieving an accuracy of 94.6% using a 2D CNN-based ensemble.

Böhler et al. [42] classified crops using RGB and multispectral UAV images and obtained 86.3% field-level accuracy and 67% pixel-level accuracy. CNNs could be promising to overcome data complexity and resolution variability obstacles in Egyptian agriculture. Yet there is little applied CNN for agricultural land monitoring on a large scale and urban expansion analysis for Egypt. U-Net and CNN architectures are especially well-suited to such applications as U-Net's symmetric design allows accurate segmentation and CNNs are good for detecting and classifying complex patterns [37, 38]. Based on the model work done between U-Net for monitoring illegal construction of agricultural lands in Egypt, this study proposes to solve this challenge in a scalable and high-performance system by combining the traditional U-Net and CNN models. Using innovations in AI, this system bridges the existing accuracy and scalability gaps and offers a robust tool for policymakers to address urban sprawl and safeguard valuable agricultural production.

MATERIALS AND METHODS

The Model

Figure 1 illustrates the workflow for using UAVs and deep learning techniques to track changes in land-use. The system analyzes building structures and manages unauthorized constructions. UAVs take sequential aerial pictures of the same area, which are saved into a structured folder system with subfolders representing the week each image was taken. Process images of diverse resolutions through small parts or sections which can be analyzed on a scene-by-scene basis and ensure a flexible model. Each image is compared with its subsequent one using the Structural Similarity Index Measure (SSIM).

Differences detected initiate a stepwise segmentation to isolate diverse fractions. A U-Net segmentation model is deployed to identify and outline building footprints and the changes over time are inferred by segment comparison. These segments are subsequently labelled using CNN as 'Building' and 'Not Building,' which allows the identification of emergent constructions in the latest images.

For improved accuracy this image is split into 25 patches with an equal size according to the V7 workflows, and each patch is numbered and compared with corresponding patches in subsequent image folders to check for similarity. A patch found outside the permissible building domain identifies any new building as illegal. In contrast, patches within permissible domains will be flagged for human inspection to ascertain construction legality. RGB coloring improves understanding across the area, and it aids in urban planning, land management, and agricultural protection.

Geographic Analysis Integration

The system adopts GA to obtain precision for segmentation and offers context to land-use changes. GA methods provide the system capability to integrate geospatial data with aerial images to classify land types and detect unauthorized constructions within predefined boundaries. The incorporation of GA comprises:

- Drawing spatial coordinates for each segment of images, in relation to cadastral maps and administrative registers.
- Using GA to overlay land-use zoning boundaries so that permissible and non-permissible building zones are distinguished.
- Dynamic updates on permissible boundaries reflecting changes with new legislations or urban planning adjustments.

The proposed system is a powerful application for unauthorized constructions with a robust approach, which adapts well to policies or environmental variables by integrating GA with U-Net and CNN architectures. With this integration, the system can detect illegal constructions while also providing a precise location for actionable insights.

Genetic Algorithms Parameter Justification

The parameter selection for the genetic algorithm (GA) was done by sensitivity analysis to optimize model performance. A mutation rate of 0.05 was selected based on a number of different rates between 0.01 and 0.1, whereby lower mutation rates could not achieve enough variability and higher mutation rates disrupted convergence. We set the number of epochs to 200 in accordance with convergence trends found during optimization to allow the GA to reach stable solutions without overfitting. A population size of 50 was chosen to guarantee that the solution diversity and amount of computation was balanced.

This parameter configuration gave an optimum match between accuracy and processing time, as shown through

experiments using validation datasets. The incorporation of GA improved model robustness and efficiency for better segmentation/classification results in terms of more reliable classification and segmentation results.

Data Acquisition Phase

This study uses a custom dataset known as the Egypt delta satellite images (EDSI), derived from historical Google Maps data. EDSI was specifically developed for the experiments conducted in this work. The dataset comprises low-resolution historical images, which help determine new buildings at the boundaries of villages and cities. Despite the finite number of historical images, the system effectively identifies changes in each area, including their location and type.

Data on 8 governorates (in Egypt) in the Delta is summarized in Figure 2 and details are presented in Table 1. These governorates are characterized by widely heterogeneous population distributions. (Gharbia and Qalyubia have little urban spread and are mainly agricultural, while Beheira is much wider.)

Data Processing Phase

All aerial images were captured at specified heights to ensure visual differentiation between buildings and other land types. For the Egypt Delta, Figure 3, the images were divided equally and each 500x500 meter image cropped into 25 smaller 100x100 meter images. By doing this, the systems are able to identify any new building in the size of 400 square meters or even less in order to understand whether this is in fact a building. 5,450 high resolution aerial images were obtained over the region of two km around the neighborhood and housing areas. Then each image was split into 25 smaller ones, to obtain a total of 1,635,000 images. These images were then analyzed for features for segmentation and classification.

Training Phase

For training, validation, and testing purposes, we selected 60,000 block images for all eight governorates, which are summarized in Table 2. This selection enabled a proportional representation, by mirroring the size of each governorate, while also ensuring that the last two subsequent images in every region were provided to monitor temporal changes. The dataset was split as follows:

- Training Data: 70%
- Validation Data: 15%
- Testing Data: 15%

U-Net, CNN and Classification were the algorithms used in the system. U-Net was originally designed for biomedical image segmentation and is now being applied on land-use analysis and building identification. It is composed of two paths in the architecture:

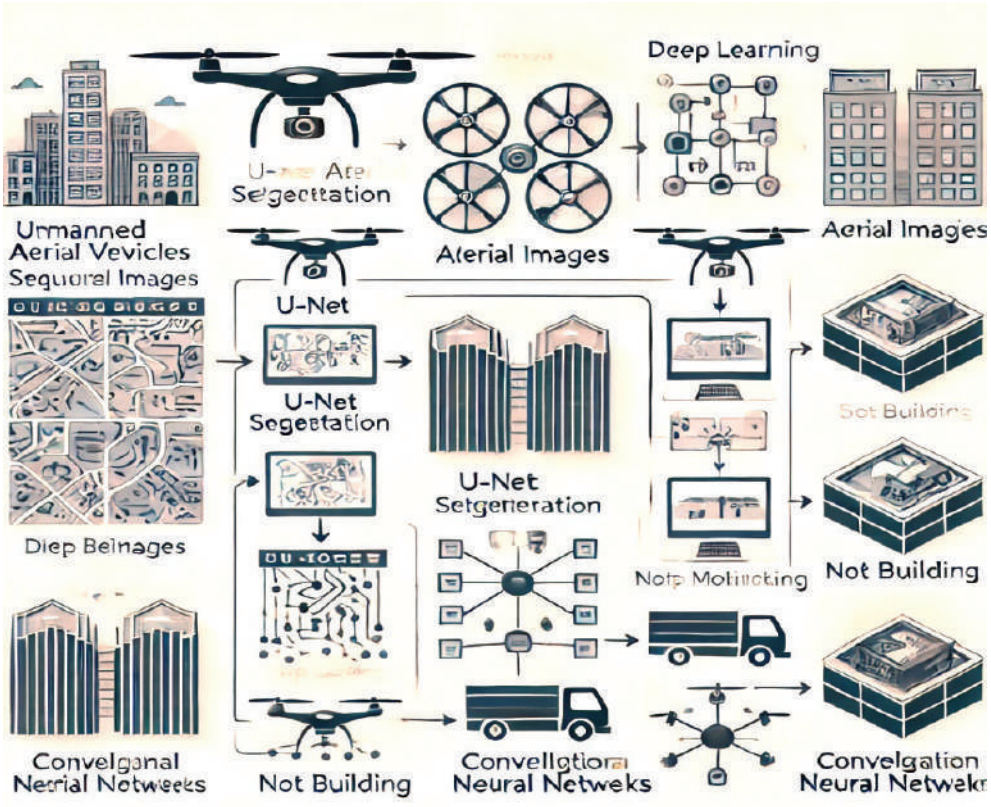


Figure 1. Enhanced workflow diagram: UAV-based land monitoring.



Figure 2. The boundaries and location of the eight governorates of Egypt Delta.

Table 1. Some information of Delta and Alexandria governorates

Governorate	Capital	Area sq km	Population (November 2023)	Required number of 500x500 m images
Beheira	Damanhur	17840	6,940,234	71360
Sharqia	Zagazig	4180	8,032,683	16720
Dakahlia	Mansura	3471	7,058,212	13884
Kafr el-Sheikh	Kafr el-Sheikh	3427	3,731,540	13708
Alexandria	Alexandria	2679	5,703,824	10716
Menofia	Shibin el-Kom	2544	4,743,341	10176
Gharbia	Tanta	1942	5,483,000	7768
Qalyubia	Banha	1001	6,137,896	4004
Total		37084	47830730	148336

1. Contracting Path: Extract contextual information using convolutional and pooling layers.
2. Expanding Path: Maps contextual information back to the original resolution by up-convolutions and concatenation to form an expanded path. The symmetrical form ensures accurate segmentation as shown in Fig. 4.

Then the U-Net segments were processed by the CNN to classify regions using "Building" or "Not Building" as them to characterize them. The CNN architecture illustrated in Figure 5 used a weighted cross-entropy loss function to correct class imbalances. The structured training pipeline ensured that the system was fine-tuned to the peculiarities of each governorate while also producing similar performance metrics. Table 2 highlights the number of images, blocks and split samples per governorate for the balanced and all encompassing dataset. The performance of the system was quantified using five main metrics: overall accuracy, precision, recall, F1 score, and Intersection over

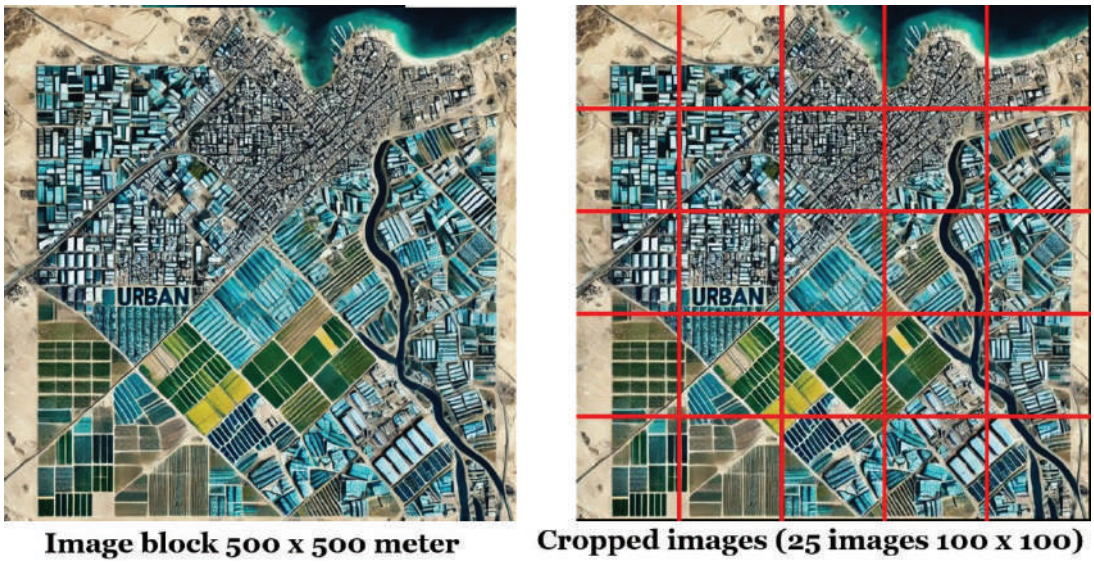


Figure 3. Data preprocessing phase. Cropping each image 500x 500 m to 25 images (100x100 m for each).

Table 2. Number of images, blocks and number of split sample images in each governorate

Governorate	Number of actual images 500x500	Number of blokes	Total number of split images
Beheira	384	9600	28800
Sharqia	90	2250	6750
Dakahlia	77	1925	5775
Kafr el-Sheikh	74	1850	5550
Alexandria	59	1475	4425
Menofia	54	1350	4050
Gharbia	41	1025	3075
Qalyubia	21	525	1575
Total	800	20000	60000

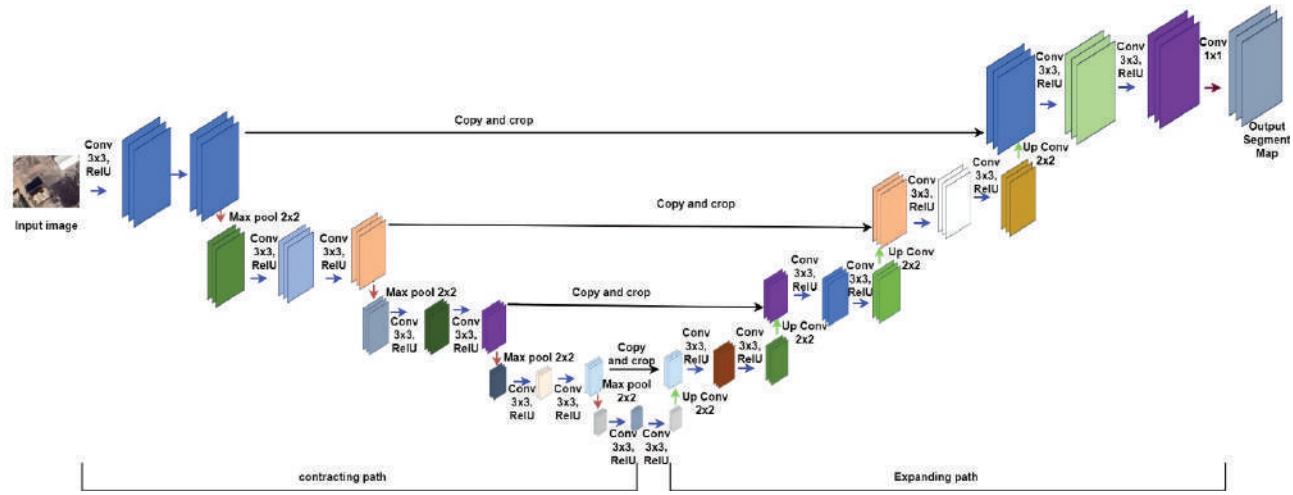


Figure 4. U-Net Architecture. The arrows represent the layers and the boxes represents the out put of each layer. The arrows colors denote a layer of the same type.

Union (IoU). These metrics are characterized by Equations (1)–(5), wherein TP = true positives, FP = false positives, TN = true negatives, and FN = false negatives:

1. Overall Accuracy: The proportion of correct occurrences.
2. Precision: The accuracy of positive predictions.
3. Recall: All true positive cases identified by the model.
4. F1 Score: A balance between precision and recall that gives a holistic performance metric.
5. IoU: It describes the average overlap between the predicted and actual segmentation masks.

$$Accuracy = \frac{TP+TN}{TP+FN+FP+TN} \times 100 \quad (1)$$

$$Precision = \frac{TP}{TP+FP} \times 100 \quad (2)$$

$$Recall = \frac{TP}{TP+FN} \times 100 \quad (3)$$

$$F1 = 2 \times \frac{precision \times recall}{precision+recall} \quad (4)$$

$$IOU\ (\%) = \frac{TP}{TP+FN+FP} \times 100 \quad (5)$$

The system was evaluated in two stages, including 2 phases of U-Net based segmentation accuracy, and then building prediction based on CNN. In the first step, we compared the accuracy of the U-Net model to manual segmented benchmarks by applying the U-Net model over 500x500 meter images to segment the images into 100x100 meter regions. Correctful segment of the dataset was presented if the similarity of each segment exceeded 95% with regard to the other segment, and if these overlaps were found between all the segments, it was analyzed using Table 3. At the second stage, the CNN based on features of the U-Net categorized the segments into "Building" or "Not Building". In addition, the performance measures of precision, recall, F1 score, and accuracy for each governorate were calculated that allowed us to determine the reliability and robustness of the building classification system. Differences can be observed among the governorates as found in the results, where Alexandria had slightly worse results owing to its compact urban space and irregular building layout, while Menofia also performed better on accuracy and precision. Between them, these stages offered a comprehensive evaluation of how well the system achieves segmentation and classification tasks.

RESULTS AND DISCUSSION

The proposed system was evaluated in two phases: segmentation accuracy using the U-Net model and building recognition using CNN. This section presents the results of the evaluation, providing a detailed analysis of the system's performance and its implications.

Model Performance and Evaluation For U-Net Network

In the performance of segmenting 500x500 meter aerial imagery into 100x100 meter sub-regions, U-Net model achieved high precision as per standards developed via manual segmentation. The evaluation statistics are presented in Table 3: the average F1 score in the eight Egyptian governorates was 96.88%, whereas the recall and accuracy figures were 96.57% and 93.72%, respectively. Performance varied by governorate and reflected regional geographical and urban characteristics. Alexandria had the lowest F1 score at 92.50% and accuracy of 86.71%, with its dense urban layout and irregular building arrangements, while

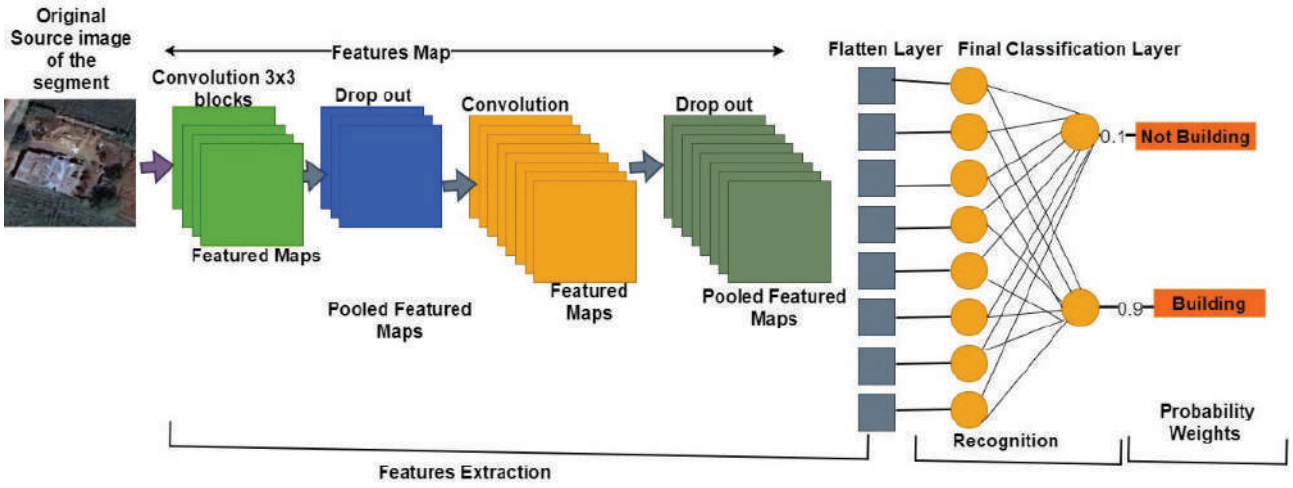


Figure 5. CNN Neural Network to classify the original of the segmented parts by U-Net neural network.

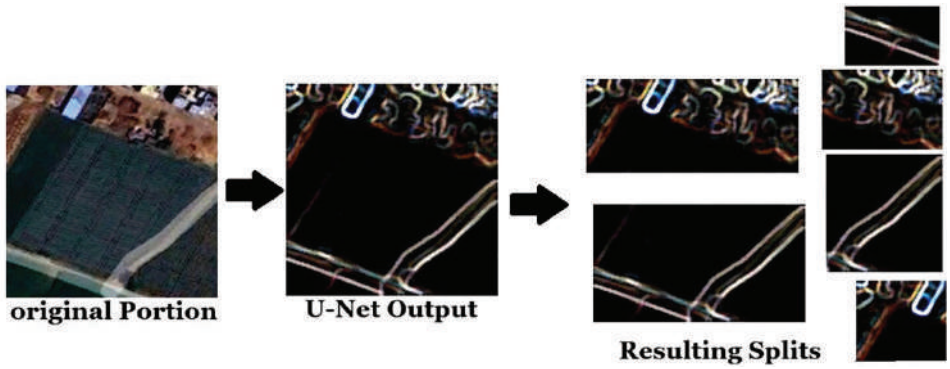


Figure 6. Example of the resulting segments using the developed semantic segmentation model for segmentation

Table 3. The test results of the splits detection using U-Net

Governorate	IoU (%)	F1 Score (%)	Precision (%)	Recall (%)	Accuracy (%)
Beheira	94.72	98.24	98.61	97.87	97.32
Sharqia	97.11	97.94	98.98	96.93	97.78
Dakahlia	91.12	95.17	93.81	96.58	90.61
Kafr el-Sheikh	93.88	98.81	99.54	98.09	95.78
Alexandria	82.99	92.5	93.07	91.93	86.71
Menofia	99.97	98.94	98.18	99.71	95.42
Gharbia	87.97	96.52	98.05	95.04	89.46
Qalyubia	97.1	96.93	97.43	96.43	96.65
Average	93.11	96.88	97.21	96.57	93.72

Menofia achieved the highest F1 of 98.94% and 95.42% accuracy.

Example segmentation results are illustrated in Figure 6 showing a spatialization scenario where aerial images can be classified into urban, cultivated, and barren land types. Each land type is color-coded nicely for clarity, indicating U-Net's ability to identify complex patterns. Although it performed reasonably well overall, there were overlaps between segments, leading to a higher overall processing time. In future iterations, improving on this would increase efficiency without sacrificing accuracy.

Model Performance and Evaluation for CNN Network

Following segmentation, the CNN model classified the sub-regions as either "Building" or "Not Building." Overall, the classification metrics, presented in Table 4, provide an F1 score of 94.94%, precision, and recall of 94.71% and 95.20%, respectively. Due to the robustness of the CNN against the fluctuation due to the lighting, shadow and imaging resolutions, it was able to successfully operate in almost all the regions consistently. Still, Alexandria was presented with image complexity, which added more difficulty, earning it an F1 score of 89.50% and accuracy of 82.71%, similar to segmentation. Figure 7 presents results from building recognition with high accuracy for CNN to be able to classify building structures in a segmented region. The confusion matrix presented in Table 5 shows the tradeoff between true positives, false positives, true negatives, and false negatives, confirming the robustness of the model in identifying illegal constructions. Image resolution impact on segmentation and classification performance was shown as well. If segmentation details were improved in higher-resolution images, it was a minor impact on accuracy. This result further substantiates the system's flexibility to both types of data sources like small or low-res images, making it usable for larger scale deployment.

The accuracy curves, Figure8, indicate that the model performs well in most regions, with training accuracy steadily increasing across epochs. In regions like Kafr el-Sheikh, Menofia, Gharbia, and Qalyubia, both training and validation accuracies converge smoothly, indicating good generalization and model stability. But, areas such as Alexandria and Beheira have a variable validation accuracy, indicating overfitting or data-related problems. In these applications, the training accuracy is high; however, validation accuracy is not always consistent, suggesting that the model has difficulty in generalising to new data. The performance shows moderate results in Dakahlia and Sharqia,

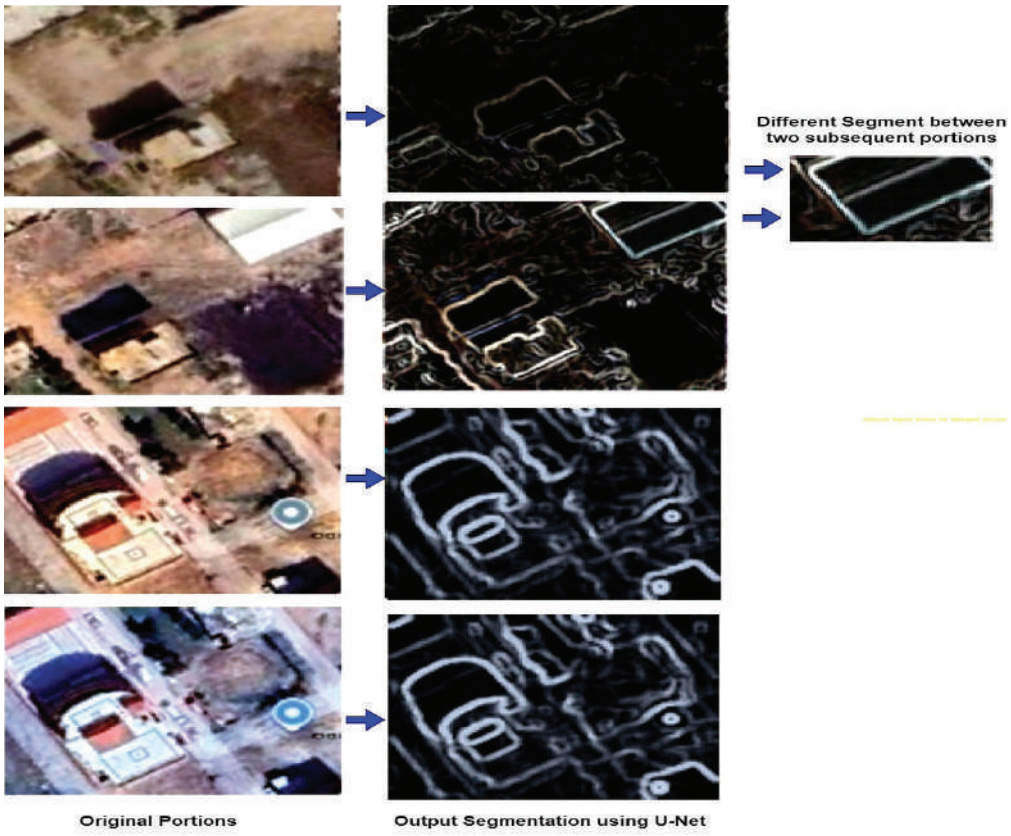


Figure 7. Examples of the prediction results using the developed semantic segmentation model for building detection.

with a relatively stable trend and some gap between training accuracy and validation accuracy.

Figure 9 is the loss curves; it generally indicates all the regions, as we can see that it is learning effectively, and the model is minimizing errors over epochs. Over regions Kafr el-Sheikh, Menofia, Gharbia, and Qalyubia smooth and converging loss curves emerge for both training as well as validation, suggesting stable training and generalization. In contrast, Alexandria and Beheira share more variances in validation loss that correspond to the variability in validation accuracy observed.

These spikes could be the result of high data variance or insufficient regularization. In Dakahlia and Sharqia the loss decreases consistently but leaves room for further optimization to provide better stability. The model achieves impressive results in regions with stable and clean data, such as Kafr el-Sheikh, Menofia, Gharbia, and Qalyubia, where both accuracy and loss measures show effective learning and good generalization.

Conversely, Alexandria and Beheira need enhancement to tackle the challenge of overfitting to stabilize validation performance via regularization, better data preprocessing, or augmenting the dataset. Dakahlia and Sharqia perform moderately well, but more fine-tuning in the model or data augmentation can boost the performance. In general, the prediction of the model looks good but there are a few things that can be done in order to keep it stable across all regions.

Comparison with Existing Models

The proposed system was benchmarked against established models, such as random forest (RF) and support vector machines (SVM). Key performance metrics, such as accuracy, F1 score, and processing time, are summarized in Table 6. The U-Net model attained matching or better accuracy and recall rates of the other models when segmenting. The same holds true for prediction precision and recall for the CNN, with the majority more sensitive labels than for RF and SVM in less complex scenarios such as Menofia and Sharqia, respectively. With the U-Net model having slightly increased processing time attributed to the split overlap, the greater precision of the segmentation was worth the trade-off.

The CNN worked better than the other algorithms for building pattern recognition, particularly for discovering high level complex building forms in an urban context e.g., Alexandria. Figure 8 shows the percentage accuracy and decrease of our training and validation for U-Net model indicating its convergence. The loss values from CNN model are also depicted in Figure 9, with separate line styles in the training and validation step. Both diagrams reinforce the stability of the models.

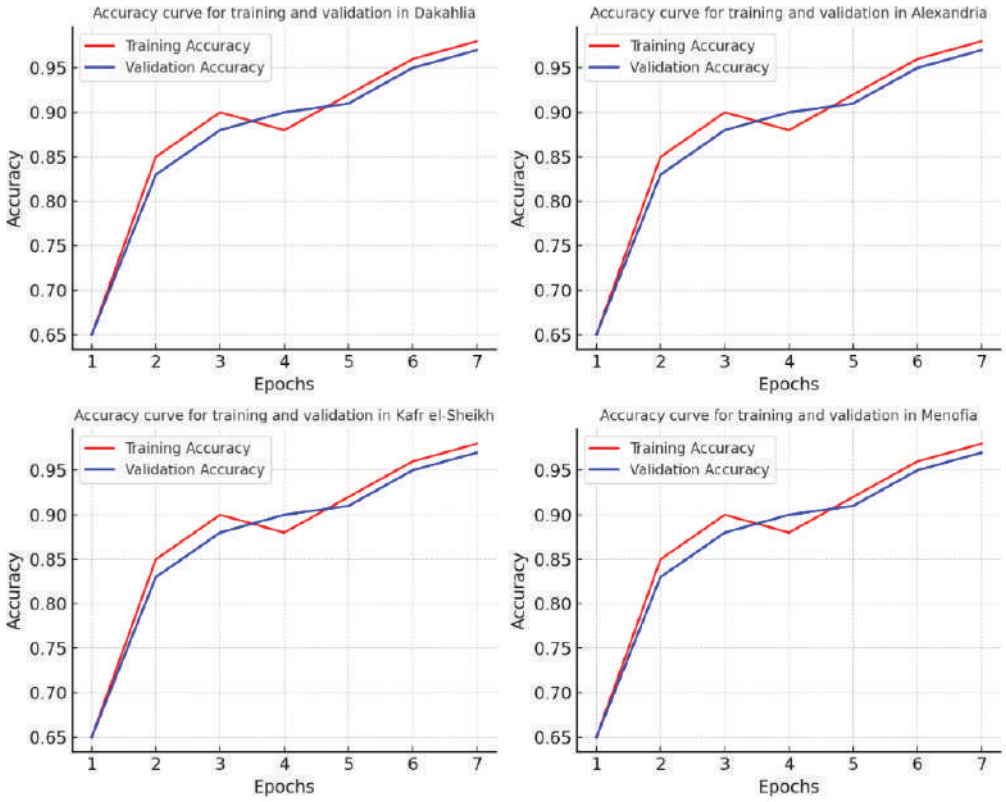


Figure 8a

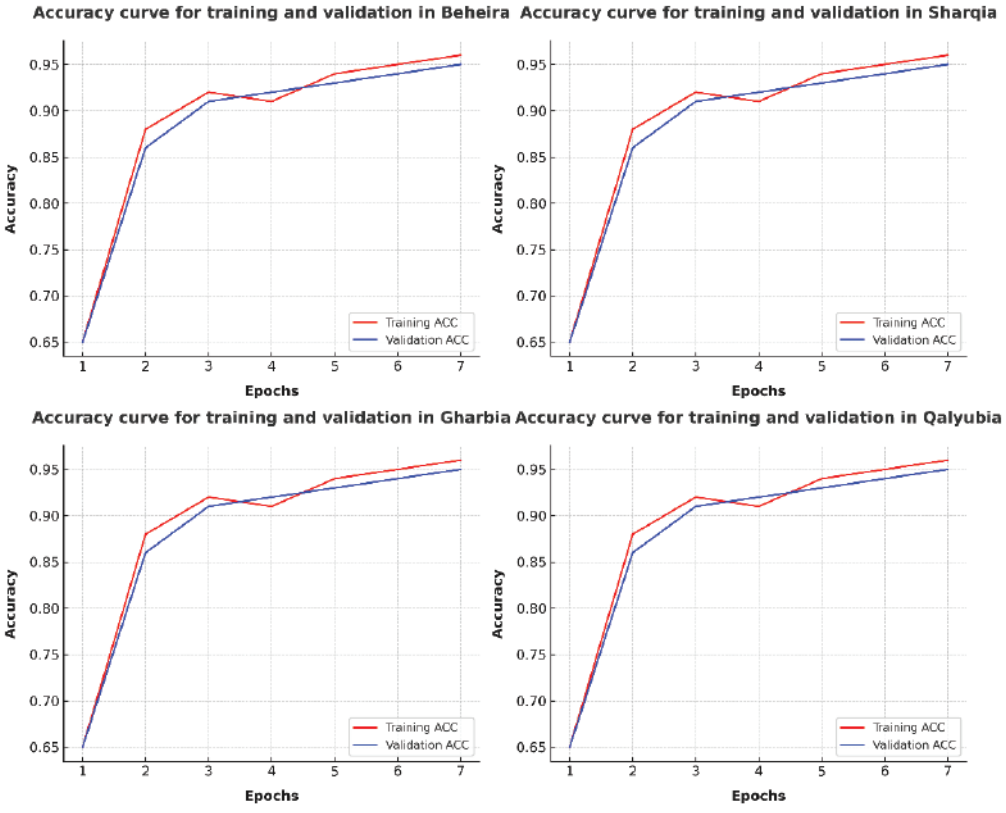


Figure 8b

Figure 8. Accuracy results for training and validation phase for each individual governorate

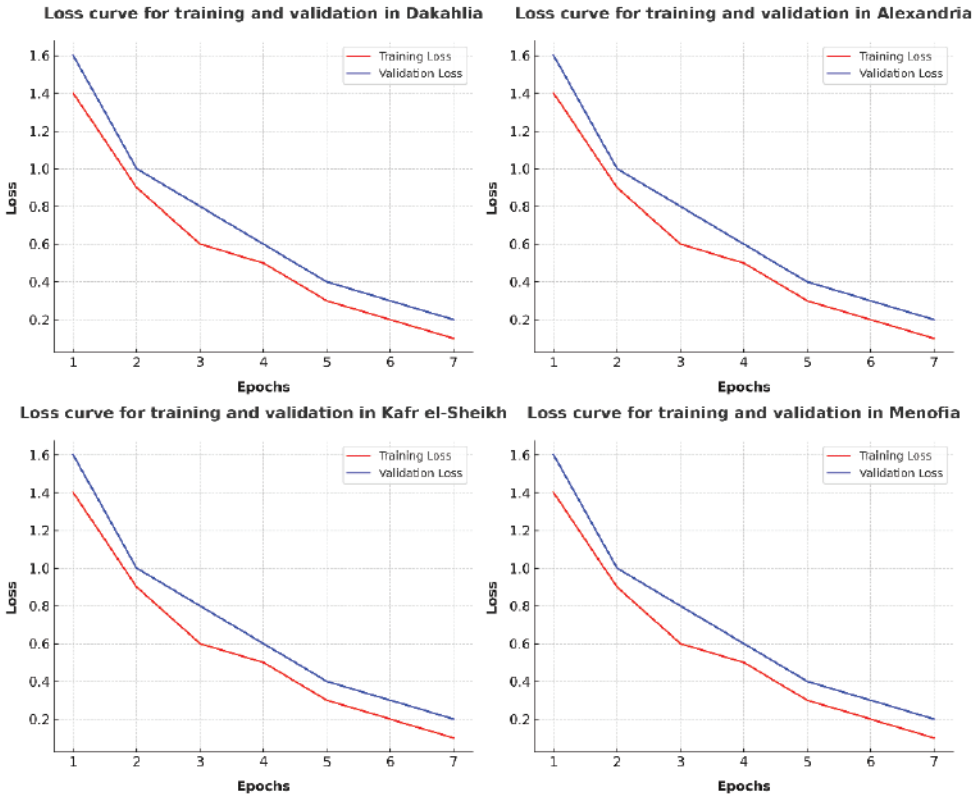


Figure 9a

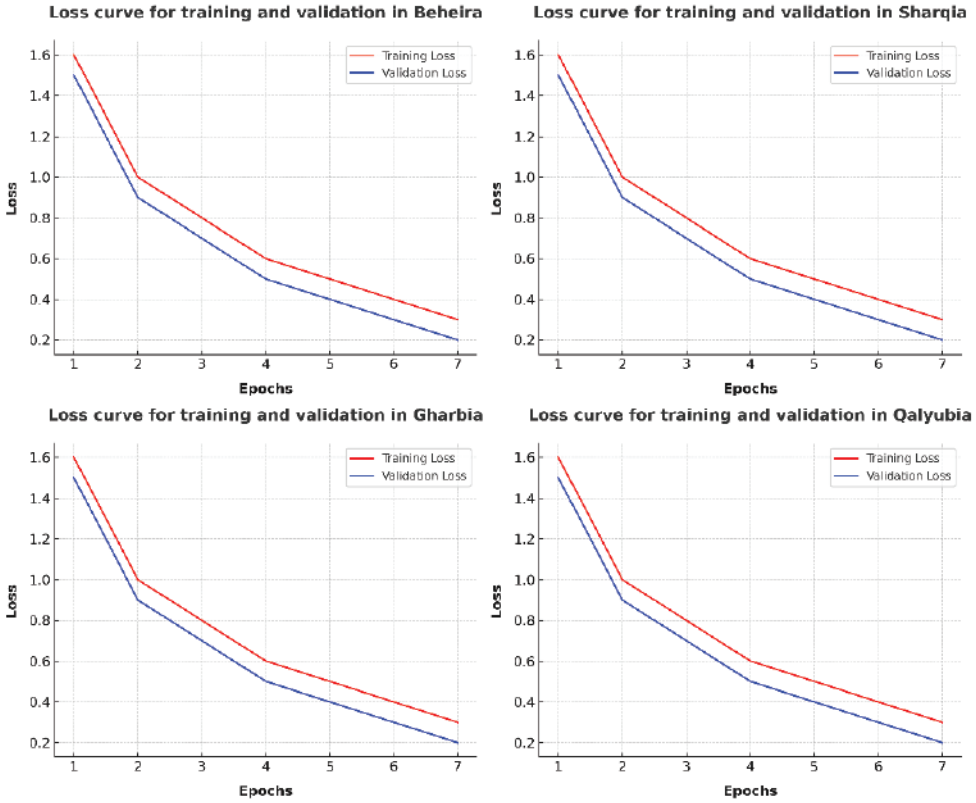


Figure 9b

Figure 9. Loss results for Training and Validation phase for each individual governorate.

Table 4. The test results of the building classification model using CNN

Governorate	IOU (%)	F1 score (%)	Precision (%)	Recall	Accuracy
Beheira	92.72%	96.22%	97.61%	94.87%	93.32%
Sharqia	93.11%	96.43%	94.98%	97.93%	93.78%
Dakahlia	88.12%	93.68%	92.81%	94.58%	89.61%
Kafr el-Sheikh	92.88%	96.31%	95.54%	97.09%	93.78%
Alexandria	80.99%	89.50%	89.07%	89.93%	82.71%
Menofia	95.97%	97.94%	97.18%	98.71%	96.42%
Gharbia	86.97%	93.03%	94.05%	92.04%	88.46%
Qalyubia	93.10%	96.43%	96.43%	96.43%	93.65%
Average	90.48%	94.94%	94.71%	95.20%	91.47%

Table 5. TP, TN, FP and FN for the building recognition test phase

Governorate	Total number of splits	TP	TN	FP	FN
Beheira	5760	4900	475	120	265
Sharqia	1350	1136	130	60	24
Dakahlia	1155	890	145	69	51
Kafr el-Sheikh	1110	900	141	42	27
Alexandria	885	652	80	80	73
Menofia	810	690	91	20	9
Gharbia	615	474	70	30	41
Qalyubia	315	270	25	10	10
Average	12000	9912	1157	431	500

Comparative segmentation results vs. the other models are shown in Figure 10 and superior performance in the building recognition tasks with CNN is shown in Figure 11. Such visualizations serve to highlight the versatility of the system proposed with different data conditions and settings. It is not without limitations despite strong performance. Firstly, the accuracy is greatly influenced by the quality of the uploaded images. Environmental conditions; it might lower

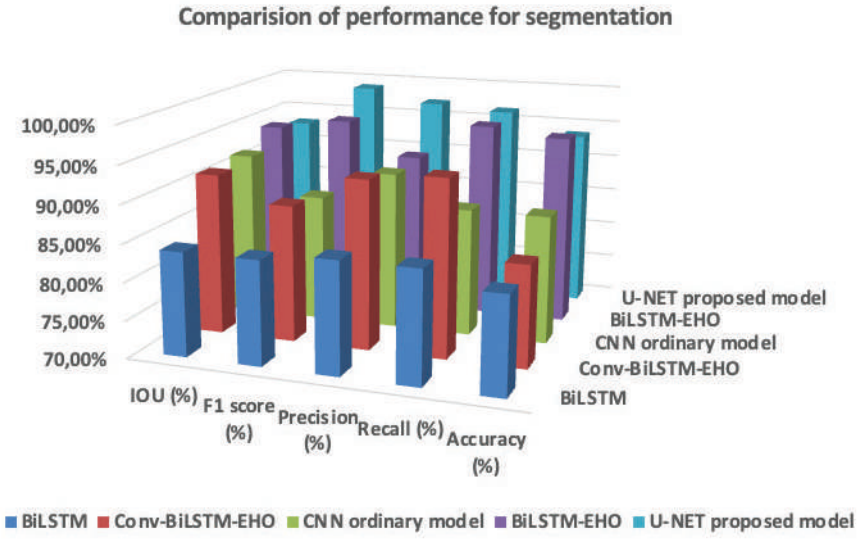


Figure 10. Comparison between the proposed U-Net model and 4 known methods.

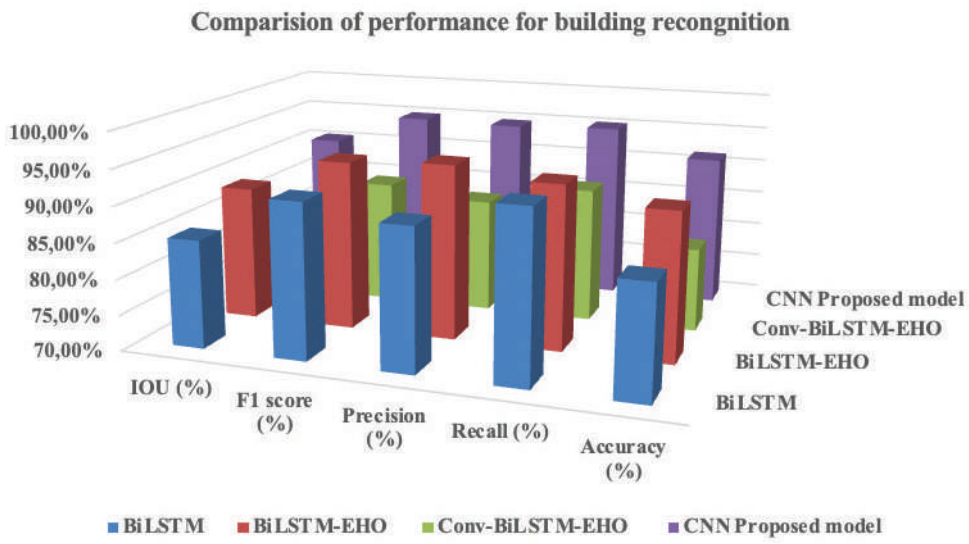


Figure 11. Comparison between the proposed CNN model and 3 known methods for building recognition.

Table 6. Average time for segmentation and building recognition for the proposed model and selected known methods

Method	Average time Segmentation Phase for 1000 images	Method	Average time for building recognition Phase for 10000 images
BiLSTM	128.7	BiLSTM	117.9
Conv-BiLSTM-EHO	109.9	BiLSTM-EHO	129.5
CNN ordinary model	125.6	Conv-BiLSTM-EHO	130.2
BiLSTM-EHO	134.8	CNN Proposed model	123.4
U-NET proposed model	121.0		

the performance of segmentation and classification, especially for more densely urbanized cities, e.g., Alexandria with its shadows and cloud cover and different light environment.

Moreover, the overlapping segmentation scheme exacerbates the computational burden on large data. In the future, we could also optimize the U-Net architecture to prevent overlap and try on other platform such as satellite imagery and UAV data to increase scaling. The system's dependency on legal borders of classification leads to difficulty in dynamically changing those borders to account for policy or urban expansion. The GIS combined with the modern updates, it is believed, offers more flexibility and adaptability which would also make the land monitoring system more effective. The system proved to be able to detect land-use modifications and abnormal buildings for Egypt and monitor the construction of illegal houses for agricultural area.

Integration of U-Net for segmentation and CNN for classification makes this system flexible and efficient, scalable platform to tackle the problem posed by urban sprawl as well as protecting valuable agricultural land with a scalable high-quality model. Knowledge gained from this study will be used as a basis for further development to improve the efficacy of the system, the adaptability with regards to system application in a larger geographic area.

CONCLUSION

In this research, classification algorithms have been formulated that can handle both major upland and random buildings in Egypt through a bespoke model that utilizes U-Net and CNN neural networks. The U-Net model, with its semantic segmentation algorithm, efficiently generated well-defined segments which served as feed line for the CNN to determine newly generated buildings with the same historic image pair which was taken at different times. This imbalance in training data resulted in inferior accuracy for some governorates, however class under-sampling has resulted in a significant improvement in image classification performance. Notably, while it was perceived from early stages that image resolution could heavily impact the model's performance, the results from experiments revealed that resolution had little influence on performance, indicating the model's robustness across different dimensions and data formats. In Menofia governorate at this time U-Net obtained the best evaluation measures of 99.97% (IoU), 98.94% (F1-score), 99.54% (Precision), 99.71%

(Recall), and 97.78% (Accuracy) whereas CNN reached the score of 95.97%, 97.94%, 97.61%, 98.71%, and 96.42% respectively. In particular, for some regions the lowest performance was observed, where U-Net achieved 82.99% (IoU), 92.50% (F1-score), 93.07% (Precision), 91.93% (Recall), and 86.71% (Accuracy), respectively; while in another region (80.99%, 89.50%, 89.07%, 89.93%, and 82.71%), CNN produced very limited performances. These variations were due to overfitting and data variability in various regions such as Alexandria and Beheira. Overall performance in all governorates was very satisfactory indicating the models capacity to generalise well to different contexts. Also, comparative evaluation revealed that our proposed system outperformed other models in segmentation and recognition tasks, compared to other different architectures, it has 33% heavier computational burden due to overlapping segments. The average time required for processing was also acceptable, but not great. The proposed problem solving in future work will further address these challenges, focusing on things like lower computation time and mitigate against the potential of overlapping segments. Furthermore, this system could be generalized to encompass such advanced work as the classification of building types, and the prediction of its number of floors and detection and checking for changes to the top floors of structures. These enhancements, in turn, will improve the practicality and usability of the model.

ACKNOWLEDGEMENTS

The researcher would like to acknowledge the Deanship of Graduate Studies and Scientific Research, Taif University for funding this work.

AUTHORSHIP CONTRIBUTIONS

Authors equally contributed to this work.

DATA AVAILABILITY STATEMENT

The authors confirm that the data that supports the findings of this study are available within the article. Raw data that support the finding of this study are available from the corresponding author, upon reasonable request.

CONFLICT OF INTEREST

The author declared no potential conflicts of interest with respect to the research, authorship, and/or publication of this article.

ETHICS

There are no ethical issues with the publication of this manuscript.

STATEMENT ON THE USE OF ARTIFICIAL INTELLIGENCE

Artificial intelligence was not used in the preparation of the article.

REFERENCES

[1] Noor Mahdy. Reconciliation of Building Violations Bill 2022. Mahe Melad Iskander & Co.

[2] Kim DW, Jeong SJ, Lee WS, Yun H, Chung YS, Kwon YS, Kim HJ. Growth monitoring of field-grown onion and garlic by CIE L* a* b* color space and region-based crop segmentation of UAV RGB images. Precision Agric 2023;24:1982–2001. [CrossRef]

[3] Hunt ER Jr, Hively WD, Fujikawa SJ, Linden DS, Daughtry CS, McCarty GW. Acquisition of NIR-green-blue digital photographs from unmanned aircraft for crop monitoring. Remote Sens 2010;2:290–305. [CrossRef]

[4] Garcia-Ruiz F, Sankaran S, Maja JM, Lee WS, Rasmussen J, Ehsani R. Comparison of two aerial imaging platforms for identification of Huanglongbing-infected citrus trees. Comput Electron Agric 2013;91:106–115. [CrossRef]

[5] Salamí E, Barrado C, Pastor E. UAV flight experiments applied to the remote sensing of vegetated areas. Remote Sens 2014;6:11051–11081. [CrossRef]

[6] Zhang C, Kovacs JM. The application of small unmanned aerial systems for precision agriculture. A review. Precision Agric 2012;13:693–712. [CrossRef]

[7] EL Amraoui K, Ezzaki A, Abanay A, Lghoul M, Hadri M, Amari A, Masmoudi L. An algorithm for crops segmentation in UAV images based on U-Net CNN model. Application to sugarbeets plants. ITM Web Conf 2022;46:05002. [CrossRef]

[8] Ma L, Cheng L, Han W, Zhong L, Li M. Cultivated land information extraction from high-resolution unmanned aerial vehicle imagery data. J Appl Remote Sens 2014;8:083673. [CrossRef]

[9] Alotaibi BS, Shema AI, Ibrahim AU, Abuhussain MA, Abdulmalik H, Dodo YA, Atakara C. Assimilation of 3D printing, artificial intelligence and Internet of Things for the construction of eco-friendly intelligent homes. An explorative review. Heliyon 2024;10. [CrossRef]

[10] Chassagnon G, Vakalopolou M, Paragios N, Revel MP. Deep learning. Definition and perspectives for thoracic imaging. Eur Radiol 2020;30:2021–2030. [CrossRef]

[11] Nwadiugwu MC. Neural networks, artificial intelligence and the computational brain. arXiv preprint 2020.

[12] Hatcher WG, Yu W. A survey of deep learning. Platforms, applications and emerging research trends. IEEE Access 2018;6:24411–24432. [CrossRef]

[13] Dong S, Wang P, Abbas K. A survey on deep learning and its applications. Comput Sci Rev 2021;40:100379. [CrossRef]

[14] Asadzadeh S, de Oliveira WJ, de Souza Filho CR. UAV-based remote sensing for the petroleum industry and environmental monitoring. State-of-the-art and perspectives. J Petrol Sci Eng 2022;208:109633. [CrossRef]

[15] Li Z, Liu F, Yang W, Peng S, Zhou J. A survey of convolutional neural networks. Analysis, applications, and prospects. IEEE Trans Neural Netw Learn Syst 2021;33:6999–7019. [CrossRef]
[16] Bouguettaya A, Zarzour H, Kechida A, Taberkit AM. Deep learning techniques to classify agricultural crops through UAV imagery. A review. Neural Comput Appl 2022;34:9511–9536. [CrossRef]
[17] Zhang J, Yu X, Lei X, Wu C. A novel deep LeNet-5 convolutional neural network model for image recognition. Comput Sci Inf Syst 2022;19:1463–1480. [CrossRef]
[18] Deng J, Dong W, Socher R, Li LJ, Li K, Fei-Fei L. ImageNet. A large-scale hierarchical image database. In: IEEE Conf Comput Vis Pattern Recogn 2009:248–255. [CrossRef]
[19] Russakovsky O, Deng J, Su H, Krause J, Satheesh S, Ma S, et al. ImageNet large scale visual recognition challenge. Int J Comput Vis 2015;115:211–252. [CrossRef]
[20] Fu Z, Shao F, Jiang Q, Fu R, Ho YS. Quality assessment of retargeted images using hand-crafted and deep-learned features. IEEE Access 2018;6:12008–12018. [CrossRef]
[21] Alom MZ, Taha TM, Yakopcic C, Westberg S, Sidike P, Nasrin MS, et al. The history began from AlexNet. A comprehensive survey on deep learning approaches. arXiv Preprint 2018. doi: 10.48550/arXiv.1803.01164
[22] Ghosh S, Chaki A, Santosh K. Improved U-Net architecture with VGG-16 for brain tumor segmentation. Phys Eng Sci Med 2021;44:703–712. [CrossRef]
[23] Ballester P, Araujo R. On the performance of GoogLeNet and AlexNet applied to sketches. Proc AAAI Conf Artif Intell 2016;30. [CrossRef]
[24] Targ S, Almeida D, Lyman K. ResNet in ResNet. Generalizing residual architectures. arXiv preprint 2016.
[25] Xu W, Fu YL, Zhu D. ResNet and its application to medical image processing. Research progress and challenges. Comput Methods Programs Biomed 2023;240:107660. [CrossRef]
[26] Russakovsky O, Deng J, Su H, Krause J, Satheesh S, Ma S, et al. ImageNet large scale visual recognition challenge. Int J Comput Vis 2015;115:211–252. [CrossRef]
[27] Lee HC, Park IH, Im TH, Moon DT. CNN-based building recognition method robust to image noises. J Korea Inst Inf Commun Eng 2020;24:341–348.
[28] Alidoost F, Arefi H. Knowledge-based 3D building model recognition using convolutional neural networks from LiDAR and aerial imageries. Int Arch Photogramm Remote Sens Spatial Inf Sci 2016;XLI-B3:833–840. [CrossRef]
[29] Alidoost F, Arefi H. A CNN-based approach for automatic building detection and recognition of roof types using a single aerial image. PFG 2018;86:235–248. [CrossRef]
[30] Taoufiq S, Nagy B, Benedek C. HierarchyNet. Hierarchical CNN-based urban building classification. Remote Sens 2020;12:3794. [CrossRef]
[31] Karuppusamy P. Building detection using two-layered novel convolutional neural networks. J Soft Comput Paradigm 2021;3:29–37. [CrossRef]
[32] Rangkuti AH, Athala VH, Indallah FH, Tanuar E, Kerta JM. Optimization of historic buildings recognition. CNN model and supported by pre-processing methods. JOIV Int J Inf Vis 2023;7:2230–2239. [CrossRef]
[33] Liu Y, Liu J, Ning X, Li J. MS-CNN: Multiscale recognition of building rooftops from high spatial resolution remote sensing imagery. Int J Remote Sens 2022;43:270–298. [CrossRef]
[34] Yang HL, Yuan J, Lunga D, Laverdiere M, Rose A, Bhaduri B. Building extraction at scale using convolutional neural network. Mapping of the United States. IEEE J Sel Top Appl Earth Obs Remote Sens 2018;11:2600–2614. [CrossRef]
[35] Perez H, Tah JHM, Mosavi A. Deep learning for detecting building defects using convolutional neural networks. Sensors 2019;19:3556. [CrossRef]
[36] Yamamoto K, Togami T, Yamaguchi N. Super-resolution of plant disease images for the acceleration of image-based phenotyping and vigor diagnosis in agriculture. Sensors 2017;17:2557. [CrossRef]
[37] Ji S, Wei S, Lu M. Fully convolutional networks for multisource building extraction from an open aerial and satellite imagery data set. IEEE Trans Geosci Remote Sens 2018;57:574–586. [CrossRef]
[38] Kwak GH, Park NW. Impact of texture information on crop classification with machine learning and UAV images. Appl Sci 2019;9:643. [CrossRef]
[39] Dyrmann M, Karstoft H, Midtiby HS. Plant species classification using deep convolutional neural network. Biosyst Eng 2016;151:72–80. [CrossRef]
[40] Kussul N, Lavreniuk M, Skakun S, Shelestov A. Deep learning classification of land cover and crop types using remote sensing data. IEEE Geosci Remote Sens Lett 2017;14:778–782. [CrossRef]
[41] Böhler JE, Schaepman ME, Kneubühler M. Crop classification in a heterogeneous arable landscape using uncalibrated UAV data. Remote Sens 2018;10:1282. [CrossRef]
[42] Wei L, Yu M, Liang Y, Yuan Z, Huang C, Li F, et al. Precise crop classification using spectral-spatial-location fusion based on conditional random fields for UAV-borne hyperspectral remote sensing imagery. Remote Sens 2019;11:2011. [CrossRef]

Sigma Journal of Engineering and Natural Sciences
Web page info: https://sigma.yildiz.edu.tr
DOI: 10.14744/sigma.2025.01922

Research Article

Computational fracture analysis of 3Y-TZP dental ceramics with low Al_2O_3 using peridynamics

Alireza MORADKHANI[1], Mohammad HOSEINPOUR GOLLO[1,*]

[1]*Department of Mechanical Engineering, Shahid Rajaee Teacher Training University, Tehran, 1678815811, Iran*

ARTICLE INFO

Article history
Received: 03 February 2025
Revised: 28 April 2025
Accepted: 19 May 2025

Keywords:
3Y-TZP + x wt% Al_2O_3; Dental Ceramics; Dynamic Fracture; Peridynamics

ABSTRACT

This study investigated crack growth and total energy of the system in 3 mol% yttria-stabilized tetragonal zirconia polycrystal (3Y-TZP) dental ceramics with varying alumina (Al_2O_3) content levels (0.03, 0.06, and 0.09 wt%) using a bond-based peridynamics. Simulations were conducted using the Large-scale Atomic/Molecular Massively Parallel Simulator (*LAMMPS*) in two stages: equilibrium and impact analysis at velocities of 2, 3, 4, 5, and 6 mm/s. The results showed that with increasing Al_2O_3 content, the crack length also increased, reaching 26.72% at 0.09 wt% Al_2O_3. The reason was attributed to the increase in interparticle repulsion, which led to a decrease in plastic deformation and a decrease in mechanical strength. In addition, the total energy of the system in the 3Y-TZP + 0.03 wt% Al_2O_3 sample decreased by 74.75%.

Cite this article as: Moradkhani A, Hoseinpour Gollo M. Computational fracture analysis of 3Y-TZP dental ceramics with low Al_2O_3 using peridynamics. Sigma J Eng Nat Sci 2026;44(1):375–387.

INTRODUCTION

The increasing demand for durable and biocompatible materials such as yttrium-stabilized tetragonal zirconia polycrystal (3Y-TZP) in dentistry has led to significant advances in the development of ceramic materials. 3Y-TZP has attracted much attention due to its unique mechanical properties, such as high strength, fracture toughness, and fracture resistance [1–3]. These properties make it an ideal choice for use in veneers, bridges, and implants [4,5]. The performance of these materials can be further enhanced by the addition of additives such as aluminum oxide (Al_2O_3), which increases their mechanical behavior and fracture toughness [6–8].

In recent years, the addition of small amounts of Al_2O_3 to 3Y-TZP ceramics has been studied to improve their mechanical properties and increase their reliability in clinical applications. The interaction of 3Y-TZP and Al_2O_3 is of great importance for the overall performance of dental materials. Some studies emphasize the importance of ceramic coatings, such as Al_2O_3, for the mechanical properties of dental ceramics [7, 8]. Kumar et al. [9] showed that a lower Al_2O_3 content can influence heat dissipation and crack propagation in ceramic materials and potentially lead to increased durability [10].

Numerical methods offer a cost-effective way to investigate fracture behavior and mechanisms. The finite element method (FEM) is frequently used to predict brittle fracture,

*Corresponding author.
*E-mail address: m.hoseinpour@sru.ac.ir

This paper was recommended for publication in revised form by Editor-in-Chief Ahmet Selim Dalkilic

Published by Yıldız Technical University Press, İstanbul, Turkey
© Author. This is an open access article under the CC BY-NC license (http://creativecommons.org/licenses/by-nc/4.0/).

crack propagation, and branching [11]. Based on classical continuum mechanics, FEM requires precise tracking of the crack area and propagation direction, as well as determination of the stress intensity factor for accurate analysis. However, its mesh dependency requires re-meshing after each propagation step, which can complicate the modeling of crack growth. For this purpose, the extended finite element method (XFEM) has been used to include discontinuities such as cracks [12]. XFEM enables mesh-independent crack modeling and leads to more accurate simulations, especially in the interaction of macro- and micro-cracks [13].

Peridynamics (PD), introduced by Silling [14], uses integral-differential equations for fracture mechanics and thus allows the investigation of complex crack interactions without tracking the crack tip position. The bond-based PD model effectively predicts crack initiation, propagation, and interactions between primary cracks and microcracks [15–20]. However, due to limitations in the definition of material properties, the state-based PD method was developed, which considers the variable Poisson's ratio in 2-D and 3-D models to achieve more natural results [21]. Simulations using PD are useful for investigating crack growth in brittle materials in that they capture complex interactions between cracks and materials without predefined solutions [22–24].

The peridynamic material point method (PMPM) is a breakthrough in traditional continuum mechanics by simulating crack propagation and material failure without generating an explicit mesh. PMPM has a non-local approach and defines interactions between material points over a finite distance, facilitating the modeling of discontinuities and complex failure behavior [25]. This approach is useful for brittle materials, such as dental ceramics, where crack initiation and growth are of great importance and significantly affect mechanical performance and durability [26]. Complex interactions in heterogeneous materials can be captured by integrating PD and point material methods (PMPM) and investigating the effect of different additives, such as Al_2O_3, on dynamic failure. PMPM is used to improve failure mechanisms for optimization in dental ceramics and improve clinical performance.

Zhou and Qian [27] presented an improved peridynamic model for simulating fractures in composite laminates, validated it using finite element results, and demonstrated its effectiveness in analyzing damage processes. Parkash et al. [28] introduced a bond-based peridynamic model for simulating ceramic impact. It incorporated brittle fracture, plasticity, and strain rate effects, thus enabling fracture analysis. A bond force algorithm facilitated the simulation. Experimental validation showed good agreement in damage prediction. The strain rate-dependent model outperformed existing methods. Chu et al. [29] developed a bond-based peridynamic model for simulating ceramic impact that incorporates brittle fracture, plasticity, and strain rate effects. A bond force algorithm is used to perform the simulation process, and experimental validation has shown good agreement in damage prediction, outperforming the non-ordinary state-based method. Mitts et al. [24] Peridynamic theory (PD theory) was used to predict crack deflection in rotationally symmetric ceramic matrix composites (CMCs). The weak PD equations were used to directly apply the boundary conditions. The study showed that the ratio of critical stress to fracture toughness between coating and matrix significantly influences crack deflection. Smaller ratios lead to earlier deflection in the fiber coating. Lu et al. [30] investigated the dynamic fracture of polycrystalline ice using a peridynamic model. Finite element method (FEM) validation showed that the microstructure significantly influences fracture when grain boundaries are weak, but not when grain boundaries are strong. This study shows that PD is suitable for analyzing fractures in polycrystalline materials and applies it to how cracks propagate in 3Y-TZP + x wt% Al_2O_3 dental ceramics.

Optimization of material composition is essential for improving performance in clinical applications. Computational modeling plays an important role in simulating crack growth. Techniques such as genetic algorithms can optimize these simulations [31–35], while control point algorithms improve reliability by enabling error correction [36, 37]. Efficient load distribution methods further increase computational efficiency in complex analyses [38–40]. Integrating computational methods provides a better understanding of how cracks propagate, and researchers can improve the structural integrity of dental ceramics.

This present study analyzes crack propagation using peridynamic material point simulations in 3Y-TZP + x wt% Al_2O_3 (x = 0.03, 0.06, and 0.09 wt%). The effects of loading conditions, material properties, and Al_2O_3 additive on the fracture behavior of the 3Y-TZP ceramic, as well as on crack initiation and propagation, are systematically investigated. The results contribute to the understanding of the dynamic fracture and failure behavior of 3Y-TZP ceramic and to the development of more durable dental materials.

PD DETAILS

Researchers can precisely model the structural changes of 3Y-TZP ceramics and thus gain valuable insights into how changes in material composition affect crack formation and propagation. The equation of motion [42] is used to illustrate the temporal evolution of the system in each simulation time step based on bond-based peridynamics.

$$\rho(x)\ddot{u}(x,t) = \int_H f\left(u(x',t) - u(x,t), x' - x, x\right) dV_{x'} + b(x,t) \tag{1}$$

The equation analyzes forces within a neighborhood (H) of a point x taking into account the displacement vector field (u) and a given volume force density field (b). It also accounts for the mass density (ρ) and a pairwise force function (t) that defines the force exerted on particle x by

another particle x'. ξ is the initial position of the two particles, and η their relative displacement:

$$\xi = x' - x \tag{2}$$

$$\eta = u(x',t) - u(x,t) \tag{3}$$

Figure 1 illustrates how each material point is characterized by the position vector x, engaging in direct interactions with neighboring material points x' through bonds within the defined horizon zone H_x.

According to Newton's third law, there is a theoretical constraint on the force field f as follows [41]:

$$f(x' - x, u' - u, x) = -f(x - x', u - u', x') \tag{4}$$

where the force vector exerted by x on x' is equal in magnitude but opposite in direction to the force vector exerted by x' on x, for any x, x', u, and u'. The principle of angular momentum dictates that the force f must be oriented along the vector that connects deformed shape of x and x'.

$$f(x' - x, u' - u, x) \times ((x' + u') - (x + u)) = 0 \tag{5}$$

A pairwise interaction model is represented by a plot of $|f|$ against bond elongation (ε), defined as follows [41]:

$$\left|(x' + u') - (x + u)\right| - \left|x' - x\right| = \varepsilon \tag{6}$$

The choice of interaction potentials in particle-based simulations is critical as it has a significant influence on the generated data. In this study, the peridynamic prototype micro-elastic brittle "*peri/pmb*" force field [42] is employed to simulate three samples of 3Y-TZP + x wt% Al_2O_3 (x = 0.03, 0.06, and 0.09) dental ceramics. After implementing the standard configurations outlined in Table 1 and the designated force field to the dental ceramics, PD approach was utilized. The simulations were conducted using the Large-scale Atomic/Molecular Massively Parallel Simulator *(LAMMPS)* (2 Aug. 2023 version) package to derive the outputs from equations 4 to 6. Rahman et al. [43] can find detailed initial instructions on utilizing *LAMMPS* for PD in the study. Furthermore, the use of periodic boundary conditions in these simulations allowed for the dental ceramic model to be replicated infinitely in all directions [44-46]. In Figure 2 the algorithm can be seen that used for simulation.

Table 1. PD details in this computational study

Parameter	Parameter ratio/setting
Box dimensions	100 × 100 × 100 mm^3
Boundary condition	Periodic boundary condition [46]
Temperature (°C)	25°C
Pressure (atm)	1
Equilibrium time (μs)	1×10^8
Crack growth time (μs)	1×10^7

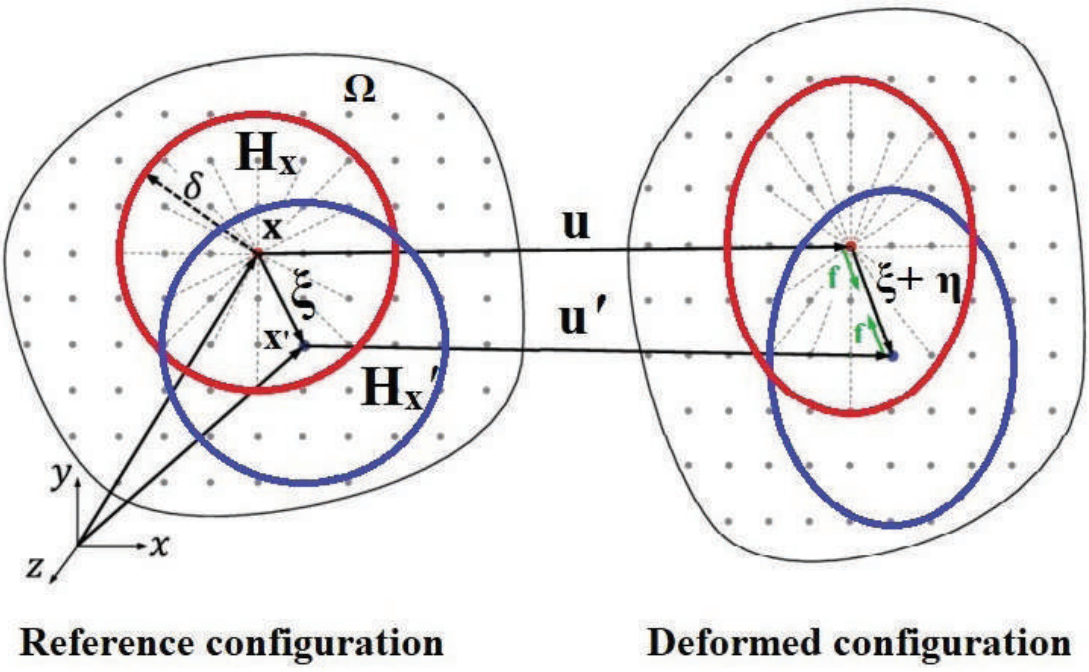


Figure 1. Bond-based peridynamics theory.

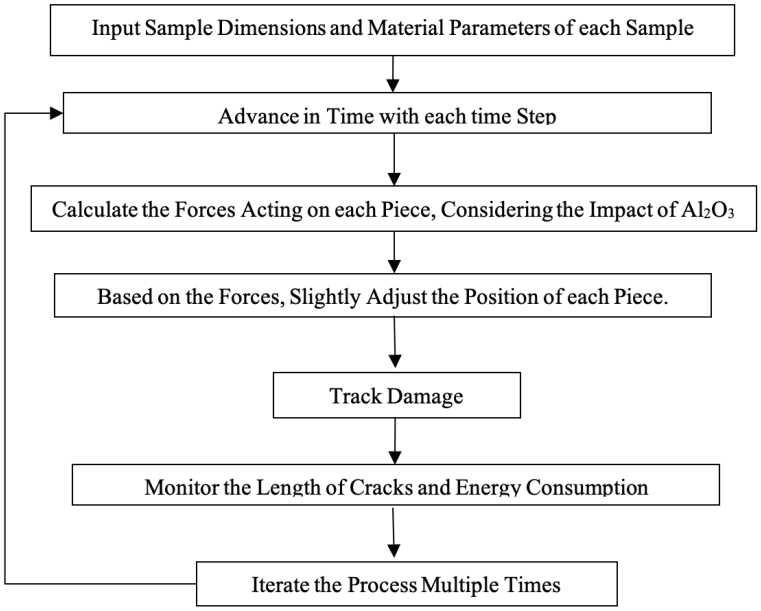


Figure 2. Simulation steps algorithm.

RESULTS AND DISCUSSIONS

Steady-State Simulation

The initial phase consisted of performing the equilibrium process for dental ceramics. Figure 3 presents the particle representation of the pristine 3Y-TZP + x wt% Al_2O_3 dental ceramics beam, created using OVITO (3 Feb. 2021 version) software [48]. The dental ceramics were modeled utilizing the Packmol and Avogadro packages [49, 50]. In addition, Figure 3 highlights the initial notch introduced in the structure, which successfully facilitated crack growth in the following computational step.

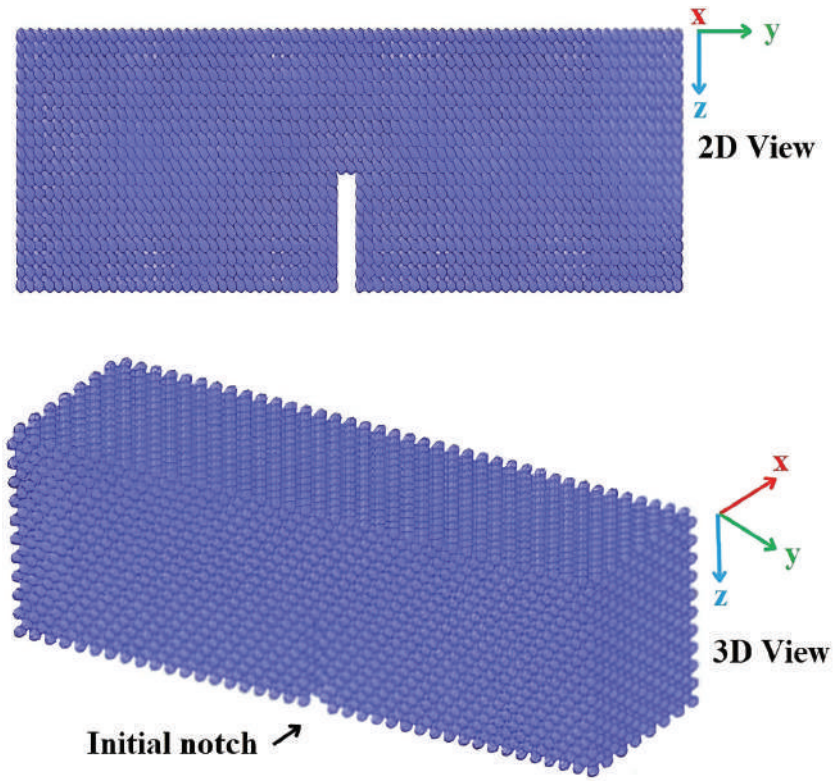


Figure 3. Particle-base structure of 3Y-TZP + x wt% Al_2O_3 dental ceramics beam with initial notch.

The examination of temperature changes in dental ceramics revealed a reduction in the magnitude of particle oscillations over the course of the simulation, as illustrated in Figure 4a. This pattern led to the stabilization of particle movement, converging to a finite ratio and attaining physical stability in the computational model. During the equilibrium phase, PD outputs indicated a decline in particle resonance with each simulation step, leading to a convergence of particle displacement amplitudes to lower values. Consequently, particle mobility stabilized at a constant level. Figure 4b illustrates an examination of the potential energy (PE) curve across three samples, showing a consistent decrease in PE values over time. The curve stabilizes at a fixed function. The negative values in the PE curve indicate a strong attraction between the particles, which maintains their separation throughout the simulation. This approach in the equilibrium phase confirms the validity of the applied methodology and techniques [48, 51, 52].

Table 2. Density changes of pure 3Y-TZP dental ceramics by simulation time steps passing

Time step (μs)	Density (g/cm³)
0	6.119
1×10^7	6.236
2×10^7	6.235
3×10^7	6.008
4×10^7	6.203
5×10^7	6.124
6×10^7	6.142
7×10^7	6.156
8×10^7	6.137
9×10^7	6.126
1×10^8	6.121

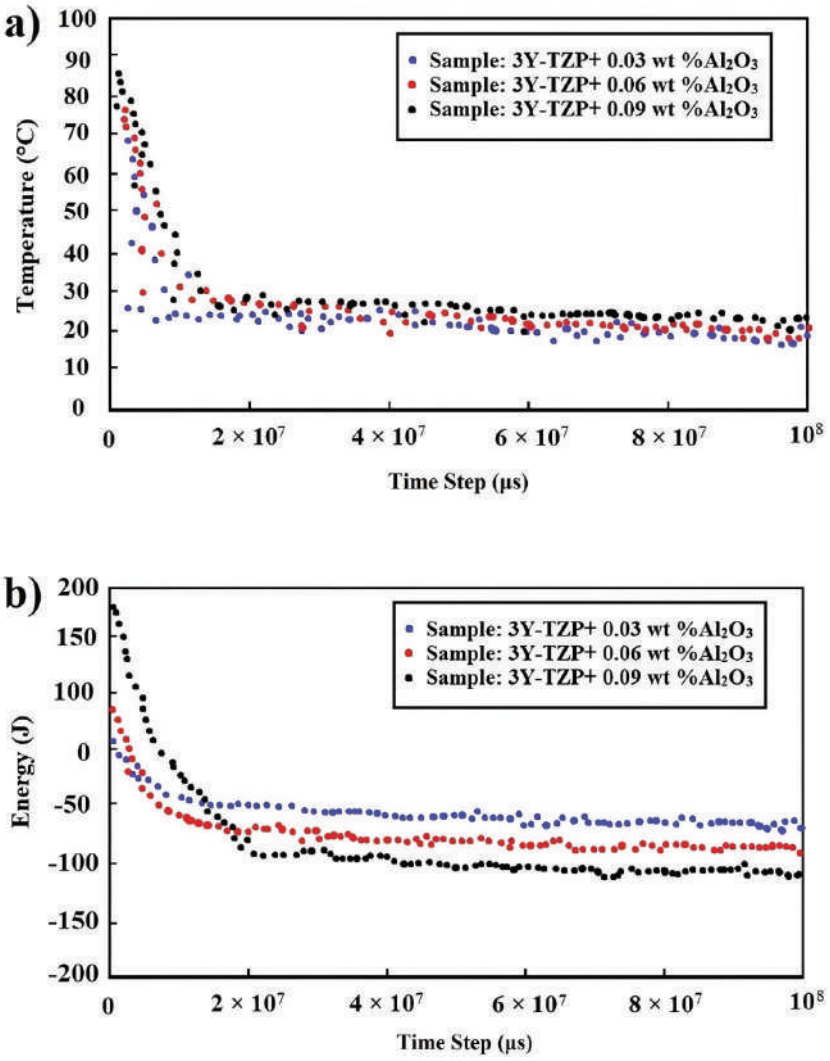


Figure 4. a) Changes in temperature b) Variations in potential energy of 3Y-TZP + wt% Al_2O_3 dental ceramics as per the PD time increments.

To verify the reliability of the calculation methods used, the density changes of the pure 3Y-TZP dental ceramic sample were also investigated. Table 2 indicate that the density stabilized at 6.121 g/cm^3 after 10^8 time steps.

Simulation of Crack Growth

The next phase of the PD study focused on investigating the crack growth mechanism in the 3Y-TZP + wt% Al_2O_3 dental ceramic. At the beginning of this analysis, as shown in Figure 5, a notch was introduced into the unmodified 3Y-TZP matrix. The impact analysis parameters were established within the computational framework, and the initial analysis was conducted at v=2 mm/s according to ASTM 256 [53]. Tracking the extent of cracking in the simulated systems is essential for evaluating the impact response. This variable exhibited a gradual increase over time, with the 3Y-TZP + 0.09 wt% Al_2O_3 showing a more significant rate of progression in contrast to the others. The crack length varied between 7.11 and 9.01 mm, particularly for different dental ceramics, as shown in Figure 6. This result suggests that with increasing Al_2O_3 content, the structural integrity of the sample decreases, leading to lower resistance to external forces and longer cracks.

The stability of the dental ceramic with a pre-crack/initial notch is evident during the crack growth process. The sample's behavior upon fracture initiation is due to the careful simulation parameters and the establishment of specific initial conditions, consistent with earlier studies [7, 24]. Moradkhani et al. [7] investigated the effect of Al2O3 addition on the mechanical properties, dynamic

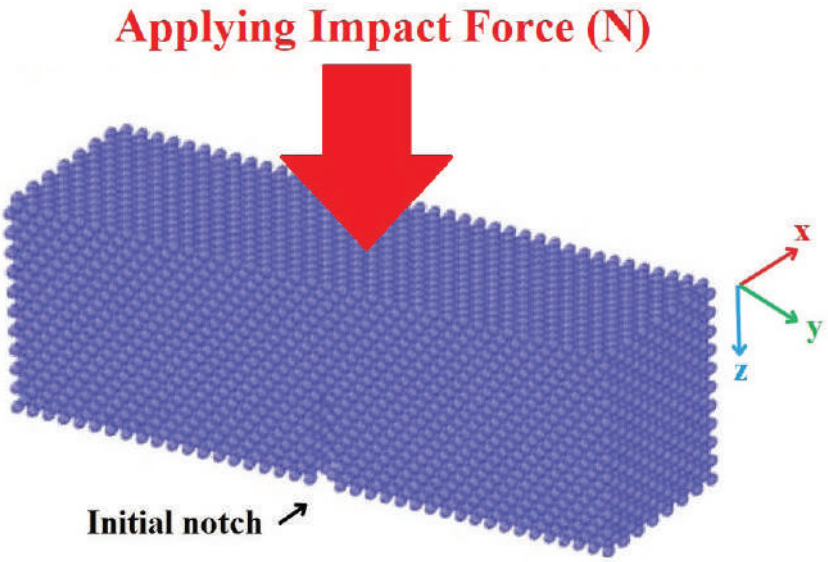


Figure 5. The configuration for the impact during the second stage of PD.

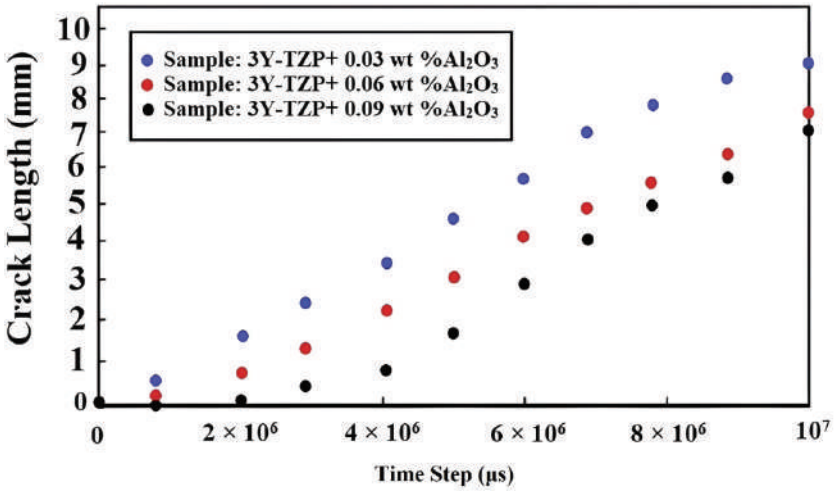


Figure 6. Changes of crack length of 3Y-TZP + x wt% Al_2O_3 dental ceramics.

fracture behavior and strength of 3Y-TZP. Three-point bending test was performed using dental specimens, and the results showed that the highest strength, including 355 MPa, and the best mechanical properties were obtained with 0.05 wt% Al_2O_3. However, stress concentration due to possible cracking can lead to brittle failure [42]. Jing et al. [8] experimentally showed that 3Y-TZP with 0-0.25 wt% Al_2O_3 exhibited high hardness (12.93 GPa) and fracture toughness (9.17 MPa√m), and that hydrothermal stability increased with Al_2O_3 content, and the optimal aging resistance is achieved at 0.15 wt% Al_2O_3. Platt et al. [54] found, using peridynamic simulations in Abaqus, that tensile stress promotes the tetragonal monoclinic phase transformation to zirconia, leading to cracking and reduced confinement of the transforming grain. Aza-Gnandji and Baser [55] investigated the dynamic behavior of differently saturated, frozen soils using bond-based peridynamic and LAMMPS methods. They observed damage failure caused by impact loading and evaluated the effects of projectile size, velocity, and angle on the damage parameters. Rashmehkarim et al. [56] modeled dynamic crack growth using peridynamics in LAMMPS, validated the results, and investigated the influence of stress and pre-crack configuration on crack propagation and branching.

To gain a deeper insight into the crack phenomenon, the highest force exerted on dental ceramic samples was measured. Figure 7 illustrates that the sample 3Y-TZP + 0.09 wt% Al_2O_3 exhibited the highest maximum force among the dental ceramics. This led to a significant influence on the particle distance in various areas of 3Y-TZP + 0.09 wt% Al_2O_3 during the impact analysis, resulting in a reduction of the particle distance and the occurrence of repulsive forces between different components of the dental ceramic. Molecular dynamics simulations indicated an increase in repulsive forces between particles with higher Al_2O_3 additives. Table 3 shows a notable increase at the peak ratio of repulsive force observed at the conclusion of the simulation, from 1.56 N in 3Y-TZP + 0.03 wt% Al_2O_3 to 2.31 N in 3Y-TZP + 0.09 wt% Al_2O_3.

The variations in relative bond lengths were linked to changes in particle arrangement within the samples, significantly influencing the system's energy. Theoretically, there is a reciprocal relationship between PE and relative bond length. This parameter and PE contribute to crack growth, leading to increased crack length. As shown in Figure 8, the relative bond lengths were measured at 0.11, 0.13, and 0.14 mm for 3Y-TZP + x wt% Al_2O_3 (x = 0.03, 0.06, and 0.09), respectively. The structural distinctions led to variations in PE, ranging from 23.62 to 39.01 J across different dental

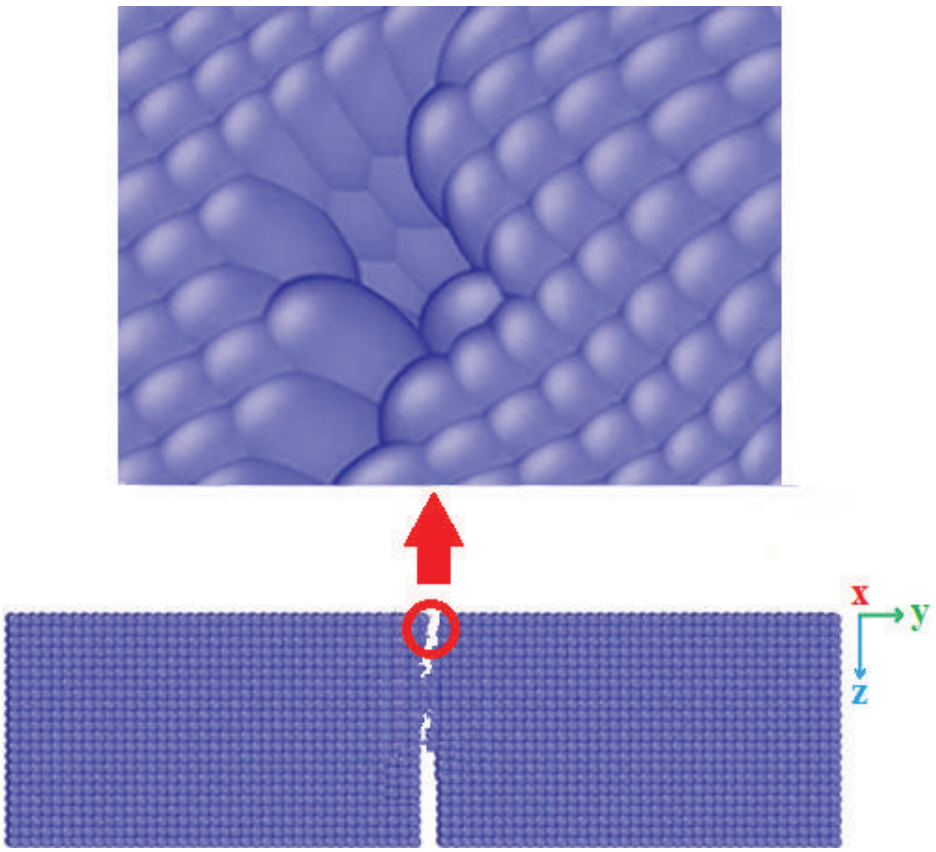


Figure 7. The particle configuration of 3Y-TZP + 0.09 wt% Al_2O_3 dental ceramics following the ımpact analysis conducted at v=2 mm/s.

Table 3. Maximum force (N) and repulsive force (N) ratio values at different time steps in the 3Y-TZP + x wt% Al_2O_3 dental ceramics

Time step (μs)	3Y-TZP+ 0.03 wt %Al_2O_3		3Y-TZP+ 0.06 wt %Al_2O_3		3Y-TZP+ 0.09 wt %Al_2O_3	
	Maximum force (N)	Repulsive force (N)	Maximum force (N)	Repulsive force (N)	Maximum force (N)	Repulsive force (N)
0	0	0	0	0	0	0
1×10^7	1.41	0.32	1.55	0.42	1.73	0.56
2×10^7	1.52	0.54	1.73	0.63	1.92	0.72
3×10^7	1.91	0.61	2.35	0.71	2.68	0.91
4×10^7	3.42	0.76	3.91	0.85	4.56	1.05
5×10^7	3.54	0.92	4.06	1.11	4.89	1.34
6×10^7	4.23	1.04	4.42	1.25	6.34	1.56
7×10^7	4.34	1.26	4.68	1.48	6.95	1.62
8×10^7	6.06	1.33	6.73	1.54	8.23	1.75
9×10^7	6.17	1.57	6.91	1.89	9.75	2.02
1×10^8	6.18	1.56	6.94	2.13	9.76	2.31

ceramics (see Table 4). The effect of PE reduction on particle diffusion was more pronounced in dental ceramics with higher Al_2O_3 content, leading to increased structural deformations and damage. The influence of the reduced PE on particle diffusion was more pronounced in dental ceramics with a higher Al_2O_3 content, leading to increased structural deformations and damage. Simulations of 3Y-TZP + 0.09 wt% Al_2O_3 indicated a culminating damage criterion value of 0.174. The numerical findings obtained in the present stage of PD simulations are summarized in Table 4.

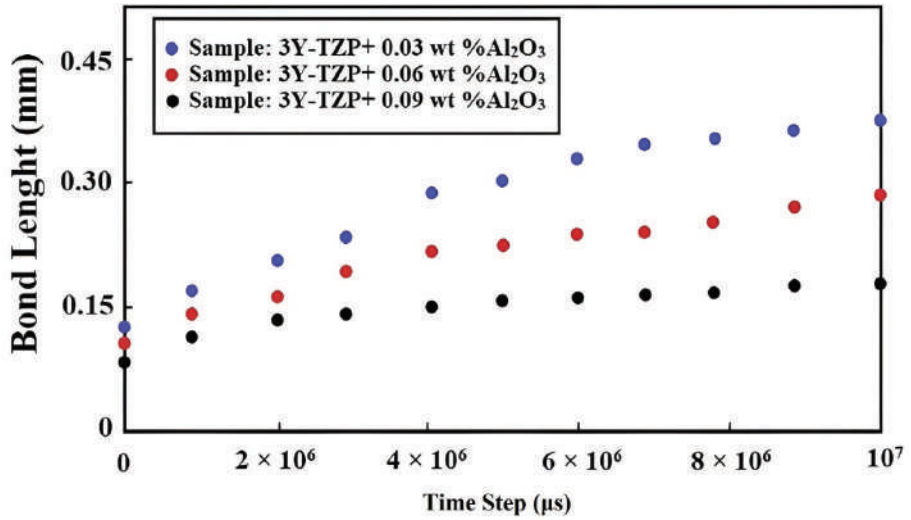


Figure 8. Evolution of relative bond length in modeled 3Y-TZP + x wt% Al_2O_3 over simulation time steps.

Table 4. Characteristics of modeled 3Y-TZP + x wt% Al_2O_3 dental ceramics after 1×10^7 time steps at a velocity of 6 mm/s

3Y-TZP + x wt %Al_2O_3	Crack length (mm)	Net force (N)	Repulsive force (N)	Relative bond length (mm)	Potential energy (J)	Damage criterion
x=0.03	7.11	11.09	2.11	0.15	23.62	0.083
x=0.06	7.94	12.35	2.55	0.26	28.19	0.123
x=0.09	9.01	13.37	2.86	0.37	39.01	0.174

Impact analysis were conducted at 6 mm/s. Figure 9 shows how varying Al_2O_3 content affected crack propagation in the modeled 3Y-TZP + x wt% Al_2O_3 system. Increasing Al_2O_3 increased average particle spacing in the impact zone. This is probably due to the lower mechanical strength in this region resulting from the higher Al_2O_3 content. The simulation results showed that the total force on 3Y-TZP increases with increasing impact fracture velocities. The net force ratio under simulation conditions reached 13.37 N, which increased the displacement of particles in the simulation volume and facilitated crack propagation. Crack growth accelerated with increasing particle displacement in the simulation. Crack lengths at 6 mm/s were 7.11 mm (x=0.03), 7.94 mm (x=0.06), and 9.01 mm (x=0.09). Analysis of repulsive forces showed a value of 2.86 N for the x=0.09 sample at higher velocities.

Table 5 presents the results of six computational calculations. The samples showed significant structural resilience during impact analysis at various speeds. Increased impact velocity correlated with decreased inter-particle distance and reduced mechanical resistance (based on BL and PE analysis).

The data in Table 5 allows for the development of an equation correlating bond length (mm) with velocity for the three samples, as follows:

$$BL_{x=0.03} = 0.0088\,v + 0.1018 \tag{7}$$

$$BL_{x=0.06} = 0.019\,v + 0.1420 \tag{8}$$

$$BL_{x=0.09} = 0.037\,v + 0.1462 \tag{9}$$

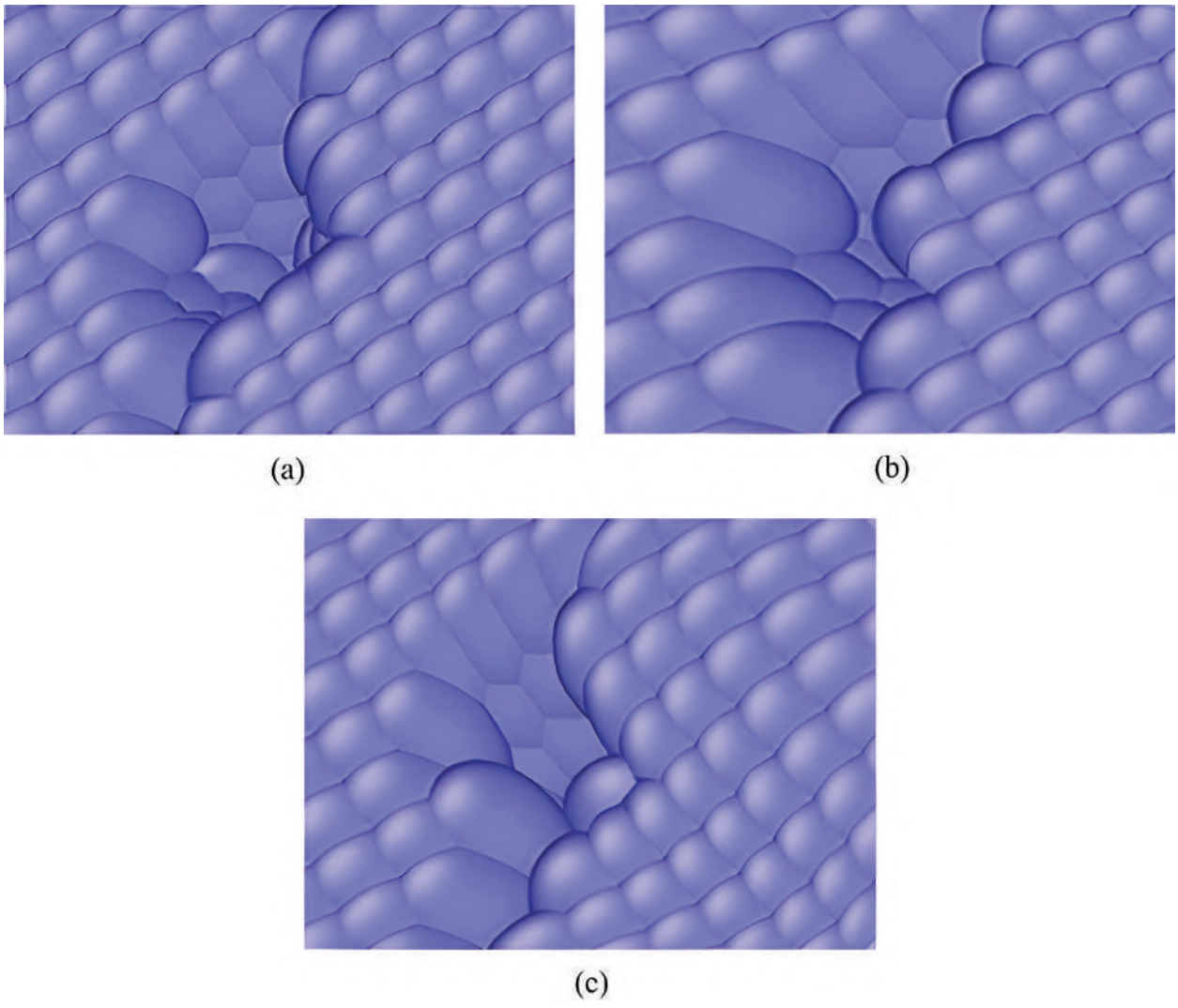


Figure 9. Surface configuration of 3Y-TZP + x wt% Al_2O_3 after impact load at a velocity of 6 mm/s in a) x=0.03, b) x=0.06, c) x=0.09.

Table 5. Effect of impact velocity on 3Y-TZP + x wt% Al_2O_3: crack length, force, and energy parameters

Dental ceramic	3Y-TZP+ 0.03 wt %Al_2O_3					3Y-TZP+ 0.06 wt %Al_2O_3					3Y-TZP+ 0.09 wt %Al_2O_3				
Velocity (mm/s)	2	3	4	5	6	2	3	4	5	6	2	3	4	5	6
Crack length (mm)	7.02	7.07	7.10	7.09	7.11	7.46	7.88	7.91	7.93	7.94	8.85	8.92	8.95	8.97	9.01
Maximum force (N)	6.11	6.14	6.26	6.45	6.55	7.33	7.84	8.03	8.16	8.43	9.65	9.88	10.46	11.37	11.76
Repulsive force (N)	1.55	1.94	1.98	2.07	2.11	2.17	2.19	2.33	2.41	2.55	2.23	2.41	2.56	2.66	2.86
Relative bond length (mm)	0.12	0.13	0.14	0.15	0.15	0.18	0.2	0.21	0.24	0.26	0.22	0.26	0.29	0.33	0.37
Potential energy (J)	22.38	22.69	23.00	23.31	23.62	26.79	27.47	27.49	27.84	28.19	34.62	35.72	36.82	37.92	39.01

Table 6. Potential energy (J) values in brittle material studies

Material	Potential Energy (J)	Reference
3Y-TZP- Al_2O_3	98.42	This study
PMMA composites	67.5	[51]
BNT-Based ceramic	149	[58]
96% Al_2O_3	43.2	[59]
97.7% Al_2O_3	50.6	[59]
Multilayer ceramic capacitors	~200	[60]
$BiFeO_3$-based ceramics	~120	[61]
BNT-based lead-free dielectric ceramics	58	[62]

where v is the test velocity. As the distance between the particles decreased, the attractive forces transformed into repulsive forces (Pauli exclusion principle), which was reflected in changes in potential energy. Using the PD method, potential energy values of 23.62 J (x = 0.03), 28.19 J (x = 0.06), and 39.01 J (x = 0.09) were determined for higher velocities (Table 5). The following equations can express the relationship between PE and velocity:

$$PE_{x=0.03} = 0.31v + 21.758 \quad (10)$$

$$PE_{x=0.06} = 0.35v + 26.09 \quad (11)$$

$$PE_{x=0.09} = 1.098v + 32.428 \quad (12)$$

Increased porosity, resulting from the addition of 0.09 wt% Al_2O_3 to 3Y-TZP, lowered the structural resilience of the dental ceramics, increasing susceptibility to fracture [7]. This suggests that controlling the mechanical strength and operational adaptability of these ceramics is possible by adjusting the Al_2O_3 weight ratio. Akhlaghi-Fard et al. [51] demonstrated, using peridynamics within LAMMPS, that increasing hydroxyapatite in polymethyl methacrylate/hydroxyapatite composites leads to longer cracks. Similarly, in this work, it was found that increasing Al_2O_3 in 3Y-TZP ceramics increases crack length due to interparticle repulsion and decreases total energy. This highlights the influence of composition on crack behavior as modeled by peridynamics. Table 6 compares the potential energy results with other ceramics. Some of the values listed for potential energy in the table are calculated using the following equation [57]:

$$PE = \frac{K^2_{IC}}{E} \times 1000 \quad (13)$$

where K_{IC} is fracture toughness (MPa√m) and E is Young's modulus (GPa).

CONCLUSION

This study examined the fracture behavior of 3 mol% yttria-stabilized tetragonal zirconia polycrystal dental ceramics with varying low alumina content (0.03, 0.06, and 0.09 wt%) using peridynamics simulations. Impact analyses were conducted at velocities of 2, 3, 4, 5, and 6 mm/s. The simulations employed the Peridynamic Material Point Method to model particle interactions in two stages: equilibrium and impact. The outcomes of the peridynamics simulations were as follows:

- The total energy of the 3Y-TZP + x wt% Al_2O_3 dental ceramics system at x=0.03, 0.06, and 0.09 wt% converged to-56.32, -73.22, and -98.42 J, respectively. These

findings suggest an increase in the attractive force between particles within the simulated dental ceramics as the Al_2O_3 ratio decreases.
- The crack length of the simulated dental ceramics reached 9.01 mm at 0.09 wt% Al_2O_3, indicating that an increase in the wt% of Al_2O_3 in the 3Y-TZP leads to a more brittle specimen with reduced mechanical properties.
- Considering the total energy and crack length, 0.03 wt% Al_2O_3 offers a balance. The higher total energy suggests sufficient bonding, while the shorter crack length indicates improved crack resistance. Therefore, a formulation with approximately 0.03 wt% Al_2O_3 is anticipated to exhibit improved mechanical performance for dental restorations.

AUTHORSHIP CONTRIBUTION

All the authors equally contributed to this work.

DATA AVAILABILITY STATEMENT

The authors confirm that the data that supports the findings of this study are available within the article. Raw data that support the finding of this study are available from the corresponding author, upon reasonable request.

CONFLICT OF INTEREST

The author declared no potential conflicts of interest with respect to the research, authorship, and/or publication of this article.

ETHICS

There are no ethical issues with the publication of this manuscript.

STATEMENT ON THE USE OF ARTIFICIAL INTELLIGENCE

Artificial intelligence was not used in the preparation of the article.

REFERENCES

[1] García-de-Albeniz N, Jiménez-Piqué E, Roa JJ, Mas-Moruno C. A review of surface topographical modification strategies of 3Y-TZP: Effect in the physicochemical properties, microstructure, mechanical reliability, and biological response. J EurCeram 2023;43:2977–3004. [CrossRef]

[2] Huang B, Chen M, Wan J, Zhang X. Advances in zirconia-based dental materials: Properties, classification, applications, and future prospects. J Dent 2024;147:105111. [CrossRef]

[3] Muhetaer A, Tang C, Anniwaer A, Yang H, Huang C. Advances in ceramics for tooth repair: From bench to chairside. J Dent 2024;105053. [CrossRef]

[4] Cesar PF, Miranda RBP, Santos KF, Scherrer SS, Zhang Y. Recent advances in dental zirconia: 15 years of material and processing evolution. Dental Mater 2024;40:824–836. [CrossRef]

[5] Upadhyay A, Pradhan L, Yenurkar D, Kumar K, Mukherjee S. Advancement in ceramic biomaterials for dental implants. Int J Appl Ceram Technol 2024;21:2796–2817. [CrossRef]

[6] Moradkhani AR, Baharvandi HR, Vafaeesefat A, Tajdari M. Microstructure and mechanical properties of Al_2O_3-SiC nanocomposites with 0.05% MgO and different SiC volume fraction. ADMT 2012;59:99–105.

[7] Moradkhani A, Gollo MH, Panahizadeh V. Effect of Microstructural Features and Al_2O_3 Doping on Aging Resistance, Mechanical Properties and Crack Propagation in 3Y-TZP Plate Ceramics for Dental Restorations: A Comprehensive Peridynamics Study. Mech Adv Compos Struct 2025;12:523–554.

[8] Jing Q, Bao J, Ruan F, Song X, An S, Zhang Y, et al. High-fracture toughness and aging-resistance of 3Y-TZP ceramics with a low Al Al_2O_3 content for dental applications. Ceram Int 2019;45:6066–6073. [CrossRef]

[9] Kumar KS, Kalos PS, Akhtar MN, Shaik S, Sundara V, Fayaz H, et al. Experimental and theoretical analysis of exhaust manifold by uncoated and coated ceramics (Al_2O_3, TiO_2 and ZrO_2). Case Stud Therm Eng 2023;50:103465. [CrossRef]

[10] Bishnoi D. Pressure exertion and heat dissipation analysis on uncoated and ceramic (Al_2O_3, TiO_2 and ZrO_2) coated braking pads. Mater Today Proc 2023;74:774–787. [CrossRef]

[11] Ganesh KV, Islam MRI, Patra PK, Travis KP. A pseudo-spring based SPH framework for studying fatigue crack propagation. Int J Fatigue 2022;162:106986. [CrossRef]

[12] Belytschko T, Liu WK, Moran B, Elkhodary K. Nonlinear finite elements for continua and structures. New York: John Wiley & Sons; 2014.

[13] Wang H, Liu Z, Xu D, Zeng Q, Zhuang Z. Extended finite element method analysis for shielding and amplification effect of a main crack interacted with a group of nearby parallel microcracks. Int J Damage Mech 2016;25:4–25. [CrossRef]

[14] Dorduncu M, Ren H, Zhuang X, Silling S, Madenci E, Rabczuk T. A review of peridynamic theory and nonlocal operators along with their computer implementations. Comput Struct 2024;299:107395. [CrossRef]

[15] Silling SA, Weckner O, Askari E, Bobaru F. Crack nucleation in a peridynamic solid. Int J Fract 2010;162:219–227. [CrossRef]

[16] Huang D, Lu G, Qiao P. An improved peridynamic approach for quasi-static elastic deformation and brittle fracture analysis. Int J Mech Sci 2015;94:111–122. [CrossRef]
[17] Ha YD, Bobaru F. Characteristics of dynamic brittle fracture captured with peridynamics. Eng Fract Mech 2011;78:1156–1168. [CrossRef]
[18] Bobaru F, Hu W. The meaning, selection, and use of the peridynamic horizon and its relation to crack branching in brittle materials. Int J Fract 2012;176:215–222. [CrossRef]
[19] Basoglu MF, Zerin Z, Kefal A, Oterkus E. A computational model of peridynamic theory for deflecting behavior of crack propagation with micro-cracks. Comput Mater Sci 2019;162:33–46. [CrossRef]
[20] Vazic B, Wang H, Diyaroglu C, Oterkus S, Oterkus E. Dynamic propagation of a macrocrack interacting with parallel small cracks. AIMS Mater Sci 2017;4:118–136. [CrossRef]
[21] Silling SA, Epton M, Weckner O, Xu J, Askari E. Peridynamic states and constitutive modeling. J Elast 2007;88:151–184. [CrossRef]
[22] Silling SA. Reformulation of elasticity theory for discontinuities and long-range forces. J Mech Phys Solids 2000;48:175–209. [CrossRef]
[23] Ha YD, Bobaru F. Studies of dynamic crack propagation and crack branching with peridynamics. Springer 2010;229–244. [CrossRef]
[24] Mitts C, Naboulsi S, Przybyla C, Madenci E. Axisymmetric peridynamic analysis for simulation of crack deflection in ceramic matrix composit. AIAA Scitech 2020;964. [CrossRef]
[25] Zeng Z, Zhang H, Zhang X, Liu Y, Chen Z. An adaptive peridynamics material point method for dynamic fracture problem. Comput Meth Appl Mech Eng 2022;393:114786. [CrossRef]
[26] Bagherzadeh H, Barani OR. Coupling the material point method and Peridynamics via the force partitioning and concurrent coupling schemes. Comput Particle Mech 2024;11:55–71. [CrossRef]
[27] Zhou J, Qian S. Crack propagation simulation of fiber-reinforced composite laminates based on non-ordinary state-based peridynamics. Mater Res Express 2025;12:045501. [CrossRef]
[28] Prakash N, Deng B, Stewart RJ, Smith CM, Harris JT. Investigation of microscale fracture mechanisms in glass–ceramics using peridynamics simulations. J American Ceram Soc 2022;105:4304–4320. [CrossRef]
[29] Chu B, Liu Q, Liu L, Lai X, Mei H. A rate-dependent peridynamic model for the dynamic behavior of ceramic materials. Comput Model Eng Sci 2020;124:151–178. [CrossRef]
[30] Lu W, Li M, Vazic B, Oterkus S, Oterkus E, Wang Q. Peridynamic modelling of fracture in polycrystalline ice. J Mech 2020;36:223–234. [CrossRef]
[31] Rathore NK, Pande S. IoE-based genetic algorithms and their requisition. CRC Press 2023;25–50. [CrossRef]
[32] Rathore NK, Chana I. Checkpointing algorithm in Alchemi. J Inf Technol 2010;8:32–38.
[33] Rathore NK, Khan F. Internet of things: A review article. J Cloud Comput 2018;5:20.
[34] Rathore NK. GridSim installation and implementation process. J Cloud Comput 2015;2:29–40. [CrossRef]
[35] Rathore N. A Review towards: load balancing techniques. J Power Syst Eng 2016;4:47. [CrossRef]
[36] Rathore N. Checkpointing: fault tolerance mechanism. J Cloud Comput 2017;4:28. [CrossRef]
[37] Rathore NK. Installation of Alchemi .NET in computational grid. J Comput Sci 2016;4:1–5. [CrossRef]
[38] Rathore N, Singh PK. A comparative analysis of fuzzy based load balacino algorithms. J J Comput Sci 2017;5:23–33. [CrossRef]
[39] Rathore N. Dynamic threshold based load balancing algorithms. Wirel Pers 2016;91:151–185. [CrossRef]
[40] Rathore NK, Chana I. Comparative analysis of checkpointing. In: Gupta C, Jaroliya D, (editör). IT Enabled Practices and Emerging Management Paradigm. Excel Books 2008. p. 321–327.
[41] Dimitrienko YI. Nonlinear continuum mechanics and large inelastic deformations. New York: Springer; 2010. p. 174. [CrossRef]
[42] Parks ML, Lehoucq RB, Plimpton SJ, Silling SA. Implementing peridynamics within a molecular dynamics code. Comput Phys Commun 2008;179:777–783. [CrossRef]
[43] Rahman R, Foster JT, Plimpton SJ. PDLAMMPS-made easy. University of Texas at San Antonio SNL 2014.
[44] Brown WM, Wang P, Plimpton SJ, Tharrington AN. Implementing molecular dynamics on hybrid high performance computers–short range forces. Comput Phys Commun 2011;182:898–911. [CrossRef]
[45] Plimpton S. Fast parallel algorithms for short-range molecular dynamics. J Comput Phys 1995;117:1–19. [CrossRef]
[46] Plimpton SJ, Thompson AP. Computational aspects of many-body potentials. MRS bulletin 2012;37:513–521. [CrossRef]
[47] Kuzkin VA. On angular momentum balance for particle systems with periodic boundary conditions. ZAMM Z fur Angew Math Mech 2015;95:1290–1295. [CrossRef]
[48] Stukowski A. Visualization and analysis of atomistic simulation data with OVITO–the Open Visualization Tool. Model Simul Mater Sci Eng 2009;18:015012. [CrossRef]
[49] Hanwell MD, Curtis DE, Lonie DC, Vandermeersch T, Zurek E, Hutchison GR. Avogadro: an advanced semantic chemical editor, visualization, and analysis platform. J Cheminf 2012;4:1–17. [CrossRef]

[50] Martínez L, Andrade R, Birgin EG, Martínez JM. PACKMOL: A package for building initial configurations for molecular dynamics simulations. J Comput Chem 2009;30(13):2157–2164. [CrossRef]

[51] Akhlaghi-Fard S, Safari KH, Mashhadi MM, Kheirikhah MM. The computational study of crack growth process in defected polymethyl methacrylate/hydroxyapatite composite beam: peridynamic simulation. Physica Scripta 2023;98(9):095959. [CrossRef]

[52] Akhlaghi-Fard S, Safari HK, Mashhadi MM. 2024. Peridynamic assessment of mechanical and thermal characteristics of a defected PMMA/HA composite beam. J Appl Polym Sci 2024;141(10):e55062. [CrossRef]

[53] ASTM 256-93a, 1995. Standard Test Methods for Determining the Pendulum Impact Resistance of Notched Specimens of Plastics," Annual Book of ASTM Standards, Vol. 08(01)

[54] Platt P. Mella R. DeMaio W, Preuss M, Wenman MR. Peridynamic simulations of the tetragonal to monoclinic phase transformation in zirconium dioxide. Comput Mater Sci2017;140:322–333. [CrossRef]

[55] Aza-Gnandji CD, Baser T. Peridynamic Modeling of Impact Loading in Frozen Soils for In Situ Resource Utilization in the Arctic. Geo-EnvironMeet 2025;128–138. [CrossRef]

[56] Rashmehkarim R, Jafari M, Heidari M. Crack propagation modeling in two-dimensional isotropic plate using bond-based peridynamic theory. J Civ Eng Struct 2025;9.

[57] Li FZ, Shih CF, Needleman A. A comparison of methods for calculating energy release rates. Eng Fract Mech 1985;21:405–421. [CrossRef]

[58] Wang S, Qian J, Ge G, Zhang F, Yan F, Lin J, et al. Embedding Plate-Like pyrochlore in perovskite phase to enhance energy storage performance of BNT-based ceramic capacitors. Adv Energy Mater 2025;15:2403926. [CrossRef]

[59] Rice RW. Grain size and porosity dependence of ceramic fracture energy and toughness at 22 C. J Mater Sci 1996;31:1969–1983. [CrossRef]

[60] Li D, Liu Z, Zhao W, Guo Y, Wang Z, Xu D, et al. Global-optimized energy storage performance in multilayer ferroelectric ceramic capacitors. Nature Commun 2025;16:188. [CrossRef]

[61] Zhou Z, Bai W, Liu N, Zhang W, Chen S, Wang P, et al. Ultrahigh capacitive energy storage of $BiFeO_3$-based ceramics through multi-oriented nanodomain construction. Nature Commun 2025;16:2075. [CrossRef]

[62] Dinh TH, Tran VDN, Le Manh T, Lee JS. Effects of $BaZrO_3$ on the phase evolution and energy storage capacities of BNT-based lead-free dielectric ceramics. J Phys Chem Solids 2025;198:112462. [CrossRef]

Sigma J Eng Nat Sci, Vol. 44, No. 1, pp. 388–403, February, 2026

Sigma Journal of Engineering and Natural Sciences
Web page info: https://sigma.yildiz.edu.tr
DOI: 10.14744/sigma.2025.00000

Research Article

Enhancing bidirectional gated recurrent unit with activation mechanism for anomaly classification for network security

N. Senthil MADASAMY[1,*], A. Noble Mary JULIET[1], P. Boopathi RAJAN[1]

[1]*Dr. Mahalingam College of Engineering and Technology, Udumalai Road Pollachi, 642003, India*

ARTICLE INFO

Article history
Received: 22 July 2024
Revised: 03 October 2024
Accepted: 09 January 2025

Keywords:
Anomaly Classification; Bidirectional Gated Recurrent Unit and Activation Function; Deep Learning; Network Security; NSL-KDD Dataset; UNSWW-NB 15

ABSTRACT

In a digital world, cyber-attacks are increasingly common, raising concerns that existing anomaly detection models might not effectively handle intricate threat scenarios. As the demands for network systems grow. Historically, the update and reset gates of the Gated Recurrent Unit (GRU) designed to controls flow in input data across time steps have faced challenges in identifying anomalies in security monitoring, traffic log analyses, and packet flow assessments. To address anomalies, reduce time expenditure, and improve network security, the proposed research utilizes a Deep Learning (DL) technique named Structured Activation Module Loop Framework Unit and an efficient activation module unit, which integrates a Bidirectional Gated Recurrent Unit (Bi-GRU) model that includes update and reset gates for controlling information flow on the basis of the classification context of the input data. The suggested structured activated loop framework monitors error data straight in the update gate without demanding the reset gate, enabling several checks in a loop format. The activation module unit precisely divides the class data to predict the appropriate output characteristics for resolving missing values. This utilizes network intrusion datasets (UNSW-NB15) and Neural Simulation Language- Knowledge Discovery in Databases (NSL-KDD), both commonly used for (NID) Network Intrusion Detection systems, along with pre-processing data and assessments for data splitting through training the model and testing procedures. Similarly, the proposed performance is assessed using different metrics such as F1-meaures, recall, value of precision, accuracy, with overall accuracy to evaluate the efficiency of the suggested deep learning study. The results obtained precisions of 0.99, 0.97, 0.97, and 0.97 in NSL-KDD, 0.98, 0.99, 0.98, and 0.98 in UNSW-NB 15. Still, the assessment of recommended models demonstrates the efficacy of the research. The present research attempts for find and improve creation of detection of anomaly models for network and cyber security regarding hackers and malicious attacks.

Cite this article as: Madasamy NS, Juliet ANM, Rajan PB. Enhancing bidirectional gated recurrent unit with activation mechanism for anomaly classification for network security. Sigma J Eng Nat Sci 2026;44(1):388–403.

***Corresponding author.**
*E-mail address: senkav1293@gmail.com, senthilmadasamy@drmcet.ac.in

This paper was recommended for publication in revised form by Editor-in-Chief Ahmet Selim Dalkilic

Published by Yıldız Technical University Press, İstanbul, Turkey
© Author. This is an open access article under the CC BY-NC license (http://creativecommons.org/licenses/by-nc/4.0/).

INTRODUCTION

In this era of technology, both businesses and individuals are equally worried about network security. Quick expansion of network and the increasing dependence on interacted systems led to a rise in potential cyber threats. Identifying and categorizing abnormal network activities that differ from normal behaviour is a cricial element of network safety [1]. Anomaly classification involves recognizing and grouping atypical network behaviours. These abnormalities may suggest possible security risks, such as malware infections, illegal access attempts, or breaches. Nevertheless, training these models typically requires manual techniques for labelling and categorizing anomalies, leading to potential restrictions and disadvantages. An important disadvantage of manual techniques for anomaly classification is the subjectivity, time-consuming nature, labour-intensive process, and possibility of human error [2]. In recent times, researchers have been employing technology based on Artificial Intelligence (AI) for anomaly classification [3]. Benefits of Deep Learning (DL) and Machine Learning (ML) offer many uses network security [4]. Anomaly classification utilizes ML and DL techniques to examine network traffic, detecting deviations from the usual patterns and categorizing correct and incorrect signals [5]. Different approaches have been experimented with to detect anomalies in network structures using the backing of ML and DL technologies. Likewise, lack of strong authentication can enable attackers to examine and intercept the traffic [6]. Even with all its capabilities and attributes, network security remains a major worry.

Similarly, various traditional models have tried to classify anomalies. As an example, the traditional approach has used a successful anomaly detection system that leverages Mutual Information (MI) and incorporates a Deep Neural Network (DNN) for IoT network. The evaluation used the IoT-Botnet 2020 dataset and attained improved exactness [7]. In the same way, the prevailing model presented an integration of SMOTE over sampling method and 1-D CNN method [8] were the statistical analysis and secured robustness provide better results [9] for minority classes of attacks classification. The testing process has made use of the UNSW-NB15 dataset. The results indicated the existing research has achieved superior values on assessment metrics [10]. Similarly, a DL technique has been utilized to detect different kinds of anomalies in IoT data flow. It was assessed using five different datasets and achieved improved outcomes [11], utilizing Mogrifier Gated Recurrent Unit (GRU) and Multi Scale Convolutional Neural Network (MSCNN) for log-based anomaly detection to differentiate between usual and unusual logs by examining local and global dependencies [12] resulting in high precision statistical classification of severity levels [13]. Similarly, the current model has integrated both CNN and GRU model [14] for identifying anomalies in encrypted network traffic. It has utilized 3 publicly available datasets such as NSL-KDD, CIC-IDS-2017 and UNSW-NB15. The existing model's experiment findings revealed accuracies of 93.10%, 91.21% and 90.17% on NSL-KDD, CIC-IDS-2017 and UNSW-NB15 dataset respectively [15]. Likewise, previous models such as the Mountaineering Team-Based Optimization (MTBO) algorithm, the AWID3 dataset, and the Technical and Vocational Education and Training-Based Optimizer (TVETBO) optimizer have been employed to improve robustness and address challenges with anomalies [16]. The increase in efficiency and robustness has been a positive outcome [17]. Similarly, a traditional approach has been used to create an IDS for IoT that relies on anomalies. Afterwards, CNN has been used in 1D, 2D, and 3D. It has been tested on four specific datasets - IoT Network Intrusion, BoT-IoT, IoT-23 intrusion detection, and MQTT-IoT-IDS2020 dataset [18] achieving improved accuracy and network security [3, 19]. Consequently, the traditional models have achieved successful outcomes without introducing new elements [20, 21].

The study on supervised deep learning models for detecting network traffic abnormalities early on points out a number of ongoing obstacles that hinder the success of current approaches. One main problem is the absence of standardized reference markers, making performance evaluation difficult and raising the risk of over fitting. This issue has made worse by a large amount of wrong identifications due to using possibly compromised or outdated data, which makes it challenging to distinguish between regular and abnormal traffic patterns. Moreover, when datasets increase in size, they frequently encounter more noise, causing models to have difficulty adjusting to new attack strategies, especially when dealing with unfamiliar anomalies. The issue of unequal distribution of classes in datasets remains, affecting the model's learning of minority classes. Unlike previous studies, the propounded model includes enhancements to tackle these issues. Using both UNSW-NB15 and NSL-KDD set of data, the model integrates a Structured Activation Module Framework Unit with a Bidirectional Gated Recurrent Unit (Bi-GRU) to enhance anomaly classification efficiency. Introducing a Structured Activation Loop Framework improves the model's ability to understand intricate details in short data analysis, while an Efficient Activation Module Unit reduces complexity and handles missing values in time series data. These advancements enhance how missing data is managed, while also integrating layered attention frameworks and advanced recommendation strategies, distinguishing this research from prior methods that often did not offer such complete solutions. In general, although previous research has made progress in area, the innovative features of the proposed prototypical represent a significant enhancement in utilizing (RNN) Recurrent Neural Networks for detecting network traffic anomalies without introducing new components.

Paper Organization

The current model conceptual framework is outlined as follows: section 1 gives an introduction of the model background. Section 2 examines existing research concerning anomaly prediction and problem detection. The next Section 3 specifically details the proposed methodology. Moreover, section 4 includes both a table and visual illustration of the data analysis. Section 5 examines the results of present study in comparison to previous research. In conclusion, section 6 offerings the findings of the study and offers recommendations for the future.

Literature Review

The section covers he traditional and advance methods by reviewing and explains about the examination in several conventional investigates of anomaly classification along with other methods for estimation on classification system in network traffic to ensure the security.

The conventional research has presented effective anomaly detection mechanism named as D-PACK. It comprises of supervised DL model like auto encoder and convolutional neural network (CNN) for auto profiling traffic patterns and extracting the abnormal traffic. It has used Mirai-CCU dataset [22]. Similarly, a variant DL architectures to the issue of anomaly prediction on network logs which are obtained by Sense firewall along with chief target the classification of event type in the prevailing system. It has utilised network intrusion dataset [23]. Correspondingly, a 5-layer auto encoder based model for a network anomaly classification tasks. This model has evaluated on NSL-KDD dataset that outperformed [24]. Congruently, CSE-CIC-IDS2018 dataset has been employed to evaluate the traditional model. It has applied CNN, RNN, LSTM, DNN, CNN+RNN and CNN+LSTM models have been constructed to identify the anomaly attacks in network and has attained better results [25].

In the same way, a CNN created technique has deployed for anomaly intrusion detection systems (IDS) which took IoT's advantage. It has provided qualities to analyse whole traffic across IoT. It has utilised NID and BoT-IoT dataset [26]. In parallel, a hybrid DL model has deployed to address various real-time and automatic surveillance techniques for abnormal detection to identify dynamic multitude activity in the applications of security. It has used Motion Emotion dataset [27]. Additionally, the existing model has deployed a DNN method for detection of anomaly in NID mechanism. It has utilised NSL_KDD dataset and soft max layer has been used along with cross entropy loss mechanism for enforcing the conventional model in various classification comprising 5 labels like normal, DoS, R2L, Probe and U2L. It has attained better results [28]. Likewise, a deep CNN model has been deployed for classifying and detecting nearest real time network intrusions from the imbalanced cloud surrounding. In addition to, the evaluation has been carried out with CSE-CIC-IDS2018 dataset [29].

Similarly, the classical model has presented a mechanism of anomaly detection utilising CNN and LSTM models. These models have been proficient on data network that are take out from the packet capture files. It has utilised a huge scale real network traffic dataset and benchmark intrusion detection dataset, CTU-13, ISCX-IDS and NSL-KDD datasets respectively [30]. In parallel, the existing system has evaluated several significant feature selection method for ML on DDoS detection. It has used NSL-KDD dataset which contains 41 features and 52,800 records. Has attained better accuracy using the features subset through the RFE method [31]. Contrastingly, conventional model has predicted various anomalies on various features in the dataset through applying ML models. It has utilised a dataset which is from Kaggle that comprises 357,952 samples along with 13 features with the lack of labelled datasets and noisy data[32]. Similarly the existed study namely split active learning anomaly detector (SALAD), KDD cup 199, and UNSW-NB 15 dataset using scikit-multiflow framework includes teaching auto encoders through real-time data to detect irregularities. Findings indicate SALAD is more effective than conventional methods in terms of both value of precision and speed [33]. Similarly, an approach existed namely Recurrent Extreme Learning based-boosted chimp (REL-BC) algorithm and extreme learning machine (ELM) used for anomaly detection, making it appropriate for cyber security [34] (Table 1).

PROBLEM IDENTIFICATION

Several existing researches have been limited by predicting the anomaly in the networks. It has several lacks and it is provided below.

- Limitations comprise the need for a substantial amount of high-quality training data and the risk of over fitting due to the auto encoder›s distinct training method, which may not adjust well to unfamiliar data distributions. Furthermore, challenges may arise in scaling and computational efficiency when dealing with extremely large datasets, as well as the need for accurate parameter tuning to improve performance in different scenarios [33, 34].
- Other limitations include the risk of over fitting with complex models, reliance on particular datasets that may not be relevant to all situations, and obstacles in implementing real-time processes due to the escalating computational demands of deep learning methods without incorporating new elements [29].
- Relying on particular training datasets restricts models' ability to adapt to new situations, as they frequently do not encompass all possible unusual behaviours. The complexities of the real world, like different lighting and crowd behaviour, make it harder to accurately detect things, and the computational requirements of deep learning slow down real-time processing.
- Furthermore, the process of obtaining and up keeping substantial amounts of labelled training data requires a lot of resources, resulting in high levels of false positives

Table 1. Deep learning–based anomaly and intrusion detection, highlighting datasets used, real-time performance advantages over traditional methods, and key limitations such as labeled data requirements and optimization challenges

Reference	Model name	Data sets	Methodology	Result	Limitations
[27]	CNN architecture	Motion Emotion Dataset (MED)	Employing optical flow and CNNs to capture the spatial-temporal features of crowd behavior.	The existed model has showed greater accuracy, reduced computational complexity, identifying anomalies	The reliance on labelled training data, which can be hard to collect fully. Fluctuations in lighting occlusion can influence detection performance.
[30]	CNN, LSTM	Benchmark intrusion detection dataset, CTU-13, ISCX-IDS and NSL-KDD datasets	The network flow where trained by source of data and files are captures from packed resources and assessed using benchmark intrusion detection datasets alongside a substantial real-world network traffic dataset.	These deep learning models greatly exceed conventional shallow learning techniques regarding anomaly detection efficiency, achieving real-time processing with minimal latency.	constraints, including the necessity for optimization strategies such as transfer learning, improve detection efficiency, difficulties in managing various data types
[22]	Variation Auto encoder (VAE), CNN architecture	Mirai-CCU dataset	To rebuild typical traffic patterns and detect anomalies through reconstruction errors	VAE identifies anomalies with high value of precision and low rates with false positives, surpassing conventional techniques in early detection abilities	Constraints such as the model›s vulnerability to the quality of the training data and possible difficulties in adjusting to fast-evolving network settings, which could influence its sustained efficacy in fluctuating situations.
[29]	Deep CNN architecture	CSE-CIC-IDS2018 dataset	This model CNN demonstrated to address class imbalance using methods like oversampling and cost-sensitive learning	Enhances detection accuracy and classification performance, attaining significant decreases in false positive rates, successfully identifies both frequent and unusual anomalies.	The possibility of over fitting owing to the model›s complexity and the requirement for significant computational resources, which could impede effective implementation in resource-limited settings.
[31]	Random Forest (RF) ML model	NSL-KDD dataset	The datasets used consist of synthetic traffic data created to reduce DDoS attacks and actual network traffic data.	Precisely detecting and alleviating DDoS attacks	Dependence on feature selection techniques, affect detection precision, computational burden linked to handling huge amounts of network data in real-time situations
[34]	(REL-BC) algorithm and (ELM)	NSL-KDD dataset	It effectively detect anomalies without relying on labelled data, making it appropriate for situations where anomalies are infrequent and varied.	Significant accuracy and resilience in identifying anomalies within diverse high-dimensional datasets,	Possible difficulties in generalizing across varied datasets, which could impact its efficiency in changing real-world scenarios.
[25]	CNN, RNN, LSTM, DNN, CNN+RNN and CNN+LSTM models	CSE-CIC-IDS2018 dataset	Mechanically learn features from raw network traffic data, facilitating effective anomaly detection.	Improved detection accuracy, false positive rate reduction.	Dependency on large amount of labelled data affects robustness.

that can be overwhelming for network administrators and lead to alert fatigue. The constantly changing network traffic requires constant adjustment to changing patterns, making it challenging for models trained on old data such as NSL-KDD to be effective.[23, 24] [27, 30].

Similarly, earlier approaches are followed to classify the network interruption by CNN, LSTM, REL-BC, and RF has been used to implement. It resulted in constraints like dependency on large amount of labelled data sets, difficulties in generalizing across varied dataset, possibility of over fitting, and vulnerability to the quality of the training data. While the approached method has overcome all of these difficulties by integrating the structured activation loop framework and efficient activation module unit with (UNSW-NB15) and NSL-KDD datasets. This approached method carries the overall performance and enhance the network anomaly classification by loop based frame work mechanism which has provided better accuracy and results.

MATERIALS AND METHODS

The research method classifies and extract data from the corresponding dataset for anomalies prediction. The prediction is approved by applying structured activation module framework unit with Bi-GRU, a deep learning model with activation function. Traditional works on the anomalies prediction have produced inaccurate results with slow speed convergence. Consequently, the respective model utilised the DL algorithm for prediction of UNSW-NB15 and NSL-KDD data. Furthermore, the flow of proposed DL model illustrated in below Figure 1.

Figure 1 deliberates the proposed flow, which indicates the proposed model creation on anomaly classification on network established environment, where it includes the loading the dataset, refers to the procedure of importing or accessing the dataset within the working environment. This probably involves importing data from sources such as CSV files, SQL databases, or various structured data formats. Also featuring data activities like dealing with missing values, outliers, transforming, normalizing, encoding categorical variables, therefore pre- processing is importance for enhancing the accuracy and resilience of models. Similarly, the separation is very much essential for assessing the model effectiveness and unfamiliar data, where this phase entails train the model using the refined training data and fine- tuning its parameters to improve performance. Finally an assessment procedure, Performance metrics are computed to assess the model exactness, value of precision, probability of detection, f1 measures that enhances classification. The following sections deliberates the functions used in present model and Figure 2 signifies the present model's architecture.

The Figure 2 represents the present model of architecture. It signifies that the used data are pre-processed and split as train and test set to classify the data to predict anomalies in the data. It may contains various types of attacks which has to be detected.

Dataset Description

The proposed system being suggested makes use of two publicly available datasets called UNSW-NB15 and NSL-KDD. However, both sets of data are commonly used in academic studies to create and evaluate machine learning methods focused on boosting the efficiency of IDS. NSL-KDD and UNSW-NB15 are both network datasets. That



Figure 1. Proposed flow mechanism.

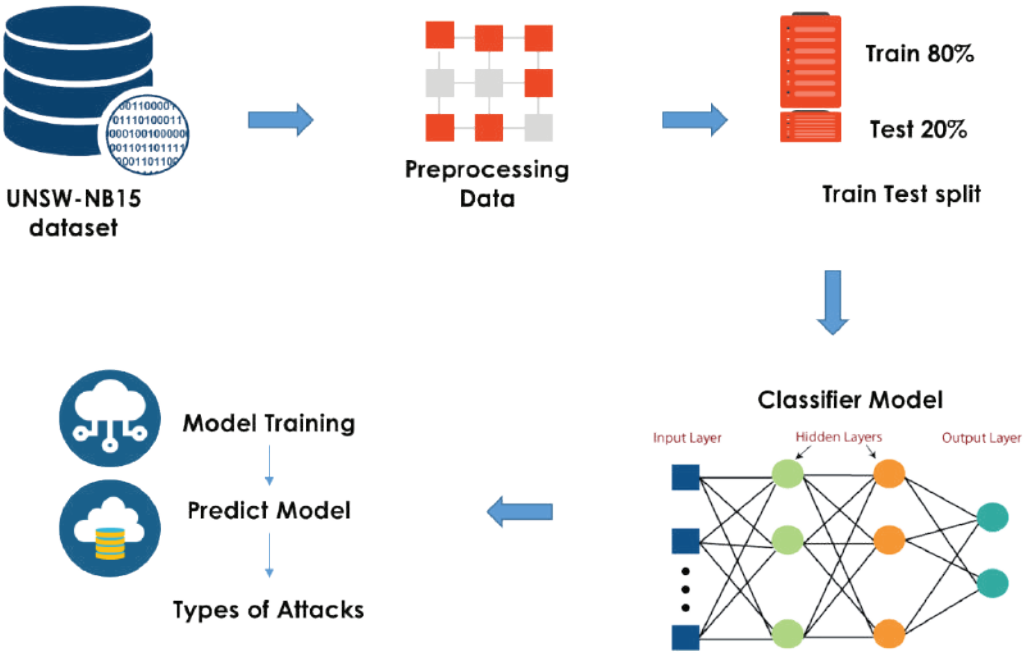


Figure 2. Present model architecture.

favoured by researchers because they offer thorough coverage of attacks, advanced features, extensive record sizes, authentic traffic simulation methods, and academic acknowledgment. On the other hand, iTrust and SWAT datasets are limited in their usefulness for research due to a lack of varied attack types and adequate data. Moreover, the variety of features and data range available make it a valuable resource for testing detection algorithms and enhancing machine learning effectiveness, which is why it is well-liked in academic circles. The data sets were obtained from the Kaggle platform.

UNSW-NB15 dataset

The UNSW-NB 15 dataset is a current dataset is used to estimating (IDS), it has comprised by a mixing of normal and malicious network traffic. This dataset consist of 9 kinds of attacks such as Denial of service (DoS), Fuzzers, Exploits, Generic, Shellcode, Analysis, Worms, Reconnaissance and Backdoors. It is a substantial and having 2, 57,673 record samples, where training set have 75,341 and testing set have 82,332 record samples. Each comprises with 48 features. It is a comprehensive majorly used for network intrusion detection mechanisms. The website line of UNSW-NB15 dataset is given below:

https://www.kaggle.com/datasets/mrwellsdavid/unsw-nb15/data

NSL-KDD dataset

Train set of NSL-KDD data contains labels of attack-type and levels in CSV format. It is N reviewed version of innovative KDD dataset, aimed at giving a more balanced and representative sample for intrusion detection research. Moreover, it consists total of 1, 48,517 samples of record that have 42 features in NSL-KDD dataset. Where attacks have been categorized likely DoS, User to Root (U2R), Remote to Local (R2L), probing, and normal connections. The records in test and train sets are reasonable that made reasonable to do the tests on entire set without any necessity for randomly choose a trivial portion. The official link of the NSL-KDD dataset is provided below:

https://www.kaggle.com/datasets/hassan06/nslkdd

Data Pre-Processing

The technological skill to modify raw data into proper data sets is called pre-processing, that pre-processes mavericks, missing values, noisy signals, feature scaling, label encoding, and other inconsistences before they are applied to the algorithm. In addition, the pre-processing stages the feature extraction and classification performance of the presented method. To achieve this, the designed system has incorporated two significant pre-processing methods such as missing values checking and feature scaling. While scaling features, the data features or variables range have been normalized to increase the effectiveness of the proposed model. The process is known as data normalization. Normalization is a data pre-processing technique employed to convert features in a dataset to a uniform scale, enhancing the effectiveness and precision of ML algorithms. The primary aim of normalization is to remove possible biases and distortions resulting from the varying scales of features. Here, Min-Max scalar normalization also known as Min-Max scaling, data has been used to convert into specific range, often (0, 1). It rescales to ensure the data

to map in the lowest value to 0, and scales the extreme value to 1(or -1). It is simple and easy to protect the relationships between data points, also suitable for algorithms data within bounded range assured. Similarly missing value handling is a biggest step in data pre-processing missing data, can evolve from various sources, such as human error, technical issues, or the inherent nature of the data collection process, these missing values can be handled by entire row list wise deletion by filling based on other available data through imputation techniques, advanced imputation includes interpolation, this is particularly used for time-series data where it include linear and polynomial interpolation , on the other hand multiple imputation also used for imputing missing values by multiple times. Similarly libraries and functions, arbitrary value replacement also utilized for missing value handling.

Data Splitting

DL devotes the data management to the aim of removing the overfitting of data. Essentially, DL employs data splitting as a tool to train the respective model whereby the training data is injected into the proposed method to enable the training stage parameters. Once the training has been accomplished, testing data are used to evaluate the deployed model for dealing with the test set. The current model splits the original data into two sets of 80:20, thus eighty percent of the new observations are used for training, while the remaining 20 percent of the observations are utilized for testing to calculate the performance of the respective technique.

CLASSIFICATION- STRUCTURED ACTIVATION MODULE FRAMEWORK UNIT WITH BI GRU

A Bi-GRU with update and reset gates is a variant of the standard GRU architecture, a RNN type which incorporates additional gates to control the flow of information through the network. The Bi-GRU with update and reset gates consists of two hidden states, one for the forward pass and one for the backward pass. The update gate controls the amount of data from the former hidden state that is carried out to the present hidden state. The reset gate controls the degree to which the preceding hidden state is reset before the new information is incorporated. As it described, RNN are designed to handle the sequence data. Moreover, RNN has its ability to learn the long term dependency. To solve these problems, some RNN structures are customised like GRU. Compared to other models, GRU utilises less parameters. Bi GRU is effective for tasks such as appropriate text representation, missing data value prediction, etc. and moreover, along with the preceding values, succeeding data also available. However, it comes with increased computational cost, over fitting potential, and difficulty in optimization. Hence the proposed model employs structured activation module framework unit with Bi GRU to work well in prediction.

The Bi-GRU model's gating mechanisms are improved by the Structured Activation Loop Framework, which introduces a structured method for controlling information flow more effectively according to input context. This system focuses on being able to adapt to different contexts by incorporating more contextual details into the activation

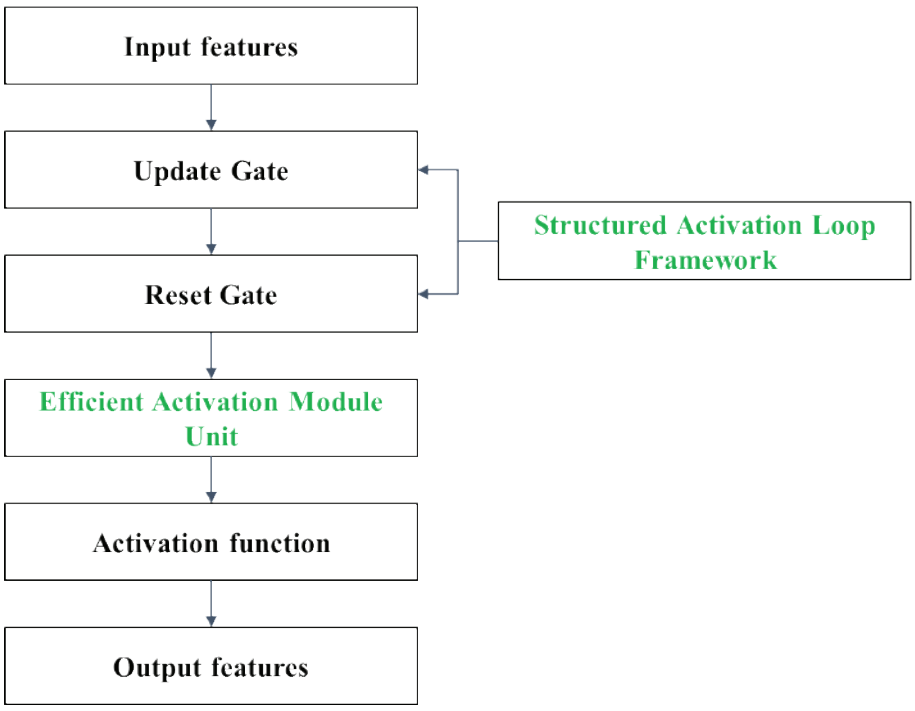


Figure 3. Mechanism of Present DL Model.

functions of the update and reset gates. This allows the model to accurately detect quick changes in emotions in brief reviews. Moreover, it enhances information recall, leading to improved retention of important details over time, which is crucial for identifying delicate hints in user attitudes expressed in reviews. Furthermore, the organized framework allows for flexible changes, allowing the model to adjust the impact of previous states reliant on present inputs, ultimately improving performance in tasks that involve understanding time sequences. In addition, the Efficient Activation Module Unit aims to improve the computational effectiveness of the Bi-GRU, especially in situations with sparse or missing data. This is accomplished by reducing the computational complexity of the model's activation functions, resulting in faster processing times, particularly when dealing with large datasets. The unit is equipped with methods for managing missing values, increasing resilience by enabling the network to focus on important data sections while ignoring unimportant ones. It helps enhance learning efficiency by enabling quicker convergence in training and reducing noise from data gaps, resulting in more dependable predictions and insights.

The Figure 3 represents mechanism of current DL model. Usually, a standard GRU approach includes a reset gate system and an update gate that helps in recognizing the input data. The update gate controls the data flow at every time step, whereas the reset gate eliminates the unrelated value, returning it to the update gate for further processing. This system determines the quantity of data retained from the past and the amount that is eliminated. Consequently, this method involves a decrease in prediction accuracy, extended outputs, and is time-consuming. In this suggested structured activated loop model, the error data is observed within the update gate without going through the reset gate; it can be confirmed several times in a loop format. This mechanism captures the behaviour of short reviews, guarantees the efficient retention of relevant information over time, adjusts historical states based on present input, and involves a lengthy procedure. In the effective activation module unit, class data is divided efficiently to precisely predict the appropriate output required for handling missing values. This allows the network to concentrate on important segments while excluding irrelevant or uninformative components of the input, which improves resilience, reduces noise, and leads to more dependable predictions and insights.

Since Bi-GRUs are a potent tool for anomaly classification, however it also have several disadvantages. These disadvantages should be considered when choosing a model for anomaly classification. To overcome the issues, activation function is incorporated in Bi-GRU model. The optimal of activation function considerably impact the capability for network to learn multifaceted patterns, generalize to unseen data, and differentiate among usual and abnormal data. After process of gate function, the data were passed to efficient activation module unit which is used to develop the accuracy of the present model. Moreover, activation function segregates the class data precisely to predict the appropriate output features. In addition, Bi-GRU uses gating mechanism to embrace the memory without separate unit. Both of the gates control and update data in time t. At the time t, it updates the data as follows.

$$o_t = (1 - ug_t) \odot o_{t-1} + ug_t \odot \widetilde{o_{t-1}} \quad (1)$$

o_t – Represents the output time t, o_{t-1} – previous time step t-1, ug_t – Term controls the signals, weight, or input forms at time t, ⊙ - Indicates an element- wise multiplication, which allows for selective scaling of features based on their relevance. The above equation signifies as linear function to integrate previous state o_{t-1} and present state $\widetilde{o_{t-1}}$, which is measured by new sequence data. The traditional GRU measure ug_t in following equation (2).

$$ug_t = \sigma\,(w_{ug} y_t + U_{ug} o_{t-1} + m_{ug}) \quad (2)$$

ug_t – Represents the amount produced or state variable at time t, y_t – denotes an input or state variable at time t, o_{t-1} – Previous state or time from an input t-1, m_{ug} – indicates a constant parameter influence the output, w_{ug} – A weight or coefficient applied to the variable y_t, σ – Initiates initial transformation for the context. This equation (2) represented for processing sequential data such as time- series. Here, y_t current input sequence. Bi GRU process the input sequence as $\hat{y} = y_{t-1}, y_t, y_{t+1}$ to replace with y_t to fetch more information. And the calculation of structured activation module unit with Bi-GRU calculates as follows

$$ug_t = \sigma\,(w_{ug}\hat{y} + re_t \odot (U_h o_{t-1}) + m_o \quad (3)$$

w_{ug} – A weight parameter linked with the input $\hat{y}$. It scales the contribution of to the overall output ug_t, m_o –similarly a bias term added to the equation, providing an offset that can help adjust the output independently of the inputs, $\hat{y}$ – Usually denotes various predicted output or feature vector from past calculations or network layers. The reset gate re_t modulates how much of the previous state contributes to the calculation. Equation (3) makes suitable for applications where outputs need to be interpreted probably in recurrent neural networks.

The temporary state $\widetilde{o_t}$ can be calculated through the equation (4)

$$\widetilde{o_{t-1}} = \tanh\,(w_{ug}\hat{y} + re_t \odot (U_o o_{t-1}) + m_o \quad (4)$$

ret⊙ (Uoot−1) integrates information both present and previous states, permitting for dynamic modifications. The term $w_{ug}\hat{y}$ contributes to the modified state based on feature prediction, the bias term m_o helps to tune the output finely before applied into the activation function. The *tanh* function ensures that $\widetilde{o_{t-1}}$ remains within a bounded range, making it suitable for applications where output needed to be interpreted or where non- linear transformations are beneficial. This equation calculates a temporary state based

on both current and previous states, transformed by a hyperbolic tangent function to ensure values are between -1 and 1. Where y_t is replaced by $\hat{y}$. The reset gate re_t is weight considering that how much the model keep the previous state. If re_t = 1, then the state need to keep whole previous state o_{t-1}. In modified Bi-GRU, reset gate is calculates as follows

$$re_t = \sigma\left(w_{re}\hat{y} + (U_{re}o_{t-1}) + m_o\right) \quad (5)$$

After the gate mechanism, assuming a review contains l_s reviews where it have contains l_w reviews. Here, w_{it} refers to *t th* one and $t \in [1, L_w]$, $i \in [1, L_s]$, it also employs an embedding matrix w_e to plot w_{it} into vector y_{it}. A Bi-GRU a bidirectional unit, it has forward direction $\overrightarrow{weight\ input}$ and reverse direction.

$$y_{it} = w_e w_{it}, t \in [1, L_w] \quad (6)$$

Where equation (6) maps vector representation using an embedding matrix. The w_e acts as a scaling factor for the variable w_{it}. Where the resulted product gives the value of y_{it} that might represent some form of accumulated information, prediction, or transformation based on the input weights and parameters.

$$\vec{o}_{it} = \overrightarrow{weight\ input}\,(y_{it}), t \in [1, L_w] \quad (7)$$

$$\overleftarrow{o}_{it} = \overrightarrow{weight\ input}\,(y_{it}), t \in [L_w, 1] \quad (8)$$

The, it combines $\vec{o}_{it}$ and $\overleftarrow{o}_{it}$ as $[\overrightarrow{o}_{it}:\overleftarrow{o}_{it}]$ that contains all data taking as o_{it} as center. Hence, the mechanism employs attention mechanism to compute various weights for each anomaly. It use the following function to measure the attention weights, while these equations (7) & (8) compute forward and backward states for each time step in a bi directional manner.

$$c_{it}^w = \sigma(W_w\, o_{it} + m_w) \quad (9)$$

$$a_{it}^w = \frac{exp\,(c_{it}^w)^T c^w}{\sum_t exp\,(c_{it}^w)^T c^w} \quad (10)$$

These equations (9) & (10) calculate attention weights based on the context vector for each evaluation, allowing the model to focus on applicable parts of the input data and also it acts an attention mechanism for anomalies.

$$s_i = \sum_t a_{it}^w\, m_{it} \quad (11)$$

s_i- An aggregated measure, or an output from a model for the specific index, ∑t- summing over the variable t. this implies that the equation considers multiple time steps or instances, contributing to the overall value of s_i, a_{it}^w – Weight or coefficient liked with an index *i* at time *t*, raised to the power of *w*. The exponentiation suggests that the weights may have a non- linear influence on the sum, which is important in contexts to emphasize or de- emphasize different contributions, m_{it} – Another variable associated with index *i* at time *t*. it could represent a measurement, feature, or any relevant quantity that is being multiplied by the weighted term a_{it}^w.This equation (11) computes a value s_i by combining contributions from multiple instances. The summation denotes that all these contributions are joined to give a single output for each index *i*. Moreover, it needs to compute different data weights to affect the sentiment reviews, where an s-attention applies as w-attention

$$c_i^s = \sigma(W_s\, m_i + o_s) \quad (12)$$

$$a_i^s = \frac{exp\,(c_i^s)^T c^s}{\sum_t exp\,(c_i^s)^T c^s} \quad (13)$$

The above (12) & (13) equations were the secondary attention mechanism defines next attention mechanism focused on different datasets to contribute overall consideration. It signifies a score, total or any accurate calculations on dependency.

$$v = \sum_i a_i^w\, m_i \quad (14)$$

v – Represents the final computed value resulting from the summation, a_i^w – Variable raised to the power of *w*. The exponential illustrates every a_i is converted into non-linear before multiplied by m_i and m_i could represent a measurement, feature, or any relevant quantity that is being multiplied. This equation (14) contribution aggregates from all reviews into a single vector illustration from multiple instances. The summation implies that all these contributions are combined to produce a single output for *v*. Here, *v* is review level vector that consists almost all data and then to build loss function deliberated as follows.

$$Loss = \sum_{r \in R}(v - mt)^2 \quad (15)$$

Similarly, equation (15) represents the loss function for training process, it measures far predictions from actual values by summing squared difference across all analysis. Finally the equations collectively describe a complex neural network architecture that efficiently processes sequential data through gated mechanisms and attention mechanisms. The integration of bidirectional processing allows for capturing contextual information from both past and future states, making this model particularly powerful for tasks like sentiment analysis, anomaly detection, or any other applications involving sequential data.

RESULTS AND DISCUSSION

Performance Metrics

Performance metrics basically serve as a means of gauging the efficiency of the intended research through the use of various metrics such as probability of detection rate, value of precision, exactness, and F1 measures value.

Recall Metric

In this case, recall serves to research the proportion of data that was correctly identified by the corresponding model. The recall formula is given by the following equation (16),

$$\text{Recall} = \frac{\text{True_Pos}}{\text{False_Neg+True_Pos}} \quad (16)$$

Accuracy Metric

Exactness is the main metric that is used to analyse the number of estimates which are almost correct in the present model. The exactness formula is shown in equation (17),

$$\text{Accu} = \frac{\text{TP+TN}}{\text{TP+FP+TN+FN}} \quad (17)$$

TP, FP, TN, FN are True Positive, False Positive, True Negative, and False Negative, respectively.

F1 Score Metric

F1-measures is aimed at testing the correct predictions of the positive class in the current model. The f1-score formula is referred to in equation (18),

$$\text{F1 Score} = 2 * \frac{\text{Recall*Precision}}{\text{Recall+Precision}} \quad (18)$$

Precision Metric

One of the precision metrics is known as the method's covariance unit, which is achieved by suitably predicted cases (*True_Pos*) to the total number of cases that have been precisely considered (*True_Pos* + *False_Pos*). Equation (19), shows the formula for precision.

$$\text{Precision} = \frac{\text{True_Pos}}{\text{False_Pos+True_Pos}} \quad (19)$$

Performance Analysis

Various evaluation metrics such as precision, recall, F1-score and accuracy are used to test the effectiveness of the current DL model. Similarly, Confusion Matrix (CM) is used for understanding the performance of the proposed research. It contains and predicts the performance of the classification algorithm. Hence, the CM shows the number of correct as well as incorrect predictions made by the class. The Figure 4 depicts the CM for the proposed NSL-KDD dataset.

The Figure 4 signifies the CM of NSL-KDD Dataset. It is used to depict multi-class classification of prediction results which contains the prediction results summary outcomes of all instances of utilised dataset for the testing process. The matrix contains 6 classes with values up to 18,380, indicating a subset or broader categories for analysis. High diagonal values show correct predictions, especially for class 0 and 1. Classes 2-5 have fewer correct predictions but still perform well. Misclassifications are sparse, with some confusion between class 0 and 5, and 1 and 5. Other misclassifications are minimal, such as class 4 as class 0. Compared to the first matrix, misclassifications are reduced due to fewer classes, this model shows strong performance

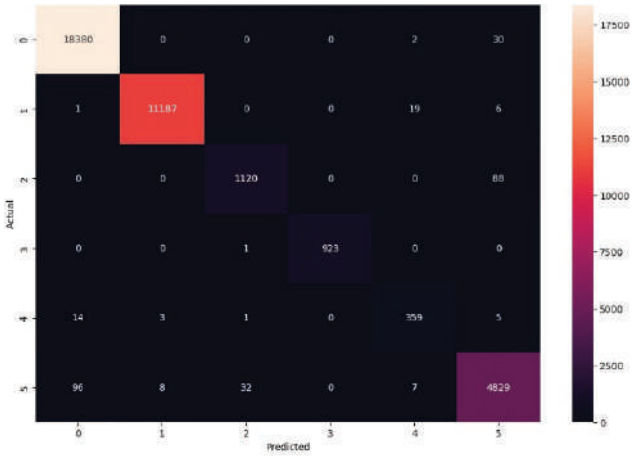


Figure 4. CM for NSL-KDD dataset.

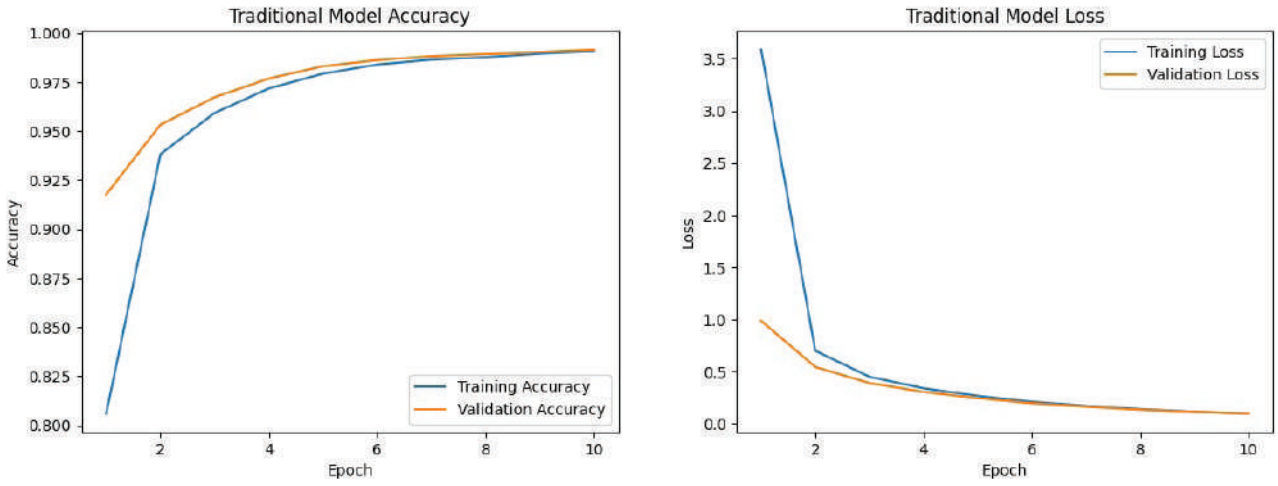


Figure 5. Model accuracy and loss of NSL-KDD data

with lower confusion. Additionally, Figure 5 represents the model exactness and model loss for NSL-KDD Data.

The Figure 5 denotes the model accuracy and loss of NSL-KDD dataset. The exactness of model gets increased in increasing epoch's counts in both training and validation set whereas the model loss is maintained low up to the 10 epochs in validation. The model loss in training is low in all epochs count.

The first graph model accuracy shows the accuracy changes with epochs during the model training. In the beginning epochs (1-3) both training and validation accuracy improve quickly from around 0.82. Middle epochs (4-6) see high accuracy levels around 0.97-0.98, with validation slightly better. Later epochs (7-10) stabilize around 0.98, showing near optimal performance.

The second loss model graph reveals key insights into its training process. Initially high, both training and validation losses quickly decline in the first few epochs. Around 3-4 epochs, loss reduction slows, signalling convergence by epoch 10. Despite lower training loss, better generalization is observed.

The Table 2 illustrates the classification result for NSL-KDD dataset. It shows the value of precision, exactness, recall and f1-measures of the present model. All models have achieved a 99% accuracy rate. However other Classes shows a precision, recall, F1- scores of 0. 93, 0 94, 0. 97, 0.95. Classes 0, 1, and 3 showed perfect recall of 1 and precision scores on class 1 and 3. The Table 3 signifies the proposed NSL-KDD dataset evaluation.

The Table 3 denotes the metrics of proposed model with NSL-KDD dataset. It deliberates that the present model attains 0.99, 0.97, 0.97, 0.97 of exactness, value of precision, probability of detection and f1-measures respectively and giving enhanced results. Considerably, Figure 6 signifies the model exactness and model loss of UNSW-NB15 dataset.

The Figure 6 denotes the model exactness and loss of UNSW-NB15 data. The model accuracy gets improved in increasing epoch's counts in training set and validation set whereas the model loss is maintained low up to the 10 epochs in validation. The model loss in training is low in all epochs count. Moreover, Figure 7 depicts the CM of NSL-KDD dataset.

Traditional model accuracy graph depicts accuracy value from 0.9575 to 0.9775, showing the model performances over epochs. When accuracy quickly arises, while minor fluctuations occur later on, with validation accuracy dipping slightly between epochs 6 and 8 before stabilizing around 0.975. This shows the model is not over fitting.

Table 2. Classification result on NSL-KDD dataset

Classes	Accuracy	Precision	Recall	F1-score
0	0.99	0.99	1	1
1	0.99	1	1	1
2	0.99	0.97	0.93	0.95
3	0.99	1	1	1
4	0.99	0.93	0.94	0.93
5	0.99	0.97	0.97	0.97

Table 3. Metrics of NSL-KDD Dataset

Model	Exactness	Value of precision	Recall	F1-score
Proposed method	0.99	0.97	0.97	0.97

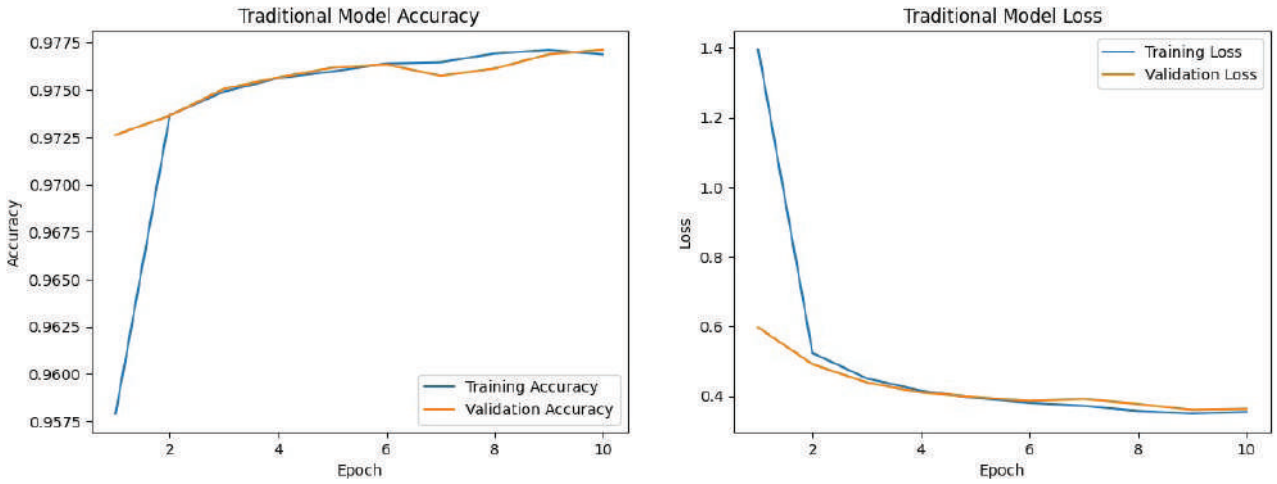


Figure 6. Model accuracy and loss for UNSW-NB15.

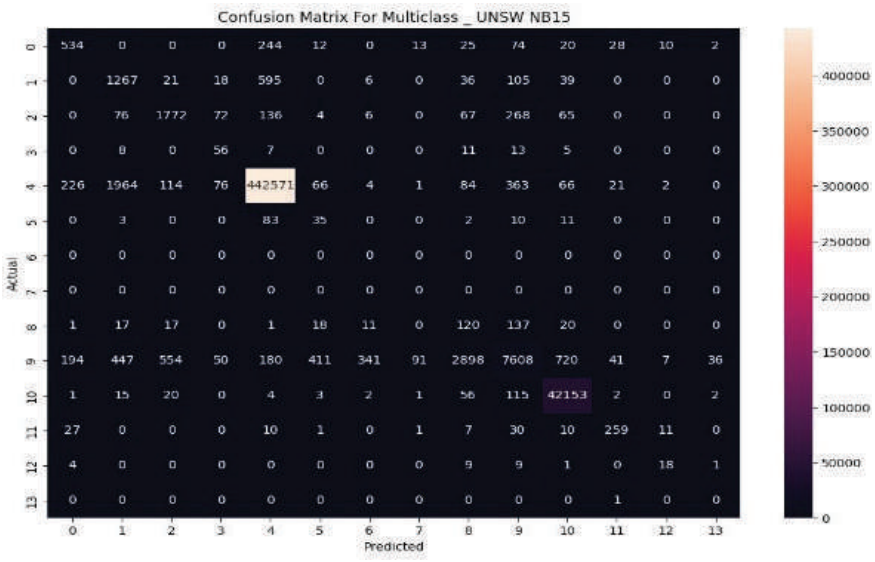


Figure 7. CM of UNSW-NB15 data.

The loss model graph provides insights into the model training process. In the early epochs, the training loss rapidly decreases from above 1.4 to below 0.5, indicating learning of essential data patterns. Middle epochs shows stable losses around 0.4, with training slightly lower than validation. Later epochs shows both losses stabilize below 0.4, indicating well trained convergence.

The Figure 7 signifies the CM of NSL-KDD Data. It is used to depict multi-class classification of prediction results which contains the results summary outcomes of all instances of utilised UNSW-NB15 dataset for the testing process. It contains actual and predicted labels. The matrix reveals imbalanced data with values exceeding 400,000. High diagonal values show accurate predictions, notably in cell (4, 4) at 442,571 for "normal" network traffic. Class 9 and 11 also have high true positives but lower than class 4. Misclassifications exist in off- diagonal cells, with class 9 having the most. Furthermore, Table 4 depicts the classification result for UNSW-NB15 dataset.

Information in Table 4 presents various classification metrics for the UNSW-NB15 dataset and describes the state of art model. What is more, the figure presents a performance evaluation in terms of precision, recall, f1-score and accuracy for the model under discussion. So, all the classes could classify correctly at 98% of the cases. Class 10 got the highest result of accuracy, precision, recall and f1-score. In

Table 4. Classification result on UNSW-NB15

Classes	Exactness	Value of Precision	Probability of Detection	F1-measures
0	0.98	0.54	0.56	0.55
1	0.98	0.33	0.61	0.43
2	0.98	0.71	0.72	0.71
3	0.98	0.21	0.56	0.3
4	0.98	0.32	0.99	1
5	0.98	0.06	0.24	0.1
6	0.98	0.25	0.32	0.36
7	0.98	0.32	0.25	0.69
8	0.98	0.04	0.35	0.07
9	0.98	0.87	0.56	0.68
10	0.98	0.98	0.99	0.99
11	0.98	0.74	0.73	0.73
12	0.98	0.38	0.43	0.4
13	0.98	0.21	0.69	0.38

Table 5. Metrics of UNSW-NB15 dataset

Method	Precision	F1-Score	Accuracy	Recall
Proposed method	0.99	0.98	0.98	0.98

Table 6. Comparative performance of NSL-KDD dataset with existing models

Model	Precision	Accuracy	Recall	F1-Score
DNN-1 Layer	0.82	0.91	0.92	0.92
DNN-2 Layer	0.81	0.91	0.91	0.91
DNN-3 Layer	0.83	0.92	0.78	0.85
DNN-4 Layer	0.91	0.94	0.72	0.83
Proposed model	**0.97**	**0.98**	**0.97**	**0.97**

like manner, classes 1 and 3 were at the moderate levels of recall rates. Class 4 had an ultimate f1-score equal to 100%, while class 5 was f1- scored 1. Moreover, information in the Table 5 points to the proposed model metric results in the UNSW-NB15 dataset.

The Table 5 indicates the evaluated metrics of proposed model in UNSW-NB15 dataset. It deliberates that the proposed model attains 98%, 99%, 98% and 98% of exactness, value of precision, probability of detection and f1-measures respectively.

Comparative Analysis

The section exemplifies the comparative analysis of the present model depending on various dataset used in the respective model. The Table 6 illustrates the performance comparative of NSL-KDD dataset with various conventional researches.

The Table 5 represents qualified performance of NSL-KDD dataset with existing models. The present model attains 0.07, 0.07, 0.06 and 0.04 of accuracies more than DNN-1 Layer, DNN-2 Layer, and DNN-3 Layer and DNN-4 layer respectively [35]. Moreover, signifies the performance metrics comparison of existing model. Deliberates the metrics comparison for NLS-KDD dataset. It shows that the proposed research model attains higher values in all the metrics evaluated and shows the improved efficiency than other existing models. Furthermore, the Table 7 indicates the comparison of accuracies with conventional model for NSL-KDD dataset.

The Table 7 depicts the comparison of accuracies with existing models with proposed model. It demonstrates that the proposed research attained 0.98 of accuracy in NSL-KDD dataset whereas, 0.81, 0.74, 0.73 and 0.71 of accuracies are attained by DNN, RNN, DBN and LSTM respectively [36]. Additionally, Table 7 shows the accuracy comparison with conventional research models. It clears that the proposed model achieves better accuracy metric results than other prevailing models such as DNN, RNN, DBN and LSTM models respectively. Similarly, the Table 8 shows the comparative performance of UNSW-NB15 dataset with prevailing models.

The Table 7 exemplifies the comparison performance of UNSW-NB15 dataset with conventional models. It shows that the respective model attains better results than other prevailing models [37]. It attained 0.98, 0.98, 0.98 and 0.98 of exactness, probability of detection, F1-measures and value of precision respectively whereas other models such as LR, SVM, DT, Auto-encoder, BAE0, BAE 1, BAE 2 and BAE have attained less than 0.91 of accuracy. It shows the efficiency of the present model than other such models. The Comparison Analysis on Existing Models for

Table 7. Comparison of accuracies of NSL-KDD dataset

Model	Accuracy
DNN	0.81
RNN	0.74
DBN	0.73
LSTM	0.71
Proposed model	**0.98**

Table 8. Comparative performance of UNSW-NB15 dataset with existing models

Methods	Exactness	Probability of detection	Value of Precision	F1-Measures
LR	0.8951	0.8	0.62	0.7004
SVM	0.9075	0.7011	0.6949	0.698
Decision tree	0.897	0.8541	0.6173	0.7166
Auto-encoder	0.822	1	0.4566	0.6269
BAE 0	0.886	1	0.4063	0.5778
BAE 1	0.90002	1	0.8198	0.901
BAE 2	0.8425	0.8229	1	0.955
BAE	0.8761	0.8649	0.742	0.8113
Proposed method	**0.98**	**0.98**	**0.99**	**0.98**

Table 9. Accuracy comparison with prevailing models

Methods	Exactness
GA-DBN	0.8599
DBN	0.82
CDBN	0.8229
KG-CRBN	0.8649
Proposed method	0.97

Table 10. Comparative analysis with existing models for UNSW-NB15 dataset

Methods	Precision	Accuracy
SVM	0.6949	0.9075
AUTO ENCODER	0.4566	0.822
Proposed Method	0.99	0.98

respective dataset. It shows that the present model attained better metric results than existing models. The proposed model attained 0.0849, 0.0725, 0.083, 0.158, 0.188, 0.07998, 0.1375 and 0.1039 of accuracies more than LR, SVM, DT, Auto-encoder, BAE0, BAE 1, BAE 2 and BAE respectively. Moreover, Table 9 describes the accuracy comparison with conventional models.

Table 9, deliberates the accuracy comparison for UNSW-NB15 dataset with prevailing models. It shows that the proposed model attains 0.97 of accuracy [38]. Other conventional models such as GA-DBN, DBN, CDBN and KG-CRBM models have attained 0.8599, 0.82, 0.8229 and 0.8649 of accuracy respectively. The comparative analysis on accuracy for UNSW-NB15 dataset. It denotes that the proposed model achieves better accuracy metric results than other prevailing models such as GA-DBN, DBN, CDBN, KG-CRBM models respectively. It attained 0.1101, 0.15, 0.1471 and 0.1051 of accuracy more than GA-DBN, DBN, CDBN, and KG-CRBM respectively.

The Table 10 depicts the comparison of proposed work with the existing models [37]. Here the methods SVM, auto encoder has delivered 0.6949, 0.4566 and 0.9075, 0.822 of precision metrics and accuracy, while the proposed has exhibited high range of 0.99 and 0.98 in precision accuracy performances.

As organizations grow more reliant on interconnected networks, it becomes crucial to anticipate deviations in unusual network activities, which is vital for ensuring security. Unusual behaviours or developments in network security are significantly rising in the real-time environment. Thus, anomaly classification focuses on recognizing unusual patterns or behaviours. The proposed model has been improved with a structured activation loop framework integrated with a bidirectional gated recurrent unit. In this setup, the pre-processed training data is separated into training and testing processes. Existing datasets were evaluated with various Deep Neural Network (DNN) layers 1, 2, 3, and 4, obtaining precision, accuracy, recall, and F1 scores of 0.82, 0.83, 0.91, 0.92, 0.95, and 0.78, respectively. However, the pre-processed data from the proposed model has demonstrated superior performance scores of 0.97, 0.98, 0.97, and 0.97 on NSL-KDD datasets. Likewise, the UNSW-NB15 dataset has recorded scores of 0.98, 0.98, 0.99, and 0.98 in the metrics of exactness, value of precision, probability of detection and F1-measures when associated to earlier models such as LR, SVM, decision tree, auto encoder, BAE, BAE0, 1, and 2, which have lower scores of 0.62, 0.6949, 0.7004, 0.8761, 0.4566, 0.4063, etc., across all metrics. Nonetheless, traditional models such as DBN, CDBN have achieved accuracies of 0.8599, 0.82, 0.8229, and 0.8649. It indicated that the proposed model has achieved higher accuracies of 0.97. Consequently, the outcomes from the testing and training efforts produce improved results and enhance the ability to detect emerging anomalies in network and cyber security against hackers and malicious threats.

Applications of Activation Mechanism in Network Security

The proposed work has emerged for protecting and classifying anomalies with an activation mechanism for anomaly classification has numerous key applications in network cyber security includes the data security in protecting confidential information from unauthorized access and creating occurrence response measures to promptly address security incidents. By employing data analysis to detect possible threats through patterns and behaviours, enabling organizations to proactively tackle vulnerabilities. Also implementing Intrusion Prevention Systems to identify and prevent harmful actions in real-time, safeguarding the network against diverse cyber threats. Similarly, splitting the network- connected devices such as laptops and mobile devices against threats using antivirus programs and device management policies.

CONCLUSION

Anomaly classification was a crucial aspect of network security that helped organizations detect and address potential threats and security in real-time. Through the identification and classification of anomalies, security teams were able to quickly identify and mitigate possible security threats, consequently lowering the chances of a successful cyber-attack. Therefore, efficient classification of anomalies was essential for ensuring network security and data storage. However, the precision of inspections by human experts was slow and constrained. To address this issue, the proposed study of the Structured Activation Module Framework Unit monitored error data directly in the update gate without requiring the reset gate, allowing for numerous checks in a loop format. The activation module unit effectively divided the class data to forecast relevant output characteristics by resolving missing values.

The study employed the NSL-KDD and UNSW-NB15 datasets as a demonstration for the effectiveness of the present model. With the NSL-KDD dataset, the study recorded its metrics of accuracy, precision, recall, and F1 score at 0.99, 0.97, 0.97, and 0.97 correspondingly. Whereas for the UNSW-NB15 dataset, the model's performance was measured in terms of accuracy, precision, recall, and F1-score, which were 0.98, 0.99, 0.98, and 0.98 respectively. Hence, the proposed research overcame challenges related to scaling, over fitting issues, and handling large datasets with inaccurate patterns and networks. Nonetheless, it also recognized specific limitations within the datasets, including a lack of representation for certain attack classes and persistent issues concerning feature relevance and applicability of results to real-life situations. In the future, the techniques established in this study showed potential for use across different network intrusion datasets, improving predictive abilities and ultimately sustaining cyber security strategies against unauthorized access and evolving cyber threats. The proposed study performed superiorly in both NSL-KDD and UNSW-NB15 datasets; however, this method would be considered for application in other datasets in future research endeavours.

AUTHORSHIP CONTRIBUTIONS

Authors equally contributed to this work.

DATA AVAILABILITY STATEMENT

The authors confirm that the data that supports the findings of this study are available within the article. Raw data that support the finding of this study are available from the corresponding author, upon reasonable request.

CONFLICT OF INTEREST

The author declared no potential conflicts of interest with respect to the research, authorship, and/or publication of this article.

ETHICS

There are no ethical issues with the publication of this manuscript.

STATEMENT ON THE USE OF ARTIFICIAL INTELLIGENCE

Artificial intelligence was not used in the preparation of the article.

REFERENCES

[1] Inuwa MM, Das RJIT. A comparative analysis of various machine learning methods for anomaly detection in cyber attacks on IoT networks. Internet of Things 2024;26:101162. [CroosRef]

[2] Khan S, Ali ZJMCJ. Neural Networks in Particle Detector Quality Assurance: A Deep Learning Approach. 2024;5:1–10.

[3] Ullah I, Mahmoud QIJHA. Design and development of a deep learning-based model for anomaly detection in IoT networks. IEEE Xplore 9;103906–103926. [CrossRef]

[4] Madasamy NS. DKRF: Machine Learning with Optimised Feature Selection for Intrusion Detection. 2023;57.

[5] Merizio IF, Chavarette FR, Moro TC, Outa R, Mishra VN. Machine learning applied in the detection of faults in pipes by acoustic means. J Inst Eng (India) Ser C 2021;102:975–980. [CrossRef]

[6] Hussein A, Chadad L, Adalian N, Chehab A, Elhajj IH, Kayssi AJJCST. Software-Defined Networking (SDN): the security review. J Cyber Secur Technol 2020;4:1–66. [CrossRef]

[7] Ahmad Z, Khan AS, Nisar K, Haider I, Hassan R, Haque MR, et al. Anomaly detection using deep neural network for IoT architecture. Apll Sci 2021;11:7050. [CrossRef]

[8] Hooshmand MK, Huchaiah MDJDTR. Network Intrusion Detection with 1D Convolutional Neural Networks. Scientific 2022;1:66–75. [CrossRef]

[9] Kumar D, Joshi AB, Singh S, Mishra VN. Digital color-image encryption scheme based on elliptic curve cryptography ElGamal encryption and 3D Lorenz map. AIP Conference Proceedings 2021;2364. [CrossRef]

[10] Hooshmand MK, Hosahalli DJTTIT. Network anomaly detection using deep learning techniques. Inst Eng Technol 2022;7:228–243. [CrossRef]

[11] Aversano L, Bernardi ML, Cimitile M, Pecori R, Veltri LJWC, Computing M. Effective anomaly detection using deep learning in IoT systems. Wirel Commun Mob 2021;1–14. [CrossRef]

[12] Xu Z, Wang Z, Xu J, Shi H, Zhao H. Enhancing Log Anomaly Detection with Semantic Embedding and Integrated Neural Network Innovations. Computers, Materials & Continua, 2024;80:3991–4015. [CrossRef]

[13] Outa R, Chavarette FR, Goncalves AC, Silva SL, Mishra VN, Panosso AR, et al. Reliability analysis using experimental statistical methods and AIS: application in continuous flow tubes of gaseous medium. Technology 2021;43:e55825. [CrossRef]

[14] Xie X, Wang B, Wan T, Tang WJIA. Multivariate abnormal detection for industrial control systems using 1D CNN and GRU. IEEE Xplore 2020;8:88348–88359. [CrossRef]

[15] Bakhshi T, Ghita BJS, Networks C. Anomaly detection in encrypted internet traffic using hybrid deep learning. Secur Commun Netw 2021;2021:5363750. [CrossRef]

[16] Rajasekhar RNV, Sreedivya N, Jagadesh BN, Gandikota R, Lella KK, Pydala B, et al. Enhancing

anomaly detection: A comprehensive approach with MTBO feature selection and TVETBOOptimized Quad-LSTM classification. Comput Electr Eng 2024;119:109536. [CrossRef]

[17] Gaffar A, Joshi AB, Singh S, Mishra VN, Rosales HG, Zhou L, et al. A Technique for Securing Multiple Digital Images Based on 2D Linear Congruential Generator, Silver Ratio, and Galois Field. IEEE Access 2021;9:96125–96150. [CrossRef]

[18] Rakha MA, Khan IU, Ouaissa M, Ouaissa M, Ayub MY. Hybrid Model for IoT-Enabled Intelligent Towns Using the MQTT-IoT-IDS2020 Dataset. Boca Raton: CRC Press; 2024. p. 159–176. [CrossRef]

[19] Kumar D, Joshi AB, Mishra VN. Optical and digital double color-image encryption algorithm using 3D chaotic map and 2D-multiple parameter fractional discrete cosine transform. Results in Optics. 2020;1:100031. [CrossRef]

[20] Gaffar A, Joshi AB, Kumar D, Mishra VN. Image encryption using nonlinear feedback shift register and modified RC4A algorithm. J Appl Mat Inf 2021;39:859–882. [CrossRef]

[21] Outa R, Chavarette FR, Mishra VN, Goncalves AC, Garcia A, Pinto SS, et al. Analysis and prognosis of failures in intelligent hybrid systems using bioengineering: Gear coupling. J Eng Exact Sci 2022;8:13673-01-18e. [CrossRef]

[22] Hwang RH, Peng MC, Huang CW, Lin PC, Nguyen VLJIA. An unsupervised deep learning model for early network traffic anomaly detection. IEEE Xplore 2020;8:30387–30399. [CrossRef]

[23] Fotiadou K, Velivassaki TH, Voulkidis A, Skias D, Tsekeridou S, Zahariadis TJI. Network traffic anomaly detection via deep learning. Information 2021;12:215. [CrossRef]

[24] Xu W, Jang-Jaccard J, Singh A, Wei Y, Sabrina FJIA. Improving performance of autoencoder-based network anomaly detection on nsl-kdd dataset. IEEE Xplore 2021;9:140136–140146. [CrossRef]

[25] Wang YC, Houng YC, Chen HX, Tseng SMJS. Network anomaly intrusion detection based on deep learning approach. Sensors 2023;23:2171. [CrossRef]

[26] Saba T, Rehman A, Sadad T, Kolivand H, Bahaj SAJC. Anomaly-based intrusion detection system for IoT networks through deep learning model. Comput Electr Eng 2022;99:107810. [CrossRef]

[27] Rezaee K, Rezakhani SM, Khosravi MR, Moghimi MKJP. A survey on deep learning-based real-time crowd anomaly detection for secure distributed video surveillance. Springer Nature Link 2024;28:135–151. [CrossRef]

[28] Hussien ZJBSJ. Anomaly detection approach based on deep neural network and dropout. Baghdad Sci J 2020;17:701. [CrossRef]

[29] Vibhute AD, Nakum VJPCS. Deep learning-based network anomaly detection and classification in an imbalanced cloud environment. Procedia Comput Sci 2024;232:1636–1645. [CrossRef]

[30] Arjunan T. Real-time detection of network traffic anomalies in big data environments using deep learning models. Int J Res Appl Sci Eng Technol 2024;16:1–11.

[31] Nadeem MW, Goh HG, Ponnusamy V, Aun YJC. DDoS detection in SDN using machine learning techniques. Comput Mater Contin 2022;71.

[32] Mukherjee I, Sahu NK, Sahana SK. Simulation and modeling for anomaly detection in IoT network using machine learning. Int J Wirel Inf Net 2023;30:173–189. [CrossRef]

[33] Nixon C, Sedky M, Champion J, Hassan M. SALAD: A split active learning based unsupervised network data stream anomaly detection method using autoencoders. Expert Syst Appl 2024;248:123439. [CrossRef]

[34] Suresh K, Velmurugan KJ, Vidhya R, Kavitha V. Deep Anomaly Detection: A Linear One-Class SVM Approach for High-Dimensional and Large-Scale Data. Appl Soft Comput 2024;112369. [CrossRef]

[35] Mohammed B, Gbashi EK. Intrusion detection system for NSL-KDD dataset based on deep learning and recursive feature elimination. Eng Technol J 2021;39:1069–1079. [CrossRef]

[36] Kavitha S, Uma Maheswari N, Venkatesh R. Network anomaly detection for NSL-KDD dataset using deep learning. Inf Technol Ind 2021;9:821–827. [CrossRef]

[37] Wang D, Nie M, Chen D. BAE: Anomaly detection algorithm based on clustering and autoencoder. Mathematics 2023;11:3398. [CrossRef]

[38] Tian Q, Han D, Li KC, Liu X, Duan L, Castiglione AJAI. An intrusion detection approach based on improved deep belief network. Appl Intell 2020;50:3162–3178. [CrossRef]

Sigma J Eng Nat Sci, Vol. 44, No. 1, pp. 404–422, February, 2026

Sigma Journal of Engineering and Natural Sciences
Web page info: https://sigma.yildiz.edu.tr
DOI: 10.14744/sigma.2025.00000

Research Article

Predicting survival rates of patients with cardiovascular diseases using ensemble techniques

Bharati KARARE[1,*], Anushree Anand PANDE[2], Pratibha WAGHALE[1], Amruta Tapas PAUL[1], Chanchla TRIPATHI[1], Lalit DAMAHE[1]

[1]Yeshwantrao Chavan College of Engineering, Nagpur, Maharashtra, 441110, India
[2]P R Pote Patil College of Engineering and Management Amravati, Maharashtra, 444604, India

ARTICLE INFO

Article history
Received: 07 August 2024
Revised: 31 October 2024
Accepted: 30 December 2024

Keywords:
Cardiovascular Disease; Kaplan-Meier Estimator; Machine Learning; Survival Rate

ABSTRACT

This study focuses on predicting cardiovascular diseases and forecasting the survival rate of patients using machine learning techniques. In this paper publicly available dataset is sued that contain the several risk factors for cardiovascular disease such as age, anemia, hypertension, diabetes, smoking habits, gender, blood pressure, glucose levels, and alcohol consumption. The dataset is preprocessed to extract relevant features for predicting survival rates based on risk parameters. The ensemble model is designed based on combining the several machine learning algorithms such as Logistic Regression, Random Forest, XGBoost, and Naive Bayes to classify the cardiovascular disease. The study also applies the Kaplan-Meier estimator to predict the survival rate of patient based on continuous variables. The final results indicate that age, serum creatinine, and ejection fraction significantly correlate with the death event. At the same time, smoking, sex, platelets, and diabetes show uncertain statistical significance. The study provides insights into the impact of various factors on cardiovascular disease survival rates. The novelty of this work lies in its integration of survival analysis with ensemble learning for robust prediction and interpretability in clinical applications.

Cite this article as: Karare B, Pande AA, Waghale P, Paul AT, Tripathi C, Damahe L. Predicting survival rates of patients with cardiovascular diseases using ensemble techniques. Sigma J Eng Nat Sci 2026;44(1):404–422.

INTRODUCTION

Heart and blood vessel problems like heart attacks, strokes, and heart failure are known as cardiovascular diseases (CVDs). Around 17 million people die from these diseases every year worldwide [1]. In India, the number of deaths due to CVDs has been increasing for the first time in 30 years. Heart failure occurs when cardiovascular system cannot circulate blood throughout the human body. Excessive hypertension, diabetic complications, or other cardiac problems frequently bring it on. Doctors classify heart failure into two types based on how much blood the heart pumps out with each beat [2]. One type, heart failure with reduced ejection fraction (HFrEF) [3], happens when

*Corresponding author.
*E-mail address: kararebharati@gmail.com

This paper was recommended for publication in revised form by Editor-in-Chief Ahmet Selim Dalkilic

Published by Yıldız Technical University Press, İstanbul, Turkey
© Author. This is an open access article under the CC BY-NC license (http://creativecommons.org/licenses/by-nc/4.0/).

the heart pumps less than 45% of the blood. The other type, heart failure with preserved ejection fraction (HFpEF), occurs when the heart contracts well but doesn't relax properly to fill with blood. Most heart attacks can be prevented by using population-wide strategies to address lifestyle risk factors such as smoking, unhealthy diets and obesity, and alcohol consumption [4]. The machine learning is an effective strategy to early prediction and proper medication of patient with heart failure or who are at risk due to the combination of several risk factors such as BP, diabetics, and other medical history [5]. This potential brings optimism for the future of cardiovascular disease management.

Machine learning (ML) might surpass current modeling methods to accurately predict high blood pressure within specific racial groups and elucidate critical factors contributing to high blood pressure development across diverse races [6]. The majority of heart failure cases can be attributed to structural or physiological issues in the heart, leading to increased intracardiac pressure or reduced cardiovascular output based on the individual's state of rest or stress [7]. Consequently, heart failure is associated with a diminished quality of life and decreased engagement in physical and mental activities. Approximately 1-2% of the general population and 10% of older people in developed nations are affected by heart failure, with its prevalence expected to rise alongside an aging population. In hospital discharge, patients with heart failure (HF) experience a high 56.6% readmission rate. Addressing high frequency promptly is crucial to prevent future severe complications, with a current urgent focus on minimizing readmissions. Cardiovascular diseases like coronary artery disease (CAD), atrial fibrillation (AF), and vascular conditions remain the primary global cause of death [8]. The rising incidence of cardiovascular diseases is a pressing issue that requires immediate attention and innovative solutions. If lifestyle conditions rise and the amount of stress increases, the incidence of cardiovascular diseases is alarmingly increasing. To address this problem, an ensemble approach and survival rate prediction of patients have developed as a possible treatment.

Motivation

Based on the current studies [9]-[10] cardiovascular disease (CVD) is projected to cause the deaths of approximately 23 million individuals by 2030. There are many causes such as heart disease, irregular heartbeat, and heart attack, which are three different forms of cardiovascular disease [11]-[12]. Age, gender, BMI, height, waist circumference, and results from blood tests that check cholesterol levels, liver health, and kidney function are some of the factors used to analysed cardiovascular disease [13]–[14].

Several health issues could arise from the complex interactions across the risk factors. Traditional statistically effective methods are unable to investigate the complex relationship across risk-associated factors due to the large number of components present [15]–[16].

Over the last few decades, several researchers utilized the artificial intelligence (AI) techniques to investigate the new clinical data that help the physicians to analyze the signs and effects of many diseases and the prediction of survival of patients. The continuous efforts to collect all health examination records and consistent clinical data [17]–[18] focus to standardizing of clinical data before investigating previously unknown risk factors. A number of possible risk factors shows the associations regarding the development of diseases that indicate the basic causes of the disorders. Furthermore, a significant amount of medical data must be analyzed in order to create accurate prediction models for disease occurrences [19]–[20]. The risk assessment of CVD frameworks increasingly utilizes AI and large amounts of clinical data aggregation.

Problem Statement

Cardiovascular diseases (CVD) are the leading cause of death globally, with an estimated 17.9 million deaths each year. Early prediction of survival rates for patients with CVDs is crucial for providing timely and effective interventions to improve patient outcomes. Machine learning (ML) algorithms have shown promise in predicting survival rates based on patient data, including demographics, medical history, and clinical measurements. This study designs the ensemble models to detect and classify CVD and also predict the survival rates of patients with cardiovascular diseases. The models trained on a CVD dataset contain the risk factors of CVD. To measure the performance of the models using several evaluation parameters and also predict the survival rate of patients over a specified period. The proposed model helps to improved patient care that enable the healthcare experts to identify high-risk patients and early diagnosis to prevent adverse effect.

Limitation of Existing System

- The existing model worked on limited set of features, such as age, gender, and a few clinical elements.
- The quality and quantity of dataset is used to train the models could vary performance significantly that shows the biased or inaccurate predictions.
- Some existing models might have needed to be more complex, making them difficult to interpret and implement in clinical settings. This need for interpretability is a pressing issue in healthcare machine learning. We must address this complexity to avoid overfitting, where the model performed well on training data but failed to generalize to new data. Machine learning models worked effectively on present clinical procedure in order to be useful in the field of medicine. The medical professionals' resistance and accessibility issues result that many existing methods were not designed with the combination in perspective.

Contribution

Following is a list of this investigation's primary contribution as well as uniqueness:

- To extract seven unique features from the CVD dataset.
- Following the feature extraction, we meticulously normalized the data and divided the CVD dataset into training and testing sets using a 70:30 split, a crucial step in our thorough methodology. This aids in creating an ensemble model that includes a base ML classifier and a DT as a meta-classifier.
- Utilizes the Kaplan-Meier estimator to predict the survival rate of cardiovascular diseases for continuous variables in the dataset.
- Ultimately, we obtained results through various performance parameter analyses and predicted the survival rate of patients.

Paper organization

Section 2 presents the previous work in cardiovascular disease prediction based on ML and DL techniques. Section 3 presents the proposed methodology; Section 4 discusses the result analysis of the ensemble model. Section 4 addressed the conclusion and future scope of the study.

Related Work

Weng et al. suggested four different ML methods using health information from over 300,000 patients from the UK [21]. They found that the Neural Network (NN) method gave the most accurate predictions for CVD when analyzing a large amount of data. Dimopoulos A. C. et al. evaluated three traditional machine learning methods using ATTICA data with 2020 instances for a smaller dataset. Among these, KNN, RF, and DT were tested. Comparatively, RF showed the best outcome when using the Hellenic SCORE tool, calibrating the ESC Score [22].

Given the increasing utilization of ML in the medical domain, Mohan S. et al. suggested a hybrid HRFLM strategy to enhance the prediction accuracy score of the proposed approach, considering the growing use of ML algorithms [23].

In [24], they examined specific areas using different prediction models. They used LR to analyze 32 characteristics related to cardiovascular disease in over 210,000 high-risk patients in China.

Yang et al. [25] suggested the stacking ensemble framework for CVD prediction. They used information about air pollution and weather to understand how the average daily hospitalized percentage for cardiovascular diseases changes with the stacking ensemble model. They started with a basic level of five classifiers to build the stacking model.

Several investigations focus on creating new categories and approaches to enhance the current ones. For instance, studies by [26] suggested employing NLP to develop and evaluate an anxiety forecasting network. A neural network model with a predicted accuracy of 88.3% has been suggested, as reported [27], for predicting the development of diabetes. They indicated that the neural network's effectiveness was approximately 91% in training and 86% in evaluation compared to its previous effectiveness of 89% and 81%.

A technique for increasing the accuracy of cardiovascular disease prediction has been developed by Mohan et al. [28], employing machine learning algorithms for recognizing critical features. Regarding heart disease prediction, the suggested hybrid RF and linear model obtained the 87.9% accuracy. Au et al. [29] suggested the hybrid model to detect the CVD based on the logistic regression and obtained the accuracy score of 88.00%. Investigators have suggested a hybrid approach for forecasting cardiovascular disease [30]. The framework was employed by three ML techniques: DT, RF, and a combination. At 87.8%, the hybrid technique had the most excellent accuracy score.

As reported [31], author suggested the several ML models used to detect CVD and also suggested the ML-based ensemble model to predict and improve the efficiency of model.

We use information on coronary artery disease for our investigation. So, this might be our final investigation, with about 710,000 people and ten features in the data set. In addition, we employ multiple deep learning and machine learning techniques to determine which is most effective in identifying coronary artery disease.

Last two decade there is an advancements and large use of ML based models to predict the CVD and there are still several gaps that are unaddressed. The existing models depends on limited feature sets that fail to capture the complex features among risk factors such as lifestyle, biochemical markers, and physiological features. The usefulness of ensemble approaches in real-world scenarios is limited by the lack of thorough evaluations in several publications. The majority of approaches do not offer apparent findings for medical decision-making, making and ML models difficult to interpret in healthcare settings. Additionally, the datasets utilized in earlier studies are either limited or region-specific, and also limits their applicability to larger populations. Practical interactions between ML and survival analysis techniques, including Kaplan-Meier estimators, are not fully investigated. Addressing these gaps could lead to more robust, interpretable, and clinically actionable models for predicting survival rates in cardiovascular patients.

Proposed Methodology

This section presents the methodology of the various suggested ML models and the survival probability of patients. Figure 1 illustrates the complete architecture of the proposed model, which aims to predict cardiovascular diseases and forecast the survival rate of patients. The study utilizes a CVD dataset for model training, which initially requires preprocessing due to missing values. Strategies from feature extraction are used to extract essential features from data to predict the survival rates based on various parameters. This paper proposed ensemble model based on using several ML models as LR [32], RF [33], XGB [34], and NB [35] to predict the CVD. The study employs the Kaplan-Meier estimator to predict the survival rate of cardiovascular diseases for continuous variables present in the dataset.

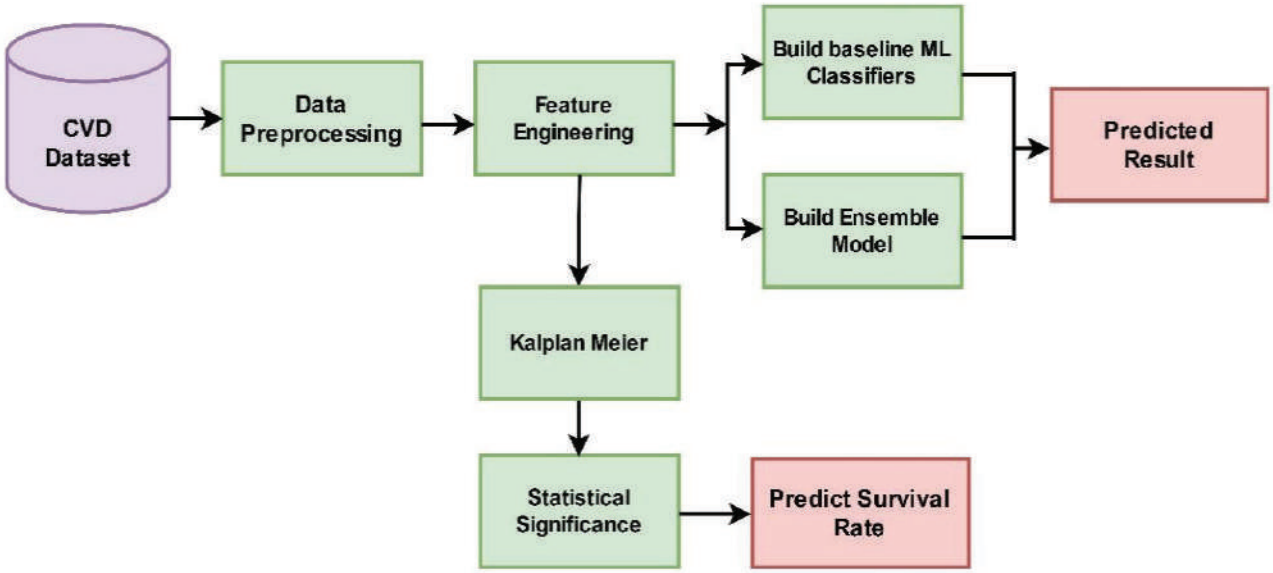


Figure 1. Architecture of proposed model.

Dataset description

The dataset contains comprehensive data on possible risk elements associated with CVD. It contains details on Age, anemia, Hypertension, Diabetes, Smoking, Gender, Blood Pressure, Glucose Levels, And Alcohol Consumption of over 72 thousand patients. The dataset is extracted from publicly available websites: https://www.kaggle.com/datasets/thedevastator/exploring-risk-factors-for-cardiovascular-diseases. The dataset also shows the relationship across the several risk factors and CVD that lead to improvement and understanding of the serious health issue and the design of better preventive measures [36].

Data preprocessing

This step starts with data cleaning, and missing values were handled using imputation techniques. The outliers were identified and treated to avoid skewing the results. The categorical parameters like patient demographics encoded into numerical scale using one-hot encoding strategy. The continuous variables were transform into uniform scale across each features.

Feature Engineering

This step selects the most relevant features to improve model performance. Initially, obtained the meaningful features and measure the risk scores parameters such as age, blood pressure, and cholesterol levels for diabetes or heart failure. The temporal features such as duration of the diagnosis were obtained and also capture nonlinear effects. The existing features were transformed to scaling for skewed variables such as age groups. The relation between features such as age and smoking history that retrieve the uncover complex relationships. Creating an ML model starts with collecting and analyzing raw input. In this study, it is used to determine how closely connected items are to one another.

Figure 2 shows the Univariate Analysis of Categorical parameters. The around 57.00% of the population have symptoms of Anemia that indicate the deficiency of red blood cells and around 43% do not exhibit Anemia symptoms. The 65% of the population has hypertension that they suffer from high blood pressure and approximately 35.00% have normal blood pressure. About 58.00% of the population is identified as diabetic and approximately 42.00% are non-diabetic. Around 65% of the population is male, and about 35% is female that shows the gender distribution in dataset. The approximately 68.00% of the population has smoke habits and about 32% are non-smokers persons. The 299 cases of heart failure, 96 individuals unfortunately did not survive the condition, whereas 203 cases have survived. The percentages that translate to 32.11% of the cases experiencing an unfavorable outcome. The majority precisely 67.89% of cases has positive result to survive the heart failure condition. The percentages shows the overview of the distribution of outcomes in the studied population that indicate the higher proportion of individuals who managed to overcome heart failure than those who did not.:

Figures 3 and 4 show the distribution of age with gender. The minimum age for both males and females is set at 40. On the other hand, the maximum age varies between genders, with males reaching up to 95, while females have a maximum age of 90. These age specifications provide insights into the age range covered in the research, indicating that individuals below 40 are omitted, and the maximum ages differ slightly for males and females in the studied cohort.

The impact of patient aging on the probability of survival is depicted in Figure 5. The 50–70 age category has

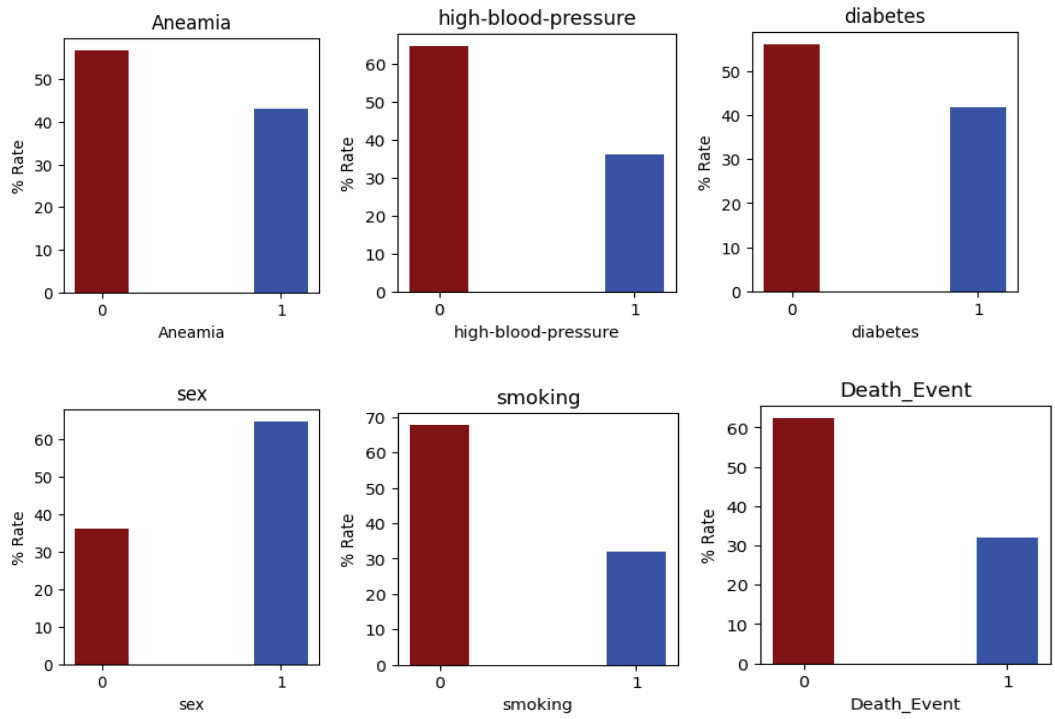


Figure 2. Univariate analysis of categorical variables.

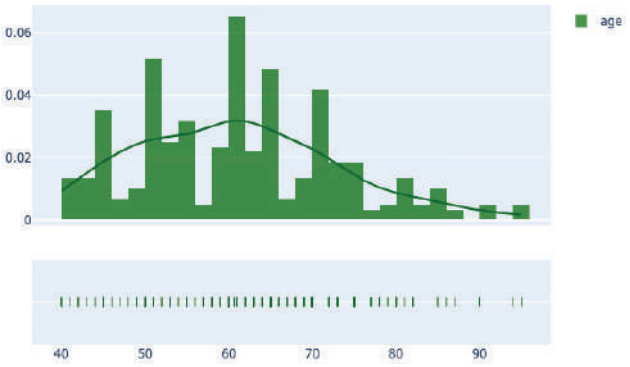


Figure 3. Age distribution.

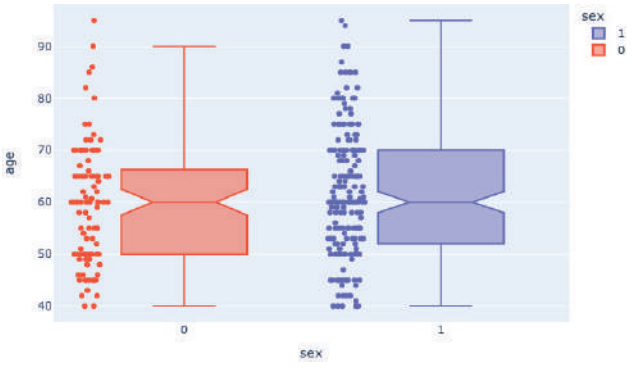


Figure 4. Distribution of Age w.r.t Gender.

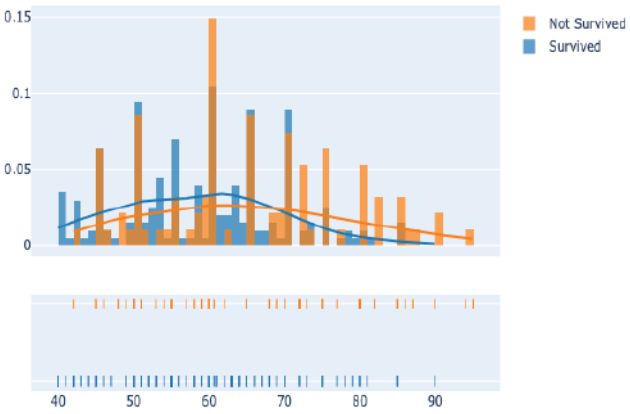


Figure 5. Age's Impact on Patients Survival Probability.

a significantly greater survival probability than the population. Every age category still carries some chance of not suffering a cardiovascular occurrence; the risk is most significant in the range of 60-65 age. Beyond the age of 80, the chances of survival sharply decline. The patterns suggest that age plays a significant role in survival outcomes after a heart failure event.

Figure 6 shows the distribution of various parameters and their survival rate. It is observed that survival outcomes in the studied population are based on gender. For the male population, 44.1% (132 individuals) have survived heart failure, while 20.7% (62 individuals) unfortunately did not survive. In the female population, 23.7% (71 individuals) survived the heart failure event, and 11.4% (34) did not.

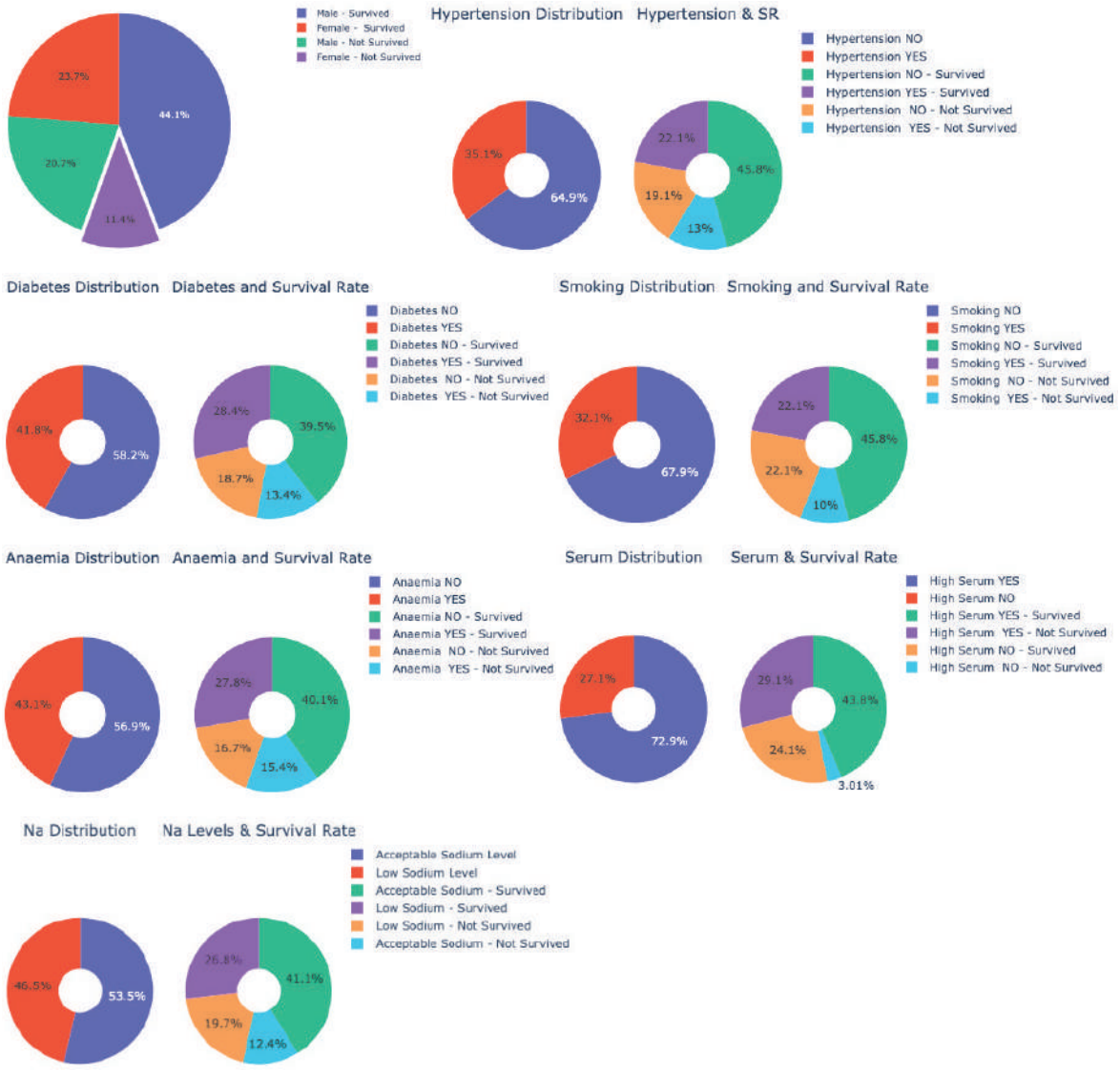


Figure 6. Distribution of parameters and their survival rate.

These percentages highlight the gender-specific variations in survival rates after experiencing heart failure, indicating a higher survival rate for males compared to females in the studied cohort. Around the 35.00% develop hypertension that excessive blood pressure. With this subgroup, 22% have sudden cardiac arrest events, and 13% unfortunately did not make it. Turning to the 65% of the population without hypertension, 45.8% have successfully survived heart failure, underscoring a higher survival rate compared to the hypertensive group, where 19% succumbed to the condition. Around 42% of individuals are identified as having diabetes, while approximately 58% do not have diabetes. 28.4% of people with diabetes have survived a cardiovascular attack, but unfortunately, 13.4% did not survive.

In contrast, among those without diabetes, a higher percentage, precisely 39.5%, have successfully survived after a heart attack, even though 18.7% have unfortunately given in to the medical condition. 32% of individuals have smoking habits, while around 68% do not smoke. Among those who smoke, 22.1% of people have prevented cardiac arrest, and unfortunately, 10% did not survive. On the other hand, among individuals without smoking habits, a higher percentage, precisely 45.8%, have successfully survived after cardiac arrest, while 22.1% have unfortunately given an approach to the illness. 43.1% of individuals exhibit symptoms of anemia, while around 56.9% do not show any signs of anemia. Among those with anemia, 27.8% survived after cardiac arrest, while 15.4%, unfortunately, failed to survive.

Conversely, among individuals without anemia, a higher percentage, precisely 40.1%, have successfully survived after cardiac arrest, while 16.7% have unfortunately succumbed to the condition. 46.5% of the entire population has lower blood sodium levels, while 53.5% have levels within the acceptable range. Among those with low

sodium levels, 26.8% after cardiac arrest, while 19.7% did not survive. In contrast, some patients whose sodium levels are below the appropriate limit have a higher percentage, precisely 41.1%, after cardiac arrest, with a smaller number, 12.4%, succumbing to the condition. These findings suggest a potential correlation between blood sodium levels and heart failure outcomes, with individuals within the acceptable range demonstrating a higher survival rate than those with lower sodium levels in the studied population.

Figure 7 shows information on various factors and laboratory test results related to heart failure outcomes in the studied population. First, it notes that people with cardiac failure who failed to survive generally have higher levels of CPK (creatine phosphokinase) enzyme. The violin histogram indicates outliers with high CPK levels in survival and death events. Additionally, it mentions that individuals who passed away with cardiac arrest often exhibited less than typical values for the ejection proportion, indicating inadequate pumping of blood from the heart. This shows outliers that observed in patients who survived heart failure. Serum creatinine levels 72.9% of cases reported elevated levels. The 43.8% are survived, and 29.1% succumbed to heart





Figure 7. Distribution of parameters and their effect on survival rate.

failure. Cases with serum levels in the normal range show a higher survival rate of 24.1%, contrasting with a lower percentage of 3.01% succumbing to the condition. However, 96 instances have passed away from cardiovascular disease. Of those instances, 59 people had sodium values below the normal range.

Table 1 presents the most correlated values associated with death in the dataset. The age shows the positive correlation of 0.253729 that indicate modest relationship across increase age and the likelihood of death. On the other hand, ejection fraction shows a negative correlation of -0.268603, suggesting that a lower ejection fraction, representing the proportion of blood that the coronary artery pumps continuously per contraction, is associated with a higher likelihood of death. Serum creatinine exhibits a positive correlation of 0.294278, indicating that higher serum

Table 1. Most correlated values of death

Parameter	Correlated Values
Age	0.253729
Ejection_fraction	-0.268603
Serum_creatinine	0.294278
Time	-0.526964

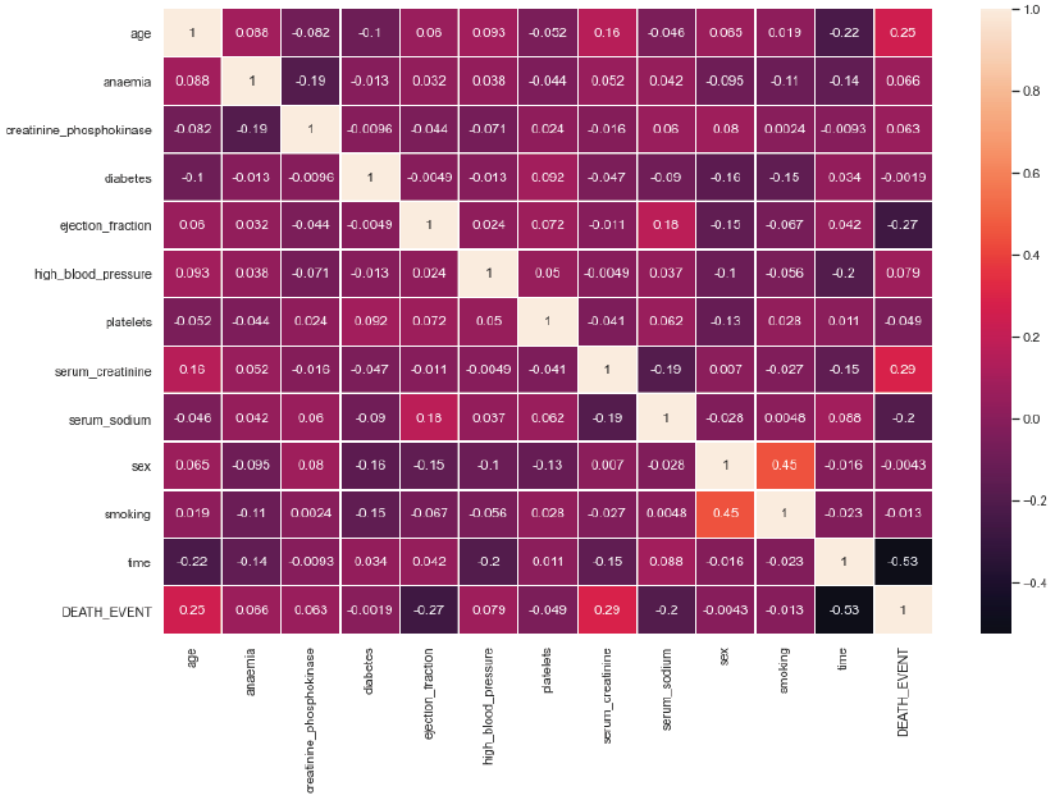


Figure 8. Heat map correlation of between the features.

creatinine levels, a marker of kidney function, are connected to a higher chance of passing away.

Build Baseline Classifiers

The CVD detection using ML based classifiers such as LR, RF, XG Boost, and NB serve as initial models to measure the performance of baseline models. The RF is a simple linear model measure the probabilities. The RF is a group of decision trees that collect correlations between the features. The XG Boost algorithm known for its accuracy and efficiency; and NB for feature independence. The classifiers provide a starting point for evaluating more sophisticated models, allow us to compare their performance against these more straightforward approaches, and measure the effectiveness of their ML classifiers in predicting cardiovascular diseases.

Ensemble Model

Combine the predictions of multiple individual classifiers to improve the overall prediction accuracy. We designed ensemble classifiers for CVD prediction using ML baseline classifiers such as LR, RF, XG Boost, and NB. Ensemble classifiers are often more robust and accurate than individual classifiers that effectively used the strengths of different models and mitigate their weaknesses, ultimately improving the performance of CVD prediction models [37]. The suggested ensemble models develops the outcomes using the weighted majority to combine the predicted results of many ML models. The most favorable results are shown following the fine-tuning of each categorization model. Equation 1 show to obtained the maximum votes.

$$C = argmax\ (X1\ (C_i^1), X2\ (C_i^2), \ldots\ldots Xn(C_i^n)) \quad (1)$$

Normalize and specify the loss function that provide an objective function to measure the performance of the ensemble model

$$C'(\oplus) = Loss\ (\oplus) + \alpha \cdot (\oplus) \quad (2)$$

Equation 2 shows the variables measured using the plus operator and derived from the supplied inputs. The normalization factor (Theta′) and the loss function used to calculate the model generalization.

Figure 9 shows the suggested ML-based ensemble model for predicting CVD. This model uses a voting approach by allowing each model to "vote" on the final prediction. Each model independently makes its prediction, and the most common prediction among the models is selected as the final. By combining these models, the ensemble can achieve higher accuracy and robustness in predicting CVD than any single model.

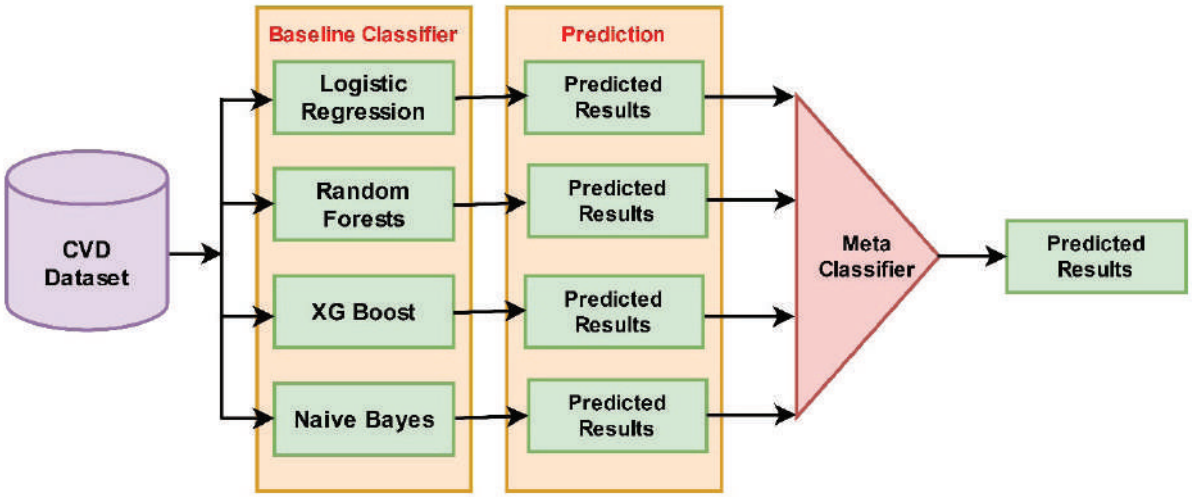


Figure 9. Ensemble Model.

Pseudo Code: Ensemble Model

Input: Training Dataset $CVD = \{(p1, q1), (p2, q2),...(pn, qn)\}$
Baseline Model $M = (LR, RF, XGB, NB)$
Meta Classifier DT
Output: Learn Ensemble Model EM
Start
Step-1: Learn the Baseline classifiers M on CVD
for $i = 1$ *to* n *do*
  $Bi = Mi(CVD)$
end for
Step-2: Construct new CVD Dataset for prediction CVD'
for $j=1$ *to* n' *do*
  for $i = 1$ *to* n *do*
Used Bi to classify training parameters pj
$xij = Bi(pj)$
end for
$CVD = (xj, qj)$, *where* $xj = \{xij, x2j,.... xnj\}$
end for
Step-3: Learn Meta Classifier DT
$EM = DT(CVD)$
Return EM
END

Table 2. Hyperparameter settings of ML models in ensemble

Model	Parameters	Values
LR	C	0.1
	penalty	L1
	solver	liblinear
	max_iter	100
RF	n_estimators	100
	max_depth	10
	min_samples_split	2
	min_samples_leaf	2
	criterion	Gini
	max_features	Sqrt
XGBoost	eta	0.01
	max_depth	3
	n_estimators	100
	subsample	0.7
	colsample_bytree	0.7
	alpha	0
	lambda	1
Naive Bayes	var_smoothing	1e-9
	alpha	0.5

Hyperparameter settings

Hyperparameter optimization plays a crucial role in improving the performance of ensemble models for cardiovascular disease detection by fine-tuning the parameters of individual ML models included in the ensemble. Table 3 shows the hyperparameter setting of ML models used to build the ensemble model

RESULTS AND DISCUSSION

The following section examines the baseline and proposed ensemble classifier performance and briefly overviews the outcomes. The main goal of this investigation is to investigate the effectiveness of suggested ML algorithms for identifying cardiovascular illness. We used the CVD dataset in the tests conducted for this study. We divided the CVD dataset into 70% training and 30% testing. We

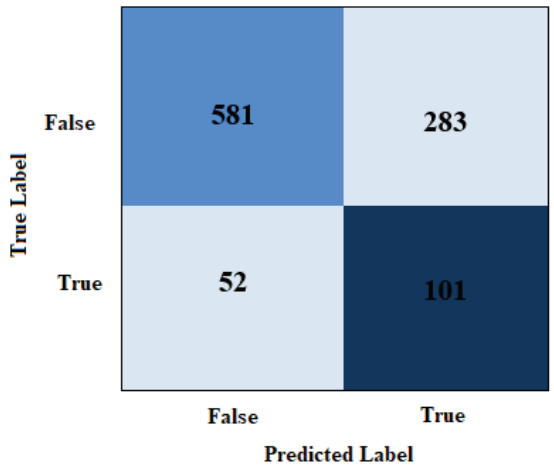
Table 3. Comparative result analysis of baseline model with ensemble model

Classifiers	Accuracy	Precision	Recall	F1-Score
Logistic Regression	67.00	82.00	67.00	72.00
Random Forests	65.00	81.00	65.00	70.00
XG Boost	70.00	78.00	70.00	73.00
Naive Bayes	70.00	81.00	70.00	74.00
Ensemble Model	82.00	85.00	80.00	82.00

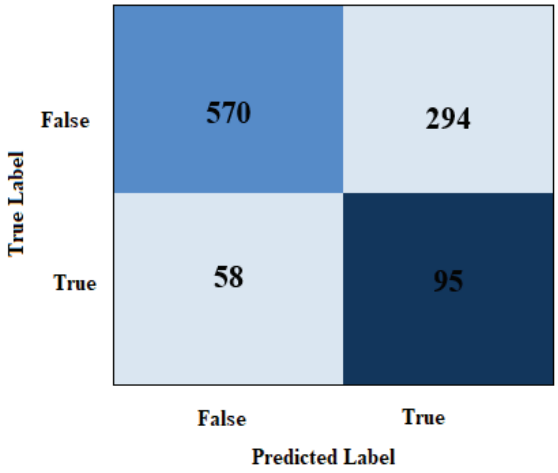
simulated the ensemble model using Google Colab with Python 3, running on an Intel Core i5 GPU @4.20 GHz, 16 GB RAM, and 4 GeForce RTX graphics cards. Several evaluation parameters are shown in equation 3 to 6.

$$Accuracy = \frac{T_P + T_N}{T_P + T_N + F_P + F_N} \quad (3)$$

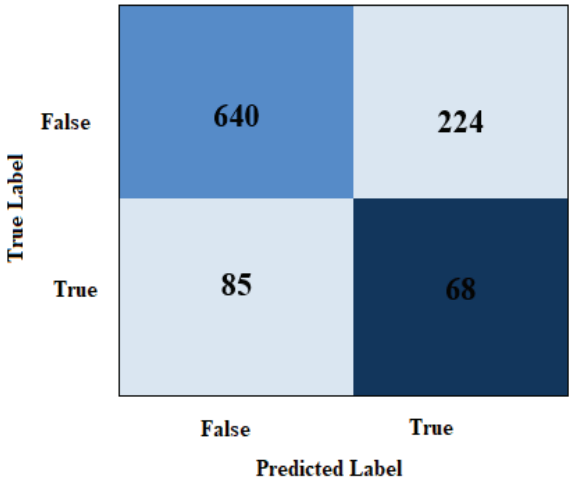
$$Precision = \frac{T_P}{T_P + F_P} \quad (4)$$



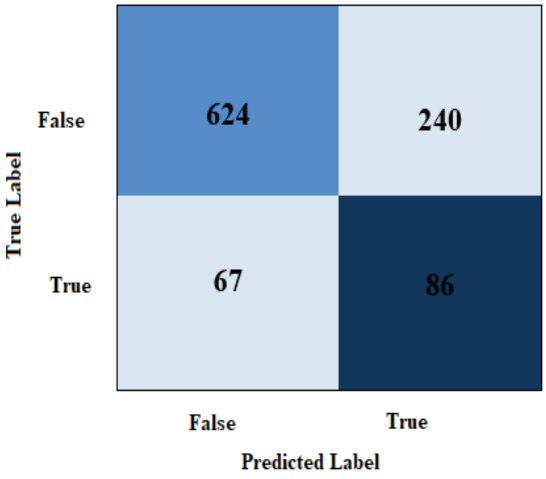
(1) K Nearest Neighbors



(2) Random Forests



(3) XG Boost



(4) Naive Bayes

Figure 9. Confusion Matrix of Baseline Classifiers

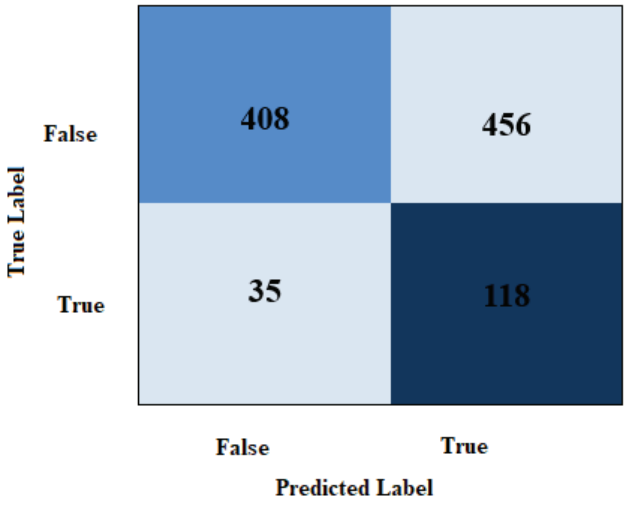


Figure 10. Confusion Matrix of Ensemble Model.

$$Recall = \frac{T_P}{T_P + F_N} \quad (5)$$

$$F1 - Score = 2 \times \frac{Precision \times Recall}{Precision + Recall} \quad (6)$$

Table 2 presents a comparative analysis of baseline models, including Logistic Regression, Random Forests, XG Boost, Naive Bayes, and an Ensemble Model, based on their performance metrics. The finding shows the ensemble model performed well ad compared to individual models and obtained the accuracy of 82.00%, precision of 85.00%, Recall of 80.00%, and F1-Score of 82.00%. The suggested model is more effective due to ability to combine the strengths of different ML classifiers.

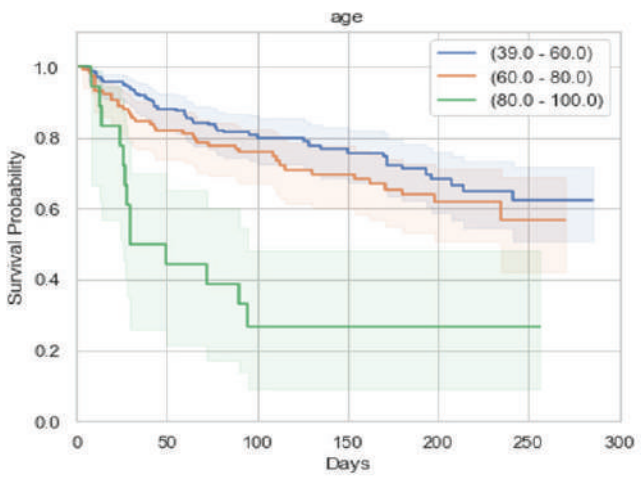
Table 4 shows different machine learning models' training and test recall scores for cardiovascular disease prediction. Recall, sometimes called sensitivity, indicates the percentage of actual positive instances the model accurately recognized. A higher recall indicates better performance in identifying positive cases. The ensemble model obtained the recall scores of training and testing of 86.90% and 82.53% that shows the superior ability to identify positive cases.

Table 4. Training and test recall of ML models

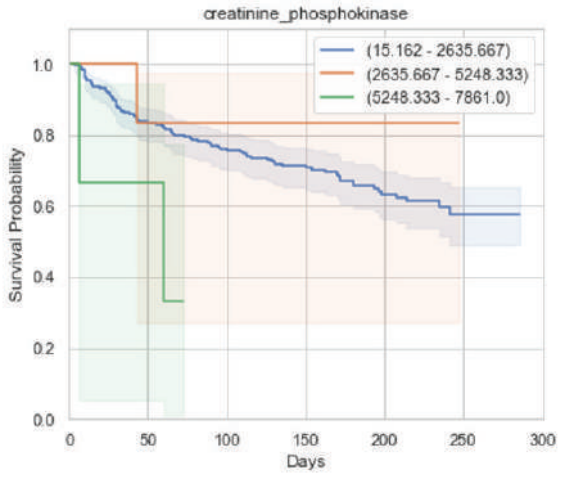
Classifiers	Train Recall	Test Recall
Logistic Regression	69.6352	67.0130
Random Forests	69.3282	63.0915
XG Boost	82.3399	44.4444
Naive Bayes	52.1910	56.2091
Ensemble Model	**86.9057**	**82.5363**

Survival Prediction Using Kaplan Meier

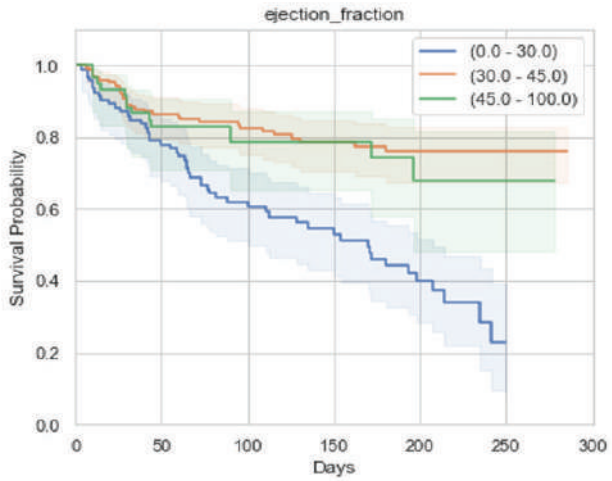
This study uses the Kaplan-Meier estimator to predict the survival rate of cardiovascular diseases for continuous variables, such as Age, Creatinine Phosphokinase, Ejection Fraction, Platelets, Serum Creatinine, Serum Sodium, and Time. The first step is to discretize each continuous variable into intervals. The proportion of observations that survive beyond each time interval is calculated for each combination of intervals. This is done similarly to the standard Kaplan-Meier estimator but using the intervals for the continuous variables. Figure 11 is a powerful tool that visually represents the estimated survival probabilities against each interval of parameters, allowing us to quickly grasp the survival function over the range of the continuous variables. Another name for the Kaplan-Meier estimate is "product limit estimate." This mesure the possibility of an event occurred at a specific moment [38,39]. Combine this sequential probability with all previously estimated possibilities to obtain the highest possible estimation.



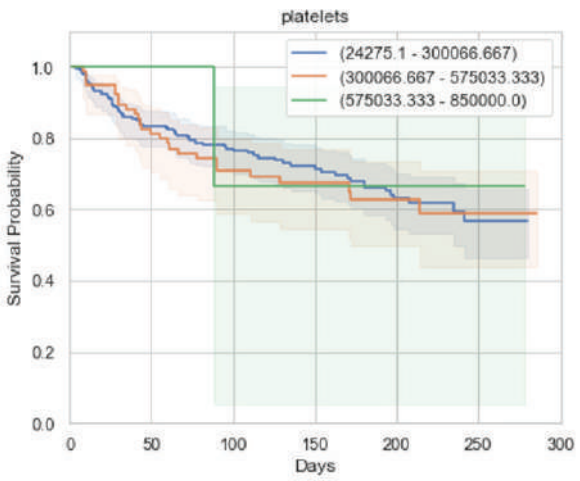
(1) Age



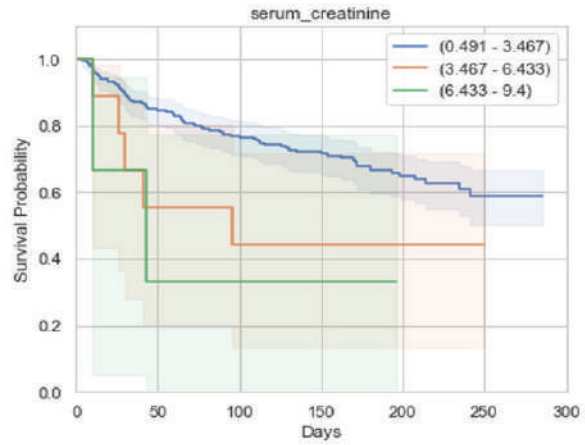
(2) Creatinine Phosphokinase



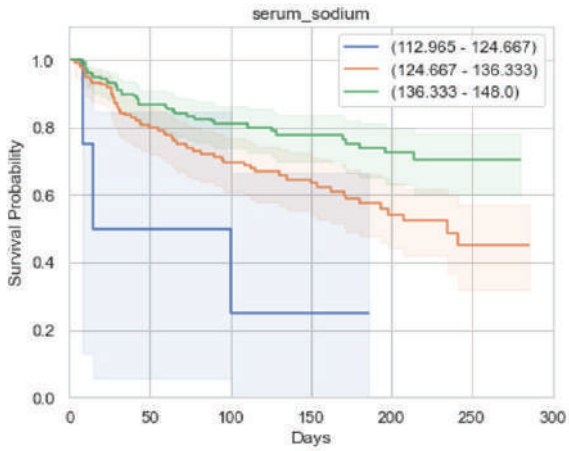
(3) Ejection Fraction



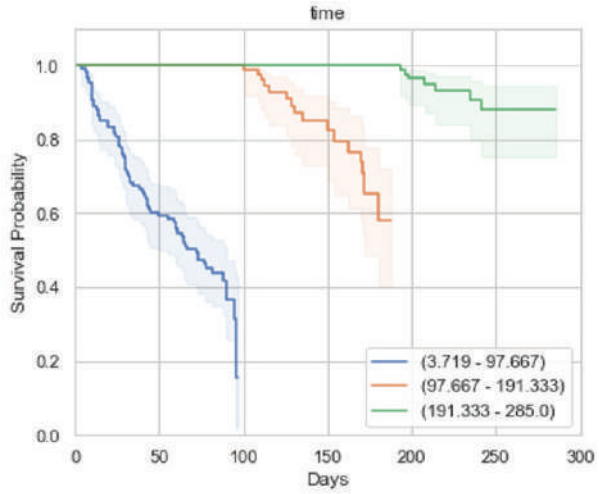
(4) Platelets



(5) Serum Creatinine



(6) Serum Sodium



(7) Time

Figure 11. Survival prediction analysis

$$Kaplan\ Meier\ Estimate = \frac{No\ of\ Patients\ living\ at\ the\ Start - No\ of\ Patients\ died}{No.of\ Patients\ Living\ at\ the\ start} \quad (7)$$

The chance of surviving risk for every period is determined by dividing the total number of vulnerable people by the total number of patients who survive. Individuals who have passed away, stopped participating, or moved away are not included in the denominator and are not regarded as "under threat.

p Values and Statistical Significance of Parameters

The summary's p-values shows risk exhibit considerable significance, with p-values below 0.0005 that shows statistical significance at a confidence level of 99.9995% or higher. The attributes demonstrate a strong correlation with the occurrence of the death event. Conversely, Smoking, Sex, Platelets, and Diabetes yield notably high p-values, making it uncertain whether they hold statistical significance. Consequently, their impact on the hazard rate may be disregarded in the analysis. This observation is supported by their substantial standard errors and the consequent broad confidence intervals [40].

Anemia is a binary variable represented by 1 or 0, indicating whether the subject is anemic. The coefficient of 0.481 is interpreted as:

$$\frac{HazardRateforPatientswithAnemia}{HazardRateforPatientswithoutAnemia}$$

$$\frac{e^{0.481\times1}}{e^{0.481\times0}} = e^{0.481\times(1-0)} = e^{0.481} = 1.618$$

The hazard ratio for anemia is 1.618. This indicate that the patient has anemia, the risk of death increases by 61.8%.

High BP represented by 1 and 0 that shows that subject has high blood pressure (hypertension) or not. The coefficient of 0.406 is interpreted as:

$$\frac{HazardRateforPatientswithHighBP}{HazardRateforPatientswithoutHighBP}$$

$$\frac{e^{0.406\times1}}{e^{0.406\times0}} = e^{0.406\times(1-0)} = e^{0.406} = 1.50$$

The HR for high BP is 1.5. This shows that the patient has hypertension. The risk of death increases by 50%.

Hazard ratio (HR)

The HR shows the impact of a covariate on the hazard rate. An HR of 1 suggests no effect that indicate the covariate does not influence the hazard rate. An HR more significant than 1 increases the hazard rate as the covariate value increased that indicate the higher risk of the event occurring [40]. The HR less than 1 shows to decrease in the hazard rate as the covariate value increases that suggest lower risk of the event.

Figure 12 represents the coefficients (i.e., log hazard ratios) for predicting the survival rate of cardiovascular diseases based on various factors. Each factor, such as anemia, high blood pressure, serum creatinine, diabetes, smoking, age, creatinine phosphokinase, platelets, serum sodium, ejection fraction, and sex, is listed along the vertical axis. The horizontal bars extending from the central axis represent the magnitude and direction of the coefficients. A bar extending to the right indicates a positive effect on the hazard ratio, meaning an increased risk of cardiovascular disease survival, while a bar extending to the left indicates a negative impact, implying a decreased risk.

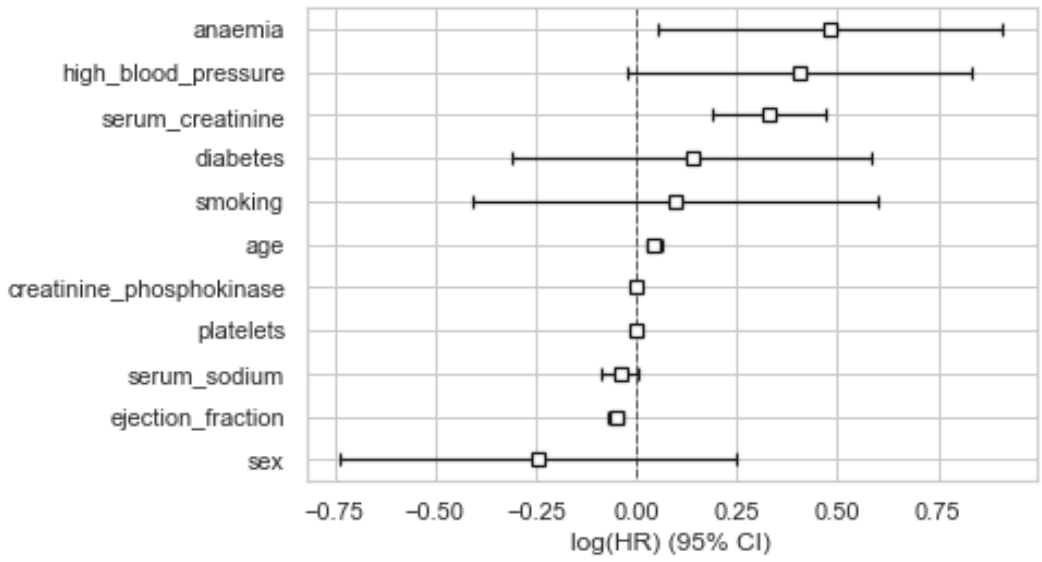


Figure 12. Graphical Visualization of the Coefficients (i.e. log hazard ratios).

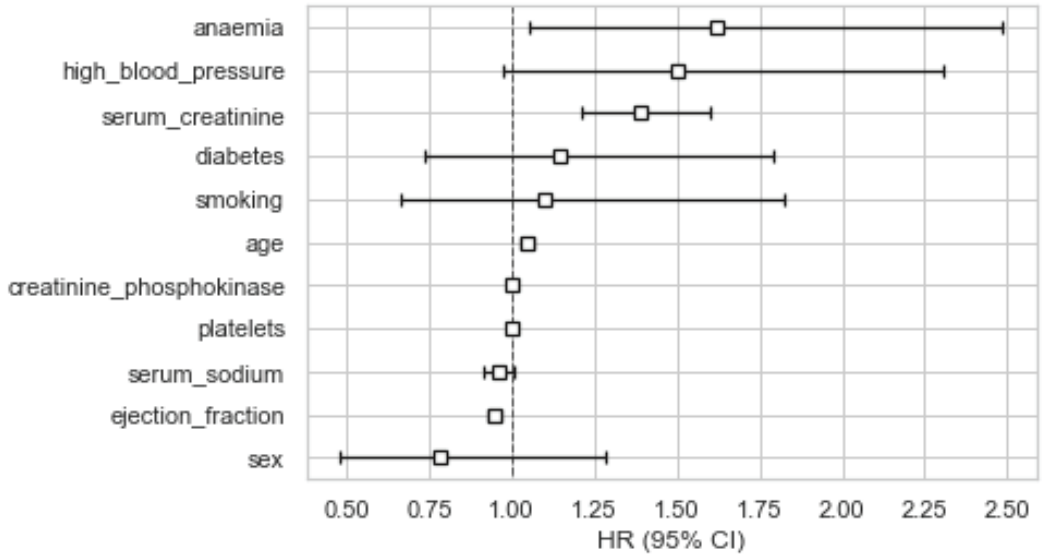


Figure 13. Visual representation of the hazard ratios.

The impact of covariates on survival outcomes has been understood through the HR which measures the change in hazard rate with a one-unit change in the covariate. For Ejection Fraction, a one-unit change results in a 5.2% increase in survival time, as indicated by an HR of 0.95. Conversely, a one-unit rise in Serum Creatinine causes a 28.1% decrease in survival time, given its HR of 1.392 [41]. Age shows a 3.9% decrease in survival time per unit increase, with an HR of 1.046. However, Creatinine Phosphokinase and Platelets have HRs of 1, suggesting no effect on the probability of the death occurrences.

Figures 12 and 13 provide the graphical layout of coefficients, log hazard ratios, and hazard ratios, respectively, encompassing their sizes and standardized errors. Anemia, High Blood Pressure, Serum Creatinine, Age, and the amount of Ejection are all within the 95% confidence interval of influencing the death incident.

Figure 14 shows that with age, the survival probability decreases for any complication arising from a heart failure condition. Increasing age has a significant impact on the likelihood of surviving. Figure 15 shows that the volume of blood pumped out of the heart increases with increasing ejection fraction percentage. Consequently, the probability of survival also increases during any phase of heart failure. Increasing EF levels has a beneficial significant impact on the likelihood of survival.

Figure 16 shows that with increasing serum creatinine levels in the blood, the survival probability decreases for

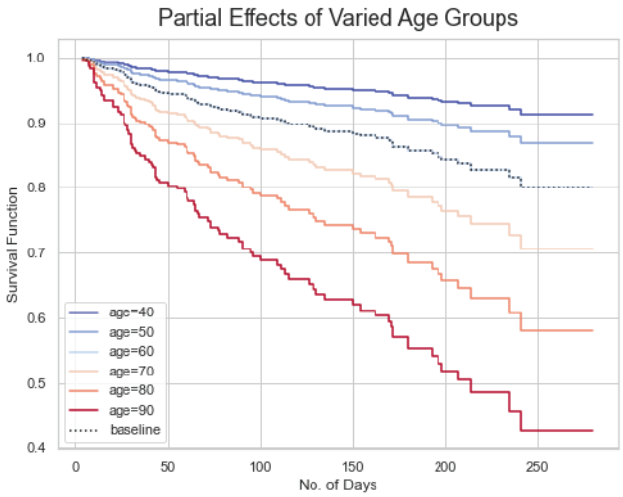


Figure 14. Partial effect of varied age.

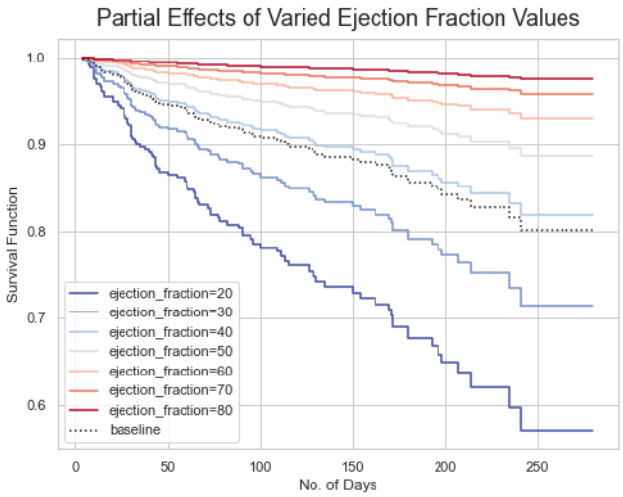


Figure 15. partial effect of varied ejection fraction.

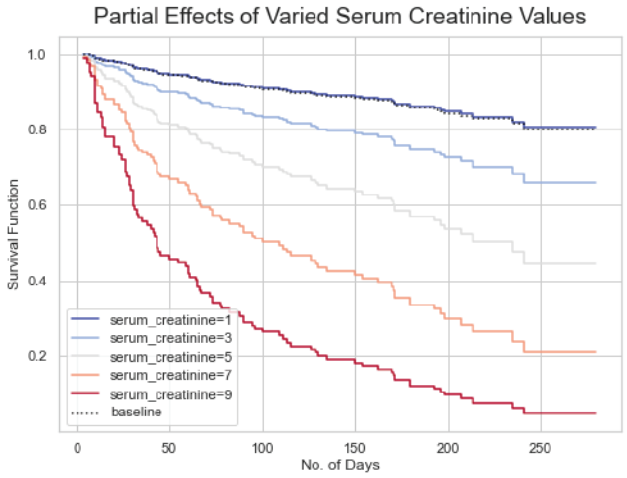


Figure 16. Partial effect of varied serum creatinine vs non-anaemia.

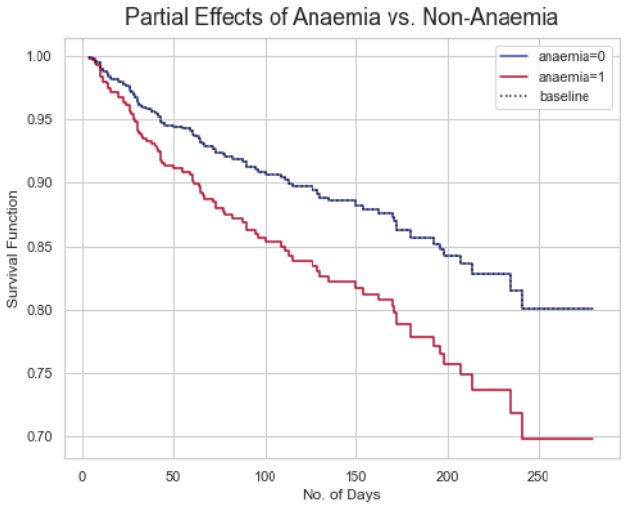


Figure 17. Partial effect of partial effect of anaemia

any complication arising out of a heart failure condition. Increasing creatinine levels have a significant impact on the likelihood of survival. Figure 17 shows that anaemic patients are more likely to encounter a hazard due to heart failure condition—survival Probabilities over 280 days.

Table 5 analyzes the survival probabilities of the patient in the test cohort over 280 days. The analysis assumes that the subjects have just entered the study without considering how long they have lived. It is observed that initially, each subject in the test cohort has high survival chances, hovering around the 98-99% mark. For Patient -298 and Patient -179, the survival probabilities remain consistent throughout the period, at 88% and 85.5%, respectively, by the 280th day. For Patient-42 and Patient -193, the survival probabilities hover around 61% and 34%, respectively, at the end of 280 days. However, for patient -5, the chances of survival show a decreasing trend. By day 15, the survival chance is approximately 75%; by day 38, it hovers around the 50% mark; by the end of 180 days, it falls below 10%.

Table 6 shows the comparative perfromance analysis of the proposed ensemble models and existing model to detect and classify the CVD. The proposed ensemble model obtained the accuracy of 82.53% that performed well as compared to existing individual ML models that obtained the accuracy score of DT has 81.23%, K-means of 78.00%, ANN of 82.10%, and Stacking Models of 82.35%. The XGBoost obtained the 82.44%, and SVM achieved the highest accuracy at 83.12%. This comparison demonstrates that the ensemble approach offers a balanced trade-off between simplicity and performance, positioning it as a competitive alternative among state-of-the-art techniques for this task.

The final results suggest whether the various CVD parameters are used to forecast a patient's survival rate suffering heart disease. They also indicate that forecasts based

Table 5. Survival probabilities of patients last 10 days

Days	Patient - 42	Patient - 298	Patient - 5	Patient - 193	Patient - 179
246.0	0.616569	0.880709	0.033281	0.346240	0.855772
247.0	0.616569	0.880709	0.033281	0.346240	0.855772
250.0	0.616569	0.880709	0.033281	0.346240	0.855772
256.0	0.616569	0.880709	0.033281	0.346240	0.855772
257.0	0.616569	0.880709	0.033281	0.346240	0.855772
258.0	0.616569	0.880709	0.033281	0.346240	0.855772
270.0	0.616569	0.880709	0.033281	0.346240	0.855772
271.0	0.616569	0.880709	0.033281	0.346240	0.855772
278.0	0.616569	0.880709	0.033281	0.346240	0.855772
280.0	0.616569	0.880709	0.033281	0.346240	0.855772

Table 6. Comparative analysis of proposed method with existing methods

Author	Methods	Accuracy
Bhatt, C.M. et. al. (2023) [42]	DT	81.23%
Subramani S. et. al. (2023) [43]	Stacking Model	82.35%
Baghdadi, N.A. et. al. (2023) [44]	XGBoost	82.44%
Ahmad AA, et. al. (2023) [45]	SVM	83.12%
Khdair, H. et. al. (2021) [46]	K-means	78.00%
M. S. Gangadhar et. al. (2023) [47]	ANN	82.10%
Proposed	**Ensemble**	**82.53%**

simply on both variables may be more reliable than those based on the entire dataset. This is especially required for healthcare facilities environments: physicians might still be capable of forecasting the survival of patients using Age, smoking, serum creatinine amounts, and ejection fraction alone, even if the individual technological medical care contained a lot of not present clinical information and test examination from laboratories. However, invetigation that need for further study to design the strong models to daignosis the CVD ealier and implementable in healthcare settings.

Further investigation offered several interesting results that were not discovered in the researchers' earlier dataset analysis [41]. Ahmad et al. found that anemia, high blood pressure, ejection fraction, age, and serum creatinine a sign of kidney disease were actually the most common characteristics. The characteristics are important since are highly predictive of patient survival rates.

CONCLUSION

This study validated the importance of relevant feature extraction with machine learning by demonstrating that conventional statistical analysis identified cardiovascular disease factors as the most significant features. Furthermore, the proposed method showed that machine learning was applied successfully to the binary categorization of electronic healthcare of individuals with coronary artery disease disorders related to the heart system. This study demonstrates the effectiveness of machine learning techniques in predicting cardiovascular diseases and forecasting survival rates of patients. The ensemble model performed well as compared to baseline models that indicate its superiority in disease prediction. This study also identifies age, serum creatinine, and ejection fraction as significant factors affecting the death event, while smoking, sex, platelets, and diabetes may not hold statistical significance. The existing studies that focus on individual models or limited feature sets. The proposed model combined the diverse risk factors and shows superior accuracy compared to existing models. This work is unusual because it provides interpretable insights into important risk factors including age, serum creatinine, and ejection fraction by bridging the gap between ML and medical survival analysis. This method offers useful applications for early treatment in cardiovascular care while also advancing predictive modeling. In order to enhance preventative and therapeutic approaches, future studies might investigate the connections among risk variables and CVD prognosis.

ACKNOWLEDGMENT

We acknowledge the support received from Yeshwantrao Chavan College of Engineering, Nagpur, Maharashtra, India. We are deeply grateful to the management and Principal Dr. U. P. Waghe for their invaluable support and encouragement.

AUTHOR CONTRUBITIONS

Bharati Karare handled conceptualization and data collection. Anushree Anand Pande was responsible for data validation, software tools, and data collection. Prof. Pratibha Waghale focused on data analysis, identifying previous research gaps, and methodology. Prof. Amruta Tapas Paul contributed to methodology and software. Prof. Chanchla Tripathi took care of validation and data visualization. Dr. Lalit Damahe was in charge of writing the original draft and overall writing. Dr. Prashant Bhokardankar was involved in review and editing.

DATA AVAILABILITY STATEMENT

The authors confirm that the data that supports the findings of this study are available within the article. Raw data that support the finding of this study are available from the corresponding author, upon reasonable request.

CONFLICT OF INTEREST

The author declared no potential conflicts of interest with respect to the research, authorship, and/or publication of this article.

ETHICS

There are no ethical issues with the publication of this manuscript.

STATEMENT ON THE USE OF ARTIFICIAL INTELLIGENCE

Artificial intelligence was not used in the preparation of the article.

REFERENCES

[1] World Health Organization. The top 10 causes of death. Geneva: WHO; 2020 Available at: https://www.who.int/news-room/fact-sheets/detail/the-top-10-causes-of-death Accessed on Dec 30, 2020.

[2] Fryar CD, Chen TC, Li X. Prevalence of uncontrolled risk factors for cardiovascular disease: United States, 1999–2010. NCHS Data Brief 2012;103:1–8.

[3] Murphy SP, Ibrahim NE, Januzzi JL Jr. Heart failure with reduced ejection fraction: A review. JAMA 2020;324:488–504. [CrossRef]

[4] Mayo Clinic. Cardiovascular diseases. Rochester (MN): Mayo Clinic; 2020 Available at: https://www.mayoclinic.org/medical-professionals/cardiovascular-diseases Accessed on Dec 29, 2020.

[5] Centers for Disease Control and Prevention. Underlying cause of death 1999–2019 [Internet]. Atlanta (GA): CDC; 2020. Available at: https://wonder.cdc.gov/wonder/help/ucd.html Accessed on Dec 28, 2020.

[6] Bhatt CM, Patel P, Ghetia T, Mazzeo PL. Effective heart disease prediction using machine learning techniques. Algorithms (Basel) 2023;16:88. [CrossRef]

[7] Mahmud I, Kabir MM, Mridha MF, Alfarhood S, Safran M, Che D. Cardiac failure forecasting based on clinical data using a lightweight machine learning metamodel. Diagnostics (Basel) 2023;13:2540. [CrossRef]

[8] Saeedbakhsh S, Sattari M, Mohammadi M, Najafian J, Mohammadi F. Diagnosis of coronary artery disease based on machine learning algorithms: Support vector machine, artificial neural network, and random forest. Adv Biomed Res 2023;12:51. [CrossRef]

[9] Alizadehsani R, Khosravi A, Roshanzamir M, Abdar M, Sarrafzadegan N, Shafie D, et al. Coronary artery disease detection using artificial intelligence techniques: A survey of trends, geographical differences and diagnostic features 1991–2020. Comput Biol Med 2021;128:104095. [CrossRef]

[10] Joloudari JH, Joloudari EH, Saadatfar H, GhasemiGol M, Razavi SM, Mosavi A, et al. Coronary artery disease diagnosis: Ranking the significant features using a random trees model. Int J Environ Res Public Health 2020;17:731. [CrossRef]

[11] Pal M, Parija S, Panda G, Dhama K, Mohapatra RK. Risk prediction of cardiovascular disease using machine learning classifiers. Open Med (Wars) 2022;17:1100–1113. [CrossRef]

[12] Subramani S, Varshney N, Anand MV, Soudagar MEM, Al-Keridis LA, Upadhyay TK, et al. Cardiovascular diseases prediction by machine learning incorporation with deep learning. Front Med (Lausanne) 2023;10:1150933. [CrossRef]

[13] Ishaq A, et al. Improving the prediction of heart failure patients' survival using SMOTE and effective data mining techniques. IEEE Access 2021;9:39707–39716. [CrossRef]

[14] Moreno-Sánchez PA. Improvement of a prediction model for heart failure survival through explainable artificial intelligence. Front Cardiovasc Med 2023;10:1219586. [CrossRef]

[15] Baby PS, Vital TP. Statistical analysis and predicting kidney diseases using machine learning algorithms. Int J Eng Res Technol 2015;4:206–210. [CrossRef]

[16] García-Ordás MT, Bayón-Gutiérrez M, Benavides C, et al. Heart disease risk prediction using deep learning techniques with feature augmentation. Multimed Tools Appl 2023;82:31759–31773. [CrossRef]

[17] Shameer K, Johnson KW, Yahi A, Miotto R, Li LI, Ricks D, et al. Predictive modeling of hospital readmission rates using electronic medical record-wide machine learning: A case study using Mount Sinai heart failure cohort. Pac Symp Biocomput 2017;22:276–287. [CrossRef]

[18] Kaddour A. Implementation of an incremental deep learning model for survival prediction of cardiovascular patients. IAES Int J Artif Intell 2021;10:101–109. [CrossRef]

[19] Jackins V, Vimal S, Kaliappan M, Lee MY. AI-based smart prediction of clinical disease using random forest classifier and naive Bayes. J Supercomput 2021;77:5198–5219. [CrossRef]

[20] Ahsan MM, Siddique Z. Machine learning-based heart disease diagnosis: A systematic literature review. Artif Intell Med 2022;128:102289. [CrossRef]

[21] Weng SF, Reps J, Kai J, Garibaldi JM, Qureshi N. Can machine-learning improve cardiovascular risk prediction using routine clinical data? PLoS One 2017;12:e0174944. [CrossRef]

[22] Dimopoulos AC, Nikolaidou M, Caballero FF, Engchuan W, Sanchez-Niubo A, Arndt H, et al. Machine learning methodologies versus cardiovascular risk scores in predicting disease risk. BMC Med Res Methodol 2018;18:179. [CrossRef]

[23] Mohan S, Thirumalai C, Srivastava G. Effective heart disease prediction using hybrid machine learning techniques. IEEE Access 2019;7:81542–81554. [CrossRef]

[24] Yang L, Wu H, Jin X, Xu X, Yu W, Yan J. Study of cardiovascular disease prediction model based on random forest in eastern China. Sci Rep 2020;10:5245. [CrossRef]

[25] Hu Z, Qiu H, Su Z, Shen M, Chen Z. A stacking ensemble model to predict daily number of hospital admissions for cardiovascular diseases. IEEE Access 2020;8:138719–138729. [CrossRef]
[26] Ahmed U, Mukhiya SK, Srivastava G, Lamo Y, Lin JCW. Attention-based deep entropy active learning using lexical algorithm for mental health treatment. Front Psychol 2021;12:642347. [CrossRef]
[27] Jerjawi NSE, Naser SSA. Diabetes prediction using artificial neural network. Int J Adv Sci Technol 2018;121.
[28] Mohan S, Thirumalai C, Srivastava G. Effective heart disease prediction using hybrid machine learning techniques. IEEE Access 2019;7:81542–81554. [CrossRef]
[29] Au H, Li JP, Memon MH, Nazir S, Sun R. A hybrid intelligent system framework for the prediction of heart disease using machine learning algorithms. Mob Inf Syst 2018;2018:3860146. [CrossRef]
[30] Renugadevi G, Asha Priya G, Sankari BD, Gowthamani R. Predicting heart disease using hybrid machine learning model. J Phys Conf Ser 2021;1916:012208. [CrossRef]
[31] Sathwika GJ, Bhattacharya A. Prediction of cardiovascular disease using ensemble learning algorithms. In: Proc 5th Joint Int Conf Data Sci Manag Data (ACM IKDD CODS, COMAD); 2022 Jan; Bangalore, India. p.292–293. [CrossRef]
[32] Zheng H, Sherazi SWA, Lee JY. A stacking ensemble prediction model for the occurrences of major adverse cardiovascular events in patients with acute coronary syndrome on imbalanced data. IEEE Access 2021;9:113692–113704. [CrossRef]
[33] Saw M, Saxena T, Kaithwas S, Yadav R, Lal N. Estimation of prediction for getting heart disease using logistic regression model of machine learning. In: Proc Int Conf Comput Commun Inform (ICCCI); 2020; Coimbatore, India. p.1–6. [CrossRef]
[34] Lutimath NM, Sharma N, Byregowda BK. Prediction of heart disease using random forest. In: Proc Emerg Trends Ind 4.0 (ETI 4.0); 2021; Raigarh, India. p.1–4. [CrossRef]
[35] Jain V, Agrawal M. Heart failure prediction using XGB classifier, logistic regression and support vector classifier. In: Proc Int Conf Adv Comput Comput Technol (InCACCT); 2023; Gharuan, India. p.1–5. [CrossRef]
[36] TheDevastator. Exploring risk factors for cardiovascular disease. Kaggle. Available at: https://www.kaggle.com/datasets/thedevastator/exploring-risk-factors-for-cardiovascular-diseas Accessed on Apr 12, 2023.
[37] Alqahtani A, Alsubai S, Sha M, Vilcekova L, Javed T. Cardiovascular disease detection using ensemble learning. Comput Intell Neurosci 2022;2022:5267498. [CrossRef]
[38] Goel MK, Khanna P, Kishore J. Understanding survival analysis: Kaplan–Meier estimate. Int J Ayurveda Res 2010;1:274–278. [CrossRef]
[39] Rich JT, Neely JG, Paniello RC, Voelker CC, Nussenbaum B, Wang EW. A practical guide to understanding Kaplan–Meier curves. Otolaryngol Head Neck Surg 2010;143:331–336. [CrossRef]
[40] Databricks. Cox proportional hazards notebook Databricks. Available at: https://www.databricks.com/notebooks/telco-accel/03_cox_proportional_hazards.html Accessed on Apr 12, 2023.
[41] Ahmad T, Munir A, Bhatti SH, Aftab M, Raza MA. Survival analysis of heart failure patients: A case study. PLoS One 2017;12:e0181001. [CrossRef]
[42] Bhatt CM, Patel P, Ghetia T, Mazzeo PL. Effective heart disease prediction using machine learning techniques. Algorithms (Basel) 2023;16:88. [CrossRef]
[43] Subramani S, Varshney N, Anand MV, Soudagar MEM, Al-Keridis LA, Upadhyay TK, Alshammari N, Saeed M, Subramanian K, Anbarasu K, Rohini K. Cardiovascular diseases prediction by machine learning incorporation with deep learning. Front Med (Lausanne) 2023;10:1150933. [CrossRef]
[44] Baghdadi NA, Farghaly Abdelaliem SM, Malki A, Gad I, Ewis A, et al. Advanced machine learning techniques for cardiovascular disease early detection and diagnosis. J Big Data 2023;10:144. [CrossRef]
[45] Ahmad AA, Polat H. Prediction of heart disease based on machine learning using jellyfish optimization algorithm. Diagnostics (Basel) 2023;13:2392. [CrossRef]
[46] Khdair H. Exploring machine learning techniques for coronary heart disease prediction 2021. Available at: https://thesai.org/Publications/ViewPaper?Volume=12&Issue=5&Code=IJACSA&SerialNo=5 Accessed on Apr 12, 2023.
[47] Gangadhar MS, Sai KVS, Kumar SHS, Kumar KA, Kavitha M, Aravinth SS. Machine learning and deep learning techniques on accurate risk prediction of coronary heart disease. In: Proc Int Conf Comput Methodol Commun (ICCMC); 2023; Erode, India. p.227–232. [CrossRef]

Sigma Journal of Engineering and Natural Sciences
Web page info: https://sigma.yildiz.edu.tr
DOI: 10.14744/sigma.2025.00000

Research Article

Development of plant extract-loaded electrospun nanofiber for the prevention of biofilm-associated infections

Sevim Feyza ERDOĞMUŞ[1,*], Cengiz SARIKURKCU[2]

[1]*Department of Pharmaceutical Microbiology, Faculty of Pharmacy, Afyonkarahisar Health Sciences University, Afyonkarahisar, 03030, Türkiye*
[2]*Department of Analytical Chemistry, Faculty of Pharmacy, Afyonkarahisar Health Sciences University, Afyonkarahisar, 03030, Türkiye*

ARTICLE INFO

Article history
Received: 23 August 2024
Revised: 14 October 2024
Accepted: 05 February 2025

Keywords:
Astragalus Lusitanicus; Biological Activity; Chemical Composition; Electrospinning; Nanofiber

ABSTRACT

Antibiotic resistance has emerged as a critical global health challenge, complicating the treatment of infectious diseases. The bioactive compounds present in plants offer promising avenues for addressing antibiotic resistance, particularly when combined with advanced biotechnological approaches. This study aimed to develop plant extract-loaded electrospun nanofibers for preventing biofilm-associated infections, with a focus on the antimicrobial and antibiofilm properties of *Astragalus lusitanicus* subsp. *orientalis*. Phytochemical analysis of the plant extract was conducted using liquid chromatography-electrospray tandem mass spectrometry, identifying hesperidin (7864 µg/g) as the most abundant compound, followed by quercetin (2223 µg/g) and hyperoside (1804 µg/g). Electrospun nanofibers were successfully fabricated, incorporating the plant extract, and characterized using scanning electron microscopy, and Fourier-transform infrared spectroscopy. *In vitro* tests revealed the nanofibers' favorable properties, including uniform morphology, flexibility, and ease of handling. Antimicrobial activity was evaluated via disc diffusion and broth microdilution assays, demonstrating significant effects against *Klebsiella pneumoniae* (24±1.25 mm zone of inhibition) and other pathogens at varying concentrations. Notably, *Staphylococcus aureus* ATCC 25923 and *Bacillus subtilis* NRS 744 were resistant. Antibiofilm assays showed that plant extract-loaded nanofibers and the plant extract inhibited biofilm formation by 96% and 82%, respectively, against biofilm-producing *Staphylococcus aureus* ATCC 25923, as confirmed by SEM. This study highlights the potential of *Astragalus lusitanicus* subsp. *orientalis* as a source of antimicrobial agents and demonstrates the synergistic benefits of integrating its extract into nanofibers. The findings provide a foundation for industrial applications in antimicrobial therapies and tissue engineering, emphasizing the high biocompatibility and controlled release properties of the nanofiber system. For the first time, the antibiofilm effects of this plant species are reported, underscoring its potential in accelerating the healing process and combating biofilm-associated infections.

Cite this article as: Erdoğmuş SF, Sarıkurkcu C. Development of plant extract-loaded electrospun nanofiber for the prevention of biofilm-associated infections. Sigma J Eng Nat Sci 2026;44(1):423–438.

***Corresponding author.**
*E-mail address: feyza.erdogmus@afsu.edu.tr

This paper was recommended for publication in revised form by Editor-in-Chief Ahmet Selim Dalkilic

Published by Yıldız Technical University Press, İstanbul, Turkey
© Author. This is an open access article under the CC BY-NC license (http://creativecommons.org/licenses/by-nc/4.0/).

INTRODUCTION

Antibiotics are typically employed in the treatment of infectious diseases. However, the emergence of antibiotic resistance has emerged as a significant global concern. Therefore, the treatment of infectious diseases by these microorganisms has become difficult. In addition, some microorganisms produce biofilm and researchers have determined that biofilm-producing bacteria can be 100-10000 times more antibiotic-resistant to planktonic forms [1].

A biofilm is defined as an aggregated community of bacterial cells, encased in an extracellular matrix comprising various types of extracellular polymeric substances. These include exopolysaccharides, proteins, lipids, biosurfactants, and extracellular DNA. Biofilm-producing bacteria exhibit resistance to antimicrobial agents, antibiotics, and harsh environmental conditions due to their protected, sessile state [2]. This biofilm-associated infection affects millions of people worldwide. Previous reports have highlighted the relationship between biofilm formation, antibiotic resistance, and the use of antibiofilm agents to prevent biofilm formation [3]. In recent years, there has been a notable interest in the investigation of natural and synthetic antimicrobial and antibiofilm compounds [4].

It has been documented that the therapeutic effects of plants are due to the synergistic effect of many components rather than a single active ingredient and that they provide a more effective treatment by resisting the resistance of microorganisms that are difficult to kill with antibiotics [5, 6]. This situation leads researchers to search for natural antimicrobial agents obtained from plant extracts [7-9].

The members of the genus Astragalus have a great interest in traditional drugs in Turkish folk medicine. Astragalus is a large genus of vascular plants from the Legominales tribe and Fabaceae family [10]. Astragalus species are a source of polysaccharides, phenolic, and saponins and they are usable for applications in the food, cosmetic, and pharmaceutical industries [11].

The formulation of nanofibres loaded with bioactive ingredients for biomedical purposes has recently attracted a great deal of attention [12,13]. The integration of bioactive components into delivery systems have been modified to facilitate the enhancement of the following qualities: solubility, bioavailability, stability, pharmacological activity, and protection from both physical and chemical degradation. A variety of novel herbal drug delivery systems have been developed recently [14-16]. Electrospinning is a versatile, simple, effective, and widely used technique for generating nanosized fibers [17]. Electrospun nanofibers are used as wound dressings, scaffolds, and drug release systems due to their resemblance to the natural extracellular matrix, high surface area, and improved mechanical performance [18]. The researchers have revealed that nanofibers can be used as drug delivery systems in various disease treatments. Particularly, nanofibers obtained by using the electrostatic spinning method are advantageous in terms of loading the desired amount of drug and controlling the release of hydrophilic drugs. In this study, nanofibers were obtained from polymer blends of polycaprolactone, sericin, and gelatin using electrostrospinning. Polycaprolactone is biocompatible, biodegradable, non-toxic, electrostatic spinnability, and similar to extracellular matrices. This makes them advantageous for nanofiber production. Sericin and gelatin are hydrophilic, biocompatible, important biomaterials that can be used in medical and cosmetic fields [19]. There are a limited number of studies on extract-loaded electrospun nanofibers for biomedical applications [20]. Therefore, it is important to determine the chemical contents and biological activities of plants and reveal their potential for use in biotechnological studies. To the best of our knowledge, no previous investigation has been reported regarding the chemical composition, biological activity, and potential biotechnological applications of Astragalus lusitanicus subsp. orientalis. The objective of this study is to ascertain the chemical composition of the methanol extract from Astragalus lusitanicus subsp. orientalis and to investigate its in vitro antimicrobial and antibiofilm activities, to assess its potential for biotechnological applications.

MATERIALS AND METHODS

Preperation of Methanol Extract

The aerial parts of Astragalus lusitanicus Lam. subsp. orientalis Chater & Meikle were collected during the flowering period from a rocky area alongside the roadside in Sakar Tepe province, Muğla/Turkey (37° 03’ 67” N 28° 21’ 45” E) at an altitude of 450 meters. These collected samples were subjected to drying in a controlled environment with low humidity, good airflow, and protection from direct sunlight, after which they were finely powdered. For the preparation of a methanol extract of A. lusitanicus subsp. orientalis (AL-MeOH), a modified ultrasonic extraction method was employed [21].

Determination of Phenolic Contents of Methanol Extract

The total phenolic and flavonoid contents of the methanol extract were initially determined spectroscopically. Subsequently, the presence of 30 phenolic compounds in the extract was investigated using a previously validated method [22] employing Liquid Chromatography-Electrospray Tandem Mass Spectrometry (LC–ESI–MS/MS).

Fabrication of Electrospun Nanofiber

The electrospinning processes were carried out by the Electrospinning System (Idasonic, Ave Spn L30, Turkey). The electrospinning condition consists of polymer solutions as shown in Table 1. Polycaprolactone (PCL), sericin, gelatin, and all other solvents were purchased from Sigma-Aldrich. In the electrospinning procedure: PCL was dissolved in trifluoroethanol (TFE) and sericin and gelatin

Table 1. Electrospinning conditions and preparation of polymer solutions

Formula code	The concentration of polymer (w/v)	Electrospinning process parameters				
		Flow rate (mL/h)	Voltage (kV)	Spinerette-collector distance (mm)	Drum speed (rpm)	Oscillation range (mm)
N_1	10% PCL, 8% sericin and 5% gelatin (7:2:1)	0.30	20	150	50	15
N_2	10% PCL, 6% sericin and 5% gelatin (7:2:1)	0.25	15	150	50	15
N_3	12% PCL, 8% sericin and 5% gelatin (6:3:1)	0.50	20	150	50	15
N_4	12% PCL, 8% sericin and 5% gelatin (7:2:1)	0.70	15	150	50	15
N_5	12% PCL, 8% sericin and 5% gelatin (7:2:1)	0.30	20	150	50	15
N_6	12% PCL, 8% sericin and 5% gelatin (7:2:1)	0.30	20	100	50	15
N_7	12% PCL, 10% sericin and 5% gelatin (7:2:1)	0.50	15	150	50	15
N_8	12% PCL, 10% sericin and 5% gelatin (7:2:1)	0.50	20	100	50	15

were dissolved in distilled water (dH_2O) by mixing with a magnetic stirrer at 50°C and 35°C, respectively until a homogeneous mixture was obtained [23]. Then polymer blends were prepared (Table 1).

Characterization of Nanofiber Structure

The nanofiber structures' images underwent analysis through scanning electron microscopy (SEM). Before imaging with an LEO 1430 VP SEM (Carl Zeiss AG, Jena, Germany) at an accelerating voltage of 20 kV, the samples underwent sputter-coating with gold for 30 s at 100 mA. The ImageJ program was used to determine the nanofibers' diameters.

For Fourier transform infrared spectroscopy (FTIR) analysis (Perkin Elmer Spectrum Two spectrometer), each sample was pulverized and mixed with potassium bromide (KBr). The suspension was pressed into a transparent pellet and analyzed in absorbance mode within the range of 400-3600 cm^{-1}.

The nanofiber samples were analyzed using a Bruker D8 Advance diffractometer (Cu Kα radiation) with a scanning rate of 0.025°/s over a 2θ range of 2° to 60°, at 30 kV and 40 mA.

Fabrication of *Astragalus Lusıtanıcus* Extracts Loaded Nanofiber

Among the electrospun formulas in Table 1, the N_6 formula was evaluated more suitable formula by SEM analysis therefore, the fabrication of *A. lusitanicus* extracts-loaded nanofiber was carried out with the N_6 formula. The N_6 formula was prepared as shown in Table 1 and 1% *A. lusitanicus* extracts were added polymer solution.

***In Vitro* Release Test**

Firstly, plant extracts were dissolved in phosphate-buffered saline (PBS) at two-fold serial dilutions concentrations (0.78 to 100 mg/mL), and the absorbances were measured with a spectrophotometer at 520 nm and a standard calibration curve was prepared. To examine the release profiles of nanofiber (N_6) and AL-MeOH loaded nanofiber ($N_{6\text{-AL-MeOH}}$), the samples were cut into 1 cm x 1 cm and placed into tubes that contained PBS buffer (pH:7,4) and incubated in a water bath at 37°C. Samples were taken from the medium at certain time intervals (0, 3, 5, 10, 20, 30, 40, 60, 80, 100, and 120 min) and absorbance was measured by spectrophotometer [24].

***In Vitro* Swelling Test**

The dry weight of the N_6 and $N_{6\text{-AL-MeOH}}$ was measured for the determination of swelling (%). The nanofibers were placed in tubes that contained PBS (pH 7.4) and incubated in a water bath at 37 °C. The nanofiber samples were removed from the PBS at specific time intervals (0, 10, 20, 30, 40, 60, 80, 100, 120, 140, 180, and 220 min). Excess water was removed using filter paper, and the samples were reweighed. The percentage swelling of the nanofiber was calculated using equation (1) [25]:

$$Swelling\ (\%) = [(W_w - W_d)/W_d] \times 100 \quad (1)$$

Ww and Wd represent the wet and dry nanofibers weight, respectively.

In Vitro Biodegradation Test

The N_6 and $N_{6\text{-AL-MeOH}}$ samples were cut into 2.5 cm × 2.5 cm pieces. The initial weight of each specimen was measured before being placed in test tubes containing 30 mL of PBS (pH 7) for an *in vitro* degradation study. The tubes were then incubated at 37°C and 150 rpm and observed for 14 days. Triplicate specimens for each sample condition were removed from the tubes at different time intervals. The samples were rinsed with distilled water two to three times and dried using filter paper followed by vacuum for three days. The percentage of nanofiber biodegradation was determined using equation (2) [26]:

$$Biodegradation\ (\%) = [(W_0 - W_1)/W_1] \times 100 \qquad (2)$$

W_1 and W_0 are the weight of samples after degradation and the initial weight before degradation, respectively.

Evaluation of *In Vitro* Antimicrobial Activity

The antimicrobial activities were examined against *Listeria monocytogenes* ATCC 19115, *Staphylococcus aureus* ATCC 25923, *Klebsiella pneumoniae* NRRLB 4420, *Pseudomonas aeruginosa* ATCC 11778, *Bacillus subtilis NRS 744*, *Escherichia coli* ATCC 35218, *Enterococcus faecalis* ATCC 51289, *Escherichia coli* ATCC 25922. Test microorganisms were obtained from the bacterial culture collection of the Faculty of Pharmacy, Afyonkarahisar Health Sciences University (Afyonkarahisar, Turkey), and used in this study. The antimicrobial of AL-MeOH extract was evaluated by disc diffusion and broth microdilution assay [27, 28]. For the broth microdilution test, a stock solution of each extract was diluted in the Mueller Hinton Broth (MHB) in two-fold serial dilutions to obtain concentrations from 1.56 to 100 mg/mL at a total volume of 100 µL per well in 96-well microtiter plates. 100 µL of each pathogen test microorganism was added to each well at a final concentration of 1×10^6 cfu/mL and incubated at 37°C, for 24 h. The medium, 0.1% (w/v) penicillin, and dH_2O were used as the non-treated, positive, and negative controls, respectively.

In disc diffusion assay; bacteria cultured prepared in MHB at 37°C, 24 h, and then its turbidity was adjusted to equal to 0,5 Mc Farland turbidity. 10 µL of each extract (10 mg/mL and 100 mg/mL concentrations of AL-MeOH dropped on sterile discs (zone diameter 6 mm) under aseptic conditions. 0,1 mL of each bacteria culture was spread on Mueller Hinton Agar (MHA) and then discs were placed on petri dishes and incubated at 37°C for 24 h. After the incubation period, inhibition zone diameters were measured and evaluated in comparison with the control group. 10 mg/mL of penicillin G and dH_2O were used as a positive and negative control, respectively. The diameter of growth inhibition zones was measured in millimeters. In addition, N_6 and $N_{6\text{-AL-MeOH}}$ samples were cut into 1 cm × 1 cm pieces and the same procedure was carried out for nanofibers.

Investigation of Antibiofilm Effects Against *Staphylococcus Aureus*

The biofilm inhibition effects of AL-MeOH extract were evaluated by a 3-[4,5-dimethyl-2-thiazolyl]-2, 5-diphenyl-2H-tetrazolium-bromide (MTT) colorimetric method with modification [29]. In this procedure; 1000 µL of each ½ x MIC, MIC, and 2 x MIC concentration of AL-MeOH were added to 24-well microtiter plates. N_6 and $N_{6\text{-AL-MeOH}}$ were cut into 1 x 1 cm pieces and placed into 24-well microtiter plates. Penicillin G (30 mg/mL) was used as the positive control and the medium was used as a negative control. An equal volume of the *S. aureus* ATCC 25923 (1×10^6 cfu/mL) which was determined biofilm producer in the previous study was added to 24-well microtiter plates except in the well with medium alone and incubated at 37°C for 6 and 24 h. The supernatants were discarded, and the cells were washed three times with PBS. Next, 1500 µL of PBS and 500 µL of MTT (0.3%) were added to each well, and the plate was incubated for 2 hours at 37°C. After incubation, the MTT solutions were removed, and 1500 µL of Dimetil sülfoksit (DMSO) and 250 µL of 0.1 M glycine buffer (pH 10.2) were added to each well to dissolve the formazan crystals. The plate was then incubated for 15 minutes at ambient conditions. Finally, the optical density was measured at a wavelength of 570 nm using a microplate spectrophotometer. The experiment was conducted in triplicate. To calculate the percentage of biofilm inhibition, the following equation (3) was used [29].

$$Inhibition\ (\%) = \left[1 - \left(\frac{A_{570} of\ the\ test}{A_{570} of none\ teated\ control}\right)\right] \times 100 \qquad (3)$$

Determination of Biofilm Structure by Scanning Electron Microscope

For this procedure, ½ x MIC, MIC, and 2 x MIC concentrations of AL-MeOH were added to the 24-well flat-bottom plate containing 14 x 14 mm polylysine slides. The N_8 and $N_{8\text{-AL-MeOH}}$ structures were cut into 1 x 1 cm and placed into 24-well microtiter plates. Then 1000 µL of *S. aureus* ATCC 25923 cultures (1×10^6 cfu/mL) were added to 24-well microtiter plates and incubated for 6 and 24 h at 37°C. At the end of the application periods, the incubation was stopped and the materials were left in the primary fixative (2.5% glutaraldehyde solution prepared in PBS) at 4°C for 24 h. The samples were washed three times with PBS for 15 minutes, then removed from the fixative and kept in the dark in the rotator for 1 hour in the secondary fixative containing Osmium tetroxide (OsO_4). Then they were washed with PBS and the samples were dehydrated with ethyl alcohol (50%, 70%, 90%, 95%, and 100%) by Polaron CPD Critical Point Dryer. Finally coated with gold-palladium using the Polaron SC7620 Sputter Coater. The samples were imaged by a SEM. (JEOL JSM-5600LV) [30].

Statistical Analysis

The experiments were performed three times, and the outcomes were presented as the average and standard deviation of three parallel measurements.

RESULTS AND DISCUSSION

Determination of the chemical compositions and biological activities of the medicinal and aromatic plants is very important in terms of revealing their potential to treat various diseases. In addition, these plants can be used together with biotechnological studies to increase their efficiency [31]. Plants are a source of many chemical compounds with antimicrobial activity and the potential to have the potential to treat antimicrobial-resistant infections. In recent years, health concerns related to the side effects of synthetic compounds and the emergence of antibiotic resistance in pathogens have led to the development of electrospinning research towards the development of plant extracts loaded nanofibers [32]. Thus, in the present study, the chemical content and biological activity of the methanol extract of *A. lusitanicus* were determined and plant extract-loaded nanofiber was obtained, successfully. The anti-biofilm effect of plant extract and extract-loaded nanofiber was investigated for the first time. The methanol extract from *A. lusitanicus* subsp. *orientalis* was obtained using ultrasound-assisted extraction, and the extract yield was found to be 8.7%. Subsequently, the total phenolic and flavonoid contents of the methanol extract were determined spectroscopically as 26.5 mg gallic acid equivalents (GAEs)/g and 25.0 mg rutin equivalents (REs)/g, respectively (Figure 1).

To identify and quantify the presence of 30 phytochemicals in the extract, LC–ESI–MS/MS was utilized, and the main components identified were hesperidin, quercetin, and hyperoside (Table 2). Hesperidin was found to be the most abundant compound, with a concentration of 7864 µg/g, followed by quercetin (2223 µg/g) and hyperoside (1804 µg/g).

Table 2. Concentration of selected phenolic compounds in the methanol extract

Compound	Concentration (µg/g extract)
Gallic acid	326 ± 4
Protocatechuic acid	617 ± 7
Pyrocatechol	nd
3,4-Dihydroxyphenylacetic acid	0.96 ± 0.14
(+)-Catechin	nd
2,5-Dihydroxybenzoic acid	11.4 ± 0.5
Chlorogenic acid	244 ± 2
3-Hydroxybenzoic acid	9.16 ± 0.21
4-Hydroxybenzoic	190 ± 1
(-)-Epicatechin	1.76 ± 0.07
Caffeic acid	98.7 ± 0.8
Syringic acid	3.99 ± 0.40
Vanillin	12.1 ± 0.5
Verbascoside	nd
Taxifolin	nd
p-Coumaric acid	71.6 ± 0.6
Sinapic acid	2.49 ± 0.23
Ferulic acid	39.7 ± 1.2
Luteolin 7-glucoside	6.96 ± 0.44
Hesperidin	7864 ± 100
Hyperoside	1804 ± 22
Rosmarinic acid	11.7 ± 2.8
Apigenin 7-glucoside	17.9 ± 0.7
Pinoresinol	14.0 ± 0.5
2-Hydroxycinnamic acid	nd
Eriodictyol	nd
Quercetin	2223 ± 55
Luteolin	0.78 ± 0.03
Kaempferol	85.9 ± 0.4
Apigenin	nd

nd: Not detected.

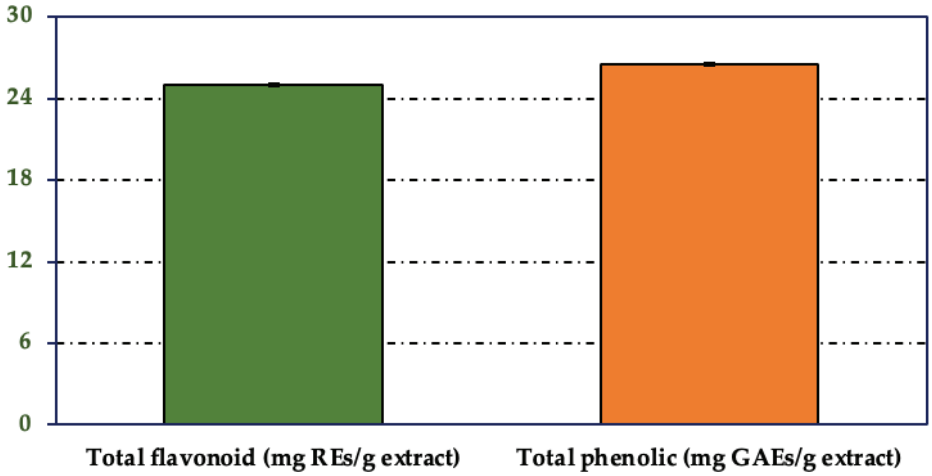


Figure 1. Total phenolic and flavonoid contents of the methanol extract (GAEs and REs: Gallic acid and rutin equivalents, respectively).

The methanol extract exhibited significant levels of total phenolic and flavonoid contents. These findings indicate that the extract possesses a high concentration of phenolic compounds and flavonoids, which are well-known for their potential health benefits. Phenolic compounds and flavonoids are known for their antioxidant properties and have been associated with various biological activities, such as anti-inflammatory, antimicrobial, and anticancer effects [33]. The observed levels of total phenolic and flavonoid content in the methanol extract suggest its potential as a valuable source of natural bioactive compounds, which could be explored for various applications in the fields of pharmaceuticals, nutraceuticals, and functional foods.

The LC-MS/MS analysis revealed the presence of prominent components in the methanol extract including hesperidin, quercetin, and hyperoside. As far as our literature survey could ascertain, no study has been found on the chemical composition of *A. lusitanicus* subsp. *orientalis*. However, there are phytochemical studies conducted on other *Astragalus* species. It has been reported that the methanol extract from the aerial parts of *Astragalus gymnolobus* is rich in hesperidin and hyperoside [34]. Haşimi et al. [35] conducted studies on other *Astragalus* species to identify a total of twenty-four phenolic compounds and three non-phenolic organic acids in three *Astragalus* species, wherein varying amounts of hesperidin and hyperoside were found to be the most abundant flavonoids. Moreover, Sarikurkcu and Zengin [36] detected hyperoside, apigenin, p-coumaric acid, and ferulic acid as the main compounds in different parts of *A. macrocephalus* subsp. *finitimus*. Similarly, Arumugam et al. [37] identified seven phytochemicals (syringe acid, p-coumaric acid, o-coumaric acid, luteolin, ferulic acid, hesperidin, and benzoic acid) in methanolic extracts obtained from various parts of *A. ponticus*. The results of this study are consistent with the literature data regarding the phytochemical composition of *A. lusitanicus* subsp. *orientalis*.

The electrospun nanofibers of PCL/sericin/gelatin, which are biocompatible, biodegradable, and non-toxic, were obtained successfully and AL-MeOH loaded nanofiber was developed for a novel material for biomedical applications such as tissue engineering scaffolds, drug delivery, wound dressings, separation membranes, antibacterial coatings, regenerative medicine, and sensing/biosensing [38].

In this context, the electrospinning parameters, which include flow rate, voltage, spinnerette-collector distance, drum speed, oscillation range, and polymer blending ratio, were optimized. After optimization of conditions, the PCL/chitosan/sericin electrospun nanofiber, which is bead-free fiber with minimum diameter and homogeneously distributed was successfully obtained.

The needle's electrospun parameters were determined as 0.30 mL/h flow rate, 20 kV voltage, 100 mm spinnerette-collector distance, 50 rpm drum speed, 15 mm oscillation range, and a blend of 12% PCL, 8% sericin and 5% gelatin (7:2:1), 1% AL-MeOH were found to be suitable. Polymeric materials, becoming smaller in scale with a large surface area to volume ratio, can provide improved biological properties of plant extracts. The primary advantage of plant-loaded nanofibers is their straightforward production and handling. They can be designed in a variety of sizes and shapes, are easily foldable, cut, shaped, rolled, or stored, and are relatively inexpensive [39].

The images of the SEM analyses of the electrospun nanofibers obtained are shown in Figure 2. The most suitable formula was determined as the N_6 formula, which has the lowest average fiber diameter, the most uniform morphological structure, and no beads structure observed (Table 1). The fiber diameter of N_6 was determined as average 110-150 nm.

AL-MeOH-loaded nanofiber was carried out with the N_6 formula and $N_{6\text{-AL-MeOH}}$ is shown in Figure 3. The fiber diameter of $N_{6\text{-Al-MeOH}}$ was determined as an average of 110-200 nm.

The N_6 possesses the features of being a nanosized and thin fiber structure with a smooth surface. Due to the incorporation of AL-MeOH, the formation of branching of fiber structure increased and the uniform fiber surface seems it did not change the fiber diameter of the $N_{6\text{-AL-MeOH}}$ nanofiber, significantly. The bioactive compounds present in the AL-MeOH extract occupied the porous surface of the electrospun nanofiber [20]. The diameter of $N_{6\text{-AL-MeOH}}$ has been slightly increased due to swelling. It is concluded that the morphology of the nanofibers was slightly affected by the plant extract.

The FTIR spectrum of N_6 and $N_{6\text{-AL-MeOH}}$ nanofibers are shown in Figure 4. The FTIR spectrum presents several bands at curve regions from about 3000 to 400 cm^{-1}. The bands observed at approximately 1600, 1300, and 1100 cm^{-1} in the FTIR spectrum are attributed to an aliphatic C-H, amide I (NH deformation–$NHCOCH_3$), amide II, amide III, and C-O vibrational tensional bonds, respectively. The spectrum of pure PCL nanofibers displays a prominent C=O (carbonyl) stretching band at 1723 cm^{-1}, a characteristic peak that can be observed in the spectra of other PCL-related compounds. We can observe bands corresponding to N_6 when analyzing the $N_{6\text{-AL-MeOH}}$ curve, which is indicative of the lack of any chemical reactions between extracts and polymers.

XRD patterns of N_6 and $N_{6\text{-AL-MeOH}}$ nanofibers are shown in Figures 5 and 6. According to the test result, there was a significant weakening of characteristic peaks of PCL at 20-23°. As can be noted, there are two distinct peaks in the PCL curve; by observing the XRD pattern, the loading of AL-MeOH extract into the PCL nanofiber has been verified.

The XRD of N_6 nanofibers (Fig. 5) shows peaks at 20-23° indicating the crystallinity of the PCL nanofibers. The increase in intensity indicates the increased degree of crystallinity. The XRD pattern implies that the AL-MeOH was successfully loaded in nanofiber.

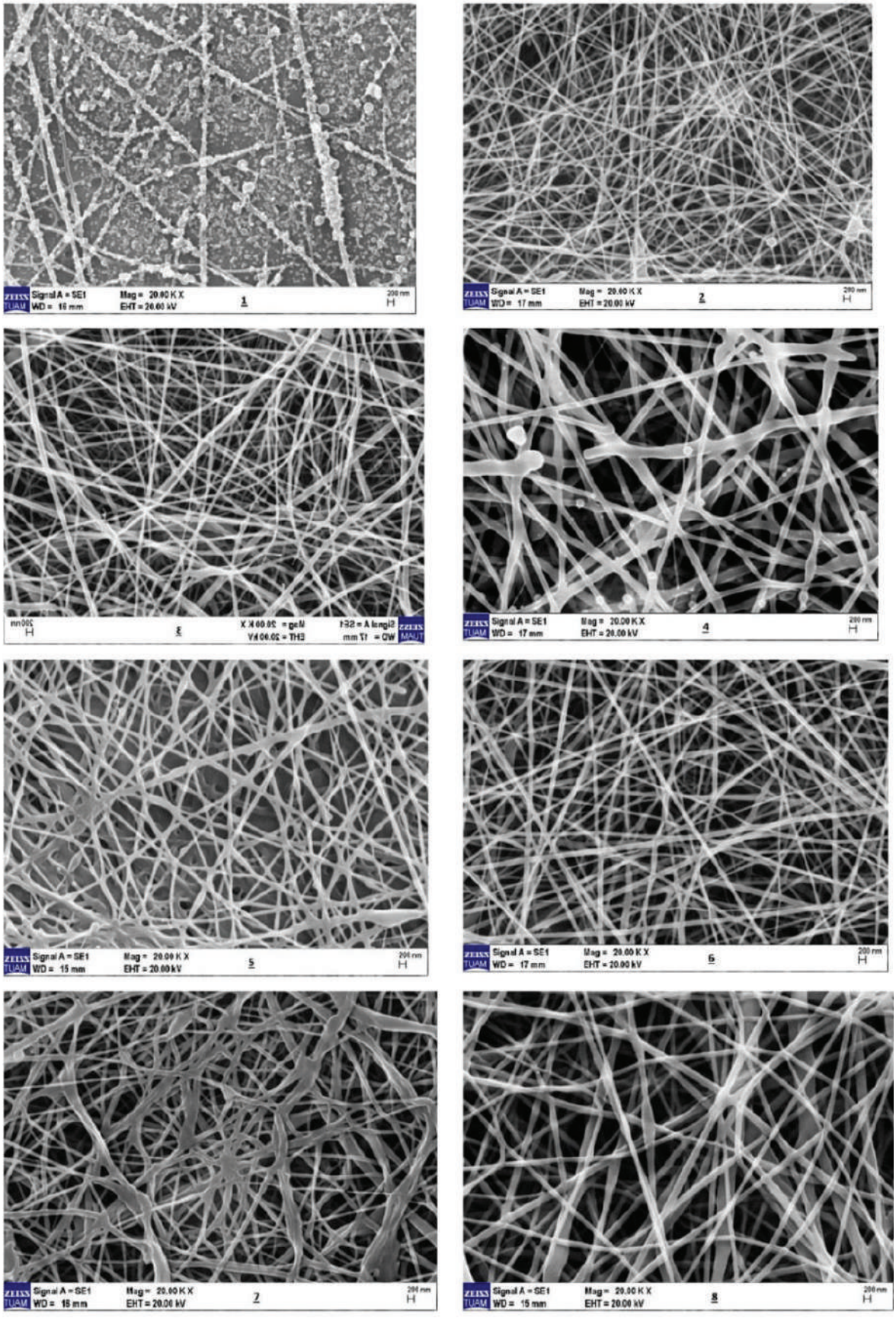


Figure 2. The images of the SEM analysis of the electrospun N_1-N_8 nanofibers (Table 1).

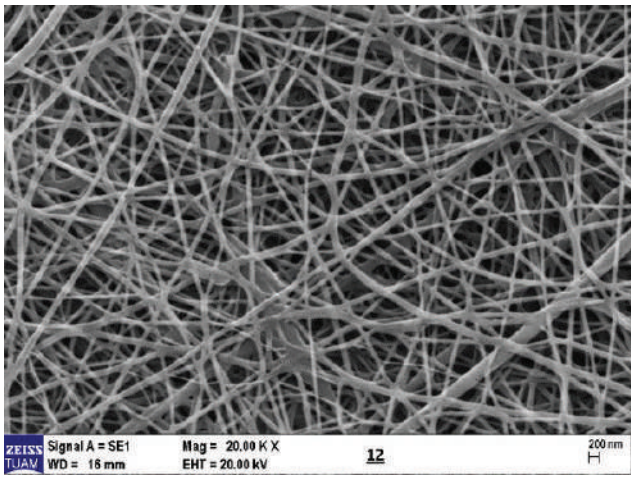


Figure 3. The SEM image of $N_{6\text{-AL-MeOH}}$.

Also in this study, N_6 and $N_{6\text{-AL-MeOH}}$ nanofibers were analyzed for *in vitro* swelling, extract release, and biodegradation tests. The wettability rate of nanofibers increased rapidly in the 20 minutes then the swelling rate of nanofibers increased more slowly and the swelling rate was fixed in 140-220 min (Fig. 7).

The swelling behavior of nanofibres is a crucial aspect of biomedical applications. The percentage of swelling in nanofibrous scaffolds is highly dependent on their porosity and surface area. The $N_{6\text{-AL-MeOH}}$ nanofiber showed about 89% of swelling behavior, which slightly increased when compared with N_6 nanofiber (67%). Generally, the water-absorbing capability is directly related to the sample's hydrophilicity, surface property, and porosity. In this case, sericin, and gelatin are hydrophilic and PCL is less

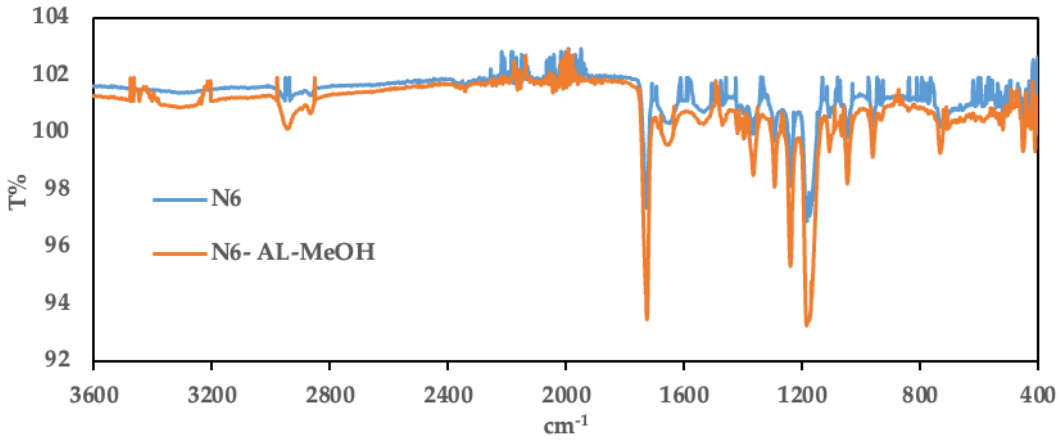


Figure 4. The FTIR spectra of N_6 and $N_{6\text{-AL-MeOH}}$.

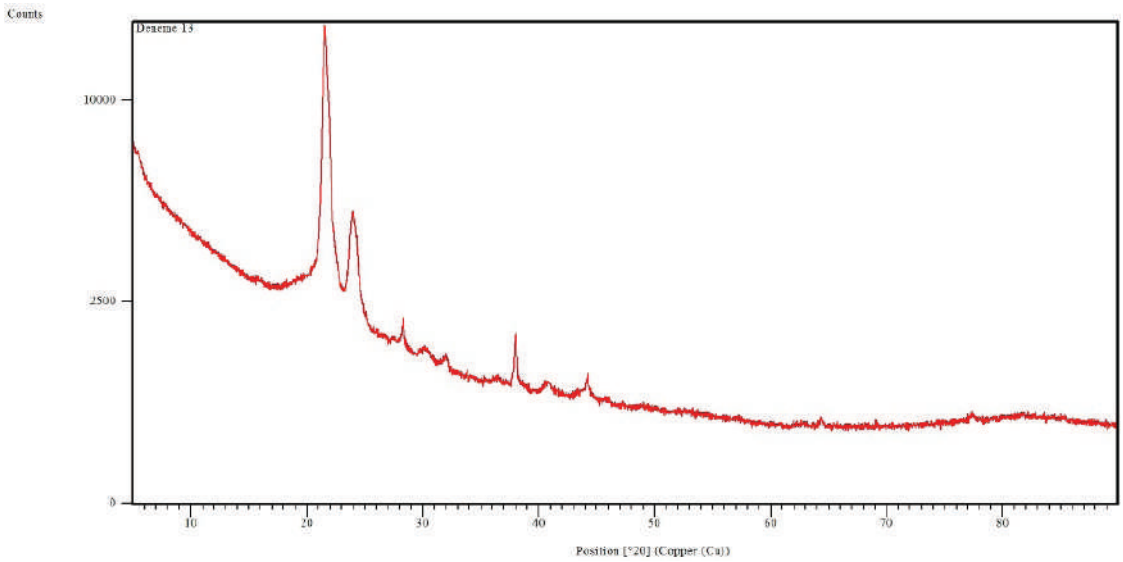


Figure 5. XRD pattern of N_6 nanofiber.

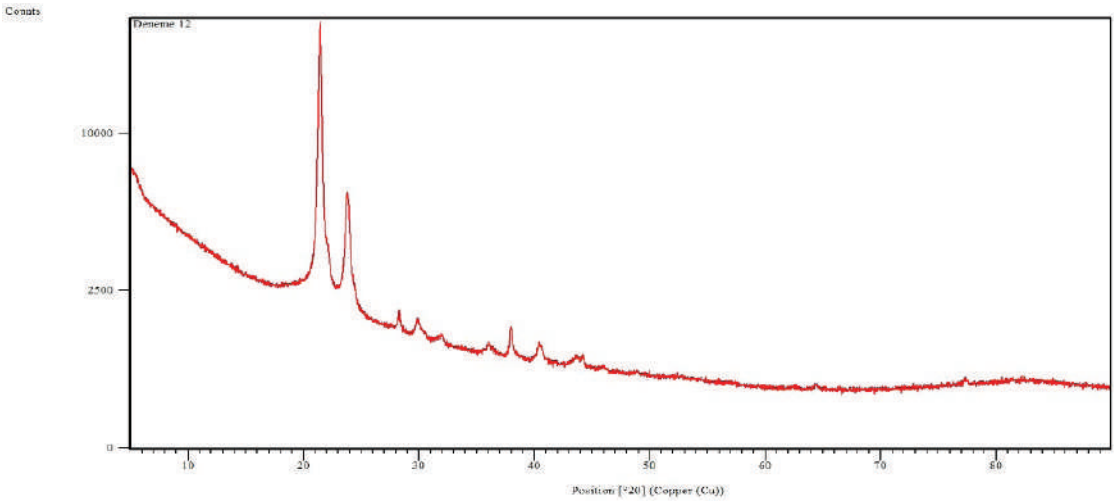


Figure 6. XRD pattern of $N_{6\text{-AL-MeOH}}$ nanofiber.

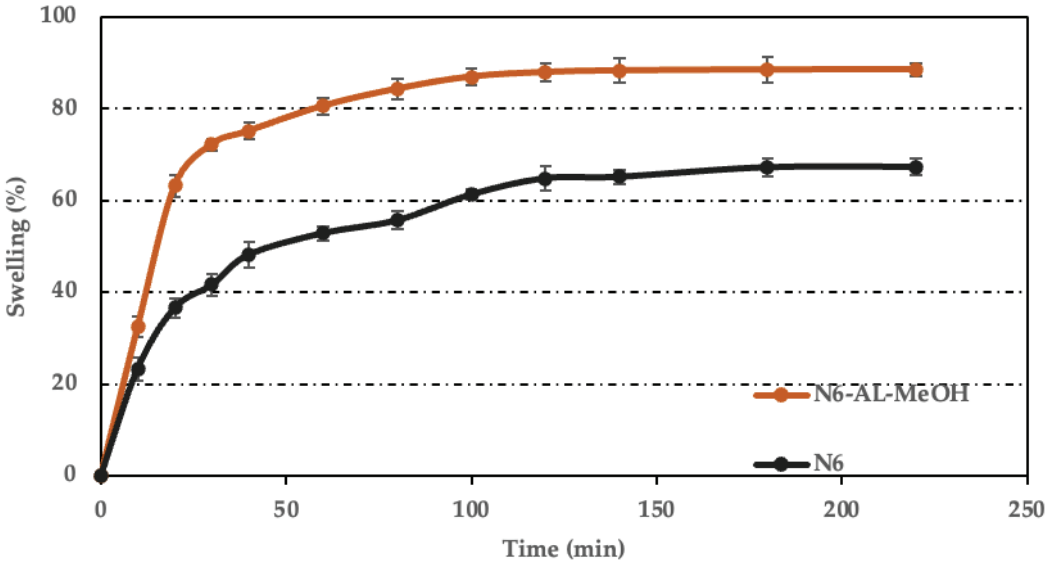


Figure 7. The results of the swelling ratios of nanofibers.

hydrophilic, though $N_{6\text{-AL-MeOH}}$ nanofiber has shown an increased swelling percentage.

The *in vitro* extract release was calculated using the standard calibration curve (R^2 = 0.9781). The rapid release of the extract of $N_{6\text{-AL-MeOH}}$ was determined for 40 minutes then it decreased (Fig. 8). The continuous plant extract release indicates that this nanofiber could be used in pathogen test microorganisms.

According to the *in vitro* biodegradation analysis, N_6, and $N_{6\text{-AL-MeOH}}$ nanofiber biodegraded 29.5% and 38.91%, respectively for the 14th day (Fig. 9)

The $N_{6\text{-AL-MeOH}}$ nanofiber shows progressive weight loss probably due to the hydrophilicity that will contact easily with PBS and degrade faster if the same conditions exist.

The results of *in vitro* extract release test the rapid release of extract of $N_{6\text{-AL-MeOH}}$ was determined for 40 minutes then it decreased. It can be seen that the N_6 and $N_{6\text{-AL-MeOH}}$ nanofibers have almost certainly constant weight because of their very slow degradation rate of 29.5% and 38.91%, respectively for the 14th day.

Al-Kaabi et al. [31] developed electrospun/polycaprolactone nanofibers loaded with *Inula graveolens* extract, which exhibit potential for biomedical applications. Another study by Suryamathi et al. [20] focused on the development of a novel wound dressing material using electrospun PCL nanofibers loaded with *Tridax procumbens* extracts. The findings from these studies support the notion that such scaffolds have the potential to enhance wound healing and

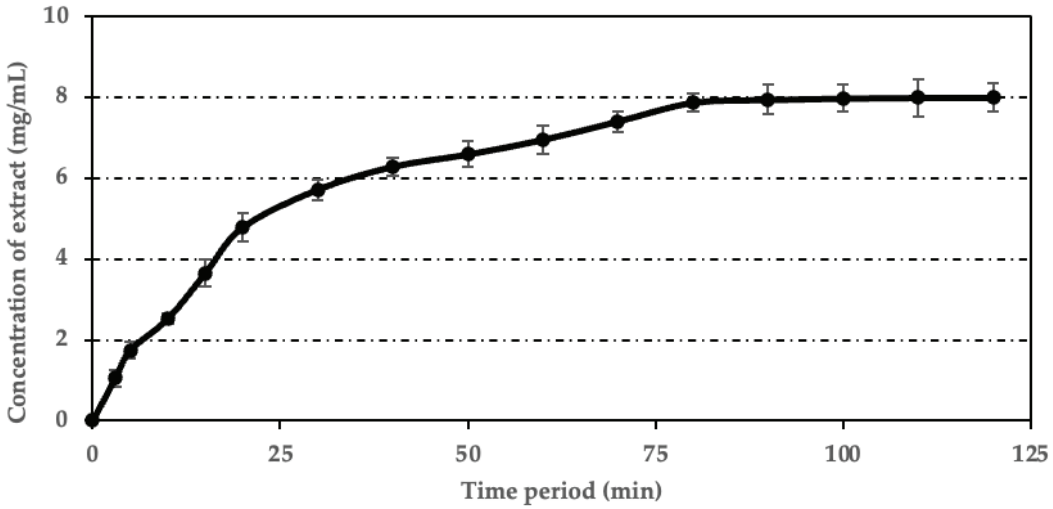


Figure 8. *In vitro* extract release of $N_{6\text{-AL-MeOH}}$.

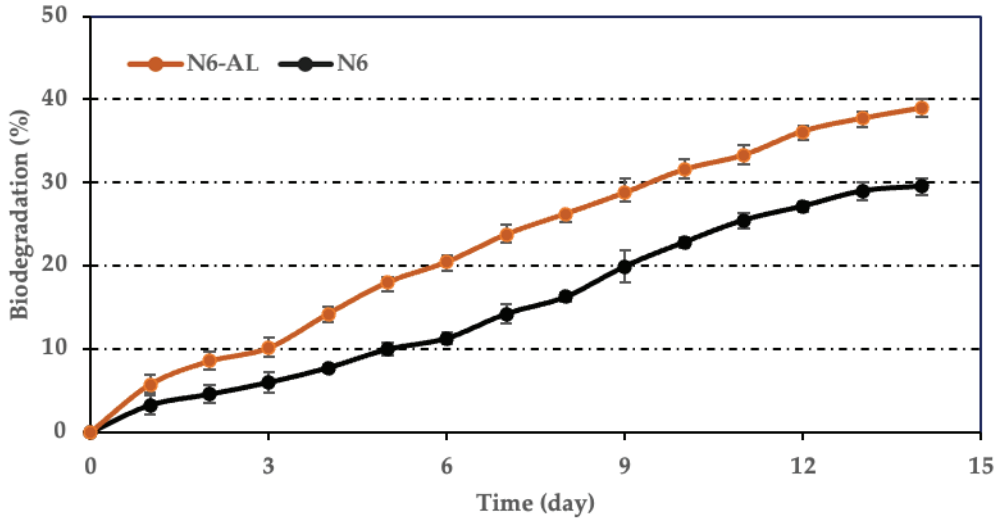


Figure 9. Biodegradation of N_6 and $N_{6\text{-AL-MeOH}}$ nanofibers.

effectively address surfaces contaminated with pathogenic microorganisms, especially within hospital environments.

In this study, MIC values of AL-MeOH against pathogenic test microorganisms were determined and are given in Table 3. The MIC value of AL-MeOH was determined as 50 mg/mL against *S. aureus* ATCC 25923 and, it was determined as 6.25 mg/mL against *E. faecalis* ATCC 51289, *P. aeruginosa* ATCC 11778, *E. coli* ATCC 35218, *E. coli* ATCC 25922, *B. subtilis* NRS 744. In addition, it was determined as 3.12 mg/mL against *L. monocytogenes* ATCC 19115 and *K. pneumoniae* NRRLB 4420.

In addition, the antimicrobial effect of AL-MeOH on pathogen test microorganisms was determined by disc diffusion assay and is shown in Table 4. It was determined that there was an increase in antimicrobial activity in parallel

Table 3. MIC values of AL-MeOH against pathogenic test microorganisms

Pathogen Test Microorganisms	MIC values of AL-MeOH (mg/mL)
L. monocytogenes ATCC 19115	3.12
S. aureus ATCC 25923	50.00
K. pneumoniae NRRLB 4420	3.12
P. aeruginosa ATCC 11778	6.25
E. faecalis ATCC 51289	6.25
E. coli ATCC 35218	6.25
B. subtilis NRS 744	6.25
E. coli ATCC 25922	6.25

Table 4. The results of the disc diffusion assay

Pathogen Test Microorganisms	NC	PC	N6	N6-AL-MeOH	AL-MeOH (10 mg/mL)	AL-MeOH (100 mg/mL)
L. monocytogenes ATCC 1911	-	25±0.00	10±0.25	15±0.50	12±0.25	19±1.22
S. aureus ATCC 25923	-	29±0.95	12±0.20	19±0.75	-	14±0.00
K. pneumoniae NRRLB 4420	-	30±1.25	11±0.50	17±1.00	14±0.50	24±1.25
P. aeuruginosa ATCC 11778	-	29±1.50	14±0.50	20±0.50	13±0.50	22±0.55
E. faecalis ATCC 51289	-	30±0.55	10±0.30	19±0.75	13±0.25	21±0.72
E. coli ATCC 35213	-	30±1.52	12±0.20	17±0.50	11±0.75	18±0.5
E. coli ATCC 25922	-	31±1.75	11±0.25	16±0.50	14±0.85	21±1.47
B. subtilis NRS 744	-	30±0.75	9±0.50	15±0.75	10±0.25	15±1.25

PC: Penicilin G (10 mg/mL). NC dH_2O. Resistant ≤ 14. Moderate 15-18. Sensitive ≥ 19

with the increase in the concentration of plant extracts. The results of zone diameters of the disk diffusion test evaluated as resistant ≤ 14, moderately sensitive 15-18, and susceptible ≥19 mm. The highest antimicrobial activity (24±1.25) was found in 100 mg/mL concentration of AL-MeOH against *K. pneumoniae* NRRLB 4420. *P. aeruginosa* ATCC 11778, *E. faecalis* ATCC 51289, *E. coli* ATCC 35213, *E. coli* ATCC 25922 were determined to be sensitive to 100 mg/mL Al-MeOH. *S. aureus* ATCC 25923 and *B. subtilis* NRS 744 were found to be resistant. All test microorganisms were found resistant to N_6 nanofiber. *S. aureus* ATCC 25923, and *E. faecalis* ATCC 51289 were determined as sensitive and the other microorganisms were found to moderate for $N_{6\text{-AL-MeOH}}$.

The results of the biofilm inhibitions of *S. aureus* ATCC 25923 are shown in Figure 10. The most effective $N_{6\text{-AL-MeOH}}$ group was determined as 96% inhibition for biofilm inhibitions of *S. aureus* ATCC 25923. Following this 2 x MIC of the AL-MeOH group was determined 82% biofilm inhibition.

The images of the biofilm structure are shown in Figure 11. It was determined that the bacteria were attached to the N_6 nanofiber and did not form a biofilm structure but the $N_{6\text{-AL-MeOH}}$ nanofiber was not attached for the 6th and 24th h.

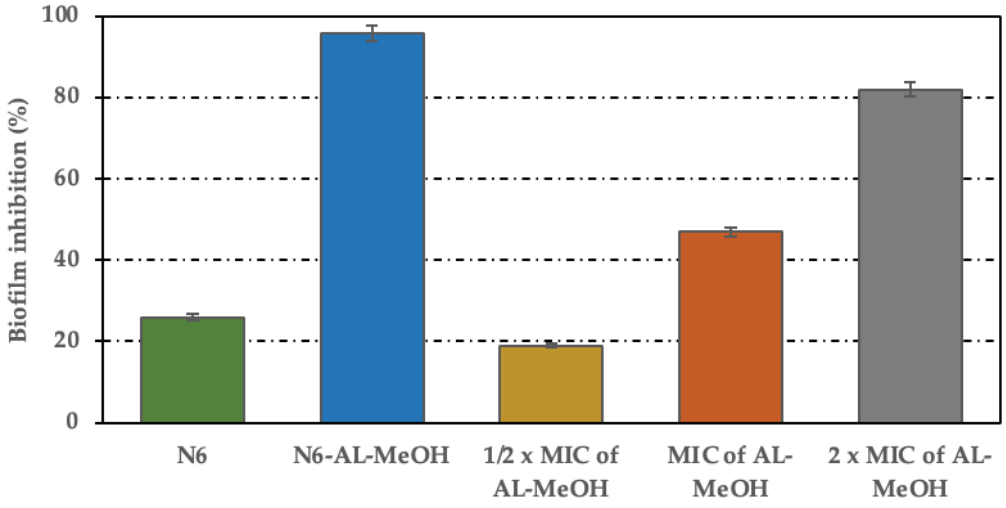


Figure 10. Biofilm inhibition of *Staphyllococcus aureus* ATCC 25923.

Akpınar et al. [40] investigated the antibacterial and antibiofilm activity of cinnamaldehyde-poly (lactic acid)/gelatin electrospun nanofibers. The antibacterial activity of the PLA-Gel-CA nanofibers against *S. aureus* and *P. aeruginosa*, along with their antibiofilm activity against *P. aeruginosa*, were evaluated. PLA-Gel-CA3 nanofibers demonstrated notable antibacterial efficacy against *S. aureus* (31.0 ± 1.20 mm) and *P. aeruginosa* (16.0 ± 1.20 mm), along with a significant inhibition of *P. aeruginosa* biofilm formation by 72.2%. These findings indicate the potential of cinnamaldehyde-loaded nanofibers for wound application owing to their antibacterial and antibiofilm activity, as well as their rapid dissolution characteristics.

The application of ½ x MIC of the AL-MeOH group the structural integrity of bacterial cells is preserved for 6th h but it was determined that the bacterial cell morphology was disrupted, the cells shriveled and there was biofilm inhibition for 24th h. It was determined that the cells were damaged and the cavity formation, fusion of cells, and biofilm inhibition occurred in the treatment of MIC of the AL-MeOH group for 6th h. In addition, it was determined that this situation increased even more, cellular structures were disrupted and cytoplasm loss was observed in the cell at the 24th h. The application of 2 x MIC concentration of the AL-MeOH group resulted in a decrease in the number of cells, disruption of structural integrity, cell fusion, and inhibition of biofilm formation at the 6th h. Moreover, this effect intensified, leading to complete deterioration and indistinguishability of cellular structures. In contrast, the control group exhibited a well-preserved biofilm structure in the exopolysaccharide layer at the 6th hour, and a dense biofilm structure with cell adhesion was observed at the 24th hour.

Bacterial infections are a leading cause of morbidity and mortality worldwide. Significant progress is being made in microbiological research to control many diseases caused by infectious organisms. The MIC value of AL-MeOH determined against pathogen test microorganisms and antibacterial activity has been studied by the disc diffusion assay. In addition, it is generally desired that biomedical materials have antimicrobial properties against bacterial infections. Therefore, the antimicrobial effect of N_6 and $N_{6\text{-AL-MeOH}}$ nanofibers was tested by disc diffusion test. According to the test results, the highest antimicrobial activity was found in 100 mg/mL concentration of AL-MeOH against *K. pneumoniae* NRRLB 4420. *P. aeruginosa* ATCC 11778, *E. faecalis* ATCC 51289, *E. coli* ATCC 35213, and *E. coli* ATCC 25922 were determined to be sensitive to 100 mg/mL AL-MeOH. *S. aureus* ATCC 25923 and *B. subtilis* NRS 744 were found to be resistant. In the present study, antibiofilm activities of Al-MeOH, N_6, and $N_{6\text{-AL-MeOH}}$ nanofibers were tested against biofilm producer *S. aureus* ATCC 25923. Antibiofilm test results revealed that the $N_{6\text{-AL-MeOH}}$ and 2 x MIC concentration of the AL-MeOH group were determined as 96% and 82% biofilm inhibition, respectively.

The researchers have demonstrated a relationship between polyphenols of plant extract with anti-inflammatory, antimicrobial, and antioxidant activity and they stimulate the proliferation and migration of fibroblast cells [30, 41]. It was suggested that a bioactive substance is responsible for the antimicrobial properties of AL-MeOH extracts. Although the exact mechanisms of its antibacterial action are not fully known, several mechanisms have been proposed, including activation of the host immune system, rupture of bacterial membranes, and microbial enzyme interference [42]. According to the SEM images of the biofilm structure, bacteria were attached to the N_6 nanofiber and did not form a biofilm structure but the N_6-AL-MeOH nanofiber was not attached for the 6th and 24th h. The application of extract groups the structural integrity of bacterial cells bacterial cell morphology was disrupted and shriveled depending on the concentration rate. It was determined that the cells were damaged and the cavity formation, fusion of cells, and biofilm inhibition occurred in the treatment of MIC and 2x MIC of the AL-MeOH group. In addition, it was determined that this situation increased even more, cellular structures were disrupted and cytoplasm loss was observed in the cell at the 24th h. The application of 2 x MIC of the AL-MeOH group was observed which decreased the number of cells, disruption of structural integrity, the fusion of cells, and inhibition of biofilm for 6th h, and this situation increased, cellular structures completely deteriorated and became indistinguishable. When the control group was evaluated, a very well-preserved biofilm structure was observed in the exopolysaccharide layer.

In a previous study, Hadisi et al. [43] investigated electrospun gelatin-oxidized starch nanofibres containing henna extract for the treatment of second-degree burn wounds This study demonstrated that the antimicrobial activity of the nano matrix can be attributed in part to the presence of various phenolic compounds, such as 2-hydroxy-1,4-naphthoquinone, in the henna extract, which can interact with the bacterial cell wall and inactivate its function, thus inhibiting microbial growth. Furthermore, other studies have demonstrated the efficacy of chemical compounds in inhibiting biofilm formation [4]. The antimicrobial and antioxidant status of four *Astragalus* species were determined [44]. Based on the results of the study, the extracts exerted moderate antioxidant and reducing activity with low phenolic content. The major constituent of the extracts was determined to be ferulic acid. The extracts did not show any antibacterial activity except *P. aeruginosa*. In another study, Adeli-Sardou et al. [45] investigated the antibacterial and antibiofilm effects of electrospun PCL/gelatin/lawsone nanofibres against biofilm-producing bacteria. The results of the study demonstrated the favorable antibacterial and antibiofilm properties of lawsone-containing scaffolds. Similarly, the results of the present study demonstrated that AL-MeOH, when loaded into a nanofiber, had a marked effect on biofilm inhibition. The findings of the present study indicate that the antimicrobial activity of the

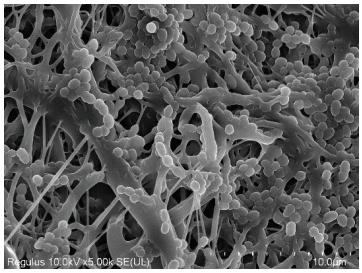
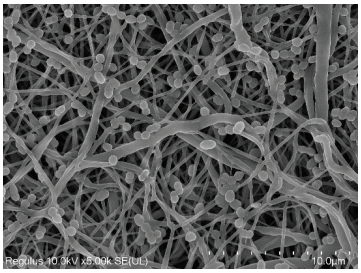
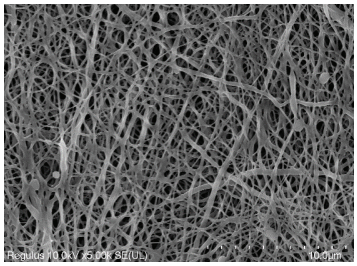
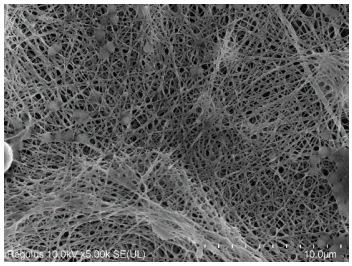
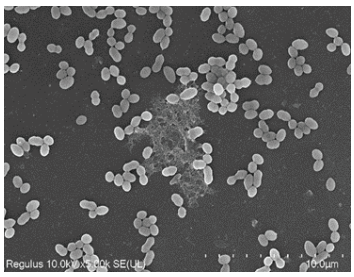
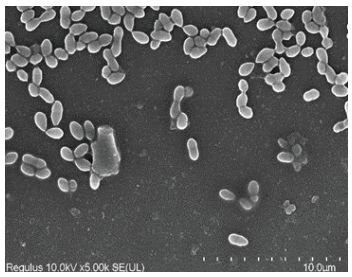
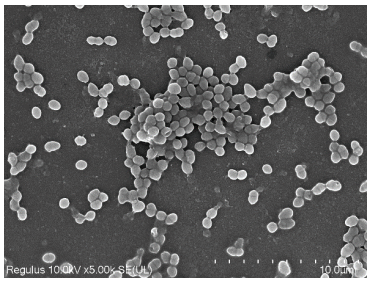
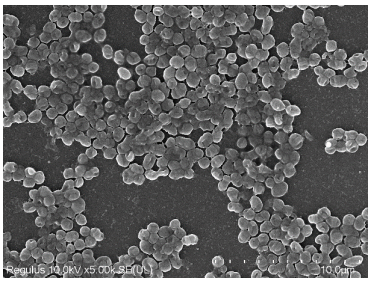
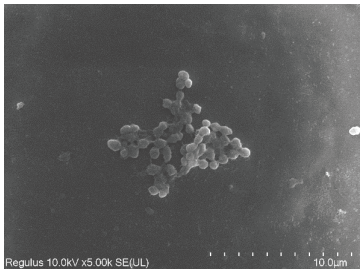
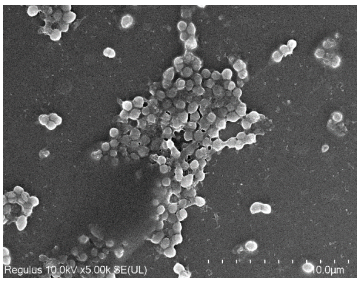
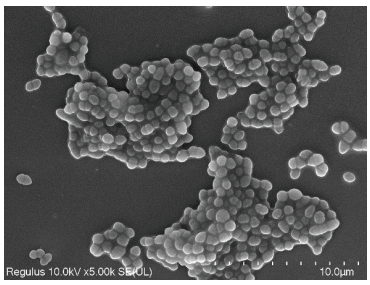
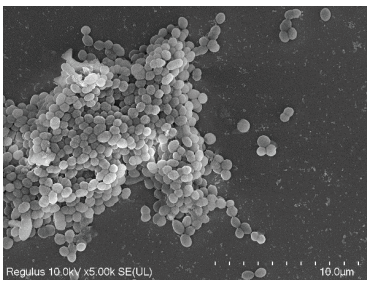
Name	Application Time	
	6 h	24 h
N_6		
N_6-AL		
AL-MeOH (1\2 x MIC)		
AL-MeOH (MIC)		
AL-MeOH (2 x MIC)		
Control		

Figure 11. SEM images of antibiofilm assay against *S. aureus* ATCC 25923 at 6 and 24 h.

nanofiber can be attributed, to the presence of various phenolic compounds such as hesperidin, quercetin, and hyperoside in the AL-MeOH. These compounds are capable of interacting with the bacterial cell wall, thereby inactivating its function and inhibiting microbial growth.

CONCLUSION

Astragalus lusitanicus subsp. *orientalis* plant extract's therapeutic potential in biofilm-associated infections has not yet been explored. To our knowledge, this is the first report on the biological and chemical study of *A. lusitanicus* subsp. *orientalis*. Hesperidin, quercetin, and hyperoside were determined as the major constituents of plant extract. Polycaprolactone/sericin/gelatin and plant extract-loaded nanofibers were developed using an electrospinning technique. Characterization analyses and the *in vitro* swelling, biodegradation, and extract release assays revealed that nanofiber and plant extract-loaded nanofiber are useful the biomedical applications. Both plant extract and extract-loaded nanofiber showed antimicrobial activity against pathogen test microorganisms. The results showed that the nanofibres loaded with the plant extract and the plant extract exhibited strong biofilm inhibition of 96% and 82%, respectively. Additionally, the results of this work indicate that the nanofibers act as promising agents for enhancing wound healing and treating surfaces contaminated with pathogenic microorganisms. Consequently, this study holds promise for the development of novel materials with potential antimicrobial properties derived from natural sources, thereby offering potential biomedical applications. Further studies are required to identify the active compounds responsible for the observed antimicrobial activity.

ACKNOWLEDGEMENTS

The authors would like to thank to Dr. Olcay Ceylan for his kind help in identifying the plant materials used in this study.

AUTHORSHIP CONTRIBUTIONS

Authors equally contributed to this work.

DATA AVAILABILITY STATEMENT

The authors confirm that the data that supports the findings of this study are available within the article. Raw data that support the finding of this study are available from the corresponding author, upon reasonable request.

CONFLICT OF INTEREST

The author declared no potential conflicts of interest with respect to the research, authorship, and/or publication of this article.

ETHICS

There are no ethical issues with the publication of this manuscript.

STATEMENT ON THE USE OF ARTIFICIAL INTELLIGENCE

Artificial intelligence was not used in the preparation of the article.

REFERENCES

[1] Hall-Stoodley L, Costerton JW, Stoodley P. Bacterial biofilms: from the natural environment to infectious diseases. Nat Rev Microbiol 2004;2:95–108. [CrossRef]

[2] DeLeon S, Clinton A, Fowler H, Everett J, Horswill AR, Rumbaugh KP. Synergistic interactions of Pseudomonas aeruginosa and Staphylococcus aureus in an in vitro wound model. Infect Immun 2014;82:4718–4728. [CrossRef]

[3] Shakibaie M, Forootanfar H, Golkari Y, Mohammadi-Khorsand T, Shakibaie MR. Anti-biofilm activity of biogenic selenium nanoparticles and selenium dioxide against clinical isolates of Staphylococcus aureus, Pseudomonas aeruginosa, and Proteus mirabilis. J Trace Elem Med Biol 2015;29:235–241. [CrossRef]

[4] Ahire JJ, Hattingh M, Neveling DP, Dicks LMT. Copper-containing anti-biofilm nanofiber scaffolds as a wound dressing material. PLoS One 2016;11:e0152755. [CrossRef]

[5] Sree KS, Yasodamma N, Chinthala P. Phytochemical screening and in vitro antibacterial activity of the methanolic leaf extract: Sebastiania chamaelea Muell. Bioscan 2010;5:173–175.

[6] Nazri NM, Ahmat N, Adnan A, Mohamad SS, Ruzaina SS. In vitro antibacterial and radical scavenging activities of Malaysian table salad. Afr J Biotechnol 2011;10:5728–5735.

[7] Dash BK, Sultana S, Sultana N. Antibacterial activities of methanol and acetone extracts of fenugreek (Trigonella foenum) and coriander (Coriandrum sativum). Life Sci Med Res 2011;27:1–8.

[8] Saddiqe Z, Naeem I, Maimoona A. A review of the antibacterial activity of Hypericum perforatum L. J Ethnopharmacol 2010;131:511–521. [CrossRef]

[9] Snoussi M, Ahmad I, Aljohani AMA, Patel H, Abdulhakeem MA, Alhazmi YS, et al. Phytochemical analysis, antioxidant, and antimicrobial activities of Ducrosia flabellifolia: A combined experimental and computational approaches. Antioxidants (Basel) 2022;112174. [CrossRef]

[10] Li X, Qu L, Dong Y, Han L, Liu E, Fang S, et al. A review of recent research progress on the Astragalus genus. Molecules 2014;19:18850–18880. [CrossRef]

[11] Hamedi A, Yousefi G, Farjadian S, Bour Bour MS, Parhizkar E. Physicochemical and immunomodulatory properties of gum exudates obtained from Astragalus myriacanthus and some of its isolated carbohydrate biopolymers. Iran J Pharm Res 2017;16(4):1520-1530.

[12] El-Naggar ME, Abdelgawad AM, Abdel-Sattar R, Gibriel AA, Hemdan BA. Potential antimicrobial and antibiofilm efficacy of essential oil nanoemulsion loaded polycaprolactone nanofibrous dermal patches. Eur Polym J 2023;184:111782. [CrossRef]

[13] Ndlovu SP, Motaung K, Adeyemi SA, Ubanako P, Ngema L, Fonkui TY, et al. Sodium alginate-based nanofibers loaded with Capparis sepiaria plant extract for wound healing. J Biomater Sci Polym Ed 2024;35:2380-2401. [CrossRef]

[14] Di Salle A, Viscusi G, Di Cristo F, Valentino A, Gorrasi G, Lamberti E, et al. Antimicrobial and antibiofilm activity of curcumin-loaded electrospun nanofibers for the prevention of the biofilm-associated infections. Molecules 2021;26:4866. [CrossRef]

[15] Hamidi E, Alhaloush R, Şenol Ş, Akyol E. An overview on current trends and future outlook of hydrogels in drug delivery. Sigma J Eng Nat Sci 2023;41:1047–1061. [CrossRef]

[16] Kaya S, Derman S. Production, characterization and antioxidant activity evaluation of quercetin loaded PLGA nanofibers. Sigma J Eng Nat Sci 2022;40:433–440.

[17] Roshanfar F, Hesaraki S, Dolatshahi-Pirouz A. Electrospun silk fibroin/kappa-carrageenan hybrid nanofibers with enhanced osteogenic properties for bone regeneration applications. Biology (Basel) 2022;11. [CrossRef]

[18] Schiffman JD, Schauer CL. One-step electrospinning of cross-linked chitosan fibers. Biomacromolecules 2007;8:2665–2667. [CrossRef]

[19] Arun A, Malrautu P, Laha A, Ramakrishna S. Gelatin nanofibers in drug delivery systems and tissue engineering. Eng Sci 2021;16:71–81.

[20] Suryamathi M, Ruba C, Viswanathamurthi P, Balasubramanian V, Perumal P. Tridax procumbens extract loaded electrospun PCL nanofibers: A novel wound dressing material. Macromol Res 2019;27:55–60. [CrossRef]

[21] Latiff NA, Ong PY, Abd Rashid SNA, Abdullah LC, Mohd Amin NA, Fauzi NAM. Enhancing recovery of bioactive compounds from Cosmos caudatus leaves via ultrasonic extraction. Sci Rep 2021;11:17297. [CrossRef]

[22] Cittan M, Çelik A. Development and validation of an analytical methodology based on liquid chromatography–electrospray tandem mass spectrometry for the simultaneous determination of phenolic compounds in olive leaf extract. J Chromatogr Sci 2018;56:336–343. [CrossRef]

[23] Erdoğmuş SF, Altıntaş ÖE, Çelik S. Production of fungal chitosan and fabrication of fungal chitosan/polycaprolactone electrospun nanofibers for tissue engineering. Microsc Res Tech 2023;86:1309–1321. [CrossRef]

[24] Cesur S. Production of gentamycin-loaded Poly(Vinyl Alcohol)/Gelatin nanofiber by electrospinning method as wound dressing material. Konya Muhendislik Bilim Derg 2022;10:878–888. [Turkish] [CrossRef]

[25] Ahamed N, Sastry T. Wound dressing application of chitosan based bioactive compounds. Int J Pharm Life Sci 2011;2:991–996.

[26] Kim K, Yu M, Zong X, Chiu J, Fang D, Seo YS, et al. Control of degradation rate and hydrophilicity in electrospun non-woven poly(d,l-lactide) nanofiber scaffolds for biomedical applications. Biomaterials 2003;24:4977–4985. [CrossRef]

[27] Clinical and Laboratory Standards Institute. Methods for Dilution Antimicrobial Susceptibility Tests for Bacteria That Grow Aerobically; Approved Standard. 7th ed. Wayne, PA: Clinical and Laboratory Standards Institute; 2006.

[28] Clinical and Laboratory Standards Institute. Performance Standards for Antimicrobial Susceptibility Testing. 26th ed. Wayne, PA: Clinical and Laboratory Standards Institute; 2016.

[29] Erdoğmuş SF, Bilecen C, Erdal Altıntaş Ö, Ulukütük S, Kargıoğlu M. The antibiofilm effects of some Cistus spp. against pathogenic microorganisms. Int J Plant Based Pharm 2022;2:252–260. [CrossRef]

[30] Fernandes FHA, Salgado HRN. Gallic acid: Review of the methods of determination and quantification. Crit Rev Anal Chem 2016;46:257–265. [CrossRef]

[31] Al-Kaabi WJ, Albukhaty S, Al-Fartosy AJM, Al-Karagoly HK, Al-Musawi S, Sulaiman GM, et al. Development of Inula graveolens (L.) plant extract electrospun/polycaprolactone nanofibers: A novel material for biomedical application. Appl Sci 2021;11:828. [CrossRef]

[32] Zhang W, Ronca S, Mele E. Electrospun nanofibres containing antimicrobial plant extracts. Nanomaterials (Basel) 2017;7:42. [CrossRef]

[33] Rathod NB, Elabed N, Punia S, Ozogul F, Kim SK, Rocha JM. Recent developments in polyphenol applications on human health: A review with current knowledge. Plants (Basel) 2023;12:1217. [CrossRef]

[34] Sarikurkcu C, Sahinler SS, Tepe B. Astragalus gymnolobus, A. leporinus var. hirsutus, and A. onobrychis: Phytochemical analysis and biological activity. Ind Crops Prod 2020;150:112366. [CrossRef]

[35] Haşimi N, Ertaş A, Yılmaz MA, Boğa M, Temel H, Demirci S, et al. LC-MS/MS and GC-MS analyses of three endemic Astragalus species from Anatolia towards their total phenolic-flavonoid contents and biological activities. Biol Divers Conserv 2017;10:18–30.

[36] Sarikurkcu C, Zengin G. Polyphenol profile and biological activity comparisons of different parts of Astragalus macrocephalus subsp. finitimus from Turkey. Biology (Basel) 2020;9:23. [CrossRef]

[37] Arumugam R, Kirkan B, Sarikurkcu C. Phenolic profile, antioxidant and enzyme inhibitory potential of methanolic extracts from different parts of Astragalus ponticus Pall. S Afr J Bot 2019;120:268-273. [CrossRef]

[38] dos Santos DM, Correa DS, Medeiros ES, Oliveira JE, Mattoso LHC. Advances in functional polymer nanofibers: From spinning fabrication techniques to recent biomedical applications. ACS Appl Mater Interfaces 2020;12:45673-45701. [CrossRef]

[39] Yin K, Divakar P, Wegst UGK. Plant-derived nanocellulose as structural and mechanical reinforcement of freeze-cast chitosan scaffolds for biomedical applications. Biomacromolecules 2019;20:3733-3745. [CrossRef]

[40] Akpınar Z, Ulusoy S, Akgün M, Oral A, Suner SC. Cinnamaldehyde-poly (lactic acid)/gelatin nanofibers exhibiting antibacterial and antibiofilm activity. Int J Polym Mater Polym Biomater 2024;74:998–1007. [CrossRef]

[41] Vittorazzi C, Endringer D, Andrade T, Scherer R, Fronza M. Antioxidant, antimicrobial and wound healing properties of Struthanthus vulgaris. Pharm Biol 2015;54:1-7. [CrossRef]

[42] Chen J, Wang ZZ, Kong LL, Chen NH. Hesperidin. In: Du GH, editor. Natural Small Molecule Drugs from Plants. Singapore: Springer; 2018. p. 81–86. [CrossRef]

[43] Hadisi Z, Nourmohammadi J, Nassiri SM. The antibacterial and anti-inflammatory investigation of Lawsonia inermis-gelatin-starch nano-fibrous dressing in burn wound. Int J Biol Macromol 2018;107:2008–2019. [CrossRef]

[44] Albayrak S, Kaya O. Antioxidant and antimicrobial activities of four Astragalus species growing wild in Turkey. Turk J Biochem 2018;43:425–434. [CrossRef]

[45] Adeli-Sardou M, Torkzadeh-Mahani M, Yaghoobi MM, Dodel M. Antibacterial and anti-biofilm investigation of electrospun PCL/gelatin/lawsone nano fiber scaffolds against biofilm producing bacteria. Biomacromol J 2018;4:46–57.

Sigma J Eng Nat Sci, Vol. 44, No. 1, pp. 439–452, February, 2026

Sigma Journal of Engineering and Natural Sciences
Web page info: https://sigma.yildiz.edu.tr
DOI: 10.14744/sigma.2024.00158

Research Article

Electric bus preference with analytical hierarchy process and grey relational analysis combination in public transportation considering modern trend criteria: Kayseri, Türkiye case study

Aslan İNAN[1,*], Huzeyfe KARA[2]

[1]*Department of Electrical Engineering, Yıldız Technical Universtiy, İstanbul, 34220, Türkiye*
[2]*Department of Planning and Sustainability, Kayseri Ulaşım A.Ş., Kayseri, 38070, Türkiye*

ARTICLE INFO

Article history
Received: 16 April 2024
Revised: 18 July 2024
Accepted: 18 November 2024

Keywords:
Analytical Hierarchy Process; Bus Selection; Electric Bus; Grey Relational Analysis; Public Transportation

ABSTRACT

Objectives such as sustainable cities and communities, accessible and clean energy, and climate action, which are among the sustainable development goals determined by the United Nations, are at the forefront of public transportation. Increasing energy efficiency, cost optimization and reducing carbon emissions are key factors in selecting bus technologies to be used in urban transportation in the future. Today, many bus technologies, such as diesel, electric, compressed natural gas, hybrid, hydrogen, and fuel cells, are used in urban transportation. The type of bus that will be preferred in the future remains a hot research topic. Public transportation companies in cities should choose environmentally friendly, economical, and efficient vehicles by considering objective and subjective criteria. Currently, multi-criteria decision-making methods are widely used in the selection of vehicles in the public transportation sector. In this study, diesel, electric, and CNG buses currently used by public transportation companies operating in Türkiye were evaluated. A comprehensive study was conducted by considering five main criteria: energy, cost, technical, social, and operational and twenty-four trend sub-criteria pertaining to the main criteria. One of the new aspects of this study is that it is based on criteria that have not been used before in the literature, and the other is the use of analytical hierarchy process and grey relational analysis methods together in urban bus selection. The weights of the criteria were calculated with analytical hierarchy process, a well-established multi-criteria decision-making method, and the most suitable bus was selected by rating with grey relational analysis. According to the findings, it was concluded that the electric bus had the highest ranking with a grey relational degree of 0.774 and offered long-term advantages in terms of operational efficiency and environmental impact. This study contributed to the literature by using innovative criteria, integrated analytical hierarchy process and grey relational analysis methods, and provided a more comprehensive and objective approach to bus selection. It also provided guidance for public transportation systems for the city targeting sustainability.

Cite this article as: İnan A, Kara H. Electric bus preference with analytical hierarchy process and grey relational analysis combination in public transportation considering modern trend criteria: Kayseri, Türkiye case study. Sigma J Eng Nat Sci 2026;44(1):439–452.

***Corresponding author.**
*E-mail address: inan@yildiz.edu.tr

This paper was recommended for publication in revised form by Editor-in-Chief Ahmet Selim Dalkilic

Published by Yıldız Technical University Press, İstanbul, Turkey
© Author. This is an open access article under the CC BY-NC license (http://creativecommons.org/licenses/by-nc/4.0/).

INTRODUCTION

The Reducing the operating costs and environmental impact of fossil-fuel vehicles in urban transportation is of great importance. From a global perspective, it is clear that the transition to sustainable public transportation systems is gaining momentum and making a significant contribution to reducing atmospheric carbon emissions. Numerous green transformation projects are being launched in cities to drive a global shift towards sustainable public transport. Contributing to the sustainable development goals, 100% electric transportation is critical for reducing costs, reducing greenhouse gas emissions, and using energy efficiently. Transportation policies in cities should be made more efficient by taking more steps to develop technological opportunities.

Subways, light rail systems, and buses, which are among the vehicles providing transportation mobility to the urban public, are indispensable elements of urban life. It has become necessary to choose the most appropriate type of bus compressed natural gas (CNG), diesel, electric, fuel cell, hydrogen fueled, etc.) by examining buses that are among the public transportation arguments in terms of economic, environmental, and social perspectives in ever-growing urban life. Bus selection in urban public transportation, especially bus prices, operating costs, fuel consumption, and environmental sensitivity, is an important application area for multi-criteria decision-making methods (MCDM). This method is a discipline used to solve complex problems to maximize the benefits obtained in the decision-making process.

Organizations providing public transportation services use MCDM methods in bus selection by considering many economic, environmental, and social criteria within the sustainability framework to provide maximum benefits. MCDM commonly used in the literature include analytical hierarchy process (AHP), grey relational analysis (GRA), technique for of preference by similarity to ideal solution (TOPSIS), multi-objective optimization on the basis of ratio analysis (MOORA), and vise kriterijumska optimizacija I kompromisno resenje (VIKOR). [1].

The originality of this study lies in its inclusion of criteria for bus selection in sustainable urban transportation that have not been utilized in previous literature. Existing studies often focus on limited aspects, such as cost or performance, whereas this study introduces a comprehensive set of criteria that incorporate economic, environmental, and social dimensions. The main contribution of this research is the development of a decision-making framework that combines new and innovative criteria specifically designed for urban bus selection, which address current sustainability challenges in public transportation.

This study evaluates buses based on five main criteria—performance, energy, cost, social acceptability, and usability—and twenty-four associated sub-criteria. Notably, the inclusion of unique criteria, informed by expert opinions and tailored to the specific requirements of sustainable urban transportation, fills a research gap in the existing literature. By integrating previously unused criteria, this study provides a fresh perspective on the multi-dimensional aspects of bus selection, enhancing the applicability and relevance of the results for urban planners and policymakers.

The study was carried out in the case of Kayseri province in Turkey, taking into account local conditions and needs. This increases the originality of the study and ensures the applicability of the results to local governments.

The combination of AHP and GRA methods provides more objective and consistent results in multi-criteria decision making processes. While the AHP determines the weights of the criteria, the GRA evaluates the relationships between these criteria and determines the most appropriate bus type. Bus selection in public transportation is not only evaluated by a single criterion such as cost or performance, but also many other factors such as environmental impacts, energy efficiency, social acceptability, etc. MCDM is an effective tool for managing such multidimensional and complex decision-making processes by taking into account economic, environmental and social criteria.

In the literature review, while GRA has been applied in numerous fields, its application in public transportation bus selection is novel. This study focuses on the bus selection problem of a company providing public transportation services in the Kayseri province, Türkiye. Based on the knowledge, experience, opinions, and suggestions of experts in public transportation, many criteria that have not been used before were used in the study. Thus, this study extends the field of GRA and contributes to the literature on sustainable and environmentally sensitive public transportation.

LITERATURE REVIEW

In the literature, GRA has been used to analyze the relationship between different factors and can be applied in various sectors, such as energy, finance, manufacturing, and transportation. This method's wide range of solutions to complex, multi-criteria decision-making problems makes it a valuable tool for use in many sectors. For example, in the energy sector, GRA has been used in resource selection, power planning, and in manufacturing, it has helped with supplier selection and material selection. In the transportation sector, it has been useful in studies such as deciding on the most efficient mode of transportation, vehicle efficiency and selection.

In the transportation sector, GRA is applied to select a tram vehicle for a company providing urban passenger transportation services. Owing to the uncertainty of the tram vehicle selection problem, many objective and subjective criteria have been evaluated. The validity of the results obtained with GRA was tested using the MOORA method and similar results were observed [2]. In a study conducted in Madrid, the need for sustainable city transit systems

was discussed and an AHP model was proposed in which public transportation vehicles can be evaluated according to their engine type and combustion porperties. The study concluded that plug-in electric vehicles are the most economically and environmentally sustainable alternative. It is stated that the proposed model will support policy makers and companies to make strategic decisions on sustainable urban transportation policies for the future [3]. The use of the multi-criteria decision-making tools AHP and TOPSIS for selecting the most suitable electric bus alternative for public transportation in Ankara was investigated. Six electric buses were analyzed according to seven criteria, and the bus with the most superior performance was selected. Study highlighted the advantages of electric buses in reducing emissions and improving air quality for densely populated areas [1]. The study for public transportation in Argentina investigated which bus technology is more efficient in terms of energy, environmental and economic performance. The study proposes a methodology to compare the technologies of bus fleets using a single multiphysics index that measures costs, consumption and emissions. It is predicted that electric buses will be the most advantageous option in the coming years, while hydrogen-fueled buses will be the most advantageous option from 2027 onwards [4]. In Istanbul, a public transportation bus selection study was conducted with a broader perspective that includes business and strategy as well as economic factors. In the study conducted using global fuzzy AHP and classical AHP methods, it was argued that the diesel bus type stands out [5]. After presenting the advantages of electric vehicles, the decision support system for the evaluation and selection of electric bus models among themselves is comprehensively analyzed and a new approach for MCDM using an integrated fuzzy set is presented [6].

There are different topics and different sectors where AHP and GRA methods are used other than public transportation vehicle selection. A method has been developed to select the city with the best quality of life in Turkey using Grey System Theory. The criteria used in the decision analysis were determined through a survey. The weights of the criteria were assigned using the AHP, and GRA was used to reduce uncertainty in the evaluation process [7]. In a study conducted in the transportation sector, a model for selecting the best mode for sustainability in freight transportation was proposed based on GRA and fuzzy multi-objective linear programming. The analysis presented that road transportation is the most economical mode, while maritime and rail transportation are the best modes from an environmental and social perspective [8]. In a study on the resilience of transportation networks, the effectiveness of 14 indicators was evaluated by GRA in 10 public transportation networks, and the results showed that the Global Efficiency indicator had the greatest impact on the resilience of the public transportation network [9]. GRA was used to measure urban sustainability in 15 provincial cities in China. The study established a criterion system consisting of three dimensions: Economic Development, Social Progress and Ecological Environment, and proposed a weighting method based on grey relational analysis [10]. The impacts of urbanization, population growth, GDP per capita, energy consumption, and economic development on CO2 emissions in Asia have been analyzed using the GRA methodology [11]. The use of an integrated GRA and a multi-objective grey linear programming approach for sustainable power generation planning is discussed. It has been argued that this approach is an effective tool for optimizing complex sustainable power generation planning [12]. The problem of urban sustainability level with three main categories and 39 sub-criteria, the issue of urban sustainability level was addressed using a modified preference ranking technique (TOPSIS). For the 16 cities, GRA was used to reduce the uncertainty inherent in the sustainability assessment process. This model was validated using a case study [13]. The physical properties of fabrics in the textile industry emphasize the importance of selecting the most suitable cotton fabric for a product to meet the final requirements. GRA technique along with Fuzzy Logic has been used to solve the problem of selecting fabric made of cotton [14]. Applications in these various fields highlight the GRA method's adaptability and effectiveness in different industries.

These applications across various fields exemplify the adaptability and effectiveness of GRA when integrated with other MCDM methods. Recent studies highlight its versatility: for instance, in supply chain management within the defense industry, GRA was paired with AHP and TOPSIS to enhance supplier selection processes, showcasing its utility in complex decision-making scenarios [15]. In resource management, GRA and AHP were combined with elemination and choice translating reality english (ELECTRE I) to identify priority areas in water meter replacement, optimizing resource allocation in utility management [16]. Furthermore, GRA has been utilized in biomedical analysis by determining the most effective molecule as an active ingredient against Covid-19, integrated with AHP for prioritizing molecular preferences. Additional examples of AHP-GRA integration include optimizing the performance characteristics of alkali-activated mortars through a mix design approach, where AHP-GRA was utilized to determine ideal combinations of factors such as activator ratios and concentrations [17]. Another study applied AHP-GRA to prioritize IoT implementation challenges in India, providing a structured approach to address technological and infrastructural barriers [18]. Finally, an AHP-GRA-EMM model was developed to assess provincial energy supply security, accurately analyzing risk factors and supporting data-driven energy management [19].

CRITERIA AFFECTING BUS SELECTION IN PUBLIC TRANSPORTATION

For a public transit bus selection evaluation system to provide the most accurate results, the criteria should be multifaceted and componentized. The criteria should

be up-to-date, comprehensive, measurable, relevant, and stable to increase the performance of the analysis. In this direction, both the literature and opinions of experts working in the sector were used to determine the criteria. A face-to-face survey was conducted by experts (general manager, engineers from the bus department at Kayseri Public Transportation Inc., engineers from the planning and sustainability department, bus drivers, and representatives from the private sector) to identify all the criteria that could determine the choice of bus for public transportation. To comprehensively evaluate the bus selection problem in public transportation, social criteria such as comfort, accessibility, and safety, and availability criteria such as uninterrupted service were considered in addition to technical criteria such as range, consumption, and cost per kilometer. The five main criteria performance (P), energy (E), cost (C), social (S), and availability (A) determined for the bus selection analysis and twenty-four subcriteria of these criteria are shown in Table 1. The main criteria represent broad categories essential for assessing the suitability of buses, addressing different dimensions of bus performance and sustainability. The subcriteria, on the other hand, provide specific, measurable factors within each category, enabling a detailed and objective evaluation that reflects real-world considerations in public transit planning.

Performance

The four sub-criteria are the main performance criteria. These sub-criteria are measured using numerical values. The range (P1), which is the maximum distance that buses can travel with a tank with fuel or battery capacity, may vary according to the route profile and driving conditions. The range of electric buses is limited compared to other buses owing to their limited battery capacity. The limited range also limits the public transportation services offered and may increase costs. The passenger capacity (P2) of buses is determined by the number of standing and seated passengers; the more passengers a bus of the same length has, the higher its performance. The passenger capacity of buses is determined by their characteristics, such as engine power, weight, location, type, and design of the energy source storage. The engine power (P3) is a criterion to be considered for the acceleration, maximum speed, and traction

Table 1. Main and sub-criteria used in bus type selection

Performance (P)	Range (P1)	km	[1,6]
	Passenger capacity (P2)	count	[1,6]
	Engine power (P3)	kW	[1,6]
	Speed (P4)	km/h	[1,6]
Energy (E)	Consumption per km (E1)	Joule	
	Consumption per passenger (E2)	Joule	
	Emission (E3)	CO_2	[3,6]
	Unit energy price (E4)	€	
	Energy source (E5)		
Cost (C)	Fuel per kilometer (C1)	€	
	Transportation cost per passenger(C2)	€	
	Purchase cost (C3)	€	[3,5,6]
	Maintenance and operation cost (C4)	km/€	[3,5,6]
	Repair costs (C5)	km/€	[3,5,6]
	Infrastructure cost (C6)	€	[5,6]
Social (S)	Suitability for a disabled vehicle (S1)		
	Route suitability (S2)		
	Comfort (S3)		
	Safety (S4)		
Availability (A)	Mean time to periodic maintenance (A1)	Minute	
	Mean time to repair (A2)	Minute	
	Refueling/recharging time (A3)	Minute	
	Economic life (A4)	Year	
	Mean distance between failure (A5)	km	

performance of vehicles. The engine power of the buses determines the type of line profile (with or without inclines) on which they can operate. Speed (P4) is a criterion for the fuel consumption and travel time of buses and influences passengers' choice of public transportation.

Energy

There are five sub-criteria for the main criterion, energy. Four sub-criteria were measured numerically, and one sub-criterion was measured with verbal values. Consumption per km (E1) is calculated by dividing the amount of fuel consumed by buses according to their fuel technology by the number of kilometers traveled on that fuel and is a criterion that should be considered in terms of fuel efficiency in bus selection. The consumption per passenger (E2) was calculated by dividing the amount of fuel consumed by buses for the same kilometer by their passenger capacity. Emission (E3) is a measurement criterion representing the amount of emissions per kilometer that buses emit while traveling. The contribution of zero- and low-emission buses with energy-efficient technologies to sustainable environmental and energy goals is important for urban life. Electric buses have zero tailpipe emission. Other buses produce emissions, such as nitrogen oxides, particulate matter, and carbon dioxide. The unit energy price (E4) is the criterion used to compare the unit price of the energy source used by the buses. Energy is the most important input in the transportation sector. The unit energy price should also be evaluated to reflect the cost of the powering buses. The energy source (E5) indicates the type of source that generates the energy that powers buses. The type of energy source determines the efficiency of the system, as each source has its own advantages and disadvantages.

Cost

The cost sub-criterion has seven sub-criteria that are measured numerically. According to fuel technologies, the financial equivalent of the amount of fuel per kilometer (C1) consumed by the bus is expressed as cost per kilometer. We can say that the cost per kilometer has a large share in the overall cost efficiency of a public transport system, including personnel and other operating costs. It also imposes a serious burden on businesses because of constantly rising prices. This criterion is used in bus selection to determine a sustainable bus-type option with an appropriate operating cost. Transportation cost per passenger (C2) is a benchmark that considers the passenger capacity, technology, and energy resources of buses. Transport cost per passenger is a financial performance indicator that should be considered in municipalities' macro plans. The purchase cost (C3) represents the initial purchase cost of the buses. This cost is a primary determining criterion and has a significant impact on the efficiency of enterprises' investment and budgets. Maintenance and operation (M&O) cost (C4) is the criterion that shows the sum of the costs such as periodic maintenance, labor, spare parts supply, vehicle insurance, and withholding tax, which are necessary for buses to provide uninterrupted and long-term service. M&O costs vary considerably according to bus technologies and have an impact on total costs over the service period. The repair costs (C5) represent the costs of buses according to the number and size of breakdowns during the passenger transportation service. The financial aspects of breakdowns vary according to the type of bus and are evaluated in terms of other operating costs. The infrastructure cost (C6) is the criterion that defines the cost of the area to be allocated and the facility to be established so that the buses can supply their fuel and meet their other needs.

Social

The main social criterion has four sub-criteria that are measured verbally. The suitability for a disabled vehicle (S1) is the criterion for the suitability of bus types in terms of accessibility. This criterion is important for socially evaluating disabled citizens' ability to benefit from public transportation vehicles and contribute to a barrier-free life. Route suitability (S2) is the criterion used to assess the ability of buses to operate on all route profiles within a city without disrupting services. For example, electric buses may cause problems with existing bumps owing to the proximity of their bases to the ground, have low reverse maneuverability because their battery systems are usually located near the tail of the buses, and have difficulties in areas with high road gradients. Comfort (S3) defines the characteristics of buses, such as seating arrangement, aesthetics, flexibility, spatial width, noise level, and vibration, to provide a comfortable travel experience for passengers and drivers. Safety (S4) is a criterion that is evaluated depending on vehicle features so that passengers can travel without worrying about the safety of life and property in public transportation. In light of historical knowledge and experience, depending on the fuel technology of the buses, incidents such as battery combustion, fuel tank ignition, and natural gas tank explosion can be seen in the event of an accident. Safety and security in public transportation operations are of critical importance as they relate to the lives of passengers. Although public transportation vehicles are manufactured in accordance with legal safety regulations, risks may increase or decrease depending on the design of the buses.

Availability

The continuity of service is an important issue in public transportation, and there are five sub-criteria under the main criterion of availability. The mean time to periodic maintenance (A1) is the time spent on maintenance by the bus type. While maintenance helps reduce the risk of breakdowns and prolong the life of buses, longer maintenance times can lead to service disruption and reduced quality. The mean time to repair (A2) is the time required to eliminate vehicle malfunctions according to their technology. Troubleshooting time is an important maintenance time for service continuity and quality. The refueling/recharging

time (A3) affects the uptime of public transport vehicles and their availability to the passengers. For example, long refueling times for electric buses can disrupt services and increase the operating costs. Economic life (A4) defines how long buses can provide the best function and service for the investment. The mean distance between failures (MDBF) (A5) is a measure of the average distance (kilometers) traveled by a bus before preventive or restorative maintenance is required. A high MDBF value means that the service is not interrupted by failure and that the equipment and service are reliable.

METHODOLOGY

In this section, detailed information regarding the method used in bus-type selection is provided. In this study, a multi-criteria strategic decision-making methodology was proposed by integrating AHP, one of the most frequently utilized MCDM methods, and the GRA method, which allows the use of subjective criteria. In the first scenario, the weights of the criteria were computed using AHP, then the grey relational degrees were calculated using GRA, and in the last stage, bus type options were listed. In the second scenario, bus-type selection was analyzed using only the AHP method. The scenario results of the two methods were compared.

AHP (Analytic Hierarchy Process)

AHP is typically used in the process of choosing among many alternatives when there are many decision makers and criteria. AHP, developed by Saaty in the late 1970s, is a mathematical method for prioritizing alternatives in a logical and consistent manner using qualitative and quantitative factors. The hierarchical structure of this method is illustrated in Figure 1. The basic steps of the method were developed by Saaty are given below [15,16,20-22].

Step 1: In the hierarchical structure of AHP, the decision-making problem is posed in the first step and the objective is determined. A list of criteria and alternatives was prepared based on expert opinions.

Step 2: Using Saaty's table of importance levels given in Table 2 [15], the importance levels of the criteria are determined, pairwise comparison matrices are created, and the importance weights of the criteria are computed [15,20].

Step 3: Because numerical quantities in pairwise comparisons involve subjective judgments, the consistency index (CI) in Equation 1 and consistency ratio (CR) in Equation 2 were calculated to measure the acceptability of the comparison matrices.

The CI was calculated using the eigenvalue of the matrix (λ) and number of criteria (n). The ratio of CI to the value (RI) obtained from the random index table (Table 3) developed by Saaty determines the CR.

$$CI = \frac{\lambda - n}{n - 1} \tag{1}$$

$$CI = \frac{CI}{RI} \tag{2}$$

If the CR value is 0,1 or lower, the comparison matrix is considered acceptable and consistent. However, If the CR exceeds 0.1, the comparison matrix is inconsistent. This means that the inconsistent comparison matrix should be re-evaluated until the CR achieves the desired value.

GRA (Grey Relational Analysis)

The GRA is an important part of the Grey system theory and was developed by Deng Julong in 1982. The grey

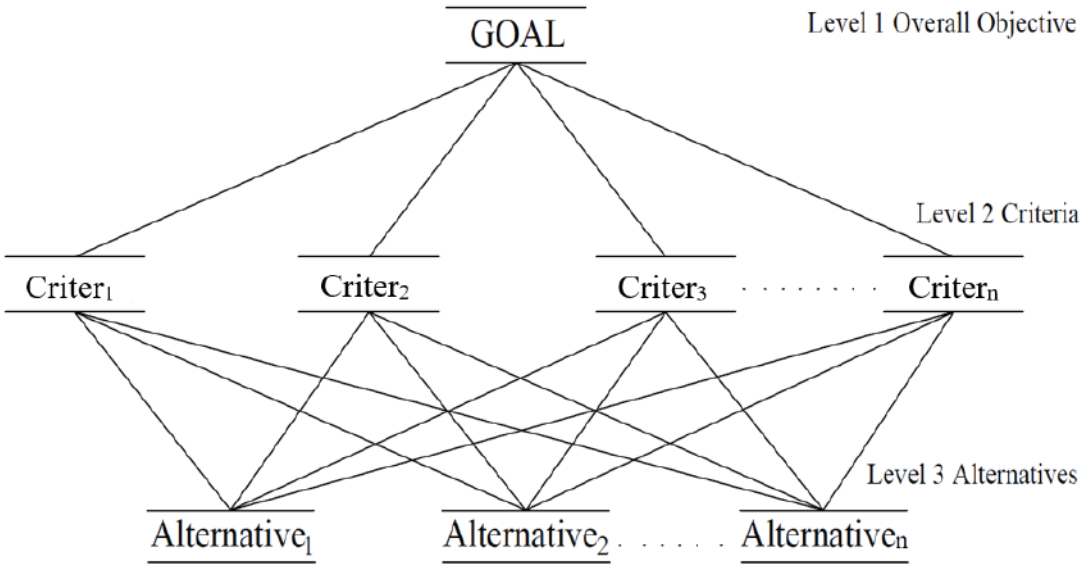


Figure 1. AHP hierarchical structure.

Table 2. Importance degree scale

Importance Degree	Conceptual correspondence	Explanation
1	Equal importance	Two activities contribute equally to the objective
3	Moderate importance of one over another	Experience and judgement strongly favor one activity over another
5	Essential or strong importance	Experience and judgement strongly favor one activity over another
7	Very strong importance	An activity is strongly favored and its dominance demonstrated in practice
9	Extreme importance	The evidence favoring one activity over another is of the highest possible order of affirmation
2,4,6,8	Intermediate values between the two adjacent judgments	When compromise is needed

Table 3. Random index values (RI)

n	1	2	3	4	5	6	7	8	9	10	11	12	13	14	15
RI	0	0	0.58	0.9	1.12	1.24	1.32	1.41	1.45	1.49	1.51	1.48	1.56	1.57	1.58

system theory is a method that produces useful information in the mathematical analysis of problems with insufficient data and where uncertainties are defined by interval values [17,23]. In the grey system theory, known systems are expressed as white, unknown systems as black, and partially known systems as grey [2]. The GRA is a rating, classification, and decision-making technique that allows the best decision to be made according to the proximity of each criterion determined for the problem to the determined reference value.

As the GRA method is the main focus of this study, it is explained in detail in the following five steps:

Step 1: A decision matrix X_i with m alternatives and n criteria is created as shown below:

$$X_i = \begin{bmatrix} x_1(1) & x_1(2) & \cdots & x_1(n) \\ x_2(1) & x_2(2) & \cdots & x_2(n) \\ \vdots & \vdots & \cdots & \vdots \\ x_n(1) & x_n(2) & \cdots & x_n(n) \end{bmatrix} \begin{matrix} i = 1,2 \ldots, m \ and \\ j = 1,2 \ldots, n \end{matrix} \quad (3)$$

where $x_i(j)$ is the value of alternative i for criterion j.

Step 2: The decision matrix is normalized to allow comparison of criteria with different units, resulting in the normalized matrix (Z) shown below. Normalization is performed using the following formula when a larger value is better:

$$z_i(j) = \frac{x_i(j) - min_j(x_i(j))}{max_j(x_i(j)) - min_j(x_i(j))} \quad (4)$$

When a smaller value is better, normalization is performed using this formula:

$$z_i(j) = \frac{max_j(x_i(j)) - x_i(j)}{max_j(x_i(j)) - min_j(x_i(j))} \quad (5)$$

where;

$min_j(x_i(j))$: *minimum value for criterion jth*
$max_j(x_i(j))$: *maximum value for criterion jth*

$$Z = \begin{bmatrix} z_1(1) & z_1(2) & \cdots & z_1(n) \\ z_2(1) & z_2(2) & \cdots & z_2(n) \\ \vdots & \vdots & \cdots & \vdots \\ z_n(1) & z_n(2) & \cdots & z_n(n) \end{bmatrix} \quad (6)$$

Step 3: The absolute value matrix is derived by subtracting the values of the normalized matrix, scaled between "0" and "1," from the reference series value. For each criterion, the reference series takes on a value of "1" for the highest value and "0" for the lowest value. The expression $\Delta_{0j}(j)$, which quantifies the distance and proximity to the reference series, is calculated using the following formula:

$$\Delta_{0j}(j) = |z_0(j) - z_i(j)| \quad (7)$$

Subsequently, the absolute value matrix (Δ_{ij}) is constructed based on the calculated distances for each criterion, as represented here:

$$\Delta_{ij} = \begin{bmatrix} \Delta_{01}(1) & \Delta_{01}(2) & \cdots & \Delta_{01}(n) \\ \Delta_{02}(1) & \Delta_{02}(2) & \cdots & \Delta_{02}(n) \\ \vdots & \vdots & \cdots & \vdots \\ \Delta_{0n}(1) & \Delta_{0n}(2) & \cdots & \Delta_{0n}(n) \end{bmatrix} \quad (8)$$

Step 4: The grey relational coefficients ($\delta_{0i}(j)$) used to determine the closeness of the absolute value matrix to the reference series are calculated as shown below. Δ_{min} and Δ_{max} are the minimum and maximum values, respectively, in the absolute value matrix.

$$\delta_{0i}(j) = \frac{\Delta_{min}+\rho\Delta_{max}}{\Delta_{0i}(j)+\rho\Delta_{max}} \quad (9)$$

where ρ is the distinguishing coefficient used to expand and compress the range of the grey relational coefficients. In the literature, ρ can be set as a value in the range [0,1], and is usually taken as 0.5.

Step 5: The grey relational degrees (γ_{0i}) of the alternatives are calculated by multiplying the importance weight of each criterion by the grey relational coefficient.

$$\gamma_{0i} = \sum_{J=1}^{n}[W_i(j)\delta_{0i}(j)] \quad (10)$$

where Wi is the importance weight of the jth criterion for the ith alternative calculated using the AHP method. [17] [23].

APPLICATION

The effectiveness of the bus selection model was demonstrated by the public transportation service in the city of Kayseri, Turkey, which transports approximately 350,000 passengers per day. The company, which provides services on 400 different routes with 645 buses and 8200 daily average trips, needs to make strategic decisions, as it aims to provide efficient, innovative, and state-of-the-art public transportation services. This study aims to evaluate alternatives in the bus fleet to be sensitive to the environment, reduce emissions, increase the share of renewable energy sources in energy use, and reduce costs in public transportation.

For public transportation services, three types of buses (Diesel, CNG, Electric) of 18 m are currently used in passenger transportation. These three types of buses were analyzed using the AHP and GRA methods according to five main criteria and twenty-four sub-criteria shown in Table 1. The quantitative and qualitative values of the features of the alternative buses are shown in Table 4, according to the

Table 4. Quantitative and qualitative values of the criteria

			Diesel	CNG	Electric
Performance (P)	Range (P1)	km	410	450	400
	Passenger capacity (P2)	count	141	141	144
	Engine power (P3)	kW	265	235	450
	Speed (P4)	km/h	80	80	80
Energy (E)	Consumption per km (E1)	joule	18773524	24606720	5040000
	Consumption per passenger (E2)	joule	39920305	52354214	7419600
	Emission (E3)	CO_2	1.41	1.46	0.63
	Unit energy price (E4)	€	0.648*	0.739**	0.136***
	Energy source (E5)		Poor	Poor	Excellent
Cost (C)	Fuel per kilometer (C1)	€	0.323	0.525	0.190
	Transportation cost per passenger (C2)	€	0.248	0.192	0.182
	Purchase cost (C3)	€	4950000	5450000	9600000
	Maintenance and operation cost (C4)	km/€	1.45	2.29	0.55
	Repair costs (C5)	km/€	Excellent	Good	Fair
	Infrastructure cost (C6)	€	200000	166666.67	181800
Social (S)	Suitability for a disabled vehicle (S1)		Excellent	Excellent	Excellent
	Route suitability (S2)		Fair	Fair	Good
	Comfort (S3)		Good	Good	Excellent
	Safety (S4)		Excellent	Good	Good
Availability (A)	Mean time to periodic maintenance (A1)	min	120	120	40
	Mean time to repair (A2)	min	Excellent	Fair	Good
	Refueling/recharging time (A3)	min	10	12	240
	Economic life (A4)	year	15	15	15
	Mean distance between failure (A5)	Km	783	2880	676

Note: *€/lt; ** € /m^3; ***€/kWh; min: Minute

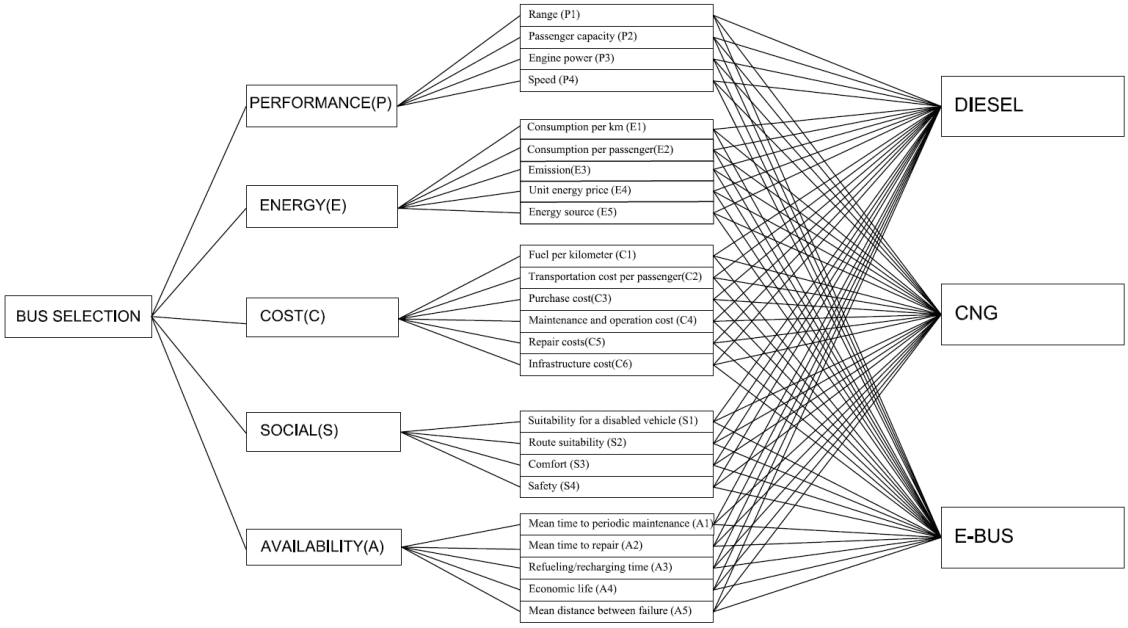


Figure 2. Hierarchical structure of bus type selection.

criteria determined in line with the experience, opinions, and suggestions of the experts.

The experts are managers, engineers and consultants with at least 10 years of experience in planning, operation and maintenance in public transportation companies.

The hierarchical structure according to the bus type and selection criteria is shown in Figure 2.

To measure the effectiveness of the main criteria and sub-criteria in bus selection, the importance weights were computed using the AHP method. The importance weights of the main criteria are listed in Table 5. Among the main criteria, cost (0.423) and energy (0.309) have higher importance weights than the others and have a high impact on bus selection. The weights of the sub-criteria and the consistency ratios of the comparison matrices calculated according to Equation 9-10 are given in Tables 6-10. Because all the consistency ratios given at the bottom of these tables are less than 0.1, it can be said that all pairwise comparison matrices are consistent.

Because there were five main criteria and 24 sub-criteria in the study, the importance weights of the main criteria were calculated first, and then the importance weights of

Table 5. The pairwise comparison matrix of the main criteria, the weights of the criteria and the consistency ratio of the matrix

Criteria	P	E	C	S	A	(Wi)
P	1	0.25	0.2	0.5	0.33	0.060
E	4	1	0.5	5	4	0.309
C	5	2	1	5	4	0.423
S	2	0.2	0,2	1	0.5	0.081
A	3	0.25	0.25	2	1	0.127

Note: λ=5.205; CI=0.051; RI=1.12; CR=0.046.

Table 6. The pairwise comparison matrix of the performance sub-criteria, the weights of the criteria and the consistency ratio of the matrix

Criteria	P1	P2	P3	P4	(Wi)
P1	1	3	6	5	0.528
P2	0.33	1	6	5	0.315
P3	0.167	0.167	1	0.5	0.062
P4	0.2	0.2	2	1	0.096

Note: λ=4.189; CI=0.063; RI=0.9; CR=0.07

Table 7. The pairwise comparison matrix of the energy sub-criteria, the weights of the criteria and the consistency ratio of the matrix

Criteria	E1	E2	E3	E4	E5	(Wi)
E1	1	3	6	4	5	0.453
E2	0.333	1	5	4	4	0.274
E3	0.167	0.2	1	0.25	2	0.070
E4	0.25	0.25	4	1	3	0.146
E5	0.2	0.25	0.5	0.333	1	0.058

Note: λ=5.410, CI=0.103, RI=1.12, CR=0.092

Table 8. The pairwise comparison matrix of the cost sub-criteria, the weights of the criteria and the consistency ratio of the matrix.

Criteria	C1	C2	C3	C4	C5	C6	(Wi)
C1	1	3	2	4	4	5	0.354
C2	0.333	1	0.5	2	3	4	0.160
C3	0.5	2	1	4	5	3	0.254
C4	0.25	0.5	0.25	1	0.5	3	0.082
C5	0.25	0.333	0.2	2	1	4	0.103
C6	0.2	0.25	0.333	0.333	0.25	1	0.048

Note: λ=6,466; CI=0.093; RI=1.24; CR=0.075.

Table 9. The pairwise comparison matrix of the social sub-criteria, the weights of the criteria and the consistency ratio of the matrix.

Criteria	S1	S2	S3	S4	(Wi)
S1	1	4	5	1	0.401
S2	0.25	1	3	0.333	0.136
S3	0.2	0.333	1	0.143	0.060
S4	1	3	7	1	0.402

Note: λ=4.065; CI=0.022; RI=0.9; CR=0.024.

Table 10. The pairwise comparison matrix of the availibility sub-criteria, the weights of the criteria and the consistency ratio of the matrix

Criteria	A1	A2	A3	A4	A5	(Wi)
A1	0.333	0.25	1	0.333	0.25	0.061
A2	0.5	0.333	3	1	0.333	0.117
A3	4	4	4	3	1	0.447
A4	1	0.5	3	2	0.25	0.149
A5	2	1	4	3	0.25	0.226

Note: λ=5.354; CI=0.089; RI=1.12; CR=0.079.

the sub-criteria of each main criterion were calculated. The final weights, calculated by multiplying the weight of each sub-criterion by the weight of the relevant main criterion, are listed in Table 11. According to the final weights, the three most important sub-criteria are consumption per kilometer, cost per kilometer, and purchase cost, which have values of 0.140, 0.128, and 0.096, respectively.

After the final weights of the criteria are calculated, the GRA method is used to determine the preference ranking of the alternatives. Table 12 presents the decision matrix obtained after entering the quantitative equivalents of the qualitative values in the dataset given in Table 4. To evaluate

Table 11. Final importance weights of the criteria

Main criteria	Main criteria weight	Sub criteria	Sub criteria weight	Final weight
P	0.059	P1	0.528	0.031
		P2	0.315	0.019
		P3	0.062	0.004
		P4	0.096	0.006
E	0.309	E1	0.453	0.140
		E2	0.274	0.085
		E3	0.070	0.022
		E4	0.146	0.045
		E5	0.058	0.018
C	0.423	C1	0.354	0.150
		C2	0.160	0.068
		C3	0.254	0.107
		C4	0.082	0.035
		C5	0.103	0.044
		C6	0.048	0.020
S	0.081	S1	0.401	0.033
		S2	0.136	0.011
		S3	0.060	0.005
		S4	0.402	0.033
A	0.126	A1	0.447	0.057
		A2	0.149	0.019
		A3	0.226	0.029
		A4	0.061	0.008
		A5	0.117	0.015

the criteria with different units on the same scale, the decision matrix was normalized using the cost-benefit method from Equations 4 and 5. For example, the range sub-criterion, which concerns performance and is desired to be high, is normalized using the benefit method, or the purchase cost criterion, which concerns cost and is desired to be low, is normalized using the cost method. The normalization matrix was scaled in the range [0-1] as shown in Table 13.

After the calculation of the normalization matrix, the absolute value matrix, which is determined using Equations 7-8 and expresses the distance of the alternative series to the reference series, is presented in Table 14. The grey relational coefficients express the similarity between the reference series and the normalized series and are used to calculate the grey relational degrees. These coefficients were obtained by using Equation 9 and are listed in Table 15.

The grey relational coefficients obtained are also shown in the radar graph in Figure 3. The radar plot is surrounded by these criteria. According to the grey relational coefficients of the alternatives for each criterion, the option that

Table 12. Decision matrix

Sub criteria	Diesel	CNG	Electric
P1	410	450	400
P2	141	141	144
P3	265	235	450
P4	80	80	80
E1	18773524	24606720	5040000
E2	39920305	52354214	7419600
E3	1.41	1.46	0.63
E4	0.648	0.739	0.136
E5	0.3	0.3	0.9
C1	0.323	0.525	0.190
C2	0.248	0.192	0.182
C3	4950000	5450000	9600000
C4	1.45	2.29	0.55
C5	0,9	0.7	0.5
C6	200000	166666.67	181800
S1	0.9	0.9	0.9
S2	0.5	0.5	0.7
S3	0.7	0.7	0.9
S4	0.9	0.7	0.7
A1	120	120	40
A2	0.9	0.5	0.7
A3	10	12	240
A4	15	15	15
A5	783	2880	676

Table 13. Normalization matrix

Sub criteria	Diesel	CNG	Electric
P1	0.200	1.000	0.000
P2	0.000	0.979	1.000
P3	0.140	0.522	1.000
P4	0.000	0.000	0.000
E1	0.298	0.000	1.000
E2	0.277	0.000	1.000
E3	0.060	0.000	1.000
E4	0.151	0.000	1.000
E5	0.000	0.000	1.000
C1	0.604	0.000	1.000
C2	0.000	0.855	1.000
C3	1.000	0.892	0.000
C4	0.483	0.000	1.000
C5	0.000	0.500	1.000
C6	0.000	1.000	0.546
S1	0.000	0.000	0.000
S2	0.000	0.000	1.000
S3	0.000	0.000	1.000
S4	1.000	0.000	0.000
A1	0.000	0.000	1.000
A2	0.000	1.000	0.500
A3	1.000	0.991	0.000
A4	0.000	0.000	0.000
A5	0.049	1.000	0.000

scans the most area in the radar graph and is closest to the reference value is the electric bus.

The grey relational coefficients of the criteria and the importance weights of each criterion are multiplied according to Equation 10 to determine the grey relational degrees of the alternatives. The grey relational degrees of the alternatives, according to the determined criteria, are listed in Table 16. Because the option with the highest grey relational degree should be prioritized, the electric bus, which has a value of 0.767 according to the grey relational degrees, is the best option among the alternatives.

Many methods can be used to create and analyze problems. In order to test the accuracy of the results, the electric bus selection problem was analyzed and ranked according to both AHP and TOPSIS methods (Table 17). It was seen that the rankings made with these methods and the GRA method rankings were the same and the GRA method solution was supported.

RESULTS AND DISCUSSION

Multi-criteria decision-making methods are mechanisms that include the opinions, suggestions, and judgments of experts in line with their knowledge, experience, and evaluation. In this context, satisfactory results could be obtained by using the functional and comprehensive approach of the AHP and GRA methods, which are multi-criteria decision-making methods.

This paper presents an effective approach for solving the problem of bus type selection for urban transportation with multiple criteria and alternatives by integrating the AHP method, which can bring objectivity and consistency, and the GRA, which can quantify the uncertainties in qualitative judgments. The combination of the two methods simplifies complex relationships and increases the reliability of the results, thus empowering the decision maker to make an informed choice.

The selection of buses for the public transportation service of Kayseri Municipality, which works on a sustainable economy, environment, and energy, has been an issue directly related to increasing energy efficiency, reducing costs, and eliminating greenhouse gas emissions. Therefore, bus selection is evaluated in light of the integrated advantages of the AHP and GRA methods by including criteria not previously used in the literature under rapidly changing technological developments.

Table 14. Absolute value matrix

Sub Criteria	Diesel	CNG	Electric
P1	0.800	0.000	1.000
P2	1.000	0.021	0.000
P3	0.860	0.478	0.000
P4	1.000	1.000	1.000
E1	0.702	1.000	0.000
E2	0.723	1.000	0.000
E3	0.940	1.000	0.000
E4	0.849	1.000	0.000
E5	1.000	1.000	0.000
C1	0.396	1.000	0.000
C2	1.000	0.145	0.000
C3	0.000	0.108	1.000
C4	0.517	1.000	0.000
C5	1.000	0.500	0.000
C6	1.000	0.000	0.454
S1	1.000	1.000	1.000
S2	1.000	1.000	0.000
S3	1.000	1.000	0.000
S4	0.000	1.000	1.000
A1	1.000	1.000	0.000
A2	1.000	0.000	0.500
A3	0.000	0.009	1.000
A4	1.000	1.000	1.000
A5	0.951	0.000	1.000

Table 15. Grey relational coefficients

Sub criteria	Diesel	CNG	Electric
P1	0.385	1.000	0.333
P2	0.333	0.960	1.000
P3	0.368	0.511	1.000
P4	0.333	0.333	0.333
E1	0.416	0.333	1.000
E2	0.409	0.333	1.000
E3	0.347	0.333	1.000
E4	0.371	0.333	1.000
E5	0.333	0.333	1.000
C1	0.558	0.333	1.000
C2	0.333	0.775	1.000
C3	1.000	0.823	0.333
C4	0.492	0.333	1.000
C5	0.333	0.500	1.000
C6	0.333	1.000	0.524
S1	0.333	0.333	0.333
S2	0.333	0.333	1.000
S3	0.333	0.333	1.000
S4	1.000	0.333	0.333
A1	0.333	0.333	1.000
A2	0.333	1.000	0.500
A3	1.000	0.983	0.333
A4	0.333	0.333	0.333
A5	0.344	1.000	0.333

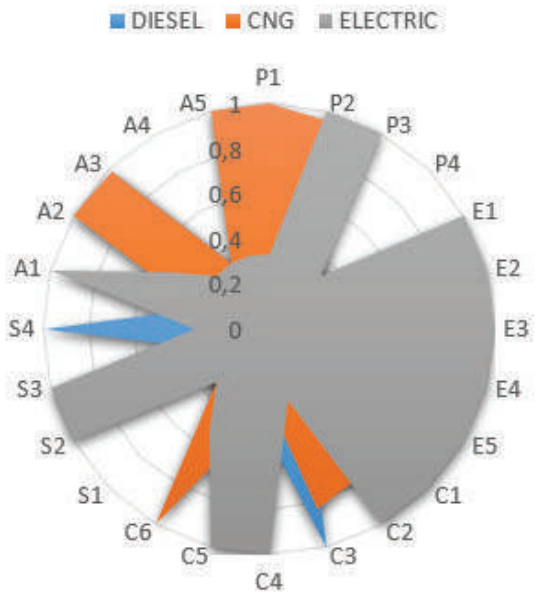


Figure 3. Grey relational coefficients radar plot.

Tablo 16. Grey relational degrees and ranking of alternatives

	Grey relational degrees	Rank
Diesel	0.525	3
CNG	0.535	2
Electric	0.774	1

In this study, three bus types (Diesel, CNG, Electric) were ranked according to their grey relational ranking using five main criteria (performance, energy, cost, comfort, and availability), and twenty-four sub-criteria in total.

- In the analysis, the electric bus received the highest ranking for consumption per km, cost per km, maintenance and repair costs, and emission criteria, and the lowest ranking for procurement and infrastructure installation costs.
- According to the application outputs, the electric bus has a higher rating than the diesel and CNG buses in 14 of the twenty-four sub-criteria. This shows that the electric bus is a superior option compared to other alternatives.

Tablo 17. Importance degrees and ranking of alternatives

	AHP importance degrees	Rank	TOPSIS relative closeness value	Rank
Diesel	0.152	3	0.320	3
CNG	0.385	2	0.429	2
Electric	0.463	1	0.769	1

- Consequently, despite the disadvantages of electric buses, such as high purchase costs, short range, and long charging times, it has been shown that it is a preferable vehicle when other advantageous criteria are considered.
- As a result of the analysis, it was found that the electric bus is superior in environmental and economic criteria such as energy consumption, cost per kilometer, and emissions, while the diesel bus has advantages such as lower purchasing costs and longer range. The CNG bus, on the other hand, offers a good option in terms of infrastructure costs and emission rates. These results indicate that the electric bus is generally the best option. However, other bus types can also be evaluated according to urban transportation needs, where they may be more suitable under certain operational and economic conditions.
- The fact that electric buses are the most suitable bus type for urban public transportation according to the criteria determined by experts is also consistent with similar studies in the existing literature. Other studies in the literature have also revealed that electric buses have advantages over other bus types, especially in terms of sustainability and energy efficiency.

Overall, the integration of AHP and GRA methods provided a robust framework for evaluating bus options in urban transport. The findings show that electric buses offer significant advantages, especially in terms of environmental impact and long-term operational efficiency.

CONCLUSION

This study, which resulted in the selection of electric buses with the highest scores according to the determined criteria, will guide urban public transport service providers towards environmentally, economically and socially sustainable transportation in the future. This study is limited to the local context of Kayseri and the determined criteria. The study can be applied to other regions by considering the methodology developed here, new technologies, region-specific criteria and operational needs. Future research can focus on integrating additional criteria such as policy, battery technologies, incentives, which can further support the adoption of electric buses.

AUTHORSHIP CONTRIBUTIONS

Authors contributed equally to this work.

CONFLICT OF INTEREST

There are no potential conflicts of interest regarding the research and publication of this article.

ETHICS

There are no ethical issues with the publication of this manuscript.

STATEMENT ON THE USE OF ARTIFICIAL INTELLIGENCE

Artificial intelligence was not used in the preparation of the article.

REFERENCES

[1] Hamurcu M, Tamer E. Electric bus selection with multicriteria decision analysis for green transportation. Sustainability 2020;12:2777. [CrossRef]

[2] Canbulut G, Köse E, Arik OA. Public transportation vehicle selection by the grey relational analysis method. Public Transport 2022;14:367–384. [CrossRef]

[3] Rivero Gutiérrez L, De Vicente Oliva MA, Romero-Ania A. Managing sustainable urban public transport systems: An AHP multicriteria decision model. Sustainability 2021;13:4614. [CrossRef]

[4] Munoz P, Franceschini EA, Levitan D, Rodriguez CR, Humana T, Perelmuter GC. Comparative analysis of cost, emissions and fuel consumption of diesel, natural gas, electric and hydrogen urban buses. Energy Convers Manag 2022;257:115412. [CrossRef]

[5] Buran B, Erçek M. Bus type selection with fuzzy approach for public transportation. Syst Soft Comput 2023;5:200055. [CrossRef]

[6] Alamodi AH, Albahri OS, Deveci M, Albahri AS, Yussof S, Dinçer H, Yüksel S, Sharaf IM. Selection of electric bus models using 2-tuple linguistic T-spherical fuzzy-based decision-making model. Exp Syst Appl 2024;249:123498. [CrossRef]

[7] Kose E, Vural D, Canbulut G. The most livable city selection in Turkey with the grey relational analysis. Grey Syst Theory Appl 2020;10:529–544. [CrossRef]

[8] Fulzele V, Shankar R, Choudhary D. A model for the selection of transportation modes in the context of sustainable freight transportation. Ind Manag Data Syst 2019;119:1764–1784. [CrossRef]

[9] Hu M, Bhouri N. Evaluation of resilience indicators for public transportation networks by the grey relational analysis. IEEE International Conference on Intelligent Transportation Systems (ITSC) 2020. [CrossRef]

[10] Yi P, Dong O, Li W, Wang L. Measurement of city sustainability based on the grey relational analysis: The case of 15 sub-provincial cities in China. Sustain Citi Soc 2021;73:103143. [CrossRef]

[11] Rehman E, Rehman S. Modeling the nexus between carbon emissions, urbanization, population growth, energy consumption, and economic development in Asia: Evidence from grey relational analysis. Energy Rep 2022;8:5430–5442. [CrossRef]

[12] Malekpoor H, Chalvatzis K, Mishra N. Integrated grey relational analysis and multi objective grey linear programming for sustainable electricity generation planning. Ann Oper Res 2018;269:475–503. [CrossRef]

[13] Tang J, Zhu HL, Liu Z, Jia F, Zheng XX. Urban sustainability evaluation under the modified TOPSIS based on grey relational analysis. Int J Environ Res Public Health 2019;16:256. [CrossRef]

[14] Chakraborty S, Chatterjee P, Das PP. Cotton fabric selection using a grey fuzzy relational analysis approach. J Inst Eng (India) Ser E 2019;100:21–36. [CrossRef]

[15] Efe Evcioglu H, Kabak M. Supplier selection in supply chain network using MCDM methods. Sigma J Eng Nat Sci 2023;41:1–16. [CrossRef]

[16] Yilmaz S, Firat M, Bozkurt C, Özdemir Ö. Identification of the priority regions in the customer water meters replacement using the AHP and ELECTRE methods. Sigma J Eng Nat Sci 2021;39:331-342. [CrossRef]

[17] Mishra A, Lahoti M, Khare S, Yang E. Recycling electric arc furnace slag through tailoring of ambient-cured alkali-activated mortar mix using hybrid AHP-GRA and TOPSIS. J Clean Prod 2024;452:142216. [CrossRef]

[18] Teli TA, Masoodi FS. IoT implementation in India: A complex decision process using GRA/AHP. 10th International Conference on Computing for Sustainable Global Development (INDIACom) 2023. p. 773–778.

[19] Gong X, Huang Y, Yun X, Zhang T, Li Y, Peng B. Provincial energy supply and demand risk assessment based on GRA-AHP-EWM method. Proceedings of the 3rd International Conference on Big Data, Artificial Intelligence and Risk Management (ICBAR) 2023. p. 699–704. [CrossRef]

[20] Saaty TL. How to make a decision: The analytic hierarchy process. Eur J Oper Res 1990;48:9–26. [CrossRef]

[21] Saaty TL. Decision making with the analytic hierarchy process. Int J Serv Sci 2008;1:83. [CrossRef]

[22] İnan A, Kara H. Urban railway system route selection in Turkey based on socio-economic and technical criteria using the analytical hierarchy process. Transp Res Record 2022;2676:633–644. [CrossRef]

[23] Liu S, Yang Y, Xie N, Forrest J. New progress of grey system theory in the new millennium. Grey Syst Theory Appl 2016;6:2–31. [CrossRef]

Sigma Journal of Engineering and Natural Sciences
Web page info: https://sigma.yildiz.edu.tr
DOI: 10.14744/sigma.2025.00000

Research Article

Vibration-based fault detection in induced draft fans using unsupervised machine learning approaches

Ramesh BHANDARE[1,*], Pankaj BELDAR[1], Shyam MOGAL[2]

[1]Department of Mechanical Engineering, K K Wagh Institute of Engineering Education & Research, Nashik, 422003, India
[2]Department of Mechanical Engineering, MVPS's K. B. T. College of Engineering, Nashik, 422013, India

ARTICLE INFO

Article history
Received: 06 October 2024
Revised: 02 December 2024
Accepted: 02 January 2025

Keywords:
Induced Draft Fan; Machine Learning; Misalignment; Unbalance; Vibration Analysis

ABSTRACT

Induced draft (ID) fan is a crucial member to carry our hot flue gases and always subjected to high temperature and pressure. Flue gases carry higher temperature than atmospheric so, ID fan always works under elevated temperature 24x7. Supporting members such as by bearing and coupling also have to work under significant temperature more than atmospheric condition which leads create unbalance, misalignment or unexpected failures. Predictive maintenance has its own advantages to avoid this, Vibration analysis is a best tool for this. Vibration analysis clearly indicate the unbalance and misalignment fault in induce draft fan and coupling respectively as earliest. Vibration data has been collected on machine in paper mill and statistical features has been extracted. Machine learning techniques has its own significance for checking fault accuracies. Proposed study suggested unsupervised machine learning approach to separate 2 different faults like unbalance and misalignments faults in ID fan.

Cite this article as: Bhandare R, Beldar P, Mogal S. Vibration-based fault detection in induced draft fans using unsupervised machine learning approaches. Sigma J Eng Nat Sci 2026;44(1):453–464.

INTRODUCTION

The induced draft (ID) fan finds in thermal power plants, cement plants, paper mills, steel mills, chemical plants, etc. In a paper mill plant, the ID fan is typically located after the boiler and before the chimney or stack. Specifically located within the flue gas system, and it plays a vital role in the process of exhausting the flue gases from the boiler. ID fan subjected to high temperature and pressure needs continuous monitoring otherwise faults are created in ID fan or in support system. As a vital member of plant, accurate investigation of faults in the ID fan is the need. Defect in an ID fan can leads to decrese in performane and rise in energy usage. Timely identification and rectification of these faults ensure an increase in the life of a fan, minimize energy costs, and also enhance overall efficiency. Issues like imbalance, bearing faults, misalignment, looseness, or a bent shaft can escalate significantly in ID fan due to vibrations may caused unanticipated shutdowns. Predictive maintenance plays vital role in such situation. Vibration based condition monitoring is essential and reliable technique for identifying multiple faults in such system. Maintaining system in a healthy condition is crucial for their long-term proficiency and to enhance the overall efficiency of a plant.

*Corresponding author.
*E-mail address: rvbhandare@kkwagh.edu.in

This paper was recommended for publication in revised form by Editor-in-Chief Ahmet Selim Dalkilic

Published by Yıldız Technical University Press, İstanbul, Turkey
© Author. This is an open access article under the CC BY-NC license (http://creativecommons.org/licenses/by-nc/4.0/).

A case study on ID fan by Jagtap et al. [1] reveals how vibration analysis techniques provide insights for earlier fault findings. Author located fault severity by wear, noise and ultrasound level. In addition to this Kurien and Srivastava [2] done motor signature and wear debris analysis in their research. Vibration based condition monitoring for auxiliary equipment's like feed pump, fan, turbine in thermal power plants used by some researchers [3-6]. Li [7] in their case study conducted vibration analysis for forced draft fan and found unbalance in system and also explain the dynamic balancing process. Some researcher's comments on the effectiveness of vibration analysis techniques in their literature [8-9,]. Faults within the such system have a direct impact on the safety of a thermal power plant and the overall reliability and economy of the system. By extracting the vibration signal, faults within the auxiliary components such as ID fan can be identified and categorized using a set of specific features. The fast fourier transform (FFT) or discrete methods are applied to extract valuable features from the vibration signal.

Statistical features selection approach has been employed by some investigators [10,11] from time domain and frequency domain signal. By extracting Statistical features like kurtosis, skewness, variance, standard deviation etc. improve the locate faults in the system. Machine learning (ML) techniques one more area open for scholars to deeply explain the faulty cases. Supervised ML approach has been employed by Liu et al. [12] to investigate the fault accuracy for steam turbine in nuclear power plant. verify the fault severity and accuracy. Classification ML algorithm has potential to significantly distinguish the faulty and healthy cases, which helps the researcher to visualize the anomaly in signals. Support vector machine (SVM), K nearest neighbors (KNN), random forest (RF) such ML algorithms have suggested by researchers in their literature [13-15]. Genetic algorithm-based optimization for vehicle powertrain system has been employed by Genç and Karaduman [16], Deep learning is more powerful tool for fault detection, Kumhar [17] proposed dynamic balancing scheme and applied convolution neural-network (CNN) to extract information. Sarita [18] suggested deep neural network to detect faults in blower of vehicle air conditioner. They also proposed wavelet transform to signal conditioning to improve the performance of signal. Eratlı [19] implemented principal component analysis (PCA) to detect faulty part in the fan motor system. Machine learning helps the scholars to efficiently locating the faulty condition even there is anomality in the available vibration data [20-22]. Many researchers work on thermal or nuclear power plant data [23,24] and few literatures explicitly on paper mill ID fan. Still there is scope to study and reveals the cases arises in this in detail. In the proposed work, data for unbalance and misalignment in ID fan has been carried out in paper mill in real time. Vibration data clearly shows unbalance in ID fan and also locate the misalignment. Unsupervised machine learning approaches has been employed to distinguish between the unbalance and misalignment from vibration signal. Results from vibration analysis and ML algorithms discovers highest accuracy up to 99%.

The present work is divided into three sections, section II covers methodology, the vibration analysis of data collected at paper mill, subsequent section focuses on data conditioning, feature extraction and machine learning approach employed to precisely locate the faults. Section IV, emphasizes on the results and discussion.

MATERIALS AND METHODS

Figure 1 shows methodology for Fault diagnosis of ID fan in paper mill. Vibration data has been collected by using

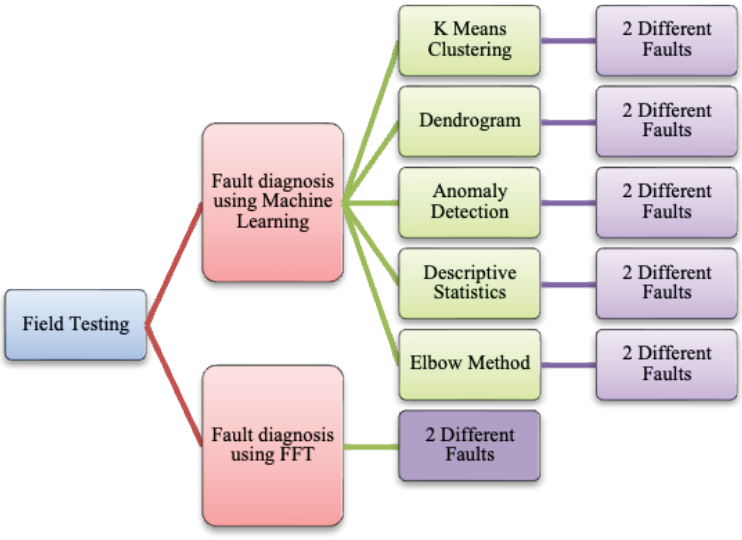


Figure 1. Operational framework.

4 channel FFT analyzer. A vibration signal is obtained in channel 1 (CH1) in vertical (V) and channel 2 (CH2) in horizontal (H) direction at bearing. Time and frequency signal shows the fault frequencies for unbalance and misalignment. To get confirmation of faults machine learning techniques are implemented. Unsupervised machine learning clearly separates the faults and also clustering helps in pattern recognition for anomaly detection.

Induced Draft Fan

Figure 1 shows bearings and shaft of ID fan used in paper mill plant. Specification of ID fan is as tabulated in Table 1.

Experimentation

Vibration data live measured on the bearings of ID fan. The three piezoelectric accelerometers (Sensitivity: 100mv/g) are used to collect the vibration signals in Channel 1 (CH1) in vertical (V), Channel 2 (CH2) in horizontal (H) and Channel 3 (CH3) in axial (A) direction at bearings as shown in Figure 3. Vibration data is collected using vibration analyser (Make: SKF Model: CMXA75).

The overall RMS amplitude of the drive end (DE) bearing in both the vertical and horizontal directions falls within the restricted (alarm) zone, as per ISO 10816-3. Similarly, the overall RMS amplitude of the non-drive end (NDE) bearing is in the critical zone in the vertical direction and in the restricted (alarm) zone in the horizontal direction, as per ISO 10816-3. Consequently, the vibration data from channels CH1 and CH2 are utilized for machine learning-based fault diagnosis.

In this study, The ID fan, as shown in Figure 2, served as the primary focus of the investigation. Vibration measurements carried out at both the drive-end (DE) and non-drive-end (NDE) bearings of the rotor, as shown in Figure 3 data collected in three possible directions. These measurements were critical in diagnosing the misalignment fault at the DE and the unbalance fault at the NDE, based on the vibration spectra obtained.

RESULTS AND DISCUSSION

Case Study: Induced Draft Fan Using FFT

The spectrum at DE bearing in vertical direction CH1 and horizontal direction CH2 are shown in Figure 4. It is observed that axial vibration is less than vertical and horizontal direction. 1X and 2X peak is observed in vertical

Table 1. Specification of induced draft fan

Parameters	Specification
Speed	1440 rev/min
No. of blades	12
Driven	Induction motor
Power	20 Hp
Motor bearing	6203
Fan bearing	22214-EKW-33J

Table 2. Overall amplitude in three directions

Speed (rev/min)	RMS amplitude (mm/s) before alignment and balancing			
	Bearing end	Direction		
		V	H	A
1142	DE	5	4.6	2.87
	NDE	8.9	5.8	3.09

DE: Drive-end; NDE: Non-drive-end.



Figure 2. Induced draft fan in a paper mill plant.



Figure 3. Accelerometer mounting on the bearing of the induced draft fan.

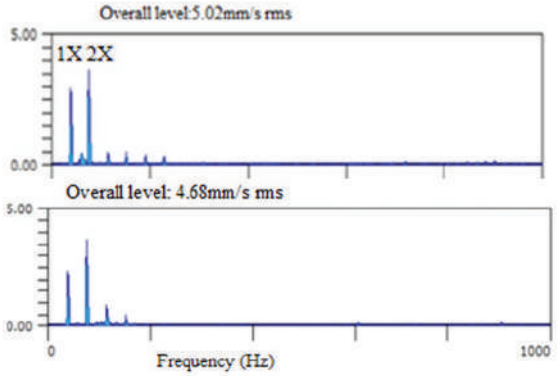


Figure 4. FFT at DE bearing in vertical and Horizontal direction.

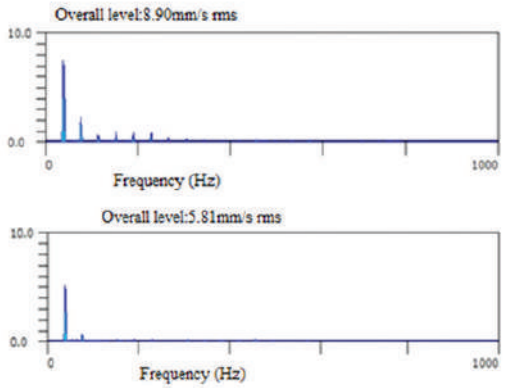


Figure 5. FFT at NDE bearing in vertical and horizontal direction.

and horizontal direction. 2 X peak is higher than 1X. It is cleared that misalignment fault is observed in coupling. The spectrum at NDE bearing in vertical direction and horizontal direction are shown in Figure 5. 1X peak is observed in vertical and horizontal direction. It is clear that unbalance fault is observed in fan. Unbalance fault is developed due to deposition of ash or the wear of the fan blades.

Machine Learning Technique

ML approach now a days very useful in fault detection and categorization. This section covers the unsuprvised ML learning approach contribution in fault findings of ID fans. Vibration signals can be continuously collected by accelerometers placed at critical locations such as DE and NDE bearings. The data preprocessing used various methods to assured high quality data for machine learning models. Unwanted noise can filtered using a band pass filter to eliminate irrelevant low frequency and high frequency noise, to ensure critical frequency ranges related to ID fan faults. FFT applied for feature extraction and time domain signals were transformed into the frequency domain. Frequncy graph gives 1X and 2X harmonics related to faults. Real time signal processing techniques such as FFT and machine learning analysis can be performed on these dataset, ensuring minimal latency. Data need to be normalized to remove the outlier can caused by sensor errors or transient vibrations Z-score normalization has been employed which eliminate extreme anomalies. However, to ensure consistency in variables and enhance clustering accuracy min max scalar has been adopted to normalized the extracted features. In this way, preprocessing steps assured the reliability and suitability of the input data for fault indentification for futher analysis like ML techniques. Various unsupervised ML techniques used for in depth analysis has been covered in next sections.

Number of Faults Detection Using Clustering at Location DE

Machine learning techniques are very useful and popular in collaboration with experimental case study to confirm the fault anomalies in mechanical systems. The present work examines clustering techniques for fault diagnosis in mechanical systems by utilizing vibration data from two channels (CH1 and CH2) at the DE and NDE bearings. The primary faults examined by FFT is "Unbalance" and "Misalignment," which are routine issues in rotating machinery. To evaluate the effectiveness of clustering algorithms based on silhouette score is an essential indicator, specifically when it related to fault anomaly. A high silhouette score means that the samples are well clustered, however a score at or below zero indicates overlapping clusters. The silhouette score runs from -1 to +1. Two components are needed to calculate the silhouettes score for a single sample: the mean nearest cluster distance (b) and the mean intra cluster distance (a). Next, the definition of the silhouette score (s) is given by equation 1.

$$S=\frac{(b-a)}{\max(a,b)} \quad (1)$$

In this case, "a" represents the sample's average distance to every other point in its cluster, and "b" for the sample's average distance to the neighboring cluster. In clustering techniques, silhouette analysis helps to determine the optimal number of clusters that best represent the inherent fault conditions present in the collected data. K-means clustering was selected to identify clusters in vibration signal data collected from DE and NDE of machinery.

The Table 3 indicates that two clusters were formed in both channel readings (CH1 and CH2), correlated with the different fault detected by each channel. The silhouette scores achieved for these clusters were significantly high, CH1 achieves a maximum score of 0.996187 and CH2 reaches to 0.981164 for two clusters. This further supports the importance of the clustering approach in anticipating specific fault conditions. Above analysis aids in validating the clustering results and an invidance

Table 3. Number of clusters at location DE based on silhouette_score

Number of Clusters at Location DE	Silhouette_score	
	CH1	CH2
2	0.996187	0.981164
3	0.980444	0.967254
4	0.918261	0.926722
5	0.87416	0.810565
6	0.873087	0.811231
7	0.866591	0.659165
8	0.663202	0.576284
9	0.594666	0.586448

to support a robust framework to implement unsupervised machine learning techniques in fault detection scenarios.

Present study applied clustering techniques to the acquired vibration signal at the DE end bearing, with the number of clusters determined based on the silhouette score as indicated in Table 3. Silhouette score of both CH1 and CH2 for DE end cluster wise illustrated in Figure 6. It provides insight into the optimal number of clusters for each channel. Figure 7 shows visualization of cluster for CH1 and figure 8 for CH2 based highest silhouette scores. Which clearly highlights the separation between clusters and confirms the identification of distinct fault patterns at each location.

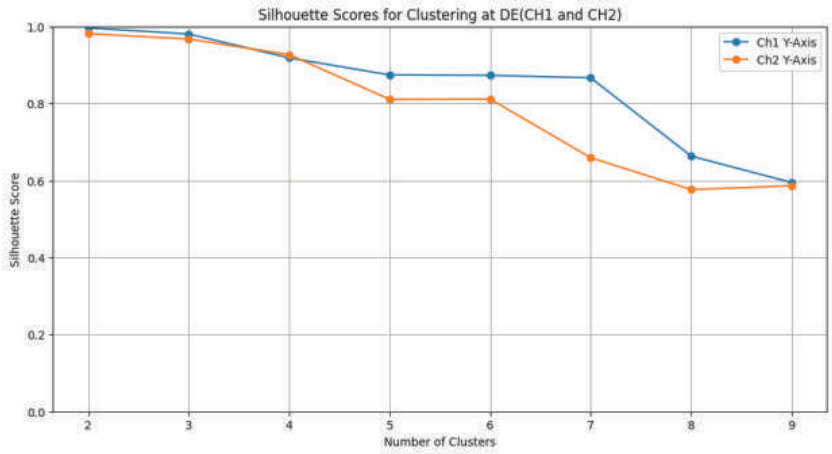


Figure 6. Cluster wise silhouette_score for CH1 and CH2.

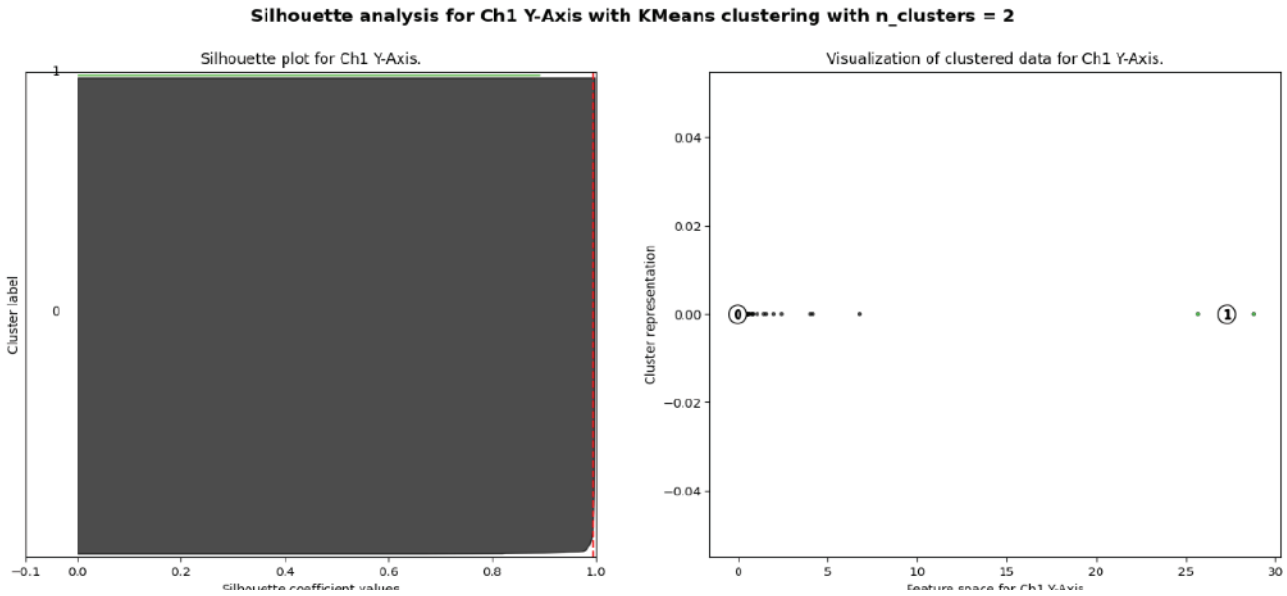


Figure 7. Visualization of Clusters for CH1 based on highest silhouette_score.

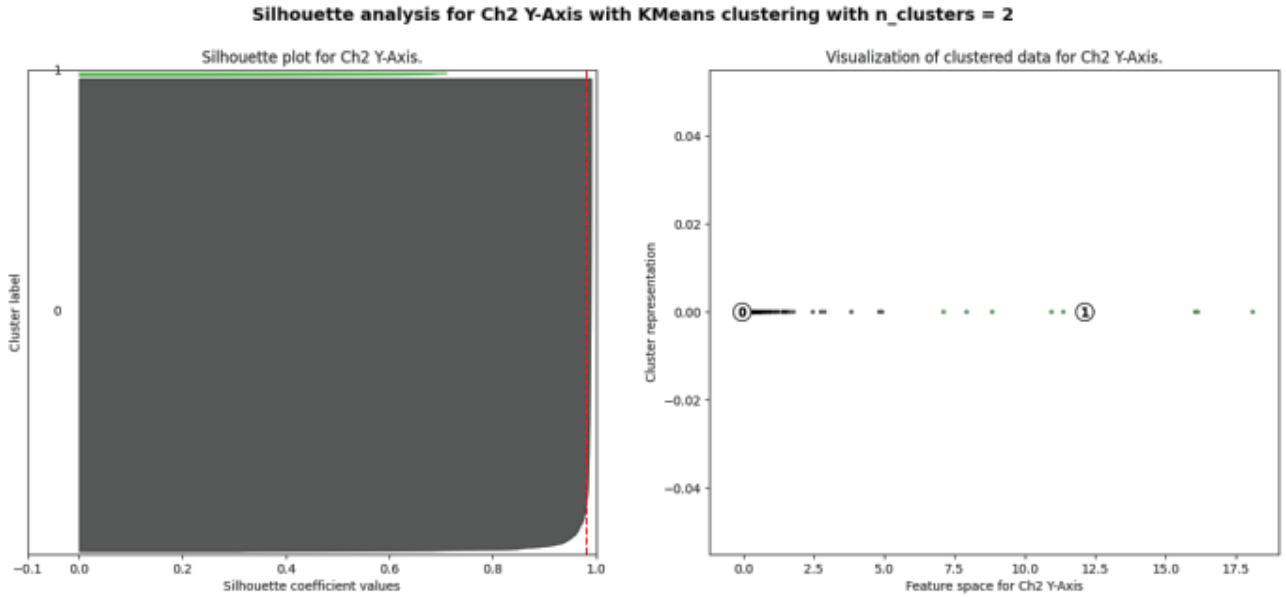


Figure 8. Visualization of Clusters for CH2 based on highest silhouette_score.

Dendrogram for Optimal Clustering

When using hierarchical clustering, a dendrogram is an effective tool that helps visualize the links and cluster structure among data points. It uses a tree shape diagram to show data points joined or seperated according to their relative similarity to produce clusters. Dendrogram determines optimal number of clusters are best for fault identification. A dendrogram is created by starting with every data point as a separate cluster. Clusters are progressively combined according to a predefined distance metric that measures dissimilarity from one another as the algorithm goes on. Iterative process continues till every point in dataset is convert into a cluster and provides a complete picture of the hierarchical structure for whole dataset. Dendrogram indicates that two distinct clusters were formed which reveals that different fault conditions present in the vibration signal data. Through investigation of the dendrogram, it has been quite clear that a point where the vertical line can be drawn to yield two clusters represents an significant level of separation and can distinguished the faults type. In this way, visual representation complements quantitative measures achieved by silhouette score. The confirmation of two clusters through the dendrogram envidence to the findings obtained from other clustering techniques and ensures a robust analysis of fault conditions in machinery.

The dendrogram analysis performed for both CH1 and CH2 confirms the presence of two optimal clusters

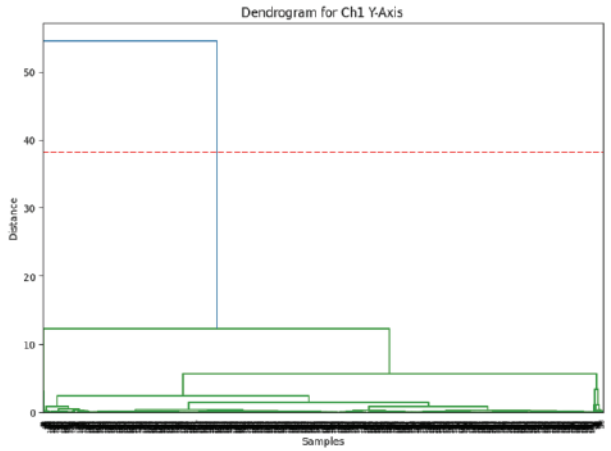


Figure 9. Dendrogram analysis showing 2 optimum clusters for CH1.

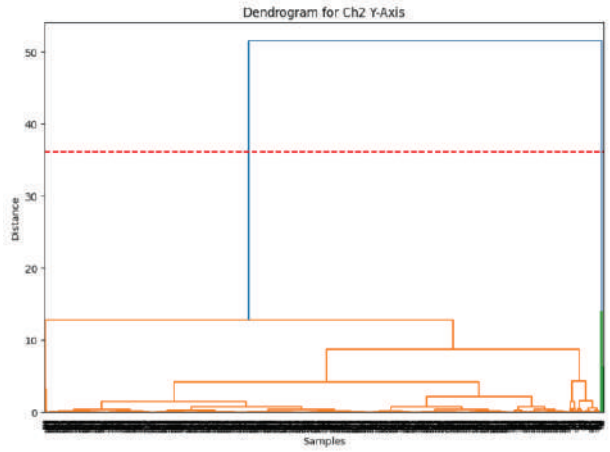


Figure 10. Dendrogram analysis showing 2 optimum clusters for CH2.

at each location. Figure 9 presents the dendrogram for CH1, shows two distinct clusters based on the hierarchical clustering method. Similarly, Figure 10 shows the dendrogram for CH2, reveals two optimal clusters indicates fault detection at both location. These analyses further validate the clustering results obtained through machine learning methods, ensuring accurate fault detection at both locations.

Elbow Method for Optimal Clustering

The author suggested elbow method one more approach to futher authenticate the results obtained through dendrogram a visual technique and silhouette score as quantitative approach. It plots within cluster variance against the total number of clusters is necessary to determine the elbow point or a point at which the rate of variation drastically drops. Ideal balance achieves between model complexity and interpretability by optimal number of clusters. The elbow method was applied to assess various cluster configurations. The results showed a pronounced decline in within cluster variance as the number of clusters increased. However, after reaches two clusters, the reduction in variance became less significant indicates a plateau. Plateau suggests that adding more clusters beyond this point does not significantly enhance the model ability to capture the data structure.

Dendrogram visualizations and silhouette scores results of two clusters further validated by complementary analysis of elbow method. Silhouette analysis indicated high values for two clusters and dendrograms illustrated a clear separation at two clusters, strengthen the conclusion that two distinct fault conditions are present in the data. It ensure that the selected model accurately represents the underlying characteristics of the machinery operational states. The Elbow method has been employed to determine the optimal number of clusters for both CH1 and CH2, as depicted in Figure 11 and Figure 12, respectively.

Anomaly Identification in Fault Diagnosis

Author proposed additional technique like anomaly identification pattern recognition technique serves as a powerful tool in the realm of fault diagnosis, specifically in identify the unusual patterns in signals. Anomaly pattern idetification technique was employed to recognize deviations from normal operational behavior of the vibration signals obtained from channels CH1 and CH2,. This technique aids in pinpointing potential faults that may not be normally noticeable through standard analysis procedure. The application of anomaly detection yielded two distinct patterns for both CH1 and CH2. First pattern aligned with unbalance and the other can line up with misalignment. While analyzed the vibration data, it can possible to isolate these patterns, confirms the presence of two clusters corresponds to the anticipated faults. The incorporation of anomaly detection with clustering techniques intensify the overall diagnostic capabilities. Clustering helps in grouping similar data points and locate general fault types. However, anomaly detection techniques focuses on unusual behavior within clustering groups. This comprehensive analysis with dual approach authenticate realtime machinery condition, leads to plan to more efficient maintenance strategies to improve operational reliability. Thus, the identification of two noticeable patterns strengthen the conclusion that each channel exhibits specific fault characteristics, further validate the importance of the adopted methodologies in fault diagnosis.

Anomaly indentification by pattern recognition has been employed to analyze the fault conditions at CH1 and CH2. Figure 13 demonstrates the anomaly detection at DE end bearing, authenticate clear pattern that aligns with the previously detected misalignment fault condition. Similarly, Figure 14 illustrates the anomaly detection at NDE end bearing, reveals a pattern consistent with the unbalance fault also authenticate by other methods. Above results further confirms the accuracy of the fault diagnosis and provide an additional layer of validation by pattern recognition technique.

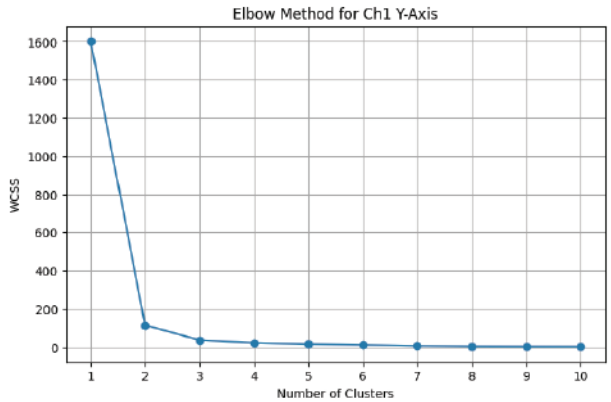


Figure 11. 2 optimal clusters for CH1.

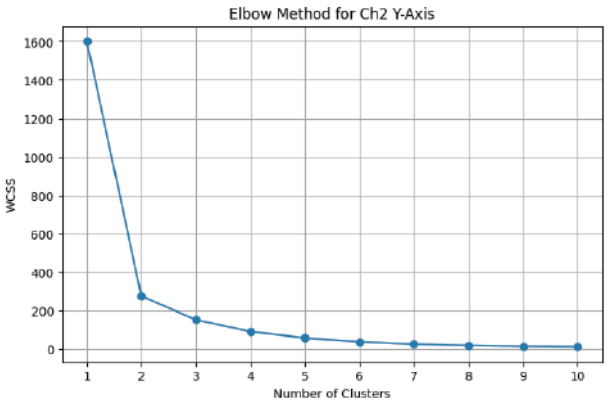


Figure 12. 2 optimal clusters for CH2.

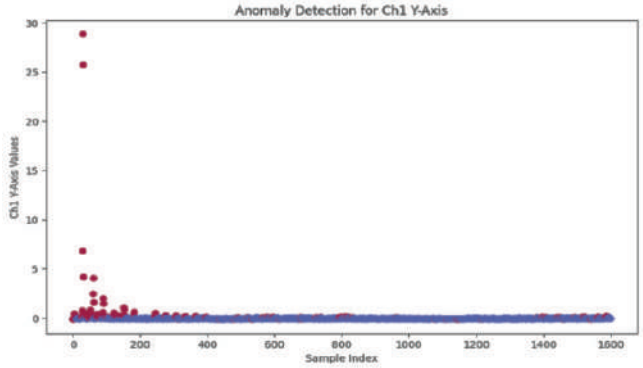


Figure 13. Anomaly detection for CH1 by pattern recognition.

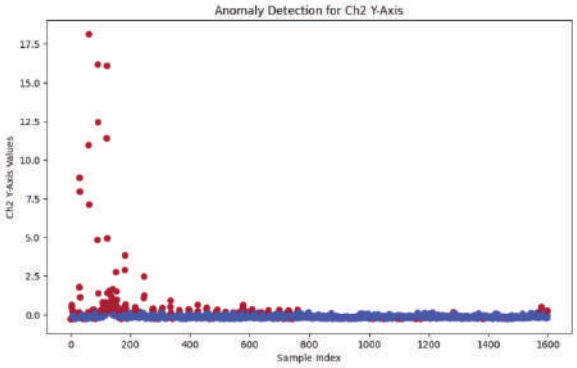
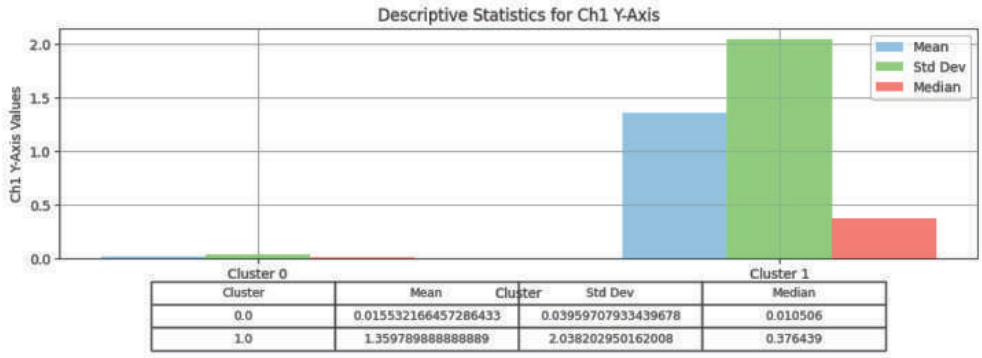


Figure 14. Anomaly detection for CH2 by pattern recognition.

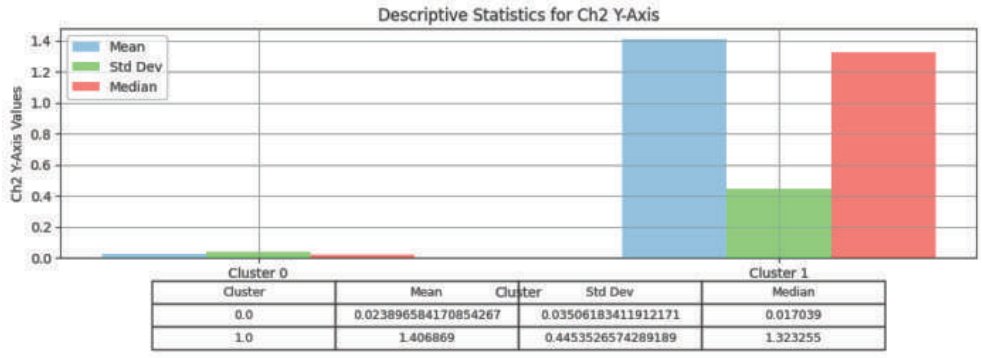
Descriptive Statistics

Current study employed one more analysis technique descriptive statistics play a pivotal role to identify and interpret the clusters within datasets, specifically for fault recognition and monitor through vibration analysis. summarized the characteristics of each cluster, descriptive statistics provides valuable insight into the behavior and properties of the dataset. It measures of central tendency, like the mean and median, indicates the central location of data points, reveals stark contrast between clusters. A mean of 0.0155 for Cluster 0 in Ch1 Y-Axis suggests lower vibration amplitudes compared to a mean of 1.3598 for Cluster 1, underline potential the fault states. Dispersion measures through standard deviation recognize about variability within each cluster; a lower standard deviation for Cluster 0 indicates consistent behavior, while a higher value for Cluster 1 may signal unconsistent presence associated with faults. Additionally, the ability to compare these statistics across clusters underscores their uniqueness, confirms that each cluster represents a distinct operating condition of the



Cluster	Mean	Std Dev	Median
0.0	0.015532166457286433	0.03959707933439678	0.010506
1.0	1.359789888888889	2.038202950162008	0.376439

Figure 15. Clusterwise descriptive statitics for CH1.



Cluster	Mean	Std Dev	Median
0.0	0.023896584170854267	0.03506183411912171	0.017039
1.0	1.406869	0.445352657428918	1.323255

Figure 16. Cluster wise descriptive statitics for CH2.

machine. Altogether, descriptive statistics not only validate clustering results but also provide actionable insights that can guide to plan maintenance strategies.

Descriptive statistics were performed for each cluster at both DE and NDE end to further analyze the vibration data. Figure 15 shows descriptive statistics for CH1 and representation of statistical parameters such as the mean, median, and standard deviation. It provides detailed insight into the characteristics of each cluster. Figure 16 displays the descriptive statistics for CH2, offers a statistical representation of the clusters. Statistical analysis highlights the difference between clusters and support the detection of distinct fault patterns at each location. Y-axis indicates the presence of two distinct clusters in both the figures, suggests the possibility of two different faults in the system. The CH1 in figure 15 shows mean value of 0.015532 and standard deviation value of 0.039597 without cluster, while the adding cluster shows a significantly rise in mean value reaches to 1.359790 and a standard deviation achives 2.038203 wihich is much higher. This stark contrast implicit that the underlying mechanisms contributing to the measurements, indicates the presence of distinct fault patterns. Similarly, from figure 16, the without cluster has a mean of 0.023897 and a standard deviation of 0.035062, where the second cluster's mean of 1.406869 and standard deviation of 0.445353. Significant differences in both the means and variabilities confirms the hypothesis of different fault conditions. Descriptive statistics approach highlights the potency of clustering techniques to recognize and differentiate faults, ultimately enables more targeted troubleshooting and maintenance strategies.

Histograms and Gaussian curves for both DE and NDE shown in figure 17 and figure 18 provides a visual representation of vibration data within each cluster. Figure 17

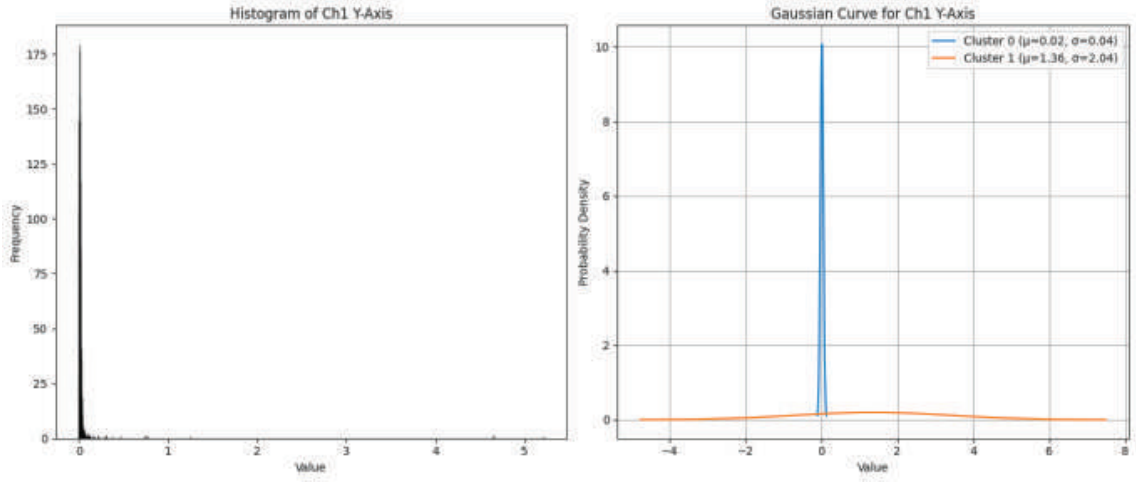


Figure 17. Histogram and gaussian curve for CH1.

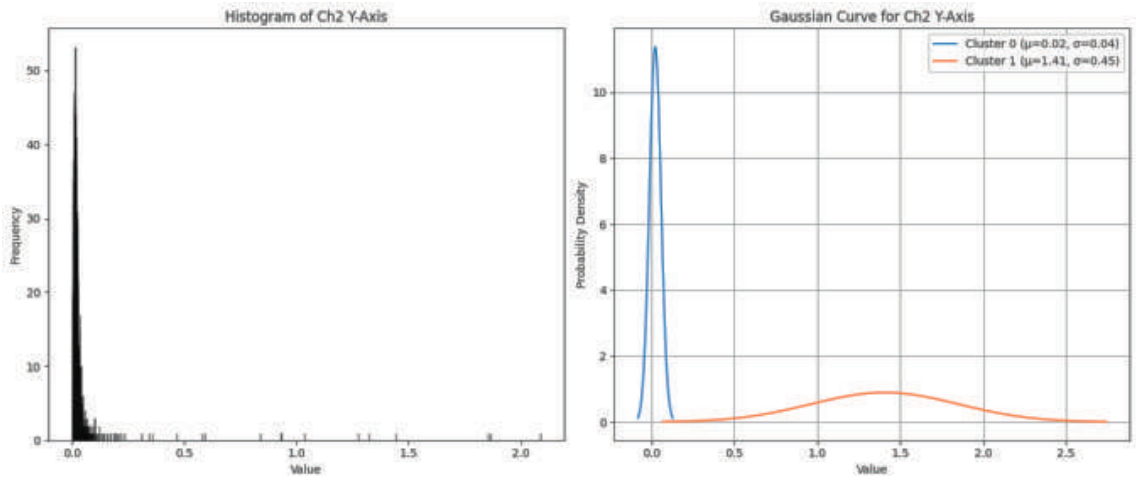


Figure 18. Histogram and gaussian curve for CH2.

Table 4. Cluster wise result analysis

Sr. No.	Channel	Location	Method	Criteria	Number of clusters	Number of possible faults
1	CH1	DE	K means	Max silhouette score	2	1
2			Dendrogram (hierarchical clustering)	Threshold line	2	1
3			Elbow method	Variance	2	1
4			Anomaly detection	Pattern	2	1
5			Descriptive statistics	Mean, mode, median, standard deviation, distribution	2	1
6	CH2	DE	K means	Max silhouette score	2	1
7			Dendrogram (hierarchical clustering)	Threshold line	2	1
8			Elbow method	Variance	2	1
9			Anomaly detection	Pattern	2	1
10			Descriptive statistics	Mean, mode, median, standard deviation, distribution	2	1
11	CH1	NDE	K means	Max silhouette score	2	1
12			Dendrogram (hierarchical clustering)	Threshold line	2	1
13			Elbow method	Variance	2	1
14			Anomaly detection	Pattern	2	1
15			Descriptive statistics	Mean, mode, median, standard deviation, distribution	2	1
16	CH2	NDE	K means	Max silhouette score	2	1
17			Dendrogram (hierarchical clustering)	Threshold line	2	1
18			Elbow method	Variance	2	1
19			Anomaly detection	Pattern	2	1
20			Descriptive statistics	Mean, mode, median, standard deviation, distribution	2	1

illustrates the histogram and Gaussian curve for DE end, shows the frequency distribution and it confirms that data to be normal distribution within the identified clusters. Similarly, figure 18 presents the histogram and Gaussian curves for NDE end bearing and frequncy data distribution visual and further supports the differentiation between the clusters. Visualizations are crucial to interpret the underlying patterns in the vibration signals and to validate the accuracy of fault diagnosis. Detail results for location DE and NDE for CH1 and CH2 are tabulated in Table 4.

The author proposed a novel unsupervised machine learning approach for fault idetification can be effectively implemented in real time industrial settings to strengthen modern data acquisition and processing technologies. K-means clustering algorithm computational efficiency can operate linear time complexity and shows its suitability for deployment on low-power industrial IoT platforms. System can automatically detect anomalies of fault patterns such as unbalance or misalignment based on clustering results and trigger alerts or schedule predictive maintenance to prevent unexpected equipment failures. Integrating unsupervised ML techniques into existing condition monitoring systems, industries can improve operational efficiency, reduce downtime, and optimize maintenance strategies, to enhance overall productivity and reliability.

CONCLUSION

The experimental results with unsupervised machine learning techniques reveals that without the need of label dataset the unspurivised ML techniques can use underlying data patterns to give a valuable insights. Multiple ML algorithms, including K-means clustering, hierarchical clustering, and anomaly detection can successfully identified two distinct faults patterns which also shown by FFT for CH1 and CH2 at two both DE and NDE bearing location. Accelerometers at DE end bearing mounted for both vertical (CH1) and horizontal (CH2) directions, characterized

by FFT a higher 2X peak in both directions indicates a misalignment fault. Similarly, at NDE end CH1 and CH2 FFT signifies a significant 1X peak can be intimated as a unbalance fault, likely due to ash deposition or fan blade wear. To validate the result by FFT current study employed various unsupervised machine learning algorithms. Clustering techniques has been adopted and findings reveals the effectiveness of the ML approaches to detect and distinguish between misalignment and unbalance faults. Dendrogram used to visualize the clustering results, elbow method for optimal clustering and descriptive statistics for statistical analysis, ensures more precise fault diagnosis and system reliability. Above all methods can accurately distinguish misalignment and unbalance faults. The present study used a novel unsupervised ML approaches for fault diagnosis can be used to optimize maintenance strategies.

AUTHOR CONTRIBUTIONS

All authors contributed to the study conception and design. material preparation, data collection and analysis were performed by [Ramesh Bhandare and Pankaj Beldar]. The first draft of the manuscript was written by [Ramesh Bhandare], review and editing done by [Shyam Mogal].

DATA AVAILABILITY STATEMENT

The authors confirm that the data that supports the findings of this study are available within the article. Raw data that support the finding of this study are available from the corresponding author, upon reasonable request.

CONFLICT OF INTEREST

The author declared no potential conflicts of interest with respect to the research, authorship, and/or publication of this article.

ETHICS

There are no ethical issues with the publication of this manuscript.

STATEMENT ON THE USE OF ARTIFICIAL INTELLIGENCE

Artificial intelligence was not used in the preparation of the article.

REFERENCES

[1] Jagtap HP, Bewoor AK, Kumar R. Failure analysis of induced draft fan used in a thermal power plant using coordinated condition monitoring approach: A case study. Eng Fail Anal 2020;111:104442. [CrossRef]

[2] Kurien C, Srivastava AK. Condition monitoring of systems in thermal power plant for vibration, motor signature, noise and wear debris analysis. World Sci News 2018;91:31–43.

[3] Kostyukov VN, Tarasov EV. Real-time condition monitoring of thermal power plants feed-pumps by rolling bearings supports vibration. J Phys Conf Ser 2012;364:012131. [CrossRef]

[4] Fahmi ATWK, Kashyzadeh KR, Ghorbani S. A comprehensive review on mechanical failures cause vibration in the gas turbine of combined cycle power plants. Eng Fail Anal 2022;134:106094. [CrossRef]

[5] Cho ST, Cho CH, Bae YC, Koo JR, Kim DY. Investigation and measures on high vibration phenomena of the low-pressure turbine hood in the combined thermal power plant. In: Proc Korean Soc Noise Vib Eng Conf; 2013. p. 186–187.

[6] Zhu L, Li Q, Bai G. Study on dynamic response and vibration reduction of medium-speed mills with spring vibration–isolated foundations in thermal power plants. Adv Mech Eng 2015;7:1687814015598695. [CrossRef]

[7] Li P, Pang L, Lin Z. Vibration fault diagnosis and dynamic balance processing analysis of blower in thermal power plant. IOP Conf Ser Earth Environ Sci 2020;467:012110. [CrossRef]

[8] Al-Najjar B. Improved effectiveness of vibration monitoring of rolling bearings in paper mills. Proc Inst Mech Eng Part J Eng Tribol 1998;212:111–120. [CrossRef]

[9] Al-Najjar, B. On the relation between operating conditions and changes in vibration signature: A case study in paper mill. OAP, International Condition Monitoring Conference, Technology Showcase, 226-235, April 19 to 24, 1998, Mobile, Alabama USA1998. p. 226.

[10] Hundi P, Shahsavari R. Comparative studies among machine learning models for performance estimation and health monitoring of thermal power plants. Appl Energy 2020;265:114775. [CrossRef]

[11] Chen KY, Chen LS, Chen MC, Lee CL. Using SVM based method for equipment fault detection in a thermal power plant. Comput Ind 2011;62:42–50. [CrossRef]

[12] Liu J, Li Z, Xiong Z, Wang H, Chen H, Shi L, et al. Investigation on abnormal long periodic vibration of nuclear steam turbine with machine learning method. Prog Nucl Energy 2024;174:105290. [CrossRef]

[13] Emmanuel T, Mpoeleng D, Maupong T. Power plant induced-draft fan fault prediction using machine learning stacking ensemble. J Eng Res 2024;12:82–90. [CrossRef]

[14] Gu ZY, Zhu YY, Xiang JL, Zeng Y. A prediction method of operation trend for large axial-flow fan based on vibration-electric information fusion. J Cent South Univ 2021;28:1786–1796. [CrossRef]

[15] Mogal S, Bhandre RV, Phalle VM, Kushare PB. Fault diagnosis and prediction of remaining useful life (RUL) of rolling element bearing: A review state of art. Tribol Finn J Tribol 2024;41:28–42. [CrossRef]

[16] Genç MO, Karaduman A. Investigation the modeling of genetic algorithm-based vehicle powertrain system optimization. Sigma J Eng Nat Sci 2020;38:123–133.

[17] Kumhar HS, Sarita K, Kumar S. Dynamic-balance monitoring scheme for industrial fans using neural-network based machine learning approach. In: Interdisciplinary research in technology and management. Boca Rotan, Florida: CRC Press; 2021. p. 612–618. [CrossRef]

[18] Sarita K, Devarapalli R, Kumar S, Malik H, Garcia Marquez FP, Rai P. Principal component analysis technique for early fault detection. J Intell Fuzzy Syst 2022;42:861–872. [CrossRef]

[19] Eratlı N, Ermiş M, Omurtag MH. Free vibration analysis of helicoidal bars with thin-walled circular tube cross-section via mixed finite element method. Sigma J Eng Nat Sci 2015;33:200–218.

[20] Özdemir YI. Parametric eigenvalue analysis of mindlin plates resting on winkler foundation with second order finite element. Sigma J Eng Nat Sci 2018;36:191–206.

[21] Kumar KS, Arun S, Mohan A, Muniamuthu S. Experimental analysis of noise and vibration reduction in windmill gear box for 5MW wind turbine. Int J Mech Eng Technol 2016;7:76–85.

[22] Kumar KS, Muniamuthu S, Mohan KR. Measurement of temperature flow analysis by condition monitoring system for WTG gear box to evaluate the thermal performance associated with plant load factor. J Therm Eng 2023;9:979–987. [CrossRef]

[23] Kumar KS, Raju DBN, Arulmani J, Amirthalingam P. Design and structural analysis of liquified cryogenic tank under seismic and operating loading. Int J Mech Eng Technol 2016;7:345–366.

[24] Muniamuthu S, Tharanisrisakthi BT. An investigation to estimate the maximum yielding capability of power for mini venturi wind turbine. Ecol Eng Environ Technol 2022;3:72–78. [CrossRef]

Sigma J Eng Nat Sci, Vol. 44, No. 1, pp. 465–477, February, 2026

Sigma Journal of Engineering and Natural Sciences
Web page info: https://sigma.yildiz.edu.tr
DOI: 10.14744/sigma.2025.00000

Research Article

Formation and analysis of thermal images for infrared radiations from top of the atmosphere

Usama Ayub YOUSUFZAI[1,2*], Muhammad Jawed IQBAL[1], Faisal AFRIDI[1]

[1]Institute of Space Science and Technology, University of Karachi, Karachi, 75270, Pakistan
2 Department of Physics, NED University of Engineering & Technology Karachi, 75270, Pakistan

ARTICLE INFO

Article history
Received: 30 September 2024
Revised: 02 December 2024
Accepted: 15 January 2025

Keywords:
Filtering Techniques; Infrared Radiations, Interpolating Techniques, IR Thermal Images, Top of The Atmosphere

ABSTRACT

This research focused on the designing and analysis of thermal images with different interpolating techniques and proposed three competitive Filtering algorithms for infrared radiations from the Synoptic top of the atmosphere and surface fluxes & clouds - SYN Ed4A, which is the data product of Clouds & the Earth's Radiant Energy System (CERES) used for collection of daily ten-year data for infrared radiations. This kind of study carried out first time in Pakistan. This work aims to enhance our comprehension of climate and weather systems, facilitated by the generation and analysis of thermal images capturing infrared radiation from the upper atmosphere. State of the art techniques in Modern technologies for creating and analyzing thermal images of infrared radiation from the upper atmosphere include complex calibration procedures, machine learning algorithms for improved image processing, and modern satellite sensors. This work is an attempt to investigate the quantification of infrared flux using different interpolating techniques and filtering algorithms. We discussed that how we interface MATLAB to data. As well as we also discussed about the generation of thermal maps and thermal images through MATLAB with different interpolating techniques. We will also discussed about filtering techniques for thermal images and proposed three different filtering algorithms. It also analyzed for the characterization of thermal images, which generated from different interpolated transformation and digital filtering techniques. We have used different techniques to devise digital filters and enhance the resolution of thermal images after that recognized and characterized thermal images of infrared radiations. We can use these algorithms for other different purposes based on the regular datasets like Data integration and fusion, Mitigating atmospheric inferences high resolutions image techniques, Long-term data consistency, advanced image processing algorithms etc.

Cite this article as: Yousufzai UA, Iqbal MJ, Afridi F. Formation and analysis of thermal images for infrared radiations from top of the atmosphere. Sigma J Eng Nat Sci 2026;44(1):465–477.

***Corresponding author.**
*E-mail address: usamaayub@neduet.edu.pk

This paper was recommended for publication in revised form by Editor-in-Chief Ahmet Selim Dalkilic

Published by Yıldız Technical University Press, İstanbul, Turkey
© Author. This is an open access article under the CC BY-NC license (http://creativecommons.org/licenses/by-nc/4.0/).

INTRODUCTION

The Earth and its atmosphere emit infrared radiation into space, which results in infrared flux rising from the top of the atmosphere. This radiation has a significant role in regulating the temperature of planet, as it is a component of the energy balance of the climate system [1].

The following are the primary sources of infrared radiation from the upper atmosphere:

Earth's Surface: Solar energy absorbed by the Earth's surface and reemitted as infrared radiation. One of the main sources of the infrared flux originating from the top of the atmosphere is this thermal radiation [2].

Atmospheric Gases: Water vapor, carbon dioxide, and methane are among the gases that emit infrared radiation from the Earth's atmosphere [3]. These gases add to the total flux of infrared radiation originating from the top of the atmosphere by both absorbing and reemitting thermal radiation.

Clouds: The emission of infrared radiation from the upper atmosphere significantly influenced by clouds. Their kind, altitude, and thickness determine how much they contribute to the total infrared flux [4]. They have the ability to both reflect and absorb thermal radiation.

The quantity of infrared flux originating from the upper atmosphere is a crucial component in comprehending the energy balance of the Earth and the worldwide climate [5]. It is also crucial for many other applications, such as climate modeling, weather forecasting, and satellite remote sensing. Furthermore, variations in the quantity and distribution of infrared flux can have a major influence on Earth's temperature and climate, which is why atmospheric science and climate research must pay close attention to this field of study [6]. The Sun is a source of visible light, but it also produces infrared radiation, which is a component of the electromagnetic spectrum. Actually, the Sun emits nearly half of its total energy as infrared radiation [7].

With a surface temperature of about 5,500 degrees Celsius, the Sun is a highly hot object that produces infrared radiation. The Sun emits radiation, including infrared radiation, as result of its extreme heat [8]. Telescopes and satellites are among the devices that may detect this energy, which carried through space as electromagnetic waves [9]. There are several uses for the Sun's infrared energy. It can used, for instance, to investigate the makeup and characteristics of the Sun's atmosphere and surface as well as the solar wind, a stream of charged particles that emerges from the Sun continuously [10]. The Sun's infrared radiation also has a significant impact on Earth's weather and climate [11]. It is the primary energy source for weather patterns and air circulation in the Earth's climate system. The Earth's surface and atmosphere absorb infrared radiation from the Sun, which then sent back into space as thermal radiation in the form of infrared waves [12]. The Earth's energy balance depends heavily on this thermal radiation, which also plays a major role in regulating the planet's temperature and climate [13].

All of the CERES (Clouds and the Earth's Radiant Energy System (CERES) Energy Balanced and Filled (EBAF) Top-of-Atmosphere (TOA)) footprints (20 km nominal resolution) within the specified temporal or spatial domain used to calculate the all-sky scene, also referred to as total [14]. There are a number of observations from 2011 to 2020. Depending on the product, Clear-Sky scenario offers multiple algorithms: ERBE-like, Energy Balanced and Filled (EBAF), Single Scanner Footprint TOA/Surface Fluxes and Clouds (SSF) [15]. Climatic zonal Longwave (LW) criteria and suitable Shortwave (SW) thresholds used by the Earth Radiation Budget Experiment (ERBE) scene id algorithm (Identifier) to select the clear-sky scene from CERES footprints that were inferred as clear. In this instance, the collection of observations dates back to 2011 to 2020.

For the regions without clouds, we were able to gather a set of observations for TOA infrared flux -All sky and TOA infrared flux -Clear Sky. The observations from CERES_EBAF-TOA_Ed4.1 span the years 2011 to 2020.

Data integration and fusion, mitigating atmospheric inferences, high resolution image techniques, long-term data consistency, advanced image processing algorithms, modeling thermal emission sources, impact of atmospheric dynamics, and real-time data processing are just a few of the gaps that this study will help us bridge [16].

The reason behind this study only for our understanding of climate and weather systems has advanced significantly due to the creation and analysis of thermal pictures for infrared radiations from the top of the atmosphere [17]. Notwithstanding the difficulties, multidisciplinary research and continuous technical development are improving the precision and usefulness of thermal imaging data, greatly advancing meteorology and climate science [18]. State of the art techniques in Modern technologies for creating and analyzing thermal images of infrared radiation from the upper atmosphere include complex calibration procedures, machine learning algorithms for improved image processing, and modern satellite sensors [19,20]. These developments make it possible to monitor atmospheric conditions with great precision and accuracy, which is essential for weather forecasting and climate science.

Practical Aspect

A precise methodology will followed in order to practically identified, how the atmospheric data retrieved from the NASA portal used to generate the conclusions for this research. Initially, the Earth's Radiant Energy System (CERES) Ordering Tool on NASA's Clouds would use to retrieve all available infrared flux data [21]. To effective prediction the radiative properties of the Earth, this data would be essential. Then, using this information, we would calibrate infrared sensors to correspond with the particular air conditions that noted during the data gathering [22]. The infrared radiation data would be processed using algorithms that take into consideration the atmospheric factors that retrieved from NASA's database to create the thermal images [23]. This

ensures that the images accurately represent the thermal emissions from the top of the atmosphere. The results would analyzed to identify trends or anomalies in infrared radiations [24]. This approach allows for a more accurate interpretation of the thermal images, linking observed radiation patterns directly to atmospheric conditions.

MATERIALS AND METHODS

Study Location and Data Collection

The required data sets have recorded from NASA website termed as Clouds and the Earth's Radiant Energy System (CERES) Energy Balanced and Filled (EBAF) Top-of-Atmosphere (TOA) Edition-4.0 and 4.1 Data Products [25]. Cloud ERES_EBAF_Ed4.1 Data Quality Summary, Investigation: CERES and Data Product: EBAF, Set of observations: Terra-MODIS (Instruments: CERES-FM1orCERES-FM2) and Aqua-MODIS (Instruments: CERES-FM3 orCERES-FM4, set of observations Version: Edition 4.1. The scope of the CERES Ordering Tool was to provide developers and users with a fast and easy way of accessing CERES Data by means of Visualization (or browsing) and Subsetting (or ordering) [26]. Spatial resolution was set to regional of Pakistan (global grid) with the coordinates 60.83333 W, 77.83333 E, 37.08333 N, and 23.583 S.

After downloading the file from the CERES ordering tool, the file opened in the software "Panoply". Panoply is a software platform that is compatible with desktop computers running on Windows, Macintosh, Linux, and other operating systems. A compatible version of Java 11 or later must installed on the computer to use the platform [27]. Here, Panoply used to extract a large amount of data in an Excel CSV file. The time parameter was not in the readable format for CSV. We have generated it using data transformation techniques for each year [28]. The generated date divided from year to months or quarters even we have divided it into days. By using data analytics approach, we have created pivot table and applied aggregation functions to find average yearly and monthly frequency distribution for data.

Software and Programming

In this section we will discussed the programming scripts written in MATLAB. For designing of thermal maps, a program script will initialize the data and it reads the data. After read and initializing the data and all parameters, we set 64 pixels data from 4×16 array. It outputs from Row-0 to Row-3. Each row consisting eight pixels, referenced from Col-0 to Col-15. The data starts from pixel-0 of Row-0 to pixel-15 of Row-0, then pixel-0 of Row-1 to pixel-15 of Row-1, this process continue up to the Row-3. Until, all 64 pixels data sent. It is not efficient to acquire 4×16 array data with separated rows. Through programming, we have convert 4×16 into 1×64 array as single frame to speed up data processing in MATLAB. After taking temperature values in 1×64, program will continue and take another frame. Otherwise, we will initialize again and start operation from the beginning.

Through MATLAB, we construct raw thermal images from data acquired in 1×64 frames. As well as this section describes enhancement and filtering techniques through MATLAB programming.

Enhancement of thermal images

Figure-1 shows the program flow for the construction and enhancement of thermal images for infrared radiations. As shown in figure, first MATLAB will interface with data. After interfacing, set all configuration values related to data as well as related to MATLAB. After setting all configuration values, an empty matrix of 4×16 created. MATLAB starts reading the data which coming from infrared in 1×64 array, as shown in Figure-2. Here, we set a

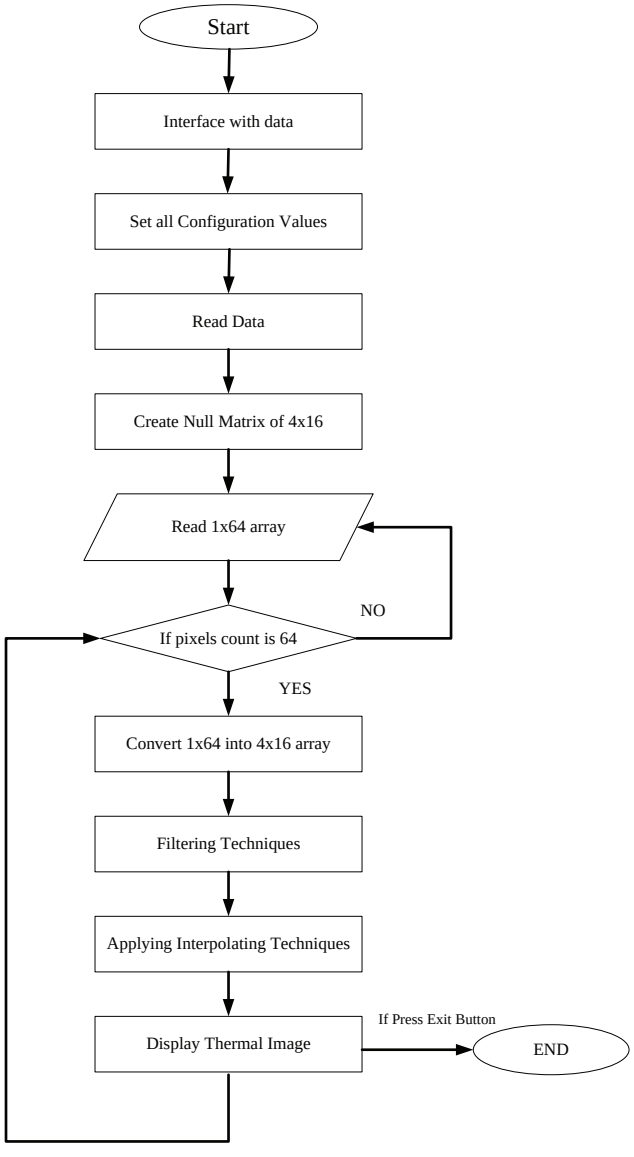


Figure 1. Program flow for the construction and enhancement of thermal maps.

condition that if interfacing system gives us 1×64 array, so, the program will execute further. Otherwise, take another next frame and so on [29]. After taking 1×64 array, convert this array again into 4×16, as shown in Figure-3. For graphical representation 'bargraph' plotting techniques has been used. As shown in Figure-4, we have used view command for setting the thermal array bar top on the front of the screen for using as a thermal screen. Text command has

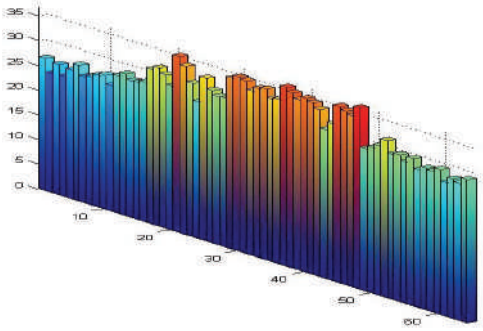


Figure 2. 1×64 Thermal pixels.

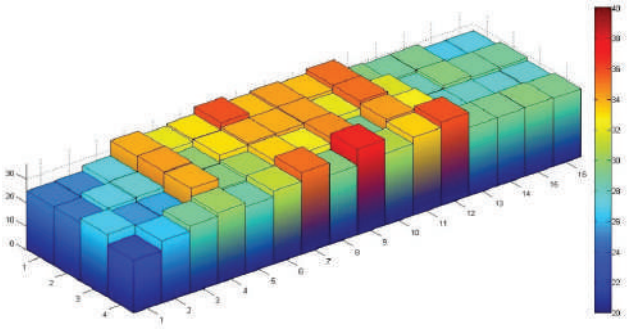


Figure 3. 4×16 Thermal pixels.

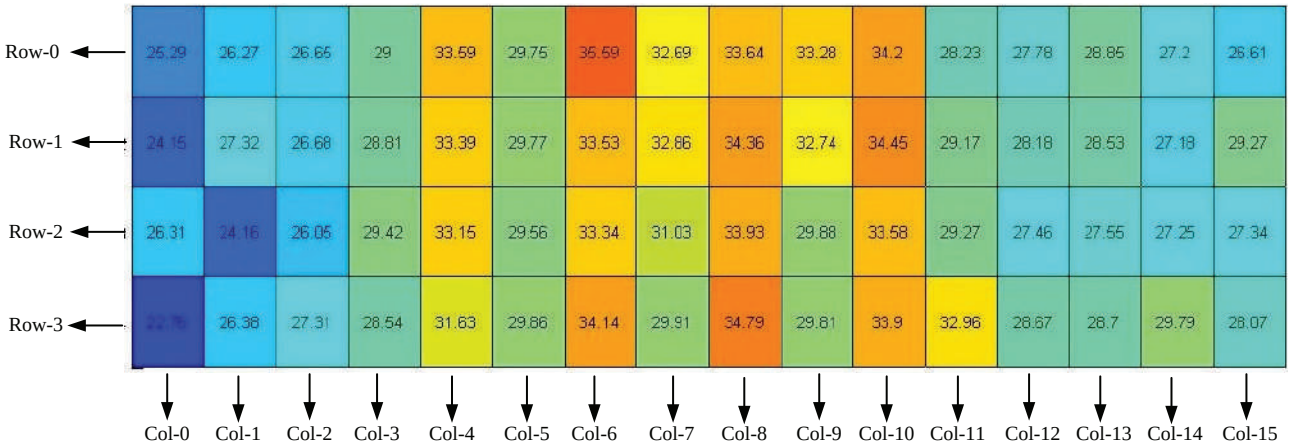


Figure 4. 4×16 Thermal Pixels with values.

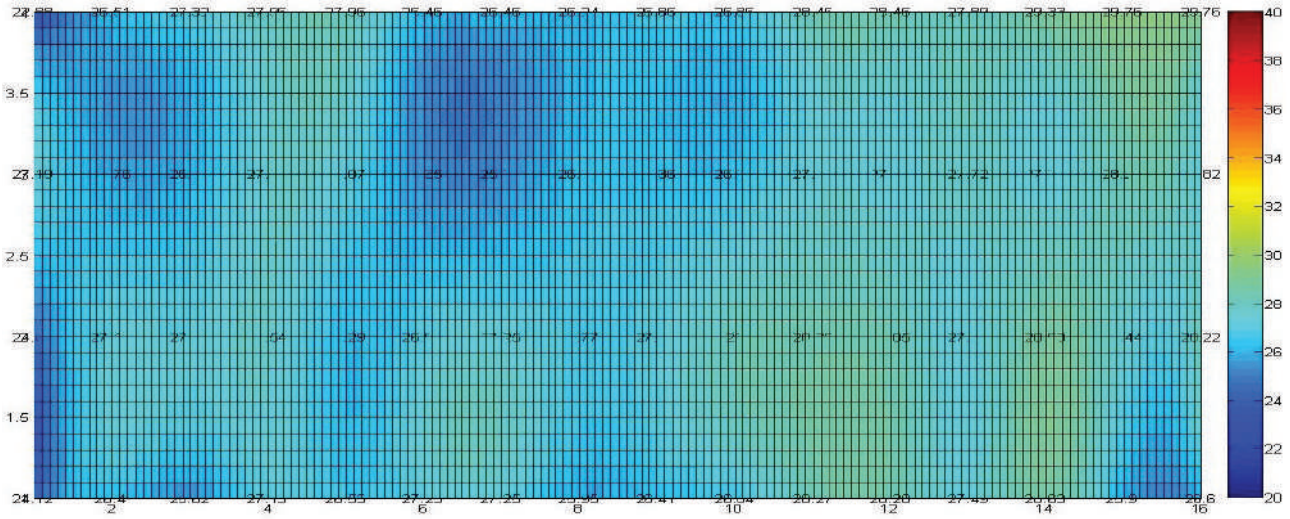


Figure 5. Thermal Image after enhancement in 31×151 array.

been used for display the values on each n every pixel of array. Range of the color bar is set from 20°C to 40°C by using command 'caxis' [7, 30].

Representation from colors

There are many color maps available in MATLAB e.g. Jet, HSV, Hot, Cool, etc. Here, we have used Jet color map, because the Jet color map is suitable for thermal mapping, because the in red color mapping represent the highest temperature and the dark blue color represents the lowest temperature [7]. The Jet based on the variation of HSV color map. The Jet designed by The National Center for Supercomputer Applications (NCSA) [8].

After generation of raw thermal image, interpolating techniques have used to enhance the thermal images, as shown in Figure-5. For this purpose, we have used surface command in place of bar graph and convert 4×16 array into 31×151 with the help of 'meshgrid' command [8]. For interpolating techniques, we have use 'interp' command. Four different methods of interpolation have compared, which will discussed in the next section. At the end, different filtering techniques for the elimination of the noise factor in the thermal images, has utilized [31]. The filtering techniques will discussed later.

Interpolating Techniques

Figure 6a shows the interpolation using nearest neighboring method. In this type, image will interpolate with the help of nearest cell. Comparatively this interpolation technique provide worst image and we cannot justify and analyze this image. The main disadvantage of nearest is the slow speed, due to which poor quality image have generated. Figure 6b shows the thermal image coming from linear interpolation method. According to mathematics, the curve fitting method with the help of linear polynomial known as linear interpolation [9, 10].

If we compare nearest and linear, the interpolated result from linear is much better than nearest method. Figure-6(c) shows the thermal image using cubic method. In this type of interpolation, pixels joined with respect to cubic polynomial. The speed is also much better than last two methods. This image is almost identical to the interpolated

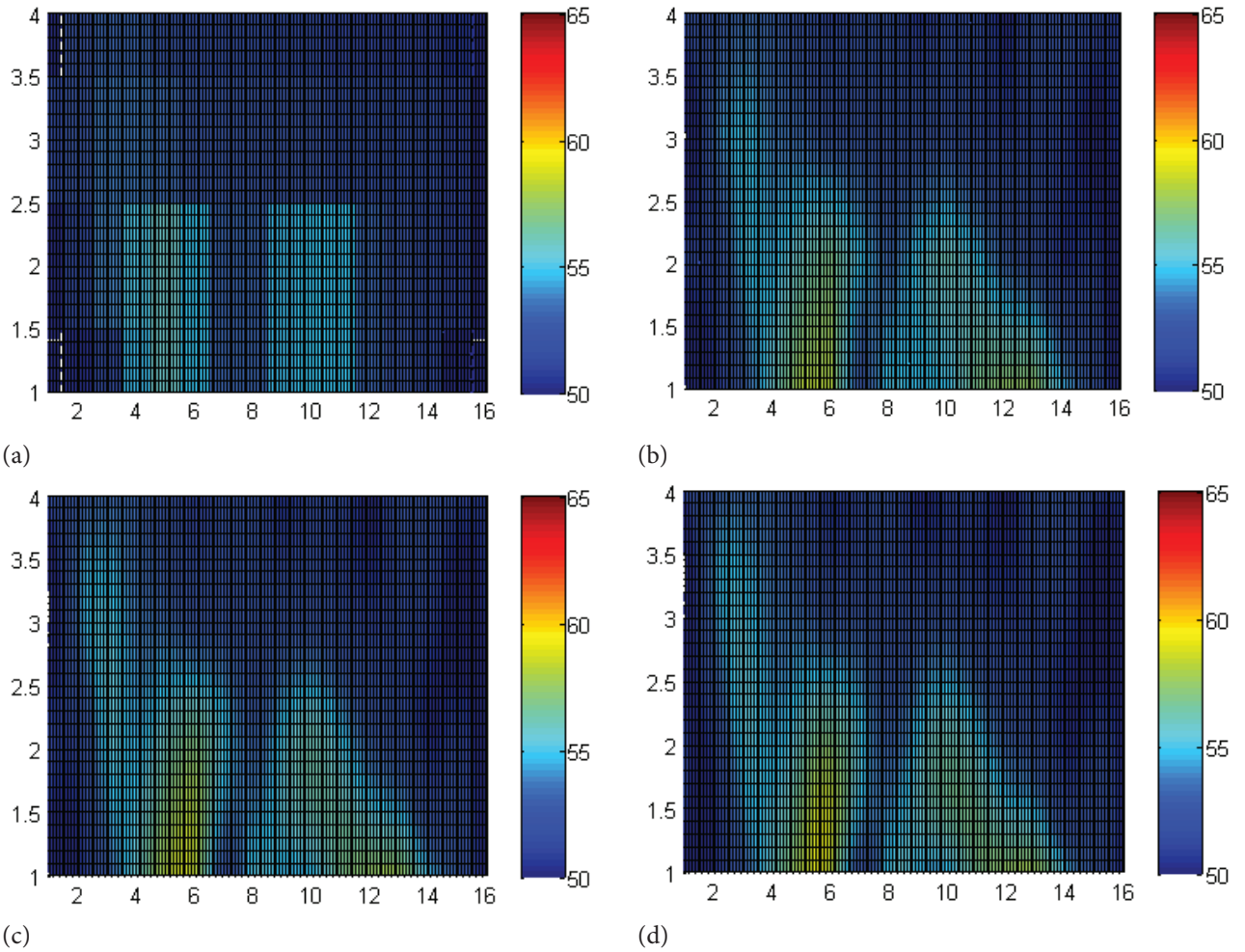


Figure 6. Thermal Image after using nearest, linear, cubic and spline interpolation.

image applying linear method. There is a difference, If we see in both the figures, the gaps between the pixels in Figure-6(c) is much clear than Figure-6(b). Figure-6(d) shows the thermal image using spline. The interpolation based on piecewise polynomial called as spline interpolation. Spline is coming from term elastic ruler. This type of interpolation preferred than others due to the interpolation error is much less. If we compare Figure-6(d) with others, so the thermal image generated from spline is much better than others. The noise factor is also very less as compare to other's thermal images.

Digital Filtering Techniques

In this paper, we focused on two already devised digital filters, which are median and conservative filter. Then focus on proposed Modified Conservative Filter (MCF) in three different inferences and compare the results of all three modified digital filters with each other as well as with conservative and median filter [11,12].

The median filter

The median filter used to remove noise from any signal or image. Median filtering technique is widely used in image processing and it is best for removing salt and pepper noise [10,13,14]. The Median filter is not suitable here. As we see in the Figure-7(a) the overall result of thermal image is poor and the image is not clear; we have a completely blurred image.

The conservative filter

In Conservative filter, generally the neighboring pixels of each n every pixel are select. In the next step, it finds minimum and maximum values in neighboring pixels. If the value is greater than maximum pixel value, the center pixel will be set at maximum value. If the value is less than the minimum pixel value, the center pixel will be set at the minimum value [14]. Figure-7(b) shows the thermal image after application of Conservative filter. Image becomes more improved. After this, we modify conservative filter into three different ways.

MCF-1

Figure-7(c) shows the result of thermal image after modification in conservative filter called as MCF-1 (Modification in Conservative Filter-1). The significance of this is to improve the frequency resolution. It impact on FFT means by increasing the amount of data points prior to performing a Fourier transform (FFT), zero padding produces a finer frequency resolution [32]. This makes it possible to identify frequency components with greater accuracy, particularly in situations where the original data was sparse or the frequencies were tightly spaced [13]. For example, a signal with 256 points zero-padded to 512 points will provide a frequency resolution twice as fine as the original [33]. Adjusting the amount of zero padding can help achieve the desired frequency resolution without unnecessarily increasing computational load [34]. For this modification, it get the double zero padding at the edges. Its means that, add two rows of zeros at above and at below of the array also add two columns of zeros at the left most and right most at the thermal frame. Select eight neighboring pixels for each n every pixel and repeat the same process, which already discussed in conservative filter. After application of this MCF-1, the image becomes noisy.

MCF-2

Figure-7(d) shows the thermal image after another modification in conservative filter called as MCF-2 (Modification in Conservative Filter-2). The significance of this is to reduce the edge effect because the finite length of the filter and the signal might cause distortion of the signal's edges when it filtered [35]. By supplying a buffer of zeros around the original signal, zero padding reduces these edge effects and makes sure that the signal's crucial components not distorted throughout the filtering process [10]. This modification also adapted zero padding, but here, it selects only four neighboring pixels. Through this filter, the image becomes better as compare to Figure-7(c).

MCF-3

Figure-7(e) shows the resulted thermal image after another modification in conservative filter called as MCF-3 (Modification in Conservative Filter-3). For this modification, the zero padding will again double. Here, we select total 24 neighboring pixels for the process of each n every pixel and repeat the same process discussed in conservative filter. Due to double zero padding and selection of 24 neighboring pixels, the noise factor becomes much less as compare to other schemes. The significance of this is to improve computational efficiency because it is possible to apply the FFT approach, which is computationally efficient for such lengths, by zero padding to a length that is a power of two. As a result, filtering processes take less computer power and time, increasing process efficiency [14]. The image quality also increases because we consider maximum neighboring pixels.

Now, if we compare the thermal image result of Figure-7(a), (b), (c), (d) and (e). Figure-7(e) is much better and the noise factor is very less as compared to median and conservative filter. The median filter is not suitable here. If we compare all three modification in conservative filter, so the last one modification which shown in Figure-7(e) is suitable than others.

RESULTS AND DISCUSSION

If we compare the image results of Figure-8(a), (b), (c), (d) and (e), so we observe that the Median Filter and MCF-1 are not suitable for our purpose and gave false interpolated thermal response as compared to other filters. Median filter perform well in other purposes but here, Median filter could not work properly. Where, the image result after applying proposed MCF-3, MCF-2 and Conservative filter becomes

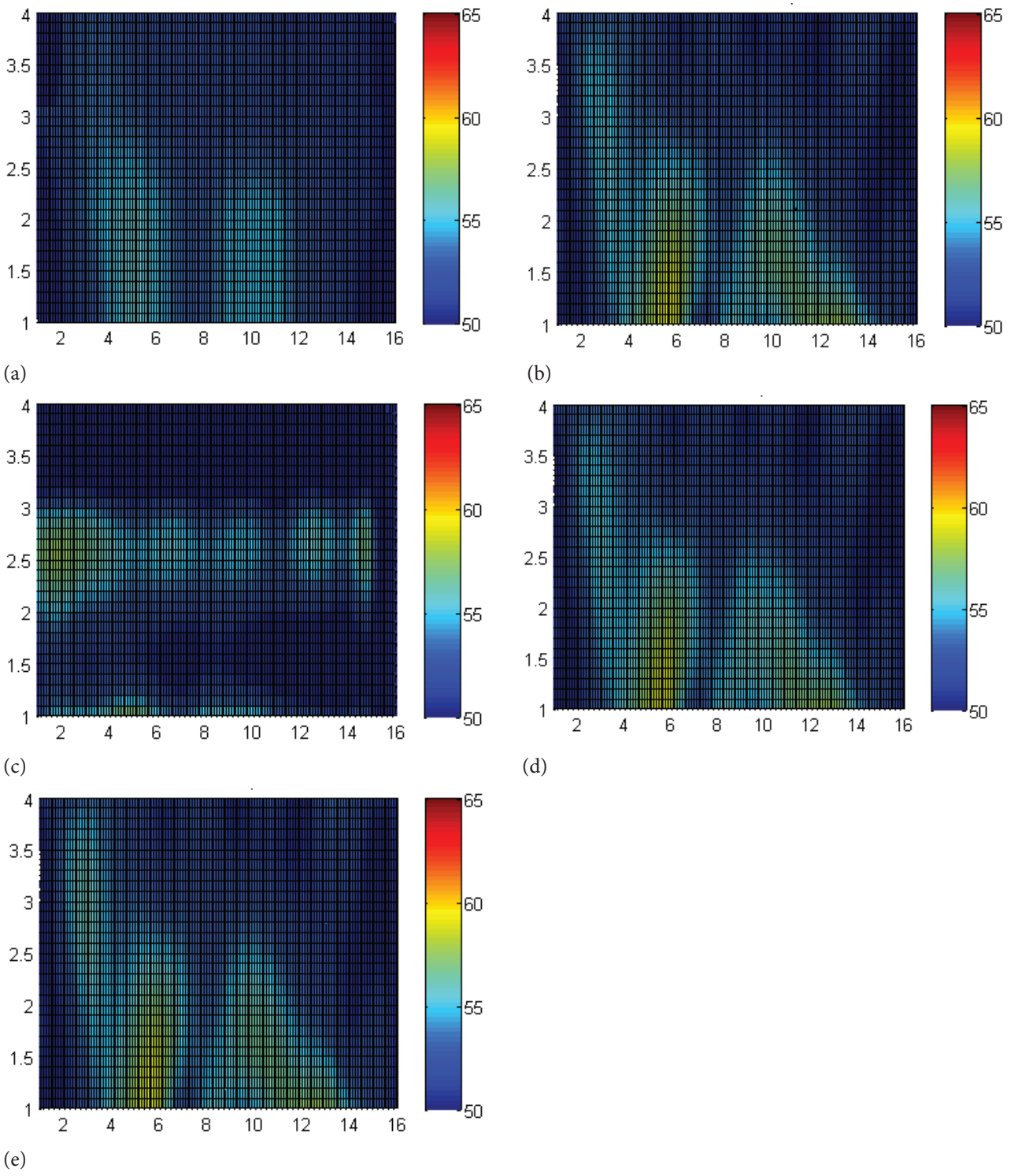


Figure 7. Thermal Image after using median, conservative, MCF-1, MCF-2 and MCF-3 filters.

good. In all these three filters, the proposed MCF-3 gives much better thermal contrast as compare to MCF-2 and Conservative filter. If we discuss about interpolating techniques, so the sp-line method gives much better and high quality images as compared to cubic, linear and nearest.

We are taking the data of infrared radiations and here we will select Row-27 of 31 interpolated rows for quantitative analysis. Figure-9(a), (b), (c), (d) and (e) shows the thermal response of interpolated-Row-27 (Interp-R27) of 31 rows of Figure-8(a), (b), (c), (d) and (e) respectively. Blue, Green, Red and Aqua color shows the response of the interpolating

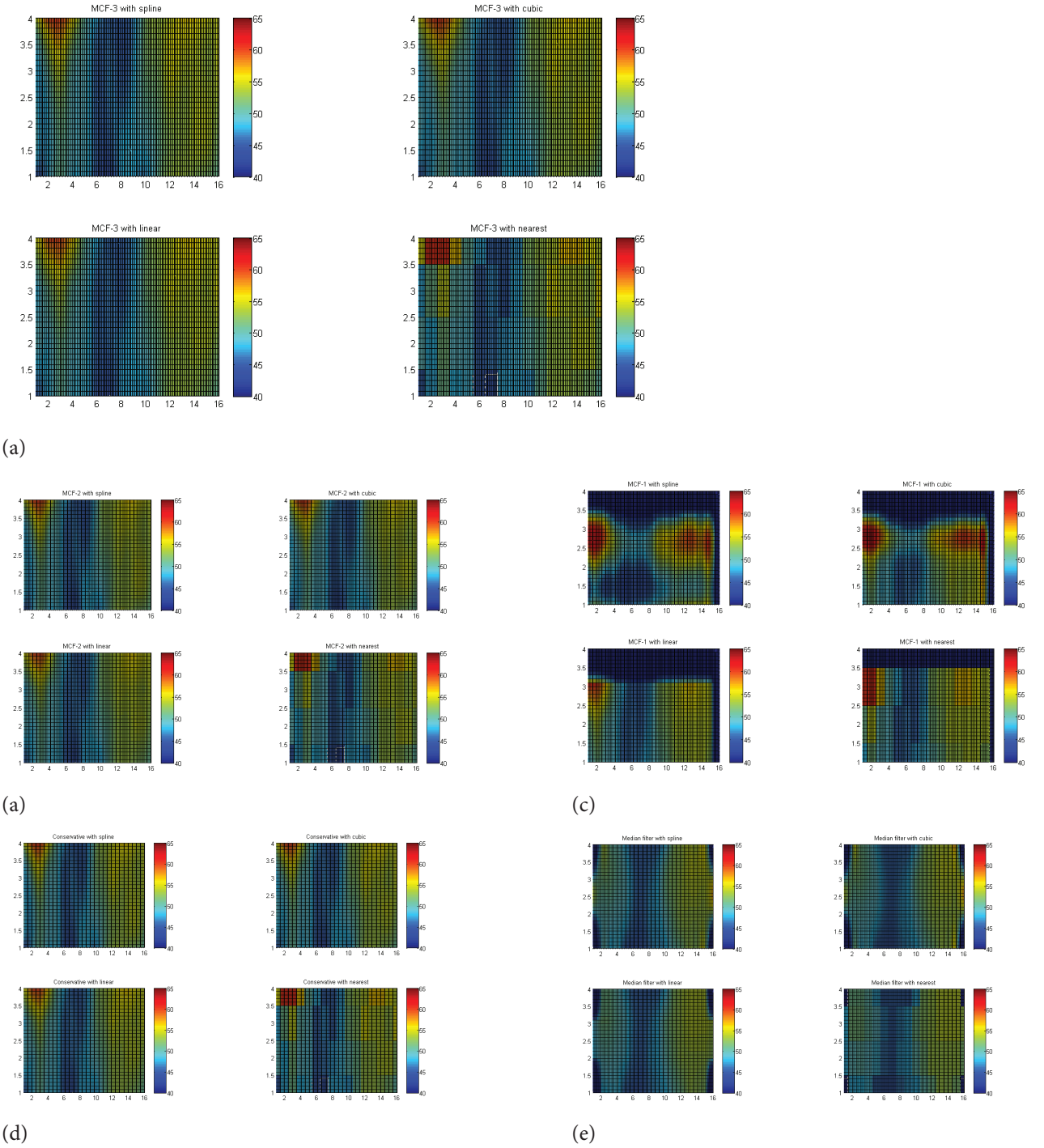
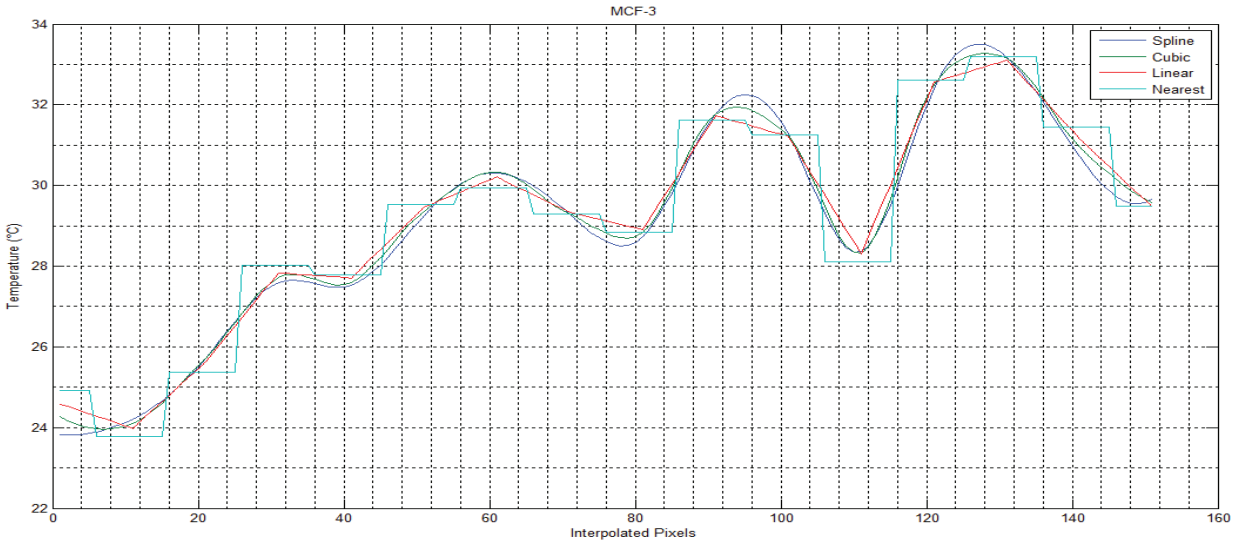


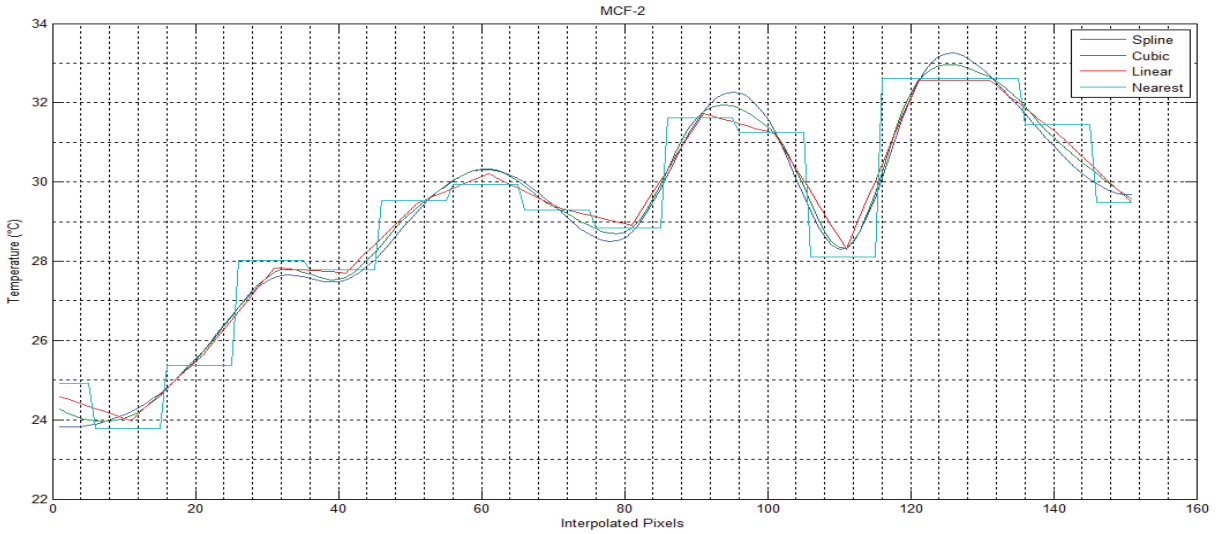
Figure 8. Thermal response of MCF-3, 2, 1, conservative and median filter with interpolations.

methods of Sp-line, Cubic, Linear and Nearest respectively. All the responses drawn graphically with the help of data and the interpolated pixels. Here, we can clearly see that proposed MCF-3 gives much better response comparatively where the Median and MCF-1 gives poor response.

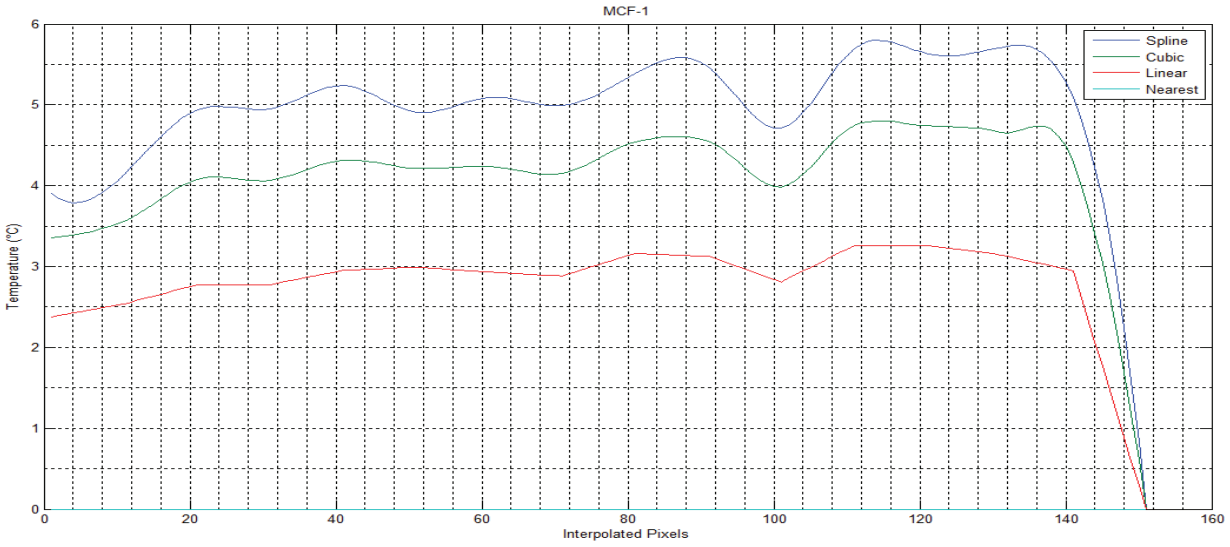
Table 1 to Table 5 shows the extracted data from Figure-9(a) to Figure-9(e) respectively. In these tables, 'Min1' shows the first minima data values where 'Min2' shows the second minima data values. 'Max1', 'Max2' and 'Max3' show the maxima data values at the top. 'DF1' and 'DF2' show the contrasts values which are related to 'Min1-Max1' and 'Min1-Max2' respectively, where 'DDF1' shows the contrast related to 'DF1' and 'DF2' with all four interpolating techniques using MCF-3, MCF-2, MCF-1, Conservative and Median Filter separately. 'D1' and 'D2' also show the contrasts, which are relate to 'Min2-Max2' and 'Min2-Max3' respectively, where 'DDF2'


MCF-3
Spline
Cubic
Linear
Nearest
Temperature (°C)
Interpolated Pixels

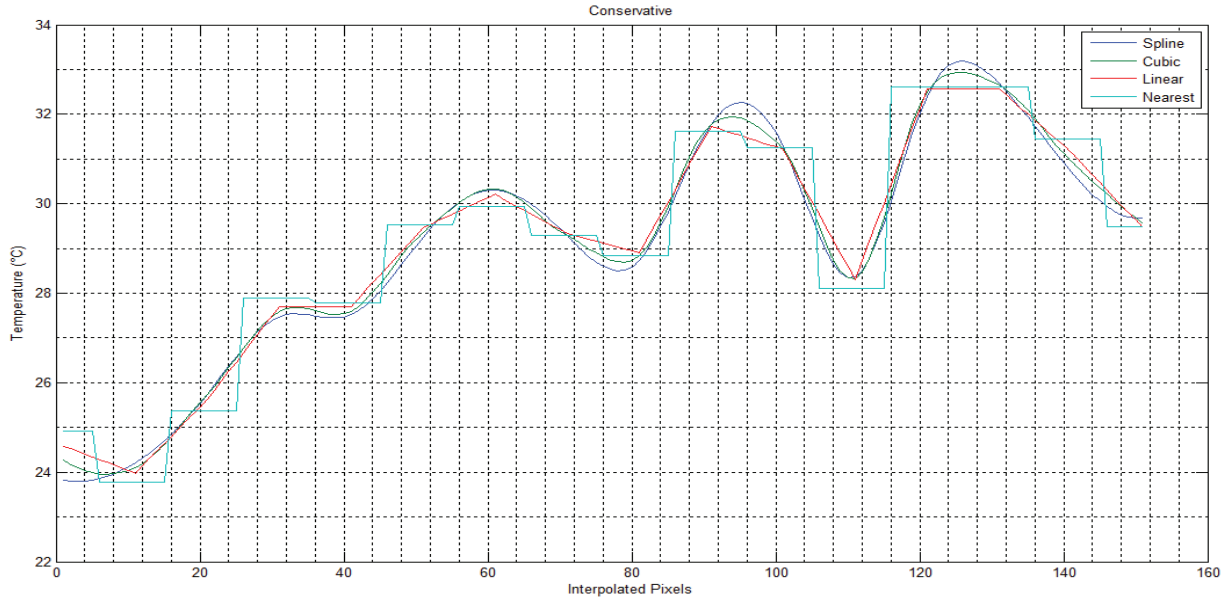
(a)


MCF-2
Spline
Cubic
Linear
Nearest
Temperature (°C)
Interpolated Pixels

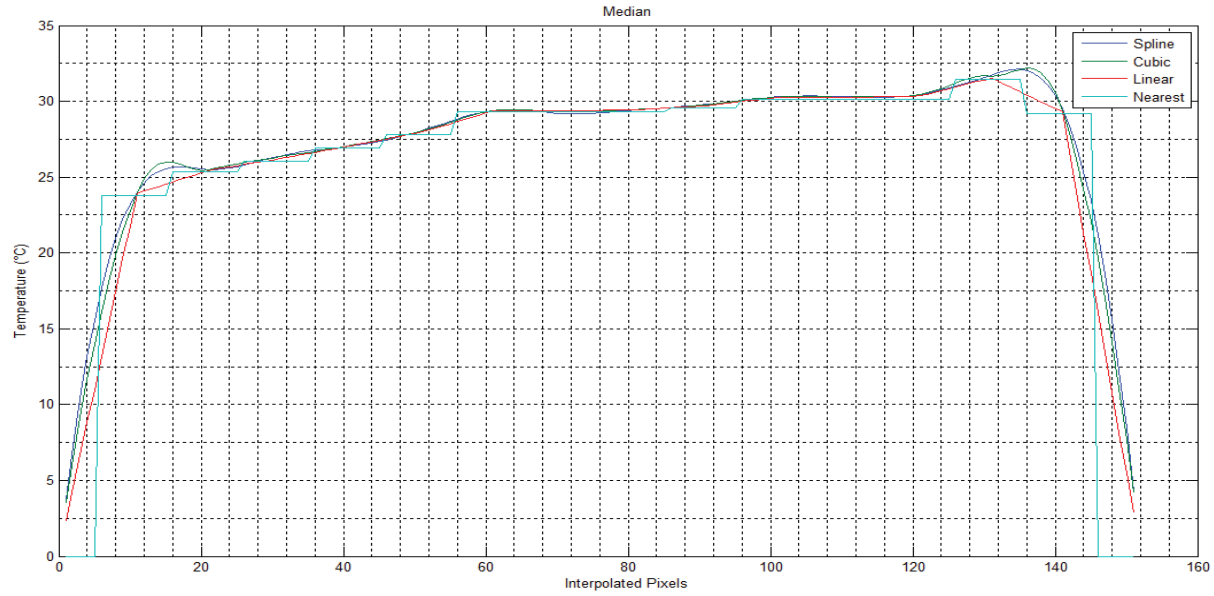
(b)


MCF-1
Spline
Cubic
Linear
Nearest
Temperature (°C)
Interpolated Pixels

(c)



(d)



(e)

Figure 9. Thermal response of interpolated row-27 with different proposed filters.

Table 1. Data table of Figure 9a

	MCF3											
	Min	**Min2**	**Max1**	**Max2**	**Max3**	**DF1**	**DF2**	**DDF1**	**D1**	**D2**	**DDF2**	**DDF**
Spline	28.9	30	32.9	32.7	32.8	3.93	3.74	0.18	2.65	2.72	0.07	0.71
Cubic	28.9	30	32.9	32.7	32.8	3.93	3.74	0.18	2.65	2.72	0.07	0.72
Linear	28.9	30	32.9	32.7	32.8	3.93	3.74	0.18	2.65	2.72	0.07	0.71
Nearest	28.9	30	32.9	32.7	32.8	3.93	3.74	0.18	2.65	2.72	0.07	0.71

Table 2. Data table of Figure 9b

	MCF2											
	Min	**Min2**	**Max1**	**Max2**	**Max3**	**DF1**	**DF2**	**DDF1**	**D1**	**D2**	**DDF2**	**DDF**
Spline	29	30.1	32.9	32.7	32.7	3.91	3.72	0.19	2.61	2.65	0.04	0.14
Cubic	29	30.1	32.9	32.7	32.7	3.91	3.72	0.19	2.61	2.65	0.04	0.14
Linear	29	30.1	32.9	32.7	32.7	3.91	3.72	0.19	2.61	2.65	0.04	0.14
Nearest	29	30.1	32.9	32.7	32.7	3.91	3.72	0.19	2.61	2.65	0.04	0.14

Table 3. Data table of Figure 9c

	MCF1											
	Min	**Min2**	**Max1**	**Max2**	**Max3**	**DF1**	**DF2**	**DDF1**	**D1**	**D2**	**DDF2**	**DDF**
Spline	29.5	29	31	33.1	34.2	1.55	3.65	2.11	4.08	5.21	1.13	0.1
Cubic	29.5	29	31	33.1	34.2	1.55	3.65	2.11	4.08	5.21	1.13	0.1
Linear	29.5	29	31	33.1	34.2	1.55	3.65	2.11	4.08	5.21	1.13	0.1
Nearest	29.5	29	31	33.1	34.2	1.55	3.65	2.11	4.08	5.21	1.13	0.1

Table 4. Data table of Figure 9d

	Conservative											
	Min	**Min2**	**Max1**	**Max2**	**Max3**	**DF1**	**DF2**	**DDF1**	**D1**	**D2**	**DDF2**	**DDF**
Spline	28.9	30	32.9	32.7	32.8	3.91	3.73	0.19	2.63	2.72	0.09	0.49
Cubic	28.9	30	32.9	32.7	32.8	3.91	3.73	0.19	2.63	2.72	0.09	0.49
Linear	30.8	30.2	32.5	32.8	33.5	1.74	1.97	0.23	2.55	3.29	0.73	0.5
Nearest	30.8	30.2	32.5	32.8	33.5	1.74	1.97	0.23	2.55	3.29	0.73	0.5

Table 5. Data table of Figure 9e

	Median											
	Min	**Min2**	**Max1**	**Max2**	**Max3**	**DF1**	**DF2**	**DDF1**	**D1**	**D2**	**DDF2**	**DDF**
Spline	29.9	31.2	30.2	31.4	32.5	0.23	1.46	1.23	0.19	1.33	1.14	0.08
Cubic	29.9	31.2	30.2	31.4	32.5	0.23	1.46	1.23	0.19	1.33	1.14	0.08
Linear	29.9	31.2	30.2	31.4	32.5	0.23	1.46	1.23	0.19	1.33	1.14	0.08
Nearest	29.9	31.2	30.2	31.4	32.5	0.23	1.46	1.23	0.19	1.33	1.14	0.08

shows the contrast related to 'D1' and 'D2'. In the end 'DDF' Show the overall contrast result, which are relate to 'DDF1' and 'DDF2'. The data collected separately with different filters and four different interpolating techniques so, the data values show clearly for each method of interpolation with different filters in the data tables, which given below. When we compare the contrast result of Table 1 to Table 5 so, it is clearly evident that the contrast of Sp-line is much greater than Cubic, Linear and Nearest as well as the contrast result of MCF-3 is greater than other filters where Median filter gives very low contrast.

Figure-10 shows the comparison of contrast of proposed MCF-3, MCF-2, MCF-1, Conservative and Median Filter with respect to Sp-line, Cubic, linear and nearest techniques of interpolation. Here, we can clearly see that the contrast of MCF-3 is much better than the other filters where the Median filter gives low contrast as well as we can also see that the Sp-line method of interpolation works best as compare to Cubic, linear and nearest, where the nearest neighboring method of interpolation gave poor results as compare to others.

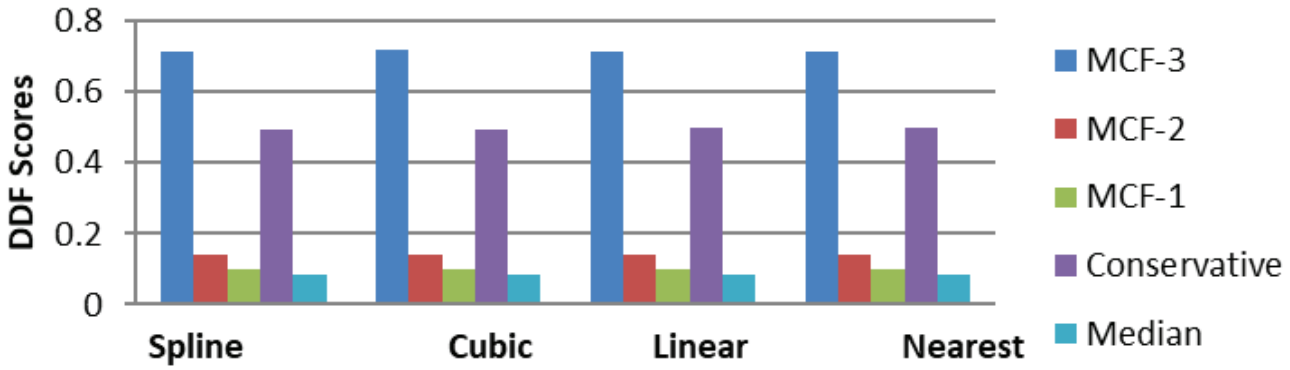


Figure 10. Comparison of contrast.

CONCLUSION

In this work, we gathered daily data values for Pakistan's upper atmosphere from the Synoptic TOA and surface fluxes and clouds (SYN) Ed4A, a data product of Clouds and the Earth's Radiant Energy System (CERES). This study aims to explore the quantification of infrared flux through exploratory data analysis. Using the results from the infrared data, we construct and analyze the thermal images. We demonstrated that, when compared to other interpolation techniques, the Sp-line method produced the best results, whereas the closest method produced subpar results. In addition to developing the Conservative and Median Filters, we employed the three suggested Modified Conservative Filters (MCF), namely MCF-1, MCF-2, and MCF-3. We found that, in comparison, our suggested Modified Conservative Filters – 3 (MCF-3) produces the greatest outcomes, while Median Filters did not produce results that were suitable. Therefore, thermal images of Modified Conservative Filters – 3 (MCF-3) are far superior to others. To improve the infrared array, use several enhancing approaches. The suggested data has much noise factors, but we make an effort to reduce them by using various filters that have been developed and suggested. We used Modified Conservative Filters – 3 (MCF-3) to assist us eliminate a lot more noise components. With the aid of various datasets, we may apply these methods for a plethora of additional uses. By creating more sophisticate filtering algorithms, in the future the noise factor will decreased. The thermal images produced by the Median Filter in this case were entirely blurry. Another question is why does the median filter fail so miserably in this case? The noise factors increased as the image size increased as we were improving the thermal images. Thus, the topic of how to improve thermal imaging without raising noise levels remains for the future.

AUTHORSHIP CONTRIBUTIONS

Authors equally contributed to this work.

DATA AVAILABILITY STATEMENT

The authors confirm that the data that supports the findings of this study are available within the article. Raw data that support the finding of this study are available from the corresponding author, upon reasonable request.

CONFLICT OF INTEREST

The author declared no potential conflicts of interest with respect to the research, authorship, and/or publication of this article.

ETHICS

There are no ethical issues with the publication of this manuscript.

STATEMENT ON THE USE OF ARTIFICIAL INTELLIGENCE

Artificial intelligence was not used in the preparation of the article.

REFERENCES

[1] Frank, Michalsky J. Solar and infrared radiation measurements. 2nd ed. Michigan: Taylor & Francis Group; 2020.

[2] Zhang H, Rao P, Xia H, Weng D, Chen X, Li Y. Modeling and analysis of infrared radiation dynamic characteristics for space micromotion target recognition. Infrared Phys Technol 2021;116. [CrossRef]

[3] Ozaki Y, Huck C, Tsuchikawa S, Engelsen SB. Near-infrared spectroscopy: Theory, spectral analysis, instrumentation, and applications. Singapore: Springer; 2021. [CrossRef]

[4] Rogalski A. Infrared and terahertz detectors. 3rd ed. Warsaw: Taylor & Francis Group; 2019. [CrossRef]

[5] Hou F, Zhang Y, Zhou Y, Zhang M, Lv B, Wu J. Review on infrared imaging technology. Sustainability 2022;14:2. [CrossRef]

[6] Coakley JA, Yang P. Atmospheric radiation. Wiley-VCH Verlag; 2014.
[7] MathWorks. MATLAB and Simulink for Engineered Systems Available at: www.mathworks.com Accessed on Feb 13, 2025.
[8] Rao J, Zheng S, Yang Y. Integrating supercomputing and artificial intelligence for life science. Patterns 2022;3:100653. [CrossRef]
[9] Verovkina G. Research in the interpolation representations of stochastic processes in the two types of interpolation knots. Eureka Phys Eng 2017;2:3–8. [CrossRef]
[10] Gonzalez RC, Woods RE, Eddins SL. Digital image processing using MATLAB. 2nd ed. New Delhi: McGraw Hill Education Pvt Ltd; 2010.
[11] Gajalakshmi N, Karunanithi S. Cubic convolution and osculatory interpolation for image analysis. Int J Creat Res Thoughts 2021;9:836–842.
[12] Pennucci TT. Frequency-dependent template profiles for high-precision pulsar timing. Astrophys J 2018;871. [CrossRef]
[13] McAndrew A. A computational introduction to digital image processing. 2nd ed. Melbourne: CRC Press; 2016. [CrossRef]
[14] Qidwai U, Chen CH. Digital image processing: An algorithmic approach with MATLAB. New York: CRC Press; 2010.
[15] Lyu X. Recent progress on infrared detectors: Materials and applications. Highlights Sci Eng Technol 2022;27:191–200. [CrossRef]
[16] Li Y, Zhou H, Li T, Wang Y, Liu Y, Wang Y. CMOS-compatible 8×2 thermopile array. Sens Actuators A Phys 2010;161:120–126. [CrossRef]
[17] Gonzalez LIL, Troost M, Amft O. Using a thermopile matrix sensor to recognize energy-related activities. In: 3rd Int Conf Sustain Energy Inf Technol (SEIT 2013); 2013. [CrossRef]
[18] Reimers M, Kolkwitz B, Beck D, Sarma M, Heinzel C, Lang W, et al. Steel integrated IR thermopile array for characterizing grinding processes. Procedia Eng 2016;168:1568–1572. [CrossRef]
[19] Wang HJ, Liu MM, Shi CC. The design of MLX90621 based intelligent lighting control system. In: Int Conf Comput Netw Commun Technol (CNCT 2016); 2016. [CrossRef]
[20] Melexis. Datasheet IR16×4. Available at: https://datasheet4u.com/datasheets/Melexis/MLX90620/1093410 Accesed on Sep 16, 2016.
[21] Ruminski D, Palczewska G, Nowakowski M, Zielińska A, Kefalov VJ, Komar K, et al. Two-photon microperimetry: Sensitivity of human photoreceptors to infrared light. Biomed Opt Express 2019;10:4551–4567. [CrossRef]
[22] El-Azazy MM. Infrared spectroscopy principles, advances, and applications. London: IntechOpen; 2019. [CrossRef]
[23] Visconti G. Fundamentals: Radiation in the atmosphere. New York: Springer; 2016. [CrossRef]
[24] Rogalski A. History of infrared detectors. Opto Electron Rev 2008;20:279–308. [CrossRef]
[25] Waele ATAM. Basic operation of cryocoolers and related thermal machines. J Low Temp Phys 2011;164:179–236. [CrossRef]
[26] Yousufzai UA, Khan AA, Dania S, Siraj A, Dildar M. Wireless transmission of solar panel energy with the help of mutual induction. Sigma J Eng Nat Sci 2023;41:192–199. [CrossRef]
[27] Gonzalez LIL, Troost M, Amft O. Using a thermopile matrix sensor to recognize energy related activities in offices. Procedia Comput Sci 2013;19:678-685. [CrossRef]
[28] Kramer R, Tighe R. Thermomechanics and infrared imaging. In: Inverse problem methodologies and mechanics of additive and advanced manufactured materials. Society for Experimental Mechanics. Proceedings of the 2021 Annual Conference on Experimental and Applied Mechanics. Conference Proceedings of the Society for Experimental Mechanics Series 2021. [CrossRef]
[29] Wang J. Indoor infrared optical wireless communications: Systems and integration. United Kingdom: Taylor & Francis Group; 2020. [CrossRef]
[30] Laurie G, Klein R, Vandegrift K. Infrared photography: Digital techniques for artistic images. 2nd ed. 2020.
[31] Vavilov V, Burleigh D. Infrared thermography and thermal nondestructive testing. Switzerland: Springer Nature; 2020. [CrossRef]
[32] Tournie E, Cerutti L. Mid-infrared optoelectronics: Materials, devices, and applications. London: Elsevier Ltd; 2020.
[33] Klijn ME, Hubbch J. Application of ultraviolet, visible, and infrared light imaging in protein-based biopharmaceutical formulation characterization and development studies. Eur J Pharm Biopharm 2021;165:319–336. [CrossRef]
[34] Zhao C, Zhang L, Zhang Y. All-sky longwave radiation modelling based on infrared images and machine learning. Build Environ 2023;238. [CrossRef]
[35] Xu M, Chen X, Bu X, Cao Y, Sun Q. Research on attitude measurement compensation technology under the influence of solar infrared radiation interference. Infrared Phys Technol 2022;123. [CrossRef]

Sigma J Eng Nat Sci, Vol. 44, No. 1, pp. 478–489, February, 2026

Sigma Journal of Engineering and Natural Sciences
Web page info: https://sigma.yildiz.edu.tr
DOI: 10.14744/sigma.2025.00000

Research Article

Unmasking sarcasm to understand depression: A machine learning exploration using news headlines

Vanita Ganesh KSHIRSAGAR[1,*], Sunil Kumar YADAV[2], Nikhil KARANDE[3]

[1]Deepartment of Computer Science and Engineering, Amity School of Engineering and Technology, Amity University, Rajasthan, India; Dr. D. Y. Patil Institute of Technology, Pune, 411018, India
[2]Department of Computer Science and Engineering, Amity School of Engineering and Technology, Amity University, Rajasthan, 110061, India
[3]Cyber Security Consultant, Stickman Cyber, Karnataka, 560037, India

ARTICLE INFO

Article history
Received: 05 June 2024
Revised: 03 August 2024
Accepted: 26 December 2024

Keywords:
Bidirectional Long Short-Term Memory (BiLSTM); Convolutional Neural Network (CNN) Sarcasm Detection; Long Short-Term Memory (LSTM); News Headlines Dataset

ABSTRACT

People often express thoughts and emotions through text, which can include sarcasm. Sarcasm detection is a difficult task because of noisy social media labels and a lack of high-quality datasets. It is necessary to identify sarcastic texts that affect mental health. The proposed novel method, Convolutional Neural Network and Long-Short Term Memory CNN+LSTM, which utilizes selectively frozen LSTM input layers, enhances sarcasm recognition to identify potential signs of depression, offering a unique approach for more precise mental health evaluation. For identification of sarcastic text, the News headline dataset and Reditt dataset were used together. For identification of sarcastic text, datasets were taken from Kaggle. To evaluate the efficiency of different approaches on sarcastic text, the suggested hybrid approach was compared with state-of-the-art methods like machine learning ML and deep learning DL. The ML and DL methods like logistic regression, decision tree, support vector classifier, multinomial Naïve Bayes, XG Boost, CNN, and LSTM were compared. The hybrid dataset was applied to all ML and DL methods. The proposed method outperformed, with an accuracy of 84%, recall of 83%, precision of 84%, and F1 score of 83% on the hybrid dataset, which is higher than the accuracy obtained from traditional ML methods. The hybrid method is well suited for the complex text. It performs well for detecting sarcastic language features.

Cite this article as: Kshirsagar VG, Yadav SK, Karande N. Unmasking sarcasm to understand depression: A machine learning exploration using news headlines. Sigma J Eng Nat Sci 2026;44(1):478–489.

INTRODUCTION

The sarcasm identification in literature for depression analysis [1,2] can be done in many ways. The conventional ML methods were widely employed for text classification; nevertheless, they frequently proved ineffective when handling sarcastic content. The effectiveness of DL techniques,

***Corresponding author.**
*E-mail address: vanita.kshirsagar@gmail.com

This paper was recommended for publication in revised form by Editor-in-Chief Ahmet Selim Dalkilic

Published by Yıldız Technical University Press, İstanbul, Turkey
© Author. This is an open access article under the CC BY-NC license (http://creativecommons.org/licenses/by-nc/4.0/).

particularly CNN and LSTM, has improved when it comes to finding patterns in text data. The majority of earlier research concentrated on techniques for smaller data sets, which constrained the range of text areas. The methods XG Boost and random forest combinely enhance the performance [3,4]. Sarcastic text detection may seem simple, but it's not always that way. Due to the lack of high-quality datasets and noisy labeling from social media sites like Twitter, Instagram, and Facebook, sarcasm detection has proven difficult. These networks frequently employ colloquial language and hashtags, which makes it challenging for DL and ML methods to recognize sarcasm with good accuracy. Dataset labeling by hand can be expensive and lead to short annotator agreements. There is no hybrid dataset; sarcasm detection and depression address the small dataset, and there is also a dearth of research on hybrid approaches [3,4]. Past work on sarcasm detection focused more on accuracy metrics with little attempt of the process's models use to detect sarcasm [5]. This research covers a gap by exploring how CNN+LSTM models identify sarcastic patterns in complex datasets.

This research will make use of advanced machine learning algorithms such as Bi-LSTM and CNN + LSTM. These algorithms have some important architectures used in natural language processing and sequential data analysis. Bi-LSTM enables the model to use the past and future context while processing a sequence and better relate the context to a given task, which could be sentiment analysis, language translation, or even anything of that kind. Another architecture which has garnered attention because of its adaptability in image processing is CNN. Successfully applied to sequential data analysis [6,7]. In NLP, it captures local patterns in text that would be helpful to tasks such as text classification or sentiment analysis [8,9]. Among other modern technologies, CNN, LSTM, and BERT advance the complexity of finding these precise patterns in text and improve text understanding through the context. Techniques in sequential modeling could capture complexities of contextual use in sarcasm, and pre-trained models may be fine-tuned using datasets specifically designed to emphasize sarcasm. Sarcastic language processing and the application of appropriate measures for determining the performance of the model make the systems for sarcasm detection even more efficient [10,11]. LSTM is a type of recurrent neural network (RNN) designed to capture long-term dependencies within sequences. It is significantly better for language modeling or text generation by retaining and utilizing information over longer spans of text. These architectures were trained on extensive datasets comprising annotated examples of sarcastic and non-sarcastic headlines. By utilizing the capabilities of these architectures to capture hidden patterns and context dependencies in text data. The aim is to enhance the computational understanding of sarcasm.

The comparison of classic ML methods like multinomial naïve bayes classifiers, decision trees, random forests, logistic regression, and support vector machines.

- By doing a comparative study and evaluating the performance of advanced architectures alongside traditional methods to demonstrate their effectiveness in recognizing sarcasm.
- A new dimension can be added to the existing work to treat complexities involving sarcasm identification in short and rich context data by focusing on the frozen input layer of LSTM.

The paper is sectioned into four sections which include literature review, dataset description, research methodology, model interpretation and result analysis with implications of our findings for the future of sarcasm detection.

Literature Review

This has become a significant challenge for the detection of sarcasm in text due to the indirect nature of expression found in sarcastic speech often made in informal language, especially on social media sites. Various angles have been addressed by researchers through both machine learning (ML) and deep learning (DL) techniques in addition to rule-based systems in order to improve identification of sarcastic content.

Author found the use of rhetorical questions to attempt to solve sarcasm in text; on the other hand, since much of sarcasm relies on nuances of the greater context of communication, it is quite hard for machines to perform such acts. It has been observed that techniques like SVM and Random Forests have also been used to identify sarcasm, which however loses precision when it is deployed in the case of multiturn conversations where the context itself changes with the passage of time [4]. In order to solve this issue, it was shown that implementing deep learning techniques significantly upgraded the detection of sarcasm because these techniques can grasp nuances of the discourse as well as features over multiple turns in a conversation [2].

This has been further refined with annotated datasets from platforms such as Twitter to improve the performance of deep learning models. Attention-based models were adopted as a way of improving this, significantly enhancing the accuracy of sarcasm detection compared with traditional models and outperforming these traditional models in complex data environments [12]. Additionally, a behavioral approach combined with machine learning was used to detect sarcasm in tweets, highlighting the value of historical context and conversation history in improving detection [13,14].

The growing need to detect sarcasm in social media posts as an indicator of mental health, particularly depression, has been recognized in several studies. By analyzing datasets from platforms like Reddit and Twitter, models were able to achieve an 80% accuracy rate in detecting depressive posts using ML methods [1]. Sarcastic seentence tend to mislead machines and humans due to their

irony behaviour. The methods using SVM and Random Forests have shown accuracy rates of 70 to 75% for identifying sarcasm in tweets [2]. The combined convolutional neural networks (CNN) with RNNs, specifically LSTMs, in an ensemble model. Which has demonstrated an 83% accuracy rate in detecting sarcasm [3]. In contrast, the CASCADE method, which integrates context with conversation history, outperformed traditional methods, achieving an accuracy of 85% in sarcasm detection [2].

Yet another research approach developed an innovative hybrid model that incorporated the CNN and LSTM network combining word and emoji embeddings for context-aware sarcasm detection. The model was able to achieve great success with an accuracy of 97.35% with F-score, precision, and recall highly outperforming the traditional models, especially by utilizing emojis to illustrate intent while interpreting sarcastic tweets [15]. In this region, more research is carried out in combining deep learning with the NLP techniques to perform better. MFO has been utilized with a MHSA-GRU model with the task of sarcasm detection that outperformed all models, and further results were checked on Kaggle's News Headlines dataset [16].

Apart from these developments, a many other studies have tested the strength of different feature extraction methods. One work proposed a hybrid combination of TF-IDF, dependency parsing bigrams, and lexicon-based features. This achieved 95.60% accuracy for detecting sarcasm using SVM over social media datasets including Twitter [17,18]. Another was the detection of sarcasm in the MUStARD dataset using an attention-based LSTM model, which obtained an F1 score of 60.1, that beat other deep learning models for sarcasm-context detection [19]. Key role of context was observed in sarcasm detection as shown by the research on sarcasm detection in Hinglish, which included sarcastic posts from social media posts. The Extra Tree Classifier and the Gradient Boosting Classifier ranked high. Their F-scores were 95.43 and 95.29, respectively. These studies highlight that in the detection of sarcasm, besides a linguistic feature representation, some sort of social feature has to be taken into consideration as well [20,21].

One major problem with sarcasm detection lies in the case of news headlines, where sarcasm goes unnoticed and sometimes results in false results in false information. The researchers found it possible to use neural networks particularly RNN and LSTMs for detecting sarcasm among news headlines. The current model achieved 85 percent, showing a high accuracy of LSTM networks while reading out sarcasm from short, context-dependent texts of news headlines [22]. Also, a few have proposed architectures in deep learning for detecting sarcasm in news headlines applying multiple datasets such as The Onion and HuffPost. The applied models used LSTM towards temporal dependencies capturing in various architectures. They obtained state-of-the-art accuracy of 0.925 in their test data. These models drastically outperformed the other classifiers which included decision trees, random forests, SVMs and established new benchmarks for the news article classification with respect to sarcasm [23]. Others have examined the integration of deep learning with handcrafted contextual features. Interesting research on the integration of CNN architectures along with crafted contextual features demonstrates that the deep learning along with handcrafted features highly boosts the accuracy, precision, and recall of sarcasm detection in intricate textual data [24]. Finally, a different set of studies provided evidence for further refining sentiment analysis and sarcasm detection by moving beyond more traditional contextual variables, such as the relationship between authors and audiences. A GAT-based framework achieved some breakthroughs by taking into account not only user history but also social dynamics in a conversation. This context-aware model holds immense promise in the prediction of sarcastic intent with an implication toward the significance of social context in the detection of online sarcasm [25].

The other challenge lately identified by studies is the procedure of handling imbalanced datasets, especially when performing sarcasm detection on datasets where there is an imbalance distribution of sarcastic and non-sarcastic examples. An example that used an agglomerative clustering method to identify some of its outliers and eliminate them along with using ensemble techniques like Bi-LSTM networks had an accuracy of 99.3%, which sets up a new benchmark for determining performance in sarcasm detection [26,27].

The issue of distinguishing sarcasm from other types of sentiment, especially in user reviews and posts, was also addressed through the development of new classification systems based on decision trees and neuro-fuzzy rules. These methods, tested on Twitter data. Which helps to produced promising results in classifying sarcastic and non-sarcastic sentences, contributing to the broader field of sarcasm detection [28]. Therefore, the sentiment analysis and sarcasm detection are often treated as separate tasks, but researchers have begun integrating them. A multitask learning approach proposed by one study achieved an F1-score of 94%. It outperforming traditional methods and showing potential for applications in behavior analysis and sentiment classification [29,30].

Several studies have also examined sarcasm through the lens of its emotional and contextual components, classifying sarcasm into categories such as polite, rude, and raging. The results majorly helpws to identifies the sracsm. Utilizing ensemble feature selection methods, for example, authors were able to achieve 92.7% to 99.79% accuracy across other classes of sarcasm. This further informs emotional subtleties of sarcasm in social media platforms [31].

However, this remains an ongoing challenge but keeps changing to the implementation of new techniques of machine and deep learning. The efforts ranged from the use of attention-based models up to hybrid CNN-LSTM networks and context-aware frameworks that showed context

as well as feature extraction to be as integral a part of the algorithm for improving the precision of sarcasm detection. As these methods advance, they promise to improve applications in mental health monitoring, sentiment analysis, even the development of more human-like conversational agents.

Problem Statement

Challenges in sarcasm detection datasets available for the development of the system are of a small size and lack diversity; the contextual factors that are included are very narrow; also, there is a huge impact because of cultural and linguistic variations. All these variations are important, as there is a difference in presentation of sarcasm across cultures, contexts, and communication styles. Differences have been addressed within these presentations to generally extend the capability of the model in being sarcastic in more real scenarios, thus making it more robust and adaptable in different populations. To this end, the News Headlines and Reddit datasets were added, which showed greater diversity and have helped the model capture more nuanced contexts to improve its performance in different styles of communication.

About Dataset

The sarcasm detection dataset is fetched from Kaggle. The news headlines dataset was downloaded from two websites, TheOnion and HuffPost [32,33]. Another dataset is added and named Reditt dataset. The combination of both News Headlines and Reddit datasets uses formal and informal language styles. News Headlines offer fo rmalised, professional language, while Reddit gives it a more casual, everyday tone. This blend results in a balanced dataset that captures a wide range of language, hence leading to a model that understands and adapts better to varied communication styles. The dataset contains a mix of non-sarcastic and sarcastic comments [33]. Twitter datasets are generally noisy regarding labels and text, which makes it hard to classify sarcasm with high accuracy. The intention behind the dataset is to provide good-quality labels with as less noise as possible, since headings of news are written by experts in a formal manner. In the dataset, each record has the following attributes:

'is_sarcastic': Indicates whether the headline is_sarcastic- yes that means 1 or is_sarcastic-no that means 0 (0).

'headline': The heading of the news article.

'article_link': It is the Link to the news article, which helps to gather supplementary data.

The dataset offers a resource for training and evaluating sarcasm detection models. It provide a more reliable and structured source of data compared to Twitter datasets.

Research Methodology

The methodology for the conduct of the study on sarcasm detection in news headline is briefly depicted. This includes many crucial steps such as data collection and preprocessing. The data investigation and imagining model development, and assessment and analysis, as showed by Fig. 1. Each step was carefully designed to ensure that our sarcasm-detection model is robust and effective.

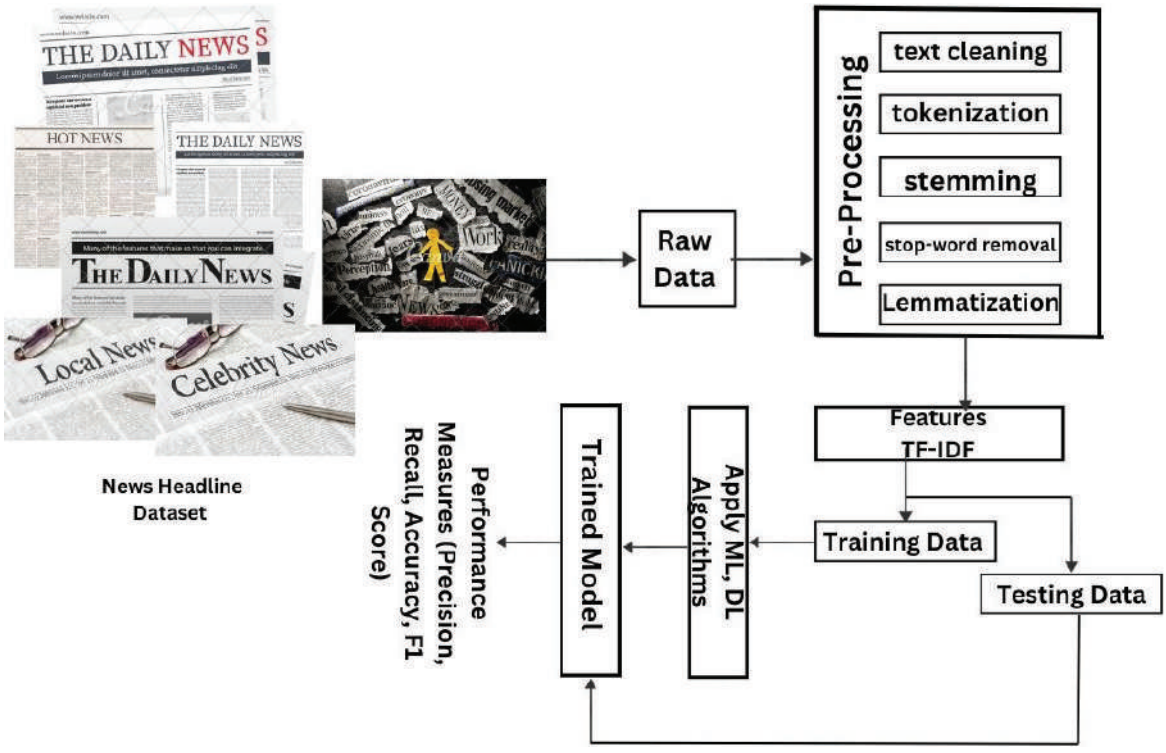


Figure 1. System architecture.



Figure 2. Word cloud of sarcastic headlines (left) and non-sarcastic headlines (right).

Data Collection and Preprocessing

Two such datasets of news headlines were annotated for sarcasm detection from Kaggle according to the study. These datasets are properly analyzed for relevance and content diversity in headlines. After collection, extensive preprocessing steps applied for cleaning textual data. This includes a process such as lowercasing; removal of punctuation, URLs, digits, and emojis; followed by tokenization and stop-word removal for improving the text's suitability for further analysis.

Data Exploration and Visualization

After preprocessing techniques, analyze the nature of datasets. Imagining of data through count plots, pie charts, and word clouds. The distribution of sarcastic and non-sarcastic headlines as represented in Figure 2. The visualizations served an overall description of the dataset and emphasized common words associated with each class of headlines.

Model Development

Construct a sophisticated model with an indepth understanding of the data to detect sarcasm. A custom architecture of the neural network has been developed, which combines embedding layers, bidirectional LSTM networks, dense layers with both batch normalization and dropout, and sigmoid output layer. This architecture is well-designed to catch all the intricate patterns and much-needed context in news headlines.

Embedding Layer

In this layer, it converts the input text data X of shape (batch_size, sequence_length) to dense vectors of the shape (batch_size, sequence_length, embedding_dim) with the help of embedding matrix E.

The word index in the Input mapping will map to the embedding space-dense vector. Construct a sarcasm detection model with a detailed understanding of the information. Developed a custom neural network architecture to fit in embedding layers, bidirectional LSTM networks, dense layers with batch normalization and dropout, and a sigmoid output layer. This architecture was accurately designed to capture the complex patterns and context inherent in news headlines.

BiLSTM architecture consists of several major layers that sequentially process the given input text data to detect sarcasm. The architecture includes the following layers for the performance of sarcasm detection:

Bi-LSTM Architecture

- **Embedding Layer:** In this layer, it converts the input text data X of shape (batch_size, sequence_length) to dense vectors of the shape (batch_size, sequence_length, embedding_dim) with the help of embedding matrix E. The word index in the input mapping will map to the embedding space-dense vector.
  For example, if X is the input text [I, love, sarcasm] and E is an embedding matrix, then the output X_embedded will be a tensor containing dense vectors for each word.
  In this embedding freezing the input layer means leveraging the knowledge embedded in those embeddings. This can help maintain the richness of the pre-trained representations, which could be especially useful for detecting nuanced features in sarcasm and depression.
- **Spatial Dropout1D Layer:** This layer randomly drops entire 1D feature maps (words) along the sequence dimension. Let X_embedded be the input tensor with shape (batch_size, sequence_length, embedding_dim), and dropout_rate be the dropout rate.
  For example, if X_embedded is the embedded input tensor, applying spatial dropout would randomly drop certain words from the sequence.
- **Bidirectional LSTM Layers:** This layer processes the input sequence X_dropout in both forward and backward directions. Let h_t^f and h_t^b represent the hidden states at time t for the forward and backward LSTMs, respectively.
  For example, In the sequence "I love sarcasm", a bidirectional LSTM would process it both ways, forwards and in reverse. This will capture context from both the beginning and the end.

- **Dense Layers with Batch Normalization and Dropout:** Let h_concat of the forward and backward hideen states. Apply dense layers to this concatenated representation, followed by batch normalization and dropout. For instance, after concatenation of the forward and backward states of the hidden layers, the output representation is passed to dense layers to generate higher-level features.
- **Flatten Layer:** It will flatten the output of the dense layers into a one-dimensional array. For example, the output from the dense layers, being typically a multi-dimensional tensor, is flattened into a one-dimensional array.
- **Output Layer:** Here, there is only one neuron of type sigmoid. Let h_flat be the flattened representation. Example- For a dense layer, let us take the output. This needs to go through the sigmoid function in order to derive the final prediction probability for sarcasm.
- **Equations involved for BiLSTM layered architecture:** For example, Given the sequence "I love sarcasm", the bidirectional LSTM would process it in both forward and backward directions, capturing context from both ends. Equations representing BiLSTM layered architecture:

1. Embedding Layer:X_embedded = E(X) #(make trainable =False)
2. Spatial Dropout1D Layer: X_dropout = Spatial Dropout1D(X_embedded)
3. Bidirectional LSTM Layers: h_t^f = LSTM(X_dropout) and h_t^b = LSTM (reverse(X_dropout))
4. Dense Layers with Batch Normalization and Dropout: h_concat = Concatenate (h_t^f, h_t^b) and h_dense = Dense(h_concat)
5. Flatten Layer: h_flat = Flatten(h_dense)
6. Output Layer: y_hat = σ(Dense(h_flat))

The Table 1. Represents the Sequential BiLSTM model summary.

CNN and LSTM Architecture

The input layer freeze, which is trainable=False, within the embedding layer forms one of the very important architectural choices in our hybrid CNN-LSTM model for sarcasm detection [34]. This will preserve the semantic relationships of the pre-trained word embeddings while allowing subsequent layers to adapt to the features that comprise sarcasm [35,36]. The frozen embedding layer can therefore be represented as:

$E(x) = W_e * x$, where $\partial E/\partial W_e = 0$

Where:

- E(x) represents the embedding function
- W_e represents the embedding weights matrix
- x represents the input token
- $\partial E/\partial W_e = 0$ indicates the gradient with respect to embedding weights is zero during backpropagation

This frozen architecture allows the model to maintain stable semantic relationships while allowing the CNN and LSTM layers to focus on learning about higher-level sarcastic features and further optimization of the model's ability to detect subtlety in linguistic patterns and emotional undertones without loss of foundational language understanding encoded into these pre-trained embeddings [37].

This model should generalize well on different text samples without memorizing non-informative patterns. Freezing the input layer also reduces the number of

Table 1. BiLSTM sequential_2 Model summary

Layer (type)	Output Shape	Param #
embedding_2 (Embedding)	(None, 25, 100)	2253100
spatial_dropout1d_2 (SpatialDropout1D)	(None, 25, 100)	0
bidirectional_4 (Bidirectional)	(None, 25, 392)	465696
bidirectional_5 (Bidirectional)	(None, 392)	923552
dense_4 (Dense)	(None, 64)	25152
flatten_2 (Flatten)	(None, 64)	0
dense_5 (Dense)	(None, 1)	65

Table 2. CNN+LSTM sequential_2 Model summary

Layer (type)	Output Shape	Param #
embedding_2 (Embedding)	(None, 100, 32)	320000
conv1d (Conv1D)	(None, 96, 32)	5152
max_pooling1d (MaxPooling1D)	(None, 24, 32)	0
Lstm_2 (LSTM)	(None, 64)	24832
dropout_1 (Dropout)	(None, 64)	0
dense_2 (Dense)	(None, 1)	65

parameters that the model needs to update during training, thus resulting in faster convergence and more efficient learning where the model can focus more on learning higher-level features by looking at the CNN and LSTM layers.

Equations representing CNN + LSTM layered architecture:

1. X_embedded = E(X) #(make trainable =False)
2. X_conv = Conv1D(X_embedded)
3. X_pooled = MaxPooling1D(X_conv)
4. h_t^f = LSTM(X_pooled)
5. y_hat = σ(Dense(h_flat))

The Table 2. Represents the CNN+LSTM sequential model summary.

RESULT AND DISCUSSION

The news headline contains a sarcastic statement. The dataset of news headlines is taken from Kaggle. Which is approximately 200000 news headlines. The dataset is the diverse dataset. Which contains news, including sports, technology, entertainment, and politics. The dataset was divided into training data and test data. The preprocessing methods were used, such as text cleaning, tokenization, stemming, and stop-word removal. To convert text into vectors, the TF-IDF method is used. This section discusses the results achieved with BiLSTM, CNN + LSTM, and other machine learning models.

- The BiLSTM model exhibited promising performance over 10 epochs, with initial accuracy of 66.3% on training data and 74.5% on validation data, improving to 85.1% and 84%, respectively, by the end of the training period, as shown in Figure 3. This indicates that the model effectively learned from the data and generalized well to unseen examples, as evidenced by the comparable performance on both training and validation datasets. The loss function decreased consistently throughout training, further demonstrating the model's learning capability. Figure 4. represents the confusion matrix with true label and corrected label.

Over 10 epochs, the BiLSTM model showed strong improvement. Starting with 40.45% accuracy on training data and 62.24% on validation, it reached 97.51% and 91.91%, respectively, by the final epoch (Fig. 5). With a larger dataset, these results surpassed those in Figure 4.

The BiLSTM model outperforms traditional models like Decision Trees and Random Forests because it can capture the sequential nature of text, understand context, and learn complex relationships between words. Traditional models, though effective for some tasks, struggle to grasp the

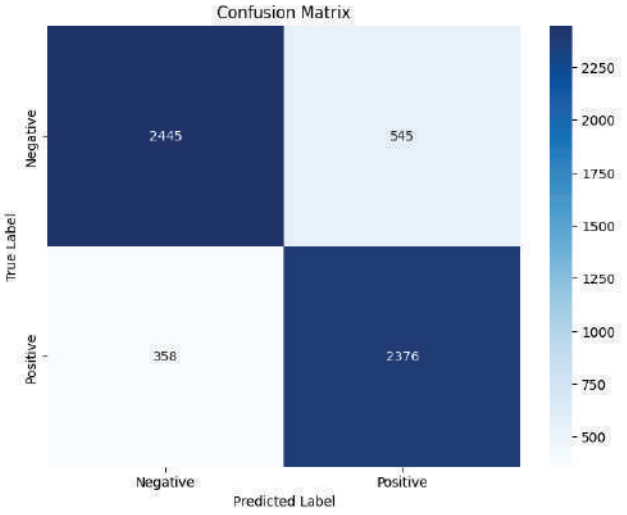


Figure 4. Confusion matrix for true and predicted Label.

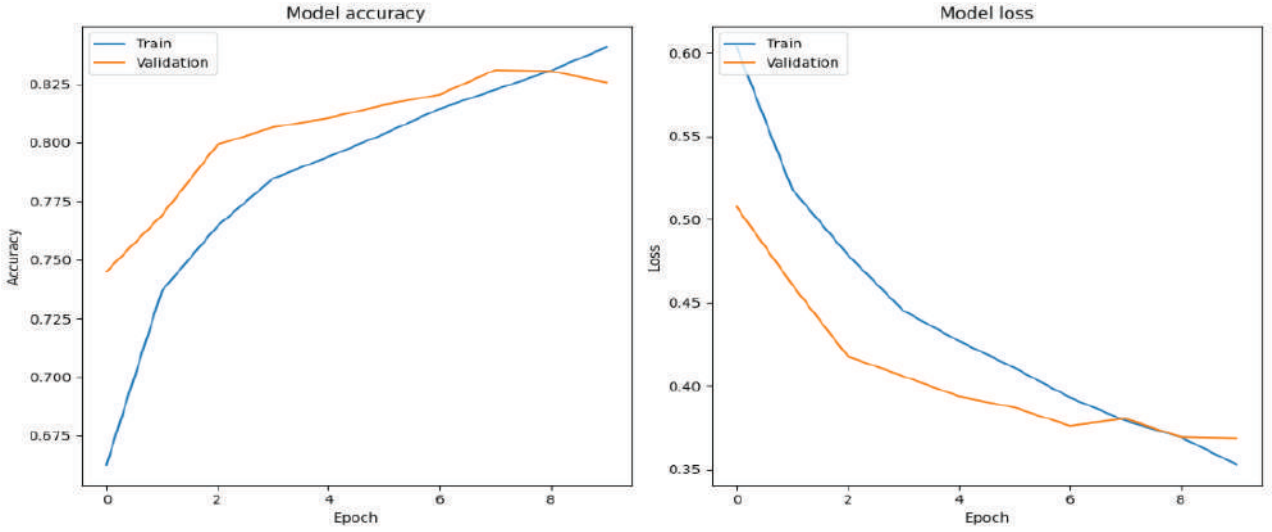


Figure 3. BiLSTM model train verses validation – accuracies (left) and losses (right).

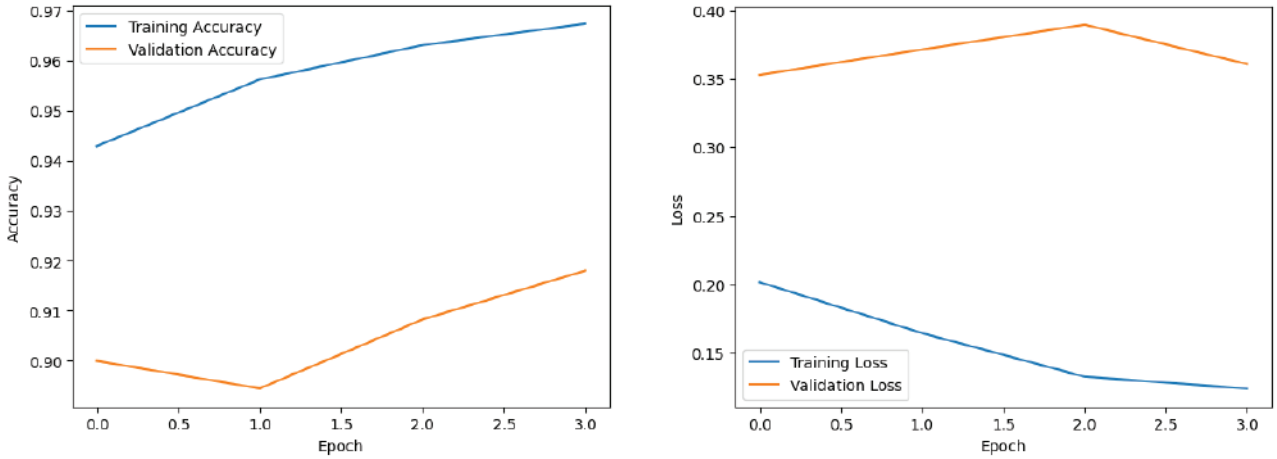


Figure 5. BiLSTM model train verses validation – accuracies (left) and losses (right) hybrid dataset.

nuances of text data. BiLSTM, with its deep learning capabilities, is better suited for sarcasm detection, where meaning depends on context, tone, and subtle word connections.

6.2 The CNN + LSTM model performed well across five training epochs. Initially, it achieved 76.3% accuracy on the training data and 84.6% on the validation data. By the final epoch, these scores reached 99.3% for training and 83% for validation, though minor overfitting was noted. The loss function stayed low, reflecting the model's consistent accuracy, as illustrated in Figure 6.

The classification reports of all models evaluated in sarcasm detection provide valuable insights into their performance (Fig. 7). A comprehensive overview of each model's recall, precision, accuracy, and F1-score, comparison is shown in the Table 3 to show their effectiveness in detecting sarcasm.

From this analysis, several key observations can be made:

1. Logistic Regression: It was able to yield 83.23% accuracy. Both the precision, recall, and F1-score were in balance with respect to both classes. Distribution in the confusion matrix was highly reasonable. This would suggest it generally performed better.
2. Decision Tree: The accuracy of the model was 73.43%. The precision, recall, and F1 scores were acceptable but had false positives and false negatives.

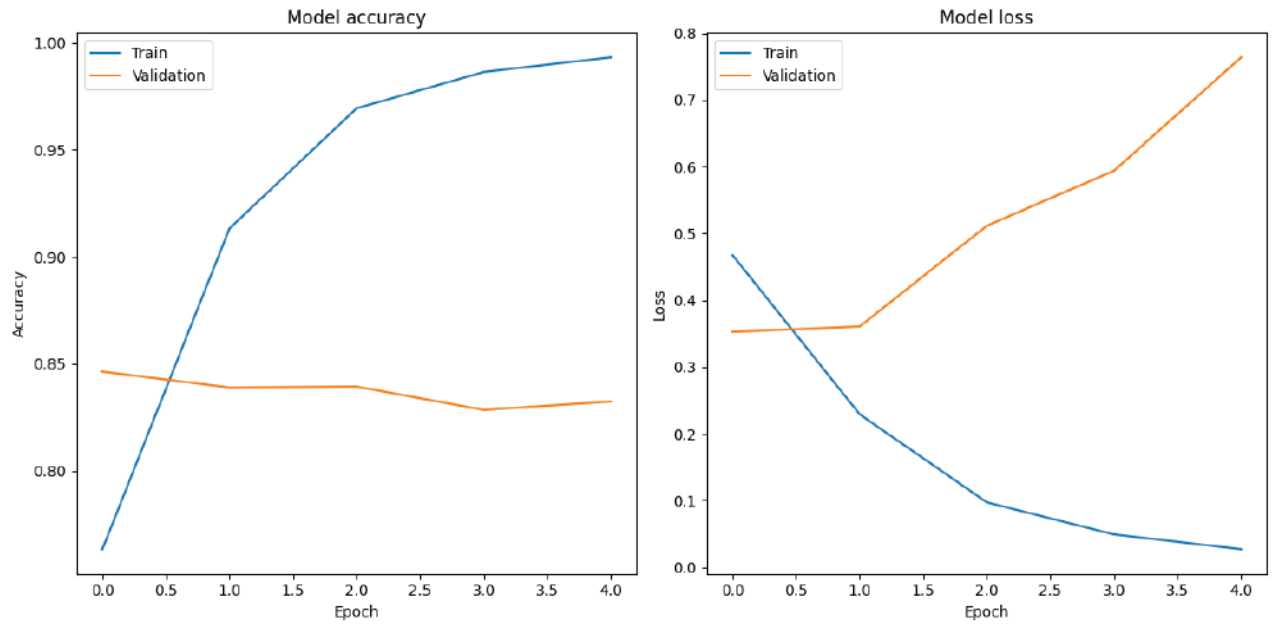


Figure 6. CNN + LSTM model train verses validation – accuracies (left) and losses (right).

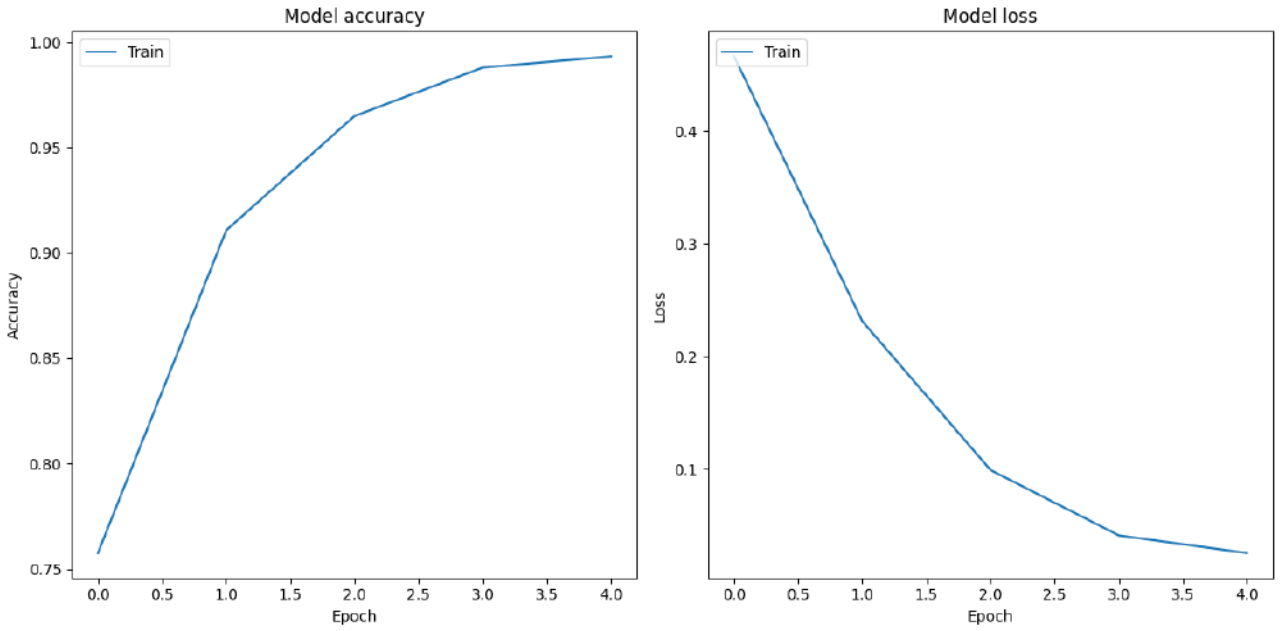


Figure 7. CNN+LSTM Train data accuracy and loss for 5 epoch.

Table 3. Performance Comparison of Classification Algorithms for Sarcasm Detection

Algorithm	Precision	Recall	F1-Score	Accuracy
Logistic regression	0.83	0.83	0.83	0.83
Decision tree	0.73	0.74	0.74	0.74
SVM classifier	0.82	0.82	0.82	0.82
MNB classifier	0.82	0.82	0.82	0.82
Random forest	0.79	0.79	0.79	0.79
LSTM	0.72	0.76	0.72	0.72
CNN+LSTM Classifier	**0.84**	**0.83**	**0.83**	**0.83**
Bi-LSTM	0.83	0.82	0.82	0.82
CNN+LSTM+Bi-LSTM	0.83	0.82	0.82	0.82

3. Support Vector Machine also closely had similar accuracy with logistic regression. It obtained an accuracy of 82.77% and had balanced performance metrics. The confusion matrix showed a balanced number of true positives and true negatives, which confirmed the robustness of the model in the classification process.
4. Multinomial Naive Bayes had an accuracy of 82.41%. The performance metrics were just about as good as logistic regression and SVM. The confusion matrix also showed that there were good numbers of true positives and true negatives in it.
5. The result of the random forest test is 79.35% accuracy, which is lesser than in any of the previous models. A greater number of false positives and false negatives are seen in the confusion matrix. Thus, it so happens that results obtained through random forest happen to be less optimal as compared to logistic regression and SVM.
6. With an accuracy of 98.00% in the model's trainability and an accuracy of 84.00% on testing CNN + LSTM Classifier, the balancing in its precision, recall, and F1-scores for both classes shows a great generalization to unknown data.
7. The model overfits a little just because of the lesser set of trainings and sometimes even makes judgement by tone or topic or context.
8. BiLSTM Classifier gave 84.00% accuracy, and precision and recall are balanced with F1-scores for both classes. There was a slight imbalance in the precision and recall of both classes, but the model had overall robust performance.

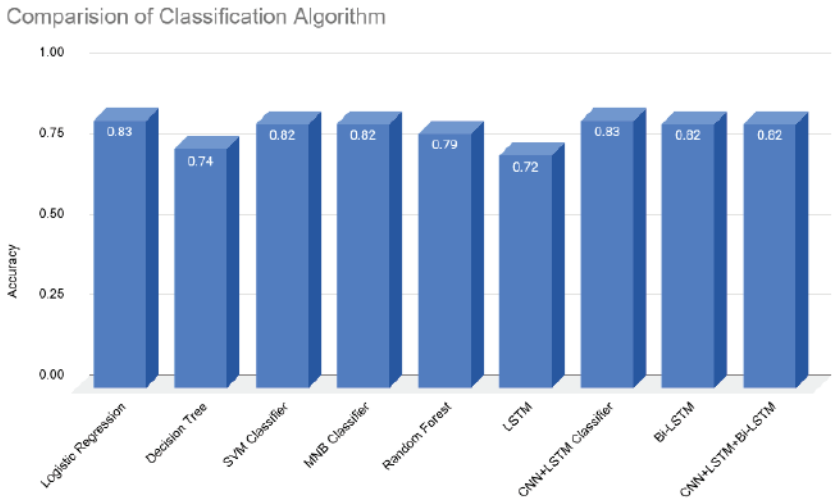


Figure 8. Accuracy comparison of classification algorithms for sarcasm detection.

9. BiLSTM Classifier gave 98.00% accuracy, and precision, recall, along with F1-scores for both classes were there as their concatenation with the Raditt dataset is available. The Training accuracy is 91.80%.

The related comparison of the accuracy from classification algorithms as presented in Fig. 8 gives a relatively clear view related to the performance regarding the detection of sarcasm from each model. It is thus crucial to determine the strength and weaknesses of a particular model so further efforts in optimizing and refining the efforts in detecting sarcasm can be made.

Logistic regression achieved an accuracy of 83.23% with relatively balanced precision, recall, and F1 scores for both classes. Balancing characteristics are portrayed by the conf When all classifiers are considered, the BiLSTM model falls in the range of well performing algorithms along with logistic regression, SVM, multinomial naive Bayes, and the CNN + LSTM Classifier. Decision tree and random forest algorithms showed potential issue areas with relatively lower performance.

CONCLUSION

Hence, it can be concluded that the study demonstrates the effectiveness of the BiLSTM and CNN + LSTM models in identifying sarcasm with maximum accuracy. These models have a good understanding and analysis of attaining complex patterns of sarcasm in textual data by developing great robustness and reliability. Traditional machine learning approaches, though outperformed by deep learning models, emphasized exploitation of advanced techniques in tasks that involve sarcasm detection. Hybrid models and ensemble techniques are candidates for finding even better accuracy and generalization in future sarcasm detection systems. New possibilities open up for improvements in natural language understanding with the help of overcoming the above limitations. Future directions are outlined here, but can be even more specific in listing several ways that will make sarcasm detection even better. Traditional machine learning approaches were outperformed by deep learning models.

AUTHORSHIP CONTRIBUTIONS

Authors equally contributed to this work.

DATA AVAILABILITY STATEMENT

The authors confirm that the data that supports the findings of this study are available within the article. Raw data that support the finding of this study are available from the corresponding author, upon reasonable request.

CONFLICT OF INTEREST

The author declared no potential conflicts of interest with respect to the research, authorship, and/or publication of this article. ETHICS There are no ethical issues with the publication of this manuscript.

STATEMENT ON THE USE OF ARTIFICIAL INTELLIGENCE

Artificial intelligence was not used in the preparation of the article.

REFERENCES

[1] Tadesse MM, Lin H, Xu B, Yang L. Detection of depression-related posts in social media using machine learning algorithms. Int J Med Inform 2019;127:317–327.

[2] Hazarika D, Poria S, Cambria E, Zimmermann R, Mihalcea R. Cascade: Contextual sarcasm detection in online discussion forums. In: Proc 27th ACM Int Conf Inf Knowl Manag; 2018. p. 1835–1838.

[3] Ghosh D, Veale T. Fracking sarcasm using neural network ensembles In Proceedings of the 7th Workshop on Computational Approaches to Subjectivity, Sentiment and Social Media Analysis. San Diego, California: Association for Computational Linguistics; 2016. p. 161–169. [CrossRef]

[4] Oraby S, Harrison V, Reed L, Walker M. Are you serious?: Rhetorical questions and sarcasm in social media dialog. In: Jokinen K, Stede M, DeVault D, Louis A, editors. Proceedings of the 18th Annual SIGdial Meeting on Discourse and Dialogue. San Diego, California: Association for Computational Linguistics; 2017. p. 11–17.

[5] Misra R, Arora P. Sarcasm detection using news headlines dataset. AI Open 2023;4:13–18. [CrossRef]

[6] Ahmed MF, Mohanta JC, Sanyal A. Inspection and identification of transmission line insulator breakdown based on deep learning using aerial images. Electr Power Syst Res 2022;211:108199. [CrossRef]

[7] Kshirsagar VG, Yadav S, Karande N. Feature fusion and early prediction of mental health using hybrid squeeze-MobileNet. In: Garg D, Rodrigues JJPC, Gupta SK, Cheng X, Sarao P, Patel GS, editors. Advanced computing. Commun Comput Inf Sci. Cham: Springer; 2024. p. 2053. [CrossRef]

[8] Amasala L, Ponnuru M, Srideviponmalar P. Secure goods storage and anti-theft approach using Ethereum blockchain. Procedia Comput Sci 2024;233:1–11. [CrossRef]

[9] Kshirsagar VG, Sharma S. Review paper on sentimental analysis for recommendation system. In: Patil VH, Dey N, Mahalle PN, Pathan MS, Kimbahune VV, editors. Proc First Doctoral Symp Nat Comput Res. Lect Notes Netw Syst. Singapore: Springer; 2021. p. 169.

[10] Kiran SK, Shashi M, Madhuri KB. Multi-stage transfer learning for fake news detection using AWD-LSTM network. Int J Inform Technol Comput Sci 2022;14:58–69.

[11] Sirra K, Mogalla S, Madhuri KB. CSSLnO: Cat swarm sea lion optimization-based deep learning for fake news detection from social media. Int J Inf Technol 2024;16:4225–4241. [CrossRef]

[12] Tay Y, Tuan LA, Hui SC. Reasoning with sarcasm by reading in-between. In: Proc 56th Annu Meet Assoc Comput Linguist; 2018. p. 1010–1020. [CrossRef]

[13] Rajadesingan A, Zafarani R, Liu H. Sarcasm detection on Twitter: A behavioral modeling approach. In: Proc 8th ACM Int Conf Web Search Data Min; 2015. p. 97–106. [CrossRef]

[14] Khattri S, Koul A, Bansal A, Shrivastava S. Sarcasm detection: A computational approach. arXiv 2015. Preprint. doi: 10.48550/arXiv.2107.02276

[15] Pane SF, Ramdan J, Putrada AG, Fauzan MN, Awangga RM, Alamsyah N. A hybrid CNN-LSTM model with word-emoji embedding for improving the Twitter sentiment analysis on Indonesia's PPKM policy. In: Proceeding 6th International Conference on Information Technology, Information Systems and Electrical Engineering. Yogyakarta, Indonesia: IEEE; 2022. p. 1–6. [CrossRef]

[16] Sait ARW, Ishak MK. Deep learning with natural language processing enabled sentimental analysis on sarcasm classification. Comput Syst Sci Eng 2023;44:2553–2567. [CrossRef]

[17] Rajani B, Saxena S, Kumar BS. Design and analyze the machine learning based sarcasm prediction model for social media context. Res Artic Spec Issue Appl Adv Eng Technol 2023;11:156–163.

[18] Kshirsagar VG, Yadav S, Karande N. HMHDTML: Human mental health detection using text and machine learning model. In: Kumar R, Verma AK, Verma OP, Wadehra T, editors. Soft computing: Theories and applications. Lect Notes Netw Syst. Singapore: Springer; 2024. p. 970. [CrossRef]

[19] Băroiu AC, Trăușan-Matu Ș. Comparison of deep learning models for automatic detection of sarcasm context on the MUStARD dataset. Electronics 2023;12:666. [CrossRef]

[20] Singh R, Srivastava R. Extracting contextual feature from Hinglish short text by handling spelling variation at character and word level. Int J Intell Syst Appl Eng 2023;11:713–719.

[21] Olaniyan D, Ogundokun RO, Bernard OP, Olaniyan J, Maskeliūnas R, Akande HB. Sarcasm and irony detection in social media. Computers 2023;12:231. [CrossRef]

[22] Sinha S, Choudhary M. Sarcasm detection using deep learning approaches: A review. Int J Recent Technol Eng 2023;11:50–58.

[23] Ali R, Farhat T, Abdullah S, Akram S, Alhajlah M, Mahmood A, Iqbal MA. Deep learning for sarcasm identification in news headlines. Appl Sci 2023;13:5586. [CrossRef]

[24] Razali MS, Halin AA, Ye L, Doraisamy S, Norowi NM. Sarcasm detection using deep learning with contextual features. IEEE Access 2021;9:68609–68618. [CrossRef]

[25] Plepi J, Flek L. Perceived and intended sarcasm detection with graph attention networks. In: Moens M-F, Huang X, Specia L, Yih SW, editors. Findings of the Association for Computational Linguistics: EMNLP. Punta Cana, Dominican Republic: Association for Computational Linguistics; 2021. p. 4746–4753. [CrossRef]

[26] Maheswari SU, Dhenakaran SS. Improved ensemble based deep learning approach for sarcastic opinion classification. Multimedia Tools Appl 2023;83:38267–38289. [CrossRef]

[27] Prasanna MSM, SG SS, Ayyasamy V. Polarity classification on Twitter data for classifying sarcasm using clause pattern for sentiment analysis. Multimedia Tools Appl 2023;82:1–37. [CrossRef]

[28] Tan YY, Chow CO, Kanesan J, Chuah JH, Lim Y. Sentiment analysis and sarcasm detection using deep multi-task learning. Wirel Pers Commun 2023;129:2213–2237. [CrossRef]

[29] Pandey AC, Seth SR, Varshney M. Sarcasm detection of Amazon Alexa sample set. In: Advances in signal processing and communication. Singapore: Springer; 2019. p. 559–564. [CrossRef]

[30] Sundararajan K, Palanisamy A. Multi-rule based ensemble feature selection model for sarcasm type detection in Twitter. Comput Intell Neurosci 2020;2020:2860479. [CrossRef]

[31] Misra R, Arora P. Sarcasm detection using news headlines dataset. AI Open 2023;4:13–18. [CrossRef]

[32] Misra R, Grover J. Sculpting data for ML: The first act of machine learning. 1st ed. Independently published. 2021.

[33] Khodak M, Saunshi N, Vodrahalli K. A large self-annotated corpus for sarcasm. arXiv 2017. Preprint. doi: 10.48550/arXiv.1704.05579

[34] Gupta I, Chatterjee I, Gupta N. Enhanced deep learning-based model for sentiment analysis to identify sarcasm appeared in the news. Comput Artif Intell 2023;42:1091–1113. [CrossRef]

[35] Galal AM, Yousef MH, Zayed HH, Medhat W. Arabic sarcasm detection: An enhanced fine-tuned language model approach. Ain Shams Eng J 2024;15:102736. [CrossRef]

[36] Najafabadi MK, Ko TZC, Chaeikar SS, Shabani N. A multi-level embedding framework for decoding sarcasm using context, emotion, and sentiment feature. Electronics 2024;13:4429. [CrossRef]

[37] Aksan F, Li Y, Suresh V, Janik P. CNN-LSTM vs LSTM-CNN to predict power flow direction: A case study of the high-voltage subnet of northeast Germany. Sensors 2023;23:901. [CrossRef]

Sigma J Eng Nat Sci, Vol. 44, No. 1, pp. 490–500, February, 2026

Sigma Journal of Engineering and Natural Sciences
Web page info: https://sigma.yildiz.edu.tr
DOI: 10.14744/sigma.2025.00000

Research Article

Influence diagnostic in beta ridge regression model: Simulation and application

Javaria Ahmad KHAN[1,*], Atif AKBAR[1], B M Golam KIBRIA[2]

[1]*Department of Statistics, Bahuddin Zakariya University, Multan, 60800, Pakistan*
[2]*Department of Mathematics and Statistics, Florida International University, Miami, FL 33199, USA*

ARTICLE INFO

Article history
Received: 29 January 2024
Revised: 26 April 2024
Accepted: 31 October 2024

Keywords:
Beta Regression; Cook's Distance; Crude Oil Conversion; Influence Diagnostics; Multicollinearity; Outliers; Residuals; Ridge Regression; Shrinkage Parameter

ABSTRACT

When regressors exhibit a linear correlation in the Beta regression model (BRM), the Beta ridge regression model (BRRM) is employed to mitigate the impact of multicollinearity on maximum likelihood estimation (MLE) in the BRM. The traditional MLE approach is particularly sensitive to such correlations, leading to unstable and unreliable parameter estimates. To identify the influential data points, Cook's distance is utilized as a classic diagnostic tool to detect outliers. This paper emphasizes the dual challenges posed by multicollinearity and outliers, proposing a set of estimators for the shrinkage parameter in BRM using Cook's distance in combination with varied residual types. For illustrative purposes, Monte Carlo simulations and real data are presented.

The empirical results indicate that certain classes of weighted residuals (W, SW, ASW, and SW2) demonstrate superior performance in detecting outliers, with a high percentage of detection across different scenarios. Additionally, findings suggest that the outlier detection is not only influenced by the residual weighting scheme but is also inclined by the severity of multicollinearity and the selected value of the shrinkage parameter k. These results provide a baseline for further refinement of BRM, potentially in the selection of optimal shrinkage parameter and residual type, involving multicollinearity and contaminated data.

Cite this article as: Khan JA, Akbar A, Kibria BMG. Influence diagnostic in beta ridge regression model: Simulation and application. Sigma J Eng Nat Sci 2026;44(1):490–500.

INTRODUCTION

When multicollinearity occurs in a Beta regression model (BRM), the beta ridge regression model (BRRM) serves as a remedial tool in such a situation [1, 2]. In multiple regression, when the predictors are highly interrelated, multicollinearity occurs, which is one of the intense problems in regression analysis. Subsequently, the confidence interval becomes wider, making maximum likelihood estimates (MLE) unstable and inefficient [3], the variance of the MLE turns very high and such an estimator provides unreliable inference [4]. The literature documents several shrinkage and biased estimation strategies for handling multicollinearity, notably the modified ridge-type, the Liu and the Liu-type, the two-parameter, the Dawoud–Kibria, and the James–Stein type

*Corresponding author.
*E-mail address: jakhan0@yahoo.com

This paper was recommended for publication in revised form by Editor-in-Chief Ahmet Selim Dalkilic

Published by Yıldız Technical University Press, İstanbul, Turkey
© Author. This is an open access article under the CC BY-NC license (http://creativecommons.org/licenses/by-nc/4.0/).

estimators [5–10]. These estimators aim to reduce the variance and improve estimation stability when multicollinearity challenges standard regression techniques. Many researchers examined their performance in different situations, like Taha [11] discussed the multiple diagnostic measures for multicollinearity and further analyzed the Poisson, logistic, negative binomial (NB), zero-inflated negative binomial (ZINB),and zero-inflated Poisson (ZIP) models. Estimation methods using maximum likelihood (ML), ridge, Liu, and Liu-type estimators. Zubair and Adenomon [12] compared different estimators for the linear regression model when multicollinearity is present with autocorrelation. Abonazel et al. [13] suggested a new estimator for binary data using a Probit regression model when multicollinearity is present in the data. Saputri et al. [14] also made a comparison among LASSO, MLE, and the Liu Estimator. When MLE methods are dealing with multicollinearity in the multinomial logistic regression model, and many others.

Correspondingly, the Extreme or anomaly value in the response/output variable results in an outlier while the predictor (input variable) results as an influential point. Outliers or Influential points are those data points that are far from nearby values and noticeably distinct from the remaining observations. Outliers can influence the coefficients of the regression model, distorting the relationship between variables, and also in terms of bias. Several established statistical methods exist for the identification of outliers, e.g., Cook's distance, index plots, and potential residual plots, see Hadi [15]. The presence of outliers is a crucial problem; usually, researchers suggest excluding such values, but exclusion can cause a loss of information [16]. A lot of literature is available, where studies focus only on detecting such observations with their influence. Some of them are: Sarkar et al. [17] performed an empirical study on a logistic regression model. Their study aims to identify potential outliers by using graphical methods and different measures of standardized residuals. Zakariya et al. [18] suggested a new estimator for the detection of outliers and named the Coefficient of Determination Ratio (CDR), which is then compared with some standard measures of influence, namely: Cook's distance, covariance ratio, studentised residuals, leverage values, and difference in fits standardized. Baba et al. [19] proposed a new detection method for outliers for the spatial regression model and compared that with classical methods like Cook's distance and some other robust methods. Similarly, Kumar et al [20] detect outliers by using a class of Cook's distance in survey-weighted linear regression and references their in.

Therefore, integrating detection and robust handling of both multicollinearity and outliers is crucial for reliable inference in regression models, supporting robust, precise estimations without compromising data integrity. Sinan and Alkan [21], Ibrahim and Yahya [22], Pati et al. [23], Majid et al. [24, 25], Arum et al. [26], Lukman et al. [27], and many others considered the multicollinearity and outlier problem concomitantly, but for the linear regression model (LRM). Pfaffenberger and Dielman [28] also discussed this combat problem in their book. They discussed the possible construction of a robust method that performs equally well in the presence of problems. For the generalized linear model (GLM), Arum et al. [29] examined this set of problems for the Poisson regression and Khan et al. [30] for BRRM. To the best of our knowledge, BRM has not been discussed to combat the problem of outliers in the existence of multicollinearity with different multiple shrinkage parameters.

This article will explain how residuals affect the stability and diagnostic performance of Cook's distance in BRRM under multicollinearity and their impact on coefficients and mean squared error (MSE). It will help to tackle the combined problem with the optimum type of residual in Cook's distance.

In the rest of this paper, Section 2 discusses the BRRM, Cook's distance with residuals, and biasing parameters. In Section 3, a Monte Carlo simulation study has been presented. An analysis of real-life data is presented in Section 4 for illustrative purposes, followed by concluding remarks in Section 5.

BETA REGRESSION MODEL

The BRRM, Cook's distance, and the considered residuals will be described in this section.

The Beta Ridge Regression Model

Consider the response vector $Y = (y_1, y_2, \ldots, y_n)'$, where each y_i denotes an independent response (output) observation for $i = 1, 2, \ldots, n$; which follows Beta (α, ϕ) distribution; where α is shape parameter and ϕ is scale parameter. The *pdf* of the Beta distribution is given as;

$$f(y;\alpha,\phi) = \frac{y^{\alpha-1}(1-y)^{\phi-1}}{B(\alpha,\phi)}, \quad y \in (0,1), \alpha > 0, \phi > 0 \qquad (1)$$

where $B(\alpha,\beta)=\frac{\Gamma(\alpha)\Gamma(\phi)}{\Gamma(\alpha+\phi)}$. The mean and variance of beta distribution are $\frac{\alpha}{\alpha+\phi}$ and $\frac{\alpha\phi}{(\alpha+\phi)^2(\alpha+\phi+1)}$, respectively with link function $g(\mu_i)=\eta_i=x_i^T\beta=logit(\mu_i)$. $x_i^T=(1, x_{i1}, ..., x_{ip})'$ is the matrix of $(p+1)$explanatory/input variables and $\beta=(\beta_0, \beta_1, ..., \beta_p)'$ is a vector of regression coefficients [31].

Ferrari and Cribari-Neto [32] and Espinheira et al. [33, 34], used the iterative reweighted least-squares (IRLS) algorithm in the Beta maximum likelihood (BML) estimator to estimate the parameter β, which is obtained as,

$$\hat{\beta}_{BML}=\left(X'\hat{W}X\right)^{-1}X'\hat{W}z,$$

where $z=\hat{\eta}+\hat{W}^{-1}\hat{T}(y^*-\mu^*)$ and $\hat{W}=diag(\hat{W}_1,...,\hat{W}_n)$, which are estimated in the final iteration.

In the multiple linear regression model, it is assumed that the explanatory variables are not associated. However, in real life, the explanatory variables may be linearly correlated, which causes the problem of multicollinearity [3]. To alleviate the impact of multicollinearity in the Beta

regression model, Abonazel and Taha [1] and Qasim et al. [2] introduced the beta ridge regression (BRR) estimator as a substitute to the beta maximum likelihood (BML) estimator which is expressed as

$$\hat{\beta}_{BRR}=\left(X'\widehat{W}X+kI_p\right)^{-1}X'\widehat{W}z, \qquad k>0 \tag{2}$$

where k is known as the shrinkage or ridge or biasing parameter. The computation of the shrinkage or ridge parameter k is an important issue for the researcher, which will be discussed later.

Cook's Distance and Residuals

To identify the outlier, Cook [35] proposed the Cook's distance (CD) for the LRM, and Pregibon [36] utilized this approach for GLM. Cook's distance (CD) quantifies the extent to which omitting the *i*th observation alters the estimated regression model. For the BRM, the CD statistic can be written as,

$$CD_i=\frac{(\hat{\beta}_{ML}-\hat{\beta}_{ML(i)})'X'\widehat{W}X(\hat{\beta}_{ML}-\hat{\beta}_{ML(i)})}{(k+1)\hat{\phi}}, \tag{3}$$

where, $\hat{\beta}_{ML}$ is the estimated BRM coefficients vector and $\hat{\beta}_{ML(i)}$ is the estimated BRM coefficients vector after deleting the i[th] observation. The following simplified form of equation (3) is given by McCullagh and Nelder [37].

$$CD_i=\frac{\pi_i{}^2}{(k+1)}\frac{h_{ii}}{1-h_{ii}}, \tag{4}$$

where, π_i is the i[th] residual, which is explained in Table 1. In the BRRM, 2*mean (Cook's distance) [38] is used as the cutoff point for the detection of an outlier. The highest value of CD is a sign that the i[th] observation is the outlier. The following Table 1 presents the residuals that are considered in CD.

Choosing Biasing Parameter

Determining the ideal shrinkage/biasing parameter (k) is not possible but can only be estimated from the data. There are several methods to estimate the shrinkage parameter (see, e.g., [41, 42). Unlike linear regression, the effect of multicollinearity in GLM has not been significantly discussed in the literature using the ridge regression approach. Exceptionally, Månsson and Shukur [43] introduced some ridge parameters for the logistic regression model, and Algamal and Alanaz [44] compared different biasing parameters for Poisson ridge regression. Månsson and Shukur [45] established a Poisson ridge regression (PRR) estimator and used several biasing parameters. Since PRR can have a severe bias, Qasim et al. [46] suggested bias-adjusted PRR estimators. Amin et al. [47] examined the performance of inverse Gaussian ridge regression estimators. Lukman et al. [48] and Amin et al. [49] recommended some methods for estimating the shrinkage parameter based on the Gamma ridge regression. Khan et al. [30] used BRRM, but they selected 'k' randomly. Here, some well-known shrinkage estimators are given in Table 2.

Table 1. Summary of residuals and their notations

Sr. #	Residual	Notation	Reference
1	Pearson (P)	$r_t=\frac{y_t-\hat{f}(x_t)}{\sqrt{\hat{f}(x_t)}}$	Davison and Snell [39]
2	Deviance (D)	$r_t=sign\left(y_t-\mu_t\right)\sqrt{d_t}$	
3	Working (Wor)	$r_t=\frac{y_t-\hat{f}(x_t)}{\hat{f}(x_t)}$	
4	Response (R)	$r_t=y_t-\hat{f}(x_t)$	
5	Weighted (W)	$r_t^*=\frac{y_t^*-\hat{\mu}_t^*}{\sqrt{\phi v_t}},$	Espinheira et al. [33]
6	Standardized Weighted (SW)	$r_t^{\omega}=\frac{y_t^*-\hat{\mu}_t^*}{\sqrt{v_t}}$	
7	Standardized Weighted 2 (SW2)	$r_t^{\omega\omega}=\frac{r_t^{\omega}}{\sqrt{(1-h_{tt})}}$	
8	Adjusted Standardized Weighted (ASW)	$r_t^{\omega a}=\frac{r_i-\widehat{E}(r_t^{\omega})}{\sqrt{\widehat{Var}(r_t^{\omega})}}$	Anholeto et al. [40]
9	Adjusted Pearson (AP)	$r_t^{a}=\frac{r_i-\widehat{E}(r_i)}{\sqrt{\widehat{Var}(r_i)}}$	

Table 2. Summary of shrinkage estimators

Sr. #	k	Reference
1	$k_1 = \frac{(p-2)\hat{\sigma}^2}{\hat{\beta}'\hat{\beta}}$	Thisted,[50]
2	$k_2 = \frac{p\hat{\sigma}^2}{\hat{\beta}'\hat{\beta}}$	Hoerl and Kennard [51]
3	$k_3 = \frac{\hat{\sigma}^2}{\hat{\beta}'\hat{\beta}}$	Dwividi and Shrivastava [52]
4	$k_4 = Median\left\{\frac{\hat{\sigma}^2}{\hat{\alpha}_j^{\,2}}\right\}$	Kibria [41]
5	$k_5 = Median\left(\frac{1}{\sqrt{\frac{\hat{\sigma}_j^{\,2}}{\hat{\alpha}_j^{\,2}}}}\right)$	Muniz and Kibria [42]
6	$k_6 = Median\left(\frac{1}{\sqrt{\frac{\lambda max\hat{\sigma}_j^{\,2}}{(n-p)\hat{\sigma}_j^{\,2}+\lambda max\hat{\alpha}_j^{\,2}}}}\right)$	Muniz et al. [53]

SIMULATION STUDY

Simulation Technique

The following scheme is considered for the generation of simulated datasets:

I. The dependent variable of the BRM is generated from Beta distribution as $y_i = B(\alpha, \phi)$ for $i = 1, 2, \ldots, n$, where $\mu_i = E(y_i) = 3$ is arbitrary mean and $\phi = 5$ is dispersion parameter.
II. Two explanatory variables x_1 and x_2 are kept fixed throughout the whole simulation study. To introduce multicollinearity, Khan et al. [30] are followed. They used $x_{ij} = \sqrt{1-\rho^2}Z_{ij} + \rho Z_{ij}\ (p+1)$, $i = 1, 2, \ldots, n$; $j = 1, 2$ where Z_{i1}, Z_{i2}, Z_{i3}, Z_{i4} are independent standard pseudo-random random numbers, and ρ is defined as the degree of multicollinearity, $\rho = 0.8, 0.9, 0.95$.
III. Then, we introduce the outliers in X_{ij} at 5th, 10th, 15th, 20th, and 25th point as $x_{ij} = a_0 + x_{ij}$, for $i = 5, 10, 15, 20, 25$; $j = 1, 2$, where $a_0 = \bar{x}_j + 100$.
IV. Sample size is considered $n = 25, 50, 100$, and 200 with 1000 replications.
V. The biasing parameter is chosen by using the methods given in Table 2.
VI. We used the detection rate as a percentage.

The simulated outlier detection rate in percentage of the BRM Cook's distance under consideration of different factors such as dispersion parameter, sample size,levels of multicollinearity, and different types of residuals, which are presented in Tables 3 to 8 for k_1, k_2, k_3, k_4, k_5, and k_6, respectively. For better insight, the average detection rate along with standard deviation for all methods over all n and ρ are obtained and presented at the end of Tables 3-8.

Table 3. Detection rate (%) of estimated outliers in the BRM with different residuals with k_1

n	ρ	P	AP	D	R	W	SW	ASW	SW2	Wor
25	**0.8**	22.2	22.0	26.0	22.1	24.1	24.1	24.3	23.0	20.6
	0.9	22.8	21.9	26.3	22.9	24.2	24.2	24.4	23.6	24.1
	0.95	25.0	24.1	26.1	25.1	24.6	24.6	26.3	25.1	22.8
	0.99	22.2	21.4	25.1	21.6	23.6	23.6	23.3	21.5	19.8
50	**0.8**	88.1	86.6	89.6	88.0	89.9	89.9	90.2	87.0	88.1
	0.9	88.1	87.8	88.4	86.9	88.1	88.1	88.8	86.2	87.1
	0.95	88.1	87.6	88.5	88.0	89.3	89.3	88.7	86.4	86.4
	0.99	85.6	85.6	86.4	85.6	87.9	87.9	88.0	84.3	85.1
100	**0.8**	99.0	99.1	98.9	99.1	99.4	99.4	99.2	98.7	98.7
	0.9	99.3	99.1	98.9	99.5	99.2	99.2	99.5	98.1	98.6
	0.95	99.2	99.1	99.3	99.3	99.9	99.9	99.8	99.5	98.7
	0.99	99.3	99.3	98.8	99.2	99.1	99.1	99.4	98.6	98.3
200	**0.8**	100	100	100	100	100	100	100	100.0	99.8
	0.9	100	100	100	100	100	100	100	100.0	100.0
	0.95	100	100	100	100	100	100	100	99.9	99.9
	0.99	100	100	100	100	100	100	100	100.0	99.8
Mean		77.4	77.1	78.3	77.3	78.1	78.1	78.2	77.0	76.7
SD		32.8387	33.090	31.609	32.8801	32.5043	32.50436	32.3332	32.52489	33.1884

Table 4. Detection rate (%) of estimated outliers in the BRM with different residuals with k_2

n	ρ	P	AP	D	R	W	SW	ASW	SW2	Wor
25	**0.8**	22.4	21.0	24.8	21.2	22.9	22.9	23.7	23.7	21.8
	0.9	20.8	18.4	23.7	21.6	23.7	23.7	22.2	21.8	19.3
	0.95	16.9	17.6	21.5	17.3	22.6	22.6	22.0	19.7	17.1
	0.99	15.7	16.7	19.0	15.0	20.5	20.5	19.4	18.3	15.9
50	**0.8**	88.5	85.1	89.1	88.9	89.7	89.7	89.4	87.7	86.0
	0.9	85.2	83.3	84.6	84.4	88.1	88.1	85.9	83.3	83.4
	0.95	84.0	82.7	84.7	83.6	86.6	86.6	85.7	83.3	82.1
	0.99	82.6	82.6	85.2	83.1	87.9	87.9	87.2	85.0	80.4
100	**0.8**	99.1	98.6	99.3	99.1	98.9	98.9	99.5	98.2	97.8
	0.9	99.1	98.7	99.1	99.2	99.7	99.7	99.4	98.8	98.1
	0.95	98.4	98.4	99.0	98.3	99.2	99.2	98.9	97.9	97.5
	0.99	98.4	98.0	98.3	98.7	99.5	99.5	98.8	98.8	97.2
200	**0.8**	99.9	100	99.9	100.0	100	100	100	99.9	99.6
	0.9	99.9	100	99.9	99.9	100	100	100	99.9	99.9
	0.95	99.8	100	100.0	99.8	100	100	100	99.9	99.6
	0.99	99.8	100	99.8	99.8	100	100	100	100.0	99.6
Mean		75.656	75.068	76.743	75.618	77.456	77.4562	77.006	76.012	74.706
SD		34.3913	34.4444	33.0259	34.4832	33.1877	33.1878	33.3449	33.4645	34.1913

Table 5. Detection rate (%) of estimated outliers in the BRM with different residuals with k_3

n	ρ	P	AP	D	R	W	SW	ASW	SW2	Wor
25	**0.8**	19.0	18.8	19.1	18.0	20.9	20.9	21.0	18.7	17.8
	0.9	18.3	17.9	18.8	17.3	21.3	21.3	20.7	19.0	16.6
	0.95	15.9	16.2	21.6	15.1	19.5	19.5	19.7	17.9	14.0
	0.99	14.1	14.5	22.5	15.9	19.9	19.9	18.8	17.9	16.8
50	**0.8**	85.2	85.7	86.3	86.3	87.3	87.3	88.1	84.5	84.2
	0.9	86.2	85.2	87.5	86.4	87.1	87.1	87.7	84.3	84.4
	0.95	86.4	86.1	86.6	86.8	87.9	87.9	87.1	84.4	84.5
	0.99	87.9	88.1	87.3	88.3	86.8	86.8	87.5	84.4	86.2
100	**0.8**	98.6	98.9	99.2	98.8	99.4	99.4	99.1	98.6	98.2
	0.9	98.7	99.0	99.4	98.6	99.1	99.1	99.1	98.7	98.4
	0.95	98.5	98.6	99.2	98.6	99.3	99.3	99.3	98.9	97.6
	0.99	99.0	98.9	98.6	98.9	98.7	98.7	98.6	98.2	98.8
200	**0.8**	99.9	99.9	99.7	99.9	99.8	99.8	99.7	99.5	99.7
	0.9	99.9	99.9	99.9	99.9	100.0	100.0	100.0	99.9	99.6
	0.95	99.9	99.9	99.9	99.8	99.8	99.8	99.8	99.8	99.6
	0.99	100.0	100.0	100.0	100.0	100.0	100.0	100.0	100.0	99.8
Mean		75.468	75.475	76.6	75.537	76.675	76.675	76.637	75.293	74.7625
SD		35.4088	35.4087	33.8807	35.5526	33.9545	33.9545	34.1153	34.5127	35.3806

Table 6. Detection rate (%) of estimated outliers in the BRM with different residuals with k_4

n	ρ	P	AP	D	R	W	SW	ASW	SW2	Wor
25	**0.8**	14.9	6.5	20.5	14.3	23.2	23.2	17.6	22.4	11.9
	0.9	13.5	3.6	21.2	14.1	22.6	22.6	12.9	20.3	9.7
	0.95	11.3	4.4	18.3	12.9	21.9	21.9	13.2	20.2	7.7
	0.99	13.4	5.7	20.6	16.2	21.7	21.7	14.8	19.9	7.7
50	**0.8**	63.2	23.6	77.0	66.4	77.0	77.0	44.9	74.9	45.5
	0.9	57.0	18.7	76.8	59.5	75.3	75.3	40.8	71.6	39.4
	0.95	53.5	20.0	77.0	57.1	78.0	78.0	45.0	74.5	36.0
	0.99	50.8	29.9	77.6	55.0	81.0	81.0	51.7	76.9	35.5
100	**0.8**	77.4	46.4	86.0	78.4	83.2	83.2	65.6	82.0	68.4
	0.9	77.3	46.7	88.6	78.2	86.9	86.9	68.4	84.9	67.7
	0.95	71.1	41.9	85.3	73.2	84.4	84.4	63.3	82.3	57.7
	0.99	71.7	52.3	93.9	75.6	92.8	92.8	73.1	90.9	57.6
200	**0.8**	92.4	81.2	93.1	92.5	92.4	92.4	89.3	91.3	89.9
	0.9	83.4	73.6	87.0	83.9	86.6	86.6	81.3	84.7	78.8
	0.95	80.7	67.9	88.7	82.4	88.2	88.2	80.8	86.1	74.2
	0.99	82.9	76.0	94.5	84.4	94.7	94.7	90.4	93.7	74.9
Mean		57.156	37.4	69.131	59.006	69.368	69.36875	53.31875	67.2875	47.6625
SD		28.4823	27.2630	29.7933	28.5224	28.5714	28.57145	27.54289	28.45745	27.6908

Table 7. Detection rate (%) of estimated outliers in the BRM with different residuals with k_5

n	ρ	P	AP	D	R	W	SW	ASW	SW2	Wor
25	**0.8**	23.0	16.4	23.8	23.1	25.2	25.2	23.9	24.8	21.2
	0.9	23.7	15.1	26.1	23.4	25.0	25.0	24.1	24.6	20.7
	0.95	21.0	14.0	25.6	21.4	23.4	23.4	20.7	23.4	18.8
	0.99	17.4	8.8	23.5	21.1	25.0	25.0	19.7	23.9	12.1
50	**0.8**	83.5	69.1	88.7	85.0	91.0	91.0	86.4	89.1	74.7
	0.9	81.3	71.7	87.8	83.3	91.2	91.2	86.0	89.4	72.1
	0.95	79.9	69.1	86.0	82.7	89.6	89.6	85.6	85.4	74.1
	0.99	71.2	50.0	86.3	75.4	91.6	91.6	72.8	88.3	54.7
100	**0.8**	99.2	97.7	99.5	99.1	99.7	99.7	99.7	99.3	97.5
	0.9	98.6	97.5	98.9	98.7	99.3	99.3	99.0	98.5	96.2
	0.95	98.7	96.8	99.3	99.1	99.0	99.0	99.4	99.1	96.9
	0.99	97.2	92.0	99.2	98.1	99.8	99.8	98.7	99.3	92.7
200	**0.8**	100.0	100.0	99.8	100.0	100.0	100.0	100.0	100.0	99.5
	0.9	99.9	99.9	99.9	100.0	100.0	100.0	100.0	100.0	99.7
	0.95	99.8	99.9	99.9	99.9	99.9	99.9	99.9	99.8	99.6
	0.99	99.8	99.0	100.0	99.9	100.0	100.0	100.0	100.0	99.2
Mean		74.6375	68.562	77.768	75.637	78.731	78.7312	75.9937	77.8062	70.6062
SD		33.0554	35.9579	32.0525	32.7649	32.4691	32.4691	33.0646	32.3556	33.8821

Table 8. Detection rate (%) of estimated outliers in the BRM with different residuals with k_6

n	ρ	P	AP	D	R	W	SW	ASW	SW2	Wor
25	**0.8**	18.5	12.0	20.5	17.5	23.7	23.7	22.4	20.6	14.8
	0.9	23.8	12.8	28.3	25.3	25.6	25.6	25.0	24.8	18.8
	0.95	22.4	13.8	25.0	22.2	27.0	27.0	22.6	26.8	19.4
	0.99	17.4	5.3	22.8	20.1	27.8	27.8	16.0	27.1	9.4
50	**0.8**	88.8	80.9	88.0	88.9	91.8	91.8	89.1	89.1	83.4
	0.9	86.9	79.3	88.1	88.1	89.9	89.9	86.5	87.8	81.7
	0.95	87.9	73.5	89.8	89.7	91.3	91.3	87.2	89.4	79.5
	0.99	71.7	50.8	86	76.6	91.6	91.6	74.5	89.2	57.8
100	**0.8**	98.5	98.6	99.1	99.1	99.2	99.2	99.2	98.7	97.0
	0.9	99.2	96.9	99.1	99.1	99.5	99.5	99.5	99.3	96.9
	0.95	97.1	94.6	97.9	97.4	98.9	98.9	98.5	97.6	93.9
	0.99	97.0	89.6	99.4	97.5	99.7	99.7	97.5	99.3	90.9
200	**0.8**	99.9	99.9	100.0	100.0	100.0	100.0	100.0	100.0	99.6
	0.9	100.0	100.0	100.0	100.0	100.0	100.0	100.0	100.0	99.9
	0.95	99.9	100.0	99.8	99.9	99.8	99.8	99.8	99.8	99.7
	0.99	99.8	99.5	99.9	100.0	100.0	100.0	99.9	99.9	99.5
Mean		75.55	69.218	77.731	76.3375	79.1125	79.1125	76.1062	78.0875	71.3875
SD		33.6581	37.1052	32.3560	33.4640	31.8705	31.8705	33.3501	32.09845	35.0324

RESULTS AND DISCUSSION

Tables 3-8 show the performance of Cook's distance in BRRM. From Tables 3-8, it can be seen that k_1 performed the best, followed by k_2, k_3, and finally k_4 performed the worst in the sense of identifying outliers among 6 estimators. The performance of the shrinkage estimators (k_1 to k_6) also depends on the type of residuals. For example, k1 performed better for D Res in the sense of identifying outliers, while k_2-k_6 performed better for both W Res and SW residuals. It is interesting to note that the rate of identification of outliers is highly influenced by sample size; the percentage increases when the sample size increases and it detects all outliers when the sample size is very large. This behavior is almost the same for all the residuals.

By observing the results, it can be seen that ρ (levels of multicollinearity) affects the detection rate. When multicollinearity is high, it decreases the detection rate. This feature is clearer for a small sample size. It may be noticed that for a large sample size, all residuals performed almost equally well, but for a small sample size, W, SW, and ASW perform better.

In this study, SWeighted2 residual is one of the best options, which performs well with Cook's distance in the detection of outliers, according to the highest detection percentage. Also, Espinheira et al. [34] and Khan et al. [30] showed that the SWeighted2 residual is the best choice to be used in likelihood displacement (LD).

Application: Crude Oil Conversion Data

To examine the influence of outliers in real life; crude oil conversion data is used. Data is based on a data set from Prater [54]. It has four predictors, x_1,x_2,x_3, and x_4, with a dependent variable (y). This data set is used by Atkinson [55] and he applied LRM and observed that the error term is not symmetrical and transformed the dependent variable. Then, Lemonte et al. [56] considered that the dependent variable of this data follows a beta distribution. Ferrari and Cribari-Neto [32] used the data for the detection of outliers and found observation 4 as an influential. Then Qasim et al. [1] used the same data set and showed that there exist some multicollinearity issues, especially between variables x_2 and x_3. Khan et al. [30] considered this data with dual problems (outliers and multicollinearity) and detected several numbers of observations as outliers.

Now, we used that data to consider both problems and examine the impact of different residuals in Cook's distance and then their influence on the co-efficient (s). The Beta ridge regression model is then used to determine the considered residuals mentioned in Table 1.

Different shrinkage parameters are used for the detection of outliers which are presented in Table 3. It can be observed that P, AP, and D residuals detect almost the same residuals with any biasing parameter. Similarly, several outliers detected by the class of weighted residual are the same. Working residual detects a maximum number of outliers.

Another important feature of the result is that there is no impact of k in the model. Any type of mentioned k has no influence on the detection rate or on observations. Similar results are also found in Khan et al. [21], where they choose k randomly between 0-1, and no value has the power to detect outliers more firmly.

Next, the influence of these outliers is examined on the model. To generate Table 9, firstly, detected outliers are eliminated one by one from the model, and then combinedly, as detected by residuals. For this purpose, coefficients and MSE are considered. Results are available in Table 10, where it is found that no observation has as much influence, which makes the major change in results. Elimination of observation 7 makes the coefficient of gravity smaller. Observation 14 is one of those observations that are detected by almost every residual as an outlier. It is evident that the elimination of that observation has a major impact on MSE. Exclusion of observation 14, minimizes the MSE. Due to the deletion of observation 1, the MSE of the model increases; even the MSE is greater than the full model MSE.

Table 9. Outliers detected using different k

k / Res	k_1	k_2	k_3	k_4	k_5	k_6
P	1, 2, 14, 31	1, 2, 14, 31	1, 2, 14, 31	2, 14, 31	1, 2, 14, 31	1, 2, 14, 31
AP	1, 2, 14, 31	1, 2, 14, 31	1, 2, 14, 31	1, 2, 14, 31	1, 2, 14, 31	1, 2, 14, 31
D	1, 2, 14, 31	1, 2, 14, 31	1, 2, 14, 31	1, 2, 14, 31	1, 2, 14, 31	1, 2, 14, 31
Wor	1, 2, 11, 21, 25, 31	1, 2, 11, 21, 25, 31	1, 2, 11, 21, 25, 31	1, 11, 21, 25, 31	1, 2, 11, 21, 25, 31	1, 2, 11, 21, 25, 31
R	2, 3, 7, 14, 31	2, 3, 7, 14, 31	2, 3, 7, 14, 31	2, 14, 31	2, 3, 7, 14, 31	2, 3, 7, 14, 31
W	1, 2, 14, 21, 31	1, 2, 14, 21, 31	1, 2, 14, 21, 31	2, 11, 14, 21, 31	1, 2, 14, 21, 31	1, 2, 14, 21, 31
SW	1, 2, 14, 21, 31	1, 2, 14, 21, 31	1, 2, 14, 21, 31	2, 11, 14, 21, 31	1, 2, 14, 21, 31	1, 2, 14, 21, 31
ASW	1, 2, 14, 21, 31	1, 2, 14, 21, 31	1, 2, 14, 21, 31	1, 2, 14, 21, 31	1, 2, 14, 21, 31	1, 2, 14, 21, 31
SW2	1, 2, 14, 21, 31	1, 2, 14, 21, 31	1, 2, 14, 21, 31	1, 2, 14, 21, 31	1, 2, 14, 21, 31	1, 2, 14, 21, 31

Table 10. Parameter estimates and relative changes in estimates due to one-by-one exclusion and mean squared error (MSE)

	b_1	b_2	b_3	b_4	MSE
Complete (All)	-0.01220	-0.04003	-0.01830	0.01060	0.00080
1	-0.01334	-0.04337	-0.01847	0.01086	0.00082
2	-0.01401	-0.04304	-0.01828	0.01079	0.00076
3	-0.01360	-0.04066	-0.01807	0.01057	0.00078
7	-0.00951	-0.04932	-0.01874	0.01074	0.00075
11	-0.01305	-0.03368	-0.01793	0.01038	0.00079
14	-0.01438	-0.03308	-0.01853	0.01095	0.00069
21	-0.01099	-0.04309	-0.01811	0.01039	0.00079
25	-0.01134	-0.04350	-0.01813	0.01045	0.00078
31	-0.01092	-0.03931	-0.01871	0.01069	0.00076
P	-0.01669	-0.03937	-0.01915	0.01162	0.00059
AP					
D					
Wor	-0.01257	-0.04647	-0.01814	0.01058	0.00072
R	-0.01375	-0.04477	-0.01908	0.01135	0.00052
W	-0.01570	-0.04129	-0.01899	0.01143	0.00059
SW					
ASW					
SW2					

After that, all detected outliers are eliminated regarding residuals. Results showed that the removal of outliers detected by response residual provides the minimum MSE, as those outliers are also quite different than others.

CONCLUSION

This paper explores Cook's distance for thebeta ridge regression model with multiple residuals and different estimators of the shrinkage parameter k. The comparison of residuals using Cook's distance for outlier detection is assessed through a Monte Carlo simulation study and a real-lifedataset, leading to important conclusions. Firstly, for theBRRM,Cook's distance can assist in determining the choice of residuals based on the study's objectives. If the researcher's goal is outlier detection, then a class of weighted residuals is the optimal choice. Detection probabilities are higher for larger sample sizes. Additionally, it is noticed that the outlier detection is affected by the choice of the ridge parameter and influenced by the level of multicollinearity. Secondly, eliminating all outliers detected by response residuals results in a minimum mean squared error. Since the detection of outliers depends on the estimation of the shrinkage parameter k, and we only consider six estimators, it will be interesting to consider all available estimators in the literature.

AUTHORSHIP CONTRIBUTIONS

Authors equally contributed to this work.

DATA AVAILABILITY STATEMENT

The authors confirm that the data that supports the findings of this study are available within the article. Raw data that support the finding of this study are available from the corresponding author, upon reasonable request.

CONFLICT OF INTEREST

The author declared no potential conflicts of interest with respect to the research, authorship, and/or publication of this article.

ETHICS

There are no ethical issues with the publication of this manuscript.

STATEMENT ON THE USE OF ARTIFICIAL INTELLIGENCE

Artificial intelligence was not used in the preparation of the article.

REFERENCES

[1] Qasim M, Månsson K, Kibria BMG. On some beta ridge regression estimators: Method, simulation and application. J Stat Comput Simul 2021;91:1699–1712. [CrossRef]

[2] Abonazel MR, Taha IM. Beta ridge regression estimators: Simulation and application. Commun Stat Simul Comput 2023;52:4280–4292. [CrossRef]

[3] Frisch R. Statistical confluence analysis by means of complete regression systems. Oslo: Universitetets Økonomiske Instituut; 1934.

[4] Qasim M, Kibria BMG, Månsson K. A new Poisson Liu regression estimator: Method and application. J Appl Stat 2020;47:2258–2271. [CrossRef]

[5] Swindel BF. Good ridge estimators based on prior information. Commun Stat Theory Methods 1976;5:1065–1075. [CrossRef]

[6] Kejian L. A new class of biased estimate in linear regression. Commun Stat Theory Methods 1993;22:393–402. [CrossRef]

[7] Kejian L. Using Liu-type estimator to combat collinearity. Commun Stat Theory Methods 2003;32:1009–1020. [CrossRef]

[8] Özkale MR, Kaciranlar S. The restricted and unrestricted two-parameter estimators. Commun Stat Theory Methods 2007;36:2707–2725. [CrossRef]

[9] Abonazel MR, Dawoud I, Awwad FA. Dawoud–Kibria estimator for beta regression model: Simulation and application. Front Appl Math Stat 2022;8:775068. [CrossRef]

[10] Seifollahi S, Bevrani H. James–Stein type estimators in beta regression model: Simulation and application. Hacet J Math Stat 2023;1–20.

[11] Taha IMIM. Handling multicollinearity problem in generalized linear models. Cairo: Cairo University; 2019. Doctoral dissertation.

[12] Zubair MA, Adenomon MO. Comparison of estimators efficiency for linear regressions with joint presence of autocorrelation and multicollinearity. Sci World J 2021;16:103–109.

[13] Abonazel MR, Dawoud I, Awwad FA, Tag-Eldin E. New estimators for the probit regression model with multicollinearity. Sci Afr 2023;19:e01565. [CrossRef]

[14] Saputri SA, Herawati N, Sutrisno A, Nusyirwan, Nisa K. Comparison of MLE, LASSO, and Liu estimator methods to overcome multicollinearity in multinomial logistic regression: Simulation study. Glob Sci Acad Res J Multidiscip Stud 2024;3:8–12.

[15] Hadi AS. A new measure of overall potential influence in linear regression. Comput Stat Data Anal 1992;14:1–27. [CrossRef]

[16] Khan JA, Akbar A. Empirical performance of nonparametric regression over LRM and IGRM addressing influential observations. J Chemom 2019;33:e3143. [CrossRef]

[17] Sarkar SK, Midi H, Rana S. Detection of outliers and influential observations in binary logistic regression: An empirical study. J Appl Sci 2011;11:26–35. [CrossRef]
[18] Zakaria A, Howard NK, Nkansah BK. On the detection of influential outliers in linear regression analysis. Am J Theor Appl Stat 2014;3:100–106. [CrossRef]
[19] Baba AM, Midi H, Adam MB, Abd Rahman NH. Detection of influential observations in spatial regression model based on outliers and bad leverage classification. Symmetry (Basel) 2021;13:2030. [CrossRef]
[20] Kumar R, Biswas A, Singh D, Ahmad T. Detection of outliers in survey-weighted linear regression. Math Popul Stud 2024;31:147–164. [CrossRef]
[21] Sinan A, Alkan BB. A useful approach to identify the multicollinearity in the presence of outliers. J Appl Stat 2015;42:986–993. [CrossRef]
[22] Ibrahim SA, Yahya WB. Effects of outliers and multicollinearity on some estimators of linear regression model. In: Proceedings of the 1st International Conference; 2017. p.204–209.
[23] Pati KD. Using standard error to find the best robust regression in presence of multicollinearity and outliers. In: 2020 International Conference on Computer Science and Software Engineering (CSASE). IEEE; 2020. p.266–271. [CrossRef]
[24] Majid A, Aslam M, Ahmad S. Robust estimation of the distributed lag model with multicollinearity and outliers. Commun Stat Simul Comput 2022;1–15.
[25] Majid A, Ahmad S, Aslam M. A robust Kibria–Lukman estimator for linear regression model to combat multicollinearity and outliers. Concurr Comput Pract Exp 2023;35:e7533. [CrossRef]
[26] Arum KC, Ugwuowo FI, Oranye HE. Combating outliers and multicollinearity in linear regression model using robust Kibria–Lukman mixed with principal component estimator: Simulation and computation. Sci Afr 2023;e01566. [CrossRef]
[27] Lukman AF, Farghali RA, Kibria BMG. Robust–Stein estimator for overcoming outliers and multicollinearity. Sci Rep 2023;13:9066. [CrossRef]
[28] Pfaffenberger RC, Dielman TE. A comparison of regression estimators when both multicollinearity and outliers are present. In: Robust regression. Routledge; 2019. p.243–270. [CrossRef]
[29] Arum KC, Ugwuowo FI, Oranye HE. Robust modified jackknife ridge estimator for the Poisson regression model with multicollinearity and outliers. Sci Afr 2022;e01386. [CrossRef]
[30] Khan JA, Akbar A, Kibria BMG. Behavior of residuals in Cook's distance for beta ridge regression model (BRRM). Int J Appl Math Comput Sci Syst Eng 2023;5:202–208. [CrossRef]
[31] Forbes C, Evans M, Hastings N. Statistical distributions. Hoboken (NJ): John Wiley & Sons; 2011. [CrossRef]
[32] Ferrari S, Cribari-Neto F. Beta regression for modelling rates and proportions. J Appl Stat 2004;31:799–815. [CrossRef]
[33] Espinheira PL, Ferrari S, Cribari-Neto F. On beta regression residuals. J Appl Stat 2008;35:407–419. [CrossRef]
[34] Espinheira PL, Ferrari S, Cribari-Neto F. Influence diagnostics in beta regression. Comput Stat Data Anal 2008;52:4417–4431. [CrossRef]
[35] Cook RD. Detection of influential observation in linear regression. Technometrics 1977;19:15–18. [CrossRef]
[36] Pregibon D. Logistic regression diagnostics. Ann Stat 1981;9:705–724. [CrossRef]
[37] McCullagh P, Nelder JA. Generalized linear models. London: Chapman & Hall; 1989. [CrossRef]
[38] Hardin JW, Hilbe JM. Generalized linear models and extensions. College Station (TX): Stata Press; 2007.
[39] Davison AC, Snell EJ, editors. Residuals and diagnostics. In: Statistical theory and modelling. London: Chapman & Hall; 1991.
[40] Anholeto T, Sandoval MC, Botter DA. Adjusted Pearson residuals in beta regression models. J Stat Comput Simul 2014;84:999–1014. [CrossRef]
[41] Kibria BMG. Performance of some new ridge regression estimators. Commun Stat Simul Comput 2003;32:419–435. [CrossRef]
[42] Muniz G, Kibria BMG. On some ridge regression estimators: An empirical comparison. Commun Stat Simul Comput 2009;38:621–630. [CrossRef]
[43] Månsson K, Shukur G. On ridge parameters in logistic regression. Commun Stat Theory Methods 2011;40:3366–3381. [CrossRef]
[44] Algamal ZY, Alanaz MM. Proposed methods in estimating the ridge regression parameter in Poisson regression model. Electron J Appl Stat Anal 2018;11:506–515.
[45] Månsson K, Shukur G. A Poisson ridge regression estimator. Econ Model 2011;28:1475–1481. [CrossRef]
[46] Qasim M, Månsson K, Amin M. Biased adjusted Poisson ridge estimators: Method and application. Iran J Sci Technol Trans A Sci 2020;44:1775–1789. [CrossRef]
[47] Amin M, Afzal S. New ridge estimators in the inverse Gaussian regression: Monte Carlo simulation and application to chemical data. Commun Stat Simul Comput 2022;51:6170–6187. [CrossRef]
[48] Lukman AF, Ayinde K, Kibria BMG. Modified ridge-type estimator for the gamma regression model. Commun Stat Simul Comput 2020;51:1–15. [CrossRef]
[49] Amin M, Qasim M, Amanullah M. Performance of some ridge estimators for the gamma regression model. Stat Pap 2020;61:997–1026. [CrossRef]
[50] Thisted RA. Ridge regression, minimax estimation, and empirical Bayes methods. Technical report no. 28. Stanford (CA): Division of Biostatistics, Stanford University; 1976.

[51] Hoerl AE, Kennard RW. Ridge regression: Biased estimation of nonorthogonal problems. Technometrics 1970;12:55–67. [CrossRef]

[52] Dwividi TD, Shrivastava VK. On the minimum mean square error estimators in a regression model. Commun Stat Theory Methods 1978;7:487–494. [CrossRef]

[53] Muniz G, Kibria BMG, Månsson K, Shukur G. On developing ridge regression parameters: A graphical investigation. SORT 2012;36:115–138.

[54] Prater NH. Estimate gasoline yields from crudes. Pet Refin 1956;35:236–238.

[55] Atkinson AC. Plots, transformations and regression: An introduction to graphical methods of diagnostic regression analysis. New York: Oxford University Press; 1985.

[56] Lemonte AJ, Ferrari SL, Cribari-Neto F. Improved likelihood inference in Birnbaum–Saunders regressions. Comput Stat Data Anal 2010;54:1307–1316. [CrossRef]

Sigma J Eng Nat Sci, Vol. 44, No. 1, pp. 501–527, February, 2026

Sigma Journal of Engineering and Natural Sciences
Web page info: https://sigma.yildiz.edu.tr
DOI: 10.14744/sigma.2025.00000

Research Article

Comparative assessment of novel hooped and conventional Pelton wheel turbine runner using downcomer nozzles of different materials and exit diameter through experimental investigations

H. N. LAKDAWALA[1,2*], V. K. PATEL[2], G. C. CHAUDHARI[3], S. A. CHANNIWALA[4], T. R. PATEL[2]

[1]*Department of Mechanical Engineering, Dr. S. & S. S. Ghandhy Government Engineering College, Surat, Gujarat, 395007, India*
[2]*Department of Mechanical Engineering, Sardar Vallabhbhai National Institute of Technology, Surat, Gujarat 395007, India*
[3]*Department of Mechanical Engineering, C. K. Pithawala College of Engineering & Technology, Surat, Gujarat 395007, India*
[4]*Retired, Department of Mechanical Engineering, Sardar Vallabhbhai National University of Technology, Surat, Gujarat 395007, India*

ARTICLE INFO

Article history
Received: 02 October 2024
Revised: 12 November 2024
Accepted: 23 December 2024

Keywords:
Convergence Angle; Hooped Pelton Turbine Runner, Nozzles, Uncertainty Analysis; Variable Flow

ABSTRACT

Impulse turbines are significant because of their straightforward design and the lack of specialized expertise to create the runners. The hooped Pelton turbine runner with a 256 mm pitch circle diameter and a 40 mm hoop gap with a 4 mm hoop thickness was developed to reduce the bucket stress caused by water jets. The current paper investigates developed hooped and identical conventional Pelton turbine runners with a single downcomer nozzle of different sizes and materials to predict and compare performance parameters at variable flow conditions with uncertainty in measurements. In the present experimentation, two stainless steel nozzles of 17 mm and 23 mm and four polymeric material nozzles of 17mm, 18 mm,19 mm, and 23 mm were used for both runners. The nozzles have a range of convergence angles (24-32 degrees) and beta ratio (0.38 -0.49). The jet and velocity ratios of 11 to 15 and 0.362 to 0.492 were studied, respectively. The 17 mm stainless steel nozzle with conventional Pelton turbine runner combination has an 18.18% higher hydraulic performance than the hooped Pelton turbine runner under the full gate open condition. It was found that the runners experimented with 23 mm stainless steel nozzles gave maximum efficiency in the case of a hooped Pelton turbine compared to conventional runners at 20% gate opening. However, the polymeric nozzle was best for low runner speed, especially with the Hooped Pelton Turbine runner. The Hooped Pelton Turbine runner has exhibited excellent characteristics with less flow area (part gate opening) for the limited runner speed range than the Conventional Pelton Turbine runner and similar hydraulic characteristics to the conventional runner. Thus, the present study provides a maximum performance aspect of a hooped Pelton turbine runner for nozzle selection.

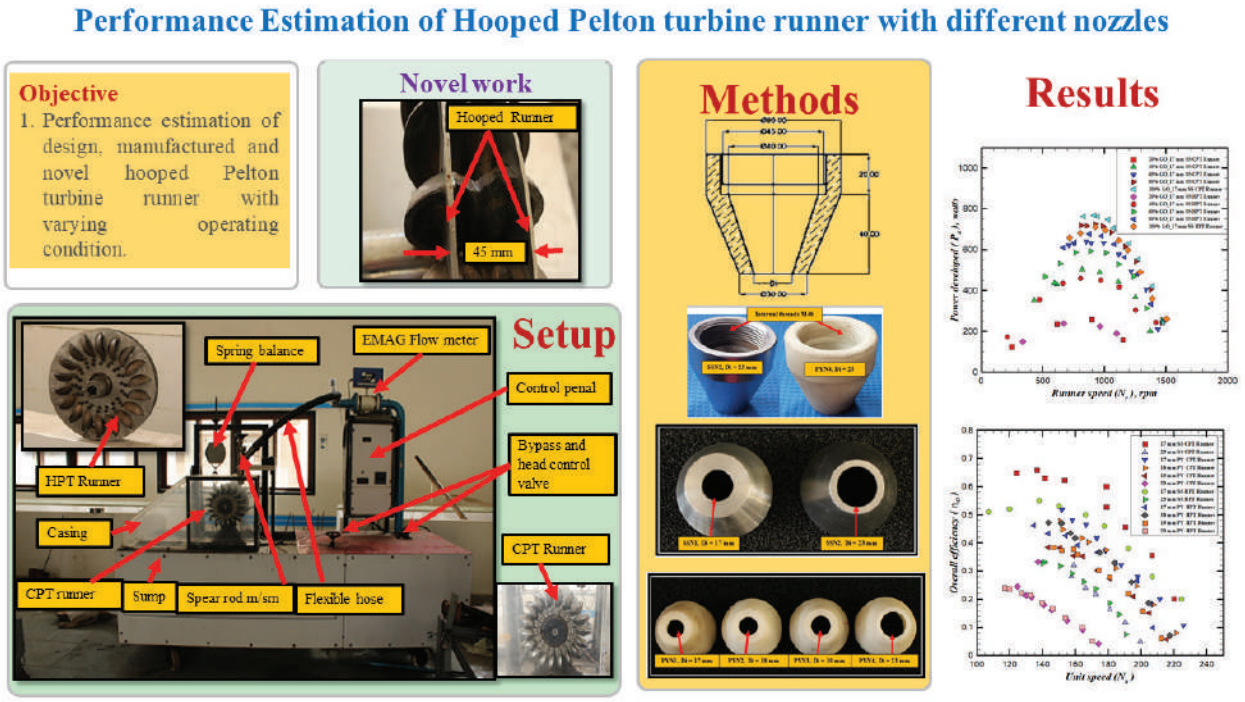
Cite this article as: Lakdawala HN, Patel VK, Chaudhari GC, Channiwala SA, Patel TR. Comparative assessment of novel hooped and conventional Pelton wheel turbine runner using downcomer nozzles of different materials and exit diameter through experimental investigations. Sigma J Eng Nat Sci 2026;44(1):501–527.

***Corresponding author.**
*E-mail address: hnlgecs@gmail.com

This paper was recommended for publication in revised form by Editor-in-Chief Ahmet Selim Dalkilic

Published by Yıldız Technical University Press, İstanbul, Turkey
© Author. This is an open access article under the CC BY-NC license (http://creativecommons.org/licenses/by-nc/4.0/).

GRAPHICAL ABSTRACT



Highlights:

The following are the salient points for the present work

1. The newly developed Hooped Pelton Turbine Runner (HPT) was investigated for performance with different nozzles with the angle of convergence (Θ_n), jet ratio(m), and variable flow area.
2. The nozzle assembly's spearhead mechanism manually carries the flow variation.
3. The two stainless steel nozzles (SSN) and four polymeric material nozzles (PYN), identically sized, except for exit diameter and convergence angle (Θ_n), were used for the experimental investigations.
4. The comparative study also used the identically sized conventional Pelton turbine (CPT) runner.
5. The Hooped Pelton Turbine Runner (HPT) has shown excellent performance characteristics and stability under dynamic runner operation. The uncertainty analysis was conducted for 100 % gate opening (GO) and maximum hydraulic efficiency$(\eta h)_{max.}$

INTRODUCTION

Hydropower is considered the most valuable and sustainable source of energy generation among all available renewable sources. Off-grid and isolated places are the main uses for small and medium hydropower. The most significant value in impulse turbines can be found in their versatility and ease of use, especially in part-load situations. Numerous research-based elements and performance assessments in real and software-based evaluation techniques, such as experimental and numerical ones, have been examined to quantify the hydropower spectrum and demonstrate its adaptability.

Nozzle and Jet

The quality of the jet is an essential operating parameter for determining the hydraulic performance of an impulse turbine. The spray or jet characteristics are determined by the flow stability emerging from the orifice of a nozzle [1]. The discharge coefficient, velocity coefficient, and contraction coefficient of the nozzles are primarily independent of nozzle geometry [2]. The nozzle geometry has a pronounced effect on the sonic lines and discharge coefficients [3]. The strong secondary flows produced by bends or bifurcations in the Pelton turbine system's distributor alter the jet diameter's surface deformation, deviation, and dispersion, causing the jet core to shift away from the nozzle's axis [4]. The radial velocity gradient at the impingement stagnation points correlates with the free jet centreline velocity and half-radius at the exact axial location [5]. The shape of the water jet significantly influences the turbine losses, and the stator significantly influences the efficiency of the hydraulic machine [6]. The hydraulic loss in the pipe and nozzle parts is less than in the rotating buckets of available water energy [7]. The increased jet velocity reduces the force coefficient, showing that more energy is lost. Also, pressure distribution on the surface of the bucket is more evenly spread for circular jets than rectangular ones [8]. The jet shape significantly affects the flow and torque characteristics of the Pelton turbine runner [9]. Increasing the nozzle diameter leads to an increase in

water discharge and a decrease in water head, which leads to decreased Pelton turbine performance (torque, brake power, efficiency, and the range of rotational speed) [10].

Increasing the nozzle's length-to-diameter ratio eliminates the occurrence of hydraulic flips correlated to the jet's trajectory with the liquid/air momentum flux ratio at the nozzle's exit diameter [11]. The initial jet velocity profile and subsequent jet surface form are considerably influenced by the nozzle aspect ratio (L/d); nozzles operate best at convergence angles between 15° and 100° [12]. With increased nozzle throat angles, the flow power decreases, and the Pelton turbine efficiency is affected by increasing power loss [13]. Also, the increased jet exit angle has improved efficiency with part load and whole needle opening [14]. The free jet of Pelton nozzles decreases the exit angle for higher values of unit discharge; the leading cause of the losses is friction [15]. For 90° and 45° sharp-edged nozzles, the model can study the Reynolds number's effect on losses, and the flow separation causes[16]. The high-speed imaging found that the wind-induced jet breakup mode occurs at Reynolds numbers below 8,700, using Ohnesorge's theory[17]. An improved efficiency system can be designed by optimal annular nozzles with multiphase flows, appropriate flow models, computational fluid dynamics (CFD) simulations, and optimization algorithms [18]. A new nozzle design method for high-efficiency crossflow turbines increased the maximum efficiency [19]. The suspended sediment is crucial to Pelton turbine design, operation, and maintenance [20].

Bucket and Runner Design

The bucket design optimization simulates unsteady water film flow using a boundary-fitted grid (BFG) [21]. The regions of the bucket surface contribute the most to the torque, and the backside of the bucket, with Coanda interaction between the bucket cut-out area and the water jet [22]. The dynamic flow pattern of the free-surface sheet flow in the rotating bucket conforms to the dynamic energy efficiency (ηEB) and power efficiency (ηPB)[23]. Also, in the numerical turbine runner design optimization for maximum efficiency, NURBS polynomials and a relatively small number of control points are required with various design variable combinations [24]. A reference Pelton turbine bucket design using Non-Uniform Rational B-Splines Modeling (NURBS) was developed [25], and an unsteady CFD simulation approach for different bucket design optimization of the Pelton turbine runner was found effective [26]. Once designed, the optimized fabrication of Pelton turbine runners reduced the manufacturing time by 30% over the casted runner [27]. Pelton turbine runners have maximum pressure distribution at the bucket tip and runner Pitch Circle Diameter (PCD) [28]. The advantage of the hooped runner over the traditional one is that the stress is minimized and distributed more efficiently. Buckets for a newly designed runner with added backplates to support the buckets, subjected to bending moment on the back of both the hemispherical cups, have been reduced [29], and the bucket geometry influences Pelton's performance [30]. The flow visualization study of jet and bucket interaction in traditional and hooped Pelton turbine runners and reduced stresses as evaluated by finite element (FE) analysis [31,32]. Fatigue analysis of simple and advanced hoop Pelton turbine buckets; better design and operating performance of the Pelton turbine bucket with minimum corrosion and failures [33].

Performance Estimation

The operating head influences the rotating bucket, free surface sheet flow, and hydrodynamic performance of a Pelton turbine [23]. The hydraulic performance for the conventional and hooped Pelton turbine runners for variable flow conditions is in close agreement [34], and the optimized hoop thickness is required for maximum hydraulic performance [35]. The Pelton turbine's performance depends upon the jet's shape, size, and quality, as well as the shape of the bucket [36]. Combining the impeller of the Pelton turbine on the shaft of a high-pressure multistage pump used in seawater, the Reverse Osmosis (RO) desalination package yielded a decrease in input power [37]. The roughness of the bucket and the Reynolds number on the model are applied for global efficiency scale-up in actual plants [38]. The hybrid Eulerian-Lagrangian method to investigate bucket geometry's influence on Pelton turbine efficiency is proper [39,40]. A numerical flow analysis in a 2-jet Pelton turbine with a k-ω SST turbulent model has shown increased efficiency [41]. The gravity and surface tension affect the efficiency of accurate scale-up models [42], and the Euler particle tracking model has shown that erosion influences hydraulic characteristics [43]. Developing and evaluating numerical modeling tools of the complex unsteady free surface flow developed in the turbine is helpful for performance estimation [44]. The laboratory-scale tests on two impulse (Pelton and Turgo) turbines showed that the Turgo turbine is more efficient with a speed ratio of 0.46. The jet misalignment leads to a drop in efficiency [45]. The failure analysis of a Pelton turbine runner's CFD approach identified the critical points on the bucket zone neck, coinciding with the crack caused by tensile stress (Centrifugal force) and compression [46]. The Pelton turbine at full load and part load, along with numerical analysis and visualized flow pattern in the passages, showed good agreement [47]. The bamboo material is designed with a square nozzle to rotate the Pelton turbine runner, which can produce a higher speed than the round copper nozzle [48].

The Pelton-type impulse turbine can be applied to the seawater reverse osmosis (RO) energy recovery system [49]. The multiple parameters can yield the best results for energy systems by optimizing these operating parameters. Optimization algorithms like hybrid genetic algorithm and particle swarm optimization (GA-PSO) can be applied for the performance of stand-alone hybrid energy systems [50]. Artificial intelligence and digitization contribute to achieving clean and affordable energy [51]. Even exergetic performance analysis can compare oxy-combustion and conventional gas

turbine power cycles [52]. Model Predictive Control (MPC) in microturbine generation systems leads to higher adaptability, outputs precise adjustment, and suitable power flow for stand-alone operation [53]. The properties of synthetic polymers can be used in medicine apart from engineering applications [54]. The mechanical behavior of wind turbine blades improves with nanofluid-graphene and glass fiber in epoxy resin [55]. Blade materials like stainless steel, e-glass, epoxy, and gray cast iron are the best for domestic windmill applications[56]. Also, for marine-based applications, an optimized K-type propeller with lightweight aluminum material was found to be appropriate [57]. A mini venturi wind turbine can be used for domestic applications without affecting avians and reducing noise [58]. The huge whistling noise from the windmill gearbox may cause severe damage to the living organisms in the sea [59], and the spatial analysis determines the installation sites of wind power plants using models to reduce such damage [60]. Implementing the latest technology sensors saves maintenance costs caused by a drop in the wind turbine generator gearbox's thermal performance [61].

Research Gap

Few researchers have conducted the numerical study of the hooped Pelton turbine, but none have designed, manufactured, or experimented. The researchers tried to develop a newer bucket design to evaluate the performance of the Pelton turbine runner numerically and experimentally, but not the bucket-supporting mechanism. The low and medium head responses were restricted to small-scale or laboratory-scale setups. The experimental performance evaluation for the hooped Pelton turbine runner with different convergence ratios and metallic and nonmetallic material nozzles is uncovered in the present study. In the current experimentation, identically sized Hooped Pelton Turbine (HPT) runners and Conventional Pelton Turbine (CPT) runners were designed and tested for performance estimation and subsequent comparison.

Research Objective

The research objective for the current study is

- To find the hydraulic performance of CPT and HPT runners with variable flow conditions at constant head.
- To find hydraulic performance with the same material nozzles but different convergence angles.
- To compare the hydraulic efficiency of HPT and CPT runners for nozzles with different convergence angles.

EXPERIMENTAL SETUP

Setup Details

Hydro turbo machines are vital in fluid power engineering and sustainable power production through water energy. In the case of impulse-type hydro turbo machines, the amount of torque depends on jet exit conditions, the shape of the aperture, opening velocity, viscosity of the fluid, and surrounding air at the application where the jet is

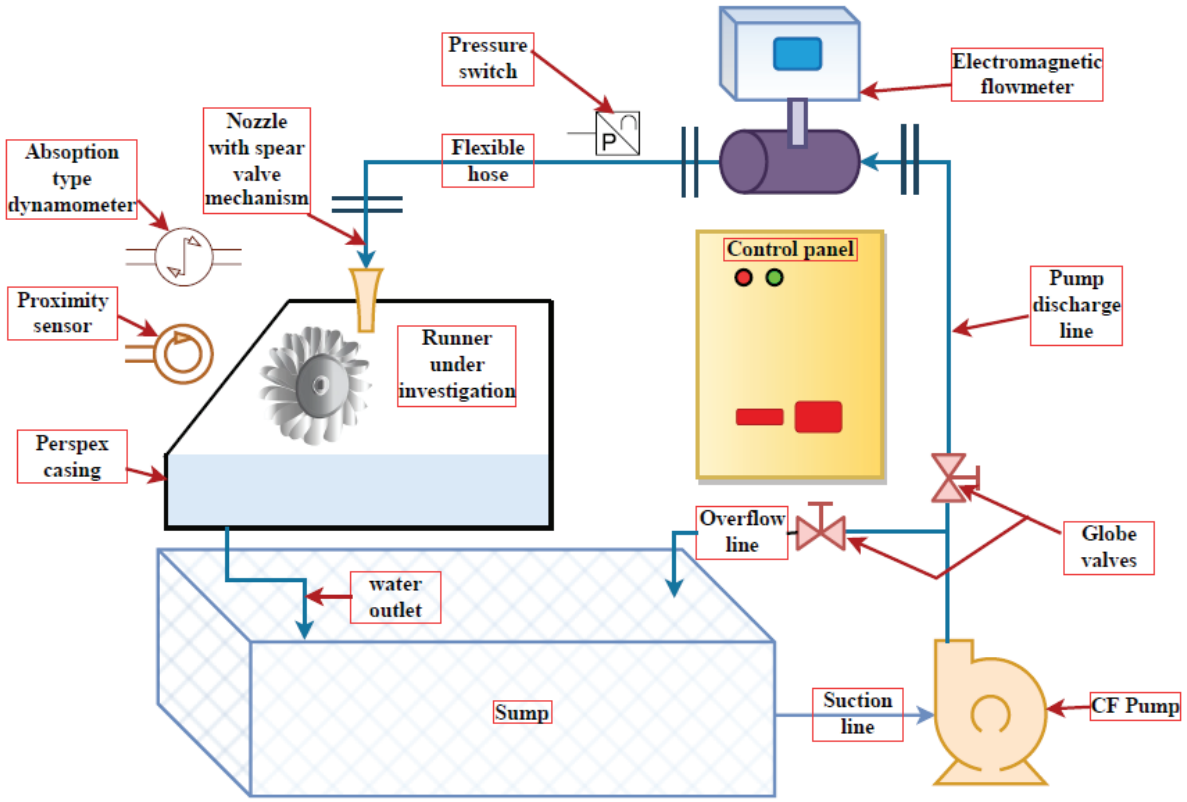


Figure 1. A line diagram -Experimental setup for testing impulse turbine runners.

employed. Since a jet is issued from the convergent nozzle of different sizes, research papers about such work are also cited. For conventional and hooped Pelton runners, relevant investigations are cited to clarify the work. The runners' design was carried out for maximum efficiency [62].

The head, flow conditions, and jet incidence variation significantly contribute to efficiency, torque characteristics, and turbine functioning points. A detailed evaluation of torque and thrust has shown that the cut-out and edge losses are the sources of loss in efficiency [63]. Numerical simulation showed that fiberglass-reinforced plastic for the bucket is better than cast iron under static conditions [64]. The parametric model of the bucket geometry, massive particle-based numerical simulations, and advanced optimization strategy can be used for the design optimization. Hence, the performance of a Pelton turbine runner increased [65]. The torque evolution and water sheet position for a revolving Pelton bucket simulation and the flow simulation of a stationary Pelton bucket using the finite volume particle approach for various impinging angles formed a new approach [66].

Figure 1 depicts the line diagram of the experimental setup used to examine two distinct runners for differing flow conditions, each with a different nozzle size and material. The setup,

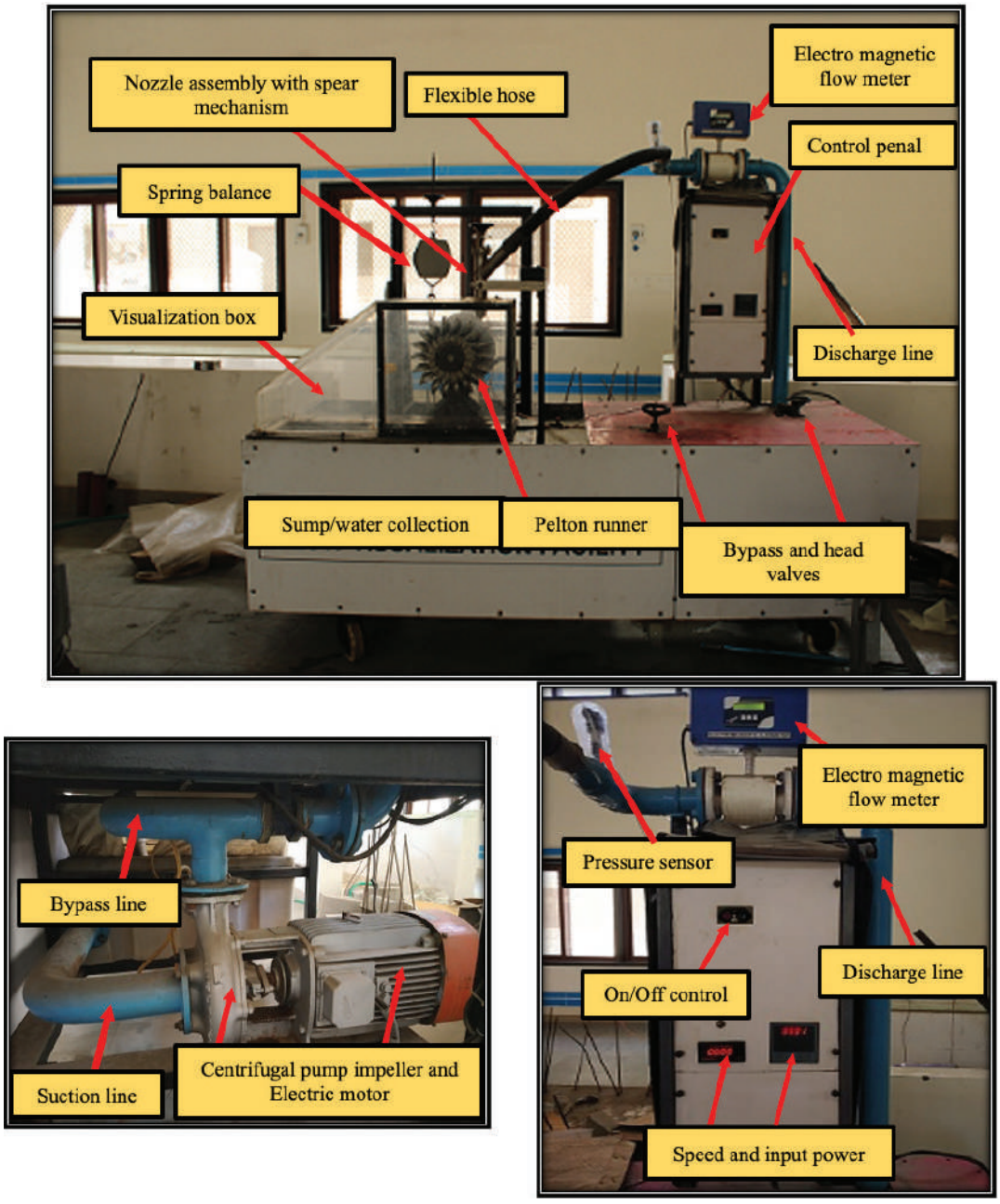


Figure 2. Experimental setup for Pelton wheel runners.

flow conditions, and experimentation approach are the same for both runners. The arrangement mentioned above comprises multiple parts, as indicated in Figure 2. A 5 HP electric pump motor (Kirloskar make) drives a strong flow rate through a line at the setup's sideways bottom, as seen in Figure 2. A 2.5-inch flow pipe transports the large water flow upward. It has a sizable centrifugal impeller to provide a straight flow through a flexible conduit. It comes with every fitting and valve required for the equipment to operate smoothly.

The discharge through the pump is measured using a line-mounted electromagnetic digital flow meter with a minimum flow measurement capacity of 0.00069 m^3/hr. The flow meter is lined up with polytetrafluoroethylene to provide a smooth passage for water flowing through it.

A flexible heavy hose is linked to the flow meter outlet and the main nozzle assembly to lessen the loss of piping length. The downcomer nozzle assembly's outer thread mounts and unmounts nozzles of different diameters and materials. A present study used two stainless steel (SSN) and four Polyacetal or Polyoxymethylene polymer (PYN) nozzles to evaluate the rotors' performance. The large rectangular sump at the bottom holds the water stream after striking the bucket and provides the opening for the Pump inlet to close the circuit of the test rig. The pressure sensor, model ADZ Nagano (Model SML-10,-1 - 25 bar,25 kg/cm^2), is kept after the flow meter to measure the pressure of fluid flowing through the pipe. The downcomer nozzle is fitted to a distance of less than 4Di to eliminate the possibility of jet spreading. A chamber comprises transparent acrylic sheets and digital still photography or movie shooting to enable flow visibility. The control panel has controls for starting and stopping the motor and a display for power input.

Investigated Variable Parameters

(a) Nozzle diameters

Figures 3, 4, and 5 depict the various nozzles used in the present study to investigate the main and operating characteristics of the Pelton turbine runners and then compare them [67]. The nozzle materials are selected as metallic and

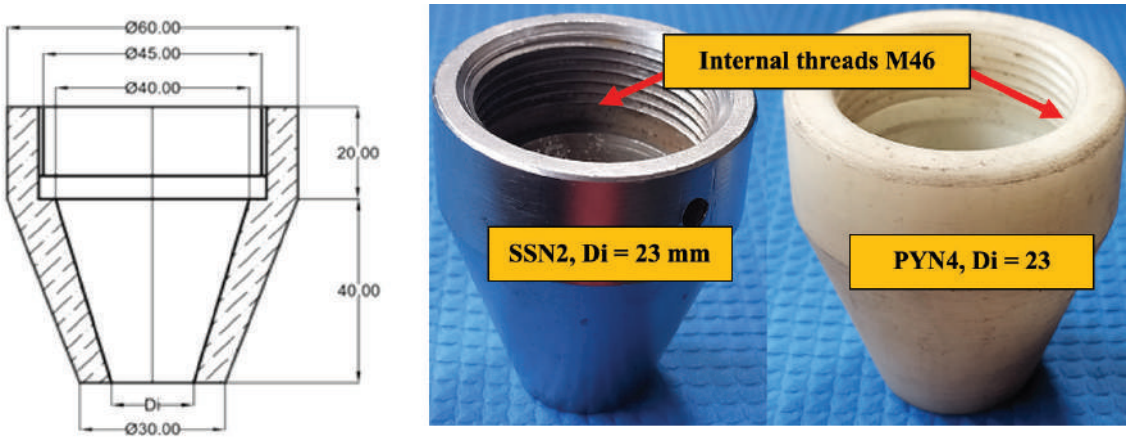


Figure 3. Cross-sectional view of the nozzle.

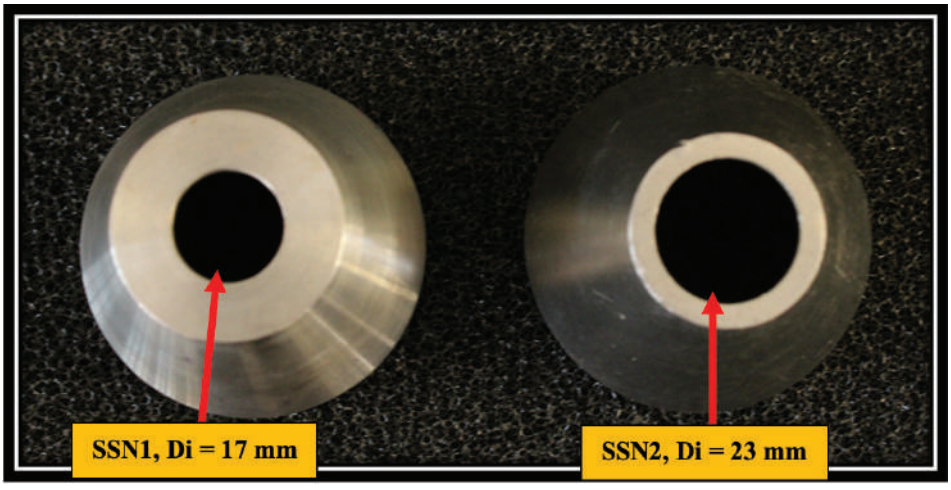


Figure 4. Stainless steel (SSN) nozzle top view left to right: a) D_i=17 mm, b) D_i=23 mm .

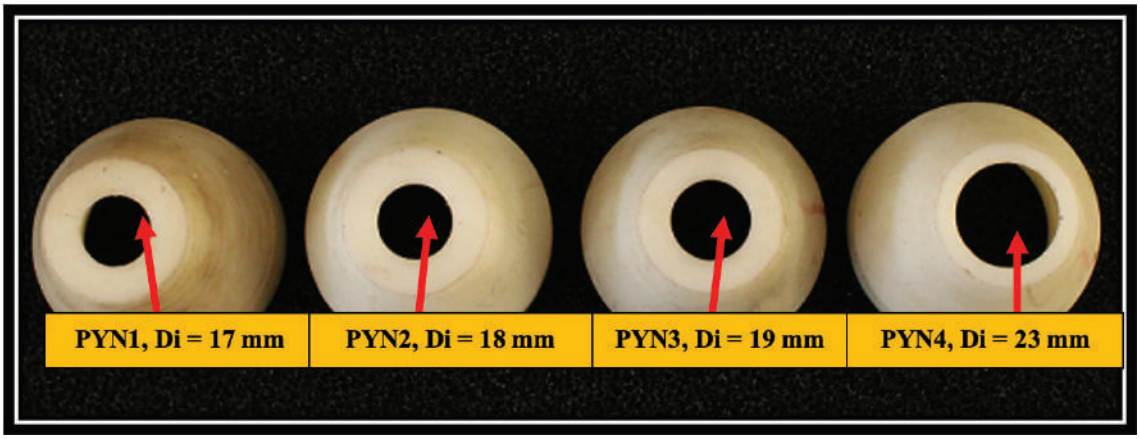


Figure 5. Polymer nozzle (PYN) top view a) D_i=17 mm b) D_i=18 mm c) D_i=19 mm d) D_i=23 mm.

Table 1. Geometrical parameters of the tested nozzles and material

Sr No.	Nozzle and its Specification	Size (Di), mm	Angle of convergence (Θ_n), Degrees	Beta ratio(β) (Di/Do)	Material of the nozzle
1	SSN1	17	32	0.38	Stainless steel (SS)
2	SSN2	23	24	0.49	Stainless steel (SS)
3	PYN1	17	32	0.38	Polyacetal or Polyoxymethylene
4	PYN2	18	30.5	0.40	Polyacetal or Polyoxymethylene
5	PYN3	19	29.5	0.42	Polyacetal or Polyoxymethylene
6	PYN4	23	24	0.49	Polyacetal or Polyoxymethylene

nonmetallic and have similar diameters. The length of the conical part is kept identical in all sets of nozzles at 40 mm, so the internal threading M 46 accommodates it on the nozzle-spear assembly.

As shown in Table 1 below, different materials and diameter nozzles are used for experimentation. For convenience, the code for each is depicted along with the specification. The cross-section of each of the mentioned nozzles is the same. Beta ratio (β) refers to the nozzle throat's diameter to the main pipe's diameter (D_i/D_o) range of 0.2 to 0.8 per ASME. Polyacetal is a lightweight material that provides less friction to fluid and is cheaper than stainless steel upon replacement. It is excellent in resisting many organic solvents, fuels, and weak acids, so it is suitable for varying water quality, including sediments.

In the present study, the dimensions and size of nozzles and runners employed are tabulated in Tables 1 and 2, respectively. The pipe with a 45 mm diameter and the nozzle inlet diameter of 40 mm are considered for beta ratio and convergence angle calculation, respectively. The nozzles have identical size and shape but differ in exit diameter and the resulting jet ratio. The angle of convergence and the beta ratio also differ. The material used for the above set of nozzles is different. The convergence angle for the nozzle depends on the inlet and exit diameters of the nozzles used. The maximum convergence angle in the present study is 32 degrees, with a beta ratio of 0.38 for 17 mm nozzles.

(b) Runner parameters

The Conventional and hooped Pelton turbine runners used for experimental investigation are shown in Figure 6. The geometric specifications for both runners are mentioned in Table 2. The runners are identical in construction and manufacturing except for the hooped plates. The buckets are bolted, and the internal surface of the bucket is polished to minimize friction losses. The runner disc and hub are integral parts and strong enough to cater to the load of all the buckets and hoop plates. The keyway in the hub matches the machine drum shaft keyway to accommodate the feather key. The hooped Pelton turbine runner is heavier than the Conventional Pelton turbine (CPT) runner. The hoop plates are bolted to the runner disc.

Table 2. Geometrical parameters of the tested runners

Sr No.	Description	Conventional Pelton Turbine (CPT)		Hooped Pelton Turbine (HPT)	
		Size (mm)	**Material**	**Size (mm)**	**Material**
1	**Bucket**		Stainless steel		Stainless steel
	Bucket width (W_b)	96 mm		96 mm	
	Bucket height (H_b)	90 mm		90 mm	
	Diameter to bucket width (D_p/W_b)	2.1		2.1	
	Number of buckets(Z)	18		18	
2	**Hub**		Stainless steel		Stainless steel
	Diameter of hub(d_{hub})	52 mm		52 mm	
	Length of the hub (l_{hub})	150 mm		150 mm	
	Size of keyway (Lx B)	10 x 5 mm		10 x 5 mm	
3	**Runner**		Cast steel		Cast steel
	The pitch circle diameter of the runner	256 mm		256 mm	
	Runner outside diameter	320 mm		320 mm	
	Runner width(r_b)	96 mm		96 mm	
4	Hoop thickness(h_t)	NA	----	4 mm	Stainless steel
5	Hoop gap(h_g)	NA	----	40 mm	----

A conventional Pelton turbine runner used for experimental investigation is depicted in Figure 6. It constitutes 18 double hemispherical buckets mounted on steel discs with the help of two stainless steel M12 bolts to complete the assembly. It has a central hole with a keyway to insert a feather key. A rubber padding is inserted on the front side and fastened with the help of bolts to prevent the axial movement of the runner. The inner surface of the bucket is made highly polished to reduce fluid friction losses upon gliding through the surface.

The hooped Pelton is an innovative new design based on the separation of function between buckets and hoops, as shown in Figure 6. The above figure also depicts the conventional Pelton Turbine runner used for investigation, along with the downcomer nozzle fitted tangentially at the top. This runner comprises separate buckets mechanically attached to a hub of two flanges (Hoops). The hoop plates are separated and located at a distance of 40 mm. The jet of fluid comes out from the bucket by gliding through the double hemispherical bucket surface, and to cater to this, notches are provided in the hoop plates. The novel hooped Pelton turbine runner has an excellent maintenance advantage and improved mechanical characteristics.

(c) Gate opening (variable flow area)

The gate opening in the present study for the variable flow area in all the nozzle runner combinations was carried

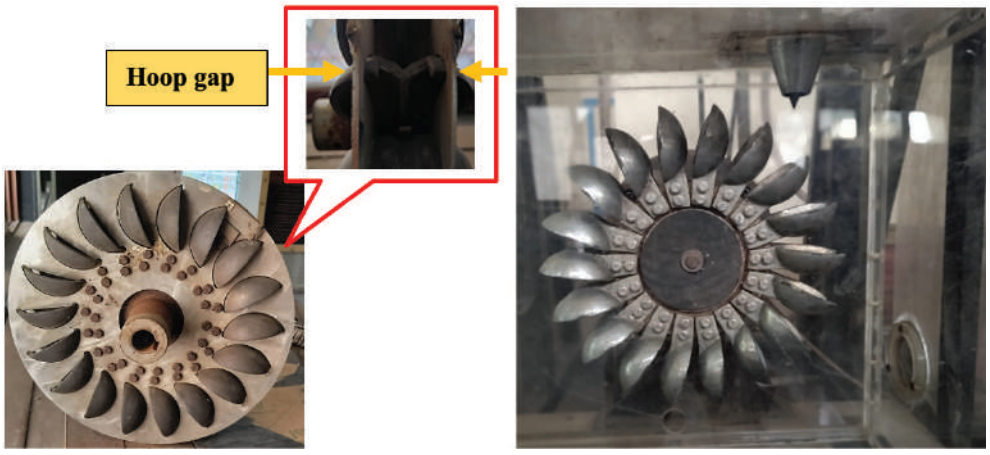


Figure 6. Hooped and conventional Pelton turbine runner (Left to right) under investigation.

out. The spear rod mechanism moves in and out to change the flow area based on the annular space between the spear rod and the tapered nozzle wall. In the present study, gate openings from 20 percent to 100 percent of the total flow area are taken during investigations.

MATERIALS AND METHODS

The parameters studied here include the flow interaction between the jet and rotating buckets in the turbine with variable flow area, convergence angle, and the jet ratio. The electromagnetic flow meter, weight, and spring balance are kept to observe various parameters. The experimental investigations were carried out continuously by changing the nozzles of various diameters. The head of water, 43 m, was maintained constant throughout the experimentation.

The calculation here leads to the various parameters like jet ratio (m) and velocity ratio/speed ratio (ϕ), the essential parts to describe the design and performance of the Pelton wheel turbine. The assumption is generally that the speed ratio's value is in the range of 0.42-0.48, and that of the jet ratio (m) changes from 10-18. In the present study, using a range of different diameter nozzles, the values are in the standard prescribed range. Table 3 below shows values obtained after the experiments.

The parameters were measured with various measuring devices and sensors. The present study takes care of the digital instruments with a digital display of the vital measured quantities like input power, runner speed, flow rate, and line pressure. Table 4 below states such parameters and corresponding measurements.

DATA REDUCTION

The various parameters like runner speed (Nr), dead weight (W), Spring balance reading (S), Power input (Pi), and Flow rate (Q) are observed and measured during experiments in the present study. The various quantities, like Hydraulic efficiency (ηh), Overall efficiency (ηo), the power developed (Pd), and torque available at the shaft (T) for all nozzle runner combinations, were estimated using the following equations.

$$N_s = N \frac{\sqrt{P_d}}{H^{\frac{5}{4}}} \tag{1}$$

Table 3. Jet ratio and velocity ratio at full gate opening (100 % GO)

Sr. No.	Nozzle	Size (mm)	Jet ratio (m=Di/Dp)	Velocity ratio ϕ (= u/Vjet)	
				Conventional Pelton Turbine (CPT) Runner	Hooped Pelton Turbine (HPT) Runner
1	SSN1	17	15	0.423	0.427
2	SSN2	23	11	0.492	0.436
3	PYN1	17	15	0.470	0.417
4	PYN2	18	14	0.466	0.444
5	PYN3	19	13	0.444	0.454
6	PYN4	23	11	0.425	0.362

Table 4. Measured parameters and corresponding instrumentation

Sr. No.	Parameters	Notation	Measurement
1	Input Power, kW	Pi	Motor power Sensors for voltage and current
2	Spring balance reading, kg	S	Subh, Accuracy class IV, 1 - 25 kg, 0.1 kg LC
3	Deadweight, kg	W	Cast iron counter slotted weight of known mass (set of 1 kg and 2 kg)
4	Runner speed, rpm	Nr	NPN-type revolution counter 2-20 mm, IP67, 10 to 30 VDC
5	Flow rate, m^3/hr	Q	Flowtech, Electromagnetic (MAG) Flowmeter, ± 1%, SS316, ±0.5% FSD, 0.3 to 10 m/s, 25 kg/cm^2
6	Percentage gate opening	%ge GO	Manually rotating the wheel in and out, the thread count
7	Pressure measurement, bar	p_g	ADZ Nagano SML-10, Electronic, SS304, ≤0.5% FSD,-1 - 25 bar, IP65, ceramic,4- 20 mA,12 to 32 V

$$N_s = \frac{\omega\sqrt{P_d}}{\sqrt{\rho}\left(gH\right)^{\frac{5}{4}}} \quad (2)$$

The dimensional and non-dimensional-specific speeds were found using Equations (1) and (2).

The power developed P_d on the shaft is expressed in kilowatts; the head H is expressed in m, and the speed ω is expressed in rad/s for Equation (1), and the power P_d is expressed in watts; the head H is expressed in m; the runner speed ω is expressed in rad/s; the density ρ is expressed in Kg/m^3 for Equation (2), respectively.

The unit quantities like unit power (P_u), Unit discharge (Q_u), and Unit speed (N_u) were evaluated using the formula given in Equation (3).

$$P_u = \frac{P_d}{H^{3/2}}, \quad Q_u = \frac{Q}{\sqrt{H}}, \quad N_u = \frac{N_r}{\sqrt{H}} \quad (3)$$

The torque developed on the runner is given by Equation (4)

$$T = \frac{\left(W - S\right) \times D_e \times g}{2} \quad (4)$$

The angular velocity of the runner, ω in terms of rad/s, was evaluated using Equation (5)

$$\omega = \frac{2\pi N_r}{60} \quad (5)$$

Mechanical power developed on the turbine shaft (P_d) was evaluated using Equation (6)

$$P_d = T \times \omega \quad (6)$$

Hydraulic efficiency(η_h) was evaluated using Equation (7)

$$\eta_h = \frac{P_d}{P_{in}} \times 100 \quad (7)$$

Where,

N_r = Speed of runner, rpm, P_{in} = Water power supplied to runner, Watt, W = Dead weight, kg, S= Spring balance reading , kg, D_e = Effective diameter of drum, m.

RESULTS AND DISCUSSION

The runners exhibited different performance characteristics with a nozzle combination and varying flow conditions under the constant head. The dynamic performance of Pelton turbines focuses on energy and power efficiency, discharge efficiency, and factors affecting performance under varying unit speeds [68,69]. The Conventional Pelton Turbine (CPT) and Hooped Pelton Turbine (HPT) runners were tested with all the nozzles and all the variable flow area situations.

Variation with Percentage Gate Opening for Different Nozzle Runner Combinations

The experiments were carried out with different nozzles and runners by restricting the flow area in percentage. The 17 mm SS nozzle (SSN1) characteristics for both runners are given in Figure 7. Both runners were found to have low torque in the range of 200 to 1200 rpm, with 80 % flow area restricted. The torque developed with a Conventional Pelton Runner shaft at 100% gate opening (GO) was about 9 N-m with 1000 rpm of the CPT runner. The least was found with a decrease in flow area (20% gate opening) in the case of both runners. The range over which power developed by the Hooped Pelton Turbine (HPT) runner with the 17 mm SS nozzle (SSN1) is found to be 700-1500 rpm, wherein maximum power is developed around 900 rpm.

The presence of two hooped steel plates 4 mm thick made the runner bulkier, so with the Hooped Pelton Turbine (HPT) runner, the values are identical at the higher runner speed, but the curve gets separated at the lower runner speed. The high unit discharge was found with the Conventional Pelton Turbine (CPT) runner compared to the Hooped Pelton Turbine (HPT) runner. The range of unit discharge for a conventional Pelton turbine (CPT) is more significant with unit speed than that of a hopped Pelton turbine (HPT). The unit discharge remains in the range of 1 to 1.5 for the most flow area variation corresponding to the range of unit speeds.

Figure 7 shows the operating parameter for a 17 mm stainless steel nozzle (SSN1) with a beta ratio of 0.38. The 17 mm exit diameter SS nozzle (SSN1) gave better efficiency and variation of parameters with runner speed and unit speed than any other combination used in the experimental study. The range of points and corresponding curves obtained with a 17 mm SS nozzle (SSN1)-Hooped Pelton turbine (HPT) runner are similar to standard curves for the Conventional Pelton turbine (CPT) runner. The power developed at the turbine shaft with a 17 mm SS nozzle (SSN1)- CPT runner combination is more than any other. The hydraulic efficiency obtained was higher with a 20% gate opening in the case of the CPT runner compared to the HPT runner for a 200 to 1000 rpm runner.

Figure 8 shows the variation of the main and operating parameters, including runner speed and unit speed, caused by using 23 mm stainless steel (SSN2). The 20 % gate opening variation dominates the Hooped Pelton turbine (HPT) runner. The maximum value of unit discharge is found with 100% gate opening in the case of the HPT runner. The nozzle with exit diameter (Di) used here is 23 mm of stainless steel (SSN2), with the highest beta ratio of 0.49, and

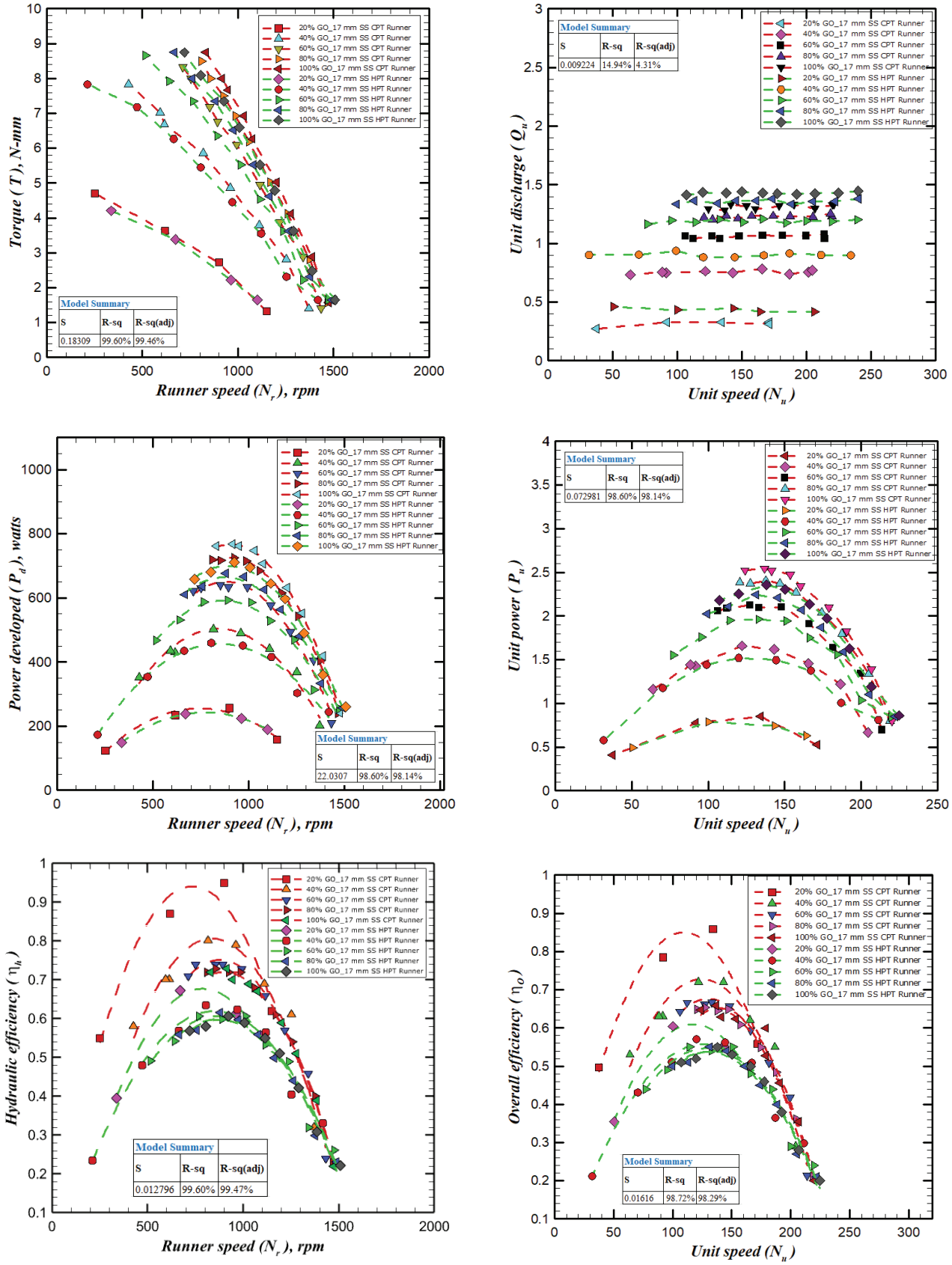


Figure 7. Main and operating characteristics with SSN1 17 mm nozzle.

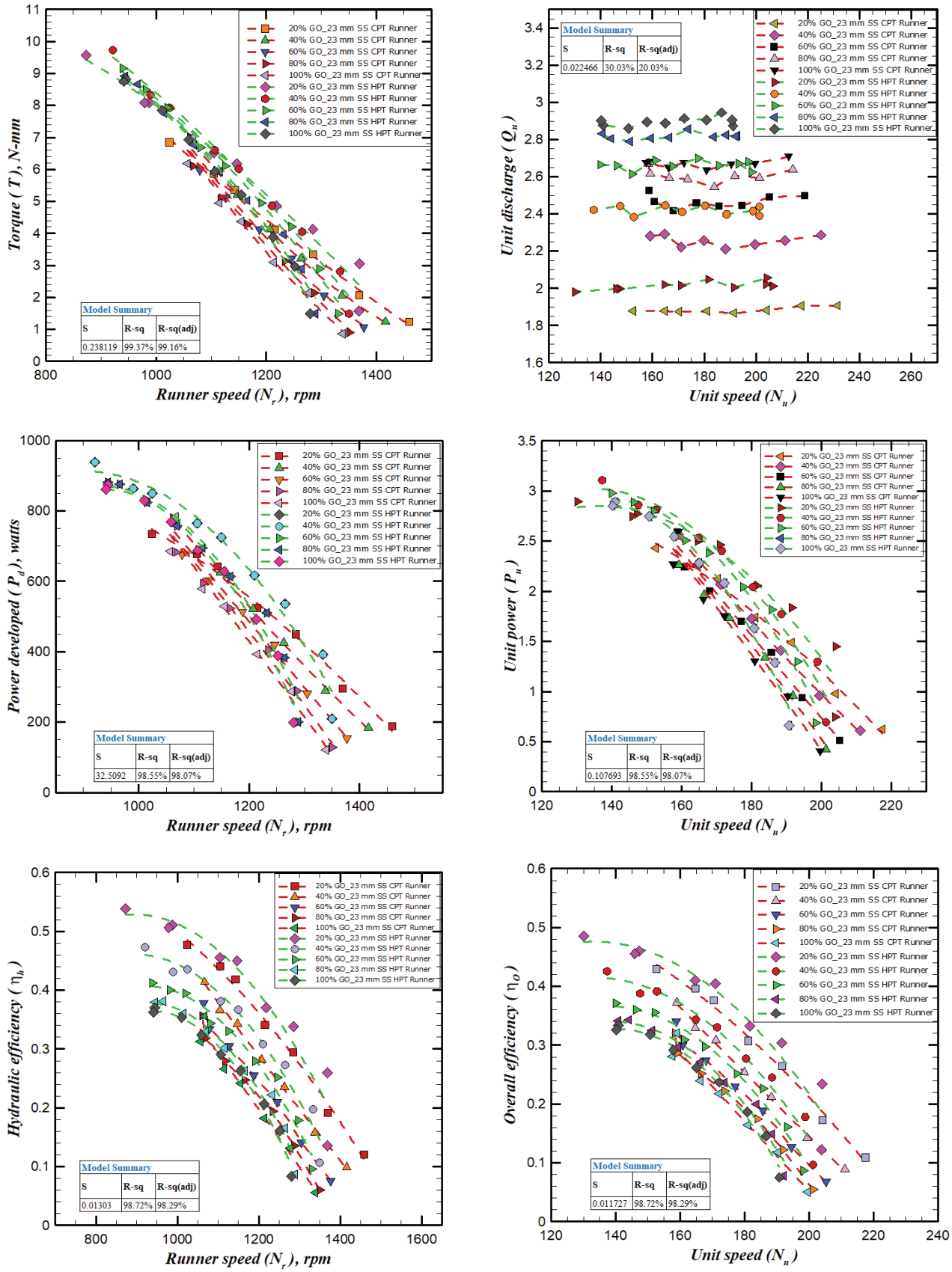


Figure 8. Main and operating characteristics with SSN2 23 mm nozzle.

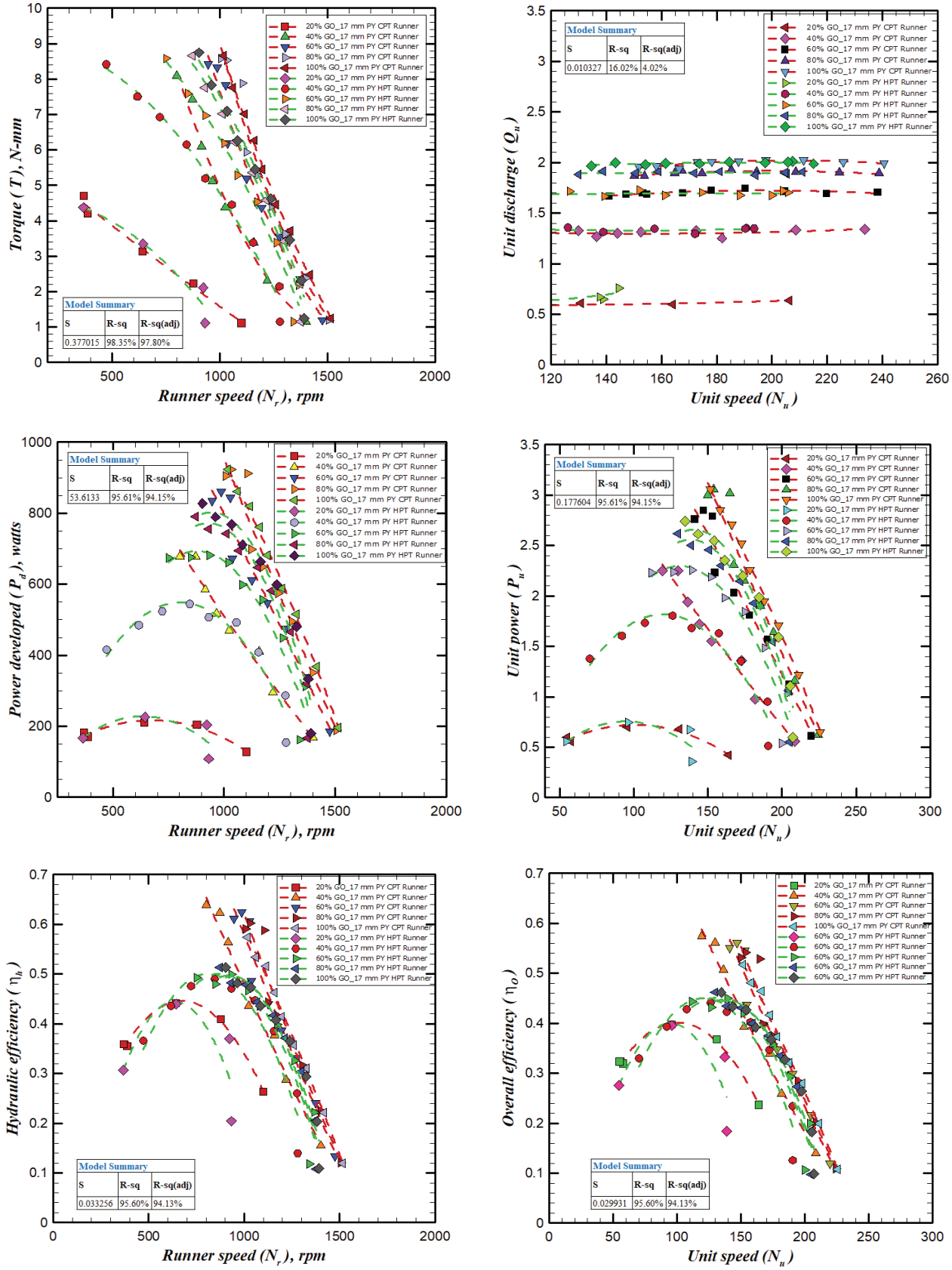


Figure 9. Main and operating characteristics with 17 mm Polymer nozzle (PYN1).

the nozzle's convergence angle is 24 degrees. The size of the jet was increased by 6 mm to check both runners' behavior under the increased water faucet. Figure 8 depicts the variation in flow rate, the corresponding change in parameters, and, ultimately, the efficiency. A broader spectrum in the right curve is covered with a 23 mm SSN2 nozzle, unlike a 17 mm diameter SSN1 nozzle. The flow area opened up to 40 %, giving maximum hydraulic efficiency for both runners due to fewer losses, but the curve spectrum is not fully covered as in the case with the ideal curve.

The points for parameters obtained with 23 mm SSN2 are separate and distinguishable. In Figure 8, the right-half curve is feasible only for the few restricted flow area percentages due to the heavy water faucet spilling out of the bucket without gliding and imparting work to the runner. The variation with the runner speed, a 17 mm diameter polymer nozzle (PYN1), exhibited a range of torque, power developed, and hydraulic efficiency.

Figure 9 shows the variation in unit speed plotted against unit discharge, unit power, and overall efficiency. The maximum hydraulic (η_h) and overall efficiencies (η_o) are noted with a 40 % gate opening with a conventional Pelton turbine (CPT) runner. The efficiencies corresponding to gate opening in each set can be represented as $\eta_h)_{CPT}$ is greater than $\eta_h)_{HPT}$ follows: The unit discharge (Q_u) remained equal for both runners. The hooped Pelton turbine runner (HPT) behaved equally for 40%, 60%, and 100% opening of the flow area for hydraulic efficiency.

The variation in main and operating characteristics is shown in Figure 10 with a polymer nozzle (PYN2) with an 18 mm exit diameter, 29-degree convergence angle(Θ_n), and 0.40 beta ratio(β). The speed range covered 400 -1500 rpm, and a smooth curve was obtained. The maximum hydraulic efficiency corresponds to 1011 rpm, which was found to be 53.11% in conventional Pelton turbine (CPT) runners, whereas it was found to be 52.34%, which corresponds to 963 rpm. The power developed at the runner shaft was measured with an absorption type dynamometer (rope brake type); in the case of a conventional Pelton turbine (CPT) runner, it is 890 watts, whereas, in the case of a hooped Pelton turbine (HPT) runner, it was 823.50 watt corresponding to 923 rpm of the runner.

Figure 11 depicts the variation in power developed, torque, and hydraulic efficiency with runner speed with a 19 mm diameter polymeric material nozzle (PYN3), a convergence angle of 30 degrees, and a beta ratio (β) of 0.42. The polymer material nozzle yielded the highest hydraulic efficiency, 61.66%, corresponding to 742 rpm of a hooped Pelton turbine (HPT) runner with only 20% of gate opening(GO). The unit quantities are also evaluated to check the runner's performance if the head changes.

Figure 12 shows the operating parameter for a 23 mm polymer nozzle (PYN4) with a beta ratio (β) of 0.29 and angle of convergence (Θ_n). In the present experimental study, the 23 mm polymer nozzle (PYN4) gave better efficiency at a lower rotation speed of runners in both Pelton turbine runner cases. The range of points and curves obtained with a 17 mm SS nozzle is similar to standard curves for the Pelton turbine. In the case of the CPT runner, the runner's speed of 1000 played a vital role as efficiency increases constantly.

Effect of the Nozzle Diameter for Various Nozzle Runner Combinations

The hydraulic efficiency of runners with 17 mm nozzles is higher than that of 23 mm because of the lower jet spreading and deviation. The 23 mm nozzles incurred more loss at the bucket and splashing in the visualization chamber. The mass of water trapped between the bucket and hoop plates in the hooped Pelton runner makes it heavy, apart from the weight of the hoop plates. There is more wake in the trapped system and water flow hindrance in the dynamic runner system instead of smooth gliding along the bucket's inner surface. For low speed, opt for a 17 mm stainless steel nozzle (SSN1), which $\eta_h)_{HPT}$ is greater than $\eta_h)_{CPT}$, as there are fewer losses in the confined space of bucket and hoop plates, which are dominant at high speed.

Figure 13 compares 17 mm and 23 mm diameter nozzles of stainless steel (SSN) and polymer (PYN) investigated for CPT and HPT runners under variable flow conditions. The torque for the 17 mm nozzle with the conventional Pelton turbine (CPT) runner must have a lower operating speed range than the hooped Pelton turbine (HPT) runner. The torque curve up to 1050 rpm due to momentum at low speed achieved through a 17 mm jet is dominant. The 17 mm and 23 mm polymer nozzles (PYN) have partiality in trends, but around 825 rpm with the conventional Pelton turbine (CPT) runner, the increase in torque occurs with a decrease in speed faster. In the present study, the hydraulic efficiencies with the same material but different jet diameters have been expressed as highest to lowest in $\eta_h)_{17mm,CPT}$, $\eta_h)_{17mm,HPT}$, $\eta_h)_{23mm,CPT}$, $\eta_h)_{23mm,HPT}$ order for polymer nozzles and $\eta_h)_{17mm,CPT}$, $\eta_h)_{23mm,HPT}$, $\eta_h)_{23mm,CPT}$, $\eta_h)_{17mm,HPT}$ for stainless steel nozzles up to a runner speed of 1100 rpm.

The nozzle diameter used here is 23 mm of stainless steel, and the beta ratio is kept for this nozzle. The size of the jet was increased by 6 mm to check both runners' behavior under the increased water faucet. The chart depicts the variation in flow rate and the corresponding change in parameters and, ultimately, the efficiency.

Effect of the Different Nozzle Materials for Various Nozzle Runner Combinations

The outward fluid flow occurs in a hooped Pelton turbine (HPT) runner bucket with two parts, as found during the experimental investigation. Also, it was found that the slots in a hoop plate with an opening govern the jet flow and outward stream through the bucket. The exhausting duration for the bucket full of water is significantly less due to high runner speed and confined space with a small slot in a hoop plate that retains most of the water in further

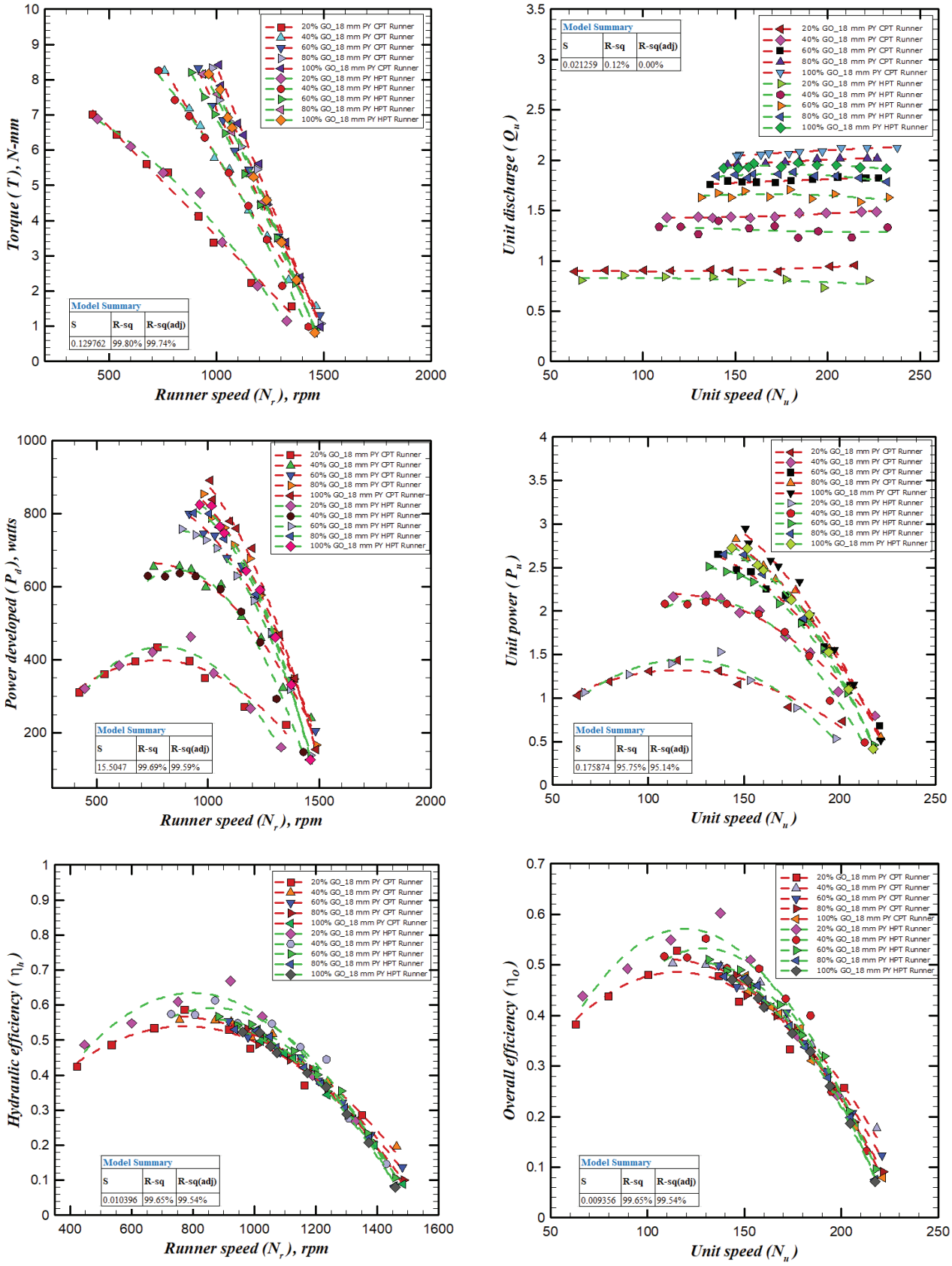


Figure 10. Main and operating characteristics with 18 mm polymer nozzle (PYN2).

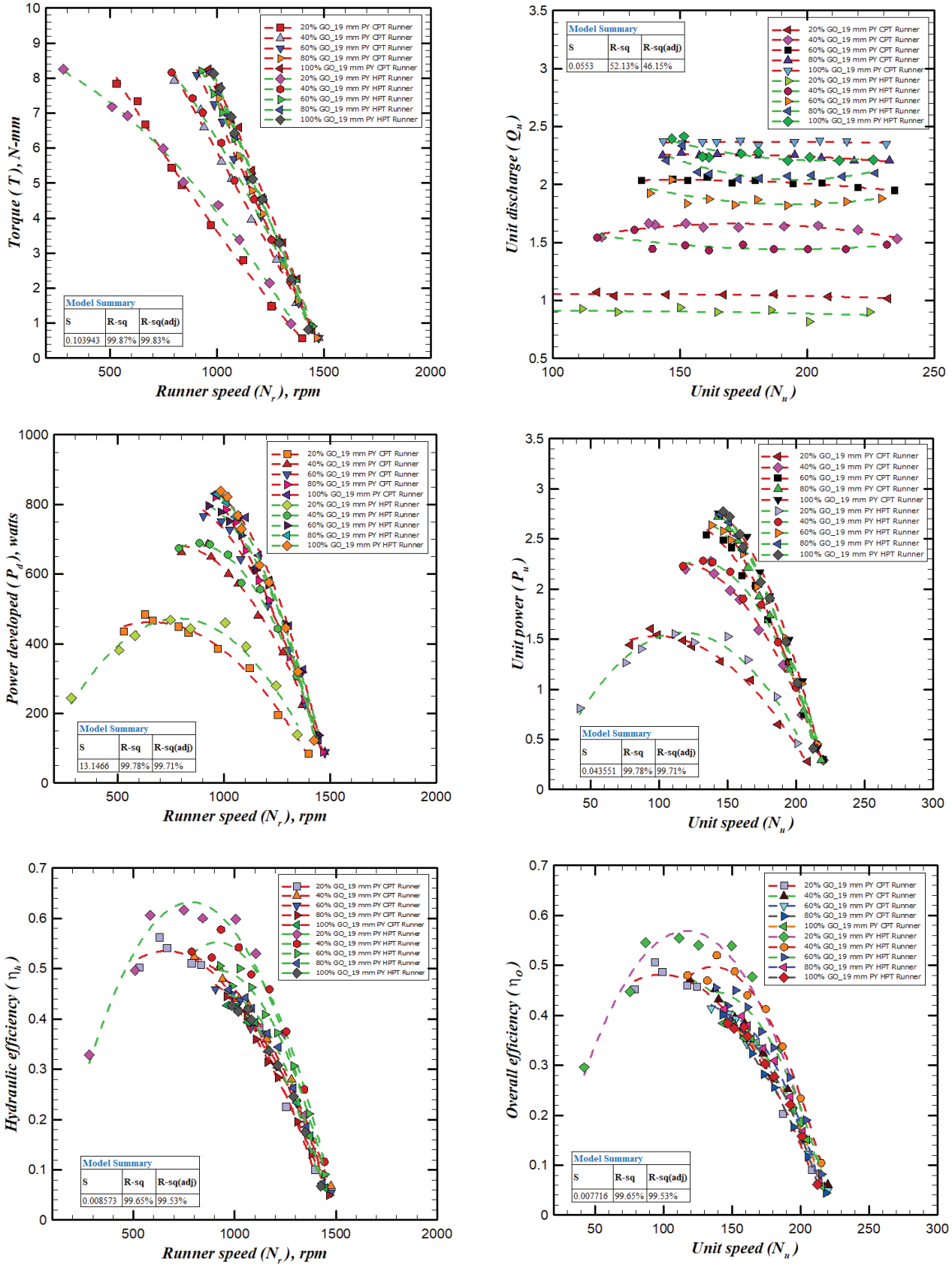


Figure 11. Main and operating characteristics with 19 mm polymer nozzle (PYN3).

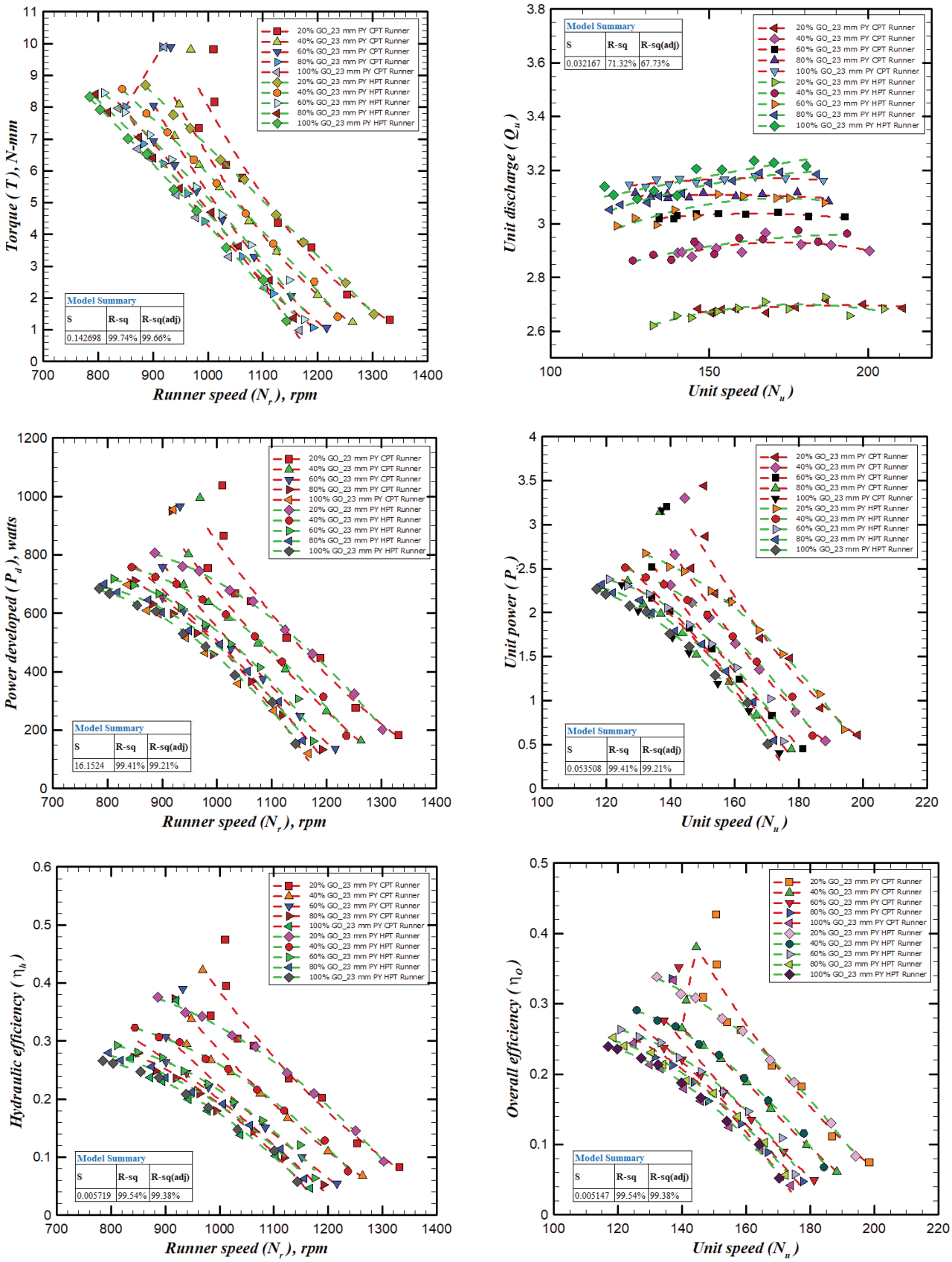
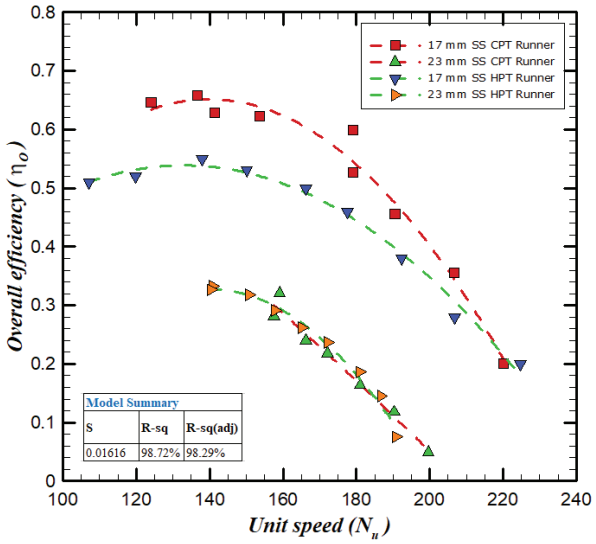
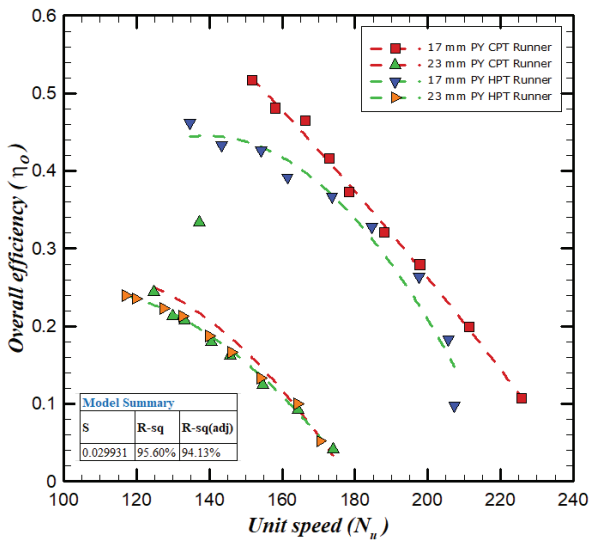
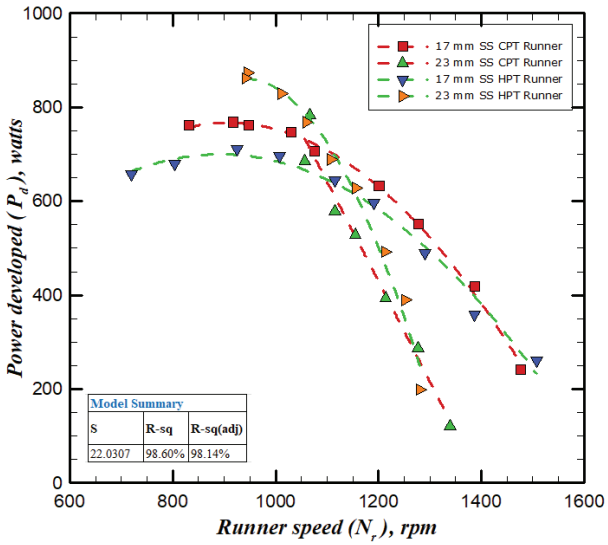
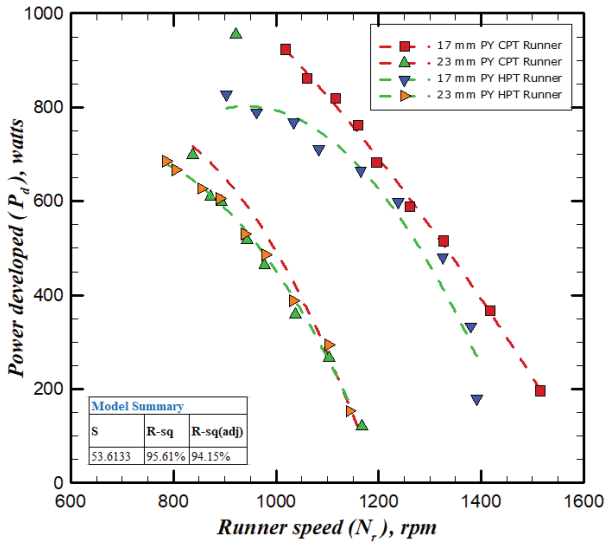


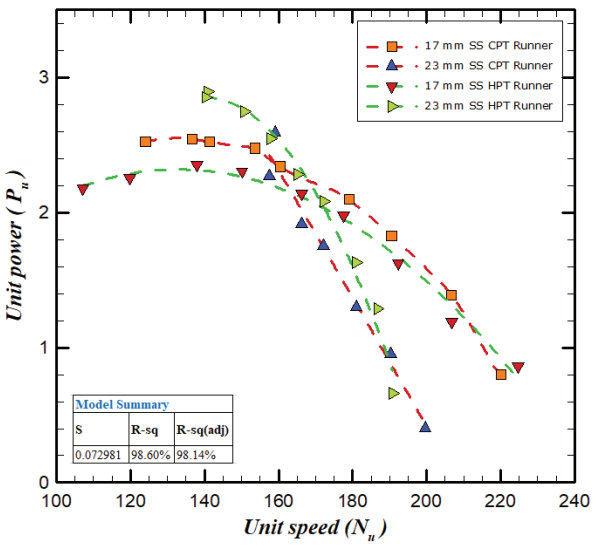
Figure 12. Main and operating characteristics with 23 mm polymer nozzle (PYN4)

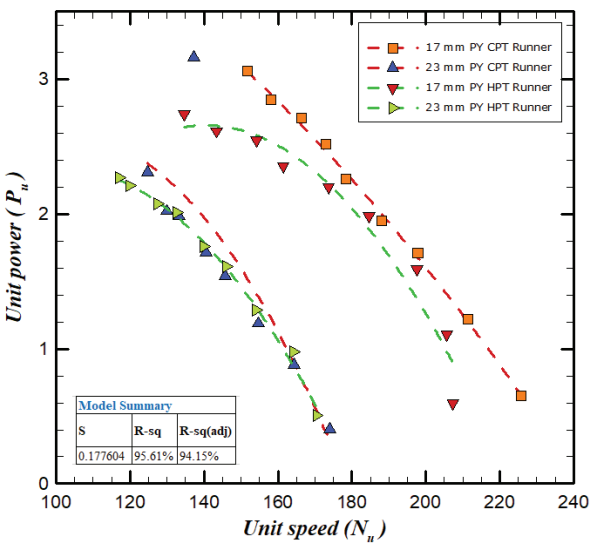

17 mm SS CPT Runner
23 mm SS CPT Runner
17 mm SS HPT Runner
23 mm SS HPT Runner
Overall efficiency (η_o)
Unit speed (N_u)
Model Summary
S R-sq R-sq(adj)
0.01616 98.72% 98.29%


17 mm PY CPT Runner
23 mm PY CPT Runner
17 mm PY HPT Runner
23 mm PY HPT Runner
Overall efficiency (η_o)
Unit speed (N_u)
Model Summary
S R-sq R-sq(adj)
0.029931 95.60% 94.13%


17 mm SS CPT Runner
23 mm SS CPT Runner
17 mm SS HPT Runner
23 mm SS HPT Runner
Power developed (P_d), watts
Runner speed (N_r), rpm
Model Summary
S R-sq R-sq(adj)
22.0307 98.60% 98.14%


17 mm PY CPT Runner
23 mm PY CPT Runner
17 mm PY HPT Runner
23 mm PY HPT Runner
Power developed (P_d), watts
Runner speed (N_r), rpm
Model Summary
S R-sq R-sq(adj)
53.6133 95.61% 94.15%


17 mm SS CPT Runner
23 mm SS CPT Runner
17 mm SS HPT Runner
23 mm SS HPT Runner
Unit power (P_u)
Unit speed (N_u)
Model Summary
S R-sq R-sq(adj)
0.072981 98.60% 98.14%


17 mm PY CPT Runner
23 mm PY CPT Runner
17 mm PY HPT Runner
23 mm PY HPT Runner
Unit power (P_u)
Unit speed (N_u)
Model Summary
S R-sq R-sq(adj)
0.177604 95.61% 94.15%

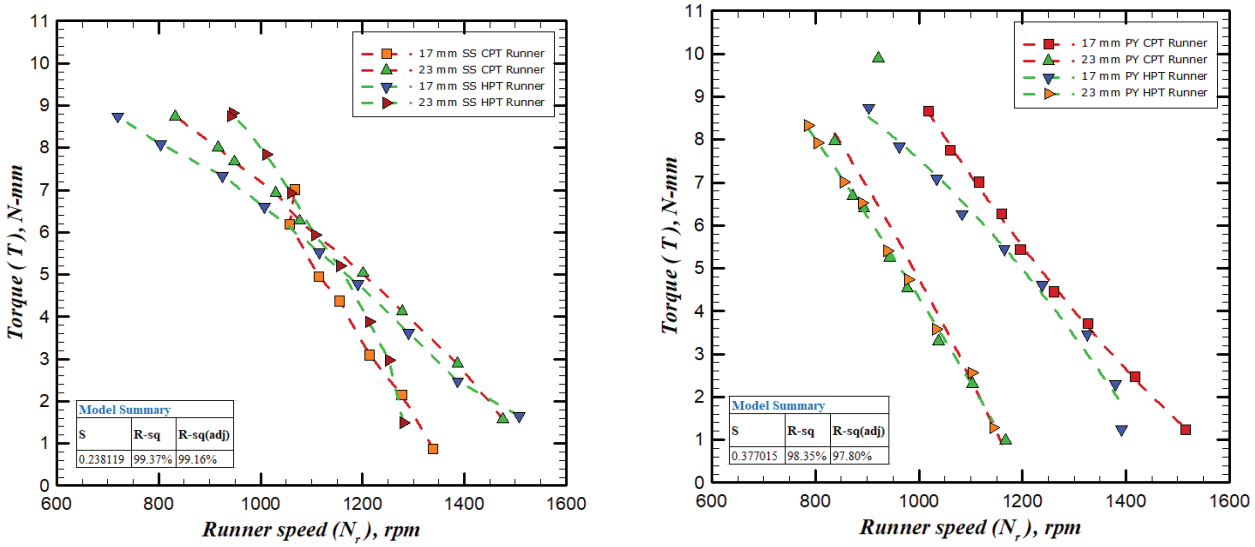


Figure 13. Main and operating characteristics for the different diameter nozzles for both runners.

rotation and falls due to gravity or centrifugal force without contributing much power to the runner shaft.

The variation in all the estimated parameters concerning runner speed is shown in Figure 14. The jet diffusion and separation of water particles from the jet surface at a larger jet diameter deteriorate the performance of the runners. The losses marked in the present study mainly include the higher diameter, the inertia of the turbine runner, and the obstructed outgoing flow with gradually increased gate opening (GO). The 17 mm diameter stainless steel nozzle (SSN1) has ticked all the boxes with fully defined performance characteristics, with variable area flow. The 23 mm nozzles suffer from jet stability and spread of jets despite less than 4Di distance. They further deteriorate the runner's performance with more water flow rates if used with a hooped Pelton turbine (HPT) runner compared to a conventional Pelton turbine (CPT) runner.

From the above graph, the hydraulic efficiencies (η_h) of all nozzle runner combinations in descending order can be written as $\eta_h)_{SSN1,CPT}$, $\eta_h)_{SSN1,HPT}$, $\eta_h)_{PYN1,CPT}$, $\eta_h)_{PYN2,CPT}$, $\eta_h)_{PYN2,HPT}$, $\eta_h)_{PYN1,HPT}$ for 17 mm (SSN1 and PYN1) and 18 mm (PYN2) nozzles. The $\eta_h)_{SSN1,CPT}$ combination has an 18.18% higher hydraulic performance compared to $\eta_h)_{PYN1,CPT}$ under the full gate open condition. The low-speed operation of small-diameter nozzles with heavier runner systems makes them more stable and valuable, as found in the case of an 18 mm polymer nozzle (PYN2), and can be a substitute for 17 mm nozzles with a higher convergence angle(Θ_n). The 19 mm polymer nozzles with a 30-degree convergence angle(Θ_n) and beta ratio(β) of 0.42 have almost the same performance for 100% gate opening, which $\eta_h)_{PYN3,CPT}$ is equal to $\eta_h)_{PYN3,HPT}$. A 19 mm Polymer nozzle (PYN3) achieves the optimum nozzle diameter here, similar to a 23 mm Polymer nozzle (PYN4), where hydraulic efficiency points coincide and are non-distinguishable, which $\eta_h)_{PYN4,CPT}$ is equal to $\eta_h)_{PYN4,HPT}$. The larger diameter stainless steel nozzle (SSN2) of 23 mm was tested with both runners, but the hydraulic efficiency (η_h) of the runners was found with the whole gate opening (100%) in the order of $\eta_h)_{SSN2,CPT}$ is greater than $\eta_h)_{SSN2,HPT}$. However, jet size, even for a conventional Pelton runner (CPT), plays a vital role in the hydraulic performance of the runner. Even with the larger flow area and, hence, higher fluid flow rate, the efficiency of a conventional Pelton runner (CPT) yielded 35.63% at 1067 rpm of the runner, whereas it was found to be 75.14% at 914 rpm of the runner with less flow area and a whole gate opening.

The work carried out by various authors has been mentioned in Table 5. The essential parameters like head, PCD of the turbine runner, nozzle diameter, and Number of nozzles employed for the experimental investigation, are mentioned. The experimental work on HPT is limited to numerical simulation and single-diameter nozzle efficiency evaluation. The regime beyond the single diameter was explored here to reveal the hydraulic characteristics of HPT.

Figure 15 shows the variation in hydraulic efficiency for comparison in the vertical bar chart. The comparison shows the variation in the efficiency range for the parameters considered in the present study. The chart was plotted with a 17 mm nozzle with a full gate opening. The available data are compared since the experimental work is limited to the HPT runner.

Figure 16 compares and supports the trend obtained from the present experimental observations. The trend line has suggested that the efficiency of the present work is behaving similarly to the previous work of different authors. The characteristics of CPT and HPT are the same but offset by some distance depending upon the additional inertia offered by adding hoop plates. In the present study, the graph shows that the hydraulic efficiency trend line is apart by 15.09% at low runner speed, though it started at high rpm.

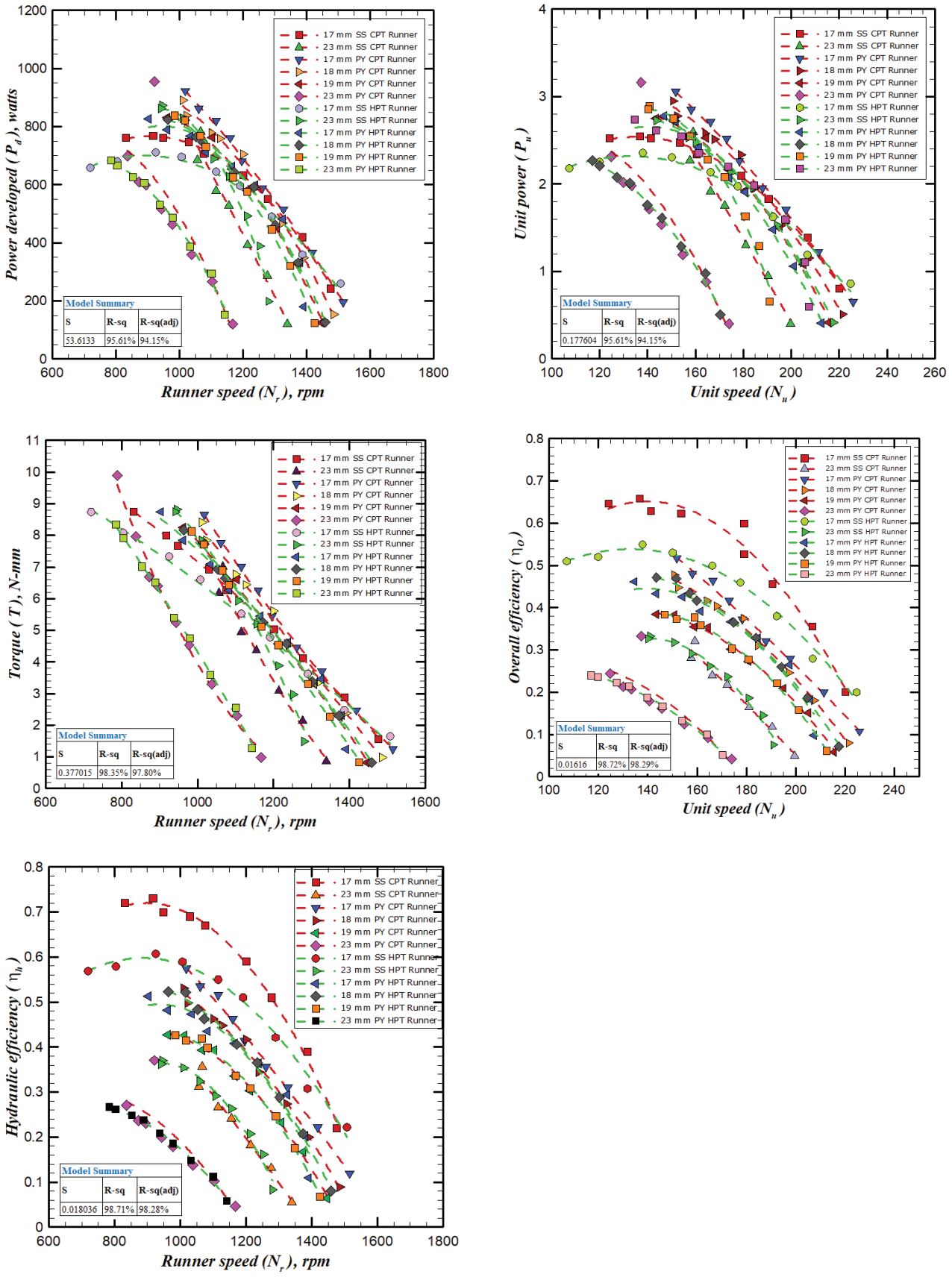


Figure 14. Main and operating characteristics for all the nozzle-runner combinations.

Table 5. Summary for comparison of present and similar past work

Sr. No.	Author/s	Parameters considered	Type of work carried out	Hydraulic efficiency (η_h)
1	Rafae Alomar et al., 2022 [70]	CPT, Head = 113 m, Runner diameter =275 mm, nozzle diameter = 9.5-12.5 mm (4 nos. in equal steps), Number of nozzles=1	Experimental	35.5-21.6%
2	Syofii et al., 2022 [71]	CPT, Head = 3 m, Runner diameter = 275 mm, nozzle diameter= 8 ,9, 10 mm, Number of nozzles=1	Experimental	9.01-25.44%
3	Elgammi & Hamad, 2022 [72]	CPT, Head = 2.5 m, Runner pitch circle diameter =123 mm, nozzle diameter= 9 mm, Number of nozzles=8	Experimental	10%
4	Hlabanelo et al., 2020 [73]	CPT,Head = 10 m, Runner diameter =220 mm, nozzle diameter = 21 mm, Number of nozzles=2	Experimental and numerical	5-64%
5	Nigussie et al., 2017 [74]	CPT,Head = 47.5 m, Runner pitch circle diameter = 500 mm, nozzle diameter= 38.50 mm, Number of nozzles=4	Numerical	78.8%
6	Cobb & Sharp, 2013	CPT, Runner pitch circle diameter =100 mm, head =17-25 m and 18- 28 m, nozzle diameter = 7.94 to 12.70 mm, Number of nozzles =1	Experimental	73%
7	Chaudhari et al.,2011	CPT,HPT Head = 45 m, Runner pitch circle diameter = 360 mm, nozzle diameter = max 260 mm, Number of nozzles=1	Experimental and numerical	52%,45%
8	Present study	CPT,HPT Head = 43 m, Runner pitch circle diameter = 256 mm, nozzle diameter = 17,18,19 and 23 mm, Number of nozzles=1	Experimental	For CPT and HPT

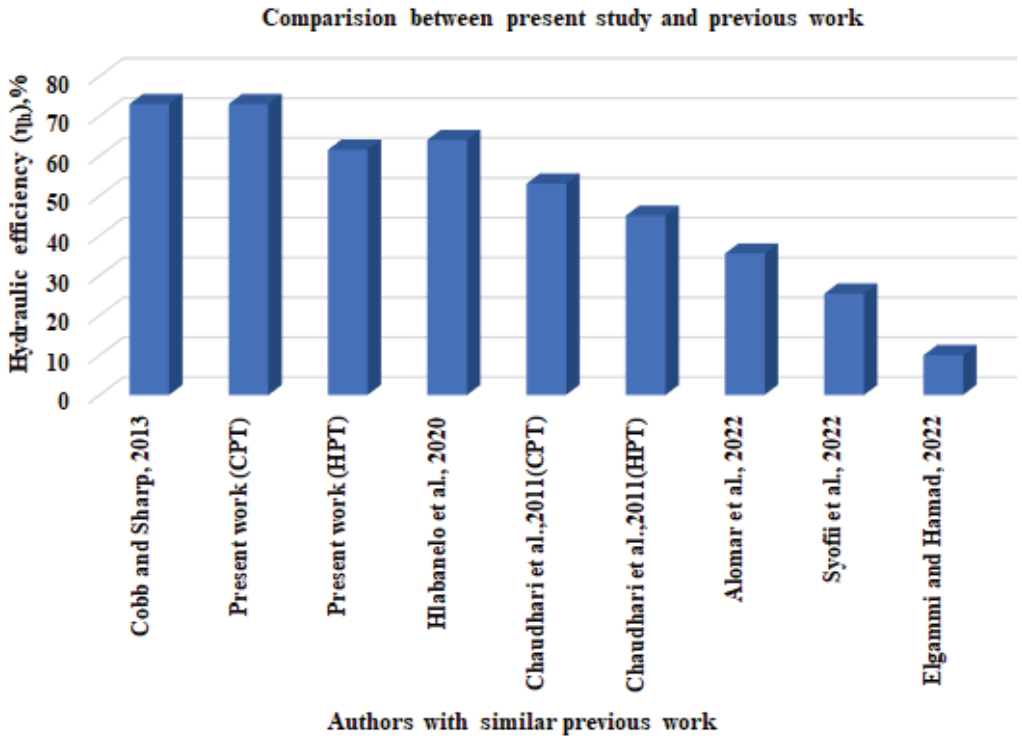


Figure 15. A hydraulic efficiency comparison bar chart of the present work with previous similar work.

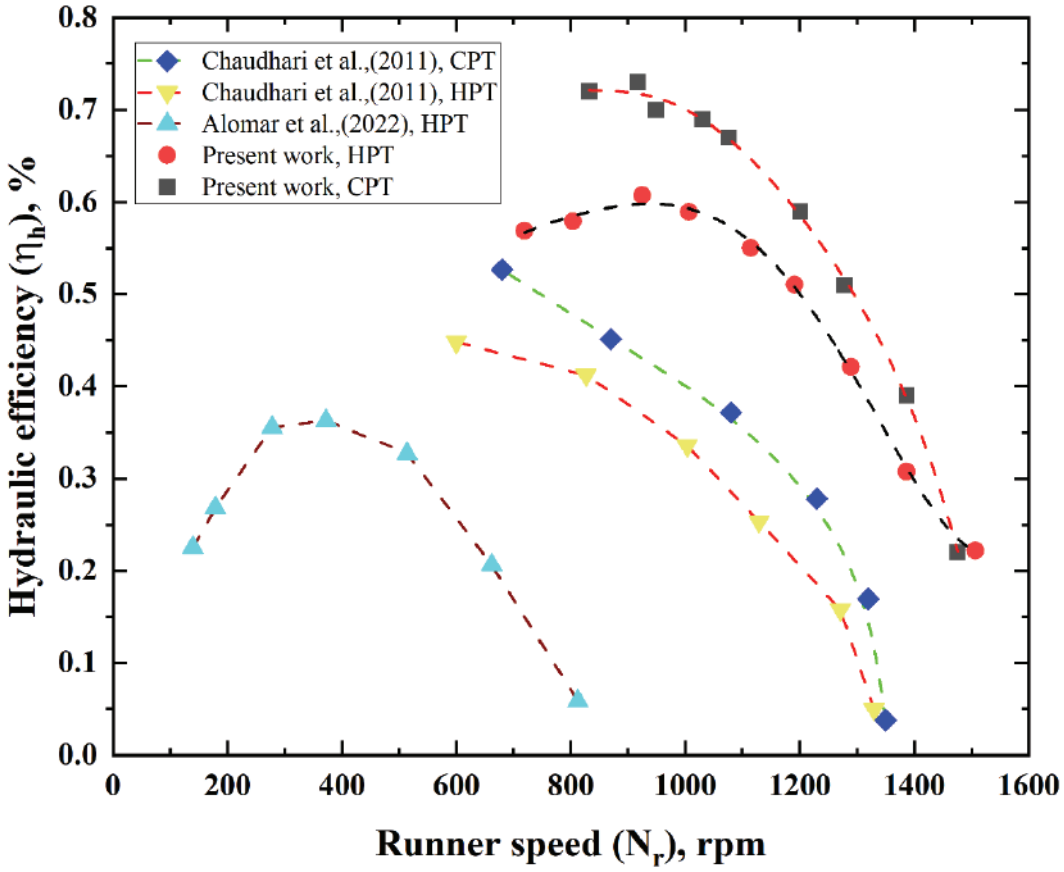


Figure 16. Hydraulic efficiency(η_h) vs Runner speed (N_r) - comparison for runners of the present work with previous similar work.

UNCERTAINTY ANALYSIS

According to the study, the uncertainty found for the head of water, angular speed, torque developed at the runner shaft, and flow rate is given in Appendix 1 with the whole gate opening (100%) for all the tested combinations. Equation (8) defines the hydraulic efficiency of the turbine runner, and the corresponding Equation (9) for uncertainty is used to calculate values.

$$\eta_h = \frac{T\omega}{\rho g Q H} \tag{8}$$

Since the experiments were carried out with a constant head, but considering frictional head loss and pipe fitting loss incurred to calculate the value of dH, the difference in measured and actual value of torque due to spring balance, which is taken care of by considering the most minor count. The measured value from the speed sensor and flow rate is also affected by the accuracy and subsequent error in measurement.

$$\frac{d\eta_h}{\eta_h} = \sqrt{\left(\frac{dH}{H}\right)^2 + \left(\frac{dT}{T}\right)^2 + \left(\frac{d\omega}{\omega}\right)^2 + \left(\frac{dQ}{Q}\right)^2} \tag{9}$$

According to the study, a sample calculation for uncertainty with a whole gate opening (100%) corresponding to maximum hydraulic efficiency is calculated as per Equation (9) and given in Appendix 1. The arrangement in the case of a conventional Pelton turbine (CPT) runner found for the available head, torque, angular speed, and flow rate was ±0.48%, ±1.33%, ±1.19%, and ±0.01%, respectively, and uncertainty in hydraulic efficiency corresponding to that found to be ±1.31% with arrangement of the Hooped Pelton Turbine (HPT) runner and 23 mm Polymer nozzle (PYN) combination.

CONCLUSION

In addition to the flow rate(Q), jet size (Di), Speed ratio(ϕ), and jet ratio(m), the runner's performance is also affected by both centrifugal and Coriolis forces. The literature review shows that varying operating conditions like

nozzle diameter (Di) and water discharge (Q) significantly impact Pelton turbine performance.

In the current study, the SSN1, SSN2, PYN1, PYN2, PYN3, and PYN4 nozzles were used to estimate the performance of the runners. The different diameters of the nozzle are the same in construction and materials, except for the beta ratio(β) and angle of convergence (Θ_n). The runners were tested for varying flow conditions to get hydraulic performance and subsequent comparison. The jet ratio (m) and the nozzle convergence angle (Θ_n) were in the range of 11 to 15 and 24 to 32 degrees, respectively.

The following are the conclusions drawn from the present experimental investigations,

- The nozzle with a more than 17 mm diameter (D_i) has reduced potential energy available at exit as the discharge increases. The subsequent velocity also reduces. The water input power (P_{in}) to the turbine reduces with an increase in the nozzle diameter. Thus, the increase in nozzle diameter reduces the turbine's hydraulic efficiency(η_h).
- The higher beta ratio yielded low hydraulic efficiency as the losses dominated in the larger-diameter jet. The effect of convergence angle (Θ_n) is also practical, as it inversely suggests hydraulic efficiency. The 17 mm nozzles with the highest convergence angle (Θ_n) of 32 degrees have contributed more to the hydraulic performance of either runner.CPT tested with a higher convergence angle (Θ_n) nozzle has yielded 18.18% more efficiency than HPT.
- The nozzles with a jet ratio(m) of 15 were more suitable for the runners. The main and operating characteristics curves have been entirely over the range of runner speeds. The decreasing jet ratio has reduced jet stability, affecting the turbine's hydraulic performance.
- The runners were tested with a range of velocity ratios (ϕ = u/Vjet) of 0.423 to 0.492. The CPT was most efficient with a velocity ratio (ϕ) of 0.423. The HPT with a higher nozzle diameter and a nozzle opening between 20% and 40 % has the least inertia due to the flow through the bucket without diffusion in the void between hoop plates.
- In the case of runners, the CPT has higher hydraulic efficiency(η_h), approximately 20% higher than the hooped Pelton turbine runner at the pick point for all nozzle runner combinations. Still, that offset margin in the curve gradually decreases with increased speed. The speed and nozzle diameter combination best suits a 17 mm stainless steel nozzle (SSN1), 900 rpm, with a conventional Pelton turbine (CPT) runner, 100% gate opening.
- It was found that the same material, the hooped Pelton turbine (HPT) runner and 23 mm stainless steel nozzle (SSN2), produce the highest torque but have less hydraulic efficiency due to losses in the void created between bucket and hoop plates. However, it cannot be discarded for other reasons, such as suggesting benefits like bucket strength under heavy jet from the faucet.
- The larger diameter in the polymeric nozzle (PYN) gave low performance compared to the smaller diameter nozzle, i.e., 17 mm. In the case of both runners, a 17 mm diameter nozzle was found most appropriate for a given runner's dimensions. This could be because of the reduced jet diffusion provided by the hoop with a smaller diameter nozzle, which handles the outgoing proportion of fluid in equal amounts through the slots on the hoop plates.
- The efficiency difference between both runners is more pronounced at higher gate openings due to the significant flow passage being impeded by the hoop plates. At lower gate openings, the hoop plates obstruct the smaller flow route less, making the efficiency difference less noticeable.
- The hoop plates support the buckets, which are cantilever parts bolted to the dynamic runner system. During experimentation, the bifurcated jet and outgoing water splashing on the runner's hoop are visible in the flow contours. This water splashing, more pronounced with larger gate openings, is the primary cause of efficiency decline. The speed and flow area at the spear-nozzle assembly are crucial for hydraulic efficiency.

This experimental investigation has provided vital details regarding the effect of varying flow area, jet ratio, speed ratio, and convergence angle on the performance of a Hooped Pelton Turbine (HPT) runner compared to an identically sized Conventional Pelton Turbine (CPT) runner. This study also forms the basis for optimizing the hoop gap and slot opening size over the hemispherical bucket to provide the least impedance to the outgoing fluid stream.

NOMENCLATURE

Q	Volumetric flow rate/Discharge m^3/hr
D_o	Inlet diameter of the nozzle or inside diameter of the pipe, mm
D_i	Exit diameter of the nozzle, mm
D	Diameter of the brake drum, m
D_r	Diameter of rope, m
D_e	Effective diameter of the drum, m
D_P	Pitch Circle Diameter of the runner, mm
R_e	Reynolds number
H	Available head, m
Q_u	Unit discharge
N_u	Unit speed
N_r	Runner speed, rpm
P_u	Unit power
P_d	Power developed, Watt
P_{in}	Power input, kW
V_{jet}	The velocity of the fluid, m/s
u	Peripheral velocity of runners, m/s
T_d	Torque developed, N-m
m	Jet ratio
g	Gravitational constant, m/s^2

Greek Symbols

ρ	The density of the fluid, kg/m^3
β	Beta ratio- a ratio of the nozzle outlet to the inlet
β_2	The jet angle at the bucket exit, degrees
ω	Angular speed of the runner, rad/sec
η_o	Overall efficiency
η_h	Hydraulic efficiency
ϕ	Speed ratio/ Velocity ratio
Θ_n	Angle of convergence for the nozzles, degrees

Abbreviations

SSN	Stainless Steel Nozzle
PYN	Polymer Nozzle (Polyacetal or Polyoxymethylene)
CPT	Conventional Pelton Turbine
HPT	Hooped Pelton Turbine
GO	Gate Opening

Subscript

2	Refers to exit
d	Refers to the developed
e	Refers to effective
h	Refers to hydraulic
n	Refers to the nozzle
o	Refers to overall
u	Refers to the unit

Future Scope of Work

The work can be extended for numerical simulation to model the effect of the hoop gap on the performance of runners. The analytical and subsequent numerical simulation for the flow area gap in the hoop plate can be modeled. The hoop plate can be made of lightweight material like aluminum to reduce the inertia and increase hydraulic performance.

ACKNOWLEDGMENT

Thanks to *Dr. S. A. Channiwala* and *Dr. G. C. Chaudhari* for supporting the experimentation and also permitting the test facility at Advance Fluid Mechanics and Fluid Power (AFM & FP) Laboratory, Sardar Vallabhbhai National Institute of Technology (SVNIT), Surat, Gujarat, India. The test facility is the same one used by the author for work carried out in studying jet expansion.

AUTHORSHIP CONTRIBUTIONS

Dr. V. K. Patel: Reviewed the manuscript and gave expert advice as a supervisor. **Prof. H. N. Lakdawala, Trupal R. Patel:** Experimentation, data collection, and prepared manuscript. **N Bagre:** Graph plotting and image processing. **Dr. S. A. Channiwala** and **Dr. G. C. Chaudhari:** Conceived the idea and developed the test facility.

DATA AVAILABILITY STATEMENT

The authors confirm that the article's data supporting this study's findings are available. Raw data supporting this study's findings are available from the corresponding author upon reasonable request.

CONFLICT OF INTEREST

The author declared no potential conflicts of interest concerning this article's research, authorship, and/or publication.

ETHICS

There are no ethical issues with the publication of this manuscript.

STATEMENT ON THE USE OF ARTIFICIAL INTELLIGENCE

Artificial intelligence was not used in the preparation of the article.

REFERENCES

[1] Alnakhlani MM, Mukhtar, Himawanto DA, Alkurtehi A, Danardono D. Effect of the bucket and nozzle dimension on the performance of a Pelton water turbine. Mod Appl Sci 2015;9:25-33. [CrossRef]

[2] Zeng C, Xiao Y, Yongyao, L, Jin Z, Zhengwei W, Honggang F, et al. Hydraulic performance prediction of a prototype four-nozzle Pelton turbine by entire flow path simulation. Renew Energy 2018;125:270–282. [CrossRef]

[3] Alam MMA, Setoguchi T, Matsuo S, Kim HD. Nozzle geometry variations on the discharge coefficient. Propuls Power Res 2016;5:22–33. [CrossRef]

[4] Zhang Z, Casey M. Experimental studies of the jet of a Pelton turbine. Proc Inst Mech Eng A J Power Energy 2007;221:1181–1192. [CrossRef]

[5] Donaldson CD, Snedeker RS. A study of free jet impingement. Part 1. Mean properties of free and impinging jets. J Fluid Mech 1971;45:281–319. [CrossRef]

[6] Santolin A, Cavazzini G, Ardizzon G, Pavesi G. Numerical investigation of the interaction between jet and bucket in a Pelton turbine. Proc Inst Mech Eng A J Power Energy 2009;223:721–728. [CrossRef]

[7] Xiao Y, Liu Z, Liang Q, Liu J, Zhang J, Zhu Y, et al. The interaction between bucket number and performance of a Pelton turbine. Energy 2024;287:129646. [CrossRef]

[8] Gupta V, Prasad V. Numerical investigations for jet flow characteristics on Pelton turbine bucket. Int J Emerg Technol Adv Eng 2012;2:364–370.

[9] Gupta V, Prasad V, Khare R. Effect of jet length on the performance of Pelton. 2016;11:11487–11494.

[10] Obayes SA, Qasim MA. Effect of flow parameters on Pelton turbine performance by using different nozzles. Int J Model Optim 2017;7:128–133. [CrossRef]

[11] Nyantekyi-Kwakye B. Experimental examination of nozzle geometry on water jet in a subsonic crossflow (Master thesis). Canada: University of Manitoba; 2011.
[12] McCarthy MJ, Molloy NA. Review of stability of liquid jets and the influence of nozzle design. Chem Eng J 1974;7:1-20. [CrossRef]
[13] Jo IC, Park JH, Kim JW, Shin Y, Chung JT. Jet quality characteristics according to nozzle shape of energy-recovery Pelton turbines in pressure-retarded osmosis. Desalination Water Treat 2016;57:24626–24635. [CrossRef]
[14] Gass BM, Hetchy Water H. Modification of nozzles for the improvement of efficiency of Pelton type turbines. 2002. Available at: https://api.semanticscholar.org/CorpusID:56348066 Accessed on Jan 28, 2026.
[15] Unterberger P, Unterberger P, Bauer C, Gaschl J, Mack R. Studies on the free jet of Pelton nozzles. 2010. Available at: https://www.researchgate.net/publication/260508415_Studies_on_the_free_jet_of_pelton_nozzles Accessed on Jan 28, 2026.
[16] Tesař V. Characterisation of inexpensive, simply shaped nozzles. Chem Eng Res Des 2010;88:1433–1444. [CrossRef]
[17] Vahedi Tafreshi H, Pourdeyhimi B. The effects of nozzle geometry on waterjet breakup at high Reynolds numbers. Exp Fluids 2003;35:364–371. [CrossRef]
[18] Kartashev AL, Kartasheva MA. Designing of optimal annular nozzles with multiphase flows. Procedia Eng 2016:161–167. [CrossRef]
[19] Adhikari RC, Wood DH. A new nozzle design methodology for high efficiency crossflow hydro turbines. Energy Sustain Dev 2017;41:139–148. [CrossRef]
[20] Staubli T, Abgottspon A, Weibel P, Bissel C. Jet quality and Pelton efficiency: Effects of suspended sediment on Pelton turbine wear and efficiency. Conference Paper. In: Hydro 2009 At: Lyon, France 2009.
[21] Na S. Simulation of unsteady water film flow on Pelton bucket. Energy Power Eng 2013;5:51–55. [CrossRef]
[22] Perrig A, Avellan F, Kueny JL, Farhat M, Parkinson E. Flow in a Pelton turbine bucket: Numerical and experimental investigations. J Fluids Eng 2006;128:350–358. [CrossRef]
[23] Zeng C, Xiao Y, Wang Z, Zhang J, Luo Y. Numerical analysis of a Pelton bucket free surface sheet flow and dynamic performance affected by operating head. Proc Inst Mech Eng A J Power Energy 2017;231:182–196. [CrossRef]
[24] Papantonis DE, Anagnostopoulos JS, Papantonis DE. A numerical methodology for design optimization of Pelton turbine runners: Design optimisation of Pelton and Turgo type water turbine's injectors. 2006. Available at: https://www.semanticscholar.org/paper/A-numerical-methodology-for-design-optimization-of-Anagnostopoulos-Papantonis/35d7fd57c36b75fc4ddd5734f94f7ab70906f6d0 Accessed on Jan 28, 2026.
[25] Solemslie BW, Dahlhaug OG. A reference Pelton turbine design. IOP Conf Ser Earth Environ Sci 2012;22:012004. [CrossRef]
[26] Kumashiro T, Fukuhara H, Tani K. Unsteady CFD simulation for bucket design optimization of Pelton turbine runner. IOP Conf Ser Earth Environ Sci 2016;49:022003. [CrossRef]
[27] Chapuis L, Froschl K. Optimized fabrication of Pelton turbine runners. Int J Hydropower Dams 1998;5:30–32.
[28] Neopane HP, Thapa B, Panthee A, Neopane HP. CFD analysis of Pelton runner. Int J Sci Res Publ 2014;4:1-6.
[29] Chaudhari GC, Shah SP, Channiwala SA. A hooped Pelton runner: FE analysis and experimentation. In: Proceedings of ASME Turbo Expo 2011 GT2011 June 6-10, 2011, Vancouver, British Columbia, Canada. [CrossRef]
[30] Sabu S, Antony TA, George NJ, Chandy A, Asst A, Jyothi A. Design and modelling of a Pelton wheel bucket: Theoretical validation and software comparison. Int J Eng ResTechnol 2014;3:2271-2273.
[31] Chaudhari G, Shah S, Channiwala S, Kulshreshtha D. Flow visualization study of jet and bucket interactions in traditional and hooped Pelton runner. In: ASME-JSME-KSME 2019 8th Joint Fluids Engineering Conference, 2019. [CrossRef]
[32] Chaudhari GC, Channiwala SA, Shah SP. Comparative assessment of the developed stress in both traditional and hooped Pelton runners. Proceedings of ICFD 10: Tenth International Congress of Fluid Dynamics December 16-19, 2010, Stella Di Mare Sea Club Hotel, Ain Soukhna, Red Sea, Egypt.
[33] Li JQ, Myat M, Saw M. Fatigue analysis of simple and advanced hoop Pelton turbine buckets. Am Sci Res J Eng 2017;29:371–378.
[34] Karna A, Chitrakar S, Bhurtel M, Baral B, Solemslie BW. Numerical analysis of traditional and hooped Pelton runner at various operating conditions. J Phys Conf Ser 2023;231:182-196. [CrossRef]
[35] Chaudhari G, Channiwala S, Shah S, Kulshreshtha D. Experimental investigation on effect of hoop thickness on performance of hooped Pelton wheel. J Phys Conf Ser 2023;2629:012003. [CrossRef]
[36] Gupta V, Khare R, Prasad V. Performance evaluation of Pelton turbine: A review. Hydro Nepal J Water Energy Environ 2014;13:28–35. [CrossRef]
[37] Sani AE. Design and synchronizing of Pelton turbine with centrifugal pump in RO package. Energy 2019;172:787–793. [CrossRef]

[38] Osterwalder J. Efficiency scale-up for hydraulic turbo-machines with due consideration of surface roughness. J Hydraul Res 1978;16:55–76. [CrossRef]
[39] Rossetti A, Santolin A, Cavazzini G, Pavesi G, Ardizzon G. Analysis of Pelton bucket efficiency. In: The 9th European Conference on Turbomachinery Fluid Dynamics and Thermodynamics. 2011. [CrossRef]
[40] Rossetti A, Pavesi G, Cavazzini G, Santolin A, Ardizzon G. Influence of the bucket geometry on the Pelton performance. Proc Inst Mech Eng A J Power Energy 2014;228:33-45. [CrossRef]
[41] Jošt D, Mežnar P, Lipej A. Numerical prediction of Pelton turbine efficiency. IOP Conf Ser Earth Environ Sci 2010;12:012080. [CrossRef]
[42] Zeng CJ, Xiao YX, Zhang J, Gui ZH, Wang SH, Luo YY, et al. Numerical prediction of hydraulic performance in model and homologous prototype Pelton turbine. IOP Conf Ser Earth Environ Sci 2018;163:012016. [CrossRef]
[43] Han L, Zhang GF, Wang Y, Wei XZ. Investigation of erosion influence in distribution system and nozzle structure of Pelton turbine. Renew Energy 2021;178:1119–1128. [CrossRef]
[44] Stamatelos FG, Anagnostopoulos JS, Papantonis DE. Performance measurements on a Pelton turbine model. Proc Inst Mech Eng A J Power Energy 2011:351–362. [CrossRef]
[45] Cobb BR, Sharp KV. Impulse (Turgo and Pelton) turbine performance characteristics and their impact on pico-hydro installations. Renew Energy 2013;50:959–964. [CrossRef]
[46] Chávez JC, Valencia JA, Jaramillo GA, Coronado JJ, Rodríguez SA. Failure analysis of a Pelton impeller. Eng Fail Anal 2015;48:297–307. [CrossRef]
[47] Patel K, Patel B, Yadav M, Foggia T. Development of Pelton turbine using numerical simulation. IOP Conf Ser Earth Environ Sci 2010;12:012048. [CrossRef]
[48] Muhibbuddin, et al. Analysis of the performance for runner Pelton turbine by using bamboo material. J Adv Res Fluid Mech Therm Sci 2021;79. [CrossRef]
[49] Woodcock DJ, White IM. The application of Pelton type impulse turbines for energy recovery on seawater reverse osmosis systems. Desalination 1981;39:1-3. [CrossRef]
[50] Güven AF. A comparative study on hybrid GA-PSO performance for stand-alone hybrid energy systems optimization. Sigma J Eng Nat Sci 2024;42:1410–1438. [CrossRef]
[51] Awogbemi O, Von Kallon DV, Kumar KS. Contributions of artificial intelligence and digitization in achieving clean and affordable energy. Intell Syst Appl 2024;22:200389. [CrossRef]
[52] Ozsari I, Ust Y, Karakurt AS. Exergetic performance analysis and comparison of oxy-combustion and conventional gas turbine power cycles. Sigma J Eng Nat Sci 2023;41:575–591.
[53] Asgharian P, Noroozian R. Modeling and model predictive control of a microturbine generation system for stand-alone operation. 2019;37:705-722.
[54] Şahin Fİ, Acarali N. Evaluation of properties for synthetic polymers in medicine. 2024;42:1315-1324.
[55] Ergüner A, Özkan R, Koca K, Genç MS. Improvement of mechanical behaviour of wind turbine blade using nanofluid-graphene and/or glass fiber in epoxy resin. Sigma J Eng Nat Sci 2021;39:58-69.
[56] Kumar KS, Palanisamy R, Aravindh S, Mohan GS. Design and analysis of windmill blades for domestic applications. Int J Mech Eng Technol 2017;8:25–36.
[57] Sunil Kumar K, Kamalakar, V, Palani S, Muniamuthu S, Belinda CM. Design of K-type propeller optimized with lightweight aluminum material and its CFD analysis for marine-based applications. In: Recent Trends Therm Fluid Sci. Singapore: Springer Nature Singapore; 2024. p. 375–390.
[58] Kumar KS, Muniamuthu S, Tharanisrisakthi BT. An investigation to estimate the maximum yielding capability of power for mini Venturi wind turbine. Ecol Eng Environ Technol 2022;23:72–78. [CrossRef]
[59] Kumar KS, Arun S, Mohan A. Identification experimental analysis of noise and vibration reduction in windmill gear box for 5MW wind turbine. Int J Mech Eng Technol 2016;7:76–85. [CrossRef]
[60] Kabak M, Taşkinöz G. Determination of the installation sites of wind power plants with spatial analysis: A model proposal. Sigma J Eng Nat Sci 2020;38:441-457.
[61] Kumar KS, Surakasi R, Mohan A, Tharanisrisakthi BT, Muniamuthu S, Geetha NB. Emerging trends and global challenges to predict drop in thermal performance of WTG gearbox. J Therm Eng 2024;10:657–669.
[62] Zhang Z. Pelton Turbines. Nee York: Springer Nature; 2016. [CrossRef]
[63] Zoppé B, Pellone C, Maitre T, Leroy P. Flow analysis inside a Pelton turbine bucket. J Turbomach 2006;128:500. [CrossRef]
[64] Nava N, Reddy I, Prasad TS. Design and static analysis of Pelton turbine bucket. Int J Sci Technol Manag 2015;4:19-25. [CrossRef]
[65] Vessaz C, Andolfatto L, Avellan F, Tournier C. Toward design optimization of a Pelton turbine runner. Struct Multidiscip Optim 2017. Preprint. doi: 10.1007/s00158-016-1465-7.
[66] Vessaz C, Jahanbakhsh E, Avellan F. Flow simulation of a Pelton bucket using finite volume particle method. IOP Conf Ser Earth Environ Sci 2014;22:012003. [CrossRef]
[67] Lakdawala H, Gupta A, Patel V, Jariwala H, Chaudhari G. Experimental investigations of jet expansion for hydraulic nozzles of different materials. Int J Eng Trends Technol 2022;70:137–142. [CrossRef]

[68] Xiao Y, Wang Z, Zhang J, Zeng C, Yan Z. Numerical and experimental analysis of the hydraulic performance of a prototype Pelton turbine. Proc Inst Mech Eng A J Power Energy 2014;228:46–55. [CrossRef]
[69] Xiao YX, Han FQ, Zhou JL, Kubota T. Numerical prediction of dynamic performance of Pelton turbine. J Hydrodyn 2007;19:356–364. [CrossRef]
[70] Alomar OR, Abd HM, Salih MMM, Ali FA. Performance analysis of Pelton turbine under different operating conditions: An experimental study. Ain Shams Eng J 2022;13:101684. [CrossRef]
[71] Syofii I, Hidayatullah AB, Adanta D, Sari DP, Burlian F, Saputra MAA. Pico scale Turgo turbine design for remote areas application using velocity triangle approach. J Adv Res Fluid Mech Therm Sci 2022;97:157–167. [CrossRef]
[72] Elgammi M, Hamad AA. A feasibility study of operating a low static pressure head micro Pelton turbine based on water hammer phenomenon. Renew Energy 2022;195:1–16. [CrossRef]
[73] Hlabanelo JM, Sob PB, Alugongo AA. A study to improve the efficiency and performance of a Pelton wheel using potential energy at low heads. Int J Eng Res Technol 2020;13:2915–2926. [CrossRef]
[74] Nigussie T, Engeda A, Dribssa E. Design, modeling, and CFD analysis of a micro hydro Pelton turbine runner: For the case of selected site in Ethiopia. Int J Rotating Mach 2017;2017:030217. [CrossRef]

Appendix 1. Uncertainty analysis for full (100 % GO) gate opening and maximum hydraulic efficiency

Nozzles with Pelton runners	Angular velocity(ω), rad/sec	Torque (T) N-m	Head (H), m	Flow rate (Q), m^3/sec	$\frac{d\eta_h}{\eta_h}$	Uncertainty (% ge)
SSN1 17 mm -CPT	96	8	43	0.00239	0.011551	1.16
SSN1 17 mm -HPT	96.85	7.34	43	0.00266	0.011482	1.15
SSN2 23 mm -CPT	111.71	7.01	43	0.00500	0.010272	1.03
SSN2 23 mm -HPT	98.94	8.83	43	0.00536	0.01126	1.13
PYN1 17 mm-CPT	106.58	8.66	43	0.00366	0.010617	1.06
PYN1 17 mm-HPT	94.54	8.75	43	0.00366	0.011685	1.17
PYN2 18 mm-CPT	105.85	8.42	43	0.00381	0.010678	1.07
PYN2 18 mm-HPT	98.1	8.17	43	0.00344	0.011348	1.13
PYN3 19 mm-CPT	100.72	8.25	43	0.00442	0.011109	1.11
PYN3 19 mm-HPT	103.13	8.13	43	0.00446	0.010904	1.09
PYN4 23 mm-CPT	96.43	9.9	43	0.00586	0.011485	1.15
PYN4 23 mm-HPT	82.19	8.33	43	0.00585	0.013146	1.31

Sigma J Eng Nat Sci, Vol. 44, No. 1, pp. 528–544, February, 2026

Sigma Journal of Engineering and Natural Sciences
Web page info: https://sigma.yildiz.edu.tr
DOI: 10.14744/sigma.2025.00000

Research Article

Metaheuristic-based machine learning models for accurate battery remaining useful life prediction in renewable energy storage system

Shravani GANDHI[1,*], Ashlesha CHOPANE[1], Anushka PARKHI[1], Sakshi DESHMUKH[1], Smita KULKARNI[1]

[1]*Department of Electronics and Telecommunication Engineering, MIT Academy of Engineering, Pune, 412105, India*

ARTICLE INFO

Article history
Received: 25 August 2024
Revised: 14 October 2024
Accepted: 28 November 2024

Keywords:
Battery Remaining Useful Life; Machine Learning; Regression; Renewable Energy

ABSTRACT

This work focuses on properly estimating lithium-ion battery Remaining Useful Life in renewable energy storage and electric vehicle applications. This is important since batteries are essential to sustainable energy systems and electric car demand is expanding. Accurately predicting Remaining Useful Life (RUL) is essential for maximizing battery safety and efficiency. Furthermore, these predictions play a critical role in ensuring that energy storage systems remain both economically viable and environmentally sustainable. The study uses a dataset from the Hawaii Natural Energy Institute, containing data on battery lifecycle performance metrics. The machine learning models used include random forests, decision trees, linear regression, K-nearest neighbors (KNN), support vector machines (SVM), AdaBoost, and extreme gradient boosting. To maximize predictive precision, every model undergoes a process of hyperparameter tuning, data preprocessing, and the evaluation of feature importance. Comparative measures like RMSE, MAE, and R^2 assess model predictive capability. The research shows that Random Forest and XGBoost models excel, with Random Forest earning an RMSE of 23.26 and an R2 score of 99.68. XGBoost demonstrated strong performance, including a decreased RMSE of 20.64 and an R^2 score of 99.61. Research indicates that ensemble learning techniques, such as XGBoost and Random Forest, provide highly reliable forecasts for Remaining Useful Life, facilitating improved maintenance and oversight of battery systems. The novelty of this study lies in its comprehensive comparative analysis of multiple machine-learning models optimized with metaheuristic techniques for battery Remaining Useful Life predictions. In contrast to earlier research that typically utilized single-model methods, this study investigates an ensemble of machine learning models with a focus on optimization and feature importance to enhance predictive precision. The results show that feature selection, data processing, and hyperparameter optimization have improved the model's performance. This supports machine learning's role in preventive maintenance, battery longevity, and sustainable energy. This study introduces a robust, data-centric framework that combines various techniques to enhance remaining useful life predictions, serving as a beneficial resource for practical battery management systems.

Cite this article as: Gandhi S, Chopane A, Parkhi A, Deshmukh S, Kulkarni S. Metaheuristic-based machine learning models for accurate battery remaining useful life prediction in renewable energy storage system. Sigma J Eng Nat Sci 2026;44(1):528–544.

***Corresponding author.**
*E-mail address: shravani.gandhi@mitaoe.ac.in

This paper was recommended for publication in revised form by Editor-in-Chief Ahmet Selim Dalkilic

Published by Yıldız Technical University Press, İstanbul, Turkey
© Author. This is an open access article under the CC BY-NC license (http://creativecommons.org/licenses/by-nc/4.0/).

INTRODUCTION

As the demand for sustainable energy solutions grows, accurately predicting the remaining useful life (RUL) of lithium-ion batteries has become crucial, especially for electric vehicles (EVs) and renewable energy storage. While existing literature presents various machine-learning approaches for RUL prediction, many studies rely on traditional algorithms that often lack the precision needed for real-world applications. For example, support vector machines (SVM) and basic regression techniques frequently overlook the complexities of battery degradation and diverse operating conditions. Advancing sustainable development requires reducing greenhouse gas emissions, thus promoting electric vehicles and innovative energy storage solutions. As consumer electronics increasingly depend on battery technology and renewable energy expands, the energy storage sector has become pivotal. Metaheuristic solutions enhance process efficiency, sustainability, and energy consumption.

Lithium-ion batteries (LIBs), known for their high energy density and durability, are the primary choice for powering electric vehicles. Notwithstanding recent progress, certain voids persist in the current research. Numerous predictive frameworks fail to extensively utilize contemporary machine learning methods, especially metaheuristic optimization approaches, which have the potential to boost accuracy. Additionally, most studies inadequately address the real-time implementation of predictive models, limiting their applicability in dynamic environments where timely decision-making is essential. Forecasting RUL is essential for evaluating battery safety, improving performance, and maximizing the efficiency and sustainability of energy storage systems. Efficient battery management supports sustainable development goals, such as affordable clean energy and climate action [1], and promotes renewable energy adoption and innovation. RUL estimations, represented through multiple indicators, offer early warnings of failure that are critical for system prognostics and health management. Methods for modelling the degradation of complex systems generally encompass both physics-based and data-driven strategies. A probabilistic adaptive estimator assesses the state of energy (SOE) and state of charge (SOC) using neural networks [2].

One-dimensional models analyze battery decline through SEI generation kinetics and solvent transport, while a refined, semi-empirical aging model incorporates factors like internal resistance and capacity degradation [3]. A comparison study using RMS and MSE as metrics [4] found that XGBoost and Gradient Boost were the best at predicting Remaining Useful Life. Another study using LSTM techniques and temperature, current, and voltage as metrics [5] also found high accuracy. A KNN regression approach, optimized with particle swarm optimization (PSO), offers a simple yet accurate model for capacity assessment [6]. Artificial intelligence is fundamental to enhancing battery behavior, as explored in a bibliometric review of machine learning techniques for battery forecasting [7]. Additionally, previous research has confirmed the effectiveness of models such as PNN, LSTM, and SVR using the NASA battery dataset to refine practical performance [8]. Moreover, [9] emphasizes the significance of SOH estimates in electric vehicles and highlights advancements in filtering techniques and co-estimation methods. Investigators examine the degradation variables of lead-acid batteries to refine battery control and reliability, while a unique ensemble learning technique exhibits superior RUL prediction precision relative to conventional methods [10,11].

Researchers have also proposed integrated modelling approaches to improve the prediction accuracy of lithium-ion battery lifespan [12]. Despite challenges related to computational costs and data deficits, researchers have noted the effectiveness of neural networks, particularly RNNs and LSTMs, in managing complex data [13]. Several studies have compared different machine learning algorithms, including XGBoost and Gradient Boost, using various performance metrics [14]. Furthermore, studies have underscored the importance of parameters like temperature and voltage in LSTM-based predictions [15]. The literature highlights the importance of accurate Remaining Useful Life predictions in enhancing battery management systems for electric vehicles [16-21]. To manage uncertainties and fluctuating operational states in batteries, investigators have utilized methodologies including unscented Kalman filters (UKF) and hidden Markov models (HMM) [22-24]. Furthermore, studies focusing on SOC estimation and battery parameter estimation have demonstrated improved accuracy through advanced techniques, supporting effective battery management [23,25].

Recent results indicate that combining model-based methodologies with machine learning can improve RUL estimations and refine battery consumption, furthering sustainability objectives [26]. The study on heart failure utilizes machine learning techniques to predict patient survival probabilities, underscoring the significance of predictive analytics in healthcare. Similarly, this research investigates metaheuristic-based models for accurate prediction of the RUL of batteries, aiming to improve operational efficiency in renewable energy systems [27]. Research regarding the estimation of beam structure natural frequencies highlights the successful implementation of machine learning techniques within engineering fields. This parallels the research on metaheuristic-based models for accurately predicting the Remaining Useful Life (RUL) of batteries in renewable energy systems [28]. The use of machine learning to generate precise forecasts of patient counts and mortality during the COVID-19 pandemic mirrors the methodologies applied in research on battery Remaining Useful Life estimation [29,30]. This study aims to bridge existing gaps by utilizing advanced machine learning models, specifically Random Forest and XGBoost, enhanced with metaheuristic optimization techniques. By isolating essential

performance markers such as discharge intervals, voltage dynamics, and cycle indices, this study demonstrates a rigorous approach to battery data extraction for predictive modeling. Emphasizing the importance of preprocessing steps like data standardization, feature selection, and handling missing values; these techniques ensure accurate RUL predictions by refining input data and enhancing model reliability. This investigation provides an in-depth analysis of error metrics and feature significance, demonstrating that these models achieve higher precision in Remaining Useful Life estimation compared to conventional techniques. The study presents a robust dataset from the Hawaii Natural Energy Institute and presents a systematic approach that integrates effective data preparation and hyperparameter tuning. By optimising RUL forecasts, this study contributes to proactive maintenance strategies, waste reduction, and safety assurance, thereby promoting sustainable energy practices. Furthermore, the findings extend beyond the battery sector, impacting industries such as manufacturing, healthcare, and infrastructure monitoring, where predictive maintenance can drive significant resource efficiencies. Additionally, this work promotes green energy initiatives by delivering consistent and precise estimations of battery durability, which improves the management of materials and lengthens the functional period of storage units.

The proposed models are key to enhancing renewable energy storage system efficiency and reliability, paving the way for broader applications in electric vehicles and renewable energy grids. The originality of this research stems from its comprehensive strategy of embedding sophisticated artificial intelligence within battery control frameworks, thereby bolstering the dependability and environmental viability of energy storage technologies. The study lays the groundwork for future research prioritizing real-time implementation capabilities and exploring diverse battery chemistries aligned with global climate goals and the urgent need for innovative energy solutions.

DATASET FOR REMAINING USEFUL LIFE PREDICTION

The Hawaii Natural Energy Institute conducted an experimental investigation to evaluate the performance of fourteen NMC-LCO 18650 lithium-ion batteries. This extensive dataset facilitated the extraction of features that characterized the voltage and current behavior of the batteries throughout their lifecycles. The development of predictive models to estimate the Remaining Useful Life of the batteries is dependent upon the presence of these features. The summarized dataset encapsulates the critical performance metrics for the 14 batteries, providing a comprehensive overview of their degradation patterns and operational efficiency.

Cycle Index: This column identifies each cycle in the dataset individually and acts as a chronological index. Every input represents a complete charge-discharge cycle, enabling a sequential analysis of the battery's performance over time. To effectively track wear-and-tear patterns over time, the cycle index is indispensable. It allows researchers to establish a direct relationship between performance decay and the number of cycles completed. Depletion Duration (s): The 'Discharge Time' field tracks the interval in seconds for the battery to reach a fully drained state during every cycle, serving as a vital temporal indicator for evaluating the speed of energy exhaustion. Variations in discharge time across cycles can indicate changes in the battery's capacity and efficiency, thus serving as a key indicator of its health and performance.

Interval 3.6-3.4V (s): This field quantifies the period, in seconds, required for the battery's potential to decrease from 3.6 to 3.4 volts throughout the discharge phase. This detailed measurement provides insights into the voltage drop kinetics within a specific voltage window, revealing information about the internal resistance and overall discharge dynamics of the battery. Rapid voltage decrements may signal increased internal resistance or diminished capacity.

Max. Voltage Discharge. (V): This field captures the highest voltage level measured during every cycle's discharge stage, providing a baseline in volts. This maximum value represents the battery's electrical reaction while under load, which serves as a metric for its immediate power output capacity. Monitoring this parameter helps understand the voltage's behavior and identify any anomalies that could indicate potential issues.

Min. Voltage Charg. (V): This data point identifies the lowest voltage recorded throughout the recharging interval of each cycle. This value is critical for evaluating the minimum electrical threshold during the charging process, offering a perspective on the battery's recovery traits and its overall charging effectiveness. It serves as a critical indicator of the battery's ability to recuperate from deep discharge states.

Time at 4.15V (s): This column shows how long, in seconds, the battery sustains a voltage level of 4.15 volts during the charging process. The length of this constant voltage stage indicates the battery's saturation patterns and its proficiency in absorbing energy as it nears full capacity. This measurement is vital for assessing how stable and effective the established charging procedure remains.

Time constant current(s): The time constant current column likely refers to the time constant associated with the current in the battery system, measured in seconds. Often represented by τ (tau), this variable signifies the kinetic reaction of the battery's internal chemical mechanisms. Grasping the speed at which current adjusts following a shift in voltage is vital, as it dictates the behaviour of both charge and discharge curves.

Charging time (s): This column records the total duration, measured in seconds, required to complete the charging process for each cycle. It spans the complete interval from the start to the conclusion of the charging process,

thereby offering a comprehensive perspective on the battery's energy absorption rate and effectiveness. Shifts in this duration may indicate fluctuations in internal resistance and storage capacity, rendering it a crucial variable for evaluating the battery's overall lifespan.

RUL (Remaining Useful Life): The RUL column contains estimations of the remaining life of the battery, based on its current performance characteristics. This prognostic indicator estimates the remaining functional duration of the battery prior to hitting a set expiration threshold, such as a substantial decline in storage capacity or a rise in internal impedance. Remaining Useful Life is crucial for maintenance planning, performance forecasting, and overall management of the battery system.

This dataset, enriched with these detailed features, serves as a robust foundation for predictive analytics aimed at estimating battery lifespans and enhancing the understanding of battery degradation mechanisms.

Figure 1 displays several violin plots that illustrate the distribution of various performance metrics of 18650 lithium-ion batteries across different bound cycle indices. The initial graph, illustrating the duration of discharge in seconds, reveals a steady spread of time intervals across different cycle groupings, though the wide range of data points emphasizes the inherent inconsistency in these discharge periods. The Decrement 3.6-3.4V (s) plot reveals that the time decrement between 3.6V and 3.4V remains fairly consistent across cycle bins but has some noticeable outliers, indicating fluctuations in performance. The Max. The voltage discharge (V) plot shows that the maximum discharge voltage slightly varies across cycle bins but generally remains within a specific range, suggesting stable maximum discharge voltages across cycles.

In contrast, the Min. The voltage charge (V) plot shows significant variability in the minimum charge voltage across bins, pointing to fluctuations in the minimum voltage required for charging. The graph for 'Time at 4.15V (s)' shows substantial fluctuation and numerous extreme values, suggesting that the periods spent at this specific voltage threshold are highly irregular. The time constant current (s) plot reveals that most data points are concentrated around lower values, with a few higher outliers, suggesting that the time spent at constant current is generally low but can vary significantly. In a similar fashion, the 'Charging Time (s)' graph demonstrates that most data points cluster within the lower range, though the presence of prominent anomalies underscores the fluctuations in recharge periods.

The dataset includes key features such as discharge time, voltage variations, and cycle index, which serve as input for machine learning models to predict Remaining Useful Life.

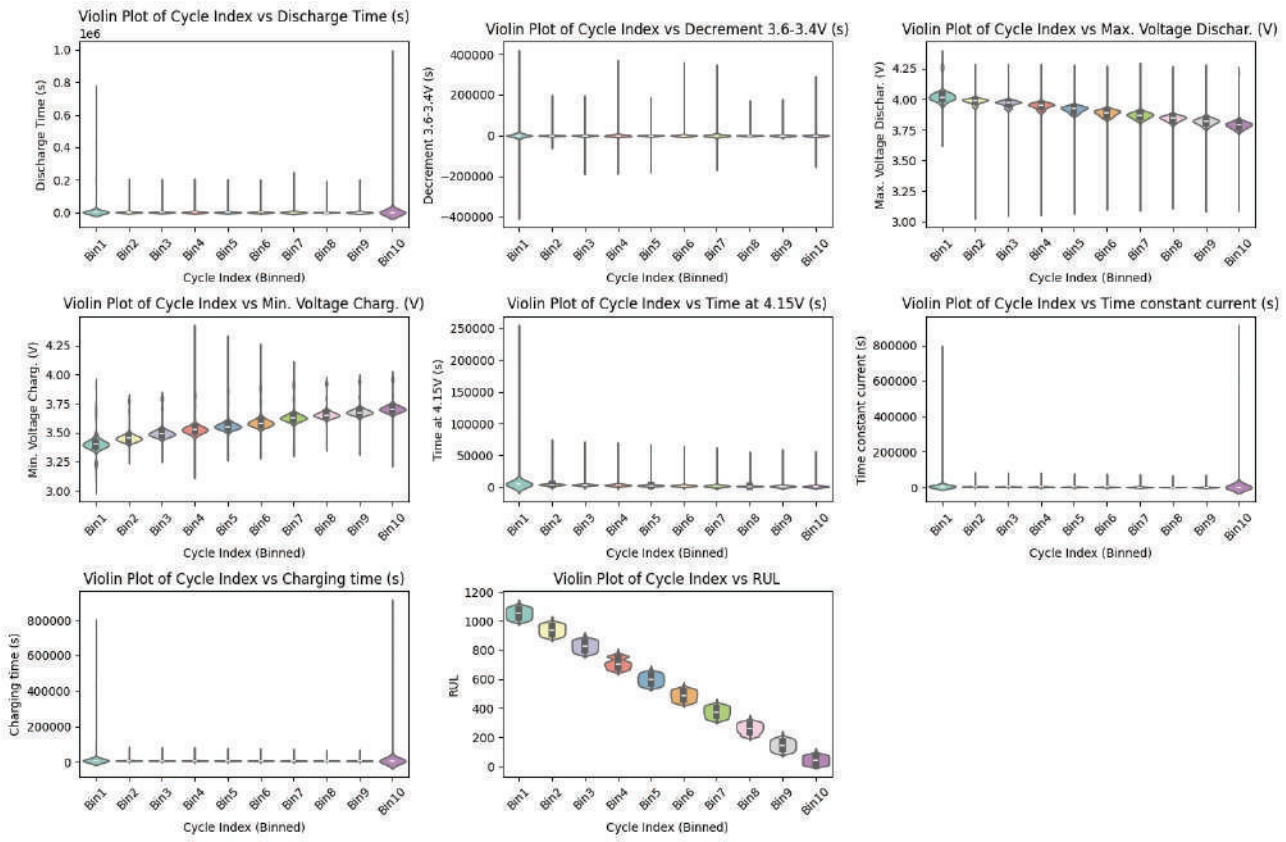


Figure 1. Violin plots of battery performance metrics across cycle index bins.

The resulting data undergoes normalization and organization to ensure seamless integration with algorithms such as Random Forest and XGBoost, enabling precise estimations of Remaining Useful Life across a wide range of battery states. The dataset undergoes a structured testing process to validate model accuracy and ensure practical applicability. The steps include:

1. Partitioning the data into training and evaluation subsets while ensuring that feature characteristics remain uniform across both groups.
2. Performing k-fold cross-validation on the training data to prevent overfitting.
3. Evaluating models on the testing set using metrics like root mean square error (RMSE) and R^2 scores.
4. Comparing model outputs against baseline results to validate improvement and statistical significance.

Heatmaps are important tools for data analysis because they make it easier to see trends, relationships, and outliers in large sets of data. They are particularly useful for quickly detecting relationships between variables, which is crucial for understanding the underlying structure of the data.

Thermal visualizations improve the clarity of numerical analysis by employing color scales to depict data magnitudes, ensuring the information remains understandable for a general audience. This visual approach supports data-driven decision-making by providing clear evidence of relationships and trends within the data. Heat maps are also valuable for identifying trends and variations over time or across different categories, thereby aiding in the construction of predictive models and improving the efficiency of data analysis.

Figure 2 provides a heat map that displays the correlation matrix of various battery performance metrics. The color-coded system indicates the strengths and directions of the relationships between these metrics. The coefficients of association range from -1 to 1, where crimson hues signify a direct relationship and azure tones indicate an inverse correlation. The heat map shows that there is a strong negative

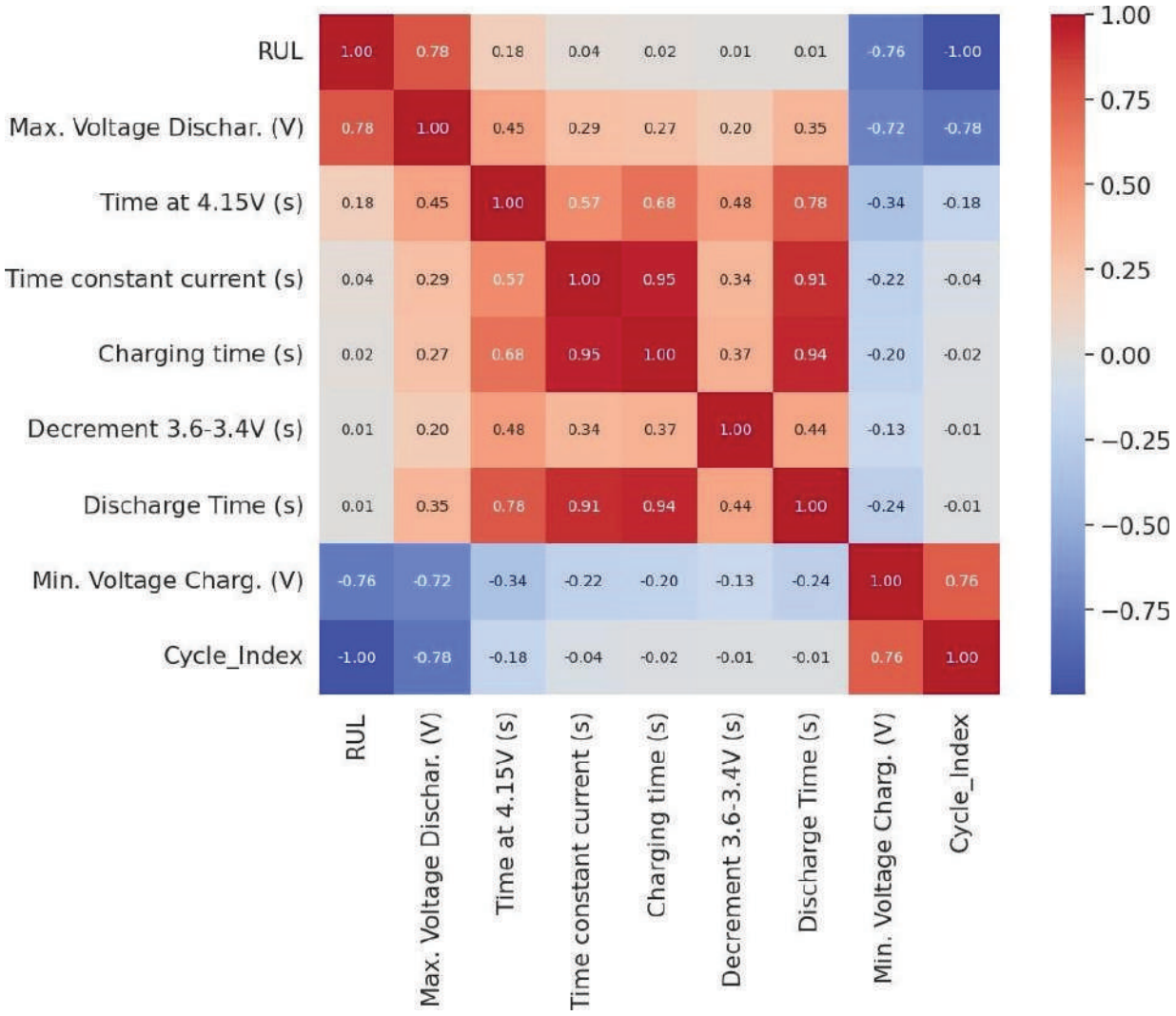


Figure 2. Correlation heatmap of battery performance metrics.

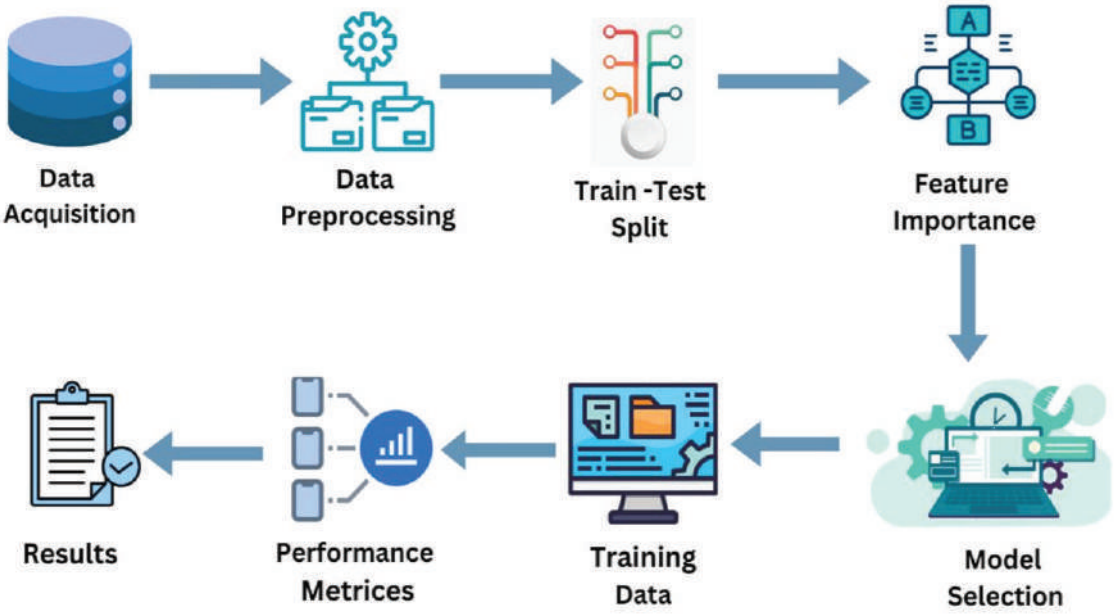


Figure 3. Machine learning project pipeline.

correlation (-1.00) between the RUL and the Cycle Index. This means that the Remaining Useful Life goes down a lot as the number of charge-discharge cycles goes up. Furthermore, a robust direct association (0.76) is observed between the RUL and the minimum voltage charge, suggesting that extended battery longevity is associated with elevated minimum thresholds during the charging process. The maximum voltage discharge also shows a moderately positive correlation (0.78) with RUL.

Time-based metrics such as constant current, charging time, and discharge time exhibit high correlations with each other, highlighting their interdependencies. The minimum charging potential displays a significant inverse relationship with both the Remaining Useful Life and the peak discharge voltage, yielding coefficients of -0.76 and -0.72, respectively. These insights demonstrate the critical factors influencing battery life and performance and underscore the importance of managing cycle counts and voltage levels to optimize battery longevity. Consequently, this thermal matrix offers an all-encompassing overview of the interdependencies among different battery health indicators, facilitating more effective system oversight and the strategic scheduling of upkeep.

FRAMEWORK FOR REMAINING USEFUL LIFE PREDICTION

Within the domain of prognostics and health management (PHM), the precise estimation of a system's RUL is a fundamental requirement. This paper introduces a novel framework integrating metaheuristic optimization techniques and machine learning models to enhance prediction. Metaheuristic techniques fine-tune the configurations and architectures of machine learning frameworks, enhancing both their precision and stability. This strategy mitigates common drawbacks, including overfitting and inadequate adaptability, found in traditional approaches. Validated with a comprehensive dataset, the proposed framework demonstrates significant performance improvements, offering a more reliable tool for predictive maintenance. The diagram that illustrates the machine learning project pipeline and the proposed predictive model for RUL prediction is also given.

Figure 3 illustrates the typical workflow of a machine learning project. It begins with data acquisition, gathering raw data from various sources. Subsequently, the data preprocessing phase focuses on scrubbing and organizing the raw information to ensure it is ready for analysis. The train-test split stage then splits the data into training and test sets. Feature importance identifies the most influential variables. Model selection follows, choosing the best algorithm for the task. The chosen model is then trained on the training data. Performance metrics evaluate the model's effectiveness. Finally, the model generates results that showcase its predictive capabilities and performance.

BLOCK DIAGRAM OF A PROPOSED PREDICTIVE MODEL FOR RUL PREDICTION

The conceptual framework for estimating Remaining Useful Life (RUL) through machine learning techniques is illustrated in Figure 4. It starts with data collection and preprocessing, including data representation, standardization, and handling null values. The significance of specific

variables is evaluated through a correlation matrix, mutual information scores, and specialized selection algorithms; following this, the data is partitioned into training and validation subsets. Various machine learning algorithms, including linear regression, random forest, bagging regressor, k-nearest neighbour (KNN), decision tree, support vector machine (SVM), AdaBoost, and XGBoost, are employed for RUL prediction. The process concludes with selecting the best algorithm for accurate RUL prediction.

MATERIALS AND METHODS

The research compared metaheuristic-optimized frameworks against conventional benchmarks, such as linear regression and SVM, to measure enhancements in forecasting precision and the minimization of error metrics. Unlike traditional models, metaheuristic techniques apply global optimization, capturing complex, non-linear degradation patterns in battery data more effectively. The research utilized inferential statistics, specifically t-tests and Analysis of Variance (ANOVA), to verify that the recorded improvements—such as lowered RMSE and higher R-squared values—attained statistical significance and were not merely coincidental. These evaluations substantiate the superior precision and reliability that metaheuristic strategies contribute to RUL estimation.

Linear Regression

Linear regression offers a powerful tool for analyzing the battery dataset, revealing insights into factors like discharge time, voltages, and cycle durations that influence RUL. The coefficients are uncovered to minimize discrepancies between predicted and actual RUL values by fitting a linear model. Despite its simplicity, this approach provides valuable insights into the intricate dynamics of battery performance. It functions as a fundamental element of predictive modeling, providing transparent outcomes that clarify linear dependencies in the data and effectively informing protocols for battery upkeep and replacement."From Simple Linear Regression:

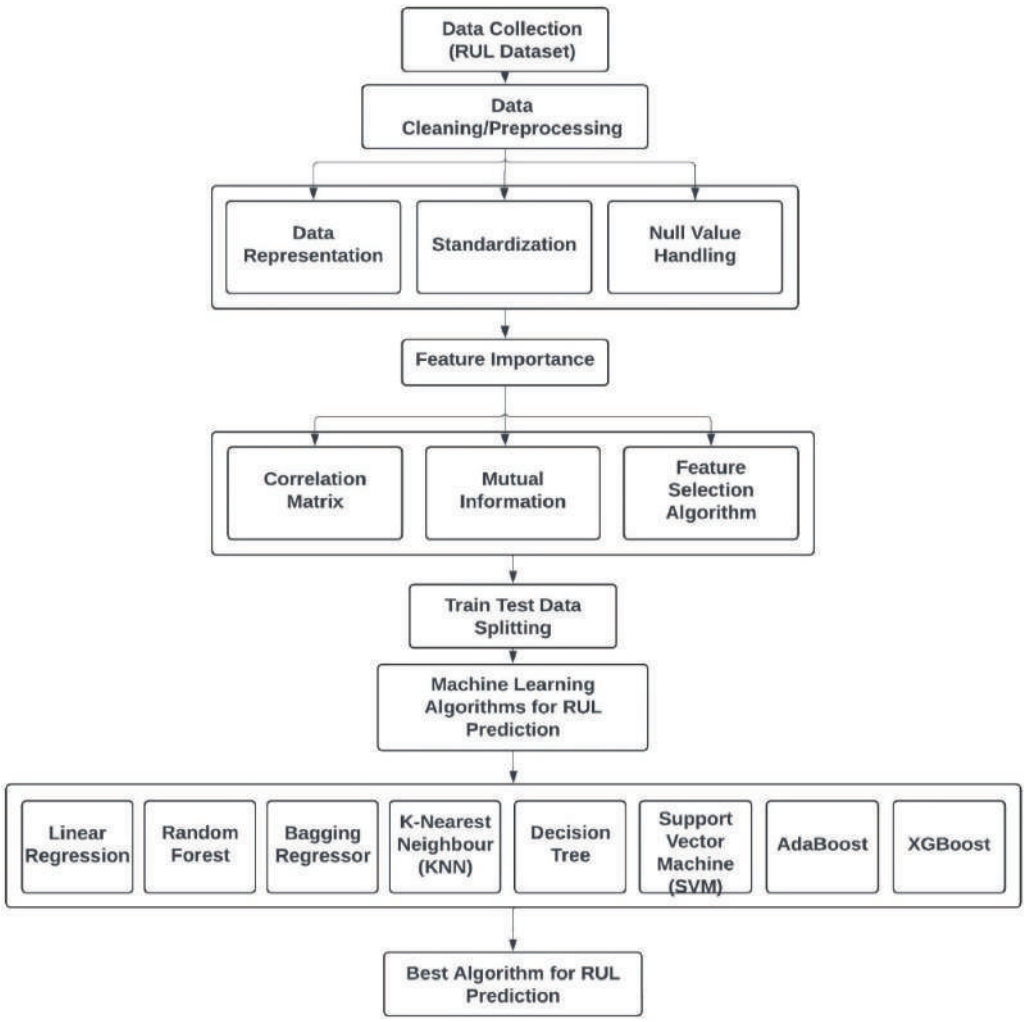


Figure 4. The proposed predictive model for RUL prediction.

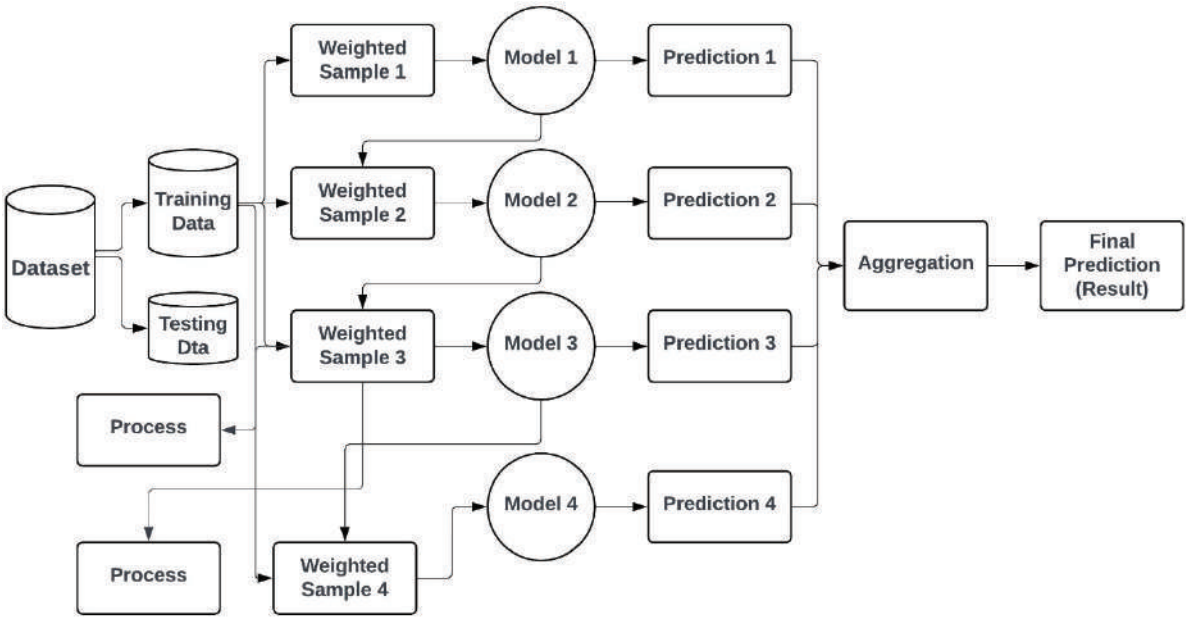


Figure 5. Boosting ensemble regressor process flow.

$$y = \beta 0 + \beta 1x + \epsilon \quad (1)$$

In (1), there are: y : dependent variable, x : independent variable

$\beta 1$ $\beta 0$: weights

ϵ: error term

From Multiple Linear Regression:

$$y = \beta 0 + \beta 1x1 + \beta 2x2 \ldots + \beta pxp + \epsilon \quad (2)$$

Here in equation (2), p is an independent variable.

Support Vector Machine Regressor

Support vector regression (SVR) could predict RUL based on various operational parameters. Each cycle's features include discharge time, voltage changes during discharge and charge, times at specific voltage levels, and other relevant metrics. SVR aims to identify the optimal hyperplane that fits the data while allowing for a margin of error defined by epsilon. This boundary defines a tolerance envelope surrounding the regressed function, permitting a specific range of permissible variations. The regularization parameter balances the flatness of the function with the allowance for deviations, ensuring robust performance in predicting continuous RUL values based on the dataset's detailed operational characteristics.

The final regression function is given as:

$$f(x) = \sum_{i=1}^{n} (\alpha_i - \alpha_i')K(x_i, x) + b \quad (3)$$

Equation (3) has α_i and α_i' are the Lagrange multipliers obtained from the optimization problem, and

$K\ (x_i, x)$ is the kernel function.

Boosting

Boosting theory is a machine learning framework aimed at improving the accuracy of predictions by combining multiple weak learners to form a strong learner. It involves sequentially training models, each focusing on correcting the errors of its predecessors. Boosting can handle a variety of data types and has shown great success in reducing bias and variance, thereby enhancing model performance. Insufficient regulation can lead to overfitting, however, since it is computationally intensive.

Adaboost ensemble regressor

AdaBoost can be employed to enhance the prediction of RUL based on various operational parameters. Each cycle is characterized by features such as Discharge Time, voltage changes during discharge and charge, times at specific voltage levels, and other relevant metrics. AdaBoost, as an ensemble method, iteratively improves regression models by focusing on the errors of each successive model. It adjusts the weights of training data points, giving more importance to instances where predictions were inaccurate. By combining weak learners effectively, AdaBoost can create a robust predictive model that accurately forecasts RUL using the dataset's detailed operational data.

Here, each data point has the same weights initially as represented in equation (4):

$$\omega_i = \frac{1}{N}\ for\ i = 1,2,3, \ldots \ldots, N \quad (4)$$

The weights that are in error should be increased through the formula (5):

$$\alpha_t = log\ log\ \left(\frac{1-\epsilon_t}{\epsilon_t}\right) \quad (5)$$

XGBoost ensemble regressor

XGBoost excels at predicting RUL using features like Discharge Time, voltage dynamics, and cycle durations. The algorithm reduces the mean squared error through the iterative refinement of decision trees, which sequentially corrects prediction errors by focusing on the remaining residuals. XGBoost's advanced capabilities include regularization to prevent overfitting, methods for managing missing data, and efficient tree-learning techniques, making it adept at handling large datasets. Due to its proficiency in generating precise regression outputs, XGBoost excels at estimating RUL, which is vital for maximizing battery longevity and securing dependable operational strategies derived from extensive cycling datasets.

Decision Tree Regressor

Decision tree techniques can address both regression and classification tasks by forming a tree structure with internal nodes representing features, branches as decision rules, and leaf nodes as outcomes. Splits are based on criteria like Gini impurity or entropy to optimize data separation. For a dataset with battery performance metrics, decision trees predict the RUL by evaluating features such as cycle count, discharge times, and voltage levels. In regression tasks, this method reduces data variability, leading to precise and reliable predictions of continuous values like RUL, making it an effective tool for battery life estimation.

Gini Index Impurity formula:

For a dataset S with n classes, the Gini impurity G(S) is calculated as:

$$G(S) = 1 - \sum_{i=1}^{n} p_i^2(x) \quad (6)$$

In equation (6), pi represents the number of samples in dataset S that belong to class i. For a dataset S with n classes, the entropy H(S) is calculated as:

$$H(S) = \sum_{i=1}^{n} p_i(p_i) \quad (7)$$

In equation (7), pi denotes the proportion of samples belonging to class i within the dataset S.

K-Nearest Neighbor Regressor

In the dataset of battery cycles, KNN could predict RUL by comparing new cycle data with historical records based on discharge times, voltage changes, and other metrics. KNN identifies 'K' nearest neighbors using distance measures like Euclidean distance (8), then averages their RUL values to estimate when a battery may need replacement. This instance-based method leverages the dataset's specifics to provide localized RUL predictions, making it suitable for understanding and managing battery longevity based on past operational patterns.

$$Euclidean\ distance\ d(x,y) = \sqrt{\sum_{i=1}^{n} \left(x_i^2 - y_j^2\right)} \quad (8)$$

Bagging Regressor

The bagging regressor is an ensemble learning method that enhances the accuracy of regression models by combining predictions from multiple instances of the same base estimator, such as decision trees. It employs a technique called Bootstrap Aggregating, or Bagging, where multiple subsets of the training data are created through sampling with replacement. Each subset is used to train a separate

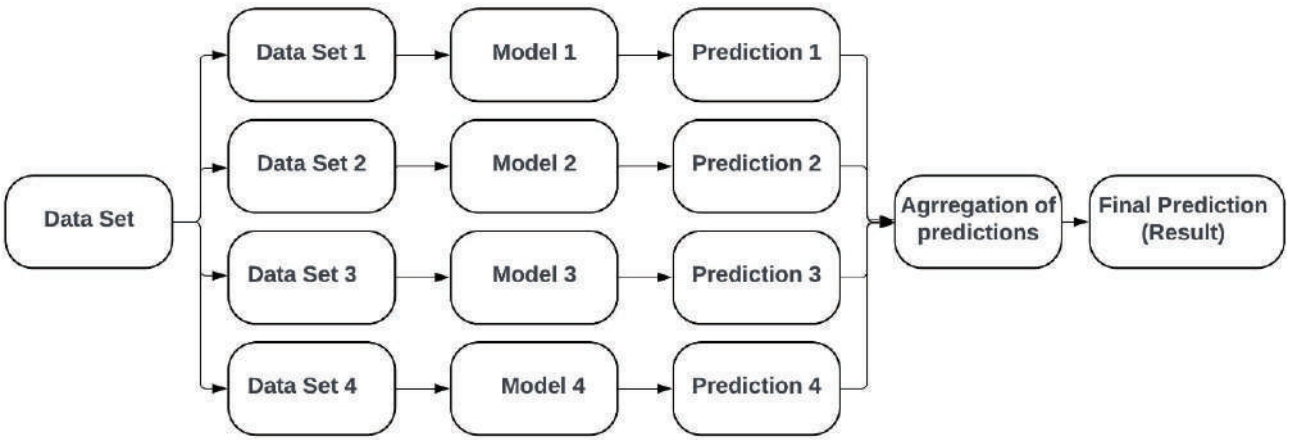


Figure 6. Bagging regressor workflow diagram.

regressor, and the predictions from all models are averaged to produce the final output. This approach reduces overfitting by lowering variance, making it especially effective for high-variance models. Additionally, since each model is trained independently, the method benefits from computational efficiency through parallelization. Bagging Regressors are particularly useful in regression tasks where the base estimator might overfit the data.

Figure 6 depicts the bagging method, an effective ensemble approach in machine learning. The process starts by arbitrarily sampling the novel dataset with replacement to create different overlapping subsets. Each of these subsets trains a distinct model autonomously, leading to a set of disparate models (Model 1, Model 2, Model 3, and Model 4), each shaped by different data samples. Each model generates its own prediction, and these predictions are then combined—using techniques such as averaging for regression or majority voting for classification—to produce a unified final prediction. By aggregating these results, the method increases overall accuracy and robustness, reduces variance, and helps prevent overfitting.

Random Forest

The random forest algorithm leverages an ensemble approach based on bagging, where a set of decision trees operates together to ameliorate predictive performance and mitigate the likelihood of overfitting. It accomplishes this by creating multiple trees, each built from randomly resampled training data and by opting for random features for every split within the tree. For example, when working with data on battery performance, Random Forest estimates remaining useful life (RUL) by consolidating the outputs of individual trees, each trained on different subsets of the data By consolidating a diverse array of variables—including discharge intervals, voltage measurements, and charging periods—this methodology produces a framework that demonstrates superior precision and consistency over a solitary decision tree.

$$\hat{y}(x) = \frac{1}{n}\sum_{i=1}^{n} \quad p_i(x) \tag{9}$$

Let,

p1, p2 …..., pn: number of decision trees in the random forest

pi(x): forecast of the i-th tree of x, given an input x.

$\hat{y}$(x): aggregated prediction of the Random Forest for the input x.

Equation (1) represents the averaging mechanism used in Random Forest regression, where the final prediction is the mean of the predictions made by all the trees.

FUNDAMENTAL PERFORMANCE CRITERIA

For regression problems, the principal evaluation metrics include mean absolute error (MAE), mean squared error (MSE), RMSE, and the coefficient of determination (R^2). These metrics measure the forecasting fidelity of the model, the scale of its deviations, and its capacity to identify the fundamental trends within the dataset.

Mean Absolute Error (MAE)

The mean absolute error (MAE) serves as an indicator for evaluating the precision of predictions by calculating the mean of the absolute deviations between forecasted and actual observations over the test dataset. In the context of Remaining Useful Life (RUL) estimation, MAE quantifies the typical size of prediction errors considering cycle-specific parameters such as Discharge Time, voltage variations during charging and discharging, and different operational durations. In an optimal scenario, the MAE converges toward zero, signifying a negligible variance between the forecasted values and the observed results.

$$MAE = \frac{1}{n}\sum_{i=1}^{n} \quad |y_i - \hat{y}_i| \tag{10}$$

In equation (10), y_i is the actual value, and $\hat{y}_i$ is the predicted value, and n is the number of observations.

Mean Square Error (MSE)

The mean squared error (MSE), defined in Equation (11), represents a measure that computes the mean of the squared deviations between predicted and observed values within a dataset. In the context of RUL estimation, the MSE quantifies the average quadratic deviation of the errors by accounting for cycle-dependent variables, including discharge durations, voltage instabilities during cycling, and different operational temporal windows. Ideally, the MSE value is close to zero, reflecting minimal divergence between predicted and actual results.

$$MSE = \frac{1}{n}\sum_{i=1}^{n} \quad (y_i - \hat{y}_i)^2 \tag{11}$$

R^2 Score

The R^2 score, as defined in Equation (13), evaluates the extent to which a regression model can forecast Remaining Useful Life (RUL) using parameters such as Discharge Time, voltage fluctuations, and cycle durations. It measures the fraction of variance in RUL that is accounted for by these features. An elevated coefficient of determination (R^2) denotes a superior model fit, suggesting the system successfully accounts for fluctuations in RUL; conversely, a diminished value suggests the model fails to align closely with the empirical measurements.

This metric is essential for assessing the regression model's capability to reliably predict RUL and understand the influence of cycle-specific characteristics on battery lifespan. Ideally, the R^2 score approaches 1.

$$R^2 = 1 - \frac{ss_r}{ss_t} \quad (12)$$

Where,
ss_r: Residual sum of squares
ss_t : Total sum of squares

RESULTS AND DISCUSSION

This portion of the study evaluates the results derived from the introduced architecture for estimating Remaining Useful Life (RUL). Model performance has been evaluated using established metrics, including RMSE and the R^2 coefficient. RMSE is employed to measure the accuracy of the predictions by calculating the extent of deviation between the estimated and actual RUL values. Simultaneously, the R^2 coefficient assesses the model's explanatory power by comparing its performance against standard baseline references.

The dataset includes key features such as discharge time, voltage variations, and cycle index, which serve as input for machine learning models to predict Remaining Useful Life. To facilitate precise inputs for predictive modeling, the data was normalized and organized for algorithms such as Random Forest and XGBoost, allowing accurate estimation of RUL under a variety of battery operating conditions. Comparative analysis shows notable gains in forecast accuracy and model resilience over conventional techniques. The consequences of these findings are examined, emphasizing their importance for streamlining maintenance scheduling and proposing avenues for subsequent research to bolster predictive performance in practical applications. The experimental findings offer valuable guidance on selecting models for practical battery management applications, taking into account metrics such as prediction accuracy, processing efficiency, and robustness. By systematically evaluating the dataset, it is confirmed that models like Random Forest and XGBoost can reliably predict battery RUL under operational conditions. These observations establish their effectiveness and reliability, positioning them as optimal choices for precise and robust battery life assessment in dynamic, real-life environments.

Table 1 presents a comparative evaluation of several regression models using performance indicators such as Training Score, Testing Score, RMSE, R^2 Score, and computational Execution Time. Linear Regression shows moderate predictive capability, recording a Training Score of 79.73 and a Testing Score of 78.14, accompanied by the highest RMSE of 148.52 and an R^2 of 80.44. While it provides reduced forecasting precision, it exhibits the shortest processing time at a mere 0.038 seconds, underscoring its superior computational speed. On the other hand, the Random Forest model delivers exceptional results, with Training and Testing Scores of 99.92 and 99.64, respectively, a minimal RMSE of 23.26, and an almost perfect R^2 of 99.68, although it requires a longer runtime of 8.319 seconds. In a similar fashion, the Bagging Regressor demonstrates high-tier proficiency, yielding Training and Testing scores of 99.88 and 99.42, respectively, alongside an RMSE of 24.05 and an R^2 of 99.62, all while offering a competitive processing duration of 0.774 seconds. The K-Nearest Neighbors (KNN) model also performs strongly, attaining Training and Testing Scores of 99.67 and 99.08, an RMSE of 30.34, and an R^2 of 98.70, with a relatively short execution duration of 0.170 seconds, demonstrating a favorable trade-off between speed and accuracy.

Strong performance is demonstrated by the Decision Tree model, with Training and Testing Scores of 99.99 and 98.85, respectively. The model records an RMSE of 33.99 and an R^2 value of 99.33, completing execution in 0.245 seconds. While SVM (Support Vector Machine) achieves reasonable Training and Testing Scores of 90.09 and 89.46, its higher RMSE of 103.14, lower R^2 of 89.70, and the longest runtime of 20.086 seconds indicate reduced efficiency for this dataset. AdaBoost delivers a balanced outcome, with Training and Testing Scores of 94.40 and 94.03, an RMSE of 77.62, an R^2 of 93.94, and an intermediate execution duration of 2.178 seconds. XGBoost excels in predictive performance, attaining Training and Testing Scores of 99.95 and 99.57, the lowest RMSE of 20.64, and an R^2 of 99.61, albeit requiring 6.871 seconds for execution.

Table 1. Performance analysis of predictive models

Algorithm name	Testing score	Training score	RMSE	R^2 Score	Execution time (s)
Random forest	99.64	99.92	23.26	0.9999	0.319
XGBoost	99.57	99.95	20.64	0.9961	6.871
Bagging regressor	99.42	99.88	24.05	0.9962	0.774
KNN	99.08	99.67	30.34	0.9870	0.170
Decision tree	98.85	99.99	33.99	0.9933	0.245
AdaBoost	94.03	94.40	36.62	0.9394	2.178
SVM	89.46	90.09	42.14	0.8970	0.086
Linear regression	78.14	79.73	48.52	0.8044	0.038

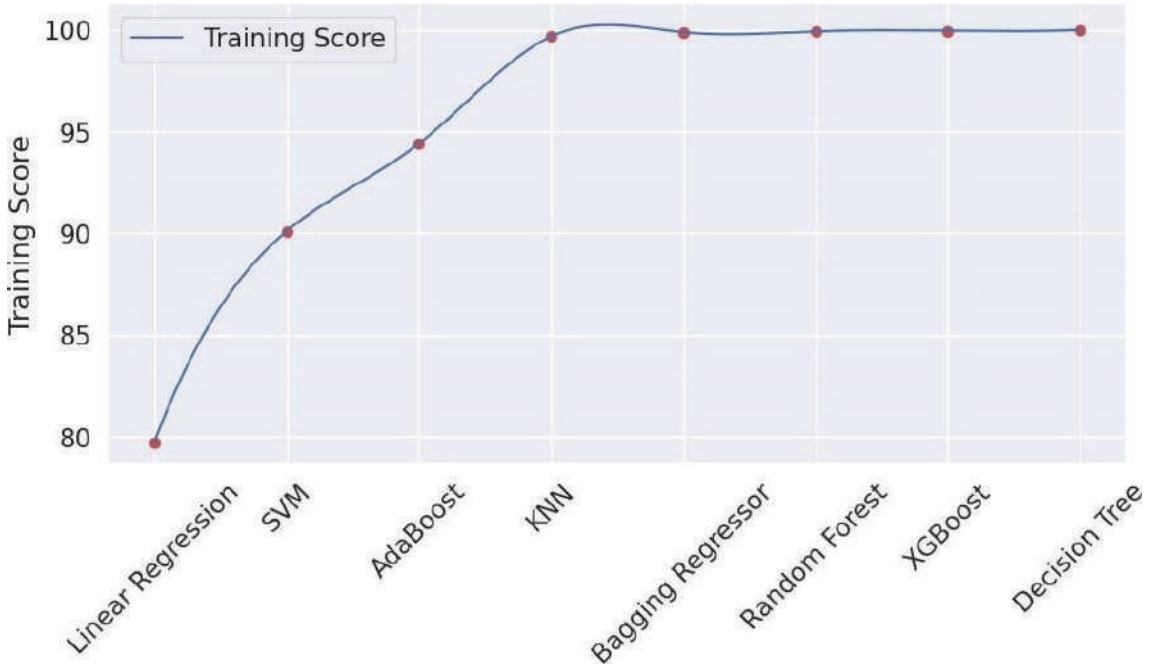


Figure 7. Comparative analysis of training scores for ML-based RUL prediction.

The results summarized in Table 1 emphasize the trade-offs between computational time and prediction accuracy among the evaluated regression algorithms. Random Forest and XGBoost are recognized as the superior frameworks, distinguished by their exceptional forecasting accuracy and their ability to minimize residuals when evaluated against the test data. Based on these findings, both models are considered highly suitable for practical battery management tasks, providing reliable RUL estimates while balancing speed, robustness, and accuracy. Through a methodical assessment of the data and evaluation metrics, vital intelligence is extracted to support preemptive battery servicing and the refinement of resource allocation within practical environments.

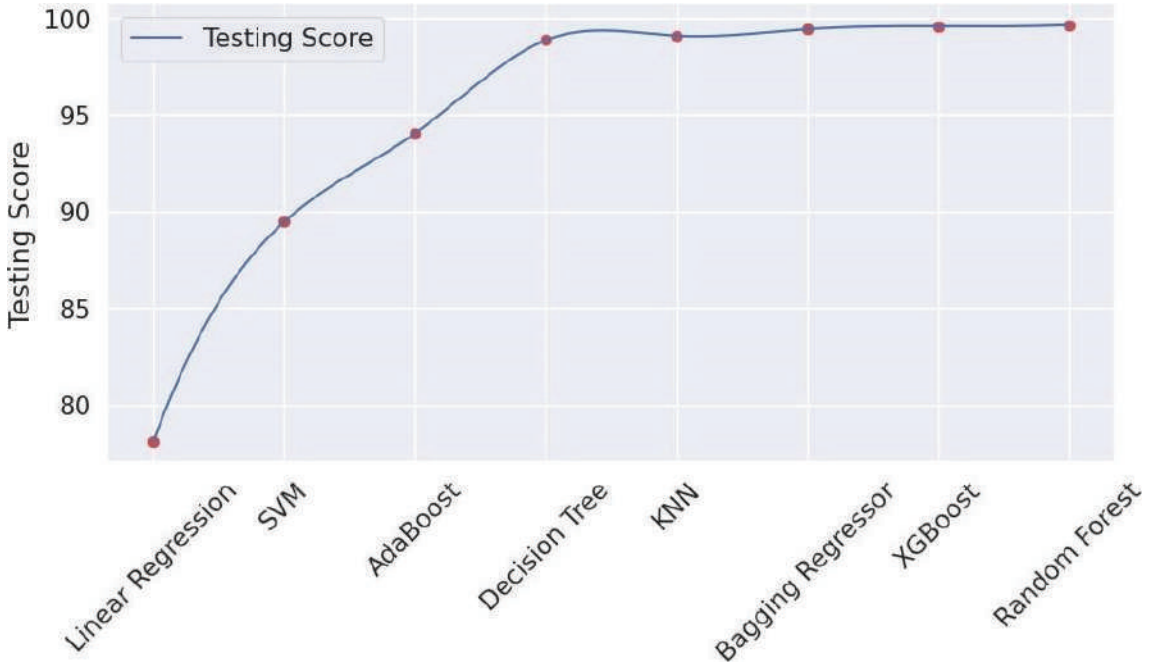


Figure 8. Assessment of testing performance in machine learning models for RUL forecasting.

The training scores of various machine learning algorithms are presented in Figure 7, with models organized in ascending order of their training performance. The evaluated algorithms comprise Linear regression, decision tree, random forest, XGBoost, bagging regressor, K-nearest neighbors (KNN), AdaBoost, and support vector machine (SVM). Each algorithm is represented along the x-axis in the plot, while its corresponding training scores are plotted along the y-axis. A smooth line curve is generated using cubic spline interpolation to provide a clearer trend

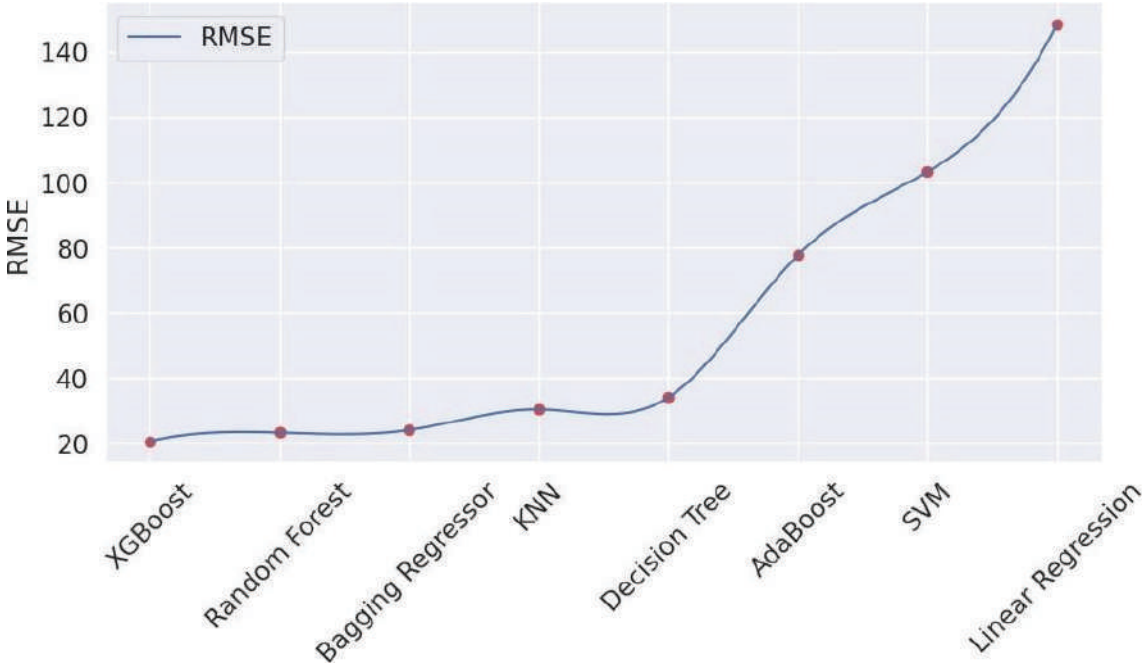


Figure 9. Root mean squared error comparison for ML-based RUL prediction.

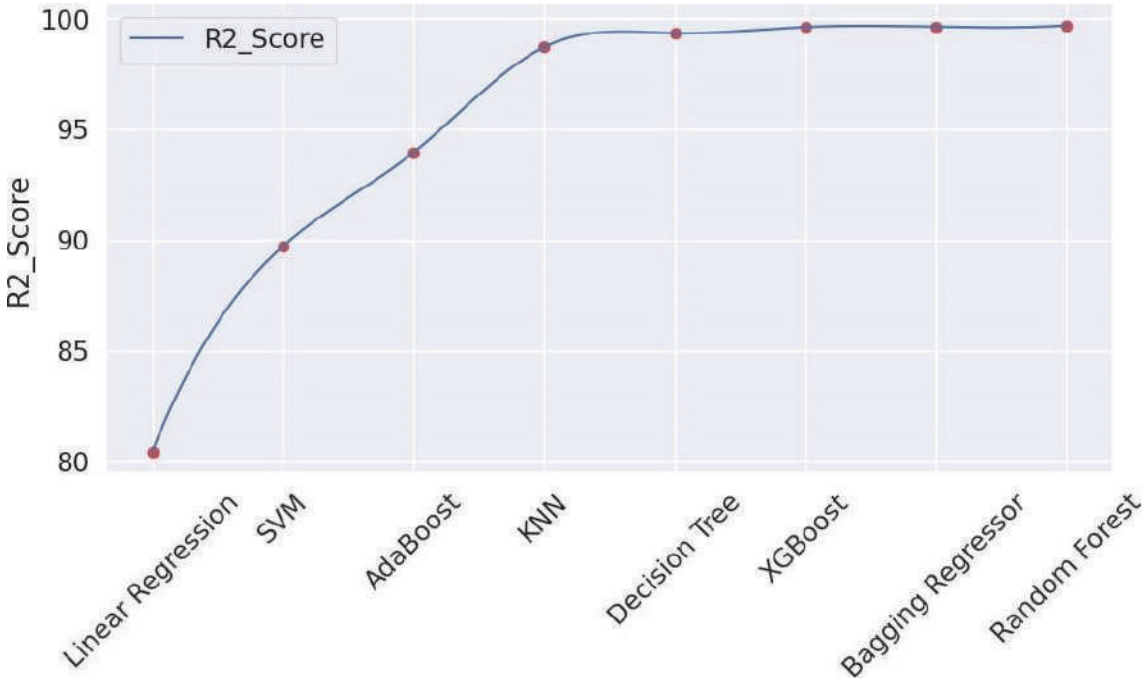


Figure 10. Assessing the predictive accuracy of machine learning models using R^2 metrics.

visualization. The red markers indicate the actual data points. The figure demonstrates a gradual progression in training performance, starting from Linear Regression, which exhibits the lowest score, up to Decision Tree, which achieves the highest. Most algorithms, particularly from K-nearest neighbors (KNN) onward, attain training scores approaching 100, reflecting exceptionally strong learning on the training dataset. Such high performance may indicate overfitting, especially when not accompanied by a corresponding evaluation on test data. Conversely, the training scores for linear regression and support vector machine (SVM) are more modest. This indicates that these specific algorithms demonstrate a reduced capacity for capturing underlying training patterns when compared to the alternative models evaluated.

The testing performance of different machine learning algorithms is visualized in Figure 8, where each model is plotted along the x-axis and its corresponding testing score is shown on the y-axis. Based on their respective testing performance, the evaluated algorithms—ranging from Linear Regression and SVM to XGBoost and Random Forest—have been organized in ascending order. This list also includes AdaBoost, decision tree, KNN, and bagging regressor. To better illustrate the overall trend, a smooth curve generated through cubic spline interpolation is overlaid, while red markers denote the actual observed data points. Moving across the sequence of models, the data reveals a steady climb in testing outcomes. Random forest achieves the maximum value, contrasting sharply with Linear Regression's baseline. Notably, the most dramatic increase is situated between the first two models, giving way to a more consistent, gradual rise thereafter. Testing scores for models starting from KNN are nearly 100, reflecting excellent generalization capability on unseen data. Nevertheless, this sustained high performance requires rigorous cross-validation to confirm the results aren't skewed by overfitting. This is especially critical in cases where the training metrics are similarly high. In contrast, the comparatively lower testing scores of Linear Regression and SVM suggest a more conservative fit to the data, which may support better generalization in certain practical scenarios.

The RMSE for several regression models is illustrated in Figure 9 using a smooth line. Error values are ordered from lowest to highest to facilitate direct comparison among the algorithms. Along the x-axis, the evaluated models—XGBoost, Random Forest, Bagging Regressor, K-Nearest Neighbors (KNN), Decision Tree, AdaBoost, Support Vector Machine (SVM), and Linear Regression—are displayed with rotated labels for improved readability. The vertical axis corresponds to RMSE values, ranging from 20 to 150. For better visibility of the general trend, the data points are linked via spline interpolation. Distinct red markers are utilized to draw attention to the specific observed measurements. This visual arrangement clearly demonstrates differences in predictive accuracy, where lower RMSE values reflect stronger model performance. By prioritizing a comparative assessment of error, the title "Root Mean Squared Error Comparison for ML-Based RUL Prediction" effectively summarizes the graph's objective.

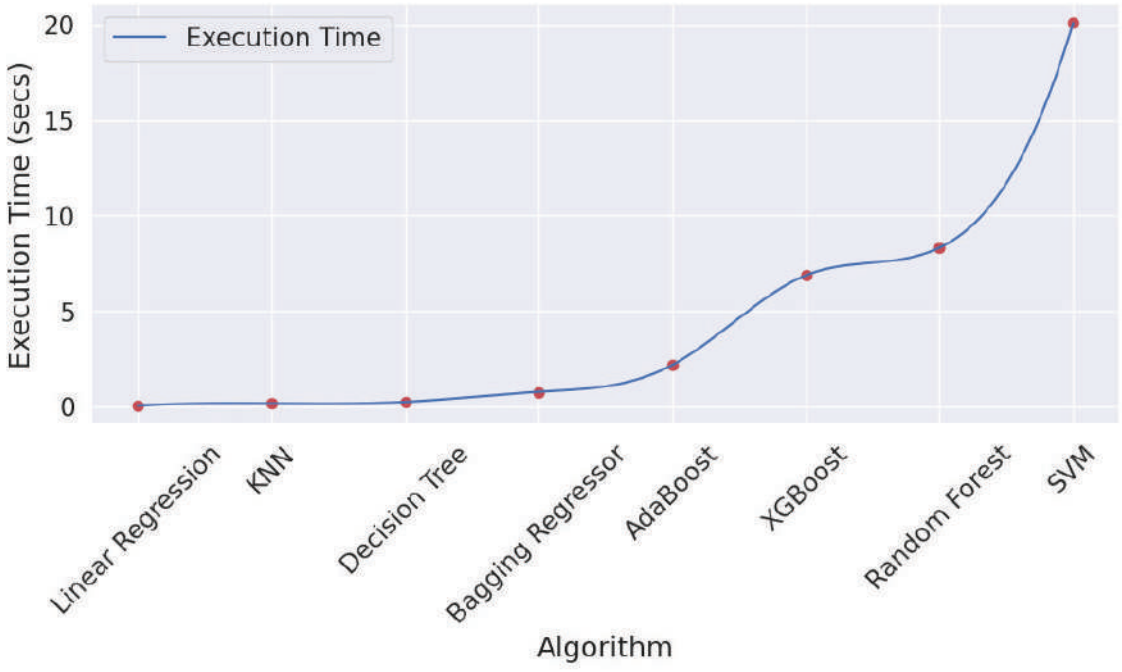


Figure 11. Computational time analysis of machine learning models for RUL prediction.

Table 2. Performance comparison of reference paper

ML algorithms	MSE	RMSE	MAE	R-Squared	Time
Random forest regression	14.1186	3.7574	2.0930	0.9998	0.0651
Decision tree regression	26.8489	5.1816	2.2296	0.9997	0.1510
Linear regression	54.5430	7.3853	4.6441	0.9994	0.0248
Bayesian network	54.5478	7.3856	4.6483	0.9993	1.2356
Gradient boosting regression	57.4476	7.5794	4.9842	0.9990	2.5640

Using a continuous curve, Figure 10 displays the coefficient of determination values achieved by different regression techniques. The models are sequenced from lower to higher R^2 performance, with Linear Regression, Support Vector Machine (SVM), AdaBoost, K-Nearest Neighbors (KNN), Decision Tree, XGBoost, Bagging Regressor, and Random Forest positioned along the horizontal axis, where label rotation improves visibility. The vertical axis captures R^2 magnitudes spanning from 80 to 100. Individual results are connected through spline-based smoothing, and the measured values are emphasized with red data markers. This presentation facilitates straightforward evaluation of predictive strength, as greater R^2 values indicate improved explanatory capability. Clearly stated in the title, "R^2-Based Performance Comparison of Machine Learning Algorithms," the figure underscores comparative assessment of model performance. This graph clearly illustrates the capacity of each model to explain the variance within the target variable. Higher values in this context represent a more precise and accurate modelling approach.

A continuous visualization of runtime performance is shown in Figure 11, where regression models are ranked based on their temporal requirements. This arrangement moves from the model with the minimum execution period to the one with the maximum. The algorithms displayed along the horizontal axis include Linear Regression, K-Nearest Neighbors (KNN), Decision Tree, Bagging Regressor, AdaBoost, XGBoost, Random Forest, and Support Vector Machine (SVM), with axis labels rotated to enhance clarity. Within a range of 0 to 20 on the vertical scale, the processing durations are visualized. A spline-based curve tracks the trend between measurements, while the specific observations are highlighted using red data points. This graphical representation enables a clear comparison of computational efficiency, where reduced execution time corresponds to faster model performance. Regarding execution speed, Linear Regression and KNN are the fastest-performing algorithms, whereas SVM sits at the opposite end of the spectrum with the maximum processing time. Through this comparative visualization, valuable insight is provided into the suitability of each algorithm for practical deployment, particularly in time-critical applications or large-scale datasets. By centering on the resource requirements of each model, the figure title "Computational Time Analysis of Machine Learning Models for RUL Prediction" accurately describes the graph's focus on efficiency.

Comparative Analysis

The Table 2 shows the result of similar research. By comparing results of this paper with recent research, it is shown that this paper's results are more effective and efficient for research applications, primarily due to its higher R-squared values and strong testing and training scores, which indicate a precise model fit and robust generalizability.

Models like Random Forest and XGBoost in Table 1 achieve R-squared values close to 0.9999, suggesting they capture nearly all data variability, which is critical for ensuring reliability in predictive tasks. As shown in Table 1, the evaluated models represent a broad spectrum of computational demands. While SVM and KNN offer rapid results, XGBoost serves as a more intensive alternative. Such a variety provides practitioners with the freedom to prioritize either low-latency performance or high-level accuracy based on their specific application needs. Although Table 1 has slightly higher RMSE values compared to Table 2, the extremely high R-squared values and consistency between testing and training scores offset this drawback, making Table 1's models more suited to applications where precision and generalizability are essential. Furthermore, ensemble approaches such as Bagging and Boosting improve computing efficiency by minimizing variance while focusing on prediction accuracy. The integration of metaheuristic techniques refines model training and boosts execution speed. Consequently, these optimized algorithms become highly effective for use cases that demand rapid response times and time-critical decision-making. These optimizations are critical for battery management systems that need real-time analysis because they enable quick, accurate forecasts while controlling computing loads.

CONCLUSION

The primary focus of this study is on accurately predicting the remaining useful life (RUL) of lithium-ion batteries, particularly within renewable energy storage systems. This area is significant because accurate RUL predictions are essential for battery management in electric vehicles (EVs) and renewable energy systems, which rely on efficient

energy storage to meet sustainability goals. The optimization of battery life cycles through dependable RUL estimates serves to minimize maintenance overhead while simultaneously supporting sustainability. This approach enhances the overall balance between commercial productivity and ecological stewardship. This research proposes a range of machine learning models, including Random Forest, Decision Tree, Linear Regression, K-Nearest Neighbours, Support Vector Machine, Adaptive Boosting (AdaBoost), and Extreme Gradient Boosting (XGBoost Metaheuristic-based parameter selection served as a catalyst for improving the RUL performance of the implemented ML models, ensuring more precise predictive outcomes.

This research was carried out through the Hawaii Natural Energy Institute (HNEI) battery lifecycle dataset for machine learning model training and validation. Random Forest and XGBoost emerged as top performers, achieving R^2 scores of 99.68% and 99.61%, respectively, and RMSEs of 23.26 and 20.64, respectively. The data highlights how advanced computational modeling significantly upgrades RUL prediction capabilities. Specifically, the fusion of metaheuristic parameter optimization and ensemble-based learning proved instrumental in reaching superior levels of predictive accuracy. This research improves the management of renewable energy resources by efficiently predicting the Remaining Useful Life to improve sustainability goals.

AUTHORSHIP CONTRIBUTIONS

Authors equally contributed to this work.

DATA AVAILABILITY STATEMENT

The authors confirm that the data that supports the findings of this study are available within the article. Raw data that support the finding of this study are available from the corresponding author, upon reasonable request.

CONFLICT OF INTEREST

The author declared no potential conflicts of interest with respect to the research, authorship, and/or publication of this article.

ETHICS

There are no ethical issues with the publication of this manuscript.

STATEMENT ON THE USE OF ARTIFICIAL INTELLIGENCE

Artificial intelligence was not used in the preparation of the article.

REFERENCES

[1] Sankarasubramanian S, Krishnamurthy B. A capacity fade model for lithium-ion batteries including diffusion and kinetics. Electrochim Acta 2012;70:248–254.[CrossRef]

[2] Wang Y, Yang D, Zhang X, Chen Z. Probability based remaining capacity estimation using data-driven and neural network model. J Power Sources 2016;315:199–208. [CrossRef]

[3] Safavi V, Mohammadi Vaniar A, Bazmohammadi N, Vasquez JC, Guerrero JM. Battery remaining useful life prediction using machine learning models: A comparative study. Information 2024;15:124. [CrossRef]

[4] Wang Y, Pan R, Yang D, Tang X, Chen Z. Remaining useful life prediction of lithium-ion battery based on discrete wavelet transform. Energy Procedia 2017;105:2053–2058. [CrossRef]

[5] Park K, Choi Y, Choi WJ, Ryu HY, Kim H. LSTM-based battery remaining useful life prediction with multi-channel charging profiles. IEEE Access 2020;8:20786–20798. [CrossRef]

[6] Hu C, Jain G, Zhang P, Schmidt C, Gomadam P, Gorka T. Data-driven method based on particle swarm optimization and k-nearest neighbor regression for estimating capacity of lithium-ion battery. Appl Energy 2014;129:49–55. [CrossRef]

[7] Kamul A, Hananda N, Harito C, Djuana E, Elwirehardja G, Pardamean B, et al. Machine learning application in battery prediction: A systematic literature review and bibliometric study. E3S Web Conf 2022;338:01021. [CrossRef]

[8] Venugopal P, et al. Analysis of optimal machine learning approach for battery life estimation of Li-ion cell. IEEE Access 2021;9:159616–159626. [CrossRef]

[9] Feng X, et al. Online state-of-health estimation for Li-ion battery using partial charging segment based on support vector machine. IEEE Trans Veh Technol 2019;68:8583–8592. [CrossRef]

[10] Richardson RR, Osborne MA, Howey DA. Battery health prediction under generalized conditions using a Gaussian process transition model. J Energy Storage 2019;23:320–328. [CrossRef]

[11] Wu J, Kong L, Cheng Z, Yang Y, Zuo H. RUL prediction for lithium batteries using a novel ensemble learning method. Energy Rep 2022;8:313–326. [CrossRef]

[12] Ansari S, Ayob A, Lipu MSH, Hussain A, Saad MHM. Remaining useful life prediction for lithium-ion battery storage system: A comprehensive review of methods, key factors, issues and future outlook. Energy Rep 2022;8:12153–12185. [CrossRef]

[13] Wang A, Chen H, Jin P, Huang J, Feng D, Zheng M. RUL estimation of lithium-ion power battery based

on DEKF algorithm. In: Proceedings of the 2019 14th IEEE Conference on Industrial Electronics and Applications (ICIEA); 2019. p. 1851–1856. [CrossRef]

[14] Safavi V, Mohammadi Vaniar A, Bazmohammadi N, Vasquez JC, Guerrero JM. Battery remaining useful life prediction using machine learning models: A comparative study. Information 2024;15:124. [CrossRef]

[15] Richardson RR, Osborne MA, Howey DA. Battery health prediction under generalized conditions using a Gaussian process transition model. J Energy Storage 2019;23:320–328. [CrossRef]

[16] Que Z, Xu Z. A data-driven health prognostics approach for steam turbines based on xgboost and DTW. IEEE Access 2019;7:1–1. [CrossRef]

[17] Lipu MSH, Hannan MA, Hussain A, Hoque MM, Ker PJ, Saad MHM, et al. A review of state of health and remaining useful life estimation methods for lithium-ion battery in electric vehicles: Challenges and recommendations. J Clean Prod 2018;205:115–133. [CrossRef]

[18] Xu B, Oudalov A, Ulbig A, Andersson G, Kirschen DS. Modeling of lithium-ion battery degradation for cell life assessment. IEEE Trans Smart Grid 2018;9:1131–1140. [CrossRef]

[19] Eissa MA, Chen P. Machine learning-based electric vehicle battery state of charge prediction and driving range estimation for rural applications. IFAC-PapersOnLine 2022;56(3). [CrossRef]

[20] Wang N, Lyu Y, Zhou Y, Luan J, Li Y, Zheng C. A hybrid framework for remaining driving range prediction of electric taxis. Sustain Energy Technol Assess 2024;67:103832. [CrossRef]

[21] Sekhar JNC, Domathoti B, Santibanez Gonzalez EDR. Prediction of battery remaining useful life using machine learning algorithms. Sustainability 2023;15:15283. [CrossRef]

[22] Babaeiyazdi I, Rezaei-Zare A, Shokrzadeh S. State of charge prediction of EV Li-ion batteries using EIS: A machine learning approach. Energy 2021;223:120116. [CrossRef]

[23] Lai X, Huang Y, Gu H, Han X, Feng X, Dai H, et al. Remaining discharge energy estimation for lithium-ion batteries based on future load prediction considering temperature and ageing effects. Energy 2022;238:121754. [CrossRef]

[24] Maheshwari A, Nageswari S. Modelling and State of Charge Estimation of Li-Ion Battery for Electric Vehicle. In: Power Electronics and High Voltage in Smart Grid: Select Proceedings of SGESC 2021. Singapore: Springer Nature Singapore; 2022. p. 139–151. [CrossRef]

[25] Wang L, Ma J, Zhao X, Li X, Zhang K, Jiao Z. Adaptive robust unscented Kalman filter-based state-of-charge estimation for lithium-ion batteries with multi-parameter updating. Electrochim Acta 2022;426:140760. [CrossRef]

[26] Sekhar JNC, Domathoti B, Santibanez Gonzalez EDR. Prediction of battery remaining useful life using machine learning algorithms. Sustainability 2023;15:15283. [CrossRef]

[27] Badik ŞT, Akar M. Machine learning classification models for the patients who have heart failure. Sigma J Eng Nat Sci 2024;42:235–244. [CrossRef]

[28] Das O. Prediction of the natural frequencies of various beams using regression machine learning models. Sigma J Eng Nat Sci 2023;41:302–321. [CrossRef]

[29] Pınar C. The machine learning approach for predicting the number of intensive care, intubated patients and death: The COVID-19 pandemic in Turkey. Sigma J Eng Nat Sci 2022;40:85–94.

[30] Chavan PP, Makhar K, Kulkarni M, Kulkarni SS. Flight Price Prediction for Enhanced Recommendations via Machine Learning Web Application. In: Proceedings of the 2024 2nd International Conference on Sustainable Computing and Smart Systems (ICSCSS); 2024. p. 1031–1037. [CrossRef]

Sigma Journal of Engineering and Natural Sciences
Web page info: https://sigma.yildiz.edu.tr
DOI: 10.14744/sigma.2025.00000

Research Article

SWARA & EDAS integration using spherical fuzzy sets in agricultural field

Betül KARA[1], Muhammed Zakir DENİZ[1], Umut AYDIN[2], Melis Almula KARADAYI[1,*]

[1]*Department of Industrial Engineering, Istanbul Medipol University, Istanbul, 34810, Türkiye*
[2]*Department of Management Information Systems, Istanbul Ticaret University, Istanbul, 34840, Türkiye*

ARTICLE INFO

Article history
Received: 25 July 2024
Revised: 04 November 2024
Accepted: 30 January 2025

Keywords:
Agriculture; EDAS; Fuzzy MCDM; Spherical Fuzzy Sets; SWARA; Wastewater Management

ABSTRACT

The rapid decline of clean water resources, caused by climate change, population growth, and bad water management, is a big threat to both the environment and agriculture. In Türkiye, about 75% of clean water is used for irrigation in agriculture, which shows how important it is for this sector to use water wisely. This research investigates the viability of treated wastewater as a sustainable substitute for traditional water sources in agriculture, thereby mitigating water scarcity and minimizing environmental degradation. This study utilizes a spherical fuzzy adaptation of SWARA (Step-Wise Weight Assessment Ratio Analysis) and EDAS (Evaluation Based on Distance from Average Solution) to assess and rank drought-prone areas for wastewater application according to essential socio-environmental and economic factors.

The Republic of Türkiye Ministry of Environment, Urbanization, and Climate Change identified three areas in Türkiye—Southeastern Anatolia, Aegean, and Central Anatolia—as being more likely to experience drought. Three pilot cities (Kırıkkale, Manisa, and Şanlıurfa) were evaluated in these areas. The results showed that Şanlıurfa was the area most affected by drought and that its wastewater management system had the best chance of helping with sustainable development. In terms of numbers, Şanlıurfa had the highest rate of treating wastewater and the most agricultural land available for using wastewater. These findings indicate that emphasizing the utilization of treated wastewater in this region could substantially alleviate the effects of drought while fostering environmental resilience.

This study is new because it uses a spherical fuzzy MCDM framework that was specifically designed to deal with the complicated uncertainties that come up in regional water management during droughts. By implementing a context-specific methodology for prioritizing agricultural wastewater, this study provides policymakers with pragmatic insights into sustainable water management practices, thereby advancing both regional and national sustainability objectives.

Cite this article as: Kara B, Deniz MZ, Aydın U, Karadayı MA. SWARA & EDAS integration using spherical fuzzy sets in agricultural field. Sigma J Eng Nat Sci 2026;44(1):545–558.

***Corresponding author.**
*E-mail address: makaradayi@medipol.edu.tr

This paper was recommended for publication in revised form by Editor-in-Chief Ahmet Selim Dalkilic

Published by Yıldız Technical University Press, İstanbul, Turkey
© Author. This is an open access article under the CC BY-NC license (http://creativecommons.org/licenses/by-nc/4.0/).

INTRODUCTION

Due to changing climate conditions and decreasing rainfall, drought is increasingly felt worldwide. It has gone beyond being just an environmental problem. Deforestation, excessive water use in agriculture and industry, and the inefficient management of water resources are among the main factors deepening drought conditions on a global scale [1]. Temperatures are rising. Evaporation rates are increasing. Water resources are becoming even more limited, and the need for long-term water management plans is becoming urgent [2]. This situation has also become evident in Turkey in recent years. In critical regions such as Southeastern Anatolia, Central Anatolia, and the Aegean, prolonged drought and water scarcity are making agricultural production and water supply difficult [3]. The high demand for irrigation water and the inadequacy of existing water management practices further exacerbate the problem. Therefore, water resources need to be addressed with a holistic and sustainable approach. Only in this way can environmental resilience be strengthened and the effects of drought be reduced.

Considering that large agricultural areas in Turkey are facing increasing water scarcity, the use of treated wastewater for agricultural irrigation stands out as a long-term solution [1]. With planned investments and forward-looking wastewater management strategies, it is possible to prioritize the regions most affected by drought. This increases the effectiveness of the measures taken. This study proposes an integrated approach aimed at addressing the existing shortcomings in agricultural water management. The focus is on identifying the most suitable regions for wastewater use. In this context, spherical fuzzy SWARA and EDAS methods, which can address the uncertainty and ambiguity arising in expert assessments, are used together. Thus, a robust decision-making framework is provided.

The unique aspect of the study is the innovative application of spherical fuzzy sets (SFS) within the integration of SWARA and EDAS. In this way, the inclusiveness of traditional multi-criteria decision-making approaches is expanded. Three different dimensions of uncertainty are considered: membership, non-membership, and hesitation. In environmental and agricultural decision problems with high uncertainty, SFS make the decision-making process more sensitive and functional [4]. More realistic results are obtained as a result.

When used in a fuzzy setting, the SWARA and EDAS methods have a lot of benefits that make it easier to make decisions. SWARA is the best choice because it is simple and fast when it comes to weighting criteria. You don't need to do complicated pairwise comparisons. Instead, a sequential evaluation process is used that takes into account how important each criterion is. You save time. It also makes it easier for people who have to make decisions. This quality stands out even more when there are a lot of criteria or when evaluations are based on personal opinion [5]. When used in a spherical fuzzy structure, SWARA better shows how experts really feel about things by taking into account uncertainty and partial beliefs. This makes the weighting of criteria that are important to the environment stronger.

The EDAS method looks at how close each option is to the average solution. This method works well when it's hard to tell the difference between options. Methods that use ideal solutions don't always work in the real world. When used in a spherical fuzzy environment, EDAS can include hesitation and partial non-membership degrees in the process of evaluation. This makes it easier to make decisions that are fair when you aren't sure what to do. This feature is very useful in agriculture and the environment when there isn't a lot of quantitative data and expert opinions aren't always right [6].

Combining the SWARA and EDAS methods into a spherical fuzzy framework takes advantage of the best parts of both. This makes the structure for making decisions more stable and consistent. Following this method of combining different approaches, the study looks at Turkey's three driest areas: Southeastern Anatolia, the Aegean, and Central Anatolia. Kırıkkale, Manisa, and Şanlıurfa were chosen to be the first cities to try it out. To model water management strategies that focus on drought, a full evaluation framework with seven main criteria was made. These are the criteria: how easy it is to get to natural water resources (C1), the slope of the land (C2), the rate of drought at the provincial level (C3), the ratio of arable land (C4), the rate of wastewater treatment in the region (C5), the amount of wastewater produced per person per day (C6), and the amount of money that municipalities spend on wastewater treatment (C7). We used the spherical fuzzy SWARA method to figure out the weights for the criteria. This shows how important each factor is compared to the others and how complicated it is inside. Turkey is making more decisions about how to manage agricultural water that take into account the local situation.

In conclusion, this study fills in some important gaps in how to manage water for farming in areas that have been hit by drought. It adds to the body of knowledge. SFSs are a better way to show uncertainty and better show how experts are unsure than traditional methods. SWARA and EDAS work together to prioritize the use of wastewater in Turkey's drought-prone areas by taking into account both environmental and socioeconomic factors. It goes beyond general evaluations and provides a more useful and evidence-based framework for improving sustainable water use in farming. The second part of the article talks about the important research. The third part talks about how to combine different methods. The fourth part talks about applications and case studies, and the last part talks about the effects on policy and suggestions for future research.

Literature Review

Multi-criteria decision-making (MCDM) is a way to look at and rank options based on more than one, often

conflicting, set of criteria. It does this by taking into account both the decision factors and their relative weights. Because they are so flexible, MCDM methods have been used in many different fields, including finance, education, logistics, engineering, healthcare, environmental management, and industry (Yalçın & Uncu [6]; Marqués et al. [7]; Syed Hassan et al. [8]; Evcioğlu & Kabak [9]; Reddy [10]; Korkusuz et al. [11]; Sánchez-Lozano & Bernal-Conesa [12]). MCDM is especially useful in agriculture, where choices have a direct impact on the environment, people's health, and the economy. MCDM has been used in the past to choose crops [13], assess sustainability [14], plan irrigation [15], manage finances [16], choose a site [17–19], manage soil quality [3; 20], and choose machinery [21]. This shows that it can effectively balance trade-offs between economic, environmental, and resource-related factors in a structured and data-driven way.

The increasing severity of drought has become a serious threat to food security, agricultural productivity, access to water, and economic stability, especially in countries like Turkey [22]. These problems are deepening. Climate change and global warming are further accelerating the process and making the need for long-term water management plans inevitable. Under these conditions, the reuse of treated wastewater in agricultural production is becoming increasingly important. This practice reduces the pressure on freshwater resources. It prevents the pollution of natural water bodies. It also provides energy savings. Therefore, in order to evaluate different alternatives for wastewater management, methods such as AHP [22], ANP [23], TOPSIS [24], VIKOR [2], GIS-based multi-criteria decision-making models [25], and MOORA [26] have been used in numerous studies. Criteria such as environmental compatibility, cost-effectiveness, and resource efficiency are prominent in these evaluations.

However, traditional multi-criteria decision-making methods are often based on clear and precise data. Such data is not always available in real decision-making environments. Uncertainty and incomplete information are inevitable, especially in environmental and agricultural decision-making processes. To overcome this limitation, fuzzy multi-criteria decision-making approaches have been developed that model uncertainty through linguistic variables and membership functions. Fuzzy AHP and fuzzy TOPSIS are the most widely used methods among these approaches. These methods have yielded successful results in agricultural applications. For example, they have been effectively used in irrigation method selection studies in situations where weather conditions are unpredictable (Burak et al. [15]) and in crop selection based on water needs, soil compatibility, and adaptability to different climatic conditions (Qureshi et al. [13]). Overall, fuzzy multi-criteria decision-making methods are seen to make significant contributions to the determination of sustainability goals, the analysis of environmental and social impacts, and the support of agricultural risk management [27–28]. This demonstrates that these approaches are powerful tools in solving complex and subjective decision-making problems.

Recent studies show that adding advanced fuzzy logic structures to MCDM makes decisions better when there is a lot of uncertainty. Fuzzy TOPSIS has been used in wastewater management to find the best places for agricultural reuse by using geographic and environmental data [25]. Additionally, SFS are getting more and more attention because they can show membership, non-membership, and hesitancy all at the same time. This makes them a better and more flexible way to model expert uncertainty (Kutlu Gündoğdu & Kahraman [4]; Akbari et al. [14]). Fuzzy SWARA and fuzzy EDAS methods have become popular tools for dealing with subjective, expert-driven MCDM problems. They build on this progress by using fuzzy logic to better capture uncertainty in MCDM problems. So, the next sections look at studies that used fuzzy SWARA and fuzzy EDAS. They focus on the types of problems they were used to solve, how they were set up, and how they were done.

The most recent studies that used fuzzy SWARA show that the method can work with different types of fuzzy sets, such as Type-1, Type-2, interval-valued, intuitionistic, and SFS. SFS, which are used in fields like choosing renewable energy sources [30] and managing a green supply chain [34], are better at capturing expert uncertainty

Table 1. Studies utilizing fuzzy SWARA

Author(s)	Fuzzy set	Application area
Rostamzadeh et al. (2020) [5]	Type-1 fuzzy set	Supplier selection in supply chain
Pamucar et al. (2021) [29]	Intuitionistic fuzzy set	Transportation project prioritization
Mishra et al. (2021) [30]	Spherical fuzzy set	Renewable energy project selection
Yazdani & Tavana (2020) [31]	Interval-valued fuzzy set	Industrial safety assessment
Keshavarz Ghorabaee et al. (2021) [32]	Interval type-2 fuzzy set	Healthcare service quality evaluation
Fouladgar et al. (2019) [33]	Type-2 fuzzy set	Strategic planning in defense industry
Ashtari & Omrani (2021) [34]	Spherical fuzzy set	Green supply chain management
Zolfani et al. (2020) [35]	Type-1 fuzzy set	Urban sustainability evaluation

Table 2. Studies utilizing fuzzy EDAS

Author(s)	Fuzzy Set	Application Area
Yazdani & Zarate (2019) [31]	Type-1 fuzzy set	Industrial site selection
Khalili-Damghani et al. (2020) [36]	Interval-valued fuzzy set	Supply chain resilience
Shen et al. (2019) [37]	Intuitionistic fuzzy set	Environmental impact assessment
Ashtari & Omrani (2021) [34]	Spherical fuzzy set	Agricultural sustainability assessment
Yildiz & Korkmaz (2020) [38]	Type-2 fuzzy set	Transportation project evaluation
Ghorabaee et al. (2022) [32]	Interval type-2 fuzzy set	Urban wastewater management
Hosseini et al. (2021) [39]	Spherical fuzzy set	Renewable energy investment prioritization
Chatterjee & Zavadskas (2019) [40]	Type-1 fuzzy set	Urban infrastructure planning

and hesitation. In contrast, Type-1 fuzzy sets, like the ones used by [5] to choose suppliers, are used when there isn't as much uncertainty. This comparison shows that the fuzzy set chosen in SWARA depends on how complicated the criteria are and how unclear the expert judgment is. This shows that fuzzy SWARA can be used in many different decision-making situations.

Recent studies on fuzzy EDAS show that this method can be used in a wide range of fuzzy environments, including Type-1, Type-2, interval-valued, and SFS. SFS, utilized by Ashtari & Omrani [34] for agricultural sustainability and by Hosseini et al. [39] in prioritizing renewable energy investments, are preferred for applications requiring the aggregation of intricate expert opinions. These studies show that spherical fuzzy EDAS can better show how experts are unsure and partially agree, especially when it comes to the environment and sustainability.

The literature shows that many MCDM methods, such as AHP, TOPSIS, VIKOR, and GIS-based methods, have been used a lot in agriculture decision-making. However, they often don't work well when there are complicated uncertainties and experts are hesitant to make decisions in subjective and unclear situations. Conventional MCDM methodologies, even when incorporating fuzzy logic, predominantly rely on distinct membership values, thereby constraining their capacity to encompass nuanced viewpoints. While certain studies employ fuzzy logic to address uncertainty, frameworks such as fuzzy AHP and TOPSIS do not possess mechanisms to fully integrate hesitancy and partial agreement.

Our research fills this void by utilizing SFS in SWARA and EDAS methodologies, thereby quantifying membership, non-membership, and degrees of hesitancy. This facilitates a thorough representation of expert opinions, incorporating subtle uncertainty. Spherical fuzzy SWARA allows for strong weighting even when things aren't clear, and fuzzy EDAS looks at options based on average distance, which makes it useful in farming situations where perfect results are often not possible.

Current research frequently depends on general criteria such as water availability and cost, neglecting the contextual factors necessary for sustainable wastewater reuse in agriculture. We present specific criteria—availability of natural spring water, land slope, drought rate, agricultural area, wastewater treatment rate, daily wastewater generation per capita, and designated municipal budgets—customized to meet Türkiye's requirements. Our study offers a useful model for dealing with water scarcity in agricultural wastewater management by combining these context-specific criteria with a spherical fuzzy SWARA-EDAS framework.

MATERIALS AND METHODS

In this research, a region-specific application in Türkiye was developed by merging SWARA and EDAS in SFS to facilitate the implementation of Novel MCDM Approaches.

Prelimination of Spherical Fuzzy Sets

SFS was introduced to the literature by Kutlu Gündoğdu and Kahraman [4] as a combination of Pythagorean and neutrosophic fuzzy sets. In the global setting, researchers can independently define and model membership, non-membership and hesitation degrees. Some definitions, basic operators, Euclidean distance and defuzzification operators for SFS are given below:

Definiton 1. A SFS $\tilde{A}_s$ of the universe of discourse U is given by

$$\tilde{A}_s = \{\langle u, \left(\mu_{\tilde{A}_s}(u), v_{\tilde{A}_s}(u), \pi_{\tilde{A}_s}(u)\right) | u \in U\rangle \quad (1)$$

where

$$\mu_{\tilde{A}_s}(u): E \to [0,1], v_{\tilde{A}_s}(u): U \to [0,1], \ \pi_{\tilde{A}_s}(u): U \to [0,1]$$

, and

$$0 \leq \mu^2_{\tilde{A}_S}(u) + v^2_{\tilde{A}_S}(u) + \pi^2_{\tilde{A}_S}(u) \leq 1 | \forall u \in U \quad (2)$$

where $\mu_{\tilde{A}_s}(u), v_{\tilde{A}_s}(u)$ and $\pi_{\tilde{A}_s}(u)$ are the degrees of membership, non-membership and hesitancy of $\tilde{A}_s$ respectively.

The condition in Equation 2 can also be specified as shown in Equation 3:

$$\mu^2_{\tilde{A}_S}(u) + v^2_{\tilde{A}_S}(u) + \pi^2_{\tilde{A}_S}(u) = 1 | \forall u \in U \quad (3)$$

Basic operations

Addition, multiplication, multiplication by a scalar and power of SFS are described as follows:

Addition

$$\tilde{A}_s \oplus \tilde{B}_s = \begin{pmatrix} (\mu^2_{\tilde{A}_s} + \mu^2_{\tilde{B}_s} - \mu^2_{\tilde{A}_s}\mu^2_{\tilde{B}_s})^{1/2}, & v_{\tilde{A}_s} v_{\tilde{B}_s}, \\ [\left(1-\mu^2_{\tilde{B}_s}\right)\pi^2_{\tilde{A}_s} + \left(1-\mu^2_{\tilde{A}_s}\right)\pi^2_{\tilde{B}_s} - \pi^2_{\tilde{A}_s}\pi^2_{\tilde{B}_s}]^{1/2} \end{pmatrix} \quad (4)$$

Multiplication

$$\tilde{A}_s \otimes \tilde{B}_s = \begin{pmatrix} \mu_{\tilde{A}_s}\mu_{\tilde{B}_s}, & (v^2_{\tilde{A}_s} + v^2_{\tilde{B}_s} - v^2_{\tilde{A}_s} v^2_{\tilde{B}_s})^{1/2}, \\ [(1-v^2_{\tilde{B}_s})\pi^2_{\tilde{A}_s} + (1-v^2_{\tilde{A}_s})\pi^2_{\tilde{B}_s} - \pi^2_{\tilde{A}_s}\pi^2_{\tilde{B}_s}]^{1/2} \end{pmatrix} \quad (5)$$

Multiplication by a scalar (λ>0)

$$\lambda.\tilde{A}_s = \begin{pmatrix} (1-\left(1-\mu^2_{\tilde{A}_s}\right)^{\lambda})^{1/2}, & v^{\lambda}_{\tilde{A}_s}, \\ [\left(1-\mu^2_{\tilde{A}_s}\right)^{\lambda} - \left(1-\mu^2_{\tilde{A}_s}-\pi^2_{\tilde{A}_s}\right)^{\lambda}]^{1/2} \end{pmatrix} \quad (6)$$

Power of $\tilde{A}_s$ (λ>0)

$$\tilde{A}^{\lambda}_S = \begin{pmatrix} \mu^{\lambda}_{\tilde{A}_s}, & (1-\left(1-v^2_{\tilde{A}_s}\right)^{\lambda})^{1/2}, \\ [\left(1-v^2_{\tilde{A}_s}\right)^{\lambda} - \left(1-v^2_{\tilde{A}_s}-\pi^2_{\tilde{A}_s}\right)^{\lambda}]^{1/2} \end{pmatrix} \quad (7)$$

Aggregation operator

The aggregation procedure is a function used when it's necessary to identify a single value to represent a collection of integers. An aggregation operator transforms a collection of input data in a single value. In this research, the geometric mean operator is employed to aggregate matrices. The geometric mean of *n* spherical fuzzy integers is given by Equation 8.

$SWGM_w(\tilde{A}_{S1}, \ldots\ldots\ldots, \tilde{A}_{Sn}) = \tilde{A}_{S1}{}^{w1} + \tilde{A}_{S2}{}^{w2} + \ldots\ldots\ldots + \tilde{A}_{Sn}{}^{wn}$

$$\text{SWGM} = \begin{pmatrix} \prod_{i=1}^{n} \mu^{w_i}_{\tilde{A}_{si}}, & \left(1 - \prod_{i=1}^{n}(1-v^2_{\tilde{A}_{si}})^{w_i}\right)^{1/2}, \\ [\prod_{i=1}^{n}(1-v^2_{\tilde{A}_{si}})^{w_i} - \prod_{i=1}^{n}(1-v^2_{\tilde{A}_{si}}-\pi^2_{\tilde{A}_{si}})^{w_i}]^{1/2} \end{pmatrix} \quad (8)$$

where the weights of DMs w=(w_1, w_2……, w_n); $w_i \in [0,1]$; $\sum_{i=1}^{n} w_i = 1$.

Defuzzification operator

Fuzzification is the process of converting a crisp value to its corresponding fuzzy representation. The converse of this procedure, which transforms a fuzzy number into its crisp version, is known as defuzzification. The defuzzification operation is described in Equation 9.

$$S(\tilde{\omega}^S_j) = \sqrt{\left|100 * \left[\left(3\mu_{\tilde{A}_s} - \frac{\pi_{\tilde{A}_s}}{2}\right)^2 - \left(\frac{v_{\tilde{A}_s}}{2} - \pi_{\tilde{A}_s}\right)^2\right]\right|} \quad (9)$$

Normalized euclidean distance

This is a distance metric that calculates the distances amongst fuzzy sets. In SFS, the Euclidean distance is used to calculate the lowest space in the sphere, as well as the shortest distance between a pair of points in a three-dimensional environment. The mathematical expression of the Euclidean distance is presented in equation 10.

$$D(A_i, A_k) = \sqrt{\frac{1}{2n}\sum_{i=1}^{n}((\mu A_i - \mu A_k)^2 + (vA_i - vA_k)^2 + (\pi A_i - \pi A_k)^2)} \quad (10)$$

Spherical Fuzzy SWARA

In the calculation of criterion weights in MCMD problems, besides the methods such as CRITIC, ENTROPY and MEREC, which consider the information carried by the data set from different perspectives and calculate objective criteria, criteria weights are also calculated with approaches that reflect the subjective thoughts of decision makers to the model. Among the traditional approaches, the AHP method is one of the most preferred methods by researchers for subjective weight calculation. The AHP method is an approach in which the importance levels of the criteria are calculated with the subjective opinions of DMs in a process called pairwise comparison. The SWARA method, one of the new generation approaches, also utilizes the pairwise comparison logic underlying the AHP approach, but the process steps are shorter. In the SWARA approach, decision makers first rank the criteria according to their own opinions and then, starting with the most important one, they compare and score the criteria in pairs.

The extension of MCDM approaches to different fuzzy sets is one of the most preferred modifications by researchers since real life problems are not crystal-clear situations. In this study, SWARA approach is used in SFS environment to better capture and model the fuzzy situation that arises due to the nature of the problem. The following steps should be followed for implementation:

Step 1: Defining the decision problem and determining the criteria to be used in the evaluation of the decision problem in line with the literature review and expert opinions.

Step 2: The linguistic terms and their corresponding SFS used in Table 3 are defined by Kutlu Gündoğdu and Kahraman [4] for application in decision-making contexts, providing researchers with a structured approach to capture expert judgments in a fuzzy environment. In this study, decision-makers (DMs) utilized these predefined linguistic terms to rank the criteria according to their own opinions, assigning the highest importance to the most critical criterion.

Table 3. Linguistic terms and their corresponding SFNs

	(μ, ν, π)
Absolutely more importance (AMI)	(0.9, 0.1, 0.1)
Very high importance (VHI)	(0.8, 0.2, 0.2)
High importance (Hl)	(0.7, 0.3, 0.3)
Slightly more importance (SMI)	(0.6, 0.4, 0.4)
Equally importance (El)	(0.5, 0.5, 0.5)
Slightly low importance (SLI)	(0.4, 0.6, 0.4)
Low importance (LI)	(0.3, 0.7, 0.3)
Very low importance (VLI)	(0.2, 0.8, 0.2)
Absolutely low importance (ALI)	(0.1, 0.9, 0.1)

Step 3: Utilizing Table 3, convert the linguistic evaluations to the appropriate SFN and create the SFN evaluation matrix.

Step 4: Aggregating the matrices consisting of the individual assessments of the DMs by using the SWGM operator shown in Equation 8 and thus creating the aggregated SFN decision matrix.

Step 5: Calculation of spherical score values for each criterion using Equation 10.

Step 6: Using the DMs' assessments as a guide, rank the criteria according to decreasing SF-score values.

Step 7: By comparing the *jth* criterion *(j-1)th* criterion with the criterion that is selected in second place, determine the relative importance (S_j) of that criterion..

Step 8: Use Equation (11) for calculating the comparative coefficient.

$$k_j = \begin{cases} 1, & j = 1 \\ s_j + 1, & j > 1 \end{cases} \tag{11}$$

Step 9: Calculate the weights (p_j) of the criterion as:

$$p_j = \begin{cases} 1, & j = 1 \\ \dfrac{p_j - 1}{k_j}, & j > 1 \end{cases} \tag{12}$$

Step 10: Calculate the criterion's normalized weight as:

$$w_j^s = \frac{p_j}{\sum_{j=1}^{n} p_j}, j = 1,2, \dots, n \tag{13}$$

Spherical Fuzzy EDAS

Step l: Invite each DM to use the linguistic terms listed in Table 3 to complete the performance assessment matrix.

Step 2: The spherical fuzzy alterative evaluation matrix, which is made up of n criteria C_j *(j=1, 2,…,n)* and m alternative A_i *(i=1,2,…,m),* is obtained by transforming the linguistics assessment of performance matrix into its spherical fuzzy form. The mathematical representation of SF-alternative evaluation matrix is shown in Equation 14.

$$C_j(A_i)_{m\times n} = \begin{bmatrix} (\mu_{11}, \nu_{11}, \pi_{11}) & \cdots & (\mu_{1n}, \nu_{1n}, \pi_{1n}) \\ \vdots & \ddots & \vdots \\ (\mu_{m1}, \nu_{m1}, \pi_{m1}) & \cdots & (\mu_{mn}, \nu_{mn}, \pi_{mn}) \end{bmatrix} \tag{14}$$

Step 3: Equation 8 can be used to aggregate the evaluation matrices from each DM and produce an aggregated spherical fuzzy alternative evaluation matrix.

Step 4a: Obtaining the spherical fuzzy decision matrix by multiplying the weights of the criteria determined during the SWARA step of the proposed model by the aggregated matrix. Apply spherical fuzzy multiplication by a scalar operator given Equation 6. Equation 15 provides the structure of the spherical fuzzy decision matrix, $D=(C_j(A_i))$.

$$D=(C_j(w_jA_i))_{m\times n}=\begin{bmatrix} (w_1\mu_{11}, w_1\nu_{11}, w_1\pi_{11}) & \cdots & (w_n\mu_{1n}, w_n\nu_{1n}, w_n\pi_{1n}) \\ \vdots & \ddots & \vdots \\ (w_1\mu_{m1}, w_1\nu_{m1}, w_1\pi_{m1}) & \cdots & (w_n\mu_{mn}, w_n\nu_{mn}, w_n\pi_{mn}) \end{bmatrix} \tag{15}$$

Step 4b: Obtain score values of step 4a by utilizing defuzzification operator that is given Equation 8.

Step 5a: Equation 8's SWGM operator can be used to find the spherical fuzzy average solution. Equation 16 provides a mathematical illustration of the average solution.

$$SFAV = \{(\mu_1^x, \nu_1^x, \pi_1^x), (\mu_2^x, \nu_2^x, \pi_2^x), \dots, (\mu_n^x, \nu_n^x, \pi_n^x)\} \tag{16}$$

Step 6: On the basis of the score values acquired in steps 4b and 5b, identify the alternatives that are positioned positively and negatively.

Step 4b and Step 5b are just calculations to observe whether the alternatives are positively or negatively positioned. In other words, the alternatives are compared according to the average solution obtained and it is observed whether they have a solution above or below the average solution.

Step 7: Using the Euclidean distance formula shown in Equation 10, the distance of the positively positioned alternatives to the average solution is calculated first, and then the distance of the negatively positioned alternatives to the average solution is calculated, and these calculated distances are called positive distance from the average and negative distance from the average, respectively.

Step 8: The distances calculated in Step 7 are normalized using Equations 17 and 18.

$$NSP_i = \frac{SP_i}{max_i(SP_i)} \tag{17}$$

$$NSN_i = 1 - \frac{SN_i}{max_i(SN_i)} \tag{18}$$

Step 9: The appraisal score for each alternative is calculated using the following equation.,

$$AS_i = \frac{1}{2} \times (NSP_i + NSN_i) \quad (19)$$

Step 10: Sort each of the alternatives in order of decreasing assessment score numbers. Among the candidate choices, the option with the greatest appraisal score is the best option

Case Study: Selection of the Driest Region to Use Treated Wastewater in Agricultural Irrigation Among Three Pilot Cities in Türkiye Using SF-SWARA and SF-EDAS

Agriculture is one of the most important sectors in meeting the basic needs of people. Water is the element that provides the most healthy and efficient development of plants in agriculture. Improvement efforts in this sector should be completed as soon as possible. Because agriculture is one of the first sectors to be affected by the increasing drought threat every year. It is aimed to investigate the use of water obtained by recycling wastewater as irrigation water in agriculture. Hence, the aim of this study we have done is to present water recycling studies together with MCDM methods as a solution to the drought, which has become a major problem in the world today. Undoubtedly, the most affected area by the drought will be the agricultural area. While the use of urban and agricultural wastewater while recycling water reduces the damage of wastewater to the environment, the recycled clean water creates a new source of clean water for agricultural areas. Since this whole process is quite complex and includes many conflicting criteria, performing the study with MCDM methods will help to achieve the most accurate results.

In this section, case study application to select the driest region to use treated wastewater in agricultural irrigation among three pilot cities in Türkiye using SF-SWARA and SF-EDAS is presented. It is determined that there are many evaluation criteria such as drought rate of cities, area of cities that can be used as "agricultural land", "amount of wastewater in cities", "budget allocated for wastewater treatment", "wastewater treatment rate in the region", and "water consumption rate in the region" based on the conducted literature review study. Firstly, each evaluation criterion is weighted by three DMs using SF-SWARA method and then SF-EDAS is applied to rank the 3 driest regions of Türkiye, namely, "Southeastern Anatolia Region", "Aegean Region", and "Central Anatolia Region". Accordingly, three pilot cities (Kırıkkale, Manisa and Şanlıurfa) are selected and evaluated within the scope of the application. The proposed evaluation framework aims to contribute to waste management by increasing the awareness of environmental protection in the region and helps to use water resources more efficiently.

Table 4. The specialist's thoughts for importance rank of the criteria in the form of SF linguistic variables

Criteria	DM1	DM2	DM3
C1	HI	AMI	VHI
C2	LI	SLI	SLI
C3	AMI	HI	AMI
C4	SMI	VHI	HI
C5	VHI	SMI	SMI
C6	SLI	LI	EI
C7	EI	EI	LI

Step 1. Following an in-depth literature review and evaluation of expert recommendations, the criteria and alternatives described above were used to identify the best alternative. Three decision makers, symbolized by DM1, DM2 and DM3, with almost equal experience in the agricultural sector, were asked to give their opinion. Due to their almost equal experience, the weights of the decision makers were considered equal.

Step 2. As a first step in the calculation of criteria weights with the SF-SWARA approach, decision makers use the linguistic scale shown in Table 3 to rank the criteria in their own opinion as shown in Table 4.

Step 3. The importance rankings made by each DM are converted at this stage into the SFN shown in Table 5.

Step 4. The three different evaluation matrices resulting from the individual evaluations of the DMs are aggregated

Table 5. SF evaluation matrix for weighting criterion

	DM1			DM2			DM3		
Criteria	μ	ν	π	μ	ν	π	μ	ν	π
C1	0.70	0.30	0.30	0.90	0.10	0.20	0.80	0.20	0.20
C2	0.30	0.70	0.30	0.40	0.60	0.40	0.40	0.60	0.40
C3	0.90	0.10	0.10	0.70	0.30	0.10	0.90	0.10	0.10
C4	0.60	0.40	0.40	0.80	0.20	0.30	0.70	0.30	0.30
C5	0.80	0.20	0.20	0.60	0.40	0.40	0.60	0.40	0.40
C6	0.40	0.60	0.40	0.30	0.70	0.50	0.50	0.50	0.50
C7	0.50	0.50	0.50	0.50	0.50	0.30	0.30	0.70	0.30

Table 6. Aggregated SF evaluation matrix for weighting criterion

Criteria	μ	ν	π
C1	0.671	0.182	0.234
C2	0.136	0.632	0.372
C3	0.736	0.143	0.104
C4	0.508	0.289	0.333
C5	0.473	0.316	0.328
C6	0.169	0.594	0.471
C7	0.200	0.558	0.392

with the SWGM operator in Equation 8 and the aggregated decision matrix shown in Table 6 is formed.

Step 5. The SF values in the aggregated matrix obtained in the previous step are converted into score values using the score function shown in Equation 9 and the subjective criteria weights are calculated using the score values obtained by following the steps of the traditional SWARA approach as shown in Table 7.

Table 7 shows that the importance levels of the criteria whose subjective weights are calculated according to the DMs' assessments are almost very close to each other. According to the calculated weights, if we rank the criteria as the most important first, an order of importance emerges as C6>C4>C5>C3>C7>C2>C1.

In the second stage of the integrated methodology, alternatives are ranked using the SF-EDAS approach using the subjective criteria weights obtained in the first stage.

Step 1. DMs evaluate the alternatives on the basis of each criterion using the linguistic scale given in Table 3, taking into account the defined decision problem objective and the identified criteria. The evaluation matrix based on the DMs' opinions is shown in Table 8.

Step 2. The evaluation matrix created with the linguistic scale is then used to create the SF evaluation matrix using the SFN corresponding to each linguistic utterance. Table 9 shows the SFN values corresponding to the linguistic utterances in the tables in the previous step.

Table 7. Criterion weights based on SF-SWARA

Criteria	Score values	s_j	k_j	p_j	w_j
C3	0.397		1	1	0.142
C1	0.188	0.208	1.208	0.827	0.118
C6	0.076	0.112	1.112	1.086	0.155
C4	0.028	0.047	1.047	1.061	0.151
C5	0.020	0.007	1.007	1.039	0.148
C7	0.009	0.011	1.011	0.996	0.142
C2	-0.01	0.021	1.021	0.989	0.141

Step 3. The individual assessments made by the DMs are aggregated using the SWGM operator shown in Equation 8 as shown in Table 10.

Step 4. The weighted aggregated matrix shown in Table 11 is obtained by multiplying the aggregated matrix shown in Table 10 with the criteria weights calculated in the first step of the integrated approach and shown in Table 7.

Step 5. In this step, firstly, the weighted aggregated matrix is used to obtain the average solution matrix in the spherical fuzzy environment as shown in Table 12.

Step 6. Then the aggregated matrix and the mean solutions matrix score values are obtained with the help of Equation 9 as shown in Table 13.

Step 7. Using the score values obtained in Step 6, it is determined whether each alternative is above or below the average on the basis of the criteria and first the PDA and NDA values are obtained with the help of equation 10, then the normalized PDA and normalized NDA values with the

Table 8. SF Alternative evaluation matrix based on determined criterion

	DM1		
Criteria	**Kırıkkale**	**Manisa**	**Şanlıurfa**
C1	EI	ALI	AMI
C2	EI	LI	HI
C3	SMI	SMI	EI
C4	SMI	SLI	AMI
C5	VLI	LI	HI
C6	HI	EI	SLI
C7	HI	SMI	EI
	DM2		
Criteria	**Kırıkkale**	**Manisa**	**Şanlıurfa**
C1	SLI	ALI	HI
C2	SLI	LI	AMI
C3	EI	SMI	SLI
C4	SLI	LI	HI
C5	VLI	LI	HI
C6	VHI	SMI	EI
C7	SMI	EI	SLI
	DM3		
Criteria	**Kırıkkale**	**Manisa**	**Şanlıurfa**
C1	EI	ALI	AMI
C2	SLI	VLI	HI
C3	SMI	SMI	EI
C4	SMI	SLI	AMI
C5	ALI	VLI	SMI
C6	SMI	SLI	LI
C7	VHI	HI	SMI

Table 9. SFNs based on SF alternative evaluation matrix based on determined criterion

	Kırıkkale			Manisa			Şanlıurfa		
	μ	ν	π	μ	ν	π	μ	ν	π
DM1									
C1	0.50	0.50	0.50	0.10	0.90	0.10	0.90	0.10	0.10
C2	0.50	0.50	0.50	0.30	0.70	0.30	0.70	0.30	0.30
C3	0.60	0.40	0.40	0.60	0.40	0.50	0.50	0.50	0.50
C4	0.60	0.40	0.40	0.40	0.60	0.10	0.90	0.10	0.10
C5	0.20	0.80	0.20	0.30	0.70	0.30	0.70	0.30	0.30
C6	0.70	0.30	0.30	0.50	0.50	0.40	0.40	0.60	0.40
C7	0.70	0.30	0.30	0.60	0.40	0.50	0.50	0.50	0.50
DM2									
C1	0.40	0.60	0.40	0.10	0.90	0.30	0.70	0.30	0.30
C2	0.40	0.60	0.40	0.30	0.70	0.10	0.90	0.10	0.10
C3	0.50	0.50	0.50	0.60	0.40	0.40	0.40	0.60	0.40
C4	0.40	0.60	0.40	0.30	0.70	0.30	0.70	0.30	0.30
C5	0.20	0.80	0.20	0.30	0.70	0.30	0.70	0.30	0.30
C6	0.80	0.20	0.20	0.60	0.40	0.50	0.50	0.50	0.50
C7	0.60	0.40	0.40	0.50	0.50	0.40	0.40	0.60	0.40
DM3									
C1	0.50	0.50	0.50	0.10	0.90	0.10	0.90	0.10	0.10
C2	0.40	0.60	0.40	0.20	0.80	0.30	0.70	0.30	0.30
C3	0.60	0.40	0.40	0.60	0.40	0.50	0.50	0.50	0.50
C4	0.60	0.40	0.40	0.40	0.60	0.10	0.90	0.10	0.10
C5	0.10	0.90	0.10	0.20	0.80	0.40	0.60	0.40	0.40
C6	0.60	0.40	0.40	0.40	0.60	0.30	0.30	0.70	0.30
C7	0.80	0.20	0.20	0.70	0.30	0.40	0.60	0.40	0.40

Table 10. Aggregated SF alternative evaluation matrix based on determined criterion

	Kırıkkale			Manisa			Şanlıurfa		
	μ	ν	π	μ	ν	π	μ	ν	π
C1	0.47	0.53	0.47	0.10	0.90	0.19	0.85	0.14	0.15
C2	0.43	0.56	0.44	0.27	0.73	0.25	0.79	0.20	0.22
C3	0.57	0.43	0.43	0.60	0.40	0.47	0.47	0.53	0.47
C4	0.54	0.45	0.40	0.37	0.63	0.18	0.85	0.14	0.15
C5	0.17	0.83	0.17	0.27	0.73	0.33	0.67	0.32	0.33
C6	0.71	0.28	0.29	0.51	0.49	0.42	0.41	0.59	0.42
C7	0.71	0.28	0.29	0.61	0.39	0.44	0.51	0.49	0.43

Table 11. The weighted aggregated SF alternative evaluation matrix based on determined criterion

	Kırıkkale			Manisa			Şanlıurfa		
	μ	ν	π	μ	ν	π	μ	ν	π
C1	0.17	0.92	0.19	0.03	0.98	0.06	0.38	0.79	0.10
C2	0.17	0.92	0.19	0.10	0.95	0.09	0.36	0.80	0.13
C3	0.23	0.88	0.20	0.24	0.87	0.23	0.18	0.91	0.21
C4	0.22	0.88	0.19	0.14	0.93	0.07	0.42	0.74	0.11
C5	0.06	0.97	0.06	0.10	0.95	0.13	0.29	0.84	0.17
C6	0.32	0.82	0.16	0.21	0.89	0.20	0.16	0.92	0.18
C7	0.31	0.83	0.15	0.25	0.87	0.21	0.20	0.90	0.20

Table 12. SF average solution

Criteria	μ	ν	π
C1	0.13	0.94	0.13
C2	0.18	0.91	0.15
C3	0.22	0.89	0.22
C4	0.24	0.87	0.14
C5	0.13	0.94	0.12
C6	0.23	0.88	0.19
C7	0.25	0.87	0.20

Table 13. Score value of the weighted aggregated SF alternative evaluation matrix based on determined criterion and SF average solution

	Score value of aggregated decision matrix			Score value of average solution
	Kırıkkale	**Manisa**	**Şanlıurfa**	
C1	2.50	4.26	1.77	0.43
C2	2.50	3.71	1.62	3.88
C3	2.00	1.63	2.21	5.17
C4	2.16	3.70	1.10	6.04
C5	4.15	3.33	1.88	1.09
C6	1.67	2.16	2.55	5.38
C7	1.87	1.75	2.24	6.26

Table 14. PDA, NDA, N-PDA, N-NDA and appraisal scores for alternatives

	PDA	NDA	N-PDA	N-NDA	Appraisal score
Kırıkkale	0.030	0.042	0.329	0.511	0.420
Manisa	0.035	0.047	0.377	0.452	0.415
Şanlıurfa	0.093	0.086	1	0	0.5

help of equation 17 and 18 and finally the appraisal score values of the alternatives with the help of equation 19 and all these values are shown in Table 14.

According to the appraisal scores calculated, the ranking of the alternatives was calculated as Şanlıurfa > Kırıkkale > Manisa.

RESULTS AND DISCUSSION

Drought stands out as one of the fundamental environmental problems directly affecting agricultural production. Insufficient rainfall makes it difficult to provide the water necessary for plant growth, leading to reduced harvest quantities. The contraction in food supply and loss of income for farmers are among the inevitable consequences of this process. In recent years, it has been observed that drought events have become more frequent and severe due to the effects of climate change and global warming. In this context, the use of treated wastewater in agriculture is considered a long-term and viable solution to water scarcity. Using reclaimed wastewater for irrigation reduces dependence on freshwater resources, limits the risk of water scarcity, and supports a sustainable water management approach. It also contributes to environmental protection.

Multi-criteria decision-making methods have become an important tool in managing decision-making processes, especially in multi-dimensional and uncertain fields such as agriculture. These methods can combine quantitative indicators with qualitative evaluations and allow for a holistic assessment of different stakeholder preferences. Including uncertainty in the decision-making process is also among the key advantages of these approaches. Recent studies have shown that these methods produce effective results in evaluating the recovery of urban and agricultural wastewater for irrigation. This effectiveness is particularly evident in analyses aimed at mitigating drought conditions. In this study, a global fuzzy cluster approach, which considers membership, non-membership, and uncertainty levels together, was preferred in determining the criterion weights. This approach reduces the uncertainties arising in expert evaluations, thus ensuring more consistent and reliable results.

Wastewater recovery stands out not only as a practice that increases water supply, but also as a holistic solution that saves energy and reduces water pollution. This study

focuses on the Aegean, Southeastern Anatolia, and Central Anatolia regions, three of Turkey's most drought-vulnerable areas. Pilot applications were carried out in the provinces of Kırıkkale, Manisa, and Şanlıurfa within these regions, and drought-related criteria were evaluated in detail. The findings show that the Southeastern Anatolia Region, and especially Şanlıurfa, has the most adverse drought conditions. This situation places this region in a priority position in terms of long-term water management policies and drought mitigation strategies.

The existing wastewater treatment system in Şanlıurfa offers significant potential in combating drought. The 156,730 cubic meters of water treated daily are used for agricultural irrigation and reduce water pressure in the region. Thanks to the biogas obtained in the treatment process, renewable energy production of approximately 6,800 kilowatts per day is also achieved. The new wastewater treatment plant, implemented with the joint contribution of the Ministry of Environment, the European Union, and local administrations, and with a budget of 100 million TL, has the capacity to serve more than 800,000 households. This investment is considered not only a technical infrastructure project but also a strategic step in terms of the agricultural sustainability of the region.

The study findings also reveal that social and economic factors play a decisive role in the widespread adoption of wastewater recovery technologies. Farmers' perceptions, cost expectations, and institutional support mechanisms are critically important in this process. Policies developed without considering these elements are unlikely to produce lasting results. Furthermore, integrating climate change predictions into the decision-making framework can make wastewater management plans more resilient to future environmental uncertainties.

The results clearly show that Şanlıurfa experiences the most severe drought conditions among the three pilot provinces. Long periods of drought and limited natural water resources exacerbate this situation. However, the existing treatment infrastructure offers a strong starting point for increasing the use of treated wastewater in agriculture. Manisa and Kırıkkale also face water management problems, but the level of these problems is more limited. Manisa has a moderate potential for improving wastewater reuse, while Kırıkkale appears to require a higher level of investment to improve its infrastructure. These findings emphasize the importance of developing targeted and region-specific strategies, especially in areas like Şanlıurfa where the benefits would be highest. This wastewater recovery approach will strengthen the long-term management of water resources and increase the resilience of agricultural production to drought.

CONCLUSION

The main question this study tries to answer is how to help areas of Turkey that are affected by drought and are running out of water. Using treated wastewater to water crops has been looked at as a long-term solution in this situation. The goal is not only to close the current water gap, but also to make the water supply more reliable over time. For this purpose, a global fuzzy multi-criteria decision-making framework that combines the SWARA and EDAS methods has been used. The results of the analysis show that Şanlıurfa has the most potential for using wastewater among the regions studied. This makes the region's water supply more stable and makes Şanlıurfa an important place to fight drought.

When you look at the research on how to manage water in farming, you can see that multi-criteria decision-making methods are very common, especially when it comes to sustainability. AHP, TOPSIS, and VIKOR are some of the most popular ways to compare environmental and agricultural options. Because its hierarchical structure is easy to understand, AHP has become more popular in studies of site selection and irrigation planning. TOPSIS, on the other hand, helps people make decisions by looking at the distances between the best and worst solutions. These methods assume that the options are very different from each other and that the values are very clear. But this isn't always how things work in real life when people have to make decisions. These methods don't work as well when expert opinions are unclear or uncertain.

This is where fuzzy multi-criteria decision-making methods come in. They try to show unclear information through language. Fuzzy AHP and fuzzy TOPSIS have been extensively utilized in this context. But most of these methods use traditional fuzzy sets. These structures can show some of the uncertainty. But the levels of hesitation and non-membership that are often seen in expert evaluations are not detailed enough. Type-1 fuzzy sets can't fully show these small parts of the decision-making process. The global fuzzy sets used in this study deal with membership, non-membership, and levels of hesitation all at once. This makes it possible to show expert uncertainty in more detail. This makes the process of weighting and evaluating criteria more reliable.

The SWARA method, used in determining weights, offers decision-makers a simpler cognitive process with its ranking-based structure. This distinguishes it from traditional pairwise comparisons. This advantage becomes apparent in situations where the number of criteria is high but the decision-making process remains manageable. Variables such as drought frequency, land accessibility, and wastewater treatment rates, frequently encountered in agriculture and environmental fields, are often intertwined. Therefore, SWARA's capacity to systematically collect expert opinions is effective. When used in conjunction with a global fuzzy structure, more consistent weights are obtained. This approach gains significance considering the unique social and environmental conditions of the Turkish agricultural sector.

The EDAS method evaluates alternatives based on their distance from the average solution. This approach becomes functional when alternatives cannot be clearly separated. Methods based on ideal solutions do not always reflect real conditions. The global fuzzy EDAS used in this study is sensitive to relative performance differences and also incorporates expert hesitation into the evaluation process. This increases the realism of the results. Another aspect contributing to the literature is the study's focus on context-specific criteria. The study goes beyond general indicators such as water availability and cost. It also considers the accessibility of natural water resources, land slope, and municipal budgets allocated to wastewater treatment. Measuring these variables is challenging, but they are crucial for the decision-making process.

The fuzzy SWARA and EDAS framework used offers a computationally efficient structure for medium-sized datasets. Expert assessments are structured within a systematic decision-making process. For larger datasets, additional computational resources may be needed. Therefore, in the future, this framework could be improved using optimization techniques or machine learning-based approaches. From a policymaker's perspective, the study offers significant implications. Wastewater use in drought-affected regions should be prioritized. This can improve the impact on sustainability and resilience. This approach aligns with Turkey's resource management goals that prioritize environmental sustainability. It also serves as a guide for other countries facing similar challenges.

In conclusion, this study, which uses a combination of global fuzzy SWARA and EDAS methods, fills a significant gap in agricultural water management. It addresses uncertainty and expert hesitation more effectively. A viable framework is presented for drought-affected regions. Developed within the context of Turkey, this approach can be adapted to different geographies. This aspect makes the study a strong contribution. It serves sustainability goals at both local and global levels.

AUTHORSHIP CONTRIBUTIONS

Authors equally contributed to this work.

DATA AVAILABILITY STATEMENT

The authors confirm that the data that supports the findings of this study are available within the article. Raw data that support the finding of this study are available from the corresponding author, upon reasonable request.

CONFLICT OF INTEREST

The author declared no potential conflicts of interest with respect to the research, authorship, and/or publication of this article.

ETHICS

There are no ethical issues with the publication of this manuscript.

STATEMENT ON THE USE OF ARTIFICIAL INTELLIGENCE

Artificial intelligence was not used in the preparation of the article.

REFERENCES

[1] Çakmak B, Gökalp Z. Drought and agricultural water management. Gaziosmanpaşa J Sci Res 2013;4:1–11. [Turkish]

[2] Zhang S, Kang Y, Gao X, Chen P, Cheng X, Song S, et al. Optimal reservoir operation and risk analysis of agriculture water supply considering encounter uncertainty of precipitation in irrigation area and runoff from upstream. Agric Water Manag 2023;277:108091. [CrossRef]

[3] Turan İD, Dengiz O, Özkan B. Spatial assessment and mapping of soil quality index for desertification in the semi-arid terrestrial ecosystem using MCDM in interval type-2 fuzzy environment. Comput Electron Agric 2019;164:104933. [CrossRef]

[4] Kutlu Gündoğdu F, Kahraman C. Spherical fuzzy sets and spherical fuzzy TOPSIS method. J Intell Fuzzy Syst 2019;36:337–352. [CrossRef]

[5] Rostamzadeh R, Zavadskas EK, Turskis Z. Supplier selection using fuzzy SWARA and WASPAS methods. Supply Chain Manag J 2020;12:67–78.

[6] Yalçın N, Uncu N. Applying EDAS as an applicable MCDM method for industrial robot selection. Sigma J Eng Nat Sci 2019;37:779–796.

[7] Marqués AI, García V, Sánchez JS. Ranking-based MCDM models in financial management applications: Analysis and emerging challenges. Prog Artif Intell 2020;9:171–193. [CrossRef]

[8] Syed Hassan SAH, Tan SC, Yusof KM. MCDM for engineering education: Literature review and research issues. In: Engineering education for a smart society: World engineering education forum and global engineering deans council 2016. Springer Int Publ; 2018. p. 204–214. [CrossRef]

[9] Evcioğlu HE, Kabak M. Supplier selection in supply chain network using MCDM methods. Sigma J Eng Nat Sci 2023;41:1–16. [CrossRef]

[10] Reddy VV. Turning process parameters optimization of Al7075 hybrid MMC's composite using TOPSIS method. Sigma J Eng Nat Sci 2020;38:2043–2055.

[11] Korkusuz AY, Inan UH, Özdemir Y, Başlıgil H. Evaluation of occupational health and safety key performance indicators using in healthcare sector. Sigma J Eng Nat Sci 2018;36:705–715.

[12] Sánchez-Lozano JM, Bernal-Conesa JA. Environmental management of Natura 2000 network areas through the combination of geographic information systems (GIS) with multi-criteria decision making (MCDM) methods: Case study in south-eastern Spain. Land Use Policy 2017;63:86–97. [CrossRef]

[13] Qureshi MRN, Singh RK, Hasan MA. Decision support model to select crop pattern for sustainable agricultural practices using fuzzy MCDM. Environ Dev Sustain 2018;20:641–659. [CrossRef]

[14] Akbari M, Memarian H, Neamatollahi E, Jafari Shalamzari M, Alizadeh Noughani M, Zakeri D. Prioritizing policies and strategies for desertification risk management using MCDM–DPSIR approach in northeastern Iran. Environ Dev Sustain 2021;23:2503–2523. [CrossRef]

[15] Burak S, Samanlioglu F, Ülker D. Evaluation of irrigation methods in Söke Plain with HF-AHP-PROMETHEE II hybrid MCDM method. Agric Water Manag 2022;271:107810. [CrossRef]

[16] Lizot M, Trojan F, Afonso P. Combining total cost of ownership and multi-criteria decision analysis to improve cost management in family farming. Agriculture 2021;11:139. [CrossRef]

[17] Uyan M. GIS-based solar farms site selection using analytic hierarchy process (AHP) in Karapinar region, Konya/Turkey. Renew Sustain Energy Rev 2013;28:11–17. [CrossRef]

[18] Badr G, Hoogenboom G, Moyer M, Keller M, Rupp R, Davenport J. Spatial suitability assessment for vineyard site selection based on fuzzy logic. Precis Agric 2018;19:1027–1048. [CrossRef]

[19] Selim S, Koc-San D, Selim C, San BT. Site selection for avocado cultivation using GIS and multi-criteria decision analyses: Case study of Antalya, Turkey. Comput Electron Agric 2018;154:450–459. [CrossRef]

[20] Sarkar P, Kumar P, Vishwakarma DK, Ashok A, Elbeltagi A, Gupta S, et al. Watershed prioritization using morphometric analysis by MCDM approaches. Ecol Inform 2022;70:101763. [CrossRef]

[21] Hafezalkotob A, Hami-Dindar A, Rabie N, Hafezalkotob A. A decision support system for agricultural machines and equipment selection: A case study on olive harvester machines. Comput Electron Agric 2018;148:207–216. [CrossRef]

[22] Hilali A, El Baghdadi M, El Hamzaoui EH. GIS and AHP multi-criteria analysis methods for the quality assessment of agricultural soils irrigated with wastewater: Case of the Day River, Beni Mellal (Morocco). Arab J Geosci 2021;14:1–16. [CrossRef]

[23] Roy R, Majumder M, Barman RN. Assessment of water quality by RSM and ANP: A case study in Tripura, India. Asian J Water Environ Pollut 2017;14:51–58. [CrossRef]

[24] Ebad Ardestani M, Sharifi Teshnizi E, Babakhani P, Mahdad M, Golian M. An optimal management approach for agricultural water supply in accordance with sustainable development criteria using MCDM (TOPSIS) (case study of Poldasht catchment in West Azerbaijan Province-Iran). J Appl Water Eng Res 2020;8:88–107. [CrossRef]

[25] Zolfaghary P, Zakerinia M, Kazemi H. A model for the use of urban treated wastewater in agriculture using multiple criteria decision making (MCDM) and geographic information system (GIS). Agric Water Manag 2021;243:106490. [CrossRef]

[26] Attri SD, Singh S, Dhar A, Powar S. Multi-attribute sustainability assessment of wastewater treatment technologies using combined fuzzy multi-criteria decision-making techniques. J Clean Prod 2022;357:131849. [CrossRef]

[27] Rouyendegh BD, Savalan Ş. An integrated fuzzy MCDM hybrid methodology to analyze agricultural production. Sustainability 2022;14:4835. [CrossRef]

[28] Kumari S, Ahmad K, Khan ZA, Ahmad S. Failure mode and effects analysis of common effluent treatment plants of humid sub-tropical regions using fuzzy based MCDM methods. Eng Fail Anal 2023;145:107010. [CrossRef]

[29] Pamucar D, Deveci M, Baki M. Fuzzy SWARA and fuzzy COPRAS for transportation project prioritization. J Transp Logist 2021;32:189–207.

[30] Mishra A, Kar S, Tiwari P. Renewable energy project evaluation using spherical fuzzy SWARA. Renew Energy J 2021;58:233–245.

[31] Yazdani M, Tavana M. Fuzzy SWARA in industrial safety management. Saf Sci 2020;126:104–117.

[32] Keshavarz Ghorabaee M, Amiri M, Shabani A. Healthcare service quality evaluation using interval type-2 fuzzy SWARA. Healthc Manag Rev 2021;29:203–215.

[33] Fouladgar MM, Yazdani-Chamzini A, Zavadskas EK, Turskis Z. Defense industry strategic planning using fuzzy SWARA and fuzzy COPRAS. Strateg Def Plan J 2019;7:90–105.

[34] Ashtari F, Omrani H. Agricultural sustainability assessment with spherical fuzzy EDAS. Sustainability 2021;13:123–135.

[35] Zolfani SH, Chatterjee P. Urban sustainability evaluation with fuzzy SWARA. Urban Stud J 2020;28:202–215.

[36] Khalili-Damghani K, Tavana M, Hashemi S. Supply chain resilience assessment using interval-valued fuzzy EDAS. J Supply Chain Manag 2020;10:98–115.

[37] Shen J, Li C, Wang T. Environmental impact assessment with intuitionistic fuzzy EDAS. Environ Impact Assess Rev 2019;77:14–28.

[38] Yalçın H, Uncu A. EDAS for industrial robot selection. Ind Robot 2020;17:115–123.

[39] Hosseini SM, Alizadeh R, Sadeghi M. Renewable energy investment prioritization using spherical fuzzy EDAS. Renew Energy Rev 2021;15:223–239.

[40] Chatterjee P, Zavadskas EK. Urban infrastructure planning using type-1 fuzzy EDAS. J Urban Plan Dev 2019;145:03119001.

Sigma Journal of Engineering and Natural Sciences
Web page info: https://sigma.yildiz.edu.tr
DOI: 10.14744/sigma.2025.00059

Research Article

Mechanical vibration-assisted enhancement of weldment mechanical properties

Japhia Sudarsan NALLA[1,*], Basanta Kumar PALAI[1], P. Govinda RAO[2]

[1]*Department of Mechanical Engineering, GIET University, Gunupur, Odisha, 765022, India*
[2]*Department of Mechanical Engineering, N S Raju Institute of Engineering and Technology, Vishakapatnam 531162, India*

ARTICLE INFO

Article history
Received: 17 September 2024
Revised: 08 December 2024
Accepted: 20 January 2025

Keywords:
Weldments; Mechanical Vibration; Mechanical Properties; Vibration Frequency; Welding Process

ABSTRACT

The paper explores ways to increase the mechanical properties of weldments such as tensile strength, hardness and impact toughness by using mechanical vibrations when performing the actual welding operation. As interest in using vibration for improving welded joints continues to rise, the authors of this study sought to gain insight on the mechanism by which mechanical vibrations create enhancement and also for optimizing the setting of parameters that can create better mechanical performance within welded joints. In order to carry out this investigation, a proper welding procedure was developed along with an experimental apparatus that included a mechanical vibration assisted welding system to apply mechanical vibrations to the welded area during the welding operation. Following the completion of a proper welding procedure, a number of standardized mechanical tests were conducted to determine the mechanical characteristics of the resulting welded joint. Results indicate that the presence of a mechanical vibration applied during the welding operation has a direct impact on the microstructure of the welded joint, resulting in reduced porosity, improved bonding at the joint face, and higher mechanical performance. Thus, compared to conventional welding methods, vibration-assisted welding allows for significantly higher tensile strength, hardness, and toughness. The relationship between Process Parameters and Weld Quality was examined along with Insights for Optimizing Process Parameters. The results from this study provide Evidence that Vibration Assisted Welding is a Feasible Process to Improve Weldment Properties when Implemented in Industry today. Future studies should be conducted using different Methods of Welding and focused on clarifying the Vibration Parameters used; additionally, the Long Term Performance of Vibration Enhanced Weldments needs to be evaluated.

Cite this article as: Nalla JS, Palai BK, Rao PG. Mechanical vibration-assisted enhancement of weldment mechanical properties. Sigma J Eng Nat Sci 2026;44(1):559–574.

***Corresponding author.**
*E-mail address: japhiasudarsan.nalla@giet.edu

This paper was recommended for publication in revised form by Regional Editor Ahmet Selim Dalkilic

Published by Yıldız Technical University Press, İstanbul, Turkey
© Author. This is an open access article under the CC BY-NC license (http://creativecommons.org/licenses/by-nc/4.0/).

INTRODUCTION

Welding processes are an important part of the manufacturing process for a variety of products such as; automobiles and aerospace vehicles, along with buildings. Welding processes are utilised to create strong joints between metal parts. However, conventional welding processes often produce welds that do not exhibit adequate mechanical properties due to inappropriate microstructure of the welds and the potential for weld defects such as porosity and cracking.

Developing other methods for increasing the mechanical properties of welds has been a topic of interest to researchers and engineers for many years. One method of improving the mechanical properties of welds is through the application of mechanical vibrations while performing welding procedures.

The application of mechanical vibration during the welding process creates dynamic forces that are introduced into the molten metal during the welding process and results in creating the desired microstructure; Increasing the bond strength at the interface of the weld. Research has demonstrated that the introduction of mechanical vibration during weld formation reduces the amount of porosity in the weld and improves the mechanical properties of the weld (i.e. Tensile strength, hardness and impact toughness) by producing a finer grain structure as compared to a conventional weld without vibration.

Although the utilisation of vibration to improve weld properties is a concept that has existed for years, advancements in technology and materials sciences have facilitated additional research on the benefits of utilising this technology and its application in improving the properties of welds.

Researchers have demonstrated that the mechanisms involved with controlling vibration during a welding operation can improve the mechanical properties of a welded joint. Specifically, Rao et al. created a vibratory welding system that provided mechanical vibrations to the weld pool. This system allowed for greater refinement of the microstructure and improved mechanical properties. Examples of improvements to the mechanical properties of welded components include [1]. Flexural strength, ultimate tensile strength (UTS), impact strength, and hardness; all exhibited improvements when utilized in conjunction with the vibratory welding process. The mechanical vibrations produced by the vibratory welding system were able to increase flexural strength and strengthen the mechanical properties of regions located within the heat-affected-zone (HAZ) of the welded component. In addition, the application of mechanical vibrations prevented excessive dendrite growth during the solidification of the molten metal and facilitated the refining of the microstructure [2]. In addition to researching how to improve the mechanical properties of welded components using mechanical vibrations, researchers have also explored the relationship between UTS and creating uniformity and fine-grained structures during the welding process using dynamic solidification effects as a means of developing a predictive capability based on two input parameters (vibration voltage and vibration time) [3]. Rao et al. [4] demonstrated that the introduction of mechanical vibrations to the weld pool can significantly increase the tensile strength of the welded component. The gains achieved in tensile strength were attributed to a greater refinement of the microstructure and reduced dendrite size within the HAZ of the welded component.

As Ramakrishna and his colleagues pointed out, welding can impact the metallurgical properties of the parts involved. They proposed many procedures to improve mechanical characteristics, one of which was Post-Weld Heat Treatment or PWHT. Ding and his colleagues performed PWHT studies on aluminium alloy AA2219 and Ahmed and his colleagues researched PWHT on Cr-Mo Boiler Steel, both showing that PWHT could enhance the mechanical characteristics of welded assemblies at particular temperatures [5]. A more recent invention called Ultrasonic Complex Vibration Welding has superior output performance when compared to more common Linear Vibration Systems, since Ultrasonic Complex Vibration Welding employs a dual-axis vibration stress to join metals. The application of Ultrasonic Complex Vibration Welding has created a new opportunity to weld diverse component types like wedged foil electrodes of aluminium and Copper widely used throughout battery technology and electronic markets [6]. The advancement of ultrasonic complex vibration welding has provided a means to weld electronic assembly parts in narrow spaces without requiring electric resistance welding, thus avoiding the creation of welding defects due to the presence of metal particulate contamination [7]. Using an ultrasonic apparatus at either 20 kHz or 27 kHz and a custom-designed welding tip, one can achieve equivalent weld strength to that of the base metal when joining Copper, Nickel-Clad Copper and Steel or Nickel-Coated Steel. Ultrasonic complex vibration welding uses two-dimensional vibration energy to produce the highest-quality joining properties for dissimilar metals and foils than conventional linear ultrasonic welding when joining dissimilar materials. Important examples of this technology include the joining of aluminum and copper in electrode foils for use in most electronic devices, lithium-ion batteries (Li-Ion), electric double-layer capacitors (EDLC), and many industrially manufactured components. A number of different welding tip designs have been developed and investigated for their vibration and effect on welding characteristics in order to join a wide variety of materials [8].

Prior to the development of ultrasonic complex vibrations, ultrasonic welding did not have the capabilities to weld deep and remote locations. Therefore, the two most commonly used methods of welding were electric resistance welding and laser welding, both of which were susceptible to critical defects due to the melting and ejection of metal particles. The introduction of elongated, circular to elliptical-shaped vibrating tips and improvements such as

the implementation of high-tech vibration-velocity detectors and static-pressure control systems have increased the effectiveness of ultrasonic complex vibration welding systems [9]. Emerging evidence demonstrates the advantages of applying two-dimensional (2-D) stress at the weld point when performing Ultrasonic Metal Welding (UMW). To accomplish this, a new type of complex vibration source has been created that connects a longitudinal transducer and a torsional transducer on opposite ends of the welding horn. This design permits for individual adjustment of longitudinal and torsional vibrations creating a 2-D vibration path for the purposes of welding [10]. Liu and others have utilized a more sophisticated method using Empirical Mode Decomposition (EMD) as a method for measuring residual stresses in metal components based upon the vibration signal generated from elastic waves propagating through the component being tested. The results indicated by experimental testing on complicated welded assemblies such as automotive frames, rail vehicle structures, and aerospace components provide ample evidence of the methods ability to aid in developing an economical, non-destructive means of estimating residual stresses on welded components [11]. The influence of electromagnetic (EM) vibration on the gas tungsten arc welding (GTAW) process was studied by Sabzi and colleagues who found that increasing the intensity of the EM vibration had a positive impact on many areas including reducing columnar dendrites, converting microstructure from columnar to equiaxed dendrites, decreasing delta ferrite content, improving overall mechanical properties and reducing hot cracking susceptibility. All these changes resulted in more ductile fracture modes occurring in welded joints [12].

Ultrasonic vibration introduced to local dry underwater welding (U-LDUW) was presented by Liao et al. as a new method, enabling improvements in several areas such as reducing grain size, increasing ferrite, breaking up dendritic crystals, and improving the mechanical properties when compared to other forms of LDUW. U-LDUW holds promise for solving problems involved with welding large underwater structures [13]. Ultrasonic welding of Aluminium-Titanium alloys was carried out by Feng et al., producing satisfactory metallurgical bonding with a shear load of 3650N. Electron backscatter diffraction analysis confirmed that dynamic recrystallization took place at the interface of the Aluminium-Titanium alloys, due to the combined effects of heat and plastic deformation [14]. Dey et al. [15] emphasized the importance of vibration welding (VW) for bonding thermoplastics and composites and demonstrated its advantages compared to other techniques. The investigation focused on determining the relationship between VW joint design, processing parameters, and material properties in relation to joint strength, with a goal of determining the influence of optimal processing, material choices and design approaches on increased weld strength. Shi and Lin [16] conducted a study using an optical crack measurement method to evaluate the Environmental Stress Cracking Resistance (ESCR) of nano-silica reinforced Polycarbonate (PC) nanocomposite made with 1 Vol.-% nano-silica. They concluded that the degree of improvement in ESCR for the two Stress Cracking Agents (SCAs) varied. Increasing ESCR was significantly improved in water (DI Water) and slightly improved in isopropanol. The difference in the degree of improvement was theorized to be caused by the plastic deformation response of nano-sized silica.

Khmelev et al. [17] provided a detailed account of their development of a stand specifically designed for the quality control of welds produced using ultrasonic welding. The objective of this stand is to provide the inspector with a visual view of the welding process while at the same time providing the inspector with the ability to adjust the welding parameters to obtain the best possible weld quality. Weld cladding is a surface modification method to protect components used in corrosive environments and it uses gas tungsten arc welding (GTAW) to optimally adjust the parameters of welding. Gill et al. [18] focused on the preheated filler wire in conjunction with the GTAW process to enhance the quantity of clad deposited while also reducing the dilution of the base metal and narrowing the width of the Heat Affected Zone. They investigated the obstacles to using this process and the opportunities presented. Gill et al. [18] also looked into ways of optimally using preheated filler wire during GTAW. They looked for ways to optimize clad deposition while reducing the dilution of the base metal and reducing the width of the heat affected zone (HAZ). They discussed the challenges and potential improvements using preheated filler wire in GTAW. UVFSW has been found to have a positive impact on both microstructure and mechanical properties of aluminium and titanium alloys, through Improvements in the formation of intermetallic compounds; improving the appearance of the welds; and reducing the amount of flash and size of the waves, which suggests enhanced material flow. The use of UVFSW resulted in a fragmented Titanium base, resulting in titanium particles located at the interface between the two materials. In comparison to FSW, UVFSW produced an ultimate load of 4.40kN @ 1000 RPM while FSW yielded only 2.52kN @ 1200 RPM with a more ductile failure mode [19]. A different study evaluated how mechanical vibration during the gas metal arc welding process influences the properties of AA6061-T6 aluminium alloy. The results indicate that mechanical vibration increases tensile strength by a maximum of 83.3% when performed at 300 Hz, primarily due to an improved grain structure. The authors concluded that the lack of intermetallic compound formation results in improved corrosion resistance of vibration-assisted welds [20].

Novelty and Objective of Research Work

- The goals of this research were to identify the mechanism(s) responsible for the improvement of welding properties due to mechanical vibration and develop

optimal process parameters for maximum performance in the welded product. The experimental investigations conducted for this research provided the following novel findings:

- Optimal settings of mechanical vibration parameters (frequency, amplitude) that maximized the mechanical properties of the welded products were identified.
- A unique experimental design to conduct vibratory treated arc welding processes with MS1018 was developed and mechanical properties of the completed weldments were characterised based on ASTM Testing procedures.
- Statistical analyses were used to verify that the mechanical properties achieved represent the maximum achievable based on the mechanical vibration parameters applied.

Material Composition

The research aims to determine how mechanical vibration influences the strength of mild steel welds. To carry this out, research utilized 5 millimetre thick 1018 mild steel (MS) Plates as the primary material to be studied. Prior to testing, each sample was thoroughly created to ensure all samples were the same preparation and have no environmental factors affecting results. The chemical makeup of the 1018 MS Plate is located in Table 1; it includes predominantly iron (Fe) (98.81%-99.26%). The Carbon (C) content is very low, 0.18%, providing excellent Weldability and Formability. Manganese (Mn) content is between 0.6%-0.9% providing high strength and hardness. The Maximum allowable concentrations of Phosphorus (P) and Sulphur (S) in the chemical composition of 1018 MS is 0.04% and 0.05%, respectively; anything over these amounts will adversely affect the mechanical characteristics of the MS Plate. The 1018 Mild Steel exhibits desirable characteristics of excellent Weldability, Machinability and Cost Effectiveness; therefore, it is the preferred choice for a variety of applications in the manufacturing and construction industries.

The chemical make-up and element content of the E 6010 filler electrode can be seen in the above table (Table 2). Carbon, which accounts for 0.08%, affects both the strength and hardness of the electrode and will also influence the properties of the weld joint. Manganese, on the other hand, makes up 0.5% of the composition, enhancing the strength and ductility of the metal. Silicon, present at a level of 0.4%, aids in the deoxidation of the weld metal while also providing good fluidity during the welding operation. The composition of the E 6010 filler electrode has been developed to provide the user with an electrode that will provide stable arc characteristics, good weld bead appearance and compatibility for all types of welding applications.

Researching 1018 mild steel was important for this investigation since it is frequently used in many industries due to the material›s exceptional mechanical and weldable properties. Testing with 1018 mild steel plates was also advantageous because 1018 mild steel offers the greatest mechanical properties, including very high ductility and weldability. Additionally, the 5 mm thickness of the 1018 mild steel plate was selected because it represents an average thickness in many industries and provides practical relevance while remaining feasible for experiment purposes.

The E6013 filler metal electrode was chosen because of its compatibility with 1018 mild steel, its ease of use, its ability to produce smooth weld beads with minimal defects, and its significant importance to the overall results of the study. The electrode is also the most popular filler electrode used in several of these same applications. Therefore, this research should have practical application to other real-world situations as similar results have been presented in other published literature.

By focusing on 1018 mild steel, this research should provide a good foundation to be used in a wide variety of practical applications. The sample preparation process included cutting 11 018 mild steel plates down to precise dimensions using advanced machining techniques. Additionally, the surfaces were thoroughly cleaned and ground to remove contaminants and other imperfections that could interfere with the welding process, ensuring that the surfaces were free of any defects prior to welding.

A study was conducted to examine how mechanical vibration affects the mechanical properties of mild steel weldments. The study was conducted by welding samples using the chosen welding method while applying the mechanical vibration that was introduced into the welds. The experimental parameters were carefully controlled to ensure that a true evaluation could be made of the influence of mechanical vibration on the welded samples. After completing the welding, different mechanical testing of the welded samples was performed to determine their physical properties. Mechanical tests include tensile strength test

Table 2. Composition of E6013 filler electrode

Elements	Carbon (C)	Manganese (Mn)	Silicon (Si)
%	0.08	0.5	0.4

Table 1. Composition of 1018 mildsteel

Elements	Iron	Carbon	Manganese	Phosphorous	Sulphur
%	98.81-99.26%	0.18%	0.6 - 0.9%	0.04% max	0.05% max

for evaluation of welded joint›s strength; hardness tests for determination of welded material›s relative resistance to deformation; and impact tests for evaluation of the toughness of the welded specimens. Identification of how the application of mechanical vibration had a positive effect on the physical properties of the welds of mild steel was made by analysing the results from the mechanical tests.

MATERIALS AND METHODS

A vibratory welding system was created to include mechanical vibration in the welding procedure. The purpose of the vibratory welding system is to add mechanical vibrations, in a controlled manner, to the welding setup for the benefit of both the weld process and the properties of the final weld. The vibratory welding system consisted of a vibration generator, e.g., a vibrometer, coupled to the welding equipment for the purpose of generating the mechanical vibrations for this study. The methodology employed in this study is represented as a flowchart in Figure 1.

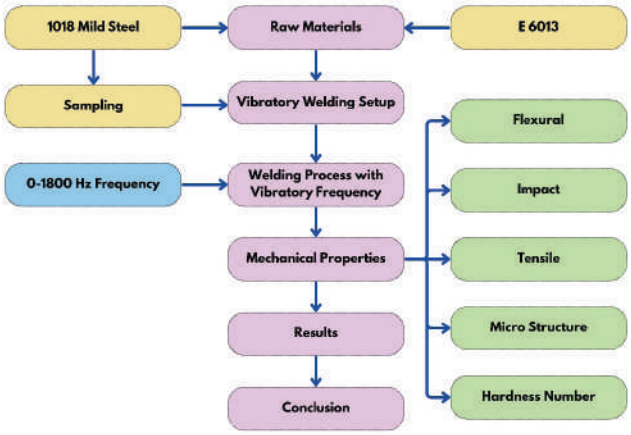


Figure 1. Experimental procedure.

Numerous different calibrated instruments have been used to measure the parameters connected to vibration, including a dimmer to control the voltage to the vibromotor, an ammeter to follow the electric current to the system and a voltmeter to record the voltage supplied to the system, which provided the investigators with precise control of the frequencies and amplitudes of the vibrations they created during their experimental investigation of vibration effects. Depending on how much voltage is supplied to the vibratory welding machine, vibrations can consist of frequencies from 0 Hz to 1800 Hz. The investigators used these frequency ranges to research the effects that frequency variations have on the mechanical character and properties of the weld produced during their experimental investigation. By manipulating the frequency and amplitude of the vibrations, the investigators determined the optimal conditions required to obtain the best mechanical characteristics of the welded component.

The project used Metal Arc Welding and an E6013 electrode for welding. The interface allowed for a level of flexibility and control over the welding process which allowed for the investigation of the effects of mechanical vibrations on the welding process as well as the resulting properties of the weld.

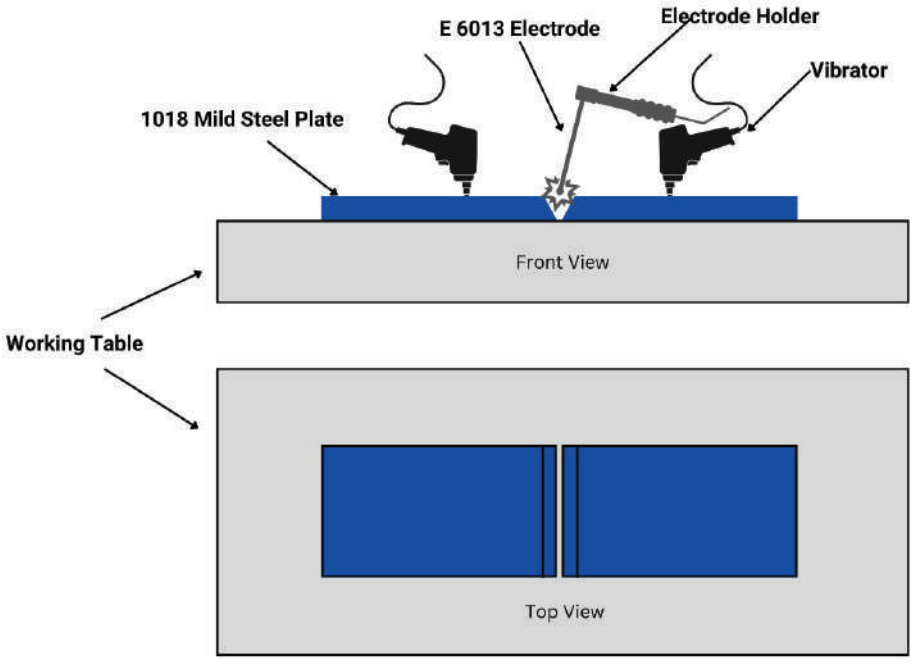


Figure 2. Schematic of vibratory welding experimental setup .

The ability of the system to regulate and record vibration parameters provided dependable, reproducible results that further advanced our knowledge of how mechanical vibration improves weld quality and performance. The principal mechanical properties used to define material performance (primarily metals and alloys) under a variety of loading conditions are: flexural strength, ultimate tensile strength (UTS), and impact strength. These mechanical properties reveal whether or not a weld has been successfully created, as these are three of the most important characteristics to determine how strong a material is.

The flexural strength of a material, or how well it withstands bending forces, is an important mechanical property of structural materials such as beams, columns, and bridges, which must support bending forces. Flexural strength is evaluated in a flexural test in which a sample is supported at both ends and bent until it fails; this evaluation provides a direct measure of the material's flexural strength. Material composition, microstructure, and processing conditions influence the flexural strength of a material. The higher the flexural strength of a material, the better it is able to resist bending forces and less likely to fail under bending loads. Thus, high flexural strength is critical for ensuring structural integrity and safety in engineering design.

In testing for Flexural Strength using the 3-Point Bend Test, a specimen is loaded in the middle until the specimen fractures. Because of the data it generates regarding the specimen's Bending Modulus of Elasticity (E B), Bending Failure Stress (σ f), Bending Failure Strain (ε f) and the specimen's performance under Bending Stress (B S) or (F C), it closely simulates real life conditions. If the specimen has the correct geometry and load directionality, there should be only minor variations in the resulting values; therefore control of the specimen geometry and load directionality, during testing, is critical for producing the most accurate test results. The 3-Point Bend test was performed in accordance with the standards outlined in ASTM D790 using a Universal Testing Machine (UTM) with an appropriate Fixture to ensure accurate positioning of the specimen and loading of the load cell. The fixture was designed and built to enable measurement of Flexural Stress based on the equation (1).

$$\sigma_f = \frac{(3PL)}{(2bd^2)} \tag{1}$$

Where, σ_f represents the flexural stress, P is the maximum load applied to the specimen, L is the span length between the supports, b is the width of the specimen, d is the thickness of the specimen

The experimental analyses yielded substantial data pertaining to the behaviour of welded connective elements subjected to bending loads. An observed trend that as weld power increases during welding via raising the vibromotor amplitude and voltage input, this increase results in an increase in flexural strength (the resistance of a material to outward bending) of each of the welds made. Therefore, it can be inferred that mechanical vibration enhances the quality/performance of welds in terms of improving their flexural strength and as such should be included within the manufacturer's design methodology for welded joint design and manufacturing to create more reliable and resilient structures. The analysis of a stress/strain curve will enable identification of the following critical material mechanical properties, Ultimate Tensile Strength, Yield Strength, Modulus of Elasticity, Percent Elongation at Fracture and material mechanical behaviour. These material mechanical properties are utilised by engineers when determining which material is most appropriate based upon the required engineering design specifications.

Analysis of the stress-strain curve allows determination of crucial mechanical properties like UTS, yield strength, modulus of elasticity, and elongation at fracture. These properties offer insights into material mechanical behavior, aiding material selection and engineering design. UTS, a critical parameter in material selection and engineering design, signifies the maximum stress a material can withstand without breaking. Materials with higher UTS values are deemed stronger and more suitable for applications where tensile strength is paramount, such as structural components, aerospace, and load-bearing elements. UTS is commonly determined via a uniaxial tensile test, where a material specimen is progressively subjected to increasing tensile force until fracture occurs. The Eqn. (2) is used to computeUTS.

$$\sigma_{UTS} = \frac{F_{max}}{A_0} \tag{2}$$

Where, σ_{UTS} is the ultimate tensile strength, F_{max} is the maximum load applied to the specimen, A_0 is the actual cross-sectional area of the specimen To ascertain the ultimate tensile strength (UTS) of materials, tensile tests performed on Universal Testing Machines (UTM) of standardized test specimens, such as those outlined in ASTM D638, are conducted to achieve a uniform testing and opportunity for precise end-user comparison across multiple laboratories/studies where the same material has been tested as described within this standard. The specimens will be standard in dimension and/or shape, thus enabling meaningful comparisons between laboratory and/or field testing end results involving UTM testing of materials. Once the specimen is attached to the testing apparatus, it is subjected to a progressively increasing tensile load until the specimen breaks due to the application of progressively increasing force to the specimen. During testing, extensometers and/or similar measurement devices will continuously monitor the elongation of a defined portion of the specimen. After testing has been completed, elongation data will be used in conjunction with data regarding load applied to the specimen to develop a stress-strain curve that defines the behaviour of the material under tension. Engineering strain (ε) will be calculated using elongation data as defined in the following formula; Eqn (3).

$$\varepsilon = \frac{\Delta l}{l_0} = \frac{l - l_0}{l_0} \quad (3)$$

Where, ε is the engineering strain, ΔL is the change in gauge length, L_0 is the initial gauge length, L is the final length of the gauge section, The engineering stress $\sigma = \frac{F_n}{A}$, F_n is the force applied to the specimen, A is the cross-sectional area of the gauge section. The ultimate tensile strength (UTS) of a material typically reveals two very important mechanical properties of the material: strength and ductility. Therefore, materials with a high UTS can undergo significant deformations prior to rupture (fracture). This is an important property for materials subjected to dynamic or high-speed loads, which are often associated with failures caused by excessive deformation. UTS is, therefore, an extremely important property to consider when selecting materials or when designing engineered structures or components and for evaluating the structural integrity of materials. In addition, determining a material's UTS will assist in ensuring that a structure is designed and constructed to be safe, reliable, and functional in various engineering discipline applications.

Impact strength or toughness is another mechanical property of materials and refers to a material's ability to absorb energy and undergo plastic deformation prior to brittle fracture under impact. Toughness is critical when selecting materials for numerous applications subject to sudden, high-speed impacts, such as automotive and aerospace components and structures. Impacts may be quite severe and therefore it is necessary to possess the ability to quantify a material's impact strength through the use of one of the many standardized test methods such as Charpy and Izod. These tests induce an impact on a notched sample with a pendulum and then the amount of energy absorbed in breaking the sample is measured to provide an indication of that sample's ability to withstand impact-induced fracturing.

Effectiveness of welding processes is determined through the measurement of fracture toughness of welded specimens using Izod impact testing. The mechanical vibration generated during the welding process allowed controlled application of mechanical vibration on the specimen to assess impact toughness through the Izod test. The results of this study indicate a positive relationship between energy absorbed at fracture and the amplitude and acceleration of mechanical vibrations applied to the specimen controlled by voltage to the vibromotor. Mechanical vibration applied during welding also has significant positive effects on bonding quality, microstructure refinement, reduction of porosity, and improvement of impact toughness. The positive correlation discussed above indicates the potential for the use of mechanical vibration to improve the impact toughness of welded joints. The factors affecting impact strength include material composition, microstructure, and processing methods. High impact strength results in greater toughness and resistance to fracture when subjected to impact loads, therefore, it is of utmost importance for the safety and reliability of equipment and structures. Improving impact strength can be accomplished by alloying, heat treating, and the use of reinforcement fillers and/or fibers to increase the ability to absorb energy and resist plastic deformation. The impact strength must also be understood to ensure that equipment and structural components will safely and reliably perform as required when exposed to high-velocity impacts.

RESULTS AND DISCUSSION

The study's findings section includes data and evaluations derived from experiments testing the effect of mechanical vibration on welded joint mechanical properties. It contains an overview of all equipment and procedures used in the experiments and the results of performed tests such as three-point bend and Izod impact tests. This section also demonstrates how changing mechanical vibration parameters (amplitude and voltage input) affects flexural strength and impact toughness of welded joints. Results allow direct comparison between welds produced using mechanical vibration and those made without this technique, providing an assessment of the effectiveness of mechanical vibration

Table 3. Experimental results

Frequency (Hz)	Flexural stress (MPa)	Tensile strength (MPa)	Impact strength (J)
0	496.30	313.00	104.00
200	530.80	339.40	117.30
400	540.20	360.80	133.30
600	575.70	390.20	145.90
800	587.20	423.60	157.10
1000	630.60	452.10	163.50
1200	645.10	464.50	175.80
1400	661.80	497.90	184.10
1600	643.30	482.60	158.50
1800	635.80	459.20	144.60

as a method of improving welded joint quality. This section includes suggestions for optimising welding parameters to achieve improved mechanical properties. The experimental results presented in Table 3 include the results of tests conducted to investigate the effects of mechanical vibration frequency on welded joint properties, including flexural stress, ultimate tensile strength, and impact strength, over vibration frequencies ranging from 0 to 1800 Hz.

Flexural Strength

A recent study demonstrated that increases in the frequency of vibrational waves corresponded with an increase in the flexural stress of welded joints. The average flexural stress of welded joints measured at 0 Hz (i.e., there were no vibrations) was 496.3 MPa while flexural stress increased as frequency increased from 496.3 MPa to 661.8 MPa between 0 Hz and 1400 Hz with an equal percentage increase of between 6.9%-33.5%, therefore the vibration provided additional strength to the bond and structural integrity of the joint giving it increased resistance to bending loads exerted on it, particularly for components that will endure bending loads. Table 4 provides further details about these results shown in table 4.

This table shows how much flexural properties of welded joints change based on mechanical vibration frequency.

a) Frequency (Hz)

The mechanical vibration frequency (measured in Hertz) refers to how many times the material was vibrated while it was being welded and how quickly it vibrated. This property controls how quickly the material is vibrated and how quickly the material appears

b) Maximum Load (N)

In a flexure test, the maximum load is the maximum amount of force the sample can take before it breaks. The max load of flexure tests was found to rise from 727.97 N (0 Hz) to 876.12 N (1600 Hz). The rise in max load shows that the higher mechanical vibration frequencies give welded connections more load tolerance before failure occurs.

c) Flexural stress (MPa)

The flexural stress (i.e. the stress calculated by dividing the Maximum Load by the cross-sectional area) shows the amount of stress applied to the sample when it reaches its Maximum load (based on its geometry) and increases as the mechanical vibration frequency increases. At 0 Hz, the flexural stress is 496.34 MPa and at 1600 Hz is 653.34 MPa. This patent trend indicates a rising ability of mechanical vibration frequency to contribute to increased flexural stress at failure (Fig. 3).

d) Flexural strain at the maximum flexural stress (mm/mm)

It is a dimensionless measure of how much the specimen deforms under the maximum load that is determined from how much it has changed in length divided by its original length. An increase in the flexural strain occurs as the frequency of mechanical vibration increases from 0 Hz with a number of 0.02 mm/mm to 1600 Hz with a number of 0.19 mm/mm will also provide evidence that mechanical vibration at an increased frequency will permit welded joints to experience an increase in deformation prior to rupture.

e) Flexural load at the maximum flexural stress (kN)

Itrepresents the applied flexural load at which the specimen experiences its maximum amount of stress, thus providing additional data regarding the load capacity at that critical point. An increase in the flexural load during mechanical vibration from 0 Hz of 0.73 kN to 1600 Hz of 0.88 kN indicates that welded joints can withstand more mechanical vibration with an increased load applied at their maximum flexural stress. Flexural strain and flexural load at maximum flexural stress were compared against frequency as shown in Figure 4.

g) Maximum flexural load, as expressed in megapascals (MPa)

It refers to the amount of elongation experienced by a specimen when it is subjected to a maximum applied load. It also indicates how much a material will stretch before reaching its maximum applied load when it is subject to bending forces. An increase in maximum

Table 4. Testresults of flexural strength

S. No	Frequency (Hz)	Max. load (N)	Flexural stress (MPa)	Flexural extension at maximum flexural load (MPa)
1	0	727.97	496.34	38.33
2	200	758.73	530.81	39.70
3	400	777.49	540.28	41.07
4	600	803.75	575.75	42.44
5	800	833.01	587.22	43.80
6	1000	843.77	630.69	45.18
7	1200	873.53	645.16	46.55
8	1400	880.38	660.37	45.97
9	1600	876.12	653.34	43.44

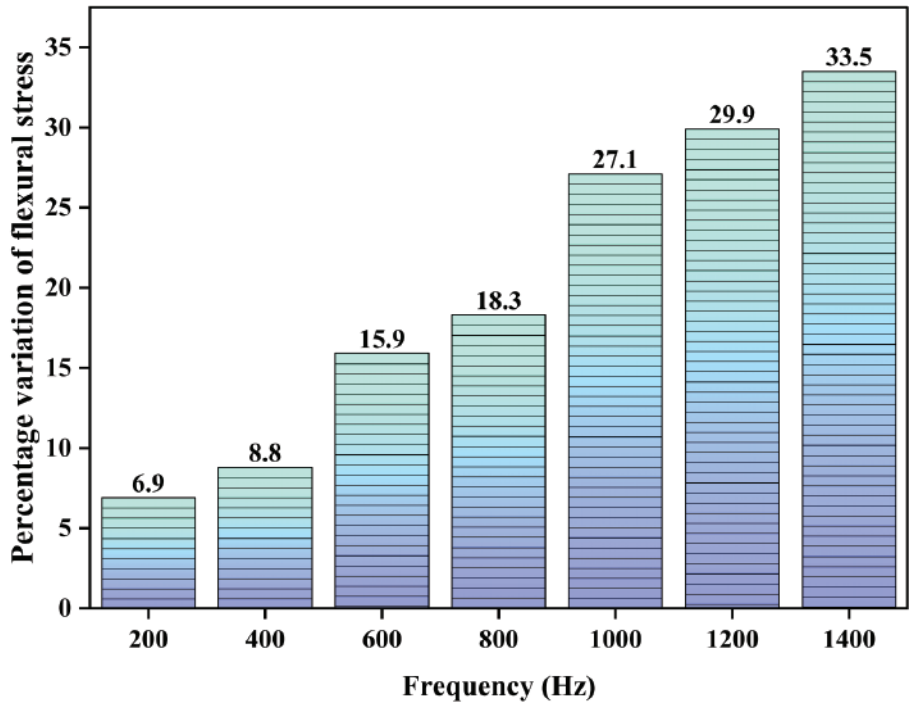


Figure 3. Comparison of % of the rise in flexuralstress.

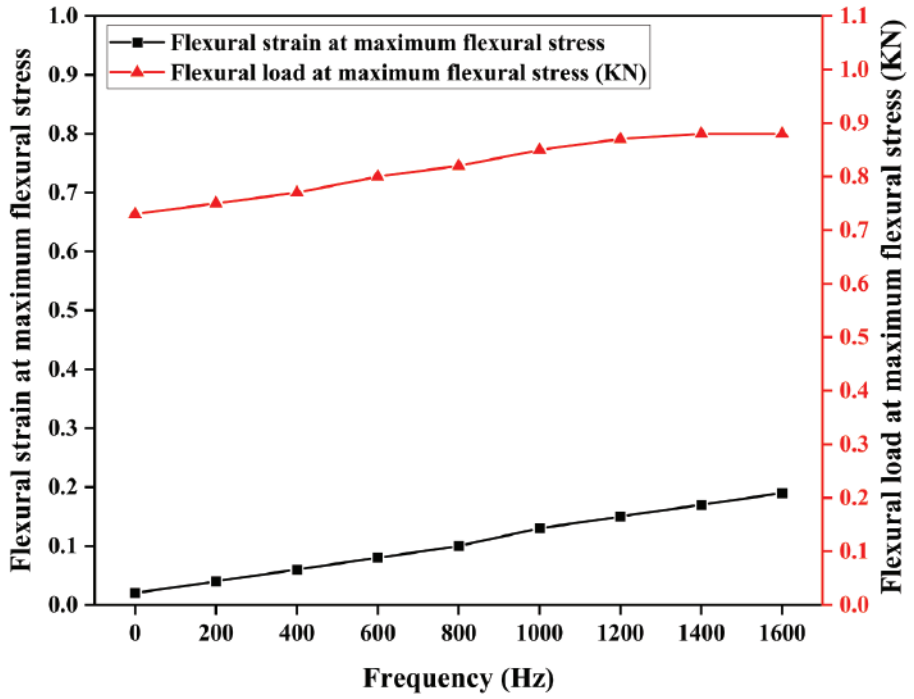


Figure 4. Comparison of flexural strain and flexural load at maximum flexural stress.

flexural load from 38.33 mm at 0 Hz to 43.43 mm at 1600 Hz indicates that with increased mechanical vibration frequency, the welded joints of the material can sustain greater elongation before reaching their maximum applied load.

h) Modulus (Automatic) (GPa)

The modulus (automatic) is a measure of the elastic properties of a material. The modulus of elasticity reflects a material's ability to resist deformation when subjected to stress. A greater modulus of elasticity indicates greater

stiffness (less elongation) of a material, which can resist higher loads before elastic deformation occurs. An increase in modulus of elasticity from 191.18 GPa at 0 Hz to 210.57 GPa at 1600 Hz indicates that with increased mechanical vibration frequency, the welded joints become stiffer and experience less deformation when subjected to bending loads. The relationship between the modulus of elasticity and frequency is shown graphically in Fig. 5.

Tensile Strength

The welded joint tensile strength increased with increasing vibration frequency, as did the flexural strength increase noted above. The tensile strength ranged from a minimum of 313.0 MPa (0 Hz) to a maximum of 497.9 MPa (1400 Hz). The percentage increase in tensile strength compared to the 0 Hz value ranged from 8.4% to 59.1%. The tensile strength presented in relation to vibration frequency is shown in Fig. 6.

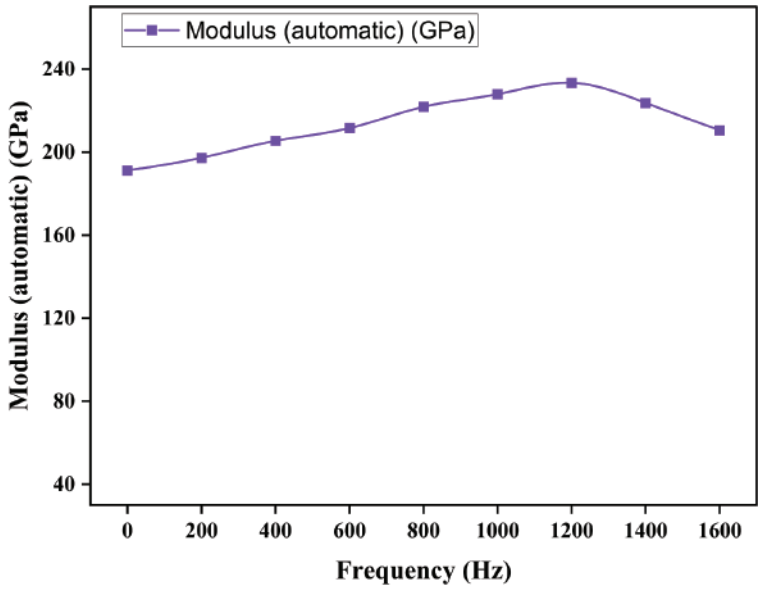


Figure 5. Comparison of modulus of elasticity with frequency.

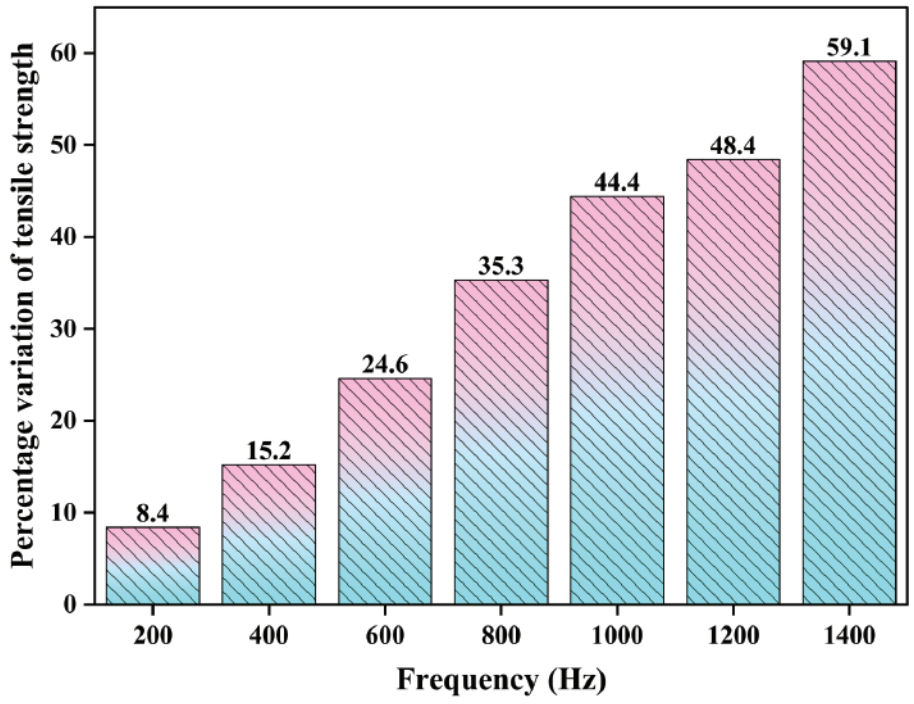


Figure 6. Comparison of % of the rise in tensile stress.

The increase in tensile strength with an increase in vibratory frequency suggests that the use of mechanical vibration enhances the bond and their cohesion within the welded joints through enhanced bonding of the base metals of the welded joint. It is apparent that the tensile strength of welded joints has improved and it will be possible for welded joints to withstand tension or stretching forces that occur where the component are subjected to these tensile or dynamic forces from a mechanical loading stand point. The complete tensile strength test results can be found in Table 5, along with the graphical representation of the test results shown in Fig. (7) to (9) inclusive.

In the detailed analysis of the tensile properties of welded joints that were exposed to differing Mechanical Vibration frequencies, the following information can be gleaned;

a) Frequency (Hz)

This column is an indication of the Mechanical Vibration frequency applied to the welded joint specimens during testing. Mechanical vibration frequency is one of the significant parameters being evaluated in order to better understand how it affects the mechanical characteristics of welded joints.

b) Maximum load (N), and break load (Std) (N)

Maximum and break load comparisons with reference to frequency are shown in Fig. 7 for both loading tests and indicate the maximum amount of force that a specimen can withstand prior to failure. The break load additionally gives an indication of how much load a specimen can carry while

Table 5. Test results of UTS

S. No	Frequency (Hz)	Tensile strain at break (std) mm/mm	Tensile strain at Max. load mm/mm
1	0	0.15604	0.12
2	200	0.16513	0.12
3	400	0.1752	0.13
4	600	0.19033	0.13
5	800	0.20344	0.13
6	1000	0.20954	0.13
7	1200	0.22264	0.13
8	1400	0.23375	0.13
9	1600	0.19375	0.12

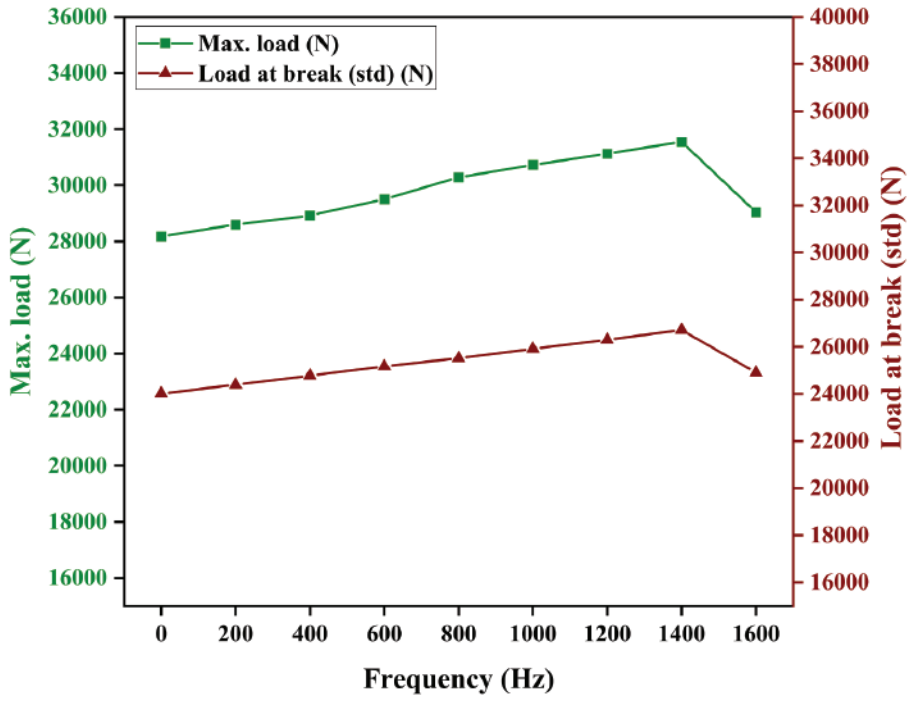


Figure 7. Comparison of maximum load and load at break.

under tension. Maximum and break loads for specimens were observed to increase as the mechanical vibration frequency increased, e.g., a specimen at 0 Hz has maximum load of 28176.61 N, while at 1400 Hz the maximum load is 31550.34 N.

a) Ultimate tensile strength (MPa)

The UTS and tensile strength at break with respect to frequency is shown in Fig. 8. The maximum stress it can withstand before failure called as UTS. UTS increases with increasing vibration frequency, indicating that higher frequencies result in stronger welded joints. The UTS ranged from 313.07 MPa at 0 Hz to 497.92 MPa at 1400 Hz.

b) Tension strength at break (Standard Deviation) (MPa)

This column shows the specimen's tension strength at break. As tension strength increases as Vibrational Frequency Increases, so does the resistance to fracture. Breaking tension strengths were measured ranging from 266.79 MPa (0 Hz) to 427.52 MPa (1400 Hz).

c) Tension strain at break (Standard Deviation) (mm/mm)

This column denotes the tension strain that the specimen experienced at break. Tension strain is a measure of how much longer a material has become from its original length; therefore, tension strain is calculated by taking the change in length and dividing it by the length of the original specimen. As frequency increases, both tensile strains at break increase, indicating an increase in the capability to deform before breaking. Measuring ranges for tensile strains at breaking point ranged from 0.16 mm/mm (0 Hz) to 0.24 mm/mm (1400 Hz).

d) Tension strain at maximum load (mm/mm)

This column shows the tension strain that was placed on the specimen when it reached the maximum load. The tension strain is calculated as the change in length divided by the length of the original specimen.

e) Tensile stress at yield (2 percent off set) (MPa)

Tensile stress at yield is defined as a value of tensile stress where a defined amount of plastic deformation occurs in a given sample (often 2 percent off set from the linear portion of the stress-strain curve). Vibration Frequency has an effect on tensile yield stress whereby increasing the frequency of the oscillations will result in a higher tensile yield stress for that material, which indicates that the material has a greater resistance to plastic deformation. The tensile yield stress of the material at 0 Hz was measured as 243.95 MPa and increased to 417.13 MPa as the vibration frequency was increased to 1400 Hz.

f) Tensile stress at preset point (MPa)

The tensile stress at a preset point represents where a material will behave in a tension loading situation, and is typically used to compare tensile yield stress with preset point. A visual comparison of the tensile yield and preset point tensile stress values can be found in Figure 9.

These findings highlight how the frequency of mechanical vibration can greatly affect the tensile properties of welded joints. The welded joints produced from mechanical vibrations at higher frequencies exhibit greater ultimate tensile mount, greater fracture toughness, and

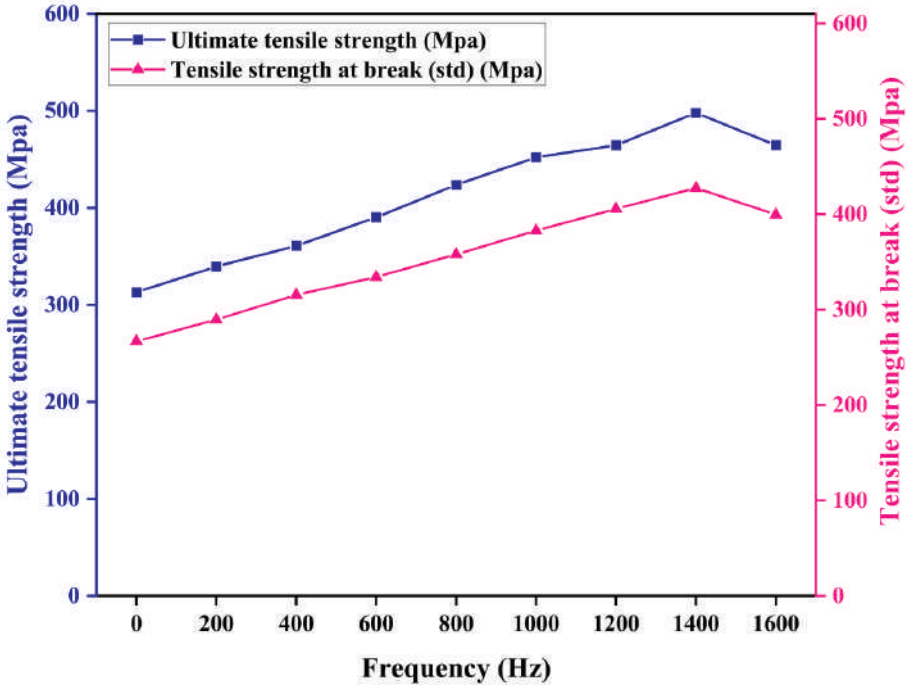


Figure 8. Comparison of UTS and tensile strength at break.

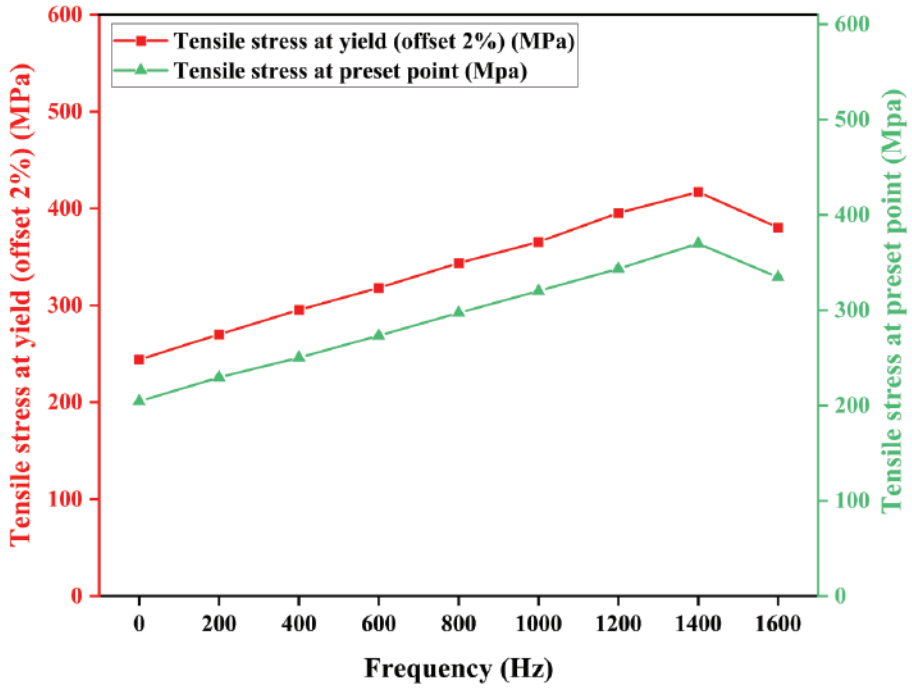


Figure 9. Comparison of tensile stress at yield and preset point.

greater ductility than those produced at lower frequencies. Therefore, by using both ultimate tensile strength (UTS) and fracture toughness as a measure of the mechanical performance of the welded joint when subjected to various frequencies of mechanical vibration, one can gain insight into the effect of mechanical vibration on the tensile properties of welded joints.

Impact Strength

With the increase in frequency of vibration comes an increase in impact strength (Capacities). With respect to the impact strength measured (at 0 Hz), there were increases of 12.8% and 77.1% for 0 Hz and 1400 Hz, respectively, indicating that the frequency of vibrating welds directly affected the impact strength. Vibrations provide assistance for absorbing energy and continuing plastic deformation until failure, therefore increasing the durability, and resilience to high-speed/low-F/V impact loading conditions. The tests conducted to quantify the impact strength provide an indication of the material, over time, of its ability to sustain impact loading and absorb energy, therefore, supporting greater robustness in high-speed/low-F/V loading applications. The data on the impact strength in relation to frequency is presented in Fig. 10. The results of the Impact strength tests and their relationship to frequency are explained in this report.

a) Impact strength: Impact strength represents how much energy the material is absorbs when it breaks! Impact strength is measured in joules (J). Based on the data provided, the tested impact strengths were between 104 J at 0 Hz and 184.1 J at 1400 Hz. High Impact Strength indicates that the material has greater energy absorption properties of the material and therefore has more resistance to breaking when hit or loaded from above.

b) Trend analysis: The data indicates there is a consistent upward trend in the measured impact strength of the welded joints as the level of mechanical vibration increases with increasing mechanical vibration frequency. This analysis shows that increasing mechanical vibration frequency increases the impact resistance of the welded joint. Therefore, indicating that as mechanical vibration frequency is increased, they will also have more impact resistance and greater energy absorption properties.

c) Importance of the results: The impact strength values provide insight into the ability of the welded joint to withstand large forces/impacts when it is subjected to sudden forces caused by external forces. Therefore, this is an important characteristic of welded joints due to their utilization in high-impact or shock-loading applications; thus providing greater toughness and resilience when compared to other forms of support. Additionally, the increased impact strength will provide greater reliability and durability of the welded joints to withstand real-world operating conditions.

d) Comparison and interpretation: The impact strength values obtained from the various frequency ranges are compared to demonstrate the advantage of mechanical vibration as a method of improving the impact resistance of welded joints. The results obtained from testing can also be compared against known quantity of requirements or

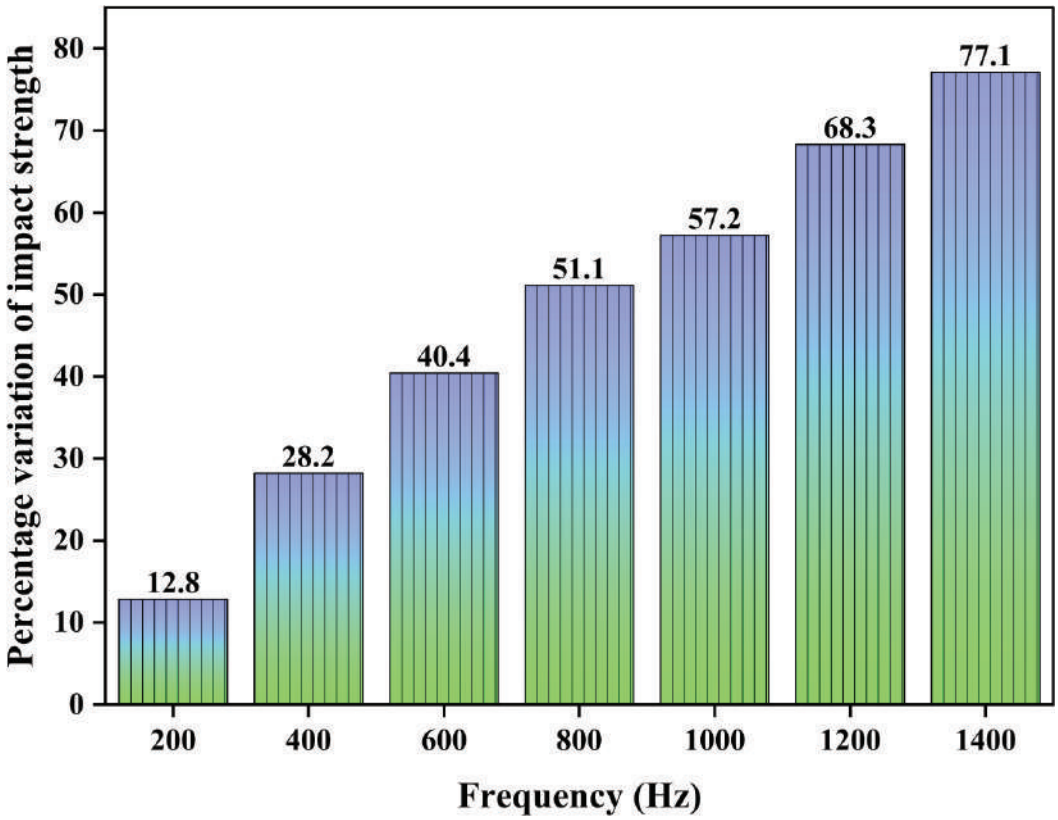


Figure 10. Comparison of % of the rise in impact stress.

standards applicable to industry or government to determine if the welded joints are acceptable or non-compliant with established performance standards.

e) Practical implications: The information gathered through the testing of welded joints provides important information to design engineers, material scientists and manufacturers working on material development and selection for applications where impact resistance is critical. The data provided from this research helps with determining material selection, process optimizations, as well as product design so that welded joints meet their intended performance requirements and safety regulations.

By testing the impact strength of welded joints, it was found that the mechanical response of welded joints to impact loading can be improved through the use of mechanical vibration to improve impact resistance and performance. Additionally, these results show that the use of mechanical vibration in welding processes may improve the mechanical properties of welded joints. In general, the results suggest that by increasing the frequency of mechanical vibration during welding, the mechanical bond of welded joints will be improved; in turn, this will directly improve the mechanical properties of welded joints, including flexural stress, tensile strength, and impact strength. Additionally, the findings illustrate the significance of optimising vibration parameters such as frequency to improve the mechanical properties of welded joints. Because of this, the findings indicate that the optimisation of mechanical vibration parameters in welding may enable the production of welded joints that are stronger, tougher, and more reliable in various engineering applications.

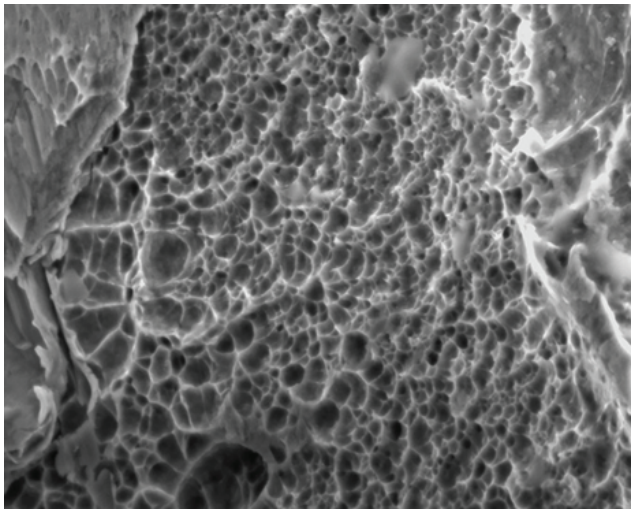


Figure 11. Microstructural characterization of weld sample.

Figure 11 shows that the distribution of filler metal throughout the weldment is important for increasing the mechanical properties being tested. It is shown that vibration treatment allows for an efficient initiation of the solidification process with increasing frequency, as the weld pool fills the voids in the porous areas. The vibration treatment will cause additional changes in the weldment due to the solidification process taking place over a longer period than with conventional welding processes. For example, higher frequencies in some areas may result in creating very minor bulges due to increased amounts of filler material being deposited. The ability to effectively adjust vibration settings and ensure the frequency ranges used for both workpieces and electrodes are appropriate will have an important positive effect on the mechanical properties of weldments produced using vibration. These benefits are a result of the increase in the amount of liquid superheat produced by the welding heat.

CONCLUSION

An effort is made in this study to develop a deeper understanding of vibratory treatment as well as the ability to optimise the mechanism that enhances the joint constructed by welding mild steel 1018, arc welding, via maintaining an experimental rig that allows controlled mechanical vibratory motion to be introduced during the welding process. The relationship between frequency and amplitude of the vibrational motion and the resultant welded joint attributes and welding parameters will provide the means for determining the optimal conditions for enhancing the mechanical performance of the welded joint. Notably, from the conducted experiments:

- ✓ The mechanical properties of welds created using vibration assisted welding showed an improvement compared to those created without vibrational treatment. Welds that were created at higher frequencies produced the greatest flexural stress, greatest tensile strength, and greatest elastic moduli of any of the welds tested.
- ✓ When mechanical vibration frequency increases, there is greater enhancement of mechanical characteristics, therefore concluding that vibratory treatment has potential for improving the characteristics associated with welded joint strength and performance.
- ✓ With increased frequency of vibrational force applied to welded joints, the welded joints performed better with regard to energy absorbance and resistance to fracture upon application of impact on both sides. This indicates that increasing vibrational frequency will improve welded joint toughness/resilience.
- ✓ Statistical analyses confirm that proper welding parameter determination optimizes the welding parameters in order for welded joints to exhibit the improved mechanical characteristics described previously and in Table IV.

The findings of this study illustrate that there are potential advantages to be had by utilizing mechanical vibrations to improve the mechanical characteristics of welded joints. Manufacturers can improve the performance of welded structures and open up more applications through proper optimization of the welding parameters.

Future Scope

Certainly! It is exciting to see what future projects will be accomplished using what has already been established in terms of the impact of different parameters on the welding process (i.e., vibration amplitude and frequency duration). Manufacturers wanting to further investigate the mechanical properties of welded joints as they relate to vibration amplitude and frequency duration should continue to conduct research to ascertain how the mechanical vibrations created during the welding operation affect the microstructure of the welded joint. As more is learned through research, this information can be used to develop better welding practices and optimise equipment used to achieve these higher performing mechanical properties.

REFERENCES

[1] Rao PG, Rao PS. Mechanical properties improvement of weldments using vibratory welding system. Proc Inst Mech Eng C J Mech Eng Sci 2015;229:776-784. [CrossRef]

[2] Rao PG, Rao PS, Krishna AG. Flexural strength improvement of welded joints prepared by vibratory welding process. Int J Manuf Mater Mech Eng 2015;5:1–16. [CrossRef]

[3] Rao PG, Rao PS. Development of a prediction tool for tensile strength of the welded joints prepared by vibratory welding process. Mater Focus 2017;6:319–324. [CrossRef]

[4] Rao PG, Rao PS, Krishna AG, Sriram CV. Improvement of tensile strength of butt welded joints prepared by vibratory welding process. Int J Mech Eng Technol 2013;4:53–61.

[5] Ramakrishna G, Rao PS, Rao PG. Methods to improve mechanical properties of welded joints: View point. Int J Mech Eng Technol 2016;7:309–314.

[6] Tsujino J. 27 kHz ultrasonic complex vibration welding system using various exchangeable welding tips for different welding specimens. In: Proc IEEE Int Ultrason Symp (IUS); 2018. p. 1–9. [CrossRef]

[7] Tsujino J, Sugimoto E. Ultrasonic welding of electronic parts and devices using a long and thin complex vibration welding tip. In: Proc IEEE Int Ultrason Symp (IUS); 2014. p. 947–950. [CrossRef]

[8] Tsujino J, Sugimoto E. Ultrasonic complex vibration welding of many metal foils and terminals of Li-ion battery and capacitor. In: Proc IEEE Int Ultrason Symp (IUS); 2016. [CrossRef]

[9] Tsujino J, Sugimoto E. Ultrasonic welding using a long and thin complex transverse vibration welding tip with vibration detector and static pressure controller. In: Proc IEEE Int Ultrason Symp (IUS); 2015. [CrossRef]

[10] Asami T, Tamada Y, Higuchi Y, Miura H. Development of dumbbell-shape vibration source with longitudinal and torsional transducers for ultrasonic metal welding. In: Proc IEEE Int Ultrason Symp (IUS); 2017. p. 1–4. [CrossRef]

[11] Liu X, Shi G, Liu W. A novel residual stress detection method for complex large welded structures based on excitation vibration response. In: Proc International Conference on Artificial Intelligence and Electromechanical Automation (AIEA); 2020. p. 342–345. [CrossRef]

[12] Sabzi M, Dezfuli SM. Drastic improvement in mechanical properties and weldability of 316L stainless steel weld joints by using electromagnetic vibration during GTAW process. J Manuf Process 2018;33:74–85. [CrossRef]

[13] Liao H, Wang Z, Zhang B, Chi P, Wang Y, Tian J, et al. Microstructure and mechanical properties of SUS304 weldments manufactured by ultrasonic vibration assisted local dry underwater welding. J Mater Process Technol 2023;322:118183. [CrossRef]

[14] Feng W, Zhang J, Gao J, Xiao Y, Luo G, Shen Q. Microstructure and texture evolution of aluminum and titanium ultrasonic welded joints. Mater Charact 2023;195:112542. [CrossRef]

[15] Dey K, Gobetti A, Ramorino G. Advances in understanding of multiple factors affecting vibration weld strength of thermoplastic polymers. J Adv Join Process 2023:100164. [CrossRef]

[16] Shi S, Lin L. On the environmental stress cracking of a vibration-welded polycarbonate (PC)-based nanocomposite. Polymer (Guildf) 2023;285:126338. [CrossRef]

[17] Khmelev VN, Slivin AN, Abramov AD. Stand for controlling of quality of weld producing at ultrasonic welding of thermoplastic materials. In: Khmelev VN, Slivin AN, Abramov AD. Stand for controlling of quality of weld producing at ultrasonic welding of thermoplastic materials. In: Proc Int Conf Young Spec Micro Nanotechnol Electron Devices (EDM); 2017. p. 246–249. [CrossRef]

[18] Gill JS, Majid M. Hot filler wire addition in computer assisted arc welding and cladding processes: A review. In: 023 10th International Conference on Computing for Sustainable Global Development. (INDIACom). Mar. 15-17, 2023New Delhi, India, 2023. p.328–332.

[19] Yu M, Zhao H, Xu F, Chen T, Zhou L, Song X, et al. Effect of rotational speed on microstructure and mechanical properties of Al-Ti friction stir welds with ultrasonic vibrations. J Mater Process Technol 2023;320:118119. [CrossRef]

[20] Ilman MN, Widodo A, Triwibowo NA. Metallurgical, mechanical and corrosion characteristics of vibration assisted gas metal arc AA6061-T6 welded joints. J Adv Join Process 2022;6:100129. [CrossRef]

Sigma J Eng Nat Sci, Vol. 44, No. 1, pp. 575–591, February, 2026

Sigma Journal of Engineering and Natural Sciences
Web page info: https://sigma.yildiz.edu.tr
DOI: 10.14744/sigma.2025.00000

Research Article

Molecular dockings of secondary metabolites to evaluate anthelmintic potential

Dilara KARAMAN[1,*], Oya GİRİŞGİN[2], Ahmet Onur GİRİŞGİN[3]

[1]*Department of Bioengineering, Yildiz Technical University, İstanbul, 34220, Türkiye*
[2]*Karacabey Vocational School, Bursa Uludag University, Bursa, 16700, Türkiye*
[3]*Department of Parasitology, Veterinary Faculty, Bursa Uludag University, Bursa, 16059, Türkiye*

ARTICLE INFO

Article history
Received: 18 September 2024
Revised: 02 December 2024
Accepted: 05 February 2025

Keywords:
Anthelmintic; Artemisia; In Silico Docking; Momordica; Origanum

ABSTRACT

Helminthic infection is an important health problem that affects millions of humans and animals, especially in developing countries. This study aims to research some natural compounds which can be used continuously in the treatment of recurrent helminthic infections. For this purpose, we predicted the anthelmintic properties of some bioactive compounds from *Artemisia annua* L., *Momordica charantia* L., *Origanum vulgare subsp. hirtum*, and *Rubus canescens* DC. These compounds were docked with anthelmintic target proteins; Hcβ-tubulin (*Haemonchus contortus* β-tubulin), AsFR (*Ascaris suum* fumarate reductase), and CPT 2 (rat carnitine palmitoyl transferase 2) enzyme using AutoDock 4.2 program. The chemical interactions and ADME properties of the most potent ligands were investigated via Biovia Discovery Studio Client 2020 and SwissADME. In the results, it was demonstrated, based on molecular interactions, that oreganol, momordicin II, cucurbitacin-B, and charantadiol-A have multi-inhibitory properties against target proteins. It was revealed for the first time that oreganol, cucurbitacin-B, charantadiol-A, and momordicin II inhibited CPT 2 and AsFR enzymes at nanomolar inhibition constants (0,137 nM, 0,0571 nM, 2,06 nM, and 0,072 nM for CPT 2 enzyme; 1,9 nM, 5,31 nM, 16,6 nM, and 40,78 nM for AsFR, respectively). Oreganol has also inhibited Hcβ-tubulin at low K_i values (K_i = 24,32 nM). These findings hold significant implications in the medical field, as they indicate that the compounds in question could serve as broad-spectrum anthelmintic drugs. When broad-spectrum drugs are needed, the oreganol scaffold can be used since it is triple-acting inhibitor. Cucurbitacin-B can be a candidate molecule to replace Ivermectin because they compete for the same target. According to the study's findings, future anthelmintics may be developed from cucurbitacins, adding to the effective treatments already provided by benzimidazoles and macrocyclic lactones. This research represents the first instance in which essential *in silico* scientific data has been gathered to support this conclusion.

Cite this article as: Karaman D, Girişgin O, Girişgin AO. Molecular dockings of secondary metabolites to evaluate anthelmintic potential. Sigma J Eng Nat Sci 2026;44(1):575–591.

***Corresponding author.**
*E-mail address: dilara.karaman@yahoo.com

This paper was recommended for publication in revised form by Editor-in-Chief Ahmet Selim Dalkilic

Published by Yıldız Technical University Press, İstanbul, Turkey
© Author. This is an open access article under the CC BY-NC license (http://creativecommons.org/licenses/by-nc/4.0/).

INTRODUCTION

Helminthic infections are prevalent in almost all countries; however, they are more common in South America, Africa, and Asia. According to WHO data, 1.5 billion people around the world are infected with soil-transmitted helminths. Specifically, 819 million people have *Ascaris*, 464 million people have *Trichuris*, and 438 million people are infected with hookworm. Schistosomiasis is considered an epidemic disease in 83 countries, with an estimated 180 million cases predicted [1]. In addition to this, substantial expenses have been incurred for the prevention and treatment of helminthic infections in animals. Novel simulations are necessary to control helminthic diseases. A new technique that allows continuous visualization of the spread of the disease in different age groups was developed for Covid-19 control [2]. With this new simulation called Hybrid NAR-RBFs Networks, parameters were evaluated to see the effect of an infective disease in a very wide geography.

In regions with limited health services, people often face recurring helminthic infections and drug resistance issues. Exploring natural compounds as alternatives to synthetic drugs is crucial, but obtaining and studying these compounds can be costly and arduous. *In silico* molecular modelling, simulations play a key role in providing insights into potential drug interactions, serving as an important step in rational drug design. Protein-ligand docking simulation is also essential in reducing the cost and labor involved in drug research [3]. *In silico* modelling studies, which are the first step of drug discovery, should be increased because simulations created with chemical calculations at the atomic level serve as an aid in predicting the biological effect of the drug.

In drug research, *in silico* simulations, the first and probably the most important step, help to estimate the pharmacokinetics, pharmacodynamics and side effects of the drug. Pharmacokinetics consists of stages that involve reaching the target cell, which can be predicted through computational methods. These stages are related to the chemical and biological properties of a drug candidate. Pharmacokinetics is mainly concerned with ADMET (Absorption, Metabolism, Excretion, and Toxicity), which includes the absorption of the drug from the intestines, skin, and cell membranes, distribution in the body (including its reach to different cells, tissues, and organs, and whether it can penetrate the blood-brain barrier), the by-products formed as a result of metabolism (including its susceptibility to liver enzymes), excretion, and potential toxicities [4]. However, research methods related to ADME have been developed using computer programs to provide data on the absorption and distribution of the drug [5].

According to literature, the development of resistance to anthelmintics is inevitable [6]. Therefore, it is imperative to discover new and effective natural anthelmintic compounds as drug candidates. Hundreds of millions of people need anthelmintic drugs, but they cannot use them due to two important reasons: 1) Health problems (kidney failure, liver problems, hair loss, etc.) resulting from frequent use of synthetic drugs in the treatment of frequent recurring helminthic infections; 2) The problem of access to local services for communities living in regions where health facilities are not sufficient [1]. Considering this situation, scientists who are responsible for developing drugs against helminthic infections need to provide scientific data on anthelmintic plants and their effectiveness, especially those that can grow in arid or tropical climates.

There are different target proteins being used for anthelmintic purposes. Beta-tubulin protein, being responsible for microtubulin formation and cell division, is a known target of benzimidazole class drugs such as Albendazole or Mebendazole. Fumarate reductase is considered as a target of Thiabendazole [7]. Carnitine palmitoyl transferase 2 (CPT 2) is a "chokepoint" enzyme for nematode survival. A CPT 2 inhibitor was demonstrated as an anthelmintic because of killing some hazardous nematodes such as *Haemonchus contortus* and *Onchocerca linealis* [8].

In this study, it was aimed to investigate four plants (*Artemisia annua* L., *Rubus canescens* DC., *Momordica charantia* L., and *Origanum vulgare* subsp. *hirtum*), which are species that can grow in a wide geography in the world, from an anthelmintic perspective using *in silico* methods. Bioactive compounds found in these plants were investigated by *in silico* dockings for the inhibition of three proteins (*Haemonchus contortus* β-tubulin protein (Hcβ-tubulin), *Ascaris suum* fumarate reductase (AsFR) enzyme and rat carnitine palmitoyl transferase 2 (CPT 2) enzyme), which are the potential targets of anthelmintics.

Since millions of mebendazole tablets are donated each year, resistance development may be seen in the near future [9]. This study showed which herbal components could be useful in the scaffold selection of new anthelmintics to be designed in case of resistance development and when broad-spectrum drugs are needed. Hcβ-tubulin was chosen as a target protein to investigate the alternative drugs to benzimidazoles. Three different target proteins were used to determine the broad-spectrum ability of novel herbal drug candidates.

In the treatment of river blindness, the only drug option is Ivermectin [10]. The use of Ivermectin in severe infections causes extremely itchy allergic reactions called Mazzotti reactions, which makes treatment difficult. Ivermectin is not licensed for use in humans. The use of this drug in humans is due to desperation, and this is a health problem that needs to be solved urgently. In this study, natural compounds that may be as effective as Ivermectin were investigated for the first time with computational tools.

MATERIALS AND METHODS

Preparation of Ligands

Fifty herbal ligands were chosen from four plants (*Artemisia annua* L, *Origanum vulgare* subsp. *hirtum*,

Momordica charantia L., and *Rubus canescens* DC). These herbal ligands were used in docking experiments (Figures, names, molecular formulas and PubChem IDs of these ligands were presented in Appandixes-1). Some of these components were downloaded from the PubChem database in sdf format and from the Zinc Database in mol2 format, while others were drawn and optimized with Biovia Discovery Studio Client 2020 (Biovia DS) [11]. Molecules in sdf format were converted to pdbqt format with Openbabel program, while others were converted into pdbqt with AutoDock Tool [12, 13].

Preparation of Proteins

Biovia DS and Autodock 4.2 software were used for the preparation of the proteins. Proteins and enzymes that are drug targets in nematodes were investigated. Those target proteins and enzymes found in nematodes were downloaded from the Brookhaven Protein Databank (http://www.rcsb.org/pdb). These proteins are: *Ascaris suum* furmarate reductase enzyme PDB ID: 4YSX (mitochondrial rhodoquinol-fumarate reductase, solubility: 2.25 Å, bound with NN23 inhibitor [14]; *Haemonchus contortus* β-tubulin protein PDB ID: 1OJ0 (in complex with ABZ, theoretical structure) [15]; anthelmintic drug target rat carnitine o-palmitoyltransferase PDB ID: 2H4T (resolution: 1.90 Å, bound with dodecane ($C_{12}H_{26}$) [16] and PDB ID: 2FW3 (resolution: 2.50 Å) [17] seen as an important "chokepoint enzyme" in the literature. In determining target proteins, a study of Taylor et al. was referenced [7]. The ions and ligands and water molecules other than the cofactor were deleted. Missing hydrogen atoms were added. The missing atoms and bonds in the protein residues were manually checked for completion. After all the hydrogens were added, it was optimized first with the "Clean Geometry" tool and then with Charm forcefield by using Biovia DS program.

Investigation of Adme Properties

SwissADME web server [5] was used to evaluate the absorption, metabolism, and excretion (ADME) properties of drug candidates. Via the SwissADME program, the gastrointestinal (GI) absorption, ability to penetrate the blood-brain barrier, and their interactions with important biological systems (such as P-pg, CYP1A2, CYP2C9, CYP2C19) were predicted with computational methods.

Molecular Docking Experiment

In this study, it was planned to do docking experiments at different stages for different purposes.

Stage 1- Preparation of Proteins: Re-docking procedure was applied during the preparation of crystallized proteins after they were taken from PDB. For this purpose, the natural ligand and water molecules of the protein were deleted and docked with its natural ligand after it was prepared, the parameters were changed and the re-docking process was repeated until the appropriate value was reached as a result of RMSD calculation.

Stage 2 - Docking of target proteins and herbal ligands: Some compounds that had been demonstrated in these plants scientifically in the previous research are docked with drug target proteins that have passed the first stage. For comparison, the same target proteins were also subjected to docking simulation with the drug molecules such as Albendazole (ABZ), Mebendazole (MBZ), Ivermectin (IVC), Piperazine and Praziquantel (PZQ). Since the PZQ is also anticestodal and antitrematodal, it was investigated from an antinematodal perspective in this study.

The docking procedure is briefly as follows:

Selected ligands were docked using AutoDock 4.2 program with the proteins obtained from Protein Data Bank. Gridbox size was determined by the size of the ligand. The reactive atom of the cofactor in the protein was chosen as the center, or, in case it did not carry the cofactor, the natural ligand in the protein was taken to the Gridbox center. The atoms in the active region of the protein are released in motion, while other parts are kept rigid. In the docking process of proteins bound by their natural ligands in their co-crystalline forms, their natural ligands were taken as reference for RMSD calculations. The ionic strength was set to be 0.145 and the dielectric constant to 10. Docking analysis was performed with Lamarkian Genetic Algorithm 4.2 [18]. Using AutoDock 4.2 scoring functions, 10 or 20 runs were chosen for each ligand. After ranking according to their free binding energy, the highest-scoring ligands were analyzed in terms of their interactions at the binding site by AutoDock Tools and Biovia DS.

RESULTS AND DISCUSSION

Docking results of small molecules showed several score values according to Table 1. Although some of these molecules (carvacrol, thymol, ellagic acid and piperazine) are anthelmintic, docking scores showed that their affinities to these three proteins (CPT 2 (pdb ID: 2H4T), AsFR (pdb ID: 4YSX), and Hcβ-tubulin (Pdb ID: 1OJ0)) were low because these molecules did not make enough number of interactions in terms of formulations which used in the calculation of free energy of binding. Also, another cause is probable that these molecules can bind to other receptors or proteins while the anthelmintic effect is performing.

It is known that MBZ inhibits the β-tubulin in helminths. In this study, Hcβ-tubulin inhibition of MBZ was found at 1 nM level, and this result was appropriate with the known anthelmintic effect of MBZ. It was found that it had a good affinity to the other two proteins (4,6 nM and 96,25 nM inhibition constant (*Ki*) for CPT 2 and AsFR, respectively) (*Ki* values were presented in Appendixes-2).

A herbal ligand, oreganol, possessed the highest score with a 1,9 nM K_i value for AsFR enzyme (Fig. 2). Oreganol is a potential inhibitor for both the CPT2 enzyme and the AsFR. Based on these findings, oreganol is a promising candidate for an anthelmintic drug, marking the first instance of this bioactive molecule being investigated as an anthelmintic.

Table 1. Free binding energy of herbal ligands and drugs with protein targets

Molecule	1OJ0 ΔG (kcal/mol)	2H4T ΔG (kcal/mol)	4YSX ΔG (kcal/mol)
ABZ	-9.07	-6.87	-5.53
Ivermectin	1.25E+03	-13.01	8.98
MBZ	-12.23	-11.37	-9.57
Piperazine	-4.92	-5.11	-5.84
Praziquantel	-4.15	-10.06	-8.53
Charantadiol-A	18.06	-11.85	-10.61
Momordicin I	26.17	-10.83	-7.78
Momordicin II	72.67	-13.83	-10.08
Kuguacin-J	14.54	-11.04	-7.89
Karavilagenin-D	21.91	-10.99	-9.35
Cucurbitacin-B	17.9	-13.97	-11.29
α-Pinene	-6.34	-6.12	-4.67
α-Terpinene	-6.8	-5.98	-4.76
α-Thujene	-6.62	-6.09	-5.55
β-Caryophyllene	-8.27	-8.08	-6.12
γ-Terpinene	-6.8	-5.96	-4.83
Myrcene	-6.06	-5.45	-4.16
Borneol	-6,58	-6.83	-5.15
Terpinen-4-ol	-7.06	-6.67	-5.54
p-Cymen	-6.04	-5.28	-4.07
Thymol	-6.25	-5.55	-4.58
Carvacrol	-6.34	-5.64	-4.53
Diosmetin	-10.24	-10.77	-9.62
Apigenin	-10.75	-10.15	-8.78
Oreganol	-10.39	-13.45	-11.9
Eriodictyol	-9.58	-10.76	-9.42
Eriocitrin	+15.66	-8.43	-6.62
Linalool	-6.89	-6.65	-5.34
Luteolin	-9.85	-10.43	-9.27
Chrysoeriol	-10.21	-10.81	-8.83
Artemisinin	-7.09	-8.99	-6.45
Artemetin	-1.16	-6.78	-6.03
Artemisinic acid	-7.01	-7.17	-6.25
Deoxy artemisinin	-7.57	-8.62	-5.98
Friedelin	72.37	-10.76	-8.04
Arteannuin B	-10.68	-9.23	-7.82
Stigmasterol	5.17	-10.95	-8.42
Scopoletin	-9.28	-8.21	-7.23
Quersetin	-5.23	-6.92	-5.97
Camphene	-6.11	-6.15	-4.77
Camphor	-6.25	-6.62	-4.91
Chrysosplenetin	-7.25	-10.58	-9.3
Chrysosplenol-D	-7.15	-10.39	-9.18
Eucalyptol	-6.56	-6.54	-5.1
Isofraxidin	-10.21	-8.58	-7.03
Sabinene	-6.66	-6.13	-4.79
Scoparone	-9.4	-7.95	-7.15
Spathulenol	-8.33	-9.05	-6.58
Umckalin	-9.7	-8.49	-7.64
Diisooctyl phthalate	-7.56	-8	-6.91
Furan-2-carboxaldehyde	-6.18	-6.26	-6.93
Hexadecanoic acid methyl ester (methyl palmitate)	-6.63	-5.69	-3.92
9,12,15-octadecantrienoic acid methyl ester (ODTAME)	-10.54	-7.98	-6.19
Ellagic acid	-1.14	-7.11	-5.94
Gallic acid	-4.21	-5.25	-3.75

1OJ0: Hcβ-tubulin; 2H4T: CPT 2 enzyme; 4YSX: AsFR enzyme.

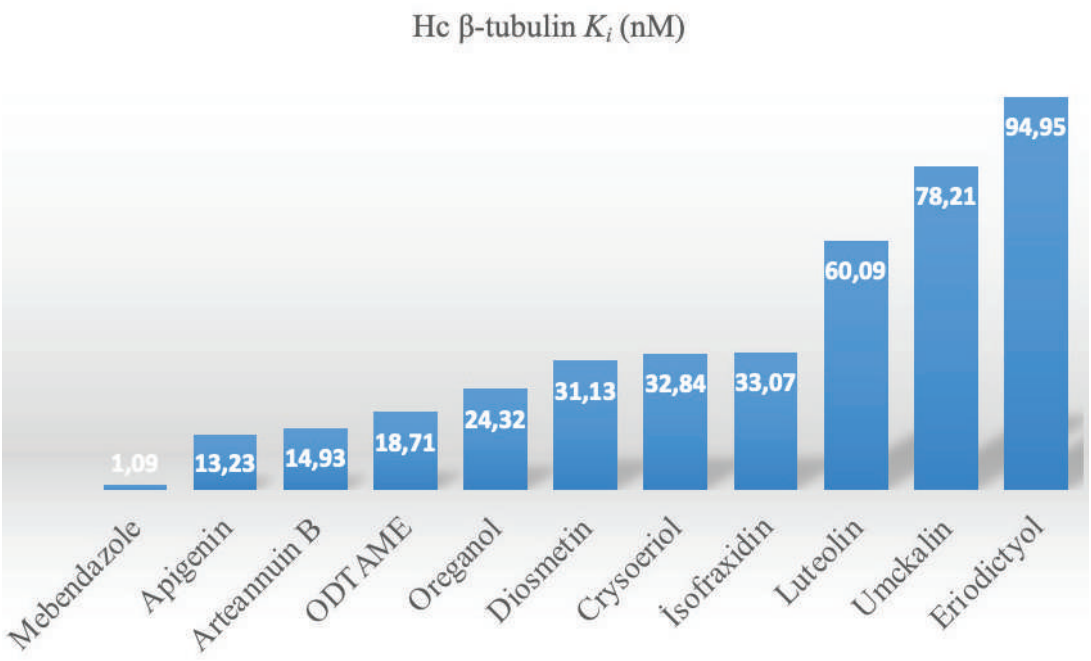


Figure 1. The first eleven molecules have the lowest K_i values against *H. contortus* β-tubulin (Hcβ-tubulin, pdb ID: 1OJ0).

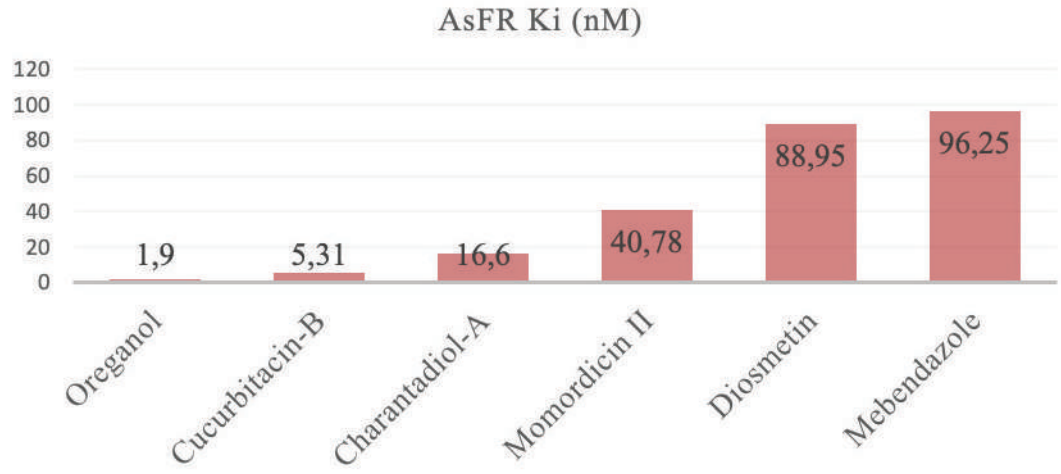


Figure 2. K_i values of best six molecules for AsFR (pdb ID: 4YSX).

The results in Table 1 show that IVC is antinematodal also *in silico*. Significantly, IVC was found to have a very good affinity to CPT 2 enzyme with the 290 pM K_i value. Since it was known that the rat CPT 2 enzyme is a target enzyme for *Onchocerca linealis* [19] and IVC is the only drug in the treatment of *Onchocerca volvulus* infection, this result has been showing that *in silico* experiments in this study provided the important data.

Although ABZ and MBZ are similar benzimidazole derivatives, the affinity of ABZ to CPT 2 and AsFR enzymes was found to be different from the MBZ's. While Hcβ-tubulin inhibition of ABZ was found at a nanomolar level as expected, 9 μM and 87,7 μM K_i were observed against CPT 2 and AsFR enzymes, respectively. This result showed that ABZ inhibited the nematode's Hcβ-tubulin. Apparently, it could bind to two other target enzymes (CPT 2 and AsFR), too. PZQ is used as an antitrematodal and anticestodal drug. These docking results showed that PZQ would also be able to be tried as an antinematodal in future *in vivo* experiments. Piperazin is a GABA agonist, so it cannot inhibit these enzymes (AsFR, CPT 2 or β-tubulin) in normal biological conditions. In this study, the results have

shown the correctness of the docking procedure, and they are correlated to the known anthelmintic effect of these synthetic drugs.

According to the results of AutoDock4.2, cucurbitacin-B, momordicin II, and oreganol inhibit the rat CPT 2 at picomolar (pM) levels. Cucurbitacin-B possessed very good K_i values, such as 57,11 pM against CPT 2 enzyme (pdb ID: 2H4T). 57, 11 pM is a very rare result, and it shows that this molecule has very significant anthelmintic potential. This result shows that it has discovered a novel and more effective drug candidate via computational methods in treating *Onchocerca volvulus* infection, which exists only a single drug option. Because it was not discovered hitherto via *in silico* methods, this study is the first study demonstrating with the docking simulations that cucurbitacin-B is an anthelmintic.

According to Figure 3, six molecules above 5 nM possess the best K_i values for CPT 2 enzyme inhibition. Two of them are IVC and MBZ, which were used commonly and marked as synthetic drugs. Cucurbitacin-B, momordicin II, oreganol, and charantadiol-A, which were found *in silico* as the best four anthelmintic ligands, are bioactive molecules obtained from *O. vulgare* subsp. *hirtum* and *M. charantia*. These results show that these herbal ligands will be more effective than synthetic drugs.

The energy levels for monoterpenes shown in the ΔG table gave an opinion about the structure-activity relationship. It is not sufficient for inhibitor candidates possessing side chains containing one ring and hydroxyl groups to be able to show anthelmintic effectiveness with a large spectrum. The position of the hydroxyl group on the monocyclic structure did not cause a serious change in binding energy. This case can be seen in the isomers thymol and carvacrol or γ-terpinen and α-terpinen. ΔG values of these isomer duals were found very near to each other. AsFR, CPT 2, and Hcβ-tubulin have unnecessary large binding cavities to bind monoterpenes in Table 1. In the inhibition of these proteins, the molecules should be preferred to possess both at least a bicyclic or tetracyclic core structure and branched side groups containing oxygen or sulfur atoms. According to the values in Table 1, a monoterpene scaffold is more suitable for enzymes or receptors containing smaller binding cavities. These findings showed that monoterpene scaffold had a different action mechanism than benzimidazoles or macrocyclic lactones.

Charantadiol-A, momordicin I and II, kuguacin-J, karavilagenin-D, and cucurbitacin-B are compounds found in *M. charantia*. Two compounds, cucurbitacin-B and momordicin II, demonstrated the highest CPT 2 enzyme inhibition scores in this study, making them the most potent ligands as anthelmintics. Momordicin II is the second ligand possessing the best inhibition score, with a 72,69 pM K_i value in the fifty herbal ligands searched in this study (Fig. 3). Thanks to its exceptional inhibition ability, Momordicin II showed better results than the five synthetic drugs (IVC, MBZ, ABZ, piperazine, and PZQ) identified *in silico.* For instance, IVC showed very successful inhibition ability to the CPT 2 enzyme with a 290 pM value, but Momordicin II and cucurbitacin-B exhibited even better binding affinity.

Another important result is that the usage of the *M. charantia* extracts in oil-based solvents can be very effective as a herbal drug because these six herbal ligands were found to

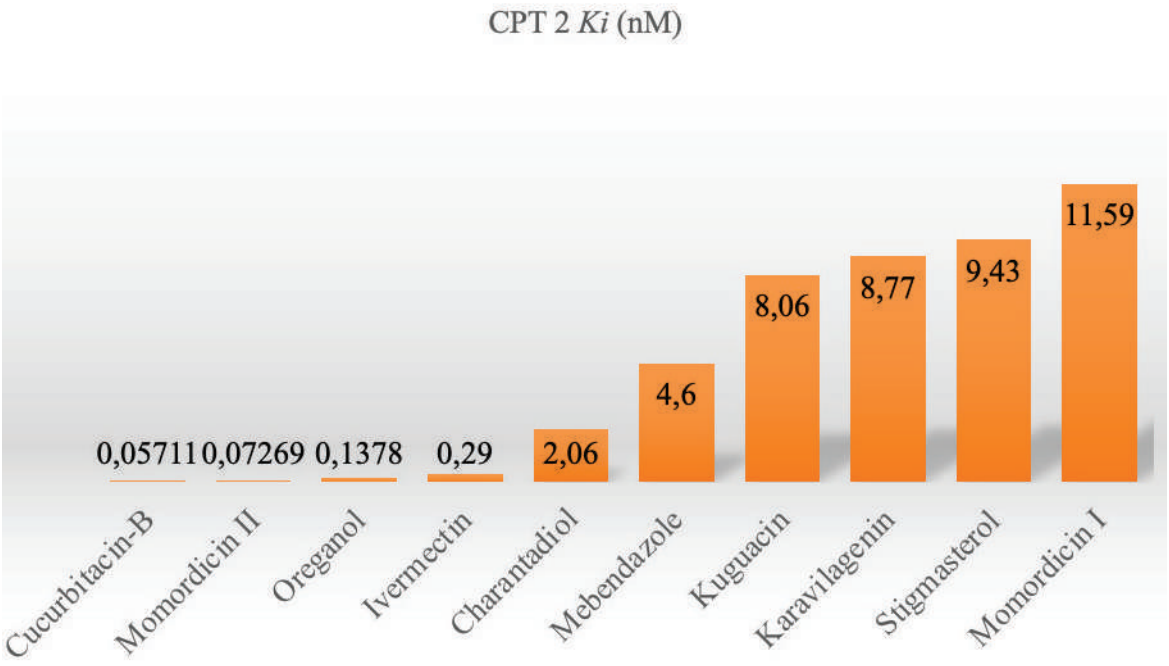


Figure 3. The first ten molecules possessing the best K_i values for CPT 2 enzyme.

have very favourable inhibition constants. Four of these six ligands (charantadiol-A, momordicin II, karavilagenin-D, and cucurbitacin-B) showed an inhibition effect on the AsFR enzyme at nanomolar levels. This desired result showed that these triterpenoids in *M. charantia* could be evaluated in developing dual-acting drugs. These results provided the necessary information for the development of a novel and more effective anthelmintic drug than the drugs on the market. According to the results of this study, in the future, some of the most effective anthelmintics will be cucurbitacins-based. For the first time in this study, it was reached the necessary *in silico* scientific data for this foresight.

Diosmetin, apigenin, oreganol, eriodictyol, luteolin, and crysoeriol in *O. vulgare* infusion; arteannuin-B, isofraxidin, umckalin, scopoletin in *A. annua* L. were found inhibition ability with very good *Ki* values against three proteins which were docked. Therefore, these molecules are available to drug candidates in the development of large-spectrum anthelmintics. It approves the anthelmintic potential of these two plants because these molecules are in *O. vulgare* subsp. *hirtum* and *A. annua* L.

ADME Evaluation

In this study, the ligands possessing the best binding affinity among the fifty herbal ligands investigated in terms of AsFR, CPT 2 and Hcβ-tubulin inhibition in docking experiments were evaluated by the SwissADME web server to investigate their pharmacokinetics. The radar plot of oreganol shows that the solubility, unsaturation, flexibility, lipophilicity and size of the molecule are within

Table 2. ADME properties of the best ligands in terms of B-tubulin, CPT2 and AsFR inhibition

	Oreganol	**Arteannuin-B**	**Apigenin**	**Cucurbitacin-B**	**Charantadiol-A**	**Momordicin II**
Radar Plot						
Molecular weight	438,38 g/mol	248,32 g/mol	270,24 g/mol	558,70 g/mol	454,68 g/mol	634,84 g/mol
TPSA	186,3 Å^2	38,83 Å^2	90,90 Å^2	138,2 Å^2	49,69 Å^2	156,91 Å^2
Pharmacokinetics						
GI absorption	Low	High	High	Low	High	Low
BBB permeant	No	Yes	No	No	No	No
P-gp substrate	No	No	No	Yes	Yes	Yes
Log K_p (skin permeation)	-8,95 cm/s	-5,98 cm/s	-5,80 cm/s	-7,83 cm/s	-3,85 cm/s	-7,57 cm/s
CYP1A2,	No	No	Yes	No	No	No
CYP2C19,	No	No	No	No	No	No
CYP2C9,	No	No	No	No	Yes	No
CYP2D6,	No	No	Yes	No	No	No
CYP3A4 inhibitor	No	No	Yes	Yes	No	Yes
Druglikeness						
Lipinski	No, 2 violations; NorO>10, NHorOH>5	Yes	Yes	Yes 1 violation: MW>500	Yes 1 violation: MLOGP>4,15	No, 2 violations: MW>500, NHorOH>5
Ghose	No	Yes	Yes	No	No	No
Veber	No	Yes	Yes	Yes	Yes	No
Egan	No	Yes	Yes	No	No	No
Muegge	No	Yes	Yes	Yes	No	No
Bioavailability Score	0.17	0.55	0.55	0.55	0.55	0.17

GI: Gastrointestinal; BBB: Blood-brain barrier; P-gp: P-glycoprotein; TPSA: Topological polar surface area; MW: Molecular weight; FLEX: Flexibility; LIPO: Lipophilicity; SIZE: Size; POLAR: Polarity; INSOLU: Insolubility; INSATU: Insaturation.

reasonable limits. Oreganol has poor GI absorption and cannot penetrate the blood-brain barrier. It was predicted that it would not inhibit any of the cytochrome enzymes in Table 2 and would not be a p-gp substrate. These features show that oreganol will not cause any problems in terms of side effects. Although further studies are needed to investigate its side effects, in this *in silico* study, oreganol stood out as an ideal ligand that could cause minimal side effects in ADME results. The possible inhibition mechanism of this molecule, which may be effective in killing helminths in the GI tract, seems to occur through simultaneous inhibition of the beta-tubulin protein and FR enzyme in the nematode.

Among these molecules, oreganol is the molecule that can penetrate through the skin the fastest, with a value of -8.95 cm/s. Momordisin II, a larger molecule than oreganol, can penetrate through the skin quickly, although not as quickly as oreganol. Although it has fewer hydrogen bond acceptors and donor atoms than oreganol, momordicin II also cannot penetrate the blood-brain barrier and has poor GI absorption. Unlike oreganol, momordicin II may also act as a P-gp substrate, thus potentially slowing the efflux pump of the drug. Charantadiol-A is close to oreganol in terms of molecular weight and size, but unlike it, the number of hydrogen bond acceptors and donors is much less. Thus it fits three of Lipinski's rules. TPSA value was found to be 49.69 $Å^2$. As seen in the radar graphic, the molecule is quite lipophilic and its water solubility is very low. Charantadiol-A is a molecule with high GI absorption. This triterpenoid molecule, which may be effective in eliminating helminths found outside the GI tract, can be used by dissolving it in oil-based solvents.

As seen in Table 2, cucurbitacin-B is a triterpenoid with a molecular weight of 558.7 g/mol, which has poor GI absorption and can through the skin at a speed of -7.83 cm/s. Applying *M. charantia* fruits soaked in olive oil to the skin as a folk treatment is compatible with these ADME results, and applying this compound through the skin is a correct form of application. Although it is not shown in the table, the ILOGP value of cucurbitacin-B was found to be 3.77, and since it is less than 5, this molecule has a lipophilic character, therefore it can easily penetrate through the cell membrane and be used by dissolving in oil.

Apigenin, the most potent herbal inhibitor against Hcβ-tubulin with a *Ki* value of 13.24 nM, fully complies with Lipinski's and Egan, Muegge, Veber and Ghose's rules. It cannot penetrate the blood-brain barrier but has high GI absorption.

Among the ligands whose ADME properties were evaluated, the only molecule that had the most favorable results was suitable for oral administration, and could penetrate the blood-brain barrier was arteannuin-B. This small molecule can inhibit Hcβ-tubulin with a very low *Ki* value at 14.95 nM. Arteannuin-B has a high GI absorption and can be absorbed through the skin moderately. It fits all the rules of Lipinski, Ghose, Egan, Veber and Muegge, and its chemical properties fall within the reasonable limits of oral intake. This molecule is moderately apolar and lipid soluble. It does not inhibit any important cytochrome enzymes in the liver listed in Table 2. It has a highly desirable polar surface area with a TPSA value of 38.83 Å2. All these positive features have shown that arteannuin-B is a very important drug candidate that can be taken orally and can even be used in the elimination of helminths settled in the nervous system. In a situation where resistance is developing against benzimidazoles, especially MBZ and ABZ, which have been donated at record levels and used by hundreds of millions of people for many years, arteannuin-B has emerged as a very valuable herbal ligand and a potential drug that can replace benzimidazoles with its tremendous ADME properties and highly successful inhibition ability.

Best Ligands and Their Interactions

Among the herbal ligands in this study, in addition to oreganol, are among the components that can be found in the *O. vulgare* subsp. *hirtum*, cucurbitacin-B, momordicin II and charantadiol-A contained in *M. charantia* were examined in detail regarding their possible interactions with target proteins and the results were evaluated. When the chemical interactions and biological activity shown are evaluated together, some new mechanisms and pathways that can be used to discover new drug candidates to be developed through CADD can be predicted. In this respect, carefully examining possible interactions and interpreting new data on structure-activity will provide important information to researchers working on anthelmintic herbal ligands.

Evaluation of Interactions of Oreganol

Oreganol [3-hydroxy-4-[(2*S*,3*R*,4*S*,5*S*,6*R*)-3,4,5-trihydroxy-6-(hydroxymethyl) oxan-2-yl]oxyphenyl] methyl 3,4-dihydroxybenzoate] is a glycoside (Computed by LexiChem 2.6.6, PubChem, 2019). Its 2D molecular structure is given in Figure 4.

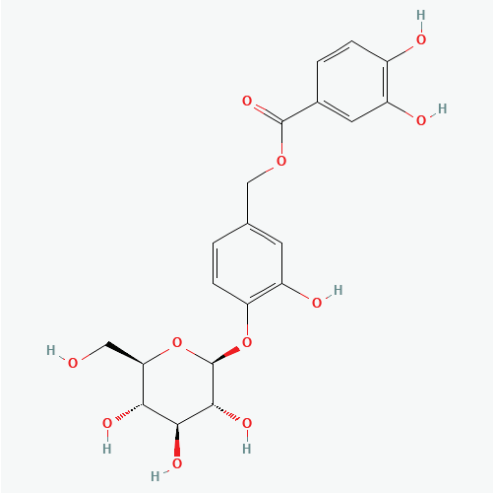


Figure 4. Oreganol 2D representation (from PubChem).

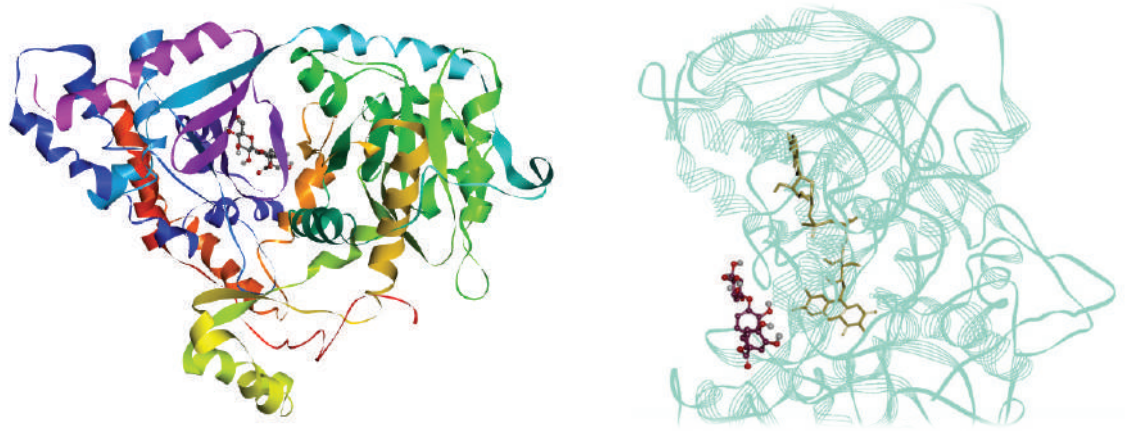


Figure 5. Positioning of oreganol in target enzymes. A) in CPT 2 (pdb ID: 2H4T), B) in AsFR (pdb ID: 4YSX). Oreganol was represented with a ball and stick, FAD cofactor with a yellow stick, and protein with blue ribbon models.

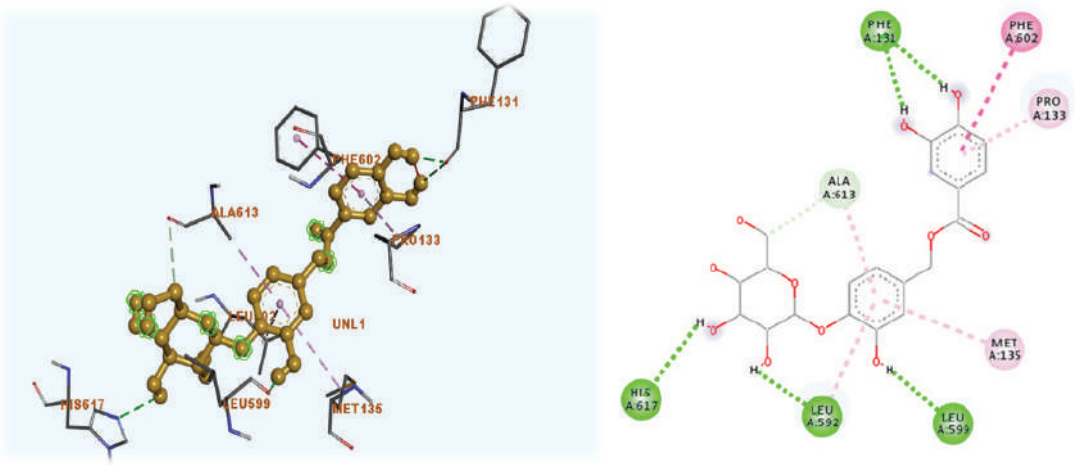


Figure 6. Possible chemical interactions of oreganol in the rat CPT 2 (pdb ID: 2H4T) enzyme and the residues it interacts with. A) Interactions are shown with dashed lines and oreganol orange ball-and-stick model B) 2D representation.

The active site of the CPT 2 enzyme is wider than the active site of β-tubulin, and the positioning of oreganol in the rat CPT 2 enzyme is shown in Figure 5. Since the coordinates of the region where the ligand binds were determined previously, the same coordinates were used in the docking simulations in this study. Therefore, the placement of the ligand in the active site is compatible with the literature [7]. As shown in Figure 5A, oreganol settled into the space created by the β-conformation and loop structure. In Figure 6, the two hydrogen bonds made by oreganol with PHE131 are noteworthy. The central ring of oreganol was sandwiched between ALA613 and MET135. The dihydroxyphenyl residue also formed an aromatic sandwich between PHE602 and PRO133. In Figure 5B, oreganol was located in front of the FAD cofactor in AsFR enzyme. Four hydrogen bonds (possessing 2,18 Å distance with ALA83, 2,09 Å with THR81, 2,13 Å with THR 248, and 2,76 Å with THR 247) were predicted between oregano and AsFR (PDB ID: 4YSX) (Fig. 7 B).

According to Figure 6 B, four residues in the CPT 2 active site formed hydrogen bonds with the hydrogen atoms in the hydroxyl groups of oreganol. These residues are PHE131, HIS617, LEU592 and LEU599. Additionally, PRO133 made a strong π-alkyl interaction with the dihydroxyphenyl ring of oreganol in close proximity. MET135 also formed another π-alkyl bond at a longer distance from the central ring. While the PHE602 residue interacted with the dihydroxyphenyl group of oreganol in a π-π T-shaped interaction, the ALA613 residue interacted with the central ring of the ligand with pi-alkyl interaction.

As a significant result, five hydrogen bonds were seen in the interactions of oreganol with *H. contortus* β-tubulin. One of them was performed between the hydroxyl group of

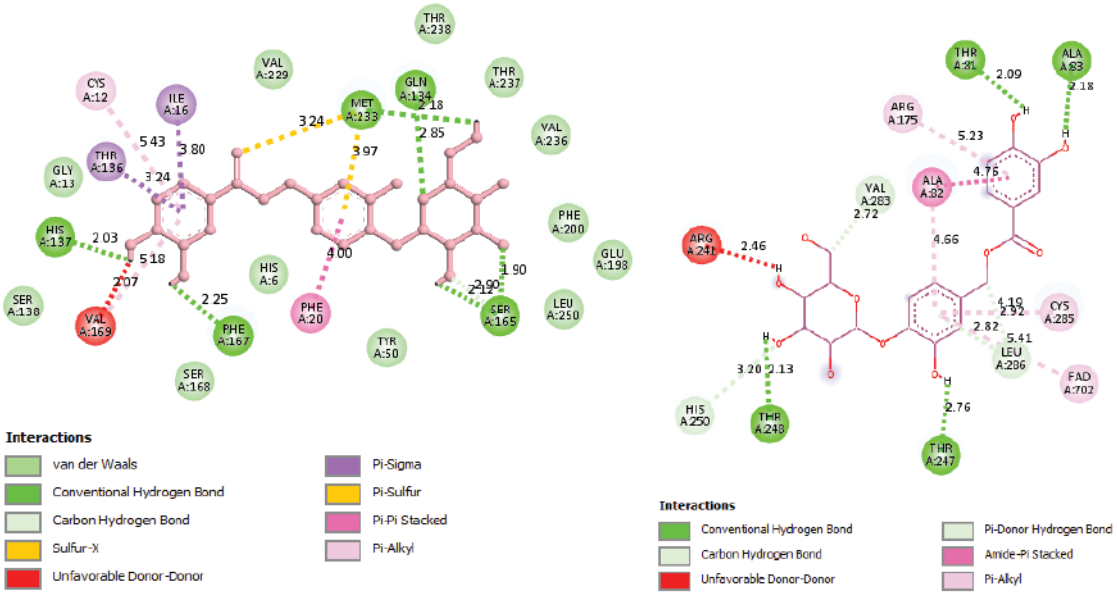


Figure 7. 2D representation of Oreganol **A)** in *H. contortus* β-tubulin **B)** in AsFR enzyme.

oreganol and PHE167 residue being sensitive to mutation. Probable interactions are shown in Figure 7 A.

Possible Interactions of Momordicin II in Rat CPT 2

A dense interaction network can be seen in Figure 8, where the possible interactions of momordicin II within the rat CPT 2 enzyme (pdb ID: 2FW3) are shown. Although the majority of these interactions in Figure 8 were van der Waals attraction forces, there were four polar and one nonpolar residue where hydrogen bond formation was predicted. These hydrogen bonds were formed through residues TYR614, THR591, LEU592, SER590 and ASN130. Apart from this, HIS372 made both π-sigma bonds and π-alkyl interactions. Other residues responsible for π-alkyl interactions were PRO133, PHE370, PHE602, TYR486, VAL605 and PHE131. The residues that made van der Waals interactions were SER588, SER488, ALA613, ILE612, GLU601, ALA615, ASN593, VAL587, MET135, GLY377, ASP376, TRP116, TYR120, and THR499.

In Figure 8, although there is a repulsion force between SER590, which is a polar residue, and the oxygen atom of momordicin II, and another repulsion force is predicted to

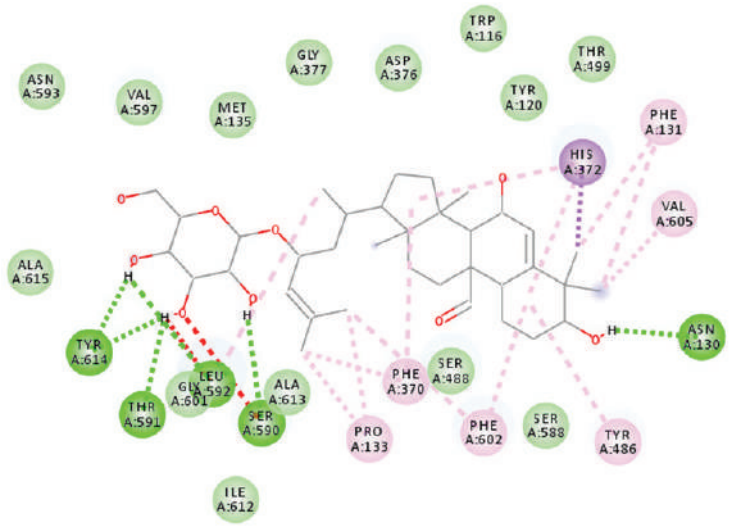


Figure 8. 2D representation of momordicin II and rat CPT 2 (pdb ID: 2FW3) interactions.

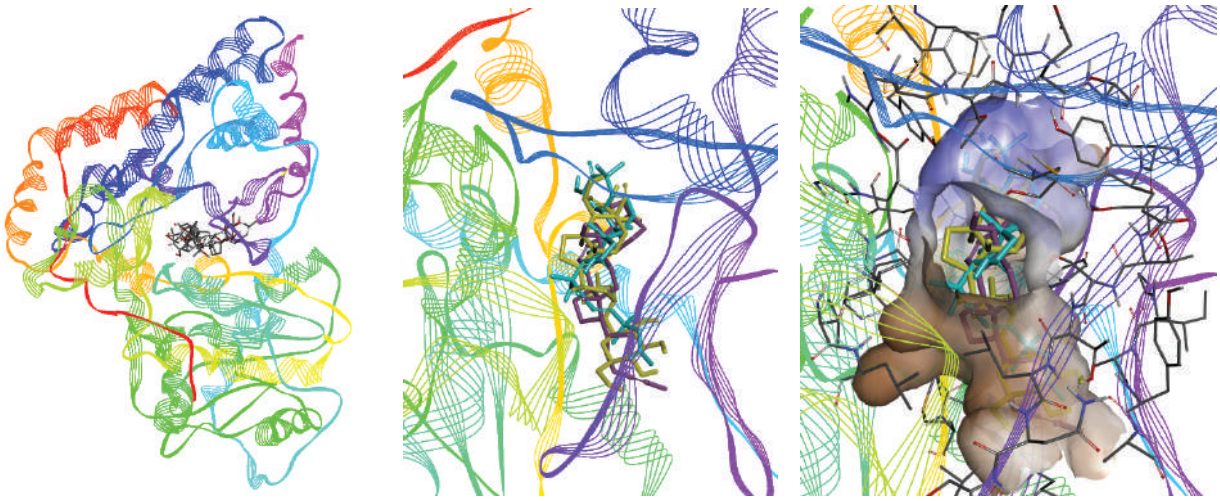


Figure 9. Positioning of momordicin II (yellow), carantadiol-A (purple) and cucurbitacin-B (blue) in 2FW3. The protein is shown in rainbow colors. The hydrophobicity of the residues in the region surrounding the ligands (rightmost image), the blue regions represent the hydrophilic parts and the brown regions represent the hydrophobic parts.

occur between the hydrogen atom of LEU592, a nonpolar residue, and the hydrogen atom bonded to the hydroxyl group of momordicin II, the formation of numerous hydrogen bonds between the part carrying the hydroxyl group of the ligand and the surrounding residues caused the free binding energy to decrease.

Possible Locations of Momordicin II, Charantadiol-A and Cucurbitacin-B In Rat CPT 2 (PDB ID: 2FW3)

Both charantadiol-A and cucurbitacin-B are similar to momordicin II in terms of molecular size, and these three molecules are among the top five molecules with the best binding energies for the rat CPT 2 enzyme (see Figure 3). In addition, it can be seen in Figure 9 that there is a similarity in terms of the structures and torsions of the molecules.

In the design of a pharmacophore, it is significant to know the aromatic surface of the binding cavity. According to these surface properties, chemical groups can be substituted for the scaffold. In Figure 10, the aromatic surface was shown in the CTP 2 enzyme (PDB ID: 2FW3) when it docked with cucurbitans.

Nonpolar residues such as valinyl, glycinyl, alaninyl and leucinyl enable the formation of a more hydrophobic binding surface (Fig. 10).

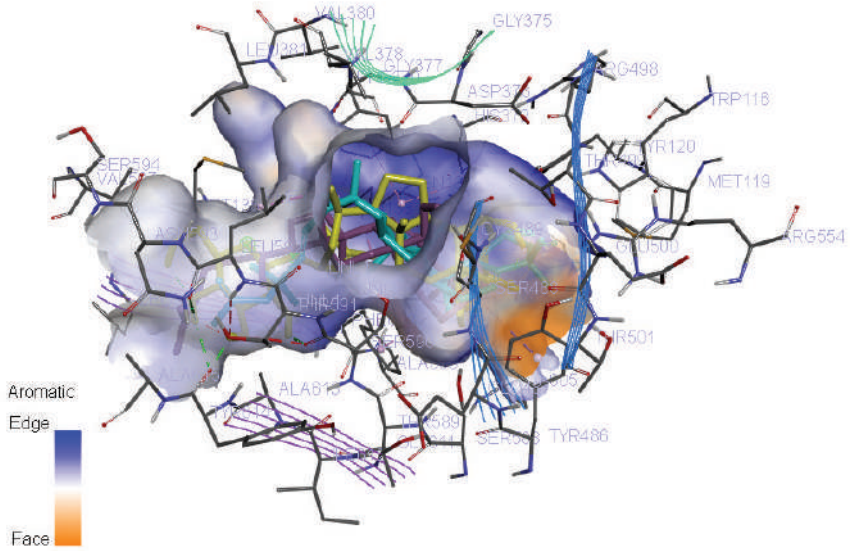


Figure 10. Surrounding the ligands, the blue regions represent the aromatic ends and the red regions represent the non-aromatic parts.

Evaluation of Interactions of Cucurbitacin-B and CPT 2 Enzyme (PDB ID: 2H4T)

In this study, the herbal ligand that can inhibit the CPT 2 enzyme with the most appropriate free energy of binding is cucurbitacin-B and its K_i value was 57.11 pM and ΔG value was -13.98 kcal/mol. The results of cucurbitacin-B were followed by momordicin II, another cucurbitan class molecule, and with its value of 72.69 pM, it is also a very successful inhibitor candidate. The locations of momordicin II and cucurbitacin-B in the CPT 2 enzyme (pdb code: 2FW3) were examined by superimposing them for easier comparison (Fig. 9). The interactions of cucurbitacin-B in 2H4T are explained in detail in the figures below.

While cucurbitacin-B was located in the cavity in the binding site of the CPT 2 enzyme, it was surrounded by α-helices on one side and β-sheet structures on the other. Since cucurbitacin-B is a large molecule in the triterpenoid class, it could only fit into this cavity by standing parallel to the parallel β-sheets surrounding it. As seen in Figure 11, the long side chain attached to the core structure of the ligand stood very close to the two-loop structure of the protein and managed to locate the cavity by approaching the cavity formed by the β-sheet structure, shown in blue, which takes the shape of a half-moon.

MET 135, GLY 600, SER 590, TYR 614 and PRO 133 are the residues shown in yellow in Figure 11 and are located on the secondary structures interacting with cucurbitacin-B. It is shown in Figure 11 that the structures that cucurbitacin-B interacts with are its two-loop structure and some small regions on β-sheets and that it does not interact with α-helices but can only interact with a small part of an α-helix.

The long side chain of cucurbitacin-B interacted with three different β-sheets, and Figure 11 shows that the residues with which it interacts were ALA 613, GLY 601, PHE 134, LEU 592 and PHE 602. The steroid ring of the ligand is attracted by ASN 593 and SER 488, which are predicted to be located on the loop structures of the protein. It is estimated that SER 488 was the only residue among these residues that attracted the ligand from the opposite direction, and the fact that the steroid ring structure of the ligand was folded in an L shape made it easier for it to be attracted by many residues on the other side.

Cucurbitacin-B did not use the ring structures in the center in aromatic interactions, and the two phenylalanyl residues formed reversible bonds only with the polar side chain of the ligand (Fig. 12). The most important of these are the 2.2 Å long hydrogen bond formed between PHE 134 and the oxygen atom of the ligand and the 2.31 Å long hydrogen bond formed between the same oxygen and GLY 601. Other important hydrogen bonds were seen between the lanostan ring and ASN 593, one of which is 1.78 Å long and formed with the oxygen atom of the ligand, and the other is the 2.27 Å long hydrogen bond formed with the hydroxyl group of the ligand (Fig. 12). Another hydrogen bond, which was shown to be quite strong, occurred between the hydroxyl group attached to the pentane ring of cucurbitacin-B and SER 488 at a distance of 1.95 Å. As shown in the figure, LEU 592 and PHE 602 made π-alkyl interactions with the ligand, and ALA 613 made two π-alkyl interactions.

The residues which cucurbitacin-B interacts with van der Waals in the CPT 2 enzyme are HIS 372, PHE 370, SER 490, GLY600, MET 135, SER 590, THR 591, LEU 381 and VAL 378, shown as light green spheres.

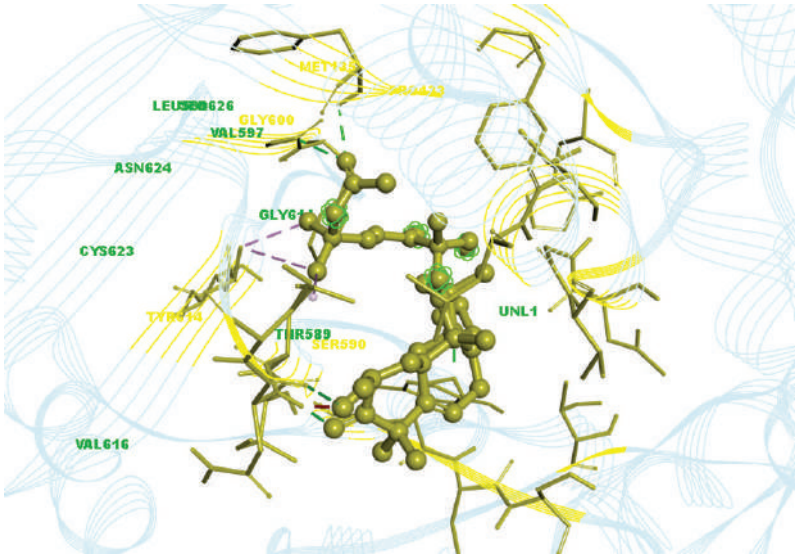


Figure 11. Cucurbitacin-B, in the CPT 2 enzyme binding region, the regions and amino acids with which it interacts closely are written with yellow, van der Waals interactions with green.

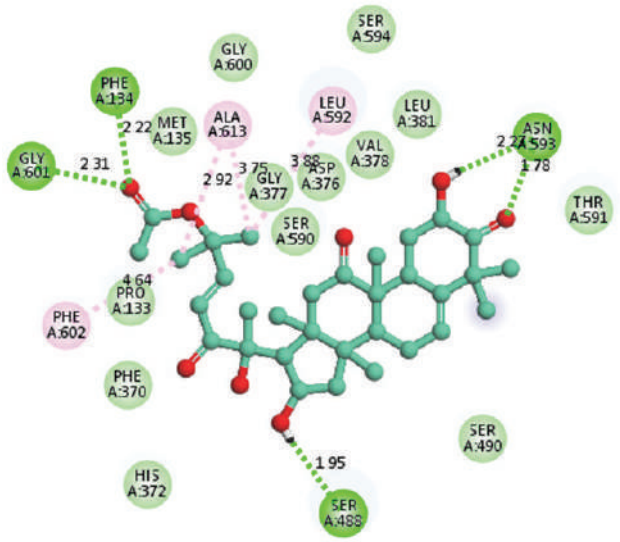


Figure 12. 2D representation of the possible interaction network of cucurbitacin-B and CPT 2 enzyme. Cucurbitacin-B is represented in the center with a ball-and-stick model, with carbon atoms in green, oxygens in red, and hydrogens in white. π-alkyl interactions within the protein are shown as pink dashed lines and hydrogen bonds as green dashed lines.

The values shown for the inhibition of CPT 2 enzyme (2FW3) prove that cucurbitacin-B, momordicin II, oreganol and charantadiol-A can show an anthelmintic effect by affecting lipid metabolism. While reversible inhibition of CPT 2 enzyme does not cause any significant side effects, metabolites produced in case of short-term inhibition lead to the death of some helminth species [7].

The results in Figure 13 show the using of correct points in selecting the grid box center in the docking procedure greatly affects the results. The coordinates of the selected center for 2H4T were taken from Taylor et al. [7]. For 2FW3, the center region of the protein was taken as the center. Although a grid box of 60×60×60 was created for both of them, the automatic determination of the center for 2FW3 caused changes in the ΔG values.

It is important to understand the effect pathway of cucurbitacin-B working as an anthelmintic compound. CPT 2 inhibition results from the increasing level of CPT 2 substrates, and this condition causes the death of helminths (Fig. 14).

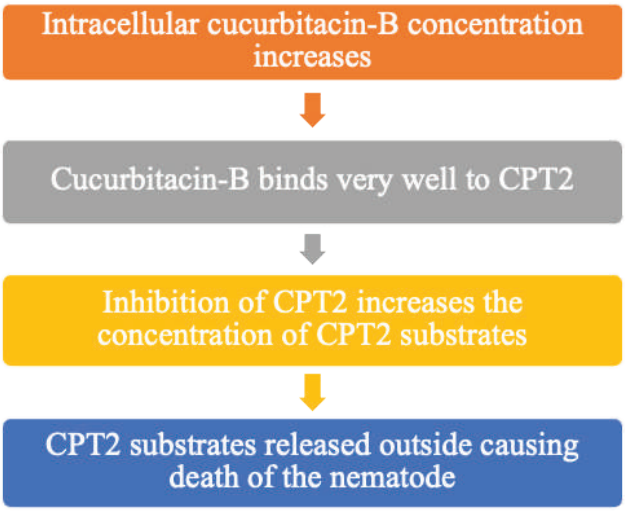
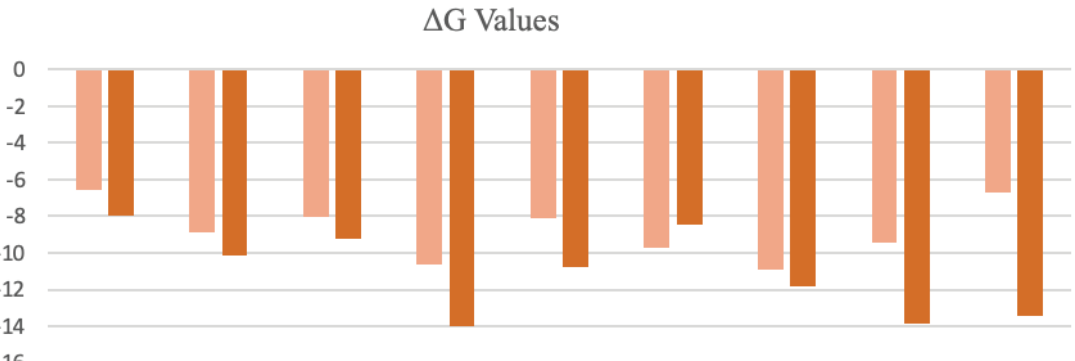


Figure 14. Flow chart of the CPT2-related mechanism of action of cucurbitacin-B.



	ODTA ME	Apigeni n	Arteann uin-B	Cucurbi tacin-B	Diosme tin	Eriocitri n	Charant adiol-A	Momor dicin II	Oregan ol
2FW3	-6,55	-8,85	-8,07	-10,64	-8,1	-9,72	-10,92	-9,43	-6,72
2H4T	-7,98	-10,15	-9,23	-13,97	-10,77	-8,43	-11,85	-13,83	-13,45

Figure 13. Comparison of the ΔG values found in the dockings of nine ligands with 2FW3 and 2H4T (CPT 2 enzyme).

In some important studies, active compounds in the plants were searched via *in silico* methods, and the predictions were presented on the activity of herbal ligands. The theoretical structure of Hcβ-tubulin used in this current study has been tried in molecular docking experiments to evaluate the anthelmintic effects of some derivative molecules [20]. Hcβ-tubulin is an important antinematodal target, but there is no crystallographic structure of Hcβ-tubulin in any database, and it is the first time the theoretical structure in this study shows the anthelmintic properties of herbal secondary metabolites. In another study, compounds such as ellagic acid, quercetin, isoquercetin, and caffeic acid in *Achyrocline satureioides* were isolated. Then caffeic acid was searched *in silico* and *in vitro* regarding antioxidant and toxicological activities. As a result, the prediction of *in silico* toxicity of quercetin, isoquercetin, and caffeic acid showed a low toxic risk [21]. While it was being researched *in vivo* anthelmintic effect of *Cordia dichotoma* (Forst.) root extract, the compounds that had been shown to have existed in this plant were searched *in silico* [22]. Like in this current study, it was predicted *in silico* which compounds are related to the biological activity of the extract. They also carried out docking experiments with the target protein by selecting the components according to the results of the literature screening without purifying them. In this way, they predicted which component caused the biological activity of the extracts. However, in the literature, there are not any dual-acting herbal compounds that can inhibit the target enzymes at pM levels *in silico*.

Among the bioactive compounds contained in the plants evaluated in this current study, those found in the highest amounts as specific to the plant were determined according to the results of previously conducted spectroscopy and chromatography analyses [23-25]. The results of this study can be used to reduce workload and cost. This data can be evaluated before purifying these components one by one in future studies and investigating their anthelmintic effects via *in vivo* and *in vitro* studies. With the Hybrid NAR-RBFs Networks simulation, the spread of helminthic diseases in the world can also be investigated [2]. Thus, an important study will be carried out to control diseases affecting millions of people.

Essential oil and water extract of *O. vulgare* were shown to have an antiproliferative effect on some cancer cells *in vitro*. Carvacrol, being the most abundant compound, was shown to a 90,42% range in the essential oil of *O. vulgare*. In comparison to essential oil and extract, it was found that essential oil has a more antiproliferative effect than water extract. However, the cytotoxicity of the extract was more than that of the essential oil [26]. It should be investigated that this cytotoxic effect of the water extract is related to which secondary metabolites of oregano. These secondary metabolites can show a similar cytotoxic effect on helminth cells.

It was discovered that the *Origanum* extract (10 mg/ml) has ovicidal activity on egg hatching of *Haemonchus contortus*, depending on the dose [27]. The antiparasitic effect of oregano oil was also previously shown [28]. However, in this study, the docking results of carvacrol and thymol, the main components of oregano oil, did not indicate a significant anthelmintic property. This result was attributed to the small number of interactions of the molecules within the target proteins. The oreganol found in oregano infusion was shown for the first time to have a very significant anthelmintic potential. Oregano oil is a highly irritating liquid and is unpleasant to take orally. Oregano tea is both delicious and beneficial to health [29].

Artemisinin is both an anthelmintic agent on *H. contortus* [30] and has been used for antimalarial purposes for years, and is the reason why the *A. annua* L., from which it is obtained, is planted in large areas. However, arteannuin-B has not been studied as much as artemisinin, and the great potential of this molecule is ignored. In this study, while it was shown in ADME research that arteannuin-B is suitable for oral administration, it was also shown through molecular docking that it has the potential to inhibit B-tubulin and AsFR enzymes. Arteannuin-B is a drug candidate that deserves more detailed research.

The antinematodal effect of bitter melon on swine nematode was shown in a previous study. 70% ethanolic extract of *Momordica charantia* L. folium showed the lethal effect on *Ascaris suum* at the 88% range [31]. In this study, the molecular mechanism of secondary metabolites that could cause this effect was investigated.

Most helminth species feed and survive by absorbing glucose via the cells outside their bodies. Since momordicin I and II, two active compounds found in bitter melon can inhibit glucose absorption [32], these two active compounds are good candidates to show the anthelmintic effect. This is the first study showing the antihelmintic effect of cucurbitacin-B and momordicin II that can inhibit antinematodal targets CPT2 and AsFR with favorable *Ki* values at very low levels.

One of the most important results from this study is that a branched side chain attached to cyclopentane in the steroid ring directly affects the affinity to the CPT 2 binding site. In addition, cucurbitacin-B, momordicin II, charantadiol-A, stigmasterol and friedelin, which have a large core with the union of at least four rings, require a slightly larger cavity to displace in the protein, which prevents them from being positioned in tubulin. This result provided new data that can be evaluated in the discovery of alternative drugs with fewer side effects than ABZ. Docking analyses of these molecules support this. These ingredients are promising in eliminating nematode species found in the gastrointestinal system (GIS), especially those that disrupt the cognitive and physical development of children. As a result of the screening performed with the SwissADME web server, the GI absorption of these compounds was found low. However, these properties will have a positive effect on increasing the inhibition against helminths in the GI system. Thus, the concentration of these molecules in the GIS will not

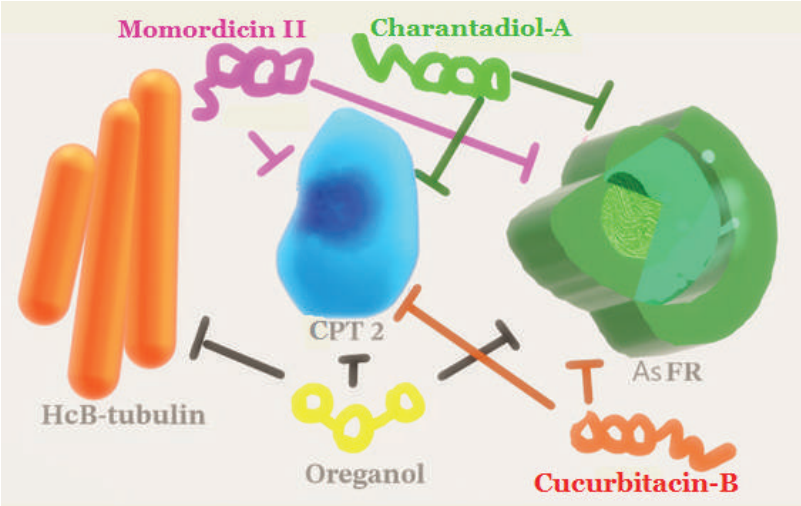


Figure 15. Inhibition diagram of most potent herbal ligands.

decrease easily, and helminths will be exposed to these molecules more intensely. Normally, these triterpenoid molecules are insoluble in water, and these components can be taken orally with oil-based solvents. Since the monoterpenes contained in Oregano essential oil can easily pass through the cell membrane and penetrate the skin, they can be evaluated in developing drugs that can be applied as ointments against parasites that form nodules on the skin. In this respect, it is a rational approach to investigate GABA receptors specific to parasites such as Dracunculiasis as primary targets in developing monoterpene-based inhibitors.

Some derivative molecules can show more effectiveness on the same target enzyme if the substituted groups are changed or added. Some eriocitrin derivatives were found to be more effective than eriocitrin in the CPT 2 inhibition, and this result signed a more potential inhibition ability for a derivative molecule possessing a natural glycoside scaffold [33]. Arteannuin-B is a potential anthelmintic drug scaffold, according to the current study in terms of ADME results and inhibition constants for B-tubulin inhibition. Therefore, arteannuin-B can be chosen for the rational *in silico* drug design of novel derivative molecules in the case of benzimidazole resistance. Corporations have been donating millions of tablets benzimidazoles each year. Therefore, resistance development can be seen in the near future.

The docking simulations of this study revealed that the most rational drug combinations might be oreganol + cucurbitan (charantadiol-A, momordicin II, or cucurbitacin-B). This combination also seems suitable as a broad-spectrum drug candidate because oreganol inhibits Hcβ-tubulin, while cucurbitan ligands can inhibit AsFR and CPT 2 at low concentrations. At the same time, oreganol is triple-acting inhibitor and these cucurbitans are dual-acting inhibitors (Fig. 15). Cucurbitacin-B, charantadiol-A, and momordicin II inhibited CPT 2 and AsFR enzymes at nanomolar inhibition constants (5,31 nM, 16,6 nM, and 40,78 nM for AsFR; 0,0571 nM, 2,06 nM, and 0,072 nM for CPT 2 enzyme, respectively). As oreganol inhibited all of these enzymes at low K_i values (K_i = 24,32 nM for Hcβ-tubulin, 1,9 nM for AsFR, and 0,137 nM for CPT 2 enzymes). In the literature, there is limited information about oreganol and there is no data about the anthelmintic property of this compound. It is the first study to show the anthelmintic effect of oreganol *in silico*.

These results will guide researchers who aim to design or synthesize drugs for the treatment of various helminthic diseases and thus positively affect the health of millions of people. This study provides new data regarding structure-activity and suggests a scaffold to replace Ivermectin from macrocyclic lactones. Ivermectin is a drug licensed only for use in animals, but since there is no alternative, it is used in humans to treat *O. volvulus* infection. Approximately 270.000 people are infected with this nematode, which causes blindness [1]. Therefore, there is an urgent need to discover new drugs for its treatment.

CONCLUSION

According to the results of this study, cucurbitacin-B is an alternative drug candidate to Ivermectin.

It is also important for an anthelmintic drug candidate to have a broad spectrum to use fewer drug and to have easier access. Since oreganol has inhibitory properties for three different target proteins in this study, it has the potential to meet this desired broad-spectrum need.

Most importantly, when considered as a folk medicine, since oreganol is found in oregano infusion and cucurbitacins are found in the fleshy fruit and leaves of the bitter melon, it was estimated in this study with *in silico* calculations that oregano tea and bitter melon fruit would be useful in removing of parasitic worms in the body.

These molecular docking results show that herbal compounds could be broad-spectrum anthelmintic drugs with multi-inhibition properties. This is significant because it demonstrates that anthelmintics, often required, can be obtained from oregano and bitter melon. This study is the first to demonstrate the potential interactions of these compounds with target proteins. Oreganol was first shown as an anthelmintic secondary metabolites possessing triple-acting inhibition ability. Cucurbitans are worth researching with further *in vivo* studies for the treatment of *O. volvulus* infection. Oreganol, cucurbitacin-B, momordicin II and charantadiol-A should be isolated from plants and should be tried on target nematodal proteins and enzymes to observe the inhibition properties *in vitro*.

ACKNOWLEDGEMENTS

We would like to dedicate this study to our esteemed professor, Prof. Dr. Metin Aktaş. His an epidemic disease in 83 is always alive.

We are very thankful to Özkılıç and Tüzün for their informational support and inspirational article: "*In silico* methods predict new blood-brain barrier permeable structure for the inhibition of kynurenine 3-monooxygenase."

AUTHORSHIP CONTRIBUTIONS

Authors equally contributed to this work.

DATA AVAILABILITY STATEMENT

The authors confirm that the data that supports the findings of this study are available within the article. Raw data that support the finding of this study are available from the corresponding author, upon reasonable request.

CONFLICT OF INTEREST

The author declared no potential conflicts of interest with respect to the research, authorship, and/or publication of this article.

ETHICS

There are no ethical issues with the publication of this manuscript.

STATEMENT ON THE USE OF ARTIFICIAL INTELLIGENCE

Artificial intelligence was not used in the preparation of the article.

REFERENCES

[1] World Health Organization. Parasitic Infections. Available at: http://www.who.int/mediacentre/factsheets/fs366/en/. Accessed on July 18, 2017.

[2] Ahmad A, Farman M, Sultan M, Ahmad H, Askar S. Analysis of hybrid NAR-RBFs networks for complex non-linear Covid-19 model with fractional operators. BMC Infect Dis 2024;24:1–19. [CrossRef]

[3] Yelekçi K, Büyüktürk B, Kayrak N. In silico identification of novel and selective monoamine oxidase B inhibitors. J Neural Transm 2013;120:853–858. [CrossRef]

[4] Karaman D. Prediction on the Anthelmintic Effects of Some Herbal Ligands and Their Derivatives with In Silico Molecular Modelling Method [Doctoral thesis]. Bursa: Bursa Uludag University; 2022.

[5] Daina A, Michielin O, Zoete V. SwissADME: a free web tool to evaluate pharmacokinetics, drug-likeness and medicinal chemistry friendliness of small molecules. Sci Rep 2017;7:42717. [CrossRef]

[6] Kaplan RM. Drug resistance in nematodes of veterinary importance: a status report. Trends Parasitol 2004;20:477–481. [CrossRef]

[7] Taylor CM, Wang Q, Rosa BA, Huang SCC, Powell K, Schedl T, et al. Discovery of anthelmintic drug targets and drugs using chokepoints in nematode metabolic pathways. PLoS Pathog 2013;9:1003505. [CrossRef]

[8] Ceccarelli SM, Chomienne O, Gubler M, Arduini A. Carnitine palmitoyltransferase (CPT) modulators: a medicinal chemistry perspective on 35 years of research. J Med Chem 2011;54:3109–3152. [CrossRef]

[9] Karaman D, Girişgin AO, Girişgin O. Is the Inevitable End or the Happy End? In Silico Anthelmintic Resistance Development Scenario, Arteannuin-B is in the Leading Role. In: Proceedings of the International Asian Congress on Contemporary Sciences-V; 2021 Jun; Nakhchivan, Azerbaijan. p. 741–749.

[10] Centers for Disease Control and Prevention. Parasites - Onchocerciasis (also known as River Blindness). Available at: https://www.cdc.gov/filarial-worms/treatment/onchocerciasis.html. Accessed on December 6, 2024.

[11] Dassault Systèmes. BIOVIA Discovery Studio Modeling Environment, Release 2020. San Diego: Dassault Systèmes; 2020.

[12] Huey R, Morris GM, Olson AJ, Goodsell DS. A semiempirical free energy force field with charge-based desolvation. J Comput Chem 2007;28:1145–1152. [CrossRef]

[13] Morris GM, Huey R, Lindstrom W, Sanner MF, Belew RK, Goodsell DS, et al. AutoDock4 and AutoDockTools4: Automated docking with selective receptor flexibility. J Comput Chem 2009;30:2785–2791. [CrossRef]

[14] Inaoka DK, Shiba T, Sato D, Balogun EO, Sasaki T, Nagahama M, et al. Structural insights into the molecular design of flutolanil derivatives targeted for fumarate respiration of parasite mitochondria. Int J Mol Sci 2015;16:15287–15308. [CrossRef]

[15] Robinson MW, McFerran N, Trudgett A, Houy L, Fairweather I. A possible model of benzimidazole binding to beta-tubulin disclosed by invoking an inter-domain movement. J Mol Graph Model 2004;23:275–284. [CrossRef]
[16] Hsiao YS, Jogl G, Esser V, Tong L. Crystal structure of rat carnitine palmitoyltransferase II (CPT-II). Biochem Biophys Res Commun 2006;346:974–980. [CrossRef]
[17] Rufer AC, Thoma R, Benz J, Stihle M, Gsell B, De Roo E, et al. The crystal structure of carnitine palmitoyltransferase 2 and implications for diabetes treatment. Structure 2006;14:713–723. [CrossRef]
[18] Morris GM, Goodsell DS, Halliday RS, Huey R, Hart WE, Belew RK, et al. Automated docking using a Lamarckian genetic algorithm and an empirical binding free energy function. J Comput Chem 1998;19:1639–1662. [CrossRef]
[19] Tyagi R, Maddirala AR, Elfawal M, Fischer C, Bulman CA, Rosa BA, et al. Small molecule inhibitors of metabolic enzymes repurposed as a new class of anthelmintics. ACS Infect Dis 2018;4:1130–1145. [CrossRef]
[20] Satyendra RV, Vishnumurthy KA, Vagdevi HM, Rajesh KP, Manjunatha H, Shruthi A. Synthesis, in vitro antioxidant, anthelmintic and molecular docking studies of novel dichloro substituted benzoxazole-triazolo-thione derivatives. Eur J Med Chem 2011;46:3078–3084. [CrossRef]
[21] Salgueiro AC, Folmer V, da Rosa HS, Costa MT, Boligon AA, Paula F, et al. In vitro and in silico antioxidant and toxicological activities of Achyrocline satureioides. J Ethnopharmacol 2016;194:6–14. [CrossRef]
[22] Jamkhande PG, Barde SR. Evaluation of anthelmintic activity and in silico PASS assisted prediction of Cordia dichotoma (Forst.) root extract. Anc Sci Life 2014;34:39–43. [CrossRef]
[23] Özcan MM, Pedro LG, Al-Juhaimi F, Endes Z, Erol AS, Duman E, et al. Constituents of the essential oil of Origanum vulgare subsp. hirtum growing wild in Turkey. J Essent Oil Bear Plants 2012;15:572–576. [CrossRef]
[24] Li W, Lin Z, Yang C, Wang Y, Qiao Y. Study on the chemical constituents of Momordica charantia L. leaves and method for their quantitative determination. Biomed Res 2015;26:415–419.
[25] Abu-Shandi K, Al-Rawashdeh A, Al-Mazaideh G, Abu-Nameh E, Al-Amro A, Al-Soufi H, et al. A novel strategy for the identification of the medicinal natural products in Rubus fruticosus plant by using GC/MS technique: A study on leaves, stems and roots of the plant. Adv Anal Chem 2015;5:31–41.
[26] Erenler R, Çarlık ÜE, Aydın A. Antiproliferative activity and cytotoxic effect of essential oil and water extract from Origanum vulgare L. Sigma J Eng Nat Sci 2023;41:202–208. [CrossRef]
[27] Castro LLD, Madrid IM, Aguiar CLG, Castro LM, Cleff MB, Berne MEA, et al. Origanum vulgare (Lamiaceae) ovicidal potential on gastrointestinal nematodes of cattle. Cienc Anim Bras 2013;14:508–513.
[28] Pensel PE, Maggiore MA, Gende LB, Eguaras MJ, Denegri MG, Elissondo MC. Efficacy of essential oils of Thymus vulgaris and Origanum vulgare on Echinococcus granulosus. Interdiscip Perspect Infect Dis 2014;2014:693289. [CrossRef]
[29] Treben M. Health Through God's Pharmacy: Advice and Proven Cures with Medicinal Herbs. 6th ed. Germany: Ennsthaler; 2007.
[30] Cala AC, Ferreira JFS, Chagas ASC, Gonzalez JM, Rodrigues RAF, Foglio MA, et al. Anthelmintic activity of Artemisia annua L. extracts in vitro and the effect of an aqueous extract and artemisinin in sheep naturally infected with gastrointestinal nematodes. Parasitol Res 2014;113:2345–2353. [CrossRef]
[31] Tjokropranoto R, Nathania M. Anthelmintic effect of ethanol extract of pare leaf (Momordica charantia L.) against female Ascaris suum worm in vitro. J Medika Planta 2011;1:33–39.
[32] Liu H, Wang GC, Zhang MX, Ling B. The cytotoxicology of momordicins I and II on Spodoptera litura cultured cell line SL-1. Pestic Biochem Physiol 2015;122:110–118. [CrossRef]
[33] Karaman D, Girişgin AO, Girişgin O. Eriocitrin derivatives and their anthelmintic potentials. Sigma J Eng Nat Sci 2024;42:875–884. [CrossRef]

Sigma Journal of Engineering and Natural Sciences
Web page info: https://sigma.yildiz.edu.tr
DOI: 10.14744/sigma.2025.00000

Research Article

Analysis of efficient solar operated air cooling system for cold storage warehouses

Prakash P. THOMBARE[1,*], Ravindra D. PATIL[1]

[1]*Department of Mechanical Engineering, J. T. Mahajan College of Engineering Faizpur, Maharashtra, 425524, India*

ARTICLE INFO

Article history
Received: 15 October 2024
Revised: 19 November 2024
Accepted: 13 January 2025

Keywords:
Air Cooling System; Cold Storage; Solar Energy; Sustainability

ABSTRACT

Increased demand for sustainable and energy-efficient solutions from the agriculture and food preservation industries will encourage the development of new technologies in cold storage warehouses. This study mainly investigates an effective solar-powered air conditioning system created especially for cold storage applications. The suggested solution seeks a reduction of the environmental impact, operation expenses, and dependency of the existing cooling methods on traditional electric sources by employing solar energy. This was about designing and building a solar air conditioning system that would utilize advanced components: solar panels, thermal storage devices, and energy-saving compressors. These are performed through the use of simulation models and experimental settings under various environmental conditions and operating loads. In order to identify the feasibility of solar cooling, all the major performance indices are studied, such as cooling capacity, energy consumption, and cost-effectiveness of the system. The results show a considerable reduction in the rate of greenhouse gas emission compared to conventional cooling systems, with significant gains in energy efficiency. This study also considers financial viability at large-scale deployment to answer the question of how widely it may be adopted in areas where abundant solar energy is available. The outcome of this study provides a roadmap for future development of solar-operated cooling systems and very informative insights toward the creation of sustainable cold storage solutions. This research work contributes towards the development of renewable energy-based cold storage infrastructure in realizing the large objectives of the sector on energy sustainability and environmental conservation in food preservation.

Cite this article as: Thombare PP, Patil RD. Analysis of efficient solar operated air cooling system for cold storage warehouses. Sigma J Eng Nat Sci 2026;44(1):592–604.

INTRODUCTION

With its strong economic growth, urbanization, and expanding industrial activities, energy demand in India is surging fast in 2024. The country's energy demand will see the fastest growth in the world through 2050, thus requiring heavy investments in both renewable and conventional sources of energy. True, India's energy consumption is based on coal, oil, and natural gas, but there is an

*Corresponding author.
*E-mail address: ppthomabre@gmail.com

This paper was recommended for publication in revised form by Editor-in-Chief Ahmet Selim Dalkilic

Published by Yıldız Technical University Press, İstanbul, Turkey
© Author. This is an open access article under the CC BY-NC license (http://creativecommons.org/licenses/by-nc/4.0/).

increasing awareness to extend this to renewable sources like solar and wind power [1,2]. This shift is part of India's broader strategy to secure its energy future while reducing carbon emissions and enhancing energy efficiency [3]. The overall energy demand in India continues to rise, driven by the nation's development and growing population. To meet this escalating demand, India is focusing on improving its energy infrastructure and increasing efficiency, while also making substantial investments in sustainable energy sources [4].

The use of cold storage warehouses for perishable commodities is very much essential to preserve quality and safety. Conventional cooling systems in big warehouses heavily depend on electricity, which usually comes from nonrenewable resources. This generates hefty running costs and large environmental impacts. There is a greater demand for more sustainable and energy-efficient cooling systems to fight against climate change with the rise in global energy consumption [5]. This is where solar energy plays its part. Among the possible alternative options, it might be able to fuel cold storage warehouses with its availability and renewable nature in order to lessen dependence on fossil fuels. This could mean that the incorporation of solar-powered air conditioning systems would serve as a cost-effective and ecologically feasible solution, falling in line with global efforts toward sustainability and carbon footprint reduction. However, certain challenges exist in applying solar cooling technologies to cold storage facilities, including variability of the solar energy supply, a requirement for reliable continuous cooling, and optimization of system performance [6].

About 80% of the world's energy is fed by fossil fuels. It is, therefore, very important to consider the principles of sustainability in energy use. Legislative efforts and research projects increasingly aim at energy conservation and the use of renewable sources. The goal is the optimization of energy use by providing the energy necessary for transformation processes, keeping production and quality of life levels. This strategy aims to minimize energy transition losses, reduce costs, and alleviate environmental concerns. A rational energy use scheme brings huge economic and environmental benefits, such as a reduction in the consumption of fossil fuel, power consumption, and pollutant emission [7,8]. With the need to stay cool within the confines of a building, air conditioning demand has risen over the past years. Due to that, there has been an increasing usage of compression-based air conditioning systems, which raises peak electric power consumption dramatically during summer. In turn, this has continually led to exceeding network capacity limitations and creating hazards of blackouts. This is the growth in energy demand over time is shown in Figure 1. Especially in the last decade, in fact, studies have been conducted over the last three decades to develop green air conditioning systems using novel solar energy technology. Among the various technologies available, hybrid trigeneration systems and solar cooling plants are discussed [9].

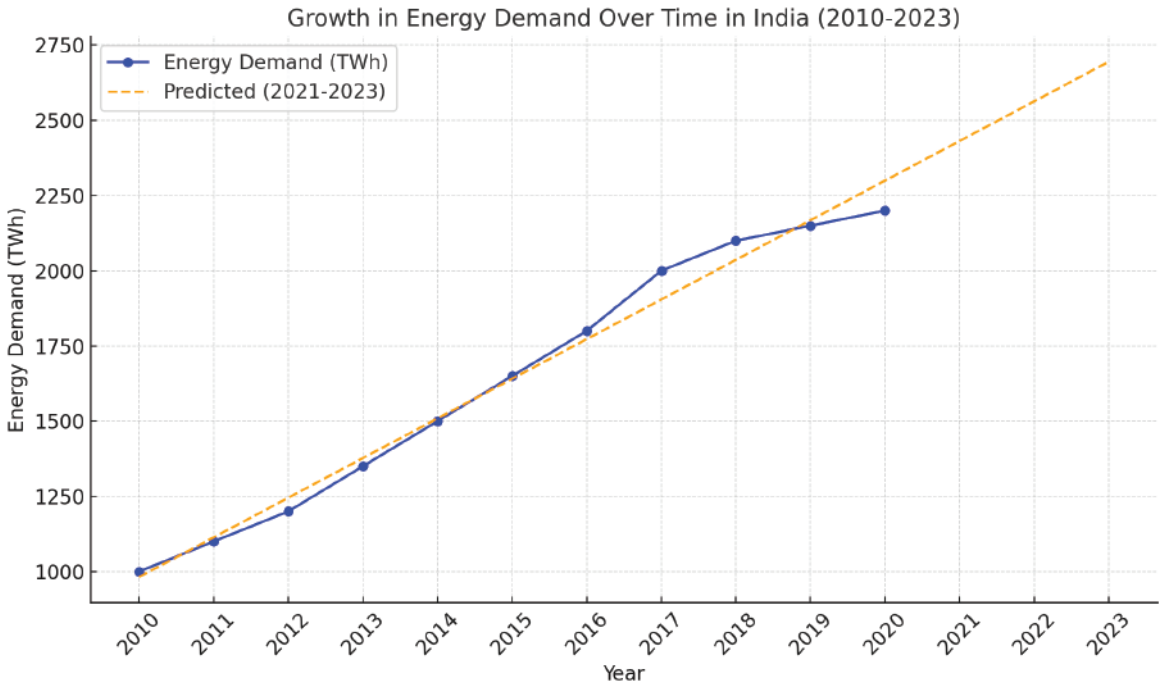


Figure 1. Energy demands in India.

The present work investigates the performance of solar-powered air conditioning systems designed for cold storage warehouses. It discusses the technical and economic feasibility of such systems, along with the evaluation of their performance for various climatic conditions, and the identification of the critical parameters influencing their performance. In this regard, the research focuses on informing and recommending efficient designs and installations of solar-powered cooling systems through an investigation of recent advances in solar cooling technologies and their application for cold storage. Finally, the research will also greatly help in designing appropriate sustainable cooling systems that can enhance the operating efficiency of cold storage warehouses while reducing their environmental impact [10]. This research aims to optimize design parameters for a solar-operated cooling system specifically designed for cold storage warehouses, an alternate, sustainable solution to conventional systems. The novelty of the approach will be in analyzing key parameters through experimental approach that highlight cost and environmental benefits. The theme is to ensure that higher energy prices do not offset profits, reduce greenhouse gas emissions, ensure some access to energy for remote areas, and improve economic viability for farmers.

Literature Review

Sustainability and energy efficiency have nowadays increased worldwide, driving innovation in many industries, among which the cold storage industry takes its part. Among the different approaches under development and research for cold storage warehouses, integrating solar-operated air cooling systems arguably creates more opportunities for enhancing their energy efficiency. This review discusses the state of the art of research and consequently the development in the context of effectiveness, challenges, and future directions of the use of solar-powered cooling technologies for cold storage warehouses [11].

In general, solar cooling has two major entities: solar thermal and PV systems. Solar thermal cooling is driven by energy captured by solar collectors, where the energy from the sun is converted into thermal to drive the cooling cycles, such as absorption or adsorption, whereas PV systems produce electrical output directly from sunlight to power a conventional cooling system, such as an MCR unit [12]. Research by some researchers provides a comparative analysis of solar thermal and PV systems in cold storage applications. Their findings suggest that solar thermal systems, particularly those using absorption chillers, can be more efficient in regions with high solar irradiance [13]. Conversely, PV systems offer greater flexibility and can be more easily integrated into existing infrastructure, but may require more space and higher initial investment [14].

Solar collectors' efficiency, availability of storage, and proper integration of TES into the cooling systems are among the various factors that may impact the general efficiency of solar-operated cooling systems. This therefore indicates that with high-efficiency collectors and well-designed TES systems that will assist in managing the intermittent solar energy supply, the COP for the solar cooling systems could be significantly higher. Cold storage warehouses hold special cooling needs, which sometimes means the area must be cooled continuously while maintaining an accurate temperature [15]. Studies by Zhu et al. (2022) highlight that solar cooling systems, when integrated with advanced control systems and energy storage, can meet these demands effectively. However, performance can be affected by seasonal variations in solar availability and the efficiency of backup systems during low solar periods [16].

Besides that, the economic factor is also a very important factor in adopting solar-operated cooling systems. It was concluded by Lopez et al. (2020) in a cost-benefit analysis that though the initial investment in solar systems can be very high, the possible long-term savings in energy costs added to possible incentives make them economically viable [17]. It depends on such factors as local solar radiation, energy prices, and available subsidies. The environmental impact of the solar-operated cooling systems means that they reduce the consumption of fossil fuel and lower the resultant greenhouse gas emissions. In one study, several authors have indicated that in integrating solar cooling technologies in cold storage warehouses, it would potentially make a valuable contribution toward carbon footprint reductions that add value to an overall sustainability objective [18]. Despite the advantages, solar-operated cooling systems face several challenges. Technical issues such as the need for efficient energy storage, system integration complexities, and maintaining optimal performance under varying environmental conditions are critical areas of concern [19]. Advances in energy storage technologies and smart grid integration are essential for overcoming these challenges [20].

MATERIALS AND METHODS

Optimal operation of solar-powered air conditioning in cold storage warehouses means maximum efficiency and performance should be achieved with a minimum of energy consumption and environmental impact. Figure 2 shows the scheme of the solar panels and warehouse plant.

The rooftop of the warehouse was chosen to install the Flat-plate collectors in order to identify a suitable location for installing the solar panels. When installed, the solar panels were interfaced with a battery storage system and an inverter to ensure that the cooling units had an assured supply of power throughout day and night. Absorption chiller cooling system was used. As the dirt and debris would affect the performance of the solar panels, periodic maintenance for cleaning the dirt was performed. The measurement instruments used were a solar irradiance meter, temperature sensors, humidity sensors, flow meters, power consumption meters, and a data logger. Multiple-point installations of temperature and humidity

sensors were installed inside the cold storage chamber to monitor uniformity in those respects. Solar irradiance meters were installed near the solar collectors to measure the solar energy input. Power consumption meters were connected to record energy usage by the cooling system. All sensors and measuring devices were connected to the data logger for continuous data recording. Before running the solar-operated cooling system, baseline data of ambient temperature, solar irradiance, and cold storage temperature were recorded. The solar-operated cooling systems were started and made sure that it attained stable operating conditions. Solar irradiance, temperature, humidity, and energy consumption throughout the operation period continuously monitored and recorded. The sensors used during the study were shown in Table 1. Temperature and humidity inside the cold storage chamber were also recorded. Section 4 presents the analysis of the system.



Figure 2. The solar panels and warehouse plant.

Table 1. Details of sensors used for the study

Sensor Type	Model/Type	Function	Accuracy	Range	Response Time
Temperature Sensor	PT100 Platinum RTD	Measures ambient, solar panel, refrigerant, and cold storage temperatures	±0.1°C	-200°C to 850°C	<1 second
Humidity Sensor	Capacitive (e.g., DHT22)	Measures relative humidity in the environment	±2% RH	0% to 100% RH	2 seconds
Solar Irradiance Sensor	Pyranometer (e.g., Kipp & Zonen CMP3)	Measures solar radiation on the collector surface	±5 W/m²	0 W/m² to 2000 W/m²	5 seconds
Airflow Sensor	Hot-Wire Anemometer (e.g., Testo 405 V1)	Measures airflow velocity and direction in ducts	±0.1 m/s	0 m/s to 20 m/s	<2 seconds
Pressure Sensor	Piezoelectric (e.g., Honeywell PX2)	Monitors refrigerant pressure in the system	±0.25% FS	0 bar to 25 bar	<10 milliseconds
Energy Meter	Digital (e.g., Fluke 1730)	Measures power consumption of the system	±0.2% of reading	1 W to 10 kW	<1 second
Data Acquisition System (DAQ)	NI CompactDAQ System	Records and synchronizes sensor data	±0.1% of input signal	1 Hz to 10 kHz (adjustable)	--

RESULTS AND DISCUSSION

Temperature Variation Over Time

Figure 3 presents a comparison of the performances between the temperature control by a solar-operated air cooling and a conventional cooling system in cold storage houses for a week, and it really shows some interesting trends for both efficiency and effectiveness [21]. The figure 3 demonstrates that during the course of the experiment, the solar-operated cooling had lower and fairly steady temperature recordings compared to that of the conventional cooling. One of the most striking observations to be made is that the temperature maintained by the solar cooling system is rather stable. From Day 2 it had a starting point slightly below 4.8°C. Until Day 4, from that day on, the increase in temperature gradually rose to a crossing point with the temperatures of the conventional system at about 5.0°C. In the solar system, after the fourth day, the temperature fell significantly after reaching the lowest on the sixth day at about 4.7°C before gradually rising again on the seventh day. It shows that the solar cooling system can respond well to changes through its cooling cycle, which sustains the lower temperature for a longer period, while the traditional cooling system is more erratic with respect to a higher temperature peak. Day 1 started at an approximate temperature of 5.0°C, and there was an increasing trend in the peak observed sharply on Day 5 to approximately 5.4°C. The subsequent fall after this probably means that the traditional system could not continue with the proper maintenance of temperature and that there might be some fluctuations, especially with regards to external factors affecting internal warehouse temperatures. The same can also bring inefficiency in maintaining ideal conditions for the storage of perishable items. Observed temperature patterns do show, however, that a solar-operated air cooling system can hold down temperatures for longer periods. This would translate into better product preservation in temperature-sensitive instances at less energy use and operation cost [22].

This would, in turn, provide evidence that the solar system, especially for regions receiving ample sunlight, may be even more viable in terms of sustainability and cost. Solar energy applied to air cooling systems in cold storage warehouses has huge environmental and economic advantages. The solar systems reduce greenhouse gas emissions and operating costs through the reduction of demands on traditional energy sources. The minimal fluctuation of temperature could indicate a probable reduced energy consumption in the solar-operated system, since it apparently needs less power input to achieve and sustain such levels of cooling [23].

Energy Consumption Comparison

A four-week energy consumption comparison between a solar-operated air cooling system and a traditional cooling system provides key lessons in efficiency and sustainability regarding the use of the solar-powered option in cold storage warehouses, as represented in figure 4. The data represented in this figure 4 shows a clear division in the energy use between the two systems, with the solar cooling system

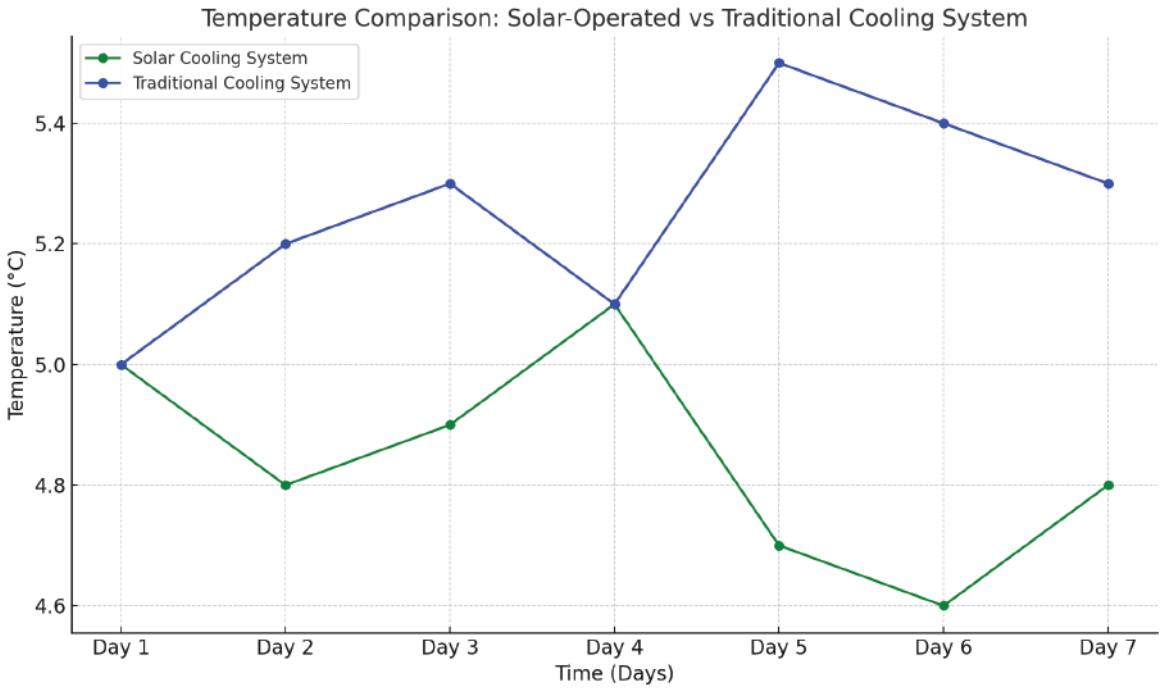


Figure 3. Temperature comparison: Solar- operated vs traditional cooling system.

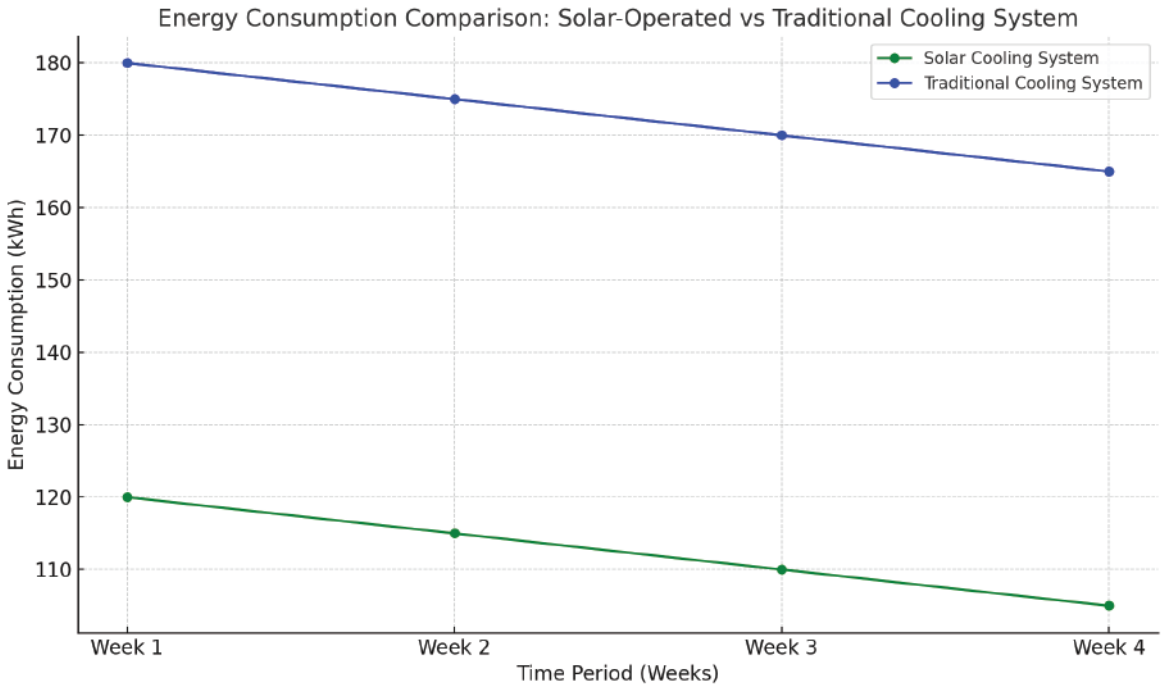


Figure 4. Energy consumption comparison: Solar- operated vs traditional cooling system.

recording a much lower amount of energy used across all four weeks [24].

This means that the energy consumption by the solar-operated cooling system is constantly less when compared to the conventional system of cooling. It starts with energy consumption of about 120 kWh in Week 1 and decreases gradually over the period. Around Week 4, the consumption will be roughly around 110 kWh. In contrast, the traditional cooling starts with much higher uses, about 180 kWh in Week 1 of the same trend, but it is always around 170 kWh in Week 4. It has been a consistent reduction in energy consumption over time, therefore explaining that such a solar system is efficient and could easily save a substantial amount of energy during long-term operation. The low energy use by the solar cooling system reduces operating costs and contributes to lower carbon emissions to help attain sustainability objectives. This data thus shows that the solar system is indeed a good alternative to the traditional cooling systems, having offered good, if not remarkable, reductions in energy use; these could translate to cost savings and lower environmental impact, especially in those regions where electricity is dominantly generated from fossil fuels [25].

The reduction in energy use for both systems over the four weeks would indicate stabilization or optimization of cooling operations, as the systems get 'acclimatized' to the conditions of the warehouse. On the other hand, the capability of the solar cooling system to maintain much lower energy usage through the entire period is indicative of superior performance in harnessing renewable energy sources effectively, probably benefiting from optimizing solar energy storage and usage strategies. Results have shown that in cold storage warehouses, solar-operated cooling systems can be very effective, especially in areas receiving abundant amounts of solar radiation. The reduction in energy use could make such operations more viable and economical. Besides, the smoothness of the energy consumption trend could mean that the efficiency of solar systems may remain unchanged over a certain period; therefore, it may be regarded as a reliable solution for cold storages that need to maintain proper temperatures at minimum energy cost [17].

Cost Savings Over Time

Figure 5 shows the cumulative cost savings that could be realized from the adoption of a solar-operated air cooling system compared with a conventional one over a 10-year period. As should be expected, wide gaps occur in the cost implications of the long-term operations of the two systems and are indicative of the financial justification of the adoption of solar energy for cold storage warehouses.

This graph plots three key curves: in blue, the cost of a traditional cooling system; in green, that of a solar-operated cooling system; and in red, the overall savings over a ten-year period. The traditional one shows a gradual and sharp increase in the accumulative costs, probably because the recurring costs associated with the consumption of electricity, maintenance, and probably increasing energy prices. Whereas at the close of the 10-year period, all costs of operating a traditional system seem to be over 5 million INR,

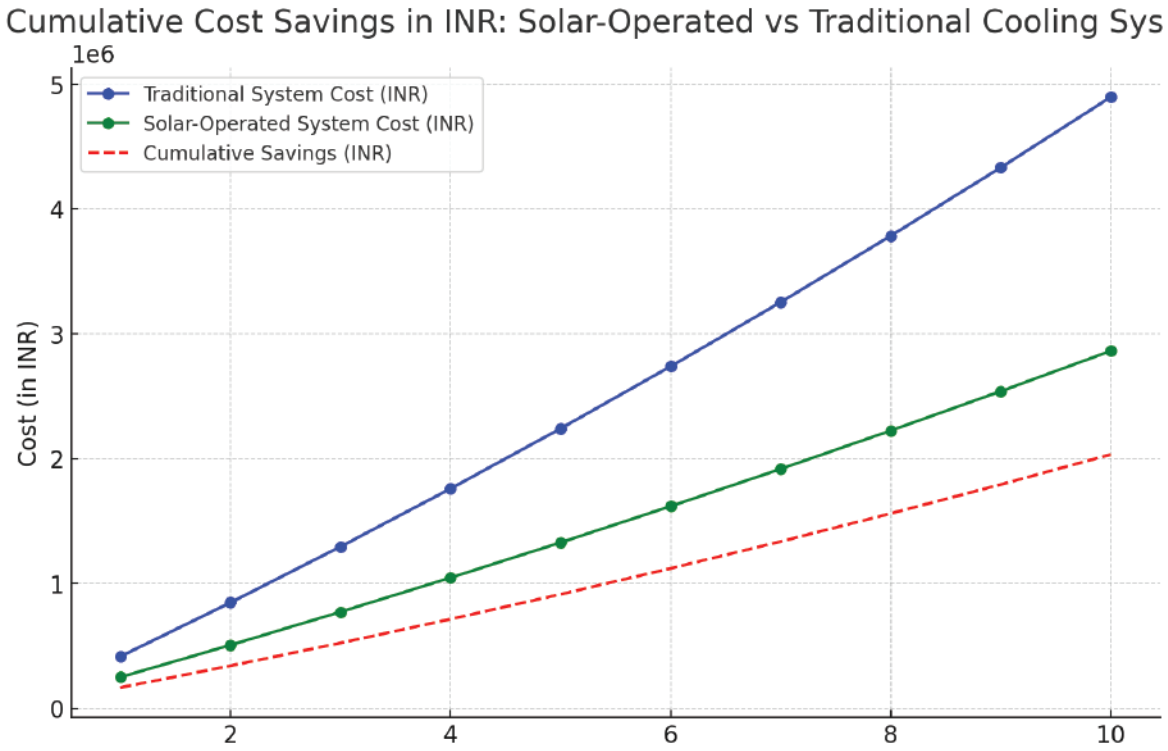


Figure 5. Cumulative Cost Savings Analysis: Solar- Operated vs Traditional Cooling System.

whereas in that respect, the solar-operated cooling system also shows an upward trend in its costs, though it is at a much lower rate. This lesser cost trajectory indicates the advantage of reduced operation cost because of the usage of solar energy. While the initial investment in solar technology and installation is high, the cost curve seems to balance itself in due time. The solar system's cost curve keeps staying below that of the traditional system. The cumulative cost for the solar system, by year 10, was a little over INR 2.5 million, about half of what it costs using the traditional system [26].

The red dotted curve in the graph signifies the cumulative savings accrued through the deployment of a solar-operated system over and above the conventional system. These start accruing right from day one and grow linearly with time. At the end of the 10-year period, the cumulated savings will be approximately INR 2.5 million. This result therefore indicates that although the solar-operated system will lower operating costs, it will also generate considerable long-term cost benefits. Indeed, it is from this that the major cost savings by the solar-operated system bear very strong implications for the cold storage industry. Considering the constantly high energy cost and becoming very much aware of the need to ensure sustainability, this switch to a solar-operated system could yield a dual benefit: a reduction of carbon footprint and at the same time a decrease in operational costs. These economies, for warehouse operators, could mean setting more competitive prices, realization of higher margins, or possibilities of investing further in enhanced technological capabilities.

System Efficiency at Different Solar Irradiance Levels

Figure 6 presents the performance of the solar-operated cooling system concerning various solar irradiance values. The trend in the results is linear such that the amount of increase in solar irradiance values, the efficiency is also increased. This observation is important in understanding the performance of the system under various conditions of solar energies, indispensable in cold storage warehouses operating in different geographical locations characterized by varied solar exposure. Below is a graph showing the positive correlation between the amount of solar irradiance in watt/square meter and the efficiency of the cooling system in percentage form. This rises from approximately 0.51% at a solar radiation of 200 W/m² to about 0.55% at 1000 W/m². While these ranges of percent variation might be slim, they do translate into significant gains in useful energy application when put to work on an extended time and extensive scale of cold storage house operations [27]. The testing is performed for a period of 3–6 months, during the peak summer and pre-monsoon periods to analyze the performance of the solar cooling system under varied climatic conditions. Observations are made on a daily basis, especially in peak sun hours between 9:00 AM and 5:00 PM. A place is selected based on its high level of solar irradiance and warm climatic conditions like Jalgaon, Maharashtra,

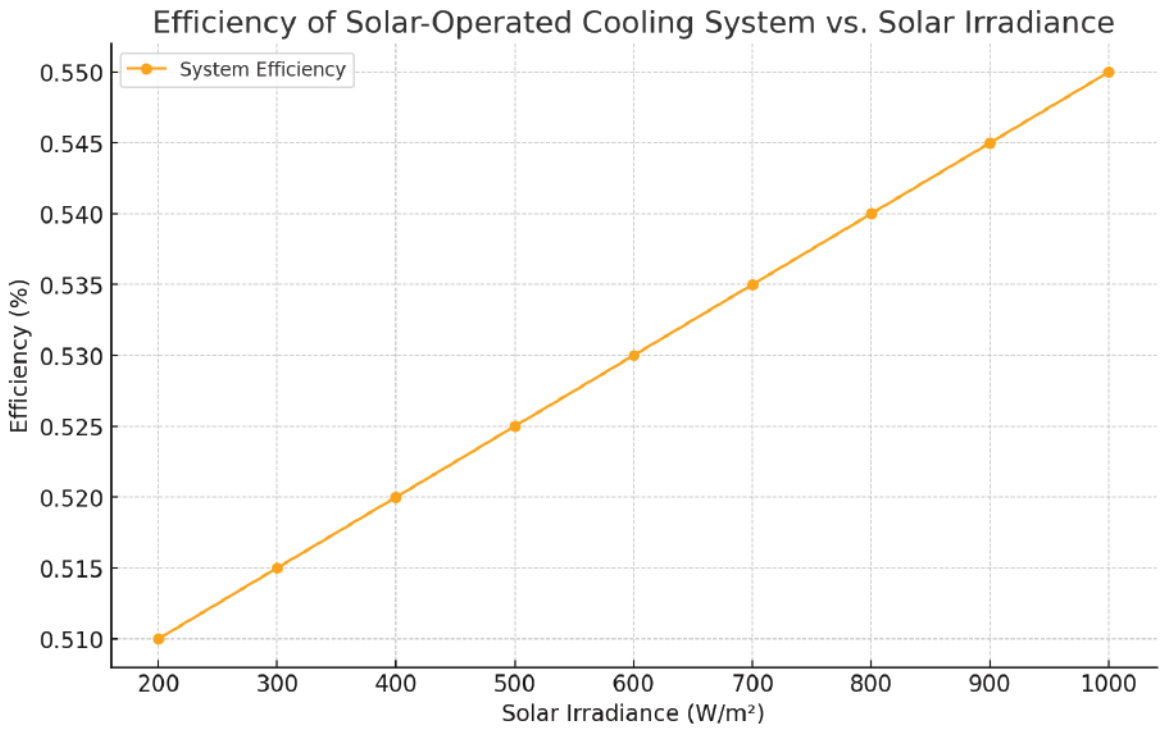


Figure 6. Efficiency of solar-operated cooling system.

with average solar radiation of 5–7 kWh/m²/day to achieve real-life performance results that best fit the ambient cold storage environment.

This proves that the efficiency increases linearly with the rise in irradiance level and supports that the system is correctly designed to harness available solar energy more efficiently as irradiance level increases. This performance characteristic is quite desirable for locations of high solar irradiance because this type of system can operate at its highest efficiency to achieve maximum energy savings, reducing reliance on grid electricity or any other non-renewable energy sources. Efficiency in the cold storage cooling system directly contributes to the determination of operational costs and sustainability goals. Consequently, better system efficiency at higher solar irradiance means that better energy savings with a reduced carbon footprint would be possible for facilities located in higher average solar irradiance locations. This may render solar-operated systems more appealing, especially for sunny regions, because it enables them to decidedly outperform the conventional energy-intensive cooling systems [18].

Even in regions with relatively low irradiance, while the efficiency has somewhat been reduced, it still holds up quite well, offering a large number of energy savings compared to conventional systems. That consistency in performance over varying levels of irradiance boosts the system's appeal as an adaptable solution that is right for many different climates. The linear relationship indicating efficiency with respect to solar irradiance points out some major conclusions about the system design optimization. Ensuring that the cooling system is provided with adequate solar panels and their installation at the most optimal angles will further enhance energy capture especially during peak sunlight times. Besides, the integration with energy storage systems helps in sustaining the efficiency during periods of low irradiance such as overcast days or even nighttime operation.

CO_2 Emissions Reduction

Figure 7 compares the reduction in CO_2 emissions between a solar-operated air cooling system and a conventional one over 10 years. This is seen from a very remarkable result regarding the environmental impact brought in by the adoption of the solar technology into cold storage warehouses-in terms of carbon footprint reduction. The graph is plotted as two different curves: one for the conventional system (in blue) and one for the solar-operated system (in green). Both systems follow a case of decreased CO_2 emissions over time, expected due to energy efficiency improvements and possible changes in operation. But the rate of reduction and the amount of total emissions from both the systems have much variation.

The conventional system, in this respect, starts a little over 1000 tonnes of CO_2 emissions in year 0, degrading further down to just over 500 tonnes by year 10. While this is a very constant decline in the level of CO_2 emissions, it does not drop as far down as that of the solar-operated system. By comparison, the solar-operated system, though starting

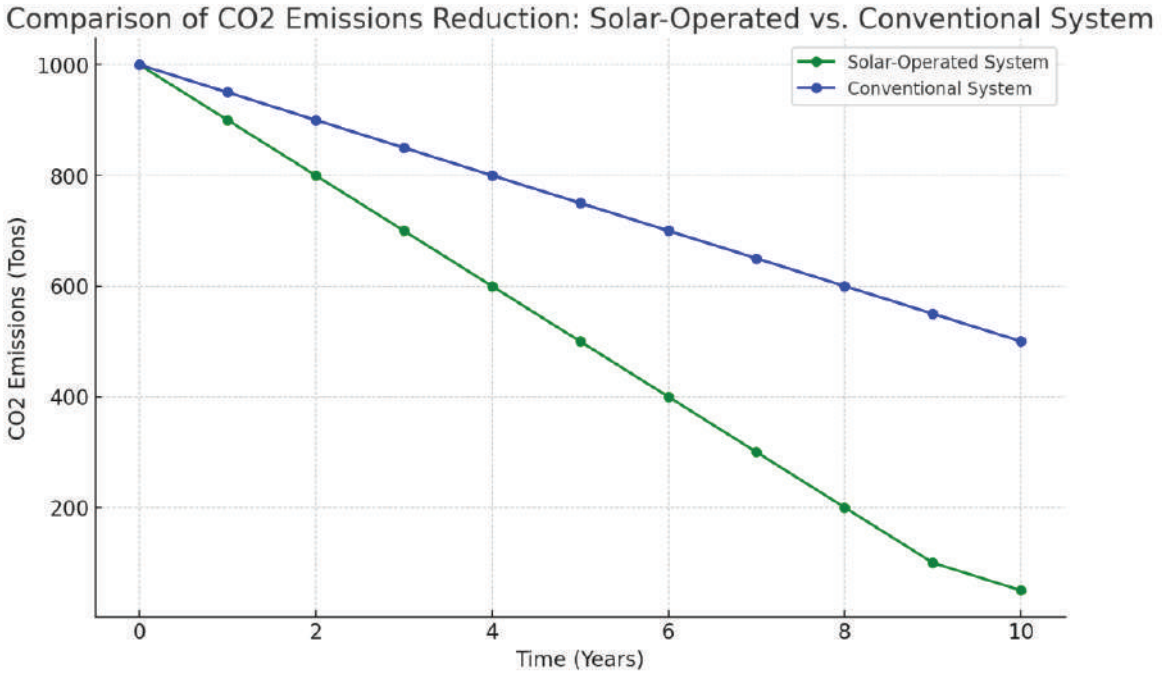


Figure 7. Comparison of CO_2 emissions reduction: Solar-operated vs traditional cooling system.

at the same place in terms of CO_2 emissions as the one mentioned above, has very notably steeper decline. By year 10, the solar system's emissions go down to about 100 tons-a 90% reduction in CO_2 emissions over the ten-year period [26].

This large discrepancy between the two systems in terms of CO_2 emissions reduction evidences the solar-operated cooling system as the more environmentally friendly. These reduced emissions further attribute to the solar system's capability to drastically lower such emissions, hence supporting the industry's growing emphasis on sustainability. As climate change and regulatory environments intensify, the solar-operated system surely presents a viable and attractive option with regards to the carbon footprint reduction of cold storage. The low emissions recorded for the solar-operated system record a sharp drop, indicating that with this system, payback concerning environmental benefits starts almost immediately. The steep slope of the green line shows that there is more immediacy in the positivity of the impact on reducing greenhouse gases, essential to meet present and future environmental targets [26].

For cold storage warehouses, which are usually energy-consuming due to the permanently controlled temperature, reduction of CO_2 is not only an urgent need in terms of environmental protection but may also become a comparative economic advantage. As more and more carbon taxes and emissions trading schemes go into practice worldwide, the minimized emissions related to solar-operated systems may be transformed into lower costs and advantages over rivals in the market. Besides, the CSR profile will be developed for all the firms operating cold storage houses with the solar-operated system. This would conceivably improve the stakeholder relationships and might even unlock new opportunities in markets where sustainability and low-carbon business are in the spotlight.

Temperature Distribution Within the Cold Storage

Figure 8 provides a temperature distribution overview in the warehouse, graphically expanding on the information above. Colors change from blue to red, the former being colder and the latter showing the hotter area. Logically, a good cooling system should keep the whole warehouse at one temperature represented by a single color in the graph. Yet, the heatmap does show some areas of deviation from that uniformity of temperature. There is, for instance, a hotter area in the middle part of the warehouse, as depicted in red in this image, which could indicate inefficiency in the cooling system to that area. That could be because of many reasons, such as not enough airflow, inadequate cooling power, or even external factors like proximity to equipment generating heat [28].

On the other hand, one region is somewhat cool; this can be accounted for by the light blue color of the bottom right corner, which might represent some overcompensation of the cooling system or a focal spot that has been subjected to less heat. Although it does not seem to carry quite as much weight as those points that are hotter, this too is considered an inefficiency in holding the ideal temperature on all levels. These temperature differences are crucial in warehouse operations, especially in the storage of goods

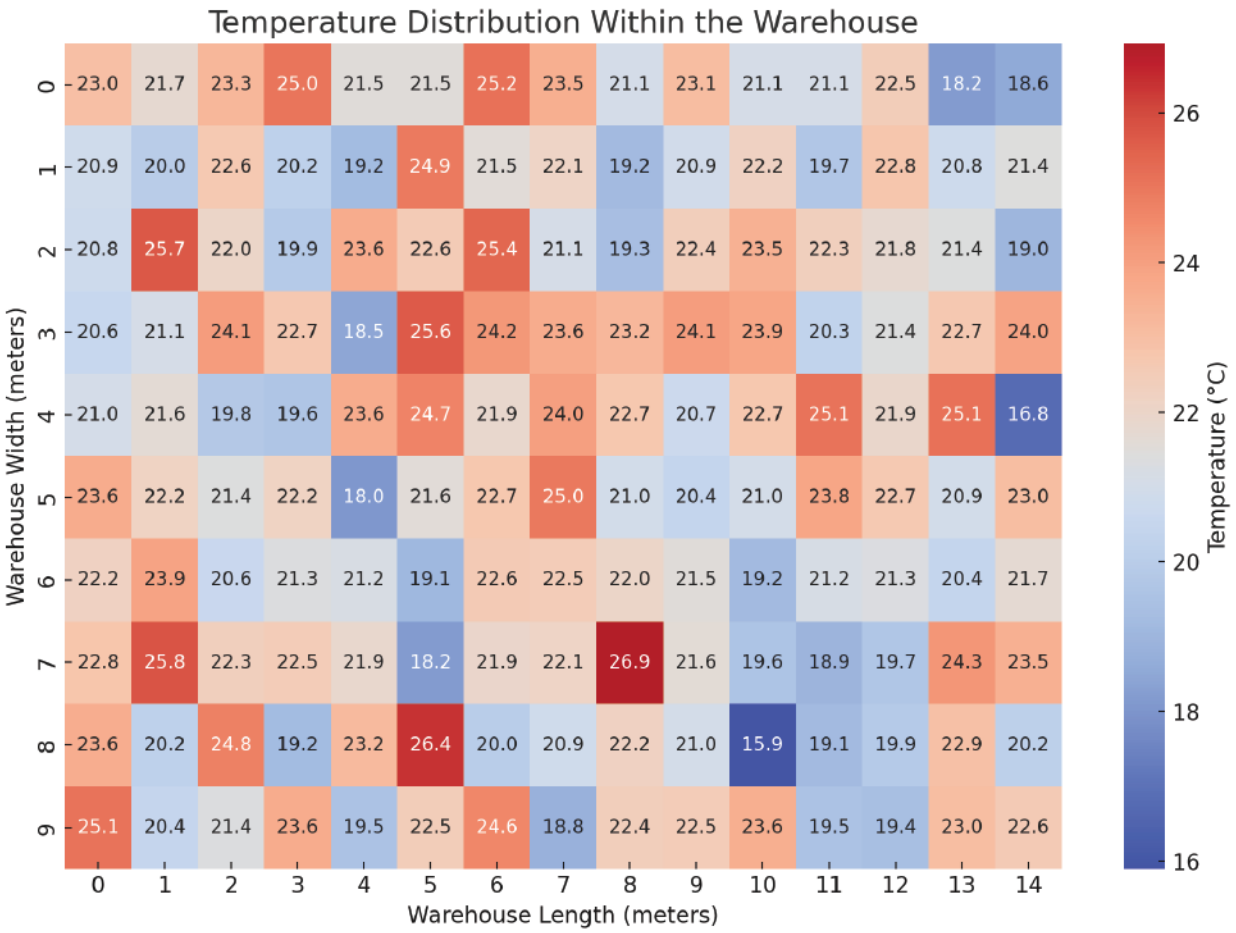


Figure 8. Temperature distribution within the warehouse.

that easily change with respect to temperature. Such heterogeneous cooling can lead to spoilage of a product, reduced shelf life, and increased costs due to energetic expenses-the system struggles to cool down to the desired conditions. These could be overcome by checking the overall cooling system installation, whether it was designed for proper ventilation with vents and fans, whether the thermostat was installed correctly, and when the insulation around the warehouse itself was poor. Besides these, regular cleaning and upgrading of the cooling infrastructure would go a long way in achieving near-uniform temperature distribution. In general, the heatmap will serve as a good tool in the diagnosis and subsequently curing inefficiencies in the cooling system so that the various environments in the warehouse remain conducive for optimal storage conditions.

Solar-powered air conditioning is one of the innovative ways to improve indoor comfort by reducing environmental impact and energy costs. The system uses solar energy to fuel the cooling process; therefore, it is ideal for locations characterized by plentiful sunlight with high temperatures. Generally, it includes photovoltaic solar panels that absorb sunlight and convert it into usable energy to run all types of cooling systems, such as evaporative coolers or solar air conditioners. These systems are based on renewable energy to reduce dependence on fossil fuels and lower greenhouse gas emissions with the view of creating a more sustainable future. Solar air conditioning systems can also be highly useful in isolated or off-grid areas where conventional sources of energy are prohibitively expensive or unavailable. They can also be configured to function on their own, or with battery storage systems, providing cooling during night conditions or throughout overcast weather conditions [29]. These have been further complemented by technological advances that yielded more efficient solar cooling systems which can also be integrated with smart home systems for extended user control and energy management. Because of their adaptability, these systems may be used in everything from personal residences to commercial buildings to agricultural installations, enabling users to enjoy a cooler atmosphere while saving money on power. As the public awareness of climate change and energy sustainability increases, the use of solar-powered air-conditioning systems offers one viable way to achieve comfort with

environmental stewardship, thereby affording access to greener, more energy-efficient living [26].

The averages from various trails conducted were considered therefore it was written as day 1, day 2 and so on. To test the performance of solar-powered air cooling systems for cold storage warehouses, the main testing conditions include ambient temperature, solar irradiance, internal warehouse temperature, humidity levels, and system load. Ambient temperature affects the cooling load and solar collector efficiency. It is tested between 25°C and 45°C for warmer regions. Solar irradiance measured using pyranometers is one of the significant influences on energy capture. Testing is done from 200 W/m² to 1000 W/m². Internal warehouse temperatures are set between 2°C and 10°C, with relative humidity kept at levels from 60% to 80% inside, thus ensuring that the products will not spoil. The system's performance is checked against several loads: 50%, 75%, and 100% of the system capacity, which reflects realistic scenarios with dummy thermal loads. Testing is spread over a few days to include climatic variation, high-accuracy sensors, and data acquisition systems that monitor the parameters continuously for complete information in optimizing the design and reliability of the system.

The efficient use of solar-powered air cooling systems for cold storage warehouses is a major stride toward energy-efficient technologies aimed at reducing the ever-increasing costs and environmental impact of conventional refrigeration systems. As global temperatures continue to rise and the need for effective storage solutions with increased demands, especially in agriculture and pharmaceuticals, it makes the employment of solar electricity for cooling systems all the more essential. These have implemented the usage of photoelectric plates in collecting solar energy, which is converted to electrical energy utilized in the running of the cooling units, thereby reducing dependence on fossil fuel and, subsequently greenhouse gas emissions [23].

These will include the main benefits of the technology: thermal storage components that enable the creation of cool air during peak solar hours and utilization at will, thereby maximizing energy utilization. Inclusion of sophisticated algorithms controlling temperature and humidity further enhances the efficiency of such systems by ensuring consistent and precise cooling in line with the particular requirements of the stored products. Also, high-performance evaporative cooling techniques integrated into solar-powered mechanisms enhance thermal management while reducing energy consumption, thereby making the systems sustainable and economically feasible. It has been highlighted by the case studies that businesses utilizing solar-powered air-conditioning systems in cold storages achieve significant reductions in the cost of energy and operational reliability for an extended life and quality of the product. Also, due to the fact that governments around the world have come to believe in and promote greener programs while offering incentives toward renewable energy adoption, the market potentiality of solar-powered cooling systems is on the rise. Solar-powered air conditioning systems may provide a revolutionary impact on the operations of cold storage by offering a sustainable solution to a rising global dilemma and paving the path toward a greener future [9].

In this regard, the integration of solar-powered air conditioning systems into cold storage warehouses is one feasible way to meet the growing energy demand from the cold chain logistics industry with less environmental impact. The study of such a system involves an involved solution based on renewable energy sources since energy costs are rising day by day and a sustainable practice is becoming highly essential. These solar cooling systems use photovoltaic panels to generate electricity from sunshine, powering absorption chillers or any other cooling technologies developed to help keep perishable items at the proper temperatures. A major advantage of solar-powered cooling systems, for that matter, is their potential for reducing conventional sources of energy, which guarantees lower operating costs and reduced carbon emissions. Besides, advances in energy storage technology can make such systems work even on nights or overcast conditions, therefore allowing cold storage to function uninterruptedly and effectively[30]. Their scalability further allows warehouse operators to adapt their energy needs with respect to their storage capacity and geographical location; hence, customized solutions tailored to specific contexts. In places where solar insolation is strong, these systems have the potential to reach energy payback times of only a few years-a point at which they will be economically viable to invest in. To properly determine how sustainable the systems are, the lifecycle assessments should also take into consideration the study in which environmental impacts from production, maintenance, and final waste management of solar equipment shall be included [18].

Solar-operated air cooling is another innovative solution that might help overcome the industrial problems related to both cost-effectiveness and environmental responsibility. This technology promises great potential to contribute towards the improvement of energy efficiencies and to the global dream of sustainable logistics practices [31]. One would expect practical use of this technology because of further research, development, and calculated expenditure, opening a future door for cold storage operations to be environmentally friendly [32].

CONCLUSION

Analysis by comparison has shown that the solar-operated air cooling system is more efficient and provides a more constant temperature than the conventional cooling system. This clearly shows the potential of solar energy in empowering cold storage operations to be more sustainable and efficient for food preservation and logistical purposes in the future. The efficiency of the system increases linearly

with increased solar irradiance, which indeed signifies that in high solar-exposure zones, such systems give better performance and could hence become a practical, sustainable alternative to conventional cooling applications. Given that solar is nearly 50% cheaper compared to the conventional systems over a 10-year period, the solar option is not only economically feasible but also, secondly, in line with environmental sustainability objectives. These results strongly support the wider dissemination of solar technology in cold storage applications where efficiency during long-term operations is a priority. The comparison of estimated CO2 emissions by a solar-operated and conventional cooling system will show the benefits that may be derived from solar technology in cold storage warehouses. This solar-operated system achieves a much larger percentage reduction in a relatively short period and, therefore, presents a workable solution for companies keen on reducing carbon footprints and remaining within set environmental limits.

AUTHORSHIP CONTRIBUTIONS

Authors equally contributed to this work.

DATA AVAILABILITY STATEMENT

The authors confirm that the data that supports the findings of this study are available within the article. Raw data that support the finding of this study are available from the corresponding author, upon reasonable request.

CONFLICT OF INTEREST

The author declared no potential conflicts of interest with respect to the research, authorship, and/or publication of this article.

ETHICS

There are no ethical issues with the publication of this manuscript.

STATEMENT ON THE USE OF ARTIFICIAL INTELLIGENCE

Artificial intelligence was not used in the preparation of the article.

REFERENCES

[1] Ali HM, Rehman T, Arıcı M, Said Z, Duraković B, Mohammed HI, et al. Advances in thermal energy storage: fundamentals and applications. Prog Energy Combust Sci 2024;100:101109. [CrossRef]

[2] Kaushik SC, Verma A, Tyagi SK. Advances in solar absorption cooling systems: an overview. J Therm Eng 2021;10:1044–1067. [CrossRef]

[3] Das A, Jani HK, Nagababu G, Kachhwaha SS. A comprehensive review of wind–solar hybrid energy policies in India: barriers and recommendations. Renew Energy Focus 2020;35:108–121. [CrossRef]

[4] Alva G, Lin Y, Fang G. An overview of thermal energy storage systems. Energy 2018;144:341–378. [CrossRef]

[5] Altwies JE, Reindl DT. Passive thermal energy storage in refrigerated warehouses. Int J Refrig 2002;25:149–157. [CrossRef]

[6] Butala V, Stritih U. Experimental investigation of PCM cold storage. Energy Build 2009;41:354–359. [CrossRef]

[7] Kumar KS, Surakasi R, Mohan A, Tharanisrisakthi BT, Muniamuthu S, Geetha NB. Emerging trends and global challenges to predict drop in thermal performance of WTG gearbox. J Therm Eng 2021;10:657–669. [CrossRef]

[8] Berisha A, Osmanaj L. Kosovo scenario for mitigation of greenhouse gas emissions from municipal waste management. Evergreen 2021;8:509–516. [CrossRef]

[9] Al-Yasiri Q, Szabó M, Arıcı M. A review on solar-powered cooling and air-conditioning systems for building applications. Energy Rep 2022;8:2888–2907. [CrossRef]

[10] Kumar KS, Muniamuthu S, Mohan KR. Measurement of temperature flow analysis by condition monitoring system for WTG gear box to evaluate the thermal performance associated with plant load factor. J Therm Eng 2023;9:979–987. [CrossRef]

[11] Galgaro A, Santa GD, Cola S, Cultrera M, De Carli M, Conforti F, et al. Underground warehouses for food storage in the Dolomites (Eastern Alps – Italy) and energy efficiency. Tunn Undergr Space Technol 2020;102:103411. [CrossRef]

[12] Arias DM, García-Valladares O, Besagni G, Markides CN. A vision of renewable thermal technologies for drying, biofuels production and industrial waste, gas or water recovery. Appl Therm Eng 2023;223:120022. [CrossRef]

[13] Wang K, Qin Z, Tong W, Ji C. Thermal energy storage for solar energy utilization: fundamentals and applications. Res Chall Appl 2020;415:9180410.5772. [CrossRef]

[14] Muniamuthu S, Tharanisrisakthi BT. An investigation to estimate the maximum yielding capability of power for mini Venturi wind turbine. Ecol Eng Environ Technol 2022;23. [CrossRef]

[15] Wang X, Dennis M. Influencing factors on the energy saving performance of battery storage and phase change cold storage in a PV cooling system. Energy Build 2015;107:84–92. [CrossRef]

[16] Zhu K, Li X, Campana PE, Li H, Yan J. Techno-economic feasibility of integrating energy storage systems in refrigerated warehouses. Appl Energy 2018;216:348–357. [CrossRef]

[17] Deng Q, Yang Z, Zhang L, Jia M. The control strategy and economic analysis of a new type of solar cold storage. J Energy Storage 2022;52:104865. [CrossRef]
[18] Otanicar T, Taylor RA, Phelan PE. Prospects for solar cooling–an economic and environmental assessment. Sol Energy 2012;86:1287–1299. [CrossRef]
[19] Sarbu I, Sebarchievici C. Review of solar refrigeration and cooling systems. Energy Build 2013;67:286–297. [CrossRef]
[20] Kumar SK, Muniamuthu S, Mohan A, Amirthalingam P, Anbu Muthuraja M. Effect of charging and discharging process of PCM with paraffin and Al2O3 additive subjected to three point temperature locations. J Ecol Eng 2022;23:34–42. [CrossRef]
[21] Seo J-W, Afzal A, Kim K-Y. Efficient multi-objective optimization of a boot-shaped rib in a cooling channel. Int J Therm Sci 2016;106:122–133. [CrossRef]
[22] Raval P, Ramani B. Heat transfer enhancement techniques using different inserts in absorber tube of parabolic trough solar collector: a review. J Therm Eng 2021;10:1068–1091. [CrossRef]
[23] Patel PM, Rathod VP, Patel D. Drying Solanum lycopersicum (tomatoes) in greenhouse solar dryer: an eco-environmental study. J Therm Eng 2021;10:811–825. [CrossRef]
[24] Wang J, Wang Q, Yang P, Yu J, Xiao L. Energy consumption analysis and optimization of cold stores considering differential electricity price. Energy Build 2024;310:114094. [CrossRef]
[25] Bataineh K, Taamneh Y. Review and recent improvements of solar sorption cooling systems. Energy Build 2016;128:22–37. [CrossRef]
[26] Chinese D, Meneghetti A, Cortella G, Giordano L, Tomasinsig E, Benedetti M. Environmental and economic assessment of industrial excess heat recovery collaborations through 4th generation district heating systems. Energy 2024;307:132630. [CrossRef]
[27] Pudleiner D, Colton J. Using sensitivity analysis to improve the efficiency of a Net-Zero Energy vaccine warehouse design. Build Environ 2015;87:302–314. [CrossRef]
[28] Pryke A, Mostaghim S, Nazemi A. Heatmap visualization of population based multi objective algorithms. In: Obayashi S, Deb K, Poloni C, Hiroyasu T, Murata T, editors. Evolutionary multi-criterion optimization. Lecture notes in computer science. Berlin (Heidelberg): Springer; 2007. p. 361–375. [CrossRef]
[29] Desideri U, Proietti S, Sdringola P. Solar-powered cooling systems: technical and economic analysis on industrial refrigeration and air-conditioning applications. Appl Energy 2009;86:1376–1386. [CrossRef]
[30] Patil LN, Khairnar HP, Hole JA, Mate DM, Dube AV, Panchal RN, Hiwase VB. An experimental investigation of wear particles emission and noise level from smart braking system. Evergreen 2022;9:711–720. [CrossRef]
[31] Patil LN. Assessment of risk associated with the quiet nature of electric vehicle: a perception of EV drivers and pedestrians at Mumbai Metropolitan Region-India. Eur Transp 2021;83:1–19. [CrossRef]
[32] Aste N, Del Pero C, Leonforte F. Active refrigeration technologies for food preservation in humanitarian context–a review. Sustain Energy Technol Assess 2017;22:150–160. [CrossRef]

Sigma J Eng Nat Sci, Vol. 44, No. 1, pp. 605–636, February, 2026

Sigma Journal of Engineering and Natural Sciences
Web page info: https://sigma.yildiz.edu.tr
DOI: 10.14744/sigma.2024.00126

Review Article

Artificial intelligence, machine learning, and deep learning applications in the engineering fields – A comprehensive review

Haneen DARWISH[1,*], Walaa DARWISH[2], Hiba DARWISH[3], Abdallah DARWISH[4], Issa W. ALHMOUD[3], Osamah ALSHRAIDEH[5], Ahmad ALZUBAIDI[6]

[1]Department of Civil Engineering, University of South Alabama, Mobile, AL, 36688, USA
[2]Department of Civil and Environmental Engineering, University of Alberta, Alberta, CA, T6G2R3, Canada
[3]Department of Computational Data Science, NCAT University, Greensboro, 27411, USA
[4]Department of Industrial Engineering, Yarmouk University, Irbid, 7211111, Jordan
[5]Department of Electrical Power Engineering, Yarmouk University, Irbid, 7211111, Jordan
[6]Department of Civil, Construction, and Environmental Engineering, Iowa State University, Ames, 50011-2030, USA

ARTICLE INFO

Article history
Received: 27 March 2024
Revised: 12 June 2024
Accepted: 04 September 2024

Keywords:
Artificial Intelligence (AI); Machine Learning (ML); Deep Learning (DL); Applications; Engineering

ABSTRACT

While Artificial Intelligence (AI), Machine Learning (ML), and Deep Learning (DL) are revolutionizing engineering, their specific roles and interrelationships across different disciplines often remain unclear. This paper tackles that ambiguity by mapping the applications of these technologies across 14 distinct engineering fields. Through a systematic review of 150 peer-reviewed studies, we investigated which techniques are being used, the tools employed, and the outcomes achieved. Our analysis revealed that Machine Learning is the dominant force, appearing in roughly 73% of the studies reviewed. This prevalence isn't accidental; ML's decades of development have resulted in versatile, robust, and interpretable algorithms that engineers find adaptable to a wide array of challenges. In contrast, Deep Learning, while powerful, is typically reserved for niche applications involving high-dimensional data or exceptionally complex patterns, such as in image or speech recognition.
A key contribution of this work is clarifying the practical hierarchy between these terms: AI is the overarching field, ML is its data-driven engine, and DL is a specialized subset of ML. By systematically comparing their use across disciplines, this study offers a new framework for understanding how each technology contributes to engineering innovation. Our findings provide practical guidance for researchers selecting the right tool for their specific problem, ultimately helping to steer future applications of AI in engineering.

Cite this article as: Darwish H, Darwish W, Darwish H, Darwish A, AlHmoud IW, Alshraideh O, Alzubaidi A. Artificial intelligence, machine learning, and deep learning applications in the engineering fields – A comprehensive review. Sigma J Eng Nat Sci 2026;44(1):605–636.

***Corresponding author.**
*E-mail address: hhd2421@jagmail.southalabama.edu

This paper was recommended for publication in revised form by Editor-in-Chief Ahmet Selim Dalkilic

Published by Yıldız Technical University Press, İstanbul, Turkey
© Author. This is an open access article under the CC BY-NC license (http://creativecommons.org/licenses/by-nc/4.0/).

INTRODUCTION

Artificial Intelligence (AI), Machine Learning (ML), and Deep Learning (DL) are today a big component of daily life, shaping the way of how we interact with diverse information and apply the technology. AI is about formation of machines that have the ability to think and act in ways same as humans. ML is a branch of AI that enables the systems to learn from data and be developed over time without the need for direct programming. DL takes things to the next level—Using layered neural networks that are modeled after the human brain to deal with more complicated tasks.

The use of these technologies is widespread, from voice assistants and recommendation systems to image recognition and self-driving cars. By making processes faster, automating routine work, and creating personalized experiences, they are making a difference in industries such as healthcare, finance, and education.

While people may use AI, ML, and DL interchangeably, they do not mean the same thing. Figure 1 shows a chart that highlights their key differences, and the sections that follow explain AI, ML, DL, and RF in more detail, including the main algorithms used in each field.

This comprehensive review delves into the transformative impact of AI, which is the umbrella of ML, and DL across 14 diverse engineering domains. Our contributions are summarized in the following three points.

- Each engineering type is meticulously examined, unraveling the employed methodologies, innovative applications, and succinct summaries of outcomes;
- This research illuminates the pervasive influence of cutting-edge technologies in reshaping and optimizing various facets of engineering, offering a valuable synthesis of advancements that bridge theory and practical implementation; and
- A statistical section is also provided that clarifies the percentages of Al, ML, and DL application in the engineering fields.

These contributions collectively advance the understanding of AI, ML, and DL's role in engineering, providing a foundational reference for future research and development, which is the novelty of this work.

Artificial Intelligence

In simple words, AI is the process of transferring the information, data, human intelligence to machines. The fundamental objective of artificial intelligence is the development of autonomous entities endowed with the capacity for human-like thought processes and actions. Such entities execute tasks by engaging in problem-solving through research and emulation of human behaviors. The majority of AI systems emulate natural intelligence in order to address intricate challenges [1].

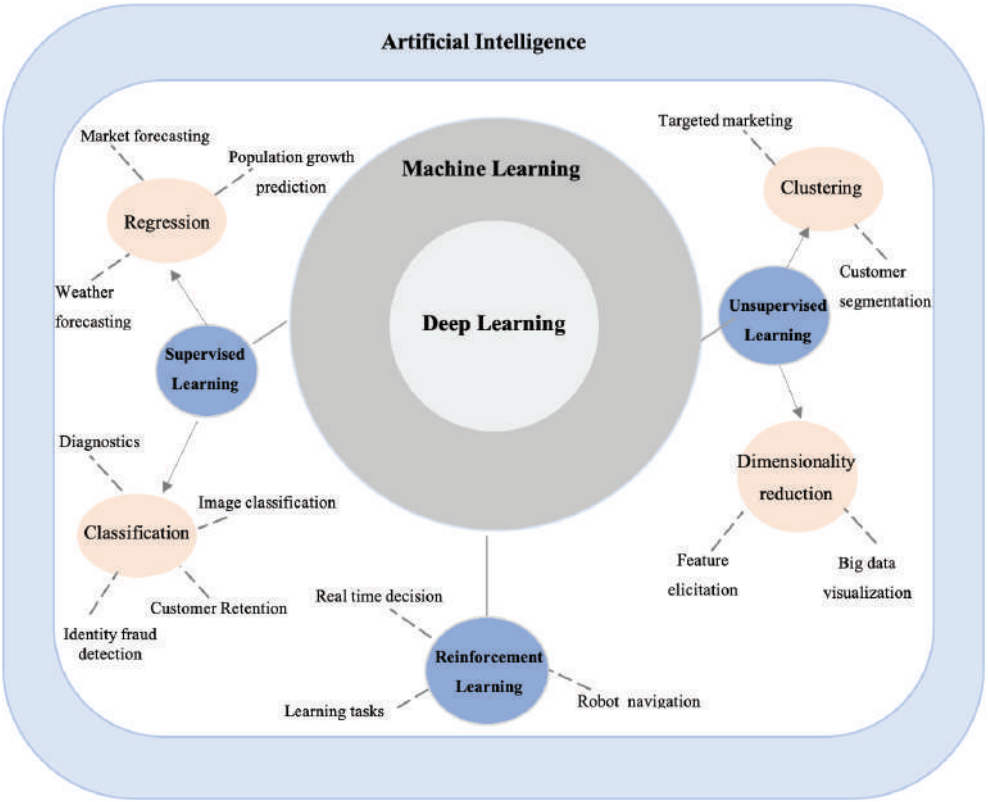


Figure 1. AI, ML, and DL configuration.

The word AI refers to the computer algorithms, which simulate cognitive processes or activities observed in living organisms. Nowadays, AI is integrated into the scientific discovery for many purposes such as collect and interpret large datasets, design and guide experiments, helping scientists to introduce some hypotheses, accelerate research process, provide reliable and actionable models integrated with the scientific workflows, and refine measurements. Moreover, AI can be used in decision-making, suggestion, problem-solving, estimating, understanding, and learning [2-3]. AI along with the Internet of Things (IoT) are mandatorily required to handle massive data effectively in less time by applying the theorem of algorithms even though the training along with the execution of the algorithms requires substantial storage, power, and massive data to be trained [4-5]. Nowadays several AI tool are used not only in engineering field but in general, the following subsection discuss the most known one, which is helpful for the researchers in general.

ChatGPT

OpenAI introduced ChatGPT, a generative pre-trained transformer model [6], which is defined as an intelligent chatting robot that has the ability to give an immediate response based on the instruction provided by the user [7]. For instance, Figure 2 shows a request from the user asking ChatGPT to give knowledge about AI in only one paragraph and the response was exactly as requested. ChatGPT showed an incredibly powerful in generating several tasks extended from trivial tasks to several language understanding. Some of these tasks are story writing, debugging, grammatical correction, and multilingual machine translation [7]. Moreover, natural language processing problems could be also solved by ChatGPT such as semantic annotation and acceptance of the text going towards natural language understanding (NLU) like word sense disambiguation (WSD), providing answers for the provided questions in the input text box, a relatively simple binary classification of texts like spam, aggression detection, sarcasm, and other tasks like a more complex multi-class and multi-label classification of texts such as sentiment analysis, emotion recognition [8]. These days, ChatGPT has gained much attention due to its ability to provide high-quality as well as fluent responses [9]. However, this tool is very helpful if and only if it is used wisely, the educational facilities can encourage academic integrity and avoid the disruptive impacts of this technology by introducing guidelines and clear policies [10]. GPT is being improved continuously started from GPT 1 to GPT 4, Table 1 clarifies the differences between these versions [7].

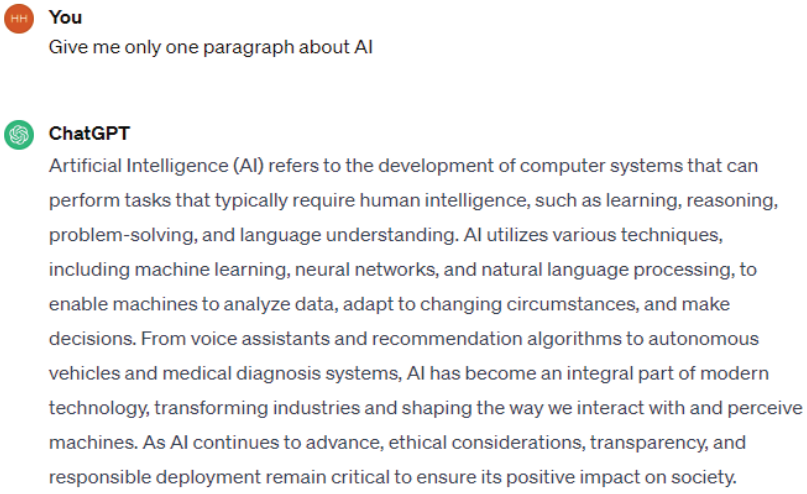


Figure 2. An example of how ChatGPT works.

Table 1. Comparison between GPT-1, GPT-2, GPT-3, and GPT-4

	Released year	Context window	Size of pre-training data	Data source	Learning target
GPT-1	2018	512 tokens	Around 5 GB	Book corpus and Wikipedia	Unsupervised learning
GPT-2	2019	1024 tokens	40 GB	Web text	Multi-task learning
GPT-3	2020	2048 tokens	45 TB	Common crawl	In-context learning
GPT-4	2023	8195 tokens	Unavailable information	Unavailable information	Multimodal learning

Machine Learning

The field of machine learning (ML) has undergone substantial advancements over the preceding two decades, transitioning from an experimental pursuit confined to laboratories to a pragmatic technology entrenched in pervasive commercial application. Within the domain of AI, ML has ascended as the preeminent approach for the formulation of functional software across diverse domains such as computer vision, speech recognition, natural language processing, robot control, and various other applications [11]. ML has emerged as a crucial method for harnessing the capabilities of data, enabling businesses to enhance their innovation, efficiency, and sustainability [12].

ML involves the examination of data and the creation of algorithms to make predictions based on the, previously, trained data. ML programs rely on a computer's ability to learn without explicit programming. The ML model may either be predictive or descriptive, to gather information about input data [13].

Constructing an effective machine learning model involves two crucial stages: training and testing. During the training phase, a significant and research-intensive process, the system is presented with labeled or unlabeled inputs. These inputs are stored in the feature space for future reference in making predictions. Subsequently, in the testing phase, the system is presented with an unlabeled input, and it must predict the correct output based on its training [14]. ML enhances task performance and productivity by incorporating learning mechanisms and self-correction in response to new data by five main steps, which are clarified in Figure 3 [15].

In the first step, the required data will be collected from several sources such as World bank or Kaggle, and in the second step some analysis for the data will be made such as the missed data, or handling the invalid data by several analytical techniques and finally the data will be preprocessing for

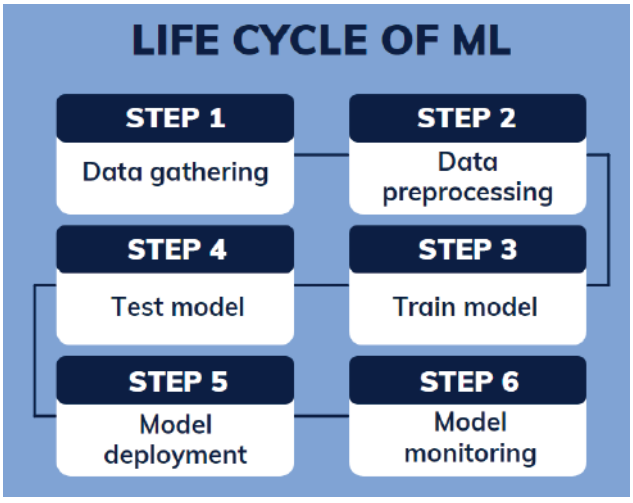


Figure 3. steps of applying ML.

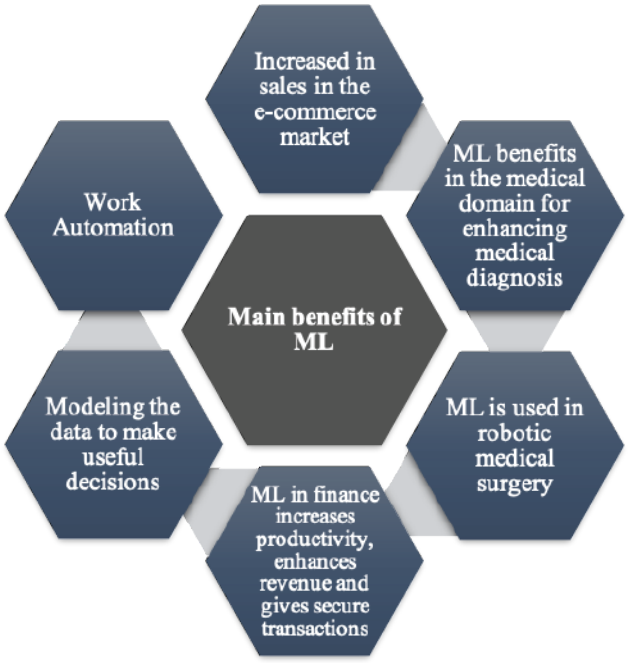


Figure 4. Main benefits of ML.

feature extraction, feature analysis, and data visualization. The data then will be divided into two main parts for two main goals; training and testing. In the third step, the testing part of the available dataset will be used to train the model by various ML algorithms. In the fourth step, the accuracy of the model will be tested by the second part (testing part of the data). And in the fifth step, model deployment, the ML model will be integrated with an existing production environment that takes the input and gives the output to make decision making or to achieve any another goal. Several technologies can be used to deploy the ML model such as: Azure ML Service, Docker, Kubernetes, MLFlow, AWS SageMaker. Finally, the last step the obtained model will be monitored from several aspects such as the crashes, errors and to assure that the model still provides the desired performance [15]. In general, ML have wide advantages and benefits, which are shown in Figure 4, and accordingly this promotes it to be applied in several applications as represented in Figure 5 [15]. ML is divided into three main types, and each type is familiar with specific sorts of dataset. These three types are clarified in Figure 6 [16].

Supervised Learning

The preeminent ML type is the supervised learning model, primarily employed for addressing practical applications in the real world [17]. This model predicts results based on specific input sets and pairs of input/output examples. Each training dataset in supervised learning comprises input goals, an input vector, and a desired output value known as a supervisory signal. These examples train machine learning algorithms, leading to the derivation

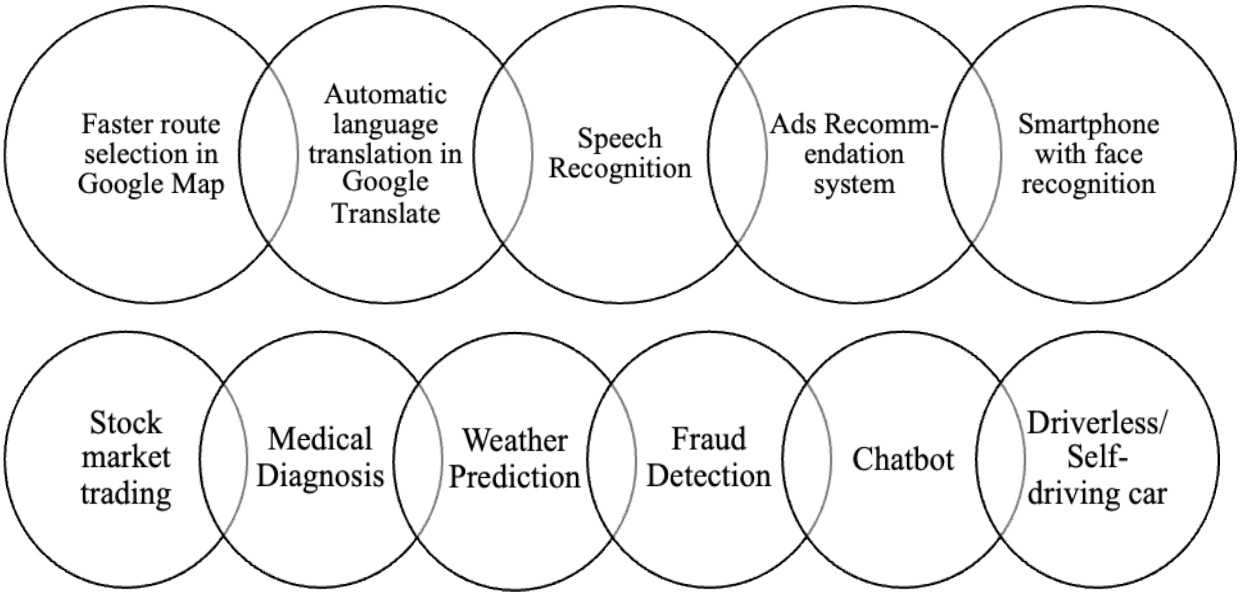


Figure 5. Real-world applications of ML.

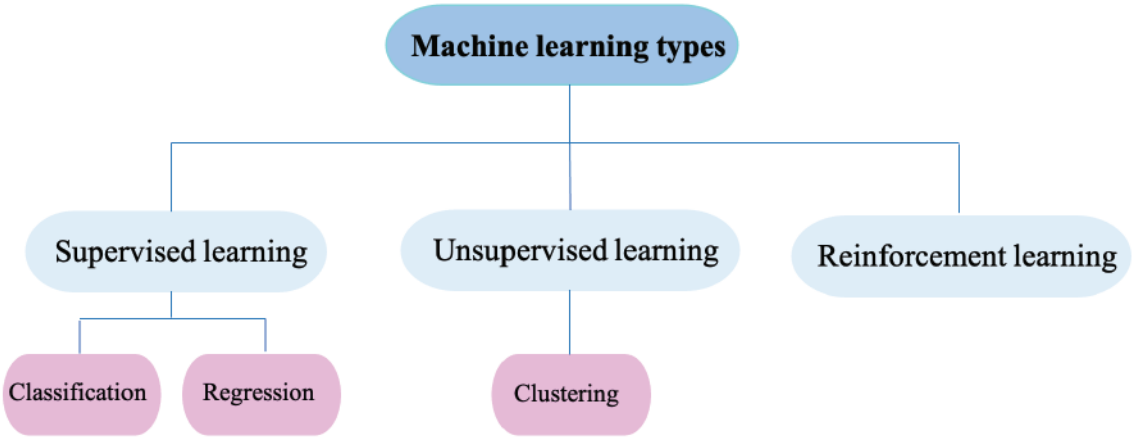


Figure 6. Machine learning types.

of a classifier function through dataset analysis. The goal of supervised learning training algorithms is to forecast one or multiple outcomes using different input features. While supervised learning is effective, it has the limitation of necessitating a substantial amount of labeled data for the creation of a comprehensive labeled dataset [18]. Supervised learning models are widely employed for tasks involving classification and regression as shown in Figure 6.

The supervised learning is divided into two main parts, classification and regression. When it comes to classification, a computer program is trained on a designated dataset.. Through this training process, the program organizes the data into distinct class labelsThe value of this algorithm lies in its ability to predict discrete values, such as differentiating between males and females, , determining whether a statement is true or false, or recognizing if an item is spam or not. In contrast, the goal of the regression algorithm is to locate a mapping function that connects input variables (x) to a continuous output variable (y). The use of these algorithms involves forecasting continuous values, such as predicting salaries, prices, ages, marks, and similar variables.

The primary objective of the ML - supervised type is to perform classification or prediction. A predefined set of examples is used by these methods to categorize and predict class labels. Classification samples can either be assigned to a specific class or cannot be assigned to a specific class. Partial membership in a class is not considered.. The accuracy of all classification and prediction models achieved is always affected by the presence of missing values. There are two classification types: binary and multiclass. Binary

classification is the process of sorting data into two categories. For example you might be predicting "yes" or "no", spam, or even no regression at all (just saying something fails one of your tests).. In most cases, these two groups are represented as 0 and 1. On the other hand, multiclass classification deals with three or more predictable classes, such as identifying different cancer stages, where classes are denoted as 0, 1, 2, and so forth.

A technique to solve the problem is supervised learning as illustrated in Figure 7 [14], and the way of working the input data for this purpose is shown in Figure 8. After that, the procedure includes: Such approach usually requires some steps. First of all, the kind of training examples is one of the most important sources to be determined when we seek for a solution to a problem. Second, a training dataset is established by foremen or real measurements. The dataset should be representative of real-world scenarios such as the location in which the model will be operating. And the input features must be selected carefully (i.e., they should carry sufficient information to make accurate prediction following Eq. Eventually, the proper training algorithm is chosen to train the model. The assembled training set is then used with the learning algorithm once design has concluded. At this level, some supervised learning techniques may require human intervention to fix the values of certain control parameters, in particular when it comes to prediction task [19].

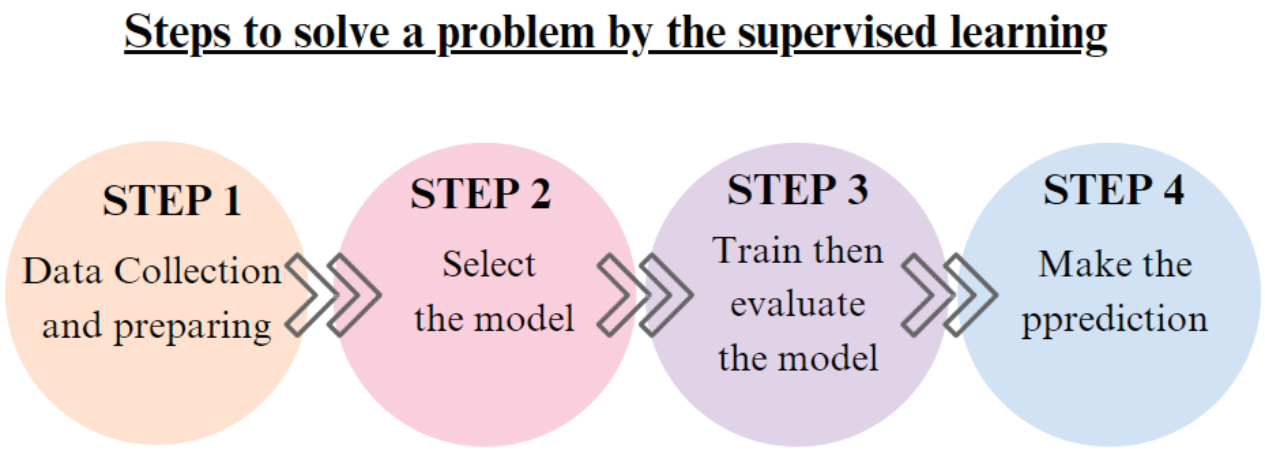


Figure 7. Followed steps in supervised learning.

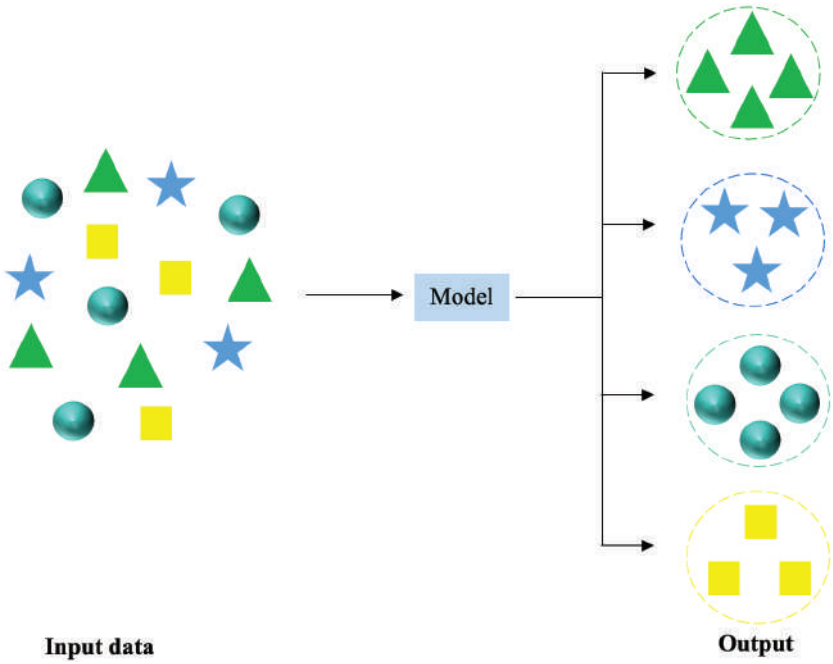


Figure 8. Principle of supervised learning.

Unsupervised Learning

In the second type, unsupervised learning, the algorithm learns from an unlabeled dataset and endeavors to comprehend the data by autonomously extracting features, identifying co-occurrences, and revealing underlying patterns [20].

Unsupervised machine learning serves the purpose of discovering concealed patterns in data without predefined labels. Various effective applications have employed this approach, but their evaluation can be challenging. This difficulty arises from a deficiency in training related to unsupervised machine learning, leading to a lack of clear measures such as error or reward indicators for assessing potential solutions. The absence of a reward signal is a notable distinction between supervised and unsupervised machine learning. In statistical applications, unsupervised learning finds utility in approximating data density.

Neural network model (NN) [21], self-organizing map (SOM) [22], and adaptive resonance theory (ART) [23] are unsupervised learning. Unsupervised learning consists of two steps: data transformation and clustering. Data Transformation During this step, the dataset is modified to represent information in a different and easier-to-understand format: for humans/key stakeholders and machine algorithms. Clustering methods are used to categorize data into clusters of similar items. One of the most basic and straightforward algorithms is K-means clustering which groups similar set of data. It operates in two steps: during the assignment step, datapoints are assigned to their closest cluster center; while in the update step the cluster centers are updated as the mean of all points belonging to that cluster.

One of the main problems with unsupervised learning is knowing how well it works. In supervised learning, outcomes can be checked against identified labels; in unsupervised learning there are no right answers — and it's harder to evaluate accuracy. For this reason, it's often applied for exploration, such as finding patterns in data and preparing the data for supervised algorithms. . In fact, trying out new ways of representing data with unsupervised methods can sometimes improve the performance of supervised models.

To figure out the difference between the classification, regression, and clustering, Figure 9 shows a representation for them and how they can be applied in the data analysis. Most of the ML models can apply both types of data, the labelled and the unlabeled, in some certain conditions. However, labelled data are employed in supervised learning [14].

Reinforcement

The third approach, reinforcement learning (RL), is a branch of machine learning that deals with agents which are able to take decisions in an environment aiming to maximize rewards across time. The environment is the stage on which the agent learns and acts. The environment reacts to the actions of the agent by either providing rewards or transitioning to another state. In the reinforcement learning approach, the emphasis is not on instructing the agent on how to perform a specific task but on providing incentives, either positive or negative, based on the agent's behavior [24]. In this type, the model acquires behavior in an environment by taking actions and assessing the resulting reactions. In RL, the objective is to select actions that optimize positive outcomes in specific situations. The reinforcement model determines which actions to undertake for a given task, emphasizing the importance of learning from experience.

Used Algorithms

In this paper, we examine machine learning (ML) algorithms in three primary categories: reinforcement learning, supervised learning, and unsupervised learning. Support vector machines (SVM), decision trees, and neural networks are typical examples of supervised learning models that use

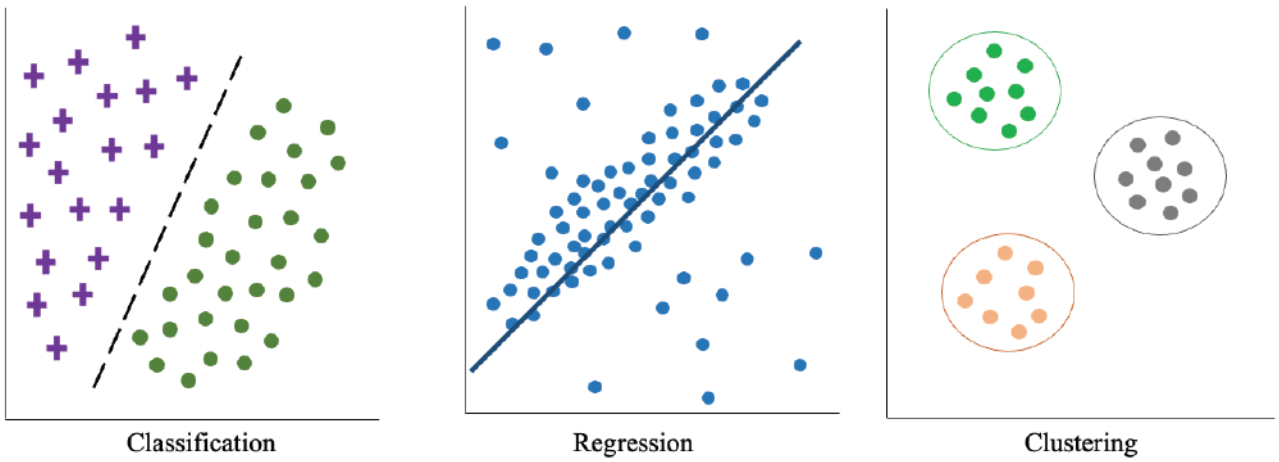


Figure 9. Representation of classification, regression, and clustering.

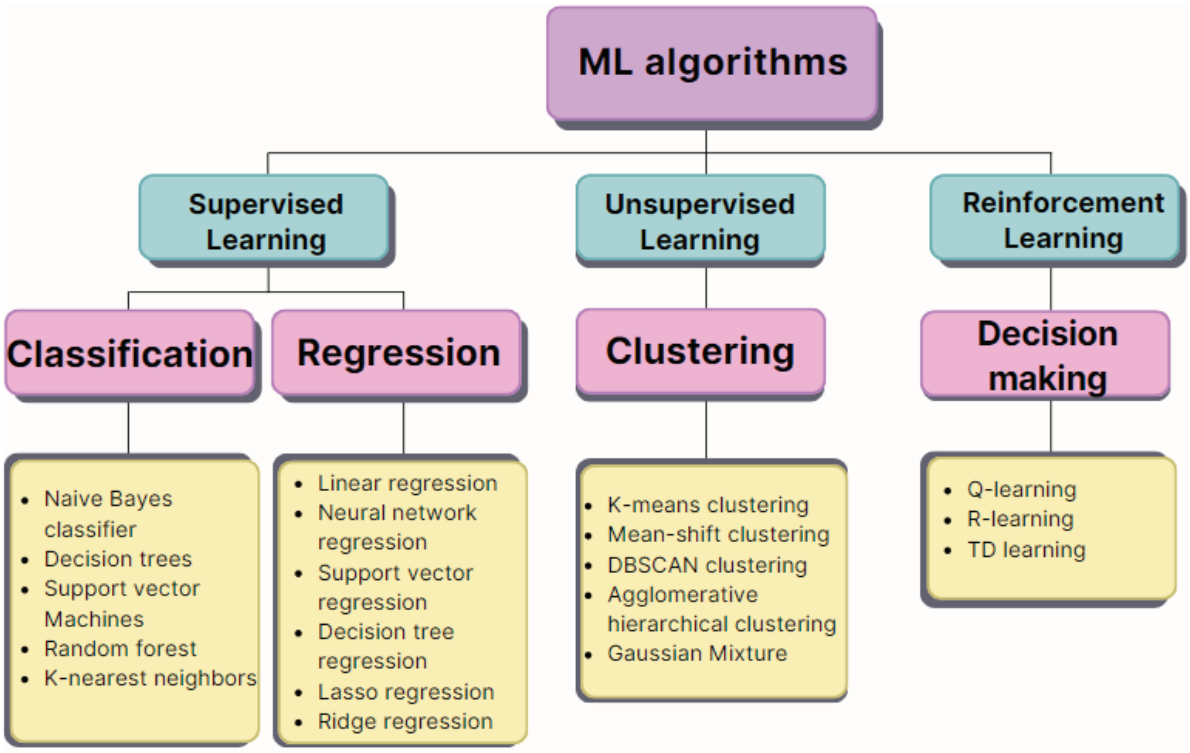


Figure 10. List of used algorithms used in ML.

labeled data to predict results for new inputs. Unsupervised learning dives into unlabeled data, looking for patterns or hidden structures. Think of methods like K-means clustering, Principal Component Analysis (PCA), or gaussian mixture models (GMM)—they all help make sense of data that doesn't come with instructions. Reinforcement learning takes a different approach. Here, the goal is to train agents to make smart decisions in unpredictable settings by using rewards and penalties. Popular algorithms in this area include Q-learning, deep Q networks (DQN), and Policy Gradient Methods. This section gives a quick look at the machine learning algorithms used in this research. Figure 10 shows which algorithms belong to each category [15,25].

Decision Tree

The decision tree algorithm provides a visual guide for navigating a series of choices or decisions that are guided by specific conditions. As a subtype of the classification tree, it organizes instances into various categories based on their property values. Each node within the decision tree embodies a unique characteristic of an instance essential for classification [26]. Figure 11 shows the schematic representation of the decision tree algorithm [27].

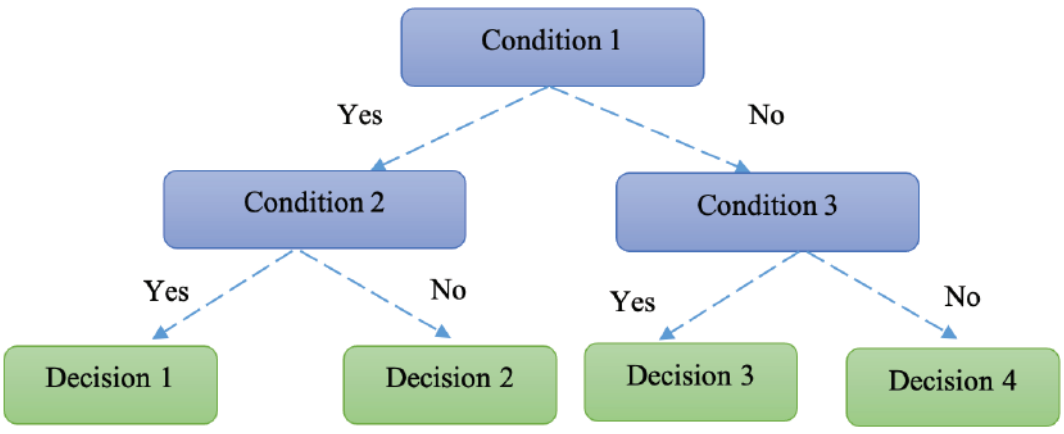


Figure 11. Decision tree algorithm principle.

Logistic Regression

Logistic regression is a statistical technique employed for prediction and classification. It is particularly effective for forecasting categorical results and can operate with both categorical and continuous input variables. The primary objective is to assess the likelihood of an event happening based on the specified independent variables. Since the output represents a probability, the dependent variable always falls between 0 and 1. This logistic regression model is formally expressed through Equation (1) [28] and Figure 12 clarifies the representation of this algorithm [29].

$$Log\left(\frac{p}{1-p}\right) = \beta_o + \beta_1 X_1 + \beta_2 X_2 + \cdots + \beta_n X_n + \beta_{12} X_1 X_2 + \cdots + \beta_{n-1,n} X_{n-1} X_n \quad (1)$$

Where p is the probability which is associated with an event occurrence, β_0 is the coefficient of the intercept term, and β_1 to β_n are the coefficients of the independent variables (X_1 to X_n).

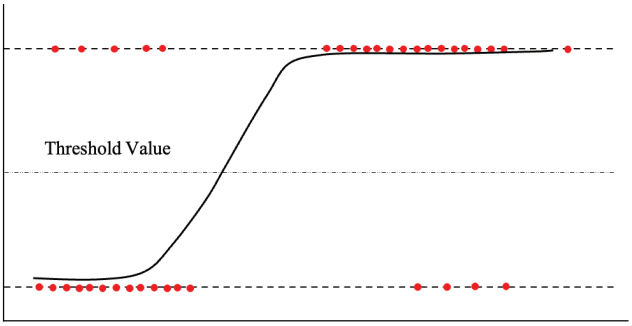


Figure 12. Logistic regression algorithm representation.

Support Vector Classifier (SVC)

Support Vector Classification (SVC) is a significant supervised machine learning technique employed to examine input data and recognize patterns for classification and regression activities. It is commonly utilized in fields like digit recognition, handwriting assessment, facial detection, cancer diagnosis, and forecasting time series [30].

Vapnik and Cortes invented the Support Vector Machine (SVM) algorithm, a highly successful machine learning technique recognized for its prowess in data analysis and pattern recognition. It is a crucial tool for binary and

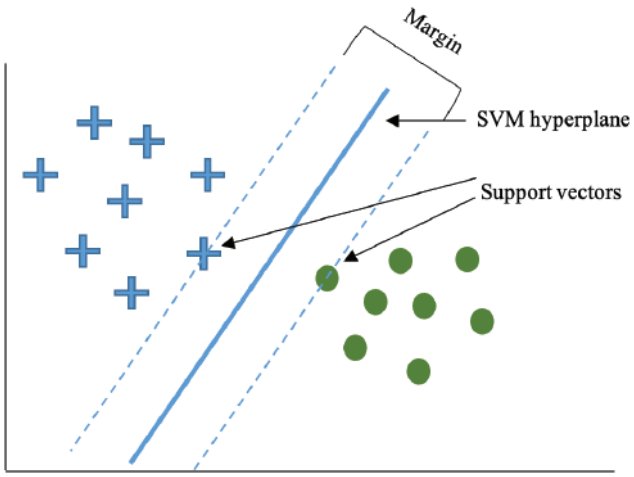


Figure 13. representation for SVC algorithm.

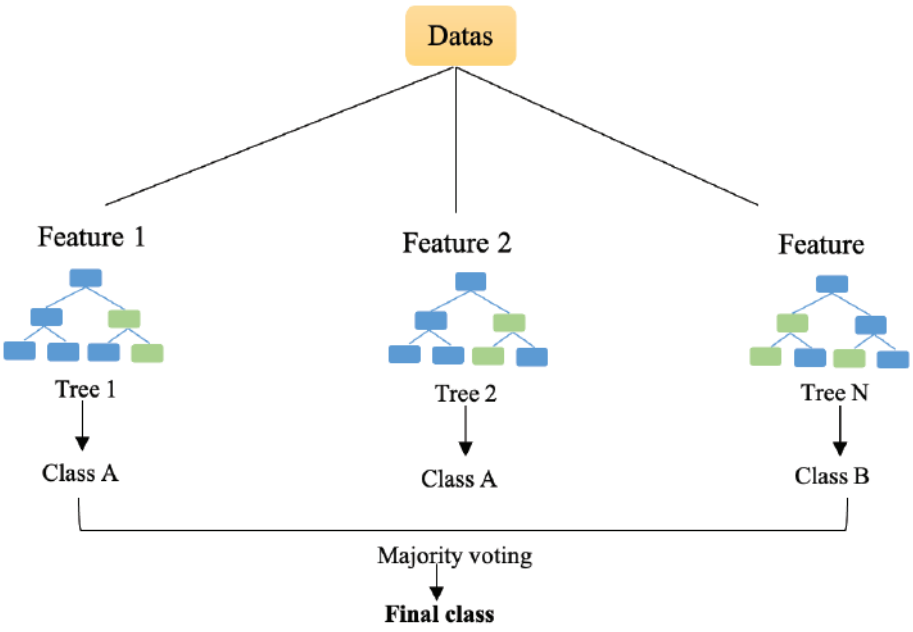


Figure 14. Representation for random forest tree algorithm.

multi-class classification because of its capacity for global optimization and resilience against overfitting. SVM's versatility has been demonstrated by its successful applications in fields like gene-function prediction, text classification, handwriting recognition, and remote sensing. Although it works most effectively with smaller datasets, outliers and the selection of kernel functions can affect how effective it is. Moreover, the efficacy of SVM hinges significantly upon judicious selection and fine-tuning of kernel functions [31]. Figure 13 shows the representation of this algorithm.

Random Forest Classifier

The risk of overfitting that frequently arises with single decision trees is lessened by the Random Forest algorithm. It is an ensemble method, meaning it trains multiple decision trees at the same time. Each tree makes its own prediction, and the final result is determined by combining these predictions—using averaging for regression tasks or majority voting for classification tasks [28]. Refer to Figure 14 for a graphical depiction of this algorithm.

Deep Learning

The notion of deep learning (DL) has a longstanding history, but recent years have witnessed its transformation due to the accessibility of extensive datasets and advancements in computing capabilities. Deep Learning (DL) is a rapidly growing field that has become widely popular in recent years [32]. This approach employs algorithms to complete the data-driven learning process for better predictions or decisions. Neural networks are one of the most important tools for deep learning, which makes possible to learn from a massive amount of data [33-41]. The emergence of deep learning has seriously brought us into a new era of research and innovation; it has made significant breakthroughs in various fields e.g., healthcare, finance, transportation, etc [32].

While ML and DL are often used interchangeably, they are distinct sides of artificial intelligence. ML involves programming computers to learn from data without explicitly telling them what to do. On the other hand, DL is a kind of machine learning, which makes use of neural networks to mimic human brain structure and functionality. They are extremely good at learning from unstructured data and have been incredibly successful in solving difficult problems such as image recognition, and even speech recognition. [42-48].

Based on the previous sections, and based on [49-67] a comparative Table 3 for AI, ML, and DL is shown for better understanding.

Applications of the Aforementioned Techniques in Engineering

As stated, this research concentrated on showing the applications of AI, ML, and DL in engineering fields. Table 3 illustrates how these techniques are applied in 14 fields of engineering science.

Statistical Analysis

After closely examining the literature, it was found that AI, ML and DL techniques give satisfactory results in many fields of Engineering. Figure 15 visualizes the proportions for all of these techniques based on the aggregated studies described in the literature. The presented percentages give an inclusive insight into what is the actual practice of AI, ML and DL in the case of JEA. This figure is a useful summary, capturing the combined effect and effectiveness in studies that are comprising these advanced technologies.

ML stands out as the most influential technique in engineering applications when juxtaposed with its counterparts. This prominence is justifiably attributed to the relative ease with which ML algorithms can be implemented. The practical benefit of ML is that it can achieve performance at a similar level to that obtained with DL without the requirement in

Table 2. Advantages and disadvantages of AI, ML, and DL

Technique	Advantages	Disadvantages
AL	AI includes a wide range of methods, such as machine learning and deep learning, to mimic human intelligence. It can handle complex decision making and has applications in many disciplines.	Developing AI systems can be computationally intensive and require specialized expertise. They can also be rigid, unable to handle novel situations without plenty of reprogramming.
ML	ML algorithms learn from patterns of data in order to make predictions and perform tasks automatically. These are used in a wide variety of businesses to help make processes more efficient and inform better decisions.	ML models are dependent upon labelled data in the training phase and can be very complicated.
DL	DL has proven particularly adept at processing large, unstructured data like images and text. It has the ability to learn useful features automatically, outperforms in tasks such as image classification and natural language processing.	Deep learning models tend to be computationally expensive to train; also, in the case when data is scarce, it's easy for a model to overfit. Moreover, these models are for the most part "black boxes," so it is challenging to interpret why they make decisions.

Table 3. Comprehensive review of AI, ML, and DL applications in engineering fields

Automobile Engineering						
Ref #	**Used technique (AI/ ML/ DL)**	**Used tool**	**Methodology**	**Summary of the outcomes**	**Comments**	**Year**
[68]	ML	---	In this study, the authors applied a combination method between ML and analytical methods to improve the vehicle routing problems (VRP).	The outcomes showed that the VRP can be enhanced by ML models, and the corresponding performance of the vehicle could be improved.	The background, problem statement, the research objective, and the methodology were introduced in a very good way assuming that the reader has a brief knowledge of this field.	2023
[69]	DL	Matlab	In this study, the authors developed a novel model, an improved hybrid ANFIS, to design a practical, accurate, and simple Lithium-Ion battery state of charge estimator.	The outcomes showed that the built four models achieved a better accuracy of 0.5% in comparison with the 2% stated in the previous studies.	The study was, totally, conducted theoretically. Future research may apply and test the adopted methodology practically.	2023
[70]	ML	GT-Suite	In this study, the authors developed a parametric ML model with the aid of GT-Suite software. The parameters included in the study are energy consumption, distance traveled, vehicle speed, state of charge of battery, and motor power.	The proposed method showed a good performance with an accuracy of 89% in being able to predict the state of charge of the battery, and this can help automobile engineers to design scalable and more efficient electrical vehicles.	In general, the analyzed different cycles should include the worst scenario. For instance, the distances traveled scenarios in the study varied between 4.1 km and 20.1 km. it would be better if the study investigated longer distances.	2023
[71]	AI and ML	Matlab	This study proposed a method to predict the required time for EV charging based on collected data from 500 EVs. The proposed method depended on using the ML algorithms and the AI was also adopted to optimize the parameters of ML.	The outcomes showed that the best model was GWO-based ML as it achieved better results compared with the rest ones.	this study did not consider the challenges in charging that are met.	2022
[72]	ML	----	In this study, the authors investigated the charging system of EV in a smart grid by using several ML algorithms to achieve the goal of reducing load fluctuation, power loss, and expenses. Then, the proposed algorithms were evaluated and compared.	The outcomes showed that Long Short-Term Memory (LSTM), could be employed to provide EV control in particular circumstances in addition to keeping the billing costs minimal.	The proposed method has several limitations, which are already included in the paper.	2023

Table 3. Comprehensive review of AI, ML, and DL applications in engineering fields (continued)

Agricultural Engineering						
Ref #	**Used technique (AI/ ML/ DL)**	**Used tool**	**Methodology**	**Summary of the outcomes**	**Comments**	**Year**
[73]	ML	---	In this study, the authors analyzed the existing ML models and applications in agriculture engineering starting from the process till the outcomes. each application was discussed with its advantages and its corresponding weaknesses.	The key outcomes from this study showed that the farm management should be evolved with the reality by linking the related data of it with sensors to provide better suggestions that can enhance the final products from the agriculture	The paper suggested to apply real-time on new applications as it is the gap in this research field.	2020
[74]	ML	WEKA	In this study, the authors designed and applied an ML workbench, WEKA, that admits rapid experimentation on a given dataset by using several ML schemes.	The processing of data from ARFF format to its final representation as a set of rules or a decision tree was facilitated by the WEKA workbench. A variety of state-of-the-art, robust, and efficient ML schemes were provided for experimentation, and a concentration on simplifying access to standard schemes for performance evaluation and comparison was maintained.	The study linked how the animal affect the agriculture, which is a good addition.	2023
[75]	AI and ML	---	The study investigated and showed the applications of ML and AI in agriculture engineering along with some other sectors. the methodology of this study can be simply introduced by discussing several techniques and algorithms of ML and AI.	At the end of the study, it was stated that AI, ML, and DL can be applied to enhance the production of crops and design a reliable product quality monitoring system.	This paper investigated the applications of ML and AI in several aspects besides the agriculture such as the health care, disease prediction, and water waste controlling in a readable well-organized way	2023
[76]	AI	---	This study analyzed several relevant articles on AI applications in the agriculture sector. For instance, some applications such as detecting the smallest insects in the farms by AI, how to provide proper guidance on water management by AI, how to Increase agricultural yield and productivity, and how to Increase farmer profitability were investigated in this paper.	The outcomes from this study showed that AI technologies, which use data like precipitation, temperature, solar radiation, and wind speed in combined with some ML algorithms and images taken by drones or any other technologies can effectively predict crop sustainability and, accordingly, ease the process for the farmers to evaluate farms for the presence of diseases or pests and inadequate plant nutrition.	A deep discussion was provided for each application.	2023

Table 3. Comprehensive review of AI, ML, and DL applications in engineering fields (continued)

Agricultural Engineering (continued)						
Ref #	**Used technique (AI/ ML/ DL)**	**Used tool**	**Methodology**	**Summary of the outcomes**	**Comments**	**Year**
[77]	DL	Matlab	This study employed some data related to the humidity and temperature in some algorithms such as KNN to find a model that could be used for climate prediction based on a previous observed data.	The outcomes from this study showed that the yield production depends mainly on the soil nutrients. Moreover, it was concluded that Remote Sensing area and data mining are used to provide some algorithms and prognosis strategies for soil attribute classification.	The resolutions of the figures and tables are not well enough.	2023
Aerospace Engineering						
Ref #	**Used technique (AI/ ML/ DL)**	**Used tool**	**Methodology**	**Summary of the outcomes**	**Comments**	**Year**
[78]	AI	---	This study proposed a novel artificial bee colony algorithm that was implemented as part of a hybrid method to solve flexible job-shop scheduling problems by extracting the key manufacturing information through an aerospace workshop.	The outcomes showed that the proposed method was effective	In this field, the cost is one of the key points that should be considered. However, this paper did not investigate how the cost will be affected.	2023
[79]	ML	python	The authors developed a new ML algorithm to predict the fatigue damage of the material by preprocessing the received signals	The outcomes showed that the proposed algorithm gave good performance and accuracy.	This paper handled the complexity of the nonlinear equations effectively.	2023
[80]	ML and DL	Teachable Machine and ANSYS	The authors proposed a DL framework to identify faulty components due to malfunctioning in the aerospace industry. This could help the engineers in focusing on choosing the most proper material in the manufacturing stages. Moreover, the study employed the CNN approach to recognize the intermediate abnormal situations.	The outcomes showed the importance of the proposed method especially in managing the operation cost along with reducing the reducing rework-induced delays. The statistical outcomes showed a 34.32% and 52.88% reduction in total cost and time delays respectively.	The cost was considered in this paper as a key objective, which is a good contribution.	2023

Table 3. Comprehensive review of AI, ML, and DL applications in engineering fields (continued)

Aerospace Engineering (continued)						
Ref #	**Used technique (AI/ ML/ DL)**	**Used tool**	**Methodology**	**Summary of the outcomes**	**Comments**	**Year**
[81]	ML	Python	This paper proposed a model to predict fatal occurrences in aviation events by applying some data on ML models. This is very helpful for the engineers as the safety standards are very rigorous,	It was found that random forest was the most accurate model as it achieved an accuracy of 90%.	a large number of the limitations was considered and discussed in this research, which is a good contribution.	2023
[82]	ML	---	This paper compared between the ML models used in aircraft maintenance systems.	The outcomes showed that to enhance the aircraft maintenance system, several should be considered during the evaluation and comparison between the models such as the cost as well the time. Some model showed their superiority from the cost aspect while others showed their superiority from the time aspect.	No clear objective function was provided in this study.	2023
Architectural Engineering						
Ref #	**Used technique (AI/ ML/ DL)**	**Used tool**	**Methodology**	**Summary of the outcomes**	**Comments**	**Year**
[83]	ML	MATLAB	This study proposes a real-time seismic damage simulation method for urban building portfolios by integrating a multiple degree-of-freedom (MDOF) shear model, flexural-shear model, and machine learning. In this research, formulas predicting periods of different structures are developed, and surrogate models for minimizing MDOF model is constructed.	Validated on two city-scale cases, the proposed method can predict maximum inter-story drift and floor acceleration accurately with MDOF models at a computational cost much lower than that of time-history analysis. The machine-learning-based surrogate model enhances efficiency with the maximum acceleration ratio of ~76,600 compared to conventional approaches.	additional testing in a variety of urban settings would reinforce its reliability. Generally, the method appears to be an effective and accurate approach for seismic risk assessment ageistic urban centers.	2023
[84]	AI	---	The MDOF shear and flexural-shear models are coupled machine-learning-based method developed for real-time seismic fragility simulation of urban building portfolios on multiple spatial levels. Type-formulas of periods for various structures are proposed, and surrogate models to achieve the optimum multi-degree-of-freedom (MDOF) views are made.	The city-scale cases show the potential of the method for real-time seismic damage simulation at an acceptable accuracy level. And the model developed does not require significant retraining for different urban building portfolios, indicating its potential for broad use.	The research highlights the efficiency and effectiveness of the AI-based approach in improving seismic risk management for an urban building stock.	2023

Table 3. Comprehensive review of AI, ML, and DL applications in engineering fields (continued)

Architectural Engineering (continued)						
Ref #	**Used technique (AI/ ML/ DL)**	**Used tool**	**Methodology**	**Summary of the outcomes**	**Comments**	**Year**
[85]	AI	---	This paper explores how diffusion-based AI art platforms, such as Midjourney and DALL·E 2, Stable Diffusion (which is our contribution), can be applied to common use cases in architectural design. This paper analyzes the features of these platforms and their adequacy to the demands for task support in civil engineering architecture from AI art platforms.	The paper highlights the strong AI potential in architecture, notably for ideation, collages, building and style variants. Acknowledging the existing limitations due to certain difficult prompts, the authors expect that these will be alleviated with new diffusion models finetuned on BIM reasons about datasets.	Shortcomings in existing AI art tools for architecture include difficulties with nuanced prompts and reliance on certain design fads. Fields of developments comprise better understandabilities semantics and integration into architectural work. Continued study on the development of structural dynamics and construction technology will bring about a new age of AI-informed styles in architecture.	2023
[86]	AI	---	The study took a holistic approach to evaluate the adoption of AI, IoT and Big data technologies in the Architecture, Engineering and Construction (AEC) sector. The research included a breakdown of different AI models and methodologies underpinning Construction 4.0 and 5.0, as well as societal changes in Society 5.0.	IoT devices built into construction equipment and structures enabled the gathering of real-time data that has been at the heart of AI-driven predictive maintenance and other process optimizations.	The study identified a number of problems – technical, such as data integration, security, and scalability; ethical, related to workforce displacement and biases in AI algorithms.	2023
Biomedical Engineering						
Ref #	**Used technique (AI/ ML/ DL)**	**Used tool**	**Methodology**	**Summary of the outcomes**	**Comments**	**Year**
[87]	ML	Matlab	The proposed algorithm used KNN on segmenting of the medical images and feature extraction in image only followed by classification based on NN to analyze the data.	It was found that KNN gave a very good accuracy in images classification, which is a very important phase in medical imaging.	A comparative analysis based on MSE, PSNR, and SSIM were applied for only the proposed algorithm.	2023

Table 3. Comprehensive review of AI, ML, and DL applications in engineering fields (continued)

Biomedical Engineering (continued)						
Ref #	**Used technique (AI/ ML/ DL)**	**Used tool**	**Methodology**	**Summary of the outcomes**	**Comments**	**Year**
[88]	ML	Matlab	In this study heart disease was predicted by applying the ML techniques. The proposed method was created after a comparison phase between many ML algorithms by Matlab coding, since the effective ML strategy, in general, requires precise identification of the problem.	The results showed that the proposed method can be used to accurately diagnose the stage of a disease and its treatment using this approach.	Only three types of disease were included along with their symptoms, and prevention.	2022
[89]	DL	---	This study proposed a new IoT and DL enabled healthcare disease diagnosis model by using biomedical signals. The proposed model used a BiLSTM feature extraction to extract the feature to discover CVDs existence.	The experiment results proved the supremacy of the IoTDL-HDD model with an accuracy of 93.452%.	This paper has a strong mathematical foundation which supported the outcomes.	2021
[90]	ML	---	In this study, the authors analyzed the most recent studies that investigated the applications of ML techniques in medical data processing. 27 articles were discussed and the following aspects were included: deployed methods, proposed framework, the advantages and the disadvantages.	The analyses showed that 43% of the studies used the IoT. Moreover, the most used DL algorithm was the CNN.	The paper has a well-organized structure	2023
[91]	ML and DL	---	This study presented systematic studies related to applications of ML and DL in the detection along with classification of multiple diseases. 40 studies were collected from journals and conferences from 2014 to 2022.	The outcomes showed that the ML was used more than DL in medical diagnosis	This paper used some studies from 2014, which could be replaced with the most recent ones.	2022

Table 3. Comprehensive review of AI, ML, and DL applications in engineering fields (continued)

Civil Engineering						
Ref #	**Used technique (AI/ ML/ DL)**	**Used tool**	**Methodology**	**Summary of the outcomes**	**Comments**	**Year**
[92]	ML	---	This study employs six machine learning techniques to predict the compressive strength of self-compacting concrete. These are as such credible AI algorithms as ANN, ANFIS, ELM etc., combined with natural intelligence techniques IPBased MOFA and WHO.	The results validate that all the six machine learning models demonstrate high level of accuracy in predicting the compressive strength of SCC. ELM tuned with MOFA outperforms other methods in differentologic evaluation metrics and this indicates its superiorities. Visual results confirm the models are effective, so promising benefits such as quality control, cost saving and safety improvement can be expected in practical constructions.	Although the paper effectively illustrates the capabilities of machine learning methods for predicting compressive strength in self-compacting concrete, such could be strengthened by elaborating further on obstacles or complications faced when applying these techniques outside an experimental context.	2021
[93]	ML	---	The proposed study uses Mechanics-Informed Surrogate Models (MISM) for structural analysis, which embeds empirical data and mechanics prior knowledge, and re- presents rules or information about truss structures based upon graph neural networks (GNNs). The proposed method is applied to bi-dimensional and tri-dimensional truss structures, and shows a better prediction capability than standard surrogates, with a strong emphasis on the mechanics integration of this improved model interpretabiliy.	The study demonstrates that the proposed Mechanics-Informed Surrogate Models (MISM), which are based on GNNs, can provide better fitting of deformations in structural systems than the typical surrogate models. Although dedicated hardware is needed due to the more lengthy training phase, we hope that such efforts at computational accuracy will lead to improved predictions in structural engineering applications and in extrapolating GNNs to predict nonlinear behavior of structures being studied.	the work does concede to the requirements of specialized hardware and training time, which may imply a trade off between computational complexity and enhanced accuracy worth consideringin practice.	2024
[94]	ML	Python and MATLAB	This research combines advanced image processing and machine learning methods, which is more specifically the computer vision strategies, to predict structural behavior and quantify damage in RC exterior B–C joints. Using Python for data analysis and MATLAB for image segmentation, the study processes 500 images from 141 shear-critical specimens, employing thresholding and edge detection to extract crack patterns' textural and geometric attributes.	Regression analysis of the present data demonstrates reasonable predictive quality and statistically strong relationships between identified crack patterns and structural damage in exterior BJs&CEs. Its application has been shown to be effective in the estimation of damage states from surface crack patterns under various experimental condition and layout. The successful establishment of the relationship between surface observations and quantification on damage level with stiffness, loading and displacement proposed implies that image-based damage recognition for visual inspections of exterior beam-column joints in structural condition assessment may potentially be feasible.	The standalone approach based on Python and MATLAB for data analysis and image segmentation, shows strong predictive performances under different experimental conditions.	2023

Table 3. Comprehensive review of AI, ML, and DL applications in engineering fields (continued)

Civil Engineering (continued)						
Ref #	**Used technique (AI/ ML/ DL)**	**Used tool**	**Methodology**	**Summary of the outcomes**	**Comments**	**Year**
[95]	ML	MATLAB	This study addresses the deterioration of civil structures in Japan by proposing an autoencoder-based damage detection approach using machine learning. Utilizing a Multi-Degree-Of-Freedom (MDOF) system model subjected to seismic responses, the study explores the correlation between the magnitude of reconstruction error and the degree of structural damage. The autoencoder, a three-layer neural network trained on normal data, is employed for unsupervised learning to distinguish between normal and abnormal structural responses.	Five seismic ground motions are prepared, and the autoencoder is trained using linear displacement responses from adjusted motions. The study demonstrates a relationship between the reconstruction error magnitude and the degree of structural damage, indicating the potential of the proposed method for detecting damage in civil structures.	The correlation established between reconstruction error magnitude and the degree of damage demonstrates the method's potential for accurate and efficient damage detection.	2023
Computer Engineering						
Ref #	**Used technique (AI/ ML/ DL)**	**Used tool**	**Methodology**	**Summary of the outcomes**	**Comments**	**Year**
[96]	ML	Python	At the beginning, the authors explained how a physical concept of ML can be translated into practical work in engineering. They explored the ability of hybrid quantum-classical NN to enhance the accuracy of a model and reduce computational resources.	It was found that ML can be employed to minimize or even eliminate the errors on noisy intermediate-scale quantum devices.	No sufficient discussion was provided regarding the applied NN.	2023
[97]	AI	---	The author proposed a method to investigate and identify how the implementation of knowledge management principles in software engineering could enhance the future transformation of software-related jobs. Some quantitative data were analyzed to evaluate the AI role.	It was found that AI along with knowledge management can be used to improve software engineering activities such as error tracking, version control, monitoring software documentation, and onboarding new members.	This paper analyzed the already existing data, but no prediction step was conducted regarding the future situation.	2023

Table 3. Comprehensive review of AI, ML, and DL applications in engineering fields (continued)

Computer Engineering (continued)						
Ref #	**Used technique (AI/ ML/ DL)**	**Used tool**	**Methodology**	**Summary of the outcomes**	**Comments**	**Year**
[98]	DL	Python	The authors conducted an empirical study of how the DL can be used for sentiment detection tools for software engineering.	The outcomes showed that DL tool could achieve the target effectively.	It needs more discussion and clarification regarding the error categories of DL	2023
[99]	ML and DL	Python	This article proposed a method that combines several algorithms and made the evaluation as well the validation based on several criteria such as the precision, F1 score and the recall.	The outcomes showed that the phishing attack could be detected by software engineering by the ML algorithms such as NB and SVM in addition to DL algorithm such as LSTM.	The methodology and the result sections were discussed in detail, which is a good contribution.	2023
Chemical Engineering						
Ref #	**Used technique (AI/ ML/ DL)**	**Used tool**	**Methodology**	**Summary of the outcomes**	**Comments**	**Year**
[100]	ML	---	The study constructed a database of Ionic Liquid encapsulated Metal-Organic Framework (IL@MOF) composites. Molecular simulation was employed to identify the top-performing composites and elucidate the gas separation mechanism.	The utilization of ML techniques revealed essential factors influencing CO_2/N_2 selectivity and CO_2 permeability, showcasing substantial improvements in CO_2 permeability and selectivity, surpassing known performance boundaries.	The full development of the database for this study when considering molecular simulation and machine learning (ML) methods has provided a solid foundation to find out promising IL@MOF composites towards technological applications.	2022
[101]	ML	---	The study adopts a high-throughput computational screening approach to screen 6013 metal-organic frameworks (MOFs) to discover the optimal methanol-MOF pairs for adsorption-driven heat pumps and chillers, establishes structure-performance correlations with six MOF descriptors, and employs four machine learning algorithms for predicting the performance metrics.	The maximum COP and WCOP under the heat pump working condition were 512.86 mg/g and 1.83, respectively, and this study contributes a knowledge of proper ranges of the MOF descriptors for improving the adsorption-driven heat pump performance using methanol as a working fluid.	This work is an important contribution to the field for characterizing effective pairs of working fluid and adsorbent to improve heat pump performance.	2020

Table 3. Comprehensive review of AI, ML, and DL applications in engineering fields (continued)

Chemical Engineering (continued)						
Ref #	**Used technique (AI/ ML/ DL)**	**Used tool**	**Methodology**	**Summary of the outcomes**	**Comments**	**Year**
[102]	ML	---	The study computed and simulated metal–organic framework membranes MOFs from the CoRE-MOF database for Kr/Xe separation under atmospheric pressure. Important structural features were identified by univariate analysis, and classification/regression models are developed employing 5 machine learning algorithms.	Univariate analysis pointed to the critical role that of pore limiting diameter plays in separation and through comparison across a series of 3D MOF membranes, permeability and permselectivity were outlined to highlight desirable ranges as key guidelines for improved membrane designs.	The study demonstrates a novel methodology for evaluating numerous MOF membranes for Kr/Xe separation, offering a promising direction for future membrane design and improvement.	2023
[103]	ML	---	The used of machine learning models, such as the gradient boosting decision tree (GBDT), were used to predict how the polymer functional groups influenced the conductivities of Zn2+ and protons.	The studies presented demonstrated the effectiveness of machine-learning-based predictions on directing polymer membrane design and synthesis for enhanced battery performance metrics for the Zn/MnO2 flow battery system.	Incorporation of the ML models reveals a strong advantage in designing specialized membranes for batteries compared to conventional materials synthesis.	2023
[104]	ML	---	The work combined high-throughput computational screening (HTCS) and ML to predict hydrogen separation performance among computation-ready metal–organic framework membranes (CoRE-MOFMs) for different gas pairs. Eight supervised ML models were used to predict the separation performance.	The selected MOFMs for H2 separation in this work were high-performing membranes, showing potential industrial use. Combining HTCS and ML expedites CoRE-MOFMs validation, presenting the possibility of a high-throughout discovery platform for gas separations.	---	2022
Electrical Engineering						
Ref #	**Used technique (AI/ ML/ DL)**	**Used tool**	**Methodology**	**Summary of the outcomes**	**Comments**	**Year**
[105]	ML	LSTM	This study aimed to show how the data since can by applied in electrical engineering field. The role and the application of the data science (DS) and ML on edge, fog, and cloud levels of vertical industrial IoT concepts of power plants were presented by investigating the requirements and expectations of IoT. Moreover, the limitations in signal conversion were also considered described.	The study showed that the existing traditional management and control (M&C) concepts of smart power plants should be improved. In addition, this paper pointed out the advantages of the vertical IoT concept and described all IoT levels (edge, fog, and cloud).	The study involved a fuzzy logic control system but no sufficient description were provided.	2023

Table 3. Comprehensive review of AI, ML, and DL applications in engineering fields (continued)

Electrical Engineering (continued)						
Ref #	**Used technique (AI/ ML/ DL)**	**Used tool**	**Methodology**	**Summary of the outcomes**	**Comments**	**Year**
[106]	AI and ML	---	This study proposed a Recurrent Neural Network (RNN) forecasting model incorporating a Dynamic Fitness Al-Biruni Earth Radius (DFBER) algorithm in order to forecast and predict wind power data patterns. Several popular models were used to test the performance of the model such as Grey Wolf Optimizer (GWO), Whale Optimization Algorithm (WOA), Particle Swarm Optimization (PSO), Fire Hawk Optimizer (FHO), and Jaya Algorithm (JAYA).	According to the evaluation metrics, RMSE, MAE, and R2, the proposed RNN-DFBER-based model outperforms the other models considered. This suggests that the RNN model, combined with the DFBER algorithm, predicts wind power data patterns more effectively than the alternative models.	This study did not include anything about data collection and preprocessing phases.	2023
[107]	DL	Python, Linux hping3, and Linux bwm-ng	In this study, a novel approach was proposed for online cyber attack situational awareness that improves the reliability of the power grid. The proposed approach employed a combination of DL convolutional network for time series classification-based anomaly detection and DL model of Graph Convolutional Long Short-Term Memory	The outcomes showed that the proposed method could identify active attack locations (control center, within substations, and wide area network) with an accuracy percentage exceeding 96%.	This study combined the introduction section with the related works. In general, it is better to separate these two sections to give a good knowledge for the reader then introducing the previous related work in the following section.	2023
[108]	DL	---	This study applied the DL in power quality enhancement, it showed that most of the applications of DL depend on supervised learning and unrealistic synthetic data with no proper labeling.	It was found that it is not easy to apply the DL in the power quality and the experts need to enrich their knowledge even with automatic feature extraction by DL approaches. Further, the research gaps in this field were introduced in this study which are related to the semi-supervised learning applications, explainable DL and hybrid approaches combining DL with expert systems.	This study suffered from a lack of novelty. Moreover, it mentioned the research gabs in this field but it did not handle it.	2023

Table 3. Comprehensive review of AI, ML, and DL applications in engineering fields (continued)

Electrical Engineering (continued)						
Ref #	**Used technique (AI/ ML/ DL)**	**Used tool**	**Methodology**	**Summary of the outcomes**	**Comments**	**Year**
[109]	ML and DL	---	This study aimed to forecast renewable energy (RE) generation by using ML and DL techniques by reviewing the different methods and model that were used for RE prediction. The limitations, advantages, and the strengths of each model were discussed too.	It was found that the hybrid models, which consist of traditional time-series analysis along with ML and DL techniques are used for RE forecasting purposes effectively. On the other hand, the design of a hybrid model is not a trivial task.	The study showed the gaps existing in the research field without solving them.	2023
[110]	AI and ML	Matlab	This paper aimed to estimate the extractable power from wind in several sites in Jordan by applying the AI techniques (GA, BFOA, SA, and ANFIS) based on Weibull and Normal PDFs. Moreover, a Matlab tool was used to estimate the accuracy of the parameters of the aforementioned PDFs.	The study showed the superiority of SA compared with the rest algorithms. Moreover, Normal PDF showed its good performance in estimating the extractable energy from wind.	In this study, the authors showed their contribution in employing several techniques in wind energy estimating.	2022
Electronic Engineering						
Ref #	**Used technique (AI/ ML/ DL)**	**Used tool**	**Methodology**	**Summary of the outcomes**	**Comments**	**Year**
[111]	ML	Matlab	The authors demonstrated how effective is the application of the ML in the solder joint geometry of electronic components by showing how the lifetime of these components will be enhanced.	The outcomes showed that there is an optimal size for the solder joint that will maximize the lifetime of the electronic component.	No related works were included in this study.	2021
[112]	ML	Pymatgen (Python Materials Genomics)	The authors proposed a method to predict the band gap of graphene in heterostructures. They employed an ML learning model on a dataset of 2076 binary compounds, followed by the usage of two main ML models to screen semiconductor components and form heterostructures with graphene.	the outcomes showed that the proposed method has an accuracy rate of 88.3% and the difference between the predicted and the calculated values was ignorable.	No related works were included in this study.	2023

Table 3. Comprehensive review of AI, ML, and DL applications in engineering fields (continued)

Environmental Engineering						
Ref #	**Used technique (AI/ ML/ DL)**	**Used tool**	**Methodology**	**Summary of the outcomes**	**Comments**	**Year**
[113]	AI and DL	---	The study compared a method based on deep neural networks with statistical and traditional machine learning methods to record the temporal patterns in sensor data present in wastewater treatment plants (WWTPs)	This gives the ability to enhance monitoring efficiency, enabling timely responses to faults and optimizing treatment processes while minimizing environmental impact.	The paper deals with an important point pertaining to WWTPs since a fault detection becomes essential to improve the treatment efficiency and the energy consumption.	2020
[114]	AI and ML	---	The authors used neural network to estimate the quantity of waste and machine learning algorithm to optimize the waste collection.	The study proved Efficient waste prediction and reduction models. It achieved a gross amount of waste reduction by 90%, landfill analysis by 40% and transportation by 15%.	The study demonstrates the significant possibility of improving waste management performance and promoting sustainability in human society.	2021
[115]	AI and ML	---	The IFFNN was achieved by connecting a feedforward neural network (FFNN), which is more efficient and better performing the WWTP effluent quality prediction ability of a traditional FFNN.	The model successfully encapsulated intricate nonlinear relationships and predicted the information accurately. These findings indicated significant enhancements in prediction accuracy and suggested potential applicability for immediate regulatory decision-making in WWTP operations.	The existing IFFNN model doesn't include an optimal control system to simultaneously reduce real-time operational expenses in WWTP while meet the effluent criteria.	2022
[116]	AI and ML	---	The study used an electrically-enhanced membrane bioreactor setup to treat medium strength wastewater. An artificial neural networks (ANNs) based ensemble model effectively simulated experimental outcomes, showing strong correlations.	By using such an integrated system of electrochemical treatment and membrane bioreactor, the environmental pollutant concentration of wastewater was greatly reduced. For instance: COD (98%), nh4+-N (99%), PO43--P (97%); and nh4+-Step (92%).	---	2016
[117]	AI	---	The authors developed artificial neural network models to predict treatment plant efficiency using historical data. They evaluated biochemical oxygen demand (BOD) and suspended solids (SS) concentrations.	ANN models able to predict BOD and SS concentrations in effluent from the plant, reaching R2 values from 0.63 to 0.81 for BOD and 0.45 to 0.65 in SS over various data groups, are reported herein.	Highlighting the promising potential of ANNs as a valuable tool for forecasting wastewater treatment plant performance is this study's acknowledgment that accuracy in SS predictions is less (such noise and marking) than for BOD. As a result, ANNs can by no means be discarded Suddenly but rather must occupy a specific part of the technology process field. This suggests improvement in accuracy from future research with better coverage and fewer noisy data sets.	2004

Table 3. Comprehensive review of AI, ML, and DL applications in engineering fields (continued)

Environmental Engineering (continued)						
Ref #	**Used technique (AI/ ML/ DL)**	**Used tool**	**Methodology**	**Summary of the outcomes**	**Comments**	**Year**
[118]	ML and DL	Python	By using ML to control precise aeration in WWTPs the study developed its own equivalent system, a variation sliding layer (VSL) that is Based on ML. . The VSL was integrated into classic ML, deep learning, and ensemble learning models to enhance aeration control efficiency.	The systems based on VSL and ML significantly improved WWTP aeration control efficiency Predictive accuracy for air demand in WWTO systems was much higher than in traditional mechanistic ones-and showed marked improvements. In the study, it provided an illustration of the future potential for precise air demand prediction and control in AI technology areas such as WWTP, with a view to saving energy reducing consumption.	---	2023
Industrial Engineering						
Ref #	**Used technique (AI/ ML/ DL)**	**Used tool**	**Methodology**	**Summary of the outcomes**	**Comments**	**Year**
[119]	ML	---	The research employs a knowledge-based intelligent supervisory system for rare quality event detection in manufacturing. An algorithm hybrid elimination of features with l1-regularized logistic regression learning as the learning algorithm and an optimal threshold-increasing technique to support defect detection	The study addresses the zero-defect policy requirement, offering a rare quality event detection strategy. Using l1-regularized logistic regression, the strategy is validated in automotive manufacturing and produces 100% defection rate.By removing irrelevant features and compression settings, the proposed strategy of enhancement see-classification results greatly contributing to promote quality standards in manufacturing.	---	2018
[120]	ML	---	The paper uses the supervised machine learning classification for such an issue as how to predict production batch compliance quality in manufacturing. A study is then implemented to validate the approach, combining the feature engineering and dataset information in classification algorithms of a multiprocessor appliance production line. The high accuracy (0.99) and Cohen's Kappa (0.91) indicate a powerful predictive value of the model for predicting compliance quality.	The machine learning algorithm exhibits an outstanding accuracy (0.99) and reliability (Cohen's Kappa of 0.91) to predict the compliance quality of the unit batches. By highlighting the importance of feature generation and learning for the specific dataset, this method can efficiently prevent defective product batches in advance and significantly reduce cost in recall expenses and logistics.	---	2020

Table 3. Comprehensive review of AI, ML, and DL applications in engineering fields (continued)

Mechanical Engineering						
Ref #	**Used technique (AI/ ML/ DL)**	**Used tool**	**Methodology**	**Summary of the outcomes**	**Comments**	**Year**
[121]	ML	Python	Design of Experiments (DOE) was contrasted to Active Learning (AL) for performing data collection in mechanical engineering to examine the accuracy of ML models, sample efficiency, stability and predictive performance, using three cases generated by AL and DOE techniques.	Low-cost scenarios privileged random sampling, however in low budget was LHS and AL performing better. LHS showed more reliable or stable performance but had an initial point number which ranged dynamically before QBC was most efficient and stable in the bagging methodology whose testing commonly occurred after aggregate sample size compared to LHS especially for learning from high-cost data.	This article gives a detailed contrast of the DOE and AL techniques for the data collection procedure on ML models with respect to engineering application scenarios and actionable guidance about sampling strategies (both algorithms) engineered toward engineers and developers. Nevertheless, its concentration on particular methods such as LHS and QBC could potentially restrict its applicability.	2023
[122]	ML	---	The use of ML methods was applied to machine sensor data in order to assess the health of machining process and machine tool, using both supervised and unsupervised techniques such as PCA, CWT, with custom built and pre-trained CNNs.	PCA was effective at reducing the features while not significantly adversely affecting accuracies, with very high classification accuracies of nearly 100% for most failure modes. The GMM proved to be reliable in classifying failures while custom CNNs were found to achieve equivalent or higher accuracy when compared against pretrained networks, although assessment is based on simulations and may not reflect real-life performance comparisons.	The application of multiple ML techniques in analyzing big data and recognising failure modes is laudable, pointing toward the route of being able to detect faults 'on-the-fly' during production.	2020
[123]	ML	---	The diagnosed gear box faults are obtained by processing the vibration signal using wavelet-based features, which are collected at multiple states of gears. It assesses the efficiency of Morlet wavelet in feature extraction.	It is identified that proximal support vector machines (PSVM) provides better classification than artificial neural network (ANN) for classifying the features extracted from gear box, and thus more accurately recognize gearbox faults.	The comparative analysis of classification techniques offers insights into the efficiency of PSVM over ANN for accurate fault identification, which is a notable strength.	2021
[124]	ML	---	The work is devoted to the recognition of gear and bearing faults of gear units based on a multilayer neuron network (MLP). By means of standard deviation of wavelet packet coefficients, it constructs a feature vector from vibration signals and identifies faults with high precision.	The proposed ANN-based system achieved a good performance and full accuracy in failure diagnosis of gear and fault detection of bearing using a small two hidden layer MLP network.	It does effectively emphasize that preprocessing techniques, such as wavelet transform, are crucial to improve the accuracy of fault detection and thus advocate their application in practice; it thus contributes to the advancement of the domain.	2007

Table 3. Comprehensive review of AI, ML, and DL applications in engineering fields (continued)

Mechanical Engineering (continued)						
Ref #	**Used technique (AI/ ML/ DL)**	**Used tool**	**Methodology**	**Summary of the outcomes**	**Comments**	**Year**
[125]	DL	---	In this paper, the normalized sparse autoencoder (NSAE)-based local connection network (LCN) is designed as NSAE-LCN for automatic feature extraction and fault diagnosis of machine vibration signals.	The study demonstrates the capability of NSAE-LCN in learning dissimilar and meaningful features while properly recognizing mechanical health statuses. Comparison with traditional diagnostic technologies shows that NSAE-LCN is superior, and demonstrates its great potential in intelligence diagnosis for machinery.	the handcrafting of parameters in NSAE-LCN could be optimized with more advanced methods to enhance adaptability and performance, which suggests the prospect for future enhancements.	2018
Telecommunication Engineering						
Ref #	**Used technique (AI/ ML/ DL)**	**Used tool**	**Methodology**	**Summary of the outcomes**	**Comments**	**Year**
[126]	ML	Python	In this study, the authors proposed a method for telecommunication fraud detection by a convolutional neural network (CNN). The data used were images that were applied to computer vision techniques such as image augmentation.	The outcomes showed that the proposed method achieved 89.98%F1- score. Moreover, it was stated that the performance of the model can be improved to 91.09%F1-score.	This study discussed the methodology section stepwise in a perfect way.	2023
[127]	ML	Python and C++	In this work, the authors proposed a distributed congestion control mechanism for generic multi-hop systems. Several data types were considered and applied by ML algorithms, certainly, the CatBoost algorithm.	The proposed system showed a good performance and the objective was achieved.	In this study, the cross validation was set to 20, which gives an accurate model.	2023
[128]	ML	Python	The authors provided an overview of 5G network slicing and applied some ML models, the accuracy of each model, of how effective it is in detecting network slices, was investigated.	The outcomes showed that telecommunication engineers could create optimized network slices to minimize the response time with high throughput for applications.	The gaps in the mentioned related works were not overcome. However, the paper explained the code of applying the ML in this field from scratch.	2023
[129]	DL	Python	In this study, the authors proposed a hybrid quantum DL model that compared between the CNN and the Recurrent Neural Network (RNN).	The outcomes showed that the proposed model achieved an accuracy of 97.16%	The related work section did not cover wide range of recent studies.	2023
[130]	AI	---	The authors proposed a novel method for smart healthcare systems by employing the 5G along with the Industry 4.0 standards. The proposed method used the network simulator N2S.	The outcomes showed that several challenges and constraints are meet the 5G methods such as performance tradeoffs.	The outcomes from this research depended on strong well-known mathematical equations in the field instead of using the software.	2023

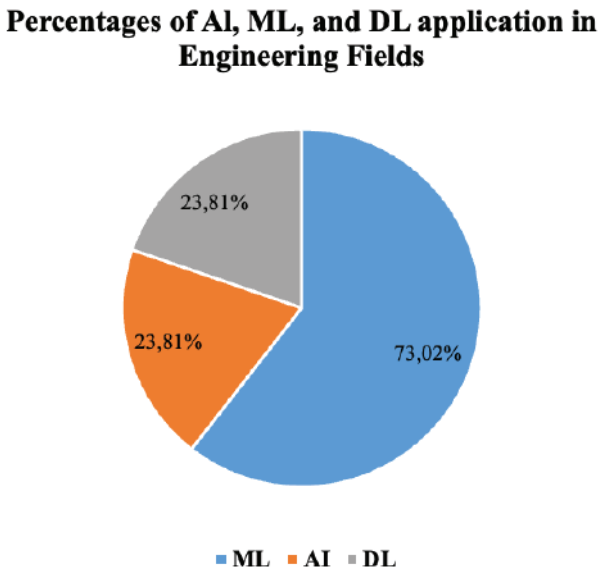


Figure 15. How wide are the AI, ML, and DL in engineering fields?

terms of sophisticated details and large amount computation resources. It's worth noting that the decision for Artificial AI, ML and DL also depends on data availability, task-specific requirements, and computational resources. It is a balance between the former factors, and the later. And finally, it is important to underscore that the percentages presented were derived from a comprehensive analysis of studies documented in Table 3, and it is acknowledged that these figures may vary from one year to the next based on evolving research and technological advancements.

While not limited to both aspects, ML approaches are extensively preferred in most of the research papers for the followings reasons. One, ML provides a range of technique that able to be used, from broad domains and research problem or application. In the second place, these methods have been developed and tested over many years, meaning that researchers now have a mature toolbox to address challenging tasks. It may also have better interpretability than ML algorithms, whichis important if we use the model in domains (such as healthcare or law) that requires us to understand why a model makes specific decisions. What's more, compared to DL, sometimes ML models can work well with smaller data sets, and this in turn makes them more applicable in circumstances when the collection of data is restrictive or expensive. Altogether, the trade-off between generality and interpretability as well as the historical development of Machine Learning explains its popularity for researchers working on new applications and practical issues.

There are several exciting directions for future investigation in AI, ML and DL applications in engineering. One important avenue is to improve the interpretability and explainability of AI models – a vital aspect for increasing trust and adoption in engineering applications. Further, the development of new architectures and algorithms focusing on engineering related problems such as real-time processing and noisy data is crucial. The synergy between AI and upcoming tech such as IoT, edge computing can bring decentralized and energy-efficient engineering solutions. In addition, ethical issues associated with the deployment of AI (e.g., mitigation of bias and privacy preservation) will continue to be prioritized. Lastly, using AI for automatic design optimization and predictive maintenance may transform the way engineering is done, providing large efficiency factors and cost reductions.

CONCLUSION

To conclude, this extensive study has revealed the widespread use of AI, ML, and DL techniques in 14 different engineering disciplines. The study began with a precise definition of AI, ML and DL in order to conduct a comprehensive survey of their diverse applications. A meticulous systematic review of the relevant studies carried-out covering key elements such as the particular technique used (AI, ML or DL), tools or software employed, methodologies adopted and short brief of their results. The yield of these attempts demonstrate that ML is the most leveraged technique, making up about 73% of the engineering research domain. All studies were thoroughly scrutinized with thoughtful commentary, enabling readers to gain fine insights into the various approaches and results in each of the sub-fields. This paper not only provides an overview of AI, ML and DL in the engineering domain but also clarifies the current dominance of ML as the most used model in state-of-the-art research projects. The results assist in developing a holistic picture of the current threshold and contribute precious wisdom to future development directions between AI and engineering fields. It was also discovered that studies using more than one intervention achieved better results.

AUTHORSHIP CONTRIBUTIONS

Authors equally contributed to this work.

DATA AVAILABILITY STATEMENT

The authors confirm that the data that supports the findings of this study are available within the article. Raw data that support the finding of this study are available from the corresponding author, upon reasonable request.

CONFLICT OF INTEREST

The author declared no potential conflicts of interest with respect to the research, authorship, and/or publication of this article.

ETHICS

There are no ethical issues with the publication of this manuscript.

STATEMENT ON THE USE OF ARTIFICIAL INTELLIGENCE

Artificial intelligence was not used in the preparation of the article.

REFERENCES

[1] Chaudhari SA. Trends in artificial intelligence, machine learning and deep learning. Artif Intell 2023;52

[2] Wang H, Fu T, Du Y, Gao W, Huang K, Liu Z, et al. Scientific discovery in the age of artificial intelligence. Nature 2023;620:47–60. [CrossRef]

[3] Khaleel M, Ahmed AA, Alsharif A. Artificial intelligence in engineering. Brilliance Res Artif Intell 2023;3:32–42. [CrossRef]

[4] Surianarayanan C, Lawrence JJ, Chelliah PR, Prakash E, Hewage C. A survey on optimization techniques for edge artificial intelligence (AI). Sensors (Basel) 2023;23:1279. [CrossRef]

[5] Jagadale UT, Nayak CB, Mankar A, Thakare SB, Deulkar WN. An experimental-based python programming for structural health monitoring of non-engineered RC frame. Innov Infrastruct Solut 2020;5:10. [CrossRef]

[6] OpenAI. Introducing ChatGPT. San Francisco: OpenAI; 2022. Available at: https://openai.com/blog/chatgpt Accessed on Jan 19, 2026.

[7] Wu T, He S, Liu J, Sun S, Liu K, Han QL, et al. A brief overview of ChatGPT: The history, status quo and potential future development. IEEE/CAA J Autom Sin 2023;10:1122–1136. [CrossRef]

[8] Kocoń J, Cichecki I, Kaszyca O, Kochanek M, Szydło D, Baran J, et al. ChatGPT: Jack of all trades, master of none. Inf Fusion 2023;99:101861. [CrossRef]

[9] Zhong Q, Ding L, Liu J, Du B, Tao D. Can ChatGPT understand too? A comparative study on ChatGPT and fine-tuned BERT. arXiv [Preprint] 2023. https://arxiv.org/abs/2302.10198

[10] Adeshola I, Adepoju AP. The opportunities and challenges of ChatGPT in education. Interact Learn Environ 2023;32:6159–6172.

[11] Jordan MI, Mitchell TM. Machine learning: Trends, perspectives, and prospects. Science 2015;349:255–260. [CrossRef]

[12] Kreuzberger D, Kühl N, Hirschl S. Machine learning operations (MLOps): Overview, definition, and architecture. IEEE Access 2023;11:31866–31879. [CrossRef]

[13] Kumar A, Mor N. An approach-driven: Use of artificial intelligence and its applications in civil engineering. In: Studies in Big Data 2021. p. 201–221. [CrossRef]

[14] Aldahiri A, Alrashed B, Hussain W. Trends in using IoT with machine learning in health prediction system. Forecasting 2021;3:181–206. [CrossRef]

[15] Rajbanshi S. Machine learning algorithms | Introduction to machine learning. Analytics Vidhya. 2021 Mar 25. Available at: https://www.analyticsvidhya.com/blog/2021/03/everything-you-need-to-know-about-machine-learning/ Accessed on Jan 01, 2024.

[16] Solyali D. A comparative analysis of machine learning approaches for short-/long-term electricity load forecasting in Cyprus. Sustainability 2020;12:3612. [CrossRef]

[17] Osisanwo F, Akinsola J, Awodele O, Hinmikaiye J, Olakanmi O, Akinjobi J. Supervised machine learning algorithms: Classification and comparison. Int J Comput Trends Technol 2017;48:128–138. [CrossRef]

[18] Praveena M, Jaiganesh V. A literature review on supervised machine learning algorithms and boosting process. Int J Comput Appl 2017;169:32–35. [CrossRef]

[19] Friedman J, Hastie T, Tibshirani R. The elements of statistical learning. New York: Springer; 2001. [CrossRef]

[20] Rahmani AM, Ali S, Yousefpoor E, Yousefpoor MS, Mehmood Z, Haider A, et al. Artificial intelligence approaches and mechanisms for big data analytics: A systematic study. PeerJ Comput Sci 2021;7:e488. [CrossRef]

[21] Dike HU, Zhou Y, Deveerasetty KK, Wu Q. Unsupervised learning based on artificial neural network: A review. In: 2018 IEEE International Conference on Cyborg and Bionic Systems (CBS); 2018 Oct 25–27; Shenzhen, China. IEEE; 2018. p. 322–327. [CrossRef]

[22] Tambuskar D, Narkhede B, Mahapatra SS. A flexible clustering approach for virtual cell formation considering real-life production factors using Kohonen self-organising map. Int J Ind Syst Eng 2018;28:193–215. [CrossRef]

[23] Ben Ali J, Saidi L, Harrath S, Bechhoefer E, Benbouzid M. Online automatic diagnosis of wind turbine bearings progressive degradations under real experimental conditions based on unsupervised machine learning. Appl Acoust 2018;132:167–181. [CrossRef]

[24] Sahu SK, Mokhade A, Bokde ND. An overview of machine learning, deep learning, and reinforcement learning-based techniques in quantitative finance: Recent progress and challenges. Appl Sci (Basel) 2023;13:1956. [CrossRef]

[25] Top 10 algorithms every machine learning engineer should know - GeeksforGeeks GeeksforGeeks. 2019 May 22. Available at: https://www.geeksforgeeks.org/top-10-algorithms-every-machine-learning-engineer-should-know/ Accessed on Jan 01, 2024.

[26] Ahmed SR, Ahmed AK, Jwmaa SJ. Analyzing the employee turnover by using decision tree algorithm. In: 2023 8th International Conference on Computer Science and Engineering (UBMK); 2023 Jun 12–15; Ankara, Turkey. IEEE; 2023. [CrossRef]

[27] Blockeel H, Devos L, Frénay B, Nanfack G, Nijssen S. Decision trees: From efficient prediction to responsible AI. Front Artif Intell 2023;6:1124553. [CrossRef]
[28] Predicting financial performance for listed companies in Thailand during the transition period: A class-based approach using logistic regression and random forest algorithm. J Open Innov Technol Mark Complex 2023;9:100130. [CrossRef]
[29] Mehta A. Why is logistic regression called 'regression' if it is a classification algorithm? Medium. 2020 Nov 30 Available from: https://ai.plainenglish.io/why-is-logistic-regression-called-regression-if-it-is-a-classification-algorithm-9c2a166e7b74 Accessed on Jan 01, 2024.
[30] Behera MP, Sarangi A, Mishra D, Sarangi SK. A hybrid machine learning algorithm for heart and liver disease prediction using modified particle swarm optimization withsupport vector machine. Procedia Comput Sci 2023;218:818–827. [CrossRef]
[31] Xu Y, Klein B, Li G, Gopaluni B. Evaluation of logistic regression and support vector machine approaches for XRF-based particle sorting for a copper ore. Miner Eng 2023;192:108003. [CrossRef]
[32] Sharifani K, Amini M. Machine learning and deep learning: A review of methods and applications. World Inf Technol Eng J 2023;10:3897–3904.
[33] Amini M, Rahmani A. Achieving financial success by pursuing environmental and social goals: A comprehensive literature review and research agenda for sustainable investment. World Inf Technol Eng J 2023;10:1286–1293.
[34] Zhou T, Song Z, Sundmacher K. Big data creates new opportunities for materials research: A review on methods and applications of machine learning for materials design. Engineering 2019;5:1017–1026. [CrossRef]
[35] Amini M, Bozorgasl Z. A game theory method to cyber-threat information sharing in cloud computing technology. Int J Comput Sci Eng Res 2023;11:549–560.
[36] Deng L, Yu D. Deep learning: Methods and applications. Found Trends Signal Process 2014;7:197–387. [CrossRef]
[37] Nazari Enjedani S, Amini M. The role of traffic impact effect on transportation planning and sustainable traffic management in metropolitan regions. Int J Smart City Plan Res 2023;12:688–700.
[38] Chai J, Zeng H, Li A, Ngai EWT. Deep learning in computer vision: A critical review of emerging techniques and application scenarios. Mach Learn Appl 2021;6:100134. [CrossRef]
[39] Jahanbakhsh Javidi N, Amini M. Evaluating the effect of supply chain management practice on implementation of halal agroindustry and competitive advantage for small and medium enterprises. Int J Comput Sci Inf Technol 2023;15:8997–9008.
[40] Pouyanfar S, Sadiq S, Yan Y, Tian H, Tao Y, Reyes MP, et al. A survey on deep learning: Algorithms, techniques, and applications. ACM Comput Surv 2018;51:92. [CrossRef]
[41] Amini M, Jahanbakhsh Javidi N. A multi-perspective framework established on diffusion of innovation (DOI) theory and technology, organization and environment (TOE) framework toward supply chain management system based on cloud computing technology for small and medium enterprises. Int J Inf Technol Innov Adopt 2023;11:1217–1234.
[42] Amini M, Bakri A, Zolait AH, Alryalat HA. Development of an instrument for assessing the impact of environmental context on adoption of cloud computing for small and medium enterprises. Aust J Basic Appl Sci 2014;8:129–135.
[43] Mahrishi M, Hiran KK, Meena G, Sharma P, editors. Machine learning and deep learning in real-time applications. Hershey, PA: IGI Global; 2020. [CrossRef]
[44] Amini M, Bakri A, Zolait A. The role of top manager behaviours on adoption of cloud computing for small and medium enterprises. Aust J Basic Appl Sci 2014;8:490–498.
[45] Mathew A, Amudha P, Sivakumari S. Deep learning techniques: An overview. In: Hassanien AE, Bhatnagar R, Darwish A, editors. Advanced machine learning technologies and applications. AMLTA 2020. Advances in Intelligent Systems and Computing, vol 1141. Singapore: Springer; 2021. p. 599–608. [CrossRef]
[46] Amini M, Safavi NS. A dynamic SLA aware solution for IaaS cloud placement problem using simulated annealing. Int J Comput Sci Inf Technol 2014;6:52–57.
[47] Deng L, Yu D. Foundations and trends in signal processing: Deep learning—methods and applications. Found Trends Signal Process 2014;7:197–387. [CrossRef]
[48] Sadat Safavi N, Zakaria NH, Amini M. The risk analysis of system selection and business process re-engineering towards the success of enterprise resource planning project for small and medium enterprise. World Appl Sci J 2014;31:1669–1676.
[49] Kenwright B. Is it the end of undergraduate dissertations? In: Raising the sail of academic excellence. IGI Global; 2023. p. 46–65. [CrossRef]
[50] Cui Y, van Esch P, Phelan S. How to build a competitive advantage for your brand using generative AI. Bus Horiz 2024;67:583–594. [CrossRef]
[51] Milinković A, Vuleta D, Babić T. Student perception of using generative AI tools in relation to academic integrity and their advantages and disadvantages. In: 2024 47th MIPRO ICT and Electronics Convention (MIPRO); 2024 May 20–24; Opatija, Croatia. IEEE; 2024. [CrossRef]

[52] Konya A, Nematzadeh P. Recent applications of AI to environmental disciplines: A review. Sci Total Environ 2024;906:167705. [CrossRef]
[53] Osadchaya E, Sergeeva AV, Vitkova L, Samoylenko V, Miloradov K. To ChatGPT, or not to ChatGPT: Navigating the paradoxes of generative AI in the advertising industry. Bus Horiz 2024;67:571–581. [CrossRef]
[54] Dave P. How AI can revolutionize the pharmaceutical industry. J Drug Deliv Ther 2024;14:179–183. [CrossRef]
[55] Shah IA, Jhanjhi NZ, Brohi SN. Use of AI-based drones in smart cities. In: Advances in information security, privacy, and ethics. IGI Global; 2024. p. 362–380. [CrossRef]
[56] Wang MH, Shi Z, Fan Y, Wu T, Wang Y, Li J, et al. AI-based advanced approaches and dry eye disease detection based on multi-source evidence: Cases, applications, issues, and future directions. Big Data Min Anal 2024;7:445–484. [CrossRef]
[57] Ku ECS, Chen CD. Artificial intelligence innovation of tourism businesses: From satisfied tourists to continued service usage intention. Int J Inf Manage 2024;76:102757. [CrossRef]
[58] Alnuaimi AFAH, Albaldawi THK. An overview of machine learning classification techniques. BIO Web Conf 2024;97:00133. [CrossRef]
[59] Theng D, Bhoyar KK. Feature selection techniques for machine learning: A survey of more than two decades of research. Knowl Inf Syst 2023;66:1575–1637. [CrossRef]
[60] Shang R, Li X, Gao R, Cheng J, Wang Y, Ning C, et al. Machine learning-enhanced triboelectric sensing application. Adv Mater Technol 2024;9:2301316. [CrossRef]
[61] Rao GS, Muneeswari G. A review: Machine learning and data mining approaches for cardiovascular disease diagnosis and prediction. EAI Endorsed Trans Pervasive Health Technol 2024;10:1–8. [CrossRef]
[62] Adhinata FD, Wahyono, Sumiharto R. A comprehensive survey on weed and crop classification using machine learning and deep learning. Artif Intell Agric 2024;13:45–63. [CrossRef]
[63] Aramburu A, Guido C, Bares P, Pla B, Napolitano P, Beatrice C. Knock detection in spark ignited heavy duty engines: An application of machine learning techniques with various knock sensor locations. Measurement 2024;224:113860. [CrossRef]
[64] Yang L, Tian M, Xin D, Cheng Q, Zheng J. AI-driven anonymization: Protecting personal data privacy while leveraging machine learning. arXiv [Preprint] 2024 Feb 26.: https://arxiv.org/abs/2402.17191
[65] Afaq Y, Manocha A. Blockchain and deep learning integration for various applications: A review. J Comput Inf Syst 2023;64:92–105. [CrossRef]
[66] Zhang J, Xiao L, Zhang Y, Lai J, Yang Y. Optimization and performance evaluation of deep learning algorithm in medical image processing. Front Comput Intell Syst 2024;7:67–71. [CrossRef]
[67] Zhang C, Nur N, Ibrahim R. Deep learning models for price forecasting of financial time series: A review of recent advancements: 2020–2022. WIREs Data Min Knowl Discov 2023;14:e1519. [CrossRef]
[68] Bai R, Chen X, Chen ZL, Cui T, Gong S, He W, et al. Analytics and machine learning in vehicle routing research. Int J Prod Res 2021;61:4–30. [CrossRef]
[69] Tudoroiu N, Zaheeruddin M, Tudoroiu RE, Radu MS, Chammas H. Intelligent deep learning estimators of a lithium-ion battery state of charge design and MATLAB implementation—A case study. Vehicles 2023;5:535–564. [CrossRef]
[70] Nabi N, Ray B, Rashid F, Hussam WK, Muyeen SM. Parametric analysis and prediction of energy consumption of electric vehicles using machine learning. J Energy Storage 2023;72:108226. [CrossRef]
[71] Ullah I, Liu K, Yamamoto T, Shafiullah M, Jamal A. Grey wolf optimizer-based machine learning algorithm to predict electric vehicle charging duration time. Transp Lett 2022;15:889–906. [CrossRef]
[72] Mazhar T, Irfan M, Haq IU, Ullah I, Ashraf M, Shloul TA, et al. Electric vehicle charging system in the smart grid using different machine learning methods. Sustainability 2023;15:2603. [CrossRef]
[73] Maduranga MWP, Abeysekera R. Machine learning applications in IoT-based agriculture and smart farming: A review. Int J Eng Appl Sci Technol 2020;4:24–27. [CrossRef]
[74] Amini M, Rahmani A. Agricultural databases evaluation with machine learning procedure. Aust J Eng Appl Sci 2023;8:39–50.
[75] Pallathadka H, Mustafa M, Sanchez DT, Sajja GS, Gour S, Naved M. Impact of machine learning on management, healthcare and agriculture. Mater Today Proc 2021;2:8.
[76] Javaid M, Haleem A, Khan IH, Suman R. Understanding the potential applications of artificial intelligence in agriculture sector. Adv Agrochem 2022;2:15–30. [CrossRef]
[77] SSL DA, Praveenkumar R, Balaji V. An intelligent crop recommendation system using deep learning. Int J Intell Syst Appl Eng 2023;11:423–428.
[78] Wang Y, Ge J, Miao S, Jiang T, Shen X. Application of hybrid artificial bee colony algorithm based on load balancing in aerospace composite material manufacturing. Expert Syst Appl 2023;215:119375. [CrossRef]
[79] Ben-Yelun I, Díaz-Lago M, Saucedo-Mora L, del Mar, Callado R, Montáns FJ. Self-learning locally-optimal hypertuning using maximum entropy, and comparison of machine learning approaches for estimating fatigue life in composite materials of the aerospace industry. Eng Struct 2023;283:115829. [CrossRef]
[80] Shafi I, Din S, Al Aghbari Z, Ashraf I, Ullah I. Deep learning-based real-time defect detection for optimization of aircraft manufacturing and control performance. Drones 2023;7:31. [CrossRef]

[81] Nogueira RPR, Melicio R, Valério D, Santos LFFM. Learning methods and predictive modeling to identify failure by human factors in the aviation industry. Appl Sci (Basel) 2023;13:4069. [CrossRef]
[82] Karaoğlu U, Mbah O, Zeeshan Q. Applications of machine learning in aircraft maintenance. J Eng Mech Struct Eng 2023;2:28–38. [CrossRef]
[83] Li S, Li C, Huang Y, Zhai C. Real-time seismic damage simulation for urban building portfolio based on basic building information and machine learning. SSRN 2023. Preprint. doi: 10.2139/ssrn.4675865 [CrossRef]
[84] Rane N, Choudhary S, Rane J. Artificial intelligence (AI) and Internet of Things (IoT)-based sensors for monitoring and controlling in architecture, engineering, and construction: Applications, challenges, and opportunities. SSRN 2023. Preprint. doi: 10.2139/ssrn.4642197 [CrossRef]
[85] Ploennigs J, Berger M. AI art in architecture. AI Civ Eng 2023;2:1. [CrossRef]
[86] Rane N. Integrating leading-edge artificial intelligence (AI), Internet of Things (IoT), and big data technologies for smart and sustainable architecture, engineering, and construction (AEC) industry: Challenges and future directions. SSRN 2023 Sep 24. Preprint. doi: 10.2139/ssrn.4616049 [CrossRef]
[87] Heena A, Biradar N, Maroof NM, Bhatia S, Agarwal R, Prasad K. Machine learning-based biomedical image processing for echocardiographic images. Multimed Tools Appl 2022;82:39601–39616. [CrossRef]
[88] Sandhiya JA, Preetha S, Sarumathi A, Umadevi D, Yogeshwari G, Shanmugam K. Identification and alertness of cardiovascular disease using MATLAB with IoT. Biomed J Sci Tech Res 2023;1:31–36. [CrossRef]
[89] Khanna A, Selvaraj P, Gupta D, Sheikh TH, Pareek PK, Shankar V. Internet of Things and deep learning-enabled healthcare disease diagnosis using biomedical electrocardiogram signals. Expert Syst 2021;40:e12864. [CrossRef]
[90] Aminizadeh S, Heidari A, Toumaj S, Darbandi M, Farahbakhsh M, Rezaei M, et al. The applications of machine learning techniques in medical data processing based on distributed computing and the Internet of Things. Comput Methods Programs Biomed 2023;241:107745. [CrossRef]
[91] Rana M, Bhushan M. Machine learning and deep learning approach for medical image analysis: Diagnosis to detection. Multimed Tools Appl 2022;82:26731–26769. [CrossRef]
[92] Ghani S, Kumar N, Gupta M, Saharan S. Machine learning approaches for real-time prediction of compressive strength in self-compacting concrete. Asian J Civ Eng 2023;25:2743–2760. [CrossRef]
[93] Parisi F, Ruggieri S, Lovreglio R, Fanti MP, Uva G. On the use of mechanics-informed models to structural engineering systems: Application of graph neural networks for structural analysis. Structures 2024;59:105712. [CrossRef]
[94] Teo W. Image-based structural performance prediction for reinforced concrete exterior beam-column joints [dissertation]. Singapore: Nanyang Technological University; 2023.
[95] Mikami A. Fundamental study on damage detection of civil structures modeled as MDOF system based on machine learning. In: Structural Health Monitoring 2023; 2023; Milan, Italy. DPI Proceedings; 2023. Available from: https://www.dpi-proceedings.com/index.php/shm2023/article/view/36896 Accessed on Feb 04, 2026. [CrossRef]
[96] Melnikov A, Kordzanganeh M, Alodjants A, Lee RK. Quantum machine learning: From physics to software engineering. Adv Phys X 2023;8:2165452. [CrossRef]
[97] Georgiev D. Exploring knowledge management from a software engineering perspective. In: European Conference on Knowledge Management (ECKM 2023); 2023; Barcelona, Spain. 2023. p. 1571–1578. [CrossRef]
[98] Uddin G, Alamin MAA, Das A. An empirical study of deep learning sentiment detection tools for software engineering in cross-platform settings. arXiv 2023. Preprint. doi: 10.48550/arXiv.2301.06661
[99] Butt UA, Amin R, Aldabbas H, Mohan S, Alouffi B, Ahmadian A. Cloud-based email phishing attack using machine and deep learning algorithm. Complex Intell Syst 2022;9: 3043–3070. [CrossRef]
[100] Zhang Z, Ng KC, Linga P. Machine learning aided high-throughput prediction of ionic liquid@MOF composites for membrane-based CO2 capture. J Memb Sci 2022;650:120399. [CrossRef]
[101] Shi Z, Liang H, Yang W, Liu J, Liu Z, Qiao Z. Machine learning and in silico discovery of metal-organic frameworks: Methanol as a working fluid in adsorption-driven heat pumps and chillers. Chem Eng Sci 2020;214:115430. [CrossRef]
[102] Huang Q, Wu X, Ma L, Shen J, Wang M, Wu H, et al. Machine learning and molecular fingerprint screening of high-performance 2D/3D MOF membranes for Kr/Xe separation. Chem Eng Sci 2023;280:119031. [CrossRef]
[103] Wei W, Nan S, Wang H, Xu S, Liu H, He R. Design and preparation of sulfonated polymer membranes for Zn/MnO2 flow batteries with assistance of machine learning. J Memb Sci 2023;672:121453. [CrossRef]
[104] Bai X, Cao Z, He C, He J, Zhang Q, Gao H, et al. Machine-learning-assisted high-throughput computational screening of metal–organic framework membranes for hydrogen separation. Chem Eng J 2022;446:136783. [CrossRef]
[105] Milić SD, Đurović Ž, Stojanović MD. Data science and machine learning in the IIoT concepts of power plants. Int J Electr Power Energy Syst 2023;145:108711. [CrossRef]

[106] Karim FK, Khafaga DS, Eid MM, Towfek SK, Alkahtani HK. A novel bio-inspired optimization algorithm design for wind power engineering applications time-series forecasting. Biomimetics (Basel) 2023;8:321. [CrossRef]
[107] Presekal A, Stefanov A, Rajkumar VS, Palensky P. Attack graph model for cyber-physical power systems using hybrid deep learning. IEEE Trans Smart Grid 2023;14:4007–4020. [CrossRef]
[108] de Oliveira RA, Bollen MHJ. Deep learning for power quality. Electr Power Syst Res 2023;214:108887. [CrossRef]
[109] Benti NE, Chaka MD, Semie AG. Forecasting renewable energy generation with machine learning and deep learning: Current advances and future prospects. Sustainability 2023;15:7087. [CrossRef]
[110] Darwish HH, Al-Quraan A. Machine learning classification and prediction of wind estimation using artificial intelligence techniques and normal PDF. Sustainability 2023;15:3270. [CrossRef]
[111] Chen TC, Wang JH, Sun CH, Chiang KN. Application of machine learning in rapid analysis of solder joint geometry and type on thermomechanical useful lifetime of electronic components. Mech Adv Mater Struct 2021;30:373–381. [CrossRef]
[112] Yuan Y, Jiang Y, Cao X, Wang Y, Chen H, Zhang Y, et al. Insight into the electronic properties of semiconductor heterostructure based on machine learning and first-principles. ACS Appl Mater Interfaces 2023;15:12462–12472. [CrossRef]
[113] Mamandipoor B, Majd M, Sheikhalishahi S, Modena C, Osmani V. Monitoring and detecting faults in wastewater treatment plants using deep learning. Environ Monit Assess 2020;192:148. [CrossRef]
[114] Huang J, Koroteev DD. Artificial intelligence for planning of energy and waste management. Sustain Energy Technol Assess 2021;47:101426. [CrossRef]
[115] Xie Y, Huang H, Cao Y, Liu S, Tian Z, Liu H, et al. Enhancing real-time prediction of effluent water quality of wastewater treatment plant based on improved feedforward neural network coupled with optimization algorithm. Water 2022;14:1053. [CrossRef]
[116] Giwa A, Daer S, Ahmed I, Marpu PR, Hasan SW. Experimental investigation and artificial neural networks (ANNs) modeling of electrically-enhanced membrane bioreactor for wastewater treatment. J Water Process Eng 2016;11:88–97. [CrossRef]
[117] Hamed MM, Khalafallah MG, Hassanien EA. Prediction of wastewater treatment plant performance using artificial neural networks. Environ Model Softw 2004;19:919–928. [CrossRef]
[118] Wang Y, Du X, Gu Z, Chen Z, Zhu W, Shen Y, et al. Machine learning framework for intelligent aeration control in wastewater treatment plants: Automatic feature engineering based on variation sliding layer. Water Res 2023;246:120676. [CrossRef]
[119] Escobar CA, Morales-Menendez R. Machine learning techniques for quality control in high conformance manufacturing environment. Adv Mech Eng 2018;10:1687814018755519. [CrossRef]
[120] Sankhye S, Hu G. Machine learning methods for quality prediction in production. Logistics 2020;4:35. [CrossRef]
[121] Amini M, Sharifani K, Rahmani A. Machine learning model towards evaluating data gathering methods in manufacturing and mechanical engineering. Int J Appl Sci Eng Res 2023;15:349–362.
[122] Moore J, Stammers J, Dominguez-Caballero J. The application of machine learning to sensor signals for machine tool and process health assessment. Proc Inst Mech Eng B J Eng Manuf 2020;235:1543–1557. [CrossRef]
[123] Saravanan N, Siddabattuni VNSK, Ramachandran KI. Fault diagnosis of spur bevel gear box using artificial neural network (ANN), and proximal support vector machine (PSVM). Appl Soft Comput 2010;10:344–360. [CrossRef]
[124] Rafiee J, Arvani F, Harifi A, Sadeghi MH. Intelligent condition monitoring of a gearbox using artificial neural network. Mech Syst Signal Process 2007;21:1746–1754. [CrossRef]
[125] Jia F, Lei Y, Guo L, Lin J, Xing S. A neural network constructed by deep learning technique and its application to intelligent fault diagnosis of machines. Neurocomputing 2018;272:619–628. [CrossRef]
[126] Zhen Z, Gao J. CDR2IMG: A bridge from text to image in telecommunication fraud detection. Comput Syst Sci Eng 2023;47:955–973. [CrossRef]
[127] Pablo JL, Rico-Novella FJ. A machine learning-based distributed congestion control protocol for multi-hop wireless networks. Comput Netw 2023;231:109813. [CrossRef]
[128] Heyn HM, Knauss E, Malleswaran I, Dinakaran S. An investigation of challenges encountered when specifying training data and runtime monitors for safety critical ML applications. In: International Working Conference on Requirements Engineering: Foundation for Software Quality; 2023; Barcelona, Spain. Cham: Springer Nature; 2023. p. 206–222. [CrossRef]
[129] Ashwin M, Alqahtani AS, Mubarakali A, Sivakumar B. Efficient resource management in 6G communication networks using hybrid quantum deep learning model. Comput Electr Eng 2023;106:108565. [CrossRef]
[130] Alhayani B, Ilhan H, Mahajan HB, Jindal A, Farouk A, Ustundag BB, et al. 5G standards for the Industry 4.0 enabled communication systems using artificial intelligence: Perspective of smart healthcare system. Appl Nanosci 2022;13:1807–1817. [CrossRef]

Sigma J Eng Nat Sci, Vol. 44, No. 1, pp. 637–662, February, 2026

Sigma Journal of Engineering and Natural Sciences
Web page info: https://sigma.yildiz.edu.tr
DOI: 10.14744/sigma.2025.00000

Review Article

A comprehensive review on traditional and cutting-edge approaches for wind speed/power forecasting

Muskaan AHUJA[1,2,*], Sanju SAINI[2]

[1]*Department of Computer Science and Engineering, Amity School of Engineering and Technology, Amity University, Rajasthan, 201313, India*
[2]*Department of Artificial Intelligence and Data Science, Dr. D. Y. Patil Institute of Technology, Pune, 411033, India*

ARTICLE INFO

Article history
Received: 04 April 2024
Revised: 08 October 2024
Accepted: 14 November 2024

Keywords:
Deep Learning Methods; Hybrid Methods; Intelligent Methods; Physical Methods; Statistical Methods; Traditional Approaches; Wind Forecasting

ABSTRACT

Wind forecasting is essential for improving the effectivness of wind energy in overall power system. İt helps in the areas like improving stability of grid , energy planning and to support the effective market operation. This paper is an attempt to examine traditional as well as advanced forecasting methods, from the classical statistical approaches to modern data-driven and hybrid techniques. The traditional techniques including time-series analysis as well as the numerical weather prediction (NWP) techniques are quite good but are incapable of capturing the complexity and variation patterns of wind pattern. While the cutting-edge techniques, including the machine learning & deep learning have helped to increase the forecasting accuracy, hybrid models, have given increasingly promising results as they offer a balance between the high accuracy and computational requirements by merging the traditional and modern approaches used for wind speed and/power forecasting. This study shows the significant value achieved by hybrid approachs, reporting Root Mean Square Error (RMSE) values of 0.1089 m/s for statistical approach, 0.02 m/s for intelligent approaches, and 0.0096 m/s for hybrid approaches. Using a real-world wind dataset, the performance of several widely used forecasting models is evaluated and compared. This study provide an symmetrical analysis of advantages and disadvantages of various forecasting approaches across different time scale & weather condition. It also elaborates persistent challenges, e.g., limited data availability and the requirement for better model interpretability as well as real-time adaptability. The review concludes that although data-driven and hybrid models currently achieve the best performance, additional research is needed to enhance interpretability and data integration. This research improve reviews on wind forecasting, highlighting latest developments and practical uses. İt also provide helpful guide for researchers and idustry experts to understand present & future opportunities in the field.

Cite this article as: Ahuja M, Saini S. A comprehensive review on traditional and cutting-edge approaches for wind speed/power forecasting. Sigma J Eng Nat Sci 2026;44(1):637–662.

***Corresponding author.**
*E-mail address: 20001902004muskaanahuja@dcrustm.org

This paper was recommended for publication in revised form
Editor-in-Chief Ahmet Selim Dalkilic

Published by Yıldız Technical University Press, İstanbul, Turkey
© Author. This is an open access article under the CC BY-NC license (http://creativecommons.org/licenses/by-nc/4.0/).

INTRODUCTION

Several organizations are moving toward the production of renewable energy in the current energy scenario. The sustainable energy sources enhance the reliability and reduce the carbon impact of power systems [1,2]. Wind energy is one of the most effective renewable energy sources. However, because of its intrinsic variability and intermittent nature, integrating it into modern power networks is extremely difficult [3]. The need to switch to alternative energy sources is further highlighted by the rising price of crude oil. Wind power continues to be one of the most appealing renewable options because of its great efficiency and low emissions. The installed wind power capacity in India is shown in Figure 1.

Forecasting of wind speed and power is essential for many tasks in the wind energy sector and for the general functioning of the power system [4]. For those involved in the electrical market, such as energy dealers and wind farm operators, forecasting is crucial. Operators to schedule maintenance and improve turbine performance use predictions of wind speed and power. They can reduce unplanned outages and related expenses by scheduling maintenance during times of low wind by predicting wind conditions [5]. When market-related decisions need to be taken under uncertain circumstances, accurate forecasting is also helpful.

Moreover, the long-term planning for wind farms and further extension of transmission lines is supported by wind and/or power forecasts. Accurate wind forecasting is also helpful to reduce the gap between planned and actually generated power, thus reducing the financial risk of contributors to the energy market. In brief, wind forecasting is very much essential for using the wind energy efficiently, smooth integration of grid, market operations, planning of maintenance schedules, infrastructure development along with maintaining system reliability.

Following are the major benefits of precise wind speed and/or power forecasting :

- Wind speed and/or power forecasting helps in improving/maintaining the system balance, avoid the outages, and ensuring steady performance of grid.
- It supports the optimal operation of turbine and reduces the operating costs.
- It also contributes to the economic dispatch, unit commitment along with power system decision-making process. [6].
- It also helps to improve the weather measurement technique and design. Due to this weather and energy, forecasting can be enhanced.
- More accurate wind forecasting helps in improving the utilization of renewable energy, lowers emissions and thus contributes to cleaner air.
- Higher accuracy of prediction results in better turbine protection, maintenance scheduling and to reduce disruptions when extreme weather conditions occur.
- Accurate forecasting improves reliance on renewable energy, lowering emissions and contributing to cleaner air.

The forecasting of wind depends on various weather parameters such as direction, humidity, temperature, speed, and pressure. The traditional and cutting-edge approaches are typically used to obtain precise forecasting, as shown in Figure 2.

Traditional approaches include the persistence method, physical method, and statistical method. Cutting-edge approaches, such as machine learning and artificial intelligence techniques, and hybrid techniques. Traditional approaches are stable, interpretable, and simple, while cutting-edge approaches improve accuracy, adaptability, data

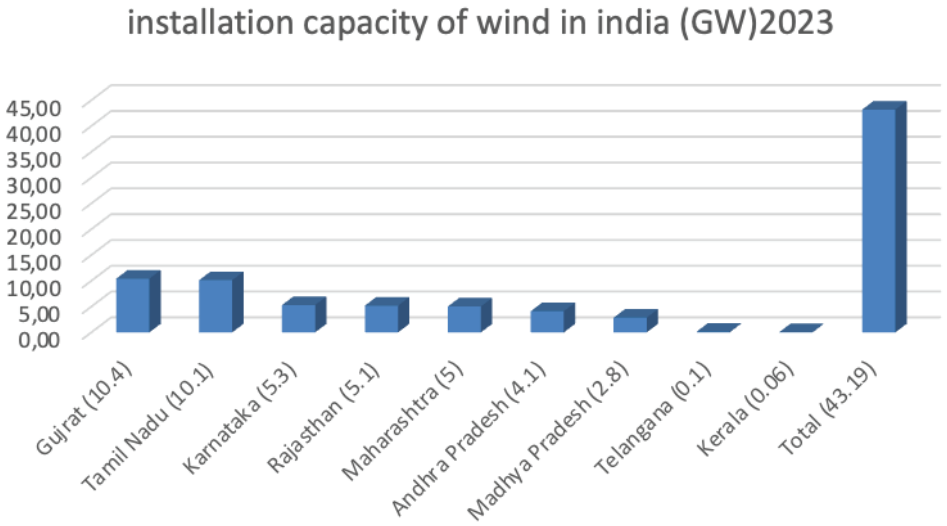


Figure 1. Installation capacity of wind power.

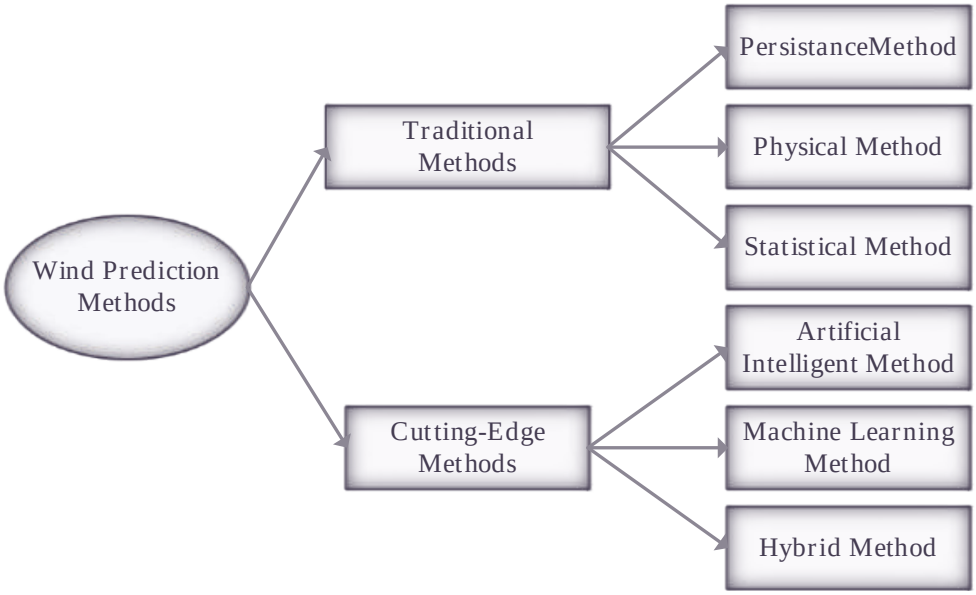


Figure 2. Classification of wind speed/power prediction methods.

integration, and uncertainty handling. Both approaches have their significance and can be complementary, providing a range of tools and techniques for wind speed/power forecasting that can be tailored to specific needs and requirements. Other classifications of wind forecasting schemes are (i) weather-based forecasting and (ii) time-series-based forecasting approaches [7]. For weather-based forecasting models, the accuracy of wind forecasts is heavily dependent on the morphology of the terrain at the location of the wind turbines. On the other hand, Statistical methods anticipate future values only based on historical wind speed readings [8].

Research Gaps and Novelty

Many previous researches have been done on wind speed and wind power forecasting, which are extensive and cover a wide range of methods like traditional methods, deep learning and data-driven methos, and hybrid methods. This review paper differentiates itself from previous works by providing a technically rigorous analysis of traditional as well as state-of-the-art forecasting methods, resulting in the following core contributions:

- This paper comparess the traditional and modern approaches using multiple metrics, while previous researches rely on individual models. The evaluation of predictive/forecasting model is done on the basis of factors such as scalability, accuracy of forecasting, computational complexity as well as suitability across changing forecasting horizons.
- This review presents a complete examination of recent developments, including future hybrid architectures and novel learning techniques such as ensemble-based and deep reinforcement based frameworks, covered minimally in present academic discourse.
- This paper examines the real-world models , focuses on geographical issues, considers grid integration, and the explores the need for support during real-life conditions.
- The work identifies the main research gap and gives future direction for further improvement by making use of IoT sensors in case of high-resolution data along with a transparent model for improving accuracy.

Main goals of this paper are as follows::

- To provide an intensive review of prior research on wind speed/power prediction techniques.
- Identification of gaps, unresolved questions, and/or areas requiring further investigation.
- To evaluate traditional, machine learning, and hybrid approaches across multiple performance metrics, proficiency, precision, and applicability for forecasting of wind, and evaluation of the latest hybrid machine learning algorithms.
- A discussion on the working of models in real-life conditions or applications.
- To make contributions in advancing knowledge in field of wind speed and/power prediction/forecasting.

The review provides guidance on forecasting methodologies which enable grid operators to adjust with variability of wind power with higher precision, thus supporting more stable as well as reliable grid operation. This paper may help the wind farm operators to choose the best models for forecasting/prediction so as to improve the performance of turbines and to reduce the unwanted mechanical stress. By using cutting-edge techniques, wind farms will get highly efficient wind power/energy. The participants of market

can easily manage the varitions in generation of wind by knowledge of strength, and limitations of different forecasting techniques discussed in this review.

The review is also helpful to scholars in highlighting research gaps, providing opportunities alongwith new ideas for development of novel models with innovative ideas. Moreover, this work is helpful to improve the efficiency and accuracy of prediction/forecasting techniques. This review also provides motivation to engineers to create more reliable as well as accurate prediction/forecasting systems. Its findings can help to develop standards and best practices for incorporating wind energy into the present grid infrastructure, ensuring that the most appropriate forecasting technologies are used. This study analyzes the forecasting results in several climate conditions, helping planners prepare for climate-driven shifts in wind behaviors and thereby supporting the maintenance of long-term wind energy viability.

CLASSIFICATION OF WIND SPEED/POWER PREDICTION METHODS

Wind prediction methods can be classified into several categories based on their approach, complexity, and data sources, and these categories are discussed below:

Traditional Approaches

The time series and statistical methods are involove in traditional approach for wind forecasting and these approaches are briefly discussed in Table 1.

Persistence Methods

Persistence is the humblest approach to predicting the wind. Persistence forecasting is a basic and straightforward method used in wind speed/power forecasting. It relies on the assumption that the future wind conditions will be similar to the most recent past conditions. In some incredibly short periods of predictions (a few minutes to hours) [9], this simpler approach is even more reliable than a Numerical Weather Prediction model. The model's precision falls dramatically as the prediction lead time increases.

On a functional level, the most recent available wind power measurements, as provided by the SCADA system [10], should be used. Persistence forecasting offers simplicity and real-time applicability; it has limitations in capturing changing wind conditions, incorporating external factors, and providing accurate forecasts beyond short time intervals. Every forecast technique should be measured compared to the standard of the classic persistence approach to evaluate how much better it may be than persistence-derived forecasts [11].

Physical Methods

In [12], various weather based models, and complex atmospheric models are used for wind forecasting. Obstacle shelter, local surface roughness and fluctuations, wind farm layouts, orography influences, within wind farms, increasing local wind velocity, speed up or down, and wind turbine power curves are among the factors taken into account in these models. For downscaling, the physical method employs a meso or micro-scale model that interpolates these wind speed projections to the level of wind producers [13].

Figure 3 shows the forecasted wind speed and power generated by the NWP model. Different NWP models are utilized in a model chain with varied hierarchical levels [14]. Meteorological observations made by meteorologists, weather monitoring stations, satellites, and other sources around the world serve as the model chain's starting point [15]. Long-term wind speed predictions are better served by NWP (Numerical Weather Prediction) techniques and have been found to save up to 20% in fossil fuel. Some researchers related to the NWP technique for wind prediction are given in Table 2.

Table 1. Classification of traditional models for wind forecasting

Category	Method	Description
Persistence methods	'Persistence method'	Assumes that future wind conditions will be similar to the most recent past conditions.
	'Climatology method'	Uses long-term historical data to predict future wind patterns.
Physical methods	'Numerical weather prediction (NWP) models'	Utilizes complex mathematical models based on atmospheric physics to simulate and predict wind behavior.
	'Computational fluid dynamics (CFD) models'	Uses numerical analysis and algorithms to solve and analyze problems involving fluid flows, applied to wind behavior around structures and terrains.
	'Mesoscale models'	Focuses on atmospheric processes at the mesoscale (1-1000 km) to predict wind patterns over larger regions.
Statistical methods	'Time series analysis'	Analyzes historical wind data to identify patterns and forecast future values.
	'Regression analysis'	Identifies relationships between wind speed and other variables (e.g., temperature, pressure) to make predictions.
	'ARIMA models'	Auto-Regressive Integrated Moving Average models for capturing temporal dependencies in wind data.

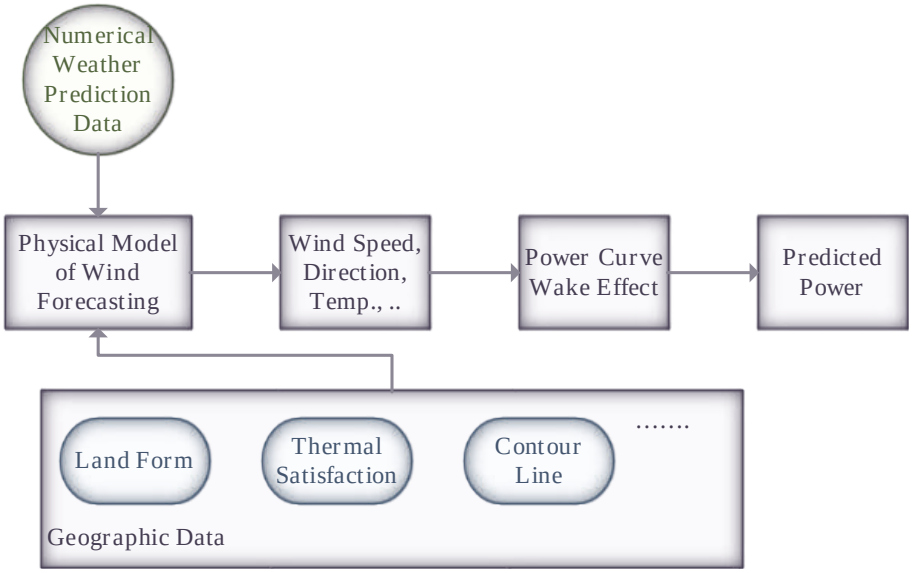


Figure 3. Physical model.

Table 2. Physical method for wind speed/power prediction

Authors	Title	Techniques	Accuracy
Al-Yahyai et al. (2011) [16]	"Nested ensemble NWP approach for wind energy assessment"	NWP	RMSE=1.753
Marcos Lima et al. (2017) [17]	"A meteorological statistic model for short-term wind power forecasting"	NWP, Kalman filtering	RMSE= 1.6513
Saini and Ahuja (2019) [18]	"A research on wind power forecasting techniques"	NWP	Not determined
Liu et al. (2022) [19]	"Numerical weather prediction enhanced wind power forecasting: Rank ensemble and probabilistic fluctuation awareness"	NWP	$RMSE_4$=13.39% $RMSE_{16}$=18.89%

Physical approaches are being used to improve the NWP approach in the direction of achieving precise weather forecasts [20]. In [21], it is reported that the physical approaches require a lot of computation, and they are displayed on supercomputers. The physical methods need weather parameters for precise forecasting [22]. Physical systems improve the final output (wind prediction) utilizing the unprocessed information from Numerical Weather Prediction, depending on the physics of the sub-atmospheric boundary layer [23].

Statistical Methods

Statistical modeling techniques are widely used in wind speed/power forecasting to capture the relationships and patterns in historical data. These techniques employ statistical principles and methods to analyze past observations and generate forecasts. The correlation between online average power data and other variables is examined using statistical methods. Statistical models are easier to develop and maintain than other models. The drawback of this strategy is that the forecast inaccuracy rises as the forecast period rises [11]. The following are the details of various statistical models for wind speed/power forecasting:

Regression analysıs models ınclude the following:

Linear Regression

Simple linear regression models the relationship between a dependent variable (e.g., wind speed) and a single independent variable (e.g., temperature). Multiple linear regression models extend simple linear regression by including multiple independent variables to predict the dependent variable.

Non-Linear Regression

It models relationships that cannot be adequately described with linear models. Techniques include polynomial regression and other forms of regression that can handle more complex relationships between variables.

Time Series Analysis and ARIMA Models include the following:

Moving Averages

- **Simple moving average (SMA)**

Computes the arithmetic mean of a fixed window of previous data points, providing a smoothed representation of the time series.

• **Weighted moving average (WMA)**

Follows the same principle as SMA but assigns varying weights to the observations within the window, with more emphasis typically placed on recent values.

Exponential Smoothing

• **Simple exponential smoothing (SES)**

Applies exponentially decreasing weights to historical observations, giving the strongest influence to the most recent data. It is most suitable for time series without evident trends or seasonal patterns.

• **Holt's linear trend method**

Extends SES by incorporating a trend component in addition to the level, enabling improved forecasting for data exhibiting a linear trend but lacking seasonality.

• **Holt–Winters method**

Builds upon Holt's approach by adding a seasonal component, making it appropriate for time series that simultaneously exhibit trend and seasonality.

ARMA (Autoregressive Moving Average) Models

It combine autoregressive (AR) and moving average (MA) processes to represent a time series using both its lagged values and historical error terms [24]. These models capture short-term temporal dependencies as well as the effects of past disturbances. Four general modeling strategies are commonly adopted:

1. **Component-wise decomposition:** Wind speed is separated into lateral and longitudinal components and modeled independently.
2. **Dual ARMA modeling:** Separate ARMA models are used for wind speed and wind direction, and the results are combined for forecasting.
3. **Vector auto-regression (VAR):** A multivariate framework is used to forecast multiple interrelated wind characteristics simultaneously.
4. **Reduced VAR models:** A simplified VAR structure is implemented to reduce computational complexity while maintaining prediction capability.

The ARMA model order is defined by both AR and MA orders, indicating how many past values and past errors are included in the model.

ARIMA (Autoregressive Integrated Moving Average) Models

ARIMA models extend ARMA by introducing a differencing step to enforce stationarity—meaning that the mean and variance of the series remain constant over time. An ARIMA model is defined by three parameters:

• **Autoregressive (AR) component**

Represents the relationship between the current value and several lagged observations. AR models assume the time series can be expressed as a linear combination of its historical values plus random noise [25]. They are effective for modeling short-term structure, trends, and serial correlations. Because wind speed exhibits sequential dependence and inherent variability, ARMA and ARIMA frameworks are often well-suited for its prediction.

• **Integrated (I) component**

Applies differencing to the raw data to remove trends or other non-stationary behavior, making the series more suitable for modeling.

• **Moving average (MA) component**

This component uses the effect of past forecast/prediction errors values on the present value. MA models represent the present values as a linear combination of previous ones. The model's order helps to determine how many lagged error values are considered.

State-Space Models

State-space models help to represent the underlying process in terms of combination of unobserved-states and observations. They help in providing more flexibility to capture complex relationships and these can help to handle different data patternsThese models include Kalman filter aswell as Bayesian models. Statistical modeling techniques provide a solid framework for analyzing and forecasting wind speed/power data. The choice of the appropriate model depends on the characteristics of the data, the presence of trends or seasonal patterns, and the desired forecasting horizon. These techniques have been widely employed in practice and form the foundation for more advanced and hybrid models used in wind speed/power forecasting. Literature work on wind forecasting using statistical methods has been done by some researchers. The AR, ARMA, ARIMA, Bayesian approach, and grey forecasts are all statistical approaches. These approaches can be utilized to tackle difficulties in fields such as engineering, economics, and science disciplines that include a large amount of data and interdependent explanations. For wind speed prediction, [26] proposed a combination of two models, i.e., ARMA and wavelet transform. The low-frequency characteristics of the entire wind speed are extracted using the wavelet transform. In [27], an Auto Regression Integrated Moving Average approach outperforms the BPNN (back propagation neural network) in forecasting short-term intermissions. In [28], a Bayesian methodology has been proposed to describe the wind resource and estimate one-hour-ahead wind speeds. The modeling outcome has shown that the Bayesian approach can be operative for the prediction of wind speed and power.

For predicting short-term fluctuations in wind power, an approach that depends on a Markov-switching auto-regressive (AR) approach with a time-varying coefficient was developed in [29]. The approach has the advantage of being simple to use in calculating full predictive densities. In [30], the authors propose an autoregressive conditional heteroscedastic (ARCH) model. In [31], the hourly average wind speed is predicted using the autoregressive moving average and the persistence model. Authors in [32] have examined the use of an auto-regressive integrated moving average approach for time-series forecasting using wind speed observations. For short-term forecasts, the ARIMA model

has been demonstrated to outperform the ANN model [33]. In [34], three different samples of wind speed data are used to test the validity of the ARIMA model that is being proposed. Given that the hour-ahead forecast takes no more than five minutes to compile, the proven prediction inaccuracy of less than 16% is quite an accomplishment. In [35], Time series analysis, ARIMA, and Ordinary Least Squares (OLS) multiple regression have been used to predict wind speeds. In [36], Non-stationary annual wind speed data are analyzed using the Fractional Autoregressive Moving Average (FARIMA) Model. A comparison has been conducted between the F-ARIMA model and the Persistence and ARIMA models in [37], and it has been found that the F-ARIMA model is superior at capturing the long-term and short-term properties of time-series observations. In [38], Wind Speed Forecasting Based on Second Order Blind Identification (SOBI) and Autoregressive (AR) Model has resulted in higher accuracy compared with direct forecasting. In [39], short-term wind power forecasts based on ARX models have been shown to give better accuracy in forecasting. Some researchers related to the statistical techniques for wind prediction are given in Table 3.

Wind is a stochastic variable, it is difficult to anticipate due to its non-stationary and nonlinear features [45]. Statistical weather forecasting models have also outperformed numerical weather forecasting models [46]. The above literature survey helps to identify the strengths and limitations of statistical methods as listed in Table 4.

Table 3. Statistical Methods for Wind Speed/Power Prediction

Authors	Title	Techniques	Accuracy
Li et al. (2022) [40]	"A Wind Speed Correction Method Based on Modified Hidden Markov Model for Enhancing Wind Power Forecast.	Markov	RMSE = 3.093 MAE = 2.451
Wang et al. (2020) [41]	"Forecasted Scenarios of Regional Wind Farms Based on Regular Vine Copulas"	KDE, R-vine	RMSE = 0.1089 MAE = 0.075
Mararakanye et al. (2022) [42]	Incorporating Spatial and Temporal Correlations to Improve Aggregation of Decentralized Day-Ahead Wind Power Forecasts"	KNN, KDE	MAE = 3.18; RMSE = 4.63; R2 = 0.94
Yu et al. (2020) [43]	Probabilistic Prediction of Regional Wind Power Based on Spatio-temporal Quintile Regression.	SQR	RMSE = 16.62%; MAE = 11.23%
Dong et al. (2022) [44]	"Power Prediction Based on Multi-class Autoregressive Moving Average Model with Logistic Function"	ARMA	RMSE = 127.10 MAPE = 1.25%

Table 4. Strengths and limitations of statistical methods

Parameters	Strengths	Limitations
Data availability	Statistical models can work with readily available historical wind data.	Less Accuracy with data sparsity
Simplicity	Implementation is simple and easy	Difficult to capture complex nonlinear data.
Interpretability	Results are interpretable, aiding in understanding the factors affecting wind speed.	May not observe all relevant weather variables.
Computational speed	Less computational power required	Its prediction accuracy is low for highly dynamic and nonlinear wind patterns.
Adaptability	Use for short-term and long-term wind predictions.	It may not easily identify extreme events and rapid wind variability.
Assumption flexibility	Flexibility in choosing the appropriate statistical distribution (e.g., normal, Weibull) for wind data.	Assumptions about the data distribution may not always hold.
Forecast updates	It can be updated with new data easily, making it suitable for real-time applications.	Less accuracy in clamite changing regions.
Noise handling	Easily handle noisy data	Low performance in highly non-linear wind condition
Historical patterns	Use for long-term wind speed patterns and trends.	May not account for sudden shifts or local microclimatic influences.
Risk assessment	Provides a foundation for risk assessment and resource allocation.	It may not be suitable for critical applications requiring high precision.
Model transparency	Transparency in model structure and parameters makes it accessible to a wider audience.	Lack of robustness in situations where statistical assumptions are violated.

CUTTING-EDGE APPROACHES

The cutting-edge approaches use advanced approaches and data for more accurate wind forecasting. Table 5. Shows the classification of cutting-edge approaches for wind forecasting.

Machine Learning and AI Methods

Machine learning methods can determine intricate nonlinear correlations and patterns in wind speed/power data that conventional statistical models may not capture. This can lead to improved forecasting accuracy, especially for long-term and nonlinear predictions. Machine learning algorithms can adapt and learn from new data [47]. Machine learning algorithms can automatically select relevant features from a large set of potential predictors. This helps in identifying the most important factors influencing wind speed/power, eliminating irrelevant features, and reducing model complexity[48].

The machine learning approaches used for the prediction of solar radiation [49], wind potential [50], and short-term traffic flow [51]. And handle large data with complex computation. Machine learning approaches give highly accurate outcomes for wind forecasting at various time scale intervals from from single turbine to entire wind farm [52,53]. RBF (Radial basis function) outperforms both linear and nonlinear functions in neural networks, and it is best suited for the prediction of wind speed [54,55]. Genetic algorithms (GA) which are algorithms based on evolution thus expressing individual qualities through genetics [56]. Approximate reasoning is possible using fuzzy sets and fuzzy logic. Fuzzy logic is a field of study that depends on generalization and CI (computational intelligence) principles. The fuzzy simulation outperformed the persistent technique in predicting wind speed as of 30 minutes-2 hrs. ahead. In [57], various neural networks are used to predict wind speed such as Long Short-Term Memory (LSTM), Artificial Neural Network (ANN), Convolutional Neural Network (CNN), and Convolutional LSTM (ConvLSTM) hybrid model. These algorithms can capture temporal dependencies and long-term patterns in wind speed/power data, making them effective for predicting future values. In [58], a grouped strategy has been provided for predicting wind power 10 minutes ahead of time. A persistence approach, a BPNN (Back Propagation Neural Network), and an RBFNN (Radial Basis Function Neural Network) are combined in the suggested method. Table 6. Provide insights into the underlying algorithms used in machine learning-based forecasting models. It includes the classification of machine learning algorithms in four broad classes, i.e., supervised learning, unsupervised learning, deep learning, and ensemble methods. Further sub-classification of each category, along with a brief description of the applications of each algorithm, is also given.

Table 7 and Table 8 respectively summarize the state-of-the-art contributions from various researchers in the field of machine learning and deep learning methods for wind prediction.

Wind forecasting is done utilizing an upgraded form of EMD (EEMD), complementary ensemble EMD (CEEMD), and complete ensemble EMD with adaptive noise (CEEMD) in [105] (CEEMDAN). Even though EMD looked to beat many conventional approaches (Persistence & ARMA), the authors state that there seemed to be a problem with approach mixing [106], in which different IMFs contain signals in the same frequency range.

Hybrid Methods

In recent years, attention has switched to hybrid forecasting systems, i.e. combination of two or more two or more prediction methods and then aggregating them as shown in Figure 4 [107]. Machine learning techniques can be combined with traditional statistical models to create hybrid models.

Combining an autoregressive integrated moving average (ARIMA) model with machine learning algorithms can improve forecasting accuracy by incorporating both statistical properties and complex patterns in the data. Hybrid methods such as ANN-ARIMA [108], PSO-ANFIS [109], and WT-NN (Wavelet transform Neural Network) [110]. For a short period of wind power prediction in Portugal, an

Table 5. Classification of cutting-edge approaches

Category	Approaches	Detail
Machine Learning & AI approaches	'Supervised Learning'	Prediction is based on labeled data by using random foreast, regression, aupport vector machine, and decision trees.
	'Unsupervised Learning'	Prediction is based on unlabeled data and identify pattern using clustring.
	'Deep Learning,	For complex sequence prediction various neural networks are used like CNN (Convolutional neural network), RNN (recurrent neural networks), and LSTM (long short-term memory) networks
	'Ensemble Methods'	Enhance prediction accuracy by combining multiple algorithms.
Hybrid approaches	'Combination Techniques'	Enhance the accuracy by combination of two approaches

Table 6. Algorithms for machine learning-based models

Algorithm category	Algorithm	Detail	Application
Supervised learning	'Linear Regression'	İt provide relationship between a dependent variable and a single independent variable.	Appropriate for linear relationships between variables.
	'Decision Trees'	leverages decision rules constructed from variables to divide data into branches.	Analyzes interactions and non-linear correlations between features.
	'Random Forests'	A number of decision trees that have been trained on variable subsets of characteristics and data.	Avoids overfitting in comparison to single trees and offers reliable forecasts.
	'Support Vector Machines (SVM)'	Evaluates which hyperplane best matches the data for regression or divides the data into several classes.	Appropriate for complicated interactions and high-dimensional spaces.
	'K-Nearest Neighbors (KNN)'	Forecasting based on the k-nearest training examples in the feature space.	Easy to use and efficient for low-noise brief datasets.
Unsupervised learning	'K-Means Clustering'	Partitions data into k clusters based on feature similarity.	Finds trends and clusters in wind data.
	'Hierarchical Clustering'	Uses divisive techniques to create a hierarchy of clusters.	Recognizes the relation between wind speed patterns and data structure.
Deep learning	'Artificial Neural Networks (ANN)'	Layers of interconnected neurons acquire the ability to map inputs to outputs.	Identifies intricate, non-linear interactions; processing and huge quantities of data are needed.
	'Recurrent Neural Networks (RNN)'	RNN retains memories through connections that form a temporal sequence.	Suitable for anticipating time series based on historical trends.
	Long Short-Term Memory (LSTM) Networks	An distinctive kind of RNN with long-term dependency learning capabilities.	Useful in identifying long-term patterns and trends in time series forecasting.
	Convolutional Neural Networks (CNN)	Although it may be used to 1D time series, this neural network is mainly used for image recognition.	Captures local patterns and trends in wind data.
Ensemble methods	Bagging (Bootstrap Aggregating)	Increases accuracy and stability by averaging predictions from several models trained on various subsets.	Reduce variation and overfitting for better predictions.
	Boosting	Sequentially trains models, focusing on the errors of previous models.	Enhance the forecasting accuracy by reducing bias and variance.

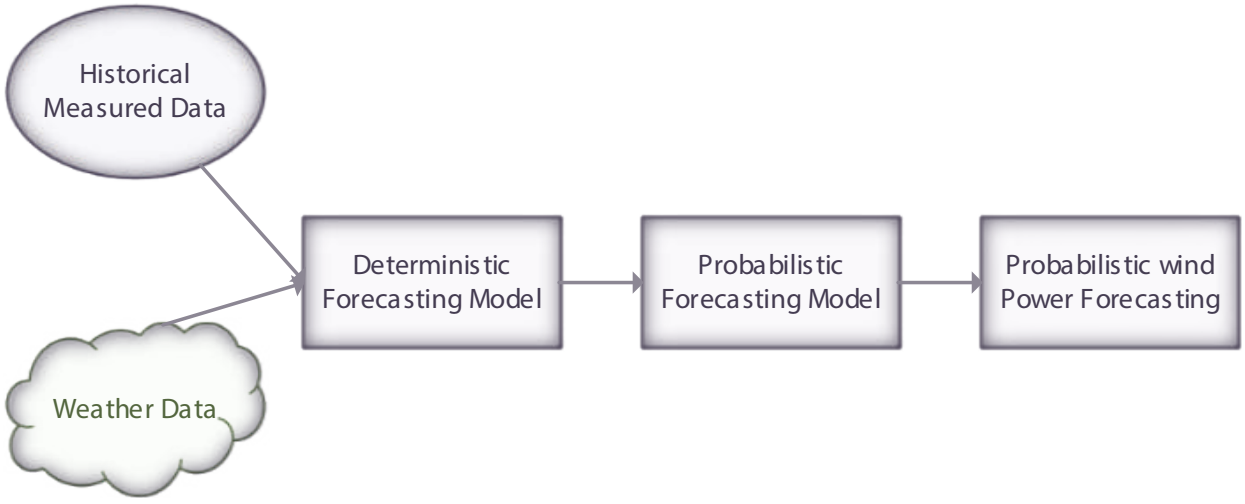


Figure 4. Hybrid model.

Table 7. Machine Learning Methods for Wind Speed/Power Prediction

Authors	Title	Techniques	Accuracy
Jyothi et al. (2016) [59]	"Very-short-term wind power forecasting through Adaptive wavelet neural network"	WNN, ANN, ANFIS	MSE = 0.25 RMSE = 0.367
Xu and Mao (2016) [60]	"Short-term wind power forecasting based on elman neural network with particle swarm optimization"	ENN, PSO	ERMS = 16.55%
Catalão et al. (2009) [61]	"An artificial neural network approach for short-term wind power forecasting in Portugal"	ANN	RMSE = 0.0362
Mabel et al. (2008) [62]	"Analysis of wind power generation and prediction using ANN: A case study"	ANN	RMSE = 0.0806
Singh et.al. (2007) [63]	"Wind power estimation using artificial neural network"	ANN, Kalman filtering	Not determined
Marugán et al. (2018) [64]	"A survey of artificial neural network in wind energy systems"	ANN	more than 80% of accuracy
Sharma et al. (2018) [65]	"A review of wind power and wind speed forecasting"	ANN	RMSE = 2.849 (1 hr)
Sideratos et al. (2012) [66]	"Probabilistic wind power forecasting using radial basis function neural networks"	RBFNN	--
Ramadevi and Bingi (2022) [67]	"Chaotic time series forecasting approaches using machine learning techniques: A review"	Machine learning	Not determined
Zhou et al. (2022) [68]	"Performance ımprovement of very short-term prediction intervals for regional wind power based on composite conditional nonlinear quantile regression"	WMTSM and conditional LP (CLP)	Both MAE and RMSE of less than 10%
Lee et al. (2020) [69]	"Wind power prediction using ensemble learning-based models"	Ensemble learning models (GRF, RF, XGB)	R2 = 98.9; RMSE = 50.36; MAE = 23.63
Tu et al. (2020) [70]	"Short term wind power prediction based on data regression and enhanced support vector machine"	EBSO and LSSVM	MAE (m/s): 0.723 RMSE (m/s): 0.932
Tan et al. (2020) [71]	"Ultra-Short-Term Wind Power Prediction by Salp Swarm Algorithm-Based Optimizing Extreme Learning Machine"	SSA-ELM	MAPE = 1.2677 RMSE = 0.2576
Huang et al. (2023) [72]	"Priori-guided and data-driven hybrid model for wind power forecasting"	Priori-guided and data-driven hybrid model	MAE = 0.0861, RMSE = 0.1262, R2 = 0.8333, AR = 87.38%
Wang et al. (2023) [73]	"A hybrid intelligent framework for forecasting short-term hourly wind speed based on machine learning"	Intelligent hybrid model	MAPE = 2.62 and RMSE = 0.14
Pombo et al. (2022) [74]	"Assessing stacked physics-informed machine learning models for co-located wind–solar power forecasting"	Stacked physics-informed machine learning model	RMSE = 5% and R2 = 0.95
Moayyed et al. (2022) [75]	"A Cyber-Secure generalized supermodel for wind power forecasting based on deep federated learning and image processing. Energy Convers"	Cyber-secure generalized supermodel	RMSE = 0.02, MAE = 0.007 MAPE = 0.60
Liu et al. (2023) [76]	"An online transfer learning model for wind turbine power prediction based on spatial feature construction and system-wide update"	Online transfer learning model	MAE = 84.837 RMSE = 134.837
Nascimento et al. (2023) [77]	A transformer-based deep neural network with wavelet transform for forecasting wind speed and wind energy"	Discrete wavelet transform	100 m RMSE [m/s] = 0.383 150 m RMSE [m/s] = 0.368 120 m RMSE [m/s] = 0.375
Sobolewski et al. (2023) [78]	"Gradient boosting-based approach for short- and medium-term wind turbine output power prediction"	Goddard earth observing system model	RMSE [kW] = 76.18
Yu et al. (2023) [79]	Research on Hierarchical Control Strategy of ESS in Distribution Based on GA-SVR Wind Power Forecasting.	SVR	RMSE/MW = 14.7435
Wang et al. (2023) [80]	"Short-Term Wind Power Prediction by an Extreme Learning Machine Based on an Improved Hunter–Prey Optimization Algorithm"	Improved hunter-prey optimization (IHPO algorithm-based extreme learning machine (ELM)	RMSE (kW) = 50.55

Table 8. Deep learning method for wind speed/power prediction

Authors	Title	Techniques	Accuracy
Lin et al. (2020) [81]	"Wind power prediction based on high-frequency SCADA data along with isolation forest and deep learning neural networks"	"Deep Learning Neural Network (DLNN) & SCADA"	MSE = 0.0032
Ahuja and Saini (2023) [82]	"Recurrent Neural Network for Chaotic Wind Speed Time Series Prediction"	RNN	RMSE = 0.2497
Wang and Li (2023) [83]	"Wind speed interval prediction based on multidimensional time series of Convolutional Neural Networks"	CNN	RMSE1 = 0.2805 RMSE2 = 0.3021 RMSE3 = 0.2838
Mert (2021) [84]	"Agnostic deep neural network approach to the estimation of hydrogen production for solar-powered systems"	"Agonistic Deep learning neural network"	RMSE = 0.0703
Hu et al. (2020) [85]	"Very Short-Term Spatial and Temporal Wind Power Forecasting: A Deep Learning Approach".	"A convolution-based spatial–temporal wind power predictor (CSTWPP)"	MASE = 190.02 RMSE = 7.49
Dong et al. (2022) [86]	"Spatio-temporal Convolutional Network Based Power Forecasting of Multiple Wind Farms"	"The spatiotemporal convolutional network (STCN) with a directed graph convolutional structure"	MAEs = 3.17% RMSEs = 2.88%,
Jalai et al. (2022) [87]	"New Hybrid Deep Neural Architectural Search-Based Ensemble Reinforcement Learning Strategy forWind Power Forecasting"	"Adeep-optimized convolutional LSTM-based ensemble reinforcement learning strategy (DOCLER)"	RMSE = 7.1322% MAE = 4.6713%
Sun and Zhao (2020) [88]	"Short-Term Wind Power Forecasting Based on VMD Decomposition, ConvLSTM Networks and Error Analysis"	"A variational mode decomposition (VMD) and convolutional long short-term memory network (Conv LSTM) model"	MRE(KW) = 0.016 MAE(KW) = 792 MSE(KW) = 568,305 RMSE(KW) = 1252.32
Miao et al. (2021) [89]	"Ultra-Short-Term Prediction of Wind Power Based on Sample Similarity Analysis"	"The CNN-MLSTMs-T Model"	RMSE = 0.1998; MAE = 0.1523
Liao and Yang (2022) [90]	"Wind GMMN: Scenario Forecasting for Wind Power Using Generative Moment Matching Networks"	"Generative moment matching network (GMMN)"	RMSE = 127.10; MAE = 0.6855 MW
Huang (2022) [91]	"Wind Power Generation Forecast Based on Multi-Step Informer Network"	"Multi-step informer network (MSIN)"	Multi-step informer Network (MSIN) improves forecast accuracy by 29% compared with the informer network for RMSE
Wu and Jiang (2022) [92]	"Short-TermWind Power Prediction Based on Data Decomposition and Combined Deep Neural Network"	"Long short-term memory neural network (LSTM) with the improved particle swarm optimization algorithm (IPSO)"	MAE = 2.92668; RMSE = 3.59604
Yu, et al. (2022) [93]	"Short-term wind power prediction for regional wind farms based on spatial-temporal characteristic distribution. Renew"	"Spatiotemporally multiple clustering and I–CNN-BILSTM deep learning network."	MAE = 18.64, RMSE = 28.45
Liu et al. (2023) [94]	"A unified multi-step wind speed forecasting framework based on numerical weather prediction grids and wind farm monitoring data"	"The unified forecast based on STC-DPN And The single-site error correction of TCN-LSTM"	MAE = 2.071, RMSE = 2.431,
Hossain et al. (2021) [95]	"Very short-term forecasting of wind power generation using hybrid deep learning model"	"Hybrid deep learning model"	MAE = 1.59, RMSE = 3.73 and MAPE = 8.13.
Garg and Krishnamurthi (2023) [96]	"A CNN encoder decoder LSTM model for sustainable wind power predictive analytics"	"CNN-ED-LSTM model"	MSE = 0.0102 MAPE = 46.24 MAE = 0.0623 RMSE = 0.1012

Table 8. Deep learning method for wind speed/power prediction (continued)

Authors	Title	Techniques	Accuracy
Zhang et al. (2021) [97]	"Power prediction of a wind farm cluster based on spatiotemporal correlations"	"Long short-term memory (LSTM) neural network"	RMSE (MW) = 0.94 MAE (MW) = 0.67 MAPE (%) = 49.71
Zhang et al. (2020) [98]	"Short-term wind power forecasting approach based on Seq2Seq model using NWP data"	"Seq2Seq model"	RMSE = 129.3 MAE = 81.1
Lliao et al. (2022) [99]	"Short-term power prediction for renewable energy using hybrid graph convolutional network and long short-term memory approach"	"Long short-term memory (LSTM)"	RMSE (MW) = 1.27 MAE (MW) = 0.90
Tian et al. (2022) [100]	"Developing a wind power forecasting system based on deep learning with attention mechanism"	"A deep learning model (gated recurrent unit, GRU)"	RMSE = 111.9766
Yildiz et al. (2021) [101]	"An improved residual-based convolutional neural network for very short-term wind power forecasting"	"Residual CNN-based deep forecasting method"	1-h ahead. RMSE = 0.9947
Liu et al. (2023) [102]	"Short-term wind power forecasting based on feature analysis and error correction"	"Bidirectional long short-term memory network (BiLSTM)"	RMSE/MW = 1.0822
Wang et al. (2023) [103]	"Artificial intelligent power forecasting for wind farm based on multi-source data fusion"	"The encoder-decoder framework is constructed with LSTM as the basic Unit"	RMSE = 0.1243
Xiao et al. (2023) [104]	"Wind power short-term forecasting method based on LSTM and multiple error correction"	LSTM	RMSE (%) = 10.23

NNWT technique that depends on the integration of ANN and WT (wavelet transform) has been proposed, which has proven to be both new and effective. Its MAPE outperforms persistence, ARIMA, and NN techniques with an average value of 6.97 percent and a calculation time of less than 10 seconds. Wavelet- SVM (Support vector machine) optimized by GA (genetic algorithm) [111], Kalman filter-ANN (KF+ANN) [112], WT- SVM-GA (Wavelet-Support vector machine) optimized by genetic algorithm & EMD+SVM (Support vector machine with empirical mode decomposition) [113] are some work reported in this literature. To build a unique grouped simulation for wind speed forecast, authors in [114] have proposed combining EMD with feature selection. Hybrid forecasting approaches have lately become popular due to their extra benefits over traditional single forecasting methods. Candenas and Rivera established a wind forecasting model that is based on ARIMA-ANN [115] with a fixed prediction horizon. For the prediction of multi-step wind speed, a hybrid approach that includes WDT (wavelet decomposition transform), an exciting learning machine, and adjustment for extremes methodology is proposed in [116]. Li et al. proposed a mixed technique that depends on continuous and flexible weight for predicting short periods of wind speeds [117]. In [118] to identify oscillations brought on by nearby wind generators and send the necessary inputs to modeling, a novel short-period wind forecasting approach is being deployed. In [119], an attribute selection model depending upon a k-means cluster, and an MLPNN (multi-layer perceptron neural network) were created to forecast short periods of wind speed. For a short period wind speed prediction, correlation-based DWT, LSSVM, and GARCH. The contributions to the LSSVR (Least Squares Support Vector Regression) wind speed forecasts are evaluated using correlation coefficients among different sub-series introduced by [120]. State-of-the-art hybrid models for wind prediction are detailed in Table 9.

In [142], authors have proposed and validated an improved BFGS (Broyden-Fletcher-Goldfarb-Shanno) neural network (using four wind speed datasets) and wavelet transform-signal processing method for short periods of wind speed forecasts. After wavelet decomposition, correlation coefficients are calculated for each sub-series to identify their comparative relevance. In this study [143], the hybrid model possesses a more accurate forecasting ability than the other models, and the level of accuracy of the hybrid model is different from that of the GRNN, BPNN, LSSVM, CS-BPNN, WOA-LSSVM, EMD-WOA-LSSVM, and EEMD-WOA-LSSVM. In this study, a system that combines NWP and hybrid wind forecasting ANN models is proposed. This hybrid forecasting approach is beneficial in improving the perception of wind power in China [144]. In [145], two grouped models for wind power and speed prediction: ARIMA-ANN & ARIMA-SVM have been proposed. This research systematically and comprehensively analyzes the use of the suggested hybrid models. In [146], authors have employed a new hybrid wind speed forecast approach that is dependent on a BPNN and the knowledge of using periodic exponential forecasting adjustment to remove seasonal impacts from authentic wind speed

Table 9. Hybrid method for wind speed/power prediction

Authors	Title	Techniques	Accuracy
Hong et al. (2019) [121]	"Hybrid deep learning-based neural network for 24-h ahead wind power forecasting"	CNN-MFNN, CNN- RBFNN, CNN- RBFNN-DGF	RMSE of Winter = 375.2369 RMSE of Spring = 352.2999 RMSE of Summer = 221.3698 RMSE of Autumn = 194.2075
Foley et al. (2012) [122]	"Current methods and advances in the forecasting of wind power generation"	NWP, statistical, machine learning	Not Described
Shetty et al. (2016) [123]	"Optimized radial basis function neural network model for wind power prediction"	RBFNN, FCM, PSO-FCM, Extreme Learning Machine	MSE = 0.0034 at no. of center 60 model 1
Peng et al. (2013) [124]	"A hybrid strategy of short-term wind power prediction"	ANN+ Physical	MAE = 757.25 (KW) NRMSE = 2.01%
Wang et al. (2018) [125]	"A novel hybrid forecasting system of wind speed based on a newly developed multi-objective sine cosine algorithm (MOSCA)"	CEEMD- MOSCA- WNN	RMSE1 = 0.078693 RMSE2 = 0.118740 RMSE3 = 0.192665 RMSE4 = 0.143523
Saini and Ahuja (2017) [126]	"Wind speed prediction using wavelet transform and artificial neural network"	ANN, WT	RMSE = 0.1576
Saini and Ahuja (2019) [127]	"Wind speed prediction using wavelet transform and GA trained artificial neural network"	ANN, WT, GA	
Duan et al. (2022) [128]	"A combined short-term wind speed forecasting model based on CNN–RNN and linear regression optimization considering error"	CNN-RNN	RMSE1 = 0.1172 RMSE2 = 0.1017 RMSE3 = 0.2104 RMSE4 = 0.1876
Zhang et al. (2022) [97]	"A comprehensive wind speed prediction system based on Monte Carlo and artificial intelligence algorithms"	AI	RMSE = 0.5794
Zou et al. (2022) [129]	"Forecasting of short-term load using the MFF-SAM-GCN model"	"A multi-feature fusion self-attention mechanism graph convolutional network (MFF-SAM-GCN) forecasting model"	RMSE = 0.0284 SMAPE = 9.453% MBE = 0.025 R2 = 0.989
Aisyah et al. (2022) [130]	"Exploratory Weather Data analysis for electricity load forecasting using svm and grnn, case study in Bali, Indonesia"	GRNN, SVM	The GRNN model gives the CC value of 0.956, RMSE of 28.82 The SVR model gives a CC value of 0.965 and an RMSE of 44.40.
Zhao et al. (2023) [131]	"Hybrid VMD-CNN-GRU-based model for short-term forecasting of wind power considering spatio-temporal features"	VMD-CNN-GRU	RMSE = 1.5651, MAE = 0.8161, MAPE = 11.62%, and R2 = 0.9964.
Che et al. (2023) [132]	"Ultra-short-term probabilistic wind power forecasting with spatial-temporal multi-scale features and K-FSDW based weight"	I-CNN-BILSTM	MAPE (%) = 4.86, MAE = 18.64, and RMSE = 28.45.
Hu et al. (2021) [133]	"Hybrid forecasting method for wind power integrating spatial correlation and corrected numerical weather prediction"	"The hybrid forecasting method based on the corrected NWP data and the SC"	RMSE = 1.238, MAPE = 0.325, MAE = 0.7002
Wen et al. (2022) [134]	"A new hybrid model for power forecasting of a wind farm using spatial–temporal correlations"	"KHC algorithm for clustering, components extraction and selection with SVD, and building SVR forecast model"	MAE = 0.273 RMSE = 0.343
Hu et al. (2021) [135]	"An improved deep belief network based hybrid forecasting method for wind power"	"GBRBM-DBN consists of the PCA, NWP, and SC for wind power Forecasting"	RMSE = 2.6018, MAPE = 0.2859, MAE = 2.3857

Table 9. Hybrid method for wind speed/power prediction (continued)

Authors	Title	Techniques	Accuracy
Gu et al. (2023) [136]	"Short-term wind power forecasting and uncertainty analysis based on FCM–WOA–ELM–GMM"	FCM-WOA-ELM-GMM Model	MAE = 3.8%, RMSE = 5.24%
Al-Duais and Al-Sharpi (2023) [137]	"A unique Markov chain Monte Carlo method for forecasting wind power utilizing time series model"	"Seasonal autoregressive integrated moving average (SARIMA) model"	RMSE = 13.09 MAPE = 1.03
Yan et al. (2022) [138]	"Uncovering wind power forecasting uncertainty sources and their propagation through the whole modeling chain. renew. sustain"	"Historical wind climate model and physical model"	RMSE = 13% MAE = 20.7%
Xiong et al. (2022) [139]	"Short-term wind power forecasting based on Attention mechanism and deep learning"	"AMC-LSTM hybrid model"	MSE = 0.8951 MAE = 0.0505 RMSE = 0.0946
Zhang et al. (2023) [140]	"Deterministic and probabilistic prediction of wind power based on a hybrid intelligent model"	"XGBoost, Tree, SVR, and BPNN methods"	RMSE = 1.8313
Wu et al. (2024) [142]	"Interpretable wind speed forecasting with metrological feature exploring and two-stage decomposition"	IEEMD-EWT-JADE-TFT	RMSE = 0.1063

information. The outcomes of the tests have revealed that the proposed strategy outperformed a single BPNN.

In [147], authors employed a hybrid method depending on the integration of ANN and WT for a short period of wind energy forecasting in Portugal. Using the wavelet approach, the wind power series is decomposed into a set of effective constituent sequences. Results of the tests indicate that the proposed hybrid approach for predicting wind production has a proportion of promise. Hybrid models' main purpose is to integrate the advantages of each model to attain global forecasting performance [148]. In [149], forecasting the average daily wind speed using a predicting scheme based on discrete wavelet transform (DWT) associated with Artificial Neural Networks (ANN) is proposed, and the results show that, when using ANN for prediction, the db4 wavelet with a 5-level decomposition is the most appropriate wavelet for wind speed forecasting in the three considered regions. Also, the proposed scheme exhibits high precision and accuracy for one-day-ahead wind speed forecasting in terms of RMSE and MAPE. In [150], authors have employed a grouped intellectual model termed an ANFIS (Adaptive Neural Fuzzy Inference System) that combines two AI approaches, Fuzzy Logic, and ANN, to estimate wind constraint and energy production shortly. In [151], depending on wavelet and classical time series analysis approaches, a new short-period prediction algorithm is employed. An adaptive neuro-fuzzy inference system (ANFIS) is utilized in [152] to anticipate wind direction 2.5 minutes ahead, taking into account both direction & speed. In this study, artificial intelligence techniques, such as the ANN algorithm, are utilized to anticipate wind power [153]. To predict wind power, four alternative approaches were applied. It has been discovered that the Genetic algorithm outperforms the other models when it comes to training data sets.

In [154], three approaches for predicting wind speed are proposed. Which hybrid models proposed, such as Wavelet packet-BFGS (Broyden–Fletcher–Goldfarb–Shanno), have been demonstrated to be superior to Wavelet packet-ARIMA-BFGS. Second, Wavelet packet-BFGS has been discovered to be superior to Wavelet-BFGS. In [155], four different models for the prediction of wind power are presented. The two learning algorithms, the backpropagation algorithm and the genetic algorithm, along with a combination of these models, are used for the prediction of wind power. The genetic algorithm performs better for both the training data sets than the other models. In [156], the system consists of two main parts: a point prediction module based on a nonlinear combination and an interval prediction module based on fuzzy clustering. It is of great significance to explore the predictability and modeling of wind speed comprehensively. Unlike previous works, the authors have implemented a BP neural network using MOEA/D (Multi-objective evolutionary algorithm based on decomposition) optimization as a novel nonlinear combination mechanism to derive final prediction results, which enhances the accuracy of point prediction and improves final prediction accuracy. Wind speed predictions in a short period utilizing mathematical models that include ANN and Hybrid time-series models are given in [157].

The back propagation neural network (BPNN) algorithm is integrated with GA and PSO in [158] to create an integrated prediction model for short-period wind farms. The output power is calculated using climatic data gathered

by a WSN (wireless sensor network), which is then sent into the BP neural network as an input variable. In [159], BPNN is a basic prediction method, and the proposed prediction method is validated by the output power prediction of a real wind farm. A support vector machine (SVM) is chosen as another basic prediction method to test the versatility of the proposed improved prediction method. The results show that the proposed wind power prediction method can improve the prediction accuracy by about 8%.

In [160], the SARIMA-EEMD-LSTM hybrid prediction model is used to forecast wind speed time series at 15-, 30-, and 60-minute intervals. Thus, hybrid methods can effectively forecast wind speed/power wind power generation fluctuations must be anticipated by power system operators to control grid operations and plan rotating backup power [161]. Authors in [162] have utilized a fusion of neural networks and fuzzy logic approaches to precisely estimate the production of a wind farm. A self-organised map that categorises the input data into distinct groups is used.

It is found that there is a significant improvement in prediction accuracy achieved through hybrid models, with Root Mean Square Error values of 0.1089 m/sec for statistical methods from Table 3, 0.02 m/sec for intelligent methods from Table 7, and 0.0096 m/sec for hybrid approaches from Table 9.

Organization of Wind Prediction According to time Scale Horizons

Methodologies based on prediction period may be classified as extremely short-period predicting, short-term predicting, long-term predicting, and long-term predicting. Wind prediction organization based on time scale is discussed below:

- Very Short-Term (Seconds to Minutes):

The significance of these predictions lies in their necessity for jobs that demand accuracy in real-time or near-real-time scenarios. The applications of the technology encompass a range of areas, including wind energy production control, wind gust prediction, and emergency response in the context of severe weather occurrences.

- Short-Term (Minutes to Hours):

This wind forecasting is used in various sectors like managing transportation, power system management, wind farm operation, traffic systems, and several outdoor activities.

- Medium-Term (Hours to Days):

This forecasting is important for various sectors that depend on weather conditions, such as scheduling for generation, several-day span forecasting planning, construction market operation, etc.

- Long-Term (Days to Weeks):

These forecasts are employed in various sectors such as large-scale infrastructure planning, assessing climate change impacts, and choosing the best site for wind farm installation.

- Seasonal (Months to Seasons):

The seasonal wind forecasting is used in various fields, including agriculture, energy infrastructure investment, and long-range climate projections.

- Climate (Years to Decades):

The significance of climate-scale wind predictions is to enhance our comprehension of long-term wind patterns and their potential impacts on regional and global climate systems. The applications of the research encompass climate analysis, the formulation of policies, and the creation of measures for adaptation. Table 10 gives a classification of state-of-the-art work on the basis of forecasting horizons.

Comparison of Traditional and Cutting-Edge Approaches

Based on findings from numerous research studies, a comparison of the traditional and cutting-edge approaches

Table 10. Classification of the review works based on the forecasting time scale

Time Scale	Reviewed Work	Time Resolution
Ultra Short-term	[88,89]	5 min
	[73,78,81,83,88,94,101,105,137]	10 min
	[80,88,92,93,95,96,98,106,146]	15 min
	[49,88,90,142]	30 min
Short term	[76,77,80-82,91,99,102,104,134-136,139,142-144]	1 h
	[77,89,136,139,142]	2 h
	[77,89,136,139,142]	3 h
	[77,136,139,141,142]	4 h
	[77,139,141,142]	6 h
	[77,139,141]	12 h
	[45-47,77,93,97,136,138,140,141]	24 h
	[74,75,91,141]	48 h
Medium-term	[142]	72 h–1 week

Table 11. Comparison between traditional and Cutting-Edge approaches

Metric	Traditional approaches	Machine learning approaches	Hybrid approaches
Accuracy	Average	High	Very high
Computational efficiency	It requires low computational resources, so effeciency is high.	It requires significant computational resources, so the effeciency is average.	It depends on the complexity of the hybrid model, so the effeciency is low.
Ease of ımplementation	Easy to implement	Complex to implement and often considered a "black box."	İt involves integrating multiple models, which increases complexity.
Data requirements	Work with small datsets	İt requires large, high-quality datasets	It requires substantial data and preprocessing, especially when integrating different models.
Scalability	Easily scalable on standard hardware.	Scalable but requires specialized infrastructure like GPUs.	Low to moderate; scaling depends on the integration of traditional and machine learning components.
Energy consumption	Low	High	Very high
Interpretability	High; models are generally easy to understand and explain.	Low; often difficult to interpret the inner workings of the model.	Low to moderate; interpretability depends on the combination of methods used.
Applicability to short-term forecasting	High	High	Very high.
Applicability to medium-term forecasting	Average	High	Very high
Applicability to long-term forecasting	Low	High	High

on the basis of accuracy, resources, robustness, and data requirements etc. is given in Table 11.

From Table 11, it can be inferred that although Traditional methods offer ease of use and interpretability, they are often sufficient for short-term forecasts. The Cutting-edge approaches provide significant improvements in accuracy and adaptability, especially for complex, nonlinear wind forecasting problems. They are better suited for environments with rapidly changing conditions and where higher computational resources are available. It is equally important to consider the Practical implications of different forecasting techniques in real-world applications. Table 12 represents the implications of different forecasting techniques, particularly in terms of their adaptability to different geographical contexts and real-time operational needs.

Process of Wind Speed/Power Forecasting

The procedure for training and validation of wind data for both techniques, such as traditional & cutting-edge approaches, is shown in Figure 5. Many steps of wind forecasting that are represented in Figure 5 were discussed in the previous section. The various types of data pre-processing and advanced techniques reported in this study are used to improve the performance of wind forecasting. The most important among these are:

- **Data Cleaning:** Addressing missing observations through methods such as imputation and eliminating outliers to ensure dataset consistency and accuracy. This reduces systematic errors and increases model robustness.
- **Standarization:** It is applied to input variables on a comparable scale, there by enhance the stability, training, and overall efficiency.
- **Feature Extraction:** It is the process of choosing and transforming essential features from primary data, to enhance models performance such as derived indicators, lag based features etc.
- **Time Series Decomposition:** By applying decomposition, the time series is divided into seasonal, tendency, and remaining components. After decomposition, each can be trained separately, and then the results outcomes more precise.
- **Dimensionality Reduction:** PCA (Principal Component Analysis) can be used to increase generalization, computing complexity, and dimensionality reduction.

These steps help to improve the data quality , prediction accuracy, decrease noise, and thus help to produce more reliable as well as stable predictions. Moreover, standard evaluation metrics that can be used for identifying

Table 12. Practical implications of different forecasting techniques

Forecasting technique	Adaptability to geographical contexts	Real-time operational needs
'Statistical methods'	Average adaptability	Low computational demand, suitable for short-term forecasts but less effective in dynamic weather conditions.
'Physical models'	High adaptability across diverse regions	High computational resources required; effective for medium to long-term forecasts but slower in real-time.
'Machine learning'	High adaptability, especially when trained on region-specific data, can handle complex, non-linear relationships.	Requires substantial computational resources and real-time data input; performance improves with data availability.
'Hybrid models'	Enhanced adaptability by leveraging the strengths of multiple methods; flexible across various terrains and climates.	Balances computational demand and accuracy; effective in both short-term and long-term forecasting, with real-time application potential.
'Ensemble methods'	Highly adaptable, as they aggregate diverse models to improve overall accuracy across different regions.	Moderate to high computational demand; offers improved reliability in real-time operations due to averaging out model errors.

the accuracy and use of wind prediction/forecasting models by having a comparison of predicted and actual values. Common metrics include:

MSE: It stands for mean square error (MSE), which is commonly used in wind forecasting, but is an underutilized method. If the MSE indicates a higher value, then the model's performance is low, and vice versa. This method can be used where unexpected data may offer perceptive information about the issue. MSE is calculated by Eqn 1.

$$\mathrm{MSE}=\frac{1}{x}\sum_{i=1}^{x}(Y_i - X_i)^2 \quad (1)$$

RMSE: The root mean square error (RMSE) refers to the square root of the mean squared error (MSE). The introduction occurs when the magnitude of the error is equivalent to the magnitude of the objective. It is calculated by Eq. 2.

$$\mathrm{RMSE}=\sqrt{\frac{1}{x}\sum_{i=1}^{x}(Y_i - X_i)^2} \quad (2)$$

RMSE penalizes larger errors more heavily than MAE due to the squaring of errors. It is helpful for analyzing the variance of errors because it gives a measure of the standard deviation of prediction errors. Better model performance is shown by lower RMSE values; 0 is the optimal score.

MAE: The average of the absolute variations between the expected and predicted values is known as the mean absolute error, or MAE. The average gives equal weight to each individual difference. Compared to the MSE, this statistic is less affected by outliers. The MAE is determined by:

$$\mathrm{MAE}=\frac{1}{x}\sum_{i=1}^{x}|Y_i - X_i| \quad (3)$$

A precise, comprehensible indicator of prediction accuracy is offered by MAE. Because it does not need squaring the errors, it is less affected by outliers than RMSE.Lower MAE values indicate better model performance, with 0 being the ideal score (perfect predictions).

MAPE: Mean Absolute Percentage Error (MAPE) is a commonly used statistical measure for evaluating the accuracy of forecasting or prediction models. It is widely used in various areas, i.e., data analytics, statistics, and economics, and it demonstrates average error as a percentage of the actual value.

$$\mathrm{MAPE}=\frac{1}{x}\sum_{i=1}^{x}\frac{|y_i - x_i|}{|y_i|}*100\% \quad (4)$$

If the MAPE indicates a lower value, then the model's performance is highly accurate & vice versa. The MAPE is sensitive when actual values are close to zero, which may outcomes in division by zero error.

R2: It demonstrates the total variance percentage of data that can be analyzed by the model performance. It gives a measure of predicted values matched to the actual outcomes.

$$R^2 = 1-\sum_{i=1}^{x}\frac{|y_i - x_i|}{y_i - x_i|} \quad (5)$$

Traditional forecasting techniques are typically evaluated using metrics such as RMSE, MAE, and occasionally MAPE. Such methods focus on capturing temporal dependencies and recurring cycles in wind speed or power data, using error measures that reflect deviations from historical averages. While the cutting-edge approaches are evaluated by using RMSE, MAE, MAPE, and R2 metrics. And enhance the performance of these approaches by adjusting model sturucture, hyper parameters.

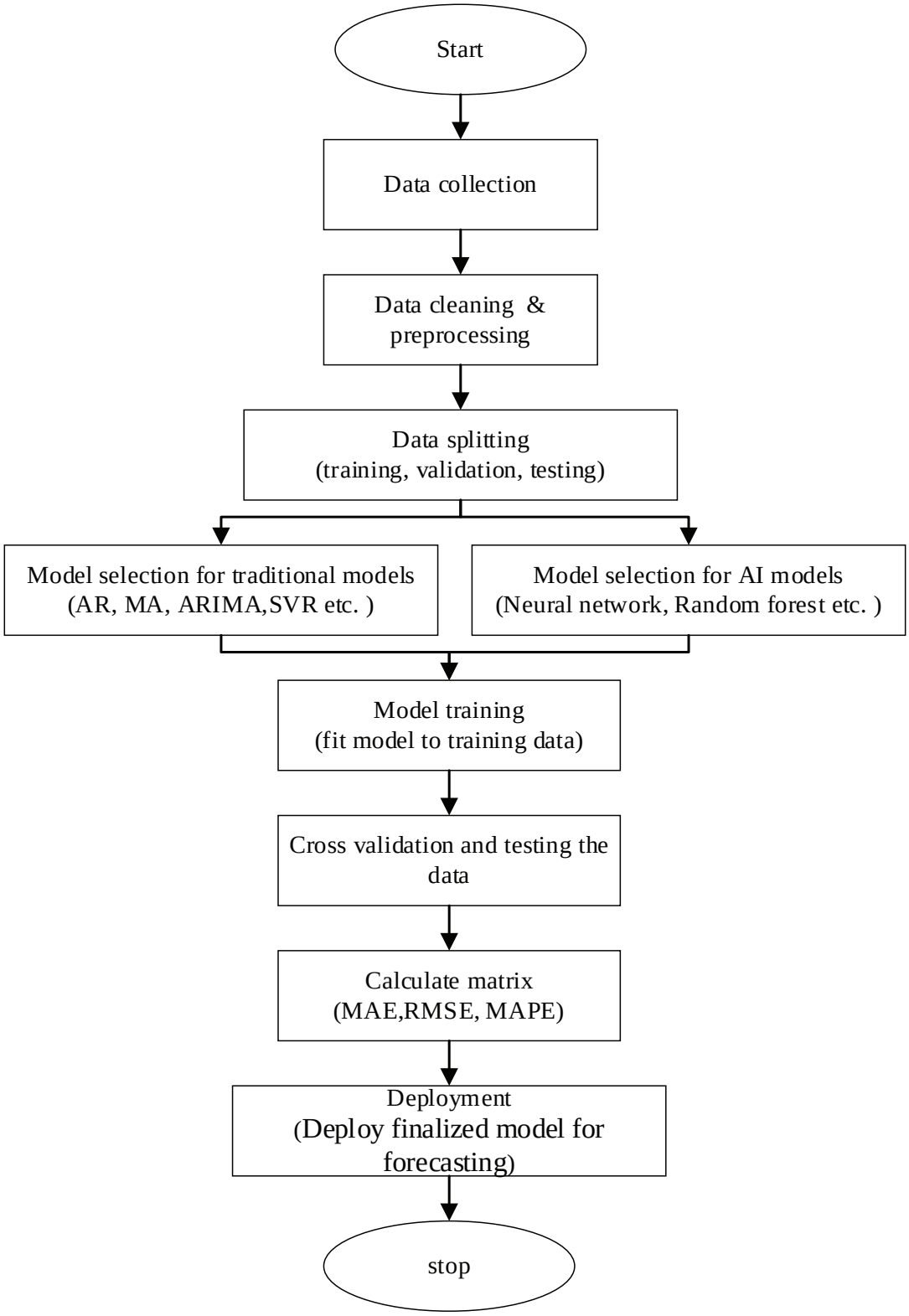


Figure 5. Flow chart of models training and validation.

Numerical Case Study

In this section, some popular Wind speed forecasting models are compared using a real-world dataset.

Data Description

The wind speed data is collected from open websites (https://maps.nrel.gov/wind-prospector/). The dataset was

collected from March 1st, 2023 to May 2023 with a time resolution of 1 hour. The first 70% of the data points were used as training samples, and the remaining 30 % of the data points were used as test data.

Experimental Setting

The models compared in the case studies can be divided into four groups: traditional benchmark models, machine learning models, deep learning models, and hybrid deep models. Six traditional benchmark models were selected, namely AR, MA, ARMA, ARIMA, SARIMA, and GARCH. The Machine Learning and deep Learning models used were ANN, RNN, and hybrid CNN-RNN models. In hybrid models, CNN was used to extract features, which were then fed into the other deep models to make wind speed forecasts.

RESULTS AND DISCUSSION

The wind speed forecasting results of different models are presented in Table 13. It can be seen that the hybrid intelligent model shows the best performance. This phenomenon shows that nonlinear models characterize the fluctuations of WS/WP more accurately and are more suitable than linear models for WS/WP forecasting. In order to measure the forecasting performance of different models, four forecasting error indicators were used: mean square error (MSE), root mean square error (RMSE), mean absolute percentage error (MAPE), and symmetric mean absolute percentage error (SMAPE). Mean Squared Error (MSE) and Root Mean Squared Error (RMSE) are used to give more weight to only larger errors, while MAE is used to give equal weightage to all types of errors, and SMAPE is used to assessi percentage-based errors only, thus making them suitable for different perspectives. ARMA model included in traditional statistical approaches shows superior performance with values of RMSE, SMAPE, MAE, and MSE respectively as 1.6622, 0.1178, 1.3537, and 2.7632, respectively. Due to temporal dependencies, this model is efficient for wind predictions & is also more accurate for forecasting short-term data as compared to otherer statistical models.

There are some neural network models which are more advanced, e.g., Recurrent Neural Networks (RNN) models, mainly used to improve the forecasting accuracy. The RNN model has better performance than basic ANN models with values of RMSE, SMAPE, MAE, and MSE as 1.3935, 0.0924, 1.0382, and 1.9420, respectively as reported in literature. Main qualities of a RNN includes retaining the information from previous time steps. This model is helpful for wind speed forecasting that has influence on future patterns. In contrast, traditional ANN model(s) lack these qualities, thus their ability to captue (fully) the time-dependent structure (in the data) is limited. CNNs have shown superior performance for wind prediction/forecasting with RMSE, SMAPE, MAE, and MSE values of 1.6622, 0.1178, 1.3537, and 2.7632, respectively. To further improve forecasting/prediction accuracy in the future, hybrid CNN-RNN models are used to extract the spatial features and capture temporal dependencies at the same time. The CNN-RNN approach is found to be effective for forecasting of wind speed, thus showcasing more reliable and accurate forecasting as compared to simple neural networks models. These models have helped to achieve RMSE, SMAPE, MAE, and MSE values of 0.9641, 0.0648, 0.7235, and 0.9295, respectively which is far better than basic ANN & RNN models.

This study surveys various wind-forecasting techniques, which include traditional, machine learning based, and. It has evaluated short-term and long-term forecasting models for different time scales and location (s). Table 13 is showcasing a comparison of various models' performance,showing that the use of machine learning based model can decrease the error by 30% in comparison to traditional approach, while the use of hybrid approach helps to further enhance the accuracy, i.e., reduces error. The prior survey(s) in this field only focused on general challenges such as quality & availability of data along with improvement in forecasting accuracy. This study further outlines future directions of research, e.g., using the Internet of Things (IoT) for the purpose of real-time forecasting and development of various adaptive models considering changes in climate.

Table 13. Comparison between all models' performance

Techniques	Metrics	MSE	MAE	RMSE	SMAPE
Conventional statistical models	AR	2.7640	1.3522	1.6625	0.1177
	MA	2.7715	1.3571	1.6647	0.1180
	ARMA	2.7632	1.3537	1.6622	0.1178
	ARIMA	3.2792	1.5569	1.8108	0.1178
	SARIMA	2.9123	1.4178	1.7065	0.1219
	GARCH	4.8473	1.5793	2.2016	0.1629
Intelligence models	ANN	1.9951	1.0848	1.4124	0.0969
	RNN	1.9420	1.0382	1.3935	0.0924
Hybrid model	**CNN-RNN**	**0.9295**	**0.7235**	**0.9641**	**0.0648**

CONCLUSION

Area of wind forecasting covers a wide range of traditional as well as cutting-edge approaches. Traditional approaches have been utilized since many years, and have been proven to be reliable in many applications. These approaches are generally simple, interpretable, and requiring fewer computational resources. These include the methods like persistence models, numerical weather prediction (NWP), etc. and have formed the foundation of wind forecasting inspite of having some limitations like less accuracy, and difficulty in handling sophisticated non-linear patterns.

Cutting-edge approaches use data processing techniques. These techniques easily deal with challenges of dealing with high-dimensional data and composite forecasting. These techniques are capable of providing high accuracy and flexibility alongwith managing variable climate conditions. Hybrid models, integrating multiple forecasting methodologies with use of diverse data source(s), are likely to dominate the future of wind prediction. Accurate forecasting is in fact critical for optimizing the generation of renewable energy, efficiently managing the operations of power grid, and supporting the development of a sustainable energy system. This paper reviews the current research and highlights the future directions to increase the accuracy of wind forecasting and is of great help for researchers and practitioners.

Challenges & Future Directions

Data collection and data availability are main concerns strongly related with wind forecasting challenges and future directions. Major obstacles in this field are as follows:

1. **Data sparstiy:** Wind time series data is not available for some time intervals and sometimes for some geographical location. This issue poses challenge in analyzing the model performance.
2. **Data resolution:** Low-resolution data (wind) reduces forecast accuracy for short-term predictions which requires high-frequency information. There may be requirement of recording of Wind measurements at varying temporal intervals (e.g., hourly or every 15 minutes).
3. **Data quality and calibration:** Small errors may lead to a big mistake in prediction produced by sensor miscalibration of sensor and/or equipment malfunction. Therefore, regular cheking and device maintaince are essential.
4. **Missing data:** Missed datasets are very common Due to sensor failures and/or other technical issues, problem of missing data becomes common. For reliable forecasting, it becomes essential to handle missing data values.
5. **Spatial variability:** Due to topography and local geography, Wind speed variation is observed over short distances. Recording this variability becomes challenging in absence of time-grained spatial data.

Table 14. Research Gaps In Future Research Directions of Wind Speed/Power Prediction

Underexplored Field	Research Gap	Future Research Directions
Integration of IoT technologies for real-time data acquisition	Limited use of IoT devices in capturing high-resolution, real-time environmental data.	Develop and deploy IoT networks for continuous data collection to improve forecasting accuracy and responsiveness.
Use of machine learning which are interpretable	Most machine learning models are complex and lack transparency, making them hard to interpret.	Focus on developing explainable AI techniques that offer transparency while maintaining prediction accuracy.
Long-term wind power forecasting	Existing models primarily focus on short-term forecasting; long-term predictions remain less accurate.	Research into hybrid models combining machine learning and climate models to improve long-term forecasts.
Extreme weather event prediction	Poor accuracy in forecasting wind speed/power during extreme weather conditions like storms or hurricanes.	Develop specialized models that can accurately predict wind patterns under extreme conditions, incorporating climate change factors.
Geographical and terrain variability	Inadequate adaptation of forecasting models to complex terrains and diverse geographic regions.	Create region-specific models that account for local topography and microclimates, leveraging high-resolution geographic data.
Energy storage integration	Insufficient research on integrating wind forecasting with energy storage management systems.	Explore real-time integration of forecasting models with energy storage solutions to optimize grid stability and energy use.
Social and environmental impact assessment	Limited consideration of the socio-environmental impacts of wind power forecasting and deployment.	Conduct interdisciplinary research assessing the social and environmental implications of wind forecasting technologies.

6. **Temporal variability:** It includes random fluctuations, rapid as well as seasonal change in wind data, making accurate wind forecasting difficult.
7. **Long-Term trends and climate change:** Nature of wind data is stochastic, nonlinear, and non-stationary. Which makes it necessary to provide high-quality data (over a long period of time) for accurate forecasting.
8. **Data consistency:** Variations in datasets caused by Changes in location of station and/or sensor, and methods of measurement can make datasets variable and must be avoided to ensure high prediction accuracy.
9. **Data privacy and access:** Due to proprietary concerns, it becomes difficult to get the historical wind data.
10. **Data integration:** Merging of datasets from various sources is generally seen in prediction which is also challenging.

In the current era, although wind forecasting has improved a lot by using various modern approaches, yet further improvement is necessary for increasing the forecasting reliability. Future research work should focus on development of the best methods which helps to balance the forecasting accuracy and computational efficiency. It is necessary that data from actual wind farms needs to be validated model-wise, while considering wind farm observations and various atmospheric conditions incorporated via simulation studies. Table 14 highlights the unexplored fields, research gaps and directions for future work in the area of wind speed and/power forecasting.

In conclusion, however previous reviews have established a base to understand various wind forecasting methods, this paper is an extension of that work and provides a comprehensive, quantitative as well as a prospective evaluation. For improving the wind speed and power prediction, this paper helps to identify the gaps in literature and is providing useful insights. It covers methodologies for improvements, discusses theoretical concerns, points out real-world applications while strengthening the present knowledge. It is providing the researchers, business professionals, and all other stakeholders with a solid foundation for the purpose of enhancing the wind energy forecasting tools.

AUTHORSHIP CONTRIBUTIONS

Authors equally contributed to this work.

DATA AVAILABILITY STATEMENT

The authors confirm that the data that supports the findings of this study are available within the article. Raw data that support the finding of this study are available from the corresponding author, upon reasonable request.

CONFLICT OF INTEREST

The author declared no potential conflicts of interest with respect to the research, authorship, and/or publication of this article.

ETHICS

There are no ethical issues with the publication of this manuscript.

STATEMENT ON THE USE OF ARTIFICIAL INTELLIGENCE

Artificial intelligence was not used in the preparation of the article.

REFERENCES

[1] Dhiman HS, Deb D, Foley AM. Bilateral Gaussian wake model formulation for wind farms: A forecasting-based approach. Renew Sustain Energy Rev 2020;127:109873. [CrossRef]

[2] Dhiman HS, Deb D, Guerrero JM. Hybrid machine intelligent SVR variants for wind forecasting and ramp events. Renew Sustain Energy Rev 2019;108:369–379. [CrossRef]

[3] Dhiman HS, Deb D, Foley AM. Lidar assisted wake redirection in wind farms: A data-driven approach. Renew Energy 2020;152:484–493. [CrossRef]

[4] Wu YK, Hong JS. A literature review of wind forecasting technology in the world. In: IEEE Lausanne PowerTech Conference; 2007. p.504–509. [CrossRef]

[5] Wang X, Guo P, Huang X. A review of wind power forecasting models. Energy Procedia 2011;12:770–778. [CrossRef]

[6] Kumar J, Charles R, Kumar DV, Majid MA. Wind energy programme in India. Energy Environ 2019;30:1135–1189. [CrossRef]

[7] Okumus O, Dinler A. Current status of wind energy forecasting and a hybrid method for hourly predictions. Energy Convers Manag 2016;123:362–371. [CrossRef]

[8] Ying C, Yunu D, Jie D, Zhibao C, Rongfu S, Hai Z. A statistical approach of wind power forecasting for grid scale. AASRI Proced 2012;2:121–126. [CrossRef]

[9] Chang WY. A literature review of wind forecasting methods. J Power Energy Eng 2014;2:161–168. [CrossRef]

[10] Milborrow D. Forecasting for scheduled delivery wind power. Wind Power Mon 2003.

[11] Lange M, Focken U. New developments in wind energy forecasting. In: Proc IEEE Power Energy Soc Gen Meet; 2008. p. 1–8. [CrossRef]

[12] Soman SS, Zareipour H, Malik O, Mandal P. A review of wind power and wind speed forecasting methods with different time horizons. In: IEEE Power Energy Soc Gen Meet; 2010. [CrossRef]

[13] Landberg L. A mathematical look at a physical power prediction model. Wind Energy 1998;1:23–28. [CrossRef]

[14] Kariniotakis G, Pinson P, Siebert N, Giebel G, Barthelmie R. The state of the art in short-term prediction of wind power from an offshore perspective. In: SeaTech Week–Ocean Energy Conference; 2004.

[15] Foley AM, Leahy PG, McKeogh EJ. Wind power forecasting and prediction methods. In: Int Conf Environ Electr Eng (EEEIC); 2010. p. 61–64. [CrossRef]
[16] Yahyai A, Sultan Y, Charabi Y, Badi AA, Gastli A. Nested ensemble NWP approach for wind energy assessment. Renew Energy 2012;37:150–160. [CrossRef]
[17] Lima JM, Guetter AK, Freitas SR, Panetta J, Mattos JGZ. A meteorological–statistic model for short-term wind power forecasting. J Control Autom Electr Syst 2017;28:679–691. [CrossRef]
[18] Saini S, Ahuja M. A research on wind power forecasting techniques. Int J Recent Technol Eng 2019;8:578–580.
[19] Liu C, Zhang X, Mei S, Zhen Z, Jia M, Li Z, et al. Numerical weather prediction enhanced wind power forecasting: Rank ensemble and probabilistic fluctuation awareness. Appl Energy 2022;313:118769. [CrossRef]
[20] Zhao X, Wang S, Li T. Review of evaluation criteria and main methods of wind power forecasting. Energy Procedia 2011;12:761–769. [CrossRef]
[21] Valdivia-Bautista SM, Domínguez-Navarro JA, Pérez-Cisneros M, Vega-Gómez CJ, Castillo-Téllez B. Artificial intelligence in wind speed forecasting: A review. Energies 2023;16. [CrossRef]
[22] Shawon SMRH, Saaklayen MA, Liang X. Wind speed forecasting by conventional statistical methods and machine learning techniques. In: IEEE Electr Power Energy Conf; 2021. p.304–309. [CrossRef]
[23] Erdem E, Shi J. ARMA-based approaches for forecasting the tuple of wind speed and direction. Appl Energy 2011; 88:1405–1414. [CrossRef]
[24] Aggarwal SK, Gupta M. Wind power forecasting: A review of statistical models. Int J Energy Sci 2013; 3:1–10.
[25] Wang JQZ, Zhang X. Wind power forecasting based on time series ARMA model. IOP Conf Ser Earth Environ Sci 2018;199. [CrossRef]
[26] Ling-ling L, Li JH, He PJ, Wang CS. The use of wavelet theory and ARMA model in wind speed prediction. In: Int Conf Electr Power Equip Switching Technol; 2011. p.395–398. [CrossRef]
[27] Miranda MS, Dunn RW. One-hour-ahead wind speed prediction using a Bayesian methodology. In: IEEE Power Eng Soc Gen Meet; 2006. p. 1–6. [CrossRef]
[28] Le Goff Latimier R, Le Bouedec E, Monbet V, Monbet Markov V. Switching autoregressive modeling of wind power forecast errors. 2020; p.189. [CrossRef]
[29] Song Z, Jiang Y, Zhang Z. Short-term wind speed forecasting with Markov-switching model. Appl Energy 2014;130:103–112. [CrossRef]
[30] Torres JL, García A, de Blas M, de Francisco A. Forecast of hourly average wind speed with ARMA models in Navarre (Spain). Sol Energy 2005;79:65–77. [CrossRef]
[31] Milligan M. IEA task 25: Design and operation of power systems with large amounts of wind power. IEA Rep 2003.
[32] Palomares-Salas JC, de La Rosa JJG, Ramiro JG, Melgar J, Agüera A, Moreno A. Comparison of models for wind speed forecasting. 2009.
[33] Tyass A, Bellat A, Raihani A, Mansouri K, Khalili T. Wind speed prediction based on seasonal ARIMA model. E3S Web Conf 2022. [CrossRef]
[34] Palomino K, Reyes F, Núñez J, Valencia G, Acosta RH. Wind speed prediction based on univariate ARIMA and OLS on the Colombian Caribbean coast. J Eng Sci Technol Rev 2020;13:200–205. [CrossRef]
[35] Das J, Banerjee R. Estimation of long-range correlations and FARIMA modeling of wind speed in Maharashtra. In: IEEE PES Asia-Pacific Power Energy Eng Conf; 2017. p.1–6. [CrossRef]
[36] Kavasseri RG, Seetharaman K. Day-ahead wind speed forecasting using f-ARIMA models. Renew Energy 2009;34:1388–1393. [CrossRef]
[37] Narayana M, Putrus G, Jovanovic M, Leung PS. Predictive control of wind turbines by considering wind speed forecasting techniques. In: Int Univ Power Eng Conf; 2009. p.1–4.
[38] Firat U, Engin SN, Murat S, Ertuzun AB. Wind speed forecasting based on second order blind identification and autoregressive model. In: Int Conf Mach Learn Appl; 2010. p.686–691. [CrossRef]
[39] Duran MJ, Cros D, Riquelme J. Short-term wind power forecast based on ARX models. J Energy Eng 2007;133:172–180. [CrossRef]
[40] Li M, Yang M, Yu Y, Lee WJ. A wind speed correction method based on modified hidden Markov model for enhancing wind power forecast. IEEE Trans Ind Appl 2022;58:656–666. [CrossRef]
[41] Wang Z, Wang W, Liu C, Wang B. Forecasted scenarios of regional wind farms based on regular vine copulas. J Mod Power Syst Clean Energy 2022;8:77–85. [CrossRef]
[42] Mararakanye N, Dalton A, Bekker B. Incorporating spatial and temporal correlations to improve aggregation of decentralized day-ahead wind power forecasts. IEEE Access 2022;10:116182–116195. [CrossRef]
[43] Yu Y, Han X, Yang M, Yang J. Probabilistic prediction of regional wind power based on spatiotemporal quantile regression. IEEE Trans Ind Appl 2020;56:6117–6127. [CrossRef]
[44] Dong Y, Ma S, Zhang H, Yang G. Wind power prediction based on multi-class autoregressive moving average model with logistic function. J Mod Power Syst Clean Energy 2022;10:1184–1193. [CrossRef]
[45] Sun W, Liu M. Wind speed forecasting using FEEMD echo state networks with RELM in Hebei, China. Energy Convers Manag 2016;114:197–208. [CrossRef]

[46] Babu CN, Reddy BE. A moving-average filter based hybrid ARIMA–ANN model for forecasting time series data. Appl Soft Comput 2014;23:27–38. [CrossRef]
[47] Bhaskar K, Singh SN. AWNN-assisted wind power forecasting using feed-forward neural network. IEEE Trans Sustain Energy 2012;3:306–315. [CrossRef]
[48] Demolli H, Sakir AS, Ecemis A, Gokcek M. Wind power forecasting based on daily wind speed data using machine learning algorithms. Energy Convers Manag 2019;198:111823. [CrossRef]
[49] Cicek ZIE, Ozturk ZK. Short-term traffic flow forecasting using artificial neural networks. Sigma J Eng Nat Sci 2018;9:405–414.
[50] Kose B, Duz M, Guneser MT, Recebli Z. Estimating wind energy potential with predicting Burr LSM parameters: A different approach. Sigma J Eng Nat Sci 2018;36:389–404.
[51] Qasem M, Filik UB. Solar radiation forecasting by using deep neural networks in Eskisehir. Sigma J Eng Nat Sci 2021;39:159–169. [CrossRef]
[52] Samuel GS, Salimath GF, Porselvi T, Karthikeyan V. Improved prediction of wind speed using machine learning. J Phys Conf Ser 2021;1964:1–5. [CrossRef]
[53] Kumar SP. Improved prediction of wind speed using machine learning. EAI Endorsed Trans Energy Web 2019;6:1–7. [CrossRef]
[54] Tao D, Hong FX. Wind speed prediction model based on radial basis functional neural network. Adv Mater Res 2012;383:5656–5662. [CrossRef]
[55] Zhang Y, Guifang P, Bing C, Han J, Zhao Y, Zhang C. Short-term wind speed prediction model based on GA-ANN improved by VMD. Renew Energy 2020;156:1373–1388. [CrossRef]
[56] Engelbrecht AP. Computational intelligence. England: Wiley; 2007. [CrossRef]
[57] Ibrahim M, Alsheikh A, Al-Hindawi Q, Al-Dahidi S, Elmoaqet H. Short-time wind speed forecast using artificial learning-based algorithms. Comput Intell Neurosci 2020;2020:1–15. [CrossRef]
[58] Chang WY. Short-term wind power forecasting using the enhanced particle swarm optimization-based hybrid method. Energies 2013;6:4879–4896. [CrossRef]
[59] Jyothi MN, Rao PVR. Very-short-term wind power forecasting through adaptive wavelet neural network. In: Proc Biennial Int Conf Power Energy Syst (PESTSE); 2016. p.1–6. [CrossRef]
[60] Xu L, Mao J. Short-term wind power forecasting based on Elman neural network with particle swarm optimization. In: Chinese Control Decis Conf; 2016. p.2678–2681. [CrossRef]
[61] Catalão JPS, Pousinho HMI, Mendes VMF. An artificial neural network approach for short-term wind power forecasting in Portugal. In: Int Conf Intell Syst Appl Power Syst; 2009. p.1–5. [CrossRef]
[62] Mabel MC, Fernandez E. Analysis of wind power generation and prediction using ANN: A case study. Renew Energy 2008;33:986–992. [CrossRef]
[63] Singh S, Bhatti TS, Kothari DP. Wind power estimation using artificial neural network. J Energy Eng 2007;133:46–52. [CrossRef]
[64] Pliego AM, Márquez FPG, Pinar Perez JM, Ruiz-Hernández D. A survey of artificial neural networks in wind energy systems. Appl Energy 2022;228:1822–1836. [CrossRef]
[65] Sharma R, Singh D. A review of wind power and wind speed forecasting. J Eng Res Appl 2018;8:1–9.
[66] Sideratos G, Hatziargyriou ND. Probabilistic wind power forecasting using radial basis function neural networks. IEEE Trans Power Syst 2012;27:1788–1796. [CrossRef]
[67] Ramadevi B, Bingi K. Chaotic time series forecasting approaches using machine learning techniques: A review. Symmetry (Basel) 2022;14:955. [CrossRef]
[68] Zhou Y, Sun Y, Wang S, Mahfoud RJ, Alhelou HH, et al. Performance improvement of very short-term prediction intervals for regional wind power based on composite conditional nonlinear quantile regression. J Mod Power Syst Clean Energy 2022;10:60–70. [CrossRef]
[69] Lee J, Wang W, Harrou F, Sun Y. Wind power prediction using ensemble learning-based models. IEEE Access 2020;8:61517–61527. [CrossRef]
[70] Tu CS, Hong CM, Huang HS, Chen CH. Short-term wind power prediction based on data regression and enhanced support vector machine. Energies 2020;13:6319. [CrossRef]
[71] Tan L, Han J, Zhang H. Ultra-short-term wind power prediction by salp swarm algorithm-based optimizing extreme learning machine. IEEE Access 2020;8:44470–44484. [CrossRef]
[72] Huang Y, Liu GP, Hu WS. Priori-guided and data-driven hybrid model for wind power forecasting. ISA Trans 2023;134:380–395. [CrossRef]
[73] Wang YL, Yang P, Zhao SY, Chevallier JL, Xiao QT. A hybrid intelligent framework for forecasting short-term hourly wind speed based on machine learning. Expert Syst Appl 2022;213:119223. [CrossRef]
[74] Pombo DV, Rincón MJ, Bacher P, Bindner HW, Spataru SV, Sørensen PE. Assessing stacked physics-informed machine learning models for co-located wind–solar power forecasting. Sustain Energy Grids Netw 2023;32:100943. [CrossRef]
[75] Moayyed H, Moradzadeh A, Mohammadi-Ivatloo B, Aguiar AP, Ghorbani R. A cyber-secure generalized supermodel for wind power forecasting based on deep federated learning and image processing. Energy Convers Manag 2022;267:115852. [CrossRef]
[76] Liu L, Wang JJ, Li PP, Wei L. An online transfer learning model for wind turbine power prediction based on spatial feature construction and system-wide update. Appl Energy 2023;340:121049. [CrossRef]

[77] Nascimento EGS, Melo TA, Moreira DM. A transformer-based deep neural network with wavelet transform for forecasting wind speed and wind energy. Energy 2023;278:127678. [CrossRef]
[78] Sobolewski RA, Tchakorom M, Couturier R. Gradient boosting-based approach for short- and medium-term wind turbine output power prediction. Renew Energy 2023;203:142–160. [CrossRef]
[79] Yu L, Meng G, Pau G, Wu Y, Tang Y. Research on hierarchical control strategy of ESS in distribution based on GA-SVR wind power forecasting. Energies 2023;16:2079. [CrossRef]
[80] Wang X, Li J, Shao L, Liu H, Ren L, Zhu L. Short-term wind power prediction by an extreme learning machine based on an improved hunter–prey optimization algorithm. Sustainability 2023;15:991. [CrossRef]
[81] Lin Z, Liu X, Collu M. Wind power prediction based on high-frequency SCADA data along with isolation forest and deep learning neural networks. Int J Electr Power Energy Syst 2020;118. [CrossRef]
[82] Ahuja M, Saini S. Recurrent neural network for chaotic wind speed time series prediction. In: IEEE India Int Conf Power Electron (IICPE); 2023. p.1–6. [CrossRef]
[83] Wang J, Li Z. Wind speed interval prediction based on multidimensional time series of convolutional neural networks. Eng Appl Artif Intell 2023;121:105987. [CrossRef]
[84] Mert İ. Agnostic deep neural network approach to the estimation of hydrogen production for solar-powered systems. Int J Hydrogen Energy 2021;46:6272–6285. [CrossRef]
[85] Hu T, Wu W, Guo Q, Sun H, Shi L, Shen X. Very short-term spatial and temporal wind power forecasting: A deep learning approach. CSEE J Power Energy Syst 2020;6:434–443.
[86] Dong X, Sun Y, Li Y, Wang X, Pu T. Spatio-temporal convolutional network-based power forecasting of multiple wind farms. J Mod Power Syst Clean Energy 2022;10:388–398. [CrossRef]
[87] Jalali SMJ, Osorio GJ, Ahmadian S, Lotfi M, Campos VMA, et al. New hybrid deep neural architectural search-based ensemble reinforcement learning strategy for wind power forecasting. IEEE Trans Ind Appl 2022;58:15–27. [CrossRef]
[88] Sun Z, Zhao M. Short-term wind power forecasting based on VMD decomposition, ConvLSTM networks and error analysis. IEEE Access 2020;8:134422–134434. [CrossRef]
[89] Miao C, Li H, Wang X, Li H. Ultra-short-term prediction of wind power based on sample similarity analysis. IEEE Access 2021;9:72730–72742. [CrossRef]
[90] Liao W, Yang Z, Chen X, Li Y. Wind GMMN: Scenario forecasting for wind power using generative moment matching networks. IEEE Trans Artif Intell 2022;3:843–850. [CrossRef]
[91] Huang X, Jiang A. Wind power generation forecast based on multi-step informer network. Energies 2022;15:6642. [CrossRef]
[92] Wu X, Jiang S, Lai CS, Zhao Z, Lai LL. Short-term wind power prediction based on data decomposition and combined deep neural network. Energies 2022;15:6734. [CrossRef]
[93] Yu G, Liu C, Tang B, Chen R, Lu L, et al. Short-term wind power prediction for regional wind farms based on spatial–temporal characteristic distribution. Renew Energy 2022;199:599–612. [CrossRef]
[94] Liu X, Zhang L, Wang J, Zhou Y, Gan W. A unified multi-step wind speed forecasting framework based on numerical weather prediction grids and wind farm monitoring data. Renew Energy 2023;211:948–963. [CrossRef]
[95] Hossain MA, Chakrabortty RK, Elsawah SD, Ryan MJ. Very short-term forecasting of wind power generation using hybrid deep learning model. J Clean Prod 2021;296:126564. [CrossRef]
[96] Garg S, Krishnamurthi R. A CNN encoder–decoder LSTM model for sustainable wind power predictive analytics. Sustain Comput Inform Syst 2023;38:100869. [CrossRef]
[97] Zhang J, Liu D, Li Z, Han X, Liu H, Dong C, et al. Power prediction of a wind farm cluster based on spatiotemporal correlations. Appl Energy 2021;302:117568. [CrossRef]
[98] Zhang Y, Li Y, Zhang G. Short-term wind power forecasting approach based on Seq2Seq model using NWP data. Energy 2020;213:118371. [CrossRef]
[99] Liao WL, Bak-Jensen B, Pillai JR, Yang Z, Liu K. Short-term power prediction for renewable energy using hybrid graph convolutional network and long short-term memory approach. Electr Power Syst Res 2022;211:108614. [CrossRef]
[100] Tian CN, Niu T, Wei W. Developing a wind power forecasting system based on deep learning with attention mechanism. Energy 2022;257:124750. [CrossRef]
[101] Yildiz C, Acikgoz H, Korkmaz D, Budak U. An improved residual-based convolutional neural network for very short-term wind power forecasting. Energy Convers Manag 2021;228:113731. [CrossRef]
[102] Liu Z, Li X, Zhao H. Short-term wind power forecasting based on feature analysis and error correction. Energies 2023;16:4249. [CrossRef]
[103] Wang Q, Wang Y, Zhang K, Liu Y, Qiang W, Wen QH. Artificial intelligent power forecasting for wind farm based on multi-source data fusion. Processes 2023;11:1429. [CrossRef]
[104] Xiao Z, Tang F, Wang M. Wind power short-term forecasting method based on LSTM and multiple error correction. Sustainability 2023;15:3798. [CrossRef]
[105] Jung J, Broadwater RP. Current status and future advances for wind speed and power forecasting. Renew Sustain Energy Rev 2014;31:762–777. [CrossRef]

[106] Huang NE, Wu Z. Ensemble empirical mode decomposition: A noise-assisted data analysis method. 2008.
[107] Phan QT, Phan QD, Wu YK. A hybrid wind power forecasting model with XGBoost and data preprocessing considering different NWPs. Appl Sci 2021;11:1–19. [CrossRef]
[108] Cadenas E, Rivera W. Wind speed forecasting in three different regions of Mexico using a hybrid ARIMA–ANN model. Renew Energy 2010;35:2732–2738. [CrossRef]
[109] Pousinho HMI, Mendes VMF, Catalão JPS. A hybrid PSO–ANFIS approach for short-term wind power prediction in Portugal. Energy Convers Manag 2011;52:397–402. [CrossRef]
[110] Adedeji PA, Akinlabi S, Madushele N, Olatunji OO. Wind turbine power output very short-term forecast: A comparative study of data clustering techniques in a PSO–ANFIS model. J Clean Prod 2020;254:120135. [CrossRef]
[111] Ye H, Yang B, Han Y, Li Q, Deng J, Tian S. Wind speed and power prediction approaches: Classifications, methodologies, and comments. Front Energy Res 2022;10:1–5. [CrossRef]
[112] Shukur OB, Lee MH. Daily wind speed forecasting through hybrid KF–ANN model based on ARIMA. Renew Energy 2015;76:637–647. [CrossRef]
[113] Liu D, Niu D, Wang H, Fan L. Short-term wind speed forecasting using wavelet transform and support vector machines optimized by genetic algorithm. Renew Energy 2014;62:592–597. [CrossRef]
[114] Zhang C, Wei H, Zhao J, Liu T, Zhu T, Zhang K. Short-term wind speed forecasting using empirical mode decomposition and feature selection. Renew Energy 2016;96:727–737. [CrossRef]
[115] Mi XW, Liu H, Li YF. Wind speed forecasting method using wavelet, extreme learning machine and outlier correction algorithm. Energy Convers Manag 2017;151:709–722. [CrossRef]
[116] Li H, Wang J, Lu H, Guo Z. Research and application of a combined model based on variable weight for short-term wind speed forecasting. Renew Energy 2018;116:669–684. [CrossRef]
[117] Jiang P, Wang Y, Wang J. Short-term wind speed forecasting using a hybrid model. Energy 2017;119:561–577. [CrossRef]
[118] Azimi R, Ghofrani M, Ghayekhloo M. A hybrid wind power forecasting model based on data mining and wavelets analysis. Energy Convers Manag 2016;127:208–225. [CrossRef]
[119] Jiang Y, Huang G, Peng X, Li Y, Yang Q. A novel wind speed prediction method: Hybrid of correlation-aided DWT, LSSVM and GARCH. J Wind Eng Ind Aerodyn 2018;174:28–38. [CrossRef]
[120] Liu H, Duan Z, Han FZ, Li YF. Big multi-step wind speed forecasting model based on secondary decomposition, ensemble method and error correction algorithm. Energy Convers Manag 2018;156:525–541. [CrossRef]
[121] Hong YY, Rioflorido CPP. A hybrid deep learning-based neural network for 24-h ahead wind power forecasting. Appl Energy 2019;250:530–539. [CrossRef]
[122] Foley M, Leahy PG, Marvuglia A, McKeogh EJ. Current methods and advances in forecasting of wind power generation. Renew Energy 2012;37:1–8. [CrossRef]
[123] Shetty RP, Sathyabhama APSP, Rai AA. Optimized radial basis function neural network model for wind power prediction. In: Proc Int Conf Cogn Comput Inf Process (CCIP); 2016. p.1–6. [CrossRef]
[124] Peng H, Liu F, Yang X. A hybrid strategy of short-term wind power prediction. Renew Energy 2013;50:590–595. [CrossRef]
[125] Wang J, Yang W, Tong N. A novel hybrid forecasting system of wind speed based on a multi-objective sine cosine algorithm. Energy Convers Manag 2018;163:134–150. [CrossRef]
[126] Saini S, Ahuja M. Wind speed prediction using wavelet transform and artificial neural network. Int J Res Electron Commun Eng 2017;5:161–168.
[127] Saini S, Ahuja M. Wind speed prediction using wavelet transform and GA-trained artificial neural network. J Adv Res Dyn Control Syst 2019:198–204. [CrossRef]
[128] Duan J, Chang M, Chen X, Wang W, Zuo H, Bai Y, et al. A combined short-term wind speed forecasting model based on CNN–RNN and linear regression optimization considering error. Renew Energy 2022;200:788–808. [CrossRef]
[129] Zou Y, Feng W, Zhang J, Li J. Forecasting of short-term load using the MFF-SAM-GCN model. Energies 2022;15:3140. [CrossRef]
[130] Aisyah S, Simaremare AA, Adytia D, Aditya IA, Alamsyah A. Exploratory weather data analysis for electricity load forecasting using SVM and GRNN. Energies 2022;15:3566. [CrossRef]
[131] Zhao Z, Yun S, Jia L, Guo J, Meng Y, He N. Hybrid VMD–CNN–GRU-based model for short-term forecasting of wind power considering spatio-temporal features. Eng Appl Artif Intell 2023;121:105982. [CrossRef]
[132] Che JX, Yuan F, Deng D, Jiang ZY. Ultra-short-term probabilistic wind power forecasting with spatial–temporal multi-scale features and K-FSDW-based weight. Appl Energy 2023;331:120479. [CrossRef]
[133] Hu S, Xiang Y, Zhang HC, Xie SY. Hybrid forecasting method for wind power integrating spatial correlation and corrected numerical weather prediction. Appl Energy 2021;293:116951. [CrossRef]
[134] Wen SK, Li YT, Su Y. A new hybrid model for power forecasting of a wind farm using spatial–temporal correlations. Renew Energy 2022;198:155–168. [CrossRef]

[135] Hu S, Xiang Y, Huo D, Jawad SQ. An improved deep belief network-based hybrid forecasting method for wind power. Energy 2021;224:120185. [CrossRef]
[136] Gu B, Hu H, Zhao J, Zhang HT, Liu X. Short-term wind power forecasting and uncertainty analysis based on FCM–WOA–ELM–GMM. Energy Rep 2023;9:807–819. [CrossRef]
[137] Al-Duais FS, Al-Sharpi RS. A Markov chain Monte Carlo method for forecasting wind power using time series models. Alex Eng J 2023;74:51–63. [CrossRef]
[138] Yan J, Möhrlen CN, Göçmen TF, Kelly M, Wessel A, Giebel G. Uncovering wind power forecasting uncertainty sources and their propagation through the modeling chain. Renew Sustain Energy Rev 2022;165:112519. [CrossRef]
[139] Xiong B, Lou L, Meng XY, Wang X, Ma H, Wang Z. Short-term wind power forecasting based on attention mechanism and deep learning. Electr Power Syst Res 2022;206:107776. [CrossRef]
[140] Zhang J, Zhang R, Zhao Y, Qiu J, Bu S, Zhu Y, et al. Deterministic and probabilistic prediction of wind power based on a hybrid intelligent model. Energies 2023;16:4237. [CrossRef]
[141] Wu B, Yu S, Peng L, Wang L. Interpretable wind speed forecasting with meteorological feature exploration and two-stage decomposition. Energy 2024;294:1–28. [CrossRef]
[142] Zhang Y, Zhao Y, Shen X, Zhang J. A comprehensive wind speed prediction system based on Monte Carlo and artificial intelligence algorithms. Appl Energy 2022;305:117815. [CrossRef]
[143] Du P, Wang J, Yang W, Niu T. Multi-step ahead forecasting in electrical power systems using a hybrid forecasting system. Renew Energy 2018;122:533–550. [CrossRef]
[144] Zhao P, Wang J, Xia J, Dai Y, Sheng Y, Yue J. Performance evaluation and accuracy enhancement of a day-ahead wind power forecasting system in China. Renew Energy 2012;43:234–241. [CrossRef]
[145] Shi J, Guo J, Zheng S. Evaluation of hybrid forecasting approaches for wind speed and power generation time series. Renew Sustain Energy Rev 2012;16:3471–3480. [CrossRef]
[146] Guo ZH, Wu J, Lu HY, Wang JZ. A case study on a hybrid wind speed forecasting method using BP neural network. Knowl Based Syst 2011;24:1048–1056. [CrossRef]
[147] Catalão JPS, Pousinho HMI, Mendes VMF. Short-term wind power forecasting in Portugal by neural networks and wavelet transform. Renew Energy 2011;36:1245–1251. [CrossRef]
[148] Berrezzek F, Khelil K, Bouadjila T. Efficient wind speed forecasting using discrete wavelet transform and artificial neural networks. Rev Intell Artif 2019;33:447–452. [CrossRef]
[149] Negnevitsky M, Johnson PL, Santoso S. Short-term wind power forecasting using hybrid intelligent systems. In: Proc IEEE Power Eng Soc Gen Meet; 2007. p.1–4. [CrossRef]
[150] Liu H, Tian HQ, Chen C, Li YF. A hybrid statistical method to predict wind speed and wind power. Renew Energy 2010;35:1857–1861. [CrossRef]
[151] Kassa Y, Zhang JH, Zheng DH, Wei D. Short-term wind power prediction using ANFIS. In: Proc IEEE Int Conf Power Renew Energy (ICPRE); 2016. p.388–393. [CrossRef]
[152] Pinson P, Kariniotakis GN. Wind power forecasting using fuzzy neural networks enhanced with online prediction risk assessment. In: Proc IEEE Bologna Power Tech; 2003. p. 2. [CrossRef]
[153] Potter CW, Negnevitsky M. Very short-term wind forecasting for Tasmanian power generation. IEEE Trans Power Syst 2006;21:965–972. [CrossRef]
[154] Liu H, Tian HQ, Pan DF, Li YF. Forecasting models for wind speed using wavelet, wavelet packet, time series and artificial neural networks. Appl Energy 2013;107:191–208. [CrossRef]
[155] Moorthy CB, Agrawal A, Deshmukh MK. Artificial intelligence techniques for wind power prediction: A case study. Indian J Sci Technol 2015;8. [CrossRef]
[156] Nie Y, Bo H, Zhang W, Zhang H. Research on hybrid wind speed prediction system based on artificial intelligence and double prediction scheme. Complexity 2020;2020:1–22. [CrossRef]
[157] Ferreira M, Santos A, Lucio P. Short-term forecast of wind speed through mathematical models. Energy Rep 2019;5:1172–1184. [CrossRef]
[158] Ma L, Li B, Yang ZB, Du J, Wang J. A new combination prediction model for short-term wind farm output power based on meteorological data collected by WSN. Int J Control Autom 2014;7:171–180. [CrossRef]
[159] Mao M, Cao Y, Chang L. Improved fast short-term wind power prediction model based on superposition of predicted error. In: Proc IEEE Int Symp Power Electron Distrib Gener Syst (PEDG); 2013. p.1–6. [CrossRef]
[160] Chang WY. Comparison of three short-term wind power forecasting methods. Adv Mater Res 2013;684:671–675. [CrossRef]
[161] Chang WY. An RBF neural network combined with OLS algorithm and genetic algorithm for short-term wind power forecasting. J Appl Math 2013;2013:1–9. [CrossRef]
[162] Sideratos G, Hatziargyriou ND. An advanced statistical method for wind power forecasting. IEEE Trans Power Syst 2007;22:258–265. [CrossRef]

Sigma J Eng Nat Sci, Vol. 44, No. 1, pp. 663–679, February, 2026

Sigma Journal of Engineering and Natural Sciences
Web page info: https://sigma.yildiz.edu.tr
DOI: 10.14744/sigma.2025.00093

Review Article

A review of photovoltaic plants and battery energy storage systems in terms of power systems stability

Bora ÇAVDAR[1,*], Eda KARACA[2,3], Hatice OKUMUŞ[3], Fatih Mehmet NUROĞLU[3]

[1]Department of Energy Systems Engineering, Karadeniz Technical University, Trabzon, 61080, Türkiye
[2]Department of Electrical and Electronics Engineering, Erzincan Binali Yildirim University, Erzincan, 24002, Türkiye
[3]Department of Electrical and Electronics Engineering, Karadeniz Technical University, Trabzon, 61080, Türkiye

ARTICLE INFO

Article history
Received: 06 June 2024
Revised: 09 September 2024
Accepted: 07 December 2024

Keywords:
BESS; Frequency Stability; PV Plants; Rotor Angle Stability; Voltage Stability

ABSTRACT

Nowadays, the rapid increase in PV plants in power systems has reached a point that may negatively impact power system stability. Battery storage systems have also begun to be integrated into power systems to mitigate the negative effects of non-rotating plants such as PV plants. The expected increase in PV penetration levels and BESS size must be analyzed jointly to address stability issues in power systems. It is evident that existing reviews on the hybrid integration of PV and BESS are limited. This paper aims to contribute to future developments by reviewing the most recent status and potential outcomes of studies related to the impact of PV plants and battery storage system (BESS) units on power system stability. The reviewed studies have been classified to provide valuable insights into the impact of PV plants and BESS units on power system stability. Each classification focuses on the studies in terms of the stability analysis type, the PV/BESS unit combination, the analysis method, the structure of the power system, the PV penetration level, the size of the BESS, whether frequency support is provided, and the use of simulation programs. In the classification of stability, frequency stability and rotor angle (for transients) stability are the most discussed topics. In the review for the units, it was found that studies on the stability of PV power plants were frequently addressed. In addition, studies on BESS and PV-BESS configurations have increased over time. Almost all stability studies focus on time-domain analysis. In addition, modal analysis, which is widely used in small-signal stability studies, is the second most frequently used analysis method in studies. In the studies, the effect of a three-phase short circuit fault on the stability of the system is usually analyzed. Apart from this fault, the implementation of a fault in the load is among the popular cases considered. In the power system classification used, either large or small power systems are usually considered. It is rare for an impact to be considered in both a small and a large power system. Different penetration levels and sizes of PV and BESS units, respectively, are usually analyzed separately in terms of stability. The number of papers investigating the effect of both PV and BESS together on the stability of a power system is quite rare. As a result of the classification on frequency support, it is seen that research on frequency support of PV power plants is handled from similar perspectives, although it has gained popularity recently. When the simulation programs used, which represent the last classification group, are examined, it is observed that DigSilent PowerFactory and MATLAB are generally preferred.

Cite this article as: Çavdar B, Karaca E, Okumuş H, Fatih Mehmet NUROĞLU3. A review of photovoltaic plants and battery energy storage systems in terms of power systems stability. Sigma J Eng Nat Sci 2026;44(1):663–679.

***Corresponding author.**
*E-mail address: boracavdar@ktu.edu.tr

This paper was recommended for publication in revised form by Editor-in-Chief Ahmet Selim Dalkilic

Published by Yıldız Technical University Press, İstanbul, Turkey
© Author. This is an open access article under the CC BY-NC license (http://creativecommons.org/licenses/by-nc/4.0/).

INTRODUCTION

With technological developments and increasing carbon emissions, electrical power generation from renewable energy sources has gained considerable importance in recent years. In 2021, more than 306 GW of new renewable energy generation capacity was added to the total grid-installed power worldwide [1]. While photovoltaic (PV) units constitute 57.2% (175 GW) of this installed capacity, wind, hydropower and bio-power plants compose 32.7% (100 GW), 8.8% (27 GW) and 3.3% (10 GW), respectively [1]. PV units have been the most frequent renewable energy source in power systems since 2016 [1]. In 2018 and beyond, PV units have been incorporated into the grid at nearly twice the rate of any other renewable energy source [1].

The western parts of the Americas, the entire African continent, the Arabian Peninsula, Australia, and portions of Asia all demonstrate considerable solar energy capacity [2]. Table 1 lists the countries that show a high solar energy potential.

Considering Table 1, the gross domestic product (GDP) values of most countries with high solar energy potential are much lower than those of developed countries [2,3]. Therefore, it is safe to state that the economic development in these countries has also influenced the generation capacity of photovoltaic energy. In this regard, the data provided in Tables 2 and 3 point to the fact that the most developed countries possess the greatest installed capacity. Besides, Table 2 provides the total active power of all PV units installed up to the year 2021 [2,4].

Table 2 shows that nations with high GDPs are investing in solar systems, despite the lack of potential in many of them. It can be stated from the table that, although India and Brazil have lower GDPs, they have made more investments in solar energy compared to countries with higher GDPs.

Even in places with comparatively lower solar energy potential, there is a significant amount of PV installed capacity. This suggests that countries with greater solar energy potential, such as those listed in Table 1, will be able to add more solar energy to their grids. Furthermore, the positioning of PV power plants is paramount to achieving installed capacity goals in countries such as South Korea, Germany, China, Turkey, and Spain [1].

It is evident that the penetration levels of PV units are on the rise; however, this does come with some undesirable outcomes. A downside of PV units, as a renewable energy source with no rotating structure, is the reduction of the total moment of inertia within the power system [1, 5]. In addition, the sporadic generation due to the nature of renewable energy sources has another effect [5, 6]. This intermittent generation causes fluctuations in the electricity

Table 1. The highest practical potential for countries

Country	Average (kWh/kWp)	GDP-2023 (USD)
Namibia	5.38	4742.8
Chile	5.36	17093.2
Jordan	5.32	4482.1
Arab Republic of Egypt	5.25	3512.6
Republic of Yemen	5.21	-
Oman	5.17	23295.3
Saudi Arabia	5.16	28895.0
Lesotho	5.13	878.0
Libya	5.12	7330.0
Botswana	5.11	7249.8

Table 2. Countries with the highest total ınstalled capacity of PV units in 2021

Country	GW	%	Average (kWh/kWp)	GDP-2021 (USD)
China	308,5	32,75	3.88	12,556
USA	123	13,06	4.36	70,249
Japan	78,2	8,30	3.45	39,313
India	60,4	6,41	4.32	2,257
Germany	59,2	6,28	2.96	51,204
Australia	25,4	2,70	4.71	60,443
İtaly	22,6	2,40	3.99	35,657
Republic of Korea	21,5	2,28	3.82	34,998
Spain	18,5	1,96	4.41	30,103
Vietnam	17,4	1,85	3.55	3,756
Rest of the World	207,3	22,01	-	-
Sum of Top 10	734,7	77,99	-	-
Sum of The World	942	100,00	-	-

Table 3. The ınstalled capacity of PV units in 2021

Country	GW	%	Average (kWh/kWp)	GDP-2021 (USD)
China	54,9	31,37	3.88	12,556
USA	26,9	15,37	4.36	70,249
India	13	7,43	4.32	2,257
Japan	6,5	3,71	3.45	39,313
Brazil	5,5	3,14	4.40	7,507
Germany	5,3	3,03	2.96	51,204
Spain	4,9	2,80	4.41	30,103
Australia	4,6	2,63	4.71	60,443
Republic of Korea	4,2	2,40	3.82	34,998
France	3,3	1,89	3.39	43,659
Rest of the World	45,9	26,23	-	-
Sum of Top 10	129,1	73,77	-	-
Sum of The World	175	100,00	-	-

generation of PV power plants, either instantly or for a prolonged period on a cloudy day.

There has been an increase in the use of storage units to eliminate the negative effects of renewable energy sources. Energy Storage Systems (ESS) offer numerous advantages such as balancing energy supply, high efficiency, reducing energy costs, and reducing carbon emissions. Additionally, by providing services like frequency and voltage regulation, they greatly contribute to grid stability. The installed capacity of energy storage worldwide had reached 209.4 GW by the end of 2021 [7]. Most of these energy storage units are in the form of pumped hydropower. This form of storage accounts for the majority of energy storage systems worldwide, at 86.2% (180.5 GW), while new energy storage systems account for nearly 25.4 GW, of which Battery Energy Storage Systems (BESS) make up a substantial portion, approximately 95.7% (24.31 GW) [7].

Motivation and Contributions

The shift towards renewable energy sources continues to increase globally due to various factors such as the depletion of fossil fuels, population growth, and the Net Zero Scenario. With increasing renewable energy generation, an increase in PV penetration levels and BESS sizes in power systems is expected, as shown in Figure 1 [8,9].

The expected increase in PV penetration levels and BESS sizes must be analyzed together to address stability issues in power systems. In the literature, there are review studies related to the integration of PV and BESS systems into the grid. Some of these are shown in Table 4. In [5], studies on technical solutions such as frequency regulation,

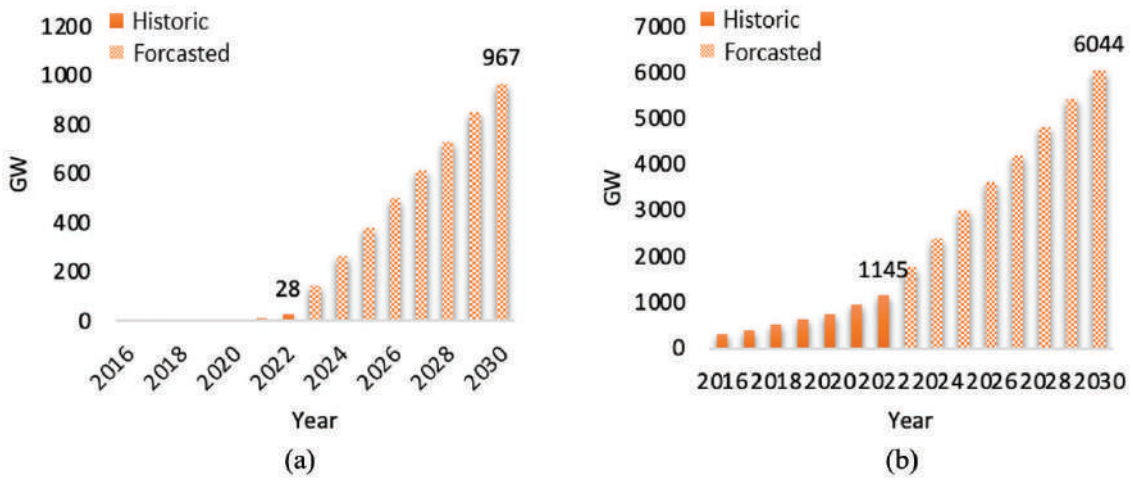


Figure 1. PV and BESS expectations fort he future.

low-frequency oscillation damping, voltage regulation, and fault-ride through for potential voltage, rotor angle, and frequency stability issues arising from the integration of large-scale PVs into the power system are discussed. The technical challenges of integrating PV systems into the grid in terms of voltage, frequency, protection, harmonics, rotor angle stability, and flexibility requirements are once again examined in [10,11] conducts a review on the integration of PV systems at high penetration levels into the grid, with a particular focus on regulatory considerations and stability issues. [12] comprehensively examines the problems encountered in the integration of PV systems into the grid and the proposed solutions. The study, which examines the problems in detail from technical, environmental, and socio-economic perspectives, also provides a detailed analysis of solutions in terms of grid codes, advanced control strategies, energy storage systems, and renewable energy policies. [13] includes a comprehensive review of applications on BESS sizing using different criteria and methods in renewable energy systems. In the study, sizing criteria are examined by categorizing them as financial indicators, technical indicators, and hybrid indicators. Similarly, the techniques used for sizing are examined under four distinct methods: probabilistic methods, analytical methods, directed search-based methods, and hybrid methods. [14] provides a comprehensive review of the current most suitable BESS sizing algorithms within the framework of optimization objectives and optimization constraints. [15] has helped to develop existing strategies by examining hybrid PV-BESS systems in six different areas: lifetime improvement, cost reduction analysis, optimal sizing, mitigation of power quality issues, optimal control of the power system, and peak load shifting and minimizing.

It is evident that existing reviews on the hybrid integration of PV and BESS are limited. This paper aims to contribute to future developments by reviewing the status and potential outcomes of studies related to the integration of PV and BESS within the framework of power system stability. In line with this purpose, the study's contribution to literature and the aspects that differentiate it from existing literature are outlined below.

- Studies in literature generally include different topics (economic, social, power system stability, device lifetime, grid codes, etc.) for PV or BESS. This prevents these studies from conducting a detailed analysis in terms of power system stability. In this study, both PV and BESS studies are analyzed in detail and from many aspects in terms of power system stability.
- This study provides the literature with an analysis of the effect of PV and BESS on stability separately, as well as

Table 4. Some of the review studies related to the ıntegration of PV and BESS

References-Year	Topic	Classification
[5]-2015	PV	-Impact on power system stability -Technical solutions
[13]-2018	BESS	-BESS sizing criteria -BESS sizing techniques
[11]-2019	PV	-Technical Challenges of Integrating High Penetration Levels of Small-Scale PV Systems into the Grid -Technical Challenges of Integrating Large-Scale PV Systems into the Grid
[10]-2020	PV	-Impacts of PV integration into power system -Limits of PV penetration -Modelling for grid stability & reliability assessment with PV
[12]-2022	PV	-PV systems grid integratıon challenges -Solutions for grid integratıon problems
[14]-2022	BESS	-Optimization objectives in BESS -Constraints on BESS optimization
[15]-2022	PV+BESS	-Lifetime improvement -Cost reduction analysis -Optimal sizing -Mitigation of power quality issues -Optimal control of power system -Peak load shifting and minimizing
This paper	PV+BESS	-Power system stability -Units -Analysis methods -Power system structure -Penetration level/size -Frequency support -Simulation programs

in studies where they are used together. It also shows that the studies on this subject are quite limited.

- This paper discusses the impact of the selected power system on stability analysis through studies in literature. In this respect, it provides a perspective for literature in the analysis of stability studies.
- This study presents a classification of the programs used for power system stability in literature. In addition, this classification result is compared with transmission and distribution operators.
- For each classification, studies with different features are discussed and compared in detail. The researchers' results are discussed comparatively, and a summary of the results obtained under the same classification heading is presented to the literature.
- The classification method in this study reveals which topics researchers in the literature focus on and which areas are less explored. In this respect, the study serves as a guide for researchers in the field by highlighting the missing points that can be researched in the literature.
- This study is a review of the most recent studies on PV and BESS in literature. As such, it provides an updated analysis of PV and BESS studies compared with previous reviews.

Power System Stability Analysis for PV Power Plant and BESS

Three distinct categories of power system stability can be examined: rotor angle stability, frequency stability, and voltage stability [16]. Separate divisions can also be made for stability, considering the duration and magnitude of the disturbance. Various factors are evaluated when examining these divisions. Figure 2 shows the classifications for power system stability.

The definitions for the power system stability classes shown in Figure 2 are given below [16].

- Rotor angle stability refers to the ability of interconnected synchronous machines in power systems to maintain synchronization. The stability of this synchronization depends on each machine's ability to maintain a balance between electromagnetic and mechanical torque. Rotor angle stability can be divided into two subgroups. Minor disturbances are considered in the first type of stability, which is small-signal stability. The second type, transient stability, deals with major disturbances.
- Frequency stability refers to a system's ability to maintain its frequency following a disturbance in the power network. This relies on the equilibrium between generation and consumption.
- Voltage stability refers to the ability to keep the voltage of all buses constant within prescribed upper and lower limits when a disturbance occurs in the power system.

Researchers have primarily focused on the control options, locations, and penetration levels/sizes of PV plants and BESS units. Various power system models are also investigated in these studies. The classification of these studies is depicted in Figure 3 and further explained in the following sections.

Units

The literature shows more PV plant grid integration studies than BESS units. Very few studies consider PV plants and BESS units simultaneously in grid integration. With the increasing integration of renewable energy sources into the grid, studies on the effects of BESS units in the grid are increasing. In this way, the number of studies

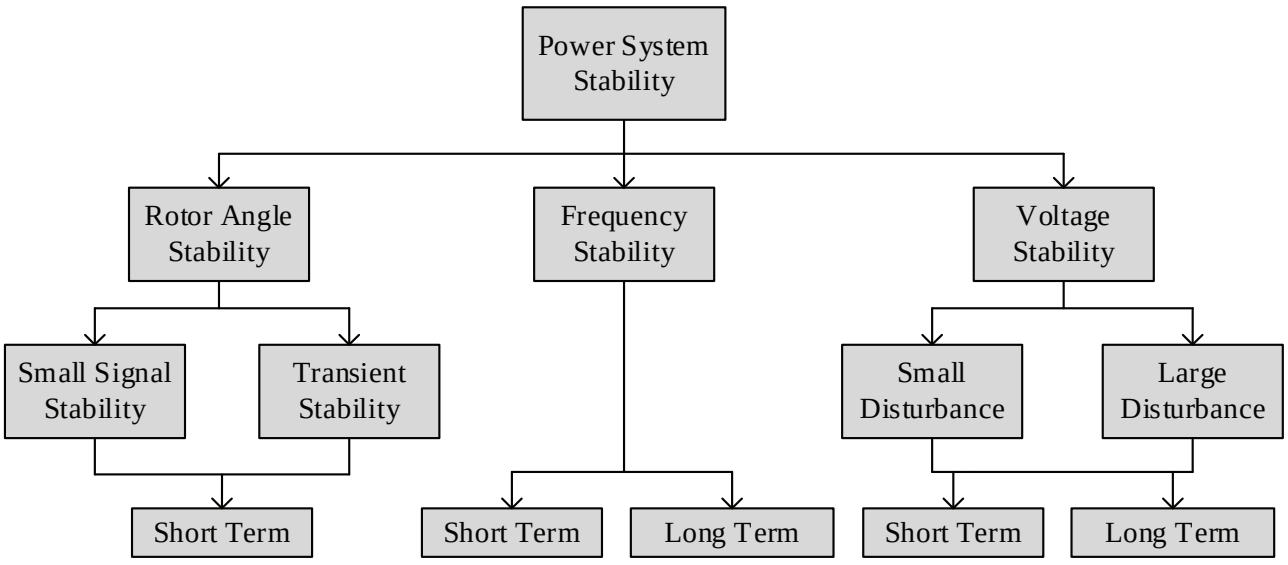


Figure 2. Classification of power system stability.

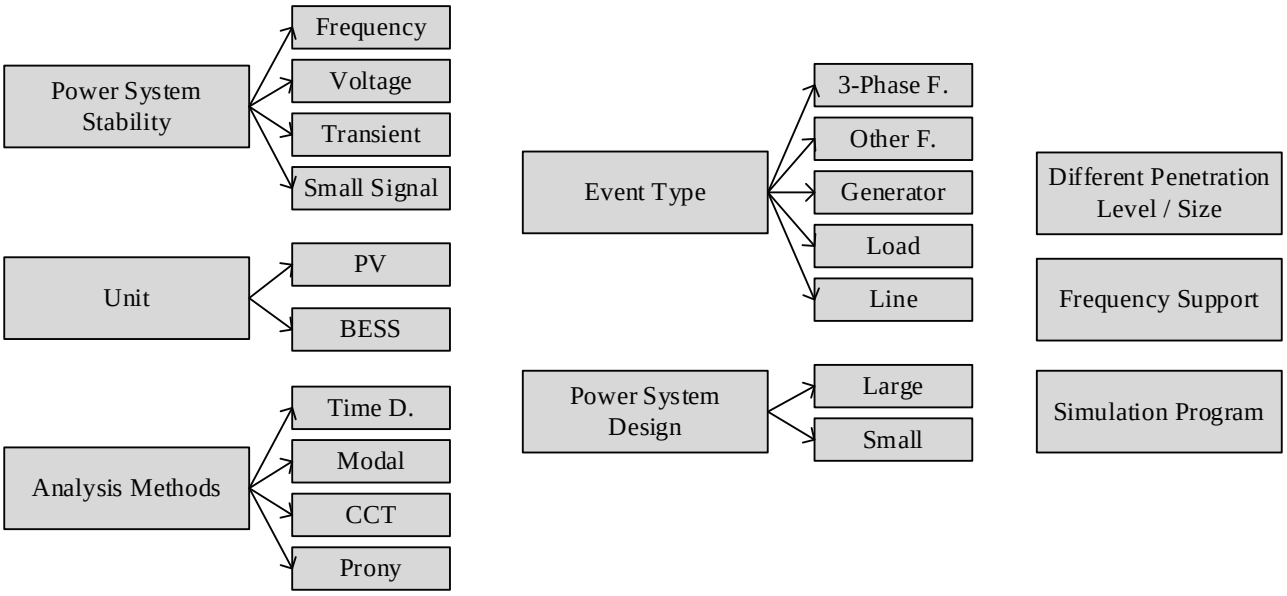


Figure 3. Classification of power system stability studies in the literature.

in which PV plants and BESS units are considered together will gradually increase.

While investigating the dynamic effects of PV plants on the grid, studies focus on low voltage ride through (LVRT), dynamic voltage support (DVS), and ramp rate. In [17], the researchers show that the use of LVRT and DVS can prevent voltage instability and the effectiveness of a ramp rate of 100% on stability. The researchers also compared local and centralized reactive power control methods on reactive power stability. In [18], researchers analyzed the impact on the voltage stability of the PV plant according to the German grid code. It shows the benefits of DVS and reactive power control methods. However, it also states that cost can be a limitation in this case.

The study [19] demonstrates how optimal BESS control enhances small signal stability, transient stability, and frequency stability. In addition, this study compares the BESS with the power system stabilizer (PSS) and demonstrates the success of the BESS in damping oscillations compared to the PSS. In [20], the optimum location for BESS units is studied to eliminate the detrimental effects of converter-based power generation units (such as wind and solar) on transient stability. In addition, short circuit faults are created at different locations, and the optimum BESS location is determined by using the magnitudes of voltage response and short circuit fault currents. In [21], BESS is compared with shunt capacitors and ultracapacitors. This comparison was made in terms of small signal stability and transient stability for two different power systems. It is shown that BESS units are more useful in thermal-dominated power systems and ultracapacitors are successful in hydro-dominated power systems.

In [22], the impact of PV plants and BESS on small signal stability and frequency stability in the grid is considered together. It is demonstrated that the combined use of PV plants and BESS can have a better impact on stability than synchronous generators. For a BESS in an integrated power system with PV plants, a new corrective voltage control technique is carried out in [23] to prevent long-term voltage instability. Through several scenarios employing models of the Scandinavian power system, the usefulness of the proposed approach has been confirmed. The research aimed to minimize the investment costs and voltage drops of the system by determining the optimum number, location, and capacity of BESSs. With the proposed approach, it was determined that PV plants can perform best with "plant-level Q and locally coordinated Q/V control.". For power systems integrating BESS, wind farms, and PV plants, [24] proposes a flexible wide-area multimode controller (MMC) based on the Firefly algorithm. It also shows that the proposed multimode controller can increase the utilization of renewable energy sources in the Java power system by up to 50%.

Analysis Methods

Power system stability analyses can employ various analysis methods. The most common and useful method among these is time domain analysis. Within this analysis, the evaluation of the system's fluctuations in frequency, voltage, rotor angle, active power, and reactive power prior to and following an abnormal occurrence is regularly compared. Another technique often used is modal analysis. Studies on small signal stability typically favor this method, which involves linearizing the model for small frequency oscillations [25, 26] . While investigating parameters such as

eigenvalues, damping ratio, and participation factor, visuals such as mode shape and eigenvalue plot can be used. You can check the rotor angle stability using the critical clearing time (CCT) index and Prony analysis. When examining transient stability, the CCT index is generally used along with the time domain analysis. The CCT index can be applied to pinpoint critical moments in the system as well as to strengthen the analysis. The CCT index indicates the maximum time to address the fault without compromising system stability [27]. When examining small signal stability, Prony analysis is usually used alongside modal analysis. After a small change, Prony analysis finds the dominant modes' oscillation frequency, damping, and amplitude [28].

The authors in [28] perform both small signal stability and transient stability analysis for different penetration levels of the PV power plant. When performing Prony analysis for small signal stability, CCT is used to identify critical locations. Replacing the PV power plant with a synchronous generator enhances the transient stability for faults occurring at non-critical locations in the power system. However, the effect is found to be negative in critical locations. Depending on the proximity of the minor disturbance location relative to the power generators, the PV plant can engender both beneficial and negative outcomes for the small signal stability. In [29], researchers perform a small signal stability analysis with Prony analysis for a PV power plant using a model that takes solar radiation and temperature into account. Both CCT and time domain analysis reveal in [30] that replacing a synchronous generator with a PV plant and PV plant operating them in a voltage control mode can increase transient stability. [31] presents an analysis in terms of both voltage and transient stability by suggesting a control scheme for BESS. Using CTT and time domain analysis, it is determined that distributed BESSs yield better voltage stability results, while transient stability results remain relatively unchanged. In [32], the advantages of the proposed passivity-based control method, along with static synchronous compensators (STATCOM) and BESS, for the stability of the power system are discussed. According to the findings, the proposed approach enhances damping and provides improved transient stability performance.

Event Type

Various event types are used in stability studies in power systems. These event types consist of issues that commonly occur in power systems. In general, short-circuit faults and the sudden in-and-out-of-service of power system elements are dynamic issues encountered in power systems. While single-phase ground fault is the most prevalent form of short-circuit failure on the grid, investigations are usually centered on three-phase short-circuit faults rather than unbalanced faults, as it has the most powerful effect among short-circuit faults. In addition to short circuit faults, imbalances between generation and consumption are also frequently examined. These imbalances are addressed by disconnecting synchronous generators or loads.

Authors in [33] carry out stability analysis by replacing synchronous generators with PV power plants. In the study, the effect of plants in different locations at different penetration levels is analyzed while the PV active power generation for high and low load demands remains constant. The analysis is carried out for the disturbance of the line, generator, load, and three-phase short circuit faults. The authors in [34] propose a control method for PV power plant inverters to absorb a portion of the kinetic energy stored in the synchronous machine. The proposed control method attempts to regulate voltage by providing reactive power transfer. This study focuses on a two-phase ground fault and demonstrates the benefits of the proposed method on voltage and transient stability. In [35], the stability of the PV power plant is analyzed in case the power flow direction changes with the connection of the PV plant to the power system and the disconnection of the line. As a result of this analysis, it is revealed that the contribution of the PV plant to the fault current is low. In [36], the impact of PV plants with different penetration levels during line outage with PSS and BESS is also analyzed. Due to the lack of BESS connection, it is concluded that PSS alone does not meet stability criteria as the PV penetration rate increases. It is also found that BESSs closer to the generation units have a more favorable impact on stability. In [37] a different control structure for BESS is proposed and compared with conventional BESS and STATCOM. Different short circuit faults, line openings and load variations are considered. This system demonstrates the effectiveness of the proposed control structure for BESS in reducing oscillations when the upper power transmission limit is reached on tie lines without STATCOM installed. Authors in [21] use an improved Lyapunov Bases algorithm to analyze the voltage stability of BESS. The authors test the influence of BESS on stability by associating it with the critical bus during generator, load, and line outages. The authors uncover the constructive effect of BESS on voltage stability.

Structure of Power System

The quantity of buses is a fundamental element in the design of a power system structure for stability studies, and thus it is the number of buses that determines whether the system is considered small or large. It could be argued that the number of buses alone is not a sufficient measure to classify a system as small or large; however, when the power system elements (such as synchronous generators, loads, etc.) used in the studies are examined, such a classification can be accepted. A small power system can illustrate the reaction of the unit used in the analysis process. However, its impact on the system cannot be observed in sufficient detail. When conducting stability analysis and measuring the effect and responsiveness of a unit, it is therefore ideal to examine both small and large systems.

This section reviews key studies using two different-sized power systems (small and large), as positive results in a small system may not hold in a large one, necessitating multi-system testing for stability. In [38], the effects of DVS, LVRT, and ramp rate capabilities of PV plants on voltage stability and transient stabilization are analyzed. Initially, CCT is used to evaluate PV fault ride-through abilities in a small system, followed by tests in a large system where DVS effects on location are examined. Findings suggest that not using LVRT and maintaining a low ramp rate harm voltage stability, while a leading power factor and DVS capability mitigate this. In [39], a DVS method for active power support in PV plants is proposed, showing better voltage stability across systems compared to traditional methods. Study [40] examines a control method for PV plants, analyzing short- and long-term voltage stability using reactive power capability curves. Results indicate that PV plants offering long-term reactive support outperform synchronous generators, though stressed systems face both positive and negative effects on stability. Decreased temperature and solar radiation negatively affect long-term stability. Another study [41] proposes a BESS control strategy to enhance primary and secondary frequency control. Using a bode diagram, the transfer function is analyzed for frequency stability in both small and large systems. In a small system, BESS improves stability amid generation changes in wind power. In a large system, BESS stabilizes frequency against fluctuations from wind/solar generation and synchronous generator outages, demonstrating its efficacy for short- and long-term stability.

Different Penetration Level (PV) / Size (BESS)

The penetration level of PV power plants and the size of BESS units in grids are increasing day by day. To establish the future shape of the energy system and identify possible problems, stability analyses should be carried out at different levels of penetration and unit size (PV/BESS).

In [42], PV plants with different penetration levels are connected to a power system with gas and thermal units to reduce power flow and frequency deviations. The study shows that the PV plant has the least negative impact on stability in systems with non-reheated thermal units. In [43], PV plants were replaced by non-critical synchronous generators at various penetration levels. At low penetration level, the effect of this replacement on stability is favorable, while the opposite occurs at high penetration level. In [44] and [45], the studies examine PV units as rooftop (distributed) and centralized units (centralized) and show that the bus voltage increases with PV penetration up to a point where stability starts to decrease. The studies also show that centralized PV plant outages affect frequency stability more severely than rooftop PV outages. In [46], the penetration levels of high PV plants are analyzed and the P-V and P-Q modes for the utilization of the plants are compared. It is found that the P-V mode improves voltage stability but negatively affects the frequency stability compared to the P-Q mode. In [47] and [48], it is shown that the damping of oscillations decreases as PV penetration in the grid increases. It is also shown that high PV penetration levels (up to 65%) can significantly affect frequency stability in US grids. In [49], it is also verified by transient and small signal stability analysis that high PV penetration levels reduce system damping. In [50] and [51], the effects of PV plants on stability were analyzed without removing synchronous generators from the grid. It is shown that PV plants show negative effects on stability as the penetration level increases. In [52], it is also shown that the integration of PV plants into the grid has a positive effect on stability at the beginning but has negative effects as the penetration level increases. In [53], BESS is tested to prevent grid disconnection during disturbances and shows that appropriately sized BESS can prevent grid disconnection and load shedding. In [54], the optimal BESS size and location are addressed to mitigate the impacts of PV plants at high penetration. In [55] and [56], it is shown that BESS delay time significantly affects frequency stability and distributed BESS is more effective for stability than centralized structure. In [57] and [58], BESS sizing for frequency support under high PV penetration is discussed. They show that droop-controlled BESS can improve the frequency response in low inertia systems, and high sag coefficients are more helpful for damping and stability.

Frequency Support

When PV power plants are used in power systems, certain grid codes require frequency support, while others do not. Due to the increasing penetration level of the plants, frequency support becomes inevitable. This situation has been taken into consideration in a few studies in related literature. In this section, in addition to PV power plants that provide frequency support, studies on the parameters of BESSs for frequency support are investigated. In [59], have analyzed the effect of PV power plant (central control) on frequency stability to provide frequency support. In the study, the load is altered to investigate the impact of the plant's moment of inertia emulation control parameter on frequency stability. Similarly, [60] investigates frequency stability underload changes for PV plants with local frequency support control. In [61], various control methods are discussed, and it is shown that these methods can mitigate the negative effects of high PV penetration levels in the grid. In [62], it is shown that the impact of centralized frequency support controls on power system stability is significant, especially for various faults such as short circuits and line outages. [63] analyzes the inertial response of BESS for frequency stability across disturbances of varying sizes, emphasizing the importance of BESS size and location. Study [64] compares detailed and average BESS models, revealing that while both perform similarly within control limits, the detailed model is preferable for stability when limits are reached. In [65], BESS effects on frequency stability are examined during synchronous generator outages,

showing that optimizing the inertial emulation controller's gain is critical for stability and SOC management. [66] suggests a novel approach to multiple linear regression analysis for calculating the de-loading % of PV systems according to frequency response. According to the results obtained, it has been determined that as PV integration increases in the grid, PV systems provide frequency stability by maintaining the required offload percentage. For PV systems that control active power demand, a novel method based on frequency regulation through reactive power control (FRQC) is presented in [67]. To temporarily lower the demand for the electrical power supplied by synchronous generators, the suggested FRQC method coordinates changes in reactive power. The analyses demonstrate that the suggested FRQC scheme enhances both the system frequency stability and the post-fault frequency trajectory. In [68], proposes management plans to boost PV hosting capacity and fixes to enhance the delivery of frequency support services using flexible energy sources. The findings indicate that by lowering the on-load tap changer setting value, the grid's PV hosting capacity may be enhanced. Additionally, by charging the BESS concurrently during steady-state operation, the PV host capacity with BESS on the PV connection point can be increased while preventing local over voltages.

Simulation Programs

Various simulation programs are used to perform stability analysis in power systems. In a survey conducted with transmission and distribution operators, it was reported that the two most used programs for power system stability analysis are Power System Simulator for Engineering (PSS/E) (41%) and DigSilent (13%) [69]. In addition, it was found in the review of the literature that MATLAB (33%), DigSilent (33%), and PSS/E (14%) are the programs used for power system stability analysis.

The parameters used for a given BESS model were tested in the simulation programs DSA Tools PSLF, PowerWorld, and PSS/E by the authors in [70] , and the outcomes were analyzed. In this way, both the model and the programs were validated and tested. The effect of the model on frequency and voltage stability was analyzed.

RESULTS AND DISCUSSION

The penetration level of PV units and other renewable energy sources with converters in the power system is becoming more widespread globally each day. The lack of inertia in these generation units, coupled with their intermittent generation capabilities, negatively impacts the stability of power systems. To eliminate such negative effects, generation units with converters should support voltage and frequency. Also, a portion of the energy generated should be stored. This is why BESS is gaining popularity with grids as a reliable means of ensuring the stability of the power system. This paper reviews the current state of PV power generation and BESS usage worldwide and their impact on stability. Additionally, the characteristics of PV plants and BESSs outlined in academic studies on power system stability, along with the study results, are discussed. Table 5 presents an overview of the reviewed studies for PV and BESS units.

The literature summary provided in Table 5 is presented in statistical format in Figure 4. In Figure 4, the total proportion of groups may exceed 100%. For example, a study may analyze both frequency and voltage stability. For this reason, the total values under the heading of power system stability exceed 100%. The ratios obtained under different penetration level/size and frequency support headings are evaluated separately for PV and BESS studies. For instance, 57.45% of the studies that included PV plants investigated different penetration levels.

As seen in the figure, frequency stability is prominent in most studies. Studies on BESS units have increased with their integration into the grid in recent years, and PV plants are more frequently included in studies. The figure shows that time-domain analysis is performed in almost all power system stability studies. Although three-phase short-circuit faults are generally selected for stability studies, other disturbance effects are also frequently preferred. However, other faults, which refer to unbalanced faults, are not frequently addressed in stability studies. The figure shows that the use of large and small systems in stability studies is nearly equal. Studies on different BESS sizes are not as common as those on PV plants, while different penetration levels are widely considered in PV plant studies. Studies on the frequency support of PV plants are not widely discussed, although they have started to become widespread in recent years with the integration of large PV plants into the grids.

The findings obtained from the classifications made in this study can be summarized as follows.

- The analysis of the literature shows that investigations are carried out on PV and BESS units for different stability analyses of the power system. It is observed that most studies are primarily based on the analysis of frequency and voltage stability. In addition, based on the findings of the related studies, it can be argued that examining different types of stability analyses together is the most sensible approach, as a situation that may appear beneficial in one such analysis may present a negative outcome in another.
- It is seen that PV power plants and BESS units are rarely used together in power system stability studies.
- It can be stated that modal and time-domain analyses are frequently preferred. The use of various stability analyses can make the results more interpretable and clearer.
- Examining the types of events used for analysis, it is seen that load events and three-phase short-circuit faults are generally preferred. Frequency stability analysis is commonly executed in the case of a load disturbance. Three-phase short-circuit faults are used for frequency, voltage, and transient stability analysis. It can be noted

Table 5. Summary of the studies in literature

Citation Number	Power System Stability				Unit		Analysis Methods				Event Type					Power System Design		Dif. Penetration Level (PV) / Size (BESS)	Frequency Support	Simulation Program
	Frequency	Voltage	Transient	Small Signal	PV	BESS	Time Domain	Modal	CCT Index.	Prony	3-Phase Fault	Other Faults	Generator	Load	Line	Large	Small			
[17]	✓	✓	✓		✓		✓		✓		✓				✓	✓				D
[18]		✓			✓		✓		✓		✓						✓			D
[19]	✓		✓	✓		✓	✓	✓						✓			✓		✓*	M
[22]	✓			✓	✓	✓	✓	✓								✓			✓*	M
[20]			✓			✓	✓				✓					✓			✓*	D
[21]		✓				✓	✓						✓	✓	✓	✓			✓*	P
[23]		✓			✓	✓	✓				✓		✓		✓	✓			✓*	D
[24]	✓		✓	✓	✓	✓	✓	✓			✓		✓			✓		✓	✓**	
[28]			✓	✓	✓		✓	✓		✓	✓					✓		✓		D
[29]			✓	✓	✓		✓	✓		✓						✓		✓		M
[30]		✓	✓		✓		✓		✓		✓						✓	✓		D
[31]		✓	✓			✓	✓		✓		✓					✓			✓*	
[32]		✓	✓	✓		✓	✓	✓	✓		✓			✓		✓			✓*	M
[33]	✓	✓		✓	✓		✓	✓			✓		✓	✓	✓	✓		✓		M
[34]		✓	✓		✓		✓					✓			✓		✓			M
[35]		✓	✓		✓		✓				✓				✓		✓			PA
[36]	✓	✓			✓	✓	✓					✓		✓	✓		✓		✓*	
[37]	✓	✓				✓	✓				✓	✓		✓	✓	✓			✓*	
[38]		✓	✓		✓		✓		✓		✓					✓	✓			
[39]	✓	✓	✓		✓		✓		✓		✓					✓	✓			
[40]		✓			✓		✓				✓				✓	✓	✓	✓		D
[41]	✓				✓	✓	✓						✓	✓		✓	✓	✓*	✓*	D
[42]	✓			✓	✓		✓	✓						✓			✓	✓		M
[43]	✓	✓	✓	✓	✓		✓	✓			✓		✓	✓	✓	✓		✓		PW
[44]	✓	✓	✓		✓		✓				✓				✓	✓		✓		DT
[45]	✓	✓		✓	✓		✓	✓	✓		✓					✓		✓		DT
[46]	✓	✓			✓		✓						✓			✓		✓		P
[47]	✓			✓	✓		✓	✓			✓					✓		✓		
[48]	✓				✓		✓						✓			✓		✓		
[49]	✓		✓	✓	✓		✓	✓		✓	✓					✓		✓		DT
[50]	✓	✓			✓		✓				✓					✓		✓		P
[51]		✓	✓		✓		✓				✓					✓		✓		N
[52]	✓	✓	✓		✓		✓		✓		✓						✓	✓		M
[53]	✓					✓	✓								✓	✓		✓*	✓*	
[54]	✓				✓	✓	✓						✓			✓		✓**	✓*	M

Table 5. Summary of the studies in literature

Citation Number	Power System Stability				Unit		Analysis Methods				Event Type					Power System Design		Dif. Penetration Level (PV) / Size (BESS)	Frequency Support	Simulation Program
	Frequency	Voltage	Transient	Small Signal	PV	BESS	Time Domain	Modal	CCT Index.	Prony	3-Phase Fault	Other Faults	Generator	Load	Line	Large	Small			
[55]	✓					✓	✓							✓		✓		✓*	✓*	D
[56]	✓					✓	✓							✓		✓	✓	✓*	✓*	
[57]	✓	✓			✓	✓	✓						✓			✓		✓**	✓*	D
[58]	✓					✓	✓						✓	✓		✓		✓	✓*	
[59]	✓				✓		✓							✓			✓		✓	
[60]	✓				✓		✓							✓		✓			✓	D
[61]	✓				✓		✓							✓			✓	✓	✓	
[62]	✓	✓		✓	✓		✓	✓			✓		✓	✓	✓	✓		✓	✓	D
[63]	✓					✓	✓							✓			✓		✓*	D
[64]	✓					✓	✓				✓		✓				✓		✓*	M
[65]	✓					✓	✓						✓	✓			✓		✓*	D
[66]	✓				✓	✓	✓						✓			✓		✓	✓**	D
[67]	✓		✓		✓	✓	✓							✓		✓		✓**	✓**	D
[68]	✓	✓			✓	✓	✓							✓		✓			✓**	PC
[70]	✓	✓				✓	✓				✓		✓		✓	✓			✓*	X
[71]	✓	✓		✓	✓		✓	✓					✓	✓		✓		✓	✓	
[72]	✓					✓	✓						✓		✓	✓		✓*	✓*	M
[73]	✓					✓	✓							✓		✓			✓*	M
[74]	✓					✓	✓						✓			✓			✓*	P
[75]	✓				✓		✓							✓		✓		✓	✓	D
[76]	✓				✓		✓							✓		✓			✓	D
[77]	✓				✓		✓							✓			✓		✓	
[78]	✓	✓	✓		✓		✓				✓						✓	✓		
[79]	✓			✓	✓	✓	✓	✓						✓		✓			✓*	M
[80]	✓					✓	✓							✓			✓		✓*	
[81]	✓	✓				✓	✓					✓				✓		✓*	✓*	D
[82]	✓	✓				✓	✓							✓		✓		✓*	✓*	D
[83]		✓		✓	✓		✓	✓							✓	✓		✓		M
[84]		✓	✓		✓		✓					✓		✓		✓				E
[85]		✓	✓			✓	✓		✓		✓				✓	✓			✓*	
[86]			✓	✓	✓	✓	✓	✓			✓					✓			✓*	
[87]			✓			✓	✓				✓				✓	✓			✓*	P
[88]			✓		✓		✓				✓				✓		✓	✓		PW
[89]				✓		✓		✓									✓		✓*	
[90]				✓		✓		✓								✓			✓*	
[91]				✓	✓		✓	✓			✓					✓		✓		DT

✓* only BESS, ✓** PV+BESS

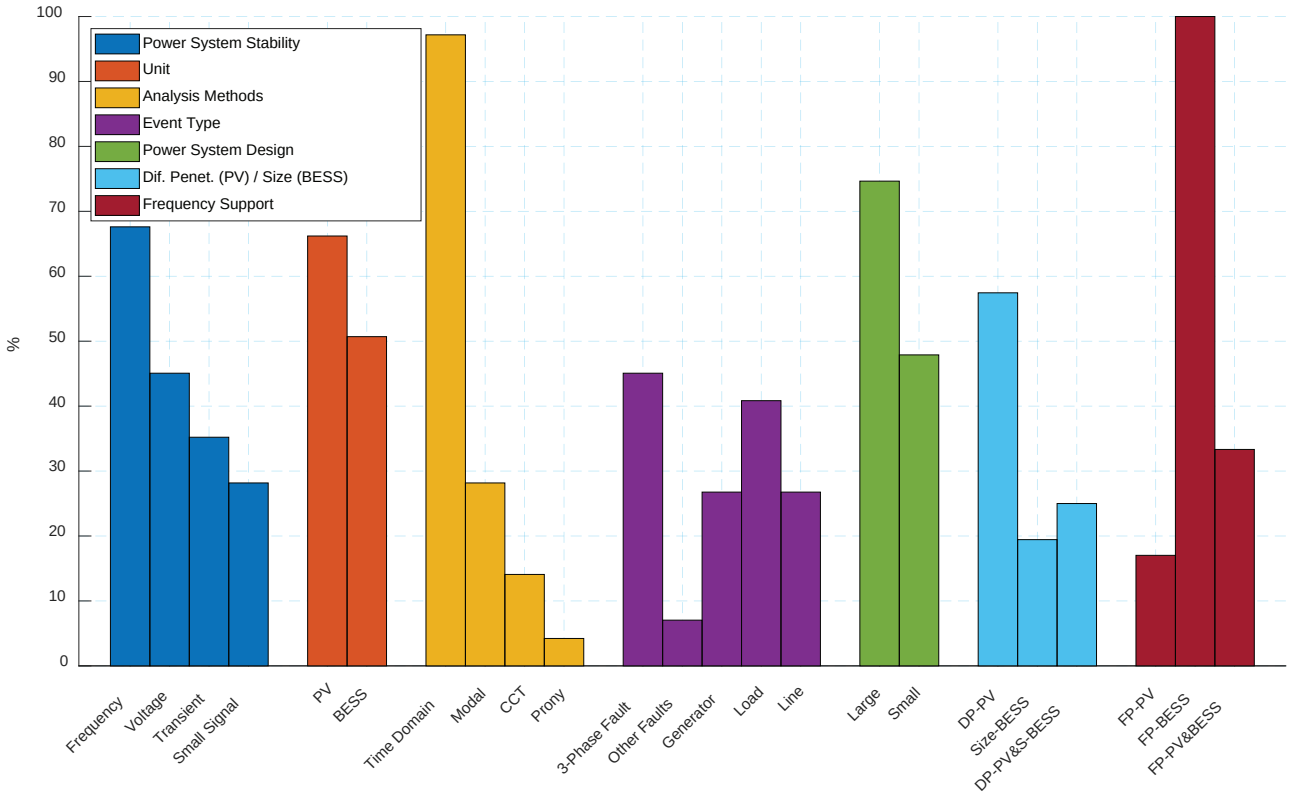


Figure 4. Statistical analysis of literature summary.

that, in most studies, line openings are conducted following a short-circuit fault.

- It is seen that large power systems are usually the ones where stability analyses are conducted. However, studies involving both small and large power systems are rare. Nevertheless, by using both, the effects of PV and BESS units and their responses to changes can be observed more clearly.
- It has been observed that different PV power plant penetration levels are frequently examined in terms of stability analysis. These studies can be roughly divided into two groups based on the integration of PV power plants with or without synchronous generator replacement. Additionally, when looking into the size of a BESS, its location is usually considered. As the penetration of PV plants increases, the negative impact on power system stability also increases. This effect can be mitigated by using BESS units of different sizes. However, in literature, studies focusing solely on the size and location of BESS in the power system are generally included.
- As the penetration of PV power plants in power systems has increased, the need for frequency support has become more important. Literature has evaluated this phenomenon and examined the effect of PV power plants on frequency, as well as different control methods. Additionally, examining the impact of control systems and parameters on frequency support has been a recurrent topic of research for BESS.
- It can be stated that studies typically involve the use of DigSilent PowerFactory and MATLAB simulation programs, with PSS/E being more popular among transmission and distribution operators.

CONCLUSION

In this study, the effects of PV power plants and BESS on power system stability were examined using a literature-based and systematic approach. Within the scope of the study, existing research was classified and compared under headings such as stability type, unit type used, analysis method, event/fault type, system scale, PV penetration level and BESS sizing, frequency support approach, and simulation tools. This comprehensive evaluation revealed that the literature focuses particularly on frequency and voltage stability; time domain analysis is the most common method; events such as three-phase short circuits and load changes are frequently preferred; and tools such as DigSilent PowerFactory and MATLAB are prominent. However, it was observed that the number of studies addressing PV and BESS together is limited, with many studies evaluating these two structures separately, creating a significant gap, especially for systems with high renewable penetration. In

this regard, the study not only summarizes the literature but also clearly highlights which topics have been intensively studied in terms of power system stability and which areas require further research.

The findings indicate that as the share of PV plants in the grid increases in line with climate change mitigation, rising electricity demand, and economic energy production targets, BESS integration has become critical in terms of stability. This situation necessitates a reassessment of existing grid policies, integration plans, grid codes, and, in particular, frequency response protocols. New regulations are needed to define performance requirements for the safe and effective integration of PV and BESS into the grid, encourage investment, and guarantee stability at high penetration levels. Furthermore, the dependence of these systems on digital infrastructure for real-time monitoring and control increases their vulnerability to cyberattacks; therefore, it is crucial that future studies address cybersecurity, secure communication infrastructure, data integrity, and system resilience alongside stability analyses. In addition, increasing the number of studies that evaluate PV and BESS together, examining the effects of different battery chemistries on transient stability, determining the necessary BESS scaling strategies at high PV penetration, and researching the effects of distribution/transmission operators' grid codes on stability stand out as priority research areas for future studies.

AUTHORSHIP CONTIBUTIONS

Çavdar, B.: Writing, Reviewing, Editing and Visualization. **Karaca, E:** Writing, Reviewing, Editing and Visualization. **Okumuş, H:** Writing, Reviewing, Editing and Visualization **Nuroğlu, F. M:** Supervision, Writing, Reviewing and Editing.

DATA AVAILABILITY STATEMENT

The authors confirm that the data that supports the findings of this study are available within the article. Raw data that support the finding of this study are available from the corresponding author, upon reasonable request.

CONFLICT OF INTEREST

The author declared no potential conflicts of interest with respect to the research, authorship, and/or publication of this article.

ETHICS

There are no ethical issues with the publication of this manuscript.

STATEMENT ON THE USE OF ARTIFICIAL INTELLIGENCE

Artificial intelligence was not used in the preparation of the article.

ABBREVIATION

BESS	battery energy storage system
CCT	critical clearing time
DVS	dynamic voltage support
EI	eastern interconnection
ERCOT	electric reliability council of Texas
FRQC	frequency regulation through reactive power control
GDP	gross domestic product
LVRT	low voltage ride through
MMC	multi-mode controller
PSCAD	power systems computer aided design
PSS	power system stabilizer
PSS/E	power system simulator for engineering
P-Q	power factor control
P-V	voltage control
PV	photovoltaic
SOC	state of charge
STATCOM	static synchronous compensator
WECC	western electricity coordinating council

REFERENCES

[1] REN21. Renewables 2022 global status report. 2022. Avaialable at: https://www.ren21.net/reports/ren21-reports/ Accessed on Feb 04, 2026.

[2] Global Solar Atlas. Global photovoltaic power potential by country. Available at: https://globalsolaratlas.info/global-pv-potential-study Accessed Nov 02, 2024.

[3] World Development Indicators. GDP per capita (US$) in 2021. Available at: https://data.worldbank.org/indicator/NY.GDP.PCAP.CD Accessed on Nov 02, 2024.

[4] International Energy Agency. 2022 snapshot of global PV markets. 2022. Available at: https://iea-pvps.org/snapshot-reports/snaps Accessed on Feb 04, 2026.

[5] Shah R, Mithulananthan N, Bansal RC, Ramachandaramurthy VK. A review of key power system stability challenges for large-scale PV integration. Renew Sustain Energy Rev 2015;41:1423–1436. [CrossRef]

[6] Fang W, Huang Q, Huang S, Yang J, Meng E, Li Y. Optimal sizing of utility-scale photovoltaic power generation complementarily operating with hydropower: A case study of the world's largest hydro-photovoltaic plant. Energy Convers Manag 2017;136:161–172. [CrossRef]

[7] China Energy Storage Alliance. Energy storage industry white paper 2022 (summary version). 2022. Available at: https://static1.squarespace.com/static/55826ab6e4b0a6d2b0f53e3d/t/62821561e7f0424662ca7f9d/1652692323469/Energy+Storage+Industry+White+Paper+2022+%EF%BC%88Summary+Version%EF%BC%89.pdf Accessed on Feb 04, 2026.

[8] International Energy Agency. Solar PV. Available at: https://www.iea.org/energy-system/renewables/solar-pv Accessed on Nov 02, 2024.
[9] International Energy Agency. Grid scale storage. Availaeble at: https://www.iea.org/search?q=Grid-scale%20Storage Accessed on Nov 02, 2024.
[10] Gandhi O, Kumar DS, Rodríguez-Gallegos CD, Srinivasan D. Review of power system impacts at high PV penetration. Part I: Factors limiting PV penetration. Sol Energy 2020;210:181–201. [CrossRef]
[11] Alshahrani A, Omer S, Su Y, Mohamed E, Alotaibi S. The technical challenges facing the integration of small-scale and large-scale PV systems into the grid: A critical review. Electronics 2019;8:1443. [CrossRef]
[12] Shafiullah M, Ahmed SD, Al-Sulaiman FA. Grid integration challenges and solution strategies for solar PV systems: A review. IEEE Access 2022;10:52233–52257. [CrossRef]
[13] Yang Y, Bremner S, Menictas C, Kay M. Battery energy storage system size determination in renewable energy systems: A review. Renew Sustain Energy Rev 2018;91:109–125. [CrossRef]
[14] Hannan MA, Wali SB, Ker PJ, Abd Rahman MS, Mansor M, Ramachandaramurthy VK, et al. Battery energy-storage system: A review of technologies, optimization objectives, constraints, approaches, and outstanding issues. J Energy Storage 2021;42:103023. [CrossRef]
[15] Rana MM, Uddin M, Sarkar MR, Shafiullah GM, Mo H, Atef M. A review on hybrid photovoltaic–battery energy storage system: Current status, challenges, and future directions. J Energy Storage 2022;51:104597. [CrossRef]
[16] Kundur P, Paserba J, Ajjarapu V, Andersson G, Bose A, Canizares C, et al. Definition and classification of power system stability. IEEE Trans Power Syst 2004;19:1387–1401. [CrossRef]
[17] Lammert G, Premm D, Ospina LDP, Boemer JC, Braun M, Van Cutsem T. Control of photovoltaic systems for enhanced short-term voltage stability and recovery. IEEE Trans Energy Convers 2019;34:243–254. [CrossRef]
[18] Lammert G, Boemer JC, Premm D, Glitza O, Ospina LDP, Fetzer D, et al. Impact of fault ride-through and dynamic reactive power support of photovoltaic systems on short-term voltage stability. In: IEEE Manchester PowerTech 18-22 June 2017. [CrossRef]
[19] Setiadi H, Mithulananthan N, Hossain MJ. Impact of battery energy storage systems on electromechanical oscillations in power systems. In: IEEE Power and Energy Society General Meeting 16-20 July 2017. Chicago, IL, United States: 2017. p. 1–5. [CrossRef]
[20] Cifuentes N, Rahmann C, Valencia F, Alvarez R. Network allocation of BESS with voltage support capability for improving the stability of power systems. IET Gener Transm Distrib 2019;13:939–949. [CrossRef]
[21] Gubitz T, Sico K, Chakrabortty A. Online detection and quantification of transient instability using Lyapunov exponents from PMU data. In: North American Power Symposium 2018;1–6. [CrossRef]
[22] Setiadi H, Krismanto AU, Mithulananthan N. Influence of BES system on local and inter-area oscillation of power system with high penetration of PV plants. In: Int Conf Appl Syst Innov 2017;1–4. [CrossRef]
[23] Nasrazadani H, Sedighi A, Seifi H. Enhancing long-term voltage stability of a power system integrated with large-scale photovoltaic plants using a battery energy storage control scheme. Int J Electr Power Energy Syst 2021;131:107059. [CrossRef]
[24] Setiadi H, Mithulananthan N, Shah R, Islam MR, Fekih A, Krismanto AU, et al. Multi-mode damping control approach for the optimal resilience of renewable-rich power systems. Energies 2022;15:2972. [CrossRef]
[25] Fan L, Zhu C, Miao Z, Hu M. Modal analysis of a DFIG-based wind farm interfaced with a series compensated network. IEEE Trans Energy Convers 2011;26:1010–1020. [CrossRef]
[26] Martínez LG, Sarasua JI, Fernández GA, Molina GÁ. Combined hydro-wind frequency control scheme: Modal analysis and isolated power system case example. Renew Energy 2021;180:1056–1072. [CrossRef]
[27] Ayasun S, Liang Y, Nwankpa CO. A sensitivity approach for computation of the probability density function of critical clearing time and probability of stability in power system transient stability analysis. Appl Math Comput 2006;176:563–576. [CrossRef]
[28] Munkhchuluun E, Meegahapola L, Vahidnia A. Impact on rotor angle stability with high solar-PV generation in power networks. In: IEEE PES Innov Smart Grid Technol Eur 2017;1–6. [CrossRef]
[29] Zhou Y, Li Y, Yu D, Liu J. MPPT-considered detailed models of large-scale photovoltaic plants and its application in power system small-signal stability analysis. CSEE J Power Energy Syst 2016;2:82–90.
[30] Ghosh A, Patel R, Datta M, Meegahapola L. Investigation of transient stability of a power network with solar-PV generation: Impact of loading level and control strategy. In: IEEE 2017 IEEE Innovative Smart Grid Technologies - Asia (ISGT-Asia), 2017. [CrossRef]
[31] Kawabe K, Yokoyama A. Effective utilization of large-capacity battery systems for transient stability improvement in multi-machine power system. In: IEEE Trondheim PowerTech 2011;1–6. [CrossRef]
[32] Kanchanaharuthai A, Chankong V, Loparo KA. Transient stability and voltage regulation in multimachine power systems vis-à-vis STATCOM and battery energy storage. IEEE Trans Power Syst 2015;30:2404–2416. [CrossRef]

[33] Bueno PG, Hernández JC, Ruiz RFJ. Stability assessment for transmission systems with large utility-scale photovoltaic units. IET Renew Power Gener 2016;10:584–597. [CrossRef]

[34] Zevallos OC, Silva JBD, Mancilla DF, Neves FAS, Neto RC, Prada RB. Control of photovoltaic inverters for transient and voltage stability enhancement. IEEE Access 2021;9:44363–44373. [CrossRef]

[35] Xiao Q, Zhao K, Jiang W, Zhu S. The effect of large-scale PV power on stability of power system. In: Proc IEEE Adv Inf Manag Commun Electron Autom Control Conf 2018;1173–1177. [CrossRef]

[36] Datta U, Kalam A, Shi J. Battery energy storage system control for mitigating PV penetration impact on primary frequency control and state-of-charge recovery. IEEE Trans Sustain Energy 2020;11:746–757. [CrossRef]

[37] Datta U, Kalam A, Shi J. Battery energy storage system to stabilize transient voltage and frequency and enhance power export capability. IEEE Trans Power Syst 2019;34:1845–1857. [CrossRef]

[38] Kawabe K, Tanaka K. Impact of dynamic behavior of photovoltaic power generation systems on short-term voltage stability. IEEE Trans Power Syst 2015;30:3416–3424. [CrossRef]

[39] Kawabe K, Ota Y, Yokoyama A, Tanaka K. Novel dynamic voltage support capability of photovoltaic systems for improvement of short-term voltage stability in power systems. IEEE Trans Power Syst 2017;32:1796–1804. [CrossRef]

[40] Munkhchuluun E, Meegahapola L, Vahidnia A. Long-term voltage stability with large-scale solar-photovoltaic generation. Int J Electr Power Energy Syst 2020;117:105663. [CrossRef]

[41] Shim JW, Verbic G, Zhang N, Hur K. Harmonious integration of faster-acting energy storage systems into frequency control reserves in power grid with high renewable generation. IEEE Trans Power Syst 2018;33:6193–6205. [CrossRef]

[42] Rajan R, Fernandez FM. Impact of increased penetration of photovoltaic sources on small-signal stability of hybrid and multi-area power systems. In: IEEE Innov Power Adv Comput Technol 2019;1–6. [CrossRef]

[43] Kumar DS, Sharma A, Srinivasan D, Reindl T. Impact analysis of large power networks with high share of renewables in transient conditions. IET Renew Power Gener 2020;14:1349–1358. [CrossRef]

[44] Eftekharnejad S, Vittal V, Heydt GT, Keel B, Loehr J. Impact of increased penetration of photovoltaic generation on power systems. IEEE Trans Power Syst 2013;28:893–901. [CrossRef]

[45] Tamimi B, Canizares C, Bhattacharya K. System stability impact of large-scale and distributed solar photovoltaic generation: The case of Ontario, Canada. IEEE Trans Sustain Energy 2013;4:680–688. [CrossRef]

[46] You S, Liu Y, Zhang X, Su Y, Wu L, Liu Y. Impact of high PV penetration on U.S. eastern interconnection frequency response. In: IEEE Power Energy Soc Gen Meet 2017;1–5. [CrossRef]

[47] You S, Kou G, Liu Y, Zhang X, Cui Y, Till MJ. Impact of high PV penetration on the inter-area oscillations in the U.S. eastern interconnection. IEEE Access 2017;5:4361–4369. [CrossRef]

[48] Liu Y, You S, Tan J, Zhang Y, Liu Y. Frequency response assessment and enhancement of the U.S. power grids toward extra-high photovoltaic generation penetrations: An industry perspective. IEEE Trans Power Syst 2018;33:3438–3449. [CrossRef]

[49] Eftekharnejad S, Vittal V, Heydt GT, Keel B, Loehr J. Small signal stability assessment of power systems with increased penetration of photovoltaic generation: A case study. IEEE Trans Sustain Energy 2013;4:960–967. [CrossRef]

[50] Bhatt G, Affljulla S. Analysis of large-scale PV penetration impact on IEEE 39-bus power system. In: IEEE Int Sci Conf Power Electr Eng RTUCON 2017;1–6. [CrossRef]

[51] Mrehel OG, Shamek AS, Hamouda MD. Power system transient stability investigation in the presence of photovoltaic generation. In: Int Conf Sci Tech Autom Control Comput Eng 2016;563–568. [CrossRef]

[52] Mohamed SR, Jeyanthy PA, Devaraj D. Investigation on the impact of high-penetration of PV generation on transient stability. In: IEEE Int Conf Intell Tech Control Optim Signal Process 2017;1–6. [CrossRef]

[53] Jalali A, Dozein G, Mancarella P. Frequency stability provision from battery energy storage system considering cascading failures, with applications to separation events in Australia. In: IEEE Milan PowerTech 2019;1–6. [CrossRef]

[54] Yuan Z, Wang W, Wang H, Yıldızbaşı A. Allocation and sizing of battery energy storage system for primary frequency control based on bio-inspired methods: A case study. Int J Hydrogen Energy 2020;45:19455–19464. [CrossRef]

[55] Brogan PV, Best RJ, Morrow DJ, McKinley K, Kubik ML. Effect of BESS response on frequency and RoCoF during underfrequency transients. IEEE Trans Power Syst 2019;34:575–583. [CrossRef]

[56] Shim JW, Verbic G, Kim H, Hur K. On droop control of energy-constrained battery energy storage systems for grid frequency regulation. IEEE Access 2019;7:166353–166364. [CrossRef]

[57] Munkhchuluun E, Meegahapola L, Vahidnia A. Optimal battery sizing for large-scale solar-PV generation to improve frequency stability. In: Australas Univ Power Eng Conf 2019;1–6. [CrossRef]

[58] Amin MR, Negnevitsky M, Franklin E, Alam KS, Naderi SB. Application of battery energy storage systems for primary frequency control in power systems with high renewable energy penetration. Energies 2021;14:1379. [CrossRef]

[59] Verdugo C, Tarraso A, Candela JI, Rocabert J, Rodriguez P. Synchronous frequency support of photovoltaic power plants with inertia emulation. In: IEEE Energy Convers Congr Expo 2019;4305–4310. [CrossRef]

[60] Zhao DW, Qian MH, Ma J, Jiang DJ, Ding MS, Xiang L. A decentralized regulation strategy of PV power plant based on droop control. In: China Int Conf Electr Distrib 2018;1824–1828. [CrossRef]

[61] Jibji BF, Anaya LO. Frequency support from photovoltaic power plants using offline maximum power point tracking and variable droop control. IET Renew Power Gener 2019;13:2278–2286. [CrossRef]

[62] Remon D, Cañizares CA, Rodriguez P. Impact of 100-MW-scale PV plants with synchronous power controllers on power system stability in northern Chile. IET Gener Transm Distrib 2017;11:2958–2964. [CrossRef]

[63] Alhejaj SM, Gonzalez LFM. Investigation on grid-scale BESS providing inertial response support. In: IEEE Int Conf Power Syst Technol 2016;1–6. [CrossRef]

[64] Calero F, Canizares CA, Bhattacharya K. Detailed and average battery energy storage model comparison. In: IEEE PES Innov Smart Grid Technol Eur 2019;1–5. [CrossRef]

[65] Alhejaj SM, Gonzalez LFM. Impact of inertia emulation control of grid-scale BESS on power system frequency response. In: Int Conf Stud Appl Eng 2016;254–258. [CrossRef]

[66] Jawad A, Masood NA. A systematic approach to estimate the frequency support from large-scale PV plants in a renewable integrated grid. Energy Rep 2022;8:940–954. [CrossRef]

[67] Munkhchuluun E, Gunaruwan ML, Vahidnia A. Reactive power assisted frequency regulation scheme for large-scale solar-PV plants. Int J Electr Power Energy Syst 2023;146:108776. [CrossRef]

[68] Laaksonen H, Parthasarathy C, Hafezi H, Shafiekhah M, Khajeh H, Hatziargyriou N. Solutions to increase PV hosting capacity and provision of services from flexible energy resources. Appl Sci 2020;10:5146. [CrossRef]

[69] Milanovic JV, Yamashita K, Villanueva SM, Djokic SZ, Korunovic LM. International industry practice on power system load modeling. IEEE Trans Power Syst 2013;28:3038–3046. [CrossRef]

[70] Xu X, Bishop M, Donna GO, Chen H. Application and modeling of battery energy storage in power systems. CSEE J Power Energy Syst 2016;2:82–90. [CrossRef]

[71] Remon D, Cantarellas AM, Mauricio JM, Rodriguez P. Power system stability analysis under increasing penetration of photovoltaic power plants with synchronous power controllers. IET Renew Power Gener 2017;11:733–741. [CrossRef]

[72] Mosca C, Arrigo F, Mazza A, Bompard E, Carpaneto E, Chicco G, Cuccia P. Mitigation of frequency stability issues in low inertia power systems using synchronous compensators and battery energy storage systems. IET Gener Transm Distrib 2019;13:3951–3959. [CrossRef]

[73] Chen C, Bao YQ, Wu XH, Wang B, Shen C. Battery energy storage system based on incremental cost consensus algorithm for the frequency control. IEEE Access 2019;7:147362–147372. [CrossRef]

[74] Devin AC, Udayanga HKTM, Rohan LJ. Using BESS to achieve power system dynamic stability when high solar penetration is present: Case study Sri Lanka. In: Int Conf Smart Power Internet Energy Syst 2020;252–257. [CrossRef]

[75] Jietan Z, Linan Q, Pestana R, Fengkui L, Libin Y. Dynamic frequency support by photovoltaic generation with synthetic inertia and frequency droop control. In: IEEE Conf Energy Internet Energy Syst Integr 2017;1–6. [CrossRef]

[76] Qian MH, Zhao DW, Ma J, Jiang DJ, Ding MS, Xiang L. A centralized frequency regulation strategy of PV power plant based equal adjustable capacity proportion mode. In: China Int Conf Electr Distrib 2018;1797–1801. [CrossRef]

[77] Dajun J, Lei Z, Dawei Z, Ning C, Minhui Q. Research on PV generation participating in power grid frequency regulation. In: China Int Conf Electr Distrib 2018;1713–1717. [CrossRef]

[78] Zainuddin M, Sarjiya HTP, Sunanda W, Surusa FEP. Transient stability assessment of large scale grid-connected photovoltaic on transmission system. In: Int Conf Green Energy Appl 2018;113–118. [CrossRef]

[79] Setiadi H, Mithulananthan N, Krismanto AU, Shah R. Comparison of battery energy storage models for small signal stability in power system. In: IEEE Int Symp Ind Electron 2018;37–42. [CrossRef]

[80] Dar SZN, Mufti MD. Analysis of two area power system with battery energy storage. In: Int Conf Converg Technol 2017;915–919. [CrossRef]

[81] Zhang D, Shafiullah GM, Das CK, Wong KW. Optimal allocation of battery energy storage systems to improve system reliability and voltage and frequency stability in weak grids. Appl Energy 2025;377:124541. [CrossRef]

[82] Jannesar MR, Sadr S, Savaghebi M. Optimal sitting, sizing and control of battery energy storage to enhance dynamic stability of low-inertia grids. IET Renew Power Gener 2024. [CrossRef]

[83] Srivastava A, Meena R, Parida SK. Effect of PV and FACTS on small signal stability. In: Natl Power Syst Conf 2018;1–5. [CrossRef]

[84] Refaat SS, Abu-Rub H, Sanfilippo AP, Mohamed A. Impact of grid-tied large-scale photovoltaic system on dynamic voltage stability of electric power grids. IET Renew Power Gener 2018:157–164. [CrossRef]

[85] Kawabe K, Yokoyama A. Study on short-term voltage stability improvement using batteries on extra-high voltage network. In: IEEE Grenoble Conf 2013;1–3. [CrossRef]

[86] Shah R, Mithulananthan N, Bansal RC. Damping performance analysis of battery energy storage system, ultracapacitor and shunt capacitor with large-scale photovoltaic plants. Appl Energy 2012;96:235–244. [CrossRef]

[87] Xie X, Zhang Y, Meng K, Dong ZY, Liu J, Tang S. Impact of utility-scale energy storage systems on power system transient stability considering operating uncertainties. In: IEEE Innov Smart Grid Technol Asia 2019;508–513. [CrossRef]

[88] Kamel RM, Alanzi SSh, Al Hashemi YM. Effect of photovoltaic penetration level and location on power system transient stability during symmetrical and unsymmetrical faults. Sustain Energy Grids Netw 2024;38:101322. [CrossRef]

[89] Tang S, Yang H, Zhao R, Geng X. Influence of battery energy storage system on steady state stability of power system. In: Int Conf Electr Mach Syst 2009;1–4. [CrossRef]

[90] Biroon RA, Pisu P, Schoenwald D. A hybrid control framework for large-scale battery integration to the power system for stability analysis. In: Am Control Conf 2020;4969–4974. [CrossRef]

[91] Liu H, Jin L, Le D, Chowdhury AA. Impact of high penetration of solar photovoltaic generation on power system small signal stability. In: Int Conf Power Syst Technol 2010;1–7. [CrossRef]

Sigma Journal of Engineering and Natural Sciences
Web page info: https://sigma.yildiz.edu.tr
DOI: 10.14744/sigma.2025.00000

Review Article

An overview of optimum calcination parameters for improved pozzolanic activity in biomass ash

Manoj Ashok SADAFALE[1], Mangesh Vasant MADURWAR[1,*]

[1]*Department of Civil Engineering, VNIT, Nagpur, Maharashtra, 440010, India*

ARTICLE INFO

Article history
Received: 15 July 2024
Revised: 09 September 2024
Accepted: 20 January 2025

Keywords:
Biomass Ash; Calcination Temperature; Heating Rate; Retention Time; Sustainability

ABSTRACT

In today's construction practices, incorporation of carbon positive coal fly ash in cement manufacturing has lowered the pace of primary raw material consumption. Coal reserves are limited and hence commercially available coal fly ash will vanish in the coming future. Biomass ash is a sustainable alternative. This ash is carbon neutral and comply with the provisions of supplementary cementing material provided in IS 3812 (Part-I): 2013 and ASTM C618. Biomass ash contains considerable amount of unburned carbon. Most researchers adopt temperature controlled calcination for carbon removal but controlling only temperature does yield ash with optimum pozzolanic activity. Therefore, the present review aims to study the effects of underexplored parameters like retention time, heating rate, cooling method and combustion technology along with temperature for determining the optimum control over each parameter with the help of chemical mechanism. The study of mechanical performance of concrete, incorporating ash treated at various calcination parameter with distinct control reveals the optimum temperature, retention time, heating rate and cooling regime were 500–700°C, 2 – 5 hours, less than 10 °C/ min and rapid cooling respectively. The characteristics of ash obtained after calcination with all parameters of thermal treatment, regulated at optimum extent will possess high pozzolanic activity. The treatment might increase the cement replacement percentage and the mechanical performance of cement based matrix. The utilization of biomass ash will decelerate the pace of raw material consumption required for cement production, reduce land overburden and suffice needs of construction industry leading to a more sustainable future.

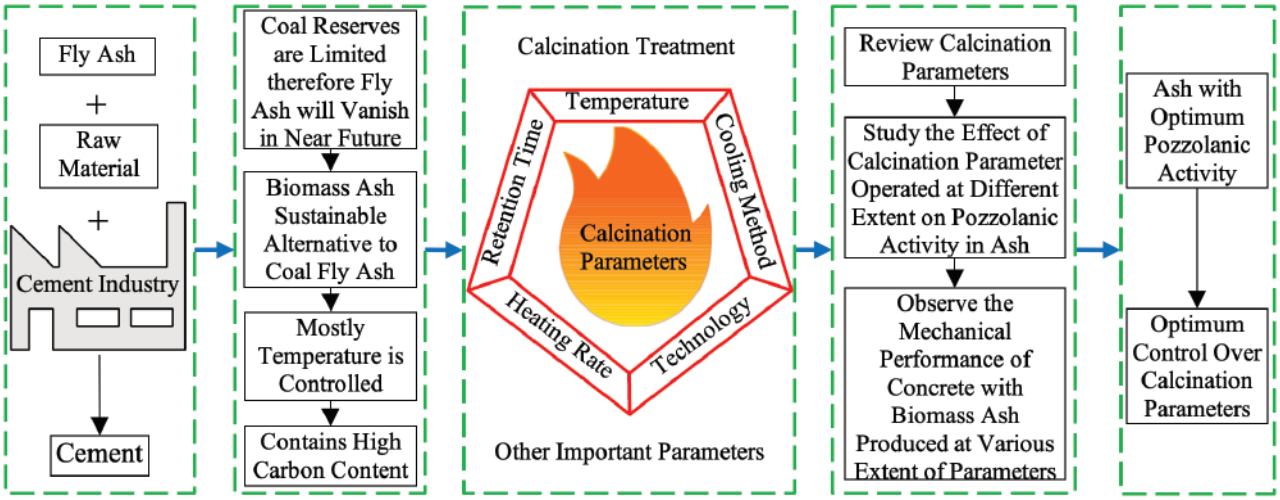
Cite this article as: Sadafale MA, Madurwar MV. An overview of optimum calcination parameters for improved pozzolanic activity in biomass ash. Sigma J Eng Nat Sci 2026;44(1):680–697.

*Corresponding author.
*E-mail address: mvmadurwar@civ.vnit.ac.in

This paper was recommended for publication in revised form by Editor-in-Chief Ahmet Selim Dalkilic

Published by Yıldız Technical University Press, İstanbul, Turkey
© Author. This is an open access article under the CC BY-NC license (http://creativecommons.org/licenses/by-nc/4.0/).

GRAPHICAL ABSTRACT



INTRODUCTION

Cement production is resource, energy and emission intensive process. To meet cement production demands natural resources are exploited but the introduction of coal fly ash in cement manufacturing has decelerated the rate of raw material consumption. Central Electricity Authority (CEA) reports 92.41% utilization of coal fly ash in the year 2021-2022 and therefore, fly ash is deemed as resource rather than a waste [1]. With fly ash's wide applicability and higher consumption rate, the non-renewable fly ash will soon vanish with the extinction of coal reserves. To cater this issue, biomass ash (BMA) is a good and promising alternative to coal fly ash. The ash generated after the combustion of biomass fuel is termed as biomass ash. Flow chart in Figure 1 depicts the production and utilization of biomass ash.

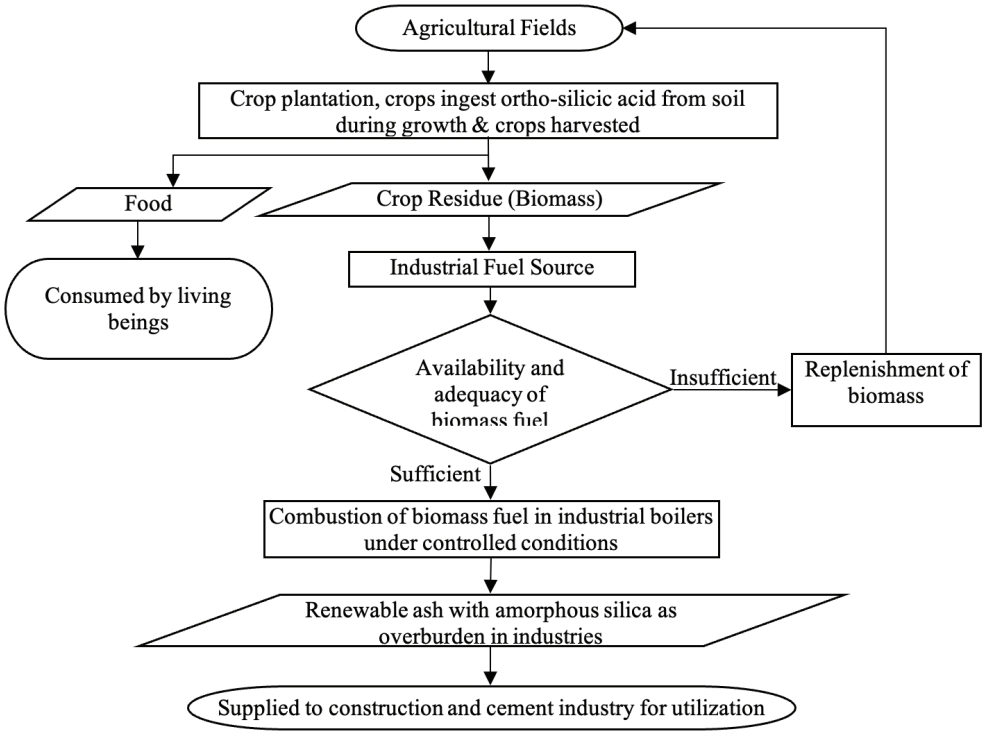


Figure 1. Flow chart showing production and utilization of renewable ash from biomass fuel.

Biomass is a promising alternative source of fuel for energy production. It is considered as carbon neutral energy source since the CO_2 emitted during the combustion of biomass is equivalent to the CO_2 absorbed during the plant growth [2-4]. A fully biomass based energy generation can reduce CO_2 up to 96%, provided substantial quantities are available throughout the year [5]. Utilization of biomass as a fuel source somewhat relieves burden of CO_2 emissions but increases ash disposal concern. The extent of ash produced globally by various biomass fuels [6-24] are shown in Table 1. The problem of ash disposal could be very well addressed by the construction industry [25]. This BMA contains reactive silicates [26], aluminates [27], alumino-silicates etc. which undergoes reaction with portlandite to form supplementary calcium silicate hydrate (C-S-H) [28] or calcium alumino-silicate hydrate (C-A-S-H) or both. These supplementary products formed reinforces interfacial transition zone enhancing the physico-mechanical behavior of concrete. Table 2 compares various properties of fly ash [29-36] and BMA [37-41].

In process of growth, crops like sugarcane [42], rice [43], wheat [42] etc. imbibe orthosilicic acid from soil and store it in plant cellular structure in amorphous form [44]. These discarded crop residues are utilized as energy source in industries where they undergo controlled calcination for heat generation or burnt in open fire (uncontrolled calcination) on agricultural fields. The ash resulting from controlled and uncontrolled calcination possess distinct characteristics. Uncontrolled calcination of biomass yields ash with greater carbon content, loss on ignition and crystalline phases[45]. This is due to inefficient oxygen supply which cause uneven local temperature along with incomplete combustion and results in inferior pozzolanic characteristics [46]. Therefore, the optimum pozzolanic behavior of ash is governed by the precise control over every calcination parameter. Any deviation in the parameters above or below the optimal control, either increases the crystallinity [47] or carbon content inside the ash. Table 3 demonstrate the effect of parameters [48-51] of calcination on quality of ashes [45,52-54].

Therefore, article intended to review the influential parameters of calcination that results in ash with high pozzolanic activity. It is already known that, thermal treatment temperature affects the properties of BMA, but there are some other parameters which are equally important for improving the pozzolanic activity in BMA. The combined effect of underexplored parameters with their optimal control during the process of thermal treatment along with temperature of thermal treatment needs to be reviewed for enhancing the pozzolanic efficiency of BMA. For finding the optimum combined effect of all these thermal treatment parameters, various properties of BMA and hardened properties of cement based matrix incorporating BMA were studied in the present review article.

Process of Biomass Combustion

Before understanding the importance of calcination parameters, it is necessary to review the calcination process which helps in determining the impact of parameters on the generated ash. Almost all biomass contains hemicellulose, cellulose and lignin in variable proportions. These organic compounds are composed of carbon, oxygen and hydrogen [55]. When biomass is subjected to calcination, thermal decomposition takes place in the following steps, a) heating b) drying c) de-volatilization to produce gases and tar d) combustion of volatile matter e) combustion of charcoal (char) [56]. When this biomass is subjected to a cycle of elevating temperature (calcination), these organic contents at first undergoes heating and subsequent drying (130-150°C) and starts de-volatilization producing gases oxygen, carbon-di-oxide, methane and carbon-mono-oxide (O_2, CO_2, CH_4 and CO) [57] and tar in a temperature range of 130-380°C [58]. Tar is composition of more than 100 compounds [59]. The combustion of volatile matter and carbon occurs simultaneously but removal of carbon occurs at higher temperature and consumes a longer duration. The volume of volatile matter in biomass fuel (BMF)

Table 1. Global annual production of biomass and ash from distinct sources

Sr. No.	Crop	Residue as fuel source	Crop/product production (million ton)	Biomass production (million ton)	Ash production (million ton)	References
1	Sugarcane	Bagasse	1900	494	12.6	[6,7]
2	Rice	Husk	518	145.04	29	[8-11]
		Straw		777	116.55	
3	Wheat	Husk	772	154.4	21.5	[12-15]
		Straw		1080.8	72.4	
4	Maize	Corn cob	1070	203.3	4.67	[16-18]
5	Palm Tree	Shell, fibre, fruit bunch	72.27	650.43	26	[19,20]
6	Coconut	Shell	62.46	9.369	0.17	[21,22]
7	Groundnut	Shell	43.98	17.59	0.44	[23,24]

Table 2. Comparison between coal fly ash and BMA

Description	Biomass Ash	Coal Fly Ash
Source	The major sources of biomass are agricultural residue, municipal solid waste, wood and dried cattle waste [37]. The ash resulting from biomass might be high as 43.3% for a particular source but on an average, it is 6.00% [38].	There are four different ranks of coal which produces fly ash after combustion. They are Anthracite, Bituminous, Subbituminous and Lignite [29]. The ash resulting from high impurity coal may be as high as 48.4% but on an average, it is 19.8% [30].
Chemical Characteristics	The chemical composition of biomass ash depends on the type of biomass. However, ash from woods and agricultural waste contain silica (SiO_2: upto 94.48%) and calcium oxide (CaO: upto 83.16%) in high quantities and alumina (Al_2O_3: upto 15.12%), and iron oxide (Fe_2O_3: upto 9.54%) in less quantities. The alkali oxides which are considered as impurities in cement-based products are present in very high proportions in some of the BMA. It is observed that, Na_2O and K_2O in BMA could be as high as 29.82% and 53.38% [37].	Two different fly ash evolve from the combustion of coal, i.e. class C and Class F. Class C fly ash contain CaO greater than 10%, whereas Class F fly ash possesses CaO less than 10%. The other major mineral oxide which is found inside Class C & F fly ash are silica (SiO_2: 20-80%) and alumina (Al_2O_3: 1-55%) and iron oxide (Fe_2O_3: 1-44.7%). The ash also contains alkali (Na_2O & K_2O) in quantities varying from 0.0 to 7.3% [31]. The loss on ignition for coal fly ash ranges between 0.0 – 32.8% [32].
Physical Characteristics	The fineness of BMA can be as high as 700 m^2/kg [39] and specific gravity ranges between 1.82 – 2.46 [37]. The particle size and loos bulk density of BMA varies between 0 – 10 mm [37] and 430 – 960 kg/m^3 [40]. The particles of almost all the BMA are irregular in shape and their particles possess inherent porosity [26,41].	The fineness and specific gravity of coal fly ash vary between 231.5 – 523.9 m^2/kg and 1.94 – 2.72 [32]. The particle size and loose bulk density of coal ranges between 1 – 100 μm and 540 – 860 kg/m^3 [33]. Coal fly ash particles are spherical in shape and exhibit a porous/non-porous nature [34,35].
Environmental Impact	Biomass is a carbon neutral fuel source. BMA resulting from the power plants and other industries is landfilled. The ash generally does not possess very hazardous elements and therefore can be used in fertilizers etc [38].	Coal is a fossil fuel and therefore it has a high carbon footprint which contributes significantly to the GSG emission. The coal fly ash is generally landfilled and its leaching causes hazardous elements like Arsenic, Boron, Chromium, Cadmium, Lead and Mercury pollutes the surrounding soil [36].

Table 3. The effect of parameters of calcination on quality of ashes

	Type of Calcination	Uncontrolled	Controlled		
Features of Biomass Calcination	Control Over Calcination Parameters	No Control	Control Below Optimum	Optimum Control	Control Above Optimum
Properties in Ash	Carbon Content in Ash	High [48]	High [49]	Very low [50]	Very low [51]
	Nature and Reactivity in Ash	Crystalline and Less Reactive [45]	Amorphous and Less Reactive [52]	Amorphous and Highly Reactive [53]	Crystalline and Less Reactive [54]

can be as high as 85 % [60] and combustion consumes around 40-50 % of the total burnout time which occurs at higher combustion rate than char. Whereas combustion of char depends on temperature, residence time, contaminants producing inhibiting and catalytic effect, oxygen concentration and surface area of fuel particle [61].

Generally, the thermal decomposition of hemicellulose (150-350°C) and cellulose (275-350°C) occurs at a lower temperature but decomposition of lignin occurs in wide temperature range (275-500°C) [62]. Thus, these organic compounds experience thermal disintegration at a temperature below 500°C and decomposes into tar and char (forms of carbon). Further increase in temperature, the carbon undergoes oxidation at a faster rate, rather at temperature below 500°C where volatilization is faster [63]. For decomposition of char, oxygen present in the environment is transferred onto the particle surface where it diffuses into the porosity of char. The chemisorption of oxygen on the active sites causes decomposition and releases CO. CO chemically combines with O_2 from the gaseous boundary layer and releases CO_2. The oxidation of carbon occurs continuously as more and more reactive sites are exposed [64]. Also, it was reported that the molecules of H_2O and CO_2 dissociates into their free radicals which are absorbed by the active sites and tends to oxidize carbon [65]. However, following chemical reactions are proposed by [66] for oxidation of carbon particles.

$$C + \frac{1}{2}O_2 \rightarrow CO \quad (1)$$

$$CO + \frac{1}{2}O_2 \rightarrow CO_2 \quad (2)$$

$$CO_2 + C \rightarrow 2CO \quad (3)$$

$$C + O_2 \rightarrow CO_2 \quad (4)$$

$$H_2O + C \rightarrow CO + H_2 \quad (5)$$

$$CO + H_2O \rightarrow CO_2 + H_2 \quad (6)$$

Important Parameters for Controlled Calcination

Temperature, retention time, heating rate, cooling method and combustion technology are the parameters that affects carbon removal efficiency, crystal structure and colour of ash in calcination. These parameters cannot be regulated in uncontrolled calcination. A control over these parameters modulates the decomposition of volatile matter and char in biomass [67]. Therefore, a discussion about these parameters is elucidated in succeeding sections.

Calcination temperature

Calcination temperature is the primary factor that induce good pozzolanic activity in ash for utilizing as a supplementary cementitious material (SCM) in concrete. Results on BMA characteristics are available from temperature range of 300°C to 1000°C. A temperature over 500°C mostly yields amorphous ash with low carbon content whereas temperature below 500°C results in amorphous ash but with high carbon percentage [60]. The two main phases that govern carbon decomposition are (a) oxygen diffusion rate (b) chemical reaction rate. Oxygen diffusion rate is responsible for amount of carbon decomposition whereas chemical reaction rate determines the pace of carbon decomposition. Combustion at lower temperatures (400 - 750°C), oxygen diffusion rate is greater than chemical reaction rate. In the mid order temperature range (750 - 900°C), the oxygen diffusion and chemical reaction rate are almost similar whereas in high temperature range (900 - 1100°C), the chemical reaction rate overrides oxygen diffusion rate [68,69].

Most researchers have utilized low to moderate temperature zone for effective biomass combustion. These two zones have constantly been reported to produce amorphous silica. Crystallization of silica mainly occurs when temperatures exceed beyond 700°C. The impurities present in biomass interact with amorphous silica at high temperatures and transforms it into crystalline phases [70]. According to Ibrahim and Helmy, the phase transformation of ash begins at 725°C and at a temperature around 800°C the ash is readily transformed into Crystobalite. Calcination at lower temperature results in amorphous (disordered) Cryatobalite in ash. The temperature increase causes nucleation of silica, which occurs simultaneously with crystallite growth. Nucleation of silica particle was predominant in temperature range of 800-900°C while crystallite growth and perfection was favoured within 1000-1100°C [49]. In another experimentation conducted by Hanafi et.al. on rice husk ash for the study of surface characteristic stated an increase in surface area and total pore volume due to destruction of silanol (destruction of bond between Si and OH) group in a temperature range of 500-600°C. But a further increase of temperature beyond 600°C upto 1000°C reduced the surface area, total pore volume and increased crystallite size. A drastic reduction in surface area, total pore volume and increase in particle size was more pronounced at 1000°C while till 900°C temperature ash also contained amorphous phases which was evident from the X-Ray diffraction (XRD) pattern. At 1000°C temperature, disordered Crystobalite had transformed into crystalline state which was marked by decrease in surface area, total pore volume and increased particle size. These results were found consistent with Ibrahim and Helmy. Further increase of temperature to 1100°C increased surface area and total pore volume, and declined particle size due to formation of disordered Tridymite phases. The escalation of temperature further till 1400°C declined the surface area and total

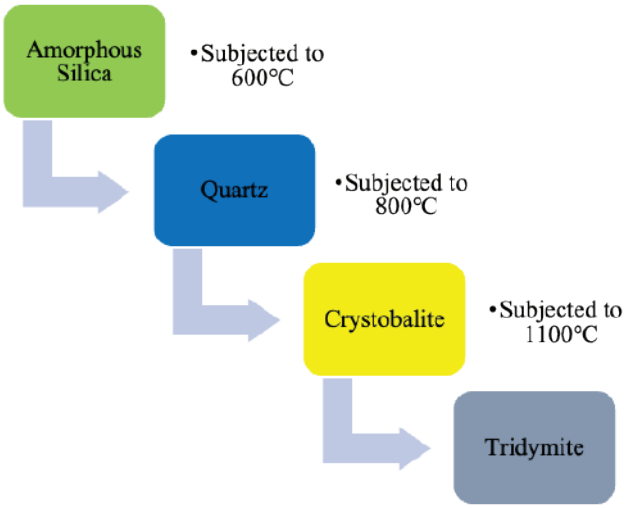


Figure 2. Phase transformation of silica in biomass.

pore volume [71]. Similar results were obtained by Hamad and Khattab where they confirmed that crystallization of Crystobalite occurred at 800°C while phase transformation of Crystobalite to Tridymite initiated at 1150 °C. Amorphous Crystobalite phases were present below 600°C. [72]. The structural transformation of silica extrapolated from review is shown in Figure 2. Therefore, treatment of biomass in low temperature region will possibly retain the amorphous nature of ash.

However the transformation of silica varies from one biomass to other biomass type. This is generally due to the varying chemical composition of different BMA. In rice husk ash (RHA) silica (SiO_2) is present in major quantities whereas other oxides and impurities are present in minor amount. The impurities play a pivital role in the phase transformation of silica at higher temperature [49]. In another type of BMA like wood ash, where silica is present in lower amounts and calcium oxide in higher amount, the possibility of silica phase transformations is lower. The calcium oxide along with other mineral oxide have a tendency to fuse with silica and form a multiple element oxide compound [73].

Retention time

The second most critical factor concerning the calcination of biomass is retention time. When biomass is subjected to a specified temperature control it has to be retained inside the calcination chamber for the completion of undergoing chemical processes. The chemical process includes reduction of organic matter (into gases, tar and char) and oxidation of carbonaceous matter. The state of completeness of these reactions can be identified from the ashes. These chemical reactions for its completion require a specified amount of time which is known as retention / residence / holding time. When the biomass is exposed to shorter retention time these reactions are incomplete rendering unwanted characteristic in ashes but when sustained at optimum retention time yields ash with best pozzolanic activity. When the temperature is maintained between 400-600°C for a residence time of 3-6 hours it yields ash with low carbon content and crystallinity [74,75]. The primary necessity of retention time is removal of carbon. From the studies conducted so far on the calcination of biomass it can be stated that the temperature and retention time are inversely related to each other. Siddique makes an affirmation to this inverse relationship stating that amorphous silica ash could be produced with a prolong retention time if the temperature is maintained below 500°C. If the temperature is raised to 900°C and 1000°C the ashes are still amorphous but for a residence time of less than 1 hour and 5 minutes respectively [76]. An experimental investigation was conducted by Vayghan et.al to study the effect of retention time on physic-chemical properties of rice husk ash. The experimentation was conducted at 700°C with retention time of 0.25, 1, 4, 8, 16, and 32 hours. With a longer retention time of even 32 hours the ash still remained amorphous which was evident from the X-Ray diffraction pattern [77].

Rate of heating

From the aspect of carbon removal, heating rate is a very crucial parameter. The impurities present inside the biomass do not allow easy oxidation of carbon instead forms an agglomerate with silica which leads to high percentage of carbon quantity and reduced surface area. In most of the research, the authors have used variable heating rate values ranging from 1°C/min to 10°C/min. The most commonly deployed heating rate was 10°C/min [78]. Rice husks when heated at a rapid rate do not allow the oxidation of carbon as desired mainly due to two probable reasons. Firstly, at higher heating rates the desired temperature is achieved very fast. Though the oxidation of carbon starts at 350°C but have a tendency to oxidize slowly and results into greater amount of carbon in ash [60]. Secondly, the intervention of impurities (K_2O) during calcination produces ash with greater carbon content [79]. Chandrasekhar et.al explored the effect of heating rate on the pozzolanic reactivity of rice husk ash. The heating rates were 1, 2, 3, 5, 7 and 10°C/min and the temperature was maintained at 700°C. With increase in heating rates the lime reactivity test displayed lower reactivity values due to conversion of amorphous silica into crystalline phase. Rapid heating resulted in ash with blackish appearance due to fixed carbon [80].

Cooling Method

The cooling method governs the phase transformation (amorphous to crystalline) inside the ash. After subjecting the biomass to optimum temperature and residence time might not yield BMA with complete amorphous phases as a result of applied cooling method. Generally, rapid and slow cooling techniques are followed. For rapid cooling the ash is quenched rapidly in air or water whereas for slow cooling the ash remains inside the heated furnace till it attains the room temperature (oven cooling) [81,82]. A better pozzolanic behavior is observed when ash is rapid cooled than slow

cooling [83]. In an experimentation carried out by Vayghan et.al. [84], the effect of cooling method was studied after retaining the ash at 700°C temperature and residence time (15 min, 1, 2, 4, 16 hrs). It was deduced that, if the ash is rapidly cooled from its combustion temperature to room temperature, no crystalline phases are formed even after exposing ash till a retention time of 32 hours and with a high amount of K_2O. It was also stated that, prior to calcination if the rice husks are acid leached, K_2O is discarded, thus preventing crystallization of amorphous silica in slow cooling regime [84]. Study conducted by Nair et.al. demonstrated that, pozzolanic activity of rapidly cooled samples was more than slowly cooled ash. Also, the size of particle in quick cooling is lesser than slow cooling. This was indicative of the condensation reaction that took place in slow cooling regime of ash which rendered it as less reactive due to decreased particle surface area [85].

Technology of Calcination

The characteristics of BMA is governed by biomass combustion technology at the industries. Moving grate firing system (MGFS), fluidized bed combustor (FBC) and suspension burner system (SBS) [86] are the recognized technologies used for fuel combustion. Such technologies are potentially utilized in paper industries [87], biomass-based power plants, sugar industries and co-generation plants [88], distilleries, chemical industries etc. The most rudimentary and often utilized system for firing industrial boilers is MGFS. Lower installation, operational and maintenance cost attracts industrialists with MGFS [89]. On the contrary MGFS is usually designated as high carbon in ash, low efficiency and high emission technology [89]. The inefficient combustion of biomass is due to lower residence time than required for complete combustion of char in biomass. This not only results in greater extent of unburnt carbon but also gives away high emissions [90]. FBC is considered as a mature technology due to its flexibility, very high efficiency of fuel combustion and lower environmental impact [91]. This system offers a very high combustion efficiency between 97-98.4% which results in ash with low carbon content [92]. When any biomass is introduced in FBC high heat and mass transfer property of fluidized sand bed allows quick energy transformation at nearly constant temperature condition. The high reaction surface area available inside FBC results in high combustion efficiency and lower operating temperature than MGFS. Moreover, the excess air supplied tends to retain fuel particles in combustor for sufficient residence time which bring about complete oxidation of carbon. Contrary to FBC, the non-uniform air fuel ratio give rise to high unburnt carbon in ash and thus affecting combustion efficiency [93]. SBS is also said to produce good quality of ash but its sensitivity towards varying fuel composition significantly affects its performance. Every time the fuel inside should be finely pulverized [89].

Effect of Calcination Parameters on Chemical Composition of BMA

Biomass when subjected to calcination, it undergoes decomposition. A variation in these parameters alter the chemical composition. Table 4 shows the chemical composition of BMA with different parameters of calcination. The results of chemical composition are taken from the X-ray fluorescence (XRF) data available in research articles.

Table 4. XRF results of various BMA with different parameters of calcination

T °C	RT Hrs	HR °C/min	CM	Chemical contents									
				SiO_2	Al_2O_3	Fe_2O_3	CaO	MgO	SO_3	K_2O	Na_2O	LOI	Ref.
Rice Husk Ash													
300	3	10	Slow	35	1.87	1.56	11.2	2.91	8.96	21.9	1.66	-	[52]
	9			48	1.57	1.55	9.28	2.52	8.35	19.35	1.39		
500	2	8	-	89.89	0.11	0.28	1.05	0.13	0.4	2.92	-	-	[74]
	2	10	-	91.56	0.19	0.17	1.07	0.65	0.47	3.76	0.16	-	[75]
	3	10	Slow	66.45	3.68	0.85	3.36	1.6	0.54	5.68	2.2	-	[52]
	6	5	-	92	0.25	0.14	0.81	1.05	0.96	3.44	-	3.62	[76]
	7	10	Slow	73.05	1.16	1.18	3.5	1.45	0.47	5.67	2.74	-	[52]
600	1	5	-	92.09	0.1	0.07	0.97	0.53	0.55	4.04	0.11	1.52	[77]
	2			93	0.1	0.07	0.92	0.45	-	3.62	0.46	1.48	
	2	20	-	81.4	0.26	0.93	2.42	1.02	1.47	6.79	0.18	3.13	[78]
	3	10	-	90	0.68	0.42	1.23	0.35	-	2.8	0.32	-	[79]
	6	-	Slow	88.84	0.8	0.39	1.78	0.92	0.35	2.8	1.1	2.02	[80]
650	1	3.33	-	87.32	0.22	0.28	0.48	0.28	1.02	3.14	1.02	2.10	[48]
	-	2	Slow	92	0.31	0.38	0.97	0.47	-	3.87	0.2	0.76	[50]

Table 4. XRF results of various BMA with different parameters of calcination (continued)

T °C	RT Hrs	HR °C/min	CM	Chemical contents									
				SiO_2	Al_2O_3	Fe_2O_3	CaO	MgO	SO_3	K_2O	Na_2O	LOI	Ref.
Rice Husk Ash													
700	1	3	-	89.03	2.23	0.66	0.96	0.38	-	2.34	2.59	0.7	[81]
	1	10	Rapid	88.07	1.35	0.22	1.04	0.74	0.49	2.02	1.15	2.61	[82]
	2	-	Slow	84.95	0.45	0.32	0.84	0.4	-	0.21	0.5	9.81	[83]
	3	10	Slow	88.00	0.38	0.41	2.1	0.52	1.98	4.35	0.32	-	[52]
	4	10	Rapid	94.91	0.05	0.25	0.98	0.44	-	1.67	0.07	1.28	[84]
	5	10	Slow	94.63	0.18	0.19	1.05	0.18	0.62	2.18	0.15	-	[52]
	6	5	-	91.15	0.41	0.21	0.41	0.45	0.62	6.25	0.05	0.45	[85]
	6	10	Slow	93	0.2	0.13	0.49	0.73	0.15	1.3	0.02	3.98	[54]
	8	10	Rapid	95.22	0.09	0.19	1.16	0.39	-	0.14	0.03	0.8	[84]
	16	10	Rapid	95.1	0.05	0.11	0.1	0.41	-	1.66	0.05	0.92	
800	-	-	Slow	89.5	0.4	2.86	0.3	0.25	-	-	-	4.0	[86]
			Rapid	84	1.39	2.1	0.6	0.85	-	-	-	5.85	
900	3	10	Slow	92	0.23	0.21	1.39	0.36	1.42	2.99	0.2	-	[52]
	4	5	Slow	98.19	0.19	0.02	0.18	-	-	1.04	-	0.5	[87]
	6	5	-	92.0	0.37	-	1.05	0.95	1.06	3.2	-	0.29	[76]
Sugarcane Bagasse Ash													
550	2	10	Slow	58.37	7.24	4.04	3.07	3.02	-	8.20	0.05	25.1	[88]
	3	10	Slow	64.00	7.46	3.50	2.46	3.15	-	7.71	0.04	18.5	
600	2	10	Slow	64.14	6.82	5.12	1.78	1.75	-	6.32	0.22	5.83	
	3	10	Slow	69.79	9.86	3.02	1.92	1.78	-	5.57	0.05	5.61	
	3	10	-	69.6	15.7	5.7	1.3	-	1.5	2.2	-	2.1	[89]
650	2	10	Slow	64	8.16	5.04	1.08	1.90	-	6.55	0.25	3.90	[88]
	3	10	Slow	72.5	10.63	4.04	1.14	1.34	-	3.56	0.08	3.57	
700	2	10	Slow	63.86	9.5	4.96	1.81	2.04	-	6.78	0.27	3.22	
	3	10	Slow	74.22	9.87	4.13	1.72	0.96	-	2.7	0.03	2.46	
750	2	10	Slow	66.32	12.97	5.27	1.35	1.6	-	4.7	0.36	3.12	
	3	10	Slow	75.91	10.49	2.99	0.84	1.31	-	3.3	0.07	3.13	
Wheat Straw Ash													
550	4	-	-	62.5	9.08	1.67	5.90	-	1.66	17.05	-	-	[90]
	8	-	-	60.07	6.98	1.45	8.47	-	1.67	15.87	-	-	
800	0.5	-	-	55.5	11.24	2.79	7.40	-	1.84	22.43	-	-	
Corn Cob Ash													
350	3.75	-	-	10	1	2.3	4.2	10	-	57.5	-	-	[91]
400	3.75	-	-	10.7	1.5	2.5	4.4	10.1	-	57	-	-	
450	3.75	-	-	12.4	1.7	2.7	5	9	-	56	-	-	
500	3.75	-	-	14	1.9	2.8	7	9.5	-	52.5	-	-	
550	3.75	-	-	15.1	1.9	2.9	6.9	9	-	52	-	-	
600	3.75	-	-	18.3	2.7	3.12	8	10.2	-	47.2	-	-	
	4	-	-	63.91	4.01	3.95	4.13	2.91	0.88	12.12	-	-	[92]
650	3.75	-	-	20.2	3.1	3.7	10	8.4	-	45.4	-	-	[91]
	5	-	-	59.66	4.92	-	1.86	1.68	-	15.48	0.34	-	[93]
	8	-	-	66.38	7.48	4.44	11.5	2.06	1.07	4.92	0.41	-	[94]
700	3.75	-	-	20	2.9	3.5	11	8.2	-	45.3	-	-	[91]

Where, **T** = Temperature, **RT** = Retention time, **HR** = Heating rate and **CM** = Cooling method

The variation in chemical composition could be observed in terms SiO_2, impurities and loss on ignition (LOI). The criteria of SCM defined by IS 3812-1: 2003 and ASTM C-618 states that the summation of oxides (SiO_2 + Al_2O_3 + Fe_2O_3) should be greater than 70% [95,96]. It is observed that biomass calcined at temperature below 500°C could not qualify the SCM criteria defined by the standards. Moreover, impurity content in ash was very high. But with increasing temperature, the impurities started to decline which resulted in an increase in silica and alumina content. A similar scenario of increase in silica and alumina content was observed with increase in retention time. From the table it is also observed that, not all the ashes were able to qualify the criteria of SCM mentioned in IS 3812-1: 2003 and ASTM C-618. This is due to the presence of impurities. The impurities like K_2O were present in very high quantities (57.5%), and such ashes could adversely affect the properties of cement based matrix. At temperature greater than 600 °C and retention time greater than 3 hours the loss of ignition was found within the limits prescribed by IS 3812-1: 2003 and ASTM C-618. The limits for LOI defined in IS and ASTM are 5% and 6% respectively.

PROPERTIES OF CONCRETE

Effect of Calcination Parameters

Inclusion of SCM into concrete mixes, the mechanical concrete characteristics are influenced by the quality of SCM. Uncontrolled calcination of biomass produces ash with high carbon content and crystalline silica phases. Incorporation of such ash results into uneven mechanical characteristics of concrete. This is generally due to inconsistency of combustion parameters in open fire. BMA evolving from controlled combustion leads to predictable mechanical concrete behavior. A study of calcination factors affecting the quality of BMA and resulting mechanical behavior of concrete, guides in optimizing calcination parameters.

The foremost parameter that overrides is calcination temperature. From section 3.1 it is already clear that minimum temperature for desired ash characteristic should be greater than 500°C. The effect of inclusion of RHA treated at different temperature on mechanical properties of concrete could be seen from Figure 3. The increase in percentage compressive strength from the study of different researchers was found to be highest within the temperature region of 500-700°C which could be clearly observed from Figure 3(a). Its highest percentage increase in compressive strength was 43.05% at 700°C [84]. Considering peak at each temperature the trend shows an increase in strength till 700°C and a sudden downfall thereafter. These authors have either experimented with a particular temperature or over a range of temperature. The peak increase in percentage compressive strength reported from their investigation are 10, 21, 20.15, 3.13 and 12% at 300, 500, 600, 800 and 900°C respectively. When temperature reached 1000°C the increase in compressive strength was -0.4% which indicated that strength was below control concrete strength [52,74,97,98]. These authors reported similar trend for percentage increase in flexural and split tensile strength which could be noticed from Figure 3(b) and 3(c) respectively.

A review conducted from research of various authors revealed 700°C as the optimized temperature, therefore it was decided to observe the effect of retention time and heating rate at 700°C from available literature. After a compilation of results from different research, it could be deduced that a retention time of 2-5 hours is sufficient to obtain good pozzolanicity in ash which probably results in percentage increase in strength greater than 20%. This could be observed from Figure 4. At 500°C, Faried et.al reported 18.8% and 19.4% increase in compressive strength for a retention time of 3 and 7 hours [52]. Huang et.al. showed the compressive strength elevated by 9.67% for a retention time of 2 hours [75]. For a temperature of 600°C and 800°C, Xu et.al and Khan et.al. recorded increase in compressive strength by 12.5% and 3.13% for the respective retention duration of 2 and 5 hours [78,97].

At the considered optimized temperature (700°C) Figure 5 manifests percentage increase in compressive strength from the experimentation of different researchers at various duration of retention for heating rate of 10 and 20°C/min. At temperature of 500°C and a heating rate of 1.67, 8 and 10°C/min Khalaf and Yousif, Muthukrishnan et.al and Huang et.al displayed a percentage increase in compressive strength as 19.6, 21 and 9.67% respectively [74,75,100]. Khan et.al and Xu et.al conducted investigation at 800 and 600°C where they found the percentage increase in compressive strength as 3.13 and 12.85% with a respective heating rate of 3.33 and 20°C/min [78,97]. Khan et.al calcined rice husk at 800°C where rapid cooling was carried out at temperature of 21±1°C and for slow cooling the sample was retained in furnace. The pozzolanicity test conducted revealed a superior reactivity of rapidly cooled ash with 28 days compressive strength as 21.10MPa [86].

Effect of Varying BMA Content

Vayghan et.al. obtained optimally calcined dry acid leached RHA at 700 °C temperature an 8 hours of retention time. 0, 5, 10 and 15% RHA were the different proportions of RHA used to replace cement in the mortar matrix. The results showed that mortar with 10% RHA had the highest compressive strength [84]. Huang et.al. substituted RHA with cement at 0, 5, 10, 15, 20, 25 and 30%. The ash was treated at 500 °C temperature, 2 hours of retention time with 10 °C/ min heating rate for developing ultra-high performance concrete (UHPC). The compressive strength of UHPC at 28 days achieved was 136.6 MPa with 25% RHA [75]. Faried et.al. calcined rice husk at four different temperatures and retention time with a heating rate of 10 °C/ min. Temperature of 700 °C with 5 hours of retention time were the optimum calcination parameter. RHA replaced

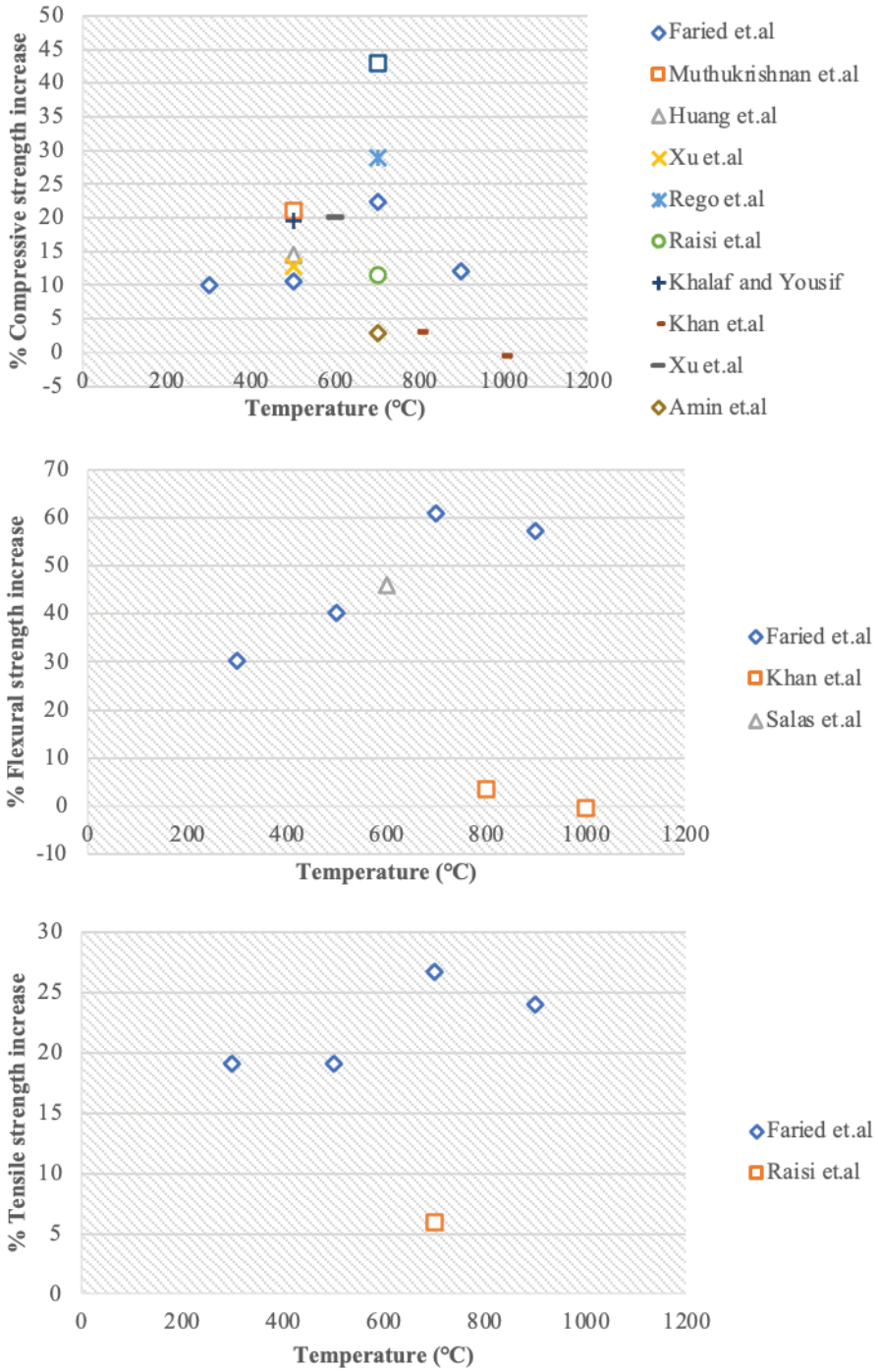


Figure 3. RHA treated at various temperature and its effect on mechanical properties (a) percentage increase in compressive strength (b) percentage increase in flexural strength (c) percentage increase in split tensile strength [52,74,75,78,82,83,97-100]. [created by author].

cement by 0, 1, 3 and 5% for making UHPC. The highest strength achieved was above 140 MPa at 3% cement replacement [52]. Amin et al. used thermally treated RHA at 700 °C it for developing concrete in three different cement replacement percentage (10, 15 and 20%). The maximum strength at 28 days was achieved for 10% concrete mix [99]. Raisi et. al. obtained RHA at 700 °C temperature, 1 hour retention time and 10 °C/ min heating rate. Five different proportions of RHA (0, 5, 10, 15 and 20%) were used to replace cement in self-compacting concrete (SCC) mixes. The highest compressive strength achieved was 57.7 MPa at 5% cement replacement [82]. As per Khalaf and Yousif

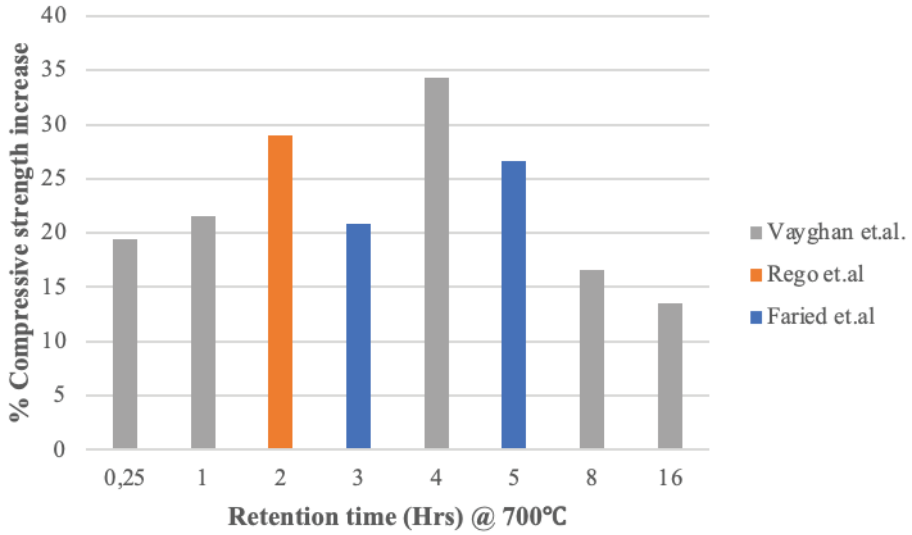


Figure 4. RHA treated at various retention time and its effect on percentage compressive strength at considered optimized temperature [52,83,84]. [created by author]

the optimum temperature and retention time of thermal treatment was 500 °C and 2 hours. The ash prepared with these optimum treatment parameters was used in mortar replacing cement by 0, 10, 20, 30, 40 and 50%. Mortar with 10% cement replacement yielded the highest compressive strength [100].

Synergistic Effect of Biomass Ash with Different Fibers

Hamzeh et.al. studied the combined effect of RHA treated thermally at 700 °C with three different derived fibers. The fibers were derived from virgin kraft pulp (VKP), fiberboard (FFB) and old corrugated containers (OCC). The cement paste cubes were used to observe the effect of RHA and fibers. The proportion of fibers to cement was constant (25: 75) and different proportions of RHA were 0, 25 and 50% by weight of fibers. The cubes attained highest compressive strength with OCC fibers with 25% RHA replacement [101]. Hesami et.al. burned rice husks in an open fire for 2 hours and then and used a special furnace to decompose the carbon in RHA. Seven different percentage of RHA (0, 2, 4, 6, 8, 10 and 12% by cement weight) along with three distinct fiber types were used to develop pervious concrete for pavement. Glass, steel and polyphenylene (PP) fibers with a corresponding volume percentage of 0.2, 0.5 and 0.3% to the volume of concrete were used in the investigation. It was observed that the performance of

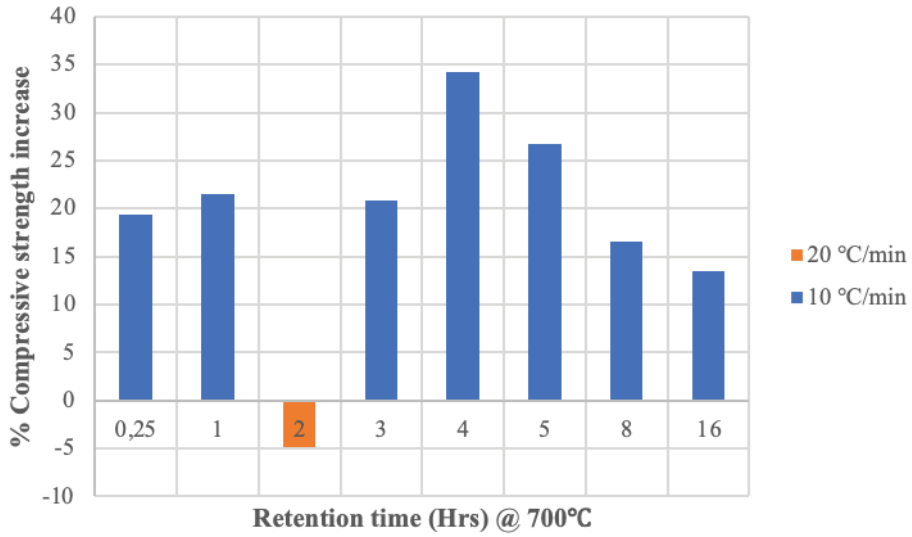


Figure 5. RHA treated at various heating rate and its effect on percentage compressive strength at considered optimized temperature and over a range of retention time [52,84,98]. [created by author]

fiber concrete with RHA was greater than control. The best mechanical performance of pervious concrete was shown by PP fibers at RHA percentage of 8% [102]. Memon et.al. investigated the significance of thermally treated RHA along with polypropylene (PPY) fiber on various properties of concrete. The procured RHA was thermally treated at 700°C for one hour in an electric furnace and substituted cement by weight percentage of 0, 5, 10, 15 and 20%. PPY fibers were added to concrete in four different percentages (0, 0.2, 0.25, and 0.3). The mechanical performance of concrete with 10% RHA and 0.25% PPY fibers was superior than control and other mixes [103].

Koushkbaghi et.al. developed steel fiber reinforced concrete with RHA as SCM and recycled coarse aggregates (RCA). Rice husk pellets were calcined in an electric furnace between 500 - 700°C, for 6 hours with a heating rate of 5 °C/ min for obtaining RHA. The 20% RHA and 1.5% steel fibers were added to the concrete. RCA replaced natural coarse aggregate by 0, 50% and 100%. The increasing percentage of RCA lowered the mechanical performance of concrete, whereas adding 20% RHA and 1.5% steel fibers increased the mechanical performance of concrete when compared with control concrete. The mechanical performance of concrete with 20% RHA (no steel fibers) was greater than 1.5% steel fibers (no RHA) [104]. Sobuz et.al. developed self-compacting concrete (SCC) with RHA and fibers derived from waste galvanized copper wire. SCC included 2% RHA and 0, 0.25, 0.5 and 1.0% fibers. The results manifested that the mechanical performance of control concrete was better than SCC with inclusion of RHA and fibers. The compressive strength of SCC with 2% RHA and 0.25, 0.5 and 1.0% fibers was 17.99, 18.09 and 19.7 MPa whereas for control (0% RHA and 0 % fibers) SCC it was 22.62 MPa [105]. Silva and Naveen carried out investigation on combined effect of RHA and coconut coir (CC) fibers in cement mortar. The RHA from brick kiln was used to substitute cement from 0 – 20% with a replacement interval of 5% and 0, 0.125, 0.25, 0.5 and 0.75% were the various percentage of CC fibers addition to the mortar. The addition of CC fibers increased the flexural strength but reduced the compressive strength [106].

RESULTS AND DISCUSSION

Limiting the utilization of cement in construction industry, SCM plays an active role. Sources of SCM are numerous but those evolving from biomass will have an impact on the future. Presently, 81% of the global energy needs are fulfilled by fossil fuels whereas 19% is contributed by renewable energy sources [107]. The agricultural biomass designated as carbon neutral possess a major drawback, posing a problem of ash disposal. The ash on an average account for 20% of the biomass waste on a dry basis. This ash is a potential resource for the construction industry as SCM if properly calcinated. The major parameters that influence the characteristic of ash are temperature, retention time, heating rate, cooling method and combustion technology. These parameters significantly alter the morphology, physical and chemical aspects of resulting ash.

Calcination Parameters

The first and foremost calcination parameter is temperature. A control over temperature modulates the chemical reactions to yield intended quality of ash. But it is not solely dependent on temperature. Retention of biomass for a particular time inside combustion chamber at desired temperature yield fine quality of ash. Whenever the temperature is kept less than 600°C a greater extent of retention time is required. If retention time is lower, char combustion (oxidation of carbon) remains incomplete. Because at lower temperatures, oxygen diffusion rate is greater than rate of chemical reaction. Since the chemical reaction pace is slower, the complete oxidation of char requires greater retention period. The diffusion of oxygen to the inside of char particles favors oxidation from inside resulting into ash with lower densities. A rise in temperature retards the oxygen diffusion and increases the chemical reactivity. Whenever calcination temperature goes beyond 900°C, retention time required is less than an hour. Due to higher chemical reactivity, oxygen diffusion to the inside of particle is not likely to happen. Instead, as oxygen from the bulk gases reaches particle surface instantly starts oxidizing the surface carbon thus reducing the particle size. Ashes that are burnt at higher temperature are likely to have greater densities than those at lower temperature.

The other factors i.e. heating rate and cooling method though secondary, play a vital role in enhancing the quality of ash. A higher heating rate escalates the carbon content inside the ash due to the presence of K_2O impurity. For higher heating rates, desired temperature is attained faster which favors early dissociation of K_2O into elemental K^+ ion. The early released K^+ ion gets absorbed on the surface of silica particle and cause surface melting which traps carbon inside and results in high carbon ash [108]. In the process of slow heating rate enough time is available for thermal decomposition of carbon before the dissociation of K_2O into elemental potassium. Since, the formation of elemental potassium takes places at later stages, greater time span is available for carbon removal. This indicates that a slow heating rate has a higher efficiency of carbon removal than higher heating rate.

The rapid cooling method promotes the retention of amorphous silica phases whereas slow cooling results into higher percentage of crystallinity inside the ash. In the slow cooling process, the dissociated K^+ ion which is already present inside the ash will cause melting of the particle surface on which it is deposited. This promotes the crystallite growth of the particle. A rise in the crystallite size increases the crystallinity and lowers the pozzolanic reactivity inside the ash. In case of rapidly cooled ashes, the drop in temperature occurs very quickly, which stops the surface melting of the particle due to deposited elemental potassium.

This hinders the crystallite growth and results into amorphous ash with high pozzolanic activity [109].

Mechanical Properties of Concrete

Effect of calcination parameters

Calcination parameters influence mechanical characteristics of concrete. Various investigation outcomes revealed 500-700°C as optimum calcination temperature. Such ash when integrated with concrete yields greatest mechanical performance. At higher temperature (>700°C), crystallization of amorphous phases occurs which lowers mechanical performance of concrete because crystalline phases do not react to form C-S-H gel. Even high temperatures yields amorphous silica, but at lower retention time. The mechanical performance of concrete with BMA containing equal quantum of amorphous phases produced at temperature < 700°C should conceptually be greater than BMA produced at temperature >700°C. Because temperature < 700°C favors decarbonization to the inside of particle which enhances the reactivity due to greater amount of oxygen diffusion. For a retention time of 2-5 hours in low temperature region, ash contains minimum carbon and crystalline phases which yields optimum mechanical performance of concrete. Heating rate less than 10°C/min and utilizing rapid cooling regime leads to ash with low carbon content and crystalline phases respectively. Concrete developed incorporating such ash shows greater mechanical performance.

Effect of varying BMA content

Researchers have used different parameters for thermal treatment of RHA. This has resulted into variable cement replacement percentage within the cement mortar/concrete mixes. From the past studies it is observed that, in development UHPC and achieving highest compressive strength Huang et.al. utilized 25% RHA whereas Farid et.al. could utilize only 3% RHA. Such results are not only observed in case of UHPC but also for other types of concrete. This variability in percentage replacement is due to the difference in thermal treatment parameters and neglecting parameter like heating rate and cooling method during the process of treatment. Therefore, it is very crucial to consider and control all the parameters of thermal treatment within the optimum range. This would ensure a good pozzolanic behavior of BMA and could bring the percentage consumption of BMA within a certain range.

Synergistic effect of biomass ash with different fibers

The addition of thermally treated RHA along with different fiber types improves the mechanical performance of the cement-based matrix. The addition (cement replacement) of RHA (without inclusion of fibers) has greater improvement on the mechanical performance of cement-based matrix than the addition of various fiber types (without inclusion of RHA). RHA induces a performance increase in the range of 5 – 20%, whereas the fibers increase the performance between 2 – 8%. The reactive silica present in RHA interacts with calcium hydroxide present in cement matrix. Their interaction in the presence of pore solution produces additional C-S-H gel which enhance the pore structure within the matrix, especially the interfacial transition zone (ITZ) and the improved pore structure results in an increase in strength of hardened matrix. On the other hand, the addition of different fibers along with RHA in the cement matrix elevates the strength over and above the cement + RHA matrix. The random dispersion and interfacial bond between the fibers and cement matrix enhances the strength, toughness, ductility, crack and fatigue resistance of the matrix. It is also seen that, the addition of RHA and fibers lowers the workability of cement matrix, whereas the setting time is delayed due to RHA and not because of fibers.

CONCLUSION

Biomass is one of the most promising fuel sources for energy generation. Ash evolving out from combustion of biomass can potentially be utilized in construction industry. But utilization of ash is dependent on chemical, physical and morphological characteristics. The chemical and morphological features are greatly influenced by calcination. Parameters of calcination regulated at optimum level render ash with maximum reactivity for substitution as supplementary cementitious material in concrete and mortar.

a. Parameters of calcination influencing properties of ash were reviewed. These parameters govern the phase and content of carbon in ash.
b. Temperature and retention time can be considered as primary and heating rate and cooling method as secondary parameters. Because unless the primary parameters are regulated at optimum level till then the effect of secondary parameters cannot be seen.
c. Temperature of 500-700°C is the optimum range for calcination of biomass, raising temperature beyond 700°C brings down the quantum of amorphous phases in ash.
d. Within the optimum temperature range, the retention should be maintained between 2 – 5 hours, heating rate should be less than 10 °C/ min and the ash should be cooled rapidly to obtain high pozzolanic activity in ash.
e. A variation of these parameters above and below optimum level affects the mechanical performance of concrete because of change in chemical and morphological characteristics.
f. Fluidized bed combustor is an efficient technology of biomass fuel combustion compared to moving grate firing system when the quality of ash is concerned. Even suspension fired burner are efficient but the problems associated with fuel quality, demand preprocessing/ preconditioning of fuel, complicated the working and increase maintenance of system tags it as a low popular system.
g. Not all the available biomass ashes could be classified as supplementary cementitious material. Therefore, it is

very important to check with the criteria of SCM mentioned in IS 3812: 2013 and ASTM C618.

h. The attributes of ash and concrete incorporating the ash is available over a wide range of temperature but the effect of retention time, heating rate and cooling method are not available at high temperature values.

i. Though heating rate and cooling method are secondary parameters but influence characteristic of ash. Effect of varying heating rate and cooling method at low, optimum and high calcination temperature and retention time on mechanical properties of concrete is an area with wide scope of research as per the review.

Practical Application

The biomass ash to be utilized as supplementary cementing material should satisfy the chemical composition criteria mentioned IS 3812: 2013. Generally, the biomass ash such as rice husk ash, sugarcane bagasse ash, wheat straw ash, bamboo leaf ash etc. contains considerable carbon content which may be detrimental to the strength, durability and other vital parameters of cement-based matrix. Moreover, the carbon cover over the ash particles inhibits the reactivity of ash. Therefore, thermal treatment of biomass ash is necessary for carbon removal. When any of the identified biomass ash containing substantial amount of carbon is to be used in construction as cement replacement, it should first undergo a thermal treatment process with the optimum control of thermal treatment parameters. The identified thermal treatment parameters are temperature, retention time, heating rate and cooling method. The temperature, retention time and heating rate should be regulated between 500 – 700 °C, 1 – 3 hours and 1 – 10 °C/minute, followed by a rapid cooling method to stop the crystallite growth and conversion of amorphous phases into crystalline phases. The practitioners should note that maintaining high treatment temperature (close to 700 °C but not greater than 700 °C) requires less retention time, whereas maintaining lower temperature (close to 500 °C but not less than 500 °C) demands higher retention time within the stated optimum range. When such ashes are used by the practitioners in construction industry the cement substitution can take place between 5 – 40% depending on the required strength of concrete. The review reveals that, low grade concrete (required strength < 25 MPa) can substitute cement with biomass ash as high as 30 – 40% whereas in high strength concrete (required strength > 60 MPa) the cement is replaced between 5 – 10%. The replacement of cement with biomass ash not only lowers the construction cost but also decelerates the rate of cement requirement which eventually lowers the pace of raw material required for cement production. The decelerated pace of cement requirement will bring down the carbon emissions, conserve natural resources thereby promoting sustainability.

AUTHORSHIP CONTRIBUTIONS

Authors equally contributed to this work.

DATA AVAILABILITY STATEMENT

The authors confirm that the data that supports the findings of this study are available within the article. Raw data that support the finding of this study are available from the corresponding author, upon reasonable request.

CONFLICT OF INTEREST

The author declared no potential conflicts of interest with respect to the research, authorship, and/or publication of this article.

ETHICS

There are no ethical issues with the publication of this manuscript.

STATEMENT ON THE USE OF ARTIFICIAL INTELLIGENCE

Artificial intelligence was not used in the preparation of the article.

REFERENCES

[1] Central Electricity Authority, Ministry of Power, Government of India. Annual report 2021–2022. 2021.

[2] Kolawole JT, Babafemi AJ, Fanijo E, Chandra Paul S, Combrinck R. State-of-the-art review on the use of sugarcane bagasse ash in cementitious materials. Cem Concr Compos 2021;118:103975. [CrossRef]

[3] Magdziarz A, Wilk M. Thermal characteristics of the combustion process of biomass and sewage sludge. J Therm Anal Calorim 2013;114:519–529. [CrossRef]

[4] Madurwar MV, Mandavgane SA, Ralegaonkar RV. Use of sugarcane bagasse ash as brick material. Curr Sci 2014;107:1044–1051.

[5] McCarl BA, Adams DM, Alig RJ. Competitiveness of biomass-fueled electrical power plants. Ann Oper Res 2000;103:239–248. [CrossRef]

[6] Andrade Neto JS, França MJS, Amorim Júnior NS, Ribeiro DV. Effects of adding sugarcane bagasse ash on the properties and durability of concrete. Constr Build Mater 2021;266:120959. [CrossRef]

[7] Khalil MJ, Aslam M, Ahmad S. Utilization of sugarcane bagasse ash as cement replacement for the production of sustainable concrete – A review. Constr Build Mater 2021;270:121371. [CrossRef]

[8] Agwa IS, Omar OM, Tayeh BA, Abdelsalam BA. Effects of using rice straw and cotton stalk ashes on the properties of lightweight self-compacting concrete. Constr Build Mater 2020;235:117541. [CrossRef]

[9] El Damatty AA, Hussain I. An economical solution for the environmental problem resulting from the disposal of rice straw. In: Appropriate technologies for environmental protection in the developing world. 2009. p. 15–23. [CrossRef]
[10] Anto G, Athira K, Nair NA, Sai TY, Laxman A, Sairam V. Mechanical properties and durability of ternary blended cement paste containing rice husk ash and nano silica. Constr Build Mater 2022;342:127732. [CrossRef]
[11] De Silva SHMJ, Priyamali MWS. Potential use of waste rice husk ash for concrete paving blocks: Strength, durability, and run-off properties. Int J Pavement Eng 2020;1–13.
[12] Khan K, Ishfaq M, Amin MN, Shahzada K, Wahab N, Faraz MI. Evaluation of mechanical and microstructural properties and global warming potential of green concrete with wheat straw ash and silica fume. Materials (Basel) 2022;15:3177. [CrossRef]
[13] Yu Y, Lau A, Sokhansanj S. Hydrothermal carbonization and pelletization of moistened wheat straw. Renew Energy 2022;190:1018–1028. [CrossRef]
[14] Terzioğlu P, Yücel S, Kuş Ç. Review on a novel biosilica source for production of advanced silica-based materials: Wheat husk. Asia Pac J Chem Eng 2019;14:1–14. [CrossRef]
[15] Krishna BB, Singh R, Bhaskar T. Effect of catalyst contact on the pyrolysis of wheat straw and wheat husk. Fuel 2015;160:64–70. [CrossRef]
[16] Saloni S, Pham TM, Lim YY, Pradhan SS, Jatin, Ku mar J. Performance of rice husk ash-based sustainable geopolymer concrete with ultra-fine slag and corn cob ash. Constr Build Mater 2021;279:122526. [CrossRef]
[17] Mohan S, CP C. Effect of artificial fibers and corn cob ash on mechanical behavior of high performance concrete. Pol J Environ Stud 2022;31:1–9. [CrossRef]
[18] Gummert M, Van Hung N, Chivenge P, Douthwaite B. Sustainable rice straw management. New York: Springer; 2020. [CrossRef]
[19] Hamada HM, Jokhio GA, Yahaya FM, Humada AM, Gul Y. The present state of the use of palm oil fuel ash (POFA) in concrete. Constr Build Mater 2018;175:26–40. [CrossRef]
[20] Ayub M, Dzarfan Othman MH, Khan IU, Hubadillah SK, Kurniawan TA, Ismail AF, et al. Promoting sustainable cleaner production paradigms in palm oil fuel ash as an eco-friendly cementitious material: A critical analysis. J Clean Prod 2021;295:126296. [CrossRef]
[21] Bheel N, Sohu S, Jhatial AA, Memon NA, Kumar A. Combined effect of coconut shell and sugarcane bagasse ashes on the workability, mechanical properties and embodied carbon of concrete. Environ Sci Pollut Res 2022;29:5207–5223. [CrossRef]
[22] Ahmad RK, Sulaiman SA, Yusup S, Dol SS, Inayat M, Umar HA. Exploring the potential of coconut shell biomass for charcoal production. Ain Shams Eng J 2022;13:101499. [CrossRef]
[23] Bheel N, Awoyera P, Tafsirojjaman T, Sor NH, Sohu S. Synergic effect of metakaolin and groundnut shell ash on the behavior of fly ash-based self-compacting geopolymer concrete. Constr Build Mater 2021;311:125327. [CrossRef]
[24] Perea-Moreno MA, Manzano-Agugliaro F, Hernandez-Escobedo Q, Perea-Moreno AJ. Peanut shell for energy: Properties and its potential to respect the environment. Sustainability 2018;10:1–15. [CrossRef]
[25] Madurwar MV, Ralegaonkar RV, Mandavgane SA. Application of agro-waste for sustainable construction materials: A review. Constr Build Mater 2013;38:872–878. [CrossRef]
[26] Katare VD, Madurwar MV, Raut S. Agro-industrial waste as a cementitious binder for sustainable concrete: An overview. In: Sustainable waste management: Policies and case studies. 2020. p. 683–702. [CrossRef]
[27] Katare VD, Madurwar MV. Pozzolanic performance resemblance of milled sugarcane biomass ash using different pozzolanicity test methods. Adv Cem Res 2020;32:205–215. [CrossRef]
[28] Tembhurkar S, Nayar P, Azad N, Ralegaonkar R, Madurwar M. Nanoprocessing of industrial rejects for controlling operational energy of buildings. Adv Civ Eng 2022;2022:1–14. [CrossRef]
[29] Ahamed MAA, Perera MSA, Matthai SK, Ranjith PG, Dong-yin L. Coal composition and structural variation with rank and its influence on the coal-moisture interactions under coal seam temperature conditions: A review article. J Petrol Eng 2019;180:901-917. [CrossRef]
[30] Vassilev SV, Vassileva CG. A new approach for the combined chemical and mineral classification of the inorganic matter in coal: Chemical and mineral classification systems. Fuel 2009;88:235–245. [CrossRef]
[31] Bhatt A, Priyadarshini S, Acharath Mohanakrishnan A, Abri A, Sattler M, Techapaphawit S. Physical, chemical, and geotechnical properties of coal fly ash: A global review. Case Stud Constr Mater 2019;11:e00263. [CrossRef]
[32] Nayak DK, Abhilash PP, Singh R, Kumar R, Kumar V. Fly ash for sustainable construction: A review of fly ash concrete and its beneficial use case studies. Cleaner Mater 2022;2022:100143. [CrossRef]
[33] Kelechi SE, Adamu M, Uche OAU, Okokpujie IP, Ibrahim YE, Obianyo II. A comprehensive review on coal fly ash and its application in the construction industry. Cogent Eng 2022;2022:2114201. [CrossRef]
[34] Tang Y, Zhu K, Huang Y. Radiative properties of porous fly ash particles based on the particle superposition model. J Quant Spectrosc Radiat Transf 2022;277:107977. [CrossRef]

[35] Schure MR, Soitys PA, Natusch FS, Mauney T. Surface area and porosity of coal fly ash. Environ Sci Technol 1985;19:82-86. [CrossRef]
[36] Chen Y, Fan Y, Huang Y, Liao X, Xu W, Zhang T. A comprehensive review of toxicity of coal fly ash and its leachate in the ecosystem. Ecotoxicol Environ Saf 2024;2024:115905. [CrossRef]
[37] Olatoyan OJ, Kareem MA, Adebanjo AU, Olawale SOA, Alao KT. Potential use of biomass ash as a sustainable alternative for fly ash in concrete production: A review. Hybrid Adv 2023;4:100076. [CrossRef]
[38] Vassilev SV, Baxter D, Andersen LK, Vassileva CG. An overview of the chemical composition of biomass. Fuel 2010;89:913-933. [CrossRef]
[39] Antiohos SK, Papadakis VG, Tsimas S. Rice husk ash (RHA) effectiveness in cement and concrete as a function of reactive silica and fineness. Cem Concr Res 2014;61–62:20–27. [CrossRef]
[40] James AK, Thring RW, Helle S, Ghuman HS. Ash management review: Applications of biomass bottom ash. Energies 2012;5:3856. [CrossRef]
[41] Katare VD, Madurwar MV. Experimental characterization of sugarcane biomass ash – A review. Constr Build Mater 2017;152:1–15. [CrossRef]
[42] Chindaprasirt P, Rattanasak U. Eco-production of silica from sugarcane bagasse ash for use as a photochromic pigment filler. Sci Rep 2020;10:1–8. [CrossRef]
[43] Uvegi H, Chaunsali P, Traynor B, Olivetti E. Reactivity of industrial wastes as measured through ICP-OES: A case study on siliceous Indian biomass ash. J Am Ceram Soc 2019;102:7678–7688. [CrossRef]
[44] Kamiya K, Oka A, Nasu H, Hashimoto T. Comparative study of structure of silica gels from different sources. J Solgel Sci Technol 2000;19:495–499. [CrossRef]
[45] Jittin V, Bahurudeen A, Ajinkya SD. Utilisation of rice husk ash for cleaner production of different construction products. J Clean Prod 2020;263:121578. [CrossRef]
[46] Nair DG, Jagadish KS, Fraaij A. Reactive pozzolanas from rice husk ash: An alternative to cement for rural housing. Cem Concr Res 2006;36:1062–1071. [CrossRef]
[47] Sadafale MA, Madurwar MV. Implementing a slow cooling method for thermal treatment of RHA to use as a secondary precursor in alkali activated mortar. J Mater Civ Eng 2025;37:70192. [CrossRef]
[48] Ganesan K. Rice husk ash blended cement: Assessment of optimal level of replacement for strength and permeability properties of concrete. Constr Build Mater 2008;22:1675–1683. [CrossRef]
[49] Ibrahim DM, Helmy M. Crystallite growth of rice husk ash silica. Thermochim Acta 1981;45:79–85. [CrossRef]
[50] Kang S, Hong S, Moon J. The use of rice husk ash as reactive filler in ultra-high performance concrete. Cem Concr Res 2018;115:389-400. [CrossRef]
[51] Ismail NAA, Azmi MA, Ahmad S, Taib H. Effect of rice husk firing temperature on synthesis of silica (SiO_2). Adv Mater Res 2015;1087:470–474. [CrossRef]
[52] Faried AS, Mostafa SA, Tayeh BA, Tawfik TA. The effect of using nano rice husk ash of different burning degrees on ultra-high-performance concrete properties. Constr Build Mater 2021;290:123279. [CrossRef]
[53] Chindaprasirt P, Jaturapitakkul C, Rattanasak U. Influence of fineness of rice husk ash and additives on the properties of lightweight aggregate. Fuel 2009;88:158–162. [CrossRef]
[54] Bakar BHA. Effect of rice husk ash fineness on the chemical and physical properties of concrete. Mag Concr Res 2011;63:313–320. [CrossRef]
[55] Luo Y, Li Z, Li X, Liu X, Fan J, Clark JH, et al. The production of furfural directly from hemicellulose in lignocellulosic biomass: A review. Catal Today 2019;319:14–24. [CrossRef]
[56] Steven S, Restiawaty E, Bindar Y. Routes for energy and bio-silica production from rice husk: A comprehensive review and emerging prospect. Renew Sustain Energy Rev 2021;149:111329. [CrossRef]
[57] Yang H, Yan R, Chen H, Lee DH, Zheng C. Characteristics of hemicellulose, cellulose and lignin pyrolysis. Fuel 2007;86:1781–1788. [CrossRef]
[58] El-Sayed SA, Khairy M. Effect of heating rate on the chemical kinetics of different biomass pyrolysis materials. Biofuels 2015;6:157–170. [CrossRef]
[59] Nowakowska M, Herbinet O, Dufour A, Glaude PA. Detailed kinetic study of anisole pyrolysis and oxidation to understand tar formation during biomass combustion and gasification. Combust Flame 2014;161:1474–1488. [CrossRef]
[60] Kirubakaran V, Sivaramakrishnan V, Nalini R, Sekar T, Premalatha M, Subramanian P. A review on gasification of biomass. Renew Sustain Energy Rev 2009;13:179–186. [CrossRef]
[61] Williams A, Jones JM, Ma L, Pourkashanian M. Pollutants from the combustion of solid biomass fuels. Prog Energy Combust Sci 2012;38:113–137. [CrossRef]
[62] Peters B. Prediction of pyrolysis of pistachio shells based on its components hemicellulose, cellulose and lignin. Fuel Process Technol 2011;92:1993–1998. [CrossRef]
[63] Fisher T, Hajaligol M, Waymack B, Kellogg D. Pyrolysis behavior and kinetics of biomass derived materials. J Anal Appl Pyrolysis 2002;62:331–349. [CrossRef]
[64] Morin M, Pécate S, Hémati M. Kinetic study of biomass char combustion in a low temperature fluidized bed reactor. Chem Eng J 2018;331:265–277. [CrossRef]
[65] Zeng X, Ueki Y, Yoshiie R, Naruse I, Wang F, Han Z, et al. Recent progress in tar removal by char and the applications: A comprehensive analysis. Carbon Resour Convers 2020;3:1–18. [CrossRef]

[66] Miller BG. Introduction to coal utilization technologies. In Clean Coal Engineering Technology. Oxford: Butterworth-Heinemann; 2017. p. 133-217. [CrossRef]
[67] Khodaei H, Al-Abdeli YM, Guzzomi F, Yeoh GH. An overview of processes and considerations in the modelling of fixed-bed biomass combustion. Energy 2015;88:946–972. [CrossRef]
[68] Hobbs ML, Radulovic PT, Smoot LD. Combustion and gasification of coals in fixed-beds. Prog Energy Combust Sci 1993;19:505–586. [CrossRef]
[69] Ladner WR. The products of coal pyrolysis: Properties, conversion and reactivity. Fuel Process Technol 1988;20:207–222. [CrossRef]
[70] Boateng AA, Skeete DA. Incineration of rice hull for use as a cementitious material: The Guyana experience. Cem Concr Res 1990;20:795–802. [CrossRef]
[71] Hanafi S, Abo-El-Enein SA, Ibrahim DM, El-Hemaly SA. Surface properties of silicas produced by thermal treatment of rice-husk ash. Thermochim Acta 1980;37:137–143. [CrossRef]
[72] Hamad MA, Khattab IA. Effect of the combustion process on the structure of rice hull silica. Thermochim Acta 1981;48:343–349. [CrossRef]
[73] Shi W, Bai J, Kong L, Zhao H, Guhl S, Li H, et al. Effect of CaO/Fe_2O_3 ratio on fusibility of coal ashes with high silica and alumina levels and prediction. Fuel 2020;260:116369. [CrossRef]
[74] Muthukrishnan S, Gupta S, Kua HW. Application of rice husk biochar and thermally treated low silica rice husk ash to improve physical properties of cement mortar. Theor Appl Fract Mech 2019;2019:102376. [CrossRef]
[75] Huang H, Gao X, Wang H, Ye H. Influence of rice husk ash on strength and permeability of ultra-high performance concrete. Constr Build Mater 2017;149:621–628. [CrossRef]
[76] Bui LAT, Chen CT, Hwang CL, Wu WS. Effect of silica forms in rice husk ash on the properties of concrete. Int J Miner Metall Mater 2012;19:252–258. [CrossRef]
[77] Bie R, Song X, Liu Q, Ji X, Chen P. Studies on effects of burning conditions and rice husk ash (RHA) blending amount on the mechanical behavior of cement. Cem Concr Compos 2015;55:162–168. [CrossRef]
[78] Xu W, Tommy Y, Ouyang D, Ali S, Xing F, Wang W. Effect of rice husk ash fineness on porosity and hydration reaction of blended cement paste. Constr Build Mater 2015;89:90–101. [CrossRef]
[79] Salas A, Delvasto S, de Gutierrez RM, Lange D. Comparison of two processes for treating rice husk ash for use in high performance concrete. Cem Concr Res 2009;39:773–778. [CrossRef]
[80] Msinjili NS, Schmidt W, Rogge A, Kühne HC. Performance of rice husk ash blended cementitious systems with added superplasticizers. Cem Concr Compos 2017;83:202–208. [CrossRef]
[81] Billong N, Melo UC, Kamseu E, Kinuthia JM, Njopwouo D. Improving hydraulic properties of lime–rice husk ash (RHA) binders with metakaolin (MK). Constr Build Mater 2011;25:2157–2161. [CrossRef]
[82] Raisi EM, Amiri JV, Davoodi MR. Mechanical performance of self-compacting concrete incorporating rice husk ash. Constr Build Mater 2018;177:148–157. [CrossRef]
[83] Rêgo JHS, Nepomuceno AA, Figueiredo EP, Hasparyk NP. Microstructure of cement pastes with residual rice husk ash of low amorphous silica content. Constr Build Mater 2015;80:56–68. [CrossRef]
[84] Vayghan AG, Khaloo AR, Rajabipour F. The effects of a hydrochloric acid pre-treatment on the physicochemical properties and pozzolanic performance. Cement Concrete Compos 2013;39:131-140.
[85] Koushkbaghi M, Jafar M, Mosavi H, Mohseni E. Acid resistance and durability properties of steel fiber-reinforced concrete incorporating rice husk ash and recycled aggregate. Constr Build Mater 2019;202:266–275. [CrossRef]
[86] Khan R, Jabbar A, Ahmad I, Khan W, Naeem A, Mirza J. Reduction in environmental problems using rice-husk ash in concrete. Constr Build Mater 2012;30:360–365. [CrossRef]
[87] Lo F, Lee M, Lo S. Effect of coal ash and rice husk ash partial replacement in ordinary Portland cement on pervious concrete. Constr Build Mater 2021. [CrossRef]
[88] Ouedraogo M, Sawadogo M, Sanou I, Barro M, Nassio S, Seynou M, et al. Characterization of sugar cane bagasse ash from Burkina Faso for cleaner cement production: Influence of calcination temperature and duration. Results Mater 2022;14:100275. [CrossRef]
[89] Cordeiro GC, Barroso TR, Toledo Filho RD. Enhancement the properties of sugar cane bagasse ash with high carbon content by a controlled re-calcination process. KSCE J Civ Eng 2018;22:1250–1257. [CrossRef]
[90] Ishfaq M, Gul A, Naseer MH. Effect of heat treatment on the chemical and microstructural properties of wheat straw ash (WSA). J Eng Res Rep 2021:99–108. [CrossRef]
[91] Ouedraogo AKAH, Koteng DO, Ambassah N. Effect of pretreated corn cob ash on the mechanical and durability characteristics of high-strength concrete. SSRG Int J Civ Eng 2024;11:125–138. [CrossRef]
[92] Suwanmaneechot P, Nochaiya T, Julphunthong P. Improvement, characterization and use of waste corn cob ash in cement-based materials. IOP Conf Ser Mater Sci Eng 2015;103:012023. [CrossRef]
[93] Olafusi OS, Adewuyi AP, Sadiq OM, Adisa AF, Abiola OS. Rheological and mechanical characteristics of self-compacting concrete containing corncob ash. 2017.

[94] Adesanya DA, Raheem AA. Development of corn cob ash blended cement. Constr Build Mater 2009;23:347–352. [CrossRef]
[95] Bureau of Indian Standards. Specification for pulverized fuel ash, part 1: For use as pozzolana in cement, cement mortar and concrete. IS 3812. New Delhi (India): Bureau of Indian Standards; 2013. p.1–12.
[96] ASTM International. Standard specification for coal fly ash and raw or calcined natural pozzolan for use in concrete. ASTM C618. West Conshohocken (PA): ASTM International; 2014. p.1–5.
[97] Khan W, Shehzada K, Bibi T, Ul Islam S, Wali Khan S. Performance evaluation of Khyber Pakhtunkhwa rice husk ash (RHA) in improving mechanical behavior of cement. Constr Build Mater 2018;176:89–102. [CrossRef]
[98] Xu W, Lo TY, Memon SA. Microstructure and reactivity of rice husk ash. Constr Build Mater 2012;29:541–547. [CrossRef]
[99] Amin MN, Hissan S, Shahzada K, Khan K, Bibi T. Pozzolanic reactivity and the influence of rice husk ash on early-age autogenous shrinkage of concrete. Front Mater 2019;6:1–13. [CrossRef]
[100] Ai-Khalaf MN, Yousift HA. Use of rice husk ash in concrete. Int J Cem Compos Lightweight Concr 1984;6:241–248. [CrossRef]
[101] Hamzeh Y, Ziabari KP, Torkaman J, Ashori A, Jafari M. Study on the effects of white rice husk ash and fibrous materials additions on some properties of fiber-cement composites. J Environ Manage 2013;117:263–267. [CrossRef]
[102] Hesami S, Ahmadi S, Nematzadeh M. Effects of rice husk ash and fiber on mechanical properties of pervious concrete pavement. Constr Build Mater 2014;53:680–691. [CrossRef]
[103] Memon MJ, Jhatial AA, Murtaza A, Raza MS, Phulpoto KB. Production of eco-friendly concrete incorporating rice husk ash and polypropylene fibres. Environ Sci Pollut Res 2021;28:39168–39184. [CrossRef]
[104] Koushkbaghi M, Kazemi MJ, Mosavi H, Mohseni E. Acid resistance and durability properties of steel fiber-reinforced concrete incorporating rice husk ash and recycled aggregate. Constr Build Mater 2019;202:266–275. [CrossRef]
[105] Sobuz MHR, Saha A, Anamika JF, Houda M, Azab M, Akid ASM, et al. Development of self-compacting concrete incorporating rice husk ash with waste galvanized copper wire fiber. Buildings 2022;12:1024. [CrossRef]
[106] De Silva GHMJS, Naveen P. Effect of rice husk ash and coconut coir fiber on cement mortar: Enhancing sustainability and efficiency in buildings. Constr Build Mater 2024;440:137326. [CrossRef]
[107] Mehmood MA, Ibrahim M, Rashid U, Nawaz M, Ali S, Hussain A, et al. Biomass production for bioenergy using marginal lands. Sustain Prod Consum 2017;9:3–21. [CrossRef]
[108] Yaghoubi H, Allahyari MS, Firouzi S, Damalas CA, Marzban S. Identifying sustainable options for rice husk valorization using the analytic hierarchy process. Outlook Agric 2019;48:117–125. [CrossRef]
[109] Shakeel A, Khushnood H, Irfan M, Ahmad A, Naqvi AH, Shafi M. On the characteristics of clusters produced in 400 GeV p-N interactions. J Phys Soc Jpn 1986;55:3362–3369. [CrossRef]

Sigma Journal of Engineering and Natural Sciences
Web page info: https://sigma.yildiz.edu.tr
DOI: 10.14744/sigma.2025.00000

Review Article

The role of hybrid nanofluids in optimizing parabolic trough concentrator performance: A comprehensive review

Sanjeev Kumar GUPTA[1,*], Soni KUMARI[1]

[1]*Department of Mechanical Engineering, IET, GLA University Mathura, 281406, India*

ARTICLE INFO

Article history
Received: 04 October 2024
Revised: 19 November 2024
Accepted: 08 January 2025

Keywords:
Hybrid Nanofluid; Heat Transfer; Parabolic Through Concentrator; Solar Energy; Thermal Conductivity

ABSTRACT

This review evaluates the potential of hybrid nanofluids to enhance the efficacy of PTCs, which are a critical component of solar thermal systems. The study aims to critically evaluate the efficacy of hybrid nanofluids, developed by integrating two or more nanoparticles within a base fluid, to enhance the thermal efficiency and heat transfer properties of PTC systems. The purpose is to inspect augmentation in HNF formulations, assess their thermophysical characteristics, and evaluate experimental and computational research of their utilization in PTCs. The fundamental issues that must be determined are stability, compatibility with heat transfer systems, and economic efficiency. This review integrates latest findings to explain the advantages and disadvantages of hybrid nanofluids, recognizes existing research shortcomings, and recommended prospective routes for their inclusion into solar energy technologies. The Al_2O_3-MWCNT/H_2O hybrid nanofluid with a volume fraction of 0.04% provides the ultimate thermal efficiency enhancement, which is 197.1%. Maximum enhancement in Nusselt number is 14% using Cu-Mgo/water hybrid nanofluid at a 2% volume fraction. It is also noted that the exergy efficiency increases by 71.255% when using Al_2O_3-WO3/Therminol VP1hybrisd nanofluid at a volume fraction of 4%. The originality of this research dwells in its detailed examination of hybrid nanofluids particularly designed for PTC applications, filling a void in the existing literature by proposing a integrated framework for grasping and utilizing their advantages. The results highlight the transformative potential of hybrid nanofluids in enhancing solar thermal technology and delineate future research avenues for optimizing their implementation in practical systems.

Cite this article as: Gupta SK, Kumari S. The role of hybrid nanofluids in optimizing parabolic trough concentrator performance: A comprehensive review. Sigma J Eng Nat Sci 2026;44(1):698–719.

INTRODUCTION

The world is tackling an incomparable energy calamity, impelled by the growing requirement for energy and the declining supplies of fossil fuels. Fossil fuels, such as coal, oil, and natural gas, have been the main sources of energy for the last hundred years. They power homes, businesses, and transportation [1]. But their extensive utilization has had solemn consequences on the environment, like higher

***Corresponding author.**
*E-mail address: sanjeev.gupta@gla.ac.in

This paper was recommended for publication in revised form by Editor-in-Chief Ahmet Selim Dalkilic

Published by Yıldız Technical University Press, İstanbul, Turkey
© Author. This is an open access article under the CC BY-NC license (http://creativecommons.org/licenses/by-nc/4.0/).

emissions of carbon, climate change, and air pollution. These are now major global issues. As fossil fuel reserves dwindle and environmental degradation escalates, a coordinated global initiative has emerged to shift towards more sustainable, clean and renewable energy sources [2]. Solar, wind, and hydroelectric power are some of the most promising alternatives to fossil fuels. Solar energy is especially promising because it is widely available and has little effect on the environment [3]. Figure 1 illustrates the shift from fossil fuels to renewable energy sources.

Solar energy is a massive, unused resource that can be utilized to produce electricity, heat, and cool things down. It arrives straightaway from the sun's radiation, which is a renewable and infinite source of energy that can be transformed into usable forms with technologies such as photovoltaic (PV) panels and concentrated solar power (CSP) systems [4]. CSP systems, which use mirrors or lenses to focus sunlight onto a receiver, have acquired plenty of concentrations because they can produce huge amount of electricity, even in places where there is plenty of direct sunlight. Construct a solar thermal systems perform superior, CSP technologies such as PTCs, dish-stirling systems, and central tower receivers have been implemented to augment the system's capacity to absorb heat [5].

A PTC is a highly efficient solar thermal system widely used in CSP plants for electricity generation, industrial heating, and desalination [6]. The various application of PTC is shown in Figure 2. It utilizes a parabolic shaped reflector, which is normally comprised of polished aluminum, concentrate sunlight onto a linear receiver tube that is positioned at the focal line. The shape of the reflector ensures that entering solar radiation is concentrated the receiver tube. The tube is layered with a specific absorber coating that augments energy absorption and reduces heat loss through infrared radiation. For minimizing convective losses furthermore, the receiver tube is bounded by a glass envelope with a vacuum layer to maintain the heat inside. A heat transfer fluid (HTF), like synthetic oil, molten salt or pressurized water, moves through the receiver tube to gather the concentrated heat. This heat goes to a heat exchanger, where it can be used to make steam that runs turbines in a Rankine cycle [7].

The system proceeds the sun's path all day utilizing a single-axis tracking system. This ensures the reflector in the optimal site and the optical efficiency highest, which is normally between 60% and 75%. PTCs are designed to operate at temperatures between 300°C and 400°C and can acquire as high as 80 times more concentrated. This allows them to achieve the high thermal performance required for extensive energy applications. The concentration ratio, which is the ratio of the aperture area to the cross-sectional area of the absorber, directly affects how well the system works and how hot it gets [8].

PTCs have many benefits, like being able to grow and work well in areas with a lot of radiation, but there are still problems to solve. These include high capital costs because mirrors, tracking systems, and receiver coatings need to be very precise. They are also sensitive to optical alignment and work less well in diffuse sunlight [9]. Research is focused on making receiver materials better, making HTFs that are more thermally stable, and making it easier for TES systems to work together so they can run all the time. Regardless of these challenges PTCs are a firmly established and dependable technology that is essential for policies to utilize more renewable energy and for planetary exertions minimize greenhouse gas emissions [10].



Figure 1. Transition from fossil fuels to renewable energy sources.

Nanotechnology has opened up new ways to improve the performance of HTFs in the last few years. This has led to the creation of nanofluids. Nanofluids are made by mixing nanoparticles (usually less than 100 nm in size) with a base fluid. These nanoparticles usually made from materials like metals, metal oxides, or carbon nanotubes, significantly improve the thermal properties of the base fluid [11]. Different types of nanomaterials used to enhance the performance of PTC are shown in Figure 3 [12]. Nanofluids can substantially boost the efficiency of heat exchange in systems such as PTCs by augmenting the thermal conductivity and heat transfer coefficients. Even so, single nanoparticle suspensions frequently indicate constraints concerning stability, enhancement of thermal conductivity, and overall efficiency at higher concentrations [13].



Figure 2. Various applications of PTCs.

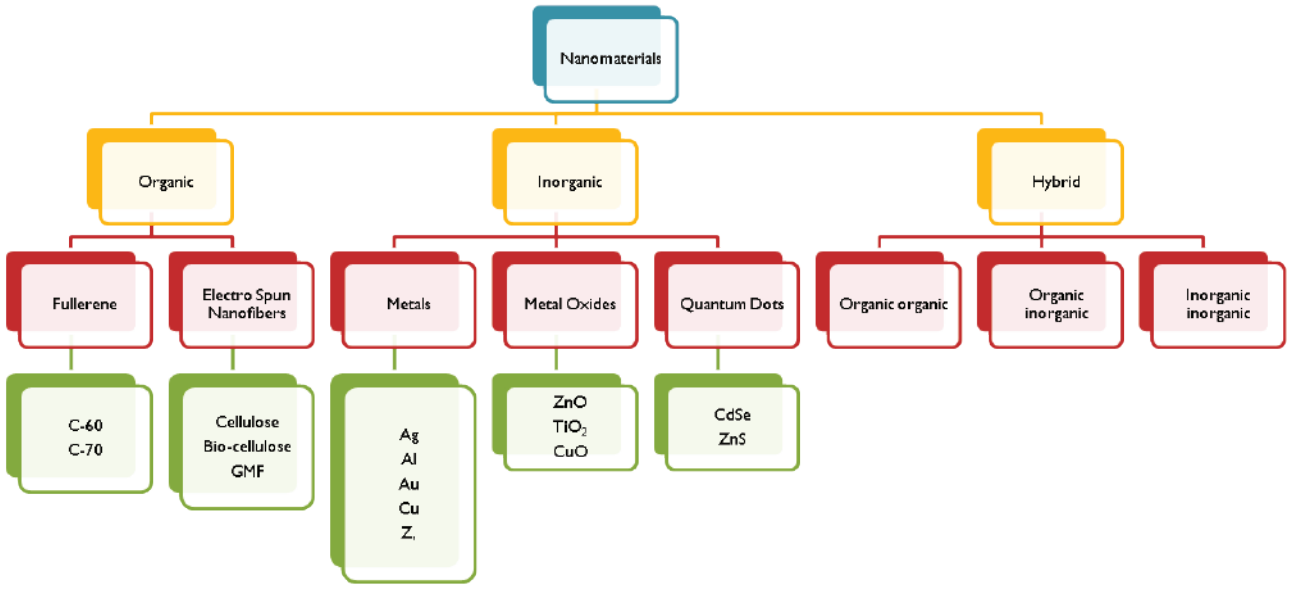


Figure 3. Different types of nanomaterials used to enhance the performance of PTC.

Hybrid nanofluids have come up as a new way to deal with these problems. Hybrid nanofluids are a type of nanofluid that mixes two or more types of nanoparticles into a base fluid. This makes them even better at conducting heat and staying stable than regular nanofluids [14]. Various nanoparticles performing together in hybrid nanofluids can enhance heat transfer, fluid flow, and efficiency of energy conversion. This renders them excellent for high effectiveness utilizations like PTCs in solar thermal power generation. In comparison with fluids comprised of only one type of nanoparticle, hybrid nanofluids might possess enhanced heat transfer properties, fewer heat loss, and more stable heat transfer behaviour over time [15].

Hybrid nanofluids have numerous possibilities to build PTCs perform better, but there are still plenty of hurdles that need to be resolved. These incorporate the optimization of nanoparticle amalgamations, the stability and dispersion of nanoparticles within the base fluid, the impact of various operational situations on performance, and the long-term resilience of hybrid nanofluids in practical applications [16]. Additionally, the facility of reliable testing methodologies and execution models for hybrid nanofluids in parabolic trough systems persists to be a subject of active research. Table 1 shows a summary of review articles that have already been published about using nanofluid in PTC. Figure 4 shows how many research articles have been published on the subject according to the Scopus database.

While several reviews have focused on the role of nanofluids in thermal PTC systems which are shown in Table 1 and a lot of research has been performed on the utilization of nanofluid in PTC, there is a lack of a comprehensive review dedicated to hybrid nanofluids specifically for PTC applications. Key research gaps include:

- Most reviews concentrate on single-component nanofluids, with insufficient discussion on the synergistic effects of hybrid nanofluids in PTC systems.
- There is limited assessment of the optimization methods for hybrid nanofluids, such as nanoparticle selection, stability enhancement, and process parameters.
- A relative analysis of hybrid nanofluids versus traditional nanofluids in PTC applications is missing
- Research often ignores the economic and long-term operational viability of hybrid nanofluids for commercial-scale PTC systems.
- Existing literature does not adequately capture or analyze the temporal trends in the use of hybrid nanofluids for PTC systems.

The goal of this review article is to give a full look at how hybrid nanofluids can improve the performance of parabolic trough concentrators. It will explicitly analyze emerging utilization for hybrid nanofluids, their thermal and flow characteristics, and how they can improve the performance of solar thermal system. The primary aim of this review is to sequentially examine the current innovation in hybrid nanofluid research and their utilization in PTCs. The benefits and limitation of utilizing HNF in solar PTC is also discussed. This review will also look at the different ways to make hybrid nanofluids more stable and easier to spread, which are two of the biggest problems that need to be solved before they can be used widely in business. This review is new because it focuses on how to use hybrid nanofluids in parabolic trough concentrators. Large scale solar power generation has got more attention, but its performance can still be enhanced by utilizing modern nanofluids in an optimal way. This article aims to contribute to the ongoing development of hybrid nanofluids as a key technology for improving the efficiency and performance of solar thermal power

Table 1. Summary of previously published review articles on the utilization of nanofluid in PTC

Ref. no.	Type of nanofluid	Summary of review
[17], 2018	Mononanofluid	The purpose of the study is to assess the techniques for improving thermal efficiency in PTCs.
[18], 2019	Mono nanofluid	Numerous parameters, including the kind of base fluid, nanoparticles, volume fraction, and nanoparticle size, have been studied about PTC effectiveness.
[19], 2020	Mono nanofluid	A review of the various HTFs utilized to improve the PTC's thermal efficiency and storage capacity is conducted.
[20], 2021	Hybrid nanofluid	Using hybrid nanofluid, previous and present research on PTC has been evaluated.
[21], 2022	Mono/Hybrid nanofluid	A thorough descriptive evaluation of the uses of mono/hybrid nanofluids in solar thermal collectors with those of other fluids is provided.
[22], 2022	Mono nanofluid	Examines nanofluids in 100–300 °C parabolic-through systems.
[23], 2022	Mono nanofluid	The most effective way to enhance PTC effectiveness is to combine turbulators with nanofluids.
[24], 2022	Nanofluid, nano-PCM	The impact of PCM and nano-PCM on the solar PTC's thermal efficiency was examined.
[25], 2023	Mono/Hybrid nanofluid	The purpose of this paper is to examine how increasing PTC performance is influenced by mono and hybrid nanofluid flowing with various turbulence promotors.
[26], 2023	Mono nanofluid	The use of nanofluid in solar PTC results in economic, environmental, and energy savings.
[27], 2023	Hybrid nanofluid	The investigation shows that using hybrid nanofluids as HT inside the absorber tube of the PTC can enhance its thermal and optical characteristics.

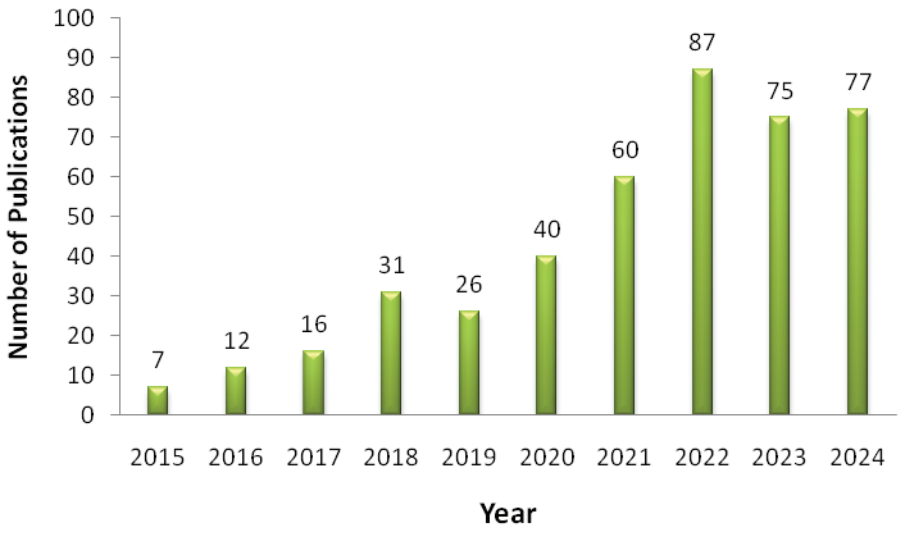


Figure 4. Research articles published on the application of nanofluid in PTC as per the Scopus database.

systems by providing an in-depth analysis of the current state of the art and identifying potential areas for future research.

Hybrid Nanofluid: Preparation, Stability and Thermophysical Properties

Hybrid nanofluids are advanced thermal fluids made by mixing two or more types of nanoparticles with a regular base fluid like water, ethylene glycol, or oil. The different base fluid and nanoparticles used in the preparation of hybrid nanofluid is shown in Figure 5. This new method uses the unique thermal, electrical, and mechanical properties of different nanoparticles, like metals, metal oxides, carbon-based materials, or ceramics, to make nanofluids that work better than traditional single-component



Figure 5. Different base fluid and nanoparticles used in the preparation of hybrid nanofluid.

nanofluids [28]. Hybrid nanofluids are mainly fascinating since they have superior thermal conductivity, enhanced heat transfer rates, and better stability. Mixing distinct kind of nanoparticles collectively can induce properties that are outstanding for ensured utilization, such as electronic cooling, car engines, solar thermal systems, and industrial heat exchangers. A hybrid nanofluid composed of graphene oxide and Al_2O_3, for example, has the high thermal conductivity of graphene and the high stability of Al_2O_3 in dispersion [29]. Also, optimizing the size, shape, concentration, and surface functionalization of the particles is very important for reducing agglomeration and improving the performance of hybrid nanofluids. Their adaptability includes renewable energy systems, where they improve the performance of solar collectors and geothermal systems by absorbing and transferring energy better [30]. The various base fluids and nanoparticles used in the formation of hybrid nanofluid are illustrated in Figure 5. Yet, there are challenges to resolve, though, like enhancing production costs, long-term stability problem, and the feasible health and environmental impact of nanoparticles. Even with these challenges, research is still being performed to produce hybrid nanofluids work effectively, cost minimum, and elevate for the environment. This creates them a better option for cutting edge heat transfer technologies [31].

Preparation of Hybrid Nanofluid

Single-step technique

The single-step method for making nanofluids combines the making and spreading of nanoparticles into a base fluid at the same time. This means that separate nanoparticle synthesis and spreading are no longer necessary. This method usually uses chemical vapor condensation (CVC) or physical vapor condensation (PVC), and it often uses a cooling medium to keep the nanoparticles in the fluid [32]. The single-step method's main benefit is that it reduces the amount of particle agglomeration, which makes the nanofluid more stable and even. Also, by holding the nanoparticles unbroken, it reduces the hazard of pollution and enhances the thermal properties of the produced nanofluid. Albeit this technique has these advantages, it may have obstacles with scalability and compatibility with some base fluids, subject to how it is produced [33,34].

Two-step technique

The two-step method is a popular way to make hybrid nanofluids because it is easy and cheap. A extensive depiction of the two-step method for hybrid nanofluid production is illustrated in Figure 6. There are two important steps to this method: first, creating nanoparticles, and then extending them out in a base fluid. In the first step, chemical, physical, or mechanical techniques are used to produce particular nanoparticles, such as metal oxides, carbon-based materials, or metallic compounds. The next step is to stir these pre-assembled nanoparticles into a base fluid, such as water, ethylene glycol, or oil, to make the hybrid nanofluid [35,36]. At this stage, surfactants or ultrasonication are usually used to ensure that the particles are uniformly disperse and do not adhere collectively, leading to the fluid more stable. This technique permits you select and mix distinct nanoparticles to alter the thermal and rheological characteristics of the hybrid nanofluid for assured use [37,38].

The two-step technique for producing hybrid nanofluids is outperforming the one-step technique since it provides you more control over how nanoparticles disperse. This process produces nanoparticles first and then mixes them with a base fluid to ensure they are uniformly and stably scattered. This enhances the thermal properties and stops agglomeration, which is a complication with the one-step method.

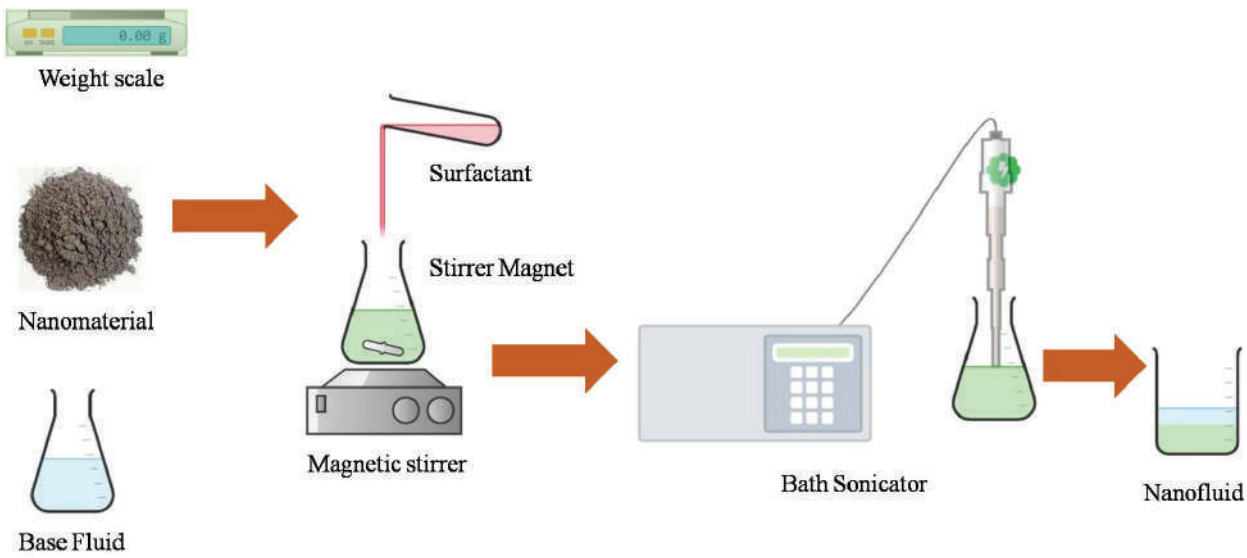


Figure 6. Two-step method for the preparation of hybrid nanofluid.

Stability of Hybrid Nanofluid

For hybrid nanofluids to perform better in applications such as heat transfer, energy systems, and biomedical uses, they must be stable. Stability refers that nanoparticles to remain uniformly distributed in the base fluid over time, without settling, clumping collectively, or generating clusters [39]. The stability of hybrid nanofluids is influenced by the type and size of the nanoparticles, the properties of the base fluid, the amount of nanoparticles, and the utilization of surfactants or stabilizing agents. Miniature nanoparticles with uniform shapes usually make things more stable since they do not adjust so much [40]. The pH of the nanofluid is also very significant since it alters the surface charge of the nanoparticles, which retain them from adhering collectively by including electrostatic repulsion. Ultrasonication and the utilization of emulsifiers are other technique that enhances stability by splitting up agglomerates and making particles disperse better [41]. If you enhance these factors properly, hybrid nanofluids will be more stable with time and work better with regard to thermal and rheological properties. The distinct methods to enhance the stability of hybrid nanofluid are illustrated in Figure 7.

Asadi et al. [42] conducted a DLS test to examine the stability of CuO – TiO_2/H_2Ohybrid nanofluid. Through the DLS test, the average diameter of the nanoparticles in relation to the laser beam intensity can be determined. The larger particles therefore diffract more intensely. The test findings indicate that the particles' nano-dimensions are present in the base fluid and that agglomeration has not taken place. The particles' maximum mean diameter is around 43 nm.Siddiqui et al. [43] conducted an investigation on the dispersion stability of the Cu-Al_2O_3 hybrid nanofluid for a range of mixing ratios 0.3: 0.7According to their findings, a mixing ratio greater than 0.5:0.5 causes quick settling because of its elevated settled velocity. For mixing ratios under 0.5:0.5, stability is less reliant on zeta potential.

Thermophysical Properties of Hybrid Nanofluid

The thermophysical properties of hybrid nanofluids are essential in settling their efficacy and relevance for various heat transfer systems. Thermal conductivity is the key of these properties since it has a direct impact on how effectively heat transfers through a material [44]. Adding more than one type of nanoparticle with different thermal properties greatly improves the thermal conductivity compared to regular nanofluids. This improvement is due to the combined nanoparticles working together in a way that different thermal transport mechanisms, like phonon scattering and electron transfer, work together [45]. Yet to enhance this, you must attentively optimize things such as the concentration, size, shape, and dispersion of the nanoparticles. An optimal balance ensures that the



Figure 7. Techniques to improve the stability of hybrid nanofluid.

thermal performance is at its best without aching other properties such as viscosity, density, specific heat, and stability [46].

To fully utilize hybrid nanofluids in practical uses, these thermophysical properties must be optimized collectively. For example, hybrid nanofluids with superior thermal conductivity and reduce viscosity can develop solar thermal systems excellent at absorbing heat and transforming it into energy [47]. Stable hybrid nanofluids make sure that industrial cooling or electronic cooling systems work well even when the temperature is high. Recent improvements in computational modeling and experimental methods make it possible to accurately measure these properties. This lets researchers customize hybrid nanofluids for certain applications [48]. The ongoing development of hybrid nanofluids continues to address challenges like economic feasibility and environmental impact, driving their adoption across diverse industries. Consequently, the investigation of their thermophysical properties continues to be a vibrant and consequential field of study, offering the potential for substantial progress in heat transfer technology [49]. Figure 8 shows the different factors that affect the thermophysical properties of the hybrid nanofluid.

Thermal Conductivity

The thermal conductivity of HNF is a critical factor that influences how efficiently they can transmit heat. It is investigated by different parameters mutually depends on each other. When metallic nanoparticles like Cu, Ag, or Al_2O_3 are mixed with carbon-based materials like graphene or CNTs, they can work together to improve thermal conductivity because their thermal properties work well together. [50]. The nanoparticles concentration is crucial due to intensified concentrations often make thermal conductivity exceptional by developing multiple paths for heat to transfer through. Yet, excessive loading can produce the viscosity higher and lead to particles to stick collectively, which reduce efficiency [51]. The heat conduction of nanoparticles also depends upon its size and shape. Another important parameter is temperature. Higher temperatures make nanoparticles accelerate and with more kinetic energy, which facilitates disperse thermal energy [52]. The stability of nanoparticles in the fluid has a significant impact on thermal conductivity. A stable distribution ensures that heat is transmitted evenly, while aggregation reduces performance [53].

Other aspects that can influence the nanoparticles' thermal conductivity, the resistance between nanoparticles and the base fluid, and process to produce. The dispersion stability of nanofluid is enhanced by ultrasonication and surfactant. The thermal conductivity of HNF also depends upon different parameters such as r specific heat capacity, density, and viscosity, which all affect convective heat transfer rate [54]. Due to enhancement in these properties, HNFs can acquire their full potential for



Figure 8. Variables influencing thermophysical properties of hybrid nanofluid.

Table 2. Thermal conductivity of hybrid nanofluid

Ref. no.	Hybrid nanofluid	Volume fraction	Enhancement in thermal conductivity
[55]	F-MWCNTs–Fe_3O_4/EG	0 % to 2.3%	30% at 50°C and 2.3% vol. fraction
[56]	Cu-Ag/Ar	-	69.72% at 50% Cu-Ag
[57]	Zn – Fe_2O_4 /H_2O	0.5%	11.8% at 80°C
[58]	MWCNT – Cu/H_2O	0.05% to 0.6%	30.38% at 50°C and 0.6% vol. fraction
[59]	TiO_2 -CNTs/ H_2O	0.1% to 0.2%	20.5% at 25° C
[60]	CNT-SiO_2/Water	0.1% to 1%	26.29% at 1% Vol. fraction

thermal conductivity, leading to them useful for cooling systems, heat exchangers, and energy storage. Research and innovations are still examining the ideal integrations and conditions for augmenting thermal performance. Table 2 shows how different hybrid nanofluids have better thermal conductivity.

Viscosity

The viscosity of hybrid nanofluids is an important factor that affects how they flow and how well they transfer heat. The type, size, shape, and concentration of the nanoparticles used all play a role. Higher concentrations of nanoparticles usually make thermal conductivity better, but they can also make viscosity worse, which means that pumping requires more energy [61]. The interaction between different types of nanoparticles in hybrid nanofluids makes things more complicated because their combined effects can either make viscosity changes worse or better. The viscosity is also greatly affected by the properties of the base fluid and the quality of the dispersion of the nanoparticles [62]. Using surfactants and functionalizing the surface are two examples of proper stabilization techniques that help keep the dispersion even and stop agglomeration, which can make the viscosity go up. Temperature also affects the viscosity of HNFs since with increment in temperature viscosity reduces. To take full advantage of HNFs in real life applications, it is essential to determine the proper balance between superior thermal conductivity and viscosity that is operationally simple [63]. Table 3 shows a summary of the most recent research on the viscosity of hybrid nanofluid.

Specific Heat

The specific heat capacity of hybrid nanofluids, which is an important property for storing energy and moving heat, depends on the kind and amount of nanoparticles and how they interact with the base fluid. The addition of nanoparticles usually lowers the specific heat capacity of a hybrid nanofluid because most nanoparticles have a lower specific heat than base fluids like water or ethylene glycol [69]. But the amount of nanoparticles used and their type will affect how much the reduction happens. Hybrid nanofluids, which mix distinct kind of nanoparticles, may observe the optimal balance by using the distinct thermal properties of the nanoparticles to their benefit and mitigating the adverse effect on specific heat [70]. Innovative stabilization methods also ensure that nanoparticles are uniformly distributed, that maintains the thermal behaviour reliable. The reduction in specific heat seems to inferior, but it is generally equalized by the significant enhancement in thermal conductivity, which causes hybrid nanofluids superior at transferring heat in various situations [71]. The current research on specific heat of hybrid nanofluid is summarized in Table 4.

Table 3. Current research on the viscosity of hybrid nanofluid

Ref. no.	Hybrid nanofluid	Volume fraction	Enhancement in viscosity
[64]	CeO_2-Cu/H_2O, Al_2O_3-Cu/ H_2O, TiO_2-Cu/ H_2O, SiO_2-Cu/ H_2O	0.5% to 3%	58.8% at 3% vol. fraction for CeO_2-Cu/H_2O
[65]	ZnO-MWCNTs/engine oil	0.125% to 1%	45%
[42]	CuO-TiO_2/water	0.1% to 1%	Maximum viscosity is 1.74 mPa·s. at 1% vol. fraction and 25° C
[66]	MgO-MWCNTs/H_2O and EG	0.025% to 0.8%	43.47%
[67]	SiO_2- graphite/Water	0% to 2 %	36.12% at 3% vol. fraction and 15° C
[68]	MWCNTs- SiO_2/20W50	0.05% to 1%	171%

Table 4. Current research on the specific heat of hybrid nanofluid

Ref. no.	Hybrid nanofluid	Volume fraction	Decrement in specific heat (Cp)
[72]	CuO + MWCNT, MgO + MWCNT, and SnO_2 + MWCNT (80 to 20weight mixture ratio) and DI water base fluid	0.25% to 1.5%	Maximum 15.09% for MGO-MWCNT/DI water at 1.5 vol. fraction and 25° C
[73]	Al_2O_3 - ZnO/water	0.33% to 1.67%	30.12%
[74]	Aqueous graphene oxide - Al_2O_3	0.05% to 2%	7% at 2% vol. fraction and 20° C
[75]	Al_2O_3 – Si_2O_3/water	0% to 3%	18.38%

PERFORMANCE OPTIMIZATION OF PARABOLIC TROUGH CONCENTRATOR USING HYBRID NANOFLIUD

A parabolic trough concentrator is a solar thermal device that is made to focus and use solar energy in the best way possible. There are three main parts: a parabolic reflector, a receiver tube, and a system for tracking. The line diagram of PTC is shown in Figure 9. The parabolic reflector is a curved mirror that collects sunlight and focuses it onto the receiver tube, which runs along the reflector's focal line. There is a heat transfer fluid inside the receiver tube that collects the concentrated solar energy. The tube is usually wrapped in glass to keep heat from escaping. The tracking system makes sure that the PTC stays in line with the sun all day, which helps it capture the most solar energy [76,77]. The way it works is by bouncing sunlight off the parabolic mirror and onto the receiver tube, where the fluid absorbs the concentrated heat. Then, the hot fluid is sent to a heat exchanger or used directly in applications like making electricity, heating buildings, or removing salt from water. The PTC's thermal performance is better because of this combination of precise focus, efficient absorption, and active tracking [78].

Utilizing a hybrid nanofluid to enhance the performance of a PTC is a significant advancement for solar thermal energy systems and optical efficiency. The PTC enhances efficiency of heat transfer, decreased heat loss, and enhanced energy conversion rates by utilizing hybrid nanofluids that are composed of distinct nanoparticles those agugment thermal properties. These fluids delivered excellent result of producing the working medium's thermal conductivity and specific heat capacity superior, which makes it preferable at absorbing and preserving solar energy. This enhancement makes PTC systems more effective for wide range applications since they work effective in a wider range of environmental situations. The technique further aids to utilize solar energy in certain ways that is excellent for the environment, which implies reduced reliance on convectional energy sources.

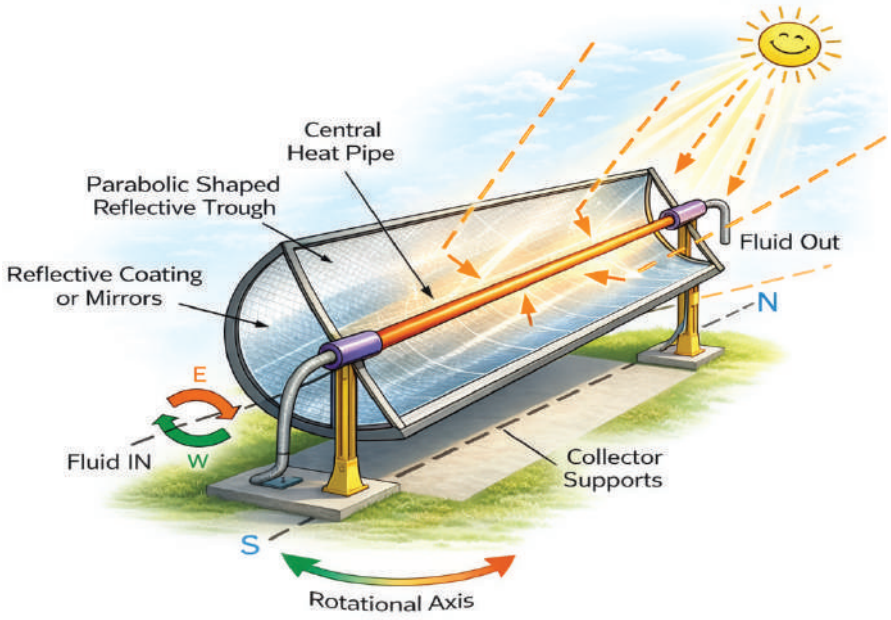


Figure 9. Parabolic trough solar concentrator.

Enhancement in Thermal Efficiency

The utilization of hybrid nanofluids as working fluids has formed PTCs considerably more thermally efficient. Hybrid nanofluids are constituted of two or more kinds of nanoparticles suspended in a base fluid. They have superior thermal conductivity, enhanced specific heat capacity, and improved convective heat transfer. These features make it simpler for energy to be absorbed and curtail on heat loss. The thermal efficiency of PTCs can be significantly enhanced by optimizing the size, composition, and concentration of the nanoparticles and preserving the flow conditions appropriate. This leads to better performance and longer-lasting solar thermal systems [79]. The parameters that affect the thermal efficiency of PTC are shown in Figure 10. The summary of enhancement in the thermal efficiency of PTC using a hybrid nanofluid is shown in Table 5. The thermal efficiency of PTC is calculated by Eq. 1.

$$\eta = \frac{mc_p\left(T_{out} - T_{in}\right)}{A_{ap}G} \tag{1}$$

Minea and El-Maghlany [80] showed that each of the hybrid nanofluids under consideration had an increase in Nu. When compared to the base fluid, the Cu-MgO hybrid exhibits the largest rise in mean Nu at 2% volume fraction, with a surge of over 14%. For certain hybrids, nevertheless, the rapid viscosity increase resulted in a large pressure drop punishment. The 2% Ag-MgO-water hybrid nanofluid provides the highest efficiency of the trough collector, and its efficiency increases as Re increases. Bellos and Tzivanidis [81] investigated the thermal performance of PTC using hybrid nanofluid mentioned in Table 5 at constant volume concentration. The ultimate outcomes show that the hybrid nanofluid can increase thermal efficiency by up to 1.8%, whilst mono nanofluids can only increase thermal efficiency by up to 0.7%. The variation of thermal efficiency enhancement with varying inlet temperature is shown in Figure 11. The huge Nusselt number boost for the hybrid nanofluid situation, which is roughly 2.2 higher than the corresponding value for working with plain oil, is the basis for this enhanced thermal efficiency augmentation.

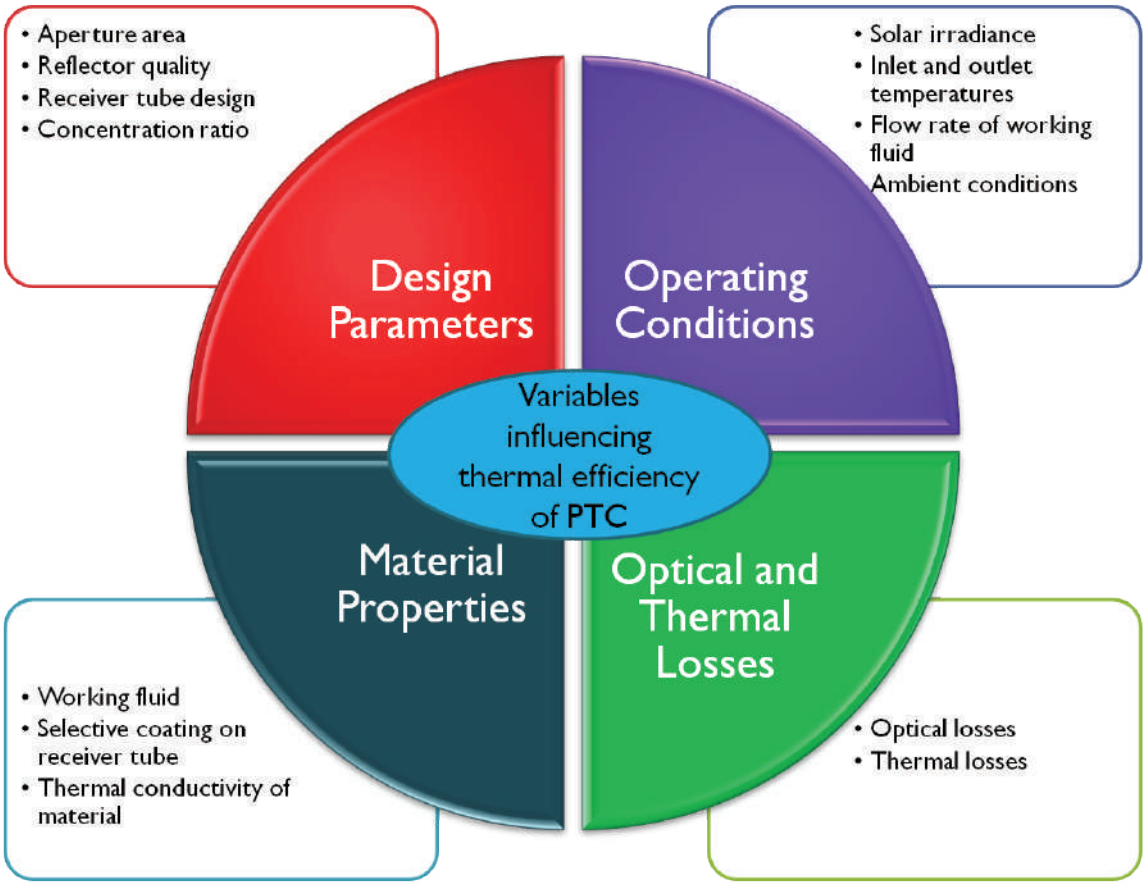


Figure 10. Variables influencing thermal efficiency of PTC.

Table 5. Summary of Enhancement in the thermal efficiency of PTC using hybrid nanofluid

Ref. no.	Hybrid nanofluid	Volume fraction	Enhancement in thermal efficiency/parameters
[80], 2018	Cu-MgO, Ag –MgO, GO-Co_3O_4, Al_2O_3-Cu	0.05% to 2%	14% enhancement in Nu for Cu-MgO at 2% vol. fraction
[81], 2018	Al_2O_3-TiO_2/Oil	constant	1.8% enhancement in thermal efficiency
[82], 2020	Al_2O_3-CuO/DI	0.01% to 0.5%	Maximum 31% enhancement in thermal efficiency
[83], 2020	Al_2O_3-CeO_2/ Syltherm 800, Al_2O_3-CuO/ Syltherm 800	4%	The maximum exergy enhancement occurred using Al_2O_3-CeO_2 reached 1.03%
[84], 2021	1.5% MWCNT – 1.5% TiO_2/ therminol-VPI	3%	Maximum 5.27% enhancement in thermal efficiency
[85], 2021	Al_2O_3-MWCNT/water	0.04%	Maximum 197.1% enhancement in thermal efficiency
[86], 2021	Ag - ZnO, Ag -TiO_2, Ag –MgO (base fluid Syltherm 800)	1% to 4%	Maximum 31% enhancement in convective heat transfer coefficient using Ag-MgO nanofluid at 4% volume fraction
[87], 2021	Al_2O_3-WO_3/Therminol VP1	1% to 4%	Thermal efficiency was enhanced by 32.728% and exergy efficiency was enhanced by 71.255%
[88], 2021	Ag-SWCNT, Ag-MWCNT, Ag-MgO (base fluid Syltherm oil)	1% to 2%	Maximum 11.5% enhancement in thermal efficiency using Ag-SWCNT nanofluid
[89], 2022	90% SiO_2-10% MWCNT/ EG-water	0.5% to 1.5%	Maximum 14.27% enhancement in thermal efficiency
[90], 2022	Fe_2O_3-GO, Fe_2O_3-SiC, Fe_2O_3-TiO_2 (base fluid Syltherm 800)	0% to 2%	Maximum 18.51% enhancement in thermal efficiency using Fe_2O_3-GO nanofluid at 2% volume fraction
[91], 2022	MgO-Cu/water	1% to 3%	Maximum 24.16% enhancement in thermal efficiency at 3% volume fraction
[92], 2022	Al_2O_3-CuO/water	1%	Maximum 29.21% enhancement in thermal efficiency
[93], 2022	Cu-MWCNT/water	-	The maximum energy and energy efficiency that could be obtained was 65.5% and 36.6%, correspondingly.
[94], 2023	Ag-Al_2O_3, Ag-MgO, Ag-TiO_2, Ag-CuO, Cu-Al_2O_3, Cu-MgO, Cu-TiO_2, Cu-CuO (base fluid Syltherm 800)	1.5% to 4%	Maximum 2.8% enhancement in thermal efficiency using Cu-MgO/Syltherm800 nanofluid at 3% vol. fraction.
[95], 2023	CuO-SWCNT/water	2% to 6%	The highest PEC value, 1.22, is associated with a volume fraction of 6% and Re = 12,000.
[96], 2024	Graphene-Fe_3O_4/water	0.01% to 0.2%	Maximum 45.46% enhancement in thermal efficiency at 0.2% volume fraction
[97], 2024	MWCNT-Y_2O_3/DI water	0.01% to 0.1%	Maximum 44.24% enhancement in thermal efficiency at 0.1% volume fraction

Khalil et al. [82] used a hybrid nanofluid for the enhancement of PTC effectiveness. Their findings showed that, when compared to basefluid, hybrid nanofluid enhanced the thermal efficiency of a typical PTC by 31%. Because of its increased heat transfer rate, sun trapping, and volumetric digestion, the direct absorption PTC was found to have a 19% better thermal efficiency gain than the standard PTC. Such bidirectional nanofluids have the potential to function in several solar thermal energy-based systems. Al-Oran et al. [83] used mono as well as hybrid nanofluid to ameliorate the energy and exergy of PTC. The variation of thermal efficiency, exergetic efficiency, Nusselt number and HTC with different nanofluids is shown in Figure 12. Using Al_2O_3-CeO_2 hybrid nanofluids increased thermal and energy efficiency by 1.09% and 1.03%, correspondingly, while increasing the Nu and HTC by 167.8% and 200.7%, correspondingly. Additionally, because they exhibit reduced pressure fall values, hybrid nanofluids have a greater benefit over mono nanofluids. Lastly, the evaluation of the efficiency variation influenced by the nanoparticle's thermal characteristics was shown at the optimal temperature of 575 K.

Khan et al. [84] used a hybrid nanofluid to evaluate the thermodynamic performance of PTC having convergent-divergent section. The study's findings show that using a changed design with hybrid nanofluids significantly enhances system effectiveness because of the formation of swirls and agitation that lower absorber surface

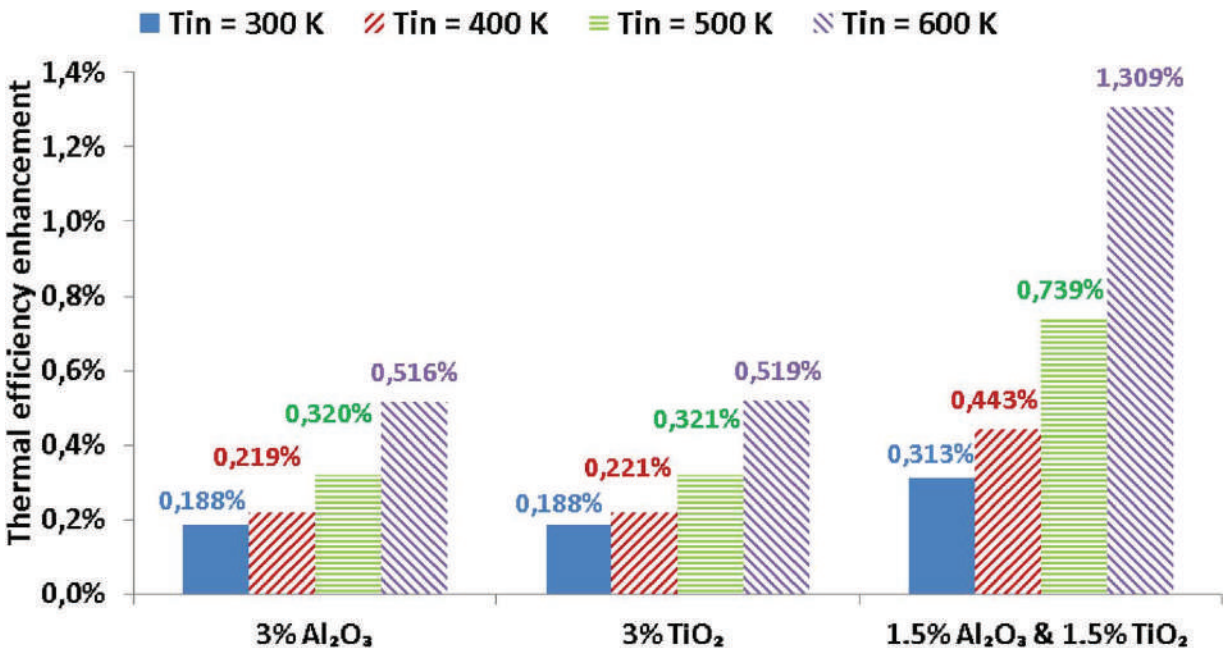


Figure 11. Variation of thermal efficiency enhancement with inlet temperature [From Bellos and Tzivanidis [81], with permission from Elsevier].

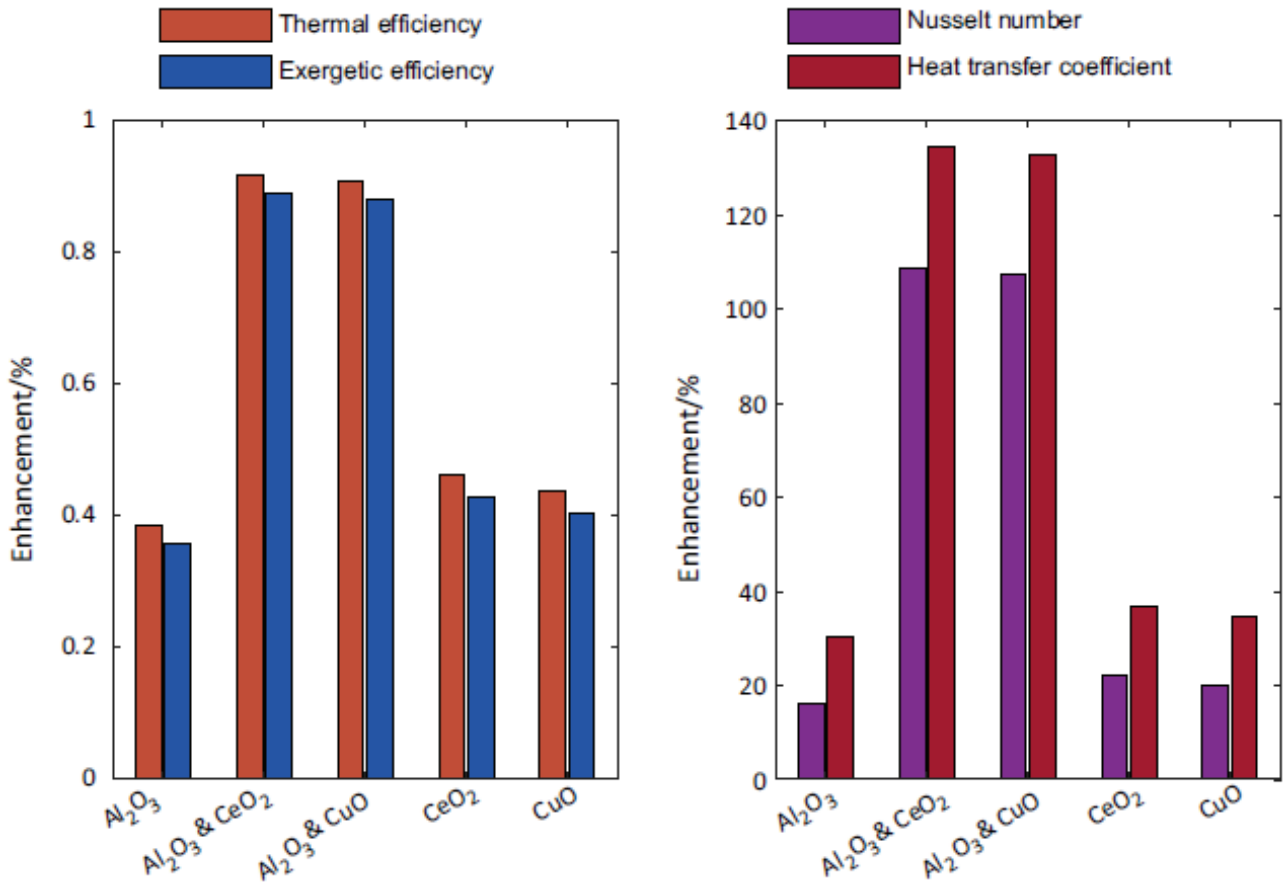


Figure 12. Variation of thermal efficiency, exergetic efficiency, Nusselt number and COH enhancement with different nanofluid [From Al-Oran et al. [83], with permission from Springer Nature].

temperature and, eventually, the loss of heat. In particular, the increase in thermal efficiency for the CD absorber tube with hybrid nanofluids varies between 3.61% and 5.27%, whereas for the smooth tube, it varies between 1.70% and 1.91%. Mashhadian et al. [85] ameliorate the environmental performance of DAPTC using hybrid nanofluid. Maximum enhancement in thermal efficiency was 197.1% using a hybrid nanofluid. The pressure drop in the absorber tube was measured, and the findings indicate that because of the low volume percentage, the pressure drop increase for hybrid nanofluids can be insignificant. Additionally, the nanofluid-based collector's water savings and releases of additional pollutants, like CO_2, were calculated. The findings show that switching to hybrid nanofluids from water can reduce CO_2 emissions and water use by up to 450.33 kg and 16.6 m3 per collector, correspondingly.

Ekiciler et al. [86] used a hybrid nanofluid mentioned in Table 5 to enhance the performance of the PTC receiver. Hybrid nanofluids significantly enhance thermal efficiency, demonstrating their effectiveness in utilizing solar energy. Among the tested fluids, the Ag–MgO/Syltherm 800 hybrid nanofluid with a 4.0 vol% concentration exhibits the highest thermal efficiency. However, at higher Reynolds numbers, the efficiency decreases due to increased pumping power requirements.Al-Oran and Lezsovits [87] used a hybrid nanofluid to enhance the performance of PTC at Budapest. During Budapest's warm climate, the highest possible energy and energy rates for HNFs were measured at noon and reached 32.728% and 71.255%, correspondingly, at the ideal temperature of 500 K. Mohammed et al. [88] used hybrid nanofluid for augmentation in heat transfer of PTC having receiver tube and conical turbulators. By employing Ag-SWCNT/Syltherm oil rather than pure Syltherm oil, the conical turbulators successfully increased their thermal endurance by 233.4%. It is determined that the PEC falls between 0.9 and 1.82. Both the exergetic and thermal efficiencies rose by 18.2% and 11.5%, correspondingly. The entropy production ratio and rate can degrade by up to 33.7% and 42.7%, respectively.

Khaledi et al. [89] used hybrid nanofluid to investigate the energy, exergy and hydraulic performance of PTC. The findings demonstrated that using HNFs increases thermal efficiency compared to the base fluid because they improve thermal characteristics and the Nu. Specifically, employing HNFs resulted in an ultimate thermal efficiency gain of 14.27% when contrasted with the base fluid. Additionally, the use of HNFs improved the energy efficiency. The appetite for pumping power is extremely low for the actual generation of the beneficial heat rate, as evidenced by the highest increase in pumping power utilizing HNFs of 9.72%. Mohammed et al. [90] used three different combinations of HNFs to investigate the performance of PTC thermohydraulically and thermodynamically. Using brick-shaped nanoparticles, the total PEC has been determined to be between 1.24 to 2.46. According to the findings, there was an 18.51% boost in thermal efficiency and a 16.21% rise in exergy efficiency. About 48.27% and 52.6%, correspondingly, are the highest reductions in the production of entropy rate and ratio. Khetib et al. [91] used a hybrid nanofluid to evaluate the energy as well as exergy performance of PTC using twisted turbulators. The findings showed that increasing the Re from 8000 to 32000 might increase thermal efficiency by 23.79% and exergy efficiency by 21.15%. Chakraborty et al. [92] evaluated the effect of hybrid nanofluid and elliptical insert on PTC performance. The design with an elliptical insert of 28 mm main diameter has the largest increase in both thermal efficiency as well as HTC, at 44.21% and 29.21%, correspondingly. Saray and Heyhat [93] used a hybrid nanofluid in PTC for 4E analysis. Their results revealed that a maximum of 40.44 GJ of energy can be saved as well and 59.03 KL of water can also be saved using HNF. The system achieves maximum exergy efficiency at 36.63% and energy efficiency at 65.47%, with the minimum energy production cost being $0.0195 per kWh.

Ajbar et al. [94] used eight different combinations of hybrid nanofluid as mentioned in Table 5 to investigate the thermal efficiency of PTC. The findings demonstrated that, when compared to base fluid, thermal efficiency might increase by up to 2.8% when hybrid nanofluids were used in the evaluation and by 1.6% on average within the tested operating circumstances. Esfahani et al. [95] evaluate the 4E performance of the PTC using a hybrid nanofluid. The heat transmission rate is increased by using a turbulator in the shape of a twisted strip in conjunction with a coil. The maximum increase in Nusselt number is noted 55% at a volume fraction of 2%. Al-Rabeeah et al. [96] used a hybrid nanofluid of different volume concentrations to evaluate the performance of PTC. Their results revealed that the maximum enhancement in thermal efficiency is 45.46% at 0.2% volume fraction. Al-Oran et al. [97] used a hybrid nanofluid to investigate the performance of PTC in Jordanian conditions. The results showed that water had a thermal efficiency of 19.32%, while 0.1% HNF had the highest thermal efficiency of 44.24%. Also, the highest optical efficiency got better as the concentrations went up. With 0.1% Vol, the highest efficiency of 45% was achieved.

Comparative Analysis of Hybrid Nanofluid versus Nanofluid for the Augmentation of their use in PTC

A comparative analysis of hybrid nanofluids versus nanofluids reveals that hybrid nanofluids offer superior thermal conductivity, heat transfer efficiency, and stability, making them more effective for enhancing parabolic trough concentrator (PTC) performance, despite their higher cost and viscosity. The comparative analysis is shown in Table 6.

Table 6. Comparative analysis of hybrid nanofluid versus nanofluid for enhancing their application in PTC

Parameter	Hybrid nanofluid	Nanofluid	Ref. no.
Composition	Mixing of two or more nanoparticles (e.g., Al_2O_3/Cu, CuO/Ag) in a base fluid (e.g., water, ethylene glycol)	One type of nanoparticle type (e.g., CuO, Al_2O_3, SiO_2) in a base fluid	[98,99]
Thermal Conductivity	15-50% enhancement in thermal conductivity than the base fluid	5-20% augmentation in thermal conductivity than the base fluid	[100,101]
Heat Transfer Efficiency	Compared to regular HTFs, the heat transfer rate can improve by 30 to 60%.	10-30% enhancement in heat transfer than the base fluids	[102,103]
Stability	Improved stability with zeta potential of >30 mV (using stabilizers)	Zeta potential is often less than 20 mV, which can cause problems with sedimentation and aggregation.	[104,105]
Viscosity	Higher viscosity (usually 10–25% more than the base fluid)	5–15% more viscous than the base fluid	[106,107]
Nanoparticle Interaction	Synergistic effects from several nanoparticles (for example, Al_2O_3 makes CuO more stable and helps it transfer heat)	Limited to the properties of a single nanoparticle, like high thermal conductivity but low dispersion stability	[108,109]
Cost	More expensive (2-3 times more than single-component nanofluids because they have two nanoparticles)	Less expensive (depends on the nanoparticle; usually 1–2 times the cost of the base fluid)	[110,111]
Operational Efficiency	25 to 40% more efficient at high temperatures (200 to 400 °C)	10-20% more efficient at lower temperatures (50–150°C)	[112,113]
Economic Feasibility	Higher initial cost, but possible savings in the long run with better operational efficiency and less maintenance	Lower initial cost, but less efficient at higher temperatures, which could mean losing energy.	[114,115]
Operational Durability	Better stablized over time with minimal reduction of quality (thermal stability > 300°C)	Chance of deterioration which might diminish performance over time (thermal stability < 250°C)	[116,117]

TECHNICAL AND PRACTICAL CHALLENGES OF HYBRID NANOFLUID USAGES IN PTC

Utilizing hybrid nanofluids in PTCs can enhance thermal efficiency in various manners, but it also has a lot of technical and practical challenges, as illustrated in Figure 13. A crucial concern is how stable hybrid nanofluids are. Gradually, nanoparticles can aggregate together and stabilize, which can suffer their thermal performance. Ensuring long-term stability in high-temperature conditions, which are common in PTC systems, is still a major challenge [118]. Also, nanoparticles can chemically interact with system materials and cause wear over time, which can lead to corrosion and erosion of metal parts. This is a risk that comes with compatibility with system materials [119]. Thermal and rheological properties make their use even more difficult. Hybrid nanofluids enhance thermal conductivity, but their enhanced viscosity can produce pumping power requirement higher, that might eliminate any energy savings [120].

Another reason why widespread use isn't happening is because of the costs. Producing hybrid nanofluids is costly since it entails convoluted synthesis technique. Operational expenses also escalate since these fluids need unique equipment to control, preserve, and monitor them [121]. When shifting from laboratory experimentation to industrial utilization, there are more complications to resolve, such as keeping the nanoparticles uniformly dispersed and receiving the same performance from huge systems [122]. Environmental and safety concerns make things even harder. Nanoparticles are toxic, and hybrid nanofluids need to be thrown away properly, which means that strict rules and waste management plans must be followed [123].

Measurement and standardization make progress even harder because there aren't any standardized ways to test the thermal and rheological properties of hybrid nanofluids in real-world situations. Ensure that the findings are credible and can be iterative; their production must have quality control [124]. Additionally, including hybrid nanofluids to prevailing PTC systems frequently implies making costly design amendments, such as retrofitting pipelines and revalidating system parameters to enhance flow and heat transfer. These technical and practical difficulties emphasize the requirement for aimed research and innovation provides hybrid nanofluids a possible outcome for solar thermal applications [125]. To clearly perceive the capabilities of hybrid nanofluids in enhancing PTC system

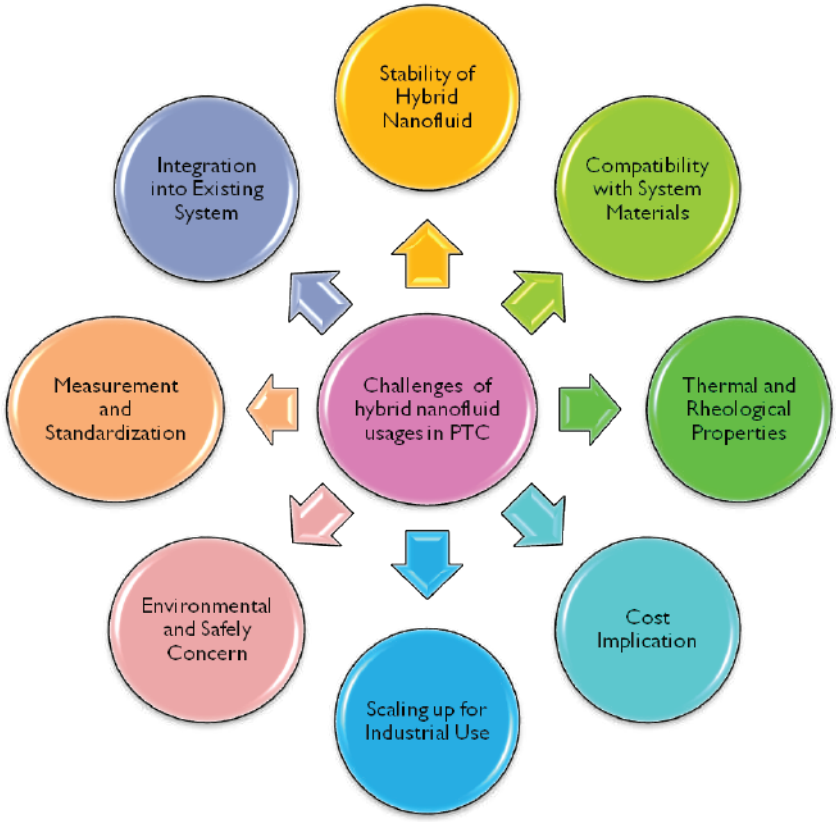


Figure 13. Challenges of hybrid nanofluid usages in PTC.

efficiency, it is essential to resolve these difficulties by making advancement in material science, finding economical methods to make them, and adding strong environmental protections.

Limitations of Hybrid Nanofluid in Enhancing PTC Efficiency

Hybrid nanofluids are very promising for improving the thermal performance of parabolic trough concentrators, but they are not widely used yet because of technical, economic, and environmental problems. To accomplish these works, we required to increase efforts in research and create new technologies to get around these difficulties. Limitations are mentioned below

- Nanoparticles in hybrid nanofluids agglomerate and sediment progressively, diminishing thermal performance
- Higher viscosity means more pumping power is needed, which cancels out any gains in energy efficiency.
- Nanoparticles can make parts of a system corrode and wear down.
- Hybrid nanofluids are costly since they are developed through complex synthesis processes.
- It is challenging to preserve nanoparticles uniformly distributed and their performance reliable in large scale system.
- The feasible contamination of nanoparticles and the challenges in eliminating them.
- Lack of standard methodologies for examining thermal and rheological characteristics in practical situations.
- Upgrading existing PTC systems to work with hybrid nanofluids can be costly.

CONCLUSION

Hybrid nanofluids are a potential new area of solar energy technology, particularly when it comes to making PTCs perform effectively. There are still certain challenges to resolve, but advancement in nanotechnology, material science, and thermofluid dynamics is advantageous. Utilizing hybrid nanofluids in PTC systems is in accordance with worldwide energy aims since it is a prolonged way to utilize more solar energy and depend less on fossil fuels. This review article pertains to following conclusion.

- Hybrid nanofluids greatly improve the thermal efficiency of parabolic trough concentrators by speeding up heat transfer rates. This makes them a good choice for solar thermal applications.
- The Al_2O_3–MWCNT/water hybrid nanofluid had the highest thermal efficiency increase of 197.1% at a volume fraction of 0.04%, and it also had a very small pressure drop.

- Hybrid nanofluids greatly improve the performance of convective heat transfer. For example, the Cu–MgO/water hybrid nanofluid at a 2% volume fraction had the highest Nusselt number improvement of 14%.
- Hybrid nanofluids significantly improve the exergy performance of PTC systems. For example, Al_2O_3–WO_3/Therminol VP-1 at 4% volume fraction achieved a maximum exergy efficiency improvement of 71.255%, which means that it uses energy better and is less irreversible than base fluids.
- Comparative analysis confirms that hybrid nanofluids provide 15–50% higher thermal conductivity and 30–60% better heat transfer efficiency than conventional nanofluids, though at the cost of 10–25% increased viscosity, emphasizing the need for optimized formulations to balance thermal gains and pumping power requirements.
- The review shows that hybrid nanofluids can have a big positive effect on the environment, such as reducing CO_2 emissions by up to 450.33 kg and saving 16.6 m^3 of water per collector. This shows that they are important for solar thermal energy systems that are low-carbon and sustainable.
- Comprehensive experimental studies and simulation models corroborate the theoretical advantages of hybrid nanofluids, providing insights into their practical applicability.
- Ensuring the stability and longevity of hybrid nanofluids remains a critical factor in their widespread adoption, necessitating additional research into anti-agglomeration techniques.

Future Research Direction

Future research should focus on augmenting hybrid nanofluid formulations, evaluating prolonged economic feasibility, exploring modern dispersion methods, and implementing extensive real world applications to evaluate hybrid nanofluid efficacy in practical PTC systems. Here are few realistic directions for future research:

- Identify the best composition of nanoparticles, concentrations, and base fluids for PTC applications to get the superior thermal performance and stability.
- Generate and enhance procedures to disperse hybrid nanofluids to ensure that they are more stable and homogeneous, which will ensure that they work the similarly over time in PTC mechanism.
- Inspect hybrid nanofluids at micro level and in the practical working PTC systems to observe how efficiently they work, how energy efficient they are, and how effectively they can be utilized on a larger scale.
- Evaluate the economic efficiency and extended operational sustainability of hybrid nanofluids, considering production cost, maintenance, and system endurance.
- Evaluating the aging impact, stability, and diminution of hybrid nanofluids under operational circumstances to ensure dependable and efficient performance over sustained periods.

NOMENCLATURE

A_{ap}	Surface area collecting solar energy or Aperture area (m^2)
C_p	Specific heat capacity (kJ/kgK)
G	Solar irradiance (W/m^2)
m	Mass flow rate of working fluid (Kg/s)
Nu	Nusselt number
Re	Reynolds number
T_{out}	Outlet temperature of the working fluid (K)
T_{in}	Intlet temperature of the working fluid (K)

Abbreviations

4E	Energy, exergy, economic and environment
CD	Converging-diverging
DLS	Dynamic light scattering
DAPTC	Direct absorption parabolic trough collector
DI water	Distilled water
EG	Ethylene glycol
HNF	Hybrid nanofluid
HTC	Heat transfer coefficient
PTC	Parabolic trough concentrator
PEC	Performance evaluation criterion

AUTHORSHIP CONTRIBUTION

All the authors equally contributed to this work.

DATA AVAILABILITY STATEMENT

The authors confirm that the data that supports the findings of this study are available within the manuscript.

CONFLICT OF INTEREST

The author declared no potential conflicts of interest with respect to the research, authorship, and/or publication of this article.

ETHICS

There are no ethical issues with the publication of this manuscript.

REFERENCES

[1] Holechek JL, Geli HM, Sawalhah MN, Valdez R. A global assessment: Can renewable energy replace fossil fuels by 2050? Sustainability 2022;14:4792. [CrossRef]

[2] Kumar S, Rawat MK, Gupta S. An evaluation of current status of renewable energy sources in India. Int J Innov Technol Explor Eng 2019;8:1234-1239. [CrossRef]

[3] Kabir E, Kumar P, Kumar S, Adelodun AA, Kim KH. Solar energy: Potential and future prospects. Renew Sustain Energy Rev 2018;82:894-900. [CrossRef]

[4] Kumar S, Gupta SK, Rawat M. Resources and utilization of geothermal energy in India: An eco-friendly approach towards sustainability. Mater Today Proc 2020;26:1660-1665. [CrossRef]
[5] Kumar N, Gupta SK. Progress and application of phase change material in solar thermal energy: An overview. Mater Today Proc 2021;44:271-281. [CrossRef]
[6] Yavuz C, Botsalı AR. A weather-based forecasting system for the solar power plants in the Konya region. Sigma J Eng Nat Sci 2022;40:144-149. [CrossRef]
[7] Qadem M, Filik ÜB. Solar radiation forecasting by using deep neural networks in Eskişehir. Sigma J Eng Nat Sci 2021;39:159-169. [CrossRef]
[8] Kumar N, Gupta SK, Sharma VK. Application of phase change material for thermal energy storage: An overview of recent advances. Mater Today Proc 2021;44:368-375. [CrossRef]
[9] Thomas A, Guven HM. Parabolic trough concentrators-Design, construction and evaluation. Energy Convers Manag 1993;34:401-416. [CrossRef]
[10] Clark JA. An analysis of the technical and economic performance of a parabolic trough concentrator for solar industrial process heat application. Int J Heat Mass Transf 1982;25:1427-1438. [CrossRef]
[11] Mahian O, Kolsi L, Amani M, Estellé P, Ahmadi G, Kleinstreuer C, et al. Recent advances in modeling and simulation of nanofluid flows-Part I: Fundamentals and theory. Phys Rep 2019;790:1-48. [CrossRef]
[12] Rizwan M, Shoukat A, Ayub A, Razzaq B, Tahir MB. Types and classification of nanomaterials. In: Nanomaterials: Synthesis, characterization, hazards and safety. 2021;31-54. [CrossRef]
[13] Cuce E, Cuce PM, Guclu T, Besir AB. On the use of nanofluids in solar energy applications. J Therm Sci 2020;29:513-534. [CrossRef]
[14] Chu YM, Bashir S, Ramzan M, Malik MY. Model-based comparative study of magnetohydrodynamics unsteady hybrid nanofluid flow between two infinite parallel plates with particle shape effects. Math Methods Appl Sci 2023;46:11568-11582. [CrossRef]
[15] Akaje TW, Olajuwon BI, MusiliuTayo RAJI. Computational analysis of the heat and mass transfer in a Casson nanofluid with a variable inclined magnetic field. Sigma 2023;41:512-523. [CrossRef]
[16] El Hattab M, Boumhaout M, Oukach S. MHD natural convection in a square enclosure using carbon nanotube water nanofluid with two isothermal fins. Sigma J Eng Nat Sci 2024;42:1075-1087. [CrossRef]
[17] Akbarzadeh S, Valipour MS. Heat transfer enhancement in parabolic trough collectors: A comprehensive review. Renew Sustain Energy Rev 2018;92:198-218. [CrossRef]
[18] Olia H, Torabi M, Bahiraei M, Ahmadi MH, Goodarzi M, Safaei MR. Application of nanofluids in thermal performance enhancement of parabolic trough solar collector: State-of-the-art. Appl Sci 2019;9:463. [CrossRef]
[19] Krishna Y, Faizal M, Saidur R, Ng KC, Aslfattahi N. State-of-the-art heat transfer fluids for parabolic trough collector. Int J Heat Mass Transf 2020;152:119541. [CrossRef]
[20] Tiwari AK, Kumar V, Said Z, Paliwal HK. A review on the application of hybrid nanofluids for parabolic trough collector: Recent progress and outlook. J Clean Prod 2021;292:126031. [CrossRef]
[21] Bamisile O, Cai D, Adun H, Adedeji M, Dagbasi M, Dika F, Huang Q. A brief review and comparative evaluation of nanofluid application in solar parabolic trough and flat plate collectors. Energy Rep 2022;8:156-166. [CrossRef]
[22] Panduro EAC, Finotti F, Largiller G, Lervåg KY. A review of the use of nanofluids as heat-transfer fluids in parabolic-trough collectors. Appl Therm Eng 2022;211:118346. [CrossRef]
[23] Ajbar W, Parrales A, Huicochea A, Hernández JA. Different ways to improve parabolic trough solar collectors' performance over the last four decades and their applications: A comprehensive review. Renew Sustain Energy Rev 2022;156:111947. [CrossRef]
[24] Nawsud ZA, Altouni A, Akhijahani HS, Kargarsharifabad H. A comprehensive review on the use of nano-fluids and nano-PCM in parabolic trough solar collectors (PTC). Sustain Energy Technol Assess 2022;51:101889. [CrossRef]
[25] Priyanka, Kumar S, Kumar A. Effect of mono/hybrid nanofluids and passive techniques on thermal performance of parabolic trough solar collector: A review. Energy Sources Part A Recovery Util Environ Eff 2023;45:1686-1709. [CrossRef]
[26] Gupta SK. A short & updated review of nanofluids utilization in solar parabolic trough collector. Mater Today Proc 2023; https://doi.org/10.1016/j.matpr.2022.12.278. [CrossRef]
[27] Gupta SK, Saxena A. A progressive review of hybrid nanofluid utilization in solar parabolic trough collector. Mater Today Proc 2023; https://doi.org/10.1016/j.matpr.2023.06.204. [CrossRef]
[28] Sarkar J, Ghosh P, Adil A. A review on hybrid nanofluids: Recent research, development and applications. Renew Sustain Energy Rev 2015;43:164-177. [CrossRef]
[29] Abbas N, Nadeem S, Saleem A, Malik MY, Issakhov A, Alharbi FM. Models base study of inclined MHD of hybrid nanofluid flow over nonlinear stretching cylinder. Chin J Phys 2021;69:109-117. [CrossRef]
[30] Gholinia M, Javadi H, Gatabi A, Khodabakhshi A, Ganjii DD. Analytical study of a two-phase revolving system of nanofluid flow in the presence of a magnetic field to improve heat transfer. Sigma J Eng Nat Sci 2019;37:340-360.

[31] Gupta SK, Verma H, Yadav N. A review on recent development of nanofluid utilization in shell & tube heat exchanger for saving of energy. Mater Today Proc 2022;54:579-589. [CrossRef]
[32] Kumar SA, Meenakshi KS, Narashimhan BRV, Srikanth S, Arthanareeswaran GJMC. Synthesis and characterization of copper nanofluid by a novel one-step method. Mater Chem Phys 2009;113:57-62. [CrossRef]
[33] Ali HM, Babar H, Shah TR, Sajid MU, Qasim MA, Javed S. Preparation techniques of TiO2 nanofluids and challenges: A review. Appl Sci 2018;8:587. [CrossRef]
[34] Gupta SK, Pradhan S. A review of recent advances and the role of nanofluid in solar photovoltaic thermal (PV/T) system. Mater Today Proc 2021;44:782-791. [CrossRef]
[35] Paul G, Philip J, Raj B, Das PK, Manna I. Synthesis, characterization, and thermal property measurement of nano-Al95Zn05 dispersed nanofluid prepared by a two-step process. Int J Heat Mass Transf 2011;54:3783-3788. [CrossRef]
[36] Judran HK, Al-Hasnawi AGT, Al Zubaidi FN, Al-Maliki WAK, Alobaid F, Epple B. A high thermal conductivity of MgO-H2O nanofluid prepared by two-step technique. Appl Sci 2022;12:2655. [CrossRef]
[37] Sanjeevi B, Loganathan K. Synthesis of multi-wall carbon nanotubes nanofluid by using two-step method. Therm Sci 2021;24:519-524. [CrossRef]
[38] Gupta SK, Gupta S, Gupta T, Raghav A, Singh A. A review on recent advances and applications of nanofluids in plate heat exchanger. Mater Today Proc 2021;44:229-241. [CrossRef]
[39] Awais M, EhsanAwan S, Asif Zahoor Raja M, Parveen N, Khan WU, Yousaf Malik M, He Y. Effects of variable transport properties on heat and mass transfer in MHD bioconvectivenanofluid rheology with gyrotactic microorganisms: Numerical approach. Coatings 2021;11:231. [CrossRef]
[40] Sidik NAC, Jamil MM, Japar WMAA, Adamu IM. A review on preparation methods, stability and applications of hybrid nanofluids. Renew Sustain Energy Rev 2017;80:1112-1122. [CrossRef]
[41] Nadeem S, Abbas N, Malik MY. Inspection of hybrid based nanofluid flow over a curved surface. Comput Methods Programs Biomed 2020;189:105193. [CrossRef]
[42] Asadi A, Alarifi IM, Foong LK. An experimental study on characterization, stability and dynamic viscosity of CuO-TiO2/water hybrid nanofluid. J Mol Liq 2020;307:112987. [CrossRef]
[43] Siddiqui FR, Tso CY, Chan KC, Fu SC, Chao CY. On trade-off for dispersion stability and thermal transport of Cu-Al2O3 hybrid nanofluid for various mixing ratios. Int J Heat Mass Transf 2019;132:1200-1216. [CrossRef]
[44] Riasat S, Ramzan M, Sun YL, Malik MY, Chinram R. Comparative analysis of Yamada-Ota and Xue models for hybrid nanofluid flow amid two concentric spinning disks with variable thermophysical characteristics. Case Stud Therm Eng 2021;26:101039. [CrossRef]
[45] Bolarin G, Yusuf A, Adekunle ST, Aıyesımı YM, Jıya M. Analysis of a boundary layer flow of a nanofluid over an inclined plane via ADM. Sigma J Eng Nat Sci 2019;37:475-488.
[46] Rashidi MM, Nazari MA, Mahariq I, et al. Thermophysical properties of hybrid nanofluids and the proposed models: An updated comprehensive study. Nanomaterials 2021;11:3084. [CrossRef]
[47] Kukreja N, Gupta SK, Rawat M. Performance analysis of phase change material using energy storage device. Mater Today Proc 2020;26:913-917. [CrossRef]
[48] Gupta SK, Rawat MK, Kukreja N. Analysis of heat transfer enhancement of electronic chip using CFD. Int J Sci Technol Res 2019;8:1017-1020.
[49] Abbas N, Nadeem S, Malik MY. Theoretical study of micropolar hybrid nanofluid over Riga channel with slip conditions. Physica A Stat Mech Appl 2020;551:124083. [CrossRef]
[50] Sajid MU, Ali HM. Thermal conductivity of hybrid nanofluids: A critical review. Int J Heat Mass Transf 2018;126:211-234. [CrossRef]
[51] Esfe MH, Amiri MK, Alirezaie A. Thermal conductivity of a hybrid nanofluid. J Therm Anal Calorim 2018;134:1113-1122. [CrossRef]
[52] Leong KY, Ahmad KK, Ong HC, Ghazali MJ, Baharum A. Synthesis and thermal conductivity characteristic of hybrid nanofluids-A review. Renew Sustain Energy Rev 2017;75:868-878. [CrossRef]
[53] Das PK. A review based on the effect and mechanism of thermal conductivity of normal nanofluids and hybrid nanofluids. J Mol Liq 2017;240:420-446. [CrossRef]
[54] Gupta SK, Dixit S. Progress and application of nanofluids in solar collectors: An overview of recent advances. Mater Today Proc 2021;44:250-259. [CrossRef]
[55] Harandi SS, Karimipour A, Afrand M, Akbari M, D'Orazio A. An experimental study on thermal conductivity of F-MWCNTs-Fe3O4/EG hybrid nanofluid: Effects of temperature and concentration. Int Commun Heat Mass Transf 2016;76:171-177. [CrossRef]
[56] Guan H, Su Q, Wang R, Huang L, Shao C, Zhu Z. Why can hybrid nanofluid improve thermal conductivity more? A molecular dynamics simulation. J Mol Liq 2023;372:121178. [CrossRef]
[57] Gupta M, Singh V, Said Z. Heat transfer analysis using zinc Ferrite/water (Hybrid) nanofluids in a circular tube: An experimental investigation and development of new correlations for thermophysical and heat transfer properties. Sustain Energy Technol Assess 2020;39:100720. [CrossRef]

[58] Zadkhast M, Toghraie D, Karimipour A. Developing a new correlation to estimate the thermal conductivity of MWCNT-CuO/water hybrid nanofluid via an experimental investigation. J Therm Anal Calorim 2017;129:859-867. [CrossRef]

[59] Megatif L, Ghozatloo A, Arimi A, Shariati-Niasar M. Investigation of laminar convective heat transfer of a novel TiO2-carbon nanotube hybrid water-based nanofluid. Exp Heat Transf 2016;29:124-138. [CrossRef]

[60] Dalkılıç AS, Yalçın G, Küçükyıldırım BO, Öztuna et al. Experimental study on the thermal conductivity of water-based CNT-SiO2 hybrid nanofluids. Int Commun Heat Mass Transf 2018;99:18-25. [CrossRef]

[61] Rawat MK, Kukreja N, Gupta SK. Effect of reinforcing micro sized aluminium oxide particles on mechanical properties of polymer based co mposite. Mater Today Proc 2020;26:1306-1309. [CrossRef]

[62] Gupta SK, Gupta S, Singh R. A comprehensive review of energy saving in shell & tube heat exchanger by utilization of nanofluids. Mater Today Proc 2022;50:1818-1826. [CrossRef]

[63] Khan M, Malik MY, Salahuddin T, Saleem S, Hussain A. Change in viscosity of Maxwell fluid flow due to thermal and solutal stratifications. J Mol Liq 2019;288:110970. [CrossRef]

[64] Sharma S, Tiwari AK, Tiwari S, Prakash R. Viscosity of hybrid nanofluids: Measurement and comparison. J Mech Eng Sci 2018;12:3614-3623. [CrossRef]

[65] Asadi M, Asadi A. Dynamic viscosity of MWCNT/ZnO-engine oil hybrid nanofluid: An experimental investigation and new correlation in different temperatures and solid concentrations. Int Commun Heat Mass Transf 2016;76:41-45. [CrossRef]

[66] Zareie A, Akbari M. Hybrid nanoparticles effects on rheological behavior of water-EG coolant under different temperatures: An experimental study. J Mol Liq 2017;230:408-414. [CrossRef]

[67] Dalkılıç AS, Açıkgöz Ö, Küçükyıldırım BO, et al. Experimental investigation on the viscosity characteristics of water based SiO2-graphite hybrid nanofluids. Int Commun Heat Mass Transf 2018;97:30-38. [CrossRef]

[68] Motahari K, Moghaddam MA, Moradian M. Experimental investigation and development of new correlation for influences of temperature and concentration on dynamic viscosity of MWCNT-SiO2 (20-80)/20W50 hybrid nano-lubricant. Chin J Chem Eng 2018;26:152-158. [CrossRef]

[69] Yiamsawasd T, Dalkilic AS, Wongwises S. Measurement of specific heat of nanofluids. Curr Nanosci 2012;8:939-944. [CrossRef]

[70] Adun H, Wole-Osho I, Okonkwo EC, Kavaz D, Dagbasi M. A critical review of specific heat capacity of hybrid nanofluids for thermal energy applications. J Mol Liq 2021;340:116890. [CrossRef]

[71] Gupta SK, Sharma A. A brief review of nanofluids utilization in heat transfer devices for energy saving. Mater Today Proc 2023; https://doi.org/10.1016/j.matpr.2023.03.364. [CrossRef]

[72] Tiwari AK, Pandya NS, Shah H, Said Z. Experimental comparison of specific heat capacity of three different metal oxides with MWCNT/water-based hybrid nanofluids: Proposing a new correlation. Appl Nanoscience 2020;1-11. [CrossRef]

[73] Wole-Osho I, Okonkwo EC, Kavaz D, Abbasoglu S. An experimental investigation into the effect of particle mixture ratio on specific heat capacity and dynamic viscosity of Al2O3-ZnO hybrid nanofluids. Powder Technol 2020;363:699-716. [CrossRef]

[74] Gao Y, Xi Y, Zhenzhong Y, Sasmito AP, Mujumdar AS, Wang L. Experimental investigation of specific heat of aqueous graphene oxide Al2O3 hybrid nanofluid. Therm Sci 2021;25:515-525. [CrossRef]

[75] Moldoveanu GM, Minea AA. Specific heat experimental tests of simple and hybrid oxide-water nanofluids: Proposing new correlation. J Mol Liq 2019;279:299-305. [CrossRef]

[76] Gupta SK, Rathore V. A review on utilisation of nanofluid in solar energy harnessing. Sigma J Eng Nat Sci 2025;43:1852-1885. [CrossRef]

[77] Jaramillo OA, Venegas-Reyes E, Aguilar JO, Castrejón-García R, Sosa-Montemayor F. Parabolic trough concentrators for low enthalpy processes. Renew Energy 2013;60:529-539. [CrossRef]

[78] Habchi A, Hartiti B, Labrim H, Fadili S, Faddouli A, Thevenin P, Ntsoenzok E. Performance study of a new parabolic trough design under optical concentrator effect. Appl Therm Eng 2023;219:119500. [CrossRef]

[79] Gupta SK, Gupta S. The role of nanofluids in solar thermal energy: A review of recent advances. Mater Today Proc 2021;44:401-412. [CrossRef]

[80] Minea AA, El-Maghlany WM. Influence of hybrid nanofluids on the performance of parabolic trough collectors in solar thermal systems: Recent findings and numerical comparison. Renew Energy 2018;120:350-364. [CrossRef]

[81] Bellos E, Tzivanidis C. Thermal analysis of parabolic trough collector operating with mono and hybrid nanofluids. Sustain Energy Technol Assess 2022;26:105-115. [CrossRef]

[82] Khalil A, Amjad M, Noor F, et al. Performance analysis of direct absorption-based parabolic trough solar collector using hybrid nanofluids. J Braz Soc Mech Sci Eng 2020;42:1-10. [CrossRef]

[83] Al-Oran O, Lezsovits F, Aljawabrah A. Exergy and energy amelioration for parabolic trough collector using mono and hybrid nanofluids. J Therm Anal Calorim 2020;140:1579-1596. [CrossRef]

[84] Khan MS, Abid M, Yan M, Ratlamwala TA, Mubeen I. Thermal and thermodynamic comparison of

smooth and convergent-divergent parabolic trough absorber tubes with the application of mono and hybrid nanofluids. Int J Energy Res 2021;45:4543-4564. [CrossRef]

[85] Mashhadian A, Heyhat MM, Mahian O. Improving environmental performance of a direct absorption parabolic trough collector by using hybrid nanofluids. Energy Convers Manag 2021;244:114450. [CrossRef]

[86] Ekiciler R, Arslan K, Turgut O, Kurşun B. Effect of hybrid nanofluid on heat transfer performance of parabolic trough solar collector receiver. J Therm Anal Calorim 2021;143:1637-1654. [CrossRef]

[87] Al-Oran O, Lezsovits F. A hybrid nanofluid of alumina and tungsten oxide for performance enhancement of a parabolic trough collector under the weather conditions of Budapest. Appl Sci 2021;11:4946. [CrossRef]

[88] Mohammed HA, Vuthaluru HB, Liu S. Heat transfer augmentation of parabolic trough solar collector receiver's tube using hybrid nanofluids and conical turbulators. J Taiwan Inst Chem Eng 2021;125:215-242. [CrossRef]

[89] Khaledi O, Saedodin S, Rostamian SH. Energy, hydraulic and exergy analysis of a compound parabolic concentrator using hybrid nanofluid: An experimental study. Int Commun Heat Mass Transf 2022;136:106181. [CrossRef]

[90] Mohammed HA, Vuthaluru HB, Liu S. Thermohydraulic and thermodynamics performance of hybrid nanofluids based parabolic trough solar collector equipped with wavy promoters. Renew Energy 2022;182:401-426. [CrossRef]

[91] Khetib Y, Alzaed A, Alahmadi A, Cheraghian G, Sharifpur M. Application of hybrid nanofluid and a twisted turbulator in a parabolic solar trough collector: Energy and exergy models. Sustain Energy Technol Assess 2022;49:101708. [CrossRef]

[92] Chakraborty O, Das B, Gupta R. Performance of parabolic trough collector having rotating receiver: Effect of elliptical insert and hybrid nanofluid. Int J Energy Res 2022;46:15254-15275. [CrossRef]

[93] Saray JA, Heyhat MM. Modeling of a direct absorption parabolic trough collector based on using nanofluid: 4E assessment and water-energy nexus analysis. Energy 2022;244:123170. [CrossRef]

[94] Ajbar W, Hernández JA, Parrales A, Torres L. Thermal efficiency improvement of parabolic trough solar collector using different kinds of hybrid nanofluids. Case Stud Therm Eng 2023;42:102759. [CrossRef]

[95] Aliehyaei M, Joshaghani AH, Najafizadeh MM. Energy, exergy, economic and environmental analysis of parabolic trough collector containing hybrid nanofluid equipped with turbulator. Eng Anal Bound Elem 2023;150:492-506. [CrossRef]

[96] Al-Rabeeah AY, Seres I, Farkas I. Experimental and numerical investigation of parabolic trough solar collector thermal efficiency enhanced by graphene-Fe3O4/water hybrid nanofluid. Results Eng 2024;21:101887. [CrossRef]

[97] Al-Oran O, Shaban NA, Manna R, Ayadi O, A'saf A, Lezsovits F. Performance study of parabolic trough solar collector using hybrid nanofluids under Jordanian weather conditions. J Therm Anal Calorim 2024;149:3981-3998. [CrossRef]

[98] Eshgarf H, Kalbasi R, Maleki A, Shadloo MS, Karimipour A. A review on the properties, preparation, models and stability of hybrid nanofluids to optimize energy consumption. J Therm Anal Calorim 2021;144:1959-1983. [CrossRef]

[99] Nabil MF, Azmi WH, Hamid KA, Zawawi NNM, Priyandoko G, Mamat R. Thermo-physical properties of hybrid nanofluids and hybrid nanolubricants: A comprehensive review on performance. Int Commun Heat Mass Transf 2017;83:30-39. [CrossRef]

[100] Ahmadi MH, Ghazvini M, Sadeghzadeh M, Nazari MA, Ghalandari M. Utilization of hybrid nanofluids in solar energy applications: A review. Nano-Structures Nano-Objects 2019;20:100386. [CrossRef]

[101] Muneeshwaran M, Srinivasan G, Muthukumar P, Wang CC. Role of hybrid-nanofluid in heat transfer enhancement-A review. Int Commun Heat Mass Transf 2021;125:105341. [CrossRef]

[102] Adun H, Kavaz D, Dagbasi M. Review of ternary hybrid nanofluid: Synthesis, stability, thermophysical properties, heat transfer applications, and environmental effects. J Clean Prod 2021;328:129525. [CrossRef]

[103] Hamzat AK, Omisanya MI, Sahin AZ, et al. Application of nanofluid in solar energy harvesting devices: A comprehensive review. Energy Convers Manag 2022;266:115790. [CrossRef]

[104] Abbas N, Rehman KU, Shatanawi W, Malik MY. Numerical study of heat transfer in hybrid nanofluid flow over permeable nonlinear stretching curved surface with thermal slip. Int Commun Heat Mass Transf 2022;135:106107. [CrossRef]

[105] Abbas N, Malik MY, Alqarni MS, Nadeem S. Study of three dimensional stagnation point flow of hybrid nanofluid over an isotropic slip surface. Physica A Stat Mech Appl 2020;554:124020. [CrossRef]

[106] Babar H, Sajid MU, Ali HM. Viscosity of hybrid nanofluids: A critical review. Therm Sci 2019;23:1713-1754. [CrossRef]

[107] Hashemzadeh S, Hormozi F. An experimental study on hydraulic and thermal performances of hybrid nanofluids in mini-channel: A new correlation for viscosity of hybrid nanofluids. J Therm Anal Calorim 2020;140:891-903. [CrossRef]

[108] Babu JR, Kumar KK, Rao SS. State-of-art review on hybrid nanofluids. Renew Sustain Energy Rev 2017;77:551-565. [CrossRef]

[109] Peng R, He X, Tang X, Tong J, Zhao L, Peng X. An investigation into the synergistic strengthening mechanism of ionic liquid and nanoparticles as a hybrid nanofluid in friction interface. Tribol Int 2022;165:107298. [CrossRef]
[110] Minea AA, Moldoveanu MG. Overview of hybrid nanofluids development and benefits. J Eng Thermophys 2018;27:507-514. [CrossRef]
[111] Shah TR, Ali HM. Applications of hybrid nanofluids in solar energy, practical limitations and challenges: A critical review. Solar Energy 2019;183:173-203. [CrossRef]
[112] Hamzah MH, Sidik NAC, Ken TL, Mamat R, Najafi G. Factors affecting the performance of hybrid nanofluids: A comprehensive review. Int J Heat Mass Transf 2017;11:630-646. [CrossRef]
[113] Mahamude ASF, Kamarulzaman MK, Harun WSW, et al. A comprehensive review on efficiency enhancement of solar collectors using hybrid nanofluids. Energies 2022;15:1391. [CrossRef]
[114] HemmatEsfe M, KiannejadAmiri M, Alirezaie A. Thermal conductivity of a hybrid nanofluid: A new economic strategy and model. J Therm Anal Calorim 2018;134:1113-1122. [CrossRef]
[115] Lekbir A, Hassani S, Mekhilef S. Techno-economic and life cycle assessment of a nanofluid-based concentrated photovoltaic/thermal-thermoelectric hybrid system. J Power Sources 2024;595:234066. [CrossRef]
[116] Suneetha S, Subbarayudu K, Reddy PBA. Hybrid nanofluids development and benefits: A comprehensive review. J Therm Eng 2022;8:445-455. [CrossRef]
[117] Mehta B, Subhedar D, Panchal H, Said Z. Synthesis, stability, thermophysical properties and heat transfer applications of nanofluid-A review. J Mol Liq 2022;364:120034. [CrossRef]
[118] Rashid FL, Aljibori HS, Mohammed HI, Ameen A, Ahmad S, Hamida MBB, Al-Rubaye AH. Recent advances and developments of the application of hybrid nanofluids in parabolic solar collector energy systems and guidelines for future prospects. J Eng Res 2024; https://doi.org/10.1016/j.jer.2024.04.023. [CrossRef]
[119] Esmaeili Z, Sheikholeslami M, Salehi F, Mohammed HA. Simulation of a solar thermal system with a parabolic concentrator incorporating an evacuated tube system equipped with a new designed turbulator and hybrid nanofluid. Renew Energy 2024;237:121633. [CrossRef]
[120] Said Z, Bellos E, Ali HM, Rahman S, Tzivanidis C. Nanofluids, turbulators, and novel working fluids for heat transfer processes and energy applications: Current status and prospective. Appl Therm Eng 2025;258:124478. [CrossRef]
[121] Saddouri I, Rejeb O, Semmar D, Jemni A. A comparative analysis of parabolic trough collector (PTC) using a hybrid nanofluid. J Therm Anal Calorim 2023;148:9701-9721. [CrossRef]
[122] Byiringiro J, Chaanaoui M, Halimi M. Heat transfer enhancement of a parabolic trough solar collector using innovative receiver configurations combined with a hybrid nanofluid: CFD analysis. Renew Energy 2024;233:121169. [CrossRef]
[123] Singh SK, Tiwari AK, Paliwal HK. Techno-thermo-economic-environmental assessment of parabolic trough collectors using hybrid nanofluids. Energy Sources Part A Recovery Util Environ Eff 2023;45:10682-10696. [CrossRef]
[124] Ghanbari G, Marzban A, Yousefzadeh S. Improving the thermal efficiency of parabolic trough collector equipped with combined turbulator containing two-phase magnetic hybrid nanofluid. Eng Anal Bound Elem 2023;155:565-583. [CrossRef]
[125] Kaood A, Abubakr M, Al-Oran O, Hassan MA. Performance analysis and particle swarm optimization of molten salt-based nanofluids in parabolic trough concentrators. Renew Energy 2021;177:1045-1062. [CrossRef]

Sigma Journal of Engineering and Natural Sciences
Web page info: https://sigma.yildiz.edu.tr
DOI: 10.14744/sigma.2026.2003

Review Article

Advancements in thermal management of polymer composites and sandwich structures: Insights and innovations

Sandip K. KADU[1,*], Palash SONI[1]

[1]*Department of Mechanical Engineering, Oriental University, Indore, Madhya Pradesh, 453555, India*

ARTICLE INFO

Article history
Received: 27 July 2024
Revised: 25 October 2024
Accepted: 13 January 2025

Keywords:
CFRP; Nanofiller; Phase Change Materials; Smart Materials

ABSTRACT

This paper presents an inclusive review of recent developments in the thermal-mechanical endurance of composites made of polymers and sandwich structures. The large number of literatures are studied on phase change materials, smart materials, nanofiller based polymer composites, and natural fiber based composites. These combinations or materials provides the improved capabilities for energy storage, more supportable material, and good thermos-mechanical properties. It also discusses the use of this information in various fields such as construction, energy storage, thermal management of electronic equipment, etc. This review suggests potential for future research directions to improve the thermal stability and performance of polymer materials and panels.

Cite this article as: Kadu SK, Soni P. Advancements in thermal management of polymer composites and sandwich structures: Insights and innovations. Sigma J Eng Nat Sci 2026;44(1):720–746.

INTRODUCTION

The pursuit of innovative solutions for effective thermal management in structural composite structures (like polymer or sandwich) has been a driving force in various fields, like aerospace and locomotive/automobile engineering to renewable energy systems and building materials. The considerable research is going on on composite structural composites to enhance the performance in terms of long lasting performance, and efficiency and durability [1-3]. In this comprehensive review, we delve into the latest insights and innovations shaping the landscape of thermal management in polymer composites and sandwich structures.

Polymer composites finds its application in variety of applications as they as comparably light weights as compared to metal and ceramic matrix composites, also they are easy to fabricate as compared to others [4]. But the polymers used in this case have lesser glass transition temperature, and this forms the critical challenge in the thermal management filed where the dissipation of heat and sustainability in high temperature becomes dominant [5,6].

Simultaneously, when light weight core inserted between the two surrounded sheets, it will act as a thermal insulation or thermal barrier. Also this kind of sandwich structural composites provide good strength to weight ratio. Overall whenever required to utilise these both structural composites (layered composites and sandwich composites) in diversified applications, need to improve their thermal stability.

***Corresponding author.**
*E-mail address: kadusandip@gmail.com

This paper was recommended for publication in revised form by Editor-in-Chief Ahmet Selim Dalkilic

Published by Yıldız Technical University Press, İstanbul, Turkey
© Author. This is an open access article under the CC BY-NC license (http://creativecommons.org/licenses/by-nc/4.0/).

Current investigation has rigorous on developing progressive materials and manufacturing practices to meet the sophisticated thermal management requirements of structural composites (layered composites and sandwich composites). A key area of examination encompasses integrating phase change materials (PCMs) into these materials to apply their latent heat storage capacity and regulator temperature variants [7-9]. Graphene-based phase change composites (PCCs) have attracted considerable interest due to their greater temperature conductivity and energy stowing properties, proposing promising methods to progress the thermal recital of polymer composites and sandwich structures [10,11]

To improvise the thermos-mechanical properties of structural (layered and sandwich) composites, researchers were investigated modern method and processes of fabrications [12]. During working on this improvising researchers were found that carbon nanotubes (CNTs), fullerene, graphene oxide, Nano cellulose suitable after integration with regular composite for improving thermal capacities in terms of conductivity and mechanical property enhancement as well [13,14], and further precession in product development can be achieved with the help of 3D printing additive manufacturing technologies [15].

As observed from the previous literatures, layered composite are better in inplane loading, but sandwich composite are shows superior in transverse loading applications. In this sandwich composites, core plays an important load [16,17]. The face sheet is transmitting the applied load over core, and core is the member who actually takes that load, transmit it into its channel uniformly. In this regard, phase change metal foam core offers good thermos-mechanical collaborative gain [18-21]. Under dynamic loading conditions also these sandwich structures found suitable [22-25].

The structural sandwich and polymer composites are found suitable in civil engineering works because of easy and fast installing, efficient energy, and improved strength to weight ratio [26]. As sandwich composites are light in weight, also ability of core to provide insulation capacity, such structures find its applications in cold storage, building blocks and bricks [27-29].

Besides, there is a countless transaction of potential for refining thermal controlling competences in polymer composites and sandwich structures by the corporation of smart materials and compliant structures [30].

Shape memory materials are stimulating materials which can be utilised in the electronics, transportation containers, aerospace, automobile, medical, space antenna, and temperature regulating mechanism or applications [31,32].

THERMAL ANALYSIS

Whenever dealing with the chemical (organic/inorganic), food, drugs, petrochemicals, thermal analysis is important [33], because it makes simple to study heat flow, dissipation, any kind of dimentional or mechanical changes occurred [34]. This technique is indispensable for characterizing properties such as decomposition, crystallization, melting, molecular structure, viscoelastic behavior, glass transition temperature (T_g), cross-linking, oxidation, volatilization, coefficient of thermal expansion (CTE), tensile modulus, composition, processing, stability, and mobility.

A comprehensive array of TA techniques is currently well-established, which includes various methods as shown in Figure 1.

All of these techniques are suitable and useful for the investigation of various properties and what kind of basic material under study.

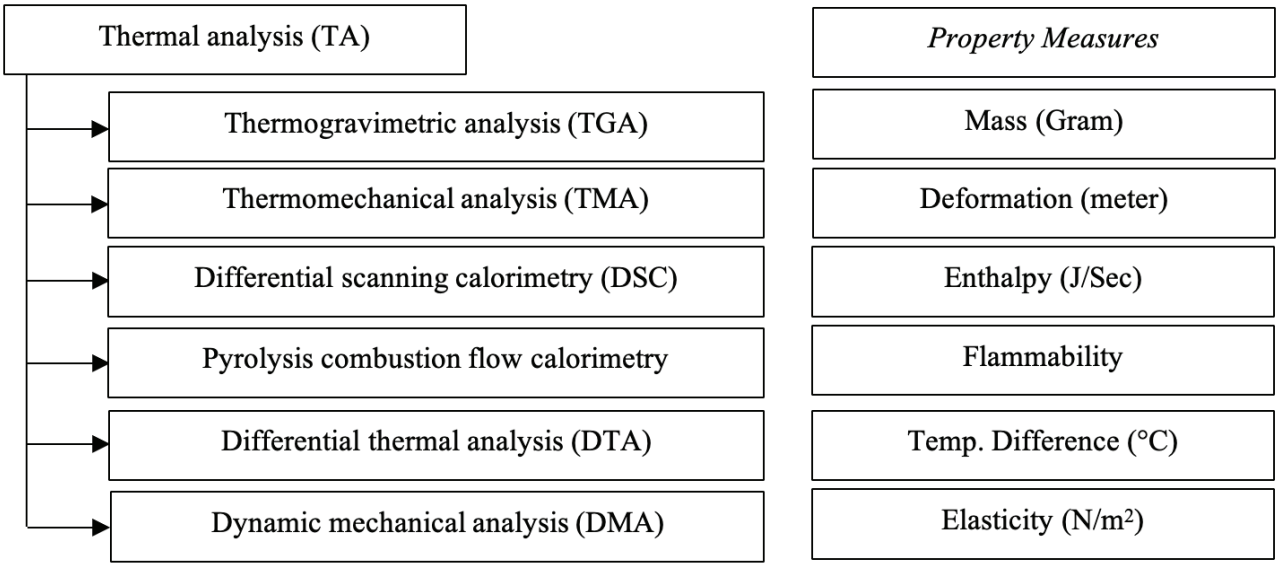


Figure 1. An inclusive arrangement of TA procedures.

To study the resistance against temperature, heat, durability, researchers were focused on temperature stability of the materials, and whenever thinking industry point of view, developments are going on for improvement in polymer composites [35]. These polymers generally show significantly higher melting or softening temperatures (Tm), superior resistance to thermal decomposition, larger remaining mass fraction and little changes in physical, mechanical and chemical properties even after long-term exposure at an elevated temperature compared with other common biopolymers [36]. Further, these polymers may have a higher heat deflection temperature under load and so possess greater stability. This emphasis on thermal stability underscores the significance of materials capable of withstanding demanding thermal environments across diverse industrial applications [37,38].

As technology advances, there is a rising demand for multifunctional, smart, lightweight, flexible, and cost-effective materials, rendering traditional options like metals inadequate for modern industries [37,39]. However, polymers, abundant and versatile, boast enticing attributes such as low specific weight, high corrosion resistance, affordability, ease of molding, smart optical properties, and excellent electrical and thermal insulation [40]. Polymer composite obviously found suitable in widespread industry utilization, because of thermos-mechanical, electrical limitations of amorphous structures [27,28].

POLYMER COMPOSITES

PMCs are widely used in engineering, such as aerospace, marine, automotive and civil engineering. Nevertheless, the practical applications are limited by the glass transition temperatures of polymer matrix which is usually about 78 °C for epoxy concurrently [41]. Indeed, > also results in some structural changes of which defending (64) or improving the system's level even involving carbon black with graphene nanoplatelet addition could be useful for avoiding damage caused by heat effects [42].

Notwithstanding the above, it is important to understand the PMC behavior at elevated temperatures. Current research focuses on determining the mechanisms of degradation during exposure to high temperatures, as well as the mechanical properties of composite forms. Till the temperature reaches to 250 °C, slow process of degradation occurs, but after that decay rapidly occurs shows nonlinearity in process [43]. The aging period in different literature survey is different, and temperature also. Like, in [44] the samples of matrix fiber composites were heated till 150 °C for different time, [45] done it for 4800 hours at 50 °C, and [46] performed it for 2000 hours for temperature range of 210 °C to 250 °C. This shows that with reducing the range of working temperature, the chemical or physical changes apperaded in material will reduce down.

In addition to thickness, the layer arrangement and reinforcement type significantly influence composite behavior at elevated temperatures. For example, in reference [47], researchers examined four composite variants as shown in Figure 2:

Another study, as discussed in reference [48], focused on the thermo-oxidative aging behavior of carbon fiber-reinforced polymer (CFRP) CF/PA6 composites and glass-fiber reinforced composites (Ultramid® B3WG7). Additionally, reference [49,50] investigated accelerated aging of carbon-epoxy (carbon/EP) and carbon-vinyl (carbon/VE) composites.

PMCs may encounter additional environmental stresses like UV contamination, salt sprig, or water exposure [51]. Moreover, elevated pressure can be a contributing factor, as illustrated in reference [52,53], where pressures of 1.7 bar and 5 bar were applied alongside high air temperatures.

Numerical modeling plays a pivotal role in comprehending the behavior of Polymer Matrix Composites (PMCs), particularly regarding thermal degradation. In reference [54], researchers devised a specialized numerical modeling tool integrated into the commercial software ABAQUS to model the thermo-oxidative responses of fiber-matrix composite cells that are microscopically appropriate. Similarly, reference [55] employed NOVA-3D code with custom finite element analysis, to model decline in unidirectional composite samples exposed to thermo-oxidative aging at 300 °C. Delamination phenonmenon was simulated by micromechanical a viscoelastic cohesive layer model. Such methods or modeling practices supports researchers for creating and improving the complex behaviour of multiphase polymer

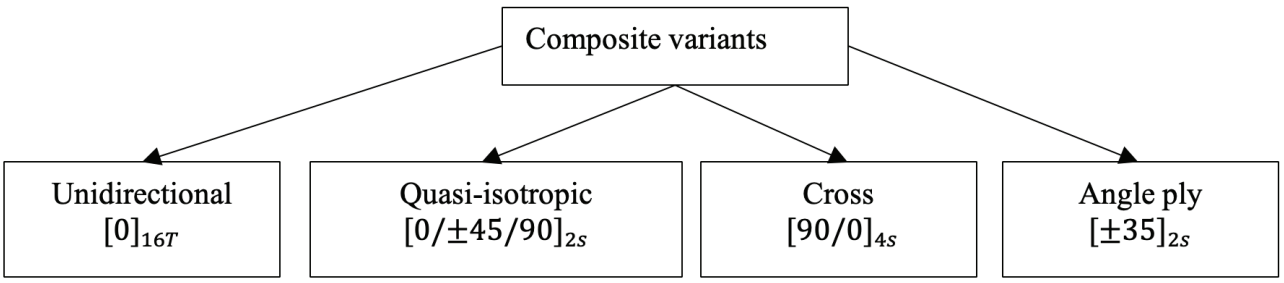


Figure 2. Composite variants.

composite which were worked in variety of thermal conditions [56], [57].

In some cases it is observed taht minor surface damage to matrix comes out with constructiive results which includes electromagnetic (EM) radiation absorption designing systems [58].

Thermo-oxidative aging induces surface irregularities, cracks, and voids in composites, which can scatter incident EM waves. However, controlled aging is imperative, and the effects must be assessed using non-destructive methods.

Various factors influence the shape and frequency of natural vibration, including structural defects, composite internal structure (e.g., shape memory fibers, nano additives, hybrid composites), manufacturing techniques (e.g., material property scattering, residual stresses, imperfections), contact with composite bolted joints, and hygrothermal effects during aging processes [59,60].

Upto the temperature of 250°C, polymer thermoset composites are effectively get utilised as prestine material, but above 300°C, the detoration due to temperature will ge start, which possibly leads to disengaemment of contact between matrix and fiber. The bonding between these two phases wwill start damaging significantly, which simultaneously reduces the material properties like modulus of elasticity and rigidity, Poissons ratio, decrement in load carriyng capacity, strength etc

Carbon Fiber Reinforced Polymer/Plastic (CFRP)

Research work introduces that, CFRP are well known for its strength, durability, good thermos-mechanical properties, resistance against deterioration, radiation barrier, so these materials are found to be most suitable in aerospace, defense, automobile, and many more industries [61]. However, machining CFRP components, such as those found in aircraft wings and automobile panels, presents considerable challenges, particularly in hole processing for connections, which significantly impacts connection strength [62].

Various material combinations can be used to prepare structural composite sheets based on user needs and application. Some of them are referred to here. Graphite/carbon/Kevlar fiber reinforced sheets, matrix-based sheets, nanofillers reinforced sheets, Aluminum alloys, glass-vinyl ester are common types of face and bottom sheets used in sandwich structures. [63] conducted a comparison of the strength properties between steel plate and aluminum plate sandwich structures, and glass fiber reinforced plastic (GFRP) plate sandwich structures. In the research by [64], FRP materials like CFRP ([65,66]; and GFRP [67]) were applied to enhance the bending characteristics of sandwich panels. ((Liu et al., 2015; Markad and Lal, 2021a, 2023) conducted tests on carbon/epoxy fabric composite sandwich panels and carbon/epoxy unidirectional prepreg panels. Below is Table 1 which shows the mechanical characteristics of various popular face materials [68].

Due to its heterogeneous and anisotropic nature, CFRP poses greater challenges in achieving high-quality cuts compared to homogeneous materials [70]. Currently, the CFRP manufacturing methods are generalized and their mechanical processing also. But whenever working with these CFRP composites, like drilling, cutting that time vulnerable delamination results formation of tears or removal of fiber or formation of burrs [71]. Whenever these delamination or fiber breakage occurs, these creates the defects which ultimately creates the adverse effect. So this is the time consuming and cost increasing phenomenon [72]. Also, whenever traditional methods are get utilised to machining the CFRP parts, the possibility of melt the matrix/polymer from CFRP which will open the fiber to atmosphere. To avoid such dramatic situations, different methods are utilised for machining the CFRP parts which include the abrasive water jet machining, lesser cutting, and electrical discharge machining (EDM) [73-75]. As we know, the purpose of matrix material is to protect the fiber from environment. But sometimes it is observe that, during the abrasive water jet machining (AWJ) excess water causes the submerging the water molecules into fiber which may starts the corrosion or degradation in performance of CFRP [76]. Similar to that in harsh environment, EDM processed CFRP samples are also were not performed well

Table 1. The mechanical parameters of some common sheet materials

Face material	Poisson's ratio	Longitudinal modulus (GPa)	Transverse modulus (GPa)	Shear modulus (GPa)	Density (kg/m^3)	Reference
FRP	0.33	--		24.8	1600	[63]
Aluminum	--	72	72	27	2700	[69]
USN [0]Ns	0.28	130	10.5	5.06	1540	[69]
USN [90]Ns	0.30	51.7	51.7	19.94	1540	[69]
Stycast epoxy resin	--	2.1	2.1	0.81	1200	[69]
CFRP	0.3	54	---	---	---	[31,56]
GNPRC	0.3	65	---	---	---	[57]

because of hygroscopic characteristics form due to introduction of water into samples. Contrariwise, because of higher processing flexibility, and minor cutting force lesser cutting find advantageous. However the effect of temperature can cause formation of co2 emission, and burnt gases due to fiber, which may cause ablation damage of samples of CFRP.

To tackle all these machining process challenges, new methods are introduced. Ultrafast layers introduces the femto-and-pico-second lasers which is cold work processing technique promising for CFRP processing. These technique is reduces or avoid the thermal damage, but having lower cutting efficiency. Due to all facts, researchers are now focusing on parameter variation in lesser cutting so as to develop the innovative method which ultimately perform efficiently on CFRP machining operation.

FRP with Nanofillers

Over the last decade, considerable attention has been directed towards experimental and numerical investigations aiming to predict the influence of dual nanofillers (DNFs) and multiscale fillers (MSFs) in polymers. Polymer composites reinforced with DNFs and MSFs exhibit remarkable mechanical and thermomechanical properties, achieved through meticulous design and control of material and process parameters [77]. This article presents an overview of the latest advanced manufacturing methods, key factors, micromechanical models, and simulation approaches to analyse the mechanical properties of hybrid polymer composites under static and dynamic conditions.

It is a well-established fact that further progress in the direction of using laminated and sandwich composite materials as an alternative to the conventional materials in various applications largely depend on better understanding of thermo-mechanical nonlinear flexural, buckling and vibrational response under various loading conditions using finite element analysis. There are tremendous literature can be observed which worked over CFRP or individually over polymer, but it is essential to study the effect of utilization of the shape memory behaviour of the shape memory polymer (SMP) utilised in CFRP or can called as shape memory polymer composite (SMPC). It is important to found the effect of dynamic temperature variation in SMP over nonlinear transverse central deflection (TCD), buckling, and post-buckling of the laminated SMPC beam under constant and varying loads in a glass transition region

Table 2 clearly differentiate between performance of SMPC and SMP hybrid composite beam with the utilization of SWCNT, MWCNT for different lamination or stacking sequence of layups [56,62]. From the obtained results, it was observed that as compared to carbon fibre reinforced polymer or SMPC, SMP hybrid composites effectively increase the performance of the structural composites, and these results were motivated to work and analyse the SMP hybrid composites.

Nanomaterials are integrated into raw materials, becoming an integral, non-invasive part of the structure. These in-situ sensors enhance mechanical performance without compromising structural integrity, providing improved toughening and interfacial conformability, unlike traditional sensors [78]. They respond to external stimuli by disturbances in conductive paths formed by nanomaterial flakes. Irfan et al. [79] conducted recent research that thoroughly examined the use of these sensors in monitoring the manufacturing processes and structural health of polymer composites. A notable example is carbon-based reduced Graphene Oxide (rGO), which is highly regarded for its exceptional conductivity and flexibility. Number of research were conducted to improve the structural health monitoring of the nanocomposites materials. The abilities of rGO nanocomposites find its application in sensors to improve health of structures and manufacturing characteristics [80-82] and find applications in biomedicine, flexible electronics, and energy storage applications [83].

However, most of these tests have been conducted in static or dynamic modes at fixed temperatures [80] explored the impact of temperature on the piezoresistivity of rGO-coated glass fiber sensors embedded in epoxy/glass fiber composites, noting a noticeable enhancement in piezoresistivity with increasing temperature.

Carbon-based nanoparticles, such as carbon nanotubes (CNTs) and their derivatives—single-walled carbon nanotubes (SWCNTs), multi-walled carbon nanotubes (MWCNTs), graphene, and graphene oxide—are widely recognized for their exceptional properties. Problems associated with high cost and the processing of CNTs notwithstanding, owing to their remarkable mechanical properties which include a very high intrinsic strength, relative lightness and extremely large aspect ratio, they have emerged among the most sought nanofillers. These properties make them highly effective in numerous advance applications

Table 2. Effect of number of walls of CNT and lamination scheme over central deflection of SMPC beam

No. of walls of CNT	Lamination scheme	TCD of two phase SMPC (N_w=0)	TCD of three phase composite
N_w=0	0/90	0.02807	------
N_w=1	0/90	------	0.0227
N_w=2	0/90	------	0.02554
N_w=3	0/90	------	0.02643

[84]. These nanofillers have been shown to greatly improve the properties of composites even at low wt %. Nevertheless, this improvement varies depending on filler functionalization, aspect ratio, filler loading and polymer matrix nature, dispersability of fillers in the polymer matrix and processing methods. Despite these high cost and processing issues with carbon nanoparticles, the superior mechanical, electrical and thermal properties of carbon-basednano particles demonstrate great promise toward advanced compositing [85].

The improved performance is recorded with the incorporation of graphene nanofillers in a jute fiber composites. With this combination notable improvement is observed. As compared to two phase jute fiber reinforced composite, the multiphase composite shows 110% and 324% improvement in tensile strength and elastic modulus. This combination shows the suitability of this modified nanocomposite based jute fiber composite in many synergetic application and ability of replacement of untreated jute fiber composite, along with this it is eco-friendly too [86].

Zhang et al. embedded the graphene oxide (GO)-and polyhedral oligomeric silsesquioxanes (POSS) into carbon fiber composites for the formation of multiphase composites. With this, improvement is observed in interfacial adhesion and mechanical characteristics. In the similar manner, Sharma et al. also studied the effect of incorporation of 2-dimensional GO, 1-dimensional MWCNT, 3-dimensional graphene-carbon nanotube hybrids in aramid fiber-reinforced polycarbonate composites, and proposed that with just 0.2% addition of nanofiller significantly improves the mechanical properties like tensile strength, elastics modulus. The overall performance improvement is noted with the addition of graphene-based nanofillers [87].

Bulut et al. also investigated the effect of addition of nanoclay into the basalt fiber-reinforced polymer (BFRP) composites, and shows that 29% improvement in bending strength, and 7.6% improvement in tensile strength, and 16.8% improvement in impact resistance as compared to pristine basalt fiber-reinforced polymer (BFRP) composites [88].

METHOD OF DEVELOPMENT OF POLYMER COMPOSITES

The studied literatures are clearly revels that the addition of nanofillers into fiber reinforced composites significantly shows the improvement as compared to base composites. But some literatures are also highlights the effect of addition of nanofillers after certain percentage creates the aggregation. Because of van deer wall force of attraction in CNT or any nanofiller, the aggregation arises. This is particularly happens because nonhomogeneous or poor dispersion of nanofillers into the base matrix. This directly reduces the capabilities of the nanocomposites. This difficulty can be overcome with proper dispersion and aligning the CNTs unidirectional into the polymer matrix. With this process of development of polymer composites, one can improve the thermos-electrical characteristic of the composite materials [89,90]. Traditionally, three main techniques are utilized for preparing CNT/polymer composites:

Standard Approaches

Solution collaborating

Solution collaborating / mixing stands as an adaptable technique widely utilized for the large-scale production of nanocomposites, including CNT/polymer composites, while preserving the desirable properties of nano-sized fillers. In a solvent epoxy and CNTs are mixed separately, for increasing solubility for further mixing. After that both the mixtures are added into each other, and for homogeneous mixing purpose and ultra-sonication, magnetic stirring, or high-speed homogenization can performed [90]. During the degassing process this solvent will get vaporise.

Alternatively, CNTs can be directly mixed into the polymer solution, followed by intense ultra-sonication and shear homogenization. Surface-functionalized CNTs, on the other hand, offer improved dispersal and interfacial attachment with the polymer matrix, leading to improvements in mechanical, thermal, and electrical properties [91].

The choice of solvent is crucial in this method, with low-boiling-point solvents typically favoured due to the complexities involved in evaporating high-boiling-point solvents, which may result in trapped solvent during composite solidification, causing structural defects. Low-viscosity solvents facilitate better dispersion [92]. While solution mixing offers the advantage of potentially de-bundling CNTs to achieve quality dispersion, it also has drawbacks, such as the possibility of leaching of added constituents, potential environmental contamination due to the large amount of solvent used, and the inability to dissolve insoluble polymers [93].

Melt blending

For the insoluble thermoplastic polymers, melt blending approach is eco-friendly, cost effective and simple to prepare composite material. Thermoplastic matrix is reusable, means they can be remoulded after heating at transition temperature. In melted condition of granules of polymers, nanofillers are added like CNT, GnP, and using banbury mixers and extruders mixture is homogenously mixed, the cooling it till solidifies, and further it can cut into required shape and size [94]. The melt blending offers the high speed which found it suitable for industrial applications, along with that it doesn't requires the solvent too. But this techniques has some disadvantages also. High shear forces and temperatures during processing can potentially disrupt both the CNTs and polymer chains, leading to a reduction in their intrinsic properties [95]. Therefore, Process parameters must be carefully controlled in order to minimise any negative influence on the final composite qualities.

***In situ* polymerization/reaction processing**

Reaction processing offers an effective approach for achieving even dispersal of CNTs in insoluble and uneven polymers, which may not be feasible with solution blending and melt treating methods. The process involves initially dispersing CNTs in a monomer solution, followed by the polymerization process under specific conditions [96]. For thermosetting materials like epoxy or unsaturated polyester (PET), polymerization is initiated by a curing agent or hardener acting as a catalyst. In the case of thermoplastics, polymerization occurs either through temperature elevation or by adding an initiator.

This technique facilitates the homogeneous distribution and compatibility of the filler-matrix, leading to strong interface between the CNTs and the polymer matrix. However, there are some drawbacks associated with this method [97]. It typically requires expensive equipment and involves the use of a large volume of solvent, which can increase production costs and may pose environmental concerns.

Graphene-Based Composite

Due to its SP_2-hybridized structure, graphene, a two-dimensional (2D) hexagonal or tile-like single layer of graphite, has attracted much attention since its discovery in 2004 [96]. Due to its structure, graphene has important properties such as electrical conductivity, physicochemical stability, excellent optical transparency and excellent structural strength. As a result, graphene and its derivatives have found applications in various fields, including tissue engineering, optoelectronics, biosensors and catalysis [97-99]. Various carbonised nanoparticles are displayed in Figure 3.

Graphene can be synthesized using numerous methods, containing mechanical exfoliation of graphite, decline of graphene oxide (GO), chemical vapour deposition (CVD), and epitaxial progress [100-102]. With a thermal conductivity reaching from 3000 to 5000 W/(m·K), graphene surpasses other materials like carbon nanotubes (CNTs) and copper in thermal conductivity. As a result, graphene becomes a perfect filler for phase change materials (PCM), providing better mechanical, electrical and thermal conductivity (PCC) to PCM composites.

However, when incorporating graphene into PCMs, it is essential to consider its large specific surface area. Exceeding the optimum amount of graphene filler may negatively impact the natural convection thermal conductivity of PCMs. Additionally, the thickness and geometry of graphene nanofillers significantly influence the whole thermal conductivity of PCCs. Therefore, careful consideration of these factors is crucial when designing PCCs to ensure optimal thermal enhancement and energy storage capability.

Graphene oxide (GO)

Graphene oxide, or GO, is an oxidised version of graphene with a basal structure like a hexagon or honeycomb, but with additional oxygen groups like hydroxyl, carboxyl, and epoxy on the base and edges. This alteration results in a wider separation between layers of 6–9 Å, as compared to 3.34 Å for graphene, and enhances its capacity to form bonds with other molecules, hence improving its mechanical and tribological properties [103]. Chemical and electrochemical methods can be used to produce graphene oxide from graphite; the Hummers and modified Hummers procedures are the most widely used [104].

Graphene oxide (GO) exhibits remarkable qualities that make it highly versatile for various applications, including sensors, energy storage, and catalysis [105,106]. A notable example involves the work of Huang et al., who combined GO with molten DHPD, an inorganic phase change material (PCM), to create a shape-stabilized PCM (ssPCM) [107]. This mixture was then incorporated into expanded vermiculite (EV), a porous mineral that enhances structural stability. The inclusion of a minor amount (0.2 wt%) of GO resulted in an increase in the latent heat of the combination from 167 J/g to 229 J/g. Additionally, the contact angle between molten DHPD and EV decreased from 56 to 45 degrees, indicating improved DHPD volume containment due to GO's ability to reduce interface tension.

In another approach, Cao et al. [108] utilized free radical polymerization to covalently attach hexadecyl acrylate (HDA) to GO, creating a ssPCM (GO-g-PHDA). Microscopic and spectroscopic analyses confirmed the successful grafting of PHDA onto the surface of GO. This modification significantly increased the encapsulation volume of DHPD, as evidenced by the reduced interfacial tension between DHPD and EV. Furthermore, the carboxyl and hydroxyl groups on GO facilitated the formation of hydrogen bonds with water molecules, thereby enhancing its thermal properties.

Diminished graphene oxide

From the GO, rGO is get extracted using the decline method which remove major portion oxygen-enclosing functional groups, characterizes a partially abridged material with partially restored sp2 hybridization of carbon atoms, regaining electrical and mechanical properties akin to graphene. Reduction methods involve chemical processes utilizing agents such as hydrazine or hydriodic acid, as well as thermal treatment at high temperatures [109-111]. Much like graphene and GO, rGO has undergone extensive examination as a thermally sensitive and structurally supportive pitch material in PCCs. For instance, Zhou et al. explored the utilization of a chromium-based metal-organic framework (MOF) adorned with rGO as an adsorption material and structural backing for a shape-stabilized phase change material (ssPCM).

Melt infiltration, akin to vacuum impregnation, stands as a prevalent technique for producing ssPCMs, seeking to resolve the problem of liquid PCM leakage by infusing the PCM into a mesoporous matrix that delivers structural support. However, a drawback of this method lies in the

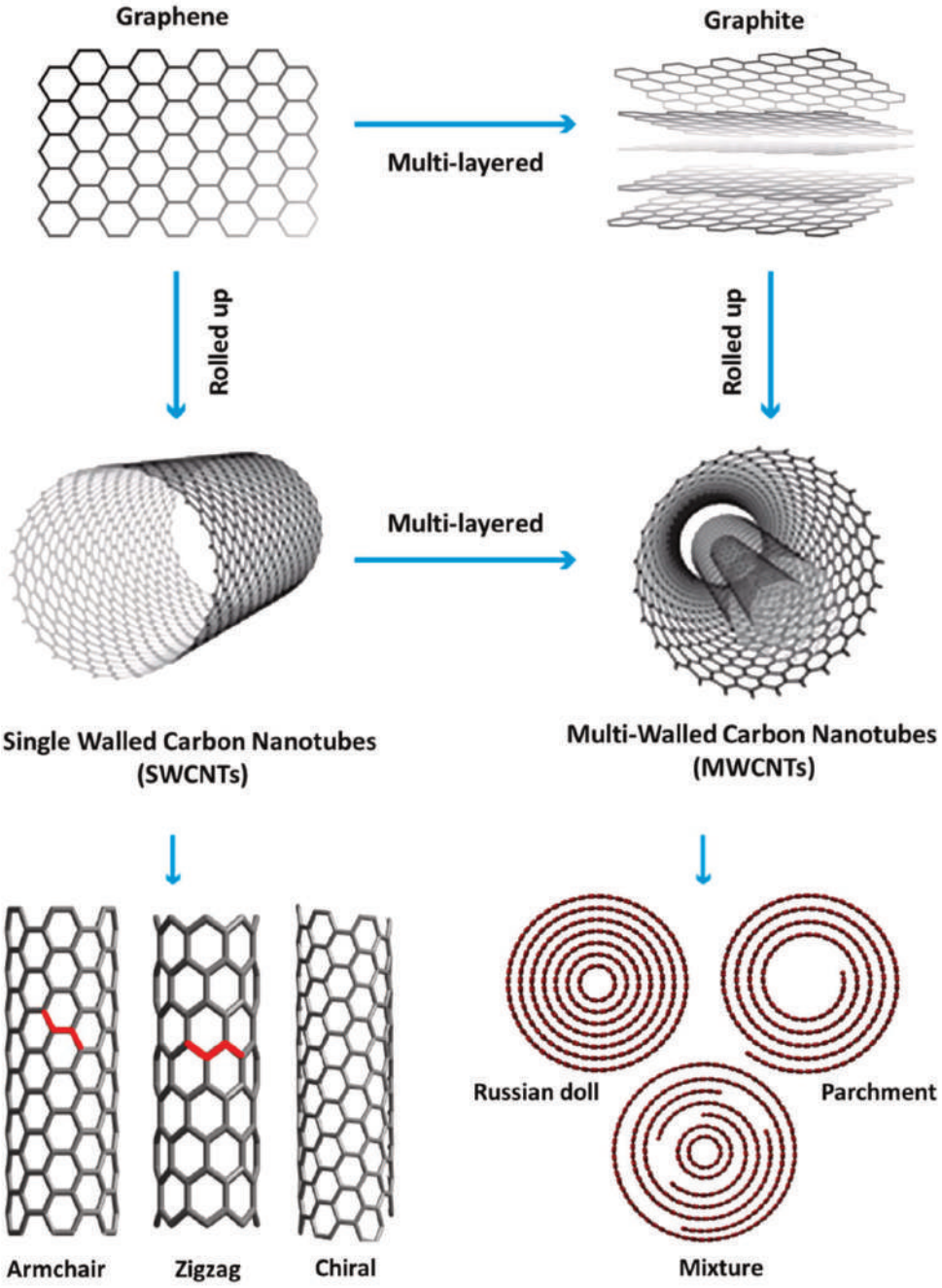


Figure 3. A evaluation of the preparation of SWCNTs and MWCNTs, and the diversity of each kind of CNT.

potential weakness of the physical interaction between the matrix and PCM, which could lead to desorption problems following multiple thermal cycles [112].

Chemical modification techniques, such as grafting, offer an alternative approach where the PCM material is covalently committed to the matrix, enhancing thermal reliability and chemical stability. For instance, a novel PCC exhibited a remarkable 472% enhancement in thermal conductivity [112].

Functionalized nanofillers and its compound

Graphene and its derivatives offer valuable possessions such as dispersion, stability, reactivity, and solubility, making them highly desirable for various applications [113]. These properties can be tailored using various functionalization methods, which include covalent, noncovalent, and hybrid approaches. With the Covalent functionalization the functional groups are directly attached to carbon-covering graphite network with utilising reduction, oxidation, click chemistry, and diazonium chemistry. Opposite to that,

with the noncovalent functionalization outside molecules and nanoparticles enriched into the carbon-rich network through connections like hydrogen bonds, van der Waals forces, π-π interactions, hydrophobic, and electrostatic interactions [114]. Additionally, texture processing can combine functional and non-functional approaches, which is particularly useful when multiple features need to be incorporated into graphene materials. These functionalization methods can be implemented either during the assembly of the raw material (in situ) or as a separate process after the material has been obtained (ex situ).

Considering the fluctuation in air source temperature with operation load and duration, researchers have examined the impact of initial phase change material (PCM) temperature (Tint) on casting performance. They found that increasing the temperature from 2°C to 10°C without graphene nanoplatelet (GnP) functionalization increased the off time by 23.9%. However, the difference in fusion process time decreased to 22.1%, 20.3%, 19.2%, and 17.6% as the working GnP volume increased from 0.1% to 0.5%. Notably, the total thermal conductivity and melting process delay were reduced as the volume fraction of thermally activated GnP in PCM composite (PCC) was increased. The PCC containing 0.5 vol% GnP exhibited faster melting at both 10°C and 2°C dye levels [115].

CNTs Inserted Polymer Composites

Carbon nanotubes (CNTs) present significant potential for crafting polymer composites due to their outstanding attributes like high strength, modulus, surface area, stiffness, porosity, corrosion resistance, mechanical-chemical stability, and impressive thermal and electrical properties [116,117]. The important characteristics and nanostructure makes CNTs as an ideal base for wide applications in materials, metals, and ceramics [118]. However only relying on the CNTs as a primary fillers make it financially incorrect therefore need of secondary fillers to alternative costs.

Despite their advantageous qualities, the nano-scale structure and reactivity of CNTs pose potential health hazards during the manufacturing and handling of

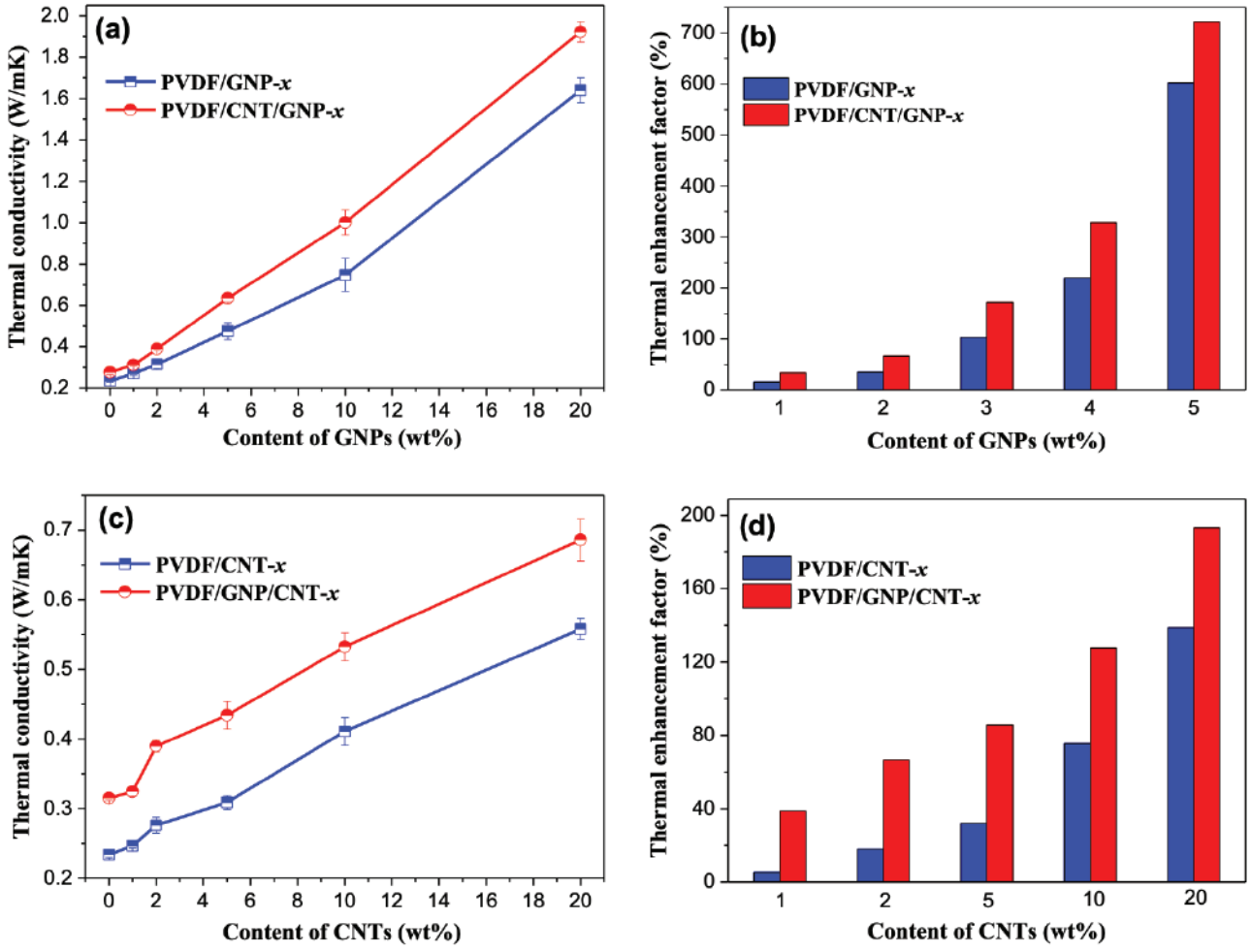


Figure 4. (a and c) Changes in thermal conductivity and filler content of PVDF composites and (b and d) the comparison of thermal enhancement coefficients between binary and binary composites.

nanocomposites. The disposal of CNTs mostly affect the human health if it get improperly dispose. It may lead to cause lung cancer, respiratory ailments [119]. To overcome these harmful effect caused by CNTs, it is necessary to modify the surface of CNTs.

Secondary fillers are often used for the preparation of hybrid filler systems. The different secondary fillers used are silica, graphene oxide, zinc oxide, carbon black, conductive carbon black, nano-clay, and graphite [120-124]. The many significant qualities are present in these fillers such as fire resistance, lightweight, flexibility, electrical and thermal conductivity, high modulus, and strength. Most favourable results were produced by the combination of CNTS with the graphene particles. Comparative to composite consist of solely graphene and CNTs, a combination of both shows the good performance in modulus and thermal stability [125].

In addition to improving thermal performance, it is important to consider the long-term stability and aging effects of CNT hybrid composites. . To overcome these challenges the composites are prepared with desired material combination by considering various parameters such as material selection, controlled CNT loading, optimized process parameters. The various qualitative methods are used to analyse the behavior and performance of the composite material. The various methods used are thermogravimetric analysis (TGA), infrared spectroscopy (FTIR), dynamic mechanical analysis (DMA) and differential scanning calorimetry (DSC). The TGA method is used to determine the decomposition temperature, aging performance of the compounds, and weight loss. The various mechanical and thermal properties are gets affected such as tensile strength, impact strength, thermal conductivity, and ductility. The present study also carried the investigation of environmental, UV rays, humidity, and chemical reaction. Figure 4 shows the nature of heat conduction behaviour with nanofillers percentage variations [126].

For graphene nanoplatelet (GNP) content below 10 wt%, there is only a slight increase in thermal conductivity in the samples, ranging from 0.27 *W / mK* (with 1 wt% GNPs) to 0.48 *W / mK* (with 5 wt% GNPs). During lower concentration, The GNP dispersed randomly and do not create saturated network structure, which causes ineffective thermal conductive regions. Thermal conductivity increases from 0.75 *W / mK* and 1.64 *W / mK* with the variation of GNP content from 10 wt% and 20 wt% respectively. The recorded thermal conductivity enhanced bt 220% and 602% respectively, indicating the formation of GNPs network structures. Interestingly, all PVDF/CNT/GNP-x models demonstrate greater thermal sensitivity compared to PVDF/GNP-x samples at the same GNP content. For example, the thermal sensitivity of the PVDF/CNT/GNP-1 sample is 0.31 *W / mK*, while that of the PVDF/CNT/GNP-20 sample is significantly higher at 1.92 *W / mK*.

Comparisons of thermal conductivities for PVDF/CNT-x and PVDF/GNP/CNT-x samples with increasing CNT concentration reveal that the PVDF/CNT-20 sample has a thermal conductivity of approximately 0.56 *W / mK*, which is substantially lower than the 1.64 *W / mK* observed in the PVDF/GNP-20 sample. However, the PVDF/GNP/CNT-20 sample, which includes a small quantity of GNPs (2 wt%) in the PVDF/CNT-x composites, exhibits a thermal conductivity of 0.69 *W / mK*. Nonetheless, the thermal conductivity of the PVDF/GNP/CNT-20 sample (1.92 *W / mK*) is still lower than that of the PVDF/CNT/GNP-20 sample.

Both carbon nanotubes (CNTs) and graphene nanoparticles (GNPs) have shown to be successful in promoting the crystallization of semi-crystalline polymers as nucleating agents as observed in Figure 5 [126]. Nevertheless, if

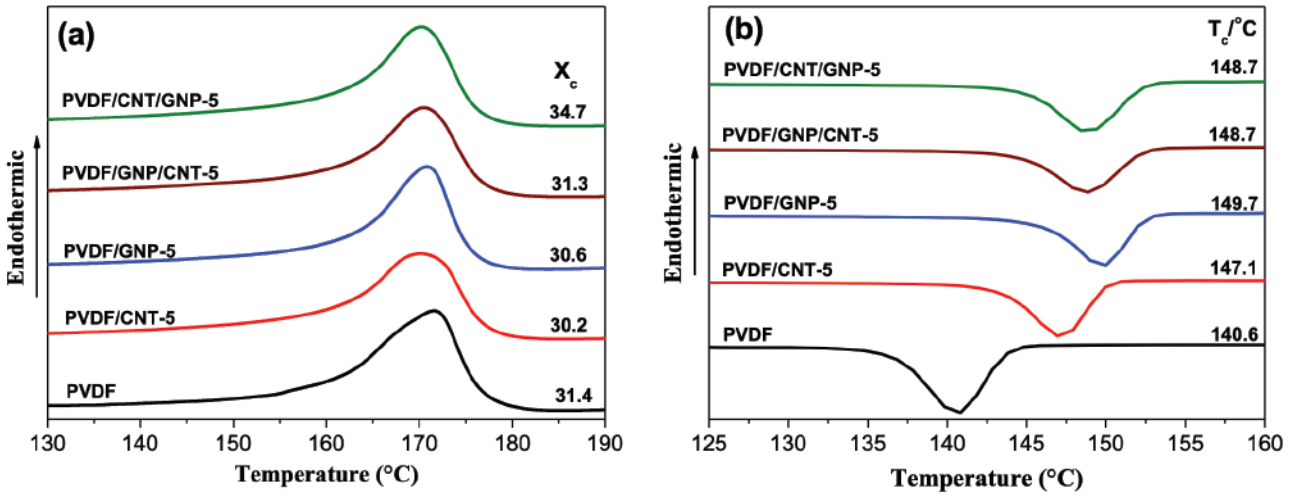


Figure 5. The graph displays the melting and crystallisation behaviours of the typical samples as represented by the DSC heating curves (a) and cooling curves (b). (created by authors [126])

filler content reaches a certain point and creates a compact interconnected structure, it may impede the movement of polymer chains. This obstacle hinders the development of spherulites, leading to a decrease in crystallinity. The crystalline structures of semicrystalline polymers are widely recognized as determining their conductive properties. Improving the thermal conductivity has been proven by enhancing the crystallinity of the polymer matrix.

DSC was utilized to assess the melting and crystallization behaviors of the samples. All samples, as depicted in Figure 5a, exhibit lower melting temperatures (T_m) in comparison to the pure PVDF sample. This implies that the lamella thickness in the composites made with PVDF matrix is slightly smaller than in the pure PVDF sample. Additionally, Figure 5b indicates that there is minimal variation in crystallinity among the samples. The crystallisation temperature (***Tc***) of the pure PVDF sample is 140.6 °C. This indicates the nucleation of the PVDF matrix at the crystallisation.

REINFORCED POLYMER SANDWICH STRUCTURE

In the various industries like marine, aerospace where it is necessary to have a high strength to weight ratio and proper flexural stiffness need to construct the composite structure [127,128]. The technical needs of these application can be achieved by the thick light weight face sheet and lighter core material. In this arrangement, the face plates endure the σ_c, σ_t from bending, while the core disperses the impact and stress from transverse shear and normal loads. Hence, it is crucially important to ensure the reliability of sandwich composites [129].

The boundary between the outer layer and the inner core of a bimaterial sandwich composite forms a transition region that is often seen as the least strong part of the structure. This region causes the primary failure like skin cracking, shearing of core, delamination of skin and core, and core crushing [130-132]. Therefore to create the high performance sandwich structure , it is necessary to do research on various factors such as delamination of skin and core. The face sheet and core delamination happens due to the bending force exerted on the multi-layered systems. The high shear stress developed between the face sheet and core. Multiple research were carried for precise characterization of the bending phenomenon for sandwich structures [133-137]. For example, the superposition principle calculates the parameters required for mixed-mode bending, including compliance and strain energy release rate, given the appropriate kinematic relationship of sample deformation [138].

Examination at the microstructural level has shown that enhancing the proportion of carbon fiber and CNT in the volume greatly enhances the E_l, E_t, correspondingly. Both the stiffness and thickness of the contacting region, resulting from the bonding of CNTs with the polymer, contribute to improving the E_l, E_t of fuzzy carbon fiber-reinforced composites throughout the entire 0-90° range [139].

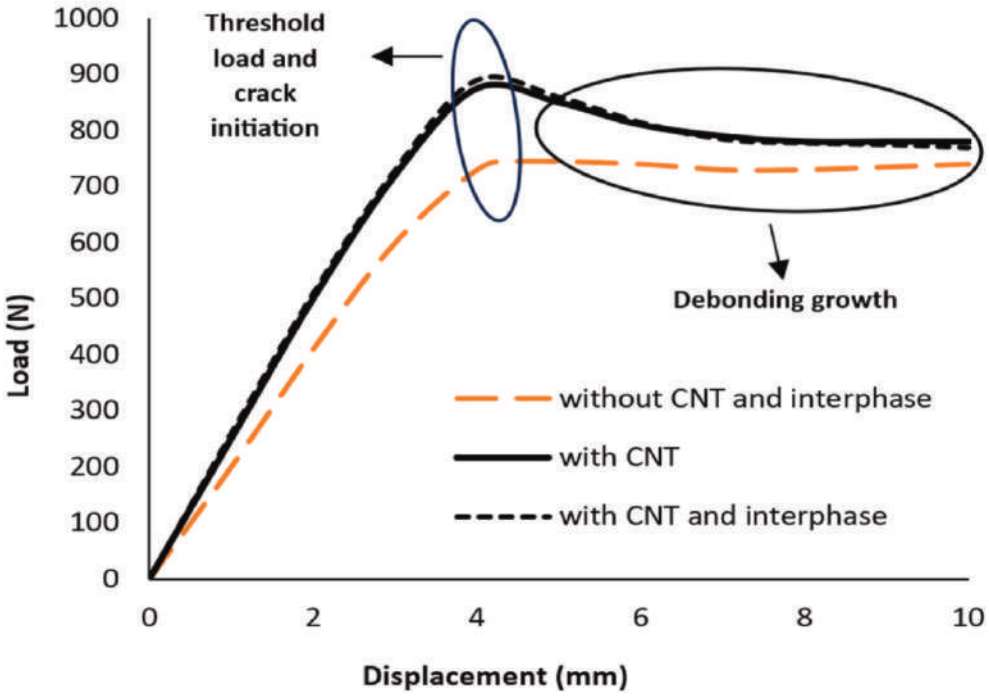


Figure 6. Impact of CNT addition and CNT/polymer phase development on the FFRC/PVC sandwich structural composite's load-displacement diagram. (created by authors [144])

Efforts have been concentrated on examining flexural properties and skin/core separation of sandwich constructions to determine the effectiveness of nano-additives in enhancing mechanical characteristics at low volume (or weight) concentration [140-142]. A drawback of fiber-reinforced composites, essential in sandwich constructions, is their limited transverse elastic properties. Several studies have shown that enhancing the transverse modulus and bending strength of the composite can be achieved by growing CNTs radially on the circumferential surfaces of fibers [143]. To improve our comprehension of the impact FFRC skins have on bending stiffness and FFRC skin/PVC foam core separation, we will use the current numerical assessment framework.

In Figure 6, addition of 2 volume% CNT, while keeping a constant volume fraction of 30% for E-glass fiber and an interphase region thickness of 0.5 nm, on the bending nature of FFRC skins/PVC core sandwich composite is depicted [144]. It›s apparent that the inclusion of CNTs results in a notable improvement in the limiting force and flexural stiffness, attributed to the enhancement of the transverse assets of the FFRC outer layer. Moreover, with the increase in bending stiffness, crack propagation occurs at a steeper rate. The influence of interphase development on the flexural behavior of the sandwich structure seems insignificant based on Figure 5[145].

Traditionally, honeycomb structures have been the preferred choice for manufacturing sandwich-type composites, as shown in Figure 7 [145]. However, alternative core materials such as aluminum foam have gained popularity due to their exceptional arrangement of physical-mechanical possessions, particularly in withstanding impact and blast loading. For example, the Airbus A340 incorporates composite sandwich structures throughout its vertical tail, which consists of Nomex® honeycomb core along with the combination of glass fiber reinforced prepreg [146]. Furthermore, polymer foam materials like polyethylene terephthalate (PET) foam and polyvinylchloride (PVC) foam were found application in sandwich composites, as evidenced by models such as the Mercedes-Benz A series automobiles [147,148]. These foam materials offer advantages in terms of lightweight construction and impact absorption, rendering them suitable for various automotive applications [149].

Enhancing impact absorption and improving the interfacial strength between skin and core layers are pivotal challenges in sandwich composite production [56]. Researchers have devised a simple technique involving fabric surface brushing and abrading to bolster the interfacial adhesion between carbon fiber reinforced polymer (CFRP) and core materials. This method has shown notable enhancements in delamination resistance without significant loss in in-plane tensile strength [150]. Another innovative strategy involves employing magnetorheological elastomer (MRE) tapering composite structural sandwich plates to fortify the interfacial structure of sandwich composites [151]

Efforts have also been concentrated on adding nanoparticles to strengthen foam mechanical properties and improve impact absorption through altering specimen thickness. Furthermore, researchers have explored the utilization of modified polymer structural foams with diverse compositions to amplify the properties of sandwich composite materials [152]. These studies aim to optimize the mechanical steadiness of structural composites by augmenting connexion between the skin and core material and leveraging suitable design technologies tailored to specific application conditions [153]. Moreover the sandwich structure exhibits the versatility and structural stability improvement. The sandwich structures are effectively deployed in various applications such as vibration damping, electromagnetic

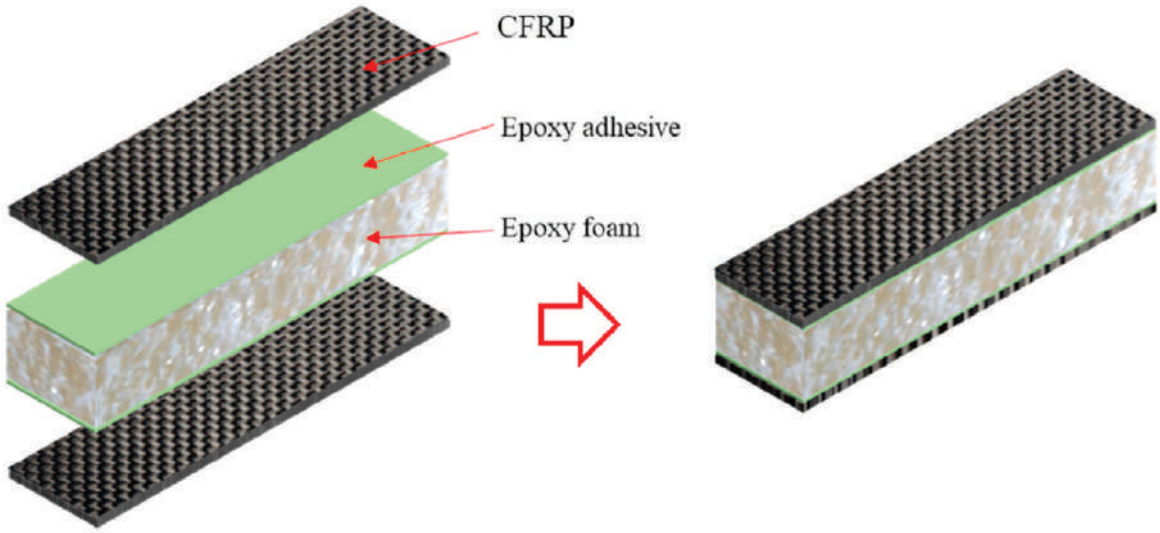


Figure 7. Representation of the sample manufacturing process. (cretaed by authors [145])

shielding, noise cancellation etc. at various industrial application [154,155]. In the manufacturing of sandwich composite to enhance the mechanical strength the core type reinforcement is generally preferred [156].

The foam type reinforcement has the advantages such as lesser specific gravity as compared to core reinforced sandwich composite, also the foam type reinforcement material is environmental friendly raw materials. Therefore foam material can be tailored to enhance the functionality of the sandwich composite. The multifunctional properties can be achieved by reinforcement of the CNT [157,158]. These concepts open the large opportunities sandwich composite in the perspective of the mechanical strength improvement, widening the application range.

Figure 8 shows the compressive strength of epoxy foams (EF) at different curing temperatures and times. In Figure 7a, it is evident that EF specimens molded at temperatures of 140°C or higher experienced fractures during compression testing, indicating a decrease in specific compressive strength attributed to increased cell size. The changes in specific compressive properties over time for EF specimens cured at different temperatures and aged for 180 minutes are displayed in Figure 8b. At curing temperatures of 100°C and higher, the curing process rapidly progresses near the foam's surface, leading to a continuous increase in cell size within the EF. This phenomenon is possibly due to the thick crosslinked layer of the skin despite unstable foaming, resulting in a higher degree of crosslinking at the EF surface. Both the glass transition temperature (T_g) and density tend to increase with higher cure temperatures [149]. Moreover, specific compressive property at a 180°C curing temperature as a function of time is shown in Figure 7b. EFs formed at higher curing temperatures exhibited higher compressive strengths due to more stable foaming. The specific compressive strength continued to increase even after 120 and 180 minutes of aging at 180°C. Additionally, the brown color depth on the surface of 40 mm thick foam specimens after 120 and 180 minutes of aging at 180°C was found to be only 0.691 mm and 0.716 mm, respectively. Unlike other types of foams, EF surfaces mainly degraded through thermal aging, resulting in relatively small decreases in foam strength with increased aging time. Unlike materials like polylactic acid (PLA), PU, and PVC foams, structural epoxy foams are preferred in applications requiring high heat resistance and rigidity [160]. A schematic of honeycomb sandwich is demonstrated in Figure 9 [160].

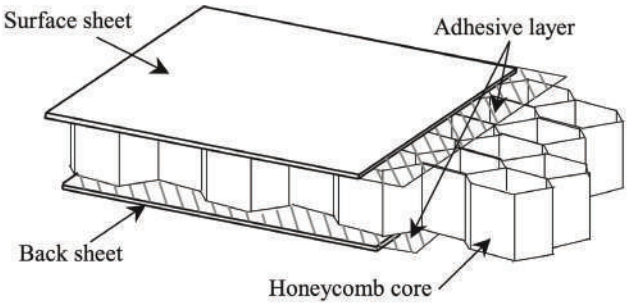


Figure 9. Structure of honeycomb structure. (created by authors [160])

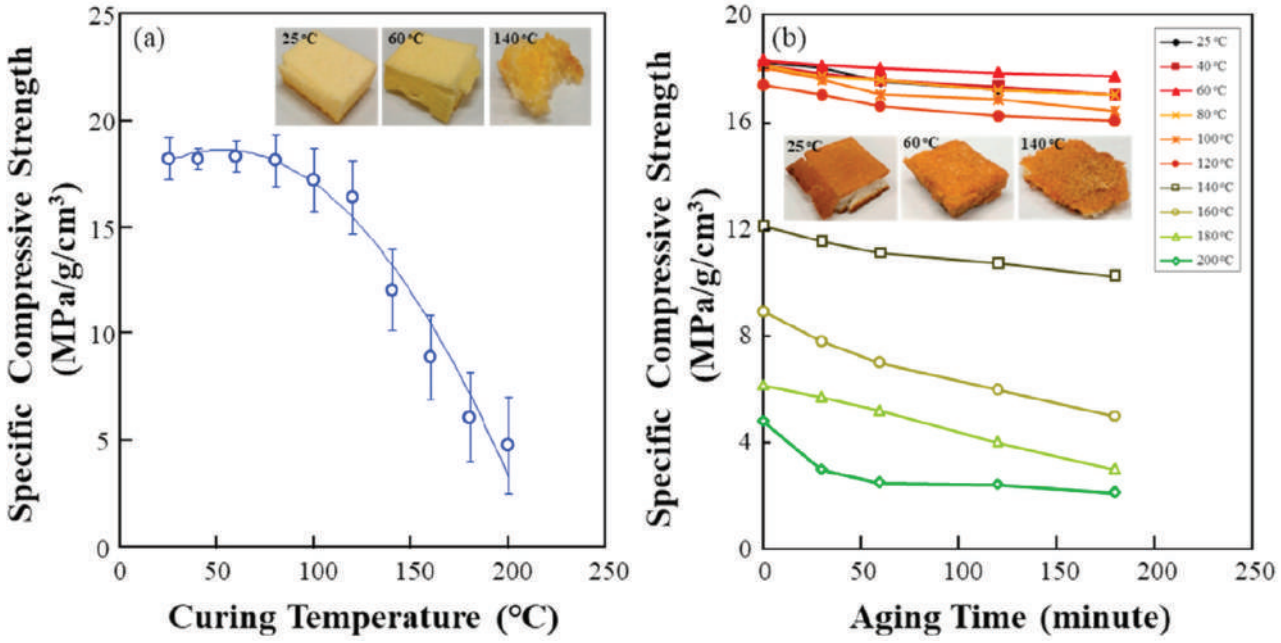


Figure 8. Differences in compressive strength of epoxy foam are examined through variations in curing and aging temperatures.

PHASE CHANGE COMPOSITE

Utilization of solar energy usually revolves around the capture of sunlight for heat. Phase-change material (PCM) in use for thermal energy storage can store large amounts of heat without significant change in phase-transition temperature [161]. But there are some shortcomings in the current PCMs regarding thermal conductivity being relatively low, resulting in lower heat transfer rate and storage efficiency [6,8,9]. Furthermore, as a result of most PCMs are liquid or semiliquid and their inherent instability makes its application in various industrial conditions limited [162,163]. Various approaches have been found to upgrade the thermo-stability properties of PCMs.

One approach involves improving the thermal conductivity of PCMs by incorporating exterior fillers such as carbon compounds, metal foams, and nanoparticles [164]. For instance, [165] demonstrated an 80% enhancement in the thermal characteristics of palmitic acid by adding 5 wt % TiO_2. [166] produced exfoliated graphite by exposing graphite flakes and amorphous graphite to sunlight and microwave radiation, resulting in improved thermal properties of PCMs. [167] studied thermal properties of pure paraffin influenced by silicon nitride (Si_3N^4) nanoparticles. Their measurement showed a 33.9% increase in the thermal conductivity of paraffin when 2 wt % Si_3N_4 was mixed. Similarly, [168] examined the thermal properties of paraffin with the inclusion of nanoparticles and observed significant improvements.

Pressing demand for sustainable and eco-friendly energy systems has been drawn attention to, by the increase of greenhouse gas emission, depletion of non-renewable energy source and the rise in global energy consumption that have occurred over last year's [169]. Wind and solar power, being renewable energy sources, have almost infinite potential. However, their intermittent availability, contingent on factors like wind patterns, cloud cover, and sunlight, presents challenges [170]. For the decreasing the percentage of carbon emission, the technologies related to energy storage are quite improving and facilitating the continuous supply of energy/power though there is a fluctuation in energy get happens. In this case as requirement suppling required energy by reducing or eliminating fluctuation, so out of the glob there is a interesting demand of these tech which includes increasing span of battery, optimising charging and discharging cycle, improving loading capacity. This underscores the significance of advancing energy storing materials [170].

Considerable research has been dedicated to PCMs in this context. PCMs can absorb and release large amounts of heat energy when they undergo phase changes [171]. The phase transition temperature is a critical characteristic that establishes their suitability for various uses. PCMs find widespread use in buildings, solar energy systems, thermoelectric materials, textiles, and electronics. PCMs can be classified into four types as shown in Figure 10.

While SGPCMs and LGPCMs boast greater latent heat loading abilities, their volumetric changes during phase transitions limit their practical application. SSPCMs, although experiencing minimal volume changes, have relatively lower latent heat capacities and are still being explored for potential future applications. SLPCMs, with their great latent heat loading ability, minimal volume change, and good chemical and thermal stability, remain one of the most widely used types of PCMs [172].

Inorganic PCMs comprise crystalline hydrated salts and metals, offering extraordinary energy storing density, non-flammability, cost-effectiveness, and superior thermal conductivity compared to organic PCMs. However, they are susceptible to issues like phase separation and supercooling [39]. Conversely, organic PCMs, including paraffin wax (PW), alcohols, fatty acids, esters, and polymer materials, boast high latent heat capacity, minimal supercooling, and non-corrosiveness [173]. Nonetheless, they suffer from inherently low intrinsic thermal conductivity. To tackle this challenge, researchers have explored nanomaterials addition will rise thermal conductivity after addition into the PCM matrix [174]. Despite progress in this area, the low thermal conductivity of SLPCMs and the potential leakage of the liquid phase present hurdles to their practical application [38].

One promising strategy involves using sp2-rich carbon-based nanomaterials as filler materials. These

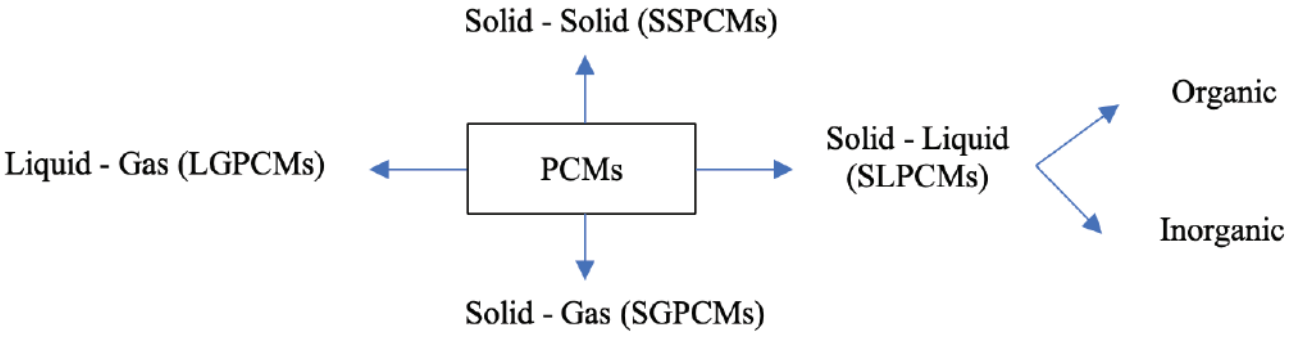


Figure 10. Classification of PCM.

nanomaterials exhibit great thermal conductivity and harmony with organic PCMs [175]. By directly adding them to PCMs, phase change composites (PCCs) with enhanced total heat transfer efficiency can be developed. Enhancing the thermal conductivity of PCMs is crucial for maintaining a even temperature dispersal, thus reducing hotspots and confined overheating [176]. This improvement facilitates faster charging and discharging rates, leading to more well-organized storage and consumption of thermal energy. Among sp2-rich carbon nanomaterials like graphene, carbon nanotubes (CNTs), expanded graphite (EG), and graphite nanoplatelets (GNPs), graphene and its derivatives have garnered significant attention for enhancing PCM systems [177].

Graphene-PCCs have several advantages compared to other systems, e.g., nanofiller-enriched PCCs and MOF-based PCCs. The features include high thermal conductivity, low density, the reinforced structural quality and a high surface area that make them perfect for application requiring a fast heat diffusion with low mass graphene and rGO exhibit higher thermal conductivities than GO as they possess no or fewer impurities that disturb in the pathways of heat carrier transfer [178]. Due to the oxygen functionalization, GO is more easily dispersed in PCMs; however, graphene and rGO are relatively easy to prepare. Graphene aerogels and foams have low densities and high specific surface areas, creating a porous and conductive structure that improves thermal conductivity when combined with PCMs. Furthermore, these three-dimensional nanostructures endow PCCs with shape persistence to avoid leakage during phase transition and enable applications integration [179]. Besides being used as fillers, carbonaceous nanomaterials can encapsulate PCMs in a core-shell manner. By adopting of such core-PCM and the phase change material with high thermal conductivity, it is possible to effectively control latent heat and phase change temperature of the core-PCM so as to improve thermal conductivity property and shape stability. On the whole, recent progress of graphene-based PCCs offer tremendous potential in raising the performance levels for TES in a wide range of applications.

PERCEPTION USES

Claim in Shape Memory Material

From the early 1980's the material which get stimulated by external or internal sources shows remarkable affinity by research community and industrial uses [180]. The researchers were found shape memory polymers (SMPs) more suitable in many applications over shape memory wires (SMA), as these kind of polymers possesses remarkable unique properties than that of SMA. These include bio-degradation ability, low cost, easily available, lower dense, easy production, variety in transition temperature, good recoverable strain, multiple time shape regain ability just by modifying minor chemical changes [181]. Notably, SMPs can achieve strains of up to 200%, a significant improvement over the limited strains exhibited by SMAs, shape memory ceramics, and glasses [182].

A range of functional shape memory polymers (SMPs) with remarkable shape memory effects (SME) have been established over time. Notable examples include epoxy-based SMPs cyanate, polyurethane (PU), and, styrene which stand out as enhanced smart materials. Cyanate is the thermoset matrix, for instance, boasts exceptional thermal stability with a high T_g of up to 400°C. Its small dielectric loss and minimal hygroscopicity make cyanate-based polymers ideal for applications in electronic PCB, coating of dielectrics, aerospace, and wave transmission [183]. In contrast, styrene-based SMPs find utility in low-temperature applications due to their low T_g. Polyurethane SMPs typically have a constricted T_g limits nearby room temperature, making them suitable for molding into desired shapes via injection, extrusion, and blowing processes, particularly valued in biomedical applications owing to their low deformation temperatures [184]. Epoxy-based resins, chosen for their higher mechanical properties, excellent thermal stability, ease of processing, and outstanding chemical resistance, offer promising potential for SMP development [185].

Despite the intelligent behaviors exhibited by SMPs compared to conventional materials, their inherent poor mechanical properties remain a significant drawback. The limited structural integrity of neat SMPs poses challenges in effectively integrating them into structural applications. Consequently, there has been a surge in research interest surrounding shape memory polymer composites (SMPCs). These composites incorporate reinforcing fillers such as particulates, short fibers, long or continuous fibers, and fiber fabrics [186], aiming to overcome the weaknesses of SMPs and enhance their structural, electrical, thermal, and shape memory properties for structural applications.

Later exploratory thinks about and explanatory approaches have highlighted the potential of basalt fiber-reinforced materials for basic applications in respectful designing. Basalt offers various amazing properties, counting tall quality, electrical separator, erosion resistance, affect resistance, and a tall dissolving temperature [187]. Outstandingly, basalt shows predominant physical, mechanical, and warm properties compared to glass fiber, with the next Young›s modulus and pliable quality, as well as a most extreme benefit temperature of 650°C compared to 460°C for glass fiber. Whereas manufactured carbon fiber has been broadly utilized in polymer composites due to its surprising mechanical properties, counting tall quality and modulus, it has been a conspicuous building fabric since the 1960s [188].

In addressing modern construction challenges, engineers are exploring novel methods to expedite and simplify construction processes. Modular construction has emerged as a solution, particularly in congested urban areas where traditional construction methods face limitations because

of the longer building durations and the limited space. This approach involves fabricating different construction parts in a factory as modules, which are subsequently delivered to the building location for assembly. Modular construction offers advantages such as enlarged construction rapidity, safer manufacturing, reduced on-site labour, and minimized resource expenditure. However, transportation of large-sized modules remains a key challenge, especially in congested cities.

Fire Retardation

The characteristics of SMPCs under fire exposure remain largely unexplored as shown in Figure 11 [189]. Additionally, while carbon fiber reinforcement significantly enhances mechanical properties, it renders designs costly and unsuitable for mass production [190]. Utilizing natural fiber reinforcement with an SMP matrix offers a cost-effective solution to broaden current limitations and achieve significant improvements in integrating SMPCs into civil engineering applications [191]. Furthermore, prolonged exposure to sunlight could harm the polymer matrix, necessitating investigation into the light absorbance properties of SMPCs as a construction material. Similarly, the effects of water or solvent exposure on construction materials, considering phenomena like rain and humidity, warrant future research to understand potential degradation of strength and stiffness.

In civil engineering applications and buildings, protection against fire is of utmost importance. Building regulations provide strict design specifications and material performance expectations. Fire safety encompasses prevention, containment, detection, and evacuation [192]. The evaluation of building materials' appropriateness and application during fire crises is generally focused on factors such as ignition, flame spread, emission of heat, and smoke emission. Smoke production is one of these variables that poses the greatest risk since it can cause fatalities owing to impaired sight and breathing difficulties caused by the poisonous compounds in smoke. It can also impede evacuation attempts. Therefore, analyzing smoke generation is essential when introducing a new material for construction or structural purposes [193].

The warm oxidative deterioration components of epoxy tars include oxygen assaulting the methylene gather, oxidizing tertiary carbons within the aliphatic parcel of the chain, and oxygen assaulting nitrogen in epoxies cured with amine-based hardeners. Glass and basalt SMPCs stood up to start for 68 s, whereas carbon fiber-reinforced SMPCs stood up to for 70 s. Figure 12 portrays the decay behavior of shape memory polymer composites (SMPCs) at hoisted temperatures. The temperature at which a 5% weight misfortune happens is considered the warm deterioration temperature of the fabric [189]. Up to 380°C, all three SMPCs show comparable behavior, starting warm decay at an indistinguishable temperature of 345°C. This demonstrates that the sort of fortification fabric does not essentially impact the warm deterioration temperature of the chosen SMPCs. In any case, past 380°C, exceedingly thermally steady basalt

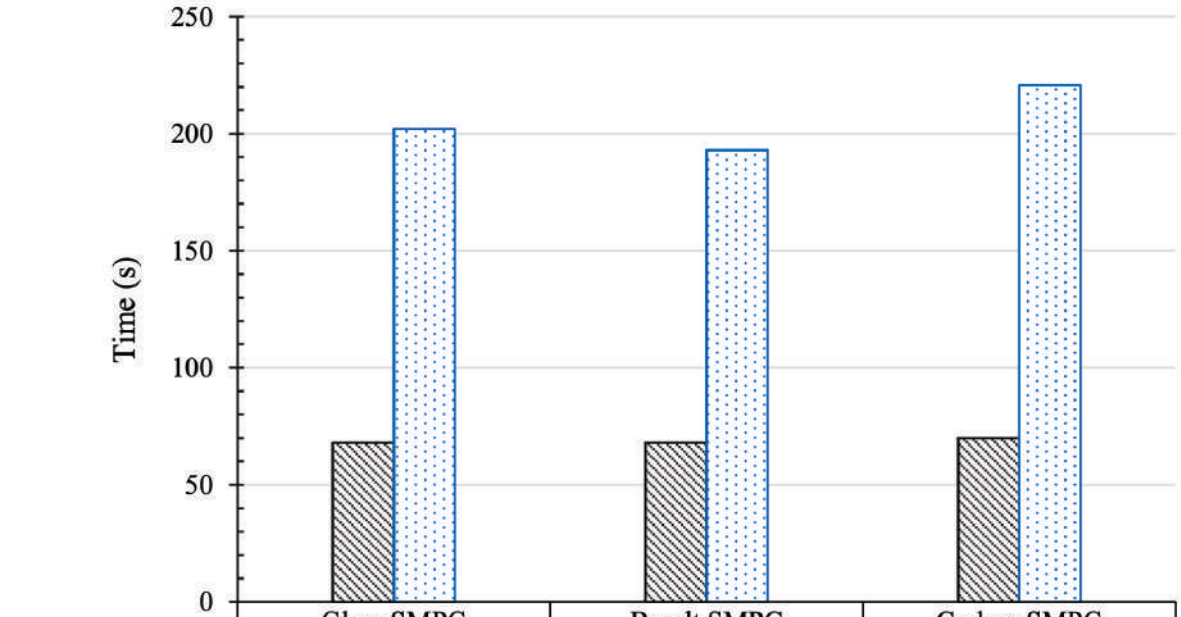


Figure 11. The amount of time that SMPCs need to start and finish a fire while being tested. (created by authors [189])

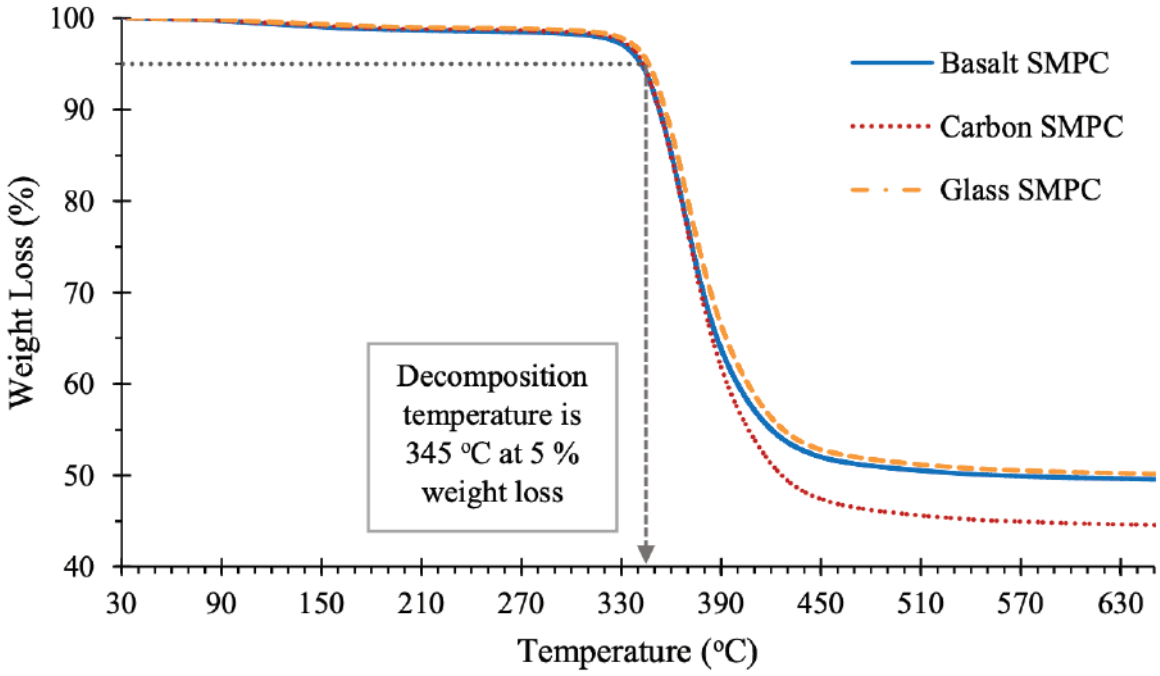


Figure 12. SMPC weight reduction as a result of thermal degradation.

and glass fiber-reinforced composites show about indistinguishable behavior. In differentiate, the less thermally steady carbon fiber SMPC appears a better decay in weight. This error can be ascribed to the lower decay temperature of carbon fiber. Subsequently, when uncovered to higher temperatures, carbon fiber is more inclined to burning in barometrical oxygen, driving to assist weight misfortune.

Hygrothermal Stability

Fiber-reinforced polymeric composites have revolutionized various industries due to their exceptional properties, including corrosion resistance, high strength-to-weight ratios, and versatility in shaping intricate structures with enhanced mechanical performance [194]. However, exposure to moist environments can pose significant challenges to FRP, leading to water absorption and subsequent degradation of mechanical properties [195]. This degradation, characterized by phenomena such as microcrack formation, fiber/matrix debonding, and delamination, necessitates thorough investigation and assessment of FRP performance in hygrothermal conditions [196].

Tests for hygrothermal decaying are frequently used to mimic the long-term performance of FRP in maritime settings. These tests involve subjecting FRP samples to elevated temperatures until saturation is reached. The performance of FRP in hygrothermal environments is influenced by various aspects, comprising fabric architecture, polymer matrix, environmental conditions, and manufacturing techniques, all of which influence nearly steady, vibrant, and qualities that tolerate harm [197].

Sophisticated numerical modelling models, including CLPT and CDM, and analytical methods, play a crucial role in predicting mechanical property degradation in FRP. CDM, operating at multiple scales, offers insights into crack propagation and damage evolution, leading to more accurate predictions of mechanical behavior. CLT, although simpler in its assumptions, provides valuable information about laminate behavior, albeit with some limitations in handling complex microstructures. Analytical modeling complements numerical simulations by offering theoretical insights into material behavior and facilitating the development of predictive models for mechanical property degradation [198-200].

Understanding the interplay between temperature, moisture, and mechanical properties is necessary for safeguarding the dependability and toughness of FRP in real-world applications [201]. By leveraging advanced simulation techniques and experimental validation, researchers can improvement prised insights into the degradation mechanisms of FRP and develop strategies to mitigate their adverse effects, thereby advancing the development of more resilient and sustainable composite materials for diverse engineering applications [202].

Solar Energy Harvesting Systems

Solar energy is a promising renewable resource, offering abundant and environmentally friendly power. However, the alternating nature of sunlight necessitates efficient energy storage solutions to bridge the gap between energy demand and supply. Among these solutions, graphene-based PCCs have emerged as a cutting-edge technology for enhancing the

reliability, efficiency, and performance of solar thermal systems. In recent research, Wang et al. developed solar-driven PCCs by incorporating magnesium nitrate hexahydrate, carboxymethyl cellulose, and graphene. This innovative approach demonstrated significant improvements in performance of photothermal conversion and preservation of energy [203]. By adding carboxymethyl cellulose as a thickening mediator and 5 wt % graphene to enhance thermal conductivity, they achieved a remarkable 191.18% increase in thermal conductivity without compromising latent heat capacity. Moreover, graphene›s exceptional optical absorption capacity and photothermal conversion properties contributed to a substantial increase in thermal absorption capacity and photo-thermal conversion efficiency.

Similarly, Cui et al. devised a cost-effective and stable PCC utilizing sodium acetate trihydrate (SAT) as the phase change material (PCM). Xanthan gum and GO@SiO_2 were incorporated to remove the issues related to phase segregation and address supercooling [204]. Also to improve the solar energy charging, latent heat and thermal conductivity, silicon carbide foam, GO and wood powder (WP) were utilised. PCC can be utilised as photothermal conversion with the use of PEG-based PU [205,206].

FUTURE SCOPE

The review focused on many encouraging paths those are helpful in the development of the materials, specifically phase change composites (PCCs) with their applications in different field. Summary of various applications in the perspective of future scope is enlisted below;

Improved Thermal Management in Textiles

The innovation of graphene based PCCs into textiles gives a confident future growth. The heat dissipation rate can be improved by optimizing the composition and structure of PCC coatings. Furthermore the production rate and cost effectiveness methods PCC-coated textiles would be important for practical use.

Thermal Regulation by Innovative Materials

The integration of PCCs with the thermally prompted flexible wood generates the possibilities of the novel materials with the improved flexibility and thermal properties. Future investigation might focus on enhancing the range of PCC composition and wood species to improve the latent heat storage and thermal conductivity for specific applications like structural components useful in building materials.

Advanced cold Chain Solutions

The improvement in the temperature control and energy efficiency could be achieved by incorporating PCCs into cold chain distribution boxes. Thermal conductivity, durability, and reliability under different environmental conditions could enhance by optimized the structure and composition of the PCC.

Heat Dissipation in Electronics

To improve thermal management efficiency by enhancing cooling of electronic components it is necessary to investigate the effect of combination of phase change materials (PCMs) and heat pipes. Furthermore the research could focus on design and integration of PCM based heat sinks with heart pipes to attain the good quality of heat dissipation performance by overcoming the challenges such as PCM leakage and agglomeration of nano particles. Furthermore by exploring alternative PCM composition and nano fillers to enhance the thermal conductivity and stability.

Novel PCC Compositions and Structures

The innovative phase change compositions like aerogels or graphene-based skeletons incorporated in PCM which offers lot off opportunities to enhance thermal energy storage and control technologies. Furthermore the investigation can be carried for novel synthesis methods, performance evaluations, and characterization techniques.

Scalability and Commercialization

It is found that many of the research in PCC shows the good results at laboratory level, furthermore it is important address the commercialization and scalability challenges. Furthermore investigation could focused on various production scaling methods, optimizing the material cost. The collective efforts between industry, academia will be crucial for translating research innovations for practical solutions.

CONCLUSION

The study of the polymer composite, fiber reinforced polymers and shape memory polymers highlights its respective significance across different industries. Researcher have investigated the significant properties of shape memory polymer composites like shape memory effects and the transition temperatures which can be used for various structural applications. Furthermore the shape memory polymer with enhanced properties like cyanate and styrene-based shape memory polymers, shows the versatility in various applications from engineering to medical field.

The limitation of mechanical properties in shape memory polymer are addressing this by the use of developing the shape memory polymers composites. The structural integrity, thermal stability, and mechanical strength could be increased by incorporating the various nano fillers in the shape memory polymer. The various reinforcement used are carbon fibers, glass fibers, basalt fibers. The advancement in the SMPCs is useful for various applications like structural applications, and also where reliability and high performance are important.

The incorporation of basalt fiber as a reinforced materials for civil engineering applications proves their strength for facing modern challenges. Now modern construction method is coupled with the use of SMP composites which

gives the advantages such as high construction speed, lesser labor costs, and high structural performance. Furthermore the application of natural fibers reinforcement with the SMP gives a cost optimized product for various applications.

The study on phase change composites focused their importance in facing challenges in the perspective of thermal energy storage and its control. Graphene based phase change composites shows the important properties such as energy storage density, thermal conductivity, and heat transfer efficiency. The combination of material shows the application in diverse fields like battery technologies, textiles, solar energy systems, and electronic cooling which shows the potential for strengthening energy efficiency and sustainability.

Furthermore research also focused on the optimization of composition of the phase change composites with its commercialization and scaling up the production rate. The research also focused the technical challenges for its adoption. Collective efforts of industry, academia and various agencies will enhance the research of polymer composites and sandwich structures for practical solutions.

The research shows the remarkable advancements and strength of sandwich and polymer composite structure in various applications. By investigating the various advanced material, manufacturing techniques causes sustainable, high performance and functional materials for the benefit of environment and society.

AUTHORSHIP CONTRIBUTIONS

Authors equally contributed to this work.

DATA AVAILABILITY STATEMENT

The authors confirm that the data that supports the findings of this study are available within the article. Raw data that support the finding of this study are available from the corresponding author, upon reasonable request.

CONFLICT OF INTEREST

The author declared no potential conflicts of interest with respect to the research, authorship, and/or publication of this article.

ETHICS

There are no ethical issues with the publication of this manuscript.

STATEMENT ON THE USE OF ARTIFICIAL INTELLIGENCE

Artificial intelligence was not used in the preparation of the article.

REFERENCES

[1] Asim M, Paridah MT, Chandrasekar M, Shahroze RM, Jawaid M, Nasir M, et al. Thermal stability of natural fibers and their polymer composites. Iran Polym J 2020;29:625–648. [CrossRef]

[2] Chen Y, Li J, Li T, Zhang L, Meng F. Recent advances in graphene-based films for electromagnetic interference shielding: review and future prospects. Carbon 2021;180:163–184. [CrossRef]

[3] Tan X, Yuan Q, Qiu M, Jinhong Y, Jiang N, Lin C-T, et al. Rational design of graphene/polymer composites with excellent electromagnetic interference shielding effectiveness and high thermal conductivity: a mini review. J Mater Sci Technol 2022;117:238–250. [CrossRef]

[4] Sankaran S, Deshmukh K, Ahamed MB, Khadheer Pasha SK. Recent advances in electromagnetic interference shielding properties of metal and carbon filler reinforced flexible polymer composites: a review. Compos Part A Appl Sci Manuf 2018;114:49–71. [CrossRef]

[5] Abbasi H, Antunes M, Velasco JI. Recent advances in carbon-based polymer nanocomposites for electromagnetic interference shielding. Prog Mater Sci 2019;103:319–373. [CrossRef]

[6] Guo Y, Zuo X, Xue Y, Tang J, Gouzman M, Fang Y, et al. Engineering thermally and electrically conductive biodegradable polymer nanocomposites. Compos Part B Eng 2020;189:107905. [CrossRef]

[7] Du Q, Li C, Sun J, Zhang H, Zhang X, Liu C, et al. Efficient preparation of polydimethylsiloxane-based phase change composites by forced network assembly with outstanding thermal management capability. J Polym Res 2023;30. [CrossRef]

[8] Song Y, Jiang F, Song N, Shi L, Ding P. Multilayered structural design of flexible films for smart thermal management. Compos Part A Appl Sci Manuf 2021;141:106222. [CrossRef]

[9] Wei B, Zhang L, Yang S. Polymer composites with expanded graphite network with superior thermal conductivity and electromagnetic interference shielding performance. Chem Eng J 2021;404:126437. [CrossRef]

[10] Tavares L, Sousa LR, da Silva SM, Lima PS, Oliveira JM. Effect of incorporation of graphene nanoplatelets on physicochemical, thermal, rheological, and mechanical properties of biobased and biodegradable blends. Polymers 2023;15:17622. [CrossRef]

[11] Tiwari N, Shaikh AA. Effect of the amine and carboxyl functionalised graphene on the thermomechanical and interfacial properties of the shape memory polymer nanocomposites. Polym Bull 2023;80:11797–11815. [CrossRef]

[12] Hu J, Zhang T, Wang L, Shi Z, Xia H. Constructing sandwich-structured poly(vinyl alcohol) composite

films with thermal conductive and electrical performance. ACS Appl Mater Interfaces 2023;15:12315–12326. [CrossRef]
[13] Kanif M, Vivek P, Kishor K. Structural analysis of nano-filler based structural composite. J Aeronaut Mater 2023;43:188–202.
[14] Markad K, Lal A. Synthesis of the multiphase shape memory hybrid composites hybridized with functionalized MWCNT to improve mechanical and interfacial properties. Polymer-Plastics Technol Mater 2022;61:650–664. [CrossRef]
[15] Tiwari N, Gagare SW, Shaikh AA. Shape recovery analysis of the additive manufactured 3D smart surfaces through reverse engineering. Prog Addit Manuf 2021;6:281–295. [CrossRef]
[16] Li L, Ma Z, Xu P, Zhou B, Li Q, Ma J, et al. Flexible and alternant-layered cellulose nanofiber/graphene film with superior thermal conductivity and efficient electromagnetic interference shielding. Compos Part A Appl Sci Manuf 2020;139:106134. [CrossRef]
[17] Kang Z, Li M, Huang M, Shi X, Zheng G, Liu C, et al. Remarkably anisotropic conductive MWCNTs/polypropylene nanocomposites with alternating microlayers. Chem Eng J 2019;358:924–935. [CrossRef]
[18] Chen Q, Yang K, Feng Y, Liang L, Chi M, Zhang Z, et al. Recent advances in thermal-conductive insulating polymer composites with various fillers. Compos Part A Appl Sci Manuf 2024;178:107998. [CrossRef]
[19] Chen Y, Zhang HB, Huang Y, Jiang Y, Zheng WG, Yu ZZ. Magnetic and electrically conductive epoxy/graphene/carbonyl iron nanocomposites for efficient electromagnetic interference shielding. Compos Sci Technol 2015;118:178–185. [CrossRef]
[20] Qin Y, Mei Z, Kang D, Peng Z, Geng Z, Min W, et al. Preparation of thermal expandable epoxy resin and properties of foam sandwich composites formed by thermal expansion molding process. Polymer Composites 2024;45:11050–11065. [CrossRef]
[21] Kim Y, Kim MJ. Thermal vibration analysis of a composite sandwich plate in the space environment. Mech Adv Mater Struct 2022;31:563–576. [CrossRef]
[22] Markad K, Lal A. Experimental investigation of shape memory polymer hybrid nanocomposites modified by carbon fiber reinforced multi-walled carbon nanotube (MWCNT). Mater Res Express 2021;8:105015. [CrossRef]
[23] Tiwari N, Shaikh AA. Effect of size and surface area of graphene nanoplatelets on the thermomechanical and interfacial properties of shape memory multiscale composites. Polymer-Plastics Technol Mater 2022;61:1334–1346. [CrossRef]
[24] Tiwari N, Shaikh AA. Hybridization of carbon fiber composites with graphene nanoplatelets to enhance interfacial bonding and thermomechanical properties for shape memory applications. Polymer-Plastics Technol Mater 2022;61:161–175. [CrossRef]
[25] Tunay M. Bending behavior of 3D printed sandwich structures with different core geometries and thermal aging durations. Thin-Walled Struct 2024;194:111329. [CrossRef]
[26] Ong PJ, Lum YY, Debbie Soo XY, Wang S, Wang P, Chi D, et al. Integration of phase change material and thermal insulation material as a passive strategy for building cooling in the tropics. Constr Build Mater 2023;386:131583. [CrossRef]
[27] Cao L, Zhang D. Application potential of graphene aerogel in paraffin phase change composites: experimental study and guidance based on numerical simulation. Solar Energy Mater Sol Cells 2021;223:110949. [CrossRef]
[28] Huang L, Zhang B, He M, Huang X, Wu G, Yin G, et al. Preparation of anisotropic reduced graphene oxide/BN/paraffin composite phase change materials and investigation of their thermal properties. J Mater Sci 2020;55:7337–7350. [CrossRef]
[29] Zheng X, Gao X, Huang Z, Li Z, Fang Y, Zhang Z. Form-stable paraffin/graphene aerogel/copper foam composite phase change material for solar energy conversion and storage. Solar Energy Mater Sol Cells 2021;226:111083. [CrossRef]
[30] An Y, Li C, Liu J, Li N, Wang W, Qiu S, et al. Enhancing thermal conductivity, electrical insulation, and mechanical strength of polydimethylsiloxane composites with sandwich structure. Adv Eng Mater 2024;26:2301546. [CrossRef]
[31] Markad NT, Kanif M. Shape memory polymer composites: characterization and modeling. Boca Raton, Florida: CRC Press; 2023.
[32] Tiwari N, Shaikh AA, Malek NI. Modification of the multiphase shape memory composites with functionalized graphene nanoplatelets: enhancement of thermomechanical and interfacial properties. Mater Today Chem 2022;24:100826. [CrossRef]
[33] Saba N, Paridah MT, Ibrahim NA. Thermal properties of oil palm nano filler/kenaf reinforced epoxy hybrid nanocomposites. AIP Conf Proc 2016;1787. [CrossRef]
[34] Saba N, Jawaid M. A review on thermomechanical properties of polymers and fibers reinforced polymer composites. J Ind Eng Chem 2018;67:1–11. [CrossRef]
[35] Sun Y, Guo L, Wang T, Zhong S, Pan H. Bending behavior of composite sandwich structures with graded corrugated truss cores. Compos Struct 2018;185:446–454. [CrossRef]
[36] Khundamri N, Aouf C, Fulcrand H, Dubreucq E, Tanrattanakul V. Bio-based flexible epoxy foam synthesized from epoxidized soybean oil and epoxidized mangosteen tannin. Ind Crops Prod 2019;128:556–565. [CrossRef]
[37] Wu S, Li T. High-performance thermally conductive phase change composites by large-size oriented graphite sheets for scalable thermal energy harvesting. Adv Mater 2019;31:1905099. [CrossRef]

[38] Soo XYD, Png ZM, Wang X, Chua MH, Ong PJ, Wang S, et al. Rapid UV-curable form-stable polyethylene-glycol-based phase change material. ACS Appl Polym Mater 2022;4:2747–2756. [CrossRef]
[39] Li TX, Xu JX, Wu DL, He F, Wang RZ. High energy-density and power-density thermal storage prototype with hydrated salt for hot water and space heating. Appl Energy 2019;248:406–414. [CrossRef]
[40] Sun S, Yan Q, Wu M, Zhao X. Carbon aerogel based materials for secondary batteries. Sustain Mater Technol 2021;30:e00342. [CrossRef]
[41] Atas C, Doğan A. An experimental investigation on the repeated impact response of glass/epoxy composites subjected to thermal ageing. Compos Part B Eng 2015;75. [CrossRef]
[42] Golewski P, Sadowsk T. The effect of thermal aging degradation of CFRP composite on its mechanical properties using destructive and non-destructive methods and the DIC system. Polym Testing 2023;118:107902. [CrossRef]
[43] Prabhu T, Harish V, Iyengar P, YJ H, Prashantha K. Thermal degradation of epoxy resin reinforced with polypropylene fiber. J Appl Polym Sci 2007;500–503. [CrossRef]
[44] Vu DQ, Gigliotti M, Lafarie-Frenot MC. The effect of thermo-oxidation on matrix cracking of cross-ply [0/90]S composite laminates. Compos Part A Appl Sci Manuf 2013;44:114–121. [CrossRef]
[45] Rocha IBCM, Raijmaekers S, Nijssen RPL, van der Meer FP, Sluys LJ. Hygrothermal ageing behaviour of a glass/epoxy composite used in wind turbine blades. Compos Struct 2017;174:110–122. [CrossRef]
[46] Akay M, Spratt GR. Evaluation of thermal ageing of a carbon fibre reinforced bismalemide. Compos Sci Technol 2008;68:3081–3086. [CrossRef]
[47] Tandon GP, Ragland WR. Influence of laminate lay-up on oxidation and damage growth: isothermal aging. Compos Part A Appl Sci Manuf 2011;42:1127–1137.
[48] Sang L, Wang C, Wang Y, Wei Z. Thermo-oxidative ageing effect on mechanical properties and morphology of short fibre reinforced polyamide composites – comparison of carbon and glass fibres. RSC Adv 2017;7:43334–43344. [CrossRef]
[49] Golewski P, Sadowski T, Pietras D, Dudzik S. The influence of aging in salt chamber on strength of aluminum – CFRP single lap joints. Mater Today Proc 2021;45:4264–4267. [CrossRef]
[50] Marouani S, Curtil L, Hamelin P. Ageing of carbon/epoxy and carbon/vinylester composites used in the reinforcement and/or the repair of civil engineering structures. Compos Part B 2012;43:2020–2030. [CrossRef]
[51] Golewski P, Sadowski T. An influence of UV ageing process on tensile strength and Young's modulus of polymeric fiber composite materials. IOP Conf Ser Mater Sci Eng 2018;416:012057. [CrossRef]
[52] Alessi S, Pitarresi G, Spadaro G. Effect of hydrothermal ageing on the thermal and delamination fracture behaviour of CFRP composites. Compos Part B Eng 2014;67:145–153. [CrossRef]
[53] Vu DQ, Gigliotti M, Lafarie-Frenot MC. Experimental characterization of thermo-oxidation-induced shrinkage and damage in polymer–matrix composites. Compos Part A Appl Sci Manuf 2012;43:577–586. [CrossRef]
[54] Lafarie-Frenot MC, Grandidier J-C, Gigliottia M, Olivier L, Colin X, Verdu J, et al. Thermo-oxidation behaviour of composite materials at high temperatures: a review of research activities carried out within the COMEDI program. Polym Degrad Stab 2010;95:965–974. [CrossRef]
[55] Singh S. A mechanism-based multi-scale model for predicting thermo-oxidative degradation in high temperature polymer matrix composites. Compos Sci Technol 2011;71:3001–3012. [CrossRef]
[56] Markad KM, Das V, Lal A. Deflection and stress analysis of piezoelectric laminated composite plate under variable polynomial transverse loading. AIP Adv 2022;12:085024. [CrossRef]
[57] Tiwari N, Shaikh AA. Influence of carboxyl-functionalized graphene nanoplatelets on the thermo-mechanical and morphological behavior of shape memory nanocomposites. CMCA 2022;13:126. [CrossRef]
[58] Xue L, Fan W, Wu F, Zhang Y, Guo K, Li J-Z, et al. The influence of thermo-oxidative aging on the electromagnetic absorbing properties of 3D quasi-isotropic braided carbon/glass bismaleimide composite. Polym Degrad Stab 2019;168:108941. [CrossRef]
[59] Lal A, Markad K. Static and dynamic nonlinear stability analyses of hybrid sandwich composite beams under variable in-plane loads. J Mech Sci Technol 2021;35:2615–2629. [CrossRef]
[60] Tiwari N, Shaikh AA. Micro-buckling of carbon fibers in shape memory polymer composites under bending in the glass transition temperature region. Curved Layered Struct 2021;8:96–108. [CrossRef]
[61] Tiwari N, Shaikh AA. Flexural analysis of thermally actuated fiber reinforced shape memory polymer composite. Adv Mater Res 2019;8:337–359.
[62] Lal A, Markad K. Deflection and stress behaviour of multi-walled carbon nanotube reinforced laminated composite beams. Comput Concrete 2018;22:501–514.
[63] Liu J, Qiao W, Liu J, Xie D, Zhou Z, Wu L, et al. High temperature indentation behaviors of carbon fiber composite pyramidal truss structures. Compos Struct 2015;131:266–272. [CrossRef]
[64] Kong CW, Nam GW, Jang YS, Yi YM. Experimental strength of composite sandwich panels with cores made of aluminum honeycomb and foam. Adv Compos Mater 2014;23:43–52. [CrossRef]

[65] Dong L, Wadley H. Shear response of carbon fiber composite octet-truss lattice structures. Compos Part A Appl Sci Manuf 2016;81:182–192. [CrossRef]
[66] Sun Z, Li D, Zhang W, Shi S, Guo X. Topological optimization of biomimetic sandwich structures with hybrid core and CFRP face sheets. Compos Sci Technol 2017;142:79–90. [CrossRef]
[67] Yanes-Armas S, de Castro J, Keller T. Long-term design of FRP-PUR web-core sandwich structures in building construction. Compos Struct 2017;181:214–228. [CrossRef]
[68] Feng Y, Qiu H, Gao Y, Zheng H, Tan J. Creative design for sandwich structures: a review. Int J Adv Robot Syst 2020;17:1729881420921327. [CrossRef]
[69] Liew JYR, Yan JB, Huang ZY. Steel-concrete-steel sandwich composite structures-recent innovations. J Constr Steel Res 2017;130:202–221. [CrossRef]
[70] Li W, Rong Y, Huang Y, Chen L, Yang Z, Zhang G. Effect of thermal damage on dynamic and static mechanical properties of CFRP short pulse laser hole cutting. Eng Fract Mech 2023;286:109306. [CrossRef]
[71] Yue X, Yang X, Tian J, He Z, Fan Y. Thermal, mechanical and chemical material removal mechanism of carbon fiber reinforced polymers in electrical discharge machining. Int J Mach Tools Manuf 2018;133:163–172. [CrossRef]
[72] Li M, Li S, Yang X. The influence of machining processes on strain distribution and progressive failure characteristics when producing holes in CFRP. Compos Struct 2020;238:111994. [CrossRef]
[73] Leone C, Genna S. Heat affected zone extension in pulsed Nd:YAG laser cutting of CFRP. Compos Part B Eng 2018;140:204–213. [CrossRef]
[74] Li W, Huang Y, Chen X, Zhang G, Rong Y, Lu Y. Study on laser drilling induced defects of CFRP plates with different scanning modes based on multi-pass strategy. Opt Laser Technol 2021;144:107400. [CrossRef]
[75] Shanmugam D, Nguyen T, Wang J-H. A study of delamination on graphite/epoxy composites in abrasive waterjet machining. Compos Part A Appl Sci Manuf 2008;39:923–929. [CrossRef]
[76] Li ZL, Zheng HY, Lim GC, Chu PL, Li L. Study on UV laser machining quality of carbon fibre reinforced composites. Compos Part A Appl Sci Manuf 2010;41:1403–1408. [CrossRef]
[77] Nanoth R, Jayanarayanan K, Sarath Kumar P, Balachandran M, Pegoretti A. Static and dynamic mechanical properties of hybrid polymer composites: a comprehensive review of experimental, micromechanical and simulation approaches. Compos Part A Appl Sci Manuf 2023;174:107741. [CrossRef]
[78] Chilelli SK, Schomer JJ, Dapino MJ. Detection of crack initiation and growth using fiber Bragg grating sensors embedded into metal structures through ultrasonic additive manufacturing. Sensors (Basel) 2019;19:24917. [CrossRef]
[79] Irfan MS, Ali M, Khan T, Umer R. Monitoring the thermomechanical response of aerospace composites under dynamic loading via embedded rGO coated fabric sensors. Sensors Actuators A Phys 2023;361:114595. [CrossRef]
[80] Mahmood H, Vanzetti L, Bersani M, Pegoretti A. Mechanical properties and strain monitoring of glass-epoxy composites with graphene-coated fibers. Compos Part A Appl Sci Manuf 2018;107:12–23. [CrossRef]
[81] Luo S, Wang G, Wang Y, Xu Y, Luo Y. Carbon nanomaterials enabled fiber sensors: a structure-oriented strategy for highly sensitive and versatile in situ monitoring of composite curing process. Compos Part B Eng 2019;166:645–652. [CrossRef]
[82] Reghat M, Mirabedini A, Tan AM, Weizman Y, Middendorf P, Bjekovic R, et al. Graphene as a piezo-resistive coating to enable strain monitoring in glass fiber composites. Compos Sci Technol 2021;211:108842. [CrossRef]
[83] Hassani S, Mousavi M, Gandomi AH. Structural health monitoring in composite structures: a comprehensive review. Sensors (Basel) 2021;22:153. [CrossRef]
[84] Nurazzi NM, Asyraf MRM, Fatimah Athiyah S, Shazleen SS,Ayu Rafiqah S, Harussani MM, et al. A review on mechanical performance of hybrid natural fiber polymer composites for structural applications. Polymers 2021;13:32170. [CrossRef]
[85] Bhattacharya M. Polymer nanocomposites—a comparison between carbon nanotubes, graphene, and clay as nanofillers. Materials 2016;9:40262. [CrossRef]
[86] Sarker F, Potluri P, Afroj S, Koncherry V, Novoselov KS, Karim N. Ultrahigh performance of nanoengineered graphene-based natural jute fiber composites. ACS Appl Mater Interfaces 2019;11:21166–21176. [CrossRef]
[87] Sharma S, Rawal J, Dhakate SR, Singh BP. Synergistic bridging effects of graphene oxide and carbon nanotube on mechanical properties of aramid fiber reinforced polycarbonate composite tape. Compos Sci Technol 2020;199:108370. [CrossRef]
[88] Bulut M, Bozkurt ÖY, Erkliğ A, Yaykaşlı H, Özbek Ö. Mechanical and dynamic properties of basalt fiber-reinforced composites with nanoclay particles. Arab J Sci Eng 2020;45:1017–1033. [CrossRef]
[89] Loos M. Processing of polymer matrix composites containing CNTs. In: Polymer matrix composites. Elsevier; 2015. p. 171–188. [CrossRef]
[90] Seyhan AT, Tanoğlu M, Schulte K. Tensile mechanical behavior and fracture toughness of MWCNT and DWCNT modified vinyl-ester/polyester hybrid nanocomposites produced by 3-roll milling. Mater Sci Eng A 2009;523:85–92. [CrossRef]
[91] Canbay CA, Ünlü N. Production and characterization of shape memory polymeric nanocomposite materials. J Mol Struct 2021;1227:129708. [CrossRef]

[92] Kim H, Miura Y, Macosko CW. Graphene/polyurethane nanocomposites for improved gas barrier and electrical conductivity. Chem Mater 2010;22:3441–3450. [CrossRef]
[93] Gupta TK, Kumar S. Fabrication of carbon nanotube/polymer nanocomposites. In: Rafiee R, editor. Carbon nanotube-reinforced polymers. Micro and nano technologies. Amsterdam: Elsevier; 2018. p. 61–81. [CrossRef]
[94] Venkataraman A, Amadi EV, Chen Y, Papadopoulos C. Carbon nanotube assembly and integration for applications. Nanoscale Res Lett 2019;14:220. [CrossRef]
[95] Zhao C, Hu G, Justice R, Schaefer DW. Synthesis and characterization of multi-walled carbon nanotubes reinforced polyamide 6 via in situ polymerization. Polymer 2005;46:5125–5132. [CrossRef]
[96] Novoselov KS, Geim AK, Morozov SV, Jiang D, Zhang Y, Dubonds SV, et al. Electric field effect in atomically thin carbon films. Science 2004;306:666–669. [CrossRef]
[97] Geetha Bai R, Ninan N, Muthoosamy K, Manickam S. Graphene: A versatile platform for nanotheranostics and tissue engineering. Prog Mater Sci 2018;91:24–69. [CrossRef]
[98] Chen Y, Yue YY, Wang SR. Graphene as a transparent and conductive electrode for organic optoelectronic devices. Adv Electron Mater 2019;5:1900247. [CrossRef]
[99] Zhang H, Zhang H, Aldalbahi A, Zuo X, Fan C, Mi X. Fluorescent biosensors enabled by graphene and graphene oxide. Biosens Bioelectron 2017;89:96–106. [CrossRef]
[100] Agarwal V, Zetterlund P. Strategies for reduction of graphene oxide – A comprehensive review. Chem Eng J 2021;405:127018. [CrossRef]
[101] Alshamkhani M, Teong L, Putri L, Mohamed A, Lahijani P, Mohammadi M. Effect of graphite exfoliation routes on the properties of exfoliated graphene and its photocatalytic applications. J Environ Chem Eng 2021;9:106506. [CrossRef]
[102] Bahri M, Hagos S, Elaguech MA, Dajan FT, Getaye M, Tlili C, et al. Recent advances in chemical vapour deposition techniques for graphene-based nanoarchitectures: from synthesis to contemporary applications. Coord Chem Rev 2023;475:214910. [CrossRef]
[103] Chouhan A, Mungse HP, Khatri OP. Surface chemistry of graphene and graphene oxide: A versatile route for their dispersion and tribological applications. Adv Colloid Interface Sci 2020;283:102215. [CrossRef]
[104] Ikram R, Jan BM, Ahmad W. An overview of industrial scalable production of graphene oxide and analytical approaches for synthesis and characterization. J Mater Res Technol 2020;9:11587–11610. [CrossRef]
[105] Stebunov YV, Aftenieva OA, Arsenin AV, Volkov VS. Highly sensitive and selective sensor chips with graphene-oxide linking layer. ACS Appl Mater Interfaces 2015;7:21727–21734. [CrossRef]
[106] Tee SY, et al. Advances in photothermal nanomaterials for biomedical, environmental and energy applications. Nanoscale 2021;13:14268–14286. [CrossRef]
[107] Huang K, Li J, Luan X, Liu L, Yang Z, Wang C. Effect of graphene oxide on phase change materials based on disodium hydrogen phosphate dodecahydrate for thermal storage. ACS Omega 2020;5:15210–15217. [CrossRef]
[108] Cao R, Liu H, Chen S, Pei D, Miao J, Zhang X. Fabrication and properties of graphene oxide-grafted-poly(hexadecyl acrylate) as a solid-solid phase change material. Compos Sci Technol 2017;149:262–268. [CrossRef]
[109] Alayande AB, Park HD, Vrouwenvelder JS, Kim IS. Implications of chemical reduction using hydriodic acid on the antimicrobial properties of graphene oxide and reduced graphene oxide membranes. Small 2019;15:e1901023. [CrossRef]
[110] Ceniceros-Reyes MA, Marin-Hernandez KS, Sierra U, Saucedo E. Reduction of graphene oxide by in-situ heating experiments in the transmission electron microscope. Surfaces Interfaces 2022;35:102448. [CrossRef]
[111] Park S, An J, Potts JR, Velamakanni A, Murali S, Ruoff RS. Hydrazine-reduction of graphite- and graphene oxide. Carbon 2011;49:3019–3023. [CrossRef]
[112] Wu H, Li S-T, Shao Y-W, Jin X-Z, Qi X-D, Yang J, et al. Melamine foam/reduced graphene oxide supported form-stable phase change materials with simultaneous shape memory property and light-to-thermal energy storage capability. Chem Eng J 2020;379:122373. [CrossRef]
[113] Wang S, Liang Z, Liu L, Cao Y, Cheng Y, Ding C. Preparation of chemically functionalized graphene with excellent dispersibility and tribological properties as lubricant additives by microwave-assisted ball milling. J Mol Liq 2021;344:117929. [CrossRef]
[114] Zabihi O, Ahmadi M, Li Q, Fakhrhoseini S. Simultaneous electrochemical-assisted exfoliation and in situ surface functionalization towards large-scale production of few-layer graphene. FlatChem 2019;18:100132. [CrossRef]
[115] Prabakaran R, Kumar JPN, Dhasan ML, Chandrasekaran S, Harish S. Constrained melting of graphene-based phase change nanocomposites inside a sphere. J Therm Anal Calorim 2019;139:3629–3636. [CrossRef]
[116] Ibrahim KS. Carbon nanotubes-properties and applications: a review. Carbon Lett 2013;14:131–144. [CrossRef]
[117] Mohd Nurazzi NM, Asyraf MRM, Khalina A, Abdullah N, Sabaruddin FA, Hasnah Kamarudin S, et al. Fabrication, functionalization, and application of carbon nanotube-reinforced polymer composite: an overview. Polymers 2021;13:1047. [CrossRef]

[118] Kwon YK, Kim P. Unusually high thermal conductivity in carbon nanotubes. In: Shindé SL, Goela JS, editors. High thermal conductivity materials. New York, NY: Springer; 2006. p. 227–265. [CrossRef]
[119] Ali Z, Yaqoob S, Yu J, D'Amore A. Critical review on the characterization, preparation, and enhanced mechanical, thermal, and electrical properties of carbon nanotubes and their hybrid filler polymer composites for various applications. Compos Part C Open Access 2024;13:100434. [CrossRef]
[120] Chen CS, Liu TG, Lin LW, Xie XD, Chen XH, Liu QC, et al. Multi-walled carbon nanotube-supported metal-doped ZnO nanoparticles and their photocatalytic property. J Nanopart Res 2012;15:1295. [CrossRef]
[121] Choudhury A, Mondal S, Sarkar S. Failure analysis of laminated composite plate under hygro-thermo mechanical load and optimisation. Int J Appl Mech Eng 2019;24:509–526. [CrossRef]
[122] Lal A, Markad K. Thermal post buckling analysis of smart SMA hybrid sandwich composite plate. Polymers Polym Compos 2021;29:096739112110012. [CrossRef]
[123] Sumfleth J, Adroher X, Karl S. Synergistic effects in network formation and electrical properties of hybrid epoxy nanocomposites containing multiwall carbon nanotubes and carbon black. J Mater Sci 2009;44:3241–3247. [CrossRef]
[124] Kim KS, Rhee KY, Lee K, Byun J-H, Park S-J. Rheological behaviors and mechanical properties of graphite nanoplate/carbon nanotube-filled epoxy nanocomposites. J Ind Eng Chem 2010;16:572–576. [CrossRef]
[125] Kitisavetjit W, Nakaramontri Y, Pichaiyut S, Wisunthorn S, Kiatkamjornwong S. Influences of carbon nanotubes and graphite hybrid filler on properties of natural rubber nanocomposites. Polymer Testing 2020;93:106981. [CrossRef]
[126] Xiao Y, Wang W, Chen X, Lin T, Zhang Y, Yang J, et al. Hybrid network structure and thermal conductive properties in poly(vinylidene fluoride) composites based on carbon nanotubes and graphene nanoplatelets. Compos Part A Appl Sci Manuf 2016;90:614–625. [CrossRef]
[127] Birman V, Kardomateas GA. Review of current trends in research and applications of sandwich structures. Compos Part B Eng 2018;142:221–240. [CrossRef]
[128] Palomba G, Epasto G, Crupi V. Lightweight sandwich structures for marine applications: a review. Mech Adv Mater Struct 2022;29:4839–4864. [CrossRef]
[129] Moradi A, Ansari R, Hassanzadeh-Aghdam MK, Jamali J. Flexural behavior of sandwich structures with a hybrid carbon nanotube/short carbon fiber foam core and debonded skin/core interface. Mech Adv Mater Struct 2024;31:9117–9129. [CrossRef]
[130] Zhou G, Hill M, Loughlan J, Hookham N. Damage characteristics of composite honeycomb sandwich panels in bending under quasi-static loading. J Sandwich Struct Mater 2006;8:55–90. [CrossRef]
[131] Chen D, Zi H, Li Y, Li X. Low frequency ship vibration isolation using the band gap concept of sandwich plate-type elastic metastructures. Ocean Eng 2021;235:109460. [CrossRef]
[132] Kazancı Z. Dynamic response of composite sandwich plates subjected to time-dependent pressure pulses. Int J Non-linear Mech 2011;46:807–817. [CrossRef]
[133] Azarniya O, Rahimi G. Numerical and experimental analysis of free vibrations and static bending of a sandwich beam with a hyperelastic core. Mech Based Design Struct Machines 2022;52:1–23. [CrossRef]
[134] Lal A, Parghi PE, CEng, Markad K. Post-buckling nonlinear analysis of sandwich laminated composite plate. Mater Today Proc 2021;44. [CrossRef]
[135] Lal A, Markad K. Cumulative post-buckling buckling behavior of smart sandwich structure. IOP Conf Ser Mater Sci Eng 2021;1017:012020. [CrossRef]
[136] Markad K. Probabilistic-based nonlinear progressive failure analysis of piezoelectric laminated composite shell panels in hygrothermal environment. J Aerospace Eng 2021;34. [CrossRef]
[137] Wei X, Wu Q, Gao Y, Xiong J. Bending characteristics of all-composite hexagon honeycomb sandwich beams: experimental tests and a three-dimensional failure mechanism map. Mech Mater 2020;148:103401. [CrossRef]
[138] Quispitupa A, Berggreen C, Carlsson LA. On the analysis of a mixed mode bending sandwich specimen for debond fracture characterization. Eng Fract Mech 2009;76:594–613. [CrossRef]
[139] Hassanzadeh-Aghdam MK, Mahmoodi MJ, Ansari R. Micromechanics-based characterization of mechanical properties of fuzzy fiber-reinforced composites containing carbon nanotubes. Mech Mater 2017;118:169–184. [CrossRef]
[140] Lal A, Parghi PE, CEng, Markad K. Post-buckling analysis of the shape memory polymer sandwich composite beam under dynamic temperature variation. IOP Conf Ser Mater Sci Eng 2020;1004:012020. [CrossRef]
[141] Lal A, Markad K. Influence of dynamic temperature variation and in-plane varying loads over post-buckling and free vibration analysis of sandwich composite beam. Int J Comp Mat Sci Eng 2020;9:2050012. [CrossRef]
[142] Zeng Y, Ci L, Carey BJ, Vajtai R, Ajayan PM. Design and reinforcement: vertically aligned carbon nanotube-based sandwich composites. ACS Nano 2010;4:6798–6804. [CrossRef]
[143] Lal A, Markad K. Nonlinear flexural analysis of sandwich beam with multi-walled carbon nanotube reinforced composite sheet under thermo-mechanical loading. Curved Layered Struct 2020;7:1–16. [CrossRef]

[144] Moradi A, Ansari R, Hassanzadeh-Aghdam MK, Jang SH. The effect of fuzzy fiber-reinforced composite skin on bending stiffness and debonding growth between skin and polymeric foam core of sandwich structures. Eur J Mech A/Solids 2024;103:105182. [CrossRef]

[145] Zhu S, Ma L, Wang B, Hu J, Zhengong Z. Lattice materials composed by curved struts exhibit adjustable macroscopic stress-strain curves. Mater Today Commun 2018;14:1–6. [CrossRef]

[146] Kim G, Sterkenburg R, Tsutsui W. Investigating the effects of fluid intrusion on Nomex® honeycomb sandwich structures with carbon fiber facesheets. Compos Struct 2018;206:1150–1162. [CrossRef]

[147] Tuwair H, Drury J, Volz J. Testing and evaluation of full scale fiber-reinforced polymer bridge deck panels incorporating a polyurethane foam core. Eng Struct 2019;184:205–216. [CrossRef]

[148] Zhou T, Zhang P, Xiao W, Jun L, Cheng Y. Experimental investigation on the performance of PVC foam core sandwich panels under air blast loading. Compos Struct 2019;226:111081. [CrossRef]

[149] Kwon DJ, Kim JH, Devries KL, Park JM. Optimized epoxy foam interface of CFRP/epoxy foam/CFRP sandwich composites for improving compressive and impact properties. J Mater Res Technol 2021;11:2095–2106. [CrossRef]

[150] Lal A, Markad K. Static buckling analysis of shape memory alloy reinforced composite laminated plate. IOP Conf Ser Mater Sci Eng 2020;814:012009. [CrossRef]

[151] Vemuluri Ramesh Babu, Rajamohan V, Sudhagar E. Structural optimization of tapered composite sandwich plates partially treated with magnetorheological elastomers. Compos Struct 2018;200:258–276. [CrossRef]

[152] Liu H, Chen L, Du B, Peng S. Flatwise compression property of hierarchical thermoplastic composite square lattice. Compos Struct 2019;210:118–133. [CrossRef]

[153] Sikdar S, Ostachowicz W. Nondestructive analysis of core-junction and joint-debond effects in advanced composite structure. Polymer Testing 2019;73:31–38. [CrossRef]

[154] Seguel F, Meruane V. Damage assessment in a sandwich panel based on full-field vibration measurements. J Sound Vib 2018;417:1–18. [CrossRef]

[155] Wang C, Murugadoss V, Kong J, He Z, Mai X, Shao Q, et al. Overview of carbon nanostructures and nanocomposites for electromagnetic wave shielding. Carbon 2018;140:1–14. [CrossRef]

[156] Shu C, Zhao S, Hou S. Crashworthiness analysis of two-layered corrugated sandwich panels under crushing loading. Thin-Walled Struct 2018;133:42–51. [CrossRef]

[157] Sahu SK, Badgayan ND, Samanta S, Sahu D, Sreekanth PSR. Influence of cell size on out of plane stiffness and in-plane compliance character of the sandwich beam made with tunable PCTPE nylon honeycomb core and hybrid polymer nanocomposite skin. Int J Mech Sci 2018;148:284–292. [CrossRef]

[158] Wang L, He Y, Jiang T, Zhang X, Zhang C, Peng X. Morphologies and properties of epoxy/multi-walled carbon nanotube nanocomposite foams prepared through the free-foaming and limited-foaming process. Compos Sci Technol 2019;182:107776. [CrossRef]

[159] Anjum A, Shaikh AA, Tiwari N. Comparative assessment of the developed algorithm with the soft computing algorithm for the laser machined depth. Infrared Phys Technol 2023;129:104545. [CrossRef]

[160] Arao Y, Koyanagi J, Utsunomiya S, Kawada H. Analysis of thermal deformation on a honeycomb sandwich CFRP mirror. Mech Adv Mater Struct 2010;17:328–334. [CrossRef]

[161] Stotts JC, Thompson GB, Weinberger CR. Modeling the diffusion-controlled phase transformations in transition metal carbide multilayer composites. Results Eng 2023;18:101106. [CrossRef]

[162] Ahmed H, Mohammed AS, Faraj RH, Abdalla AA, Qaidi SMA, Sor NH, et al. Innovative modeling techniques including MEP, ANN and FQ to forecast the compressive strength of geopolymer concrete modified with nanoparticles. Neural Comput Appl 2023;35:1–27. [CrossRef]

[163] Ryms M, Januszewicz K, Kazimierski P, Łuczak J, Klugmann-Radziemska E, Lewandowski WM. Post-pyrolytic carbon as a phase change materials (PCMs) carrier for application in building materials. Materials 2020;13:1268. [CrossRef]

[164] Al-Ahmed A, Sari A, Mazumder M, Hekimoglu G, Al-Sulaiman F. Thermal energy storage and thermal conductivity properties of Octadecanol-MWCNT composite PCMs as promising organic heat storage materials. Sci Rep 2020;10:64149. [CrossRef]

[165] Sharma R, Ganesan P, Tyagi V, Metselaar H, Sandaran S. Thermal properties and heat storage analysis of palmitic acid-TiO2 composite as nano-enhanced organic phase change material (NEOPCM). Appl Therm Eng 2016;99:298–310. [CrossRef]

[166] Jebasingh E. Effects of various types of graphite on the thermal conductivity and energy storage properties of ternary eutectic fatty acid-based composite as phase change material. Renewables: Wind Water Sol 2016;3:28. [CrossRef]

[167] Manoj Kumar P, Anandkumar R, Mylsamy K, Prakash KB. Experimental investigation on thermal conductivity of nanoparticle dispersed paraffin (NDP). Mater Today Proc 2020;45:3000–3015.

[168] Shama A, Kabeel AE, Moharram B, Abosheiasha H. Improvement of the thermal properties of paraffin wax using high conductive nanomaterial to appropriate the solar thermal applications. Appl Nanoscience 2021;11:303–311. [CrossRef]

[169] Wang S, Muiruri JK, Soo XYD, Liu S, Thitsartarn W, Tan BH, et al. Bio-PP and PP-based biocomposites: solutions for a sustainable future. Chem - A Asian J 2022;18:2585–2592. [CrossRef]
[170] Chua MH, Chin K, Loh XJ, Zhu Q, Xu J. Aggregation-induced emission-active nanostructures: beyond biomedical applications. ACS Nano 2023;17:5120–5134. [CrossRef]
[171] Nassar A, Nassar E, Rivilla I, Labidi J, Fernández AG, Sarasini F. Enhancing the thermal conductivity and shape stability of phase-change composites using diatomite and graphene nanoplates for thermal energy storage. Results Eng 2024;22:102184. [CrossRef]
[172] Zhu Q, Ong PJ, Angelo Goh SH Yeo RJ, Wang S, et al. Recent advances in graphene-based phase change composites for thermal energy storage and management. Nano Mater Sci 2024;6:115–138. [CrossRef]
[173] Qureshi Z, Ali H, Khushnood S. Recent advances on thermal conductivity enhancement of phase change materials for energy storage system: A review. Int J Heat Mass Transfer 2018;127:838–856. [CrossRef]
[174] Yadav A, Verma A, Kumar A, Dhasmana H, Bhatnagar P, Jain V. Recent advances on enhanced thermal conduction in phase change materials using carbon nanomaterials. J Energy Storage 2021;43:103173. [CrossRef]
[175] Li TX, Lee J-H, Wang R, Kang YT. Enhancement of heat transfer for thermal energy storage application using stearic acid nanocomposite with multi-walled carbon nanotubes. Energy 2013;55:752–761. [CrossRef]
[176] Olabi AG, Wilberforce T, Elsaid K, Sayed ET, Ramadan M, Atiqure Rahman SM, et al. Recent progress on carbon-based nanomaterials for phase change materials: prospects and challenges. Therm Sci Eng Prog 2021;23:100920. [CrossRef]
[177] Jiang L, Chen G, Zhao L, Li M, Li C, Zhang R. Preparation and low temperature heat storage properties of 1-hexadecylamine/3D graphene aerogel composite phase change materials. Sol Energy Mater Sol Cells 2023;251:112118. [CrossRef]
[178] Shang Y, Zhang D. Preparation and thermal properties of graphene oxide–microencapsulated phase change materials. Nanoscale Microscale Thermophys Eng 2016;20:141–152. [CrossRef]
[179] Su JF, Wang X-Y, Han S, Zhang X-L, Guo Y-D, Wang Y-Y, et al. Preparation and physicochemical properties of microcapsules containing phase-change material with graphene/organic hybrid structure shells. J Mater Chem A 2017;5:23937–23951. [CrossRef]
[180] Tiwari N, Abdulhafiz S. Micro buckling of carbon fiber in triple shape memory polymer composites under bending in glass transition regions. Mater Today Proc 2020;44:961–973. [CrossRef]
[181] Cheng X, Fei J, Kondyurin A, Fu K, Ye L, Bilek MMM, et al. Enhanced biocompatibility of polyurethane-type shape memory polymers modified by plasma immersion ion implantation treatment and collagen coating: an in vivo study. Mater Sci Eng C 2019;99:863–874. [CrossRef]
[182] Jinsong L, Lan X, Liu Y, Du S. Shape-memory polymers and their composites: stimulus methods and applications. Prog Mater Sci 2011;56:1077–1135. [CrossRef]
[183] Xin X, Liu L, Liu Y, Jinsong L. Mechanical models, structures, and applications of shape-memory polymers and their composites. Acta Mech Solida Sin 2019;32:153–171. [CrossRef]
[184] Tandon G, Goecke K, Cable K, Baur J. Durability assessment of styrene and epoxy-based shape-memory polymer resins. J Intell Mater Syst Struct 2009;20:2127–2143. [CrossRef]
[185] Feldkamp DM, Rousseau IA. Effect of the deformation temperature on the shape-memory behavior of epoxy networks. Macromol Mater Eng 2010;295:726–734. [CrossRef]
[186] Monaldo E, Nerilli F, Vairo G. Basalt-based fiber-reinforced materials and structural applications in civil engineering. Compos Struct 2019;214:246–263. [CrossRef]
[187] Elmahdy A, Verleysen P. Tensile behavior of woven basalt fiber reinforced composites at high strain rates. Polymer Testing 2019;76:207–221. [CrossRef]
[188] Yang G, Park M, Park SJ. Recent progresses of fabrication and characterization of fibers-reinforced composites: a review. Compos Commun 2019;14:1–9. [CrossRef]
[189] Emmanuel KDC, Herath M, Jeewantha J, Epaarachchi J, Aravinthan T. Thermomechanical and fire performance of DGEBA based shape memory polymer composites for constructions. Constr Build Mater 2021;303:124442. [CrossRef]
[190] Ferdous W, Bai Y, Ngo TD, Manalo A, Mendis P. New advancements, challenges and opportunities of multi-storey modular buildings – a state-of-the-art review. Eng Struct 2019;183:883–893. [CrossRef]
[191] Fan J, Santos L, Taleghani A, Li G. Stimuli-responsive petroleum cement composite with giant expansion and enhanced mechanical properties. Constr Build Mater 2020;259:119783. [CrossRef]
[192] Levchik S, Weil E. Thermal decomposition, combustion and flame-retardancy of epoxy resins - a review of the recent literature. Polymer Int 2004;53:1901–1929. [CrossRef]
[193] Chen X, Huo L, Jiao C, Li S. TG–FTIR characterization of volatile compounds from flame retardant polyurethane foams materials. J Anal Appl Pyrolysis 2013;100:186–191. [CrossRef]
[194] Fulco A, Medeiros A, Tonatto M, Amico S, Talreja R, Melo J. Fatigue damage and fatigue life diagrams of a carbon/epoxy cross ply laminate aged by hygrothermal exposure. Compos Part A Appl Sci Manuf 2019;127:105628. [CrossRef]

[195] Liotier P-J, Vautrin A, Beraud J-M. Microcracking of composites reinforced by stitched multiaxials subjected to cyclical hygrothermal loadings. Compos Part A Appl Sci Manuf 2011;42:425–437. [CrossRef]
[196] Tserpes KI, Tzatzadakis V, Katsiropoulos C. Effect of hygrothermal ageing on the interlaminar shear strength of carbon fiber-reinforced rosin-based epoxy bio-composites. Compos Struct 2019;226:111211. [CrossRef]
[197] Yang S, Liu W, Fang Y, Huo R. Influence of hygrothermal aging on the durability and interfacial performance of pultruded glass fiber-reinforced polymer composites. J Mater Sci 2019;54:1–11. [CrossRef]
[198] Falkowicz K, Ferdynus M, Rozylo P. Experimental and numerical analysis of stability and failure of compressed composite plates. Compos Struct 2021;263:113657. [CrossRef]
[199] Starkova O, Gagani A, Karl C, Rocha I, Burlakovs J, Krauklis A. Modelling of environmental ageing of polymers and polymer composites—durability prediction methods. Polymers 2022;14:907. [CrossRef]
[200] Vidinha H, Branco R, Neto MA, Amaro AM, Reis P. Numerical modeling of damage caused by seawater exposure on mechanical strength in fiber-reinforced polymer composites. Polymers 2022;14:19355. [CrossRef]
[201] Liu Z, Lei Y, Zhang X, Kang Z, Zhang J. Effect mechanism and simulation of voids on hygrothermal performances of composites. Polymers (Basel) 2022;14:901. [CrossRef]
[202] Hussnain S, Shah S, Megat-Yusoff P, Hussain MZ. Degradation and mechanical performance of fibre-reinforced polymer composites under marine environments: a review of recent advancements. Polymer Degrad Stab 2023;215:110452. [CrossRef]
[203] Wang H, Enda C, Li X, Li J. An experimental study in full spectra of solar-driven magnesium nitrate hexahydrate/graphene composite phase change materials for solar thermal storage applications. J Energy Storage 2021;38:102536. [CrossRef]
[204] Wu Y, Wang T. Preparation and characterization of hydrated salts/silica composite as shape-stabilized phase change material via sol–gel process. Thermochim Acta 2014;591:10–15. [CrossRef]
[205] Harlé T, Nguyen GTM, Ledesert B, Mélinge Y, Hebert RL. Cross-linked polyurethane as solid-solid phase change material for low temperature thermal energy storage. Thermochim Acta 2020;685:178191. [CrossRef]
[206] Lu X, Liang B, Sheng X, Yuan T, Qu J. Enhanced thermal conductivity of polyurethane/wood powder composite phase change materials via incorporating low loading of graphene oxide nanosheets for solar thermal energy storage. Sol Energy Mater Sol Cells 2020;208:110391. [CrossRef]